ADCHEM 2009

IFAC Symposium on

Advanced Control of Chemical Processes

July 12-15, 2009

Koç University, Istanbul, Turkey

Symposium Preprints

Part 1

Editors: Sebastian Engell

Yaman Arkun

International Program Committee

Sebastian Engell (Chair)

Technische Universität Dortmund, Germany

Jorge Mandler (Industrial Co-Chair)

Air Products, USA

IPC Coordination

Christian Sonntag, Thomas Tometzki

Technische Universität Dortmund, Germany

IPC Members

O. Abel (DE), F. Allgöwer (DE), J. Alvarez (MX), H. Arellano-Garcia (DE), T. Backx (NL), T. Badgwell (US), R. Berber (TR), L.Biegler (US), D. Bonvin (CH), R. Braatz (US), M. Çamurdan (TR), T. Chai (CN), M. Chiu (SG), P. Christofides (US), A. Çınar (US), I. Craig (ZA), P. Daoutides (US), C. de Prada (ES), D. Dochain (BE), F. J. Doyle, III (US), G. Dünnebier (DE), F. Forbes (CA), B. Foss (NO), F. Gao (HK), C. Georgakis (US), M. Guay (CA), S. Hasebe (JP), K. Hoo (US), M. Hovd (NO), B. Huang (CA), C. D. Immanuel (UK), S. B. Jorgensen (DK), M. V. Kothare (US), C. Kravaris (GR), J. Lee (US), D. Lewin (IL), P. Li (DE), J. Mandler (US), J. Marchetti (AR), W. Marquardt (DE), M. Nikolaou (US), D. Odloak (BR), C. Özgen (TR), A. Palazoğlu (US), S. Park (KR), M. Perrier (CA), H. Preisig (NO), Raisch (DE), J. Rawlings (US), J. Romagnoli (US), C. Scali (IT), A. R. Secchi (BR), S. L. Shah (CA), S. Skogestad (NO), M. Soroush (US), B. Srinivasan (CA), M. Tade (AU), N. Thornhill (UK), J. O. Trierweiler (BR), M. Türkay (TR), A. Vande Wouwer (BE), E. Ydstie (US), E. S. Yoon (KR), C.-C. Yu (TW), D. Zhou (CN)

National Organizing Committee

Yaman Arkun (Chair)

Koç University, Istanbul, Turkey

NOC Members

Erdoğan Alper, Tahsin Bahar, Ridvan Berber, Mehmet Çamurdan, Devrim Kaymak, Hitay Özbay, Canan Özgen, Metin Türkay, Mustafa Türker

NOC Coordination

Nur Diğdem Burak

Koç University, Istanbul, Turkey

COPYRIGHT CONDITIONS

Contents

Plenary Lectures

Challenges and problems with advanced control and optimization technologies

Campos, M.*, Teixeira, H.*, Liporace, F. and Gomes, M.****

** PETROBRAS / CENPES / Engenharia Básica Abastecimento e Gás&Energia/ Automação, Equipamentos Dinâmicos e Confiabilidade, Av. Horácio Macedo, 950 - Cidade Universitária, Ilha do Fundão, Rio de Janeiro, 21949-915, Brazil (Tel:55-21-3865-6347; e-mail: mariocampos@petrobras.com.br).*

*** PETROBRAS / CENPES / P&D de Gás, Energia e Desenvolvimento Sustentável / Gás Natural / Célula de Otimização e Eficiência Energética, Av. Horácio Macedo, 950 - Cidade Universitária, Ilha do Fundão, Rio de Janeiro, 21949-915, Brazil.*

Abstract: Oil & Gas companies continuously try to create and increase business value of their installations (platforms, refineries, etc). Particularly the increasing energy consumption on a worldwide basis and, as a result, the substantial increase in prices volatility is a major drive for better advanced control and optimization technologies. Advanced control and optimization system can play an important role to improve the profitability and stability of industrial plants. This paper discusses the problems and challenges of advanced control and optimization in petroleum industries nowadays. It emphasizes the importance of control performance assessment technology to maintain a good regulatory control and the difficulties in using these technologies. It also shows the importance of malfunction detection and diagnosis advisory system for critical equipment in order to increase the operational reliability. Model predictive control (MPC) has become a standard multivariable control solution in the continuous process industries, but there are still many open issues related to accelerate a new implementation and maintain the controller with a good performance along the years. Real time optimization tools also impose new challenges for Oil & Gas industries application, which are discussed in this paper.

Keywords: performance assessment, regulatory control, advanced control system, real time optimization

1. INTRODUCTION

The advanced control and optimization systems in oil & gas and petrochemical plants are an industrial reality (Qin and Badgwell, 2003). These advanced systems provide many advantages for the process units, as improved stability and safety, respect to constraints and higher profitability. PETROBRAS has been investing in the development of these systems for several years. Advanced control system is already a consolidated technology in its refineries with many model predictive controllers implemented (Zanin and Moro, 2004). However, the application of real time optimization (RTO) is recent, although this technology can bring great economical earnings, besides to increase the energy efficiency and minimization of emissions.

To install and maintain these advanced systems with good performance is a great challenge. Its performance is influenced by instrumentation problems, bad tuning of the regulatory and advanced control, unreliable process dynamic models (Ender, 1993; Kern, 2007), unmeasured disturbances, etc.

This article will discuss the problems and challenges of advanced control and optimization in petroleum industries nowadays. It discusses some tools for diagnosis and tuning of the regulatory and advanced control, and the challenge associated with the real time optimizers. In spite of the several tools in the market that deal with industrial control and optimization solutions, PETROBRAS has decided to invest on the development of its own tools and solutions in many situations, usually in association with some Brazilian universities. The goal of this paper is to show some challenges faced, solutions and results obtained in PETROBRAS facilities.

2. REGULATORY CONTROL LEVEL

Process control aims to maintain certain variables within their desirable operational limits and could be visualized as a pyramid. In the base of this pyramid, the first level is the regulatory control, that uses PID controllers (Campos and Teixeira, 2006; Ogata, 1982) and is configured in the digital systems (DCS - Distributed control system or PLC - Programmable logical controllers). In a second level, we have the advanced control systems that use for instance Model Predictive Control (MPC). This algorithm considers the interaction between control loops, and includes an optimization layer of the industrial plant. These algorithms are usually implemented in a process computer that communicates with DCS or PLC systems by the use of OPC protocol (OPC, 2008). The outputs of this advanced control are usually the set points of the PID controllers. The

architecture is conceived in such a way that if there is a failure in the advanced control level, the plant operation continues with the last PID set points in the DCS.

An advanced control system won't reach the expected benefits if is turned off constantly for the operators. Therefore, the instruments, valves and the regulatory control loops (PIDs) should operate appropriately. Hence, the performance of the regulatory control is fundamental for the success of the advanced control system. An industrial plant usually has hundreds of control loops, and less and less engineers to maintain the system. Therefore, the industries need tools to perform automatic analysis and diagnoses of the problems associated with the regulatory control. For example, these tools should be able to detect failures with the instrumentation (miscalibration, badly sizing, sensor noisy, out of scale, measurement resolution, etc.), non linear behavior in the process due to changes in the operational point, bad PID tuning (oscillation, stability, etc.) and control strategy problems (coupling between control loops, degrees of freedom, etc.).

There are several tools in the market that help engineers to maintain the regulatory control, but most of them require a well-trained engineers to interpret, analyze and define the correct actions, for instance: to change a control valve, tune PID controllers or to implement a new control strategy (decoupling, feedforward), etc. These engineers should also know very well the process in order to evaluate the better actions to be taken.

The great challenge for these tools will be to incorporate more "intelligence" to help engineers in the definition of the better actions. For instance, in certain case, only PID tuning could reach 80% of improvement in process variability reduction, and in some case, the process performance would improve only 10%. A lot of times in industries the engineer spends time and money with an action that won't bring great results. So, it is clear the importance of a tool that could perform the automatic diagnosis and assessment of the regulatory control (Farenzena et al., 2006). The most important features of this tool should be to have automatic ways to prioritize the actions for each process that might result in a better performance, and also to provide a standardized metric to compare different actions in different processes, even in different scales such as economical, environmental or safety (Harris, 1989; Kempf, 2003; Farenzena and Trierweiler, 2008). These features are a great development challenge for these tools.

Despite the several tools in the market, PETROBRAS and Federal University of Rio Grande do Sul (UFRGS) have developed their own tool, the software called “BR-PerfX”. Its main purpose is to compute some universal key performance indicators that reduce the subjectivity in the analysis and help engineers in their assessments and decisions about problems affecting the regulatory control.

In order to face the PID tuning problem, PETROBRAS and Federal University of Campina Grande (UFCG) developed the software "BR-Tuning" (Schmidt et al., 2008; Arruda and Barros, 2003), which is comprised by a group of techniques regarding open and close loop identification and the proposition of new tuning parameters. It communicates directly with the process automation system (DCS or PLC) using the OPC protocol.

As it was said previously, the challenge is to develop an "intelligent" layer that helps to make a diagnosis based on several indexes or indicators. The integration between different tools is also an important concern. The use of the OPC standard for the exchange of information could be an option. So, each tool could make available their indicators to others tools through OPC. This way, the engineers' work would be facilitated, avoiding losses of time and money.

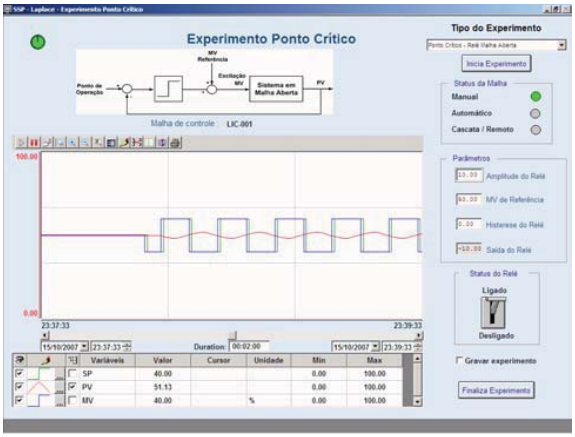

Fig. 1. BR-Tuning interface**.**

The challenges in relation to controllers' tuning are associated mainly with the identification of the models, the determination of the process non-linearities, interaction between control loops, as well as defining the desired performance for each control loop.

There are some processes where the disturbances’ pattern can change with the time, as in some off-shore petroleum platform. The slug flow can change its intensity for example due to changes in the gas-lift. So, we don't have a PID tuning parameters that are good for all these different situations. In this case, it was developed an "intelligent" system that supervises the process plant and changes the PID tuning automatically when necessary. This control strategy is equivalent a "gain-scheduling" where the control performance (deviation between the process variable and the setpoint) is evaluated during a time, and the system decides what is the best tuning for that moment. All the possible values for the PID tuning are chosen off-line. This system was installed in several PETROBRAS' platforms. The figure 2 shows the system changing the PID tuning parameters and the level performance. This project used a tool called MPA, which was developed by Catholic University of Rio de Janeiro (PUC-RJ) to PETROBRAS.

Another challenge is the development of non-linear controllers for some special cases, for example to pH control

in certain plants, although PID will continue to be the algorithm more used in this regulatory layer control for several years.

Researches and developments for the regulatory control level are still necessary, and they can bring great economical earnings. For example, an application of these tools (evaluation, tuning and changes in control strategy) allows an increased of about 9% in the production of LGN (Liquefied Natural Gas) in a natural gas plant (Campos et al., 2007).

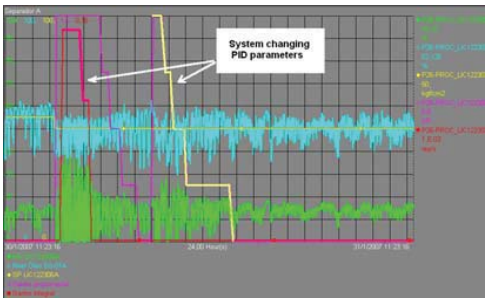

Fig. 2. Performance of this control strategy in production platform (1 day).

3. ADVANCED CONTROL SYSTEM

The multivariable predictive controllers (MPCs) are powerful tools for the process optimization and are available in many industrial plants. This system can increase feed and preferred product rates, reduce energy consumption and waste material. These benefits are more visible in complex processes where challenging dynamic responses (significant time delays, non-minimum phase responses, control loop interaction, etc.) due to disturbances (feed flow and composition, energy integration, usefulness, etc.) that must be dealt with while taking into account process constraints and trying to pursue the best economic performance. As an example of the benefits achieved, figure 3 shows an increase of about 16% in the LPG yield due to the implementation of an Advanced Process Control (APC) system in a natural gas plant.

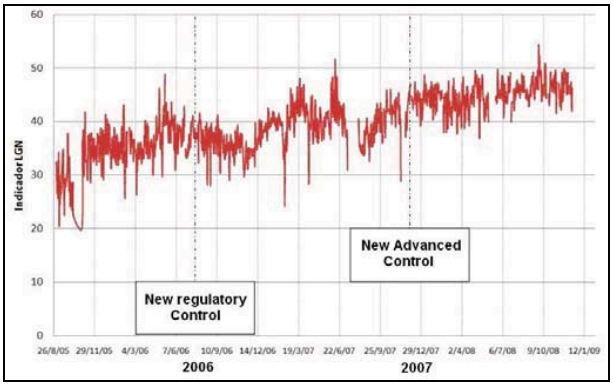

Fig. 3. LPG yield increase in a natural gas plant due to MPC.

However, even if MPC systems are nowadays seen as a commodity, there is still much to be done, due to the significant gap between the recent MPC technologies development in the academy and those effectively used on industrial plants. Most industrial MPC applications are based on the most traditional approaches: linear algorithms based on step-response models obtained through traditional step tests.

MPC maintenance

MPC performance decay throughout time is a well-known and widely reported fact (figure 4). If no maintenance work is done, the operators end up turning them off. There are many causes for this behaviour:

- Changes in the units operational objectives;
- Equipments efficiency losses (fouling);
- Changes in the feed quality;
- Problems in instruments and in the inferences;
- Lacks of qualified personnel for the controller's maintenance.

Therefore, the first great challenge associated with MPC control is to have reliable tools to keep performance and diagnose problems.

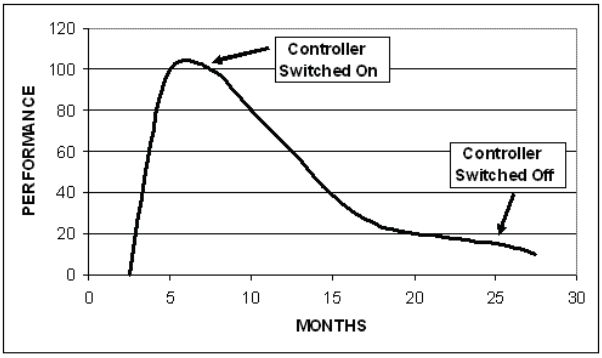

Fig. 4. Advanced Control Performance during the time.

Therefore, industry needs better tools to help maintenance personnel to answer the following questions:

- Is advanced control system accomplishing their objectives?
- What is its performance?
- Is the process optimized?
- What are the benefits?
- How is the level of disturbances?
- What is operational factor of the controller?
- How are the operators adjusting the limits of the manipulated variables?
- Are manipulated variables very limited?
- What is the variability of the main controlled variable?
- Is the process operating close to the constraints?

It is necessary a tool not only to answer these questions, but the system point out the causes of the bad performance: bad models, bad controller tuning, inference problems, non-linearities, frequent changes in the operation point, new constraints not considered in the design?

Nonlinear models, Identification and Model mismatch

Many different and even sophisticated approaches have been proposed in order to allow MPC algorithms to cope with process nonlinearity. Bequette (2007) presents a recent review on the subject. However, despite all this effort, industrial Nonlinear MPC (NMPC) applications are relatively few, and most of these are based on the simplest approaches.

One possible reason for that might be simply that the nonlinear behaviour is not known, and any lack of performance is seen as a typical model mismatch.

Another possibility might be that the nonlinear behaviour is known, but can not be easily determined with traditional plant tests. One way to overcome these problems might be the use of rigorous dynamic simulators, to improve the understanding of the process behaviour. Information obtained with dynamic simulation could be combined to the existing linear model in order to provide a reliable nonlinear one. Dynamic simulation might be useful also to find out the best way to characterize the observed nonlinearity. Once more, although there is availability of dynamic simulators, there is not much use of them in industrial applications.

Process identification of complex processes is still a hard task, where a significant part of the effort on MPC implementation is spent.

In order to address this problem, some commercial tools have been conceived in this decade for closed-loop identification. These tools are based on efficient ways to perform step tests allied to modelling strategies for minimization of the model order. While this approach has proved to be useful and promising, it is still a hard task to apply these techniques to complex processes, especially when dealing with noisy data. It seems to be a lot of space for development in this area.

Another interesting way to reduce implementation time can be the use of algorithms for automation of the plant test.

Tuning

MPC tuning is another interesting issue, where new technologies might help to reduce implementation time and also on the maintenance task.

Some interesting ideas have been proposed (Trierweiller and Farina, 2003) that try to combine desired and achievable performances. However, the controller tuning still consume time and is critical points for controller performance. Normally, all MPC tuning methods consider a square controlled variables x manipulated variables matrix, but, in fact all controller has a rectangular matrix that means different tuning scenarios depending on which constraints is active.

Another big challenge is to reduce the application time and maintenance time. For this, it is believed that the main critical points are:

- Tools for the development of inferences:
  - Use of rigorous dynamic simulators, or statistical methods for better inferences using less laboratory analysis data.
- Dynamic models identification:
  - Automation of the identification tests, minimizing problems and loss of data;
  - Efficient tools for closed loop identification;
  - Characterization and identification of the non linearities of the process.
- Better tools for tuning the predictive controller:
  - How to define the priorities in the several operating points of the controller and change automatically the tuning parameters. This activity is still done by trial and error in many industrial cases.

New advanced controllers that contemplate these aspects will help the users to implement and maintain these industrial systems.

4. REAL TIME OPTIMIZATION

Real Time Optimization (RTO) technology is a powerful tool for the continuous search of the most profitable way to run petroleum and petrochemical process units. Cutler and Perry (1983) state that despite being a hard and complex task, its potential benefits are relevant and might provide profit increases around 6 to 10% when allied to Advanced Process Control (APC).

The task of an RTO application is to make the best of an existing process unit, adjusting its process variables for every new change of external conditions, like operational variables, feed compositions and process constraints. The RTO benefits are usually associated with the maximization of products and minimization of the specific energy consumption and other resources, depending on the following factors:

- Market availability
- Products prices and feed costs
- Safety and environmental constraints
- Product specifications

The central figure of an optimization application is the mathematical model. It is expected to represent the process behaviour on a wide range of operating conditions with good accuracy. It should not only guarantee that the predicted potential profitability matches that of the real process, but also that when the optimal solution is implemented the process constraints must not be violated. Most RTO systems used nowadays are based on rigorous, steady-state, first-principles mathematical models.

The good performance of an RTO system depends on a reliable mathematical model and on reliable input data. In order to obtain that, many procedures must be executed before the economic optimization problem can be solved:

- Gross Error Detection
- Steady-state Detection
- Data Reconciliation
- Parameter estimation

Once that a reconciled data set and a fitted model have been obtained, the process optimization can be performed. The optimization problem usually consists of the maximization the operational profit (or minimization of operational costs) subject to a set of constraints. On most situations the optimization problem is posed as a non-linear programming problem (NLP). Most commercial applications are based on variations of the SQP (Successive Quadratic Programming) algorithm. This algorithm is also used to solve the previous Data Reconciliation and Parameter Estimation problems.

Real Time Optimization at PETROBRAS

Since 2004, RTO has been classified by PETROBRAS and its Strategic Downstream Committee as a "High Sustainable" technology. It means that RTO is seen as a key technology to improve PETROBRAS performance and profit, and therefore significant effort and resources will be spent on this subject.

PETROBRAS implementations on RTO covered a wide range of alternatives, focusing both on profitability and on the search of the best way to deliver the technology:

- Fluid Catalytic Cracking (FCC) and Crude Distillation Units (CDU);
- Proprietary and commercial process models and RTO systems;
- Sequential Modular (SM) and Equation Oriented (EO) approaches (Alkaya et al., 2003).

The first RTO initiatives were taken using PETROBRAS' in-house process simulator for FCC, with a small scope covering only the reactor/regenerator section. The proprietary process model used is based on a Sequential Modular (SM) approach. Though many difficulties were found (see next section), this initiative made possible to test the technology as well as to help our engineers to take a step further.

Distillation Unit / SM approach (2004)

This implementation took place at the Crude Distillation Unit (CDU) and the two Solvents Units of RECAP refinery (Gomes et al., 2008).

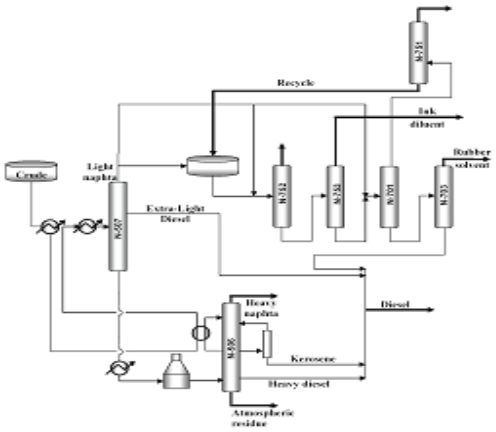

Fig. 5 - Scheme of the CDU and the Solvents Units of RECAP/PETROBRAS.

The process model was built using PETROX, a proprietary sequential-modular process simulator from PETROBRAS. The simulation comprises 53 components and pseudo-components and 64 unit operation modules, including the 7 distillation columns and a recycle stream. All modules are built with rigorous, first-principles models.

For optimization applications, PETROX was linked to NPSOL, an SQP optimization algorithm. Procedures for Steady-state and Gross error detection, Data Reconciliation, Parameter Estimation and Economic Optimization were implemented. The economic optimization problem consisted of the maximization of the operational profit, constrained by limits related to product specifications, safety constraints, feed rate and performance parameters. The whole optimization problem involves 19 decision variables and 21 constraints.

Most of the reported problems of optimization based on sequential-modular models were observed in this application:

- Low computational efficiency, due to slow recycle loops and the numerical derivatives that imply running the SM model several times. These derivatives are also inaccurate, which slows down the optimization process even more.
- Lack of reliability: the SM model is computed many times and must converge always. If a single failure happens during the optimization, all the effort is lost.

In order to minimize these problems, a lot of effort must be spent on the conception, customization and tuning of the SM model. However, that is no guarantee of success. When the Data Reconciliation and Parameter Estimation problems were implemented, the same problems were observed.

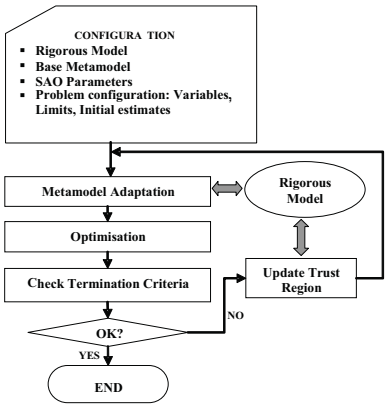

Fig. 6 - SAO strategy applied to the metamodel-based optimisation.

Metamodel approach

In order to overcome some of these shortcomings, a metamodel approach has been studied. Metamodels or surrogate models (Gomes et al., 2008) are reduced models whose parameters are obtained with data that is generated with rigorous, first principles models. In this work, an optimization procedure was developed, combining

metamodels and rigorous models with a Sequential approximate optimization (SAO) algorithm. The optimization problem is solved based on the metamodel that is updated with data obtained from the rigorous model throughout the optimization procedure. The RECAP optimization problem was addressed with this approach, with kriging models and neural nets used as metamodels. Accurate results have been obtained with considerable reduction of the computational effort on most of the studied cases.

Distillation Unit / EO (2005 to 2006)

This was the first EO RTO project PETROBRAS implemented. After an International Bid, where 3 well-known companies were invited to submit their proposals, AspenPlus Optimizer (Aspentech, Inc.) was selected. The project scope included all 3 preheat trains as well as Pre-flash, Naphtha Stabilizer, Atmospheric, Vacuum and Pre-vacuum distillations towers. The unit was fully modeled with the RTO software, which allowed for instance the understanding about the implications that changes on the preheat train, like feed distribution, have on the Atmospheric tower. Or to study the best pumparound heat removal distribution along this tower and its effects on the preheat train. In order to do that, all pumparounds were modeled as external streams from the tower and not as an internal model within its model (see Figure 7), as it is common on SM simulators.

The system is running on open loop since 2007. A few closed-loop tests were performed, but the unit had some operational problems which were solved on this last Oct/08 turnaround. PETROBRAS intends to close loop in 2009 after making model tuning adjustments in order to incorporate the new atmospheric trays and other unit improvements. Nevertheless, by keeping the system running open loop (around 9 runs / day), we were able to improve our knowledge of the system itself, how to overcome non convergence problems (feed reconciliation and optimization) and attaining expertise on how to maintain such a real time, strongly data and instrumentation dependent system as well as evaluate potential benefits (around 13 000,00 dollars / day).

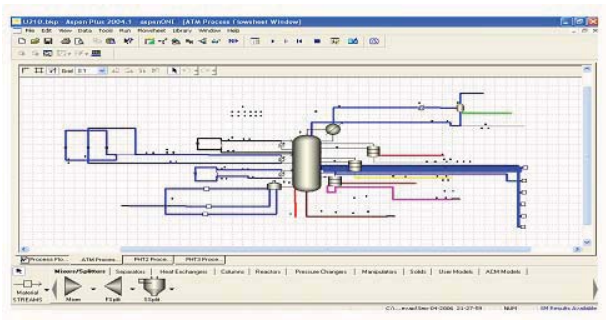

Fig. 7 - Aspen Plus Optimizer Screenshot - Atmospheric tower.

FCC Unit / EO (2007 to 2008)

Following the success on the distillation unit implementation, PETROBRAS moved forward to implement an RTO on another very important unit. Again, after an international bid, ROMeo (Invensys, Inc.) was selected.. The project scope included the Reactor / Regenerator section, Main Fractionator and Gas Recovery Plant. Again the unit was fully energy and mass integrated modeled.

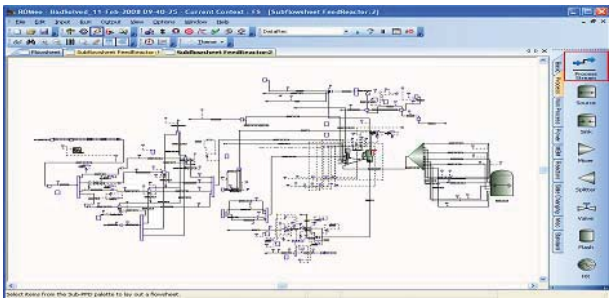

Fig. 8 - ROMeo screenshot - Reactor/Regenerator Section.

The system is running on closed loop (around 8 runs / day) since June/08 with most of the independent variables active. On average, around 60% of the successful runs are being accepted by Operations and targets are being sent to Advanced Control. PETROBRAS has evaluated an average gain of US$ 0.12 / bbl of FCC feed for this application, by comparing the unit performance with and without RTO.

A few comments on both projects:

- Lack of instrumentation on preheat train (FCC) – implied on simplifications, which has impacts on Main Fractionator heat balance and, thus, must be evaluated from time to time;
- Low feed lab analysis frequency – There is a need for a better way to estimate feed characterization;
- Non-convergence problems - Mainly, due to instrumentation faulty and/or out of service heat exchanger or other piece of equipment. Although there is a kind of standard procedure to deal with them, it is not possible to automate it. So each problem must be solved on a case to case, hands-on basis.

These facts enforce the need for a fully dedicated RTO engineer for each application, not only to assess its results and make sure they are being implemented, but to keep the system running despite of the many daily issues the application faces.

Modelling approach

PETROBRAS experiences showed that the Equation Oriented (EO) approach is more suitable for RTO, when compared to the Sequential-modular process models, especially when process unities of higher complexity are addressed.

Challenges associated with RTO

Non-convergence tracking

When the optimization process brakes down due to non-convergence, it is sometimes a hard task to find out the origin of the failure, especially when the cause of the problem is not

related to instrumentation or well-known process problems. Therefore, there is a need for better procedures or even an expert system that might identify the numerical failures and provide high-level analysis to support the user on the best actions to take.

The improvement of the initialization techniques (Fang et al., 2009) might also be useful to avoid convergence problems, especially for the data reconciliation problem.

Scaling

Scaling of variables is a subjective issue. Despite the available heuristic rules provided by the technology licensors, the users are sometimes required to define scaling factors or limits. However, it is possible that a numerical analysis of the system of equations to be solved might provide the best scaling factors.

Integrating multiple process unities

In order to take the most of process flexibilities, it might be important to expand the scope of the optimization problem to involve more than just one process unit. However, the increase of the problem size and the consequent shortcomings can be a challenge to be faced. In this case, the non-converge tracking procedures would become a key issue.

Steady-State detection

The steady-state detection procedures used nowadays in the commercial solutions require the definition of several parameters, which is a very subjective issue. This task demands from the user not only process experience, but also a long time of observation. It would be useful to have procedures that could drive a straightforward choice, especially when dealing with multiple-process optimization applications.

Multi-scale optimization

The integration and information exchange between different optimization levels is an issue that requires more attention.

Multi-level optimization concepts could be applied in order that procedures for model re-fitting or tuning and the redefinition of search spaces could be done automatically, while the different optimization problems are being solved.

Dynamic RTO

Dynamic Real Time Optimization (DRTO) is an open issue. The use of rigorous dynamic models for large-scale applications might allow the simultaneous solution of process optimization and control problems. Ideally it would also avoid the requirement of steady-state detection procedures. However, with the present resources, DRTO solutions would demand a significant computational effort and, possibly, many numerical issues should be addressed before this technology can be widely used in industrial applications.

5. CONCLUSIONS

This article has discussed some challenges associated with advanced process control and optimization in petroleum industries as well as how PETROBRAS is overcoming them. Our vision is that there is still plenty of space for further nd research and development on the improvement of those technologies. The best accomplishment of this task will come if Industry and Academy work together.

REFERENCES

Alkaya, D. et al., Generalization of a Tailored Approach for Process Optimization, Ind. Eng. Chem. Res., Vol. 39, pp. 1731-1742, 2003.

Arruda, G.H.M. and Barros, P.R., Relay based gain and phase margins PI controller design, IEEE Transactions on Instrumentation and Measurement Technology, Vol. 52, n. 05, pp. 1548-1553, 2003

Bequette, B. W, Non-linear Model Predictive Control: A Personal Retrospective, The Canadian Journal of Chemical Engineering, Vol. 85, pp. 408-415, 2007.

Campos, M. and Teixeira, H., Controles típicos de equipamentos e processos industriais, Ed. Edgard Blücher, São Paulo, 2006.

Campos, M. et al., Ganhos econômicos devidos à melhoria no controle de uma planta de processamento de gás natural, IV Congresso Rio Automação 2007, IBP, Rio de Janeiro, 2007.

Cutler, C. R. and Perry, R. T., Real-time optimization with multivariable control is required to maximize profits, Computers and Chemical Engineering, Vol. 7 (5), pp. 663-667, 1983.

Ender, D., Process Control Performance: Not as good as you think, Control Eng., pp. 180, 1993.

Fang, X. et al., Mnemonic Enhancement Optimization (MEO) for Real-Time Optimization of Industrial Processes, Ind. Eng. Chem. Res.,Vol. 48, pp. 499-509, 2009.

Farenzena, M. and Trierweiler, J., Fronteiras e desafios em gerenciamento de malhas de controle, In: COBEQ 2008 - Congresso Brasileiro de Engenharia Química, Recife, 2008.

Farenzena, M. et al., Using the Inference Model Approach to Quantify the Loop Performance and Robustness, SICOP 2006 - International Workshop on Solving Industrial Control and Optimization Problems, Gramado, 2006.

Gomes, M.V.C. et al.; Using kriging models for real-time process optimisation. Proceedings of the 18th European Symposium on Computer Aided Process Engineering, pp. 361-366, 2008.

Harris, Assessment of Control Loop Performance, The Can. J. of Chemical Engineering, Vol. 67, pp. 856-861, 1989.

Kempf, A., Avaliação de Desempenho de Malhas de Controle, Dissertação de Mestrado, Departamento Eng. Química, Universidade Federal do Rio Grande do Sul, UFRGS, 2003.

Kern, G., Summiting with multivariable predictive control, Hydrocarbon Processing, 2007

Ogata, K., Engenharia de Controle Moderno, Ed. Prentice/Hall do Brasil, 1982.

OPC Foundation, 2008, Site: <http://www.opcfoundation.org/>, Accessed in 03/17/08.

Qin, S. and Badgwell, T., A survey of industrial model predictive control technology, Control Engineering Practice 11, pp. 733-764, 2003.

Schmidt et al., BR-Tuning Ferramenta para sintonia de controladores PID, Primeiro CICAP – Congresso de Instrumentação, Controle e Automação da PETROBRAS, May, Rio de Janeiro, 2008.

Trierweiler, J. and Farina, L., RPN tuning strategy for model predictive control, Journal of Process Control, Oxford-Inglaterra - Elsevier, Vol. 13, pp. 591-598, 2003.

Zanin, A. and Moro, L., Gestão da Automação Industrial no Refino, Rio Oil&Gás 2004, IBP, Rio de Janeiro, 2004.

Real-time Embedded Convex Optimization

Stephen P. Boyd

Electrical Engineering Department,
Stanford University, 94305 Stanford, CA, USA
E-mail: boyd@stanford.edu.

Abstract: This talk concerns the use of convex optimization, embedded as part of a larger system that executes automatically with newly arriving data or changing conditions, in areas such as automatic control, signal processing, real-time estimation, real-time resource allocation and decision making, and fast automated trading. Such systems are already in use in applications such as model predictive control or supply chain optimization, with sample times measured in minutes (or longer); our focus is on systems with much faster dynamics, with execution times measured in milliseconds or microseconds for small and medium size problems. We describe a preliminary implementation of an automatic code generation system, which scans a description of the problem family and performs much of the analysis and optimization of the algorithm, such as choosing variable orderings used with sparse factorizations, at code generation time; compiling the generated source code yields an extremely efficient custom solver for the problem family.

The State of the Art in Advanced Chemical Process Control in Japan

Manabu Kano * **Morimasa Ogawa** **

* *Kyoto University, Nishikyo-ku, Kyoto 615-8510, Japan (e-mail: manabu@cheme.kyoto-u.ac.jp)*
** *Yamatake Corporation, Kurashiki, Okayama 712-8061, Japan (e-mail: ogawa-morimasa@jp.yamatake.com).*

Abstract: In this age of globalization, the realization of production innovation and highly stable operation is the chief objective of the process industry in Japan. Obviously, modern advanced control plays an important role to achieve this target; but it is emphasized here that a key to success is the maximum utilization of PID control and conventional advanced control. This paper surveys how the three central pillars of process control – PID control, conventional advanced control, and linear/nonlinear model predictive control – have been used and how they have contributed toward increasing productivity. In addition to introducing eminently practical methods, emerging methods, and their applications, the authors point out challenging problems. In Japan, industry and academia are working in close cooperation to share their important problems and develop new technologies for solving them. Several methods introduced in this paper are results of such industry-academia collaboration among engineers and researchers in various companies and universities. Furthermore, soft-sensor or virtual sensor design is treated with emphasis on its maintenance, because soft-sensors must cope with changes in process characteristics for their continuous utilization. Maintenance is a key issue not only for soft-sensors but also for controllers. Finally, we will expand our scope and briefly introduce recent activities in tracking simulation and alarm management. A part of the results of our recent questionnaire survey of process control are also introduced; the results are extremely helpful in clarifying the state of the art in process control in Japan.

Keywords: Advanced process control, Alarm management, Industrial application, Model-based control, Model predictive control, PID control, Process control, Production innovation, Soft-sensor, Tracking simulator.

1. INTRODUCTION

The Japanese chemical and petroleum refining industries has focused on *production innovation* and *highly stable operation*. The embodiment of these two concepts is believed to be indispensable. In fact, production innovation and highly stable operation have led to remarkably increased productivity at advanced chemical companies. Daicel Chemical Industries, for example, has tripled the productivity per plant employee since *Intellectual and Integrated Production System* was established in the Aboshi plant in 2000 (Daicel Chemical Industries, Ltd. (2008)). This reputable activity was motivated by the effort in Mitsubishi Chemical Corporation (MCC) in the 1990's (Shoda (1998)). MCC has developed *Super-stable Operation Technologies* (SSOTs) and *Super-stable Maintenance Technologies* (SSMTs) to maintain production stability and prevent facility accidents (Mitsubishi Chemical Corporation (2005)). SSOTs aim to keep stable plant operation by prevention and prediction of various troubles such as fouling, plugging, corrosion, and so on, and SSMTs are facility management technologies used to ensure high standards of stability.

In the 1990's, Japanese companies realized that many skilled operators were approaching retirement age. This social problem was called "year 2007 problem" in Japan. We are in the middle of this. Since the achievement of stable and efficient operation has largely depended on skilled operators in Japan, the year 2007 problem has heightened a sense of crisis and has motivated companies to initiate production innovation. Production innovation requires thorough review of personnel training, organizations, production methods as well as operation control systems.

To realize highly stable operation, process control plays an important role. In Japan, a task force was launched in 2007 to sift through problems regarding process control and investigate solutions. The task force, named "Workshop No.27 Process Control Technology," consists of 32 engineers from industry and 12 researchers from universities. It is supported by the 143rd committee on process systems engineering, the Japan Society for the Promotion of Science (JSPS). Currently, the following topics are being investigated by the members.

- Practical closed-loop system identification
- Practical tuning techniques of PID controllers
- Systematization of the control performance improvement activity based on control performance assessment

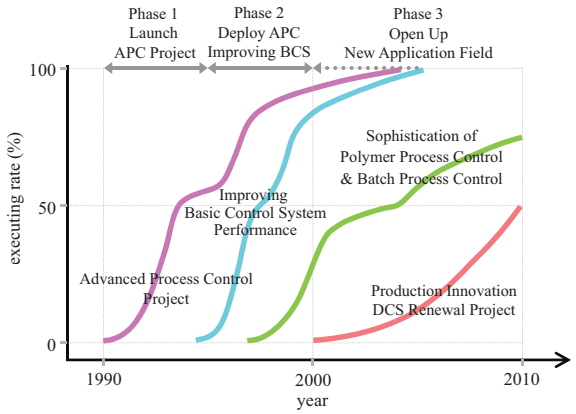

Fig. 1. Chronology of project execution in MCC

- Control system design from the viewpoint of plant-wide control
- Evaluation and maintenance of model predictive control
- Design and maintenance of soft-sensors

Most of these topics are also covered by the status report of the IFAC Coordinating Committee 6 (Dochain et al. (2008)). These are key issues not only in the Japanese chemical industry but also internationally.

This paper aims to reveal the state of the art in advanced chemical process control in Japan. First, the projects that process control sections of a general chemical corporation of Japan have executed in the last two decades are described in section 2. Then, several key technologies are investigated in more detail: PID control in section 3, conventional advanced control in section 4, model predictive control (MPC) in section 5, soft-sensor or virtual sensor in section 6, and other issues including an operation support system based on an on-line process simulator and alarm management in section 7. In each section, eminently practical techniques with successful application results are introduced, and challenges are clarified. Furthermore, this paper introduces results of a questionnaire to member companies of the JSPS 143rd committee on their process control applications including MPC and soft-sensors. The results will be extremely useful for grasping the state of the art in process control.

2. MILESTONE IN THE HISTORY OF PROCESS CONTROL APPLICATION

There are three phases in process control application projects in Mitsubishi Chemical Corporation (MCC), to which the second author had belonged for many years, as shown in Fig. 1: the advanced process control (APC) projects for large-scale continuous processes, the improvement activity of the control performance of basic control systems for small-to-medium-scale processes, and the advancement of polymer and batch process control.

2.1 Project Chronology

In the first phase in the early 1990's, multivariable MPC was applied to large-scale continuous processes such as olefin production units for generating a large profit. The APC project was conducted for 15 production units of 5 production sites by using DMCplus® as a standard tool, and satisfactory results were achieved. The key to success is nurturing process control engineers who can accomplish the projects independently on their own. They learned procedures and methods of planning, control system design, plant tests, tuning, and operation. In addition, they joined seminars on advanced control theory given by prominent researchers and professors. By accumulating experience on the projects, they grew into capable engineers who understood theory and had business acumen. These 15 process control engineers took a leading part and accomplished APC projects in MCC.

In the second phase, the performance of PID control systems was assessed and improved. All production units which APC projects did not cover were targeted. Both the operation section and the instrumentation section jointly carried out this project as a daily improvement activity in cooperation with the process control section. As a result, the operator workload was reduced through the improvement in service factors of PID control systems and a reduction in frequency of alarms and operator interventions. In addition, the improvement in control performance contributed toward the economic profit because it made operations energy-efficient through optimally changing set-points. It was also the perfect opportunity for finding applications of conventional advanced control such as override control and valve position control (VPC).

In the third phase, the advancement of polymer process control was investigated. It is important to achieve rapid grade transition while satisfying quality specification in polymer plants, because transitions among a wide variety of products are made frequently. Therefore, an original control algorithm that is based on precise first-principle models of polymerization reactions and quality models relating polymerization reaction conditions and product quality has been used since the 1980's. In this phase, process models such as catalyst activity were reviewed, and a new nonlinear MPC algorithm was developed and applied. As a result, the control performance was significantly improved, off-specification products were reduced, and quality was stabilized.

The focus of the process control section has shifted to problem-solving regarding process control of small-to-medium-scale processes and the maintenance of APC systems. The targets include 1) accumulating energy-saving effects by applying an in-house linear MPC algorithm to distillation, reforming furnace, and air separation processes, 2) developing soft-sensors, which are substituted for process gas chromatographs, for shortening the control interval and improving control performance, and 3) adapting APC systems for reinforcement of process units.

Since the 1990's, the movement to reform the whole production activity has started at advanced chemical companies as mentioned in the introduction. In addition to integration of control rooms, such production innovation requires the review of operation management, alarm management, emergency shutdown system, maintenance management, etc., and also it requires modernizing the control information system. Such an activity is triggered by the

Table 1. Classification of process control methodologies and the numbers of applications in the MCC Mizushima plant

classification	methodology	application
modern	linear MPC	54
advanced	nonlinear MPC	2
control	LQI with preview action	2
conventional advanced control	feed-forward control override control valve position control analyzer feedback control model-based control etc	500+
regulatory control	PID/I-PD control	5006

opportunity for DCS introduced in the 1980's to enter a renewal period as well as the year 2007 problem. Process control engineers are or will be involved in this movement.

2.2 Process Control Methodology

Control methodologies which bear the central role in process control systems can be classified into regulatory control such as PID control, conventional advanced control such as feedforward control and override control, and modern advanced control such as MPC. The number of applications of these control methodologies in the MCC Mizushima plant is summarized in Table 1. The ratio of applications of PID control, conventional advanced control, and MPC is 100:10:1. PID control is used in 5006 loops in 24 production units. The number of control loops repeatedly increases and decreases corresponding to new establishment, reinforcement, or stopping of production units. Conventional advanced control is effective in many cases, but the number of its applications is not as many as expected. MPC has become established as a standard technique for multivariable control which realizes economical operation of large-scale processes.

2.3 Survey Result of Control Methodology

A part of the questionnaire survey results of process control application is summarized in Table 2. This questionnaire asked control engineers to evaluate the level of their application of conventional advanced control, model-based control, adaptive control, modern-control-theory-based control, knowledge-based control, statistical process control, and soft-sensor in four grades.

This survey result clarifies the state of the art of process control application in Japan. As expected, linear MPC is the only methodology of modern advanced control that has been applied practically. Most companies have not used nonlinear MPC, adaptive control including self-tuning control, state feedback control, preview control, H_∞ control, or knowledge-based control including neural-network-based control. These control techniques have not been used because they are not available as a practical, easy-to-use tool and in-house development is troublesome. In particular, self-tuning control is a black box and has incurred a vague distrust of engineers and operators. In addition, it is not superior to gain scheduling control or robust PID tuning, which is more intuitive and understandable. On the other hand, the modern control theory has not been accepted in the chemical and petroleum refining industries. This situation is in stark contrast to that

Table 2. Level of control application (from the survey JSPS143 WS27 2009)

control methodology	level of application			
	A	B	C	D
conventional advanced control				
feedforward control	3	9	6	2
override control	2	6	5	7
valve position control	4	5	6	5
sampled-data control	1	5	9	5
dead-time compensation	0	2	11	7
gain-scheduled PID control	1	1	9	9
model-based control				
internal model control	2	5	3	9
linear model predictive control	4	6	6	3
nonlinear model predictive control	0	1	2	16
adaptive control				
self-tuning PID control	0	1	1	17
model reference adaptive control	0	0	1	18
modern-control-theory-based control				
state feedback control	0	0	4	15
preview control	0	0	1	18
H_∞ control	0	0	0	19
knowledge-based control				
fuzzy control	0	0	5	14
artificial-intelligence-based control	0	0	2	17
neural-network-based control	0	0	4	15
statistical process control	0	1	3	15
soft-sensor	3	7	4	5

Explanation of level of application:
A: standardized and always applied if necessary.
B: applied, but not standardized.
C: applied sometimes.
D: not applied.
The numbers in this table show the numbers of answers.

in the steel industry, for example, where there are many applications of modern control such as H_∞ control. This is because there have already been a number of successful MPC applications in the chemical and petroleum refining industries; thus control engineers are not motivated to use more theoretical control algorithms. Knowledge-based control is useful for complementing PID control and MPC, but it is difficult to generalize knowledge-based control so that it can be applied to a variety of processes.

3. PID CONTROL

In Japanese chemical companies, KAIZEN activities aimed at safe and stable operation are actively continuing. One important activity is improvement in the control performance of PID control systems. The aims of this improvement activity, in which controllers are retuned appropriately, are 1) to realize stable operation by reducing the influence of disturbances, 2) to realize automatic rapid transition of operating conditions such as production rate, 3) to gain the ability to achieve economical operation, and 4) to allow operators to be released from taking care of PID controllers. Additional effects are to find out problems with sensors and actuators, and to clarify possible targets of advanced control application.

In the KAIZEN activities, improving the control performance with retuning should be stressed, rather than spending time and effort to strictly assess the control performance of PID control loops. The following simple indexes are sufficient to determine good or bad control performance: 1) Is the controller in auto mode at all

times? 2) Are PID parameters in the proper range? 3) Is fluctuation of the controlled variable and the manipulated variable sufficiently small? 4) Is the PID tuning agreeable to the control purpose such as flow-averaging level control? Other than these, it is necessary to check the range propriety of sensors and actuators, the necessity of filtering of measurement noise, the presence of stiction of control valves, and so on.

Experience leads us to believe that 80% of PID control loops can be successfully tuned with a method based on rule of thumb and trial and error. For example, initial settings for PID parameters should be "wide proportional band and fast reset time" for flow control and "narrow proportional band and slow reset time" for level control. After the initial PID setting, PID parameters are tuned gradually to strengthen control action while the control performance is verified.

The control performance improvement activity introduced in this section has attracted the attention of many enterprises in the chemical and petroleum refining industries in Japan, and the number of enterprises starting this activity has increased rapidly. Such a movement seems to be the result of the process control section not directly recognizing the reality that the operation section had an awareness of control performance issues and was dissatisfied with the control performance.

3.1 Actual Project Examples

The result of a project on a large-scale monomer plant, which has 190 PID control loops, is introduced here. In this plant, 90% of the PID controllers were in auto mode for 30 days. This value outperforms the average of 70% in the literatures (Desborough and Miller (2001); Ender (1993)). Operators had adjusted PID parameters to realize very loose control action. As a result, the process was easily affected by disturbances and a long time was required for production rate changes, thus the operators made frequent adjustments such as set-point changes and manual operation.

In all, 112 loops having a margin of improvement in control performance were retuned in 12 days. The standard deviations of controlled variables (CVs), σ_e, and manipulated variables (MVs), σ_u, were reduced by an average of 37% and 28%, respectively, as shown in Fig. 2. Here $\tilde{\sigma}$ denotes the standard deviation before the retuning. The reduction is almost the same as the value reported by Shah et al. (2004). A pronounced effect was achieved in tray temperature control loops of distillation columns. Temperature fluctuation was reduced to one-fourth up to one-seventh, and composition was also stabilized.

Figure 3 shows PID parameters for 29 level control loops before and after the retuning. Here PB and T_i denote proportional band and reset time, respectively. With the exception of a part such as six loops for a heat recovery boiler, the purpose of these control loops is flow-averaging level control (FALC). Operators made the proportional gain small (wide proportional band) in order for the manipulated variable not to change. However, the manipulated variable had been oscillatory due to small reset time. To solve this problem, Ogawa et al. (1998) developed

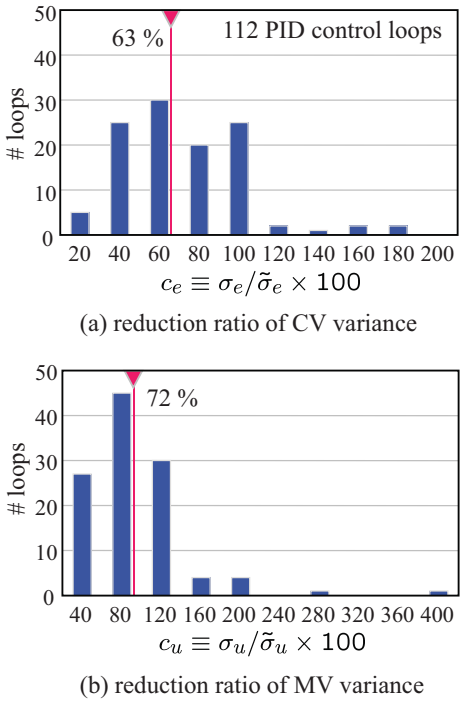

(a) reduction ratio of CV variance

(b) reduction ratio of MV variance

Fig. 2. Improvement in PID control performance: project on a large-scale monomer plant in MCC

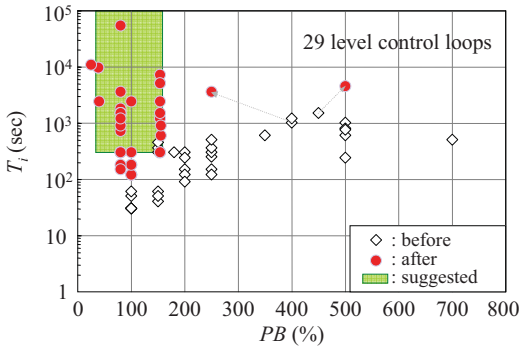

Fig. 3. PI parameters of 29 level controllers before and after retuning

a design method of flow-averaging level controllers and applied it to those loops. As a result, it became possible to suppress the oscillation of the manipulated variable by allowing the fluctuation of the level, utilizing the capacity of the drum, and absorbing flow disturbances. This FALC, explained in section 3.3, was very effective for decreasing changes in feed/product flow rate to distillation columns and lightening the burden of tray temperature control.

The above-mentioned example is the result for MCC. Generally, each company has its own in-house tool for assessing and improving PID control performance. In Sumitomo Chemical, for example, Kugemoto (2005) developed a control loop diagnostic tool "LoopDiag" that can execute control performance assessment, valve stiction detection, as well as time series data analysis. LoopDiag is a re-

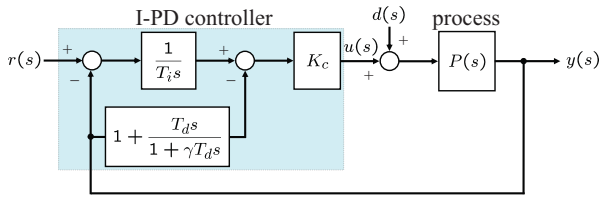

Fig. 4. I-PD control system

sult of industry-academia collaboration in the task force "Workshop No.25 Control Performance Monitoring" supported by the JSPS 143rd committee. In LoopDiag, control performance is evaluated on the basis of the minimum variance control benchmark concept (Harris (1989)), and valve stiction is detected by using the methods developed by Maruta et al. (2005) and Yamashita (2006). By the year 2005, control performance assessment was carried out for 300 PID control loops by using LoopDiag, and performance improvement was achieved. In addition, 12 valve failures were diagnosed in 118 control loops, and four of 12 valves had actually developed trouble.

Mitsui Chemicals has utilized "Plant Control Estimation & Tuning System (PCETS)" (Nishimura and Ootakara (2007)). The functions of PCETS include 1) control performance assessment based on operation data of controlled variables, set-points, and manipulated variables, 2) plant performance assessment, and 3) optimal PID tuning support. The function of control performance assessment has been applied to more than 5000 control loops, and more than 250 control loops whose performance was identified as poor were retuned by the function of optimal PID tuning support. The control performance was greatly improved in most control loops.

In Idemitsu Kosan, one-parameter tuning PID control has been used (Fujii and Yamamoto (2008)). This unique technique was developed to integrate control performance assessment and controller design and to make PID tuning easier and more intuitive for plant operators. It allows PID parameters to be tuned by adjusting just one user-specified parameter that corresponds to control strength or robustness. So far, one-parameter tuning PID control has been successfully applied to hundreds of control loops. This technique clarifies when controllers should be retuned and enables operators who do not have controller design experience to tune PID parameters effectively.

These examples would reveal the state of the art in PID control, which still plays a very important role in chemical process control. In the following part of this section, a few practical control techniques are introduced.

3.2 Robust I-PD Controller Tuning

Since most PID controllers have the I-PD algorithm at least in Japan, Ogawa and Katayama (2001) derived a robust model-based PID tuning method for the I-PD controller shown in Fig. 4. This method is suitable for specific control loops such as temperature and composition control, which are required a proper control performance in the presence of plant-model mismatch.

The advantage of I-PD control over conventional PID control is that I-PD control can realize milder response to set-point changes than PID control, while both control algorithms achieve the same performance against disturbances. When the set-point is changed stepwise in PID control systems, an abrupt change of the manipulated variable is unavoidable due to derivative and proportional actions. In practice, such an abrupt change is undesirable. On the other hand, in I-PD control systems, both derivative and proportional terms act only on the controlled variable; thus milder changes in the manipulated variable can be realized.

Here, the I-PD controller tuning method for a first-order plus time-delay (FOPTD) model is explained. The desired response $W_r(s)$ of the controlled variable y for the set-point r is specified by

$$W_r(s) \equiv \frac{y(s)}{r(s)} = \frac{1}{(1+T_F s)^n} e^{-T_L s} \tag{1}$$

where T_F denotes a tuning parameter and $n = r + 1 = 2$ for the relative order $r = 1$ of the process model. T_L, T_p, and K_p denote time-delay, time constant, and steady-state gain of the process model, respectively. By using the 1/1 Pade approximation and ignoring the derivative filter, the partial model matching method (Kitamori (1981)) provides the following PID setting rule.

$$K_c = \frac{p - 2q + 4}{K_p\,(p + 2q)} \tag{2}$$

$$T_i = \frac{(p + 2q)\,(p - 2q + 4)}{2p + 4} T_p \tag{3}$$

$$T_d = \frac{p\,(p + 4q - 2q^2)}{(p + 2q)\,(p - 2q + 4)} T_p \tag{4}$$

where $p \equiv T_L/T_p$ represents the difficulty of control and $q \equiv T_F/T_p$ is a tuning parameter. Although the parameter q can be tuned so that ISE (Integral of Squared Error) is minimized, such tuning is not preferable in practice. To realize robust PID control that is intuitive and practical, a constraint on the maximum change of the manipulated variable $u(t)$ against a stepwise set-point change is introduced. Given $U_{\max}(\%)$, the parameter q is determined by solving the following equation.

$$\max_q \|u(t)/u(\infty)\|_\infty \le U_{\max}/100 \tag{5}$$

where $u(\infty)$ is the steady-state value of $u(t)$ after the set-point change. The relationship among q, p, and $U_{\max}$ is shown in Fig. 5.

This robust I-PD controller tuning method is derived not only for FOPTD models but for integral plus FOPTD models and second-order plus time-delay (SOPTD) models with/without an unstable pole.

3.3 Flow-Averaging Level Control

Consider a process described by

$$P(s) = \frac{y(s)}{u(s)} = \frac{1}{T_p s}, \quad T_p = \frac{K_m A}{K_u} \tag{6}$$

where T_p (h) denotes reset time constant, K_m (m/%) sensor gain, K_u (m^3/h/%) actuator gain, and A (m^2) sectional area.

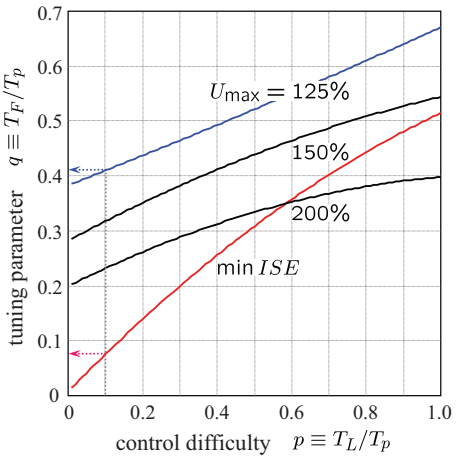

Fig. 5. Tuning of robust I-PD controllers

I-P control is used for FALC. Its block diagram is shown in Fig. 4 and derivative time T_d is set equal to 0. The control response to set-point r (%) and disturbance d (%) becomes the following second-order standard form.

$$y(s) = \frac{1}{1 + 2\zeta T_n s + T_n^2 s^2}\left(r(s) + \frac{T_i s}{K_c} d(s)\right) \tag{7}$$

The damping coefficient ζ and the natural frequency T_n are given by

$$\zeta = \sqrt{\frac{K_c T_i}{4T_p}}, \quad T_n = \sqrt{\frac{T_p T_i}{K_c}} \tag{8}$$

By defining the performance index of FALC under a step-wise disturbance as

$$\min \ J = \frac{1}{2}\int_0^\infty \left(q^2 y^2(t) + r^2 \dot{u}^2(t)\right) dt \tag{9}$$

and solving the optimization problem similar to the LQI problem, the control parameters can be related to the process parameter.

$$K_c T_i = 2T_p \tag{10}$$

As a result, the damping coefficient becomes $\zeta = 1/\sqrt{2}$ and the second-order standard form becomes Butterworth-type.

Given the size of the step-wise disturbance d_s and the maximum allowable level change y_s, the proportional gain and the reset time can be determined as follows:

$$K_c = \frac{\sqrt{2}e^{-\pi/4}}{y_s/d_s} \approx \frac{0.645}{\eta}, \quad T_i = \frac{2T_p}{K_c} \tag{11}$$

Here, $\eta \equiv y_s/d_s$ is the disturbance rejection ratio.

This tuning method has been widely used in industry to improve the performance of level control, in particular, to achieve FALC with the specified characteristics, because the calculation of PI parameters is very easy.

3.4 Direct PID Controller Tuning

Discussions with control engineers in the Japanese process industries confirm that PID controller tuning is still a key issue. A typical chemical plant has thousands of control loops whose maintenance is vital to efficient operation of the entire plant. The conventional approach to tackling this problem is to use an efficient open/closed-loop identification method and reduce the burden of modeling. However, any control system based on an identified model suffers from modeling errors and requires retuning of control parameters. In addition, identification is still one of the critical tasks in control system design. Control engineers and operators would prefer to avoid identification and manual tuning of PID controllers.

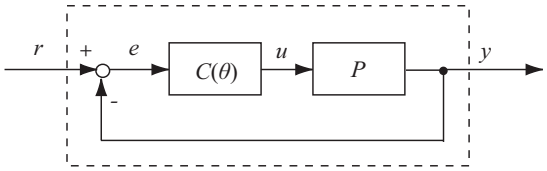

Fig. 6. Feedback control system

Extended fictitious reference iterative tuning (E-FRIT) is a new direct tuning method, which can optimize PID or I-PD control parameters directly from operation data without a process model (Tasaka et al. (2009); Kano et al. (2009b)). E-FRIT is a kind of extension of other direct tuning methods such as iterative feedback tuning (IFT) proposed by Hjalmarsson et al. (1998), virtual reference feedback tuning (VRFT) by Campi et al. (2002), and fictitious reference iterative tuning (FRIT) by Soma et al. (2004).

E-FRIT is briefly explained here. Figure 6 shows a block diagram of a feedback control system, where P denotes a process, $C(\boldsymbol{\theta})$ a controller with parameters $\boldsymbol{\theta}$, r set-point, and u and y are a manipulated variable and a controlled variable, respectively. When PID control is used,

$$C(\boldsymbol{\theta}) = K_{\mathrm{P}}\left(1 + \frac{1}{T_{\mathrm{I}} s} + T_{\mathrm{D}} s\right) \tag{12}$$

$$\boldsymbol{\theta} = (K_{\mathrm{P}}, T_{\mathrm{I}}, T_{\mathrm{D}}) \ . \tag{13}$$

In E-FRIT, a virtual output variable is formulated as a function of PID parameters by using input and output data together with a reference model. PID parameters are determined so that the difference between the real and virtual output variables is minimized. The following is the PID tuning procedure based on E-FRIT. Here, $G(s)x(t)$ or $Gx(t)$ is defined by $\mathcal{L}^{-1}\{G(s)\mathcal{L}\{x(t)\}\}$, which represents the discrete time series data collected at certain sampling intervals.

[Step 1] After the control system is stabilized with initial PID parameters $\boldsymbol{\theta}_0$, change the set-point and collect input and output data, $u_0(t)$ and $y_0(t)(t = 1, 2, \cdots, N)$.

[Step 2] Derive the fictitious reference (virtual set-point) $\tilde{r}(\boldsymbol{\theta}, t)$ that generates $u_0(t)$ and $y_0(t)$ even when $\boldsymbol{\theta} \neq \boldsymbol{\theta}_0$.

$$\tilde{r}(\boldsymbol{\theta}, t) = C(\boldsymbol{\theta})^{-1} u_0(t) + y_0(t) \tag{14}$$

[Step 3] Formulate the reference output $\tilde{y}(\boldsymbol{\theta}, t)$ by using a reference model M as shown in Fig. 7.

$$\tilde{y}(\boldsymbol{\theta}, t) = M\tilde{r}(\boldsymbol{\theta}, t) \tag{15}$$

The closed-loop system is close to the reference model when $\tilde{y}(\boldsymbol{\theta}, t)$ is close to $y_0(t)$.

[Step 4] Solve the following optimization problem and determine the optimal control parameters $\boldsymbol{\theta}^*$.

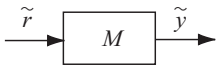

Fig. 7. Reference model of closed-loop system

$$\boldsymbol{\theta}^* = \arg\min_{\boldsymbol{\theta}} J_{\text{ext}}(\boldsymbol{\theta}) \tag{16}$$

$$J_{\text{ext}}(\boldsymbol{\theta}) = \frac{1}{N}\sum_{t=1}^{N}\left\{(y_0(t)-\tilde{y}(\boldsymbol{\theta},t))^2+\lambda\Delta\tilde{u}(\boldsymbol{\theta},t)^2\right\} \tag{17}$$

$$\Delta\tilde{u}(\boldsymbol{\theta},t) = \tilde{u}(\boldsymbol{\theta},t)-\tilde{u}(\boldsymbol{\theta},t-1) \tag{18}$$

$$\tilde{u}(\boldsymbol{\theta},t) = C(\boldsymbol{\theta})\,(r_0(t)-Mr_0(t)) \tag{19}$$

where λ is a weighting coefficient.

A reference model plays an important role in defining the desirable control response. It is difficult, however, to determine an appropriate reference model in advance without information on the process. Therefore, parameters in the reference model are optimized together with the control parameters in E-FRIT. For example, when the reference model M is defined as the second-order binomial coefficient standard form given by

$$M = \frac{\omega_0^2}{s^2+2\omega_0 s+\omega_0^2}e^{-L_{\text{M}}s} \tag{20}$$

the optimization variables are

$$\boldsymbol{\phi} = (K_{\text{P}}, T_{\text{I}}, T_{\text{D}}, L_{\text{M}}) \tag{21}$$

instead of $\boldsymbol{\theta}$. This extension makes it possible to determine the reference model that is more suitable for the process.

Kano et al. (2009b) proposed useful guidelines for applying E-FRIT to industrial processes: 1) use the fourth-order binomial coefficient standard form with dead time as a reference model, 2) set a parameter ω_0 of the reference model on the basis of the rise time of the closed-loop response, 3) optimize the dead time of the reference model together with control parameters, and 4) use a fixed value as a weighting coefficient λ for a penalty term for variation of the manipulated variable. A recommended value is $\lambda = 0.01$ for tight control and $\lambda = 1$ for mild control. E-FRIT with these guidelines was validated through industrial applications. The results have clearly shown the usefulness of E-FRIT for chemical process control. A software tool that can execute E-FRIT was developed as a result of industry-academia collaboration in the task force "Workshop No.27 Process Control Technology," and it has been used in industry.

4. CONVENTIONAL ADVANCED CONTROL

The status report of the IFAC Coordinating Committee 6 (Dochain et al. (2008)) stated that high performance multivariable control is key to achieving the desired high profits and that the technology for the design and realization of high performance model-based constrained control systems at reasonable engineering effort is one of the key challenges faced by industrial practice. In fact, MPC has contributed toward achieving high profitability for many years. However, the profit can also be realized by utilizing conventional advanced control such as valve position control and override control in particular. The following question arises here: do we make the most use of conventional advanced control? In this section, let us introduce one

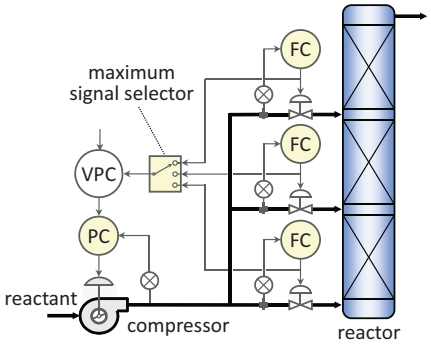

(a) control system based on VPC

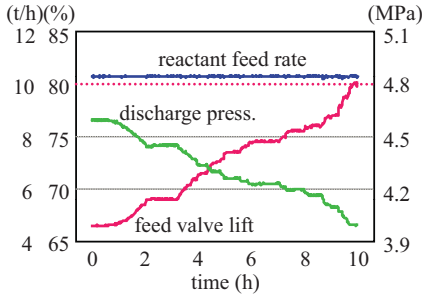

(b) control result

Fig. 8. Compressor-power-saving control

example showing the potential of conventional advanced control.

Conventional advanced control is effective for various processes and easy to implement on DCS. However, there has been a trend for control engineers to take little account of its application. This is the result that MPC became a standard tool for the advancement of process control. However, there is no doubt that production cost can be decreased by accumulating the effect of conventional advanced control.

The application of energy-saving control of the compressor with VPC is described here. As shown in Fig. 8, the feed gas is pressurized with the turbo compressor and supplied to three different stages of the reactor. Each flow rate of the feed gas is controlled. The discharge pressure of the compressor is controlled by using guide vane opening as the manipulated variable. To reduce compressor power, the discharge pressure is lowered gradually with VPC, until the largest valve opening among three feed flow control valves reaches the upper limit, while feed flow rate is kept constant. In this application, the discharge pressure was decreased from 4.6 MPa to 4.0 MPa by increasing the largest valve opening from 67% to 80%. As a result, motor electric power consumption was saved by 16%.

Shinsky (1977) listed the following objects in which there is an opportunity of the energy conservation by applying conventional advanced control: 1) excessive reflux of distillation column, 2) excessive combustion air of furnace, 3) high steam to oil ratio of reactor, and 4) fouled heat exchanger. In addition to these, excessive compression

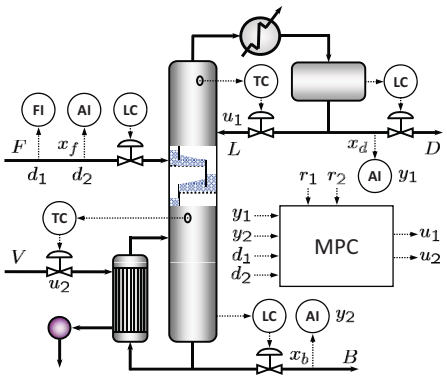

(a) MPC for distillation column

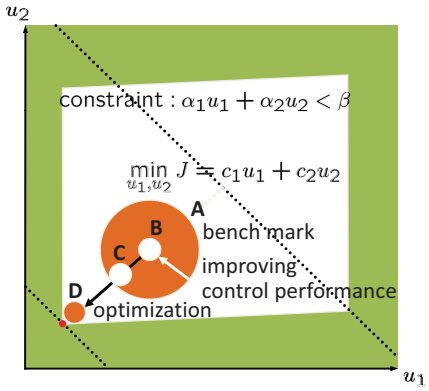

(b) optimal operation using MPC

Fig. 9. MPC for distillation process

ratio provides an opportunity for the energy conservation as illustrated.

In the enterprise, it is important to find any loss that usually has been overlooked, to make the most use of conventional advance control, and to continue the effort at minimizing the loss. In comparison with the APC project of using MPC, profitable results can be obtained much more quickly without any further expense.

5. MODEL PREDICTIVE CONTROL

In this section, the present state of linear and nonlinear MPC is described through the typical applications and the survey results.

5.1 Linear MPC

The process that MPC is applied to most is distillation. A simple example of MPC for a distillation process is shown in Fig. 9(a). The controlled variables are the purity of products extracted from the column top and bottom, and the manipulated variables are the set-points of temperature PID control at the column top and bottom. The disturbance variables are flow rate and composition of feed. The constraints are upper and lower limits of the manipulated variables and the controlled variables and upper limits of changes in the manipulated variables.

The economic benefit that MPC brings is illustrated in Fig. 9(b). Since the achievable performance of PID control is limited due to interaction, which is a feature of multivariable processes, it is assumed that the current operating region corresponds to region A in the figure. In such a situation, the operating condition bound has to be set far from the real constraints to ensure a sufficient margin of safety. Using MPC can improve control performance and reduce variation. As a result, the operating region becomes small from A to B. This improvement makes it possible to move the operating region from B to C, which is close to the bound of operating conditions. Furthermore, more economical operation D can be realized by optimizing set-points to minimize operational costs. MPC takes on the responsibility of this set of functions. The benefit is not only the improvement of the control performance by using model-based control, but also the realization of stable operation close to the optimal point under disturbances by using optimization.

Implementation of MPC releases operators from most of the adjustment work they had to do in the past because the optimal operating condition is automatically determined and maintained under disturbances. In addition, MPC makes it possible to maximize production rate by making the most use of the capability of the process and to minimize cost through energy conservation by moving the operating condition toward the control limit. Both the energy conservation and the productive capacity were improved by an average of 3 to 5% as the result of APC projects centered on MPC at MCC.

The control performance of MPC depends on the accuracy of the process model and the appropriateness of tuning, but MPC has outstanding robustness. For example, stable operation is realized by MPC in spite of large model parameter errors of about 50%. However, it is difficult to assess the control performance of MPC due to a large number of variables. A plant test for modeling sometimes requires two weeks. The engineers who have experienced it can readily understand that the implementation of MPC including modeling and tuning is a demanding job.

MPC is highly effective, but it has several weak points (Hugo (2000)). First, it is not good at level control when the process has an integrator. For such a case, PI control is easy to design and superior to MPC in control performance. Second, the control performance of MPC deteriorates against ramp-wise disturbances because the MPC algorithm is developed by assuming step-wise disturbances (Lundstrom et al. (1995); Hugo (2000)). In addition, linear programming (LP) is usually used for optimizing set-points under constraints, and the optimal point is located at one of the extreme points of a polyhedron consisting of linear constraints. When the gradient of the objective function and that of constraints are similar to each other, the optimal point jumps from one extreme point to another and the set-points change suddenly (Forbes and Marlin (1994); Hugo (2000)). Research and development are continuing to solve these problems.

Ohshima et al. (1995), who wrote about the state of MPC application in the petroleum and chemical enterprises in Japan, reported that 154 MPC controllers were in operation and 43 under implementation. The total number

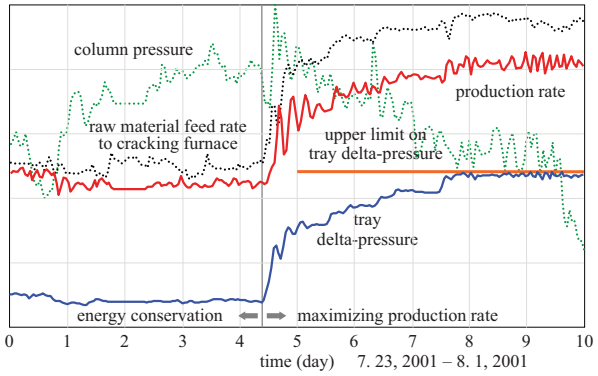

Fig. 10. Actual performance of the large scale MPC in the olefins unit

of 197 was 2.5 times as much as the number of 75 in 1990. At present, the number of MPC controllers is 169 only at MCC (Ogawa (2006)).

At the very end of this subsection, the MPC application for energy conservation and production maximization of the olefins unit at MCC Mizushima plant is briefly explained (Emoto et al. (1994)). Qin and Badgwell (2003) reported that this application was the largest MPC application in the world, consisting of 283 manipulated variables and 603 controlled variables. The process was operated in energy conservation mode for the first four days in Fig. 10. Since the productive capacity was beyond the demand, the temperature difference between vapor and coolant in the overhead condenser was increased by making the column pressure higher. As a result, an amount of heat exchanged was increased, and the amount of coolant used was decreased. This operation made it possible to reduce the refrigerator power. On the other hand, the process was operated in production maximization mode for the last five days. To maximize the production rate for fulfilling the demand, the separation performance was improved by decreasing the column pressure and increasing the relative volatility. The feed flow rate to the cracking furnace was increased until the tray delta-pressure reached its upper limit, that is, the flooding limit. In this production maximization mode, the MPC system is large because MPC controllers for many cracking furnaces and distillation columns function in cooperation.

A skilled operator made the following comment on this MPC application: "We had operated the Ethylene fractionator in constant pressure mode for more than 20 years. I was speechless with surprise that we had made an enormous loss for many years, when I watched the MPC decreased the column pressure, improved the distillation efficiency, and maximized the production rate." Another process control engineer said "I had misunderstood that set-points were determined by operation section and process control section took the responsibility only for control. I realized MPC for the first time; it makes the most use of the capability of equipments, determines set-points for economical operation, and maintains both controlled variables and manipulated variables close to the set-points."

Table 3. Statistics of MPC applications (from the survey JSPS143 WS27 2009)

in-house vs vendor			
in-house development			6 %
introduction from vendor			94 %
targeted process			
distillation			32 %
reaction			23 %
others			45 %
product			
DMCplus®			46 %
RMPCT®			36 %
Connoisseur®			5 %
SMOC®			4 %
others			9 %
number of MV, CV, and DV			
	MV	DV	CV
0	0	28	0
1	40	45	24
2	57	50	33
3-5	83	103	58
6-9	47	40	59
10-19	59	27	48
20-29	12	5	25
30-39	1	3	29
40-49	1	3	16
50 or more	5	1	13

MV: manipulated variable
CV: controlled variable
DV: disturbance variable

5.2 Nonlinear MPC

Nonlinear MPC has attracted attention in recent years (Qin and Badgwell (2003)). It is suitable for control of a nonlinear process operated in a wide range, e.g. polymerization reaction processes. In MCC, an independently developed nonlinear MPC has been applied to polymerization reactors at the polyolefin production units, and it has been put successfully to practical use (Seki et al. (2001)).

However, application of nonlinear MPC has not spread as well as was expected. It is difficult to build a nonlinear model of a process, or process control engineers have slackened their efforts at modeling nonlinear processes. On the other hand, most polymer production processes are operated without any quality problem by existing control systems supported with operators' suitable manual intervention. Therefore, it is difficult to justify any benefit of using nonlinear MPC. These obstacles should be overcome to expand nonlinear MPC application.

5.3 Survey Result of MPC

A part of the questionnaire survey results, related to MPC, is introduced here. The total number of MPC applications answered is 305, which is 1.5 times as much as the number of 197 in 1995. The statistics of 305 MPC applications are summarized in Table 3. Most of them are introduced from vendors; DMCplus® and RMPCT® are dominant tools. Distillation and reaction processes cover half the applications.

Table 4 clarifies objectives and effects of MPC. In addition to disturbance rejection and set-point tracking, the time to achieve the optimal condition and the realization of

Table 4. Effects of MPC applications (from the survey JSPS143 WS27 2009)

objective of tuning	
disturbance rejection	56 %
set-point tracking	38 %
time to optimal condition	6 %
major effect on control performance	
disturbance rejection	43 %
automatic operation	36 %
set-point tracking	18 %
others	3 %
major effect on productivity	
saving resources and energy	38 %
increasing production capacity	31 %
reducing operators' load	17 %
improving product quality	10 %
increasing flexibility toward changes	4 %
major key to success	
careful modeling	37 %
suitability for objective	33 %
education of operators and engineers	15 %
suitability for process characteristics	11 %
hardware/software environment	4 %

automatic operation are important. Saving resources and energy, increasing production capacity, reducing operators' load, and improving product quality are major effects achieved by MPC. Furthermore, process control engineers have identified the following major keys to success: 1) a process model should be developed with care, 2) MPC should be suitable for objectives, 3) operators and engineers should be adequately educated, and 4) MPC should be suitable for process characteristics.

Although MPC has been widely and successfully applied in the chemical and petroleum refining industries, problems still remain to be solved as summarized in Table 5. The major problem would be described as follows. To achieve desirable performance, it is necessary to build an accurate model and to tune control parameters appropriately. However, both of them are difficult in practice due to process nonlinearity and changes in process characteristics. To keep sufficient control performance and to prevent or at least cope with performance deterioration, the maintenance of MPC is crucial. Control engineers need to know the reason of performance deterioration and the effective countermeasure. In addition, they would like to know the relationship between model accuracy and achievable control performance. Modeling of a multivariable process is an exceedingly laborious engineering task; thus it needs to be clarified how accurate a model should be to achieve the goal. Of course, not only clarifying the relationship but also improving modeling and tuning methods is necessary. In addition, the implementation of MPC should be easier. As for the maintenance of MPC, very recently, Badwe et al. (2008) proposed a model-plant mismatch detection method by using partial correlation analysis, and Huang (2008) proposed the used of Bayesian methods. Another problem is how to transfer engineering technology from skilled engineers to others. Unfortunately, a lack of process control engineers aggravates the situation. Furthermore, it is also crucial in practice to answer the question: how can we estimate the economical benefit of installing MPC to justify the project? Most APC suppliers and users are required to report the benefit to management. Bauer and

Table 5. Problems of MPC applications (from the survey JSPS143 WS27 2009)

problem: general	
low robustness against model error	26 %
difficulty in tuning	23 %
inability to cope with specific objective	15 %
difficulty in modeling	12 %
others	24 %
problem: maintenance	
transfer of engineering technology	44 %
response to performance deterioration	33 %
education of operators	7 %
difficulty in tuning	7 %
others	9 %
need for improvement: general	
to improve modeling technology	28 %
to clarify method of estimating effect	25 %
to simplify implementation	22 %
to increase process control engineers	14 %
others	11 %
need for improvement: theory	
to cope with changes in process characteristics	26 %
to clarify relations between model accuracy and control performance	24 %
to cope with unsteady operation (SU/SD)	16 %
to incorporate know-how in control system	16 %
to cope with nonlinearity	13 %
others	5 %
need for improvement: response to changes/nonlinearity	
to switch multiple linear models	28 %
to improve robustness of linear MPC	25 %
to use time-varying/nonlinear model	18 %
to add adaptive function to linear MPC	18 %
to integrate other technique with MPC (e.g. knowledge-based control)	11 %

Craig (2008) reported that benefit estimation methods based on variance reduction are still carried out, but they are sometimes rudimentary and based on experience.

6. SOFT-SENSOR

A soft-sensor, or a virtual sensor, is a key technology for estimating product quality or other important variables when on-line analyzers are not available. In chemical processes, for example, soft-sensors have been widely used to estimate product quality of distillation columns, reactors, and so on. Artificial neural network (ANN) has been dominant in the literature since the middle 1990's, while partial least squares (PLS) is popular in industry (Kano and Nakagawa (2008)). ANN is a useful tool for building nonlinear models and supposed to be suitable for industrial processes. However, linear models have produced satisfactory results in many cases because industrial processes are operated within certain range to produce the required products and linear approximation functions well. In addition, collinearity has to be taken into account for developing reliable soft-sensors. Thus, PLS has been very popular as a tool for soft-sensor design (Mejdell and Skogestad (1991); Kresta et al. (1994); Kano et al. (2000)). In recent years, support vector machine (SVM), support vector regression (SVR), and other kernel-based methods have emerged (Boser et al. (1992); Cortes and Vapnik (1995)). These methods have attracted researchers' and engineers' attention and have been used for soft-sensor design (Yan et al. (2004); Desai et al. (2006)). Another method for

developing soft-sensors is subspace identification (SSID), which can build a state space model from input and output data (Verhaegen and Dewilde (1992); Overschee and Moor (1994)). SSID is a useful tool to build a dynamic inferential model of a multivariable process, and it is suitable for soft-sensor design because the performance of soft-sensors can be greatly improved by taking process dynamics into account (Kano et al. (2000)). Amirthalingam and Lee (1999) used SSID for inferential control of a continuous pulp digester. Amirthalingam et al. (2000) developed a two-step procedure to build SSID-based inferential control models, in which the stochastic part was idetified from historical data and the deterministic part was identified from plant test data. Kano et al. (2009a) proposed two-stage SSID to develop highly accurate soft-sensors that can estimate unmeasured disturbances without assumptions that the conventional Kalman filtering technique must make. Thus it can outperform the Kalman filtering technique when innovations are not Gaussian white noises or the properties of disturbances do not stay constant with time. The superiority of the two-stage SSID over conventional methods was demonstrated through their application to an industrial ethylene fractionator.

6.1 Reliability of Soft-sensor

A great deal of research has been conducted to develop data-based soft-sensors for various processes. A data-based soft-sensor, however, does not always function well, because a black-box model is not valid when a process is operated outside certain conditions where operation data used for modeling were obtained. The product quality and process performance will deteriorate if estimates of the soft-sensor are blindly believed by operators and used in a control system. On-line monitoring of the validity of the soft-sensor will avoid such a dangerous situation. The simplest approach is to check whether an estimation error exceeds its control limit when a measurement becomes available. This approach enables us to detect the inconsistency between the analyzer and the soft-sensor, but the cause of the inconsistency cannot be identified. In industry practice, it is assumed that an estimation error is caused by inaccurate estimation; however, this assumption is not always true because analyzers are not always reliable. For example, when blockage occurs within a sampling line, a hardware sensor cannot provide accurate measurements. To address such practical problems, Kamohara et al. (2004) proposed a PLS-based framework for developing a soft-sensor and monitoring its validity on-line. The on-line monitoring system was based on the multivariate statistical process control (MSPC) technique (Jackson and Mudholkar (1979); Kresta et al. (1991)) in which the dynamic PLS model designed for estimating the product quality is used. In addition, simple rules were established for checking the performance of a process gas chromatograph by combining the soft-sensor and the statistical monitoring system. The effectiveness of the developed system was demonstrated through its application to an ethylene production plant.

6.2 Changes in Process Characteristics

Generally, building a high performance soft-sensor is very laborious, since input variables and samples for model construction have to be selected carefully and parameters have to be tuned appropriately. Even if a good soft-sensor is developed successfully, its estimation performance deteriorates when process characteristics change. In chemical processes, for example, equipment characteristics are changed by catalyst deactivation or scale adhesion. Such a situation may lead to a decline of product quality. Therefore, from the practical viewpoint, maintenance of soft-sensors is very important to keep their estimation performance. Soft-sensors should be updated as the process characteristics change, and manual and repeating construction of them should be avoided due to its heavy workload.

To cope with changes in process characteristics and to update statistical models automatically, recursive methods such as recursive PLS were developed (Qin (1998)). These methods can adapt models to new operating conditions recursively. However, the prediction performance would deteriorate if the model is updated with an abnormal sample. Kaneko et al. (2009) used independent component analysis (ICA) to detect abnormal situations and improve the prediction accuracy. Recently, ICA is recognized as a useful technique for fault detection and diagnosis (Kano et al. (2003, 2004); Lee et al. (2004)). The combination between soft-sensors and fault detection is effective to a certain extent. But, as far as a recursive method is used, the model will adapt excessively and will not function in a sufficiently wide range of operating condition when a process is operated within a narrow range for a certain period of time. In addition, recursive methods cannot cope with abrupt changes in process characteristics.

Just-In-Time (JIT) modeling or lazy learning was proposed to cope with changes in process characteristics as well as nonlinearity, and it has been used for nonlinear process monitoring as well as soft-sensing (Atkeson et al. (1997); Bontempi et al. (1999)). In JIT modeling, a local model is built from past data around a query point only when an estimated value is requested. JIT modeling is useful when global modeling does not function well. However, its estimation performance is not always high because the samples used for local modeling are selected on the basis of the distance from the query point and the correlation among variables is not taken into account. A good model cannot be developed when correlation among input and output variables is weak even if the distance between samples is small. Conversely, a very accurate model can be developed when the correlation is strong even if the distance is large. On the basis of this idea, recently, correlation-based JIT (CoJIT) modeling was proposed by Fujiwara et al. (2009). In this technique, the samples used for local modeling are selected on the basis of correlation together with distance, and the Q statistic is used as an index of the correlation dissimilarity. The Q statistic is derived from principal component analysis (PCA), and it is a measure of dissimilarity between the sample and the modeling data from the viewpoint of the correlation among variables (Jackson and Mudholkar (1979)). CoJIT can cope with abrupt changes of process characteristics and also achieve high estimation performance. It can also cope with process nonlinearity.

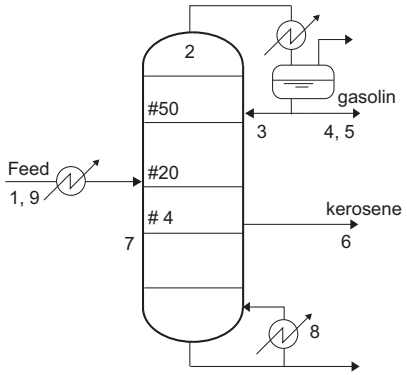

Fig. 11. Schematic diagram of the cracked gasoline fractionator of the ethylene production process at the Showa Denko K.K. (SDK) Oita plant

6.3 Industrial Case Study of CoJIT

Here, an application of CoJIT to an industrial chemical process is introduced (Fujiwara et al. (2009)). A soft-sensor for estimating the aroma concentration was constructed to realize highly efficient operation of the cracked gasoline fractionator of the ethylene production process at the Showa Denko K.K. (SDK) Oita plant in Japan. A schematic diagram of the cracked gasoline (CGL) fractionator of the ethylene production process is shown in Fig. 11. The CGL fractionator is controlled by applying multivariable MPC with an optimizer, and the aroma concentration in the CGL (aroma denotes the generic name for benzene, toluene, xylene and styrene, etc.) is used as one of the constraints in the optimizer. Although the operation data of the CGL fractionator are stored in the database every hour, the aroma concentration is analyzed in a laboratory usually once a day because of its long analysis time. For safety, the process must be operated in a condition that has a wide margin and is far from constraints. Therefore, a soft-sensor that can estimate the aroma concentration accurately in real time needs to be developed for realizing efficient operation.

In addition to eight variables measured in the CGL fractionator, the coil outlet temperature of the cracking furnace, measured four hours before, was used as an input variable, since the product composition is affected by the operating condition of the cracking furnace which is located in the upstream of the ethylene production process, and it takes about four hours for materials to reach the CGL fractionator from the cracking furnace. The selected input variables of the soft-sensor are listed in Table 6 and Fig. 11.

First, the aroma concentration was estimated with recursive PLS. The model was updated every 24 hours when the aroma concentration was analyzed in the laboratory. The estimation result is shown in Fig. 12(top). There is a bias between the measurements and the estimates after the 100th day when the pressure of the compressor was changed.

Next, the aroma concentration was estimated with CoJIT. In the initial state, the operation data obtained from April 30, 2006 to February 23, 2007 were stored in the database.

Table 6. Input variables of the soft-sensor for the CGL fractionator

No.	variable
1	Feed flow rate
2	Tower top temperature
3	Reflux volume
4	Outlet cracked gasoline temperature
5	Outlet cracked gasoline flow rate
6	Outlet cracked kerosene flow rate
7	Tray #4 differential pressure
8	Reboiler flow rate
9	Cracked furnace coil outlet temperature

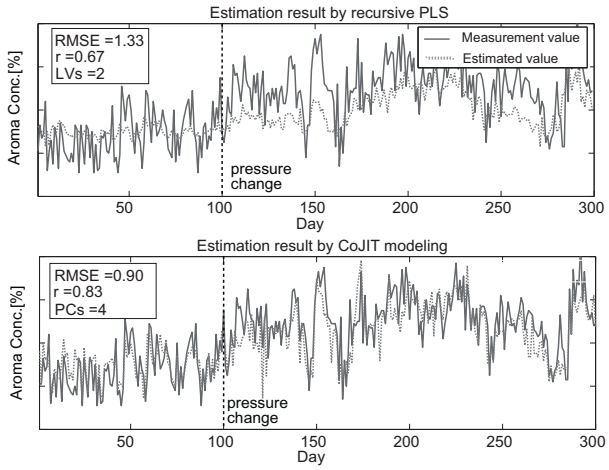

Fig. 12. Prediction results of aroma concentration: recursive PLS (top) and CoJIT modeling (bottom)

Then, the soft-sensor was updated and the aroma concentration was estimated for the next 300 days, February 24, 2007 to December 25, 2007. The estimation result is shown in Fig. 12(bottom). The estimation performance of CoJIT is high and RMSE (root mean squared error) is improved by about 28% in comparison with recursive PLS. CoJIT would have a potential for realizing efficient maintenance of soft-sensors in the real world.

6.4 Survey Result of Soft-sensor

A part of the questionnaire survey results related to soft-sensors is introduced here. This questionnaire asked control engineers the number of soft-sensor applications, targeted processes, methods for designing soft-sensors, and problems to be solved. The total number of soft-sensor applications answered was 439. The number is rapidly increasing. The survey result is summarized in Table 7.

This survey result clarifies the state of the art of soft-sensor application in Japan. First, a major targeted process is distillation (331/439), followed by reaction (86/439) and polymerization (20/439). Second, a major modeling method is multiple regression analysis (MRA) (293/439), followed by PLS (93/439). Nonlinear modeling methods are rarely used in the Japanese chemical and petroleum refining industries. It is confirmed that linear regression such as MRA and PLS can achieve sufficient estimation accuracy for most distillation and reaction processes. On the other hand, polymerization reaction processes are more difficult to model by linear regression than distillation and

Table 7. Statistics of soft-sensor applications (from the survey JSPS143 WS27 2009)

	methodology							
process	Phys	MRA	PLS	O.L.	ANN	JIT	Gray	total
distillation	20	256	41	6	0	5	3	331
reaction	5	32	43	0	0	5	1	86
polymerization	0	4	8	0	3	0	5	20
others	0	1	1	0	0	0	0	2
total	25	293	93	6	3	10	9	439

Phys: physical model
MRA: multiple regression analysis
PLS: partial least squares regression
O.L.: other linear regression
ANN: artificial neural network
JIT: just-in-time model
Gray: gray-box model or hybrid model between physical model and statistical model

Table 8. Problems of soft-sensor applications (from the survey JSPS143 WS27 2009)

accuracy deterioration due to changes in process characteristics	29 %
burden (time/cost) of data acquisition	22 %
burden of modeling itself	14 %
burden of data preprocessing	7 %
inadequate accuracy since installation	7 %
inadequate accuracy due to changes in operating conditions	7 %
difficulty in evaluating reliability	7 %
unjustifiable cost performance	7 %

other reaction processes. Thus, some companies have used gray-box models (5/20) or ANN models (3/20).

In addition, we have asked engineers what are problems related with applications of soft-sensors. The answers are summarized in Table 8. This result confirms that the maintenance of models is the most important issue concerning soft-sensors.

7. RELATED ISSUES

In this section, other important issues related to process operation are described: tracking simulator and alarm management.

7.1 Tracking Simulator

As process engineers, we have a dream that one day a plant simulator based on a rigorous first-principle model is realized and it provides functions such as 1) estimation and visualization of all states and parameters, 2) prediction of plant behavior in the future, 3) optimization of operating conditions, and 4) detection and diagnosis of abnormal situations. This plant simulation technology will become the core of future operation support system and lead to production innovation.

As mentioned before, the achievement of stable and efficient operation has largely depended on skilled operators in Japan, and many skilled operators are approaching retirement age. Thus, an advanced operation support system and an efficient operator training system are required. A training simulator for teaching operators to cope with start-up, shut-down, and other operations under abnormal situation has been developed and widely used in the process industry. The training simulator aims at faithful reproduction of real plant behavior. On the basis of the training simulator, a *tracking simulator* is now under development to realize the above-mentioned functions (Fukano et al. (2007)). The tracking simulator works simultaneously with an actual plant, adjusts parameters, estimates states, analyzes the plant, and optimizes operation by using plant models and measurements. The tracking simulator consists of a mirror model for visualizing plant states, an identification model for parameter estimation, and an analysis model for realizing the other necessary functions.

Such a tracking simulator has been developed by a few companies and introduced and tested in real plants in Japan. Further development is required to realize our dream, and various challenging problems confront us.

7.2 Alarm Management

Recently, alarm management has attracted considerable attention to achieve highly stable operation in the process industry. General recognition for current alarm systems in Japan is as follows (Higuchi et al. (2009)). With the advance of distributed control systems (DCS) in the chemical industry, it has become possible to install many alarms cheaply and easily. While most alarms help operators detect and identify faults, some are unnecessary. A poor alarm system may cause alarm floods and nuisance alarms, which reduce the ability of operators to cope with plant abnormalities because critical alarms are buried in many unnecessary alarms.

If an alarm system does not work as designed, the effects can be very serious. The explosion and fires at the Texaco Milford Haven refinery in 1994 injured 26 people and caused around £48 million of damage and a significant loss in production. The Health and Safety Executive's (HSE) investigation (1997) mentions that there were too many alarms and these were poorly prioritized and the control room displays did not help operators understand what was happening.

To improve the quality and safety of industrial plants, and to reduce cost of the design and maintenance of plant alarm systems, the Engineering Equipment and Materials Users Association (EEMUA) provided the general design and evaluation principles of plant alarm systems (The Enginnering and Equipment Materials Users' Association (EEMUA) (2007)). While this guide gathered many valuable plant engineers' experiences, it is only a general guide, and some of the design methods are only conceptual, such as the selection of alarm source signals and the decisions on alarm limits (Yan et al. (2007)). In addition, the role of operators in Japan is far different from that in other countries; thus, it is recognized that direct application of the EEMUA 191 Guide is not appropriate in Japan. In fact, a bottom-up approach has succeeded in reducing the number of alarms, average alarm frequency standards proposed by EEMUA are achieved in some plants, and further improvement is required. Generally, Japanese companies are excellent at such a bottom-up approach as TPM (total productive maintenance), which combines preven-

tive maintenance with Japanese concepts of total quality control (TQC) and total employee involvement (TEI). It is true, however, the alarm management in Japan has been short of a viewpoint of such a top-down approach as EEMUA suggested. In Japan, the industry-academia collaboration task force "Workshop No.28 Alarm Management" supported by the JSPS 143rd committee was established in 2007. This task force aims at developing new methodologies and standardizing alarm management by emphasizing distinctive culture in Japanese industries.

8. CONCLUSIONS

The state of the art in process control in Japan was described in this paper on the basis of the authors' experience and the questionnaire survey results. The realization of *production innovation* and *highly stable operation* is the chief objective of the process industry in Japan. To achieve this objective and solve the year 2007 problem, i.e., retirement of skilled operators, process control and operation need to be further improved. This improvement does not necessarily mean the adoption of novel advanced technologies. Rather, it is important to reform the whole production activity through reviewing it as leading chemical companies have done and consequently have increased productivity remarkably.

In Japan, several industry-academia collaboration task forces have been organized to sift through problems related to process operation and solve them. Such task forces include Workshop No.25 Control Performance Monitoring, Workshop No.27 Process Control Technology, Workshop No.28 Alarm Management, and so on; they are supported by the JSPS 143rd committee. More than a few methods and tools have been developed by task forces and utilized in various companies. Several examples were introduced in this paper together with practical methods developed outside task forces. The topics discussed here include PID control, advanced conventional control, model predictive control, soft-sensor, tracking simulator, and alarm management. The current situation and the problems were clarified.

In recent years, there has been a strong trend to produce polymer products having special functions in a small amount in a batch process. At the forefront of production, the necessity of practical technological development is being recognized: for example, precise control of reaction temperature, estimation of reaction state, and batch-to-batch control. Process control engineers have been committed to continuous process control so far. In the future, however, they need to open their eyes to batch process control and to meeting the challenges to its advancement.

This paper has surveyed what process control engineers have done in the last two decades and what they might do in the future, especially focusing on the projects at a Japanese chemical company. The authors expect that engineers share practical methods and best practice and also that they spare no effort in developing their own methods to solve their own problems.

ACKNOWLEDGEMENTS

The authors express their appreciation to the process control group of MCC for permitting the disclosure of many data and to the task force members of JSPS PSE 143rd committee for their constructive comments.

REFERENCES

Amirthalingam, R. and Lee, J. (1999). Subspace identification based inferential control applied to a continuous pulp digester. *Journal of Process Control*, 9, 397–406.

Amirthalingam, R., Sung, S., and Lee, J. (2000). Two-step procedure for data-based modeling for inferential control applications. *AIChE Journal*, 46, 1974–1988.

Atkeson, C., Moore, A., and Schaal, S. (1997). Locally weighted learning. *Artificial Intelligence Review*, 11, 11–73.

Badwe, A., Shah, S., Patwardhan, S., and Patwardhan, R. (2008). Model-plant mismatch detection in MPC applications using partial correlation analysis. In *IFAC World Congress*, 14926–14933. Seoul, Korea.

Bauer, M. and Craig, I. (2008). Economic assessment of advanced process control – a survey and framework. *Journal of Process Control*, 18, 2–18.

Bontempi, G., Birattari, M., and Bersini, H. (1999). Lazy learing for local modelling and control design. *International Journal of Control*, 72, 643–658.

Boser, B., Guyon, I., and Vapnik, V. (1992). A training algorithm for optimal margin classifiers. In *Annual Workshop on Computational Learning Theory*, 144–152. Pittsburgh, US.

Campi, M., Lecchini, A., and Savaresi, S. (2002). Virtual reference feedback tuning: a direct method for the design of feedback controllers. *Automatica*, 38, 1337–1346.

Cortes, C. and Vapnik, V. (1995). Support vector networks. *Machine Learning*, 20, 273–297.

Daicel Chemical Industries, Ltd. (2008). *Environmental, Safety and Social Report*.

Desai, K., Badhe, Y., Tambe, S., and Kulkarni, B. (2006). Soft-sensor development for fed-batch bioreactors using support vector regression. *Biochemical Engineering Journal*, 27(3), 225–239.

Desborough, L. and Miller, R. (2001). Increasing customer value of industrial control performance monitoring – Honeywell's experience. In *Chemical Process Control*, 153–186. Tucson, US.

Dochain, D., Marquardt, W., Won, S., Malik, O., Kinnaert, M., and Lunze, J. (2008). Monitoring and control of process and power systems: adapting to environmental challenges, increasing competitivity and changing customer and consumer demands. In *IFAC World Congress*, 7160–7171. Seoul, Korea.

Emoto, G., Ohta, Y., Matsuo, H., Ogawa, M., Raven, D., Preston, R., and Ayala, J. (1994). Integrated advanced control and closed-loop real-time optimization of an olefins plant. In *IFAC Symposium on Advanced Control of Chemical Processes (ADCHEM)*, 97–102. Kyoto, Japan.

Ender, D. (1993). Process control performance: Not good as you think. *Control Engineering*, 180–190.

Forbes, J. and Marlin, T. (1994). Model accuracy for economic optimizing controllers: the bias update case.

Industrial & Engineering Chemistry Research, 33, 1919–1929.

Fujii, K. and Yamamoto, T. (2008). One-parameter tuning pid control of chemical processes. In *International Symposium on Advanced Control of Industrial Processes (AdCONIP)*, paper MoC2. Jasper, Canada.

Fujiwara, K., Kano, M., Hasebe, S., and Takinami, A. (2009). Soft-sensor development using correlation-based just-in-time modeling. *AIChE Journal*, accepted.

Fukano, G., Onoe, Y., Nakaya, M., and Ohtani, T. (2007). Application of tracking simulator to steam reforming process. *Yokogawa Technical Report English Edition*, 43, 13–16.

Harris, T. (1989). Assessment of closed loop performance. *Canadian Journal of Chemical Engineering*, 67, 856–861.

Higuchi, F., Yamamoto, I., Takai, T., Noda, M., and Nishitani, H. (2009). Use of event correlation analysis to reduce number of alarms. In *International Symposium on Process Systems Engineering (PSE)*. Salvador, Brazil.

Hjalmarsson, H., Gevers, M., Gunnarsson, S., and Lequin, O. (1998). Iterative feedback tuning: theory and applications. *IEEE Control Systems Magazine*, 18, 26–41.

Huang, B. (2008). Bayesian methods for control loop monitoring and diagnosis. *Journal of Process Control*, 18(9), 829–838.

Hugo, A. (2000). Limitations of model predictive controllers. *Hydrocarbon Processing*, 79, 83–88.

Jackson, J. and Mudholkar, G. (1979). Control procedures for residuals associated with principal component analysis. *Technometrics*, 21, 341–349.

Kamohara, H., Takinami, A., Takeda, M., Kano, M., Hasebe, S., and Hashimoto, I. (2004). Product quality estimation and operating condition monitoring for industrial ethylene fractionator. *Journal of Chemical Engineering of Japan*, 37, 422–428.

Kaneko, H., Arakawa, M., and Funatsu, K. (2009). Development of a new soft sensor method using independent component analysis and partial least squares. *AIChE Journal*, 55(1), 87–98.

Kano, M., Hasebe, S., Hashimoto, I., and Ohno, H. (2004). Evolution of multivariate statistical process control: application of independent component analysis and external analysis. *Computers & Chemical Engineering*, 28(6-7), 1157–1166.

Kano, M., Lee, S., and Hasebe, S. (2009a). Two-stage subspace identification for softsensor design and disturbance estimation. *Journal of Process Control*, 19, 179–186.

Kano, M., Miyazaki, K., Hasebe, S., and Hashimoto, I. (2000). Inferential control system of distillation compositions using dynamic partial least squares regression. *Journal of Process Control*, 10, 157–166.

Kano, M. and Nakagawa, Y. (2008). Data-based process monitoring, process control, and quality improvement: recent developments and applications in steel industry. *Computers & Chemical Engineering*, 32, 12–24.

Kano, M., Tanaka, S., Hasebe, S., Hashimoto, I., and Ohno, H. (2003). Monitoring independent components for fault detection. *AIChE Journal*, 49(4), 969–976.

Kano, M., Tasaka, K., Hasebe, S., Masuda, S., Ogawa, M., Ootakara, S., and Shigemasa, T. (2009b). Practical direct pid controller tuning for process control. *AIChE Journal*, submitted.

Kitamori, T. (1981). A design method for nonlinear control systems based upon partial knowledge about control objects. In *IFAC World Congress*, IV25–IV30. Kyoto, Japan.

Kresta, J., MacGregor, J., and Marlin, T. (1991). Multivariate statistical monitoring of process operating performance. *Canadian Journal of Chemical Engineering*, 69, 35–47.

Kresta, J., Marlin, T., and MacGregor, J. (1994). Development of inferential process models using PLS. *Computers & Chemical Engineering*, 18, 597–611.

Kugemoto, H. (2005). Technology of controller performance monitoring and diagnosis in chemical plants. *Sumitomo Kagaku*, 2005-II, 1–10.

Lee, J., Yoo, C., and Lee, I. (2004). Statistical process monitoring with independent component analysis. *Journal of Process Control*, 14(5), 467–485.

Lundstrom, P., Lee, J., Morari, M., and Skogestad, S. (1995). Limitations of dynamic matrix control. *Computers & Chemical Engineering*, 19, 409–421.

Maruta, H., Kano, M., Kugemoto, H., and Shimizu, K. (2005). Modeling and detection of stiction in pneumatic control valves. *Trans. of the Society of Instrument and Control Engineers*, E-4(1), 18–26.

Mejdell, T. and Skogestad, S. (1991). Estimation of distillation compositions from multiple temperature measurements using partial-least-squares regression. *Industrial & Engineering Chemistry Research*, 30, 2543–2555.

Mitsubishi Chemical Corporation (2005). *RC Report 2005*.

Nishimura, Y. and Ootakara, S. (2007). The introduction of software for performance improvement of control loops. In *SICE Annual Conference on Control Systems (CCS)*, paper 72–2–1. Chofu, Japan.

Ogawa, M. (2006). Process control practice: the key to stable operation for maximizing the profit. In *KIChE Annual Meeting*. Korea.

Ogawa, M., Kano, M., and Hashimoto, I. (1998). Design of flow averaging level control system using i-p controller with gap. *Kagaku Kogaku Ronbunshu*, 24(2), 259–265.

Ogawa, M. and Katayama, T. (2001). A robust tuning method for i-pd controller incorporating a constraint on manipulated variable. *Transactions of the Society of Instrument and Control Engineers, Japan*, E-1(1), 265–273.

Ohshima, M., Ohno, H., and Hashimoto, I. (1995). Model predictive control experiences in the university-industry joint projects and statistics on mpc applications in japan. In *International Workshop on Predictive and Receding Horizon Control*, paper 72–2–1. Korea.

Overschee, P. and Moor, B. (1994). N4sid: subspace algorithms for the identification of combined deterministic-stochastic systems. *Automatica*, 30, 75–93.

Qin, S. (1998). Recursive pls algorithms for adaptive data modeling. *Computers & Chemical Engineering*, 22, 503–514.

Qin, S. and Badgwell, T. (2003). A survey of industrial model predictive control technology. *Control Engineering Practice*, 11, 733–764.

Seki, H., Ogawa, M., Ooyama, S., Akamatsu, K., Ohshima, M., and Yang, W. (2001). Industrial application of a nonlinear model predictive control to polymerization reactors. *Control Engineering Practice*, 9, 819–828.

Shah, S., Mitchell, W., and Shoock, D. (2004). Challenges in the detection, diagnosis and visualization of controller performance data. In *Control Systems*. Quebec City, Canada.

Shinsky, F. (1977). *Distillation control for productivity and energy conservation*. McGraw-Hill, Inc.

Shoda, Y. (1998). Industrial benefits and unsolved problems of process control. In *IFAC Symposium on Dynamics and Control of Process Systems (DYCOPS)*, 223–225. Corfu, Greece.

Soma, S., Kaneko, O., and Fujii, T. (2004). A new approach to parameter tuning of controllers by using one-shot experimental data – a proposal of fictitious reference iterative tuning. *Transactions of Institute of Systems, Control and Information Engineers*, 17, 528–536.

Tasaka, K., Kano, M., and Ogawa, M. (2009). Direct pid/i-pd controller tuning and its application to unstable polymerization process. *Journal of Process Control*, submitted.

The Enginnering and Equipment Materials Users' Association (EEMUA) (2007). *Alarm systems, a guide to design, management and procurement*. EEMUA Publication, No. 191.

Verhaegen, M. and Dewilde, P. (1992). Subspace model identification. I - the output-error state-space model identification class of algorithms. *International Journal of Control*, 56(5), 1187–1210.

Yamashita, Y. (2006). An automatic method for detection of valve stiction in process control loops. *Control Engineering Practice*, 14, 503–510.

Yan, L., Xiwei, L., Noda, M., and Nishitani, H. (2007). Systematic design approach for plant alarm systems. *Journal of Chemical Engineering of Japan*, 40, 765–772.

Yan, W., Shao, H., and Wang, X. (2004). Soft sensing modeling based on support vector machine and Bayesian model selection. *Computers & Chemical Engineering*, 28(8), 1489–1498.

Keynote Lectures

Approximate dynamic programming approach for process control

Jay H. Lee * **Wee Chin Wong** *

* *School of Chemical & Biomolecular Engineering, Georgia Institute of Technology, Atlanta, GA 30332 USA (e-mail: jay.lee,wwong@chbe.gatech.edu).*

Abstract: In this talk, we assess the potentials of the approximate dynamic programming (ADP) approach for process control, especially as a method to complement the model predictive control (MPC) approach. In the Artificial Intelligence (AI) and Operations Research (OR) research communities, ADP has recently seen significant activities as an effective method for solving Markov Decision Process (MDP), which represents a type of multi-stage decision problems under uncertainty. Process control problems are similar to MDPs with the key difference being the *continuous* state and action spaces as opposed to discrete ones. In addition, unlike in other popular ADP application areas like robotics or games, in process control applications first and foremost concern should be on the safety and economics of the on-going operation rather than on efficient learning. We explore different options within ADP design, such as the pre-decision state vs. post-decision state value function, parametric vs. nonparametric value function approximator, batch-mode vs. continuous-mode learning, exploration vs. robustness, etc. We argue that ADP possesses great potentials, especially for obtaining effective control policies for stochastic constrained nonlinear or linear systems and continually improving them towards optimality.

Keywords: Stochastic optimal control, constraints

1. INTRODUCTION

Model predictive control (MPC) is a technique in which the current control action is obtained by minimizing on-line, a cost criterion defined on a finite time interval. Nominal deterministic trajectories of future disturbance signals and uncertainties are necessarily assumed in order to obtain an optimization problem amenable to on-line solution via math programming. The solution generates a control sequence from which the first element is extracted and implemented. The procedure is repeated at the next time instant. Owing to its ability to handle constrained, multi-variable control problems in an optimal manner, MPC has become the de-facto advanced process control solution for the process industries today.

MPC is by now considered to be a mature technology owing to the plethora of research and industrial experiences during the past three decades. Despite this, it has some fundamental limitations, which prevents it from being a panacea for all process control problems. One well-known limitation is the potentially exorbitant on-line computation required for solving a large-scale, and potentially non-convex math program that scales with the dimension of the state as well as the length of prediction horizon. Recent developments (Laird and Biegler (2008)) have made some headway in tackling this problem although nontrivial computational challenges still exist.

⋆ JHL gratefully acknowledges financial support from Owens Corning and Weyerhaeuser.

The second limitation arises from the fact that the deterministic formulation adopted by MPC is inherently incapable of addressing uncertainty in a closed-loop optimal fashion. Its open-loop optimal control formulation used to find the control moves at each sample time means the fact that information about future uncertainty will be revealed, this being generally beneficial for control performance, is not considered. Most of the past attempts at ameliorating the impact of uncertainty has been reflected in robust MPCs formulations based on the objective of minimizing the worst-case scenarios (Scokaert and Mayne (1998)) at the expense of overly conservative policies. Multi-scenario formulations (Laird and Biegler (2008)) have also been developed but the number of scenarios is limited and they do not give closed-loop optimal policies in general. Stochastic programming based methodologies (Pena et al. (2005)) allow for recourse actions at the computational expense of enumerating an exponentially growing number of scenarios.

In this paper, we examine the possibility of lessening or removing the above-mentioned limitations by combining MPC with an approach called "approximate dynamic programming (ADP)." ADP is a technique that surfaced from the research on reinforcement learning in the Artificial Intelligence (AI) community (Sutton and Barto (1998); Bertsekas and Tsitsiklis (1996)). It has its theoretical foundations in the traditional dynamic programming by Richard Bellman (Bellman (1957)) but its computational bottlenecks, termed as "the curse of dimensionality" by Bellman himself, are relieved through ideas such as intelli-

gent sampling of the state space through simulations and function approximation. ADP, due to its root in AI, has mainly been studied in the context of Markov Decision Processes (MDPs), which involve discrete finite state/ action spaces and probabilistic transitions. Hence, its application to process control problems, which typically involve continuous state/ action spaces, is not straightforward. In addition, the characteristics of process control problems are somewhat different from those of robotics, games, and resource allocation problems. For example, in process control applications, the idea of "learning by mistakes" for the sake of efficient learning, may not be tolerated as mistakes often bring unacceptable consequences in terms of safety and economics. Hence, extension of ADP to process control may require significant care and possibly some new tools.

Design of an ADP algorithm involves a variety of choices, including type of function approximator, pre-decision vs. post-decision formulation, batch vs. continuous updating of the value table, and exploration vs. robustness tradeoff. We will visit these issues, carefully examining the implications of these choices in the context of designing a learning algorithm for process control applications. In addition, we will also consider the complementary nature or synergies between ADP and MPC.

The rest of the paper is organized as follows. In Section 2, we will briefly review the basics of MDP, ADP and also present a mathematical representation of the system we consider for control. In Section 3, we will examine the various options and choices and their implications for process control applications. In Section 4, we will present a few examples, including those involving both linear and nonlinear stochastic systems. In Section 5, we conclude the paper and discuss other control-related areas where ADP can potentially be useful in the process industries.

2. BACKGROUND

2.1 Markov Decision Processes and Approximate Dynamic Programming

Markov Decision Processes (MDPs) provide a framework for modeling real world processes that have a stage-wise structure. The stage can denote a time epoch or other quantities like location, processing step, etc. At any stage, the system is recognized as being in a state (designated as s), which is a set of attributes that aid decision-making. The set of all possible states is called state space (designated as S). Starting in state s belonging to S, there is a set of actions from which the decision-maker must choose. The set of all possible actions is called action space (A) and an element of the action space is denoted by a. When action a is taken in state s, and the system transitions to the next stage, it ends up in a unique next state $s' \in S$ in the absence of any uncertainty. However, for stochastic problems, there is a set of possible next states for each state-action pair. The probability of transition to a particular next state in this case is governed by a state transition probability function, P. In the process, reward $r(s, a, s')$ is received, which is determined by the reward function r. The dependence of r on s' is often suppressed by taking a weighted average over all possible states at the next stage. At each stage, actions are taken so that the sum of stage-wise rewards is maximized. In the presence of uncertainty, the expected sum of rewards is maximized. When infinite stages are present, i.e., extremely large time horizon, the future rewards are often discounted using a discount factor γ. When the number of stages is infinite, the problem is called an infinite horizon MDP as opposed to a finite horizon MDP for finite number of stages. In most applications, a stage symbolizes a time epoch. Therefore, the term time epoch or time step is often used synonymously with 'stage'.

More formally, MDP is defined by a tuple (S, A, P, R, γ) where S is a set of states, A is a set of actions, $P : S \times A \times S \rightarrow [0, 1]$ is a set of transition probabilities that describe the dynamic behavior of the modeled environment, $R : S \times A \times S \rightarrow \mathbb{R}$ denotes a reward model that determines the stage-wise reward when action a is taken in state s leading to next state s' and $\gamma \in [0, 1)$ is the discount factor used to discount future rewards. A γ value close to 0, places very little weightage on future rewards, while γ close to 1 results in very little discounting.

One of the fundamental properties of the MDPs is that the transition and reward functions associated with the stage-wise transition of state are independent of the past states and actions. Referred to as Markov property, this memoryless feature enables the decomposition of the overall optimization problem into separate stage-wise problems. This is accomplished by using a recursive relationship between the value of being in a state at any stage.

An important notion in this regard is the so called value function denoted by $V(s)$, which is defined as the (often discounted) sum of rewards over a time horizon which can be either finite or infinite (shown below) and discussed hereafter:

$$V^{\pi}(s) = \mathbb{E}\left[\sum_{t=0}^{\infty} \gamma^t r(s_t, \mu(s_t)) | s_0 = s\right] \tag{1}$$

where t denotes the time epoch, s_t is the state at time t and $\pi : S \rightarrow A$, is the policy that dictates the choice of action for a given state at time t.

The goal is to find an optimal policy that maximizes the value function for all $s \in S$. This is achieved by solving the Bellman equation (Bellman (1957)) for finite or infinite horizon problems. The optimal policy can be derived via dynamic programming. Let $a^*(s)$ be the optimal action to be taken when the system is in state s, independent of time t. $V^*(s)$ is called the optimal value function and is obtained as the solution to the (Bellman equation) (2), which must be solved for all $s \in S$:

$$V^*(s) = \max_{a \in A} \left\{ r(s, a) + \gamma \sum_{s' \in S} p(s'|s, a) V^*(s') \right\} \quad \forall s \tag{2}$$

$$a^*(s) = \pi^*(s) \triangleq \arg\max_{a \in A} \left\{ r(s, a) + \gamma \sum_{s' \in S} p(s'|s, a) V^*(s') \right\} \tag{3}$$

where symbol $p(.)$ denotes the probability of a quantity. It is well-known (Putterman (1994)) that for infinite horizon problems, a stationary optimal policy of the form in (3) exists, where $V^*(s)$ is the average discounted infinite horizon reward obtained when the optimal policy is followed starting from s until infinity (Putterman (1994)). This implies

that the state to action mapping in the form of optimal policy is independent of the time epoch. The existence of stationary optimal policy is conditioned on the properties of model elements. One of the sufficient conditions is that there be a finite action space A_s corresponding to each state $s \in S$, maximum attainable stage-wise reward is finite and discount factor $\gamma \in [0, 1)$. The alternative sets of sufficient conditions for existence of a stationary optimal policy for discounted infinite horizon MDPs can be found in (Putterman (1994)).

It must be noted that the set of Bellman equations also called optimality equations are difficult to solve analytically because of the presence of the max operator. One of the popular solution methods is called value iteration (Putterman (1994)): Starting with an arbitrary value function $V_0(s)$ for each state $s \in S$, the value function is iteratively improved by successive substitution into (2) until ϵ-convergence is reached. The operator for one iteration, that is the maximization in (2), can be denoted as H such that $V_{n+1} = HV_n$. The sequence of estimates of value function $V(s)$, $\forall s \in S$, converges to a fixed point solution. This is a consequence of Banach's theorem for contraction mappings (Putterman (1994)). Since H is a proven contraction map, the convergence properties hold.

Due to ease of implementation, value iteration is perhaps the most widely used algorithm in dynamic programming. Certain other methods like policy iteration (Bertsekas (2005)), a hybrid between value iteration and policy iteration (Powell (2007)) and linear programming method for dynamic programs (Farias and Roy (2003)) are also used depending on the problem structure. The complexity of the value-iteration algorithm grows as a function of $o(|S|^2 \times |A|)$. This is attributed to the following three aspects of the value iteration:

(1) Equation (2) needs to be solved for all s belong to S, so the solution time is directly proportional to $|S|$.
(2) The complexity of max operation depends on the size of the action space $|A|$.
(3) The calculation of expectation within the max operator depends on the number of possible next states, i.e., $|S|$.

In the presence of very large state and (or) action spaces, the value iteration algorithm cannot be implemented in its exact form. Several approximation methods have been developed to circumvent this difficulty, including: approximate dynamic programming methods using value function approximations (Powell (2007)), Q-learning, temporal difference learning (Sutton and Barto (1998)) functions (Farias and Roy (2003)) and dynamic programming methods using post decisions state (Powell (2007)).

All the above methods assume that the system state is completely known or observed at all times. When this assumption does not hold, the equivalent framework is called a Partially Observed Markov Decision Process (POMDP) (Cassandra et al. (1994)), for which a significant but less body of literature exists.

2.2 System Definition: Process Control Problems

Consider the optimal control of the following discrete-time stochastic system:

$$x_{t+1} = f(x_t, u_t, \omega_t) \tag{4}$$

where $x_t \in \mathcal{X} \subseteq \mathbb{R}^{n_x}$ refers to the system state at discrete time index t, $u_t \in \mathcal{U} \subseteq \mathbb{R}^{n_u}$ a control or action vector, and ω_t an exogenous, unmeasured, stochastic signal. x may contain physically meaningful states as well as measured disturbances, and parameters subject to uncertainty. f refers to the single-stage transition function. For problems where the system's dynamics are represented by ordinary differential equations, f is then the result of numerical integration across a single sample-time, with vectors u and ω held constant. Throughout this paper, it is assumed that full state feedback is available. In the event that only output feedback is available, x is interpreted as an information vector that contains the sufficient statistics of the state estimate's probability density function. Such lifting is possible as the information vector is governed by another related set of differential equations. (*i.e.*, the filter dynamics).

Let $\mu \in \Gamma$ be a 'state-feedback policy' that maps the state vector to the action vector, where Γ represents the set of all admissible (stationary) such policies. To distinguish from the earlier value function $V(s)$, $J^\mu(x)$ will be used to denote the 'cost-to-go' function, which is defined as the infinite horizon, discounted sum of the stage-wise costs under the policy μ starting from an arbitrary state x:

$$J^\mu(x) = \mathbb{E}\left[\sum_{k=0}^{\infty} \gamma^k \phi(x_k, u_k = \mu(x_k)) | x_0 = x\right] \tag{5}$$

where ϕ represents a pre-specified stage-wise cost (*e.g.* $\phi(x, u) := ||x||_Q^2 + ||x||_R^2$) and $\gamma \in [0, 1)$ is a discount factor. The goal then is to find the optimal (stationary) policy $\mu^* : \mathcal{X} \to \mathcal{U}$, that yields the minimum cost-to-go function as below:

$$J^{\mu^*}(x) = \min_{\mu \in \Gamma} \mathbb{E}\left[\sum_{k=0}^{\infty} \gamma^k \phi(x_{t+k}, u_{t+k} = \mu(x_{t+k})) | x_t = x\right] \tag{6}$$

$J^{\mu^*} : \mathcal{X} \to \mathbb{R}^{0+}$ is the *optimal* 'cost-to-go' function and is an indication of the attractiveness of a given state in terms of future rewards. By definition, $J^{\mu^*}(x) \leq J^\mu(x), \forall x$ and $\forall \mu \in \Gamma$.

The main difference between the above and the previously introduced MDPs is that the state and action spaces are continuous. However, the fundamental concepts of DP still apply here. Based on the principle of optimality (Bellman (1957)), one is able to re-write (6), thereby obtaining Bellman's optimality equations:

$$\begin{aligned} J^{\mu^*}(x) &= \min_{u \in \mathcal{U}} \left\{ \phi(x, u) + \gamma \mathbb{E}_{(\omega|x)}[J^{\mu^*}(f(x, u, \omega))] \right\} \\ &= \left(T J^{\mu^*} \right)(x) \end{aligned} \tag{7}$$

T above represents the single-pass DP operator represented by the minimization operation. The optimal policy is implicitly obtained through the solution of the associated single-stage optimization:

$$\mu^*(x) = \arg\min_{u \in \mathcal{U}} \left\{ \phi(x, u) + \gamma \mathbb{E}_{(\omega|x)}[J^{\mu^*}(f(x, u, \omega))] \right\} \tag{8}$$

In principle, the optimal control problem is solved once J^{μ^*} is known. It is noted that for deterministic problems (where the expectation operator is dropped), the DP formalism provides a convenient way of solving multi-stage problems through an equivalent single-stage optimization.

Unfortunately, analytical solutions to Bellman's optimality equations are available for only a small class of problems, of which the celebrated Linear Quadratic Gaussian (LQG) problem is one. For situations of practical interest, numerical techniques are required. Similar to the case of discrete state and action space, the repeated application of T on an arbitrarily initialized cost-to-go leads to convergence and underpins the idea behind Value Iteration (VI).

$$J^{\mu^*}(x) = TJ^{\mu^*}(x) = \lim_{i\to\infty}(T)^i J^{\mu}(x),\ \forall \mu, x \qquad (9)$$

In process control problems, due to the continuous nature of the state and action spaces which must be discretized, numerical solutions become quickly bottle-necked as the problem dimensions grow. In fact, the growth would be exponential as the number of discretized points grows with the dimension as such. Hence, a naive application of VI in this case is computationally prohibitive and the 'curse-of-dimensionality' is even more apparent in continuous problems. For problems with continuous state and action space, one needs to resort to approximations that involve an intelligent state-sampling/ discretization scheme and/ or an efficient representation of the cost-to-go (Lee and Lee (2006); Powell (2007)).

2.3 Approximate dynamic programming for problems with continuous state and action space

Value iteration or policy iteration in general can work with only finite state space. For systems with continuous state and action space, one must then work with discretized state state, either through gridding, or more preferably, sampling. It is often the case that only a small portion of $\mathcal{X}$ and $\mathcal{U}$ will ever be visited under optimal and/ or high-quality sub-optimal policies. This is especially true when the dimension of the state space is large compared to that of the input. Let us denote the subset of the state space that is 'relevant', *i.e.*, visited with non-trivial probability under the optimal control, as $\mathcal{X}^*_{REL}$. Such a set would be continuous but much smaller-sized than $\mathcal{X}$ in general. The key notion is that if one could identify $\mathcal{X}^*_{REL}$ or a parsimonious superset of it, one can sample the set with sufficient density to perform the dynamic programming at significantly reduced computation. Of course, the difficulty is that it is not easy to obtain such a set ahead of time without knowing the optimal controller itself.

The ADP approach proposed by the authors of (Lee and Lee (2004, 2006); Tosukhowong and Lee (2009)) for process control applications, the skeleton of which is described in this subsection, employs carefully designed simulation schemes for the sampling of the state space and function approximation (for the purpose of cost-to-go interpolation) to this end. For the VI-variant, we have the following off-line computations:

(1) Identify a finite-sized, 'relevant' state-space, $X_{sam} \subset \mathcal{X}$, $|X_{sam}| = N$. This is achieved, for instance, by simulating all possible combinations of sub-optimal policies (potentially with dithering) and operating conditions. The latter are defined as all starting states of interest (for servo problems) as well as potential values of measured disturbance values. Dithering may also be introduced for the purpose of exploration.
(2) Assign a cost-to-go for all elements of X_{sam}, using the simulation data according to (5). The initial, finite-sized 'cost-to-go' table, denoted by $\mathcal{T}_{[0]} \triangleq \left\{x, \hat{J}^{\mu^*}_{[0]}(x)\,|x \in X_{sam}\right\}$, is obtained. The symbol $\hat{(\cdot)}$ is used to emphasize the approximate nature of the cost-to-go sequence, even at its limit. Exact initialization is not critical per se since the fixed point derived from the following step is unique.
(3) Obtain converged cost-to-go values for X_{sam} through VI, yielding the sequence of value tables $\{\mathcal{T}_{[0]}, \mathcal{T}_{[1]}, \ldots\}$. Since the VI requires the evaluation of the cost-to-go function for states $(f(x,u,\omega))$ not necessarily in X_{sam}, a well-designed function approximator is needed to interpolate among the stored values (see discussion in Section 3.1). A certain choice of function approximator ensures that each pass of the iteration is a *contraction-map* with a unique fixed point (see Section 3.1). In other words, each step of the modified VI involves:
$$\hat{J}^{\mu^*}_{[i+1]}(x) = \left(TF(\hat{J}^{\mu^*}_{[i]})\right)(x),\ \forall x \in X_{sam} \qquad (10)$$
Here $F(\hat{J}^{\mu^*})$ denotes the cost-to-go function approximator based on the stored values $\{\hat{J}^{\mu^*}_{[i]}(x), x \in X_{sam}\}$. Termination occurs when $\|\hat{J}^{\mu^*}_{[i+1]} - \hat{J}^{\mu^*}_{[i]}\|_\infty$ is less than a pre-defined tolerance.
(4) Return to step 1, since the relevant domain of the state-space may not be properly ascertained a-priori. Otherwise, use the converged values for online control.

The authors of Ma and Powell (2009) used an approximate policy iteration scheme where $J^{\mu}(x), \forall x \in \mathcal{X}$ is assumed to be linear in a set of basis functions (known or otherwise assumed to be orthogonal polynomials of sufficiently large degree). The coefficients are learnt through a least-squares procedure once the system of interest is allowed to evolve according to the current policy, which is similar to step (1) where relevant states are collected. The limitation is that suitable basis functions are difficult to ascertain in general.

3. ISSUES AND CHOICES

3.1 Function approximation and stable learning

The need for function approximation for the purpose of generalization has been discussed. Given a training set $\mathcal{T} \triangleq \{x_i, \hat{J}(x_i)\}_{i=1}^N$, a value table composed of a finite number (N) of input $(x_i \in \mathcal{X})$ and target values $(\hat{J}(x_i) \in \mathbb{R})$, a function approximator, F, whose domain is $\mathcal{X}$, maps a query point $x_q \in \mathcal{X}$ to a subset of the real line.

The dominant and natural choice for function approximators has typically involved parametric global approximators such as neural networks or the use of basis functions

such as high order orthogonal polynomials or Fourier series (Tsitsiklis and Roy (1996); Konidaris and Osentoski (2008)). While this approach has met with some success in certain applications (*e.g.* in Backgammon (Tesauro (1992)), it is not immune from divergent behavior (Lee and Lee (2004, 2006)) when employed in the context of ADP. In certain cases, the off-line iteration would fail to converge, with the cost-to-go approximation showing non-monotonic behavior or instability with respect to iterations. Thrun and Schwartz (1993) were the first to attribute the failure with function approximation to an 'over-estimation' effect. Sabes (1993) demonstrated that sub-optimality can be severe when a global approximator with a linear combination of basis functions is employed. Boyan and Moore (1995) provide insightful illustrations showing the failure of popular function approximators during off-line learning.

There are considerably fewer papers that address function approximation schemes for problems with continuous state and action spaces (Ma and Powell (2009), Lee et al. (2006)). The problem of linear quadratic regulation, for which the value function is known to be quadratic in structure, is a noted exception Bradtke (1993). Ormoneit and Sen (2002) proposed a kernel-based approach for problems with continuous states but finite actions and demonstrate convergence to the optimal cost-to-go value function with an increasing number of samples and decreasing kernel bandwidth under a model-free scheme. Ma and Powell (2009) proposed a provably convergent approximate policy iteration under the assumption of known basis functions and other technical conditions.

Stable learning during the off-linear value iteration step of the proposed ADP strategy is highly desirable as it can be frustrating to run a large number of iterations only to have the result "blow up" all of sudden due to some complicated coupling between the function approximation error and value iteration. To have provable convergence of the approximate value iteration (not necessarily to the optimal value function, however), one needs to use a function approximator with a certain property called "non-expansion" . Gordon (1995) discussed the viability of using such a class of function approximators. With such a choice, the overall operator composed of value-iteration and then function approximation results can be shown to be a contraction map therefore ensuring convergence.

Definition 1. A γ-contraction mapping m defined on a normed vector space (mapping elements from this space, $\mathcal{V}$, to itself) is defined as such:

$\forall v_1, v_2 \in \mathcal{V}$, $||m(v_1) - m(v_2)|| \leq \gamma ||v_1 - v_2||$, $\gamma \in [0, 1)$

where v_1, v_2 are arbitrarily chosen elements of $\mathcal{V}$.

Definition 2. When $\gamma = 1$, $m : \mathcal{V} \rightarrow \mathcal{V}$ is termed a non-expansion (Gordon (1995)).

From Banach's fixed-point theorem, it can be easily shown that every the iterated sequence $\{v, m(v), m^2(v), \ldots\}$ converges to a unique fixed point. As explained earlier, the proposed ADP method starts with initial estimates $\hat{J}^{\mu^*}_{[0]}(x)$, $\forall x \in X_{sam}$. This is followed by function approximation (recall that this mapping is denoted by F), and an application of the DP operator, T to yield $\hat{J}^{\mu^*}_{[1]}$. The process is repeated again. Our experience with the ADP approach (Lee and Lee (2004, 2005)) has been that stability of learning and the quality of a learned control policy are critically dependent on the structure of the function approximator. A sufficient condition for convergence is to demonstrate that the overall operator T with function approximator F is a contraction map. This, in turn, holds true if F is a non-expansion map.

Proposition 1. T is a γ-contraction map if F is non-expansive.

Proof. Given arbitrary vectors $\hat{J}_1, \hat{J}_2 \in \mathbb{R}^N$,

$$||TF(\hat{J}_1) - T^{\mu^*}F(\hat{J}_2)||_\infty \leq \gamma ||F(\hat{J}_1) - F(\hat{J}_2)||_\infty \quad (11)$$

$$\leq \gamma ||\hat{J}_1 - \hat{J}_2||_\infty \quad (12)$$

The first line is true since T is a γ-contraction map defined on the space of value functions. The second inequality follows if one employs a function approximator with a non-expansion property.

Function approximators that employ averaging, as defined below, can be shown to possesses a non-expansion property.

Definition 3. F is an averager if every fitted valued is the weighted average of of target values, potentially with the addition of a bias term. Specifically,

$$F(\hat{J})(x_q) = \beta_0(x_q) + \sum_{i=1}^{N} \beta_i(x_q)\hat{J}(x_i) \quad (13)$$

Here, $\{\beta_i\}_{i=0}^N \geq 0$, and $\sum_{i=1}^{N} \beta_i \leq 1$. Note that the weights β are allowed to depend on the query point (x_q) and input values $(\{x_i\}_{i=1}^N)$ but not the target values.

That such an averager is a non-expansion (*i.e.* (12) is true) is easily demonstrated.

One such type of approximator we have experimented with extensively is instance-based (Lee et al. (2006)) local averagers, such as k-Nearest Neighbors-based (kNN) predictors. Instance-based algorithms are non-parametric representations using stored points 'close' to a query point for making predictions. Closeness is usually defined according to some distance metric (such as Euclidean distance). Predictions of the weighted kNN are given by:

$$F(\hat{J})(x_q) = \beta_0(x_q) + \sum_{x_i \in \mathcal{N}_k(x_q)} \beta_i(x_q)\hat{J}(x_i) \quad (14)$$

where $\mathcal{N}_k(x_q)$ refers to the set containing the k points closest to x_q. The weights (normalized by constant c) are defined as: $\beta_i = c((x_q - x_i)^T W (x_q - x_i))^{-0.5}$, $i \geq 1$. W is a feature weighting matrix use to scale and also to emphasize dimensions that are more important.

3.2 Cautious learning for robustness

It has been demonstrated (Smart and Kaelbling (2000); Lee et al. (2006)) that simply using a local averager (with $\beta_0 = 0$), though guaranteeing convergence, does not necessarily give a converged function leading to a stable closed-loop behavior. This is because function approximation

error can be significant, particularly when the training data is insufficient. Safeguards against 'over-extrapolation' during value iteration is often needed for the successful implementation of the proposed ADP method. For a query point located in regions with little data present, distance-weighted averaging may fail to provide meaningful generalizations of the cost-to-go. Prevention of taking such a query point may be achieved by including in the cost-to-go term β_0, a penalty that is imposed whenever the minimization step encounters a query point (x_q) far away from X_{sam}:

$$\beta_0(x_q) = A.U\left(\frac{1}{f_\Omega(x_q)} - \rho\right) \cdot \left(\frac{\frac{1}{f_\Omega(x_q)} - \rho}{\rho}\right)^2 \quad (15)$$

Here, ρ is a data-density threshold value, A a scaling parameter, and U, the Heaviside step function that returns a zero value whenever its argument is non-positive and unity, otherwise. $f_\Omega(x_q)$ is a measure of data density as ascertained by fitting a Kernel density estimator over training set Ω:

$$f_\Omega(x_q) = \frac{1}{N_\Omega}\sum_i^{N_\Omega} K\left(\frac{x_q - x_i}{\sigma}\right) \quad (16)$$

where kernel $K(\cdot)$ refers to a zero-mean Gaussian with variance $\sigma^2 I_{n_x}$. For generality, Ω is allowed to differ from X_{sam}. Furthermore, a bound is imposed on β_0 whenever it exceeds a threshold value. Tuning rules for ρ, A, σ can be found in (Lee et al. (2006)) and are not reproduced here in the interest of brevity.

3.3 Pre-decision vs. post-decision state formulation

For stochastic control problems, the single-stage optimization required during off-line value-iteration (see (7)) and on-line implementation of the optimal policy (see (8)) requires the generally cumbersome evaluation of an expectation.

The use of an intermediate post-decision (x^p) state, first introduced by Roy et al. (1997) and employed extensively by Powell (2007) in solving operations research problems, oftentimes allows for more computationally effective strategies. x^p refers to the the system state immediately after the control vector is introduced but before the uncertainty is realized. As a result, f is decomposed into the following sub-transitions:

$$x_t^p = f_1(x_t, u_t)$$
$$x_{t+1} = f_2(x_t^p, \omega_t)$$

where the composition of f_1 and f_2 is equivalent, in effect, to f, in (4). Note that f_1 describes a deterministic transition between the pre-decision state variable (x) and x^p. f_2 involves the transition due to uncertainty after the control action is implemented. Consequently, the value function of x^p, $J^{\mu,p}(x^p)$, may be expressed in terms of the value function of x, as such:

$$J^{\mu,p}(x_t^p) = \mathbb{E}_{(\omega|x_t^p)}\left[J^\mu(x_{t+1})\right], \forall \mu \quad (17)$$

By considering the optimal policy μ^*, and substituting (7) into (17), the min and $\mathbb{E}$ operators are interchanged, yielding:

$$J^{\mu^*,p}(x_t^p) = \mathbb{E}_{(\omega|x_t^p)}\left[\min_{u_{t+1}\in\mathcal{U}}\left\{\phi(x_{t+1}, u_{t+1}) + \gamma J^{\mu^*,p}(x_{t+1}^p)\right\}\right] \quad (18)$$

The single-stage on-line optimization is also streamlined:

$$\mu^*(x) = \arg\min_{u\in\mathcal{U}}\left\{\phi(x,u) + \gamma J^{\mu^*,p}(f_1(x,u))\right\} \quad (19)$$

The introduction of the post-decision state allows the generally non-commutative min and $\mathbb{E}$ operators to be interchanged. (18), used off-line during value iteration, consists of an independent collection of deterministic optimization problems, which may be run *in parallel* using off-the-shelf solvers. It is noted that the latter have been cornerstone of MPC technology. In this case, differentiable local averagers such as Kernel regression (Hastie et al. (2008)) may be employed. In this case, given the training set $\{x_i, \hat{J}(x_i)\}_{i=1}^N$, we have:

$$F\hat{J}(x_q) = \beta_0(x_q) + \frac{1}{\sum_{j=1} K\left(\frac{x_q - x_j}{\sigma}\right)} \cdot \sum_{i=1}^{N} K\left(\frac{x_q - x_i}{\sigma}\right)\hat{J}(x_i) \quad (20)$$

$\beta_0(x_q)$ is defined as in (15), where the Heaviside step function is replaced by a smooth approximator.

In addition to the off-line iteration step, the on-line calculation of the optimal input (in (19)) based on a pre-computed post-decision state cost-to-go function, is a deterministic optimization that does not involve an expectation operator, much like the one solved for MPC. Again, an off-the-shelf NLP solver may be employed. Another benefit, this time, compared to MPC, is that it involves only a single stage optimization as the cost-to-go function contains the precomputed optimal cost information for the rest of the horizon.

As with the pre-decision case, we can define a γ-contraction H^p so as to simplify (18). The aforementioned discussion on value-function approximation still holds for this case.

3.4 Adding new state samples: batch mode vs. continuous mode learning

In the standard ADP algorithm presented (that is, without Step (4)), we fix the set of sampled states, X_{sam}, in the beginning and do not introduce any more samples as the learning proceeds. One potential problem with this is that it may not contain sufficient samples in all the important regions of the state space.

Additional samples can be introduced as the learning proceeds in two different ways. First is to perform the simulation and the value iteration simultaneously, resulting in an X_{sam} that varies with simulation time. This approach is seen in the methods known as real-time dynamic programming (RTDP) (Barto et al. (1995)) and RTADP (Pratikakis et al. (2009)). In these approaches, one typically starts with an empty value table and introduces entries one by one as simulations proceed. Whenever a "new" state, a state that is not already recorded and does

not have a "sufficiently close" neighbor recorded in the value table, is visited during the simulation, it is entered into the value table and its cost-to-go value is assigned by evaluating the Bellman equation. The optimal action suggested by the current value table is implemented and next state is sampled according to the transition equation. If a state is revisited or there are sufficient neighbors close by, the value update for that particular state (or the sufficiently close neighbor) is performed without adding a new entry. This goes on until "new" entries are no longer added to the value table. Just how fast the convergence happens depends on the level of exploration, which will be discussed later.

The second way is to alternate between the modes of simulation and value iteration. A value iteration gives a converged cost-to-go function, which corresponds to a new policy. This new policy can be simulated to find a set of new state samples to be added to the current X_{sam}^i to yield X_{sam}^{i+1}. This continues until the simulation no longer yields different state samples.

In the case that an accurate simulation model is not available, one may have to replace the simulation with an actual on-line implementation. The continuous mode learning behaves much like adaptive control as the value table, and therefore the control policy, gets updated at every sample time. In addition, the performance during the initial phase of learning, when the value table has very few entries, may be highly unpredictable and poor. Hence, it may not be suitable in an industrial setting, whereas the other option in which the control policy remains fixed until the next off-line value iteration. Of course, given the typical constraints of industrial processes, one still has to exercise caution in implementing only a half-learned cost-to-go function on-line. The trade-off between exploration and robustness in this context is discussed next.

3.5 Exploration vs. robustness

The trade-off between exploration and robustness becomes one of the central issues when one chooses to expand X_{sam} as a part of the learning. In general, exploration gives new information to improve the eventual closed-loop performance (by expanding X_{sam}) but at the expense of slower convergence and decreased robustness. Exploration can be performed in two ways. First, one can add dither signals to the input to encourage more randomness in the state trajectories. Second, one can use an optimistic initialization of the cost-to-go value for previously unseen states, which will encourage the optimizer to choose actions leading the state trajectory to those states. If the learning is to be done directly in closed loop, the latter practice may be unacceptable for industrial practices as excursion to previously unseen states could jeopardize the safety and economics of the on-going operation. In other words, unlike in applications like robotics, "learning by mistake" is not a permissible practice for most industrial process control applications. One can in fact actively prevent such potentially harmful excursions through "pessimistic" valuation of unseen states. The previously discussed penalty approach in Section 3.2 is one way to achieve this. On the other hand, carefully chosen dither signals may be able to generate sufficiently new trajectories without imposing unacceptable risks or unduely slowing down the convergence.

3.6 Model-based vs. Model-less approach

For many industrial processes, sufficiently accurate models may not be available. In such a case, one can resort to empirical models derived from input-output data. In such as case, the state vector may simply be composed of the past input and output samples. The model can be learned separately from the ADP or it can be done as a part of it. In the latter, one learns instead of the cost-to-go function a function called Q function, which has the argument of state-input pair and assigns the cost-to-go to the pair. In other words, Q function already has the model embedded in it, which is learned together with the cost-to-go function. The two approaches are tried and compared in a recent paper by Lee and Lee (2005).

3.7 Integration with MPC

ADP can be integrated with model predictive control at several fronts. Some obvious ways include: (1)using MPC in the initial simulation to sample relevant states, (2)using the learned cost-to-go function in order to reduce the horizon size, and (3)use of the nonlinear programming solver of MPC in the post-decision-state formulation. Other methods may include the dual mode implementation, where MPC replaces the ADP controller whenever one encounters a state that is sufficiently new and the information in the learned value function cannot be trusted. Such states can be collected separately and added to X_{sam} in the next phase of value iteration.

4. EXAMPLES

Here, we demonstrate the proposed ADP algorithm on a variety of stochastic optimal control problems.

4.1 Example 1: Constrained linear stochastic system-double integrator problem

We consider the following constrained double integrator problem studied by (Batina (2004)) in the context of MPC for stochastic systems:

$$x_{t+1} = Ax_t + Bu_t + \Upsilon w_t$$

where matrix $A = [1\,0; 1\,1]$ [1], $B = [1; 0]$, $\Upsilon = [1; 0]$ and ω_t is zero-mean, white Gaussian noise with its second moment, $\mathbb{E}[\omega_t \omega_t'] = 0.2$, $\forall t$. The nominal stage-wise cost is $\tilde{\phi}(x_t, u_t) \triangleq 0.7||x_t||_2^2 + 0.33||u_t||_2^2$. The second dimension of the state vector is constrained, as is the input vector: $u_t \in [-0.5, 0.5]$, $x_2 \geq 0$.

The goal is to bring the system optimally from an arbitrary initial state ($[0; 14]$ in the following simulations) to the origin, whilst respecting the imposed constraints. We compare the performance of a Linear Model Predictive Controller (LMPC) (with prediction and control (p) horizon set to 15) against the proposed ADP approach based on the post-decision state variable. The post-decision state

[1] in Matlab notation

is defined as the quantity obtained after an action is taken but before the uncertainty is realized. That is, $x_t^p \triangleq Ax_t + Bu_t$. Since ω is an unbounded signal, we employ a soft-constraint approach for both LMPC (to avoid running into infeasibility issues) and the proposed ADP strategy. As is typically done, LMPC is implemented assuming ω remains at its nominal value of 0 over the prediction horizon. Namely, for LMPC, we solve at each time step, t:

$$\min \sum_{k=0}^{p} \tilde{\phi}(x_{t+k}, u_{t+k}) + 100||\epsilon_{t+k}||_2^2 \tag{21}$$

where $\epsilon_{t+k} \geq 0$ are non-negative auxiliary decision variables representing the least amount of slack required to make the LMPC problem feasible. That is, $[0\ 1]\, x_{t+k} + \epsilon_{t+k} \geq 0$. These inequalities are easily incorporated into the math program defined by (21). Also, the input vector is constrained to satisfy the aforementioned bounds of ± 0.5.

For the proposed ADP approach, we set the discount factor to a value close to unity, that is, $\gamma = 0.98$ and modify the stage wise cost to penalize deviations from the state constraints. Namely, $\phi(x_t, u_t) \triangleq \tilde{\phi}(x_t, u_t) + 100 \max(0, -[0,\ 1]x_t)^2$. Hard constraints on u are imposed during the off-line value iteration process and on-line implementation of the ADP-based controller.

To construct X_{sam}, we used an LMPC controller (with horizon length 5) and conducted closed-loop experiments bringing the system from 40 different initial post-decision states to the origin. Note that the initial state used for on-line testing is excluded from these 40 initial states. Namely, we consider various combinations of the sets $\{-2, 0, -1, 1, 2\}$ and $\{-4, -2, 0, 2, 4, 6, 8, 10\}$ to create various values for the first and second dimension of the initial state respectively. Consequently, a total of 3587 training points, whose initial cost-to-go values were initialized by computing the cost for LMPC over a sufficiently long horizon, was obtained as a result of the initialization scheme. For the purpose of function approximation, we employed kernel regression with the bandwidth, σ, set to 0.16. To avoid over-extrapolation, we selected $A = 1220$, and $\rho = 0.2652$. Value-iteration converged within 50 iterations, where the relative error termination criterion is set to $\left|\left| \frac{\hat{J}^{\mu^*,p}_{[i+1]} - \hat{J}^{\mu^*,p}_{[i]}}{\hat{J}^{\mu^*,p}_{[i]}} \right|\right|_\infty \leq 0.1$.

Results from 500 stochastic realizations presented as follows. As can be seen from Table 1, the proposed ADP controller has an average [2] finite horizon score an order of magnitude lower than a deterministic approach typified by LMPC. In particular, LMPC suffers from excessively high variance in terms of closed-loop performance. A look at the time series plots of the second dimension of x for both methods (see Fig. 1) reveals that LMPC results in significant constraint violation. On the other hand, the majority of the realizations based on the ADP approach do not violate the lower bound constraint.

[2] based on sample averaging

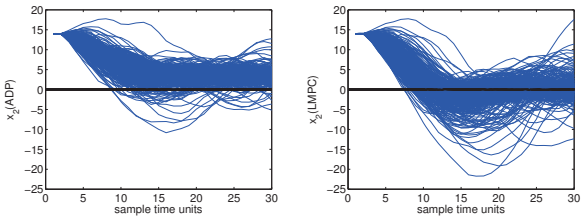

(a) ADP algorithm. (b) LMPC.

Fig. 1. Double integrator example: x_2 vs. t for 500 realizations. Lower bound for x_2 is 0.

4.2 Example 2: Constrained nonlinear stochastic system - chemostat problem

Consider the governing equations of an archetypal chemostat.

$$\dot{x}_1 = x_1 \frac{\mu_{max} x_2}{\kappa + x_2} - x_1 u$$
$$\dot{x}_2 = u[x_{2,f} - x_2] - \frac{\mu_{max}}{Y} \frac{x_1 x_2}{\kappa + x_2}$$

where $x = [x_1; x_2] \in \mathbb{R}^2$ is the state vector composed of the instantaneous concentration of the product (x_1) and substrate (x_2) respectively. $0 \leq u \in \mathbb{R}$, the dilution rate, is the non-negative manipulated variable. $x_{2,f}$ refers to the instantaneous concentration of the substrate feed. The maximum specific growth rate μ_{max} is set to 1, the yield coefficient to 1 and κ to 0.02. For the following simulations, the sampling rate is set to 0.5.

For the purpose of simulation, we assume that the feed concentration ($x_{2,f}$) fluctuates around a mean value of 1, and is perturbed by zero-mean, white Gaussian noise (ω):

$$x_{2,f,t} = 1 + \omega_t,\ \mathbb{E}[\omega_t \omega_t'] = 10^{-3} \tag{22}$$

It is desirable to maximize the productivity of the product, $\mathcal{P}_t \triangleq x_{1,t} u_t$, whilst ensuring that the conversion of the substrate, $f_{x_2} \triangleq 1 - \frac{x_2}{x_{2,f}}$, does not go lower than a relatively high value of 95%. Such an economically motivated constraint is common in several key process industries, such as bioethanol production. There is a tradeoff between productivity and conversion. Productivity increases with dilution rate and then decreases as the system approaches washout. Conversion, on the other hand, is a decreasing function of space-velocity or equivalently the dilution rate. Maximum productivity ($\mathcal{P}^* = 0.7543$) occurs at a dilution rate that corresponds to conversion levels significantly below the required 95% threshold.

We compare the performance of Non-linear MPC (NMPC) against the proposed ADP strategy. Instead of full-fledged NMPC, we employ successive-linearization based MPC (slMPC), a computationally efficient alternative proposed by Lee and Ricker (1994). For this example, we have found the closed-loop performance of slMPC to be similar to that of NMPC. For slMPC, we employed a prediction and

Table 1. Example 1: comparing performance

Score	ADP	LMPC
$\mathbb{E}\left[\sum_{t=0}^{30} \phi(x_t, u_t)\right]$	1600	10000

control horizon, p, of 10 sample units. The following math program is solved at each time instant:

$$\min \sum_{k=0}^{p} \left(||\mathcal{P}_{t+k} - \mathcal{P}^*||_2^2 + 100||\epsilon_{t+k}||_2^2 \right) \qquad (23)$$

where as in the previous example, $\epsilon \geq 0$, is a non-negative variable representing the least amount of slack required for conversion to be greater than 95%. That is, $\epsilon_{t+k} + f_{x_2,t+k} \geq 0.95$. The idea is to regulate the system at an equilibrium point that corresponds to the largest possible value of the dilution rate without exceeding the conversion bound so that productivity is maximized. The dynamics of the system are assumed to be governed by matrices obtained through linearization of the governing ordinary differential equations about the current state and past input vector. This results in a convex quadratic program.

For the proposed ADP approach, γ is set to 0.98 and the stage-wise cost defined as such: $\phi(x_t, u_t) \triangleq ||\mathcal{P}_t - \mathcal{P}^*||_2^2 + 100 \max(0, 0.95 - f_{x_2,t})^2$. To determine X_{sam}, we used an slMPC controller (with horizon length of 10 time units) and conducted closed-loop experiments regulating the system at an initial state corresponding to a conversion of 0.95. A total of 300 training points was obtained from the initialization scheme. We used kernel regression for function approximation with the bandwidth, σ, set to 0.15, A to 1.93 and ρ to 0.087 in order to prevent over-extrapolation. Value iteration terminated within 50 iterations with a relative error tolerance of 0.1.

Results from a typical realization are depicted in Fig. 2. It is apparent that the ADP-based approach, compared to slMPC, results in minimal constraint violation at the expense of slightly lower productivity. It is noted that the steady-state productivity corresponding to 95% conversion is 0.68.

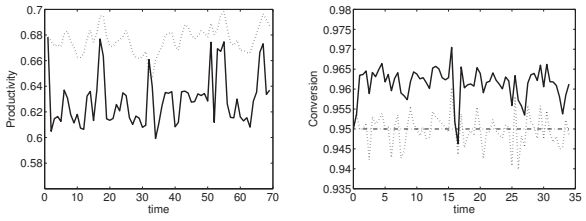

(a) Productivity vs time. (b) Conversion vs time.

Fig. 2. Example 2. Closed-loop performance of a typical realization. ADP: solid line (-); slMPC: dotted line(..); lower bound on conversion: dash-dot (-.)

4.3 Other examples in the literature

There are a number of other applications to process process control problems in the published literature. Interested readers may look at the following references for applications to more complex examples. These include: integrated reactor-separator system control (Tosukhowong and Lee (2009)), dual adaptive control (Lee and Lee (2009)), fed-batch reactor control (Peroni et al. (2005)), and microbial reactor (Kaisare et al. (2003)).

5. CONCLUSIONS

We have examined the potentials of ADP for process control and found that it can complement MPC to reduce the on-line computational load and also address stochastic system uncertainties. ADP offers a number of design options and one must think carefully through them to choose the right options for a given application. We have argued that, for process control problems, post-decision-state formulation offers the ability to use deterministic math programming solvers to be utilized, both off-line and on-line and therefore may be more convenient than the more conventional pre-decision-state formulation. In addition, the use of function approximators with nonexpansion properties offer stable learning. Robustness against over-extrapolation can be achieved through the use of a tailor-made penalty function. Finally, to achieve performance close to optimal ones, we recommend alternation between the value function update and simulation (or on-line implementation) to increase the sample set as the learning proceeds.

Though not discussed in this paper, there are a number of other application areas within process industries where ADP can prove to be a valuable tool, including resource allocation and inventory management (Pratikakis et al. (2008, 2009); Choi et al. (2004, 2006)), design and planning under uncertainty (Cheng et al. (2003)), scheduling of multiple controllers (Lee and Lee (2008)), and equipment / product inspection (Agrawal (2009)). Raised awareness of the ADP technique within the process systems engineering research community will undoubtedly bring forth additional applications that can benefit from it.

REFERENCES

Agrawal, R. (2009). *Planning and scheduling problems in manufacturing systems with high degree of resource degradation*. Ph.D. thesis, Georgia Institute of Technology.

Barto, A., Bradtke, S., and Singh, S. (1995). Learning to act using real-time dynamic programming. *Artificial Intelligence*, 72(1), 81–138.

Batina, I. (2004). *Model predictive control for stochastic systems by randomized algorithms*. Ph.D. thesis, Technische Universiteit Eindhoven.

Bellman, R. (1957). *Dynamic Programming*. Princeton University Press, New Jersey.

Bertsekas, D.P. (2005). *Dynamic Programming and Optimal Control, Vol. I*. Athena-Scientific, Belmont, MA, 3 edition.

Bertsekas, D. and Tsitsiklis, J. (1996). *Neuro-dynamic programming*. Athena Scientific, 1 edition.

Boyan, J.A. and Moore, A.W. (1995). Generalization in reinforcement learning: Safely approximating the value function. In *Advances in Neural Information Processing Systems 7*, 369–376. MIT Press.

Bradtke, S. (1993). Reinforcement learning applied to linear quadratic regulation. In *Adavances in neural information processing systems*, 295–302.

Cassandra, A., Kaelbling, L.P., and Littman, M.L. (1994). Acting optimally in partially observable stochastic domains. In *Twelfth National Conference on Artificial Intelligence*. Seattle, WA.

Cheng, L., Subrahmaniam, E., and Westerberg, A. (2003). Design and planning under uncertainty: issues on problem formulation and solution. *Computers & Chemical Engineering*, 27, 781–801.

Choi, J., Realff, M.J., and Lee, J.H. (2004). Dynamic programming in a heuristically confined state space: a stochastic resource constrained project scheduling application. *Computers & Chemical Engineering*, 8, 1039–1058.

Choi, J., Realff, M.J., and Lee, J.H. (2006). Dynamic programming in a heuristically restricted state space: stochastic supply chain management application. *AIChE Journal*, 52(7), 2473–2485.

De Farias, D.P. and Van Roy, B. (2003). The linear programming approach to approximate dynamic progrmaming. *Operations research*, 51(6), 850–865.

Gordon, G.J. (1995). Stable function approximation in dynamic programming. Technical report, School of Computer Science, Carnegie Mellon University.

Hastie, T., Tibshirani, R., and Friedman, J. (2008). *The Elements of Statisical Learning: Data Mining, Inference and Prediction*. Springer-Verlag, 2 edition.

Kaisare, N., Lee, J.M., and Lee, J.H. (2003). Simulation based strategy for nonlinear optimal control: application to a microbial cell reactor. *International journal of nonlinear and robust control*, 13, 347–363.

Konidaris, G. and Osentoski, S. (2008). Value function approximation in reinforcement learning using the fourier basis. Technical report, University of Massachusetts Amherst.

Laird, C.D. and Biegler, L.T. (2008). Large-scale nonlinear programming for multi-scenario optimization. In H.G. Bock, E. Kostina, H.X. Phu, and R. Rannacher (eds.), *Modeling, Simulation and Optimization of Complex Processes*, 323–336. Springer Berlin Heidelberg.

Lee, J.H. and Lee, J.M. (2006). Approximate dynamic programming based approach to process control and scheduling. *Computers & Chemical Engineering*, 30(10-12), 1603–1618.

Lee, J. and Ricker, N. (1994). Extended kalman filter based nonlinear model predictive control. *Industrial & Engineering Chemistry Research*, 33(6), 1530–1541.

Lee, J.M., Kaisare, N.S., and Lee, J.H. (2006). Choice of approximator and design of penalty function for an approximate dynamic programming based control approach. *Journal of process control*, 16, 135–156.

Lee, J.M. and Lee, J.H. (2004). Simulation-based learning of cost-to-go for control of nonlinear processes. *Korean Journal of Chemical Engineering*, 21(2), 338–344.

Lee, J.M. and Lee, J.H. (2005). Approximate dynamic programming-based approaches for input-ouptut data-driven control of nonlinear processes. *Automatica*, 41, 1281–1288.

Lee, J.M. and Lee, J.H. (2008). Value function-based approach to the scheduling of multiple controllers. *Journal of process control*, 18, 533–542.

Lee, J.M. and Lee, J.H. (2009). An approximate dynamic programming approach based approach to dual adaptive control. *Journal of process control*, 19, 859–864.

Ma, J. and Powell, W. (2009). A convergent recursive least squares policy iteration algorithm for multi-dimensional markov decision process with continuous state and action spaces. In *IEEE Conference on Approximate Dynamic Programming and Reinforcement Learning (part of IEEE Symposium on Computational Intelligence)*. Nashville, TN.

Ormoneit, D. and Sen, S. (2002). Kernel-based reinforcement learning. *Machine Learning Journal*, 49, 161–178.

de la Penad, D.M., Bemporad, A., and Alamo, T. (2005). Stochastic programming applied to model predictive control. In *44th IEEE Conference on Decision and Control, and the European Control Conference*, 1361–1366. Seville, Spain.

Peroni, C., Kaisare, N., and Lee, J.H. (2005). Optimal control of a fed batch bioreactor using simulation-based approximate dynamic programming. *IEEE Transactions in Control Systems Technology*, 13, 786–790.

Powell, W.B. (2007). *Approximate Dynamic Programming: Solving the Curses of Dimensionality*. Wiley Series in Probability and Statistics. Wiley-Interscience.

Pratikakis, N., Realff, M.J., and Lee, J.H. (2008). A controlled exploration of the state space via an off-line adp approach: applications on stochastic shortest path and manufacturing systems. *Computers & Chemical Engineering*, in press.

Pratikakis, N., Realff, M.J., and Lee, J.H. (2009). Strategic capacity decisions in manufacturing using real-time adaptive dynamic programming. *Naval Research Logistics*, to be published.

Putterman, M.L. (1994). *Markov decision processes: discrete stochastic dynamic programming*. John Wiley and Sons, New York.

Roy, B.V., Bertsekas, D.P., Lee, Y., and Tsitsiklis, J. (1997). A neuro-dynamic programming approach to retailer inventory management. In *IEEE Conference on Decision and Control*, volume 4, 4052–4057.

Sabes, P. (1993). Approximating q-values with basis function representations. In *Fourth Connectionist Models Summer School*. Hillsdale, NJ.

Scokaert, P. and Mayne, D. (1998). Min-max feedback model predictive control for constrained linear systems. *IEEE Transactions of Automatic Control*, 43(8), 1136–1142.

Smart, W. and Kaelbling, L. (2000). Practical reinforcement learning in continuous spaces. In *17th international conference on machine learning*, 903–910.

Sutton, R.S. and Barto, A.G. (1998). *Reinforcement learning: an introduction*. MIT Press, Cambridge, MA.

Tesauro, G. (1992). Practical issues in tempora-difference learning. *Machine Learning Journal*, 8, 257–277.

Thrun, S. and Schwartz, A. (1993). Issues in using function approximation for reinforcement learning. In *Fourth Connectionist Models Summer School*. Hillsdale, NJ.

Tosukhowong, T. and Lee, J.H. (2009). Approximate dynamic programming based optimal control applied to an integrated plant with a reactor and a distillation column with recycle. *AIChE Journal*, 55(4), 919–930.

Tsitsiklis, J. and Roy, B.V. (1996). Feature-based methods for large scale dynamic programming. *Machine Learning Journal*, 22(1), 59–94.

Quality by Design in the Pharmaceutical Industry: Process Modelling, Monitoring and Control using Latent Variable Methods

Theodora Kourti

GlaxoSmithKline & McMaster University

E-mail: kourtit@ mcmaster.ca

Abstract: The pharmaceutical industry has entered a new era. Attention is now being paid to real time process monitoring, real time process control, continuous improvement of processes, and quick product technology transfer. Terms like Quality by Design, Design Space, Control Strategy, Process Analytical technology, Process Signature reflect the current state. Multivariate Statistical Analysis has played an integral part in several industries, enabling process understanding, process monitoring, utilization of real time analysers and real time product release. It is therefore appropriate to see it as an integral part of the pharmaceutical industry effort to address issues like Design Space, Control Strategy, real time process signature monitoring, process understanding and correct technology transfer. In this work it is demonstrated that multivariate, data based statistical methods play a critical role in providing solutions to these issues. From determining the acceptability of raw material entering the plant to ensuring quality of the product that leaves the plant, the multivariate analysis philosophy should govern all the operations that take that raw material and convert it to a final product in a cost efficient way, while meeting safety and environmental constraints, from development to manufacturing to site transfer.

Keywords: Multivariate Process Monitoring, Design Space, process analytical technology, multivariate statistical process control, scale – up, latent variables, process understanding

1. INTRODUCTION

"The pharmaceutical industry has a little secret: Even as it invents futuristic new drugs, its manufacturing techniques lag far behind those of potato-chip and laundry-soap makers" proclaimed the Wall Street Journal in 2003 (Abboud and Hensley, 2003). The article went on to explain that "in other industries, manufacturers constantly fiddle with their production lines to find improvements. But FDA regulations leave drug- manufacturing processes virtually frozen in time. As part of the drug- approval process, a company's detailed manufacturing plan -- and even the factory itself -- must pass FDA muster. After approval, even a tiny change to how a drug is made requires another round of FDA review and authorization, requiring time and paperwork. The process discourages updating by the companies, which worry they will face a production delay that could cost them heavily". The article mentioned FDA as a regulatory agency because it was published in the USA, but similar were the situations with Pharmaceutical companies and other regulatory bodies around the world.

A lot of changes have happened since that article was published and the pharmaceutical industry has entered a new era. The FDA guidance on Process Analytical Technology (PAT) was introduced in 2004 which aims to improve product quality and process performance (manufacturing efficiency) in the pharmaceutical industry; it describes PAT as: systems for the analysis and control of manufacturing processes based on timely measurements during processes of critical quality parameters and performance attributes of raw and in-process materials and processes to assure acceptable end product quality at the completion of the process. (Guidance for Industry: PAT — A Framework for Innovative Pharmaceutical Development, Manufacturing, and Quality Assurance. FDA. September 2004)

The introduction of concepts like Quality by Design, Design Space and Control Strategy are also examples of this change. These terms are defined as follows by the International Conference on Harmonisation of Technical Requirements for Registration of Pharmaceuticals for Human Use (ICH is a unique project that brings together the regulatory authorities of Europe, Japan and the United States and experts from the pharmaceutical industry in the three regions to discuss scientific and technical aspects of product registration):

Quality-by-Design (QbD) is defined as a systematic approach to development that begins with predefined objectives and emphasizes product and process understanding and process control, based on sound science and quality risk management (ICH, 2008a).

Design Space is the multidimensional combination and interaction of input variables (e.g., material attributes) and process parameters that have been demonstrated to provide assurance of quality (ICH, 2008b).

Control Strategy: a planned set of controls, derived from current product and process understanding that ensures (good) process performance and product quality. The controls can include parameters and attributes related to drug substance and drug product materials and components, facility and equipment operating conditions, in-process controls, finished product specifications, and the associated methods and frequency of monitoring or control (ICH 2008a, 2008b).

The above definitions and actions indicate that the regulatory framework for the Pharmaceutical industry is changing.

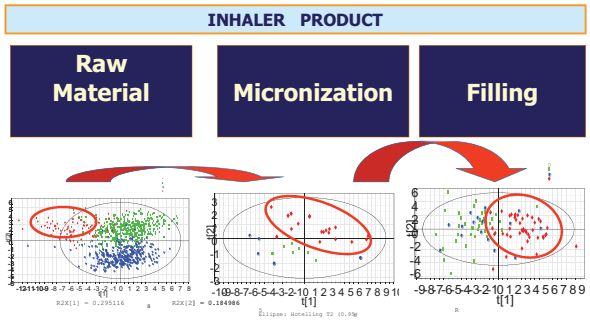

Figure 1. Projection space. Raw material properties, micronization properties and filling performance are projected on a latent variable space. Product batches produced from similar raw material (red) have similar filling performance.

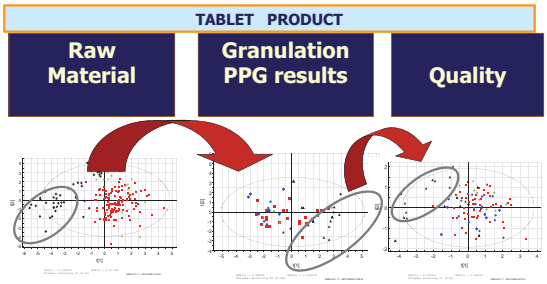

Figure 2. Tablet Product. Batches produced from raw material with similar characteristics, have similar final quality.

The ICH definition of the design space reflects a well known concept, namely that variability in the input of a process will be transferred to the quality of the final product (output) if the process is not controlled to compensate for such variability. Despite the fact that the concept is well known, it requires new ways of thinking in the pharmaceutical industry that was used to dealing with "fixed" processes, as described in the above mentioned Wall Street Journal article.

In this work the role of multivariare statistical methods in modelling, process control and monitoring under this new regulatory framework will be discussed. Multivariate latent variable methods are shown to be most suitable for process understanding, modelling for Design Space, multivariate statistical process control (MSPC), process control and product transfer. The use of these methods for the development of the Design Space for multi-unit operations will be illustrated in a case where the Tablet Quality is related to API, Excipients, Granulation, Drying and Compression parameters. Examples of how the Control Strategy can be derived from such models will also be shown.

Other topics like Process Signature and MSPC, application of soft sensors, relation of design space to clinical relevance as well as quality by design for analytical methods will be discussed.

2. LATENT VARIABLE METHODS

Latent variables exploit the main characteristic of process databases, namely that although they consist of measurements on a large number of variables (hundreds), these variables are highly correlated and the effective dimension of the space in which they move is very small (usually less than 10 and often as low as 2). Typically only a few process disturbances or independent process changes routinely occur, and the hundreds of measurements on the process variables are only different reflections of these few underlying events. For a historical process dataset consisting of a $(n \times k)$ matrix of process variable measurements **X** and a corresponding $(n \times m)$ matrix of product quality data **Y**, for linear spaces, latent variable models have the following common framework :

$$\mathbf{X} = \mathbf{T}\mathbf{P}^{\mathrm{T}} + \mathbf{E} \qquad (1)$$

$$\mathbf{Y} = \mathbf{T}\mathbf{Q}^{\mathrm{T}} + \mathbf{F} \qquad (2)$$

where **E** and **F** are error terms, **T** is an $(n \times A)$ matrix of latent variable scores, and **P** $(k \times A)$ and **Q** $(m \times A)$ are loading matrices that show how the latent variables are related to the original **X** and **Y** variables. The dimension A of the latent variable space if often quite small and determined by cross-validation or some other procedure.

Latent variable models assume that the data spaces (**X**, **Y**) are effectively of very low dimension (i.e., non-full rank) and are observed with error. The dimension of the problem is reduced by these models through a projection of the high-dimensional **X** and **Y** spaces onto the low-dimensional latent variable space **T**, which contains most of the important information. By working in this low-dimensional space of the latent variables (t_1, t_2, ... t_A), the problems of process analysis, monitoring, and optimization are greatly simplified.

Multivariate Statistical Process Control is possible utilizing latent variable methods. The following charts are used:

The Hotelling's T^2 for scores (derived either from PCA or PLS models on typical production) is calculated as:

$$T_A^2 = \sum_{i=1}^{A} \frac{t_i^2}{\lambda_i} = \sum_{i=1}^{A} \frac{t_i^2}{s_{t_i}^2} \qquad (3)$$

where $s_{t_i}^2$ is the estimated variance of the corresponding latent variable t_i. This chart essentially checks if a new observation vector of measurements on k process variables projects on the hyper-plane within the limits determined by the reference data.

As mentioned above the A principal components explain the main variability of the system. The variability that cannot be explained forms the residuals (Squared Prediction Error, SPE). This residual variability is also monitored and a control limit for typical operation is being established. By monitoring the residuals we test that the unexplained disturbances of the system remain similar to the ones observed when we derived the model. When the residual variability is out of limit, it is usually an indication that a new set of disturbances have entered the system; it is necessary to identify the reason for the deviation and it may become necessary to change the model.

SPE_X is calculated as :

$$SPE_X = \sum_{i=1}^{k} (x_{new,i} - \hat{x}_{new,i})^2 \qquad (4)$$

where $\hat{\mathbf{x}}_{new}$ is computed from the reference PLS or PCA model. Notice that SPE_x is the sum over the squared elements of a row in matrix **E** in equation (1). This latter plot will detect the occurrence of any new events that cause the process to move away from the hyperplane defined by the refence model. The calculation of the limits for the charts is discussed in Kourti (2009).

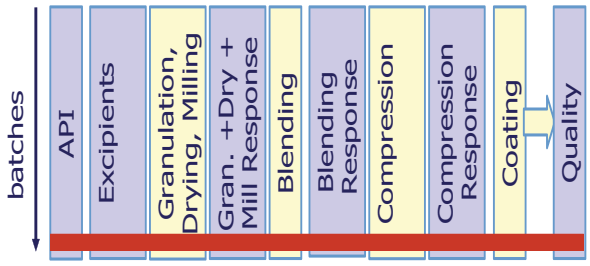

Figure 3. The quality can be modelled as a function of input material and process parameters

These two charts (T^2 and SPE) are two complementary indices; together they can give a picture of the state of the system at a glance. With this methodology, the hundreds of measurements collected from the process variables at each instant in real time are translated into one point for the T^2 chart and one point for the SPE chart (these two points summarize the process at that instant). As long as the points are within their respective limits everything is in order. Once a point is detected out of limit, then the so called *contribution plots* can be utilized that give us a list of all the *process* variables that mainly contribute to the out of limit point, and hence allow us to diagnose the process problem immediately. Contribution plots can be derived for out of limit points in both charts.

A detailed discussion on latent variable methodology for modelling and process monitoring can be found in Kourti (2002, 2005, 2009). Experiences from industrial practitioners can be found in Miletic et al (2004, 2008).

3. PROCESS UNDERSTANDING - EFFECT OF RAW MATERIAL ON FINAL QUALITY

The effect of raw material characteristics in the process performance, if the process operating conditions remain fixed, is demonstrated for an inhaler product utilizing multivariate projection space in Figure 1. The raw material is characterized by several physical and chemical properties. Raw material is produced at three supplier locations and depending on its origin, the data are coloured red, green and blue. The raw material properties are within univariate specifications, at all locations. Projected on a multivariate space, however, they form three clusters, indicating that in a multivariate sense the material possesses slightly different characteristics depending on the location it was produced (covariance structure changes with location). The material properties after micronization are projected on principal components and it can be observed that the material with red coloured origin projects on a different location than the green and blue. The filling performance of the material originating from the red location is different than the rest of the material. A note here that although the control ellipses shown are set by default in the vendor software, they are not interpretable when there is clustering; the assumptions for the calculation of these ellipses are for process monitoring and not for process exploration where there is intentional variation such that introduced by design of experiments.

4. DESIGN SPACE MODELLING

The effect of raw material on the quality as it propagates through different unit operations is shown for a tableting process in Figure 2. When the raw material properties have certain characteristics (marked black) the material projects on a different area. The properties of granules produced from raw material with such characteristics (black) are different from the rest, and the final quality also shows differences.

The difference in the quality can be theoretically explained based on the physical phenomena that govern the whole process. The idea of the design space is to express these phenomena by a model.

The design space can be established as a model that relates input material and process parameters to quality. The model may be theoretical (based on first principles) or empirical, derived from design of experiments or, a hybrid. Together with the model one has to specify the range of parameters for

which the model has been verified. The model may cover one unit operation or a series of unit operations.

The design space for the entire tableting process can be derived by relating quality to the raw material properties as well as to the process parameters of the unit operations (Figure 3). One row in the database depicted in Figure 3 would include the process conditions and quality experienced by the material as it is processed through the units. Multivariate projection methods can be used for the empirical modelling.

It should be emphasised here that the Design Space is a collection of models that relate 1) the final quality to all previous units, raw material and intermediate quality 2) intermediate quality to previous unit operations and raw material.

The empirical models derived are causal and based on carefully designed experiments (DOE). Some DOE's will also be necessary to estimate parameters even if mechanistic models are used.

Batch processes are very common in the pharmaceutical industry. Empirical methods for modelling and monitoring batch processes are discussed in Nomikos and MacGregor (1994) and in Kourti (2003).

Foundations for multiblock analysis necessary for multi unit operation systems can be found in Westerhuis et al (1998).

The level of detail in the models varies depending on the depth of process understanding one wishes to achieve. For example the variable trajectories of a granulation may be described by summary data (min, max, slopes, etc) or by the full variable trajectories aligned against time or another indicator variable (Kourti, 2003).

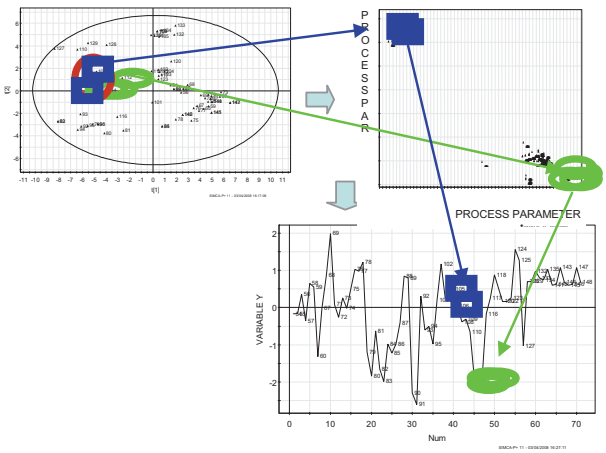

Fig. 4 Control Strategy using Projection Space.

5. CONTROL STRATEGY

Based on the process understanding derived from the design space, control strategy can be derived to assure final quality.

An example in Figure 4 is used to illustrate the new concepts. Control Strategy is devised once the Design Space is established. The example here illustrates a feed forward control scheme for Unit N+1 based on input information on the "state-of-the-intermediate product" from unit N. The settings are calculated and adjusted such that the target value for Quality Y is met.

A multivariate model was built (from batch data) to relate product quality to the process parameters of unit N+1 and the "state-of-the-intermediate product" from Unit N. From this model, a quantitative understanding was developed showing how process parameters in N+1 and the state-of-the-intermediate product from N interact to affect Quality.

Control of batch processes on multivariate space is discussed by Flores-Cerrillo and MacGregor (2004), while product transfer is discussed by García-Muñoz et al (2005).

6. PROCESS SIGNATURE AND MSPC.

It is known from other industries, that sometimes it is not sufficient to characterize a product with "end point quality measurements". The reason is that for some products we do not measure all the possible quality properties (example, downstream processability). The same "measured" quality properties may sometimes be achieved by taking different process paths. In these situations, these different paths may affect the properties that are not measured (i.e. processability). To achieve consistency in all the product properties (measured quality and ability to process down the stream) the process conditions (path to end point) must also be kept in statistical control. When this is not the case, although the measured product properties are on target, the properties that determine other characteristics (i.e., the processability of the product) may not be within acceptable limits. Therefore the "process path to the end point" must also be examined. This "process path to the end point" is also discussed in the European Regulatory Perspective (Graffner, 2005) where it is reported that "during discussions within the industry, the term process signature has been mentioned regularly". To get a common understanding of this, the EU PAT Team had invited public comments on the following definition: "A collection of batch specific information that shows that a batch has been produced within a design space of the product." The EU PAT team mentions as examples of process signatures the amount of water added in relation to time (wet massing), air flow rate, and bed temperature during fall rate drying (fluidized bed drying). They concluded that their understanding is that there is no unique process signature, but instead a family of process signatures with common characteristics (salient features).

It should be pointed out here that the process signature in the multivariate statistical process control context is nothing else

but the two multivariate indices Hotelling's T^2 and SPE. As a matter of fact, these indices take it to account not one feature (e.g., water addition rate or, drying rate) but the combination of all the variables affecting the process and product and their correlations both at each time interval but also their time correlations for the duration of the process (auto and cross correlations for the entire batch). They are therefore a more powerful tool to describe the "overall process signature".

Furthermore, these indices can be directly related to the concept of the design space, as outlined here. The design space model relates raw material characteristics, process conditions and quality. Given the characteristics of the raw material and the desired quality, the design space model can be solved to determine appropriate operating conditions. Maintaining T^2 and SPE within their good operation limits for these appropriate process conditions is nothing more than ensuring that the operation is within the design space.

7. PAT and SOFT SENSORS

Accurate on-line measurements of quality variables are essential for the successful monitoring and process control. However, due to measurement difficulties, sometimes process variables may be used to "infer" product quality in real time and therefore replace an analyzer. This is the idea of soft sensors. In many monitoring and control situations we are often lacking real time sensors capable of measuring many of the responses of interest, because the measurement equipment for such quality variables may be very expensive, or difficult to put on-line, or costly to maintain. As a result we often try to develop soft sensors or inferential models which use other readily available on-line measurements such as temperatures, and can be used to infer the properties of interest in a real time manner. In a recent paper it was demonstrated through application to a benchmark simulation of a fed-batch fermentation process that mutli-way PLS can provide accurate inference of quality variables, such as biomass concentration, that are often difficult to measure using on-line sensors. It was also demonstrated that the same PLS model can be used to provide early detection and isolation of fault conditions within a fermenter (Zhang and Lennox, 2004).

The soft sensors can either replace the hardware sensor (analyzer) or be used in parallel with it to provide redundancy and verify whether the hardware sensor is drifting or has failed; when used in parallel the soft sensor will either estimate the property and compare its value with that of the analyser, or it will keep track of the correlation between the analyser reading and the process measurements. An example where a soft sensor is used to assess the reliability of an analyser was presented in Kourti (2005). Latent variable modeling was used for this purpose.

This idea of using process measurements as a safety net to verify analyser reliability but also to monitor an index of wellness for the process, to check for unforeseen disturbances, is a crucial and important issue for real time release (Kourti, 2006a).

8. INTEGRATION OF CLINICAL TRIALS

As more complex structures of data are being generated, the multivariate analysis offers great opportunities for information integration and analysis.

Manufacturing Data as well as patient histories can be integrated and then incorporate into design space the clinical trial responses. (Kourti 2006b).

Figure 5 shows an example of the possibilities that can be explored. Quality in product Y can be related to past information of raw materials, preprocessing and holding times, the type of the vessel used, the operator that run the process, and other recipe information as well as process measurement trajectories and analyzer information.

The quality Y (and details of manufacturing) as well as the patient medical histories and clinical responses can be used to establish a better understanding of the design space.

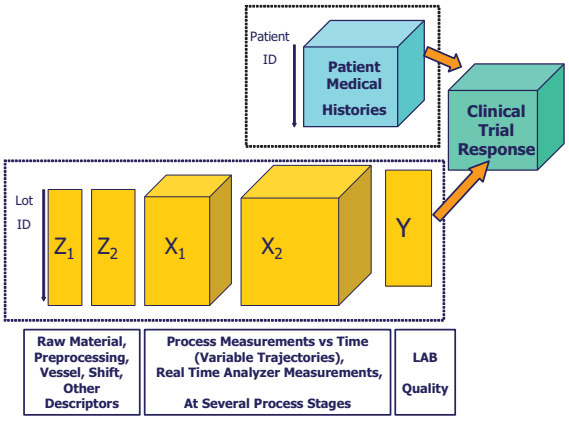

Figure 5 : Examples of complex data structures emerging in industry, that can be mined for a wealth of information. (Kourti, 2006b).

9. QUALITY BY DESIGN IN ANALYTICAL METHODS

The methodology described for design space can be applied in analytical methods. Chromatography, is a laboratory method but also a Unit operation in Bio – Pharmaceuticals.

Process Transfer ideas can be also applied in method transfer ideas, that is method transfer – and site transfer could be treated with similar principals (García-Muñoz et al., 2003)

ACKNOWLEDGEMENTS

I would like to thank John F. MacGregor, McMaster University and Gordon T. Muirhead, GlaxoSmithKline, for their support and dedication to innovation.

REFERENCES

Abboud, L., and Hensley. S (2003) Factory Shift: New Prescription For Drug Makers: Update the Plants; After Years of Neglect, Industry Focuses on Manufacturing; FDA Acts as a Catalyst; The Three-Story Blender. Wall Street Journal. Eastern edition). New York, N.Y.: Sep 3, 2003. pg. A.1, The Wall Street Journal

Flores-Cerrillo J., and MacGregor J. F. (2004) Control of batch product quality by trajectory manipulation using latent variable models, Journal of Process Control 14, 539 -553.

García-Muñoz, S, MacGregor, J.F., Kourti, T. (2005) Product Transfer between Sites using Joint Y_PLS. Chemometrics and Intelligent Laboratory Systems, 79, 101-114.

Graffner, C (2005). PAT- European Regulatory Perspective, The Journal of Process Analytical Technology, 2 (6) 8-11.

ICH (2008a). International Conference on Harmonization, ICH Draft Step 4, Q8 (R1) Pharmaceutical development revision 1, 11-November-2008.

(ICH, 2008b) International Conference on harmonization of technical requirements for registration of pharmaceuticals for human use, ICH harmonized tripartite guideline, pharmaceutical quality system Q10 Step 4, 9-June-2008.

Kourti, T. (2002) Process analysis and abnormal situation detection: from theory to practice. IEEE control systems, 22 issue 5 : 10-25

Kourti, T. (2003) Multivariate dynamic data modelling for analysis and statistical process control of batch processes, start–ups and grade transitions. J. Chemometrics, 17, 93-109

Kourti, T. (2005) Application of Latent Variable Methods to Process Control and Multivariate Statistical Process Control in Industry. International Journal of Adaptive Control and Signal Processing; 19, 213-246.

Kourti, T., (2006a). Process Analytical Technology and Multivariate Statistical Process Control. Index of wellness of product and process. Part 3. Process Analytical technology, volume 3 (3), 18-24.

Kourti, T. (2006b) Process Analytical Technology Beyond Real-Time Analyzers: The Role of Multivariate Analysis Critical Reviews in Analytical Chemistry, Critical Reviews in Analytical Chemistry, 36:257–278.

T. Kourti (2009) Multivariate Statistical Process Control and Process Control, Using Latent Variables. In: Brown S, Tauler R, Walczak R (eds.) Comprehensive Chemometrics, volume 4, pp. 21-54 Oxford: Elsevier

Miletic, I., S. Quinn, M. Dudzic, V. Vaculik, M. Champagne. (2004) Journal Process Control, 14, 821-836.

Miletic, I.; Boudreau, F.; Dudzic, M.; Kotuza, G.; Ronholm, L.; Vaculik, V.; Zhang, Y. (2008) Experiences in Applying Data-Driven Modelling Technology to Steelmaking Processes. Can. J. Chem. Eng. 86, 937–946.

Nomikos, P. and J.F. MacGregor (1994)"Monitoring of batch processes using multi-way principal component analysis," AIChE Journal, 40 , no. 8: 1361-1375.

Westerhuis, J.A., Kourti, T., and MacGregor, J.F. (1998) Analysis of multiblock and hierarchical PCA and PLS models. Journal of Chemometrics, 12, 301-321

Zhang, H., Lennox, B. (2004) Integrated condition monitoring and control of fed-batch fermentation processes, Journal of Process Control 14, 41–50.

Plantwide Optimizing Control for the Bio-ethanol Process

Silvia Ochoa*, Jens-Uwe Repke*, Günter Wozny*

**Chair of Process Dynamics and Operation, Berlin Institute of Technology, Sekr. KWT9, Strasse 17. Juni. 135, Berlin 10623, Germany*

Abstract: In this work, the Plantwide Control (PWC) problem of a continuous bio-ethanol process is investigated from a Plantwide Optimizing Control (PWOC) perspective. PWOC addresses the plantwide control problem integrating real-time optimization and control for optimal operation. Two different PWOC approaches have been considered: A Single-Layer Direct Optimizing Control approach (one-layer) and a Multi-Layer without Coordination approach (two-layer). The performance of these two PWOC approaches is compared with more traditional Decentralized architectures, demonstrating the benefits of using Plantwide Optimization-based Control strategies in bioprocesses.

Keywords: Plantwide Control, Optimizing Control, Dynamic Real Time Optimization, Ethanol.

1. INTRODUCTION

Nowadays, bioprocess industry is an important part of the worldwide economy. Specifically, the bio-ethanol industry has experienced a significant growth in the last years since ethanol, as an environmentally friendly fuel, is considered an attractive alternative energy source. Ethanol production has been continuously improved in very different ways in order to assure the economical and environmental feasibility of the process. Examples of these improvements include purification technologies for reducing energy consumption during the separation of the ethanol-water mixture (Arifeen et al., 2007), and genetic modifications of the microbial strains for building more ethanol-tolerant yeast and strains capable of carrying out simultaneously saccharification and fermentation tasks (Olofsson et al., 2008). From a process control point of view, different works have been done regarding the modelling, estimation, and control problem for the fermentation stage. However, only relatively few works (e.g. Meleiro et al., 2008, Costa et al., 2001) have addressed the control problem from the Process Systems Engineering point of view, considering the process as an integrated dynamic production system taking into account more than one single process unit (i.e. accounting for interactions between fermentation, cells recycle and flash units). In this work, the Plantwide Control (PWC) problem for the ethanol process is addressed as a large-scale real-time dynamic optimization problem due to the following facts: the nature of the process is highly nonlinear and dynamic; the process is characterized by the coupling of slow and fast dynamics; interactions between different operating units can not be neglected; and finally, economical feasibility of the process can be effectively assured if this is the main control objective of the plantwide strategy. PWC has attracted the attention of the process control community for more than 40 years, since the pioneer work by Buckley (1964). Through these years, different architectures have been used for tackling the problem of controlling a complete process. The intention of this section is to present a brief review of the several options reported for addressing PWC. A proposal of classification for different PWC architectures is shown in Fig 1, which agrees in some points with that presented by Scatollini (2009).

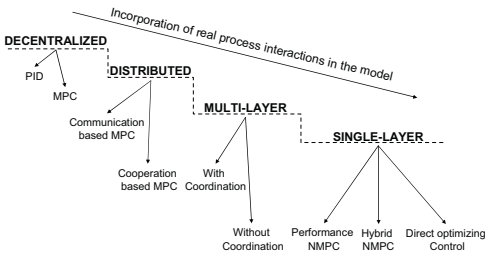

Fig 1. Plantwide Control Architectures

In the *Decentralized* scheme, many different individual regulators are used in the process without sharing any kind of information between them (i.e. each controller operates independently of the others), even though the selection of the manipulated and controlled variables might take into account the interactions in the process. The decentralized approach consists usually of SISO PID loops, although MPC controllers can also be used. As noted by Stephanopoulous and Ng (2000), most of the research activities in the topic of PWC up to year 2000, addressed the PWC problem as the selection of the best input-output pairing for the formation of SISO PID loops. Of course, as in any rule there are exceptions, and one of the most relevant examples in this case is the work by Garcia and Morari (1984), in which a multivariable control scheme based on a *Multi-layer* PWC architecture was proposed for controlling a benzene plant. Some of the many works that have addressed the PWC in a decentralized manner are Araujo et al. (2007), Larsson et al. (2003), Robinson et al. (2001), Zhen et al. (1999), Lausch et al. (1998), Luyben et al. (1997) and McAvoy and Ye (1993). Most of the works in the remaining three architectures shown in Fig 1 make use of a multivariable controller. Two main reasons motivated to move the PWC problem from the

paradigm of decentralized PID towards different alternatives: the performance limitations of the decentralized architecture, and the broad industrial impact of the Model Predictive Control (MPC) framework (Venkat et al. 2007). In the *Distributed* architecture some information is exchanged between the multiple MPC controllers. Two Distributed-MPC approaches worthy of mention are the communication- and cooperation-based, which mainly differ that in the first, each controller has a local objective function, whereas in the latter the objective function in each controller is a copy of the total objective function for the complete plant (Rawlings and Stewart, 2008). Representative works addressing the PWC from the Distributed perspective are those by Sun and El-Farra (2008), Venkat et al. (2007), Mercangöz and Doyle (2007) and Venkat (2006). *Multi-layer* architecture is a hierarchical structure that follows the guidelines given by Findeisen et al. (1980), which classified the hierarchical control into multilayer and multilevel. According to Findeisen's work, in the multilayer case, the control of a system is split into algorithms (layers), whereas in the multilevel case control is divided into local goals and the action of each local control unit is coordinated by an additional supremal unit. In Fig 1 it is proposed to sub-divide the Multi-layer (or hierarchical) architecture into: *With Coordination* (denoted as Multilevel approach by Findeisen) and *Without Coordination*. Multilayer architectures should be composed by at least two different layers, in which the task of finding the control actions that should be applied to the process is split usually into: a *Real Time Optimization* (RTO) layer that computes optimal set point values for the controlled variables, and a *Control* layer which is in charge of tracking the optimal set point values (Kadam et al., 2002). In the control layer, a PID or MPC controller can be used (Kadam and Marquardt, 2004). It is important to notice that as mentioned by Biegler and Zavala (2009), the "connection" between RTO and MPC layers may suffer inconsistencies due to model mismatch (non-linear steady state vs. linear dynamic) and conflicting objectives. Therefore, in the last years a proposal for replacing the steady state RTO by a Dynamic Real Time Optimization (D-RTO) layer has emerged (Kadam et al. 2003; Kadam and Marquardt, 2004). On the other hand, regarding the *Multi-layer with coordination* architecture, the reader is referred to the work by Tosukhowong et al. (2004) in which a coordination collar is used to find for each MPC a locally feasible set point close to the global solution found by the RTO layer; and to the work by Cheng et al. (2007), in which a price-driven method is used for coordination between the RTO and the MPC layers. Additionally to the references already mentioned, the following works include examples of PWC using *Multi-layer* architecture: Ochoa et al. (2009), Kadam and Marquardt (2007), Lu (2003), Duvall and Riggs (2000) and Ying and Joseph (1999). A final mention should be done regarding the difference between the Multilayer with coordination and the Distributed architectures. As both schemes include coordination, in the Distributed case the coordination consists on exchanging some information between the local MPCs, whereas in the Multilayer with coordination, the local MPCs are not communicated between them but communicated to the RTO layer. The last PWC architecture in the classification shown in Fig 1 is the *Single-layer* scheme. Despite the very common belief that a *Single-layer* or centralized structure will be intractable for PWC (Venkat et al., 2007), in the last years some publications from both the industrial and the academic side have shown that such monolithic approach it is not only possible to implement but also gives very good results from an economic point of view (Bartusiak, 2007; Zavala et al., 2007; Franke and Doppelhamer, 2007). Works using this architecture solve online a moving horizon optimization problem, but differ in the type of objective function optimized. A first group of works denoted as *Performance NMPC* uses a performance-type objective function (in which mainly the tracking of a reference value is penalized). The second scheme includes besides the performance term, an economic penalization term in the formulation of the objective function and therefore it is denoted here as *Hybrid NMPC* (Economic+Performance). The final scheme denoted in the literature as *Direct Optimizing Control* (Engell, 2007) uses a pure economic objective function in which the usual control specifications enter as constraints and not as set points, and therefore no tracking term is penalized. References showing examples of the application of the Single-layer architecture are: Biegler and Zavala (2009), Roman et al (2009), Ochoa et al. (2009), Engell (2007), Franke and Doppelhamer (2007), Zavala et al. (2007), Bartusiak (2007), Manenti and Rovaglio (2007), Franke and Vogelbacher (2006), Toumi and Engell (2004) and Jockenhövel et al (2003). The main purpose of this paper is to present a novel approach for the PWC of the bio-ethanol process, in which the main control objective is to maximize the profitability of the whole process. The paper is organized as follows: Section 2 gives a description of the ethanol continuous process from starch, including a brief description of the relevant works that have addressed the control of the process considering it as composed of more than one process unit. Section 3 presents the Plantwide Optimizing Control (PWOC) concept proposed in this work and describes the main steps of this approach. A new method for shrinking the search region during the optimization problem that arises when applying PWOC is proposed in Section 4. The Multi-layer without coordination and the Single-layer direct optimizing architectures are used for addressing the PWC problem in the continuous bio-ethanol process. These approaches are compared in Section 5 to conventional decentralized architectures.

2. BIO-ETHANOL PRODUCTION PROCESS

The case study addressed is based on the extractive alcoholic fermentation process shown in Fig 2. A detailed description of this process is found elsewhere (Meleiro et al., 2008). The process includes saccharification, fermentation, cells recycle, flash separation, distillation and rectification. The end product considered is the ethanol obtained at the top of the rectification column, which in a further step must be sent to a dehydration unit (e.g. molecular sieves). A nonlinear dynamic model of the process has been simulated using Simulink®. The model consists of a nonlinear DAE system comprising 69 differential states and 173 algebraic equations. pH, temperature and liquid levels are regulated as usually done in industry by means of local SISO loops, which in the

following will be denoted as *basic control*. After closing these basic loops, 13 input variables are left, 3 of which are identified as disturbances: starch (S_0), enzymes (Enz_1) and fresh yeast concentration (X_3) fed into the process. The remaining 10 inputs are available for improving the control strategy in the process. The process with its basic level control loops is shown in Fig. 2 (for simplicity, the pH and temperature loops are not shown). In addition to the basic loops, an internal biomass control strategy (Ochoa et al., 2009) is also shown. The combination of the traditional *basic control loops* with this biomass internal strategy is denoted in the following as *Local Control Strategy*. Two main reasons motivated implementing the biomass control. First, an optimal biomass concentration in the fermentor should be always guaranteed in order to avoid a misuse of the substrate if a higher concentration than the optimal is available. Additionally, if biomass concentration is below the optimum, a slower metabolite production rate will occur, affecting the productivity of the process. Second, yeast is only involved in a closed mass loop comprising fermentation, filter and cells recycle; i.e. no biomass is found on the streams up the fermentor nor downstream the filter. As already mentioned, the process has 10 manipulated variables available for improving the control strategy; however, 3 of them (F_3, F_7, F_{10}) are used as manipulated variables in the biomass strategy. The remaining 7 manipulated variables (F_0, F_1, F_{13}, VB_1, R_1, VB_2, R_2, which are the starch input flow, enzymes input flow, recycle flow from the flash to the fermentor and vapour and reflux rates for each column) are potential manipulated variables denoted as "Plantwide variables".

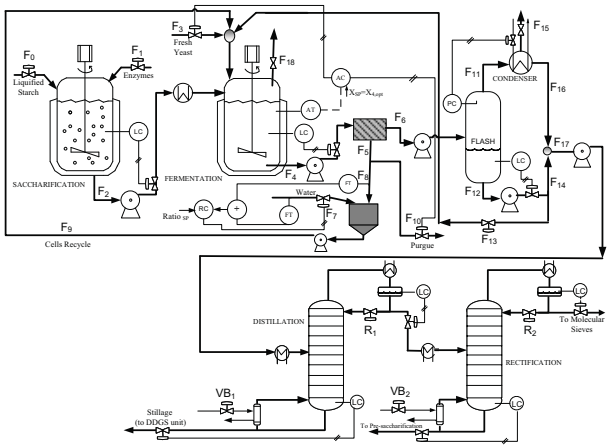

Fig 2. Bio-ethanol Process from Starch: Local Control Strategy (Basic loops + Internal Biomass Strategy).

Additionally, it should be noticed that despite the rapid increase of the bio-ethanol industry in the last 30 years and the high economic risk that this industry faces, no much effort has been done in order to improve the efficiency of the process from the optimization and control points of view. Several works have been published regarding mainly the control of the fermentation unit in the process, but to the author's knowledge, only few works have addressed the control of the process considering more than the fermentation stage. Costa et al. (2001) used Dynamic Matrix Control (DMC) for controlling the substrate or the product concentrations in the fermentor manipulating the substrate input flow or the cells recycle rate. A second contribution by Costa et al. (2002), proposes a SISO NMPC for controlling the substrate concentration in the fermentor, manipulating the substrate input flow. Meleiro et al. (2008) presented a multivariate NMPC to control simultaneously the ethanol, substrate and biomass concentrations in the fermentor. Although the process modelled in these works considers interactions fermentor-cells recycle-flash, the control task is still focused on tracking or regulating the main state variables in the fermentor without considering the optimal economic operation of the whole process. Finally, Bartee et al.(2008), propose using MPC for controlling the process including milling, cooking, distillation etc.; however, no details regarding algorithms and implementation are given.

3. PLANTWIDE OPTIMIZING CONTROL

Online optimizing control optimizes an economic objective over a finite moving horizon during plant operation based upon a rigorous nonlinear dynamic model (Küpper and Engell, 2008). Plant limitations and product specifications are included in the optimization as constraints. This definition is used in this section as key concept for developing the basic steps of a Plantwide Optimizing Control (PWOC) approach. PWOC addresses PWC as a nonlinear dynamic online problem, in which the available manipulated variables in the process are used for achieving maximum profitability in the plant in spite of disturbances. In this way, PWOC calculates optimal values for the set of selected manipulated variables, in order to maximize a Plantwide Profitability Objective function Φ, instead of maintaining a set of controlled outputs at predefined set points. A key feature of PWOC is that input-output pairing is avoided because the output actually controlled in the process is the Plantwide Profitability and the available manipulated variables are simultaneously used for satisfying that purpose. Online optimizing control has been gaining increasing attention in the last years in different chemical process applications (Engell, 2007). However, not much work has been reported in the open literature on the on-line optimizing control of bioprocesses. In this work PWC of a bioprocess is addressed from an optimizing control perspective, considering a large-scale nonlinear Dynamic Real-Time Optimization (D-RTO) problem. The proposed PWOC approach comprises six main stages, as shown in Fig 3. In the following, a description of each stage is presented.

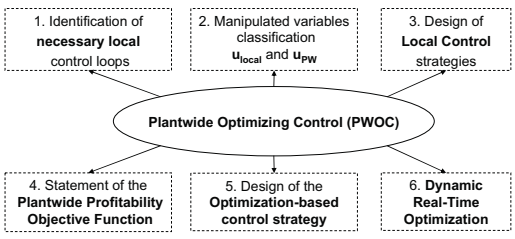

Fig 3. Plantwide Optimizing Control Stages

Stage 1: Identification of necessary control loops

Even though the goal of any chemical or biochemical process is to return a maximum profit, there are additional control

objectives that should be taken into account before establishing a PWOC structure for satisfying this economic goal. These objectives are mainly related to safe operation, equipment and environmental protection and should be achieved independently of the economical performance of the plant, i.e. by using local control loops.

Stage 2: Classification of the Manipulated Variables

Manipulated variables in the process can be used in the local control loops or for the PWOC of the process. Those manipulated variables used for satisfying the local control set points are denoted as *Local manipulated* (u_{Loc}), whereas the *Plantwide manipulated* variables (u_{Pw}) are those that remain available after selecting the u_{Loc}, and that are used for maximizing the plantwide profitability objective function.

Stage 3: Design of Local Control Strategies

After identifying the necessary local control loops in the process and the local manipulated variables required for satisfying the control objectives at the local control loops, it is then necessary to address the design of those local loops (i.e. pairing manipulated-controlled variables, selection of controller type, controller tuning, etc.), as traditionally done.

Stage 4: Statement of Plantwide Profitability Function (Φ)

The next step is to establish a plantwide profitability function Φ and its constraints, in order to formulate a D-RTO problem. Statement of the objective function Φ will depend upon the specific process addressed. However, it may contain terms related to productivity of the process, raw materials and energy consumption, economic losses, etc. Constraints in the optimization problem are determined by plant and product specifications, and by limitations in the state and input variables. Since PWOC addresses the optimizing control problem for a complete plant over a finite moving horizon during plant operation, it is also important to select the prediction horizon Δt_{opt} over which the objective function and constraints will be evaluated. Δt_{opt} should not be shorter than the characteristic response time of the slowest relevant dynamic in the process (to avoid unexpected long-term performance deterioration), while at the same time it should be as short as possible to minimize computational load.

Stage 5: Design of the Optimization-Based Control Strategy

PWOC is addressed here using two different architectures: *Single-Layer Direct Optimizing Control* and *Multi-Layer without Coordination*. These frameworks will be referred in the following as the one-layer and the two-layer approaches, respectively. The structures for both approaches are shown in Fig. 4. A detailed description of the building blocks for each framework can be found elsewhere (Ochoa et al., 2009). Comparing the schemes for the two frameworks (Fig. 4), it is possible to see that both approaches have very much in common. For example, both approaches are driven by a D-RTO layer, in which the objective function to be maximized is the plantwide profitability Φ. The main difference between the two frameworks is that in the one-layer approach, the input variables applied to the real plant are given by the optimization layer ($u_{Pw}=u_{opt}$), whereas for the two-layer, the inputs applied to the real plant are calculated by a control layer ($u_{Pw}=u_{mpc}$) that uses as set points, the optimal values of the states given by the optimization layer (x_{opt}). In both cases, the decision variables of the optimization problem are the plantwide manipulated variables u_{Pw}. In the two-layer case however, a second layer (NMPC controller) is used, in which an optimization problem is also solved for minimizing a performance-type objective function Γ, which can be composed of three terms: a penalization of the deviation of the main state variables from their set points (x_{opt}), a term that prevents large changes in the manipulated variables from one sample time to the next, and a term that constraints the manipulated variables to a small envelope around the reference trajectories u_{opt}, given by the optimization layer.

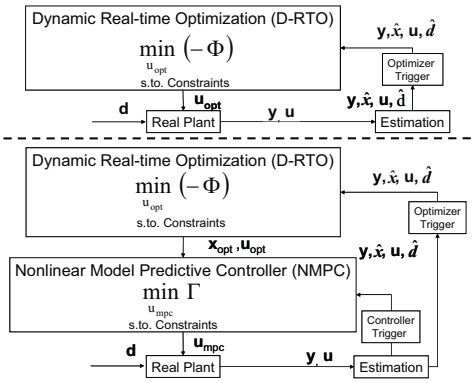

Fig. 4. Optimization-Based Control Strategies: One-layer (top) and Two-layer (bottom)

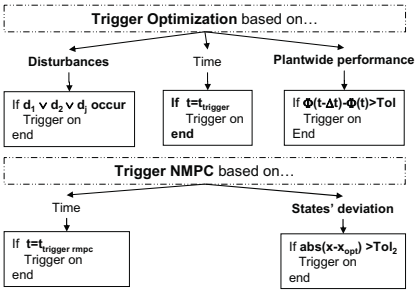

Fig. 5. Trigger for re-calling the D-RTO (top) and Controller layers (bottom)

Finally, trigger blocks in Fig. 4 deserve special mention due to their importance in the implementation of optimization-based control strategies. These trigger blocks act like switches for re-calling the optimization and control layers. An optimization-trigger for recalling the D-RTO layer can work based on a time criterion (e.g. the optimization is called periodically at a predetermined frequency), based on the disturbances dynamics (occurrence of a disturbance) or based on the performance of the plantwide profitability objective function (when Φ decreases below a certain tolerance). On the other hand, the controller-trigger can be based on a time criterion or on the state variables deviations from their optimal set points. Fig. 5 shows schematically the different criteria for activating the optimization and controller triggers.

Stage 6: Dynamic Real Time Optimization (D-RTO)

Because a nonlinear dynamic large-scale optimization problem arises in the last stage of the PWOC, an efficient feasible optimization method should be used in order to solve the problem in real time. For this purpose, different types of optimization algorithms can be used. However, the use of stochastic or evolutionary algorithms is considered here because of their reduced computational load (they do not need information about derivatives as required by gradient-based methods) and their relatively simple implementation. In this work, a stochastic method (i.e. localized random search) is used for solving the optimization problem in the PWOC. Independently of the optimization algorithm used, the method will search for the optimal solution in the space of the decision variables, which is a region bounded by the lower and upper limits of each manipulated variable (which are the decision variables of the optimization problem). This search region may be too large, resulting in long calculation times for finding an optimal solution, making difficult the solution of the PWOC problem in real time. In order to improve the efficiency of the optimization method for solving the large scale D-RTO problem, in the following section, a new stochastic-based approach for shrinking the search region of the optimization problem is introduced.

4. STOCHASTIC-BASED SHRINKING OF THE SEARCH REGION OF THE D-RTO PROBLEM

The main idea of the stochastic shrinking approach, is that for a sample time Δt (during which a disturbance took place in the process or the profitability function decreased), the changes on each plantwide manipulated variable (Δu_{PWi}) required for rejecting a disturbance, should be calculated as a function of the changes in the disturbances (Δd_j) and in the profitability objective function ($\Delta \Phi$). Mathematically, this can be written as shown in (1).

$$\Delta u_{PWi} = u_{PWi,t+\Delta t} - u_{PWi,t} = f_i(\Delta d_1, \Delta d_2, ...\Delta d_j, \Delta\Phi) \quad (1)$$

Where i is the number of plantwide manipulated variables and j is the number of disturbances that can be present in the process. f_i is a function that represents how much the manipulated variable i should change to reject disturbances. Specifically in this work, the use of a Gaussian distribution for describing function f_i is proposed. In this way, the changes on the manipulated variables are given in (2).

$$\Delta u_{PWi} = \xi_i \left(0 \, , \, \sigma_{u_i}\right) \quad (2)$$

Where $\xi_i(0, \sigma_{ui})$ represents a random number obtained from a Gaussian distribution with zero mean and standard deviation $\sigma_{ui.}$ This standard deviation can be calculated as the maximum between different contribution terms, which represent the capability of the manipulated variable i for rejecting the different known disturbances of the process at time t, and for rejecting a decrease in Φ (that can be caused by both known and unknown disturbances), as shown in (3),

$$\sigma_{u_i} = \max(w_{i1}\Delta d_1, w_{i2}\Delta d_2, ...w_{ij}\Delta d_j, w_{i\Phi} z_\Phi \Delta\Phi) \quad (3)$$

where w_{ij} are gain factors that express how much a change in the manipulated variable u_{Pwi} can reject (or counteract) the occurrence of disturbance d_j, $w_{i\Phi}$ is the gain factor for the manipulated variable i rejecting the decrease in the profitability objective function Φ, and z_Φ is a dummy variable that is only activated when the objective function Φ decreases below a given tolerance *Tol*, that is:

$$z_\Phi = \begin{cases} 0, & \Phi(t-\Delta t) - \Phi(t) \le \text{Tol} \\ 1, & \Phi(t-\Delta t) - \Phi(t) > \text{Tol} \end{cases} \quad (4)$$

A final mention should be done, regarding the calculation of the gain factors used for obtaining the standard deviation σ_{ui}. It would be desirable to calculate these gains mathematically, from the nonlinear model of the process as expressed in (5)

$$w_{ij} = \sum_{k=1}^{n} \frac{\partial u_i}{\partial x_k} \times \frac{\partial x_k}{\partial d_j} \quad (5)$$

where $\partial u_i/\partial x_k$ represents the inverse of the open loop gain between state variable x_k and input u_i; and $\partial x_k/\partial d_i$ represents the open loop disturbance gain between x_k and disturbance d_j. As the complexity of the process model increases, the complexity for calculating the w_{ij} factors analytically also increases. For this reason, these gain factors are proposed to be calculated by using Digraphs. Information regarding digraph models is found elsewhere (Maurya et al., 2003).

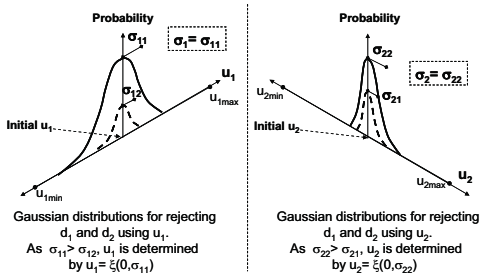

Fig. 6. Shrinking approach: Gaussian distributions for a system with two manipulated variables and two disturbances.

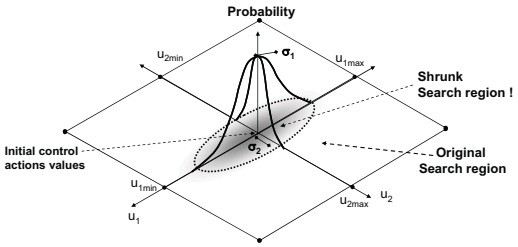

Fig. 7. Shrinking approach: Final Shrunk Search Region vs. Original Search Region.

For concluding this section, a graphical representation of the shrinking approach for a system with two manipulated variables and two disturbances that occur at the same time, is presented in Fig. 6 and 7. Fig. 6 shows the Gaussian distributions with standard deviation σ_{11} and σ_{22} for describing the manipulated variables u_1 and u_2 respectively, when disturbances occur in the process. Fig. 7 shows the Shrunk Search Region for the optimization problem, formed by the Gaussian distributions for u_1 and u_2. It is important to notice that despite the maximum standard deviation has been

selected for each case, a reduction of the search space for the optimization algorithm is achieved because the original search region of the optimization problem was only bounded by the upper and lower bounds of u_1 and u_2 (see Fig. 7). The stochastic-based shrinking approach is used in section 5 for reducing the search region of the optimization problem that arises when the PWOC concept is applied to the ethanol case study. As it will be shown through this example, the PWOC problem has been solved more efficiently by applying the shrinking approach than without shrinking.

5. PWOC FOR THE ETHANOL PROCESS: RESULTS AND COMPARISON

The main purpose of this section is to show the application of PWOC to the bio-ethanol process described in Section 2 and to compare the obtained results to a typical decentralized SISO loops scheme. The decentralized architecture implemented for comparison uses seven PID control loops, in addition to the Local Control strategy introduced in Section 2. The paired PID loops (controlled-manipulated variable) are the following: E_4-G_2-F_0, G_4-F_{13}, x_{DE1}-R_1, x_{BE1}-VB_1, x_{DE2}-R_2, x_{BE2}-VB_2, where E_4, G_2, G_4, are the ethanol concentration in the fermentor and the glucose concentration in the saccharificator and in the fermentor, respectively. x_{DE1}, x_{BE1}, x_{DE2}, x_{BE2}, corresponds to the mol fractions of ethanol in the top and bottoms of the distillation and rectification columns, respectively. A special mention should be done regarding the control loop E_4-G_2-F_0, which is a cascade proposed due to the fact that the ethanol to be produced depends strongly on the glucose concentration (G_2) that comes from the saccharificator. Finally, it should be noticed that following recommendations given by Araujo (2007), and in order to do a fair comparison to the PWOC results, the controlled variables for the distillation and rectification columns in the decentralized loops are concentrations and not temperatures (or temperature differences), which are usually the real controlled variables at an industry level. On the other hand, the main objective of PWOC is to control the profitability at its maximum value, and therefore the pairing controlled-manipulated variable is avoided. In the following, the PWOC stages are applied in detail to the bio-ethanol process.

Stages 1-3: Identification and design of necessary control loops.

For the bio-ethanol process, the following control loops has been identified as *necessary local loops*: level control in all tanks, pH and temperature control in saccharificator and fermentor, and pressure control in flash, distillation and rectification. Additionally to these loops, as explained in section 2, a biomass control strategy is used. With exception of the loops involved in the biomass strategy, all local loops are SISO (e.g. PI or PID). After implementing the local loops, the process still has 7 available manipulated variables that are used as plantwide manipulated for maximizing the profitability of the process. These plantwide manipulated variables are: F_0, F_1, F_{13},VB_1, R_1,VB_2, R_2, corresponding to starch and enzymes input flow, recycle flow from the flash to the fermentor and vapour and reflux rates for each column.

Stage 4: Statement of Plantwide Profitability Function (Φ).

The following profitability objective function is proposed to be maximized for the ethanol process addressed in this work:

$$\begin{aligned}\Phi = {} & w_1 \int_{t_0}^{t_0+\Delta t_{opt}} x_{ED_2} D_2 \, dt - w_2 \int_{t_0}^{t_0+\Delta t_{opt}} F_0 S_0 dt + w_3 \int_{t_0}^{t_0+\Delta t_{opt}} x_{ED_2} dt \\ & - w_4 \int_{t_0}^{t_0+\Delta t_{opt}} F_4 dt - w_5 \int_{t_0}^{t_0+\Delta t_{opt}} VB_1 dt - w_6 \int_{t_0}^{t_0+\Delta t_{opt}} VB_2 dt \\ & - w_7 \int_{t_0}^{t_0+\Delta t_{opt}} x_{WD_2} D_2 dt - w_8 \int_{t_0}^{t_0+\Delta t_{opt}} x_{EB_1} B_1 dt - w_9 \int_{t_0}^{t_0+\Delta t_{opt}} x_{EB_2} B_2 dt\end{aligned} \quad (6)$$

where w_i are weighting factors. The first term in (6) is related to the productivity of the process (expressed as the product between the ethanol concentration and the distillate flow rate in the top of the rectification column); the second term penalizes raw material consumption; the third term is a quality soft constraint; the following three terms in the second line of the equation (accompanied by w_4, w_5 and w_6) are used for penalizing the energy consumption in the process (pumping power and steam consumption). Last part of the equation contains a term that penalizes the presence of water at the top of the rectification column (related to post-processing costs in the dehydration unit) and two terms associated to economic losses due to the presence of ethanol in the bottom of the columns. t_0 is the initial time for the optimization routine and Δt_{opt} is the prediction horizon over which the objective function and constraints are evaluated. Δt_{opt}=15 hours has been selected taking into account the slow dynamic response of the process to changes in its inputs.

Stage 5: Design of the Optimization-Based Control Strategy

In order to compare the one- and two-layer approaches, PWOC for the ethanol case study is addressed using these two approaches shown in Fig. 8. It must be noticed that the biomass control is run in cascade with the D-RTO layer (in both frameworks), from which it receives the optimal set point value that should be locally tracked. In both cases, the objective function to be maximized in the D-RTO layer is given by (6). The complete formulation of the optimization problem addressed in the D-RTO layers is given in (7). As can be seen, the decision variables of the optimization problem are the values for the u_{Pw}. The last inequality constraint is used inside the optimization loop for assuring that the solution of the optimization problem will guarantee a long-term ethanol concentration at the top of the rectification column (x_{ED2}) equal or higher than the concentration obtained if the plantwide manipulated variables were kept constant at u_{Pw}^* (values of the manipulated variables at the time t_0). The performance-type objective function Γ in the NMPC layer of the two-layer approach (bottom of Fig. 8) penalizes deviations of the ethanol concentration in the fermentor (E_4) and in the top of the rectification column (x_{ED2}), respectively, from their optimal set points values given by the D-RTO layer during a prediction horizon Δt_{mpc}=2 hours, as stated in (8). The terms Q and R are weighting matrices, which can be seen as tuning parameters for the NMPC. Schwartz et al. (2006) present a method for determining MPC tuning parameters that lead to optimal results from either an

operational or financial standpoint. Finally, the trigger conditions used in the simulation study for addressing the PWOC problem of the ethanol process are shown in Fig. 9.

$$\min_{u_{PW}} (-\Phi(\dot{x}, u, t_0, \Delta t))$$
$$\text{s.t. } f(\dot{x}, x, u, d, t) = 0 \quad (7)$$
$$x_i(t_0) = x_{0i}, u_{min} \le u \le u_{max}$$
$$x_{ED_2}\left(t_0 + \Delta t_{opt}, u_{PW}\right) \ge x_{ED_2}\left(t_0 + \Delta t_{opt}, u_{PW}{}^*\right)$$

$$\Gamma = \int_{t_{0,mpc}}^{t_{0,mpc}+\Delta t_{mpc}} Q(x_{ED2} - x_{ED2,opt})^2 dt + \int_{t_{0,mpc}}^{t_{0,mpc}+\Delta t_{mpc}} R(E_4 - E_{4,opt})^2 dt \quad (8)$$

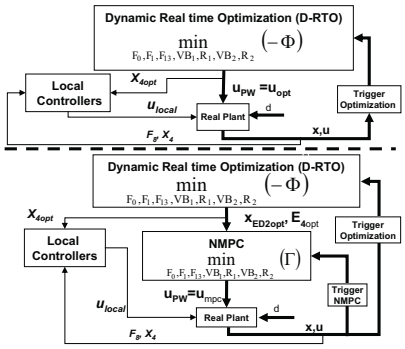

Fig. 8. Optimization-Based Control Strategies for the ethanol process: One-layer (top) and Two-layer (bottom)

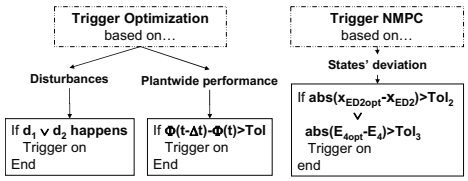

Fig 9. Trigger conditions for the ethanol PWOC: Optimization (left) and NMPC (right) layers.

The D-RTO problem was solved by the direct Sequential approach using a Monte Carlo localized random search optimization method, which is simple to implement, have broad applicability and do not require the computation of gradients (Spall, 2003). Basically, the algorithm consists of three main steps. First, an initial guess θ_0 of the optimal point is randomly picked and the number of iterations k, is set to zero. Second, an independent random vector d_k is generated, and added to the current optimal value θ_k. Third, it is checked if $-\Phi(\theta_k+d_k) < -\Phi(\theta_k)$; if this condition is satisfied, the new optimal value is set as $\theta_{k+1}=\theta_k+d_k$, otherwise, the second step is repeated (random generation of d_k). The algorithm stops when either, the maximum number of iterations has been reached or a convergence criterion has been fulfilled. For testing the PWOC approach, simulation studies were carried out using the nonlinear model of the process as the real plant. Results presented in this Section correspond to the simulation of the system starting at an optimal steady state. After 6 hours of operation at this steady state, a disturbance on the starch feed concentration enters the process (20% reduction of the starch concentration). At this moment, the optimization trigger is switched on and the D-RTO layer is called in order to calculate the new values for the plantwide manipulated variables that drive the process to optimal operation (maximal profitability). The localized random search method was used as previously explained for maximizing the profitability objective function, subject to the constraints given in (7). The optimization algorithm was selected to be run each time during 50 iterations after making a balance between performance and computational time for real-time implementation. The shrinking approach described in Section 4 was used for reducing the search space of the optimization problem. Specifically, the gain factors w_{ij} and $w_{i\Phi}$ in (3) were calculated using Digraphs. After calculating the gain factors, the standard deviation σ_{ui} of the Gaussian distribution that describes the probability of change of each manipulated variable for rejecting the disturbances was calculated as the maximum between different contribution terms. Then, precisely this Gaussian distribution for each manipulated variable was used for generating the vector d_k, in order to allow the optimization algorithm to make moves only in the region described by these distributions. Fig. 10 and 11 show the simulation results obtained of applying the PWOC to the ethanol case study, in presence of a disturbance on the feed concentration. PWOC was run using the two optimization-based control frameworks shown in Fig. 8. The first of these frameworks is the PWOC-one-layer (solid line) and the second is the PWOC-two-layer (dashed line). These two approaches are compared to the behaviour of the process when two different decentralized PID schemes are used, which in the following are denoted as: Decentralized 1 (described at the beginning of this section) and Decentralized 2. The only difference between both decentralized schemes is that in Decentralized 2, the E_4-G_2-F_0 loop is replaced by a D_2-F_0 loop, in order to keep constant the flow of product that goes to the dehydration unit. At this point it is important to remark that all the control approaches compared in this section use the Local Control Strategy mentioned in the Stages 1-3 of this Section, as part of the local control loops in the regulatory level. In the following Figures, the term *Two-layer SP* is used for denoting the set point values of the state variables E_4, x_{ED2} in the NMPC layer and for X_4 in the local control loop. These set point values are given by the D-RTO layer: $E_{4sp}=E_{4,opt}$, $x_{ED2,sp}= x_{ED2,opt}$ and $X_{4sp}=X_{4,opt}$. Also, the set point values for the state variables controlled in the decentralized schemes (including biomass concentration in the fermentor) correspond to the starting steady state values. Results shown in Fig. 10 are related to the fermentation section. It can be seen that using PWOC (both the one- and two-layer) results in a lower ethanol concentration in the fermentor than when using Decentralized schemes. Decentralized 1 achieves the highest ethanol concentration (E_4), which is not surprising because one of its control objectives is precisely to keep E_4 at its set point (original steady state value); and it is doing so by feeding a lower substrate flow rate (F_0), as shown in Fig 10-top-right. Fig 10-bottom-left shows the dynamic behaviour of the biomass concentration. It can be seen that both PWOC approaches keep a lower biomass concentration, due to the fact that they are actually tracking the optimal set point value, given by the D-RTO layer, and not just maintaining a fixed set point value (as done in the Decentralized schemes). At this point, analyzing the process as conventionally done as if it were

conformed just of a fermentation unit, wrong conclusions could arise, in which decentralized strategies will be claimed suitable enough or even, much better than the optimization-based approaches. However, it must be noticed that independently of the control scheme, the product of a bio-ethanol plant (after dehydration) is ethanol at purity higher or equal than 99.6% wt. Since the profitability of the plant is closely related to the net flow of this final product, and the latter is proportional to the net flow of ethanol in the fermentor output, which is given by $E_4 \times F_4$ (ethanol concentration × total output flow in the fermentor), then it can be concluded that the one- and two-layer approaches would lead the process to higher cumulative profitability values than the decentralized, because their total net flow of ethanol at the fermentor output is higher (See Fig. 10-bottom-right) in spite of their lower ethanol concentration. These results are confirmed in Fig 11, where the benefits of the PWOC approaches and the drawbacks of the decentralized schemes become evident when the profitability objective function (Fig 11-top) is compared for the different control approaches. Analyzing Fig 11, it is possible to conclude that PWOC results in a much more effective response to the disturbance than the Decentralized schemes, from an economical point of view. Specifically, the PWOC-one-layer reaches the highest cumulative profitability for the process, having at the same time the highest cumulative production rate and a higher ethanol concentration than the decentralized architectures. The PWOC-two-layer allows at the beginning a small decrease of its objective function (when compared to the initial value), despite the fact that this approach drives the process towards the highest product concentration (Fig 11-bottom-left). However, for the first 20 hours after the disturbance appearance, the two-layer approach kept the profitability on average at the same value than the starting steady state, and after this, it was able to improve its objective function value, reaching even at the end the same optimal value than the one-layer. Furthermore, it can be seen that the Decentralized schemes result not only in lower profitability, but also in lower product concentration and in the case of Decentralized 1, in the lowest cumulative flow of product. Of course, it can be argued that the product concentration resulting in the decentralized schemes is lower because precisely these controllers are doing their jobs regulating the controlled variables at their set point values. However, it must be noticed that regulation of the controlled variables at fixed set points might deteriorate the profitability of the process, because when a disturbance enters the process, the optimal operating point may also move. How much this point moves can not be generalized because it depends on the process and the nature of the disturbances, and in many cases disturbances can not be predicted. If well it is completely true that over the years process industry has been operating under fixed set point policies relying on PID SISO loops, without reporting enormous economical losses, it is also true as stated by Prett and García (1988), that the apparent savings in doing so (i.e. minimization of both design effort and maintenance) are in majority of cases nonexistent and in the long run result in more costs than the use of multivariate techniques. Following the analysis in Fig 11, comparing only the decentralized approaches, it is clear that Decentralized 2 is more convenient from an economic view, because at the end of the period, at least it reaches a profitability value close to the starting point, despite of resulting in less ethanol concentration in the fermentor (Fig 10-top-left).

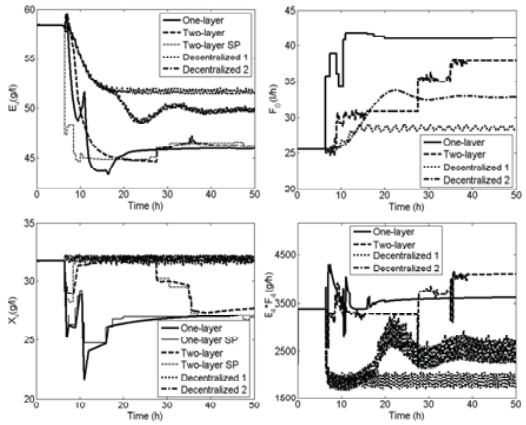

Fig. 10. PWOC results vs. decentralized control for the fermentation section: Ethanol Concentration (top-left), Starch Input Flow (top-right), Biomass Concentration (bottom-left) and Ethanol Net Flow (bottom-right).

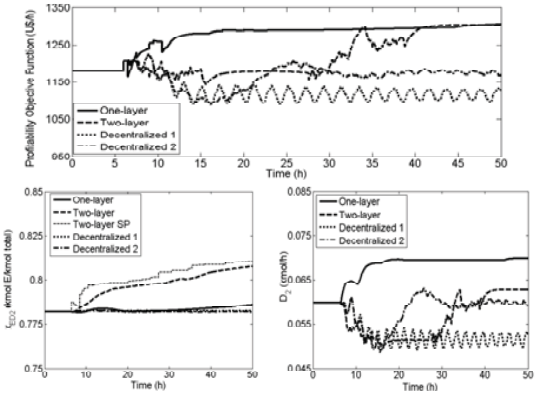

Fig. 11. PWOC results vs. Decentralized Control: Plantwide Profitability (top), Ethanol concentration in the distillate (left) and Distillate flow rate (right) at rectification section.

A final remark about the PWOC schemes should be done. If well both approaches reach the same profitability value at the end of the period (50 hours), and the two-layer has an optimal behaviour from a performance point of view (which is its "final" objective function), it might not be satisfactory at all from an economic view. Finally, it is important to highlight that independently of the optimization-based control framework selected (one or two-layer), the PWOC improves the profitability of the process when compared to the decentralized control strategies, and thus, it is a promising alternative for addressing the plantwide control problem of chemical or biochemical processes in which the profitability of the process is at risk when disturbances appear. On the other hand, in order to evaluate the performance of the shrinking approach, several simulation studies applying the PWOC with shrinking and without shrinking the search

region of the optimization problem were carried out. Fig. 12 shows the advantages of the shrinking approach. By running the optimization algorithm using the same number of iterations in the two cases, the shrinking approach has not only achieved a higher profitability, but also applied smoother control actions, which is an important fact for the stability of the process and is in general desirable.

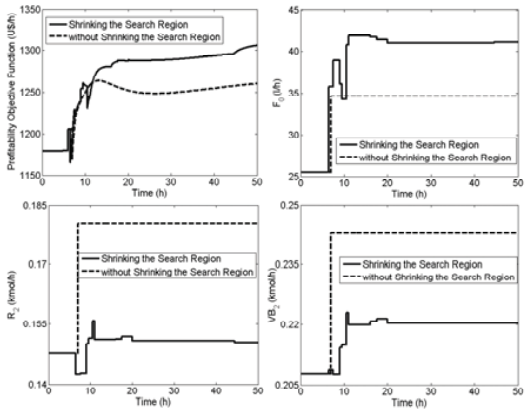

Fig. 12. One- layer PWOC: Shrinking vs. without Shrinking the Search Region. Profitability (top-left), Starch Input Flow (top-right), Reflux rate in the rectification (bottom-left) and Vapour flow rate to the rectification (bottom-right).

Analyzing the profiles for F_0, R_2 and VB_2 (Fig 12), it can be seen that when no shrinking is used (dashed lines) each manipulated variable change in a step-type policy with higher amplitude and longer period than when using shrinking (solid lines). Finally, it must be noticed that the main advantage of using the shrinking approach is that the probability of change for each manipulated variable is a function of the capability that each of them has for rejecting each disturbance (or the number of disturbances that occur at the same time, including those unknown), that means that the optimization algorithm does not waste time testing large changes in the manipulated variables that just reject in a weak way (or are not able to reject) the disturbances. When no shrinking is used, each manipulated variable is allowed to change from its lower to its upper bound, without any restriction, whereas the shrinking approach bounds the search region according to the standard deviation calculated for each manipulated variable, and it is precisely this standard deviation that contains the information about the cause-effect relationship between each manipulated variable and each disturbance.

6. CONCLUSIONS

A Plantwide Optimizing Control (PWOC) approach for bioprocesses has been presented based on the Optimizing Control concept. The main stages for PWOC and a stochastic-based shrinking approach for reducing the search space of the optimization problem have been introduced. PWOC has been applied to the bio-ethanol process, showing much better results from an economical point of view than when the process is only controlled by conventional control loops. It has been shown that PWOC is a very promising alternative for controlling chemical or biochemical processes in which the economical feasibility is at risk when disturbances appear. Finally, the shrinking approach was successfully tested resulting in an improvement of the optimization routine for real-time applications (i.e. higher productivities were obtained for the same number of iterations during optimization). Future work will be directed towards extending the shrinking approach for being applied with deterministic optimization methods.

ACKNOWLEDGMENTS

The authors acknowledge support from the Cluster of excellence "Unifying Concepts in Catalysis" coordinated by the Berlin Institute of Technology and funded by the German Research Foundation–Deutsche Forschungsgemeinschaft. Silvia Ochoa gratefully acknowledges financial support from DAAD and the Antioquia University of Colombia.

REFERENCES

Araujo, A.C.B., Hori, E.S. and Skogestad, S. (2007). Application of plantwide control to the HDA process. II Regulatory control. *Ind. Eng. Chem. Res.*,46, 5159-5174.

Araujo, A.C.B. (2007). *Studies on Plantwide Control*. Ph.D. Thesis. Norwegian University of Science & Technology.

Arifeen, N., Wang, R., Kookos, I. K, Webb, C., and Koutinas, A.A. (2007). Process Design and Optimization of Novel Wheat-Based Continuous Bioethanol Production System. *Biotechnol. Prog.* 23, 1394. 1403

Bartee, J.F., Macharia, M.A., Noll, P.D. and Tay, M.E. (2008). Integrated model predictive control of batch and continuous processes in a biofuel production process. *US Patent Application US2008/0109200 A1*.

Bartusiak, R.D. (2007). NLMPC: A platform for optimal control of feed- or product-flexible manufacturing. In: Findeisen, R. et al. (eds.). *Assessment and future directions of NMPC*. Springer-Verlag, Berlin, 367-381.

Biegler, L.T. and Zavala, V.M. (2009). Large-scale nonlinear programming using IPOPT. *Comp. Chem. Eng.*, 33, 575.

Buckley, P.S. (1964). *Techniques of Process Control*. John Wiley & Sons, Inc. New York.

Cheng, R., Forbes, J.F. and Yip, W.S. (2007). Price-driven coordination method for solving plant-wide MPC problems. *Journal of Process Control*, 17, 429-438.

Costa, A.C., Meleiro, L.A.C. and Filho, R.M. (2002). Non-linear predictive control of an extractive alcoholic fermentation process. *Process Biochemistry*, 38, 743-750

Costa, A.C., Atala, D.I.P., Filho, R.M. and Maugeri, F. (2001). Factorial design and simulation for optimization and determination of control structures for extractive alcoholic fermentation. *Proc. Biochem.,* 37, 125-137.

Duvall, P.M. and Riggs, J.B. (2000). On-line optimization of the Tennessee Eastman challenge problem. *Journal of Process Control*, 10, 19-33.

Engell, S. (2007). Feedback control for optimal process operation. *Journal of Process Control,* 17, 203-219.

Findeisen, W., Bailey, F.N., Brdys, M., Malinowski, K., Tatjewski, P. and Wozniak, A. (1980). *Control and coordination in hierarchical systems*. Wiley.

Franke, R. and Doppelhamer, J. (2007). Integration of advanced model based control with industrial IT. In

Findeisen, R. et al. (eds.). *Assessment and future directions of NMPC*. Springer-Verlag, Berlin, 399-406.

Franke, R. and Vogelbacher, L. (2006). Nonlinear model predictive control for cost optimal startup of steam power plants. *Automatisierungstechnik*, 54, 630-637.

Garcia, C.E. and Morari, M. (1984). Optimal operation of integrated processing systems. Part II: Closed-loop on-line optimizing control. *AIChE Journal*, 30, 226-234.

Jia, D. and Krogh, B.H. (2001). Distributed model predictive control. *IEEE Proc. American Control Conference*.

Jockenhövel, T., Biegler, L.T. and Wächter, A. (2003). Dynamic optimization of Tennessee Eastman process using OptControlCentre. *Comp. Chem. Eng.*, 27, 1513.

Kadam, J.V. and Marquardt, W. (2007). Integration of economical optimization and control for transient process operation. In: Findeisen, R. et al. *Assessment and future directions of NMPC*. Springer, Berlin, 419-434.

Kadam, J.V. and Marquardt, W. (2004). Sensitivity-based solution updates in closed-loop dynamic optimization. *DYCOPS 7 Proceedings*.

Kadam, J.V., Marquardt, W., Schelegel, M., Backx, T., Bosgra, O.H., Brouwer, P.J., Dünnebier, G., van Hessem, D., Tiagounov, A. and de Wolf, S. (2003). Towards integrated dynamic real-time optimization and control. *FOCAPO Conference Proceedings,* 593-596.

Kadam, J.V., Schlegel, M., Marquardt, W., Tousain, R.L., v. Hessem, D.H., Berg, J.v.d. and Bosgra, O.H. (2002). A two-level strategy of integrated dynamic optimization and control of industrial processes. *ESCAPE 12*, 511-516

Küpper, A. and Engell, S. (2008). Engineering of Online Optimizing Control - A Case Study: Reactive SMB Chromatography. *Proc. 17th IFAC World Congress.*

Larsson, T., Govatsmark, M.S., Skogestad, S. and Yu, C.C. (2003). Control structure selection for reactor, separator, and recycle processes. *Ind. Eng. Chem. Res.*, 42, 1225.

Lausch, H.R., Wozny, G., Wutkewicz, M. and Wendeler, H. (1998). Plant-wide control of an industrial process. *Trans. IChemE Part A*, 76, 185-192.

Lu, J.Z. (2003). Challenging control problems and emerging technologies in enterprise optimization. *Control Engineering Practice*, 11, 847-858.

Luyben, M.L., Tyreus, B.D. and Luyben, W.L. (1997). Plantwide control design procedure. *AIChE Journal*, 43, 3161-3173.

Manenti, F. and Rovaglio, M. (2007). Integrated multilevel optimization in large-scale poly(ethylene terephthalate) plants. *Ind. Eng. Chem. Res.*, 47, 92-104.

Maurya, M.R., Rengaswamy, R. and Venkatasubramanian, V. (2003). A systematic framework for the development and analysis of signed digraphs for chemical processes. *Ind. Eng. Chem. Res.,* 42, 4811-4827.

McAvoy, T.J. and Ye, N. (1993). Base control for the Tennessee Eastman process. *Comp. Chem. Eng.*, 18, 383.

Meleiro, L.A.C., Von Zuben, F.J. and Filho, R.M. (2008). Constructive learning neural network applied to identification and control of a fuel-ethanol fermentation process. *Eng. Applic. Artificial Intelligence,* 22, 201-215.

Mercangöz, M. and Doyle, F.J. (2007). Distributed model predictive control of an experimental four-tank system. *Journal of Process Control*, 17, 297-308.

Ochoa, S., Repke, J.U. and Wozny, G. (2009). Integrating Real-Time Optimization and Control for Optimal Operation: Application to the Bio-ethanol Process. *Biochem. Eng. J.* In press. doi:10.1016/j.bej.2009.01.005

Olofsson, K., Rudolf, A. and Liden, G. (2008). Designing SSF for improved xylose conversion by a recombinant strain of *S. cerevisiae*. *J. Biotechnol.* 134, 112–120

Prett, D.M. and Garcia, C.E. (1988). *Fundamental Process Control*. Butterworth. Stoneham.

Rawlings, J.R. and Stewart, B.T. (2008). Coordinating multiple optimization-based controllers: New opportunities and challenges. *J. Proc. Control*, 18, 839.

Robinson, D., Chen, R., McAvoy, T. and Schnelle, P.D. (2001). An optimal control based approach to designing plantwide control system architectures. *Journal of Process Control*, 11, 223-236.

Roman, R., Nagy, Z.K., Cristea, M.V. and Agachi, S.P. Dynamic modelling and nonlinear model predictive control of a fluid catalytic cracking unit. *Computers and Chemical Engineering*, 33, 605-617.

Scattolini, R. (2009). Architectures for distributed and hierarchical model predictive control – a review. *J. Proc. Control*, In press. doi:10.1016/j.jprocont.2009.02.003

Schwartz, J.D. Wang, W. and Rivera, D.E. (2006). Simulation-based optimization of process control policies for inventory management in supply chains. *Automatica*, 42, 1311-1320.

Spall, J.C. (2003). *Introduction to Stochastic Search and Optimization*. John Wiley & Sons, Inc., Hoboken, NJ.

Stephanopulous, G., and Ng, C. (2000). Perspectives on the synthesis of plant-wide control structures. *Journal of Process Control*, 10, 97-111.

Sun,Y. and El-Farra, N.H. (2008). Quasi-decentralized model-based networked control of process systems. *Computers and Chemical Engineering*, 32, 2016-2029.

Toumi, A. and Engell, S. (2004). Optimization-based control of a reactive simulated moving bed process for glucose isomerization. *Chem. Eng. Sci.*, 59, 3777-3792.

Tosukhowong, T., Lee, J.M., Lee, J.H. and Lu, J. (2004). An introduction to dynamic plant-wide optimization strategy for an integrated plant. *Comp. Chem. Eng.*, 29, 199-208.

Venkat, A.N., Rawlings, J.B. and Wright, S.J. (2007). Distributed model predictive control of large-scale systems. In: Findeisen, R. et al. (eds.). *Assessment and future directions of NMPC*. Springer, Berlin, 591-605.

Venkat, A.N. (2006). *Distributed model predictive control: Theory and applications*. Ph.D. Dissertation, University of Wisconsin-Madison.

Ying, C.M. and Joseph, B. (1999). Performance and stability analysis of LP-MPC and QP-MPC cascade control systems. *AIChE Journal*, 45, 1521-1534.

Zavala, V.M., Laird, C.D. and Biegler, L.T. (2007). Fast implementations and rigorous models: Can both be accommodated in NMPC?. *International Journal of Robust and Nonlinear Control*, 18, 800-815.

Zhen, A. Mahajanam, R.V. and Douglas, J.M. (1999). Hierarchical procedure for plantwide control systems synthesis. *AIChE Journal*, 45, 1255-1265.

A new approach for the modelling of crystallization processes in impure media using Population Balance Equations (PBE)

François Févotte[*] and Gilles Févotte[**]

** 99, Avenue de Verdun. 92130 Issy les Moulineaux (France)*
*** Ecole des Mines de Saint Etienne, Centre SPIN. 158, Cours Fauriel. 42000 Saint Etienne & Université Lyon 1, 43, Avenue A. Einstein, 69622 Villeurbanne, Cedex (France). fevotte@emse.fr*

Abstract: For obvious industrial and theoretical reasons the problem of accounting for the effect of impurities in the population balance modelling of solution crystallization processes is a very important issue, and yet it has never been reported until today. Meanwhile, several kinetic models are proposed in the literature that relate the effect of impurities on the crystal growth and could be used for PBE modelling. The goal of the present paper is to address this issue and to present a new method, based on characteristics, which is shown to efficiently solve the difficulties raised by the specificity of the mathematical formulation of the Population Balance Equation (PBE) in the presence of impurities. Indeed, as far as hindering effects of the impurities on the crystal growth are concerned, it turns out that the "age" of the particles (i.e. the time they spent in the presence of impurities) might plays a key-role in the overall dynamic crystallization process. Accounting for such a new internal variable required a specific PBE resolution algorithm to be developed and evaluated.

Keywords: Chemical industry, Crystallization, Characteristic curves, Nucleation, Modeling, Population balance equations, Numerical simulation, Batch processes.

1. INTRODUCTION

1.1 Population Balance Equations (PBE) and crystallization

The formalism of Population Balances Equations (PBEs) is a widely used modelling tool in engineering, with applications including crystallization, powder technologies, polymerization processes, biotechnologies, etc (Ramkrhisna and Mahoney, 2002). PBEs allow describing the time variations of properties of a large number of separate entities, such as particles, bubbles or droplets, interacting with each other and/or with their environment which usually consists of a continuous phase. The dynamics of complex distributed particulate systems is related through the evolution of appropriate distribution functions evolving in a p-dimensional space where p represents the number of internal coordinates required to characterize the particles. Internal coordinates refer to continuous properties of the individual dispersed entities such as size, composition, cristallinity, etc, or to discrete features such as the number of primary crystals in agglomerates or the number of free radicals in a polymerizing particle during emulsion polymerization reactions. In addition to internal coordinates, external coordinates are necessary to describe the physical location of the distributed entities.

As far as dispersed phases are concerned (i.e. separate entities in a continuous fluid phase), the governing equations involve the number density of particles, which is defined as follows:

$$E[n(\boldsymbol{x},\boldsymbol{r},t)] \equiv \psi(\boldsymbol{x},\boldsymbol{r},t), \quad \boldsymbol{x} \in \Omega_x \ , \qquad \boldsymbol{r} \in \Omega_x \tag{1}$$

As already mentioned, external and internal coordinates (i.e. $\boldsymbol{r}$ and $\boldsymbol{x}$, respectively) are necessary to characterize the "location" and the properties of the particles. Equation (1) actually means that the average number of particles in the particle state subspace $dV_x dV_r$ with coordinates $(\boldsymbol{x},\boldsymbol{r})$ is given by $\psi(\boldsymbol{x},\boldsymbol{r},t)\ dV_x dV_r$.

For the sake of simplicity $(\boldsymbol{x},\boldsymbol{r})$ is usually referred to as the particle state and, as outlined by Ramkrishna (2000), it is worth noting that the further definition of PBEs requires the average number density function $\psi(\boldsymbol{x},\boldsymbol{r},t)$to be sufficiently smooth for allowing differentiation with respect to the coordinates and time.

According to the previous definitions, the number $\mathcal{N}$ of particles belonging to a given subset $A_x \subset \Omega_x$ is given by:

$$\mathcal{N}(\boldsymbol{r},t) = \int_{A_x} \psi(\boldsymbol{x},\boldsymbol{r},t)\, dV_x \tag{2}$$

The previous mathematical formalism will now be applied to the time variations of crystals (i.e. solid particles generated during a crystallization process) characterized by some internal coordinates x. The rate of variation of $\boldsymbol{x}$ is referred to as $\dot{\boldsymbol{X}}$ in the following:

$$\frac{dx}{dt} = \dot{\boldsymbol{X}}(\boldsymbol{x}\,,\boldsymbol{r}\,,\boldsymbol{y}\,,t) \tag{3}$$

where y represents any scalar variables required to quantify the possible interactions (e.g. through heat or mass transfer) between the particles and the continuous phase.

Considering that the following operating conditions are verified:

1. The solution crystallization process takes place in a well mixed batch reactor,

2. new crystals are generated through nucleation phenomena only (i.e. according to the "classical" nucleation theory, the size of new particles appearing in the dispersed phase is the critical size L^* which can be assumed negligible. Agglomeration and breakage of the particles are both neglected),

the population balance equation relating the time variations of the particle state is:

$$\frac{\partial}{\partial t}\psi(\boldsymbol{x},t) + \nabla_x \dot{\mathbf{X}}(\boldsymbol{x},y,t)\,\psi(\boldsymbol{x},t) = h(\boldsymbol{x},y,t) = 0 \qquad (4)$$

with the following boundary conditions:

$$\begin{aligned}\dot{\mathbf{X}}(0,\boldsymbol{x}',y,t)\,\psi(0,\boldsymbol{x}',t) &\\ \cong \dot{\boldsymbol{X}}(L^*,\boldsymbol{x}',y,t)\,\psi(L^*,\boldsymbol{x}',t) &\\ = R_N(y,t)&\end{aligned} \qquad (5)$$

where the vector of internal coordinates is decomposed as:

$$\boldsymbol{x} = (L,\boldsymbol{x}')$$

The first assumption above implies that the number density function does not depend on space coordinates while assumption 2 means that, in order to express the source of new particles in the system, one has only to define boundary conditions to account for the expression of the rate(s) of nucleation of crystals (i.e. $h(\boldsymbol{x},y,t)=0$ in (4)).

In the mono-dimensional case where one characteristic size of the particle only is considered (e.g. the diameter L of a fictitious spherical particle exhibiting the same projected area than the crystal under consideration), (4) reduces to the well-known following partial differential equation allowing to compute the time variations of the Crystal Size Distribution (CSD). In the following, y is the supersaturation of the continuous liquid phase σ, defined by (9), which will now be omitted for the sake of simplicity:

$$\begin{cases} \dfrac{\partial\psi(L,t)}{\partial t} + G(t)\dfrac{\partial\psi(L,t)}{\partial L} = 0 & (6)\\ \psi(L,0) = 0 \quad or \quad \psi(L,0) = \psi_{seed} & (7)\\ \psi(0,t) \cong \psi(L^*,t) = \dfrac{R_N(t)}{G(t)} & (8)\end{cases}$$

The initial condition (7) accounts for the possibility of the crystallization to start through primary nucleation (i.e. no solid phase is initially present in the crystallizer) or through seeding. Seeding consists in the introduction of small amount of particles, usually sieved, in the supersaturated solution. The seed particles initiate the crystallization process and are characterized by their size distribution ψ_{seed}.
R_N is the rate of nucleation in $\#.s^{-1}.m^{-3}$ and G is the crystal growth rate in m/s.

1.2 Growth rates and impurities

In most published PBE modelling studies —according to McCabe's hypothesis— the growth rate $G(t)$ is assumed not to depend on the particle size but essentially on the driving force of crystallization, the following absolute definition of the supersaturation σ is now defined as:

$$\sigma(t) = C(t) - C^* \qquad (9)$$

where C^* is the equilibrium concentration (i.e. the temperature-dependant solubility of the crystallizing compound) and $C(t)$ is the solute concentration.

Several theoretical or phenomenological expressions can be found in the literature to express the supersaturation-dependency of the growth rate which, more or less, turns out to obey the following kinetic law:

$$G(t) = \frac{dL}{dt} = k_g(C(t) - C^*)^i = k_g\sigma(t)^i \qquad (10)$$

exponent i was shown to depend on the involved growth mechanism(s) which, in particular, depend(s) on the level of supersaturation (Mersmann A, 2002; Mullin J.W., 1993; Chernov, 2004). In practice, consistently with usual theoretical models, most published values of i are given between 1 and 2.

Actually, modeling and control papers published in the field of crystallization engineering deal essentially with pure solute/solvent systems. As far as one considers the context of industrial processes, this is obviously an unrealistic assumption. Indeed, it is worth noting that industrial processes cannot avoid undesirable impurities to be generated during the many chemical reactions preceding the crystallization steps. It is well-known that even minute concentrations of impurities present in the initial solution can affect the crystallization processes (Chernov, 2004; Sangwal, 1996; Wood, 2001) and induce significant reductions of the growth rate (Keshra & Sangwal, 1996; Kubota et al., 2000; Kubota, 2001).

It is also known that impurities can lead to supersaturation thresholds below which the development of crystallization is completely inhibited (see e.g. Sangwal, 2002). To the best of our knowledge, such key-features of "real" industrial crystallization processes (i.e. processes performed in the unavoidable presence of impurities) were investigated through the observation of single crystals, and never described using PBEs. Therefore it remains important to evaluate quantitatively the distribution and the time-variations of the detrimental effects of impurities during crystallization processes.

Now, if one considers the variety of the techniques which were proposed to solve the PBEs in the case of crystallization processes, it appears that few of these methods are based on

the method of characteristics (MOC). It is however known that MOCs avoid numerical diffusion errors and oscillatory solutions caused by the discretization of the involved growth term, especially when steep or discontinuous particulate phenomena take place in suspension (Kumar and Ramkrishna, 1997; Briesen, 2006).

Quamar and Warnecke (2007) have proposed a numerical method for solving PBEs involving nucleation, growth and aggregation processes. The scheme combines a method of characteristics for computing the growth term, with a finite volume technique for calculating aggregation terms. The method is compared to a finite volume scheme through the modelling of "academic" situations for which analytical solutions are available (i.e. combination of crystal growth with aggregation or nucleation). The authors show that the numerical scheme based on MOC is more efficient than pure finite volume schemes, and that it better tracks steep variations of number density functions. This interesting feature of MOC is attributed to the disappearance of the advection term $\partial G\psi/\partial L$ from the main PBE.

Sotowa et al. (2000) compared the numerical resolution of a simple crystallization PBE using a finite difference method and the method of characteristics. The study aimed at evaluating the impact of numerical dispersion on the design of feedback controllers. It was finally concluded that, as far as the simulation of control systems is concerned, the method of characteristics is recommended as a numerical technique for simulating crystallization processes.

More recently, in order to simulate the growth of anisotropic particles, Briesen (2006) proposed a reduced two-dimensionnal PBE model. Here, the MOC approach is used to validate the calculations. The application deals with the crystallization of potassium dihydrogen phosphate which is assumed to exhibit the shape of parallelepipeds terminated by two tetragonal pyramids. However, the simulation assumes initial seeding of the crystallization process only, i.e. no primary or secondary nucleation is taken into account, which is a rather questionable assumption. It should also be noticed that no specific information is reported about the MOC used.

It is the goal of the present paper to address the problem of accounting for the "birthdate" of crystals in the governing crystallization PBE, and to propose a new numerical scheme, based on MOC, for the resolution of the latter PBE. In fact, it is clear that the approach proposed by Kumar and Ramkrishna (1996a,b, 1997) in their series of three papers is much more "advanced" than the approach presented here, in terms of the accuracy of the used size integration technique and with respect to the ability of the method to describe agglomeration and breakage phenomena. Nevertheless, the present algorithm offers another way of considering nucleation phenomena and, through its great simplicity, could be valuable for applications where fast computation is required (i.e. for in-line feedback control applications for example).

2. MODELING THE CRYSTAL GROWTH RATE IN THE PRESENCE OF IMPURITIES.

2.1 The pinning mechanism

With respect to the growth of crystals in pure solvent, the time-averaged advancement velocity of a step in impure media appears to be hindered by the adsorption of impurity species on the growing crystal surface. Indeed, as Fig. 1 schematically shows, during the step advancement, kink sites can be blocked by foreign species that cannot easily be incorporated in the crystal lattice. To allow further crystal growth, the growth-step has to circumvent the pinned impurity, which obviously reduces the overall growth rate. Several models describing such a pinning mechanism were early described in the literature (see e.g. Cabrera & Vermilyea, 1958). Moreover, it is worth noting that many convincing observations of the pinning mechanism were reported, using e.g. advanced imaging techniques such as AFM (Atomic Force Microscopy, see e.g. Land et al., 1999, Thomas et al., 2004).

Kubota-Mullin's model (1995) was proposed to describe the pinning mechanism through Γ, the ratio between the step velocities in pure (u_0) and impure (u) media. Γ is given by the following expression:

$$\Gamma = \frac{u}{u_0} = 1 - \left[\frac{\gamma a}{kT\sigma d}\right]\theta = 1 - \alpha\theta \qquad (11)$$

where γ is the edge free energy, a is the size of the growth unit, T is the absolute temperature, k is the Boltzmann constant and θ is the fraction of coverage of active growing crystal surface by adsorbed impurities, d is the average distance between actives growth sites.

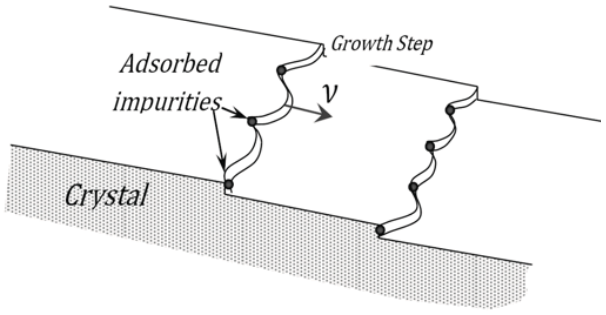

Fig. 1. Adorption of impurities at kink sites on the growing steps after Kubota (2001).

Parameter α is an effectiveness factor which quantifies the efficiency of the impurity specie in hindering the crystal growth. It is very important to notice that α does not only depend on properties of the involved solid, but also on supersaturation.

The coverage of the crystal surface by impurities is itself a stable dynamic process which therefore reaches a steady-state

θ^*. According to the hypotheses set to describe the adsorption process, various theoretical approaches can be used to compute the equilibrium coverage parameter θ^*.

In Kubota-Mullin's Model (Kubota & Mullin, 1995; Kubota et al., 1997), the equilibrium coverage of the growing surface is estimated thanks to Langmuir's adsorption theory:

$$\theta^* = KC_i/(1+KC_i) \quad (12)$$

where K is the Langmuir adsorption constant and C_i is the concentration of impurity.

Even though the adsorption process is often regarded as instantaneous (i.e., the steady-state coverage θ^* is reached instantaneously), it was shown that the dynamics of the adsorption of impurity species on the crystal surface cannot always be neglected. This is the reason why, as a first phenomenological approximation, the transient behavior of the coverage process was proposed by Kubota (2001) to obey a first-order dynamics:

$$\theta = \theta^* (1-\exp(-t/\tau)) \quad (13)$$

where τ is the time constant of the coverage dynamic process.

As the crystal growth rate is usually assumed to be proportional to the step velocity, it finally turns out that G depends on both time and supersaturation while in "usual" crystallization approaches dealing with pure media, G is assumed to depend only on σ(t). Combining equations (10) to (13) leads to the following expression where ν is the time at which the crystal surface is set in contact with impure liquid phase (i.e. the time of nucleation):

$$\begin{aligned} G(t) &= k_g \sigma(t)^i \left(1 - \alpha \frac{KC_i}{1+KC_i}\left[1 - \exp\left(-\frac{(t-\nu)}{\tau}\right)\right]\right) \\ &= G_0(t)\left(1 - \alpha \frac{KC_i}{1+KC_i}\left[1 - exp\left(-\frac{(t-\nu)}{\tau}\right)\right]\right) \end{aligned} \quad (14)$$

2.2 Expression of the PBEs accounting for Kubota-Mullin's model of impurities adsorption.

Applying the previous impurity adsorption model (14) is not straightforward as it increases the dimension of the problem: the time (t-ν) spent by the crystals in contact with impurities should now be accounted for. To this effect, we introduce a population density function ϕ depending on the "classical" variables, L and t, as well as ν:

$$\begin{cases} \dfrac{\partial \phi(L,t,\nu)}{\partial t} + G(t,\nu)\dfrac{\partial \phi(L,t,\nu)}{\partial L} = 0 & (15) \\ \phi(L,0,\nu) = 0 & (16) \\ \phi(0,t,\nu) = \dfrac{R_N(t)}{G(t,\nu)}\delta(t-\nu) & (17) \end{cases}$$

The standard definition of the crystal size distribution can still be retrieved as:

$$\psi(L,t) = \int_0^\infty \phi(L,t,\nu)d\nu = \int_0^t \phi(L,t,\nu)d\nu \quad (18)$$

3. A METHOD OF CHARACTERISTICS FOR SOLVING POPULATION BALANCE EQUATIONS ACCOUNTING FOR IMPURITY EFFECTS.

3.1 A method of characteristics for monodimensional PBEs without impurities.

Actually, the supersaturation σ(t) given by Eq. (9), is the driving force of the crystallization process. The decrease of the solute concentration $C(t)$ is caused by the generation of crystals: the molecules of solute initially present in the liquid phase are transferred through crystallization to the dispersed solid phase. The total amount of solid is therefore given by the total volume of solid after integrating the whole CSD:

$$\begin{aligned} C_s(t) &= \rho_s \varphi_p \int_{L^*}^\infty \psi(L,t) L^3 dL \\ &\cong \rho_s \varphi_p \int_0^\infty \psi(L,t) L^3 dL \end{aligned} \quad (19)$$

where ρ_s (kg/m^3) is the density of the solid compound, and φ_p is a volumetric particle shape factor (φ_p is equal to $\pi/6$ if one assumes ideally spherical particles.)

An elementary mass balance of the solute allows computing the evolutions of $C(t)$ and consequently yields σ(t) through (9), provided that the solubility curve is known.

Assuming first that the crystallization takes place in pure solvent, the PBE system (6-8) is expressed as follows where the growth rate $G(t)$ is a complex function of physical and kinetic variables depending on σ(t) and, through the indirect size-dependency of the solute concentration $C_s(t)$, on the overall current size distribution $\psi(L,t)$:

$$\begin{cases} \dfrac{\partial \psi(L,t)}{\partial t} + G(t)\dfrac{\partial \psi(L,t)}{\partial L} = 0 & (20) \\ \psi(L,0) = 0 & (21) \\ \psi(0,t) = \dfrac{R_N(t)}{G(t)} & (22) \end{cases}$$

In the sequel, it is clear that the process is operated in supersaturated conditions (i.e. $\sigma > 0$), the following condition is therefore always fulfilled:

$$\forall t \in \mathbb{R}^+, \forall \nu \in [0,t\,], \quad G(t) > 0 \quad (23)$$

Now, the following characteristic curves are considered:

$$\forall t \in \mathbb{R}^+, \quad \forall \nu \in [0,t\,] \;, \quad \tilde{L}_\nu(t) = \int_\nu^t G(t')dt' \quad (24)$$

As represented in Figure 2, the CSD along a given characteristic curve is defined as follows:

$\tilde{\psi}_\nu(t) = \psi\left(\tilde{L}_\nu(t), t\right)$, so that one can write:

$$\frac{d\tilde{\psi}_\nu(t)}{dt} = \frac{\partial\psi\left(\tilde{L}_\nu(t),t\right)}{\partial t} + \frac{d\tilde{L}_\nu(t)}{dt}\ \frac{\partial\psi\left(\tilde{L}_\nu(t),t\right)}{\partial L}$$
$$= \frac{\partial\psi\left(\tilde{L}_\nu(t),t\right)}{\partial t} + G(t)\ \ \frac{\partial\psi\left(\tilde{L}_\nu(t),t\right)}{\partial L}$$
$$\frac{d\tilde{\psi}_\nu(t)}{dt} = 0 \qquad (25)$$

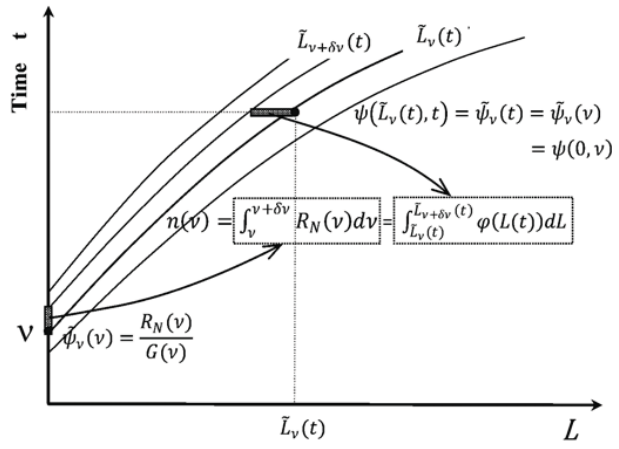

Fig. 2. Schematic representation of the relationship between the number of particles nucleated at time ν and the overall distribution at time t.

It therefore turns out that $\tilde{\psi}_\nu$ does not depend on t, which implies that the solution of (20) is fully determined by the boundary condition (22) and the resolution of (24) describing the time evolutions of the characteristic curves:

$$\forall t \in \mathbb{R}^+,\ \ \forall\, \nu \in [0,t\,]\ \ ,$$
$$\psi\left(\tilde{L}_\nu(t),t\right) = \tilde{\psi}_\nu(\nu) \qquad (26)$$
$$= \tilde{\psi}_\nu(t)$$
$$= \psi(0,\nu)$$
$$\psi\left(\tilde{L}_\nu(t),t\right) = \frac{R_N(\nu)}{G(\nu)} \qquad (27)$$

Now, let us show that equation (27) allows determining the CSD for every size and time, *i.e.* every point (L,t) in the phase space can be represented as $\left(\tilde{L}_\nu(t),t\right)$. To this effect, the following application is considered:

$\lambda_t\colon [0,t\,] \to \mathbb{R}^+, \quad \nu \mapsto \tilde{L}_\nu(t)$

$\forall t \in \mathbb{R}^+$, λ_t is clearly continuous and

$\forall t \in \mathbb{R}^+,\ \forall\, \nu \in [0,t\,]\ ,\ \ \frac{d\lambda_t}{d\nu}(\nu) = -G(\nu)$

which, given (23), shows that λ_τ is strictly decreasing and therefore invertible from [0,*t*] to [0, $\tilde{L}_0(t)$]. It follows that the characteristic curves do not exhibit shock or rarefaction.

A means of computing the distribution density function is therefore given by:

$\forall t \in \mathbb{R}^+, \forall L \in [0,\tilde{L}_0(t)]$,

$$\psi(L,t) = \frac{R_N(\lambda_t^{-1}(L))}{G\left(\lambda_t^{-1}(L)\right)} \qquad (28)$$

3.2 Semi-discretization of the size population density function.

Considering successive sampling times, the time variable ν is discretized as follows:

$$\forall t \in \mathbb{R}^+, \forall\, \nu \in [0,t\,],\ L_i(t) = \tilde{L}_{\nu_i}(t)$$
$$\Psi_{\mathrm{i}}(\mathrm{t}) = \int_{\mathrm{L_i(t)}}^{\mathrm{L_{i-1}(t)}} \psi(L,t)dL \qquad (29)$$

From (28), and setting the following change of coordinates:

$$\begin{cases} \nu = \lambda_t^{-1}(L) \\ L = \tilde{L}_\nu(t), \qquad \dfrac{dL}{d\nu} = -G(\nu) \end{cases}$$

we get:

$$\Psi_{\mathrm{i}}(\mathrm{t}) = \int_{\mathrm{L_i(t)}}^{\mathrm{L_{i-1}(t)}} \psi(L,t)\,dL$$
$$= \int_{\nu_{\mathrm{i-1}}}^{\nu_{\mathrm{i}}} \psi\left(\tilde{L}_\nu(t),t\right) G(\nu)\,d\nu$$
$$= \int_{\nu_{\mathrm{i-1}}}^{\nu_{\mathrm{i}}} R_N(\nu)\,d\nu \qquad (30)$$

As illustrated by Fig.2, it finally turns out that integrating ψ in size between L_i (t) and L_{i-1} (t), at a given time *t,* amounts to integrating ψ in ν between $\nu_{\mathrm{i-1}}$ and ν_{I} , for a given size, and that the result of this integration does not depend on time t.

Consequently, one simply has now to solve the following two systems which are coupled by the growth rate *G*:

$$\begin{cases} \dfrac{dL_i}{dt}(t) = G(t) \\ L_i(\nu_i) = 0 \end{cases} ; \quad \begin{cases} \dfrac{d\Psi_i}{dt}(t) = 0 \\ \Psi_i(\nu_i) = \int_{\nu_{i-1}}^{\nu_i} R_N(\nu)d\nu \end{cases} \qquad (31)$$

3.3 Time-discretization.

Actually, any time-discretization algorithm can be used to solve jointly the two coupled systems defined by (31). As an example, *t* can be discretized in the same way as *ν*, which leads to the very simple numerical scheme displayed below.

Any numerical integration technique can also be used for the computation of the time variations of both L and ψ. The global accuracy of the final numerical solution will mostly be limited by the order of the applied integration scheme.

$k = 0$;
while $t_k < t_{end}$ do

for $i = 1, k-1$ do
$L_0(t_k) = L_0(t_{k-1}) + \int_{t_{k-1}}^{t_k} G(t)\,dt$;
end

$L_0(t_k) = 0$;
$Y_k = \int_{t_{k-1}}^{t_k} R_N(\nu)\,d\nu$;

$k = k + 1$;
end

3.4 Method of characteristics for monodimensional PBEs accounting for impurity effects.

Now, in order to account for the distribution of growth rates resulting from the adsorption of impurities, the general system (15-18) is considered. As already explained, the growth rate $G(t)$ is a complex function of physical and kinetic variables depending on time and, through the indirect size-dependency of the solute concentration, on the whole current size distribution:

$$G(t) = f\left(t, \nu, C^*, C_s \propto \int_0^\infty \phi(L', t, \nu) L'^3\,(t) dL'\right) \tag{32}$$

where C_S is the overall concentration of crystallized solid given by (19).

The nucleation time of every crystal is introduced in (32) because, as explained in Part 2, the growth rate G now depends on the time spent by the growing crystal surface in the presence of adsorbing impurities.

As in the "classical" case, it is obvious in the following that during the crystallization process the supersaturation remains positive:

$$\forall t \in \mathbb{R}^+, \forall\, \nu \in [0, t\,], \quad G(t, \nu) > 0 \tag{33}$$

Now, let us consider characteristic curves defined as follows:

$$\forall t \in \mathbb{R}^+, \ \ \forall\, (\nu, \mu) \in [0, t\,]^2,$$
$$\tilde{L}_\mu(t, \nu) = \int_\mu^t G(t', \nu) dt' \tag{34}$$

The distribution along a given characteristic curve is noted as follows:

$$\tilde{\phi}_\mu(t, \nu) = \phi\big(\tilde{L}_\mu(t, \nu), t, \nu\big),$$

and one can write:

$$\frac{\partial \tilde{\phi}_\mu(t, \nu)}{\partial t} = \frac{\partial \phi\big(\tilde{L}_\mu(t, \nu), t, \nu\big)}{\partial t} + \frac{\partial \tilde{L}_\mu(t, \nu)}{\partial t}\ \frac{\partial \phi\big(\tilde{L}_\mu(t, \nu), t, \nu\big)}{\partial L}$$
$$= \frac{\partial \phi\big(\tilde{L}_\mu(t, \nu), t, \nu\big)}{\partial t} + G(t, \nu)\ \frac{\partial \phi\big(\tilde{L}_\mu(t, \nu), t, \nu\big)}{\partial L} \tag{35}$$

$$\frac{\partial \tilde{\phi}_\mu(t, \nu)}{\partial t} = 0 \tag{36}$$

As before, it therefore turns out that $\tilde{\phi}_\mu(t, \nu)$ does not depend on t. It can also be concluded that:

$$\forall t \in \mathbb{R}^+, \ \ \forall\, (\nu, \mu) \in [0, t\,]^2,$$

$$\phi\big(\tilde{L}_\mu(t, \nu), t, \nu\big) = \tilde{\phi}_\mu(t, \nu) = \tilde{\phi}_\mu(\mu, \nu) \tag{37}$$
$$= \phi(0, \mu, \nu) \tag{38}$$
$$\phi\big(\tilde{L}_\mu(t, \nu), t, \nu\big) = \delta(\mu - \nu)\frac{R_N(\mu)}{G(\mu, \nu)} \tag{39}$$

3.5 Semi-discretization of the size population density function taking the nucleation time into account.

The time variable μ is discretized considering successive sampling times: $\mu \in \{\mu_i, i \in \mathbb{N}\}$, and one can define the following distribution function:

$$\forall \mathrm{t} \in \mathbb{R}^+, \forall\, \nu \in [0, \mathrm{t}\,]$$
$$L_i(t) = \tilde{L}_{\mu_i}(t, \nu) \tag{40}$$
$$\Phi_\mathrm{i}(\mathrm{t}, \nu) = \int_{\mathrm{L_i(t,\nu)}}^{\mathrm{L_{i-1}(t,\nu)}} \phi(\mathrm{L}, \mathrm{t}, \nu)\mathrm{dL}$$
$$\Psi_\mathrm{i}(\mathrm{t}) = \int_0^\mathrm{t} \Phi_\mathrm{i}(\mathrm{t}, \nu)\mathrm{d}\nu \tag{41}$$

Using (40) and setting:

$$\begin{cases} \mu = \lambda_{t,\nu}^{-1}(L) \\ L = \tilde{L}_\mu(t, \nu), \end{cases}$$

$$L = \tilde{L}_\mu(t, \nu), \ \frac{dL}{d\mu}(\mu) = -G(\mu, \nu) \tag{42}$$

yields:

$$\Phi_\mathrm{i}(\mathrm{t}, \nu) = \int_{\mathrm{L_i(t,\nu)}}^{\mathrm{L_{i-1}(t,\nu)}} \phi(L, t, \nu) dL \tag{43}$$
$$= \int_{\mu_{\mathrm{i-1}}}^{\mu_\mathrm{i}} \phi\big(\tilde{L}_\mu(t, \nu), t, \nu\big) G(\mu, \nu) d\mu \tag{44}$$

$$\Phi_i(t,\nu) = \int_{\mu_{i-1}}^{\mu_i} \delta(\mu-\nu)\, R_N(\mu)\, d\mu \tag{45}$$

$$= \begin{cases} R_N(\nu) & if\ \nu \in [\mu_{i-1}\,;\mu_i] \\ 0 & otherwise \end{cases} \tag{46}$$

(47)

It follows that:

$$\Psi_i(t) = \int_0^t \Phi_i(t,\nu)d\nu = \int_{\mu_{i-1}}^{\mu_i} R_N(\nu)d\nu \tag{48}$$

The following two systems are thus obtained which are coupled by the growth rate G:

$$G(t) = f\left(t, \mu_i, C^*, C_s \propto \sum_i \Psi_i(\mu_i)\, L_i^3(t)\right) \tag{49}$$

$$\begin{cases} \frac{dL_i}{dt}(t) = G(t) \\ L_i(\mu_i) = 0 \end{cases} \quad \begin{cases} \frac{d\Psi_i}{dt}(t) = 0 \\ \Psi_i(\mu_i) = \int_{\mu_{i-1}}^{\mu_i} R_N(\mu)\, d\mu \end{cases} \tag{50, 51}$$

The principle of the resolution numerical method is the same as previously (see Fig. 2 and Part 3.3).

4. APPLICATION: SIMULATION OF THE CRYSTALLIZATION OF CITRIC ACID MONOHYDRATE IN THE PRESENCE OF IMPURITIES.

In order to illustrate the resolution method, the crystallization of citric acid monohydrate is simulated using kinetic data previously published by Févotte *et al*. (2007). In the absence of reported experimental results in impure media, the parameters of the Kubota-Mullin model were set arbitrarily in order to compare the features of crystallization operations performed with and without impurities. The corresponding parameters are summarized in Table (1).

In the following, no effect of the impurities on the nucleation kinetics is simulated, which is probably a very rough assumption. Actually published data about nucleation in the presence of impurities are really lacking and the goal here is rather to show the usefulness of the resolution method than to investigate real solute/solvent/impurity systems.

Isothermal desupersaturation crystallization operations were simulated at 15°C. In order to initiate the crystallization in the supersaturated zone (i.e. $C_{init.}$ >C* at 15°C)), a seed mass of 10 kg (2% of the expected final mass of solid) is supposed to be introduced in a 1 m^3 pilot-scale well-mixed crystallizer initially feed with a supersaturated citric acid solution. The intial solute concentration is: C_{init} = 1.825 kg/kg water. After seeding, the number of particles increases, due to secondary nucleation, and the initial supersaturation is consumed through the growth of crystals. Despite the adsorption of impurity species at the crystal surfaces, the overall concentration C_i is assumed to remain constant during the crystallization (i.e. the amount of adsorbed molecules is clearly negligible with respect to the dissolved impurities.

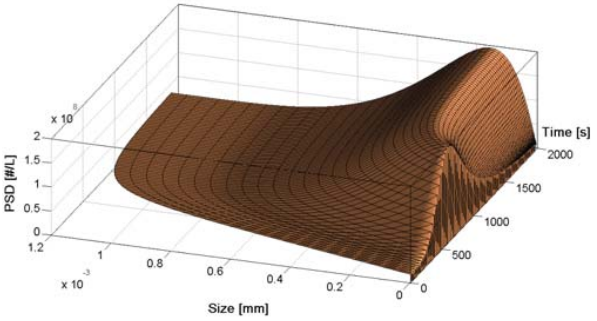

Fig. 3. Simulation of seeded isothermal crystallization of citric acid monohydrate in pure water at 15°C.

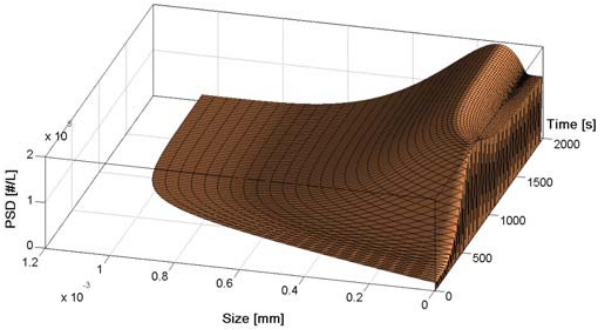

Fig. 4. Simulation of seeded isothermal crystallization of citric acid monohydrate in water and in the presence of impurity at 15°C. The parameters of Kubota-Mullin's are given in Table 1.

As one can see in Figs. 3 and 4, the computed CSD is smooth and does not exhibit oscillatory behaviour, even when coarse time intervals are used for the numerical simulation. As expected, the presence of impurities has a clear effect on the development of the CSD. Fig. 3 shows that the size of the biggest particles obtained in pure water is about 1.2 mm while it is only 1 mm in the presence of impurities (Fig.4). However, Fig.5c shows that the main difference between the two final CSDs can be observed in a rather significant increase in the number of fines which is expected to have a very detrimental effect on the the downstream operation such as filtration.

It turns out that the most significant effects of the impurities on the development of the batch process arise from the reduction of the supersaturation decrease, as displayed in Fig.5a.

Indeed, as outlined in Part 1.2, due to the pinning mechanism, the level of supersaturation remains higher when impurities are present in the crystallizing solution. As during the present simulation no impurity effect is assumed to affect the secondary nucleation of new citric acid particles, higher levels of supersaturation lead to a much higher overall

number of particles (Fig.5d) while, due to growth rate reductions and to the final supersaturation threshold outlined previously, the overall production of solid is clearly reduced. Figure 5b shows that only 70% of the expected solid is obtained at the end of the batch process performed in the presence of impurities (0.5 kg/L of crystals was expected from the selected values of C_{init} and C*).

Table 1. Kinetic equations and parameters used for the simulation of the crystallization of Citric Acid monohydrate.

$$\frac{dL}{dt} = G(t) = k_g(C(t) - C_m^*)^i$$
$$= 7.18\ 10^{-6}(C(t) - C_m^*)^{1.58} \quad (52)$$
$$R_N(t) = K_2\ C_S(t)^{i_m}(C(t) - C_m^*)^{j_m}$$
$$= 1.72\ 10^8\ C_S(t)^{0.47}(C(t) - C_m^*)^{1.14} \quad (53)$$

where $R_N(t)$ is the rate of secondary nucleation of monohydrate citric acid,
K_2 is a "lumped" kinetic constant for secondary nucleation,
C_m^* is the solubility of monohydrate citric acid at 15°C (1.35 kg/kg of water),
i & j_m are exponents expressing the supersaturation dependency of the growth rate and nucleation rate,
i_m is the exponent accounting for the impact of solid already present in suspension on the secondary nucleation rate.

$$C_s(t) = \rho_s \varphi_p \int_{L^*}^{\infty} \psi(L,t) L^3 dL$$

where ρ_s= 1545 kg/m^3
φ_p= π/6 (spherical particles)

Parameters of Kubota-Mullin's Model:

K = 1 m^3/kg
C_i = 0.01 kg/m^3
τ = 500 s
α = 10/σ

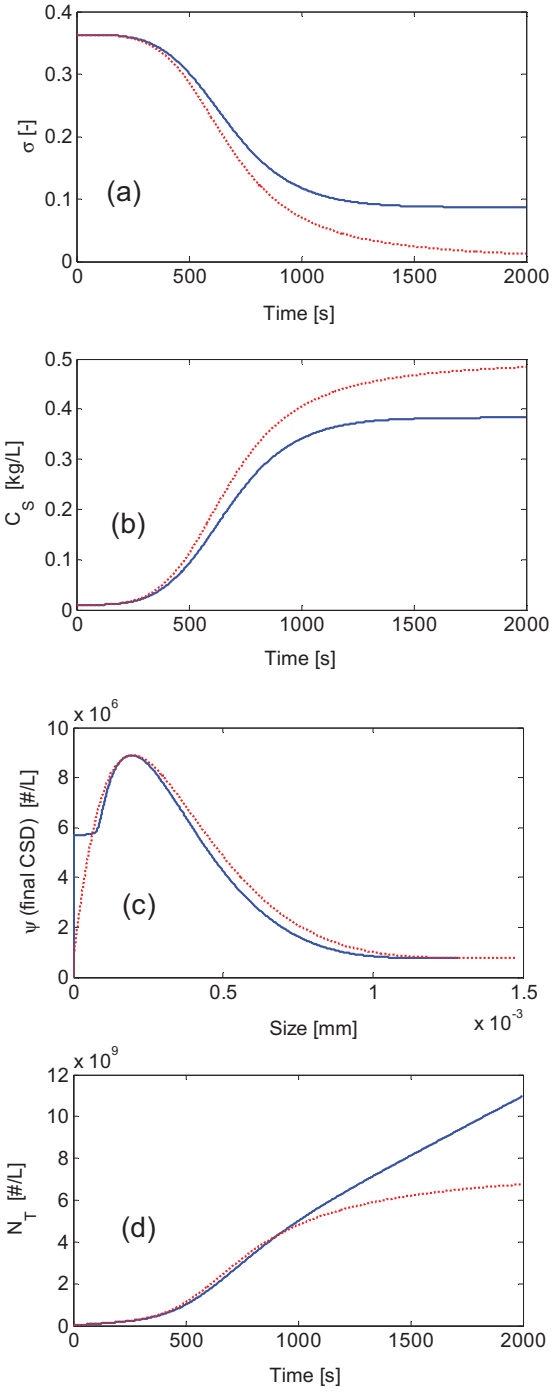

Fig. 5 . Simulation of seeded isothermal crystallization of citric acid monohydrate in water with (dotted line) and without (continuous line) the presence of impurities, at 15°C.

(a) Desupersaturation profile. (b) Generation of total crystallized solid during time. (c) Nucleation rate assuming negligible effect of the impurity species on the generation of particles. (d) Overall number of crystals.

5. CONCLUSIONS

A method of characteristics for the resolution of population balance equations was developed and evaluated using published kinetic data on the crystallization of citric acid in water. The method can be applied to crystallization processes without agglomeration and breakage, and it is intended to allow the simulation of growth rate reductions observed during solution crystallizations performed in the presence of industrial impurities.

Indeed, the effect of impurities was shown by Kubota and Mullin (1995) to depend on the time spent by every crystal in the impure liquid medium and, consequently, to depend on the "age" of the crystals. Such a particular problem requires accounting for an additional time variable in the expression of the PBEs and finding a way of solving the resulting PBE system.

From a physical viewpoint, the simulation results are shown to be consistent and demonstrate the ability of the model to simulate the development industrial crystallization processes in the presence of impurities. Such simulation could be applied, for example, to the design of optimal temperature trajectories aimed at minimizing the detrimental effect of the concentration of impurities on the yield of industrial crystallization operations.

As outlined by several authors (Kumar and Ramkrishna, 1997; Briesen, 2006), despite the apparent simplicity of these two processes, the discretization of crystal nucleation and growth raises numerical diffusion and stability issues which arise from the hyperbolic features of the governing equations (6) to (8). From this latter viewpoint it is clear that the proposed resolution method allows one to account for nucleation and growth rates in a very straightforward way.

NOMENCLATURE

C	Solute concentration	kg solute/kg solvent
C^*	Solubility concentration	kg solute/kg solvent
C_i	Impurity concentration	$kg.m^{-3}$
C_S	Solid concentration	$kg.m^{-3}$
G	Growth rate	$m.\ s^{-1}$
i	Exponent of the supersaturation dependency of the crystal growth rate	[-]
i_m	Exponent of the dependency of the nucleation rate on the concentration of solid in suspension	[-]
j_m	Exponent of the supersaturation dependency of the nucleation rate	[-]
K	Langmuir's constant	$m^3.\ kg^{-1}$
k_g	Growth rate constant	[-]
K_2	Kinetic nucleation parameter	
L	Particle size	m
$\mathcal{N}(\boldsymbol{r},t)$	Number of particles at time t in a given subset	$\#.m^{-3}$
R_N	Nucleation rate	$\#.s^{-1}.m^{-3}$
t	Time	s
u	Step velocity	$m.\ s^{-1}$
	Greek letters	
α	Impurity effectiveness factor	[-]
θ	Fraction of coverage of growing crystal surface by adsorbed impurity	[-]
θ^*	Fraction of coverage of growing crystal surface by adsorbed impurity at the equilibrium	[-]
ν	Nucleation time	s
σ	Supersaturation	[-]
τ	Adsorption time constant	s
$\psi(L,t)$	Population density function	$\#.m^{-1}.m^{-3}$

REFERENCES

Briesen, H. (2006) Simulation of crystal size and shape by means of a reduced two-dimensional population balance model. *Chem. Engng. Sci.,*61, 104-112.

Cabrera, N. and Vermilyea, D.A. (1958). in *Growth and Perfection of Crystals*, New York, 393 p.

Chernov, A.A. (2004). Notes on interface growth kinetics 50 years after Burton, Cabrera and Frank. *J. of Crystal Growth,* 264(4), 499-518.

Févotte, G., Caillet, A. and Sheibat-Othman, N. (2007). A population balance model of the solution-mediated phase transition of citric acid. *AIChE Journal*, 53(10), 2578-2589.

Kubota, N. (2001). Effect of Impurities on the Growth Kinetics of Crystals. *Cryst. Res. Technol*., 36(8-10), 749–769.

Kubota, N. (2001). Effect of Impurities on the Growth Kinetics of Crystals. *Cryst. Res. Technol*., 36, 749–769.

Kubota, N., Yokota, M. and Mullin, J.W. (2000). The combined influence of supersaturation and impurity concentration on crystal growth. *J. Crystal Growth*, 212(3-4), 480-488.

Kubota, N. and Mullin, J.W. (1995). A kinetic model for crystal growth from aqueous solution in the presence of impurity. *J. Crystal Growth,* 152(3), 203-208.

Kubota, N., Yokota, M. and Mullin, J.W. (1997). Supersaturation dependence of crystal growth in solutions in the presence of impurity. *J. Crystal Growth*, 182(1-2), 86-94.

Kumar, S. and Ramkrishna, D. (1996). On the solution of population balance equations by discretization--I. A fixed pivot technique, *Chem. Engng. Sci.,* 51, 8, 1311-1332.

Kumar,S., and Ramkrishna, D. (1996). On the solution of population balance equations by discretization--II. A

moving pivot technique, *Chem. Engng. Sci.,* 51, 8, 1333-1342.

Kumar, S. and Ramkrishna, D. (1997). On the solution of population balance equations by discretization- III. Nucleation, growth and aggregation of particles, *Chem. Engng. Sci*. 52, 24, 4659-4679.

Land, T.A., Martin, T.L., Potapenko, S., Palmore, G.T., De Yoreo, J.J. (1999). Recovery of surfaces from impurity poisoning during crystal growth. *Nature*, 399, 442-445.

Mersmann, A. (2002). Fundamentals of crystallization. *Crystallization Technology Handbook,* 2nd Ed., New York: Marcel Dekker.

Qamar,S.; Warnecke,G. (2007). Numerical solution of population balance equations for nucleation, growth and aggregation processes, *Comp. & Chem. Engng*. 31, 1576-1589.

Mullin, J.W. (1993). *Crystallization,* 3rd Ed., London (UK): Butterworth-Heinemann,

Ramkrishna, D. (2000). Population Balances: *Theory and Applications to Particulate Systems Engineering,* Academic Press.

Ramkrishna, D.; Mahoney, A.W. (2002). Population balance modelling. Promise for the future. *Chem. Engng. Sci*., 57, 595-606.

Sangwal, K. (1996). Effects of impurities on crystal growth processes. *Progress in Crystal Growth and Characterization of Materials*, 32(1-3), 3-43.

Sotowa, K.I., Naito, K., Kano, M., Hasebe, S., Hashimoto, I. (2000). Application of the method of characteristics to crystallizer simulation and comparison with finite difference for controller performance evaluation. *J. of Process Control*, 10, 203-208.

Thomas, T.N., Land, T.A., Martin, T., Casey, W.H., DeYoreo, J.J. (2004). AFM investigation of step kinetics and hillock morphology of the {1 0 0} face of KDP. *J. Crystal Growth,* 260(3-4), 566-579.

Wood, W.M.L. (2001). A bad (crystal) habit--and how it was overcome. *Powder Technology*, 121(1), 53-59.

ACKNOWLEDGEMENTS

We greatly acknowledge the French research agency ANR for the support granted to the project “IPAPI” (Improving the Properties of Active Pharmaceutical Ingredients), ref. 07-BLAN-0183

Micro Process Engineering for Fine Chemistry and Fuel Processing - from Lab to Pilot/Production and First Issues on Dynamic Operation

Volker Hessel[1,2]

[1] *Institut für Mikrotechnik Mainz GmbH (IMM), Mainz, Germany*
[2] *Eindhoven University of Technology (TU/e), Eindhoven, the Netherlands; v.hessel@tue.nl*

This presentation tries to cover the following two aspects.

- To show up how milli and micro process technologies contribute to green processing and process intensification in chemical industry. Relevant trends in the IMM developments (with some supplements of TU/e research) will be given at the focal points catalyst / fabrication / reactor / plant / processes.
- As outlook and much more briefly, first thoughts on process control for micro processing will be given, showing some issues and examples for process analytics in fine chemistry (taken from Paul Watts, University of Hull) and some IMM results about dynamic operation in fuel processing.

Fine Chemical Applications – Process Intensification by Novel Process Windows

Draw on sustainability for chemical production processes demands the integration of sustainability aspects already during process development, whereas further environmental impacts and production costs become predefined. Micro and milli process technologies [1,2] can provide novel ways for process intensification combined with ecological [3] and economic [4] advantages and first assessments were made here [5], mainly by industry. Microstructured reactors have entered the field of fine chemistry with first pilot and production plants; some examples being reported [6]. To bring these innovative apparatus to their operational limit and thus to process with maximal cost competitiveness and environmental sustainability, the idea of "Novel Process Windows" [7] is discussed referring examples of actual research. A recent case study disclosed the key drivers for ecological and economic optimisation [5] when intensifying the aqueous Kolbe-Schmitt synthesis in a minicapillary reactor [8] by using microwaves as alternative energy source and ionic liquids as alternative solvents.

[1] Hessel, Hardt, Löwe / Hessel, Löwe, Müller, Kolb, Chemical Micro Process Engineering (2 Volumes), Wiley-VCH, Weinheim, 2004/2005. *[2]* Jähnisch, V. Hessel, Löwe, Baerns, Angew. Chem. Int. Ed. 2004, 43 (4), 406. *[3]* Kralisch, Kreisel, Chem. Eng. Sci., 2007, 62 (4), 1094. *[4]* Krtschil, Hessel, Kralisch, Kreisel, Küpper, Schenk, Chimia, 2006, 60 (9), 611. *[5]* Hessel, Kralisch, Krtschil, Energy Environ. Sci. 2008, 1 (4), 467. *[6]* Hessel, Löb, Löwe, Industrial Microreactor Process Development up to Production, in: Microreactors in Organic Chemistry and Catalysis (ed. T. Wirth), Wiley-VCH, Weinheim, 2008, pp. 211-275. *[7]* Hessel, Löb, Löwe, Curr. Org. Chem., 2005, 9 (8), 765. *[8]* Hessel, Löb, Löwe et al., Org. Proc. Res. Dev., 2005, 9 (4), 479.

Hydrogen for Fuel Cells by Fuel Processing – Process System Engineering

For catalysis using microreactors [1], it is essential to have total reaction control at all length scales, ranging from mm to nm, which includes smart engineering of reactor plates and microchannels as well as proper setting of catalyst coatings and metal clusters in mesopores. Most essential here is the reliable finding of activated catalysts and proper introduction of these into the microchannels [2-7]. In continuation, catalytic pilot and production microstructured reactors [8,9] demand for solutions on scale-out (system assembly) [8,9], control over flow distribution and heat management at multi-plate architecture [10,11], integration of reaction and heat exchange / separation, process flow with many coupled reactions and operations (sometimes involving recirculation) [8,9], reduction in expenditure for energy and apparatus required for work-up [12], and increase in the service life of the catalyst including concepts for catalyst change, e.g. by replacement of entire modules. This is accompanied by the development of new microfabrication and joining techniques applicable to large, meter-sized format such as rolling / embossing / etching and brazing / diffusion bonding [13]. System and process design is widely practised at IMM for applications in fuel processing for hydrogen production to feed fuel cells [14]. This has led to industrial implementation already, e.g. the 250 W LPG fuel processor-fuel cell *VEGA* for leisure vehicles and boats (Truma Gerätetechnik) and a 2 kW diesel fuel processor-fuel cell prototype as auxiliary power unit for trucks (Volvo, DAF; assembled by Tenneco) [14]. Applications using fossil fuels being reality, the next step is to explore chances of the technology for biofuels with its more complex processing schemes, different logistics and cost structures.

[1] Kolb, Hessel, Chem. Eng. J., 2004, 98 (1-2), 1. *[2]* Muraza, Rebrov, de Croon, Schouten et al., Chem. Eng. J., 2008, 135S, S99. *[3]* Mies, Rebrov, Jansen, de Croon, Schouten, J. Catal., 2007, 247 (2), 328. *[4]* Rebrov, Kuznetsov, de Croon, Schouten, Catal. Today, 2007, 125, 88. *[5]* Pennemann, Hessel, Kolb, Löwe, Zapf, Chem. Eng. J., 2008, 135 (1), S66. *[6]* Men, Kolb, Zapf, Hessel, Löwe, Catal. Today 2007, 125 (1-2), 81. *[7]* Men, Kolb, Zapf, Hessel, Löwe, Trans IChemE, 2007, 85 (B5), 1. *[8]* Men, Kolb, Zapf, Tiemann, Wichert, Hessel, Löwe, Int. J. Hydrogen Energy, 2008, 33 (4), 1374. *[9]* Kolb, Schürer, Tiemann, Wichert, Zapf, Hessel, Löwe, J. Power Sources, 2007, 171 (1), 198. *[10]* Rebrov, Ismagilov, Ekatpure, de Croon, Schouten AIChE J., 2007, 53 (1), 28. *[11]* Mies, Rebrov, Deutz, Kleijn, de Croon, Schouten, Ind. Eng. Chem. Res., 2007, 46 (12), 3922. *[12]* Delsman, Uju, de Croon, Schouten, Ptasinski, Energy Int. J., 2006, 31 (15), 3300. *[13]* Hessel, Kolb, Brandner, Microfabrication for Energy Generating Devices and Fuel Processors in: Microfabricated Power Generation Devices (eds.: Mitsos, Barton,), in print (2008). *[14]* G. Kolb, Fuel Processing, Wiley-VCH, Weinheim, 2008.

Integration of Real-time Optimization & and Model Predictive Control ⋆

V. Adetola * **M. Guay** *

* *Department of Chemical Engineering, Queen's University, Kingston, Ontario, Canada (e-mail: martin.guay@chee.queensu.ca)*

Abstract: This paper proposes a controller design approach that integrates RTO and MPC for the control of constrained uncertain nonlinear systems. Assuming that the economic function is a known function of constrained system's states, parameterized by unknown parameters and time-varying, the controller design objective is to simultaneously identify and regulate the system to the optimal operating point. The approach relies on a novel set-based parameter estimation routine and a robust model predictive controller that takes into the effect of parameter estimation errors. A simulation example is used to demonstrate the effectiveness of the design technique.

Keywords: Adaptive control, Real-time optimization, Model predictive control

1. INTRODUCTION

In this paper, we provide a formal design technique that integrates RTO and MPC for constrained uncertain nonlinear systems. The framework considered assumes the economic function is a known function of constrained system's states, parameterized by unknown parameters. The objective and constraint functions may explicitly depend on time, which means that our proposed method is applicable to both dynamic and steady state economic optimization. The control objective is to simultaneously identify and regulate the system to the operating point that optimizes the economic function. The control input may also be required to satisfy some constraints.

The method proposed solves the control and optimization problem at the same frequency. This eliminates the ensuing interval of "no-feedback" that occurs between economic optimization and thereby improving disturbance attenuation. The RTO layer is tackled via a computational efficient approach. The constrained economic optimization problem is converted to an unconstrained problem and Newton based optimization method is used to develop an update law for the optimum value. The integrated design distinguishes between the extremum seeking and the adaptive tracking of the reference trajectory.

While many advances have been made in nonlinear systems for the stabilization of one fixed operating point, few attempts have been made to address the stabilization problem for time-varying or non-fixed setpoints. In Magni (2002), a stabilizing nonlinear MPC algorithm was developed for asymptotically constant reference signals. By selecting a prediction horizon that is longer than the time the reference setpoint is assumed to have converged, the constant pre-programmed value is used to design the stabilizing controller parameters, *i.e*, the terminal stability constraint $\mathbb{X}_f$ and terminal penalty W. The result is limited to reference signals that converge to *a-priori* known constant setpoint. The method proposed in Findeisen et al. (2000), combines a pseudo-linearization technique with a nonlinear MPC strategy to stabilize a family of (known and constant) setpoints. While the method provides a possible solution for tracking changing setpoints, such pseudo-linearization transformation and feedback is in general difficult to obtain and involve cumbersome computation.

⋆ The authors would like to acknowledge the financial support of the Natural Sciences and Engineering Research Council of Canada.

2. PROBLEM DESCRIPTION

Consider a constrained optimization problem of the form

$$\min_{x\in\mathbb{R}^{n_x}} \; p(t,x,\theta) \tag{1a}$$

$$s.t. \qquad c_j(x) \le 0 \qquad j = 1\dots m_c \tag{1b}$$

with θ representing unknown parameters, assumed to be uniquely identifiable and lie within an initially known convex set $\Theta^0 \triangleq B(\theta^0, z_\theta^0)$. The functions p and c_j are assumed to be C^2 in all of their arguments (with locally Lipschitz second derivatives), uniformly for $t \in [0,\infty)$. The constraint $c_j \le 0$ must be satisfied along the system's state trajectory $x(t)$.

Assumption 1. The following assumptions are made about (1).

(1) There exists $\varepsilon_0 > 0$ such that $\frac{\partial^2 p}{\partial x^2} \ge \varepsilon_0 I$ and $\frac{\partial^2 c}{\partial x^2} \ge 0$ for all $(t,x,\theta) \in (\mathbb{R}^+ \times \mathbb{R}^{n_x} \times \Theta^\epsilon)$, where Θ^ϵ is an ϵ neighborhood of Θ.
(2) The feasible set
$$\mathbb{X} = \big\{x \in \mathbb{R}^{n_x} \mid \max_j \; c_j(x) \le 0\big\},$$
has a nonempty interior.

Assumption 1 states that the cost surface is strictly convex in x and $\mathbb{X}$ is a non-empty convex set. Standard nonlinear optimization results guarantee the existence of a unique minimizer $x^*(t,x,\theta) \in \mathbb{X}$ to problem 1. In the case of non-convex cost surface, only local attraction to an extremum could be guaranteed. The control objective is to stabilize the nonlinear system

$$\dot{x} = f(x,\xi,u) + g(x,\xi,u)\theta \triangleq \mathcal{F}(x,\xi,u,\theta) \quad (2a)$$
$$\dot{\xi} = f_\xi(x,\xi) \quad (2b)$$

to the optimum operating point or trajectory given by the solution of (1) while obeying the input constraint $u \in \mathbb{U} \in \mathbb{R}^{n_u}$ in addition to the state constraint $x \in \mathbb{X} \in \mathbb{R}^{n_x}$. The dynamics of the state ξ is assumed to satisfy the following input to state stability condition with respect to x.

Assumption 2. If x is bounded by a compact set $B_x \subseteq \mathbb{X}$, then there exists a compact set $B_\xi \subseteq \mathbb{R}^{n_\xi}$ such that $\xi \in B_\xi$ is positively invariant under 2.

3. EXTREMUM SEEKING SETPOINT DESIGN

3.1 Finite-time Parameter Identification

Let $\hat{x}$ denote the state predictor for (2), the dynamics of the state predictor is designed as

$$\dot{\hat{x}} = f(x,\xi,u) + g(x,\xi,u)\hat{\theta} + k_w(t)e + w\dot{\hat{\theta}}, \quad (3)$$

where $\hat{\theta}$ is a parameter estimate generated via any update law $\dot{\hat{\theta}}$, $k_w > 0$ is a design matrix, $e = x - \hat{x}$ is the prediction error and w is the output of the filter

$$\dot{w} = g(x,\xi,u) - k_w w, \qquad w(t_0) = 0. \quad (4)$$

Denoting the parameter estimation error as $\tilde{\theta} = \theta - \hat{\theta}$, it follows from (2) and (3) that

$$\dot{e} = g(x,\xi,u)\tilde{\theta} - k_w\, e - w\dot{\hat{\theta}}. \quad (5)$$

The use of the filter matrix w in the above development provides direct information about parameter estimation error $\tilde{\theta}$ without requiring a knowledge of the velocity vector $\dot{x}$. This is achieved by defining the auxiliary variable

$$\eta = e - w\tilde{\theta} \quad (6)$$

with η, in view of (4, 5), generated from

$$\dot{\eta} = -k_w\,\eta, \qquad \eta(t_0) = e(t_0). \quad (7)$$

Based on the dynamics (3), (4) and (7), the main result is given by the following theorem.

Theorem 3. Let $Q \in \mathbb{R}^{n_\theta \times n_\theta}$ and $C \in \mathbb{R}^{n_\theta}$ be generated from the following dynamics:

$$\dot{Q} = w^T w, \qquad Q(t_0) = 0 \quad (8a)$$
$$\dot{C} = w^T(w\hat{\theta} + e - \eta), \qquad C(t_0) = 0 \quad (8b)$$

Suppose there exists a time t_c and a constant $c_1 > 0$ such that $Q(t_c)$ is invertible *i.e.*

$$Q(t_c) = \int_{t_0}^{t_c} w^T(\tau)w(\tau)\,d\tau \succ c_1 I, \quad (9)$$

then

$$\theta = Q(t)^{-1}C(t) \qquad \text{for all } \; t \geq t_c. \quad (10)$$

Proof: The result can be easily shown by noting that

$$Q(t)\,\theta = \int_{t_0}^{t} w^T(\tau)w(\tau)\left[\hat{\theta}(\tau) + \tilde{\theta}(\tau)\right] d\tau. \quad (11)$$

Using the fact that $w\tilde{\theta} = e - \eta$, it follows from (11) that

$$\theta = Q(t)^{-1}\int_{t_0}^{t} \dot{C}(\tau)\,d\tau = Q(t)^{-1}C(t) \quad (12)$$

and (12) holds for all $t \geq t_c$ since $Q(t) \succeq Q(t_c)$. ■

The result in theorem 3 is independent of the control u and parameter identifier $\dot{\hat{\theta}}$ structure used for the state prediction (eqn 3). Moreover, the result holds if a nominal estimate θ^0 of the unknown parameter (no parameter adaptation) is employed in the estimation routine. In this case, $\hat{\theta}$ is replaced with θ^0 and the last part of the state predictor (3) is dropped ($\dot{\hat{\theta}} = 0$).

Let

$$\theta^c \triangleq Q(t_c)^{-1}\,C(t_c) \quad (13)$$

The finite-time (FT) identifier is given by

$$\hat{\theta}^c(t) = \begin{cases} \hat{\theta}(t), & \text{if } \; t < t_c \\ \theta^c, & \text{if } \; t \geq t_c. \end{cases} \quad (14)$$

3.2 Constraint Removal

An interior point barrier function method is used to enforce the inequality constraint. The state constraint is incorporated by augmenting the cost function p as follows:

$$p_a(t,x,\theta) \triangleq p(t,x,\theta) - \frac{1}{\eta_c}\sum_{j=1}^{m_c}\ln(-c_j(x)) \quad (15)$$

with $\eta_c > 0$, a fixed constant. The augmented cost function (15) is strictly convex in x and the unconstrained minimization of p_a therefore has a unique minimizer in $\text{int}\{\mathbb{X}\}$ which converges to that of (1) in the limit as $\eta_c \to \infty$ Bertsekas (1995).

3.3 Setpoint Update Law

Let $x_r \in \mathbb{R}^{n_x}$ denote a reference setpoint to be tracked by x and $\hat{\theta}$ denote an estimate of the unknown parameter θ. A setpoint update law $\dot{x}_r$ can be designed based on newton's method, such that $x_r(t)$ converges exponentially to the (unknown) $\hat{\theta}$ dependent optimum value of (15). To this end, consider an optimization Lyapunov function candidate

$$V_r = \tfrac{1}{2}\|\frac{\partial p_a}{\partial x}(t,x_r,\hat{\theta})\|^2 \triangleq \tfrac{1}{2}\|z_r\|^2 \quad (16)$$

For the remainder of this section, omitted arguments of p_a and its derivatives are evaluated at $(t,x_r,\hat{\theta})$. Differentiating (16) yields

$$\dot{V}_r = \frac{\partial p_a}{\partial x}\left(\frac{\partial^2 p_a}{\partial x \partial t} + \frac{\partial^2 p_a}{\partial x^2}\dot{x}_r + \frac{\partial^2 p_a}{\partial x \partial \theta}\dot{\hat{\theta}}\right). \quad (17)$$

Using the update law

$$\dot{x}_r = -\left(\frac{\partial^2 p_a}{\partial x^2}\right)^{-1}\left[\frac{\partial^2 p_a}{\partial x \partial t} + \frac{\partial^2 p_a}{\partial x \partial \theta}\dot{\hat{\theta}} + k_r\frac{\partial p_a^T}{\partial x}\right] \triangleq f_r(t,x_r,\hat{\theta}) \quad (18)$$

with $k_r > 0$ and $r(0) = r_0 \in \text{int}\,\{\mathbb{X}\}$ results in

$$\dot{V}_r \leq -k_r\|z_r\|^2, \quad (19)$$

which implies that the gradient function z_r converges exponentially to the origin.

Lemma 4. Suppose $(\theta,\hat{\theta})$ is bounded, the optimal setpoint $x_r(t)$ generated by (18) is feasible and converges to $x^*_{pa}(\hat{\theta})$, the minimizer of (15) exponentially.

Proof: Feasibility follows from the boundedness of $(\theta, \hat{\theta})$ and Assumption 1.1 while convergence follows from (19) and the fact that z_r is a diffeomorphism. ■

4. ONE-LAYER INTEGRATION APPROACH

Since the true optimal setpoint depends on θ, the actual desired trajectory $x_r^*(t, \theta)$ is not available in advance. However, $x_r(t, \hat{\theta})$ can be generated from the setpoint update law (18) and the corresponding reference input $u_r(x_r)$ can be computed on-line.

Assumption 5. $x_r(t, \hat{\theta})$ is such that there exists $u_r(x_r)$ satisfying

$$0 = f(x_r, u_r, \hat{\theta}) \tag{20}$$

The design objective is to design a model predictive control law such that the true plant state x tracks the reference trajectory $x_r(t, \hat{\theta})$. Given the desired time varying trajectory (x_r, u_r), an attractive approach is to transform the tracking problem for a time-invariant system into a regulation problem for an associated time varying control system in terms of the state error $x_e = x - x_r$ and stabilize the $x_e = 0$ state. The formulation requires the MPC controller to drive the tracking error x_e into the terminal set $\mathbb{X}_{e_f}(\tilde{\theta})$ at the end of the horizon. Since the system's dynamics is uncertain, we use the finite-time identifier (34) for online parameter adaptation and incorporate robust features in to the adaptive controller formulation to account for the impact of the parameter estimation error $\tilde{\theta}$ in the design.

4.1 Min-max Adaptive MPC

Feedback min-max robust MPC is employed to provide robustness for the MPC controller during the adaptation phase. The controller maximizes a cost function with respect to θ and minimizes it over feedback control policies κ.

The integrated controller is given as

$$u = \kappa_{mpc}(t, x_e, \hat{\theta}) \triangleq \kappa^*(0, x_e, \hat{\theta}) \tag{21a}$$

$$\kappa^* \triangleq \arg \min_{\kappa(\cdot,\cdot,\cdot,\cdot)} J(t, x_e, \hat{\theta}, \kappa) \tag{21b}$$

where $J(t, x_e, \hat{\theta}, \kappa)$ is the (worst-case) cost associated with the optimal control problem:

$$J(t, x_e, \hat{\theta}, \kappa) \triangleq \max_{\theta \in \Theta} \int_0^T L(\tau, x_e^p, u^p, u_r) d\tau \tag{22a}$$

$$+ W(\tau, x_e^p(T), \tilde{\theta}^p(T)) \tag{22b}$$

$$s.t. \quad \forall \tau \in [0, T]$$

$$\dot{x}^p = f(x^p, \xi^p, u^p) + g(x^p, \xi^p, u^p)\,\theta, \quad x^p(0) = x \tag{22c}$$

$$\dot{\xi}^p = f(x^p, \xi^p), \quad \xi^p(0) = \xi \tag{22d}$$

$$\dot{x}_r^p = f_r(t, x_r, \theta), \quad x_r^p(0) = x_r \tag{22e}$$

$$x_e^p = x^p - x_r^p \tag{22f}$$

$$\dot{w^p} = \beta(g^T(x^p, \xi^p, u^p) - k_w w^p), \quad w^p(0) = w \tag{22g}$$

$$\dot{Q^p} = \beta({w^p}^T w^p), \quad Q^p(0) = Q \tag{22h}$$

$$\dot{\tilde{\theta}}^p = \Gamma\, Q^p\, \tilde{\theta}^p, \quad \tilde{\theta}^p = \theta - \hat{\theta}^p, \quad \hat{\theta}^p(0) = \hat{\theta} \tag{22i}$$

$$u^p(\tau) \triangleq \kappa(\tau, x_e^p(\tau), \hat{\theta}^p(\tau)) \in \mathbb{U} \tag{22j}$$

$$x_e^p(\tau) \in \mathbb{X}_e, \quad x_e^p(T) \in \mathbb{X}_{e_f}(\tilde{\theta}^p(T)) \tag{22k}$$

where $\mathbb{X}_e = \{ x_e^p : x^p \in \mathbb{X} \}$, $\mathbb{X}_{e_f}$ is the terminal constraint and $\beta \in \{0, 1\}$. The effect of the future parameter adaptation is incorporated in the controller design via (22a) and (22k), which results in less conservative worst-case predictions and terminal conditions.

4.2 Implementation Algorithm

Algorithm 1. The finite-time min-max MPC algorithm performs as follows: At sampling instant t_i

(1) **Measure** the current states of the plant $x = x(t_i)$, $\xi = \xi(t_i)$ and obtain the current value of the desired setpoint $x_r = x_r(t_i)$ via the update law (18)

(2) **Obtain** the current value of matrices w, Q and C from

$$\dot{w} = g(x, u) - k_w\, w, \; w(t_0) = 0, \tag{23}$$

and

$$\dot{Q} = w^T w, \; Q(t_0) = 0 \tag{24a}$$

$$\dot{C} = w^T(w\,\theta^0 + x - \hat{x} - \eta), \; C(t_0) = 0 \tag{24b}$$

respectively

(3) **If** $det(Q) = 0$ or $cond(Q)$ is not satisfactory update the parameter estimates $\hat{\theta}$ and the uncertainty set $\Theta(t) \triangleq B\left(\hat{\theta}(t), z_\theta(t)\right)$ according to Algorithm 3 in the Appendix.
Else if $det(Q) > 0$ and $cond(Q)$ is satisfactory, set $\beta = 0$ and update

$$\hat{\theta} = Q^{-1}(t_i)C(t_i), \quad z_\theta = 0$$

End

(4) Solve the optimization problem (21,22) and apply the resulting feedback control law to the plant until the next sampling instant

(5) **Increment** $i = i + 1$. **If** $z_\theta > 0$, repeat the procedure from step 1 for the next sampling instant. **Otherwise**, repeat only steps 1 and 4 for the next sampling instant.

Since the algorithm is such that the uncertainty set Θ contracts over time, the conservatism introduced by the robustness feature in terms of constraint satisfaction and controller performance reduces over time and when Θ contracts upon θ, the min-max adaptive framework becomes that of a nominal MPC. The drawback of the finite-time identifier is attenuated in this application since the matrix invertibility condition is checked only at sampling instants. The benefit of the identifier, however, is that it allows an earlier and immediate elimination of the robustness feature.

4.3 Lipschitz-based Adaptive MPC

While the min-max approach provides the tightest uncertainty cone around the actual system's trajectory, its application is limited by the enormous computation required to obtain the solution of the min-max MPC algorithm. To address this concern, the robust tracking problem is reposed as the minimization of a nominal objective function subject to "robust constraints".

The model predictive feedback is defined as

$$u = \kappa_{mpc}(t, x_e, \hat{\theta}, z_\theta) = u^*(0) \tag{25a}$$
$$u^*(.) \triangleq \arg\min_{u^p_{[0,T]}} J(t, x_e, \hat{\theta}, z_\theta, u^p, u_r) \tag{25b}$$

where $J(t, x_e, \hat{\theta}, z_\theta, u^p, u_r)$ is given by the optimal control problem:

$$J(t, x_e, \hat{\theta}, z_\theta, u^p, u_r) = \int_0^T L(t, x_e^p, u^p, u_r) d\tau \tag{26a}$$
$$+ W(x_e^p(T), z_\theta^p(T)) \tag{26b}$$
$$s.t.\ \forall \tau \in [0,\ T]$$
$$\dot{x}^p = f(x^p, u^p) + g(x^p, u^p)\hat{\theta}, \quad x^p(0) = x \tag{26c}$$
$$\dot{\xi}^p = f(\xi^p, x^p), \quad \xi^p(0) = \xi \tag{26d}$$
$$\dot{x}_r^p = f_r(t, x_r, \hat{\theta}), \quad x_r^p(0) = x_r \tag{26e}$$
$$x_e^p = x^p - x_r \tag{26f}$$
$$\dot{z}_e^p = \beta(\mathcal{L}_f + \mathcal{L}_g \Pi) z_e^p + \|g(x^p, \xi^p, u^p)\| z_\theta, \tag{26g}$$
$$z_x^p(0) = 0 \tag{26h}$$
$$X_e^p(\tau) \triangleq B(x_e^p(\tau), z_e^p(\tau)) \subseteq \mathbb{X}_e, \quad u^p(\tau) \in \mathbb{U} \tag{26i}$$
$$X_e^p(T) \subseteq \mathbb{X}_{e_f}(z_\theta^p(T)) \tag{26j}$$

Since the Lipschitz-based robust controller is implemented in open-loop, there is no setpoint trajectory $x_r(\hat{\theta})$ feedback during the inter-sample implementation. Therefore, the worst-case deviation $z_e^p \geq \max_{\theta\in\Theta} \|x_e - x_e^p\| = \max_{\theta\in\Theta} \|x - x^p\|$. Hence z_e^p given in (26g) follows from

$$\dot{z}_x^p = (\mathcal{L}_f + \mathcal{L}_g \Pi) z_x^p + \|g(x^p, u)\| z_\theta, \quad z_x^p(t_0) = 0 \tag{27}$$

where $\Pi = z_\theta + \|\hat{\theta}\|$. We assume an appropriate knowledge of Lipschitz bounds as follows:

Assumption 6. A set of functions $\mathcal{L}_j : \mathbb{X} \times \mathbb{R}^{n_\xi} \times \mathbb{U} \to \mathbb{R}^+$, $j \in \{f, g\}$ are known which satisfy

$$\mathcal{L}_j(\mathbb{X}, \xi, u) \geq$$
$$\min\left\{\mathcal{L}_j \;\middle|\; \sup_{x_1, x_2 \in \mathbb{X}} \left(\|j(x_1, \xi, u) - j(x_2, \xi, u)\| - \mathcal{L}_j \|x_1 - x_2\|\right) \leq 0\right\},$$

4.4 Implementation Algorithm

Algorithm 2. The finite-time Lipschitz based MPC algorithm performs as follows: At sampling instant t_i

(1) **Measure** the current states of the plant $x = x(t_i)$, $\xi = \xi(t_i)$ and obtain the current value of the desired setpoint $x_r = x_r(t_i)$ via the update law (18)
(2) **Obtain** the current value of matrices w, Q and C from (23) and (24)
(3) **If** $det(Q) = 0$ or $cond(Q)$ is not satisfactory, set $\beta = 1$ and update the parameter estimates $\hat{\theta} = \hat{\theta}(t_i)$ and uncertainty bounds $z_\theta = z_\theta(t_i)$ and $z_\theta^p(T) = z_\theta^p(t_i + T)$ via equation (29)

$$\dot{\hat{\theta}} = \Gamma\,(C - Q\,\hat{\theta}), \quad \hat{\theta}(t_0) = \theta^0, \tag{29}$$

equation (A.1) and equation (30)

$$z_\theta^p(\tau) = \exp^{-\bar{\mathcal{E}}(\tau - t_i)}\, z_\theta(t_i) \quad \tau \in [t_i,\ t_i + T) \tag{30}$$

where

$$\bar{\mathcal{E}} \geq \mathcal{E}(t_i) = \lambda_{\min}\left(\Gamma Q(t_i)\right).$$

Else if $det(Q) > 0$ and $cond(Q)$ is satisfactory, set $\beta = 0$ and update

$$\hat{\theta} = Q^{-1}(t_i) C(t_i), \quad z_\theta = 0$$

End

(4) **Solve** the optimization problem (25,26) and apply the resulting feedback control law to the plant until the next sampling instant
(5) **Increment** $i = i + 1$. **If** $z_\theta > 0$, repeat the procedure from step 1 for the next sampling instant. **Otherwise**, repeat only steps 1 and 4 for the next sampling instant.

Implementing the adaptive MPC control law according to Algorithm 2 ensures that the uncertainty bound z_θ reduces over time and hence, the error margin z_x^p imposed on the predicted state also reduces over time and shrinks to zero when the actual parameter estimate is constructed in finite-time.

4.5 Robust Stability

Robust stability is guaranteed under the standard assumptions that $\mathbb{X}_{e_f} \subseteq \mathbb{X}_e$ is an invariant set, W is a local robust CLF for the resulting time varying system and the decay rate of W is greater than the stage cost L within the terminal set $\mathbb{X}_{e_f}$ in conjunction with the requirement for W to decrease and $\mathbb{X}_f$ to enlarge with decreased parametric uncertainty.

4.6 Enhancing Parameter Convergence

In min-max adaptive formulation, the terminal penalty is parameterized as a function of $\tilde{\theta}$. This ensures that the algorithm will seek to reduce the parameter error in the process of optimizing the cost function and will automatically inject some excitation in the closed-loop system, when necessary, to enhance parameter convergence. However, this is not the case in the Lipschitz-based approach since the control calculation only uses nominal model. To improve the quality of excitation in the closed-loop the proposed excitation cost is

$$J_{\mathcal{E}} = \frac{\beta}{1 + \mathcal{E}_\theta^p(T)} \tag{31}$$

where

$$\mathcal{E}_\theta^p(\tau) = \lambda_{\min}\{Q^p(\tau)\} \quad \text{or} \quad \mathcal{E}_\theta^p(\tau) = \nu^T\, Q^p(\tau)\, \nu \tag{32}$$

with $\nu \in \mathbb{R}^{n_\theta}$ a unit vector. Note that any reduction in the cost function due to $J_{\mathcal{E}}$ implies an improvement in the rank of Q^p. Though, the predicted regressor matrix Q^p differs from the actual matrix Q, a sufficient condition for $Q > 0$ is for $Q^p > z_Q \geq \|Q - Q^p\|$.

5. TWO-LAYER INTEGRATION METHOD

The integration task can also be posed as a two degree of freedom paradigm where the problem is divided into two phases. The first phase deals with generating a state trajectory that optimizes a given objective function while respecting the system's dynamics and constraints, and the second phase deals with the design of a controller that would regulate the system around the trajectory.

The MPC controller design follows that of (21) and (25). The only difference is that rather than solving the setpoint differential equation (18) inside the MPC loop, the measurement of x_r obtained at sampling instants

is used as the desired setpoint to be tracked, that is, equations (22e) and (26e) are replaced by

$$\dot{x}_r^p = 0, \;\; x_r^p(0) = x_r. \tag{33}$$

The adaptive controllers are implemented according to Algorithms 1 and 2.

6. MAIN RESULT

The integration result is provided in the following:

Theorem 7. Consider problem (1) subject to system dynamics (2), and satisfying Assumption 1. Let the controller be (21) or (25) with setpoint update law (18) and parameter identifier (34)

$$\hat{\theta}^c(t) = \begin{cases} \hat{\theta}(t), & \text{if } \; t < t_c \\ Q(t_c)^{-1}\, C(t_c), & \text{if } \; t \geq t_c. \end{cases} . \tag{34}$$

If the invertibility condition (equation 35)

$$Q(t_c) = \int_{t_0}^{t_c} w^T(\tau) w(\tau)\, d\tau \succ c_1 I, \tag{35}$$

is satisfied, then for any $\varrho > 0$, there exists constant η_c such that $\lim_{t\to\infty} \|x(t) - x^*(t,\theta)\| \leq \varrho$, with $x^*(t,\theta)$ the unique minimizer of (1). In addition $x \in \mathbb{X}$, $u \in \mathbb{U}$ for all $t \geq 0$.

Proof: We know from from triangle inequality that

$$\begin{aligned} \|x - x^*(\theta)\| \leq \|x - x_r(\hat{\theta})\| + \|x_r(\hat{\theta}) - x_{pa}^*(\hat{\theta})\| \\ + \|x_{pa}^*(\hat{\theta}) - x^*(\hat{\theta})\| + \|x^*(\hat{\theta}) - x^*(\theta)\| \end{aligned} \tag{36}$$

where $x_{pa}^*(\hat{\theta})$ denotes the unique minimizer of the unconstrained problem (15) for $\theta \equiv \hat{\theta}$. Since the MPC controllers guarantees asymptotic convergence of x_e to the origin, we have $\lim_{t\to\infty} \|x - x_r(\hat{\theta})\| = 0$. Also, it follows from Lemma 4, that $\|x_r(\hat{\theta}) - x_{pa}^*(\hat{\theta})\|$ converges exponentially to the origin. Moreover, it is well established that $x_{pa}^*(\hat{\theta})$ converges continuously to $x^*(\hat{\theta})$ as $\eta_c \to \infty$ (Bertsekas, 1995, Proposition 4.1.1). Therefore there exists a class $\mathcal{K}$ function [1] $\alpha_c(\cdot)$ such that

$$\lim_{t\to\infty} \|x_{pa}^*(\hat{\theta}) - x^*(\hat{\theta})\| \leq \alpha_c\left(\frac{1}{\eta_c}\right). \tag{37}$$

The finite-time identification procedure employed ensures that $\hat{\theta} = \theta$ for all $t \geq t_c$, with $t_c < \infty$ and thus $\lim_{t\to\infty} \|x^*(\hat{\theta}) - x^*(\theta)\| = 0$.

Finally, we have

$$\lim_{t\to\infty} \|x(t) - x^*(t,\theta)\| \leq \alpha_c\left(\frac{1}{\eta_c}\right) \tag{38}$$

and the result follows for sufficiently large η_c. The constraint satisfaction claim follows from the feasibility of the adaptive model predictive controllers. ■

7. SIMULATION EXAMPLE

Consider the parallel isothermal stirred-tank reactor in which reagent A forms product B and waste-product C DeHaan and Guay (2005). The reactors dynamics are given by

$$\begin{aligned} \frac{dA_i}{dt} &= A^{in}\frac{F_i^{in}}{V_i} - A_i\frac{F_i^{out}}{V_i} - k_{i1}A_i - 2k_{i2}A_i^2, \\ \frac{dB_i}{dt} &= -B_i\frac{F_i^{out}}{V_i} + k_{i1}A_i, \\ \frac{dC_i}{dt} &= -C_i\frac{F_i^{out}}{V_i} + k_{i2}A_i^2, \end{aligned}$$

where A_i, B_i, C_i denote concentrations in reactor i, k_{ij} are the reaction kinetic constants, which are only nominally known. The inlet flows F_i^{in} are the control inputs, while the outlet flows F_i^{out} are governed by PI controllers which regulate reactor volume to V_i^0.

The economic cost function is the net expense of operating the process at steady state.

$$\begin{aligned} p(A_i,\, s,\, \theta) = \sum_{i=1}^{2} [(p_{i1}s_i + P_A - P_B)k_{i1}A_iV_i^0 \\ + (p_{i2}s_i + 2P_A)k_{i2}A_i^2V_i^0] \end{aligned} \tag{39}$$

where P_A, P_B denote component prices, p_{ij} is the net operating cost of reaction j in reactor i. Disturbances s_1, s_2 reflect changes in the operating cost (utilities, etc) of each reactor. The control objective is to robustly regulate the process to the optimal operating point that optimizes the economic cost (39) while satisfying the following state constraints $0 \leq A_i \leq 3$, $c_v = A_1^2V_1^0 + A_2^2V_2^0 - 15 \leq 0$ and input constraint $0.01 \leq F_i^{in} \leq 0.2$. The reaction kinetics are assumed to satisfy $0.01 \leq k_i \leq 0.2$.

The two-layer approach was used for the simulation. The setpoint value available at sampling instant is passed down to the MPC controller for implementation. The robustness of the adaptive controller is guaranteed via the Lipschitz bound method. The stage cost is selected as a quadratic cost $L(x_e, u_e) = x_e^T\, Q_x\, x_e + u_e^T\, R_u\, u_e$, with $Q_x > 0$ and $R_u \geq 0$.

Terminal Penalty and Terminal Set Design Let $x = [A_1,\; A_2]^T$, $\theta = [k_{11},\, k_{12},\, k_{21},\, k_{22}]^T$ and $u = [F_1^{in},\; F_2^{in}]^T$, the dynamics of the system can be expressed in the form:

$$\begin{aligned} \dot{x} = \underbrace{-\begin{bmatrix} \dfrac{x_1 k_{V1}(\xi_1 - V_1^0 + \xi_3)}{\xi_1} \\ \dfrac{x_2 k_{V2}(\xi_2 - V_2^0 + \xi_4)}{\xi_2} \end{bmatrix}}_{f_{p1}} \\ + \underbrace{\begin{bmatrix} \dfrac{A_{in}}{\xi_1} & 0 \\ 0 & \dfrac{A_{in}}{\xi_2} \end{bmatrix}}_{f_{p2}} u - \underbrace{\begin{bmatrix} x_1 & 2x_1^2 & 0 & 0 \\ 0 & 0 & x_2 & 2x_2^2 \end{bmatrix}}_{g} \theta, \end{aligned}$$

where ξ_1, ξ_2 are the two tank volumes and ξ_3, ξ_4 are the PI integrators. The system parameters are $V_1^0 = 0.9$, $V_2^0 = 1.5$, $k_{v_1} = k_{v_2} = 1$, $P_A = 5$, $P_B = 26$, $p_{11} = p_{21} = 3$ and $p_{12} = p_{22} = 1$.

A Lyapunov function for the terminal penalty is defined as the input to state stabilizing control Lyapunov function (iss-clf):

$$W(x_e) = \frac{1}{2}\, x_e^T\, x_e \tag{40}$$

[1] A continuous function $\mu : \mathbb{R}^+ \to \mathbb{R}^+$ is of class $\mathcal{K}$ if it is strictly increasing and $\mu(0) = 0$.

Choosing a terminal controller

$$u = k_f(x_e) = -f_{p_2}^{-1}\Big(- f_{p_1} + k_1 x_e + k_2\, g\, g^T\, x_e\Big), \quad (41)$$

with design constants $k_1,\ k_2 > 0$, the time derivative of (40) becomes

$$\dot{W}(x_e) = -k_1\, x_e^T\, x_e - x_e^T\, g\, \theta - k_2 x_e^T\, g\, g^T\, x_e \quad (42)$$

$$\leq -k_1 \|x_e\|^2 + \frac{1}{4k_2}\|\theta\|^2 \quad (43)$$

Since the stability condition requires $\dot{W}(x_e(T)) + L(T) \leq 0$. We choose the weighting matrices of L as $Q = 0.5I$ and $R = 0$. The terminal state region is selected as

$$\mathbb{X}_{e_f} = \{x_e\ :\ W(x_e) \leq \alpha_e\} \quad (44)$$

such that

$$k_f(x_e) \in \mathbb{U}, \quad \dot{W}(T) + L(T)\ \leq 0, \quad \forall(\theta,\, x_e) \in\ (\Theta,\, \mathbb{X}_{e_f}) \quad (45)$$

Since the given constraints requires the reaction kinetic θ and concentration x to be positive, it follows that

$$\dot{W} + L = -(k_1 - 0.5)\|x_e\|^2 - x_e^T\, g\, \theta - k_2 x_e^T\, g\, g^T\, x_e \leq 0 \quad (46)$$

for all $k_1 > 0.5$ and $x_e > 0$. Moreover, for $x_e < 0$, the constants k_1 and k_2 can always be selected such that (46) is satisfied $\forall\ \theta \in \Theta$. The task of computing the terminal set is then reduced to finding the largest possible α_e such that for $k_f(.) \in \mathbb{U}$ for all $x \in \mathbb{X}_{e_f}$.

The simulation results are presented in Figures 1 to 3. The phase trajectories displayed in Figure 1 shows that the reactor states obeys the imposed constraints while Figure 2 shows that the actual, unknown setpoint cost $p(t, x_r, \theta)$ converges to the optimal, unknown $p^*(t, x^*, \theta)$. Figure 3 shows the convergence of the parameter estimates to the true values.

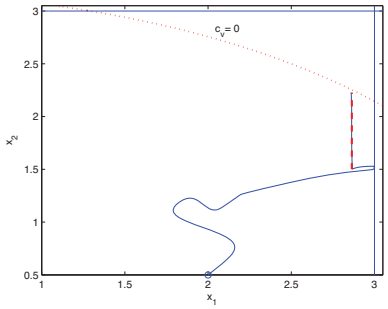

Fig. 1. Phase diagram and feasible state region

8. CONCLUSIONS

This paper provides a formal design technique for integrating RTO and MPC for constrained nonlinear uncertain systems. The solution is based upon the tools and strategies developed in the previous chapters. A single layer and two-layer approaches are presented.

REFERENCES

Dimitri P. Bertsekas. *Nonlinear Programming*. Athena Scientific, Belmont, MA, 1995.

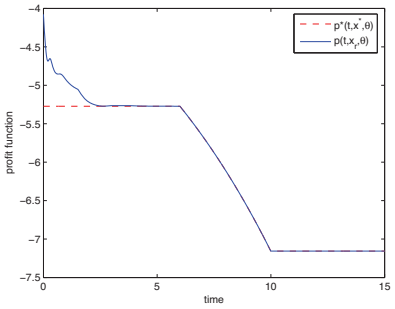

Fig. 2. Optimal and actual profit functions

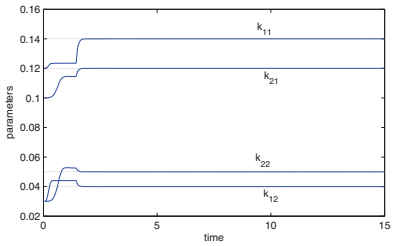

Fig. 3. Unknown parameters and estimates

D. DeHaan and M. Guay. Extremum seeking control of state constrained nonlinear systems. *Automatica*, 41(9): 1567–1574, 2005.

R. Findeisen, H. Chen, and F. Allgöwer. Nonlinear predictive control for setpoint families. In *American Control Conference*, pages 260–264, 2000.

L. Magni. On robust tracking with nonlinear model predictive control. *Int. J. Control*, 75(6):399–407, 2002.

Appendix A. ALGORITHMS

Algorithm 3. Let $\mathcal{E}(\sigma) = \lambda_{\min}(\Gamma Q(\sigma))$, beginning from time $t_{i-1} = t_0$, the parameter and set adaptation is implemented iteratively as follows:

(1) **Initialize** $z_\theta(t_0) = z_\theta^0$, $\Theta(t_0) = B(\hat{\theta}(t_0), z_\theta(t_0))$, $\bar{\mathcal{E}} = \mathcal{E}(t_0) = 0$

(2) **Implement** the following adaptation law over the interval $\tau \in [t_{i-1},\ t_i)$

$$\dot{z}_\theta(\tau) = -\bar{\mathcal{E}} z_\theta(\tau) \quad (A.1)$$

(3) At time t_i, **perform** the updates

$$\bar{\mathcal{E}} = \begin{cases} \mathcal{E}(t_i), & \text{if } \mathcal{E}(t_i) \geq \mathcal{E}(t_{i-1}) \\ \mathcal{E}(t_{i-1}), & \text{otherwise} \end{cases} \quad (A.2)$$

$$\Big(\hat{\theta},\ \Theta\Big) = \begin{cases} \Big(\hat{\theta}(t_i),\ \Theta(t_i)\Big), & \text{if } z_\theta(t_i) - z_\theta(t_{i-1}) \\ & \leq -\|\hat{\theta}(t_i) - \hat{\theta}(t_{i-1})\| \\ \Big(\hat{\theta}(t_{i-1}),\ \Theta(t_{i-1})\Big), & \text{otherwise} \end{cases} \quad (A.3)$$

(4) **Iterate** back to step 2, **incrementing** $i = i + 1$.

Dantzig-Wolfe decomposition for real-time optimization - applied to the Troll west oil rim

Vidar Gunnerud * **Bjarne Foss** * **Bjørn Nygreen** **
Randi Vestbø ** **Nina C. Walberg** **

* *Department of Engineering Cybernetics, NTNU, Trondheim Norway*
** *Department of Industrial Economics and Technology Management, NTNU, Trondheim Norway*

Abstract: This paper studies different decomposition approaches for real-time optimization of process systems with a decentralized structure where the idea is to improve computational efficiency and transparency of a solution. The contribution lies in the application and assessment of the Dantzig-Wolfe method which allows us to efficiently decompose a real-time optimization problem into parts. Furthermore, the nonlinear system is modeled by piecewise linear models with the added benefit that error bounds on the solution can be computed.
The merits of the method are studied by applying it to a semi-realistic model of the Troll west oil rim, a petroleum asset with severe production optimization challenges due to rate dependent gas-coning wells. This study indicates that the Dantzig-Wolfe approach offers an interesting and robust option for complex production systems. Moreover, the method compares favourable with earlier results using Lagrangian relaxation which again was favourable compared to a global approach.

Keywords: Optimization, Dantzig-Wolfe Decomposition, Petroleum production, Plantwide control.

1. INTRODUCTION

Development of a petroleum field asset requires planning on multiple horizons. On a life-cycle horizon, strategic decisions are made on field development such as the choice of technology and export options, and investment and recovery strategies. For offshore assets the choice of technology may include subsea solutions, and the issue of processing the reservoir fluid offshore or onshore (Nygreen et al., 1998). On a medium time horizon, typically three months to two years, production targets are decided. Depending on the life cycle of an asset, decisions may also involve a drilling program. During for instance the green field stage, it is important to plan, drill and commision new wells to reach some pre-defined plateau rate as soon as possible. A reservoir simulator, containing anything between 100.000 and $1,000,000$ states, is usually an important planning tool on the medium time horizon. A reservoir simulator will be quite complex if the geology is complex, due to heteregeneities like faults and shale layers, to represent flow patterns accurately.

On a shorter time horizon, typically days to weeks, production optimization where both the sub-surface part, like the reservoir and wells, *and* the surface part like the manifolds, pipelines and downstream production equipment, is taken into account is important. This is commonly called the real-time production optimization (RTPO) problem. Production may be constrained by reservoir conditions such as coning effects and/or the production equipment like pipeline capacity or downstream water handling capacity, and constraints may move from one part of the system to another part over time. Water production may e.g. be low early on and increase dramatically during the decline phase of a reservoir thereby making water handling capacity an issue. Decision variables in RTPO include production and possibly injection rates, and routing of well streams. A typical production system structure is shown in Fig.1. It has two separate non-connected reservoirs from which 11 wells feed into three manifolds and pipelines, and finally into the downstream facilities section. Manifold 1 and 2 belong to one cluster, while manifold 3 belongs to the other cluster.

RTPO is in use in the upstream industry today. Wang (2003), Saputelli et al. (2003) and Bieker et al. (2006) provide readable overviews. It might be noted that these references focus on the value chain from the reservoir to, and not including, the downstream processing equipment. The downstream boundary is typically a constant pressure on the inlet separator. A few publications on RTPO for the production chain from the reservoir to export are available; Foss and Halvorsen (2009), Selot et al. (2007). Commercial products for RTPO are available, but not widely used. Two of them are GAP and MaxPro. They model the well and near well region, and the pipeline system, and solve the optimization problem using a nonlinear programming (NP) algorithm like sequential quadratic programming (SQP).

There are several factors which complicate the RTPO problem.

- RTPO may give rise to optimization problems with both continuous and discrete decision variables. Discrete decision variables are found in routing when there is a choice to route the fluid from a manifold to one of several flow lines. The presence of discrete decision variables complicates the optimization problem by transforming a linear program (LP) or a nonlinear program (NP) to a mixed integer linear program (MILP) or a mixed integer nonlinear program (MINLP), respectively. Güyaguler and Byer (2007) discusses RTPO in the context of MILP while Kosmidis et al. (2005) use a MINLP formulation.
- The models in the optimization problem are often nonlinear, some of which may be highly nonlinear, as will be discussed later. This includes well models as well as pressure drop models for the pipelines which support multiphase fluid transport.
- The optimization problems are usually quite large and may include several hundred decision variables. An example is the rate allocation problem at Troll which in total includes more than one hundred wells (Hauge and Horn, 2005).

This paper focusses on the RTPO problem for systems with a decentralized structure meaning that common constraints are quite few. Such strucures are quite typical in the upstream petroleum industries as visualized by Fig.1. The contribution lies in the application and assessment of the Dantzig-Wolfe method which allows us to decompose a RTPO problem into parts meaning that we apply a divide-and-conquer strategy which is a sound engineering design principle. This principle has survived ever since complex systems came into making. The Dantzig and Wolfe principle dates back to 1960 (Dantzig and Wolfe, 1960).

A few recent publications apply Dantzig-Wolfe decomposition (DWD) to process systems. Alabi and Castro (2009) apply DWD to a refinery planning problem, formulated as a large LP problem, by decomposing it along the value chain. They show substantial savings in computation time. They also point to the inclusion of binary decision variables, which will be addressed in this paper, as a future task. Cheng et al. (2008) propose DWD as a means for designing a decentralized MPC for plant-wide MPC coordination. Again substantial computational savings are reported for the LP formulation chosen. This paper also gives a very readable introduction to DWD. Both papers state that DWD is particularly well suited for large problems with well-structured subproblems and a small number of linking constraints.

This study will show that the Dantzig-Wolfe approach offers an interesting and robust option for complex production systems wiht certain structural properties. Moreover, the method compares favourable with earlier results using Lagrange relaxation (LR) (Foss et al., 2009) on a realistic field case. The nonlinear system will be modeled by piecewise linear models with the added benefit that error bounds on the solution of the production optimization problem can be computed.

The remainder of this paper is organized as follows. First, the RTPO problem is presented in a mathematical context before the decomposition approach in general and the Dantzig-Wolfe method in particular are presented.

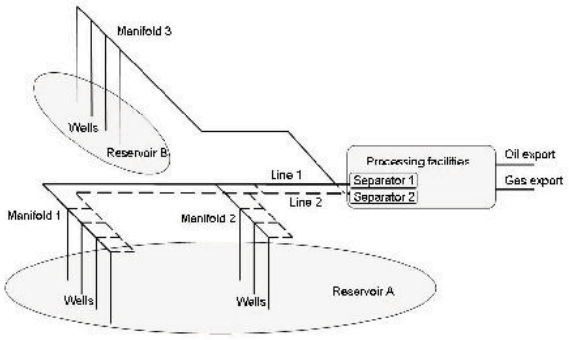

Fig. 1. A petroleum production system with two separate reservoirs from which 11 wells feed into 3 manifold and 3 pipelines. Manifold 1 and 2 belong to one cluster, while manifold 3 belongs to the other cluster. The pipeline flows provide input to the processing facilities where fluids are conditioned for export.

Subsequently, the Troll west oil rim case is presented and results are shown. Finally, results are discussed and some conclusions end the paper.

2. FORMALIZING THE RTPO PROBLEM

The RTPO problem will in most cases mean maximizing oil production while honouring system constraints like capacities in pipelines and wells, safety regulations and preventing damage on long-term effects, in particular recovery of available hydrocarbon resources. The latter point is important. An example of the interplay between short term production and long-term recovery was shown in Naus et al. (2006) in the sense that accelerated short-term production reduced long-term recovery.

The optimization problem is usually treated in a quasi-dynamic way by re-optimizing a stationary optimization problem, typically once a day. The solution of the mathematical RTPO will serve as a recommendation to the operating engineers who may or may not follow the advise. One reason for neglecting a recommendation may hinge on the fact that the transition cost of changing from one routing configuration to another is not included in the optimization problem. Therefore such a change will only be implemented if there is a substantial gain by doing this.

Referring again to Fig.1 to explain upstream systems closer, there are four wells connected to manifold 1 and 3, respectively, and three wells connected to manifold 2. Well streams from each well are connected to one pipeline. Hence, each of the wells in manifold 1 and 2 can be connected to either of the two pipelines transporting the reservoir streams to downstream processing. There is only one pipeline from manifold 3, and therefore no routing decision is necessary in this part of the system. The decision variables on each well are usually one production choke valve to adjust production and on-off valves linking a well to one of the pipelines. Further, different well completions may give rise to additional decision variables like the injected gas-rate for a gas-lift well, a commonly used technology to increase well lifetime as reservoir pressure decreases. Altogether this means that there will be both continuous as well as discrete decision variables in a typical

RTPO problem. The well and pipeline system is divided into clusters. There are two cluster in Fig.1, one covering manifold 1 and 2, and the second includes manifold 3. Hence, a cluster may include one or more manifolds.

We focus on production systems with a decentralized structure where common constraints may include downstream processing capacity limitations and common pipelines. In the following we present a system model which encompasses a large class of upstream production systems. Some simplifications are made to ease the explanation. For instance we assume only one manifold for each cluster in this section. An extension to several manifolds per cluster, as is the case for manifold 1 and 2 in Fig.1, is however straightforward. In fact in the Troll case treated later the clusters have two manifolds each.

We first present a system model for a subsystem, denoted cluster i, before the integrated optimization problem is described.

Indexes, constants and decision variables are explained in Table 1 and 2.

2.1 Modelling a subsystem

In the following we present and comment the model of *one* subsystem, cluster i.

- Mass balance is preserved for each phase, i.e. gas, oil and water, at each node. This means that no phase transition takes place at the surface of a cluster.
$$\sum_{j=1}^{J(i)} q_{ij}^p = q_i^p, \quad p \in \{g, o, w\} \tag{1}$$
- The routing problem is parameterized through binary variables for each well, one for each line; y_{ij}^l. If $y_{ij}^l = 1$ the well is connected to line l, if not it is zero. Each well cannot be connected to more than one line, hence
$$\sum_{l=1}^{L(i)} y_{ij}^l \leq 1, \quad y_{ij}^l \in \{0,1\}, \quad j \in \{1, \ldots, J(i)\} \tag{2}$$
This implies that the flow q_i^p from one cluster is divided onto $L(i)$ pipelines.
- The well model, or performance curve for gas, oil and water, are given by the following nonlinear structure
$$q_{ij}^p = d_{ij}^p(p_{ij}^{res}, p_{ij}^{wh}), \tag{3}$$
$$p \in \{g, o, w\}, \quad j \in \{1, \ldots, J(i)\}$$
where p_{ij}^{res} and p_{ij}^{wh} denotes the reservoir pressure locally at the well and the pressure at the wellhead, respectively. Depending on the reservoir conditions near a well the complexity of these well models vary a lot. The simplest version will be a linear model. In systems with rate-dependent gas coning however, as in the Troll oil case (Hauge and Horn, 2005), nonlinearities can be severe.
- The pressure drop across the production choke is given by
$$y_{ij}^l p_i^l \leq p_{ij}^{wh}, \tag{4}$$
$$j \in \{1, \ldots, J(i)\}, \quad l \in \{1, \ldots, L(i)\}$$
This constraint may only be binding if $y_{ij}^l = 1$ since it is always satisfied for $y_{ij}^l = 0$.
- Flow into the pipelines from cluster i to the platform is given by
$$q_i^{pl} = \sum_{j=1}^{J(i)} y_{ij}^l q_{ij}^p \tag{5}$$
$$p \in \{g, o, w\}, \quad l \in \{1, \ldots, L(i)\}$$
- The pressure drop in a pipeline segment from cluster i to the inlet separator depends nonlinearily on the flow of gas, oil and water in the pipe segment. The nonlinearities are particularly severe during the transition from one multiphase flow regime to another, and when a pipeline exhibits slugging. More on multiphase flow may e.g. be found in Brenne (2005)
$$p^{sep} - p_i^l = d_i^l(q_i^{gl}, q_i^{ol}, q_i^{wl}), \tag{6}$$
$$l \in \{1, \ldots, L(i)\}$$
- There are non-negativity conditions on all flow and pressure variables, i.e. backflow is not modeled.

It should be added that the downstream boundary condition is given by a fixed inlet separator pressure p^{sep}, and we assume that it is equal for all $L(i)$ pipelines. Further, it is straightforward to include additional local constraints like for instance the flowrate from a well due some external reason. This could be well-related problems like sand production, or reservoir based constraints as discussed earlier. Such contraints will typically induce relations like $q_{ij}^o + q_{ij}^w \leq q_{ij}^{\max}$

Table 1. The indexes used.

i	-	cluster i
I	-	no. of clusters
$p \in \{g, o, w\}$	-	phase index - gas, oil or water
ij	-	well j in cluster i
$J(i)$	-	no. of wells linked to cluster i
$l \in \{1, .., L(i)\}$	-	line index for cluster i
$L(i)$	-	no. of lines linked to cluster i

Table 2. The variables and data used to define the sub-problem.

q_i^p	-	total mass flowrate of phase p from cluster i
q_{ij}^p	-	mass flowrate of phase p from well j in cluster i
q_i^{pl}	-	mass flowrate of phase p through line l in cluster i
y_{ij}^l	-	binary variable equal to 1 if well ij is routed to line l
p_{ij}^{res}	-	reservoir pressure at well ij
p_{ij}^{wh}	-	wellhead pressure
d_{ij}^p	-	well performance model
d_i^l	-	pipeline pressure drop model
p_i^l	-	pressure in line l subsea in cluster i
p^{sep}	-	separator pressure

2.2 The integrated problem

The RTPO problem is specified below. The objective function is defined by the total oil production, and the global constraints are given by gas and water handling capacities in the downstream part of the value chain. Hence, the objective function and common constraints are given by

$$max \sum_{i=1}^{I} q_i^o \quad (7)$$

$$\sum_{i=1}^{I} q_i^g \leq \overline{q}^g \quad (8)$$

$$\sum_{i=1}^{I} q_i^w \leq \overline{q}^w \quad (9)$$

The objective function and common constraints are linear and additive and each term $q_i^o = \sum_{j=1}^{J(i)} q_{ij}^o$ is a function of only local variables.

The complete RTPO problem consists of I clusters, each modelled by (1)-(6), or an extension of these equations due to several manifolds in one cluster, and the integration through (7)-(9).

The actual decision variables are production choke openings and on-off valves linking a well to a pipeline. The production choke openings are not directly a part of the optimization problem. They are calculated using the pressure drop across the production choke (4) and the flowrate through the production choke $(q_{ij}^g, q_{ij}^o, q_{ij}^w)$ in an appropriate valve model.

2.3 Piecewise linearization and SOS2 sets

The optimization problem contains both continuous and discrete variables. Furthermore, nonlinear well and pressure drop models are present. Hence, this is basically a MINLP problem. We transform this into a MILP problem by replacing the nonlinear constraints by linear constraints and constraints on some auxiliary integer variables. The procedure is as follows: The nonlinear constraints, (3) and (6), are replaced by piecewise linear approximations. These piecewise linear approximations are modelled by linear constraints and discrete variables, i.e. integer constraints, using Special Ordered Sets of type 2 (SOS2). The discrete variables are necessary to assure interpolation between neighbouring points only, Williams (2005), as in any piecewise linear approximation of a nonlinear function. The number of linear constraints and integer constraints necessary to replace one nonlinear constraint depends on the nonlinearities and approximation accuracy. Higher accuracy means more interpolation points and hence more linear and integer constraints.

3. DECOMPOSITION

3.1 Principle

When a problem becomes too large or complicated to handle, a decomposition approach can be applied if the problem structure is suitable. The basic mechanism in all decomposition principles is to decompose the original problem into smaller sub-problems which are coordinated by a "master" problem. There exists multiple decomposition techniques to solve large problems. Two common methods are Lagrange relaxation and Dantzig-Wolfe decomposition.

Both LR and DWD are suited for problems with a block angular constraint structure which is the case for the RTPO problem described above. The structure is exploited when the original problem is split into sub-problems, while the common constraints remain in the master problem.

In LR (Beasley, 1993) the basic idea is to attach Lagrange multipliers to the common constraints in the model and relax these in the objective function, while DWD handles the common constraints in a master problem. The resulting integrated optimization problem will hence fall apart into I local optimization problems, one for each cluster i (Fisher, 1985). For (convex) LP problem the solution of I such local optimization problems provides the same solution as (1)-(9) provided that the Lagrange multipliers for the common constraints λ^g, λ^w are known. Hence, the Lagrange multipliers put a common cost to the use of a scarce resource by each local problem.

3.2 Dantzig-Wolfe decomposition

When applying DWD to the RTPO problem the sub-problems will be identical to LR. However, while the Lagrange multipliers are updated by a simple heuristic in the LR case, the update is now done by solving an LP-problem.

We start by assuming linear constraints and continous variables, i.e. an LP-problem instead of a MILP problem. The master problem is a reformulation of the integrated problem. By taking advantage of the fact that a convex combination of basic feasible points, which are corner points of the feasible set defined by the linear constraints of the integrated problem, also is a feasible solution, an alternative formulation can be achieved. Each basic feasible point in the integrated problem is then represented as a variable in the master problem. The number of basic feasible points for any practical problem can clearly be prohibitively high, and in reality only a small number of these basic feasible points will ever enter the basis in the master problem. The idea is then to restrict the master problem by reducing the number of basic feasible points. This is called a Restricted Master Problem (RMP).

Hence, we start with a few basic feasible points and check if the solution of the integrated problem is within a convex combination of these points. If this is not the case new basic feasible points are included in a structured way until the optimal solution has been found (Williams, 2005). This is usually called column generation and several procedures are proposed in the literature; either adding one or several columns, i.e. new basic feasible points, at each iteration (Dantzig and Thapa, 2002). Some details of the algorithm are given below with some related comments specific to the RTPO problem.

Algorithm structure

1. Choose two initial basic feasible points for each local optimization problem.

2. Specify the RMP as a LP for the given set of basic feasible points. Then solve it and compute values for the Lagrange multipliers for the global constraints, i.e. λ^g, λ^w. The RMP is specified in a separate section below.

3. Solve I local optimization problems by using the Lagrange multipliers computed in 2.

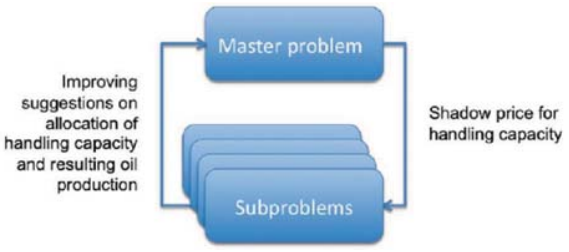

Fig. 2. Iteration structure for Dantzig-Wolfe Decomposition (DWD) and Lagrangian Relaxation (LR)

4a. For $i \in \{1, \ldots, I\}$: If the solution of a local optimization problem i extends the convex set defined by the basic feasible points used in 2, then add these basic feasible points to the RMP, and go to 2. (This implies that the feasible region of this new RMP is extended).

4b. If the solutions of all the local optimization problems are unchanged, the optimal solution has been found; and the algorithm terminates.

The main iteration loop is shown in Fig.2. This figure is also applicable for LR if the master problem box is understood as the updating algorithm for the the Lagrange multipliers for the global constraints.

In view of our RTPO problem item 1 above implies that two feasible solutions for each cluster must be determined to start the algorithm.

3.3 Restricted master- and sub-problem

The procedure is to update the Lagrange multiplier in a way that the consumption of the relaxed common constraints converge to their optimal values. Each subproblem is defined by (again only including two common constraints)

$$\begin{aligned} max \quad & q_i^o - \lambda^g q_i^g - \lambda^w q_i^w - \lambda_i^{CONVEX} \\ & \lambda \geq 0, \quad i \in \{1, \ldots, I\} \end{aligned} \tag{10}$$

and the local constraints (1)-(6). λ_i^{CONVEX} is the Lagrange multiplier for the convexity constraint in the RMP defined below. Since no sub-problem variables are associated with it, it will only act as a constant in the subproblem.

The RMP can now be formulated. z_{is}^p represents one basic feasible point s from sub-problem i. z_{is}^p could in principle include the optimal value of all decision variables for subproblem i after solving it given λ^g and λ^w. However, only the variables also present in the objective function and the common constraints will be relevant for the RMP. Hence, z_{is}^p will for this RTPO problem contain some flow variables (q_i^o, q_i^g, q_i^w), but no pressure variables. μ_{is} is the corresponding weight the master problem will give this basic feasible point. The objective function of the master problem is given in (11). Further, (12) and (13) represents the constrained common resources, while (14) is the convexity constraint.

$$max \sum_i \sum_{s \in S_i} z_{is}^o \mu_{is} \tag{11}$$

$$\sum_i \sum_{s \in S_i} z_{isp}^g \mu_{is} \leq \overline{q}^g \tag{12}$$

$$\sum_i \sum_{s \in S_i} z_{isp}^w \mu_{is} \leq \overline{q}^w \tag{13}$$

$$\sum_{s \in S_i} \mu_{is} = 1 \quad i \in \{1, \ldots, I\} \tag{14}$$

$$\mu_{is} \geq 0 \tag{15}$$

3.4 Integer variables

DWD will find exact optimal solutions for feasible LP problems. If it is extended to a MILP problem, however, Branch & Price (Desrosiers and Lubbecke, 2006) or some heuristics have to be applied to handle the integer properties. When solving the master problem, we have not imposed integer restrictions on μ_{is}, i.e. the RMP is solved as an LP to achieve Lagrange multipliers for (12) - (14). The resulting solution may then be infeasible with respect to the original MILP problem, since a convex combination of two different basic feasible points is not necessarily feasible. As mentioned, this could be handled in several ways. However, if a satisfying number of basic feasible points are generated up front, a feasible solution could simply be found by demanding integer values for μ_{is} and solve the RMP as an MIP problem. Vanderbeck (2006) adresses the use of DWD on mixed integer problems.

3.5 Solution quality

For both LP and MILP problems, upper and lower bounds on the objective function can be computed. The LP solution of the RMP plus the sum of the objective values of the sub-problems will act as an upper bound (Karlof, 2006). In the LP case, the solution of the RMP alone will give a feasible lower bound, while for the MILP problems a heuristic has to be applied to create the feasible lower bound. By using these bounds actively during the optimization process, it is possible to terminate the optimization problem when an acceptable gap is achieved.

4. RESULTS

The Troll field is a huge oil and gas field on the continental shelf west of Norway. Production allocation is complex as described in (Hauge and Horn, 2005). We study the Troll C production system shown in Fig.3 where primarily oil is produced from an oil rim through more than 50 wells. Well models and pressure drop models for multiphase flow in pipelines are based on typical models as encountered in this application. Hence, the models should be understood as approximations of the actual well and pipeline models. Each nonlinear model is approximated by a piecewise linear model. A well model (3) is typically divided into somewhere between 10 and 100 linear segments with the wellhead pressure as its input. The pipeline models require more linear segments since they depend on three inputs, cf. (6). There are 8 clusters, and each cluster has a complex structure in the sense that they contain two manifolds. Each cluster has $6-8$ wells and the total number of wells is 64. For the moment only the gas handling capacity is a binding constraint. Water handling will become an issue

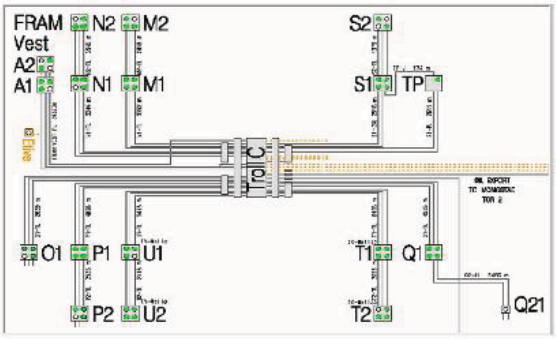

Fig. 3. Topology for the wells connected to the Troll C platform

in the near future as the reservoir drains and therefore produces more water.

The purpose of the numerical study is to investigate the DWD performance compared to a global strategy and the LR method proposed in Foss et al. (2009). Three different strategies were therefore defined:

(1) A global strategy where all clusters are solved in one large MILP problem.
(2) The LR method proposed in Foss et al. (2009).
(3) The DWD method proposed in this paper.

The computations were performed on an IBM Thinkpad T60P with a $2.33GHz$ processor and a tolerance bound of 0.5% for LR and DWD. The state-of-the-art XPress-MP software suite is used to solve the MILP problems. The main results are presented in Table 3. Results are presented column-wise for different system sizes starting with two cluster and ending with the full 64 well/8 cluster system. The gas capacity for each scenario increases with the number of clusters as shown in line 2. In the next three lines the number of variables and constraints are listed. Then follows the results in terms of computation time and oil production which is the ultimate goal, cf. (7).

Finally, it should be noted that the results in Table 3 represent typical values as observed after several test runs.

Table 3. Results from tests on the model of the Troll C production system.

No. of clusters	2	4	6	8
Gas cap.[Sm^3/day]	3000	12000	18000	24000
Continuous variables	13898	27805	41766	55688
Discrete variables	1029	2134	3725	4819
Constraints	491	981	1639	2185
Strategy 1 - Global				
Solution time [min]	0.26	7.38	237.0	720.0
Oil [Sm^3/day]	1777	6487	11641	14365
Strategy 2 - LR				
Solution time [min]	1.42	8.54	18.2	19.2
Oil [Sm^3/day]	1774	6467	11640	14440
Strategy 3 - DWD				
Solution time [min]	1.86	1.43	6.16	11.3
Oil [Sm^3/day]	1777	6458	11629	14473

5. DISCUSSION

The main observation to make is the fact that the decomposition stratgies, DWD and LR, outperform the global method for the combined rate allocation and routing problem for all but the smallest 2 cluster problem. The global method does not converge to its termination criteria after 12 hours for the eight cluster case and in general it has a hard time solving problems consisting of 6 clusters or more. Furthermore, DWD shows superior performance to LR.

By taking a closer look at the 2 cluster problem, the global method is actually fastest. This is not surprising as it is expected that the global method would be faster for small problems. For the medium size problem with 4 clusters, the global method is still working fine, and is actually faster than LR. DWD is in this case extremely quick, due to few main iterations. For the larger problems, we observe that the two decomposition methods are much faster than the global method, and that DWD is significantly faster than LR.

The reason why DWD is faster than LR is related to the updating of Lagrange multipliers. The DWD master problem finds good multipliers with fewer iterations than the LR master problem, and on average converges after fewer iterations. It should be mentioned that the computations involved in solving the DWD master problem, i.e. the LP-problem, is small compared to solving the local MILP-problems. Hence, this is no issue when comparing DWD and LD.

DWD is more stable with respect to solution time than LR. Furthermore, DWD has few tuning parameters, and works well for changing data sets. LR in contrast, is quite sensitive to perturbations of the data set. A minor change might result in a doubling of the solution time. However, extensive knowledge of the problem will give the operator a good feel for which parameter values result in fast convergence.

Focussing on solution quality, we observe that the global method finds the optimal solution for all except the full field problem with 8 clusters. In that case the method was stopped after 12 hours, with still a little more than 7.5% in duality gap. The decomposition methods terminate with less than 0.5% duality gap for all problems. The solution time does of course depend on the resolution of the piecewise linear models. A cruder approximation reduces run-time and vice versa.

DWD provides a framework for decomposing a problem and still keep track of the optimal solution for the integrated problem. This approach has potential advantages in terms of algorithmic efficiency as indicated by the test case in the previous section. The DWD algorithm, as well as LR, has some interesting properties. First, the sub-problems may be solved using different algorithms or even different software packages. This feature is interesting for integrated optimization applications which may encompass reservoir, wells, pipelines and processing facilities. It should be added that the duality gap can only be computed if upper and lower bounds on the solution can be found. This is in general not possible if the sub-problems are nonlinear programs as opposed to MILPs. A second useful property of the algorithmic structure is the potential for parallel computing since each sub-problem is self-contained and has no dependency on the other sub-problems. If the computational load between the sub-

problems is well-balanced a parallel implementation will be particularly efficient.

The optimization problem is usually treated in a quasi-dynamic way by re-optimizing the stationary optimization problem, typically once a day. More frequent disturbances may be handled by selecting a couple of wells for frequent production changes to compensate variations in for instance gas processing capacity. Well models are typically updated twice a year by running well tests to collect data to estimate well parameters. The use of dynamic models is an issue. Some applications may benefit from dynamic well models, in particular during start-up of wells. Start-up may occur quite often since many wells are shut-in from time to time due to maintenance or operational problems. Applications with long pipelines may also benefit from dynamic pipeline models provided the dynamics are important for optimal performance.

6. CONCLUSIONS

This paper argues that Dantzig-Wolfe Decomposition is well suited for the well allocation and routing problem in the upstream industries. There are several reasons for this. DWD clearly outperforms a global method. DWD has several similarities to LR. However, as the results show, DWD gives better performance than LR in all relevant cases tested herein. This is due to more efficient updating of the dual variables. Furthermore, an error bound on the solution of the production optimization problem can easily be computed. This is clearly information of interest to any user. Finally, the algorithm is efficient and can be parallelized for even higher efficiency.

Acknowledgments: We acknowledge the support of the Center for Integrated Operations at NTNU, Norway.

REFERENCES

Alabi, A. and Castro, J. (2009). Dantzig-wolfe and block coordinate-descent decomposition in large-scale integrated refinery planning. *Computers and Operations Research*, 36, 2472–2483.

Beasley, J. (1993). *Modern Heuristics Techniques for Combinatorial Problems*, 243–303. Halsted Press.

Bieker, H., Slupphaug, O., and Johansen, T. (2006). Real-time production optimization of offshore oil and gas production systems: A technology survey. *SPE 99446*.

Brenne, C.E. (2005). Fundamentals of multiphase flow. *Cambridge university press*.

Cheng, R., Forbes, J.F., and Yip, W. (2008). Dantzig-wolfe decomposition and plant-wide mpc coordination. *Computers and Chemical Engineering*.

Dantzig, G.B. and Wolfe, P. (1960). Decomposition pricniple for linear programs. *Operations Research*, 8, 101–111.

Dantzig, G. and Thapa, M. (2002). Linear programming 2: Theory and extensions. *Springer Verlag*.

Desrosiers, J. and Lubbecke, M.E. (2006). *Column Generation*, 1–32. Springer US.

Fisher, M.L. (1985). An application oriented guide to lagrangian relaxation. *Interfaces*, 15, 10–21.

Foss, B., Gunnerud, V., and Dueñas Díez, M. (2009). Lagrangian decomposition of oil production optimization - applied to the Troll west oil rim. *Accepted for SPE Journal*.

Foss, B. and Halvorsen, I.J. (2009). Dynamic optimization of the lng value chain. *Proceedings of the 1st Annual Gas Processing Symposium*.

Güyaguler, B. and Byer, T. (2007). A new production allocation optimization framework. *SPE 105200*.

Hauge, J. and Horn, T. (2005). The challenge of operating and maintaining 115 subsea wells on the troll field. *Offshore Technology Conference*.

Karlof, J.K. (2006). *Integer Programming: Theory and Practice*, chapter 4: Decomposition in Integer Linear Programming. CRC Press.

Kosmidis, V.D., Perkins, J.D., and Pistikopoulos, E.N. (2005). A mixed integer optimization for the well scheduling problem on petroleum fields. *Computers and Chemical Engineering*, 29, 1523–1541.

Naus, M., Dolle, N., and Jansen, J. (2006). Optimization of commingled production using infinitely variable inflow control valves. *SPE Production and Operations*, 21, 293–301.

Nygreen, B., Christiansen, M., Haugen, K., Bjorkvoll, T., and Kristiansend (1998). Modeling norwegian petroleum production and transportation. *Annals of Operations Research*, 82, 251 267.

Saputelli, L., Mochizuki, S., Hutchins, L., Cramer, R., Anderson, M., and Muller, J. (2003). Promoting real-time optimization of hydrocarbon production systems. *SPE 83978*.

Selot, A., Kuok, L.K., Robinson, M., Mason, T.L., and Barton, P.I. (2007). A model for short-term supply chain management of a lng production system. *IPTC, Dubai, U.A.E.*

Vanderbeck, F. (2006). Implementing mixed integer column generation. *Column Generation, chapter 12, Springer*, 331–358.

Wang, P. (2003). Development and applications of production optimization techniques for petroleum fields. *Ph. D. Dissertation, Standford University*.

Williams, H.P. (2005). *Model Building in Mathematical Programming*. Wiley.

Implementation and Validation of a Closed Loop Performance Monitoring System

Claudio Scali*(*), Marco Farnesi(**), Raffaello Loffredo(**), Damiano Bombardieri (***)

(*) Chemical Process Control Laboratory (CPLab), Department of Chemical Engineering (DICCISM), University of Pisa, Via Diotisalvi n.2, 56126, Pisa (Italy), e-mail: scali@ing.unipi.it
(**) ENI, Refining & Marketing, Raffineria di Livorno, Via Aurelia n.7, 57017, Livorno (Italy),
(***) Sysdat Informatica s.r.l.; Via Meucci 22 - Pisa (Italy)

Abstract: Main features of a performance monitoring systems operating on loops of refinery plants are illustrated together with examples of application and achieved results. The system analyses data recorded by the DCS during routine operation and originates verdicts about performance of control loops; also indications of causes of low performance and different strategies to adopt are given (retuning, valve maintenance, upstream actions). The system architecture is firstly illustrated, with characteristics of modules which accomplish different tasks of data acquisition and transfer, system configuration and priority assignment, performance analysis and verdicts emission, database query and operator support. Examples of field validation are then presented, with illustration of loop performance before and after actions suggested by the monitoring system. A synthesis of main techniques adopted in the system is finally presented.

Keywords: Closed Loop Performance Monitoring, Valve Diagnostic, Identification and Retuning.

1. INTRODUCTION

Closed Loop Performance Monitoring (CLPM) is widely recognized as a primary need in the process industry, as product quality, energy saving, waste minimization depend at a large extent on the efficiency of the control system.

The possibility of evaluating loop performance and being able to diagnose causes of deterioration brings to a direct improvement of plant performance both in the case of base control (SISO PID loops) and in the case of advanced control (MIMO, Optimization), which necessarily relies on good performance of low hierarchy control loops. Different causes of scarce performance, as incorrect tuning of controllers, anomalies and failures of sensors, presence of friction in actuators, external perturbations, should be detected and the right actions to perform should be suggested by the CLPM system.

This is a field where academic research and industrial applications should go ahead in tight contact in order to focus on real problems and to find solutions which are user friendly to be promptly accepted by plant operators. In large scale industrial processes, involving thousands of variables and hundreds of control loops, a monitoring system needs to operate automatically, leaving only key decisions to the operators. Also, results of performance analysis accomplished by the CLPM system should be presented in a very efficient manner to avoid to be seen as an additional work to be performed for plant supervision.

Anyway, even though a completely unattended system can be seen as the optimal solution, the right degree of interaction with plant personnel is of crucial important in the stage of parameter calibration and field validation. Also, the full potential of a CLPM system is fully exploited when the operator has at least a minimum knowledge of performance monitoring issues.

For these reasons, the final system architecture should take into account specific needs and requirements, as well as the skill of the user.

The evolution of academic research can be followed in the abundant literature produced in the last decade: two review papers (Qin, 1998; Thornhill and Horch, 2007) can give a flavour about. Certainly among more important open issues must be considered: the definition of significant performance indices, the development of simple and reliable techniques for automatic detection of causes, the diagnosis of root causes of perturbations in large scale plants. A very active research area is concentrated on methods for automatic diagnosis of valve stiction and many new techniques have been proposed in the last few years. A first comparison can be found in Horch (2006), while Jelali and Scali (2009) compare 11 recently proposed techniques on a benchmark of 93 industrial loops.

The paper illustrates architecture and application results of a Closed Loop Monitoring System recently developed and implemented in an Italian refinery and has the following structure: section 2 presents the overall system, with logic and interaction of different modules performing data acquisition, data transfer and verdicts archiving; section 3 illustrates main features of the system which accomplishes performance analysis and diagnostics; section 4 shows basic

features of the Data Base and the query system; section 5 presents some examples of field validation and gives examples of achieved improvements; finally conclusions and next steps are reported in section 6. An appendix will add some details about the techniques adopted for performance analysis.

2. THE SYSTEM ARCHITECTURE

A synthetic picture of the system architecture is depicted in Figure 1, where different modules, their interconnection and physical location are indicated.

The User Module (MU) starts the whole procedure by sending a message to the module of scheduling (MS) about the sequence of plants (and loops) to be analysed (the procedure is repeated periodically). In addition, it allows to see the state of advancement of operations and to send queries to the database (DB) for a synthesis of performance analysis. The user module also permits the configuration of the loops which is the very first step of the performance monitoring process. Loops configuration consists in the assignment of loop name, DCS address, loop info (for instance: single loop or cascade), priorities and constraints of the acquisition. More important loops can have higher frequency of acquisition, cascade loops are acquired simultaneously, loops of the same process unit are analysed in the same data acquisition run.

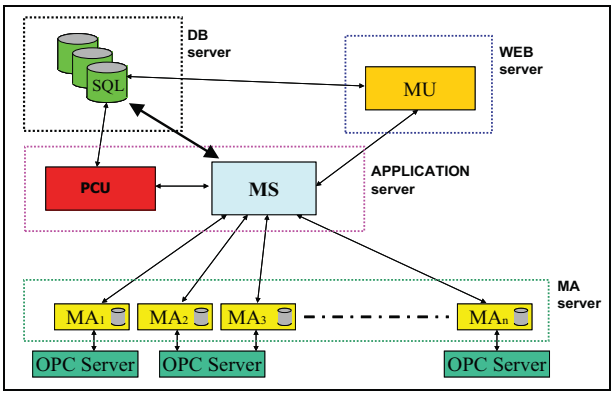

Fig.1: The system architecture

The Scheduling Module (MS), once activated by MU, sends a command to acquisition modules (MAi) which perform physically the acquisition of data from the DCS. For each loop, specific information are transferred to the Data Base (DB) trough MS, such as: loop tag name, controller settings, ranges of controlled variable (PV) and controller output (OP), saturation limits, loop hierarchy (e.g. master/slave of a cascade loop, loops under advanced control), Also information about default, minimum and maximum values for the duration of acquisition and sampling time (ts) are exchanged (default for ts= 10 seconds). Once acquisition is terminated, MS receives from MAi, data files which are sent to the DB input section. It activates the performance analysis accomplished sequentially by the PCU (Plant Check Up) module; finally, verdicts about loop status generated by PCU are transferred to the output section of the DB.

Acquisition Modules (MAi) interact with DCS, from which receive data and updated loop parameters at each sampling time; they act in parallel (up to a maximum number of 7 on a single server) and sequentially on scheduled loops, following priority and constraints indicated by MS. During the acquisition, the quality of each single datum and the change of status (man/auto, cascade open/closed) is checked and a flag is activated. In addition a first analysis is performed locally: mainly, the duration may be increased from the default (2 hours) to the maximum value (8 hours) in order to get a significant number of cycles in the case of very slow oscillating loops.

More about the PCU and DB modules are reported in next sections.

3. THE PCU MODULE

The PCU module contains the intelligence of the performance monitoring systems: it analyses each loop sequentially, interacting with the MS and with the DB from which receives raw data and to which send verdicts. A schematic representation is reported in Figure 2, where main steps and a simplified logical flow of data analysis modules are indicated. Further details about basic techniques adopted inside modules are given in the appendix.

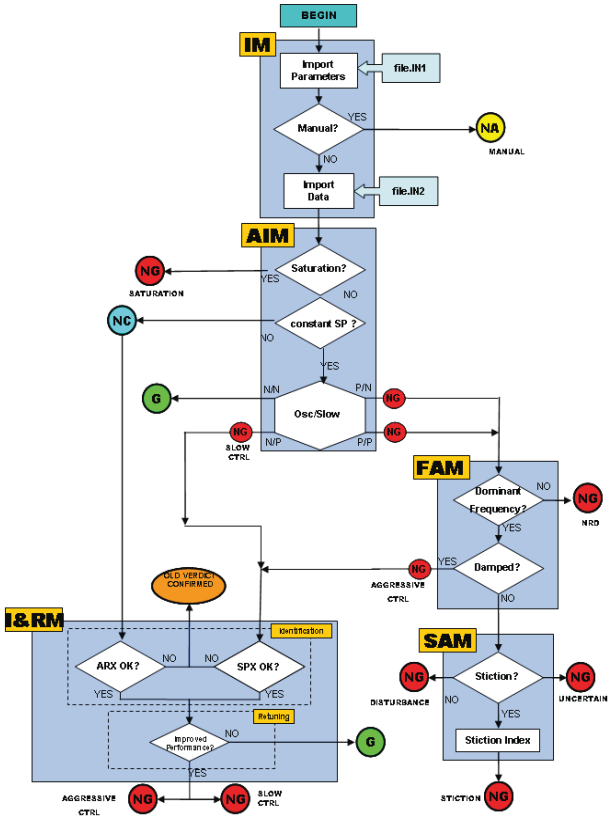

Fig.2: Schematic representation of the PCU module

IM: The Initialization Module imports parameters values from file IN1 and performs a first check about loop status; if the quality of data is not good, or a change of configuration is

detected, or the valve is operating manually (info contained in flags activated by MAi), the analysis stops. In this case, the loop receives a (definitive) label (NA: Not Analyzed) and the analysis is aborted. Otherwise, recorded data are imported from the IN2 file and the performance analysis begins.

AIM: The Anomaly Identification Module performs a first assignment of performance with verdicts: as G (*Good*), NG (*Not Good*). Loops subject to excessive set point changes (as amplitude or frequency) are temporary labelled as NC (*Not Classified*) and send to the identification module (I&RM). Valve saturation is checked first and, if detected, the label NG (and the cause) is definitive, without any further analysis (only duration is indicated). For loops not in saturation, after a data pre-treatment, tests to detect oscillating or sluggish loops are executed; these tests refer to the Hägglund approach (Hägglund, 1995, 1999), with suitable modifications of internal parameters, based on field calibration. In the case of both negative tests, the loop is classified as good performing and a definitive label G is assigned. Slow loops can only be caused by the controller: therefore they receive a NG label and are sent to the identification and Retuning Module (I&RM). Oscillating loops can be caused by aggressive tuning, external disturbance or valve stiction: for this reason, they are primarily sent to FAM, for a frequency analysis.

FAM: The Frequency Analysis Module has the scope of separating irregular oscillations from regular ones on the basis of a power spectrum which computes dominant frequencies; irregular loops are labelled NG, without any further enquiring about causes. Regular loops with decaying oscillations are sent to the I&R Module, otherwise (loops showing permanent oscillations) to the SAM for stiction/disturbance detection.

SAM: The Stiction Analysis Module analyzes data of NG oscillating loops and performs different tests to detect the presence of valve stiction. They mainly consist in the application of two techniques: the Relay based fitting of values of the controlled variable (PV) (*Rel*; Rossi and Scali, 2005) and the improved qualitative shape analysis (Ya^+; Scali and Ghelardoni, 2008). The two techniques are recalled in the appendix. Other techniques proposed for stiction diagnosis are also applied, when appropriate. Among them: the Cross-Correlation (*Cxy*; Horch, 1999), which is the simplest (and probably most widely used) test for a first discrimination between stiction and disturbance and the Bichoerence (*Bic*; Choudhury et al. 2005), which allows to put into evidence non linear characteristics of loop data. The appropriate application technique is automatically selected by the system, depending on type of loops, duration of acquisition, etc.. (for instance: Cxy is not used for Level Control, Ya^+ is reserved only to Flow Control loops). Final verdict takes into account indications coming from different techniques and from other auxiliary indices: to the exit loop, already tagged NG, the cause *Stiction* or *Disturbance* is assigned in the cases of strong evidence, otherwise the cause is *Uncertain*.

I&RM: The Identification & Retuning Module accomplishes process identification and, if successful, controller retuning and evaluation of performance improvements. It analyses loops tagged NG, owing to controller tuning (that is sluggish or too oscillating responses) and loops tagged NC. The two possibilities of constant and variable Set Point are treated differently, the second case being typical of secondary loops under cascade control. In the case of constant SP, recorded data represent a loop response under disturbance rejection: identification of process dynamics is carried out by means of a Simplex based search procedure (Rossi, 2007; Scali and Rossi, 2009). In the case of variable SP, recorded data represent a loop response under set point tracking: identification is performed by means of an ARX algorithm (Ljung, 1999). In both cases, if model identification is successful, new tuning parameters are calculated according to different techniques, the achievable performance improvement is evaluated by means of suitable upgrading indices and new controller settings are proposed. Otherwise, in the case of impossible identification, the previous assigned verdict is confirmed, without any additional suggestion.

To conclude this synthetic illustration, after the performance analysis by means of the PCU module, every loop is classified as:

- NA (Not Analysed): Manual valve, invalid data acquisition, change of loop configuration;

- NC: (Not Classified): impossible identification and no preliminary verdict;

- G (Good Performing);

- NG (Not Good performing): with an indication of cause (*saturation*, *sluggish, too oscillating, stiction, external disturbance*), or without indication for the cases of irregular disturbances or uncertainty between stiction and disturbance in the SAM.

As distinctive features of the PCU performance monitoring system, the following can be pointed out:

1) it is open to the adoption of new diagnosis techniques; once the algorithm has been built and checked in simulation, it is tested on archived and recent plant data: improvements of reliability of issued verdict lead to updating of algorithms and performance indicators;

2) it has been designed to operate completely unattended and for this reason a verdict is assigned and causes indicated only in the case of strong evidence; false indications are carefully avoided, at the expense of conservative (too cautious) indications: in case of uncertainty, the verdict is postponed to next data acquisitions;

3) the calibration of values of key and auxiliary performance indicators is made on the basis of operator experience, in order to make verdicts as more homogeneous as possible with their practice.

4. THE DATA BASE ORGANISATION

The Data Base contains all information about each single loop: recorded data, controller parameters, loop configuration and diagnosis performed by PCU (verdicts). The possibility of a fast and efficient consultation from the operator is certainly one of main specifications to be achieved for the

success of the whole implementation. Therefore, operators suggestions and requirements are carefully taken into consideration in the design of the Data Base architecture. Some significant features incorporated in the DB management are illustrated in the sequel.

1) Analyzed loops and issued verdicts for a group of plants (or all of them) at a certain date, can be immediately summarized on the screen and this allows a first evaluation of loop status, that is the total number of good performing loops, causes of scarce performance, loops in manual, reasons for invalid acquisition etc.. (Figure 3).

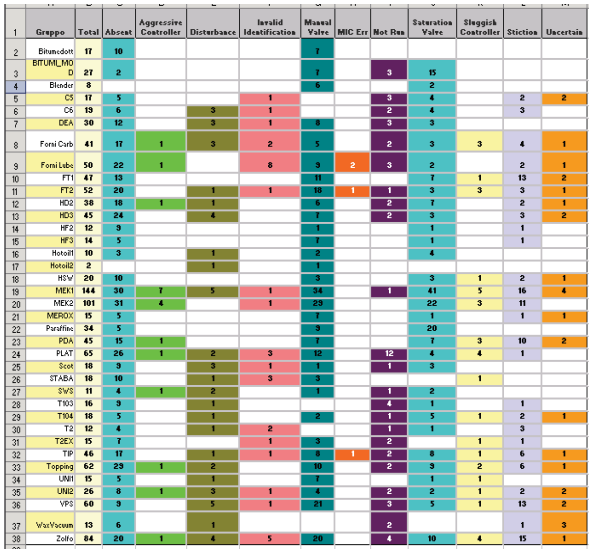

	Gruppo	Total	Absent	Aggressive Controller	Disturbance	Invalid Identification	Manual Valve	MIC Err	Not Run	Saturation Valve	Sluggish Controller	Stiction	Uncertain
2	Bitumdott	17	10				7						
3	BITUMI_MOD	27	2				7		3	15			
4	Blender	8					6			2			
5	C5	17	5			1			3	4		2	2
6	C6	19	6		3	1			2	4		3	
7	DEA	30	12		3	1	8		3	3			
8	Forni Carb	41	17	1	3	2	5		2	3	3	4	1
9	Forni Lube	50	22	1		8	3	2	3	2		2	1
10	FT1	47	13				11			7	1	13	2
11	FT2	52	20		1	1	18	1	1	3	3	3	1
12	HD2	38	18	1	1		5		2	7		2	1
13	HD3	45	24		4		7		2	3		3	2
14	HF2	12	9				1			1		1	
15	HF3	14	5				7			1		1	
16	Hotoil1	10	3		1		2			4			
17	Hotoil2	2			1		1						
18	HSV	20	10				3			3	1	2	1
19	MEX1	144	30	7	5	1	34		1	41	5	16	4
20	MEX2	101	31	4		1	23			22	3	11	
21	MEROX	15	5				7			1		1	1
22	Paraffine	34	5				3			20			
23	PDA	45	15	1			7			7	3	10	2
24	PLAT	65	26	1	2	3	12		12	4	4	1	
25	Scot	18	9		3	1	1		1	3			
26	STABA	18	10		1	3	3				1		
27	SWS	11	4	1	2		1		1	2			
28	T103	16	9		1				4	1		1	
29	T104	18	5		1		2		1	5	1	2	1
30	T2	12	4		1	2			1	1		3	
31	T2EX	15	7			1	3		2		1	1	
32	TIP	46	17		1	1	8	1	2	8	1	6	1
33	Topping	62	23	1	2		10		2	9	2	6	1
34	UNI1	15	5		1		7			1	1		
35	UNI2	26	8	1	3	1	4		2	2	1	2	2
36	VPS	60	9		5	1	21		3	5	1	13	2
37	WasVacuum	13	6		1				2			1	3
38	Zolfo	84	20	1	4	5	20		4	10	4	15	1

Fig.3: Global picture of all plants monitored at a certain date, with indication of loop status

2) The same type of visualization can be produced for a group of plants (or a single plant) for acquisitions repeated in a desired interval of time, thus allowing a first indication about the trend of loop performance (Figure 4).

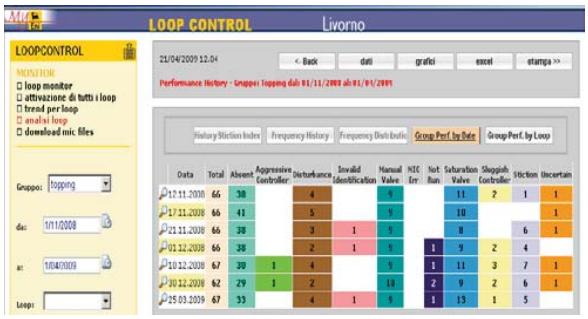

Fig.4: Global performance of a single plant for repeated acquisition at different dates

3) All plant loops at a desired date can also be visualized with individual verdicts (Figure 5).

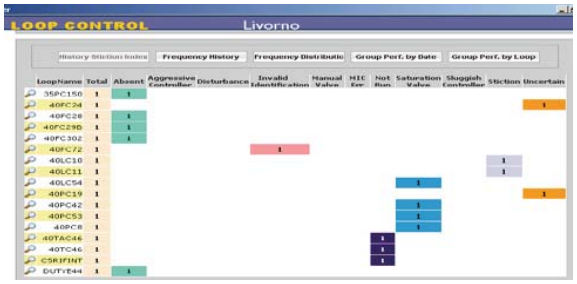

Fig.5: Single plant loop performance at a desired date

4) Single loop performance can be easily investigated, by means of plots and significant performance indices. In the case of successful identification of a loop with incorrect tuning, the trends of SP, PV, OP variables show possible improvements and required control effort with best tuned PI(D) controllers (Figure 6). On this basis (together with values of upgrading indices which allow a quantification of improvements (shown in a separate page), the operator can take a decision about the opportunity of a controller retuning.

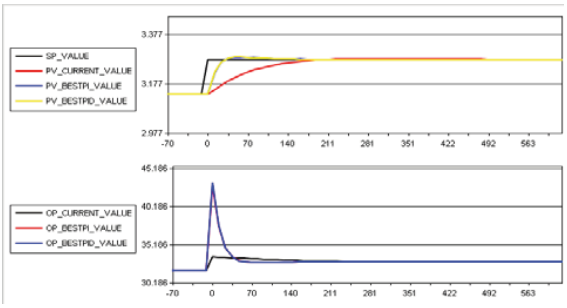

Fig.6: Screenshot for a loop with incorrect tuning

5) In the case of a loop affected by valve stiction, the trends of loop variables, the value of a Stiction Quantification Index (shown in a separate page) allow to evaluate at a glance the situation of the loop (Figure 7). This can be further confirmed by watching the PV(OP) movie (see Figure 11).

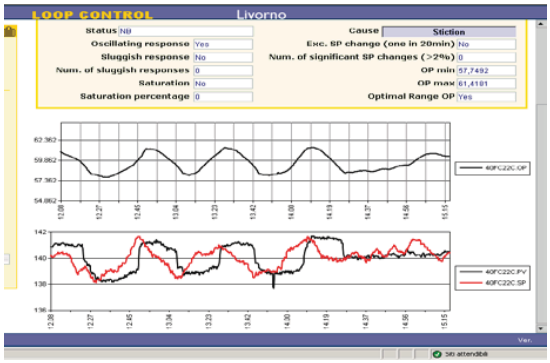

Fig.7: Screenshot for a case of valve stiction: time trends of OP, SP, PV.

7) The loops history can be easily tracked: in the case of a confirmation of issued verdicts, indications for proper actions on the loop can be decided (tuning, valve maintenance, upstream action); an example for a case of

confirmed verdict with increasing stiction in the last four data acquisition is reported in Figure 8.

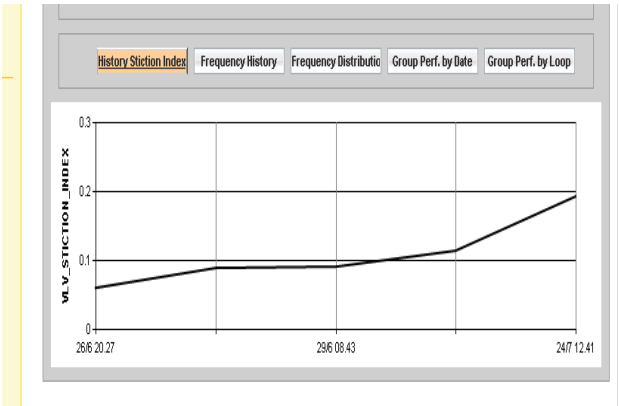

Fig. 8: Loop history for a case valve stiction

4) Many other features allow easy access to more information; for instance: frequency analysis of different oscillating loops and the comparison of dominant frequencies allows to focus on loops possibly affected by the same root cause of oscillations. Other auxiliary performance indexes are evaluated and a large variety of reports about loops statistics can be obtained right way.

5. FIELD VALIDATION

Field validation is the key step of the monitoring system implementation. As first, it allows a direct confirmation of verdicts emitted after loop data analysis, while all indications illustrated in previous section must be considered mere "predictions", i.e. based on identified models, techniques results and values of performance indices. As second point, this is the step where the operator can give indications for the final calibration of threshold values of performance indices and get confidence about the reliability of verdicts issued by the system. Few illustrative examples are reported in the sequel; more than 600 loop acquisitions were checked during the monitoring system validation.

1) Loop xxFC01 (PI control, Constant Set Point). The verdict from AIM and I&RM modules is NG, indicating as cause: sluggish controller. The identification is successful and the old settings (K_c=*1*, T_i=*0.65*), should be changed to new ones: K_c=*0.49*, T_i=*0.13*. An increase of integral action is then suggested; the upgrade index based on the model (see appendix) is: Φ=*0.476*. In this case (single FB loop), it is possible to check directly the predicted improvements: a moderate increase to SP has been given by the operator with old settings, followed by a decrease with new settings. The improvement is evident from Figure 9 (the small amplitude and high frequency oscillation represents an unidentified perturbation present in the plant) and the upgrade index evaluated from plant data is Φ'=*0.573*. This application suggested to reduce the threshold for the index Φ^0 to *0.40* (initially Φ^0 was assumed equal to *0.50*).

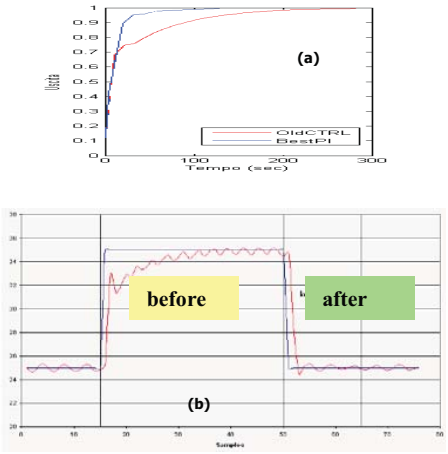

Fig.9: Response to a SP change: model prediction (a), field validation before and after retuning (b)

Loop xxFC02 (PI control, Variable Set Point). Also in this case the verdict from AIM and I&RM modules is NG, owing to sluggish controller; old settings: K_c=*0.8*, T_i=*0.7*; new settings: K_c=*2.6*, T_i=*0.72*. A strong increase of the proportional constant is proposed in this case, while the integral time constant does not change much; the upgrade index based on the model is now Φ=*0.487*. Being a secondary loop under cascade control, in this case it is not possible to give arbitrary set point changes during plant exercise. Moreover, being suggested a large increase of the gain K_c, the operator applied a gradual increase of gain: *0.8, 1.2, 1.6, 2.6*. The corresponding improvement of response in set-point following is evident from Figure 10; the upgrade index evaluated from plant data for increasing value of K_c, is now evaluated by the index (see appendix) *IQI = 0.038, 0.78, 0.85, 0.94*, to confirm the performance improvement.

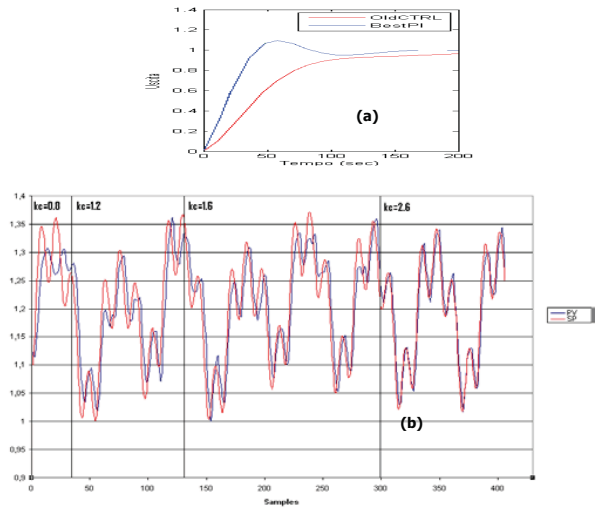

Fig.10: Response to a SP change: model prediction (a), field validation for increasing values of the gain K_c (b)

Loop xxFC08 (PI control, slow varying Set Point). This loop has been repeatedly indicated as affected by stiction in

several analysis. The values of the Stiction Quantification Index increased from 0.07 to 0.195 in about one month. The presence of stiction is clearly recognizable by the PV and OP shapes (close to square waves and triangles, respectively in Figure 11a). Moreover, the plot of PV(OP), which can be seen as a movie on the screen, shows evident stiction characteristics (Figure 11b); because in this case (FC loop), the controlled variable PV is proportional to the valve opening MV. Valve maintenance brought to an improvement of performance and a sharp decrease of the stiction index (Figure 12).

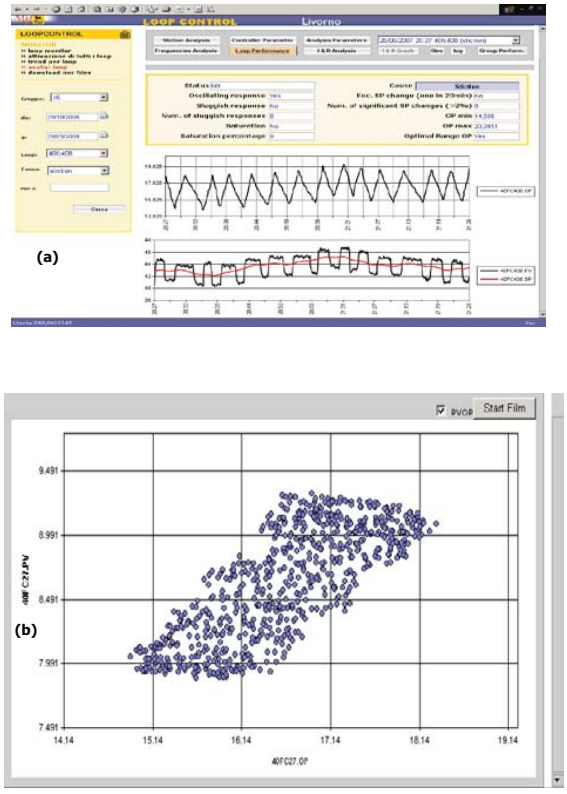

Fig.11: Validation of a loop affected by valve stiction: (a) SP, PV, OP trends; b) PV(OP) movie (FC loop)

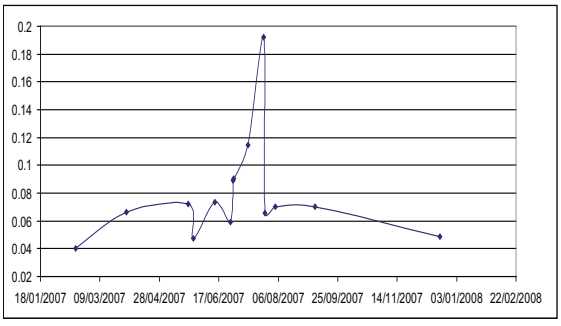

Fig.12: Time trend of the Stiction Quantification Index before and after valve maintenance

6. CONCLUSIONS

The Closed Loop Performance Monitoring system described in the paper has been developed and built with tight cooperation between university and plant personnel. The role of plant operators has been crucial for the success of the implementation, mainly in the calibration of threshold values for key performance indices and in the definition of specifications of the Data Base query system for an efficient analysis of loop performance. This fact has brought to a final version of the system "customized" on user requirements.

The design specifications for a "completely unattended" system forced to the adoption of conservative (default) values for key performance indices and, as a consequence, verdicts are emitted only in case of strong evidence, leaving a certain number of uncertain/unclassified cases. In the stage of assistance to the project, loop analysis was repeated for these cases by changing threshold values, allowing to explain many of them, thus confirming the advantages of a deeper involvement of plant personnel.

The flexibility of the system is an important feature, allowing different levels of interaction with the operator: from the lowest (analysis of periodical performance reports issued by the system) to the highest (actions on loops labelled as poorly performing). The inspection of these loops allows to focus on anomalous situations, both in the case of complete verdicts (cause indicated), and in the case of incomplete diagnosis for a deeper analysis based on process knowledge.

After implementation on a selected plant (about twenty loops), followed by field validation, it has been applied on about fifteen plants, featuring several hundreds loops. A further validation is carried on with the scope of a systematic evaluation of obtained benefits in the perspective of implementation on other group refineries.

Appendix A. ADDITIONAL DETAILS ABOUT PCU

The PCU (Plant Check Up) is the engine of the performance monitoring system and accomplishes an analysis of loop data in order to evaluate performance and to diagnose causes. Some more details are given here about techniques for stiction diagnosis, identification retuning and performance improvement evaluation. Necessarily, only a synthetic illustration is reported here; full details can be found in the references.

A.1 Stiction Diagnosis

Two techniques are mainly used for this scope: the Relay fitting of PV values (*Rel*; Rossi and Scali, 2005) and the improved qualitative shape analysis (Ya^{+}; Scali and Ghelardoni, 2008).

The *Rel* technique consists in the fitting of significant half cycles of the recorded oscillation by means of three different models: a sine wave, a triangular wave and the output response of a first order plus time delay under relay control. The last one is able to approximate the square waves shapes generated by the presence of stiction and modified by the

process dynamics (Figure 13). Relay and triangular shapes are associated with the presence of stiction, while a sinusoidal shape with the presence of external perturbations. By comparing the error between real and fitted data, an evaluation of the accuracy of approximation and then an indication of the underlying phenomenon can be obtained. Once approximations have been performed, a Stiction Identification Index (S_I) can be defined. Being E_S the minimum square error obtained by the sinusoidal approximation and E_{RT} the one obtained by the better approximation between the relay and the triangular waves, S_I is defined as:

$$S_I = (E_S - E_{RT})/(E_S + E_{RT}) \qquad (1)$$

Here E_S, E_{RT} indicate average values of error over the number of examined cycles. S_I varies in the range [-1; +1]: negative values indicate a better approximation by means of sinusoids, positive values by means of relay or triangular approximations. Values close to zero indicate that the two approximations have similar errors and the procedure gives an uncertain answer: the uncertainty region is defined by $|S_I|<0.21$.

The technique presents some analogies with the Curve Fitting Method proposed by He et al (2007): in this case, assuming that stiction is associated to a square wave shape in MV, a triangular wave shape is looked for as distinctive feature of stiction after the first integrator element of the loop. This means in OP signal (for self regulating processes – no integrators) or in the PV signal (for integrating processes).

The relay method always analyses the PV signal and uses the relay shape as additional primitive. The global fitting procedure is more complex and time consuming, but in all cases the elaboration time is absolutely negligible compared with the duration of data acquisition. Finally, the method can also put into evidence the presence of asymmetric stiction, by comparing S_I values on positive and negative half cycles.

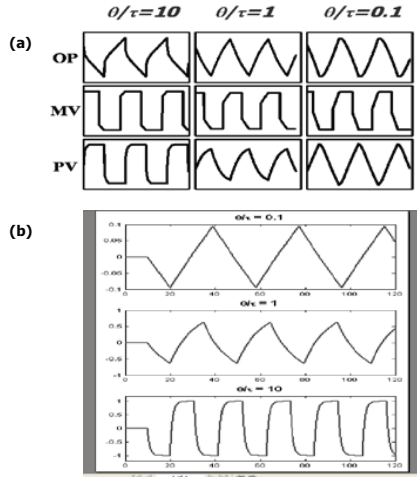

Fig.13: (a) Wave shape in a loop affected by stiction as modified by process dynamics (ratio θ/τ) for a FOPTD process. (b) Different wave shapes generated by a relay feedback controller on a FOPTD process by varying θ/τ

The Ya^+ technique is an extension of the technique originally proposed by Yamashita (2006), which is based on the analysis of trends MV(OP), that is valve output as function of the control action. Its applicability would seem low, because usually only PV and OP are recorded on industrial DCS; in the case of flow control (FC), the controlled variable can be considered known, being proportional to the valve opening. As FC loops are a large majority of base control loops (about 2/3 in the application presented here), the applicability of this technique is large. It is much larger for newly designed plants (for instance power plants with redundant instrumentation) and it will increase in a next future with the diffusion of field bus communication systems and related available information.

In the presence of stiction, the trend changes from linear to a typical parallelogram shape (Fig.14): the horizontal part indicates that the valve opening does not change for increasing controller output.

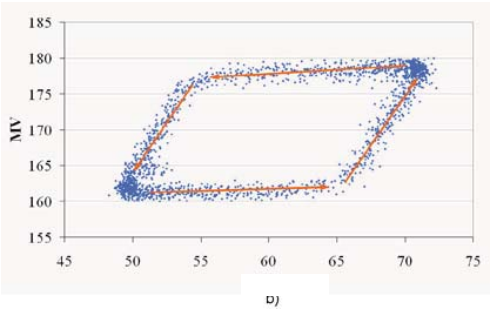

Fig. 14: Valve position (MV) as a function of the controller output (OP) in the presence of stiction (industrial data)

Following Yamashita (2006), the pattern can be approximated by means of three simple symbols: increasing (I), decreasing (D), and steady (S). Possible combinations of symbols for the stiction pattern reported above are represented in Figure 15, as: ID, IS, II; SD, SS, SI; DD, DS, DI.

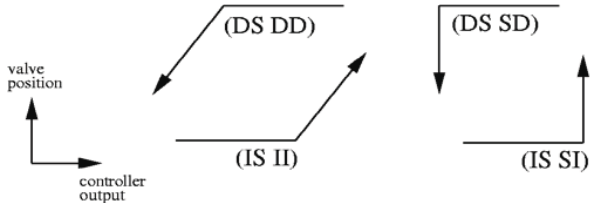

Fig. 15: Qualitative shapes observed in sticky valves.

By combining the symbols for OP and MV signals, a representation of the development in an (OP, MV) plot over time can be obtained. Based on these considerations and counting the duration of time sequences, a stiction index ρ can be defined; values of $\rho > \rho^{\circ}=0.25$ (threshold value for a random signal) are indication of possible stiction in the valve. These considerations have been extended to include different stiction patterns observed in industrial data, for instance the one reported in Fig.16.

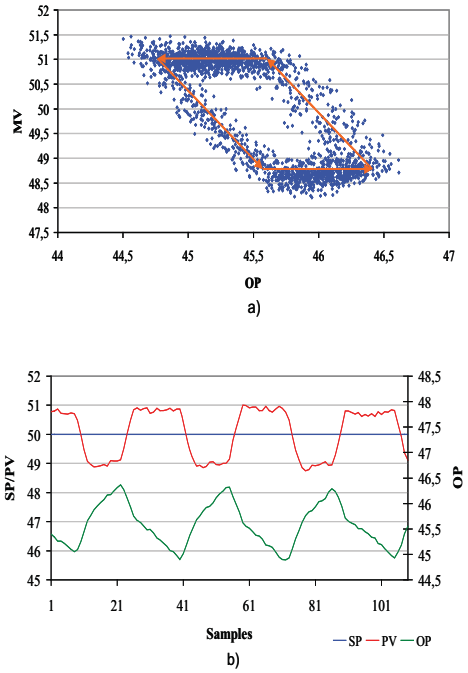

Fig. 16: a) A different MV(OP) pattern observed in industrial data, in the presence of evident stiction (b)

Other patterns are possible depending on valve type (direct/inverse action) and on DCS configuration, as reported in Figure 17.

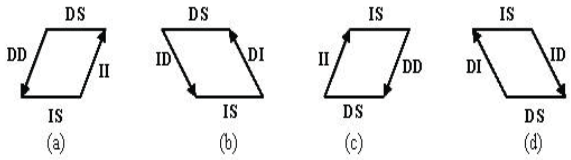

Fig. 17: Additional stiction patterns

They can be explained by the presence of a (even small) delay between OP and MV is present, caused for instance by the combined action of different factors such as: backslash phenomena, valve positioner dynamics, signal quantizer and so on. They can be reproduced by simulation by means of a widely used stiction model, with suitable modifications (Choudury et al, 2005).

Different stiction indices have been defined to be able to identify their presence in industrial data, namely: ρ_B, ρ_C, ρ_D, (in addition to a $\rho_A=\rho$), accounting for the appropriate coupled sequences of I, S, D primitives (further details in Scali and Ghelardoni, 2008).
For a set of 52 data acquisitions, 11 additional loops were indicated as sticky, according to the new index ρ_B, while would not be indicated by ρ_A, as summarized in table 1 (threshold value is 0.25). During the implementation and field validation of this project, only A and B stiction patterns were encountered, owing to some practical constraints adopted in the DCS configuration; C and D patterns may be found in the most general case.

Table 1: Details for the additional 11 sticky loops

Loop #	ρ_A	ρ_B
xxFC1	0.2459	0.4146
xxFC2	0.1941	0.2648
xxFC3	0.2238	0.3444
xxFC4	0.2303	0.2817
xxFC5	0.1889	0.2961
xxFC6	0.2071	0.4882
xxFC7	0.1352	0.2596
yyFC1	0.1200	0.3621
yyFC2	0.1797	0.3712
yyFC3	0.1614	0.3407

A.2 Identification

The Identification Module receives form the AIM module loops with constant SP labelled as NG (No Good) caused by improper tuning and loops labelled as NC (Not Classified) with variable SP.

In the case of constant SP, the recorded lops dynamics refer to a poor performing response caused by the presence of an external perturbation (Figure 18). A Simplex based search technique has been adopted for the solution of this problem, with some modifications to the original algorithm (Nelder and Mead, 1964), in order to overcome the problem of getting stuck in local minima and of managing the presence of constraints. Further details are reported in Rossi (2007) and Rossi and Scali (2009).

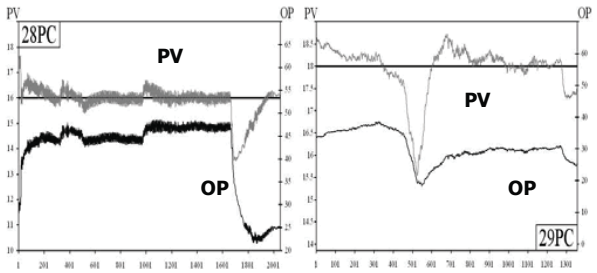

Fig. 18: Poor loop responses caused by external perturbation

Both process and disturbance dynamics are modelled as second order plus time delay systems, with parameters K, K_d (gains); θ, θ_d (delays); τ, τ_d (time constants); ξ, ξ_d (damping factors):

$$P(s)=\frac{K\cdot e^{-\theta s}}{\tau^2 s^2+2\xi\tau s+1};\ P_d(s)=\frac{K_d\cdot e^{-\theta_d s}}{\tau_d{}^2 s^2+2\xi_d\tau_d s+1} \quad (2)$$

The identification problem can be stated as the minimization over the model parameters vector V, of MSE between recorded and computed values (N is the number of samples):

$$\min_V (MSE);\quad MSE=\sum_{i=1}^{N}(Y_i-\hat{Y}_i)^2 \quad (3)$$

In the case of variable SP, an ARX process model is identified (Ljung, 1999); in discrete form:

$$y_k + a_1 y_{k-1} + \cdots + a_n y_{k-n} = b_1 u_{k-L-1} + \cdots + b_m u_{k-L-m} + e_k \quad (3)$$

where: y is the output (PV), u is the input (OP), L is the time delay, n and m are model order. From past values of y and u, it is possible to define the output predictor as:

$$\begin{cases} \hat{y}_k = \varphi_k^T \theta, \\ \varphi_k = [-y_{k-1} \quad \cdots \quad -y_{k-n} \quad u_{k-L-1} \quad \cdots \quad u_{k-L-m}]^T \\ \theta = [a_1 \quad \cdots \quad a_n \quad b_1 \quad \cdots \quad b_m]^T \end{cases} \quad (4)$$

Once a time window has been fixed of length equal to N sampling times, (details are given below), a suitable quadratic function of the error between predicted and recorded values:

$$V_N(\theta) = \frac{1}{N}\sum_{k=1}^{N}(y_k - \hat{y}_k)^2 = \frac{1}{N}\sum_{k=1}^{N}(y_k{}^2 + \theta^T \varphi_k \varphi_k^T \theta - 2\theta^T \varphi_k y_k) \quad (5)$$

and, by minimizing V_N with respect to model parameters:

$$\theta^* = \left[\sum_{k=1}^{N} \varphi_k \varphi_k^T\right]^{-1} \left(\sum_{k=1}^{N} \varphi_k y_k\right) \quad (6)$$

The value of the delay L should be known; this limitation can be overcome by repeating the computation of θ^* for different values of L (from *0* to L_{max}) and choosing the delay θ^* corresponding to minimum values of V_N. The initialization of the predictor requires the knowledge of data for $N_0=max(n,m+ L_{max})$ sampling times, before $k=1$.

Several criteria can be defined to evaluate the accuracy of identification. Here, a closed loop index has been adopted, as the scope of identification is modelling for control purpose. Given the SP sequence in the examined window, values of the output variable vector $y'_1, ..y'_N$, for the actual controller and the identified model are computed, originating the index:

$$EV_{CL} = 1 - \frac{\sum_{k=1}^{N}(y_k - y'_k)^2}{\sum_{k=1}^{N}(y_k - y_{mean})^2} \quad (7)$$

where: y_{mean} represents average value for the output. EV_{CL} represents an explained variance, with values less than 1 (and generally not less than 0).

The application of the procedure is different according to the number of SP changes, for instance primary loops or loops under cascade / advanced control.

In the case of only one SP change, only one time window is selected and the procedure is applied as described above. The starting point is fixed n_0 sampling times before the time of SP change, while the final point is taken when the response has settled within a 5% of the output value. The identification is considered successful if $EV_{CL} \geq 0.80$.

For cases of variable SP, time windows of about 20 minutes for FC loops (about one hour for other type of loops) are chosen and the identification procedure is applied on each window. The step response of the two models having larger value of EV_{CL} are compared, as:

$$MD = 1 - \frac{\frac{1}{M}\sum_{k=1}^{M}(y_k^{SR1} - y_k^{SR2})^2}{\sum_{k=1}^{M}\left(\frac{y_k^{SR1} + y_k^{SR2}}{2}\right)^2} \quad (8)$$

where: y_k^{SR1}, y_k^{SR2} are *k-th* step response coefficient of model 1 and 2. The identification is considered successful for $MD \geq 0.95$ (and $EV_{CL} \geq 0.80$). Threshold values have been assumed after intensive simulations and applications on loop data. Referring to Figure 19 and Table 2, acquired data are divided in 8 time windows, identification is heavily wrong for windows 2 and 4 ($EV_{CL}<0$), is not considered reliable enough for windows 1,3,5,6 ($EV_{CL}<0.80$), is considered successful for windows 7 and 8 ($EV_{CL} \geq 0.80$); for these two windows $MD=\geq 0.986$ and then the identified model is accepted.

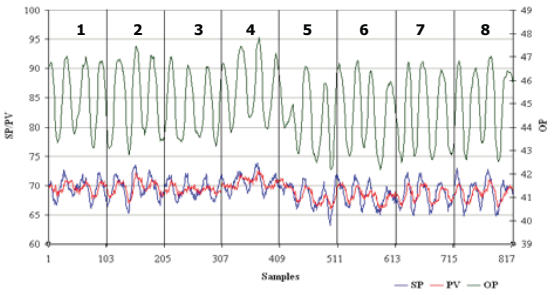

Fig. 19: Variable SP loop and time windows divisions

Table 2: Values of EV_{CL} in the 8 time windows

t.w.	1	2	3	4	5	6	7	8
EV_{CL}	*0.51*	*-40*	*0.66*	*-29*	*0.58*	*0.74*	*0.89*	*0.80*

Identification may be not successful for several reasons, for instance: non linearity of real process or not optimal choice of ARX model order (*n, m*). Nevertheless, main causes of failure are to be found in the presence of valve stiction or external disturbances.

In the first case, a failure is "desirable" (a linear model being not reliable in this case) to avoid the adoption of an incorrect model and a wrong suggestion about cause (retuning instead of stiction).

In the second, it may be possible to find few time windows not heavily affected by disturbances: this is the logical behind the choice of comparing models identified in two different time windows and requiring large values of *MD* and EV_{CL}; more details in Mervi (2007).

A.3 Upgrading Indices

Once the identification has been successfully carried out and a process model is available, the optimal tuning is evaluated according to different available techniques, selected at the configuration stage.

The performance improvement predicted on the basis of the identified model, is evaluated by means of an upgrading index Φ:

$$\Phi = \frac{IAE_{Act} - IAE_{Best}}{IAE_{Act} - IAE_{Min}} \quad (9)$$

where: IAE is the Integral of Absolute Error of the response for the actual reguator (*Act*), for the best controller having PI/PID structure (*Best*) and for the optimal one for the identified model (*Min*). For $\Phi \rightarrow 0$, the proposed controller is closet to the optimal one; for any $\Phi > 0$ there are improvements, but a threshold has been assumed to implement the new retuning (the proposed threshold $\Phi^{\circ} = 0.50$, has been decreased to *0.40*, after field validation).

Other indices allow to evaluate the real performance improvements on the plant, before and after retuning, in the two cases of primary loops (with rare SP changes, mainly step-wise) and secondary loops (with frequent SP changes, imposed by the primary loop acting on them).

For primary loops a new index Φ' is defined, having the same expression (9), with controllers tagged as *Act* and *Best* substituted by *Old* and *New* (to indicate before and after retuning) (Figure 20a).

For secondary loops, the IQI (Improvement Quantification Index) is defined, to evaluate the error between recorded SP and PV values before and after retuning (Figure 20b):

$$IQI = 1 - \frac{\frac{1}{N}\sum_{i=1}^{N}(SP_i - PV_i)^2}{\frac{1}{N}\sum_{i=1}^{N}(SP_i - SP_{medio})^2} \quad (10)$$

where: N: is the number of sampling times where the tuning is maintained as constant, SP_i: , PV_i , i-th value of SP and PV, and, SP_{ave}, is the average SP value in the time range where tuning parameters are left constant.

Values of IQI close to 1 indicate perfect control, while small or negative values indicate scarce performance.

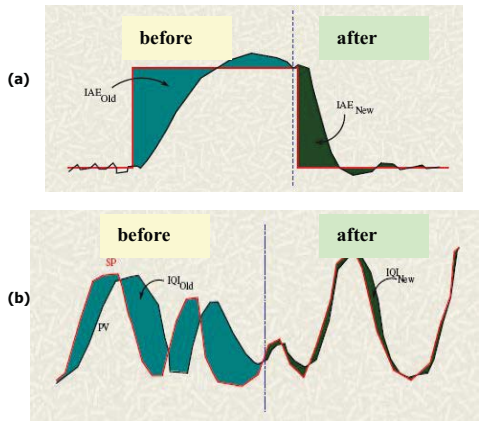

Fig. 19: Representation of the upgrading indices for: constant (a) and variable SP loops (b)

REFERENCES

Choudhury M.A.A.S, Shah S.L., and Thornhill N.F. (2004): "Diagnosis of Poor Control Loop Performance using High Order Statistics", *Automatica*, **40**(10), 1719-1728.

Choudhury M.A.A.S., Shah S.L., Thornhill N.F. (2005): "Modelling Valve Stiction", *Control Engineering Practice*, Vol. 13, pp. 641-658.

Hägglund T. (1995): "A Control Loop Performance Monitor", *Control Eng. Practice*, **3**, 1543-1551.

Hägglund T. (1999): "Automatic Detection of Sluggish Control Loops", *Control Eng. Practice*, **7**, 1505-1511.

He Q. P., Wang J., Pottman M., Qin S. J. (2007): "A Curve Fitting Method for Detecting Stiction in Oscillating Control Loops"; Ind. Eng. Chem. Res., Vol.46 (13), 4549-4560.

Horch A. (1999): "A Simple Method for Detection of Stiction in Control Valves", *Control Eng. Practice*, **7**, 1221-1231.

Horch A. (2006): "Benchmarking Control Loops with Oscillation and Stiction"; In: *Process Control Performance Assessment*, Ed.s: A. Ordys, D. Uduehi and M. A. Johnson; Springer, London –UK.

Jelali M, Scali C. (2009): "Comparative Study of Valve Stiction Detection Methods"; In: *Detection and Diagnosis of Stiction in Control Loops*, Ed.s: M. Jelali and B. Huang; Springer, London –UK.

Ljung L. (1999): "*System Identification"*, Prentice Hall, Upper Saddle River, N.J. (USA), (1999).

Mervi A (2007): "MS Thesis" (in Italian), Chem. Eng. Dept. – University of Pisa (I).

Nelder G.A., Mead R. (1964): "A Simplex Method for Function Minimization", The Computer Journal, Vol.7, No. 4, pp. 308-313.

Qin S. J. (1998): "Control performance monitoring: a review and assessment", *Comp. & Chem. Engineerin*g, **23**, 173-186.

Rossi M., Scali C. (2005): "A Comparison of Techniques for Automatic Detection of Stiction: Simulation and Application to Industrial Data", *J. Proc. Control*, **15** (5), 505-514.

Rossi M. (2007): "Development of Techniques for Closed Loop Monitoring of Chemical Processes", *PhD Thesis*; Chem. Eng. Dept. – University of Pisa (I).

Scali C. and Rossi M. (2009): " Modeling Disturbance Dynamics to Improve Controller Performance in Industrial Loops**";** *Chemical Product and Process Modeling*: Vol. 4: Iss. 2, Article 8.

Scali C., Ghelardoni C. (2008): "An Improved Qualitative Shape Analysis Technique for Automatic Detection of Valve Stiction in Flow Control loops", *Control Engineering Practice*, 16, pp. 1501-1508.

Thornhill N. F., Horch A. (2007): "Advances and New Directions in Plant-Wide Disturbance Detection and Diagnosis"; *Control Engineering Practice*, Vol. 15(10), pp. 1196-1206.

Yamashita Y. (2006): "An Automatic Method for Detection of Valve Stiction in Process Control loops"; *Control Engineering Practice*, Vol. 14, pp. 503-510.

MPC: Current Practice and Challenges

Mark L. Darby*, Michael Harmse, Michael Nikolaou*****

**CMiD Solutions, Houston, TX*
USA (Tel: 713-477-7791; e-mail: darbymark@sbcglobal,net).
***IPCOSAptitude Ltd., Cambridge, United Kingdom (e-mail:Michael.Harmse@ipcosaptitude.com)*
**** Chemical and Biomolecular Engineering, Houston, TX (e-mail:nikolaou@uh.edu)*

Abstract: Linear Model Predictive Control (MPC) continues to be the technology of choice for constrained multivariable control applications in the process industry. Successful deployment of MPC requires "getting right" multiple aspects of the problem. This includes the design of the regulatory controls that receive setpoints from MPC, design of the multivariable controller(s) themselves, test design for model identification, model development, and dealing with nonlinearities. In the following, we highlight approaches and techniques that are successfully applied in practice and provide an overview of recent technological enhancements that are being made to MPC. While significant progress has been made in both the technology and practice, there are challenges with MPC, mostly related to the effort required to develop an application and to ensure adequate performance over time. Suggestions for addressing these issues are included as possible research directions.

Keywords: model predictive control, model-based control, constraints, control system design, modeling, process identification.

1. INTRODUCTION

Model predictive control (MPC) is a mature technology. It is the standard approach for implementing constrained, multivariable control in the process industries today. MPC provides an integrated solution for controlling interacting systems with complex dynamics and constraints. A key aspect of MPC is its ability to deal with degrees of freedom, that may arise when there are more or fewer inputs (manipulated variables) than outputs (controlled variables), or when zone limits for controlled variables are used, which is the typical situation in practice. Broadly defined, MPC refers to a control algorithm that explicitly incorporates a process model to predict the future response of the controlled plant. While the model may be linear or nonlinear, we consider linear MPC as it is used in the majority of industrial applications in the refining and petrochemical industries today (and increasing, in other industries). For these applications, the plant model is identified based on data generated from a dedicated plant test. Today, there are a number of technology vendors which provide MPC solutions, including software to facilitate the development of MPC applications and monitoring of the performance of these applications over time. The last 10-15 years has seen significant efforts by technology suppliers to improve the usability of MPC products.

While the "science" of MPC has advanced and the technology is now easier to apply, there is still an "art" aspect to the application of MPC that largely comes from experience. The success of an MPC application depends on the multiple technical decisions that are made by the control engineer in the course of an implementation. In addition, there are both technical and organizational issues that are critical to ensuring that MPC benefits are sustained in the longer term once an MPC is commissioned (Darby and Teeter, 2005). Based on our experience, we find that the success rate of MPC across the industry is uneven. Some companies are consistently successful in deploying MPC, whereas others are not. In the following, our main emphasis concerns the technical aspects of MPC that arise in the course of an implementation.

MPC is positioned above a regulatory control level as shown in Figure 1. The manipulated variables for the MPC are typically setpoints of PID controllers, executed in a distributed control system (DCS). The MPC may also directly manipulate valve position signals rather than, e.g., flow.

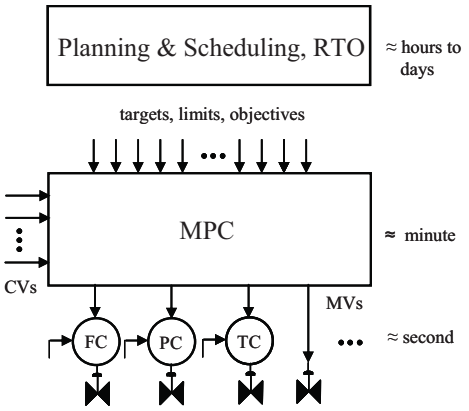

Figure 1. Control hierarchy

The DCS executes a at a higher sampling rate than the MPC, typically sub–second to multi-second sample time, compared to a 30 sec to 2 min execution period for MPC.

Certain targets and objectives for MPC come from higher level functions such as planning and scheduling, typically communicated to the operator in an open-loop fashion, or from a real-time optimizer, if present. Note that there it not necessarily a one-to one-translation of decisions from upper level functions to targets and limits in the MPC. Economic objectives and priorities may also be involved. Examples include gasoline vs. diesel objectives (winter vs. summer) in a refinery and the priority of feed stocks in an ethylene plant. In addition, there are day-today issues that may arise such as a late shipment, or a product tank becoming full.

Part of the challenge in implementing MPC is that the regulatory control layer is not a given (or should not be taken as a given). The design problem is really one of deciding on the best overall structure for the regulatory level *and* MPC, given the control objectives, expected constraints, at least qualitative knowledge of the expected disturbances, and robustness considerations. Similarly, the selection of the controlled variables for MPC is not one of simply deciding which subset of available measurements should be selected. It may be that available measurements are insufficient and additional sensors are needed. In addition, not all variables that need to be controlled may be available on a frequent-enough basis; therefore, we have the problem of inferring qualities from secondary measurements. The above decisions are by no means trivial and represent key aspects of the controller synthesis problem that have attracted significant attention over the past four decades (Buckley, 1964; Weber and Brosilow, 1972; Morari et al., 1980; Larsson and Skogestad, 2000; Stephanopoulos and Ng, 2000).

Once the regulatory level is decided upon, the remaining decisions relate to how to structure the MPC layer: Should one controller or multiple MPC controllers be used? For each controller, there is the issue of deciding on the manipulated variables, the controlled variables, and the feedforward variables. Non-linearities are other issues that must also be addressed, if significant in an application. Note that the techniques discussed here are based on approaches that retain a linear(ized) dynamic model at the core of the MPC engine.

The typical MPC project sequence is as follows:

Pretest and Preliminary MPC design.

Plant Testing.

Model and Controller Development.

Commissioning and Training.

In the pretest phase of work, the key activity is one of determining the base level regulatory controls for MPC, tuning of these controls, and determining if current instrumentation is adequate. The outcome of this phase is a list of issues that must be fixed or resolved before plant testing can proceed. Typical problems that are identified are valve issues (sizing and excessive valve stiction), faulty instruments, and sensor location. The other task that begins in this phase is one of learning the process and understanding the operational challenges and expected constraints. In addition, a preliminary design for the MPC is typically performed, i.e., identification of controlled and manipulated, and number of MPCs.

Plant testing consists of generating plant data for model identification. Additional process knowledge and insight comes from this phase of work. Testing requires moving all inputs that may be manipulated variables for the MPC. Testing may be performed manually or automatically. During this phase of work, frequent lab measurements are collected, if an inferential model of product qualities is required.

In the next phase or work, modeling of the plant is completed, including any required inferential s and non-linear compensators. It is here that the models are analyzed for consistency. The final design for the controller or controllers is completed and simulations performed to test the model and tune the controller.

Commissioning involves turning on the controller and observing its performance on the plant and making tuning adjustments as needed to obtain a properly functioning controller. Training of operations staff on the live controller is begun in this phase.

In the following, we provide a high level description of MPC, MPC, without much emphasis on the particular theoretical properties of the MPC algorithm, for which there is already a substantial body of work (Mayne et al., 2000.). Subsequently, we present a detailed discussion of the key tasks and decisions that are made in the course of an implementation. Where appropriate, current practice is highlighted and guidelines are given. The impact of recent technological enhancements that have appeared are discussed. Lastly we suggest areas where improvements may be made.

2. MPC OVERVIEW

A simplified block diagram of the typical MPC is shown in Figure 1. Key functionality of the components shown in the figure are described below.

Target Selection: Target selection determines the best feasible, steady-state operating point, $\mathbf{x}_k^s, \mathbf{u}_k^s$ based on steady-state gains of the model. It can be implemented on the basis of minimizing deviations from desired steady-state "resting values" or as the result of an economic-based steady-state optimization, typically either a linear program (LP) or a quadratic program (QP).

Controller: The controller determines optimal, feasible future inputs to minimize predicted future errors, over a moving horizon, from targets determined by target selection. Tuning parameters (e.g., weights) are used to establish the dynamic

objectives and trade-offs. A QP is typically used to perform the controller optimization.

Estimator: The estimator updates the model estimate to account for unmeasured disturbances and model errors. It includes a deterministic part that models the effect of controller-manipulated process inputs (and other measured process inputs) on the process outputs, and a stochastic part (which may only be implicit) that models the effect of unmeasured disturbances on the process outputs. The simplest form for the estimator is the original MPC output correction (and still widely used today), where the current offset between the measurement and the model prediction is used to bias future model predictions. A state space model represents a more general and flexible approach to modeling unmeasured disturbances in the estimator.

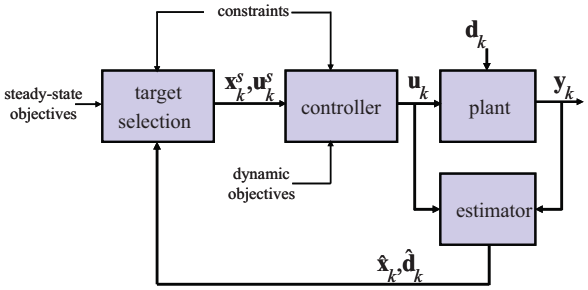

Figure 2. Simplified MPC block diagram

Various model forms are used in the various MPC products available today. Most common are the finite step response (FSR) or finite impulse response (FIR), but state space model formulations are also found. Recent controller products suggest a trend towards increased use of state space model formulations, because of the flexibility they offer to represent stable, integrating, and unstable processes in a single structure.

Our intent is not to delve into differences between the formulation and options of the various products. The interested reader is referred to Maciejowski (2002) and Qin and Badgwell (2003) Suffice it to say that differences exist among the products as to the approaches taken, but that they address important features such as prioritization of constraints, economic objectives and tuning parameters to influence CV vs. MV variance trade-offs. Most MPC controllers today force consistency between the sequence of input moves generated by the controller and the steady-state solution determined by the target selection. This consistency, which is equivalent to the imposition of a terminal constraint, provides nominal and robust stability (Genceli and Nikolaou, 1993; Rawlings and Muske, 1993; Ying and Joseph, 1999)

1. DCS STRATEGY

In deciding upon an appropriate DCS strategy for the MPC, there are several factors that need to be considered and balanced. Major factors are disturbance rejection, process interaction, robustness to model errors, and constraint considerations. Another factor is the influence of the DCS strategy on the settling time of the system, which affects the control horizon in MPC.

Fortunately, when implementing MPC, an existing DCS strategy is in place that can be evaluated and changed, if necessary. We are aware that some practitioners choose to use existing DCS schemes "as is" as opposed to modifying or pairing the PID loops in a different way. However, such modifications can have a significant impact on both MPC control performance and the ease of implementation (e.g., testing). Note that with modern DCS systems a different DCS strategy ("fall-back") may be used when MPC is switched off or fails.

A typical decision concerns whether to incorporate a cascade, such as temperature to flow cascade on a distillation column, or a temperature to pressure cascade on a direct-fired heater. As we have discussed, the DCS typically operates at a higher sample frequency than the MPC; therefore an existing cascade, if tuned well, will likely have much better disturbance rejection capability than the MPC. An additional advantage is that a cascade may help to linearize important CVs controlled by the MPC (because of the linearizing effect of feedback in the inner loop in a cascade scheme). This can be advantageous in providing acceptable control over a wider range of, e.g., plant feed rates.

The thinking with respect to cascades with MPC has clearly evolved over the years. In earlier days of MPC, it was often thought preferable to "break" an existing TC cascade and design the MPC to manipulate flow controllers. The motivation was that this would lead to simpler (overdamped) models and allow the interaction to be addressed by the MPC. What was missed with this approach was the rejection capability of the DCS via the higher sampling frequency, and the robustness that results from incorporating a TC into the MPC strategy. Consider the case of the two-by two subsystem associated with the product purities of a binary distillation column, controlled in the reflux-boilup configuration (so called *L-V* configuration). Consider two cases: 1), MPC control of compositions via *L* and *V* and 2) MPC control of the compositions via L and a stripping section TC controller that manipulates boilup. We assume that the controlled temperature correlates well with the bottoms product composition. The model relationships for these two cases are

$$\begin{bmatrix} y \\ x \end{bmatrix} = \begin{cases} L-V: & \begin{bmatrix} g_{11} & g_{12} \\ g_{12} & g_{22} \end{bmatrix} \begin{bmatrix} L_{sp} \\ V_{sp} \end{bmatrix} \\ L-TC: & \begin{bmatrix} g_{11}^{TC} & g_{12}^{TC} \\ g_{21}^{TC} \approx 0 & g_{22}^{TC} \end{bmatrix} \begin{bmatrix} L_{sp} \\ TC_{sp} \end{bmatrix} \end{cases} \quad (1)$$

Due to its lower triangular structure, *L-TC* is a more robust formulation compared to a full decoupling strategy with manipulated variable *L* and *V*, especially if the process is ill-conditioned, or more accurately, has large RGA elements (Skogestad and Morari, 1987). In most cases a temperature

cascade would be retained if it performs well. In a distillation column, it may be necessary to select another tray temperature if the existing one does not correlated well with product quality. Note that dual-ended temperature controls would normally be avoided because of interactions and the potential for the controllers to wind up (i.e., saturate) , if a section of the temperature profile shifts to a region of insensitivity (e.g., due to a feed composition change).

Another cascade decision concerns level to flow cascades, associated with feed drums, reflux accumulator drums and distillation column sumps. The questions is: should a flow be controlled directly by the MPC (with the associated level controlled by the MPC)? A motivation for doing so is to obtain a direct handle on inflows, without the dynamics of the level controller. Such an approach is useful when a plant capacity constraint exists, such as column flooding, and unit feed rate is also manipulated by the MPC. By directly manipulating column feed, tighter control of a plant capacity constraint can be achieved by taking advantage of liquid holdup in intermediate drums. Additional justification is to shorten system settling time by removing the dynamics of level controllers.

A disadvantage of including levels in the MPC is that levels, which are integrating variables with respect to flow, are that they harder to keep in bounds during an open-loop plant test. Levels are affected by both material and energy balance effects. While material balance effects may be straightforward to model, energy balance contributions affects must also be modeled, which tend to contribute over a longer time frame. Part of the challenge with integrating variables is related to the identification problem, as it is common to identify the first difference of an integrating CV, which decreases the signal-to-noise content. Note: in some FIR-based ID methods a double difference is used - one difference for the integrator and an additional difference (for both inputs and outputs) to remove integrating or slow disturbance effects. An additional challenge is that it is common for an MPC controller to contain logic to switch off if an integrating variable cannot be balanced (zero difference) at steady state., thus making integrating variables more sensitive to measurement spikes.

An alternative to controlling the level in MPC is to keep the level cascade in the DCS and manipulate the level setpoint to influence the corresponding flow rate (taking advantage of buffering capacity). In this case, the level measurement could also be brought into the MPC as a CV (and controlled within bounds). For this situation, model relationship between level setpoint and flow is zero gain (i.e., dynamic response only, zero steady-state gain). We should note that practitioners are divided on what is the best approach, although most of the experience is with FIR- or FSR-based MPC. Examples of step response models for these two cases are shown in Figure 3.

We should note that the theory and experience-to-date indicate that integrating variables are more easily handled within a state-space formulation, as it allows more flexibility in the unmeasured disturbance model – i.e., selection of the disturbance channels and incorporation of additional output measurements (Qin and Badgwell, 2003; Froisy, 2009).

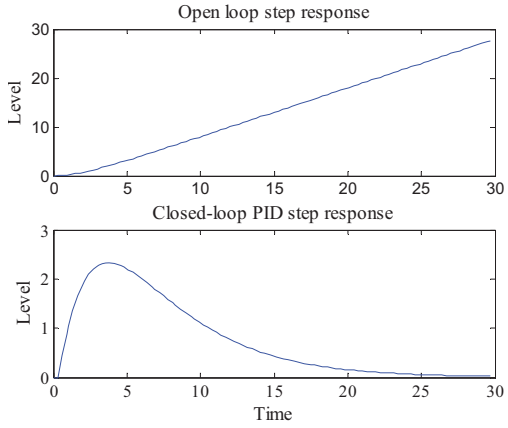

Figure 3. Step response models for integrating level: open-loop vs. closed-loop with PID

An important issue concerns valve positions of PID loops that are directly manipulated by MPC or that are affected by other manipulated variables of the MPC. For example, manipulating an FC controller setpoint will affect the valve position associated with the FC as well as the valve position associated with a downstream pressure controller. When a valve approaches a saturated state (either fully open or closed), not only is PID control lost for its associated controlled variable, but model mismatch (and nonlinearity) is introduced to all MPC-controlled variables that depend on the PID controller response. As a result, the MPC needs to keep PID controller outputs in a controllable range. This can be achieved by bringing the PID controller output into the MPC as a controlled variable. This approach is illustrated in Figure 3a. In this case, MPC manipulates the setpoint of the PID controller setpoint as necessary to keep the controller output in range. How well the PID output can be controlled and how close to saturation the MPC limit can be placed depends on: PID tuning, disturbances characteristics, and the degree of nonlinearity. It may be necessary to retune the PID loop based on the response of the controller output (a smooth response in the valve, without significant proportional "kick" is desirable).

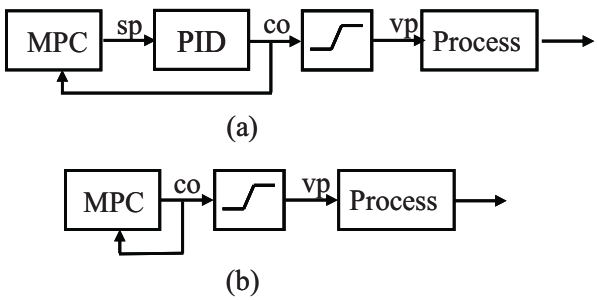

Figure 4. Alternate MPC strategies for maintaining valve positions in controllable range – (a) MPC to PID and (b) direct output to valve.

If a valve associated with a PID controller saturates more than 25% of the time, or if economics dictate operation at a fully open or closed-loop state, it may be preferable to directly manipulate the controller output directly, as shown in Figure 3b. In this way, the valve limit can be strictly enforced, resulting in control closer to the true valve limit. In this situation, additional disturbances may result from opening the PID loop that need to be addressed by the MPC

Regardless of the strategy, valves issues often arise in a project. Significant valve stiction (if greater than say 2%) must be corrected. In addition, valve nonlinearities may require compensation as part of the MPC strategy.

Example To illustrate how the various considerations discussed previously influence the MPC design, consider the two-column configuration shown in Figure 5, which is to be part of an MPC application that maximizes plant feed rate (not shown).

The following convention is used: ZC.sp denotes the setpoint of a PID loop to control Z; ZC.pv denotes the process variable or feedback variable for loop ZC; and ZC.op represents the output signal sent to the valve position.

For this example, assume it is known that the second column is susceptible to flooding, as indicated by a high value in DP1.pv, and that PC2op often saturates fully open. Because flooding is a constraint for column two, we would consider breaking the LC2 cascade and directly manipulating flow FC3.sp in the MPC. Due to the saturation potential of PC2, we would also consider directly manipulating its valve via PC2.op and controlling pressure within the MPC. If both temperature controllers perform well and the associated temperatures are good indicators of composition, they would be retained. These considerations then lead to an MPC with the following manipulated variables:

FC2.sp - column 1 reflux flow controller setpoint.

TC1.sp - column 1 temperature controller setpoint.

PC1.sp - column 1 pressure controller setpoint.

FC3.sp - column 2 feed flow controller setpoint.

FC5.sp - column 2 reflux flow controller setpoint.

TC2.sp - column 2 temperature controller setpoint.

PC2.op - column 2 pressure controller output.

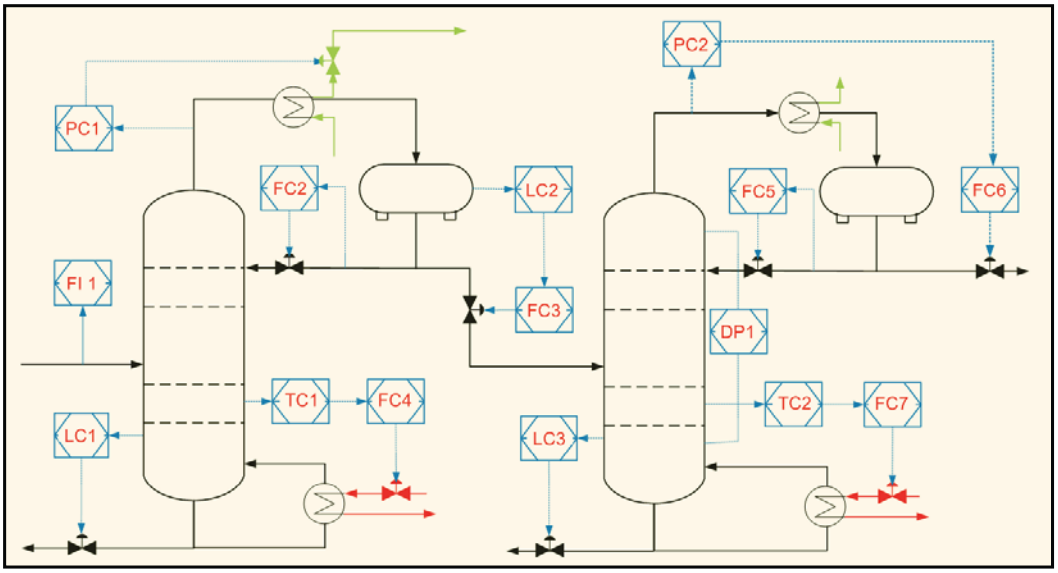

Figure 5. Example process to be controlled by MPC

2. PLANT TESTING

The plant test and subsequent model identification are the most important steps in an MPC project, and incur the most time, often representing more than 50% of the total project time. The importance of the accuracy of the plant model for MPC cannot be overstated. One cannot simply tune an MPC controller to compensate for a poor model. Further the effort involved in testing and identifying an MPC model is not a one-time event. To ensure adequate performance of an MPC application and sustain its benefits over time, it is necessary to re-perform plant testing to update the MPC model (all or in part) when control performance deteriorates due to a process change such as a process revamp.

Until the mid 90's, it was typical practice to conduct manual, open-loop tests, concentrating on the testing of one manipulated variable at a time, but moving other process inputs as necessary to maintain process operation in a desired region. Automatic testing via uncorrelated binary sequences

such as PRBS or GBN increased in popularity in the mid to late 1990's, and closed-loop testing approaches started appearing in the early 2000's. Today we are witnessing increased use of multivariable closed-loop testing methods in the industry as a means to reduced costs (human effort and time) and improved model accuracy due to richer data sets. Of course, an initial model must be available to perform a closed-loop test. An initial model may be available from an existing controller; otherwise, an initial model may need to be developed (e.g., from pretest data).

All of the above testing methods continue to be used today. Some MPC engineers continue to advocate manual testing methods, arguing that it is more conducive to developing process knowledge. While this is indeed an important step, we believe that sufficient process knowledge can come from the pretesting phase and the early stages of an automatic or closed-loop test, where the testing may start with just a few inputs.

Regardless of the testing approach, it is important to generate data in the frequency range of interest. This requires varying the pulse widths of the input signals, e.g., from 10% to 125% of the estimated settling time. A typical guideline is to achieve an average pulse width of an (uncorrelated) input signal equal to $1/3^{rd}$ of the open loop settling time of the process. Automatic signals can easily be generated to achieve a desired average pulse width. Input amplitudes are selected to keep process inputs and process outputs within desired ranges, but should be large enough to overcome valve stiction limits. Larger amplitude moves are preferred as long as the process responses remain within a linear range (unless linearizing transformations are used). A goal is to obtain a signal-to-noise ratio of at least 6-to-1.

The closed-loop testing approaches that have been developed for MPC also utilize uncorrelated binary signals. In Zhu (2001), generalized binary signals (GBN) (Tulleken, 1990) are applied to selected manipulated variables as dithers (added to MPC-generated manipulated variables) and to certain MPC-controlled variable setpoints. In Kalafatis et al. (2006), a closed-loop testing approach is described in which GBN binary signals are generated within the multivariable controller to maximize MV amplitude while keeping predicted CVs within preset constraints. Control action is only applied when predicted CVs exceed their limits.

Important quantities not measured online may require development of an inferential model. Generating data for inferential model development represents a much better approach than using only historical data, which typically has insufficient excitation and feedback effects. To ensure adequate data for model development, the process is moved to different steady-state operating values during the course of the plant test. Note that it is important to get accurate time stamps of the lab samples so that the data can be properly synchronized with measured plant test data for model identification. Due to the importance of the plant model, it is important not to stop a plant test prematurely. As a result, it is good practice to perform model identification throughout the testing phase until model quality is deemed adequate.

3. IDENTIFICATION METHODS

Dynamic Modeling. Various model structures are routinely used in the identification of models for MPC. Low order, parametric techniques continue to find application; however, these are nonlinear approaches, which require specification of model order (which is not straight forward). Processes with heat integration, recycle and/or embedded PID loops typically require higher order models to capture the resulting complex input-output behavior. As a result, we continue to find that finite impulse response (FIR) and high-order ARX (auto-regressive with exogenous input) models remain popular in MPC applications, both of which can be identified with linear least squares methods. For the FIR structure, smoothing techniques are used to reduce parameter variance (e.g., Dayal and MacGregor (1996)). Model reduction techniques are typically used with high-order ARX models to reduce parameter variance (see, e.g., Zhu (1998)).

We have witnessed increased use of subspace identification methods in industrial MPC applications over the past 10 years. This follows the development of these algorithms in the 90's (Larimore, 1983; Larimore, 1990; Overschee and De Moor, 1994). A key advantage of a subspace method is that it directly yields a multivariable state space model, which is an advantage for a state-space controllers. However, even for FIR- or FSR-based MPC, a subspace method offers advantages as it considers the correlation of the output measurements in the identification, thus leading to a potentially more accurate and robust model. Industrial experience with a subspace identification method has been discussed in Zhao et al. (2006). Their experience has shown that complex relationships can be accurately modeled with a state space model of relatively modest order (range of 5 to 15), which captures both slow and fast dynamics. Advantages compared to a parametric technique are that the model order selection can be automated and only linear methods are required. Compared to FIR models, their experience has shown that subspace leads to more accurate estimates of gain and gain ratios, which are critical to capturing the true degrees of freedom in the MPC and ensuring reliable LP performance.

For the closed-loop situation, traditional subspace methods are biased; thus, special treatment is required. Modifications can be made to subspace methods that lead to consistent estimates (as summarized in (Qin, 2006)), although in theory, prediction error methods (e.g., ARX) lead to estimates with lower parameter variance. A challenge with closed-loop identification (using a direct approach) is the importance of obtaining an accurate noise model, which is problematic in practice, since typical process disturbances cannot be captured by white noise, passed thru a linear filter. In practice, one can attempt to minimize the bias by "overwhelming" noise feedback in the frequency range of interest (Jorgensen and Lee, 2002).

Important decision made during the model identification step relate to the following:

Data slicing Determining the sections of data should be included/excluded in the identification.

Data pre-processing Includes such option as spike removal, offset correction, prefiltering/detrending options, and shifting data based on known delays.

Selection of input and outputs – inputs include both candidate manipulated variables and measured disturbances.

Model Structure This includes decisions such as FIR model length, model orders of ARX or subspace, integrating variable or not

Nonlinearities Do nonlinearities warrant additional modeling?

Each of the above steps are typically iterative. With data slicing, the important issue is removing data that would otherwise lead to model bias. This includes time periods with significant unmeasured disturbances or plant upsets, such as pump shutdown, or where valve saturation occurs with PID loops. Prefiltering/detrending, can significantly impact the identification results. It is important to pre-filter/detrend to suppress slow drifts and minimize their contribution to model bias. In some MPC identification packages user options for prefiltering/detrending are not provided. Data differencing is often used, but since it suppresses low frequency information can lead to model gain errors.

In the selection of inputs and outputs, one will have a good idea of which are the manipulated and controlled variables, but it may not be as clear as to which other inputs should be selected as disturbance variables. Note it may be desirable to include a disturbance variable simply as part of the identification step to improve the quality of the models to the key manipulated variables, and not use it as a feedforward variable in the controller. With a subspace identification method, due to the fact that it explicitly considers the correlation of the outputs, the proper selection of output variables can improve the model accuracy of a given input-output channel, regardless of whether the additional outputs are used in the controller.

An aspect of model structure selection is whether to model a controlled variable as an integrating variable. Many times, process knowledge will guide this decision (such as liquid level to flow). However, slow responding stable variables (slower than the controller prediction horizon of the controller) often lead to improved control if modeled as an integrator, especially if they are subjected to input-type of disturbances.

Nonlinearities are typically handled with a static linearizing transformation on inputs and/or outputs. This is the familiar Hammerstein and Weiner model structures, as shown in Figure 6. In typical MPC practice, these static nonlinear functions are SISO (one-to-one) as opposed to MIMO. This is because a MIMO structure would be problematic when constraints are imposed. With physical insight, one may have knowledge as the functional forms such as valve-flow relationships or logarithm of distillation product impurity.

Figure 6. General Hammerstein-Wiener model structure; f_H is the Hammerstein static nonlinear transformation, f_W is the Weiner static nonlinear transformation.

For the general case, when a specific nonlinear transformation is unknown, a piece-wise linear relationship can be empirically derived, assuming testing is over a range wide enough to capture the nonlinearity. An example is shown in Figure 7 for the case of a valve position (controller output) and an associated measurement (e.g., flow). This transformation could be used with either of the valve position scenarios shown in Figure 4.

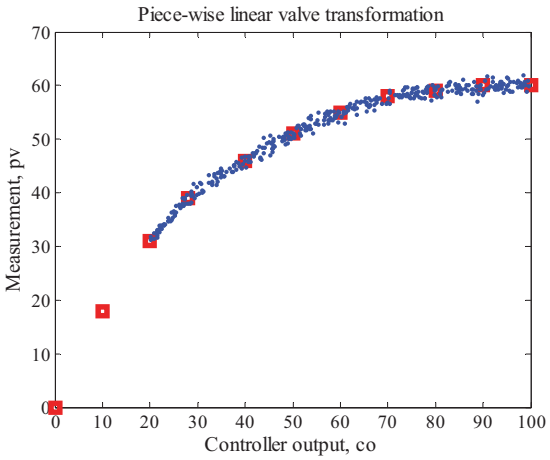

Figure 7.Example piece wise linear transformation

Many of the commercial MPC include the necessary pre- and post-processing capability to handle Hammerstein and Weiner transformations. To deal with dynamic nonlinearity one can use multiple models and "schedule" these based on knowledge of the operating point. Although this would be an easy thing to do, it is not commonly done with empirical models. An example of where multi models *are* routinely used is in ethylene applications, where there is a different furnace model for each major feed type.

Inferential modeling. For the situation where an inferential model must be developed for product qualities that are not measured online (measured infrequently by lab), a couple of approaches can be used.

The most common is to develop a regression model of the quality from directly measured variables such as flow, temperatures, and pressure. It is common for the multiple measurements (for example temperatures) used as inputs to the regression to be correlated. This requires multivariate regression techniques such as principal component regression (PCR), principal component analysis (PCA) and partial least squares (PLS). The key idea is to project the measurement values into a reduced number of important directions

(number of directions less than the number of measurements) to avoid problems associated with correlation/ill-conditioning. Improved regression modeling is possible if a steady-state simulation model is available. In this case, measurements can be selected to minimize steady-state offset in the primary variables (lab measured) for expected disturbances and setpoint changes (Pannocchia and Brombilla, 2003; Hori et al., 2005).

The other approach to inferential modeling utilizes a simplified, fundamental (nonlinear) model of the processes, where parameters in the model are tuned (or optimized) to best fit the model to lab samples. In this case, the nonlinear model provides feedback to the MPC. The advantage of this approach (assuming the model is adequate) is that less process testing is required to fit the inferential model and the model can be expected to operate satisfactorily over a wider range of operation compared to a purely regression model. See, e.g., Friedman (2001), where a static nonlinear model is used for prediction of distillation product compositions.

4. CONTROLLER DEVELOPMENT

An MPC application is typically applied to a unit such as a fluid catalytic cracking unit (FCCU) or ethylene unit. A single MPC or multiple MPC controllers may be applied, depending on the unit objective and constraints. Consider as an example the FCCU shown in Figure 8. If the unit objective is to maximize unit feed and downstream throughput constraints exist, such as DC4 flooding, one would consider a single controller. If there are no throughput constraints in the downstream columns, one would consider two MPC controllers: one for the reactor/regenerator/ main fractionator/wet gas compressor, and one for the all of the downstream distillation columns.

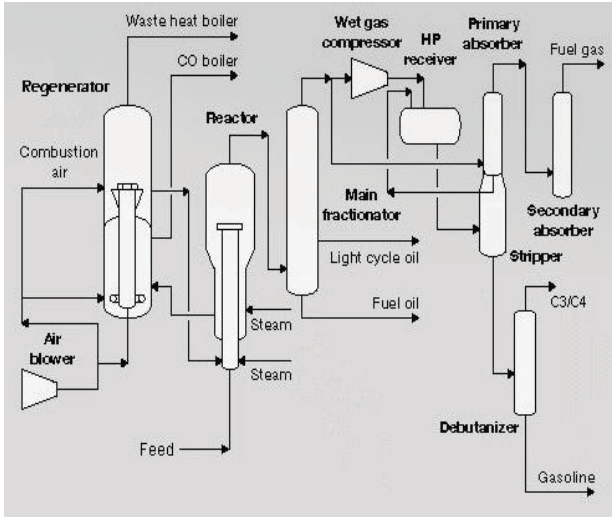

Figure 8. Fluid catalytic cracking unit.

A single unit controller is harder to implement and maintain, and if not implemented properly, or if sufficient engineering expertise is not available onsite, the result may be low MPC service factors or a controller that does not meet economic objectives. When a controller is not performing correctly or is not understood by operations, operators will typically "pinch" manipulated variables (set upper and lower limits close to each other) to overly constrain the MPC in order keep control within a region that the operator feels comfortable. When limited resources available are available, an alternative would be to first implement distributed controllers and later consolidate controllers after experience and confidence is gained.

It is good practice to develop models on an individual equipment basis. For example model reactors and distillation columns separately and build up the overall model from the various sub-models. Thus, the modeling should not be treated as one black-box, linking all inputs to all outputs (Haarsma and Mutha, 2006). If the modeling of the individual equipment is done properly, the key manipulated and controller variables have been identified and modeled and the manipulated variables for the overall model is the super set of MVs and CVs for the sub-models. Note that feedforward variables in the sub-models need to be truly independent variables from the viewpoint of the assembled model for the MPC.

With the above approach, it is typical to develop a sub-model based on its feed measurements (e.g., the feed rates to the primary absorber / stripper in Figure 8), but the overall MPC may require a model expressed in terms of unit feed. In this case, one can develop the required model from a convolution of the primary absorber sub-model and a model from unit feed to primary absorber feed. Note that the model prediction errors in the predicted feed to primary absorber feed can be used as a feedforward variable to the primary absorber / striper and DC4 with this arrangement. This is sometimes known as a prediction error feedforward in MPC jargon.

It is good modeling practice to ensure that the MPC model satisfy material balances (delta flows in equal delta flows out). When levels are controlled in MPC, the material balance consistency implies that the rate of change of levels *and* flows equal zero at steady state. Another area of consistency is where embedded PID loops imply a unity or zero gain.

As we have mentioned previously, the accuracy of the steady-state gains is critically important as they determine the steady-state operating point (target selection layer in Figure 2). This, in turn, can have a significant effect on the control layer as both target selection and dynamic control are executed at the same frequency. The challenge is that gains from an empirical model may not represent the true degrees of freedom that exist in the plant. As a result, the target selection layer may exploit fictitious degrees of freedom, a problem that tends to get .worse with problem size (due to the increased number of possible submatrices).

Consider the case that an LP is used as the target selection. At each execution , the LP will invert a square sub-matrix of the overall gain matrix. If the sub-matrix is ill-conditioned, the resulting changes to the plant may be excessive, possibly leading to cycling or instability. This normally becomes an issue when key manipulated variable handles are constrained (and therefore unavailable) and weaker manipulated variables

must be used. Note that a degree of freedom can be removed from the LP by fixing gain ratios (forcing exact colinearity). A key modeling issues is deciding whether a degree of freedom exists or not. This decision can be guided by the models themselves and their uncertainty) or from engineering insight. Two approaches are used in practice to help with this problem. One approach is to analyze various sub-matrix combinations of the gain matrix in terms of singular value decomposition (SVD or the relative gain array. Sub-matrices with high condition number or large RGA elements become candidates for forcing a collinear relationship, particularly when expected gain errors suggest a co-linearity. Another approach is an online method that automatically disregards small singular values in the sub-matrix inverse, based on user defined tolerances (Qin and Badgwell, 2003). In the authors' opinion, neither approach is completely satisfactory. Analyzing sub-matrices can be a time consuming task and tuning with singular value tolerances can lead to unexpected effects.

During the controller development phase, initial controller tuning is performed. This relates to establishing criteria for utilizing available degrees of freedom and control variable priorities. In addition, initial tuning values are established for the dynamic control. Steady state responses corresponding to expected constraint scenarios are analyzed to determine if they behave as expected, especially with respect to the steady-state changes in the manipulated variables. This step may force additional analysis and treatment of gains and gain ratios.

5. COMMISSIONING

One reason we want to execute the various project steps well is to minimize rework in the commissioning phase. In the best case, commissioning of the controller involves simply making tuning adjustments and observation of the controller under different constraint situations and plant disturbances. In the worst case, control performance is unacceptable and the control engineer is forced to revisit earlier decisions such a base level regulatory strategy or plant model quality. Both of these can lead to retesting and re identification of at least portions of the plant model, resulting in delays and possible cost overruns.

During commissioning it is typical to revisit model decisions and assumptions, and switch out certain models, or modify gains, to obtain acceptable control. Typically, 50-70% of the commissioning effort deals with models.. Commissioning typically takes place over a 2-3 week period. In reality, commissioning is an ongoing effort, although the subsequent effort is normally treated as controller support and maintenance. During the commissioning phase there are only so many different constraint and operating scenarios that can be considered. Certain operating scenarios and constraint sets can *only* be observed certain times of the year due to seasonal effects. It is therefore important that the operating company have in-house expertise that can be used to answer questions ("whys is the controller doing that?"), troubleshoot, and resolve problems that arise over time.

Once a controller is commissioned, it is important to monitor controller performance to ensure benefits are maintained. Unfortunately, multiple factors can contribute to controller performance deterioration. A change in the operating point or a plant modification may invalidate portions of the plant model. Performance degradation of other control systems (PIDs and MPCs) can lead to poor performance. For example, a PID loop associated with, or upstream of, an MPC may develop a cycle resulting from valve stiction. While technology can help with the diagnosis, ultimately expertise must be brought to bear to resolve and correct the problem. Left uncorrected such problems lead to low service factors, or worse, an MPC being permanently switched off.

6. TRENDS AND SUGGESTED RESEARCH DIRECTIONS

The impact of faster and multi-core processors are being seen in MPC products. Increased processing speed is allowing an increased number of future moves to be calculated over the control horizon and also allows for much faster controller execution. In Barham (2006), an MPC approach is described in which all manipulated variables are valve positions. It is applied to an entire FCCU, and executes on a six-second interval. Transformations are used to linearize the relationship between valves and controlled variables. In Froisy (2006), a new state space controller is described that is based on an infinite horizon move plan, Notable features include model assembly of smaller submodels into one large overall MIMO state space model, and an automation feature that simplifies the configuration and tuning of disturbance estimators within a dynamic Kalman Filter framework. We are also seeing increased offerings of MPC at the DCS level where it can execute at a 1 second interval. However, unit wide or multi-unit MPC implementations are still most often implemented in a separate, dedicated computer.

In the remainder we provide suggestions for areas of improvement, including ideas for how this might be accomplished. General themes are of facilitating improvements at the various steps in an MPC implementation, maximizing the use of data and a priori knowledge, and minimizing the impact of changing or modifying key design decisions.

6.1 DCS Strategy

As we have discussed, decisions related to structure selection of the combined MPC-DCS system are multifaceted. Fortunately, there is experience with many of the major refinery and chemical units that can guide these decisions, although specific experience may not always be sufficient for a particular plant (due to idiosyncrasies of the particular plant). This is of course problematic for processes or industries where MPC has not been previously applied. As a result, the path to an acceptable MPC controller may involve iteration. It is therefore advantageous if rework can be minimized in light of design changes. It is also clear that methods that rely on systematic design rather than trial and error only would be valuable.

In recent years, techniques and products have been developed which apply multivariable identification methods to develop models that are in turn used to tune PID loops. Such approaches can be used to improve the performance of PID loops associated with an MPC system with reduced engineering effort (Zhu, 2003; Harmse et al., 2009). Note that once a multivariable model is available (relating the effect of PID controller outputs on PID controlled variables), one could use standard techniques such as relative gain array (RGA) or block relative gain (BRG) (as a function of frequency) to focus on the most promising PID loop pairings and simulate various suggested pairing possibilities. Experience has shown that testing and developing a multivariable model for the typical loops found at the DCS level can often be completed within a day for the typical loops that are found at the DCS level (Darby and Harmse, 2009).

Changing the PID loop pairings or tuning parameters (if behavior is significantly different) requires a change to the affected models in an MPC system. Historically, such changes have required plant retesting. However, with completed knowledge of the models at the PID level (including the PID controllers themselves), it is theoretically possible to convert the MPC models to reflect a different PID configuration or tuning), potentially avoiding an expensive retest. Such an approach is described in Rejek et al. (2004). One major claim for this approach is that one could perform the plant test in one DCS configuration, but implement the MPC in another configuration as in Barham et al. (2006). To our knowledge, various options for solving this problem have not been investigated. Open questions concern accuracy and robustness issues as to how best to perform this model conversion.

6.2 Plant Testing

It is well known that that independent binary input test signals are generally inadequate (inefficient at best) for the identification of ill-conditioned systems. The reason is that the weak process directions (e.g., separation changes in a distillation column) are poorly identified in the presence of noise. The solution is to use correlated inputs, which can be generated in open or closed loop (Anderson and Kummel, 1992; Koung and MacGregor, 1994; Li and Lee, 1996). For example, in a distillation column, large changes in both reflux and reboil flow rates are required to adjust separation in any significant way. As discussed previously, ill-conditioning is often found in the MPC steady-state gain matrix. Properly designed input sequences can be expected to improve estimation of ill-conditioned sub-matrices. Recent results show that independent binary signals can also be inferior for well-conditioned systems, depending on the active constraints. In Darby and Nikolaou (2008a, b), using a criterion which maximizes the likelihood of satisfying integral controllability, optimal inputs (both amplitudes and covariance of the inputs) are shown to depend on both the system's conditioning and the specific active constraints. While correlated inputs can be achieved with independent perturbations of controller CV setpoints or limits, such an approach may translate into ineffective input perturbations due to the influence of the target selection layer. A closed-loop experimental design approach for MPC would be desirable, although treated rigorously, would require knowledge of the feedback law. This would be problematic for MPC as each constraint set represents a different control law. A possible approach is to replace the binary test signals that are currently used in closed-loop MPC with a traditional or control-relevant experimental design. An experimental design could be performed consistent within a feasible region established for the target selection layer and implemented through the controller to ensure constraint satisfaction. This might be done in a manner similar to that used in Sagias (2004) for PRBS signals, where the dynamic objective function is modified to the allow trade-off of control and test objectives. The other aspect of experimental design concerns frequency content. This aspect would need to be investigated as well. We note that with current MPC practice, the frequency content is specified indirectly based on the type of binary signal chosen and the specified average pulse width. Extending this concept further, if basis functions with desired frequency content were pre-specified, this might allow the experimental design to be expressed in terms of input amplitudes and covariances.

6.3 Identification

As mentioned earlier, there are multiple consistency relationships (e.g. gains and gain ratios) that should be enforced in the constructed MPC model. Instead of imposing these conditions by altering the identified model as a post-processing step, it would be better to incorporate these as constraints in the identification. Within the context of least squares, imposition of linear constraints results in parameter estimators with smaller variance (Seber and Lee, 2003).

Other consistency relationships could be incorporated. Material balance consistency has been discussed, but consistency can be extended to component balances. For example, for binary distillation columns, relationships can be derived which link the steady-state gains associated with top and bottom purities for a given regulatory control structure (Häggbloom and Waller, 1988).

Another area that should be exploited is a priori information available in the form of physical models. Such an approach was discussed for a steady-state inferential predictor. The basic idea is to combine available model information and data in a grey-box identification problem. The key motivation is one of getting better models with less data and effort, not necessarily one of capturing the nonlinear behavior. A linearized model from a fitted nonlinear model may well be adequate. However, it the nonlinearity were significant, the nonlinear model could be used to update models in the MPC. We should mention that in our view (for the foreseeable future) a full nonlinear model is not needed or feasible for the majority of control problems common found in industry (polymer applications and batch applications being notable exceptions). Tools to empirically determine the Hammerstein and Wiener static compensators would be useful (such as described in Zhu (2000) for the case of cubic splines). One

could also consider combing the dynamic identification step with piece-wise linear transformations in a single identification problem. We might expect that nonlinear models could be developed for certain submodels of an MPC, if the improvements or costs saving to develop the model are significant. The online implementation might be posed as a constrained estimation problems using techniques such as found in Rawlings and Bakshi (2006), where the estimator would provide feedback (and possibly future predictions) to MPC. An example of a common situation where nonlinear affects are often encountered is variable liquid hold-up (e.g., reflux accumulator), which causes a variable dynamic response in downstream composition signals.

6.3 Improved Disturbance Estimators

A key advantage in utilizing a general state space formulation is improved (unmeasured) disturbance modeling. For example, it is well known that the output bias approach, traditionally used for the MPC model update step, can lead to sluggish response to an input disturbance (Shinskey, 1994). A properly designed estimator overcomes this limitation (Muske and Badgwell, 2002; Pannocchia and Rawlings, 2003). An additional advantage of state space disturbance model is that of incorporating additional output measurements. A typical example is shown in Figure 9. The variable u represents the MPC manipulated variable and y is the MPC controller variable; yI is an intermediate variable. Examples include:

> Case 1: u is plant feed rate, y_I a downstream flow measurement and y is a downstream controlled variable.
>
> Case 2: u is column reflux flow rate, y_I a tray temperature, and y a product analyzer.
>
> Case 3: u is a PID setpoint, y_I is the PID error and, y is an MPC controlled variable..

Case 1 represents the example considered earlier (cf section 6). Case 2 provides structure similar to a traditional cascade control (Froisy, 2006). Case 3 models the behavior of the base level PID, e.g., a time series model of the PID error, which has the advantage that unnecessary moves are not generated by MPC when the base layer is capable of rejecting the unmeasured disturbance (Haarsma and Mutha, 2006). Improved disturbance modeling could also be applied to the situation where MPC is directly manipulating a valve (and local flow, temperature, and/or pressure measurements are available).

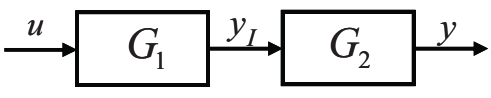

Figure 9. Plant model with intermediate variable y_I.

While it is possible to replicate such approaches within traditional FIR- and FSR-based MPC, they involve ad-hoc solutions. An interesting possibility is the use of improved disturbance estimators within traditional FIR- or FSR-based MPC (Badgwell, 2009). What is unclear is the extent to which these improved estimators are actually being used within existing state space controllers. Anecdotal evidence suggests a gap between these capabilities and actual usage by MPC engineers. Part of the challenge in developing these more general estimators is that it requires linking disturbances to particular model channels. Tools and techniques to facilitate or simplify this step would be helpful.

6.4 Robustness

Model errors impact performance of MPC at both the target selection layer and the dynamic controller, although, as we have seen, the problem is more acute with the steady-state target selection layer. While the target selection layer offers advantages in terms of constraint control, economic optimization, and dealing with non-square systems, it represents a source of challenges for an MPC implementation, ones that grow with the size of the controller. The goal is to prevent the optimizer from exploiting fictitious degrees of freedom, and from exploiting true degrees of freedom that may exist, but lead to large steady-state moves for only small economic improvement. Another challenge is minimizing the impact of effects that can lead to chatter in the steady-state targets (Shah et al., 2001; Kozub, 2002). This includes high frequency noise associated with controlled variables, unmeasured disturbances and/or model error. An approach that has been used industrially to minimize change from the optimizer layer to the dynamic layer is based on a minimum-movement criterion (to achieve all control objectives) in the dynamic layer and to invoke a QP optimization once all predicted controlled variables are within a pre-defined funnel (Lu, 2003).

Given the importance of the steady-state gain matrix in the optimizer, Kassman et al. (2000) proposed a robust LP formulation based on ellipsoidal uncertainty of the gain matrix. An advantage of their approach is that the resulting optimization problem is convex. An open question is how well their approach addresses problems with ill-conditioning. Note that we have avoided mentioning worse case formulations due to their tendency to provide overly cautious control for the average case.

The challenges outlined above could benefit from additional research. Pertinent questions are whether it is possible to avoid inverting the gain matrix for the entire plant and whether techniques could be used to avoid exploiting uncertain (and undesirable) degrees of freedom. These issues might be considered with the general problem of how to coordinate multiple MPCs, which is currently receiving increased research attention. .We note that when the plant optimum is consistent with maximum throughput, a simplified coordinator can be used (Aske et al., 2008). Such an approach explicitly limits the degree of freedom that are used in the plant wide control scheme.

7. CONCLUSION

The MPC algorithm is a mature technology and there is good understanding of the algorithm's properties and behavior. But as discussed, there are facets of the technology that could be improved. As one would expect, the performance of MPC systems does not depend only on the "control law" (MPC tuning) but on successful completion of all of the following steps: articulation of control objectives, selection of measurements and manipulations, configuration of controller structure (i.e. interconnections among MVs and CVs), and, finally, design of the control law (Stephanopoulos, 1984). Even though the control law can be designed in a fairly systematic way, completion of the design steps above it is less systematic, and offers a margin of creativity. Process understanding remains indispensable for these steps. Improving the ability to systematically complete these steps would certainly contribute towards designing better MPC systems. Industry and academia can continue collaboration towards this end, with full understanding of the need for sanitized academic solutions to bear industrial relevance and that common practice may not necessarily be best practice.

REFERENCES

Anderson, H. W. and Kummel, M. (1992). Evaluating estimation of gain directionality part 2: A case study of binary distillation. *Journal of Process Control*, **2**, 67-86.

Aske, E. M. B., Strand, S. and Skogestad, S. (2008). Coordinator MPC for maximizing plant throughtput. *Computers & Chemical Engineering*, **32**, 195-204.

Badgwell, T. A. (2009). Personal communication with T. A. Badgwell.

Barham, M., Watts, J., Bailey, M., Carroll, T., Garcia, L., Cutler, C., Hetzel, M., Szuhay, J. and Boyden, S. (2006). Adaptive dynamic matrix control on a fluidized catalytic cracking unit. *ISA 2006*, Houston.

Buckley, P. S. (1964). *Techniques of Process Control.* John Wiley & Sons.

Darby, M. L. and Harmse, M. (2009). Is it time for a new approach to PID tuners. *AIChE 2009 Spring Meeting*, Tampa.

Darby, M. L. and Nikolaou, M. (2008a). Multivariable system identification for integral controllability. *Automatica*, submitted.

Darby, M. L. and Nikolaou, M. (2008b). Design of experiments for identification of multivariable models satisfying integral
controllability: The dynamic model case. *AIChE Annual Meeting*, Philadelphia.

Darby, M. L. and Teeter, E. (2005). Best practices of MPC/RTO in ethylene. *AIChE Spring Meeting*, Atlanta.

Dayal, B. S. and MacGregor, J. F. (1996). Identification of finite impulse response models: Methods and robustness issues. *Industrial & Engineering Chemistry Research*, **35**, 4078-4090.

Friedman, Y. Z. (2001). Experience with GDS, a first principles inference model for distillation columns. *ERTC Computer Conference*, Paris.

Froisy, J. B. (2006). Model predictive control - Building a bridge between theory and practice. *Computers & Chemical Engineering*, **30**, 1426-1435.

Froisy, J. B. (2009). Personnel communication with J.B. Froisy.

Genceli, H. and Nikolaou, M. (1993). Robust stability analysis of l1- norm model predictive control. *AIChE Journal*, **39**, 1954-1965.

Haarsma, G. and Mutha, R. (2006). Implementation of unit wide advanced process control in ethylene plant. *AIChE Spring Meeting*, New Orleans.

Häggbloom, K. E. and Waller, K. V. (1988). Transformations and consistency relations of distillation control structures. *AIChE Journal*, **34**, 1634-1648.

Harmse, M., Hughes, R., Dittmar, R., Singh, H. and Gill, S. (2009). Robust optimization-based multiloop PID controller tuning: A new tool and an industrial example. *Advanced Control of Chemical Processes, ADCHEM 2009*, Istanbul.

Hori, E. S., Skogestad, S. and Alstad, V. (2005). Perfect steady-state indirect control. *Industrial & Engineering Chemistry Research*, **44**, 863-867.

Jorgensen, S. B. and Lee, J. H. (2002). Recent advances and challenges in process identification. *Proceedings of the Sixth International Conference on Chemical Process Control*, Tucson, 55-74.

Kalafatis, K., Patel, K., Harmse, M., Zheng, Q. and Craig, M. (2006). Multivariable step testing for MPC projects reduces crude unit testing time. *Hydrocarbon Processing*, 93-99.

Kassman, D. E., Badgwell, T. A. and Hawkins, R. B. (2000). Robust steady-state target calculation for model predictive control. *AIChE Journal*, **46**, 1007-1024.

Koung, C. W. and MacGregor, J. F. (1994). Identification for robust multivariable control - The design of experiments. *Automatica*, **30**, 1541-1554.

Kozub, D. J. (2002). Controller performance monitoring and diagnosis. Industrial perspective. *Fifteenth Triennial World Congress of the International Federation of Automatic Control*, Spain.

Larimore, W. E. (1983). System identification. reduced-order filtering and modeling via canonical variate analysis. *Proceedings of the 1983 American Control Conference*, San Francisco, 445-451.

Larimore, W. E. (1990). Canonical variate analysis in identification, filtering and adaptive control. *Proceedings of the 29th Conference on Decision and Control*, Honolulu, 596-604.

Larsson, T. L. and Skogestad, S. (2000). Plantwide Control - A review and a new design procedure. *Modeling, Identification and Control*, **21**, 209-240.

Li, W. and Lee, J. (1996). Frequency domain closed-loop identification of multivariable systems for feedback control. *AIChE Journal*, **42**, 2813-2827.

Lu, J. Z. (2003). Challenging control problems and emerging technologies in enterprise optimization. *Control Engineering Practice*, **11**, 847-858.

Maciejowski, J. (2002). *Predictive Control with Constraints.* Englewood Cliffs: Prentice Hall.

Mayne, D. Q., Rawlings, J. B., Rao, C. V. and Scokaert, a. P. O. M. (2000.). Constrained model predictive control: stability and optimality. *Automatica*, **36**, 789-814.

Morari, M., Arkun, Y. and Stephanopoulos, G. (1980). Studies in the synthesis of control structures for chemical processes Parts I, II, III. *AIChE Journal*, **26**, 220-260.

Muske, K. and Badgwell, T. A. (2002). Disturbance modeling for offset-free linear model predictive control. *Journal of Process Control*, **12**, 617-632.

Overschee, P. v. and De Moor, B. (1994). N4SID: Subspace algorithms for the identification of combined deterministic-stochastic systems. *Automatica*, **31**, 1853-1864.

Pannocchia, G. and Brombilla, A. (2003). Consistency of property estimators in multicomponent distillation control. *Industrial & Engineering Chemistry Research*, **42**, 4452-4460.

Pannocchia, G. and Rawlings, J. B. (2003). Disturbance models for offset-free model-predictive control. *AIChE Journal*, **49**, 426-437.

Qin, J. Q. and Badgwell, T. A. (2003). A survey of industrial model predictive control. *Control Engineering Practice*, **11**, 733-764.

Qin, S. J. (2006). An overview of subspace identification. *Computers & Chemical Engineering*, **30**, 1502-1513.

Rawlings, J. B. and Bakshi, B. R. (2006). Particle filtering and moving horizon estimation. *Computers & Chemical Engineering*, **30**, 1529–1541.

Rawlings, J. B. and Muske, K. R. (1993). The stability of constrained receding horizon control. *IEEE Trans. Automatic Control*, **AC-38**, 1512-1516.

Sagias (2004). *Closed loop identification of a process controlled by MPC.* Chemical Engineering, University of Houston, Houston, TX.

Seber, G. A. F. and Lee, A. J. (2003). *Linear Regression Analysis.* 2nd Ed. Hoboken, NJ, John Wiley.

Shah, S. L., Patwardhan, R. and Huang, B. (2001). Multivariate controller performance monitoring: Methods, applications and challenges. *Chemical Process Control VI*, Tuscon.

Shinskey, F. G. (1994). *Feedback Controllers for the Process Industries.* New York, McGraw-Hill.

Skogestad, S. and Morari, M. (1987). Implications of large RGA elements on control performance. *Industrial & Engineering Chemistry Research*, **26**, 2323-2330.

Stephanopoulos, G. (1984). *Chemical Process Control.* New York, Prentice Hall.

Stephanopoulos, G. and Ng, C. (2000). Perspectives on the synthesis of plant-wide control structures. *Journal Of Process Control*, **10**, 97-111.

Tulleken, H. J. A. F. (1990). Generalized binary noise test-signal concept for improved-experiment design. *Automatica*, **28**, 37-49.

Weber, R. and Brosilow, C. (1972). The use of secondary measurements to improve control. *AIChE Journal*, **18**, 614-623.

Ying, C. M. and Joseph, B. (1999). Performance and stability analysis of LP-MPC-QP-MPC cascade control systems. *AIChE Journal*, **45**, 1521-1534.

Zhao, H., Harmse, M., Guiver, J. and Canney, W. (2006). Subspace identification in industrial applications - A review of recent progress and industrial experience. *14th IFAC Symposium on System ID*, Newcastle.

Zhu, Y. (1998). Multivariable process identification for MPC: The asymptotic method and its applications. *Journal Of Process Control*, **8**, 101-115.

Zhu, Y. (2000). *Multivariable System Identification for Process Control.* Amsterdam, Pergamon.

Zhu, Y. (2001). Progress in MPC identification: A case study on totally closed-loop plant test. *ERTC Computing Conference*, Milan.

Zhu, Y. (2003). Robust PID tuning using closed-loop identification. *Advanced Control of Chemical Processes, ADCHEM 2004*, Hong Kong, 165-170.

Power-Shaping Control of an Exothermic Continuous Stirred Tank Reactor (CSTR) ⋆

Audrey Favache * **Denis Dochain** **

* *Université catholique de Louvain, Unité d'ingéniérie des matériaux et procédés, B-1348 Louvain-la-neuve; Université catholique de Louvain, CESAME, B-1348 Louvain-la-neuve (e-mail: audrey.favache@uclouvain.be).*
** *Université catholique de Louvain, CESAME, B-1348 Louvain-la-neuve (e-mail: denis.dochain@uclouvain.be).*

Abstract: The exothermic continuous stirred tank reactor (CSTR) is a classical yet complex case study of nonlinear dynamical systems. Power-shaping control is a recent approach for the control of nonlinear systems based on the physics of the dynamical system. In this paper we present a general methodology to apply the power-shaping control approach to the exothermic CSTR study case. It results in a global Lyapunov function for the exothermic CSTR. This Lyapunov function is then reshaped by the means of a controller in order to stabilize the process at a desired temperature. Some considerations on the local and global convergence to the desired state are presented.

Keywords: Nonlinear control; Power-Shaping Control; exothermic CSTR

1. INTRODUCTION

Thermodynamic systems, and among them chemical reaction systems, are usually nonlinear dynamical systems. They can therefore have a complex behaviour and be difficult to analyze and to control. Stability analysis of nonlinear systems requires the use of abstract mathematical tools such as the two Lyapunov methods or the passivity theory. Over the past years, several works have combined those abstract concepts with the underlying physical phenomena giving rise to the dynamical behaviour of the system. These works include for instance the study of port-Hamiltonian systems (Dalsmo and van der Schaft (1998), Maschke and van der Schaft (2005), Eberard et al. (2006)), energy-balancing passivity based control (PBC) (Ortega et al. (2001), Jeltsema et al. (2004)) or the introduction of the contact formalism for expressing the dynamics of systems in which irreversible phenomena arise (Eberard et al. (2005), Eberard (2006), Favache et al. (2007)). The exothermic continuous stirred tank reactor (CSTR) is a classical study case of nonlinear systems. Indeed, the dynamical behaviour shows complex features, such as multiple equilibrium points. Up to now no exact physical interpretation of the complex behaviour of the exothermic reactor has been found (Favache and Dochain (2009)).

Power-shaping control (Ortega et al. (2003)) has been developed in the past years as an extension of energy-balancing passivity-based control (Ortega et al. (2001), Jeltsema et al. (2004)). In energy-balancing passivity based control, the controller reshapes the energy function of the system so that it has a minimum at the desired equilibrium point. The controller provides to the system a finite amount of energy so as to drive the system to the desired state. This concept has been widely applied to electro-mechanical systems (Ortega et al. (1999), Maschke et al. (2000), Ortega et al. (2002)) but also to thermodynamic systems where the storage function is the entropy instead of the energy (Alonso et al. (2002), Otero-Muras et al. (2006)). Nevertheless energy-balancing passivity-based control can only be applied to systems without pervasive dissipation, i.e. systems where the power provided by the controller is equal to zero at the desired equilibrium point. To overcome this difficulty the concept of power shaping control was introduced firstly for the stabilization of nonlinear RLC circuits (Ortega et al. (2003)). Contrary to energy-balancing passivity-based control, the storage function used for the control is related to the power and not to the energy. Power-shaping control has subsequently been applied to the control of mechanical and electro-mechanical systems (Garcia-Canseco et al. (2008)). Power-shaping control is based on a particular formulation of the system dynamics, namely the Brayton-Moser equations (Brayton and Moser (1964a), Brayton and Moser (1964b)). Although the first systems which have been described using this formalism are electrical circuits, it is shown in Jeltsema and Scherpen (2003), Jeltsema and Scherpen (2007) and Garcia-Canseco et al. (2008) that mechanical systems can also been expressed in this form.

As the work of Alonso, Ydstie and coworkers (see e.g. Alonso et al. (2002), Antelo et al. (2007), Farschman et al. (1998)), the present research is basically motivated by the objective to connect thermodynamics with process control design (see also Favache and Dochain (2009)). In this paper we apply power-shaping control to the exothermic CSTR case study with the aim of bringing more physical insight in its dynamical behaviour. After a brief presentation of

⋆ The work of A. Favache is funded by a grant of aspirant of Fonds National de la Recherche Scientifique (Belgium).

the main principles of power-shaping control in Section 2 and of the CSTR case study in Section 3, we shall apply the power-shaping control theory to our example. First we shall use the power-shaping approach to analyze the open-loop behaviour (Section 4) and then to design a control action (Section 5). Finally Section 6 presents some general comments on the possibility of extending the power-shaping approach to more complex systems, namely systems with more than one reactant, and/or more than one reaction.

2. POWER-SHAPING CONTROL

In this section, we briefly explain the principles of power-shaping control. The statements are given without any proof. For more details, the reader can refer to Jeltsema and Scherpen (2003), Ortega et al. (2003), Jeltsema and Scherpen (2007), Garcia-Canseco et al. (2008).

2.1 The Brayton-Moser formulation

Let us consider a dynamical system of dimension n with m inputs. The state of the system is given by the vector $x \in \mathbb{R}^n$ and the input is given by vector $u \in \mathbb{R}^m$. The power-shaping control theory is based on the Brayton-Moser formulation of the system dynamics (Brayton and Moser (1964a), Brayton and Moser (1964b)). In this formulation the system dynamics are of the following form:

$$Q(x)\frac{dx}{dt} = \nabla P(x) + G(x)u \tag{1}$$

where $Q(x) : \mathbb{R}^n \to \mathbb{R}^n \times \mathbb{R}^n$ is a non-singular square matrix, $P(x) : \mathbb{R}^n \to \mathbb{R}$ is a scalar function of the state and $G(x) : \mathbb{R}^n \to \mathbb{R}^n \times \mathbb{R}^m$. Additionally the symmetric part of the matrix $Q(x)$ is negative semi-definite, i.e.:

$$Q(x) + Q^t(x) \preceq 0 \tag{2}$$

The function $P(x)$ is called the potential function. In electrical and mechanical systems, the potential function has the units of power. In electrical systems it is related to the so-called content and co-content of the resistances (Ortega et al. (2003), Jeltsema and Scherpen (2007)) while it is related to the Rayleigh dissipation function (Jeltsema and Scherpen (2003)) in mechanical systems. In both cases, the potential function $P(x)$ is related to the dissipated power in the system.

Let us now assume that the system dynamics are given by the following relation:

$$\frac{dx}{dt} = f(x) + g(x)u \tag{3}$$

where $f(x) : \mathbb{R}^n \to \mathbb{R}^n$ and $g(x) : \mathbb{R}^n \to \mathbb{R}^n \times \mathbb{R}^m$. The system (3) can be written in the form (1) if there exists a non-singular matrix $Q(x)$ fulfilling (2) and that solves following partial differential equation:

$$\nabla(Q(x)f(x)) = \nabla^t(Q(x)f(x)) \tag{4}$$

This condition is equivalent to the existence of the potential function $P(x)$ (i.e. if the potential function $P(x)$ exists, its Jacobian matrix must be symmetric). This one is the solution of the following partial differential equation system:

$$\nabla P(x) = Q(x)f(x) \tag{5}$$

Finally the function $G(x)$ is given by the following relation:

$$G(x) = Q(x)g(x)$$

2.2 Power-shaping control

Let us assume that the system dynamics can be expressed using the Brayton-Moser equations presented above. The desired equilibrium state is denoted by x^*. The rationale of power-shaping control is to choose the input $u(x)$ such that in closed loop the system dynamics are given by the following relation:

$$Q(x)\frac{dx}{dt} = \nabla P_d(x)$$

where $P_d(x) : \mathbb{R}^n \to \mathbb{R}$ is the reshaped potential function. The desired equilibrium point x^* must be a local minimum of the potential function $P_d(x)$ in order to be locally asymptotically stable. The function $P_d(x)$ cannot be arbitrarily chosen since the following relation has to be fulfilled:

$$g^\perp(x)Q^{-1}(x)\nabla P_a(x) = 0 \tag{6}$$

where $g^\perp(x) : \mathbb{R}^n \to \mathbb{R}^{n-m} \times \mathbb{R}^n$ is a full-rank left annihilator of $g(x)$ (i.e. $g^\perp(x)g(x) = 0$ with $\operatorname{rank}\left(g^\perp(x)\right) = n - m$) and $P_a(x) = P_d(x) - P(x)$. The condition (6) ensures the existence of a function $u(x)$ such that:

$$Q(x)(f(x) + g(x)u(x)) = \nabla P(x) + \nabla P_a(x)$$

Under these conditions, the control input $u(x)$ that achieves to reshape $P(x)$ into $P_d(x)$ is the following one:

$$u(x) = \left(G^t(x)G(x)\right)^{-1} G^t(x)\nabla P_a(x) \tag{7}$$

where $G(x) = Q(x)g(x)$

3. THE EXOTHERMIC CONTINUOUS STIRRED TANK REACTOR (CSTR)

In our research, we have applied the power-shaping methodology to a classical process control case study: the exothermic continuous stirred tank reactor (CSTR), illustrated in Figure 1. The reaction that is taking place is $A \to B$. In order to simplify the model, the following assumptions have been considered:

- the reactor is liquid phase and the volume V is constant.
- the density ρ and the specific heat c_p of the mixture are constant (i.e. independent of the temperature or of the composition).
- the reaction heat is independent of the temperature.
- the reaction is irreversible.
- the reaction kinetics obey to the mass action law, i.e. $r = k(T)n_A$ where $k(T)$ is the kinetic constant, depending only on the temperature T and n_A is the number of moles of component A. The function $k(T)$ is assumed to be monotonically increasing. Moreover let us assume that [1] $\lim_{T\to 0} k(T) = 0$, $\lim_{T\to\infty} k(T) = k_0$ and
$$\lim_{T\to 0}\frac{dk}{dT} = \lim_{T\to\infty}\frac{dk}{dT} = 0$$
- the dynamics of the jacket can be neglected.

[1] These assumptions on $k(T)$ are for instance fulfilled by the commonly used Arrhenius law.

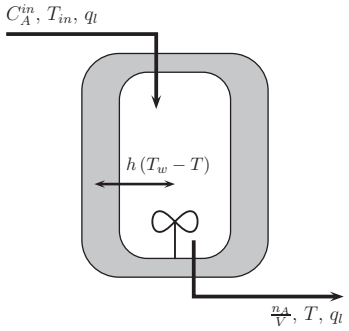

Fig. 1. Schematic view of the CSTR

- the heat exchange between the reactor and the jacket is proportional to the temperature difference between them, with h the heat exchange coefficient.
- the system is controlled by the cooling fluid flow rate. It acts directly on the heat transfer coefficient h. Therefore we shall consider in the sequel that the control input is the quantity $\frac{h}{\rho c_p V}$.

Under these assumptions the dynamic model of the system is given by following equations:

$$\begin{cases} \dfrac{dn_A}{dt} = \dfrac{q_l}{V}\left(C_A^{in}V - n_A\right) - k\left(T\right)n_A \\ \dfrac{dT}{dt} = \dfrac{q_l}{V}\left(T_{in} - T\right) + \dfrac{\left(-\Delta_r H\right)}{\rho c_p V}k\left(T\right)n_A \\ \qquad\qquad + \dfrac{h}{\rho c_p V}\left(T_w - T\right) \end{cases} \tag{8}$$

where q_l is the volumetric inlet and outlet flow rate, C_A^{in} is the inlet concentration of A, T_{in} is the inlet temperature, $(-\Delta_r H)$ is the reaction heat and T_w is the temperature of the cooling fluid. Using the notations of (3), we have:

$$f\left(x\right) = \begin{pmatrix} \delta\left(C_A^{in}V - n_A\right) - k\left(T\right)n_A \\ \delta\left(T_{in} - T\right) + \gamma k\left(T\right)n_A \end{pmatrix}$$

$$g\left(x\right) = \begin{pmatrix} 0 \\ T_w - T \end{pmatrix}$$

with $x = \left[n_A, T\right]^t$, $u = \frac{h}{\rho c_p V}$, $\delta = \frac{q_l}{V}$ and $\gamma = \frac{(-\Delta_r H)}{\rho c_p V}$.

It can be shown that this system can have up to three equilibrium points in open loop (i.e. for $u = 0$), depending on the numerical values of the parameters (see e.g. Aris and Amundson (1958), Uppal et al. (1974)). Here we shall consider the case with three equilibrium states, two being stable and one being unstable.

4. THE OPEN LOOP BEHAVIOUR

The methodology described in Section 2.1 has been applied to the system described in Section 3. The first step was to find the square matrix $Q\left(x\right)$ that meets the required properties (2) and (4). The partial differential equation (4) for the open-loop CSTR is written as follows:

$$\begin{aligned} &- q_{11}n_A\frac{dk}{dT} - q_{12}\delta + q_{12}\gamma n_A\frac{dk}{dT} \\ &+ \frac{\partial q_{11}}{\partial T}\left(\delta\left(C_A^{in}V - n_A\right) - kn_A\right) \\ &+ \frac{\partial q_{12}}{\partial T}\left(\delta\left(T_{in} - T\right) + \gamma kn_A\right) \\ &= -q_{21}\delta - q_{21}k + q_{22}\gamma k + \frac{\partial q_{21}}{\partial n_A}\left(\delta\left(C_A^{in}V - n_A\right) - kn_A\right) \\ &+ \frac{\partial q_{22}}{\partial n_A}\left(\delta\left(T_{in} - T\right) + \gamma kn_A\right) \end{aligned} \tag{9}$$

where q_{ij} is the entry in position (i, j) of the matrix $Q\left(n_A, T\right)$. We first transformed (9) into an algebraic equation by restricting ourselves to a subset of possible matrices $Q\left(n_A, T\right)$. This algebraic equation then has been solved and a possible matrix has been found [2] . In our case, the symmetric part of matrix $Q\left(x\right)$ was found to be definite negative.

Remark 1. Indeed a family of possible matrices $Q\left(n_A, T\right)$ has been found that both satisfy (2) and (4). But since they all have a similar form apart from a constant parameter, we shall treat them in the sequel as one unique matrix.

Next the potential function is found by integrating (5). The general form of the potential form is given by the following expression:

$$\begin{aligned} P\left(n_A, T\right) = &\int p\left(T\right)dT \\ &+ \omega\left[\gamma\left(C_A^{in}V - n_A\right) + \left(T^{in} - T\right)\right]^2 \end{aligned} \tag{10}$$

where ω is a positive constant and $p\left(T\right) : \mathbb{R} \to \mathbb{R}$ is a non-linear function of $k\left(T\right)$ and T. The quadratic term of (10) is clearly linked to the convection phenomena, whereas the integral term is related to the reaction kinetics.

Remark 2. Actually the function $p\left(T\right)$ is not unique. It depends directly on the matrix $Q\left(x\right)$. Since we have found a family of matrices $Q\left(x\right)$, there is a corresponding family of functions $p\left(T\right)$ that are similar apart from a constant parameter.

Let us now consider the equilibrium points $\bar{x} = \left(\bar{n}_A, \bar{T}\right)$ of the open-loop CSTR:

$$Q\left(\bar{x}\right)\left.\frac{dx}{dt}\right|_{\bar{x}} = \nabla P\left(\bar{x}\right) = 0$$

Since the matrix $Q\left(x\right)$ is non-singular, the equilibrium points $\bar{x}$ are also critical points of the potential function $P\left(x\right)$ (i.e. $\nabla P\left(\bar{x}\right) = 0$) and conversely. The analysis of the Hessian matrix of the obtained potential function (10) at each of the equilibrium points shows that the stable ones are local minima of the function $P\left(x\right)$ whereas the unstable one is a saddle point. The level curves of the function $P\left(x\right)$ are given in Figure 2.

The variation of function $P\left(x\right)$ along the trajectories of the system are given by the following relation:

[2] Calculation details can be found in Favache and Dochain (2008).

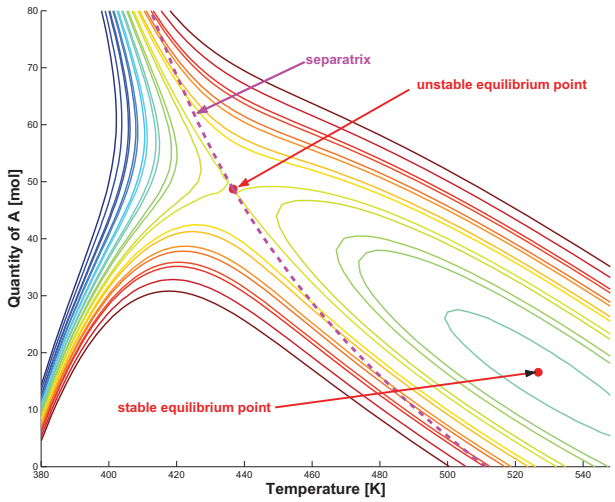

Fig. 2. Level curves of the potential function

$$\begin{aligned}\frac{dP}{dt} &= \nabla^t P(x) f(x) \\ &= \nabla^t P(x) Q^{-1}(x) \nabla P(x) \\ &= \frac{1}{2}\nabla^t P(x) \left(Q^{-1}(x) + \left(Q^t(x)\right)^{-1}\right) \nabla P(x)\end{aligned}$$

Since the symmetric part of $Q(n_A, T)$ is negative definite, we have $\frac{dP}{dt} \leq 0$ where the equality holds only for $\nabla P(x) = 0$, i.e. for the equilibrium points. As a consequence $P(n_A, T)$ is decreasing along the trajectories. Moreover $P(x)$ is radially unbounded. Therefore the potential function $P(n_A, T)$ is a global Lyapunov function for the system (Khalil (2002)).

5. POWER-SHAPING CONTROL OF THE CSTR

5.1 Controller design

Let us denote by $x^* = [n_A^*, T^*]^t$ the desired equilibrium state. Since the input has an effect only on the temperature dynamics, the values of n_A^* and T^* cannot be chosen independently. This is stated in the following lemma:

Lemma 1. Let us consider some control input $u(x)$ such that the closed loop system has at least one equilibrium point. The equilibrium points of the closed loop system are contained in the following set:

$$(n_A^*, T^*) \in \left\{ (n_A, T) \,\middle|\, \begin{array}{c} n_A = \dfrac{\delta C_A^{in} V}{k(T) + \delta} \\ T \in]0, +\infty[\setminus \{T_w\} \end{array} \right\} \tag{11}$$

Proof. Let $x^* = (n_A^*, T^*)$ be an equilibrium point of the closed loop system for the control input $u(x)$. By definition of an equilibrium point, we have:

$$\left\{ \begin{array}{rl} 0 = & \dfrac{q_l}{V}\left(C_A^{in} V - n_A^*\right) - k(T^*) n_A^* \\ 0 = & \dfrac{q_l}{V}(T_{in} - T^*) + \dfrac{(-\Delta_r H)}{\rho c_p V} k(T^*) n_A^* \\ & + u(x^*)(T_w - T^*) \end{array} \right. \tag{12}$$

The first equation can be directly rewritten as follows:

$$n_A^* = \frac{\delta C_A^{in} V}{k(T^*) + \delta}$$

Let us now assume that $T^* = T_w$ is a possible equilibrium of the open loop system. If we replace in the second equation of (12), we find the following relation:

$$0 = \frac{q_l}{V}(T_{in} - T_w) + \frac{(-\Delta_r H)}{\rho c_p V} k(T_w) \frac{\delta C_A^{in} V}{k(T_w) + \delta}$$

This relation implies that T_w is an equilibrium point of the open-loop system. But, except an unlikely particular case, there is no reason that the temperature of the cooling fluid is exactly equal to an equilibrium temperature of the open-loop CSTR. Hence T_w cannot be an equilibrium temperature of the closed-loop system. □

Lemma 2. (11) is a necessary condition for $x^* = (n_A^*, T^*)$ to be a local minimum of $P_d(x)$.

Proof. A necessary condition for x^* to be a local minimum of $P_d(x)$ is the following one:

$$\nabla P_d(x^*) = \nabla P(x^*) + \nabla P_a(x^*) = 0$$

By replacing $\nabla P(x)$ and $\nabla P_a(x)$ by their expressions, the following relation is obtained:

$$\begin{aligned} -\nabla P(x^*) &= -Q(x^*) f(x^*) \\ &= \nabla P_a(x^*) = Q(x^*) g(x^*) u(x^*) \end{aligned}$$

Since $Q(x^*)$ is invertible, this can be rewritten as :

$$f(x^*) + g(x^*) u(x^*) = 0 \tag{13}$$

When replacing $f(x)$ and $g(x)$ by their respective expression, (12) is obtained. Thus the rest of the proof of Lemma 1 also applies here. □

The control action is then found by applying the methodology described in Section 2.2. First we solve (6) using the previously found expression for the matrix $Q(x)$. The left annihilators of $g(x)$ are given as follows:

$$g^{\perp}(x) = [\varphi \quad 0]$$

with $\varphi \in \mathbb{R}^*$. (6) is thus written as follows:

$$\frac{\varphi}{\det Q(x)} \left(q_{22}(n_A, T) \frac{\partial P_a}{\partial n_A} - q_{12}(n_A, T) \frac{\partial P_a}{\partial T} \right) = 0$$

where $q_{12}(n_A, T)$ and $q_{22}(n_A, T)$ are the elements of $Q(x)$ in position $(1,2)$ and $(2,2)$, respectively. With our matrix $Q(x)$ the solution of this partial differential equation is given as follows:

$$P_a(n_A, T) = f_a\left(n_A + \int w(T)\, dT\right)$$

where $w(k(T))$ is a rational function of the kinetic coefficient $k(T)$. $f_a(z) : \mathbb{R} \to \mathbb{R}$ can be any smooth real-valued function. In our case we have chosen $f_a(z)$ to be a second order polynomial. Using now (7), the control action of the following form is obtained for stabilizing the desired equilibrium point:

$$u(n_A, T) = \frac{-\mu(n_A - n_A^* + W_{T^*}(T)) + u^*(T_w - T^*)}{T_w - T} \tag{14}$$

where $W_{T^*}(T) : \mathbb{R}^{*+} \to \mathbb{R}$ is given by the following expression:

$$W_{T^*}(T) = \int_{T^*}^{T} w(k(\tau))\, d\tau$$

Obviously $W_{T^*}(T^*) = 0$. $\mu \in \mathbb{R}$ is a parameter of the controller and u^* is the value of the input at the equilibrium state:

$$u^*(T_w - T^*) = -\delta(T_{in} - T) - \gamma\delta\left(C_A^{in}V - n_A^*\right)$$

In order to ensure that x^* is a local minimum of $P_d(x^*)$, μ has to be lower bounded. The bounds are obtained by imposing that the Jacobian matrix of $P_d(x^*)$ is positive definite at the desired closed-loop equilibrium point. The control action $u(x)$ acts in (8) via the term

$$g(x)\,u(x) = \begin{pmatrix} 0 \\ -\mu\left(n_A - n_A^* + W_{T^*}(T)\right) + u^*(T_w - T^*) \end{pmatrix}$$

which does not depend on $(T_w - T)$ anymore. This means that the actual control input is the transferred heat which is equal to:

$$-\mu\left(n_A - n_A^* + W_{T^*}(T)\right) + u^*(T_w - T^*)$$

5.2 Considerations on local and global convergence

The controller designed in the previous section only guarantees a local convergence to the desired set point, i.e. the system will converge to desired point if and only if the initial conditions are close enough to it. Global convergence is ensured if and only if the shaped potential function $P_d(x)$ does not have other local minima, i.e. if and only if x^* is a global minimum of the function $P_d(x)$.

Let us assume that the point $x^\# = \left[n_A^\#, T^\#\right]^t$ is another local minimum of the function $P_d(x)$. For the same reasons as stated before, the following relation has to be fulfilled:

$$n_A^\# = \frac{\delta C_A^{in} V}{k(T^\#) + \delta} \tag{15}$$

Moreover, for $x^\#$ to be a closed loop equilibrium of (8), the following relation has to be fulfilled:

$$\delta\left(T_{in} - T^\#\right) + \delta\gamma\left(C_A^{in}V - n_A^\#\right) + u^*(T_w - T^*) - \mu\left(n_A^\# - n_A^* + W_{T^*}\left(T^\#\right)\right) = 0 \tag{16}$$

By analogy with (15), let us define the function $\tilde{T}^\#(n_A)$ by the following implicit relation:

$$k\left(\tilde{T}^\#(n_A)\right) = \frac{\delta C_A^{in} V}{n_A} - \delta$$

Consider the following function:

$$\Delta(n_A) = \delta\left(T_{in} - \tilde{T}^\#\right) + \delta\gamma\left(C_A^{in}V - n_A\right) + u^*(T_w - T^*) - \mu\left(n_A - n_A^* + W_{T^*}\left(\tilde{T}^\#\right)\right)$$

where the dependence of $\tilde{T}^\#(n_A)$ on n_A has been omitted for sake of clarity. The equilibrium points x^* and $x^\#$ are zeros of the function $\Delta(n_A)$. Therefore x^* is the unique convergence point if it is the unique zero of $\Delta(n_A)$.

The function $\Delta(n_A)$ is linear in the parameter μ. Therefore it can be written as follows:

$$\Delta(n_A) = \Delta_0(n_A) + \mu\Delta_\mu(n_A)$$

Remark 3. In Favache and Dochain (2009), we have presented several old and new results that aim at linking the thermodynamics and the system theory concepts via

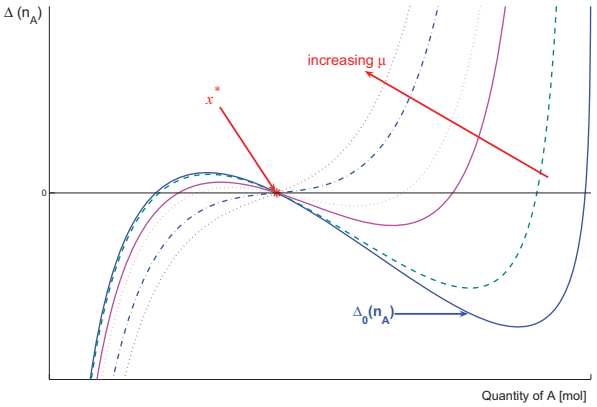

Fig. 3. Influence of μ on $\Delta(n_A)$

the CSTR study case [3] In this paper we have introduced a function of the state, denoted $\Delta_{eq}(T)$. By integrating the notations and assumptions of the present paper, this function is given by the following expression:

$$\Delta_{eq}(T) = k(T)\,n_A V(-\Delta_r H) - \rho c_p V\left[u(n_A, T)(T - T_w) + \delta\left(T - T^{in}\right)\right]$$

It can be seen directly that $\Delta_{eq}(T)$ and $\Delta(n_A)$ are linked by the following relation:

$$\Delta(n_A) = \frac{\Delta_{eq}\left(\tilde{T}^\#(n_A)\right)}{\rho c_p V}$$

It can be shown that the assumptions on the form of $k(T)$ described in Section 3 and the existence of three open loop equilibria implies that $\Delta_0(n_A)$ is increasing for low and high temperatures, but decreasing on one determined interval [4] As a consequence, $\Delta(n_A)$ can have several zeros, depending on the term $\mu\Delta_\mu(n_A)$.

If the function $w(T)$ has been adequately chosen, then $\Delta_\mu(n_A) > 0$ for $n_A > n_A^*$ and $\Delta_\mu(n_A) < 0$ for $n_A < n_A^*$. This means that if μ is chosen sufficiently large and positive, then the term $\mu\Delta_\mu(n_A)$ reshapes the initial function $\Delta_0(n_A)$ so as to make the two undesired zeros to vanish (see Figure 3). As a conclusion, there is a lower bound on the parameter μ in order to ensure global convergence.

5.3 Simulation results

In this section we present some simulation results of the controlled system. First the performance of the controller for reference tracking is shown in Figure 4. Then Figures 5 and 7 show the cases where only local convergence and global convergence, respectively, to the desired equilibrium point is ensured. These figures show the temperature evolution for different initial conditions. The corresponding level curves of the potential function $P_d(x)$ are shown for

[3] In Favache and Dochain (2009) we have considered a CSTR with a reversible reaction, but the results can be applied directly for an irreversible reaction by setting the kinetic reaction coefficient of the reverse reaction equal to zero.

[4] This can be deduced from the form of $\Delta_{eq}(T)$ in Favache and Dochain (2009) using the fact that $\tilde{T}^\#(n_A)$ is a strictly decreasing function.

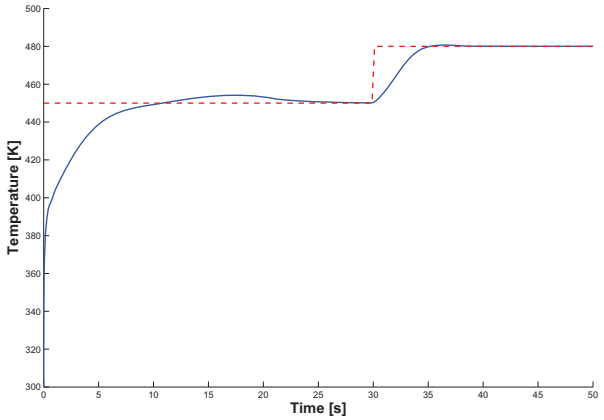

Fig. 4. Reference tracking

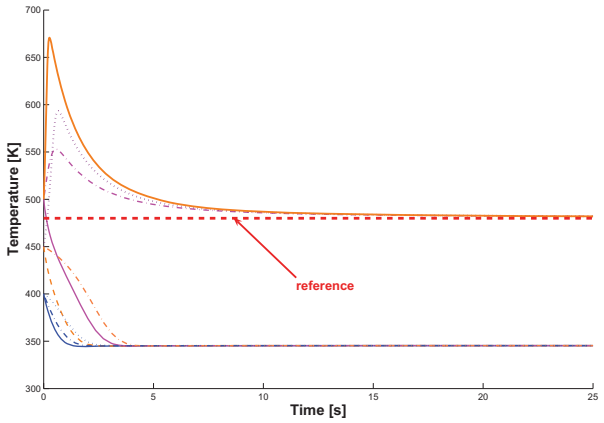

Fig. 5. Temperature evolution for different initial conditions (local convergence)

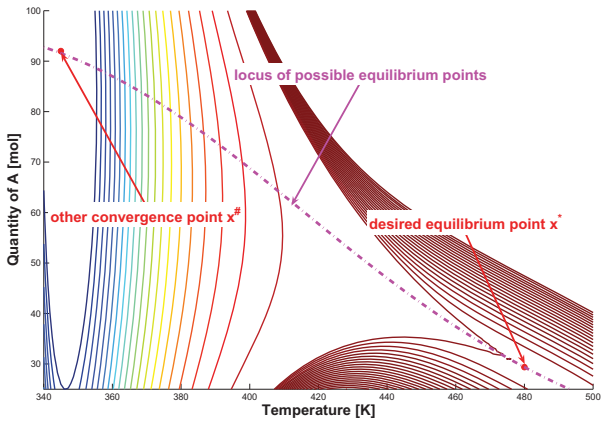

Fig. 6. Level curves of $P_d(x)$ (local convergence)

both cases in Figures 6 and 8, respectively. It can be clearly seen on Figure 5 that there exist two convergence points, depending on the initial condition. This is confirmed by the level curves of the function $P_d(x)$ in Figure 6 where two local minima can be distinguished.

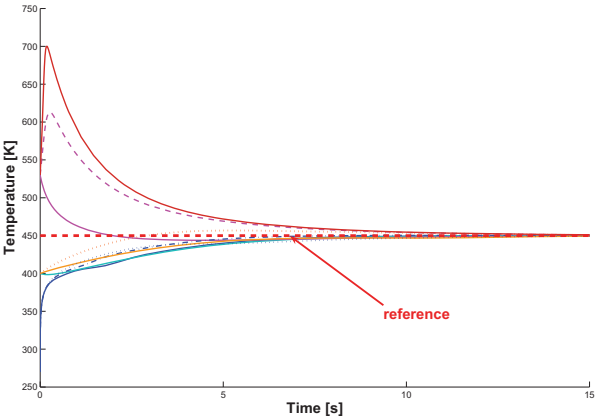

Fig. 7. Temperature evolution for different initial conditions (global convergence)

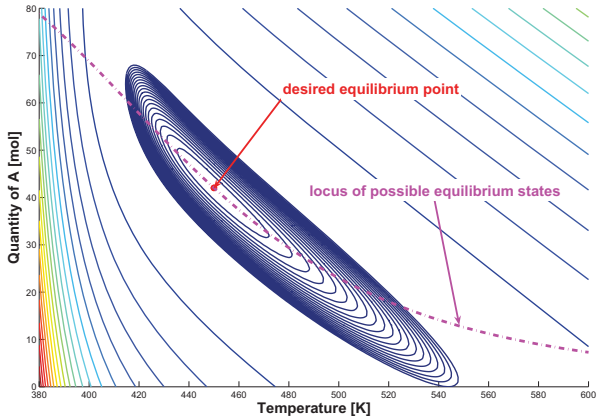

Fig. 8. Level curves of $P_d(x)$ (global convergence)

5.4 Robustness analysis

The control law given in (14) requires the complete state feedback. Moreover it also requires the knowledge of the temperature dependence of the kinetic coefficient $k(T)$ that appears in the expression of $W_{T^*}(T)$. In most practical applications, the kinetic coefficient is determined experimentally and the on-line measurement of the concentration is not always achievable. In this section we shall analyze the effect on the closed-loop convergence and stability of modeling errors in the kinetic coefficient $k(T)$.

Let us assume that there is a modeling error on the kinetic coefficient. The aim is to stabilize the state (n_A^*, T^*). The controller is designed using the function $\hat{k}(T)$ instead of the real kinetic coefficient $k(T)$:

$$\hat{k}(T) = (1 + \xi(T))\, k(T) \tag{17}$$

with $\xi(T) > -1$.

Assumption 1. Despite the error on $k(T)$, the equilibrium value of n_A is known:

$$n_A^* = n_A^{eq}(T^*) = \delta \frac{C_A^{in} V}{\delta + k(T)} \neq \delta \frac{C_A^{in} V}{\delta + \hat{k}(T)}$$

Assumption 2. Despite the error on $k(T)$, the equilibrium value of the control input u^* is known:

$$u_c^* = -\delta\left(T_{in} - T^*\right) - \gamma k\left(T^*\right) n_A^*$$
$$\neq -\delta\left(T_{in} - T^*\right) - \gamma \hat{k}\left(T^*\right) n_A^*$$

Assumption 3. The control input has been designed such that, based on the estimated value of the kinetic coefficient, the desired equilibrium is asymptotically stable.

From (14), the control input applied to the system is given by the following expression:

$$u_c\left(T_w - T\right) = \mu\left(n_A^* - n_A - \int_{T^*}^{T} \hat{w}\left(\tau\right) d\tau\right) + u_c^*\left(T_w - T^*\right)$$

where we have introduced the following notation, for the sake of clarity: $\hat{w}\left(T\right) = w\left(\hat{k}\left(T\right)\right)$. Assumptions 1 and 2 imply that (n_A^*, T^*) is still an equilibrium of the closed-loop system. Assumption 3 implies that the function $w\left(y\right)$ and the parameter μ have been chosen such that the following matrix is negative definite:

$$\hat{\Lambda} = \begin{pmatrix} -\left(\delta + \hat{k}^*\right) & -n_A^* \left.\dfrac{d\hat{k}}{dT}\right|_{T^*} \\ \gamma\hat{k}^* - \mu & -\delta + \gamma n_A^* \left.\dfrac{d\hat{k}}{dT}\right|_{T^*} - \mu\hat{w}\left(T\right) \end{pmatrix}$$

$\hat{\Lambda}$ is the matrix of the linearized system around the desired equilibrium state if the kinetics was indeed equal to $\hat{k}\left(T\right)$. As a consequence we have:

$$\operatorname{tr}\hat{\Lambda} < 0 \quad \text{and} \quad \det\hat{\Lambda} > 0$$

The actual matrix of the linearized system around (n_A^*, T^*) is written as follows:

$$\Lambda = \begin{pmatrix} -\left(\delta + k^*\right) & -n_A^* \left.\dfrac{dk}{dT}\right|_{T^*} \\ \gamma k^* - \mu & -\delta + \gamma n_A^* \left.\dfrac{dk}{dT}\right|_{T^*} - \mu\hat{w}\left(T\right) \end{pmatrix}$$

The trace and the determinant of Λ are given by the following relations:

$$\operatorname{tr}\Lambda = \Psi^* - \delta - \mu\hat{w}\left(T^*\right)$$
$$\det\Lambda = -\delta\Psi^* + \mu\left[\left(\delta + k^*\right)\hat{w}\left(T^*\right) - n_A \left.\frac{dk}{dT}\right|_{T^*}\right]$$

with

$$\Psi^* = -\left(k^* + \delta\right) + \left.\frac{dk}{dT}\right|_{T^*} \gamma n_A^* \tag{18}$$

Using (17), we can define the following quantity $\hat{\Psi}^*$ by analogy with (18):

$$\hat{\Psi}^* = \gamma n_A^* \left.\frac{d\hat{k}}{dT}\right|_{T^*} - \left(\hat{k}^* + \delta\right)$$
$$= \Psi^*\left(1 + \xi^*\right) + \gamma n_A^* k^* \left.\frac{d\xi}{dT}\right|_{T^*} + \delta\xi^*$$

where $\xi^* = \xi\left(T^*\right)$. As a consequence the trace and the determinant of $\Lambda^{(cl)}$ can be rewritten as follows:

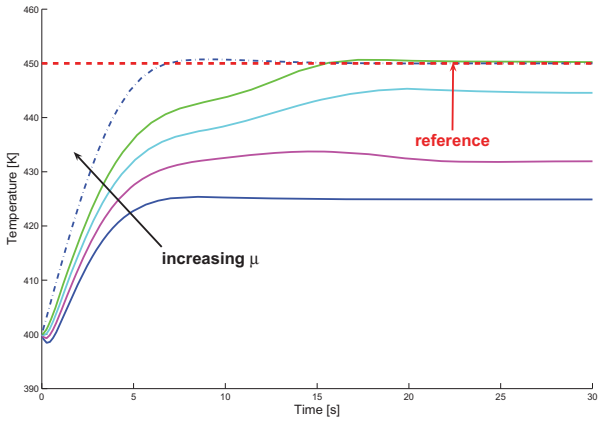

Fig. 9. Influence of the modelling error on $k\left(T\right)$ for different values of μ

$$\left(1 + \xi^*\right)\operatorname{tr}\Lambda = \underbrace{\hat{\Psi}^* - \delta - \mu\hat{w}\left(T^*\right)}_{\operatorname{tr}\hat{\Lambda}^{(cl)} < 0} - \left[\left.\frac{d\xi}{dT}\right|_{T^*} \gamma k^* n_A^* + 2\xi^*\delta + \mu\xi^*\hat{w}\left(T^*\right)\right]$$

By applying the same development on the determinant, the following expression is obtained:

$$\left(1 + \xi^*\right)\det\Lambda = \det\hat{\Lambda} + \xi^*\delta\left(\delta + \mu\hat{w}\left(T^*\right)\right) + n_A^* k^* \left.\frac{d\xi}{dT}\right|_{T*} \left(\gamma\delta + \mu\right)$$

The closed-loop equilibrium is asymptotically stable if and only if the trace is strictly negative and the determinant is strictly positive. Using the inequalities of Assumption 3, this means that if $\xi^* > 0$ and $\left.\frac{d\xi}{dT}\right|_{T^*} \geq 0$, the closed-loop equilibrium is asymptotically stable. But if these two conditions are not fulfilled, then the closed-loop equilibrium can become unstable. Nevertheless, if the function $w\left(y\right)$ has been taken sufficiently large such that:

$$\left(\delta + k^*\right)\hat{w}\left(T^*\right) - n_A \left.\frac{dk}{dT}\right|_{T^*} > 0$$

then $\det\Lambda^{(cl)}$ is increasing with μ such that there is a lower bound on μ that ensures the local asymptotic convergence (see Figure 9).

6. EXTENSION TO MORE COMPLEX SYSTEMS

The power-shaping approach has given interesting results on the simplified CSTR case study. It is therefore of major interest to see if this approach can be extended to more complex systems, and more particularly to systems with more than one reacting chemical species and/or with multiple reactions.

We keep the same assumptions as before, but we consider more complex kinetics. Under these assumptions, the general form of the dynamics of a non-isothermal CSTR can be deduced from (8).

Let us now consider a CSTR with N_r independent reactions. From all the chemical species in the mixture, it is only necessary to consider those that intervene in the

kinetics of the reactions. Let N_c be the number of chemical species which intervene in the expression of the reaction kinetics. For each species i the time evolution is given by the following differential equation (with $i = 1, \ldots, N_c$):

$$\frac{dn_i}{dt} = \delta\left(C_i^{in}V - n_i\right) + \sum_{l=1}^{N_r} \Gamma_{il} r_l\left(T, n\right) \tag{19}$$

where Γ_{il} is the stoichiometric coefficient of species i in the reaction l. The temperature dynamical equation becomes as follows:

$$\frac{dT}{dt} = \delta\left(T^{in} - T\right) + \sum_{l=1}^{N_r} \gamma_l r_l\left(T, n\right)$$

where $\gamma_l = \frac{(-\Delta_r H)_l}{\rho c_p V}$ and $(-\Delta_r H)_l$ is the reaction heat of the reaction l. The time evolution equations of n_A and T have a similar form and the dynamics of the system can be written as follows (see Dochain et al. (1992)):

$$\frac{dx}{dt} = \delta\left(x^{in} - x\right) + \Gamma r\left(x\right) \tag{20}$$

where $x = [n_A, \ldots, n_{N_c}, T]^t$, . $\Gamma \in \mathbb{R}^{N_c+1} \times \mathbb{R}^{N_r}$ is a matrix that contains the stoichiometric coefficient of species i in the reaction l in position (i, l) if $1 \leq i \leq N_c$ and that contains γ_l in the l^{th} column if $i = N_c + 1$.

We shall now apply the same approach as in Section 4, i.e. we shall first look for a matrix $Q\left(x\right)$ that fulfills the conditions (2) and (4). By using (20), we have the following relations $(i, j = 1, \ldots, N_c + 1)$:

$$\left(Q\left(x\right) f\left(x\right)\right)_i = \sum_{k=1}^{N_c+1} q_{ik}\left(\delta\left(x_k^{in} - x_k\right) + \Gamma_{kl} r_l\left(x\right)\right)$$

and thus:

$$\begin{aligned}\left(\nabla\left(Q\left(x\right) f\left(x\right)\right)\right)_{ij} = -\delta q_{ij} &+ \sum_{k=1}^{N_c+1}\left[q_{ik}\sum_{l=1}^{N_r}\Gamma_{kl}\frac{\partial r_l}{\partial x_j}\right] \\ &+ \sum_{k=1}^{N_c+1}\frac{\partial q_{ik}}{\partial x_j}\left(\delta\left(x_k^{in} - x_k\right) + \Gamma_{kl} r_l\left(x\right)\right)\end{aligned}$$

Consequently, condition (4) can be rewritten as follows:

$$\begin{aligned}&-\delta q_{ij} + \sum_{k=1}^{N_c+1}\left[q_{ik}\sum_{l=1}^{N_r}\Gamma_{kl}\frac{\partial r_l}{\partial x_j}\right] \\ &+ \sum_{k=1}^{N_c+1}\frac{\partial q_{ik}}{\partial x_j}\left(\delta\left(x_k^{in} - x_k\right) + \Gamma_{kl} r_l\left(x\right)\right) \\ &= -\delta q_{ji} + \sum_{k=1}^{N_c+1}\left[q_{jk}\sum_{l=1}^{N_r}\Gamma_{kl}\frac{\partial r_l}{\partial x_i}\right] \\ &+ \sum_{k=1}^{N_c+1}\frac{\partial q_{jk}}{\partial x_i}\left(\delta\left(x_k^{in} - x_k\right) + \Gamma_{kl} r_l\left(x\right)\right)\end{aligned} \tag{21}$$

for all $i, j = 1, \ldots, N_c + 1$.

In the simplified CSTR case, we have first restricted the set of possible matrices $Q(x)$ to find a solution for (4) by transforming the partial differential equation into an algebraic one which is simpler to solve. The same can be done in the more complex case by adequately restricting the set of possible solutions.

A general solution of the algebraic form of (21) has not been found yet. Despite of this, some characteristics of the solution (if it exists) have already been derived in Favache and Dochain (2008). We shall now look at some particular cases of more complex reactions to get a first intuition of the existence of non-singular and negative semi-definite solutions of the algebraic form of (21). The detailed solution for the three particular cases (namely parallel reactions, reactions with two reactants and consecutive reactions) is given in Favache and Dochain (2008). In the three cases it has been assumed that the kinetic functions can be expressed as powers of the concentration of the reactants, i.e.:

$$r_l\left(n, T\right) = k_l\left(T\right)\prod_{i\in\Theta_l}\left(n_i\right)^{\zeta_{il}}$$

where Θ_l is the set of reactants of reaction l and ζ_{il} is some positive constant.

6.1 Parallel reactions and reactions with two reactants

In this case a solution has been found, but the obtained matrix has not a negative semi-definite symmetric part. Thus the corresponding potential function cannot be used as a Lyapunov function for the open-loop system because they are not decreasing along the system trajectories.

As shown in Garcia-Canseco et al. (2008), given a matrix $Q\left(x\right)$ that fulfills (4), other solutions to (4) can be built departing from the first one. Applying this methodology on the matrices that have been found could lead to another matrix $Q\left(x\right)$ that would be negative-definite and hence give a Lyapunov function for the open-loop system.

Remark 4. In the particular case of parallel reactions with first order kinetics, another solution for the matrix $Q\left(x\right)$ has been found. This solution does not exist for higher order kinetics. This particular solution has a very similar form of that of the matrix proposed for the case with one reaction. This seems to indicate that the matrix $Q\left(n_A, T\right)$ that has been used in Section 4 is a particular solution of (9) that exists only in the case of first-order kinetics.

6.2 Consecutive reactions

In this case the algebraic form of (21) has no non-singular solution. This does not mean that the dynamics cannot be put into the Brayton-Moser form. But if the Brayton-Moser form exists, then the partial differential equation (21) has to be solved.

7. CONCLUSION

A general description of the power-shaping control approach of the CSTR has been given in this paper. The main results that were obtained by this approach have been presented and illustrated by some simulation results. A detailed mathematical analysis is provided in Favache and Dochain (2008). Contrary to previous works and approaches, a global Lyapunov function for the exothermic CSTR has been found using the power-shaping approach. This Lyapunov function could then be used to design a controller for stabilizing the reactor at a desired temperature. Some results about the local and global convergence of the controller have also been shown.

The Lyapunov function that was found is the potential function of the Brayton-Moser formulation of the CSTR

dynamics. Although the potential function has a physical meaning for the Brayton-Moser formulation of electrical or mechanical systems, a precise physical interpretation of the potential function of the CSTR has still to be found. This interpretation should give more physical insight on the reasons of the existence of multiple open loop equilibria, and also on the action of the controller.

The controller obtained by the power-shaping control approach depends on the on-line measurements of the concentration and of the knowledge on the reaction kinetics. Both quantities are usually not exactly known. We have shown, that if the parameters of the controller are adequately chosen, the control action is robust with respect to modeling errors on the kinetics. But a robustness study on the influence of the concentration measurement errors should also be of great interest before applying it to a real reactor.

Finally we studied the possibility of extending the previous work to more complex systems, and more precisely to CSTRs with multiple reactions and/or multiple reactants. The extension seems to be rather complex, even for simple cases such as two parallel reactions or two consecutive reactions with mass action law kinetics. Indeed, in the simple CSTR case with a single first-order kinetics reaction, the solution of the partial differential equation needed to write the system dynamics in the Brayton-Moser form has been found by transforming it into an algebraic one. For the three considered particular cases the corresponding algebraic equation system has either no non-singular solution (consecutive reactions) or an indefinite solution (parallel reactions, reaction with two reactants). The study presented here is only embryonic since it does not imply that the power-shaping control approach cannot been applied. But the Brayton-Moser form of the dynamics (if it exists) actually needs the solution of the partial differential equation, and not of its simplified version which is the algebraic equation. Nevertheless in the cases where an indefinite matrix has been found, the work presented in Garcia-Canseco et al. (2008) offers the possibility of finding an alternative negative semi-definite matrix without having to solve the partial differential equation. Also in this study we have only considered a particular form of the kinetics, namely we have assumed that the kinetics can be written as a product of powers of the concentration (i.e. a more general form of the mass action law) and a kinetic term. This is only a restricted class of the possible kinetic laws. Indeed it could also be interesting to apply the power-shaping control to other forms of kinetics such as the Monod kinetics (biological systems) or the Michaelis-Menten kinetics (enzymatic reactions), for instance.

ACKNOWLEDGEMENTS

This paper presents research results of the Belgian Network DYSCO (Dynamical Systems, Control, and Optimization), funded by the Interuniversity Attraction Poles Programme, initiated by the Belgian State, Science Policy Office. The scientific responsibility rests with its authors.

REFERENCES

Alonso, A., Ydstie, B., and Banga, J. (2002). From irreversible thermodynamics to a robust control theory for distributed process systems. *Journal of Process Control*, 12, 507–517.

Antelo, L.T., Otero-Muras, I., Banga, J.R., and Alonso, A.A. (2007). A systematic approach to plant-wide control based on thermodynamics. *Computers & Chemical Engineering*, 31(5-6), 677–691.

Aris, R. and Amundson, N.R. (1958). An analysis of chemical reactor stability and control–I : The possibility of local control, with perfect or imperfect control mechanisms. *Chemical Engineering Science*, 7(3), 121–131.

Brayton, R. and Moser, J. (1964a). A theory of nonlinear networks I. *Quaterly of applied mathematics*, 22, 1–33.

Brayton, R. and Moser, J. (1964b). A theory of nonlinear networks II. *Quaterly of applied mathematics*, 22, 81–104.

Dalsmo, M. and van der Schaft, A. (1998). On representations and integrability of mathematical structures in energy-conserving physical systems. *Journal on Control and Optimization*, 37(1), 54–91.

Dochain, D., Perrier, M., and Ydstie, B. (1992). Asymptotic observers for stirred tank reactors. *Chemical Engineering Science*, 47, 4167–4178.

Eberard, D. (2006). *Extension des systèmes hamiltoniens ports aux systèmes irréversibles: une approche par la géométrie de contact*. Ph.D. thesis, Université Claude Bernard, Lyon 1.

Eberard, D., Maschke, B., and van der Schaft, A. (2005). Port contact systems for irreversible thermodynamical systems. In *Proc. 44^{th} IEEE Conference on Decision and Control and European Control Conference*. Sevilla (Spain).

Eberard, D., Maschke, B., and van der Schaft, A. (2006). Energy-conserving formulation of rlc-circuits with linear resistors. In *Proc. 17^{th} International Symposium on Mathematical Theory of Networks and systems*. Kyoto (Japan).

Farschman, C.A., Viswanath, K.P., and Ydstie, B.E. (1998). Process systems and inventory control. *AICHE Journal*, 44(8), 1841–1857.

Favache, A., Maschke, B., and Dochain, D. (2007). Contact structures: application to interconnected thermodynamical systems. In *Proc. European Control Conference 2007*. Kos (Greece).

Favache, A. and Dochain, D. (2008). Stability analysis of a CSTR via power-shaping control. Technical report, CESAME, Université catholique de Louvain, Belgium.

Favache, A. and Dochain, D. (2009). Thermodynamics and chemical systems stability: The CSTR case study revisited. *Journal of Process Control*, 19(3), 371–379.

Garcia-Canseco, E., Jeltsema, D., Scherpen, J., and Ortega, R. (2008). Power-based control of physical systems: two case studies. In *Proc. 17^{th} IFAC World Congress*. Seoul (Korea).

Jeltsema, D., Ortega, R., and M.A. Scherpen, J. (2004). An energy-balancing perspective of interconnection and damping assignment control of nonlinear systems. *Automatica*, 40(9), 1643–1646.

Jeltsema, D. and Scherpen, J.M. (2003). On mechanical mixed potential, content and co-content. In *Proc. European Control Conference*, 73–78.

Jeltsema, D. and Scherpen, J.M. (2007). A power-based description of standard mechanical systems. *Systems & Control Letters*, 56(5), 349–356.

Khalil, H. (2002). *Nonlinear Systems*. Prentice Hall, Upper Saddle River, 3^{rd} edition.

Maschke, B., Ortega, R., and van der Schaft, A. (2000). Energy-based Lyapunov functions for forced Hamiltonian systems with dissipation. *IEEE Transactions on Automatic Control*, 45(8), 1498–1502.

Maschke, B. and van der Schaft, A. (2005). From conservation laws to port-Hamiltonian formulation of distributed parameter systems. In *Proc. 16^{th} IFAC world congress*. Prague (Czech Republic).

Ortega, R., Jeltsema, D., and Scherpen, J. (2003). Power shaping: A new paradigm for stabilization of nonlinear RLC-circuits. *IEEE Transactions on Automatic Control*, 48(10), 1762–1767.

Ortega, R., van der Schaft, A., Maschke, B., and Escobar, G. (1999). Energy-shaping of port-controlled Hamiltonian systems by interconnection. In *Proc. 38^{th} IEEE Conference on Decision and Control*, 1646–1651. Phoenix (USA).

Ortega, R., Van Der Schaft, A., Mareels, I., and Maschke, B. (2001). Putting energy back in control. *IEEE Control Systems Magazine*, 21(2), 18–33.

Ortega, R., van der Schaft, A., Maschke, B., and G.Escobar (2002). Interconnection and damping assignment: passivity-based control of port-controlled Hamiltonian systems. *Automatica*, 38, 585–596.

Otero-Muras, I., Szederknyi, G., Alonso, A., and Hangos, K. (2006). Dynamic analysis and control of chemical and biochemical reaction networks. In *Proc. International Symposium on Advanced Control of Chemical Processes*, 165–170. Gramado (Brazil).

Uppal, A., Ray, W.H., and Poore, A.B. (1974). On the dynamic behavior of continuous stirred tank reactors. *Chemical Engineering Science*, 29(4), 967–985.

Treatment Planning of Cancer Dendritic Cell Therapy Using Multi-Objective Optimization

K. Lakshmi Kiran*, S. Lakshminarayanan*

**Department of Chemical and Biomolecular Engineering, National University of Singapore, 117576 Singapore (Tel: 0065-65168484; e-mail: chels@ nus.edu.sg).*

Abstract: Cancer immunotherapy is one of the emerging therapies for cancer treatment where immune cells are guided to fight against cancer. Clinical immunologists are proposing different ideas to stimulate the immune cells and dendritic cell therapy is one among them. Like, other treatment modalities, the challenge in dendritic cell therapy is when and how much dendritic cells should be administered. In this work we use a mathematical model which elucidates the activation of the helper T-cells and cytotoxic T-cells by the intervention of dendritic cells. The objective is to minimize the tumor cells for a given input of dendritic cells. Then multi-objective optimization is applied on the model to design the treatment planning in order to achieve the objective.

Keywords: Cancer, Immune system, Dendritic cell therapy, Mathematical model, Multi-objective optimization

1. INTRODUCTION

Cancer stands next only to heart disease in the list of most fatal diseases in the world. From Fig.1, it is obvious that the decrease in death rate for cancer patients over the years 1950-2003 has been minimal as compared to other major diseases. Cancer related deaths have been escalating meteorically - according to World Health Organization, 7.6 million people died of cancer (out of 58 million deaths overall) in 2005. They speculate that cancer deaths will increase to 18% and 50% by 2015 and 2030 respectively. Recently, the American Cancer Society reported that around 1.5 million new cancer cases and 0.6 million cancer death cases occurred in the US in 2007. According to another report on worldwide cancer rates by the WHO's International Agency for Research on Cancer (IARC) (Paola Pisani, 2002), North America leads the world in the rate of cancers diagnosed in adults, followed closely by Western Europe, Australia and New Zealand. In 1994, in Britain, almost one in three were expected to develop the disease over their survival period and it is estimated to increase to one in two by 2010 with reference to the trends at that time (Imperial Cancer Research Fund). Another publication from the Australian Institute of Health and Welfare (1999) projects that, based on the incidence rates existing in 1999, one in three men and one in four women would be directly affected by cancer in the first 75 years of life. Moreover, a loss of 254,000 potential years of life to the community each year was estimated as a result of people dying of cancer before the age of 75. As a whole, cancer is currently responsible for 29% of male deaths and 25% of female deaths in Australia. In Singapore, the proportion of cancer deaths among all causes of death rose steadily from 14.8% (in the years 1968-1972) to 27.1% (in the period 1998-2002) reflecting a worldwide trend. The above mentioned figures are alarming and have drawn the attention of researchers to understand the mechanism of cancer and come out with better therapies.

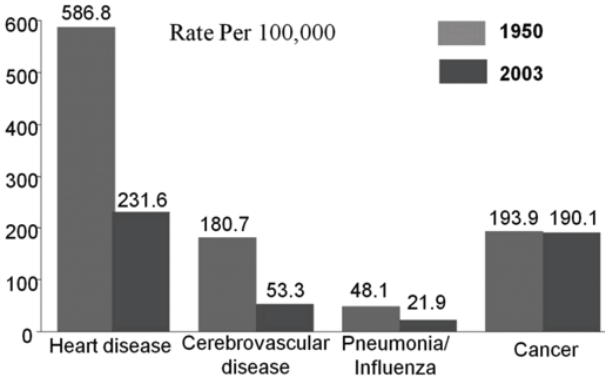

Fig.1. Change in death rates of different diseases in US from 1950 to 2003

The main characteristics of the cancer cell are its uncontrolled and unregulated growth (Hanahan and Weinberg, 2000; Martins et al., 2007). It is caused by the external factors such as UV radiations, carcinogenic chemicals as well as transfer of the cancer prone genes from parents. When a normal cell interacts with these external factors, its information system (DNA) gets damaged and the normal cell transforms to a cancer cell. Initially, the clump of the cancer cells is confined to particular location and it is regarded as being benign. If the cancer is not diagnosed and treated in the benign stage, it will change into a malignant form, and the cancer cells could migrate to different parts of the body and ultimately may lead to the death of the patient. So, it is better for the cancer patients to be provided suitable

treatment at the early stages itself so as to prolong and enhance the quality of their life.

1.1 Cancer treatment modalities

Over the past 50 years, many cancer treatment modalities have been discovered. The most prominent of these are surgery, chemotherapy, and radiation therapy. Some of the emerging therapies are immunotherapy and viral therapy. However, a specific therapy for all types of cancer is still missing and the available therapies have their own advantages and shortcomings. Surgical techniques to remove tumors have been in practice even thousand years ago. Usually, surgery is favoured to remove the tumors diagnosed at the very early stages ensuring almost complete cure. Surgery can be very difficult if the tumor location is near critical locations in the body (e.g. brain); furthermore, surgery is not a preferred option if the cancer had already metastasized by the time of diagnosis. In any case, complete clearance of the tumor cells is not assured with surgery. Radiation therapy is an alternative to surgery in order to kill the localized tumor cells. In radiation therapy, high energy radiations are used and its dosage is determined such that the normal cells near the tumor are spared. Thus, radiation therapy also depends on the location of the tumor and sensitivity of the tumor cells to the radiation.

As a result, surgery is followed by chemotherapy or radiation therapy to suppress further tumor growth. In the case of chemotherapy and radiation therapy, precise care should be taken to avert the damage to normal tissues. Among these two therapies, chemotherapy is preferred because it is a systemic therapy. In systemic therapy, the drug flows throughout the body and destroys the migrated cancer cells along with residual cancer cells near the surgery location. Chemotherapy is always given as a course in cycles based on the patient health status rather than as a one-time treatment. This is done so as to maintain the drug concentration within the dosage limits in the body and kill the remaining cancer cells in the subsequent treatments (Dua et al., 2008). However, the side effects of the chemotherapy are significant and sometimes they become serious than the disease itself. In contrast to chemotherapy and radiation therapy, immunotherapy has fewer side effects, because, typically, the patient's own cells are modified and used as therapeutic agents. The prime objectives of any therapy are to keep the number of cancer cells below a lethal level and avoid the side effects caused by the therapeutic agents. This can be achieved by optimal scheduling and the optimal administration of the therapeutic agents if the dynamical characteristics of the system are known.

2. CANCER IMMUNOTHERAPY

The role of the immune system in cancer treatment was first observed by William Coley, a New York surgeon. Cancer immunotherapy is the stimulation of immune cells to fight the tumor cells. The main function of the immune system is to fight against the abnormal changes in the body, and the successful functioning of it lies in its ability to distinguish the "self" and "non-self" based on the self-marking molecules. The immune system recognizes the abnormality with the help of antigens presented by the injured or abnormal cells. If the immune system exhibits a response based on antigen recognition, then antigens are called immunogenic. However, not all antigens are immunogenic. For example, if the tumor is larger in size, immune cells may not respond to it. Before studying the tumor-immune interactions, it is informative to take a brief look at the mechanisms of the immune system. In this regard, the review paper by Adam et al., (2003) provides a comprehensive discussion on the immune response in cancer.

In our body, the immune action is carried out by specialized cells called lymphocytes which are mostly present in the blood. The common lymphocytes are macrophages, dendritic cells, natural killer (NK) cells, lymphokine activated killer cells, B-cells and T-cells. Immune response is categorized as natural immunity, humoral immunity and cellular immunity based on the lymphocytes. Macrophages, dendritic cells, and natural killer cells are responsible for natural immunity, in which these cells directly attack the infected cells (cancer cell) and act as antigen presenting cells (APC). Antigen is an agent which can easily be recognized by immune cells. Thus, APC highlights the infected cells and alerts the T-cells for further action against the infected cells. In humoral immunity, antibodies produced by B-cells encounters the infected cells. Each B-cell has a specific antibody of a particular shape. The concept of antibody-antigen interaction resembles the mechanism of lock and key. When the shape of an antibody of a B-cell matches exactly with the shape of the antigen corresponding to the infected cells, B-cell proliferates and produces plasma cells which actively secrete the antibodies. These antibodies neutralize the activity of the infected cell by inhibiting their cell division process, by producing a lethal group of enzymes called complement and by opsonization. In opsonization, antibodies coat the infected cells in order to make them easily recognizable by the killer lymphocytes. This process is known as antibody dependent cell-mediated cytotoxicity. In cellular immunity, the key players are T-cells which are further classified as helper T-cells ($CD4^+$) and cytotoxic T-cells ($CD8^+$). Helper T-cells gets activated by the natural immune cells and regulates the production of the cytokines. Cytokines are the enzymes which keep the momentum of all the immune cells as per their requirement. Interleukins and interferons are regarded as the important cytokines to fulfil the immune action. Cytotoxic T-cells directly attack the infected cells after its activation by the cytokines.

From the above discussion, we can infer that key elements for immunotherapy are antibodies, cytokines, and the natural immune cells. On this basis, immunotherapy is classified into three main schemes, monoclonal antibody therapy (MAT), adoptive cellular immunotherapy (ACI) and vaccines (Adam et al., 2003). MAT involves the introduction of externally developed tumor specific antibodies into the patient's body using hybridoma technology. ACI constitutes the

modification of the lymphocytes (helper T-cells, cytotoxic T-cells, NK cells) by using cytokines like interleukin (Kirschner and Panetta, 1998). This ultimately ameliorates the anti-tumor activity of the lymphocytes. This is done in two ways namely, lymphokine-activated killer cell (LAK) therapy and tumor infiltrating lymphocyte (TIL) therapy. In both therapies, the lymphocytes are activated externally and later they are injected back at the tumor site. In LAK therapy, the lymphocytes are obtained from the *in vitro* culturing with high concentration of IL-2 which is extracted from the patient's blood. Conversely, in TIL therapy, lymphocytes are taken from the patient tumor sites and cultured with the high concentrations of interleukin *in vitro*.

Generally, cancer vaccines are in the form of cells, molecules or micro-organisms. They facilitate the quick recognition of tumor cells by the immune cells. In other words, tumor associated antigens (TAA) are made tangible to the immune cells. Consequently, tumor-immune interactions are enhanced thereby achieving the goal of cancer immunotherapy.

3. TUMOR-IMMUNE INTERACTION MODELS

Tumor-immune interaction models explain interactions between different types of immune cells and the tumor. There are many tumor-immune interaction models and a few of them will now be described. In the model proposed by De Boer and Hogeweg (1986), interactions between macrophages, T-lymphocytes and tumors are considered. The macrophages and T-lymphocytes are given in different dosages. This model captures the "sneaking through" phenomenon i.e. when lower dosages of tumor is introduced, the immune system may not recognize it and then the tumor grows to a bigger size; however, the immune cells reject the tumor when they are given in higher quantities. Another successful model (Kuznetsov et al., 1994) was developed based on the studies of the B-lymphoma BCL_1 in the spleen of mice. The model is very simple, and considers only two states (effector and tumor cells). Effector cells represent any of the killer immune cells. In this model, the parameters were estimated using *in vivo* data. Then, bifurcation analysis was performed to find the critical parameters for sneak through phenomenon. This model was further extended and modified (Kirschner and Panetta, 1998) by including the dynamics of the interleukin. Based on bifurcation analysis, this work emphasized that tumor immunogenicity is an important parameter. Their work also discussed about the effects of immunotherapy (adoptive cellular therapy and interleukin) through mathematical analysis. Models such as those by (Castiglione and Piccoli, 2007; de Pillis et al., 2005; de Pillis et al., 2006), consider the natural killer cells and cytotoxic $CD8^+$T cells as different states rather than considering them under the same family as effector cells. In de Pillis et al. (2005), the authors focus on the impact of NK cells and $CD8^+$ T cells on tumor growth. Their model is in the form of a system of ODEs. Parameters of the model were estimated and validated with the published mice and human data. In addition, sensitivity analysis was done on the model. The sensitivity analysis concluded that the variable to which model is sensitive is patient-specific. This model was extended with slight modifications in the functional forms of growth and death terms of the immune cells (de Pillis et al., 2006). The model was also used for understanding the effects of combination therapy (chemo-immuno and vaccine therapy) for different patient parameters. Other models have included the dynamics of NK cells, B cells, helper and cytotoxic T-cells , and LAK cells (Szymanska, 2003). In this work, dendritic cell vaccine (DCV) is considered. DCV is produced by the process called dendritic cell transfection. In this process, some TAA are configured and cultivated with autologous dendritic cells that is extracted from the patient itself (Cappuccio et al., 2007; Castiglione and Piccoli, 2007; Piccoli and Castiglione, 2006). The resulting vaccine is injected back into the patient. Here, we consider the mathematical model proposed by Piccoli and Castiglione (2006) because this is the only model which includes the dynamics of dendritic cells and apply multi-objective optimization using non-dominated sorting genetic algorithm (NSGA) to find the optimal scheduling of dendritic cell vaccine interventions.

4. MULTI-OBJECTIVE OPTIMIZATION

Multi-objective optimization (MOP) is the optimization of two or more conflicting objectives of a system represented in the form of a mathematical model subjected to certain known constraints. Most practical problems such as product and process design, finance, aircraft design, automobile design, and medical applications have multiple objective scenarios. In these problems, an optimal decision needs to be taken in the presence of trade-offs between the conflicting objectives. In MOP, there may be a number of solutions in the feasible region, and the decision maker has to analyze all the solutions based on the prior knowledge of the system before a final solution is adopted (Tamaki et al., 1996).

Suppose there are 'n' decision variables and 'p' objectives. MOP tries to find a point $x = (x_1, \ldots\ldots, x_n)$ which minimizes (or maximizes) the values of the objective functions $f = (f_1, \ldots\ldots, f_p)$ within the feasible region F of x. In contrast to single-objective optimization problems, an exact solution may not exist for the MOP problems because of the trade-off characteristics among the objectives. Hence a concept of the Pareto-optimal set was introduced for MOP problems. Pareto-optimal set is, 'a family of points which is optimal in the sense that no improvement can be achieved in any objective without degradation in others'.

Definition (Tamaki et al., 1996): Let $x^0, x^1, x^2 \in F$

1. x^1 is said to be *dominated* by (or inferior to) x^2, if $f(x^1)$ is partially less than $f(x^2)$, i.e.,

$f_i(x^1) \geq f_i(x^2)$, $\forall_i = 1, \ldots\ldots, p$, and $f_i(x^1) > f_i(x^2)$, $\exists_{i=1,\ldots\ldots p}$.

2. x^0 is the Pareto-optimal (or non-dominated), if there doesn't exist any $x \in F$ such that x dominates x^0

As Pareto-optimal solution is a logical strategy to the MOP, the prime goal of solving the MOP is to obtain a Pareto-optimal set. The Pareto-optimal solutions can be obtained by solving on a one-at-a-time basis using single objective optimization methods like weighted sum method and the ε-constraint method. Unlike the conventional methods, population-based methods (e.g. evolutionary algorithms) such as genetic algorithm, particle swarm optimization, simulated annealing and differential evolution can generate Pareto-optimal set simultaneously. The searching strategy of different evolutionary algorithms is different and they are based imitating some natural processes. However, the common theme of all the evolutionary algorithms is to search the whole hyper-domain of decision variables and find the best possible solution. Population based methods are further subdivided into non-Pareto approaches and Pareto approaches. In non-Pareto approach, the selection/reproduction of the new population in the subsequent generations are based on the objective function values whereas in Pareto-approaches, the new population is generated not only on the basis of the objective value themselves but also on their dominance property. In this work, we used the Pareto-based approach known as non-domination based genetic algorithm (NSGA-II) which was proposed by Deb et al., (2000) because of its elitism and minimal computational complexity. Genetic algorithms (GAs) which imitate the process of natural evolution have shown successful results in many optimization problems which are difficult to solve by the conventional methods of the mathematical programming (Nemhauser et al., 1989).

4.1 Non-domination based genetic algorithm for multi-objective optimization

A brief introduction to the NSGA algorithm (Deb et al., 2000) is provided here. The algorithm is initiated with suitable values for population size and number of generations. The stopping criterion of the algorithm is the maximum number of generations. Broadly, the prime steps involved in the algorithm in each generation are selection, offspring production and recombination. First, the population is initialized randomly within the bounds of the decision variables. Once the population is initialized, they are sorted into separate fronts based on non-domination as discussed earlier. Among these fronts, the first front members completely dominate others in the current population and the second front members are dominated by only the first front members and so on. Each individual in the front is given a rank (fitness) based on the front in which they are present. The first front individuals are assigned a fitness value of 1 and second front individuals are assigned fitness value of 2 and so on. Apart from this, a parameter called crowding distance is calculated for each individual. The interpretation of the crowding distance is the closeness of an individual to its neighbours. A larger crowding distance indicates the diverse nature of the population. Crowding distance is compared only when the individuals belong to the same front. Thus, best N parent individuals are selected from the current population based on the rank and crowding distance, where N is the population size. Then, in the offspring production step, the selected parent individuals are used to generate offspring via the crossover and mutation operators. Finally, in the recombination step, the offspring population is combined with the current generation population and the combined population is used as an initialized population for the next generation. In this way, the procedure is repeated until the maximum number of generations. Thus, the important tuning parameters in this algorithm are the number of generations, indices for crossover and mutation processes. The schematic representation of the algorithm is shown in Fig. 2.

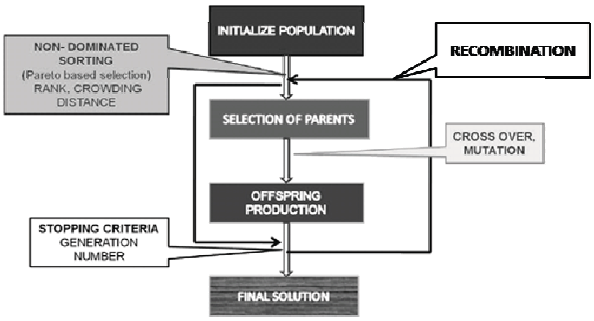

Fig.2. Non-dominated sorting genetic algorithm

5. MATHEMATICAL MODEL

The model taken from Piccoli and Castiglione (2006) describes the interactions among the tumor cells, helper and cytotoxic T-cells, dendritic cells and interleukin. The model assumes that tumor cells are immunogenic and do not metastasize. In other words, tumor cells are recognized by dendritic cells and are presented to cytotoxic T-cells. The interactions between the cytotoxic T lymphocytes and the tumor cells are described by a kinetic scheme and are presented in the form of ordinary differential equations. The states in the system are denoted by

- *H(t)*, helper T-cells (CD4+)
- *C(t)* , cytotoxic T-cells (CD8+)
- *M(t)*, tumor cells
- *D(t)*, dendritic cells
- *I(t)* , interleukin

The pharmacodynamics is represented by the term e_2MC in equation (3) and the pharmacokinetics is captured in equation (4). In equation (4), 'u' is the input rate of the dendritic cells. Once the dendritic cells are injected, the CD4+ cells, CD8+ cells, and interleukins are triggered as shown in equations (1, 2 & 5) respectively by the following terms. ($c_0Dd_0\gamma(H, f_0)$, $c_1I(M+D)d_1\gamma(C, f_1)$, a_4HD). The first two terms in equations (1) and (2) correspond to the natural evolution of

the cytotoxic T-lymphocytes. In the same way, the second and third terms in equation (5) explain the loss of interleukin (IL-2) due to its interactions with CD8+ cells and its natural decay respectively. The model assumes that tumor growth follows the logistic equation with the constants 'd_2' and 'f_2' in the absence of immune interactions. Another assumption in the model is that externally administered DCV is the only source of dendritic cells. The initial value of tumor is *M(0)* = 0.1, the initial level of helper and cytotoxic T-cells are taken to be their equilibrium values *H(0)* = a_0/b_0 and *C(0)* =a_1/b_1. It is assumed that there is no immune response before the treatment and therefore *I(0)* and *D(0)* are taken to be zero.

5.1 Model equations

$$\frac{dH}{dt} = a_0 - b_0 H + c_0 D d_0 \gamma(H, f_0), \quad (1)$$

$$\frac{dC}{dt} = a_1 - b_1 C + c_1 I(M + D) d_1 \gamma(C, f_1), \quad (2)$$

$$\frac{dM}{dt} = d_2 \gamma(M, f_2) - e_2 MC, \quad (3)$$

$$\frac{dD}{dt} = -e_3 DC + u, \quad (4)$$

$$\frac{dI}{dt} = a_4 HD - c_4 CI - e_4 I, \quad (5)$$

where $\gamma(x, c) = x(1 - x/c)$

5.2 Problem formulation:

Objective 1: $\min_{u(t_i)} \int_0^{t_f} M(t, u(t_i))\, dt + M(t_f)$ (6)

Objective 2: $\min_{u(t_i)} (Max(M(t, u(t_i))))$ (7)

t_f is the final time i.e. the planning horizon and t_i is the i^{th} time injection of the dendritic cells.

Constraints:

Equations (1) through (5) i.e. the mathematical model and

$t_{i-1} \le t_i \le t_{i+1}$, $i = 1, 2...., 9$

In this paper, two objectives are considered based on the typical goals sought by oncologists. Objective 1, as given by equation (6), seeks to minimize the summation of the running load and final load of tumor cells. Objective 2 (equation (7)) seeks to minimize the maximum possible value of the tumor cells in the given time horizon. If only objective 1 is taken into consideration, it may so happen that the tumor cells may shoot up to a very high value at a particular time while remaining at lower values at other times. This sudden shoot up of tumor cells to a higher value may lead to later stages of cancer which is very difficult to treat. So, in order to maintain the tumor in the benign stage, objective 2 is also considered. The time horizon considered to implement the multi-objective optimization is 4500 hours (approximately 6 months). In the given time horizon, the plan is to give injections of DCV ten times. Thus, the decision variables of the problem are the time of injections. It is assumed that the duration of injection every time is one hour and total vaccine quantity given in each injection is 0.5. Thus, $u(t_i)$ is equal to 0.5 c mm^{-3} h^{-1}.

Table 1. Parameter values

Parameter	Description	Value	Units (c=cells, h=hours)
a_0	CD4 T birth rate	10^{-4}	c h^{-1} mm^{-3}
b_0	CD4 T death rate	0.005	h^{-1}
c_0	Max. proliferation of CD4 T	10	
d_0	½ saturation constant of CD4 T	10^{-2}	c $^{-1}$ h^{-1} mm^3
f_0	Carrying capacity of CD4 T	1	c mm^{-3}
a_1	CD8 T birth rate	10^{-4}	c h^{-1} mm^3
b_1	CD8 T death rate	0.005	h^{-1}
c_1	Max. proliferation of CD8 T	10	
d_1	½ saturation constant of CD8 T	10^{-2}	h^{-1} $(mm^{-3}/c)^2$
f_1	Carrying capacity of CD8 T	1	c mm^{-3}
d_2	½ saturation constant of tumor	0.02	h^{-1}
e_2	Killing by CD8 of tumor	0.1	c $^{-1}$ h^{-1} mm^3
f_2	Carrying capacity of tumor	1	c mm^{-3}
e_3	CD8 T killing of DC	0.1	c $^{-1}$ h^{-1} mm^3
a_4	IL-2 production by CD4 T	10^{-2}	c $^{-1}$ h^{-1} mm^3
c_4	IL-2 uptake by CD8 T	10^{-7}	c $^{-1}$ h^{-1} mm^3
e_4	IL-2 degradation rate	10^{-2}	h^{-1}

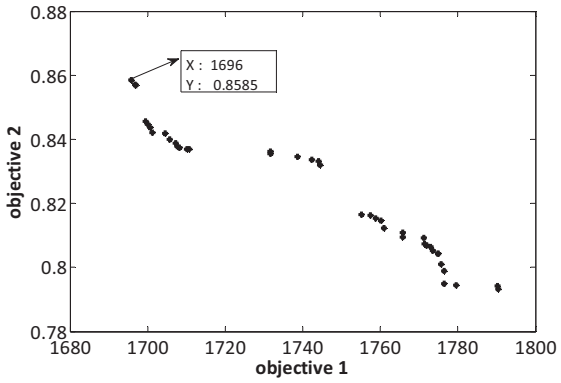

Fig.3. Optimal Pareto solutions for the multi-objective optimization problem

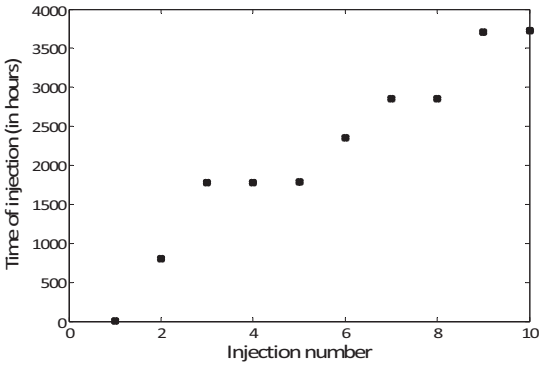

Fig.4. Plot of time of injections of the dendritic cell vaccine for the chosen solution

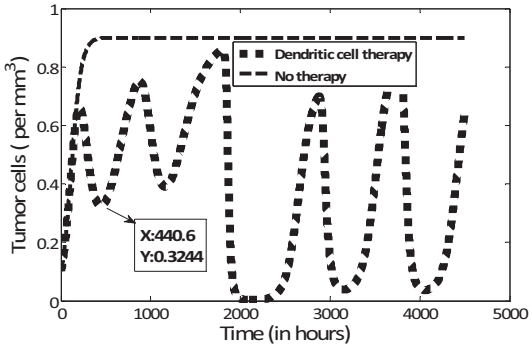

Fig.5. Dynamics of tumor cells for no therapy and dendritic cell therapy

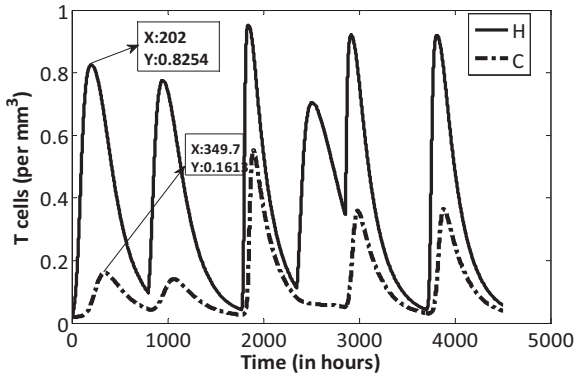

Fig.6. Dynamics of helper T-cells and cytotoxic T-cells

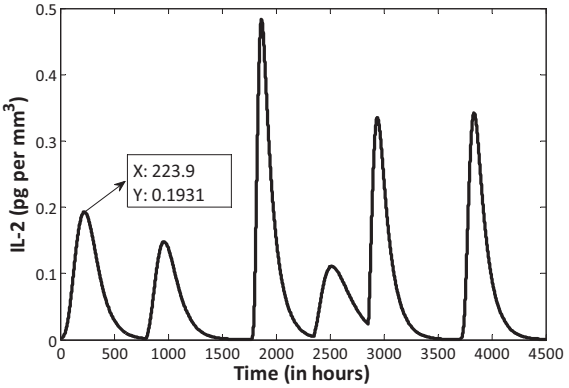

Fig.7. Dynamics of interleukin

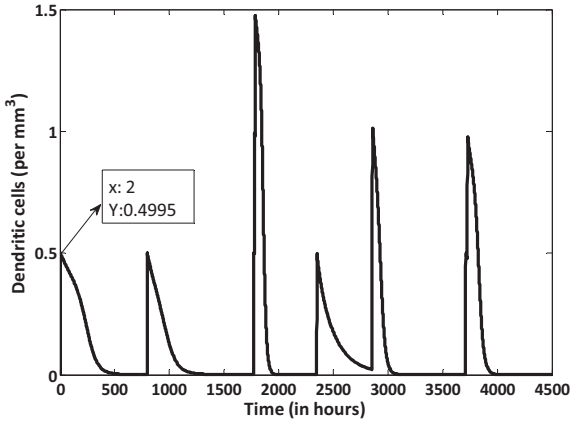

Fig.8. Dynamics of dendritic cells

6. RESULTS AND DISCUSSION

We used MATLAB's implementation of NSGA-II to solve the multi-objective optimization problem as outlined above. The algorithm starts with an initial population of possible solutions within their mentioned bounds and in each generation, the solutions are updated based on the genetic principles. In this work, we considered the population number to be 40 and the maximum number of generations as 40.

Finally, the algorithm provides the best Pareto curve as shown in Fig.3. It can be seen from the Fig.3 that there are gaps in the Pareto curve in spite of the problem being continuous. These gaps can be filled by increasing the population number and the number of generations of the genetic algorithm, but at the cost of higher computational effort. Then, one of the solutions can be chosen from the Pareto curve as per the requirement. Here, solution marked in Fig 3. is chosen because it corresponds to the least value of objective 1 (tumor burden) among all points of the Pareto curve. The time of injections for the chosen point from the Pareto curve is given in Fig 4. According to this treatment plan, DCV is injected and the evolution of the tumor cells, T-cells, interleukin, and dendritic cells are shown in figures 5 through 8 respectively.

From Fig.4, it is observed that injection timings are almost close during (1700-1800 hours, 2850-2900 hours, and 3700-3750 hours). The reason is the increase of tumor cells during these periods. So, in order to bring them down immediately, the frequency of injection times is increased. Thus, the treatment planning seems to be reasonable and logical.

From figures 5 through 8, the first intervention of dendritic cells is considered. This intervention is given in the second hour. Because of this intervention, the helper T-cells, interleukin, and cytotoxic T-cells reach their highest value at around 200 hours (8 days), 221.9 hours (9 days), 349.7 hours (15 days) respectively from the time of intervention of DCV. At the same time, tumor cells reach a lower value at around 440.6 hours (19 days) due to the first intervention. Similarly, tumor cells took around 15 days to reach its lower value after second intervention of DCV. Thus, for the given input of DCV, the time gap between the interventions should not be more than 3 weeks in order to avoid the peak value of the tumor cells. Moreover, it takes more time for the helper T-cells and cytotoxic T-cells to get activated before reacting to the tumor cells. This activation time can be reduced by injecting more DCV (but within the threshold range) or by introducing the interleukin therapy (approved by FDA) where interleukin is also given externally. One of our future plans is to consider a combination of dendritic cell therapy and interleukin therapy.

7. CONCLUSIONS

We have applied multi-objective optimization to find the optimal schedule of dendritic cell therapy for a given input of dendritic cells. The freedom of choice of any one solution as per the requirements is a major advantage of multi-objective optimization strategy. The obtained treatment planning seems to be reasonable in controlling the tumor cells from reaching a higher value. Further analysis suggests that the time gap between the interventions should be less than 3 weeks in order to achieve the objective. Thus, the obtained protocol design can guide caregivers in treating cancer subjects.

ACKNOWLEDGEMENTS

This work was supported by the National University of Singapore in the form of a research scholarship to the first author.

REFERENCES

Adam, J.K., Odhav, B. and Bhoola, K.D. (2003) Immune responses in cancer, *Pharmacology & Therapeutics*, **99**, 113-132.

Cappuccio, A., Castiglione, F. and Piccoli, B. (2007) Determination of the optimal therapeutic protocols in cancer immunotherapy, *Mathematical Biosciences*, **209**, 1-13.

Castiglione, F. and Piccoli, B. (2007) Cancer immunotherapy, mathematical modeling and optimal control, *Journal of Theoretical Biology*, **247**, 723-732.

De Boer, R.J. and Hogeweg, P. (1986) Interactions between macrophages and T-lymphocytes: Tumor sneaking through intrinsic to helper T cell dynamics, *Journal of Theoretical Biology*, **120**, 331-351.

de Pillis, L.G., Gu, W. and Radunskaya, A.E. (2006) Mixed immunotherapy and chemotherapy of tumors: modeling, applications and biological interpretations, *Journal of Theoretical Biology*, **238**, 841-862.

de Pillis, L.G., Radunskaya, A.E. and Wiseman, C.L. (2005) A Validated Mathematical Model of Cell-Mediated Immune Response to Tumor Growth, *Cancer Res*, **65**, 7950-7958.

Deb, K., Agrawal, S., Pratap, A. and Meyarivan, T. (2000) A fast elitist non-dominated sorting genetic algorithm for multi-objective optimization: NSGA-II. Springer-Verlag, Paris, France, 849-858.

Dua, P., Dua, V. and Pistikopoulos, E.N. (2008) Optimal delivery of chemotherapeutic agents in cancer, *Computers & Chemical Engineering*, **32**, 99-107.

Hanahan, D. and Weinberg, R.A. (2000) The Hallmarks of Cancer, *Cell*, **100**, 57-70.

Kirschner, D. and Panetta, J.C. (1998) Modeling immunotherapy of the tumor – immune interaction, *Journal of Mathematical Biology*, **37**, 235-252.

Kuznetsov, V.A., Makalkin, I.A., Taylor, M.A. and Perelson, A.S. (1994) Nonlinear dynamics of immunogenic tumors: Parameter estimation and global bifurcation analysis, *Bulletin of Mathematical Biology*, **56**, 295-321.

Martins, M.L., Ferreira Jr, S.C. and Vilela, M.J. (2007) Multiscale models for the growth of avascular tumors, *Physics of Life Reviews*, **4**, 128-156.

Nemhauser, G.L., Rinnooy Kan, A.H.G. and Todd, M.J. (1989) *Optimization*. North-Holland.

Paola Pisani, F.B., D. Maxwell Parkin, (2002) Estimates of the world-wide prevalence of cancer for 25 sites in the adult population, *International Journal of Cancer*, **97**, 72-81.

Piccoli, B. and Castiglione, F. (2006) Optimal vaccine scheduling in cancer immunotherapy, *Physica a-Statistical Mechanics and Its Applications*, **370**, 672-680.

Szymanska, Z. (2003) Analysis of immunotherapy models in the context of cancer dynamics, *Int.J. Appl. Math. Comput. Sci.*, **13**, 407- 418.

Tamaki, H., Kita, H. and Kobayashi, S. (1996) Multi-objective optimization by genetic algorithms: a review. *Proceedings of IEEE International Conference on Evolutionary Computation*. 517-522.

An Industrial and Academic Perspective on Plantwide Control

James J. Downs*. Sigurd Skogestad**

**Eastman Chemical Company, Kingsport, TN 37662, USA*
(e-mail: jjdowns@ eastman.com).
*** Dept. of Chemical Engineering, Norwegian University of Science and Technology, N-7491 Trondheim, Norway*
(email: skoge@ntnu.no)

Abstract: The purpose of this paper is to stress the importance of selecting the right plantwide control structure and the need for a formalized approach that can encompass the many issues that arise in plantwide control design. Since the concept of process control design based on a holistic view of the process came about, the variety of procedures and approaches to the design problem have illustrated the difficulty of a unified approach. Using examples, a formal design approach is presented to help put in context the need and advantages of using such an approach. The examples deal with disturbance rejection, throughput maximization and economic optimization of plants consisting of parallel units.

Keywords: process control, control structure design, plantwide control, inventory control, throughput

1. INTRODUCTION

Industry uses a variety of approaches to accomplish plantwide control design. The range of tools used spans from engineering judgment to the applications of complex model based algorithms. Over the last 40 years the field of research in this area has attacked this design problem on various levels. Larsson and Skogestad (2000) provide a good review of the various approaches. Design heuristics based on experience, design rules based on case studies, algorithms for objective function minimization, etc. have all contributed to the improvement of how designs can be accomplished (e.g., Downs, (1992), Narraway and Perkins (1993), Luyben (1998), Zheng, Mahajanam and Douglas (1999), Kookos and Perkins (2002), Chen and McAvoy (2003), Vasbinder and Ho (2003), Skogestad (2004), Konda et al. (2005), Ward et al. (2006)). However, the complex nature of the problem and the various depths to which it needs to be solved have resulted in a design procedure that is difficult to piece together from the various approaches that have been put forth. This is not a new issue and almost 20 years ago the "Tennessee Eastman challenge problem" (Downs and Vogel, 1993) was put forward so that various approached could be tested against each other. Nevertheless, today in industry, much of the research in this area has still not gained traction to have the profound influence possible. The purpose of this paper is to stress the need for a formalized yet simple approach that can encompass the many levels that arise in plantwide control design.

In section 2 industrial aspects of plantwide control design are discussed and two examples illustrate how industry may approach the plantwide control problem using a single criterion for design guidance. This points to the need for a more formal procedure which is presented in Section 3. In Section 4 the inclusion of plantwide economic variables is presented and illustrated in Section 5. The paper concludes that the formal approach presented is a step in the direction of helping to organize the design procedure for plantwide control. This paper also illustrates the application of the formal procedure to more complex examples that illustrate plantwide design involves many issues and one-criteria approaches may not be sufficient.

2. STATUS IN INDUSTRY

The traditional approach for designing process control strategies for chemical plants has been to set production rates by setting process feed rates and then to design automatic control systems around each unit operation sequentially through the process. For processes having significant in-process inventory and not too much in the way of recycles, this approach can be used successfully. However, as processes become more complex and at the same time have less in-process inventory, the design of a plant-wide control strategy becomes a more important part of the overall process control design problem. The interrelation of the plant-wide control strategy with the process chemistry and economics requires both control theory and also process knowledge. It has become apparent that the design of plant-wide control strategies involves not only the development and application of process control theory but also, in a more fundamental sense, the development of a methodology one uses to approach the plant-wide control problem.

While we usually think about material balance and energy balance equations applying to a unit operation, they also apply to whole processes and to entire chemical complexes. The time it takes to accumulate and deplete inventories may be longer for large processes or chemical complexes, but the laws of accumulation and depletion of material hold nonetheless. Whereas for a process, we assume the rate of accumulation of each component to be zero, the fact that the control system must ensure that to be the case is often

overlooked. The manipulation of flows, utilities, and the readjustment of process operating conditions to maintain a balance of material and energy entering and leaving an entire process is one of the overriding priorities for the control system (Buckley, 1964). The material balance must be maintained not only from an overall viewpoint but also for each component in the system.

While traditional control theory can be used to approach the control problem as, "Given a process described by a model of the form ... ", the plant-wide control problem requires much more in the development of the problem statement itself. It is not intuitively obvious at the outset what the underlying control problems are - much less how they should be solved. As researchers have begun to explore the plant-wide control area, the application of methods and techniques as applied to case studies has elucidated issues that are difficult to quantify and are in need of further discussion and research.

Despite the ever-increasing incentive, segregation of the process design and control tasks is still common. Two contributing factors to this segregation are: (1) the difficulty of changing from the historical approach of fixing the process design before the control engineer becomes involved, and (2) the difference in the thought pattern of design and control engineers. In addition it can be costly and time consuming to address controllability and operability in a rigorous way at the design stage. The common notion is that process economics are solely determined by the steady-state process design. While the nominal steady-state design point is very important, it loses its distinction if one is unable to maintain plant operation at the design point. Design decisions are often based on steady-state analysis without consideration of controllability, process and product variability, or plant-wide control issues. The basic thought pattern in the design stage usually follows the form, "Given these conditions, create a design to perform this function" (design question), as opposed to, "Given this design, how well will it perform its intended function?" (rating question). As existing plants are pushed to produce greater throughputs, an additional question becomes important, “Given this plant, how can I maximize profit?” (optimization question).

Current industrial practice is usually focused on unit operation control. This viewpoint emanates from the overriding issue of reliable operation. These unit control strategies are simple and understandable by operators and engineers alike and lead to operations that when “sick” can usually be healed without the capabilities of experts. This approach has worked reasonably well for many years. Furthermore, the high costs of building new facilities have led to more retrofits and plants producing products that they were not designed to produce. As plants are campaigned to produce a wider variety of product specifications, control strategies that are simple and perhaps applicable to many different operating points, can result in more reliable operation.

This current design practice is being challenged as process economics drive toward fewer new designs and more operation of existing facilities in new ways. Techniques for plant wide process control design are needed (1) that result in processes that are operated in near optimal fashion while not employing complex control technology and (2) that do not require the care and feeding of control experts. Several approaches that address the attainment of optimal operation of plants while not requiring implementation of complex, perhaps difficult to understand control systems, have emerged. Two of these, self optimizing control design (Skogestad, 2000) and operational strategies based on process chemistry (Ward et al., 2004, 2006) have found particular appeal at Eastman.

The importance of being able to discriminate how process variables need to behave to achieve optimal operation is fundamental when designing plantwide strategies. Often the underlying unit operation strategies can be kept simple and usually SISO while the overall plant wide strategy is optimizing plant operation in a more natural fashion. This approach has wide appeal when plant reliability and control system understandability are required. Each of these approaches builds into the control system a natural “self-optimizing” that is part of normal operation. Contrasted with the centralized approach of using models to determine an optimum and then driving a process to that optimum point, optimization designed in from the bottom up provides the important robustness and reliability component.

From start-up the primary objective for a new plant is to achieve nameplate capacity in a reliable and predicable way. Often times the need for optimization of plant operations comes after the facility has been operational for a few years. By this time top down optimization strategies can be implemented, provided the plant has a good regulatory control system. If the optimization strategy is counterintuitive, then operator understanding can suffer. We can all attest to the uphill battle to achieve routine usage of a control system that, while driving the process to the correct economic conditions, does so in an unusual or difficult to understand fashion.

The importance of having plantwide control strategies that are optimizing in a natural, fundamental way can have long term effects. Operator training and understanding during the early years of plant operation sets thought patterns for years to come. When the need for plant optimization arises, the basic building blocks of how the control system automatically drives plant operation are in place. The process optimizer at this time may only have to make small adjustments to a process that is close to optimum already. The trick, of course, is that these strategies must be basically simple and for the most part SISO. Our experience is that for plants where “self-optimizing” regulatory control strategies have been build in from the beginning, we have been successful with process optimization projects that have been undertaken. On the other hand, for older processes which have control strategies not designed with optimization in mind, we may struggle for years working to gain operator acceptance to a new strategy. Even the simple idea of setting

process throughput at a place other than the process feed can become a difficult endeavour.

Example 2.1 - Changing the production throughput manipulator (TPM) for an esterification plant: Eastman operates many processes that have produced chemicals for over 50 years. Esterification chemistry is well known and has been a workhorse for the company. Units that were built 50 years ago were typically designed with the process throughput set at the feed to the process. Control systems consisted of pneumatic single input / single output controllers that were difficult to change and had a long operating history. As production rates increased over the years due to demand growth and incremental process improvement, the original plantwide strategy would become limiting. The original plant had the standard scheme with the throughput manipulator (TPM) located at the feed as illustrated in Figure 2-1.

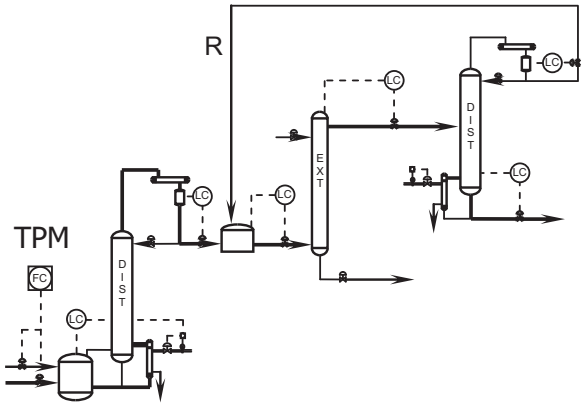

Figure 2-1. Esterification process. Inventory control strategy with column 1 feed rate used as the TPM.

In the late '70's and early '80s' Eastman benefited from implementing a change in the TPM location on numerous plants. Early adoption of this significant change was difficult because of (1) an ingrained mindset toward needing process feeds constant, (2) operator understanding of an "inventory-to-feed" strategy, and (3) the difficulty of reversing the control decision using pneumatic hardware. Today at Eastman, the notion of setting the TPM at a location other than the process feeds is common and is driven by variability propagation and ease of operation requirements. The benefits of choosing the best location for the TPM have also become realized in our capital design process.

For the esterification process the first change was to move the TPM from the process feed rate to the distillate flow rate leaving the first distillation column as shown in Figure 2-2. This strategy worked well for many years because many of the disturbances entering the reactor were directed away from the more sensitive separation portion of the process. The extraction step of the process was intended to wash unreacted alcohol from the ester product. As the extraction step became the process bottleneck, it became evident that its behaviour as a function of organic feed rate was very nonlinear. This nonlinearity stemmed from the fact that increasing organic

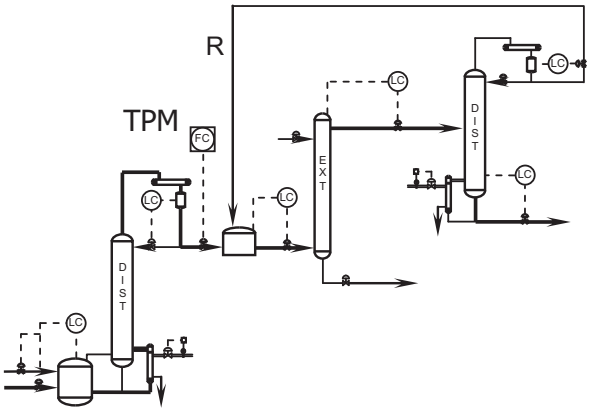

Figure 2-2. Esterification process. Inventory control strategy with column 1 distillate rate used as the TPM.

feed rate resulted in an increasing composition of the alcohol taken from the extractor to the final distillation column. The increase in distillate rate needed to remove the alcohol from the final product would aggravate the situation by increasing the feed rate to the extractor (stream "R" in Figure 2-2). The point at which the process would enter this "windup" varied with the amount of unreacted alcohol reaching this part of the process. This windup in the recycle loop is similar to Luyben's "snowball effect" (Luyben, 1994), but the cause in our case is a limitation in mass transfer rate whereas in Luyben's case it is a limitation in reaction rate. For this process, the windup condition usually took 12-24 hours to get fully engaged. This made it difficult for operators to confidently set the production rate. In addition, what may be a maximum and stable rate today might result in the windup condition tomorrow. The outcome of this uncertainly resulted in operations setting a lower than optimum production rate to guarantee process stability.

A further improvement in locating the TPM occurred when it was relocated to be the feed to the extraction system (Figure 2-3). Obviously, this eliminated variability from propagating to the extractor, but more importantly, it resulted in a self regulating system that avoids the windup should the operator set the TPM too high. In particular, if the TPM is set too high and excess alcohol leaks to the final distillation system, take note of the system response to the extra distillate flow recycled to the extractor. Namely, it results in less flow being drawn from the front end of the process and the extractor, while not at the optimum feed rate, does remain stable. This situation is quite recoverable by operators who note that production rates have fallen, and realize that they have set the extractor feed rate too high. We found that the operators were capable of optimizing the operation once fear of setting the extractor feed too high was removed.

The principle that proved most useful is the idea that the optimum did not lie against or close to a process cliff. The original strategy was very unforgiving once the process was pushed too far. Extractor flooding, loss of liquid/liquid immiscibility, and flooding of the final distillation column

meant several hours of lost production. The ability to experiment with the process without the penalty of passing this "point of no return", gave operators confidence in the control system to recover if they ended up pushing rates too high.

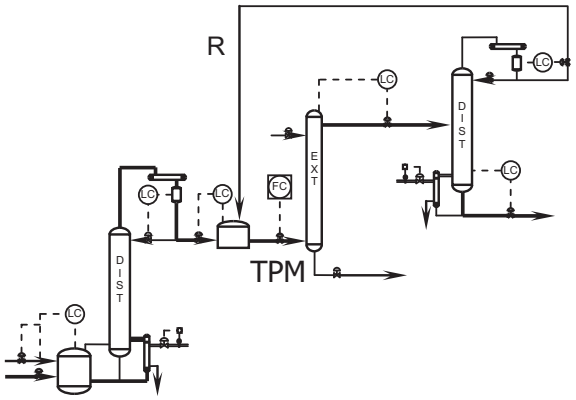

Figure 2-3. Esterification process. Inventory control strategy with extractor feed rate used as the TPM.

Example 2.2 - Control strategy for a liquid-liquid extraction process: During the control design phase one may chose from a variety of criteria to drive the control strategy design and the criterion chosen is usually based upon engineering judgement. The importance of the criterion choice is often not appreciated. The objective of this example is to illustrate how the choice of a design criterion that aims to *propagate disturbances to insensitive locations* results in a particular design. The resulting control strategy can then be compared with those obtained using a more methodical approach.

Consider the extraction process in Figure 2-4 where acid is transferred from the water/acid feed (F) to the extract (E) by use of a solvent (S). The remaining water is the raffinate product (R). The total inventory is self-regulated by overflow of extract, but the interface level (component inventory) does not self regulate. How should this inventory be controlled? Two alternatives are shown in Figure 2-5.

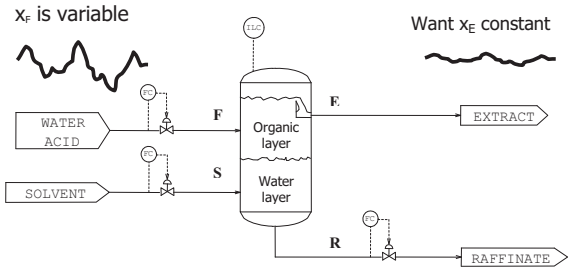

Figure 2-4. Liquid-Liquid Extraction Process

Strategy I. Let aqueous feed F control interface level (with constant outflow R)
Strategy II. Let aqueous outflow R control interface level (with constant feed F).

Both of these structures have been used for extraction control in various services including the example given here. Obviously, both structures work and give the same result if everything is constant (no disturbances). How do the two strategies differ when there are disturbances? To understand the difference we ask the question: "Where does the disturbance go"?

Let x denote the acid fraction, and consider variation (disturbance) in the acid feed fraction x_F by ±1% (30±1%). For strategy I, the resulting variation in the acid composition of the extract product (x_E) is ±0.856% (21.4 ±0.856%) and for strategy II it is ±0.506% (21.4 ±0.506%). For details see the mass balances in Table 1. Thus, strategy II is the preferred strategy of the two if the objective is to have small variations in extract composition, x_E.

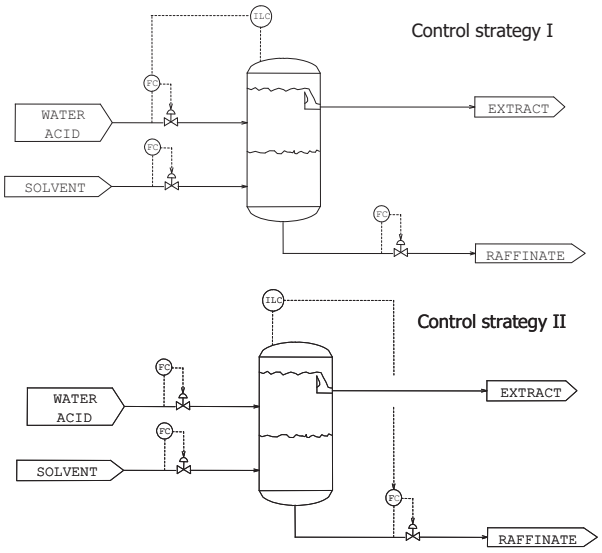

Figure 2-5. Alternative Control Strategies for Liquid-Liquid Extraction

In summary, for strategy I the variation in x_F results in variations in the feed flow, F, and in x_E (with gain 0.856), while for strategy II the variation in x_F results in variations of the outlet flow, R, and to a lesser extent in x_E (with gain 0.506). Strategy II is the preferred strategy of the two if the main objective is to have small variations in x_E. This example suggests that different inventory strategies may result in process variability being transferred to portions of the process that are insensitive to variation or portions in which variability is harmful. The idea of propagating disturbances to insensitive locations gives good insight and can result in good designs. However, for more complex problems and for less experienced engineers a more systematic approach is needed.

	Feed, F				S	Extract, E				Raffinate, R			
Case	Base	I	II	III,IV	All	Base	I	II	III,IV	Base	I	II	III,IV
Water	70	70.568	69	66.774	0	10	10.568	10.33	10	60	60	58.67	56.77
Acid	30 (30%)	31.705 **(31%)**	31 **(31%)**	30 **(31%)**	0	30 (21.4%)	31.705 (22.3%)	31 (21.9%)	30 (21.4%)	0	0	0	0
Solvent	0	0	0	0	100	100	100	100	100	0	0	0	0
Total	100	102.273	**100**	96.77	0	140	142.273	141.33	140	60	**60**	58.67	56.77

Table 1. Mass balances for extraction process: Base case ($x_F = 30\%$) and with disturbance ($x_F = 31\%$) for control strategies I, II, III, and IV. (Assumption: Equilibrium relationship Acid/Water = 3 in extract, E.)

3. A PLANTWIDE CONTROL DESIGN PROCEDURE

No matter what approach we use, the following decisions need to be made when designing a plantwide control strategy:

Decision 1. What to control? Selection of controlled variables (CVs) to achieve
a. Good steady-state performance (economics), and
b. "Stable" operation with little dynamic drift (including selecting CVs related to inventories)

Decision 2. Where to set the production rate? Placement of throughput manipulator (TPM)

Decision 3. How to control the inventories? How to pair the loops? That is, selection of a control configuration that interconnects CVs and MVs.

Often in industrial practice all issues are considered simultaneously without making formal decisions that answer the above three questions. For the extraction process in Example 2.2 the need for good extract composition raised the question of how best to control the aqueous inventory. This naturally leads one to consider the same issues on a broader, plantwide scale. To be effective, a more systematic procedure is helpful.

The plantwide control structure design procedure of Skogestad (2004) consists of the following seven steps:

I. Top-down part

Step 1. Define operational objectives (economics) and constraints.
Step 2. Identify degrees of freedom (MVs) and optimize operation for important disturbances (offline analysis)
Step 3. Select primary (economic) controlled variables
*- **Decision1a***
Step 4. Select location of throughput manipulator
*- **Decision 2***

II. Bottom-up part

Step 5. Structure of regulatory control layer (including inventory control)
*a. Select secondary ("stabilizing") CVs (**Decision 1b**)*
*b. Select "pairings" between CVs and MVs (**Decision 3**)*
Step 6. Structure of supervisory control layer (decentralized, MPCs?)
*- Related to **Decisions 1a and 3***
Step 7. Structure of (and need for) optimization layer (RTO)
*- Related to **Decision 1a***

The top-down part (steps 1-4) is mainly concerned with economics and steady-state considerations are often sufficient. Dynamic considerations are required for steps 4 to 6.

Steps 1 and 2 involve *analysis* of the optimal operation of the plant, and should form the basis for the actual *decisions* in Steps 3 to 7. A detailed analysis in steps 1 and 2 requires that one has available a steady-state model and that one performs optimizations using the model for various disturbances. This is often not done in industrial practice. The model used for design may not be suitable or available, the working relationship between the design and control functions may be weak, or there may not be time to perform this analysis.

Nevertheless, one should at least perform a simplified engineering version of steps 1, 2, and 3 where one thinks through the economics of the present and future operation with aim of using process insight to propose which variables to control, keep constant, from a steady-state economic point of view. In particular, a good engineer can often easily identify the "active constraints" that the control system should maintain. That is, where should one optimally stay at maximum or minimum values of flow, temperature, pressure, composition, etc?

Simplified Step 1-3. Identify degrees of freedom and main disturbances. Based on process insight, select variables to keep constant at steady-state in order to achieve close-to-optimal economic operation (in spite of disturbances).
*- **Decision 1a***

There have been many applications of the above design procedure, e.g. see Araujo et al. (2007), but most of them on academic problems. There exist several other procedures for plantwide control (e.g., Luyben et al., 1998), but they focus mainly on the bottom-up part, and in particular on Step 5. However, making good decisions in step 5 can be difficult without having first gone through the top-down plantwide economic analysis in steps 1 to 4.

Step 4 (location of TPM) was addressed in Example 2.1, and this issue is further discussed in the recent PhD thesis by Aske (2009); see also Aske et al. (2008).

The focus of the rest of this paper is on step 3 (economic CVs). In this respect it is important to notice that the best control structure may vary, and, depending on market conditions, there are two main modes of operation:

Mode I. Maximize efficiency (for a given throughput).

With a given throughput (production rate), the value of the products is usually known, and provided there are degrees of freedom left after satisfying the constraints (specifications), the economic objective is to minimize the use of utilities, maximize raw material yield, and to minimize waste treatment costs. These and other issues that increase specific production costs are the same as maximizing the efficiency. As discussed in section 2 on the industrial status, the control system for a new plant is usually set up to handle this mode of operation well. Changes in production rate are considered a disturbance.

Mode II. Maximize throughput (with production rate as a degree of freedom).

When market demand is good and product prices are high, the profit is maximized by running the plant at maximum throughput. In fact, the first thing that the operation people usually focus on after startup of a new plant is to increase capacity because the opportunities for extra profit in mode II are usually much larger than in mode I (In spite of this there is usually no effort during the design phase to design a control system that can operate at maximum throughput). Operation at maximum throughput usually corresponds to using all degrees of freedom to satisfy active constraints. There will be a bottleneck somewhere in the plant against which operation at maximum throughput will run. Trying to increase the throughput will result in infeasible operation in the bottleneck unit. The maximum flow through the bottleneck unit is then an active constraint, and operation in mode II should be focused on keeping this flow at its maximum (Aske, 2009).

The esterification plant in Example 2-1 is a case of operating in mode II with the extraction section being the bottleneck.

Example 3-1 - Application of the design procedure to Example 2-2: The design criterion for Example 2-2 was that disturbances should be propagated to insensitive locations. At this point we want apply the more systematic plantwide procedure. The process is very simple, so we use the simplified approach for selection of controlled variables (there are no degrees of freedom left for economic optimization once the specifications are satisfied).

Simplified Step 1-3. Identify degrees of freedom (MVs) and main disturbances and based on process insight, select primary controlled variables (Decision 1a).

The extract product flow (E) is on overflow, so there are 3 MVs that can be used for control; the two feed flows (F and S) and the raffinate R. However, at steady state there are only 2 degrees of freedom because the interface level, which has no steady-state effect, needs to be controlled. Further, the throughput is assumed to be given (mode I), which consumes another degree of freedom. We are then left with only 1 steady-state degree of freedom, and thus need to decide on 1 "economic" CV. From process insight it is important to maintain a constant product composition (x_E) so we decide that this should be controlled. There are then no degrees of freedom left for economic optimization.

Decision 1a: The acid product composition x_E should be kept constant. The "economic" CV is therefore $CV_1 = x_E$.

Step 4. Select location of throughput manipulator (TPM) (Decision 2).

The location of the TPM influences the structure (pairing) of the inventory control system in Step 5. The throughput is often located at the main feed, but could generally be anywhere in the process. Since the two proposed control strategies both have a constant solvent feed flow, we assume here that the solvent feed S is the throughput manipulator ***(Decision 2).***

Step 5. Structure of regulatory control layer (including inventory control)

Decision 1b: The total inventory is self-regulated by overflow, but also the interface level between the two liquid phases must be controlled. Thus, CV_2 = interface level.

We must next decide *how* to control the interface level. With solvent feed rate S as the TPM, we have left two candidate MVs: Feed F and outflow R. The main issue for regulatory control is usually dynamics, and from this point of view there does not seem to be any significant difference between the two choices. Another issue for regulatory control is to avoid saturation of the MV, and this tells us that we should prefer the largest flow, which is the feed F. However, one should also think ahead to Step 6, which is the structure of the supervisory layer. Here, the concern is to control acid composition ($CV_1 = x_E$) which depends directly on the feed F but only indirectly on the outflow R. Thus, we would like to "save" F for the supervisory layer.

Decision 3. Use R to control the interface layer (MV_2 = R). This gives inventory control in the direction of flow, which is normal with the throughput set at the feed.

Step 6. Structure of supervisory control layer

Decision 3, continued. The remaining MV_1 = F is used to control acid composition ($CV_1 = x_E$). The final control structure is shown as strategy III in Figure 3-1.

Note that we assumed that the product composition x_E can be measured ($CV_1 = x_E$), but this may not be possible in practice. We then need to find something else to "control" (keep constant). This is what we indirectly did in the previously proposed strategies where we selected

Strategy I: Keep CV_1 = R constant (and use F to control the interface level)

Strategy II: Keep CV_1 = F constant (and use R to control the interface level)

However, both of these strategies give undesired variations in the product composition x_E; we found $\Delta x_E/ \Delta x_F = 0.856$ for strategy I and $\Delta x_E/ \Delta x_F = 0.506$ for strategy II. It is possible to add a supervisor layer, where one adjusts R (strategy I) or F (strategy II) such that x_E is kept constant. This modification to strategy II is shown as *Strategy III* in Figure 3-1.

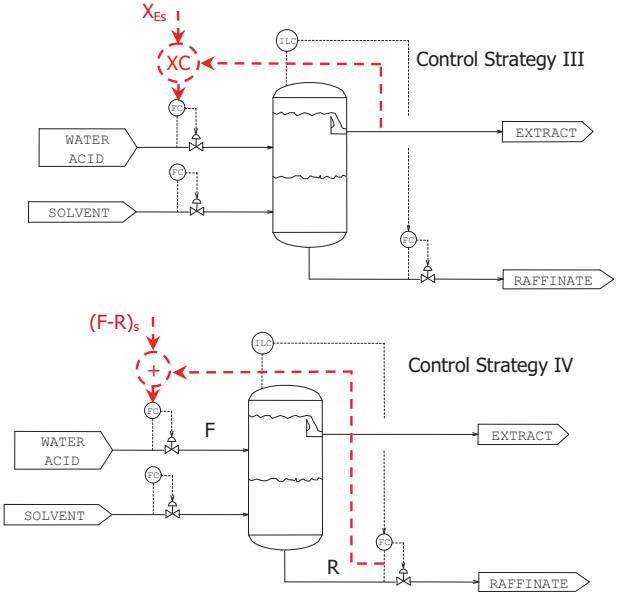

Figure 3-1. Self-Optimizing Strategies for Extraction Process

However, assume there is no online measurement of the extract composition x_E. One option would then be to estimate x_E using a model and available measurements ("soft sensor"), but this is a bit complicated. Is it possible to find a simple strategy (maybe a combination of strategies I and II) that gives $\Delta x_E/ \Delta x_F = 0$? Yes, it is!

Strategy IV: Keep the flow difference CV_1 = F – R constant (while at the same time adjusting F and R to control interface level). One possible implementation is shown in Figure 3-1.

Why does strategy IV give constant composition x_E? Controlling the interface level (which indirectly depends on the feed composition x_F) closes the material balance at steady-state. From the total material balance we have E = S + (F-R) so by keeping F-R constant, we have that the flow E remains constant (because the throughput S is constant) and assuming equilibrium it follows that the composition of E must remain constant (again assuming S constant). If the throughput S varies (disturbance) then all flows should be scaled by S to keep x_E constant, so by process insight we derive that an "improved strategy IV" is to keep the variable $CV_1 = (F-R)/S$ constant.

Strategy IV is a special case of a "self-optimizing" measurement combination, as discussed below. In fact, since we have $n_d = 1$ disturbance (x_F) and $n_u = 1$ steady-state degrees of freedom, we have from the nullspace theorem (Alstad and Skogestad, 2007) that self-optimizing control can be obtained by controlling a combination of $n_d + n_u = 2$ independent measurements. The flows (MVs) R and F are here candidate "measurements", so a possible controlled variable is $CV_1 = h_1 F + h_2 R$, where in general the optimal h_1 and h_2 can be found from the nullspace theorem. In this example, we found by process insight that the optimal choice is $h_1 = 1$ and $h_2 = -1$ (strategy IV).

4. SELECTION OF ECONOMIC (PRIMARY) CVs

In the above example, we found that the flow difference F-R is a good primary CV. How do we select primary (economic) CVs in a systematic manner (step 3)?

We make the standard assumption here that a steady-state analysis is sufficient for studying the economics. The question is: How can we turn optimization into a setpoint problem? The issue is to find some "magic" variable, c, to keep constant. The obvious "magic" variable is the gradient of the cost function, $J_u = dJ/du$, which should be zero at the optimum point, independent of disturbances. However, before we look at this idea, let us look in a bit more detail in Steps 1 to 3 in the proposed procedure for selecting economic CVs.

Step 1. Define operational objectives (cost J) and constraints

In many cases a simple economic cost is used:

> Profit = - J = value products – cost feeds – cost utilities (energy)

Other operational issues, such as safety and environmental impact are usually formulated as constraints. For cases with good marked conditions we often have a constrained optimum and the cost function can be simplified to J = - TP (mode II, maximum throughput).

Other cost functions are also possible. For example, consider the extraction process. Here, the optimum is to keep a constant product composition x_E, but this is not possible, even at steady-state, because there is no online measurement. We therefore want to control something else that gives *indirect control* of the primary output (Hori et al., 2005). The cost function is then $J = (x_E - x_{ES})^2$.

Step 2. Identify degrees of freedom and optimize operation for various disturbances.

One approach is to use a steady-state flowsheet simulator, if available, to optimize operation (with respect to the degrees of freedom) for various disturbances. In many cases, simpler models and approaches may be used. Typical "disturbances" include feed composition, feed rate, reaction rate constants, surroundings, values of constraints and prices.

Step 3. Select primary (economic) controlled variables

The issue is to select the primary (economic) controlled variables (CVs). That is, for what should we use the (steady-state) degrees of freedom? What should we control?

1. Control active constraints. The active constraints come out of the analysis in step 3 or may in some cases be identified based on physical insight. The active constraints should be selected as CVs because the optimum is not "flat" with respect to these variables. Thus, there is usually a significant economic penalty if we "back off" from the active constraints, *so tight control of the active constraints is usually desired.*

Specifically, in mode II the feed rate should be adjusted to keep the bottleneck unit operating at its active constraints. Any back-off from the active constraints will reduce the flow through the bottleneck unit and give a loss in feed flow (production) which can never be recovered.

2. Identify "self-optimizing" variables related to the (possibly) remaining unconstrained degrees of freedom. These are "magic" variables which when held constant result in close-to-optimal operation (with a small loss), in spite of the presence of disturbances. The term "magic" is used to signify that the choice may have a significant effect on the economics (loss), and that it is not generally obvious what a good choice is. A good self-optimizing variable should give a "flat" optimum, which means that tight control of these variables is usually not required (as opposed to the active constraints). Note that the different self-optimizing variables must be found for each region of active constraints.

There are two main possibilities for selecting self-optimizing CVs:

1. Select single measurements as CVs (however, it is difficult to find single measurements in a systematic manner, so one must often use the "brute force" approach)
2. Use measurements combinations as CVs (here, methods exist to find optimal combinations).

To identify good candidates for a controlled variable, c, we may use the following four requirements (Skogestad, 2000):

Requirement 1. Its optimal value is insensitive to disturbances (so that the optimal variation Δc_{opt} is small).

Requirement 2. It is easy to measure and control accurately (so that the implementation error n is small).

Requirement 3. Its value is sensitive to changes in the manipulated variable, u; that is, the gain, G, from u to c is large (so that even a large error in controlled variable, c, results in only a small error in u. Equivalently, the optimum should be 'flat' with respect to the variable, c.

Requirement 4. For cases with two or more controlled variables, the selected variables should not be closely correlated.

All four requirements should be satisfied. For example, for a marathon runner, the heart rate may be a good "self-optimizing" controlled variable (to keep at constant setpoint). Let us check this against the four requirements. The optimal heart rate is weakly dependent on the disturbances (requirement 1) and the heart rate is easy to measure (requirement 2). The heart rate is relatively sensitive to changes in power input (requirement 3). Requirement 4 does not apply since this is a problem with only one unconstrained input (the power).

In addition to the above requirements, some systematic approaches to evaluate and find good "self-optimizing" CVs (especially associated with the unconstrained degrees of freedom) are:

Approach 1 - Brute force. Conceptually, the simplest approach for finding candidate CVs is the "brute force" approach where one considers the economic loss imposed by keeping a candidate set of CVs constant when disturbances occur (rather than re-optimizing their values),

$$\text{Loss} = J(\text{CV} = \text{constant}, d) - J_{opt}(d)$$

The term "brute force" is used is because one must do a separate evaluation of each candidate set of CVs. The "brute force" approach is the most general and exact method, but also the most time consuming method because there are essentially an infinite number of possible CVs (at least if measurement combinations are included) that can be suggested, and for each of them we need to do computations to find the cost for each disturbance.

The "brute force" approach was essentially what we initially tried with strategies I and II for the extraction process, where we evaluated the change in product composition ($\Delta x_E / \Delta x_F$) resulting from a disturbance in feed composition.

Approach 2 - Use analytic expressions or insight about the optimum. This is not a general approach, but it may be

very effective for cases where it works. One useful method is to start from the fact that at the optimum the gradient of the cost J with respect to the degrees of freedom should be zero:

At optimum: Gradient = $J_u = dJ/du = 0$

These are also known as the necessary condition of the optimum (NCO) (Srinivasan, et al). It seems obvious that the gradient CV = J_u is the "ideal" self-optimizing variable (Halvorsen and Skogestad, 1997), However, it may be difficult to obtain the expression for J_u or it may depend on non-measured variables.

Approach 3 - Exact local method and optimal measurement combinations. The details are found in Halvorsen et al (2003), Alstad and Skogestad (2007) and Alstad et al. (2009). For the case single measurements as CVs, this is a "local" version of the brute force approach. However, the evaluation is much more efficient. In addition, the "nullspace method" can be used to find truly optimal measurement combinations, as was done in strategy IV for the extraction process.

Approach 4 - Maximum gain rule. The maximum gain rule (Halvorsen et al., 2003) says that one should control "sensitive" variables with a large scaled gain |G|/span(CV). This captures two main concerns:

1. *The optimal value of the CV should be approximately constant* (independent of disturbances), that is, span(CV) should be small.
2. *The CV should be sensitive to changes in the unconstrained degrees of freedom* (to ensure a flat optimum), that is the gain G = ΔCV / ΔMV should be large.

The maximum gain rule can be derived from the exact local method by making some not too serious assumptions. An important advantage of the maximum gain rule is the insight that it gives.

5. OPTIMAL OPERATION OF PARALLEL UNITS

Let us return to an important problem, often encountered in industrial practice. During the life of production of a product, a company often times expands capacity as demand grows. Early plant design may involve process designs based on incomplete data as time to market drives commercialization timelines. Once operation begins, improved operating conditions, equipment designs, and process topology emerge. When capacity expansion takes places the new capacity may come simply by adding equipment to the existing process or by construction of a parallel plant. The new plant is seldom run in a "stand alone" fashion, but instead may share some unit operations with the existing facility. As expansion continues, the complexity of the topology among the plants can lead to plant wide control problems.

In its simplest form, consider a number of plants operating in parallel, each of differing ages, and each with its own efficiency and yield relationships that are dependent on throughput. How should we optimally load each plant to achieve a target production while minimizing the total production costs? We can derive useful result from the necessary optimality condition $J_u = 0$. We derive that, provided the total production rate is given, it is optimal to load the units such that we have **equal marginal costs in all units** (which corresponds to $J_u = 0$).

Proof. To derive this result, consider *n independent parallel units* with a given total load (e.g., given total feed). Let the total cost be $J = \Sigma J_i$ and let the total feed (or some other limited load for the units) be fixed, $F = \Sigma F_i$. The necessary conditions of optimality is that $J_u = \delta J/\delta u = 0$ where u in this case is the vector of feed rates F_i. Since the total feed is fixed, there are n-1 independent degrees of freedom F_i, and we assume these are the F_i's for n-1 first units (and for unit n we have $F_n = F - \sum_{i=1}^{n-1} F_i$) The units are assumed to be independent which means that the cost in unit i, J_i, depends only on the flow into unit i, F_i. However, note that when we make a change in F_i, we also need to change F_n, and we have $dF_n = - dF_i$. The optimality condition $\delta J/\delta F_i = 0$ for variable F_i then becomes

$$\delta J/\delta F_i = \delta(J_1 + J_2 + \ldots J_i + \ldots J_n)/\delta F_i = \delta(J_i + J_n)/\delta F_i$$
$$= \delta J_i/\delta F_i - \delta J_n/\delta F_n = 0$$

or $\delta J_i/\delta F_i = \delta J_n/\delta F_n$. Since this must hold for all i units, we have proved that one should operate such that the *marginal cost* $\delta J_i/\delta F_i$ *is the same in same units.* **End proof.**

Urbanczyk and Wattenbarger (1994) applied this criterion to the maximization of oil production of wells that produce both oil and gas, but where the total gas handling capacity is fixed (limited). In their application J_i is the oil production and F_i is the gas production in well i, and the idea is to operate the wells such that $\delta J_i/\delta F_i$ is the same for all wells; that is, by increasing the gas production by a given amount δF_i one gets the same benefit in terms of extra oil production δJ_i in all wells.

Good self-optimizing variables are then the difference in marginal cost between the units (which should be zero). Below we discuss two industrial applications of this idea.

Example 5-1 – Operation of parallel refining systems: Eastman received an industry award for its application of advanced control to optimally load three parallel refining systems. Each system consists of four distillation columns used to refine crude reactor product. The application uses process data to establish operating costs for processing material from crude reactor effluent to saleable product. Based on operating costs, process operation limits, and utility availability, the feed rate to each refining train is adjusted to match reactor production with refining system production. *The allocation of load to each system is adjusted to achieve equal marginal refining costs.*

Example 5-2 – Syngas production in parallel furnaces: For many years Eastman produced synthesis gas by reacting methane and steam in reforming furnaces. The process consisted of 15 furnaces operated in parallel, see Figure 5-1. The effluent gas from the furnaces was combined as feed to three carbon dioxide removal systems. The product syngas from the three carbon dioxide removal systems was combined to form a single product gas used in downstream chemical production. The 15 reforming furnaces, constructed over the span of three decades, each had different energy efficiency characteristics as well as different yield performance as technology advanced. In addition, the three carbon dioxide removal systems were of varying efficiency and performance. Newer systems were better instrumented, had valves that performed better, and had on-line analytical measurements. At any time, there were one to three furnaces down for routine maintenance.

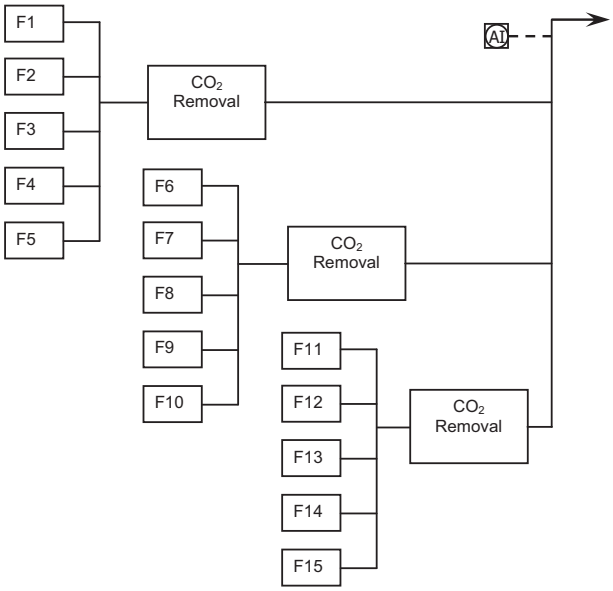

Figure 5-1. Syngas process with fifteen furnaces and three CO_2 removal systems.

The optimum operation of the plantwide system to coordinate pressure and production among the interconnected gas flow network was a significant challenge. The simple objective of matching production of syngas with consumption often ended up varying the production rate on the newest furnace because it could most gracefully handle the needed changes. From an optimization point of view this approach usually resulted in the most efficient units not being operated at their maximum rates.

Normally with units in parallel, an expected "self-optimizing" strategy is to operate with the same outlet conditions (temperatures or compositions) of all parallel units. This would have been a good strategy if the reactors were identical, but, for this example it is more economical to operate each furnace differently based on its particular efficiency and yield profile and then ensure that the combination stream met the total stream specifications. In particular, the newer more efficient furnaces were able to produce a much purer product for the same cost as the older units producing a much less pure product. The purity of the product from each furnace was a relatively weak function of feed rate. The final layer of complexity arises from the efficiency of the carbon dioxide removal system. Each system was connected to a designated set of furnaces so that it was beneficial to operate furnaces linked to the better performing carbon dioxide removal system.

The optimization layer to coordinate the total process production and the allocation of that production to various parallel units was complicated by the presence of crossover lines. These lines added operational flexibility but created an ever increasing complexity of the optimization problem. Local MPC controllers for furnace operation and supervisory control for the carbon dioxide removal systems allowed for near optimal operation at the local level illustrated in Figure 5-2. Overall optimization was approached by production loading strategies and coordination using a supervisory MPC controller. As solutions to this problem were developed, it became clear that technology to guide us on the appropriate degree of decentralization was sparse. Developing a centralized system with all the CV's and MV's in

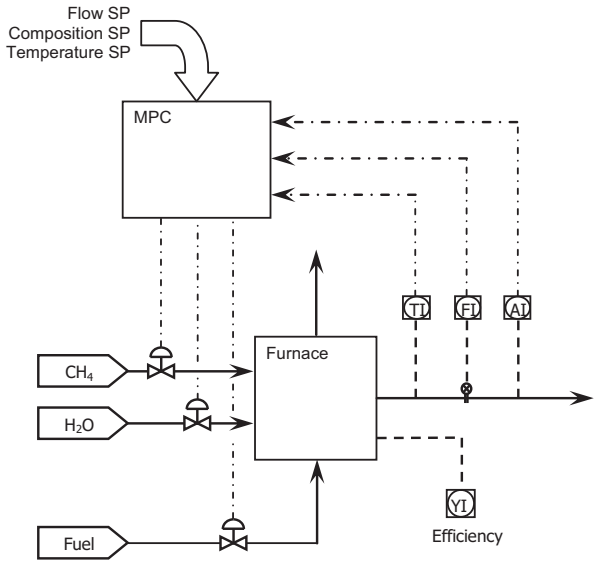

Figure 5-2. Individual syngas furnace control with three manipulated variables and three controlled variables.

the same MPC was problematic due to the routine on-line/off-line operation of the furnaces. Being able to gracefully add and remove systems from the overall control system was critical to success. In addition, measurement reliability often resulted in some furnaces being operated in "local' mode; i.e., not connected to the centralized MPC. The eventual control system needed to be developed and commissioned in reasonable time, needed to be implemented on available hardware, needed to be understood by plant operating staff, and had to be maintainable as process

improvements were made. This led to a decentralized strategy choice as shown in Figure 5-3.

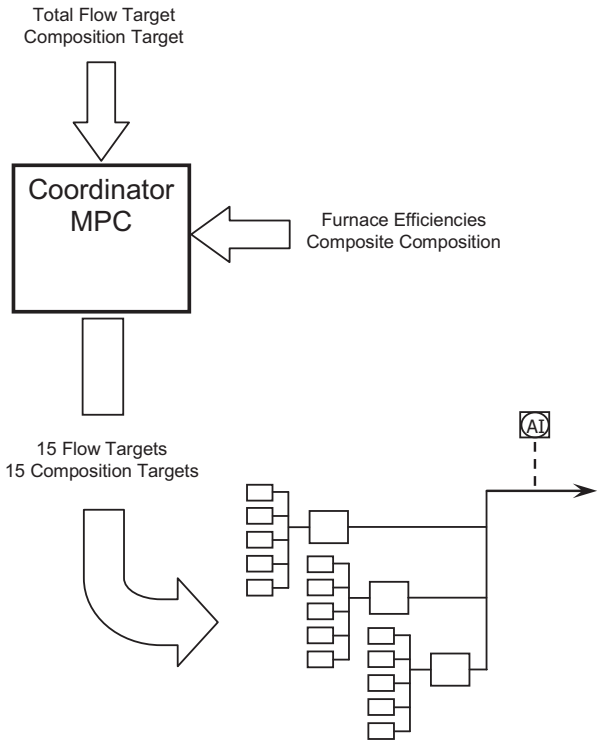

Figure 5-3. Coordination MPC supervising fifteen local furnace MPC controllers.

These examples illustrate the complex nature of an industrial plantwide control problem. The use of a formalized procedure can make known improved strategies that may go undetected when using only one or two design criteria for guidance. The ability to weave in practical issues that complicate implementation is paramount. Using a formalized procedure can help unscramble the vast array of decisions that can overwhelm designers and cause them to continue reliance upon a unit operation focus.

6. DISCUSSION

The design of plantwide control strategies can be seen from two viewpoints. These are (1) the design of control strategies for the regulation of plant material and energy inventories and (2) the design of control strategies for process economic optimization. The design of inventory control strategies determines the manipulated variables that remain for process economic optimization. Concepts are needed that guide the design of the inventory control strategy such that the design of the process economic optimization strategy is made easy. It is clear that if a good job is done during the design of the inventory control strategy, such as setting the TPM near the bottleneck, then the remaining process economic optimization strategy design is made easier. On the other hand, if the inventory control strategy results in key optimization variables being far away from available manipulated variables, then strategies for optimizing process economics will be difficult if not impossible to implement.

The examples illustrate that the inventory control strategy design not only affects the dynamics between manipulated and controlled variables used for optimization, but also can change the gain as well. The emphasis upon placement of the TPM for a process has long been recognized as a key decision in the resulting inventory control strategy. It is becoming more evident that this decision also determines the difficulty of the remaining process economic optimization strategy design. Techniques to determine self-optimizing control variables can be effectively and easily employed if the variables available to optimize the process have good dynamic linkage with their manipulated variable counterparts.

The examples also illustrate that the application of optimization from a top down viewpoint may guide one to select manipulated variables that should remain free for economic optimization while other should be used for inventory control. The formalization of a procedure to organize the design of these two phases of control includes the concepts of: (1) TPM location within the process, (2) control of unit operation process variables against their local constraints, and (3) the development of measurement combinations whose control implies nearness to the economic optimum.

The application of plantwide control design procedures for new plants is certainly an obvious direction of growth. However, the redesign of plantwide control structures for existing plants has been shown to be very beneficial. The known locations of process bottlenecks, known market conditions and product demands, and the operating nuances of a running process all make the plantwide design procedure more understandable and manageable. Using a procedure to determine alternate control structures can lead to new ideas for control that may have been missed for existing processes. As noted, the migration from tried and true control, but inferior, control strategies to new and unfamiliar strategies can be difficult.

7. CONCLUSION

Since the concept of process control design based on a holistic view of the process came about, the variety of procedures and approaches to the design problem have illustrated the difficulty of a “one size fits all approach.” The examples presented illustrate the application of a few industrial design approaches. A more formal design procedure is presented and it is applied to the industrial examples. The importance of addressing process economics in the control design procedure is discussed and the industrial need to run plant at their maximum feed rate (mode II) is emphasized. The use of a plantwide design procedure that

incorporates and organizes the variety of concerns and technical issues in this important area is demonstrated.

REFERENCES

V. Alstad and S. Skogestad, "Null Space Method for Selecting Optimal Measurement Combinations as Controlled Variables", *Ind. Eng. Chem. Res.*, **46** (3), 846-853 (2007).

V. Alstad, S. Skogestad and E.S. Hori, "Optimal measurement combinations as controlled variables", *J. Proc. Control*, **19**, 138-148 (2009).

A.C.B. Araujo, M. Govatsmark and S. Skogestad, "Application of plantwide control to the HDA process. I Steady-state and self-optimizing control"', *Control Engineering Practice*, 15, 1222-1237 (2007).

E.M.B. Aske, S. Strand and S. Skogestad, "Coordinator MPC for maximizing plant throughput", *Computers and Chem. Eng.,* **32**, 195-204 (2008).

E.M.B. Aske, *Design of plantwide control systems with focus on maximizing throughput*, PhD Thesis, Norwegian University of Science and Technology (NTNU) (2009)

P.S. Buckley, *Techniques of Process Control*, Wiley, New York (1964), Chapter 13.

R. Chen and T.J. McAvoy, "Plantwide control system design: Methodology and application to a vinyl acetate process", *Ind. Eng. Chem. Res.*, **42** (20), 4753-4771 (2003).

J.M. Douglas, *Conceptual Design of Chemical Processes*, McGraw-Hill, New York (1988).

J.J. Downs, "Distillation Control in a Plantwide Control Environment", In: *Practical Distillation Control*, W.L. Luyben (ed.), Van Nostrand Reinhold, 413-439 (1992)

J.J. Downs and E.F. Vogel, "A Plant-Wide Industrial Process Control Problem", *Computers and Chem. Eng.,* **17**, 245-255 (1993)

I.J. Halvorsen and S. Skogestad, "Optimizing control of Petlyuk distillation: Understanding the steady-state behavior", *Computers and Chem. Eng.,* **21**, Suppl., S249-S254 (1997).

I.J. Halvorsen, S. Skogestad, J.C. Morud and V. Alstad, "Optimal selection of controlled variables", *Ind. Eng. Chem. Res*., **42** (14), 3273-3284 (2003).

E.S. Hori, S. Skogestad and V. Alstad, "Perfect steady-state indirect control", *Ind. Eng. Chem. Res.*, **44** (4), 863-867 (2005).

NVSNM Konda, G.P. Rangaiah and P.R. Krishnaswamy, "Plantwide control of industrial processes: An integrated framework of simulation and heuristics", *Ind. Eng. Chem. Res.* , **44** (22), 8300-8313 (2005).

I.K. Kookos and Perkins, J.D., "An Algorithmic method for the selection of multivariable process control structures", *J. Proc. Control*, 12, 85-99 (2002).

W.L. Luyben, B.D. Tyreus and M.L. Luyben, *Plantwide Process Control*, McGraw-Hill, New York (1998).

W.L. Luyben, "Snowball Effects in Reactor Separator Processes with Recycle", *Ind. Eng. Chem. Res.* , **33**, 299-305 (1994).

L.T. Narraway, J.D. Perkins, "Selection of control structure based on economics", *Computers and Chem. Eng.,* **18**, S511–S515 (1993).

S. Skogestad "Plantwide control: the search for the self-optimizing control structure", *J. Proc. Control*, **10**, 487-507 (2000).

S. Skogestad, "Control structure design for complete chemical plants", *Computers and Chem. Eng.,* **28** (1-2), 219-234 (2004).

B. Srinivasan, D. Bonvin and E. Visser, "Dynamic optimization of batch processes – III. Role of measurements in handling uncertainty", *Computers and Chem. Eng.,* **27** (1) 27–44 (2003).

E.M. Vasbinder and K.A. Hoo, "Decision-based approach to plantwide control structure synthesis", *Ind. Eng. Chem. Res*., **42**, 4586-4598 (2003).

J.D. Ward, D.A. Mellichamp, and M.F. Doherty, "Importance of Process Chemistry in Selecting the Operating Policy for Plants with Recycle", *Ind. Eng. Chem. Res*., **43**, 3957 (2004).

J.D. Ward, D.A. Mellichamp, and M.F. Doherty, "Insight from Economically Optimal Steady-State Operating Policies for Dynamic Plantwide Control", *Ind. Eng. Chem. Res*., **45**, 1343 (2006).

C.H. Urbanczyk and R.A. Wattenberger, "Optimization of well rates under gas coning conditions", *SPE Advanced Technology Series*, **2**, (2), 61-68 (1994).

A. Zheng, R.V. Mahajanam, J.M. Douglas, "Hierarchical procedure for plantwide control system synthesis", *AIChE Journal*., **45**, (6) 1255-1265 (1999)

Distributed Control

Oral Session

Industrial Implementation of a Coordinator MPC for Maximizing Throughput at a Large-Scale Gas Plant

Elvira Marie B. Aske [*,**] **Stig Strand** [**] **Sigurd Skogestad** [*]

[*] *Department of Chemical Engineering, Norwegian University of Science and Technology, N-7491 Trondheim, Norway, e-mail: sigurd.skogestad@chemeng.ntnu.no (Sigurd Skogestad)*
[**] *StatoilHydro R&D, Integrated Operations and Process Control, N-7005 Trondheim, Norway*

Abstract: An industrial implementation of a coordinator MPC to maximize throughput at the large-scale Kårstø gas plant is described. The "coordinator MPC" coordinates the flows through the network and not the local MPCs. It uses as degrees of freedom (MVs) the flows not used by the local MPCs (feeds, crossovers), and maximizes the throughput subject to the keeping the remaining capacities in all units zero or positive. A key idea is to use the local MPCs to estimate the remaining capacities in the units (Aske et al., 2008). Although not fully implemented, the coordinator MPC is found to be a promising tool for implementing maximum throughput.

Keywords: Model based control, throughput, implementation, optimization, capacity.

1. INTRODUCTION

This paper describes an actual industrial implementation of the method for maximum throughput proposed earlier by Aske et al. (2008). The application is the Kårstø gas processing plant located in Norway, which receives rich gas and unstabilized condensate through pipelines from more than 30 producing offshore fields. This set high demands, not only to the plant efficiency and its regularity, but also to the plant throughput. Limited gas plant processing capacity means that one or more fields must reduce production or even shut down. Therefore, it is important that the Kårstø plant does not become a "bottleneck" in the Norwegian gas transport system. The Kårstø plant has no recycles or reactors, but it has several independent feeds and parallel flows that make it possible to have multiple bottlenecks at the same time. The bottlenecks may move due to disturbances, thus the throughput maximizing is a dynamic and multivariable problem.

The overall feed rate (or more generally the throughput) affects all units in the plant. For this reason, the throughput is usually not used as a degree of freedom for control of any individual unit, but is instead left as an "unused" degree of freedom (u^c) to be set at the plant-wide level. The throughput at the Kårstø plant is presently set by the operators who manipulate the feed valves to satisfy orders from the gas transport system (operated by another company). The objective of this work is to coordinate the throughput manipulators (u^c) to achieve economic optimal operation.

In general, to optimize the economic operation of a plant, one may use real-time optimization (RTO), normally based on (rigorous) steady-state models. Standard RTO methods require the plant to be close to steady state before performing a reoptimization based on data reconciliation or parameter estimation (Marlin and Hrymak, 1997). However, many plants are rarely at steady state or important economic disturbances occur more frequent than the controlled plant response times. At least in theory, it is then more suitable to use dynamic optimization with a nonlinear model, which may be realized using dynamic RTO (DRTO) or non-linear model predictive controller (MPC) with an economic objective, e.g. Engell (2007); Strand (1991).

In this study, a different approach is used. We assume that optimal economic operation is the same as maximizing plant throughput, subject to achieving feasible operation (satisfying operational constraints in all units) with the available feeds. This corresponds to a constrained operation mode with maximum flow through the bottleneck(s). At maximum throughput, all throughput manipulators (u^c) are used to satisfy active constraints (bottleneck). Thus a nonlinear model of the entire plant is not needed, and instead linear MPC may be used. One option is to combine all the MPCs in the plant into a single application. However, here we choose to decompose the problem by keeping the local MPC applications and introducing a coordinator MPC (Aske et al., 2008) to maximize throughput. The coordinator uses the remaining degrees of freedom (u^c) to maximize the flow through the network subject to satisfying given constraints. The remaining degrees of freedom (u^c) include feed rates, feed splits and crossovers. The constraints are the feasible remaining capacities of the individual units ($R_k > 0$). The feasible remaining capacity R_k is how much more feed unit k can receive while operating within its constraints. For most units, R_k is not a quantity that can be measured, because it depends on the operation of the unit. For

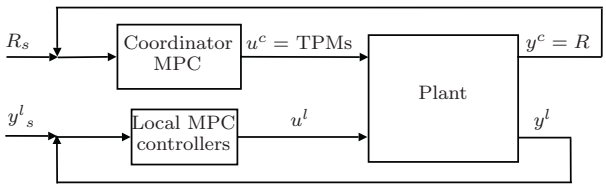

Fig. 1. Plant decomposition by coordinator MPC. The local MPC applications uses u^l to control the local targets y^l_s, whereas the coordinator uses the throughput manipulators (u^c = TPMs) to control the remaining capacity ($y^c = R$) in the units.

example, the capacity may be increased by producing less pure products. A key idea in the approach of Aske et al. (2008) is to use the local MPC to estimate R_k. By estimating R_k for each unit, the plant-wide control problem is decomposed and the application becomes smaller in size and hence easier to understand and maintain. The plant decomposition is illustrated in Fig. 1.

This paper considers about half of the Kårstø gas processing plant. The application presently includes 12 distillation columns, 2 compressor stages, 4 feed valves and 2 crossovers (splits). The main reason for not including the entire plant is that local MPC applications are yet not implemented on all units. All MPC applications at the Kårstø plant use the in-house SEPTIC technology (Strand and Sagli, 2003).

This paper is organized as follows. The local MPC controllers for the individual units are discussed briefly in Section 2. The local MPCs adjust the local degrees of freedom (u^l) such that the operation is locally feasible. However, local feasibility requires that the feed rate to the unit F^l_k is below its maximum capacity, $F^l_{k,max}$, and one of the tasks of the plant-wide coordinator is to make sure that this is satisfied. The maximum capacity for a unit ($F^l_{k,max}$) may change depending on disturbances (e.g. feed composition) and needs to be updated continuously. To estimate $F^l_{k,max}$ by using the already existing models in the local MPCs is discussed in Section 3. Section 4 discusses the coordinator MPC, including control design choices, model development, tuning issues and test runs. Experience from the implementation at the Kårstø site is summarized in Section 5. An extended version of this paper is found in Aske (2009, Ch. 6)

2. LOCAL MPC APPLICATIONS

Presently, all the local MPC applications for the coordinator are on two-product distillation columns. The main control objective for each distillation column is to control the quality of the distillate- (D) and bottoms (B) products. In addition, the column must be kept under surveillance to avoid overloading, where column differential pressure (Δp) is used as an indicator.

The local MPCs are configured with the following controlled variables (CVs), manipulated variables (MVs) and disturbance variables (DVs):

CV (set point + max constraint): Impurity of heavy key component in D.
CV (set point + max constraint): Impurity of light key component in B.
CV (max constraint): Column differential pressure (Δp).
MV: Reflux flow rate set point (L).
MV: Tray temperature set point (T_s).
DV: Column feed flow.

These MVs correspond to the local degrees of freedom (u^l) and the CVs correspond to the local outputs (y^l), see Fig. 1. Some of the columns have additional variables, but in principle, all the columns have the same control configuration.

The local MPC problems are solved at each sample time using a standard two-step approach, where first a steady-state problem is solved with constraint relaxation until the predicted final steady state is feasible, and then the "standard" dynamic MPC problem is solved with the possibly recalculated (reachable) set points and constraints. The high limit differential pressure has the highest priority, followed by impurity limits and then impurity set points. This priority hierarchy may leads to a relaxation of the impurity set points (and in worst case the limits) to avoid exceeding the differential pressure high limit. By using relaxation, the column can handle the given feed rate without flooding the column, but note that the exceeding the limits may result in an unsellable product. In the dynamic optimization part, constraints are handled by adding penalty terms to the objective function.

The local MPC applications are based on experimental step response models. The prediction horizon is 3 to 6 hours and the sample time is 1 minute.

3. ESTIMATE OF REMAINING CAPACITY

In this section, the procedure used by the local MPCs for estimating the remaining capacity in each unit (R_k) is explained.

The remaining capacity for unit k is the difference between the current feed F^l_k and the feasible maximum feed $F^l_{k,max}$

$$R_k = F^l_{k,max} - F^l_k \tag{1}$$

The feed to the local unit F^l_k is assumed to be a DV in the local MPC application. The maximum feed to the unit k is then easily obtained by solving an additional steady-state LP-problem subject to the present initial state, linear model equations and constraints used in the local MPC. $F^l_{k,max}$ is calculated using the end predictions (steady-state model) for the variables. This to include both past MV moves, disturbances and future MV moves for the local MPC. This indirectly assumes that the closed-loop response time for the local MPC is faster than for the coordinator. Note that $F^l_{k,max}$ can change due to updated measurements, disturbances (e.g. feed compositions changes), changes in the constraints and model changes in the local MPCs. The current feed to the unit (F^l_k) is measured, either by a flow transmitter or by a level controller output (valve opening) if a flow transmitter is not available.

The accuracy of the estimated remaining capacity depends on:

- The validity of the models used in the local application. The algorithm uses the end prediction and therefore the steady-state gain is in particular important.
- The appropriate use of gain scheduling for CV-MV pairs with larger nonlinearities. Here "gain scheduling" means that the model gain is updated (scaled) based on the current operation point.
- The CV constraints must reflect the true operational limits and the MV constraints must be reasonable.

Let us explain the first two points in more detail. An incorrect steady-state gain leads to a poor estimate of the remaining capacity and because the coordinator MPC has slow dynamics, it will take a long time before the feedback can correct for the error. A too high remaining capacity estimate lead to a oscillating behavior because of the long delays in the flow network. Another issue is that the operators will not trust the remaining capacity estimates if the estimates are far away compared to their own experience.

The remaining capacity estimate uses the CV constraints and not the CV set points. For a distillation column this implies that the distillate and bottoms quality constraints are used instead of the CV set points because set point deviations are acceptable if the alternative is feed reduction. This leads to an estimated capacity that is often larger than expected by the operators.

For units with several feeds, the LP optimization will maximize the feed with the smallest steady-state gain (smallest predicted effect on capacity), whereas the other feeds will go to zero. However, some feeds cannot be set to zero, because they are outlet from an upstream unit with no possibility for routing it elsewhere. In this case, the LP optimization is set to maximize the feed from the flow line the unit must process and the other feeds are held constant in the optimization.

Compressors are also included in the application, but at present there are no MPC applications implemented on these. To estimate the remaining capacity of the compressors one option could be to consider the percent load (given by the speed). However, it may not always be possible to reach 100% load due to other constraints, for instance the turbine exhaust gas temperature. To consider several constraints, we therefore use MPC applications with no control tasks, but with only CVs and DVs and the models between them to estimate the remaining capacity. A copressor stage consists of several copressors, but local control handles the distribution between parallel compressors (equal distance to the compressor control line), therefore is only one remaining capacity needed at each compressor stage.

At present, the estimates are based on experimental models. However, rigorous models for local units can also be used to predict the remaining capacity. This is attractive for units where experimental modelling is difficult, for example, due to nonlinearities. This illustrates the flexibility with this decomposition where the best available model can be used to predict the remaining capacity.

4. COORDINATOR MPC

4.1 Objective, variables and constraints

The Kårstø plant is shown in Fig. 2 where most of the CVs, MVs and DVs for the coordinator MPC are indicated. The coordinator MPC maximizes sum of the total plant feed which is the sum of the feeds to train 100 (T100), train 200 (T200), train 300 (T300), train 400 (T400) and the dew point control unit (DPCU). The application consists of:

- 6 MVs: 4 feed rates, 1 crossover, 1 feed split.
- 22 CVs: Remaining capacity of 12 distillation columns and 2 compressors stages, 7 other constraints plus the main objective: total plant feed with a high, unreachable set point with lower priority.
- 7 DVs: 3 feed rates, 2 feed compositions, 1 crossover, 1 feed split.

The "other" 7 CV constraints are related to the use of MVs, that is, levels constraints to avoid filling or emptying of buffer tanks and sump volumes, pressure constraints in the pipelines and pressure controller outputs. The CV "total plant feed" is the sum of the plant feeds and is given by

$$\begin{aligned}\text{TOTALFEED} = {} & 20\text{FC1001A} + 20\text{FC2001A} + 27\text{FC3108} \\ & + 27\text{FC3208} + 21\text{FC4125A} + 21\text{FC4225A} + 21\text{FC5219}\end{aligned} \tag{2}$$

where the variables are marked in Fig. 2. In general, the feeds could have different weighting, but at present, their weights are equal. Of the 22 CVs, only the total plant feed is set point controlled; the other CVs are constraints.

The MVs (throughput manipulators) are the feed rates, a crossover between parallel trains (from T100 to T300) and a feed split to T300. Other throughput manipulators that affect the CVs in the sub-application are included as DVs. Later, if the coordinator MPC is extended to the whole plant, most of these DVs will become MVs. The feed compositions (DVs) reflects the gas/liquid split, and determine the split between gas flow to the compressors and liquid flow to the fractionation and are estimated from flow- and temperature measurements.

The objective function in the SEPTIC MPC algorithm is quadratic, while the objective function for the the maximum throughput problem is linear. To obtain a quadratic objective function that fits directly into our quadratic MPC algorithm, we have used the common trick of introducing a quadratic set point deviation term with a high and unreachable set point with a lower priority than the capacity constraints. (Of course, the actual case function used by the coordinator MPC has additional terms and weights). The first step of the coordinator MPC solution will then result in a recalculated (reachable) set point for the total feed.

Each variable (CV, MV and DV) belongs to one or more sub-groups that will be deactivated if one critical variable in the sub-group is deactivated. For instance, if a local MPC application is turned off, the corresponding remaining capacity CV is deactivated, and this critical variable suspends the whole sub-group. By using this condition-based logic, the coordinator MPC can operate

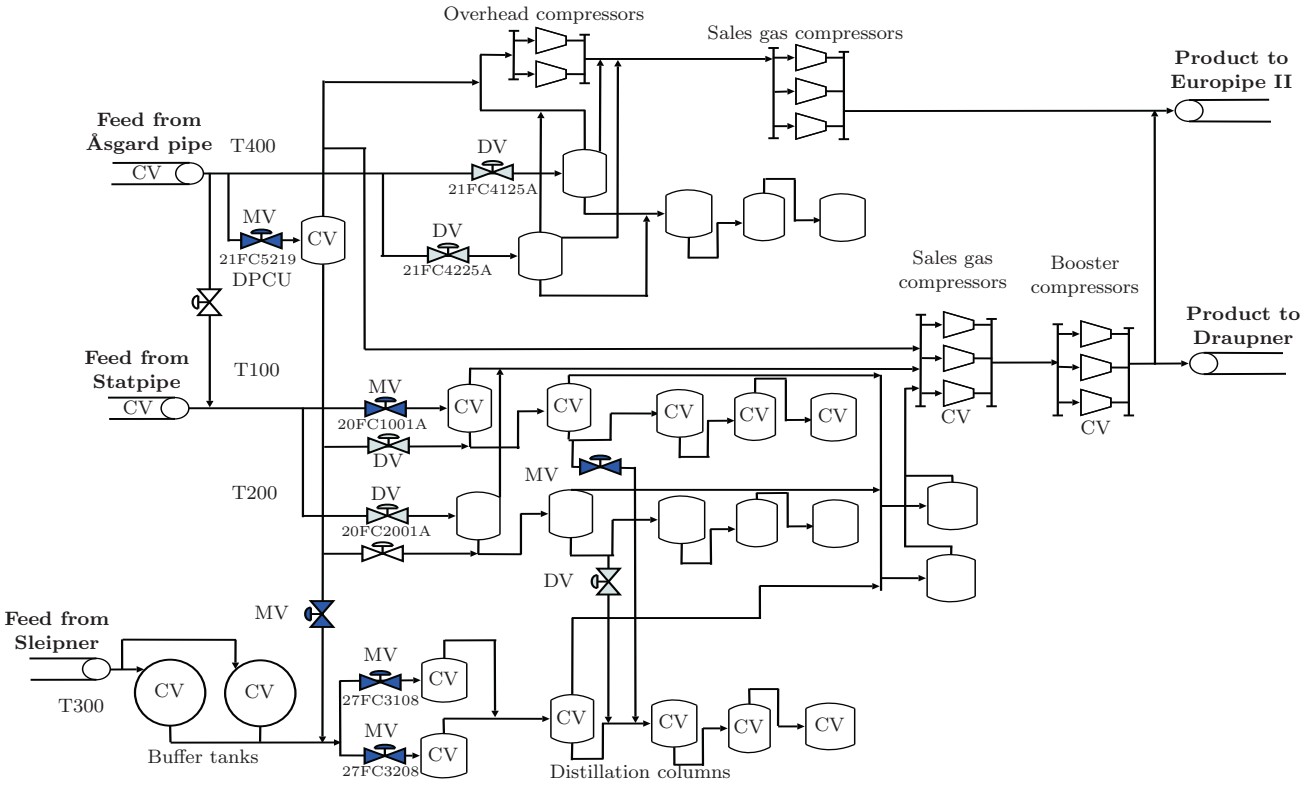

Fig. 2. Overview of the Kårstø plant, including the coordinator MPC variables.

even if parts of the plant are not running or not available for throughput maximization.

The decomposition requires that the coordinator receives three variables from each of the 12 local MPC applications:

- Estimated remaining capacity (value)
- Quality of the remaining capacity value (good/bad)
- Status of the local MPC (on/off)

If the estimated remaining capacity has a bad value, that is, the LP formulation is not feasible, then the status of the remaining capacity CV is set to ERROR and the corresponding MVs, given by the sub-grouping in the coordinator, are then suspended. If a local MPC application is deactivated, then the unit remaining capacity CV is set to OFF in the coordinator and the sub-group in the coordinator is suspended. The coordinator still runs, but the MVs in the sub-group are deactivated. This is done because we require that the local MPC application is active before the coordinator can manipulate on the corresponding unit feed rate.

4.2 Dynamic modelling for the coordinator MPC

The model for the coordinator MPC is a linear dynamic model for the flows through the plant network with the local MPC applications in service. The current implementation of the coordinator uses individual (SISO) step response models, or more precisely a single-input multiple-output representation of a multi-input multi-output system. The advantage with SISO models is that it is easy to adjust the models independently for input-output pairs. However, SISO models imply that the structure of the model is lost and, for instance, disturbances may not propagate as they would in a state-space model. The loss of structure leads to some additional variables around the DPCU.

The models are obtained from step tests and historical plant data. The steady-state gains found from step-tests are verified by calculating the gains using typical feed compositions.

The sampling time for the coordinator MPC is 3 minutes. The prediction and control horizon are set to 6 hours, whereas the longest response models reach steady state at approximately 4.5 hours.

4.3 Tuning the coordinator MPC

The tuning of the coordinator MPC is a trade-off between robustness and MV (e.g. feed) variations on one side and keeping the flows through the bottlenecks close to their maximum on the other side. The coordinator MPC was gradually operating in closed-loop and tuned in several tests in February 2008.

MV tuning From the early tests, it became clear that the trick of using a CV of total plant feed with a high, unreachable set point to maximize throughput, requires ideal values on the MV plant feeds to obtain satisfactory dynamic performance. The ideal values that are added to the MV plant feeds are high and unreachable with a lower priority than the total plant feed set point and have a low penalty on the deviation from the ideal value. The ideal

values are needed to avoid that *all* MVs that constitute the CV total plant feed (see (2)) are reduced dynamically to reach the new recalculated set point for CV total plant feed.

When ideal values (IV) for the MVs are introduced, the rate of change towards the ideal value is specified to obtain ramping rate independent of the penalty on the deviation from ideal value (Strand and Sagli, 2003). The ideal ramping rate is typical set to 500-750 kg/h. Maximum increase and decrease of the MV at each sample is chosen based on typically rate changes operators choose to implement.

CV tuning The most important tuning variables for the CVs are the penalties on constraint violation used in the dynamic step of the MPC algorithm. The constraint violation is "balanced" by using penalties on MV moves to obtain a satisfactory dynamic behavior when CV constraints are violated. Even though a CV constraint is violated, the use of MVs should not be too aggressive to avoid unnecessary throughput variations. Importantly, the CV constraints are not absolute because back off is included to handle disturbances and imperfect control. Specifically, the lower value of the remaining capacities is not set to zero, but rather to a positive back off value, $R_k^l > \text{back off}_k > 0$. The value of the back off is a tuning parameter decided by disturbance handling and model accuracy.

The coordinator MPC has four integrating CVs; two buffer volumes (levels) and two pipelines pressures. For an integrator, the horizon length is a tuning parameter. A shorter horizon length will give a larger slope and allow for larger feed rate changes. The integrating variables have a prediction horizon of 3 hours, which is half the prediction length to the other variables. The prediction horizon is shortened because it is likely that disturbances occur within the 6-hour period that counteracts the change in the integrated variable.

5. EXPERIENCE FROM IMPLEMENTATION

Some experiences from the implementation at the Kårstø site are summarized in this Section.

5.1 Estimate of remaining capacity

For distillation columns that frequently operate close to their capacity limit, the estimated capacity is generally good. For these units we have more experience in the actual operation range, and the models in the local MPC applications are typically obtained in this range. For some columns, the differential pressure is included in the remaining capacity calculation and this improves the estimate.

For control, the initial response for the models is most crucial to obtain good performance. For remaining capacity estimate, the steady-state model gain is most important. A systematic evaluation of the inferential models (estimators of product quality) and models in the local MPC applications is necessary to obtain satisfactory performance of the coordinator MPC. Since some of the local MPC applications were commissioned several years ago, a validation of the models was found necessary.

One observation is that when a large disturbance occurs, the predicted steady-state values may violate their limits and, if this violation is sufficiently large, the LP optimization does not find a feasible solution and the estimate of maximum capacity ($F_{k,max}^l$) fails. The end prediction values are in such cases often not reasonable because the MPC application assumes that the disturbances will maintain constant (possible reduced with a low-pass filter) throughout the prediction horizon, which is rarely the case.

To improve the estimation of remaining capacity, several approaches are used:

- With a known, measured, short-time disturbance: The maximum capacity ($F_{k,max}^l$) is held constant during the period of the disturbance. For example, this is used for the disturbances that occur at each dryer exchange.
- For each unit, a minimum value of the maximum capacity ($F_{k,max}^l$) is included.
- CV constraints included in the local MPCs that should not limit the throughput were replaced with wider constraints. This applies to "non-physical" constraint that may have been added in the MPC for tuning reasons.
- Gain scheduling is included for some differential pressure models.

The main structural weakness in the estimation of remaining capacity is that the LP solver may "give up" to find a solution because there is no possibility for relaxation of constraints. When the LP solver does not find a solution, it returns a "bad quality" value to the coordinator and its variable subgroup is turned off. It would be preferable that the coordinator finds the best possible solution instead of "giving up". This can be realized with a LP solver that includes relaxation of the constraints. This improvement of the LP algorithm is planned to be included in the future.

5.2 Experience with the coordinator MPC

A test run of the coordinator MPC from 07 Feb. 2008 is displayed in Fig. 3. The coordinator is turned on at $t = 18$ min and the coordinator starts to increase the feed to T100 (Fig. 3(a)) until the pipeline pressure in Statpipe reaches its low constraint (Fig. 3(b)). During this start-up period, the crossover flow ramps towards its ideal value (Fig. 3(c)). The remaining capacity in the butane splitter T100 reaches its low constraint (Fig. 3(d)) and the crossover increases again to avoid reduction in the throughput. However, the use of the crossover is "aggressive" and actually generates oscillations in the downstream remaining capacities. The model gain was almost doubled around $t = 250$ minutes and the crossover is now able to control the remaining capacity towards its low constraint. The adjustment of the model gain was based on comparing the model prediction (not shown) and actual value.

The accuracy of the estimate of remaining capacity for demethanizer T100 (Fig. 3(e)) was poor. The model gain from column feed to differential pressure was increased at $t = 320$ minutes, and the new value seems to give a more

correct estimate of the remaining capacity for the column. Again, the adjustment of the model gain was based on comparing model prediction and the actual value. Note that the remaining capacity of the demethanizer T100 became close to zero at about $t = 330$ min and the lower constraint value (back off) was increased at $t = 500$ min to obtain larger operation margins.

Feed composition changes are important disturbances and affect the remaining capacity to the units. The feed composition in the Statpipe (T100) (Fig. 3(f)) is rather stable until $t = 580$ min when the feed becomes significantly heavier and thereafter (at $t = 610$ min) significantly lighter. In this case, the coordinator uses the crossover (Fig. 3(c)) and the T100 feed rate (Fig. 3(a)) to control the remaining capacity for the butane splitter T100 (Fig. 3(d)) at its constraint.

When in closed loop, the coordinator MPC manipulates directly on the plant production. This directly involves the shift manager at Kårstø and close cooperation with the manager at the gas pipeline network (operated by another company) is necessary. The plant is operated by three control panels, so a close dialog between the operator personnel and the shift manager is crucial. The coordinator MPC introduces a "new way of thinking" for both operators and shift managers. The coordinator introduces the back off constraint as a new handle in addition to pressure pipeline constraints, instead of the feed valves.

ACKNOWLEDGEMENTS

The implementation was performed together with Kjetil Meyer, Roar Sørensen, shift managers and operating personnel at the Statpipe and Sleipner panels. All are gratefully acknowledged. The plant operator Gassco and technical services provider StatoilHydro are acknowledged for plant data.

REFERENCES

Aske, E. (2009). *Design of plantwide control systems with focus on maximum throughput*. Ph.D. thesis, NTNU, Trondheim, Norway. Available at the homepage of S. Skogestad.

Aske, E., Strand, S., and Skogestad, S. (2008). Coordinator MPC for maximizing plant throughput. *Comput. Chem. Eng.*, 32(1-2), 195–204.

Engell, S. (2007). Feedback control for optimal process operation. *J. Proc. Control*, 17, 203–219.

Marlin, T.E. and Hrymak, A.N. (1997). Real-time operations optimization of continuous processes. In J. Kantor, C. Garcia, and B. Carnahan (eds.), *CPC-5*, 156–164. Lake Tahoe, Nevada.

Strand, S. (1991). *Dynamic Optimization in State-Space Predictive Control Schemes*. Ph.D. thesis, Norwegian Institute of Technology, Trondheim, Norway.

Strand, S. and Sagli, J. (2003). MPC in Statoil - Advantages with in-house technology. *ADCHEM, Hong Kong, 2004*, 97–103.

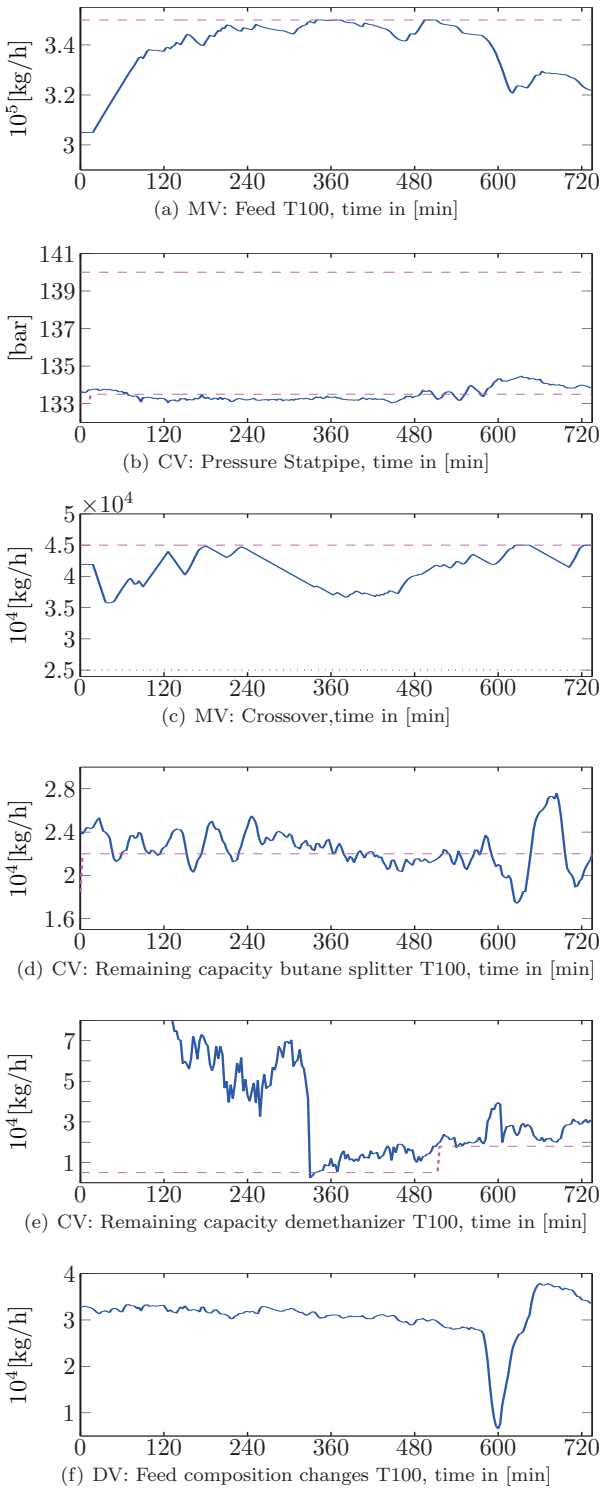

Fig. 3. From test run 07 Feb. 2008: $t = 18$ min: turn on, $t = 250$ min: change in model gain for crossover, $t = 320$ min: change in model grain for feed to differential pressure in the demethanizer, $t = 580$ and $t = 610$ min: feed composition change. MV and CV values (solid), high and low limits (dashed) and ideal values (dotted).

Coordination of Distributed Model Predictive Controllers for Constrained Dynamic Processes ⋆

Natalia I. Marcos *, **J. Fraser Forbes** * and **Martin Guay** **

* *Department of Chemical and Materials Engineering, University of Alberta, Edmonton, Alberta, Canada T6G 2V4*
** *Department of Chemical Engineering, Queen's University, Kingston, Ontario, Canada K7L 3N6*

Abstract: In this paper, a coordinated-distributed model predictive control (MPC) scheme is presented for large-scale discrete-time linear process systems. Coordinated-distributed MPC control aims at enhancing the performance of fully decentralized MPC controllers by achieving the plant-wide optimal operations. The 'price-driven' decomposition-coordination method is used to adjust the operations of the individual processing units in order to satisfy an overall plant performance objective. Newton's method, together with a sensitivity analysis technique, are used to efficiently update the price in the price-driven decomposition-coordination method. The efficiency of the proposed control scheme is evaluated using a model of a fluid catalytic cracking process.

Keywords: Decomposition-coordination methods; Large-scale optimization; Optimal control theory.

1. INTRODUCTION

Since the late seventies, the design of chemical processes has evolved towards integrated operations that have increased plant's efficiency. The improvement in the design of chemical processes included, among other things, energy and mass integration, and the use of recycle streams. As a result, processes became more complex and processing units became more tightly interconnected. Control of such integrated large-scale processes has been typically performed with *decentralized* schemes because of the difficulties in implementation and maintenance of *centralized* control frameworks.

Centralized and decentralized control are two distinct control strategies. In centralized control, no real distinction is made among processing units. The centralized control framework is formulated as a monolithic control problem that incorporates all process variables with no unit-level decomposition. While a centralized strategy can lead to optimal plant-wide performance, it presents some disadvantages (e.g., the large-dimensionality of the control problem and lack of flexibility in terms of operation and maintenance), which make centralized control unsuitable for industrial processes. In decentralized control, each engineering unit is optimized separately by neglecting the interactions with the other units. The decentralized approach is the most commonly used in the industry because of its robustness and its resiliency to systems failures. Nevertheless, decentralized control does not generally lead to the desired plant-wide optimal operations (Lu (2003); Sun and El-Farra (2008)).

⋆ This work is supported by Natural Sciences and Engineering Research Council of Canada (NSERC) and Alberta Ingenuity.

A compromise between centralized and decentralized control is desired in order to improve plant operations. *Distributed* control has emerged as a promising control strategy that can lead to the plant-wide optimal operations, while keeping manageable controllers for each subunit in the plant. In the distributed control framework, it is assumed that each subsystem computes its own optimal solution while considering all or certain degree of interactions with the other subsystems. To attain the desired control performance, information related to each subsystems' optimal solutions is generally exchanged among the subsystems. In this work, we present a coordinated-distributed model predictive control (CDMPC) framework for constrained dynamic processes. In CDMPC control, data is exchanged with each individual MPC controller via a 'coordinator' or 'master'.

1.1 Distributed MPC Control

Distributed MPC control has attracted the attention of many researchers in recent years. Dunbar and Murray (2004) formulated MPC platforms for nonlinear interacting subsystems (multi-vehicle formations) whose state variables are coupled in a single objective function. For linear interconnected systems, Venkat et al. (2005) proposed a communication-based MPC that can converge to a Nash equilibrium. The communication-based MPC was further improved by a cooperation-based MPC that leads to the Pareto optimal feasible solution. Cheng et al. (2008, 2007) proposed a coordinated scheme for MPC steady state target calculation based on Dantzig-Wolfe decomposition and price-driven coordination methods, respectively.

The main contribution of this work is to propose the *price-driven* decomposition-coordination algorithm, as described in Cheng et al. (2007), for the control of constrained process systems whose dynamics are represented by discrete-time models. The CDMPC control scheme presented in this paper achieves the centralized optimal operations and can be implemented when step-response models are available for the process. Since our control formulation uses models obtained from step-test data, it does not need estimation of unavailable process variables (as it might be required when formulating MPC controllers based on state-space models). Furthermore, the proposed CDMPC control scheme allows for bias correction in the predicted outputs through feedback.

An illustration of CDMPC is shown in Fig. 1. The price-driven decomposition-coordination method is used in the formulation of the CDMPC controllers. In the price-driven decomposition-coordination method, the coordinator sets up a price, 'p', for the subsystems' interacting variables (Fig. 1). The price provided by the coordinator is then

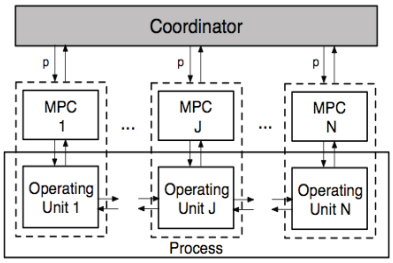

Fig. 1. Illustration of CDMPC Control

adjusted to alter the subunits' calculated control actions towards the overall plant optimum. In this work, the price, p, is updated based on Newton's method. An iterative procedure is established between the coordinator and the subunits until the desired plant-wide optimal solution is achieved.

2. CDMPC CONTROL FOR DYNAMIC PROCESS SYSTEMS

In this section, the CDMPC control scheme is presented. Since we consider the centralized performance as the ideal benchmark, we begin the CDMPC control formulation by decomposing the centralized control problem into N smaller subproblems that are easier to solve. Then, an efficient mechanism is used to achieve the same solution as the one obtained in the centralized control problem.

2.1 Process Model

Consider the overall plant process, modelled by step-response coefficients:

$$\begin{aligned} y_z(k+l) = & \sum_{h=1}^{T-1} \sum_{w=1}^{r} S_{zw,h} \Delta u_w(k+l-h) + \\ & \sum_{w=1}^{r} S_{zw,T}\ u_w(k+l-T), \\ & \forall z = 1, \ldots, m, \end{aligned} \tag{1}$$

where y_z $(\forall z = 1, ..., m) \in \Re^m$ denote the process outputs; $u_w \in \Re^r$ and $\Delta u_w \in \Re^r$ $(\forall w = 1, ..., r)$ denote the manipulated variables and the change in the manipulated variables, respectively. The coefficients $S_{11,h}, ..., S_{mr,h}$ represent the step-response coefficients for h^{th} time step. The step-response weight $S_{11,h}$ is the coefficient between Δu_1 and output y_1 for the h^{th} time step. In a similar manner, $S_{mr,h}$ is the coefficient between Δu_r and output y_m for the h^{th} time step.

2.2 Centralized MPC Formulation

For the centralized MPC implementation, it is convenient to arrange process model (1) in a matrix form as following:

$$\hat{Y}(k+1) = \mathcal{S}\Delta\hat{U}(k) + Y^0(k+1) + \hat{D}(k+1), \tag{2}$$

where the output variables, input variables and change in input variables predicted along the prediction horizon H_p and control horizon H_u are defined as:

$$\begin{cases} \hat{Y}(k+1) = [\hat{y}(k+1|k)^\top, ..., \hat{y}(k+H_p|k)^\top]^\top, \\ \hat{y}(.) = [\hat{y}_1(.), ..., \hat{y}_m(.)]^\top, \\ \Delta\hat{U}(k) = [\Delta\hat{u}(k|k)^\top, ..., \Delta\hat{u}(k+H_u-1|k)^\top]^\top, \\ \Delta\hat{u}(.) = [\Delta\hat{u}_1(.), ..., \Delta\hat{u}_r(.)]^\top, \hat{u}(.) = [\hat{u}_1(.), ..., \hat{u}_r(.)]^\top. \end{cases} \tag{3}$$

The $m \times H_p$ vector of unforced responses $Y^0(k+1)$ is:

$$\begin{cases} Y^0(k+1) = [y^0(k+1)^\top, ..., y^0(k+H_p)^\top]^\top, \\ y^0(.) = [y_1^0(.), ..., y_m^0(.)]^\top. \end{cases} \tag{4}$$

The vector $\hat{D}(k+1)$ has been incorporated in (2) to correct through feedback the discrepancies between the measured and predicted outputs. The vector $\hat{D}(k+1)$ is defined as:

$$\hat{D}(k+1) = \underbrace{[I_m, ..., I_m]^\top}_{H_p\ times}[y(k) - \hat{y}(k|k-1)],$$

where I_m is the $m \times m$ identity matrix. It is assumed that the difference between the measured and predicted outputs at time k remains constant throughout the prediction horizon.
In (2), the matrix of step-response coefficients $\mathcal{S}$ is defined as:

$$\mathcal{S} = \begin{bmatrix} S_1 & 0 & \cdots & 0 \\ S_2 & S_1 & 0 & 0 \\ \vdots & \vdots & \ddots & 0 \\ S_{H_u} & S_{H_u-1} & \cdots & S_1 \\ \vdots & \vdots & \ddots & \vdots \\ S_{H_p} & S_{H_p-1} & \cdots & S_{H_p-H_u+1} \end{bmatrix}, \tag{5}$$

where S_h is the $m \times r$ matrix of step-response coefficients for the h^{th} time step $(\forall h = 1, ..., H_p)$:

$$S_h = \begin{bmatrix} S_{11,h} & S_{12,h} & \cdots & S_{1r,h} \\ \vdots & \cdots & \cdots & \vdots \\ S_{m1,h} & \cdots & \cdots & S_{mr,h} \end{bmatrix}. \tag{6}$$

The centralized MPC controller is formulated to minimized the following objective function:

$$\min_{\hat{Y},\Delta\hat{U}} \quad \mathcal{J} = \frac{1}{2}\Big((Y_{sp} - \hat{Y}(k+1))^\top Q(Y_{sp} - \hat{Y}(k+1)) + \Delta\hat{U}(k)^\top R\Delta\hat{U}(k)\Big) \tag{7}$$

subject to:

$$\begin{cases} \text{Process model (2)-(6), and} \\ \hat{u}(k+l|k) = \sum_{h=0}^{l} \Delta\hat{u}(k+h|k) + u(k-1), \\ \Delta\hat{u}(k+h|k) = 0, \qquad H_u \le h \le H_p - 1, \\ y_{min} \le \hat{y}(k+l+1|k) \le y_{max}, \\ u_{min} \le \hat{u}(k+l|k) \le u_{max}, \\ \Delta u_{min} \le \Delta\hat{u}(k+n|k) \le \Delta u_{max}, \\ \forall l = 0,\ldots,H_p-1, \quad \text{and} \quad \forall n = 0,\ldots,H_u-1, \end{cases} \tag{8}$$

where Y_{sp} is the vector of desired set-points, $Q = diag\{Q(l+1)\}$ and $R = diag\{R(n)\}$ are positive definite matrices of appropriate dimensions.

2.3 Decomposition of Centralized MPC Formulation

We propose a decomposition of the overall optimization problem (7)-(8) into N subproblems 'i'. We consider that the plant dynamics and constraints can be decomposed into N subunits, followed by a block decomposition of the tuning matrices Q and R. As a result of the centralized problem decomposition, each subunit i ($\forall i : 1,\ldots,N$) solves its own optimization problem given by:

$$\min_{\hat{Y}_i,\Delta\hat{U}_i,\hat{V}_i} \mathcal{J}_i = \frac{1}{2}\Big((Y_{i\_sp} - \hat{Y}_i(k+1))^\top Q_{ii}(Y_{i\_sp} - \hat{Y}_i(k+1)) + \Delta\hat{U}_i(k)^\top R_{ii}\Delta\hat{U}_i(k)\Big) + p^\top\Theta_i Z_i(k) \tag{9}$$

subject to:

$$\hat{Y}_i(k+1) = \mathcal{S}_{ii}\Delta\hat{U}_i(k) + \hat{V}_i(k) + Y_i^0(k+1) + \hat{D}_i(k+1), \tag{10}$$

$$\hat{V}_i(k) = \mathcal{S}_{ij}\Delta\hat{U}_j(k), \quad \forall j \ne i, \tag{11}$$

and

$$\begin{cases} \hat{u}_i^s(k+l|k) = \sum_{n=0}^{l} \Delta\hat{u}_i^s(k+h|k) + u_i^s(k-1), \\ \Delta\hat{u}_i^s(k+h|k) = 0, \qquad H_u \le h \le H_p - 1, \\ y_{i\_min}^s \le \hat{y}_i^s(k+l+1|k) \le y_{i\_max}^s, \\ u_{i\_min}^s \le \hat{u}_i^s(k+l|k) \le u_{i\_max}^s, \\ \Delta u_{i\_min}^s \le \Delta\hat{u}_i^s(k+n|k) \le \Delta u_{i\_max}^s, \\ \forall l = 0,\ldots,H_p-1, \quad \text{and} \quad \forall n = 0,\ldots,H_u-1. \end{cases} \tag{12}$$

The vector $\hat{y}_i^s$ is a subset of the plant predicted outputs ($\hat{y}_i^s \subset [\hat{y}_1,...,\hat{y}_m]$) and represents the predicted output variables of subsystem i, $\forall i = 1,...,N$. Similarly, the vector $\hat{u}_i^s$ is a subset of the plant predicted inputs ($\hat{u}_i^s \subset [\hat{u}_1,...,\hat{u}_r]$) and represents the predicted input variables of subsystem i, $\forall i = 1,...,N$. According to the proposed decomposition, the predicted change in input variables and predicted outputs can be arranged in vector form as $\Delta\hat{U}_i(k) = [\Delta\hat{u}_i^s(k|k)^\top,...,\Delta\hat{u}_i^s(k+H_u-1|k)^\top]^\top$ and $\hat{Y}_i(k+1) = [\hat{y}_i^s(k+1|k)^\top,...,\hat{y}_i^s(k+H_p|k)^\top]^\top$, respectively.

In (10) and (11), the matrix $\mathcal{S}_{ii}$ corresponds to the step-response coefficient matrix between $\Delta\hat{U}_i(k)$ and predicted output variables $\hat{Y}_i(k+1)$; while the matrix $\mathcal{S}_{ij}$ corresponds to the step-response coefficient matrix between the interacting variables $\Delta\hat{U}_j(k)$ and predicted output variables $\hat{Y}_i(k+1)$. The matrices $\mathcal{S}_{ii}$ and $\mathcal{S}_{ij}$ can be obtained by decomposing matrices (5) and (6) into N subsystems.

Finally, the variables $\hat{V}_i(k)$ represent the interacting or linking variables among the different subunits in the plant. The interacting variables account for the effect that inputs from unit j have on unit i, with $i \ne j$. In the objective function (9), $Z_i(k) = [\hat{Y}_i(k+1)^\top, \Delta\hat{U}_i(k)^\top, \hat{V}_i(k)^\top]^\top$ represents the vector of decision variables for subunit i; the matrix Θ_i is the coefficient matrix for the linking variables, which is constructed according to (10) and (11), and p is a price vector provided by the coordinator.

For simplicity, we re-write problem (9)-(12) as:

$$\min_{Z_i} \quad \mathcal{J}_i = \frac{1}{2}\Big(Z_i(k)^\top\Upsilon_i Z_i(k)\Big) + \Phi_i^\top Z_i(k) + p^\top\Theta_i Z_i(k) \tag{13}$$

subject to:

$$\begin{cases} B_i^{eq} Z_i(k) = b_i^{eq}, \\ B_i^{ineq} Z_i(k) \le b_i^{ineq} \qquad \forall i = 1,...,N. \end{cases} \tag{14}$$

The optimization problem (13)-(14) can be straightforwardly obtained by arranging (9)-(12) in a matrix form for the entire prediction and control horizons. The optimization problem described by (13)-(14) forms part of the price-driven decomposition coordination method. The price-driven decomposition-coordination method was discussed in Jose and Ungar (2000, 1998) to solve algebraic optimization problems such as resource allocation or auction problems. This method was successfully adapted and implemented in Cheng et al. (2007) to solve the MPC steady-state target calculation problem. In this work, we use the price-driven method to solve MPC dynamic calculation problems.

2.4 Coordination of CDMPC Controllers

In the previous section, a decomposition of the overall problem into N smaller subproblems was presented. A key step in the formulation of CDMPC controllers is to design an efficient coordination mechanism that ensures convergence of the distributed optimal solutions to the centralized optimum. In this section, we extend the results obtained in Cheng et al. (2007) for the MPC steady-state target calculation to the MPC dynamic calculation.

As discussed in Jose and Ungar (2000), a large-scale problem:

$$\max_{z_1,\ldots,z_n} \quad \sum_i^n f_i(z_i)$$

$$\text{s.t.} \quad \sum_i^n R_i(z_i) \le \bar{R}, \qquad z_i \in \Omega_i,$$

with $z_i \in \Re^{n_i}$ decision variables, R_i vector of shared resources, and vector $\bar{R}$ representing the availability of shared resources, can be decomposed into N subproblems:

$$\max_{z_i \in \Omega_i} f_i(z_i) - (p + qR_i(z_i))^\top R_i(z_i). \quad (15)$$

In (15), 'p' represents the price vector, and the variable q is a nonnegative scalar that could be assumed to be zero for quadratic programming problems. In this work, we assume $q = 0$.

It was shown in Jose and Ungar (2000) that, when the subproblems present concave objective functions and compact convex feasible sets, they can be successfully coordinated. Moreover, at equilibrium, the following condition is satisfied:

$$\Delta R(p,q) = \sum_i R_i(p,q) - \bar{R} \leq 0,$$

with $p^\top(\Delta R(p,q)) = 0$, and $p \geq 0$.

Coordination of subproblem (13)-(14) for $i : 1, ..., N$ to achieve the plant-wide optimal solution can be performed by using an efficient price-update technique, such as Newton's method. Based on Newton's method, the price vector can be updated as follows (Cheng et al. (2007)):

$$p^{[\kappa+1]} = p^{[\kappa]} - \alpha J^{-1} \Delta R^{[\kappa]}, \quad (16)$$

provided that the matrix J is invertible. In the price update mechanism (16), the superscripts '$[\kappa]$' and '$[\kappa+1]$' denote the iteration steps; α is the step size in Newton's method, $\Delta R^{[\kappa]} = \Delta R(p,q)$, and J can be calculated as:

$$J = \frac{d\Delta R^{[\kappa]}}{dp^{[\kappa]}} = \sum_i \frac{dR_i^{[\kappa]}}{dp^{[\kappa]}}. \quad (17)$$

For the problem formulation described by (13)-(14), the shared resources or linking constraints are defined as $R_i^{[\kappa]} = \Theta_i Z_i^{[\kappa]}$, with $Z_i^{[\kappa]}$ representing the decision variables at each iteration step 'κ'. Therefore, the Jacobian matrix J in (17) becomes:

$$J = \sum_i \frac{dR_i^{[\kappa]}}{dp^{[\kappa]}} = \sum_i \Theta_i \frac{dZ_i^{[\kappa]}}{dp^{[\kappa]}}. \quad (18)$$

The Jacobian matrix (18) requires information of the sensitivity matrix $dZ_i^{[\kappa]}/dp^{[\kappa]}$; that is, in order to efficiently adjust the price vector, the coordinator should be aware of how the price affects the decision variables $Z_i^{[\kappa]}$ at each iteration. A sensitivity analysis was proposed in Wolbert et al. (1994) for an algebraic optimization of a process flowsheet, and it was extended in Cheng et al. (2007) for the MPC steady-state target calculation. This approach can be followed to solve problem (18). By performing a sensitivity analysis, the matrix $dZ_i^{[\kappa]}/dp^{[\kappa]}$ can be calculated. This requires solving the following system of equations:

$$\Gamma_i \begin{bmatrix} \nabla_p Z_i(k) \\ \nabla_p \lambda_i \\ \nabla_{pA} \mu_i \\ \nabla_{pI} \sigma_i \end{bmatrix} = - \begin{bmatrix} \Theta_i^\top \\ 0 \\ 0 \\ 0 \end{bmatrix}, \quad (19)$$

where

$$\Gamma_i = \begin{bmatrix} \Upsilon_i & B_i^{eq\top} & {}_A B_i^{ineq\top} & 0 \\ B_i^{eq} & 0 & 0 & 0 \\ {}_A B_i^{ineq} & 0 & 0 & 0 \\ {}_I B_i^{ineq} & 0 & 0 & I \end{bmatrix}, \quad (20)$$

assuming that Γ_i is full-rank. We refer the reader to Cheng et al. (2007) for a detailed derivation of equations (19) and (20).

2.5 Implementation of CDMPC Control Scheme

In the traditional MPC implementation, a control action sequence is determined at each sampling interval by optimizing an objective criterion over a finite-time horizon. Only the first control signal is applied to the process, while the rest of the calculated control inputs are discarded (Camacho and Bordons (1999); Maciejowski (2002)). At the next sampling interval, new process measurements are available and the optimization is repeated to calculate a new control action sequence.

In a CDMPC control platform, the coordinator imposes an extra step to the traditional MPC implementation. Before the control input is applied to the process, the control action calculated by each distributed MPC controller needs to converge to the optimal centralized control action. Convergence of the CDMPC solutions to the centralized performance can be achieved by allowing the coordinator to iteratively adjust the price vector, and therefore the optimal solution of each subsystem, according to the plant-wide objective.

Implementation of the CDMPC controllers is carried out according to the following steps:

(1) **Initialization:** The coordinator sets up an initial price vector $p^{[\kappa]}$ for the interacting variables ($\Theta_i Z_i$, $\forall i = 1, ..., N$) and sends that information to every subsystem.
(2) **Optimization performed by each subsystem:** Based on the price provided by the coordinator, each subsystem solves its own optimization problem (13)-(14) and calculates the resources $R_i^{[\kappa]} = \Theta_i Z_i^{[\kappa]}$; as well as $dZ_i^{[\kappa]}/dp^{[\kappa]}$, according to (19)-(20). This information is communicated back to the coordinator.
(3) **Price update:** The coordinator gathers the information from each subsystem; it calculates $\Delta R^{[\kappa]}$, and J given by (18). Then, the coordinator determines the step size α (with $0 < \alpha \leq 1$) and updates the price vector $p^{[\kappa]}$ as per (16). The new price vector is informed to each subsystem.
(4) **Iteration until convergence:** Steps (2)-(3) are repeated until convergence of the price-driven decomposition coordination algorithm. Convergence of the algorithm is achieved when $||\Delta R^{[\kappa]}|| \leq \epsilon$, where ϵ is a tolerance error.
(5) **Implementation of control action:** Once the decomposition-coordination algorithm converges, the control actions calculated for the first sampling interval are implemented in each subsystem and the optimization problem (steps (1)-(4)) is initiated again for the next receding horizon.

3. SIMULATION EXAMPLE

In this section, a case study is performed to illustrate the effectiveness of the proposed algorithm. We consider a fluid

catalytic cracking (FCC) process given in Grosdidier et al. (1993). A diagram of the FCC system is shown in Fig. 2.

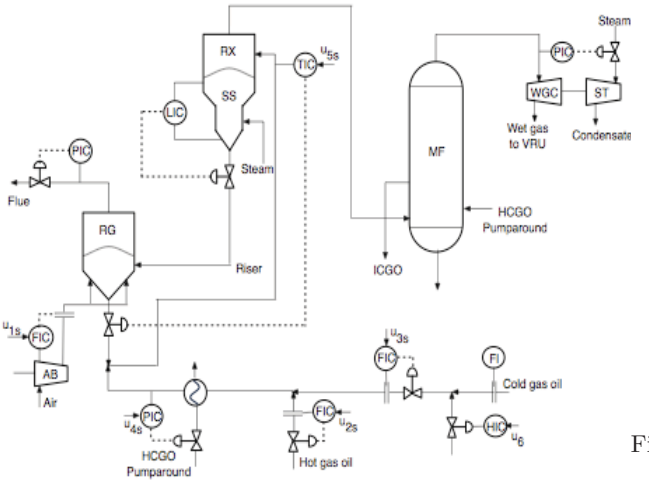

Fig. 2. FCC process (Grosdidier et al. (1993))

In the FCC unit, gas oil is converted into hydrocarbons of shorter chains. A description of the FCC process, together with the limit values for the controlled and manipulated variables are given in Grosdidier et al. (1993). The model of the FCC process, as well as, the models of the regulatory controllers are shown in tables 1 and 2, respectively. The continuous-time transfer function models were obtained through identification analysis of step-test data and include seven outputs and six inputs. The transfer function matrix for the overall process, including the models for the regulatory controllers, can be obtained by multiplying each transfer function model in table 1 by the corresponding input model in table 2, except for transfer functions between $y5-u5$ and $y6-u5$, which do not require that multiplication (Grosdidier et al. (1993)). To implement the CDMPC controllers, step-response models were obtained based on the process dynamics given in tables 1 and 2. The sampling interval used for simulations was 1 $[min]$.

3.1 Simulation Results

We begin by decomposing the centralized problem into two subsystems. The first subsystem includes outputs y_1 to y_3 and inputs u_1 to u_3, while the second subsystem includes outputs y_4 to y_7 and inputs u_4 to u_6. The following parameters were used in the simulation study: weighting matrices $Q(l+1) = diag\{5;10;0.001;5;5;5;0.001\}$, $R(n) = diag\{100;100;100;100;100;100\}$, for $l = 0,...,H_p-1$ and $n = 0,...,H_u-1$. The weighting matrices $Q(.)$ and $R(.)$ are decomposed as $Q_{11}(.) = diag\{5;10;0.001\}$ and $R_{11}(.) = diag\{100;100;100\}$ for the first subsystem, and $Q_{22}(.) = diag\{5;5;5;0.001\}$ and $R_{22}(.) = diag\{100;100;100\}$ for the second subsystem. The prediction horizon H_p and the control horizon H_u considered for the simulation are 50 and 5, respectively.

A set-point change of 0.5 was performed in output y_1 at initial time, while the targets for the remaining outputs were kept at the origin. The results of the simulation are

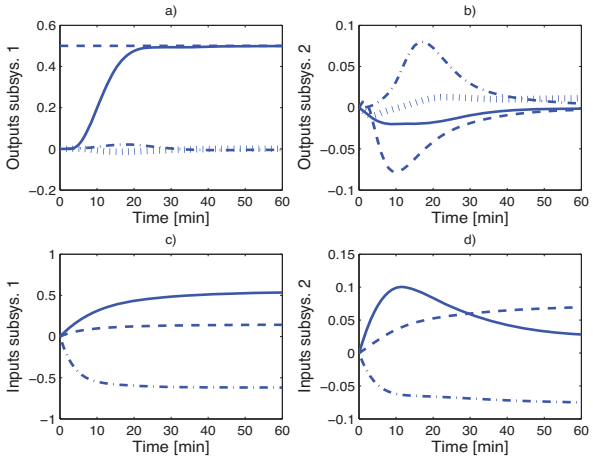

Fig. 3. a) Output variables for subsystem 1: set-point for y_1 (dashed line), y_1 (solid line), y_2 (dotted line), y_3 (dash-dot line); b) Output variables for subsystem 2: y_4(dash-dot line), y_5 (dashed line), y_6 (solid line), y_7 (dotted line); c) Input variables for subsystem 1:u_1 (dashed line), u_2 (dashed-dot line), u_3 (solid line); d) Input variables for subsystem 2: u_4 (dashed-dot line), u_5 (solid line), u_6 (dashed line)

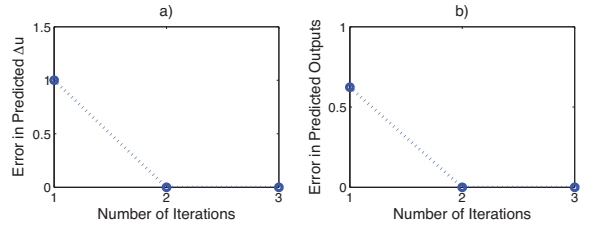

Fig. 4. a) Error in predicted change in input variables $\Delta\hat{U}(k)$; b) Error in predicted output variables $\hat{Y}(k+1)$

presented in Fig. (3)-(4). The closed-loop performance of the CDMPC controllers for subsystems 1 and 2 is shown in Fig. 3, where the trajectories are plotted in deviation variables. It can be seen in Fig. (3a)-(3d) that the CDMPC controllers provide a good performance since output y_1 achieves the new set-point and outputs y_2 to y_7 are stabilized at their new steady-state optimal values. Fig. (4a)-(4b) show the normalized errors of the predicted inputs ($||\Delta\hat{U}_{CDMPC} - \Delta\hat{U}_{cen}||/||\Delta\hat{U}_{cen}||$) and predicted outputs ($||\Delta\hat{Y}_{CDMPC} - \Delta\hat{Y}_{cen}||/||\Delta\hat{Y}_{cen}||$) for the optimization performed at the first sampling time. These prediction errors are calculated as the difference between the CDMPC optimal solutions and the optimal solutions calculated with a centralized MPC controller. It can be observed in Fig. (4a)-(4b) that the solutions achieved with the CDMPC controllers converge to the centralized performance within 2 iterations. The fast convergence observed in this simulation study confirms the results reported in Cheng et al. (2007) when using Newton's method as price-adjustment algorithm for the MPC steady-state target calculation. In the numerical simulations performed for the FCC unit, the same fast solution convergence (2 iterations) was observed within each control execution.

Table 1. FCC process models

	u_1	u_2	u_3	u_4	u_5	u_6
y_1	$\frac{0.097(1.7s+1)e^{-2s}}{19s^2+6.5s+1}$	$\frac{-0.87e^{-2s}}{13s^2+4.9s+1}$	$\frac{-0.092(0.25s+1)e^{-3s}}{3.7s^2+4.7s+1}$	$\frac{0.026e^{-7s}}{12s+1}$	$\frac{-0.074(4.8s+1)}{9.3s^2+3.4s+1}$	$\frac{-(0.48s)e^{-12s}}{(6s+1)(8s+1)}$
y_2	0	$\frac{0.55e^{-4s}}{27s^2+8.7s+1}$	$\frac{0.55e^{-4s}}{10s^2+4.9s+1}$	0	$\frac{0.74(1.7s+1)e^{-2s}}{11s^2+7.3s+1}$	$\frac{0.36e^{-11s}}{33s^2+6.5s+1}$
y_3	0	$\frac{0.14e^{-11s}}{46s^2+8.5s+1}$	$\frac{0.14e^{-6s}}{46s^2+8.5s+1}$	0	$\frac{0.27(16s+1)}{53s^2+23s+1}$	$\frac{0.015(12s+1)e^{-9s}}{66s^2+27s+1}$
y_4	0	$\frac{0.25e^{-11s}}{17s^2+7s+1}$	$\frac{0.25e^{-7s}}{3s+1}$	0	$\frac{0.70}{3s+1}$	$\frac{0.079(6.3s+1)e^{-10s}}{24s^2+12s+1}$
y_5	0	$\frac{0.66e^{-s}}{2.5s+1}$	$\frac{0.66e^{-s}}{2.5s+1}$	$\frac{-0.9e^{-10s}}{6s+1}$	$\frac{1}{2s+1}$	$\frac{-0.54e^{-11s}}{9s+1}$
y_6	0	$\frac{-0.84e^{-s}}{6.1s+1}$	$\frac{-0.90}{1.5s+1}$	$\frac{0.35e^{-10s}}{5s+1}$	$\frac{-(0.64s+1)}{13s^2+7s+1}$	$\frac{0.23(0.5s+1)e^{-14s}}{3.6s^2+11s+1}$
y_7	0	$\frac{0.81}{6s+1}$	$\frac{0.90}{s+1}$	$\frac{-0.35e^{-10s}}{5s+1}$	0.80	$\frac{-0.26e^{-18s}}{7.1s+1}$

Table 2. Models between regulatory controller set-points us_i and process inputs u_i, for $i = 1, ..., 6$

(us_1, u_1)	(us_2, u_2)	(us_3, u_3)	(us_4, u_4)	(us_5, u_5)	(us_6, u_6)
$\frac{1}{(0.75s+1)(4.5s+1)}$	$\frac{1}{(s+1)}$	$\frac{1}{1.7s^2+2.1s+1}$	$\frac{(3.3s+1)e^{-s}}{40s^2+13s+1}$	$\frac{(0.64s+1)}{13s^2+7s+1}$	1

Remark: For the ease of presentation, we decomposed the overall FCC process into two subsystems of similar dimensions. Nevertheless, the CDMPC control scheme can be applied to N number of subsystems of different dimensions. As future work, we will evaluate the efficiency of the CDMPC control scheme on process systems that include more subunits and there is a significant mismatch in the size of the subunits.

4. CONCLUSION

In this paper, we presented a coordinated-distributed model predicted control scheme for constrained dynamic processes. The CDMPC control framework improves the performance of decentralized controllers by achieving the overall plant-wide optimal operations.

An important advantage of CDMPC controllers is the simplicity in the control scheme, which does not require a radical new configuration of the decentralized MPC controllers operating in the plant. The upgrade from the existing decentralized MPC controllers to CDMPC controllers only involves small modifications in the control formulation of each subsystem and the addition of a coordinator.

The price-driven decomposition-coordination algorithm was used to efficiently coordinate the dynamic behavior of the CDMPC controllers. Newton's method was selected to update the price vector during the coordination process. It was shown with a benchmark process system that Newton's method provides a rapid convergence of the unit operations towards the plant-wide optimal performance.

REFERENCES

Camacho, E.F. and Bordons, C. (1999). *Model Predictive Control*. Springer, Berlin.

Cheng, R., Forbes, J.F., and Yip, W.S. (2007). Price-driven coordination method for solving plant-wide mpc problems. *Journal of Process Control*, 17, 429–438.

Cheng, R., Forbes, J.F., and Yip, W.S. (2008). Dantzig-wolfe decomposition and plant-wide mpc coordination. *Computers and Chemical Engineering*, 32, 1507–1522.

Dunbar, W.B. and Murray, R.M. (2004). Receding horizon control of multi-vehicle formations: A distributed implementation. In *43rd IEEE Conference on Decision and Control*, 1995–2002.

Grosdidier, P., Mason, A., Aitolahti, A., Heinonen, P., and Vanhamaki, V. (1993). Fcc unit reactor-regenerator control. *Computers and Chemical Engineering*, 17(2), 165–179.

Jose, R.A. and Ungar, L.H. (1998). Auction-driven coordination for plantwide optimization. In *Proceedings of Foundations of Computer-Aided Process Operation (FOCAPO)*.

Jose, R.A. and Ungar, L.H. (2000). Pricing interprocess streams using slack auctions. *AIChE Journal*, 46(3), 575–587.

Lu, J.Z. (2003). Challenging control problems and emerging technologies in enterprise optimization. *Control Engineering Practice*, 11, 847–858.

Maciejowski, J.M. (2002). *Predictive Control with Constraints*. Prentice Hall, Essex, England.

Sun, Y. and El-Farra, N.H. (2008). Quasi-decentralized model-based networked control of process systems. *Computers and Chemical Engineering*, 32, 2016–2029.

Venkat, A.N., Rawlings, J.B., and Wright, S.J. (2005). Stability and optimality of distributed model predictive control. In *Proceedings of the 44th IEEE Conference on Decision and Control*, 6680–6685.

Wolbert, D., Joulia, X., Koehret, B., and Biegler, L.T. (1994). Flowsheet optimization and optimal sensitivity analysis using analytical derivatives. *Computers and Chemical Engineering*, 18(11/12), 1083–1095.

Integrating Control and Scheduling of Distributed Energy Resources Over Networks ⋆

Yulei Sun, Sathyendra Ghantasala and Nael H. El-Farra *

* *Department of Chemical Engineering & Materials Science, University of California, Davis, CA 95616 USA (e-mail: nhelfarra@ucdavis.edu)*

Abstract: This paper presents an integrated approach for the control and scheduling of Distributed Energy Resources (DERs) that are managed by a central supervisor over a resource-constrained communication network. The objective is to enhance the performance and disturbance-handling capabilities of the DERs while keeping the communication requirements with the supervisor to a minimum in order to reduce the susceptibility of the DERs to communication outages. To this end, the rate of data transfer from the DERs to the supervisor is initially minimized by embedding in the supervisor a set of models that are used to generate the necessary control action when measurements are not transmitted over the network, and then updating the models' states at discrete time instances. Only a subset of the DERs are allowed to transmit their data at any given time to provide updates to their target models according to a certain scheduling strategy. By formulating the networked closed-loop system as a hybrid system, an explicit characterization of the interdependence between the performance of the DERs, the communication rate, the transmission schedule and times, and the plant-models' mismatch is obtained. It is shown that by judicious selection of the transmission schedule and models, it is possible to optimize the performance of the DERs while simultaneously reducing network utilization beyond what is possible with concurrent transmission configurations. The results are demonstrated through an application to a collection of solid oxide fuel cells in a distributed power network.

Keywords: Networked control, model-based control, scheduling algorithms, distributed energy resources, solid oxide fuel cells.

1. INTRODUCTION

Distributed Energy Resources (DERs) are a suite of on-site, grid-connected or stand-alone technology systems that can be integrated into residential, commercial, or institutional buildings and/or industrial facilities. These energy systems include distributed generation, renewable energy sources, and hybrid generation technologies; energy storage; thermally activated technologies that use recoverable heat for cooling, heating, or power. Such distributed resources offer advantages over conventional grid electricity by offering end users a diversified fuel supply; higher power reliability, quality, and efficiency; lower emissions and greater flexibility to respond to changing energy needs. As the number and diversity of DERs on the grid increases, dispatching these resources at the right time and accounting for the flow of energy correctly become complex problems that require reliable monitoring and telemetering equipment, as well as reliable communication and control technologies to enable the integration and inter-operability functions of a broad range of DERs. Some estimates (Lovins et al (2002)) place the market potential for advanced control and communications technologies in DERs at $3.75-$7.5 billion domestically, and at $15-$30 billion worldwide .

While managing DERs over a communication network offers an appealing modern solution to the control of distributed energy generation, it poses a number of challenges that must be addressed before the full economic and environmental potential of DERs can be realized. These challenges stem in part from the inherent limitations on the information transmission and processing capabilities of communication networks, such as bandwidth limitations, network-induced delays, data losses, signal quantization and real-time scheduling constraints, which can interrupt the connection between the central control authority (the supervisor), the generation units and the loads, and consequently degrade the overall control quality if not properly accounted for in the control system design (see, for example, Zhang et al. (2001); Walsh et al. (2002); Hokayem and Abdallah (2004); Xu and Hespanha (2004); Munoz de la Pena and Christofides (2008) and the references therein for discussions and results on control over communication networks). Despite the availability of fast and reliable communication networks, the fact that the distributed power market is primarily driven by the need for super-reliable, high-quality power implies that the impact of even a brief communication disruption (e.g., due to local network congestion or server outage) can be substantial.

⋆ Financial support, in part by NSF, CBET-0747954, and by the UC Energy Institute is gratefully acknowledged.

In sites such as hospitals, police stations, data centers and high-tech plants which cannot afford blackouts, millisecond outages that merely cause lights to flicker will cause costly computer crashes. Such high-stake risks provide a strong incentive for the development of robust control and communication strategies that ensure the desired levels and quality of power supply from the DERs while minimizing their reliance on the communication medium, which in turn minimizes the impact of communication disruptions on power supply.

Over the past decade, several efforts have been made towards the development and implementation of control strategies for DERs (e.g., Wang (2001); Barsali et al. (2002); Ro and Rahman (2003); Marei et al. (2004); Lasseter (2007)). While the focus of these studies has been mainly on demonstrating the feasibility of the developed control algorithms, the explicit characterization and management of communication constraints in the formulation and solution of the DER control problem have not yet been addressed. An effort to address this problem was initiated in Sun et al. (2009) where a model-based networked control approach was developed for a DER that communicates with the central controller over a bandwidth-constrained communication network that is shared by several other DERs. The minimum allowable communication frequency was characterized for the case when all DER sensor suites communicate their measurements over the network concurrently and are given simultaneous access to the network. In addition to controlling the transmission frequencies of individual DERs in the network, another important way of reducing network utilization is to select and dispatch only a subset of the deployed DERs at any given time to communicate with the supervisor. Under this restriction, the stability and performance properties of each DER become dependent not only on the controller design but also on the selection of the scheduling strategy that determines the order and times in which the sensor suites of the DERs transmit their data to the supervisor.

Motivated by these considerations, we focus in this work on the problem of integrating control and scheduling of DERs over resource-constrained communication networks. The objective is to find an optimal strategy for establishing and terminating communication between the DERs and the central controller that minimizes the rate at which each DER must collect and disseminate data to the supervisor without jeopardizing the stability and performance properties of the DERs. The rest of the paper is organized as follows. Following some preliminaries in Section 2, the problem of DER scheduling over the network is formulated and an overview of its solution is presented. Section 3 then presents the networked control structure and describes its implementation under scheduling. The closed-loop system is then formulated and analyzed in Section 4 where a precise characterization of the interdependence between the networked closed-loop performance, the communication rate between the DERs and the supervisor, the scheduling strategy, as well as the accuracy of the models and the choice of the control laws, is provided. This characterization is shown to allow a systematic search for the sensor transmission schedules that enhance the overall performance while simultaneously reducing the unnecessary utilization of the communication medium. The implementation of the networked control and scheduling strategy are demonstrated in Section 5 through an application to a network of solid oxide fuel cell (SOFC) plants managed by a supervisor over a communication network.

2. PRELIMINARIES

2.1 Structure of distributed generation units

We consider an array of n DERs managed by a higher-level supervisor over a shared bandwidth-limited communication network. Each DER is modeled by a continuous–time system with the following state–space description:

$$\begin{aligned} \dot{x}_i(t) &= A_i x_i + B_{i_1} w_i + B_{i_2} u_i \\ z_i(t) &= C_i x_i + D_i u_i, \quad i = 1, \cdots, n \end{aligned} \tag{1}$$

where $x_i \in \mathbb{R}^{n_i}$ denotes the vector of state variables associated with the i–th DER (e.g., exhaust temperatures and rotation speed in turbines and internal combustion engines, operating temperature and pressures in fuel cells), $u_i \in \mathbb{R}^{m_i}$ denotes the vector of manipulated inputs associated with the i–th DER (e.g., inlet fuel flow rate in fuel cells, shaft speed in turbines), $w_i \in \mathbb{R}^{q_i}$ denotes the vector of disturbance inputs, $z_i \in \mathbb{R}^{p_i}$ is the vector of DER performance output signals of interest (e.g., power, voltage and frequency), and A_i, B_{i_1}, B_{i_2}, C_i, and D_i are constant matrices. Each DER has local (on-board) sensors and actuators with some limited built-in intelligence that gives the DER the ability to run autonomously for periods of time when no communication exists with the remote software controller (the supervisor). The local sensors in each DER transmit their data over a shared communication network to the supervisor where the necessary control calculations are carried out and the control commands are sent back to each DER over the communication network. Based on load changes, changes in utility grid power prices and the state and capacity of each DER, the supervisor regulates and coordinates local power generation in the DERs.

2.2 Problem formulation and methodological framework

One of the main problems to be addressed when managing a large number of DERs over a communication network is the large amount of bandwidth required by the different subsystems sharing the communication medium. A tradeoff typically exists between the control performance and the extent of network utilization. On the one hand, optimal control of each DER to deliver the required power quality in the presence of process variations and disturbances is best achieved when information (e.g., measurements, control commands) are exchanged continuously between each DER and the supervisor. Minimal network utilization necessary to save on communication costs, on the other hand, favors only limited communication. Proper characterization and management of this tradeoff is an essential first step to the design of resource-aware networked control systems that ensure the desired performance while respecting inherent constraints on the resources of the communication medium. To address this problem, we will focus in this work on minimizing the sensor-controller communication costs under the assumption that the actuators and supervisor are collocated (i.e., the network exists between the sensors and the controller; generalizations to account for actuator-controller communication constraints are possible and the subject of other research work). To this end, we will consider the following approach:

- Initially design for each DER an appropriate feedback control law that regulates its output (in the absence of communication constraints) at the desired set-point decided by the supervisor.
- Reduce the collection and transfer of information from each DER to the supervisor as much as possible to limit the bandwidth required from the network without sacrificing the desired stability and performance properties by using models of the DERs in the supervisor to calculate the control action when measurements are not available.
- Limit the number of DERs that, at any time, transmit their data to update the corresponding target models.
- Find a scheduling strategy for establishing and terminating communications between the DERs and the supervisor that optimizes a certain performance metric for the closed-loop system while simultaneously keeping the communication rate to a minimum.

3. NETWORKED CONTROLLER DESIGN AND SCHEDULING

3.1 Model-based networked control of DERs

In order to reduce network usage, we embed a dynamic model of each DER in the supervisor to provide it with an estimate of the evolution of the states of the DER when measurements are not available. The use of a model at the controller/actuator side to recreate the dynamics of each DER allows the on-board sensors to transmit their data at discrete time instances and not continuously (since the model can provide an approximation of the DER dynamics) thus allowing conservation of network resources. The computational load associated with this step (e.g., model forecasting and control calculations) is justified and supported by the increasing capabilities of modern computing systems used by the central control authority. Feedback from the DER is then performed by updating the state of the model state using the actual state that is provided by its sensors at discrete time instances. The model-based controller is implemented as follows:

$$\begin{aligned} u_i(t) &= K_i\widehat{x}_i(t),\ t \neq t_k^i \\ \dot{\widehat{x}}_i(t) &= \widehat{A}_i\widehat{x}_i(t) + \widehat{B}_{i_2}u_i(t),\ t \in [t_k^i, t_{k+1}^i) \\ \widehat{x}_i(t_k^i) &= x_i(t_k^i),\ \ k = 0, 1, 2, \cdots \end{aligned} \tag{2}$$

where $\widehat{x}_i$ is an estimate of x_i, $\widehat{A}_i$ and $\widehat{B}_{i_2}$ are estimates of A_i and B_{i_2}, respectively, which do not necessarily match the actual dynamics of the i–th DER, (i.e., in general $\widehat{A}_i \neq A_i$, $\widehat{B}_{i_2} \neq B_{i_2}$). The notation t_k^i is used to indicate the k-th transmission time for the sensor suite of the i-th DER in the collection. The model state is used by the controller as long as no measurements are transmitted, but is updated (or re-set) using the true measurement whenever it becomes available from the network.

3.2 Scheduling DER transmissions over the network

A key parameter in the analysis of the control and update laws in Eq.2 is the update period for each DER, $h^i := t_{k+1}^i - t_k^i$, which determines the frequency at which the sensor suite of the i-th DER collects and sends measurements to the supervisor through the network to update the corresponding model state. To simplify the analysis, we consider in what follows the case when the update period is constant and the same for all DERs, so that $t_{k+1}^i - t_k^i := h,\ i = 1, 2, \cdots, n$. The update period is also an important measure of the extent of network utilization, with a larger h indicating a larger reduction in network utilization. Because of the bandwidth limitations on the communication network and in order to further reduce network utilization, we perform sensor scheduling whereby only one DER is allowed to transmit its measurements to the supervisor at any one time, while the other DERs remain dormant for some time before the next DER is allowed to transmit its data (the results can also be generalized to configurations where multiple DERs transmit at the same time). The transmission schedule is defined by: (a) the sequence (or order) of transmitting suites of DERs: $\{s_i,\ i = 1, 2, \cdots, n\},\ s_i \in \mathcal{N} := \{1, 2, \cdots, n\}$,where s_i is a discrete variable that denotes the i-th transmitting entity in the sequence, and (b) the time at which each DER in the sequence collects and transmits measurements. To characterize the transmission times, we introduce the variable: $\Delta t_i := t_k^{s_{i+1}} - t_k^{s_i},\ i = 1, 2, \cdots, n-1$, which is the time interval between the transmissions of two consecutive DERs in the sequence.

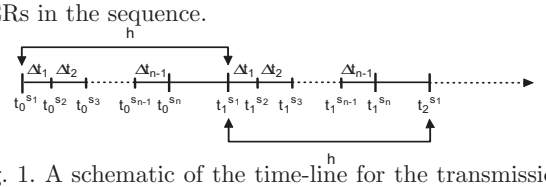

Fig. 1. A schematic of the time-line for the transmissions of DERs in an h-periodic schedule.

Fig.1 is a schematic representation of how DER scheduling is performed. Note that the schedule is h-periodic in the sense that the same sequence of transmitting DERs is executed repeatedly every h seconds (equivalently, each DER transmits its data every h seconds). Note also from the definitions of both h and Δt_i that the transmission times always satisfy the constraint $\sum_{i=1}^{n-1} \Delta t_i < h$. Since the update periods for all DERs are the same, the intervals between the transmission times of two specific DERs are constant, and within any single execution of the schedule (which lasts less than h seconds), each DER can only transmit its measurements through the network and update its model in the supervisor once. This can be represented mathematically by the condition: $s_i \neq s_j$ when $i \neq j$. By manipulating the time intervals Δt_i (i.e., the transmission times) and the order in which the DERs transmit, one can systematically search for the optimal transmission schedule that leads to the largest update period (or the smallest communication rate between the sensor suite of each DER and the supervisor).

4. PERFORMANCE CHARACTERIZATION OF THE SCHEDULED CLOSED-LOOP SYSTEM

4.1 A hybrid system formulation

Defining the model estimation errors by $e_i = x_i - \widehat{x}_i$, where e_i represents the difference between the state of the i-th DER and the state of its model embedded in the supervisor, and introducing the augmented vectors: $\mathbf{e} := [e_1^T\ e_2^T\ \cdots\ e_n^T]^T,\ \mathbf{x} := [x_1^T\ x_2^T\ \cdots\ x_n^T]^T$, it can be shown that the overall networked closed-loop system of Eqs.1-2 can be formulated as a combined discrete–continuous (hybrid) system of the form:

$$\begin{aligned} \dot{\mathbf{x}}(t) &= \Lambda_{11}\mathbf{x}(t) + \Lambda_{12}\mathbf{e}(t) + \bar{B}_N w(t) \\ \dot{\mathbf{e}}(t) &= \Lambda_{21}\mathbf{x}(t) + \Lambda_{22}\mathbf{e}(t) + \bar{B}_N w(t),\ \ t \neq t_k^i \\ e_i(t_k^i) &= 0,\ \ i = 1, 2, \cdots, n,\ \ k = 0, 1, 2, \cdots, \end{aligned} \tag{3}$$

where $\bar{B}_N = [B_{1_1}^T\ B_{2_1}^T\ \cdots, B_{n_1}^T]^T$, and the DER states evolve continuously in time while the estimation errors are

reset to zero at each transmission instance. Note, however, that unlike the case of simultaneous DER transmissions (where no scheduling takes place) which was investigated in Sun et al. (2009), not all models within the supervisor are updated (and hence not all estimation errors are reset to zero) at each transmission time. Instead, only the model of the transmitting DER is updated using the measurements provided by its sensor suite.

Referring to Eq.3, Λ_{11}, Λ_{12}, Λ_{21}, and Λ_{22} are all $m \times m$ constant, block-diagonal matrices, where $m = \sum_{i=1}^{n} n_i$ and n_i is the dimension of the i-th state vector. These matrices are linear combinations of A_i, B_{i_2}, $\widehat{A}_i$, $\widehat{B}_{i_2}$, K_i, which are the matrices used to describe the dynamics, the models, and the control laws of the different DERs. The explicit forms of these matrices are given by: $\Lambda_{11} = \text{diag}\{A_i + B_{i_2}K_i\}$, $\Lambda_{12} = \text{diag}\{-B_{i_2}K_i\}$, $\Lambda_{21} = \text{diag}\{\widetilde{A}_i + \widetilde{B}_{i_2}K_i\}$, $\Lambda_{22} = \text{diag}\{\widehat{A}_i + \widetilde{B}_{i_2}K_i\}$, where $\widetilde{A}_i = A_i - \widehat{A}_i$, and $\widetilde{B}_{i_2} = B_{i_2} - \widehat{B}_{i_2}$. Defining the augmented state vector $\xi(t) := [\mathbf{x}^T(t)\ \mathbf{e}^T(t)]^T$, the dynamics of the overall closed-loop system can be written as:

$$\begin{aligned} \dot{\xi}(t) &= \Lambda\xi(t) + B_N w(t),\ t \neq t_k^i \\ e_i(t_k^i) &= 0,\ \ i = 1, 2, \cdots, n,\ \ k = 0, 1, 2, \cdots \\ \mathbf{z}(t) &= C_N\xi(t) \end{aligned} \tag{4}$$

where $\Lambda = \begin{bmatrix} \Lambda_{11} & \Lambda_{12} \\ \Lambda_{21} & \Lambda_{22} \end{bmatrix}$, $B_N = [\bar{B}_N^T\ \ \bar{B}_N^T]^T$, $C_N = [\text{diag}\{C_i + D_iK_i\}\ \ \text{diag}\{-D_iK_i\}]$, and $\mathbf{z} := [z_1^T\ z_2^T\ \cdots\ z_n^T]^T$ is the overall performance output of the DER collection.

4.2 Performance characterization using extended H_2-norm

Our objective in this section is to assess the performance of the networked scheduled closed-loop system subject to disturbances and explicitly characterize its dependence on the update period and the DER transmission schedule to determine an optimal schedule and update period that ensure minimal influence of the disturbances on the performance output of the closed-loop system. As a performance metric, we choose the extended H_2-norm introduced originally in Montestruque and Antsaklis (2006). This performance measure, which is an H_2-like norm that is suitable for analyzing periodic networked control systems, captures the 2-norm of the performance output response when the closed-loop system is initialized at the steady-state and an impulse disturbance is introduced in the input at $t = t_0$ (see Montestruque and Antsaklis (2006) for other types of performance measures that can be used). The following theorem explicitly characterizes the performance output response in terms of the control, communication and scheduling design parameters. The proof can be obtained by solving the system of Eq.4 within each subinterval of the time-line in Fig.1, and is omitted for brevity.

Theorem 1. Consider the system of Eq.4 with a transmission schedule $\{s_1, s_2, \cdots, s_n\}$ and the initial condition $\xi(t_0^{s_1}) = [\mathbf{0}\ \ \mathbf{e}^T(t_0^{s_1})]^T = \xi_0$, with $e_{s_1}(t_0^{s_1}) = 0$, subject to an impulse disturbance $w = \delta(t - t_0^{s_1})$. Then:

(a) For $t \in [t_k^{s_i},\ t_k^{s_{i+1}})$, $i = 1, 2, \cdots, n-1$, $k = 0, 1, 2, \cdots$, the performance output response is given by:

$$\mathbf{z}(t) = C_N e^{\Lambda(t - t_k^{s_i})}\Gamma_i(\Delta t_i, I_s^{s_i})M^k B_N \tag{5}$$

(b) For $t \in [t_k^{s_n},\ t_{k+1}^{s_1})$, $k = 0, 1, 2, \cdots$, the performance output response is given by:

$$\mathbf{z}(t) = C_N e^{\Lambda(t - t_k^{s_n})}\Gamma_n M^k B_N \tag{6}$$

where

$$M(h) = I_s^{s_1} e^{\Lambda(h - \sum_{i=1}^{n-1}\Delta t_i)}\Gamma_n \tag{7}$$

$$\Gamma_i = \left\{ \begin{array}{ll} \displaystyle\prod_{i-1-\mu=0}^{i-2} I_s^{s_{\mu+1}} e^{\Lambda\Delta t_\mu}, & \text{for } i \geq 2 \\ I, & \text{for } i = 1 \end{array} \right\} \tag{8}$$

$$I_s^{s_i} = \begin{bmatrix} I & O & \cdots & O \\ O & H_1 & \cdots & O \\ \vdots & \vdots & & \vdots \\ O & O & \cdots & H_n \end{bmatrix},\ H_i = \left\{ \begin{array}{ll} I, & i \neq s_i \\ O, & i = s_i \end{array} \right. \tag{9}$$

for $i = 1, 2, \cdots, n$, $t_{k+1}^{s_i} - t_k^{s_i} = h$ and $\Delta t_i = t_k^{s_{i+1}} - t_k^{s_i}$, for $i = 1, 2, \cdots, n-1$.

Remark 1: The expression in Eq.5 captures the response of the performance output during the time periods between the transmissions of two consecutive DERs in a given execution of the schedule, while the expression in Eq.6 provides the response for the time period between the transmission of the last DER in a given execution and the transmission of the first DER in the next execution. As expected the responses are parameterized by the transmission sequence (which determines the structure of the matrices $I_s^{s_i}$) as well as the transmission times (which are determined by Δt_i). Note from the term M^k (which captures the growth of the response due to the repeated execution of the transmission schedule) that a necessary and sufficient condition for the responses to be stable is to have all the eigenvalues of the matrix M strictly inside the unit circle (e.g., see Sun and El-Farra (2008) for further details on the characterization of closed-loop stability).

Based on the result of Theorem 1, the extended H_2-norm for the scheduled networked closed-loop system, $\| G \|_{H_2}$, can be calculated using the following defining relation:

$$\| G \|_{H_2} = \text{trace}(B_N^T X B_N)^{1/2} \tag{10}$$

where X is the solution to the discrete Lyapunov equation:

$$M^T(h, I_s^{s_i}, \Delta t_i)XM(h, I_s^{s_i}, \Delta t_i) - X + \sum_{i=1}^{n} W_i = 0, \tag{11}$$

W_i is a matrix computed as:

$$W_i = \int_0^{\Delta t_i} \Gamma_i^T e^{\Lambda^T t} C_N^T C_N e^{\Lambda t}\Gamma_i dt,\ \ i = 1, 2, \cdots, n \tag{12}$$

and $\Delta t_n := h - \sum_{i=1}^{n-1}\Delta t_i$.

Remark 2: The relations of Eqs.10-12 provide a generalization of the extended H_2-norm calculation to networked control systems with scheduled sensor transmissions. In the limit as $\Delta t_i \to 0$, for $i = 1, \cdots, n-1$, (i.e., simultaneous transmissions), these relations reduce to the ones developed originally in Montestruque and Antsaklis (2006) for non-scheduled networked control systems.

Remark 3: By examining Eqs.10-12, it can be seen that $\| G \|_{H_2}$ depends on the interplay between the plant-model mismatch for each DER, the controller gains, the update period, the time intervals between transmissions, as well as the transmission sequence, which altogether provide handles that can be tuned to optimize the performance of the networked closed-loop system subject to disturbances. For example, the extended H_2-norm can be used to

compare different schedules (by varying the transmission sequence and times) to determine which schedules achieve the best performance with the least communication rate between the DERs and the supervisor. Alternatively, if the schedule is fixed by the network access constraints, the performance index can be used to compare the performance levels achieved by using different models and different controllers. The performance criterion can therefore be used to formulate various kinds of optimization problems.

5. SIMULATION STUDY: A NETWORK OF SOLID OXIDE FUEL CELLS

As an illustrative example, we consider a network of three solid oxide fuel cell (SOFC) plants that communicate with the supervisor over a shared communication network . The plants have different dynamic characteristics due to the differences in sizes and capacities of the individual fuel cell stacks. The supervisor is responsible for maintaining the power output of each SOFC plant at a desired set-point by manipulating the inlet fuel flow rate in the presence of disturbances in the inlet air flow rate. Measurements from the sensor suite of each SOFC plant can be received by the supervisor only through the communication network, while the actuator suite of each plant is assumed to have un-interrupted access to the supervisor (ideal actuator-controller links). Under standard modeling assumptions, a dynamic model of the following form can be derived for each SOFC stack from material and energy balances (Mursheda et al. (2007)):

$$\begin{aligned}
\dot{p}_{H_2} &= \frac{T_s}{\tau^*_{H_2} T^* K_{H_2}}(q^{in}_{H_2} - K_{H_2} p_{H_2} - 2K_r I) \\
\dot{p}_{O_2} &= \frac{T_s}{\tau^*_{O_2} T^* K_{O_2}}(q^{in}_{O_2} - K_{O_2} p_{O_2} - K_r I) \\
\dot{p}_{H_2O} &= \frac{T_s}{\tau^*_{H_2O} T^* K_{H_2O}}(q^{in}_{H_2O} - K_{H_2O} p_{H_2O} + 2K_r I) \\
\dot{T}_s &= \frac{1}{m_s C_{ps}} \sum q^{in}_i \int_{T_{ref}}^{T_{in}} C_{p,i}(T) dT \\
&\quad - \sum q^{out}_i \int_{T_{ref}}^{T_{in}} C_{p,i}(T) dT - \dot{n}^r_{H_2} \triangle \hat{H}^o_r - V_s I
\end{aligned} \tag{13}$$

where, p_i is the partial pressure of component i (i: H_2, O_2, H_2O), T_s is the stack temperature, q^{in}_i is the inlet molar flow rate of component i, m_s and C_{ps} are the mass and average specific heat of fuel cell materials excluding gases, $C_{p,i}$ is the specific heat of gas component i, $\triangle \hat{H}^o_r$ is the specific heat of reaction, I is the load current, $\tau^*_i := V/K_i R T^*$ is a time constant for i-th component, K_i is the valve molar constant for component i, and $K_r = N_0/4F$, N_0 is the number of cells in the stack, F is Faraday's constant, V_s is the overall stack voltage:

$$V_s = N_0 \left[\triangle E_0 + \frac{RT_s}{2F} \ln \frac{p_{H_2} p^{(0.5)}_{O_2}}{p_{H_2O}} \right] - r_0 \exp\left[\alpha\left(\frac{1}{T_s} - \frac{1}{T_0}\right)\right] I \tag{14}$$

where r_0 is the internal resistance at T_0, α is the resistance slope (only ohmic losses are included, while activation and concentration losses are neglected), and $\triangle E_0$ is the standard cell potential. Linearizing the SOFC plants around the desired set-points yields a system of the form of Eq.1 with $n = 3$, where x_i, u_i, w_i and z_i are the dimensionless state, manipulated input (inlet fuel flow rate), disturbance (inlet air flow rate) and power output for the i-th plant, respectively. To regulate the power output of each fuel cell, a feedback controller of the form $u_i = K_i x_i$, is designed and implemented. The explicit forms of the plants and controller matrices are omitted due to space limitations.

5.1 Performance under scheduled sensor transmissions

In this section, we investigate the impact of varying the DER transmission schedule, the intervals between transmissions, and the plant-model mismatch on the total power output of the SOFC network which is chosen as the performance output. As mentioned in Section 3, we focus on scheduling configurations where at each transmission time, only the sensor suite of one SOFC plant is allowed to transmit its measurement updates to the supervisor. To quantify the mismatch between each plant and its model that is embedded in the supervisor, we consider as an example parametric uncertainty in Cp_{H_2} and define $\delta_1 = (Cp^m_{H_2} - Cp_{H_2})/Cp_{H_2}$, where $Cp^m_{H_2}$ is a nominal value used in the model, as a measure of model accuracy (any other set of uncertain parameters can also be considered and analyzed in a similar fashion). We initialize the closed-loop SOFC plants at the desired set-points and introduce a unit impulse disturbance in the inlet flow rate of air to each plant. The power outputs of the individual fuel cells are chosen as the performance outputs. Fig.2(a) shows the

Table 1. SOFC plant transmission schedules

Schedule	$s_1, s_2, s_3, s_1, s_2, s_3, \cdots$
1	$1, 2, 3, 1, 2, 3, \cdots$
2	$1, 3, 2, 1, 3, 2, \cdots$
3	$2, 1, 3, 2, 1, 3, \cdots$
4	$2, 3, 1, 2, 3, 1, \cdots$
5	$3, 1, 2, 3, 1, 2, \cdots$
6	$3, 2, 1, 3, 2, 1, \cdots$

dependence of the extended H_2-norm of the entire SOFC network on the update period, h, under the six possible sensor transmission schedules listed in Table 1 when imperfect models are embedded in the supervisor (each model with parametric uncertainty $\delta_1 = 5$) and the transmission times are fixed such that $\Delta t_1 = \Delta t_2 = h - \Delta t_1 - \Delta t_2$. It can be seen that among all possible schedules, schedule 4 provides the best performance since for any update period it yields the smallest $\| G \|_{H_2}$. Note also that this schedule yields an improved performance over the non-scheduled (i.e., concurrent) transmission configuration shown by the solid profile. Not only is the minimum extended H_2-norm smaller for the scheduled configuration, but the optimal update period is also larger, which implies that the rate at which each plant needs to collect and transmit measurements to the supervisor under the scheduled configuration is smaller, thus leading to bigger savings in the overall utilization of the communication network resources. The reason for the performance improvement can be understood in light of the fact that forcing the different SOFC plants to transmit their data and update their target models in the supervisor at different times (rather than simultaneously) creates opportunities for providing a more targeted correction to the estimation errors of the different models, where the models with the largest plant-model mismatch can receive more timely updates than would be feasible under simultaneous transmissions. This in turn helps reduce the rate at which each SOFC plant in the communication network must collect and transmit data.

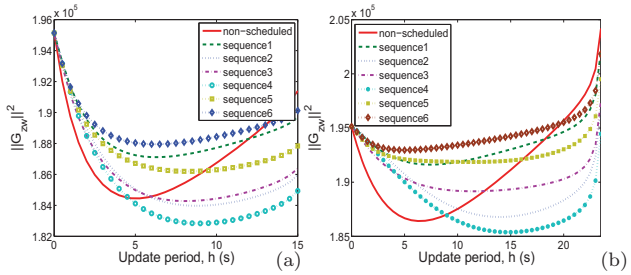

Fig. 2. Dependence of the norm of the power output vector for the SOFC network on the update period for different sensor transmission sequences under (a) a model-based scheme, and (b) a zero-order hold scheme.

Fig.2(b) shows how the extended H_2-norm of the overall SOFC network under each schedule varies as h is varied when a zero-order hold scheme is used. In this case, the supervisor holds the last measurement received from the individual SOFC plant until the next time a measurement is transmitted and received from the network (this corresponds to using models with $\widehat{A}_i = O$ and $\widehat{B}_{i_2} = O$). It can be seen that the optimal update period obtained under scheduling is also larger in this case than the one obtained under simultaneous transmissions.

5.2 Dependence of overall performance on model quality

In this part, we investigate the effect of model uncertainty on the overall SOFC network performance. Fig.3 depicts the dependence of $\| G \|_{H_2}$ of the entire SOFC network on both δ_1 and the update period when the sensors' transmission follows schedule 4. As expected, for a given overall performance level, the range of feasible update period shrinks as the plant-model mismatch increases. The predictions of Fig.3(a) are further confirmed by the closed–loop power output profile in Fig.3(b) which shows that under the same update period of $h = 9$ s and sensor transmission sequence 4, the networked closed-loop system performs better with a relatively accurate model ($\delta_1 = -2$) than the one with an inaccurate model ($\delta_1 = -10$).

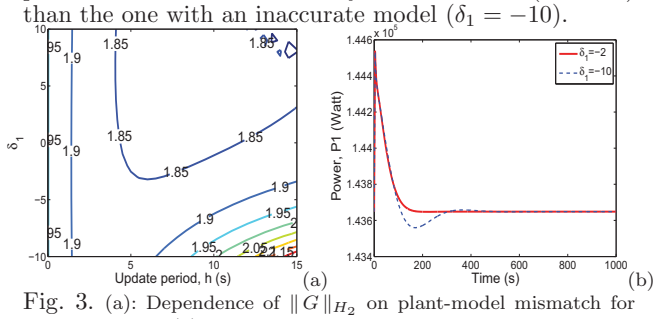

Fig. 3. (a): Dependence of $\| G \|_{H_2}$ on plant-model mismatch for various h. (b): First SOFC plant power output profile under the networked control system with different models.

5.3 Performance dependence on the transmission times

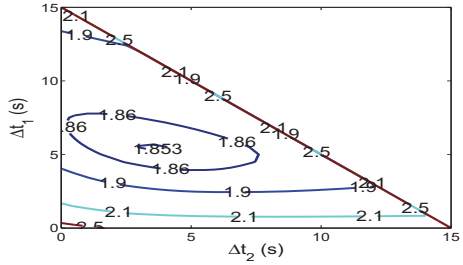

Fig. 4. Dependence of $\| G \|_{H_2}$ on Δt_1 and Δt_2 under schedule 4.

Fig.4 is a contour plot showing the dependence of $\| G \|_{H_2}$ on Δt_1 and Δt_2 for a fixed update period ($h = 15$ s) when the SOFC plants transmit according to schedule 4 and a zero-order hold model is considered. In comparison with the performance achieved in the case when $\Delta t_1 = \Delta t_2 = h - \Delta t_1 - \Delta t_2$ ($\| G \|_{H_2} = 1.854 \times 10^5$; see Fig.2(b)), it can be seen that an improved performance is attained ($\| G \|_{H_2} = 1.853 \times 10^5$) by varying the transmission times such that $\Delta t_1 = 5.5$ s and $\Delta t_2 = 3.5$ s.

REFERENCES

Barsali, S., Ceraolo, M., Pelacchi, P., and Poli, D. (2002). Control techniques of dispersed generators to improve the continuity of electricity supply. In *Proceedings of IEEE Power Eng. Soc. Win. Mtg.*, 789–794.

Hokayem, P. and Abdallah, C. (2004). Inherent issues in networked control systems: A survey. In *Proceedings of American Control Conference*, 329–336. Boston, MA.

Lasseter, R.H. (2007). Microgrids and distributed generation. *Journal of Energy Engineering*, 133, 144–149.

Lovins et al, A.B. (2002). *Small Is Profitable: The Hidden Economic Benefits of Making Electrical Sources the Right Size*. Rocky Mountain Institute.

Marei, M.I., El-Saadany, E.F., and Salama, M.M.A. (2004). A novel control algorithm for the DG interface to mitigate power quality problems. *IEEE Transactions on Power Delivery*, 19, 1384–1392.

Montestruque, L.A. and Antsaklis, P.J. (2006). Performance evaluation for model-based networked control systems. In *Netw. Emb. Sens. and Cntrl., LNCIS*, volume 331, 231–249. P.J. Antsaklis, P. Tabuada (Eds.), Springer-Verlag, Berlin.

Munoz de la Pena, D. and Christofides, P.D. (2008). Lyapunov-based model predictive control of nonlinear systems subject to data losses. *IEEE Trans. Automat. Contr.*, 53, 2067–2089.

Mursheda, A., Huang, B., and Nandakumara, K. (2007). Control relevant modeling of planer solid oxide fuel cell system. *Journal of Power Sources*, 163, 830–845.

Ro, K. and Rahman, S. (2003). Control of grid-connected fuel cell plants for enhancement of power system stability. *Renewable Energy*, 28, 397–407.

Sun, Y. and El-Farra, N.H. (2008). Quasi-decentralized model-based networked control of process systems. *Comp. & Chem. Eng.*, 32, 2016–2029.

Sun, Y., Ghantasala, S., and El-Farra, N.H. (2009). Networked control of distributed energy resources: Application to solid oxide fuel cells. In *Proceedings of American Control Conference,* to appear. St. Louis, MO.

Walsh, G., Ye, H., and Bushnell, L. (2002). Stability analysis of networked control systems. *IEEE Trans. Contr. Syst. Tech.*, 10, 438–446.

Wang, H.F. (2001). Multi-agent co-ordination for the secondary voltage control in power-system contingencies. *IEE Proceedings on Generation, Transmission and Distribution*, 148, 61–66.

Xu, Y. and Hespanha, J.P. (2004). Optimal communication logics for networked control systems. In *Proceedings of the 43rd IEEE Conference on Decision and Control*, 3527–3532. Atlantis, Paradise Island, Bahamas.

Zhang, W., Branicky, M.S., and Phillips, S.M. (2001). Stability of networked control systems. *IEEE Contr. Syst. Mag.*, 21, 84–99.

Distributed Model Predictive Control of Nonlinear Process Systems Subject to Asynchronous Measurements

Jinfeng Liu [*] **David Muñoz de la Peña** [**]
Panagiotis D. Christofides [*,***,1]

[*] *Department of Chemical and Biomolecular Engineering, University of California, Los Angeles, CA, 90095-1592, USA.*
[**] *Departamento de Ingeniería de Sistemas y Automática, Universidad de Sevilla, Camino de los Descubrimientos S/N, 41092, Sevilla, Spain.*
[***] *Department of Electrical Engineering, University of California, Los Angeles, CA, 90095-1592, USA.*

Abstract: In this work, we address distributed model predictive control of nonlinear process systems subject to asynchronous measurements. Assuming that there exists an upper bound on the interval between two successive measurements of the process state, two separate Lyapunov-based model predictive controllers that coordinate their actions and take asynchronous measurements explicitly into account are designed. The proposed distributed control design only requires one directional communication between the two distributed controllers and provides the potential of maintaining stability and performance in the face of new or failing actuators. The results are illustrated through a chemical process example.

Keywords: Distributed model predictive control; Nonlinear systems; Networked control systems; Process control; Asynchronous measurements.

1. INTRODUCTION

We are currently witnessing an augmentation of the existing, dedicated local control networks, with additional networked (wired and/or wireless) actuator/sensor devices which have become cheap and easy-to-install the last few years. Such an augmentation in sensor information and networked-based availability of data has the potential (Ydstie (2002); Neumann (2007); Christofides et al. (2007)) to be transformative in the sense of dramatically improving the ability of the control systems to optimize process performance and prevent or deal with abnormal situations more quickly and effectively. However, augmenting dedicated, local control systems (LCS) with control systems that may utilize real-time sensor and actuator networks gives rise to the need to design/redesign and coordinate separate control systems that operate on a process. Model predictive control (MPC) is a natural control framework to deal with the design of coordinated, distributed control systems because of its ability to handle input and state constraints, and also because it can account for the actions of other actuators in computing the control action of a given set of control actuators in real-time. Motivated by the lack of available methods for the design of networked control systems (NCS) for chemical processes, in a previous work (Liu et al. (2008)), we introduced a decentralized control architecture for systems with continuous and asynchronous measurements. In this architecture, the local, pre-existing control system uses continuous sensing and actuation and an explicit control law. On the other hand, the NCS uses networked (wired or wireless) sensors and actuators and has access to heterogeneous, asynchronous measurements that are not available to the LCS. The NCS is designed via Lyapunov-based model predictive control (LMPC). Following up on this work, in another recent work (Liu et al. (in press)), we proposed a distributed model predictive control method for the design of networked control systems where both the pre-existing local control system and the networked control system are designed via Lyapunov-based model predictive control.

With respect to available results on distributed MPC design, several distributed MPC methods have been proposed in the literature that deal with the coordination of separate MPC controllers that communicate in order to obtain optimal input trajectories in a distributed manner (Rawlings and Stewart (2007); Dunbar (2007); Richards and How (2007); Keviczky et al. (2006); Magni and Scattolini (2006); Raimondo et al. (2007)). All of the above results on distributed MPC design are based on the assumption of continuous sampling and perfect communication between the sensor and the controller. However, one may encounter asynchronous measurement samplings because of measurement difficulties in process control applications.

In this work, we address distributed model predictive control of nonlinear process systems subject to asynchronous measurements. Assuming that there exists an upper bound on the interval between two successive measurements of the process state, two separate Lyapunov-based model predictive controllers that coordinate their actions and

[1] Corresponding author: Panagiotis D. Christofides. Tel.:+1 310 825 2046; fax: +1 310 206 4107; e-mail: pdc@seas.ucla.edu.

take asynchronous measurements explicitly into account are designed. Sufficient conditions are derived for the proposed distributed control design to guarantee that the state of the closed-loop system is ultimately bounded in a region that contains the origin. In addition, the proposed distributed control design only requires one directional communication between the two distributed controllers and provides the potential of maintaining stability and performance in the face of new or failing actuators. The results are illustrated through a chemical process example.

2. PRELIMINARIES

2.1 Control problem formulation

We consider nonlinear process systems described by the following state-space model

$$\dot{x}(t) = f(x(t), u_1(t), u_2(t), w(t)) \tag{1}$$

where $x(t) \in R^{n_x}$ denotes the vector of process state variables, $u_1(t) \in R^{n_{u_1}}$ and $u_2(t) \in R^{n_{u_2}}$ are two separate sets of manipulated inputs and $w(t) \in R^{n_w}$ denotes the vector of disturbance variables. The two manipulated inputs are restricted to be in two nonempty convex sets $U_1 \subseteq R^{n_{u_1}}$ and $U_2 \subseteq R^{n_{u_2}}$ and the disturbance vector is bounded, i.e., $w(t) \in W$ where

$$W := \{w \in R^{n_w} \text{ s.t. } |w| \leq \theta, \theta > 0\}\,^{2}.$$

We assume that f is a locally Lipschitz vector function and $f(0,0,0,0) = 0$. This means that the origin is an equilibrium point for the nominal system (system (1) with $w(t) = 0$ for all t) with $u_1 = 0$ and $u_2 = 0$. System (1) is controlled with the two sets of manipulated inputs u_1 and u_2, which could be multiple inputs of a system or a single input divided artificially into two terms (e.g., $\dot{x}(t) = \hat{f}(x(t), u(t), w(t))$ with $u(t) = u_1(t) + u_2(t)$).

2.2 Lyapunov-based controller

We assume that there exists a Lyapunov-based controller $u_1(t) = h(x(t))$ which satisfies the input constraint on u_1 for all x inside a given stability region and renders the origin of the nominal closed-loop system asymptotically stable with $u_2(t) = 0$. Using converse Lyapunov theorems (Massera (1956); Lin et al. (1996)), this assumption implies that there exist functions $\alpha_i(\cdot)$, $i = 1, 2, 3, 4$ of class $\mathcal{K}$ [3] and a continuously differentiable Lyapunov function V for the nominal closed-loop system that satisfy the following inequalities

$$\begin{gathered} \alpha_1(|x|) \leq V(x) \leq \alpha_2(|x|) \\ \frac{\partial V(x)}{\partial x} f(x, h(x), 0, 0) \leq -\alpha_3(|x|) \\ |\frac{\partial V(x)}{\partial x}| \leq \alpha_4(|x|) \\ h(x) \in U_1 \end{gathered} \tag{2}$$

for all $x \in D \subseteq R^{n_x}$ where D is an open neighborhood of the origin. We denote the region Ω_ρ [4] $\subseteq D$ as the stability region of the closed-loop system under the control $u_1 = h(x)$ and $u_2 = 0$.

[2] $|\cdot|$ denotes Euclidean norm of a vector.

[3] A continuous function $\alpha : [0, a) \to [0, \infty)$ is said to belong to class $\mathcal{K}$ if it is strictly increasing and $\alpha(0) = 0$.

[4] We use Ω_r to denote the set $\Omega_r := \{x \in R^{n_x} | V(x) \leq r\}$.

By continuity and the local Lipschitz property assumed for the vector field $f(x, u_1, u_2, w)$ and the fact that the manipulated inputs u_1 and u_2 are bounded in convex sets, there exists a positive constant M such that

$$|f(x, u_1, u_2, w)| \leq M \tag{3}$$

for all $x \in \Omega_\rho$, $u_1 \in U_1$, $u_2 \in U_2$ and $w \in W$. In addition, by the continuous differentiable property of the Lyapunov function V and the Lipschitz property assumed for the vector field $f(x, u_1, u_2, w)$, there exist positive constants L_x, R_x, R_w such that

$$|\frac{\partial V}{\partial x} f(x, u_1, u_2, 0) - \frac{\partial V}{\partial x} f(x', u_1, u_2, 0)| \leq L_x |x - x'| \tag{4}$$

and

$$|f(x, u_1, u_2, w) - f(x', u_1, u_2, 0)| \leq R_x |x - x'| + R_w |w| \tag{5}$$

for all $x, x' \in \Omega_\rho$, $u_1 \in U_1$, $u_2 \in U_2$ and $w \in W$.

These constants will be used in section 4 in the proof of the main results of the present work.

2.3 Modeling of asynchronous measurements

Most control systems assume that measurements from sensors are obtained in a continuous periodic pattern. However, in many chemical processes, this assumption does not hold due to a host of measurement difficulties. In this case, the system is subject to asynchronous measurements. In the present work, we assume the state of system (1), $x(t)$, is sampled and available asynchronously at time instants t_k where $\{t_{k\geq 0}\}$ is a random increasing sequence of times. The distribution of $\{t_{k\geq 0}\}$ characterizes the time needed to obtain a new measurement in the case of asynchronous measurements. In general, there exists the possibility of arbitrarily large (but finite) periods of time in which a new measurement is not available. In such a case, it is not possible to provide guaranteed stability properties, because there exists a non-zero probability that the system operates in open loop for a period of time large enough for the state to leave the stability region. In order to study the stability properties in a deterministic framework, in the present work, we assume that there exists an upper bound T_m on the interval between two successive measurements, i.e., $\max_k\{t_{k+1} - t_k\} \leq T_m$. This assumption is reasonable from a process control perspective.

3. DISTRIBUTED LMPC

3.1 Distributed LMPC formulations

In our previous work (Liu et al. (in press)), we introduced a distributed model predictive control method where both the pre-existing LCS and the NCS are designed via Lyapunov-based model predictive control as shown in Fig. 1. The LMPCs computing the input trajectories of the LCS (i.e., u_1) and the NCS (i.e., u_2) are referred to as LMPC 1 and LMPC 2, respectively. Under the assumption of continuous and flawless measurements, in Liu et al. (in press), it was proved that this control scheme guarantees practical stability of the closed-loop system and has the potential to maintain the closed-loop stability and performance in the face of new or failing actuators (for example, the failure of the actuator of the NCS (zero input) does not affect the closed-loop stability) and to reduce

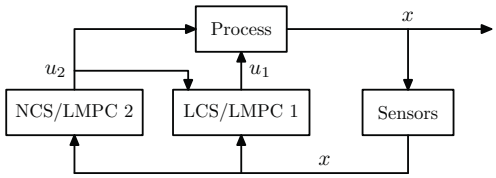

Fig. 1. Distributed LMPC design for networked control systems with continuous measurements (i.e., $x(t)$ is available to the controllers at $t_k = t_{k-1} + \Delta$ where Δ is a fixed sampling time for all k).

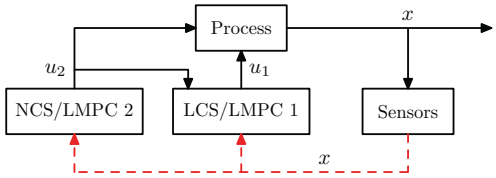

Fig. 2. Distributed LMPC design for networked control systems subject to asynchronous measurements.

computational burden in the evaluation of the optimal manipulated inputs compared with a centralized LMPC. However, when asynchronous measurements are present as shown in Fig. 2, these results do not hold. In this work, the distributed model predictive control method is extended to take into account asynchronous measurements explicitly, both in the constraints imposed on the LMPCs and in the implementation strategy.

In the presence of asynchronous measurements, the controllers need to operate in open-loop between successive new state measurements. We propose to take advantage of the model predictive control scheme to update the input based on a prediction obtained using the model. This is achieved by having the control actuators to store and implement the last computed optimal input trajectory. The proposed implementation strategy in the presence of asynchronous measurements is as follows:

(1) When a measurement $x(t_k)$ is available at t_k, LMPC 2 computes the optimal input trajectory of u_2;
(2) LMPC 2 sends the entire optimal input trajectory to its actuators and also sends the entire optimal input trajectory to LMPC 1.
(3) Once LMPC 1 receives the entire optimal input trajectory for u_2, it evaluates the future input trajectory of u_1;
(4) LMPC 1 sends the entire optimal input trajectory to its actuators.
(5) When a new measurement is received ($k = k+1$), go to step 1.

Note that in the proposed distributed scheme, only LMPC 2 is required to send its optimal input trajectory to LMPC 1 each time when a new measurement is available. This minimizes the communications required between the two controllers. Note also that the communication between LMPC 1 and LMPC 2 is in general done using a reliable link, and hence, it is not subject to data losses or delays.

We first design the optimization problem that charcterizes LMPC 2. This optimization problem depends on the latest state measurement $x(t_k)$, however, LMPC 2 does not have any information about the value that u_1 will take. In order to take a decision, LMPC 2 must assume a trajectory for u_1 along the prediction horizon. To this end, the Lyapunov-based controller $u_1 = h(x)$ is used. LMPC 2 is based on the following optimization problem:

$$\min_{u_{d2} \in S(\Delta)} \int_0^{N\Delta} L(\tilde{x}(\tau), u_{d1}(\tau), u_{d2}(\tau)) d\tau \tag{6a}$$

$$\dot{\tilde{x}}(\tau) = f(\tilde{x}(\tau), h(\tilde{x}(j\Delta)), u_{d2}(\tau), 0), \quad \forall \tau \in [j\Delta, (j+1)\Delta) \tag{6b}$$

$$\dot{\hat{x}}(\tau) = f(\hat{x}(\tau), h(\hat{x}(j\Delta)), 0, 0), \forall\, \tau \in [j\Delta, (j+1)\Delta) \tag{6c}$$

$$u_{d2}(\tau) \in U_2, \forall \tau \in [0, N\Delta) \tag{6d}$$

$$\tilde{x}(0) = \hat{x}(0) = x(t_k) \tag{6e}$$

$$V(\tilde{x}(\tau)) \leq V(\hat{x}(\tau)), \forall \tau \in [0, N_R\Delta) \tag{6f}$$

where $S(\Delta)$ is the family of piece-wise constant functions with sampling time Δ, N is the prediction horizon,

$$L(x, u_1, u_2) = x^T Q_c x + u_1^T R_{c1} u_1 + u_2^T R_{c2} u_2$$

is the performance index, Q_c, R_{c1} and R_{c2} are positive definite weight matrices that define the cost, $\tilde{x}$ is the predicted trajectory of the nominal system with u_2 being the input trajectory computed by the LMPC of Eq. 6 (i.e., LMPC 2) and u_1 being the Lyapunov-based controller h applied in a sample-and-hold fashion with $j = 0, ..., N-1$, $\hat{x}$ is the predicted trajectory of the nominal system with u_1 being h applied in a sample-and-hold fashion and $u_2 = 0$, $x(t_k)$ is the state measurement obtained at t_k and N_R is the smallest integer that satisfies the inequality $T_m \leq N_R\Delta$. To take full advantage of the nominal model in the computation of the control action, we take $N \geq N_R$.

The optimal solution to this optimization problem is denoted by $u^*_{d2}(\tau|t_k)$. Once this optimal input trajectory of u_2 is available, it is sent to LMPC 1 as well as the control actuators controlled by LMPC 1.

In order to inherit the stability properties of the Lyapunov based controller, u_2 must satisfy the constraint (6f) which guarantees that the predicted decrease of the Lyapunov function from t_k to $t_k + N_R\Delta$, if $u_1 = h(x)$ and $u_2 = u^*_{d2}$ are applied, is at least equal to the one obtained if the Lyapunov-based controller h is applied in a sample-and-hold fashion. Note that we have considered input constraints, see Eq. 6d.

The optimization problem of LMPC 1 depends on the latest state measurement $x(t_k)$ and the decision taken by LMPC 2 (i.e., u^*_{d2}). This allows LMPC 1 to compute an input u_1 such that the closed-loop performance is optimized, while guaranteeing that the stability properties of the Lyapunov-based controller are preserved. Specifically, LMPC 1 is based on the following optimization problem:

$$\min_{u_{d1} \in S(\Delta)} \int_0^{N\Delta} L(\check{x}(\tau), u_{d1}(\tau), u_{d2}(\tau)) d\tau \tag{7a}$$

$$\dot{\check{x}}(\tau) = f(\check{x}(\tau), u_{d1}(\tau), u_{d2}(\tau), 0), \forall \tau \in [0, N\Delta) \tag{7b}$$

$$\dot{\tilde{x}}(\tau) = f(\tilde{x}(\tau), h(\tilde{x}(j\Delta)), u_{d2}(\tau), 0), \quad \forall \tau \in [j\Delta, (j+1)\Delta) \tag{7c}$$

$$u_{d2}(\tau) = u^*_{d2}(\tau|t_k), \forall \tau \in [0, N\Delta) \tag{7d}$$

$$u_{d1}(\tau) \in U_1, \forall \tau \in [0, N\Delta) \tag{7e}$$

$$\check{x}(0) = \tilde{x}(0) = x(t_k) \tag{7f}$$

$$V(\check{x}(\tau)) \leq V(\tilde{x}(\tau)), \ \forall \tau \in [0, N_R\Delta) \tag{7g}$$

where $\check{x}$ is the predicted trajectory of the nominal system if $u_2 = u^*_{d2}$ and $u_1 = u_{d1}$ are applied, and $\tilde{x}$ is the predicted trajectory of the nominal system if $u_2 = u^*_{d2}$ and the Lyapunov-based controller h are applied in a sample-and-hold fashion.

The optimal solution to this optimization problem is denoted by $u^*_{d1}(\tau|t_k)$. The contractive constraint (7g) guarantees that the predicted decrease of the Lyapunov function from t_k to $t_k + N_R\Delta$, if $u_1 = u^*_{d1}$ and $u_2 = u^*_{d2}$ are applied, is at least equal to the one obtained when $u_1 = h(x)$ and $u_2 = u^*_{d2}$ are applied.

Note that the trajectory $\tilde{x}(\tau)$ predicted by constraint (7c) is the same optimal trajectory predicted by LMPC 2. This trajectory and the two contractive constraints (6f) and (7g) allow proving the closed-loop stability properties of the proposed controller.

The manipulated inputs of the proposed control scheme are defined as follows:

$$\begin{array}{l} u_1(t) = u^*_{d1}(t - t_k|t_k),\ \forall t \in [t_k, t_{k+1}) \\ u_2(t) = u^*_{d2}(t - t_k|t_k),\ \forall t \in [t_k, t_{k+1}). \end{array} \quad (8)$$

Note that, as explained before, the controllers apply the last evaluated optimal input trajectory between two successive state measurements.

4. STABILITY PROPERTIES

In this section, we present the stability properties of the proposed distributed control scheme. We prove that the contractive constraints (6f) and (7g) guarantee that the proposed distributed control scheme inherits the stability properties of the Lyapunov-based controller (implemented in sample and hold and using the model to estimate the state of the system when a new measurement is not available). This property is presented in Theorem 1 below. To state this theorem, we need the following propositions.

Proposition 1. (c.f. Muñoz de la Peña and Christofides (2008)). *Consider the nominal sampled trajectory $\hat{x}$ of system (1) in closed-loop with the Lyapunov-based controller h applied in a sample-and-hold fashion and $u_2(t) = 0$. Let $\Delta, \epsilon_s > 0$ and $\rho > \rho_s > 0$ satisfy*

$$-\alpha_3(\alpha_2^{-1}(\rho_s)) + \alpha_4(\alpha_1^{-1}(\rho))L_x M\Delta \leq -\epsilon_s/\Delta. \quad (9)$$

Then, if $\rho_{\min} < \rho$ where

$$\rho_{min} = \max\{V(\hat{x}(t+\Delta)) : V(\hat{x}(t)) \leq \rho_s\} \quad (10)$$

and $\hat{x}(0) \in \Omega_\rho$, the following inequality holds

$$V(\hat{x}(k\Delta)) \leq \max\{V(\hat{x}(0)) - k\epsilon_s, \rho_{min}\}. \quad (11)$$

Proposition 1 ensures that if system (1) with $w(t) = 0$ for all t under the control law $u_1 = h(x)$ implemented in a sample-and-hold fashion and $u_2 = 0$ starts in Ω_ρ, then it is ultimately bounded in $\Omega_{\rho_{\min}}$. The following proposition provides an upper bound on the deviation of the state trajectory obtained using the nominal model, from the real-state trajectory when the same control input trajectories are applied.

Proposition 2. (c.f. Liu et al. (2008)). *Consider the following state trajectories*

$$\begin{array}{l} \dot{x}_a(t) = f(x_a(t), u_1(t), u_2(t), w(t)) \\ \dot{x}_b(t) = f(x_b(t), u_1(t), u_2(t), 0) \end{array} \quad (12)$$

with initial states $x_a(t_0) = x_b(t_0) \in \Omega_\rho$. There exists a class $\mathcal{K}$ function $f_W(\cdot)$ such that

$$|x_a(t) - x_b(t)| \leq f_W(t - t_0), \quad (13)$$

for all $x_a(t), x_b(t) \in \Omega_\rho$ and all $w(t) \in W$ with

$$f_W(\tau) = \frac{R_w\theta}{R_x}(e^{R_x\tau} - 1).$$

The following proposition bounds the difference between the magnitudes of the Lyapunov function of two different states in Ω_ρ.

Proposition 3. (c.f. Liu et al. (2008)). *Consider the Lyapunov function $V(\cdot)$ of system (1). There exists a quadratic function $f_V(\cdot)$ such that*

$$V(x) \leq V(\hat{x}) + f_V(|x - \hat{x}|) \quad (14)$$

for all $x, \hat{x} \in \Omega_\rho$ with

$$f_V(s) = \alpha_4(\alpha_1^{-1}(\rho))s + Ms^2.$$

In Theorem 1 below, we provide sufficient conditions under which the proposed distributed LMPC design (8) guarantees the closed-loop stability of system (1) in the presence of asynchronous measurements.

Theorem 1. Consider system (1) in closed-loop with the distributed LMPC design (8) based on a controller $h(x)$ that satisfies (2). Let $\Delta, \epsilon_s > 0$, $\rho > \rho_{min} > 0$, $\rho > \rho_s > 0$ and $N \geq N_R \geq 1$ satisfy (9),(10) and the following inequality

$$-N_R\epsilon_s + f_V(f_W(N_R\Delta)) < 0. \quad (15)$$

If $x(t_0) \in \Omega_\rho$, then $x(t)$ is ultimately bounded in $\Omega_{\rho_c} \subseteq \Omega_\rho$ where

$$\rho_c = \rho_{min} + f_V(f_W(N_R\Delta)).$$

Proof: In order to prove that the closed-loop system is ultimately bounded in a region that contains the origin, we will prove that $V(x(t_k))$ is a decreasing sequence of values with a lower bound.

The proof consists of two parts. In the first part, we will prove that the stability results stated in Theorem 1 hold for the case where $t_{k+1} - t_k = T_m$ for all k and $T_m = N_R\Delta$. The proof of the stability results for the general case, that is $t_{k+1} - t_k \leq T_m$ for all k and $T_m \leq N_R\Delta$, will be shown in the second part.

Part 1: In this part, we prove that the stability results stated in Theorem 1 hold in the case that $t_{k+1} - t_k = T_m$ for all k and $T_m = N_R\Delta$. This case corresponds to the worst possible situation in the sense that LMPC 1 and LMPC 2 need to operate in open-loop for the maximum possible amount of time.

In order to simplify the notation, we will denote $\tilde{x}(t)$ the nominal closed-loop trajectory of system (1) with $u_1 = h$ implemented in a sample-and-hold fashion and $u_2 = u^*_{d2}$ from $x(t_k)$, $\hat{x}(t)$ the nominal closed-loop trajectory of system (1) under the Lyapunov-based controller $u_1 = h$ implemented in a sample-and-hold fashion and $u_2 = 0$ from $x(t_k)$, and denote $\check{x}(t)$ the nominal closed-loop trajectory of system (1) with $u_1 = u^*_{1d}$ and $u_2 = u^*_{2d}$ from $x(t_k)$.

By Proposition 1 and the fact that $t_{k+1} = t_k + N_R\Delta$, the following inequality can be obtained:

$$V(\hat{x}(t_{k+1})) \leq \max\{V(\hat{x}(t_k)) - N_R\epsilon_s, \rho_{\min}\}. \quad (16)$$

From the contractive constraints (6f) and (7g) in LMPC 2 and LMPC 1, the following inequality can be written:

$$V(\check{x}(t)) \leq V(\tilde{x}(t)) \leq V(\hat{x}(t)), \forall t \in [t_k, t_k + N_R\Delta). \quad (17)$$

From inequalities (16) (17) and taking into account that $\hat{x}(t_k) = \tilde{x}(t_k) = \check{x}(t_k) = x(t_k)$, the following inequality is obtained:

$$V(\check{x}(t_{k+1})) \leq \max\{V(x(t_k)) - N_R\epsilon_s, \rho_{\min}\}. \quad (18)$$

When $x(t) \in \Omega_\rho$ for all times (this point will be proved below), we can apply Proposition 3 to obtain the following inequalities:

$$\begin{aligned} V(x(t_{k+1})) \leq\ & V(\check{x}(t_{k+1})) \\ & + f_V(|\check{x}(t_{k+1}) - x(t_{k+1})|). \end{aligned} \quad (19)$$

Applying Proposition 2 we obtain the following upper bound on the deviation of $\check{x}(t)$ from $x(t)$:

$$|x(t_{k+1}) - \check{x}(t_{k+1})| \leq f_W(N_R\Delta) \quad (20)$$

From inequalities (19) and (20), the following upper bound on $V(x(t_{k+1}))$ can be written:

$$V(x(t_{k+1})) \leq V(\check{x}(t_{k+1})) + f_V(f_W(N_R\Delta)). \quad (21)$$

Using inequality (18), we can re-write inequality (21) as follows:

$$\begin{aligned} V(x(t_{k+1})) \leq\ & \max\{V(x(t_k)) - N_R\epsilon_s, \rho_{\min}\} \\ & + f_V(f_W(N_R\Delta)). \end{aligned} \quad (22)$$

If condition (15) is satisfied, from inequality (22), we know there exists $\epsilon_w > 0$ such that the following inequality holds:

$$V(x(t_{k+1})) \leq \max\{V(x(t_k)) - \epsilon_w, \rho_c\} \quad (23)$$

which implies that if $x(t_k) \in \Omega_\rho/\Omega_{\rho_c}$, then $V(x(t_{k+1})) < V(x(t_k))$, and if $x(t_k) \in \Omega_{\rho_c}$, then $V(x(t_{k+1})) < \rho_c$. Using inequality (23) recursively, it is proved that if $x(t_0) \in \Omega_\rho$, the closed-loop trajectories of system (1) under the proposed distributed LMPC design (8) satisfy

$$\limsup_{t\to\infty} V(x(t)) \leq \rho_c.$$

This proves that the closed-loop system is ultimately bounded in Ω_{ρ_c} for the case where $t_{k+1} - t_k = T_m$ for all k and $T_m = N_R\Delta$.

Part 2: In this part, we extend the results proved in Part 1 to the general case, that is, $t_{k+1} - t_k \leq T_m$ for all k and $T_m \leq N_R\Delta$ which implies that $t_{k+1} - t_k \leq N_R\Delta$. The proof is divided into two cases. The first case is that $t_{k+1} - t_k \leq \Delta$. In this case, the stability results hold as shown in Liu et al. (in press). The second case is that $\Delta < t_{k+1} - t_k \leq N_R\Delta$. Because f_V and f_W are convex and strictly increasing functions of their arguments (see Propositions 2 and 3 for the expressions of f_V and f_W) and following similar steps in Part 1, we can show that inequality (22) still holds. This proves that the stability results stated in Theorem 1 hold.

5. APPLICATION TO A CHEMICAL PROCESS

The process considered in this example is a three vessel, reactor-separator process consisting of two continuously stirred tank reactors (CSTRs) and a flash tank separator.A feed stream to the first CSTR F_{10} contains the reactant A which is converted into the desired product B. The desired product B can then further react into an undesired side-product C. The effluent of the first CSTR along with additional fresh feed F_{20} makes up the inlet to the second CSTR. The reactions $A \to B$ and $B \to C$ (referred to as 1 and 2, respectively) take place in the two CSTRs in series before the effluent from CSTR 2 is fed to a flash tank. The overhead vapor from the flash tank is condensed and recycled to the first CSTR and the bottom product stream is removed. A small portion of the overhead is purged before being recycled to the first CSTR. All the three vessels are assumed to have static holdup. The dynamic equations describing the behavior of the system, obtained through material and energy balances under standard modeling assumptions, can be found in Liu et al. (in press).

Each of the tanks has an external heat input. The manipulated inputs to the system are the heat inputs, Q_1, Q_2 and Q_3, and the feed stream flow rate to vessel 2, F_{20}.

The process was numerically simulated using a standard Euler integration method. Process noise was added to simulate disturbances/model uncertainty and it was generated as autocorrelated noise of the form $w_k = \phi w_{k-1} + \xi_k$ where $k = 0, 1, \ldots$ is the discrete time step of 0.001 hr, ξ_k is generated by a normally distributed random variable with standard deviation σ_p, and ϕ is the autocorrelation factor and w_k is bounded by θ_p, that is $|w_k| \leq \theta_p$.

We assume that the measurements of the temperatures T_1, T_2, T_3 and the measurements of mass fractions x_{A1}, x_{B1}, x_{A2}, x_{B2}, x_{A3}, x_{B3} are available asynchronously at time instants $\{t_{k\geq 0}\}$ with an upper bound $T_m = 3\Delta$ on the maximum interval between two successive measurements, where Δ is the controller sampling time and chosen to be $\Delta = 0.02\ hr = 1.2\ min$.

For each set of steady-state inputs Q_{1s}, Q_{2s}, Q_{3s} and F_{20s} corresponding to a different operating condition, the process has one steady-state x_s. The control objective is to steer the process to the steady state

$$x_s^T = [0.61, 0.39, 425.9, 0.61, 0.39, 422.6, 0.35, 0.63, 427.3].$$

The process belongs to the following class of nonlinear systems

$$\dot{x}(t) = f(x(t)) + g_1(x(t))u_1(t) + g_2(x(t))u_2(t) + w(t)$$

where $x^T = [x_1\ x_2\ x_3\ x_4\ x_5\ x_6\ x_7\ x_8\ x_9] = [x_{A1} - x_{A1s}\ x_{B1} - x_{B1s}\ T_1 - T_{1s}\ x_{A2} - x_{A2s}\ x_{B2} - x_{B2s}\ T_2 - T_{2s}\ x_{A3} - x_{A3s}\ x_{B3} - x_{B3s}\ T_3 - T_{3s}]$ is the state, $u_1^T = [u_{11}\ u_{12}\ u_{13}] = [Q_1 - Q_{1s}\ Q_2 - Q_{2s}\ Q_3 - Q_{3s}]$ and $u_2 = F_{20} - F_{20s}$ are the manipulated inputs which are subject to the constraints $|u_{1i}| \leq 10^6\ KJ/hr$ $(i = 1, 2, 3)$ and $|u_2| \leq 3\ m^3/hr$, and $w = w_k$ is a time varying noise.

To illustrate the theoretical results, we first design the Lyapunov-based controller $u_1 = h(x)$ which can stabilize the closed-loop system and the explicit expression of the controller can be found in Liu et al. (in press). We consider a Lyapunov function $V(x) = x^T P x$ with P being the following weight matrix

$$P = diag^{\,5}\,(5.2 \times 10^{12}\,[4\ 4\ 10^{-4}\ 4\ 4\ 10^{-4}\ 4\ 4\ 10^{-4}]).$$

The values of the weights in P have been chosen in a way such that the Lyapunov-based controller $h(x)$ satisfies the input constraints, stabilizes the closed-loop system and provides good closed-loop performance.

Based on the Lyapunov-based controller $h(x)$, we design LMPC 1 and LMPC 2. The prediction horizons of both LMPC 1 and LMPC 2 are chosen to be $N = 6$ and N_R is

[5] $diag(v)$ denotes a matrix with its diagonal elements being the elements of vector v and all the other elements being zeros.

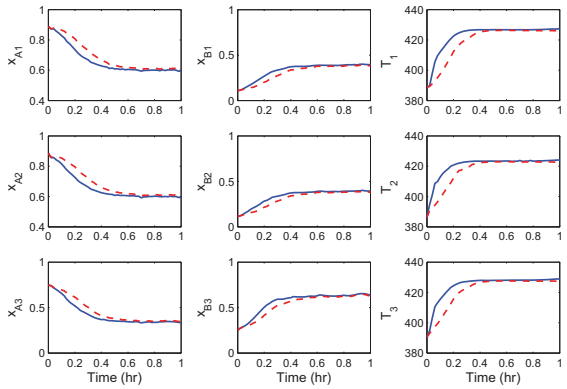

Fig. 3. State trajectories of the process under the proposed distributed LMPC design (8) (solid lines) and the original distributed LMPC design in Liu et al. (in press) (dashed lines) under continuous measurements.

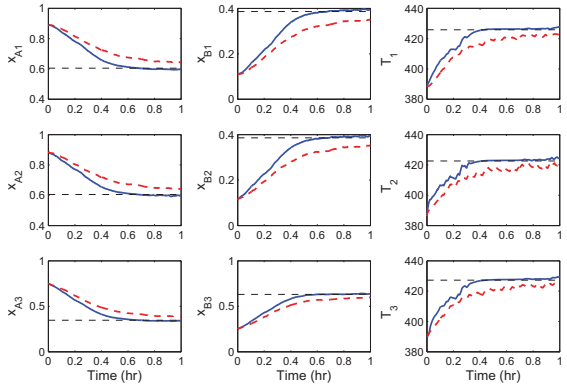

Fig. 4. State trajectories of the process under the proposed distributed LMPC design (8) (solid lines) and the original distributed LMPC design in Liu et al. (in press) (dashed lines) in the presence of asynchronous measurements.

chosen to be 4 so that $N_R\Delta \geq T_m$. The weight matrices for the LMPC designs are chosen as: $Q_c = diag(10^3 Q_v)$ with $Q_v = [2\ 2\ 0.0025\ 2\ 2\ 0.0025\ 2\ 2\ 0.0025]$, $R_{c1} = diag(\begin{bmatrix}5\cdot 10^{-12} & 5\cdot 10^{-12} & 5\cdot 10^{-12}\end{bmatrix})$ and $R_{c2} = 100$.

We first carried out simulations to compare the proposed distributed LMPC design (8) with the original distributed LMPC design in Liu et al. (in press) in the case where no asynchronous measurements are present (i.e., state measurements $x(t_k)$ are available continuously with the interval between two successive measurements being Δ). The state trajectories under the two control designs are shown in Fig. 3. From Fig. 3, we can see that both the proposed and the original distributed LMPC designs stabilize the closed-loop system at the desired steady state.

We also carried out another set of simulations to compare both control laws in the presence of asynchronous measurements. To model the time sequence $\{t_{k\geq 0}\}$, we use an upper bounded random Poisson process. The Poisson process is defined by the number of events per unit time W. The interval between two successive concentration sampling times (events of the Poisson process) is given by $\Delta_a = \min\{-ln\chi/W, T_m\}$, where χ is a random variable with uniform probability distribution between 0 and 1. This generation ensures that $\max_k\{t_{k+1} - t_k\} \leq T_m$. In this example, W is chosen to be $W = 20$. The state trajectories of the system in closed-loop with both controllers are shown in Fig. 4. From Fig. 4, we can see that the proposed distributed LMPC design, which takes into account asynchronous measurements explicitly, can stabilize the closed-loop state at the desired steady state; however, the original distributed LMPC design failed to drive the closed-loop state to the desired steady state.

REFERENCES

Christofides, P.D., Davis, J.F., El-Farra, N.H., Clark, D., Harris, K.R.D., and Gipson, J.N. (2007). Smart plant operations: Vision, progress and challenges. *AIChE Journal*, Perspective article, 53, 2734–2741.

Dunbar, W.B. (2007). Distributed receding horizon control of dynamically coupled nonlinear systems. *IEEE Transactions on Automatic Control*, 52, 1249–1263.

Keviczky, T., Borrelli, F., and Balas, G.J. (2006). Decentralized receding horizon control for large scale dynamically decoupled systems. *Automatica*, 42, 2105–2115.

Lin, Y., Sontag, E.D., and Wang, Y. (1996). A smooth converse lyapunov theorem for robust stability. *SIAM Journal on Control and Optimization*, 34, 124–160.

Liu, J., Muñoz de la Peña, D., Ohran, B., Christofides, P.D., and Davis, J.F. (2008). A two-tier architecture for networked process control. *Chemical Engineering Science*, 63, 5394–5409.

Liu, J., Muñoz de la Peña, D., and Christofides, P.D. (2009). Distributed model predictive control of nonlinear process systems. *AIChE Journal*, 55, 1171-1184.

Magni, L. and Scattolini, R. (2006). Stabilizing decentralized model predictive control of nonlinear systems. *Automatica*, 42, 1231–1236.

Massera, J.L. (1956). Contributions to stability theory. *Annals of Mathematics*, 64, 182–206.

Muñoz de la Peña, D. and Christofides, P.D. (2008). Lyapunov-based model predictive control of nonlinear systems subject to data losses. *IEEE Transactions on Automatic Control*, 53, 2076–2089.

Neumann, P. (2007). Communication in industrial automation: What is going on? *Control Engineering Practice*, 15, 1332–1347.

Raimondo, D.M., Magni, L., and Scattolini, R. (2007). Decentralized MPC of nonlinear system: An input-to-state stability approach. *International Journal of Robust & Nonlinear Control*, 17, 1651–1667.

Rawlings, J.B. and Stewart, B.T. (2007). Coordinating multiple optimization-based controllers: New opportunities and chanllenges. In *Procedings of 8th IFAC Symposium on Dynamics and Control of Process*, volume 1, 19–28. Cancun, Mexico.

Richards, A. and How, J.P. (2007). Robust distributed model predictive control. *International Journal of Control*, 80, 1517–1531.

Ydstie, E.B. (2002). New vistas for process control: Integrating physics and communication networks. *AIChE Journal*, 48, 422–426.

Predictive Control of Nonlinear Chemical Processes under Asynchronous Measurements and Controls

P. Varutti * **and R. Findeisen** *

* *P.Varutti and R.Findeisen are with the Institute of Automation Engineering, Otto-von-Guericke University, 39016 Magdeburg, Germany ({paolo.varutti,rolf.findeisen}@ovgu.de).*

Abstract: In many process control problems measurement and control instances might not be available in a periodically-equally-distributed way. Moreover, due to the sensor processing time, actuators/sensors calibration, or computation, inevitable delays can often arise. Also information losses caused, for example, by temporary components failure, or the presence of unreliable communication media, might represent a non-trivial problem. This leads to asynchronous availability of measurement and control inputs, i.e. the controller, sensor, and actuator work in an event-driven, rather than a continuous way. In order to avoid instability and performance loss all these issues must be considered during the control design. In this paper, it is shown that predictive control methods based on continuous time models can be used to stabilize event-based nonlinear systems under variable delays, and limited information losses. It is demonstrated that by using the suggested approach asymptotic convergence is ensured.

Keywords: nonlinear model predictive control, continuous time systems, event-based control, delays, information losses, process control

1. INTRODUCTION

In many cases, continuous time systems are controlled by means of periodically-equally-distributed sampling times, commonly assumed to be known a priori. However, practical control problems are often intrisictly asynchronous, i.e. the dynamics of the system depends on some –maybe exogenous– event. Examples are multi fold: sensors such as chromatographers or laboratory measurements of compositions could need long time due to calibration or limited processing capabilities. The energy of an actuator might be limited, e.g. it must first be "charged" before applying the input. Measurements/actuation might demand human interaction, often unpredictable or inefficient. Moreover, it happens frequently that systems are subject to input/output delays caused, for example, by computational time, communication, and/or sensor/actuator slow dynamics. It might also occur that part of the exchanged information is lost, e.g. due to components failure, or the use of unreliable communication media. If these issues are not taken into account, performance loss or instability of the closed loop can arise. Event-based and asynchronous control is a very active field, Brockett and Liberzon (1998); Heemels et al. (2008). However, most of the work focuses only on linear unconstrained systems, without considering explicitly either time delays or information losses.

In this paper, a solution for the formerly introduced problems, especially suitable to process control applications, is presented. In particular, the suggested solution relies on Predictive Control (PC), which fits well the nature of event-based/asynchronous systems, since the sampling times do not have to neither be equally distant nor to be known a priori (see Fontes (2001); Findeisen (2006)). The compensation capabilities of PC with respect to measurement and computational delays have already been assessed in inter alia Chen et al. (2000); Findeisen and Allgöwer (2004)), where asymptotic stability with respect to such delays has been established. In this work, we focus on the complete asynchronous case, including delays and losses on the actuation and measurement side, which is significantly more challenging. By using smart-sensors and smart-actuators, i.e. components capable of full-duplex communication with the controller, it is possible to achieve closed loop asymptotic convergence.

In the next section PC and the problem under consideration are formally presented. In Section 3, an asynchronous PC solution to compensate delays and information losses is introduced. Results on asymptotic convergence are provided. Simulation results on a Continuous Stirred Tank Reactor (CSTR) are reported in Section 4.

2. PROBLEM STATEMENT

We consider the problem of controlling the nonlinear time-continuous process of the form

$$\dot{x} = f(x,u), \quad x(0) = x_0, \quad x \in \mathbb{R}^n, u \in \mathbb{R}^m. \tag{1}$$

It is assumed that the whole state x is available only at discrete instants t_i. The objective is to stabilize the system around the origin, i.e. $\|x\| \to 0$ for $t \to \infty$, under the state and input constraints $x \in X \subset \mathbb{R}^n$, $u \in U \subset \mathbb{R}^m$. The state constraints X, e.g. max temperature, and the input constraints U, e.g. max valve opening, are assumed to be closed sets. It is also assumed that $f(0,0) = 0$, and f is sufficiently differentiable. The controller should provide for every state measurement $x(t_i)$ a piece of input trajectory

$$u(t) = u(t; x(t_i)), \text{ for } t \in (t_i, t_{i+1}], \quad (2)$$

i.e. the calculated input trajectory is applied open loop in between consecutive recalculation times. This kind of control is commonly called sampled-data open loop feedback. Note that the recalculation times t_i do not need to be known a priori, e.g. in the event-based case when a measurement is triggered once some conditions, such as deviation from the product specifications, are met. This fits well such an asynchronous frame, and it can be used to provide better performance, thanks to the possibility of adjusting on-the-fly the recalculation frequency.

2.1 Predictive Control

In this section, we summarize the basic idea of PC (for more details see Mayne et al. (2000); Findeisen (2006)). The idea is to use a model of the process to be controlled, in order to repeatedly solve an optimization problem, based on the state prediction provided by the model itself. Then, only the first piece of trajectory is implemented and the problem is re-solved with the new measurement. The following definition will be useful for the remainder of the paper.

Definition 1. (Partition). Every series $\pi = (t_i)$, $i \in \mathbb{N}$, $t_i \in \mathbb{R}^+$, such that $t_0 = 0$, $t_i < t_{i+1}$ and $t_i \to \infty$ is called partition.

For every $t_i \in \pi$, $x(t_i)$ is measured, and

$$\min_{\bar{u}(\cdot)} \int_{t_i}^{t_i+T_p} F(\bar{x}(\tau), \bar{u}(\tau)) d\tau + E(\bar{x}(t_i + T_p)), \quad (3a)$$

$$\text{s.t. } \dot{\bar{x}}(t) = f(\bar{x}(t), \bar{u}(t)), \quad \bar{x}(t_i) = x(t_i), \quad (3b)$$

$$\bar{u}(t) \in U, \quad t \in (t_i, t_{i+1}], \quad (3c)$$

$$\bar{x}(t) \in X, \quad (3d)$$

$$\bar{x}(t_i + T_p) \in \mathcal{E}, \quad (3e)$$

is solved, where $\bar{\cdot}$ denotes the controller internal variables. The solution is an optimal control signal $u^*(t; x(t_i))$, for $t \in [t_i, t_i + T_p]$, where T_p represents the finite prediction horizon. For sake of simplicity, prediction and control horizon are supposed to be equal, i.e. $T_c = T_p$. The control input is then implemented for the time-span $(t_i, t_i + \delta]$, i.e.

$$u(t) = u^*(t; x(t_i)), \text{ for } t \in (t_i, t_i + \delta], \quad (4)$$

where δ represents the interval between two consecutive recalculation times, i.e. $\delta = (t_{i+1} - t_i), \forall t_i, t_{i+1} \in \pi$. Stability can then be achieved by properly choosing the cost functional $F(x, u)$, the terminal cost $E(x)$, the terminal region $\mathcal{E} \subset X$, and the prediction horizon T_p, see Mayne et al. (2000); Fontes (2001); Findeisen (2006). As formerly mentioned, it is commonly assumed that the recalculation intervals $\delta = (t_{i+1} - t_i)$ are constant and known a priori. Here, however, these assumptions are relaxed, allowing for the recalculation instants to be time-varying and unknown a priori. The only requirement on δ is given by Assumption 2.

Assumption 2. Given the prediction horizon T_p, $\beta \in \mathbb{R}^+$,

$$\beta < \delta = (t_{i+1} - t_i) < T_p, \forall t_i, t_{i+1} \in \pi. \quad (5)$$

In the remainder of the paper, $\overline{\delta}$ will be used to refer to the maximum recalculation interval $\delta = (t_{i+1} - t_i)$. Additionally, the following theorem will be useful for the final results.

Theorem 3. (Asynchronous Predictive Control). Consider the closed-loop system given by (1), (3)-(4). If

i) Assumption 2 is satisfied.

ii) $\forall x_0 \in \mathcal{E} \subseteq X, \exists \bar{u}(\tau) \in U, \tau \in [0, T_p]$ where

$$x(\tau) \in \mathcal{E}, \quad (6a)$$

$$\text{for } \dot{x}(\tau) = f(x(\tau), \bar{u}(\tau)), \quad x(0) = x_0, \quad (6b)$$

$$\text{and } \frac{\partial E}{\partial x} f(x(\tau), \bar{u}(\tau)) + F(x(\tau), \bar{u}(\tau)) \leq 0. \quad (6c)$$

iii) The optimal control problem is solvable for a time t_0.

Then, $\lim_{t \to \infty} \|x(t)\| = 0$.

Proof. The proof comes directly from Findeisen (2006) and the results about PC stability, see inter alia Fontes (2001); Mayne et al. (2000). It must be ensured that δ is smaller than T_p.

Remark 4. The solution of the optimal control problem, as well as the closed loop stability, are based only on the discrete time measurements $x(t_i)$ at $t_i \in \pi$, where π does not have to be known a priori. This makes PC a very appealing solution for event-based problems.

Remark 5. Note that Theorem 3 states only asymptotic converge, and not asymptotic stability in the Lyapunov sense. The former is a weaker property, meaning that even withouth disturbances, the system can temporary drift away from the equilibrium point before converging to the equilibrium. Proving asymptotic stability would in the first step require to rigorously define stability for discrete event systems, since the partition π is not known a priori. This is way beyond the focus of this paper.

2.2 Delays and Information Losses

In a closed loop controlled system, it is quite common to face delays and/or information losses, e.g. due to components failures. Essentially, there can be three delay sources (see Figure 1):

i) *Measurement delays*, which can be due to measurement elaboration, observer reconstruction, slow sensor dynamics, but also the time required for a signal to reach the controller.

ii) *Computational delays*, which represent the time required by the controller to calculate the control input.

iii) *Actuation delays*, which can be due to slow actuator dynamics, but also signal transportation.

The following assumption on the delays is made:

Assumption 6. $\tau_s(t), \tau_c(t), \tau_a(t)$ are nondeterministic with arbitrary probability distribution, but ultimately limited, i.e.

$$\tau_s(t) \in [0, \overline{\tau_s}], \tau_c \in [0, \overline{\tau_c}], \tau_a(t) \in [0, \overline{\tau_a}]. \quad (7)$$

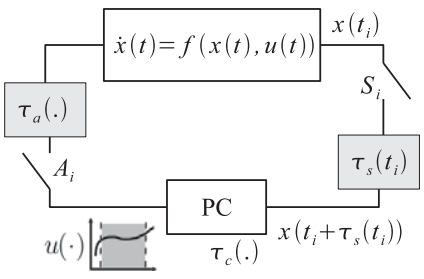

Fig. 1. Sketch of an event-based system subject to delays and information losses.

Both the sensor-to-controller and controller-to-actuator channel can suffer from information losses, which, for example, can be modeled as Bernoullian variables $A_i \sim \mathcal{B}(1-p_a)$, and $S_i \sim \mathcal{B}(1-p_s)$, such that

$$A_i = \begin{cases} 1, & \text{if a control input is received} \\ 0, & \text{otherwise} \end{cases},$$

$$S_i = \begin{cases} 1, & \text{if a measurement is received} \\ 0, & \text{otherwise} \end{cases}.$$

p_a, and p_s represent the loss probabilities for the actuation and the measurement link respectively. Sensor, controller, and actuator are event-driven, such that measurement and control information are dispatched only when necessary. It is also assumed that the following statements are fulfilled.

Assumption 7. Either a common global time, or a set of synchronized clocks is available, such that a common unique time t is established among the components.

Assumption 8. All exchanged information is time-stamped.

3. ASYNCHRONOUS PC

Model-based approaches, such as PC, represent an intuitive and natural way to handle input/output delayed systems. In this section, we show how PC can be used in an event-based way to control asynchronous systems by preserving stability, in the sense of asymptotic convergence, and simultaneously reducing both exchanged information and computational requirements. Note that delays are very common on a daily basis, therefore the presented approach represents a good solution for a wide class of problems, e.g control under actuator/sensor slow dynamics, heavy computation, control over networks, and/or limited resources.

3.1 Compensating Delays

Measurement Delays Assume for the moment that no information is lost. When a measurement $[x(t_i)|t_i]$ is dispatched at a time $t_i \in \pi$, where $x(t_i) \in \mathcal{X}$ is the state value, while t_i is its time-stamp, if there is a measurement delay $\tau_s(t)$, then the information will be available to the controller only at $(t_i + \tau_s(t_i))$, i.e. the controller has to use some piece of information which is outdated and does not correspond to the actual state of the system under control. Therefore, it is necessary to compensate this delay in order to solve the correct control problem. Since a model of the system is available at the controller side, and no mismatch is present, under Assumptions 7-8, it is possible to determine the delay simply by comparing the time-stamp with the global time t, i.e. $\tau_s(t_i) = (t - t_i)$. By means of forward prediction through the local model, possible since it is known what input is applied to the plant (no actuation delay), one can obtain the state prediction

$$\overline{x}(t_i + \tau_s(t_i)) = x(t_i + \tau_s(t_i)). \tag{8}$$

Theorem 9. (Measurement Delay Compensation).
Given the closed loop system (1),(3)-(4), if

i) Theorem 3 is satisfied in the nominal case, i.e. without measurement delays.
ii) $T_p > \overline{\tau_s} + \overline{\delta}$.

Then, $\lim_{t\to\infty} \|x(t)\| = 0$.

Proof. The proof follows from Theorem 3, when the state prediction (8) is used to compensate the delay $\tau_s(t_i)$. More details can be found in Findeisen (2006).

Compensation of Actuation Delays Less trivial is the compensation of computational and actuation delays. In this case, in fact, if the delays are nondeterministic, the actual applied input is not known for sure to the controller. Thus, it is not possible to obtain (8) correctly since $u^*(\cdot)$ is not uniquely determined. As formerly stated, this kind of delays are common in real application, e.g. due to slow actuator dynamics or reduced computational capabilities, and if not explicitly considered can worsen considerably the closed loop performance, or bring to instability. To solve this problem, in some way the applied input must be made deterministic. This can be achieved by using future input trajectories and buffer them in the actuator till the moment they can be used, see Alldredge and M. S. Branicky (2008); Findeisen and Varutti (2009); Varutti and Findeisen (2008). In fact, since Assumption 6 must hold, one can consider the worst case for $\tau_a(t)$ and $\tau_c(t)$, namely $\overline{\tau_a}$ and $\overline{\tau_c}$, in which the state prediction

$$\overline{x}(t_i + \tau_s(t_i) + \overline{\tau_a} + \overline{\tau_c}) = x(t_i) + \int_{t_i}^{t_i+\tau_s(t_i)+\overline{\tau_a}+\overline{\tau_c}} f(x(\tau), u(\tau))d\tau \tag{9}$$

is obtained by using the measurement $x(t_i)$. (9) is then used to solve the optimal control problem and the corresponding solution is despatched to the actuator with a new time-stamp, buffered and used once its time-stamp matches with the global time t, i.e.

$$u^*(\tau; \overline{x}(t_i + \tau_s(t_i) + \overline{\tau_a} + \overline{\tau_c})), \tag{10}$$

for $\tau \in (t_i + \tau_s(t_i) + \overline{\tau_a} + \overline{\tau_c}), t_{i+1} + \tau_s(t_{i+1}) + \overline{\tau_a} + \overline{\tau_c})]$ is sent as $[u^*(\cdot)|(t_i + \tau_s(t_i) + \overline{\tau_a} + \overline{\tau_c})]$. The overall algorithm is reported in Algorithm 1, Appendix A. It can be proved that under Assumption 7, and

$$T_p > \overline{\delta} + \overline{\tau_s} + \overline{\tau_a} + \overline{\tau_c}, \tag{11}$$

Algorithm 1 stabilizes the delayed system.

Theorem 10. (Worst Case Compensation).
Given the nonlinear continuous time system (1) and the the predictive controller obtained from (3)-(4), and (9), by applying Algorithm 1, under (11) the closed loop system is stable, in sense of asymptotic convergence, if the nominal controller, i.e. the controller subject to no delays obtained from Theorem 3, stabilizes the system.

Proof. The proof follows directly from Theorem 3, and 9, first, by proving recursive feasibility, and then convergence –see Findeisen (2006); Findeisen and Varutti (2009); Varutti and Findeisen (2008) for more details–.

Remark 11. Assumption 7 is required to have a common time-frame among the components. This can represent a problem for fast dynamical systems, since the state-of-the-art synchronization algorithms cannot guarantee high precision.

3.2 Information Loss Compensation

It has been assumed till now that the communication is not affected by any information loss. In reality, however, information losses might occur due, for example, to unreliable communication media, or some temporary components failure. As in the delay case, the major problem is represented by losses/failures in the actuation channel. In fact, if an information loss $S_i = 0$ occurs for $t_i \in \pi$, the controller can still use the last available state

$$x(t_k), \text{ for } t_k \in \pi, \text{ s.t. } S_k = 1, \tag{12}$$

and the nominal model for (1) to calculate the prediction

$$\overline{x}(t_k + \sum_{j=k}^{i} \tau_s(t_j) + \overline{\tau_a} + \overline{\tau_c}), \text{ for } t_j \in \pi, \text{ s.t. } S_j = 0, \quad (13)$$

by using the compensation approach presented in Section 3.1, if the applied input is uniquely determined.

Remark 12. Notice that $t_k + \sum_{j=k}^{i} \tau_s(t_j)$ can be substituted by the global time t, moment in which the controller receives a new measurement.

On the contrary, if a dropout $A_i = 0$ occurs, then the control input is not uniquely known at the controller side, and thus (13) cannot be accurately calculated. In Varutti and Findeisen (2008); Findeisen and Varutti (2009) a solution for the problem was found by using *prediction consistent feedbacks*, i.e. feedbacks that under information losses are able to keep the difference between state prediction and actual state negligible and hence guarantee convergence under a limited amount of dropouts.

In this paper, a different approach is considered. In particular, the following assumptions are made:

Assumption 13. An acknowledge mechanism is available on the actuator side.

Assumption 14. The acknowledgments have high priority, and they cannot be dropped.

Assumption 15. The acknowledgments are delivered instantaneously.

This is equal to saying that for every input received by the actuator an acknowledgment with the time-stamp of the latest successfully delivered information is sent back to the controller.

We show later how Assumption 15 can be relaxed. On the contrary, Assumption 14 is a fundamental condition since it is well known from theoretical results that no handshake protocol can solve a coordination problem under acknowledgment losses –see "The two Generals Paradox", Tanenbaum (2008)–. In the case of chemical processes, however, timely submission of acknowledgments is often not a problem, since there are frequently slow measurement and actuation devices. The used communication networks are often sufficiently fast and provide the possibility of having high priority acknowledgments. Although restrictive, these conditions are necessary to allow the controller to correctly reconstruct the applied input sequence. Algorithm 2 in Appendix A illustrates the procedure to compensate simultaneously delays and information losses. Differently from Algorithm 1, the entire control input trajectory $u^*(\tau; x(t_i))$, for $\tau \in (t + \overline{\tau_a} + \overline{\tau_c}, t_i + T_p]$ is sent to the actuator with time-stamp $(t + \overline{\tau_a} + \overline{\tau_c})$. In this way, when some information is dropped either in the down- or in the up-link, the actuator can still utilize the old input trajectory to control the system. Note that in an event-based setup measurement losses are transparent to the controller. This means that no new control input is generated and dispatched to the actuator. However, since the whole control trajectory is sent, if the number of consecutive losses S_i is less than T_p, the actuator can still apply the latest received input. On the other hand, the controller can establish immediately that some information has gone lost thanks to the timer that is implicitly set by time-stamping the control inputs. In fact, if the current time exceeds the former time-stamp, from Assumption 15, it is known for sure that no new control input has arrived. An alternative would be to index the control trajectories and use an error mechanism instead, i.e. an error is sent every time some control information is lost. However, in the asynchronous case utilizing acknowledgments is more efficient, since the actuator does not have to wait till the next successfully received trajectory to realize that some information went lost. Finally, note that a non-resend policy has been chosen, i.e. if a control trajectory is lost, the controller does not transmit it again but it simply records the event in order to update its local copy of the currently applied control input. This seems to be a more logical choice since the sequence would probably arrive when its applicability time is already expired.

Theorem 16. (Convergence Under Information Losses). Given the closed loop system (1), (3)-(4), (13) if

i) Assumptions 13-15 are satisfied.
ii) Algorithm 2 is used.
iii) The prediction horizon T_p is such that

$$T_p > \overline{\delta} + n \cdot \overline{\tau_s} + \overline{\tau_c} + m \cdot \overline{\tau_a}, \quad (14)$$

where n,$m \in \mathbb{N}/\{0\}$ represent, respectively, the number of consecutive losses in the measurement and in the actuation.

Then, $\lim_{t\to\infty} \|x(t)\| = 0$.

Proof. The proof follows from Theorem 3 and 9. The use of acknowledgments allows the controller to reconstruct in real time the correct applied control sequence. Thus, feasibility and convergence can be proved.

As formerly stated, Assumption 15 can be relaxed by allowing the acknowledgments to be subject to nondeterministic delays $\tau_{ack}(t)$. In this case, however, the following assumption is required.

Assumption 17. $\tau_{ack}(t)$ is nondeterministic with arbitrary probability distribution, but limited, i.e $\tau_{ack}(t) \in [0, \overline{\tau_{ack}}]$.

By using a worst case compensation approach similar to Algorithm 1, and 2, one can ensure asymptotic convergence of the closed loop system by considering, instead, the state prediction

$$\overline{x}(t_k + \sum_{j=k}^{i} \tau_s(t_j) + \overline{\tau_a} + \overline{\tau_c} + \overline{\tau_{ack}}), \quad (15)$$

for $t_j \in \pi$, such that $S_j = 0$.

Corollary 18. (Convergence Under Information Losses). The closed loop system (1), (3)-(4), is stable, in the sense of asymptotic convergence, if

i) The conditions for Theorem 3, 9, 10, and Assumption 17 are satisfied.
ii) A modified variant of Algorithm 2, such that the prediction (15) is used and $[u^*(\tau; x(t_i))|ts]$, for $ts = t+\overline{\tau_{ack}}+\overline{\tau_s}+\overline{\tau_c}+\overline{\tau_a}$, $\tau \in [t+\overline{\tau_{ack}}+\overline{\tau_s}+\overline{\tau_c}+\overline{\tau_a}, t_i+T_p]$ is utilized.
iii) $T_p > n \cdot \overline{\tau_s} + \overline{\tau_c} + m \cdot \overline{\tau_a} + \overline{\tau_{ack}}$, where n,$m \in \mathbb{N}/\{0\}$ represent the number of consecutive losses in the measurement/actuation.

4. SIMULATION RESULTS FOR A CSTR

The formerly presented method has been applied to a CSTR, where an irreversible exothermic reaction, $A \rightarrow B$, takes place in a constant volume, cooled by a single coolant stream at temperature T_c –see Figure 2–. The overall

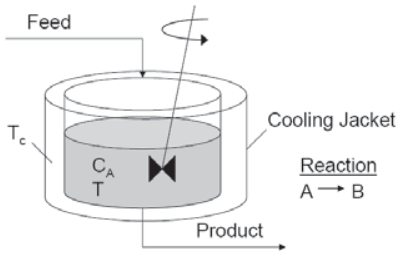

Fig. 2. Scheme of CSTR under study.

system is modeled as:

$$\dot{C}_A(t) = \frac{F}{V}(C_{Af} - C_A(t)) - k_0 C_A(t) e^{-\frac{E}{RT_r(t)}},$$
$$\dot{T}_r(t) = \frac{F}{V}(T_{rf} - T_r(t)) - \frac{k_0 \Delta H}{\rho c_p} C_A(t) e^{-\frac{E}{RT_r(t)}} + \frac{UA}{\rho c_p V}(T_c(t) - T_r(t)).$$

The meaning and the values of all the parameters are explained in Henson and Seborg (1997). Under the nominal condition $T_c^{nom} = 103.4$ K, the system has the three equilibrium points depicted in Figure 3. The objective is to stabilize the unstable saddle point $(0.52, 398.97)$ by manipulating the control input $u(t) = T_c(t)$ under the input constraints $T_c(t) \in [275, 370]$ K. If we represent

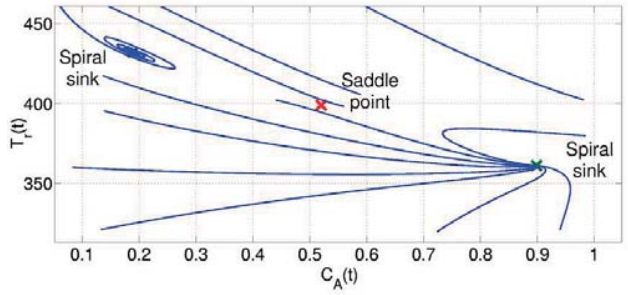

Fig. 3. Phase plot of the system for the nominal case $T_{c,nom} = 302$ K.

the state as the vector $x(t) = [C_A(t) \quad T_r(t)]^T$, the cost functional to be minimized is given by

$$J(u, x) = \int_{t_i}^{t_i + T_p} (x^T Q x + u^T Q u) d\tau,$$

where $Q = I$, $R = 1$, and $T_p = 1.5$ min. For sake of simplicity, the control trajectory is held constant between consecutive recalculation times. Terminal penalty and terminal region constraints have been chosen such that closed loop stability in the nominal case is achieved.

In Figure 4, the results for the asynchronous nominal case (no delays and no failures) are presented. Compared to a classical sampling approach with constant recalculation interval $\delta = 0.15$ min, the asynchronous controller presented in Theorem 3 obtains extremely similar results by saving up to 30% of computational effort and exchanged information. The partition π is implicitly determined by the absolute error on the product concentration, i.e. the sensor regularly checks the concentration $C_A(t)$, but it sends a measurement to the controller only when

$$\|C_A(t) - 0.52\| > \epsilon, \text{ with } \epsilon = 2 \cdot 10^{-3},$$

for longer than 0.15 minutes. In a second simulation

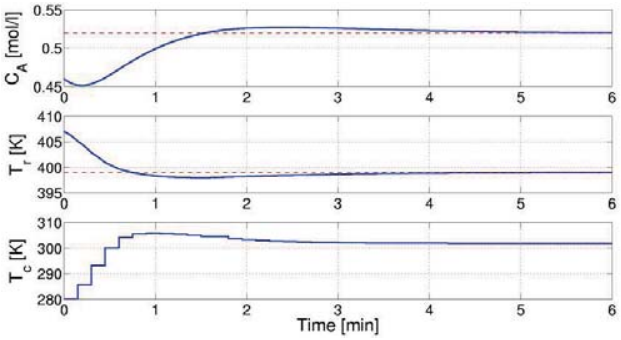

Fig. 4. Event-based controller under nominal conditions.

both measurement and actuation delays are considered. It is assumed that τ_s lies between 0 and 15 seconds, while τ_a between 0 and 5 seconds. Both are modeled as uniform variables. For sake of simplicity, no computational delay is considered. However, notice that this delay could be implicitly considered as part of the input delay τ_a. Furthermore, it is assumed that the probability loss at the actuator side p_a is equal to 5%, while no information from the sensor is lost. It is also supposed that Assumption 15 is verified. The results for the compensated and the uncompensated case are presented in Figure 5. As one can see, the proposed method is able to stabilize effectively the unstable saddle point with performance comparable to the nominal case, reported in Figure 4. Note that the controllers presented in Findeisen and Allgöwer (2004); Chen et al. (2000) are not able to handle delays on the actuation side at all.

5. CONCLUSIONS AND FUTURE DIRECTIONS

In this paper, it was shown how PC can be used to control event-based/asynchronous systems, such as chemical processes, in which the recalculation times do not need to be known a priori. Moreover, it was depicted how delays and information losses/failures on the actuators/sensors, common in control systems, need to be taken into account to avoid instability. Whereas delays can be compensated easily with forward prediction, one can exploit bidirectional communication with the actuators in order to establish an acknowledgment mechanism to counteract information losses/failures. Two algorithms able to guarantee asymptotic convergence for nonlinear continuous time systems were presented. Through the simulation of a CSTR, it was shown firstly that asynchronous PC can actually reduce both computational requirements and exchanged information, but also compensate effectively delays and information losses while keeping closed loop stability and good performance. Future work should concentrate on how to include directly in the optimization problem the

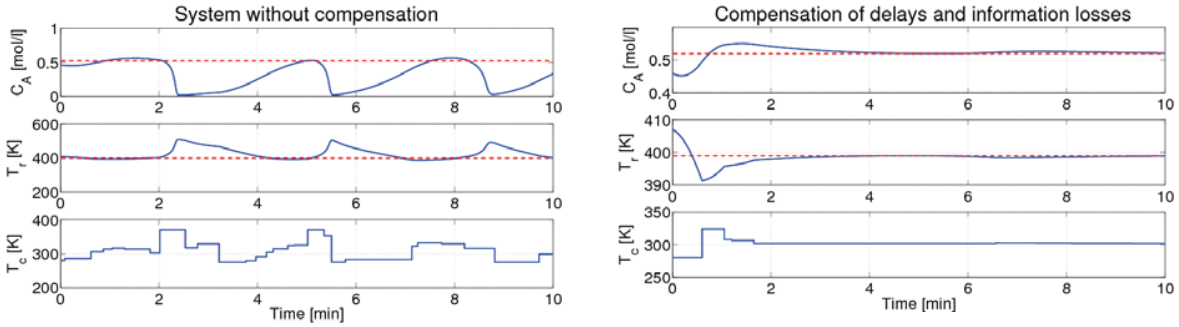

Fig. 5. Results for the closed loop system subject to delays and information losses with and without compensation.

exchanged information. Moreover, the method should be extended to include also robustness.

REFERENCES

Alldredge, G. and M. S. Branicky, V.L. (2008). Play-back buffers in networked control systems. evaluation and design. *Amer. Cont. Conf.*, 3106–3113.

Brockett, R. and Liberzon, D. (1998). Quantized feedback systems perturbed by white noise. In *Proc. 37th IEEE Conference on Decision and Control*, volume 2, 1327–1328.

Chen, W., Ballance, D., and O'Reilly, J. (2000). Model predictive control of nonlinear systems: Computational delay and stability. In *IEE Proceedings, Part D 147(4)*, 387–394.

Findeisen, R. (2006). *Nonlinear Model Predictive Control: a Sampled-Data Feedback Perspective*, volume 8. VDI Verlag.

Findeisen, R. and Allgöwer, F. (2004). Computational delay in nonlinear model predictive control. In *Proc. Int. Symp. Adv. Contr. of Chem. Proc.*, 427–432. Hong Kong, PRC.

Findeisen, R. and Varutti, P. (2009). Stabilizing nonlinear predictive control over nondeterministic communication networks. In L. Magni, D. Raimondo, and F. Allgwer (eds.), *Nonlinear Model Predictive Control: Towards New Challenging Applications*, Lecture Notes in Control and Information Sciences. Springer. In printing.

Fontes, F. (2001). A general framework to design stabilizing nonlinear model predictive controllers. *Sys. Contr. Lett.*, 42(2), 127–143.

Heemels, W.P., Sandee, J.H., and Van den Bosch, P. (2008). Analysis of event-driven controllers for linear systems. *Inter. J. of Cont.*, 81, 571–590.

Henson, M. and Seborg, D. (1997). *Feedback Linearizing Control*. Prentice Hall.

Mayne, D.Q., Rawlings, J.B., Rao, C.V., and Scokaert, P.O.M. (2000). Constrained model predictive control: Stability and optimality. *Automatica*, 36(6), 789–814.

Tanenbaum, A.S. (2008). *Computer Networks*. Prentice Hall PTR, 4th edition.

Varutti, P. and Findeisen, R. (2008). Compensating network delays and information loss by predictive control methods. (submitted to ECC09).

Appendix A

Algorithm 1 (Worst Case Compensation)

$\forall t_i \in \pi$; t = current time;

Sensor:

(1) Measure $x(t_i)$.
(2) Send $[x(t_i)|ts]$, with $ts = t_i$, to the controller.
(3) Go to 1.

Controller:

`buffer` $= [x(t_i)|ts]_{old}$;
`control_input` $= \{[u^*(\cdot)|ts_0]\}$;
(1) If $[x(t_i)|ts]_{new}$ arrives
  a) If $ts_{new} \leq ts_{old}$, then discard.
  b) Else `buffer` $= [x(t_i)|ts]_{new}$.
(2) $\tau_s = (t - t_i)$ for $t_i = ts$.
(3) Calculate (9), from $u^*(\cdot; x(t_i)) \in$ `control_input`.
(4) Solve the o.c.p. for (9) $\longrightarrow$
  $u^*(\tau; x(t_i))$, for $\tau \in (t_i + \tau_s(t_i) + \overline{\tau_a} + \overline{\tau_c}, t_{i+1} + \tau_s(t_{i+1}) + \overline{\tau_a} + \overline{\tau_c}]$.
(5) Send $[u^*(\tau; x(t_i))|ts]$, with $ts = (t + \overline{\tau_a} + \overline{\tau_c})$.
(6) Insert $[u^*(\tau; x(t_i))|ts]$ in `control_input`.
(7) Go to 1.

Actuator:

`buffer` $= \{[u^*(\cdot)|ts_0], \ldots, [u^*(\cdot)|ts_n]\}$, for $ts_0 < t < ts_1 \ldots < ts_n$;
`applied_input` $= [u^*(\cdot)|ts_0]$;
(1) If $[u^*(\cdot)|ts]_{new}$ arrives
  a) Insert $[u^*(\cdot)|ts]_{new}$ in `buffer`.
  b) Sort `buffer` by increasing ts.
(2) `temp` = first element of `buffer`.
(3) If $ts_{\texttt{temp}} = t$
  a) `applied_input` = `temp`.
  b) Remove first element from `buffer`.
(4) Go to 1.

Algorithm 2 (Information Loss Compensation)

$\forall t_i \in \pi$; t = current time;

Sensor:

(1) Measure $x(t_i)$.
(2) Send $[x(t_i)|ts]$, with $ts = t_i$.
(3) Go to 1.

Controller:

`buffer` $= [x(t_i)|ts]_{old}$;
`control_input` $= \{[u^*(\cdot)|ts_0]\}$;
`delivered` = `true`;
(1) If $[\cdot|ts]$ arrives:
(2) Case($[x(t_i)|ts]$):
  If $ts_{new} \leq ts_{old}$, then discard.
  Else `buffer` $= [x(t_i)|ts]_{new}$.
  $\tau_s = (t - t_i)$ for $t_i = ts$.
  Calculate (13), from $u^*(\cdot; x(t_i)) \in$ `control_input`.
  Solve the o.c.p. for (13) $\longrightarrow$
  $u^*(\tau; x(t_i))$, for $\tau \in (t + \overline{\tau_a} + \overline{\tau_c}, t_i + T_p]$.
  `delivered` = `false`.
  Send $[u^*(\tau; x(t_i))|ts]$, with $ts = (t + \overline{\tau_a} + \overline{\tau_c})$.
  Wait until `delivered`=`true` OR t $\geq$ ts.
  If `delivered` = `true`, then insert $[u^*(\tau; x(t_i))|ts]$ in `control_input`.
  Else if t $\geq$ ts, then `delivered` = `false`, use old input in `control_input`.
  Go to 1.
(3) Case($[ack|ts]$):
  Set `delivered` = `true`.
  Go to 1.

Actuator:

`buffer` $= \{[u^*(\cdot)|ts_0], \ldots, [u^*(\cdot)|ts_n]\}$,
for $ts_0 < t < ts_1 \ldots < ts_n$;
`applied_input` $= [u^*(\cdot)|ts_0]$;
(1) If $[u^*(\cdot)|ts]_{new}$ arrives
  a) Send $[ack|ts]$ to the controller.
  b) Insert $[u^*(\cdot)|ts]_{new}$ in `buffer`.
  c) Sort `buffer` by increasing ts.
(2) `temp` = first element of `buffer`.
(3) If $ts_{\texttt{temp}} = t$
  a) `applied_input` = `temp`.
  b) Remove first element from `buffer`.
(4) Go to 1.

Biological Systems

Oral Session

Analysis, Control, and Operational Optimization of a *Zymomonas mobilis* Reactor with Equilibrium Multiplicity

Jorge O. Trierweiler and Fabio C. Diehl

Group of Intensification, Modeling, Simulation, Control and Optimization of Processes – GIMSCOP
Department of Chemical Engineering, Federal University of Rio Grande do Sul – UFRGS
Rua Luiz Englert, s/n CEP: 90040-040 - Porto Alegre - RS - BRAZIL
E-MAIL: {jorge, fcdiehl}@enq.ufrgs.br

Abstract: For a successful application of any industrial *Z. mobilis* facility, it is necessary to have an efficient and simple control strategy. This paper analyzes the control and optimization problem of a continuous ZM bioreactor modeled by Jöbses et al. (1986). This system has steady state multiplicity in part of the operating range. The idea is to maintain the process close to the manifold border where is achievable the highest ethanol production. Based on a systematically analysis of the operational controllability using the nonlinear RPN indices it is identified that the process can be controlled using a linear controller. Finally the paper proposes a variable transformation that makes easy to maintain the bioreactor close to the optimum.

Keywords: nonlinear degree measurement, RPN methodology, bifurcation, bioreactor control, process optimization

1 INTRODUCTION

Zymomonas mobilis has attracted considerable interest over the past decades as a result of its unique metabolism and ability to rapidly and efficiently produce ethanol from simple sugars. However, despite its apparent advantages of higher yields and faster specific rates when compared to yeasts, no commercial scale fermentations currently exist which use *Z. mobilis* for the manufacture of fuel ethanol. In addition to ethanol depending on the substrate other fermentation products can occur, such as lactic acid, acetic acid, formic acid, acetone, and sorbitol. See (Rogers *et al.*, 2007), for a detailed review.

In the literature, *Zymomonas mobilis* has been proposed as a more promising microorganism than conventional yeast *Saccharomyces cerevisiae* for industrial production of ethanol (Rogers *et al.*, 2007). A major drawback of this microorganism is that it exhibits sustained oscillations (i.e., Hopf bifurcation) for low dilution rates (i.e., $D_f \leq 0.1\ h^{-1}$) when grown in continuous mode. This leads to decreased ethanol productivity and less efficient use of available substrate (Zhang and Henson, 2001). Various models have been proposed to describe the oscillatory dynamics of continuous *Zymomonas mobilis* cultures. Two of them are the Daugulis *et al.* (1997) and Jöbses *et al.* (1986) models. Even though the model predictions can be considered similar at low dilution rates, where the models have been fitted to the experimental data, they are quite different for higher dilution rates (Trierweiler and Diehl, 2009).

The Jöbses's model was fitted to experimental data with low dilution rate (i.e., $D_f \leq 0.1\ h^{-1}$) and middle inlet substrate concentration (i.e., $C_{S0} \cong 150\ kg/m^3$). Later, it was extrapolated outside of this operating region by Elnashaie *et al.* (2006), who have found a much more profitable operating region at higher dilution rates ($D_f \cong 2.0\ h^{-1}$) and inlet concentrations ($C_{S0} \cong 200\ kg/m^3$). Notwithstanding the Jöbses's model has not been validated at this region, our contribution will assume that this extrapolation is acceptable and we will propose a control strategy to maintain the system working at this more profitable operating region.

This paper is structured as follows: In section 2 the Jöbses's models is presented, section 3 it is analyzed the operational controllability which is used as basis for the proposed control strategy developed in section 4 and later validated by simulation. Final conclusions and remarks are then summarized in section 5.

2 MODEL DESCRIPTION AND OPERATING POINT DEFINITIONS

Since the Jöbses's model can predict a branch with higher ethanol production, which has been experimentally confirmed (at least for low dilution rates) by Elnashaie *et al.* (2006), we decide to analyze the control problem of a continuous bioreactor with the Jöbses *et al.* (1986) kinetic model, which is shortly described in the next subsection.

2.1 Model Description

The Jöbses's model consists of the following 4 differential equations:

$$\frac{dC_S}{dt} = -\frac{\mu_{max}.C_S.C_E}{Y_{SX}.(K_S+C_S)} - m_S.C_X + D_f.(C_{S0} - C_S)$$

$$\frac{dC_X}{dt} = \frac{\mu_{max}.C_S.C_E}{(K_S+C_S)} + D_f.(C_{X0} - C_X) \quad (1)$$

$$\frac{dC_E}{dt} = \frac{K_E.(C_P-c_1)(C_P-c_2).C_S.C_E}{(K_S+C_S)} + D_f.(C_{E0} - C_E)$$

$$\frac{dC_P}{dt} = \frac{\mu_{max}.C_S.C_E}{Y_{PX}.(K_S+C_S)} + m_P.C_X + D_f.(C_{P0} - C_P)$$

where C_S is the substrate (glucose) concentration, C_X is the biomass (*Z. mobilis*), C_P is the product (ethanol) concentration, and C_E is an auxiliary variable used to lag the effect of the ethanol concentration in the kinetic model. The insertion of the $K_E.(C_P - c_1)(C_P - c_2)$ parcel together with C_E makes possible the model to depict the oscillatory behavior of the Hopf bifurcation. In the model, dilution rate D_f is the inversion of the residence time and is defined as the relation between the inlet flow rate and the bioreactor volume. The model parameters are summarized in Table 1.

Table 1: Model parameters

Parameters	Values	Parameters	Values
K_E $\left[\frac{m^6}{kg^2.h}\right]$	0.00383	m_S $\left[\frac{kg}{kg.h}\right]$	2.160
c_1 $\left[\frac{kg}{m^3}\right]$	59.2085	m_P $\left[\frac{kg}{kg.h}\right]$	1.100
c_2 $\left[\frac{kg}{m^3}\right]$	70.5565	(Y_{SX}, Y_{PX}) $\left[\frac{kg}{kg}\right]$	(0.02445, 0.05263)
K_S $\left[\frac{kg}{m^3}\right]$	0.500	μ_{max} $\left[\frac{1}{h}\right]$	1.0

Fig. 1 shows the steady-state solutions for ethanol concentration (C_P) in function of dilution rate (D_f) and inlet substrate concentration (C_{S0}).

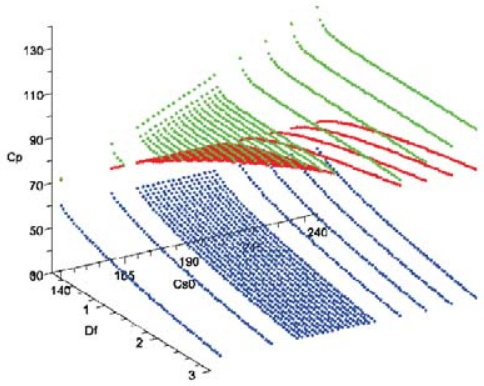

Fig. 1: Steady-state ethanol concentration (C_P) as a function of Dilution rate (Df) and inlet substrate concentration (C_{S0}).

2.2 Operating points

The optimal condition for the bioreactor is achieved with a high ethanol production. For the Jöbses's model, it can be shown that the main decision operating criterion for the best operating point is the ethanol production (EP), which is given by the multiplication of the dilution rate (D_f) and the ethanol concentration (C_P), i.e.,

$$EP = D_f.C_P. \quad (2)$$

Fig. 2 is produced for the iso-inlet substrate concentrations C_{S0} of 180, 200, and 220 kg/m^3 that were already shown in Fig. 1. Note that the dashed and dashdot lines are the same for all three operating conditions, therefore only one line for each branch is shown in Fig. 2.

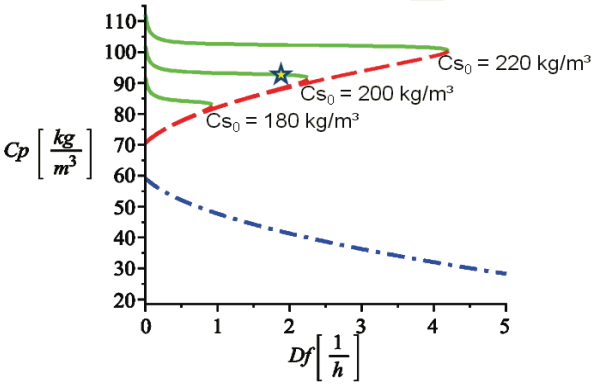

Fig. 2: Steady-state ethanol concentration (C_P) for three inlet substrate concentrations (C_{S0}).

Considering the curves generated for $C_{S0} = 200\ kg/m^3$ in Fig. 2, we can see that in the range of $0 < D_f < 2.25\ h^{-1}$ the system has three possible steady-state solutions. Two of them are stables (solid and dashdot lines) and one unstable (i.e., the middle branch illustrated by dashed line). The best operating point is located in the above curve close to the saddle point formatted by the intersection of the stable and unstable branches. The star in the above branch depicts a typical optimal operating point. From a control point of view the main difficult is to maintain the system working in this point avoiding a migration to the bellow operating point – the dash-dot line in Fig. 2. This migration can occur if the dilution rate is above the corresponding to the bifurcation saddle point or by a reduction to the inlet substrate concentration. Fig. 3 shows the case where the dilution rate is increased from 2 h^{-1} to 2.5 h^{-1} and then at 10 h again reduced to 2 h^{-1}. To bring the system to the more profitable operating point it is necessary to apply a pulse in the inlet ethanol concentration (C_{P0}) as shown at 15 h.

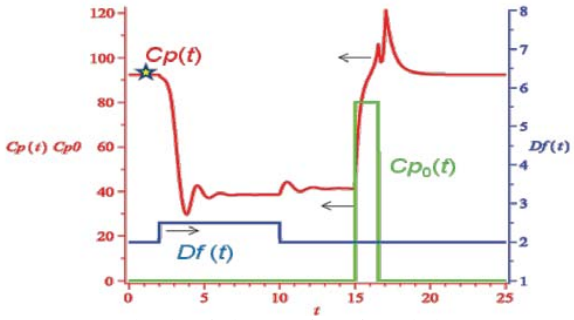

Fig. 3: Dynamic simulation to show how it is easy to move the operating point from the high to the low production branch.

2.3 Operating regions

The manifold that separate the region where occurs multiplicity in the ethanol concentration is defined by the saddle bifurcation points and is shown in Fig. 4. This manifold limits the operating region with possible high ethanol concentration (region A) from the region where only a low ethanol concentration is achievable (region B), where the operating conditions goes outside de operating region A, the ethanol concentration will fall down as it was depicted in Fig. 3.

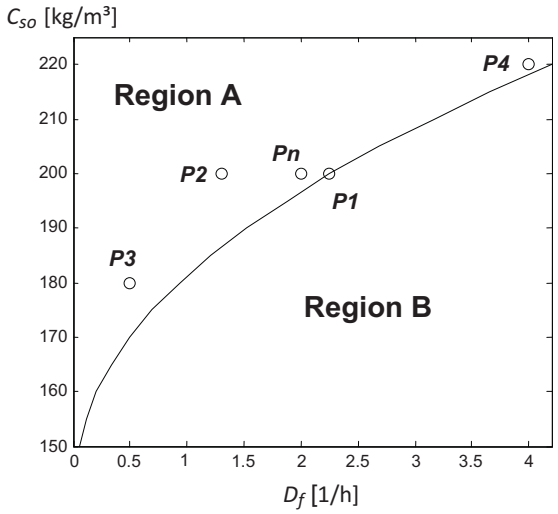

Fig. 4: Manifold of saddle points defining the operating region A (where exists multiplicity) and operating region B (where exits one solution only).

To characterize the differences between the high and low ethanol concentration branches, the system was linearized in five different operating points defined in Table 2 and placed in Fig. 4, where P_n is considered as the nominal/optimal operating point. The other four can occurs during a normal operation in the region A. Of course, P_4 has higher *EP* than P_n, but since the Jöbses model cannot describe higher C_{S0} correctly, we will just assume that P_n is the best operating point, but the same analysis could be performed considering P_4 as nominal model.

Table 2: Definition of Operating Region

	D_f $[h^{-1}]$	$C_{S0}\left[\frac{kg}{m^3}\right]$	OP1- high C_P $(C_P, C_S)_{SS}$*	OP2 - low C_P $(C_P, C_S)_{SS}$*
P_n	2.0	200	(92.57, 1.23)	(41.29, 111.34)
P_1	2.25	200	(91.83, 2.75)	(39.94,114,22)
P_2	1.3	200	(93.07, 0.40)	(45.56, 102.29)
P_3	0.5	180	(84.24, 0.31)	(52.09,68.90)
P_4	4.0	220	(101.38, 2.04)	(32.02, 151.16)

*$(C_P, C_S)_{SS}$ means steady-state values for ethanol and substrate concentration for a given D_f and C_{S0}.

Figures 5 and 6 respectively show the step response of the dynamic linearized models for high and low ethanol concentration branches. Essentially the high ethanol branch has an over-damped behavior, whereas for the low branch the system is under-damped.

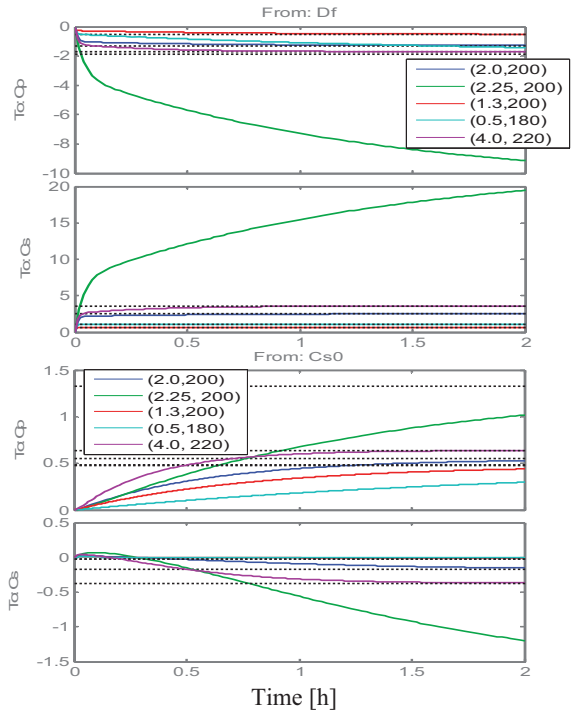

Fig. 5: Step response of the linearized models at the operating points defined in Table 2 corresponding to the high ethanol concentration branch for C_P and C_S outputs.

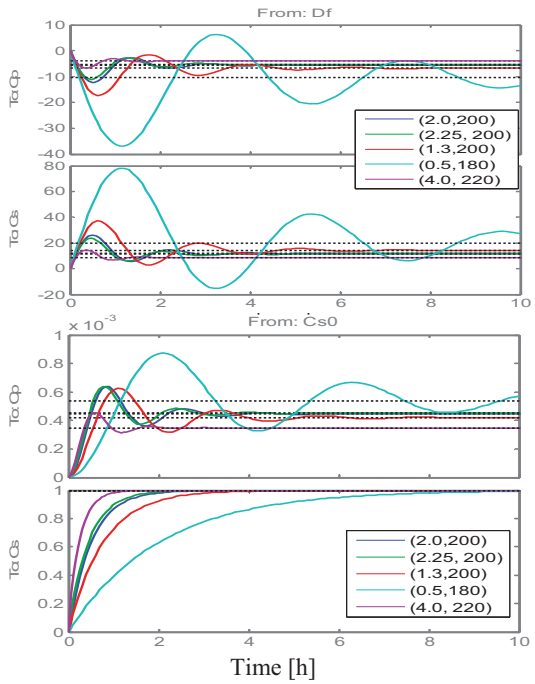

Fig. 6: Step response of the linearized models at the operating points defined in Table 2 corresponding to the low ethanol concentration branch for C_P and C_S outputs.

3 OPERATIONAL CONTROLLABILITY ANALYSIS

3.1 Manipulated and controlled variables

Ethanol and substrate concentrations are two natural controlled variables of the system and can be in principle measured on-line using 2D-fluorescence spectroscopy (Hantelmann *et al.*, 2006). As candidates for manipulated variables, we have the dilution rate (D_f), inlet substrate concentration (C_{S0}), and inlet ethanol concentration (C_{P0}). In principle, C_{P0} should be used only in critical situations, just to bring the system back to the higher production branch (as shown in Fig. 3). Therefore we will not consider it in our operational controllability analyses, where only the input-output pairs $(D_f, C_{S0}) \rightarrow (C_P, C_S)$ is further considered.

3.2 Nominal Operational Controllability

The determinant and the elements λ_{11} and λ_{12} of the RGA – relative gain array (Skogestad and Postlethwaite, 2005) – are calculated using the steady state gain matrix for each one of the linearized models defined in Table 2. These results are summarized in Table 3, where we can see that the determinant (Det) does not change its sign when the system goes from the operating region 1 (OR1) with high ethanol concentration to OR2 with low ethanol concentration. Nevertheless the recommended pairing using steady state RGA changes from OR1 to OR2. Usually, when the pairing recommendation is changed it is normally associated with a change in the determinant sign, what it does not happens for this system. When the determinant changes its sign it is equivalent to the change in the multivariable gain, what is quite critical for the success of any control strategy. The reason for this unusual behavior is related to the gain sign change of channel $C_{S0} \rightarrow C_S$ ($i.e., K_{22}$) as it can been seem by the gain matrix for the nominal operating point P_N for the high and low ethanol concentration branches, which are given by:

$$K_{PN\_high} = \begin{bmatrix} -1.30 & 0.55 \\ 2.55 & -0.18 \end{bmatrix} \quad (3)$$

$$K_{PN\_low} = \begin{bmatrix} -5.55 & 0.0004 \\ 11.82 & 0.999 \end{bmatrix} \quad (4)$$

Similar behavior occurs for all other OPs.

Table 3: Determinant and Steady State RGA

	Det OR1	Det OR2	RGA – OR1 $(\lambda_{11}, \lambda_{12})$*	RGA – OR2 $(\lambda_{11}, \lambda_{12})$*
P_n	-1.16	-5.55	(-0.20, 1.20)	(0.99, 0.01)
P_1	-10.58	-5.25	(-1.89, 2.89)	(0.99, 0.01)
P_2	-0.26	-6.78	(-0.05, 1.05)	(0.99, 0.01)
P_3	-0.48	-10.26	(-0.11, 1.11)	(0.99, 0.01)
P_4	-1.66	-3.98	(-0.38, 1.38)	(0.999, 0.001)

$(\lambda_{11}, \lambda_{12})$* it was calculated considering the pairing $D_f \rightarrow C_P$ and $C_{S0} \rightarrow C_S$.

3.3 RPN and rRPN Analysis

The Robust Performance Number (RPN) was introduced in (Trierweiler, 1997) and (Trierweiler and Engell, 1997) as a measure to characterize the operational controllability of a system. The RPN indicates how potentially difficult it is for a given system to achieve the desired performance robustly. The RPN is influenced by three terms: the desired closed loop performance, nonminimum phase behavior (i.e., RHP pole, zero, and pure time delays), and its degree of directionality.

The RPN is a measure of how potentially difficult it is for a given system to achieve the desired performance robustly. The easiest way to design a controller is to use the inverse of the process model. An inverse-based controller will have potentially good performance robustness only when the RPN is small. As inverse-based controllers are simple and effective, it can be concluded that a good control structure selection is one with a small (< 5) RPN (Trierweiler and Engell, 1997).

Table 4: RPN Analysis for the *high* ethanol concentration branch

	$t_R = 1.0\ h$		$t_R = 0.50\ h$		$t_R = 0.25\ h$	
	RPN	$rRPN$	RPN	$rRPN$	RPN	$rRPN$
P_n	1.66	0.088	1.61	0.085	1.58	0.086
P_1	2.27	0.152	1.90	0.1201	1.78	0.097
P_2	1.52	0.069	1.53	0.074	1.51	0.0790
P_3	1.50	0.068	1.53	0.0725	1.52	0.0781
P_4	1.91	0.124	1.80	0.110	1.69	0.101

Table 4 shows the RPN calculated by three different desired performance specified by the rise times $t_R = 1, 0.5,$ and $0.25\ h$ and 10% overshoot for both outputs, what makes the system 2, 4, and 8 times faster than open loop response for the high ethanol concentration branch and all operating points. The results shown in Table 4 allow us to conclude that considering each operating point independently they will be easily controllable. It is important to mention that the RPN does not give a clear idea of the control difficulties for that it is necessary to analyze the *relative* RPN ($rRPN$), which has been introduced by Trierweiler (2002) (see also (Trierweiler and Farina, 2002) for an additional discussion).

The $rRPN$ is the relative distance between the RPN curve and the minimum RPN curve and it is quantified by the areas under the curves. Values less than 1 and close to zero means that the desired performance is easily achievable. Again, since we are considering only the two stable branches, no nonminimum phase component occurs in the analyzed operating points. In this case, typically faster performance will usually reduce the $rRPN$. Table 4 depicts that it is possible to design a controller that achieves the desired performance for each one of the analyzed operating points. Similar analyses (not shown here) performed for the low ethanol concentration branch produce similar conclusions with a RPN and $rRPN$ in the order of 1.5 and 0.004, respect.

The local operational controllability analyses clearly conclude that for each one of the considered models it is possible and easy to design a controller with the desired performance. Although each point is easily controllable,

nothing can be said about all operating points together. Is there possible to design a controller that will produce a good performance for all operating points? Moreover, if a controller designed for OR1 will work in OR2? Based on the steps responses of the linearized models shown in Figures 5 and 6, it seems the responses are quite different, especially if we compare the under-damped behavior shown by OR2 and the over-damped of the OR1. In the next subsection, we answer these questions through the *nonlinear RPN* analysis.

3.4 Nonlinear degree – nRPN Analysis

In (Farenzena and Trierweiler, 2004) three novel indices were introduced to measure system's nonlinearity. These nonlinear measurements are derived from the Robust Performance Number (RPN) concept. The total system's nonlinearity can be measured by the *nonlinear RPN* ($nRPN$), while the purely static nonlinearity is captured by *nonlinear static RPN* ($nRPN_{STAT}$) and the dynamic component by the *nonlinear dynamic RPN* ($nRPN_{DYN}$). These indices do not require a nonlinear model, being enough a set of linear models. Therefore, they can easily be applied to quantify the nonlinearities of industrial plants and used to answer several practical important questions such as: how nonlinear is the system? Is it necessary to apply a nonlinear controller? What kind of nonlinear controller is required?

In the definition of the nonlinear RPN indices was introduced the logarithm function to make easier their interpretation. Values smaller than 1 indicate that the performance difference between nonlinear and linear controllers is not significant, so that a linear controller is recommended. Indices greater than 2 clearly indicate that a nonlinear controller is necessary. Between 1 and 2 is a transition zone, where in many times a robust controller can stabilize all possible plants, but the performance loss can be significant if the values are close to 2. This analysis is made for all three indices. For instance, if $nRPN$ and $nRPN_{STAT}$ are high and $nRPN_{DYN}$ is small, it indicates that the nonlinearity is essentially static and can be compensated by gain scheduling controller. If the all values are big (greater or close to 2), then a nonlinear model predictive controller is recommended.

Table 5: $nRPN$, $nRPN_{STAT}$, and $nRPN_{DYN}$. Analyses

	$t_R = 1.0\ h$			$t_R = 0.50\ h$		
	nRPN	*STAT.*	*DYN.*	*nRPN*	*STAT.*	*DYN.*
H	0.86	0.58	-0.052	0.79	0.58	-0.21
L	0.31	-0.28	0.455	0.27	-0.28	0.40
T	1.68	0.88	0.74	1.50	0.88	0.51
	$t_R = 0.25\ h$			$t_R = 0.10\ h$		
	nRPN	*STAT.*	*DYN.*	*nRPN*	*STAT.*	*DYN.*
H	0.74	0.58	-0.35	0.69	0.58	-0.54
L	0.27	-0.28	0.39	0.29	-0.28	0.42
T	1.32	0.88	0.24	1.12	0.88	-0.12

→ Stat. and Dyn. mean $nRPN_{STAT}$ and $nRPN_{DYN}$, respect. *H*: polytope model for the high C_P branch, *L*: polytope model for the low C_P branch, and $T = H \cup L$.

To quantify the nonlinearity using the *nonlinear RPN* it is necessary to construct a set of linearized models, called as polytope model. The operating points defined in Table 2 have been used to define the polytopes. Three polytope sets have being formed: *H* formed with the 5 linearized models at the *high* ethanol concentration branch; *L* formed from the linearized models corresponding to the *low* C_P branch; and *T* formed by the union of all 10 models.

Table 5 summarizes the results of the $nRPN$ analysis, which indicates that in general the polytope *H* is more nonlinear than the polytope *L* and the nonlinearity found in *H* is essentially static, whereas for *L* the nonlinearity is of the dynamic type. Of course, the combination of both polytopes (*T*) exhibits the highest nonlinearity, which has similar dynamic and static components for low performance, but for the highest desired performance (i.e., $t_R = 0.10$) it becomes essentially static. Moreover, for this performance it is expected that a linear controller will be able to control the system in both operating regions. To verify this prediction, we have design a multivariable PI controller, given by:

$$PI(s) = \begin{bmatrix} -0.161 \times \left(1 + \frac{1}{0.1128s}\right) & 1.6981 \times \left(1 + \frac{1}{0.0063s}\right) \\ 12.287 \times \left(1 + \frac{1}{0.6288s}\right) & 6.4204 \times \left(1 + \frac{1}{0.3606s}\right) \end{bmatrix} \quad (5)$$

This quite simple controller can control all 10 linearized models with a good performance as it is shown in Fig. 7, where it has been simulated a setpoint change in C_P of one unit at 1 h and a simultaneous load disturbance of $\Delta D_f = 0.2\ h^{-1}$ and $\Delta C_{S0} = 1\ kg/m^3$ at 6 h.

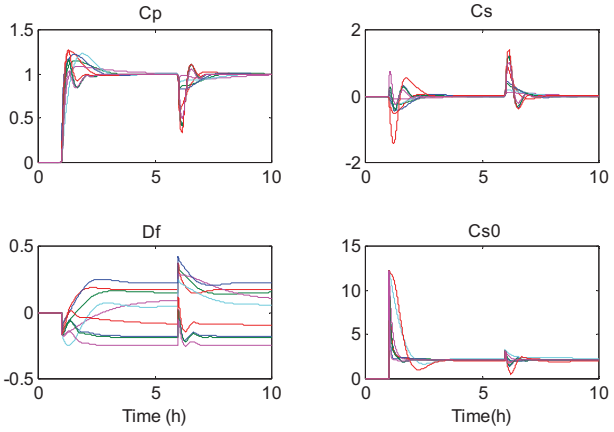

Fig. 7: Closed loop simulation with a multivariable *PI* controller for all 10 linearized models

4 CONTROL STRATEGY

Note that the predictions made by nonlinear RPN indices were confirmed by the closed loop simulation using the linearized models. Similar results are obtained using the fully nonlinear model (Trierweiler and Diehl, 2009). In this section, it is shown the basic ideas of the recommended control strategy.

4.1 General control strategy

It is recommended to use an Extended Kalman Filter (EKF) technique to filter the measurements from the 2D-fluorescence spectroscopy. The EKF is important also to estimate the biomass concentration and to take the input and model uncertainties into account. A multivariable controller should be used with the pairing $(D_f, C_{S0}) \rightarrow (C_P, C_S)$ and the inlet ethanol concentration (C_{P0}) should be only used in exceptional cases to bring the system back to the high ethanol concentration branch as shown in Fig. 3.

4.2 Solving the constraint problem

A single linear controller can be used to control the bioreactor in all operating conditions. The only special problem is to constraint the range of the manipulated variables, which should be limited by the saddle point manifold. This can be easily guaranteed by a single variable transformation as shown in Fig. 8. Instead to use directly the physical variables $(\Delta C_{S0},\ \Delta D_f)$ the controller calculate the control actions for $(\Delta y,\ \Delta x)$ using the simple restriction $\Delta y > 0$. The conversion to $(\Delta C_{S0},\ \Delta D_f)$ is performed by the multiplication with the rotation matrix R, given by:

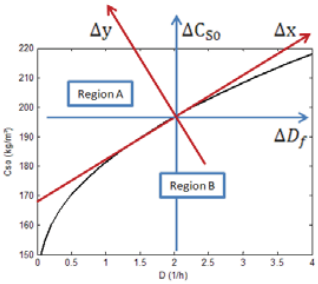

$$R = \begin{bmatrix} \cos(\theta) & -\sin(\theta) \\ \sin(\theta) & \cos(\theta) \end{bmatrix}$$

where θ is the rotation angle.

Fig. 8: Simple variable transformation for guarantee the feasible region A

Note that the optimal operating point is close to $\Delta y = 0$. This idea is explored in (Trierweiler and Diehl, 2009) to maintain the system always close to the optimal economic conditions.

5 CONCLUSIONS

The paper has introduced several contributions, which are summarized as follows:

***Zymomonas mobilis* control problem** – as far as we know, this contribution is the first paper that discusses the control problem of a continuous bioreactor with *Z. mobilis*.

Control strategy – a simple and efficient control strategy has been proposed based on the control of (C_P, C_S) using the manipulated variables $(\Delta C_{S0},\ \Delta D_f)$. Since the branch where the high C_P occurs is restricted, it was proposed to use a variable transformation as shown in Fig. 8. This transformation makes simple to consider the restriction range and open a simple strategy for assuring the optimal economic conditions, which occurs at $\Delta y \approx 0.5$.

RGA pairing with negative diagonal elements – the *Z. mobilis* bioreactor with the Jöbses's model it is a interesting example to illustrate that the common pairing rule where the positive diagonal elements are recommended it is not always the best global pairing. For this system the best pairing changes when the system moves from the high to the low C_P branch. It is interesting that the paring change occurs without alteration in the sign of the gain matrix determinant.

The RPN analysis is reliable – the RPN analysis, especially using the nonlinear RPN indices made possible very easily to check and quantify the nonlinearity degree and based on these analyses prescribe the appropriated controller. It was shown that if a fast controller is designed a simple linear controller can be used. To confirm this prediction a simple multivariable PI controller has been tuned and simulated.

Procedure for analysis a bioprocess optimization and control problem – finally the paper illustrate the typical steps necessary to develop a control and optimization strategy for a bioprocess system. Before designing a controller, it is necessary to systematically analyze the system as have been done in the paper.

Jöbses's Model – we have assumed that the model could predict the system behavior at high dilution rate and inlet substrate concentration. Of course, this extrapolation is totally questionable considering a real application.

Acknowledgements: The authors are very grateful for the grants from CAPES / BRAZIL. The first author also thanks Prof. Dr. W. Marquardt for receiving him for his sabbatical at RWTH Aachen, where this work has been written.

REFERENCES

Daugulis, A. J., Mclellan, P. J. and Li, J. (1997) Experimental investigation and modeling of oscillatory behavior in the continuous culture of *Zymomonas mobilis*. *Biotechnology and Bioengineering,* 56**,** 99-105.

Elnashaie, S. S. E. H., Chen, Z., Garhyan, P., Prasad, P. and Mahecha-Botero, A. (2006) Practical Implications of Bifurcation and Chaos in Chemical and Biological Reaction Engineering. *International Journal of Chemical Reactor Engineering 4*

Farenzena, M. and Trierweiler, J. O. (2004) System Nonlinearity Measurement Based on the RPN Concept. *DYCOPS - 7TH IFAC Symp. on Dynamics and Control of Process Systems***,** 181-191.

Hantelmann, K., Kollecker, M., Hüll, D., Hitzmann, B. and Scheper, T. (2006) Two-dimensional fluorescence spectroscopy: A novel approach for controlling fed-batch cultivations. *Journal of Biotechnology,* 121**,** 410-417.

Jöbses, I. M. L., Egberts, G. T. C., Luyben, K. C. A. M. and Roels, J. A. (1986) Fermentation kinetics of *Zymomonas mobilis* at high ethanol concentrations: Oscillations in continuous cultures. *Biotechnology and Bioengineering,* 28**,** 868-877.

Rogers, P., Jeon, Y., Lee, K. and Lawford, H. (2007) Zymomonas mobilis for Fuel Ethanol and Higher Value Products. *Biofuels.* Springer Berlin / Heidelberg.

Skogestad, S. and Postlethwaite, I. (2005) *Multivariable feedback control : analysis and design,* Chichester, England ; Hoboken, NJ, John Wiley.

Trierweiler, J. O. (1997) A Systematic Approach to Control Structure Design. Dortmund, University of Dortmund.

Trierweiler, J. O. (2002) Application of the RPN Methodology for Quantification of the Operability of the Quadruple-Tank Process. *Brazilian Journal of Chemical Engineering,* 19**,** 195-206.

Trierweiler, J. O. and Diehl, F. C. (2009) Control Strategy for a *Zymomonas mobilis* Bioreactor used in the Ethanol Production. *Submitted to PSE 2009*

Trierweiler, J. O. and Engell, S. (1997) The Robust Performance Number: A New Tool for Control Structure Design. *Computer Chemical Engineering* 21**,** 237-243.

Trierweiler, J. O. and Farina, L. A. (2002) The RPN Methodology Applied to Quantify Process Operability and Controller Design. *Proc.15th IFAC World Congress, Barcelona***,** CDROM, paper 2663.

Zhang, Y. and Henson, M. A. (2001) Bifurcation Analysis of Continuous Biochemical Reactor Models. *Biotechnology Progress,* 17**,** 647-660.

Adaptive extremum-seeking control of fed-batch cultures of micro-organisms exhibiting overflow metabolism

L. Dewasme [*] **A. Vande Wouwer** [*] **B. Srinivasan** [**] **M. Perrier** [**]

[*] *Service d'Automatique, Faculté Polytechnique de Mons, Boulevard Dolez 31, B-7000 Mons, Belgium (e-mails : Laurent.Dewasme, Alain.VandeWouwer@fpms.ac.be)*
[**] *Département de génie chimique, Ecole Polytechnique de Montréal, C.P.6079, Montréal, Que., Canada*

Abstract: *Overflow metabolism* characterizes cells strains that are likely to produce inhibiting metabolites resulting from an excess of substrate feeding and a saturated respiratory capacity. The critical substrate level separating the two different metabolic pathways is generally not well defined. This paper proposes two non-model based extremum-seeking strategies preventing a too important accumulation of inhibiting metabolites in fed-batch cultures, by estimating the critical substrate level on the basis of 3 simple measurements related to the feeding, oxygen and carbon dioxide. A simple substrate controller based on Lyapunov stability arguments is then designed and tested in combination with the two extremum-seeking schemes.

Keywords: Extremum seeking, nonlinear adaptive control, fermentation process, biotechnology.

1. INTRODUCTION

Industrial vaccine production is usually achieved using fed-batch cultures of genetically modified yeast or bacteria strains, which can express different kinds of recombinant proteins. From an operational point of view, it is necessary to determine an optimal feeding strategy (i.e. the time evolution of the input flow rate to the fed-batch culture) in order to maximize productivity.

The main encountered problem comes from the metabolic changes of such strains in presence of feeding overflow. This "overflow metabolism", also called "short-term Crabtree effect", is a metabolic phenomenon that is induced when the rate of glycolysis exceeds a critical value, leading to a generally inhibiting by-product formation from pyruvate (for not well understood reasons). It occurs for instance in *S. cerevisiae* cultures with aerobic ethanol formation, in *P. pastoris* with aerobic methanol formation, in *E. coli* cultures with aerobic acetate formation or in mammalian cell cultures with the aerobic lactate formation. To avoid this undesirable effect, a closed-loop optimizing strategy is required, which could take various forms (Pomerleau (1990), Chen et al. (1995), Akesson (1999), Renard (2006), Dewasme et al. (2007)).

In this study, a non-model based extremum-seeking strategy is chosen. Two original techniques are proposed and compared.

The first one is related to the work of Blackman in the 60's, revisited and improved in Ariyur and Krstic (2003) while the second one is based on a simple recursive least squares technique (RLS). Non-model based extremum-seeking has already been applied succesfully to dynamic optimization of continuous cultures in Wang et al. (1999).

Alternatively, model-based extremum-seeking strategy as presented in the works of Guay et al. (2004), Titica et al. (2003a) and Titica et al. (2003b) could also be considered for the on-line determination of the critical glucose concentration. However, the convergence of this adaptation scheme is slow and lacks robustness (Dewasme and Vande Wouwer (2008)).

2. MODEL AND CONTROL OBJECTIVES

2.1 Modeling cultures of micro-organisms exhibiting overflow metabolism

In this study, we consider a generic model that would, in principle, allow the representation of the culture of different strains presenting an overflow metabolism (yeasts, bacteria, animal cells, etc). This model describes therefore the cell catabolism through the following three main reactions:

$$\text{Substrate oxidation :} \quad \mathrm{S} + k_5\,\mathrm{O} \overset{r_1 X}{\rightarrow} k_1\,\mathrm{X} + k_8\,\mathrm{C} \tag{1a}$$

Overflow reaction (typically fermentation) :

$$\mathrm{S} + k_6\,\mathrm{O} \overset{r_2 X}{\rightarrow} k_2\,\mathrm{X} + k_4\,\mathrm{P} + k_9\,\mathrm{C} \tag{1b}$$

$$\text{Metabolite product oxidation :} \quad \mathrm{P} + k_7\,\mathrm{O} \overset{r_3 X}{\rightarrow} k_3\,\mathrm{X} + k_{10}\,\mathrm{C} \tag{1c}$$

where X, S, P, O and C are, respectively, the concentration in the culture medium of biomass, substrate (typically glucose or glycerol), product (i.e. ethanol or methanol in yeast cultures, acetate in bacteria cultures or lactate in animal cells cultures), dissolved oxygen and carbon dioxide. k_i are the yield coefficients and r_1, r_2 and r_3 are the nonlinear specific growth rates given by:

$$r_1 = \min\left(r_S, r_{Scrit}\right) \tag{2}$$

$$r_2 = \max\left(0, r_S - r_{Scrit}\right) \tag{3}$$

$$r_3 = \max\left(0, \min\left(r_P, \frac{k_5\left(r_{Scrit} - r_S\right)}{k_7}\right)\right) \tag{4}$$

where the kinetic terms associated with the substrate consumption r_S, the critical substrate consumption r_{Scrit} (generally de-

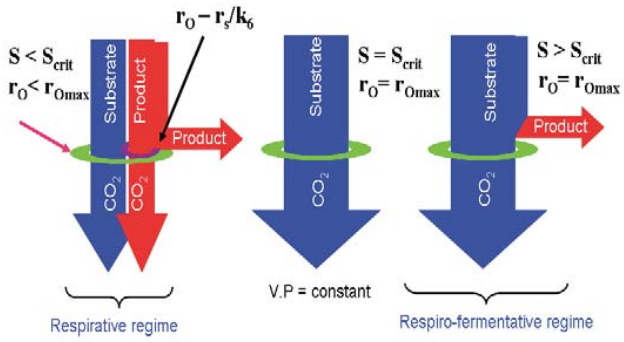

Fig. 1. Illustration of Sonnleitner's bottleneck assumption for cells limited respiratory capacity.

pendant on the cells oxidative or respiratory capacity r_O) and the product oxidative rate r_P are given by:

$$r_S = \mu_S \frac{\mathrm{S}}{\mathrm{S}+K_S} \tag{5a}$$

$$r_{Scrit} = \frac{r_O}{k_5} = \frac{\mu_O}{k_5}\frac{\mathrm{O}}{\mathrm{O}+K_O}\frac{Ki_P}{Ki_P+P} \tag{5b}$$

$$r_P = \mu_P \frac{\mathrm{P}}{\mathrm{P}+K_P} \tag{5c}$$

These expressions take the classical form of Monod laws where μ_S, μ_O and μ_P are the maximal values of specific growth rates, K_S, K_O and K_P are the saturation constants of the corresponding element, and Ki_P is the inhibition constant.

This kinetic model is based on Sonnleitner's bottleneck assumption (Sonnleitner and Käppeli (1986)) which was applied to a yeast strain *Saccharomyces cerevisiae* (Figure 1). During a culture, the cells are likely to change their metabolism because of their limited respiratory capacity. When the substrate is in excess (concentration $S > S_{crit}$), the cells produce a metabolite product P through fermentation, and the culture is said in respiro-fermentative (RF) regime. On the other hand, when the substrate becomes limiting (concentration $S < S_{crit}$), the available substrate (typically glucose), and possibly the metabolite P (as a substitute carbon source), if present in the culture medium, are oxidized. The culture is then said in respirative (R) regime. Component-wise mass balances give the following differential equations :

$$\frac{dX}{dt} = (k_1 r_1 + k_2 r_2 + k_3 r_3)X - DX \tag{6a}$$

$$\frac{dS}{dt} = -(r_1 + r_2)X + DS_{in} - DS \tag{6b}$$

$$\frac{dP}{dt} = (k_4 r_2 - r_3)X - DP \tag{6c}$$

$$\frac{dO}{dt} = -(k_5 r_1 + k_6 r_2 + k_7 r_3)X - DO + OTR \tag{6d}$$

$$\frac{dC}{dt} = (k_8 r_1 + k_9 r_2 + k_{10} r_3)X - DC - CTR \tag{6e}$$

$$\frac{dV}{dt} = F_{in} \tag{6f}$$

where S_{in} is the substrate concentration in the feed, F_{in} is the inlet feed rate, V is the culture medium volume and D is the dilution rate ($D = F_{in}/V$). OTR and CTR represent respectively the oxygen transfer rate from the gas phase to the liquid phase and the carbon transfer rate from the liquid phase to the gas phase. Classical models of OTR and CTR are given by:

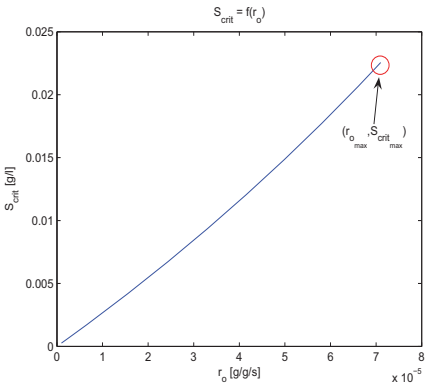

Fig. 2. S_{crit} as a function of r_o.

$$OTR = k_L a(O_{sat} - O) \tag{7a}$$

$$CTR = k_L a(P - P_{sat}) \tag{7b}$$

where $k_L a$ is the volumetric transfer coefficient and, O_{sat} and P_{sat} are respectively the dissolved oxygen and carbon dioxide concentrations at saturation.

2.2 Control objectives

First, we show that the respiratory capacity has an influence on the critical substrate concentration level. In the optimal operating conditions ($S = S_{crit}$), the fermentation and metabolite product oxidation rates are equal to zero and the substrate consumption rate r_S is equal to r_{Scrit} or $\frac{r_O}{k_5}$. Consequently, after a trivial mathematical manipulation of (5a), a relation between the critical substrate concentration level and the cell respiratory capacity is obtained as:

$$S_{crit} = \frac{K_S r_O}{k_5 \mu_S - r_O} \tag{8}$$

Figure 2 shows a plot of this relation where the point $[0,0]$ corresponds to a totally inhibited respiratory capacity, preventing any growth, and the point $[r_{o_{max}}, S_{crit_{max}}]$ corresponds to maximum productivity (i.e. absence of metabolite product in the culture medium and a sufficient level of oxygenation). Obviously, the presence of the product in the culture medium can decrease the respiratory capacity and in turn the value of the critical substrate concentration $S = S_{crit}$. In order to maintain the system at the edge between the respirative and respiro-fermentative regimes, it would be necessary to determine on-line the critical substrate concentration (S_{crit}) and to control the substrate concentration in the culture medium around this value (Dewasme and Vande Wouwer (2008)). Unfortunately, the substrate concentration measurement is a difficult task as typical concentration levels are below the resolution of currently available probes (or sensors).

An alternative solution is to reformulate the problem not as a maximazition of the respiratory capacity but as the maximization of the substrate consumption rate coupled to the minimization of the fermentation rate.

This can finally be formulated as follows:

$$max_{S_{crit}} Y = max_{S_{crit}} \varphi_1 - \varphi_2 \tag{9}$$

where:

- Y is the assumed measurable cost function;
- φ_1 and φ_2 correspond to the reaction rates $r_1 X$ and $r_2 X$, respectively.

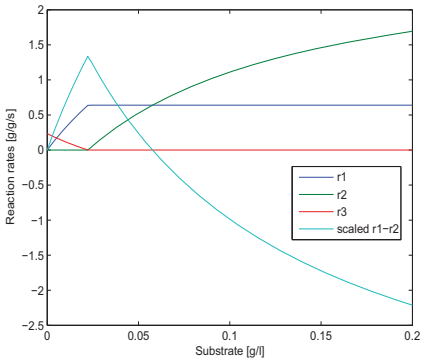

Fig. 3. Reaction rates and optimization criteria as a function of S.

In order to estimate the cost function Y online, we use a pseudo-steady state assumption. Indeed, assuming that the variations of substrate, oxygen and carbon dioxyde concentrations are equal to zero, we obtain from (6b), (6d) and (6e):

$$D(S_{in}-S) = (r_1+r_2)X \tag{10a}$$
$$-DO+OTR = (k_5r_1+k_6r_2+k_7r_3)X \tag{10b}$$
$$DC+CTR = (k_8r_1+k_9r_2+k_{10}r_3)X \tag{10c}$$

Dilution terms can be considered as negligible in comparison with OTR, CTR and DS_{in}. Replacing the reaction rates r_iX by φ_i $(i=1,2,3)$, (10) can be written:

$$DS_{in} = \varphi_1+\varphi_2 \tag{11a}$$
$$OTR = k_5\varphi_1+k_6\varphi_2+k_7\varphi_3 \tag{11b}$$
$$CTR = k_8\varphi_1+k_9\varphi_2+k_{10}\varphi_3 \tag{11c}$$

From this on, after some basic mathematical manipulations, it is possible to express a relation evolving proportionaly to $\varphi_1-\varphi_2$, as a function of the yield coefficients, OTR, CTR and DS_{in}. We decide to call DS_{in} the "substrate intake rate" (SIR) and we finally obtain:

$$Y = \varphi_1-\varphi_2 \propto y$$
$$y = 2\,k_{10}\,OTR - 2\,k_7\,CTR + (k_7k_9-k_5k_{10}+k_8k_7-k_6k_{10})SIR \tag{12}$$

This optimization criteria can thus be evaluated on the basis of 3 measurements (OTR, CTR and SIR) coupled to a sufficiently good identification of several yield coefficients. Figure 3 shows the evolution of the reaction rates and the criteria (scaled 20 times higher) as a function of the substrate concentration for a model of *S. cerevisiae* where the respiratory capacity is assumed to be constant (no oxygen limitation and no inhibition).

3. ADAPTIVE MODEL-FREE EXTREMUM-SEEKING STRATEGIES

Two adaptive extremum-seeking techniques are proposed in the following.

3.1 Extremum-seeking through a bank of filters

The objective of the extremum-seeking strategy is to determine on-line the parameter $\hat{\theta}$ (which in this case represents the critical glucose concentration). To this end, the system is excited by injection of a relatively slow sinusoidal dither signal $d = Asin(\omega t)$, as shown in Figure 4.

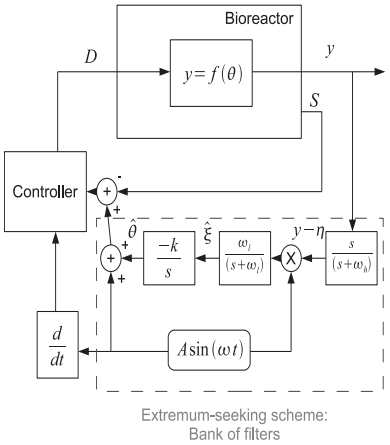

Fig. 4. Extremum-seeking scheme with a bank of filters.

The following equations describe the extremum-seeking method: The corresponding equations to Figure 4 are:

$$y = f(\hat{\theta}+Asin(\omega t)) \tag{13a}$$
$$\dot{\hat{\theta}} = k\xi \tag{13b}$$
$$\dot{\xi} = -\omega_l\xi+\omega_l(y-\eta)Asin(\omega t) \tag{13c}$$
$$\dot{\eta} = -\omega_h\eta+\omega_h y \tag{13d}$$

where:

- $y = f(\hat{\theta}+Asin(\omega t))$ is the measurable cost function;
- $\hat{\theta}$ is the estimation of the unknown parameter;
- k is the gain of the integrator;
- ξ can be seen as the gradient estimation ($\approx \frac{d\hat{\theta}}{dt}$);
- ω_l is the cut-off frequency of the low-pass filter;
- ω_h is the cut-off frequency of the high-pass filter;
- η is an intermediate variable explaining the absence of the low frequencies rejected from y in $y-\eta$ by the high-pass filter;

A first high-pass filter is used in order to reject the continuous component of y. The output is then multiplied by the dither signal in order to be "demodulated". As the dither signal and the output of the high-pass filter can only be in phase ($\hat{\theta}<\theta^*$) or out of phase ($\hat{\theta}>\theta^*$), there exists another continuous component inside the result of this demodulation. The second low-pass filter is used in order to isolate this new component containing the information of interest and sometimes residual mid-frequencies signals. This signal ξ is then filtered one last time by an integrator in order to attenuate the last "parasite" components and to recover the estimation of the unknown parameter from the integration of the continuous component. Following the theorem demonstrated in Krstic and Wang (1997), by choosing adequate values for all the parameters of the optimizing loop, the system should exponentially converge to an $O(\omega+A)$-neighborhood of the optimum.

3.2 Extremum-seeking through a RLS scheme

This second technique presents a scheme somewhat equivalent to the previous one where the bank of filters is actually replaced by a continuous recursive least squares (RLS) (Sastry and Bodson (1989)) scheme (see Figure 5) that computes the gradient ξ using a linear relationship, which is inspired from the shape of r_1-r_2 as a function of the substrate concentration:

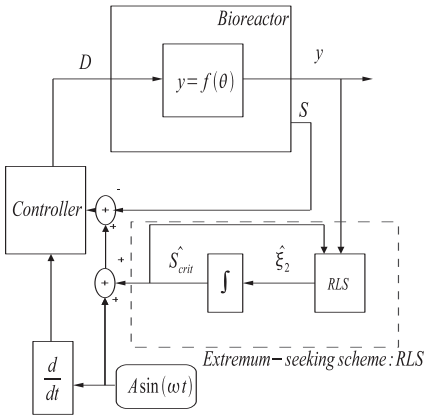

Fig. 5. Extremum-seeking scheme with RLS.

$$y = \hat{\xi}\Phi \tag{14}$$

where:

- $y = \varphi_1 - \varphi_2$
- $\hat{\xi} = [\hat{\xi}_1\ \hat{\xi}_2]$
- $\Phi = [1\ S_{crit}]$

In comparison with the previous extremum-seeking technique, (14) can be seen as the new relation replacing (12). The vector parameter $\hat{\xi}$ is then identified through the continuous RLS scheme that follows:

$$e = y - \hat{\xi}\Phi \tag{15a}$$

$$\dot{\hat{\xi}} = KR^{-1}\Phi^T e \tag{15b}$$

$$\dot{R} = K(\Phi^T\Phi - \lambda R) \tag{15c}$$

where:

- K is the strictly positive and constant adaptation gain;
- R is the inversed covariance matrix acting as a directional adaptation gain;
- λ is a forgetting factor used in order to avoid a "covariance wind-up problem" due to the absence of bounds in R growth (if $\lambda = 0$, $\dot{R} \geq 0$ (Sastry and Bodson (1989))).

$\hat{\xi}_2$ can be considered as the gradient estimation. This one is pushed to zero in average using an integral control of the form:

$$\dot{\hat{S}}_{crit} = k_i\hat{\xi}_2 \tag{16}$$

The conclusions about the convergence error are identical to the previous extremum-seeking technique.

3.3 Controller design

We derive adaptation and control laws from the consideration of a candidate Lyapunov function ensuring system stability.
First, equation (6b) can be rewritten as follows:

$$\frac{dS}{dt} = -\nu X - D(S - S_{in}) \tag{17}$$

where $\nu = r_1 + r_2$ is considered as an unknown kinetic parameter. Defining:

$$Z_s = S_{crit} + d - S \tag{18}$$

the control error variable, where $d = Asin(\omega t)$, is the periodical "dither signal".

$$\tilde{\nu} = \nu - \hat{\nu} \tag{19}$$

the estimation error on ν, we consider the following Lyapunov candidate function:

$$V = \frac{1}{2}Z_s^2 + \frac{1}{2\gamma}\tilde{\nu}^2 \tag{20}$$

where γ is a strictly positive tuning parameter.
A stabilizing controller is obtained if one can prove the strict negativity of the Lyapunov function derivative. Differentiating V and considering S_{crit} constant in order to decouple the control law from the extremum-seeking scheme (this can be done assuming that the controller converges significatively faster than the extremum-seeking scheme), we obtain:

$$\dot{V} = Z_s\left[\nu X + D(S - S_{in}) + \dot{d}\right] + \tilde{\nu}(-\frac{\dot{\hat{\nu}}}{\gamma}) \tag{21}$$

Replacing (18) and (19) in (21) and forcing $\dot{V}$ to be negative as in:

$$\dot{V} = -k_p Z_s^2 \tag{22}$$

where k_p is a strictly positive tuning parameter, we obtain:

$$-k_p Z_s = \hat{\nu} X + D(S - S_{in}) + \dot{d} \tag{23}$$

provided that:

$$\dot{\hat{\nu}} = -\gamma Z_s X \tag{24}$$

Finally, the control law is given by:

$$D = \frac{\left[k_p Z_s + \dot{d} + \hat{\nu} X\right]}{S_{in} - S} \tag{25}$$

This last expression explains the presence of the derivative $\dot{d}$ in the controller (Figure 4 and 5).

4. SIMULATION RESULTS

Coupling the controller designed in the subsection 3.3 with the extremum-seeking schemes, we apply the complete loop to a small-scale simulated yeasts culture (typically 20 l bioreactor). The initial and operating conditions are: $X_0 = 0.4g/l$, $S_0 = 0.5g/l, E_0 = 1g/l, O_0 = O_{sat} = 0.035g/l, C_0 = C_{sat} = 1.286g/l$, $V_0 = 5l$, $S_{in} = 350g/l$ where E_0 is the initial concentration of ethanol. For the kinetic and yield parameter values, the reader is referred to Sonnleitner and Käppeli (1986).

4.1 Application of the bank filters technique

The parameters for this extremum-seeking scheme are $A = 0.007$, $\omega = \frac{2\pi}{0.2}\ h^{-1}$, $\omega_h = 0.1\omega\ h^{-1}$, $\omega_l = 1.5\omega\ h^{-1}$, $k = 100$ and $k_p = 100$. The culture time is fixed to 24 h. Figures 6 and 7 show the results when no inhibition from ethanol accumulation is considered. This seems to be realistic as the ethanol concentration is below 4 g/l.
However, inhibition is an important phenomena that has to be taken into account. When included in our bioprocess model, the extremum-seeking results are as shown in Figure 8 and 9. It is apparent that the biomass level that can be achieved is significantly affected by the presence of ethanol, despite the set-point adaptation. Note that these results are very satisfactory in view of the situation where a constant substrate concentration is regulated. Indeed, a small error on S_{crit} would lead to a dramatical accumulation or reconsumption of ethanol and biomass growth would probably be affected beyond model prediction.
As it is explained in Ariyur and Krstic (2003), the output error of the extremum-seeking algorithm achieves a local exponential convergence to an $O(A^2)$-neighborhood of the origin if it is

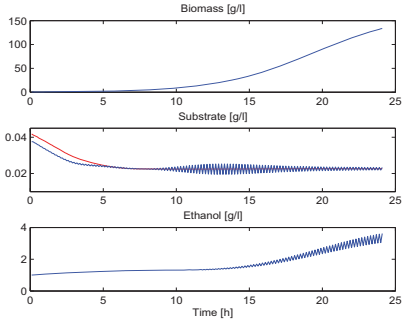

Fig. 6. Biomass (X), substrate (S in blue and $\hat{S}_{crit}$ in red), and ethanol (E) concentrations evolutions when no respiratory capacity inhibition is considered.

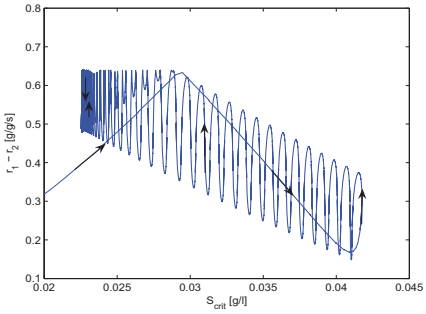

Fig. 7. Convergence of the optimization criteria $r_1 - r_2$ to the optimum when no respiratory capacity inhibition is considered.

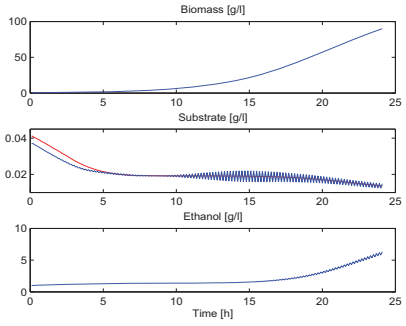

Fig. 8. Biomass (X), substrate (S in blue and $\hat{S}_{crit}$ in red), and ethanol (E) concentrations evolutions when inhibition is considered.

assumed that we are operating around a point of zero slope as it is typically the case for a convex function. As it can be observed in Figure 3, the criteria does not present a point of zero slope as the function has a discontinuous derivative at the optimum. Despite this difficulty, we see that the algorithm converges well and more particularly, the error is around an $O(A)$-neighborhood of the origin (Krstic and Wang (1997)).
This last remark, which won't be elaborated in this paper, is clearly a source of bias in the set-point when the ethanol inhibition is considered (cfr Figure 9). As A needs to be chosen sufficiently large to create a significant variation on the system dynamics, a small error cannot be avoided and the ethanol is

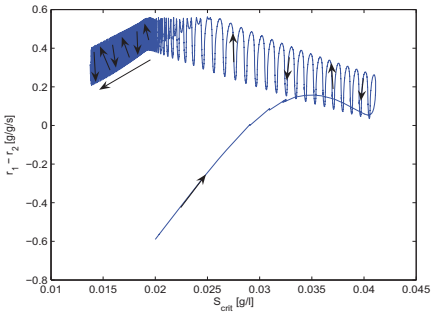

Fig. 9. Convergence of the optimization criteria $r_1 - r_2$ to the optimum when inhibition is considered.

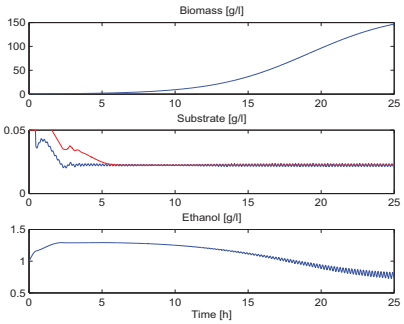

Fig. 10. Extremum-seeking with RLS: Biomass (X), substrate (S in blue and $\hat{S}_{crit}$ in red), and ethanol (E) concentrations evolutions when no respiratory capacity inhibition is considered.

accumulated while the algorithm goes on converging. As the ethanol concentration grows, the respiratory capacity slightly decreases and, following (8), S_{crit} does so.

4.2 Application of the RLS technique

The tuning parameters are defined as: $A = 0.001$, $K = 100$, $\lambda = 0.1$, $\omega = \frac{2\pi}{0.2}$, $k_i = 0.01$ and $k_p = 100$. The culture time is still fixed to 24 h. Figures 10 and 11 show the new results when no inhibition from ethanol accumulation is considered, and Figures 12 and 13 when the inhibition term is taken into account. The main observations are: (i) convergence is clearly faster. (ii) convergence is achieved around S_{crit} so that the ethanol concentration slowly decreases in the last hours.
When no inhibition is considered as in Figure 10, this set-point bias has no consequence on the extremum while, in Figure 12, when inhibition is taken into account, the set-point error is, by chance, playing a positive role so that ethanol is consumed.
In this application, the RLS algorithm is less computationally demanding, and easier to tune than the bank of filters strategy.

5. CONCLUSION

The high productivity of fed-batch cultures using genetically modified strains exhibiting overflow metabolism relies on a double condition: an optimal feeding strategy and the implied limitation of the inhibiting by-product formation. To this end, an adaptive controller using two different non-model based extremum-seeking strategies is designed for a general case of

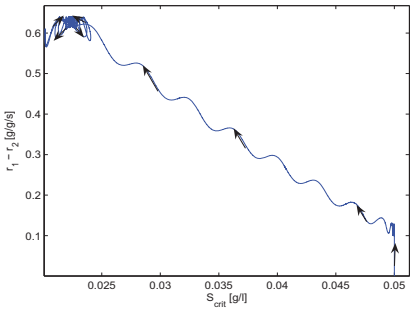

Fig. 11. Extremum-seeking with RLS: convergence of the optimization criteria $r_1 - r_2$ to the optimum when no respiratory capacity inhibition is considered.

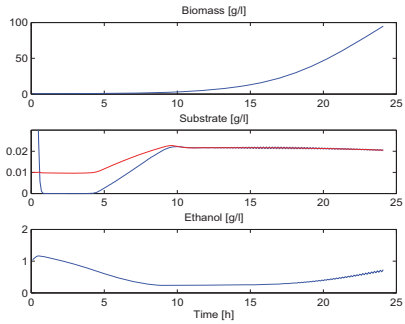

Fig. 12. Extremum-seeking with RLS: Biomass (X), substrate (S in blue and $\hat{S}_{crit}$ in red), and ethanol (E) concentrations evolutions when inhibition is considered.

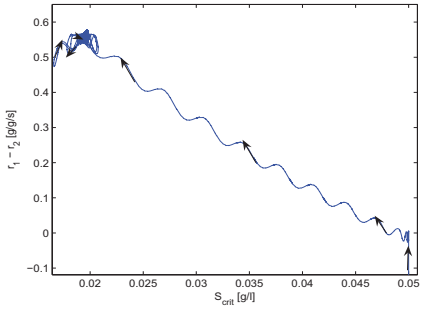

Fig. 13. Extremum-seeking with RLS: convergence of the optimization criteria $r_1 - r_2$ to the optimum when inhibition is considered.

overflow metabolized strain and is applied to the particular case of *S. cerevisiae*. The tracking of the critical substrate level (or, at least, its kinetic image), representing the optimum, is correctly performed by both extremum-seeking techniques, limiting the ethanol accumulation despite the considerations of an ethanol-inhibited respiratory capacity and discontinuous derivatives around the optimum.

6. ACKNOWLEDGMENT

This paper presents research results of the Belgian Network DYSCO (Dynamical Systems, Control, and Optimization), funded by the Interuniversity Attraction Poles Programme, initiated by the Belgian State, Science Policy Office. The scientific responsibility rests with its authors.
The authors also gratefully acknowledge the support of the Wallonie-Bruxelles-Québec commission in the framework of the research project between A. Vande Wouwer and M. Perrier.

REFERENCES

M. Akesson. *Probing control of glucose feeding in* Escherichia coli *cultivations*. PhD thesis, Lund Institute of Technology, 1999.

K. B. Ariyur and M. Krstic. *Real-Time Optimization by Extremum-Seeking Control*. John Wiley & Sons, INC., publication, wiley-interscience edition, 2003.

L. Chen, G. Bastin, and V. van Breusegem. A case study of adaptive nonlinear regulation of fed-batch biological reactors. *Automatica*, 31(1):55–65, 1995.

L. Dewasme and A. Vande Wouwer. Adaptive extremum-seeking control applied to productivity optimization in yeast fed-batch cultures. *IFAC 2008, Seoul, Korea*, July 2008.

L. Dewasme, F. Renard, and A. Vande Wouwer. Experimental investigations of a robust control strategy applied to cultures of S. cerevisiae. *ECC 2007 , Kos, Greece*, July 2007.

M. Guay, D. Dochain, and M. Perrier. Adaptive extremum seeking control of nonisothermal continuous stirred tank reactors. *Proc. Adchem 2003, Hong Kong, China*, pages 333–338, 2004.

M. Krstic and H. H. Wang. Design and stability analysis of extremum seeking feedback for general nonlinear systems. *Proceedings of the 1997 Conference on Decision and Control, San Diego, CA*, (TA02-3), 1997.

Y. Pomerleau. *Modélisation et commande d'un procédé fed-batch de culture des levures pain*. PhD thesis, Département de génie chimique. Ecole Polytechnique de Montréal., 1990.

F. Renard. *Commande robuste de bioprocédés opérés en mode fed-batch. Application industrielle à des cultures de* S. cerevisiae. PhD thesis, Faculty of Engineering, Mons, April 2006.

S. Sastry and M. Bodson. *Adaptive Control: Stability, Convergence and Robustness*. Prentice-Hall, Englewood Cliffs, New Jersey 07632, prentice-hall information and system sciences series, thomas kailath edition, 1989.

B. Sonnleitner and O. Käppeli. Growth of S*accharomyces cerevisiae* is controlled by its limited respiratory capacity : Formulation and verification of a hypothesis. *Biotechnol. Bioeng.*, 28:927–937, 1986.

M. Titica, D. Dochain, and M. Guay. Adaptive extremum seeking control of fed-batch bioreactors. *European Journal of Control*, 9(6):618–31, 2003a.

M. Titica, D. Dochain, and M. Guay. Real-time optimization of fed-batch bioreactors via adaptive extremum-seeking control. *Chemical Engineering Research and Design*, 81(A9): 1289–1295, October 2003b.

H. Wang, M. Krstic, and G. Bastin. Optimizing bioreactors by extremum seeking. *Int. J. Adaptive Control and Signal Processing*, 13:651–669, 1999.

Probing Protein Folding Dynamics Using Multivariate Statistical Techniques

Ahmet Palazoglu*, Yaman Arkun, Burak Erman*****
Attila Gursoy****

**Dept. of Chemical Engineering and Materials Science, University of California, CA 95616 USA (Tel: 530-752-8774; e-mail: anpalazoglu@ucdavis.edu)*
***Dept. of Chemical and Biological Engineering, Koç University, Turkey (e-mail: yarkun@ku.edu.tr)*
****Dept. of Chemical and Biological Engineering, Koç University, Turkey (e-mail: berman@ku.edu.tr)*
***** Dept. of Computer Engineering, Koç University, Turkey, (e-mail: agursoy@ku.edu.tr)}*

Abstract: The study of protein folding and its ramifications in biological contexts is at the heart of computational biology. In this paper, we discuss a number of tools in systems engineering that would provide an analysis framework to help explain the observed dynamic behavior of the protein, ultimately making the connection between protein structure and functionality. A case study of villin headpiece folding using principal components analysis as well as clustering demonstrates the potential of these tools in responding to this challenge.

Keywords: optimal folding trajectories, dynamic simulations, principal components analysis, clustering.

1. INTRODUCTION

The study of proteins is easily justified by the fact that they constitute an essential element of all living beings. Specifically, proteins are responsible for controlling gene expression, allow transmission of signals between cells and organs, transport and store other species and defend the body against microbes, among many other functions. Thus, due to their universal significance, understanding the relationships between their sequence, configurations and the vital functions they play in the body, can help development of new therapies and novel biomaterials. As such, uncovering the mysteries of proteins requires an interdisciplinary approach, enlisting not only biologists and medical professionals but also engineers, mathematicians and computer scientists. Recent studies include bioinformatics approaches that explore data mining (Brito, Dubitzky et al. 2004) and evolutionary algorithms (Pal, Bandyopadhyay et al. 2006), in addition to structure prediction problems (Krogh, Larsson et al. 2001; Floudas 2007) and computational techniques focusing on optimization (Krogh, Larsson et al. 2001; Greenberg, Hart et al. 2004).

All protein molecules are chains of amino acids and referred to as linear heteropolymers due to the unbranched nature of their monomeric units (amino acids) (Creighton 1993). The amino acid building blocks consist of a central α-carbon (C^{α}) atom surrounded by four groups: an amino group ($-NH_2$), a carboxyl group (-COOH), a hydrogen atom and a fourth group (-R) that can be one of twenty specific molecules, and is referred to as the side group. The specific side group gives the amino acid its unique characteristic. The sequence of amino acids (also called residues) as read from the amino (N-terminus) to the carboxyl (C-terminus) is referred to as the primary structure. Helices, β-strands, loops, etc. are the secondary structures. Organization of the secondary structures in space to form a stable 3-D structure leads to the tertiary structure. The lowest free energy tertiary structure is the unique native conformation with which the protein performs its function.

The type of a protein and its folding characteristics are determined by its primary structure, i.e., the sequence of amino acids (Dill, Bromberg et al. 1995). It is also noted that the folding process is often aided by molecular chaperons that help the protein fold correctly as it exits the ribosome by minimizing the influence of other nearby proteins as well as by binding to the protein to prevent misfolding (Shinde and Inouye 2000). This is especially important as incorrectly folded proteins resulting from errors during folding are responsible for illnesses such as Creutzfeldt-Jakob disease, Bovine spongiform encephalopathy, Parkinson's and Alzheimer's diseases. Due its implications in understanding such diseases, the dynamics of folding has received substantial attention in recent years (Karplus and Kuriyan 2005; Colombo and Micheletti 2006).

The dynamics of protein folding have been studied extensively in vitro, where the protein is denatured to assume an arbitrary initial configuration and then as the natural conditions are restored, folds into its native configuration. This refolding process has been explored both by molecular dynamics (MD) simulations (Duan and Kollman 1998; Pan and Daggett 2001; Mori, Colombo et al. 2005) and using mostly stop-flow experiments and NMR spectroscopy (Eaton, Thompson et al. 1996; Plaxco and Dobson 1996) and the results provided unique insight towards the folding

dynamics. During the refolding process, the simulations explore the conformational energy landscape accessible to the protein molecule and all-atom MD simulations with explicit solvent can only feasibly achieve time scales shorter than about 1μs for relatively small proteins which leaves out a number of phenomena inaccessible and poorly understood.

In this paper, we show how systems engineering tools can be used to probe the dynamics of protein folding to provide a better understanding of the key mechanisms. The next section discusses protein folding simulations and the type of information gathered as a result. Dynamic folding trajectories that result from such simulations can be interrogated by a number of analysis tools, and we focus on the use of Karhunen-Loeve and clustering to extract spatial and temporal features to help explain the folding dynamics.

2. SIMULATIONS OF PROTEIN FOLDING

Folding of a protein takes place in the form of a competition between the loss of configurational entropy and the decrease of energy due to the formation of inter-residue contacts. Consequently, a free energy barrier separates the unfolded and folded states. The energy surface, as a function of the variables active in folding, such as the 3*N* coordinates of an *N* atom protein and a multitude of additional dimensions describing the surrounding water molecules, is called the 'energy landscape'. The competition of entropy and energy results in a rugged landscape, and leads to transient trapping of structures that are either partially folded or misfolded. A comprehensive account of protein folding simulations can be found in a recent article (Scheraga, Khalili et al. 2007).

The protein can be modeled at different levels of complexity ranging from all-atom to coarse-grained representations. The all-atom visualization coupled with MD simulations gives the most detailed picture of folding but the computational time is a serious bottleneck. The only full-trajectory molecular dynamics simulation in the presence of explicit water up to this date is that of a 35-residue protein (Duan and Kollman 1998). In typical coarse-grained approximation approaches (Haliloglu and Bahar 1998; Doruker, Jernigan et al. 2002), the protein consists of N beads that represent the amino acids joined into a linear chain by virtual bonds analogous to the chemical bond. A virtual bond joins two consecutive alpha carbons, C^{α}, along the chain. The length of a virtual bond is fixed, a condition referred to as the 'fixed bond length condition'. Each bead has a finite volume. No bead shares its own volume with any other bead. This is called the 'excluded volume condition'. Folding of the protein progresses from a random initial state at $t = 0$ to the final state at $t = t_f$, subject to the fixed bond length and excluded volume conditions at all stages of folding. Folding to the native configuration requires the specification of interactions between pairs of amino acids. This information is based on empirical energy functions, chosen such that the unique native state corresponds to the minimum of total energy (Erman and Dill 2000).

The protein folding problem in its simplest form may be viewed as *a constrained optimization problem:* We are given an initial configuration of *N* beads connected in the form of a linear chain. The beads want to move towards their specified final destinations by spending minimal energy subject to the (i) connectivity between beads, (ii) fixed bond length and (iii) excluded volume constraints. Each bead obeys Newton's second law of motion throughout the folding trajectory. The forces acting on each bead are received either from the other beads or they are external interaction forces with the environment. Under these conditions, one needs to determine the optimal forces acting on the beads and the resulting optimal trajectory of the beads from their initial configuration to their final native states.

Here, we analyze the optimal pathways followed by the protein during folding. These pathways were generated using the optimal control framework proposed in our earlier work (Guner, Arkun et al. 2006). A coarse grained dynamic model based on Newton's equation of motion is used to make the dynamic optimization manageable.

3. INTERROGATION OF SIMULATION DATA

While simulations provide a wealth of data on the nature of protein motion, extraction of useful information that would shed light on the dominant folding/unfolding mechanisms, evolution of interactions among key residues such as those that determine the hydrophobic core, as well as understanding of the structural conformations and their relationship with biological function is non-trivial. The computational burden and complexity are significant barriers; thus, methods that help reduce dimensionality and provide analytical capabilities in a low-dimensional subspace are largely used. Here, we discuss two techniques. Karhunen-Loeve expansion (KLE) or Principal Components Analysis (PCA) can extract key coordinates (modes) that govern the global motion of the protein. Clustering helps classify large-scale correlated motions that can explain the presence of meta-stable states in which certain protein configurations exist and evolve.

3.1 Principal Components Analysis

The application of PCA to the study of macromolecular motion dates back many years where MD simulations were studied to identify fluctuation modes (Garcia 1992) and to extend simulation time scales (Amadei, Linssen et al. 1993). In the latter work, the conformational space is subdivided into an 'essential' subspace (Van Aalten, De Groot et al. 1997) which contains only a few degrees of freedom, exhibiting unharmonic motion and a 'residual' subspace where the fluctuations are Gaussian. Recent studies explore the energy landscape and the conformational states (Alakent, Doruker et al. 2005; Mu, Nguyen et al. 2005), identify modes contributing to protein fluctuations in MD simulation of apo-adenylate kinase (Lou and Cukier 2006), and extract key mechanistic features from simulations of chemotrypsin inhibitor 2 (Palazoglu, Gursoy et al. 2004). One can also refer to a comprehensive review article for further details (Stein, Loccisano et al. 2006).

The data matrix can be constructed in various forms depending on the information desired. For example, we can construct a matrix of spatial positions as they evolve in time.

The simulations yield the position vectors of N residues for M time intervals and, after subtracting the temporal mean, this results in a $M \times K$ array, where $K = 3N$. One can also use the fluctuation matrix which captures the jump dynamics governing protein folding. The fluctuation matrix becomes $M \times K$ with $K = N$ and has been previously studied (Palazoglu, Gursoy et al. 2004). Another possibility is to form a matrix in which temporal evolution of the magnitude of the distance between the contact pairs is captured. This matrix would have M time intervals and K would correspond to the total number of short- and long-range contact pairs.

The expansion has K modes (eigenvector directions) and each eigenvalue measures the mean energy of its corresponding mode. Among the class of all linear expansions, KLE is optimal in the sense that, on a subspace of lower dimension $L < K$, it retains the most energy possible. One can retain only the first few L modes that extract the important trends and filter the details deemed insignificant by the user.

3.2 Clustering

Cluster analysis (Everitt, Landau et al. 2001) is a class of statistical methods that seeks to partition a set of N observations (objects) into distinct groups. Each observation corresponds to a particular sampling interval (distinct period in time) for which corresponding measurements are available on the same set of parameters. One of the early applications of clustering to MD simulation data is by Karpen et al. (Karpen, Tobias et al. 1993) where feature vectors (dihedral angle time series) are clustered for a 2.2 ns trajectory of the small peptide YPGDV to identify conformational states during unfolding. When applied to protein models, clustering can classify ensembles of structural models based on their backbone structure, using C^{α} distances as the dissimilarity measure (Domingues, Rahnenfuhrer et al. 2004). The molecular motion of proteins can also be classified using clustering to identify functionally relevant structures (Pan, Dickson et al. 2005) and to gain insight towards the shape of the energy landscape (Plaku, Stamati et al. 2007).

Agglomerative hierarchical clustering is used to identify sampling intervals exhibiting similar 'behavior' based on a chosen metric. It accepts as input a symmetric matrix $\boldsymbol{D}$ whose elements D_{ij} indicate the relative dissimilarity between sampling intervals i and j. Matrix $\boldsymbol{D}$ can derive from various parameters in a given simulation, such as the dihedral angles, internal coordinates and potential energies, and must be properly defined for the cluster solution to be physically meaningful. The hierarchical clustering starts with all objects residing in their own cluster, and by using various linkage rules, proceeds by merging the closest objects, and subsequently, the closest clusters, finally terminating when all objects are collected under a single cluster. The output of the hierarchical clustering algorithm is graphical in nature (a dendrogram), and facilitates the visualization of recurring phenomena manifested in the data. Another popular method, k-means clustering (Everitt, Landau et al. 2001), creates clusters based on the maximization of between-cluster variance and minimization of the within-cluster variance, and often gets trapped in local extrema, requiring multiple initializations. The number of clusters needs to be specified a priori for the k-means algorithm and it starts by randomly populating these clusters and proceeding by the optimization step to reform the clusters. These shortcomings were overcome in a recently proposed aggregated k-means clustering strategy (Beaver and Palazoglu 2006) where an ensemble of cluster solutions, generated by performing many randomly initialized runs of the algorithm, can be aggregated to form a single, hierarchical solution. A recent study discusses the performance of different clustering algorithms applied to MD trajectories (Shao, Tanner et al. 2007).

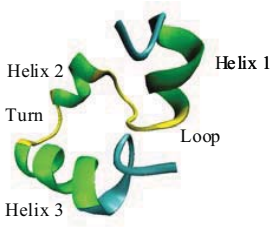

Fig. 1. The structure of villin headpiece.

4. CASE STUDY OF CHICKEN VILLIN HEADPIECE

We consider a 36-residue protein, (PDB code 1Vii.pdb), chicken villin headpiece that is the smallest protein that can fold autonomously. It has been shown through a landmark all-atom explicit water simulation of villin headpiece (Duan and Kollman 1998) that there is a sudden initial hydrophobic collapse followed by longer structural adjustment phase. Other simulation studies also agree with the folding events revealed by Duan and Kollman, e.g., the implicit-water simulation by Shen and Freed (Shen and Freed 2002) and MD scheme integrated with Monte Carlo search by Mori et al. (Mori, Colombo et al. 2005).

Chicken villin headpiece (Figure 1) has 3 short helices, Helix 1, 2 and 3 which contain the residues 4-8, 15-18, and 23-32, respectively. They are held together by a loop between residues 9-14, and a turn between residues 19-22.

Fig. 2. Snapshots from the folding process starting from an arbitrary initial configuration, $t = 0$, followed by $t = 30$, $t = 60$, and $t = 90$, and $t = 150$.

4.1 Folding Trajectories

The optimal folding trajectories were calculated starting from several random initial configurations (Guner, Arkun et al. 2006). Each simulation is performed for 301 time steps. Results include the optimal values for both the position of each bead and the force applied to each bead as a function of time. Figure 2 shows a representative result where the initial denatured configuration is significantly stretched out and the protein starts to establish the helices first. Once the helices form, the loop and the turn secondary structures begin to get established. Finally, the native 3-D structure is reached after refinement of the overall configuration.

The root-mean-square-distance (RMSD) is the distance between the native structure $S_1 = (s_{11} \quad s_{12} \quad ... \quad s_{1N})$, and a folding structure $S_2 = (s_{21} \quad s_{22} \quad ... \quad s_{2N})$, where s_{ij} is the position of the j^{th} bead in structure i:

$$RMSD = \sqrt{\frac{2}{N(N-1)} \sum_{i}^{N} \sum_{j>i}^{N} \left(\| s_{1i} - s_{1j} \| - \| s_{2i} - s_{2j} \| \right)^2}$$

Figure 3 shows the RMSD variation between the native structure and simulated structures with respect to time for the whole chain. On the average, initial configurations fold around time step 100, with an average final RMSD of 3Å.

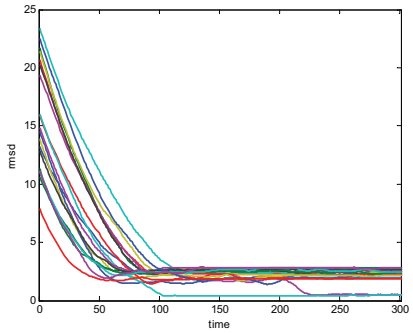

Fig. 3. The evolution of RMSD over all simulations.

4.2 KL Analysis

The long-range contact pairs are defined as those residues that are 5 and more residues apart. For chicken villin, there are a total of 89 native contact pairs and 8 are considered as long-range contacts: 2-34, 7-14, 7-34, 10-33, 10-34, 11-33, 11-34, 19-26. Here, we consider the temporal evolution of the magnitude of the contact pairs, r_{ij}'s. The matrix is 301×89 with 301 rows for the time steps and 89 columns for each pair of native contacts. For this analysis, we focused on 14 simulations. We found that, in general, 2 modes capture 99% of the variance in the simulation data. Figure 4 shows the first and second spatial eigenvectors indicating which native contact pairs contribute to these directions the most. The major contributions to the first come from the long-range contacts, as indicated by the vertical lines. The other contact pairs have generally minor contributions to this direction, perhaps with the exception of the pair 2-7 (position 4 on the plot). It is reported (Frank, Vardar et al. 2002) that three phenylalanine residues F47, F51, and F58 (residues 7, 11 and 18) make up the bulk of the hydrophobic core along with the hydrophobic residues L42, V50, and L69 (residues 2, 10 and 29). Thus, it is noteworthy that the first mode is significantly influenced by the interaction between residues 2 and 7 as the hydrophobic collapse occurs. Another observation is that all pairs load positively in this direction, indicating that all move in the same direction, effectively in the direction of reducing the distances among contact pairs. In fact this coordinated collapse is observed in Fig. 1. Another important observation is that this loading behavior is independent of the initial configuration, underscoring the fundamental nature of the collapse. In the second mode, the influence of the long-range contacts is attenuated (especially for 10-33, 10-34, 11-33 and 11-34) and short-range contacts become more important, almost across the board for all such contacts. The native contact pair 2-7 still retains its influence. The contact pairs load in both positive and negative directions, a key difference from the first mode, indicating a more complex motion. It is also important to note that this loading depends on the initial configuration, implying that the formation of secondary structures can follow different paths in time.

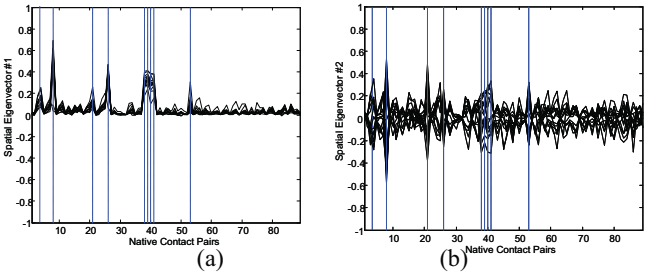

(a) (b)

Fig. 4. First (a) and second (b) spatial eigenvectors, vertical lines indicate the position of long-range native contact pairs, and vertical line at position 4 points to the native contact pair 2-7.

As shown in Fig. 5, the temporal coefficient of the first spatial eigenvector decays exponentially, indicating that the manner with which energy is minimized is common for all simulations regardless of the initial configuration. This also supports the all-positive loading directions of the contact pairs as shown in Figure 4a. On the other hand, the temporal coefficient of the second spatial eigenvector shows second-order behavior and is attenuated significantly, underscoring the lesser influence of the second mode. This mode explains the fast dynamics associated with the short-range contacts as secondary structures (helices in this case) are made quickly and then readjusted to conform to the overall formation of the protein structure. Folding dynamics exhibit two time-scales, which is consistent with the two-step folding mechanism of the hydrophobic collapse model (Baldwin 2002).

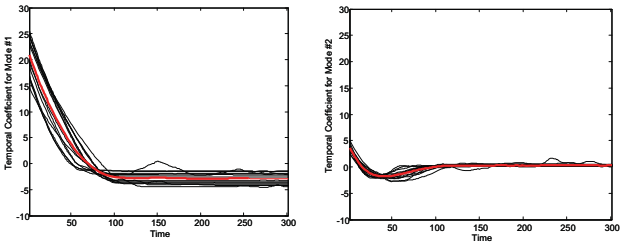

(a) (b)

Fig. 5. First (a) and second (b) temporal coefficients, bold red line indicates the averages.

4.3 Cluster Analysis

To demonstrate the potential of clustering, we focus on native contact distances analyzed before. For a given simulation, the expectation is to see if the dynamic signature of contact distances can be used to label each contact pair as belonging to a class, distinguished by its characteristic temporal evolution or contact distance. Thus, the feature vector is the

time series of contact distance magnitudes, r_{ij}'s. The simulation data from the 14 runs were stacked into a matrix of dimension 4214×89 and the data were normalized to [0, 1]. The data matrix is then transposed for clustering the 89 contact pairs. Thus, the scaling is in reality performed on the *rows* of the clustered data matrix, as opposed to for the columns as is more typical. A different scaling is used in this analysis because the variables have different mean levels although they are measured in the same units.

Using aggregated *k*-means clustering with average linkage, the dendrogram in Figure 6 is obtained. It shows two coarse and six relatively distinct fine clusters with a cophenetic coefficient (Beaver and Palazoglu 2006) of 0.96, which indicates that the dendrogram is a good representation of the relationships among the objects. The aggregated distances show that the cluster members have short merging distances while the main clusters merge at relatively large distances. This shows that the within-cluster variance is low while the between-cluster variance is high.

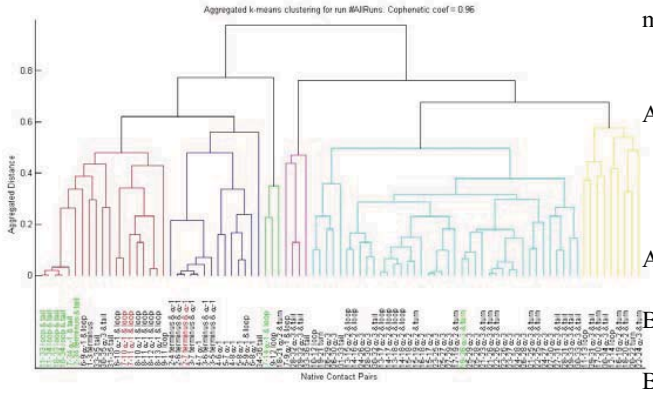

Fig. 6. The dendrogram for clustering the distances of all native contact pairs for 14 simulations. Contacts labelled as green are the long-range native contacts whereas the contacts labelled as red are the ones involving residues in the hydrophobic core.

In Figure 6, it is noted that a large number of the residues that form the long-range native contacts and the hydrophobic core fall in the same cluster. Indeed, first cluster (labeled as red) contains six of the eight long-range contact pairs along with two short-range contact pairs that contain hydrophobic core residues. This cluster captures the concerted motions of the loop and the tail, as well as the loop and helix-1 contacts. The second cluster (dark blue) is largely residues involved in forming the helix-1. It is noted that the long-range native contact pair 7-14 (PHE7-THR14) appears in a rather isolated third cluster (green) and its motion shows greatest similarity to contact pairs 9-12 and 18-21. The long-range interaction, i.e., 7-14, is the only long-range interaction close to the N-terminal, thus having dynamic characteristics different than the other long-range contacts is expected. The small fourth cluster (magenta) contains residues towards the end of the protein chain and also notably differs from the first three clusters. The fifth cluster (light blue) contains all the remaining short-range contacts associated with helix 2 and helix 3, including the long-range contact 19-26. This long-range contact pair shares characteristics common with the other helix 3 contact pairs, thus dynamically acts in concert with a large number of short-range contact pairs specific to the secondary structure with which it is associated. The final cluster (yellow) brings together short-range contacts primarily involving turn and tail secondary structures.

We must re-iterate that a coarse clustering decision indicates two main clusters, containing the subclusters (1, 2, 3) and (4, 5, 6), respectively. Such a grouping would suggest two classes of residues where the first mainly contains the long-range-contacts and the second, the short-range contacts. Yet, the fact that specific residues (such as long-range contacts) do not appear all in a single cluster and usually appear together with other residues is supported by (Larson, Ruczinski et al. 2002) who claim that both poorly and highly conserved residues are equally likely to participate in the protein folding nucleus. They also note, however, that there is an observable bias in the mean sequence conservation of the residues in the folding nuclei. This is especially consistent with the membership of the large cluster on the left.

REFERENCES

Alakent, B., P. Doruker, et al. (2005). "Application of time series analysis on molecular dynamics simulations of proteins: A study of different conformational spaces by principal component analysis " J. Chem. Phys. **121**(10): 4759-4769.

Amadei, A., A. B. Linssen, et al. (1993). "Essential dynamics of proteins." Proteins **17**: 412-425.

Baldwin, R. L. (2002). "Making a network of hydrophobic clusters." Science **295**(5560): 1657-8.

Beaver, S. and A. Palazoglu (2006). "A cluster aggregation scheme for ozone episode selection in the San Francisco, CA Bay Area." Atmospheric Environment **40**(4): 713-725.

Brito, R., W. Dubitzky, et al. (2004). "Protein folding and unfolding simulations: A new challenge for data mining." Omics - J Integrative Biology **8**(2): 153-166.

Colombo, G. and C. Micheletti (2006). "Protein folding simulations: combining coarse-grained models and all-atom simulations." Theor. Chem. Acc. **116**: 75-86.

Creighton, T. E. (1993). Proteins: Structures and Molecular Properties. New York, W.H. Freeman.

Dill, K. A., S. Bromberg, et al. (1995). "Principles of protein folding - a perspective from simple exact models." Protein Science **4**: 561-602.

Domingues, F. S., J. Rahnenfuhrer, et al. (2004). "Automated clustering of ensembles of alternative models in protein structure data." Protein Engineering **17**: 537-543.

Doruker, P., R. L. Jernigan, et al. (2002). "Dynamics of large proteins through hierarchical levels of coarse-grained structures." J. Comp. Chem. **23**: 119-127.

Duan, Y. and P. A. Kollman (1998). "Pathways to a protein folding intermediate observed in a 1-Microsecond simulation in aqueous solution." Science **282**(5389): 740-744.

Eaton, W. A., P. A. Thompson, et al. (1996). "Fast events in protein folding." Structure **4**: 1133-1139.

Erman, B. and K. A. Dill (2000). "Gaussian theory of protein folding." J. Chem. Phys. **112**: 1050-1056.

Everitt, B., S. Landau, et al. (2001). Cluster Analysis. New York, NY, Oxford.

Floudas, C. A. (2007). "Computational methods in protein structure prediction." Biotech. and Bioeng. **97**(2): 207-213.

Frank, B. S., D. Vardar, et al. (2002). "The role of aromatic residues in the hydrophobic core of the villin headpiece subdomain." Protein Science **11**(3): 680-687.

Garcia, A. E. (1992). "Large-amplitude nonlinear motions in proteins." Phys. Rev. Lett. **68**: 2696-2699.

Greenberg, H., W. Hart, et al. (2004). "Opportunities for combinatorial optimization in computational biology." Informs J Computing **16**(3): 211-231.

Guner, U., Y. Arkun, et al. (2006). "Optimum folding pathways of proteins. Their determination and properties." J. Chem. Phys. **124**: 134911.

Haliloglu, T. and I. Bahar (1998). "Coarse-grained simulations of conformational dynamics of proteins: application to apomyoglobin." Proteins: Structure, Function, and Genetics **31**: 271-281.

Karpen, M. E., D. J. Tobias, et al. (1993). "Statistical clustering technique for the analysis of long molecular dynamics trajectories: Analysis of 2.2-ns trajectories of YPGDV." Biochemistry **32**: 412-420.

Karplus, M. and J. Kuriyan (2005). "Molecular dynamics and protein function." PNAS **102**(19): 6679-6685.

Krogh, A., B. Larsson, et al. (2001). "Predicting transmembrane protein topology with a hidden Markov model: application to complete genomes " J. Mol. Biology **305**(3): 567-580.

Larson, S. M., I. Ruczinski, et al. (2002). "Residues participating in the protein folding nucleus do not exhibit preferential evolutionary conservation." J Mol Biol **316**(2): 225-33.

Lou, H. and R. I. Cukier (2006). "Molecular dynamics of apo-adenylate kinase: A principal component analysis." J. Phys. Chem. B **110**: 12796-12808.

Mori, G. M. S., G. Colombo, et al. (2005). "Study of the villin headpiece folding dynamics by combining coarse-grained Monte Carlo evolution and all-atom molecular dynamics." Proteins: Structure, Function, and Bioinformatics **58**: 459-471.

Mu, Y., P. H. Nguyen, et al. (2005). "Energy landscape of a small peptide revealed by dihedral angle principal component analysis." Proteins: Structure, Function, and Bioinformatics **58**: 45-52.

Pal, S. K., S. Bandyopadhyay, et al. (2006). "Evolutionary computation in bioinformatics: A review." IEEE Trans. Systems Man and Cybernetics C - Applications and Reviews **36**(5): 601-615.

Palazoglu, A., A. Gursoy, et al. (2004). "Folding dynamics of proteins from denatured to native state: principal component analysis." J. Comp. Biology **11**: 1149-1168.

Pan, P. W., R. J. Dickson, et al. (2005). "Functionally relevant protein motions: Extracting basin specific collective coordinates from molecular dynamics trajectories." J. Chem. Phys. **122**: 034904.

Pan, Y. P. and V. Daggett (2001). "Direct comparison of experimental and calculated folding free energies for hydrophobic deletion mutants of chymotrypsin inhibitor 2: Free energy perturbation calculations using transition and denatured states from molecular dynamics simulations of unfolding." Biochemistry **40**(9): 2723-2731.

Plaku, E., H. Stamati, et al. (2007). "Fast and reliable analysis of molecular motion using proximity relations and dimensionality reduction." Proteins: Structure, Function, and Bioinformatics **67**: 897-907.

Plaxco, K. W. and C. M. Dobson (1996). "Time-resolved biophysical methods in the study of protein folding." Current Opinion in Structural Biology **6**: 630-636.

Scheraga, H. A., M. Khalili, et al. (2007). "Protein-folding dynamics: Overview of molecular simulation techniques." Annual Review of Physical Chemistry **58**: 57-83.

Shao, J. Y., S. W. Tanner, et al. (2007). "Clustering molecular dynamics trajectories: 1. Characterizing the performance of different clustering algorithms." Journal of Chemical Theory and Computation **3**(6): 2312-2334.

Shen, M. Y. and K. F. Freed (2002). "All-atom fast protein folding simulations: the villin headpiece." Proteins: Structure, Function, and Genetics **49**: 439-445.

Shinde, U. and M. Inouye (2000). "Intramolecular chaperones: polypeptide extensions that modulate protein folding." Cell and Developmental Biology **11**: 35-44.

Stein, S. A. M., A. E. Loccisano, et al. (2006). "Principal components analysis: A review of its application on molecular dynamics data." Ann. Rep. in Comp. Chemistry **2**: 233-261.

Van Aalten, D. M. F., B. L. De Groot, et al. (1997). "A comparison of techniques for calculating protein essential dynamics." J. Comp. Chemistry **18**(2): 169-181.

Applied Advanced Process Analytics in Biopharmaceutical Manufacturing: Challenges and Prospects in Real-time Monitoring and Control

Cenk Ündey*, Sinem Ertunç, Thomas Mistretta, Manuj Pathak

Amgen Inc.,
Process Development
Process and Systems Analysis
40 Technology Way, West Greenwich, RI 02817 USA.

Abstract: Biopharmaceutical manufacturing processes are inherently complex due to their nonlinear bioprocess dynamics, variability in batch operations and manufacturing schedule, raw materials involved, and automatic process control. A typical processed lot generates large amounts of data that need to be analyzed and interpreted for process troubleshooting and continuous improvement purposes in addition to product release. Multivariate Batch Process Modeling, Monitoring and Control approaches in real-time are elaborated by providing industrial examples from the commercial manufacturing processes. Examples and opportunities in cell culture (e.g., bioreactor applications) and purification (e.g., large-scale chromatography) operations are summarized. Impact of Process Analytical Technologies (PAT), soft-sensor development, first principles modeling applications and commercial-scale examples are presented.

Keywords: Process Analytical Technologies, Quality-by-Design, Biopharmaceutical Manufacturing, Real-Time Multivariate Process Monitoring, Soft-sensors.

1. INTRODUCTION

Biotechnology-based products have become increasingly important in recent years in treating chronic diseases such as cancer and arthritis. Although biopharmaceutical drugs constitute a small portion of (about 8% in 2004) of the pharmaceutical market, approximately 27% of new medicines in active development are now biotech products (Business Insights, 2005). Process development and commercial manufacturing of these products, such as therapeutic proteins; require a good understanding of chemistry, manufacturing and controls. Advanced process analytical technologies can be incorporated in process development as well as into commercial-scale manufacturing for advanced monitoring, control, continual process improvement, cost reduction and risk management.

Biopharmaceutical processes are typically comprised of a series of unit procedures operated in batch mode to produce therapeutic proteins, and have complex biological mechanisms that result in non-linear and time-variant process dynamics. This makes their modeling, monitoring and control challenging. In a typical commercial-scale biopharmaceutical manufacturing process there are multiple batch processing unit operations where off-line samples are taken to ensure in-process control and quality objectives are met and real-time measurements are made for open and closed-loop control and monitoring. A number of measurements are also made for raw material release testing towards use in manufacturing. When this is looked at from a holistic perspective; there are many batches, variables and operational characteristics to analyze in a meaningful and proactive manner. While this goal can be achieved via post-mortem analysis, it is more desirable to monitor and control these multivariable multi-stage biopharmaceutical processes in real-time. Advanced process analytics in the form of real-time multivariate process monitoring and control provides an efficient means of identifying/reducing variation, managing process risks, relating process information to critical quality attributes (CQAs) and determining process improvement opportunities such as increasing yields and decreasing impurities. Due to long lead times and inflexibility in the regulatory approval process, applying process changes for improvement has not been very straightforward in the conventional regulatory paradigm. The United States Food and Drug Administration has published a series of new guidelines to address this issue and provide more flexibility for innovation while appropriately managing the risk around proposed process changes for continual improvement via process analytics and quality-by-design (QbD) principles (US FDA, 2002, 2004, 2006, Chirino and Mire-Slius, 2004). *Process Analytical Technology* (PAT) is defined as a system for designing, analyzing, and controlling manufacturing through real-time measurements of critical quality and performance attributes of the process as well as raw materials and other process inputs. QbD promotes improved process understanding

* Corresponding author. *E-mail*: *Cenk.Undey@ amgen.com*

during process and product development and building quality in the design instead of testing for quality. This can be achieved via correlative, causal, or mechanistic knowledge and at the highest level via first principle models (Cinar, et al., 2003, Rathore and Winkle, 2009).

Process analytical approaches including deploying multivariate techniques along with on-line/at-line/in-line sensors and analyzers and the use of chemometrics in biotechnology have received significant attention in recent years (Junker and Wang, 2006). Applications included monitoring and control of microbial fermentations (Albert and Kinley, 2001, Lopes, et al., 2004, Undey et al., 2004, Gnoth, et al., 2007), cell culture (Arnold, et al., 2003, Undey, et al, 2006) and purification processes (Larson, et al., 2003, Lee et al., 2006, Rathore, et al., 2008). Development of new measurement technologies for real-time bioprocess monitoring and control is also crucial (Becker, et al., 2007).

In this paper, a generic approach for developing further process understanding, modelling, monitoring and control is summarized. Specific applications and case studies are provided from commercial manufacturing experience in the use of process analytics. The potential of soft-sensors and first principles modeling in biopharmaceutical manufacturing is discussed with industrial examples. Use of process analytics and real-time multivariate monitoring technology in operational success is also demonstrated. Challenges and prospects of adaptive process control are discussed.

2. *PROCESS UNDERSTANDING VIA MODELING AND ADVANCED MONITORING*

Aforementioned QbD approach demands a high-level of process understanding for ensuring control of CQAs. Levels of process understanding and knowledge can be categorized in increasing order (lowest to highest) as descriptive, correlative, causal, mechanistic and first principles-based. While mechanistic and first principles models provide the highest level of understanding and predictability, their development and adaptation may not be very straightforward in biopharmaceutical process development and manufacturing that use design of experiments (DOE)-based approaches along with other heuristic knowledge about the process and product. During commercialization of a product an essential level of process understanding is demonstrated to ensure process consistency, product safety, efficacy and purity. However, in order to expedite time-to-market (while the drug is meeting the efficacy, purity and safety requirements) and make the product available to the patients, its manufacturing process may not be sufficiently optimized early in the product lifecycle. Additionally, there may be scale-up effects, raw material lot-to-lot variability (i.e., as an unmeasured load disturbance to the process) and other operational aspects such as maintenance schedules and human factors collectively driving the overall process variability. Real-time multivariate statistical process monitoring (RT-MSPM) provides a means to proactively monitor this overall process variability and build the necessary foundation towards predictive monitoring and multivariable control. In the generic methodology proposed in this paper, a multivariate model for each unit operation is developed for advanced monitoring and prediction purposes where applicable. Based on the frequency of data availability, models are used in real-time and/or via post-mortem batch analytical purposes. Making the data available and establishing required databases, connections to source systems, data pre-treatment and reconciliation are practical considerations that need to be addressed in industrial setting prior to enabling RT-MSPM (Undey, 2008).

Fig. 1. Simplified process flow of a biologics manufacturing process (inoculation, scale-up bioreactors, clarification and purification train).

As shown in Fig. 1 typical biopharmaceutical manufacturing processes involve multiple unit operations including bioreactors for scale-up, cell growth/protein production, clarification ultrafiltration and chromatography columns and skids. There may be more steps based on each product's requirement and several parallel trains for plant throughput maximization.

3. *MULTIVARIATE BATCH MODELING AND MONITORING*

Multivariate (MV) modeling techniques such as Principal Components Analysis (PCA) and Partial Least Squares (PLS) are used to handle batch process data issues such as large number of variables, colinearity and missing data while summarizing the overall variability in the principal component and latent variable space. Historical in-control batches are used for MV model development. Control limits for MV statistics are calculated and MSPM charts are used for efficient monitoring (Nomikos and MacGregor, 1995).

In this study batch process data are analyzed and monitored in two hierarchical levels. The first level is called the observation level and used to monitor the batch evolution with respect to a maturity variable in real-time. The second level is the batch level which is used for monitoring the batch fingerprint and can be used in predicting a final performance variable (Wold et al., 1998). Since early in the progress of a batch the confidence in the prediction is typically low, care needs to be taken when to start using batch level MV charts for real-time monitoring after a certain amount of data is available. All the real-time batch level cases presented in this paper starts computing the batch level MV statistics when 50% of the batch is completed and it has provided a good predictive performance.

Umetrics' Simca-P+ and SBOL (Simca-Batch On-Line) modules are used for the MSPM cases presented in this paper. Simca-P+ is the tool used for offline MV model development. SBOL is the tool used for real-time MSPM and uses the MV models developed by Simca-P+.

4. *DESIGN SPACE MONITORING AND POSTMORTEM ANALYSES OF BATCH PERFORMANCE*

During initial bioprocess design and characterization the full variability due to raw material lots, scale-up parameterization and large-scale operations cannot be estimated and therefore the process is monitored to ensure consistency. Process design space is constructed to understand the ranges on key and critical operating variables (process inputs) and their impact on the key/critical performance variables (process outputs) at bench and pilot-scale manufacturing and later scaled-up to commercial operation. Multivariate models can be helpful in also comparing the bench and/or pilot-scale experience against large-scale manufacturing to study similarities and identify any differences in performance. It can also be used to improve bench/pilot-scale model representation against large-scale so that process development can improve on the scale up parameterization. Representative scaled-down process models (i.e., actual scaled-down equipment) are crucial for troubleshooting and process improvement experimentation. In the following example (Fig. 2), PCA-based multivariate models were applied to process performance variables from batches performed at both bench and large-scale manufacturing.

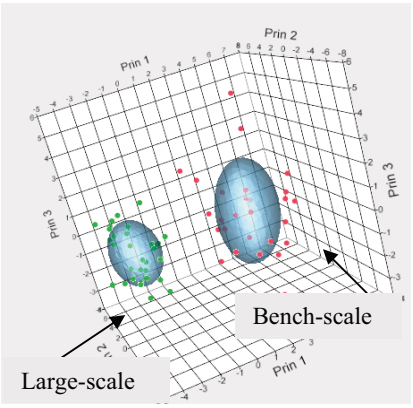

Fig. 2. Multivariate comparison and monitoring of different manufacturing scales against design space

With this approach, variability in process data from more than twenty performance variables is summarized with only three principal components. Ellipsoids represent 95% confidence volume. In this case, large-scale batches seem to be more tightly controlled compared with bench-scale batches (partly due to a wider range of input space explored in bench-scale and scale-up differences). Multivariate monitoring of both scales provide a means of comparison as well as identifying improvement areas where changes can be made to move the two spaces closer to each other in terms of expected correlations, variability and means.

As a postmortem case study, multivariate modeling is performed retrospectively on commercial manufacturing batches to support technical investigations, identify process and/or operational improvement opportunities, the sources of process variation to increase process understanding. Data from historical batches is used to develop PLS-based models for key process performance variables. Information from process characterization studies can also be leveraged to further refine the PLS models. As an example, a low product titer trend was observed in manufacturing of a commercial biologic. A PLS-model was developed for product titer using multiple process inputs from 36 historical batches. Based on a review of exceptional batches in the MV charts (fingerprint in Fig. 3 and variable contribution chart in Fig. 4), it was determined that the cell specific productivity was significantly lower in the decreased product titer batches. This information guided process analysts to focus on operational parameters likely to adversely impact cell specific productivity. This analysis revealed that a shift in induction timing potentially contributed to the low product titer trend. After the induction timing was adjusted back to target, higher product titers were obtained.

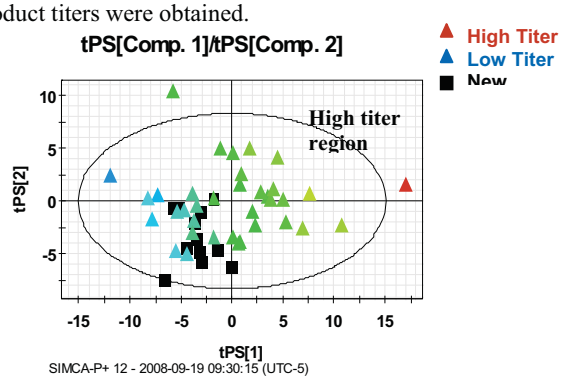

Fig. 3. A score scatter plot showing new manufacturing batches relative to historical ones.

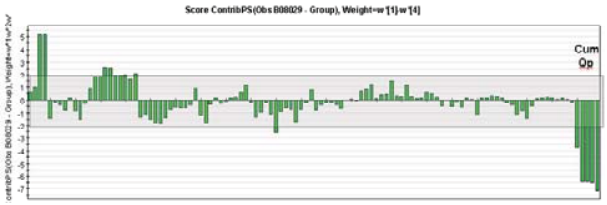

Fig. 4. Variable contribution plot to Hotelling's T^2 showing low cell specific productivity as a significant contributor to low titer (horizontal band indicates +/- 2 standard deviation about the mean batch).

With introduction of new on-line technologies such as cell density probes, pCO_2 probes and Glucose/Lactate sensors comes the possibility of applying multivariate process modeling to predict and control biologic manufacturing processes towards achieving target productivity and quality end points. Several opportunities exist to improve the process models using new and available characterization data and increase model sensitivity and predictability. While it is very informative to use MSPM for postmortem exploratory analysis of process upsets, it is more desirable to monitor the process in real-time to detect and diagnose those upsets and take preventive actions where possible. In addition to monitoring, prediction of key end points while the process is in progress is also possible (a.k.a. soft-sensors) and provides

various opportunities towards more efficient process operations and advanced process control and optimization.

5. *REAL-TIME MULTIVARIATE BIOPROCESS MONITORING CASE STUDIES*

5.1. *CASE STUDY-1: REAL-TIME LARGE-SCALE BIOREACTOR CELL CULTURE MONITORING*

The first example is from a bioreactor monitoring and shows how real-time monitoring technology is used towards operational excellence, hence identifying equipment and mechanical related issues as well. A transient decline (~3%) is observed in Final Viabilities (measured offline) in a Perfusion Bioreactor across batches. Deviations in real-time MV charts are detected for those low viability batches (*Hotelling's* T^2 chart for one of the low viability batches is shown in upper Fig. 5). Variable contribution plots identified that the low Final Viability batches that are run on particular bioreactor and its skid had higher Perfusion Feed and Retentate Temperature compared to the historical batches. Further investigation revealed that the wrong size gaskets were installed in the pump seal flush line for these batches. This made the control of temperature and pressure on the seal flush line very difficult. The correct size gaskets were replaced prior to the next batch and the temperature profile and final viability were within their normal ranges.

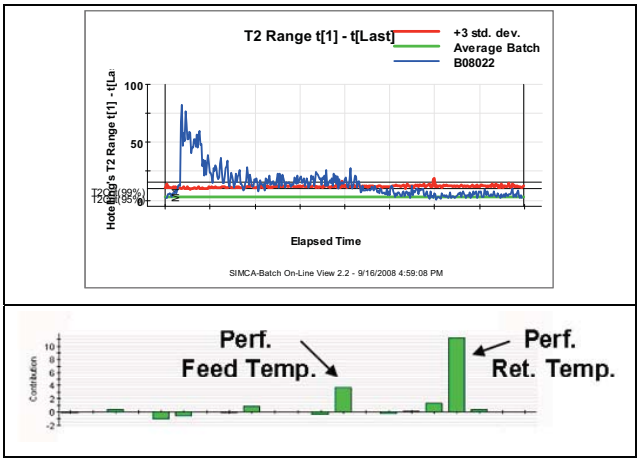

Fig. 5. Hotelling's T^2 chart (top) for one of the low final viability batches and contributions to the deviation (bottom)

5.2. *CASE STUDY-2: REAL-TIME MONITORING OF LARGE-SCALE CHROMATOGRAPHY PROCESS*

PCA models were developed for each phase of the Protein A affinity chromatography unit operation (e.g., pre-equilibration, elution) from historical process data. In general, only two or three principal components were needed for a given phase to summarize the batch process. Future batches could then be projected onto the model to allow rapid detection of deviations from the normal operating space and corrective actions would be taken where possible. Model has detected failure of a pre-column pH probe during purification of a batch through Protein A chromatography. The online pH probes are commonly used to verify proper equilibration of a column or end-point of a titration for a viral inactivation step prior to taking a confirmatory offline sample. In this example, the *Hotelling's* T^2 plot identifies the out of trend batch (on the left at Fig. 6) in real-time and the variable contribution plot (on the right hand side) identifies the pH probe having a significant effect. This information was used to replace the probe prior to further processing and avoided compromising any offline verification samples.

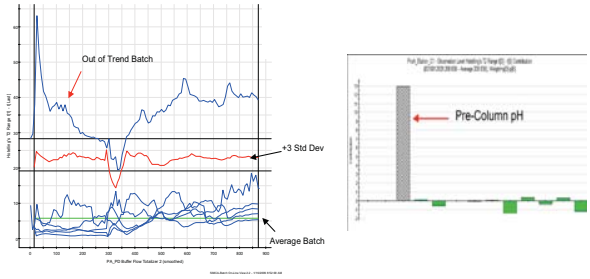

Fig. 6. Hotelling's T2 chart (on the left) indicating an out-of-control batch and the contribution plot diagnosing the faulty pH probe (on the right)

6. *REAL-TIME SOFT (VIRTUAL)-SENSOR APPLICATIONS IN BIOPHARMACEUTICAL MANUFACTURING*

There are many on-line/at-line/in-line probes and analyzers available for measuring bioprocess variables and quality/performance indicators. In a typical setting, for instance a bioreactor has temperature, level, pH, pressure, agitator speed, aeration rate, and dissolved oxygen measurement systems and data acquisition. Additional measurement systems such as cell density, dissolved carbon dioxide, mass spectroscopy in the off-gas, on-line HPLC, and fluorometric sensors are among the available and desirable technology. Research has shown that there are mathematical means via empirical and first principles modeling to generate predictions on the performance end-points in real-time (Cheruy, 1997, Undey, et al., 2006). A generic framework is depicted in Fig. 7, where more frequently measured and readily available process variables are used for developing a soft-sensor to generate an on-line quality estimate. Industrial examples are given for a cell culture production bioreactor case where product final titer is predicted in real-time and a first-principles model for monitoring a chromatography column performance in real-time.

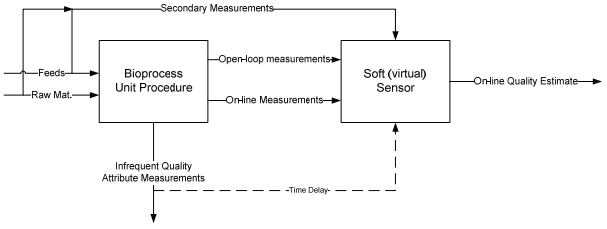

Fig. 7. Soft (virtual)-sensors for bioprocesses.

6.1. *CASE STUDY-3: REAL-TIME SOFT-SENSOR FOR BIOREACTOR FINAL TITER PREDICTION*

The production bioreactor is a critical step for biopharmaceutical processes since the target protein is expressed during this step. It is very important to closely monitor this unit operation in real-time. Any deviations from the normal operation during this step may lead to low productivity and out-of-spec product.

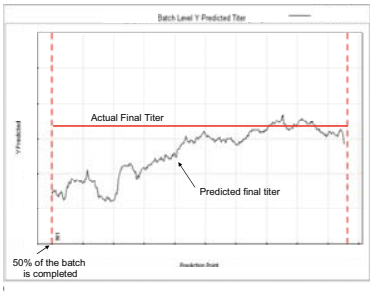

Fig. 8. Real-time Final Titer prediction starts when 50% of the batch is completed.

Final Titer is used as the performance parameter that is predicted in the batch level while monitoring the process in real-time. Accurately predicting Final Titer several days in advance of harvesting provides many PAT opportunities such as offline assay elimination (titer is typically determined via an HPLC method offline), titer optimization, schedule optimization and real-time control. Fig. 8 illustrates real-time final titer prediction for a batch by only using the continuously measured inputs and outputs such as pH, O_2 flow and bioreactor volume as predictors. Final titer is predicted within 0.5 % of the actual offline testing result.

6.2. *CASE STUDY-4: REAL-TIME SOFT-SENSORS FOR CHROMATOGRAPHY OPERATION*

In this case study for biologics purification has been real-time determination of unit operation step yields. These are typically calculated by measuring offline samples of the load and product pools, and results are often not available until well after batch completion. UV detection unit is typically available by the production unit, Beer's Law (A=ϵBC, i.e., absorbance is proportional to concentration of a solution, where ϵ is molar absorptivity, B, path length of the sample and C, concentration of the solution) can be used as a basis to correlate the absorbance to Protein Concentration UV in real time (Fig. 9). Estimated concentration can then be used to determine unit operation step yield.

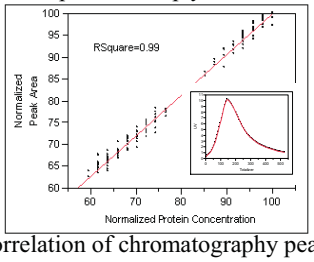

Fig. 9. Correlation of chromatography peak area (shown as inset) to protein concentration.

For process chromatography operating in bind and elute mode, the eluate peak can be integrated numerically. The same can be done for phases of the chromatography operation, such as regeneration, to complete the mass balance. Incorporating these mass balance terms into the PLS model significantly improves the predictive power.

Another area of exploration for advanced monitoring has been the use of first principles models to predict chromatography resin binding capacity. The resin capacity is typically determined during characterization studies by measuring the percentage breakthrough of protein during the loading phase. Due to the large volume requirements, this is typically not measured routinely once the process is implemented at manufacturing scale. This capacity measurement is useful to understand the changes in resin characteristics during the operational lifetime of the column and make decisions about when to change out the resin to ensure high performance.

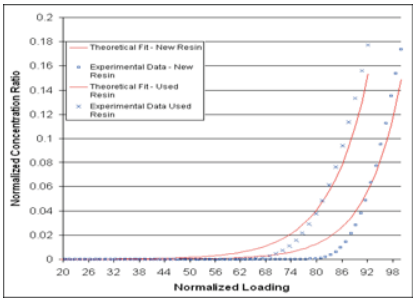

Fig. 10. Capacity changes of resin used in 90 batches of biopharmaceutical purification process.

Using the analytical solution to the differential mass-balance equation developed by Ghose et al. (2004), actual resin capacity at different points in the column lifetime was modeled. The model inputs were determined from literature and via process knowledge. This capacity information can then be compared against the expected column loading for a given batch to determine if any losses would be expected (Fig. 10). It can also be incorporated as an input variable to the soft-sensor (multivariate model in this case) to provide a more accurate prediction of step yield.

7. *CONCLUSIONS*

Process analytical technology (PAT) within the Quality-by-design framework provided by regulatory agencies define guidelines towards demonstrating good process understanding in product development and therefore requires improved monitoring and control for pharmaceutical manufacturing processes. Real-time multivariable monitoring framework for bioprocesses as shown in the examples not only provides proactive process supervision but also serves as an operational success management tool, hence, it has the potential to reduce production costs since it is also used to monitor and detect the equipment-related issues.

Soft (virtual)-sensors were also studied in this paper and promising examples were provided from cell culture and

purification areas to show how existing process and its data can be utilized for prediction of key performance end points. While advanced monitoring capabilities are demonstrated, it is important to understand how process control (e.g., feedback and/or feed forward) can be achieved to ensure consistent process outputs based on biological performance end points. This paper summarized the necessary preliminary steps of process understanding and advanced monitoring applied in biopharmaceutical manufacturing environment. New measurement technologies will be necessary to enable closed-loop control of key performance variables and CQAs to meet biopharmaceutical manufacturing needs. It is necessary that these on-line quality measurement systems that are available or being developed to have faster turn around times than the process time (i.e., the on-line test results can be available before the relevant biological phase is completed) so that a control action can be taken in a timely manner. Advanced multivariable monitoring with robust, accurate and improved on-line/at-line/in-line probes and analyzers with fully-automated data management and multivariable control capabilities hold great possibilities for 21st century PAT-enabled biopharmaceutical manufacturing.

REFERENCES

Albert, S., and Kinley, R. (2001). Multivariate statistical monitoring of batch processes: an industrial case study of fermentation supervision. *Trends in Biotechnology*, 19(2), 53-62.

Arnold, S.A., Crowley, J., Woods, N., Harvey, L.M., and McNeil, B. (2003). In-situ near infrared spectroscopy to monitor key analytes in mammalian cell cultivation, *Biotechnology and Bioengineering*, 84(1), 13-19.

Becker, T., Hitzmann, B., Muffler, K., Pörtner, R., Reardon, K.F., Stahl, F. and Ulber, R. (2007). Future aspects of bioprocess monitoring, *Advances in Biochemical Engineering and Biotechnology*, 105, 249-293.

Business Insights (2005). *The biotechnology market outlook: growth opportunities and effective strategies for licensing and collaborations*, MindBranch, Inc.

Cheruy, A. (1997). Software sensors in bioprocess engineering, *Journal of Biotechnology*, 52, 193-199.

Chirino, A.J., and Mire-Slius, A., 2004. Characterizing biological products and assessing comparability following manufacturing changes. *Nature Biotechnology*, 22(11), 1383–1391.

Cinar, A., Parulekar, S. J., Undey, C., and Birol, G. (2003). *Batch Fermentation: Modeling, Monitoring and Control*, CRC Press, New York, NY.

Ghose, S., Nagarath, D., Hubbard B., Brooks, C., and Cramer, S.M. (2004). Use and optimization of a dual-flow rate loading strategy to maximize throughput in protein-A affinity chromatography. *Biotechnology Progress,* 20(3), 830-840.

Gnoth, S., Jenzsch, M., Simutis, R., and Lubbert, A. (2007). Process Analytical Technology (PAT): Batch-to-batch reproducibility of fermentation processes by robust process operational design and control, *Journal of Biotechnology*, 232, 180-186.

Junker, B.H., and Wang, H.Y. (2006). Bioprocess monitoring and computer control: Key roots of the current PAT initiative, *Biotechnology and Bioengng*, 95(2), 226-261.

Larson, T.M., Davis J., Lam, H., and Cacia, J. (2003). Use of process data to assess chromatographic performance in production-scale protein purification columns. *Biotechnology Progress*, 19, 485–492.

Lee, W., Pasumarthy, M., Undey, C., Kundu, S., and Stout, J. (2006). Assessment of production-scale protein purification column packing through transition analysis, *RXII–Recovery of Biological Products XII,* Phoenix, AZ.

Lopes, J.A., Costa, P.F., Alves, T.P., and Menezes, J.C. (2004). Chemometrics in bioprocess engineering: Process analytical technology (PAT) applications, *Chemometrics and Intelligent Lab. Systems,* 74, 269-275.

Nomikos, P., and MacGregor, J.F. (1995). Multivariate SPC charts for monitoring batch processes, *Technometrics*, 37, 41-59.

Rathore, A.S., Yu, M., Yeboah, S., and Sharma A. (2008). Case study and application of process analytical technology (PAT) towards bioprocessing: use of on-line high-performance liquid chromatography (HPLC) for making real-time pooling decisions for process chromatography, *Biotechno.l Bioeng.*, 100(2), 306–316.

Rathore, A.S., and Winkle, H. (2009). Quality by design for biopharmaceuticals, *Nature Biotechnology*, 27(1), 26-34.

Undey, C., Tatara, E. and Cinar, A. (2004). Intelligent Real-time Performance Monitoring and Quality Prediction for Batch/fed-batch Cultivations, *J Biotechnol.*, 108, 61-77.

Undey, C., Geldart, R.W., Collins, E., Kundu, S., Humphreys, L., Johnson, K., and Frohlich, B. (2006). A case study for PAT initiative project: seeding density variability reduction approach combining an on-line cell density probe and predictive modeling, *IBC's 3rd Intl.on Implementing PAT for Bioprocessing*, Reston, VA.

Undey, C. (2008). Are we there yet? An Industrial Perspective of Evolution from Post-mortem Data Analysis towards Real-time Multivariate Monitoring and Control of Biologics Manufacturing Processes, *IBC's BioProcess International Analytical and Quality Summit*, Cambridge, MA, June 2-4.

US Food and Drug Administration (August 2002). *Pharmaceutical cGMPs for the 21st century: A risk-based approach (FDA, Rockville, MD).* [Web] [cited 2009 01/06/2009]; Available from: http://www.fda.gov/oc/guidance/gmp.html.

US Food and Drug Administration (September, 2004). *Guidance for Industry: PAT — A Framework for Innovative Pharmaceutical Development, Manufacturing, and Quality Assurance* (FDA, Rockville, MD). [Web] [cited 2009 01/06/2009]; Available from: http://www.fda.gov/Cder/guidance/6419fnl.pdf.

US Food and Drug Administration (September 2006). *Guidance for industry: Q10 quality systems approach to pharmaceutical cGMP regulations* (FDA, Rockville, MD). [Web] [cited 2009 01/06/2009]; Available from: http://www.fda.gov/cber/gdlns/qualsystem.pdf.

Wold, S., Kettaneh, N., Fridén, H., and Holmberg, A. (1998). Modelling and diagnostics of batch processes and analogous kinetic experiments, *Chemometrics and Intelligent Laboratory Systems*, 44, 331-340.

Cascade Hybrid Control for Anaerobic Digestion Systems ⋆

J.P. García-Sandoval *,

* *Chemical Engineering Department, University of Guadalajara, Calz. Gral. Marcelino García Barragán 1451, Guadalajara, Jalisco 44430, México (e-mail: paulo.garcia@cucei.udg.mx)*

Abstract: A cascade hybrid controller is proposed to guarantee the operational stability of anaerobic digestion systems and at the same time to assure a satisfactory remotion. The effluent chemical oxygen demand (COD) concentration and the dilution rate are taken respectively as the regulated and the manipulated variables. This controller is composed by a continuous inner loop which controls the concentration of volatile fatty acids and updates its reference at each sampling period according to the available discrete information of the COD, enhancing the robustness of the closed-loop with respect of influent disturbances. The performance of the proposed control scheme is illustrated via numerical simulations and compared with a discrete controller which only uses the COD information.

Keywords: Cascade control, anaerobic digestion, continuous and discrete measurements

1. INTRODUCTION

The stringent regulation policies imposed in chemical and biological processes has brought abut the need of more efficient monitoring, decision and control systems. Nowadays, it is not enough to regulate readily available variables such as pH or temperature, to guarantee both product quality and process safety (Alcaraz-González and González-Álvarez, 2007). In the particular case of anaerobic digestion, one must pay attention to certain operating conditions that may lead the system to the eventual crash even under tightly controlled pH and temperature conditions (Dochain, 2008). The last two decades have seen an increasing interest to improve the operation of bioprocesses by applying advanced control schemes. In particular, Anaerobic digestion (AD) has regained the interest of the wastewater treatment scientific and industrial community to reduce and transform the organic matter from industrial and municipal effluents into a high-energy gas (Henze et al., 1997). Nevertheless, its widespread application has been limited, because of the difficulties involved in achieving the stable operation of the AD process, which cannot be guaranteed by regulating temperature and pH, because the microbial community within the AD process is quite complex (Méndez-Acosta et al., 2008). In addition, the behavior of such a process may be affected by the substrate composition and inhibition by substrates or products, for example the accumulation of volatile fatty acids (VFA). Moreover, it is well-known that, to guarantee the so-called operational stability (Hill et al., 1987) and to avoid the eventual crash of the anaerobic digester, the organic matter in the liquid phase must be kept in a set of predetermined values.

Over the past decade, the regulation of the organic matter has been addressed by proposing many control techniques to keep certain operating variables which are readily available (such as the chemical oxygen demand (COD) and the biogas production) at a predetermined value (Schügerl, 2001; Alvarez-Ramírez et al., 2002; Puñal et al., 2002; Ahring and Angelidaki, 1997). For example, Alvarez-Ramírez et al. (2002) designed a continuous PI feedback controller to regulate COD concentration which uses the VFA as a secondary measurement that is incorporated into the feedback loop scheme to enhance the robustness of the control scheme with respect of influent disturbances. Nevertheless, the problem of the operational instability due to the accumulation of volatile fatty acids remains open (Méndez-Acosta et al., 2008). In this context, the regulation of the VFA concentration as a controlled variable seems to be very promising, because the operational stability of the AD process is largely dependent on the accumulation of VFA. For instance, some authors recommend a VFA concentration below 1.5 g/l (25 mmol/l) (Angelidaki et al., 2004). For this reason, it is necessary to design multiobjective controls which fulfill environmental regulations about COD effluents and at the same time guarantee the operational stability.

In this work we propose the regulation of COD concentration using a cascade scheme which assures the robustness and the operational stability via VFA continuous regulation, where the VFA reference is updated at each sampling period according to the available discrete information of the COD, in contrast with the continuous information used by Alvarez-Ramírez et al. (2002). The proposed scheme is a cascade hybrid control since is composed by a continuous and a discrete part. The paper is organized as follows. In section 2 the AD model is presented. Then, in section 3 the controller is designed and in section 4 it is implemented

⋆ Supported by PROMEP under proyect 103.5/08/2919 and CONACYT under grant 43658.

and tested via numerical simulations. Finally, the paper is closed with some concluding remarks.

2. MODEL PRESENTATION

There are hundreds of dynamical models available to describe anaerobic digestion, from the basic ones considering only one biomass (Andrews, 1968) to detailed models including several bacterial populations and several substrates. Among the complex models available in the literature, the IWA Anaerobic Digestion Model 1 (Batstone et al., 2002) has imposed itself as an useful tool to describe the behavior of a digestion plant with more insight into the process dynamics. However, its excessive complexity makes any advanced mathematical analysis of the model critical (Hess and Bernard, 2008). Thus it is considered a simplified macroscopic model of the anaerobic process based on 2 main reactions (Bernard et al., 2001), where the organic substrate (S_1) is degraded into volatile fatty acids (S_2) by acidogenic bacteria (X_1), and then the VFA are degraded into methane CH_4 and CO_2 by methanogenic bacteria (X_2). A mass balance model in a continuous stirred tank reactor (CSTR) can straightforwardly be derived (Bastin and Dochain, 1990; Bernard et al., 2001):

$$\dot{X}_1 = \mu_1(S_1) X_1 - \alpha D X_1 \tag{1a}$$
$$\dot{S}_1 = -k_1 \mu_1(S_1) X_1 + D(S_{1in} - S_1) \tag{1b}$$
$$\dot{X}_2 = \mu_2(S_2) X_2 - \alpha D X_2 \tag{1c}$$
$$\dot{S}_2 = k_2 \mu_1(S_1) X_1 - k_3 \mu_2(S_2) X_2 + D(S_{2in} - S_2) \tag{1d}$$

where D is the dilution rate, S_{1in} and S_{2in} are respectively, the concentrations of influent organic substrate and of influent VFA. The k_is are pseudo-stoichiometric coefficients associated to the bioreactions. Parameter $\alpha \in (0, 1]$ represents the fraction of the biomass which is not retained in the digester. The specific bacterial growth rates, $\mu_1(S_1)$ and $\mu_2(S_2)$, are given by the nonlinear equations (Dochain and Vanrolleghem, 2001; Van-Impe et al., 1998):

$$\mu_1(S_1) = \mu_{\max 1} \frac{S_1}{S_1 + K_{S1}}$$
$$\mu_2(S_2) = \mu_{\max 2} \frac{S_2}{S_2 + K_{S2} + (S_2/K_{I2})^2}$$

where $\mu_{1\max}$, K_{S1}, $\mu_{2\max}$, K_{S2} and K_{I2} are the maximum bacterial growth rate and the half-saturation constant associated to the substrate S_1, the maximum bacterial growth rate in the absence of inhibition, and the saturation and inhibition constants associated to substrate S_2, respectively.

Hess and Bernard (2008) presented an extensive steady state analysis for system (1). They have found that, for a given dilution rate, the VFA concentration have three equilibrium points mathematically stables, but two of them are operationally unstable since one drives to substrate inhibition which can produce methanogenic bacterial extinction, which is the second operational unstable equilibrium. For this reason volatile fatty acids must be controlled, but at the same time, it should be guaranteed the COD remotion. In the next section we propose a control algorithm to achieve these goals.

3. CONTROL DESIGN

3.1 Problem formulation

Consider a nonlinear system describe by

$$\dot{x}(t) = f(x(t), u(t), \mu) \tag{2}$$
$$y_1(t) = C_1 x(t) \tag{3}$$
$$y_2(k\delta) = C_2 x(k\delta) \tag{4}$$

where $x \in \mathbb{R}^n$ represents the state vector, $u \in \mathbb{R}$ describes the input vector, $y_1 \in \mathbb{R}$ is a continuous measurement, while $y_2 \in \mathbb{R}$ is a discrete measurement obtained at each sampling period δ. Finally, $\mu \in \mathbb{R}^p$ is a parameter vector which may take values in a neighborhood $\mathcal{P} \in \mathbb{R}^p$ of the nominal ones, μ_0.

Given a constant value y_{2r}, it is desirable to regulate the output y_2 around y_{2r}, then, it can be defined the regulation error

$$e_2 = y_2 - y_{2r} \tag{5}$$

and the proposed *Regulation Problem* consists in finding, if possible, a controller which guarantees that $\lim_{t\to\infty} e_2(t) = 0$. However this controller must take into account both, continuous and discrete outputs (3)-(4) in order to guarantee the stability of the closed-loop system. The next assumption about the steady state around $e_2 = 0$ is instrumental in the controller design.

Assumption 1. Given the constant reference y_{2r} there exists at least one linear vector $x_{ss}(\mu)$ and one scalar $u_{ss}(\mu)$ such that equations

$$0 = f(x_{ss}, u_{ss}, \mu), \tag{6}$$
$$0 = C_2 x_{ss} - y_{2r}, \tag{7}$$

hold. Additionally, the scalar y_{1ss} is defined such that

$$0 = C_1 x_{ss} - y_{1ss}. \tag{8}$$

Remark 2. x_{ss} represents the steady state vector, u_{ss} is the input necessary to achieve this steady state, while y_{1ss} denotes the constant value which reaches the output, y_1. Notice that, by using the central manifold theory (Isidori, 1995), it is evident that x_{ss}, u_{ss} and y_{1ss} will depend on both y_{2r} and the unknown parameter vector, μ. Additionally, assumption 1 can be reformulated in order to fix the value of y_{1ss} and find the solution of (6), (7) and (8) for x_{ss}, u_{ss} and y_{2r}. Finally, if for a given y_{2r}, the solution of (6) and (7) is not unique, neither is y_{1ss}.

In order to design a controller which solves the proposed regulation problem, some basic concepts will be presented in the next subsection.

3.2 Basic facts about jump observers

Consider the linear system

$$\dot{x}(t) = Ax(t) + Bu(t) \qquad \forall t \in [0, \infty) \tag{9}$$
$$y(k\delta) = Cx(k\delta) \qquad k = 1, 2, 3, \ldots, \tag{10}$$

where $x \in \mathbb{R}^n$, $u \in \mathbb{R}^m$, and $y \in \mathbb{R}^q$ are the state, input and output vectors, respectively. In this case the outputs are obtained at each sampling time δ.

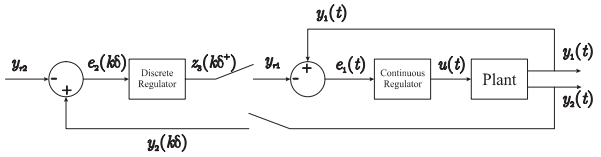

Fig. 1. Cascade proposed control scheme.

The usual way to estimate the unknown states of system (9) from output (10) consists in discretizing and designing a discrete observer. However, the observer thus obtained only provides information at each sampling period. Additionally, to obtain a discrete version of (9) it is necessary to have a well defined input in order to place the appropriate holder (for example a zero holder or a exponential holder), hence unexpected input variations during intersampling periods may produce a failure in the discrete observer (García-Sandoval, 2006). For this reason, an interesting problem would be to construct an observer of the form

$$\dot{z}(t) = Az(t) + Bu(t) \qquad \forall t \neq k\delta \tag{11}$$

$$z\left(k\delta^+\right) = z(k\delta) - G\left[y(k\delta) - Cz(k\delta)\right] \quad t = k\delta \tag{12}$$

where $z \in \mathbb{R}^n$ are the observer states and $z\left(k\delta^+\right)$ denotes the updated observer states at each sampling instant, i.e this is a continuous observer which updates its states at each sampling instant. The next lemma establishes conditions for the existence of such observer.

Lemma 3. Consider system (9)-(10) and suppose the pair $\left(e^{A\delta}, C\right)$ is observable, then an observer of the form (11)-(12), where the matrix gain G is such that matrix $(I + GC)\, e^{A\delta}$ is Schur, guarantees that $\lim_{t\to\infty}\left[x(t) - z(t)\right] = 0$.

Proof. See Appendix.

Remark 4. The main feature of observer (11)-(12) is that the intersampling state information is available at any time and it is not necessary to have a pre-established dynamic behavior for the input. Equation (11) can be seen as an continuous open loop observer in the intersampling period, whose states, according to (12), are updated at the sampling instant.

Observer (11)-(12) can be used to design a cascade controller which uses the continuous information in the inner loop and the discrete information in the external loop, as presented in the next subsection.

3.3 Proposed controller

In order to solve the regulation problem, it is proposed to design a cascade control scheme where the inner loop consists of a continuous controller which uses the input $u(t)$ to regulate the continuous output, y_1, around y_{1r} (notice that y_{1r} may not necessarily be equal to y_{1ss}, since y_{1ss} is initially unknown). Then, by using a jump observer, it is possible to devise an external loop controller which estimates the reference y_{1r} necessary to regulate the discrete output, y_2, around y_{2r}. The scheme is illustrated in Figure 1.

The next Theorem presents the proposed solution to the regulation problem.

Theorem 5. Consider assumption 1 holds. Assume the pairs

$$[A_0, B_0] \quad \text{and} \quad [A, C_{T1}]$$

with

$$A = \begin{pmatrix} A_0 & -B_0 \\ 0 & 0 \end{pmatrix}, \quad C_{T1} = (C_1 \;\; 0), \tag{13}$$

$$A_0 = \left[\frac{\partial f}{\partial x}\right]_{(x,u,\mu)=(0,0,0)} \quad \text{and} \quad B_0 = \left[\frac{\partial f}{\partial u}\right]_{(x,u,\mu)=(0,0,0)}$$

are stabilizable and detectable, respectively. Then a controller which solves the regulation problem for system (2) using outputs (3) and (4) is

$$\dot{z}_1(t) = (A_0 - G_1C_{01})\, z_1(t) - B_0 z_2(t) + B_0 u(t) + G_1 e_1(t), \qquad \forall t \neq k\delta, \tag{14a}$$

$$\dot{z}_2(t) = -G_2C_{01} z_1(t) + G_2 e_1(t), \quad \forall t \neq k\delta, \tag{14b}$$

$$z_3\left(k\delta^+\right) = G_dC_{02} z_1(k\delta) + z_3(k\delta) - G_d e_2(k\delta), \qquad \forall t = k\delta, \quad k = 1, 2, 3, \ldots \tag{14c}$$

$$u(t) = Kz_1(t) + z_2(t) \tag{14d}$$

with

$$e_1(t) = y_1(t) - z_3\left(k\delta^+\right), \tag{15}$$

$$e_2(k\delta) = y_2(k\delta) - y_{2r}, \tag{16}$$

where K and $G = (G_1, G_2)^T$ are such that matrices $(A_0 + B_0K)$ and $(A - GC_{T1})$ are Hurwitz, while given matrices

$$\overline{A}_d = \begin{pmatrix} A_d & -M_d \\ 0 & 1 \end{pmatrix} \tag{17}$$

with

$$A_d = e^{(A - GC_{1T})\delta} \quad \text{and} \quad M_d = \int_0^\delta e^{(A-GC_{1T})\lambda} G d\lambda, \tag{18}$$

the scalar G_d is such that $\left(I + \overline{G}_d\overline{C}_2\right)\overline{A}_d$ is Schur, where

$$\overline{G}_d = \begin{pmatrix} 0 \\ G_d \end{pmatrix}, \quad \overline{C}_2 = (C_{T2} \;\; 0) \quad \text{and} \quad C_{T2} = (C_2 \;\; 0), \tag{19}$$

obviously the pair $\left(\overline{A}_d, \overline{C}_2\right)$ must be detectable.

Proof. Given a reference y_{2r}, if the solution of (6), (7) and (8) is x_{ss}, u_{ss} and y_{1ss}, the linear version of system (2) around the pair $(x, u) = (x_{ss}, u_{ss})$ and the nominal values μ_0 is

$$\dot{\underline{x}}(t) = A_0\underline{x}(t) + B_0u(t) - B_0u_{ss} + \widehat{f}\left(\underline{x}(t), u(t), \mu\right) \tag{20a}$$

$$y_1(t) = C_1\underline{x}(t) + y_{1ss} \tag{20b}$$

where $\underline{x} = x - x_{ss}$, while

$$A_0 = \left.\frac{\partial f}{\partial x}\right|_{\substack{x=x_{ss},\\ u=u_{ss}}}, \quad B_0 = \left.\frac{\partial f}{\partial u}\right|_{\substack{x=x_{ss},\\ u=u_{ss}}} \quad \text{and} \quad C_{01} = \left.\frac{\partial h_1}{\partial x}\right|_{x=x_{ss}},$$

are the linear approximations and $\widehat{f}(\underline{x}, u, \mu)$ contains the second or higher order terms. Since z_3 remains constant along each sampling instant, it can be considered that $\dot{z}_3 = 0\ \forall t \neq k\delta$. Defining

$$\xi_1 = \underline{x} - z_1$$

$$\xi_2 = u_{ss} - z_2$$

$$\xi_3 = y_{1ss} - z_3$$

the linear approximation of the closed-loop system can be written as

$$\dot{\xi}(t) = \overline{A}\xi(t), \qquad \forall t \neq k\delta \tag{21}$$

$$\xi\left(k\delta^{+}\right) = \left(I + \overline{G}_d\overline{C}_2\right)\xi(k\delta), \quad \forall t = k\delta,\ k = 1, 2, .. \tag{22}$$

where

$$\overline{A} = \begin{pmatrix} A - GC_{T1} & -G \\ 0 & 0 \end{pmatrix}$$

while A and C_{T1} are given in (13). Notice that $\underline{x}(k\delta) = \underline{x}\left(k\delta^{+}\right)$. Integrating (21) for $t \in \left(k\delta^{+}, (k+1)\delta\right)$,

$$\xi\left((k+1)\delta\right) = \overline{A}_d\xi\left(k\delta^{+}\right), \tag{23}$$

where $\overline{A}_d$ is described in (17), while A_d and M_d are defined in (18). Taking an increment in (22) and replacing (23),

$$\xi\left((k+1)\delta^{+}\right) = \left(I + \overline{G}_d\overline{C}_2\right)\overline{A}_d\xi\left(k\delta^{+}\right).$$

Since by hypothesis $(A - GC_{T1})$ is Hurwitz, then A_d is Schur and $\overline{A}_d$ have only one eigenvalue in the unitary circle. However, if G_d is such that $\left(I + \overline{G}_d\overline{C}_2\right)\overline{A}_d$ is Schur, it is guaranteed that $\xi\left(k\delta^{+}\right)$ is asymptotically stable. Therefore $\lim_{k\to\infty} z_3(k\delta) = y_{1ss}$, $\lim_{k\to\infty} z_2(k\delta) = u_{ss}$ and $\lim_{k\to\infty} z_1(k\delta) = \underline{x}(k\delta)$. Then by continuity $\lim_{t\to\infty} z_2(t) = u_{ss}$ and $\lim_{t\to\infty} z_1(t) = \underline{x}(t)$ and the closed-loop dynamics of (20) approach to

$$\dot{\underline{x}}(t) = (A_0 + B_0K)\,\underline{x}(t) + \widehat{f}\left(\underline{x}(t), K\underline{x}(t) + u_{ss}, \mu\right)$$

which is asymptotically stable in a neighborhood of the origin since $(A_0 + B_0K)$ is Hurwitz. Then $\lim_{t\to\infty}[x(t) - x_{ss}] = 0$ and this guarantees that $\lim_{t\to\infty}[y(t) - y_{2r}] = 0$, concluding the proof.

Remark 6. z_1 and z_2 represent the dynamic of the continuous regulator, while z_3 is the state of the discrete regulator. Notice that z_2 which is present in the input (14d) can be considered as an integral action since integrating (14b), which is precisely the dynamic of z_2, appears an integral of $e_1(t)$. Analogously, z_3 is also an discrete integral action which consider $e_2(k\delta)$. These variables give the robustness to the cascade controller.

4. CONTROL IMPLEMENTATION

Considering that the VFA concentration is measured continuously, while the COD concentration is measured at each sampling period δ, the outputs of system (1) are

$$y_1(t) = C_1x(t) \qquad \text{and} \qquad y_2(k\delta) = C_2x(k\delta),$$

where $x = \mathrm{col}(X_1, S_1, X_2, S_2)$ and

$$C_1 = (0\ 0\ 0\ 1) \qquad , \qquad C_2 = (0\ 1\ 0\ 0).$$

System (1) is similar to (2), hence controller (14) presented in Theorem 5 can be designed. The linear matrix approximations of system (1) are

$$A_0 = \mu_1(S_{1ss}) \begin{pmatrix} 0 & \Psi_1 & 0 & 0 \\ -k_1 & -k_1\Psi_1 - \dfrac{1}{\alpha} & 0 & 0 \\ 0 & 0 & 0 & \Psi_2 \\ 0 & k_2\Psi_1 & -k_3\Psi_2 & -k_3\Psi_2 - \dfrac{1}{\alpha} \end{pmatrix},$$

$$B_0 = \left(-\alpha X_{1ss}\ (S_{1in} - S_{1ss})\ -\alpha X_{2ss}\ (S_{2in} - S_{2ss})\right)^T,$$

where $\Psi_1 = \frac{K_{S1}}{\mu_{\max 1}}\frac{\mu_1(S_{1ss})}{S_{1ss}^2}X_{1ss}$, $\Psi_2 = \frac{\mu_2(S_{2ss})}{S_{2ss}^2}X_{2ss}$. $\left[\frac{K_{S2} - (S_{2ss}/K_{I2})^2}{\mu_{\max 2}}\right]$, while the steady state is described by

Table 1. Nominal parameter values and variations.

Parameter	Nominal value	% of variation from nominal value		
		$t < 10$	$10 \leq t < 30$	$t \geq 30$
$\mu_{\max 1}$	$1.2\,\mathrm{d}^{-1}$	-10	-20	-20
$\mu_{\max 2}$	$0.744\,\mathrm{d}^{-1}$	-7	-10	-10
K_{S1}	$7.1\,\mathrm{g/l}$	-5	10	10
K_{S2}	$9.28\,\mathrm{mmol/l}$	10	10	10
K_{I2}	$16\,\mathrm{mmol/l}$	-15	-15	-15
k_1	$42.14\,\mathrm{g/g}$	-12	-12	-12
k_2	$116.5\,\mathrm{mmol/g}$	15	15	15
k_3	$268\,\mathrm{mmol/g}$	13	13	13
α	0.5	0	15	15
S_{1i}	$30\,\mathrm{g/l}$	25	10	10
S_{2i}	$750\,\mathrm{mmol/l}$	-5	-5	50

$$\alpha D_{ss} = \mu_1(S_{1ss}) = \mu_2(S_{2ss}),$$

$$X_{1ss} = \alpha^{-1}k_1^{-1}(S_{1in} - S_{1ss}),$$

$$X_{2ss} = \alpha^{-1}k_3^{-1}\left[k_1^{-1}k_2(S_{1in} - S_{1ss}) + (S_{2in} - S_{2ss})\right],$$

where it must be fixed one variable (which might be any of this: D_{ss}, S_{1ss} or S_{2ss}) in order to estimate the others.

In order to analyze the closed-loop dynamic behavior, the parameters reported in Table 1 where taken from (Bernard et al., 2001). Following Theorem 5 and considering a sample period of 1day, the next matrices were obtained

$$A_0 = \begin{pmatrix} 0 & 0.1207 & 0 & 0 \\ -13.1687 & -5.7096 & 0 & 0 \\ 0 & 0 & 0 & 0.1554 \\ 36.4063 & 14.0570 & -83.7500 & -42.2704 \end{pmatrix},$$

$$B_0 = (-0.6526\ 27.5000\ -3.0566\ 743.1464)^T,$$

while using LQR techniques the next feedback parameters were obtained

$$K = (-0.0007\ -0.0044\ -0.0162\ -0.0083),$$

$$G = (-0.1132\ 5.3922\ -0.8990\ 88.2809\ -10.0000)^T,$$

$$G_d = 2.5.$$

Since it is desirable to guarantee the operational stability, it was set that VFA reference must be bounded by the next domain: $y_{1r} \in (0, 12)$ mmol/l, while $D \in (0.05, 1)\ \mathrm{d}^{-1}$.

4.1 Simulation results

To verify if the proposed controller enhances the robustness of the closed-loop with respect of influent disturbances, a discrete controller was designed with the same sampling period to regulate the COD concentration. Figure 2 presents the dynamic response for both controllers. The simulation was carried out using steady state initial conditions and nominal parameter values (see Table 1). At time $t = 5\,\mathrm{d}$ a step in the reference from 2.5 to 2 COD g/l was induced. As can be seen in Figure 2a both controllers can handle this step approximately with the same dynamic response, however, at time $t = 15\,\mathrm{d}$ a drastic overload in the VFA influent concentration was induced. Since this overload does not affect the acidogenesis phase, the discrete controller remains unaltered as well as its COD concentration, while the cascade controller detects a change in the VFA concentration and modify the dilution

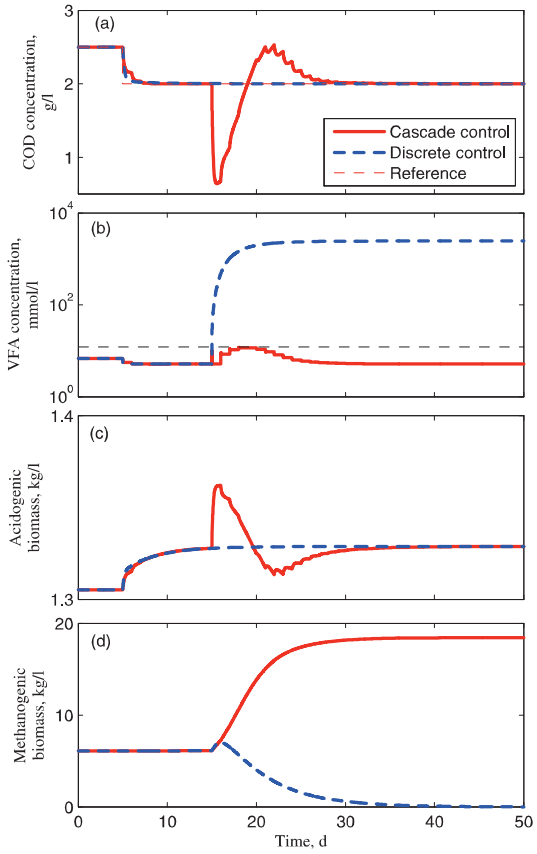

Fig. 2. Comparison of the cascade control with a traditional COD regulator. (a) COD concentration. (b) VFA concentration. (c) Acidogenic biomass. (d) Methanogenic biomass.

rate (see Figure 3). This induced a variation on the COD concentration which is corrected by the cascade controller in approximately 10 days. As can be seen in Figure 2b the VFA concentration increases in both cases, however, since for the cascade controller y_{1r} is bonded, at approximately $t = 25\,\mathrm{d}$, this reference reached the upper bound and the inner loop did not allow it to keep increasing, while for the discrete controller it keeps increasing, producing an acidification and consequently, a substrate inhibition which finally causes the methanogenic bacterial death, as shown in Figure 2d. This simulation remarks the capabilty of the cascade controller to guarantee the operational stability at the expense of a small temporary variation on the COD concentration.

Another simulation for the cascade controller was carried out, in order to verify the robustness to parametric and load variations as reported in Table 1, notice that variations up to 50% were induced. Figures 4 and 5 present the dynamic response. It is evident the robustness of the closed-loop with respect to load disturbances and several parametric variations.

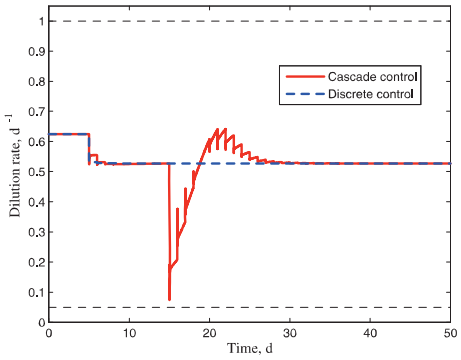

Fig. 3. Dilution rate for the cascade control and a traditional COD regulation.

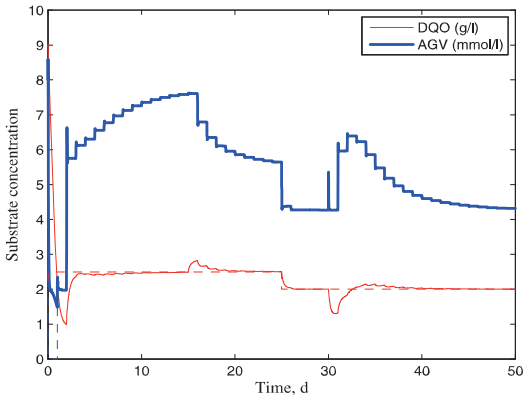

Fig. 4. Substrate concentrations.

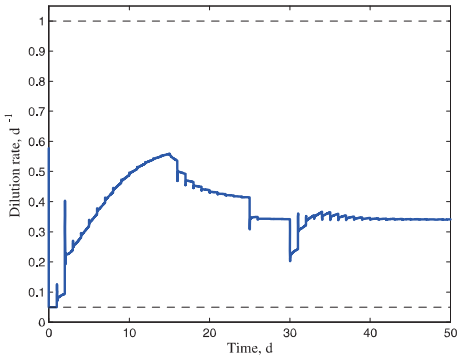

Fig. 5. Dilution rate.

5. CONCLUSION

A cascade scheme was proposed to regulate the COD concentration of AD processes. Although the control law is based on a linear approximation its robustness is conferred by integral actions of the controller. The cascade scheme also presents advantages since, additionally to the COD regulation, can be used to guarantee the operational stability, i.e. to avoid the AGV inhibition, at the expense of a small temporary variation on the COD concentration. Real time implementation are been carried out and results

will appear soon. Although the design of the control law (14) was motivated by the control of AD systems, it can be applied to another systems. As future work this theory will be extended to the case of not constant references.

(Chapter head:)*

Bibliography

Ahring, B. and Angelidaki, I. (1997). Monitoring and controlling the biogas process. In *Proceedings of the 8th International Conference on Anaerobic Digestion*, volume 1.

Alcaraz-González, V. and González-Álvarez, V. (2007). *Selected Topics in Dynamics and Control of Chemical and Biological Processes*, volume 361 of *Lecture Notes in Control and Information Sciences*, chapter Robust Nonlinear Observers for Bioprocesses Application to Wastewater Treatment, 119–164. Springer, Germany.

Alvarez-Ramírez, J., Meraz, M., Monroy, M., and Velasco, A. (2002). Feedback control design for an anaerobic digestor process. *J. Chem. Technol. & Biotechnol.*, 77(6), 725–734.

Andrews, J. (1968). A mathematical model for the continuous culture of microorganisms utilizing inhibitory substrates. *Biotechnology and Bioengineering*, 10, 707–723.

Angelidaki, I., Boe, K., and Ellegaard, L. (2004). Efect of operating conditions and reactor configuration on effciency of full-scale biogas plants. In *10th World Congress of Anaerobic Digestion*, 275–280. Canada.

Bastin, G. and Dochain, D. (1990). *On-Line Estimation and Adaptive Control of Bioreactors*. Elsevier.

Batstone, D., Keller, J., Angelidaki, I., Kalyuzhnyi, S., Pavlostathis, S., Rozzi, A., Sanders, W., Siegrist, H., and Vavilin, V. (2002). *Anaerobic Digestion Model No. 1 (ADM1)*, volume 13 of *Scientific and Technical Report*. IWA Publishing, London.

Bernard, O., Hadj-Sadok, Z., Dochain, D., Genovesi, A., and Steyer, J. (2001). Dynamical model development and parameter identification for anaerobic wastewater treatment process. *Biotechnology & Bioengineering*, 75(4), 424–439.

Dochain, D. and Vanrolleghem, P. (2001). *Dynamical Modelling and Estimation in Wastewater Treatment Processes*. IWA Publishing, Colchester.

Dochain, D. (2008). *Bioprocess Control*. Control Systems, Robotics and Manufacturing. Wiley.

García-Sandoval, J. (2006). *The Robust Regulation Problem Using Immersions: Reactors Applications*. Ph.D. thesis, CINVESTAV.

Henze, M., Harremoes, P., LA-Cour-Jansen, J., and Arvin, E. (1997). *Wastewater Treatment: Biological and Chemical Processes*. Springer Verlag, Berlin, 2nd edition.

Hess, J. and Bernard, O. (2008). Design and study of a risk management criterion for an unstable anaerobic wastewater treatment process. *Journal of Process Control*, 18(1), 71–79.

Hill, D., Cobbs, S., and Bolte, J. (1987). Using volatile fatty acid relationships to predict anaerobic digester failure. *Trans. ASAE*, 30(2), 496–501.

Isidori, A. (1995). *Nonlinear Control Systems*. Springer, London, 3rd edition.

Kailath, T. (1980). *Linear Systems*. Prentice Hall.

Méndez-Acosta, H., Palacios-Ruiz, B., Alcaraz-González, V., Steyer, J., González-Álvarez, V., and Latrille, E. (2008). Robust control of volatile fatty acids in a anaerobic digesters. *Industrial and Engineering Chemical Research*, 47(20), 7715–7720.

Puñal, A., Palazzotto, L., Bouvier, J., Conte, T., and Steyer, J. (2002). Automatic control of VFA in anaerobic digestion using a fuzzy logic based approach. In *IWA VII Latin America Workshop and Symposium on Anaerobic Digestion*, 126–133.

Schügerl, K. (2001). Progress in monitoring, modeling and control of bioprocesses during the last 20 years. *J. Biotechnol.*, 85(2), 149–173.

Van-Impe, J., Vanrolleghem, P., and Iserentant, D. (1998). *Advanced Instrumentation, Data Interpretation, and Control of Biotechnological Processes*. Kluwer Academic Publishers.

Appendix A. OUTLINE OF PROOF

Proof. [Lemma 3] Let us define

$$\xi(t) = x(t) - z(t), \quad \text{and } \xi\left(k\delta^+\right) = x(k\delta) - z\left(k\delta^+\right),$$

where $\xi(t)$ represents the continuous error and $\xi\left(k\delta^+\right)$ is the updated error for each sampling period. Note that $x\left(k\delta^+\right) = x(k\delta)$ since system (9) is continuous. Now

$$\dot{\xi}(t) = A\xi(t) \qquad \forall t \neq k\delta \tag{A.1}$$

$$\xi\left(k\delta^+\right) = (I + GC)\,\xi(k\delta) \qquad t = k\delta. \tag{A.2}$$

Solving (A.1) for $t \in \left[k\delta^+, (k+1)\,\delta\right]$, it follows that

$$\xi(k+1) = A_d\xi\left(k\delta^+\right), \tag{A.3}$$

where $A_d = e^{A\delta}$. From (A.2) and (A.3) it is obtained

$$\xi\left((k+1)\,\delta^+\right) = (I + GC)\,\xi(k+1) = (I + GC)\,A_d\xi\left(k\delta^+\right),$$

and thus, if the pair (A_d, CA_d) is observable, then a matrix G can be calculated such that $A_d + GCA_d$ is Schur and the error $\xi\left(k\delta^+\right)$ will converge to zero, hence $\lim_{k\to\infty}\left[x(k\delta) - z\left(k\delta^+\right)\right] = 0$; then for $k\delta < t \leq (k+1)\,\delta$ the solution $z(t)$ converges to $x(t)$, that is $\lim_{t\to\infty}\left[x(t) - z(t)\right] = 0$. On the other hand, to prove that the pair (A_d, CA_d) is observable if the pair (A_d, C) is observable, consider its observability matrix

$$\mathcal{O} = \begin{pmatrix} CA_d \\ CA_d^2 \\ \vdots \\ CA_d^n \end{pmatrix},$$

where $A_d \in \mathbb{R}^{n\times n}$, then using the Hamilton-Cailey theorem (Kailath, 1980)

$$A_d^n = a_0 I + a_1 A_d + \cdots + a_{n-1}A_d^{n-1},$$

the observability matrix becomes

$$\mathcal{O} = \begin{pmatrix} CA_d \\ CA_d^2 \\ \vdots \\ a_0 C + a_1 CA_d + \cdots + a_{n-1}CA_d^{n-1} \end{pmatrix}.$$

Since A_d is obtained through a discretization of matrix A then $a_0 \neq 0$ and $\mathcal{O}$ has full rank if the pair (A_d, C) is observable.

Analysis and Control of Crystallization Processes

Oral Session

A Stochastic Approach for Anti-Solvent Addition Policy in Crystallization Operations: An Application to a Bench-Scale Fed-Batch Crystallizer

Omar GALAN*, Massimiliano GROSSO, Roberto BARATTI**, José ROMAGNOLI***

** Department of Chemical Engineering, Louisiana State University, USA (e-mail: galan, jose@lsu.edu)*

*** Dipartimento di Ingegneria Chimica e Materiali, Università di Cagliari, Cagliari, Italy (e-mail: grosso, baratti@dicm.unica.it)*

Abstract: This work aims a stochastic approach for the calculation of robust anti-solvent addition policies for controlling the mean crystal size (MCS) in fed-batch crystallization operations. The proposed strategy is based-on a non-structured population balance where uncertainties associated with the start-up condition and random fluctuations along the fed-batch operation can be taken into account in a very natural fashion. We include and quantify the effect of the uncertainties by embedding a deterministic crystal growth model into a Fokker-Planck equation (FPE) resulting in a stochastic model for the MCS dynamics. This approach uses the Generalized Logistic equation (GLE) that has an adequate mathematical structure that suits the dynamic characteristic of the crystal growth. Thus, the numerical solution of the FPE provides the most likely MCS evolution for a given anti-solvent flow-rate. The effect of the anti-solvent is incorporated into the parameters of the FPE. The parameters of the FPE are computed as linear piece-wise interpolating functions of the anti-solvent flow-rate. The strategy uses a PID-like regulator in closed-loop fashion with the FPE to compute the anti-solvent addition flow-rates for different set-point targets in the MCS. In order to validate the stochastic model and assess the merits of the proposed strategy, the crystallization of sodium chloride in water using ethanol as anti-solvent is performed in a bench-scale fed-batch crystallizer. The implementation of the calculated anti-solvent policies resulted in a good control of the MCS despite modelling mismatch and uncertainties present during the crystallization operation.

Keywords: Anti-Solvent; Crystallization; Fokker-Planck Equation; Mean Crystal Size; Stochastic.

1. INTRODUCTION

The design of chemical plants endeavors to build equipment that preferably content hazards and make possible the transformation and separation of materials. It also attempts to harness the impact of apparently disordered and erratic phenomena (*e.g.* turbulent flow, pressure and temperature fluctuations, measurement noise, etc.). Fluctuations are a very common element in a large number of chemical, biological and physical phenomena. Practically, all systems are subjected to complicated external or internal influences that are not fully known and that are often termed noise or fluctuations. However, if a sufficiently long record of noisy measurement is analyzed, it may admit a statistical description. This means that it is possible to estimate the probability or likelihood that the process variable will attain in some specified range of values (Feigenbaum, 1980; Risken, 1984).

The study of stochastic system as the Brownian motion resulted in the Fokker-Planck equation (FPE). The FPE is just an equation of motion for the distribution function of fluctuating macroscopic variables. The FPE deals with those fluctuations of systems which stem from many tiny disturbances, each of which changes the variables of the system in an unpredictable but small way. The FPE provides a powerful tool with which the effects of fluctuations close to transition points can be adequately treated and that the approaches based on FPE are superior to other approaches based on Langevin equations (LE). The FPE plays an important role in chemical and biological processes that involve noise.

For many practical applications it is required to have simplified models that group the complexity behind a natural phenomenon and its interactions with its surroundings. For a dynamic system, it means of a set of deterministic differential equations with semi-empirical parameters. When studying chemical processes, these models are the core element for the design of all model-based control and optimization strategies. However, extra care is needed to take into account the no modeled dynamics and unknown exogenous disturbances acting on the process. The FPE is an interesting approach to introduce the robustness feature to the design of prediction, control and optimization tools.

This work describes a novel stochastic approach for the robust prediction of the mean crystal size (MCS) in a bench-scale fed-batch crystallization unit where anti-solvent is added to speed-up the crystal formation process. The crystal growth is modeled by a classic logistic equation of common use in theoretical ecology (May and McLean, 2007; Grosso et al., 2007). In a different fashion, the use of FPE for a monomer particle growth can be found in the literature (Matsoukas and Yulan, 2006). Unknown dynamics, internal and external fluctuations and sensitivity to initial conditions can be taken into account by embedding the logistic equation in the FPE.

2. Mean Crystal Size Estimation for an Anti-Solvent Aided Crystallization Process

Crystallization is a physical process for solid-liquid separation where the solid (solute) is dissolved in the solvent (liquid). The driving force in crystal formation is the super-saturation. The super-saturation condition establishes the thermodynamic equilibrium for the solid-liquid separation and it can be affected by cooling and evaporation. The super-saturation can be also induced by addition of precipitant or anti-solvent to the solution. The anti-solvent reduces the solubility of the solute in the original solvent resulting in super-saturation. The anti-solvent aided crystallization is an advantageous technique of separation where the solute is highly soluble or heat sensitive.

2.1 Mathematical Model

The development of rigorous mathematical models describing the dynamic of crystal growth in crystallization processes are based-on population balances. The idea of population balances has been widely used in theoretical ecology and extended to the modeling of particulate systems in chemical engineering. The population balances can be either structured or unstructured models.

At the core of the structured population dynamics, the number of crystals in a fed-batch crystallizer is increased by nucleation and decreased by dissolution or breakage. Structured population balances models provide detailed information regarding the crystal size distribution in the crystallization unit. However, they demand a great deal of knowledge on the complex thermodynamic associated with the solute and solvent properties to be adequately incorporated in the population balances. Some important contributions in this subject have been reported in the literature (Worlitschek and Mazzotti, 2004; Nagy et al. 2007; Nowee et al., 2007).

Here, we introduce a simple unstructured population model, where the crystals are classified by their size, *L*. The growth of each individual crystal is supposed to be independent by the other crystals and is governed by the same deterministic model. In order to take into account the growth fluctuations and the unknown dynamics not captured by the deterministic term, a random component can be introduced (Gelb, 1988). The stochastic model can thus be written as a Langevin equation of the following type:

$$\dot{L} = f(L;\vartheta) + \eta(t) \tag{1}$$

In Equation 1, $f(L;\vartheta)$ is the expected rate of growth of L (the deterministic model introduced below), L is the size of the single crystal, t is the time, ϑ is the vector parameter defined in the model, and $\eta(t)$ is a random term assumed as Gaussian additive white noise:

$$\begin{aligned} &E[\eta(t)] = 0 \\ &E[\eta(t)\eta(t+\tau)] = 2D\delta(\tau) \end{aligned} \tag{2}$$

Where D is the additive noise intensity. Equation 1 implies that the crystal size L behaves as a random variable, characterized by a certain probability density function (PDF) $w(L,t)$ depending on the state variables of the system, i.e. the size L and time t. Incidentally, it should be noted that one can regard the probability density $w(L,t)$ as the relative ratio of crystals having a given dimension L, in the limit of infinite observations. Thus, from a practical point of view, it coincides with the Particle Size Distribution experimentally observed.

The new random variable thus can be described in terms of its probability density distribution, $w(L,t)$, at any instant of time t and should follow the linear Fokker-Planck Equation, FPE:

$$\partial_t w + \partial_L [f(L;\vartheta(u))w] = D(u)\partial_{LL} w \tag{3}$$

along with the boundary conditions:

$$f(0)w(0,t) - D(u)\partial_L w(0,t) = 0 \tag{4a}$$

$$\partial_L w(\infty,t) = 0 \tag{4b}$$

The reflecting boundary condition in Equation 4a ensures that the elements of the population will never assume negative values, whereas Equation 4b ensures the decay condition on $w(L,t)$ as L goes to infinity, for any time.

The diffusion coefficient D determines the random motion of the variable L that takes into account the fluctuation in the particle growth process (Randolph and Larson, 1988; Olesen et al, 2005).

Regarding the deterministic part of the model, our purpose is to choose a model as simple as possible, with a parsimonious number of adjustable parameters. To this end, the Generalized Logistic equation (Tsoularis and Wallace, 2002), is possibly the best-known simple sigmoidal asymptotic function used to describe the time dependence of growth processes in an unstructured fashion:

$$f(L;\vartheta) = r L^{\alpha} [1 - (L/K)^{\beta}]^{\gamma} \tag{5}$$

In Equation 4, L is the size of the single crystal, the crystal growth rate r and the equilibrium mean crystal size K are considered constant for each experimental condition and they are supposed to be only dependent on the anti-solvent flow rate. Moreover, α, β and γ are positive real numbers that regulate the shape of the growing curve. Hereafter we will consider the simple case with $\alpha = \beta = \gamma = 1$. With these assumptions, the present growth model can be regarded as the simplest model taking into account mild nonlinearities. In spite of this simplicity, this model provides the main qualitative features of a typical growth process: the growth follows a linear law at low crystal size values and saturates at a higher equilibrium value.

Finally the evolution in time of the probability density is described in terms of a linear, partial differential equation depending on the parameters r (linear Malthusian growth

rate), K (crystal size asymptotic value) and D (diffusivity), that are assumed to depend on the feeding conditions. This functionality is achieved by linear interpolation of the parameters as a function of the different anti-solvent flow rates. This parameterization with the anti-solvent flow rate allows the merger of multiple models for different operating regimes to a single model in the all operating envelop.

It is worth to stress out that the synergy between unstructured population balances and the Fokker-Planck equation results in structured-like population balances.

3. Experimental Validation

For parameter estimation and model validation purposes, three different anti-solvent flow-rates were implemented. All experiments were carried in a bench scale crystallizer which was kept at a fix temperature. Only purified water, regent grade sodium chloride (99.5%) and absolute ethanol (99.9%) were used. The experimental set-up and procedure are described as follows.

3.1 Experimental Set-up

The experimental rig is made up of one litre glass, cylindrical crystallizer submerged in a temperature controlled bath. The temperature in the bath is measured using an RTD probe which is wired up to a slave temperature control system capable of heating and cooling. In similar fashion, the anti-solvent addition is carried out by a slave peristaltic pump. The master control is performed by a Distributed Control System (Honeywell® DCS) which is wired up to the slave temperature and flow-rate controllers respectively. The desired set-points are calculated at the master controller. All relevant process variables are archived in the DCS system. In addition there is a particle size analyzer (Mastersizer® 2000) for the determination of the mean and crystal size distribution along the experiment. The mean crystal sizes and their distribution are also verified by visual inspection using a digital camera mounted in a microscope. The captured images are then processed by means of sizing computer software (Amscope®).

3.2 Experimental Procedure

At the start-up condition, the crystallizer is loaded with an aqueous solution of $NaCl$ made up of $34\,g$ of NaCl in $100\,g$ of water. The temperature is kept at $25^{\circ}C$. Then ethanol was added to the aqueous NaCl solution using a calibrated peristaltic pump. Along the operation, $5\,mL$ samples were taken in an infrequent fashion. The samples are then measured off-line using the particle size analyzer. Also, part of the sample was filtered over filter paper and then dried in an oven at $50^{\circ}C$ for farther visual inspection.

3.3 Parameter Estimation

The three parameters for the Fokker-Planck equation were estimated based-on experimental data obtained by monitoring the mean size distribution for different flow rates of anti-solvent. For every operating condition, that is, anti-solvent flow rate, a set of parameters $\vartheta=[r,K,D]$ is estimated using a nonlinear least-square algorithm. The values for the estimated parameters are given in the Table 1.

u (mL/min)	r (1/h)	K (μm)	D (μm^2 /h)
0.82	1.83	131.51	568.12
1.64	1.15	132.03	287.48
3.23	62.58	105.45	291.27

Table 1: Estimated parameters for the different operating conditions for the constant values $\alpha=1$, $\beta=1$ and $\gamma=1$.

3.4 Model Validation

In order to assess the prediction capabilities of the mathematical model based on the Fokker-Planck equation, the model predictions are compared with the reported experimental data within a valid range for the different operating conditions. It implies that the parameterization of the crystal growth rate, the free crystal size and the diffusivity coefficient with the anti-solvent are only reliable within the experimental range. The numerical solution of the mathematical model based on the Fokker-Planck equation requires an initial condition for the crystal size distribution. However, the initial condition requires information on crystal sizing. Observing the experimental data (Figure 1), the first available data value is at $t_0=0.1h$ (new origin), where the mean crystal size is around $L_0=92\,\mu m$ for anti-solvent flow rate. In order to take into account the uncertainty associated with this condition, a standard deviation $\sigma_0=30\,\mu m$ typical for this measurement is then assumed. Once the initial and boundary conditions are posed, the partial differential equation is then solved using a collocation method. The number of collocation knots $n=300$ and they are chosen as the roots of the Chebyshev polynomial of degree "n" where the solution domain is $L\in[0,\ell]$ with $\ell=210\,\mu m$ a sufficient high value. Note that a different set of data values were used for parameter estimation. Thus, the numerical solution of the Fokker-Planck equation (2-3) by the collocation methods provides the predictions for the mean crystal size by computing the first moment of the distribution (see Figure 1).

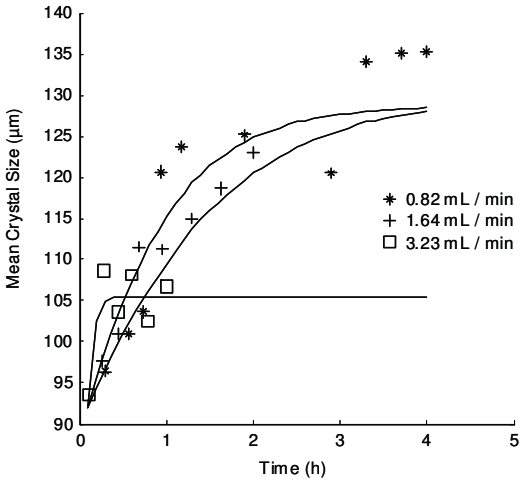

Figure 1: Model validation of the mean crystal size for different anti-solvent flow rates. Experimental results at low (*), medium (+) and high (□) anti-solvent flow rates. The three-parameter model based-on the Fokker-Planck equation predicts the dynamic behaviour of the mean crystal size growth for all anti-solvent flow rates (solid lines).

4. Calculation of the Robust Anti-Solvent Flow Rate Profile

4.1 Problem Formulation

Let us consider without loss of generality that the mean crystal size growth dynamics in an anti-solvent aided process is given by the following forced deterministic equation:

$$\dot{\mu}_L = F(\mu_L, u) \tag{6}$$

Where the forcing input (anti-solvent flow rate) is constrained, that is, $u \in [u^-, u^+]$. We say that the solutions of (6) in the time interval $t \in [0, t_0]$ for any input u and any given uncertain initial condition $\mu_L(0) \neq 0$ generates trajectories which at $t_0 > 0$ lie around a nominal value L_0, that is,

$$\mu_L(t_0) = L_0 \pm \Delta_0, \forall t_0 > 0 \tag{7}$$

It means that regardless what the input is, the effect of the uncertainty in the initial condition is propagated to another point $\mu_L(t_0)$ in the trajectory (7), where a nominal mean crystal size L_0 is associated with an uncertainty Δ_0. It is advantageous since it is then possible to choose a new initial time origin at the point t_0, which coincides with experimental data value that helps to quantify the values for L_0 and Δ_0. Thus, the new initial condition at t_0 is still uncertain but it can be characterized and incorporated to our mathematical description of the problem.

The robust anti-solvent flow rate profile for the mean crystal size distribution is calculated using a hybrid strategy that requires engineering insight and process knowledge. The strategy involves a piece-wise function (8), a regulator-like (PI) algorithm (9), and a saturation function (10).

$$u = \begin{cases} u^+, \text{ if } t \leq t_0 \\ \zeta(\upsilon), \text{ otherwise} \end{cases} \tag{8}$$

$$\dot{\upsilon} = \kappa_1 \dot{\mu}_L + \kappa_2 (\mu_L - L_r), \upsilon(t_0) = u^+ \tag{9}$$

$$\zeta(\upsilon) = \begin{cases} u^-, \text{ if } \upsilon \leq u^- \\ u^+, \text{ if } \upsilon \geq u^+ \\ \upsilon, \text{ otherwise} \end{cases} \tag{10}$$

From the actual starting-up condition at $t = 0$ to a chosen origin $t_0 > 0$, the anti-solvent flow rate is maintained constant at its maximum value u^+. It has been experimentally observed that the anti-solvent addition at the initial stage of the crystallization process promotes nucleation and speeds up the mean crystal size growth rate. Then, from time $t > t_0$ onwards the anti-solvent addition must be controlled in order to reach a desirable mean crystal size L_r. It is achieved by using a dynamic velocity-like regulator algorithm which is tuned selecting arbitrary values for the constants κ_1 and κ_2. Since the anti-solvent flow rate is constrained, it is necessary to include a saturation function to limit the control action within its physical range. It is important to highlight that velocity-like regulator with initial condition $\upsilon(t_0) = u^+$ introduces a bump-less transition from the saturation state. Also, the volume of spent anti-solvent at any time can be calculated using (11). The constant value "60" is the conversion factor for the anti-solvent flow rate from mL/min to mL/h.

$$V = 60[u^+ t_0 + \int_{t_0}^{t} u(\xi)\, d\xi] \tag{11}$$

It is important to remark that the strategy can be used either as a size-regulator, if the mean crystal size μ_L is a real-time available measurement or as tool to calculate an *off-line robust trajectory* for the anti-solvent addition. Due to its simplicity, this strategy can be easily implemented.

4.2 Simulation and Experimental Validation of Anti-Solvent Addition Policy

We next use numerical simulations and experimental validation to assess the closed loop performance of the anti-solvent addition strategy proposed for this specific crystallization process. The simulation parameters are given in Table 2. Since the experimental data is constrained to a certain operating window, the calculated profile is also limited to this operating range. The anti-solvent addition strategy was tested within the validity range of the experimental data and targeting a medium mean crystal size. The initial condition is then represented as a Gaussian –like distribution with mean value $L_0 = 92\,\mu m$ and standard deviation $\sigma_0 = 30\,\mu m$ based-on the experimental information.

Parameter	Value
u^- (mL/min)	0.82
u^+ (mL/min)	3.23
κ_1 (mL/h ·µm)	0.0052
κ_2 (mL/h^2· µm)	-0.0015
L_0 (µm)	92.0
σ_0 (µm)	30.0
ℓ (µm)	210.0
t_0 (h)	0.1
Δt (h)	0.1

Table 2: Simulation parameters for the assessment of the anti-solvent addition strategy.

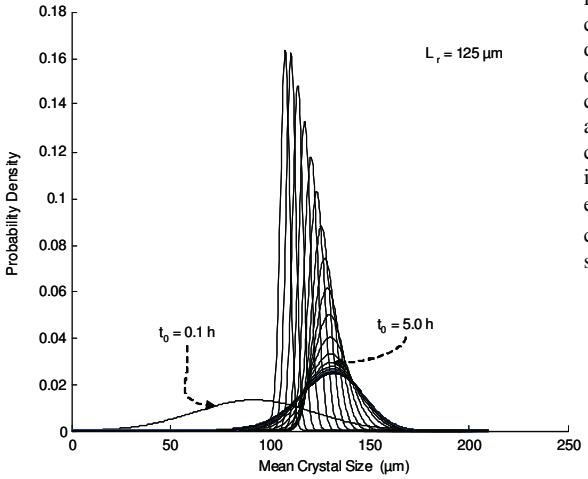

Figure 2: Propagation of the probability density.

Figure 2 depicts the time evolution of the time evolution of the probability density function as function of time for $L_r = 125 \mu m$. For sake of brevity only one value is reported here. For a set point of $L_r = 125 \mu m$ (medium size), the crystal growth rate is alike the previous case, however the anti-solvent flow rate is cut down to an even lower flow rate. It makes clear that the transition between high and low concentration of anti-solvent in the solution promotes the crystal growth instead of the new crystal formation. Therefore, it results in larger crystal size. The volume of anti-solvent added to the crystallizer for a desired mean crystal sizes are calculated using (11) and it is 669.48 *mL* for medium crystal size. The calculation is based on 5.0 hours of operation. Note that the upper and lower prediction bounds for the mean size distribution (Figure 3) are wider at the start-up condition and its narrows when reaching the desired set-point value. The steady-state crystal size distribution suggests that at controlled conditions it is possible to have a very narrow mean size distribution for a given anti-solvent addition policy (Figure 4).

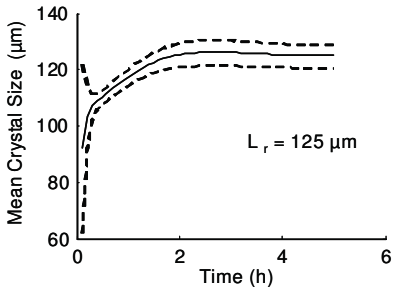

Figure 3: Predicted mean crystal size and its lower and upper bound.

The distribution indicates how disperse the experimental data is. The observed dispersion is incorporated in the diffusivity coefficient of the Fokker-Planck equation. It is envisaged that depending on the amount and quality of the experimental data, the diffusivity coefficient can be clearly related with the crystal size distribution and predicted by this modeling approach. Figure 5 shows the time evolution of the mean crystal size when the anti-solvent addition policy is implemented experimentally for a desired value of time evolution of the $L_r = 125 \mu m$. The quantitative growth of crystal size can be seen in the Figures 6a to 6c. Note the size scale at the corner of every picture.

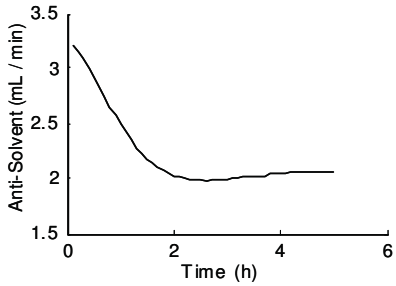

Figure 4: Anti-solvent addition policy for a desired mean crystal size of $L_r = 125 \mu m$.

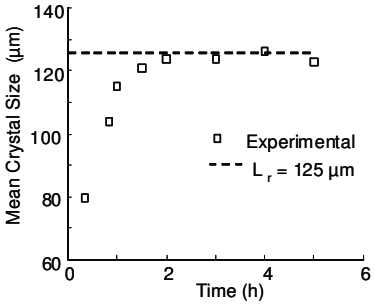

Figure 5: Mean crystal size evolution when the anti-solvent addition policy is implemented.

5. CONCLUSIONS

The hybrid strategy of using the Fokker-Planck Equation (FPE) and the PI-like regulator for the calculation of the anti-solvent addition policy has proved to be simple and still a powerful way to control the mean crystal size in a crystallization operation. It is envisaged that the FPE is a rather useful fashion to study systems with uncertain initial condition in dynamic systems. The initial uncertainty can be quantified and naturally included in the structure of the solution. Future work will be devoted to exploit the FPE approach for the determination of the mean crystal size and its distribution in cooling and anti-solvent aided crystallization.

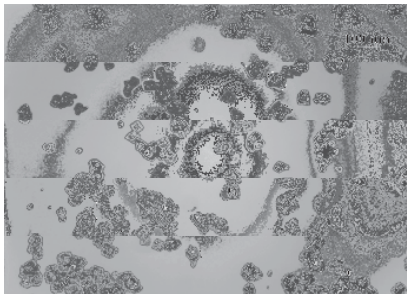

Figure 6.a $NaCl$ crystals at $t = 0.16\ h$

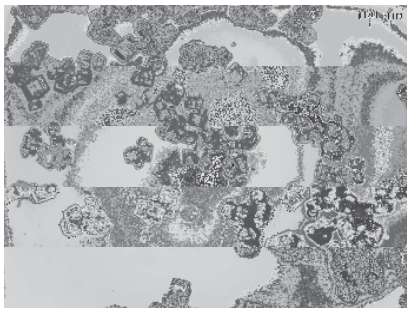

Figure 6.b $NaCl$ crystals at $t = 1\ h$

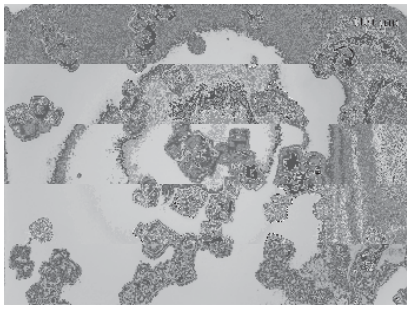

Figure 6.c $NaCl$ crystals at $t = 2\ h$

REFERENCES

Feigenbaum, M. J. (1980), "Universal Behaviour in Nonlinear Systems", Los Alamos Science, 1, pp. 4 – 27

Gelb A., Applied Optimal Estimation (1988) M.I.T. Press, Cambridge Massachusetts, USA

Grosso, M., Cella, Baratti R. (2007), "Development of a Probabilistic Model for the Plant Growth in the Nursery Phase", Food and Agriculture Products: Processing and Innovations, September 24-26, Naples, Italy.

Lo, C.F. (2007) "Stochastic Gompertz Model of Tumor Cell Growth." Journal of Theoretical Biology, 248, pp. 317-321.

Matsoukas T., Yulan, L. (2006), "Fokker-Plank Equation for Particle Growth by Monomer Attachment", Phys. Rev. E, 74, pp. 031122-1-031122-9.

May R., McLean, A. (2007), "Theoretical Ecology" Principles and Applications", Oxford University Press, Great Britain

Nagy Z., Fujiwara, M., Braatz, R. (2007). "Recent Advances in the Modelling and Control of Cooling and Anti-Solvent Crystallization of Pharmaceuticals", Dynamics and Control Process Systems, Vol. 2, pp. 29-38, June 6-8, 2007, Cancún, Mexico

Nowee S.M., Abbas A., Romagnoli, J.A. (2007), "Optimization in Seeded Cooling Crystallization: A Parameter Estimation and Dynamic Optimization Study", Chem. Eng. Proc., 46, pp. 1096-1106.

Olesen P., Ferkinghoff-Borg J., Jensen M.H., Mathiesen J., Phys. Rev. E (2005), 72, 031103

Randolph A.D., Larson M. (1988), Theory of Particulate Processes: Analyses and Techniques of Continuous Crystallization, Academic Press, San Diego, USA.

Risken H., (1984), "The Fokker-Planck Equation: Methods of Solution and Applications", Springer –Verlag, Germany.

Tsoularis A., Wallace J. (2002), "Analysis of logistic growth models", Math. Biosci., 179, pp. 21-55

Worlitschek J., Mazzotti M. (2004), "Model-Based Optimization of Particle Size Distribution in Batch-Cooling Crystallization of Paracetamol", Crystal Growth & Design, Vol. 4, No. 5, pp. 891-903.

Model Based Robust Batch-to-Batch Control of Particle Size and Shape in Pharmaceutical Crystallisation

Zoltan K. Nagy

Chemical Engineering Department, Loughborough University, Loughborough, LE11 3TU, United Kingdom, (e-mail: Z.K.Nagy@lboro.ac.uk)

Abstract: The paper presents a novel batch-to-batch control approach for crystallization processes, which can be used for designing the shape of the crystal size distribution (CSD) and the habit of the crystals, to robustly achieve desired product properties. The method is implemented in a hierarchical structure. On the lower level a supersaturation control approach is used that drives the system in the phase diagram according to a concentration versus temperature trajectory, providing the within batch control. On the higher level a robust model-based optimization algorithm adapts the setpoint of the supersaturation controller, after each batch, using the adapted model parameters by applying a batch-to-batch moving horizon estimation (MHE) approach, to counteract the effects of changing operating conditions, and parameter uncertainties. The process is modelled using the two dimensional population balance equation (PBE), which is solved using the method of characteristics (MOC). The control approach is corroborated through simulations studies. The results illustrate the benefits of the robust iterative learning approach which is able to control both the entire CSD and the habit of the product crystals, reducing significantly the variability in the product properties after only four batches.

1. INTRODUCTION

Crystallization is one of the key unit operations in the pharmaceutical, food and fine chemicals industries. Despite the long history and widespread application of batch crystallization, there remains a disproportionate number of problems associated with its control (Braatz, 2002), mainly related the complex nonlinear dynamics with nonideal mixing, and various disturbances characteristic to these systems. The operating conditions of the crystallization process determine the physical properties of the products which are directly related to the crystal size distribution (CSD), shape or polymorphic form. These properties determine the efficiency of downstream operations, such as filtration, drying, and tablet formation, and the product effectiveness, such as bioavailability and shelf-life. With the recent change of industrial procedures from Quality-by-Testing (QbT) to Quality-by-Design (QbD) and the advent of process analytical technology (PAT) initiative, especially in the pharmaceutical industries, approaches which can be used to design desired product properties are of great interest (Fujiwara *et al.*, 2005). The classical control objectives expressed in characteristics of the size distribution (e.g. maximize average size, minimize coefficient of variation) can lead to conservative and economically inefficient designs of the crystallization systems, and they most often neglect the shape of the crystals. The paper presents a batch-to-batch iterative control (ILC) approach which can be used to directly design the shape of the crystal size distribution and the crystal habit at the same time, to robustly achieve desired product properties. The method is able for example to minimize filtration time without generating unnecessarily large crystals, or minimize breakage by controlling the aspect ratio. Since dissolution rate depends on the shape of the CSD, when the resulting crystals represent the final product (e.g. drugs for inhalers) controlling the shape of the CSD can provide novel applications in the area of drug delivery, or environmentally friendly dosage of pesticides, where particular multimodal distributions can be designed to achieve desired concentration level of the active ingredient. The crystallization system in this study is modelled via a two-dimensional population balance equation (2D-PBE) which is directly used in the optimization procedure where the objective function is expressed in terms of the shape of the entire CSD, and the aspect ratio is added as constraints. The control of crystal size and shape has been considered previously by Lee *at al.* (2002), however in their approach the authors used a computationally more demanding high resolution finite volume method to solve the 2D population balance equation, and parameter uncertainties were not considered directly in the control problem formulation. In this paper the population balance equation (PBE) is solved using a generic 2D-method of characteristics (LeVeque, 1992). Crystallization models are generally subject to significant uncertainties. A robust model based optimization approach (Nagy and Braatz, 2003) is evaluated and it is shown that taking parametric uncertainties into account in the problem formulation can lead to significant improvement in the robustness of the product quality after a few batches only. The control approach is implemented in a hierarchical

structure where on the lower level a model-free crystallization control methodology, the supersaturation controller, drives the system in the phase diagram, rather then in the time domain, providing the within batch control methodology, whereas on the higher level a robust batch-to-batch model based optimization algorithm, the adapts the setpoint of the supersaturation controller after each batch to counteract the effects of changing operating conditions and parameter uncertainties. The method adapts the uncertain kinetic parameters using the information available over the past batches, applying a moving horizon estimation (MHE) scheme (Rawlings *et al.*, 1993), which also provides the uncertainty description used in the robust optimal control problem. The optimization problem is solved using an efficient multistage approach implemented in the optimization package OptCon (Nagy *et al.*, 2004). The proposed approach is corroborated in the case of a simulated crystallization system.

2. 2D POPULATION BALANCE MODELLING OF BATCH CRYSTALLIZATION PROCESSES

Considering a single growth direction with two characteristic lengths L_1 and L_2, and a well-mixed crystallizer with growth and nucleation as the only dominating phenomena the crystal size distribution (CSD) expressed in the number density function $f_n(L_1, L_2, t)$, is given by the population balance equation (PBE) with the form

$$\frac{\partial f_n(L_1,L_2,t)}{\partial t} + \frac{\partial\{G_1(S,L_1;\theta_{g1})f_n(L_1,L_2,t)\}}{\partial L_1} + \frac{\partial\{G_2(S,L_2;\theta_{g2})f_n(L_1,L_2,t)\}}{\partial L_2} = B(S;\theta_b)\delta(L_1 - r_{01}, L_2 - r_{02}) \tag{1}$$

with initial condition given by the size distribution of seed, $f(L_1,L_2,0) = f_{seed}(L_{1,0},L_{2,0})$, t is time, $G_1(S,L_1;\theta_{g1})$ and $G_2(S,L_2;\theta_{g2})$ are the generic size dependent growth rates of crystal in the two characteristic directions. $B(S;\theta_b)$ is the nucleation rate, $\delta(\cdot,\cdot)$ is the two dimensional Dirac delta function, r_{01} and r_{02} are the characteristic sizes of the nucleai, $S = C - C_{sat}$ is the supersaturation, C is the solute concentration, $C_{sat}(T)$ is the saturation concentration at the temperature T, and θ_{g1}, θ_{g2} and θ_b are vectors of growth and nucleation kinetic parameters, respectively. The partial differential equation can be reduced to a system of ODEs by applying the method of characteristics (MOC). The aim of the MOC is to solve the PBE by finding characteristic planes in the $L_1 - L_2 - t$ space that reduce the PBE to a system of ODEs. The $L_1 - L_2 - t$ space is expressed in a parametric form by $L_1 = L_1(\mathcal{Z})$, $L_2 = L_2(\mathcal{Z})$ and $t = t(\mathcal{Z})$, where the parameter $\mathcal{Z}$ gives the measure of the distance along the characteristic curve. Hence, applying the chain rule with $f_n(L_1,L_2,t) = f_n(L_1(\mathcal{Z}),L_2(\mathcal{Z}),t(\mathcal{Z}))$ gives,

$$\frac{df_n}{d\mathcal{Z}} = \frac{dL_1}{d\mathcal{Z}}\frac{\partial f_n}{\partial L_1} + \frac{dL_2}{d\mathcal{Z}}\frac{\partial f_n}{\partial L_2} + \frac{dt}{d\mathcal{Z}}\frac{\partial f_n}{\partial t}. \tag{2}$$

Comparing (2) with (1) we find $\mathcal{Z} = t$ and the characteristic equations can be derived. Solving these together with the system of equations which results by applying the method of moments (MOM), we can calculate the dynamic evolution of $f_n(L_1,L_2,t)$ by the following ODEs,

$$\begin{aligned}
&\frac{d\mu_{0,0}}{dt} = B,\\
&\frac{d\mu_{i,j}}{dt} = iG_1\mu_{i-1,j} + jG_2\mu_{i,j-1},\\
&\frac{dL_1}{dt} = G_1,\\
&\frac{dL_2}{dt} = G_2,\\
&\frac{\partial f_n}{\partial t} = -f_n(L_1,L_2,t)\left(\frac{dG_1}{dL_1} + \frac{dG_2}{dL_2}\right) + B\delta(L_1 - r_{01}, L_2 - r_{02}),
\end{aligned} \tag{3}$$

where the system was solved for zeroth moment $\mu_{0,0}$, first order moments $\mu_{1,0}$ and $\mu_{0,1}$, second order moments $\mu_{1,1}$, $\mu_{2,0}$ and $\mu_{0,2}$, and third order moments $\mu_{2,1}$, $\mu_{1,2}$, $\mu_{3,0}$, $\mu_{0,3}$, defined by

$$\mu_{i,j} = \int_0^\infty \int_0^\infty L_1^{\,i} L_2^{\,j} f_n\left(L_1,L_2,t\right) dL_1 dL_2, \tag{4}$$

with initial conditions given by the following vector $x_0 = [\mu_{0,0}(0),\ldots,\mu_{03}(0),L_{1,0},L_{2,0},f_{seed}(L_{1,0},L_{2,0})]$. The solute concentration is given by

$$C(t) = C(0) - \rho_c\left(\mu_{21}(t) - \mu_{21}(0)\right), \tag{5}$$

where ρ_c is the density of crystals. In (5) it is considered that the shape of the crystal is rectangular with L_1 and L_2 being width (and depth) and length, respectively. The nucleation kinetics is given by

$$B = k_b S^b, \tag{6}$$

with nucleation parameters $\theta_b = [k_b, b,]$. In the case when the growth rates are independent of size and are expressed by

$$G_1 = k_{g1}S^{g1}, \quad G_2 = k_{g2}S^{g2}, \tag{7}$$

with growth parameters $\theta_{g1} = [k_{g1,}\ g1]$ and $\theta_{g2} = [k_{g2,}\ g2]$. In the case of size independent growth $dG_1/dL_1 = 0$ and $dG_2/dL_2 = 0$ and the system of ODEs (3) can be solved analytically (Rusli *et al.*, 2006) and the CSD can be constructed in any time step using different initial conditions obtained by varying $L_{1,0}$ and $L_{2,0}$, the shape of the distribution can be obtained with desired resolution. Additionally the analytical solution can be simplified by the assumption of growth dominated process, and constant supersaturation, which can be considered valid for supersaturation controlled processes. The dissolution process

was modelled similarly, with expressions similar to (7), but different constants, which apply when $S < 0$.

Several approaches have been proposed for designing the operating curves for crystallization systems. Generally speaking, two main categories can be distinguished, (i) the model-based approach (Rawlings *et al.*, 1993) and (ii) the direct design (Fujiwara *et al.*, 2005). In the model-based design approach the detailed model (4) is used together with optimization techniques to determine temperature versus time trajectories, which optimize desired product properties, usually expressed as functions of the moments of the CSD. The direct design approach is based on the understanding of the basic concept of crystallization, to operate the system within the metastable zone bounded by the nucleation and solubility curves. In this technique a supersaturation setpoint profile is chosen experimentally and it is followed in the phase diagram using a supersaturation controller based on concentration measurement. The approach proposed in the paper combines the two methods in a hierarchical control algorithm, in which a model-based robust optimization determines the operating profile in the phase diagram, which is used then as the setpoint for the supersaturation controller.

3. DISTRIBUTIONAL BATCH-TO-BATCH NMPC

The main feature of the batch-to-batch control is that variations on two time-scales must be considered. As shown on Figure 1, within and between batches variations can be considered leading to an optimization problem on two time-scales. In batch process operation often within batch measurements are not available or adjustment to the operating conditions cannot be made. In these cases batch-to-batch improvement is practically easier to implement, by learning from the information obtained usually from after-batch laboratory analyses. In this framework the within batch measurements (if available) can be used for model based parameter and state estimation/adaptation, and the updated model then can be used in an iterative learning control framework for the improvement of the future operating recipe (Figure 2).

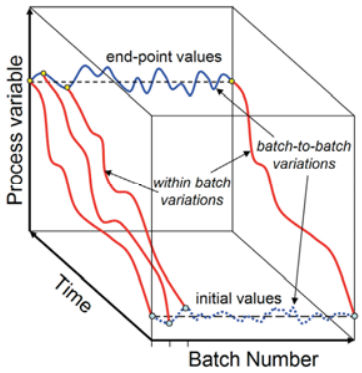

Fig. 1. Schematic representation of the dynamic two-time scale variations in batch control.

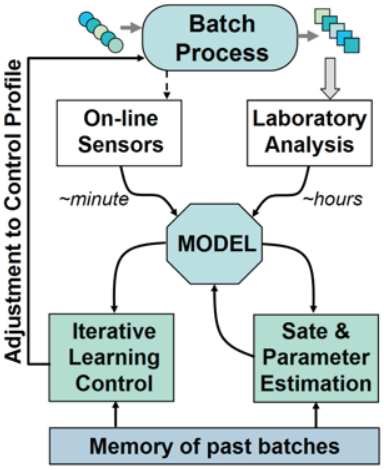

Fig. 2. Structure of the iterative learning control framework.

The optimal control problem for the iterative learning scheme can be formulated as the alternative application of a moving horizon estimation (MHE) and a robust optimal control problem. The MHE problem solved after each batch k is,

$$\min_{\hat{x}_{0,k},\,\theta_k} \sum_{i=k-1}^{k-N_b} W_i (y_i^{\text{model}}(\hat{x}_{0,k};\theta_k) - y_i^{\text{meas.}})^2 \tag{8}$$

subject to:

$$\dot{x}_i = f(x_i, u_i; \theta_k); \quad x_{0,i} = x_{0,k};\ x_i \in \mathcal{X} \tag{9}$$

$$y_i = g(x_i, u_i;\ \theta_k);\ i = k-1, \ldots, k-N_b \tag{10}$$

where N_b is the number of past batches used in the estimation and W_i is a weighting matrix with exponential forgetting factor over the past batches. The model output used in the parameter estimation in the case of crystallization processes can be the entire CSD or properties of the CSD (e.g. number or weight average mean size). From the parameter estimation problem estimates of the uncertainty bounds on the parameters are also calculated, which can then be used in the robust optimization problem for control. The model based optimal control problem is expressed as

$$\min_{\Delta u_k} \mathcal{H}(x_k, u_k; \theta_k) \tag{11}$$

subject to:

$$\dot{x}_k(t) = f(x_k(t), u_k(t); \theta_k); \quad x_k(t_0) = \hat{x}_{0,k} \tag{12}$$

$$y_k(t) = g(x_k(t), u_k(t); \theta_k) \tag{13}$$

$$u_k = u_{k-1} + \Delta u_k \tag{14}$$

$$h(x_k(t),\ u_k(t); \theta_k) \le 0, \quad t \in [t_0,\ t_F] \tag{15}$$

where $\mathcal{H}$ is the performance objective, t is the time, t_F is the final time at the end of prediction (end of batch), $x(t) \in \mathbb{R}^{n_x}$ is the vector of states, $u(t) \in \mathcal{U} \subset \mathbb{R}^{n_u}$ is the set of input vectors, $y(t) \in \mathbb{R}^{n_y}$ is the n_y vector of measured variables used to compute the estimated states $\hat{x}(t_k)$,

$\theta \in \Theta \subset \mathbb{R}^{n_\theta}$ is the n_θ vector of uncertain parameters, where the set Θ can be either defined by hard bounds or probabilistic, characterized by a multivariate probability density function. The function $f : \mathbb{R}^{n_x} \times \mathcal{U} \times \Theta \rightarrow \mathbb{R}^{n_x}$ is the twice continuously differentiable vector function of the dynamic equations of the system, $g : \mathbb{R}^{n_x} \times \mathcal{U} \times \Theta \rightarrow \mathbb{R}^{n_y}$ is the measurement equations function, and $h : \mathbb{R}^{n_x} \times \mathcal{U} \times \Theta \rightarrow \mathbb{R}^{c}$ is the vector of functions that describe all linear and nonlinear, time-varying or end-time algebraic constraints for the system, where c denotes the number of these constraints. The repeated optimization problem is solved by dividing the batch time $t \in [0, t_F]$ into N equally spaced time intervals Δt (stages), with discrete time steps $t_k = k\Delta t$, and $k = 0, 1, \ldots, N$ (Biegler and Rawlings, 1991). The model based control approach is implemented in the Matlab toolbox, OptCon (Nagy *et al.*, 2007), which is based on a state-of-the-art large-scale nonlinear optimization solver (HQP) (Franke *et al.*), which uses a multiple shooting algorithm (Diehl *et al.*, 2002).

Consider the case of parameter uncertainty, with $\delta\theta \in \mathbb{R}^{n_\theta}$ defined as the perturbation about the nominal parameter vector $\hat{\theta}$. The real uncertain parameter vector is then given by $\theta = \hat{\theta} + \delta\theta$. Assuming zero mean, normal measurement errors, and known covariance matrix, the set of possible parameter values is given by the hyperellipsoidal confidence region, defined as

$$\Theta(\alpha) \triangleq \{\theta : (\theta - \hat{\theta})^T \mathbf{V}_\theta^{-1} (\theta - \hat{\theta}) \leq \chi^2_{n_\theta}(\alpha)\}, \qquad (16)$$

where α is the confidence level, $\chi^2_{n_\theta}(\alpha)$ is a quantile of the chi-squared distribution with n_θ degrees of freedom, and $\mathbf{V}_\theta \in \mathbb{R}^{n_\theta \times n_\theta}$ is the parameter covariance matrix. Uncertainty description (16) results most commonly from typical least-squares identification procedures from experimental data, and it is provided by the MHE estimation approach applied in this paper. The parameter covariance matrix is updated after each batch when a new set of parameters are also computed using the MHE algorithms. We denote with $\psi(x(t_f);\theta)$ the end-point property of interest. Considering the mean-variance approach the following objective function is used to account for parameter uncertainties in the NMPC:

$$\mathcal{H} = (1 - w)\mathcal{E}[\psi(x(t_f), \theta)] + w V_\psi(t_f), \qquad (17)$$

where $\mathcal{E}$ and $V_\psi \in \mathbb{R}$ is the expected value and variance, respectively, of the property at the end of the batch, and $w \in [0,1]$ is a weighting coefficient that quantifies the tradeoff between nominal and robust performance. The main advantage of this approach compared to the classical minmax optimizations is that the tradeoff between nominal and robust performance can be controlled by appropriately weighting the two objectives. Expected value and variance can be computed efficiently using a second order power series expansion,

$$\delta\psi = L\delta\theta + \frac{1}{2}\delta\theta^T \mathbf{M}\delta\theta + \ldots, \qquad (18)$$

where $L = (d\psi / d\theta)_{\hat{\theta},u} \in \mathbb{R}^{n_\theta}$, and $\mathbf{M} = (d^2\psi / d\theta^2)_{\hat{\theta},u} \in \mathbb{R}^{n_\theta \times n_\theta}$ are the first and second order sensitivities, respectively. Assuming zero mean, normally distributed parameters $\delta\theta$, deriving the expected value and variance of $\delta\psi$ based on (18) gives the analytical expressions:

$$\mathcal{E}[\delta\psi] = \frac{1}{2}\mathrm{tr}(\mathbf{M}\mathbf{V}_\theta) \qquad (19)$$

$$V_\psi = L\mathbf{V}_\theta L^T + \frac{1}{2}[\mathrm{tr}(\mathbf{M}\mathbf{V}_\theta)]^2 \qquad (20)$$

where $\mathrm{tr}(\mathbf{A})$ is the trace of matrix $\mathbf{A}$. The feasibility of the optimization under parametric uncertainty is achieved by reformulating the constraints in a probabilistic sense:

$$\mathbb{P}(h_i(x, u;\theta) \leq 0) \geq \alpha_i, \qquad (21)$$

where $\mathbb{P}$ is the probability and α_i is the desired confidence level for the satisfaction of constraint i. The robust formulation of (21) can be written using the t-test in the form:

$$\mathcal{E}[h_i] + t_{\alpha/2,n_\theta}\sqrt{V_{h_i}} \leq 0, \quad i = 1,\ldots,c. \qquad (22)$$

The expected value ($\mathcal{E}[h_i]$) and covariance (V_{h_i}) of the constraint h_i can be evaluated using first or second order approximations. For first order approximation $\mathcal{E}[h_i(x,u;\theta)] = h_i(x,u;\hat{\theta})$ and $V_{h_i} = L_{h_i}\mathbf{V}_\theta L_{h_i}^T$, whereas for second order approximation expressions similar to (19) and (20) can be used, with $L_{h_i} = (dh_i / d\theta)_{\hat{\theta},u} \in \mathbb{R}^{n_\theta}$, and $\mathbf{M}_{h_i} = (d^2 h_i / d\theta^2)_{\hat{\theta},u} \in \mathbb{R}^{n_\theta \times n_\theta}$. In this formulation the algorithm shows robust performance in the sense of constraint satisfaction and decreased variance of the performance index (Nagy and Braatz, 2004).

4. APPLICATION OF THE ROBUST BATCH-TO-BATCH NMPC FOR CRYSTALLIZATION PRODUCT DESIGN

For the case studies the crystallization of a pharmaceutical was considered as the model system, for which nucleation and growth kinetics were determined experimentally using image analysis using the Sympatec Qicpic equipment. It was found that a 1D-PBM was not able to describe accurately the variation of the CSD, since a time-varying volumetric shape factor was found to be necessary to capture the significant change in aspect ratio during the batch. Using the 2D-PBE the volume of the individual crystals are directly calculated hence the volumetric shape factor is not needed. Although, the 2D-PBM provides the full 2D CSD, in this paper the target distribution was given as a 1D CSD based on the equivalent spherical diameter, since this is the most commonly used characterisation mode of CSD used in practice. Additionally the *in situ* CSD measurement during the experiments was based on focused beam reflectance measurement (FBRM), which provides 1D information. The equivalent spherical diameter (r) is calculated by

$$r = \frac{6L_1^2 L_2}{\pi}. \qquad (23)$$

The 2D-PBM also allows the incorporation of the shape information in the optimization problem. Different product design problems were considered, when various objective functions expressed as desired shapes of the CSD and limits of the crystal aspect ratio ($\alpha = L_1 / L_2$) were optimized and the required temperature profiles were determined. The novel feature of the proposed approach is that the optimization is performed in the phase diagram, and a concentration trajectory for batch k is obtained as a function of temperature $C_{set,k} = f(T)$. This allows the direct application of the widely accepted supersaturation control in conjunction with the NMPC. The optimization problem can be expressed by the generic robust formulation:

$$\min_{C_{set,k}(T)} \{(1-w)\sum_i (f_n(r_i,t_f;\theta_k) - f_n^{desired}(r_i,t_f))^2 + wV[f_n(r,t_f;\theta_k]\} \quad (24)$$

$$s.t. \quad T_{\min} \le T(t) \le T_{\max}$$
$$R_{\min} \le \frac{dT}{dt} \le R_{\max}$$
$$C(t_f) \le C_{\max} \quad (25)$$
$$\alpha_{\min} \le \alpha \le \alpha_{\max}$$

where $f_n^{desired}(r_i,t_f)$ is the desired (setpoint) CSD with a given shape at the end of the batch, $T_{\min}$, $T_{\max}$, $R_{\min}$, $R_{\max}$ are the operating constraints determined by the bounds and minimum and maximum rate changes of the temperature profiles, respectively, C is the concentration, $C_{\max}$ is the maximum concentration at the end of batch required to achieve a desired crystallization yield, and $\alpha_{\min}$ and $\alpha_{\max}$ are the minimum and maximum bounds on the aspect ration for the desired crystal shape. For most crystallization processes there are significant variations in the metastable zone width (MSZW), which is incorporated in the optimization by considering uncertainties in the nucleation parameters ($\theta_b = [k_b,\ b]$). The variations in the nucleation kinetics are usually significantly larger than the uncertainties in the growth hence this will be considered in this study. In the MHE scheme a fixed iteration approach was used and the convergence of the two nucleation parameters is shown on Figure 3. It can be seen that the MHE converges practically after 3-4 iterations, after which the robust profile is also constant. Figure 4 shows the metastable zone width in the phase diagram delimited by the solubility and nucleation curves. Because of the uncertainties in the nucleation kinetics there is a nucleation region, with a width given by the 99% confidence intervals obtained via Monte Carlo simulations. The operating profiles resulted by solving (24)-(25) for the nominal case ($w = 0$) and one robust case ($w = 0.3$) are shown in the phase diagram in Figure 4. The target CSD was monomodal with a shape biased toward larger particles to improve filtration. The robust operating profile which resulted after 4 iterations, corresponds to a trajectory, which is further away from the nucleation zone throughout the entire batch. The operating profiles are implemented using a supersaturation controller. Figure 5 shows the time-domain representation of the operating curves corresponding to Figure 4. Since the robust profile operates at lower superasaturation the cooling is slower than in the nominal case resulting in longer batch time for similar yield. The robust operating policy also indicates slower cooling and even a slight increase in the temperature during the initial part of the batch when the nuclei are generated. This is in correlation with the often used industrial practice, according to which slow cooling and moderate increase in temperature after the onset of nucleation can result in improved consistency in the final CSD. Monte Carlo simulations were performed by randomly sampling (100 samples) the uncertain parameter space θ_b and applying the nominal and robust temperature profiles. Figure 6 demonstrates that the robust operating curve leads to significantly reduced variability in the product quality compared to the nominal operating policy. The incorporation of the constraint with respect to the aspect ratio allows controlling the crystal habit (aspect ratio) and shape of the CSD at the same time. Figure 7 represents the variations during repeated batches in the product quality expressed as the aspect ratio and maximum Feret diameter. The Monte Carlo simulations show that the robust iterative learning control approach with the profile shown in Figures 4 and 5, provides a significantly lower variability in the crystal size and aspect ratio due to parameter uncertainty.

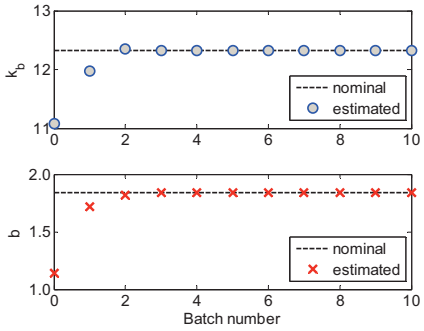

Fig. 3. Evolution of the parameters estimated by the MHE over the batches.

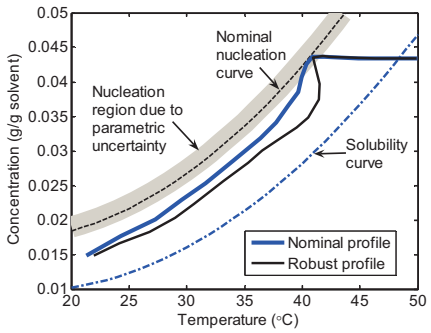

Fig. 4. Phase diagram with nominal ($w = 0$) and robust ($w = 0.3$) operating curves for monomodal target CSD.

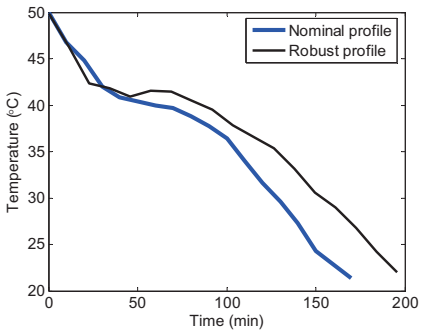

Fig. 5. Time-domain representation of the nominal and robust operating profiles corresponding to Figure 3.

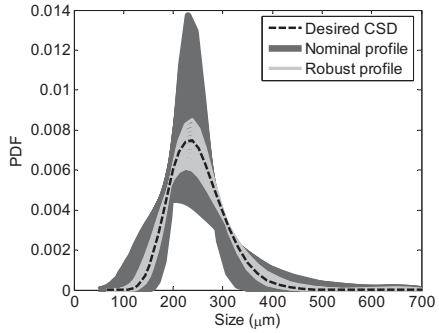

Fig. 6. Monomodal target and product CSDs resulting from Monte Carlo simulations with the uncertain nucleation parameters using the nominal and robust operating profiles.

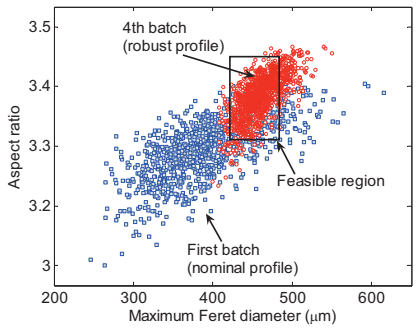

Fig. 7. Monte Carlo simulations showing the performance of the robust iterative learning control after 4 batches.

In the case of the robust ILC most of the batches provide product within the feasible region whereas the original nominal trajectory leads to a very high proportion of off-spec product, which could lead to decreased efficiency of the downstream processes or problems in formulation.

6. CONCLUSIONS

The paper presents a novel robust batch-to-batch control approach for the design of crystalline products by shaping the crystal size distribution and habit. A distributional optimization approach is used to design a robust concentration versus temperature profile, which is used as a setpoint for a lower level supersaturation controller. A two dimensional population balance model is solved using the method of characteristics, to capture the dynamic evolution of the aspect ratio which is incorporated into the robust optimization problem to control the shape of the size distribution and habit at the same time. Simulation results demonstrate the benefits of the proposed approach, which can decrease variability in size and shape of the product in a few batches.

ACKNOWLEDGEMENTS

Financial support by EPSRC (EP/E022294/1) and the Royal Academy of Engineering, U.K. is gratefully acknowledged.

REFERENCES

Biegler, L., J. Rawlings (1991). Optimization Approaches to Nonlinear Model Predictive Control, *Chemical Process Control*, South Padre Island, TX, 1991.

Braatz, R.D. (2002). Advanced control of crystallization processes, Annual Reviews in Control 26, 87-99.

Diehl, M., H.G. Bock, J.P. Schlöder, R. Findeisen, Z.K. Nagy, F. Allgöwer (2002). Real-time optimization and nonlinear model predictive control of processes governed by differential-algebraic equations, *J. of Process Control* 12, 577-585.

Franke, R., E. Arnold, H. Linke. HQP: A solver for nonlin-early constrained optimization. http://hqp.sourceforge.net.

Fujiwara, M., Z.K. Nagy, J.W. Chew, R.D. Braatz (2005). First-principles and direct design approaches for the control of pharmaceutical crystallization, *J. of Process Control* 15, 493-504.

Lee, K., J.H. Lee, M. Fujiwara, D.L. Ma, R.D. Braatz (2002). Run-to-run control of multidimensional crystal size distribution in a batch crystallizer, *Proc. of the American Control Conf.*, IEEE Press, Piscataway, NJ, 1013-1018.

LeVeque, R. (1992). Numerical Methods for Conservation Laws, Birkhauser.

Nagy, Z.K., B. Mahn, R. Franke, F. Allgower (2007). Efficient output feedback nonlinear model predictive control for temperature control of industrial batch reactors, Control Engineering Practice, 15, 839-859.

Nagy, Z.K., R.D. Braatz (2003). Robust nonlinear model predictive control of batch processes, *AIChE J.* 49, 1776-1786.

Nagy, Z.K., R.D. Braatz (2004). Open-loop and closed-loop robust optimal control of batch processes using distributional and worst-case analysis, *J. of Proc. Control*, 14, 411-422.

Rawlings, J., S. Miller, W. Witkowski (1993). Model identification and control of solution crystallization processes A review, *Ind. Eng. Chem. Res.* 32, 1275-1296.

Rusli, E., J.H. Lee, R.D. Braatz (2006). Optimal distributional control of crystal size and shape, *Proc. of the Fifth World Congress on Particle Technology*, Orlando, FL, paper 240f.

Modeling and Control System Design of a Crystallizer Train for Para-xylene Production

Souichi Amano * **Genichi Emoto** * **Hiroya Seki** **

* *Production Technology Department, Mitsubishi Chemical Corporation, Kurashiki, 712-8054 Japan*
** *Chemical Resources Laboratory, Tokyo Institute of Technology, Yokohama, 226-8503 Japan*
(Corresponding author, e-mail: hseki@ pse.res.titech.ac.jp)

Abstract: A dynamic process model of an industrial crystallizer train for para-xylene production, which consists of five scraped surface crystallizers, two hydrocyclone separators, and two centrifugal separators, is developed for control system design. The model is identified by using real plant data. Optimal operating policies, which consider feed maximization and load distribution among the crystallizers, are derived, and multiloop controller is configured to realize the operating policy.

Keywords: Crystallization, industrial application, plantwide control

1. INTRODUCTION

Crystallization is one of the most popular unit operations for separation and purification used in the chemical industry. Despite their importance, process and control system design for separation processes based on crystallization technology has received much less attention compared with distillation column processes [Mendez et al. (2005)].

Most of the studies on control system design for crystallization processes focus on operations of a single crystallizer as an isolated unit [Rawlings et al. (1993), Hasebe et al. (2000)], although crystallizers never exist in isolation and simultaneous consideration of subprocessing units such as filtration and drying, etc. should be equally important [Chang et al. (1998)]. Some studies handle operations of multiple crystallizers [Garside (1985), Liu et al. (1991)], but study on process and control system design for crystallization processes from the plantwide perspective is quite limited [Wibowo et al. (2001), Ward et al. (2007)].

In this paper, modeling and control system design of an industrial crystallizer train, which comprises five crystallizers, two centrifugal separators and two cyclone separators, are discussed. The process concerns the product recovery section in a para-xylene production plant. The process underwent several revamps during the course of a long history of commercial operation, and the process became rather complicated, so that quantitative analysis based on a mathematical model would help provide us with improved operations.

First, a dynamic process model is developed, which describes crystallization kinetics, mass balance, and heat balance for the whole plant. The model is then identified by using the actual plant data. Based on the developed model, optimal operating policies are derived through optimization calculations. In setting up the optimization problem, practical considerations such as constraint handling issues are discussed in detail. Finally, a multi-loop control system is configured which realizes the optimal operation.

2. PROCESS DESCRIPTION

2.1 Para-xylene production process

Para-xylene is an aromatic hydrocarbon used primarily to make intermediates for manufacturing polyester. It is the main feedstock for purified terephthalic acid and dimethyl terephthalate, which in turn are used to produce polyethylene terephthalate (PET) for use in fibres for textiles, bottles for soft drinks and water.

Figure 1 shows a typical commercial production process of para-xylene, where fresh feed that contains mixed xylene (mixture of ortho-xylene, meta-xylene, and para-xylene) and ethylebenzene is sent from the upstream plant and pure para-xylene (normally $> 99.5\%$) is recovered from the feedstock by fractionation and crystallization. Crystallization is one of the conventional methods for the recovery of pure para-xylene; currently adsorption may be the most popular. Filtrate from the para-xylene recovery section is sent to the reaction section, where ortho-xylene, meta-

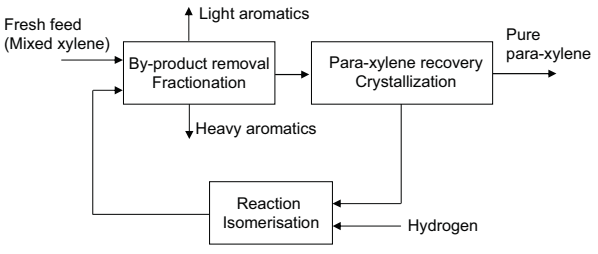

Fig. 1. Typical para-xylene production process

xylene are converted into para-xylene through isomerization reaction.

2.2 Para-Xylene recovery based on crystallization technology

Since many physical properties of the individual xylene isomers are similiar, high purity separation of each individual xylene isomer is difficult. Crystallization is one of the methods for that purpose, resorting to the differences in the melting points among the xylene isomers.

Figure 2 shows the crystallizer train under study, which consists of two separate cyrstallization stages. The first stage uses several (in this example, three) scraped surface crystallizers to bring the temperature of the xylene mixture close to the para-xylene/meta-xylene eutectic point. The first-stage crystallizers are followed by a solid-liquid separation process using a centrifuge (screen-bowl type in this example). The cold xylene filtrate from the first stage cools the feedstream (not shown in the figure) and is sent to the isomerization section. To achieve the maximum production rate from a certain feedstock, the first-stage crystallization temperature should be decreased as low as possible, down to the eutectic point of para-xylene and meta-xylene.

The solid cake para-xylene crystals and the adherent mother liquor from the first stage are melted in the melt tank, and pumped to the second-stage crystallizers. The second stage is made up of the main crystallizer, and the auxiliary crystallizer located on the recycle stream. The slurry from the main crystallizer is sent to the final centrifugal separator, and the filter cake is melted to form the final para-xylene product. A major portion of the mother liqour from the main crystallizer is returned to the first-stage after a part of para-xylene in the mother liquor is recovered by the auxiliary crystallizer.

Due to the presence of the recycle streams at several locations, which have been added during the course of a long history of commercial operation, the process becomes highly interacting, so that careful analysis on the basis of a mathematical model would be necessary in designing control system.

3. MODELING

3.1 Crystallizer

The crystallizers are assumed to be mixed-suspension mixed-product removal (MSMPR) systems. In addition, the following assumptions are made for model development:

- Only growth and nucleation are considered as crystallization kinetics; breakage and agglomeration are ignored.
- Para-xylene crystal growth is fast enough so that the liquid phase para-xylene is always saturated (the assumption of the high growth rate limit). Nucleation occurs at the crystallizer wall.

These assumptions are adopted from the study by Patience et al. (2001), who studied experimentally the crystallization kinetics of para-xylene in a scraped surface crystallizer.

Denoting the crystal size distribution (CSD) in the crystallizer as $f(x,t)$, its $i-$th moment μ_i is defined as

$$\mu_i = \int_0^\infty f(x,t)x^i dx.$$

By using the method of moment, the population balance equation can be written as:

$$\frac{d\mu_0}{dt} = B + \mu_0^{in} - \mu_0^{out},$$
$$\frac{d\mu_i}{dt} = iG\mu_{i-1} + \mu_i^{in} - \mu_i^{out} \qquad (i \geq 1),$$

where B and G are the nucleation rate and growth rate of para-xylene crystal respectively, μ_i^{in} and μ_i^{out} are the moment flows in and out of the crystallizers which can be calculated from the MSMPR assumption. The empirical expression is used for the nucleation rate B:

$$B = k_b \Delta C^b,$$

where ΔC is defined as the supersaturation created by the temperature difference between the magma and the crystallizer wall:

$$\Delta C = \frac{C^*(T) - C^*(T_J)}{C^*(T_J)}.$$

Here, T is the temperature of the magma, T_J is the temperature of the crystallizer wall, which is assumed to be equal to the jacket temperature, and $C^*(T)$ is the temperature dependent solubility of para-xylene.

The mass balance of the liquid phase para-xylene is written as

$$\frac{dm_{PX}}{dt} = F^{in}C^{in} - F^{out}C^*(T) - 3\rho k_v G\mu_2,$$

where m_{PX} is the liquid hold up of para-xylene in the crystallizer, F^{in} and F^{out} are the inlet and outlet liquid flow rates respectively, C^{in} is the para-xylene concentration of the inlet flow, ρ is the density of para-xylene crystals, k_v is the shape factor. Note that the liquid concentration of para-xylene in the crystallizer is assumed to be saturated.

The heat balance is written as

$$\frac{dH}{dt} = H^{in} - H^{out} + 3\rho k_v G\mu_2 \Delta H_c - UA(T - T_J),$$

where H is the overall enthalpy of the crystallizer, H^{in} and H^{out} are the enthalpy in and out of the crystallizer respectively, ΔH_c is the heat of crystallization, and UA is the overall heat transfer coefficient. Because of the fouling of the crystallizer wall, the heat transfer coefficient is treated as slowly time-varying.

The assumption of the high growth rate limit, that is, the growth rate of para-xylene crystals is so large that the liquid phase para-xylene concentration is always saturated, renders the model equations a DAE system; the growth rate is not explicitly given in the above equations. But the model equation can be easily converted into the ODE by the procedure shown by Patience et al. (2001).

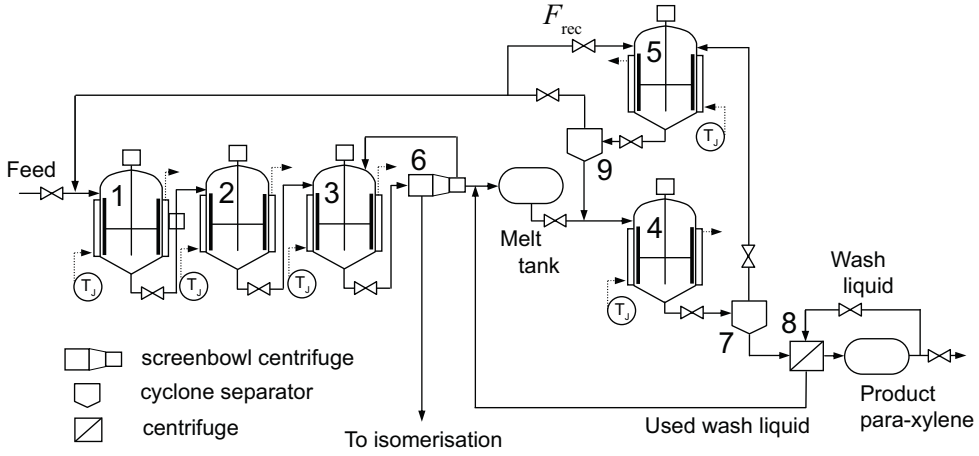

Fig. 2. Process flow of the para-xylene recovery section. The numbers ($1 \sim 9$) denote the equipment numbers which are used as subscript to distiguish the equipments.

3.2 Cyclone separator

The hydrocyclone separates the inlet slurry flow into two streams: the overflow and underflow streams. With the help of centrifugal force, the solid particles contained in the inlet stream are concentrated in the underflow. Ideally the overflow stream contains no solid particle, but it is practically assumed that some of the crystals whose size is smaller than $\bar{d}$ escape into the overflow stream. An ideal separation is assumed, where the crystals over the size $\bar{d}$ will not be included in the overflow. Crystals under the size $\bar{d}$ will be included both in the underflow and overflow, and they are distributed according to the liquid flow rates of these streams.

To obtain the amount of crystals smaller than $\bar{d}$, the crystal size distribution has to be recovered from its associated moment information. However, it is known that infinite number of the moments are needed to reconstruct the CSD [McGraw et al. (1998)].

To avoid this problem, the logarithmic normal distribution is assumed for the CSD. From the values of the moments $\mu_i's$, the mean crystal size m and variance σ^2 can be recovered from the relation:

$$\log(\mu_n/\mu_0) = \frac{n^2}{2}\sigma^2 + nm.$$

In this study, m and σ are determined through the least squares fit by using the moments up to the 4-th order.

Then the amount of crystals below the size $\bar{d}$ can be calculated as

$$\int_0^{\bar{d}} x^n f(x)dx = \exp(\frac{n^2\sigma^2 + 2nm}{2}) \cdot\frac{1}{2}\left(\mathrm{erf}(\frac{\log\bar{d} - m - n\sigma^2}{\sqrt{2}\sigma}) + 1\right),$$

where the error function is defined as

$$\mathrm{erf}(x) = \int_0^x \frac{2}{\pi}\exp(-\lambda^2)d\lambda.$$

No holdup is assumed for the cyclone separators. Then, the balance equations for the hydrocyclone are readily derived.

3.3 Centrifugal separator

At the centrifugal separators, it is assumed that the para-xylene crystals of the size smaller than $\hat{d}$ pass through the screen, accompanying the mother liquor. The amount of such crystals is calculated in the same way as in the hydrocyclone separator model.

Constant void fraction is assumed for the filter cake ($\varepsilon = 0.4$), and the average degree of saturation S_{av} (the percentage of the void in the cake filled with mother liquor) is assumed to be a function of the average crystal size $d_{23} = \mu_3/\mu_2$:

$$S_{av} = S_{av}(\hat{S}, d_{23}),$$

where $\hat{S}$ is a parameter to define the empirical expression.

When the cake is washed (as in the second stage centrifuge), part of the mother liquor in the cake is replaced by the wash liquor. The percentage of the mother liquor replaced by the wash liquid is expressed by the empirical expression, which is a function of S_{av} and the ratio of the amounts of the wash liquid and the mother liqour. The amount of the remaining mother liquor in the cake largely accounts for the product purity.

Then, the balance equations for the centrifuge are readily derived; no holdup is assumed.

The screen-bowl type centrifugal separator at the outlet of the 1st stage is modeled as a combined system comprising a cyclone and a centrifuge; the bowl part is modeled as the cyclone. The parameter α is introduced as the ratio between the bowl filtrate (overflow stream) and the liquid inlet, which will be used for model identification in the next section.

3.4 Overall process model

By combining the models for the crystallizers, the hydrocyclone separators, the centrifugal separators and other

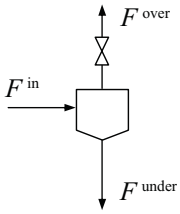

Fig. 3. Hydrocyclone separator modeling

storage tanks, a nonlinear dynamic process model in the following form is derived:

$$\begin{aligned} \dot{x} &= f(x,u,p) \\ y &= h(x,u,p), \end{aligned} \tag{1}$$

where x is the state variable, u is the measured independent variables, p is the unknown parameters and unmeasured independent variables, and y is the measured variables. Here, the variables are defined for the purpose of model identification.

3.5 Model identification

The unknown parameters are obtained through least squares fit of the model calculation with the plant data:

$$\min_{x,p} \quad (\tilde{y}-y)^T(\tilde{y}-y) \tag{2}$$

subject to

$$0 = f(x,u,p), \tag{3}$$

where $\tilde{y}$ is the plant data. Eq. (3) assumes that model identification is done for steady states.

Several data sets for $(\tilde{y},u)$, which have been obtained by heavily filtering 1 hour average data from the real plant, are used for the least squares fit. The available measurements $\tilde{y}$ consist of the holdups of the five crystallizers, the holdups of the melt tank and product tank, the temperatures of the crystallizers, the production rate, the recycle flow rate to the isomerization reaction, para-xylene concentrations of the melt tank and product tank.

As a result of the sensitivity analysis of the minimization problem (2), the identifiable parameter set $p \in \Re^6$ has been selected as

$$p = \left(\alpha_6 \ \bar{d}_6 \ \hat{d}_6 \ \hat{S}_6 \ \hat{S}_8 \ \bar{d}_9\right)^T,$$

where the subscript are defined as equipment number in Fig. 2. The overall heat transfer coefficient UA_i of each crystallizer ($i = 1 \sim 5$) is considered as time-varying and is also used for model identification as the fitting parameters. It should be noted that the parameters concerning crystallization kinetics such as b and k_b are not identifiable from the available measurements, so that their values are adopted from the paper by Patience et al. (2001).

Figure 4 shows one of the fitting results: the parity plot of the fitting result for the production rate. The operation condition used for model identification covers ±20% of the nominal production rate.

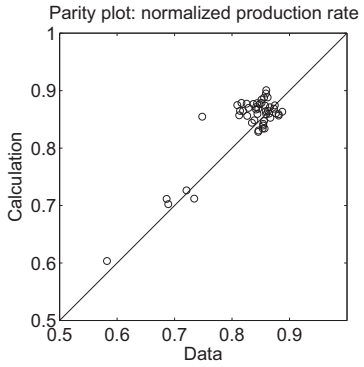

Fig. 4. Parity plot of production rate measurements

4. CONTROL SYSTEM DESIGN

4.1 Definition of manipulated and controlled variables

By using the identified process model, basic regulatory control system is designed; the seven inventory control loops are closed with each effluent flow, and the temperature control loop of each crystallizer is closed by manipulating its corresponding jacket temperature.

The manipulated variables for further control system design are defined as $u_C \in \Re^9$, and they consist of the temperature setpoints of the crystallizers, the ratios of the flow rates of the overflow and the underflow of the cyclones, the wash liquid flow rate, and the recycle flow rate from the overflow of the cyclone to the auxiliary crystallizer:

$$u_C = \left(T_1 \ T_2 \ T_3 \ T_4 \ T_5 \ \alpha_7 \ \alpha_9 \ F_w \ F_{rec}\right)^T,$$

where the subscripts are defined as the equipment number in Fig. 2 and α_i ($i = 7, 9$) is the flow rate ratio in the cyclone separators, and F_w is the wash flow rate, and F_{rec} is the recycle flow rate.

The controlled variables are defined as y_C, for which constraints may be considered, and the process model for control system design is described as

$$\begin{aligned} \dot{x} &= f_C(x,u_C) \\ y_C &= h_C(x,u_C). \end{aligned} \tag{4}$$

4.2 Steady state optimal operation policy

In deriving optimal operating policies, the following constraints are considered.

- *Lower limit for the para-xylene purity* x_{prod} This is a product specification. The purity is determined by the amount of accompanying mother liquor, which is affected by the average crystal size (the larger, the better) and the intensity of the wash at the centrifuge.
- *Lower limits for the jacket temperatures at the 1st stage crystallizers* $T_{J,1} \sim T_{J,3}$ The yield of the para-xylene recovery section is determined by how low the 1st stage crystallizer temperature can be reduced. The refrigerator capacity determines the lower limits of the jacket temperatures.
- *Upper limits for the temperature difference between the jacket and crystallizer* $\Delta T_1 \sim \Delta T_5$ One of the

major operational concerns is the fouling of the crystallizer wall, which is caused by the crystal deposition on the wall surface and exacerbated by too high a super-saturation at the crystallizer wall. Para-xylene crystal deposition on the wall results in poor heat transfer and limits the production rate.

- *Upper limits for the slurry concentrations in the second stage crystallizers* Cs_4, Cs_5 The slurry concentrations in the second stage crystallizers tend to be high and they are limited by the torque limit of the agitator. If the slurry concentration is too high, mixing in the crystallizer would become imperfect.
- *Upper and lower flow rate limits for the cyclone separators* Operation of the cyclone in an abnormal flow rate regime results in inappropriate classification of crystals.
- *Upper limits for the slurry concentrations in the underflow of the cyclone separators* Cs_7, Cs_9 The slurry concentration in the underflow of the cyclone separator tends to be large. Too high a slurry concentration results in clogging of the pipe.
- *Upper limit for the para-xylene concentration in the melt tank* If this concentration is too high, some of the solid para-xylene with low purity from the 1st stage do not dissolve in the melt tank.

The following two modes of operations are considered for developing optimal operating policies.

Feed maximization Feed maximization is realized by solving the following optimization problem:

$$\max_{u_C} \quad F_p \tag{5}$$

subject to

$$\begin{aligned} 0 &= f_C(x, u_C) \\ y_C^{LL} &\le y_C \le y_C^{UL} \\ u_C^{LL} &\le u_C \le u_C^{UL}, \end{aligned} \tag{6}$$

where $(\cdot)^{LL}$ and $(\cdot)^{UL}$ are the lower limits and upper limits respectively; F_p is the production rate that is defined as the effluent of the product tank minus the wash liquid.

Prospective active constraints are found to be the lower limits of the jacket temperatures of the 1st stage crystallizers, the upper limits for the temperature differences and slurry concentrations of the second stage crystallizers, and the slurry concentration in the underflow of the cyclone on the recycle stream. It has been found that around 2% increase in the production rate could be possible compared with the conventional operation.

Load distribution Load for the crystallizer is expressed as the temperature difference (ΔT) between the crystallizer and the jacket. For a prescribed production rate $\bar{F}_p$, flexible operation by distributing the loads between the two crystallizers at the second stage would be advantageous; when fouling of the crystallizer wall of one of the crystallizers is severe, which situation may be observed by decrease in the heat transfer coefficient, the load for that crystallizer is lowered while the load for the other crystallizer is increased to keep the production rate. For such cases, the following optimization problem can be conceived:

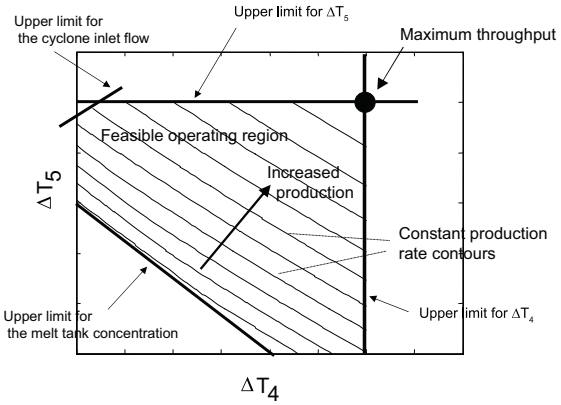

Fig. 5. Optimization landscape described as a contour plot of production rate

$$\min_{u_C} \quad w\Delta T_4 + (1-w)\Delta T_5 \tag{7}$$

subject to

$$\begin{aligned} 0 &= f_C(x, u_C) \\ F_p &= \bar{F}_p \\ y_C^{LL} &\le y_C \le y_C^{UL} \\ u_C^{LL} &\le u_C \le u_C^{UL}, \end{aligned} \tag{8}$$

where w ($0 \le w \le 1$) is the weight used for distributing the load.

Figure 5 shows the optimization landscape obtained by solving the minimization problem (7) for various values of production rate $\bar{F}_p$ and weight w, in which the load distribution for a fixed production rate is described as a contour plot in the $\Delta T_4 - \Delta T_5$ plane. The maximum throughput is realized when the upper limit constraints for both of the temperature differences become active, whereas the throughput is decreased for a moderate load where there is room for the temperature difference. The lower limits for the jacket temperatures of the 1st stage crystallizers and the upper limits for the slurry concentrations in the 2nd stage crystallizers and the underflow of the cyclone are always active.

4.3 Optimizing control

To realize the optimal operating policies derived in the previous subsection, a 6×6 multi-loop control is configured. As the manipulated and controlled variables, the following variables are selected:

Manipulated: T_4, T_5, α_7, α_9, F_w, F_{rec}
Controlled: Cs_4, ΔT_4, Cs_5, ΔT_5, Cs_9, x_{prod},

where Cs_4, Cs_5 and Cs_9 are the slurry concentrations of the 2nd stage crystallizers and the underflow of the cyclone separator on the recycle stream, x_{prod} is the para-xylene concentration in the product stream.

Constant setpoints are given to Cs_4, Cs_5, Cs_9, and x_{prod}, because constraints for these variables are known to be always active with the optimal operations, while the setpoints to ΔT_4 and ΔT_5 are varied according to the load distribution policy. Care should be taken in giving setpoints to ΔT_4 and ΔT_5, because other constraints for

Table 1. RGA analysis for the multi-loop controller design

	T_4	T_5	α_7	α_9	F_w	F_{rec}
Cs_4	0.0093	0.33	0.81	-0.19	0.041	0
ΔT_4	0.85	-0.33	0.18	-0.093	0.39	0
Cs_5	-0.057	0.055	0	0.0028	0	1.0
ΔT_5	-0.30	0.73	-0.0024	0.57	0.0074	-0.0027
Cs_9	-0.0034	0.33	0.0031	0.67	0.0022	0.0019
x_{prod}	0.5	-0.12	0.01	0.038	0.56	0.0

such variables as the cyclone inlet flow rate and melt tank concentration may become active.

A pairing of these variables in the multi-loop control system is determined through the relative gain array (RGA) analysis [Bristol (1966)] shown in Table 1.

5. SIMULATION STUDY

Figure 6 shows a simulation result of the designed control system when the setpoints of the temperature differences ΔT_4 and ΔT_5 are changed (all the numerical values are eliminated from the plot to keep any proprietary information confidential). For the first half of the simulation, the temperature difference ΔT_5 is changed stepwise, while the temperature difference of the other crystallizer ΔT_4 is held constant. This operation increases the production rate. For the second half, ΔT_4 is decreased stepwise while ΔT_5 is held constant. As a result, the load of the crystallizer 4 is reduced while the load of the crystallizer 5 is increased, compared with the initial state of the simulation.

Toward the end of the simulation when the load on the crystallizer 4 is reduced, the cyclone inlet flow almost hits the upper limit, which is anticipated from the analysis shown in Fig. 5.

6. CONCLUSION

A process model of an industrial crystallizer train for para-xylene recovery has been developed and a multi-loop control system has been configured.

Since the process is highly interactive due to the existence of the recycle streams, and the active constraints are subject to change depending upon operating conditions as shown in Fig. 5, application of multivariable model predictive control with constraint handling capability may be justified, if override control logic is regarded tedious.

One of the major concerns in the crystallizer operations is fouling of the crystallizer wall due to large supersaturation, which leads to decreased heat transfer and production rate. A monitoring and control system which is capable of identifying the deteriorating heat transfer coefficient to automatically adjust ΔT would be helpful.

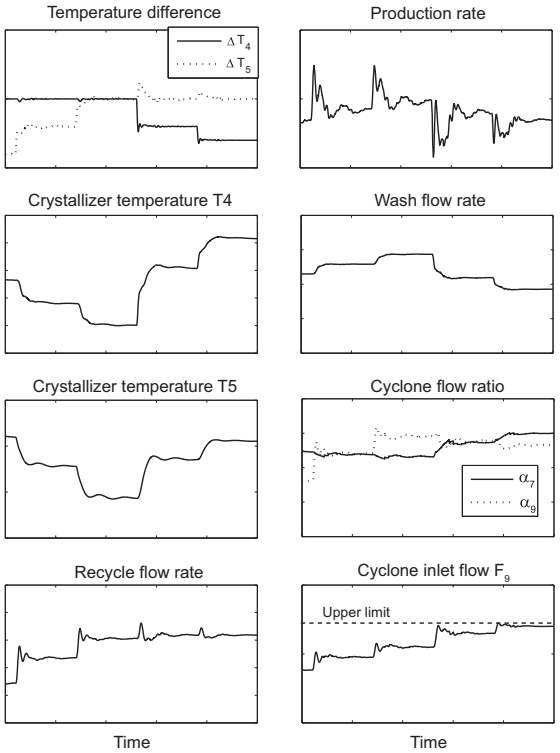

Fig. 6. Simulation result

REFERENCES

E.H. Bristol. On a new measure of interactions for multivariable process control. *IEEE Trans.*, volume AC-11, pages 133-134, 1966.

W.C. Chang and K.M. Ng. Synthesis of processing system around a crystallizer. *AIChE Journal*, volume 44, pages 2240–2251, 1998.

J. Garside. Industrial crystallization from solution. *Chem. Eng. Sci.*, volume 40, pages 3–26, 1985.

S. Hasebe, T. Hamamura, K. Naito, K. Sotowa, M. Kano, I. Hashimoto, H. Betsuyaku, and H. Takeda. Optimal operation of a continuous DTB crystallizer. *J. Process Control*, volume 10, pages 441–448, 2000.

C.H. Liu, D.H. Zhang, C.G. Sun, and Z.Q. Shen. The modelling and simulation of a multistage crystallizer. *The Chemical Engineering Journal*, volume 46, pages 9–14, 1991.

R. McGraw, S. Nemesure, and S.E. Schwartz. Properties and evolution of aerosols with size distributions having identical moments. *J. Aerosol Sci.*, volume 29, pages 761-772, 1998.

C.A. Mendez, J. Myers, S. Roberts, J. Logsdon, A. Vaia, and I.E. Grossmann. MINLP model for synthesis of paraxylene separation processess based on crystallization technology. *Proc. ESCAPE 15*, pages 829–834, Barcelona, Spain, 2005.

D.B. Patience, J.B. Rawlings, and H.A. Mohameed. Crystallization of para-xylene in scraped-surface crystallizers. *AIChE Journal*, volume 47, pages 2441–2451, 2001.

J.B. Rawlings, S.M. Miller, and W.R. Witkowski. Model identification and control of solution crystallization processes: a review. *Ind. Eng. Chem. Res.*, volume 32, pages 1275–1296, 1993.

J.D. Ward, C.C. Yu, and M.F. Doherty. Plantwide operation of processes with crystallization. *AIChE Journal*, volume 53, pages 2885–2896, 2007.

C. Wibowo, W.C. Chang, and K.M. Ng. Design of integrated crystallization systems. *AIChE Journal*, volume 47, pages 2474–2492, 2001.

Evaluation of the Effect of the Solubility Model on Antisolvent Crystallization Optimization

D. J. Widenski*, A. Abbas, J. A. Romagnoli***

**Chemical Engineering Department, Louisiana State University, Baton Rouge, LA 70803 USA (e-mail:dwiden1, jose@lsu.edu)*
***School of Chemical and Biomolecular Engineering, University of Sydney, Sydney, NSW 2006 Australia (e-mail: alia@usyd.edu.au)*

Abstract: The use of predictive solubility models can be of great use for crystallization modeling, and can decrease the amount of experimental data needed to create a robust crystallization model. In this paper, predictive solubility models such as MOSCED, UNIFAC, NRTL-SAC, and the Jouyban-Acree model are compared against an empirical model for predicted solubility accuracy. The best models are subsequently compared against the empirical model for the antisolvent crystallization of acetaminophen in acetone using water. Two different optimization objective functions are executed for each solubility model to generate corresponding optimal profiles. The effect of these optimal profiles on the predicted crystal properties is evaluated.

Keywords: Optimization, Solubility Model, Crystallization, Antisolvent, NRTL-SAC, Jouyban-Acree, Population Balance

1. INTRODUCTION

Crystallization is an important unit operation for the production of pharmaceuticals, fertilizers, and fine chemicals. Optimal crystallization operation often requires a crystallization model. This crystallization model, typically based on population balances (Hulburt and Katz, 1964; Ramkrishna, 1985; Randolph and Larson, 1988), requires a companion solubility model. Empirical solubility models have been extensively used in crystallization modelling (Zhou et al., 2006; Nowee et al., 2008; Lindenberg et al., 2009). It is of interest to understand how other predictive solubility models such as the MOSCED, NRTL-SAC, UNIFAC, and Jouyban-Acree models can be incorporated into crystallization models and how their accuracy of predicting the solubility profiles influences both the crystallization model prediction and optimal profile calculation. The outcome of combining predictive solubility modelling with the crystallization model is expected to reduce the need for solubility experimental data and consequently streamline the optimization of the crystallization process.

The solubility prediction is an important aspect of any crystallization model because its prediction is the basis for any crystallization phenomena. Crystallization is caused by supersaturation which is defined as the difference between the solution concentration and the equilibrium concentration (absolute supersaturation), or the ratio of the solution and equilibrium concentrations (relative supersaturation).

This paper investigates the effect of different solubility models on the optimization of antisolvent crystallization. Both the effect of the model on the predicted optimal profile and on the result of these models' optimal profiles implemented into a validated crystallization model will be evaluated. Specifically, we examine the effect on the supersaturation, mean size, and volume percent crystal size distribution (CSD) profiles. Although there has been extensive work done in the area of crystallization control and optimization (Braatz, 2002; Zhou et al., 2006; Nowee et al., 2008; Sheikhzadeh et al., 2008), as far as we are aware there is no study that has investigated the use of predictive solubility models in developing optimal antisolvent feed profiles.

2. SOLUBILITY MODELS

2.1 MOSCED & UNIFAC Models

The MOSCED model (Lazzaroni et al., 2005), generates infinite dilution activity coefficients. In order to obtain a non-infinite dilution activity coefficient, another activity coefficient model is required. The Van Laar, Wilson, and NRTL models were each combined with the MOSCED model to evaluate which would give the best prediction to known experimental data. The next solubility model considered is the UNIFAC model (Anderson and Prausnitz, 1978). The UNIFAC model predicts activity coefficients based on group contributions. The MOSCED and UNIFAC models predicted equilibrium profiles for acetaminophen in acetone and water are shown in Figure 1.

The MOSCED models all give very poor solubility predictions. They all greatly underestimate the solubility. The NRTL and Wilson models give better estimates to the shape of the solubility curve than the Van Laar model does. The UNIFAC model is the worst of the models both greatly overestimating the solubility and weakly representing the shape of the curve.

2.2 NRTL-SAC, Jouyban-Acree, and Empirical Models

The next solubility model considered is the NRTL-SAC model (Chen et al., 2004, 2006). The NRTL-SAC model is a NRTL activity coefficient model that has been modified using segment theory (Chen et al., 2004, 2006). The last predictive solubility model considered is the Jouyban-Acree model (Jouyban et al., 2006).

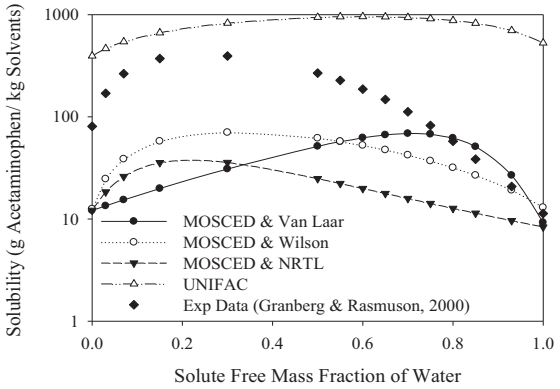

Figure 1: MOSCED & UNIFAC Solubility Predictions.

The Jouyban-Acree model is a semi-empirical model developed to predict the solubility of pharmaceuticals in organic solutions. This model requires the solubilities of both pure components in a binary solute-solvent system, and predicts the solubility of a solute in a solvent mixture. The last solubility model considered is an empirical model generated from data from Granberg and Rasmuson (2000) by Zhou et al. (2006).

$$C^* = -5.01902 \text{ x } 10^{-12}w^6 + 1.69767 \text{ x } 10^{-9}w^5 - 2.46765 \text{ x } 10^{-7}w^4 + 2.19262 \text{ x } 10^{-5}w^3 - 1.27018 \text{ x } 10^{-3}w^2 + 3.42614 \text{ x } 10^{-2}w + 7.96086 \text{ x } 10^{-2} \quad (1)$$

Where C^* is the equilibrium concentration (kg acetaminophen/kg solvents), and w is the solute free mass percent of water. The NRTL-SAC, Jouyban-Acree, and empirical model predicted solubilities are plotted in Figure 2. The NRTL-SAC and Jouyban-Acree solubility models both predict the equilibrium solubility much better than the MOSCED or UNIFAC models did. The empirical model fits the data very well and will be considered as the standard solubility model for benchmarking. Since the UNIFAC and MOSCED models gave such poor solubility predictions, only the NRTL-SAC and Jouyban-Acree models will be compared against the empirical model in the optimization sensitivity study in the subsequent sections.

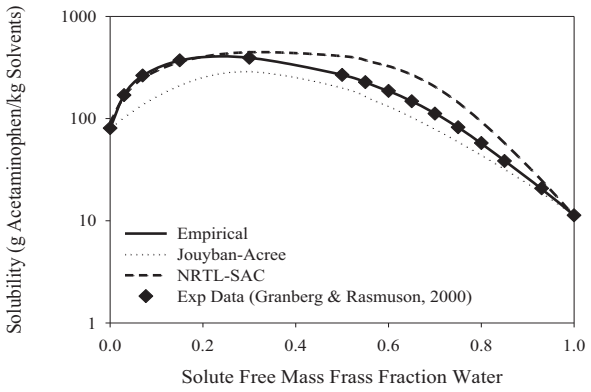

Figure 2: NRTL-SAC and Jouyban-Acree Solubility Predictions.

3. CRYSTALLIZATION MODEL

In order to evaluate the effect of the solubility model on the predicted optimal trajectories, a crystallization model is required.

3.1 Population Balance

The population balance for a crystallization system having size-independent crystal growth and without attrition or agglomeration is defined in (2).

$$\frac{\partial n(L,t)}{\partial t} + \frac{n(L,t)}{V}\frac{dV}{dt} + G\frac{\partial n(L,t)}{\partial L} - B = 0 \quad (2)$$

Where $n(L,t)$ is the crystal density (# of particles/m^3), V is the volume (m^3), G is the growth rate (m/s), and B is the nucleation rate (# of particles/ s m^3). The population balance was solved by discretization using backward finite differences. The discretization consisted of 250 geometrically spaced intervals from 0.5-1000 microns.

3.2 Crystallization Kinetics

The antisolvent crystallization kinetics for acetaminophen in acetone with water as the antisolvent were taken from Zhou et al (2006). The authors developed their own kinetic rates (3-6), from previous crystallization data performed by Granberg et al. (1999, 2001).

$$N = 8.56080 \text{ x } 10^8 \text{ x } \exp\left\{-1.22850 \text{ x } 10^{-3}\frac{\ln^3\left(\frac{\rho_c}{C^*\rho_s}\right)}{\ln^2\left(\frac{C}{C^*}\right)}\right\} \quad (3)$$

$$G = k_g(C - C^*)^g \quad (4)$$

$$k_g = 4.01067 \text{ x } 10^{-8}w^2 - 1.76198 \text{ x } 10^{-6}w + 5.78135 \text{ x } 10^{-5} \quad (5)$$

$$g = -4.22536 \text{ x } 10^{-3}w + 1.77428 \quad (6)$$

Where N is the nucleation rate (no. of particles/m^3), ρ_c is the crystal density of acetaminophen (kg/m^3), C^* is the equilibrium concentration defined previously, C is the solution concentration (kg acetaminophen/kg solvents), ρ_s is the density of the solution (kg/m^3), G is the crystal growth rate (m/s), and w is the solute free mass percent of antisolvent (water) in the solution. Also, the growth kinetics is only valid for solute free water mass percents greater than 30%.

4. OPTIMIZATION

The first optimization objective (O-1) was to create a final volume mean crystal size (D_{43}) of 200 microns, and jointly minimize the total amount of nucleation by minimizing the zeroth moment. The optimization constraints were to end with a solute free antisolvent mass percent of water of 88%, and the mass flow rate of water could range between 0 and 400 g/min. The duration of the experiment was fixed at 4200 s. The control interval was discretized into 10 fixed 360 s intervals where the antisolvent flow rate could be adjusted in a piecewise constant manner. The final 600 s had a fixed antisolvent flow rate of zero. This was done to ensure that all remaining supersaturation is consumed at the end of the run. The optimizations were implemented using the gPROMS package (Process System Enterprise, UK) using the gOPT entity. The objective function used is defined in (7) subject to initial conditions in (8).

$$OBJ = \begin{matrix}\max D_{43} \\ \min \mu_0\end{matrix} \begin{cases} D_{43} \leq 200\ \mu\text{m} \\ w_f = 88\% \\ 0 \leq \dfrac{dW}{dt} \leq 400\ g/\min \text{Water} \end{cases} \quad (7)$$

$$T = 16\ ^\circ\text{C} \quad w_i = 40\% \quad n_i(L,0) = 0 \quad C_i = C_i^* \quad (8)$$

This optimization was carried out using the crystallization model in Section 3 separately with each of the empirical, Jouyban-Acree, and NRTL-SAC solubility models. The MOSCED and UNIFAC models were not considered because when those models where incorporated into the crystallization model they did not predict any crystallization phenomena.

4.1 Optimal Antisolvent Feed Profiles for O-1.

Each solubility model resulted in an optimal profile (Figure 3).. The empirical and Jouyban-Acree models generated similar optimal profiles (denoted Profile A.1 and Profile B.1 respectively) with a small initial flow rate at the beginning of the experiment, moderate flow rate in the middle, and higher flow rate at the end. In contrast, the NRTL-SAC model calculates an optimal profile (denoted Profile C.1) that has a moderate initial flow rate followed by a high flow rate in the middle, and no flow at the end.

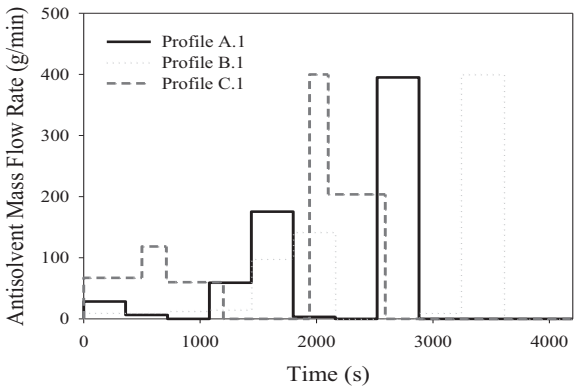

Figure 3: Optimal antisolvent feed profiles for O-1.

The second optimization objective (O-2) was to create a larger final volume mean size (D_{43}) of 400 microns while again minimizing the total amount of nucleation by minimizing the zeroth moment. The objective function formulation for O-2 was the same as for O-1 with the exception that D_{43} now cannot be greater than 400 microns.

4.2 Optimal Antisolvent Feed Profiles for O-2.

Each solubility model resulted in a new optimal profile for O-2 (Figure 4). The empirical and Jouyban-Acree models again generated similar optimal profiles (denoted Profile A.2 and Profile B.2 respectively) with a small initial flow rate at the beginning of the experiment, a high flow rate in the middle for A.2, and a high flow rate at the end for B.2. In contrast, the NRTL-SAC model calculates an optimal profile (denoted Profile C.2) that has a moderate initial flow rate followed by a low flow rate in the middle, and a moderate flow rate at the end.

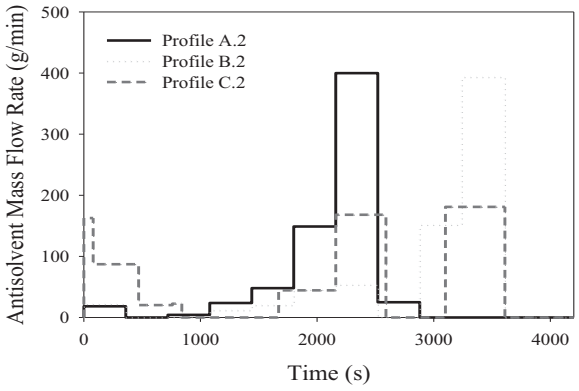

Figure 4: Optimal antisolvent feed profiles for O-2.

5. OPTIMIZATION SENSITIVITY ANALYSIS

The crystallization model was executed for each generated optimal feed profile (A.1-C.2) using the empirical solubility model. The empirical model is used as the benchmark since it

showed very close agreement to experimental solubility data. This should predict what these optimal profiles would actually produce in a real crystallizer. Results are shown in the next sections.

5.2 Optimal Profiles for O-1 Evaluation

When the optimal profiles are implemented into the empirical solubility model there are several observed differences in the simulated supersaturation profiles (Figure 5) under Profiles A.1, B.1, and C.1. The NRTL-SAC optimal profile (C.1) causes the supersaturation to peak earlier than the other two models, while the supersaturation caused by the Jouyban-Acree profile (B.1) is shown to be similar in shape to the empirical profile (A.1) but with a delay. Next, the effect on the volume mean size growth is shown in Figure 6.

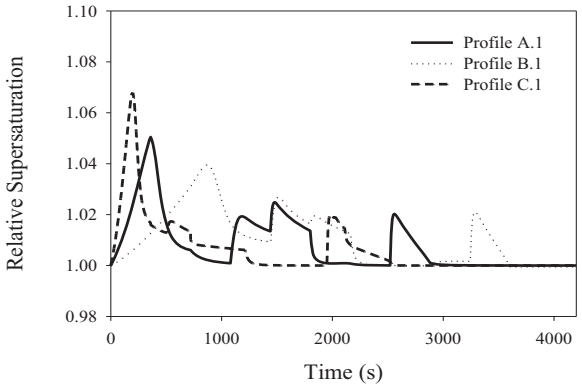

Figure 5: Relative supersaturation profiles for each optimal antisolvent feed profile for O-1.

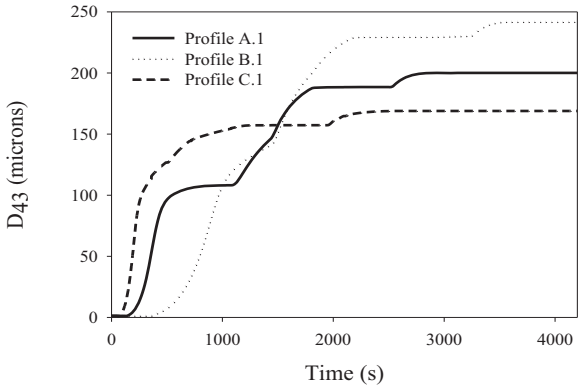

Figure 6: Volume mean size for each optimal antisolvent feed profile for O-1.

Each volume mean size profile can be explained by its corresponding supersaturation curve. Whenever the supersaturation increases there is a corresponding increase in the volume mean size. The NRTL-SAC optimal profile's (C.1) supersaturation profile only has one large early supersaturation peak which causes the first primary increase in crystal size, and a second peak which causes a small increase in crystal size. The empirical optimal profile's (A.1) generated supersaturation profile has four peaks which cause four increases in crystal size. Likewise the Jouyban-Acree optimal profile (B.1) causes the supersaturation profile to have four increases in D_{43}. Using the empirical solubility model, the empirical optimal profile (A.1) satisfies its objective of 200 microns, the Jouyban-Acree optimal profile (B.1) is higher at 242 microns, and the NRTL-SAC optimal profile (C.1) is lower at 169 microns. Both predictive models optimal profiles did not meet the optimization objective but are within 20% of the desired value.

Figure 7 shows the volume percent CSD for each optimal profile. All three optimal profiles give similar distributions with the NRTL-SAC optimal profile (C.1) distribution having a lower mean size than the others, and the Jouyban-Acree optimal profile (B.1) distribution having a larger mean size. All three optimal profiles generated distributions with similar width.

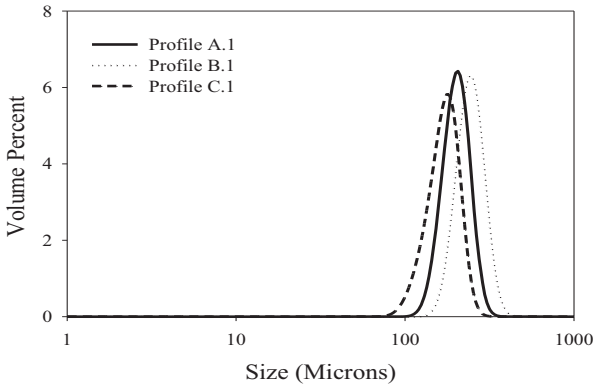

Figure 7: Volume percent CSD for each optimal antisolvent feed profile for O-1.

For this objective function (O-1) only the empirical model's optimal profile (A.1) was able to satisfy the objective to create a volume mean size of 200 microns, but the predictive models' profiles (B.1 & C.1) were able to be within 20% of the desired value. Also, all three profiles were successfully able to suppress nucleation to produce unimodal profiles.

5.3 Optimal Profiles for O-2 Evaluation

The next objective function considered is the 400 volume mean size objective function (O-2). As seen in Figure 8 the generated supersaturation profiles follow the same trend as for the first objective function (O-1). The NRTL-SAC optimal profile (C.2) generates a supersaturation profile that is nearly identical to the supersaturation profile that C.1 generated for O-1. The empirical optimal profile (A.2) generates a supersaturation amount that is above 1.02 from 500 to 2500 s. The Jouyban-Acree optimal profile (B.2) generates a supersaturation peak that is similar to (A.2) but not as high of a supersaturation amount.

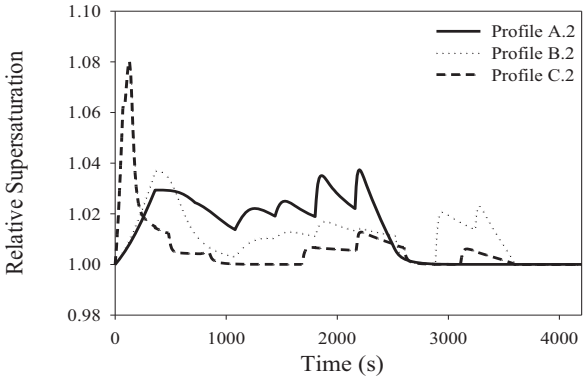

Figure 8: Relative supersaturation profiles for each optimal antisolvent feed profile for O-2.

The Jouyban-Acree (B.2) and NRTL-SAC (C.2) optimal profiles both generated a much smaller mean size because they did not generate the required supersaturation. The Jouyban-Acree optimal profile (B.2) generated a volume mean size of 271 microns and the NRTL-SAC optimal profile (C.2) generated a volume mean size of 162 microns. Both predictive solubility models' optimal profiles do not satisfy O-2 as well as they satisfied O-1.

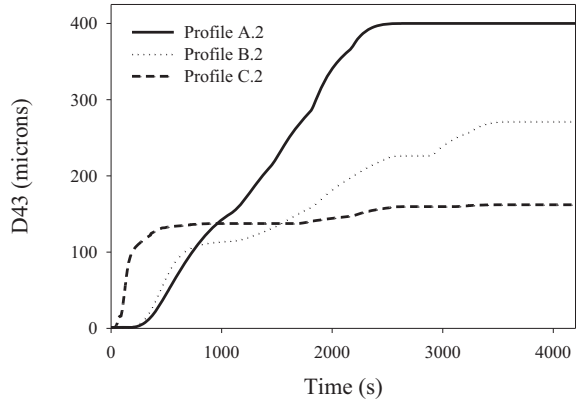

Figure 9: Volume mean size for each optimal antisolvent feed profile for O-2.

Figure 10 shows the volume percent CSD for each optimal profile for O-2. For this case there is a larger difference between the three profiles. Clearly, the Jouyban-Acree (B.2) and NRTL-SAC (C.2) optimal profiles did not satisfy the optimization objective. Also, the distribution width had more variation between the three profiles. The empirical profile (A.2) had the lowest distribution width, followed by the Jouyban-Acree (B.2) and the NRTL-SAC (C.2) model had the largest distribution width.

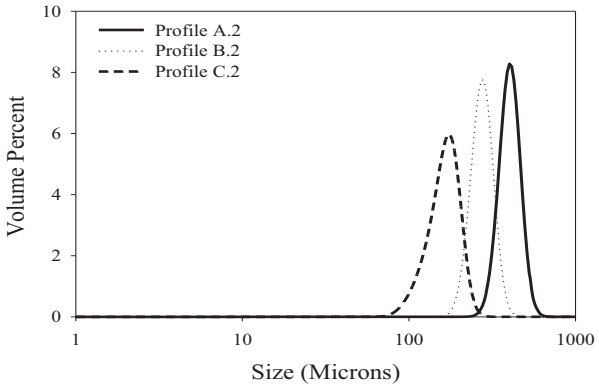

Figure 10: Volume percent CSD for each optimal antisolvent feed profile for O-2.

Just as for the first case (O-1) only the empirical model's optimal profile (A.2) was able to satisfy the objective (O-2) to create a volume mean size of 400 microns. Both predictive model profiles (B.2 & C.2) produced a much smaller mean size. The Jouyban-Acree profile (B.2) produced particles 32% smaller, and the NRTL-SAC profile (C.2) produced particles 60% smaller. Even though they did not produce the proper volume mean size, all three profiles were successfully able to suppress nucleation to produce unimodal profiles.

5.5 Optimization Evaluation

The reason why the optimal flow rates are similar for both the empirical and Jouyban-Acree model is that the slopes of both solubility curves are very similar. Since the slope of the solubility curve is what dictates the supersaturation profile, it would be expected to give similar supersaturation profiles. The NRTL-SAC model has a different slope in its solubility profile which causes the larger deviation in these reported results. In order for a predictive solubility model to produce predictive optimal profiles it must be accurate both quantitatively and qualitatively.

Table 1: Final volume mean crystal size derived from each optimal profile.

	Final Volume Mean Size & Percent Error			
Optimal Feed Profile	O-1 (200)	Prediction Percent Error	O-2 (400)	Prediction Percent Error
Empirical	200	0	400	0
Jouyban-Acree	242	21%	271	-32%
NRTL-SAC	169	-16%	162	-60%

Only the optimal profiles (A.1, A.2) generated from the empirical solubility model were able to satisfy both optimization objectives. When other optimal profiles were used the final volume mean size was as much as 60% under predicted and 21% over predicted when implemented into the

empirical solubility model. The deviation from the objective criteria increased as the volume mean size increased.

6. CONCLUSION

The effect of several solubility models were evaluated on the predicted optimal antisolvent feed profiles. The solubility model did have an effect on the optimal profile, and generated a unique optimal antisolvent feed profile. The use of the predictive solubility models' optimal profiles in the empirical solubility model did not satisfy the original objective function. The use of an incorrect solubility model will create a sub-optimal antisolvent feed profile that will not satisfy its intended crystallization optimization objective in a real system. This underpins the significance of the solubility profile in crystallisation optimizations work.

REFERENCES

Anderson T.F., Prautsnitz J.M. (1978), Application of the UNIQUAC Equation to Calculation of Multicomponent Phase Equilibria 2: Liquid-Liquid Equlibria, *Industrial & Engineering Chemistry Process Design and Development*, 17-4, 561-567

Braatz R.D. (2002), Advanced Control of Crystallization Processes, *Annual Reviews in Control*, 26, 87-99.

Chen C.C., Crafts P.A. (2006), Correlation and Prediction of Drug Molecule Solubility in Mixed Solvent Systems with the Nonrandom Two-Liquid Segment Activity Coefficient (NRTL-SAC) Model, *Industrial & Engineering Chemistry Research*, 45, 4816-4824.

Chen C.C., Song S. (2004), Solubility Modelling with a Nonrandom Two-Liquid Segment Activity Coefficient Model, *Industrial & Engineering Chemistry Research*, 43, 8354-8362.

Granberg R. A., Bloch D. G., Rasmuson A. C. (1999), Crystallization of Paracetamol in Acetone-Water Mixtures, *Journal of Crystal Growth, 198/199*, 1287-1293.

Granberg R. A., Ducreux C., Gracin S., Rasmuson A. C. (2001), Primary Nucleation of Paracetamol in Acetone-Water Mixtures, *Chemical Engineering Science*, *56*, 2305-2313.

Granberg R.A., Rasmuson A.C. (2000), Solubility of Paracetamol in Binary and Ternary Mixtures of Water, *Journal of Chemical & Engineering Data*, 45, 478-483.

Hulbert H.M., Katz S. (1964), Some Problems in Particle Technology, *Chemical Engineering Science,* 19, 555.

Jouyban A., Chan H.K., Chew N.Y.K., Khoubnasabjafari M., Acree, Jr. W.E. (2006), Solubility Prediction of Paracetamol in Binary and Ternary Solvent Mixtures Using Jouyban-Acree Model, *Chemical and Pharmaceutical Bulletin,* 54-4, 428-431.

Lazzaroni M., Bush D., Eckert C. (2005), Revision of MOSCED Parameters and Extension to Solid Solubility Calculations, *Industrial & Engineering Chemistry Research*, 44, 4075-4083.

Lindenberg C., Krattli M., Cornel J., Mazzotti M., Brozio J. (2009), Design and Optimization of a Combined Cooling/Antisolvent Process, *Crystal Growth & Design*, 9:2, 1124-1136.

Nowee S.M., Abbas A., Romagnoli J.A. (2008), Model-Based Optimal Strategies for Controlling Particle Size in Antisolvent Crystallization Operations, *Crystal Growth & Design,* 8:8, 2698-2706.

Ramkrishna D. (1985), The Status of Population Balances, Reviews in Chemical Engineering, 3:1, 49-95.

Randolph A.D., Larson M.A. (1988), *Theory of Particulate Processes (2nd ed.), Academic Press, San Diego,* CA.

Sheikhzadeh M., Trivkovic M., Rohani S. (2008), Real-time optimal control of an anti-solvent isothermal semi-batch crystallization process, *Chemical Engineering Science*, 63, 829-839.

Zhou G.X., Fujiwara M., Woo X.Y., Rusli E., Tung H.H., Starbuck C., Davidson O., Ge Z., Braatz R.D. (2006), Direct Design of Pharmaceutical Antisolvent Crystallization through Concentration Control, *Crystal Growth and Design*, 6-4, 892-898.

Numerical Studies of Wavelet-based Method as an Alternative Solution for Population Balance Problems in a Batch Crystalliser

Johan Utomo, Tonghua Zhang, Nicoleta Balliu and Moses O. Tadé*

Department of Chemical Engineering, Curtin University of Technology,
GPO Box U 1987, Perth, WA 6845, Australia
**corresponding author:(Tel:61-8-9266 4998; e-mail: m.o.tade@curtin.edu.au).*

Abstract: This paper deals with the numerical simulation studies of the nucleation and crystal growth process in a batch crystalliser. The population density functions may extend over orders of several magnitudes and the size distribution can be very sharp, thus accurate numerical solution of the population density functions can be challenging. The main interest for finding a more representative population balance solutions has motivated many researchers to develop many methods for the last four decades. In this paper, four methods have been implemented including wavelet-based method. The results obtained in three case studies, have demonstrated the wavelet scheme to be an alternative in providing accurate, fast and robust solutions.

Keywords: Crystallisation, Numerical scheme, Population Balance, Wavelet method

1. INTRODUCTION

Hulburt and Katz (1964) introduced a statistical mechanical formulation, known as population balance, for modelling the crystallisation process. The population balance equation (PBE) can be defined as a mathematical description characterising particles undergoing the mechanisms of birth, growth, death and leaving a certain particle phase space. In crystallisation, those mechanisms can be categorized as nucleation, growth, agglomeration and breakage. The population density functions may extend over orders of several magnitudes and the size distribution can be very sharp, thus the accurate numerical simulation of the population density functions can be challenging and has motivated several researchers in this area for decades to develop specialised algorithms for solving PBE, for example Ramkrishna (1981), Hounslow et al.(1988), Litster et al. (1995), Kumar and Ramkrishna (1996), Nicmanis and Hounslow (1996), and Mahoney and Ramkrishna (2002). All of these methods can be classified into four categories, such as method of weight residuals/orthogonal collocation, finite elements methods, finite difference schemes/discrete population balances methods, and other methods. There are major drawbacks from those methods such as computationally expensive, lack of stability and accuracy of the solution and in applicability of the solved models to be implemented in control based models. Extensive comparative discussion of those methods can be found in the literature (Kostoglou et al. 1994; Ramkrishna 2000; Vanni 2000). Therefore, the need for accurate, fast, robust and low order solution is essential for design, control and optimisation purposes.

This paper reports the application of wavelet based methods as an alternative, for solving population balance problems in a batch crystalliser condition. Previous study (Utomo et al. 2006) has been extended by comparing with finite difference based methods, such as upwind finite difference (U-FD), biased upwind finite difference (BU-FD), and method of weighted residuals, such as, orthogonal collocation with finite element method (OCFE). Different types of population balance are illustrated in the three cases discussed in this paper. They are having a high non-linearity, a steep-front profile, and stiff characteristic. The solutions are benchmarked with respects to their size (spatial grid points used), accuracy (mean and average error) and the computation time (t-CPU).

2. NUMERICAL SCHEMES

2.1 Previous Methods

Finite difference (FD) methods have been commonly used for the solution of all types of partial differential equations (ODEs) systems. FD method approximates the continuous function, $f(x)$, with Taylor expansion series (Hangos and Cameron, 2001). They can be a first order or second order approximations. In our case, FD method was used to approximate the first partial derivative of population density over its size and converts the PDE into a set of ODEs.

In this paper, the upwind finite difference and biased upwind finite difference schemes were applied to effectively handle the instability and to avoid the spurious oscillation as generated by a centred FD scheme. The five-point (fourth-order accuracy) upwind and biased upwind on uniform grids were implemented as described in (Wouwer et al. 2005). Orthogonal collocation technique was developed and applied in various cases of boundary value problems. The trial functions are chosen as sets of orthogonal polynomials and

the collocation points are the roots of these polynomials. The use of orthogonal polynomials is to reduce the error as the polynomial order increases (Gupta 1995; Hangos et al. 2001). OCFE is the combination method of dividing the regions into a number of elements and by applying orthogonal collocation techniques for each element can improve the solution where the profile is very steep. In the region, where there is a sharp transition, numbers of small elements can be applied while the remainder utilizes larger size elements. Selection of the elements size is therefore essential.

2.2 Wavelet-based methods

In 1992, Daubechies in her famous text-book, "Ten lectures on wavelets" (Daubechies 1992), predicted that a wavelet based software package to solve partial differential equations will be available in the market. The prediction has not been met as today there is no software available except for the Wavelet Toolbox in MATLAB®, which cannot be used for solving any partial differential equation (PDE).

The earliest wavelet application in chemical engineering was Wavelet Galerkin (WG). It was due to the work of Chen et al. (1996). Wavelet method with Galerkin scheme was utilised to solve the breakage population balance in a batch crystalliser. One of the challenges of WG is the expansion coefficients in WG was not specified in the physical space, while most of the PDEs can be directly solved in the physical space rather than converting and transforming its solution back to physical space. The second method was Wavelet Optimised Finite Difference (WOFD), developed by Jameson (1998). To date, this method has not been employed in the chemical engineering field. The third method was Wavelet Orthogonal Collocation (WOC). Its first application in chemical engineering was due to Liu and Cameron (2001). This method was successfully applied to solve the population balance and steep front concentration profiles in adsorption. However, WOC has not been applied for solving the complex cases which may involve the non-linearity and full dimensional variables. To sum up, the comparison of the three methods discussed are given below, which may initiate further development of a new wavelet-based numerical scheme for solving PDEs.

Table 1. Comparative components of three wavelet-based methods, WG: Wavelet Galerkin, WOFD: Wavelet Optimised Finite Difference and WOC: Wavelet Orthogonal Collocation

Comparative components	***WG***	***WOFD***	***WOC***
Basis calculation	Wavelet	**Physical**	**Physical**
BC treatment	Difficult	**Easy**	Moderate
Non-linearity handling	Difficult	**Moderate**	**Moderate**
Adaptive scheme	No	**Yes**	**Yes**
Computation capacity	Fixed	Fixed	**Reduced**

2.3 Daubechies orthonormal wavelets

Wavelet can be used as a basis function to represent a certain function. In the wavelet function, two-basis functions can be found, the scaling function and the wavelet function. The scaling function coefficient illustrates a local average of the solution can be calculated from the collocation points. The function (coarse illustration) and the wavelet function coefficient describes detailed information of the function (refinements) that cannot be found from the average coefficient. Compared to Fourier expansion, wavelet approximation gives smaller error and is highly localized at discontinuity regions (Nielsen 1998). Compared to the traditional trigonometric basis functions which have infinite support, wavelets have compact support, therefore wavelets are able to approximate a function by the placement of the right wavelets at appropriate locations. From Daubechies's work (1988), scaling function (ϕ) and wavelet function (ψ) can be described by a set of L (an even integer) coefficients (p_k: k = 0,1,…, L-1) through the two-scale relationship:

$$\phi(x) = \sum_{k=0}^{L-1} p_k \phi(2x-k) \tag{1}$$

and the wavelet function

$$\psi(x) = \sum_{k=2-L}^{1} (-1)^k \, p_{1-k} \phi(2x-k) \tag{2}$$

The support for the scaling function is in the interval 0 to (L-1), whilst for the wavelet function is in the interval (1-L/2) to (L/2). The coefficients p_k are called the wavelet filter coefficients.

Denote $L^2(R)$ as the space of square integrable functions on the real line. Let V_j be the subspace as the L^2-closure of the linear combination of:

$$\phi_{jk}(x) = 2^{j/2} \phi\left(2^j x - k\right) \tag{3}$$

for $k \in Z = \{...,-1,0,1...\}$. A function $f(x) \in V_j$ can be represented by the wavelet series:

$$f(x) = \sum_{k \in Z} f_{jk} \phi_{jk}(x) \tag{4}$$

The multi-resolution properties of wavelets give another advantage to represent functions in differential equations which can be solved numerically (Motard et al. 1994). Detailed information about Daubechies orthonormal wavelets can be found in Daubechies (1988).

2.4 Wavelet Orthogonal Collocation(WOC)

This method was introduced by Betoluzza and Naldi (1996) for solving partial differential equations. In 2001, it was developed and applied for solving population balance problems by Liu and Cameron (2001). The interpolation functions are generated by autocorrelation of the compactly supported Daubechies scaling functions $\phi(x)$. Then the function θ called autocorrelation function verifies the interpolation property due to the orthonormality.

$$\theta(0) = \int \phi(x)\phi(x)dx = 1 \tag{5}$$

and

$$\theta(n) = \int \phi(x)\,\phi(x-n)\,dx = 0,\ n \neq 0 \tag{6}$$

The approximate solution of our problem will be a function u_j in the term of its dyadic points to obtain the wavelet expression:

$$u_j(x) = \sum u_j\left(2^{-j} n\right)\theta\left(2^j x - n\right) \tag{7}$$

Detailed information can be found in Liu and Cameron (2001) and Bertoluza and Naldi (1996).

3. CASE STUDIES

Three case studies of population balances, which have sharp transition phenomena in their particle size distribution in the batch crystallizer, were tested in this paper. Even though the case studies considered here are simple, the analytical solutions are available for comparison purposes.

3.1 Case I: Population balance with nucleation and size-independent growth

The population balance for nucleation mechanism and size independent growth is described by the partial differential equation:

$$\frac{\partial n(x,t)}{\partial t} + G\frac{\partial n(x,t)}{\partial x} = B_0$$
$$G = 1; B_0 = \exp(-x) \tag{8}$$

where n is the number of particle (population density), x is the particle size, G is the growth rate, and B_0 is the nucleation rate.

With initial and boundary conditions such as:

$$n(t,0) = 0; \quad n(0,x) = 0 \tag{9}$$

The analytical solution for this case is:

$$n(t,x) = 1 - \exp(-x) \qquad x - t < 0$$
$$n(t,x) = \exp(-x)[\exp(-t) - 1] \qquad x - t > 0 \tag{10}$$

The dimensionless particle size L is defined as follow:

$$L = x/x,\max = [0:1]$$

Where: $x = [x,\min : x,\max] = [0:2]$

3.2 Case II: Population balance with size-independent growth only and initially seeded

One dimensional population balance for size dependent growth mechanism is described by the partial differential equation below:

$$\frac{\partial n(x,t)}{\partial t} + G\frac{\partial n(x,t)}{\partial x} = 0 \qquad G = 1 \tag{11}$$

With initial and boundary conditions such as:

$$n(t,0) = 0; \quad n(0,x) = \exp(-100(x-1)^2 \times 1/6.6) \tag{12}$$

The analytical solution for the second case is :

$$n(t,x) = \exp(-100(x - G.t - 1)^2 \times 1/6.6) \tag{13}$$

The dimensionless particle size L is defined as follow:

$$L = x/x,\max = [0:1]$$

Where: $x = [x,\min : x,\max] = [0:5]$

3.3 Case III: Seeded batch crystalliser with nucleation and growth

$$\frac{\partial n(L,t)}{\partial t} + G\frac{\partial n(L,t)}{\partial L} = B \tag{14a}$$

$$B = k_b\, M_T^j\, \Delta c^b \tag{14b}$$
$$G = k_g\, \Delta c^g \tag{14c}$$

where G is the growth rate, and B is the nucleation rate, k_g and k_b are the growth and nucleation constant, M_T is the suspension density, Δc is the supersaturation, and superscript g and b are the exponential constants for growth and nucleation rate respectively.

With initial and boundary conditions such as:

$$n(0,L) = n_0\,\delta(L - L_0)$$
$$n(t,0) = B/G \tag{15}$$

The supersaturation balance can be written as

$$\frac{d\Delta c}{dt} = \frac{3W_{S0}\,L_S^2\,G}{L_{S0}^3\,S} + \frac{3\rho\,k_v\,A_N\,G}{k_a} \tag{16}$$

where W_{S0} is the mass of seed crystals, $L_{S0}$is average size of seed crystals, L_S is the average size of growing crystals, S is the amount of solvent used, ρ is the crystal density, k_v is the volume shape factor, A_N is the total surface area of crystals, and k_a is the area shape factor.

The particle size L is defined as follow:

$$L = [L,\min : L,\max] = [400:1400]\,\mu m$$

4. RESULTS AND DISCUSSION

All the simulation results presented have been executed on an Intel(R) Core(TM) 2 CPU, with 2.00 GHz and 2.00 Gigabytes of RAM. A MATLAB® version 7.4.0.287 (R2007a) was used as the computation software to simulate the models. The built-in integrator of "ode15s" was utilised for integrating set of ordinary differential equations. The relative and absolute error of the integrator was specified at value of 10^{-3}.

4.1 Case I

The first case describes a simple population balance system which presents sharp front size distribution profiles. The PBE has a nucleation as function of size and a constant growth rate

and the analytical solution was available from (Chang et al. 1984). Four numerical schemes were applied in this case, their performance were tested in order to see the suitability, accuracy and stability of tested methods in handling the non-linearity and the sharp profile characteristic. The orthogonal collocation with finite elements (OCFE) scheme with 2 elements, which comprise of 31 grid points was applied. The other two methods were based on finite difference scheme. The upwind finite difference (U-FD) of 2 points and the biased upwind finite difference (BU-FD) of 5 points were employed. Both of them were discretised in space to generate 129 grid points. Lastly, wavelet orthogonal collocation (WOC) was used, and their performance were benchmarked with the analytical solution.

The average error (AE) was defined as the square root of sum of square error divided by the number of grid points. As it was calculated on an individual time basis, AE does not depend on the number of equations (grid points). The value of AE can illustrate the total absolute error of the grids for a certain time. A small value of AE may also illustrate a stable solution. While AE is the global error figure, the maximum error (ME) could show a local error or an overshoot from the reference value. ME was defined as the maximum value of the square root of sum of square error at a certain time.

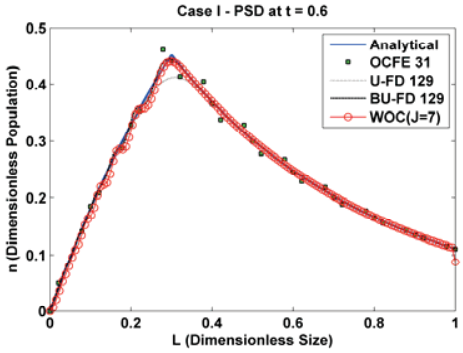

Fig. 1. Particle size distribution, case I at 0.6 seconds, simulated by four methods and compared with analytical solution.

Figure 1 shows a comparative particle size distribution (PSD) at 0.6 s. The particle distribution was initially zero and the nucleation start to generate nuclei and at the same, the born nuclei grow at a constant rate of 1.0. OCFE 31 profile produced a slightly overestimated particle density than the analytical solution. While, all the other numerical schemes, including WOC, with the same resolution gave comparable results. The simplest two points upwind scheme gave an under predicted population at the peak point, while the simulation results from biased upwind and wavelet are equivalent in term of minimising the error at the peak point. From the AE point of view, U-FD was the least while BU-FD was the first accurate then followed by WOC. When the wavelet level (J) was increased from 7 to 9, the ME values were about the same but an increased accuracy was achieved by 62%, consequently at the same time the computation time (t-CPU) was 440% higher.

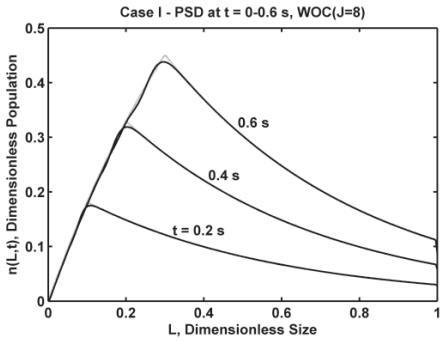

Fig. 2. Particle size distribution of WOC (J=8) at 0.2, 0.4 and 0.6 second, the black line: WOC solution and grey line: analytical solution.

In this simulation, all the computation time was short (less than 5 seconds) because all the methods have the same structure of a matrix form. Matrix to matrix calculation was superior than loop calculation (using *for* loop) for its computation time and its adaptability to a more complex case. Figure 2 shows the solutions produced by WOC (J=8) at various time from t = 0.2, 0.4 and 0.6 seconds. At this point, it can be concluded that OCFE methods can be with reasonable accuracy level and WOC method can be employed as an equivalent alternative solution for handling the case of sharp fronts profile caused by non-linear nucleation function. A question that arose is whether these methods are able to track a very sharp profile as shown in the next case.

Table 2. Numerical performance results for case I, N: grid points, AE: average error, ME: maximum error, t-CPU: computation time

Case I @ 0.6 s	N	AE	ME	t-CPU
OCFE (2)	31	0.4383	0.7861	< 1s
U-FD (2)	129	0.0082	0.0391	< 1s
BU-FD (5)	129	0.0031	0.0120	< 1s
WOC (J=7)	129	0.0064	0.0243	< 1s
WOC (J=8)	257	0.0033	0.0242	1.4 s
WOC (J=9)	513	0.0024	0.0239	4.4 s

4.2 Case II

In a seeded batch crystalliser, where the nucleation can be minimised, particle size distribution will be controlled only by the initial condition of seeding and a crystal growth. In this case, the crystal growth was assumed again constant, and the seed condition was artificially made to present a very sharp front of particle size distribution. The previous study done by Utomo, et al. (2006) reported that OCFE method cannot be applied as the unstable solutions were obtained. Moreover, the upwind finite difference scheme gave delayed solutions. Therefore, only WOC method as an equivalent method was tested in this case. The effect of wavelet resolution (J) and vanishing moments (M) were observed to closely study its performance.

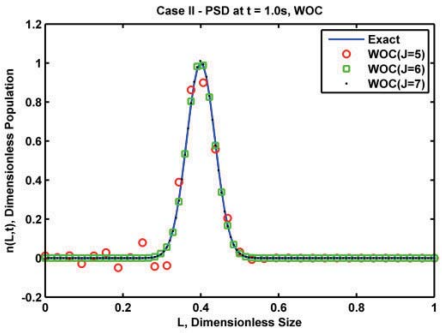

Fig. 3. Particle size distribution of WOC at t = 1s, using various J =5,6,7.

Figure 3 shows the WOC solutions with various wavelet resolution (J=5, 6, and 7) as compared to the exact analytical solution. It is clear that except for J=5, WOC presented a good validation result with high accuracy. WOC for J=5, however, not only gave a high ME but also oscillation and a negative value problem. The final solution of J=5 was stable, but early oscillation recorded the highest average error in the solution. The same problem was mentioned by (Muhr et al. 1996), can be easily rectified by decreasing the spacing or utilising adaptive gridding.

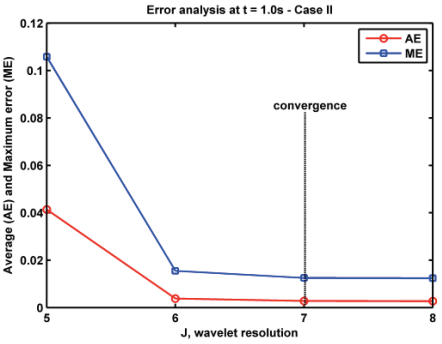

Fig. 4. The error analysis at t = 1s for various J, where AE: average error and ME: maximum error.

The convergence issue is important for numerical simulation. The WOC method for the tested resolution could easily give good convergence at a resolution as low as 6. Both AE and ME could be used for error analysis to show the convergence at a certain time. As shown in Figure 4, the convergence was actually reached as the J was increased from 6 to 7 and further increased in resolution would not give any improvement in the accuracy. The effect of vanishing moments (M) could only be observed, when the lowest resolution was applied. M = 0 and 1 were the most optimal values in giving the lowest level of error. At this stage, it can be summarised that WOC could have been also employed as an alternative for a very sharp front's profile. The selection of resolution is more sensitive to the computational performance rather than the sequential choice of vanishing moments. Selection of M becomes sensitive only when the symptom of instability was observed. To demonstrate WOC capabilities as an alternative method, the more complex population balance in a batch crystalliser case study was performed in the next section.

Table 3. Numerical performance results for case II; M: vanishing moments, N: grid points, AE: average error, ME: maximum error, t-CPU: computation time

Case II @ 1.0 s	M	N	AE	ME	t-CPU
WOC (J=5)	0	33	0.0369	0.0933	< 1.0 s
	1		0.0368	0.0933	
	2		0.0406	0.0931	
	3		0.0414	0.1058	
WOC (J=6)	0-3	65	0.0038	0.0155	< 1.0 s
WOC (J=7)	0-3	129	0.0028	0.0125	< 1.0 s
WOC (J=8)	0-3	257	0.0027	0.0124	1.3 s

4.3 Case III

The last case presents a seeded batch crystalliser with capacity of 25.5 kg solvent, running in an isothermal condition for batch time of 6000 seconds. The nucleation and growth kinetics are described in (14b) and (14c). The initial condition was the seed condition at the average size of 500 µm and the boundary condition is outlined in (15). To solve the system, a population balance equation (14a) coupled with the mass (supersaturation) balance for the solute and solid phase as in (16), thus the dynamic of crystal size distribution (CSD) can be computed. All the parameters used in this case were adopted from (Tavare et al. 1986).

For illustrative purposes, Figure 5, shows the profile of supersaturation and crystal growth rate during 6000 seconds batch operation. The initial condition of 0.015 kg/kg solvent would give a corresponding crystal growth of 1.68×10^{-10} m/s. The WOC method with J = 7 and M = 1 was employed and a reasonable result was obtained in Figure 6 as the experimental results was not available.

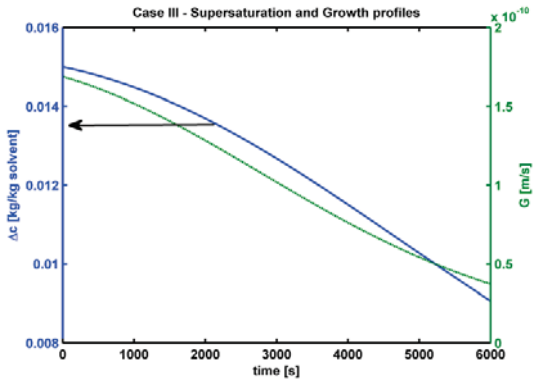

Fig. 5. Supersaturation (left) and crystal growth rate (right) profiles for case III up to 6000 seconds.

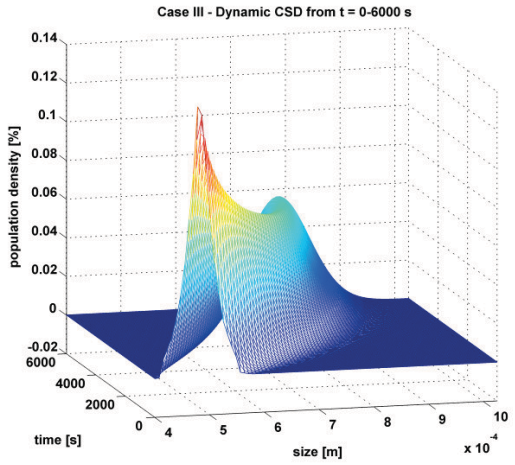

Fig. 6. Dynamic crystal size distribution for case III, for 400-1000 μm in size and 0-6000 seconds.

5. CONCLUSIONS

In this paper, three case studies which present a very sharp size distribution profile have demonstrated the potential of wavelet-based numerical scheme as an alternative in providing accurate, fast and robust solutions. Further research on a new wavelet numerical scheme and wavelet application in chemical engineering field is essentially required and promising. From the computational efficiency result shown, with the WOC algorithm, the model is suitable to be employed in online control system, however, from control engineers' perspective, low-order models are needed.

REFERENCES

Bertoluzza, S. and G. Naldi (1996). A Wavelet Collocation Method for the Numerical Solution of Partial Differential Equations. *Applied and Computational Harmonic Analysis*, 3(1), 1-9.

Chang, R.-Y. and M.-L. Wang (1984). Shifted Legendre function approximation of differential equations; application to crystallization processes. *Computers & Chemical Engineering*, 8(2), 117-125.

Chen, M.-Q., C. Hwang and Y.-P. Shih (1996). A wavelet-Galerkin method for solving population balance equations. *Computers & Chemical Engineering*, 20(2), 131-145.

Daubechies, I. (1988). Orthonormal bases compactly supported wavelets. *Communications Pure and Applied Mathematics*(41), 909-996.

Daubechies, I. (1992). Ten Lectures on Wavelets. *Philadelphia: Society for Industrial and Applied Mathematics*.

Gupta, S. K. (1995). *Numerical Methods for Engineers*. New Age International, New Delhi.

Hangos, K. and I. T. Cameron (2001). *Process Modelling and Model Analysis*. Academic Press, London.

Hounslow, M. J., R. L. Ryall and V. R. Marshall (1988). A discretized population balance for nucleation, growth and aggregation. *AIChE Journal*, 34, 1821-1832.

Hulburt, H. M. and S. Katz (1964). Some problems in particle technology : A statistical mechanical formulation. *Chemical Engineering Science*, 19(8), 555-574.

Jameson, L. (1998). A Wavelet-Optimized, Very High Order Adaptive Grid And Order Numerical Method. *Siam J. Sci. Comput.*, 19(6), 1980-2013.

Kostoglou, M. and A. J. Karabelas (1994). Evaluation of Zero Order Methods for Simulating Particle Coagulation. *Journal of Colloid and Interface Science*, 163(2), 420-431.

Kumar, S. and D. Ramkrishna (1996). On the solution of population balance equations by discretization--I. A fixed pivot technique. *Chemical Engineering Science*, 51(8), 1311-1332.

Litster, J. D., D. J. Smit and M. J. Hounslow (1995). Adjustable Discretized Population Balance for Growth and Aggregation. *AIChE Journal*, 41(3), 591-603.

Liu, Y. and I. T. Cameron (2001). A new wavelet-based method for the solution of the population balance equation. *Chemical Engineering Science*, 56(18), 5283-5294.

Mahoney, A. W. and D. Ramkrishna (2002). Efficient solution of population balance equations with discontinuities by finite elements. *Chemical Engineering Science*, 57(7), 1107-1119.

Motard, R. L. and B. Joseph (1994). *Wavelet applications in chemical engineering*. Kluwer Academic Publisher, London.

Muhr, H., R. David, J. Villermaux and P. H. Jezequel (1996). Crystallization and precipitation engineering-VI. Solving population balance in the case of the precipitation of silver bromide crystals with high primary nucleation rates by using the first order upwind differentiation. *Chemical Engineering Science*, 51(2), 309-319.

Nicmanis, M. and M. J. Hounslow (1996). A finite element analysis of the steady state population balance equation for particulate systems: Aggregation and growth. *Computers & Chemical Engineering*, 20(Supplement 1), S261-S266.

Nielsen, O. M. (1998). Wavelets in Scientific Computing. Ph.D. Thesis, Department of Mathematical Modelling, Technical University of Denmark, Lyngby.

Ramkrishna, D. (1981). Analysis of population balance--IV : The precise connection between Monte Carlo simulation and population balances. *Chemical Engineering Science*, 36(7), 1203-1209.

Ramkrishna, D. (2000). *Population balance : theory and applications to particulate systems in engineering*. Academic Press, London.

Tavare, N. S. and J. Garside (1986). Simultaneous Estimation of Crystal Nucleation and Growth Kinetics From Batch Experiments. *Chemical Engineering Research and Design*, 64(a), 109-118.

Utomo, J., N. E. Balliu and M. O. Tade (2006). Challenges of Modelling A Population Balance Using Wavelet. F. J. Doyle III, J. O. Trieweiler and A. R. Secchi (ed.),*Preprints Volume II*,643-648, IFAC, Gramado, Brazil.

Vanni, M. (2000). Approximate Population Balance Equations for Aggregation-Breakage Processes. *Journal of Colloid and Interface Science*, 221(2), 143-160.

Wouwer, A. V., P. Saucez, W. E. Schiesser and S. Thompson (2005). A MATLAB implementation of upwind finite differences and adaptive grids in the method of lines. *Journal of Computational and Applied Mathematics*, 183(2), 245-258.

Model-predictive Control Algorithms

Oral Session

Economic Dynamic Real-Time Optimization and Nonlinear Model-Predictive Control on Infinite Horizons

Lynn Würth * **James B. Rawlings** ** **Wolfgang Marquardt** ***

* *AVT - Process Systems Engineering, RWTH Aachen University, D-52056 Aachen, Germany (email: lynn.wuerth@avt.rwth-aachen.de).*
** *Dept. Chem. & Biol. Eng. - Univ. of Wisconsin. Madison (WI), USA (email: rawlings@engr.wisc.edu)*
*** *AVT - Process Systems Engineering, RWTH Aachen University, D-52056 Aachen, Germany (email: wolfgang.marquardt@avt.rwth-aachen.de).*

Abstract: This paper investigates the formulation of nonlinear model-predictive control problems with economic objectives on an infinite horizon.
The proposed formulation guarantees nominal stability for closed-loop operation. Furthermore, a novel solution method of the infinite horizon method through a transformation of the independent time variable is employed. The closed-loop optimization with infinite horizon is compared to a finite-horizon formulation. A small case study is presented for illustration purposes.

Keywords: Dynamic Real-Time Optimization, Economic Objective, Nonlinear Model-Predictive Control, Infinite Horizon, Stability.

1. INTRODUCTION

The interest in economic Dynamic Real-Time Optimization (DRTO) or Nonlinear-Model Predictive Control (NMPC) with economic objectives has increased (Backx et al. (2000), Helbig et al. (2000), Engell (2007), Rawlings and Amrit (2008), Zavala (2008)), as the development of efficient methods for solving these types of optimization problems has significantly progressed in recent years. Compared to the traditional formulation of NMPC problems with quadratic cost criteria minimizing the deviation from a fixed steady-state set-point, the economic dynamic optimization problem exploits all the dynamic degrees of freedom available to maximize the profit of the plant on a given time horizon. Furthermore, the profit is maximized at a sampling rate of high frequency, whereas the traditional steady-state optimization is performed at a slow rate and only when the process is in a steady-state. Thus, disturbances with a favorable impact on the profit can also be exploited efficiently instead of compensating them by minimizing a steady-state offset.
However, theoretical studies of DRTO and NMPC problems with economic objectives are still lacking. Huesman et al. (2008) have pointed out that certain formulations with linear economic objective functions lead to multiple solutions. They concluded that some degrees of freedom are left for optimization. These degrees of freedom can be exploited by introducing a second optimization problem to improve the operability.
Rawlings and Amrit (2008) have shown that in order to optimize process economics it is sometimes advantageous not to reach the steady-state quickly. Secondly, they pointed out that the formulation with an economic objective results in characteristic trajectories behaving like a turnpike. The trajectory is attracted to a constant path and finally moves away from the constant path at the end of the horizon. The turnpike is a characteristic property of the economic optimization problem with finite-horizon, which has been introduced and studied in the economics literature before (Carlson et al., 1991).
In the economics literature an infinite horizon formulation is often employed. Infinite horizons have also been considered in the MPC literature as stabilizing although impractical for online application. A review of methods providing stability but circumventing infinite horizons by adding a terminal constraint, a terminal cost function, or by employing a terminal constraint set with a local stabilizing controller have been reviewed by Mayne et al. (2000).

An infinite-horizon formulation for (nonlinear) economic dynamic optimization on a receding horizon is explored in this paper. There are several advantages related to an infinite horizon formulation:

(1) The somewhat arbitrary choice of the final time of the optimization horizon is avoided. A natural formulation of the optimization problem is achieved for continuous processes if the final time is not specified.
(2) The infinite-time horizon formulation leads to closed-loop operation with guaranteed stability. This property was also exploited in the literature of linear MPC, where the infinite-horizon formulation can

be transformed into a finite horizon formulation by adding a terminal term to the cost functional (Muske and Rawlings, 1993).

In the following, the formulation of the economic optimization problem will be investigated and a comparison between finite and infinite horizon problems will be carried out. A new approach is presented for solving the infinite-horizon problem numerically. We use a transformation of the infinite-time onto a finite-time horizon and combine this transformation with an adaptive discretization. As already noted in the literature investigating stability in MPC, very long horizons provide stable control but lead to high computational costs. Many solution methods employed in MPC use a discretization of the control variables with a uniform spacing of grid points. An alternative adaptive discretization (Schlegel et al., 2005) introduces grid points mainly within the transient parts of the profile and reduces the computational load. Note that this method can also be applied to solve the infinite-horizon problem in the MPC regulator case to track a given set-point.

2. ECONOMIC DRTO PROBLEM

2.1 Finite-Horizon Formulation

The moving horizon formulation of the DRTO problem is similar to the formulation used in nonlinear model-predictive control, although an economic objective is chosen to provide an economically optimal operation at all times (Helbig et al., 2000). The moving horizon problem is defined as follows:

$$\min_{\boldsymbol{u}^j(t)} \Phi(\boldsymbol{x}, \boldsymbol{u}, t_0, t_f) \tag{1}$$

$$\text{s.t.} \quad \dot{\boldsymbol{x}}(t) = \boldsymbol{f}(\boldsymbol{x}(t), \boldsymbol{u}^j(t)), \tag{2}$$

$$\boldsymbol{y}(t) = \boldsymbol{g}(\boldsymbol{x}(t), \boldsymbol{u}^j(t)), \tag{3}$$

$$\boldsymbol{x}(t^j) = \hat{\boldsymbol{x}}^j, \tag{4}$$

$$\boldsymbol{0} \geq \boldsymbol{h}(\boldsymbol{x}(t), \boldsymbol{y}(t), \boldsymbol{u}^j(t)), \tag{5}$$

$$\boldsymbol{0} \geq \boldsymbol{e}(\boldsymbol{x}(t_f^j)), \tag{6}$$

$$t \in [t^j, t_f^j], \tag{7}$$

$$t^j := t^{j-1} + \Delta t, \tag{8}$$

$$j = 0, 1, ...J. \tag{9}$$

$\boldsymbol{x}(t) \in \mathbb{R}^{n_x}$ are state variables with initial conditions $\hat{\boldsymbol{x}}^j$; $\boldsymbol{y}(t) \in \mathbb{R}^{n_y}$ are algebraic output variables. The dynamic process model (2) is given by $\boldsymbol{f}(\cdot)$. The time-dependent control variables $\boldsymbol{u}(t) \in \mathbb{R}^{n_u}$ are degrees of freedom for the optimization problem. The optimization problem is solved on the time horizon $[t^j, t_f^j]$ at each sampling instant t^j; the control is implemented on the current sampling interval (assuming negligible computational time), and the optimization horizon is then shifted by the sampling interval Δt. Equations (5) and (6) describe the path constraints $\boldsymbol{h}(\cdot)$ on the input and state variables and the endpoint constraints $\boldsymbol{e}(\cdot)$ on the state variables. Process operation is determined by economic decision criteria, which enter into the definition of the objective function $\Phi(\cdot)$. Exemplarily the profit function can be defined as

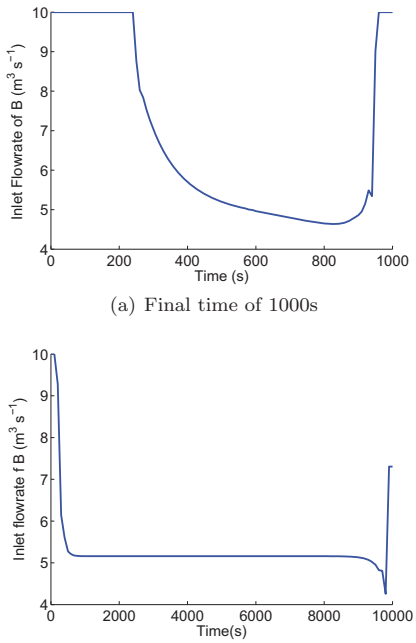

(a) Final time of 1000s

(b) Final time of 10000s

Fig. 1. Finite horizon

$$\Phi = -\int_0^T (c_{prod}\dot{n}_{prod} - c_{reac}\dot{n}_{reac} - \dot{q})dt, \tag{10}$$

where c_{prod} and c_{reac} are the costs of the products and reactants, and $\dot{n}_{prod}$ and $\dot{n}_{reac}$ are the flowrates of the products and reactants. The term $\dot{q}$ includes utility costs, depreciation, and other expenses.

If we choose a finite horizon in a dynamic optimization problem with economic objective, we often observe a so-called turnpike effect when looking at the solution profile (Rawlings and Amrit (2008), Carlson et al. (1991)). The turnpike effect means that the trajectory spends most time at a balanced equilibrium path, which is independent of the initial condition and the final time. Under certain conditions, this turnpike reduces to a singleton. In that case, the characteristic behavior is that the trajectory is attracted by a stationary path, at a certain time t_m and stays on this constant path, until it reaches a point t_n close to the end of the horizon and moves away from the path at the end of the horizon. This gives rise to trajectories as shown in Figure 1. The trajectories represent the inlet flowrate of the reactant of the CSTR presented in Section 5; they were computed for different final times. In these figures the solution path strongly depends on the choice of the final time. In the first figure, the final time is not long enough to let the process reach the turnpike. However, if a long horizon is chosen, the process gets on a constant path $\bar{k}$ (Carlson et al., 1991). The optimal steady-state path represents an attractor for the finite horizon path.

In practice, often a long horizon length is chosen to achieve closed-loop stability (Mayne et al., 2000). For stable plants, the final time T is often chosen to be large compared to the settling time of the plant. The somewhat arbitrary choice of the final time suggests that more

research is required to reconsider the current formulations and to look for adequate formulations of economic dynamic optimization problems providing stability in closed loop.

2.2 Infinite Horizon Formulation

For a given optimal trajectory, according to Bellmann's optimality principle, the trajectory starting from any point on the optimal trajectory is optimal for the corresponding problem initiated at that point on the trajectory. This implies that the formulation of the optimization problem on an infinite horizon is providing stability in closed loop.

If the profit function is optimized on a long or an infinite horizon, the time value of money should be accounted for. This is accomplished through the parameter ρ discounting the future profit to the present value. If we deal with discrete payment periods, discounting the future amounts to today's value can be included in the calculation of the net present value. The objective function maximizing the net present value of cash flows C_k in N discrete time periods and with discounting rate ρ is formulated as

$$\Phi = \sum_{k=0}^{N} \frac{C_k}{1+\rho^k}, \tag{11}$$

where k is the index of the time period. In this work we investigate an objective function with continuous discounting on an infinite horizon:

$$\Phi = -\int_0^\infty e^{-\rho t}(c_{prod}\dot{n}_{prod} - c_{reac}\dot{n}_{reac} - \dot{q})dt. \tag{12}$$

The exponential formulation is usually employed for optimal control problems in continuous time and is equivalent to the discrete-time formulation in equation (11). Both formulations use, however, the same discount factor ρ, which can be chosen as the annual market interest rate.

Note that researchers in macroeconomics have included infinite horizons in their problem formulations very early to model e.g. economic growth (Barro and Sala-i-Martin, 1995). This is due to the fact that there is no natural finite time in these types of problems and the consequences of investment are very long-lived. Since this theory is not well-known in the systems and control community, an example of an economic growth model by Cass (1966) is shown here for illustration of the economic growth problem formulation:

$$y(t) = f(k(t)) \tag{13}$$
$$c(t) = y(t) - z(t) \tag{14}$$
$$\dot{k}(t) = z(t) - \mu k(t) \tag{15}$$
$$k(0) = k_0 \tag{16}$$

$k(t)$ is the stock of capital accumulated at time t. The production function $f(\cdot)$ associates an output y with the capital stock k. The output $y(t)$ can be either consumed at a rate $c(t)$ or invested at a rate $z(t)$. The capital stock depreciates at a constant rate μ. Cass (1966) considered the welfare functional

$$W = \int_0^T e^{-\rho t}U(c(t))dt, \tag{17}$$

where $U(c)$ is the concave utility function depending on the level of consumption $c(t)$. The maximization of W is the standard optimal control problem and the final time T is often assumed to be infinite in economic growth theory. If the discount factor ρ is strictly positive, the objective function on an infinite horizon is bounded. However, if the discount factor is zero, the objective function becomes unbounded. Methods for reducing the unbounded objective on an infinite horizon to finite rewards have been presented by Carlson et al. (1991). We consider in this paper the case where the discount factor is positive, as it seems to be a reasonable assumption to include the time value of money on a long or infinite-time horizon. The discount factor is chosen in the range of the interest rate of the market.
Very few numerical solution methods exist in the literature of mathematical economics to solve the infinite-time horizon problem. Often, the indirect methods of optimal control are used to derive the First-Order Necessary Conditions of Optimality and a two-point boundary-value problem has to be solved. In the following, we will apply a numerical solution method with adaptive grid refinement to solve nonlinear infinite-horizon problems.

3. INFINITE HORIZON SOLUTION APPROACH

Solving the infinite-horizon problem is not straightforward and several attempts approximating the infinite horizon with finite horizons or reformulating the infinite-time problem exist in the literature.

3.1 Time Transformation

A common approach replaces the infinite-time horizon by a finite-time horizon, thereby introducing a truncation error. A second possibility is to use a variable transformation to transform the infinite-horizon into a finite-horizon problem. We choose the second approach in this work, since it does not introduce truncation errors and allows to obtain a solution of higher accuracy of the optimization solution on the infinite horizon.
The infinite horizon with $t \in [0, \infty)$ can be transformed into a finite horizon with $\tau \in [0, 1]$ using the variable transformation

$$\tau = t/(1+t) \tag{18}$$

of the independent variable t. A similar variable transformation was presented by Kunkel and Hagen (2000) to obtain solutions of the infinite-horizon optimal control problem. The variable transformation of eq. (2) yields the transformed system:

$$\frac{d\boldsymbol{x}}{d\tau} = \frac{\boldsymbol{f}(\boldsymbol{x}(\tau), \boldsymbol{u}(\tau))}{(1-\tau)^2}. \tag{19}$$

We can see that a singularity is introduced at $\tau = 1$, which corresponds to $t = \infty$.
In order to study the singularity at $\tau = 1$, we will restrict the analysis to the scalar system

$$\frac{dx}{d\tau} = \frac{f(x(\tau))}{(1-\tau)^2}. \tag{20}$$

The eigenvalue problem corresponding to eq. (19) is

$$\frac{dx}{d\tau} = \frac{\lambda x}{(1-\tau)^2}. \tag{21}$$

The general solution of this differential equation is

$$x(\tau) = ce^{\frac{\lambda}{1-\tau}}. \tag{22}$$

If we assume that the system is within the region of attraction of a stable steady-state, we obtain the limit

$$\lim_{\tau \to 1} c e^{\frac{\lambda}{1-\tau}} = 0, \quad (23)$$

if $\lambda < 0$ and the system will reach steady-state as $\tau \to 1$.

However, if $\lambda > 0$, the system is unstable, and

$$\lim_{\tau \to 1} c e^{\frac{\lambda}{1-\tau}} = \infty. \quad (24)$$

In that case we have to handle the singularity at $\tau = 1$ by imposing a boundary condition at final time. The steady-state solution can be imposed as terminal boundary condition. If we are dealing with an unstable system, a numerical solution approach different from the single-shooting method presented in the following section must be employed. The boundary value problem problem could be solved using multiple-shooting or orthogonal collocation methods. In order to generalize the analysis of the singularity above, an extension to the multivariable case should be performed including an analysis of the stable and unstable modes of the system.

3.2 Adaptive Discretization

The continuous control variables in optimization problem (1) are discretized after the time transformation with eq. (18) using piecewise-constant or piece-wise linear approximations. The discretization and the formulation of the NLP for the piecewise constant approximation reads as

$$\mathbf{u}_i(\tau_k) = \mathbf{c}_{\mathbf{u}_{i,k}}, k = 1, ..., N, i = 1, ..., n_u, \quad (25)$$

where N is the number of discretization intervals and n_u the number of control variables. Choosing the discretized controls $\mathbf{z}_i := [\mathbf{c}_{\mathbf{u}_{i,k}}]$, as the n_z optimization variables, the dynamic optimization problem can be transcribed into the NLP

$$\min_{\boldsymbol{z}} f(\boldsymbol{z}) := \Phi(\boldsymbol{z}) \quad (26)$$

$$\text{s.t. } \boldsymbol{g}(\boldsymbol{z}) \geq 0. \quad (27)$$

The nonlinear program can be solved by employing a standard SQP algorithm. Since the optimization algorithm requires repetitive function evaluations and gradients, the objective function Φ, constraints $\mathbf{g}(\cdot)$ and their gradients are evaluated by a simultaneous integration of the process model and the sensitivity equation system.
The optimization problem is solved using the dynamic optimization software DyOS (2002), which adopts an adaptive control vector parameterization (Schlegel et al., 2005). The adaptation is done using a refinement method based on a wavelet analysis of the control profile. If the horizon of the optimization problem is infinite or has a long finite time, an adaptive discretization is essential to deal with the computational load associated with these long or infinite horizons. The adaptive discretization allows to introduce the grid points selectively in transient regions of the control profile, and therefore avoids overloading the optimization problem with many optimization parameters. Furthermore, a highly accurate solution profile can be obtained.

3.3 Closed-loop Implementation

The solution approach outlined in the previous section is implemented in an algorithm for closed-loop dynamic optimization. The optimization is performed on the transformed timehorizon $[0, 1]$, and the results are converted back to the original timehorizon.

for $j = 1, N$ (number of sample intervals) **do**

(1) **Solve** the optimization problem (26), where the control variables $\boldsymbol{u}^j(\tau)$ have been discretized on $[0, 1]$, to obtain the solution $\boldsymbol{z}^j$.
(2) **Transform** the control variables $\boldsymbol{u}^j(\tau)$, $\tau \in [0, 1]$ back to the original representation $\boldsymbol{u}^j(t)$, $t \in [0, \infty)$.
(3) **Implement** the control variables $\boldsymbol{u}^j(t)$ for one sampling interval $[t_j, t_{j+1}]$. Get measurements and compute state estimates.
(4) **Horizon shift:** Reduce the time horizon by one sampling interval and use the shifted solution as initial guess for the next optimization problem.
(5) **Transform** the shifted variables $\boldsymbol{u}^j(t)$ to the finite horizon representation $\boldsymbol{u}^j(\tau)$, $\tau \in [0, 1]$ using eq. (18).

end for

4. INFINITE-HORIZON NMPC

Apart from the economic dynamic optimization problem, the presented solution method for infinite-horizon formulations can also be used for the NMPC regulator problem, if we deal with a pure tracking problem. In that case the economic objective function is replaced by the quadratic objective function

$$\Phi = \int_0^\infty (\Delta \boldsymbol{u}^T \boldsymbol{Q} \Delta \boldsymbol{u} + (\boldsymbol{y}^{set} - \boldsymbol{y})^T \boldsymbol{W} (\boldsymbol{y}^{set} - \boldsymbol{y})) dt, \quad (28)$$

minimizing the deviation from fixed set-points $\boldsymbol{y}^{set}$ and the control moves $\Delta \boldsymbol{u}$. As a finite horizon is traditionally used in NMPC, some methods guarantee closed-loop stability by introducing e.g. a terminal constraint. However, introducing a terminal constraint can lead to feasibility problems. By employing the infinite-horizon solution method, the disadvantages of the finite-horizon methods to guarantee closed-loop stability can be avoided.

5. CASE STUDY

The approach is applied to the benchmark case of the Williams-Otto continuous stirred tank reactor, as introduced by Forbes (1994). The reactions taking place in the reactor are

$$A + B \xrightarrow{k_1} C, \; C + B \xrightarrow{k_2} P + E, \; P + C \xrightarrow{k_3} G.$$

Reactant A is already present in the reactor, whereas reactant B is fed continuously to the reactor. During the exothermic reactions the desired products P and E as well as the side-product G are formed. At the end of the batch, the conversion to the main products P and E should be maximized. During the batch, constraints on the inlet flow rate of reactant B ($F_{B_{in}}$) and the reactor temperature (T_r) must be fulfilled. The manipulated control variables of this process are $F_{B_{in}}$ and T_r. The CSTR is assumed to be well-mixed and the dynamics of the cooling system are neglected. The reactor system is open-loop stable and therefore the singularity issues at $\tau = 1$ do not arise in this case study.

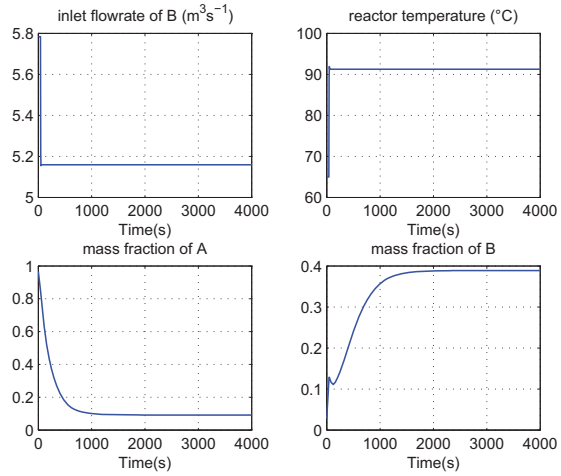

(a) Infinite horizon, open-loop

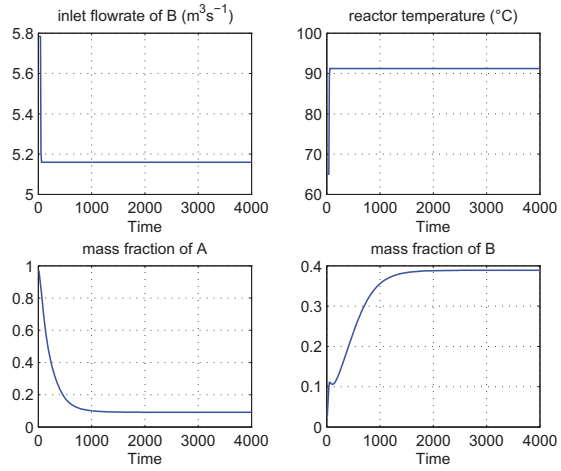

(b) Infinite horizon, closed-loop

Fig. 2. Infinite horizon results

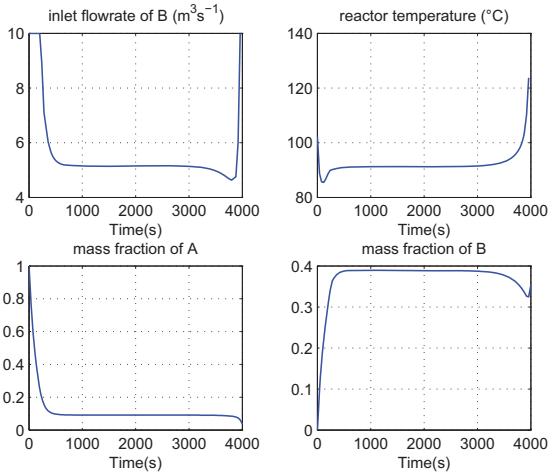

(a) Finite horizon, open-loop

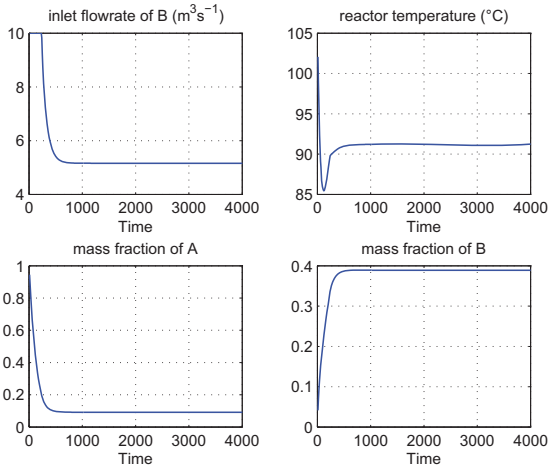

(b) Finite horizon, closed-loop

Fig. 3. Finite horizon results

5.1 Economic DRTO Problem

The economic objective is to maximize the profit, which consists of the revenue obtained from the products minus the costs of the reactants over the infinite time horizon. Furthermore, an annual discount rate of 5% is chosen to account for the time value of money. The optimization problem is formulated as follows:

$$\max_{F_{B_{in}}(t),T_r(t)} \Phi = \int_0^\infty e^{-\rho t}(c_p\dot{n}_p + c_e\dot{n}_e - c_a\dot{n}_a - c_b\dot{n}_b)dt \tag{29}$$

s.t. *process model*, and

$$0\frac{\text{kg}}{\text{sec}} \leq F_{B_{in}}(t) \leq 5.784\frac{\text{kg}}{\text{sec}}, \tag{30}$$

$$0\ ^\circ\text{C} \leq T_r(t) \leq 150\ ^\circ\text{C}. \tag{31}$$

5.2 Closed-Loop Results

The economic performance of the operation of the CSTR is optimized for both infinite and finite horizon formulations on a receding horizon. The results for the infinite-horizon case are shown in Figure 2. The open-loop optimization problem is solved using the time transformation for $\tau \in [0, 1]$ and the results are simulated on a long horizon in the original time variable. The closed-loop results are obtained using the algorithm with adaptive grid refinement as sketched in Section 3.3. Figure 2 shows that the nominal trajectories in open-loop and closed-loop are almost identical except minor deviations due to the online adaptation scheme. This result confirms that the solution of the optimal problem on an infinite horizon in closed-loop is providing a nominally stable control with an economic objective. Furthermore, the computational effort has been low as only few degrees of freedom are required in the adaptive grid refinement approach. It is interesting to observe that the control variables reach their steady-state values very fast, but the state variables require more time to reach the steady-state values.

The results for the finite-horizon formulation with a final time of 4000 s are shown in Figure 3. In this case, the open-loop trajectory shows the turnpike behavior. Since

only the first control interval is implemented in closed-loop, the end of the trajectory in open-loop is actually never implemented. This leads to a discrepancy between the open-loop and the closed-loop behavior, as Bellmann's optimality principle is not fulfilled. Nevertheless, the figures show that the system reaches the steady-state quite fast.

Comparing the closed-loop results obtained with the infinite- and the finite-time horizon formulation, the figures show that the transient part of the trajectories at the beginning is quite different, but that the steady-states obtained after a certain time are identical. The temperature profile is different in the infinite-horizon (Figure 2.b) and the finite-horizon cases (3.b), as the temperature increases from 65 °C to 90 °C in (2.b) and the temperature decreases from 102 °C to 91 °C in (3.b). It was observed that this difference only occurs for relatively short horizons. If the final time chosen for the finite-horizon case increases, the trajectory of the finite-horizon case approximates the infinite-horizon case more closely. As expected, the longer the horizon becomes, the closer the solution of the finite-horizon problem will be to the infinite-time solution. This is due to the fact that the transient parts of the trajectories have less impact on the profit function for increasing length of the time horizon. As the same steady-state is reached by both finite- and infinite-time horizon formulations, the same profit is also obtained at steady-state.

These results show that also the finite-horizon formulation with economic objective can provide closed-loop stability, as the system gets on the turnpike (which corresponds to a stationary path in this case) and stays there for most of the time. Hence, by choosing a long time horizon it is possible to achieve closed-loop nominal stability, because the trajectory is attracted to the stationary path. However, as shown in Figure (1.a), if the finite time horizon is not long enough the resulting trajectories will not reach the optimal stationary path.

6. CONCLUDING REMARKS

The closed-loop solution of nonlinear DRTO or NMPC problems was studied. Nominal stability in closed-loop economic optimization is achieved via an infinite-horizon formulation. The comparison of the infinite- to the finite-horizon formulation shows that the formulation of DRTO problems on finite horizons can also provide closed-loop stability, if the optimization time horizon is chosen long enough such that the trajectory is attracted to a constant path.

Secondly, a new numerical approach was introduced for solving infinite-horizon problems addressed in NMPC and DRTO. The method achieves high computational accuracy because the infinite horizon is transformed into a finite horizon through a simple variable transformation. The advantage is that the truncation error occurring by choosing an arbitrary final time is avoided. Furthermore, the computational load is still low because of adaptive grid refinement resulting in low number of degrees of freedom for optimization.

In the future, it is of interest to further investigate the properties of the finite-horizon economic optimization problem required to achieve closed-loop stability. On the other hand, the infinite-horizon formulation with adaptive grid refinement is a promising approach to guarantee closed-loop stability. The solution method for infinite-horizon problems will be further developed and extended to open-loop unstable systems.

REFERENCES

Backx, T., Bosgra, O., and Marquardt, W. (2000). Integration of model-predictive control and optimization of processes. In *IFAC Symposium "Advanced Control of Chemical Processes", ADCHEM 2000*, 249–260. Pisa, Italy.

Barro, R. and Sala-i-Martin, X. (1995). *Economic Growth*. McGraw-Hill Advanced Series in Economics.

Carlson, D.A., Haurie, A.B., and Leizarowitz, A. (1991). *Infinite Horizon Optimal Control*. Springer Verlag.

Cass, D. (1966). Optimal growth in an aggregative model of capital accumulation, a turnpike theorem. *Econometrica*, 34, 833–850.

DyOS (2002). *DyOS User Manual*. Process Systems Engineering, Aachener Verfahrenstechnik, RWTH Aachen University.

Engell, S. (2007). Feedback control for optimal process operation. *Journal of Process Control*, 17, 203–219.

Forbes, J. (1994). *Model Structure and Adjustable Parameter Selection for Operations Optimizations*. Ph.D. thesis, McMaster University, Hamilton, Canada.

Helbig, A., Abel, O., and Marquardt, W. (2000). Structural concepts for optimization based control of transient processes. In F. Allgöwer and A. Zheng (eds.), *Nonlinear Model Predictive Control*, volume 26 of *Progress in Systems and Control Theory*, 295–311. Birkhäuser, Basel.

Huesman, A.E.M., Bosgra, O.H., and den Hof, P.M.J.V. (2008). Integrating MPC and RTO in the process industry by economic dynamic lexicographic optimization; an open-loop exploration. In *Proceedings of the 2008 AICHE Annual Meeting*. Philadelphia, USA.

Kunkel, P. and Hagen, O.V.D. (2000). Numerical solution of infinite-horizon optimal control problems. *Computational Economics*, 16(3).

Mayne, D.Q., Rawlings, J.B., RAO, C.V., and Scokaert, P.O.M. (2000). Constrained model predictive control: Stability and optimality. *Automatica*, 36(6), 789–814.

Muske, K.R. and Rawlings, J.B. (1993). Model predictive control with linear models. *A.I.Ch.E. Journal*, 39(2), 262–287.

Rawlings, J.B. and Amrit, R. (2008). Optimizing process economic performance using model predictive control. In *Assessment and Future Directions of Nonlinear Model Predictive Control*. Pavia, Italy.

Schlegel, M., Stockmann, K., Binder, T., and Marquardt, W. (2005). Dynamic optimization using adaptive control vector parameterization. *Comp. & Chem. Eng.*, 29(8), 1731–1751.

Zavala, V. (2008). *Computational Strategies for the Optimal Operation of Large-Scale Chemical Processes*. Ph.D. thesis, Carnegie Mellon University.

Soft Constraints for Robust MPC of Uncertain Systems

Guru Prasath [*,**] **John Bagterp Jørgensen** [**,1]

[*] *FLSmidth Private Limited. Automation Division*
Chennai, India (e-mail: mgp-in@flsaindia.co.in)

[**] *Informatics and Mathematical Modelling*
Technical University of Denmark, DK-2800 Kgs. Lyngby, Denmark
(e-mail: jbj@imm.dtu.dk).

Abstract: In this paper we develop a robust constrained predictive controller for linear systems. The controller is equipped with soft output constraints that are used in a novel way to have robustness against model plant mismatch. By simulation we compare the performance of the new robust constrained predictive controller to a nominal predictive controller. In the nominal case, the performance of the robust predictive controller is comparable to the performance of the nominal predictive controller. In the case of plant model mismatch, the robust predictive controller performs significantly better than the nominal predictive controller.

Keywords: Linear Model Predictive Control, Robust Predictive Control, Soft Constraints

1. INTRODUCTION

Model predictive control has become a standard technology in high level control of chemical processes. However, little advice is available regarding tuning methodologies of such controllers in the face of the inevitable plant model mismatch. The closed-loop performance of nominal linear model predictive control can be quite poor when the models are uncertain. Consequently, some years after commissioning, many high-level control systems are turned off due to bad closed-loop performance. This is often due to changes in the plant dynamics caused by wear and tear combined with lack of the necessary human resources at the plant to re-tune and maintain the MPC. Model predictive controllers with robust performance against model-plant mismatch is therefore crucial in long-term maintenance and success of MPC system. Using soft output constraints in a novel way, we demonstrate by simulation that the poor performance of predictive control in the case of plant model mismatch can be improved significantly. Therefore, we suggest use of the soft constraints to tune and improve the performance of linear model predictive control.

Specifically, we investigate the effect of uncertain models on the performance of a regularized l_2 model predictive controller with input constraints, input-rate constraints and soft output constraints (Maciejowski, 2002; Goodwin et al., 2005; Qin and Badgwell, 2003). Previously, the soft output constraints have been used to replace hard output constraint and guarantee feasibility (Scokaert and Rawlings, 1999). We use the soft output constraints to create a dead zone around the set point and demonstrate by simulation that the performance of such an MPC does not degrade much in the nominal case but improves significantly in the case of plant model mismatch. This technique is similar but not identical to the funnels used by Honeywell in RMPC (Qin and Badgwell, 2003; Havlena and Lu, 2005; Havlena and Findejs, 2005). Compared to classical process control, our use of the soft constraints has some similarities to PID control with dead zones (Shinskey, 1988).

We use a finite impulse response (FIR) model for prediction of the process outputs. In contrast to state space parameterizations, the FIR model is in a form that can easily be applied in robust predictive control, i.e. predictive control based on robust linear programming or second-order cone programming (Hansson, 2000; Vandenberghe et al., 2002; Boyd and Vandenberghe, 2004). To facilitate comparative performance studies of l_2 and robust MPC, a FIR based l_2-MPC benchmark has been established (Prasath and Jørgensen, 2008). The soft output constraint included in the MPC acts as a dead zone to the controller to reduce its sensitivity to noise and uncertainty when the process output is close to its target. This use of soft constraints for robustness is new, simple, and gives good performance. Bemporad and Morari (1999) provide an excellent survey of methodologies for robust model predictive control.

This paper is organized as follows. We derive the predictive controller consisting of a regulator and an estimator with soft output constraints in Section 2. Section 3 illustrates by simulation the performance of MPC with and without soft constraints for both deterministic and stochastic processes. Conclusions are given in Section 4.

2. FIR MODEL BASED MPC

Model predictive control systems consist of an estimator and a regulator as illustrated in Figure 1. The inputs to

[1] Corresponding author.

the MPC are the target values, r, for the process outputs, z, and the measured process outputs, y. The output from the MPC is the manipulated variables, u.

2.1 Plant and Sensors

The plant is assumed to be a linear state space system

$$\boldsymbol{x}_{k+1} = A\boldsymbol{x}_k + Bu_k + B_d d_k + G\boldsymbol{w}_k \tag{1a}$$
$$\boldsymbol{z}_k = C\boldsymbol{x}_k \tag{1b}$$

with x being the states, u being the manipulated variables (MVs), d being unmeasured disturbances, and w being stochastic process noise. z denotes the controlled variables (CVs). The measured outputs, y, are the controlled outputs, z, corrupted by measurement noise, v. Consequently

$$\boldsymbol{y}_k = \boldsymbol{z}_k + \boldsymbol{v}_k \tag{1c}$$

The initial state, the process noise, and the measurement noise are assumed to be normally distributed stochastic vectors

$$\boldsymbol{x}_0 \sim N(\bar{x}_0, P_0) \tag{2a}$$
$$\boldsymbol{w}_k \sim N_{iid}(0, Q) \tag{2b}$$
$$\boldsymbol{v}_k \sim N_{iid}(0, R) \tag{2c}$$

The measured output, y, is the signal available for feedback and used by the estimator. u is the signal generated by the control system and implemented on the plant.

2.2 Regulator

Stable processes can be represented by the finite impulse response (FIR) model

$$z_k = b_k + \sum_{i=1}^{n} H_i u_{k-i} \tag{3}$$

in which $\{H_i\}_{i=1}^n$ are the impulse response coefficients (Markov parameters). b_k is a bias term generated by the estimator. b_k accounts for discrepancies between the predicted output and the actual output. In this paper, the output predictions used by the regulator are based on the FIR model (3). Consequently, using the FIR model (3), the regularized l_2 output tracking problem with input and soft output constraints may be formulated as

$$\min_{\{z,u,\eta\}} \phi = \frac{1}{2}\sum_{k=0}^{N-1} \|z_{k+1} - r_{k+1}\|^2_{Q_z} + \|\Delta u_k\|^2_{S_u} + \sum_{k=1}^{N} \frac{1}{2}\|\eta_k\|^2_{S_\eta} + s'_{\eta_k}\eta_k \tag{4a}$$

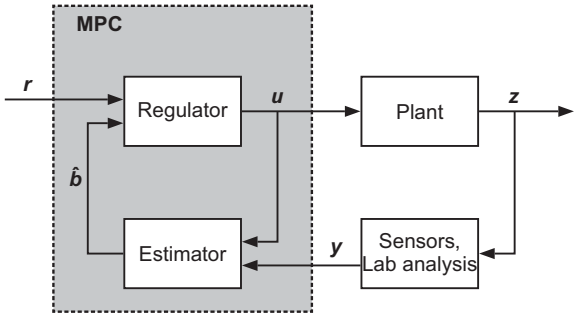

Fig. 1. Generic model predictive control system.

subject to the constraints

$$z_k = b_k + \sum_{i=1}^{n} H_i u_{k-i} \qquad k = 1, \ldots, N \tag{4b}$$
$$u_{\min} \le u_k \le u_{\max} \qquad k = 0, \ldots, N-1 \tag{4c}$$
$$\Delta u_{\min} \le \Delta u_k \le \Delta u_{\max} \qquad k = 0, \ldots, N-1 \tag{4d}$$
$$z_k \le z_{\max,k} + \eta_k \qquad k = 1, \ldots, N \tag{4e}$$
$$z_k \ge z_{\min,k} - \eta_k \qquad k = 1, \ldots, N \tag{4f}$$
$$\eta_k \ge 0 \qquad k = 1, \ldots, N \tag{4g}$$

in which $\Delta u_k = u_k - u_{k-1}$. In this formulation, the control and the prediction horizon are identical. If desired, a prediction horizon longer than the control horizon could be included in the formulation. However, we prefer instead to select the control horizon sufficiently long such that any boundary effects at the end of the horizon has no influence on the solution in the beginning of the horizon. (4) can be converted to a constrained linear-quadratic optimal control problem. Efficient algorithms exists for the solution of such problems with long prediction horizons, N. In this paper we adopt another approach and formulate a dense quadratic program in standard form that is equivalent with (4).

Define the vectors Z, R, U and η as

$$Z = \begin{bmatrix} z_1 \\ z_2 \\ \vdots \\ z_N \end{bmatrix} \quad R = \begin{bmatrix} r_1 \\ r_2 \\ \vdots \\ r_N \end{bmatrix} \quad U = \begin{bmatrix} u_0 \\ u_1 \\ \vdots \\ u_{N-1} \end{bmatrix} \quad \eta = \begin{bmatrix} \eta_1 \\ \eta_2 \\ \vdots \\ \eta_N \end{bmatrix} \tag{5}$$

Then the predictions by the impulse response model (4) may be expressed as

$$Z = c + \Gamma U \tag{6}$$

For the case $N = 6$ and $n = 3$, Γ is assembled as

$$\Gamma = \begin{bmatrix} H_1 & 0 & 0 & 0 & 0 & 0 \\ H_2 & H_1 & 0 & 0 & 0 & 0 \\ H_3 & H_2 & H_1 & 0 & 0 & 0 \\ 0 & H_3 & H_2 & H_1 & 0 & 0 \\ 0 & 0 & H_3 & H_2 & H_1 & 0 \\ 0 & 0 & 0 & H_3 & H_2 & H_1 \end{bmatrix}$$

and c is

$$c = \begin{bmatrix} c_1 \\ c_2 \\ c_3 \\ c_4 \\ c_5 \\ c_6 \end{bmatrix} = \begin{bmatrix} b_1 + (H_2 u_{-1} + H_3 u_{-2}) \\ b_2 + (H_3 u_{-1}) \\ b_3 \\ b_4 \\ b_5 \\ b_6 \end{bmatrix}$$

Similarly, for the case $N = 6$, define the matrices Λ and I_0 by

$$\Lambda = \begin{bmatrix} I & 0 & 0 & 0 & 0 & 0 \\ -I & I & 0 & 0 & 0 & 0 \\ 0 & -I & I & 0 & 0 & 0 \\ 0 & 0 & -I & I & 0 & 0 \\ 0 & 0 & 0 & -I & I & 0 \\ 0 & 0 & 0 & 0 & -I & I \end{bmatrix} \quad I_0 = \begin{bmatrix} I \\ 0 \\ 0 \\ 0 \\ 0 \\ 0 \end{bmatrix}$$

Define $s_\eta = \begin{bmatrix} s'_{\eta_1} & s'_{\eta_2} & \ldots & s'_{\eta_N} \end{bmatrix}'$ and

$$\mathcal{Q}_z = \begin{bmatrix} Q_z & & & \\ & Q_z & & \\ & & \ddots & \\ & & & Q_z \end{bmatrix} \quad \mathcal{S}_i = \begin{bmatrix} S_i & & & \\ & S_i & & \\ & & \ddots & \\ & & & S_i \end{bmatrix}$$

with $i = \{u, \eta\}$. Then the objective function (4) may be expressed as

$$\begin{aligned}
\phi &= \frac{1}{2}\sum_{k=0}^{N-1} \|z_{k+1} - r_{k+1}\|^2_{Q_z} + \|\Delta u_k\|^2_{S_u} \\
&\qquad + \frac{1}{2}\|\eta_{k+1}\|^2_{S_\eta} + s'_{\eta_{k+1}}\eta_{k+1} \\
&= \frac{1}{2}\|Z - R\|^2_{\mathcal{Q}_z} + \frac{1}{2}\|\Lambda U - I_0 u_{-1}\|^2_{\mathcal{S}_u} \\
&\qquad + \frac{1}{2}\|\eta\|^2_{\mathcal{S}_\eta} + s'_\eta\eta \\
&= \frac{1}{2}\|c + \Gamma U - R\|^2_{\mathcal{Q}_z} + \frac{1}{2}\|\Lambda U - I_0 u_{-1}\|^2_{\mathcal{S}_u} \\
&\quad + \frac{1}{2}\|\eta\|^2_{\mathcal{S}_\eta} + s'_\eta\eta \qquad (7) \\
&= \frac{1}{2}U'\left(\Gamma'\mathcal{Q}_z\Gamma + \Lambda'\mathcal{S}_u\Lambda\right)U \\
&\quad + \left(\Gamma'\mathcal{Q}_z(c - R) - \Lambda'\mathcal{S}_u I_0 u_{-1}\right)'U \\
&\quad + \left(\frac{1}{2}\|c - R\|^2_{\mathcal{Q}_z} + \frac{1}{2}\|I_0 u_{-1}\|^2_{\mathcal{S}_u}\right) \\
&\quad + \frac{1}{2}\eta'\mathcal{S}_\eta\eta + s'_\eta\eta \\
&= \frac{1}{2}U'HU + g'U + \rho + \frac{1}{2}\eta'\mathcal{S}_\eta\eta + s'_\eta\eta \\
&= \frac{1}{2}x'\bar{H}x + \bar{g}'x + \rho
\end{aligned}$$

with

$$H = \Gamma'\mathcal{Q}_z\Gamma + \Lambda'\mathcal{S}_u\Lambda \qquad (8a)$$
$$g = \Gamma'\mathcal{Q}_z(c - R) - \Lambda'\mathcal{S}_u I_0 u_{-1} \qquad (8b)$$
$$\rho = \frac{1}{2}\|c - R\|^2_{\mathcal{Q}_z} + \frac{1}{2}\|u_{-1}\|^2_{S_u} \qquad (8c)$$
$$x = \begin{bmatrix} U \\ \eta \end{bmatrix} \quad \bar{H} = \begin{bmatrix} H & 0 \\ 0 & \mathcal{S}_\eta \end{bmatrix} \quad \bar{g} = \begin{bmatrix} g \\ s_\eta \end{bmatrix} \qquad (8d)$$

Consequently, we may solve the FIR based MPC regulator problem (4) by solution of the following convex quadratic program

$$\min_x \quad \psi = \frac{1}{2}x'\bar{H}x + \bar{g}'x \qquad (9a)$$
$$s.t. \quad x_{\min} \le x \le x_{\max} \qquad (9b)$$
$$b_l \le \bar{A}x \le b_u \qquad (9c)$$

in which

$$x_{\min} = \begin{bmatrix} U_{\min} \\ 0 \end{bmatrix} \quad x_{\max} = \begin{bmatrix} U_{\max} \\ \infty \end{bmatrix} \qquad (10a)$$

$$b_l = \begin{bmatrix} \Delta U_{\min} \\ -\infty \\ Z_{\min} - c \end{bmatrix} \quad A = \begin{bmatrix} \Lambda & 0 \\ \Gamma & -I \\ \Gamma & I \end{bmatrix} \quad b_u = \begin{bmatrix} \Delta U_{\max} \\ Z_{\max} - c \\ \infty \end{bmatrix} \qquad (10b)$$

In a model predictive controller only the first vector, u_0^*, of $U^* = \left[(u_0^*)' \; (u_1^*)' \; \dots \; (u_{N-1}^*)'\right]'$, is implemented on the process. At the next sample time the open-loop optimization is repeated with new information due to a new measurement.

2.3 Soft Constraint Principle

Figure 2 illustrates the stage cost function for l_2 model predictive control (nominal MPC) and l_2 model predictive control with a dead zone (soft MPC). The stage cost

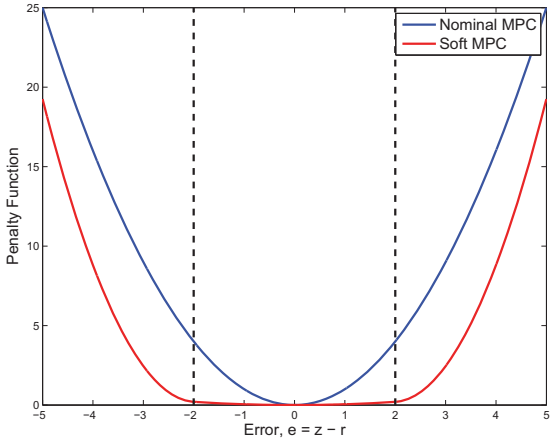

Fig. 2. The set point deviation penalty function for nominal MPC and soft MPC.

function, or penalty function, is plotted as function of the set-point error, $e = z - r$. The penalty function of the nominal MPC is a quadratic function. The penalty function of the soft MPC is constructed such that it is zero or almost zero within the dead-zone between the soft limits and growths quadratically when the set-point error exceeds the soft limits. The small penalty within the soft limits ensures that the controller produces a steady state offset free response. By having the penalty small within the soft constraints, the controller does not react much to small errors. In this way we avoid that the controller introduces significant real disturbances to the process because it reacts to say measurement noise or plant-model mismatch. Outside the soft limits, it is assumed that the deviation from target is due to a real process disturbance, and the soft MPC may be designed to react in the same way as the nominal MPC.

2.4 Simple Estimator

To have offset free steady state control when unknown step responses occur, we must have integrators in the feedback loop. This may be achieved using a FIR model in difference variables. Assume that the relation between the inputs and outputs may be represented as

$$\Delta y_k = \Delta z_k = e_k + \sum_{i=1}^{n} H_i \Delta u_{k-i} \qquad (11)$$

in which Δ is the backward difference operator, i.e. $\Delta y_k = y_k - y_{k-1}$, $\Delta z_k = z_k - z_{k-1}$, and $\Delta u_k = u_k - u_{k-1}$. This representation is identical with the FIR model (3)

$$y_k = z_k = \hat{b}_k + \sum_{i=1}^{n} H_i u_{k-i} \qquad (12)$$

if $\hat{b}_k$ is computed by

$$e_k = \Delta y_k - \sum_{i=1}^{n} H_i \Delta u_{k-i} \qquad (13a)$$
$$\hat{b}_k = \hat{b}_{k-1} + e_k \qquad (13b)$$

Note that in the regulator optimization problem $b_1 = b_2 = \dots = b_N = \hat{b}_k$ at each time instant. This is based on the assumption that the disturbances enter the process

as constant output disturbances. Of course this may not be how the disturbances enter the process in practice, and significant performance deterioration may result as a consequence of this representation.

3. SIMULATIONS

In this Section we consider plants of the form

$$\boldsymbol{Z}(s) = G(s)U(s) + G_d(s)\left(D(s) + \boldsymbol{W}(s)\right) \tag{14a}$$

$$\boldsymbol{y}(t_k) = \boldsymbol{z}(t_k) + \boldsymbol{v}(t_k) \tag{14b}$$

with the transfer functions

$$G(s) = \frac{K(\beta s+1)}{(\tau_1 s+1)(\tau_2 s+1)}\, e^{-\tau s} \tag{15a}$$

$$G_d(s) = \frac{K_d(\beta_d s+1)}{(\tau_{d1} s+1)(\tau_{d2} s+1)}\, e^{-\tau_d s} \tag{15b}$$

The disturbance model, $G_d(s)$, is kept fixed at its nominal value, while the transfer function, $G(s)$, from $U(s)$ varies around its nominal value, $G_0(s)$. This is used to illustrate the consequence of model uncertainty on the MPC closed-loop performance. The nominal system is $K = K_d = 1$, $\tau_1 = \tau_2 = \tau_{d1} = \tau_{d2} = 5$, $\beta = \beta_d = 2$, and $\tau = \tau_d = 5$. The system is converted to a discrete time state space model (1) using a sample time of $T_s = 1$ and a zero-order-hold assumption on the inputs.

The predictive controller is based on the impulse response coefficients of the following system

$$Z(s) = \hat{G}(s)U(s) \tag{16}$$

in which $\hat{G}(s)$ is identical to the nominal plant $G_0(s)$.

The simple estimator described in Section 2.4 is used for bias estimation. The input limits are $u_{\min} = -1$, $u_{\max} = 1$, $\Delta u_{\min} = -0.2$, and $\Delta u_{\max} = 0.2$. The horizon of the impulse response model is $n = 40$ and the control horizon is $N = 120$. The MPC is tuned with $Q_z = 1$ and $S = 10^{-3}$.

The unknown deterministic process disturbance, $D(s)$, the stochastic process disturbances, $\boldsymbol{W}(s)$ or $\boldsymbol{w}_k$, and the measurement noise, $\boldsymbol{v}(t_k) = \boldsymbol{v}_k$, used in the simulations are illustrated in Figure 3. The stochastic process disturbances is $\boldsymbol{w}_k \sim N(0, 0.01)$, and the stochastic measurement noise is $\boldsymbol{v}_k \sim N(0, 0.01)$.

3.1 Nominal Stochastic System

We consider the case when the model used by the controller is identical to the deterministic part of the plant model. However, the plant has in addition to the deterministic part stochastic process disturbances and stochastic measurement noise as illustrated in Figure 3.

Consider the case with no determistic disturbance, i.e. $D(s) = 0$. The performances of the nominal MPC and the soft MPC applied to this system are compared in Figure 4. The output variances produced by the two controllers are almost identical, while the input variance of the soft MPC is much smaller than the input variance of the nominal MPC. Due to the low penalties within the soft limits, the soft MPC does not react to measurement noise and do not need to compensate such previous erroneous measurement noise induced input moves.

Figure 5 illustrates the performance of the nominal MPC and the soft MPC when the model is identical to the

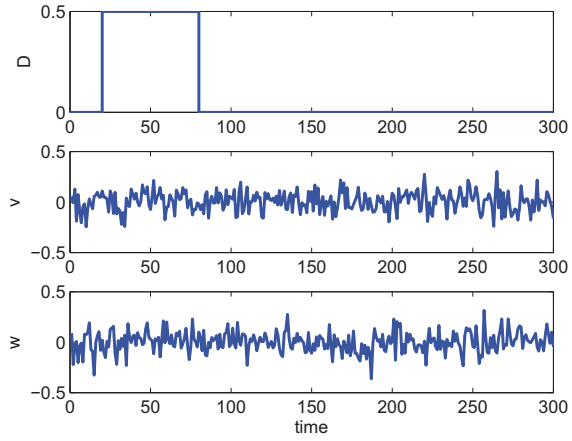

Fig. 3. External signals used in the closed loop simulations. $D(s)$ or d_k is the unknown deterministic disturbance, $\boldsymbol{v}_k$ is the stochastic measurement noise, and $\boldsymbol{w}_k$ is the stochastic process noise,

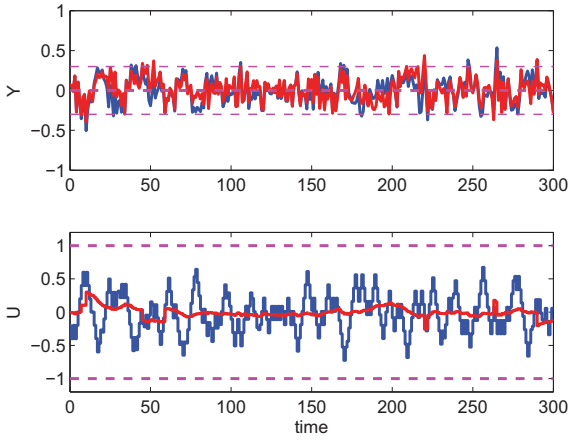

Fig. 4. Comparison of normal and soft MPC with nominal models applied to a stochastic system with no deterministic disturbance (Nominal MPC = blue, Soft MPC = red).

plant model and the external signals illustrated in Figure 3 are applied to the model (14). Also in this case, the controlled variable, Y (or Z), of the two controllers are similar while the manipulated variable, U, of the soft MPC has significantly less variance than the manipulated variable, U, of the nominal MPC.

3.2 Uncertain Determistic System

We consider a deterministic system without stochastic process noise nor stochastic measurement noise. However, the model used by the controllers is different from the plant model. The process is perturbed by an unknown deterministic disturbance, $D(s)$, as illustrated in figure 3.

We compare the performance of the nominal MPC and the soft MPC for model-plant mismatches defined by the time delay, τ, the gain K, the time constant τ_1, and the zero β.

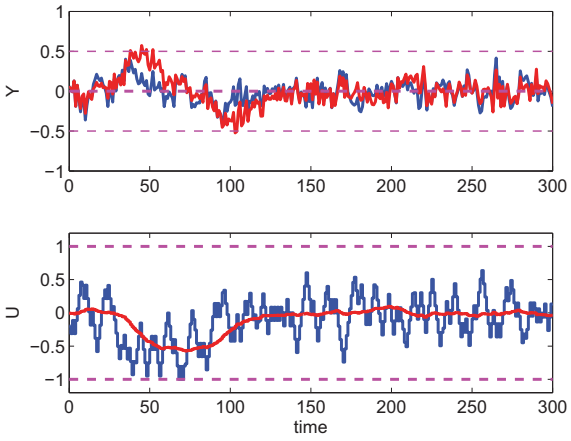

Fig. 5. Comparison of normal and soft MPC with nominal models applied to a stochastic system with an unknown deterministic disturbance (Nominal MPC = blue, Soft MPC = red). The external signals are shown in Figure 3.

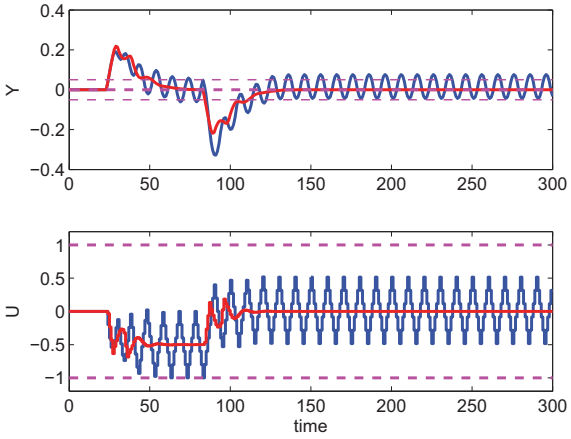

Fig. 6. Closed-loop MPC performance with time delay uncertainty. The plant delay is $\tau = 3$ and the model delay is $\hat{\tau} = 5$ (Nominal MPC = blue, Soft MPC = red).

Figure 6 and Figure 7 illustrate closed-loop performances achieved by the nominal and soft MPC when there is time delay plant-model mismatch. The soft MPC has smaller input variation than the nominal MPC, and the soft MPC provies better control than the nominal MPC in terms of set point deviations.

Figures 8-10 illustrate the performances of the nominal MPC and the soft MPC in the case of model-plant mismatch in the gain, the time constant, and the zero, respectively. In all cases, the soft MPC has significantly less input variation than the nominal MPC. Furthermore, the outputs are significantly better controlled by the soft MPC than by the nominal MPC.

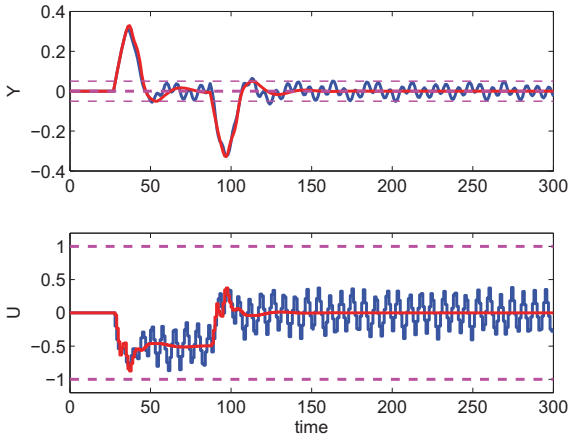

Fig. 7. Closed-loop MPC performance with time delay uncertainty. The plant delay is $\tau = 7$ and the model delay is $\hat{\tau} = 5$ (Nominal MPC = blue, Soft MPC = red).

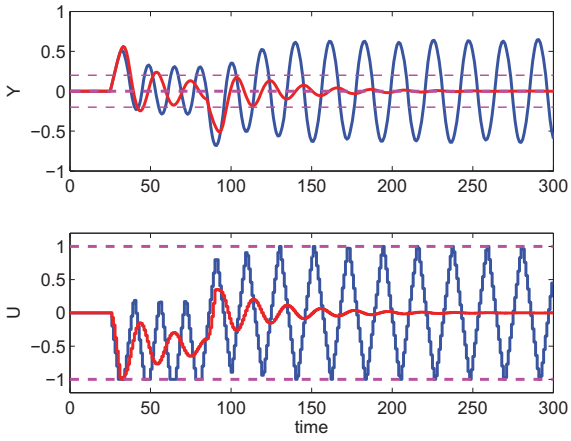

Fig. 8. Closed-loop MPC performance with gain uncertainty. The plant gain is $K = 2$ and the model gain is $\hat{K} = 1$ (Nominal MPC = blue, Soft MPC = red).

3.3 Uncertain Stochastic System

Figure 11 illustrates the closed loop performance of a nominal MPC and a soft MPC applied to the system (14) with the external signals in Figure 3 and a plant-model mismatch in the gain. The plant gain is $K = 2$ and the model gain is $\hat{K} = 1$. By inspection, it is obvious that the performance of the soft MPC is significantly better than the performance of the nominal MPC. The superior performance is achieved by having a small set point deviation penalty within the soft constraints such that the controller does not react aggressively when close to the set point. In this way it avoids perturbing the system due to stochastic measurement noise and plant-model mismatch.

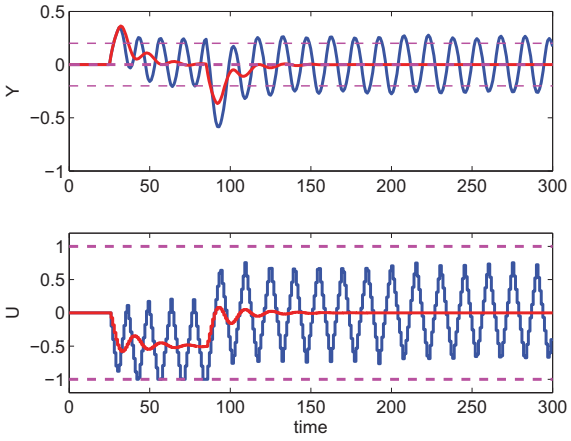

Fig. 9. Closed-loop MPC performance with time constant uncertainty. The plant time constant is $\tau_1 = 2$ and the model time constant is $\hat{\tau}_1 = 5$ (Nominal MPC = blue, Soft MPC = red).

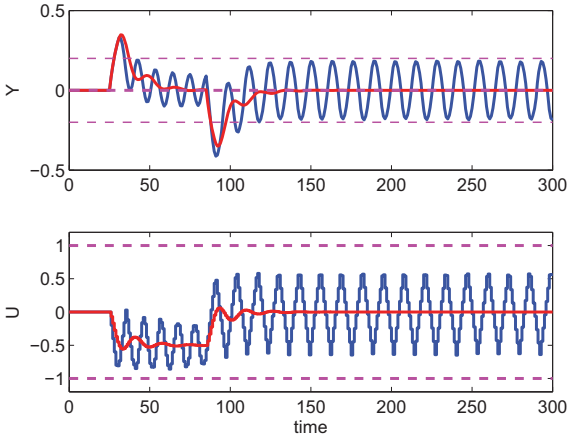

Fig. 10. Closed-loop MPC performance with zero uncertainty. The plant zero is $\beta = 4.5$ and the model zero is $\hat{\beta} = 2$ (Nominal MPC = blue, Soft MPC = red).

4. CONCLUSION

We have developed a l_2 regularized predictive controller with soft constraints and demonstrated efficient application of this controller to uncertain stochastic systems. We call this controller soft MPC. It is illustrated and verified by simulations that this soft MPC provides significantly better closed loop performance than nominal MPC. The soft MPC also provides much better performance degradation in the face of plant-model mismatch than nominal MPC. These features are expected to contribute to better closed loop performance, easier maintenance, easier tuning, and longer lifetime of model predictive controllers for chemical processes.

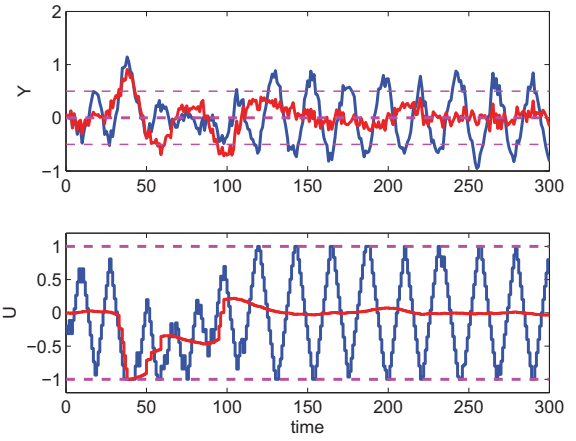

Fig. 11. Closed-loop MPC performance for a system with the external signals in Figure 3 and gain uncertainty. The plant gain is $K = 2$ and the model gain is $\hat{K} = 1$. Nominal MPC = blue, Soft MPC = red.

REFERENCES

Bemporad, A. and Morari, M. (1999). Robust model predictive control: A survey. In A. Garulli, A. Tesi, and A. Vicino (eds.), *Robustness in Identification and Control*, volume 245 of *Lecture Notes in Control and Information Sciences*, 207–226. Springer-Verlag.

Boyd, S. and Vandenberghe, L. (2004). *Convex Optimization*. Cambridge University Press, Cambridge, UK.

Goodwin, G.C., Seron, M.M., and De Dona, J.A. (2005). *Constrained Control and Estimation. An Optimization Approach*. Springer, New York.

Hansson, A. (2000). A primal-dual interior-point method for robust optimal control of linear discrete-time systems. *IEEE Transactions on Automatic Control*, 45, 1639–1655.

Havlena, V. and Lu, J. (2005). A distributed automation framework for plant-wide control, optimisation, scheduling and planning. In *IFAC World Congress 2005*. IFAC, Prague, Czech Republic.

Havlena, V. and Findejs, J. (2005). Application of model predictive control to advanced combustion control. *Control Engineering Practice*, 13, 671–680.

Maciejowski, J.M. (2002). *Predictive Control with Constraints*. Prentice Hall, Harlow, England.

Prasath, G. and Jørgensen, J.B. (2008). Model predictive control based on finite impulse response models. In *ACC 2008*. American Control Conference 2008, Seattle, Washington.

Qin, S.J. and Badgwell, T.A. (2003). A survey of industrial model predictive control technology. *Control Engineering Practice*, 11, 733–764.

Scokaert, P.O.M. and Rawlings, J.B. (1999). Feasibility issues in linear model predictive control. *AIChE Journal*, 45, 1649–1659.

Shinskey, F.G. (1988). *Process Control Systems. Application, Design, and Tuning*. McGraw-Hill, New York.

Vandenberghe, L., Boyd, S., and Nouralishadi, M. (2002). Robust linear programming and optimal control. In *15th IFAC World Congress 2002*. IFAC, Barcelona, Spain.

Dynamic Operability for the Calculation of Transient Output Constraints for Non-Square Linear Model Predictive Controllers

Fernando V. Lima and Christos Georgakis*

Department of Chemical and Biological Engineering &
Systems Research Institute, Tufts University, Medford,
*MA, 02155, USA (*e-mail:christos.georgakis@tufts.edu)*

Abstract: This paper introduces a dynamic operability-based approach for the determination of feasible output constraints during transient operation. This approach is based on previously published steady-state operability developments and the concept of output funnels. In this study, high-dimensional non-square systems with more outputs than inputs are of particular interest. Such systems are challenging because it is impossible to control all the outputs at specific set-points when there are fewer degrees of freedom available than the controlled variables. Thus, interval, instead of set-point, control is needed for at least some of the output variables. In order to motivate the new concepts, two non-square case studies are addressed, one illustrative and one industrial - obtained from the control system of a Steam Methane Reformer process. The calculated constraints are validated by running DMCplus™ (AspenTech) closed-loop simulations for the extreme values of the disturbances. These constraints are intended for use online in model-based controllers (e.g., Model Predictive Controllers) to ensure that each of the outputs will remain inside a feasibility envelope during transient operation.

Keywords: Output Variables, Constraints, Model-based Control, Operability, Dynamic Systems.

1. INTRODUCTION

Model Predictive Control (MPC) is a long standing multivariable constrained control methodology that utilizes an explicit process model to predict the future behavior of a chemical plant. At each control interval, the MPC algorithm attempts to optimize the future plant behavior by computing a sequence of future manipulated variable adjustments. The first of the optimal sequence of calculated input moves is implemented into the plant and the entire calculation is repeated at subsequent control intervals using updated process measurements. MPC has been extensively studied in academia and widely accepted in the chemical industry for its ability to handle complex multivariable and highly interactive process control problems (Qin and Badgwell, 2003). MPC-type controllers in industrial practice aim to control non-square systems in which there are more controlled outputs than manipulated inputs. In such systems it is impossible to control all the outputs at specific set-points because there are fewer degrees of freedom available than the controlled variables.

Based on the input constraints, generally specified *a priori* due to the physical limitations of the process, an important design task is to determine the output ranges within which one wants to control the process. The improper selection of these constraints can make the controller infeasible when a disturbance moves the process far away from its usual operating region. Past practice requires that output constraints are enforced whenever feasible and softened whenever they become infeasible (Rawlings, 2000). The steady-state operability methodology originally introduced for square systems (Vinson and Georgakis, 2000) and extended for non-square systems (Lima and Georgakis, 2006; Lima and Georgakis, 2008a) provides a method for selecting such output constraints systematically, so that they are as tight as possible but also do not render the controller infeasible. Specifically for non-square systems, the interval operability framework was introduced (Lima and Georgakis, 2006) to assess the input-output open-loop operability of multivariable non-square systems at the steady-state, a necessary condition for the overall process operability. The application of this framework to high-dimensional square and non-square systems is discussed in another set of publications (Lima and Georgakis, 2008b; Lima, Georgakis, Smith and Schnelle, 2008), where a Linear Programming (LP) based approach is introduced to calculate the tightest feasible set of steady-state output constraints when interval operability is necessary.

This paper extends this interval operability framework to enable the determination of feasible output constraints during transient for high-dimensional non-square systems. Although the previously developed steady-state operability approaches are necessary to quantify the overall operability of a process and to determine the steady-state output constraints for MPC, the development of a dynamic operability methodology for non-square systems will have great impact on MPC controller design. Specifically, dynamic operability analysis can be used to systematically calculate the amount of constraint relaxation necessary in order to prevent the occurrence of transient infeasibilities, when disturbances affect the process (see Dimitriadis and Pistikopoulos (1995) for dynamic flexibility analysis). This extension is accomplished here by designing a funnel for each of the output variables, which provides output

constraints that guarantee feasible process operation in closed-loop. Previously, output funnels have been used to define MPC controllers' output trajectories in commercial packages (Qin and Badgwell, 2003). Specifically, Honeywell's RMPCT (Robust Multivariable Predictive Control Technology) controller defines a funnel for the outputs or Controlled Variables (CV) constraints. When a predicted CV trajectory leaves its funnel, the controller algorithm penalizes this trajectory to bring the CV back within its range (Qin and Badgwell, 2003; Maciejowski, 2002). Here such funnels are used to design output constraints during transient operation. This design is especially important for underdamped systems in general, where overshoots may occur during process operation, and overdamped or critically damped systems when disturbance dynamics are faster than input dynamics. For the opposite case when input dynamics are faster than disturbance ones, the output constraints calculated using one of the steady-state operability methodologies are also applicable during transient.

2. PROCESS OPERABILITY

Before introducing the dynamic operability approach, it is necessary to briefly define the sets of variables used for steady-state interval operability calculations (Lima and Georgakis, 2008a). The Available Input Set (**AIS**) is the set of values that the process input, or manipulated, variables (**u**) can take, based on the constraints of the process. For an $n \times m \times q$ (*n outputs*, *m inputs* and *q disturbances*) linear system:

$$\mathbf{AIS} = \left\{ \mathbf{u} \mid u_i^{\min} \le u_i \le u_i^{\max};\ 1 \le i \le m \right\} \tag{1}$$

The Desired Output Set (**DOS**) is given by the ranges of the outputs (**y**) that are desired to be achieved and is represented by:

$$\mathbf{DOS} = \left\{ \mathbf{y} \mid y_i^{\min} \le y_i \le y_i^{\max};\ 1 \le i \le n \right\} \tag{2}$$

The Expected Disturbance Set (**EDS**) represents the expected steady-state values of the disturbances (**d**):

$$\mathbf{EDS} = \left\{ \mathbf{d} \mid d_i^{\min} \le d_i \le d_i^{\max};\ 1 \le i \le q \right\} \tag{3}$$

Based on the steady-state linear model of the process, expressed by the process gain matrix (**G**) and the disturbance gain matrix ($\mathbf{G}_d$), the Achievable Output Set for a specific disturbance vector, **AOS(d)**, is defined by the ranges of the outputs that can be achieved using the inputs inside the **AIS**:

$$\mathbf{AOS(d)} = \left\{ \mathbf{y} \mid \mathbf{y} = \mathbf{Gu} + \mathbf{G}_d\mathbf{d};\ \mathbf{u} \in \mathbf{AIS},\ \mathbf{d} \text{ is fixed} \right\} \tag{4}$$

The Achievable Output Interval Set (**AOIS**) is defined as the tightest feasible set of output constraints that can be achieved, with the available range of the manipulated variables and when the disturbances remain within their expected values (see references (Lima and Georgakis, 2008a; Lima and Georgakis, 2008b; Lima, Georgakis, Smith and Schnelle, 2008) for the algorithms developed for the calculation of this important set). Using these defined sets and some of the previously published interval operability concepts and calculations, a dynamic operability approach, based on the design of output funnels, for the determination of output constraints during transients is introduced next through a 2-D illustrative example. This is followed by the analysis of the Steam Methane Reformer (SMR) process example, which is 9-D and underdamped.

3. ILLUSTRATIVE EXAMPLE

In order to introduce the dynamic operability approach, consider a 2-D example from Lima and Georgakis (2006) with 2 outputs, 1 input and 1 disturbance (2 x 1 x 1). This example has the following steady-state gain model and constraining sets (see information on process dynamics below):

$$\begin{pmatrix} y_1 \\ y_2 \end{pmatrix} = \begin{pmatrix} 1.41 \\ 0.66 \end{pmatrix} u_1 + \begin{pmatrix} -0.6 \\ 0.4 \end{pmatrix} d_1 \tag{5}$$

$$\mathbf{AIS} = \left\{ u_1 \mid -1 \le u_1 \le 1 \right\}$$

$$\mathbf{EDS} = \left\{ d_1 \mid -1 \le d_1 \le 1 \right\}$$

$$\mathbf{DOS} = \left\{ \mathbf{y} \in \Re^2 \mid \|y\|_\infty \le 1 \right\}$$

Two funnels, one for each output, with specific amplitudes and decay characteristics will be designed for the two output variables of this system. Each of these funnels is designed from the moment that a disturbance is inserted into the system and provides an envelope where the control problem is always feasible if the output constraints remain inside of this envelope. This envelope starts at the funnel amplitude value (defined below), decays at a specific rate and ends at a designed steady-state constraint calculated using one of the interval operability approaches cited above. Cases where the disturbance variable takes its extreme values are of particular interest because they represent the worst cases, which if satisfied, ensure feasible operation for all the other cases.

For the system above, the dynamics of each of the input-output and disturbance-output pairs are plotted in Figs. 1, 2, 3, and 4 for pairs (y_1, u_1), (y_1, d_1), (y_2, d_1), and (y_2, u_1), respectively. In these figures, these dynamics are represented by step response coefficients, which would be obtained in practice by plant testing.

The funnel amplitude associated with output *i* (a_i) is defined as follows:

$$a_i = k_{d,j-i} s_j \tag{6}$$

where $k_{d,j-i}$ corresponds to the value of the steady-state disturbance gain associated with the disturbance-output pair *j-i* and s_j is the step disturbance value. For this example, s_j will be assumed at the extreme values of the disturbance within the **EDS**, i.e. d_1 is moved from 0 to ± 1. If $d_1 = 1$, then $a_1 = -0.6$ and $a_2 = 0.4$. When $d_1 = -1$, $a_1 = 0.6$ and $a_2 = -0.4$. It is assumed that using steady-state disturbance gains to calculate the starting point of the funnel decay, as opposed to the maximum absolute value of the dynamic gains, will be enough to provide an envelope that contains the entire closed-loop response. This is based on the assumption that the inputs are able to compensate for the presence of overshoots, caused by these dynamic gains, in most practical cases during closed-loop operation, especially if a model-based controller, such as MPC, is implemented. The decay for each output funnel (λ_i) is determined by the slowest dynamics among all

the input-output and disturbance-output pairs for the corresponding output. Each output is analyzed separately because the disturbance dynamics might be slower for one of the outputs, while the input dynamics may be slower for the other. These dynamics are estimated from the step response curves using two approaches, depending on the characteristics of the analyzed curve:

1) Exponential fit (typically for oscillatory responses): an exponential is fitted to two selected points of the step response curve. These points are selected such that most of the curve is below (or above, depending on the sign of the dynamic gains) the fitted exponential. The dynamics of the analyzed pair are estimated by the following exponential decay:

$$y_{\exp} = a_{\exp} \exp\left(-\lambda_{\exp} t\right) + y_{\infty} \tag{7}$$

where y_{∞} corresponds to the steady-state gain of the analyzed step response curve. Using the two selected points and eq. (7), a system of 2 equations and 2 unknowns can be solved for the two parameters of the exponential, $a_{\exp}$ and $\lambda_{\exp}$. For the example above, this approach is used for pairs (y_1, u_1), (y_1, d_1), and (y_2, d_1), whose exponential fits are shown in Figs. 1, 2, and 3, respectively, along with the fitted points selected for each case. For such pairs, the following exponential fits are obtained:

$$\begin{aligned}
\left(y_1,\, u_1\right) &= 0.47\exp\left(-1.89\times10^{-2}t\right) + 1.41 \Rightarrow \lambda_{\exp} = 1.89\times10^{-2} \\
\left(y_1,\, d_1\right) &= -1.70\exp\left(-2.12\times10^{-2}t\right) - 0.60 \Rightarrow \lambda_{\exp} = 2.12\times10^{-2} \\
\left(y_2,\, d_1\right) &= 0.18\exp\left(-4.22\times10^{-2}t\right) + 0.40 \Rightarrow \lambda_{\exp} = 4.22\times10^{-2}
\end{aligned} \tag{8}$$

2) First-order models estimated using ARX (Auto-Regressive model with eXogenous inputs, subroutine ARX in Matlab) (Ljung, 1999): the following first-order ARX model with a zero-order holder in the z domain is fitted to the step response coefficients of a specific pair:

$$y(z) = \frac{bz^{-1}}{1+az^{-1}}u(z) \text{ with } \lambda_{\text{arx}} = -\ln\left(p_z\right) \tag{9}$$

where λ_{arx} represents the model dynamics and is calculated by taking the negative natural log of the transfer function pole in the z domain, $p_z = -a$. This approach is used whenever a pair dynamics can be well approximated by a first-order model. This approach is applied here to pair (y_2, u_1), which is shown in Fig. 4, and the following model and λ_{arx} are obtained:

$$y_2(z) = \frac{0.0283}{z-0.9601}u_1(z) \Rightarrow \lambda_{\text{arx}} = -\ln\left(0.9601\right) = 4.07\times10^{-2} \tag{10}$$

After calculating all λs for all possible pairs (4 in this case), using the two approaches above, their values are compared and the one with smallest absolute value for each output (representing the slowest dynamics) is retained and used in the funnel design for the corresponding output. For example, for output 1, $\lambda_1 = 1.89 \times 10^{-2}$ is chosen, which is the smallest between 1.89×10^{-2} and 2.12×10^{-2}. Therefore, for this example, the following values of λ_i are selected:

$$\lambda_1 = 1.89\times10^{-2},\ \lambda_2 = 4.07\times10^{-2} \tag{11}$$

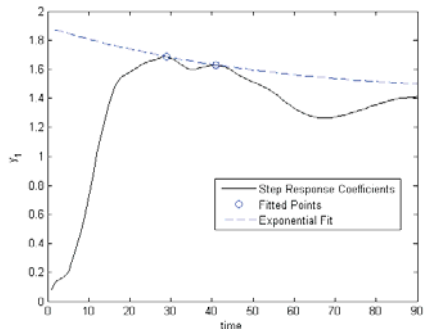

Fig. 1. Step Response Coefficients, Exponential Fit and Fitted Points for (y_1, u_1) pair.

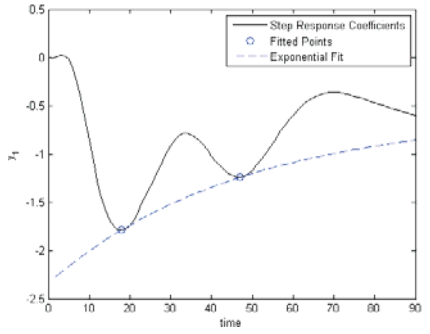

Fig. 2. Step Response Coefficients, Exponential Fit and Fitted Points for (y_1, d_1) pair.

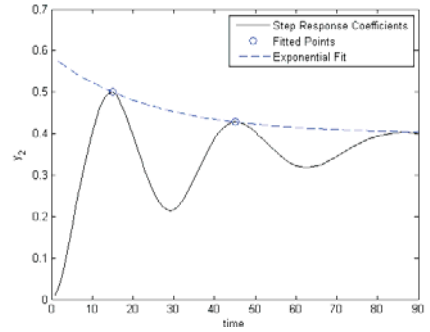

Fig. 3. Step Response Coefficients, Exponential Fit and Fitted Points for (y_2, d_1) pair.

Using the calculated amplitudes and decays, the following equation represents the funnel for each of the output variables:

$$f_i = \left(1+\alpha_f\right)a_i \exp\left[-\left(1+\beta_f\right)\lambda_i t\right] + y_{ss,i} \tag{12}$$

where $y_{ss,i}$ is one of the steady-state output constraints (upper or lower limit) for output i, which is calculated using the previously published interval operability approaches (Lima and Georgakis, 2008a; Lima and Georgakis, 2008b). Also, α_f

and β_f are adjustable tuning parameters, associated with amplitude and decay, respectively, and are independent of the output selected. As explained above for a_i, depending on the magnitude of the disturbance inserted, which in this case takes either its maximum or minimum value, $y_{ss,i}$ will have different values. For the case study here, if $d_1 = 1$, then $y_{ss,1} = -0.464$ and $y_{ss,2} = 0.464$. When $d_1 = -1$, $y_{ss,1} = 0.464$ and $y_{ss,2} = -0.464$. These values were extracted from the steady-state operability results presented in the ADCHEM 2006 paper by Lima and Georgakis (see case 2, section 3). Thus, each output envelope actually has upper and lower limits that start at different points and end at the upper and lower calculated steady-state constraints, respectively. The same decay holds for both cases. Therefore, for the 2-D case study above, selecting $\alpha_f = 0$ and $\beta_f = -0.74$, the following funnels are obtained for each output for the two extreme values of the disturbance:

$$\text{For } d_1 = 1:\ y_{ss,1} = -0.464,\ y_{ss,2} = 0.464$$

$$f_1 = -0.6\exp\left[-(1-0.74)1.89\times10^{-2}t\right] - 0.464 \quad (13)$$

$$f_2 = 0.4\exp\left[-(1-0.74)4.07\times10^{-2}t\right] + 0.464 \quad (14)$$

$$\text{For } d_1 = -1:\ y_{ss,1} = 0.464,\ y_{ss,2} = -0.464$$

$$f_1 = 0.6\exp\left[-(1-0.74)1.89\times10^{-2}t\right] + 0.464 \quad (15)$$

$$f_2 = -0.4\exp\left[-(1-0.74)4.07\times10^{-2}t\right] - 0.464 \quad (16)$$

The funnels for outputs 1 (eqs. 13 and 15) and 2 (eqs. 14 and 16) are plotted in Figs. 5 and 6, respectively, along with the DMCplus™ (Dynamic Matrix Control - AspenTech, a multivariable constrained controller) trend obtained for each case. For all cases, the controller is operating in closed-loop mode and the disturbance was inserted at time = 0.

4. HIGH-DIMENSIONAL INDUSTRIAL SYSTEM

The design of output constraints during transient for the Steam Methane Reformer (SMR; Vinson, 2000) process example will now be performed using the output funnels defined above. This process has 9 outputs, 4 inputs and 1 disturbance variable and it is defined by the following set of steady-state equations and constraining sets (see information on process dynamics below):

$$\begin{pmatrix}\delta y_1\\ \delta y_2\\ \delta y_3\\ \delta y_4\\ \delta y_5\\ \delta y_6\\ \delta y_7\\ \delta y_8\\ \delta y_9\end{pmatrix} = \begin{pmatrix} 1.00 & 0 & 3.99 & 2.22\\ 2.50 & 0.25 & 16.51 & -11.80\\ -0.14 & 0 & -1.53 & -1.45\\ 0.55 & 0 & 2.76 & 0.69\\ -0.04 & 0.02 & 0 & 0\\ 2.34 & -0.66 & 36.71 & 5.09\\ 3.96 & -0.19 & 44.40 & 5.79\\ -0.04 & 0 & -3.11 & -1.71\\ 0.36 & 0.05 & 1.10 & -16.54\end{pmatrix}\begin{pmatrix}\delta u_1\\ \delta u_2\\ \delta u_3\\ \delta u_4\end{pmatrix} + \begin{pmatrix}0.40\\ 1.65\\ -0.15\\ 0\\ 0\\ 3.67\\ 4.44\\ -0.31\\ 0.11\end{pmatrix}\delta d_1 \quad (17)$$

$$\mathbf{AIS} = \left\{\begin{array}{l}\mathbf{u}\in\Re^4 \mid 10\le u_1\le 48;\ \ 60\le u_2\le 140;\\ \qquad 0.2\le u_3\le 2.0;\ \ -2.4\le u_4\le -0.7\end{array}\right\} \quad (18)$$

$$\mathbf{EDS} = \{d_1 \mid -4\le d_1\le 4\}$$

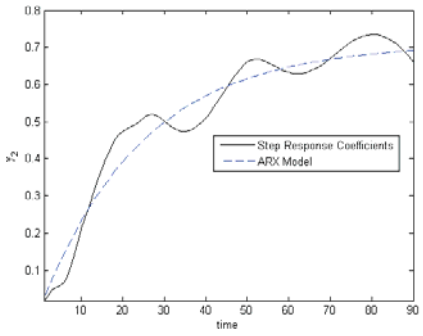

Fig. 4. Step Response Coefficients, Exponential Fit and First-order ARX Model for (y_2, u_1) pair.

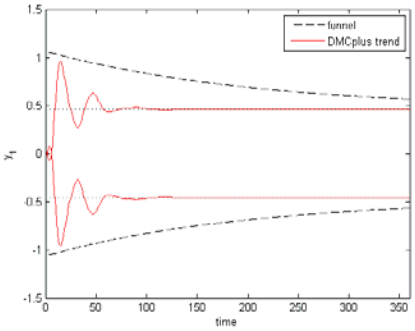

Fig. 5. Funnel Design and DMCplus trend for output y_1 with (α_f, β_f) = (0, -0.74).

where $\delta\mathbf{y}$, $\delta\mathbf{u}$ and δd_1 are deviation variables from the steady-state values for the outputs ($\mathbf{y}_{ss}$), the inputs ($\mathbf{u}_{ss}$), and the disturbance ($d_{1,ss}$), respectively. These steady-state values are given by:

$$\mathbf{y}_{ss} = (44.35,\ 94.10,\ 1.50,\ 21.5,\ 1.80,\ 431.45,\ 510.75,\ 5.35,\ 37.1)^T \quad (19)$$
$$\mathbf{u}_{ss} = (29.00,\ 100.00,\ 1.10,\ -1.55)^T;\ d_{1,ss} = 0$$

Also, the original output constraints (**DOS**), lower and upper limits, are given in Table 1. The SMR process has underdamped dynamics for several input-output/disturbance-output pairs, which are represented by the step response coefficients obtained by plant testing that are shown in Fig. 7. For this case, the disturbance gains, given in eq. (17), and the designed output constraints at the steady-state in Table 1 (from Lima, Georgakis, Smith, Vinson and Schnelle, 2009) will be used here to define each output funnel.

Following the same procedure as in the illustrative example above, exponential and ARX fits were obtained and λs calculated for all the input-output and disturbance-output pairs. The calculated λs for all these pairs are presented in Table 2, where the smallest absolute values of λ for each output, which will be used in the funnel design, are highlighted. Thus, using eq. (12), the funnel equations (20) and (21) are calculated for all outputs when d_1 moves from 0 to ± 4 (extreme cases) and (α_f, β_f) = (1.00, 0.36).

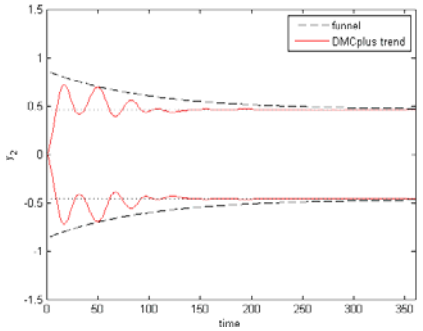

Fig. 6. Funnel Design and DMCplus trend for output y_2 with $(\alpha_f, \beta_f) = (0, -0.74)$.

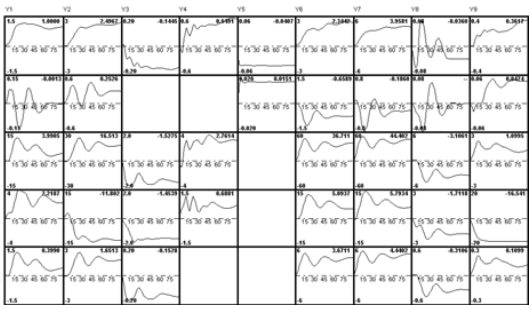

Fig. 7. Step Response Model for the SMR Problem. Responses for outputs y_1- y_9 to a step in inputs u_1 - u_4 and disturbance d_1. Empty boxes represent that there is no interaction between the input-output or disturbance-output pair.

Table 1. SMR Example: original and designed set of output constraints at the steady-state (Lima, Georgakis, Smith, Vinson and Schnelle, 2009).

Process Outputs	Original Lower Bound	Original Upper Bound	Designed Lower Bound	Designed Upper Bound
y_1	43.00	45.70	43.98	44.72
y_2	26.90	161.30	84.89	103.31
y_3	0.80	2.20	1.02	1.98
y_4	0	43.00	20.91	22.09
y_5	1.70	1.90	1.73	1.87
y_6	424.70	438.20	426.82	436.08
y_7	430.10	591.40	455.48	566.02
y_8	3.20	7.50	3.87	6.83
y_9	21.50	52.70	26.41	47.79

For $d_1 = 4$:

$$
\begin{aligned}
f_1 &= (1+1)1.60\exp\left[-(1+0.36)1.51\times10^{-2}t\right]+44.72\\
f_2 &= (1+1)6.60\exp\left[-(1+0.36)2.86\times10^{-2}t\right]+103.31\\
f_3 &= (1+1)(-0.60)\exp\left[-(1+0.36)1.40\times10^{-2}t\right]+1.02\\
f_4 &= 22.09\\
f_5 &= 1.87\\
f_6 &= (1+1)14.68\exp\left[-(1+0.36)1.95\times10^{-2}t\right]+436.08\\
f_7 &= (1+1)17.76\exp\left[-(1+0.36)2.21\times10^{-2}t\right]+566.02\\
f_8 &= (1+1)(-1.24)\exp\left[-(1+0.36)2.48\times10^{-2}t\right]+3.87\\
f_9 &= (1+1)0.44\exp\left[-(1+0.36)1.10\times10^{-2}t\right]+47.79
\end{aligned}
\tag{20}
$$

For $d_1 = -4$:

$$
\begin{aligned}
f_1 &= (1+1)(-1.60)\exp\left[-(1+0.36)1.51\times10^{-2}t\right]+43.98\\
f_2 &= (1+1)(-6.60)\exp\left[-(1+0.36)2.86\times10^{-2}t\right]+84.89\\
f_3 &= (1+1)0.60\exp\left[-(1+0.36)1.40\times10^{-2}t\right]+1.98\\
f_4 &= 20.91\\
f_5 &= 1.73\\
f_6 &= (1+1)(-14.68)\exp\left[-(1+0.36)1.95\times10^{-2}t\right]+426.82\\
f_7 &= (1+1)(-17.76)\exp\left[-(1+0.36)2.21\times10^{-2}t\right]+455.48\\
f_8 &= (1+1)1.24\exp\left[-(1+0.36)2.48\times10^{-2}t\right]+6.83\\
f_9 &= (1+1)(-0.44)\exp\left[-(1+0.36)1.10\times10^{-2}t\right]+26.41
\end{aligned}
\tag{21}
$$

Note that, for outputs y_4 and y_5, the steady-state disturbance gains are 0, and thus, their funnel's upper and lower bounds are constants at their upper and lower designed steady-state limits, respectively. Figs. 8, 9, and 10 show the DMCplus trends for y_1, y_2, and y_3, respectively, as well as the funnels for each case, where the controller is operating in closed-loop mode and the disturbance was inserted at time = 0. The funnels for the other outputs are not shown here due to space limitations of the manuscript.

Table 2. Calculated λs for each input-output and disturbance-output pairs for the SMR Example (smallest λ for each of the outputs in bold; dash (-) for pairs with no model)

y/ u, d	u_1	u_2	u_3	u_4	d_1
y_1	0.0189	0.0323	0.0212	**0.0151**	0.0212
y_2	0.0335	0.0699	0.0288	**0.0286**	0.0288
y_3	0.0794	-	**0.0140**	0.0847	**0.0140**
y_4	0.0537	-	0.0939	**0.0364**	-
y_5	1.4437	**0.5177**	-	-	-
y_6	0.0407	0.0453	0.0422	**0.0195**	0.0422
y_7	0.0530	0.0391	0.0681	**0.0221**	0.0681
y_8	**0.0248**	0.0280	0.0316	0.0706	0.0316
y_9	0.0243	0.0290	**0.0110**	0.1213	**0.0110**

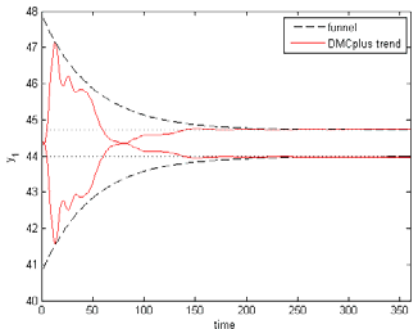

Figure 8: SMR Example: funnel design and DMCplus trend for output y_1 with $(\alpha_f, \beta_f) = (1.00, 0.36)$.

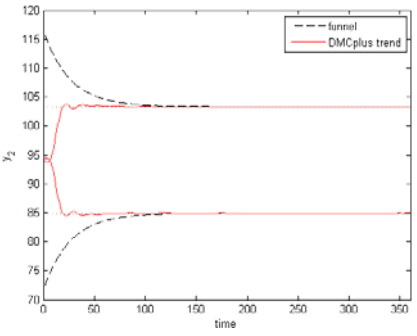

Figure 9: SMR Example: funnel design and DMCplus trend for output y_2 with $(\alpha_f, \beta_f) = (1.00, 0.36)$.

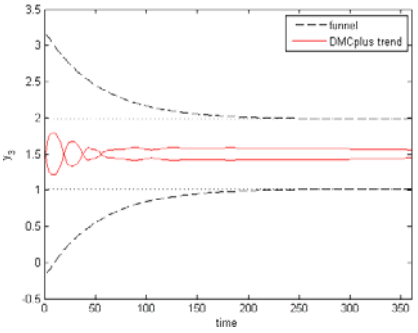

Figure 10: SMR Example: funnel design and DMCplus trend for output y_3 with $(\alpha_f, \beta_f) = (1.00, 0.36)$.

6. CONCLUSIONS

In this paper we have presented an extension of the previously developed steady-state interval operability approach to dynamical systems. Through the detailed examination of an illustrative case study we have motivated the calculation of output funnels for the design of output constraints during transient operation. The developed methodology was then applied to determine feasible output constraints for the Steam Methane Reformer industrial process. The analysis presented here provides a starting point for the verification of the achievability of control objectives in the entire control horizon. As potential future directions, an extension of this framework to address systems with multiple disturbances is necessary. Moreover, a moving horizon operability approach could be developed, where operability calculations would be performed online at each time instant, as the control horizon advances.

ACKNOWLEDGMENTS

The authors gratefully acknowledge the financial support from PRF-ACS through grant # 45400-AC9. We also wish to acknowledge David R. Vinson (APCI) for providing the process model and William M. Canney (AspenTech) for providing the DMCplus™ software.

REFERENCES

Dimitriadis, V.D. and Pistikopoulos, E.N. (1995). Flexibility analysis of dynamic systems. *Ind. Eng. Chem. Res*., 34, 4451-4462.

Lima, F.V. and Georgakis, C. (2006). Operability of multivariable non-square systems. *In Proceedings of the 2006 IFAC International Symposium on Advanced Control of Chemical Processes (ADCHEM)*, 989-994.

Lima, F.V. and Georgakis, C. (2008a). Design of output constraints for model-based non-square controllers using interval operability. *J. Process Control*, 18, 610-620.

Lima, F.V. and Georgakis, C. (2008b). Input-output operability of control systems. *J. Process Control, submitted for publication*.

Lima, F.V., Georgakis, C., Smith, J.F., Vinson, D.R. and Schnelle, P.D. (2009). Operability-based determination of feasible constraints for the control of several high-dimensional non-square industrial processes. *AIChE Journal*, *accepted for publication.*

Lima, F.V., Georgakis, C., Smith, J.F. and Schnelle, P.D. (2008). Analysis of the constraint characteristics of a sheet forming control problem using interval operability concepts. *Computer Aided Chemical Engineering*, 25, 387-392.

Ljung, L. (1999). *System identification: Theory for the user.* 2nd ed., Prentice Hall, Upper Saddle River, NJ.

Maciejowski, J.M. (2002). *Predictive control with constraints.* Prentice Hall, Englewood Cliffs, NJ.

Qin, S.J. and Badgwell, T.A. (2003). A survey of industrial model predictive control technology. *Control Engineering Practice,* 11, 733-764.

Rawlings, J.B. (2000). Tutorial overview of model predictive control. *IEEE Control Syst. Magazine*, 20, 38-52.

Vinson, D. R. (2000). *A new measure of process operability for the improved steady-state design of chemical processes*. Ph.D. Thesis, Lehigh University, USA.

Vinson, D.R. and Georgakis, C. (2000). A new measure of process output controllability. *J. Process Control*, 10, 185-194.

Computation of the Infinite Horizon Continuous Time Constrained Linear Quadratic Regulator ⋆

Gabriele Pannocchia * **James B. Rawlings** ** **David Q. Mayne** *** **Wolfgang Marquardt** ****

* *Dept. Chem. Eng., Ind. Chem. & Sc. Mat. – Univ. of Pisa, Italy (email: g.pannocchia@ing.unipi.it)*
** *Dept. Chem. & Biol. Eng. – Univ. of Wisconsin. Madison (WI), USA (emai: rawlings@eng.wisc.edu)*
*** *Dept. Elec. & Electronic Eng. – Imperial College London, UK (email: d.mayne@imperial.ac.uk)*
**** *AVT–Process Systems Engineering, RWTH Aachen University, Germany (email: Wolfgang.marquardt@avt.rwth-aachen.de)*

Abstract: We present a method for computing the solution to the infinite horizon continuous-time constrained linear quadratic regulator (CLQR). The method relies on two main features: a multi-grid method for placing a finite number of time intervals, and a piece-wise linear parameterization of the input within the intervals. The input values at the grid points and slopes within the time intervals are computed via quadratic programs (QPs). The grids are gradually refined to efficiently improve the accuracy of the solution, and the required matrices and vectors for all QPs are computed offline and stored to improve the online efficiency. We present two examples, a single-input single-output unstable system and a three-input three-output stable system, to show the main characteristics of the proposed computation method.

Keywords: Constrained Linear Quadratic Regulation, Continuous Time Systems, Model Predictive Control, Optimal Control

1. MOTIVATIONS FOR CONTINUOUS TIME MODEL PREDICTIVE CONTROL

The scope of applications of model predictive control (MPC) has expanded well beyond its original starting point in the process industries. With this increased scope has come the need to evaluate in real time the solution to the MPC optimal control problem for systems with fast open-loop dynamics. It is reasonable to anticipate that this trend to faster applications may culminate with a return to the continuous time description of the system model. The previous widespread adoption of discrete time models to represent the system dynamics made perfect sense. The typical sample time in earlier applications was small compared to the closed-loop dynamic response of the system (seconds compared to minutes) so there was essentially no loss in model accuracy. Moreover, the earlier analysis of the closed-loop properties and computational strategies to approximate infinite horizon control laws was simplified using discrete time models (Mayne et al., 2000).

In today's application environment, it is no longer safe to assume that some fixed sample rate can be chosen very small compared to the closed-loop system dynamics. Next, given the rapid development of MPC theory for discrete time models over the last 15 years, there is no real difficulty in establishing properties of interest in a continuous time setting. Finally, the actuator hardware has become "smarter" and it is now becoming appropriate to assume that any reasonable time function may be sent to the actuator, and it is actuator hardware's job to accurately track this signal. If the application has fast dynamics, obviously a requirement of the process design is the selection of sensors and actuators that are fast enough to keep up.

In this paper we would like to remove all issues of sampling and address directly the MPC problem for the continuous-time model (Yuz et al., 2005). The job of the MPC controller in this context is to send its solution as a time signal to the actuators until a measurement becomes available and a new state initial condition is available to the controller. This context has become popular in the nonlinear MPC area, where nonlinear models from physical principles are almost always continuous time nonlinear differential equations [see (Diehl et al., 2008) and references therein]. In this paper we would like to explore what efficiencies can be gained when we restrict attention to *linear* continuous time models.

2. PROBLEM DEFINITION

We consider linear time-invariant continuous-time systems

$$\dot{x} = Ax + Bu\,, \tag{1}$$

in which $x \in \mathbb{R}^n$ is the state and $u \in \mathbb{R}^m$ is the input. We define the following cost function for a given initial state $x_0 \in \mathbb{R}^n$ and infinite-time input $\mathbf{u}$:

$$V(x_0, \mathbf{u}) = \frac{1}{2}\int_0^\infty (x'Qx + u'Ru)\,dt, \quad \text{s.t. (1) and } x(0) = x_0\,. \tag{2}$$

in which we use the following notation. Given a function $u : \overline{\mathbb{R}} \to \mathbb{R}^m$, we define $\mathbf{u} = \{u(t) | t \geq 0\}$. The aim of this work is to compute, given the current initial state x_0, the solution of the

⋆ This research was supported by National Science Foundation (Grant CTS-0456694).

following infinite horizon optimal constrained linear quadratic regulation (CLQR) problem

$$\mathbf{u}^*(x_0) = \underset{\mathbf{u}}{\operatorname{argmin}}\ V(x_0, \mathbf{u}), \quad \text{s.t. } Du(t) \leq d\,, \qquad (3)$$

in which $D = \begin{bmatrix} D_1' & D_2' \end{bmatrix}'$ and $d = \begin{bmatrix} d_1' & d_2' \end{bmatrix}'$ with $d_1 > 0$ and $d_2 = 0$ (in element-wise sense). Notice that we allow the possibility of either (D_1, d_1) or (D_2, d_2) being empty.

We make the following assumptions.

Assumption 1. Given a matrix $T \in \mathbb{R}^{m \times r}$ with rank r such that $D_2 T = 0$, the pair (A, BT) is stabilizable, R is positive definite, Q is positive semi-definite and (A, Q) is detectable.

It is important to point out that the constraint $D_2 u \leq 0$ is active at the equilibrium point ($u = 0$). Assumption 1 states that the system must be stabilizable under the restricted control $D_2 u = 0$. We can write the restricted optimal control as $u = \bar{K}x = -(T'RT)^{-1}(BT)\bar{P}x$, with $\bar{P}$ solution of the continuous-time Riccati equation for the system matrices (A, BT) with penalties $(Q, T'RT)$ [see (Rao and Rawlings, 1999; Pannocchia et al., 2003) for further details]. Such control is feasible for all x in the positively invariant set $\mathcal{X} = \{x | D_1 \bar{K} e^{(A+B\bar{K})t} x \leq d_1 \text{ for all } t\}$.

Compared to the discrete-time counterpart, the continuous-time CLQR problem has received much less attention, although several results are available. Cannon and Kouvaritakis (2000) proposed a method for single-input single-output systems, using basis functions, in which input constraint satisfaction is ensured by a backoff strategy. Kojima and Morari (2004) propose a design method that is based on the singular value decomposition (SVD) of the finite horizon linear system and that guarantees in the limit constraint satisfaction and convergence to the optimal solution. For low dimensional linear systems, Sakizlis et al. (2005) present an approach for computing the explicit solution to the finite horizon continuous-time CLQR problem, by merging variational analysis with parametric optimization tools. Goebel and Subbotin (2007) present an approach based on the solution of the backward Hamiltonian system; optimal trajectories are stored for subsequent on-line suboptimal evaluation.

In this work, we propose a novel approach based on the direct evaluation of a suboptimal solution to the infinite horizon CLQR problem that requires, like the discrete-time case, the solution of only quadratic programs (QPs). Thus, we compute the control input in a number of grid points that can be efficiently adapted on-line to improve the accuracy of the solution. Two appropriate continuous-time input parameterizations (holds) are proposed, which show markedly improved convergence towards the optimal continuous-time solution compared to the usual piece-wise constant parameterization, and still guarantees satisfaction of the input constraints. Other related details, including proofs of the results, can be found in (Pannocchia et al., 2009).

3. INPUT PARAMETERIZATION, EXACT COST EVALUATION AND CONVERGENCE ANALYSIS

We consider three different input parameterization methods (also referred to as holds), and for each hold type a discrete-time system realization is obtained in a way that the continuous-time and the discrete-time state and input match at given grid points $(t_0, t_1, \ldots)$ assumed, in general, not evenly spaced. Moreover,

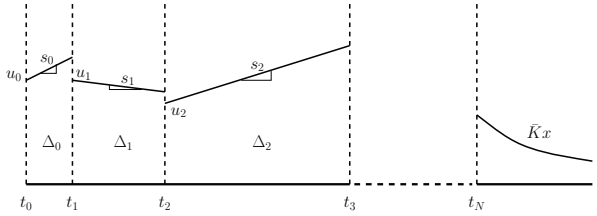

Fig. 1. Piece-wise linear input parameterization and time gridding scheme.

for each hold type we compute the corresponding discrete-time LQR cost matrices in a way that the cost in (2) is exactly evaluated. We recall that the solution to (1) is given by:

$$x(t) = e^{At}x_0 + \int_0^t e^{A(t-\tau)} B u(\tau) d\tau\,. \qquad (4)$$

3.1 Three input parameterization methods

First we summarize the properties of the well known zero-order hold (ZOH), defined as:

$$u(t) = u_k, \qquad t_k \leq t < t_{k+1}\,, \qquad (5)$$

with $t_{k+1} = t_k + \Delta_k$. Notice that we do not assume, however, that Δ_k is constant. From (4) and (5), we obtain the time-varying discrete-time system: $x_{k+1} = A_k^0 x_k + B_k^0 u_k$, in which the matrices (A_k^0, B_k^0) are defined as: $A_k^0 = e^{A\Delta_k}$, $B_k^0 = I_0(\Delta_k)B$, with $I_0(t) = \int_0^t e^{A\tau} d\tau$.

We consider a second input parameterization referred to as "piece-wise linear" hold (PWLH), and defined as:

$$u(t) = u_k + s_k(t - t_k), \qquad t_k \leq t < t_{k+1}\,, \qquad (6)$$

in which $s \in \mathbb{R}^m$ defines the "slope" of u between grid points. In the sake of clarity, we sketch the PWLH input parameterization in Figure 1, in which we also emphasize the uneven time gridding scheme that we consider later in Section 4. From (4) and (6), the time-varying discrete-time system $x_{k+1} = A_k^{\mathrm{I}} x_k + B_k^{\mathrm{I}} u_k^{\mathrm{I}}$ is obtained, in which $u^{\mathrm{I}} \in \mathbb{R}^{2m} = \begin{bmatrix} u' & s' \end{bmatrix}'$ is the augmented input, and the matrices $(A_k^{\mathrm{I}}, B_k^{\mathrm{I}})$ are: $A_k^{\mathrm{I}} = A_k^0 = e^{A\Delta_k}$, $B_k^{\mathrm{I}} = [I_0(\Delta_k)B \quad I_1(\Delta_k)B]$, with $I_0(t) = \int_0^t e^{A\tau} d\tau$ and $I_1(t) = \int_0^t e^{A(t-\tau)} \tau d\tau$.

Finally, we consider a third input parameterization, which also assumes that the input varies linearly between discrete times, but with a slope equal to forward finite input difference, i.e.

$$u(t) = u_k + \left(\frac{u_{k+1} - u_k}{\Delta_k} \right)(t - t_k), \qquad t_k \leq t < t_{k+1}\,. \quad (7)$$

In the sequel, this input parameterization is referred to as "forward first-order" hold (FFOH). From (4) and (7), we obtain the time-varying discrete-time system: $x_{k+1}^{\mathrm{II}} = A_k^{\mathrm{II}} x_k^{\mathrm{II}} + B_k^{\mathrm{II}} u_k^{\mathrm{II}}$, in which the augmented state $x^{\mathrm{II}} \in \mathbb{R}^{n+m}$, the shifted input $u^{\mathrm{II}} \in \mathbb{R}^m$, and $(A_k^{\mathrm{II}}, B_k^{\mathrm{II}})$ are:

$$x_k^{\mathrm{II}} = \begin{bmatrix} x_k \\ u_k \end{bmatrix}, \quad u_k^{\mathrm{II}} = u_{k+1},$$

$$A_k^{\mathrm{II}} = \begin{bmatrix} A_k^0 & I_0(\Delta_k)B - \frac{I_1(\Delta_k)}{\Delta_k}B \\ 0 & 0 \end{bmatrix}, \quad B_k^{\mathrm{II}} = \begin{bmatrix} \frac{I_1(\Delta_k)}{\Delta_k}B \\ I \end{bmatrix}.$$

We emphasize that ZOH generates a $u(t)$ constant between discrete times and discontinuous at the discrete times, PWLH generates a $u(t)$ linear between discrete times and discontinuous at the discrete times, FFOH generates a $u(t)$ continuous at all times and linear between discrete times.

3.2 Exact continuous time cost computation

Lemma 2. (Exact cost matrices for ZOH). If the continuous-time input is given by (5), then

$$\int_{t_k}^{t_{k+1}} (x'Qx + u'Ru)dt = x_k'Q_k^0 x_k + u_k'R_k^0 u_k + 2x_k'M_k^0 u_k \,,$$

with: $Q_k^0 = \int_0^{\Delta_k} (e^{At})'Qe^{At}dt$, $R_k^0 = \int_0^{\Delta_k} \left(R + (I_0B)'QI_0B\right) dt$, $M_k^0 = \int_0^{\Delta_k} (e^{At})'QI_0Bdt$.

It is interesting to notice that this quadrature result is known (Kwakernaak and Sivan, 1972, p.549), (Yuz et al., 2005, Sec.2.2), but most of the literature on optimal control of continuous-time systems usually ignores the mixed state-input cost term and assumes $Q_k^0 = Q\Delta_k$, $R_k^0 = R\Delta_k$, thus introducing an inherent quadrature error.

From the previous result it immediately follows that, given an infinite discrete-time input sequence $(u_0, u_1, u_2, \ldots)$, assuming that the continuous-time input $\mathbf{u}$ is defined in (5), then

$$V(x_0, \mathbf{u}) = \frac{1}{2}\sum_{k=0}^{\infty} x_k'Q_k^0 x_k + u_k'R_k^0 u_k + 2x_k'M_k^0 u_k \,.$$

Lemma 3. (Exact cost matrices for PWLH). If the continuous-time input is given by (6), then $\int_{t_k}^{t_{k+1}} (x'Qx + u'Ru)dt = x_k'Q_k^{\mathrm{I}} x_k + (u_k^{\mathrm{I}})'R_k^{\mathrm{I}} u_k^{\mathrm{I}} + 2x_k'M_k^{\mathrm{I}} u_k^{\mathrm{I}}$, with:
$Q_k^{\mathrm{I}} = \int_0^{\Delta_k} (e^{At})'Qe^{At}dt$,
$R_k^{\mathrm{I}} = \int_0^{\Delta_k} \begin{bmatrix} R + (I_0B)'Q(I_0B) & (I_0B)'Q(I_1B) + Rt \\ (I_1B)'Q(I_0B) + Rt & (I_1B)'Q(I_1B) + Rt^2 \end{bmatrix} dt$,
$M_k^{\mathrm{I}} = \int_0^{\Delta_k} \begin{bmatrix} (e^{At})'Q(I_0B) & (e^{At})'Q(I_1B) \end{bmatrix} dt$.

From this results it follows that, given infinite discrete-time input sequence and slope sequence $(u_0, u_1, u_2, \ldots)$, $(s_0, s_1, s_2, \ldots)$, assuming that the continuous-time input $\mathbf{u}$ is defined in (6), then

$$V(x_0, \mathbf{u}) = \frac{1}{2}\sum_{k=0}^{\infty} x_k'Q_k^{\mathrm{I}} x_k + (u_k^{\mathrm{I}})'R_k^{\mathrm{I}} u_k^{\mathrm{I}} + 2x_k'M_k^{\mathrm{I}} u_k^{\mathrm{I}} \,.$$

Lemma 4. (Exact cost matrices for FFOH). If the continuous-time input is given by (7), then $\int_{t_k}^{t_{k+1}} (x'Qx + u'Ru)dt = (x_k^{\mathrm{II}})'Q_k^{\mathrm{II}} x_k^{\mathrm{II}} + (u_k^{\mathrm{II}})'R_k^{\mathrm{II}} u_k^{\mathrm{II}} + 2(x_k^{\mathrm{II}})'M_k^{\mathrm{II}} u_k^{\mathrm{II}}$, with:
$Q_k^{\mathrm{II}} = \int_0^{\Delta_k} \begin{bmatrix} (e^{At})'Qe^{At} & (e^{At})'Q(I_0 - \frac{I_1}{\Delta_k})B \\ ((I_0 - \frac{I_1}{\Delta_k})B)'Qe^{At} & ((I_0 - \frac{I_1}{\Delta_k})B)'Q(I_0 - \frac{I_1}{\Delta_k})B + R\left(1 - \frac{t}{\Delta_k}\right)^2 \end{bmatrix} dt$,
$R_k^{\mathrm{II}} = \int_0^{\Delta_k} \left(R\left(\frac{t}{\Delta_k}\right)^2 + \left(\frac{I_1}{\Delta_k}B\right)' Q \left(\frac{I_1}{\Delta_k}B\right)\right) dt \,,$
$M_k^{\mathrm{II}} = \int_0^{\Delta_k} \begin{bmatrix} (e^{At})'Q\frac{I_1}{\Delta_k}B \\ ((I_0 - \frac{I_1}{\Delta_k})B)'Q\frac{I_1}{\Delta_k}B + R\frac{t}{\Delta_k}\left(1 - \frac{t}{\Delta_k}\right) \end{bmatrix} dt.$

Clearly, it follows that given an infinite discrete-time input sequence $(u_0, u_1, u_2, \ldots)$, assuming that the continuous-time input $\mathbf{u}$ is defined in (7), then

$$V(x_0, \mathbf{u}) = \frac{1}{2}\sum_{k=0}^{\infty} (x_k^{\mathrm{II}})'Q_k^{\mathrm{II}} x_k^{\mathrm{II}} + (u_k^{\mathrm{II}})'R_k^{\mathrm{II}} u_k^{\mathrm{II}} + 2(x_k^{\mathrm{II}})'M_k^{\mathrm{II}} u_k^{\mathrm{II}} \,.$$

3.3 Unconstrained convergence analysis for the three holds

In this section, we evaluate the unconstrained optimal cost that is achieved by using the three different input parameterizations, in the case of evenly spaced points, i.e. $\Delta_0 = \Delta_1 = \cdots = \Delta$, and we compare the order of convergence to the optimal continuous-time cost as Δ goes to zero. [1] We first recall the following well-known results for unconstrained LQR problems.

Lemma 5. The optimal cost-function value for the unconstrained continuous-time LQR problem $\min_{\mathbf{u}} V(x_0, \mathbf{u})$ is given by $\frac{1}{2}x_0'Px_0$ in which P is the positive semi-definite solution of the Riccati equation:

$$0 = Q + A'P + PA - PBR^{-1}B'P \,. \tag{8}$$

Lemma 6. The following discrete-time LQR problem with mixed state-input terms:

$$\min_{(u_0, u_1, \ldots)} \frac{1}{2}\sum_{k=0}^{\infty} x_k'\bar{Q}x_k + u_k'\bar{R}u_k + 2x_k'\bar{M}u_k \,, \quad \text{s.t.}$$
$$x_{k+1} = \bar{A}x_k + \bar{B}u_k \,,$$

is equivalent to the following discrete-time LQR problem without mixed state-input terms:

$$\min_{(u_0, u_1, \ldots)} \frac{1}{2}\sum_{k=0}^{\infty} x_k'\bar{Q}x_k + u_k'\bar{R}u_k, \quad \text{s.t.}$$
$$x_{k+1} = \bar{A}x_k + \bar{B}u_k \,, \tag{9}$$

in which the following change of variables is considered: $u_k \leftarrow u_k - \bar{R}^{-1}M'x_k$, $\bar{A} \leftarrow \bar{A} - \bar{B}\bar{R}^{-1}\bar{M}'$, $\bar{Q} \leftarrow \bar{Q} - \bar{M}\bar{R}^{-1}\bar{M}'$.

Lemma 7. The optimal cost-function value for the unconstrained discrete-time LQR problem (9) is $\frac{1}{2}x_0'\Pi x_0$, in which Π is the positive semi-definite solution of the Riccati equation:

$$0 = -\Pi + \bar{Q} + \bar{A}'\Pi\bar{A} - \bar{A}'\Pi\bar{B}(\bar{R} + \bar{B}'\Pi\bar{B})^{-1}\bar{B}\Pi\bar{A} \,. \tag{10}$$

If P is the solution of the continuous-time Riccati equation (8) and $\Pi(\Delta)$ is the solution of the discrete-time Riccati equation (10) using a given hold and a fixed discrete-time interval Δ, it is straightforward to show that $P \preccurlyeq \Pi(\Delta)$, which is equivalent to saying $\Pi(\Delta) - P$ is positive semidefinite. Clearly, it is desirable for an input parameterization to have convergence $\Pi(\Delta) \to P$ as $\Delta \to 0$. We define the order of convergence ℓ for a given hold implementation as the smallest non-negative integer for which $\lim_{\Delta\to 0} \frac{\Pi(\Delta) - P}{\Delta^\ell} \neq 0$.

We next establish the following results about the convergence order the LQR cost using different holds [2] . Notice that each hold defines a discrete-time optimal control problem, in which the decision variables are $\{u_k\}_{k=0}^{\infty}$ for ZOH and FFOH, and are $\{(u_k, s_k)\}_{k=0}^{\infty}$ for PWLH.

Theorem 8. (Second order convergence of ZOH). The convergence of $\Pi^0(\Delta)$ to P is second order for system matrices $\bar{A} = A^0 - B^0(R^0)^{-1}(M^0)'$, $\bar{B} = B^0$ and cost matrices $\bar{Q} = Q^0 - M^0(R^0)^{-1}(M^0)'$, $\bar{R} = R^0$.

It is interesting to notice that if inexact cost matrices are used in ZOH, the order of convergence is less than 2. For instance, if one simply chooses $Q^0 = Q\Delta$, $R^0 = R\Delta$, $M^0 = 0$, the convergence order is 1.

Theorem 9. (Fourth order convergence of PWLH). The convergence of $\Pi^{\mathrm{I}}(\Delta)$ to P is fourth order for system matrices $\bar{A} = A^{\mathrm{I}} - B^{\mathrm{I}}(R^{\mathrm{I}})^{-1}(M^{\mathrm{I}})'$, $\bar{B} = B^{\mathrm{I}}$ and cost matrices $\bar{Q} = Q^{\mathrm{I}} - M^{\mathrm{I}}(R^{\mathrm{I}})^{-1}(M^{\mathrm{I}})'$, $\bar{R} = R^{\mathrm{I}}$.

Before presenting the convergence result for FFOH, it is important to recall that, in system (3.1), the state is aug-

[1] The proof for ZOH is reported in (Pannocchia et al., 2009), and follows Taylor expansions of all terms in the discrete algebraic Riccati equation. For PWLH and FFOH, symbolic manipulation software may be useful.

[2] Since the time interval is fixed, all the discrete-time matrices are time-invariant. Thus, we drop the subscript k in this section.

mented. Thus, the corresponding solution of (10) is in the form $\Pi = \begin{bmatrix} \Pi_{xx} & \Pi_{xu} \\ \Pi'_{xu} & \Pi_{uu} \end{bmatrix}$, and, hence, the unconstrained cost for any given initial state x_0 is given by $\frac{1}{2}(x_0'\Pi_{xx}x_0 + 2x_0'\Pi_{xu}u_0 + u_0'\Pi_{uu}u_0)$. Since the input u_0 is a decision variable, the optimal unconstrained cost for any given initial state x_0 using FFOH is easily obtained as $\frac{1}{2}x_0'(\Pi_{xx} - \Pi_{xu}\Pi_{uu}^{-1}\Pi'_{xu})x_0$.

Theorem 10. (Fourth order convergence of FFOH). The convergence of $\Pi^{\rm II}(\Delta) = \Pi_{xx} - \Pi_{xu}\Pi_{uu}^{-1}\Pi'_{xu}$ to P is fourth order for system matrices $\bar{A} = A^{\rm II} - B^{\rm II}(R^{\rm II})^{-1}(M^{\rm II})'$, $\bar{B} = B^{\rm II}$ and cost matrices $\bar{Q} = Q^{\rm II} - M^{\rm II}(R^{\rm II})^{-1}(M^{\rm II})'$, $\bar{R} = R^{\rm II}$.

We now show how the optimal discrete-time cost matrices for different holds are "ordered".

Theorem 11. (Cost comparison). The following linear matrix inequalities hold: $\Pi^{\rm I}(\Delta) \preccurlyeq \Pi^{0}(\Delta)$, $\Pi^{\rm I}(\Delta) \preccurlyeq \Pi^{\rm II}(\Delta)$.

The reader may naturally expect the following ordering also to hold, $\Pi^{\rm II}(\Delta) \preccurlyeq \Pi^{0}(\Delta)$, but this is not valid for arbitrary Δ. The discontinuities allowed in ZOH may provide better performance than the continuous FFOH for large Δ. Of course, due to the different convergence orders, the ordering does hold for sufficiently small Δ.

4. ALGORITHM FOR COMPUTATION OF THE CONTINUOUS-TIME CLQR

4.1 Introduction and main definitions

Motivated by the nice convergence results of the PWLH and FFOH input parameterizations, we propose computing a suboptimal solution to problem (3) in terms of an appropriate finite number of decision variables, namely the inputs $(u_0, \ldots, u_{N-1})$, and for the PWLH case also the slopes $(s_0, \ldots, s_{N-1})$. As shown in this section, we can write the infinite-horizon continuous-time CLQR problem as a finite dimensional Quadratic Program, whose complexity is the same as that of the discrete-time CLQR problem. Furthermore, we define a procedure for placing the grid points $(t_0, \ldots, t_N)$ in a way that the number of decision variables is kept small while the accuracy of the solution is improved.

Let $(t_0, \ldots, t_N)$ be a sequence of $N+1$ grid points with $t_0 = 0$, and consider the following suboptimal CLQR problems:

$$\mathbf{u}^{\rm I} = \underset{\mathbf{u}}{\operatorname{argmin}}\ V(x_0, \mathbf{u}) \quad \text{s.t. } Du(t) \le d, \text{ (6), and } D_2u(t) = 0, \quad \text{for } t \ge t_N\,, \quad (11)$$

$$\mathbf{u}^{\rm II} = \underset{\mathbf{u}}{\operatorname{argmin}}\ V(x_0, \mathbf{u}) \quad \text{s.t. } Du(t) \le d, \text{ (7), and } D_2u(t) = 0, \quad \text{for } t \ge t_N\,, \quad (12)$$

From what presented so far, we can rewrite the problem (11) as follows:

$$\min_{(u_0^{\rm I}, u_1^{\rm I}, \ldots, u_{N-1}^{\rm I})} \frac{1}{2}x_N'P^{\rm I}x_N + \frac{1}{2}\sum_{k=0}^{N-1} x_k'Q_k^{\rm I}x_k + (u_k^{\rm I})'R_k^{\rm I}u_k^{\rm I} + 2x_k'M_k^{\rm I}u_k^{\rm I}, \quad \text{s.t.} \quad (13a)$$

$$x_{k+1} = A_k^{\rm I}x_k + B_k^{\rm I}u_k^{\rm I},\ x_0 = x(0),\ \begin{bmatrix} D & 0 \\ D & D\Delta_k \end{bmatrix} u_k^{\rm I} \le \begin{bmatrix} d \\ d \end{bmatrix}, \quad (13b)$$

in which $P^{\rm I} = \bar{P}$, provided that $x_N \in \mathcal{X}$.

Similarly, the problem (12) can be rewritten as follows:

$$\min_{(x_0^{\rm II}, u_0^{\rm II}, u_1^{\rm II}, \ldots, u_{N-1}^{\rm II})} \frac{1}{2}(x_N^{\rm II})'P^{\rm II}x_N^{\rm II} + \frac{1}{2}\sum_{k=0}^{N-1}(x_k^{\rm II})'Q_k^{\rm II}x_k^{\rm II} + (u_k^{\rm II})'R_k^{\rm II}u_k^{\rm II} + 2(x_k^{\rm II})'M_k^{\rm II}u_k^{\rm II}, \quad \text{s.t.} \quad (14a)$$

$$x_{k+1}^{\rm II} = A_k^{\rm II}x_k^{\rm II} + B_k^{\rm II}u_k^{\rm II},\ \mathcal{I}x_0^{\rm II} = x(0),\quad D[0,\ I]x_0^{\rm II} \le d, \quad Du_k^{\rm II} \le d\,, \quad (14b)$$

in which $P^{\rm II} = \mathcal{I}'\bar{P}\mathcal{I}$ and $\mathcal{I} = [I,\ 0]$, provided that $\mathcal{I}x_N^{\rm II} \in \mathcal{X}$.

After elimination of the state variables using (13b), problem (13) can be written as a convex QP in $2mN$ decision variables. Similarly, using (14b), the problem (14) can be written as a convex QP in $m(N+1)$ decision variables. Notice that $x_0^{\rm II} = [x_0',\ u_0']'$ is a decision variable in (14), but the initial constraint in (14b) implies that only u_0 is a free variable.

Notice that if $V^{\rm I}(x_0) = V(x_0, \mathbf{u}^{\rm I})$ and $V^{\rm II}(x_0) = V(x_0, \mathbf{u}^{\rm II})$ denote the optimal cost-function values for the problems (11) and (12), respectively, obtained with the same grid points $(t_0, \ldots, t_N)$, then it follows that $V^{\rm II}(x_0) \ge V^{\rm I}(x_0) \ge V^*(x_0)$.

4.2 Offline and online computations

The degree of suboptimality of the solution depends on the number of grid points, where it is clear that a larger number of intervals would result in a more accurate solution. However, it is important to observe that, in order to improve the solution, more grid points need to be placed where input and states are far away from the origin, whereas when they approach the origin, many intervals are unnecessary. During this work we tested several strategies for deciding the number and size of the intervals, with two desired goals in mind: (i) at each iteration the solution accuracy is improved, i.e. the computed objective function is decreased; (ii) the total number of intervals, and hence the number of QP decision variables, is kept small. We next present the simplest algorithm that is used offline to generate the QP associated with (13).

Algorithm 1. Data: maximum time t_N, initial number of intervals Θ, number of halving loops Θ_s.

(1) Compute the Θ intervals $(\Delta_0, \ldots, \Delta_{\Theta-1})$ such that $\Delta_k/\Delta_{k+1} = 0.5$ and $\sum_{k=0}^{\Theta-1}\Delta_k = t_N$.
(2) Define the initial sequence of $N_1 = \Theta$ intervals as $\mathcal{P}_1 = (\Delta_0^1, \ldots, \Delta_{N_1-1}^1) = (\Delta_0, \ldots, \Delta_{\Theta-1})$.
(3) Set $j \leftarrow j+1$ and define the next sequence $\mathcal{P}_j$ of $N_j = 2N_{j-1}$ intervals by halving each interval of $\mathcal{P}_{j-1}$.
(4) If $j < \Theta_s + 1$ go to 3. Otherwise, for each interval sequence $\mathcal{P}_j$ with $j = 1, \ldots, \Theta_s+1$, compute the matrices $(A_k^{\rm I}, B_k^{\rm I}, Q_k^{\rm I}, R_K^{\rm I}, M_k^{\rm I})$ in (13), build the associated QP in the form:

$$\mathbb{QP}_j: \quad \min_{\mathbf{v}} \frac{1}{2}\mathbf{v}'\mathbf{H}\mathbf{v} + \mathbf{v}'\mathbf{Q}x_0, \quad \text{s.t. } \mathbf{A}\mathbf{v} \le \mathbf{b} \quad (15)$$

with $\mathbf{v} = (u_0^{\rm I}, \ldots, u_{N_j-1}^{\rm I})$, storing $\mathbf{H}$, $\mathbf{Q}$, $\mathbf{A}$, $\mathbf{b}$.

For open-loop unstable systems, in order to avoid ill-conditioning of $\mathbf{H}$, the input variable re-parameterization discussed in (Rossiter et al., 1998) is recommended.

The next algorithm describes the operations that are performed online to compute $\mathbf{u}^I(x_0)$.

Algorithm 2. Given x_0, the relative cost decrease tolerance $\mu > 0$. Initialize $j = 1$.

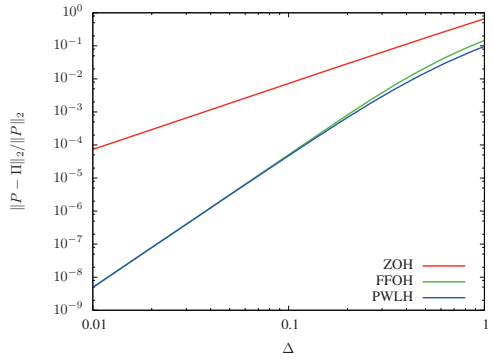

Fig. 2. System 1: Relative error between P and discrete-time cost Π for ZOH, FFOH, PWLH *vs* Δ.

(1) Solve $\mathbb{QP}_j$, let $V_j^{\mathrm{I}}(x_0)$ be the associated optimal cost and $\mathbf{u}_j^{\mathrm{I}}(x_0)$ the optimal input.
(2) If $j = 1$, set $j \leftarrow j + 1$ and go to 1. Otherwise,
(3) If the relative cost decrease satisfies $\frac{V_{j-1}^{\mathrm{I}}(x_0) - V_j^{\mathrm{I}}(x_0)}{V_{j-1}^{\mathrm{I}}(x_0)} < \mu$ or $j = \Theta_s + 1$, set $\mathbf{u}^{\mathrm{I}}(x_0) = \mathbf{u}_j^{\mathrm{I}}(x_0)$ and stop. Otherwise, set $j \leftarrow j + 1$ and go to 1.

Notice that if at any iteration j, the solution to $\mathbb{QP}_j$ is such that $x_N \notin \mathcal{X}$, then an additional interval of the largest size is added, i.e. $t_N \leftarrow t_N + \Delta_{N-1}$ and $\mathbb{QP}_j$ is solved again $x_N \notin \mathcal{X}$. Such additional intervals are retained also for subsequent iterations. For efficient online computation it is advised that the matrices associated with each $\mathbb{QP}_j$ are built and stored for different increasing t_N, so that the online CPU time is required only for solving the QPs.

We have the following important result.

Theorem 12. For each iteration $j > 1$ of Algorithm 2, we have that:

$$V_j^{\mathrm{I}}(x_0) \leq V_{j-1}^{\mathrm{I}}(x_0), \quad \text{for all } j > 0\,. \tag{16}$$

It is important to remark that the same cost decrease property holds true if Algorithm 2 is applied to compute $\mathbf{u}^{\mathrm{II}}(x_0)$.

5. CASE STUDIES

To illustrate the main features of the proposed method, we present two examples. The first example is a SISO unstable system, whose transfer function is shown below:

$$g_1(s) = -\frac{6.512s + 1.628}{-2.4390s^2 + 3.9756s + 1}\,.$$

The second example is the 3 input, 3 output Shell Control Problem (Prett and Morari, 1987), for which we use a 10 state continuous-time model. For both examples we use $Q = I$, $R = 0.1I$.

In Figure 2 we show, for the first example, the relative error (evaluated using the 2-norm) between the continuous-time LQR cost matrix P and the corresponding discrete-time cost matrix Π obtained with ZOH, FFOH, PWLH as a function of Δ. As expected from Theorems 8, 9, 10, the orders of convergence for ZOH is 2, whereas it is 4 for PWLH and FFOH.

Unless otherwise specified, in the subsequent studies we consider input constraints $-1 \leq u \leq 1$, the optimal input $\mathbf{u}^{\mathrm{II}}(x_0)$ is computed with Algorithm 2 using FFOH input parameterization and using a relative tolerance of $\mu = 10^{-4}$. For

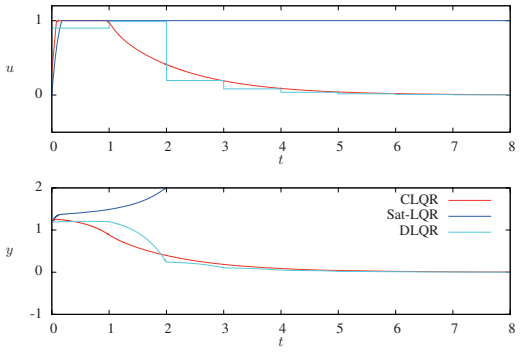

Fig. 3. System 1. Input and output closed-loop response using CLQR, "saturated" LQR and DLQR.

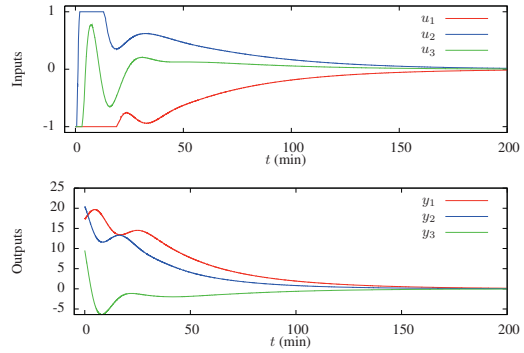

Fig. 4. System 2. Closed-loop inputs and outputs using CLQR at decision times $0, 1, \ldots$.

System 1 we show in the top plot of Figure 3 the optimal closed-loop input and output, computed by solving the optimal control problem with the proposed algorithm at decision times $0, 1, \ldots, 7$, and implementing the computed infinite horizon input in a receding horizon fashion. For comparison, we also show the results obtained by: (i) infinite horizon discrete-time constrained LQR (DLQR), (ii) "saturated" continuous-time LQR law $u = \mathrm{sat}\,(Kx)$. We observe that DLQR generates a stable closed-loop response that is fairly different from the optimal one obtained with CLQR. We also note that Kx_0 is feasible, but nonetheless the saturated LQR makes the closed-loop system unstable, whereas CLQR and DLQR stabilize the system in closed-loop (due to the infinite horizon formulation). Inputs and outputs for System 2 computed with constrained LQR at the decision times $0, 1, \ldots, 200$ are shown in Figure 4.

Finally, for System 1, we report in Table 1 the relative cost error, the number of required intervals, and CPU-time for solving all the QPs [3] for different values of μ. In computing the relative cost error, we approximate $V^*(x)$ with the value obtained using PWLH-CLQR with $\mu = 10^{-8}$. The data reported in Table 1 refer to the computation of $\mathbf{u}(x_0)$ for the same initial state considered in Figure 3. We report in Table 2 the same computational study for System 2. We can observe that, when the number of intervals is the same, PWLH-CLQR achieves a slightly lower cost than FFOH-CLQR. However, this comes at the expense of a higher CPU time because PWLH-CLQR

[3] Using GNU Octave on an AMD Athlon$^{\mathrm{TM}}$ 64 X2 Dual Core Processor 4400+ running Debian Linux.

Table 1. System 1. Comparison of cost relative error, number of intervals of the final QP and overall CPU-time for solving all QPs vs. relative tolerance μ for PWLH-CLQR and FFOH-CLQR

	PWLH-CLQR Algorithm			FFOH-CLQR Algorithm		
μ	$\frac{V^{\mathrm{I}}(x_0)-V^*(x_0)}{V^*(x_0)}$	N	CPU-time (s)	$\frac{V^{\mathrm{II}}(x_0)-V^*(x_0)}{V^*(x_0)}$	N	CPU-time (s)
10^{-2}	$1.755 \cdot 10^{-3}$	6	0.00012	$7.689 \cdot 10^{-4}$	12	0.00020
10^{-3}	$1.841 \cdot 10^{-4}$	24	0.00120	$1.883 \cdot 10^{-4}$	24	0.00040
10^{-4}	$4.495 \cdot 10^{-8}$	96	0.0376	$4.926 \cdot 10^{-8}$	96	0.0075
10^{-5}	$4.495 \cdot 10^{-8}$	96	0.0376	$4.926 \cdot 10^{-8}$	96	0.0075
10^{-6}	$4.495 \cdot 10^{-8}$	96	0.0376	$4.926 \cdot 10^{-8}$	96	0.0075
10^{-7}	$6.408 \cdot 10^{-9}$	192	0.360	$8.841 \cdot 10^{-9}$	192	0.0440
10^{-8}	—	384	3.264	$1.468 \cdot 10^{-9}$	384	0.444

Table 2. System 2. Comparison of cost relative error, number of intervals of the final QP and overall CPU-time for solving all QPs vs. relative tolerance μ for PWLH-CLQR and FFOH-CLQR

	PWLH-CLQR Algorithm			FFOH-CLQR Algorithm		
μ	$\frac{V^{\mathrm{I}}(x_0)-V^*(x_0)}{V^*(x_0)}$	N	CPU-time (s)	$\frac{V^{\mathrm{II}}(x_0)-V^*(x_0)}{V^*(x_0)}$	N	CPU-time (s)
10^{-2}	$3.3681 \cdot 10^{-3}$	6	0.00040	$6.4084 \cdot 10^{-3}$	6	0.00027
10^{-3}	$5.0657 \cdot 10^{-5}$	48	0.334	$1.1411 \cdot 10^{-4}$	48	0.0267
10^{-4}	$8.8931 \cdot 10^{-7}$	96	2.40	$1.0786 \cdot 10^{-6}$	192	2.29
10^{-5}	0	192	15.8	$1.0786 \cdot 10^{-6}$	192	2.29

optimizes over the input and the slope in each interval, while FFOH-CLQR optimizes only over the input with the slope fixed by continuity at the end point of the interval. For instance, for System 1, with $\mu = 10^{-3}$ PWLH-CLQR optimizes (in the last QP) over $2mN = 48$ decision variables while FFOH-CLQR over $m(N+1) = 25$ variables. Also notice that a relative tolerance between 10^{-2} and 10^{-3} results in small suboptimality. For these reasons, the most effective algorithm appears to be FFOH-CLQR, which achieves a solution in 0.40 ms with a relative cost error of about $1 \cdot 10^{-4}$. For System 2, a reasonable value for μ is also between 10^{-2} and 10^{-3}. For instance using FFOH-CLQR with $\mu = 10^{-3}$, we compute a solution in 27 ms with a relative cost error less than $2 \cdot 10^{-4}$. Such a computational time is clearly negligible compared to the systems dynamics. The resolution of the actuator in the application also implies a fairly loose tolerance ($\sim 10^{-3}$) on the solution should be used. It obviously makes little sense to compute an optimal input more accurately than the actuator hardware can resolve.

6. CONCLUSIONS

In this paper we presented a method for solving the infinite horizon continuous-time constrained linear quadratic regulator, by solving a finite number of finite dimensional quadratic programs. A number of unevenly spaced grid points are selected and adapted on-line to achieve a tolerance specification in the controller cost. The input parameterization is piecewise linear on the chosen time intervals; we examined both continuous and discontinuous parameterizations. The parameterizations guarantee exact input constraint satisfaction. Both of these input parameterizations converge to the optimal solution much more quickly than piecewise constant inputs, allowing a reduction in the final number of intervals and, therefore, decision variables. Furthermore, we derived exact discrete-time matrices and penalties to avoid quadrature errors, and moved offline all the computation required for solving ODEs and creating the Hessian and linear terms in the QPs solved online. Finally, we presented simulation results for two examples to illustrate the main ideas. The online complexity of solving the infinite horizon continuous-time CLQR with the proposed method is no larger than that required for solving an infinite horizon discrete-time CLQR problem of the same size.

REFERENCES

Cannon, M. and Kouvaritakis, B. (2000). Infinite horizon predictive control of constrained linear systems. *Automatica*, 36, 943–955.

Diehl, M., Ferreau, H.J., and Haverbeke, N. (2008). Efficient numerical methods for nonlinear MPC and moving horizon estimation. In *Proceedings of the International Workshop on Assessment and Future Directions of NMPC*. Pavia, Italy.

Goebel, R. and Subbotin, M. (2007). Continuous time linear quadratic regulator with control constraints via convex duality. *IEEE Trans. Auto. Contr.*, 52(5), 886–892.

Kojima, A. and Morari, M. (2004). LQ control of constrained continuous-time systems. *Automatica*, 40, 1143–1155.

Kwakernaak, H. and Sivan, R. (1972). *Linear Optimal Control Systems*. John Wiley & Sons.

Mayne, D.Q., Rawlings, J.B., Rao, C.V., and Scokaert, P.O.M. (2000). Constrained model predictive control: Stability and optimality. *Automatica*, 36(6), 789–814.

Pannocchia, G., Wright, S.J., and Rawlings, J.B. (2003). Existence and computation of infinite horizon model predictive control with active steady-state input constraints. *IEEE Trans. Auto. Contr.*, 48(6), 1002–1006.

Pannocchia, G., Rawlings, J.B., Mayne, D.Q., and Marquardt, W. (2009). On computing the solutions to the continuous time constrained linear quadratic regulator. Submitted for publication in IEEE Trans. Auto. Cont.

Prett, D.M. and Morari, M. (1987). *The Shell Process Control Workshop*. Butterworth Publishers.

Rao, C.V. and Rawlings, J.B. (1999). Steady states and constraints in model predictive control. *AIChE J.*, 45, 1266–1278.

Rossiter, J.A., Kouvaritakis, B., and Rice, M.J. (1998). A numerically robust state-space approach to stable-predictive control strategies. *Automatica*, 34, 65–73.

Sakizlis, V., Perkins, J.D., and Pistikopoulos, E.N. (2005). Explicit solutions to optimal contol problems for contrained continuous-time linear systems. *IEE Proc.-Control Theory Appl.*, 152(4), 443–452.

Yuz, J., Goodwin, G., Feuer, A., and De Doná, J. (2005). Control of constrained linear systems using fast sampling rates. *Syst. Contr. Lett.*, 54, 981–990.

Explicit Robust Model Predictive Control ⋆

Efstratios N. Pistikopoulos * **Nuno P. Faísca** **
Konstantinos I. Kouramas * **Christos Panos** *

* *Centre for Process Systems Engineering, Department of Chemical Engineering, Imperial College London, SW7 2AZ London, UK (e-mail: e.pistikopoulos, k.kouramas, christos.panos08@imperial.ac.uk)*
** *Process Systems Enterprise Ltd, London, UK (e-mail: pitigrilli@gmail.com)*

Abstract: Explicit robust multi–parametric feedback control laws are designed for constrained dynamic systems involving uncertainty in the left-hand side(LHS) of the underlying MPC optimization model. Our proposed procedure features: (i) a robust reformulation/optimization step, (ii) a dynamic programming framework for the model predictive control (MPC) problem formulation, and (iii) a multi-parametric programming solution step.

Keywords: Robust model predictive control, multi-parametric programming, dynamic programming, multi–parametric control, explicit control.

1. INTRODUCTION

Robust model predictive control (Robust MPC) is an important class of constrained, model–based control methods that can explicitly account for the presence of modeling uncertainties in the controlled process, which has received significant attention in control systems research–an indicative list of related publications is given in (Bemporad and Morari, 1999; Mayne et al., 2000; Sakizlis et al., 2004; Wang and Rawlings, 2004; Pistikopoulos et al., 2007a) and references within. On the other hand, explicit MPC, which has also received equal attention recently (Pistikopoulos et al., 2002, 2007a), is a control method where the online MPC optimization problem is solved off–line with multi–parametric programming methods to obtain the optimal control actions as a set of functions of the system states. The MPC controller can then be implemented online as a set of simple feedback control laws based on function evaluations instead of using online optimization with complex and increased computational demands.

Despite these significant advances, explicit, robust MPC is still an important area of research. It is evident from the relevant literature (Bemporad et al., 2003; Wang and Rawlings, 2004; Pistikopoulos et al., 2007a) that, even for the case of linear MPC, the underlying optimization model of the MPC is nonlinear due to the uncertainties appearing both in the left–hand side and right–hand side of the optimization constraints (Borrelli, 2003; Pistikopoulos et al., 2007a). This imposes difficulties for the application of the existing multi–parametric programming techniques and special treatment is required to ensure that the constraints are always satisfied (Bemporad et al., 2003; Kouramas et al., 2009).

⋆ This work is supported by EPSRC (GR/T02560/01, EP/E047017/1) and European Commission (PRISM ToK project, Contact No: MTKI-CT-2004-512233 and DIAMANTE ToK project, Contract No: MTKI-CT-2005-IAP-029544)

Explicit robust MPC was investigated in Sakizlis et al. (2004) for the case of linear dynamic systems with additive state disturbances (right–hand side uncertainty in the optimization model). A dynamic programming based method, for linear dynamic systems with linear objective costs and uncertainties in left–hand side of the optimization model was studied in Bemporad et al. (2003). Furthermore, an explicit robust MPC with a quadratic objective and left–hand side uncertainties, based on robust optimization methods (Ben-Tal and Nemirovski, 2000; Lin et al., 2004), was presented in Kouramas et al. (2009) where the MPC optimization is treated as a robust multi–parametric optimization problem. Explicit robust MPC problems with quadratic costs have not yet been fully studied since the underlying multi–parametric optimization problem becomes nonlinear due to the uncertain coefficients in the constraints (Kouramas et al., 2009). On the other hand, employing dynamic programming methods for even the simple case of explicit MPC (with no uncertainties) results either into solving a demanding global optimization problem (Faísca et al., 2008) at each stage of the dynamic programming procedure or overlapping critical regions in the explicit solution.

This work presents a novel method for *Explicit Robust Model Predictive Control* based on dynamic programming methods (Bellman (2003); Faísca et al. (2008)) and robust optimization techniques (Ben-Tal and Nemirovski, 2000; Lin et al., 2004) that (i) allows the use of quadratic objective functions, (ii) accounts for the uncertainties in the left–hand side of the underlying MPC optimization problem, and (iii) overcomes the limitations of previous methods and the need for global optimization at each stage of the dynamic programming.

We focus on the following explicit robust MPC problem

$$
\begin{aligned}
V^*(x) = &\min_U J(U,x) \\
= &\min_U \sum_{k=0}^{N-1} \{x_k^T Q x_k + u_k^T R u_k\} + x_N^T P x_N \qquad (1)\\
\text{s.t. } & x_{k+1} = Ax_k + Bu_k,\ \forall\, \Delta A \in \mathcal{A},\ \Delta B \in \mathcal{B} \\
& Cx_k \le d,\ \ k = 0,1,\ldots,N \\
& Mu_k \le \mu,\ \ k = 0,1,\ldots,N-1 \\
& Tx_N \le \tau \\
& x = x_0
\end{aligned}
$$

where $x \in \mathbb{R}^n$ is the system state, $u \in \mathbb{R}^m$ is the system input and N the prediction horizon. We assume that the underlying system is uncertain in that the system matrices are described as

$$
\begin{aligned}
& x_{k+1} = Ax_k + Bu_k,\ A = A_0 + \Delta A,\ B = B_0 + \Delta B \qquad (2)\\
& \Delta A \in \mathcal{A} = \{\Delta A \in \mathbb{R}^{n\times n} | -\varepsilon_a |A_0| \le \Delta A \le \varepsilon_a |A_0|\} \\
& \Delta B \in \mathcal{B} = \{\Delta B \in \mathbb{R}^{n\times n} | -\varepsilon_\beta |B_0| \le \Delta B \le \varepsilon_\beta |B_0|\}
\end{aligned}
$$

where A_0, B_0 are of known constant values but the values of matrices $\Delta A, \Delta B$ are not known but are bounded as given in (2) and $\epsilon_a, \epsilon_\beta \in [0,1)$. The system states and inputs are also subject to the following linear constraints

$$x \in \mathcal{X} = \{x \in \mathbb{R}^n | Cx \le d\} \qquad (3)$$

$$u \in \mathcal{U} = \{u \in \mathbb{R}^m | Mu \le \mu\} \qquad (4)$$

where the sets $\mathcal{X}$,$\mathcal{U}$ are assumed to be compact, non-empty polytopic sets that include the origin in their interior and with $C \in \mathbb{R}^{n_c \times n}$, $d \in \mathbb{R}^{n_c}$, $M \in \mathbb{R}^{m_M \times m}$ and $\mu \in \mathbb{R}^{m_M}$. The proposed approach and the underlying mathematical framework for solving (1) will be discussed in detail in the following sections.

2. EXPLICIT ROBUST MODEL PREDICTIVE CONTROL

The proposed approach is realized in three key steps:

(1) dynamic programming: the MPC optimization is recast in a multi-stage optimization setting,
(2) robust reformulation: the constraints at each stage are reformulated to account for the worst-case uncertainty, and
(3) multi-parametric programming: each one of the reformulated stages is solved as multi-parametric programming problems where the optimization variables are the incumbent control inputs, given the optimal solutions of the previous steps.

These steps are described in detail in the following.

2.1 Dynamic Programming – Multi-stage optimization

The robust MPC problem (1) can be expressed as a multi–stage optimization problem since it involves a discrete-time dynamic system and a stage–additive quadratic objective function. The same procedure was applied for the nominal system case (where $\varepsilon_a, \varepsilon_\beta = 0$) in Faísca et al. (2008) Dynamic programming techniques (Bellman, 2003) can be applied to decompose (1) into a set of *stage-wise* problems of smaller dimensions, significantly reducing the complexity of the initial problem (Bellman (2003) and Faísca et al. (2008)) - at each stage k the following optimization problem is considered

$$
\begin{aligned}
V_k(x_k) = &\min_{u_k \in \mathcal{U}} J_k(u_k, x_k) \\
= &\min_{u_k \in \mathcal{U}} \sum_{i=k}^{N-1} \{x_i^T Q x_i + u_i^T R u_i\} + x_N^T R x_N \qquad (5)\\
\text{s.t. } & x_{i+1} = Ax_i + Bu_i,\ i = k,\ldots,N \\
& Cx_k \le d,\ \ Cx_{k+1} \le d,\ \ Mu_k \le \mu, \\
& \forall\, \Delta A \in \mathcal{A},\ \Delta B \in \mathcal{B}
\end{aligned}
$$

The optimization is taken only on the current stage input u_k and only the constraints on x_k and x_{k+1} have to be considered. The main idea is to solve the single–stage optimization problem (5) as a robust mp–QP problem and obtain the control variable u_k at each stage as an explicit function of current state x_k

$$u_k = f_k^*(x_k) \qquad (6)$$

or

$$u_k = K_k^i x_k + c_k^i \quad \textbf{if } \ x_k \in CR_k^i\ ,\ \ i = 1,\ldots,L_k$$

A method for solving (5) as a robust mp–QP problem and deriving (6) is presented in the following sections. The proposed procedure for solving (1) as a multi-stage problem is the following: starting from time $k = N-1$, problem (5) is solved iteratively at each time k until $k = 0$ where the procedure stops. At the initial stage $k = N-1$ the extra terminal constraint $Tx_N \le \tau$ should also be added in (5).

In order to ensure that a feasible solution u_k exists for all $k = 0,1,\ldots N-1$ an extra feasibility constraint is introduced in each of the single stage problems (5)

$$x_{k+1} \in \mathcal{X}^{k+1}\ ,\ \ \mathcal{X}^{k+1} = \cup_{i=1}^{L_{k+1}} CR_{k+1}^i \qquad (7)$$

where $\mathcal{X}^{k+1}$ is the union of all critical regions of the explicit solution $u_{k+1} = f_{k+1}^*(x_{k+1})$ from the previous stage $k+1$ i.e. $\mathcal{X}^{k+1}$ is the set of states x_{k+1} for which the optimization problem at the stage $k+1$ has a feasible solution. Since the set of all critical regions is a convex polyhedral set (Pistikopoulos et al., 2002), the set $\mathcal{X}^{k+1}$ is given by a set of linear inequalities

$$\mathcal{X}^{k+1} = \{x \in \mathbb{R}^n | H^{k+1} x \le h^{k+1}\} \qquad (8)$$

Adding the constraints (8) in (5) will ensure that the future state x_{k+1} lies in the set $\mathcal{X}^{k+1}$ and hence one of the critical regions CR_{k+1}^i, and therefore a feasible control input $u_{k+1} = f_{k+1}^*(x_{k+1})$ at time $k+1$ can be obtained. For simplicity the inequalities $Cx_{k+1} \le d$ and (8) will be replaced by the single inequality

$$\mathcal{G}^k x_{k+1} \le b^k$$

where $\mathcal{G}^k = [C^T \ \ {H^{k+1}}^T]^T$ and $b^k = [d^T \ \ {h^{k+1}}^T]^T$.

We will now proceed to describe how to reformulate (5) to a robust mp–QP problem. Considering u_k as the optimization variable and $\theta_k = \left[x_k^T\ u_{k+1}^T \ldots u_{N-1}^T\right]^T$ as the vector of parameters, and by incorporating the system dynamics $x_{k+1} = Ax_k + Bu_k$ into the objective and constraints, one obtains the following multi-parametric optimization problem

$$
\begin{aligned}
V_k(x_k) = &\min J_k(u_k, \theta_k) \\
= &\min_{u_k \in \mathcal{U}} \left\{ \frac{1}{2} u_k^T H u_k + \theta_k^T F u_k \right\} + \theta_k^T Y \theta_k \qquad (9)\\
\text{s.t. } & \mathcal{G}^k A x_k + \mathcal{G}^k B u_k \le b^k,\ \ Cx_k \le d,\ \ Mu_k \le \mu \\
& \forall\, \Delta A \in \mathcal{A},\ \Delta B \in \mathcal{B}
\end{aligned}
$$

where the matrices H, F, Y are functions of the matrices A, B, Q and R. When there is no uncertainty in the underlying system dynamics $\varepsilon_a = \varepsilon_\beta = 0$, (5) is a simple mp–QP problem and can be solved with the known mp–QP method (Pistikopoulos et al., 2007b). However, in the presence of uncertainty (when $\varepsilon_a, \varepsilon_\beta \in [0, 1)$ are non-zeros) special treatment of (9) is required to reformulate it into mp–QP problem.

Remark 1. In conventional dynamic programming, the optimal value $u_{k+1} = f^*_{k+1}(x_{k+1})$ would have been incorporated into the formulation of (14) to create an optimization problem where only u_k is the optimization variable and x_k the parameter. However, even for the simple case with no uncertainties, this would have resulted into a nonlinear multi–parametric programming problem (since $u_{k+1} = f^*_{k+1}(x_{k+1})$ is a piecewise affine function) that would need to employ global optimization methods to be solved (Borrelli, 2003; Faísca et al., 2008). Our approach is based on the work of Faísca et al. (2008) for the case of explicit MPC with no uncertainties, where this issue is overcome by substituting previous solutions u_{k+1} in the current solution u_k after the multi–parametric programming has been solved.

2.2 Robustification Step

The main issue for applying multi-parametric optimization techniques for the solution of (9) is the presence of the uncertain matrices A, B in the objective and the inequalities of (9). The objective function can be set to penalize only the behaviour of the nominal system $x_{k+1} = A_0 x_k + B_0 u_k$, that is to say the objective function in (9) is formed by replacing $x_{k+1} = A_0 x_k + B_0 u_k$ in the objective (5) and H, F, Y are constant matrices. However, it is very important to guarantee the feasibility of the constraints in the presence of the uncertainty. Problem (9) can then be recast as

$$V_k(x_k) = \min_{u_k \in \mathcal{U}} \left\{ \frac{1}{2} u_k^T H u_k + \theta_k^T F u_k \right\} + \theta_k^T Y \theta_k \qquad (10)$$
$$\text{s.t. } \mathcal{G}^k A_0 x_k + \mathcal{G}^k \Delta A x_k + \mathcal{G}^k B_0 u_k + \mathcal{G}^k \Delta B u_k \le b^k$$
$$C x_k \le d, \;\; M u_k \le \mu, \;\; \forall\, \Delta A \in \mathcal{A}, \; \Delta B \in \mathcal{B}$$

It is obvious from (10) that due to variations of $\Delta A, \Delta B$ constraint violations might occur. Solving (10) is a robust multi-parametric optimization problem where u_k is the optimization variable and θ_k is the vector of parameters. The objective is to find a solution $u^*_k(\theta_k)$ which can guarantee constraint satisfaction for all admissible values of the uncertainty i.e. for all $\Delta A \in \mathcal{A}$ and $\Delta B \in \mathcal{B}$.

Definition 2.1. A solution $u^*_k(\theta_k)$ of robust mp-QP problem (10) is a *robust* or *reliable* solution if it is feasible for (10) both for the nominal system ($A = A_0$, $B = B_0$) and the uncertain system i.e. if it is feasible for all admissible values of the uncertainty i.e. for all $\Delta A \in \mathcal{A}$ and $\Delta B \in \mathcal{B}$.

In order to avoid constraint violations, the constraints have to be *immunized* against the model uncertainty (see Ben-Tal and Nemirovski (2000) and Lin et al. (2004)). In order to account for the uncertainty in (10), the inequality constraints of (10) are replaced by the following two inequalities

$$\mathcal{G}^k A_0 x_k + \mathcal{G}^k B_0 u_k \le d \qquad (11)$$

$$\mathcal{G}^k A_0 x_k + \varepsilon_a |\mathcal{G}^k| |A_0| |x_k| + \mathcal{G}^k B_0 u_k + \varepsilon_\beta |\mathcal{G}^k| |B_0| |u_k| \le b^k + \delta \max\{1, |d|\} \qquad (12)$$

The first inequality ensures that the problem is feasible for the nominal system case while the second inequality represents the realisation of the constraint for the worst-case value of the uncertainty. The newly introduced variable δ is a measure of the infeasibility tolerance for the constraint in the problem i.e. how much the constraint can be relaxed to ensure a feasible solution. If no infeasibility is allowed then $\delta = 0$.

Replacing the new constraints (11)–(12) into (10) results into a multi–parametric nonlinear programming problem. To overcome this, (12) is replaced by the following linear inequalities

$$\begin{aligned} &\mathcal{G}^k A_0 x_k + \varepsilon_a |\mathcal{G}^k| |A_0| z_k + \mathcal{G}^k B_0 u_k \\ &+ \varepsilon_\beta |\mathcal{G}^k| |B_0| \omega_k \le b^k + \delta \max\{1, |d|\} \\ &- z_k \le x_k \le z_k, \;\; -\omega_k \le u_k \le \omega_k, \;\; z_k, \omega_k \ge 0 \end{aligned} \qquad (13)$$

It is obvious that if a pair x_k, u_k satisfies (13) then, since $|x_k| \le z_k$ and $|u_k| \le \omega_k$, it also satisfies (12). By replacing (13) in (10) the new robust mp–QP formulation is obtained for each stage

$$V_k(x_k) = \min_{u_k, z_k, \omega_k} \left\{ \frac{1}{2} u_k^T H u_k + \theta_k^T F u_k \right\} + \theta_k^T Y \theta_k \qquad (14)$$
$$\begin{aligned} &\text{s.t. } \mathcal{G}^k A_0 x_k + \mathcal{G}^k B_0 u_k \le b^k \\ &\mathcal{G}^k A_0 x_k + \varepsilon_a |\mathcal{G}^k| |A_0| z_k + \mathcal{G}^k B_0 u_k \\ &\quad + \varepsilon_\beta |\mathcal{G}^k| |B_0| \omega_k \le b^k + \delta \max\{1, |d|\} \\ &\quad - z_k \le x_k \le z_k, \;\; -\omega_k \le u_k \le \omega_k, \;\; z_k, \omega_k \ge 0 \\ &\quad C x_k \le d, \;\; M u_k \le \mu \end{aligned}$$

where now the parameters are θ_k, the optimization variable is $\pi_k = \left[u_k^T, z_k^T, \omega_k^T\right]^T$, the objective function is a quadratic function and the constraints are all linear inequalities. The new formulation (14) is an mp–QP problem and can be solved by employing the mp–QP methods of Pistikopoulos et al. (2002) and Pistikopoulos et al. (2007b) which is discussed next.

2.3 Multi–Parametric Quadratic Programming

In order to solve (14) as an mp–QP problem, the following three steps have to be followed

Step 1. The Karush–Kuhn–Tucker (KKT) conditions are first applied for problem (14) (see Bazaraa and Shetty (1979)):

$$\nabla \mathcal{L}(\pi_k, \lambda, \theta_k) = 0, \;\; \lambda_i \psi_i(\pi_k, \theta_k) = 0, \;\; \forall \;\; i = 1, \ldots, p$$
$$\mathcal{L} = J_k(\pi_k, \theta_k) + \sum_{i=1}^{p} \lambda_i \psi_i(\pi_k, \theta_k) \qquad (15)$$

where $J_k(\pi_k, \theta_k)$ is the objective function of (14), $\psi(\pi_k, \theta_k) \le 0$ is the vector of the inequality constraints in (14) and λ is the vector of the Lagrange multipliers.

Step 2. The basic sensitivity theorem (Fiacco (1976)) is then applied to the KKT conditions (15). For simplicity we set $\theta = \theta_k$ and $\pi = \pi_k$.

Theorem 2. Let θ_0 be a vector of parameter values and $(\pi_0, \lambda_0, \mu_0)$ a KKT triple corresponding to (15), where

λ_0 is nonnegative and π_0 is feasible in (14). Also assume that (i) strict complementary slackness (SCS) holds, (ii) the binding constraint gradients are linearly independent (LICQ: Linear Independence Constraint Qualification), and (iii) the second-order sufficiency conditions (SOSC) hold. Then, in neighbourhood of θ_0, there exists a unique, once continuously differentiable function, $z(\theta) = [\pi(\theta), \lambda(\theta)]$, satisfying (15) with $z(\theta_0) = [\pi(\theta_0), \lambda(\theta_0)]$ where $\pi(\theta)$ is a unique isolated minimiser for (14), and

$$\begin{pmatrix} d\pi(\theta_0)/d\theta \\ d\lambda(\theta_0)/d\theta \end{pmatrix} = -(M_0)^{-1} N_0, \tag{16}$$

where, M_0 and N_0 are the Jacobians of system (15) with respect to z and θ (Fiacco, 1983, pp. 80–81), (Pistikopoulos et al., 2002).

Step 3. A general analytic expression for π_k is then derived by applying the following corollary of Dua et al. (2002)

Corollary 3. First-order estimation of $\pi(\theta)$, $\lambda(\theta)$, near $\theta = \theta_0$ (Fiacco, 1983): Under the assumptions of Theorem 2, a first-order approximation of $[\pi(\theta), \lambda(\theta)]$ in a neighbourhood of θ_0 is,

$$\begin{bmatrix} \pi(\theta) \\ \lambda(\theta) \end{bmatrix} = \begin{bmatrix} \pi_0 \\ \lambda_0 \end{bmatrix} + (M_0)^{-1} \cdot N_0 \cdot \theta + o(||\theta||), \tag{17}$$

where $(\pi_0, \lambda_0) = [\pi(\theta_0), \lambda(\theta_0)]$, $M_0 = M(\theta_0)$, $N_0 = N(\theta_0)$, and $\phi(\theta) = o(||\theta||)$ means that $\phi(\theta)/||\theta|| \to 0$ as $\theta \to \theta_0$.

The critical region (set of θ) where (17) remains optimal can then be obtained as follows (Dua et al., 2002). If $\breve{\psi}$ corresponds to the non-active constraints, and $\tilde{\lambda}$ corresponds to the active constraints then each critical region is defined by

$$\begin{array}{ll} \breve{\psi}(u(\theta_k), \theta_k) \leq 0 & \text{(Feasibility conditions)}, \\ \tilde{\lambda}(\theta_k) \geq 0 & \text{(Optimality conditions)}. \end{array} \tag{18}$$

It is obvious from step 1.–3. and corollary 3 that the the explicit solution π_k^* of (14) is given by a conditional piecewise linear function (Dua et al. (2002) and Pistikopoulos et al. (2007a)) i.e. $\pi_k = f_k^*(\theta_k)$. Consequently, the control u_k is also obtained as an explicit function of the parameter θ_k as follows

$$u_k = f_k^*(\theta_k) = f_k^*(x_k, u_{k+1}, \ldots, u_{N-1}) \tag{19}$$

or

$$u_k = K_k^i \theta_k + c_k^i, \ \textbf{if} \ \ \theta_k \in CR_k^i, \ i = 1, \ldots, L_k \tag{20}$$

where K_k^i, c_k^i are matrices and vectors of appropriate dimensions and the critical regions $CR_k^i \subset \mathbb{R}^n$ are sets defined by (18). The same procedure repeats iteratively, starting at $k = N-1$ and stopping at $k = 0$ and hence the full profile of control policies $u_k(\theta_k)$, $k = 0, 1, \ldots, N-1$ is derived.

Although u_k is a function of θ_k, the objective is to obtain u_k as an explicit control function of the incumbent state x_k thus obtaining a feedback control strategy. We can overcome this issue by following an approach similar to Faísca et al. (2008) for the nominal explicit MPC case. As the procedure is repeated repetitively and backwards from $k = N-1$ to $k = 0$, the control inputs $u_{k+1}, \ldots, u_{N-1}$ before stage k are obtained as in (19)

$$\begin{aligned} u_{k+1} &= f_{k+1}^*(x_{k+1}, u_{k+2}, \ldots, u_{N-1}) \\ &\vdots \\ u_{N-1} &= f_{N-1}^*(x_{N-1}) \end{aligned} \tag{21}$$

All the above control inputs are piecewise linear functions of their arguments. Note also that since the control inputs $u_{k+1}, \ldots, u_{N-1}$ are functions of the future states $x_{k+1}, \ldots, x_{N-1}$ they are also functions of the incumbent input u_k and state x_k. By incorporating the previous solutions (21) into (19) and by performing algebraic manipulation we obtain the explicit control law $u_k = f_k^*(x_k)$ (see for more details Faísca et al. (2008)). The final critical regions of $u_k = f_k^*(x_k)$ are defined as a union of the inequalities (of the critical regions) of (19) and of each of the critical regions of (21). This results in (i) realisable feasible sets of inequalities describing the feasible critical regions of $u_k = f_k^*(x_k)$ and (ii) empty sets of inequalities where no feasible solution exists. Feasibility tests, as the ones presented in Faísca et al. (2008), are finally performed, during the substitution of (21) into (19), to obtain the final feasible critical regions.

2.4 Algorithm for Robust mp–MPC

The dynamic programming based procedure that was described above is summarized in table 1. The Algorithm starts at $k = N-1$ and iterates through Steps 2 and 3 until $k = 0$. At the k^{th} stage of the algorithm, problem (14) is solved following the analysis in sections 2.1–2.3. Each of the inputs u_k is obtained as an explicit function of the corresponding state x_k i.e. $u_k = f_k(x_k)$ where $f_k(x_k)$ is a piecewise linear function similar to (6). At the termination of the algorithm a sequence of admissible control policies is obtained $u_0^* = f_0^*(x_0)$, $u_1^* = f_1^*(x_1)$, $\ldots$, $u_{N-1}^* = f_{N-1}^*(x_{N-1})$. Each of these control policies are *reliable* (or *robust*) control policies for each of the stage problems (14). Since each control policy also guarantees that the state and input constraints $x_k \in \mathcal{X}$ and $u_k \in \mathcal{U}$ at each stage are satisfied, then the control sequence $U = \{u_0^*, u_1^* \ldots u_{N-1}^*\}$ is also a robust solution for the initial robust mp-MPC problem (1). The following lemma can then be stated

Lemma 4. The control sequence $U = \{u_0^*, u_1^* \ldots u_{N-1}^*\}$, where u_k^*, $k = 0, 1, \ldots, N-1$ are the optimal control policies obtained by solving (14) iteratively using the algorithm in table 1, is a robust (or reliable solution) of (1).

Table 1. Algorithm for Robust Multi–Parametric MPC

Step 1.	Set $k = N-1$: solve the mp-QP problem (14) with x_{N-1} being the parameters and obtain $u_{N-1}^* = f_{N-1}^*(x_{N-1})$.
Step 2.	Set k to the current stage: solve the k^{th} stage–wise mp–QP problem (14) with $x_k, u_k, \ldots, u_{N-1}$ being the parameters and obtain $u_k^* = f_k^*(x_k, u_k, \ldots, u_{N-1})$.
Step 3.	Obtain the control law $u_k = f_k(x_k)$ by comparing the sets of solutions (19) and (21).
Step 4.	Set $k = k-1$: if $k = 0$ stop, else go to Step 2.

The main advantage of the proposed algorithm is that it can handle robust Model Predictive Control problems with quadratic objectives in the presence of uncertainties in the

LHS of the underlying optimization model at each stage of the proposed dynamic programming procedure. This is achieved by treating the optimization problem for each stage of the procedure as a convex robust mp–QP problem (14) with linear constraints, avoiding the nonlinearities introduced by the presence of uncertainty in (11).

The introduction of the two new variables z, ω also results in an increase of the number of constraints in the optimization as it can be seen from (13). The total number of optimization variables in the resulting robust mp–QP problem (14) is $2m + n$, while the total number of linear inequalities is $2n_c + m_M + n + m$. One can notice that both the number of optimization variables and inequalities for problem (14), after the robustification step, is linear with the number of system states and inputs. Thus the complexity of the mp–QP problem is not significantly increased. Finally, the number of parameters of the mp–QP (14) at each stage is equal to $n + (N - k - 1)m$, hence it increases as k decreases. This will have an important effect on the number of critical regions at each stage and eventually in the overall number of critical regions.

3. EXAMPLE

Consider the following robust MPC example where

$$A_0 = \begin{bmatrix} 1 & 1 \\ 0 & 1 \end{bmatrix} \ , \ B_0 = \begin{bmatrix} 0 \\ 1 \end{bmatrix} \ , \ \varepsilon_a = \varepsilon_\beta = 0.2$$

$$\begin{bmatrix} -10 \\ -10 \end{bmatrix} \leq x_k \leq \begin{bmatrix} 10 \\ 10 \end{bmatrix} \ , \ -1 \leq u_k \leq 1$$

$$Q = \begin{bmatrix} 1 & 0 \\ 0 & 1 \end{bmatrix} \ , \ R = 1 \ , \ P = \begin{bmatrix} 2.6005 & 2.081 \\ 2.081 & 3.3306 \end{bmatrix} \ , \ N = 3$$

The target set in this example is considered to be simply the set of state constraints while $\delta = 0$ is set equal to zero. The algorithm, presented in Table 1, is applied and the results can be seen in Figures 1, 2, 3. In the first iteration of the algorithm the robust multi-parametric programming problem (14) for $k = 2$ is solved, where the parameter is $\theta_2 = x_2$. The critical regions of the explicit solution $u_2 = f_2(x_2)$ are shown in Figure 1. Then, the procedure is repeated for the stages $k = 1$ and $k = 0$ to obtain the explicit controls $u_1 = f_1(x_1)$ and $u_0 = f_0(x_0)$. The critical regions for these stages are shown in Figures 2 and 3 respectively. One can notice that the area of the critical regions at each stage k decreases as k decreases. This happens since the set of states which can be driven to the target set (which here is the set of constraints) reduces as k reduces. Also, the number of critical regions increases since at each stage the number of parameters increases. Two different simulations for two different initial states of the explicit robust MPC control is shown in Figure 4 where the system matrices A, B are perturbed around their nominal values. Finally, table 1 shows some of the critical regions and corresponding control functions for the explicit solution at stage 0.

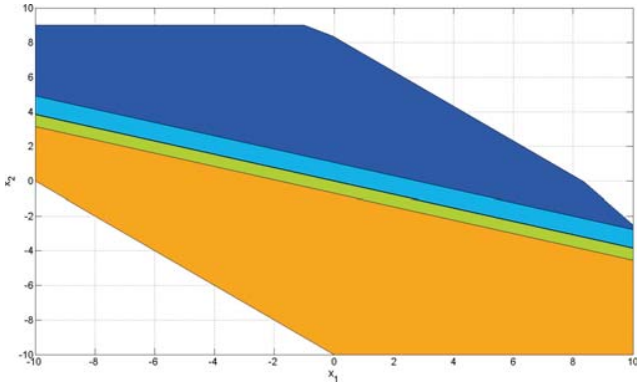

Fig. 1. Critical regions of the explicit robust MPC for stage 2, $u_2 = f_2(x_2)$

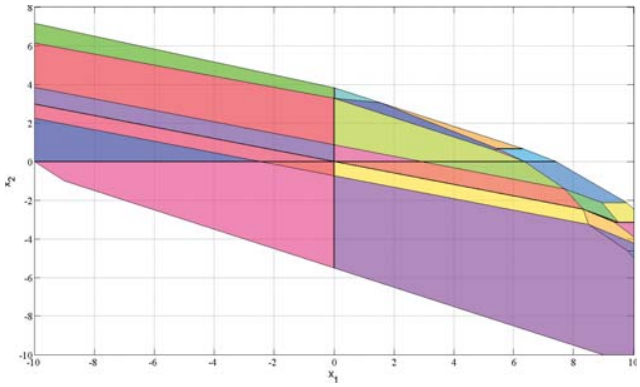

Fig. 2. Critical regions of the explicit robust MPC for stage 1, $u_1 = f_1(x_1)$

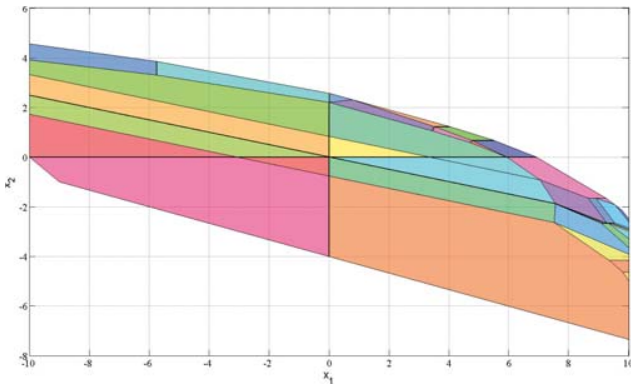

Fig. 3. Critical regions of the explicit robust MPC for stage 0, $u_0 = f_0(x_0)$

4. CONCLUDING REMARKS

A new algorithm for robust multi–parametric MPC was presented when uncertainty is introduced in the LHS of the underlying MPC optimization model. Based on dynamic programming and robust optimization, the algorithm obtains the control input explicitly as function of the states by solving a set of convex mp–QP problems and avoid the need for employing multi–parametric global optimization. Current work is focusing on the generalisation of the presented results to the following problems: (i) explicit robust MPC of constrained dynamic systems with uncertainty

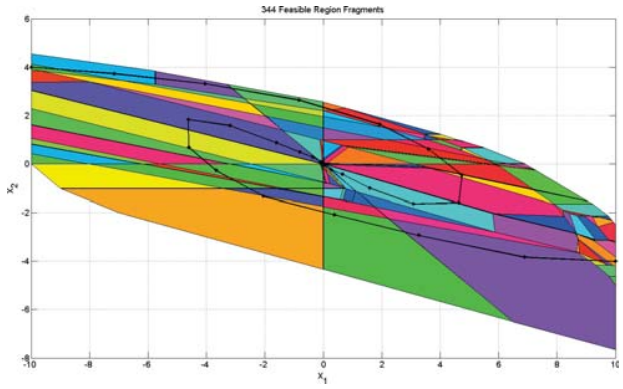

Fig. 4. Simulation of the uncertain system state trajectory with explicit robust MPC.

Table 2. Critical Regions and the corresponding Control Laws for stage 0

Critical Regions No.	Control Law	Critical Regions
1	$u = 1$	$\begin{bmatrix} 0.2174 & 1 \\ 0 & 1 \\ -0.5 & -1 \\ -0.3333 & -1 \\ 1 & 0 \end{bmatrix} x \leq \begin{bmatrix} -1.748 \\ -1.01 \\ 5.5 \\ 4.3333 \\ -0.01 \end{bmatrix}$
2	$u = 1$	$\begin{bmatrix} 0.2174 & 1 \\ -0.3333 & -1 \\ -1 & 0 \\ 1 & 0 \end{bmatrix} x \leq \begin{bmatrix} -1.7480 \\ 4.3333 \\ 0.01 \\ 0.0050 \end{bmatrix}$
3	$u = -1$	$\begin{bmatrix} -0.2513 & -1 \\ 0.9 & 1 \\ 0 & 1 \\ 0 & -1 \\ -0.7821 & -1 \\ -1 & -0.9524 \end{bmatrix} x \leq \begin{bmatrix} -0.1791 \\ 6.65 \\ -1.6562 \\ 2.1250 \\ -4.5301 \\ -6.3333 \end{bmatrix}$
4	$u = -0.5662x_1 - 1.3573x_2 + 1.0378$	$\begin{bmatrix} -1 & -0.2757 \\ 0.4172 & 1 \\ 1 & 0.631 \\ -0.4172 & -1 \\ -1 & -0.555 \end{bmatrix} x \leq \begin{bmatrix} -7.8743 \\ 1.5014 \\ 7.3523 \\ -0.7720 \\ -7.0852 \end{bmatrix}$
5	$u = -0.4701x_1 - 1.3476x_2 - 0.0001$	$\begin{bmatrix} 1 & 0.9042 \\ -1 & -1 \\ -1 & -0.7395 \\ -1 & -0.1585 \\ 1 & 1 \end{bmatrix} x \leq \begin{bmatrix} 0.079 \\ 0.01 \\ -0.0211 \\ -0.0579 \\ 0.005 \end{bmatrix}$

and additive disturbance, both in the LHS and RHS of the underlying multi–parametric optimization model (Sakizlis et al. (2004)), (ii) explicit robust MPC of hybrid systems – based on multi–parametric Mixed Integer Linear Programming (Faísca et al. (2009)) and (iii) multi–parametric Global Optimisation (Dua et al. (2004))..

REFERENCES

Bazaraa, M. and Shetty, C. (1979). *Nonlinear Programming–Theory and Algorithms*. Wiley, New York.

Bellman, R. (2003). *Dynamic programming*. Dover Publications.

Bemporad, A., Borrelli, F., and Morari, M. (2003). Min-max control of constrained uncertain discrete–time linear systems. *IEEE Trans. Aut. Con.*, 48, 1600–1606.

Bemporad, A. and Morari, M. (1999). Robustness in identification and control: A survey. In A. Garulli, A. Tesi, and A. Vicino (eds.), *Robustness in identification and control*. Springer-Verlag, Boston, USA.

Ben-Tal, A. and Nemirovski, A. (2000). Robust solutions of linear programming problems contaminated with uncertain data. *Math. Prog.*, 88, 411–424.

Borrelli, F. (2003). *Constrained optimal control of linear and hybrid systems*, volume 290 of *Lecture notes in control and information sciences*. Berlin: Springer.

Dua, V., Bozinis, A., and Pistikopoulos, E. (2002). A multiparametric programming approach for mixed-integer quadratic engineering problems. *Comput. Chem. Eng.*, 26, 715–733.

Dua, V., Papalexandri, K., and Pistikopoulos, E. (2004). Global optimization issues in multiparametric continuous and mixed–integer optimization problems. *Journal of Global Optimization*, 30, 59–89.

Faísca, N., Kosmidis, V., Rustem, B., and Pistikopoulos, E. (2009). Global optimization of multi–parametric milp problems. *Journal of Global Optimization*, to appear in Special Issue of JOGO for the Workshop on Global Optimization.

Faísca, N., Kouramas, K., Saraiva, P., Rustem, B., and Pistikopoulos, E. (2008). A multi-parametric programming approach for ocnstrained dynamic programming problems. *Optimization Letters*, 2, 267–280.

Fiacco, A. (1976). Sensitivity analysis for nonlinear programming using penalty methods. *Math. Prog.*, 10, 287–311.

Fiacco, A. (1983). *Introduction to Sensitivity and Stability Analysis in Nonlinear Programming*. Academic Press, New York.

Kouramas, K., Sakizlis, V., and Pistikopoulos, E. (2009). Design of robust model-based controllers via multi-parametric programming. *Encyclopedia of Optimization*, 677–687.

Lin, X., Janak, S., and Floudas, C. (2004). A new robust optimization approach for scheduling under uncertainty: I. bounded uncertainty. *Comp. Chem. Eng.*, 28, 1069–1085.

Mayne, D., Rawlings, J., Rao, C., and Scokaert, P. (2000). Constrained model predictive control: stability and optimality. *Automatica*, 36, 789–814.

Pistikopoulos, E., Dua, V., Bozinis, N., Bemporad, A., and Morari, M. (2002). On-line optimization via off-line parametric optimization tools. *Comp. Chem. Eng.*, 26, 175–185.

Pistikopoulos, E., Georgiadis, M., and Dua, V. (2007a). *Multi-parametric model-based control: theory and applications*, volume 2 of *Process Systems Engineering Series*. Wiley-VCH, Weinheim.

Pistikopoulos, E., Georgiadis, M., and Dua, V. (2007b). *Multi-parametric Programming: Theory, Algorithms and Applications*, volume 1 of *Process Systems Engineering Series*. Wiley-VCH, Weinheim.

Sakizlis, V., Kakalis, N., Dua, V., Perkins, J., and Perkins, E. (2004). Design of robust model-based controllers via parametric programming. *Automatica*, 40, 189–201.

Wang, Y. and Rawlings, J. (2004). A new robust model predictive control method i: theory and computation. *J. of Proc. Con.*, 14, 231–247.

Robust Adaptive MPC for Systems with Exogeneous Disturbances ⋆

V. Adetola * **M. Guay** *

* *Department of Chemical Engineering, Queen's University, Kingston, Ontario, Canada (e-mail: martin.guay@chee.queensu.ca)*

Abstract: In this paper, we consider the problem of Adaptive model predictive control subject to exogenous disturbances. Using a novel set-based adaptive estimation, the problem of robust adaptive MPC is proposed and solved for a class of linearly parameterized uncertain nonlinear systems subject to state and input constraints. Two formulations of the adaptive MPC routine are proposed. A minmax approach is first considered. A Lipschitz-based formulation, amenable to real-time computations, is then proposed. A chemical reactor simulation example is presented that demonstrates the effectivenessof the technique.

Keywords: Adaptive control, Robust MPC, Nonlinear MPC

1. INTRODUCTION

Most physical systems possess consists of parametric and non-parametric uncertainties and the system dynamics can be influenced by exogeneous disturbances as well. Examples in chemical engineering include reaction rates, activation energies, fouling factors, and microbial growth rates. Since parametric uncertainty may degrade the performance of MPC, mechanisms to update the unknown or uncertain parameters are desirable in application. One possibility would be to use state measurements to update the model parameters off-line. A more attractive possibility is to apply adaptive extensions of MPC in which parameter estimation and control are performed online. In this paper, we extend an adaptive MPC framework to nonlinear systems with both constant parametric uncertainty and additive exogenous disturbances.

The literature contains very few results on the design of adaptive nonlinear MPC Adetola and Guay (2004); Mayne and Michalska (1993). Existing design techniques are restricted to systems that are linear in the unknown (constant) parameters and do not involve state constraints. Although MPC exhibits some degree of robustness to uncertainties, in reality, the degree of robustness provided by nominal models or certainty equivalent models may not be sufficient in practical applications. Parameter estimation error must be accounted for in the computation of the control law.

This paper is inspired by DeHaan and Guay (2007); DeHaan et al. (2007). While the focus in DeHaan and Guay (2007); DeHaan et al. (2007) is on the use of adaptation to reduce the conservatism of robust MPC controller, this study addresses the problem of adaptive MPC and incorporates robust features to guarantee closed-loop stability and constraint satisfaction. Simplicity is achieved here-in by generating a parameter estimator for the unknown parameter vector and parameterizing the control policy in terms of these estimates rather than adapting a parameter uncertainty set directly.

First, a min-max feedback nonlinear MPC scheme is combined with an adaptation mechanism. The parameter estimation routine are used to update the parameter uncertainty set, at certain time instants, in a manner that guarantees non-expansion of the set leading to a gradual reduction in the conservativeness or computational demands of the algorithms. The min-max formulation explicitly accounts for the effect of future parameter estimation and automatically injects some useful excitation into the closed-loop system to aid in parameter identification.

Second, the technique is extended to a less computationally demanding robust MPC algorithm. The nominal model rather than the unknown bounded system state is controlled, subject to conditions that ensure that given constraints are satisfied for all possible uncertainties. State prediction error bound is determined based on assumed Lipschitz continuity of the model. Using a nominal model prediction, it is impossible to predict the actual future behavior of the parameter estimation error as was possible in the min-max framework. It is shown how the future model improvement over the prediction horizon can be considered by developing a worst-case upper bound on the future parameter estimation error. The conservativeness of the algorithm reduces as the error bound decreases monotonically over time.

The paper is as follows. The problem description is given in section 2. The parameter estimation routine is presented in section 3.Two approaches to robust adpative model predictive control are detailed in section 4. This is followed by a simulation example in section 5 and brief conclusions in section 6.

2. PROBLEM SET-UP

Consider the uncertain nonlinear system

$$\dot{x} = f(x,u) + g(x,u)\theta + \vartheta \triangleq \mathcal{F}(x,u,\theta,\vartheta) \qquad (1)$$

⋆ The authors would like to acknowledge the financial support of the Natural Sciences and Engineering Research Council of Canada.

where the disturbance $\vartheta \in \mathcal{D} \subset \mathbb{R}^{n_d}$ is assumed to satisfy a known upper bound $\|\vartheta(t)\| \leq M_\vartheta < \infty$. The objective of the study is to (robustly) stabilize the plant to some target set $\Xi \subset \mathbb{R}^{n_x}$ while satisfying the pointwise constraints $x \in \mathbb{X} \in \mathbb{R}^{n_x}$ and $u \in \mathbb{U} \in \mathbb{R}^{n_u}$. The target set is a compact set, contains the origin and is robustly invariant under no control. It is assumed that θ is uniquely identifiable and lie within an initially known compact set $\Theta^0 = B(\theta_0, z_\theta)$ where θ_0 is a nominal parameter value, z_θ is the radius of the parameter uncertainty set.

3. PARAMETER AND UNCERTAINTY SET ESTIMATION

3.1 Parameter Adaptation

Let the estimator model for (1) be selected as

$$\dot{\hat{x}} = f(x,u) + g(x,u)\hat{\theta} + k_w\, e + w\dot{\hat{\theta}}, \quad k_w > 0 \tag{2}$$
$$\dot{w} = g(x,u) - k_w\, w, \qquad w(t_0) = 0. \tag{3}$$

resulting in state prediction error $e = x - \hat{x}$ and auxiliary variable $\eta = e - w\tilde{\theta}$ dynamics:

$$\dot{e} = g(x,u)\tilde{\theta} - k_w\, e - w\dot{\hat{\theta}} + \vartheta \qquad e(t_0) = x(t_0) - \hat{x}(t_0) \tag{4}$$
$$\dot{\eta} = -k_w\, \eta + \vartheta, \qquad \eta(t_0) = e(t_0). \tag{5}$$

Since ϑ is not known, an estimate of η is generated from

$$\dot{\hat{\eta}} = -k_w\, \hat{\eta}, \qquad \hat{\eta}(t_0) = e(t_0). \tag{6}$$

with resulting estimation error $\tilde{\eta} = \eta - \hat{\eta}$ dynamics

$$\dot{\tilde{\eta}} = -k_w\, \tilde{\eta} + \vartheta, \qquad \tilde{\eta}(t_0) = 0. \tag{7}$$

Let $\Sigma \in \mathbb{R}^{n_\theta \times n_\theta}$ be generated from

$$\dot{\Sigma} = w^T w, \qquad \Sigma(t_0) = \alpha\, I \succ 0, \tag{8}$$

based on equations (2), (3) and (6), thye preferred parameter update law is given by

$$\dot{\Sigma}^{-1} = -\Sigma^{-1} w^T w \Sigma^{-1}, \qquad \Sigma^{-1}(t_0) = \frac{1}{\alpha} I \tag{9a}$$
$$\dot{\hat{\theta}} = \mathrm{Proj}\left\{\gamma\, \Sigma^{-1} w^T (e - \hat{\eta}),\ \hat{\theta}\right\}, \qquad \hat{\theta}(t_0) = \theta^0 \in \Theta^0 \tag{9b}$$

where $\gamma = \gamma^T > 0$ and $\mathrm{Proj}\{\phi,\ \hat{\theta}\}$ denotes a Lipschitz projection operator such that

$$-\mathrm{Proj}\{\phi,\ \hat{\theta}\}^T \tilde{\theta} \leq -\phi^T \tilde{\theta}, \tag{10}$$
$$\hat{\theta}(t_0) \in \Theta^0 \ \Rightarrow\ \hat{\theta}(t) \in \Theta^0_\epsilon,\ \ \forall\, t \geq t_0. \tag{11}$$

where $\Theta^0_\epsilon \triangleq B(\theta^0, z^0_\theta + \epsilon)$, $\epsilon > 0$. More details on parameter projection can be found in Krstic et al. (1995). To proof the following lemma, we need the following result

Lemma 1. Desoer and Vidyasagar (1975) Consider the system

$$\dot{x}(t) = Ax(t) + u(t) \tag{12}$$

Suppose the equilibrium state $x_e = 0$ of the homogeneous equation is exponentially stable,

(1) if $u \in \text{Ł}_p$ for $1 < p < \infty$, then $x \in \text{Ł}_p$ and
(2) if $u \in \text{Ł}_p$ for $p = 1$ or 2, then $x \to 0$ as $t \to \infty$.

Lemma 2. The identifier (9) is such that the estimation error $\tilde{\theta} = \theta - \hat{\theta}$ is bounded. Moreover, if

$$\vartheta \in \mathcal{L}_2 \qquad \text{or} \qquad \int_{t_0}^{\infty} \left[\|\tilde{\eta}\|^2 - \underline{\gamma}\, \|e - \hat{\eta}\|^2\right] d\tau < +\infty \tag{13}$$

with $\underline{\gamma} = \lambda_{\min}(\gamma)$ and the strong condition

$$\lim_{t\to\infty} \lambda_{\min}\big(\Sigma\big) = \infty \tag{14}$$

is satisfied, then $\tilde{\theta}$ converges to zero asymptotically.

Proof: Let $V_{\tilde{\theta}} = \tilde{\theta}^T \Sigma\, \tilde{\theta}$, it follows from (9) and the relationship $w\tilde{\theta} = e - \hat{\eta} - \tilde{\eta}$ that

$$\begin{aligned} \dot{V}_{\tilde{\theta}} &\leq -2\underline{\gamma}\, \tilde{\theta}^T w^T (e - \hat{\eta}) + \tilde{\theta}^T w^T w \tilde{\theta} \\ &= -\underline{\gamma}\, (e - \hat{\eta})^T (e - \hat{\eta}) + \|\tilde{\eta}\|^2, \end{aligned} \tag{15}$$

implying that $\tilde{\theta}$ is bounded. Moreover, it follows from (15) that

$$V_{\tilde{\theta}}(t) = V_{\tilde{\theta}}(t_0) + \int_{t_0}^{t} \dot{V}_{\tilde{\theta}}(\tau) d\tau \tag{16}$$
$$\leq V_{\tilde{\theta}}(t_0) - \underline{\gamma} \int_{t_0}^{t} \|e - \hat{\eta}\|^2\, d\tau + \int_{t_0}^{t} \|\tilde{\eta}\|^2\, d\tau \tag{17}$$

Considering the dynamics of (7), if $\vartheta \in \mathcal{L}_2$, then $\tilde{\eta} \in \mathcal{L}_2$ (Lemma 1). Hence, the right hand side of (17) is finite in view of (13), and by (14) we have
$\lim_{t\to\infty} \tilde{\theta}(t) = 0$ ■

3.2 Set Adaptation

An update law that measures the worst-case progress of the parameter identifier in the presence of disturbance is given by:

$$z_\theta = \sqrt{\frac{V_{z\theta}}{\lambda_{\min}(\Sigma)}} \tag{18a}$$
$$V_{z\theta}(t_0) = \lambda_{\max}\Big(\Sigma(t_0)\Big)\, (z^0_\theta)^2 \tag{18b}$$
$$\dot{V}_{z\theta} = -\underline{\gamma}\, (e - \hat{\eta})^T (e - \hat{\eta}) + \Big(\frac{M_\vartheta}{k_w}\Big)^2. \tag{18c}$$

Using the parameter estimator (9) and its error bound z_θ (18), the uncertain ball $\Theta \triangleq B(\hat{\theta}, z_\theta)$ is adapted online according to the following algorithm:

Algorithm 1. Beginning from time $t_{i-1} = t_0$, the parameter and set adaptation is implemented iteratively as follows:

1 **Initialize** $z_\theta(t_{i-1}) = z^0_\theta$, $\hat{\theta}(t_{i-1}) = \hat{\theta}^0$ and $\Theta(t_{i-1}) = B(\hat{\theta}(t_{i-1}), z_\theta(t_{i-1}))$.
2 At time t_i, using equations (9) and (18) **perform** the update

$$\Big(\hat{\theta},\ \Theta\Big) = \begin{cases} \Big(\hat{\theta}(t_i),\ \Theta(t_i)\Big), & \text{if } z_\theta(t_i) \leq z_\theta(t_{i-1}) \\ & -\|\hat{\theta}(t_i) - \hat{\theta}(t_{i-1})\| \\ \Big(\hat{\theta}(t_{i-1}),\ \Theta(t_{i-1})\Big), & \text{otherwise} \end{cases} \tag{19}$$

3 **Iterate back** to step 2, **incrementing** $i = i + 1$.

The algorithm ensure that Θ is only updated when z_θ value has decreased by an amount which guarantees a contraction of the set. Moreover z_θ evolution as given in (18) ensures non-exclusion of θ as shown below.

Lemma 3. The evolution of $\Theta = B(\hat{\theta}, z_\theta)$ under (9), (18) and algorithm 1 is such that

i) $\Theta(t_2) \subseteq \Theta(t_1),\ t_0 \leq t_1 \leq t_2$
ii) $\theta \in \Theta(t_0) \Rightarrow \theta \in \Theta(t),\ \forall t \geq t_0$

Proof:

i) If $\Theta(t_{i+1}) \nsubseteq \Theta(t_i)$, then

$$\sup_{s \in \Theta(t_{i+1})} \|s - \hat{\theta}(t_i)\| \geq z_\theta(t_i). \tag{20}$$

However, it follows from triangle inequality and algorithm 1 that Θ, at update times, obeys

$$\begin{aligned}\sup_{s \in \Theta(t_{i+1})} & \|s - \hat{\theta}(t_i)\| \\ &\leq \sup_{s \in \Theta(t_{i+1})} \|s - \hat{\theta}(t_{i+1})\| + \|\hat{\theta}(t_{i+1}) - \hat{\theta}(t_i)\| \\ &\leq z_\theta(t_{i+1}) + \|\hat{\theta}(t_{i+1}) - \hat{\theta}(t_i)\| \ \leq\ z_\theta(t_i),\end{aligned}$$

which contradicts (20). Hence, Θ update guarantees $\Theta(t_{i+1}) \subseteq \Theta(t_i)$ and the strict contraction claim follows from the fact that Θ is held constant over update intervals $\tau \in (t_i, t_{i+1})$.

ii) We know that $V_{\tilde{\theta}}(t_0) \leq V_{z\theta}(t_0)$ (by definition) and it follows from (15) and (18c) that $\dot{V}_{\tilde{\theta}}(t) \leq \dot{V}_{z_\theta}(t)$. Hence, by the comparison lemma, we have

$$V_{\tilde{\theta}}(t) \ \leq\ V_{z\theta}(t), \quad \forall t \geq t_0. \tag{21}$$

and since $V_{\tilde{\theta}} = \tilde{\theta}^T \Sigma\, \tilde{\theta}$, it follows that

$$\|\tilde{\theta}(t)\|^2 \leq \frac{V_{z\theta}(t)}{\lambda_{\min}(\Sigma(t))} = z_\theta^2(t), \quad \forall t \geq t_0. \tag{22}$$

Hence, if $\theta \in \Theta(t_0)$, then $\theta \in B(\hat{\theta}(t), z_\theta(t)),\ \forall t \geq t_0$.

■

4. ROBUST ADAPTIVE MPC

4.1 A Min-max Approach

The formulation of the min-max MPC consists of maximizing a cost function with respect to $\theta \in \Theta$, $\vartheta \in \mathcal{D}$ and minimizing over feedback control policies κ. The robust receding horizon control law is

$$u = \kappa_{mpc}(x, \hat{\theta}, z_\theta) \triangleq \kappa^*(0, x, \hat{\theta}, z_\theta) \tag{23a}$$

$$\kappa^* \triangleq \arg \min_{\kappa(\cdot,\cdot,\cdot,\cdot)} J(x, \hat{\theta}, z_\theta, \kappa) \tag{23b}$$

where

$$J(x, \hat{\theta}, z_\theta, \kappa) \triangleq \max_{\theta \in \Theta,\ \vartheta \in \mathcal{D}} \int_0^T L(x^p, u^p) d\tau + W(x^p(T), \tilde{\theta}^p(T)) \tag{24a}$$

$s.t.\ \forall \tau \in [0,\ T]$

$$\dot{x}^p = f(x^p, u^p) + g(x^p, u^p)\theta + \vartheta,\ \ x^p(0) = x \tag{24b}$$

$$\dot{w^p} = g^T(x^p, u^p) - k_w\, w^p,\ \ w^p(0) = w \tag{24c}$$

$$(\dot{\Sigma^{-1}})^p = -(\Sigma^{-1})^p w^T w (\Sigma^{-1})^p, \quad (\Sigma^{-1})^p(0) = \Sigma^{-1} \tag{24d}$$

$$\dot{\hat{\theta}}^p = \mathrm{Proj}\left\{\gamma\,(\Sigma^{-1})^p w^T (e - \hat{\eta}),\ \hat{\theta}\right\}, \quad \tilde{\theta}^p = \theta - \hat{\theta}^p,\ \ \hat{\theta}^p(0) = \hat{\theta} \tag{24e}$$

$$u^p(\tau) \triangleq \kappa(\tau, x^p(\tau), \hat{\theta}^p(\tau)) \in \mathbb{U} \tag{24f}$$

$$x^p(\tau) \in \mathbb{X},\ \ x^p(T) \in \mathbb{X}_f(\tilde{\theta}^p(T)) \tag{24g}$$

The effect of future parameter adaptation is also accounted for in this formulation. The conservativeness of the algorithm is reduced by parameterizing both W and $\mathbb{X}_f$ as functions of $\tilde{\theta}(T)$. While it is possible for the set Θ to contract upon θ over time, the robustness feature due to $\vartheta \in \mathcal{D}$ will still remain.

Algorithm 2. The MPC algorithm performs as follows: At sampling instant t_i

(1) **Measure** the current state of the plant $x(t)$ and obtain the current value of matrices w and Σ^{-1} from equations (3) and (9a) respectively
(2) Obtain the current value of parameter estimates $\hat{\theta}$ and uncertainty bound z_θ from (9b) and (18) respectively
If $z_\theta(t_i) \leq z_\theta(t_{i-1}) - \|\hat{\theta}(t_i) - \hat{\theta}(t_{i-1})\|$
$\hat{\theta} = \hat{\theta}(t_i), \quad z_\theta = z_\theta(t_i)$
,
Else
$\hat{\theta} = \hat{\theta}(t_{i-1}), \quad z_\theta = z_\theta(t_{i-1})$
End
(3) **Solve** the optimization problem (23) and apply the resulting feedback control law to the plant until the next sampling instant
(4) **Increment** $i = i+1$. Repeat the procedure from step 1 for the next sampling instant.

4.2 Lipschitz-based Approach

In this section, we present a Lipschitz-based method whereby the nominal model rather than the unknown bounded system state is controlled, subject to conditions that ensure that given constraints are satisfied for all possible uncertainties. State prediction error bound is determined based on the Lipschitz continuity of the model. A knowledge of appropriate Lipschitz bounds for the x-dependence of the dynamics $f(x,u)$ and $g(x,u)$ are assumed as follows:

Assumption 4. A set of functions $\mathcal{L}_j : \mathbb{X} \times \mathbb{U} \to \mathbb{R}^+$, $j \in \{f, g\}$ are known which satisfy

$$\mathcal{L}_j(\mathbb{X}, u) \geq \min\left\{\mathcal{L}_j \ \Big|\ \sup_{x_1, x_2 \in \mathbb{X}} \Big(\|j(x_1,u) - j(x_2,u)\| - \mathcal{L}_j \|x_1 - x_2\|\Big) \leq 0\right\},$$

where for $j \equiv g$ is interpreted as an induced norm since $g(x,u)$ is a matrix.

Assuming a knowledge of the Lipschitz bounds for the x-dependence of the dynamics $f(x,u)$ and $g(x,u)$ as given in Assumption 4 and let $\Pi = z_\theta + \|\hat{\theta}\|$, a worst-case deviation $z_x^p \geq \max_{\theta \in \Theta} \|x - x^p\|$ can be generated from

$$\dot{z}_x^p = (\mathcal{L}_f + \mathcal{L}_g \Pi) z_x^p + \|g(x^p, u)\| z_\theta + M_\vartheta, \quad z_x^p(t_0) = 0. \tag{26}$$

Using this error bound, the robust Lipschitz-based MPC is given by

$$u = \kappa_{mpc}(x, \hat{\theta}, z_\theta) = u^*(0) \tag{27a}$$

$$u^*(.) \triangleq \arg \min_{u^p_{[0,T]}} J(x, \hat{\theta}, z_\theta, u^p) \tag{27b}$$

where

$$J(x,\hat{\theta},z_\theta,u^p) = \int_0^T L(x^p,u^p)d\tau + W(x^p(T),z_\theta^p) \quad (28a)$$

$$s.t.\ \forall \tau \in [0,\ T]$$

$$\dot{x}^p = f(x^p,u^p) + g(x^p,u^p)\hat{\theta},\quad x^p(0) = x \quad (28b)$$

$$\dot{z}_x^p = (\mathcal{L}_f + \mathcal{L}_g\Pi)z_x^p + \|g^p\|z_\theta + M_\vartheta,\ z_x^p(0) = 0 \quad (28c)$$

$$X^p(\tau) \triangleq B(x^p(\tau),z_x^p(\tau)) \subseteq \mathbb{X},\quad u^p(\tau) \in \mathbb{U} \quad (28d)$$

$$X^p(T) \subseteq \mathbb{X}_f(z_\theta^p) \quad (28e)$$

The effect of the disturbance is built into the uncertainty cone $B(x^p(\tau),z_x^p(\tau))$ via (28c). Since the uncertainty bound is no more monotonically decreasing in this case, the uncertainty radius z_θ which appears in (28c) and in the terminal expressions of (28a) and (28e) are held constant over the prediction horizon. However, the fact that they are updated at sampling instants when z_θ shrinks reduces the conservatism of the robust MPC and enlarges the terminal domain that would otherwise have been designed based on a large initial uncertainty $z_\theta(t_0)$.

Algorithm 3. The Lipschitz-based MPC algorithm performs as follows: At sampling instant t_i

(1) **Measure** the current state of the plant $x = x(t_i)$
(2) **Obtain** the current value of the parameter estimates $\hat{\theta}$ and uncertainty bound z_θ from equations (9) and (18) respectively,
If $z_\theta(t_i) \le z_\theta(t_{i-1})$
$$\hat{\theta} = \hat{\theta}(t_i),\quad z_\theta = z_\theta(t_i)$$
Else
$$\hat{\theta} = \hat{\theta}(t_{i-1}),\quad z_\theta = z_\theta(t_{i-1})$$
End
(3) **Solve** the optimization problem (27) and apply the resulting feedback control law to the plant until the next sampling instant
(4) **Increment** i:=i+1; repeat the procedure from step 1 for the next sampling instant.

5. CLOSED-LOOP ROBUST STABILITY

Robust stabilization to the target set Ξ is guaranteed by appropriate selection of the design parameters W and X_f. The robust stability conditions require the satisfaction of the following criteria.

Criterion 5. The terminal penalty function $W : \mathbb{X}_f \times \tilde{\Theta}^0 \to [0, +\infty]$ and the terminal constraint function $\mathbb{X}_f : \tilde{\Theta}^0 \to \mathbb{X}$ are such that for each $(\theta,\ \hat{\theta},\ \tilde{\theta}) \in (\Theta^0 \times \Theta^0 \times \tilde{\Theta}^0_\epsilon)$, there exists a feedback $k_f(.,\hat{\theta}) : \mathbb{X}_f \to \mathbb{U}$ satisfying

(1) $0 \in \mathbb{X}_f(\tilde{\theta}) \subseteq \mathbb{X},\quad \mathbb{X}_f(\tilde{\theta})$ closed
(2) $k_f(x,\hat{\theta}) \in \mathbb{U},\ \forall x \in \mathbb{X}_f(\tilde{\theta})$
(3) $W(x,\tilde{\theta})$ is continuous with respect to $x \in \mathbb{R}^{n_x}$
(4) $\forall\, x \in \mathbb{X}_f(\tilde{\theta})\backslash\Xi$, $\mathbb{X}_f(\tilde{\theta})$ is strongly positively invariant under $k_f(x,\hat{\theta})$ with respect to $\dot{x} \in f(x,k_f(x,\hat{\theta})) + g(x,k_f(x,\hat{\theta}))\Theta + \mathcal{D}$
(5) $L(x,k_f(x,\hat{\theta})) + \frac{\partial W}{\partial x}\mathcal{F}(x,k_f(x,\hat{\theta}),\theta,\vartheta) \le 0,\ \forall x \in \mathbb{X}_f(\tilde{\theta})\backslash\Xi$.

Criterion 6. For any $\tilde{\theta}_1,\ \tilde{\theta}_2 \in \tilde{\Theta}^0$ *s.t.* $\|\tilde{\theta}_2\| \le \|\tilde{\theta}_1\|$,

(1) $W(x,\tilde{\theta}_2) \le W(x,\tilde{\theta}_1),\ \forall x \in \mathbb{X}_f(\tilde{\theta}_1)$
(2) $\mathbb{X}_f(\tilde{\theta}_2) \supseteq \mathbb{X}_f(\tilde{\theta}_1)$

The revised condition C5 require W to be a local robust CLF for the uncertain system 1 with respect to $\theta \in \Theta$ and $\vartheta \in \mathcal{D}$.

5.1 Main Results

Theorem 7. Let $X_{d0} \triangleq X_{d0}(\Theta^0) \subseteq \mathbb{X}$ denote the set of initial states with uncertainty Θ^0 for which (23) has a solution. Assuming criteria 5 and 6 are satisfied, then the closed-loop system state x, given by (1,9,18,23), originating from any $x_0 \in X_{d0}$ feasibly approaches the target set Ξ as $t \to +\infty$.

Proof: *Feasibility*: The closed-loop stability is based upon the feasibility of the control action at each sample time. Assuming, at time t, that an optimal solution $u^p_{[0,T]}$ to the optimization problem (23) exist and is found. Let Θ^p denote the estimated uncertainty set at time t and Θ^v denote the set at time $t+\delta$ that would result with the feedback implementation of $u_{[t,t+\delta]} = u^p_{[0,\delta]}$. Also, let x^p represents the worst case state trajectory originating from $x^p(0) = x(t)$ and x^v represents the trajectory originating from $x^v(0) = x + \delta v$ under the same feasible control input $u^v_{[\delta,T]} = u^p_{[\delta,T]}$. Moreover, let $X^a_{\Theta^b} \triangleq \{x^a | \dot{x}^a \in \mathcal{F}(x^a,u^p,\Theta^b) \triangleq f(x^a,u^p) + g(x^a,u^p)\Theta^b\}$.

Since the $u^p_{[0,T]}$ is optimal with respect to the worst case uncertainty scenario, it suffice to say that $u^p_{[0,T]}$ drives any trajectory $x^p \in X^p_{\Theta^p}$ into the terminal region $\mathbb{X}^p_f$. Since Θ is non-expanding over time, we have $\Theta^v \subseteq \Theta^p$ implying $x^v \in X^p_{\Theta^v} \subseteq X^p_{\Theta^p}$. The terminal region $\mathbb{X}^p_f$ is strongly positively invariant for the nonlinear system (1) under the feedback $k_f(.,.)$, the input constraint is satisfied in $\mathbb{X}^p_f$ and $\mathbb{X}^v_f \supseteq \mathbb{X}^p_f$ by criteria 2.2, 2.4 and 3.2 respectively. Hence, the input $u = [u^p_{[\delta,T]}, k_{f[T,T+\delta]}]$ is a feasible solution of (23) at time $t+\delta$ and by induction, the optimization problem is feasible for all $t \ge 0$.

Stability: The stability of the closed-loop system is established by proving strict decrease of the optimal cost $J^*(x,\hat{\theta},z_\theta) \triangleq J(x,\hat{\theta},z_\theta,\kappa^*)$. Let the trajectories $(x^p,\ \hat{\theta}^p,\ \tilde{\theta}^p,\ z^p_\theta)$ and control u^p correspond to any worst case minimizing solution of $J^*(x,\hat{\theta},z_\theta)$. If $x^p_{[0,T]}$ were extended to $\tau \in [0,T+\delta]$ by implementing the feedback $u(\tau) = k_f(x^p(\tau),\hat{\theta}^p(\tau))$ on $\tau \in [T,T+\delta]$, then criterion 5(5) guarantees the inequality

$$\int_T^{T+\delta} L(x^p,k_f(x^p,\hat{\theta}^p))d\tau + W(x^p_{T+\delta},\tilde{\theta}^p_T) - W(x^p_T,\tilde{\theta}^p_T) \le 0 \quad (29)$$

where in (29) and in the remainder of the proof, $x^p_\sigma \triangleq x^p(\sigma)$, $\tilde{\theta}^p_\sigma \triangleq \tilde{\theta}^p(\sigma)$, for $\sigma = T,\ T+\delta$.
The optimal cost

$$J^*(x,\hat{\theta},z_\theta) = \int_0^T L(x^p,u^p)d\tau + W(x^p_T,\tilde{\theta}^p_T)$$

$$\ge \int_0^T L(x^p,u^p)d\tau + W(x^p_T,\tilde{\theta}^p_T) \quad (30)$$

$$+\int_{T}^{T+\delta} L(x^p, k_f(x^p,\hat{\theta}^p))d\tau + W(x^p_{T+\delta},\tilde{\theta}^p_T) - W(x^p_T,\tilde{\theta}^p_T) \tag{31}$$

$$\geq \int_0^{\delta} L(x^p,u^p)d\tau + \int_{\delta}^{T} L(x^p,u^p)d\tau \tag{32}$$

$$+\int_{T}^{T+\delta} L(x^p, k_f(x^p,\hat{\theta}^p))d\tau + W(x^p_{T+\delta},\tilde{\theta}^p_{T+\delta}) \tag{33}$$

$$\geq \int_0^{\delta} L(x^p,u^p)d\tau + J^*(x(\delta),\hat{\theta}(\delta),z_\theta(\delta)) \tag{34}$$

Then, it follows from (34) that

$$J^*(x(\delta),\hat{\theta}(\delta),z_\theta(\delta)) - J^*(x,\hat{\theta},z_\theta) \leq -\int_0^{\delta} L(x^p,u^p)d\tau \leq -\int_0^{\delta} \mu_L(\|x,u\|)d\tau. \tag{35}$$

where μ_L is a class $\mathcal{K}_\infty$ function. Hence $x(t) \to 0$ asymptotically.

Remark 8. In the above proof,

- (31) is obtained using inequality (29)
- (33) follows from criterion 5.1 and the fact that $\|\tilde{\theta}\|$ is non-increasing
- (34) follows by noting that the last 3 terms in (33) is a (potentially) suboptimal cost on the interval $[\delta, T+\delta]$ starting from the point $(x^p(\delta),\hat{\theta}^p(\delta))$ with associated uncertainty set $B(\hat{\theta}^p(\delta), z^p_\theta(\delta))$.

The closed-loop stability is established by the feasibility of the control action at each sample time and the strict decrease of the optimal cost J^*. The proof follows from the fact that the control law is optimal with respect to the worst case uncertainty $(\theta,\ \vartheta) \in (\Theta,\ \mathcal{D})$ scenario and the terminal region $\mathbb{X}^p_f$ is strongly positively invariant for (1) under the (local) feedback $k_f(.,.)$. ■

Theorem 9. Let $X'_{d0} \triangleq X'_{d0}(\Theta^0) \subseteq \mathbb{X}$ denote the set of initial states for which (27) has a solution. Assuming Assumption 4 and Criteria 5 and 6 are satisfied, then the origin of the closed-loop system given by (1,9,18,27) is feasibly asymptotically stabilized from any $x_0 \in X'_{d0}$ to the target set Ξ.

The proof of the Lipschitz-based control law follows from that of theorem 7.

6. SIMULATION EXAMPLE

To illustrate the effectiveness of the proposed design, we consider the regulation of the CSTR subject to an additional disturbance on the temperature dynamic:

$$\dot{C}_A = \frac{q}{V}(C_{Ain} - C_A) - k_0 \exp\left(\frac{-E}{RT_r}\right) C_A$$

$$\dot{T}_r = \frac{q}{V}(T_{in} - T_r) - \frac{\Delta H}{\rho\, c_p} k_0 \exp\left(\frac{-E}{RT_r}\right) C_A + \frac{UA}{\rho\, c_p\, V}(T_c - T_r) + \vartheta$$

where $\vartheta(t)$ is an unknown function of time. We also assume that the reaction kinetic constant k_0 and ΔH are only nominally known.

It is assumed that reaction kinetic constant k_0 and heat of reaction ΔH are only nominally known and parameterized as $k_0 = \theta_1 \times 10^{10}\,\mathrm{min}^{-1}$ and $\Delta H\, k_0 = -\theta_2 \times 10^{15}$ J/mol min with the parameters satisfying $0.1 \leq \theta_1 \leq 10$ and $0.1 \leq \theta_2 \leq 10$. The objective is to adaptively regulate the unstable equilibrium $C_A^{eq} = 0.5$ mol/l, $T_r^{eq} = 350$ K, $T_c^{eq} = 300$ K while satisfying the constraints $0 \leq C_A \leq 1$, $280 \leq T_r \leq 370$ and $280 \leq T_c \leq 370$. The nominal operating conditions, which corresponds to the given unstable equilibrium are taken from Magni et al. (2001): q=100 l/min, V=100 l, ρ=1000 g/l, $c_p = 0.239$ J/g K, E/R = 8750 K, $UA = 5\times10^4$ J/min K, $C_{Ain} = 1$ mol/l and $T_{in} = 350$ K.

The control objective is to robustly regulate the reactor temperature and concentration to the (open loop) unstable equilibrium $C_A^{eq} = 0.5$ mol/l, $T_r^{eq} = 350$ K, $T_c^{eq} = 300$ K by manipulating the temperature of the coolant stream T_c.

Defining $x = [\frac{C_A - C_A^{eq}}{0.5},\ \frac{T_r - T_r^{eq}}{20}]'$, $u = \frac{T_c - T_c^{eq}}{20}$, the stage cost $L(x,u)$ was selected as a quadratic function of its arguments:

$$L(x,u) = x^T\, Q_x\, x + u^T\, R_u\, u \tag{36a}$$

$$Q_x = \begin{bmatrix} 0.5 & 0 \\ 0 & 1.1429 \end{bmatrix} \qquad R_u = 1.333. \tag{36b}$$

The terminal penalty function used is a quadratic parameter-dependent Lyapunov function $W(x,\theta) = x^T P(\theta) x$ for the linearized system. Denoting the closed-loop system under a local robust stabilizing controller $u = k_f(\theta)\, x$ as $\dot{x} = A_{cl}(\theta)x$. The matrix $P(\theta) := P_0 + \theta_1 P_1 + \theta_2 P_2 + \ldots\ \theta_{n\theta} P_{n\theta}$ was selected to satisfy the Lyapunov system of LMIs

$$P(\theta) > 0$$
$$A_{cl}(\theta)^T P(\theta) + P(\theta) A_{cl}(\theta) < 0$$

for all admissible values of θ. Since θ lie between known extrema values, the task of finding $P(\theta)$ reduces to solving a finite set of linear matrix inequalities by introducing additional constraints Gahinet et al. (1996). For the initial nominal estimate $\theta^0 = 5.05$ and $z^0_\theta = 4.95$, the matrix $P(\theta^0)$ obtained is

$$P(\theta^0) = \begin{bmatrix} 0.6089 & 0.1134 \\ 0.1134 & 4.9122 \end{bmatrix} \tag{37}$$

and the corresponding terminal region is

$$\mathbb{X}_f = \{x :\ x^T P(\theta^0)\, x \leq 0.25\}. \tag{38}$$

For simulation purposes, the disturbance is selected as a fluctuation of the inlet temperate $\vartheta(t) = 0.01\, T_{in} \sin(3t)$ and the true values of the unknown parameters were also chosen as $k_0 = 7.2 \times 10^{10}\mathrm{min}^{-1}$ and ΔH = - 5.0 $\times$ 10^4 J/mol. The stage cost (36), terminal penalty (37) and terminal region (38) were used. The Lipschitz-based approach was used for the controller calculations and the result was implemented according to Algorithm 3. As depicted in Figures 1 to 3, the robust adaptive MPC drives the system to a neighborhood of the equilibrium while satisfying the imposed constraints and achieves parameter convergence. Figure 4 shows that the uncertainty bound z_θ also reduces over time.

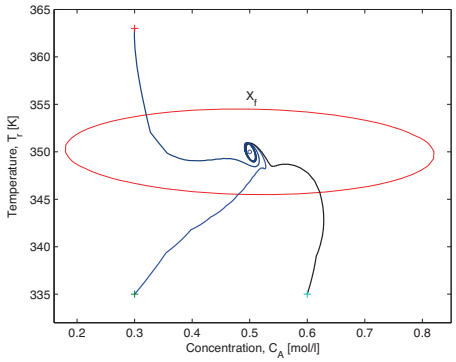

Fig. 1. Closed-loop reactor trajectories under additive disturbance $\vartheta(t)$

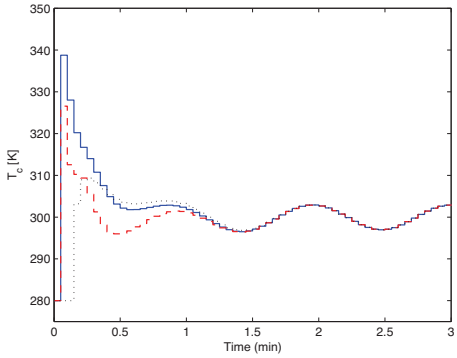

Fig. 2. Closed-loop input profiles for states starting at different initial conditions $(C_A(0),\ T_r(0))$: (0.3, 335) is solid line, (0.6, 335) is dashed line and (0.3, 363) is the dotted line

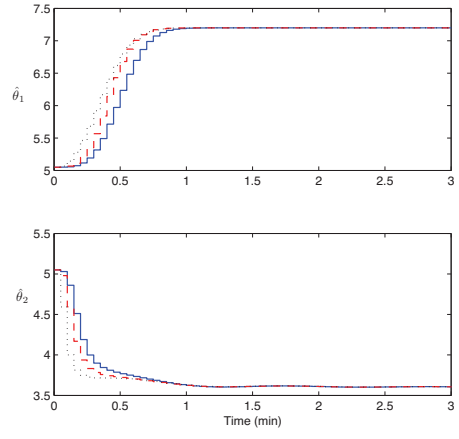

Fig. 3. Closed-loop parameter estimates profile for states starting at different initial conditions $(C_A(0),\ T_r(0))$: (0.3, 335) is solid line, (0.6, 335) is dashed line and (0.3, 363) is the dotted line

7. CONCLUSIONS

The adaptive MPC design technique is extended to constrained nonlinear systems with both parametric and time

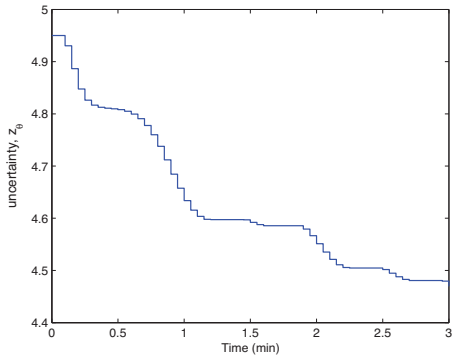

Fig. 4. Closed-loop uncertainty bound trajectories for initial condition $(C_A,\ T_r) = (0.3,\ 335)$

varying disturbances. The proposed robust controller updates the plant model online when model improvement is guaranteed. The embedded adaptation mechanism enables us to construct less conservative terminal design parameters based upon subsets of the original parametric uncertainty. While the introduced conservatism/computation complexity due to the parametric uncertainty reduces over time, the portion due to the disturbance $\vartheta \in \mathcal{D}$ remains active for all time.

REFERENCES

Adetola, V. and Guay, M. (2004). Adaptive receding horizon control of nonlinear systems. In *Proc. of IFAC Symposium on Nonlinear Control systems*, 1055–1060. Stuttgart.

DeHaan, D., Adetola, V., and Guay, M. (2007). Adaptive robust mpc: An eye towards computational simplicity. In *Proc. of IFAC Symposium on Nonlinear Control systems*. South Africa.

DeHaan, D. and Guay, M. (2007). Adaptive robust mpc: A minimally-conservative approach. In *Proc. of American Control Conference*.

Desoer, C. and Vidyasagar, M. (1975). *Feedback Systems: Input-Output Properties*. Academic Press, New York.

Gahinet, P., Apkarian, P., and Chilali, M. (1996). Affine parameter-dependent lyapunov functions and real. parametric uncertainty. *IEEE Transactions on Automatic Control*, 41(3), 436–442.

Krstic, M., Kanellakopoulos, I., and Kokotovic, P. (1995). *Nonlinear and Adaptive Control Design*. John Wiley and Sons Inc, Toronto.

Magni, L., De Nicolao, G., Magnani, L., and Scattolini, R. (2001). A stabilizing model-based predictive control algorithm for nonlinear systems. *Automatica*, 37, 1351–1362.

Mayne, D.Q. and Michalska, H. (1993). Adaptive receding horizon control for constrained nonlinear systems. In *In Proc. of IEEE Conference on Decision and Control*, 1286–1291. San Antonio, Texas.

Applications

Oral Session

Energy Consumption Optimization of RO Membrane Desalination Subject to Feed Salinity Fluctuation ⋆

Aihua Zhu, Panagiotis D. Christofides and Yoram Cohen

Department of Chemical and Biomolecular Engineering
Water Technology Research Center
University of California, Los Angeles, CA 90095-1592, U.S.A.

Abstract: We study the energy consumption optimization of a reverse osmosis water desalination process producing a constant permeate flow in the presence of feed concentration fluctuation. We propose a time-varying optimal operation strategy that can significantly reduce the specific energy consumption compared to time-invariant process operation.

Keywords: specific energy consumption optimization, reverse osmosis, thermodynamic restriction, feed concentration fluctuation

1. INTRODUCTION

Reverse osmosis (RO) membrane water desalination is now well established as a mature water desalination technology. However, energy consumption is a major portion of the total cost of water desalination and can reach as high as about 45% of the total permeate production cost (Manth et al. (2003); Busch and Mickols (2004); Wilf and Bartels (2005)). The energy cost per volume of produced permeate (i.e., the specific energy consumption or SEC) is significant in RO operation due to the high pressure requirement (up to about 1000 psi for seawater and in the range of 100-600 psi for brackish water desalting). Considerable effort, dating back to the initial days of RO development in the early 1960s (as reviewed in Zhu et al. (2008)), has been devoted to minimizing the specific energy consumption of water desalination. The introduction of highly permeable membranes in the mid 1990s with low salt passage (Wilf (1997)) has generated considerable interest (Zhu et al. (2008)), given their potential for reducing the energy required to attain a given permeate flow, since the operating pressure can be greatly reduced to approach the osmotic pressure difference at the exit of a membrane module (Wilf (1997), Song et al. (2003a); Song and Tay (2006)).

In a previous work (Zhu et al. (2008)), we systematically studied the effect of the thermodynamic restriction (i.e., the fact that the applied pressure cannot be lower than the osmotic pressure of the exit brine stream plus pressure losses across the membrane module) on the optimization of the specific energy consumption of an RO process. Specifically, we computed the optimum SEC, corresponding water recovery, and permeate flux for single-stage and two-stage RO membrane desalination systems. We also studied the effect of energy recovery device, membrane cost and brine disposal costs on SEC. The developed approach can also be utilized to evaluate the energy savings of a two-stage RO system over single-stage RO and the impact of extra membrane area consumption of two-stage over single-stage. In a recent work (Zhu et al. (2009)), we carried out a systematic study of the energy consumption of two-pass reverse osmosis membrane desalination accounting for key practical issues like membrane salt rejection, presence/absence of energy recovery devices and concentration polarization. We established that if the salt rejection level of the available membranes can achieve the desired permeate salt content, then a single-pass configuration is more energy favorable than a two-pass configuration for the same level of total water recovery and salt rejection. However, if it is not possible to obtain the desired permeate salt content with the available membranes, then a two-pass configuration has to be used, and in this case, the energy optimal solution is to operate the first-pass using the membranes with the maximum rejection.

In the present work, we extend our previous results to account for the effect of feed salinity fluctuation on energy consumption optimization. Due to seasonal rainfalls, the feed water salinity will fluctuate both for seawater and brackish water. For example, at one location in the central San Joaquin Valley, the total dissolved solid (TDS) deviated up to 52% from its annual average (McCool (2008)). The objective of the present work is to determine the optimal time-varying operating policy to produce a constant permeate flow in the presence of a given feed salinity fluctuation profile.

2. RO PROCESS

2.1 Description and Modeling

In order to illustrate the approach to energy cost optimization it is instructive to consider a membrane RO

⋆ The present work was supported in part by the International Desalination Association (Channabasappa Memorial Scholarship to Aihua Zhu), California Department of Water Resources, the Metropolitan Water District of Southern California, the University of California Water Resources Center, and the United States Environmental Protection Agency. Corresponding author: Panagiotis D. Christofides (e-mail: pdc@seas.ucla.edu)

process without the deployment of an energy recovery device (ERD) as shown schematically in Fig. 1.

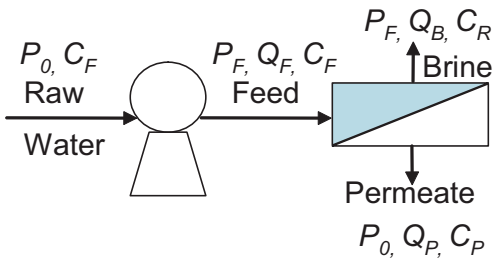

Figure 1. Schematic of simplified RO system.

The energy cost associated with RO desalination is evaluated in the present analysis as the specific energy consumption (SEC) defined as the electrical energy needed to produce a cubic meter of permeate. Pump efficiency can be included in the following analysis in a straightforward fashion as presented in Zhu et al. (2008). As a first step, however, in order to simplify the presentation of the approach, the required electrical energy is taken to be equal to the pump work, (i.e., assuming a pump efficiency of 100%). Accordingly, the SEC for the plant shown in Fig. 1 is given by:

$$SEC = \frac{\dot{W}_{pump}}{Q_p} \tag{1}$$

where Q_p is the permeate flow rate and $\dot{W}_{pump}$ is the rate of work done by the pump, given by:

$$\dot{W}_{pump} = \Delta P \times Q_f \tag{2}$$

in which

$$\Delta P = P_f - P_0 \tag{3}$$

where P_f is the water pressure at the entrance of the membrane module, P_0 is the pressure of the raw water which is assumed (for simplicity) to be the same as the permeate pressure, and Q_f is the volumetric feed flow rate. In order to simplify the analysis, we initially assume that the impact of the pressure drop (within the RO module) on locating the minimum SEC is negligible; this issue is addressed further in Zhu et al. (2008). It is acknowledged that, fouling and scaling will impact the selection of practical RO process operating conditions and feed pretreatment. However, the inclusion of such effects is beyond the scope of the present paper.

The permeate product water recovery for the RO process, Y, is an important measure of the process productivity, defined as:

$$Y = \frac{Q_p}{Q_f} \tag{4}$$

and combining Eqs. (1), (2) and (4), the SEC can be rewritten as follows:

$$SEC = \frac{\Delta P}{Y} \tag{5}$$

The permeate flow rate can be approximated by the classical reverse osmosis flux equation Mulder (1997):

$$Q_p = A_m L_p(\Delta P - \sigma\overline{\Delta\pi}) = A_m L_p(\overline{NDP}) \tag{6}$$

where A_m is the active membrane area, L_p is the membrane hydraulic permeability, σ is the reflection coefficient (typically assumed to be about unity for high rejection RO membranes and in this study $\sigma = 1$), ΔP is the transmembrane pressure, $\overline{\Delta\pi}$ is the average osmotic pressure difference between the retentate and permeate stream along the membrane module, $(\Delta P - \sigma\overline{\Delta\pi})$ is the average trans-membrane net driving pressure designated as $\overline{NDP}$. We also invoke the typical approximation in Mulder (1997) that the osmotic pressure varies linearly with concentration (i.e., $\pi = f_{os}C$ where f_{os} is the osmotic pressure coefficient and C is the solution salt concentration). For the purpose of the present analysis and motivated by our focus on RO processes that utilize highly permeable membranes, the average osmotic pressure difference (up to the desired level of product water recovery), $\overline{\Delta\pi}$, can be approximated as the log-mean average along the membrane (ASTM (2000)) as confirmed in a previous work Zhu et al. (2008),

$$\overline{\Delta\pi} = f_{os}C_f\frac{ln(\frac{1}{1-Y})}{Y} \tag{7}$$

where C_f is the salt concentration of the feed to the membrane module. The osmotic pressures at the entrance and the exit of the membrane module, relative to the permeate stream, are approximate by:

$$\Delta\pi_{entrance} = f_{os}C_f - \pi_p \tag{8}$$

$$\Delta\pi_{exit} = f_{os}C_r - \pi_p \tag{9}$$

where C_r is the salt concentration of the exit brine (i.e., concentrate) stream. For sufficiently high rejection level, the osmotic pressure of the permeate can be taken to be negligible relative to the feed or concentrate streams and C_r can be approximated by:

$$C_r = \frac{C_f}{1-Y} \tag{10}$$

Thus, by combining Eqs. (8)–(10), the osmotic pressure difference between the retentate and permeate stream at the exit of the module can be expressed as:

$$\Delta\pi_{exit} = \frac{\pi_0}{1-Y} \tag{11}$$

where $\pi_0 = f_{os}C_f$ is the feed osmotic pressure. Eq. (11) is a simple relationship that illustrates that the well known inherent difficulty in reaching high recovery in RO desalting is due to the rapid rise in osmotic pressure with increased recovery.

2.2 Thermodynamic Restriction of Cross-flow RO Operation

In the process of RO desalting, an external pressure is applied to overcome the osmotic pressure, and pure water is recovered from the feed solution through the use of a semipermeable membrane. Assuming that the permeate pressure is the same as the raw water pressure, P_0, the applied pressure (ΔP) needed to obtain a water recovery of Y should be no less than the osmotic pressure difference at the exit region (Wilf (1997); Song et al. (2003b)), which is given by Eq. (11). Therefore, in order to ensure permeate

productivity along the entire RO module (or stage), the following lower bound is imposed on the applied pressure:

$$\Delta P \geq \Delta \pi_{exit} = \frac{\pi_0}{1-Y} \tag{12}$$

This is the so-called thermodynamic restriction of cross-flow RO (Song et al. (2003a); Song and Tay (2006)) and referred to as the "thermodynamic restriction" in the current work. The equality on the right-hand-side of Eq. (12) is the condition at the "limit of thermodynamic restriction" in the exit of the membrane module and is attained at the limit of infinite membrane permeability for a finite membrane area. It is particularly important from a practical point of view when a highly-permeable membrane is used for water desalination at low pressures. It is emphasized that the constraint of Eq. (12) arises when one wants to ensure that the entire membrane area is utilized for permeate production.

The specific energy consumption (SEC) for the RO desalting process can be derived by combining Eqs. (1)–(4) and (12), to obtain:

$$SEC \geq \frac{\pi_0}{Y(1-Y)} \tag{13}$$

where SEC is in pressure units. It is convenient to normalize the SEC, at the limit of thermodynamic restriction (i.e., operation up to the point in which the applied pressure equals the osmotic pressure difference between the concentrate and permeate at the exit of the membrane module), with respect to the feed osmotic pressure such that:

$$SEC_{tr,norm} = \frac{SEC_{tr}}{\pi_0} = \frac{1}{Y(1-Y)} \tag{14}$$

and this dependence is plotted in Fig. 2 showing that there is a global minimum. In order to obtain the analytical global minimum $SEC_{tr,norm}$, with respect to the water recovery, one can set $(dSEC_{tr,norm})/(dY) = 0$ from which it can be shown that the minimum $SEC_{tr,norm}$ occurs at a fractional recovery of $Y = 0.5$ (or 50%) where $(SEC_{tr,norm})_{min} = 4$ (i.e., four times the feed osmotic pressure). The above condition, i.e., $(SEC_{tr,norm})_{min} = 4$ at $Y = 0.5$, represents the global minimum SEC (represented by the equality in Eq. 13). In order to achieve this global minimum energy cost, the RO process should be operated at a water recovery of 50% with an applied pressure equivalent to $2\pi_0$ (i.e., double that the feed osmotic pressure).

2.3 Feed Salinity Fluctuation

For the purpose of illustration of the proposed optimal operation approach, we consider a simple feed salinity fluctuation profile shown in Fig. 3. Specifically, we consider a 20-hour time window in which the feed osmotic pressure in the first 10 hours is 500 *psi*, and it is then reduced to 200 *psi* for the remaining 10 hours. For a single-stage RO system with constant feed flow rate Q_f, the average feed osmotic pressure is 350 *psi*. We will study the minimum specific energy consumption (SEC) of two difference cases. In case 1, the operating pressure is a constant, while in case 2, it will change with the instantaneous feed osmotic pressure and will always be double that of the instantaneous feed osmotic pressure. Both cases are operated at the limit of thermodynamic restriction.

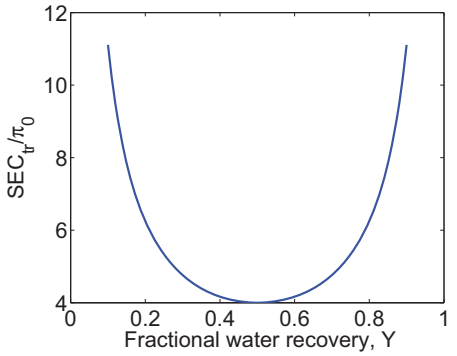

Figure 2. Variation of the normalized SEC with water recovery for a single-stage RO at the limit of thermodynamic restriction.

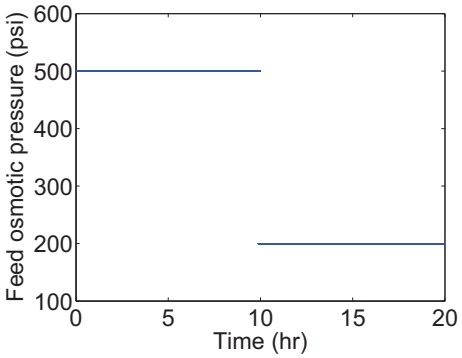

Figure 3. Feed osmotic pressure profile within 20 hours.

3. RESULTS

In the presence of the feed salinity fluctuation of Fig. 3,the following two operating strategies may be considered.

- Operating strategy A: The transmembrane pressure is maintained at double that of the average (over the whole 20-hour time window) feed osmotic pressure, i.e. 700 *psi*.
- Operating strategy B: The transmembrane pressure is maintained at double that of the instantaneous feed osmotic pressure.

For a built plant to produce the same amount of permeate volume for both operating strategy A and operating strategy B, the permeate flow rates in the first 10 hrs and the last 10 hrs have to be the same. The specific energy consumption (SEC) comparison of operating strategy A and operating strategy B will be first done for an RO process without an energy recovery device (see Fig. 1) and the case of an RO process with an energy recovery device (see Fig. 4) will be then addressed. In Fig. 4, P_e and P_p are the brine discharge and permeate pressure, respectively, which are assumed here to be equal to P_0.

The rate of work done by the pump on the raw water, in the presence of an ERD, is given by:

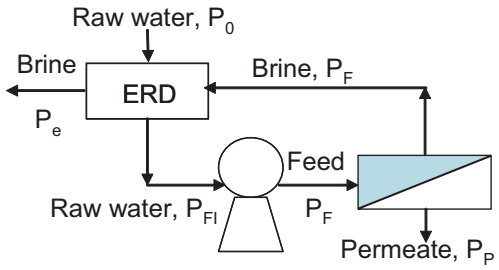

Figure 4. Simplified RO system with an energy recovery device (ERD).

$$\dot{W}_{pump} = \Delta P \times (Q_f - \eta Q_b) \tag{15}$$

where η is the efficiency of the energy recovery device.

3.1 RO Process without ERD

Operating strategy A. At the limit of thermodynamic restriction, according to Eq. 11, the water recovery in the first 10 hrs, $Y_1 = 1 - \frac{500}{700} = \frac{2}{7}$ and the water recovery in the last 10 hrs, $Y_2 = 1 - \frac{200}{700} = \frac{5}{7}$. In order to produce the same amount of permeate volume, the feed flow rate in the first 10 hrs has to be 2.5 times that of the feed flow rate in the last 10 hrs ($Q_{f,2}$). Therefore, the permeate flow and energy consumption in the first and last 10 hrs are:

$$V_{p,1} = 2.5 \times Q_{f,2} \times \frac{2}{7} \times 10\,hr = \frac{50}{7} Q_{f,2} \times hr \tag{16}$$

$$W_1 = \Delta P_1 \times V_{f,1} = 17500\, Q_{f,2} \cdot psi \cdot hr \tag{17}$$

$$V_{p,2} = Q_{f,2} \times \frac{5}{7} \times 10\,hr = \frac{50}{7} Q_{f,2} \times hr \tag{18}$$

$$W_2 = \Delta P_2 \times V_{p,2} = 7000\, Q_{f,2} \cdot psi \cdot hr \tag{19}$$

Therefore, the average SEC is:

$$\overline{SEC}^A = \frac{W_1 + W_2}{V_{p,1} + V_{p,2}} = 1715\, psi \tag{20}$$

Operating strategy B. The water recovery in the last 10 hrs is the same as the water recovery in the first 10 hrs (both at 50%). In order to produce the same amount of permeate volume, the feed flow rate in the first 10 hrs should be the same as the feed flow rate in the last 10 hrs ($Q'_{f,2}$). The permeate flow and energy consumption in the first and last 10 hrs are:

$$V'_{p,1} = Q'_{f,2} \times \frac{1}{2} \times 10\,hr = 5Q'_{f,2} \times hr \tag{21}$$

$$W'_1 = \Delta P'_1 \times V'_{f,1} = 10000\, Q'_{f,2} \cdot psi \cdot hr \tag{22}$$

$$V'_{p,2} = Q'_{f,2} \times \frac{1}{2} \times 10\,hr = 5Q'_{f,2} \times hr \tag{23}$$

$$W'_2 = \Delta P'_2 \times V'_{f,2} = 4000\, Q'_{f,2} \cdot psi \cdot hr \tag{24}$$

Therefore, the average SEC is:

$$\overline{SEC}^B = \frac{W'_1 + W'_2}{V'_{p,1} + V'_{p,2}} = 1400\, psi \tag{25}$$

From Eq. 20 and Eq. 25, we see that the operating strategy A has a higher SEC than operating strategy B about 22.5% ($\frac{1715-1400}{1400} = 22.5\%$). Furthermore, in order to equate the total permeate volume in operating strategy A and operating strategy B, $Q'_{f,2} = \frac{10}{7} Q_{f,2}$. Thus, the total feed volume in operating strategy B is $2 \times \frac{10}{7} Q_{f,2} = \frac{20}{7} Q_{f,2}$, while the total feed volume in operating strategy A is $(2.5 + 1) Q_{f,2} = 3.5 Q_{f,2}$. Therefore, in order to get the same amount of permeate volume, operating strategy A requires a higher amount of feed water, and thus, it has a lower overall water recovery.

3.2 RO Process with ERD: Efficiency is 100%

Operating strategy A. The water recovery in the last 10 hrs is 2.5 times that of the water recovery in the first 10 hrs. In order to produce the same amount of permeate volume, the feed flow rate in the first 10 hrs has to be 2.5 times that of the feed flow rate in the last 10 hrs ($Q_{f,2}$). Therefore, the permeate flow and energy consumption in the first and last 10 hrs are:

$$V_{p,1} = 2.5 \times Q_{f,2} \times \frac{2}{7} \times 10\,hr = \frac{50}{7} Q_{f,2} \times hr \tag{26}$$

$$W_1^{ERD} = \Delta P_1 \times V_{p,1} = 5000\, Q_{f,2} \cdot psi \cdot hr \tag{27}$$

$$V_{p,2} = Q_{f,2} \times \frac{5}{7} \times 10\,hr = \frac{50}{7} Q_{f,2} \times hr \tag{28}$$

$$W_2^{ERD} = \Delta P_2 \times V_{p,2} = 5000\, Q_{f,2} \cdot psi \cdot hr \tag{29}$$

Therefore, the average SEC is:

$$\overline{SEC}^A = \frac{W_1^{ERD} + W_2^{ERD}}{V_{p,1} + V_{p,2}} = 700\, psi \tag{30}$$

Operating strategy B. The water recovery in the last 10 hrs is the same as the water recovery in the first 10 hrs. In order to produce the same amount of permeate volume, the feed flow rate in the first 10 hrs has to be the same as that the feed flow rate in the last 10 hrs ($Q_{f,2}$'). The permeate flow and energy consumption in the first and last 10 hrs are:

$$V'_{p,1} = Q'_{f,2} \times \frac{1}{2} \times 10\,hr = 5Q'_{f,2} \times hr \tag{31}$$

$$W_1^{'ERD} = \Delta P'_1 \times V'_{p,1} = 5000\, Q'_{f,2} \cdot psi \cdot hr \tag{32}$$

$$V'_{p,2} = Q'_{f,2} \times \frac{1}{2} \times 10\,hr = 5Q'_{f,2} \times hr \tag{33}$$

$$W_2^{'ERD} = \Delta P_2 \times V'_{p,2} = 2000\, Q_{f,2} \cdot psi \cdot hr \tag{34}$$

Therefore, the average SEC is:

$$\overline{SEC}^B = \frac{W_1 + W_2}{V'_{p,1} + V'_{p,2}} = 700\, psi \tag{35}$$

From Eq. 30 and Eq. 35, we see that in the presence of an ERD with a 100% efficiency, operating strategy A and operating strategy B have the same SEC. Furthermore, in order to equate the total permeate volume in operating strategy A and operating strategy B, $Q'_{f,2} = \frac{10}{7} Q_{f,2}$. Thus, the total feed volume in operating strategy B is $2 \times \frac{10}{7} Q_{f,2} = \frac{20}{7} Q_{f,2}$, while the total feed volume in operating strategy A is $(2.5 + 1) Q_{f,2} = 3.5 Q_{f,2}$. Therefore, in order to get the same amount of permeate volume, operating strategy A requires a higher amount of feed water, and thus, it has a lower overall water recovery.

3.3 ERD Efficiency between 0 and 1

Operating strategy A. The water recovery in the last 10 hrs is 2.5 times that of the water recovery in the first 10 hrs. In order to produce the same amount of permeate volume, the feed flow rate in the first 10 hrs has to be 2.5 times the feed flow rate in the last 10 hrs ($Q_{f,2}$). Therefore, the permeate flow and energy consumption in the first and last 10 hrs are:

$$V_{p,1} = 2.5 \times Q_{f,2} \times \frac{2}{7} \times 10\,hr = \frac{50}{7} Q_{f,2} \times hr \quad (36)$$

$$W_1^{ERD} = \Delta P_1 \times (V_{f,1} - \eta(V_{f,1} - V_{p,1})) \quad (37)$$

$$V_{p,2} = Q_{f,2} \times \frac{5}{7} \times 10\,hr = \frac{50}{7} Q_{f,2} \times hr \quad (38)$$

$$W_2^{ERD} = \Delta P_2 \times (V_{f,2} - \eta(V_{f,2} - V_{p,2})) \quad (39)$$

Therefore, the average SEC is:

$$\overline{SEC}^A_{ERD} = \frac{W_1^{ERD} + W_2^{ERD}}{V_{p,1} + V_{p,2}} = (1715 - 1015\eta)\,psi \quad (40)$$

Operating strategy B. The water recovery in the last 10 hrs is the same as the water recovery in the first 10 hrs. In order to produce the same amount of permeate volume, the feed flow rate in the first 10 hrs has to be the same as that the feed flow rate in the last 10 hrs ($Q_{f,2}$'). Therefore, the permeate flow and energy consumption in the first and last 10 hrs are:

$$V'_{p,1} = Q'_{f,2} \times \frac{1}{2} \times 10\,hr = 5Q'_{f,2} \times hr \quad (41)$$

$$W_1^{'ERD} = \Delta P'_1 \times (V'_{f,1} - \eta(V'_{f,1} - V'_{p,1})) \quad (42)$$

$$V'_{p,2} = Q'_{f,2} \times \frac{1}{2} \times 10\,hr = 5Q'_{f,2} \times hr \quad (43)$$

$$W_2^{'ERD} = \Delta P_2 \times (V'_{f,2} - \eta(V'_{f,2} - V'_{p,2})) \quad (44)$$

Therefore, the average SEC is:

$$\overline{SEC}^B_{ERD} = \frac{W_1^{'ERD} + W_2^{'ERD}}{V'_{p,1} + V'_{p,2}} = 700(2 - \eta)\,psi \quad (45)$$

The SEC difference between operating strategy A and operating strategy B is $(1715 - 1015\eta) - 700(2 - \eta)\,psi = 315(1 - \eta)\,psi$. Thus, when $0 < \eta < 1$, the SEC of operating strategy A will be always greater than the SEC of operating strategy B. The fractional SEC increase is,

$$\frac{\overline{SEC}^A_{ERD} - \overline{SEC}^B_{ERD}}{\overline{SEC}^B_{ERD}} = \frac{315}{700} \frac{(1 - \eta)}{[1 + (1 - \eta)]} \quad (46)$$

which is plotted in Fig. 5. For example, when the ERD efficiency is 90%, the fractional SEC increase is 4.1%. Furthermore, in order to equate the total permeate volume in operating strategy A and operating strategy B, $Q'_{f,2} = \frac{10}{7} Q_{f,2}$. Thus, the total feed volume in operating strategy B is $2 \times \frac{10}{7} Q_{f,2} = \frac{20}{7} Q_{f,2}$, while the total feed volume in operating strategy A is $(2.5+1)Q_{f,2} = 3.5Q_{f,2}$. Therefore, in order to get the same amount of permeate volume, operating strategy A requires a higher amount of feed water, and thus, it has a lower overall water recovery.

In summary, operating strategy A is worse since we need to process more feed water to obtain the same permeate and has a higher SEC. In others words, by adjusting operating pressure to be double that of the instantaneous feed osmotic pressure, the system needs to process less volume of feed water to produce the same amount of permeate water and has a lower SEC.

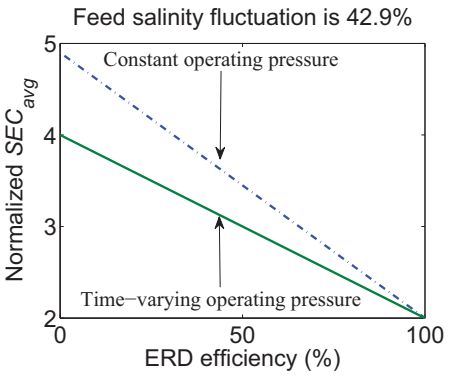

Figure 5. Percentage SEC increase when feed pressure is not adjusted. vs. ERD efficiency.

4. DISCUSSION

4.1 Effect of the Feed salinity Fluctuation Percentage on Energy Savings

The effect of the fluctuation amplitude on energy savings can be studied following the same procedure presented in Section 3.3. Assuming the average osmotic pressure is π_0, the osmotic pressure in the first 10 hrs is $(1 + \sigma)\pi_0$ $(0 < \sigma < 1)$, and the osmotic pressure in the last 10 hrs is $(1 - \sigma)\pi_0$. Therefore, the feed fractional fluctuation is σ. Similarly, the following two operating strategies may be considered.

- Operating strategy A: The transmembrane pressure is maintained at double that of the average feed osmotic pressure, i.e. $2\pi_0$.
- Operating strategy B: The transmembrane pressure is maintained at double that of the instantaneous feed osmotic pressure.

Operating strategy A. The water recovery in the last 10 hrs, $Y_1 = 1 - \frac{(1+\sigma)\pi_0}{2\pi_0} = \frac{1-\sigma}{2}$, and in the last 10 hrs, $Y_2 = 1 - \frac{(1-\sigma)\pi_0}{2\pi_0} = \frac{1+\sigma}{2}$. In order to produce the same amount of permeate volume, the feed flow rate in the first 10 hrs has to be $\frac{1+\sigma}{1-\sigma}$ times that of the feed flow rate in the last 10 hrs ($Q_{f,2}$). The permeate flow and energy consumption in the first and last 10 hrs are:

$$V_{p,1} = \frac{1+\sigma}{1-\sigma} \cdot Q_{f,2} \cdot \frac{1-\sigma}{2} \cdot 10\,hr = 5(1+\sigma) \cdot Q_{f,2} \cdot hr \quad (47)$$

$$W_1^{ERD} = \Delta P_1 \times (V_{f,1} - \eta(V_{f,1} - V_{p,1})) \quad (48)$$

$$V_{p,2} = Q_{f,2} \times \frac{1+\sigma}{2} \times 10\,hr = 5(1+\sigma) \cdot Q_{f,2} \cdot hr \quad (49)$$

$$W_2^{ERD} = \Delta P_2 \times (V_{f,2} - \eta(V_{f,2} - V_{p,2})) \quad (50)$$

Therefore, the average SEC is:

$$\overline{SEC}^A_{ERD} = \frac{W_1^{ERD} + W_2^{ERD}}{V_{p,1} + V_{p,2}} = 2\pi_0[\frac{(1-\eta)}{1-\sigma} + \frac{(1+\eta\sigma)}{1+\sigma}] \quad (51)$$

Operating strategy B. The water recovery in the last 10 hrs is the same as the water recovery in the first 10 hrs. In order to produce the same amount of permeate volume, the feed flow rate in the first 10 hrs has to be the same as the feed flow rate in the last 10 hrs ($Q_{f,2}$'). The permeate flow and energy consumption in the first and last 10 hrs are:

$$V'_{p,1} = Q'_{f,2} \times \frac{1}{2} \times 10\,hr = 5Q'_{f,2} \times hr \quad (52)$$

$$W_1^{'ERD} = \Delta P'_1 \times (V'_{f,1} - \eta(V'_{f,1} - V'_{p,1})) \quad (53)$$

$$V'_{p,2} = Q'_{f,2} \times \frac{1}{2} \times 10\,hr = 5Q'_{f,2} \times hr \quad (54)$$

$$W_2^{'ERD} = \Delta P_2 \times (V'_{f,2} - \eta(V'_{f,2} - V'_{p,2})) \quad (55)$$

Therefore, the average SEC is:

$$\overline{SEC}^B_{ERD} = \frac{W_1^{'ERD} + W_2^{'ERD}}{V'_{p,1} + V'_{p,2}} = 2(2-\eta) \cdot \pi_0 \quad (56)$$

The SEC difference of operating strategy A from operating strategy B is $(2[\frac{(1-\eta)}{1-\sigma} + \frac{(1+\eta\sigma)}{1+\sigma}] - 2(2-\eta)) \cdot \pi_0$. When $0 < \eta < 1$, the SEC of operating strategy A will be always greater than the SEC of operating strategy B. The fractional SEC increase is:

$$\frac{\overline{SEC}^A_{ERD} - \overline{SEC}^B_{ERD}}{\overline{SEC}^B_{ERD}} = \frac{[\frac{(1-\eta)}{1-\sigma} + \frac{(1+\eta\sigma)}{1+\sigma}]}{(2-\eta)} - 1 \quad (57)$$

which is plotted in Fig. 6 when the efficiency of the ERD is set to be 90%. Fig. 6 shows that as feed salinity fluctuation percentage increases, time-invariant operation increases SEC more remarkably. Even in some cases there is only marginal energy savings, it is still worthwhile to adopt the proposed operating strategy accompanied by the control algorithms developed at UCLA M3 group regarding reverse osmosis water desalination system (McFall et al. (2008); Bartman et al. (2008)) since we will not be able to know what the future salinity profile would exactly be. Furthermore, in order to equate the total permeate volume in operating strategy A and operating strategy B, $Q'_{f,2} = (1+\sigma)Q_{f,2}$. Thus, the total feed volume in operating strategy B is $2(1+\sigma) \cdot Q_{f,2}$, while the total feed volume in operating strategy A is $(\frac{1+\sigma}{1-\sigma} + 1)Q_{f,2} = (1 + \frac{2\sigma}{1-\sigma} + 1)Q_{f,2} > (1+2\sigma+1)Q_{f,2}$. Therefore, in order to get the same amount of permeate volume, operating strategy A requires a higher amount of feed water, and thus, it has a lower overall water recovery.

5. CONCLUSION

Based on a model for a reverse osmosis membrane desalination plant and the feed concentration fluctuation (which is common in both seawater and brackish water desalination) profile, the proposed approach requires less amount of feed water and decreases specific energy consumption by as much as 22%, providing the same permeate flow. Experimental results confirming the proposed operating policy will be presented at the conference.

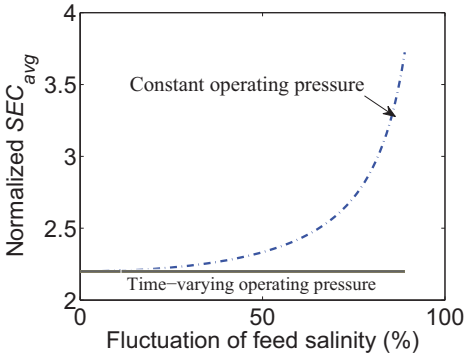

Figure 6. Percentage SEC increase without adjusting the operating pressure vs. feed concentration fluctuation percentage.

REFERENCES

Manual. Standard Practice for Standardizing Reverse Osmosis Performance Data, *ASTM international, April 2000.*

Bartman, A., McFall, C.W., Christofides, P.D., and Cohen, Y. (2009). Model-predictive control of feed flow reversal in a reverse osmosis desalination process. *Journal of Process Control*, 19, 433–442.

Busch, M. and Mickols, W. (2004). Reducing energy consumption in seawater desalination. *Desalination*, 165, 299–312.

Manth, T., Gabor, M., and Oklejas, E. (2003). Minimizing RO energy consumption under variable conditions of operation. *Desalination*, 157(1-3), 9–21.

McCool, B.C. (2008). The feasibility of reverse osmosis desalination of brackish water in the San Joaquin Valley. UCLA master thesis.

McFall, C.W., Bartman, A., Christofides, P.D., and Cohen, Y. (2008). Control and monitoring of a high recovery reverse osmosis desalination process. *Industrial & Engineering Chemistry Research*, 47(17):6698–6710.

Mulder, M. (1997). *Basic Principles of Membrane Technology.* Kluwer Academic Publishers (Boston).

Song, L., Hu, J.Y., Ong, S.L., Ng, W.J., Elimelech, M., and Wilf, M. (2003a). Emergence of thermodynamic restriction and its implications for full-scale reverse osmosis processes. *Desalination*, 155(3), 213–228.

Song, L., Hu, J.Y., Ong, S.L., Ng, W.J., Elimelech, M., and Wilf, M. (2003b). Performance limitation of the full-scale reverse osmosis process. *Journal of Membrane Science*, 214(2), 239–244.

Song, L. and Tay, K.G. (2006). Performance prediction of a long crossflow reverse osmosis membrane channel. *Journal of Membrane Science*, 281(1-2), 163–169.

Wilf, M. (1997). Design consequences of recent improvements in membrane performance. *Desalination*, 113(2-3), 157–163.

Wilf, M. and Bartels, C. (2005). Optimization of seawater RO systems design. *Desalination*, 173(1), 1–12.

Zhu, A., Christofides, P.D., and Cohen, Y. (2008). Effect of thermodynamic restriction on energy cost optimization of RO membrane water desalination. *Industrial & Engineering Chemistry Research*, Publication Date (Web): August 29, 2008 (DOI: 10.1021/ie800735q).

Zhu, A., Christofides, P.D., and Cohen, Y. (2009). Minimization of Energy Consumption for a Two-Pass Membrane Desalination: Effect of Energy Recovery, Membrane Rejection and Retentate Recycling. *Journal of Membrane Science*, doi:10.1016/j.memsci.2009.04.039.

A novel image based algorithm for interface level detection in a separation cell

Phanindra Jampana * **Sirish Shah** **

* *Department of Chemical Engineering, University of Alberta, Edmonton, Canada (e-mail: pjampana@ualberta.ca)*
** *Department of Chemical Engineering, University of Alberta, Edmonton, Canada (e-mail: slshah@ualberta.ca)*

Abstract: Controlling the interface between Bitumen-froth and Middlings in separation cells in the oil sands industry is important for economical and environmental reasons. Traditional sensors do not provide reliable measurements of this interface level and image based sensors are being used to alleviate this problem. Previous work in this area has focussed on separation cells with a single side-view glass. The current work describes a new image based algorithm for interface level detection and confidence estimation based on the concept of image differencing. The algorithm can be extended in a straight-forward manner to separation cells with arbitrary number of side-view glasses. Off-line and on-line results show that the algorithm accurately detects the interface level in normal process conditions and outputs correct confidence values in other situations with very low false positive and negative rates.

Keywords: Bitumen-froth Middlings interface, image sensors, image differencing

1. INTRODUCTION

The control of Bitumen-froth and Middlings interface using image based sensors has been approached previously (Jampana et al., 2008) via particle filtering techniques. Images obtained from a *side-view* glass camera are processed in real time for estimates of the interface level and its quality. These estimates are used subsequently for automatic control. A typical camera image from this setup is shown in Fig 1. For separation cells with multiple side-view glasses (Fig 2) the algorithm described there does not generalize in a straight forward manner. The current work describes an interface level detection algorithm based on image differencing which can be easily generalized to arbitrary number of side-view glasses.

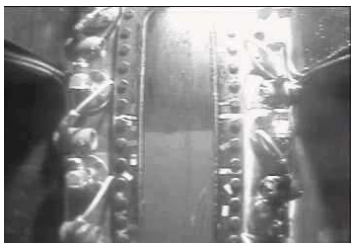

Fig. 1. Separation cell with single side view glass

The generalization property is achieved by computing a confidence estimate (in addition to the interface level estimate) for each side-view glass. This confidence estimate quantifies the chance of the presence of an interface. The final interface level estimate is obtained from the view

⋆ Financial support from NSERC, Matrikon, Suncor and iCORE in the form of the Industrial Research Chair(IRC) program at the University of Alberta is gratefully acknowledged.

Fig. 2. Separation cell with three side view glasses

glass with the highest quality. As confidence estimation is not entirely independent of the interface level estimation procedure, the interface level estimation procedure should facilitate the computation of quality values in an easy manner. The image differencing algorithm described in this paper is one such method.

The image differencing method is based on the idea that the *change* from any previous video frame to the current video frame is maximum near the current interface, though this maximum need not be unique. This change is detected here through (absolute) image differencing. To ensure that the maximum change occurs very close to the current interface, (absolute) image differences between the current and many previous frames are used. The sum image of all these differenced images has maximum values located close to the current interface level for ideal interface images, i.e. images which are completely free from noise. The proof of this fact is given in section 2.

In reality, interface images are seldom noise free. This leads us into estimating a quality value which reflects whether the current interface level estimate is purely a result of

noise. To compute the final confidence estimate however, the noise based quality value alone would not suffice. This is because abnormal changes might occur in the separation cell, which cannot be ascribed to noise alone and which do not necessarily imply the existence of a true interface. Fig 3 shows an example of such a change where the noise based quality described above might be high but the interface is spurious.

Fig. 3. Abnormal process condition resulting in a spurious interface

Therefore, apart from the noise based quality value, an edge quality is also estimated. This quality value quantifies the number of edges detected near the interface estimate. The edge detection method employed here is described in (Elder and Zucker, 1998). A combination of both these quality estimates suppresses most false negatives. In a few pathological cases however, both the noise based quality and the edge based quality can be high, even though the detected interface is spurious. To make the algorithm robust to these, a change based quality is estimated. The final confidence estimate is then based on the three values - noise based quality, edge based quality and change based quality.

The rest of the paper is organised as follows: Section 2 presents the image differencing based interface level detection algorithm in detail followed by section 3 which describes the confidence estimation procedure. Results are displayed in section 4 and section 5 gives the concluding remarks.

2. INTERFACE LEVEL DETECTION USING ABSOLUTE IMAGE DIFFERENCING

This section presents two results which describe the image differencing method for ideal images and also provide theoretical bounds for the interface level estimates obtained. The following notation is fixed first.

Let,

(1) I_t represent the video frame obtained at time t
(2) $D_{t_1,t_2} = I_{t_1} - I_{t_2}$, be the difference of two images at times t_1 and t_2
(3) $AD_{t_1,t_2} = abs(I_{t_1} - I_{t_2})$, be the absolute difference of two images at times t_1 and t_2
(4) $il(t)$ represent the interface level at time t (The interface level is always assumed to be on the Middlings side of the interface).
(5) $\mu_B(t), \mu_M(t)$ represent the average intensity values of pixels in the Bitumen-froth and Middlings regions at time t, respectively.
(6) W and H represent the width and height of the interface image
(7) C be the maximum change in the interface level between two successive video frames
(8) The origin of images is always assumed to be at the top-left corner

Lemma 1. Consider a noise free interface having dynamics such that it remains horizontal at all times and having homogeneous pixel intensities in the Bitumen and Middlings regions. Let $\{I_t, t = 0, 1, ...\}$ be a sequence of completely noiseless images from such an interface such that $\mu_B(0) = \mu_B(1) = \mu_B(2) = ...$ and $\mu_M(0) = \mu_M(1) = \mu_M(2) = ...$ If there is a change in the interface level in a time window $[t_0, t_N]$ and if:-

$$J_N(i,j) = \sum_{k=0}^{N-1} AD_{t_N,t_k}(i,j), \quad \forall i \in \{0,1,2,...,H-1\}, \quad j \in \{0,1,2,...,W-1\}$$

$$P_N(i) = \sum_{j=0}^{W-1} J_N(i,j), \forall i \in \{0,1,2,...,H-1\}$$

$$\hat{il}(t_N) = \inf(\arg\max_i P_N(i))$$

then,

(1) $P_N(i)$ is decreasing in $i \in [\hat{il}(t_N), H-1]$ and increasing in $i \in [0, \hat{il}(t_N)]$,
(2) $0 \leq il(t_N) - \hat{il}(t_N) \leq C$

In reality the interface is seldom horizontal. Lemma 2 guarantees similar bounds as above for the interface level estimate even for the more general case of non-horizontal interfaces:

Lemma 2. Consider the more general case of an interface having dynamics such that it can become non-horizontal. Let $ip(t,v)$ for $v \in [0, W-1]$ be the interface pixels at time t. If $|ip(t,v) - ip(t,m)| < Q$, for all $v, m \in [0, W-1]$, $t \in [t_0, t_N]$ and $|ip(t_1,v) - ip(t_2,v)| < C$ whenever $|t_1 - t_2| = 1$, $v \in [0, W-1]$ and if there is a change in the interface in the time window $[t_0, t_N]$ then it is true that $-C \leq \hat{il}(t_N) - ip(t_N, v) \leq C + Q$ for some $v \in [0, W-1]$.

(Proof for both proofs are omitted due to a lack of space but are available from the authors). The above lemma shows that in the absence of noise and non-homogeneties in images, the estimated interface level is close to the actual interface, especially if C and Q are small. However, when the images are corrupted by noise and other non-homogenties in pixel intensities, the estimated interface level might not be close to the actual interface. Hence a confidence value of the interface level estimate is computed.

3. CONFIDENCE ESTIMATION

The analysis above assumed that images obtained are completely noise free - an assumption that is never met in practice. Image noise is modelled to be additive, homogeneous and Gaussian with zero mean and variance σ^2.

In the presence of noise, it might no longer be true that $\hat{il}(t_N)$ will lie close to an interface point as predicted by

Lemmas 1 and 2. This is because the images observed are only instantiations of a (two dimensional) random field, which is completely described only by the noise statistics, the interface level $il(t_N)$ and the Middlings and Bitumen pixel intensities $\mu_M(t), \mu_B(t)$. Hence, each $P_N(i)$ for $i \in [0, H-1]$ now has a probability distribution. In the case of a horizontal interface, given the noise distribution, the probability that is of interest is the following:-

$$P(P_N(il(t_N)) > \max_{|j-il(t_N)|>G} P_N(j))$$

The above probability quantifies the chance of obtaining an interface level estimate (by following the differencing method described before), $\hat{il}(t_N)$, which satisfies $|\hat{il}(t_N) - il(t_N)| \leq G$. This probability can be used as the confidence value but it cannot be determined, as $il(t_N)$ cannot be known a priori.

As the theoretical confidence (the probability above) cannot be computed, a confidence estimate is obtained by heuristic methods. The confidence estimate is based on the following three quality values, which are explained subsequently:

- Noise based quality
- Edge based quality
- Change based quality

3.1 Noise based quality

Let $TP(t, i, j)$ represent the true (expected) pixel value in the image at time t and at the location i, j. Then the observed value of each pixel $I_t(i, j)$ can be written as $TP(t, i, j) + Y(t, i, j)$, where $Y(t, i, j)$ is a random variable whose distribution is the same as the estimated noise distribution. Using this, the following can be derived:

$$\begin{aligned} P_N(i) - \sum_{j=0}^{W-1}\sum_{k=0}^{N-1} |Y(t_N, i, j) - Y(t_k, i, j)| \\ \leq \sum_{j=0}^{W-1}\sum_{k=0}^{N-1} |TP(t_N, i, j) - TP(t_k, i, j)| \\ \leq P_N(i) + \sum_{j=0}^{W-1}\sum_{k=0}^{N-1} |Y(t_N, i, j) - Y(t_k, i, j)| \end{aligned}$$

The above inequality gives loose bounds on the actual values, $\sum_{j=0}^{W}\sum_{k=0}^{N-1} |TP(t_N, i, j) - TP(t_k, i, j)| \equiv M(i)$, i.e., the values which would have resulted if the images are noise free. In practice, only one instance of $P_N(i)$ is observed. From this value, the value of the corresponding instance of $R_N(i) \equiv \sum_{j=0}^{W}\sum_{k=0}^{N-1} |Y(t_N, i, j) - Y(t_k, i, j)|$ cannot be computed. Therefore the bounds above cannot be determined exactly.

Given $P_N(i) = \hat{P}_N(i)$, $R_N(i)$ follows the conditional probability distribution given by $P(R_N(i)|P_N(i) = \hat{P}_N(i))$. Considering the instances $(\hat{R}_N(i))$ of this distribution allows us to compute inequalities which are be obeyed with a certain degree of probability. For example, if $P_{R_N(i)|P_N(i)}(R_N(i) \leq \hat{R}_N(i)) = r(i)$, then the inequalities

$$\hat{P}_N(i) - \hat{R}_N(i) \leq M(i) \leq \hat{P}_N(i) + \hat{R}_N(i)$$

are true with a probability of $r(i)$. If $\hat{R}_N(i)$ are chosen such that $r(i)$ are very high, then the inequalities are very likely to be satisfied. On the other hand, if the $\hat{R}_N(i)$ are chosen such that $r(i)$ are very low, it is very unlikely that the inequalities will be correct. Given a choice of $\hat{R}_N(i)$, the noise based quality can be defined as:

$$Q_{noise}(t_N) = \begin{cases} 0; \text{if } \exists i, |i - \hat{il}(t_N)| > N_{TH}, \\ \hat{P}_N(i) + \hat{R}_N(i) > \\ \hat{P}_N(\hat{il}(t_N)) - \hat{R}_N(\hat{il}(t_N)) \\ 1; \text{otherwise} \end{cases}$$

This quality value penalizes the interface level estimates when the minimum bound of $M(\hat{il}(t_N))$ is less than the maximum bound of $M(i)$, for i far away ($N_{TH} > C$) from the current interface. In this case, the interface estimate is said to be obtained purely due to camera noise and other irregularities in the images.

As the conditional probability distribution cannot be estimated, the instance $\hat{R}_N(i)$, is chosen based on the unconditional one. The support of the unconditional distribution is a superset of the support of the conditional distribution. Hence, for high values of $\hat{R}_N(i)$ (based on the unconditional distribution) the inequalities obtained will very likely be true. But high values of $\hat{R}_N(i)$ make the bounds very loose and are not useful for noise based quality estimation as most quality estimates will be zero. On the other hand, for small values of $\hat{R}_N(i)$, the quality estimates might be high but the inequalities themselves are true only with a very small probability.

The problem is to obtain estimates $\hat{R}_N(i)$, for which the inequalities will be true with a high probability and are tight enough for use in noise based quality estimation. In the absence of any other information, the choice $E(R_N(i)) = \hat{R}_N(i)$, where E represents mathematical expectation can be considered a possible candidate. From basic probability and the properties of the Gaussian distribution, it can be computed that $E(R_N(i)) = NW\sigma\sqrt{(\frac{8}{\pi})}$.

The accuracy of the noise based quality estimates $Q_{noise}(t_N)$, obtained by the choice $\hat{R}_N(i) = E(R_N(i))$ depends on the absolute difference of average pixel intensities $|\mu_B(t_N) - \mu_M(t_N)|$, the size of the images and the noise standard deviation σ. Based on this dependence, false positive and false negative error rates for the noise based quality are estimated.

When σ is small and $|\mu_B(t_N) - \mu_M(t_N)|$ is high, the false positive rate is approximately $0 - 2\%$, which is small as expected. This rate increases with an increase in σ but decreases with an increase in $|\mu_B(t_N) - \mu_M(t_N)|$. The ratio $\frac{|\mu_B(t_N) - \mu_M(t_N)|}{\sigma}$ can be considered as an upper bound on the Signal to Noise ratio (SNR). If $\frac{|\mu_B(t_N) - \mu_M(t_N)|}{\sigma} = 10$, the false positive error rate is $7 - 8\%$ on an average.

For computing the false negative error rates, random interface images, which do not contain an interface are created. As these images do not contain any interface the percentage of time $Q_{noise}(t_N) = 1$ is considered an estimate of the false negative error rate. In a simulation

study using the same parameters as above (except that $\mu_B(t_N) = \mu_M(t_N)$), it has been found that there were no false negatives. As other type of examples cannot be readily created to study the false positive and negative error rates, they are estimated on real videos collected from a plant site. These are presented in Section 4.

3.2 Edge based quality

Noise based quality alone is not sufficient for estimating confidence. This is due to the fact that false negatives result when abnormal changes occur inside the separation cell (scenarios as shown in Fig 3) which cannot be explained by noise alone. Hence, an additional edge detection algorithm is used to aid in the estimation of the confidence.

The motivation for using edge detection to estimate a quality value is that the available information in images would be utilised in a very efficient manner as the edge based algorithm captures information which cannot be obtained by image differencing. Given only the difference images $I(t) - I(s)$ for $s < t$, it is impossible to recover the edge map of $I(t)$ and similarly given only the edge map of $I(t)$, it is impossible to estimate the difference images except in a few pathological cases. Using the image differencing and the edge detection algorithms simultaneously most false negatives (high confidence values when the interface level estimates are wrong), can be avoided.

The algorithm described in (Elder and Zucker, 1998) is used here with the already estimated variance σ^2 of the Gaussian noise distribution. The advantage of this particular edge detection algorithm over standard algorithms (Sobel, Canny etc.) is its ability to detect edges over a large blur scale and contrast. The Bitumen-Middlings interface tends to become fuzzy when the percent of sand in the oil sands ore is high. The chosen algorithm can detect edges under these situations and hence is suitable for the purpose. Another reason for the choice is that spurious edges that occur due to sensor noise are minimised because of statistical bound checking based on the sensor noise variance in the algorithm. This increases the efficiency of the edge based quality.

A simple heuristic based on the number of edge points in a predefined window near the detected interface level is used to estimate the edge based quality. If EI is the edge map returned by the edge detection algorithm, and if *nedges* represent the number of edges in a predefined window near the detected interface level and E_{TH} is a given threshold then the edge based quality is defined as:

$$Q_{edge}(t_N) = \begin{cases} 0; nedges < E_{TH} \\ 1; \text{otherwise} \end{cases}$$

3.3 Change based quality

The edge detection algorithm, in most cases does not produce the exact edge map, EI. When spurious edges are detected (due to shadows, lighting glare etc.), the edge based quality might be high even when the interface level estimate is not correct. If the noise variance is under estimated, the noise based quality would also be high resulting in a wrong estimate of the interface level. False negatives in interface level detection can have an undesired effect on the overall process as the controller takes immediate corrective action based on these false readings.

To make the algorithm robust to such cases a quality based on the percent change near the interface is estimated. The change based quality analyzes the instance of P_N observed, $\hat{P}_N$. An example $\hat{P}_N$ (for a normal interface image sequence) is shown in Fig 4.

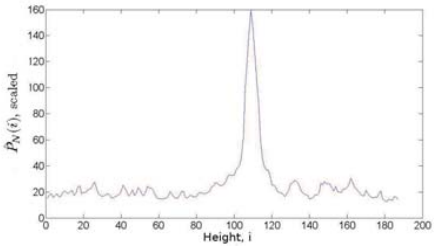

Fig. 4. An example of the profile, P_N obtained by the image differencing method

For a normal interface, based on test videos, the average and minimum values of $\hat{P}_N$ have been observed to be close to each other as shown in the figure above. The maximum value of P_N, $\hat{P}_N(\hat{il}(t_N))$, is in general high compared to both these values. Based on this, the change based quality is defined simply as:

$$Q_{change}(t_N) = \begin{cases} 0; \dfrac{\max(\hat{P}_N) - avg(\hat{P}_N)}{\max(\hat{P}_N) - ((1-\epsilon)\min(\hat{P}_N))} \\ \quad < C_{TH} \\ 1; \text{otherwise} \end{cases}$$

Here, $0 < \epsilon \approx 10^{-2} << \min(\hat{P}_N)$. The change based quality value would be high when the average value of $\hat{P}_N$ is close to the minimum value of $\hat{P}_N$. When the average is close to the maximum this quality value would be small.

The thresholds – N_{TH}, E_{TH}, C_{TH} and N determine the performance of the final algorithm. The value of E_{TH} is chosen as a percentage of the width of the image W and the value of $C_{TH} \in [0, 1]$. Hence both these thresholds are relative in nature. The value of N_{TH} is chosen based on the dynamics of the interface. Based on the three quality values, the final confidence is defined as

$$il_{conf}(t_N) = \begin{cases} 1; Q_{noise}(t_N) = 1, \\ \quad Q_{edge}(t_N) = 1, \\ \quad Q_{change}(t_N) = 1 \\ 0; \text{otherwise} \end{cases}$$

4. RESULTS

4.1 Off-line results

The algorithm is first tested off-line on three videos recorded at the Suncor Energy Inc. plant site located at Fort McMurray, Alberta, Canada. The first video contained only one side view glass whereas the other two were equipped with three side view glasses. In the first video (Fig 5a) the view glass was wider and the interface was always present inside it. There was also significant lighting

glare present on the top of the glass window. The other two videos had considerably smaller view glasses. In one of these two videos (Fig 5c), the interface was only present in two of the three view glasses. In the other video (Fig 5b), spurious changes occurred (due to Bitumen sticking on the inside) in one of the glasses initially and the interface reappeared at the end.

The original videos were from colour cameras and for the purpose of analysis, they were converted to grayscale by averaging across all the three (RGB) colour channels. For single side view glass, the algorithm as described in the sections before can be applied directly. Whereas, in the case of three view glasses, the algorithm is extended in a straightforward manner. Each glass window is analysed separately and finally the window with the highest confidence value is chosen along with its interface level estimate. In cases where the interface is present in two or more glasses, more than one window can have a high confidence value. In such situations, the final interface level is chosen at random from these glasses, as all of the interface level estimates refer to the same interface.

In all the videos the same parameters, $N = 100$, $N_{TH} = 30$ pixels, $E_{TH} = \frac{W}{4}$, $C_{TH} = 0.75$ were used. Fig 6a shows the true and the estimated interface level values for the video with a single side view glass ($H = 188$ pixels, $W = 61$ pixels). It can be seen that the estimated value is very close to the actual value. The average absolute error was calculated to be approximately two pixels. This corresponds to an average error of less than one percent with respect to the height of the view glass. The confidence estimate was equal to one throughout(except at one frame where the edge based quality was zero). Noise standard deviation was estimated to be $\sigma = 1.0$ pixels and $|\mu_B(t_N) - \mu_N(t_N)| = 21.9$ intensity units. The corresponding false positive has been estimated to be zero which explains the fact that the noise based quality was equal to one throughout. Edge based quality was also high because the interface was clear and easily detectable by the edge detection algorithm. The change based quality was one throughout.

For the video with three side view glasses shown in Fig 5c, the results obtained are shown in Fig 6b. Note that in this case, the interface level estimate corresponds to the view glass with the highest confidence value. The average absolute error was calculated to be three pixels approximately, which corresponds to an average error of less than one percent with respect to the height of the view glass, as before. The confidence estimate was equal to one at all times except for three frames. The noise based quality was equal to one throughout but the edge based quality was zero at these three frames owing to significant fuzziness in the interface (not shown here). The change based quality was one throughout as before.

Finally, the video shown in Fig 5b is split into two segments. In the first part, the interface was either spurious or not present in the view glass. For this segment of the video the false negative rate obtained was equal to zero, i.e. the confidence value was identically zero all the time. Fig 6c shows the estimated and the actual interface level for the second part of the video, when the interface reappeared in the view glass. The average absolute difference was equal to three pixels which corresponds to an error of less than one percent with respect to the height of the view glasses. The false positive rate during this time was estimated to be 10%, due to zero edge based quality during those frames. The high false positive rate in this video can be attributed to following:-

- Loss of resolution from the original to the recorded video resulting in a poor quality of the video
- Highly fuzzy interfaces occur due to a high fines situation – too many sand particles in the Bitumen-froth

The false positive rate can be minimized by employing a simple filtering rule. In the industry, a single occurrence of a confidence value of zero triggers an alarm for operator intervention. As the confidence value is susceptible to sudden changes in the fuzziness of the interface it is reasonable to wait until the confidence value stabilizes. Hence, instead of signalling an alarm for a single occurrence, alarm is only signalled when the confidence value is zero for a sustained period of time ($\tau \approx 5s$). The interface level estimate used for control during this phase is the most recent estimate with a confidence value of one. This simple filtering rule has been observed to increase the efficiency of the algorithm.

4.2 On-line results

The algorithm described in this paper has been implemented on two separation cells (previously shown in Fig 5b and Fig 5c) at Plant 86, Suncor Energy Inc., Fort McMurray, Alberta, Canada. A frame grabber card is used to transfer the images from the analog cameras to the PC. Software has been built in in the C programming language based mainly on the Intel OpenCV library for image manipulation.

Fig 7a compares the true and estimated interface level values for the separation cell shown in Fig 5b. In this plot, hourly data is collected at random times and stitched together for the final result. A total of eight hours of data is used for comparison. On this data set, the average absolute error(in percentage) was calculated to be four percent. Similarly, Fig 7b compares the true and estimated interface level values for the separation cell shown in Fig 5c. The average absolute error was equal to three percent of the total height of the view glasses. These results suggest that the estimates from the vision sensor very closely reflect the true interface level values.

5. CONCLUSIONS

This work has presented a novel image differencing method for Bitumen-froth and Middlings interface level detection. It has been shown that in the case of noiseless images the estimation error is bounded. For nominal values of the dynamics of the separation cell, the bounds are very small.

When noise is present in the images, a confidence value which estimates the correctness of the detection is computed. The confidence value is based on a novel noise based quality estimate along with simple edge and change criterion. Analysis and results show that the final algorithm accurately detected the interface level and exhibited

(a) Video with one side view glass

(b) Video with spurious changes

(c) Video with interface present in two glasses

Fig. 5. Interface levels in different separation cells

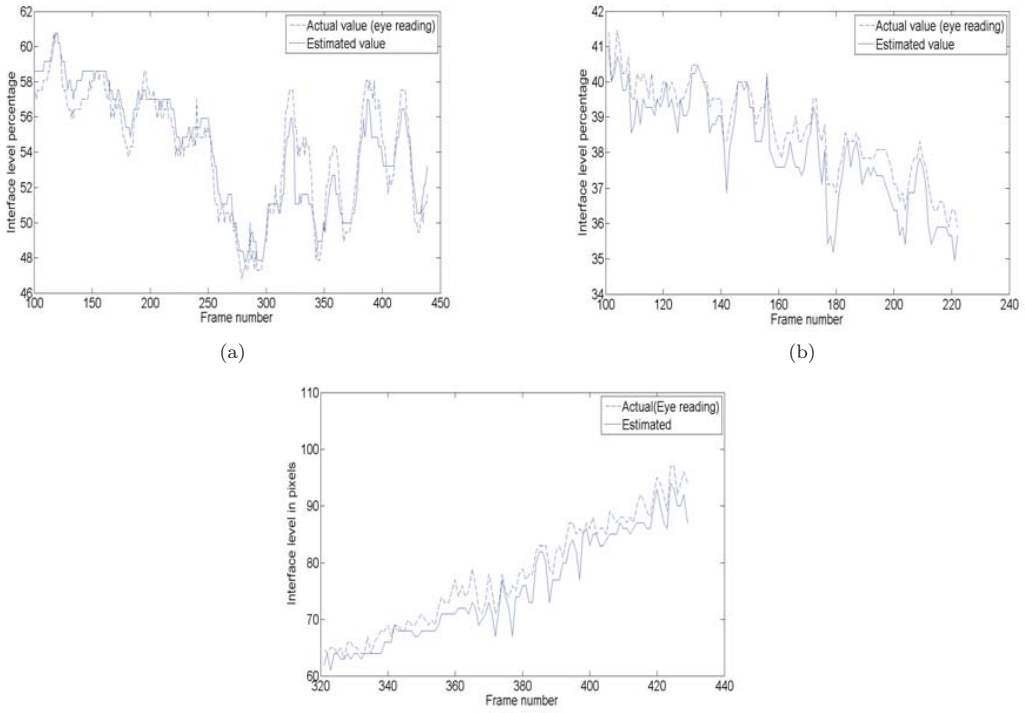

(a) (b)

(c)

Fig. 6. True and estimated interface levels - Off-line results

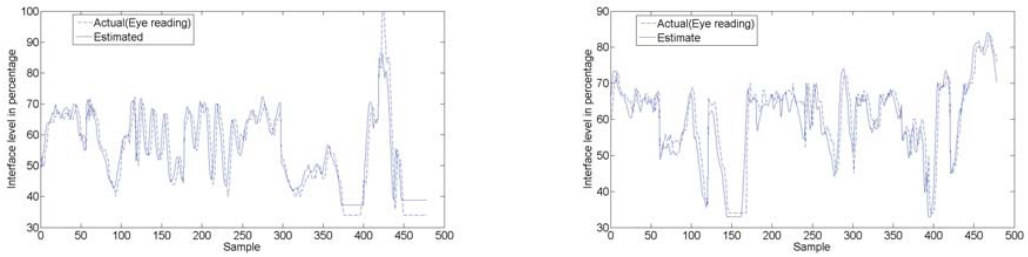

(a) True and estimated interface levels for separation cell shown in Fig 5b

(b) True and estimated interface levels for separation cell shown in Fig 5c

Fig. 7. True and estimated interface levels - On-line results

very few false positive and negative error rates. The sensor has been installed at Suncor Energy. Inc, Fort McMurray, Canada and has been yielding highly satisfactory results.

REFERENCES

Elder and Zucker (1998). Local scale control for edge detection and blur estimation. *IEEE Transactions on Pattern Analysis and Machine Intelligence*, 20(7), 699 – 716.

Jampana, P., Shah, S., and Kadali, R. (2008). Computer vision based interface level control in a separation cell. *IFAC world congress.*

Model-Based Dosing Control of a Pellet Softening Reactor

K.M. van Schagen [*,**] **R. Babuška** [**] **L.C. Rietveld** [***] **A.M.J. Veersma** [****]

[*] *DHV B.V., Amersfoort, The Netherlands (e-mail: kim.vanschagen@dhv.com)*
[**] *Delft Center for Systems and Control, Delft University of Technology, The Netherlands*
[***] *Faculty of Civil Engineering and Geosciences, Delft University of Technology, The Netherlands*
[****] *Waternet, Amsterdam, The Netherlands*

Abstract: The control of a drinking-water treatment plant aims to produce the correct quantity of water, with a constant quality. Achieving constant water quality is not an obvious task, since the online water-quality measurements and possible control actions are limited. Applying model-based control improves disturbance rejection and online process optimisation. For the softening process step, the integral control scheme is shown with multiple controllers for different time scales and process detail. The dosing control is elaborated and verified using simulation experiments. The control is implemented and tested in the pilot plant of Weesperkarspel (Amsterdam). It shows that in the case of accurate state estimation, quick changes in setpoint can be tracked.

Keywords: multivariable control; MPC; crystallisation

INTRODUCTION

In the last decades, most drinking-water treatment plants have been automated. During these first automation realisations, the goal was to operate the treatment plant in the same way as the operators did before. Therefore the control configurations consisted of a heuristic control strategy, based on historical operator knowledge. The controls are designed for the static situation, including extra safety margins to take operator response into account. This was a logical and practical solution. However, this heuristic solution does not optimise the control of a treatment plant.

The heuristic control is based on static local control objectives, without taking the current state of the treatment plant into account. Therefore it is necessary to adopt a new control strategy, which can take into account quality-related and economic criteria and optimise the overall performance of the plant, based on the current state of the processes.

Since the treatment steps are coupled, local changes affect other treatment steps and therefore local optimisations should be considered in a global context. It is necessary that operational actions do not introduce new disturbances to other processes. This must be considered in all levels of control, from basic valve controllers to plant-wide quantity control. At the same time, the control should consider the actual state of the process and optimise plant operations.

The information density in the online measured data of water treatment plants is limited and multiple measurements have to be used to obtain a good view of the actual treatment performance (van Schagen et al., 2006b). By using white or grey models, the process knowledge is no longer stored as historical heuristic rules of thumb or static local control objectives. The local control objectives evolve from applying the new criteria to the existing models in the case of changes to the process, such as boundary conditions, influent properties and desired treated water quality.

The model-based dosing control is part of the new model-based control configuration for the pellet-softening treatment step, consisting of a number of pellet reactors and a bypass. The pellet softening process step at the Weesperkarspel treatment plant is described in the first section. The model-based control configuration is elaborated in the second section. Finally the model-based dosing control scheme is validated in simulation experiments and finally validated in the pilot plant of Weesperkarspel (Amsterdam).

PROCESS DESCRIPTION

In the Netherlands, softening of drinking water in treatment plants is mainly carried out with fluidised pellet reactors. The pellet reactor consists of a cylindrical vessel that is partly filled with seeding material (figure 1). The diameter of the seeding grain is small, between 0.2 and 0.4 mm and consequently the crystallisation surface is large. The water is pumped through the reactor in an upward direction at high velocities, maintaining the seeding material in a fluidised condition. In the bottom of the reactor, chemicals are dosed (caustic soda, soda ash or lime). Calcium carbonate then becomes super-saturated and crystallises on the seeding material, resulting in the

formation of pellets. At regular intervals, pellets at the bottom of the reactor are removed. These pellets can be re-used in industry (van Dijk and Wilms, 1991).

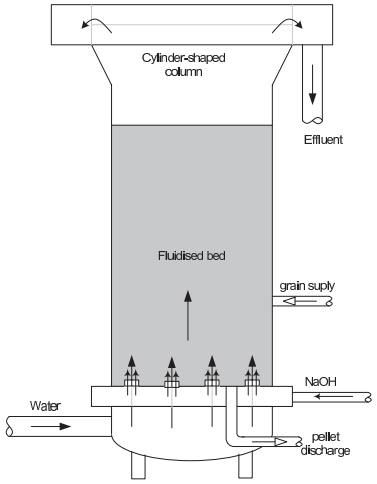

Fig. 1. Fluidised bed reactor for water softening.

Softening in a reactor is normally deeper than the required levels. Therefore, part of the water can be bypassed and mixed with the effluent of the reactors. In general, several identical parallel reactors are installed to increase the reliability of the system and the flexibility in operation. Reactors can be switched on and off in case of flow changes, maintaining water velocities between 60 and 100 m/h.

The mixture of the effluent of the reactors and the bypass water must be chemically stable to avoid crystallisation in the filters after the softening step.

At Weesperkarspel caustic soda (NaOH) is dosed for softening. The seeding material is garnet sand. The dosing of caustic soda in the pellet reactor is adjusted to realise the mixed effluent hardness of 1.5 mmol/l. The pellet removal is based on the hydraulic resistance of the fluidised bed (head loss) and the goal was to keep the hydraulic resistance constant. The garnet sand dosage was a manually set percentage of the mass of discharged pellets. The pH, flow, water temperature and hydraulic resistance were measured every minute, while hardness, calcium, bicarbonate, super saturation, pellet diameter and bed height were measured at longer intervals (Rietveld, 2005).

The characteristics of the softening process at Weespekarspel are given in table 1.

Table 1. Characteristics of softening reactors at Weesperkarspel.

Number of reactors	8	-
Surface area of reactor	5.3	m^2
Maximum bed height	5	m
Typical water velocity	60-100	m/h
Grain size of seeding material	$0.25\ 10^{-3}$	m
Density of the seeding material	4114	kg/m^3

CONTROL CONFIGURATION

The aim of the control of the softening process is to achieve a desired calcium concentration and, at the same time, minimise the use of dosage material (caustic soda, seeding grains and acid). The available control inputs are the water flow through the bypass and for each reactor the water flow through the reactor, the grain supply rate, the pellet discharge rate, the caustic soda dosage and the acid dosage.

To control the complete treatment step, a modular control setup is chosen. In this way, the controller complexity is minimised, maximising operator understanding of the control structure. Due to the diverse time constants in the process, these controllers are implemented on different platforms, with appropriate performance for the controllers. Figure 2 shows the control modules that are related to the softening process step. On the vertical axis represents the typical time constant of the controller and the horizontal axis shows the process level of the controller.

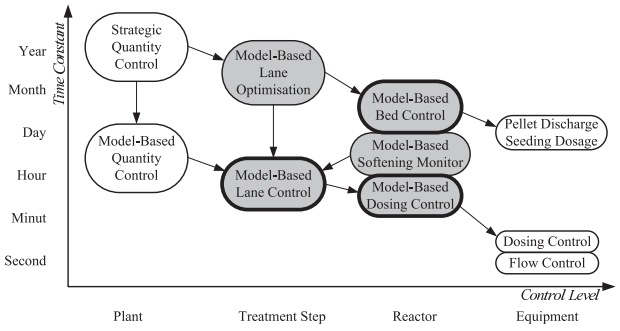

Fig. 2. Control setup for the pellet-softening treatment step. Modular controllers for different time constants and control levels.

The *Strategic Quantity Control* determines the amount of water, which has to be produced at the treatment plant. This is based on yearly consumption patterns, available resources at this plant and, in a multiple plants setup, the other treatment plants. The amount of water to be treated, is then passed to the Model-Based Quantity controller and the Model-Based Lane Optimisation.

The *Model-Based Quantity Control* determines the actual production rate of the entire plant, based on expected daily consumption pattern and the available water in the storage tanks. Restrictions in production rate, due to short-term maintenance, are taken into account and fluctuations of production rate are minimised (DHV, 2008).

The *Model-Based Lane Optimisation* determines the ideal pellet size, bypass ratio and the optimal number of reactors in operation, based on the expected production rate from the Stategic Quantity Control and the expected temperature variations. Changing bed configurations is a long term optimisation, due to the retention time of seeding material in the reactor of approximately 100 days. An extensive description of this optimisation scheme can be found in (van Schagen et al., 2008c).

The *Model-Based Bed Control* achieves the optimal bed composition as found with the Model-Based Lane Optimisation by determining the required pellet discharge and seeding material rates (van Schagen et al., 2008c). It uses the estimation of the current bed composition, determined by the Model-Based Monitor. This can be the model-based monitor of the complete reactor as shown in van Schagen et al. (2006b).

The *Model-Based Monitor* estimates the accuracy of the measurement devices and determines the actual state of the softening process. This monitor is used to verify the measurements that are used by the other controllers. In the case of unexpected differences between measurement and model outcome, operators are notified to take appropriate action. If measurement accuracy is sufficient, the model can be used to estimate unmeasured quality parameters using online measurements and historical laboratory results. Finally the actual state of the process can be estimated, such as the diameters of the pellets in the softening reactor at different heights. An extensive description of this monitoring scheme can be found in van Schagen et al. (2006b).

The *Model-Based Lane Control* determines the current flow and quality setpoints for each lane. It uses the estimated bed composition from the Model-Based Monitor and the actual production rate from the Model-Based Quantity Control. This controller is introduced, since the fluidised bed has limited control possibilities and it is expected that the actual bed composition is different for each reactor. The Model-Based Bed Control strives for the optimal bed composition, while the Model-Based Lane Control adapts to the current bed composition. The Model-Based Lane Control is elaborated in van Schagen et al. (2006a).

The *Model-Based Dosing Control* determines the actual dosing of caustic soda in the reactor to achieve the desired calcium concentration after the reactor, while respecting the constraints of the reactor. The objective of this controller is to follow the setpoint for the Model-Based Lane Control smoothly. The Model-Based Dosing control is shown in this article.

The *Pellet Discharge*, *Seeding Dosage*, *Dosing Control* and *Flow Control* follow the setpoints from the model-based controllers, by adjusting the physical devices such as valves and pumps. These local controllers are implemented in the process automation system of the plant.

MODEL-BASED DOSING CONTROL

The control of water flow and base dosage in the softening reactor is not straightforward. The dosing control and flow control are strongly interrelated. The retention time in the reactor is at least five minutes and response to control actions can only be detected after this time, since water quality can only be measured in the effluent of the reactor. The measurement of the total hardness (the main controlled variable), is a semi-online measurement and has a delay of at least ten minutes. The online pH measurement is inaccurate and has a tendency to drift. Changes in flow and dosing must be gentle, to prevent introduction of process disturbances and fast-changing water quality parameters, which cannot be compensated in consecutive treatment steps. Since the water production rate is predicted, setpoint changes can be predicted as well. Ideally the control should take these predicted changes into account. Finally, the constraints of the reactor, such as maximal height and maximal dosing must never be violated.

Controller Configuration

A model-based multivariable controller is used to meet all requirements. A linear Model Predictive Controller (linear MPC) is used, since in this case calculation time is limited and valid solutions must be guaranteed. The information density in the process is insufficient to use a data-based model. The controller model is therefore obtained through numerical lineralisation of the white nonlinear model described in van Schagen et al. (2008a). The nonlinear model is linearised using the current bed composition found by the Model-Based Lane Control for the given reactor, and the current influent water quality parameters, water flow and caustic soda dosage.

Model predictive control is an online model-based optimal control technique based on the receding horizon principle. An online optimisation algorithm (normally a linear or quadratic programming algorithm) is applied to compute a series of control actions that minimizes a pre-defined cost function or 'performance index', subject to certain constraints. Applying the receding horizon principle means that only the first control sample is implemented and the horizon is shifted one time-step. Then the optimisation starts all over again. Figure 3 shows the principle of receding horizons graphically: $r(k)$, $y(k)$ and $u(k)$ are the reference, output and control (or manipulated) signals, N_m is the 'Minimum cost horizon', N_c is the 'Control horizon' and N the 'Prediction horizon'.

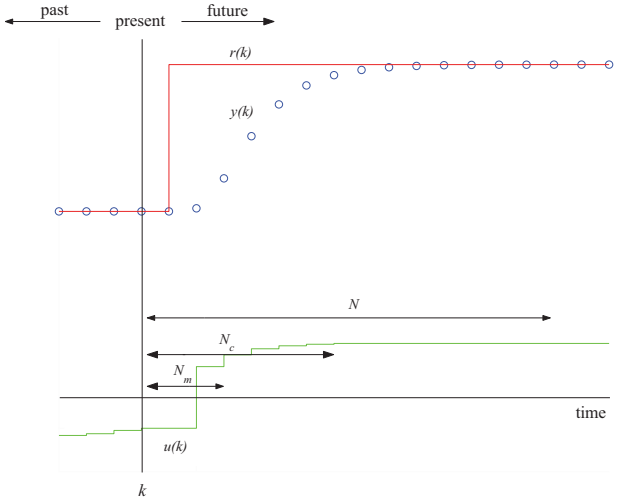

Fig. 3. The principle of linear model predictive control

At time instant k the system output is predicted from time step k until $k+N$ as a function of the control actions. Then the performance index is minimized resulting in an optimal control trajectory $\{u(k|k), ..., u(k+N_c-1|k)\}$.The outputs

from k until $k + N_m - 1$ are left out of the optimisation (to ignore minimum-phase and dead-time behaviour of the system) and the control actions are not allowed to change after time step $k + N_c - 1$.

Many different varieties of model predictive control configurations exist. The one chosen to implement for the pellet reactor controller is the so called 'Standard Predictive Control' (SPC) configuration (van den Boom and Backx, 2001). The advantage of this configuration is its flexibility and its state-space formulation.

The control objectives are to follow the current and future setpoints of the Model-Based Lane Control under smooth variation of the manipulated inputs, as formulated in the following cost function:

$$\begin{aligned} J = &\sum_{j=N_m}^{N} \|\mathbf{y}(k+j|k) - \mathbf{r}_y(k+j)\|_P^2 \\ &+ \sum_{j=1}^{N} \|\Delta\mathbf{u}(k+j|k)\|_{Q_{\Delta u}}^2 \\ &+ \sum_{j=1}^{N} \|\mathbf{u}(k+j|k) - \mathbf{r}_u(k+j)\|_{Q_u}^2 \end{aligned} \tag{1}$$

where N and N_m are the prediction horizon and the minimum costing horizon, and $\mathbf{r}_u$ and $\mathbf{r}_y$ are the references for the inputs and the outputs. In this way the control can use the setpoint predictions from the Model-Based Lane Control, due to predicted production rate changes.

The inputs are the caustic soda dosage and the water flow through the reactor. The outputs are the fluidised bed height in the reactor and the following water quality parameters in the effluent of the reactor: calcium concentration, pH, M-alkalinity and conductivity.

To meet the physical constraints in the process the linear MPC takes these constraints into account:

$$\begin{aligned} \mathbf{u}_{min} < \mathbf{u}_k < \mathbf{u}_{max} \\ \mathbf{y}_{min} < \mathbf{y}_k < \mathbf{y}_{max} \end{aligned} \tag{2}$$

To introduce extra integration action in the MPC controller, the model is modified to an IIO model. The new state vector consists of the previous output and the difference of the sate vector of the linearised model. The state update equation is now given by:

$$\begin{aligned} \begin{bmatrix} \mathbf{y}_k \\ \mathbf{x}_{k+1} - \mathbf{x}_k \end{bmatrix} = \begin{bmatrix} \mathbf{I} & \mathbf{C} \\ \mathbf{0} & \mathbf{A} \end{bmatrix} \begin{bmatrix} \mathbf{y}_{k-1} \\ \mathbf{x}_k - \mathbf{x}_{k-1} \end{bmatrix} + \\ \begin{bmatrix} D \\ B \end{bmatrix} (\mathbf{u}_k - \mathbf{u}_{k-1}) \end{aligned} \tag{3}$$

with the corresponding output function:

$$\mathbf{y}_k = [\,\mathbf{I}\ \mathbf{C}\,] \begin{bmatrix} \mathbf{y}_{k-1} \\ \mathbf{x}_k - \mathbf{x}_{k-1} \end{bmatrix} + D\,(\mathbf{u}_k - \mathbf{u}_{k-1}) \tag{4}$$

where $\mathbf{A}$, $\mathbf{B}$, $\mathbf{C}$ and $\mathbf{D}$ are the system matrices of the linearised model.

To compensate for plant-model mismatch an observer is used, to estimate the offset in $\hat{\mathbf{y}}_k$. The state update in the MPC controller is therefore given by:

$$\begin{aligned} \begin{bmatrix} \hat{\mathbf{y}}_k \\ \hat{\mathbf{x}}_{k+1} - \hat{\mathbf{x}}_k \end{bmatrix} = \begin{bmatrix} \mathbf{I} & \mathbf{C} \\ \mathbf{0} & \mathbf{A} \end{bmatrix} \begin{bmatrix} \hat{\mathbf{y}}_{k-1} \\ \hat{\mathbf{x}}_k - \hat{\mathbf{x}}_{k-1} \end{bmatrix} + \\ \begin{bmatrix} D \\ B \end{bmatrix} (\mathbf{u}_k - \mathbf{u}_{k-1}) + \\ \begin{bmatrix} \mathbf{L} \\ \mathbf{0} \end{bmatrix} (\mathbf{y}_{k-m} - \hat{\mathbf{y}}_{k-m}) \end{aligned} \tag{5}$$

where $\mathbf{y}_{k-m}$ is the measurement result of m samples ago, due to the measurement delay.

A detailed explanation of the linear MPC algorithm is given in van den Boom and Backx (2001).

Simulation Results

To evaluate the performance of the controller, simulations were performed for the full-scale plant. The sample time for the controller was chosen to be 1 minute. The minimum cost horizon N_m, the control horizon N_c and the prediction horizon N are chosen to be 3,10,20 respectively, since the hydraulic retention time of the reactor is about 3 to 5 minutes. The setpoint for reactor flow and calcium concentration were taken from the lane controller. The simulation is started with a lane flow of 400 m^3/h, increasing the lane flow to 570 m^3/h, due to a production rate change after 1 hour. The reactor flow is kept constant and the bypass flow is increased. As a result from this flow change, the calcium concentration has to change from 50 to 35 mg/l. This is a regular change in calcium setpoint to produce constant water quality in the mixed effluent of reactor and bypass:

$$[\mathrm{Ca}^{2+}]_l = \frac{[\mathrm{Ca}^{2+}]_{in} F_{BP} + [\mathrm{Ca}^{2+}]_r F_{w,r}}{F_{w,l}} \tag{6}$$

Finally, if all lanes are operated at maximum capacity, the lane controller can increase the reactor flow for all reactors that are not yet limited by fluidised bed height. Therefore, in the simulation, the reactor flow is increased to 450 m3/h (the maximum flow for this reactor). The lane flow in this case is 640 m^3/h.

The operating point for the linearised model is the steady-state of the dissolved components in the nonlinear model with current estimated bed composition and the current influent flow and dosage. The states, which describe the bed composition ($\mathbf{m}_g$ and $\mathbf{m}_c$) are kept constant during numerical linearisation. The weighting matrices in equation 1 are diagonal, and the non-zero diagonal elements are given by:

$$\begin{aligned} P(\mathrm{Ca}^{2+}) &= 0.1 \\ Q_u(F_w) &= 1 \\ Q_{\Delta u}(F_w) &= 1 \\ Q_{\Delta u}(F_s) &= 0.1 \end{aligned} \tag{7}$$

The non-zero weights in P and Q_u penalise the deviation of the calcium concentration and water flow from their reference values. Change in the manipulated variables are penalised to achieve a smooth transition between operation points. In addition, level constraints are defined for all outputs and inputs, based on their physical ranges. To make the simulation more realistic, noise was added to

the simulated outputs. For the measurements of calcium and M-alkalinity the measurement noise was set at 2%, for bed height, pH and conductivity 1%.

The observer gain was chosen to be diagonal and the same for all measurements, since it is used to estimate model offset. The change in offset is expected to be equal for all measurements.

$$\mathbf{L} = \text{diag}\left([0.2\ 0.2\ 0.2\ 0.2\ 0.2]\right) \tag{8}$$

The simulation results using the nonlinear process model are shown in figures 4 and 5. In figure 4 the dashed-dot line is the setpoint for the calcium concentration, changing from 50 to 35 mg/l, due to a lane flow increase. The solid line is the simulated process values without measurement noise, while the dots are the actual measurement values available for the MPC controller. For calcium, M-alkalinity and conductivity, these measurements are only taken every 10 minutes, with a 10 minute delay. In the graph the measurements are therefore shifted by 10 minutes. The pH measurement and bed height measurements are online measurements and available every minute. The dashed line is output estimation $\hat{\mathbf{y}})_k$ of the MPC controller. In figure 5 the dashed-dot line is the setpoint for the reactor flow from the lane controller and the solid lines are the actual setpoints from the MPC controller.

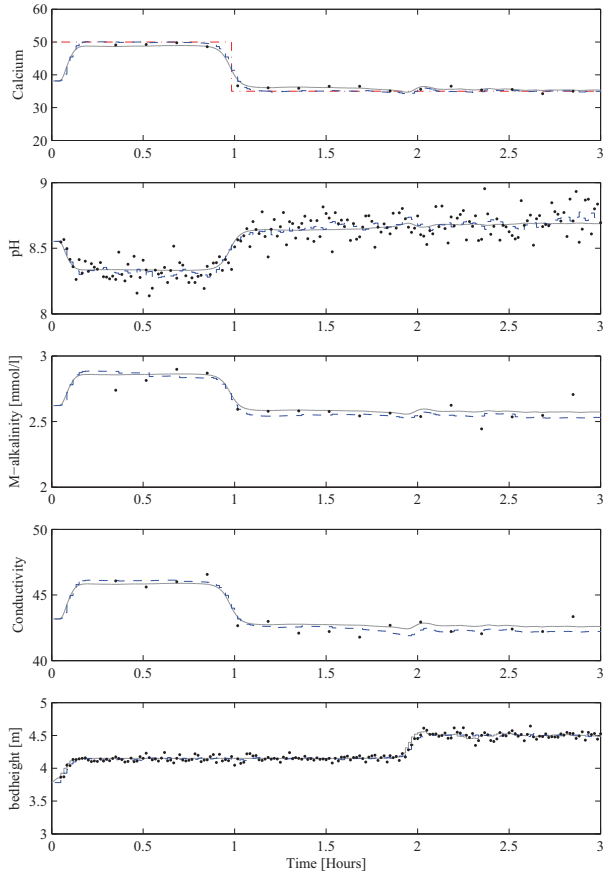

Fig. 4. Simulation results outputs. dashed-dot: Reference, dashed: Estimate, solid: Process, dots: Measurements

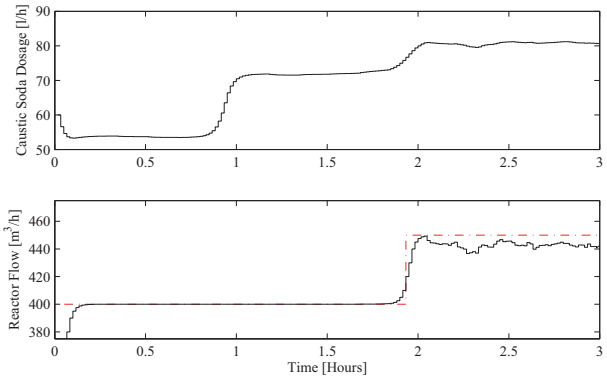

Fig. 5. Simulation results control inputs. dashed-dot: Reference, solid: MPC.

It can be observed, that the tracking of the reference signal is appropriate, including the desired smooth transition. The calcium concentration and the flow change starts before the actual setpoint change, as expected, to get a smooth transition close to the desired setpoint. Another interesting observation is that the water flow through the reactor and the caustic soda dosage are not strictly linked (as opposed to the current heuristic strategy). A flow reference change shows a rapid flow response, but a relatively slow dosage response, which results in a negligible change of the calcium concentration. Finally it can be seen that the MPC controller prevents a flow increase to the setpoint of 450 m^3/h, due to the limitation in bed height.

Pilot plant Results

The MPC controller is also implemented on the pilot plant of Weesperkarspel. The setpoints for the calcium concentration and reactor flow follow a similar pattern as in the full-scale reactor simulation. In this experiment the weighting matrices in equation 1 are diagonal, and the non-zero diagonal elements are given by:

$$\begin{aligned} P(\text{Ca}^{2+}) &= 3 \\ Q_u(F_w) &= 1 \\ Q_{\Delta u}(F_w) &= 0.01 \\ Q_{\Delta u}(F_s) &= 0.01 \end{aligned} \tag{9}$$

The matrices are selected to focus on setpoint achievement and less on smooth transition. The non linear model is the model from a validation experiment. The bed composition in this experiment is determined using the pressure drop measurement with different flows in the reactor. In the pilot-scale plant the pH measurement is not available as online measurement, and is determined semi-online during the M-alkalinity titration. The results from the pilot plant experiments are shown in figures 6 and 7.

The MPC controller in the pilot plant is performing as expected. The relatively small weighting matrix for control variations in equation 10 cause more variation in the caustic soda dosage and flow than for the full-scale simulation experiment.

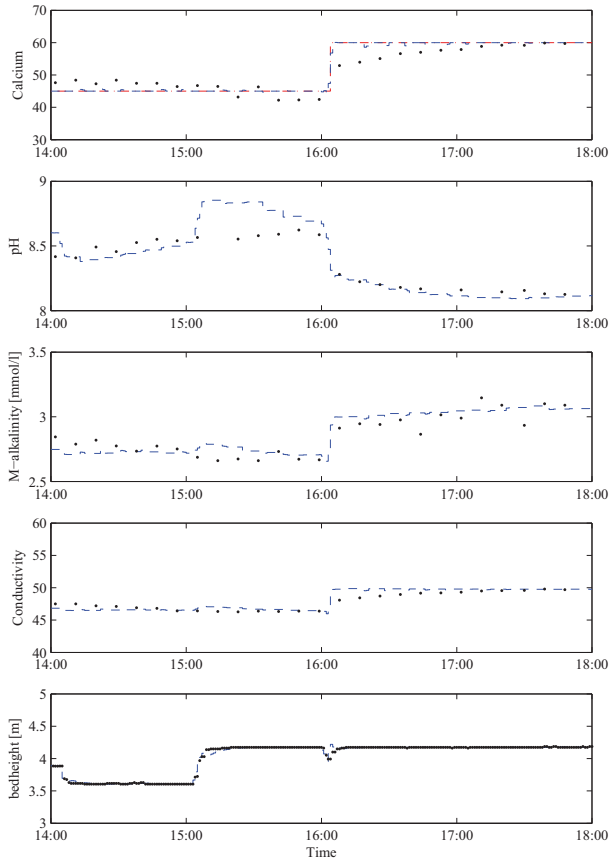

Fig. 6. Pilot plant experiment results outputs. dashed-dot: Reference, dashed: Estimate, dots: Measurements

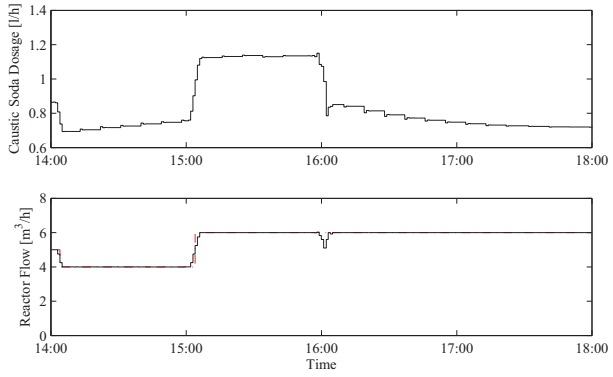

Fig. 7. Pilot plant experiment results control inputs. dashed-dot: Reference, solid: MPC.

CONCLUSIONS

The performance of the softening process step can be improved by applying a model-based control scheme. The control configuration is split in separate controllers for different control levels and time constants. To achieve smooth but quick responses to changing setpoints, a linear MPC is shown to be an effective controller.

A linear MPC controller shows a smooth transition between sudden changes of setpoints, while using a limited number of online and semi-online measurements. The controller is shown to function appropriately in the pilot-scale plant of Weesperkarspel.

REFERENCES

DHV (2008). http://www.aquasuite.com. Internet.

Rietveld, L. (2005). *Improving operation of drinkingwater treatment through modeling*. Ph.D. thesis, Faculty of Civil Engineering and Geosciences, Delft University of Technology.

van den Boom, T.J. and Backx, T.C. (2001). *Model Predictive Control*. TU Delft, Faculty of Information Technology and Systems. Lecture notes.

van Dijk, J. and Wilms, D. (1991). Water treatment without waste material - fundamentals and state of the art of pellet softening. *Journal of Water Supply: Research and Technology-AQUA*, Vol 40(5), 263–280.

van Schagen, K., Rietveld, L., Babuška, R., and E.Baars (2008c). Control of the fluidised bed in pellet softening process. *Chemical Engineering Science*, 63(5), 1390–1400. doi:10.1016/j.ces.2007.07.027.

van Schagen, K., Babuška, R., Rietveld, L., and E.Baars (2006a). Optimal flow distribution over multiple parallel pellet reactors: a model-based approach. *Water Science & Technology*, 53(4-5), 493–501.

van Schagen, K., Bakker, M., Rietveld, L., Veersma, A., and Babuška, R. (2006b). Using on-line quality measurements in drinking water process control. In *AWWA WQTC Conference*. Denver, USA.

van Schagen, K., Rietveld, L., and Babuška, R. (2008a). Dynamic modelling for optimisation of pellet softening. *Journal of Water Supply: Reasearch and Technology-AQUA*, 57(1), 45–56. doi:10.2166/aqua.2008.097.

Repetitive Control and Online Optimization of Catofin Propane Process

Wangyun Won*, Kwang Soon Lee*†, Seokho Lee, and Chansul Jung****

**Department of Chemical and Biomoleulcar Engineering, Sogang University,Seoul, Korea (Tel: +82-2-705-8477; e-mail: kslee@sogang.ac.kr)*
***Samgsung Engineering Co., Ltd., Seoul, Korea (e-mail: sh.yi@samsung.com)*

Abstract: The Catofin propane process is an emerging industrial process for propylene production through dehydrogenation of propane. It is composed of multiple adiabatic fixed-bed reactors which undergo cyclic operations where propane dehydrogenation and catalyst regeneration alternate over roughly ten minute period for each. One of the major concerns in the operation of the Catofin process is maintaining the reactor at an optimum condition while overcoming gradual catalyst deactivation. Addressing this issue, an online optimization of the Catofin process combined with a repetitive control has been investigated. The optimizer computes optimum initial bed temperatures for dehydrogenation and optimum air flow rate for regeneration, and the repetitive controller performs cycle-wise feedback action during regeneration to attain the target bed temperatures at the terminal time of the regeneration period. Numerical studies have shown that the proposed online optimizing control system performs satisfactorily coping with the catalyst deactivation and other disturbances.

Keywords: Catofin process, online optimization, repetitive control, adiabatic fixed-bed reactor

1. INTRODUCTION

Advanced control and online optimization are now accepted as an essential process intensification technology that can create an additional profit in process industries wherever they are applicable. During the past two decades or more, there have been numerous industrial projects for advanced process control alone or integrated with online optimization as reviewed in Qin and Badgwell (2003). Such projects have typically proceeded for continuous processes with linear MPC only or cascaded by online steady state optimization. While the continuous process with steady state operation represents the majority of the chemical processes, non-continuous processes such as batch, semi-batch, and repetitive processes also take an important part. Such processes are run under unceasing dynamics, which renders conventional advanced control and online optimization techniques to show limitations in the performance. In this research, a repetitive process called the Catofin propane process (ABB, 2008) has been addressed and an advanced control technique combined with online optimization that exploits the unique nature of the Catofin process has been investigated.

In this study, an on-line optimizing control system for the Catofin propane process has been proposed and investigated numerically. The optimizing control system is composed of two tiers, a repetitive controller cascaded by an online optimizer. Repetitive control is put into an action during the regeneration (RG) steering the bed temperatures at two axial positions to reach the target values at the terminal time of the RG period. The open-loop operation with only a state estimation is conducted during the dehydrogenation (DH). The optimizer calculates the optimum target values for the bed temperatures and the RG air flow rate under a cyclic steady state. Both repetitive control and online optimization were constructed on the basis of a first principle reactor model reduced to a set of ordinary differential equations (ODE's) using the cubic spline collocation method (CSCM) (Yun and Lee, 2007). For the repetitive control, the model is linearized before the start of each RG cycle around the operating trajectories in the previous cycle. The performance of the proposed optimizing control scheme has been investigated numerically.

2. PROCESS DESCRIPTION

Fig. 1 shows a simplified process flow diagram of the Catofin propane process. It consists of multiple parallel adiabatic fixed-bed reactors that contain Cr_2O_3/Al_2O_3 catalyst, where the DH of propane and RG of catalyst are carried out alternatively over roughly ten minute period each with short periods of purging and evacuation operations in-between.

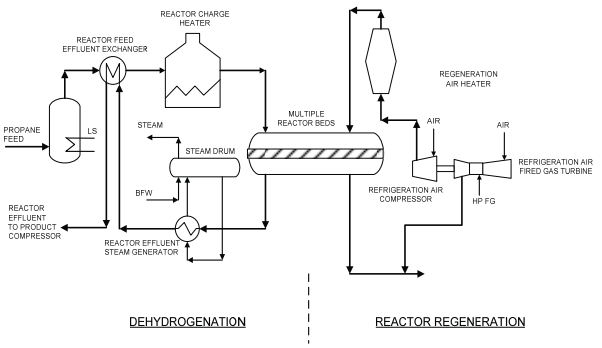

Fig. 1. Process flow diagram of the Catofin propane process.

The DH reaction is endothermic and produces a significant amount of coke. The bed temperatures are decreased and the catalyst loses activity by coke deposit and chromium reduction during this period. The RG reaction is coke burning by hot air and both the bed temperatures and catalyst activity are recovered under the oxidizing condition. The catalyst is known to have two years of life time and gradually loses the activity as the number of active sites is diminished by surface migration and agglomeration of Cr_2O_3 (Nijhuis, Tinnemans, Visser, and Weckhuysen, 2004).

The following apparent reaction kinetics proposed by Kim, Lee, and Song (1980) for the propane DH and Mickley, Nestor, and Gould (1965) and Pena, Monzon, and Santamaria (1993) for the coke combustion were assumed:

$$\begin{cases} C_3H_8 \underset{r_2}{\overset{r_1}{\rightleftharpoons}} C_3H_6 + H_2 \qquad C_3H_6 \xrightarrow{r_3} 3C + 3H_2 \\ C_3H_8 + C_3H_6 \xrightarrow{r_4} 2CH_4 + C_2H_6 + 2C \end{cases} \tag{1}$$

$$C + O_2 \xrightarrow{r_5} CO_2 \tag{2}$$

The rate constants are given in Table 1, which were slightly adjusted from the original values (Kim, Lee, and Song, 1980; Mickley, Nestor, and Gould, 1965; Pena, Monzon, and Santamaria, 1993) to more closely fit the conversion and yield of the real process (ABB, 2008).

Table 1. Parameters and normal operating conditions for the Catofin reactor model

Constants	Bed length = 1.5 (m), Bed diameter = 5.7 (m) C_c = 0.80 (kJ/kg•K), ρ_c=8x10^2 (kg/m^3), C_g = 3.71 for DH, 5.66 (kJ/kg•K) for RG D =1.7 for DH, 0.76 (m^2/min) for RG k_B=1.982 (kJ/min•m•K), R= 8.3462 (kJ/kmol K), DH and RG periods = 9min each
Normal operating condition for DH	Inlet temp=650℃, Propane flow=56.8(kmol/min), P=0.5 (atm)
Reaction rates (kmol/kg-cat.min) for DH	r_1= $k_1[C_3H_8]RT$, k_1=3.126*10^{7}e$^{(-47100/RT)}$ r_2=$k_2[C_3H_8][H_2]R2T2$, k_2=9.70*10^{-3}e$^{(-12800/RT)}$ r_3=$k_3[C_3H_6]R^2T^2$, k_3=8.407*10^{9}e$^{(-62900/RT)}$ r_4= k_4 $[C_3H_8][C_3H_6]R^2T^2$,k_4=9.498*10^{5}e$^{(-47800/RT)}$
Normal operating condition for RG	Inlet temp=690℃, Air flow=103.4 (kmol/min), P=2.0 (atm)
Reaction rate for RG	r_5=$k_5[C][O_2]RT$, k_5=4.129*10^{3}e$^{(-25575/RT)}$

It is assumed that the bed temperatures are measured at z = 0.2, 0.4, 0.6, 0.8, and 1.0, respectively, and the product gas compositions are available as the time average values over the DH and RG periods each with one cycle of measurement delay. It is also assumed that the RG is conducted under feedback control while the DH is carried out in an open loop state under a constant propane flow rate. The control objective during the RG is to steer the bed temperatures at z=0.2 and 0.4 to the target values provided by the optimizer using the RG air temperature as a manipulating variable (MV). The RG air flow rate was chosen as a decision variable for the optimizer together with the bed temperature target values.

3. REACTOR MODELLING

3.1 Mass and Energy Balances

In an adiabatic fixed-bed reactor, radial distribution of the concentrations and temperatures can be neglected. Under this assumption, the component mass and energy balance equations are written as

$$\begin{aligned} &\frac{\partial C_i}{\partial t} = \left(\frac{D}{L^2}\right)\frac{\partial^2 C_i}{\partial z^2} - \left(\frac{v_g}{L}\right)\frac{\partial C_i}{\partial z} + \left(\frac{1-\varepsilon}{\varepsilon}\right)\rho_c \bar{r}_i \\ &\frac{\partial C_c}{\partial t} = \rho_c \bar{r}_c \\ &\text{I.C. :} \quad C_i = C_i^I(z) \ \text{ at } \ t = 0 \\ &\text{B.C. :} \quad C_i = C_i^0(t) \ \text{ at } \ z = 0, \ \frac{dC_i}{dz} = 0 \ \text{ at } \ z = L_f = 5 \end{aligned} \tag{3}$$

$$\begin{aligned} &\frac{\partial T}{\partial t} = \left(\frac{k_B}{\rho_c c_{pc} L^2}\right)\frac{\partial^2 T}{\partial z^2} - \left(\frac{\varepsilon}{1-\varepsilon}\right)\left(\frac{\rho_g c_{pg} v_g}{\rho_c c_{pc} L}\right)\frac{\partial T}{\partial z} - \left(\frac{1}{c_{pc}}\right)\sum_j \Delta H_j r_j \\ &\text{I.C. :} \quad T = T_o(z) \ \text{ at } \ t = 0 \\ &\text{B.C. :} \quad T = T_o(\text{t}) \ \text{ at } \ z = 0, \ \frac{dT}{dz} = 0 \ \text{ at } \ z = L_f = 5 \end{aligned} \tag{4}$$

where $\bar{r}_i$ and C_i represent the rate of generation (kmol/kg-cat·min) and concentration (kmol/m^3) of component i, which refers to C_3H_8, C_3H_6, H_2, CH_4, C_2H_6 for DH operation, and CO_2, O_2 for RG operation, respectively; $\bar{r}_c$ and C_c represent the rate of generation (kmol/kg-cat·min) and concentration (kmol/m3) of coke, respectively; r_j referes to the rate of the j^{th} reaction; z denotes the normalized axial distance. Note that $\bar{r}_c$ for DH is different from $\bar{r}_c$ for RG. Other parameters and variables in the above model equations are given in Table 1.

In the above, the second boundary condition is specified at $z = 5$ instead of $z = 1$ whereas the spatial domain is $z \in (0,1]$. The reason for this is to more reasonably represent the true phenomenon, $dT/dz \to 0$ as $z \to \infty$, using a condition at a distant axial position, which was named as the far-side boundary condition (Yun and Lee, 2007).

3.2 ODE Models by Cubic Spline Collocation Method

ODE models for the virtual process and nominal model were derived separately using the CSCM (Yun and Lee, 2007) using ten and five equally spaced collocation points over

(0,1] plus an additional point at $z = 5$, respectively. The resulting ODE models can be concisely written as

$$\frac{d\bar{x}_k^i}{dt} = \bar{f}^i(\bar{x}_k^i, u_k^i), \quad i = DH, RG \tag{5}$$

In the above, the subscript k denotes the cycle number; $\bar{x}^{DH}$ represents the state for the DH model, that consists of bed temperatures, concentrations of C_3H_8, C_3H_6, H_2, CH_4, C_2H_6, and C at the internal collocation points; $\bar{x}^{RG}$ is similar to $\bar{x}^{DH}$ except that the concerned chemical components are C and O_2; u denotes the MV and represents the air temperature T^{air} for *i*=RG and is void for *i*=DH, respectively.

3.3 Process Behavior under a Cyclic Steady State

Fig. 2 shows the bed temperature trajectories of the virtual process under a cyclic steady state at the nominal operating condition. The bed temperatures are initially increased as the higher bed temperatures in the fore part of the respective collocation points recede by the gas flow. After a while, however, bed temperatures are decreased by the endothermic reactions as the propane DH proceeds and restored again by the coke combustion during the RG. The amount for the coke deposit changes during this operation are as shown in Fig. 3. The coke generation is larger at the higher temperature positions and vice versa.

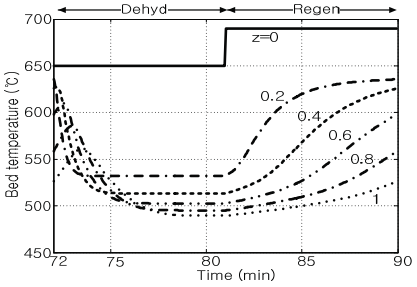

Fig. 2. Bed temperature trajectories at six axial positions under a cyclic steady state.

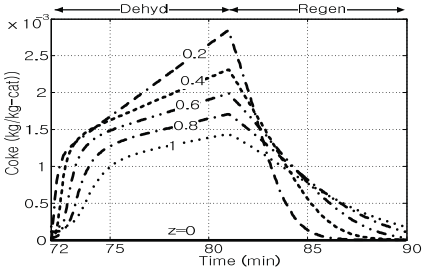

Fig. 3. Trajectories of coke deposit at six axial positions under a cyclic steady state.

The associated propane and propylene concentration trajectories during propane DH are shown in Fig. 4. Over an initial period while the bed temperatures are high, almost complete propane conversion and high propylene yield are obtained at the reactor outlet. As the bed temperatures begin to fall, both the propane conversion and propylene yield decrease. If we scrutinize Fig. 4, it can be seen that the front half of the bed where temperatures are higher than the rear half contribute more than 78.2% of the propylene production. The propane conversion and propylene selectivity averaged over a DH period are 51.5% and 86.2%, respectively.

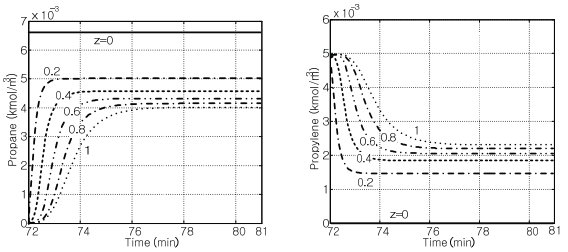

(a) (b)

Fig. 4. Trajectories of propane and propylene concentrations under a cyclic steady state.

4. OPTIMIZING CONTROL SYSTEM

4.1 Structure

The optimizing control system consists of three major parts: the online cyclic steady state optimizer, the repetitive controller, and the model estimator. Fig. 5 shows the overall structure of the proposed system.

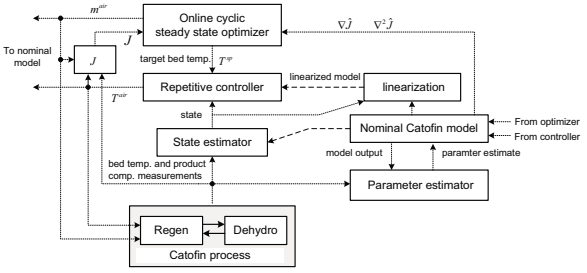

Fig. 5. Structure of the optimizing control system.

Fig. 6 illustrates the information flow through the state estimators along the operational sequence in more detail. The state estimation continues for the DH as well as RG periods based on the measurements of the bed temperatures and average product gas compositions in the previous cycle. Estimates of the coke deposit and bed temperature at the collocation points are transferred from the DH to RG and also from the RG to DH.

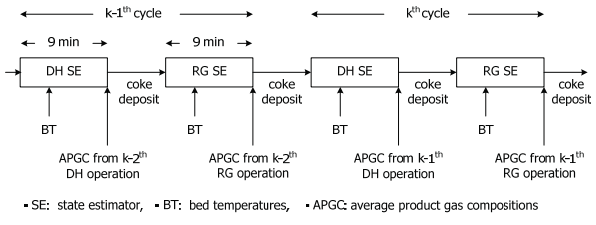

Fig. 6. Information flow along the sequence of operations.

4.2 Repetitive Control

4.2.1 Discrete-time Nominal Model

We first describe how the discrete-time nominal model for the state estimator and controller design is derived. The forward difference approximation applied to (5) results in

$$\bar{x}_k^i(t+1) = \bar{g}^i(\bar{x}_k^i(t), u_k^i(t)),\ \ i = \mathrm{DH}, \mathrm{RG} \tag{6}$$

The output equation can be written as

$$\begin{aligned} \bar{y}_k^i(t) &= V^i \bar{x}_k^i(t), \\ \bar{p}_k^i &= \frac{1}{N}\sum_{n=0}^{N-1} H^i \bar{x}_{k-1}^i(n),\ \ i = \mathrm{DH},\ \mathrm{RG} \end{aligned} \tag{7}$$

where $\bar{y}$ and $\bar{p}$ represent the bed temperatures at z=0.2, 0.4,…,1.0 and the average product gas composition measured at the end of the DH and RG periods with one cycle of measurement delay, respectively; N denotes the total number of sampling instance during the period of DH (or RG). V is a matrix that extracts the bed temperatures from the state and H is defined in a similar way for the compositions at the bed outlet. Hereafter, let us drop the superscript i for notational simplicity wherever there is no confusion.

The composition equation in (7) can be rewritten in the form of a state space equation. For this, let us define

$$\bar{p}_k(t+1) \triangleq \frac{1}{N}\sum_{n=0}^{t} H\,\bar{x}_{k-1}(n)$$

$$w_{1,k}(t) \triangleq \bar{x}_{k-1}(t),\ w_{2,k}(t) \triangleq \bar{x}_{k-1}(t+1),\ \cdots,\ w_{N,k}(t) \triangleq \bar{x}_k(t-1) \tag{8}$$

$$\bar{w}_k(t) \triangleq \begin{bmatrix} w_{1,k}(t) \\ w_{2,k}(t) \\ \vdots \\ w_{N-1,k}(t) \\ w_{N,k}(t) \end{bmatrix},\ M \triangleq \begin{bmatrix} 0 & I & 0 & \cdots & 0 \\ 0 & 0 & I & \cdots & 0 \\ \vdots & \vdots & \ddots & \vdots & \vdots \\ 0 & 0 & 0 & \cdots & I \\ 0 & 0 & 0 & \cdots & 0 \end{bmatrix},\ J \triangleq \begin{bmatrix} 0 \\ 0 \\ \vdots \\ 0 \\ I \end{bmatrix},\ \bar{J} \triangleq \begin{bmatrix} I & 0 & \cdots & 0 & 0 \end{bmatrix}$$

Then the associated state transition equations are recast to

$$\begin{aligned} \bar{x}_k(t+1) &= \bar{g}(\bar{x}_k(t), u_k(t)) \\ \bar{w}_k(t+1) &= J\,\bar{x}_k(t) + M\bar{w}_k(t) \\ \bar{p}_k(t+1) &= \bar{p}_k(t) + \frac{1}{N} H\bar{J}\,\bar{w}_k(t) \end{aligned} \tag{9}$$

The resulting model equation can be rewritten in the following simplified form:

$$\begin{aligned} x_k(t+1) &= g(x_k(t), u_k(t)) \\ y_k(t) &= c(t)\,x_k(t) \end{aligned} \tag{10}$$

where

$$\begin{aligned} &x_k(t) \triangleq \begin{bmatrix} \bar{x}_k(t) \\ \bar{w}_k(t) \\ \bar{p}_k(t) \end{bmatrix}, \\ &y_k(t) = \bar{y}_k(t) \ \text{ and } \ c(t) = \begin{bmatrix} V & 0 & 0 \end{bmatrix} \quad \text{for } t = 1, \cdots, N-1 \\ &y_k(N) = \begin{bmatrix} \bar{y}_k(N) \\ \bar{p}_k(N) \end{bmatrix} \text{ and } c(N) = \begin{bmatrix} V & 0 & 0 \\ 0 & 0 & I \end{bmatrix} \end{aligned} \tag{11}$$

Note that (10) and (11) holds for DH and RG separately.

4.2.2 Control Algorithm for RG Operation

The repetitive control conducts cycle-wise integral control action. To facilitate the construction of the control law, it is convenient to transform (10) to a state space model with $\Delta u_k(t) \triangleq u_k(t) - u_{k-1}(t)$ and $y_k(t)$ as the input and output variables, respectively. Linearization of (10) around the trajectories of the process variables in the k-1$^{\text{th}}$ cycle yields

$$\begin{aligned} \Delta x_k(t+1) &= A_{k-1}(t)\Delta x_k(t) + B_{k-1}(t)\Delta u_k(t) \\ y_k(t) &= y_{k-1}(t) + C_{k-1}(t)\Delta x_k(t) \end{aligned} \tag{12}$$

where $\Delta x_k(t) \triangleq x_k(t) - x_{k-1}(t)$; $A_{k-1}(t)$ represents a shorthand notation of $A_{k-1}(u_{k-1}(t), x_{k-1}(t \mid t))$, and similarly for $B_{k-1}(t)$ and $C_{k-1}(t)$. $\Delta u_k(t)$ is allowed to change P times at $t_1(=0)$, t_2, $\cdots$, t_P during the RG period and determined at each time moment to satisfy the following quadratic prediction objective:

$$\begin{aligned} &\min_{\Delta u_k(\bullet)} \left[\left\| T_k^{sp} - \hat{y}_k(N \mid t_m) \right\|_Q^2 + \sum_{n=m}^{P} \left\| \Delta u_k(t_n) \right\|_{R(m)}^2 \right],\ m = 1, \cdots, P \\ &\text{subject to input constraints} \end{aligned} \tag{13}$$

At other occasions than t_m, $m = 1, \cdots, P$ $\Delta u(t) = 0$. In the above, $\hat{y}_k(N \mid t_m)$ represents a prediction of $\hat{y}_k(N)$, the bed temperatures at z=0.2 and 0.4, on the basis of the information up to t_m at the k^{th} cycle; T_k^{sp} denotes the target value of $\hat{y}_k(N)$. $\hat{y}_k(N \mid t_m)$ is given by the following form:

$$\hat{y}_k(N \mid t_m) = \hat{y}_{k-1}(N) + F_{k-1}(t_m)\Delta x_k^{RG}(t_m \mid t_m) + \sum_{n=m}^{P} G_{k-1}(t_n)\Delta u_k(t_n) \tag{14}$$

It is straightforward to derive (14) from (12). Note that the state estimate $x_{k-1}(t \mid t)$ and $\Delta x_k^{RG}(t_m \mid t_m)$ are needed to construct (12) (for linearization) and to solve (13) for $\Delta u_k(\bullet)$ (using (14)), respectively.

4.2.3 State Estimator

The state estimator is constructed separately for DH and RG in the form of the extended Kalman filter (EKF) for (10) and is given as

$$\begin{aligned} x_k(t+1 \mid t) &= g\left(x_k(t \mid t), u_k(t)\right) \\ x_k(t \mid t) &= x_k(t \mid t-1) - K_k(t)\left(y_k(t) - c_k(t)x_k(t \mid t-1)\right) \end{aligned} \tag{15}$$

The observer gain $K_k(t)$ was obtained according to the EKF law using the process and measurement noise covariance matrices as the tuning factors. Using $x_k^{RG}(t_m \mid t_m)$ and $x_{k-1}^{RG}(t_m \mid t_m)$, $\Delta x_k^{RG}(t_m \mid t_m) = x_k^{RG}(t_m \mid t_m) - x_{k-1}^{RG}(t_m \mid t_m)$ for (14) was estimated. The state estimator acts as a fixed-lag smoother at t=N because the average product gas compositions are measured with one cycle of delay.

4.2.4 Implementation procedure

Over a DH-RG cycle, the following steps take turns in the repetitive control level:

[Step 1] DH period

$x_k^{DH}(t\,|\,t)$ is estimated for $t = 1, \cdots, N$ using (15).

[Step 2] Transition from DH to RG

Initialize $x_k^{RG}(1\,|\,0)$ by carrying over the coke deposit and bed temperature estimates in $x_k^{DH}(N\,|\,N)$ to $x_k^{RG}(1\,|\,0)$. Obtain the linearized model in (12) by linearizing (10) around $x_{k-1}^{RG}(t\,|\,t)$ and $u_{k-1}(t-1)$, $t = 1, \cdots, N$.

[Step 3] RG period

Perform the state estimation using (15). Compute $\Delta x_k^{RG}(t\,|\,t) = x_k^{RG}(t\,|\,t) - x_{k-1}^{RG}(t\,|\,t)$. Determine $\Delta u_k(t_m)$, $m = 1, \cdots, M$ according to (13) and (14). Implement $T_k^{air}(t) = u_k(t) = u_{k-1}(t) + \Delta u_k(t)$ to the process.

[Step 4] Transition from RG to DH

Initialize $x_k^{DH}(1\,|\,0)$ by transferring the coke deposit and bed temperature estimates in $x_k^{RG}(N\,|\,N)$ to $x_k^{DH}(1\,|\,0)$.

4.3 Online Cyclic Steady State Optimizer

The online optimizer determines T^{sp} and m^{air}, the target bed temperatures and the combustion air flow rate, respectively, that minimize the cost function under a cyclic steady state whenever the optimizer is invoked.

$$\begin{aligned}\min_{T^{sp},\,m^{air}}\ & J = -\alpha_1 m^p Y_{css}^p + \alpha_2 \sum_{t=1}^{N} c_{pa} m^{air}\left(T_{css}^{air}(t) - T_{ref}\right) \\ & \quad + \alpha_3 \left(\max(0, T_{z=0.2}^{sp} - 500)\right)^2 + \|s\|_Q^2,\ \ a_i > 0,\ \ Q > 0 \\ \text{subject to}\ & (10) \\ & \begin{bmatrix}615\\600\end{bmatrix} \le T^{sp} \le \begin{bmatrix}720\\690\end{bmatrix} (^\circ\text{C}) \\ & 10 \le \left|T_{z=0.2}^{sp} - T_{z=0.4}^{sp}\right| \le 30\,(^\circ\text{C}) \\ & m_{\min}^{air} \le m^{air} \le m_{\max}^{air} \\ & s = x^{DH}(0) - x^{RG}(N)\end{aligned} \tag{16}$$

where T_{ref}, m^p, and Y^p represent the reference temperature, propane mass flow rate, and average propylene yield over a DH period, respectively and the subscript *css* means the cyclic steady state. The summation is taken over the RG period.

The last term in J is to enforce the cyclic steady state condition, which is slackened by introducing a slack variable *s* defined the last equation in (16).

4.4 Model Parameter Estimator

In this study, the catalyst deactivation was assumed to be the most important process change and the parameter estimator was designed to update the pre-exponent rate constants by minimizing the following quadratic objective on the prediction error:

$$\min_{\theta^i}\ V^i = \frac{1}{k_2 - k_1} \sum_{k=k_1}^{k_2-1} \sum_{t=1}^{N} \left\| y_k^{m,i}(t) - y_k^i(t;\theta^i) \right\|_{\bar{Q}}^2,\ i = \text{DH, RG} \tag{17}$$

$$\text{subject to}\ \ \theta_{\min}^i \le \theta^i \le \theta_{\max}^i$$

where $y_k^{m,i}(t)$ and $y_k^i(t;\theta^i)$ represent the measurement and model prediction of $y_k^i(t)$ based on θ^i, respectively.

We devised a three parameter function as in (18), which is to be multiplied to each of the pre-exponent rate constants.

$$\xi(z) = \begin{cases} a + b\left(1 + \sin\left((-\pi / 2d)(z + d)\right)\right), & z \in [0,1] \\ a + 2b \quad \text{if } 2d \le z \end{cases} \tag{18}$$

Since there are four rate constants for the DH, $\theta^{DH} \triangleq \left[a_1 \cdots a_4\ b_1 \cdots b_4\ d_1 \cdots d_4\right]$. Likewise, $\theta^{RG} \triangleq \left[a_5\ b_5\ d_5\right]$.

It is true that (18) is only a rough description of the catalysts activity distribution in the real process. Nonetheless, both the repetitive controller and the optimizer can achieve highly precise tracking as well as the true minimum, respectively, overcoming model uncertainties since the controller performs the cycle-wise integral action and the optimizer searches for the minimum on the basis of the process measurements.

5. SIMULATION CONDITIONS

The sampling period was chosen to be 3 sec resulting in total sampling instants of 360 with $t^{RG} = t^{DH} = 180$ over an entire cycle. The number control moments *P* was chosen as 3 and t_1, t_2, and t_3 were selected as 1, 60, and 120, respectively. The following constraints were imposed on the MV movements for repetitive control:

$$600 \le u(t) = T_{air}(t) \le 750\,(^\circ\text{C}) \tag{19}$$

In the virtual process, the case of catalyst deactivation is represented by multiplying all k_i's by $1 - 0.5e^{-2.4z}$.

6. RESULTS AND DISCUSSION

The performance of the optimizing control system has been investigated for two cases. In the first case, the reactor was assumed to be initially at an arbitrary open-loop cyclic steady state and the optimizer steers the reactor to an optimum condition. In this case, the model parameter estimator was not invoked. In the second case, the optimum operation condition was assumed to be changed by catalyst deactivation, and the optimizer seeks for a new optimum condition from the previous operating condition determined in the first case. In the second case, the model parameter estimator plays an important role for both the repetitive controller and the online optimizer.

The simulation results for the first case are summarized in Fig. 7. It shows the response of the bed temperatures to their respective target values sent by the optimizer and the decrease of the objective function as the online optimization proceeds. The online optimizer calculates the new optimal target values once a cyclic steady state is reached on the basis of the nominal model and process measurements whereas the repetitive controller maneuvers the air temperature to attain the target values.

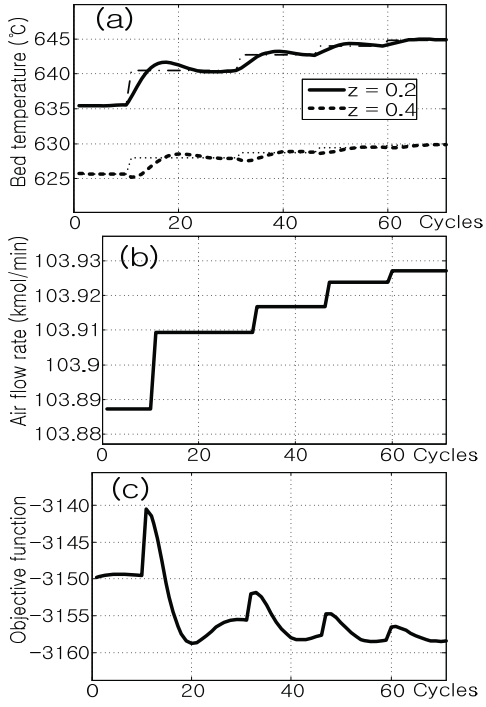

Fig. 7. Results of online optimization starting from an arbitrary open-loop state; (a) bed temperatures and their target values, (b) combustion air flow rate, (c) objective function.

The simulation results for the second case are given in Fig. 8. It can be seen that the overall responses are similar to Fig. 7. Unlike in the previous case, however, θ^{DH} and θ^{RG} were recurrently updated during the optimization. One thing to note is that the bed temperatures are raised even higher from the values determined in the first case to compensate for the catalyst deactivation.

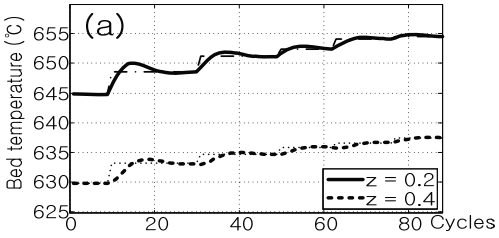

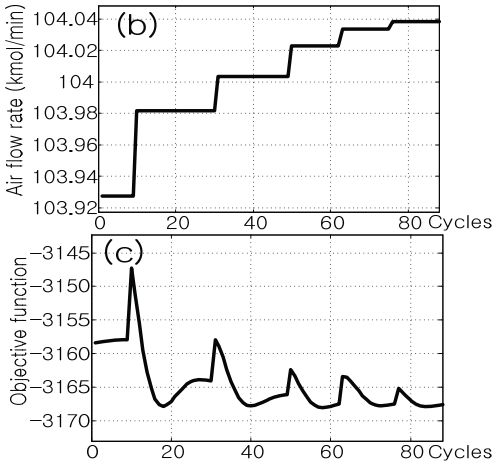

Fig. 8. Results of online optimization after the catalyst deactivation occurs; (a) bed temperatures and their target values, (b) combustion air flow rate, (c) objective function.

REFERENCES

ABB (2008). http://www02.abb.com/GLOBAL/NOOFS/noofs187.nsf/viewunid/494CDF435B2EE22DC12569EE0036977A/$file/CATOFIN.pdf

Bhasin, M. M., McCaina, J. H., Vora, B. V., Imai, T., & Pujad, P. R. (2001). Dehydrogenation and oxydehydrogenation of paraffins to olefins. *Applied Catalysis A: General*, 221, 397–419.

Kim, Y. G., Lee, H. S., & Song, Y. S. (1980). A study on dehydrogenation of propane. *Korean Journal of Chemical Engineering*, 18, 11-19.

Mickley, H. S., Nestor, J. W., & Gould, L. A. (1965). A kinetic study of the regeneration of a dehydrogenation catalyst. *Canadian Journal of Chemical Engineering*, 61-68.

Nijhuis, T. A., Tinnemans, S. J., Visser, T., & Weckhuysen, B. M. (2004). Towards real-time spectroscopic process control for the dehydrogenation of propane over supported chromium oxide catalysts. *Chemical Engineering Science*. 59, 5487-5492.

Pena, J. A., Monzon, A., & Santamaria, J. (1993). Coking kinetics of fresh and thermally aged commercial Cr2O3/Al2O3 catalyst. *Applied Catalysis A*, 101, 185-198.

Qin, S. J. & Badgwell, T. A. (2003). A survey of industrial model predictive control technology. *Control Engineering Practice*, 11, 733-764.

Yun, W. & Lee, K. S. (2007). The Use of Cubic Spline and Far-side Boundary Condition for the Collocation Solution of a Transient Convection-Diffusion Problem. *Korean Journal of Chemical Engineering*, 24, 204-208.

Model-based Control Design of a Diesel Oxidation Catalyst

Olivier Lepreux * **Yann Creff** * **Nicolas Petit** **

* *IFP Lyon, Technology, Computer Science and Applied Mathematics Division, BP 3, 69360 Solaize, France (e-mail: olivier.lepreux @ ifp.fr, yann.creff @ ifp.fr)*
** *Centre Automatique et Systèmes, Mathématiques et Systèmes, MINES ParisTech, 60, bd. Saint-Michel, 75272 Paris Cedex 06, France (e-mail: nicolas.petit @ mines-paristech.fr)*

Abstract:
This paper proposes a control strategy for a Diesel Oxidation Catalyst (DOC) which is grounded on a one-dimensional distributed parameter model. This first principles model for the propagation of the temperature variations accounts for spatially distributed heat generation (due to oxidation of reductants). As is discussed, heat generation can be regarded as equivalent inlet temperature variations. This fact is supported by experimental results. By nature, DOC outlet temperature response includes long and time-varying delays. An approximation of the proposed model allows to derive delays analytically, and can be used to schedule control parameters. As a consequence, it is easy to design several standard controllers for the DOC outlet temperature which account for the effects of the inlet temperature (disturbance) and the reductant (control). In this paper, simulation results are presented for a PI, a PID, and a Smith predictor. Interestingly, the three controllers use solely parameters determined from the previous analysis and do not need any extra tuning parameter. The strategies are tested on a standard NEDC driving cycle in simulation. It appears that, among these standard strategies, the DOC partial derivative equations can be efficiently controlled using the presented Smith predictor.

Keywords: Automotive exhaust aftertreatment systems, Diesel oxidation catalyst, Distributed-parameter systems, Boundary control, Control applications

1. INTRODUCTION

1.1 Motivation

On most new Diesel vehicles, increasing requirements regarding particulate matter emissions (Ecopoint Inc., 2008) are satisfied using a Diesel Particulate Filter (DPF). This filter, located in the vehicle exhaust line, stores particulate matter until it is burnt in an active regeneration process (Bisset, 1984). During this phase, DPFs behave like potentially unstable reactors (Achour, 2001), and their inlet temperature must be carefully controlled to prevent filter runaway.

In most current aftertreatment architectures (Koltsakis and Stamatelos, 1997), a Diesel Oxidation Catalyst (DOC) is placed upstream the DPF in the vehicle exhaust line. To increase the DPF inlet temperature, reductant is oxidized in the DOC, which, in turn, increases its outlet temperature. The DOC also conveys, up to some heat losses, its inlet enthalpy flow: in other words, inlet temperature variations propagate through the DOC.

A DOC is a chemical system difficult to control. Classical models are usually composed of a dozen of coupled partial differential equations (PDEs) (Depcik and Assanis, 2005), which complexify the development of model-based control laws. Experimentally, it can be observed that a step change on the inlet temperature propagates to the output of the system with long response times (Oh and Cavendish, 1982). Depending on the engine outlet gas flow rate, these response times significantly vary: they roughly decrease by a factor of 10 from idle speed to full load. Strategies that are commonly used to deal with this problem rely on look-up tables, which, in practice, are difficult and time-consuming to calibrate.

The purpose of this paper is to propose implementable control laws tuned according to a simple control-oriented model. This approach allows faster calibration. To achieve this goal, simplification of the above-mentioned classical models is needed.

After a presentation of a mathematical formulation of the control problem in the second part of this introduction, we show in section 2 how the model proposed in Lepreux et al. (2008), initially using inlet temperature as control variable, can be used to accurately describe actual cases of engineering interest, i.e. cases where the reductant flow is the control variable. Then, we show in section 3 how to approximate the model. Finally, in section 4, this approximation is used to tune several classic controllers. Simulation results serve as comparisons and stress that a Smith predictor tuned using the proposed methodology represents an efficient controller for the DOC.

1.2 Problem Formulation

It has been shown in Lepreux et al. (2008) that, considering only inlet temperature variations and neglecting chemical reactions, a DOC thermal behavior can be accurately described by the following model

$$\begin{cases} \dfrac{\partial T}{\partial t}(z,t) + v\dfrac{\partial T}{\partial z}(z,t) \;=\; -k_1(T(z,t) - T_s(z,t)) \\ \dfrac{\partial T_s}{\partial t}(z,t) \;=\; k_2(T(z,t) - T_s(z,t)) \end{cases} \tag{1}$$

with boundary control

$$T(z=0,t) = T^{in}(t)$$

where T and T_s are respectively gas and solid temperature variations about steady state, v is the channel gas speed which can be derived from mass flow, parameters (k_1,k_2) can be either derived from usual correlation (Osizik, 1977) or identified from experimental data (Lepreux et al., 2008). The output of the system is the outlet gas temperature

$$T^{out}(t) = T(z=L,t)$$

Considering steady-state initial conditions

$$\begin{cases} T(z,0) = 0 \\ T_s(z,0) = 0 \end{cases}$$

system (1) yields the transfer function

$$\hat{T}(z,s) = \hat{T}^{in}(s)\exp\left(-\frac{z}{v}s - \frac{k_1 z}{v} + \frac{m(z)}{s+k_2}\right) \tag{2}$$

where $m(z) = k_1 k_2 z/v$, $\hat{x}$ is the Laplace transform of x, and s is the Laplace variable. We denote Υ the Heaviside function and $\mathrm{I_i}$ the modified Bessel functions of the first kind. The system step response is

$$\begin{aligned} T(z,t) = {} & \Upsilon(t - \frac{z}{v})\exp\left(-\frac{k_1 z}{v}\right)\times \\ & \left[1 + \int_0^{t-z/v} \exp\left(-k_2\tau\right)\sqrt{\frac{m(z)}{\tau}}\mathrm{I}_1(2\sqrt{m(z)\tau})d\tau\right] \end{aligned} \tag{3}$$

For an easy evaluation of (3), a formulation using power series expansion is given in Lepreux et al. (2008).

2. REDUCTANT FLOW AS CONTROL VARIABLE

It is shown in Lepreux et al. (2008) that experimentally measured step responses of the system can be identified to model (1) with good quality. However, this representation might seem a bit simplistic in view of real applications since inlet temperature variations are difficult to control and cannot be used directly as control variable. In practice, reductants (hydrocarbons HC) are injected at the inlet of the DOC. They are oxidized on the catalyst and, consequently, increase the DOC temperature. In this section, we compute HC step response and compare it against T^{in} step response.

2.1 Model with Heat Source

During the regeneration process, the DOC is working at high temperatures, which ensures that the rate of conversion of reductants is high. Moreover, large quantity of HC is injected to generate exothermicity. Consequently, the inlet fraction of this reductant is very important, and its effect is dominating over other species'. By construction, a DOC is designed to yield large heat and mass transfer. These transfers are very effective, and the time scales implying the thermal phenomena are much lower than the ones implying chemical reactions. For the experiments presented in § 2.3 gas flows through the DOC approximatively 1000 times faster than the outlet temperature response time. For these reasons, to model the DOC thermal behavior, we propose to encompass all the chemical reactions in a "source term Ψ", leading to the following model

$$\begin{cases} \dfrac{\partial T}{\partial t}(z,t) \;+\; v\dfrac{\partial T}{\partial z}(z,t) = -k_1\left(T(z,t) - T_s(z,t)\right) \\ \dfrac{\partial T_s}{\partial t}(z,t) \;=\; k_2\left(T(z,t) - T_s(z,t)\right) + \Psi(z,t) \end{cases} \tag{4}$$

where $\Psi(z,t)$ is the control variable and $T^{in}(t)$ is regarded as a disturbance. Ψ includes the sum of the enthalpies of the various reactions taking place inside the DOC. We formulate a strong simplifying assumption. Namely, we assume that the rate of reaction is independent of the species concentration. Further, we also assume that it is independent of the temperature. In other words, Ψ is constant over some spatial interval. These assumptions are supported by experimental identification results of § 2.3. Over the whole range of considered operating conditions, the obtained results are quite accurate. We note L_c the length of the portion of the DOC where the enthalpy of reaction is released (see Fig. 1). Formally, we consider the

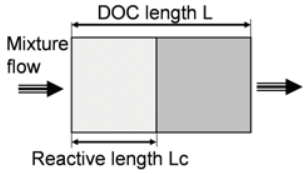

Fig. 1. HC reaction zone

following discontinuous function

$$\begin{cases} \hat{\Psi}(z,s) = \alpha/s, & 0 \le z \le L_c \\ \hat{\Psi}(z,s) = 0, & L_c < z \le L \end{cases} \tag{5}$$

Then, several steps of operational calculus on (4) lead to

$$\hat{T}(L_c,s) = \hat{T}^{in}\exp\left(-\hat{A}(s)L_c\right) + \frac{\hat{B}(s)}{\hat{A}(s)}\left(1 - \exp\left(-\hat{A}(s)L_c\right)\right) \tag{6}$$

with $\hat{A}(s) = \dfrac{1}{v}\left(s + k_1 - \dfrac{k_1 k_2}{s+k_2}\right)$ and $\hat{B}(s) = \dfrac{k_1}{v}\dfrac{\alpha}{s(s+k_2)}$.

In (6), the first term corresponds to the transfer from the inlet temperature $T^{in}(t)$ to the output $T(L_c,t)$, while the second term corresponds to the transfer from the input signal $\hat{\Psi}$ defined in (5) to the output $T(L_c,t)$. The linearity of the two effects will be used to study these phenomena separately in our control strategy. Further, for $z > L_c$, equation (4) gives $\hat{T}(z,s) = \hat{T}(L_c,s)\exp\left(-\hat{A}(z-L_c)\right)$ and, we get

$$\begin{aligned} \hat{T}(z,s) = {} & \hat{T}^{in}\exp\left(-\hat{A}z\right) - \frac{\hat{B}}{\hat{A}}\exp\left(-\hat{A}z\right) \\ & + \frac{\hat{B}}{\hat{A}}\exp\left(-\hat{A}(z-L_c)\right) \end{aligned} \tag{7}$$

Eventually, by an inverse Laplace transform of (7) (Abramowitz and Stegun, 1965), one obtains the reductant step response

$$\begin{aligned} T(z,t) = {} & \Upsilon\left(t - z/v\right)\exp\left(-\frac{k_1 z}{v}\right)M(z, t - z/v) \\ & - \Upsilon\left(t - z/v\right)\exp\left(-\frac{k_1 z}{v}\right)F(z, t - z/v) \\ & + \Upsilon\left(t - z/v\right)\exp\left(-\frac{k_1 z}{v}\right)F(z - L_c, t - z/v) \end{aligned} \tag{8}$$

where

$$\begin{cases} M(z,t) = T^{in}(t) \\ \quad + \int_0^t \exp(-k_2\tau)\sqrt{\frac{m(z)}{\tau}}\mathrm{I}_1(2\sqrt{m(z)\tau})T^{in}(t-\tau)d\tau \\ F(z,t) = g(t) \\ \quad + \int_0^t \exp(-k_2\tau)\sqrt{\frac{m(z)}{\tau}}\mathrm{I}_1(2\sqrt{m(z)\tau})g(t-\tau)d\tau \\ g(t) = \frac{k_1\alpha}{k_1+k_2}t - \frac{k_1\alpha}{(k_1+k_2)^2}\left(1-\exp(-(k_1+k_2)t)\right). \end{cases}$$

2.2 Fitting the heat source model with an equivalent no-source model

The static gain $G_{T^{in}}$ of the transfer from the inlet temperature T^{in} to the output $T(z,t)$ is equal to 1 (Lepreux et al., 2008). The static gain G_u of the transfer from the input signal $\hat{\Psi}$ to the output $T(z,t)$ can be computed using (7)

$$G_u = \lim_{t\to\infty} T(t) = \lim_{s\to 0} s\hat{T}(s) = \frac{k_1\alpha L_c}{k_2 v} \tag{9}$$

These last formulas are used during the identification and normalization process in this Section and for controllers design in Section 4. In practice, it is possible to relate α, L_c, the current HC conversion efficiency and the amount of injected reductants (which is itself related to the injector energizing time): for a given (identified) L_c, α *can be regarded as a control variable*.

In Fig. 2a, it is shown that the overall shape of the reductant step response, computed with (8), is very similar to the T^{in} step response (3). This similarity suggests that it is possible

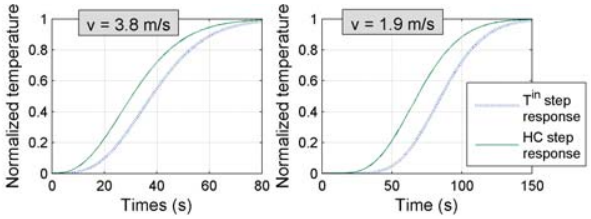

(a) Comparison between HC step response and T^{in} step response. Analytic results obtained respectively from (8) and (3).

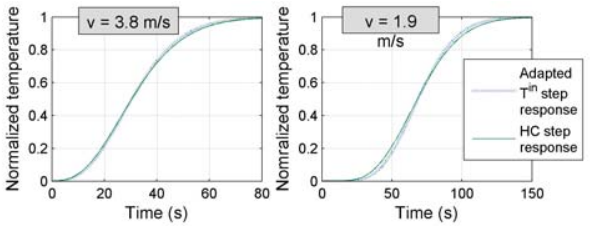

(b) Comparison between HC step response (model with source) and adapted T^{in} step response (model with no source)

Fig. 2. HC step response approximation in various operating conditions

to approximate HC step response by T^{in} step response at the expense of an additional identification procedure. We show in Fig. 2b that it suffices to adapt the DOC length, using the model with no source (1), to get results very close to the ones obtained with the model with source (4) [1]. In other words, generating enthalpy by HC is quite equivalent to generating enthalpy by T^{in} with a DOC having a shorter length. Hence, the temperature response of the DOC associated to the T^{in} variations are slower than those associated to HC. From a control point of view, this allows us to reject the T^{in} disturbance.

[1] further details of this adaptation will be treated in a forthcoming publication

2.3 Experimental model validation

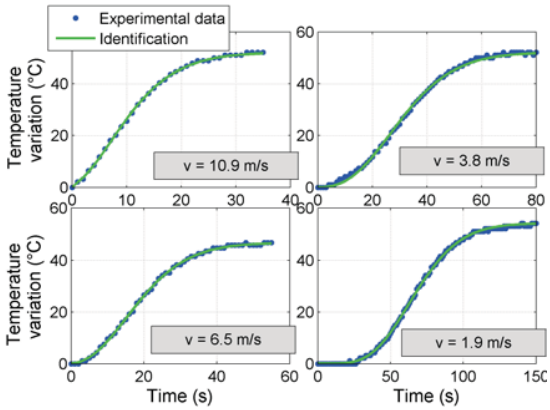

Fig. 3. Experimental HC step response identified to T^{in} model (1) in various operating conditions

As we stressed it in the previous discussion, considering an additional model adaptation of parameters (L_c is a piecewise linear function of v), model (1) and model (4) yield pretty similar results. In Fig. 3, we present experimental HC step responses under various operating conditions. To obtain these data, a 2.2-L 4-cylinder Diesel engine equipped with a 3-inch long 5.66-inch diameter 400-cpsi DOC was tested. These responses are well represented by the equivalent T^{in} step response (3) corresponding to the model with no source (1). It is shown that the model with no source kindly fits experimental data, usually described using a source term.

3. APPROXIMATING DOC EQUATIONS

We wish to simplify the previous model further. The desired representation is a first order plus delay model, which belongs to a class of models relatively easy to design a controller for (Silva et al., 2005).

For small values of $|s|$ (i.e. the range of low frequencies), the DOC transfer function (2) can be approximated in the following way

$$\begin{aligned} &\exp\left(\tfrac{m(z)}{s+k_2}\right) \\ &= \exp\left(-(1-\nu)\tfrac{k_1 z}{k_2 v}s\right)\exp\left(\tfrac{k_1 z}{v}\left((1-\nu)s/k_2 + \tfrac{1}{1+s/k_2}\right)\right) \\ &\approx \exp\left(-(1-\nu)\tfrac{k_1 z}{k_2 v}s\right)\exp\left((1-\nu)s/k_2 + 1 - s/k_2\right)^{\frac{k_1 z}{v}} \\ &\approx \exp\left(-(1-\nu)\tfrac{k_1 z}{k_2 v}s\right)\exp\left(\tfrac{k_1 z}{v}\right)\exp\left(-\nu s/k_2\right)^{\frac{k_1 z}{v}} \\ &\approx \exp\left(-(1-\nu)\tfrac{k_1 z}{k_2 v}s\right)\exp\left(\tfrac{k_1 z}{v}\right)\frac{1}{1+\nu\frac{k_1 z}{k_2 v}s} \end{aligned}$$

where $\nu \in]0,1[$ can be seen as a weighting variable which will be discussed later on. This leads to the following transfer function as an approximation of (2)

$$\exp\left(-\left(\frac{z}{v}+(1-\nu)\frac{k_1 z}{k_2 v}\right)s\right)\frac{1}{1+\nu\frac{k_1 z}{k_2 v}s}$$

As a result, one obtains a delayed first-order step response $\frac{\exp(-\delta s)}{1+\tau s}$ where $\tau = \nu\frac{k_1 z}{k_2 v}$ and $\delta = \frac{z}{v} + (1-\nu)\frac{k_1 z}{k_2 v}$. The weighting variable ν relates τ and δ. Explicitly, we get $\delta = \frac{z}{v} + \frac{k_1 z}{k_2 v} - \tau$. In an identification standpoint, the next step is to determine a constraint to set the value of τ, which implicitly sets the value of ν.

Inflexion point The second-order derivative of the step response (3) with respect to time is

$$\frac{\partial^2}{\partial t^2}T(z,t+\frac{z}{v}) = -\Upsilon(t)\exp\left(-\frac{k_1 z}{v}\right)\exp(-k_2 t)\times \left[\left(k_2+\frac{1}{t}\right)\sqrt{\frac{m(z)}{t}}\mathrm{I}_1\left(2\sqrt{m(z)t}\right) - \frac{m(z)}{t}\mathrm{I}_0\left(2\sqrt{m(z)t}\right)\right]$$

Using the following asymptotic expansion of Bessel function (Abramowitz and Stegun, 1965)

$$\begin{cases} \mathrm{I}_\nu(z) \approx \frac{\mathrm{e}^z}{\sqrt{2\pi z}}\left(1 - \frac{\mu-1}{8z} + \frac{(\mu-1)(\mu-9)}{2!(8z)^2} - \dots\right) \\ \mu = 4\nu^2 \end{cases} \tag{10}$$

at first-order, we get, for $\frac{3}{16\sqrt{m(z)t}} \ll 1$,

$$\frac{\partial^2}{\partial t^2}T(z,t+\frac{z}{v}) \approx -\Upsilon(t)\exp\left(-\frac{k_1 z}{v}\right)\exp(-k_2 t)\times \left[\left(k_2+\frac{1}{t}\right)\sqrt{\frac{m(z)}{t}}\frac{\mathrm{e}^{2\sqrt{m(z)t}}}{\sqrt{4\pi\sqrt{m(z)t}}} - \frac{m(z)}{t}\frac{\mathrm{e}^{2\sqrt{m(z)t}}}{\sqrt{4\pi\sqrt{m(z)t}}}\right]$$

The equation of the inflexion point, of which t_I is the unknown abscissa, is given by $\frac{\partial^2}{\partial t^2}T(z,t_I) = 0$. With $t_{I'} = t_I - z/v$, this leads to $k_2 + \frac{1}{t_{I'}} - \sqrt{\frac{m(z)}{t_{I'}}} = 0$. Then,

$$t_{I'} \approx \frac{k_1 z}{k_2 v}\left(\frac{1}{2}+\frac{1}{2}\sqrt{1-\frac{4v}{k_1 z}}\right) - \frac{1}{k_2}$$

and assuming $\frac{4v}{k_1 z} \ll 1$, we finally obtain $t_I \approx \frac{k_1 z}{k_2 v} + \frac{z}{v}$.

Parameters τ and δ Note f the delayed first order model step response $f(t) = 1 - \exp\left(-\frac{t-\delta}{\tau}\right)$. Let t_E be the solution of $f(t_E) = T(z,t_I)$. We impose the slope of f at abscissa t_E to equal the slope of T at t_I, i.e.

$$\frac{d}{dt}f(t_E) = \frac{\partial}{\partial t}T(z,t_I) \tag{11}$$

then, we get $\tau = \dfrac{1-T(z,t_I)}{\exp(-2k_1 z/v)k_2\mathrm{I}_1(2k_1 z/v)}$

To sum up, with the additional requirement (11), it is possible to write explicit values of τ and δ

$$\begin{cases} \tau = \dfrac{1-T(z,t_I)}{\exp(-2k_1 z/v)k_2\mathrm{I}_1(2k_1 z/v)} \\ \delta = \dfrac{z}{v} + \dfrac{k_1 z}{k_2 v} - \dfrac{1-T(z,t_I)}{\exp(-2k_1 z/v)k_2\mathrm{I}_1(2k_1 z/v)} \end{cases} \tag{12}$$

Typical identification results are presented in Fig. 4. Two different cases that are representative of real DOC parameter values, as motivated by Lepreux et al. (2008), are reported.

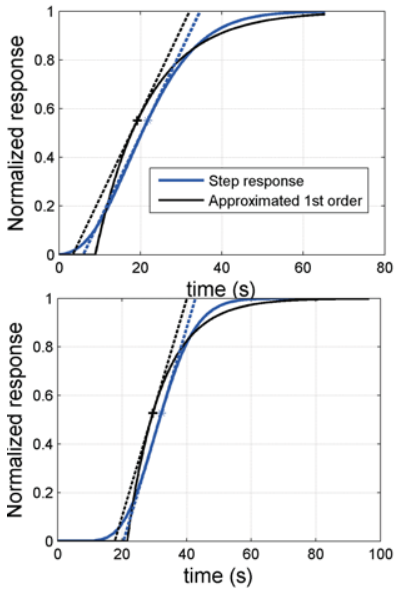

Fig. 4. Matching the DOC response with a first order plus delay model. k_1=400, k_2=0.35, v=4 (up). k_1=1591.09, k_2=0.82, v=4.597 (down).

Further approximation of τ and δ It has been shown that the choice of the constraint (11) leads to good matching of responses results. Further approximation can be made to prevent evaluation of the Bessel function. In experiment of Fig. 4, we get $\frac{3}{8}\frac{1}{2k_1 z/v} \ll 1$ for the two presented cases. Referring to (10), this validates the use an asymptotic expansion of I_1. We can make the approximation $\mathrm{I}_1(2k_1 z/v) \approx \frac{\exp(2k_1 z/v)}{\sqrt{2\pi 2k_1 z/v}}$. Then, we get the following expressions

$$\begin{cases} \tau = \frac{1}{k_2}\left(1-T(z,t_I)\right)\cdot 2\cdot\sqrt{\pi}\cdot\sqrt{\frac{k_1 z}{v}} \\ \delta = \frac{z}{v} + \frac{1}{k_2}\frac{k_1 z}{v} - \frac{1}{k_2}\left(1-T(z,t_I)\right)\cdot 2\cdot\sqrt{\pi}\cdot\sqrt{\frac{k_1 z}{v}} \end{cases} \tag{13}$$

It is interesting to note that, considering requirement (11), δ does not have an hyperbolic behavior with respect to v. Experimental results for evolution of τ and δ are shown in Fig. 5 (see also Frobert et al. (2009) for more complete results and details about the identification process). Corresponding analytical values are obtained using constant parameters k_1 and k_2, and L_c a function of v as mentioned in section 2.

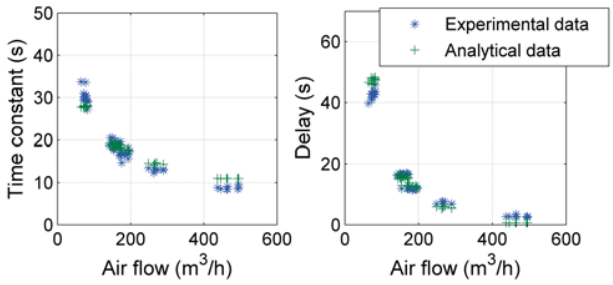

Fig. 5. Experimental evolution of δ and τ versus v

To sum up, the derived model is a combination of two first order plus delay models as shown in Fig. 6. The first one uses T^{in} as

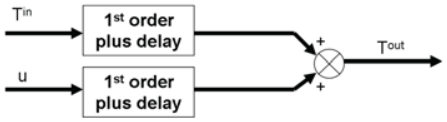

Fig. 6. Scheme of the first order plus delay model

input and $\tau_{T^{in}}$ and $\delta_{T^{in}}$ parameters are evaluated by (12) using the whole DOC length. The second one uses T^{in}-equivalent-to-Ψ as input, and corresponding τ_u and δ_u are evaluated by the same formula (12) using a part of the DOC length as explained in section 2. In both submodels, k_1 and k_2 are constant and equal.

Despite the fact that the proposed method of approximation does not allow to evaluate errors a priori, it is shown in simulations of subsection 4.2 that these methods provide accurate results for real cases of engineering interest such as those of a DOC used in driving conditions.

4. CONTROLLER PRESENTATION

4.1 Control Designs

Based on the results of section 3, we consider three classical control designs and evaluate their performance. The first two designs are simple PI and PID controllers with a feedforward term as presented in Fig. 7. We use respectively Tavakoli and Fleming (2003) and Tavakoli and Tavakoli (2003) parameters tuning for the PI and the PID controllers. Parameters τ and δ are evaluated using (12). The third controller, presented in Fig. 8,

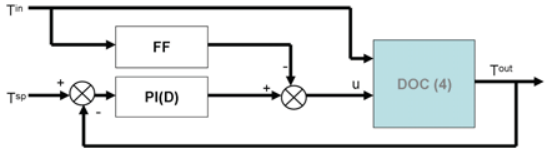

Fig. 7. Control scheme for the PI(D) controller

consists of a Smith controller (Abe and Yamanaka, 2003). For

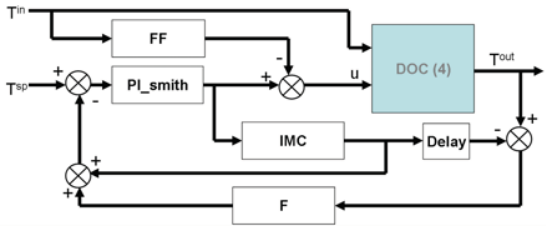

Fig. 8. Control scheme for the Smith controller

the three controllers, the gain G_u is calculated using (9). The FF block is dedicated to treating the T^{in} disturbance. Here, we use a standard feedforward strategy given by

$$FF = \frac{G_{T^{in}}}{G_u} \frac{\tau_u s + 1}{\tau_{T^{in}} s + 1} \exp\left(-\left(\delta_{T^{in}} - \delta_u\right) s\right)$$

Transfer functions for the Smith controller are given as follows

$$PI_{Smith} = \frac{1}{G_u}\left(1 + \frac{1}{\tau_u s}\right)$$

$$IMC = G_u \frac{1}{\tau_u s + 1}$$

The $Delay$ operator applies a delay of δ_u. The robustness filter F is a first order filter which time constant set to 1 s. It is not primordial here because, thanks to the presented detailed analysis of the DOC equations, delays are well approximated.

4.2 Simulation Results

First, we study the influence of a disturbance step variation. Then, we present control performance during a NEDC driving cycle. Simulation results are shown on the model with source (4) with $k_1 = 870\ \mathrm{s}^{-1}$, $k_2 = 0.45\ \mathrm{s}^{-1}$, $L_c = 0.0305$ m, $L = 0.0762$ m.

Basic performance Fig. 9 compares performance of the three controllers for a setpoint change. Setpoint is risen from 0 to 50 at $t = 200$. At the end of the rise, the system is disturbed by an important gas speed variation. These variations are directly linked to driver's power request, they are very fast and cannot be avoided. Although both controllers show similar tracking performance, the Smith controller shows much better disturbance rejection. Similar results are presented in Fig. 10

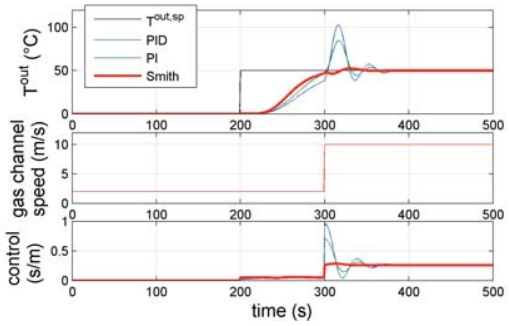

Fig. 9. Step setpoint transition and step v variation for PI, PID, and Smith controllers. $T^{in} = 0$.

with a 20% error on the k_1 parameter, implying important delay misestimation. All three proposed controllers are quite robust regarding this error.

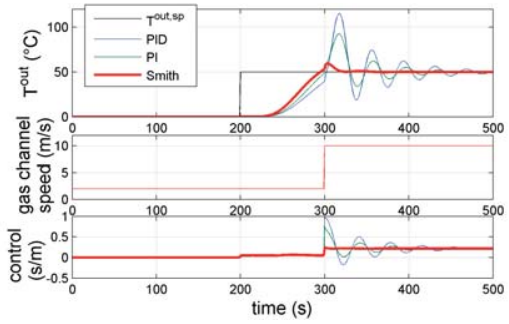

Fig. 10. Step setpoint transition and step v variation for PI, PID, and Smith controllers with a 20%-error on k_1. $T^{in} = 0$.

Performance on the NEDC cycle The three controllers are now tested on a simulated NEDC cycle. Results are presented in Fig. 11. In this case of a constantly-varying air flow rate, the differences between controllers are very small. Similar results are presented in Fig. 12 with a 20% error on the k_1 parameter. Once again, the presented controllers show good results regarding robustness on this fundamental parameter.

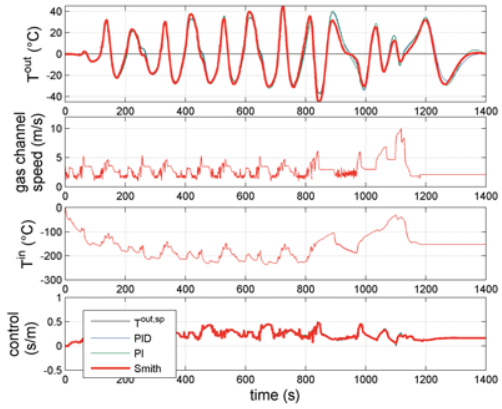

Fig. 11. PI, PID, and Smith controllers on NEDC cycle

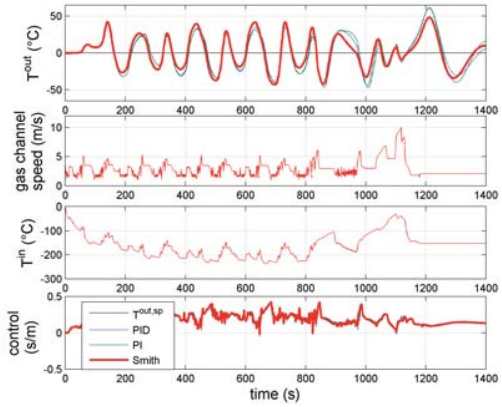

Fig. 12. PI, PID, and Smith controllers on NEDC cycle with a 20%-error on k_1

Conclusion The presented Smith controller requires more computational effort than the presented PI(D) controllers and shows some advantages in specific cases (setpoint transition, large air flow rate variation). It should be discussed based on further experimentations if it is necessary to use it or not for every specific case of application. It should be noted that its major drawback (lack of robustness toward a misestimation of the delay) has been circumvented thanks to the presented detailed analysis of the DOC equations.

5. CONCLUSIONS AND FUTURE WORKS

Control-oriented DOC modeling has been validated with experimental data in a former work (Lepreux et al., 2008). Grounding the current work on these equations and using several steps of approximation lead us, in this paper, to present a simple delayed first-order control-oriented model to approximate the DOC thermal behavior. This model is used as a starting point for control design. Interestingly, presented controllers require no particular tuning effort. They are tested in simulation on NEDC driving cycle. First, a simple PI or PID in which parameters are scheduled using developed approximations, reveal to be overreactive in certain specific cases. Alternatively, a Smith design shows good results and turns out to be fairly robust.

The presented experimental results allow a good level of confidence in our model. However, the next step is to present experimental results on the driving cycle using the proposed controllers.

A significant part of performance achieved by controllers presented in this paper, is due to the feedforward treatment of disturbances. To simplify the analysis, the presented controllers use classical feedforward control laws. However, going deeper into analysis, allows to achieve much better results. This feedforward control will be fully detailed in a forthcoming publication.

Being a part of an integrated system in the vehicle, the DOC is subject to whole class of reductants oxidizing onto it. It is worth properly estimating their flow, resulting from in-cylinder combustion, because it represents important disturbances for the DOC outlet temperature controller. This estimator is the subject of future works.

REFERENCES

Abe, N. and Yamanaka, K. (2003). Smith predictor control and internal model control - a tutorial. In *SICE 2003 Annual Conference*, volume 2, 1383–1387.

Abramowitz, M. and Stegun, I.A. (1965). *Handbook of mathematical functions*. Dover Publications.

Achour, L. (2001). *Dynamique et contrôle de la régénération d'un filtre à particules Diesel*. Ph.D. thesis, École des Mines de Paris.

Bisset, E. (1984). Mathematical model of the thermal regeneration of a wall-flow monolith diesel particulate filter. *Chem. Eng. Sci.*, 39, 1232–1244.

Depcik, C. and Assanis, D. (2005). One-dimensional automotive catalyst modeling. *Prog. Energy Combust. Sci.*, 31, 308–369.

Ecopoint Inc. (2008). DieselNet. Available online: http://www.dieselnet.com/.

Frobert, A., Creff, Y., Lepreux, O., Schmidt, L., and Raux, S. (2009). Generating Thermal Conditions to Regenerate a DPF: Impact of the Reductant on the Performances of Diesel Oxidation Catalysts. In *SAE International*. Detroit, USA.

Koltsakis, G. and Stamatelos, A. (1997). Catalytic automotive exhaust aftertreatment. *Prog. Energy Combust. Sci.*, 23, 1–39.

Lepreux, O., Creff, Y., and Petit, N. (2008). Motion planning for a Diesel Oxidation Catalyst. In *Proc. of American Control Conference 2008*. Seattle, USA.

Oh, S. and Cavendish, J. (1982). Transients of monolithic catalytic converters: response to step changes in feedstream temperature as related to controlling automobile emissions. *Ind. Eng. Chem.*, 21, 29–37.

Osizik, M. (1977). *Basic heat transfer*. McGraw-Hill.

Silva, G.J., Datta, A., and Bhattacharyya, S.P. (2005). *PID controllers for time-delay systems*. Birkhäuser.

Tavakoli, S. and Fleming, P. (2003). Optimal tuning of PI controllers for first order plus dead time/long dead time models using dimensional analysis. In *Proc. of the 7th European Control Conference*.

Tavakoli, S. and Tavakoli, M. (2003). Optimal tuning of PID controllers for first order plus time delay models using dimensional analysis. In *Proc. of the 4th International Conference on Decision and Automation (ICCA'03)*. Montreal, Canada.

Controller Design in a Fuel-Cell Powered Automobile

Srinivas Palanki[a] [1] **John C. Telotte**[b]

[a] *Department of Chemical and Biomolecular Engineering, University of South Alabama, Mobile, AL 36688, USA*
[b] *Department of Chemical and Biomedical Engineering, Florida State University, Tallahassee, FL 32310-6046, USA*

Abstract: In this paper, the control problems that arise during dynamic operation of a fuel-cell powered automobile, are analyzed. In particular, it is shown that there are three distinct control problems that need to be solved when the power demand fluctuates. A logic-based switching controller is proposed that switches to the battery backup when the fuel cell is unable to provide the necessary power to the motor. An adaptive controller is developed based on a linear model that adjusts the hydrogen flow into the fuel cell in response to changing power demand. Finally, a thermal controller is developed based on a nonlinear model that regulates the temperature of the fuel cell. Interaction between these controllers is analyzed via simulations under realistic road conditions.

Keywords: controller design, PEM fuel cell, automotive power generation system

1. INTRODUCTION

Fuel cell power systems for automotive applications have received increased attention in recent years because of their potential for high fuel efficiency and lower emissions [Zalc and Loffler, 2002]. While there have been significant advances in fuel cell technology, one reason this technology has not seen wide-spread applications in the automotive industry has been the lack of an efficient hydrogen distribution center and the difficulties associated with storing hydrogen onboard an automobile. One option to alleviate these problems is to develop a system that utilizes a commonly available carbon-based hydrogenous fuel such as gasoline or methane to generate the necessary hydrogen *in situ* on an "as needed" basis. In this paper, we identify three separate control problems that need to be solved in a fuel-cell powered automobile.

2. SYSTEM DESIGN CONSIDERATIONS

A schematic of the fuel cell system under consideration is shown in Fig. 1. The two main components of the overall system are (1) the fuel processing subsystem and (2) the power generation subsystem. Methane enters the fuel processing subsystem and is converted to hydrogen. Hydrogen enters the fuel cell where it mixes with oxygen to generate electrical power which drives an electric motor. In addition to the fuel cell, there is a battery backup that the electric motor switches to when the hydrogen delivered to the fuel cell is insufficient to meet the *instantaneous* power demands of the electric motor. This battery backup is essential because significant load transitions occur frequently as a result of sudden acceleration on highway ramps as well as terrain changes [Zalc and Loffler, 2002].

[1] Corresponding author: palanki@usouthal.edu

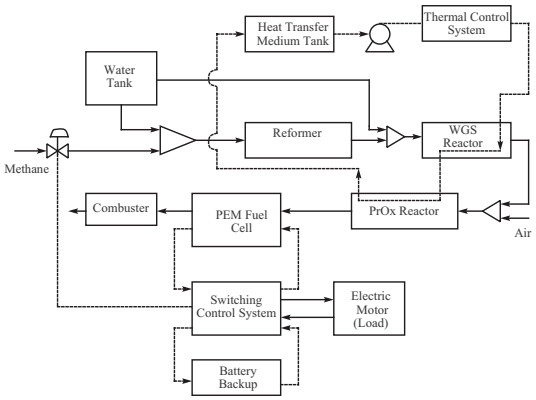

Fig. 1. Schematic of Fuel Cell System

In an earlier paper [Kolavennu *et al.*, 2006], the primary components of a fuel cell power system, that utilizes methane to generate hydrogen, were analyzed. In particular, basic chemical engineering principles were utilized to design a reactor train that converts methane to hydrogen of the desired purity. The relation between power produced by a PEM fuel cell and methane entering the reactor train *at steady state* was calculated. However, a typical automobile does not operate at steady state. The power demand for an automobile motor undergoes significant variations due to acceleration, changes in road surface and traffic conditions.

In this paper, we analyze the control problems that arise during dynamic operation of a fuel-cell powered automobile in the face of fluctuating power demand. In particular, it is shown that there are three distinct control problems that need to be solved when the power demand fluctuates. When power demand goes down, the excess hydrogen can

be diverted from the fuel cell. A sudden *increase* in power demand requires an instantaneous increase in hydrogen flow rate into the fuel cell. However, the conversion of methane to hydrogen takes several seconds which leads to an unacceptable lag between power demand of the motor and the power supplied by the fuel cell. For this reason, a backup battery is required that takes over this power load during the time it takes for the fuel cell to generate the necessary power and a suitable controller is required that switches between the fuel cell and the battery backup. If sufficient hydrogen is being produced by the fuel processor, a separate controller is required to adjust the hydrogen flow into the fuel cell in response to changing power demand. Finally, the fuel cell is subject to temperature changes and a thermal controller is required to regulate the temperature to the desired setting. In the paper, we propose the following controllers:

- A logic-based switching controller that switches to the battery backup when the fuel cell is unable to provide the necessary power to the motor.
- An adaptive controller based on a linear model that adjusts the hydrogen flow into the fuel cell in response to changing power demand.
- A thermal controller based on a nonlinear model that regulates the temperature of the fuel cell.

The design of these controllers is described in the sections below.

3. SWITCHING CONTROLLER DESIGN

There has been considerable research effort in modeling fuel cells [Nguyen and White, 1993]. In electric and fuel cell vehicles the battery is charged and discharged continuously and so knowledge of the transient behavior of the batteries is very important. Dynamic models developed from electrochemical principles like the cell sandwich model give spatial distribution of potentials and chemical compositions inside the cell as well as the transient behavior of cell potential and temperature. However for control oriented studies we require models which can be simulated quickly. Equivalent electric circuit models have been developed in the literature which give an accurate prediction of state-of-charge (SOC) of the battery [He and Hodgson, 2002].

He and Hodgson [2002] have observed that while discharging a battery over a period of time there exists a cutoff or critical voltage beyond which the battery performance deteriorates rapidly as the voltage begins to fall rapidly. To avoid operation near the critical voltage the state of charge is set to zero at the cutoff voltage and is defined as

$$SOC = 1 - \frac{Voc_{cutoff}}{Voc_{full}} \tag{1}$$

where Voc_{full} is the voltage of the battery at full capacity and Voc_{cutoff} is the battery terminal voltage at the critical point. Practically, it is difficult to measure the open circuit voltage at each instant hence utilizing the relationship between the SOC and the available battery capacity SOC can be redefined as

$$SOC = 1 - \frac{UsedCapacity}{TotalCapacity} \tag{2}$$

The total current drawn from the battery can be used as an indicator for the used capacity and is given by.

$$CAP_{used} = \int_0^t I.dt \tag{3}$$

So now the SOC is one when the battery is fully charged and zero when discharged to the critical voltage. It is desirable to maintain the SOC around 0.5-0.7.

A battery model which requires experimentally obtained open-circuit voltage and battery resistance data and predicts the battery terminal voltage, current, and SOC as a dynamic function of operator imposed power demand has been developed based on the model by He and Hodgson [2002]. The model consists of the battery as an ideal voltage source with an internal resistance. This battery model is characterized by the idealized open circuit voltage, V_{oc}, and the internal battery resistance, R_b. The terminal voltage can be expressed in terms of V_{oc} and R_b as

$$V_{term} = V_{oc} - I * R_b \tag{4}$$

The terminal voltage of a battery during discharge is lower than the instantaneous open circuit voltage because of the internal resistance inside the battery. Hence current I is given a positive sign when the cell is discharging. Similarly when the cell is charging we need to apply a voltage greater than the V_{oc} to overcome the internal resistance inside the cell so the current in this case is chosen to be negative.

The open circuit voltage and the internal resistance of the battery are both functions of SOC and temperature. For a battery operating at constant temperature the relationship between V_{oc}, Rb and the SOC can be determined experimentally.

The power available at the terminals of the battery is given by the product of voltage and current and substituting the expression for voltage from equation 4. we have

$$Pwr_{term} = V_{term}I = IV_{oc} - I^2 * R_b \tag{5}$$

For a particular power demand we can calculate the current by solving equation 5 which is a quadratic equation in I.

$$I = \frac{V_{oc} - \sqrt{(V_{oc}^2 - 4.R_b.Pwr)}}{2R_b} \tag{6}$$

where Voc and Rb are both functions of the SOC. The same sign convention as was used for the current is used i.e. the power is positive during discharge and negative during charge. The current calculated from eq. 6 is used to calculate the used capacity from eq. 3, which in turn is used to calculate the SOC by eq. 2. The V_{oc} and R_b are obtained for the new SOC from the experimental data. Using the new values of V_{oc} and R_b the current is estimated using eq. 6.

The switching controller is a logic based on-off controller that switches back and forth between the fuel cell and the battery to meet the power demand. As discussed earlier there is a time lag between the methane entering the reformer and the hydrogen coming out of the fuel processor. If the power demand remains constant the power produced by the fuel cell is sufficient to meet the power demand. The actual power demand curve is not a straight line and has a lot of fluctuations. To meet this fluctuating power demand, the fuel cell may switch to the battery. The switching controller has to address the following scenarios:

- *Increase in Power Demand*: Whenever there is an increase in power demand the fuel cell cannot produce the required power (P_r) because of the time delay (τ) in producing power and hence any deficit in power demand is handled by switching to the battery until the fuel cell can produce sufficient power. During this time delay the power produced by the battery is

$$P_{bat} = P_r - P_{fc} \quad for \quad t < \tau \tag{7}$$

- *Decrease In Power Demand*: During deceleration or decrease in power demand the fuel cell continues to produce the power requested until the time delay has elapsed. This excess power produced by the fuel cell during decrease in power demand should be routed to the battery, so that the battery can be charged. The same equation used in the scenario above can be used here. Since here the power requested is less than the power produced by the fuel cell the P_{bat} is negative which indicates that the battery is being charged.
- *State of Charge*: The state of charge of the battery should be always maintained above a specified target(SOC_{target}). But during sudden increase in power demand the battery might be discharged rapidly and the SOC might fall below the specified target and also the initial SOC itself might be less than the SOC_{target}. When the SOC of the battery falls below SOC_{target} the controller should direct the fuel cell to produce power to charge the battery in addition to the power demand.

$$P_{fc} = P_r + P_{bat} \quad if \quad SOC < SOC_{target} \tag{8}$$

- *Total Power Demand*: Since the fuel processor and the fuel cell system were designed for a maximum power output of 50 kW, the switching controller should make sure that the power demand from the fuel cell is not greater than 50 kW.

The fuel processor, fuel cell system and battery model along with the switching controller were simulated in MATLAB for different power demands. For a simple case where the power demand is a step increase followed by a step decrease the power profiles are given in Figure 2. Notice that the fuel cell supplies the power with a time delay of 4 seconds in the meantime the battery supplies the requested power demand. Once the fuel cell is able to meet the power demand the battery is turned off until 15 seconds at which time the battery again is used to supply the necessary power demand. At 30 seconds when there is a decrease in power demand the deficit power is sent to the battery to charge it until the fuel cell reaches the level of the new power demand.

To get a more realistic power vs time profile we obtained the power profile for a small car from an existing speed vs time profile using ADVISOR software package [NREL, 2002]. The Urban Dynamometer Driving schedule (UDDS) which is designed for light duty vehicle testing in city driving conditions has been used. The speed versus time profile is shown in Figure 3. The profiles of power requested, fuel cell power and battery power versus time are plotted in Figure 4.

The power supplied by the battery also depends on the initial SOC of the battery. For the same cycle the system was simulated for different initial SOC as shown in Figure 5. The controller was designed to maintain the SOC above

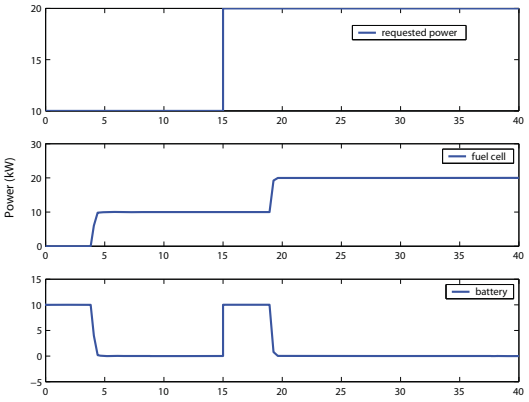

Fig. 2. Power profile

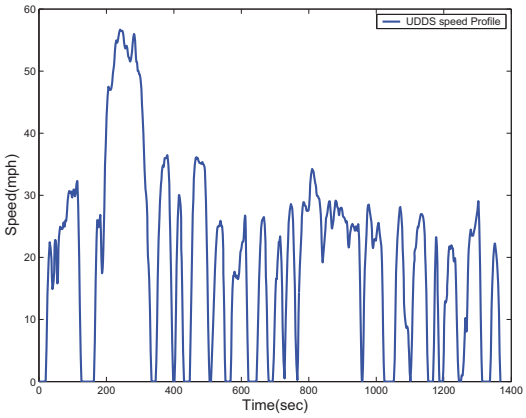

Fig. 3. Speed Vs time profile for UDDS

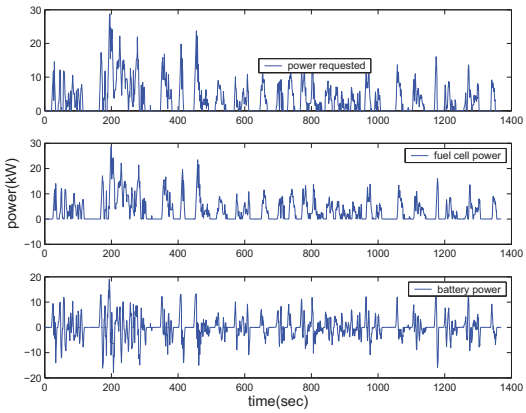

Fig. 4. Power profiles for the UDDS

0.5. For the initial conditions where the battery is almost charged (SOC=0.9) and semi charged (SOC=0.64) the profiles look similar. But for the case where the initial SOC is less than 0.5 the controller is activated and brings the SOC level to above 0.5.

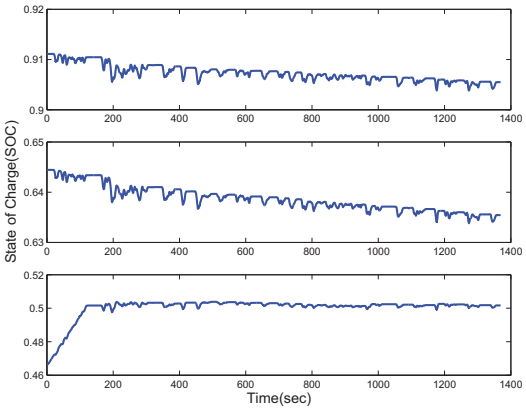

Fig. 5. State of charge for different initial conditions

Current battery technology in hybrid vehicles involves the use of nickel metal hydride (NiMH) battery packs. For instance, the Toyota Prius consists of 38 prismatic modules of a new generation NiMH design with a total pack nominal voltage of 273.6 V and a total energy capacity of 1.8 kWh [Kelly *et al.*, 2001]. The dimensions of this battery pack are 19.6 mm x 106 mm x 275 mm (volume of 57 l). The battery considered in this paper is of the same order of magnitude with a peak voltage of 300 V. If we assume that the energy capacity of the battery is 1.8 kWh (same as the Prius battery) and the battery has to have a state of charge of at least 50%, this battery would deliver 50 kW for 1 minute starting from a fully charged state before depleting to 50%. Thus, from a cold start, the reformer would have to be operational within 1 minute so that the car can switch from the battery to the fuel cell. It was shown in the previous section that once the fuel cell is operational, under realistic city driving conditions, the charge of the battery never goes under 50%. Newer gas-electric and fuel cell-electric hybrid vehicles use lithium ion battery technology. These batteries have superior power density versus energy density characteristics when compared to either NiMH batteries or supercapacitors. The second generation Honda Clarity fuel cell-electric hybrid is equipped with such a battery module. It is rated for 283 volts, and replaces the super capacitor energy storage system of the first generation Clarity. Improvement in lithium ion battery technology is ongoing. Current research indicates that energy capacity of 6-18 kWh are achievable with a calendar life of 15 years and 2500-5000 charge depleting cycles [Axsen *et al.*, 2008]. Preliminary research on magnesium ion battery systems suggest another order of magnitude in performance improvent is achievable [Axsen *et al.*, 2008].

4. ADAPTIVE CONTROLLER DESIGN FOR POWER GENERATION SUBSYSTEM

Pukrushpan [2003] developed and experimentally verified a dynamic model for a PEM fuel cell stack system similar to the one shown in Fig. 1. The model incorporates transient behavior that is important for controller design and analysis. In particular, a time-scale analysis of the various components was conducted and dynamic balances were developed for those operations that relate to automobile operations. Slower dynamics associated with temperature regulation and heat dissipation were ignored. Inertia dynamics along with nonlinear curve fitting of the compressor characteristic map were used to model the compressor. The manifold dynamics were based on lumped-volume filling dynamics. Static models of the air cooler and air humidifier were developed from thermodynamic relations. The fuel cell stack model was composed of four interacting submodels, namely stack voltage, cathode flow, anode flow and membrane hydration. The dynamic equations at the cathode and anode were developed using mass conservation principles and thermodynamic and psychometric properties of air. All gases were assumed to behave like an ideal gas. Spatial variations in temperature and concentration were ignored. It was assumed that the anode inlet flow rate could be instantaneously adjusted by a valve to maintain the minimum pressure difference between the cathode and the anode. Mass transport of water across the fuel cell membrane was calculated in membrane hydration model. Both water content and mass flow were assumed to be uniform over the surface of the membrane. However, this model developed by Pukrushpan [2003] consists of a large number of coupled, nonlinear differential and algebraic equations (DAE) and adaptive control theory cannot be applied directly to this system.After suitable substitution of variables, we obtained a reduced model of the fuel cell system that is a set of nine ordinary differential equations and is suitable for controller design and analysis [Kolavennu *et al.*, 2008]. In this model, it is assumed that all the cells in the stack perform similarly, i.e., by analyzing the polarization curve of a single cell, the stack performance can be estimated. The power from the fuel cell, which is a function of the current and voltage, is given by:

$$P = V_{st} I = (N_c V_c)(i A_c) \tag{9}$$

where P is the power produced by the fuel cell, V_{st} is the voltage of the stack which is the product of the number of cells N_c and the individual cell voltage V_c, I is the current drawn from the cell and is the same for each cell and depends on the area of cross section A_c, i is the current density.

The reversible standard potential E^o for the above cell reaction is 1.23 V at 25 ^oC as determined from the change in the Gibb's free energy. The actual voltage depends upon the concentration of the species and temperature at which the fuel cell is operating. The concentration dependence is given by the Nernst equation [Pukrushpan, 2003] as shown below:

$$\begin{aligned} E \;=\; & 1.229 - 8.5 \times 10^4 (T_{fc} - 298.15) + \\ & 4.3085 \times 10^{-5} T_{fc} \left[ln(P_{H_2}) - \frac{1}{2} ln(P_{O_2}) \right] \end{aligned} \tag{10}$$

where E is the open circuit voltage, the fuel cell temperature T_{fc} is in K, and reactant partial pressures P_{H_2} and P_{O_2} are expressed in atm. The actual cell voltage at any given current density is obtained by subtracting the activation, ohmic and concentration losses from the reversible potential as expressed below.

$$\nu_{fc} = E - \nu_{act} - \nu_{ohm} - \nu_{conc} \tag{11}$$

where ν_{act}, ν_{ohm} and ν_{conc} are activation, ohmic and concentration overvoltages. These losses are a function of the current density, pressure, membrane humidity and

also on the type of membrane and are represented by the empirical equations given below

$$\nu_{act} = \nu_0 + \nu_a(1 - e^{10i}) \tag{12}$$

$$\nu_{ohm} = i.R_{ohm} \tag{13}$$

$$\nu_{conc} = i\left(c_2 \frac{i}{i_{max}}\right)^2 \tag{14}$$

where ν_0, ν_a and c_2 are functions of temperature, pressure and membrane humidity of the cell. Using this model we can calculate the power produced by the fuel cell based on the voltage current characteristics. For a given current demand the voltage is calculated using Eq. 11 and thereby the power output of the fuel cell.

For the fuel cell systems to operate at levels comparable to existing internal combustion engines, the key issue that should be addressed is the *transient* behavior of fuel cell systems. Automobiles are subjected to significant load transitions during operation and the fuel cell system should be able to produce power which can follow this varying load profile. Power produced by the fuel cell is dependent on the voltage current characteristics. The transient response data from the nonlinear model presented in [Kolavennu *et al.*, 2008] was generated by subjecting the nonlinear system to a series of step inputs in the current around the 100 Amperes operating point. Utilizing this input output data from the nonlinear model system identification techniques were employed to derive a linear second order model was fit between the current demand and the voltage produced by the fuel cell stack. The transfer function G_p is given below

$$G_p = \frac{-390.78}{s^2 + 27.291s + 2068.8} \tag{15}$$

This transfer function is used in this paper to design an adaptive controller to regulate the power output of the fuel cell to the power demand. This adaptive controller is then implemented on the *nonlinear* model described in [Kolavennu *et al.*, 2008]. The control problem is to track the power demand of the motor using current as the manipulated variable.

To get a more realistic power vs time profile we obtained the power profile for a small car from an existing speed vs time profile using ADVISOR software package [NREL, 2002]. The Urban Dynamometer Driving schedule(UDDS) which is designed for light duty vehicle testing in city driving conditions was used.

Model reference adaptive control (MRAC) is derived from the model reference control (MRC) problem. The objective of MRC is to find the feedback control law that changes the structure and dynamics of the plant so that its I/O properties are exactly the same as those of a reference model. The structure of an MRC scheme for a LTI, SISO plant is shown in Fig. 6 [Ioannou and Sun, 1996]. Here, $W_m(s)$ is the transfer function of the reference model, $r(t)$ a given reference input signal, $y_m(t)$ the output of the reference model and $y(t)$ is the plant output. The feedback controller, denoted by $C(\Theta_c)$, is designed so that all signals are bounded and the closed-loop plant transfer function from r to y is equal to $W_m(s)$. This transfer function matching guarantees that for any given reference input $r(t)$, the tracking error $e = y - y_m$, which represents the

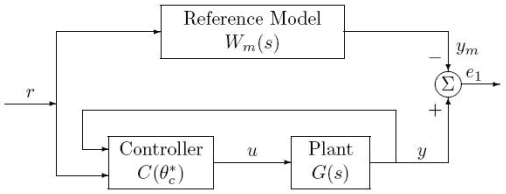

Fig. 6. Model Reference Adaptive Control

Table 1. Performance of MRAC on different road profiles

Profile or Cycle	ITAE error
UDDS	40.5
Federal Test Procedure	42.76
US06	55.13
Highway Fuel Economy Test	11.09
Extra Urban Driving Cycle	8.20
Indian Highway Profile	10.20

deviation of the plant output from the desired trajectory ym, converges to zero with time.

The model reference is chosen to be:

$$W_m = \frac{1}{s + 0.023} \tag{16}$$

The performance of the adaptive controller can be improved by adding some derivative action, i.e., using a PD controller in conjunction with the adaptive controller. This essentially makes the linearized plant represented by eq. 15 of unity relative degree which is the same as that of the reference model eq. 16.

The Environmental Protection Agency (EPA) reviews and revises as necessary the regulations governing the Federal Test Procedures (FTP) to insure that vehicles are tested under circumstances which reflect the actual current driving conditions under which motor vehicles are used, including conditions relating to fuel, temperature, acceleration, and altitude. The adaptive controller was tested on a variety of profiles. The controller was designed for the UDDS profile using the linearized model represented by eq. 15 and the same settings were employed for the remaining profiles. The resulting adaptive controller was implemented on the *nonlinear* model given in [Kolavennu *et al.*, 2008]. The Integrated Time Averaged Error (ITAE) was computed for each power profile. The results are shown in Table 1. It is observed that the adaptive controller with derivative action is able to track power profiles resulting from a wide variety of road conditions. A PID tuning procedure for the UDDS profile resulted in an ITAE error of 91.46. However, this controller when implemented on the US HWY profile resulted in loss of stability. On the other hand, the adaptive controller that was designed for the UDDS profile was able to successfully track the Federal Test Procedure profile, the US06 profile, the Highway Fuel Economy Test profile, the Extra Urban Driving Cycle profile, and the Indian Highway profile with no off-line tuning.

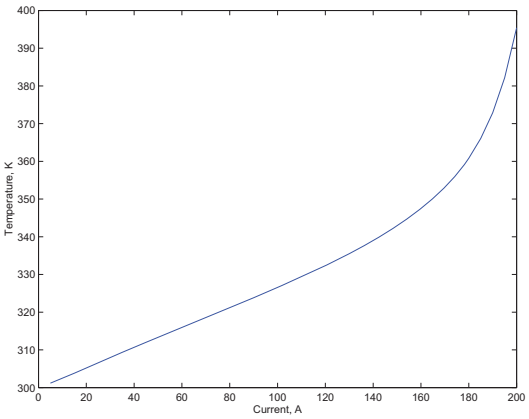

Fig. 7. Steady State Temperature versus Current in Fuel Cell

5. THERMAL CONTROLLER FOR FUEL CELL TEMPERATURE REGULATION

In this section, a dynamic model is developed that accounts for temperature changes in a PEM fuel cell. The dynamic model is obtained by extending a static current-voltage description to include temperature difference and by dynamically modeling the stack temperature. The following chemical reaction occurs in the fuel cell:

$$2H_2 + O_2 \rightarrow 2H_2O \tag{17}$$

The accumulation term for each species is negligible in the fuel cell compared to the mass of the fuel cell stack. Thus, a steady state model can be assumed for the gaseous and liquid species as follows:

$$\dot{N}_{i,out} = \dot{N}_{i,in} + \nu_i \dot{\xi} \tag{18}$$

where $\dot{N}_i$ is the molar flow rate of species i, ν_i is the stoichiometric coefficient and $\dot{\xi}$ is the reaction rate. It can be shown that this steady state assumption leads to the following dynamic balance for the temperature of the fuel cell stack:

$$m_{fc} C_{p_{fc}} \frac{dT_{fc}}{dt} = -C_p^* I(T_{fc} - T_\infty) - \Delta\tilde{H} I - hA(T_{fc} - T_\infty) - VI \tag{19}$$

where m_{fc} is the mass of the fuel cell stack, $C_{p_{fc}}$ is the specific heat of the fuel cell stack, C_p^* is the mole average specific heat of the reacting species, and T_∞ is the ambient temperature.

This provides a dynamic relation between the stack temperature, current and voltage. Fig. 7 shows the steady state relationship between temperature and current at a humidity of 50% in the cell. It is observed that the cell temperature increases nearly linearly with current until the design point (167 A), which is at optimum power output, and then increases rapidly due to cell inefficiency. The above equation was integrated numerically with realistic operating conditions of the fuel cell system and it was observed that the temperature dynamics are very slow compared to the dynamics of the fuel cell. In particular, it takes about 50 minutes to go from a cold start to the steady state temperature when the current is 150 A.

We are currently developing a nonlinear controller that utilizes the above model to regulate temperature to the desired set-point in the face of fluctuating power demand.

REFERENCES

Axsen, J., Burke, A., and Kurani, K., "Batteries for Plug-in Hybrid Electric Vehicles (PHEVs): Goals and the State of Technology circa 2008," *UCD-ITS-RR-08-14*, 2008

He, X. and Hodgson, J.W., " Modeling and Simulation for Hybrid Electric Vehicles: Modeling." *Intelligent Transportation Systems*, volume 3, 235-243, (2002)

Ioannou P. and J. Sun, *Robust Adaptive Control*, Prentice Hall, Inc., 1996

Kelly, K.J., Mihalic, M., and Zolot, M., "Battery Usage and Thermal Performance of the Toyota Prius and Honda Insight during Chassis Dynamometer Testing," *NREL/CP-540-31306*, 2001

Kolavennu, P.K., Telotte, J.C., and Palanki, S., "Design of a Fuel Cell Power System for Automotive Applications," *Int. J. Chemical Reactor Engng*, Vol 4: A19 (2006)

Kolavennu, P.K., Palanki, S., Cartes, D.A. and Telotte, J.C., "Adaptive Controller for Tracking Power Profile in a Fuel Cell Powered Automobile," *J. Process Control*, 18, 558-567 (2008)

Nguyen, T.V., and White, R.E., "A Water and Heat Management Model for Proton-exchange-membrane Fuel Cells," *J. Electrochem. Soc.*, 140, 8, 2178-2186 (1993)

National Renewable Energy Laboratory, "ADVISOR (Advanced Vehicle Simulator)", 2002

Pukrushpan, J. T., *Modeling and Control of Fuel Cell Systems and Fuel Processors*, PhD thesis, The University of Michigan, Ann Arbor, 2003

Zalc, J.M., and Loffler, D.G., "Fuel processing for PEM fuel cells: transport and kinetic issues of system design," *J. Power Sources*, 111, 58-64 (2002)

Fault Detection and Diagnosis

Oral Session

Fault Detection in Process Systems using Hidden Markov Disturbance Models

Wee Chin Wong * **Jay H. Lee** *

* *School of Chemical & Biomolecular Engineering, Georgia Institute of Technology, Atlanta, GA 30332 USA*
(e-mail: {weechin.wong, jay.lee}@chbe.gatech.edu).

Abstract: Fault detection and diagnosis is critical for maintaining the health of process systems. Common fault signals include process and disturbance parameter changes, as well as sensor and actuator malfunctions (such as persistent drifts and biases). These may be characterized by the existence of latent 'fault' states. This work examines the effectiveness of a Hidden Markov Model framework for modeling such fault regimes. The proposed methodology may be interpreted as a generalization of a commonly-employed Mixture-of-Gaussians (Kesavan and Lee (1997)) approach and is demonstrated through a shell-and-tube heat exchanger problem. Furthermore, the flexibility of the method is shown in the context of detecting valve stiction. This is a significant problem in process industries where a valve's output suffers from excessive friction and is unable to track its input leading to degradation in closed-loop performance.

Keywords: Fault detection, Markov model, Sensor failure, Control valves.

1. INTRODUCTION

Tracking the closed-loop performance and health of process systems, although intuitively important, is oftentimes overlooked during the design of control solutions. Maintenance, required to mitigate the effects of system faults, typically necessitates expert personnel not found within normal plant situations (Kesavan and Lee (1997)). For this reason, multiple process monitoring algorithms have been developed so that such faults may be automatically detected, diagnosed and eventually removed.

Process monitoring methods may be further classified as i) data-driven ii) analytical and/ or iii) knowledge-based (Chiang et al. (2001)). The first involves statistical treatment of large quantities of process data and are typified by data-mining and machine learning techniques (such as principal and independent component analysis), statistical control charts and so on. Knowledge-based methods employ qualitative reasoning and are oftentimes rules-based with a strong logic underpinning. A thorough overview of all three classes is presented by Chiang et al. (2001) and the references therein.

This work, relying on dynamical models of the process for fault detection, is a particular type of analytical approach. Consequently, a necessary standing assumption is the availability of a mathematical model derived from first principles or otherwise. Given the wide-spread popularity of model-based control (such as Model Predictive Control), the controller's model can be readily ported over for the purpose of fault-detection. A model structure, such as in (1), (2), is therefore relevant in subsequent developments.

$$\begin{aligned} x_t &= f(x_{t-1}, \theta_{t-1}, u_{t-1}, \omega_t) \\ y_t &= g(x_t, \theta_t, v_t) \end{aligned} \tag{1}$$

$$\begin{aligned} \gamma_t &= \mathbb{A}_t \gamma_{t-1} + \mathbb{B}_t \varphi_t \\ \theta_t &= \mathbb{C}_t \gamma_t + e_t \end{aligned} \tag{2}$$

Here, $x_t \in \mathbb{R}^{n_x}$ represents the state at discrete time index t, $u_t \in \mathbb{R}^{n_u}$, the control input, and $y_t \in \mathbb{R}^{n_y}$, a noise-corrupted measurement signal. $\theta_t \in \mathbb{R}^{n_\theta}$ represents a fault vector with potentially time-varying dynamics governed by matrices $(\mathbb{A}_t, \mathbb{B}_t, \mathbb{C}_t)$ and noise vectors (φ_t, e_t) [1]. ω_t and v_t are process and measurement noise signals respectively. $f(\cdot)$, which may represent an integration of the continuous-time model over a unit sample-time, is the state transition map. Similarly, $g(\cdot)$ represents the state-to-output map.

Faults are typically manifested (Kesavan and Lee (1997)) as i) process parameter changes, and/ or ii) disturbance parameter changes, as well as iii) actuator and sensor problems – all captured by θ. Depending on circumstances, these may be sudden jumps (*e.g.* due to an abrupt introduction of significant sensor bias), or slow drifts or random walk-type changes (*e.g.* as a result of catalyst fouling) or even a mixture of both (Fig. 1). Such failure modes, which cannot be directly observed, and need to be estimated, are conveniently incorporated into the fault model (2) by adding the notion of latent states (denoted by r), each of which modifies the fault model (see (2)) differently. This work explores the use of a Hidden Markov chain, used previously to model realistic disturbances in the context of process control (Wong and Lee (2007)), to describe the temporal, probabilistic transitions between the latent states. Furthermore, this work can be interpreted as a generalization of the popular approach of assuming statistical independence, from one time period to the next, between hidden states. For example, at each time step t, Willsky (1976) and Kesavan and Lee (1997) allowed the statistics

[1] In practice, the user would model θ according to disturbance scenarios of interest.

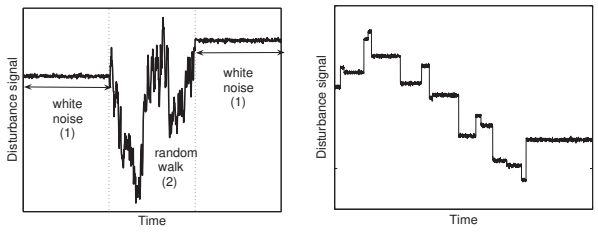

(a) Intermittent drifts: white noise probabilistically interspersed with integrated white noise.

(b) Abrupt jumps.

Fig. 1. Possible disturbance signals (θ).

of φ_t and e_t to be described by a Mixture-Of-Gaussians (MOG)[2]. This captures the situation where faults that do occur happen infrequently but with significantly larger magnitudes. Persistent faults like drifts, which are easily described by the proposed Hidden Markov Model (HMM) approach, are captured in the MOG context by introducing additional states or non-linearities in the model.

The main contribution is to show that the aforementioned faults (abrupt jumps/ biases and drifts) can be better modeled and detected by the proposed method. Another novel application is in the context of detecting valve stiction, where it is demonstrated that the output of the valve (which is not normally measured) can be effectively tracked using the same proposed framework.

Section 2 provides the details behind an HMM, its subsequent use for fault detection and relevance to prior work. Section 3 demonstrates the effectiveness of the proposed method in the context of a heat exchanger. Section 4 explores the valve stiction issue before concluding remarks regarding future research are presented in Section 5.

2. FAULT MODELING USING HIDDEN MARKOV MODELS

HMMs represent a useful class of statistical models where a latent state, taking values from an alphabet $\mathcal{J} \in \{1, 2, \ldots, J \in \mathbb{Z}^+\}$ of cardinality J, transitions probabilistically in a Markovian[3] fashion from one sampling time to the next. Mathematically, a finite-state Markov chain is a sequence of random variables $(r_0, r_1, ..., r_t, ...)$, where the transition probability matrix $\Pi = (\pi_{ij}) = (pr(r_t = j | r_{t-1} = i), i, j \in J) : \sum_{j=1}^{J} \pi_{ij} = 1, \forall i \in \mathcal{J}$, governs the probabilistic temporal transitions. The term 'Hidden' signifies that the actual regime label is usually not known with complete certainty and must be inferred from available noisy measurements of itself or other related states. In the simplest case, each latent state has a probability distribution over a finite set of possible output symbols. All Markov chains under consideration are ergodic. For simplicity, the Markov chain is assumed to be at steady state, satisfying $\pi = \Pi'\pi$, where π is a column vector containing the unconditional and initial probabilities of each regime. HMMs have found widespread applications in science and engineering - ranging from speech recognition (Rabiner (1989)) to bioinformatics and diverse fields such as econometrics.

HMMs and their generalizations have been used in fault detection, with significant differences to our proposed approach. Smyth (1994), for example, did not consider an explicit fault model (*i.e.,* (2)). Instead, the process parameters are continuously estimated (in batch mode) and treated as output of an underlying Markov chain. This necessitates linking the process parameter vector to fault modes, which is not always possible. A recursive maximum a posteriori filter is then used for fault-mode detection. Huang (2008) suggested a similar (see Section 2.1) HMM approach to sensor problem diagnosis but limited considerations to faults in the output channels and input signals taking values from a finite, discrete set. Almeida and Park (2008) learned an HMM corresponding to each operating condition and, unlike the approach proposed in this work, does not make use of the process model. There, fault detection is achieved by a classification scheme that chooses the HMM that maximizes the probability of a given sequence of observations.

2.1 Proposed Fault Model: Intermittent Drifts & Abrupt Jumps

Following the successes in other fields, a generalization of (2) is considered by allowing the statistics of (φ_t, e_t) (and potentially the fault model parameters $(\mathbb{A}, \mathbb{B}, \mathbb{C})$) to vary according to a hidden Markov chain.

Intermittent Drifts. In the case of one-dimensional intermittent drifts (Fig. (1a)), one has:

$$\begin{aligned} \gamma_{t+1} &= \gamma_t + \varphi_{r_{t+1}} \\ \theta_t &= \gamma_t + e_t \\ r_t &\in 1, 2 \\ \pi_{11} &\approx 1,\ \pi_{11} < 1 \\ \pi_{22} &\approx 1,\ \pi_{22} < 1 \end{aligned} \tag{3}$$

Here, φ_{r_t} and e_t are uncorrelated, zero-mean Gaussian signals with covariances (that may depend on r_t) of $Q^{\varphi}_{r_t}$ and Q^{e}_{t}. The abuse of notation on the subscript of φ emphasizes the dependence of the covariance of the noise signal on the underlying Markov chain. When $r_t = 1$ (*i.e.,*, the white-noise regime), $Q^{\varphi}_{r_t=1} \approx 0$. Random-walk type behavior occurs when the hidden state switches to $r_t = 2$, where $Q^{\varphi}_{r_t=2} >> 0$; Q^{e}_{t} is invariant to the hidden regime and of appropriate magnitude. Since it is common that there is low probability of switching once the system enters a particular regime, a diagonally-dominant Π is employed.

Abrupt Jumps. In the case of modeling abrupt jumps, (3) is adjusted such that $\pi_{11} = \pi_{12} = p \approx 1$, $p < 1$, so that $\Pi = [p,\ 1-p;\ p,\ 1-p]$. This ensures that the jump state (the second one, in this case) is infrequently accessed and when it is, a significant step-change occurs.

In this latter case, since it is assumed that the Markov chain is at steady state, this form of the transition matrix implies that the probability of entering a particular regime is independent of the current mode. It is thus clear that the HMM framework subsumes an MOG description.

[2] *i.e.,* at each time step, a member from a set of Gaussians, from which the noise signal is to be sampled, is selected with some time-invariant probability.

[3] transitions depend only upon the immediate past.

Fault detection and diagnosis is performed via state estimation (in particular to track θ) without the knowledge of the latent state trajectory. Hence, a brief mention of state estimation, based on a model resulting from the concatenation of (1), and (2) is necessary.

2.2 Fault Detection via State Estimation of Jump Markov Systems

Equations (1) and (2) can be merged to yield:

$$\begin{aligned}\begin{bmatrix} x_{t+1} \\ \gamma_{t+1} \end{bmatrix} &= \mathcal{F}_{r_{t+1}}\Big(\begin{bmatrix} x_t \\ \gamma_t \end{bmatrix}, u_t, \xi_{r_{t+1}} \Big) \\ y_t &= \mathcal{G}_{r_t}\Big(\begin{bmatrix} x_t \\ \gamma_t \end{bmatrix}, n_{r_t} \Big) \\ pr(r_t = j | r_{t-1} = i) &= \pi_{ij} \end{aligned} \tag{4}$$

Here, $\mathcal{F}$ is implicitly understood to include model structures and parameters from $\{f, \mathbb{A}, \mathbb{B}, \mathbb{C}\}$ and the hidden Markov chain. A similar remark is extended to $\mathcal{G}$. Besides $\mathcal{F}$ and $\mathcal{G}$, the statistics of the noise ξ (a concatenation of (ω, φ, e)) and n (a concatenation of (v, e)) can depend on r. The system represented by (4) is also termed a Markov jump system. Without knowledge of the sequence $(r_0, \ldots, r_t)$, the optimal filter involves averaging over an exponentially growing number of linear filters. The number of filters scales as J^t, where J is the cardinality of the set containing all possible realizations of r.

The following paragraphs outline the Generalized Pseudo Bayesian estimation algorithm of order 2 (GPB2), a popular sub-optimal method, developed by Bar-Shalom and Li (1993). The main idea to have trajectories whose last 2 terms differ be merged (via moment-matching) into a single Gaussian. Using the law of total probability and Bayes' Rule, it can be shown that:

$$\begin{aligned} x_{t+1|t+1} &= \sum_{r_{t+1}} p(r_{t+1}|t+1) x_{t+1|(t+1,r_{t+1})} \\ x_{t+1|(t+1,r_{t+1})} &\triangleq \sum_{r_t} x_{t+1|(t+1,r_{t+1},r_t)} p(r_t|r_{t+1}, t+1) \\ P_{t+1|t+1} &= \sum_{r_{t+1}} \{(x_{t+1|t+1} - x_{t+1|(t+1,r_{t+1})})(\cdot)' \\ &\quad + P_{t+1|t+1,r_{t+1}}\} p(r_{t+1}|t+1) \\ P_{t+1|t+1,r_{t+1}} &= \sum_{r_t} \{(x_{t+1|t+1,r_{t+1}} - x_{t+1|(t+1,r_{t+1},r_t)})(\cdot)' \\ &\quad + P_{t+1|t+1,r_{t+1},r_t}\} p(r_t|r_{t+1}, t+1) \\ p(r_t|r_{t+1}, t+1) &= \frac{1}{c_1} p(y_{t+1}|t, r_{t+1}, r_t) p(r_t|r_t) p(r_t|t) \\ p(r_{t+1}|t+1) &= \frac{1}{c_2} \sum_{r_t} p(y_{t+1}|t, r_{t+1}, r_t) p(r_{t+1}|r_t) p(r_t|t) \end{aligned}$$

The term $p(y_{t+1}|t, r_{t+1}, r_t)$ refers to the probability density of the corresponding one-step ahead output prediction. $x_{t+1|(t+1,r_{t+1})}$ refers to the estimate of x_{t+1} given output measurements $\{y_0, \ldots, y_{t+1}\}$ and a certain realization of r_{t+1}; $P_{t+1|(t+1,r_{t+1})}$ denotes the corresponding error covariance matrix. The pair $(x_{t+1|(t+1,r_{t+1},r_t)}, P_{t+1|(t+1,r_{t+1},r_t)})$ are similarly defined. It is noted that starting from $(x_{t|(t,r_t)}, P_{t|(t,r_t)})$, a single application of the time and measurement update steps of the (extended) Kalman filter yields these latter quantities. c_1 and c_2 are normalizing constants such that the merging probabilities $p(r_t|r_{t+1}, t+1)$ and $p(r_{t+1}|, t+1)$ sum to unity.

2.3 A-posteriori Regime Estimation

If required, a prediction and/ or filtered estimate of the hidden regime can be obtained viz:

$$\begin{aligned} \hat{r}_{t+1|t} &= \arg\max_{r_{t+1}} \left\{ p(r_{t+1}|t) \triangleq \sum_{r_t} pr(r_{t+1}|r_t) \cdot pr(r_t|t) \right\} \\ \hat{r}_{t|t} &= \arg\max_{r_t} \{p(r_t|t)\} \end{aligned} \tag{5}$$

3. EXAMPLE 1: FAULT TRACKING IN A SHELL & TUBE HEAT EXCHANGER

In this example, the usefulness of the proposed method in detecting faults is studied in the context of a shell and tube heat exchanger (6) also considered by Kesavan and Lee (1997). In particular, we contrast the proposed HMM approach against an MOG method (Kesavan and Lee (1997)) in modeling the latent states that govern the fault signals (see Section 3.1 for simulation details). The main difference is that the latter framework assumes that each latent state occurs with a (time-invariant) probability that is independent of the previous realization. The governing non-linear ordinary differential equations used for simulation but not estimator design, are:

$$\begin{aligned} \frac{dT_c}{dt} &= \frac{q_c}{V_c}(T_{ci} - T_c) + \frac{\alpha_c}{V_c}(T_h - T_c) \\ \frac{dT_h}{dt} &= \frac{q_h}{V_h}(T_{hi} - T_h) - \frac{\alpha_h}{V_h}(T_h - T_c) \\ y &= \begin{pmatrix} T_c \\ T_h \end{pmatrix} + \mu_v + v \end{aligned} \tag{6}$$

Here, the measured state variables are the temperatures of the hot and cold streams respectively: $[T_c; T_h]$. $[T_{ci}; T_{hi}]$ are the temperatures of the incoming cold and hot streams respectively. $[\alpha_c; \alpha_h]$ are system parameters reflecting the heat transfer coefficient, heat transfer area, density, specific heat capacity of the cold and hot streams respectively. Similarly, $[q_h; q_c]$ are the flow rates of the hot and cold streams and represent the degrees of freedom available to a controller. $[V_c; V_h]$ are the volumes of the cold and hot sides. Steady-state values are reported in Table 1. v refers to zero-mean measurement noise of covariance $R \triangleq \mathbb{E}[vv']$. μ_v is nominally a null vector but might be subject to changes due to disturbances.

3.1 Simulation Conditions

Although a variety of fault types may be considered (*e.g.* those affecting the various input and output channels and/ or changes in parameters (α_c, α_h), as discussed in Section 1), for clarity of exposition, only two different fault types are assumed. Furthermore, these affect only the cold side. Given initially quiescent conditions (see Table 1), one considers:

(1) An abrupt step that is normally distributed with zero mean [L/min] and variance q_u^{hi} [L^2/min^2] affecting the input channel on the cold side (q_c) at some unknown time t_u. This may be thought of as a sudden bias developing in the input channel:

$$q_{ct} = q_{ct-1} + \varphi_t^u \cdot \delta(t, t_u),\ \varphi_t^u \sim \mathcal{N}(0, q_u^{hi}) \quad (7)$$

$\delta(\cdot,\cdot)$ is the Dirac delta function. q_u^{hi} has a value of 2 in the following experiments.

(2) A sudden drift (see Fig. 1a) affecting the sensor relaying T_c (*i.e.,* y_1) measurements between an unknown time span: $\mathcal{T} \triangleq [t_{y,1}, t_{y,2}]$. Namely, one has:

$$\mu_{v,1_t} = \mu_{v,1_{t-1}} + \varphi_t^y \quad (8)$$

where $\mathbb{E}[\varphi_t \varphi_t'] = q_y^{hi} = 0.5$ if $t \in \mathcal{T}$ and $\mathbb{E}[\varphi_t \varphi_t'] = q_y^{lo} = 10^{-10} \approx 0$, for other time periods. $\mu_{v,2}$ remains at the origin for all time.

The above non-linear model is not available for state estimation. Instead, a version linearized about the nominal operating conditions is available. With a sampling time of 0.5 min, A = [0.91, 0.03; 0.03, 0.91], B = [-0.12, 0.002; -0.002, 0.12], $C = diag([1, 1])$. Measurement covariance, R, is set to $diag([0.5, 0.5])$ and known. Since estimation is the focus of this example, the system is run in the absence of feedback control.

3.2 Proposed HMM Method to Handle Abrupt Jumps & Intermittent Drifts

The following Markov jump linear model, a specialization of (4), is employed:

$$\begin{aligned} x_{t+1} &= Ax_t + Bu_t + b\theta_t^u + \omega_{t+1} \\ \theta_{t+1}^u &= \theta_t^u + \varphi_{r_{t+1}}^u \\ \theta_{t+1}^y &= \theta_t^y + \varphi_{r_{t+1}}^y \\ y_t &= Cx_t + \theta_t^y + v_t \end{aligned} \quad (9)$$

where x_t, the state variable at discrete time index t are deviations from $[T_c^*; T_h^*]$. Similarly, the vector $u_t \in \mathbb{R}^2$ represents deviations from $[q_c^*; q_h^*]$. b represents the first column of matrix B, consistent with the fact that disturbances enter the q_c channel. $[\theta^u; \theta^y]$ are input and output disturbance state variables respectively. Both θ^u and θ^y are modeled as integrators but distinguished by the effects of the hidden Markov regime on the second moments of φ^u and φ^y. Consistent with the assumption of an abrupt jump, the covariance of φ^u is assumed to be large with a small probability, and vice versa. θ^y is naturally modeled as an intermittent drift (see (3)). Details are given in the following paragraphs.

Table 1. Nominal steady state operating conditions

Variable	Value	Units
$q_c^* = q_h^*$	10	L/min
T_{ci}^*	25	^{o}C
T_{hi}^*	100	^{o}C
T_c^*	43.75	^{o}C
T_h^*	81.25	^{o}C
α_c^*	5	m^3/min
α_h^*	5	m^3/min
$V_c^* = V_h^*$	75	L

A four-regime Markov chain is considered. These regimes represent the following scenarios:

(1) No disturbance in input channel, No disturbance in output channel ('LO-LO')
(2) No disturbance in input channel, Drifting disturbance in output channel ('LO-HI')
(3) Abrupt disturbance in input channel, No disturbance in output channel ('HI-LO')
(4) Abrupt disturbance in input channel, Drifting disturbance in output channel ('HI-HI')

Accordingly, a simple method for determining the values of the transition probability matrix (Π) is proposed. Per the earlier discussion (Section 2.1), two (sub) transition probability matrices are appropriate for the input (Π^u) and output channels (Π^y) respectively, the first state being the 'normal' regime in both cases.

$$\Pi^u = \begin{pmatrix} 0.99 & 0.01 \\ 0.99 & 0.01 \end{pmatrix};\ \Pi^y = \begin{pmatrix} 0.99 & 0.01 \\ 0.01 & 0.99 \end{pmatrix} \quad (10)$$

An overall transition probability matrix (Π) accounting for the four scenarios can be obtained by assuming statistical independence between the input and output channels. For example in computing π_{23}, one has transitions between the 'normal' to 'abnormal' state for the input channel and the opposite transitions for the output channels so that

$$\pi_{23} = \pi_{21}^u \pi_{12}^y \quad (11)$$

The overall Π [4] is:

$$\begin{pmatrix} 0.98 & 0.01 & 0.01 & 0.01 \\ 0.01 & 0.98 & 0.01 & 0.01 \\ 0.98 & 0.01 & 0.01 & 0.01 \\ 0.01 & 0.98 & 0.01 & 0.01 \end{pmatrix}$$

In accordance to the noise statistics of the possible fault scenarios, the covariance of the overall noise vector $\xi_t \triangleq [\omega_t, \varphi_t^u, \varphi_t^y]$ for the 4 regimes are:

(1) 'LO-LO': $\mathbb{E}[\xi_t \xi_t'] = diag([10^{-10}, 10^{-10}, 10^{-10}, q_y^{lo}])$
(2) 'LO-HI': $\mathbb{E}[\xi_t \xi_t'] = diag([10^{-10}, 10^{-10}, 10^{-10}, q_y^{hi}]$
(3) 'HI-LO': $\mathbb{E}[\xi_t \xi_t'] = diag([10^{-10}, 10^{-10}, q_u^{hi}, q_y^{lo}]$
(4) 'HI-HI': $\mathbb{E}[\xi_t \xi_t'] = diag([10^{-10}, 10^{-10}, q_u^{hi}, q_y^{hi}]$

Process noise ω is negligible compared to θ^u and will be assumed to be absent for simplicity.

3.3 Alternative MOG Description

If one were to be restricted to an MOG description of the latent regime, then an additional state (θ^β) is required:

$$\begin{aligned} x_{t+1} &= Ax_t + Bu_t + b\theta_t^u + \omega_{t+1} \\ \theta_{t+1}^u &= \theta_t^u + \varphi_{t+1}^u \\ \theta_{t+1}^\beta &= \theta_t^\beta + \varphi_{t+1}^\beta \\ \theta_{t+1}^y &= \theta_t^y + \theta_t^\beta \\ y_t &= Cx_t + \theta_t^y + v_t \end{aligned} \quad (12)$$

Similar to (9), θ^u refers to the input channel disturbance and is modeled as an abrupt jump. However, the output

[4] the rows do not sum to unity due to rounding errors

disturbance (θ^y) is now modeled as a double integrator (driven by θ^β). θ^β itself may be interpreted as a velocity term and is driven by φ^β which is set to have a small covariance (10^{-10}) with large probability and a large covariance (of q_y^{hi}) with small probability. This captures the (rare) event of a velocity change when the output disturbance transitions from the white-noise regime to the random-walk mode and vice versa (see Fig. 1(a)). In this case, the sub transition matrices for the input and output channels are:

$$\Pi^u = \Pi^y = \begin{pmatrix} 0.99 & 0.01 \\ 0.99 & 0.01 \end{pmatrix}$$

The overall transition matrix may be obtained as before, per (11). The covariance of the overall noise vector $\xi_t \triangleq [\omega_t, \varphi_t^u, \varphi^\beta, \varphi_t^y]$ for the 4 regimes are:

(1) $\mathbb{E}[\xi_t \xi_t'] = diag([10^{-10}, 10^{-10}, 10^{-10}, q_y^{lo}, 10^{-10}])$
(2) $\mathbb{E}[\xi_t \xi_t'] = diag([10^{-10}, 10^{-10}, 10^{-10}, q_y^{hi}, 10^{-10}]$
(3) $\mathbb{E}[\xi_t \xi_t'] = diag([10^{-10}, 10^{-10}, q_u^{hi}, q_y^{lo}, 10^{-10}]$
(4) $\mathbb{E}[\xi_t \xi_t'] = diag([10^{-10}, 10^{-10}, q_u^{hi}, q_y^{hi}, 10^{-10}]$

3.4 Example 1: Results

Table 2 presents a summary (average over 100 realizations) of the state-estimation error for both the input and output channel. A typical realization is depicted in Fig. 2.

Table 2. 2-norm of state-estimation error (Average of 100 realizations)

Channel	Proposed see (9)	MOG approach see (12)
Input	11.4	12.9
Output	13.3	19.7

Due to the similarities in modeling the abrupt jump in the output channel, it can be seen from Fig. 2(a) and the first line of Table 2 that the performance of the state estimator corresponding to both approaches yield similar performances. However, the MOG approach fares significantly worse than the proposed HMM approach in tracking the fault signal (which is an intermittent drift) corresponding to the output channel (see Fig. 2(b) and the second row of Table 2).

4. EXAMPLE 2: VALVE STICTION

Valve stiction is a common problem in control valves, the latter being widely used in process industries (Choudhury et al. (2005)). Due to the effects of friction, the output (u^x) of the control valve does not track its input (u^c) (*i.e.,* the control signal prescribed by the controller) instantaneously. Instead, u^x has been observed to demonstrate a delayed and sluggish response to u^c, where the valve 'sticks' to its current position if changes in the control signal (and/ or the absolute magnitude itself) are insufficiently large to overcome friction effects. This is usually to the detriment of closed-loop performance. It is assumed that the plant is linear and therefore parameterized by matrices (A, B, C), where A is the state-transition map, B, the input-to-state map and C, the state-to-output map. Technical definitions, first-principles and empirical models of stiction can be found in the articles by Choudhury et al. (2005, 2008) and the references therein. For simplicity,

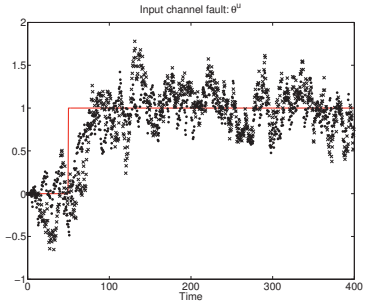

(a) Tracking θ^u

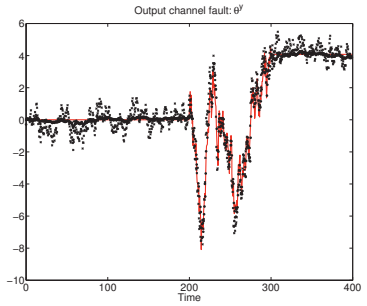

(b) Tracking θ^y

Fig. 2. Tracking θ^u and θ^y. Comparing the proposed HMM vs. MOG approaches. Legend: solid line - actual fault signal; Dots (·) - HMM; Crosses (x) - MOG

an efficient single-parameter model employed by Stenman et al. (2003) and Srinivasan and Rengaswamy (2005) for stiction detection is used for simulations in the sequel:

$$u_t^x = \begin{cases} u_{t-1}^x, \text{ if } |u_t^c - u_{t-1}^x| \leq d \\ u_t^c, \text{ otherwise} \end{cases} \tag{13}$$

where d represents the valve stiction band. The larger the value of d, the more severe the stiction problem.

The detection, diagnosis and compensation-for valve stiction has received much attention in academia and industry. Based on (13), Stenman et al. (2003) proposed a suitable model for detecting stiction:

$$u_t^x = \tilde{\delta}_t \cdot u_{t-1}^x + (1 - \tilde{\delta}_t) \cdot u_t^c$$

where $\tilde{\delta}_t$ is a binary (0/1) mode parameter occurring with a certain (i.i.d) probability.

For the same purpose of stiction detection and estimating the typically unmeasured u_t^x, we allow $\tilde{\delta}_t$ to have statistics governed by an underlying Markov chain so that observations reflecting persistent 'stickiness' can be more effectively modeled. Also, instead of identifying the segmentation sequence $\{\tilde{\delta}_1, \ldots, \tilde{\delta}_t\}$ that maximizes the posterior quantity $pr(\tilde{\delta}_1, \ldots, \tilde{\delta}_t | y_1, \ldots, y_t)$ through dynamic programming, we propose a novel Markov jump linear description that is consistent with (13) to be used by a GPB2 state-estimator:

$$\begin{pmatrix} x_t \\ u^x_{t-1} \end{pmatrix} = \begin{pmatrix} A & B^x_{r_{t-1}} \\ 0 & \tilde{\delta}_{r_{t-1}} \end{pmatrix} \begin{pmatrix} x_{t-1} \\ u^x_{t-2} \end{pmatrix} + \begin{pmatrix} B^c_{r_{t-1}} \\ 1-\tilde{\delta}_{r_{t-1}} \end{pmatrix} u^c_{t-1}$$

$$y_t = \begin{pmatrix} C & 0 \end{pmatrix} \begin{pmatrix} x_t \\ u^x_{t-1} \end{pmatrix} + v_t \tag{14}$$

When $r = 1$, stiction is absent, $\tilde{\delta} = 0$, $B^x = 0$, $B^c = B$. Conversely, when $r = 2$, stiction is present, $\tilde{\delta} = 1$, $B^x = B$, $B^c = 0$.

4.1 Simulation Studies: Mixing Tank

For simulation studies, we consider a simple isothermal mixing-tank (of cross-sectional area $\mathcal{A}$) with an outlet stream whose flow-rate is controlled by a valve (with resistance $\mathcal{R}$):

$$\frac{dm}{dt} = \frac{1}{\mathcal{A}}(q_1 + q_2 - \frac{m}{\mathcal{R}}) \tag{15}$$

The controlled (and also measured) variable is the liquid level (m). The flow-rate of the first stream, q_1, is a measured disturbance whereas that of the other stream (q_2) represents the manipulated variable. A PI controller (with gain K_c, and integral time constant τ_I) is given by:

$$u^c_t = u^c_{t-1} + K_c[e_t - e_{t-1} + \frac{h}{\tau_I} e_t],\ e_t \triangleq l - y_t$$

Here l is the set-point, nominally calibrated to a value of 6. For ease, $\mathcal{A}$, $\mathcal{R}$, K_c, τ_I and the measured disturbance signal q_1, are all set to nominal values of 1. A relatively large value for the stiction band is employed: $d = 0.5$. A sampling time of $h = 0.05$ is employed, resulting in the following parametrization to be used by the state estimator: $A = 0.951$, $B = 0.0488$ and $C = 1$. Measurement noise is set to have a known covariance of $R \triangleq \mathbb{E}[v_t v_t'] = 10^{-4}$. To reflect the high degree of stiction, the transition probability matrix Π is:

$$\begin{pmatrix} 0.01 & 0.99 \\ 0.01 & 0.99 \end{pmatrix} \tag{16}$$

4.2 Results: Estimating Valve Output & Detecting Stiction

Tracking results for a typical closed-loop realization are shown in Fig. 3. The existence of the cycles in u^c and u^x (Fig. 3(a)) is due to the presence of integral action as well as the valve stiction phenomenon. From Fig. 3(a), it can be seen that the proposed methodology is able to estimate u^x. Observing the (a-posteriori) probability (see (5) and Fig. 3(b)) of the first mode (or equivalently the second) via reveals the time instances where a switch occurs (by means of the probability peaks). Doing so represents an effective way for detecting stiction.

5. CONCLUSIONS & FUTURE WORK

The main contribution of this work is to show that the common faults (abrupt jumps/ biases and drifts) can be better modeled and detected by the proposed HMM-based method. Another novel application is in the context of detecting valve stiction, where it is demonstrated that the output of the valve (which is not normally measured) can be effectively estimated. Future work involves extending the problem to large scale systems (*e.g.* a network of unit operations) of industrial interest.

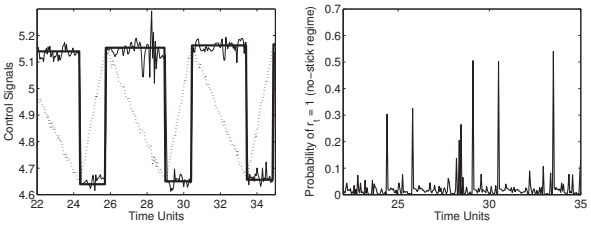

(a) Time series plot of valve input and output and estimate of valve output. Legend: dotted: u^c; bold line: u^x; line: $\hat{u}^x$

(b) Probability of mode 1

Fig. 3. Tracking unmeasured valve output in mixing-tank example.

REFERENCES

Almeida, G.M. and Park, S.W. (2008). Fault detection and diagnosis in the damadaics benchmark actuator systems - a hidden markov model approach. In *17th IFAC World Congress*, 12419. Seoul, Korea.

Bar-Shalom, Y. and Li, X.R. (1993). *Estimation and Tracking: Principles, Techniques, and Software*. Artech House.

Chiang, L., Russell, E., and Braatz, R. (2001). *Fault detection and diagnosis in industrial systems*. Advanced textbooks in control and signal processing. Springer.

Choudhury, M.S., Jain, M., and Shah, S. (2008). Stiction - definition, modeling, detection and quantification. *Journal of Process Control*, 18, 232–243.

Choudhury, M.S., Thornhill, N.F., and Shah, S. (2005). Modeling valve stiction. *Control Engineering Practice*, 13, 641–658.

Huang, B. (2008). Bayesian methods for control loop monitoring and diagnosis. *Journal of process control*, 18, 829–838.

Kesavan, P. and Lee, J.H. (1997). Diagnostic tools for multivariable model-based control. *Industrial & Engineering Chemistry Research*, 36, 2725–2738.

Rabiner, L.R. (1989). A tutorial on hidden markov models and selected applications in speech recognition. *Proceedings of the IEEE*, 77(2), 257–286.

Smyth, P. (1994). Hidden markov models for fault detection in dynamic systems. *Pattern recognition*, 27, 149–164.

Srinivasan, R. and Rengaswamy, R. (2005). Control loop performance assessment: 1. a qualitative approach for stiction diagnosis. *Industrial & Engineering Chemistry Research*, 44, 6708–6718.

Stenman, A., Gustafsson, G., and Forsman, K. (2003). A segementation-based method for detection of stiction in control valves. *International journal of adaptive control and signal processing*, 17, 625–634.

Willsky, A.S. (1976). A survey of design methods for failure detection in dynamic systems. *Automatica*, 12, 601–611.

Wong, W.C. and Lee, J.H. (2007). Disturbance modeling for process control via hidden markov models. In *8th International Symposium on Dynamics and Control of Process Systems*. Cancun, Mexico.

Root Cause Diagnosis of Plantwide Disturbance Using Harmonic Analysis

M. A. A. Shoukat Choudhury * **Shubharthi Barua** * **Mir Abdul Karim** *
Nahid Sanzida *

* *Department of Chemical Engineering, Bangladesh University of Engineering and Technology (BUET), Dhaka - 1000, Bangladesh (e-mail: shoukat@che.buet.ac.bd)*

Abstract: Disturbances in the form of oscillations are usually originated in process plants due to various faults such as sensor faults, valve faults, process faults and controller tuning faults. Many of these faults can be represented as nonlinearities. Faults in the form of nonlinearities may produce oscillations with a fundamental frequency and its harmonics. This study presents a novel method based on the estimated frequencies, amplitudes and phases of the fundamental oscillation and its harmonics to troubleshoot or isolate the root-cause of plantwide or unit-wide disturbances. Once the root cause is known, the oscillations can be eliminated, and the process can be operated more economically and profitably. The successful application of the method has been demonstrated both on simulated and industrial data sets.

Keywords: Plantwide oscillations, nonlinearity, harmonic, control performance, stiction

1. INTRODUCTION

Modern process plants are designed based on the concept of energy and material integration in order to minimize the energy requirements and pollution levels. Large process plants, such as oil refineries, power plants and pulp mills, are complex integrated systems, containing thousands of measurements, hundreds of controllers and tens of recycle streams. The integration of energy and material flow, required for efficiency, results in the spread of fluctuations throughout a plant. The fluctuations force the plant to be operated further from the economic optimum that would otherwise be possible, and thus cause decreased efficiency, lost production and in some cases increased risk. Because of the scale of operation of process plants, a small percentage decrease in productivity has large financial consequences. It can be extremely difficult to pinpoint the cause of these fluctuations. In the most difficult case, the fluctuations are in the form of oscillations. The problem is that oscillations have no defined beginning and end, and so the cause cannot be isolated by standard techniques. Finding the cause of oscillations is a tedious, labor-intensive, often fruitless task. Once the cause is understood, removal of the oscillations is usually straightforward. Therefore, it is important to detect and diagnose the causes of oscillations in a chemical process.

Most of the available techniques for oscillation detection focus on a loop by loop analysis (Hagglund, 1995). Thornhill and co-workers have presented some detection tools that consider the plant-wide nature of oscillations (Thornhill *et al.*, 2003). To detect oscillations in process measurements and identify signals with common oscillatory behavior, use of spectral principal component analysis (Thornhill *et al.*, 2002) or autocorrelation functions (acf) (Thornhill *et al.*, 2003) is suggested. Xia and Howell (2003) have proposed a technique that takes into account the interactions between control loops. Thornhill and Horch (2007) provided an overview of the advances and new direction for solving plantwide oscillation problems. A recent book (Choudhury *et al.*, 2008) provides two chapters on the state of the art technologies for plantwide oscillation detection and diagnosis. This paper demonstrates a method for detecting plantwide oscillations and isolating the root causes of such oscillations.

2. WHAT ARE PLANTWIDE OSCILLATIONS?

When one or more oscillations is generated somewhere in the plant and propagates throughout a whole plant or some units of the plant, such oscillations are termed as plantwide or unitwide oscillations. Oscillation may propagate to many units of the process plants because of the tight heat and mass integration in the plant as well as the presence of recycle streams in the plant. Figure 1 shows an example of a plant-wide oscillation problem. The top panel shows the time trends of 37 variables representing a plant-wide oscillation problem in a refinery (courtesy of South-East Asia Refinery). The bottom panel shows the power spectra of these variables. A common peak in the power spectra plot indicates the presence of a common disturbance or oscillation at a frequency of 0.06 or approximately 17 samples/cycle in many of these variables. The presence of such plant-wide oscillations takes a huge toll from the overall plant economy.

3. DETECTION OF PLANTWIDE OSCILLATIONS

Detection of plantwide oscillation is relatively an easy problem. Often times the plant operators notice some oscillations in the plant, which leads to a deeper investigation of the problem and may cause the invention of a plantwide oscillation of a larger nature. Over the last few years, some studies were carried out to detect plantwide oscillations (Tangirala *et al.*, 2005; Jiang *et al.*, 2006) and to group the similar oscillations together. The following are the brief description of some of these techniques that can be used for detecting plant-wide oscillations.

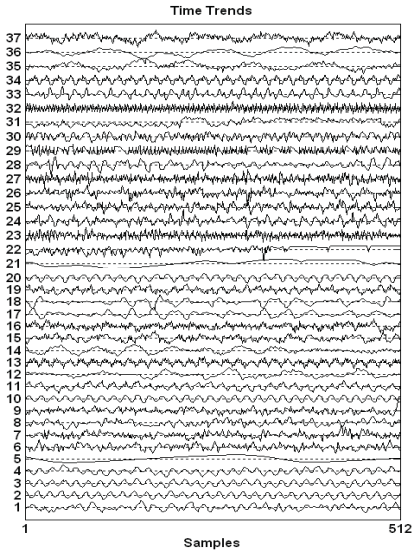

(a) Time Trends

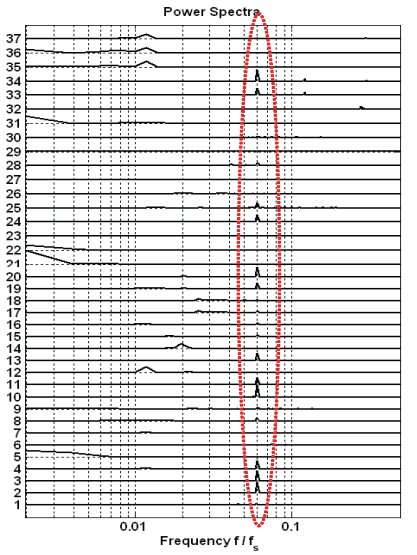

(b) Power Spectra

Fig. 1. Time trends and their power spectra for the South-East Asia Refinery data set

3.1 High Density Plot - An Excellent Visualisation Tool

This plot describes time series data and their spectra in a nice compact form in one plot. From this plot, one can easily visualize the nature of the data and the presence of common oscillation(s) in the data. However, this method is not automated and cannot provide a list of the commonly oscillating variables. Figure 1 is an example of a high density plot.

3.2 Power Spectral Correlation Map (PSCMAP)

The power spectral correlation index (PSCI) is defined as the correlation between the power spectra of two different measurements. It is a measure of the similarity of spectral shapes, i.e., measure of the commonness of frequencies of oscillations. The PSCI for any two spectra $|X_i(\omega)|^2$ and $|X_j(\omega)|^2$ is calculated as

$$PSCI = correlation(|X_i(\omega)|^2, |X_j(\omega)|^2) = \frac{\sum_{\omega_k} |X_i(\omega_k)|^2 |X_j(\omega_k)|^2}{\sqrt{|X_i(\omega_k)|^4 |X_j(\omega_k)|^4}} \quad (1)$$

The PSCI always lies between 0 and 1. In the detection of plantwide oscillations, the objective is to collect variables with similar oscillatory behaviour.

For multivariate processes, the PSCI is a matrix of size $m \times m$, where m is the number of measured variables. In order to provide an effective interpretation of the PSCI, the matrix is plotted as a colour map, which is termed as the power spectral correlation map. An important aspect of this colour map is its ability to automatically re-arrange and group variables together with similar shapes, i.e., variables, which oscillate at a common frequency and have therefore similar values of PSCI. For a detailed discussion on this method, refer to (Tangirala *et al.*, 2005).

3.3 Spectral Envelope Method

In (Jiang *et al.*, 2007), the spectral envelope method has been used to troubleshoot plantwide oscillations.

Let $\mathbf{X}$ is a data matrix of dimension $n \times m$, where n is the number of samples and m is the number of variables. If the covariance matrix of $\mathbf{X}$ is $\mathbf{V_X}$ and the power spectral density (PSD) matrix of $\mathbf{X}$ is $\mathbf{P_X}(\omega)$, then the spectral envelope of $\mathbf{X}$ is defined as:

$$\lambda(\omega) \triangleq \sup_{\beta \neq 0} \{ \frac{\beta^* \mathbf{P_X}(\omega) \beta}{\beta^* \mathbf{V_X} \beta} \} \quad (2)$$

where ω represents frequency and is measured in cycles per unit time, for $-1/2 < \omega \leq 1/2$, the $\lambda(\omega)$ is the spectral envelope at the frequency ω, $\beta(\omega)$ is the optimal scaling vector that maximizes the power (or variance) at the frequency ω, the '*' represents conjugate transpose. The quantity $\lambda(\omega)$ represents the largest portion of the power (or variance) that can be obtained at frequency ω from a scaled series. Jiang et. al (2007) provided a detailed description of this method.

4. DIAGNOSIS TECHNIQUES FOR PLANTWIDE OSCILLATIONS

In a control loop, oscillations arises due to the following primary reasons:

(1) Presence of a poorly tuned controller
(2) An oscillatory external disturbance
(3) Presence of a faulty valve, e.g., a sticky valve or saturated valve.
(4) A highly nonlinear process
(5) Model-plant mismatch for an active MPC controller.

As described, the detection of plant-wide oscillation is relatively an easy problem compared to the diagnosis of its root-cause. Recently a number of papers appeared in the literature describing a few techniques to perform root-cause diagnosis of plant-wide oscillation (Thornhill *et al.*, 2001; Thornhill and Horch, 2007; Choudhury *et al.*, 2007; Jiang *et al.*, 2007; Zang and Howell, 2007; Choudhury *et al.*, 2008).

Oscillations originated in process plants due to various faults such as sensor faults and valve faults may be represented as nonlinearities. Faults in the form of nonlinearity produce oscillations with a fundamental frequency and its harmonics. It is well known that the chemical processes are low-pass filters in nature. Therefore, when a fault propagates away from its origin or source, the higher order harmonics get filtered out.

4.1 Oscillation and Harmonics

Sinusoidal fidelity states that if a sinusoidal input passes through a linear system, the output of the linear system is a sinusoid with the same frequency, but with a different magnitude and phase. A linear system does not produce any new frequency. On the other hand, when a sinusoidal signal with a certain frequency passes through various types of nonlinear systems or functions such as a square function, an exponential function, a logarithmic function and a square-root function, nonlinear systems may generate harmonics in addition to the original fundamental frequency of the input sinusoid. Therefore, nonlinearity induced oscillatory signals generally contain a fundamental frequency and its harmonics. Harmonics are oscillations whose frequencies are integer multiples of the fundamental frequency.

4.2 Fourier Series and Harmonics

Fourier series states that any signal can be represented as a summation of sinusoids. Therefore, any time series, $y(t)$, where, $t \in \Re$ can be represented as

$$y(t) = \sum_{i=0}^{\infty} A_i \, cos(\lambda_i \, t + \phi_i) \tag{3}$$

For a signal containing harmonics, Equation 3 can be rewritten as:

$$y(t) = \sum_{i=0}^{M} A_i \, cos(i * \lambda \, t + \phi_i) + \varepsilon(t) \tag{4}$$

where λ is the fundamental frequency. Each term of equation 4 contains three unknowns namely, amplitude, frequency and phase. The basic idea is to estimate the amplitudes, frequencies and phases for each term of equation 4 for any time series and then examine the relationships among the frequencies to find whether they are harmonically related.

From the experience of the author, for useful application of the harmonic analysis of chemical process data, it suffices to use $M = 5$.

4.3 Total Harmonic Content (THC)

A new index called Total Harmonic Content (THC) can be defined as:

$$THC = n * WHM \tag{5}$$

where n is the number of harmonics found and WHM is the Weighted Harmonic Mean. WHM is defined as

$$WHM = \frac{\sum_{i=1}^{M} w_i}{\sum_{i=1}^{M} \frac{w_i}{A_i}} \tag{6}$$

where w_i is weights and is defined as $w_i = i / \sum_{i=1}^{M} i$ so that the summation of the weights are equal to 1 and the weights for the higher harmonics are large. More weights are given to the higher harmonics because due to the low-pass filtering effect of the chemical processes the higher harmonics get filtered out gradually as the signal propagates away from the source or the root cause.

For plant-wide oscillations, the amplitudes, frequencies and phases of first five term of Equation 4 are estimated. For all tags or variables which have the same fundamental frequency are identified and the Total Harmonic Contents (THC) are calculated using Equation 5. After calculating the THCs, the variables are ranked according to the descending order of THC. The variable with the highest THC is likely to be the root cause. Plant information such as Piping and Instrumentation (P&I) diagrams, Process Flow Diagrams (PFD) and operators' knowledge should be utilised in conjunction with the information provided by THC to confirm the root cause. The chance of being right first time is high. However, if the variables with the maximum value of THC is not the root cause, the variable with the second highest value of THC should be investigated as a root cause. Thus maintenance effort should be started from variable with the maximum value of THC to the variables in the descending order of THC.

Thornhill *et al.* (2001) described a similar method using a distortion factor, which was defined as the ratio of the total power of the signal except the power at the fundamental frequency to the power of the fundamental frequency. They used power spectrum to estimate the distortion factor. The method was successful to a limited extent because the power spectrum is heavily affected by the signal noise. On the other hand, the method described here uses only the amplitudes of the harmonics and the fundamental frequency, therefore the THC is not influenced by the signal noise except some small contamination occurs during the frequency and amplitude estimation.

5. SIMULATION EXAMPLE

This simulation example describes a hypothetical process where a nonlinear function, a square function, followed by some linear filters are present. The simulink block diagram is shown in figure 2. The process was excited by a sinusoid

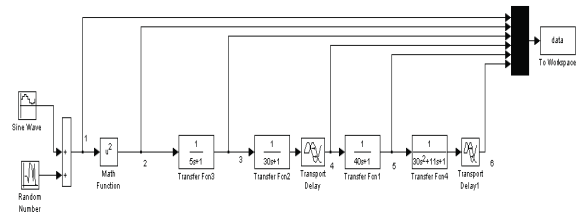

Fig. 2. Simulink block diagram for simple oscillation propagation

with frequency 0.25 rad/sec. Random noise with variance 0.05 was added to the sinusoid. The simulated time series data with their power spectra are shown in Figure 3. From the power spectra, it is hard to see the harmonics generated by the square function because the fundamental frequency has high power. It is interesting to note that for tags 4, 5 and 6, a low frequency oscillation has been developed due to the low pass filtering of the random noise by the process. The fundamental oscillation and its harmonic are gradually filtered out as the signal propagates through the system.

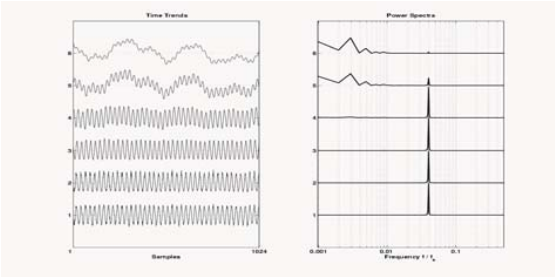

Fig. 3. Simulated data and their power spectra

Table I shows the harmonic analysis of the simulated data. The algorithm correctly identifies the presence of sinusoids in the signal. Five sinusoids are estimated for each signal. For the first signal (tag 1), the magnitude of the first sinusoid is much larger (more than 50 times) than the other sinusoids. The other sinusoids came into play due to the addition of random noise which has power in all frequencies. Research is undergoing to formulate a statistical hypothesis test to detect the presence of true sinusoids. The current algorithm correctly estimates the frequency of the main sinusoid as 0.25 rad/sec. Two dominant sinusoids with frequencies 0.25 and 0.5 rad/sec are estimated for tag 2. For tag 3, the sinusoid with frequency 0.5 rad/sec is present but its power has been decreased because of its attenuation by the first order filter. For tag 4, 5 and 6, the fundamental frequency sinusoid (0.25 rad/sec) has become gradually weak and has been masked with the noise, as evident from the estimated magnitudes shown in the table. The Total Harmonic Content (THC) was calculated for each tag where oscillation with fundamental frequency and its harmonic are found. The maximum THC corresponds to tag 2 indicating the source or root-cause of the propagated oscillation.

6. CASE STUDIES

6.1 Simulation Example - A Non-Linear Dynamic Vinyl Acetate Process

This example describes a simulation case study for root-cause diagnosis of plantwide oscillations using a non-linear dynamic model of a Vinyl Acetate process. The nonlinear dynamic model of the Vinyl Acetate process is published by (Chen *et al.*, 2003) and is freely available from the authors' website. Figure 4 shows a simplified schematic of the Vinyl Acetate Process. The process model contains 246 state variables, 26 manipulated variables and 43 measurements. The process takes approximately 300 minutes time to reach steady state. For details, refer to (Chen *et al.*, 2003).

After the process reached steady state, a 5% stiction ($S = 5$, $J = 2$) in the manipulated variable corresponding to the cooling water flow rate for the separator jacket temperature cooling valve was introduced using the stiction model developed in (Choudhury *et al.*, 2005). Simulation data set consisted of 1000 minutes of data with a sampling time of 15 seconds containing a total of 4000 observations for each variable. The last 1024 data points were used in this analysis in order to avoid transient behaviour due to the sudden introduction of stiction. Figure 5 shows the time trends and power spectra of the manipulated variables of the Vinyl Acetate process. The power spectra show that the variables 1, 2, 4, 5, 6, 7, 8, 9, 11, 12, 14, 19, 21, 22 and 23 are oscillating with a common oscillation at

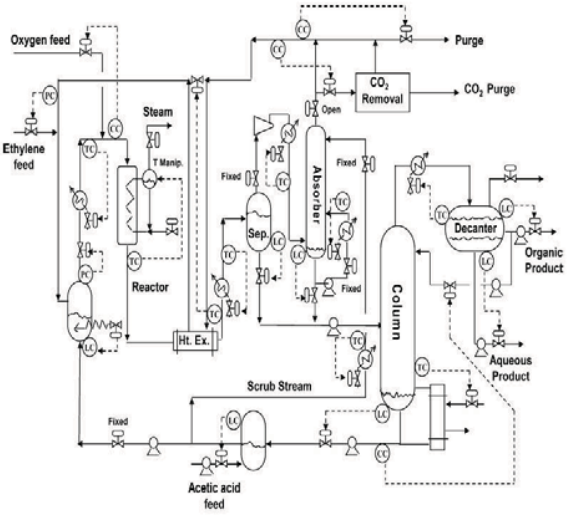

Fig. 4. Schematic of the Vinyl Acetate Process

a normalized frequency of 0.0505. Total Harmonic Content (THC) was calculated for these variables. Figure 6 shows the calculated THC values against the variable or tag number. The maximum THC corresponds to the tag 9 correctly indicating the root-cause of the plantwide oscillation because stiction was introduced in this variable during simulation.

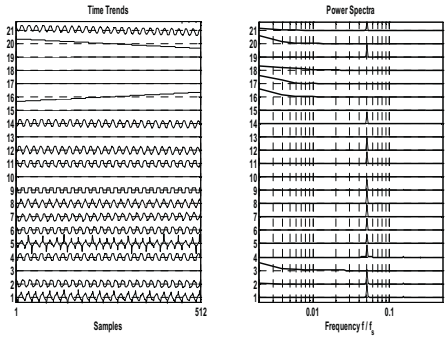

Fig. 5. Time trends and power spectra for the Vinyl Acetate Process Variables

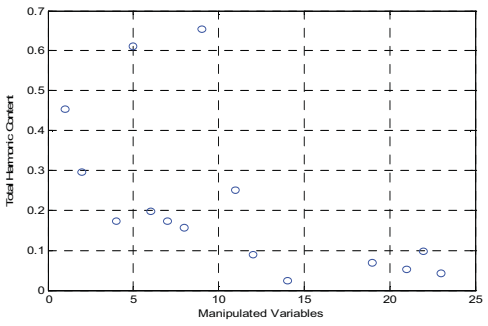

Fig. 6. THC values for the Vinyl Acetate Process Variables

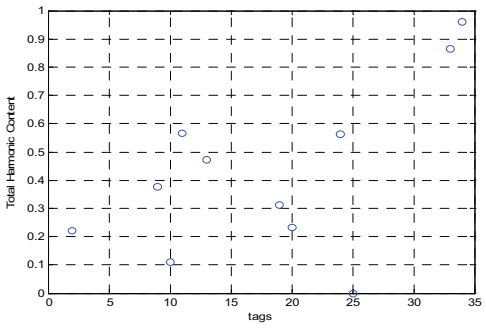

Fig. 7. Total Harmonic Contents (THC) Results for SEA data sets

6.2 An Industrial Example - Application to a Refinery Data Set

The proposed method was applied to a benchmark industrial data set for plantwide oscillations study appeared in the literature such as (Tangirala *et al.*, 2007; Tangirala *et al.*, 2005; Thornhill *et al.*, 2001). The data set, courtesy of a SE Asian Refinery, consists of 512 samples of 37 measurements sampled at 1 min interval. It comprises measurements of temperature, flow, pressure and level loop along with some composition measurements. The time trends of the controller errors are shown in Figure 1(a) and the corresponding power spectra are shown in Figure 1(b). From these figures or using the technique of power spectral correlation map (PSCMAP) described in (Tangirala *et al.*, 2005), it can be found that the tags 2, 3, 4, 8, 9, 10, 11, 13, 15, 16, 17, 19, 20, 24, 25, 28, 33 and 34 are oscillating together with a common frequency of 0.0605 or 17 samples/cycle approximately. All data corresponding to the variables with the common frequency were first normalized so that they had zero-mean and unit variance. Then the amplitudes, frequencies and phases for first five sinusoids were estimated and THC were calculated for these variables. The calculated THC values are plotted against the tag number in Figure 7. The highest THC value corresponds to the tag no. 34, which is the first candidate for the possible root-cause of this plantwide oscillation. In real plant investigation if this tag is not found to be the root cause, then the tag corresponding to next highest value of THC should be investigated. For this case, earlier studies (Thornhill *et al.*, 2001; Tangirala *et al.*, 2005; Tangirala *et al.*, 2007) found tag 34 as the root-cause. Therefore, the proposed THC index correctly detected the root-cause of this plantwide oscillations.

7. CONCLUSIONS AND FUTURE WORKS

This study describes a method to troubleshoot plantwide oscillation using harmonic information present in the signal. The amplitudes, frequencies and phases of the fundamental signal component and its harmonics are estimated and used for the diagnosis of the root-cause of plantwide oscillation. A new index called Total Harmonic Contents (THC) has been defined and used for isolating the root-cause. The method can be automated to facilitate troubleshooting of plantwide oscillation.

8. ACKNOWLEDGEMENTS

All assistance including laboratory, computing and financial supports from Bangladesh University of Engineering and Technology (BUET), Dhaka, Bangladesh are gratefully acknowledged. Authors are also grateful to South-East Asia Refinery for permitting to publish its plant data.

REFERENCES

Chen, Rong, Kedar Dave, Thomas J. McAvoy and Michael Luyben (2003). A nonlinear dynamic model of a vinyl acetate process. *Ind. Eng. Chem. Res.* **42**, 4478–4487.

Choudhury, M. A. A. S., N. F. Thornhill and S. L. Shah (2005). Modelling valve stiction. *Control Engineering Practice* **13**, 641–658.

Choudhury, M. A. A. S., S. L. Shah and N. F. Thornhill (2008). *Diagnosis of Process Nonlinearities and Valve Stiction - Data Driven Approaches*. Springer-Verlag. Germany.

Choudhury, M.A.A.S., V. Kariwala, N.F. Thornhill, H. Douke, S.L. Shah, H. Takadac and J.F. Forbes (2007). Detection and diagnosis of plant-wide oscillations. *Canadian Journal of Chemical Engineering* **85**, 208–219.

Hagglund, T. (1995). A control loop performance monitor. *Control Engineering Practice* **3**(11), 1543–1551.

Jiang, H., M. A. A. S. Choudhury and S. L. Shah (2007). Detection and diagnosis of plantwide oscillations from industrial data using the spectral envelope method. *Journal of Process Control* **17**, 143–155.

Jiang, H., M.A.A.S. Choudhury, S.L. Shah, J. W. Cox and M. A. Paulonis (2006). Detection and diagnosis of plant-wide oscillations via the spectral envelope method. In: *the proceedings of ADCHEM 2006*. Gramado, Brazil. pp. 1139–1144.

Tangirala, A. K., J. Kanodia and S. L. Shah (2007). Non-negative matrix factorization for detection of plant-wide oscillations. *Ind. Eng. Chem. Res.* **46**, 801–817.

Tangirala, A.K., S.L. Shah and N.F. Thornhill (2005). PSCMAP: A new tool for plantwide oscillation detection. *Journal of Process Control* **15**, 931–941.

Thornhill, N. F. and A. Horch (2007). Advances and new directions in plant-wide disturbance detection and diagnosis. *Control Engineering Practice* **15**, 1196–1206.

Thornhill, N. F., B. Huang and H. Zhang (2003). Detection of multiple oscillations in control loops. *Journal of Process Control* **13**, 91–100.

Thornhill, N. F., S. L. Shah and B. Huang (2001). Detection of distributed oscillations and root-cause diagnosis. In: *Preprints of CHEMFAS-4 IFAC*. Korea. pp. 167–172.

Thornhill, N. F., S. L. Shah, B. Huang and A. Vishnubhotla (2002). Spectral principal component analysis of dynamic process data. *Control Engineering Practice* **10**, 833–846.

Xia, C. and J. Howell (2003). Loop status monitoring and fault localisation. *Journal of Process Control* **13**, 679–691.

Zang, X. and J. Howell (2007). Isolating the source of whole-plant oscillations through bi-amplitude ratio analysis. *Control Engineering Practice* **15**, 69–76.

Table 1. Harmonic analysis results for simple oscillation propagation example

Tags	λ_1	λ_2	λ_3	λ_4	λ_5	A_1	A_2	A_3	A_4	A_5	ϕ_1	ϕ_2	ϕ_3	ϕ_4	ϕ_5	RESS	λ_1/λ_1	λ_2/λ_1	λ_3/λ_1	λ_4/λ_1	λ_5/λ_1	THC
1	**0.25**	**1.25**	2.88	1.95	1.22	**1.394**	**0.028**	0.027	0.023	0.023	2.06	0.39	2.17	-2.85	-0.74	24.40	1.0	5.0	11.5	8.0	4.9	3.91
2	**0.25**	**0.50**	2.88	**1.25**	1.99	**1.387**	**0.130**	0.028	**0.028**	0.023	2.06	-2.13	2.27	0.33	-3.01	26.67	1.0	2.0	11.5	5.0	8.0	8.96
3	**0.25**	**0.50**	0.02	0.06	0.03	**1.409**	**0.079**	0.028	0.026	0.024	1.15	2.96	2.46	2.79	0.98	6.08	1.0	2.0	0.1	0.2	0.1	1.91
4	**0.25**	0.02	0.03	0.00	0.05	**1.367**	0.206	0.132	0.110	0.100	-0.5	3 2.17	0.82	-0.95	1.98	21.30	1.0	0.1	0.1	0.0	0.2	0.73
5	0.02	0.25	0.00	0.03	0.02	0.864	0.688	0.545	0.407	0.301	1.66	-1.97	-1.20	0.04	-1.06	83.98	1.0	15.2	0.3	1.8	1.4	
6	0.02	0.00	0.03	0.02	0.25	0.953	0.682	0.454	0.336	0.264	1.30	-1.17	-0.33	-1.31	1.13	88.34	1.0	0.2	1.7	1.4	15.1	

Systematic Development of Automata Generated Languages for Fault Diagnosis in Continuous Chemical Processes

Chuei-Tin Chang. Jung-Yang Chen

National Cheng Kung University, Tainan, Taiwan 70101,
ROC (Tel:886-6-275-7575 ext. 62663; e-mail: ctchang@mail.ncku.edu.tw).

Abstract: A SDG-based simulation procedure is presented in this study to qualitatively predict all possible effects of one or more fault propagating in a given process system. All possible state evolution behaviors are characterized with an automaton model. By selecting a set of on-line sensors, the corresponding diagnoser can be constructed and the diagnosability of every fault origin can be determined accordingly. Furthermore, it is also possible to construct a formal diagnostic language on the basis of this diagnoser. Every string (word) in the language is then encoded into an IF-THEN rule and, consequently, a comprehensive fuzzy inference system can be synthesized for on-line diagnosis. The feasibility of this approach is demonstrated with a simple example in this paper.

Keywords: fault diagnosis, automata, signed directed graph, formal language, fuzzy logic.

1. INTRODUCTION

The fault diagnosis methods have been widely recognized as indispensable tools for enhancing process safety. Generally speaking, they could be classified into three distinct groups, i.e., the model based approaches, the knowledge based approaches, and the data-analysis based approaches (Venkatasubramanian et al., 2003a, b). However, in order to carry out these strategies on-line, it is usually necessary to first analyze the historical data and/or operational experiences obtained during *every* serious accident. This requirement cannot always be satisfied in practice.

To circumvent the above drawbacks, a qualitative cause-and-effect model, i.e., the signed directed graph (SDG), is used in the present study to characterize fault propagation mechanisms. The advantage of this modelling approach is mainly due to the fact that the causal relations in process systems can always be established according to generic engineering principles without any quantitative knowledge. On the other hand, it should be noted that such causal models are basically static in nature. Many SDG-based fault identification techniques were therefore implemented on the basis of the *steady-state* symptoms only, e.g., Maurya et al. (2006). Since the effects of fault(s) and/or failure(s) usually propagate throughout the entire system dynamically in sequence, a series of intermediate events may occur before the inception of catastrophic consequences. Thus, the performance of a qualitative diagnosis scheme should be evaluated not only in terms of its correctness but also its timeliness.

To enhance diagnostic efficiency, it is obviously necessary to consider the precedence order (in time) of various fault propagation effects derived from the qualitative models. Extensive studies have already been carried out to develop effective diagnosis strategies by incorporating both the eventual symptoms and also their *occurrence order* into a fuzzy inference system (FIS). This approach has been applied successfully to a number of loop-free processes (Chang et al., 2002) and also to systems with feedback and/or feed forward control loops (Chang and Chang, 2003; Chen and Chang, 2006; 2007).

Despite the fact that diagnostic performance can be significantly improved with the aforementioned technique, the representation, analysis and synthesis of inference systems are still very cumbersome. In particular, many different versions of the symptom occurrence orders can often be deduced from a single fault origin on the basis of SDG model. Manual enumeration of all such scenarios for all origins may become intractable even for a moderately complex system. Furthermore, the diagnosability issues concerning the resulting FIS have never been systematically addressed in the past. Thus, there is a definite need to develop a unified theoretical framework to extract the intrinsic features of dynamic fault propagation mechanisms. Our concern here is primarily with the sequence of system states visited after the occurrence of fault origin(s) and also the associated events causing the state transitions. A systematic procedure is proposed in this paper to construct automata and language models for the purpose of representing these sequences accurately and succinctly. As a result, additional insights can be revealed and, also, more compact inference rules can be produced accordingly. A simple example is provided at the end of this paper to demonstrate the feasibility and effectiveness of the proposed procedures for FIS synthesis and for fault diagnosis.

2. AUTOMATA CONSTRUCTON

2.1 Qualitative Simulation Procedure

Although other qualitative models may be equally acceptable, the SDG is adopted in the present study to simulate (or predict) the effects of faults and failures. This is due to the fact that the needed implementation procedure is conceptually straightforward. Notice first that the fault origins can usually be associated with the primal nodes, i.e., the nodes without inputs. A set of five values, i.e., {-10, -1, 0, +1, +10}, may be assigned to every node in the digraph to represent deviation from the normal value of corresponding variable. The value 0 represents the normal steady state. The negative values are used to denote the lower-than-normal states and the positive values signify the opposite. The magnitudes of non-zero deviations, i.e., 1 or 10, can be interpreted qualitatively as "small" and "large" respectively. The causal relation between two variables can be characterized with a directed arc and the corresponding gain. Each gain may also assume one of the five qualitative values mentioned above. The output value of every arc in digraph can be computed with the gain and its input value according to the following equation:

$$v_{out} = \begin{cases} g \times v_{in} & \text{if } -10 \le g \times v_{in} \le +10 \\ +10 & \text{if } g \times v_{in} > +10 \\ -10 & \text{if } g \times v_{in} < -10 \end{cases} \quad (1)$$

where g, v_{in} and v_{out} denote respectively the gain, input and output values. It is obvious that the deviation values of all variables affected by one or more fault origin can always be computed with this formula, but the time at which each deviation occurs is indeterminable. Without the reference of time in the SDG-based simulation results, it can nonetheless be safely assumed that *the change in an input variable should always occur earlier than those in its outputs*. In essence, this is the most basic assumption adopted in this study. Notice that, if the precedence order of various fault propagation effects is to be considered in fault diagnosis, a large number of different versions of qualitative simulation results may be generated accordingly. All such scenarios can be captured with the automaton model described in the sequel.

2.2 System Automata

A formal definition of a deterministic automaton $\mathcal{A}$ can be found in Cassandras and Lafortune (1999). Specifically, it is a six-tuple

$$\mathcal{A} = (\mathbb{X}, \mathbb{E}, f, \Gamma, x_0, \mathbb{X}_m) \quad (2)$$

where, $\mathbb{X}$ is the set of system states; $\mathbb{E}$ is the finite set of events associated with the transitions in automaton; $f : \mathbb{X} \times \mathbb{E} \to \mathbb{X}$ is the transition function; $\Gamma : \mathbb{X} \to 2^{\mathbb{E}}$ is the active event function; x_0 is the initial system state; $\mathbb{X}_m \subseteq \mathbb{X}$ is the set of marked states. In the present application, each system state $x \in \mathbb{X}$ is either a collection of node values at a particular instance after an initiating failure occurs or the initial state itself. Every event $e \in \mathbb{E}$ represents a previously nonexistent fault effect. Notice that the precedence order of these events must be consistent with the basic assumption mentioned above. The active event function $\Gamma(x)$ is used to specify the events which could change the system state x, while the transition function $f(x,e)$ is used for stipulating the resulting state caused by $e \in \Gamma(x)$. Finally, it should be noted that the initial state x_0 in this study is always associated with the *normal* condition and the set $\mathbb{X}_m$ contains the final steady states reached in all possible fault propagation scenarios.

To facilitate illustration of the automaton construction steps, let us consider the most fundamental digraph configuration, i.e., tree. More specifically, let us use the fictitious SDG model in Figure 1 as an example and also assume that a positive deviation in the upstream variable d, i.e., $d(+1)$, is the only possible fault origin in this case. Notice that, although the precedence order of any two effects along the same branch path in this digraph can be uniquely identified with the proposed qualitative simulation procedure, the order of two distinct events located on *separate* branches should be considered as indeterminable. The corresponding automaton can thus be described with the state transition diagram presented in Figure 2. Every system state here is characterized with a collection of the qualitative values of all variables in the digraph and all of them are listed in Table 1. Three equally possible event sequences between the initial and final system states can be identified from this automaton model, i.e.,

1. $d(+1)x(+1)y(+1)z(-1)u(+1)$,
2. $d(+1)x(+1)y(+1)u(+1)z(-1)$,
3. $d(+1)x(+1)u(+1)\ y(+1)\ z(-1)$.

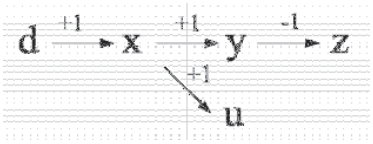

Fig. 1. A tree-shaped SDG model.

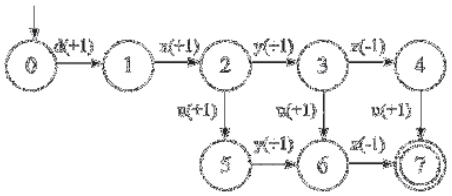

Fig. 2. The state transition diagram of automaton derived from Figure 1.

The automaton resulting from a "large" disturbance can be obtained by following a similar procedure. An auxiliary assumption is introduced in this work to facilitate an accurate description of the fault propagation mechanism, i.e., *the smaller deviation of a process variable must occur before*

reaching a larger one of the same variable. Thus, the automaton in Figure 2 can be revised to incorporate this requirement (see Figure 3).

Table 1. System states in Figure 2.

State	*d*	*x*	*y*	*z*	*u*
0	0	0	0	0	0
1	+1	0	0	0	0
2	+1	+1	0	0	0
3	+1	+1	+1	0	0
4	+1	+1	+1	-1	0
5	+1	+1	0	0	+1
6	+1	+1	+1	0	+1
7	+1	+1	+1	-1	+1

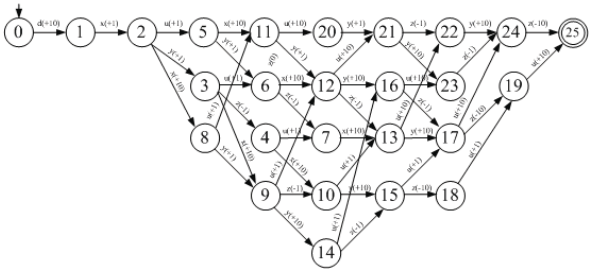

Fig. 3. The automaton resulted from $d(+10)$ in Figure 1

2.3 Diagnoser and Diagnisability

In realistic applications, the fault origins (i.e., failures or upsets) and some of the process variables cannot be monitored on-line. Thus, the event set of an automaton model can be further divided into the observable and unobservable event subsets, i.e., $\mathbb{E} = \mathbb{E}_o \bigcup \mathbb{E}_{uo}$. To check diagnosability of each fault origin and also facilitate diagnostic inference with the available sensors, the system automaton $\mathcal{A}$ should be converted to a *diagnoser* $\mathcal{A}_{diag}$, which is in essence a transformed automaton with the observable subset $\mathbb{E}_o$ as its event set. Although a systematic construction procedure has already been developed by Sampath et al. (1996) for the discrete event systems in general, the diagnosers for the present applications are built with an intuitive but more convenient alternative approach. Specifically, if a state is reached immediately after an unobservable event, then this state is merged with its predecessor(s) in the original automaton model. For example, let us assume that $d(+1)$ is the fault origin and $y(+1)$ is not observable in Figure 2. The corresponding diagnoser can be easily obtained by applying the aforementioned principle (see Figure 4). The numerical node labels here are the same as those in Figure 2, while the subscript of each label is used to reflect whether or not the fault origin has occurred at the corresponding state.

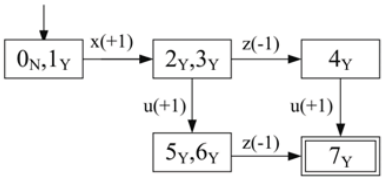

Fig. 4. The diagnoser obtained by assuming $y(+1)$ in Figure 2 is unobservable.

It should be noted that this construction method is applicable even when multiple scenarios are possible. For example, let us consider the SDG model in Figure 5 and assume that there are two measured variables, i.e., y and z , and four potential fault origins, i.e., (1) $d_x(+1)$, (2) $d_y(+1)$, (3) $d_z(+1)$ and (4) $d_u(+1)$.

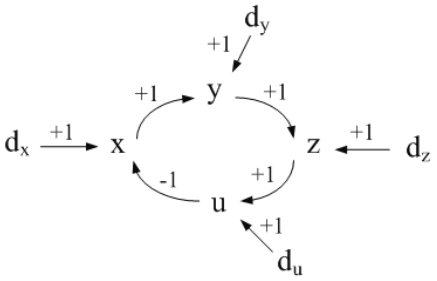

Fig. 5. A SDG model with negative feedback loop

The automaton model of this system and the corresponding diagnoser can be found in Figures 6(A) and 6(B) respectively. Obviously, the issue of diagnosability becomes important in this situation. Although the formal necessary and sufficient conditions of system diagnosability has also been derived and proven rigorously by Sampath et al. (1995), the identifiability of each fault origin in our studies can be determined simply by inspecting the diagnoser. In particular, the diagnosability of a fault origin can be established if it is the unique cause of at least one diagnoser state. Otherwise, the corresponding on-line symptoms should be indistinguishable from those of one or more scenarios caused by other origins. It can be determined on the basis of this criterion that fault origins (3) and (4) are both diagnosable, while the observable event sequences in scenarios (1) and (2) are identical and thus cannot be differentiated from one another.

The feasibility of this simple checking procedure is attributed mainly to the fact that the automata used in the present applications form a special subclass of those for modelling the discrete event systems. More specifically, since the *continuous* chemical processes are considered in this work, the corresponding automata can be characterized with the following unique features:

1. The initial automaton state is always associated with the normal system condition.
2. Every initial state transition is triggered by

failure event(s).

3. Recurrence of system state is not possible, i.e., the automaton is free of any feedback loop. Notice that this feature is due to our assumption that a final steady state is reachable in every possible scenario.

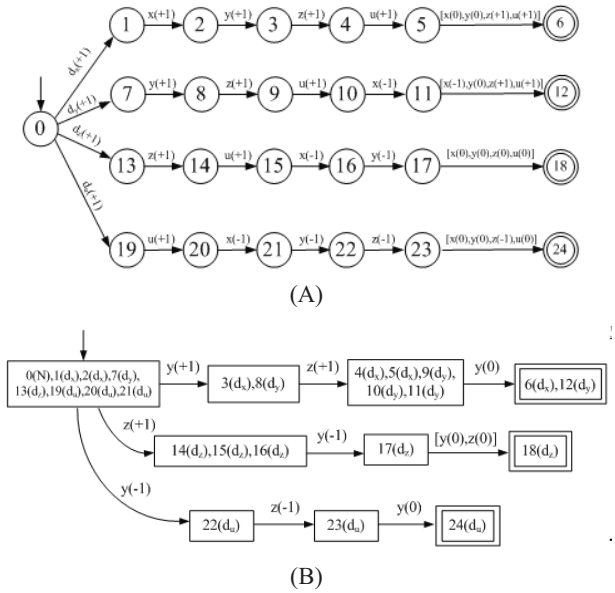

Fig 6. The automaton (A) and diagnoser (B) constructed according to the SDG in Figure 5

3. LANUGAE GENERATION

A *language* $\mathfrak{L}$ is regarded in this work as a collection of finite-length event sequences. These sequences are referred to as *strings* or *words*. The set of all possible events (alphabets) is the set $\mathbb{E}$ defined in equation (2). An additional set $\mathbb{E}^*$ is also utilized here to include all possible strings (including the empty string ε) constructed over $\mathbb{E}$. Thus, it is obvious that $\mathfrak{L} \subseteq \mathbb{E}^*$.

Since fault diagnosis can only be performed according to the on-line symptoms, the automaton $\mathcal{A}_{diag}$ (not $\mathcal{A}$) is used to generate a diagnostic language for the purpose of enumerating all *observable* event sequences caused by a given fault origin. Specifically,

$$\mathfrak{L}\left(\mathcal{A}_{diag}\right)=\left\{s\in \mathbb{E}^* \mid f\left(x_0,s\right) \text{ is defined by } \mathcal{A}_{diag}\right\} \quad (3)$$

The transition function $f\left(x_0,s\right)$ here can be evaluated recursively according to the following rules:

$$\begin{aligned} f\left(x,\varepsilon\right)&=x \\ f\left(x,se\right)&=f\left(f\left(x,s\right),e\right) \end{aligned} \quad (4)$$

where, $s\in \mathbb{E}^*$ and $e\in \mathbb{E}$. In addition, the *marked* language of automaton $\mathcal{A}_{diag}$ can be defined as

$$\mathfrak{L}_{\mathrm{m}}\left(\mathcal{A}_{diag}\right)=\left\{s\in \mathfrak{L}\left(\mathcal{A}_{diag}\right) \mid f\left(x_0,s\right)\in \mathbb{X}_m\right\} \quad (5)$$

Notice that an automaton-based language can be synthesized by first identifying the longest strings and then obtaining all their *prefixes*. Since the marked states in the present application are always terminal, $\mathfrak{L}\left(\mathcal{A}_{diag}\right)$ can be produced by taking the prefix closure of $\mathfrak{L}_{\mathrm{m}}\left(\mathcal{A}_{diag}\right)$ (Cassandras and Lafortune, 1999), i.e.

$$\mathfrak{L}\left(\mathcal{A}_{diag}\right)=\overline{\mathfrak{L}_{\mathrm{m}}\left(\mathcal{A}_{diag}\right)} \quad (6)$$

where, $\overline{\mathfrak{L}_{\mathrm{m}}\left(\mathcal{A}_{diag}\right)}$ denotes the set of all prefixes of the strings in $\mathfrak{L}_{\mathrm{m}}\left(\mathcal{A}_{diag}\right)$. From equation (6), it can be shown that every diagnoser considered in this study must be *nonblocking*, i.e., any string $s\in \mathfrak{L}\left(A_{diag}\right)$ can be always extended by another string t such that $st\in \mathfrak{L}_{\mathrm{m}}\left(A_{diag}\right)$.

Let us use the diagnoser in Figure 4 as an example to illustrate the proposed approach. The two languages marked and generated respectively by $\mathcal{A}_{diag}$ in this case should be

$$\mathfrak{L}_{\mathrm{m}}\left(\mathcal{A}_{diag}\right)=\left\{x(+1)z(-1)u(+1),\ x(+1)u(+1)z(-1)\right\} \quad (7)$$

$$\mathfrak{L}\left(\mathcal{A}_{diag}\right)=\left\{\begin{matrix}\varepsilon, x(+1),\ x(+1)z(-1),\ x(+1)u(+1),\\ x(+1)z(-1)u(+1),\ x(+1)u(+1)z(-1)\end{matrix}\right\} \quad (8)$$

If the possibilities of multiple fault origins are incorporated in a diagnoser, then it is necessary to further generate a sublanguage specific to every fault origin, i.e.

$$\mathfrak{L}\left(\mathcal{A}_{diag}\right)=\bigcup_i \mathfrak{L}\left(\mathcal{A}_{diag}^{F_i}\right) \quad (9)$$

where, $\mathcal{A}_{diag}^{F_i}$ is an automaton obtained by removing all the abnormal states in A_{diag} which are *not* caused by the i th fault origin F_i. The marked sublanguages of the fault origins in Figure 6(B) can be easily produced with this method, i.e.,

$$\mathfrak{L}_{\mathrm{m}}\left(\mathcal{A}_{diag}^{d_x(+1)}\right)=\mathfrak{L}_{\mathrm{m}}\left(\mathcal{A}_{diag}^{d_y(+1)}\right)=\left\{y(+1)z(+1)y(0)\right\} \quad (10)$$

$$\mathfrak{L}_{\mathrm{m}}\left(\mathcal{A}_{diag}^{d_z(+1)}\right)=\left\{z(+1)y(-1)\left[y(0),z(0)\right]\right\} \quad (11)$$

$$\mathfrak{L}_{\mathrm{m}}\left(\mathcal{A}_{diag}^{d_u(+1)}\right)=\left\{y(-1)z(-1)y(0)\right\} \quad (12)$$

4. FUZZY INFERENCE SYSTEM

Every string in $\mathfrak{L}\left(\mathcal{A}_{diag}\right)$ is encoded with an IF-THEN rule in this work. These rules can be incorporated in a fuzzy inference system to evaluate the *existence potential* of the corresponding fault origin. In particular, if at least one event sequence in the marked sublanguage $\mathfrak{L}_{\mathrm{m}}\left(\mathcal{A}_{diag}^{F_i}\right)$ can be confirmed, then it is highly possible that they are caused by the corresponding fault origin F_i. To assert such a belief, the fuzzy conclusion "cs_i is OCR" is adopted in the inference rule, where OCR is the linguistic value of the *occurrence index* cs_i reflecting the highest confidence level in confirming the existence of F_i. More specifically, this rule can be written as

$$\text{IF } s_o \in \mathfrak{L}_{\mathrm{m}}\left(\mathcal{A}_{diag}^{F_i}\right) \text{ THEN } cs_i = \text{OCR}$$

where s_o denotes the observed event string.

On the other hand, it is certainly reasonable to disregard the possibility of a fault if none of the corresponding event strings in $\mathfrak{L}\left(\mathcal{A}_{diag}^{F_i}\right)$ can be observed. Thus, the diagnosis for this scenario should be "cs_i is NOC", where NOC is the linguistic value representing the lowest level of confidence. In other words,

$$\text{IF } s_o \notin \mathfrak{L}\left(\mathcal{A}_{diag}^{F_i}\right) \text{ THEN } cs_i = \text{NOC}$$

The diagnostic conclusion for each of the remaining strings should be UCT_ℓ, i.e., uncertain with confidence level ℓ. In particular, this rule can be written as

$$\text{IF } s_o \in \mathfrak{L}\left(\mathcal{A}_{diag}^{F_i}\right) \setminus \mathfrak{L}_{\mathrm{m}}\left(\mathcal{A}_{diag}^{F_i}\right) \text{ THEN } cs_i = \text{UCT}_\ell$$

In this study, the confidence level ℓ in confirming the existence of the root cause(s) is assumed to be proportional to the string length. The highest possible confidence level is of course assigned to the strings in $\mathfrak{L}_{\mathrm{m}}\left(\mathcal{A}_{diag}^{F_i}\right)$.

Finally, it should be noted that the aforementioned IF-THEN rules can be implemented with the two-layer fuzzy inference framework developed by Chen and Chang (2006).

5. CASE STUDY

Let us consider the level control system presented in Figure 7 and the corresponding SDG model in Figure 8. All on-line signals, i.e., s_5 - s_8, are assumed to be available for fault diagnosis in this example. For illustration convenience, only two possible scenarios are considered here, i.e., (1) a moderate (controllable) increase in the flow rate of stream 3 while control valve CV-01 sticks and (2) an uncontrollable increase in the flow rate of stream 3.

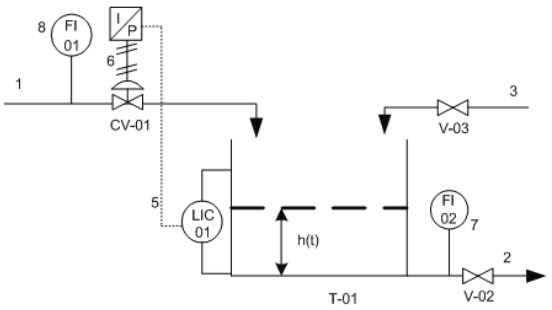

Fig. 7. A level-control system.

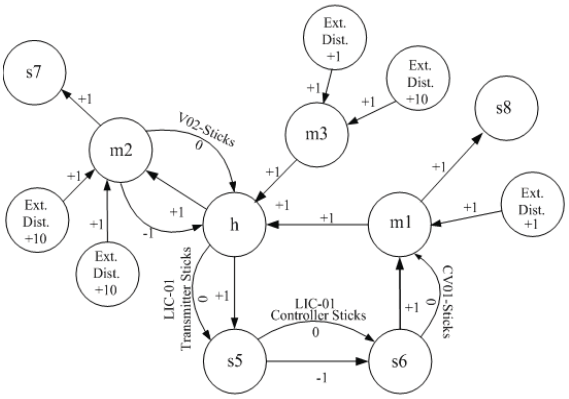

Fig. 8. The SDG model of level-control system.

The diagnoser for these two fault origins can be found in Figure 9. Notice that this automaton is presented in two parts for clarity. States 0 and $0'$ are used to represent the combined states of the normal condition and the system conditions reached immediately after the occurrence of fault origin in scenario 1 and scenario 2 respectively. These two states, i.e., 0 and $0'$, should be lumped into a single one in the actual diagnoser.

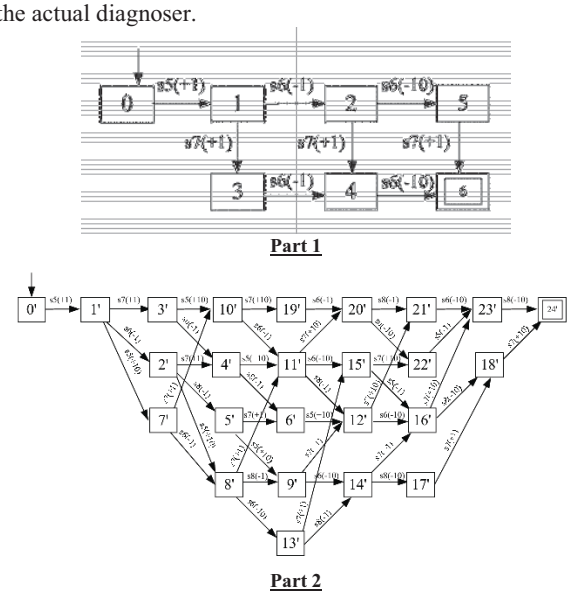

Fig. 9. The diagnoser used for level-control system

To verify the effectiveness of the proposed fault diagnosis approach, extensive numerical simulation studies have been carried out in this work. The on-line measurement data of all fault propagation scenarios were generated with SIMULINK. These data were then used in Sugeno's inference procedure with the fuzzy-logic module of MATLAB toolbox. As an example, let us first examine the occurrence index of the event $m3(+10)$ in scenario 2. It can be observed from Figure 10(A) that the diagnosis is clearly swift and quite accurate. Specifically, the existence of fault origin is detected almost immediately and fully confirmed at about 500 second after its introduction. On the other hand, the occurrence index of the incorrectly assumed fault origin in scenario 2, i.e., $m3(+10)$, is presented in Figure 10(B). Notice that the nonzero occurrence index in the period between 1000 and 2600 sec can be attributed to the fact that the observed event strings caused by the two fault origins can be matched partially during the *initial stage*. More specifically, the set of matched strings is

$$\left\{\overline{s5(+1)s6(-1)s7(+1)}, \overline{s5(+1)s7(+1)s6(-1)}\right\}$$

As the on-line symptoms developed further, none of the longer strings generated by the first part of automaton in Figure 9 can be used to characterize the measurement data obtained after 2600 sec and thus the occurrence possibility of the second fault origin was rejected with the proposed inference mechanisms (Chen and Chang, 2006)..

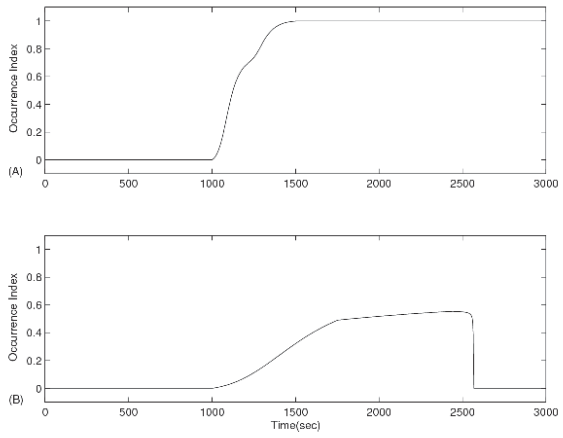

Fig. 10. Diagnosis results of two different scenarios in the level control system. (A) Occurrence index of the second fault origin using simulation data obtained by introducing the same event; (B) Occurrence index of the second fault origin using simulation data obtained by introducing the basic events in the first scenario.

6. CONCLUSIONS

In this study, a SDG-based reasoning procedure is proposed to qualitatively predict all possible symptom patterns and also their progression sequences. These intrinsic features of symptom evolution patterns are captured with automata and language models. The resulting IF-THEN rules can be incorporated in a fuzzy inference system and this system can be installed on-line to identify not only the locations of fault origins but also their magnitude levels with relatively high resolution.

REFERENCES

Cassandras, C.G., and Lafortune S. (1999). *Introduction to Discrete Event Systems*, Kluwer Academic Publisher. Boston.

Chang, S.Y., and Chang, C.T. (2003). A fuzzy-logic based fault diagnosis strategy for process control loops. *Chem. Eng. Sci.,* 58, 3395.

Chang, S.Y., Lin, C.R., and Chang, C.T. (2002). A fuzzy diagnosis approach using dynamic fault trees. *Chem. Eng. Sci.,* 57, 2971.

Chen, J.Y., and Chang, C.T. (2006). Fuzzy diagnosis method for control systems with coupled feed forward and feedback loops. *Chem. Eng. Sci.,* 61, 3105.

Chen, J.Y., and Chang, C.T. (2007). Systematic enumeration of fuzzy diagnosis rules for identifying multiple faults in chemical processes. *Ind. Eng. Chem. Res.,* 46, 3635.

Ju, S.N., Chen, C.L., and Chang, C.T. (2004). Constructing fault trees for advanced process control systems - application to cascade control loops. *IEEE Trans on Reliab*., 53, 43.

Maurya, M.R., Rengaswamy, R., and Venkatasubramanian, V. (2004). Application of signed digraph-based analysis for fault diagnosis chemical process flowsheets. *Engineering Applications of Artificial Intelligence.,* 17, 501.

Maurya, M.R., Rengaswamy, R., and Venkatasubramanian, V. (2006). A signed directed graph-based systematic framework for steady state malfunction diagnosis control loops. *Chem. Eng. Sci.*, 61, 1790.

Oyeleye, O.O., and Kramer, M.A. (1988). Qualitative simulation of chemical process systems: steady-state analysis. *AIChE Journal.*, 34, 1441.

Sampath, M., Sengupta, R., Lafortune, S., Sinnamohideen, K., and Teneketzis, D. (1996). Failure Diagnosis using discrete-event models. *IEEE Trans. Cont. Syst. Tech.,* 4, 105.

Sampath, M., Sengupta, R., Lafortune, S., Sinnamohideen, K., and Teneketzis, D. (1995). Diagnosability of discrete-event systems. *IEEE Trans. Auto. Cont*., 40, 1555.

Venkatasubramanian. V., Rengaswamy, R., Yin, K., and Kavuri, S. (2003a). A review of process fault detection and diagnosis, part 1: quantitative model based methods. *Comput & Chem Engng.*, 27, 293.

Venkatasubramanian, V., Rengaswamy, R., and Kavuri, S. (2003b). A review of process fault detection and diagnosis, part 2: qualitative model and search strategies. *Comput. & Chem. Engng.*, 27, 313.

Sensor Location for Effective Fault Diagnosis in Micro Chemical Processes

Osamu Tonomura*. Satoshi Nagahara. Jun-ichi Kano. Manabu Kano. Shinji Hasebe

Department of Chemical Engineering, Kyoto University, Kyoto, Japan, (*e-mail: tonomura@cheme.kyoto-u.ac.jp).

Abstract: It is clear from worldwide research that micro chemical processes (MCPs) offer a unique approach to the spatial and temporal control of chemical reactions. The well-known advantages of MCPs are often counterbalanced by serious faults such as channel blockage and catalyst deterioration. To realize stable long-term operation of MCPs, it is necessary to develop a monitoring system that can detect and diagnose these faults. In this work, a physical model-based process monitoring system for a tubular microreactor is developed. A state space model is derived by using the orthogonal collocation method, and the extended Kalman filter is used as an observer. The optimal sensor locations are determined so that unknown parameters such as catalyst effectiveness can be estimated most accurately. In addition, the validity of the conventional observability measures in solving the sensor location problems of MCPs is assessed.

Keywords: Microreactor, Sensor location, Process monitoring, Parameter estimation, Fault diagnosis.

1. INTRODUCTION

In microspaces, viscous force, surface tension, conduction heat transfer, and molecular diffusion become dominant. In addition, the contact time and interfacial area between fluids are precisely controlled. These features achievable in microspaces enable us to handle highly exothermic and rapid reactions and to produce fine particles with narrow size distribution (Hessel et al., 2005). However, the above features are often counterbalanced by serious faults such as channel blockage and catalyst deterioration. To realize stable long-term operation of micro chemical processes (MCPs), it is necessary to develop a monitoring and control system suitable for MCPs. Such a system is usually based on the measurements available from installed sensors. However, the existing miniaturized sensors are too expensive in terms of the initial as well as the maintenance costs. In addition, the sensors connected to microreactors in series are not allowed to observe the internal states of microreactors, because they generate dead volume and affect the flow conditions. Therefore, it is important to develop a monitoring system that can estimate unmeasured variables and unknown parameters from a few indirect on-line measurements and quickly detect and diagnose faults. Thus, our technical imperatives are to develop MCPs-oriented sensing devices, to develop a system that can estimate the internal states of MCPs, to propose an approach for effective fault detection and diagnosis in MCPs, etc. So far, there are only few papers about fault detection and diagnosis of MCPs (Kano et al., 2007). In this work, optimal sensor locations for effective fault diagnosis of a tubular microreactor (TMR) are investigated. In addition, the validity of the conventional observability measures in solving the sensor location problems of the TMR is assessed. Finally, operation policies and control structures for MCPs with an external numbering-up structure are investigated. Two types of operation policies, total flow control and pressure drop control, are compared from the viewpoint of flow uniformity when blockage occurs.

2. TUBULAR MICROREACTOR (TMR)

Applications of TMRs can be found in nitration of aromatic compounds, radical polymerization reactions, etc.

2.1 Concept of Fault Detection and Diagnosis

The following method to detect and diagnose faults in TMRs is proposed. A limited number of temperature sensors are embedded in walls of TMRs. Wall temperatures are used to estimate unknown parameters such as catalyst effectiveness. At the same time, the optimal sensor location problems have to be solved so that unknown parameters can be estimated most accurately. Previous similar researches on conventional reactors often neglect heat conduction inside walls when constructing their process models. In case of TMRs, it is crucial to rigorously model the wall heat conduction due to high volume ratio of walls to channels. In addition, there are two methods to formulate process models: empirical model-based method and physical model-based method. In this work, the latter method is adopted.

2.2 Physical Model

Figure 1 shows a schematic diagram of a TMR. Premixed reactants, A and B, are fed into the inner tube, and a coolant is fed into the outer tube. Each flow is assumed to be plug

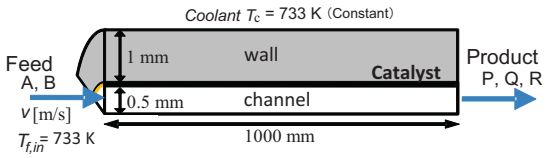

Fig. 1. Schematic diagram of TMR.

flow, and the inner wall surface is coated with a catalyst. On the catalyst surface, the following exothermic reactions take place:

$$\mathrm{A} + \mathrm{B} \rightarrow \mathrm{P} \qquad r_1 = k_1 C_{\mathrm{A}} \tag{1}$$

$$\mathrm{A} + \mathrm{B} \rightarrow \mathrm{Q} \qquad r_2 = k_2 C_{\mathrm{A}} \tag{2}$$

$$\mathrm{P} + \mathrm{B} \rightarrow \mathrm{R} \qquad r_3 = k_3 C_{\mathrm{P}} \tag{3}$$

P is a desired product, and Q and R are by-products. The temperature-dependent rate constant k_i in each reaction is presented by Arrhenius form:

$$k_i = A_i \exp\left(-E_i / RT_S\right) \quad , \quad i = 1,2,3 \tag{4}$$

Table 1 shows the reaction parameters. A and P are treated as key components, and the TMR can be described by the following mass and energy balance equations:

$$\frac{\partial C_i}{\partial t} = -v\frac{\partial C_i}{\partial z} + D\frac{\partial^2 C_i}{\partial z^2} + D\frac{\partial^2 C_i}{\partial r^2} + D\left(\frac{1}{r}\right)\frac{\partial C_i}{\partial r} \tag{5}$$

$$\frac{\partial T_f}{\partial t} = -v\frac{\partial T_f}{\partial z} + \frac{k_f}{\rho_f C_{pf}}\frac{\partial^2 T_f}{\partial z^2} + \frac{k_f}{\rho_f C_{pf}}\frac{\partial^2 T_f}{\partial r^2} + \frac{k_f}{\rho_f C_{pf}}\left(\frac{1}{r}\right)\frac{\partial T_f}{\partial r} \tag{6}$$

$$\frac{\partial C_{\mathrm{AS}}}{\partial t} = -v\frac{\partial C_{\mathrm{AS}}}{\partial z} + D\frac{\partial^2 C_{\mathrm{AS}}}{\partial z^2} - \frac{k_c}{\delta}\left(C_{\mathrm{AS}} - C_{\mathrm{A}}\big|_{r=\frac{d}{2}}\right) - k_1 C_{\mathrm{AS}} - k_2 C_{\mathrm{AS}} \tag{7}$$

$$\frac{\partial C_{\mathrm{PS}}}{\partial t} = -v\frac{\partial C_{\mathrm{PS}}}{\partial z} + D\frac{\partial^2 C_{\mathrm{PS}}}{\partial z^2} - \frac{k_c}{\delta}\left(C_{\mathrm{PS}} - C_{\mathrm{P}}\big|_{r=\frac{d}{2}}\right) + k_1 C_{\mathrm{AS}} - k_3 C_{\mathrm{PS}} \tag{8}$$

$$\frac{\partial T_S}{\partial t} = -v\frac{\partial T_S}{\partial z} + \frac{k_f}{\rho_f C_{pf}}\frac{\partial^2 T_S}{\partial z^2} - \frac{U}{\delta}\left(T_S - T_f\big|_{r=\frac{d}{2}}\right) - \frac{U}{\delta}\left(T_S - T_w\big|_{r=\frac{d}{2}}\right) \tag{9}$$

$$-\left(\Delta H_1 k_1 C_{\mathrm{AS}} + \Delta H_2 k_2 C_{\mathrm{AS}} + \Delta H_3 k_3 C_{\mathrm{PS}}\right)/(\rho_f C_{pf})$$

$$\frac{\partial T_W}{\partial t} = \frac{k_w}{\rho_w C_{pw}}\frac{\partial^2 T_W}{\partial z^2} + \frac{k_w}{\rho_w C_{pw}}\frac{\partial^2 T_W}{\partial r^2} + \frac{k_w}{\rho_w C_{pw}}\left(\frac{1}{r}\right)\frac{\partial T_W}{\partial r} \tag{10}$$

where z and r are the axial and radial space coordinates [m], and other variables are summarized in Table 2. Subscripts s, f, and w are catalyst surface, fluid, and wall, respectively. Catalyst thickness, δ, is set to 0.2 mm.

3 PROCESS MODEL FORMULATION

TMR's physical model described in the previous section is regarded as a real process. Fault diagnosis will be based on a state space model, which is derived from the distributed parameter model (5)-(10).

3.1 Process Model

Using the orthogonal collocation method, each state variable is approximated by the following:

Table 1. Reaction parameters.

Reaction	*Ai* [1/s]	*Ei* [J/mol]	ΔHi [kJ/mol]
(1)	86760	71711.7	- 2980
(2)	37260	71711.7	- 4622
(3)	149.4	36026.3	- 1664

Table 2. Model parameters.

Parameter	Value	
Reactant velocity v	1	m/s
Mass diffusion coefficient D	1 x 10^{-5}	m^2/s
Heat diffusion coefficient k_f	0.041	J/m K s
Heat conductivity of wall k_w	16.3	J/m K s
Density of reactant ρ_f	1.01	kg/m^3
Density of wall ρ_w	8000	kg/m^3
Viscosity of fluid μ	2.92 x 10^{-5}	Pa s
Heat capacity of reactant C_{pf}	1090	J/kg K
Heat capacity of wall C_{pw}	500	J/kg K
Reactor length L	1	m
Channel diameter d	1	mm
Wall thickness d_w	1	mm
Inlet conc. of species A C_A	4	mol/m^3
Inlet conc. of species P C_P	0	mol/m^3
Inlet temp. of reactant $T_{f,in}$	733	K
Coolant temp. T_c	733	K

$$X(t,z,r) \approx \sum_{i=1}^{n}\sum_{j=1}^{m} L_i(z) L_j(r) X_{i,j}(t), \quad X = C_A, C_P, T_f, T_w \tag{11}$$

$$X(t,z,r) \approx \sum_{i=1}^{n} L_i(z) X_i(t), \quad X = C_{AS}, C_{PS}, T_S \tag{12}$$

where $X_{i,j}(t)$ and $X_i(t)$ are the value of $X(t, z, r)$ at the axial collocation points $z_1 \sim z_n$ ($0 = z_1 < z_2 < \ldots < z_n = L$) and the radial collocation points $r_1 \sim r_m$ ($0 = r_1 < r_2 < \ldots < r_m = d/2$), respectively. $L_i(z)$ and $L_j(r)$ are Lagrange polynomials. In this study, n and m are set to 30 and 5, respectively, and the collocation points are chosen as roots of a Chebyshev polynomial. The above approximation is also applied to the states at boundaries. Equations (5)-(10) are transformed into the following:

$$\dot{\boldsymbol{x}}(t) = f\left(\boldsymbol{x}(t), \boldsymbol{u}_{in}\right) \tag{13}$$

where $\boldsymbol{u}_{\mathrm{in}}$ denotes the input vector and $\boldsymbol{x}$ the state vector:

$$\boldsymbol{x} = [\ \boldsymbol{C}_{\mathrm{A}}{}^T \quad \boldsymbol{C}_{\mathrm{P}}{}^T \quad \boldsymbol{C}_{\mathrm{AS}}{}^T \quad \boldsymbol{C}_{\mathrm{PS}}{}^T \quad \boldsymbol{T}_f{}^T \quad \boldsymbol{T}_S{}^T \quad \boldsymbol{T}_w{}^T\ ]^T . \tag{14}$$

3.2 Observer Design

Nonlinear estimation problems in this research are solved with the extended Kalman filter (EKF), which is based upon the principle of linearization of the state transition matrix and the observation matrix with Taylor series expansions. Wall temperature measurements are used as observed variables. To obtain the best estimates, the locations of the available

sensors must be selected carefully. The sensor location candidates in the axial direction of TMR are prepared according to the collocation points, and the optimal sensor locations are selected according to the following performance index,

$$J = 1 \Big/ \left\{ \frac{1}{N} \sum_{k=1}^{N} \left\| \boldsymbol{\theta}_{real} - \boldsymbol{\theta}_{est}(k) \right\|^2 \right\} \tag{15}$$

where N is the number of iteration steps, $\boldsymbol{\theta}_{\mathrm{real}}$ and $\boldsymbol{\theta}_{\mathrm{est}}$ the real and estimated values of parameters. J means the rate of convergence towards real values. As J becomes larger, the estimation performance becomes higher.

4. SIMULATION RESULTS

Three different examples of fault diagnosis of TMR are presented in this section. In addition, the conventional observability measures are examined for the selection of optimal sensor locations in TMR.

4.1 CASE 1: Catalyst Deterioration

In CASE 1, an optimal sensor location problem for estimation of catalyst effectiveness α is investigated. It is assumed that reaction rate constant k_1 includes α:

$$k_1(t,z) = \alpha\, A_1 \exp\left(-E_1 / RT_S(t,z)\right) \tag{16}$$

An initial value of $\alpha = 1$ is considered, followed by an abrupt change from 1 to 0.8 at time $t = t_s$. After catalyst deterioration, α is estimated from one temperature measurement by using EKF. The normal steady state ($\alpha = 1$) is used as the initial state of parameter estimation. J is calculated at every candidate for sensor locations. As shown in Fig. 2 (left), the largest value of J can be found near the inlet of TMR. This result is well illustrated by Fig. 2 (right). The solid and dotted curves in Fig. 2 (right) correspond to the wall temperature profiles along TMR having $\alpha = 1$ and 0.8, respectively. The great differences between the solid and dotted curves mean the high responses of temperature to a parameter change. This physical interpretation confirms that the optimal sensor location is near the inlet of TMR.

4.2 CASE 2: Channel Blockage

In CASE 2, a blockage diagnosis problem in TMR is investigated. Specifically, the inlet flow rate is constant, and one temperature sensor is used to estimate fluid velocity v. An initial value of $v = 1$ m/s is considered, followed by an abrupt change from 1 m/s to 1.2 m/s at time $t = t_s$. After channel blockage, v is estimated by using EKF. The normal steady state ($v = 1$ m/s) is used as the initial state of parameter estimation. J is plotted as a function of sensor position. The relative large values of J can be found in the latter part of TMR, as seen in Fig. 3 (left). This result is well illustrated by Fig. 3 (right). As well as CASE 1, the large differences between both profiles mean the high responses of temperature to a fluid velocity change. All things considered,

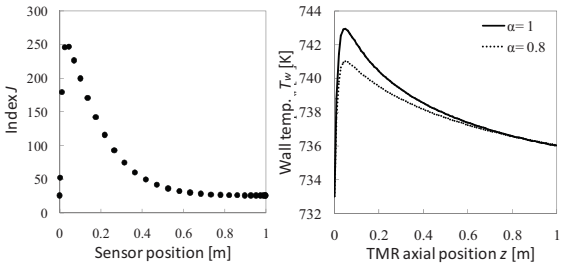

Fig. 2. Estimation results of CASE 1.

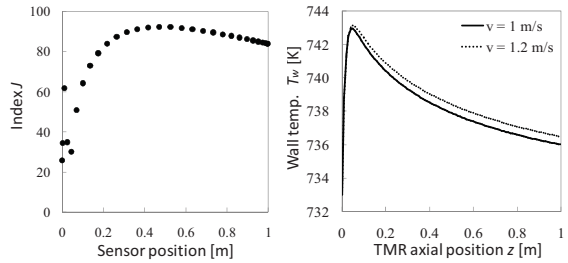

Fig. 3. Estimation results of CASE 2.

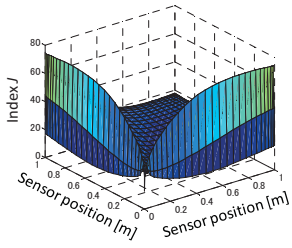

Fig. 4. Results of CASE 3.

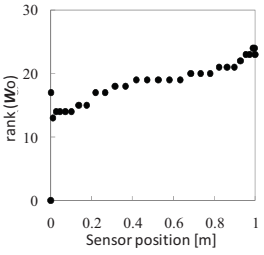

Fig. 5. Rank of $\boldsymbol{W}_O$.

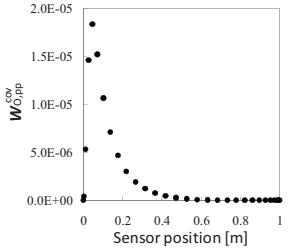

Fig. 6. $\boldsymbol{W}_{\mathrm{O,pp}}^{\mathrm{cov}}$ *of CASE 1.*

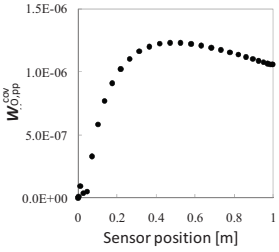

Fig. 7. $\boldsymbol{W}_{\mathrm{O,pp}}^{\mathrm{cov}}$ *of CASE 2.*

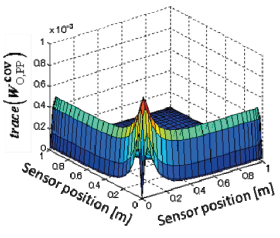

Fig. 8. $\boldsymbol{W}_{\mathrm{O,pp}}^{\mathrm{cov}}$ *of CASE 3.*

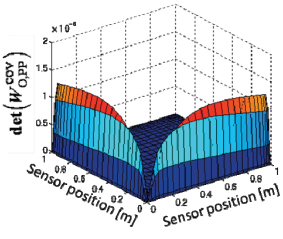

Fig. 9. $\boldsymbol{W}_{\mathrm{O,pp}}^{\mathrm{cov}}$ *of CASE 3.*

the optimal sensor location is in the latter part of TMR, which differs from CASE 1.

4.3 CASE 3: Simultaneous Diagnosis of Multi-Faults

This study is similar to the previous cases, but the two unknown parameters, α and v, are simultaneously estimated by using two temperature sensors. The simulation conditions of the observer are the same as used in the previous cases. Figure 4 suggests that one sensor should be located near the inlet of TMR and the other in the latter part of TMR to realize successful fault diagnosis.

4.4 Observability Measures

Over the years, several studies on sensor locations for estimation in conventional processes have been reported. The representative approaches are to define optimal criteria based on the observability Gramian $\boldsymbol{W}_{\mathrm{O}}$. An overview of several criteria is summarized below. Muller et al. (1972) examine the smallest singular value, the determinant, and the trace of $\boldsymbol{W}_{\mathrm{O}}$ as a measure for sensor location. Dochain et al. (1997) present the condition number of $\boldsymbol{W}_{\mathrm{O}}$, and van den Berg et al. (2000) use the trace of $\boldsymbol{W}_{\mathrm{O}}$ as a criterion for sensor location. While the above presented $\boldsymbol{W}_{\mathrm{O}}$ is suitable only for linear systems, one alternative is to use the observability covariance matrix $\boldsymbol{W}_{\mathrm{O}}^{\mathrm{cov}}$ if systems are nonlinear. Singh et al. (2005) present the trace of $\boldsymbol{W}_{\mathrm{O}}^{\mathrm{cov}}$ for sensor location. The aim of this section is to assess the effectiveness of the existent sensor location criteria for parameter estimation problems in TMR.

In the above presented TMR, observability analysis is performed by determining the rank of $\boldsymbol{W}_{\mathrm{O}}$. Figure 5 shows the rank of $\boldsymbol{W}_{\mathrm{O}}$ at every possible sensor location. Since $\boldsymbol{W}_{\mathrm{O}}$ at every location is rank deficient, then the system is not observable. In such a situation, the smallest singular value of $\boldsymbol{W}_{\mathrm{O}}$ is zero. Accordingly, it is not suitable to use criteria such as the smallest singular value, the smallest eigenvalue, the determinant, and the condition number of $\boldsymbol{W}_{\mathrm{O}}$. Therefore, the trace of $\boldsymbol{W}_{\mathrm{O}}^{\mathrm{cov}}$ is appropriate to the determination of the optimal sensor location for parameter estimation. However, for this work, $\boldsymbol{W}_{\mathrm{O}}^{\mathrm{cov}}$ is used instead of $\boldsymbol{W}_{\mathrm{O}}$ because the process is a time-variant system in case of parameter estimation problem. $\boldsymbol{W}_{\mathrm{O}}^{\mathrm{cov}}$ can be decomposed into (Singh et al., 2005):

$$\boldsymbol{W}_{\mathrm{O}}^{\mathrm{cov}} = \begin{bmatrix} W_{\mathrm{O,nn}}^{\mathrm{cov}} & W_{\mathrm{O,pn}}^{\mathrm{cov}} \\ W_{\mathrm{O,np}}^{\mathrm{cov}} & W_{\mathrm{O,pp}}^{\mathrm{cov}} \end{bmatrix} \tag{17}$$

where $\boldsymbol{W}_{\mathrm{O,nn}}^{\mathrm{cov}}$ the observability covariance matrix of the system, $\boldsymbol{W}_{\mathrm{O,pp}}^{\mathrm{cov}}$ the covariance of the outputs caused by changes in the parameters, and $\boldsymbol{W}_{\mathrm{O,np}}^{\mathrm{cov}}$ and $\boldsymbol{W}_{\mathrm{O,pn}}^{\mathrm{cov}}$ the covariance of the outputs resulting from changes in the states and parameters. The optimal sensor location for parameter estimation is computed by maximizing the traces of $\boldsymbol{W}_{\mathrm{O,pp}}^{\mathrm{cov}}$. The traces of $\boldsymbol{W}_{\mathrm{O,pp}}^{\mathrm{cov}}$ in CASEs 1 and 2 are plotted for possible sensor locations in Figs. 6 and 7. Figs. 6 and 7 are similar to Figs. 2 (left) and 3 (left), respectively. That is, the trace of $\boldsymbol{W}_{\mathrm{O,pp}}^{\mathrm{cov}}$ is useful as a criterion for judging where the sensors should be located. On the other hand, the trace and determinant of $\boldsymbol{W}_{\mathrm{O,pp}}^{\mathrm{cov}}$ in CASE 3 are plotted in Figs. 8 and 9, respectively. As compared with Fig. 4, it is clarified that the determinant of $\boldsymbol{W}_{\mathrm{O,pp}}^{\mathrm{cov}}$ is effective as a criterion of optimal sensor locations for estimating multi-parameters.

5. OPERATION POLICY FOR MCPs

The production capacity of MCPs is usually increased by numbering-up, which means the repetition of a microdevice. One of the critical operational issues of MCPs with numbering-up structure is to keep a uniform flow distribution among parallelized microdevices even when blockage occurs in one or more microdevice. Since it is not practical to install flow controllers in all the microdevices, a simple and effective operation policy against blockage occurrence needs to be developed. In this work, two types of operation policies, total flow control and pressure drop control, are compared from the viewpoint of flow uniformity when blockage occurs.

5.1 Total Flow Control and Pressure Drop Control

To maintain the desired product quality, it is important to keep a uniform flow rate in each microdevice of the micro chemical plant when blockage occurs, because flow maldistribution worsens the performance of the micro chemical plant. In this research, pressure drop control is proposed to achieve the uniform flow distribution.

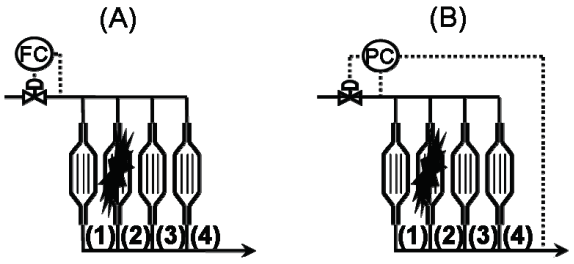

Fig. 10. Parallelized microdevices under two operation policies: (A) total flow control and (B) pressure drop control.

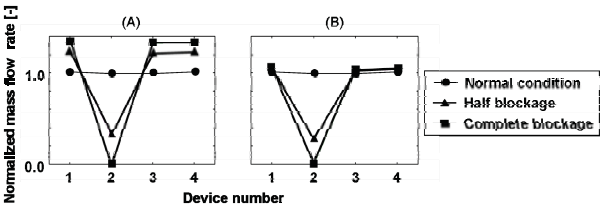

Fig. 11. Mass flow rate of each microdevice under blockage occurrence: (A) total flow control and (B) pressure drop control.

A micro chemical plant consisting of four parallelized microdevices in Fig. 10 is used to demonstrate the difference of two operation policies, total flow control and pressure drop control. When blockage occurs in microdevice 2, the flow distribution under the pressure drop control is derived by simulation and compared with that under the total flow control. In Fig. 10, reactant is fed to the parallelized microdevices at 0.1 m/s in the normal condition. The physical properties of the reactant are assumed to be the same as water (293 K). The results are shown in Fig. 11. In the case of blockage occurrence, mass flow rates of unblocked microdevices are significantly increased under the total flow control (Fig. 11 left), while they are kept constant at the value in a normal condition under pressure drop control (Fig. 11 right). These results show that the proposed pressure drop control is effective in making flow distribution uniform even when blockage occurs.

5.2 Comparison of Control Structures in Pressure Drop Control

In the previous section, it was confirmed that pressure drop control is superior to total flow control in realizing uniform flow distribution among unblocked microdevices when blockage occurs. In this section, two different control structures based on pressure drop control, pumping pressure control and pressure drop control over the parallelized section, are investigated.

5.2.1 Experimental Apparatus

Micro chemical plants having four or eight parallelized microdevices are used to grasp the distinction between two control structures. A schematic drawing of a micro chemical plant having four parallelized microdevices is shown in Fig. 12. Reactant is fed with a double plunger pump. The product line is open to the atmosphere. The flow rate of each microdevice is measured by using an in-line mass flow meter, and blockage in each microdevice is artificially realized by closing the valve located between the pump and each microdevice. Each microdevice consists of an SUS tube having 0.3 mm inner diameter and 2 m in length. In addition, an SUS tube with 0.5 mm in inner diameter and various lengths is installed after the parallelized microdevices to represent units that are not necessary to be parallelized. Hereafter, this section is referred to as a residence time section. The pressure drops over the parallelized section and the residence time section are denoted by ΔPa and ΔPb, respectively. The ratio of ΔPa to ΔPb is changed by adjusting the length of the residence time section.

5.2.2 Pumping Pressure Control

Under pumping pressure control, the double plunger pump is operated at constant pumping pressure. In experiments, pumping pressure is kept at a gauge pressure of 500 kPa – 1 MPa. Pressure drop over the whole micro chemical plant is kept constant under pumping pressure control, because the product line is open to the atmosphere.

The influence of blockage on flow distribution under pumping pressure control is investigated through both simulations and experiments with changing the ratio $\Delta Pa/\Delta Pb$ in the range of one-fifth to seven. The first step in the experimental procedure is to adjust the pumping pressure to realize a total flow rate of 12 mL/min. This operating condition is regarded as the normal condition. Then, microdevice 1 is artificially blocked by closing the valve. In 300 s, the micro chemical plant is returned to the normal condition by opening the valve. These procedures are repeated for the other valves to imitate blockage in the other microdevices.

Figure 13 shows the normalized average mass flow rate, which is defined as the ratio of average mass flow rate of unblocked microdevices under blockage occurrence to that under the normal condition at each $\Delta Pa/\Delta Pb$. There is little difference between the results of experiments and those of CFD simulations. The normalized average mass flow rate becomes closer to the flow rate under the normal condition as $\Delta Pa/\Delta Pb$ becomes larger. In other words, ΔPa should be significantly larger than ΔPb to keep the flowrate of unblocked microdevices unchanged when blockage occurs. It is concluded that pumping pressure control is effective to realize uniform flow distribution when the pressure drop over the parallelized section is dominant.

5.2.3 Pressure Drop Control Over the Parallelized Section

The flow uniformity achieved by pumping pressure control depends on $\Delta Pa/\Delta Pb$, which is the ratio of the pressure drop over the parallelized section to that over the residence time section. The flow uniformity in the parallelized microdevices deteriorates when $\Delta Pa/\Delta Pb$ is small. In this subsection,

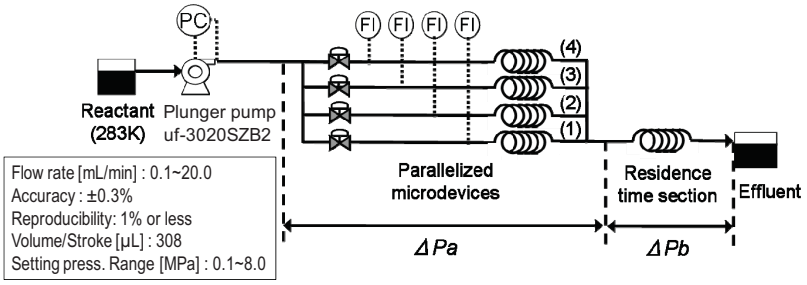

Fig. 12. Micro chemical plant under pumping pressure control.

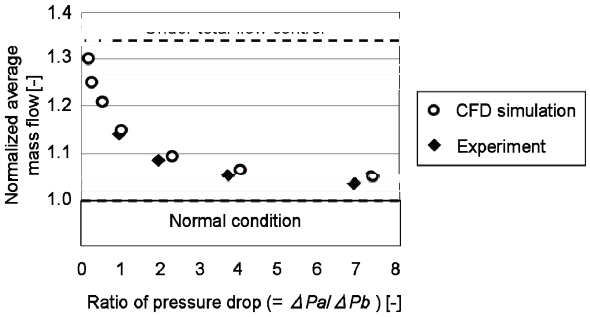

Fig. 13. Influence of blockage on the mass flow rate.

another pressure drop control structure where ΔPa is directly controlled by manipulating the flow rate of the bypass line is proposed.

The performance of the proposed control structure is evaluated experimentally by using the micro chemical plants with four (Type A) and eight (Type B) parallelized microdevices. The plunger pump is operated so that the total flow rate is kept constant. The other conditions are the same as those in the previous subsection.

The experimental results for a Type A plant are shown in Fig. 14. The top and bottom figures correspond to the case where $\Delta Pa/\Delta Pb = 50$ and $\Delta Pa/\Delta Pb = 1$, respectively. In the range of 0–300 s, the micro chemical plant is operated under the normal condition. The difference in flow rate between microdevices 1 and 2 is due to the degree of precision in the fabrication. When blockage occurs in microdevice 1 at 300 s, the flow rate of microdevice 1 goes to zero instantaneously and the flow rate of microdevice 2 deviates from its set-point. However, the flow rate of microdevice 2 returns to the normal level in a few tens of seconds. Flow rate deviation becomes small when blockage occurs gradually. The transient responses of microdevices 3 and 4 are similar to that of microdevice 2; they are not shown in Fig. 14 to identify the transient response of each microdevice easier. The top and bottom figures in Fig. 14 show almost the same profiles. This result shows that the efficiency of the proposed control structure does not depend on $\Delta Pa/\Delta Pb$.

The experimental result of a Type B plant is almost the same as that of the Type A plant. These results show that the proposed control structure has the function of keeping the flow rate of the unblocked devices constant regardless of the changes in $\Delta Pa/\Delta Pb$ and the number of parallelized microdevices.

6. CONCLUSIONS

In this study, sensor locations for effective fault diagnosis of TMR are investigated. It is clarified that two different faults are accurately diagnosed by using only two wall temperature sensors, which are optimally located in the axial direction of TMR. In addition, the optimality criteria for sensor locations in TMRs are investigated. The results obtained from case studies demonstrate that the criteria based on observability covariance matrix are effective and their maximization allows

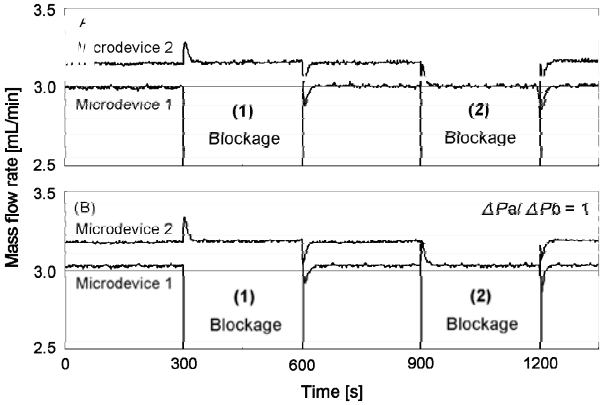

Fig. 14. The time series of mass flow rate in each microdevice in Type A: (A) $\Delta Pa/\Delta Pb = 50$, (B) $\Delta Pa/\Delta Pb = 1$.

one to determine where the sensors should be located. Finally, we have discussed operation policies and control structures for micro chemical plants with an external numbering-up structure. Two operation policies, total flow control and pressure drop control, were compared. The simulation result shows that the pressure drop control is effective to keep a uniform flow distribution among the parallelized microdevices even when blockage occurs. In addition, two control structures based on pressure drop control, pumping pressure control and pressure drop control over the parallelized section, were investigated experimentally. The former control structure is simple. However, this structure functions only when the ratio of the pressure drop over the parallelized section to that over the residence time section, $\Delta Pa/\Delta Pb$, is large. On the other hand, the latter control structure can make the flow distribution uniform for any $\Delta Pa/\Delta Pb$.

REFERENCES

Dochain, D., Tali-Maamar, N., and Babary, J. P. (1997). On Modeling, Monitoring and Control of Fixed Bed Bioreactors, *Comp. Chem. Eng.*, 21 (11), 1255-1266.

Hessel, V., Hardt, S., and Lowe, H. (2005). Chemical Micro Process Engineering: Fun-damentals, Modelling and Reactions. *Wiley, VCH, Weinheim*.

Kano, M., Fujioka, T., Tonomura, O., Hasebe, S., and Noda, M. (2007). Data-based and Model-based Blockage Diagnosis for Stacked Microchemical Processes. *Chem. Eng. Sci.*, 62 (4), 1073-1080.

Muller, P. C. and Weber, H. I. (1972). Analysis and Optimization of Certain Qualities of Controllability and Observability for Linear Dynamical Systems, *Automatica*, 8, 237-246.

Singh, A. K. and Hahn, J. (2005). Determining Optimal Sensor Locations for State and Parameter Estimation for Stable Nonlinear Systems, *Ind. Eng. Chem. Res.*, 44, 5645-5659.

van den Berg, F. W. J., Hoefsloot, H. C. J., Boelens, H. F. M., and Smilde, A.K. (2000). Selection of Optimal Sensor Position in a Tubular Reactor Using Robust Degree of Observability Criteria, *Chem. Eng. Sci.*, 55, 827-837.

Data-driven Control Loop Diagnosis: Dealing with Temporal Dependency in Bayesian Methods ⋆

Fei Qi *, **Biao Huang** *,

* *Department of Chemical and Materials Engineering, University of Alberta, Edmonton, Alberta, T6G 2G6, Canada(e-mail: fei.qi@ualberta.ca, biao.huang@ualberta.ca)*

Abstract: Conventional Bayesian methods commonly assume that the evidences are temporally independent. This condition does not hold for most practical engineering problems. With evidence transition information being considered, the temporal domain information can be synthesized within the Bayesian framework to improve the diagnosis performance. A data-driven algorithm is developed to estimate the evidence transition probabilities. The application in a pilot scale process is presented to demonstrate the data dependency handling ability of the proposed approach.

Keywords: Performance monitoring, Performance assessment, Bayesian diagnosis, Evidence dependency

1. INTRODUCTION

Control loop performance assessment and diagnosis has been an active area of research in the process control community. A number of control performance methods are available, including the ones based on minimum variance control (MVC), linear quadratic Gaussian control (LQG), historical data trajectories, and user-specified control, etc (Huang and Shah, 1999; Harris et al., 1999; Qin, 1998; Jelali, 2006; Schafer and Cinar, 2004; Patwardhan and Shah, 2002). Several surveys on the control performance assessment research are available (Harris et al., 1999; Qin, 1998; Hoo et al., 2003; Hugo, 2006; Jelali, 2006). Besides performance evaluation of control loops, significant progress has also been made in the development of monitoring algorithms for process and instrument components within the control loops, such as sensor monitor, valve stiction monitor, process model validation monitor (Qin and Li, 2001; Ahmed et al., 2009; Choudhury et al., 2008; Mehranbod et al., 2005). A number of successful industry applications of the process monitors have been reported. However, many practical problems remain. One of the outstanding problems is that the monitoring algorithms are often designed for one specific problem. An implicit assumption that other unattended components are in good shape is made. Clearly this assumption does not always hold, and thus it may lead to misleading results. It is desirable to develop approaches that not only monitor the performances of single components, but also are capable of synthesizing the information from different monitor outputs to isolate underlying source of problematic control performance.

According to Huang (2008), several challenging issues exist for the process monitor synthesizing problem. The first one is the similar symptoms among different problem sources. For instance, oscillations can either be invoked by a sticky valve or an improperly tuned controller. Another problem is that no process monitor has 100% detection rate and 0% false alarm rate, and thus a probabilistic framework should be built to represent the uncertainties. Third, a large number of the developed monitoring algorithms are purely data based without any *a priori* process information. Incorporating *a prior* process knowledge into the diagnosis framework is challenging, but better diagnosis performance can be expected by doing so.

The Bayesian method sheds lights on the problem solutions by providing a probabilistic information synthesizing framework. Applications of the Bayesian methods have been reported in medical science, image processing, target recognition, pattern matching, information retrieval, reliability analysis, and engineering diagnosis (Dey and Stori, 2005; Mehranbod et al., 2005; Steinder and Sethi, 2004; Chien et al., 2002). It is one of the most widely applied techniques in probabilistic inferencing. Built upon previous work in Bayesian fault diagnosis by Pernestal (2007) and a framework laid out by Huang (2008), Qi and Huang (2008) developed a data-driven Bayesian algorithm for control loop diagnosis with consideration of missing data. The algorithm is tested through simulation, where the information synthesizing ability of the proposed approach is demonstrated. However, the existing Bayesian methods have not considered temporal dependency problem. In this paper, a new algorithm is developed with consideration of temporal dependency, so as to achieve more reliable and better diagnosis performance.

⋆ This work is supported by the Natural Sciences and Engineering Research Council of Canada (NSERC) and the Alberta Ingenuity Fund.

The remainder of this paper is organized as follows. In Section 2, the control loop diagnosis problem and related preliminaries are described, and the data-driven Bayesian approach developed in (Qi and Huang, 2008) is briefly revisited. The rationale to consider evidence temporal dependency is detailed in Section 3. The estimation algorithm for the evidence transition probability is developed in Section 4. Section 5 presents application of the proposed approach to a pilot scale process. Finally the Section 6 concludes this paper.

2. DATA-DRIVEN BAYESIAN DIAGNOSIS METHOD REVISIT

2.1 Control Loop Diagnosis Problem

Generally a control loop consists of the following components: controller, actuator, process, and sensor. These components may all suffer from malfunctions. In this work, monitors are assumed to be available for some or all of the components of interest. These monitors, however, are all subject to disturbances and thus can produce false alarms, and each monitor can be sensitive to abnormalities of other problem sources. Our target is to pinpoint the source of problematic control performance based on the collected monitor output data.

To adopt the Bayesian method for control loop diagnosis, several notations need to be introduced (Qi and Huang, 2008).

Mode M Assume that a control loop under diagnosis consists of P components of interest: C_1, C_2, $\cdots$, C_P, among which the problem source may lie in. Each component is said to have a set of discrete operating status. For instance, the sensor might be "biased" or "unbiased". An assignment of operating status to all the components of interest in the control loop is called a mode, and denoted as M; M can take different values and a specific value is denoted by m. For example, m=(C_1=*well tuned controller*, C_2=*valve with stiction*, $\cdots$). Suppose that component C_i has q_i different status. Then the total number of possible modes is

$$Q = \prod_{i=1}^{P} q_i,$$

and the set of all possible modes can be denoted as

$$\mathcal{M} = \{m_1, m_2, \cdots, m_Q\}.$$

Evidence E The monitor readings, called evidence, are the input to the diagnostic system, and are denoted as $E = (\pi_1, \pi_2, \cdots, \pi_L)$, where π_i is the output of the i-th monitor, and L is the total number of the monitors. Often the continuous monitor readings are discretized according to predefined thresholds. In this work, monitor readings all take discrete values. For example, the control performance monitor may indicate "optimal", "normal", or "poor". A specific value of evidence E is denoted as e; for example, e=(π_1=*optimal control performance*, π_2=*no sensor bias*, $\cdots$). Suppose that the single monitor output π_i has k_i different discrete values. Then there are totally

$$K = \prod_{i=1}^{L} k_i$$

different evidences, and the set of all possible evidence values can be denoted as

$$\mathcal{E} = \{e_1, e_2, \cdots, e_K\}.$$

Historical evidence data set $\mathcal{D}$ In this paper, process data refer to the readings from physical instruments such as temperature, pressure, etc. The evidence data refer to the readings of monitors which are calculated typically from a section (window) of process data. Historical evidence data are retrieved from the past record where the mode of the control loop, namely, status of the components of interest in the control loop, is available, and the monitor readings are also recorded. Each sample d^t at time t in the historical evidence data set $\mathcal{D}$ consists of the evidence E^t and the underlying mode M^t. This can be denoted as $d^t = (E^t, M^t)$, and the set of historical evidence data is denoted as

$$\mathcal{D} = \{d^1, d^2, \cdots, d^{\tilde{N}}\},$$

where $\tilde{N}$ is the number of historical evidence data samples. In (Qi and Huang, 2008), all the historical evidence data samples are assumed to be independent as commonly assumed in the data-driven Bayesian approaches.

2.2 Data-driven Bayesian Diagnosis Approach

This section will give a brief review of the data-driven Bayesian approach proposed by Qi and Huang (2008). Given current evidence E, historical evidence data set $\mathcal{D}$, the posterior probability of each possible operating mode can be calculated according to Bayes' rule:

$$p(M|E, \mathcal{D}) \propto p(E|M, \mathcal{D})p(M), \tag{1}$$

where $p(E|M, \mathcal{D})$ is the likelihood probability; $p(M)$ is the prior probability of mode M. Among all the possible modes, generally the one with the largest posterior probability is taken as the underlying mode based on the maximum *a posterior* (MAP) principle, and the abnormality associated with this mode is normally diagnosed as the problem source.

Since prior probabilities are determined by *a priori* information, the main task of building a Bayesian diagnostic system is the estimation of the likelihood probabilities with historical evidence data $\mathcal{D}$. In (Qi and Huang, 2008), a data-driven Bayesian algorithm for estimation of the likelihood probability is proposed based on the work by Pernestal (2007) and Huang (2008).

Suppose that the likelihood of evidence $E = e_i$ under mode $M = m_j$ is to be calculated, where

$$e_i \in \mathcal{E} = \{e_1, \cdots, e_L\},$$

and

$$m_j \in \mathcal{M} = \{m_1, \cdots, m_Q\}.$$

The following result can be obtained for calculating the likelihood (Pernestal, 2007):

$$p(E = e_i|M = m_j, \mathcal{D}) = \frac{n_{i|m_j} + a_{i|m_j}}{N_{m_j} + A_{m_j}}, \tag{2}$$

where $n_{i|m_j}$ is the number of historical evidence samples with the evidence $E = e_i$, and mode $M = m_j$; $a_{i|m_j}$ is the number of prior samples that is assigned to

evidence e_i under mode m_j; $N_{m_j} = \sum_i n_{i|m_j}$, and $A_{m_j} = \sum_i a_{i|m_j}$.

3. DEPENDENCY IN HISTORICAL EVIDENCE DATA

Note that in the approach described in Section 2, an assumption is that the current evidence only depends on current mode, and is independent on the previous samples. This assumption is true for appropriate designed monitors, as explained below.

The independency among evidences relies on how the evidence data are sampled, and how the disturbance affects the monitor outputs. If the evidence samples are collected with sufficiently large intervals, or if the disturbance has no or weak correlation among the evidence samples, the evidences may be considered as independent. Generally the first requirement regarding the sampling interval can be easily satisfied by leaving sufficient gap between consecutive monitor readings. However, there is no guarantee that the disturbance is uncorrelated in practical applications. If disturbance has long-term autocorrelation and the gap between consecutive monitor readings is not large enough, then the temporal independency assumption of monitor readings can not apply. A simple practical example of long-term autocorrelation of the disturbance is the ambient temperature change. Consider that each monitor reading is calculated based on 1-hour data and there is no overlap in the use of data. Assume that some of the monitor outputs are affected by the ambient temperature. Due to the cyclic change of temperature within 24 hours, the evidence samples should follow a predictable pattern. Apparently it is more justifiable to consider the dependency between those evidence samples than ignoring it in this example.

Besides the practical issues, another limitation with the conventional Bayesian approach ignoring evidence dependency is its inability to capture all time domain information. An illustrative problem is presented in the following. Suppose that the system under diagnosis has two modes m_1 and m_2. One monitor π, with two discrete outcomes, 0 and 1, is available. A set of 100 samples of the monitor outputs is shown in Figure 1. The title in each plot indicates the underlying operating mode under which the data are collected.

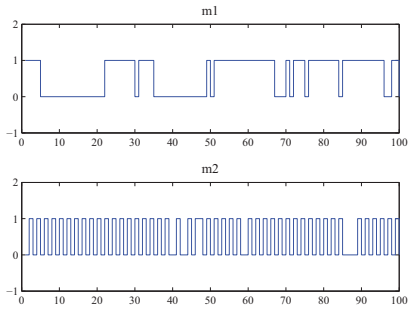

Fig. 1. Monitor outputs of the illustrative problem

The likelihood probability of evidence being 0 or 1 is calculated according to Equation 2, as summarized in Table 1. Clearly the likelihood of the evidence being 0 or 1 under the two modes is almost identical. This may invoke confusion in the diagnosis, which will lead to higher false diagnosis rate. By looking at the data plot in Figure 1, one can argue that distinguishing the two modes should not be such a difficult task. Although the evidences under m_1 and m_2 share similar likelihood, the frequencies of the evidence change apparently differ far from each other. The limitation with the conventional Bayesian method without considering evidence dependency is that the temporal information has not been completely used, leading to less efficient diagnosis performance. In summary it is desirable to take the evidence dependency into consideration when building the diagnostic model.

Table 1. Likelihood estimation of the illustrative problem

	$e = 0$	$e = 1$
m_1	0.46	0.54
m_2	0.48	0.52

With the consideration of evidence dependency, the mode posterior probability is calculated as

$$p(M^t|E^{t-1}, E^t, \mathcal{D}) \propto p(E^t|M, E^{t-1}, \mathcal{D})p(M). \quad (3)$$

Comparing the difference between Equation 1 and Equation 3, the main task of building a Bayesian diagnostic system boils down to the estimation of the evidence transition likelihood probability with historical evidence data $\mathcal{D}$, $p(E^t|M, E^{t-1}, \mathcal{D})$.

4. EVIDENCE TRANSITION PROBABILITY ESTIMATION

The intention of the estimation of evidence transition probability is to make the estimated likelihood probabilities be consistent with historical evidence data set $\mathcal{D}$ in which the evidence dependency exists. Our goal is to calculate the likelihood probability of an evidence E^t given current underlying mode M^t and previous evidence E^{t-1} to reflect the dependency with the Markov property, so every composite evidence sample for evidence transition probability estimation purpose should include three elements,

$$d_E^{t-1} = \{M^t, E^{t-1}, E^t\}. \quad (4)$$

Accordingly, the new composite evidence data set $\mathcal{D}_E$, which is assembled from historical evidence data set $\mathcal{D}$ to estimate transition probability, is defined as

$$\begin{aligned}\mathcal{D}_E &= \{d_E^1, \cdots, d_E^{t-1}\} \\ &= \{(M^2, E^1, E^2), \cdots, (M^t, E^{t-1}, E^t)\}, \end{aligned} \quad (5)$$

Figure 2 depicts how the original collected historical evidence data are divided to form composite evidence samples. In Figure 2, the part highlighted with shadows or gray and enclosed by the dash-lined or solid-lined frame is a single composite evidence sample described by Equation 4.

Suppose that the evidence transition probability from $E^{t-1} = e_s$ to $E^t = e_t$ under mode $M^t = m_k$ is to be estimated from the composite evidence data set,

$$p(E^t|E^{t-1}, M^t, \mathcal{D}_E) = p(e_t|e_s, m_k, \mathcal{D}_E) \quad (6)$$

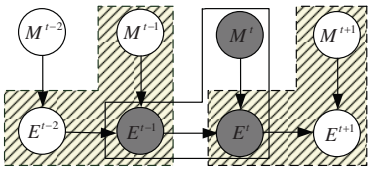

Fig. 2. Bayesian model considering dependent evidence

where

$$e_s, e_t \in \mathcal{E} = \{e_1, \cdots, e_L\}, \tag{7}$$

and

$$m_k \in \mathcal{M} = \{m_1, \cdots, m_Q\}. \tag{8}$$

The transition probability $p(e_t|e_s, m_k, \mathcal{D}_E)$ can only be estimated from the composite evidence data subset $\mathcal{D}_{E|m_k}$ where the mode $M^t = m_k$,

$$\begin{aligned} p(e_t|e_s, m_k, \mathcal{D}_E) &= p(e_t|e_s, m_k, \mathcal{D}_{E|m_k}, \mathcal{D}_{E|\neg m_k}) \\ &= p(e_t|e_s, m_k, \mathcal{D}_{E|m_k}), \end{aligned} \tag{9}$$

where $D_{E|\neg m_k}$ is the composite evidence data set whose underlying mode M^t is not m_k. To simplify notations, the subscript m_k will be omitted when it is clear from the context.

Define $\Phi_s = \{\phi_{s,1}, \phi_{s,2}, \cdots, \phi_{s,K}\}$ as the likelihood parameters for all possible evidence transition from evidence e_s under mode m_k, where $\phi_{s,j} = p(e_j|e_s, m_k)$ is the transition probability from evidence e_s to e_j, and K is the total number of possible evidences. The likelihood probability can be computed by marginalization over all possible evidence transition likelihood parameters,

$$\begin{aligned} &p(e_t|e_s, m_k, \mathcal{D}_E) \\ &= \int_{\Psi_1,\cdots,\Psi_K} p(e_t|\Phi_1, \cdots, \Phi_K, e_s, m_k, \mathcal{D}_E) \\ &\qquad \cdot f(\Phi_1, \cdots, \Phi_K|e_s, m_k, \mathcal{D}_E) d\Phi_1 \cdots \Phi_K \\ &= \int_{\Psi_1,\cdots,\Psi_K} \phi_{s,t} \cdot f(\Phi_1, \cdots, \Phi_K|e_s, m_k, \mathcal{D}_E) d\Phi_1 \cdots \Phi_K, \end{aligned} \tag{10}$$

where Ψ_i is the space of all the likelihood parameters Φ_i.

$f(\Phi_1, \cdots, \Phi_K|e_s, m_k, \mathcal{D}_E)$ can be calculated according to Bayes' rule,

$$\begin{aligned} &f(\Phi_1, \cdots, \Phi_K|e_s, m_k, \mathcal{D}_E) \\ &\propto p(\mathcal{D}_E|e_s, m_k, \Phi_1, \cdots, \Phi_K) f(\Phi_1, \cdots, \Phi_K|e_s, m_k). \end{aligned} \tag{11}$$

In Equation 11, the first term, $p(\mathcal{D}_E|e_i, m_k, \Phi_1, \cdots, \Phi_K)$ is the composite evidence data likelihood given parameter sets $\{\Phi_1, \cdots, \Phi_K\}$. It should be noted that likelihood of composite evidence data $\mathcal{D}_E$ is solely determined by the mode and parameter sets $\{\Phi_1, \cdots, \Phi_K\}$, and thereby is independent of e_s given the mode and the likelihood parameters, i.e.,

$$\begin{aligned} p(\mathcal{D}_E|e_s, m_k, \Phi_1, \cdots, \Phi_K) &= p(\mathcal{D}_E|m_k, \Phi_1, \cdots, \Phi_K) \\ &= \prod_{i=1}^{K} \prod_{j=1}^{K} \phi_{i,j}^{\tilde{n}_{i,j}}, \end{aligned} \tag{12}$$

where $\tilde{n}_{i,j}$ is the number of evidence transition from e_i to e_j in the composite evidence data set.

Assume that the priors for different parameter sets Φ_i and Φ_j, for $i \neq j$, are independent (Pernestal, 2007),

$$f(\Phi_1, \cdots, \Phi_K|e_s, m_k) = f(\Phi_1|e_s, m_k) \cdots f(\Phi_K|e_s, m_k). \tag{13}$$

Dirichlet distribution is commonly used to model priors of the likelihood parameters with parameters $b_{i1}, \cdots, b_{iK}$,

$$f(\Phi_i|e_s, m_k) = \frac{\Gamma(\sum_{j=1}^{K} b_{ij})}{\prod_{j=1}^{K} \Gamma(b_{ij})} \prod_{j=1}^{K} \phi_{ij}^{b_{ij}-1}, \tag{14}$$

where b_{ij} can be interpreted as the number of prior samples for evidence transition from e_i to e_j. $\Gamma(\cdot)$ is the gamma function,

$$\Gamma(x) = (x-1)!, \tag{15}$$

where x is positive integer.

Substituting Equation 14 and Equation 12 in Equation 11, and then combining it with Equation 10, the following result is obtained,

$$p(e_t|e_s, m_k, \mathcal{D}_E) = \frac{\tilde{n}_{s,t} + b_{s,t}}{\tilde{N}_s + B_s}, \tag{16}$$

where $\tilde{N}_i = \sum_j n_{i,j}$ is the total number of historical data samples with evidence transition from e_i under mode m_k, and $B_i = \sum_j b_{i,j}$ is the corresponding total number of prior samples.

By comparing Equation 2 and Equation 16, we can see that the evidence transition probabilities are also determined by both prior samples and historical samples, similar to the evidence likelihood calculation when the evidences are independent. The difference lies in how the numbers of prior and historical evidence samples are counted. In Equation 2 the prior and historical evidence samples refer to a simple count of the evidence samples corresponding to a certain mode, while in Equation 16 the prior and historical evidence samples refer to the count of composite evidence samples corresponding to a evidence transition under the target mode. Readers are referred to (Qi and Huang, 2008) for detailed explanation of the likelihood calculation.

5. PILOT SCALE EXPERIMENT

5.1 Process Description

The experiment setup is a water tank with one inlet flow and two outlet flows. The schematic diagram of the process is shown in Figure 3. The inlet flow is driven by a

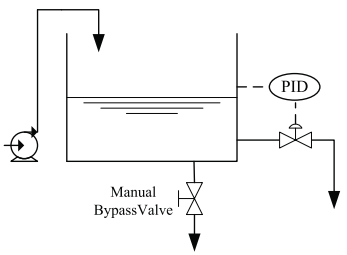

Fig. 3. Pilot scale tank process

pump. Of the two outlet flow valves, one is adjusted by a

PID controller to provide level control for the tank, and the other one is a manual bypass valve. It is assumed that the bypass valve is closed when the system in its normal operation condition.

Three operating modes are defined, including the *normal functioning* (NF) mode, and two problematic modes *leakage* and *bias*. The problems associated with the two faulty modes are: the tank leakage problem defined as *leakage* mode, implemented by opening the bypass valve manually, and the sensor bias problem defined as *bias* mode, implemented by adding a constant bias to the sensor output. The two problems share similar symptoms in terms of shifting the steady state operation point of the process. For instance, when there is a leakage in the tank, the valve adjusted by the PID controller will decrease to maintain the water level; when there is a negative sensor bias, the valve will also decrease. Thus it is not obvious how to distinguish the two faulty modes without any advanced information synthesizing approach. To make things worse, the external disturbance introduced by changing the pump input will also shift the operation point. Thus the operation point may also change during normal operation.

Random binary sequence is introduced into the inlet pump input to simulate temporal dependent disturbances. By defining the high value as 1, and the low value as 0, the disturbance transitions are designed to follow the transition probability matrices presented in Equation 17.

$$P_{NF}^{dis} = \begin{matrix} \\ 0 \\ 1 \end{matrix} \begin{matrix} \begin{matrix} 0 & 1 \end{matrix} \\ \begin{pmatrix} 0.9 & 0.1 \\ 0.2 & 0.8 \end{pmatrix} \end{matrix}, P_{leakage}^{dis} = \begin{matrix} \\ 0 \\ 1 \end{matrix} \begin{matrix} \begin{matrix} 0 & 1 \end{matrix} \\ \begin{pmatrix} 0.1 & 0.9 \\ 0.8 & 0.2 \end{pmatrix} \end{matrix},$$
$$P_{bias}^{dis} = \begin{matrix} \\ 0 \\ 1 \end{matrix} \begin{matrix} \begin{matrix} 0 & 1 \end{matrix} \\ \begin{pmatrix} 0.5 & 0.5 \\ 0.5 & 0.5 \end{pmatrix} \end{matrix}. \quad (17)$$

Two process monitors, process model validation monitor and sensor bias monitor, are designed. Since we mainly focus on the study of the information retrieving and synthesizing abilities of Bayesian approaches with different diagnosis strategies, the selected monitor algorithms are not necessary to have good performances.

The output of process model validation monitor π_1 is given by the squared sum of the nominal model output residuals, scalded by the magnitude of the process output. Let the simulated output of the nominal model be $\hat{y}_t$ at each sampling instance t, and the real output be y_t. The output of the model validation monitor π_1 is calculated as

$$\pi_1 = \frac{\sum_{t=1}^{N}(y_t - \hat{y}_t)^2}{\bar{y}}, \quad (18)$$

where $\bar{y} = \frac{1}{N}\sum_{t=1}^{N} y_i$ is the mean value of the process output over one monitor reading period, and N is the length of data segment over the one monitor reading.

The sensor bias monitor output π_2 is obtained by examining the operation point shift. For illustration, consider the scenario when a negative sensor bias occurs. The steady state in terms of the sensor output will not change, since it is controlled by the PID. The steady state output of the controller, i.e., the valve position, however, will decrease. The valve position will reverse in the presence of the positive sensor bias. Thus we can detect the sensor bias by monitoring the deviation of the controller output mean value from the nominal operation point. The output of the sensor bias monitor π_2 is calculated as

$$\pi_2 = \left| u_0 - \frac{1}{N}\sum_{t=1}^{N} u_t \right|, \quad (19)$$

where u_0 is the nominal operation point of the controller output, u_t is the controller output at each sampling instance t, and N is the length of process data segment for a single monitor reading. Note that this monitor will fail for the transition data, thus only steady state data are collected and used in this example.

5.2 Diagnosis Settings and Results

Process data are collected for the three predefined modes. The sampling interval is set to be one second. Every 100 seconds of process data are used for calculation of one monitor reading. Totally 600 monitor readings are calculated from 16.5 hours of process data samples. The collected evidence data of the three modes are divided into two parts for estimation of the likelihood, and for cross-validation respectively. Table 2 summarizes the Bayesian diagnosis parameters.

Table 2. Summary of Bayesian diagnosis parameters

Discretizaion	$k_i = 2$, $K = 2^2 = 4$
Historical data	120 monitor readings for each mode
Prior samples	Uniformly distributed with prior sample, for single evidence space, and evidence transition space
Prior probabilities	$p(NF) = p(m_{other}) = 1/3$
Evaluation data	80 independently generated cross-validation monitor readings for each mode

With the data-driven Bayesian approaches of two different strategies, namely, considering and ignoring the evidence dependency, the diagnosis results in Figure 4 are obtained based on the cross-validation data. In the plot, the gray bars are the numbers of the underlying modes occurred in the validation data set; the light gray and dark bars are the numbers of the diagnosed mode by two diagnostic approaches respectively.

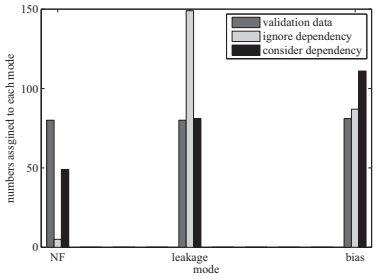

Fig. 4. Numbers assigned to each mode

Owing to the dependent external disturbance, the Bayesian approach ignoring evidence dependency significantly overestimates the number of leakage mode occurrence, and underestimates the number of NF mode. Therefore, its overall correct diagnosis rate is only 51.45%, and is much lower in comparison to the diagnosis rate of the proposed method, which is 73.86%. Not only can better overall performance be obtained by the proposed approach, the diagnosis performance of each single mode, as will be also investigated, is more favorable.

Figure 5 summarizes the diagnosis results in the form of average posterior probabilities. The title of each plot denotes the true underlying mode, and the posterior probability corresponding to the true underlying mode is highlighted with light gray bars. The left panel summarizes the diagnosis results calculated by the approach ignoring evidence dependency; the right panel summarizes the diagnosis results obtained by the approach with consideration of evidence dependency. It is observed that for the three modes, the posterior probabilities assigned to the true underlying modes by the proposed approach are all higher than these assigned by the method ignoring dependency. Thus we can conclude that the proposed approach has better performance for diagnosis of all modes. This conclusion is confirmed by computing the correct diagnosis rate for each mode, as presented in Table 3.

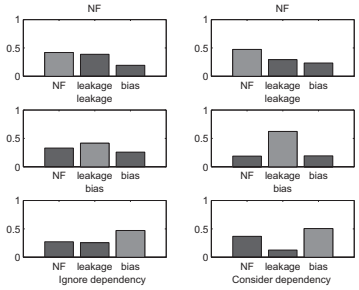

Fig. 5. Average posterior probability for each mode

Table 3. Correct diagnosis rate for each single mode

	NF	*leakage*	*bias*
Ignore evidence dependency	6.25%	73.75%	70%
Consider evidence dependency	55%	78.75%	92.5%

6. CONCLUSION

In this work, a data-driven approach considering evidence dependency is presented. Temporal dependency of monitor outputs is taken into consideration to obtain more accurate diagnosis results. The evidence transition probabilities are estimated from historical data with the developed data-driven algorithm. The method is applied to a pilot scale process, where the performance of the proposed approach is shown superior to that of the method ignoring evidence dependency. In summary, the more information from the time domain is synthesized, the better diagnosis performance is expected.

REFERENCES

Ahmed, S., Huang, B., and Shah, S. (2009). Validation of continuous-time models with delay. *Chemical Engineering Science*, 64(3), 443–454.

Chien, C.F., Chen, S.L., and Lin, Y.S. (2002). Using bayesian network for fault location on distribution feeder. *IEEE Transactions on Power Delivery*, 17(13), 785–793.

Choudhury, M.A.A.S., Jain, M., and Shah, S. (2008). Stiction - definition, modelling, detection and quantification. *Journal of Process Control*, 18(3-4), 232–243.

Dey, S. and Stori, J. (2005). A bayesian network approach to root cause diagnosis of process variations. *International Journal of Machine Tools*, 45(1), 75–91.

Harris, T., Seppala, C., and Desborough, L. (1999). A review of performance monitoring and assessment techniques for univariate and multivariate control systems. *Journal of Process Control*, 9(1), 1–17.

Hoo, K., Piovoso, M., Sheneller, P., and Rowan, D. (2003). Process and controller performance monitoring: overview with industrial applications. *International Journal of Adaptive Control and Signal Processing*, 17, 635–662.

Huang, B. (2008). Bayesian methods for control loop monitoring and diagnosis. *Journal of Process Control*, 18(9), 826–838.

Huang, B. and Shah, S. (1999). *Performance assessment of control loops*. Springer-Verlag.

Hugo, A. (2006). Performance assessment of single-loop industrial controllers. *Journal of Process Control*, 16, 784–794.

Jelali, M. (2006). An overview of control performance assessment technology and industrial applications. *Control Engineering Practice*, 14(5), 441–466.

Mehranbod, N., Soroush, M., and Panjapornpon, C. (2005). A method of sensor fault detection and identification. *Journal of Process Control*, 15(3), 321–339.

Patwardhan, R. and Shah, S. (2002). Issues in performance diagnostics of model-based controllers. *Journal of Process Control*, 12(3), 413–427.

Pernestal, A. (2007). *A Bayesian approach to fault isolation with application to diesel engine diagnose*. Ph.D. thesis, KTH School of Electrical Engineering.

Qi, F. and Huang, B. (2008). Data-driven bayesian approach for control loop diagnosis. In *Proceeding of Amecican Control Conference*. Seattle, U.S.A.

Qin, S. (1998). Control performance monitoring - a review and assessment. *Computers Chem. Engng*, 23(2), 173–186.

Qin, S. and Li, W. (2001). Detection and identification of faulty sensors in dynamic process. *AIChE Journal*, 47(7), 1581–1593.

Schafer, J. and Cinar, A. (2004). Multivariable mpc system performance assessment, monitoring, and diagnosis. *Journal of process control*, 14(2), 113–129.

Steinder, M. and Sethi, A. (2004). Probabilistic fault localization in communication systems using belief networks. *IEEE/ACM Transactions on Networking*, 12(5), 809–822.

Data-based Fault Detection and Isolation Using Output Feedback Control ⋆

Benjamin J. Ohran [*] **Jinfeng Liu** [*]
David Muñoz de la Peña [***] **Panagiotis D. Christofides** [*,**,1]
James F. Davis [*]

[*] *Department of Chemical and Biomolecular Engineering, University of California, Los Angeles, CA 90095-1592 USA.*
[**] *Department of Electrical Engineering, University of California, Los Angeles, CA 90095-1592, USA.*
[***] *Departamento de Ingeniería de Sistemas y Automática, Universidad de Sevilla, Camino de los Descubrimientos S/N, 41092, Sevilla, Spain.*

Abstract: This work focuses on data-based fault detection and isolation (FDI) of nonlinear process systems. Working within the framework of controller-enhanced fault detection and isolation that we recently introduced, we address and solve an unresolved, practical problem. We consider the case where only output measurements are available and design appropriate state estimator-based output feedback controllers to achieve controller-enhanced fault detection and isolation in the closed-loop system. The necessary conditions for achieving fault detection and isolation using output feedback control are provided. We use a nonlinear chemical process example to demonstrate the applicability and effectiveness of the proposed method.

Keywords: Process control, process monitoring, state estimation, fault detection and isolation

1. INTRODUCTION

Advanced automation technology has changed how the chemical process industry operates in many ways. Over the last few decades, advancements in plant operations have led to higher efficiency and improved economics through better control and monitoring of process systems. These technological advances have resulted in process systems becoming increasingly automated, no longer requiring operators to open and close valves in order to manually perform process control. In general, there is a trend towards such"smart" plants that are capable of highly automated control with decision making at the plant level taking into account environmental, health, safety and economic considerations (Christofides et al. (2007)). With increased amounts of sensors and actuators, it becomes possible to design systems capable of detecting and handling process or control system abnormalities through fault-tolerant control (FTC) (see for example, Mhaskar et al. (2006, 2007)). This is an important area of research as abnormal situations cost U.S. industries over $20 billion each year (Nimmo (1995)). A key element of a successful FTC system is a fast, accurate method for detecting faulty process behavior and isolating its cause. The fault detection and isolation (FDI) problem is the focus of the present work.

In a previous work (Ohran et al. (2008)), we developed an FDI method that takes advantage of both model-based and data-based approaches. This method brought together elements of model-based controller design and statistical process monitoring. In this method, the controller is designed with the FDI scheme in mind in addition to stability and performance criteria. By enforcing an isolable structure in the closed-loop system, it becomes possible to perform FDI based on statistical evaluation of process measurements. The purpose of the present work is to further develop the approach proposed in Ohran et al. (2008) by relaxing the requirement of full state feedback control. Specifically, we consider the case where only output measurements are available and design appropriate state estimator-based output feedback controllers to achieve controller-enhanced fault detection and isolation in the closed-loop system. This is demonstrated using a nonlinear chemical process example to show the applicability and effectiveness of the proposed method.

2. PRELIMINARIES

2.1 Process system structure

We consider nonlinear process systems with the following general state-space description:

$$\dot{x} = f(x, u, d) \tag{1}$$

where $x \in \mathbb{R}^n$ is the vector of process state variables, $u \in \mathbb{R}^m$ is the vector of manipulated input variables and $d \in \mathbb{R}^p$ is the vector of p possible actuator faults or disturbances. Vector d is equal to zero when the system is under normal operating conditions. When fault k, with $k = 1, ..., p$ occurs, d_k can take any time-varying value. The approach of controller enhanced FDI was introduced in Ohran et al. (2008) as a method of dividing the state vector into a number of partially decoupled subvectors. These subvectors can be monitored using measured process data.

⋆ Financial support from NSF, CTS-0529295, is gratefully acknowledged.
[1] Corresponding author: P.D. Christofides, pdc@seas.ucla.edu

Based on their responses and the system structure enforced by the decoupling controller, it is possible to discriminate between individual faults or groups of faults. In order to understand the necessary structure to perform isolation, we review the definitions of the incidence graph, the reduced incidence graph and the isolability graph (Ohran et al. (2008)).

Definition 1. The incidence graph of the system of Eq.1 is a directed graph defined by n nodes, one for each state, $x_i,\ i = 1 \dots n$, of the system. A directed arc with origin in node x_i and destination in node x_j exists if and only if $\frac{\partial f_j}{\partial x_i} \neq 0$.

The arcs in the incidence graph illustrate dependencies within the states of the system. A path through more than one arc that starts and ends at the same node is denoted as a loop.

Definition 2. The reduced incidence graph of the system of Eq.1 is the directed graph of N nodes, one for each q_i, $i = 1 \dots N$, where N is the maximum number of nodes that satisfy the following conditions:

- Each node q_i corresponds to a set of states $X_i = \{x_j\}$. These sets of states are a partition of the state vector of the system, i.e.,
$$\bigcup X_i = \{x_1, \dots x_n\}, \quad X_i \bigcap X_j = \emptyset,\ \forall i \neq j.$$
- A directed arc with origin q_i and destination q_j exists if and only if $\frac{\partial f_l}{\partial x_k} \neq 0$ for some $x_l \in X_i$, $x_k \in X_j$.
- There are no loops in the graph.

The reduced incidence graph reveals the partially decoupled subsystems within the structure of the states in x.

Definition 3. The isolability graph of the system of Eq.1 is a directed graph made of the N nodes of the reduced incidence graph and p additional nodes, one for each possible fault d_k. In addition, a directed arc with origin in fault node d_k and destination to a state node q_j exists if and only if $\frac{\partial f_l}{\partial d_k} \neq 0$ for some $x_l \in X_j$.

These definitions present the basic dependencies within a state vector. In most nonlinear process systems, the states are fully coupled and the isolability graph contains a single node representing all of the states in the system. However, in systems with partially decoupled dynamics these figures demonstrate graphically the subsets of the state vector.

With the isolability graph of a system, we can perform fault isolation based upon monitoring the subsystems. For this purpose, it is necessary to review the definition of a fault signature given below (Ohran et al. (2008)):

Definition 4. The signature of a fault d_k of the system of Eq.1 is a binary vector W^k of dimension N, where N is the number of nodes of the reduced incidence graph of the system. The i^{th} component of W^k, denoted W^k_i, is equal to 1 if there exists a path in the isolability graph from the node corresponding to fault d_k to the node q_i corresponding to the set of states X_i, or 0 otherwise.

2.2 Process monitoring

For the purpose of monitoring whether or not a state has deviated from its normal behavior, we use statistical process monitoring methods. Specifically, we use Hotelling's T^2 statistic developed in Hotelling (1947), a well established method in statistical process control that monitors multivariate normal (Gaussian) data using a single statistic. Because of its suitability for continuous, serially correlated chemical processes, the method of using single observations is employed (Tracy et al. (1992)). Given a multivariate state vector x of dimension n, the T^2 statistic can be computed using the mean $\bar{x}$ and the estimated covariance matrix S of process data obtained under normal operating conditions (see, for example, Kourti and MacGregor (1996)), as follows:

$$T^2 = (x - \bar{x})^T S^{-1} (x - \bar{x}). \tag{2}$$

The upper control limit (UCL) for the T^2 statistic can be calculated from its distribution, under the assumption that the data are multivariate normal, according to the following formula:

$$T^2_{UCL} = \frac{(h^2 - 1)n}{h(h - n)} F_\alpha(n, h - n) \tag{3}$$

where h is the number of historical measurements used in estimating S, $F_\alpha(n, h-n)$ is the value on the F distribution with $(n, h - n)$ degrees of freedom for which there is probability α of a greater or equal value occurring.

In order to perform FDI, the T^2 statistic based on the full state vector x with upper control limit T^2_{UCL} is first used to detect the presence of a fault. Subsequently, the T^2_i statistic is used to monitor the status of each subset of the state vector with an upper control limit T^2_{UCLi} where $i = 1, \dots, N$ that is based on each of the subvectors and their states $x_j \in X_i$. The fault detection and isolation procedure then follows the steps given below (Ohran et al. (2008)):

1. A fault is detected if $T^2(t) > T^2_{UCL}\ \forall t\ t_f \leq t \leq t_f + T_P$ where t_f is last time when T^2 crossed the UCL and T_P is the fault detection window chosen. Choosing T_P depends on the process time constants and on historical information of past process behavior.
2. Fault isolation can be performed by comparing fault signatures with the process signature $W(t_f, T_P)$ which can be built as follows:
$T^2_i(t) > T^2_{UCLi}\ \forall t\ t_f \leq t \leq t_f + T_P \rightarrow W_i(t_f, T_P) = 1.$
$T^2_i(t) \not> T^2_{UCLi}\ \forall t\ t_f \leq t \leq t_f + T_P \rightarrow W_i(t_f, T_P) = 0.$
A fault d_k is isolated at time $t_f + T_P$ if $W(t_f, T_P) = W^k$. If two or more faults are defined by the same signature, further isolation between them is not possible on the basis of the fault signature.

2.3 Controller design for enhanced FDI

Decoupling controller design The approach to fault detection and isolation discussed in the previous section can be applied if the signatures of the faults in the closed-loop system are distinct. The uniqueness of a fault depends on the structure of the closed-loop system and the faults considered. In general, complex nonlinear systems are fully coupled (i.e., cannot be broken down into partially decoupled subvectors). However, an isolable structure in the closed-loop system may still be achieved through the application of appropriately designed nonlinear control laws. As an example, consider a controller that can be

applied to nonlinear systems with the following state space description:

$$\begin{aligned} \dot{x}_1 &= f_{11}(x_1) + f_{12}(x_1, x_2) + g_1(x_1, x_2)u + d_1 \\ \dot{x}_2 &= f_2(x_1, x_2) + d_2 \end{aligned} \tag{4}$$

where $x_1 \in R$, $x_2 \in \mathbb{R}^n$, $u \in \mathbb{R}$ and $g_1(x_1, x_2) \neq 0$ for all $x_1 \in R$, $x_2 \in \mathbb{R}^n$. With a nonlinear state feedback controller of the form:

$$u(x_1, x_2) = -\frac{f_{12}(x_1, x_2) - v(x_1)}{g_1(x_1, x_2)} \tag{5}$$

the closed-loop system takes the form

$$\begin{aligned} \dot{x}_1 &= f_{11}(x_1) + v(x_1) + d_1 \\ \dot{x}_2 &= f_2(x_1, x_2) + d_2 \end{aligned} \tag{6}$$

where $v(x_1)$ has to be designed in order to achieve asymptotic stability of the origin of the x_1 subsystem when $d_1 = 0$. In this case, the controller of Eq.5 guarantees asymptotic stability of the closed-loop system, as well as different signatures for faults d_1 and d_2. For more detailed results, see Ohran et al. (2008).

Input/output linearizable nonlinear systems Input/output linearizable nonlinear systems constitute a special class of nonlinear systems for which it is possible to systematically design nonlinear controllers to achieve controller-enhanced fault detection and isolation. Using a feedback-linearizing control law that takes the following general form,

$$u(x) = \frac{1}{L_g L_f^{r-1} h(x)} [v(x) - L_f^r h(x)] \tag{7}$$

where $L_f^r h(x)$ is the r-th order Lie derivative, $L_g L_f^{r-1} h(x)$ is a mixed Lie derivative and $v(x)$ is an external controller for the purpose of stabilizing the system, the system under closed loop operation will have linear input-output dynamics.

If the state-feedback law given in Eq.7 is applied to an input/output linearizable system, faults affecting the system can be isolated into two different groups: those that affect the output and those that do not affect the output. The induced structure of the closed-loop system provides different signatures for the faults depending on the relative degree of the output with respect to the fault and the relative degree of the output with respect to the input. Faults with relative degree higher than the relative degree of the input will not affect the output. Thus, when a fault occurs, taking into account whether the trajectory of the output has deviated from the normal case or not, it is possible to isolate to which group the fault belongs. For the definitions of relative degree and an in depth discussion of feed-back linearization in this context, see Ohran et al. (2008).

3. CONTROLLER ENHANCED FDI USING OUTPUT FEEDBACK CONTROL

3.1 State estimation

In order to perform controller enhanced FDI using output feedback control, any unknown process state variable must be quickly and accurately estimated from the available output measurements so that the decoupling state feedback controller designs of subsections 2.3.1 and 2.3.2 can be implemented. The state estimation is performed for the state vector x (or a subset thereof) with the outputs, or measured states, defined as $y = Cx$. In this work, we consider only outputs of the form $y_i = x_i, i = 1, \ldots, q < n$. In other words, C is a matrix with one and only one non-zero entry in each row and that entry is equal to unity. This set-up is appropriate in chemical process control applications where measurements of a few states like temperature and concentrations of a few species, like key products, are available, but concentrations of some species are not measured. This set-up also allows obtaining a clear picture of the use of output feedback instead of full state feedback in controller enhanced FDI. The theory for the state estimator design is based upon a linear system, but can also be applied to nonlinear systems, using a local stability analysis around the operating point (origin). Specifically, the linearized model of the nonlinear system of Eq.1 takes the following form:

$$\begin{aligned} \dot{x} &= Ax + Bu + Wd \\ y &= Cx \end{aligned} \tag{8}$$

where A is the Jacobian matrix of the nonlinear system at the operating point, u is the manipulated input vector and d is the fault vector. The matrices B and W can be computed from the linearization of Eq.1 around the origin. Under the assumption that (A, C) forms an observable pair, each state variable x can be estimated by the following dynamic equation:

$$\dot{\hat{x}} = A\hat{x} + Bu + L(y - C\hat{x}) \tag{9}$$

where $\hat{x}$ is the state estimate and L is the estimator gain that can be chosen so that all the eigenvalues of the matrix $(A - LC)$ are placed at appropriate locations in the left-half of the complex plane to guarantee a desirable rate of convergence of the estimation error to zero. The computation of L can be done using standard pole placement techniques or via a Kalman filtering framework by adding process and measurement noise in the linearized model of Eq.8. In either case, the linearized state estimation error equation with $d(t) = 0$ takes the form:

$$\dot{e} = (A - LC)e. \tag{10}$$

where $e = x - \hat{x}$ is the estimation error. While it is possible to perform state estimation using the full state vector in the state estimator of Eq.9 when $d(t) \equiv 0$, it becomes necessary to use a reduced-order process model when designing a state estimator-based output feedback controller to enhance FDI. This need for a reduced-order model arises due to faults that affect the state estimator and introduce error into the estimate (i.e., the full state estimation scheme of Eq.9 works when $d(t) = 0$, but not when $d(t) \neq 0$). Specifically, if the error vector d on the right-hand side of Eq.8 is nonzero, the new equation for the estimator error becomes $\dot{e} = (A - LC)e + Wd$. Thus, in the presence of a fault, the state estimates no longer converge to their actual values, and the isolable structure attained in the closed-loop system under state feedback control cannot be maintained. However, it is possible in some process systems to perform the state estimation task using a subset of the states that are not directly affected by the expected faults, i.e., effectively eliminating d in the estimation error system. The general structure of the model in Eqs.8-10 remains the same for the reduced-order system, but it is based on a subset of the full state vector, $x_r \subset x$. To mathematically realize this notion, consider a system with the following structure, where time derivatives of the states

x_r are not functions of d and include all unknown states to be estimated along with some measured states, and x_d includes the remaining measured states, whose dynamic equations may be functions of d. Specifically, we consider the following decomposition of the vectors and matrices of the linearized system of Eq.8

$$x = \begin{bmatrix} x_r \\ x_d \end{bmatrix},\ A = \begin{bmatrix} A_r & A_{rd} \\ A_{dr} & A_d \end{bmatrix},\ W = \begin{bmatrix} 0 \\ W_d \end{bmatrix}$$
$$B = \begin{bmatrix} B_r \\ B_d \end{bmatrix},\ C = \begin{bmatrix} C_r & 0 \\ 0 & C_d \end{bmatrix},\quad y = \begin{bmatrix} y_r \\ y_d \end{bmatrix}. \tag{11}$$

Provided that the pair (A_r, C_r) is observable, the state estimator based on the reduced-order system then takes the form:

$$\dot{\hat{x}}_r = A_r\hat{x}_r + A_{rd}x_d + B_r u + L_r(y_r - C_r\hat{x}_r) \tag{12}$$

Eq.12 uses the actual measured values for all of the states in x_d. We can break x_r down further into measured states and unmeasured states, $x_r = [x_{rm}^T\ x_{ru}^T]^T$. Note that x_{rm} must include enough measured states independent of d for the system to be observable. Given the restrictions on C, this implies that $y_r = C_r x_r = x_{rm}$ and $C_d = I$ (i.e., $y_d = x_d$). Finally, we define a vector with full state information by combining the measured and estimated data, $\hat{x} = [x_{rm}^T\ \hat{x}_{ru}^T\ x_d^T]^T$. Note that $\hat{x}_{rm}$ is only used as the driving force for convergence of the state estimator. With these definitions, the reduced-order state estimator of Eq.12 is not a direct function of d and the dynamics of the estimation error, $e_r = x_r - \hat{x}_r$, take the form $\dot{e}_r = (A_r - L_r C_r)e_r$ which implies that $e_r(t)$ will converge to zero even in the presence of a change in d.

Once the estimator gain obtained from the linearized model of the system is calculated, it can then be used to estimate the states of the process using the nonlinear model dynamics. Once again, for the nonlinear system, the state vector, x, decomposes into the one of the reduced-order system (independent of d) and the remaining states, i.e., $x = [x_r^T\ x_d^T]^T$ and $f([x_r^T\ x_d^T]^T, u, d) = [f_r(x_r, x_d, u)^T\ f_d(x_r, x_d, u, d)^T]^T$. The nonlinear dynamic equations for the reduced-order system are then combined with the estimator gain and the output error to create a nonlinear state estimator as follows:

$$\dot{\hat{x}}_r = f_r(\hat{x}_r, x_d, u) + L_r(y_r - h_r(\hat{x}_r)) \tag{13}$$

where the measured values are used for the states in x_d, i.e., by assumption $y_d = x_d$. Note that following the previous assumption, $h_r(x_r) = C_r x_r$. Combining the nonlinear state estimator of Eq.13 with a nonlinear state feedback controller, $u = p_{DC}(x)$, that enforces an isolable structure in the closed-loop system and can be designed following the approaches presented in subsections 2.3.1 and 2.3.2, we obtain the following dynamic nonlinear output feedback controller:

$$\begin{aligned} \dot{\hat{x}}_r &= f_r(\hat{x}_r, x_d, p_{DC}(\hat{x})) + L_r(y_r - C_r\hat{x}_r) \\ u &= p_{DC}(\hat{x}) \end{aligned} \tag{14}$$

Due to the effect of estimation error, it is not possible to achieve complete decoupling. However, it is possible to achieve a near isolable structure that is sufficient for practical purposes. In this sense, we consider a near isolable structure to be one where the closed-loop system under output feedback control can be seen as an $O(e_r)$ regular perturbation of the closed-loop system under state feedback control which is locally exponentially stable and has an isolable structure. Thus, the estimation error can be viewed a small perturbation error that will be accounted for by the FDI thresholds designed to filter out normal process variation. Theorem 1 below summarizes the main analysis and controller design result of this section as well as the closed-loop FDI properties.

Theorem 1. Consider the closed-loop system of Eq.1 under the nonlinear output feedback controller of Eq.14 and assume that the pair (A_r, C_r) is observable and L_r is designed such that the matrix $(A_r - L_r C_r)$ has all of its eigenvalues in the left-half of the complex plane. Then, there exist δ, ϵ and T_y such that if f is continuously differentiable on $D = \{x \in \mathbb{R}^n |\ \|x\|_2 < \delta\}$, the Jacobian of f is bounded and Lipschitz on D and $\max\{\|x(t_0)\|_2, \|\hat{x}_r(t_0)\|_2\} < \delta$ then $\|x_r(t) - \hat{x}_r(t)\|_2 < \epsilon,\ \forall t > t_0 + T_y$, and a near isolable structure is enforced in the closed-loop system.

Proof. Under the control law of Eq.14, the closed-loop system of Eq.1 takes the form,

$$\begin{aligned} \dot{x} &= f(x, p_{DC}(\hat{x}), d),\ \ y = h(x) \\ \dot{\hat{x}}_r &= f_r(\hat{x}_r, x_d, p_{DC}(\hat{x})) + L_r(y_r - h_r(\hat{x}_r)). \end{aligned} \tag{15}$$

Linearizing the closed-loop system of Eq15 around the equilibrium point (origin) yields,

$$\dot{x} = Ax + Bp_{DC}(\hat{x}),\ \ y = Cx \tag{16}$$
$$\dot{\hat{x}}_r = A_r\hat{x}_r + A_{rd}x_d + B_r p_{DC}(\hat{x}) + L_r(y_r - C_r\hat{x}_r). \tag{17}$$

The error between the actual and estimated states of the reduced-order, linearized system is then $e_r = x_r - \hat{x}_r$ with the dynamics $\dot{e}_r = (A_r - L_r C_r)e_r$. Assuming that the pair (A_r, C_r) is observable and that L_r is chosen such that the matrix $A_r - L_r C_r$ has eigenvalues in the left-half of the complex plane, the estimation error, e_r, in the linearized system has exponentially stable dynamics. If the vector field of the nonlinear system, $f(x, p_{DC}(\hat{x}), d)$, is continuously differentiable and the Jacobian matrix is bounded and Lipschitz on $D = \{x \in \mathbb{R}^n |\ \|x\|_2 < \delta\}$, then the nonlinear system dynamics are also locally, exponentially stable within some region around the equilibrium point Khalil (1992). For some initial condition $max\{\|x_0\|_2, \|x_{r0}\|_2\} < \delta$, the state estimation error, e_r, will be bounded such that $\|x_r - \hat{x}_r\| < \epsilon\ \forall t > t_0 + T_y$, where T_y is a time interval of $O(\epsilon)$. Thus, the output feedback control approaches state feedback control with error of order ϵ, i.e., $x_r = \hat{x}_r + O(\epsilon)\ \forall t > t_0 + T_y$. For sufficiently small ϵ, this leads to a near isolable structure in the closed-loop system for almost all times since the state feedback controller $p_{DC}(x)$ enforces an isolable structure in the closed-loop system.

3.2 Application to a CSTR example

The example considered is a well-mixed CSTR in which a feed component A is converted to an intermediate species B and finally to the desired product C, according to the reaction scheme

$$A \overset{1}{\rightleftharpoons} B \overset{2}{\rightleftharpoons} C.$$

Both steps are elementary, reversible reactions and are governed by the following Arrhenius relationships:

$$r_1 = k_{10} e^{\frac{-E_1}{RT}} C_A, \;\; r_{-1} = k_{-10} e^{\frac{-E_{-1}}{RT}} C_B \tag{18}$$

$$r_2 = k_{20} e^{\frac{-E_2}{RT}} C_B, \;\; r_{-2} = k_{-20} e^{\frac{-E_{-2}}{RT}} C_C \tag{19}$$

where k_{i0} is the pre-exponential factor and E_i is the activation energy of the i^{th} reaction where the subscripts $1, -1,\ 2, -2$ refer to the forward and reverse reactions of steps 1 and 2. R is the gas constant, while C_A, C_B and C_C are the molar concentrations of species A, B and C, respectively. The feed to the reactor consists of pure A at flow rate F, concentration C_{A0} and temperature T_0. The state variables of the system include the concentrations of the three main components C_A, C_B, and C_C as well as the temperature of the reactor, T. Using first principles and standard modeling assumptions, the following mathematical model of the process is obtained

$$\begin{aligned}
\dot{C_A} &= \frac{F}{V}(C_{A0} - C_A) - r_1 + r_{-1} + d_1 \\
\dot{C_B} &= -\frac{F}{V}C_B + r_1 - r_{-1} - r_2 + r_{-2} \\
\dot{C_C} &= -\frac{F}{V}C_C + r_2 - r_{-2} \\
\dot{T} &= \frac{F}{V}(T_0 - T) + \frac{(-\Delta H_1)}{\rho c_p}(r_1 - r_{-1}) \\
&\quad + \frac{(-\Delta H_2)}{\rho c_p}(r_2 - r_{-2}) + u + d_2
\end{aligned} \tag{20}$$

where V is the reactor volume, ΔH_1 and ΔH_2 are the enthalpies of the first and second reactions, respectively, ρ is the fluid density, c_p is the fluid heat capacity, $u = Q/\rho c_p$ is the manipulated input, where Q is the heat input to the system, d_1 denotes a disturbance in the inlet concentration and d_2 denotes a fault in the control actuator. The system of Eq.20 is modeled with sensor measurement noise and autoregressive process noise. For details on noise generation and for complete system parameter values, please refer to Ohran et al. (2008).

In order to obtain the estimated trajectory for C_B, a state estimator as in Eq.13 was implemented using the reduced-order system $\hat{x}_r = [\hat{C}_B\ \hat{C}_C]^T$. The process measurements for C_A and T were used in computing the dynamics of $\hat{x}_r$. Note that although C_C is measured, it is used in the reduced-order state estimator so that the reduced-order system is observable. The control input was updated at each sampling interval with the measured values for C_A, T and C_C and the estimated value of $\hat{C}_B$. As discussed in subsection 3.1, C_A and T should not be modeled as dynamic states in the estimator since they are directly affected by the faults d_1 and d_2. Thus, the measured data for C_A and T must be used in modeling the estimator, and the final form of the state estimator based on the reduced subsystem $\hat{x}_r = [\hat{C}_B\ \hat{C}_C]^T$ is as given below:

$$\begin{aligned}
\dot{\hat{C}}_B &= -\frac{F}{V}\hat{C}_B + r_1 - r_{-1} - r_2 + r_{-2} + L_1(C_C - \hat{C}_C) \\
\dot{\hat{C}}_C &= -\frac{F}{V}\hat{C}_C + r_2 - r_{-2} + L_2(C_C - \hat{C}_C)
\end{aligned} \tag{21}$$

with

$$r_1 = k_{10} e^{\frac{-E_1}{RT}} C_A, \;\; r_{-1} = k_{-10} e^{\frac{-E_{-1}}{RT}} \hat{C}_B$$
$$r_2 = k_{20} e^{\frac{-E_2}{RT}} \hat{C}_B, \;\; r_{-2} = k_{-20} e^{\frac{-E_{-2}}{RT}} \hat{C}_C$$

where L is the filter gain obtained using Kalman-filtering theory based on the reduced-order system.The resulting value for L_r is $[L_{r1}\ L_{r2}]^T = [0.0081\ 0.0559]^T$.

The controlled output of the system, for the purpose of feedback linearization, is defined as the concentration of the desired product $y = h(x) = C_C$ (although, the measured output vector is $y_m = [C_A\ T\ C_C]^T$.) We consider only faults d_1 and d_2, which represent undesired changes in C_{A0} (disturbance) and Q (actuator fault), respectively. In this process, the manipulated input u appears in the temperature dynamics and the output, $y = C_C$, has relative degree 2 with respect to u. The fault d_1 appears only in the dynamics of C_A and the output, $y = C_C$, has relative degree 3 with respect to d_1. Finally, the output has relative degree 2 with respect to d_2. Based on the relative degrees of the output with respect to the input and with respect to the faults, under feedback linearizing control the system structure will be such that the state vector can be separated into two subsets: $X_1 = \{C_A, \hat{C}_B, T\}$ and $X_2 = \{C_C\}$. Thus, the fault signature for $d_1 = [1\ 0]^T$ and for $d_2 = [1\ 1]^T$. During the simulation, the T^2 for the full state vector is monitored in order to perform fault detection (substituting the estimate $\hat{C}_B$ for the unknown state C_B.) Each of the subsystems is monitored to compute the system signature upon detection of a fault. Based on observation of the system dynamic behavior, a fault detection window, T_P, of 1 min is used.

The control objective is to regulate the system at the equilibrium point

$$\begin{aligned}
&C_{As} = 2.06\frac{kmol}{m^3},\ C_{Bs} = 1.00\frac{kmol}{m^3},\ C_{Cs} = 0.937\frac{kmol}{m^3}, \\
&T_s = 312.6K,\ u_s = 0K/s
\end{aligned} \tag{22}$$

where the subscript s refers to the steady state values of the variables. It should be noted that the CSTR system of Eq.20 belongs to the class of systems of Eq.1 with $x = [C_A - C_{As},\ T - T_s,\ C_B - C_{Bs},\ C_C - C_{Cs}]^T$ where C_B is replaced with $\hat{C}_B$ in the definition of $\hat{x}$. This implies that we can apply the output feedback scheme presented using the controlled output $y = C_C$. Using Eq.7, the feedback-linearizing controller takes the following form:

$$u = \frac{v - L_f^2 h(\hat{x})}{L_g L_f h(\hat{x})} \tag{23}$$

with

$$v = [-2\zeta_1 - 2\zeta_2].$$

where

$$\begin{aligned}
\zeta_1 &= C_C, \;\; \zeta_2 = -\frac{F}{V}C_C + r_2 - r_{-2} \\
r_2 &= k_{20} e^{\frac{-E_2}{RT}} \hat{C}_B, \;\; r_{-2} = k_{-20} e^{\frac{-E_{-2}}{RT}} C_C.
\end{aligned}$$

The state variables are in the transformed space and are shifted so that the origin represents the desired set-point.

The closed-loop system was simulated for each of the two faults considered. Each simulation was run for a process time of 1 hour with the fault occurring at $t = 40$ min. The values for the faults were each zero prior to the fault

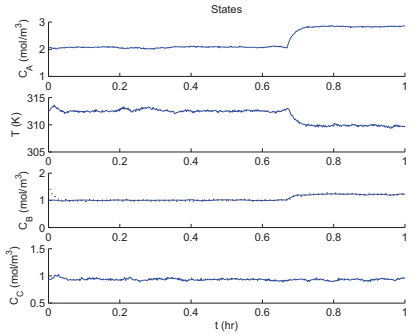

Fig. 1. Plot of measured state values for the CSTR under output feedback decoupling control with fault d_1. C_B shows both actual (solid) and estimated (dotted) values.

occurring and took constant values of $d_1 = 1\ kmol/m^3 min$ and $d_2 = 10\ K/min$ at $t = 40\ min$. The state estimator was initialized far from the operating point at $\hat{C}_B(0) = 1.5\ kmol/m^3$ and $\hat{C}_C(0) = C_C(0) = C_{Cs}$ in order to demonstrate convergence.

Figure 1 shows the trajectories for each of the states in the simulation with a failure in d_1. The fault is apparent at approximately $t = 40\ min$ $(0.667hr)$. We can readily see from the state trajectories, that the decoupling scheme was effective as evidenced by the fact that the output, C_C, is unaffected by the fault. Also, we see that the state estimator converged at around $t = 3\ min$.

For the system with a failure in d_1, Figure 2 shows the Hotelling's T^2 statistic for the two subvectors X_1 and X_2 as well as for the full state vector. From the graph, we can see that a fault is clearly detected at the expected time $t = 40\ min$ as shown in the plot of the T^2 statistic for the full state vector (T_3^2). Although there were a few single incidents of data breaching the upper control limit, none of them represented sustained departures for the length of the fault detection window, T_P. Also note that values above the upper control limit before $t = 0.1hr$ were due to the state estimator not having converged. Upon detection of the fault, the system signature can be computed as $W = [1\ 0]^T$ due to the fact that the T^2 statistic for the subvector X_1 exceeded the upper control limit for a sustained period and the T^2 for the subvector X_2 remained within the bounds of normal operation. Because the system signature matches that of the fault signature for d_1, a fault in d_1 is declared at time $t \approx 41\ min$. In Figure 3, we see the simulation results for the same system with a failure in d_2. Again, the failure is evident around $t = 40\ min$. However, in this case we see that both subsystems are affected. The process signature obtained from the T^2 statistics in Figure 3 shows that both subvectors were affected and this process signature matches the fault signature of d_2.

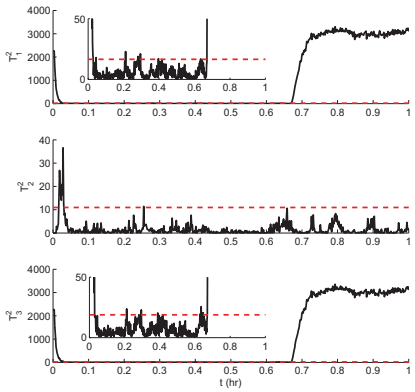

Fig. 2. T^2 statistics for the CSTR under output feedback decoupling control with fault d_1 for the subsystem X_1 (T_1^2), the subsystem X_2 (T_2^2) and the full system x (T_3^2).

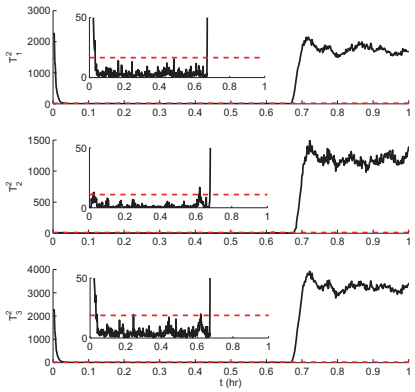

Fig. 3. T^2 statistics for the CSTR under output feedback decoupling control with fault d_2 for the subsystem X_1 (T_1^2), the subsystem X_2 (T_2^2) and the full system x (T_3^2).

REFERENCES

Christofides, P.D., Davis, J.F., El-Farra, N.H., Clark, D., Harris, K.R.D., and Gipson, J.N. (2007). Smart plant operations: Vision, progress and challenges. *AIChE Journal*, 53, 2734–2741.

Hotelling, H. (1947). Multivariate quality control. In O. Eisenhart (ed.), *Techniques of Statistical Analysis*, 113–184. McGraw-Hill.

Khalil, H. (1992). *Nonlinear Systems*. Macmillan Publishing Comapny.

Kourti, T. and MacGregor, J. (1996). Multivariate SPC methods for process and product monitoring. *Journal of Quality Technology*, 28, 409–428.

Mhaskar, P., Gani, A., and Christofides, P.D. (2006). Fault-tolerant process control: Performance-based reconfiguration and robustness. *International Journal of Robust & Nonlinear Control*, 16, 91–111.

Mhaskar, P., Gani, A., McFall, C., Christofides, P.D., and Davis, J.F. (2007). Fault-tolerant control of nonlinear systems subject to sensor data losses. *AIChE Journal*, 53, 654–668.

Nimmo, I. (1995). Adequately address abnormal operations. *Chem. Eng. Prog.*, 91, 36–45.

Ohran, B.J., Muñoz de la Peña, D., Christofides, P.D., and Davis, J.F. (2008). Enhancing data-based fault isolation through nonlinear control. *AIChE Journal*, 54, 223–241.

Tracy, N.D., Young, J.C., and Mason, R.L. (1992). Multivariate control charts for individual observations. *Journal of Quality Technology*, 24, 88–95.

Monitoring and Hybrid Control of Industrial Processing Systems (Invited Session)

Oral Session

Data reconciliation and optimal management of hydrogen networks of a petrol refinery

D. Sarabia*, S. Cristea*, E. Gómez*, G. Gutierrez*, C.A. Méndez, J.M. Sola***, C. de Prada***

*University of Valladolid, c/ Real de Burgos s/n, 47011 Valladolid, Spain (Tel: 34-983184647; e-mail: dsarabia@autom.uva.es).
** INTEC (UNL-CONICET), Güemes 3450, 3000 Santa Fe,Argentina (e-mail: cmendez@intec.unl.edu.ar)
*** PETRONOR, Edificio Muñatones, San Martin, 5, 48550 Muskiz, Spain (e-mail: jmsola@repsol.com).

Abstract: This paper describes the main problems associated to the management of hydrogen networks in petrol refineries and presents an approach to deal with them with the aim of operating the installation in the most profitable way. In particular, the problems of data reconciliation, economic optimization and interaction with the underlying basic control structure are reviewed. The paper provides also a proposal for the implementation of the system and illustrates the approach with results obtained using real data from an industrial site.

Keywords: Hydrogen networks, Process optimization, Data reconciliation, Control of networks.

1. INTRODUCTION

Hydrogen has become one of the main products in petrol refineries due to several factors, among them the new legislation about the reduction in the polluting compounds content (sulphur, nitrogen, aromatics, etc.), the need to convert heavy into light products to improve the economic balance of the refineries, and the installation of platformer plants, with the purpose of increasing the octane degree of the gasoline, as an alternative path to the use of lead compounds, operations that involve the use of large amounts of hydrogen.

As a result, hydrogen management plays a key role in the production of the different commercial oil fractions. Three different types of units are involved in a typical plant: dedicated hydrogen production units, hydrogen consuming units, and production units where hydrogen is the by-product of another process. All these kinds of units are interconnected through a hydrogen pipeline network.

Hydrogen is quite often produced on site from hydrocarbons in reformer ovens Control of these units, its temperature in particular, is not easy and MPC is frequently used to direct its operation. Demands of H_2 from the consumers change from time to time and constitute at the same time, a disturbance to reject with respect to the H_2 purity and a target to follow with regards to the mass flow. Adaptation to these demands plays an important role in order to operate with minimum losses while satisfying the orders from other units. The hydrogen production is fed at a given pressure and purity to the hydrogen pipeline network for distribution.

Most of the consumer plants have as a goal the desulphurization of different oil fractions and are named with the acronym HDS. They receive a mixture of hydrocarbons which react with H_2 at the appropriate temperatures and with the adequate catalysers in the HDS reactors. In order to secure the life of the catalysers, a given excess ratio hydrogen / hydrocarbons must be kept on the reactors. The surplus hydrogen from the reactors is separated and partially recycled, the excess being sent to the fuel-gas network. In the recovery of H_2, flash units can be employed as well as special membranes, which are used to separate high-purity H_2 from other gases.

The operation of the HDS is quite complex and its is affected by different disturbances, in particular the supply of hydrocarbons that may change in quantity as well as in composition according to the type of crude being processed and the global production aims. Important operating constraints are linked to the hydrogen / hydrocarbon ratio and to the operation of the compressors that maintain the hydrogen flows and inject it from the H_2 distribution network. This one should be able to provide the required amounts requested by the changing operation of the HDS along time.

There are a final set of plants, mainly platformers, which increase the octane index of the gasoline (catalytic reforming process) and generate hydrogen as result of these reactions. These plants generate a positive net flow of low purity hydrogen (between 75 % and 85 %) as a by-product, which is incorporated to the hydrogen pipeline network for use in other plants. Being a secondary product, there is no direct control of the H_2 production, so that it can be considered as a disturbance in flow and purity from the point of view of the network conditions.

All these types of plants are interconnected by several kilometres diverse pipes forming a distribution network with different purities, capacities and operating at several pressures. Fig. 1 displays the structure of one of such networks with three main hydrogen collectors, high purity

manifold (C-H4), medium purity manifold (C-H3) and low purity manifold (C-BP). The boxes represent the different types of production (H3 and H4), consumer and net production units (P1 and P2). Production and net production units dump hydrogen to the collectors (C-H4, C-H3, C-P1N1 and C-P2N2), while the HDS are fed from the different sources according to the choice of the operators.

In the picture we can see also the outputs from the plants to fuel-gas network, where the excess hydrogen is sent to be consumed in furnaces. Part of this flow also comes from the pressure controllers of the collectors (i.e. from manifold C-BP on the left). In order to guarantee that enough hydrogen is available to the consumer units when need it, a surplus of it must be maintained in the collectors, the excess being released by the pressure controllers to the fuel-gas network.

Hydrogen networks have received attention in the literature from the point of view of its (re)design, but very few from the one of real-time operation and, as far as we know, no commercial software is available in the sector for this purpose. The most used method of analysis is the so-called hydrogen pinch to evaluate the scope for hydrogen savings, Alves (1999). On the other hand, Hallale and Liu (2001) developed an improved methodology for hydrogen network retrofit that considers pressure constraints as well as the existing compressors.

To improve the day-to-day operation of the whole hydrogen supply network, this paper presents an integrated optimization based framework to optimize the distribution of the available hydrogen from producers to consumer facilities, so as to take advantage of low purity hydrogen supplies by combining streams of different purity levels and flows and, at the same time, ensuring operational restrictions. This work is carried out within an industrial project in close collaboration with Petronor, an oil refining company belonging to the Repsol-YPF Group, Spain. The major aim of the project is to provide an effective and integrated decision support system for on-line, open-loop optimization and data reconciliation. The proposed optimization tool has been validated with real-world data provided by the Petronor refinery.

The paper is organized as follows: after the introduction, the main problems of the hydrogen network operation and a proposal for a decision support system (DSS) are described in section two. The formulation of the hydrogen network model is given in section three, then, data reconciliation and hydrogen optimal management problems are described in sections four and five respectively while results obtained using plant data are presented in section 6. The paper ends with some conclusions and a short bibliography.

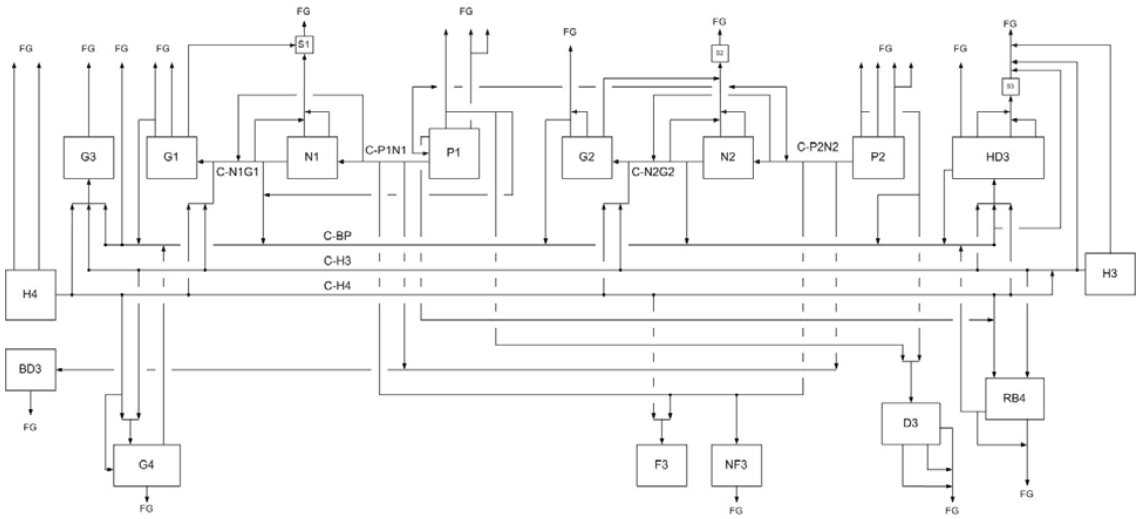

Fig. 1. A typical hydrogen network of a petrol refinery.

2. THE HYDROGEN NETWORK

2.1 Operational problems

Being a product heavily used and expensive to produce, optimizing the use of hydrogen is a clear target in any refinery. The problem can be formulated as of balancing the hydrogen that is being produced and consumed in the refinery and distribute it through the existing pipeline network in such a way that an economic target is optimized, while satisfying a set of operational constraints. Many aims appear as possible targets for the problem. For instance, minimizing the production of H_2, maximizing the use of lower cost hydrogen, minimizing the flow of H_2 to the fuel gas network, maximizing the use of low purity H_2, etc. the choice of one of them or a suitable combination being dependent of the particular situation of the refinery.

Several problems are related to the hydrogen management and optimization that are worth to mention, among them, the lack of reliable information about many streams and compositions and the large scale of the system that creates additional difficulties.

Regarding the first one, it is clear that reliable information of the network is required if we wish to perform optimal

decisions. Part of the uncertainty comes from the measurement system, but mainly from unmeasured variables and from partial measurements. In particular, gas flows, which are the main variables of the process, are measured usually in terms of volumetric flows that require compensation in order to be converted to mass or normalized flows required for the models, based on mass balances. This compensation involves pressure, temperature and molecular weight of the streams. Nevertheless, the last one are quite often non available, partly because of the price and reliability of the instruments measuring hydrogen purity and partly because the purity of the flows do not reflect directly its composition. With other gases this would not be a problem, but hydrogen has a molecular weight of only two, so that a small change in the composition of the (unmeasured) impurities, for instance from methane to propane, can have a significant impact on the molecular weight of the stream and hence on its mass flow.

Consequently, improving the information about the hydrogen network implies then the need of a data reconciliation system able to correct the readings of the process transmitters and estimate the unknown variables Cronkwright (2007).

Regarding the large scale of the system, it imposes computational barriers for a global solution of the problem. Firstly, because the size of the problem, but also for the wide range of time scales involved. The problem is dynamic in nature, being one of its aspects the need to adapt the rhythm of production of hydrogen to its consumption in order to minimize losses to the fuel-gas network. It operates with the changes in global production at the time scale of hours-days, changes in the operation of the producer and consumer units at the time scale of minutes-hours and the fast dynamics of the pressures and gas flows in the order of seconds. Trying to find solutions involving all these elements at the same time would be unrealistic, but the division in time scales allows separating the decision problems in different layers, facilitating in this way the solution as a set of linked sub-problems. The separation can be considered also from a functional point of view: producer and consumer units can perform local optimizations of its functioning provided that they have predictions of its future loads, while the optimal distribution of these loads must be performed in the network, which operates with a much faster dynamics and can be considered static in relation to the slower producer and consumer units.

Finally, notice that the implementation of optimally computed targets for the units and the distribution network will require a control layer that takes into account its dynamics and associated constraints. Alternatively, a decision support system (DSS) could give recommendations to the operators of the control room about these targets, being them the ones in charge of the implementation using the existing plant controllers.

2.2 Proposed architecture

In view of the above mentioned problems, the following supervisory architecture, depicted in Fig. 2, is proposed. It consists of four stages: the first one, corresponding to data reconciliation, allows fitting periodically the network and units models to the state of the plant. The second stage uses simplified models of the consumer units to compute the future profile of the hydrogen consumption at the unit hydrogen entrance, required to treat the future loads. This profile can be locally optimized or taken as the one corresponding to the current operating policy. The third stage considers the whole distribution network and, using a model of it, computes the optimal production profile of each production unit as well as the optimal distribution that satisfies the consumer units needs. Notice that, formulated in this way this problem can be considered as a series of constraint programming problems. Finally, the last stage is performed either by local MPC controllers (model predictive controllers) that implement the required distribution of flows, or as a DSS that gives the recommendations to the operators.

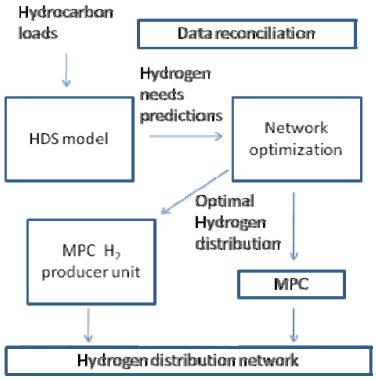

Fig. 2. A schematic of the proposed control and optimization system, with only one producer and one consumer unit.

In this paper, the reconciliation and optimization problems corresponding to the third stage are described assuming constant demands from the consumer units.

3. THE NLP MATHEMATICAL MODEL

All nodes in the complete hydrogen network are modelled by mass balances in terms of purity, flow and molecular weight for every stream, considering also a mixture of ideal gases. For example, a node consisting in one input stream F_1 and two output streams F_2 and F_3 with hydrogen purities X_1, X_2 and X_3 and molecular weights MW_1, MW_2 and MW_3 respectively is described by,

$$\begin{aligned} F_1 &= F_2 + F_3 \\ F_1 X_1 &= F_2 X_2 + F_3 X_3 \\ F_1 MW_1 &= F_2 MW_2 + F_3 MW_3 \end{aligned} \qquad (1)$$

On the other hand, the molecular weight of every stream is calculated from the hydrogen purity X, hydrogen molecular weight and molecular weights of all impurities MW^{imp} according to:

$$MW_i = (2X_i + MW_i^{imp}(100 - X_i))/100 \qquad i = 1,2,3 \qquad (2)$$

Volumetric flows F_i (Nm^3/h) in (1) are measured at standard temperature (0ºC) and pressure (1 Atm) conditions and purities are measured in percentage of volume.

In the particular industrial case considered, the nonlinear model consists of 142 equations like (1) and (2) and 263 variables, 137 of them are flows, 42 are purities, 42 are molecular weights of the streams and 42 are molecular weights of impurities of every stream. From a mathematical point of view it is necessary to define 121 boundary variables and the remaining 142 are considered explicit variables. On the other hand, there are 138 measured data from the process, so, 121 are assigned to boundary variables and the remaining 17 are redundant (explicit variables but with a measured data available).

4. DATA RECONCILIATION PROBLEM

The data reconciliation problem can be formulated as to compute the decision variables $F_{i,dec}$, $X_{i,dec}$ and $MW_{i,dec}^{imp}$ (flows, purities and molecular weights of impurities that minimize the function J (3) given by the sum of the squares of the deviations between the (compensated) measured data ($F_{i,med}, X_{i,med}, F_{i,med}^{red}, X_{i,med}^{red}$) and the calculated variables ($F_{i,dec}, X_{i,dec}, F_{i,exp}^{red}, X_{i,exp}^{red}$), while satisfying the nonlinear model (4), and the ranges on the explicit and decision variables (5), (6).

$$\begin{aligned}\min_{\{F_{i,dec},X_{i,dec},MW_{i,dec}^{imp}\}} J = &\sum_{i=1}^{89}\frac{w_i}{\sigma_i^2}\left(F_{i,dec}/Fc_i - F_{i,med}\right)^2 \\ &+\sum_{i=1}^{16}\frac{w_i}{\sigma_i^2}\left(X_{i,dec} - X_{i,med}\right)^2 \\ &+\sum_{i=1}^{15}\frac{w_i}{\sigma_i^2}\left(F_{i,exp}^{red}/Fc_i^{red} - F_{i,med}^{red}\right)^2 \\ &+\sum_{i=1}^{2}\frac{w_i}{\sigma_i^2}\left(X_{i,\exp}^{red} - X_{i,med}^{red}\right)^2\end{aligned} \tag{3}$$

Subject to:

$$\begin{aligned} F_{i,exp} &= g(F_{j,dec}, X_{k,dec}, MW_{l,dec}^{imp}) && i = 1,...,33 \\ F_{i,exp}^{red} &= g(F_{j,dec}, X_{k,dec}, MW_{l,dec}^{imp}) && i = 1,...,15 \\ X_{i,exp} &= g(F_{j,dec}, X_{k,dec}, MW_{l,dec}^{imp}) && i = 1,...,24 \\ X_{i,exp}^{red} &= g(F_{j,dec}, X_{k,dec}, MW_{l,dec}^{imp}) && i = 1,...,2 \\ MW_{i,exp} &= g(F_{j,dec}, X_{k,dec}, MW_{l,dec}^{imp}) && i = 1,...,42 \\ MW_{i,\exp}^{imp} &= g(F_{j,dec}, X_{k,dec}, MW_{l,dec}^{imp}) && i = 1,...,26 \end{aligned} \tag{4}$$

$$\begin{aligned} 0 \le F_{i,exp} &\le F_{max} && i = 1,...,33 \\ F_{i,\min}^{red} \le F_{i,exp}^{red} &\le F_{i,\max}^{red} && i = 1,...,15 \\ 0 \le X_{i,exp} &\le 100 && i = 1,...,24 \\ X_{i,\min}^{red} \le X_{i,exp}^{red} &\le X_{i,\max}^{red} && i = 1,...,2 \end{aligned} \tag{5}$$

$$\begin{aligned} F_{i,\min} \le F_{i,dec} &\le F_{i,\max} && i = 1,...,89 \\ X_{i,med} \le X_{i,dec} &\le X_{i,med} && i = 1,...,16 \\ MW_{i,\min}^{imp} \le MW_{i,dec}^{imp} &\le MW_{i,\max}^{imp} && i = 1,...,16 \end{aligned} \tag{6}$$

The stationary model of the hydrogen network is represented by (4), where explicit variables $F_{i,exp}$, $X_{i,exp}$, $MW_{i,\exp}$, $MW_{i,exp}^{imp}$, $F_{i,exp}^{red}$ and $X_{i,exp}^{red}$ are calculated solving the model $g(\bullet)$ with values of the boundary variables $F_{i,dec}$, $X_{i,dec}$ and $MW_{i,dec}^{imp}$ respectively.

The lower and upper limits of the decision variables associated to flows and purities come from the range of their corresponding instruments. But the limits for molecular weights of impurities are obtained through historical data of laboratory analysis in the associated streams, because there are not measured online. Finally, all terms in the cost function (3) have been normalized by means of the variance (σ_i^2) of data measured and can also be weighted by w_i (from 0 to 1) which indicates the level of importance of the corresponding instrument. The problem is a NLP (nonlinear programming) one that consists of 121 decision variables, 142 nonlinear equations (network model), 148 nonlinear constraints (74 lower limits and 74 upper limits of explicit variables) and 121 linear inequalities (lower and upper limits of decision variables).

There is another issue associated to flow measurements which must be taken into account: Most flowmeters in the refinery are orifice plates and they provide volumetric flows at standard conditions considering a specific pressure, temperature and molecular weight of design. However, these values change during the operation, being necessary compensate the corresponding measured flow. The compensated flow is given by,

$$F_{i,compensate} = F_{i,med} Fc_i \Rightarrow F_{i,med} = F_{i,compensate} / Fc_i \tag{7}$$

where $F_{i,med}$ is the measured flow and Fc_i is the factor of compensation defined for each orifice plate,

$$Fc_i = \sqrt{\frac{T_{i,dis}+273}{(P_{i,dis}+1)MW_{i,dis}}}\sqrt{\frac{(P_{i,op}+1)MW_{i,op}}{T_{i,op}+273}} \tag{8}$$

$P_{i,dis}$, $T_{i,dis}$ and $MW_{i,dis}$ are the design values for pressure, temperature and molecular weight of the stream (in kg/cm^2, ºC and g/mol respectively) and "op" are the operating values. Then, pressures and temperatures are also measured data from the process, and the molecular weight of every stream is a variable of the model, which is calculated through the model (4) or equation (2) in the small example.

So, the compensation factor Fc_i is a function of the hydrogen purity and molecular weight of each stream and indirectly a function of molecular weight of impurities for every stream and has been included in cost function (3). In this way, the reconciliation of mass and volume is made simultaneously in a rigorous manner.

5. OPTIMAL MANAGEMENT PROBLEM

According to the policy depicted in Fig.2, the main goal in this step is to distribute the hydrogen in the network and recirculate most of the excess of hydrogen from consumer units into the low purity manifold (C-BP), minimizing the hydrogen production from units H3 and H4 and all flows to the fuel gas manifold, while satisfying predefined hydrocarbon production targets, actual topological restrictions (10) as well as the exact demand in flow and purity of the hydrogen makeup flowing from the different sources to each consumer unit. The cost function *Jc* is shown bellow and the 11 flows to be minimized are shown in Table 2.

$$\min_{\{F_{i,dec},Pu_{i,dec}\}} Jc = \sum_{i=1}^{11} w_i F_i \tag{9}$$

Subject to:

$$\begin{aligned} F_{i,exp} &= g(F_{j,dec}, X_{k,dec}) \quad i = 1,...,33 \\ F^{red}_{i,exp} &= g(F_{j,dec}, X_{k,dec}) \quad i = 1,...,15 \\ X_{i,exp} &= g(F_{j,dec}, X_{k,dec}) \quad i = 1,...,24 \\ X^{red}_{i,exp} &= g(F_{j,dec}, X_{k,dec}) \quad i = 1,...,2 \end{aligned} \tag{10}$$

$$\begin{aligned} F_{i,\min} \le F_{i,exp} \le F_{i,max} \quad & i = 1,...,33 \\ F^{red}_{i,\min} \le F^{red}_{i,exp} \le F^{red}_{i,\max} \quad & i = 1,...,15 \\ X_{i,\min} \le X_{i,exp} \le X_{i.\max} \quad & i = 1,...,24 \\ X^{red}_{i,\min} \le X^{red}_{i,exp} \le X^{red}_{i,\max} \quad & i = 1,...,2 \end{aligned} \tag{11}$$

$$\begin{aligned} F_{i,\min} \le F_{i,dec} \le F_{i,\max} \quad & i = 1,...,89 \\ X_{i,\min} \le X_{i,dec} \le X_{i,\max} \quad & i = 1,...,16 \end{aligned} \tag{12}$$

This problem assumes that the dynamics of the network is faster than the one of the production and consumer ones, distributing in a better way the hydrogen available in the refinery. This is possible because in several units the excess hydrogen in the reactions can be sent to fuel gas manifold or recirculated to the low purity manifold (C-BP). Moreover, medium purity manifold (C-H3), low purity manifold (C-BP), manifold from unit N1 to G1 (C-N1G1) and manifold from unit N2 to G2 (C-N2G2) can send hydrogen to fuel gas if there is an overpressure, that is, if the hydrogen in these manifolds is not consumed/used in other units. Table 1. lists the decision variables of the problem: hydrogen production flow in units H4 and H3 (H4.F and H3.F) and all flows to fuel gas manifold which we want to minimize.

Notice that the model of the hydrogen network represented in (10), and used to solve the optimal management problem only includes flows and purities. The molecular weight of every stream, and the molecular weight of impurities are considered constant because all flows measured come from the solution of reconciliation problem previously solved. Equations (11) and (12) are the lower and upper limits of all flows and purities. In many cases these upper and lower limits are equal, forcing to maintain the exact flow and purity of hydrogen makeup in each consumer unit and forcing to maintain the exact excess of hydrogen and its purity from units as the current ones, letting unmodified in this way the internal operation of the HDS. For example, in unit G2 the decision variables are the inflow from manifold C-H4 (C-H4_G2.F), the inflow from manifold C-H3 (C-H3_G2.F) and the inflow from manifold C-N2G2 (C-N2G2_G2.F), imposing the constraints on the total inflow and purity to the unit. Others decision variables are the outflow from G2 to fuel gas (G2_FG.F) and from G2 to low purity manifold (G2_C-BP.F) being their sum fixed by the operation of the unit.

6. RESULTS AND DISCUSSION

The approach presented before has been tested with sets of real operation data of the refinery. Here we present some of them in a certain normalized scale. They corresponds to the average of two hours of operation and the corresponding standard deviation of the measured variables in this period. First, the data reconciliation methodology has been applied and then, the optimal management problem has been solved with all data reconciled. In both cases, the CPU time necessary to solve the optimization problem is lower than 3 minutes in a Intel Corel Duo with 2.13 GHz. Notice that all flows presented here have been scaled between 0 and 100 Nm^3/h and the purities of H_2 are in percentage (%).

6.1 Data reconciliation

The optimization problem (3) has been solved with a set of weights w_i equal to 1 for all terms in cost function (3), that is, we suppose that all measured data has the same accuracy. Fig. 3 shows the standard deviation times between the reconciled data (the solution) and measured data. Notice that, measured flows are not compensated but the solution flows are compensated in pressure, temperature and molecular weight, so, to compare both quantities the flows have been de-compensated. The solution of NLP problem provide a coherent close balance of hydrogen in all hydrogen network, 108 reconciled measures have a difference lower than 4 sigmas. These differences can be due to a bad flowmeter calibration or other causes. In order to eliminate its effect, the data reconciliation is repeated, this time with a weight w_i equal to zero in the potentially faulty variables, and the new reconciled data are used in the following step, while an order is given to recalibrate the defective instruments.

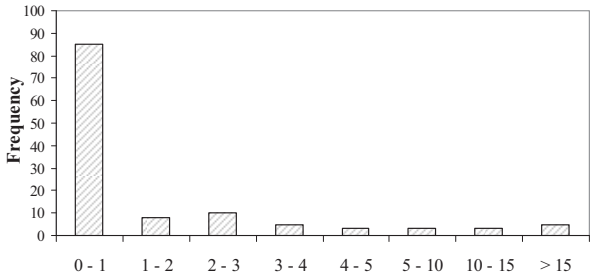

Fig. 3. Difference between reconciliated and measured data in number of standard deviations.

6.2 Optimal management of hydrogen network

The optimization problem (9) has been solved with the set of reconciled data obtained before. Results of the optimization are given in Table 1 besides their initial values(reconciled data): the cost function *Jc* and individual values of each term in this cost function. The cost function has been reduced from 100 Nm^3/h to 81.76 Nm^3/h. The optimal solution obtained reduces the total flow produced in units H4 and H3, from 73.22 Nm^3/h to 64.10 Nm^3/h and decrease the flow sent to fuel gas, from 24.98 Nm^3/h to 16.76 Nm^3/h, that is, the results show the possibility to reuse the hydrogen available in the refinery in a better way: i) without modifying the operation of each consumer unit ii) without increasing the production of hydrogen and iii) without increasing the purity of hydrogen produced. The minimum and maximum production of hydrogen allowed in unit H4 is 27.84 Nm^3/h and 62.77 Nm^3/h respectively and 15.57 Nm^3/h and 34.53 Nm^3/h for unit H3. Notice that the flow production of unit H3 (H3.F) has been reduced to the minimum production allowed, 15.57 Nm^3/h.

Table 1. Solution of the hydrogen optimal management problem

Flows (F_i)	Units	Data reconciled	Optimal solution
H4.F	Nm^3/h	50.76	48.53
H3.F	Nm^3/h	22.46	15.57
G1_FG.F	Nm^3/h	0.00	0.00
G2_FG.F	Nm^3/h	2.42	10.11
P1_FG.F	Nm^3/h	2.64	0.00
P2_FG.F	Nm^3/h	5.75	0.00
C-BP_FG.F	Nm^3/h	0.26	0.29
C-BP_FG2.F	Nm^3/h	12.72	6.36
C-N1G1_S1.F	Nm^3/h	0.08	0.00
C-N2G2_S2.F	Nm^3/h	1.72	0.89
C-H3_FG.F	Nm^3/h	1.20	0.00
Sum of all flows (*Jc*)	Nm^3/h	100.00	81.76
Economical cost (*Je*)	€/h	100.00	66.50

It is interesting to evaluate the economical cost of this solution *Je*. To do this, we are going to use the economical criteria used in the refinery. That is, the economical cost *Je* is the total hydrogen sent to fuel gas manifold times the total cost of hydrogen production minus the price of hydrogen as fuel,

$$Je = F_{H2-FG}\left(Cost_{ProductionH2} - Price_{combustibleH2}\right) \quad (13)$$

On the other hand, the total cost of hydrogen production is calculated by means,

$$Cost_{ProductionH2} = \frac{Cost_{H2inH4}H4.F + Cost_{H2inH3}H3.F}{H4.F + H3.F} \quad (14)$$

where H4.F and H3.F are the flow production in H4 and H3 respectively, the cost of hydrogen production in unit H4 is $Cost_{H2inH4}$ = 77.0€/KNm^3, in unit H3 is $Cost_{H2inH3}$ = 88.1€/KNm^3 and the price of hydrogen used as combustible in the fuel gas manifold is $Price_{combustibleH2}$=6.55 €/KNm^3. These are scaled values and they are related to pure hydrogen (100 % of purity). Table 1. shows the economical cost before hydrogen optimal management *Je* = 100.00 €/h and for the optimal solution *Je* = 66.5 €/h, so, it is possible a economical reduction of 33.5 %. Of course, this solution is not directly applicable to the refinery mainly due to the pressure constraints in hydrogen network. At present, further research is conducted to include the dynamical constraints imposed by the lower network control layer on the network optimization.

6. CONCLUSIONS

An approach has been presented to optimally manage complex hydrogen networks of refinery operations. The data reconciliation and optimal hydrogen distribution steps have been described with more detail using a NLP based optimization. The proposed method is able to systematically reduce utility cost by increasing hydrogen recovery in consumer units and reducing production cost in the alternative hydrogen suppliers. This paper is mainly focused on the treatment of hydrogen mass balances. Future work is aiming at extending the model to actual compression costs and other operational constraints as well as the use of alternative separation units (membranes) to recycle higher-purity off-gas to consumer units. In particular, including membranes in the model, convert it in a hybrid process, because membranes are formed by discrete package which can be turn on or turn off. Other improvements are related to the gross errors detection must be added to the DSS to enhance the quality and coherence of the reconciled data as well as better detect instrumentation malfunctions in the refinery.

ACKNOWLEDGMENTS

The valuable collaboration of Repsol-YPF and the Petronor refinery is gratefully acknowledged. The authors are also thankful for financial support received from project DPI2006-13593 of the Spanish CICYT and project GR. 085/2008 of JCyL.

REFERENCES

Alves, J. (1999). *Analysis and design of refinery hydrogen systems*, Ph.D. Thesis, UMIST.

Cronkwright, M., Frey, G., Brown, S. and Gulati, H. (2007) Refinery-wide data reconciliation case-study: operational decision support based on reconciled data. *NPRA 2007 O&A and Technology Forum*, 8-9.

Fonseca, A., Sá, V., Bento, H., Tavares, M.L.C., Pinto, G. and Gomes, A.C.N. (2008). Hydrogen distribution network optimization: a refinery case study. *Journal of Cleaner Production*, 16, 1755-1763.

Hallale, N. and Liub, F. (2001). Refinery hydrogen management for clean fuels production. *Advances in Environmental Research*, 6, 81-98.

Towler, G.P., Mann, R., Serriere, A.J-L, and Gabaude, C.M.D. (1996). Refinery hydrogen management: Cost analysis of chemically-integrated facilities. *Ind. Eng. Chem. Res.*, 35 (7), 2378-2388.

Performance Monitoring in Supermarket Refrigeration Systems - Synchronization of Refrigerated Display Cases

Liang Chen * **Torben Green** ** **Lars F. S. Larsen** **
Rafael Wisniewski * **Roozbeh Izadi-Zamanabadi** **

* *Department of Electronic Systems, Automation and Control, Aalborg University, Fredrik Bajers Vej 7C, DK-9220 Aalborg, Denmark (email: lchen.dhu@gmail.com, raf@es.aau.dk).*
** *Danfoss A/S, Refrigeration and Air conditioning, DK-6430 Nordborg, Denmark (email: Torben.Green@danfoss.com, Lars.Larsen@danfoss.com, Roozbeh@danfoss.com).*

Abstract: The overall task of a supermarket refrigeration system is to maintain the quality of the foodstuff. This is done by making use of a refrigeration cycle in which a refrigerant transport heat from the refrigerated display-cases to the outdoor surroundings. Typically the system is equipped with a decentralized control system neglecting interactions between subsystems. Though these interactions are minor they from time to time lead to a synchronization of the operation of the display-cases which causes an inferior control performance and increased energy consumption. In this paper we will analyze the synchronization using bifurcation theory and show that the system has a chaos-like behavior when it is not synchronized. Therefore, it is a good choice to de-synchronize the system by making the system chaotic. The positive maximal Lyapunov exponent is usually taken as an indication that the system is chaotic, it is used in this paper as a measure of performance for the tendency of the system to synchronize.

Keywords: Refrigeration system, Chaotic behavior, Hybrid system, Performance monitoring, Complex system.

1. INTRODUCTION

A supermarket refrigeration system consists of a central compressor rack that maintains the required flow of refrigerant to the refrigerated display cases located in the supermarket sales area. Each display case has an inlet valve for refrigerant that needs to be opened and closed such that the air temperature in the display case is kept within tight bounds to ensure a high quality of the goods. For many years, the control of supermarket refrigeration systems has been based on distributed control systems, which are flexible and simple. For example, each display case used to be equipped with an independent hysteresis controller that regulates the air temperature in the display case by manipulating the inlet valve. The major drawback, however, is that the control loops are vulnerable to self-inflicted disturbances caused by the interaction between the distributed control loops. In particular, practice and simulations show that the distributed hysteresis controllers have the tendency to synchronize [Larsen (2006)], meaning that the opening and closing actions of the valves coincide. Consequently, the compressor periodically has to work hard to keep up the required flow of refrigerant, which results in low efficiency, inferior control performance and a high wear on the compressor. The control problem is significantly complicated by the fact that many of the control inputs are restricted to discrete values, such as the opening/closing of the inlet valves and the stepwise control of the compressor. Furthermore, the system features switched dynamics turning the supermarket refrigeration system into a hybrid system.

The intense focus on limiting energy consumption and the global environmental awareness calls for energy efficient solutions. By monitoring the performance of the refrigeration system the "goodness" of the operation can be measured and early warnings about undesired behaviors can be given such that the control system can accommodate these and continuously optimize the system performance. In this paper we will focus on the monitoring of the synchronization phenomenon. By analyzing the system behavior using bifurcation and chaos theory [Crawford (1991), Devaney (2003)] it can be shown that the system has a chaos-like behavior. Bifurcation and chaos theory is most commonly applied to the mathematical study of dynamical systems to investigate dramatic changes in the qualitative or topological structure of a system. It can be dated back to 1975 when the first mathematical definition of 'chaos' was given [Li and Yorke (1975)]. The synchronization in the paper can be interpreted as a low order limit cycle [Wisniewski and Larsen (2008)]. It will be shown how the system jumps between low order and high order limit cycles varying the hysteresis bounds of the temperature controller. If the system converges towards a

low order limit cycle it can be seen as an indication of a risk that the system may synchronize. Therefore, it is a good choice to de-synchronize the system by making the system chaotic. The positive maximal Lyapunov exponent is usually taken as an indication that the system is chaotic. A huge number of references are available on calculation of the Lyapunov exponents [Müller (1995); Benettin et al. (1980); Wolf et al. (1985)]. We suggest using the maximal Lyapunov exponent as a measure of performance for the tendency of the system to synchronize.

2. SYSTEM DESCRIPTION

The overall task for a supermarket refrigeration system is to maintain the quality of the stored foodstuff. The goods are usually stored in open display cases in the sales area of the supermarket. The working principle of the supermarket system is a refrigeration cycle which utilizes a refrigerant to transport heat from the display cases to the outdoor surroundings.

A simplified supermarket refrigeration circuit is shown in Fig. 1. The compressors and the display cases are in the majority of supermarket refrigeration systems connected in parallel. The compressors supply the flow by compressing the low pressure refrigeration which is drained from the suction manifold. The refrigerant then passes through the condenser and into the liquid manifold. Each display case has an expansion valve which is connected to the liquid manifold where from the refrigerant then flows through the expansion valve and into the evaporator of the display case. In the evaporator the refrigerant absorbs heat from the stored goods and thereby changes phase. The vaporized refrigerant flows into the suction manifold, thus closing the refrigerant cycle. The typical layout of a

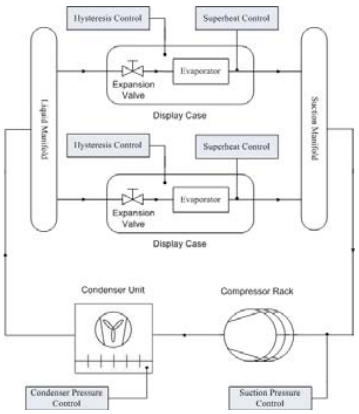

Fig. 1. Simplified supermarket refrigeration layout

display case can be seen in Fig. 2. The refrigerant is fed into the evaporator at the bottom of the display case and as the air is passed over the surface of the evaporator heat is absorbed which render a vaporization of the refrigerant. The resulting air flow creates an air curtain of cold air over the stored good. The air takes up the heat flow $\dot{Q}_{\text{goods}-\text{air}}$ from the stored goods and as a side effect the heat flow $\dot{Q}_{\text{load}}$ from the surroundings. The temperature of the air, T_{air}, is measured by a sensor mounted in the inlet air stream to the evaporator the goods to provide an indirect measure for the temperature of the goods.

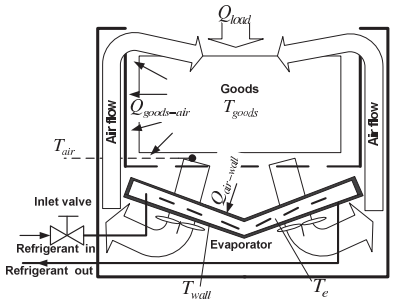

Fig. 2. Cross sectional view of a refrigerated display case.

2.1 Traditional Control

The typical controller structure for a supermarket refrigeration system is decentralized. Each of the display cases is fitted with an air temperature controller and a superheat controller, which ensures the desired filling of the evaporator. The compressor rack controls the suction pressure controller and the condenser fans control the condensing pressure. The only controllers considered in this paper is the suction pressure controller and the temperature controllers in the display cases.

The temperature in the display cases is controlled by a hysteresis controller that opens and closes the expansion valve, i.e. the valve opens when T_{air} reaches a predefined upper temperature limit and stay open until T_{air} decreases to the lower temperature limit and the valve closes again.

The suction pressure is controlled by switching compressors in the compressor rack on or off. A dead band around the reference is introduced to avoid excessive switching of the compressors. If the pressure exceeds the upper bound of the dead band one or more compressors are switched on. If the pressures drops below the lower bound of the dead band a compressor is switched off. This control strategy prevents moderate changes in the suction pressure from initiating compressor switching.

In a common supermarket many of the display cases will be alike and in addition be working under the same conditions. Thus, the switching frequency , for each of the expansion valves for the different display cases, will be close to each other. The display cases have a tendency to synchronize because there individual dynamics are coupled through the suction pressure. Synchronization of the display cases lead to periodic high and low amount of vaporized refrigerant flow into the suction manifold. Hence, large fluctuations in the suction pressure will be a consequence which then leads to higher switch frequency of the compressors and therefore excessive wear on the compressors. The result from synchronizing display cases can be seen in Fig. 3

3. MODEL OF THE REFRIGERATION SYSTEM

The model for the supermarket refrigeration system is composed of a number of sub-models which each represent a component in the refrigeration system. That is, individual models are made for the display cases, the suction manifold, the compressor rack, and the condensing unit. Because the emphasis of the paper is to examine

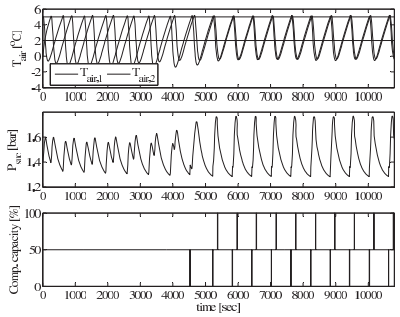

Fig. 3. The effect of synchronization

the synchronization phenomenon the modeling will be concentrated on the display cases and the suction manifold such that only the dynamics relevant for the control of the hysteresis control and the compressors are captured. The dynamic of the compressors are usually much faster than the dynamics of the rest of the refrigeration system. Thus, the modeling of the compressors dynamic is neglected.

The mathematical model presented in this section is a summary of the supermarket refrigeration model developed in [Larsen et al. (2007)]. The suction pressure P_{suc}, comprises the common state for the combined models. Each display case, $i = 1, \ldots, N$ where N is the number of display cases in the system, is described by four states. That is, the temperature of the goods $T_{\text{goods,i}}$, the air temperature $T_{\text{air,i}}$, the temperature of the evaporator wall $T_{\text{wall,i}}$, and the mass of the refrigerant in the evaporator $M_{r,i}$. The input is the volumetric flow generated by the compressors $\dot{V}_{\text{comp}}$, and the binary state of the ith inlet valve δ_i (closed or opened, $\delta_i \in \{0, 1\}$). The systems are affected by the heat load from the surroundings of the display case $\dot{Q}_{\text{load}}$.

$$\frac{\mathrm{d}T_{\text{goods,i}}}{\mathrm{d}t} = -\frac{\dot{Q}_{\text{goods-air,i}}(\cdot)}{M_{\text{goods,i}}\, C_{\text{p,goods,i}}} \tag{1}$$

$$\frac{\mathrm{d}T_{\text{wall,i}}}{\mathrm{d}t} = \frac{\dot{Q}_{\text{air-wall,i}}(\cdot) - \dot{Q}_{\text{e,i}}(\cdot)}{M_{\text{wall,i}} C_{\text{p,wall,i}}} \tag{2}$$

$$\frac{\mathrm{d}T_{\text{air,i}}}{\mathrm{d}t} = \frac{\dot{Q}_{\text{goods-air,i}}(\cdot) + \dot{Q}_{\text{load,i}}(\cdot) - \dot{Q}_{\text{air-wall,i}}(\cdot)}{M_{\text{air}} C_{\text{p,air,i}}} \tag{3}$$

$$\frac{\mathrm{d}M_{r,i}}{\mathrm{d}t} = \begin{cases} \dfrac{M_{\text{r,max,i}} - M_{\text{r,i}}}{\tau_{\text{fill,i}}} & \text{if } \delta_i = 1 \\ -\dfrac{\dot{Q}_{\text{e,i}}(\cdot)}{\Delta h_{\text{lg}}(P_{\text{suc}})} & \text{if } \delta_i = 0 \text{ and } M_{\text{r,i}} \geq 0 \\ 0 & \text{if } \delta_i = 0 \text{ and } M_{\text{r,i}} = 0 \end{cases} \tag{4}$$

$$\frac{\mathrm{d}P_{\text{suc}}}{\mathrm{d}t} = \frac{\dot{m}_{\text{in-suc}}(\cdot) + \dot{m}_{\text{r,const}} - \dot{V}_{\text{comp}}\, \rho_{\text{suc}}(P_{\text{suc}})}{V_{\text{suc}}\, \nabla\rho_{\text{suc}}(P_{\text{suc}})} \tag{5}$$

The enthalpy difference across the two-phase region of the evaporator is denoted by Δh_{lg}, the density of the refrigerant is denoted by ρ_{suc}, and $\nabla\rho_{\text{suc}}$ denotes the pressure derivative of the refrigerant density. T_e is the evaporation temperature for the refrigerant. The subscripts for the mass M and the heat capacity C_p denotes the media. The heat flow is denoted by $\dot{Q}$ where the subscript indicates the media between which the thermal energy is exchanged. In addition, the varies heat flows are defined by the following functions:

$$\dot{Q}_{\text{goods-air,i}}(T_{\text{goods,i}}, T_{\text{air,i}}) = UA_{\text{goods-air,i}} \cdot (T_{\text{goods,i}} - T_{\text{air,i}}) \tag{6}$$

$$\dot{Q}_{\text{air-wall,i}}(T_{\text{air,i}}, T_{\text{wall,i}}) = UA_{\text{air-wall,i}} \cdot (T_{\text{air,i}} - T_{\text{wall,i}}) \tag{7}$$

$$\dot{Q}_{e,i}(M_{r,i}, T_{\text{wall,i}}, P_{\text{suc}}) = UA_{\text{wall-ref,i}}(M_{r,i}) \cdot (T_{\text{wall,i}} - T_e(P_{\text{suc}})) \tag{8}$$

$$UA_{\text{wall-ref,i}}(M_{r,i}) = UA_{\text{wall-ref,max,i}} \cdot \frac{M_{\text{r,i}}}{M_{\text{r,max,i}}} \tag{9}$$

The overall heat transfer coefficient is denoted by UA and the subscript denotes the media from which the heat is transferred. In addition the mass flow rate in the suction manifold is given by:

$$\dot{m}_{\text{in-suc}}(M_{\text{r,i}}, T_{\text{wall,i}}, P_{\text{suc}}) = \sum_{i=1}^{N} \frac{\dot{Q}_{\text{e,i}}(\cdot)}{\Delta h_{\text{lg}}(P_{\text{suc}})} \tag{10}$$

The functions Δh_{lg}, ρ_{suc}, and T_e are refrigerant specific. Detailed description of these functions are given in [Larsen et al. (2007)]. In (4) it can be seen that the system have a hybrid nature due to the the discrete input which represents the opening and closing of the expansion valves.

3.1 Simplified model

In order to obtain a model that is suitable for analyzing the synchronization phenomenon the equation system (1) through (5) are further simplified to a second order affine switched system.

The simplification of the model is based on the following assumptions:

- The heat capacity of the goods is large, thus the temperature of the goods in a display case is constant and equal T_{g0}.
- The heat capacity of the air is small.
- The evaporator is instantly filled (emptied) when the inlet valve is opened (closed).
- The mass flow out of the display case when the valve is open is constant and equal $\dot{m}_0$.
- The evaporation temperature T_{e} and the density ρ_{suc} of the refrigerant in the suction manifold are affine functions of suction pressure P_{suc},

$$T_{\text{e}} = a_T P_{\text{suc}} + b_T \text{ and } \rho_{\text{suc}} = a_\rho P_{\text{suc}} + b_\rho$$

- The gradient $\nabla\rho_{\text{suc}}(P_{\text{suc}}) \equiv \nabla\rho_{\text{suc0}}(P_{\text{suc0}})$ is constant.
- The compressor delivers a constant volume flow $\dot{V}_{\text{comp}}$.
- The heat load $\dot{Q}_{\text{load}}$ on the display cases is constant.

Based on these assumptions the dynamic of the air temperature $T_{\text{air,i}}$ in the ith display case can be formulated as follows:

$$\frac{\mathrm{d}T_{\mathrm{air,i}}}{\mathrm{d}t} = \frac{\dot{Q}_{\mathrm{goods-air,i}} + \dot{Q}_{\mathrm{load,i}} - \delta_i \dot{Q}_{\mathrm{e,max,i}}}{\left(1 + \frac{UA_{\mathrm{goods-air,i}}}{UA_{\mathrm{air-wall,i}}}\right) M_{\mathrm{wall,i}} Cp_{\mathrm{wall,i}}} \quad \text{with} \tag{11}$$

$$T_{\mathrm{wall,i}} = T_{\mathrm{air,i}} - \frac{\dot{Q}_{\mathrm{goods-air,i}} + \dot{Q}_{\mathrm{load,i}}}{UA_{\mathrm{air-wall,i}}}, \tag{12}$$

$$\dot{Q}_{\mathrm{goods-air,i}} = UA_{\mathrm{goods-air,i}}(T_{\mathrm{g0,i}} - T_{\mathrm{air,i}}), \tag{13}$$

$$\dot{Q}_{\mathrm{e,max,i}} = UA_{\mathrm{wall-ref,max,i}}(T_{\mathrm{wall,i}} - a_T P_{\mathrm{suc}} - b_T), \tag{14}$$

The suction manifold dynamics is governed by the expression

$$\frac{\mathrm{d}P_{\mathrm{suc}}}{\mathrm{d}t} = \frac{\sum_{i=1}^{N} \delta_i \dot{m}_{0,\mathrm{i}} + \dot{m}_{\mathrm{r,const}} - \dot{V}_{\mathrm{comp}}(a_\rho P_{\mathrm{suc}} + b_\rho)}{V_{\mathrm{suc}} \cdot \nabla\rho_{\mathrm{suc0}}}. \tag{15}$$

Thus, the non-linear hybrid system has been reduced to a two order (for each display case) affine system with discrete inputs. For a refrigeration system with two display cases, the system states of the simplified model are $T_{\mathrm{air,i}} (i = 1, 2)$ and P_{suc}. The discrete inputs are $\delta_i \in \{0, 1\}$, which indicate if the valves are closed or open. The input δ is controlled by a hysteresis controller which changes the value of δ in the following way:

$$\delta_i(k+1) = \begin{cases} 1 & \text{if } T_{air,i} \geq \overline{T_{\mathrm{air,i}}} \\ 0 & \text{if } T_{air,i} \leq \underline{T_{\mathrm{air,i}}} \\ \delta_i(k) & \text{if } \underline{T_{\mathrm{air,i}}} < T_{air,i} < \overline{T_{\mathrm{air,i}}}, \end{cases} \tag{16}$$

where k denotes the time index, $\overline{T_{air,i}}$ is the upper bound the air temperature and $\underline{T_{air,i}}$ is the lower bound .

4. DYNAMICAL ANALYSIS

In this section, we will analyze dynamics of the simplified refrigeration model through bifurcation and chaos theory. The theory is most commonly applied to the mathematical study of dynamical systems. The aim of the theory is to investigate dramatic changes in the qualitative or topological structure of a system by changing smoothly a system parameter. For the refrigeration system we will analyze the system behavior by changing smoothly the lower bound in one of the display cases. The resulting behavior will be depicted in a so-called bifurcation diagram, from which the synchronization phenomenon will be studied, thereafter a measure will be developed to evaluate the tendency of synchronization. All simulation results in the section are based on the following parameter settings:

4.1 Phase plots w.r.t $\underline{T_{\mathrm{air,2}}}$

We shall study bifurcation, i.e. the influence of changes of system parameters on the system behavior at large. There are two system parameters, i.e. the upper bound and the lower bound of the temperature in the air temperature control of the display case. Here, we examine the lower bound of the second display case $\underline{T_{\mathrm{air,2}}}$. This will provide an example which will help understand how the system behaves with the varying parameter.

Fig. 4 shows some typical phase plots of the system states $T_{\mathrm{air,1}}$ and $T_{\mathrm{air,2}}$. When the parameter $\underline{T_{\mathrm{air,2}}} = 0$,

Table 1. Parameters for a simplified supermarket refrigeration system

Display cases					
$UA_{\mathrm{wall-ref,max}}$	500	$\frac{J}{s \cdot K}$	T_{g0}	3.0	^0C
$UA_{\mathrm{goods-air}}$	300	$\frac{J}{s \cdot K}$	$\dot{m}_0$	1.0	kg/s
$UA_{\mathrm{air-wall}}$	500	$\frac{J}{s \cdot K}$	$\dot{Q}_{\mathrm{load}}$	3000	J/s
$\dot{m}_{\mathrm{r,const}}$	0.2	$\frac{kg}{s}$	M_{wall}	260	kg
$\nabla\rho_{\mathrm{suc0}}$	4.6	$\frac{kg}{m^3 bar}$	$C_{\mathrm{p,wall}}$	385	$\frac{J}{kg \cdot K}$
The same parameters has been used for all disp.					
Compressor					
$\dot{V}_{\mathrm{comp}}$	0.28	$\frac{m^3}{s}$			
Suction manifold					
V_{suc}	5.00	m^3			
Air temperature control					
$\underline{T_{\mathrm{air,i}}}$	0.00	^0C	$\overline{T_{\mathrm{air,i}}}$	5.00	^0C
i for the disp.					
Coefficients					
$a_T = 16.2072$		$b_T = 41.9095$	$a_\rho = 4.6$		$b_\rho = 0.4$

the limiting behavior of the system switches between the two points $(0, 0)$ and $(5, 5)$ within an accepted tolerance ($1E-6$ in the paper). Here, we call it as a 2-periodic limit cycle. The period of a limit cycle is defined by the sum of a number of switching points on the boundary $\partial\Box = \partial([\underline{T_{\mathrm{air,1}}}, \overline{T_{\mathrm{air,1}}}] \times [\underline{T_{\mathrm{air,2}}}, \overline{T_{\mathrm{air,2}}}])$. The phase plot of the 2-periodic limit cycle corresponds to the synchronization phenomenon mentioned in the above section, where the two states $T_{\mathrm{air,1}}$ and $T_{\mathrm{air,2}}$ agree all the time. When the parameter $\underline{T_{\mathrm{air,2}}}$ increases slightly to the value of 0.15, a 4-periodic limit cycle appears, which is similar to the synchronization but with a bigger difference of the two states; we will call it the quasi-synchronization. When $\underline{T_{\mathrm{air,2}}} = 0.2$, another topology of 4-periodic limit cycle appears in the phase plot, which is totally different from the state agreement in the synchronization. If we continue increasing $\underline{T_{\mathrm{air,2}}}$ to the value of 0.3, we will find that the system tends to a high-periodic limit cycle with many switching points in the boundary of $\partial\Box$. It looks like chaos, the common phenomenon in the nonlinear system [Devaney (2003)]. It is far away from the synchronization.

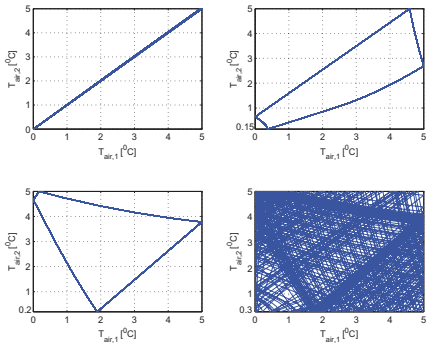

Fig. 4. Typical limiting behaviors with the various values of the parameter $\underline{T_{\mathrm{air,2}}}$. (a) 2-periodic limit cycle (synchronization, $\underline{T_{\mathrm{air,2}}} = 0$), (b) 4-periodic limit cycle ($\underline{T_{\mathrm{air,2}}} = 0.15$), (c) another 4-periodic limit cycle ($\underline{T_{\mathrm{air,2}}} = 0.2$), (d) high-periodic limit cycle ($\underline{T_{\mathrm{air,2}}} = 0.3$).

Synchronization of the display cases leads to large fluctuations in the suction pressure which then result in higher switch frequency of the compressors. It reduces lifetime of the compressors and enlarges energy consumption. Fig. 5 shows the comparison of the suction pressures between the synchronization and the chaos-like situation. We can see that in the chaos-like situation, the fluctuation range of the suction pressure decreases occasionally; even for the part with the same fluctuation amplitude as the synchronization, the pressure jumps so fast that the traditional PI controller in the compressor can fix it. Therefore, we conclude that good control performance can be achieved if the system behaves like chaos.

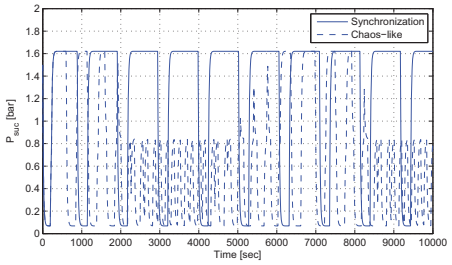

Fig. 5. The suction pressure P_{suc} in the situations of (a) synchronization and (b) chaos-like ($\underline{T_{\text{air},2}} = 0.3$).

4.2 Bifurcation diagram w.r.t $\underline{T_{\text{air},2}}$

To show how the system behaves with the smooth change of the parameter, we usually use the bifurcation diagram. A bifurcation diagram exhibits the possible long-term values (equilibria/fixed points or periodic orbits) of a system as a function of parameters in the system. A bifurcation occurs when a small smooth change made to the values of the bifurcation parameter causes a sudden 'qualitative' or topological change in its behavior. In this paper, the lower bound of the second display case $\underline{T_{\text{air},2}}$ is considered as the bifurcation parameter. Fig. 6 shows the limiting behavior of the state $T_{\text{air},1}$ with respect to the parameter $\underline{T_{\text{air},2}}$. The system exhibits very complicated behaviors. When $\underline{T_{\text{air},2}} = 0$, the system stabilizes at a 2-periodic limit cycle with the phase plot shown in Fig. 4a. As the parameter $\underline{T_{\text{air},2}}$ increases, the 2-periodic limit cycle becomes unstable, and a stable 4-periodic limit cycle appears (the phase plot is like Fig. 4b). The limit cycle retains the similar shape until another stable 4-periodic limit cycle occurs at $\underline{T_{\text{air},2}} = 0.186$ (the phase plot is like Fig. 4c). The shape keeps until $\underline{T_{\text{air},2}} = 0.234$, a higher order oscillation, like chaos, is generated (the phase plot is like Fig. 4d). If the parameter continuously rise, we can see that the system behavior becomes very complex and keeps switching between order and chaos-like oscillations.

The bifurcation diagram demonstrates that the simple refrigeration model is very sensitive to a change in the parameter $\underline{T_{\text{air},2}}$. If we change the parameter slightly, we obtain a totally different topology of the behavior. Therefore, we may ask: is it possible to suppress the synchronization phenomenon we found in the practice of the supermarket refrigeration system by adjusting a little

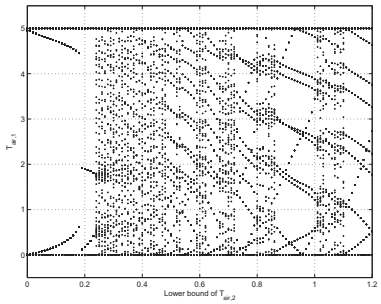

Fig. 6. Bifurcation diagrams of the system state $T_{\text{air},1}$ w.r.t the parameter $\underline{T_{\text{air},2}}$.

bit value of the bounds $\overline{T_{\text{air}}}$ or $\underline{T_{\text{air}}}$? It is obvious for a small 'toy' system with only two display cases that by changing the bound of the temperature, the system can be de-synchronized by making it chaotic. However, for a real plant with many different display cases, it is not obvious how to select the bounds. Hence, we are seeking a method to identify whether the bounds are selected such that the system will synchronize or not. For this purpose we will use the maximal Lyapunov exponent.

4.3 Description of Lyaponov exponent

The Lyapunov exponent characterizes the averaged rate of separation of two close trajectories in the phase space [Oseledec (1968)]. Quantitatively, two trajectories $x_1(t)$ and $x_2(t)$ in phase space with initial separation $\delta x(0)$ diverge

$$|\delta x(t)| \approx e^{\lambda t} |\delta x(0)|, \tag{17}$$

where $\delta x(t) = x_1(t) - x_2(t)$, λ is the Lyapunov exponent. The negative Lyapunov exponent measures the exponential convergence of trajectories, and the positive measures the exponential divergence of trajectories.

There are n Lyapunov exponents in the spectrum of an n-dimensional dynamical system. It is common to just refer to the largest one, i.e. the maximal Lyapunov exponent (MLE), which is defined as follows:

$$\lambda_{\max} = \lim_{t\to\infty} \frac{1}{t} \ln \frac{|\delta x(t)|}{|\delta x(0)|}. \tag{18}$$

The positive MLE is usually taken as an indication that the system is chaotic. It is used in this paper as a measure of performance for the tendency of the system to synchronize, that is, the higher value of the MLE the lower risk for synchronization.

4.4 Algorithm for computation the MLE

Algorithms for computing the Lyapunov exponents of the "smooth" dynamical system are well established [Benettin et al. (1980),Wolf et al. (1985)]. Let us consider the system

$$\dot{x} = f(x(t)), \tag{19}$$

where $f \in C^1$ is a continuously differentiable vector function with the initial condition $x(t_0) = x(0)$. The algorithm is based on the integration of the linearized equation (20) as follows:

$$\delta\dot{x} = J(t)\delta x, \tag{20}$$

where

$$J(t) = \left.\frac{\partial f(x)}{\partial x^T}\right|_{x=x(t)} \quad (21)$$

is the Jacobian matrix of f w.r.t the trajectory under consideration. The MLE $\lambda_{\max}$ is given as the average for some different initial conditions $\delta x(0)$ as Eq. (18).

For the "non-smooth" dynamical system with discontinuities like the refrigeration system in this paper, the above algorithm cannot be directly applied. One way to calculate the MLE is to supplement the transition conditions at the instants of discontinuities into the linearized equations [Müller (1995)]. This model-based method requires exact system information and the calculation complexity greatly increases with the number of the sub-systems. It is not suitable for the refrigeration system especially with many display cases in the supermarket. Besides, to apply this method one needs to know the switching sequence of the sub-systems in advance. It is also impossible in our case. We prefer to take the practical view of calculating the MLE from experimental data. Two well-known papers are [Wolf et al. (1985), S. Sato and Sawada (1987)]. Basic computing steps are given in the following:

(1) Based on the $N-$point time series $x_1, x_2, ..., x_N$, reconstruct the phase space:
$$Y_i = [x_i, x_{i+\tau}, ..., x_{i+(m-1)\tau}] \in R^n \ (i = 1, ..., M),$$
where $M = N - (m-1)\tau$, τ is the reconstruction delay, m is the embedding dimension.

(2) Find the nearest neighbor, $Y_{\hat{i}}$, by searching for the point that minimizes the distance to the particular reference point Y_i, that is, $d_i(0) = \min_{Y_i} \|Y_i - Y_{\hat{i}}\|$.
After j discrete-time steps, the distance $d_i(0)$ goes to $d_i(j)$.

(3) Estimate the averaged rate of distance separation as the MLE:
$$\lambda_{\max} = \frac{1}{j \cdot \Delta t} \cdot \frac{1}{(M-j)} \sum_{i=1}^{M-j} \frac{d_i(j)}{d_i(0)},$$
where Δt is the sampling period of the time series.

5. CONCLUSION

The main focus of this paper was on dynamic analysis of a simple system with two display cases by using bifurcation and chaos theory. Interpreting synchronization as a low periodic limit cycle and by varying the hysteresis bounds of the temperature controller it was shown that the system exhibited a complex chaos-like behavior when it was not synchronized, i.e. it switches between low and high periodic limit cycles. Synchronization of the system has proven to result in an inferior performance due to the resulting large pressure variations. It was, however, indicated in this paper that by de-synchronizing the system (by making it chaotic) it is possible to significantly reduce the pressure variations and hence improve the performance. The positive maximal Lyapunov exponent, usually used as the indication of chaos, was in this paper used as a measure of performance for the tendency of the system to synchronize. These findings for the small "toy" system may seem obvious, however they can easily be scaled to (realistic) large scale systems, where it is harder to distinguish and evaluate "good" and "bad" behavior.

REFERENCES

Benettin, G., Galgani, L., Giorgilli, A., and Strelcyn, J.M. (1980). Lyapunov characteristic exponents for smooth dynamical systems and for hamiltonian systems; a method for computing all of them. part i: Theory, part ii: Numerical application. *Meccnnica*, 15:9–20, 21–30.

Crawford, J.D. (1991). Introduction to bifurcation theory. *Reviews of Modern Physics, Vol. 63, No. 4*, 991–1037.

Devaney, R.L. (2003). *An Introduction to Chaotic Dynamical Systems*. Westview Press.

Georgiou, I.T. and Schwartz, I.B. (1999). Dynamics of large scale coupled structural/ mechanical systems: A singular perturbation/proper orthogonal decomposition approach. *SIAM J. Appl. Math.*, 59:1178–1207.

Kennedy, M.P., Kolumban, G., and Kis, G. (2000). Chaotic modulation for robust digital communications over multipath channels. *Int. J. Bifur. Chaos*, 10:695–718.

Larsen, L.F.S. (2006). *Model Based Control of Refrigeration Systems*. Ph.D. thesis, Department of Control Engineering - Aalborg University, Aalborg.

Larsen, L., Izadi-Zamanabadi, R., Wisniewski, R., and Sonntag, C. (2007). Supermarket refrigeration systems - a benchmark for the optimal control of hybrid systems. Technical report, Hycon, http://astwww.bci.uni-dortmund.de/hycon4b/wprelated/sr.pdf.

Li, T.Y. and Yorke, J.A. (1975). Period three implies chaos. *Amer. Math. Monthly*, 82:481–485.

Müller, P.C. (1995). Calculation of lyapunov exponents for dynamic systems with discontinuities. *Chaos, Solitons and Fractals*, 9:1671–1681.

Oseledec, V.I. (1968). A multiplicative ergodic theorem: Lyapunov characteristic numbers for dynamical systems. *Trans. Moscow Math. Soc.*, 19:197–231.

Ottino, J.M., Muzzio, F.J., and Tjahjadi, M. (1992). Chaos, symmetry, and self-similarity: Exploiting order and disorder in mixing processes. *Science*, 257:754–760.

S. Sato, M.S. and Sawada, Y. (1987). Practical methods of measuring the generalized dimension and the largest lyapunov exponent in high dimensional chaotic systems. *Prog. Theor. Phys.*, 77:1.

Schiff, S.J., Jerger, K., and Duong, D.H. (1994). Controlling chaos in the brain. *Nature*, 370:615–620.

Wisniewski, R. and Larsen, L.F.S. (2008). Method for analysis of synchronization applied to supermarket refrigeration system. In *17th IFAC World Congress*. Seoul, Korea.

Wolf, A., Swift, J.B., Swinney, H.L., and Vastano, J.A. (1985). Determining lvapunov exponents from a time series. *Physica D*, 16:285–317.

A hierarchical approach to optimal control of a hybrid chromatographic batch process ⋆

Dmitry Gromov * **Suzhou Li** ** **Jörg Raisch** *, **

* *Fachgebiet Regelungssysteme, Technische Universität Berlin*
e-mail: {gromov,raisch}@control.tu-berlin.de
** *Max-Planck-Institut für Dynamik komplexer technischer Systeme, Magdeburg, Germany*
e-mail: suzhou@mpi-magdeburg.mpg.de

Abstract: In this paper we consider a hierarchical approach to solve an optimal control problem for a hybrid chromatographic batch process. The plant consists of several chromatographic columns which can be connected in an arbitrary way. The plant configuration can therefore be considered as a discrete-valued control input. The dynamics of each chromatographic column is described by two coupled nonlinear partial differential equations. Hence, we have a hybrid optimisation problem with highly nonlinear dynamics.
To handle complexity, we propose a hierarchical two-level optimisation scheme: first, we solve a number of continuous optimisation problems that correspond to fixed configurations. In a subsequent step, on the basis of these solutions, we solve a discrete optimisation problem to generate the optimal configuration or configuration signal.
Because of the imposed structure, we can of course not expect the overall solution to be optimal. However, we demonstrate that, by using the plant configuration as an an additional control input, performance may be considerably improved when compared to the constant configuration scenario.

Keywords: Hierarchical optimisation, optimal control, hybrid systems, batch chromatography

1. INTRODUCTION

Column chromatography using solid and liquid phases is a key technique for the isolation and purification of valuable products, which has found a large number of successful applications in petrochemical, food and pharmaceutical industries during the last decades. Chromatographic separation processes can be operated in continuous or batch mode. Continuous separation is usually realised by the well-known simulated moving bed (SMB) process and its various modifications. This scheme has been proven to be very efficient for large-scale separation tasks. A drawback is, however, that the start-up procedure may take considerable time. Hence, this technology may not be suitable for the separation for relatively small amounts of mixtures. In this case, batch chromatography is an attractive alternative. Currently, a considerable number of chromatographic separations are operated in batch mode. Therefore the efficient operation and control of these processes is an important topic in order to exploit the economic potential and reduce the production cost.

There are a number of papers devoted to the optimisation and parameter identification of batch separation processes, see, e.g., (Dünnebier et al., 2001; Gao and Engell, 2005; Nagrath et al., 2003; Piątkowski, 2006) for details and references. These papers study the problem of optimisation of the process w.r.t. different performance criteria (e.g., productivity, or more specific criteria, like in (Felinger and Guiochon, 1996, 1998)). These criteria describe the overall (integral) performance of the system, but they are not very suitable if there are additional operational restrictions such as fixed batch volume, separation time and so on. Such restrictions naturally appear if the chromatographic system is a part of a complex chemical plant whose operation must follow a certain schedule. Moreover, in some applications the configuration of the plant is an additional degree of freedom, as the plant consists of a number of chromatographic columns that can be arranged in different ways. This degree of freedom has not been widely investigated up to now. An exception is (Ziomek et al., 2006), where the plant configuration is a design parameter, but constant over time. Also, additional operational restrictions (e.g., fixed batch size etc.) are not considered there.

In this contribution, we aim to develop a general framework to optimal (open loop) control of a chromatographic batch process. It includes several practically important problem statements and covers the scenario where the plant configuration may change during the operation of the plant. The latter introduces an additional, discrete-valued, degree of freedom, which makes the overall control problem an intrinsicly hybrid one. To deal with the inherent complexity of this hybrid problem, we suggest a hierarchical approach, where a lower control level determines the continuous inputs and a higher control level solves the remaining discrete optimisation problem.

⋆ Work has been done in the framework of the project "Methods from Discrete Mathematics for the Synthesis and Control of Chemical Processes", DFG-FG 468

This paper is organised as follows: In Section 2, we define the plant and a suitable PDE model. In Section 3, we motivate different optimisation problems for this plant. Section 4 suggests a hierarchical approach to solve these problems, and Section 5 presents a numerical example.

2. PLANT DESCRIPTION

2.1 Mathematical model

The system consists of N identical chromatographic columns, which can be arranged in $N_\ell \leq N$ parallel lines. Via valves connected to the columns, their configuration can be changed within a very short time. The column configuration can therefore be interpreted as a control input. The number of columns in the i-th line is denoted by $N^i_{col}(t)$, with the obvious restriction $\sum_{i=1}^{N_\ell(t)} N^i_{col}(t) = N$, $\forall t$.

Figure 1 shows a configuration with (at time t) $N = 5$, $N_\ell(t) = 2$, $N^1_{col}(t) = 3$, and $N^2_{col}(t) = 2$.

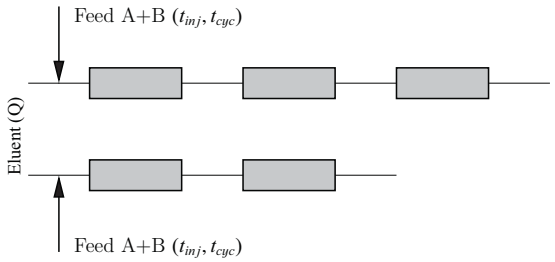

Fig. 1. Example configuration.

The dynamics of a single column is described by two nonlinearly coupled second order PDEs (so called equilibrium-dispersive model, (Guiochon et al., 2006)):

$$\frac{\partial c_k(t,x)}{\partial t} + F\frac{\partial q_k(t,x)}{\partial t} + u\frac{\partial c_k(t,x)}{\partial x} = D_{ap}\frac{\partial^2 c_k(t,x)}{\partial x^2}, \quad k \in \{A, B\},$$

where c_k and q_k are the liquid phase and solid phase concentrations, t, x are the temporal and spatial coordinates, u is the velocity of the liquid phase in the column, $F = (1-\epsilon_t)/\epsilon_t$ is the phase ratio, and ϵ_t is the column total void fraction. D_{ap} is the apparent axial dispersion coefficient defined as a function of u: $D_{ap} = uf(u)/2$, where $f(u) = (\alpha_D + \beta_D u)$ represents the linearised van Deemter equation, α_D and β_D are constant coefficients. In the following, we shall often use the volumetric flowrate $Q = u\pi D^2\epsilon_t/4$ instead of u, where D is the diameter of the column.

The concentrations of the components in the solid and liquid phases are related via the isotherm equation. To describe adsorption, the competitive Langmuir model is employed:

$$q_k(c_A, c_B) = \frac{H_k c_k}{1 + K_A c_A + K_B c_B}, \quad k \in \{A, B\},$$

where H_k and K_k are the Henry and the equilibrium constants. Component A is assumed to be less retained than component B, therefore, $H_A < H_B$.

The initial and boundary conditions are defined in a standard way: the initial concentration of the components in the columns is equal to zero. We employ the Danckwerts boundary conditions for the inlet of the first and the outlet of the last column in each line:

$$\left[uc_k(t,x) - D_{ap}\frac{\partial c_k(t,x)}{\partial x}\right]_{x=0} = uc_{k,in}(t)$$
$$\left.\frac{\partial c_k(t,x)}{\partial x}\right|_{x=L} = 0,$$

where $k \in \{A, B\}$, L is the column length. The "inter-column" boundary conditions reflect the continuity of the concentrations profiles.

The functioning of a single chromatographic column is shown schematically in Fig.2. The solution containing a binary mixture is injected at the inlet of the column during the time interval t_{inj}. Injections are repeated cyclically, with the interval between two subsequent injections t_{cyc} (Fig.2a). The mixture is transported through the column with velocity u. During transportation, separation occurs because one of the components (in our example component A) is less retained than the other one. Fig.2b shows a snapshot of the concentration profiles within the column at two time instants: at an "early" time instant, the separation effect is weak, and the concentration profiles for the two components are very close (dashed lines). At a later time instant, the profiles have moved further apart. Finally, component A is collected from the outlet during the fractionation interval t_{fr}. Fig.2c shows the concentration signals $c_{A,out}(t)$ and $c_{B,out}(t)$ at the outlet of the column. t_1 denotes the time instant when the concentration of the less retained component A exceeds a given threshold $c_{A,thr}$ and t_4 denotes the time when the concentration c_B becomes less than another threshold.

The following entities are used to characterise the separation process within each line and during each injection cycle. For component A, they are:

- The mass output
$$m_{A,out} = \int_{t_1}^{t_2} c_{A,out}(t)Q dt.$$
- The purity
$$Pur_A = \frac{\int_{t_1}^{t_2} c_{A,out}(t)dt}{\int_{t_1}^{t_2} c_{A,out}(t)dt + \int_{t_1}^{t_2} c_{B,out}(t)dt}.$$
- The yield
$$Y_A = \frac{m_{A,out}}{V_{inj} c_{A,in}},$$
where $V_{inj} = Q\, t_{inj}$ is the injection volume.
- The productivity
$$Pr_A = \frac{m_{A,out}}{t_{cyc}} = \frac{V_{inj} c_{A,in} Y_A}{t_{cyc}}. \quad (1)$$

For component B, they are defined in an analogous way.

There are also a number of technological constraints imposed on the system. Some of them are listed below (for details see Ziomek et al. (2006)). For example, for each line of columns, we have:

- Two restrictions on the volumetric flowrate. The first one is caused by the the maximal pressure drop ΔP_{max}, namely $Q \leq Q_{max}(\Delta P_{max})$. The maximal

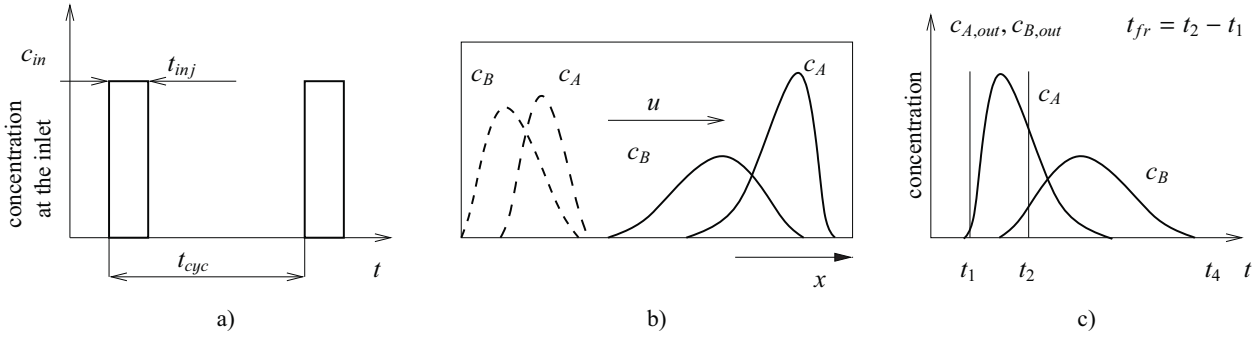

Fig. 2. a)input signal; b) concentration profiles within the column; c) concentration signals at the outlet.

pressure drop is calculated from the Darcy equation. Furthermore, there is a restriction on the maximal capacity of the pump Q^p_{max}. Hence, the resulting constraint is written as follows (Guiochon et al., 2006):

$$Q \leq \min(Q_{max}(\Delta P_{max}), Q^p_{max}).$$

- Minimal fractionation time caused by technical limitations: $t_{fr} \geq t_{fr,min}$.

2.2 Decision parameters

There are a number of parameters that can be chosen to optimise the process. We can divide them into two groups: discrete parameters, which can take values in a finite set, and continuous parameters, which can take values in a dense subset of $\mathbb{R}$. The continuous parameters are defined for each line $i \in \{1, N_\ell\}$:

(1) The velocity of the liquid phase, u^i,
(2) The injection time, t^i_{inj},
(3) The cycle period, t^i_{cyc},
(4) The fractionation time, t^i_{fr}.

The first parameter enters the PDEs directly whereas the second and the third one enter the boundary conditions of the first column within a line. The last parameter is usually determined to satisfy purity requirements.

The discrete parameters are the number of lines, N_ℓ, and the number of columns in the i-th line, N^i_{col}. These parameters describe the configuration of the plant. Furthermore, for a given configuration, the number of injections N^i_{inj} in line i is also a degree of freedom. In the following, we shall consider two cases:

(1) The configuration is constant during the entire operation of the process.
(2) The configuration changes over time.

In the second case, the sequence

$$\{(N_\ell(j), N^1_{col}(j), \ldots, N^{N_\ell(j)}_{col}(j), N^1_{inj}(j), \ldots, N^{N_\ell(j)}_{inj}(j), \tau(j))\}, \quad j = 0, N_s$$

can be interpreted as a control signal, with N_s the (a priori fixed) number of configuration changes, $\tau(j)$ the time interval during which the plant is operated in the j-th configuration, $N_\ell(j)$ the number of lines for this configuration, $N^i_{col}(j)$ the number of columns in the i-th line in the j-th configuration, and $N^i_{inj}(j)$ the number of injections for the i-th line in the j-th configuration.

In the remainder of this paper, we will use the following assumptions:

A1 The continuous control parameters for all parallel lines can be adjusted separately.
A2 The only component we are interested in is component A (less retained). In the following, we shall omit the subscript identifying the component if this is clear from the context.
A3 The continuous control parameters do not change within the interval of constant configuration $\tau(j)$.
A4 The cycle time is chosen to be equal to the duration of the chromatogram: $t^i_{cyc} = t^i_4 - t^i_1,\ i \in \{1, N_\ell\}$.
A5 The inlet concentrations $c_{k,in},\ k \in \{A, B\}$ are assumed to be known and fixed $\forall t$.

3. OPTIMISATION PROBLEMS

We shall investigate the following overall optimisation problems:

(1) Yield maximisation for fixed overall time span T_{max}:

$$\begin{aligned} &\text{maximise } Y_\Sigma \\ &s.t.\ T_\Sigma \leq T_{max}, \end{aligned} \tag{2}$$

where overall yield Y_Σ is defined as

$$Y_\Sigma = \frac{\sum_{j=0}^{N_s} V_\Sigma(j) Y_\Sigma(j)}{\sum_{j=0}^{N_s} V_\Sigma(j)}. \tag{3}$$

In (3), $V_\Sigma(j)$ and $Y_\Sigma(j)$ are the processed volume and the yield for the j-th configuration:

$$V_\Sigma(j) = \sum_{i=1}^{N_\ell(j)} N^i_{inj}(j) V^i_{inj}(j),$$

$$Y_\Sigma(j) = \frac{\sum_{i=1}^{N_\ell(j)} N^i_{inj}(j) m^i_{out}(j)}{c_{in} V_\Sigma(j)}.$$

Overall time T_Σ is given by $T_\Sigma = \sum_{j=0}^{N_s} \tau(j)$, where

$$\tau(j) \geq \max_{i=1,N_\ell(j)} (N^i_{inj}(j) t^i_{cyc}(j)).$$

(2) Produce required yield Y_{min} in minimal time:

$$\begin{aligned} &\text{minimise } T_\Sigma \\ &s.t.\ Y_\Sigma \geq Y_{min}. \end{aligned} \tag{4}$$

In both cases, we have additional constraints for overall batch size (volume): $V_\Sigma = V_{batch}$, and for overall purity:

$$Pur_\Sigma = \frac{\sum_{j=0}^{N_s} V_\Sigma(j) Y_\Sigma(j)}{\sum_{j=0}^{N_s} \frac{V_\Sigma(j) Y_\Sigma(j)}{Pur_\Sigma(j)}} \geq Pur_{min},$$

where

$$Pur_\Sigma(j) = \frac{\sum_{i=1}^{N_\ell(j)} N^i_{inj}(j) m^i_{out}(j)}{\sum_{i=1}^{N_\ell(j)} N^i_{inj}(j) \frac{m^i_{out}(j)}{Pur^i(j)}}.$$

Note that m^i_{out} and Pur^i are the mass output and the purity in the i-th line for one cycle and depend on the continuous decision parameters as well as on the number of columns in line i, N^i_{col}.

4. HIERARCHICAL APPROACH

The optimisation problems posed in Sec.3 are highly complex tasks. In the variable configuration case, there is a large number of discrete and continuous decision parameters. In each iteration step during the optimisation procedure, $2N_\ell$ partial differential equations have to be solved. Moreover, the values of the cost functions cannot be found analytically and have to be calculated from the results of numerical simulation. Since information about the derivatives of the cost functions is not available, derivative-free methods must be used, which substantially reduces the efficiency of numerical optimisation. Therefore, standard solvers normally fail to deliver a solution to these optimisation problems in reasonable time (if they provide a solution at all).

Therefore, we propose to use a hierarchical optimisation scheme to cope with complexity. In this scheme, optimisation of discrete and continuous decision variables is decoupled.

4.1 Low-level (local) optimisation

On the low level, we define a set of continuous optimisation problems for one line of columns over one cycle period. The cost function for the low-level problem is productivity (Eq.1). The set of low-level problems is parametrised by the number of columns n (n=1, N) in a line and a (finite) number of purity constraints $Pur \geq p_m$, $m = 1, M$:

$$\begin{aligned} &\underset{(Q, t_{inj}, t_{fr})}{\text{maximise}} \quad Pr \\ &s.t.\ N_{col} = n, \\ &\quad Pur \geq p_m. \end{aligned} \tag{5}$$

For each low-level problem, the optimal solution ($Q^*, V^*_{inj} = t^*_{inj} Q^*, t^*_{fr}$) and the corresponding values (t^*_{cyc}, m^*_{out}) need to be stored and will be used for the solution of a high-level problem. This information can be conveniently collected in the following table.

		Pur		
		p_1	...	p_M
N_{col}	1	.	.	.
	⋮	.	.	.
	n	.	.	Q^*, V^*_{inj}, t^*_{fr}, t^*_{cyc}, m^*_{out}
	⋮	.	.	.
	N	.	.	.

Table 1. Results of the local optimisation

4.2 High-level optimisation

a) Constant configuration case:

On the high level we maximise overall productivity

$$Pr_\Sigma = \frac{\sum_{i=1}^{N_\ell} N^i_{inj} m^i_{out}}{T_\Sigma} \tag{6}$$

$$\text{s.t. } Pur_\Sigma = \frac{\sum_{i=1}^{N_\ell} N^i_{inj} m^i_{out}}{\sum_{i=1}^{N_\ell} N^i_{inj} \frac{m^i_{out}}{Pur^i}} \geq Pur_{min} \tag{7}$$

$$V_\Sigma = \sum_{i=1}^{N_\ell} N^i_{inj} V^i_{inj} = V_{batch} \tag{8}$$

and such that

$$T_\Sigma = \max_{i=1,N_\ell} (N^i_{inj} t^i_{cyc}), \tag{9}$$

or such that

$$Y_\Sigma = \frac{\sum_{i=1}^{N_\ell} N^i_{inj} m^i_{out}}{c_{in} V_\Sigma}. \tag{10}$$

Note that for fixed time T_Σ and fixed batch volume V_Σ, the maximisation of overall productivity is equivalent to the maximisation of overall yield. Conversely, for fixed batch volume and fixed overall yield, the maximisation of productivity is equivalent to the minimisation of the overall processing time. Therefore, the optimisation problem (6-8) and (9) or (10) can be seen as a general formulation encompassing both our original optimisation problems described in Sec. 3.

The decision variables for the high-level optimal problem are N_ℓ, N^i_{inj}, $i = 1, N_\ell$, and pairs (n^i, m^i) representing the entry in the n^i-th row and m^i-th column of Table 1. Naturally, the restriction $\sum_{i=1}^{N_\ell} n^i = N$ has to hold. As N^i_{inj}, the number of injections in the i-th line, is always bounded by the problem setup, the high-level problem has

a finite search space. Note that to evaluate the overall cost function, only the values of the decision variables and the corresponding entries in Tab. 1 are needed. In particular, no numerical simulations are required. In effect, this means that we assemble an overall solution from the solutions of the low-level optimisation problem.

While we cannot expect the resulting solution to be globally optimal, it seems reasonable that we shall obtain a decent approximation.

b) Variable configuration case:

In the variable configuration case, the overall cost function (6) changes to

$$Pr_{\Sigma} = c_{in} \frac{\sum_{i=0}^{N_s} V_{\Sigma}(j) Y_{\Sigma}(j)}{\sum_{i=0}^{N_s} \tau(j)} \tag{11}$$

with the obvious corresponding changes in (7)-(10). The only difference in terms of the optimisation procedure is an increase of the cardinality of the search space.

From a practical point of view, the question whether a significant improvement is possible when allowing a variable configuration is of prior interest. Our example in the next section indicates that switching configuration may indeed improve performance.

5. NUMERICAL EXAMPLE

As an example of the proposed approach we consider a case with 5 chromatographic columns, $N = 5$. The numerical values of parameters and restrictions for a single column are listed in Appendix A. We investigate the maximisation of yield within a given time. The required minimal purity is 95%. Time T_{max} is equal to 20000s. Different overall batch volumes are considered.

5.1 Low-level optimisation

First, we solved a set of low-level optimisation problems of the form (5). Optimisation was performed for the following values of required purity: $p_m \in \{0.9, 0.91, \ldots, 0.99\}$ and for different numbers of columns in the line: $N_{col} \in \{1, 2, 3, 4, 5\}$. The optimal values of the continuous decision variables $(Q^*, V^*_{inj}, t^*_{fr})$, as well as the corresponding values (t^*_{cyc}, m^*_{out}) were stored as a table as indicated in the previous section.

An improved derivative-free Nelder-Mead method (Nelder and Mead, 1965; Kelley, 1999) was used to solve these nonlinear constrained optimisation problems. In the proposed variant, the initial simplex was generated randomly and a multi-restart strategy was taken to increase the probability of locating the global optimum. For each subsequent restart, only the vertex with the best solution found previously was retained and the other vertices were replaced with new random points. Moreover, the algorithm was capable of handling the nonlinear constraints by using the penalty function technique. During the optimisation, a numerical simulation procedure was used to generate the outlet concentration signals for given values of decision variables. From this, we evaluate the objective function and check the constraints. This information was then used by the optimiser to find a new direction in the continuous search space to improve the cost.

The coupled PDE model of the considered process with N_{col} columns connected in series was discretised using the method of orthogonal collocations on finite elements (Ma and Guiochon, 1991; Kaczmarski et al., 1997). The resulting system of differential algebraic equations was solved by ode15s, a variable step-size and variable order integrator implemented in Matlab (Shampine and Reichelt, 1997). Information about the Jacobian contained in the discretised model equations was fully exploited by the solver, thereby significantly accelerating the integration.

5.2 High-level optimisation

a) Constant configuration case:

Next, we solved the discrete optimisation problem (2) for the constant configuration case, as described in Sec.4.2a. The results of the optimisation procedure are presented in Tab. 2.

Volume of the batch, V_{batch}, ml	Optimal configuration	Optimal purities, Pur^i, %	Resulting productivity Pr, g/s	Resulting yield Y
23000	{3 2}	0.94 0.97	5.942 e-4	0.517
25000	{3 2}	0.95 0.95	6.2404 e-4	0.4992
27000	{3 2}	0.96 0.94	6.4118 e-4	0.475
28000	{2 2 1}	0.95 0.96 0.97	6.0756 e-4	0.424
29000	{2 2 1}	0.95 0.95 0.98	6.2808 e-4	0.421
31000	{2 2 1}	0.95 0.96 0.94	6.6047 e-4	0.3901

Table 2. Results of high-level optimisation for constant configuration scenario

b) Variable configuration case:

It can be seen from Table 2 that the configuration {3 2} ensures high productivity for smaller batch volumes. For higher volumes, this configuration cannot process the required volume within the required time. Hence, from the certain batch volume V_{batch}, one has to use another configuration, for example {2 2 1}. This configuration ensures higher throughput at the cost of productivity. Therefore, it is intuitive to consider configuration as a time-variant degree of freedom, i.e., a control variable. In this way one expects to combine the advantages of both configurations.

We considered the case with one possible configuration change, i.e., $N_s = 1$. Indeed, our optimisation results show an increase of performance for the variable configuration case. The results are shown in Table 3. It is worth noting that the improvement could be much bigger if there were bigger differences in the productivity and in the throughput between the different configurations.

ACKNOWLEDGEMENTS

We acknowledge many helpful discussions with A. Seidel-Morgenstern, L.C. Keßler and G. Ziomek.

Volume of the batch, V_{batch}	Optimal configuration	Time, $\tau(j)$, $j = 0, 1$	Volume, $V_\Sigma(j)$	Optimal purities, $Pur^i(j)$	Resulting productivity, Pr_Σ	Resulting yield, Y_Σ	Improvement compared to constant configuration case
28000	{2 2 1}	10600	16100	0.95 0.95 0.96	6.4305 e-4	0.4603	+5.84%
	{3 2}	9400	11900	0.95 0.95			
29000	{2 2 1}	10800	16675	0.95 0.95 0.96	6.5115 e-4	0.4509	+3.7%
	{3 2}	9200	12325	0.96 0.94			

Table 3. Results of the high-level optimisation with the change of structure

REFERENCES

Dünnebier, G., Engell, S., Epping, A., Hanisch, F., Jupke, A., Klatt, K.U., and Schmidt-Traub, H. (2001). Model-based control of batch chromatography. *AIChE Journal*, 47(11), 2493–2502.

Felinger, A. and Guiochon, G. (1996). Optimizing preparative separations at high recovery yield. *Journal of Chromatography A*, 752, 31–40.

Felinger, A. and Guiochon, G. (1998). Comparing the optimum performance of the different modes of preparative liquid chromatography. *Journal of Chromatography A*, 796(1), 59–74.

Gao, W. and Engell, S. (2005). Iterative set-point optimization of batch chromatography. *Computers & Chemical Engineering*, 29(6), 1401–1409.

Guiochon, G., Felinger, A., and Shirazi, S. (2006). *Fundamentals of Preparative and Nonlinear Chromatography*. Elsevier.

Kaczmarski, K., Mazzotti, M., Storti, G., and Morbidelli, M. (1997). Modelling fixed-bed adsorption columns through orthogonal collocations on moving finite elements. *Comput. Chem. Eng.*, 21(6), 641–660.

Kelley, C. (1999). *Iterative Methods for Optimization*. SIAM.

Ma, Z. and Guiochon, G. (1991). Application of orthogonal collocation on finite elements in the simulation of nonlinear chromatography. *Comput. Chem. Eng.*, 15(6), 415–426.

Nagrath, D., Bequette, B.W., and Cramer, S.M. (2003). Evolutionary operation and control of chromatographic processes. *AIChE Journal*, 49(1), 82–95.

Nelder, J. and Mead, R. (1965). A simplex method for function minimization. *Comput. J.*, 7(4), 308–313.

Piątkowski, W. (2006). Analysis of the design and optimization of preparative chromatography on the basis of the separation of a real post-reaction mixture. *Acta Chromatographica*, 16, 92–118.

Shampine, L. and Reichelt, M. (1997). The MATLAB ODE suite. *SIAM J.Sci.Comput.*, 18.

Ziomek, G., Antos, D., Tobiska, L., and Seidel-Morgenstern, A. (2006). Comparision of possible arrangements of five identical columns in preparative chromatography. *Journal of Chromatography A*, 1116, 179–188.

Appendix A. LIST OF PARAMETERS

Name	Unit	Description	Value
Physical (geometric) parameters			
L	cm	Column length	25
D	cm	Column diameter	2
ϵ_t	-	Column total void fraction	0.78
α_D	-	Coefficient of the linearised van Deemter equation	0.012
β_D	-	Coefficient of the linearised van Deemter equation	0.156
H_1	-	Henry constant	5.7
H_2	-	Henry constant	7.4
K_1	ml/g	Equilibrium constant	170
K_2	ml/g	Equilibrium constant	370
Operating parameters			
$C_{i,in}$, i=A, B	g/ml	Feed concentrations	0.001
$C_{i,thr}$	g/ml	Threshold concentrations	$0.001C_{i,in}$
N	-	Number of columns	5
t_{fr}^{min}	s	Minimal collecting (fractionating) time	5
ΔP_{max}	bar	Maximal pressure drop	100
Q_{max}	ml/s	Volumetric flowrate corresponding to the maximal pump capacity	8.33

Sensitivity-based Predictive Control of a Large-scale Supermarket Refrigeration System ⋆

Christian Sonntag * **Malte Kölling** ** **Sebastian Engell** *

* *Process Dynamics and Operations Group (BCI-DYN), Dept. of Biochemical and Chemical Engineering, Technische Universität Dortmund, 44221 Dortmund, Germany E-mail: {christian.sonntag|sebastian.engell}@bci.tu-dortmund.de.*
** *Hydro Aluminium, 41515 Grevenbroich, Germany E-mail: malte.koelling@hydro.com*

Abstract: Today, many supermarket refrigeration systems are operated by decentralized control systems that often lead to excessive starting and stopping of the compressors which drive the cooling cycle and, consequently, to a large wear of the process equipment. In our previous work, a hierarchical model-predictive control scheme was proposed for supermarket refrigeration systems that overcomes this drawback. In this scheme, simple low-level temperature controllers are employed, and the high-level optimization task is the optimal adjustment of the parameters of these controllers. While this approach yields a good control performance, it is computationally too expensive for larger systems. In this paper, a more efficient approach is presented that is based on an approximation of the system dynamics using simple models that are computed from system sensitivities around simulated reference trajectories. The application of the new approach to a large hybrid model proves the real-time capabilities of the new technique.

Keywords: Predictive control, process control, supermarket refrigeration systems, discretely controlled continuous systems, hybrid systems.

1. INTRODUCTION

In supermarket refrigeration systems, a rack of compressors feeds liquid refrigerant to several open display cases that are used to cool edible goods. These systems exhibit both, discrete and continuous dynamics, and are thus hybrid systems: The control inputs (valves and compressors) can only be switched discretely, and the nonlinear continuous dynamics changes due to switching of the discrete inputs. Today, supermarket refrigeration systems are often controlled using decentralized schemes in which each display case is equipped with independent simple control loops (Larsen et al., 2005). Since this approach often causes a severe reduction of the efficiency of the process and of the lifespan of the equipment (see e.g. Wisniewski and Larsen (2008)), the suitability of advanced model-predictive schemes for the control of supermarket refrigeration systems has been investigated in previous work to overcome these problems.

In Larsen et al. (2005), the hybrid MPC approach from Bemporad and Morari (1999) is applied to a piecewise affine approximation of the nonlinear hybrid model of a supermarket refrigeration system that is also considered in this paper. Although this approach succeeds in keeping most process variables within pre-specified bounds, the frequency of the compressor switching is high due to the inaccuracy of the linear approximations of the nonlinear dynamics. In Sarabia et al. (2009), a nonlinear MPC scheme is proposed in which the cost function is evaluated by simulation of a nonlinear model. This approach is capable of keeping all process variables within the bounds, but the solution of complex NLP problems with many decision variables in each iteration leads to a large computational effort. In Sonntag et al. (2007, 2008), a hierarchical NMPC approach for supermarket refrigeration systems is presented. Here, the switching of the valves of the display cases is not optimized directly, but simple low-level controllers are employed that regulate the temperatures in the display cases with a high sampling frequency. The parameters of these controllers are adjusted by a high-level NMPC optimizer that operates on a longer time horizon, thus leaving more computation time for the NLP step in every NMPC iteration. Instead of considering a (complex) MINLP problem in each iteration, the discrete search is performed by solving a sequence of continuous optimization problems with an increasing number of switches, and the search is stopped as soon as a policy is found that meets the specification. This reflects the main control goal, the minimization of the number of switches of the compressors.

While the NLP-based approaches that are described above yield a good control performance, they cannot currently be applied to larger systems in real time due to the prohibitively large computational effort. To overcome this problem, this paper presents a new and computationally

⋆ The authors gratefully acknowledge the financial support by the EU-funded Network of Excellence HYCON, contract number FP6-IST- 511368.

more efficient hierarchical model-predictive control approach for supermarket refrigeration systems. As in Sontag et al. (2007, 2008), the switching of the valves of the display cases is not optimized directly, but simple low-level controllers are employed that regulate the temperatures in the display cases. The high-level approach presented in this paper differs from the previous version in two respects: the compressors are not switched by the high-level controller anymore since the corresponding control goal for the suction pressure is merely safety-related, and it is not necessary to achieve optimality in this part of the system. A simple discrete low-level controller is employed instead. Furthermore, the optimization approach of the high-level controller is significantly different. It is based on the observation that the considered supermarket refrigeration system belongs to an important subclass of hybrid systems, the *Discretely Controlled Continuous Systems* (DCCS). These systems have been investigated in academia for many years, see e.g. Matveev and Savkin (2000); Dankowicz and Piiroinen (2002); Schild and Lunze (2008). The property of DCCS that is exploited in this paper is that simple yet accurate finite-dimensional models of the system behavior (the so-called *embedded maps* of the system) can be approximated linearly around simulated reference trajectories based on the sensitivities of the continuous subsystems. These low-dimensional embedded maps are then used as linear constraints in the optimizing high-level control system, and the complex dynamic optimization problem can be recast as a sequence of algebraic optimization problems. In combination with a decomposition of the large-scale supermarket system into (virtually) independent subcomponents which are approximated separately, this new approach allows for a very efficient computation of optimal switching times which enables the real-time control even of large-scale supermarket systems.

2. THE SUPERMARKET REFRIGERATION SYSTEM

Fig. 1 shows a schematic representation of a supermarket refrigeration system. It consists of five major parts: a liquid manifold, several display cases, a compressor rack, a suction manifold, and a condenser. Liquid refrigerant is supplied to the display cases from the liquid manifold through inlet valves (see Fig. 2). Within each display case, cold air circulates and forms an air curtain in front of the edible goods. Thermal energy is transferred from the goods to the air curtain ($\dot{Q}_{goods-air}$) and, since the temperature of the surrounding air is larger than that of the air curtain, the curtain also absorbs heat from the surroundings ($\dot{Q}_{airload}$). The absorbed thermal energy is transported to the evaporator ($\dot{Q}_{air-wall}$) in which the refrigerant evaporates and thus takes on the thermal energy ($\dot{Q}_e$). The vapor accumulates in the suction manifold and is fed to the condenser via the compressors which increase the pressure of the refrigerant vapor. Since the evaporation temperature of the refrigerant increases with the pressure, the energy from the display cases can be removed in the condenser at room temperature. Finally, the liquefied refrigerant is fed back to the display cases.

The hybrid model of the supermarket refrigeration system used in this work was proposed in Larsen et al. (2007). It may contain an arbitrary number of display cases n_{dc}. The state of each display case $i \in \{1, \dots, n_{dc}\}$ is described by four differential state variables: the temperature of the goods ($T_{g,i}$), the temperature of the evaporator wall ($T_{w,i}$), the temperature of the air inside the case ($T_{air,i}$), and the mass of liquid refrigerant within the evaporator of the display case ($m_{ref,i}$). Thus, the vector of continuous state variables of the i-th display case is given by $\mathbf{x}_{dc,i} = [T_{g,i}, T_{w,i}, T_{air,i}, m_{ref,i}]^T$. Since the dynamics of the condenser unit is not modeled, the overall continuous state vector of the model can be written as $\mathbf{x} = [\mathbf{x}_{dc,1}^T, \dots, \mathbf{x}_{dc,n_{dc}}^T, P_{suc}]^T$, where P_{suc} is the pressure in the suction manifold. Each display case is equipped with an expansion valve for the refrigerant, and the discrete input vector is given by $\mathbf{v} = [v_1, \dots, v_{n_{dc}}, v_c]^T$. Here, $v_1, \dots, v_{n_{dc}} \in \{1, 0\}$ are binary variables representing the state of the inlet valves (open/closed), and $v_c \in \Xi_c$ (given in %) determines the relative capacity of the compressors that are currently running within the compressor rack [1]. The set Ξ_c contains all discrete capacity levels that can be realized by switching the compressors on or off. In this paper, a system with six compressors of equal capacity is investigated. For this system, Ξ_c is defined as:

$$\Xi_c := \{0\%, 16.7\%, 33.3\%, 50\%, 66.7\%, 83.3\%, 100\%\}. \quad (1)$$

[1] Thus, the values 0% (100%) always indicate that all compressors are off (on), independently of the number of compressors.

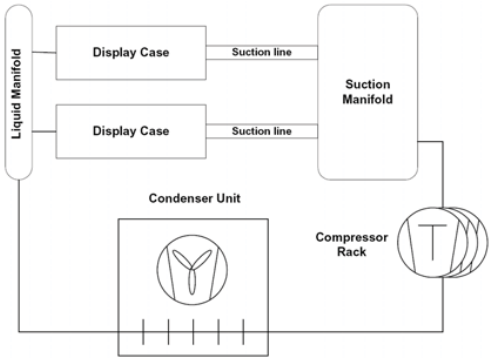

Fig. 1. A simplified scheme of a supermarket refrigeration system with two display cases.

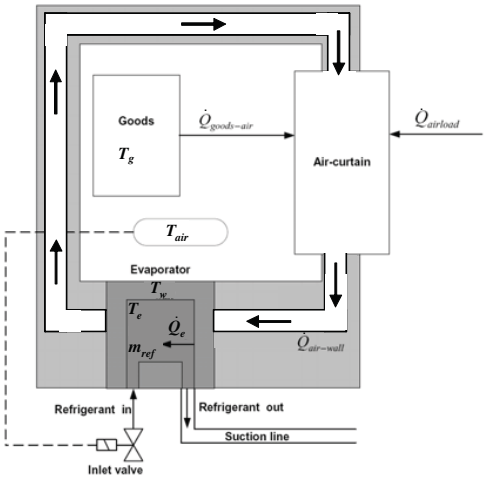

Fig. 2. Cross section of a display case.

The continuous dynamics is modeled by a lumped-parameter ODE system [2] under the assumption that all display cases are of equal design. Each display case exhibits two different continuous dynamics, depending on the setting of the corresponding expansion valve, i.e.

$$\frac{d\mathbf{x}_{dc,i}}{dt} = \begin{cases} \mathbf{f}_{i,vo}(\mathbf{x}_{dc,i}) \text{ if } v_i = 1, \text{ (a)} \\ \mathbf{f}_{i,vc}(\mathbf{x}_{dc,i}) \text{ if } v_i = 0. \text{ (b)} \end{cases} \quad (2)$$

The vector functions $\mathbf{f}_{i,vo}$ and $\mathbf{f}_{i,vc}$ only differ in the dynamic equation that determines the mass of refrigerant in the evaporator of a display case $m_{ref,i}$ according to

$$\frac{dm_{ref,i}}{dt} = \begin{cases} \dfrac{m_{ref,max} - m_{ref,i}}{\tau_{fill}} \text{ if } v_i = 1, \text{ (a)} \\ -\dfrac{\dot{Q}_{e,i}}{\Delta h_{lg}} \qquad \text{if } v_i = 0. \text{ (b)} \end{cases} \quad (3)$$

Here, the maximum mass of refrigerant each display case can accommodate is represented by $m_{ref,max}$, $\dot{Q}_{e,i}$ is defined in Eq. 9, the specific enthaply of evaporation of the remaining liquefied refrigerant in the evaporator is given by Δh_{lg}, and τ_{fill} is a time constant. The display case is filled with refrigerant as long as the inlet valve is open (Eq. 3.a), and after the inlet valve has been closed, the remaining refrigerant evaporates according to Eq. 3.b. The temperature dynamics within the i-th display case does not change with the valve setting and is given by:

$$\frac{dT_{g,i}}{dt} = -\frac{\dot{Q}_{goods-air,i}}{m_{goods} \cdot cp_{goods}}, \quad (4)$$

$$\frac{dT_{w,i}}{dt} = \frac{\dot{Q}_{air-wall,i} - \dot{Q}_{e,i}}{m_{wall} \cdot cp_{wall}}, \quad (5)$$

$$\frac{dT_{air,i}}{dt} = \frac{\dot{Q}_{goods-air,i} + \dot{Q}_{airload} - \dot{Q}_{air-wall,i}}{m_{air} \cdot cp_{air}}, \quad (6)$$

with

$$\dot{Q}_{goods-air,i} = UA_{goods-air} \cdot (T_{g,i} - T_{air,i}), \quad (7)$$

$$\dot{Q}_{air-wall,i} = UA_{air-wall} \cdot (T_{air,i} - T_{w,i}), \quad (8)$$

$$\dot{Q}_{e,i} = UA_{wall-ref}(m_{ref,i}) \cdot (T_{w,i} - T_e(P_{suc})), \quad (9)$$

$$UA_{wall-ref}(m_{ref,i}) = UA_{wall-refmax} \cdot \frac{m_{ref,i}}{m_{ref,max}}. \quad (10)$$

Here, m_{goods}, m_{wall}, m_{air}, cp_{goods}, cp_{wall}, cp_{air}, $UA_{goods-air}$, $UA_{air-wall}$, and $UA_{wall-refmax}$ are constant model parameters, and T_e is the evaporation temperature of the refrigerant which is a nonlinear function of P_{suc}. The dynamics of the suction pressure is given by

$$\frac{dP_{suc}}{dt} = \frac{\dot{m}_{in-suc} + \dot{m}_{ref-const} - \dot{V}_c \cdot \rho_{suc}}{V_{suc} \cdot \frac{d\rho_{suc}}{dP_{suc}}}, \quad (11)$$

with

$$\dot{m}_{in-suc} = \sum_{i=1}^{n_{dc}} \frac{\dot{Q}_{e,i}}{\Delta h_{lg}}, \quad \dot{V}_c = \frac{v_c \cdot \eta_{vol} \cdot V_d}{100}. \quad (12)$$

Here, the total mass flow of refrigerant from all display cases into the suction manifold is given by $\dot{m}_{in-suc}$, and $\dot{m}_{ref-const}$ is a measurable external disturbance that represents an additional flow of refrigerant from other unmodeled cooling facilities into the suction manifold. $\dot{V}_c$ is the volume flow from the suction manifold, and ρ_{suc} and $\frac{d\rho_{suc}}{dP_{suc}}$ are nonlinear refrigerant-dependent functions modeling the density of the vapor in the suction manifold and the derivative of ρ_{suc} w.r.t. the suction pressure, and η_{vol} and V_d are constant model parameters.

The controlled variables of the system are the pressure inside the suction manifold (P_{suc}) and the temperatures of the air inside the display cases ($T_{air,i}$). As the system never reaches a steady state since the different continuous dynamics of the display cases have distinct equilibrium points, the control goal is not to track setpoints, but to maintain the controlled variables within specified bounds $\underline{T}_{air,i} \leq T_{air,i} \leq \overline{T}_{air,i}$ and $\underline{P}_{suc} \leq P_{suc} \leq \overline{P}_{suc}$.

3. THE CONTROL STRATEGY

A scheme of the hierarchical control strategy is shown in Fig. 3. This strategy is very similar to the hierarchical approach that was presented in Sonntag et al. (2008), with one important difference: while in Sonntag et al. (2008), the parameters of the low-level controllers as well as the settings of the compressors are adapted by the high-level optimizer, the controlled subsystems are separated into two categories in the new approach: The first category consists of subsystems for which the desired control functionality is only safety-related, i.e. the control goal is to keep a process variable within an admissible region, and a quantitative measure of optimality is not necessary. Among the subsystems of the supermarket refrigeration system, the suction manifold and the compressor rack fall into this category and are not considered in the high-level predictive controller. The second category consists of subsystems for which quantitative optimality measures can be defined. In the supermarket system, the display cases belong to this category since here the control goal, the temporal desynchronization of the air temperatures, can be formulated in a quantitative way that is amenable to minimization. This temporal desynchronization ensures that the variations in the suction pressure and, thus, the necessity for compressor switching are minimized.

3.1 The Low-Level Control System

The switching strategy for the valves of display case i is shown in Fig. 4. The valve of the corresponding display case remains closed as long as the air temperature remains below the switching threshold δ_s. After the refrigerant has evaporated, the air temperature starts to rise. Once the air temperature crosses δ_s from below, v_i is opened for a constant period of time t_{v_i}, and the air temperature will decrease again. The time period t_{v_i} is a continuous parameter that is assigned by the high-level controller for

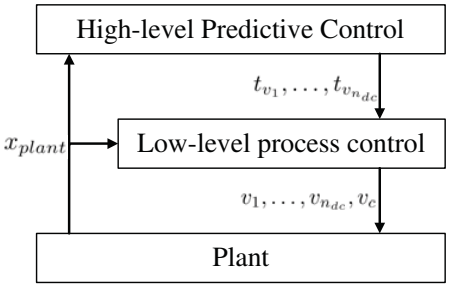

Fig. 3. Scheme of the control strategy.

[2] See also Larsen et al. (2007).

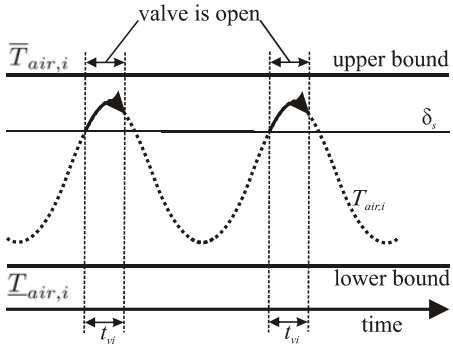

Fig. 4. Switching strategy for the expansion valves for an exemplary evolution of the air temperature of display case i.

each display case ($t_{v_1}, \ldots, t_{v_{n_{dc}}} \in \mathbb{R}^{\geq 0}$ in Fig. 3). The value of δ_s was determined in simulation studies assuming that $T_{air,i}$ will always decrease shortly after the valve v_i is opened (which can be deduced from the continuous model dynamics and parameters).

The low-level pressure controller switches off a compressor if $P_{suc} \leq \underline{P}_{suc}$, and it switches on an additional compressor if $P_{suc} \geq \overline{P}_{suc} - 0.1\ bar$. To avoid excessive switching of the compressors over a short time period, a compressor can only be switched 10 seconds after the previous compressor switch at the earliest. To compensate for fast changes of the external disturbances, an additional controller is employed that monitors the stationary continuous compressor capacity v_{cs} that is needed to keep all process variables within the admissible region over long time periods. From the ODE system, v_{cs} can be computed as:

$$v_{cs} = 100\ \% \cdot \left(\frac{\dot{m}_{in-suc} + \dot{m}_{ref-const}}{\rho_{suc} \cdot \eta_{vol} \cdot V_d} \right). \qquad (13)$$

If v_{cs} changes by more than $\delta_c = \frac{1}{2} \cdot \frac{100\ \%}{n_c}$ (n_c is the number of compressors) over a time period of 30 seconds, the controller switches the compressors to the discrete capacity level that is closest to v_{cs}.

3.2 Desynchronizing High-level Control

The high-level controller operates on a moving time horizon. In every iteration, a fixed time interval of t_p seconds is available for the adaptation of the valve opening times $t_{v_1}, \ldots, t_{v_{n_{dc}}}$ of the low-level temperature controllers. The algorithm is based on the assumption that all display cases can be regarded separately, i.e. that the interactions between the display cases are negligible. To confirm this assumption, a sensitivity analysis was performed for the system in which the cross-correlations between the system variables were computed by the solution of the matrix-valued linear sensitivity equation

$$\frac{d\mathbf{S}}{dt} = \frac{\partial \mathbf{f}}{\partial \mathbf{x}} \cdot \mathbf{S}, \quad \mathbf{S}(t_0) = \mathbf{I}. \qquad (14)$$

Here, $\frac{\partial \mathbf{f}}{\partial \mathbf{x}}$ is the Jacobian of the dynamic vector equation of the system. It was found that the effect of changes of the state variables $\mathbf{x}_{dc,i}$ of a display case i and the variables $\mathbf{x}_{dc,j}$ of other display cases with $j \neq i$ as well as the effect of changes of the suction pressure P_{suc} on $\mathbf{x}_{dc,i}$ are several orders of magnitude smaller than the effects between the internal variables of the display case in all operating regimes that are relevant for nominal process operation. Thus, the display cases can be considered as independent subsystems for control design purposes.

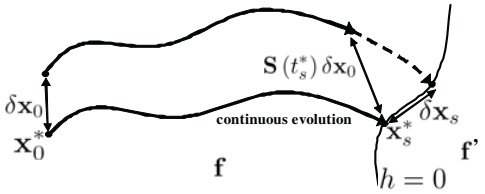

Fig. 5. On the linear approximation of the embedded map.

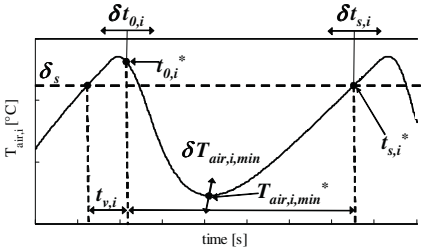

Fig. 6. Application of the approximation procedure to a single display case.

The desynchronization algorithm is based on the computation of an abstract algebraic model (an embedded map) for each display case which is locally valid around a simulated reference trajectory. Such a model maps small deviations $\delta\mathbf{x}_0$ of an initial continuous state $\mathbf{x}_0^*$ to the corresponding deviations $\delta\mathbf{x}_s$ of a reference state $\mathbf{x}_s^*$ that lies on a switching threshold which is defined by the zero-level set of a switching function h (see Fig. 5). The linear approximation is computed by (Parker and Chua, 1989):

$$\delta\mathbf{x}_s = \underbrace{\left[I - \frac{\mathbf{f}(\mathbf{x}_s^*) \cdot \frac{\partial h}{\partial \mathbf{x}}(\mathbf{x}_s^*)}{\frac{\partial h}{\partial \mathbf{x}}(\mathbf{x}_s^*) \cdot \mathbf{f}(\mathbf{x}_s^*)} \right]}_{(1)} \underbrace{\mathbf{S}\,(t_s^*)}_{(2)} \delta\mathbf{x}_0 \qquad (15)$$

Here, $\mathbf{f}(\mathbf{x}_s^*)$ is the evaluation of the dynamic equations at $\mathbf{x}_s^*$, $\frac{\partial h}{\partial \mathbf{x}}(\mathbf{x}_s^*)$ is the gradient of h evaluated at $\mathbf{x}_s^*$, and $\mathbf{S}\,(t_s^*)$ is the solution of Eq. 14 at t_s^* with $\mathbf{S}(t_0^*) = \mathbf{I}$. Term (2) of Eq. 15 maps the evolution of the initial deviation $\delta\mathbf{x}_0$ along the reference trajectory while the term (1) projects the resulting state along $\mathbf{f}$ onto the zero-level set of h.

Fig. 6 depicts how this mapping is adapted for each display case i. Under the assumption that the air temperature $T_{air,i}$ exhibits periodic behavior after the first period for constant disturbances and for unchanged $t_{v,i}$, the remainder of the time evolution of $T_{air,i}$ after $t_{s,i}^*$ can be neglected for control purposes. The state and sensitivity trajectories that are needed for the approximation of the embedded maps are computed simultaneously by the simulation of the hybrid model. Since the display cases are assumed to be independent, the sensitivity equations are evaluated separately for each display case which drastically reduces the number of sensitivities that must be computed.

The main idea is to formulate the resulting linear model of the controlled system as an algebraic optimization problem in which the finite-state embedded maps of the display cases appear as linear constraints [3] . Depending on the type of the cost function that is chosen, the overall problem can then be stated as a linear, a quadratic, or even a nonlinear programming problem. The control goal for the supermarket system is to desynchronize the air temperatures which corresponds to a uniform temporal distribution of the "time points of impact" $t^*_{s,i}$ of the air temperatures on the switching threshold δ_s. Thus, we are only interested in how a deviation $\delta t_{0,i}$ of the nominal valve closing time $t^*_{0,i}$ changes the next "time point of impact" $t^*_{s,i}$ of the air temperature $T_{air,i}$ on the switching threshold δ_s. Hence, a mapping $\delta t_{s,i} = H \cdot \delta t_{0,i}$ must be derived.

For simplicity, a new state vector $\mathbf{x}_{em,i} = [\mathbf{x}_{dc,i}, t]$ is defined for each display case that includes the time as an additional state. Since the switching function $h_i = T_{air,i} - \delta_s$ represents a constant switching threshold for each display case, its gradient is given by $\partial h_i / \partial \mathbf{x_{em,i}} = [0, 0, 1, 0, 0]$. Substituting this equation into Eq. 15, evaluating the right-hand side (with $\mathbf{f} = \mathbf{f_{i,vc}}$, see Eq. 3), and considering only the last row of the resulting matrix yields

$$\delta\, t_{s,i} = -\frac{1}{\frac{dT_{air,i}}{dt}(t^*_{s,i})} \cdot \mathbf{s}(t^*_{s,i}) \cdot \delta \mathbf{x}_{0,i} \tag{16}$$

with

$$\mathbf{s}(t^*_{s,i}) = \begin{bmatrix} s_{T_{air,i},T_{g,i}}(t^*_{s,i}) \\ s_{T_{air,i},T_{w,i}}(t^*_{s,i}) \\ s_{T_{air,i},T_{air,i}}(t^*_{s,i}) \\ s_{T_{air,i},m_{ref,i}}(t^*_{s,i}) \\ -1 \end{bmatrix}^T \tag{17}$$

In this equation, $s_{x_1,x_2}(t^*_{s,i})$ corresponds to the solution of the sensitivity equation at time $t^*_{s,i}$ that represents the effect of a change of x_2 on x_1. The final step is to express $\delta \mathbf{x}_{0,i}$ in terms of $\delta t_{0,i}$ which is achieved by linear interpolation: in addition to the simulation that is performed to determine the reference trajectory, a second simulation for the maximally allowed variation $\delta t_{0,i,max}$ from $t^*_{0,i}$ yields the maximal deviation of the state variables $\delta \mathbf{x}_{0,i,max}$. Here, $\delta t_{0,i,max}$ is a constant design parameter that is determined a priori by simulation such that the error of the linear approximation is negligible. Now, $\delta \mathbf{x}_{0,i}$ can be related linearly to $\delta t_{0,i}$ by $\delta\ \mathbf{x}_{0,i} = \frac{\delta \mathbf{x}_{0,i,max}}{\delta t_{0,i,max}} \cdot \delta\ t_{0,i}$. To ensure that the air temperatures do not violate the lower temperature bounds $\underline{T}_{air,i}$, additional linear constraints are derived that represent the variation $\delta T_{air,i,min}$ of the minimal air temperature $T_{air,i,min}$ of the reference trajectory with a variation of $t^*_{0,i}$ (see Fig. 6).

Since the embedded maps are only valid in a neighborhood $\epsilon := [\delta t^*_{0,i} - \delta t_{0,i,max}, \delta t^*_{0,i} + \delta t_{0,i,max}]$ around the reference trajectory, an algorithm is used that iterates between the generation of reference trajectories and optimization until convergence to the optimal solution is achieved. In each iteration j, the following steps are performed:

(1) **Determination of the impact order:** A reference trajectory and the order of the impact points $t^*_{s,i}$ are determined by simulation with the optimal values $t^*_{0,j-1}$ from the previous iteration. This order remains fixed in iteration j.

(2) **Computation of optimal impact points:** The air temperature of the display case with the earliest impact point $t^*_{s,\bullet}$ is driven to the lower bound $T_{air,i,min}$ using the linear approximations. Considering the resulting time trajectory over two periods yields lower (impact time point after the first period) and upper (impact time point after the second period) reference values t_{min} and t_{max} for the impact time points of all other air temperatures. The optimal impact points $t^*_{s,i}$ for all other air temperatures are distributed equidistantly in the range $[t_{min}, t_{max}]$.

(3) **Computation of optimal parameters:** Since the optimal impact points are known for all air temperatures, the corresponding valve closing times $t^*_{0,i}$ are computed by inverting the embedded maps ($\delta t^*_{0,i} = H^{-1} \cdot \delta t^*_{s,i}$). If all $t^*_{0,i}$ are within ϵ, the algorithm **terminates** since the optimal values have been found. If one or more $t^*_{0,i}$ are outside ϵ, go to step (4).

(4) **Recomputation of the reference trajectory:** A new reference trajectory is computed using values for the valve opening times that are determined from the results of step (3). Here, all values that are outside the neighborhood ϵ are replaced by the upper (if they are larger than the maximum value in ϵ) or the lower (if they are smaller than the minimum value in ϵ) limits of ϵ. Then, the algorithm returns to step (3).

4. APPLICATION RESULTS

The optimization algorithm was implemented in *Matlab* and was tested with a large-scale supermarket refrigeration system with 10 display cases and 6 compressors. Fig. 7 shows the optimization results for a day-night scenario. From 0 to 7200 seconds, the system is in day-time operation, and after 7200 seconds, a night-time operation is assumed. During the day, the masses of the goods are varied to model the removal by customers and the replenishment by the supermarket staff, as shown in Fig. 7 (d). Tab. 1 shows the parameter values that were used in the simulation. The controller is capable of keeping all process variables within the bounds and desynchronizes the air temperatures very quickly, as is shown in the lower part of 7 (a). Furthermore, the low-level compressor controller detects the drastic change in the external disturbances at 7200 seconds and switches off four compressors to counteract the sudden change in the stationary compressor capacity. A comparison to previously obtained results for smaller systems shows that the control scheme significantly reduces the frequency of the compressor switching. As expected, the very major contribution to the run-time of the algorithm is the computational effort for the simulation of the nonlinear model. During nominal operation with only slowly varying disturbances, the algorithm only needs to execute very few simulations since the valve opening times are already close to the optimal values. Thus, an MPC iteration only takes a few seconds in this case. In the worst case, i.e. when the temperatures are completely synchronized, the computation time to achieve a complete

[3] Note that for the supermarket system, the optimal solution can be computed analytically from the embedded maps, as is described below. For other systems, however, optimization may be necessary.

desynchronization was less than 100 seconds on a standard PC. With some optimization of the prototype implementation, it seems realistic to achieve worst-case computation times in the region of 20 seconds.

Table 1. Parameter values used in the simulation studies.

n_{dc}	n_c	δ_s
10	6	4.6 °C ℃
t_p	$\underline{T}_{air,1}$ - $\underline{T}_{air,10}$	$\overline{T}_{air,1}$ - $\overline{T}_{air,10}$
100 s	2 °C	5 °C
$t_{0,i,max}$	$\underline{P}_{suc}$	$\overline{P}_{suc}$ (day/night)
1 s	1 bar	1.7 bar / 1.9 bar
$\dot{Q}_{airload}$ (day)	$\dot{Q}_{airload}$ (night)	
3000 W	1800 W	
$\dot{m}_{ref-const}$ (day)	$\dot{m}_{ref-const}$ (night)	
0.2 $\frac{kg}{s}$	0.0 $\frac{kg}{s}$	

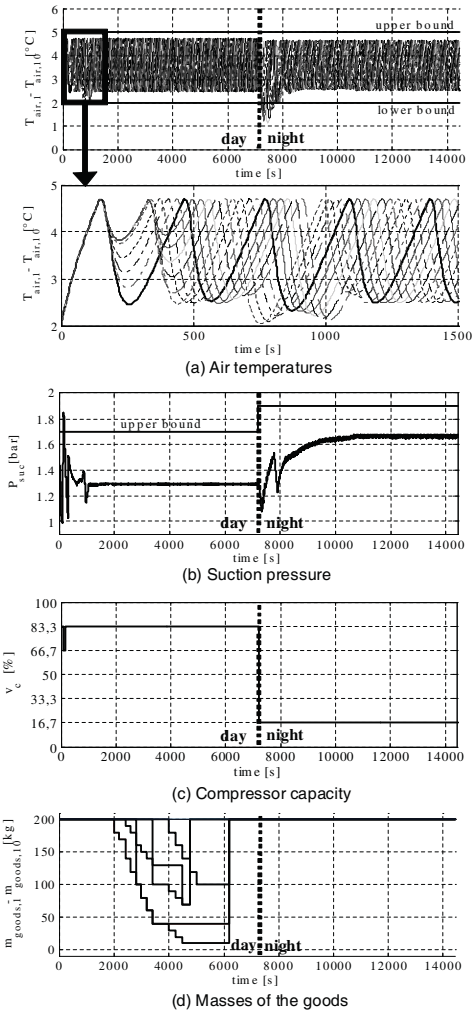

Fig. 7. Simulation results for a supermarket refrigeration system with 10 display cases and 6 compressors.

5. CONCLUSIONS

In this paper, a new hierarchical approach for the real-time capable control of large-scale supermarket refrigeration systems with hybrid dynamics is presented. Simple low-level temperature controllers are employed, and the high-level control task is the optimal adjustment of the parameters of these controllers to achieve a desynchronization of the air temperatures in the display cases which reduces the wear of the process equipment. Efficient desynchronizing control is achieved using a combination of model decomposition and approximation of the system dynamics by simple algebraic models. The main advantages of this approach over existing control techniques for supermarket refrigeration systems are that (a) the system is not linearized a priori. Any nonlinear characteristics of the system that are encoded in the reference trajectories are considered implicitly in the high-level control scheme, and (b) the computational performance is improved considerably since the original mixed-integer nonlinear dynamic optimization problem is replaced by a sequence of low-dimensional analytic problems that can be solved efficiently. Future work will concentrate on the extension of the developed technique to more general hybrid systems.

REFERENCES

Bemporad, A. and Morari, M. (1999). Control of systems integrating logic, dynamics, and constraints. *Automatica*, 35, 407–427.

Dankowicz, H. and Piiroinen, P.T. (2002). Exploiting discontinuities for stabilization of recurrent motions. *Dynamical Systems*, 17(4), 317–342.

Larsen, L.F.S., Geyer, T., and Morari, M. (2005). Hybrid MPC in supermarket refrigeration systems. In *Proc. 16th IFAC World Congress*. Th-E12-TO/5.

Larsen, L.F.S., Zamanabadi, R.I., Wisniewski, R., and Sonntag, C. (2007). Supermarket refrigeration systems - a benchmark for the optimal control of hybrid systems. Technical report for the Network of Excellence HYCON. Http://tinyurl.com/23nrkc.

Matveev, A.S. and Savkin, A.V. (2000). *Qualitative Theory of Hybrid Dynamical System*. Birkhäuser.

Parker, T.S. and Chua, L.O. (1989). *Practical Numerical Algorithms for Chaotic Systems*. Springer.

Sarabia, D., Capraro, F., Larsen, L.F.S., and De Prada, C. (2009). Hybrid NMPC of supermarket display cases. *Control Engineering Practice*, 17(4), 428–441.

Schild, A. and Lunze, J. (2008). Switching surface design for periodically operated discretely controlled continuous systems. In *Hybrid Systems: Computation and Control*, volume 4981 of *LNCS*, 471–485.

Sonntag, C., Devanathan, A., and Engell, S. (2008). Hybrid NMPC of a supermarket refrigeration system using sequential optimization. In *Proc. 17th IFAC World Congress*, 13901–13906.

Sonntag, C., Devanathan, A., Engell, S., and Stursberg, O. (2007). Hybrid nonlinear model-predictive control of a supermarket refrigeration system. In *Proc. IEEE Multi-Conference on Systems and Control (MSC/CCA)*, 1432–1437.

Wisniewski, R. and Larsen, L.F.S. (2008). Method for analysis of synchronization applied to supermarket refrigeration system. In *Proc. 17th IFAC World Congress*, 3665–3670.

PWA Modelling and Co-ordinated Continuous and Logical Control of a Laboratory Scale Plant with Hybrid Dynamics

J. Hlava

Faculty of Mechatronics, Technical University of Liberec
461 17 Liberec, Studentská 2, Czech Republic,
(e-mail: jaroslav.hlava@tul.cz)

Abstract: Many process plants are nonlinear and together with this they include a combination of continuous valued and logical control inputs and subsystems. This paper attempts to explore the potential of hybrid model predictive control (MPC) to cope with both of these problems. It uses a laboratory scale plant that was designed for experiments with hybrid systems. This plant has both continuous and logical control inputs and it is considerably nonlinear. An approximate hybrid model of the plant in the form of a piecewise affine (PWA) system is developed and evaluated in the first part of the paper. After that a hybrid MPC based on PWA model is applied to the control of the plant. While designing hybrid MPC and evaluating its performance, there is a special focus on the following question. Logical and continuous control systems are usually designed separately. This may result in unforeseen interactions between logical and continuous control and in the deterioration of the control performance. However, hybrid MPC is based on hybrid model that captures both logical and continuous dynamics in one unified framework. Hence it can reasonably be expected that hybrid MPC can avoid undesirable interactions and possibly also make use of these interactions in a positive way (e.g. to speed up the control response using logical inputs). Control results obtained with hybrid MPC are indeed fairly good and they show clear improvement over the results achieved with separate design of logical and continuous control.

Keywords: Hybrid systems, model predictive control, piecewise affine systems

1. INTRODUCTION

Model predictive control (MPC) of hybrid systems has recently attracted a considerable research attention. This attention is reflected in the growing number of publications on hybrid MPC. Monographs such as (Christophersen, 2007), (Borrelli, 2003) and survey paper (Morari & Baric, 2006) can be quoted as important examples representing a vast and constantly growing body of literature. The application area of hybrid MPC is twofold. First, many process plants comprise continuous-valued as well as logical/discrete-valued control inputs and components. Such plants are naturally modelled as hybrid systems and this requires the use of control approaches for hybrid systems. Second, non-linearities that are ubiquitous in the models of process plants can often be well approximated by a special class of hybrid systems called piecewise affine (PWA) systems. The result is again a plant model in the form of a hybrid system.

This paper is focused on both of the above mentioned aspects of the hybrid MPC. It uses a case study of a laboratory scale plant. This plant exhibits hybrid phenomena that are found in many process control applications. The plant includes both continuous valued and logical control inputs and its dynamic behaviour abruptly changes at certain operating points. Most continuous components of the plant are nonlinear. This nonlinear behaviour must be approximated by a PWA model. This approximation is necessary for the design of hybrid MPC controller and it is a non-trivial task. PWA approximation, selection of individual affine models, their validity regions and comparison with the responses of the original nonlinear plant are described in detail. Finally a hybrid model is obtained whose hybrid features are both due to the hybrid nature of the plant itself and due to the PWA approximation of plant nonlinearities. Further, the attention is turned to MPC control of this plant. A special emphasis is laid on the ability of hybrid MPC to achieve an integrated design of logical and continuous control.

Typically, logical control is responsible for safety related and limiting functions such as preventing the process variables from leaving safe operation limits, starting and shutdown of process equipment. Logical controllers are also used to manipulate logical control inputs such as on/off valves. On the other hand, the regulatory and supervisory control is performed by continuous controllers. Common design practice relies on separate design of logic and continuous control. As non-trivial and not easily predictable interactions often arise between continuous and logical parts of the control system, this practice may result in a poor control performance. On the other hand, hybrid model describes both continuous and logical (or more generally discrete-valued) parts of the whole system, including continuos/logical interactions, the hybrid controller designed on the basis of this model can be expected to control the whole plant in a co-ordinated manner and avoid the deteriorating effects of interactions between separately designed logical and continuous control systems. However, it is well known that expectations though well founded in the theory and practical reality may be two different worlds. For this reason, this

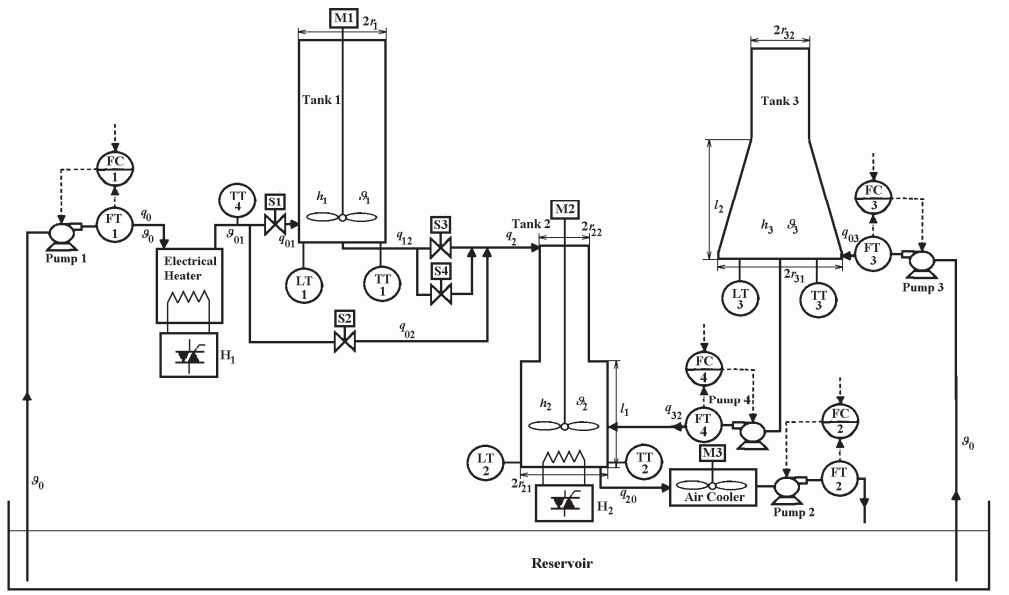

Fig. 1. Structure of the laboratory scale plant, FT, LT, TT are flow, level and temperature transmitters FC – flow controller, S– solenoid valve, M – motor, r_1= 5.64 cm, r_{21}= 5.8 cm, r_{22}= 3 cm, r_{31}= 6 cm, r_{32}= 2.9 cm, tank height l_{max}=80 cm, l_1= l_2=40 cm

paper in its final part attempts to make an experimental comparison of a separate design of logic and continuous control on the one hand and co-ordinated design based on hybrid model on the other hand.

2. EXPERIMENTAL PLANT

A detailed description of the experimental plant has recently been given by the author in (Hlava & Šulc, 2008). As the full text of this paper is available from the IFAC-PapersOnLine website, the description of this plant in the present paper can be short. Plant structure is shown in Fig. 1. Basic components are three water tanks. Tanks 2 and 3 have special shapes that introduce changes in dynamics. The tanks are thermally insulated to make the heat losses negligible. Water from the reservoir mounted under the plant is drawn by Pump 1 and Pump 3 to the respective tanks. The delivery rates can be continuously changed. The flow rates are measured using turbine flow-meters. To compensate for pump non-linearity, it is beneficial to use slave flow rate controllers.

The flow from Pump 3 is fed directly to Tank 3. The flow from Pump 1 goes through heater and it is further controlled by solenoid valve S1. The power output of the heater can be changed continuously and ϑ_{01} can be made to follow a specified function of time. Another continuously controlled heater is mounted on the bottom of Tank 2. The temperatures are measured with Pt1000 sensors at the points shown in Fig. 1. In addition to the pumps, whose delivery flow rates can be changed continuously, the plant includes another way of manipulating the flow: solenoid valves. These discrete valued actuators control the flow from Tank 1 to Tank 2 (valves S3, S4). The flow is changed in three steps: no valve open, one open, both valves open. Tank 1 can be bypassed by closing S1 and opening S2. The air-water heat exchanger with cooling fan at the output from Tank 2 keeps the water temperature in the reservoir roughly constant. Water levels are measured using pressure sensors.

The plant is controlled from a PC using two data acquisition boards (11 analog inputs, 6 analog outputs, 6 digital outputs) and interface hardware (power amplifiers, solid state relays, signal conditioning devices). The basic software tool for identification and control experiments is the Real Time Toolbox. It allows an easy connection of Matlab/Simulink environment with the real world. Alternatively WinCon-8000 industrial control system produced by ICP DAS can be used. This control system makes it possible to experiment with the implementation of advanced control algorithms using real industrial hardware. The changeover from PC to WinCon-8000 and vice versa is simple: two connectors with analog and digital inputs/outputs have to be reconnected.

3. CONTROL OBJECTIVE

Many control scenarios can be defined with this plant. Some examples are given in (Hlava & Šulc, 2008). The scenario considered in this paper uses Tank 1 and 2. This scenario is inspired in part by (Slupphaug *et al.*, 1997) and it can be formulated as follows. Tank 1 serves as a buffer that receives water from an upstream process. Water flow rate and temperature are disturbances. The main control objective is to deliver the water to a downstream process at a desired temperature (temperature ϑ_2), while the flow demand of the downstream process is variable and hence it also acts as a disturbance. Power output of heater H_2 is a continuous manipulated variable. Valves S3 and S4 are used as a discrete valued manipulated variable to control the flow from Tank 1 to Tank 2 in three steps. Valve S1 is used to close water flow to Tank 1, if tank overflow is to be avoided. There is no valve at the output of Tank 2, but an effect equivalent to closing an output valve is achieved by switching off Pump 2.

The main control objective necessarily includes several auxiliary objectives. Tank levels must be kept within specified limits, and overflow as well as emptying of the tanks must be avoided. It is also necessary to avoid the necessity to close valve S1 in order to prevent Tank 1 overflow. In a real control situation, closing S1 would mean that water from the upstream process cannot flow to the buffer but must be re-routed to the environment. Similarly it is necessary to avoid the necessity to switch off Pump 2 in order to prevent Tank 2 from underflow. The standard way to satisfy these auxiliary objectives would be to use separately designed control logic.

4. MATHEMATICAL MODEL OF THE PLANT

Plant model is derived using mass and energy balances. The reader is referred to (Hlava & Šulc, 2008) for details. In this paper just the part of the plant model will be given that is relevant to the specified control objective (i.e. excluding Tank 3). Assuming liquid incompressibility and constant heat capacity c, negligible heat losses and ideal mixing, the following model is obtained

$$\dot{h}_1(t) = (1/A_1)\left(q_0(t)\sigma_0(t) - 0.1k_v\sigma_1(t)\sqrt{gh_1(t)}\right) \tag{1}$$

$$\dot{h}_2(t) = \begin{cases} (1/A_{21})\left(0.1k_v\sigma_1(t)\sqrt{gh_1(t)} - q_{20}(t)\sigma_2(t)\right) & h_2(t) \le l_1 \\ (1/A_{22})\left(0.1k_v\sigma_1(t)\sqrt{gh_1(t)} - q_{20}(t)\sigma_2(t)\right) & h_2(t) > l_1 \end{cases} \tag{2}$$

$$\dot{\vartheta}_1(t) = q_0(t)\sigma_0(t)\left(\vartheta_{01}(t) - \vartheta_1(t)\right)/A_1h_1(t) \tag{3}$$

$$\dot{\vartheta}_2(t) = \begin{cases} \dfrac{\left(0.1k_v\sigma_1(t)\sqrt{gh_1(t)}\left(\vartheta_1(t) - \vartheta_2(t)\right) + \dfrac{H(t)}{\rho c}\right)}{A_{21}h_2(t)} & h_2(t) \le l_1 \\ \dfrac{\left(0.1k_v\sigma_1(t)\sqrt{gh_1(t)}\left(\vartheta_1(t) - \vartheta_2(t)\right) + \dfrac{H(t)}{\rho c}\right)}{A_{21}l_1 + A_{22}(h_2(t) - l_1)} & h_2(t) > l_1 \end{cases} \tag{4}$$

where $A_i = \pi r_i^2$, discrete valued input σ_0 assumes values 0,1 (S1 closed, S1 open), σ_1 assumes values 0,1,2 (no valve open, S3 open, S3 and S4 open), σ_2 assumes values 0,1 (Pump 2 off, Pump 2 running with flow rate q_{20} depending on the flow demand of the downstream process), H is power output of heater H_2, k_v is flow coefficient of valves S3 and S4.

5. APPROXIMATE PLANT MODEL IN A PWA FORM

Plant model (1)-(4) includes continuous and discrete valued inputs, dynamics switching depending on operating point in (2), (4) and non-linear elements. It must first be approximated by a PWA model. The general form of a discrete-time PWA system is given by

$$\begin{aligned} \boldsymbol{x}(k+1) &= \boldsymbol{M}_i\boldsymbol{x}(k) + \boldsymbol{N}_i\boldsymbol{u}(k) + \boldsymbol{f}_i \\ \boldsymbol{y}(k) &= \boldsymbol{C}_i\boldsymbol{x}(k) + \boldsymbol{D}_i\boldsymbol{u}(k) + \boldsymbol{g}_i \end{aligned} \tag{5}$$

where each dynamics i=1,2..$N_Đ$ is active in a polyhedral partition $Đ$ that is defined by guard lines described by

$$\boldsymbol{G}_i^x\boldsymbol{x}(k) + \boldsymbol{G}_i^u\boldsymbol{u}(k) \le \boldsymbol{G}_i^c \tag{6}$$

That means, the dynamics i represented by matrices and vectors [$\boldsymbol{M}_i$, $\boldsymbol{N}_i$, $\boldsymbol{f}_i$, $\boldsymbol{C}_i$, $\boldsymbol{D}_i$, $\boldsymbol{g}_i$] is active in the region of state-input space which satisfies constraints (6). Unlike some other approaches to hybrid MPC that use probabilistic Bayesian approach to combine weighted local linearized models (e.g. Nandola & Bhartiya, 2008), the approach considered in this paper is deterministic and local models are just switched depending on the region in state-input space.

It has been noted already in the well known seminal paper on PWA systems (Sonntag, 1981) that nonlinear systems can be globally approximated arbitrarily close by PWA systems and this claim has often been repeated. This claim is certainly true. However, it is also true that although there are several methods of experimental identification of PWA models (see Paoletti *et al.*, 2007 for an overview), there is no general systematic procedure to find a PWA approximation of a given non-linear system described by analytical state equations. The route to the PWA approximation is always closely connected with a particular system to be approximated. In this section, model described by (1)- (4) will be considered. Its approximation by a set of affine models of the form (5), (6) can proceed as follows.

An obvious source of partial models is logical control inputs σ_0, σ_1, σ_2. The best way to handle these inputs is to associate one partial model with each combination of their values. This results in 12 partial models. Equations (2) and (4) include dynamics switching at water level l_1. That means the number of 12 must be doubled and 24 partial models are obtained as an absolute minimum for modeling this plant. These 24 partial models must further be linearized. To achieve an acceptable precision, each model is approximated by a set of linearized models. The linearization is done in two steps.

1. Obtain linearizations around general operating points characterized by a vector of input and state variables (σ_{0P}, σ_{1P}, σ_{2P}, q_{0P}, q_{20P}, ϑ_{0P}, H_p, h_{1P}, h_{2P}, ϑ_{1P}, ϑ_{2P}). If possible, steady state operating points should be preferred.

2. Find a suitable set of operating points together with adequate partitioning of state-input space that will be well representative of the dynamics of the original system.

This procedure can be most simply illustrated for (1). If S1 is open (σ_{0P}=1) the respective steady state characteristics is

$$q_{0P} = \frac{1}{\sigma_{0P}}0.1k_v\sigma_{1P}\sqrt{gh_{1P}}\ , \tag{7}$$

and (1) can be linearized around a steady state operating point (h_{1P}, q_{0P}, σ_{0P}, σ_{1P}). This linearization is given by

$$\dot{h}_1(t) = \frac{\sigma_{0P}}{A_1}(q_0(t) - q_{0P}) - \frac{0.1k_v\sigma_{1P}}{2A_1}\sqrt{\frac{g}{h_{1P}}}\,(h_1(t) - h_{1P}) \tag{8}$$

Substituting for q_{0P} from (7), linearization can be modified to

$$\dot{h}_1(t) = \frac{\sigma_{0P}}{A_1}q_0(t) - \frac{0.1k_v\sigma_{1P}\sqrt{g}}{2A_1\sqrt{h_{1P}}}\,h_1(t) - \frac{0.1k_v\sigma_{1P}\sqrt{gh_{1P}}}{2A_1} \tag{9}$$

It can be seen that (9) holds even if σ_{1P}=0. What is less obvious is the case of σ_{0P}=0. Equation (7) cannot be used and (1) is autonomous system that has just zero steady state. However, it can be linearized around a non-steady state

$$\dot{h}_{1P}(t) = -0.1k_v\sigma_{1P}\sqrt{gh_{1P}}\,/A_1 \tag{10}$$

and this linearization has the same form as (9). Thus (9) is general linearized approximation of (1). As actual values of the variables and not deviations from operating point are used, (9) is affine and not linear.

The next step is to find a suitable set of representative operating points. The simplest approach would be to divide the whole range of h_1 into several intervals of identical length and to take midpoints of these intervals as selected nominal operating points. A better way is to modify (9) to the form

$$\frac{2A_1\sqrt{h_{1P}}}{0.1k_v\sigma_{1P}\sqrt{g}}\dot{h}_1(t) + h_1(t) = \frac{2\sigma_{0P}\sqrt{h_{1P}}}{0.1k_v\sigma_{1P}\sqrt{g}}q_0(t) - h_{1P} \tag{11}$$

Dynamics of (11) can be characterised by time constant

$$\tau = 2A_1\sqrt{h_{1P}}\,/\left(0.1k_v\sigma_{1P}\sqrt{g}\right) \tag{12}$$

and the partitioning of the whole range of h_1 can be done in such a way as to keep the ratio of maximum and minimum time constant within each interval the same. The nominal operating point in each interval is then again selected so that the nominal time constant would have the same ratio to the minimum and maximum value of time constant within this interval. If the whole range is divided into four intervals, this reasoning leads to the following

$$\begin{aligned}
&h_{1m1} = h_{1min}^{\frac{3}{4}}h_{1max}^{\frac{1}{4}}; \quad h_{1m2} = h_{1min}^{\frac{2}{4}}h_{1max}^{\frac{2}{4}}; \quad h_{1m3} = h_{1min}^{\frac{1}{4}}h_{1max}^{\frac{3}{4}}\\
&h_{1P1} = \sqrt{h_{1min}h_{1m1}}; \quad h_{1P2} = \sqrt{h_{1m1}h_{1m2}}; \quad h_{1P3} = \sqrt{h_{1m2}h_{1m3}}\\
&h_{1P4} = \sqrt{h_{1m3}h_{1max}}
\end{aligned} \tag{13}$$

where $h_{1\min}$ and $h_{1\max}$ are the minimum and maximum values of h_1 respectively, h_{1m1}, h_{1m2}, h_{1m3} are limiting points of subintervals, h_{1P1}, h_{1P2}, h_{1P3}, h_{1P4} are nominal operating points.

Other parts in plant model can be approximated by PWA systems in a similar way. The dynamics of water level in Tank 2 as described by (2) depends mainly on h_1, while h_2 just governs switching between two partial models. Linearization of (1) as described by (9) actually means that square root was replaced by the linear part of Taylor series. Using the same method for (2) results in

$$\dot{h}_2(t) = \begin{cases} \dfrac{1}{A_{21}}\left(\dfrac{0.1k_v\sigma_{1P}\sqrt{g}}{2\sqrt{h_{1p}}}h_1(t) + \dfrac{0.1k_v\sigma_{1P}\sqrt{gh_{1p}}}{2} - q_{20}(t)\sigma_{2P}\right) & h_2(t) \le l_1 \\ \dfrac{1}{A_{22}}\left(\dfrac{0.1k_v\sigma_{1P}\sqrt{g}}{2\sqrt{h_{1p}}}h_1(t) + \dfrac{0.1k_v\sigma_{1P}\sqrt{gh_{1p}}}{2} - q_{20}(t)\sigma_{2P}\right) & h_2(t) \le l_1 \end{cases} \tag{14}$$

Steady state characteristics of (3) are unity gain for any nonzero h_1. Its linearization is therefore also very simple as all terms that include the difference ϑ_{0P}-ϑ_{1P} equal zero.

$$\dot{\vartheta}_1(t) = \left(q_{0P}/A_1h_{1P}\right)\left(\vartheta_{01}(t) - \vartheta_1(t)\right) \tag{15}$$

Using (7) this equation can be modified to

$$\dot{\vartheta}_1(t) = \left(0.1k_v\sigma_{1P}/A_1\right)\sqrt{\left(g/h_{1P}\right)}\left(\vartheta_{01}(t) - \vartheta_1(t)\right) \tag{16}$$

This equation has time constant

$$\tau = A_1\sqrt{h_{1P}}\,/\left(0.1k_v\sigma_{1P}\sqrt{g}\right) \tag{17}$$

Apart from multiplicative constant, this is the same expression as (12). Thus, the same partitioning of the range h_1 is obtained.

Equation (4) poses a more difficult problem. However, the effect of power output of the heater $H(t)$ on the dynamics of ϑ_2 is linear and the equation can be linearized around a point where $H(t)$=0. Then the steady state relation between ϑ_2 and ϑ_1 is again unity gain and the linearized equation is

$$\dot{\vartheta}_2(t) = \begin{cases} \dfrac{\left(0.1k_v\sigma_{1P}\sqrt{gh_{1P}}\left(\vartheta_1(t) - \vartheta_2(t)\right) + \dfrac{H(t)}{\rho c}\right)}{A_{21}h_{2P}} & h_2(t) \le l_1 \\ \dfrac{\left(0.1k_v\sigma_{1P}\sqrt{gh_{1P}}\left(\vartheta_1(t) - \vartheta_2(t)\right) + \dfrac{H(t)}{\rho c}\right)}{A_{21}l_1 + A_{22}(h_{2P} - l_1)} & h_2(t) > l_1 \end{cases} \tag{18}$$

Selection of nominal operating points is partly given by dynamics switch at level l_1. To achieve good approximation subranges $\langle h_{2\min}, l_1\rangle$ and $(l_1, h_{2\max}\rangle$ are further partitioned in a similar way as it was done with Tank 1. In this paper, the partitioning of both subranges into four intervals is used. Total number of partial models is then 384 (=2*3*2*4*8). The result is a continuous time PWA model with four states and seven inputs

$$\begin{aligned}
&\dot{\mathbf{x}}(t) = \mathbf{A_i}\mathbf{x}(t) + \mathbf{B_i}\mathbf{u}(t) + \mathbf{o_i} \quad i = 1,...,384\\
&\mathbf{x}(t) = \left[h_1(t)\ \ h_2(t)\ \ \vartheta_1(t)\ \ \vartheta_2(t)\right]^T\\
&\mathbf{u}(t) = \left[\sigma_0(t)\ \ \sigma_1(t)\ \ \sigma_2(t)\ \ H(t)\ \ q_0(t)\ \ \vartheta_{01}(t)\ \ q_{20}(t)\right]^T
\end{aligned} \tag{19}$$

Most elements of matrices in (19) are zeros. The expressions for the few nonzero elements can be written according to (9)-(18). Partial models are valid in regions that are defined by specified values of logical inputs σ_0, σ_1, σ_2 and minimum and maximum limits on state variables. These specifications are formulated in the form of guard lines (6). Due to the high dimensions and great number of variants the expressions for matrices $\boldsymbol{G}_i^x$, $\boldsymbol{G}_i^u$, $\boldsymbol{G}_i^c$ cannot be given here.

System (19) must finally be converted to discrete time. This is done by discretizing each partial model separately assuming zero order hold at the inputs. Control Systems Toolbox for Matlab has no routine for discretization of affine systems. However it can be easily derived that the formulae for $\boldsymbol{N}_i$ and $\boldsymbol{f}_i$ in (5) have the same form

$$\boldsymbol{N}_i = e^{\boldsymbol{A}_iT_v}\int_0^{T_v} e^{-\boldsymbol{A}_i\tau}\boldsymbol{B}_i d\tau;\ \boldsymbol{f}_i = e^{\boldsymbol{A}_iT_v}\int_0^{T_v} e^{-\boldsymbol{A}_i\tau}\boldsymbol{o}_i d\tau \tag{20}$$

Hence the computation of discretized model is possible by using c2d command first with arguments ($\boldsymbol{A}_i$, $\boldsymbol{B}_i$, $\boldsymbol{C}_i$, $\boldsymbol{D}_i$) to obtain $\boldsymbol{N}_i$ and then with arguments ($\boldsymbol{A}_i$, $\boldsymbol{o}_i$, $\boldsymbol{C}_i$, 0) to obtain $\boldsymbol{f}_i$.

The comparison of responses of the original model (1)–(4) and its PWA approximation is shown in Fig. 2. To evaluate the PWA model in a wide range of changes, the following step changes are used: q_0 changes at t=1000 s from 1 to 1.2 l/min, σ_1 changes at t=2000 s from 1 to 0 and at t= 2100 s back to 1, q_{20} changes at t=2400 s from 1 to 1.4 l/min and at t=3000 s to 1.2 l/min, ϑ_0 changes at t=3000 s from 40 to 50°C, H changes at t=4500 s from 0 to 500 W. Initial conditions are: h_{10}=0.6 m, h_{20}=0.12 m, ϑ_{10}=30°C, ϑ_{20}=55°C, sampling period T_s=1 s. The responses of PWA system were simulated using the Simulink block included in Multi-Parametric (MPT) Toolbox (Kvasnica *et al.*, 2004). There is generally a good agreement between the responses of the original system and its PWA approximation. Any comparison using a specified set of input signals has naturally a limited value because the agreement depends also on how close is the actual response to the selected set of representative operating points. However, it can be said that in most cases the maximum peak error does not exceed 1 cm or 1°C and normally the difference is in the range of tenths of cm and °C most of the time. It is also possible to decrease the number of partial models. Figure 2 was obtained with 384 partial models. If the range of h_2 is divided in just four sub-ranges, the number of models is reduced to 192 and the precision of PWA approximation remains good. However, any further reduction of the number of partial models results in a marked decrease of approximation precision.

6. CONTROL DESIGN AND EXPERIMENTS

Standard procedure to design a control system satisfying the objectives specified above is divided into two separate tasks: design of logical control and design of continuous control (in this paper the term continuous relates to control where the variables are continuous-valued regardless of whether the controller is designed in continuous or discrete time setting). Logic part of the control system is described by a set of simple rules. Normal and desirable state of the logical control inputs is σ_0=1; σ_1=1, σ_2=1. That means, water from the upstream process flows to the buffer (Tank 1) and further to the supply (Tank 2) and the supply is able to meet the demand of the downstream process while water levels of both tanks remain within acceptable ranges $w_{1\min} \le h_1 \le w_{1\max}$, $w_{2\min} \le h_2 \le w_{2\max}$. If water levels deviate from these ranges, the following rules apply

A. If $h_1 < w_{1\min}$, set σ_1 to zero to avoid Tank 1 emptying
B. If $h_1 > w_{1\max}$, set σ_0 to zero to avoid Tank 1 overflow, if also $h_2 < w_{1\min}$, set σ_1 to 2 to accelerate the recovery of both water levels to normal ranges
C. If $h_2 < w_{2\min}$, set σ_2 to zero to avoid Tank 2 emptying
D. If $h_2 > w_{2\max}$, set σ_1 to zero to avoid Tank 2 overflow

Continuous control system is designed as SISO control loop, where $H(t)$ is manipulated variable and temperature ϑ_2 is a controlled variable. It can be seen from (4) that logical control inputs act as disturbances and they may have adverse effects on control performance.

The situation changes when logical and continuous control is designed in a unified way. System described by (1)-(4) is treated as a hybrid system and model predictive controller can be designed based on its PWA approximation. Hybrid MPC controller is designed using MPT Toolbox. To compare performance of the systems using separate design and hybrid model predictive control, the following control experiment was performed. Starting from the state q_0=q_{20}=1 l/min, h_1=0.5 m, h_2=0.3 m, ϑ_1=50°C, ϑ_2=40°C, the setpoint was increased from 40°C to 60°C. Separate design used logic rules defined in the beginning of this section. The continuous control algorithm was MPC with linear performance function and control horizon 2. The unified design used MPC with the same performance function and control horizon, however this MPC algorithm could make use of the logical control inputs. The responses are shown in the following figures.

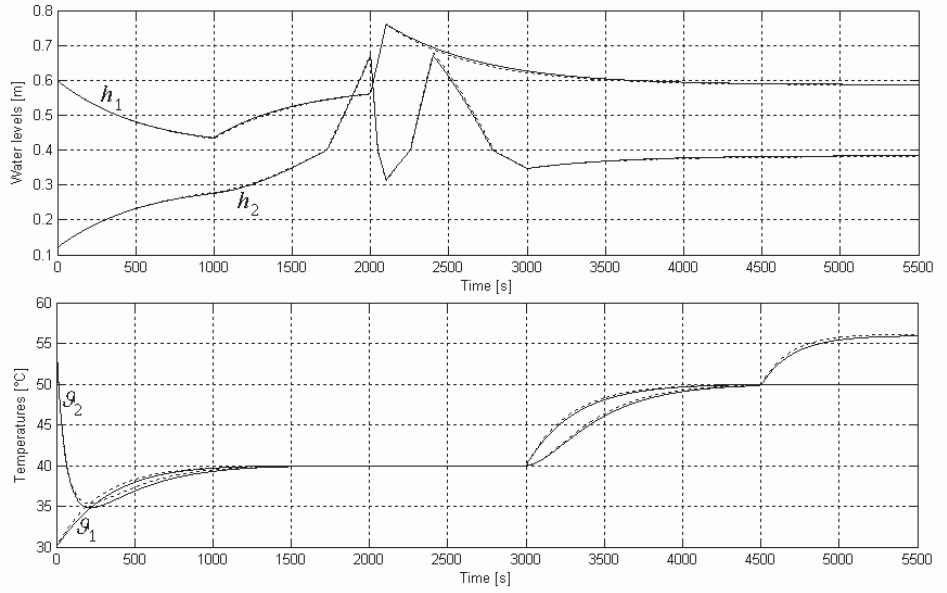

Fig. 2 Comparison of responses of the original plant model and its PWA approximation (in all responses original plant models is plotted with solid line and PWA approximation with dotted line).

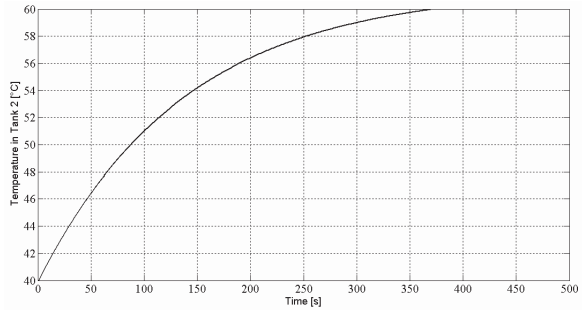

Fig. 3 Setpoint response Separate design

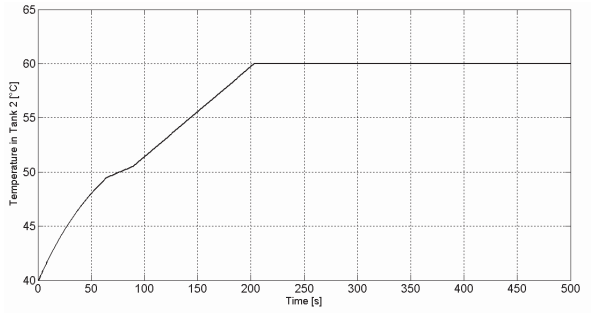

Fig. 4 Setpoint response – Unified design

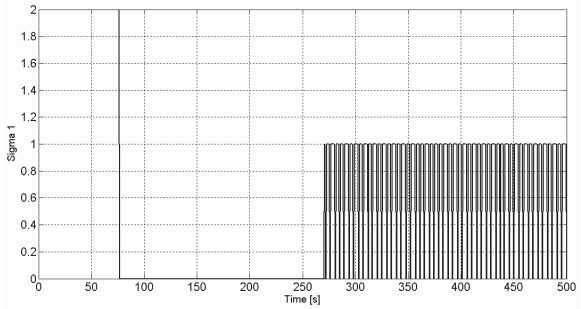

Fig. 5 Logical manipulated variable σ_1

It can be seen that unified design achieves better results. The control time is much shorter. Fig. 5 shows that this improvement is due to the ability of the unified design to make use of logical manipulated variables. Unlike separate design, logical control inputs can be used not only to keep the water levels within specified limits but also to accelerate control responses. In the beginning σ_1 is used to accelerate the setpoint response by increasing the inflow of warmer water to Tank 2. When controlled variable reaches setpoint, σ_1 is used just to keep the water levels within specified range.

7. CONCLUSION

This paper was focused on the possibilities that hybrid model predictive control can offer for unified design of logical and continuous control. As the character of this paper is mainly experimental, its results are connected with the particular laboratory plant considered and they cannot be regarded as completely general. In spite of that, some conclusions can be made. It could be seen that the application of hybrid MPC is not particularly easy. The development of the PWA model that is necessary for hybrid MPC takes up a substantial part of the paper. The complexity of the PWA model expressed by several hundreds of partial systems is also quite high even in the case of this laboratory scale plant that has still quite simple structure compared with real industrial process plants.

On the other hand, it has been shown that hybrid MPC can make use of the information how the controlled variable is affected by logical control inputs to improve control responses. The setpoint response was improved by adding the effect of opening valve S4 to the effect of increasing heater power output. Thus, the control results achieved with hybrid MPC were better than the results obtained with separate design of logical and continuous control.

Given paper length allowed to present one selected control experiment. Other control scenarios can be devised and tested with similar results and there is still a large open space for further experiments with this plant focused on exploring the possibilities offered by hybrid MPC for co-ordinated design of logical and continuous control. A particular attention will also be paid to the real time implementation of explicit MPC using industrial control system WinCon-8000 that can be used with this plant as an alternative to the academic experimental setting using Matlab/Simulink, Real Time Toolbox and PC data acquisition boards.

ACKNOWLEDGEMENT:

This research has been supported by the Czech Science Foundation within project 101/07/1667.

REFERENCES

Borrelli, F. (2003), *Constrained Optimal Control of Linear and Hybrid System,* Springer Verlag.

Christophersen, F. (2007), *Optimal Control of Constrained Piecewise Affine Systems*, Springer Verlag.

Hlava, J., & Šulc B. (2008), Advanced Modelling and Control using a Laboratory Plant with Hybrid Processes, *Proceedings of the 17th IFAC World Congress*, Seoul Korea July 2008, pp. 14636-14641.

Kvasnica, M., Grieder, P., Baotic M. & Morari M.(2004), Multi-Parametric Toolbox (MPT), *HSCC 2004 (Hybrid Systems: Computation and Control)*, pp.448-462, Springer Verlag.

Nandola, N. N., & Bhartiya, S. (2008), A multiple model approach for predictive control of nonlinear hybrid systems, *Journal of Process Control*, vol. 18, No. 2, pp.131-148.

Morari M., Baric M. (2006), Recent developments in the control of constrained hybrid systems, *Computers & Chemical Engineering*, vol. 30, pp. 1619–1631.

Paoletti, S., Juloski, A.Lj., Ferrari-Trecate G., & Vidal R. (2007), Identification of hybrid systems: a tutorial. *European Journal of Control*, vol. 13, pp.242-260.

Slupphaug, O., Vada J. & Foss B. A. (1997), MPC in Systems with Continuous and Discrete Control Inputs, *Proceedings of ACC 97*, Albuquerque USA June 1997.

Sontag, E. (1981), Nonlinear regulation: The piecewise linear approach, *IEEE Transactions on Automatic Control*, vol. 26, no. 2, pp. 346-358.

Nonlinear and Adaptive Control

Oral Session

Thermodynamic approach for Lyapunov based control

H. Hoang * **F. Couenne** * **C. Jallut** * **Y. Le Gorrec** **

* *LAGEP, University of Lyon, University of Lyon 1, UMR CNRS 5007, Villeurbanne, France (e-mails: {hoang;jallut;couenne}@lagep.univ-lyon1.fr)*
** *FEMTO-ST / AS2M, ENSMM Besançon, Besançon, France (e-mail: yann.le.gorrec@ens2m.fr)*

Abstract: This paper focuses on non linear control of non isothermal Continuous Stirred Tank Reactors (CSTRs). The model of the CSTR is thermodynamically consistent in order to apply the control strategy based on the concavity of the entropy function and the use of thermodynamic availability as Lyapunov function. More precisely the stabilization problem of continuous chemical reactors is addressed operated at an unstable open loop equilibrium point. The chosen control variable is the jacket temperature. In this paper we propose a state feedback strategy to insure asymptotic stability with physically admissible control variable solicitations. Theoretical developments are illustrated on a first order chemical reaction.

Keywords: Lyapunov based control, Irreversible thermodynamics, Non isothermal CSTR, Multiple steady states, Entropy.

1. INTRODUCTION

Continuous Stirred Tank Reactors (CSTR) have been widely studied in the literature with respect to process control design (Luyben (1990); Alvarez (1999); Hua (2000); Guo (2001); Hoang (2008)). Numerous strategies have been developed to control such non linear systems. Let us cite for example: feedback linearization (Viel (1997)) for control under constraints, nonlinear PI control (Alvarez (1999)), classical Lyapunov based control (Antonellia (2003)), nonlinear adaptive control (Guo (2001)) and more recently thermodynamical Lyapunov based control (Hoang (2008)).

Besides these control problems, observation/estimation strategies have been developed in the case of under sensored CSTRs (Gibon-Fargeot (2000); Dochain (2009)). Usually, the reactor temperature is the only on-line available measurement. Then the purpose is to estimate the missing state variables that are used in the control strategy.

In this paper we focus on the control purposes only and we assume that concentrations and temperature are measured. This control synthesis is based on thermodynamic concepts defined in Callen (1985) and more recently in (Ruszkowski (2005); Ydstie (1997)) and (Hoang (2008)). More precisely, we propose a Lyapunov based approach for the stabilization of CSTR about unstable steady state as in (Hoang (2008)). This is done thanks to the Lyapunov function issued from thermodynamics consideration: the availability function $\mathcal{A}$ (Ruszkowski (2005)).

In Hoang (2008), we proposed feedback laws involving inlet and jacket temperatures as well as inlet flows. These feedback laws were obtained by imposing that the time derivative of the availability $\mathcal{A}$ remains negative, insuring consequently the global asymptotic stability. However, no care was given on the amplitude of the controls. Moreover the temperature of the reactor had to be inverted and the feedback laws had in some case some oscillatory behaviors about the critical point.

The main contribution of this paper with respect to previous work (Hoang (2008)) is the redesign of the exponential asymptotic controller in order to prevent excessive control demand and oscillation problems. In this way the obtained controller is practically more efficient. The price to pay is that global asymptotic stability is obtained on some validity domain only.

This paper is organized as follows: in section 2, we remind thermodynamical concepts and variables necessary to construct thermodynamic availability. This latter function is the Lyapunov candidate of the method. In section 3 the dynamic model of the considered CSTR is presented and analyzed. Section 4 is devoted to the design of the state feedback insuring asymptotic stability. Simulation results are given in section 5. It is shown that the resulting control leads to admissible manipulated control variables.

2. THERMODYNAMIC BASIS FOR AN AVAILABILITY FUNCTION

Irreversible thermodynamics concept will play a leading role in the methodology used for the design of the Lyapunov function (Ruszkowski (2005); Hoang (2008)). In this section we review the main ideas concerning this thermodynamical approach and the construction of the candidate Lyapunov function: the availability function in the case of an homogeneous phase.

In equilibrium thermodynamics, the system variables are divided into extensive and intensive variables, depending on whether their values depend on the "size" of the system or not. The internal energy of a homogeneous system is then expressed in terms of products of pairings of energy conjugate variables such as pressure P/ volume V, temperature T/ entropy S and chemical potential μ_i/ mole number n_i for each species i of the mixture.

The fundamental relation of thermodynamics expresses the entropy S of a given phase as a function of the so called extensive variables $Z = (U, V, n_i)$ by the Gibbs equation:

$$dS = \frac{1}{T}dU + \frac{P}{T}dV + \sum_{i=1}^{n_c} \frac{-\mu_i}{T} dn_i. \quad (1)$$

It can also be written as:

$$dS = w^T dZ \quad (2)$$

with $w = (\frac{1}{T}, \frac{P}{T}, \frac{-\mu_i}{T})$.

Since the entropy S is an extensive variable, it is a homogenous function of degree 1 of Z (Callen (1985)). From Euler's theorem we get:

$$S(Z) = w^T Z \quad (3)$$

Equation (2) can also be applied in irreversible thermodynamics as soon as the local state equilibrium is assumed: it postulates that the present state of the homogeneous system in any evolution can be characterized by the same variables as at equilibrium and is independent on the rate of evolution. So (2) can also be applied at any time.

Moreover, it is well known that balance equations can be established for $Z = (U, V, n_i)$ as well as for the entropy S but this latter is not conservative: in irreversible thermodynamics there is a source term σ which is always positive from the the second law of thermodynamics. This term represents the irreversible entropy production: the energy $T\sigma$ associated to this term represents the energy lost from material, space or thermal domains and that will never more contribute to some physical works. As a consequence of (2), the entropy balance can alternatively be written as:

$$\frac{dS}{dt} = w^T \frac{dZ}{dt} \quad (4)$$

Finally let us notice that for homogeneous thermodynamical systems (one phase only), the entropy function $S(Z)$ is necessarily strictly concave (see Callen (1985)) as shown in Fig. 1.

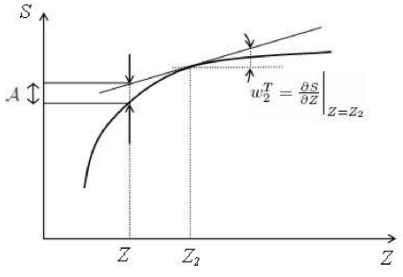

Fig. 1. Entropy and availability functions w. r. to Z.

From these observations, it can be shown (see Ydstie (1997)) that the non negative function:

$$\mathcal{A}(Z) = S_2 + w_2^T(Z - Z_2) - S(Z) \geq 0 \quad (5)$$

where Z_2 is some fixed reference point (for example the desired set point for control), is a measure of the distance between entropy $S(Z)$ and its tangent plane passing through Z_2. It is geometrically presented in Fig. 1. The slope of the tangent plane is related to intensive vector $w(Z)$ calculated at $Z = Z_2$.

As soon as we consider homogeneous mixture, S remains concave and then $\mathcal{A}$ remains also non negative. As a consequence, A is a natural Lyapunov candidate. It remains to build a feedback law to insure:

$$\frac{d\mathcal{A}}{dt} \leq 0. \quad (6)$$

3. CASE STUDY: A NON ISOTHERMAL CSTR MODEL

3.1 Assumptions of the model

We consider a jacketed homogeneous CSTR with the following first-order chemical reaction: $A \rightarrow B$. The temperature of the jacket T_w is supposed to be uniform and is used for the control purpose. The dynamics of the CSTR is deduced from volume, material and energy balances.

The following assumptions are made:

- The fluid is incompressible and the reaction mixture is supposed to be ideal.
- The two species are supposed to have the same partial molar volume v.
- At the inlet of the reactor, the pure component A is fed at temperature T_e.
- The reaction volume V is supposed to be constant.
- The heat flow exchanged with the jacket is represented by $\dot{Q} = \lambda(T_w - T)$.
- The kinetics of the liquid phase reaction is modelled thanks to the Arrhenius law. The reaction rate r_v is given by $k_0 \exp(\frac{-k_1}{T}) \frac{n_A}{V}$.

In Tables (1,2) are given the notations and numerical values that will be used for modelling and simulation. Finally let us notice that constant volume assumption implies that the total number of moles n_T is constant since the two species have the same partial molar volume.

Notation	unit	
F_{Ae}	mol/s	Inlet molar flow rate of A
F_A	mol/s	Outlet molar flow rate of A
F_B	mol/s	Outlet molar flow rate of B
F	mol/s	Total outlet molar flow rate
h_{Ae}	J/mol	Inlet molar enthalpy of A
h_i	J/mol	Molar enthalpy of species i $(i = A, B)$
H	J	Total enthalpy of the mixture
n_A	mol	Mole number of species A
n_B	mol	Mole number of species B
T	K	Temperature in the CSTR
n_T	mol	Total mole number
r_v	$mol/m^3/s$	Reaction rate
U	J	Internal energy
$x_i = \frac{n_i}{n_T}$		Molar fraction of species i, $i = A, B$

Table 1. Notation of the variables of the model.

	Numerical value	
C_{pA}	75.24 $(J/K/mol)$	Heat capacity of species A
C_{pB}	60 $(J/K/mol)$	Heat capacity of species B
h_{Aref}	0 (J/mol)	Reference enthalpy of A
h_{Bref}	-4575 (J/mol)	Reference enthalpy of B
k_0	0.12 10^{10} $(1/s)$	Kinetics constant
k_1	8.7 10^3 (K)	Parameter in Arrhenius law
P	10^5 (Pa)	Pressure
T_{ref}	300 (K)	Reference temperature
v	0.0005 (m^3/mol)	Molar volume
V	0.001 (m^3)	Reaction volume
λ	0.05808 (W/K)	Heat transfer coefficient
s_{Aref}	210.4 $(J/K/mol)$	Reference entropy of A
s_{Bref}	180.2 $(J/K/mol)$	Reference entropy of B

Table 2. Parameters of the CSTR.

Moreover the constant volume assumption constrains the total outlet molar flow rate F.

3.2 CSTR modelling

The material balances are given by:

$$\begin{cases} \dfrac{dn_A}{dt} = F_{Ae} - F_A - r_{\mathrm{v}} V \\ \dfrac{dn_B}{dt} = -F_B + r_{\mathrm{v}} V \end{cases} \tag{7}$$

and the energy balance by:

$$\frac{dU}{dt} = \dot{Q} - P\frac{dV}{dt} + F_{Ae}h_{Ae} - (F_A h_A + F_B h_B) \tag{8}$$

Remark 1. Since we suppose ideality of the mixture, the enthalpy of species A_i, $i = A, B$ in the mixture can be expressed as: $h_i(T) = c_{pAi}(T - T_{ref}) + h_{iref}$. Let us furthermore note that, as the species are involved in a chemical reaction, the reference molar enthalpies are chosen with regard to the enthalpy of formation of species.

Finally the volume balance leads to:

$$\frac{dV}{dt} = 0 \tag{9}$$

Since molar volume of species are assumed to be equal, it implies that $F = F_{Ae}$ and $F_A = x_A\, F_{Ae}$ and $F_B = x_B\, F_{Ae}$

The internal energy balance can be written in term of temperature. This is done by using the expression of the enthalpy of the system $H = \sum_{i=A,B} n_i h_i$ and by noticing that under our assumptions $\frac{dU}{dt} = \frac{dH}{dt}$. We finally obtain:

$$C_p\frac{dT}{dt} = \Big(-\Delta H\Big) r_{\mathrm{v}} V + F_{Ae}C_{pA}(T_e - T) + \lambda(T_w - T) \tag{10}$$

where $\Delta H = (h_B - h_A)$ is the enthalpy of the reaction and $C_p = C_{pA}n_A + C_{pB}n_B$ is the total heat capacity.

The dynamics of states variables (H, n_A) ((8) and (7)) or (T, n_A) ((10) and (7)) give two equivalent representations of the CSTR. These representations will be used for late purpose.

3.3 Analysis of the steady states

For this purpose, manipulated variables are chosen as:

$$F_{Ae} = 0.0183\ (mol/s),\ T_e = 310\ (K)\ T_w = 300\ (K) \tag{11}$$

Steady states are calculated by setting (7) and (10) equal to zero.

By introducing the expression of the steady state mole number of n_A in the temperature equation, the steady state temperatures are the values that satisfy $P_e(T) = 0$ with:

$$P_e(T) = \frac{h_A - h_B}{C_p} k_0 \exp(\frac{-k_1}{T}) \frac{F_{Ae}}{\Big(\frac{F_{Ae}}{n_T} + k_0 \exp(\frac{-k_1}{T})\Big)} + \frac{F_{Ae}C_{pA}}{C_p}(T_e - T) + \frac{\lambda}{C_p}(T_w - T) \tag{12}$$

These values are represented in Fig. 2(a). It shows that the system has three steady state operating points: P_1, P_2 and P_3.

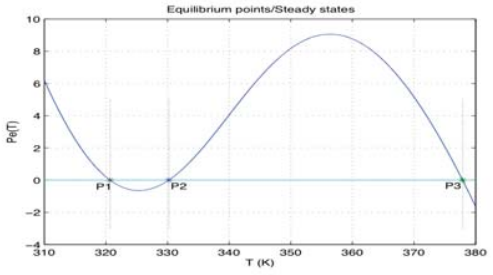

Fig. 2. Steady states

The numerical values of these steady states and the eigenvalues of the linearized system about these points are given in Table 3.

Points	Values	Eigenvalues
P_1: $[n_A\ T]$	[1.6449 320.6704]	[−0.0090 −0.0024]
P_2: $[n_A\ T]$	[1.3583 330.1997]	[−0.0090 0.0027]
P_3: $[n_A\ T]$	[0.1416 377.8795]	[−0.0802 −0.0100]

Table 3. Steady state points and eigenvalues

From Table 3, one can see that steady state operating points P_1 and P_3 are stable, whereas the steady state operating point P_2 is not stable since one of its eigenvalues is positive.

Control Problem: we are interested to operate the reactor at $T = 330.1997$ corresponding to the unstable steady state operating point P_2 and at fixed F_{Ae} and T_e. As a consequence a control feedback law on T_w is necessary.

4. CONTROLLER SYNTHESIS

In this paper we propose a feedback law that is less conservative than the one proposed in Hoang (2008) and that still insures asymptotic stability in some admissible domain. We first give some preliminary results necessary for the controller synthesis.

Proposition 1 shows that n_A belongs to an invariant domain $[0, n_T]$.

Proposition 1. If $n_A(0) \in [0, n_T]$ then $n_A(t) \in [0, n_T]\ \forall t$

Proof. It is straightforward looking at (7) since $\frac{dn_A}{dt}\Big|_{n_A=0} = F_{Ae} > 0$ and $\frac{dn_A}{dt}\Big|_{n_A=n_T} = -k_0 \exp(-\frac{k_1}{T}) n_T < 0$ □

Moreover we notice that the sign of $\frac{dn_A}{dt}$ is the same as that of $G(T) = \frac{F_{Ae}}{\frac{F_{Ae}}{n_T} + k_0 \exp(\frac{-k_1}{T})}$.

In order to stabilize the closed loop system about (n_{a_2}, T_2), we propose the following feedback law for T_w.

Proposition 2. At fixed T_e and F_{Ae}, the system defined by ((7) and (8)) with the non linear feedback law (13) for T_w:

$$T_w = \frac{1}{\lambda}\Big(K_1\widetilde{v}_1 - \mathfrak{F}F_{Ae} + \frac{f}{-\widetilde{v}_1}\frac{dn_A}{dt}\Big) + T \tag{13}$$

where:

$$\widetilde{v}_1 = \left[\frac{1}{T} - \frac{1}{T_2}\right] \tag{14}$$

$$\mathfrak{F}(T_e, T, n_A, n_B) = \Big(h_{Ae} - (x_A h_A + x_B h_B)\Big) \tag{15}$$

and

$$f(T) = \Big((C_{pA} - C_{pB})T_{ref} - (h_{Aref} - h_{Bref})\Big)\widetilde{v}_1 + \Big(C_{pA} - C_{pB}\Big)\ln\Big(\frac{T}{T_2}\Big) \tag{16}$$

is stable and asymptotically converges to the desired operating point $P_2 = (T_2, n_{A2})$ for any initial condition (T_0, n_{A0}) contained in some validity domain for which the constant K_1 is chosen positive.

Proof. K_1 insures the continuity of T_w at $t = 0$: $T_w(0) = T_0$ or,

$$\left[K_1\widetilde{v}_1 - \mathfrak{F}F_{Ae} + \frac{f}{-\widetilde{v}_1}\frac{dn_A}{dt}\right]_{t=0} = 0 \tag{17}$$

The proof of the proposition 2 contains two parts:

1. Determination of the validity domain of initial conditions: developing (17) and using the material balance (7) and since $n_B = n_T - n_A$, we have at $t = 0$:

$$K_1\widetilde{v}_1 = F_{Ae}h_{Ae} - F_{Ae}h_B + \frac{f}{\widetilde{v}_1}F_{Ae} - n_A D(T) \tag{18}$$

with $D(T) = \left[\frac{F_{Ae}}{n_T}(h_A - h_B) + \Big(\frac{F_{Ae}}{n_T}F_{Ae} + k_0\exp(\frac{-k_1}{T})\Big)\frac{f}{\widetilde{v}_1}\right]$.

For positive K_1, (18) is positive if $\widetilde{v}_1 > 0$. So the right hand side of the equality has the sign of $\widetilde{v}_1$.

In a same way, we obtain :

$$\begin{cases} n_{A0} < F(T_0) \text{ if } T_0 > T_2 \\ n_{A0} > F(T_0) \text{ if } T_0 < T_2 \end{cases} \tag{19}$$

with $F(T) = \frac{(h_{Ae} - h_B + \frac{f}{\widetilde{v}_1})}{\frac{1}{n_T}(h_A - h_B) + \frac{1}{G(T)}\frac{f}{\widetilde{v}_1}}$.

The domain of validity is given in Fig. 3.

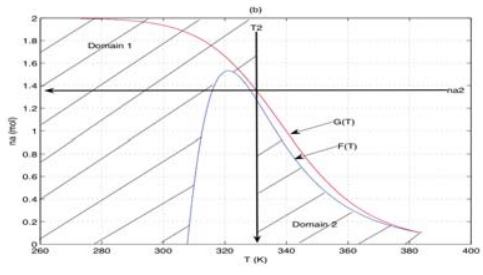

Fig. 3. Domain of validity of initial conditions

2. Stability and convergence to the desired point (T_2, n_{A2}): Let us consider the function $\mathcal{A}$ (5). The time derivative of such function can be written:

$$\frac{d\mathcal{A}}{dt} = -\widetilde{v}_1\frac{dU}{dt} - \widetilde{v}_2\frac{dn_A}{dt} \tag{20}$$

with $\widetilde{v}_2 = -\big(\frac{\mu_A}{T} - \frac{\mu_B}{T}\big) + \Big(\frac{\mu_{A2}}{T_2} - \frac{\mu_{B2}}{T_2}\Big)$. From the energy balance (8), (20) can be written:

$$\frac{d\mathcal{A}}{dt} = -\widetilde{v}_1\Big[F_{Ae}\mathfrak{F} + \lambda(T_w - T)\Big] - \widetilde{v}_2\frac{dn_A}{dt} \tag{21}$$

where $\mathfrak{F}$ is defined in (14). Furthermore, using the constitutive equation

$$\mu_A(T, P, x_A) = \mu_A^0(T) + RT\ln(\frac{n_A}{n_A + n_B}) \tag{22}$$

where $\mu_A^0(T) = C_{pA}(T - T_{ref}) + h_{Aref} - T\Big(C_{pA}ln(\frac{T}{T_{ref}}) + s_{Aref}\Big)$ one can write $\widetilde{v}_2$ on the following form:

$$\widetilde{v}_2 = f(T) + g(n_A) \tag{23}$$

where $f(T)$ is defined in (16) and $g(n_A) = R\ln\Big(\frac{n_{A2}}{n_A}\frac{n_B}{n_{B2}}\Big)$. Then (21) becomes :

$$\frac{d\mathcal{A}}{dt} = -\widetilde{v}_1\Big[F_{Ae}\mathfrak{F} + \lambda(T_w - T)\Big] - (f + g)\frac{dn_A}{dt} \tag{24}$$

We propose the following feedback law :

$$T_w = \frac{1}{\lambda}\Big(K_1\widetilde{v}_1 - \mathfrak{F}F_{Ae} + \frac{f}{-\widetilde{v}_1}\frac{dn_A}{dt}\Big) + T \tag{25}$$

for systems with initial conditions $(T_w(0) = T(0))$ such that $K_1 > 0$. Using this feedback law, $\frac{d\mathcal{A}}{dt}$ becomes:

$$\frac{d\mathcal{A}}{dt} = -K_1\widetilde{v}_1^2 - g\frac{dn_A}{dt} \tag{26}$$

The idea is to not constrain the system by imposing $\frac{d\mathcal{A}}{dt} < 0\ \forall t$ as in Hoang (2008).

We are now going to show that depending on the initial conditions from the domain of validity (associated with condition $K_1 > 0$), $-g\frac{dn_A}{dt}$ is either negative $\forall t$ or becomes negative and converges to 0.

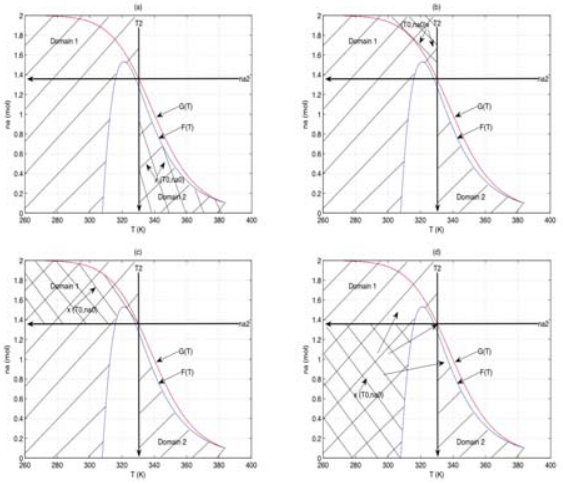

Fig. 4. Admissible initial conditions in the domain of validity.

Remark 2. A simple analysis permits to conclude that $g(n_A)$ is positive as soon as $n_A \leq n_{A2}$.

In all cases in using (19), lemma 1 and remark 2 we will show the negativeness of $-g\frac{dn_A}{dt}$.

With initial conditions such as shown in Fig. 4(a) and using additionally the remarks 4.5 and 4.6 of appendix A), we have:

$$\frac{d\mathcal{A}}{dt} = -K_1\widetilde{v}_1^2 - g\frac{dn_A}{dt} \leq 0, \ \forall t \tag{27}$$

With initial conditions such as shown in Fig. 4(b), using the remarks 4.3 and 4.4 we obtain the same inequality (27).

The trajectory of (T, n_A) issued from initial domain as shown in Fig. 4(c) is trapped in the domain of Fig. 4(b). This is obtained thanks to remarks 4.2 and 4.3 and 4.4.

Finally for initial conditions as shown in Fig. 4(d), there are two possible scenarios : one is that the trajectory of (T, n_A) is trapped in the domain of figure 4(a) or 4(c) then 4(b). The result then follows from remarks 4.2 and 4.3 and 4.4. The other scenario is that the trajectory of (T, n_A) is not trapped in these domains and then $\mathcal{A}$ always decreases and converges to 0.

Finally, from all the admissible initial conditions and after some time, $\mathcal{A}$ plays the role of a Lyapunov function.

Remark 3. The feedback law T_w (13) is well defined for $T = T_2$ since $\lim_{T\to T_2} \frac{f}{\widetilde{v}_1} = \Big((C_{pA} - C_{pB})T_{ref} - (h_{Aref} - h_{Bref})\Big) + \Big(C_{pA} - C_{pB}\Big)(-T_2)$.

5. SIMULATION

The purpose of this section is to illustrate the good performances obtained from the aforementionned control strategy and the admissibility of the resulting control variables. The open and closed loop simulations are carried out respect to four different initial conditions chosen in the initial domain of validity of the control law. These initial conditions correspond to the four different scenarios depicted in Fig. 4 in view of studying the convergence properties of the control law and the control variable solicitation. The four initial conditions are:

(C1): $(T(0) = 340, n_{A0} = 0.6)$ belongs to Fig. 4(a).
(C2): $(T(0) = 325, n_{A0} = 1.8)$ belongs to Fig. 4(b).
(C3): $(T(0) = 300, n_{A0} = 1.6)$ belongs to Fig. 4(c).
(C4): $(T(0) = 300, n_{A0} = 0.6)$ belongs to Fig. 4(d).

5.1 Open loop simulation

First of all let us consider open loop simulations with inputs defined by (11) and initial conditions (C1) to (C4). Simulations are given in Figure (5).

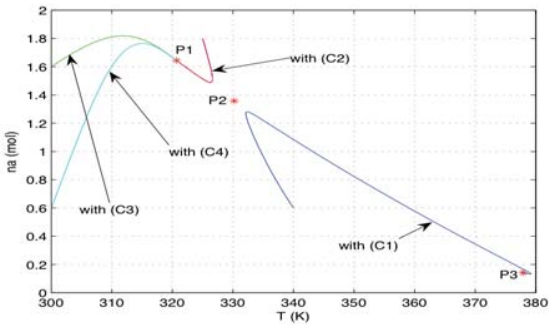

Fig. 5. The representation of the open loop phase plan

5.2 Closed loop system

The open loop system is closed with the feedback law T_w constructed with the state variables n_A and T.

The trajectories issued from the initial points (C1) to (C4) are given in Fig. 6. We notice that for all the initial conditions the system converges to the desired operating point P2.

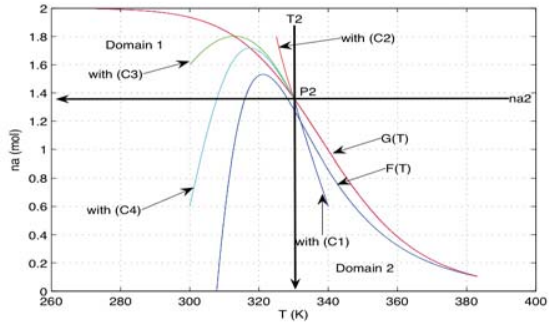

Fig. 6. Closed loop trajectories in phase plane.

Fig. 7 shows the control variable T_w. Its values are admissible and its evolution is slow enough.

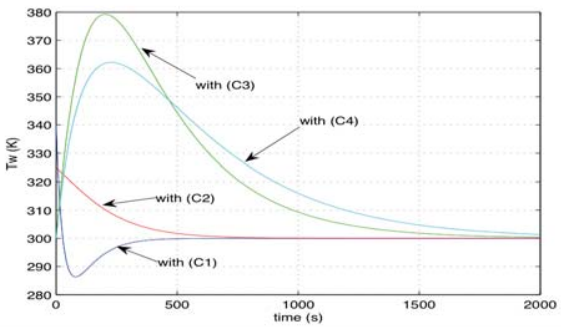

Fig. 7. The feedback law T_w

Fig.8 shows the time trajectory of $\mathcal{A}$ for the different initial conditions. For initial conditions (C1) and (C2),

the availability $\mathcal{A}$ can be assimilated to Lyapunov function from the beginning of the reaction. For initial conditions (C3) and (C4), $\frac{d\mathcal{A}}{dt}$ is forced to be negative only after a certain time from which $\mathcal{A}$ plays the role of Lyapunov function, and converges to 0.

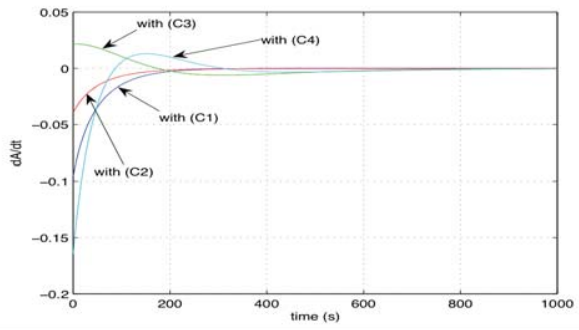

Fig. 8. The dynamics of $\frac{d\mathcal{A}}{dt}$

6. CONCLUSION

In this paper, we have shown how to stabilize a CSTR about the desired operating point by means of Lyapunov-based method. The Lyapunov function is the availability function $\mathcal{A}$. $\mathcal{A}$ is derived from thermodynamic considerations. The stabilization is ensured in some domain of validity issued from the condition of positivity of the design parameter K_1 and the continuity of the feedback law T_w.

The simulation results showed that convergence objective is satisfied and that the state feedback law is physically implementable since jacket temperature remains in some physical domain with admissible rate of variation.

Nevertheless,in the proposed control strategy the closed loop dynamic is imposed by the initial conditions (with K_1). This is the reason why we are now studying for dynamic controllers with additional freedom degrees. It remains also to compare our result with previous results as given in Viel (1997) for example) in term of performance and robustness.

REFERENCES

Alvarez-Ramirez, J. and Femat, R. (1999). Robust PI stabilization of a class of chemical reactors. *Systems & Control Letters*, 38(4-5), 219-225.

Antonellia, R., and Astolfi, A. (2003). Continuous stirred tank reactors: easy to stabilise? *Automatica*, 39, 1817-1827.

Callen, H.B. (1985). *Thermodynamics and an introduction to thermostatics.* John Wiley & Sons Inc, New York, 2nd edition.

Dochain, D., Couenne, F.,and Jallut, C. (2009) Enthalpy Based Modelling and Design of Asymptotic Observers for Chemical Reactors. *accepted to International Journal of Control.*

Gibon-Fargeot, A.M., Celle-Couenne, F. , and Hammouri, H. (2000). Cascade estimation design for cstr models. *Computers & Chemical Engineering*, 24(11), 2355-2366.

Guo, B., Jiang, A., Hua, X., and Jutan, A. (2001). Nonlinear adaptive control for multivariable chemical processes. *Chemical Engineering Science*, 56, 67816791.

Hoang, H., Couenne, F.,Jallut, C., and Le Gorrec, Y. (2008). Lyapunov based control for non isothermal continuous stirred tank reactor. *Proceedings of the 17th World Congress of the IFAC*, July 6-11, 2008, Seoul, Korea.

Hua, X., and Jutan A. (2000). Nonlinear Inferential Cascade Control of Exothermic Fixed-bed Reactors. *AICHE Journal*, 46, 980-996, 2000.

Luyben, W.L. (1990). *Process Modeling, Simulation, and Control for Chemical Engineers.* McGraw-Hill, Singapore.

Ruszkowski, M., Garcia-Osorio, V., and Ydstie, B.E. (2005) Passivity based control of transport reaction systems. *AIChE Journal*, 51, 3147-3166.

Viel, F., Jadot, F., and Bastin, G. (1997). Global stabilization of exothermic chemical reactors under input constraints. *Automatica*, 33(8), 1437-1448.

Ydstie, B.E., and Alonso, A.A. (1997). Process systems and passivity via the Clausius-Planck inequality. *Systems Control Letters*, 30(5), 253-264.

Appendix A

Lemma 1. The energy balance (8) with feedback law (13) gives rise to:

1.
$$(\sum_i n_i C_{pi})\frac{dT}{dt} = K_1\widetilde{v}_1 + L(T)\frac{dn_A}{dt} \qquad (A.1)$$
with $L(T) = \left(-\frac{f}{v_1} - (h_A - h_B)\right)$.

2. With assumptions presented in section 3.1, we have: $L(T) > 0$ if $T < T_2$ and $lim_{T\to T_2} L(T) = 0$.

Remark 4. The following remarks hold:

(1) From Proposition 1, C_p is bounded and positive.
(2) Lemma 1 insures that if $T < T_2$ and $\frac{dn_A}{dt} > 0$ then $\frac{dT}{dt} > 0$ since $C_p\frac{dT}{dt} = K_1\underbrace{\widetilde{v}_1}_{>0} + \underbrace{L(T)\frac{dn_A}{dt}}_{>0}$.
(3) When $\frac{dn_A}{dt} = 0$ (n_A reaches $G(T)$) and $T < T_2$ then $(\sum_i n_i C_{pi})\frac{dT}{dt} = K_1\underbrace{\left(\frac{1}{T} - \frac{1}{T_2}\right)}_{>0}$ and $\frac{dT}{dt}$ remains positive.
(4) When $\frac{dn_A}{dt} < 0$ and $T = T_2$, then $C_p\frac{dT}{dt} = 0$ and T stays equal to T_2.
(5) When $\frac{dn_A}{dt} = 0$ (n_A reaches $G(T)$) and $T > T_2$, then $(\sum_i n_i C_{pi})\frac{dT}{dt} = K_1\underbrace{\left(\frac{1}{T} - \frac{1}{T_2}\right)}_{<0}$ and T decreases.
(6) When $\frac{dn_A}{dt} > 0$ and $T = T_2$, then $(\sum_i n_i C_{pi})\frac{dT}{dt} = 0$ and T remains equal to T_2.
(7) When $\frac{dn_A}{dt} = 0$ and $T = T_2$, the system reaches the desired point and stays on.

Boundary geometric control of co-current heat exchanger

Ahmed MAIDI [*,**] **Moussa DIAF** [*] **Jean Pierre CORRIOU** [**]

[*] *Université Mouloud MAMMERI, Faculté de Génie Electrique et d'Informatique, Département Automatique, Tizi-Ouzou, Algérie*
[**] *Laboratoire des Sciences de Génie Chimique, CNRS-ENSIC, 1 rue Grandville BP 20451, 54001 Nancy Cedex, France*

Abstract: A control strategy is proposed to control the internal fluid temperature at the outlet of a co-current heat exchanger by manipulating the inlet external fluid temperature. The dynamic model of the heat exchanger is given by two partial differential equations. Based on nonlinear geometric control, a state-feedback law that ensures a desired performance of a measured output defined as spatial average temperature of the internal fluid is derived. Then, in order to control the outlet internal fluid temperature, a control strategy is proposed where an external controller is introduced to provide the set point of the considered measured output by taking as input the error between the outlet internal fluid temperature and its desired set point. The validity of the proposed control design and strategy is examined in simulation by considering the tracking and perturbation rejection problems.

Keywords: distributed parameter system, partial differential equation, geometric control, characteristic index,PI controller, co-current heat exchanger.

1. INTRODUCTION

As a thermal device, heat exchangers are widely used in process industries both for cooling and heating operations. The dynamic behavior of the heat exchanger is modeled by a set of partial differential equations (PDE) that describe the spatio-temporal variation of the temperatures. Thus, the need to find the best operating conditions for the heat exchangers and to improve their effectiveness lead to take into account their distributed nature. In this context, good performances can be attained using more efficient control strategy based on the direct use of the distributed parameter model rather than a reduced or a lumped model (Ray, 1989; Christofides, 2001).

Heat exchangers can be classified into two major types according to their flow arrangement: co-current and counter-current heat exchangers. For the first one, the two fluids travel in the same direction. By contrast, for the second one, the fluids move in opposite directions.

In the control problem of tube heat exchangers, the variable which is manipulated, theoretically, is the thermal power at the inlet of the outer tube, i.e. grossly the product of a flow rate and a difference of temperature. In practice, to control the outlet temperature of a heat exchanger, two possible strategies which are not equivalent exist. The first one is to use the inlet temperature of the external fluid, while the second is to manipulate its flow rate.

When the flow rate is considered as a manipulated variable, if it becomes too low, the flow regime in the outer tube can be laminar instead of turbulent, which affects the parameters of the models, in particular the heat transfer coefficient (Xuan and Roetzel, 1993). So the tuning of the controller should vary with the flow rate, which is a difficult task (Abdelghani-Idrissi et al., 2001; Arbaoui et al., 2007). In addition, by manipulating the flow rate, a minimum bound is to set on this input. With the temperature as a manipulated input, it is possible to work at a constant large flow rate and the hydrodynamic regime is invariable. Physically, manipulating the temperature is almost possible if this latter is the outlet of a process with fast dynamics like plate heat exchangers. Potential flow rate variations will be assumed as a disturbance that affects the system and needs to be rejected by the designed controller.

Control of counter-current heat exchanger has attracted much attention, and several strategies are proposed based either on the PDE model or ODE model (see e.g. Maidi et al. (2008a) for more references) compared to the co-current heat exchanger for which few methods have been proposed in the literature. Derese and Noldus (1980) addressed the problem of controlling of the co-current heat exchanger using dynamical lumped parameter controllers designed based on technical frequency domain specifications. Based on the conjugate gradient method (CGM) of minimization, Huang and Yeh (2003) proposed an algorithm for determining an optimal external distributed heat-flux of a steady state co-current heat exchanger.

In this paper, a control strategy is proposed to control the outlet internal fluid temperature of a co-current heat exchanger by manipulating the inlet external fluid temperature. The designed approach is based on the use of the PDE model that describes the dynamic behavior. The idea is to design a state-feedback control that allows controlling the average temperature of the internal tube of the heat exchanger, assumed as the measured output. As it will be demonstrated, the direct design of a control law by considering the outlet temperature as the controlled variable is a difficult task due to the fact that the process is infinite-dimensional. Then, in order to control the outlet fluid temperature, a control strategy is proposed where a PI controller is introduced to provide the set point of the measured

⋆ Corresponding author: corriou@ensic.inpl-nancy.fr

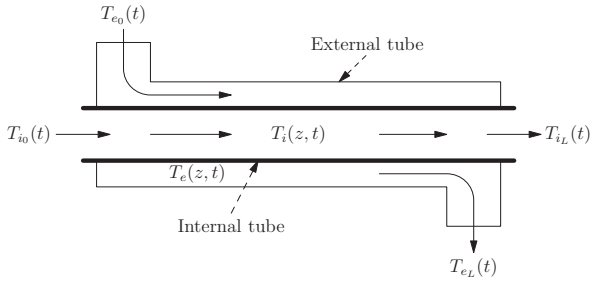

Fig. 1. co-current heat exchanger.

output (spatial average temperature). The design of the state-feedback control law makes use of the concept of characteristic index (Christofides and Daoutidis, 1996), which characterize the spatiotemporal interactions between the controlled and manipulated variables.

The paper is organized as follows. In section 2, the studied co-current heat exchanger is presented and its dynamic model given as a system of two PDEs. Section 3 concerns the formulation of the control problem and the design methodology. Section 4 is dedicated to simulation results concerning tracking and perturbation rejection problems. Finally, a conclusion ends the article.

2. CO-CURRENT HEAT EXCHANGER DYNAMIC MODEL

2.1 Description of the heat exchanger

The process studied in this work corresponds to a tubular co-current heat exchanger (Fig. 1). A fluid of constant density ρ_i and of heat capacity C_{p_i} flows through the internal tube of a heat exchanger, of length L, with a constant velocity v_i. This fluid enters at temperature T_{i_0} and exchanges heat with the an external fluid or non condensating vapor fluid, of constant density ρ_e and of heat capacity C_{p_e}, which flows in the same direction in the jacket with a velocity v_e. This fluid enters at temperature T_{e_0}. At the outlet of the exchanger, the internal fluid leaves at temperature T_{i_L}. In the present study, the internal and external cross sections S_i and S_e of the heat exchanger are supposed to be uniform and the surface area used for the heat transfer per unit length is $\mathcal{A}$. Both temperatures T_i of the internal fluid and T_e of the external fluid depend on time and spatial position along the tube.

The energy balance of the heat exchanger, after classical simplifying hypotheses (Ray and Ogunnaike, 1994), gives the following partial differential equation for the internal tube (internal fluid)

$$\frac{\partial T_i(z,t)}{\partial t} = -v_i \frac{\partial T_i(z,t)}{\partial z} + h_i \left[T_e(z,t) - T_i(z,t)\right] \qquad (1)$$

and the following partial differential equation for the jacket (external fluid)

$$\frac{\partial T_e(z,t)}{\partial t} = -v_e \frac{\partial T_e(z,t)}{\partial z} + h_e \left[T_i(z,t) - T_e(z,t)\right] \qquad (2)$$

where $h_i = \dfrac{U_i\,\mathcal{A}}{\rho_i\,S_i\,C_{p_i}}, \quad h_e = \dfrac{U_e\,\mathcal{A}}{\rho_e\,S_e\,C_{p_e}}.$

T_i and T_e are the temperatures of the internal and external fluids, respectively, h_i and h_e are the heat transfer coefficients, v_i and v_e are the velocities, U_i and U_e are the overall heat transfer coefficients, $\mathcal{A}$ is the surface area devoted to heat transfer.

Each PDE requires an initial condition and a boundary condition to be fully defined. The studied heat exchanger is of co-current type. For Eq. (1) describing the temperature of the internal fluid, the boundary condition is usually specified at $z = 0$ as the temperature of the fluid entering the tube is in general known and measurable. Thus, at $z = 0$, it gives

$$T_i(0,t) = T_{i_0}(t) \qquad (3)$$

and most often the initial condition is some given temperature profile at $t = 0$

$$T_i(z,0) = T_i^*(z) \qquad (4)$$

Similarly, for Eq. (2), describing the distribution of temperature of the external fluid in the jacket, the boundary condition is the temperature of the entering fluid T_{e_0}, specified at $z = 0$, consequently

$$T_e(0,t) = T_{e_0}(t) \qquad (5)$$

while the initial condition is some given temperature profile at $t = 0$

$$T_e(z,0) = T_e^*(z) \qquad (6)$$

Eqs. (1)-(6) constitute the dynamic model of the co-current heat exchanger.

3. CONTROL OF THE CO-CURRENT HEAT EXCHANGER

3.1 Control problem formulation

As indicated above, to control the outlet internal temperature T_{i_L}, two manipulated variables are possible, either the inlet external fluid temperature T_{e_0} or the flow rate represented by the velocity v_e. In this work, the temperature T_{e_0}, corresponding to the boundary condition (5), is taken as a manipulated variable to easily control the outlet internal fluid temperature T_{i_L} since the hydrodynamic regime remains invariable. Now, due to Eq. (2), it is noticeable that by manipulating the boundary condition of the jacket, given by Eq. (5), a variation of the temperature of the external fluid T_e along the jacket results. Thus, by denoting as u the control variable and y the controlled variable, the model of the heat exchanger (1)-(6) takes the following form

$$\frac{\partial T_i(z,t)}{\partial t} = -v_i \frac{\partial T_i(z,t)}{\partial z} + h_i \left[T_e(z,t) - T_i(z,t)\right] \qquad (7)$$

$$\frac{\partial T_e(z,t)}{\partial t} = -v_e \frac{\partial T_e(z,t)}{\partial z} + h_e \left[T_i(z,t) - T_e(z,t)\right] \qquad (8)$$

$$T_i(0,t) = T_{i_0}(t) \qquad (9)$$

$$T_e(0,t) = T_{e_0}(t) = u(t) \qquad (10)$$

$$T_i(z,0) = T_i^*(z) \qquad (11)$$

$$T_e(z,0) = T_e^*(z) \qquad (12)$$

$$y(t) = \mathcal{C}\big(T_i(z,t)\big) = \int_0^L \delta(z-L)\,T_i(z,t)\,dz \qquad (13)$$

where $\mathcal{C}(\,.\,)$ is a bounded linear operator.

3.2 Design approach

Recently the nonlinear geometric control has proved to be very successful as a control approach of the linear and quasi-linear DSP (Christofides and Daoutidis, 1996; Gundepudi and Friedly, 1998; Christofides, 2001; Wu and Liou, 2001; Maidi et al., 2008a,b). The most important advantage of geometric control is that the control law can be designed using directly the PDE model, which leads to distributed control that increases the performances (Christofides, 2001). Thus, this theoretical approach will be used to derive a boundary control law for the co-current heat exchanger.

The manipulated variable $u(t)$ appears as an inhomogeneous part in the boundary condition (10), so in order to obtain the expression of the control law, we propose to insert the manipulated variable $u(t)$ through the use of Dirac delta function in the state equation (7) as follows

$$\frac{\partial T_e(z,t)}{\partial t} = -v_e \frac{\partial T_e(z,t)}{\partial z} + h_e \left[T_i(z,t) - T_e(z,t)\right] + v_e\, \delta(z)\, u(t) \tag{14}$$

so that the model will be affine with respect to the input $u(t)$.

Under these conditions, the boundary condition (10) becomes homogeneous,

$$T_e(0,t) = 0 \tag{15}$$

Now, as the open-loop system $u(t)$-$y(t)$ is infinite dimensional, the characteristic index σ does not exist. This can be easily verified by calculating the successive derivatives of the output (13) with respect to time. To overcome this problem, we propose to consider another measured output given as the average of the external fluid temperature, i.e.

$$y_m(t) = \mathcal{C}_m\big(T_i(z,t)\big) = \int_0^L c_m(z)\, T_i(z,t)\, dz \tag{16}$$

where $\mathcal{C}_m(\,.\,)$ is a bounded linear operator and $c_m(z)$ is a smooth positive function ($c_m(z) > 0$).

In this case, the derivative of the measured output (16) with respect to time yields

$$\begin{aligned}\frac{dy_m(t)}{dt} &= \int_0^L c_m(z)\, \frac{\partial T_i(z,t)}{\partial t}\, dz \\ &= \int_0^L c_m(z) \Bigg(- v_i \frac{\partial T_i(z,t)}{\partial z} + h_i \left[T_e(z,t) - T_i(z,t)\right] \Bigg) dz \end{aligned} \tag{17}$$

the characteristic index is greater than one. Performing one more differentiation, we obtain:

$$\frac{d^2 y_m(t)}{dt^2} = \int_0^L c_m(z) \Bigg(- v_i \frac{\partial}{\partial t}\left(\frac{\partial T_i(z,t)}{\partial z}\right) + h_i \left[\frac{\partial T_e(z,t)}{\partial t} - \frac{\partial T_i(z,t)}{\partial t}\right] \Bigg) dz \tag{18}$$

By substituting the term $\dfrac{\partial T_e(z,t)}{\partial t}$ by its expression given by (14) and after arrangement, equation (18) takes the form

$$\frac{d^2 y_m(t)}{dt^2} = I_1 + h_i\, v_e \underbrace{\left[\int_0^L c_m(z) \delta(z)\, dz\right]}_{I_2} u(t) \tag{19}$$

where I_1 is the remaining term of the integral in equation (18). According to equation (19), it is clear that the input appears linearly.

Now, in order to have the control law $u(t)$ well-defined, the integral term I_2 must be different from zero. This condition ensures that the characteristic index of the measured output $y_m(t)$ with respect to the manipulated input $u(t)$ is equal to 2. The calculus of I_2 gives

$$I_2 = \int_0^L c_m(z)\, \delta(z)\, dz = c_m(z)\big|_{z=0} \tag{20}$$

The condition on the characteristic index being equal to 2 is related to the choice of the function $c_m(z)$, i.e. the value of $c_m(z)$ should not be zero at $z = 0$

$$I_2 = c_m(0) \neq 0 \tag{21}$$

Thus, by choosing a function $c_m(z) \geq 0$ that satisfies the condition (21), the characteristic index will be $\sigma = 2$. In summary, the modification of equation (14) by introduction of the manipulated input and the consideration of the new output (16) have ensured the existence of the characteristic index.

As $\sigma = 2$, this suggests requesting the following input-output response of the closed-loop system

$$\tau_2 \frac{d^2 y_m(t)}{dt^2} + \tau_1 \frac{dy_m(t)}{dt} + y_m(t) = v(t) \tag{22}$$

Substituting (19) into equation (22), we obtain the following state-feedback control law

$$u(t) = \frac{1}{h_i\, v_e\, \tau_2\, I_2}\Big[v(t) - y_m(t) - \tau_1\, \dot{y}_m(t) - \tau_2\, I_1\Big] \tag{23}$$

where τ_1, τ_2 are adjustable controller parameters chosen to guarantee the input-output stability and to enforce the desired performance specifications for the output $y_m(t)$ (Christofides, 2001), and $v(t)$ is an external input.

The control robustness dealing with problems of model and parameter uncertainty and unmodeled dynamics, is provided in (23) through application of the linear control theory to the resulting linear [input $v(t)$-output $y_m(t)$] linear system to define the external input $v(t)$ by a robust controller. In this work, in order to ensure the robustness, i.e. to handle uncertainties and unmodeled dynamics, the external input $v(t)$ is defined by means of a PI controller (Kravaris and Kantor, 1990) as follows

$$v(t) = K_{c_m}\left[\big(y_m^d(t) - y_m(t)\big) + \frac{1}{\tau_{I_m}} \int_0^t \big(y_m^d(\xi) - y_m(\xi)\big)\, d\xi\right] \tag{24}$$

where K_{c_m}, τ_{I_m} are respectively the proportional gain, integral time constant of the PI controller, respectively. $y_m^d(t)$ is the set-point of the measured variable $y_m(t)$.

Thus, the transfer function of the closed loop system is the following

$$\frac{Y_m(s)}{Y_m^d(s)} = \frac{K_{c_m}\left(\tau_{I_m}+1\right)}{\tau_{I_m}\,\tau_2\,s^3+\tau_{I_m}\,\tau_1\,s^2+\left(\tau_{I_m}+K_{c_m}\,\tau_1\right)+K_{c_m}} \quad (25)$$

The scalar parameters K_{c_m}, τ_{I_m} and τ are tuned in order for the denominator to approach a polynomial minimizing an ITAE criterion (Corriou, 2004) and it can be verified that the following polynomial is Hurwitz (the poles have a negative real part) to ensure the closed loop stability related to the roots of the characteristic equation

$$\tau_2\tau_{I_m}\,s^3+\tau_1\tau_{I_m}\,s^2+\left(\tau_{I_m}+\tau_1 K_{c_m}\right)s+K_{c_m}=0 \quad (26)$$

At this point, it is clear that the control law (23) ensures the desired performances of the introduced measured output $y_m(t)$ rather the controlled output $y(t)$. Actually, the output $y_m(t)$ is introduced only in order to avoid the problem of non-existence of the characteristic index. In order to solve the formulated boundary control problem, i.e. controlling the output $y(t)$, we propose to keep the control law (23) derived for the measured output (16) with $c(z)$ satisfying the condition (21). Then, define the set point of the measured output $y_m(t)$, denoted by $y_m^d(t)$, by means of a PI controller taking as input the error $e(t) = y^d(t) - y(t)$, where $y^d(t)$ is the corresponding set point of the controlled variable $y(t)$. Note that another control technique can be adopted to provide the set point $y_m^d(t)$. The proposed global control strategy is summarized in Fig. 2.

The control law (23) requires that the complete state $T_i(z,t)$ must be available especially to evaluate the integral term I_1 and the measured output $y_m(t)$. From a practical point of view, this is impossible since the state $T_i(z,t)$ is infinite. Ray (1989) discusses some way that can provide the complete state of a distributed parameter system. The design of Kalman filter that estimates the whole state variables vector in the case of a counter-current heat exchanger has been studied by Maidi et al. (2008a). In this work, it is considered that the vector of state variables is fully available to clearly show the effectiveness and the contribution of the proposed control strategy.

Note that the choice of the function $c_m(z)$ is not unique. Nevertheless, the relation (21) shows that the function $c_m(z)$ is involved in the evaluation of the integral term I_1 and in calculating the measured output $y_m(t)$ and its derivative $\dot{y}_m(t)$, so it is suggested to choose a simple function for example $c_m(z) = L - z$. From a practical point of view, these calculations can be provided simply by a computer by processing the data measurements $T_i(z,t)$ and $T_e(z,t)$.

4. SIMULATION RESULTS

In this section, the performance of the proposed control strategy will be illustrated through application examples. For simulation purpose of the closed-loop system, the method of lines (Wouwer et al., 2004) is used by considering a number of discretization points $N = 100$. The control is held constant over the sampling period equal to $0.02\,\mathrm{s}$ in all simulation runs. The integral term I_1, the measured output $y_m(t)$ and its derivative $\dot{y}_m(t)$ involved in the control law (23) are evaluated numerically using the trapezoidal method. The terms involving differentiation according to the space variable z are evaluated by means of finite differences.

The heat exchanger parameters (Friedly, 1972) are $v_e = 2\,\mathrm{m\,.\,s^{-1}}$, $v_i = 1\,\mathrm{m\,.\,s^{-1}}$, $h_e = 1\,\mathrm{s^{-1}}$, $h_i = 1\,\mathrm{s^{-1}}$ and $L = 1\,\mathrm{m}$. For the internal PI controller, the tuning parameters obtained following the tuning procedure described at the end of the section 3.2 are $K_{c_m} = 0.0240$, $\tau_{I_m} = 0.0469\,\mathrm{s}$. The tuning parameters K_c and τ_I of the external PI controller that provide the set point $y_m^d(t)$ have been achieved by trial and error and observation of the obtained performance, so that the retained parameters are $K_c = 0.02$ and $T_i = 0.3\,\mathrm{s}$.

The initial conditions $T_i(z,0)$ and $T_e(z,0)$ are the steady state profiles (Fig. 3) defined by $T_{i_0}(t) = 25°\mathrm{C}$ and $T_{e_0}(t) = 50°\mathrm{C}$.

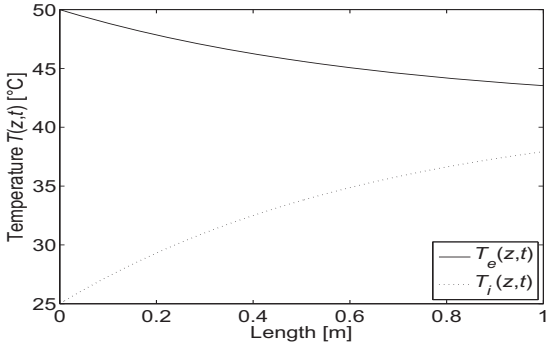

Fig. 3. Profiles of the temperatures of the internal and external fluids at steady state.

4.1 Tracking problem

In the first simulation run, the reference input tracking capabilities of the controller are studied. Thus, two step set points have been specified at times $t = 1\,\mathrm{s}$ and $t = 30\,\mathrm{s}$ corresponding respectively to $y^d(t) = 60\,°\mathrm{C}$ and $y^d(t) = 30\,°\mathrm{C}$. On Fig. 4, it is clear that the output $y(t)$ (Fig. 4b) follows perfectly the imposed set point whereas the control moves of $u(t)$ are physically acceptable (Fig. 4c). In addition, the spatial profiles of temperature obtained at time $t = 60\,\mathrm{s}$ is also realistic (Fig. 4d).

4.2 Disturbance rejection

The second performed test concerns the problem of disturbance rejection. The performances of the control strategy are thus evaluated with respect to changes of the internal fluid temperature at the inlet of the heat exchanger which is a disturbance for the process. For that reason, a step of -10% of the temperature of the entering internal fluid (at $z = 0$) is imposed as a disturbance at time $t = 30\,\mathrm{s}$, after having imposed a step set point at time $t = 1\,\mathrm{s}$ corresponding to $y^d(t) = 60\,°\mathrm{C}$. From Fig. 5, it is clear that the controller behaves adequately to reject the disturbance effect and achieve perfectly the set point tracking (Fig. 5b). The dynamic behavior of the manipulated variable $u(t)$ (Fig. 5c) remains also physically admissible. Again, the profiles of temperatures at $t = 60\,\mathrm{s}$, after successively the step set point and the step disturbance, are typical of the behavior of a co-current heat exchanger (Fig. 5d).

5. CONCLUSION

In this paper, the geometric control of a co-current heat exchanger is investigated, and a control strategy is proposed to

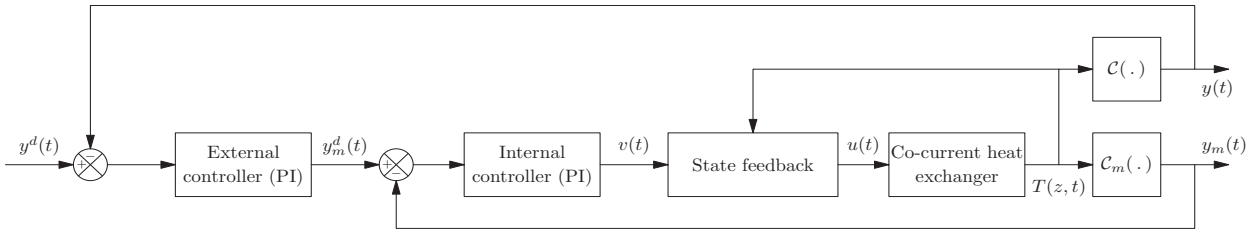

Fig. 2. Global control strategy of a co-current heat exchanger ($T(z,t) = [T_e(z,t)\, T_i(z,t)]^T$).

control the outlet internal fluid temperature. The main idea consists in inserting the manipulated variable, i.e. the inlet external fluid temperature, in the state equations of the heat exchanger by means of a Dirac function. Furthermore, the spatial average temperature of the internal fluid has been introduced, as measured output, in order to ensure the existence of the characteristic index. Then, to achieve a desired performance of the outlet internal fluid temperature, a control strategy is proposed where a PI external controller is introduced to provide the set point of the introduced measured output by taking as input the error between the outlet internal fluid temperature and its desired set point. The effectiveness of the proposed design and control strategy is demonstrated through numerical experiments. The simulation results show that the control strategy behaves correctly and ensures a satisfactory tracking and disturbance rejection.

REFERENCES

M. A. Abdelghani-Idrissi, F. Bagui, and L. Estel. Analytical and experimental response time to flow rate step along a counter flow double pipe heat exchanger. *International Journal of Heat and Mass Transfer*, 44:3721–3730, 2001.

M. A. Arbaoui, L. Verniéres-Hassimi, D. Seguin, and M. A. Abdelghani-Idrissi. Counter-current tubular heat exchanger: modeling and adaptive predictive functional control. *Applied thermal Engineering*, 27:2332–2338, 2007.

P. D. Christofides. *Nonlinear and Robust Control of PDE Systems: Methods and Applications to Transport-Reaction Processes*. Birkhäuser, Boston, 2001.

P. D. Christofides and P. Daoutidis. Feedback control of hyperbolic PDE systems. *AIChE Journal*, 42:3063 – 3086, 1996.

J. P. Corriou. *Process control - Theory and applications*. Springer, London, 2004.

I. Derese and E. Noldus. Control of parallel current and counter-current heat exchangers. *Analysis and Optimization of Systems*, 28:497–515, 1980.

J. C. Friedly. *Dynamic Behaviour of Processes*. Prentice-Hall, New Jersey, 1972.

P. K. Gundepudi and J. C. Friedly. Velocity control of hyperbolic partial differential equation systems with single characteristic variable. *Chemical Engineering Science*, 53(24): 4055 – 4072, 1998.

C.-H. Huang and C.-Y. Yeh. An optimal control algorithm for entrance co-current flow problems. *International Journal of heat and Mass Transfer*, 46:1013–1027, 2003.

C. Kravaris and J. C. Kantor. Geometric methods for nonlinear process control. 2. controller synthesis. *Industrial & Engineering Chemistry Research*, 29:2310–2323, 1990.

A. Maidi, M. Diaf, and J.-P. Corriou. Boundary geometric control of a counter-current heat exchanger. *Journal of Process Control*, In Press, 2008a.

A. Maidi, M. Diaf, and J.-P. Corriou. Distributed geometric control of wave equation. *17th IFAC World Congress*, July 6-11, Seoul, Korea, 2008b.

W. H. Ray. *Advanced Process Control*. Butterworths, Boston, 1989.

W.H. Ray and B.A. Ogunnaike. *Process Dynamics, Modeling and Control*. Oxford University Press, 1994.

A. V. Wouwer, P. Saucez, and W. E. Schiesser. Simulation of distributed parameter systems using a matlab-based method of lines toolbox: Chemical engineering applications. *Industrial and Engineering Chemical Research*, 43(14):3469–3477, 2004.

W. Wu and C. Liou. Output regulation of nonisothermal plug-flow reactors with inlet perturbations. *Computers and Chemical Engineering*, 25:433–443, 2001.

Y. Xuan and W. Roetzel. Dynamics of shell-and-tube heat exchangers to arbitrary temperature and step flow variations. *AIChE Journal*, 39:413–421, 1993.

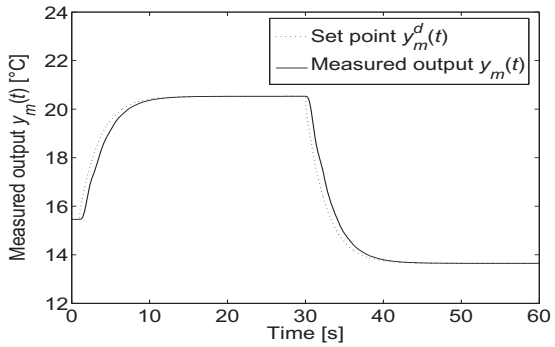

(a) Measured output $y_m(t)$.

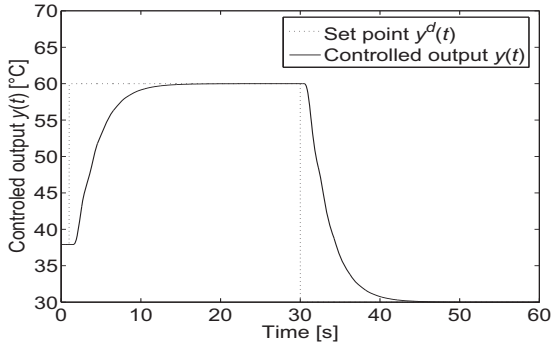

(b) Controlled output $y(t)$.

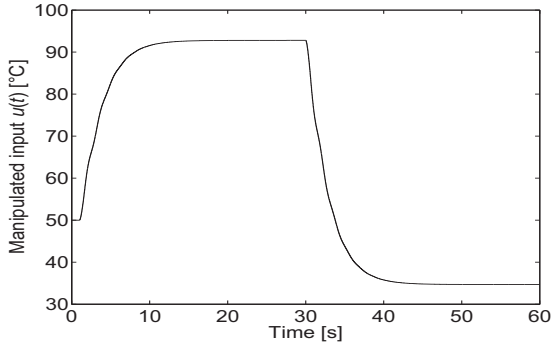

(c) Manipulated variable $u(t) = T_e(0,t)$.

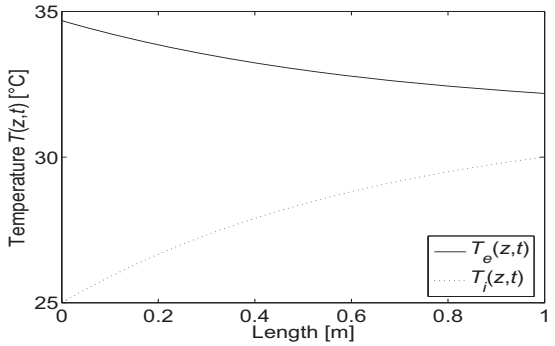

(d) Spatial profiles $t = 60$ s.

Fig. 4. Set point tracking.

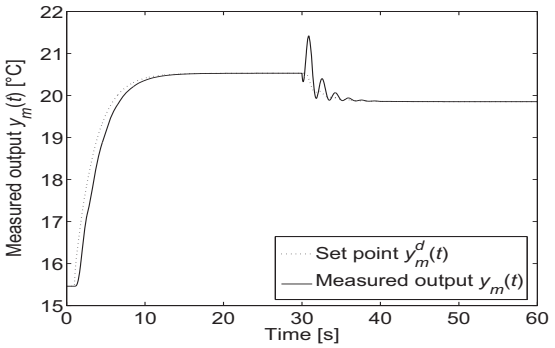

(a) Measured output $y_m(t)$.

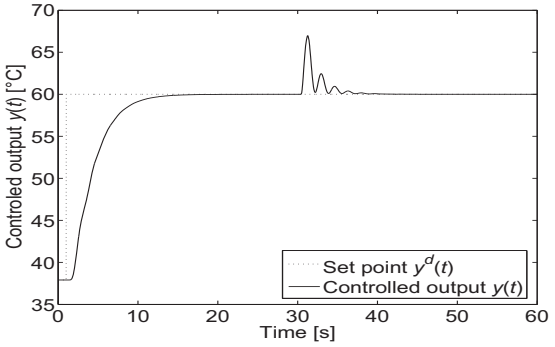

(b) Controlled output $y(t)$.

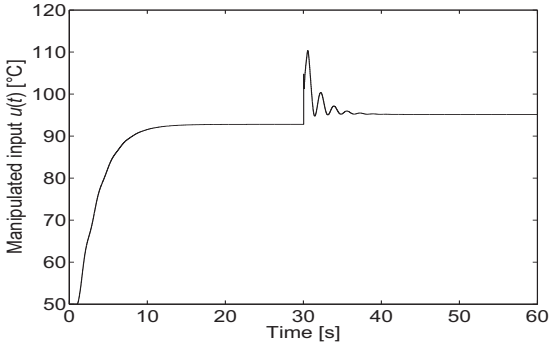

(c) Manipulated variable $u(t) = T_e(0,t)$

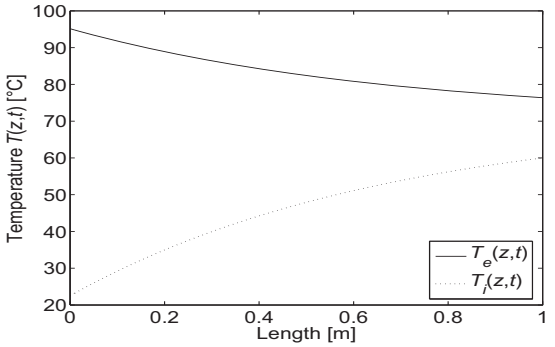

(d) Spatial profile at $t = 60$ s.

Fig. 5. Disturbance rejection.

Feedback Controller Design for the Four-Tank Process using Dissipative Hamiltonian Realization

Nicolas Hudon * **Martin Guay** *

* *Department of Chemical Engineering, Queen's University, Kingston, ON, Canada, K7L 3N6 (e-mail:* martin.guay@chee.queensu.ca*)*

Abstract: This paper considers the problem of stabilizing the quadruple-tank process using an approximate dissipative Hamiltonian realization. The proposed approach consists in canceling by feedback the deviation of the system from a Hamiltonian system. First, we obtain a characteristic one-form for the system by taking the interior product of a non vanishing two-form with respect to the controlled vector field. We then construct a homotopy operator on a star-shaped region centered at a desired equilibrium point. The dynamics of the system is then decomposed into an exact part and an anti-exact one. The exact part is generated by a potential, hence stability of this part is guaranteed using the generating potential as a Lyapunov function. The stabilizing feedback controller is designed by canceling the anti-exact part of the characteristic one-form. Application of the resulting controller is illustrated by numerical simulations.

Keywords: Feedback Regulation, Approximate Dissipative Hamiltonian Realization, Stability.

1. INTRODUCTION

Application of generalized Hamiltonian systems are an important approach for stability studies and controller design of nonlinear control systems (van der Schaft, 2000) and several physical problems were studied using this class of dynamical system representations. One example in chemical engineering was given recently by Otero-Muras et al. (2008) who studied the stability of a reaction network using its dissipative Hamiltonian representation. However, one limitation associated with the study of non-mechanical nonlinear systems using dissipative Hamiltonian is to derive a suitable Hamiltonian function for the problem. As discussed in (Johnsen and Allgöwer, 2007) and (Ortega et al., 1999), applications of Interconnection and Damping Assignment Passivity-Based Control (IDA-PBC) techniques is difficult since the concept of "energy" is usually ill-defined for process control applications, for example when mass balances are considered. In (Cheng et al., 2005), it was shown that a nonlinear system of the form

$$\dot{x} = f(x) + G(x)u, \tag{1}$$

where $x \in \mathbb{R}^n$, $u \in \mathbb{R}^m$, and $G(x)$ full rank, is transformable to a stable Port-Controlled Hamiltonian (PCH) system

$$\dot{x} = F(x)\nabla H(x), \quad F(x) = [J(x) - R(x)] \tag{2}$$

if there exists a feedback $\beta : \mathbb{R}^n \to \mathbb{R}^m$ such that the *matching equation*

$$f(x) + G(x)\beta(x) = F(x)\nabla H(x) \tag{3}$$

holds. In particular, for a fixed structure matrix $F(x)$ and a free Hamiltonian function $H(x)$, the problem leads to a set of PDEs parameterized by the structure matrix and the feedback controller $\beta(x)$. Relaxing the need for exact matching, a non-exact matching IDA-PBC approach was recently developed and applied successfully to chemical reactor process stabilization (Ramírez et al., 2009).

In this paper, we will address the problem of stabilizing controllers design using approximate dissipative Hamiltonian realization. In (Cheng et al., 2000), conditions for approximate Hamiltonian realizations were given in terms of a normal form. Sufficient conditions and a constructive algorithm for a generalized Hamiltonian realization for time-invariant nonlinear systems were presented in (Wang et al., 2003). In particular, the method proposed in (Wang et al., 2003) proposed a vector field decomposition along the gradient direction $\nabla H(x)$ and the tangential direction of the energy surfaces of $H(x)$, for a regular positive-definite function $H(x)$. Following the work in (Maschke et al., 2000) which related port-controlled Hamiltonian systems to the construction of Lyapunov functions, it was shown in (Wang et al., 2007) how k-th degree approximate dissipative Hamiltonian systems can be used to solve the realization problem and how associated k-th degree approximate Lyapunov functions can be used to study the stability of such systems.

In the following, we propose to use the tools of exterior calculus to construct the Hamiltonian function and design a stabilizing controller. It is shown that a stabilizing controller can be developed by canceling the anti-exact part of the dynamics (this dynamics acts tangentially to the dynamics generated by the potential). More precisely, assuming a controller structure, we obtain a characteristic one-form for the system by taking the interior product of a non vanishing two-form with respect to the vector field. A homotopy operator centered at a desired equilibrium

point for the system is used to obtain an exact one form, generated by a Hamiltonian function, and an anti-exact form that generates the tangential dynamics. We design the controller in such a way that the anti-exact form vanishes. The stability argument presented in (Hudon et al., 2008) uses local equivalence between the exact part of the dynamics and a pre-defined Hamiltonian dissipative realization, viewed as a reference system to develop a local change of coordinates to derive the desired local dissipative potential for the system.

The paper is organized as follows. Section 2 presents the four-tank system as a motivating example. In Section 3, mathematical background is presented, recalling the elements required for the development of the radial homotopy operator that is used in the sequel. The application of this operator to discriminate the exact and anti-exact parts of the dynamics and the development of the stabilizing controller are presented in Section 4. Numerical applications to the four-tank system are given in Section 5. Conclusions and future areas of investigation are outlined in Section 6.

2. QUADRUPLE-TANK PROCESS EXAMPLE

To motivate the present paper, we use the four-tank system studied in details in (Johansson, 2000). More recently, Johnsen and Allgöwer (2007) developed an IDA-PBC controller for the system by introducing error dynamics and solving the matching equations assuming a perturbed Hamiltonian function for the closed-loop dynamics.

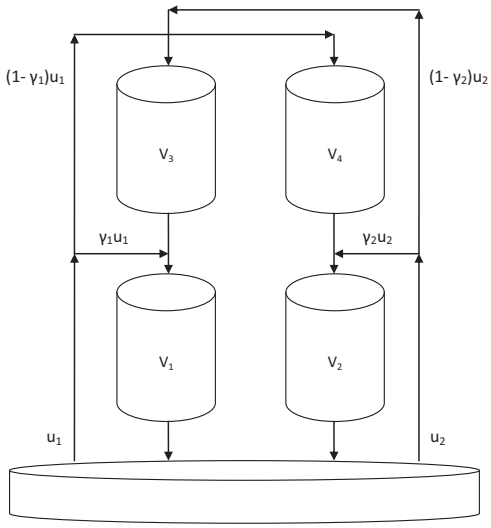

Fig. 1. Four-Tank System

The dynamic model for the four-tank system is given as a control affine nonlinear system of the form

$$\dot{x} = f(x) + G(x)u \tag{4}$$

where $x \in \mathbb{R}^4$ are the levels in the respective tanks and $u \in \mathbb{R}^2$ are the manipulated flows. Using the model proposed in (Johnsen and Allgöwer, 2007), $f(x)$ and $G(x)$ are given by

$$f(x) = \begin{pmatrix} \frac{-a_1}{A_1}\sqrt{2gx_1} + \frac{a_3}{A_1}\sqrt{2gx_3} \\ \frac{-a_2}{A_2}\sqrt{2gx_2} + \frac{a_4}{A_2}\sqrt{2gx_4} \\ \frac{-a_3}{A_3}\sqrt{2gx_3} \\ \frac{-a_4}{A_4}\sqrt{2gx_4} \end{pmatrix}, \tag{5}$$

$$G(x) = \begin{pmatrix} \frac{\gamma_1}{A_1} & 0 \\ 0 & \frac{\gamma_2}{A_2} \\ 0 & \frac{1-\gamma_2}{A_3} \\ \frac{1-\gamma_1}{A_4} & 0 \end{pmatrix}. \tag{6}$$

The parameters A_i represent the cross sections of the respective tanks $i = 1, \ldots, 4$, such that the volumes are given by $V_i = A_i x_i$. The parameters a_i are the cross section of the outlet holes. The gravitational acceleration is denoted by g. The parameters $\gamma_1,\ \gamma_2 \in [0,\ 1]$ are the valve parameters that determined how much of the flows u_i are re-directed in bottom tanks $i = 1, 2$. If the levels of tanks 1 and 2 are the only measured states, it was shown in (Johansson, 2000) that the condition for stable zero dynamics is that $\gamma_1 + \gamma_2 \neq 1$.

To stabilize the system at a desired admissible steady-state, (x^*, u^*), we propose a controller of the form

$$u_1(t) = k_{11}(x) \cdot x_1(t) + k_{12}(x) \cdot x_2(t) \tag{7}$$

$$u_2(t) = k_{21}(x) \cdot x_1(t) + k_{22}(x) \cdot x_2(t). \tag{8}$$

At this point, we assume that all tanks levels are measured. In Section 5, we will discuss how this requirement can be relaxed in the case where only x_1 and x_2 are measured.

3. EXTERIOR CALCULUS AND HOMOTOPY OPERATOR

In this section, we show how to construct a homotopy operator $\mathbb{H}$, *i.e.*, a linear operator on differential forms ω, that satisfies the identity

$$\omega = d(\mathbb{H}\omega) + \mathbb{H}d\omega. \tag{9}$$

We first recall some notions of exterior calculus on $\mathbb{R}^n$ (Edelen, 1985). We denote a smooth vector field $X \in \Gamma^\infty(\mathbb{R}^n)$ as a smooth map

$$X : \mathbb{R}^n \to T\mathbb{R}^n, \qquad X|_x = \sum_{i=1}^{n} v^i(x)\partial_{x_i}|_x. \tag{10}$$

The cotangent (dual) space $T_x^*\mathbb{R}^n$ is the set of all linear functionals on $T_x\mathbb{R}^n$,

$$T_x^*\mathbb{R}^n = \{\omega|_x : T_x\mathbb{R}^n \to \mathbb{R}\} \tag{11}$$

where each $\omega|_x$ is linear, *i.e.*

$$(a\omega_1|_x + b\omega_2|_x)(X_x) = a\omega_1|_x(X|_x) + b\omega_2|_x(X|_x). \quad (12)$$

The standard basis of $T_x^*\mathbb{R}^n$ is given by $\{dx_1, \ldots, dx_n\}$, where $dx_i(\partial_{x_j}) = \delta_j^i$, δ_j^i being the Kronecker delta. An element $\omega|_x$ in the cotangent space $T_x^*\mathbb{R}^n$ can be written as

$$\omega|_x = \sum_{i=1}^{n} \omega_i dx_i, \quad \omega_i \in \mathbb{R}. \quad (13)$$

In the sequel, differential one-forms will be used. We write

$$\omega = \sum_{i=1}^{n} \omega_i(x) dx_i, \quad (14)$$

where ω_i are smooth functions on $\mathbb{R}^n$. The exterior (wedge) product $\wedge$ is defined on $\Omega^1(\mathbb{R}^n) \times \Omega^1(\mathbb{R}^n)$ by the requirements

$$dx_i \wedge dx_j = -dx_j \wedge dx_i$$
$$dx_i \wedge f(x)dx_j = f(x)dx_i \wedge dx_j$$

for all smooth functions $f(x)$ and

$$\alpha \wedge (\beta + \gamma) = \alpha \wedge \beta + \alpha \wedge \gamma, \quad (15)$$

for all $\alpha, \beta, \gamma \in T^*\mathbb{R}^n$. If $\alpha \in \Lambda^k(\mathbb{R}^n)$, then we write $\deg \alpha = k$. Notice that $\Lambda^1(\mathbb{R}^n) = T^*\mathbb{R}^n$ and $\Lambda^0(\mathbb{R}^n) = \mathcal{C}^\infty(\mathbb{R}^n)$.

The differential operator d is the unique operator on $\Lambda(\mathbb{R}^n) = \bigoplus_{k=0}^n \Lambda^k(\mathbb{R}^n)$ with the following properties:

$$d : \Lambda^k(\mathbb{R}^n) \to \Lambda^{k+1}(\mathbb{R}^n), \quad 0 \le k \le n-1, \quad (16)$$

1. $d(\alpha + \beta) = d\alpha + d\beta$.
2. $d(\alpha \wedge \beta) = d\alpha \wedge \beta + (-1)^{\deg \alpha} \alpha \wedge d\beta$.
3. $df = \frac{\partial f_i}{\partial x_i} dx_i$, $\forall f(x) \in \Lambda^0(\mathbb{R}^n)$.
4. $d \circ d\alpha = 0$.

A k-form α is said to be closed if $d\alpha = 0$. It is said to be exact if there exists a $(k-1)$-form β such that $d\beta = \alpha$.

The interior product $\lrcorner$ is a map

$$\lrcorner : \Gamma^\infty(\mathbb{R}^n) \times \Lambda^k(\mathbb{R}^n) \to \Lambda^{k-1}(\mathbb{R}^n) \quad (17)$$

with the following properties $\forall X \in \Gamma^\infty(\mathbb{R}^n)$ and $\forall f \in \Lambda^0(\mathbb{R}^n)$:

1. $X \lrcorner f = 0$.
2. $X \lrcorner \omega = \omega(X), \forall \omega \in \Lambda^1(\mathbb{R}^n)$.
3. $X \lrcorner (\alpha + \beta) = X \lrcorner \alpha + X \lrcorner \beta, \forall \alpha, \beta \in \Lambda^k(\mathbb{R}^n)$, $k = 1, \ldots, n$.
4. $X \lrcorner (\alpha \wedge \beta) = (X \lrcorner \alpha) \wedge \beta + (-1)^{\deg(\alpha)} \alpha \wedge (X \lrcorner \beta), \forall \alpha, \beta \in \Lambda(\mathbb{R}^n)$.

The first step in the construction of a homotopy operator is to define a star-shaped domain on $\mathbb{R}^n$ (Edelen, 1985; Banaszuk and Hauser, 1996). An open subset S of $\mathbb{R}^n$ is said to be star-shaped with respect to a point $p^0 = (x_1^0, \ldots, x_n^0) \in S$ if the following conditions hold:

- S is contained in a coordinate neighborhood U of p^0.
- The coordinate functions of U assign coordinates $(x_1^0, \ldots, x_n^0)$ to p^0.
- If p is any point in S with coordinates $(x_1, \ldots, x_n)$ assigned by functions of U, then the set of points $(x^0 + \lambda(x - x^0))$ belongs to S, $\forall \lambda \in [0, 1]$.

A star-shaped region S has a natural associated vector field $\mathfrak{X}$, defined by

$$\mathfrak{X}(x) = [x_i^0 + \lambda(x_i - x_i^0)]\partial_{x_i}, \quad \forall x \in S. \quad (18)$$

In this paper, we will consider the case where the star-shaped domain is centered at the desired equilibrium point x_i^*.

For a differential form ω of degree k on a star-shaped region S centered at an equilibrium point, the homotopy operator will be defined, in coordinates, as

$$(\mathbb{H}\omega)(x) = \int_0^1 \mathfrak{X}(x) \lrcorner\, \omega(\lambda x) \lambda^{k-1} d\lambda, \quad (19)$$

where $\omega(\lambda x)$ denotes the differential form evaluated on the star-shaped domain in the local coordinates defined above.

The properties of the homotopy operator are as follows (Edelen, 1985):

H1. $\mathbb{H}$ maps $\Lambda^k(S)$ into $\Lambda^{k-1}(S)$ for $k \ge 1$ and maps $\Lambda^0(S)$ identically to zero.
H2. $d\mathbb{H} + \mathbb{H}d =$ identity for $k \ge 1$ and $(\mathbb{H}df)(x) = f(x) - f(x_0)$ for $k = 0$.
H3. $(\mathbb{H}\mathbb{H}\omega)(x_i) = 0$, $(\mathbb{H}\omega)(x_i^0) = 0$.
H4. $\mathfrak{X} \lrcorner \mathbb{H} = 0$, $\mathbb{H}\mathfrak{X} \lrcorner = 0$.

The first part of the right hand side of (9), $d(\mathbb{H}\omega)$, is obviously a closed form, since $d \circ d(\mathbb{H}\omega) = 0$. By property (H1), for $\omega \in \Lambda^k(S)$, we have $(\mathbb{H}\omega) \in \Lambda^{k-1}(S)$, $d(\mathbb{H}\omega)$ is also exact on S. We denote the exact part of ω by $\omega_e = d(\mathbb{H}\omega)$ and the anti-exact part by $\omega_a = \mathbb{H}d\omega$. It is possible to show that ω vanishes on $\mathbb{R}^n$ if and only if ω_e and ω_a vanish together (Edelen, 1985).

In the sequel, we will apply the homotopy operator on one-forms. Since in our applications, ω_e is an exact one-form, $(\mathbb{H}\omega)$ computed by homotopy is a dissipative potential. A non dissipative potential is associated with the anti-exact part, but on the star-shaped domain S, ω_a does not contribute to the dissipative part of the system. In other words, ω_a belongs to the kernel of $\mathbb{H}$, which can be seen by applying property (H3) from above to the definition of ω_a. In the next section, we will show how stabilization of the desired equilibrium will be ensured by canceling the dynamics associated with ω_a using feedback.

4. FEEDBACK CONTROLLER DESIGN

4.1 Potential Computation

We now present the central element to the proposed construction, namely using the homotopy operator to discriminate the exact and the anti-exact parts associated to a given autonomous system and then computing a feedback controller to cancel the anti-exact part of the dynamics.

Let the vector field $X|_x = \sum_{i=1}^n f_i(x)\partial_{x_i}$, $i = 1, \ldots, n$ be known. We assume that X is of class $\mathcal{C}^k$ with $k \ge 2$. It is also assumed that X has an equilibrium point, in the

present case, an admissible steady-state for the four-tank process. First, we define a non vanishing closed two-form $\Omega = \sum_{1\leq i<j\leq n} dx_i \wedge dx_j$ on $\mathbb{R}^n$.

Taking the interior product of Ω with respect to the vector field X, we compute a one-form ω as follows

$$\omega = X \lrcorner\, \Omega \tag{20}$$
$$= \sum_{1\leq i<j\leq n} \left(f_i dx_j - f_j dx_i\right). \tag{21}$$

Given a star-shaped region centered at the origin, with associated vector field $\mathfrak{X}(x) = x_i \partial_{x_i}$, we have

$$(\mathbb{H}\omega)(x) = \int_0^1 \left(\mathfrak{X} \lrcorner\, \omega(\lambda x)\right) d\lambda. \tag{22}$$

Letting $\tilde{f}_i$ denote the values of the components of f after integration with respect to λ, we have

$$(\mathbb{H}\omega)(x) = \sum_{1\leq i<j\leq n} \left(\tilde{f}_i \cdot x_j - \tilde{f}_j \cdot x_i\right) := \tilde{F}(x). \tag{23}$$

Taking the exterior derivative, we have

$$\omega_e = \sum_{i=1}^{n} \frac{\partial \tilde{F}}{\partial x_i} dx_i. \tag{24}$$

The anti-exact form is then given by

$$\omega_a = \omega - \omega_e$$
$$= \sum_{1\leq i<j\leq n} \left(f_i - \frac{\partial \tilde{F}}{\partial x_j}\right) dx_j - \left(f_j + \frac{\partial \tilde{F}}{\partial x_i}\right) dx_i. \tag{25}$$

Remark 1. As a special case, if one defines Ω to be the canonical symplectic two-form and if X_H is the vector field generated by a known Hamiltonian H, ω obtained by the interior product $X_H \lrcorner\, \Omega$ is closed, and we can show that $\omega = \omega_e = -dH$.

For the quadruple-tank system, using our knowledge of the coupling between the tanks, we define the non-vanishing two-forms as

$$\Omega = dx_1 \wedge dx_3 + dx_2 \wedge dx_4. \tag{26}$$

The characteristic one-form for the system is thus given by

$$\omega = -f_3 dx_1 - f_4 dx_2 + f_1 dx_3 + f_2 dx_4. \tag{27}$$

On a star-shaped region centered at the desired equilibrium point $(x_1^*, x_2^*, x_3^*, x_4^*)$, we have

$$\mathfrak{X} = x_i^* + \lambda(x_i - x_i^*). \tag{28}$$

A net result on our notation for the sequel is that on the star-shaped domain, x denotes deviation variables from the center x^*. In (Hudon et al., 2008), the exact part

$$\omega_e = \sum_{i=1}^{4} f_{e,i}(x) dx_i \tag{29}$$

was used to compute a dissipative potential by equivalence to a normal form of dissipative Hamiltonian realization. In the present paper, we are interested in canceling the anti-exact part ω_a by feedback to ensure stability of the closed-loop dynamics.

4.2 Anti-exact Dynamics Cancelation

As mentioned before, the anti-exact part does not influence the value of the computed dissipative potential, at least on the star-shaped domain where the homotopy operator is defined. However, in order to prove stability, the anti-exact part must also vanishes at the equilibrium point of the system (and only there). In the considered example, we will show that a desired equilibrium can be rendered attractive provided that $\omega_a(x^*) = 0$.

The controlled vector field for the four-tank system is given as in Johnsen and Allgöwer (2007) by Equations (4-6). We fixed the controller to be

$$u_1(t) = k_{11}(x) \cdot x_1(t) + k_{12}(x) \cdot x_2(t) \tag{30}$$
$$u_2(t) = k_{21}(x) \cdot x_1(t) + k_{22}(x) \cdot x_2(t). \tag{31}$$

From Section 4.1, we are left we an anti-exact part of the form:

$$\omega_a = \sum_{i=1}^{4} f_{a,i}(x) dx_i. \tag{32}$$

It is desired to make this form closed by using the elements $k_{i,j}(x)$ of the proposed controller. A one-form is closed if

$$\frac{\partial f_{a,i}}{\partial x_j} = \frac{\partial f_{a,j}}{\partial x_i}. \tag{33}$$

For the four-tank system, it leads us to 5 equations with 4 unknown:

$$k_{22}\frac{\gamma_2 - 1}{A_3} - k_{11}\frac{\gamma_1 - 1}{A_4} = 0 \tag{34}$$
$$\frac{1}{2}\frac{a_3 A_1 \sqrt{2g}}{A_3\sqrt{x_3}} + \frac{1}{2}\frac{a_1\sqrt{2g}}{\sqrt{x_1}} - \gamma_1 k_{11} = 0 \tag{35}$$
$$-\frac{k_{21}\gamma_2}{A_2} = 0 \tag{36}$$
$$-\frac{k_{12}\gamma_1}{A_1} = 0 \tag{37}$$
$$\frac{1}{2}\frac{a_4 A_2 \sqrt{2g}}{A_4\sqrt{x_4}} + \frac{1}{2}\frac{a_2\sqrt{2g}}{\sqrt{x_2}} - \gamma_2 k_{22} = 0. \tag{38}$$

From Equations (36-37), we have that $k_{12} = k_{21} = 0$. From Equations (35) and (38), we have that

$$k_{11}(x) = -\kappa_1 \frac{A_3\gamma_1\sqrt{2x_1x_3}}{a_3A_1\sqrt{gx_1} + a_1A_3\sqrt{gx_3}} \tag{39}$$
$$k_{22}(x) = -\kappa_2 \frac{A_4\gamma_2\sqrt{2x_2x_4}}{a_4A_2\sqrt{gx_2} + a_2A_4\sqrt{gx_4}} \tag{40}$$

where the gains κ_1 and κ_2 are used to guarantee the first equality (34).

The stability argument for the closed loop system uses the Barbashin-Krasovskiĭ, hence the requirement that ω_a vanishes only at the desired equilibrium point. In fact, the condition that $\omega = \omega_a + \omega_e$ be closed along with the requirement that ω vanishes at the desired equilibrium is essentially a convexity condition of a generating potential. In that sense, decomposition of the dynamics using a characteristic one-form is related to the stability requirements

for IDA-PBC as presented in (Ortega et al., 1999) and (Ortega et al., 2002). In the next section, we will illustrate the application of the proposed stabilizing controller.

5. NUMERICAL SIMULATION RESULTS

We now present some numerical applications of the feedback controllers derived in the previous section. Simulation parameters are taken from (Johnsen and Allgöwer, 2007) and are presented in Table 1. We will look at 3 different cases parameterized by the values of γ_1 and γ_2.

Table 1. System Parameters (Johnsen and Allgöwer (2007))

	A_i (cm^2)	a_i (cm^2)
$i = 1, 2$	50.3	0.233
$i = 3, 4$	28.3	0.127

First, we look at the case where $\omega_1 = \omega_2 = 0.6$. For these values, an admissible steady-state x^* is computed to be approximately $x^* = [9,\ 9,\ 4.8,\ 4.8]^T$, and we initialize the system at $x = [4,\ 7,\ 6.8,\ 6.8]^T$. Figures 2 and 3 show that the controller (even with small gains) drives the trajectory to the desired equilibrium and the controller to the consistent steady-state value u^*. Hence by canceling the anti-exact part, the center of the star-shaped domain is attractive.

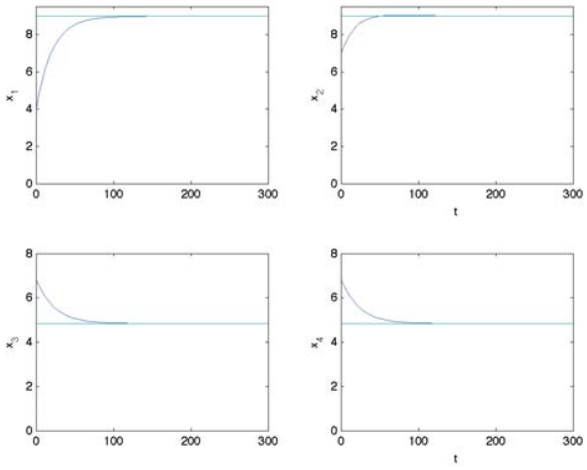

Fig. 2. Full state stabilization of case $\gamma_1 = 0.6,\ \gamma_2 = 0.6$

We now consider the case where $\gamma_1 = \gamma_2 = 0.5$. An admissible steady-state x^* is computed to be approximately $x^* = [10.9,\ 10.9,\ 9.17,\ 9.17]^T$. Initializing the simulation at $x = [5.9,\ 9.9,\ 11.2,\ 11.2]^T$, the proposed controller drives the system to the desired equilibrium (Figures Figures 4 and 5). This case is interesting since, as mentioned in Section 2, if we had considered only output feedback, the zero dynamics for the system are unstable at those values.

To consider output feedback for the case $\gamma_1 = \gamma_2 = 0.5$, we replace $x_3(t)$ and $x_4(t)$ in the controller expressions (39-40) by their desired steady-state values x_3^* and x_4^*. In this particular case, since the zero dynamics is unstable,

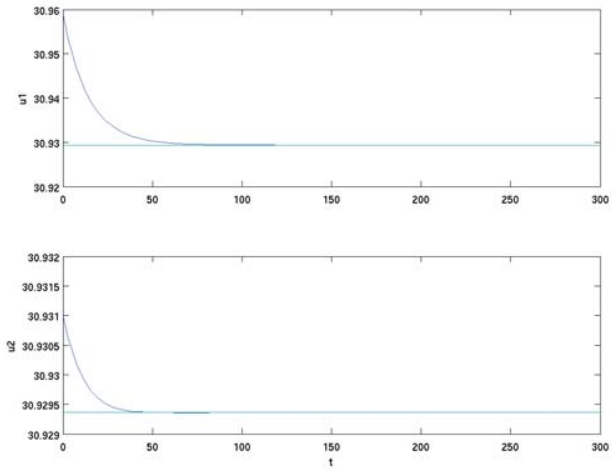

Fig. 3. Control variables values for case $\gamma_1 = 0.6,\ \gamma_2 = 0.6$

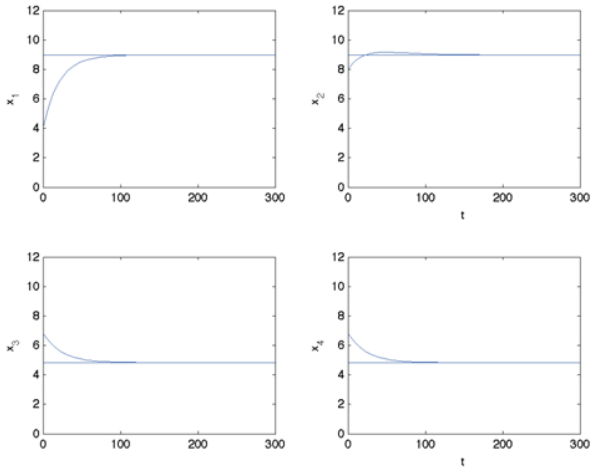

Fig. 4. Full state feedback stabilization of case $\gamma_1 = 0.5,\ \gamma_2 = 0.5$

we use the design parameters κ_1 and κ_2 to make the dynamics of the system associated with the anti-exact part dominated by the gradient term. We seek to reach the same equilibrium point as above $x^* = [10.9,\ 10.9,\ 9.17,\ 9.17]^T$ from two different initial states: $[5.9,\ 9.9,\ 7.2,\ 7.2]^T$ and $[15.9,\ 11.9,\ 11.2,\ 11.2]^T$. Results are presented in Figure 6. As argued in (Ramírez et al., 2009) for a related design approach, the stabilization results present here still hold locally since the proposed controller design procedure does not involve inversion of the dynamics.

6. CONCLUSION

In this paper, a procedure to construct stabilizing controllers using local dissipative Hamiltonian realization for nonlinear dynamical systems was presented. The proposed approach can be seen as an extension of the approximate feedback linearization approach proposed by Banaszuk

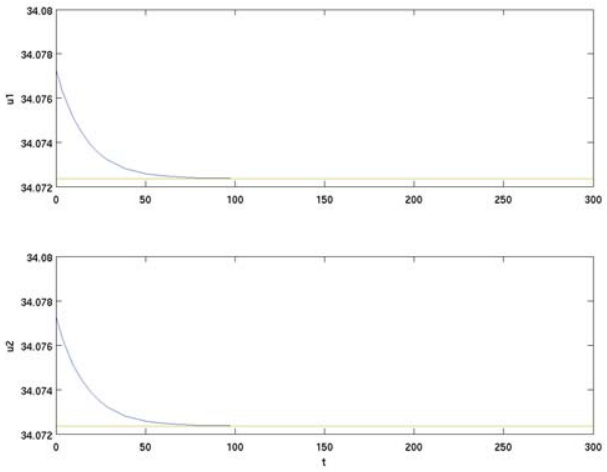

Fig. 5. Control variables values for case $\gamma_1 = 0.5,\ \gamma_2 = 0.5$

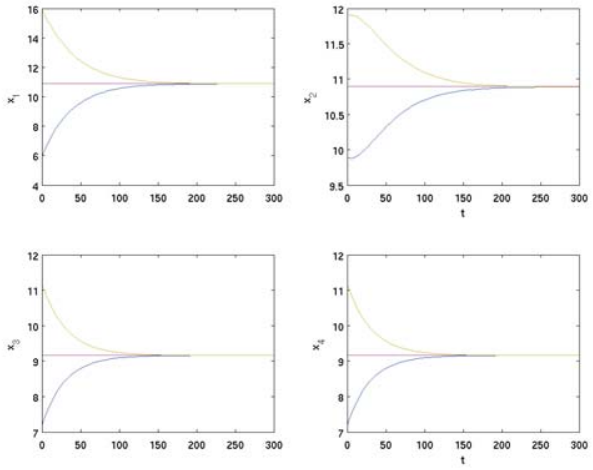

Fig. 6. Output feedback stabilization of case $\gamma_1 = 0.5,\ \gamma_2 = 0.5$

and Hauser (1996). Taking the interior product of a non vanishing two-form with respect to the vector field defining the system, we first obtained a (possibly) non-closed characteristic one-form for the system. Constructing a locally defined homotopy operator on a star-shaped domain centered at the desired equilibrium point, we presented how to decompose locally the obtained form into an exact and an anti-exact one-forms. From (Hudon et al., 2008), we know that the exact part is associated to a dissipative (stable) potential. The obtained anti-exact form is associated to a non dissipative potential which generated tangential dynamics that do not contribute to the value of the dissipative potential on the star-shaped domain. However, using a pre-defined feedback controller to make this error one-form exact, it was shown, using the four-tank system example, that the procedure enables us to construct a stabilizing control. Future research will focus on the limitations of the technique, especially cases where the controller information does not appear in the expression of the anti-exact form, for example the nonisothermal CSTR system presented in (Ramírez et al., 2009).

REFERENCES

A. Banaszuk and J. Hauser. Approximate feedback linearization. *SIAM Journal on Control and Optimization*, 34(5):1533–1554, 1996.

D. Cheng, S Spurgeon, and J. Xiang. On the development of generalized Hamiltonian realizations. In *Proceedings of the 39th IEEE Conference on Decision and Control*, pages 5125–5130, 2000.

D. Cheng, A. Astolfi, and R. Ortega. On feedback equivalence to port-controlled Hamiltonian systems. *Systems and Control Letters*, 54:911–917, 2005.

D.G.B. Edelen. *Applied Exterior Calculus*. Wiley, New York, NY, 1985.

N. Hudon, K. Höffner, and M. Guay. Equivalence to dissipative Hamiltonian realization. In *Proceedings of the 47th IEEE Conference on Decision and Control*, pages 3163–3168, 2008.

K.H. Johansson. The quadruple-tank process: A multivariable laboratory process with an adjustable zero. *IEEE Transactions on Control Systems Technology*, 8(3):456–465, 2000.

J. Johnsen and F. Allgöwer. Interconnection and damping assignment passivity-based of a four-tank system. In F. Bullo and K. Fugimoto, editors, *Lagrangian and Hamiltonian Methods for Nonlinear Control 2006*, volume 366 of *Lectures Notes in Control and Information Science*, pages 111–122, Berlin, 2007. Springer-Verlag.

B. Maschke, R. Ortega, and A.J. van der Schaft. Energy-based Lyapunov functions for forced Hamiltonian systems with dissipation. *IEEE Transactions on Automatic Control*, 45(8):1498–1502, 2000.

R. Ortega, A. Astolfi, G. Bastin, and H/ Rodrigues-Cortes. Output feedback control of food-chain systems. In H. Nijmeijer and T.I. Fossen, editors, *New Directions in Nonlinear Observer design*, volume 244 of *Lectures Notes in Control and Information Science*, pages 291–310, London, 1999. Springer-Verlag.

R. Ortega, A.J. van der Schaft, B. Maschke, and G. Escobar. Interconnection and damping assignment passivity-based control of port-controlled Hamiltonian systems. *Automatica*, 38:585–596, 2002.

I. Otero-Muras, G. Szederkényi, A.A. Alonso, and K.M. Hangos. Local dissipative Hamiltonian description of reversible reaction networks. *Systems and Control Letters*, 57:554–560, 2008.

H. Ramírez, D. Sbarbaro, and R. Ortega. On the control of non-linear processes: An IDA-PBC approach. *Journal of Process Control*, 19:405–414, 2009.

A.J. van der Schaft. *L_2-Gain and Passivity Techniques in Nonlinear Control*. Springer-Verlag, London, 2nd edition, 2000.

Y. Wang, C. Li, and D. Cheng. Generalized Hamiltonian realization of time-invariant nonlinear systems. *Automatica*, 39:1437–1443, 2003.

Y. Wang, D. Cheng, and S.S. Ge. Approximate dissipative Hamiltonian realizations and construction of local Lyapunov functions. *Systems and Control Letters*, 56: 141–149, 2007.

Robust Nonlinear Model Predictive Control using Volterra Models and the Structured Singular Value (μ)

Rosendo Díaz-Mendoza, Hector Budman

Department of Chemical Engineering, University of Waterloo, Waterloo, ON, Canada, N2L 3G1

Abstract: A methodology is proposed for designing robust nonlinear model predictive controllers based on a Volterra series model with uncertain coefficients. The objective function of the on-line optimization is formulated in terms of a Structured Singular Value (μ). The proposed formulation considers a penalty on the manipulated variables actions and manipulated variables and terminal condition constraints.

Keywords: Model predictive control, nonlinear control, robust control, structured singular value.

1. INTRODUCTION

Linear model predictive control is a widely accepted control strategy in the chemical industry. Many theoretical studies and industrial applications of linear MPC have been reported elsewhere (Qin and Badgwell, 2003). On the other hand, the nonlinear behaviour of chemical processes has motivated researchers and practitioners to consider predictive control strategies based on nonlinear process models referred to as nonlinear model predictive controllers (NMPC) (Findeisen and Allgöwer, 2002).

Some of the challenging requirements related to the industrial implementation of NMPC are: (1) a reliable nonlinear model of the process is needed that can be effectively used for real time control and (2) ensuring robustness to model error.

Both first principles as well as empirical input-output models have been used in the past for nonlinear predictive control strategies. Although first principles models have the advantage of formally satisfying basic energy and mass balances of the process, they are often too complex for real time control and their structure is generally not amenable for formal robust analysis and design. NMPC strategies based on empirical models such as Hammerstein and Volterra series (Hérnandez and Arkun, 1993; Maner et al., 1996; Parker and Doyle III, 2001) have been reported but their robustness with respect to model error have not been thoroughly studied.

The need to address robustness arises from the fact that the models used for predictive control are never exact. Although a good amount of research work has been conducted on robustness of linear predictive controllers, the robustness of nonlinear predictive controllers has not been extensively studied. The lack of robustness guarantees is currently perceived as one of the key obstacles for wide industrial acceptance of NMPC strategies (Nagy and Braatz, 2003a).

The current work investigates the design of a robust NMPC algorithm based on an empirical Volterra series model. Volterra series models have been shown to efficiently describe general nonlinear systems (Schetzen, 1980). A key idea for this study is that based on the Volterra model it is possible to formulate the robust predictive control problem as a μ-Structured Singular Value test that can be used on-line to calculate optimal control actions. The μ (Structured Singular Value, Doyle, 1982) norm is used, at each sampling instant, to calculate a bound on the norm of a vector containing both output and input predictions along a predefined prediction time horizon in the presence of disturbances and uncertainty in the Volterra model coefficients. Then, the calculated bound is minimized with respect to the optimal control actions to be sent to the process.

The paper is organized as follows. In section 2 the formulation of the μ test and the optimization problem based on the calculated bound is presented. In the same section terminal conditions to enforce stability as well as conditions to enforce manipulated variable constraints are also presented. Section 3 presents two case studies and conclusions are presented in Section 4. Mathematical details are presented in Appendix A.

2. METHODOLOGY

2.1 Model Predictive Control

MPC minimizes a cost function that considers the future errors whit respect to the manipulated variables. For simplicity of notation a single input single output (SISO) case is shown but the formulation can be easily extended to the multivariable case. Considering that y^{pr} is the predicted value of the controlled variable and y^{sp} is the controlled variable set point, a vector of predictions can be written as follows:

$$\mathbf{Y} = \begin{bmatrix} y^{pr}(k_0) + d(k_0) - y^{sp}(k_0) \\ \vdots \\ y^{pr}(k_0 + p) + d(k_0 + p) - y^{sp}(k_0 + p) \end{bmatrix} \quad (1)$$

where k_0 is the initial sampling instant, p is the prediction horizon and d is a measured disturbance. The objective function of the controller proposed in this work minimizes the maximum absolute value of each element of the **Y** vector with respect to the manipulated variables u as follows:

$$\min_{\text{wrt } u(k_0),\ldots,u(k_0+m)} \left\|\mathbf{Y}\right\|_\infty \tag{2}$$

where m is the control horizon. In principle norms other than the infinity norm of the output may be considered in the formulation but are beyond the scope of the current study. It will be also shown in subsections 2.4 to 2.6 that the vector **Y** in (2) may be augmented by additional variables, other than predicted outputs, to enforce a terminal condition and manipulated variables constraints. The following subsection discusses the Volterra models used to calculate the prediction **Y**.

2.2 Volterra series

The general structure of a Volterra series model is given as follows:

$$y^{pr}(k_0) = \sum_{\sigma_1=1}^{\infty}\sum_{\sigma_i=1}^{\infty} h_i(\sigma_1,\ldots,\sigma_i)u(k_0-\sigma_1)u(k_0-\sigma_i) \tag{3}$$

where u is the manipulated variable, y is the controlled variable and h_i are the coefficients of the Volterra series. For practical purposes the series is truncated and the resulting expression is

$$\begin{aligned} y^{pr}(k_0) = \quad & h_0 + \\ & \sum_{n=1}^{N}\sum_{i_1=1}^{M}\cdots\sum_{i_n=1}^{M}\left(h_n(i_1,\ldots,i_n)\times\right. \\ & \left. u(k_0-i_i)u(k_0-i_n)\right) \end{aligned} \tag{4}$$

without loss of generality it can be consider that h_0=0. For example, for N=2, the value of the controlled variable is

$$\begin{aligned} y^{pr}(k_0) = \quad & \sum_{n=1}^{M} h_n^L u(k_0-n) + \\ & \sum_{i=1}^{M}\sum_{j=i}^{M} h_{i,j}^{NL} u(k_0-i)u(k_0-j) \end{aligned} \tag{5}$$

where M is the memory of the system. The linear h_n^L, and nonlinear $h_{i,j}^{NL}$, Volterra series coefficients can be obtained by least squares regression using process input-output data by imposing an appropriate input sequence. For a system with polynomial degree N, it has been shown that is necessary to use a N+1 level pseudorandom multilevel sequence (Nowak and Van Veen, 1994). Confidence intervals for the coefficients, to be used in the calculations as uncertainty bounds associated to these coefficients, can be obtained using least squares regression.

2.3 Calculation of the worst predicted output

The worst predicted output calculation can be performed by a Structured Singular Value (SSV) test (Nagy and Braatz, 2003b). The main motivation to use the SSV test is that it allows finding the worst $\left\|\mathbf{Y}\right\|_\infty$ when uncertainty in the Volterra coefficients is considered. Accordingly, (5) can be modified to include parameter uncertainty as follows where h_n^L and $h_{i,j}^{NL}$ are the nominal value of the coefficients and δh_n^L and $\delta h_{i,j}^{NL}$ are the uncertainty associated to the coefficients:

$$\begin{aligned} y^{pr}(k_0) = \quad & \sum_{n=1}^{M}\left[h_n^L + \delta h_n^L\right]u(k_0-n) + \\ & \sum_{i=1}^{M}\sum_{j=i}^{M}\left[h_{i,j}^{NL} + \delta h_{i,j}^{NL}\right]u(k_0-i)u(k_0-j) + \\ & w(k_0) \end{aligned} \tag{6}$$

w is a feedback term that considers the current difference between the actual process output and the predicted output:

$$w(k_0) = y^{real}(k_0-1) - y^{pr}(k_0-1) \tag{7}$$

By selecting an appropriate interconnection matrix **M** and uncertainty block structure **Δ**, the worst value of a variable in the presence of model error can be calculated by the following SSV test (Braatz et al., 1994; Nagy and Braatz, 2003b)

$$\max_{\text{wrt } \delta h_i^L,\delta h_{i,j}^{NL},w} \left\|\mathrm{Y}\right\|_\infty \geq k_{ssv} \Leftrightarrow \mu_\Delta(\mathrm{M}) \geq k_{ssv} \tag{8}$$

Thus, a bound on the worst deviation of $\left\|\mathbf{Y}\right\|_\infty$, i.e. the norm of the prediction vector can be obtained by the following skew μ problem:

$$\max_{\text{wrt } \delta h_i^L,\delta h_{i,j}^L,w} \left\|\mathbf{Y}\right\|_\infty = \max_{\substack{\text{wrt } k_{ssv} \\ \text{st } \mu_\Delta(\mathbf{M}) \geq k_{ssv}}} (k_{ssv}) \tag{9}$$

A key idea in (9) is that the feedback term in (7) is also treated as an uncertainty and the maximization in (9) is carried out with respect to both this feedback error and the uncertainties in coefficients. Accordingly, the uncertainty block **Δ** is as follows:

$$\mathbf{\Delta} = \mathrm{diag}(\mathbf{\Delta}_1, \mathbf{\Delta}_2, \mathbf{\Delta}_3) \tag{10}$$

where $\mathbf{\Delta}_3$ is a complex scalar square matrix of dimensions $p\times p$ related to performance and $\mathbf{\Delta}_1$ and $\mathbf{\Delta}_2$ are real scalar square matrices related to the uncertainty in feedback and Volterra series coefficients respectively with the following dimensions:

$$\mathbf{\Delta}_1 = \left(p + 2\sum_{i=1}^{p} i + \sum_{i=1}^{p-1}\sum_{j=1}^{i} j\right) \times \left(p + 2\sum_{i=1}^{p} i + \sum_{i=1}^{p-1}\sum_{j=1}^{i} j\right) \tag{11}$$

$$\mathbf{\Delta}_2 = \mathrm{diag}\left[\mathbf{\Delta}_{2_1} \quad \ldots \quad \mathbf{\Delta}_{2_p}\right] \tag{12}$$

$$\mathbf{\Delta}_{2_i} = \left[p\times p \quad \ldots \quad 1\times 1\right]^{\mathrm{T}} \quad i \leq 2 \tag{13}$$

$$\mathbf{\Delta}_{2_i} = \left[(p+2-i)\times(p+2-i) \quad \ldots \quad 1\times 1\right]^{\mathrm{T}} \quad i > 2 \tag{14}$$

The problem stated in (8) and (9) can be used within the predictive control problem defined in (2) as follows:

$$\min_{u(k_0),\ldots,u(k_0+m)} \left[\max\left(k_{ssv}\right)\right] \quad \text{wrt } k_{ssv} \quad \text{st } \mu_{\mathbf{A}}(\mathbf{M}) \geq k_{ssv} \tag{15}$$

The vector **Y** can be modified, as mentioned in section 2.1 to include additional terms as follows: (1) a penalty term to prevent an excessive movement of the manipulated variables, (2) manipulated variables to enforce constraints and (3) a terminal condition to ensure convergence. These terms are explained in the following subsections.

2.4 Manipulated variables movements penalization

Define:

$$\mathbf{y}^{\Delta u} = \begin{bmatrix} W_1^{\Delta u}\left[u(k_0) - u(k_0-1)\right] \\ \vdots \\ W_m^{\Delta u}\left[u(k_0+m) - u(k_0+m-1)\right] \end{bmatrix} \tag{16}$$

Redefining: $\mathbf{Y}=[\,\mathbf{y}^{pr}\ \mathbf{y}^{\Delta u}\,]^{\mathrm{T}}$ it is ensured by (9) that the elements of $\mathbf{y}^{\Delta u}$ satisfy $\max(y_i^{\Delta u}) \leq k_{ssv}$ for $i=1,\ldots,m$. Thus, the maximum weighted manipulated variable movement is bounded at each sampling instant by k_{ssv}.

2.5 Manipulated variables constraints

Define:

$$\mathbf{y}^{uc} = \left[k_{ssv}\frac{u(k_0)}{u_{\max}(k_0)} \quad \ldots \quad k_{ssv}\frac{u(k_0+m)}{u_{\max}(k_0+m)} \right]^{\mathrm{T}} \tag{17}$$

Redefining: $\mathbf{Y}=[\,\mathbf{y}^{pr}\ \mathbf{y}^{\Delta u}\ \mathbf{y}^{uc}\,]^{\mathrm{T}}$ it is ensured by (9): that the elements of $\mathbf{y}^{uc}$ satisfy $\max(k_{ssv}u(i)/u_{\max}(i)) \leq k_{ssv}$ for $i=k_0,\ldots,k_0+m$ which can be simplified to: $\max(u(i)) \leq u_{\max}(i)$ for $i=k_0,\ldots,k_0+m$. Thus, the manipulated variables are bounded at each sampling instant by $u_{\max}(i)$ for $i=k_0,\ldots,k_0+m$.

2.6 MPC terminal condition

A terminal condition is used to ensure that at steady state the predicted output stays within a neighborhood ε near the origin (Chen and Allgöwer, 1998). Although not shown here for brevity, it can be shown that the use of the terminal condition together with the manipulated variables constraints ensures stability providing that the terminal condition is feasible with respect to constraints. Define:

$$\mathbf{y}^{tc} = \begin{array}{l} \dfrac{k_{ssv}}{\varepsilon}\left[u(k_0+m)\displaystyle\sum_{i=1}^{p}\left(h_i^L + \delta h_i^L\right)\right] + \\ \dfrac{k_{ssv}}{\varepsilon}\left[u^2(k_0+m)\displaystyle\sum_{i=1}^{p}\sum_{j=i}^{p}\left(h_{i,j}^{NL} + \delta h_{i,j}^{NL}\right)\right] \end{array} \tag{18}$$

ε can be selected by the user but a smaller value results in more conservative control. Redefining: $\mathbf{Y}=[\mathbf{y}^{pr}\ \mathbf{y}^{\Delta u}\ \mathbf{y}^{uc}\ \mathbf{y}^{tc}]^{\mathrm{T}}$ it is ensured by (9) that

$$\max\left[\begin{array}{l} \dfrac{k_{ssv}}{\varepsilon}\left(u(k_0+m)\displaystyle\sum_{i=1}^{p}\left(h_i^L + \delta h_i^L\right)\right) + \\ \dfrac{k_{ssv}}{\varepsilon}\left(u^2(k_0+m)\displaystyle\sum_{i=1}^{p}\sum_{j=i}^{p}\left(h_{i,j}^{NL} + \delta h_{i,j}^{NL}\right)\right) \end{array}\right] \leq k_{ssv} \tag{19}$$

which can be simplified to:

$$\max\left[\begin{array}{l} u(k_0+m)\displaystyle\sum_{i=1}^{p}\left(h_i^L + \delta h_i^L\right) + \\ u^2(k_0+m)\displaystyle\sum_{i=1}^{p}\sum_{j=i}^{p}\left(h_{i,j}^{NL} + \delta h_{i,j}^{NL}\right) \end{array}\right] \leq \varepsilon \tag{20}$$

Details on the construction of **M** for a Volterra series model NMPC strategy considering the additional terms of subsections 2.4, 2.5 and 2.6 can be found on Appendix A at the end of this paper.

3. CASE STUDIES

Different case studies are presented to show the more important features of the proposed algorithm. For simplicity a SISO case is presented where an approximated Volterra model describing the effect of coolant temperature on reactor concentration for a CSTR is as follows (Gao, 2004):

$$\begin{array}{rl} y(k_0) = & h_1^L u(k_0) + h_2^L u(k_0-1) + h_3^L u(k_0-2) + \\ & h_{1,1}^{NL} u^2(k_0) + h_{1,2}^{NL} u(k_0)u(k_0-1) + \\ & h_{1,3}^{NL} u(k_0)u(k_0-2) + h_{2,2}^{NL} u^2(k_0-1) + \\ & h_{2,3}^{NL} u(k_0-1)u(k_0-2) + h_{3,3}^{NL} u^2(k_0-2) \end{array} \tag{21}$$

$h_1^{\mathrm{L}} = 0.2835$, $h_2^{\mathrm{L}} = 0.1445$, $h_3^{\mathrm{L}} = 0.0594$, $h_{1,1}^{\mathrm{NL}} = -0.0072$, $h_{1,2}^{\mathrm{NL}} = -0.049$, $h_{1,3}^{\mathrm{NL}} = -0.0281$, $h_{2,2}^{\mathrm{NL}} = -0.0379$, $h_{2,3}^{\mathrm{NL}} = -0.017$, $h_{3,3}^{\mathrm{NL}} = -0.0081$. The MPC prediction and control horizons are $p=3$ and $m=2$.

The first study is intended to illustrate the possibility of tuning the proposed algorithm through the value of $W_1^{\Delta u}$, i.e. the weight used to penalize manipulated variables from sampling instant (k_0–1) to sampling instant (k_0). The response of the process to a pulse disturbance is studied and the set point is equal to zero. The disturbance is as follows: from $0<k_0\leq 20$ $d=5$, then from $20<k_0\leq 40$ $d=0$. For this case it is considered that there is no uncertainty in the Volterra model coefficients.

Figures 1 and 2 show that the weight imposed on the movement on the manipulated variables can be effectively used to tune the closed loop response. To illustrate the significance of the nonlinear terms, a simulation is carried on with a controller based solely on the linear part of the Volterra model. The results (dotted line in Figures 1 and 2) illustrate that the nonlinear model based controller provides as expected, a better and more consistent performance than the linear model based one.

To illustrate the constraint handling capabilities of the algorithm, the response to a pulse disturbance is studied. The disturbance is: for $0<k_0\leq 5$ $d=5$, for $5<k_0\leq 10$ $d=50$ and for

$10<k_0\leq 15$ d=5. The value of the manipulated variable is restricted to $|u(k_0)| \leq 5.5$ and $W_1^{\Delta u}$=2. For this case it was considered that the Volterra series coefficients are known accurately, i.e. there is no model uncertainty. It can be seen from Figure 3 that the controller keeps the value of the manipulated variable within the allowed limits.

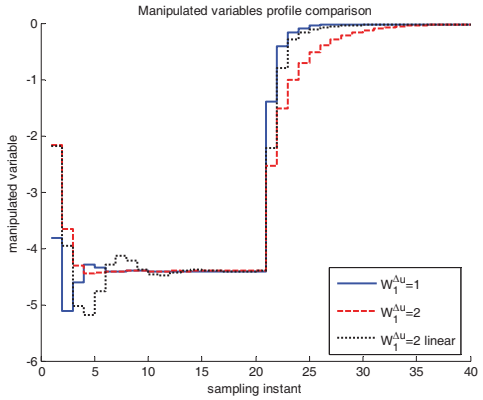

Fig. 1. Manipulated variable profile for case study 1.

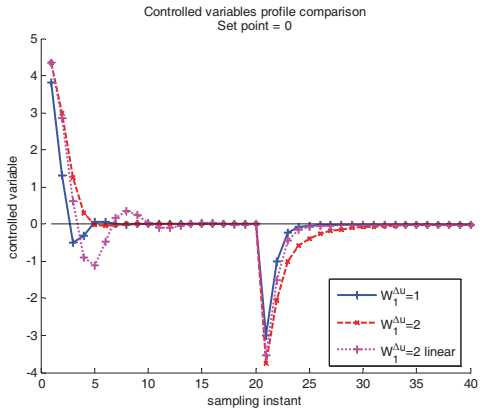

Fig. 2. Controlled variable profile for case study 1.

A key feature of the proposed MPC is that it allows considering that the Volterra series coefficients are not exactly known. To illustrate this feature of the algorithm it is assumed that certain coefficients are uncertain as follows: $h_1^{L} = 0.2551 \pm 0.0383$, $h_{2,2}^{NL} = -0.0360 \pm 0.0072$ and $h_{3,3}^{NL} = -0.0089 \pm 0.0018$. In this case the Volterra series coefficients of the plant are the same as those used for case study 1 and 2. Furthermore, the disturbance affecting the process is the same as that of case study 1. Figures 4 and 5 show the manipulated and controlled variable profile when $W_1^{\Delta u}$=2. The response obtained with the uncertain model MPC is more oscillatory but still acceptable. The figures show that the control variable converges to a value very close to zero and the manipulated variables are kept within limits. The small offset observed in the manipulated variable with respect to u=0 arises from the requirement of the terminal condition in the presence of model uncertainty.

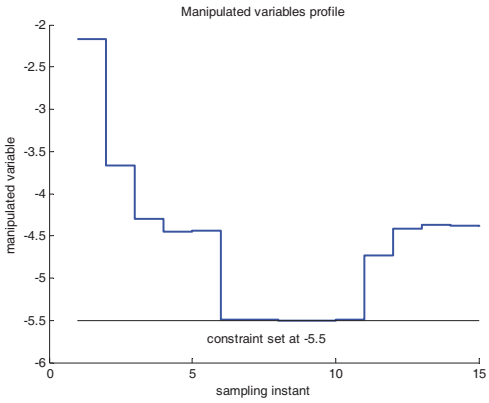

Fig. 3. Manipulated variable profile for case study 2.

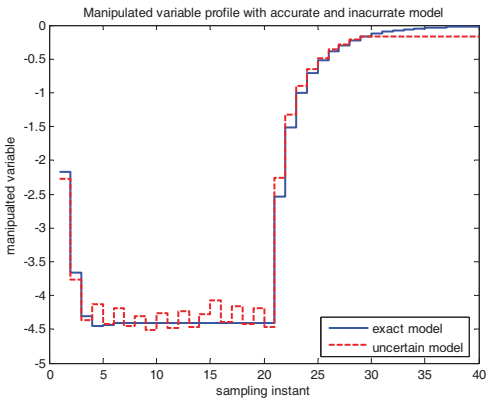

Fig. 4. Manipulated variable profile for case study 3.

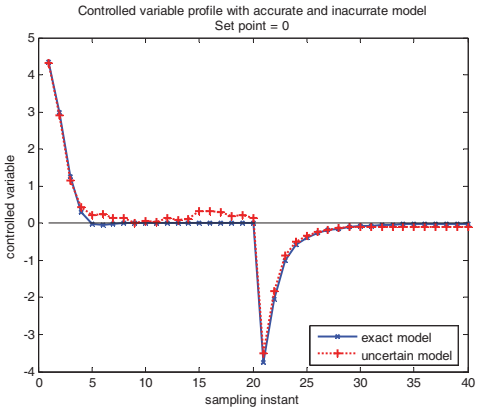

Fig. 5. Controlled variable profile for case study 3.

4. CONCLUSIONS

A novel robust NMPC controller based on a Volterra model was presented. The methodology uses μ analysis to calculate, for an uncertain plant model, the worst possible norm of a vector of inputs and outputs. The interconnection matrix can include terms to account for manipulated variables movement weighting, manipulated variables constraints and robust stability properties enforced through a terminal condition. The application of this technique to MIMO problems is currently being investigated.

ACKNOWLEDGMENTS

The financial support provided by Natural Sciences and Engineering Research Council of Canada is gratefully acknowledged.

REFERENCES

Braatz, R. D., Young, P. M., Doyle, J. C., and Morari, M. (1994). Computational complexity of μ calculation, *IEEE Transactions on Automatic Control*, 39 (5), 1000–1002,

Chen, H., and Allgöwer, F. (1998). A quasi-infinite horizon nonlinear model predictive control scheme with guaranteed stability, *Automatica,* 34 (10), 1205–1217.

Doyle, J., (1982). Analysis of feedback systems with structured uncertainties, *IEE Proceedings D Control Theory & Applications,* 129 (6), 242–250.

Findeisen, R., and Allgöwer, F. (2002). An introduction to nonlinear model predictive control. In Bram de Jager and Hans Zwart (ed.), *21st Benelux Meeting on Systems and Control,* 119–141. Technische Universiteit Eindhoven, Veldhoven.

Gao, J. (2004). *Robust control design of gain-scheduled controllers for nonlinear processes*. PhD Thesis University of Waterloo, Waterloo.

Hérnandez, E. and Arkun, Y. (1993). Control of nonlinear systems using polynomial ARMA models, *AIChE Journal,* 39 (3), 446–460.

Maner, B. R., Doyle III, F. J., Ogunnaike, B. A., and Pearson, R. K. (1996). Nonlinear model predictive control of a simulated multivariable polymerization reactor using second-order Volterra models, *Automatica,* 32 (9), 1285–1301.

Nagy, Z. K., and Braatz, R. D. (2003a). Robust nonlinear model predictive control for batch processes, *AIChE Journal,* 49 (7), 1776–1786.

Nagy, Z. K., and Braatz, R. D. (2003b). Worst-case and distribution analysis of finite-time control trajectories for nonlinear distributed parameter systems, *IEEE Transactions on Control Systems Technology,* 11 (5), 694–704.

Nowak, R. D., and Van Veen, B. D. (1994). Random and pseudorandom inputs for Volterra filter identification, *IEEE Transactions on Signal Processing,* 42 (8), 2124–2135.

Parker, R. S. and Doyle III, F. J. (2001). Optimal control of a continuous bioreactor using an empirical nonlinear model, *Industrial Engineering & Chemistry Research*, 40 (8), 1939–1951.

Qin, S. J., and Badgwell, T. A. (2003). A survey of industrial model predictive control technology. *Control Engineering Practice*, 11 (7), 733–764.

Schetzen, M. (1980). *The Volterra & Wiener theories of nonlinear systems.* Robert E. Krieger, Florida.

Appendix A. CONSTRUCTION OF THE MATRIX **M**

The use of an appropriate interconnection matrix **M** allows quantifying the effect that an input has on the system's output in the presence of uncertainty through a linear fractional transformation (LFT). If **M** is built according to the following structure

$$\mathbf{M} = \left[\begin{array}{c|c} \mathbf{M}_{11}^{\mathrm{LFT}} & \mathbf{M}_{12}^{\mathrm{LFT}} \\ \hline \mathbf{M}_{21}^{\mathrm{LFT}} & \mathbf{M}_{22}^{\mathrm{LFT}} \end{array}\right] \tag{22}$$

the effect that the input has on the output in the presence of uncertainty is:

$$\mathbf{Y}(k) = \left[\mathbf{M}_{21}^{\mathrm{LFT}}\boldsymbol{\Delta}\left[\mathbf{I} - \mathbf{M}_{11}^{\mathrm{LFT}}\boldsymbol{\Delta}\right]^{-1}\mathbf{M}_{12}^{\mathrm{LFT}} + \mathbf{M}_{22}^{\mathrm{LFT}}\right]\begin{bmatrix}\boldsymbol{w}(k)\\ 0\end{bmatrix} \tag{23}$$

where $\boldsymbol{w}(k) = [w(k), \ldots, w(k)]^{\mathrm{T}}_{p}$. The interconnection matrix **M** that considers manipulated variables movement penalization, manipulated variables constraints and terminal condition has the following structure:

$$\mathbf{M} = \left[\begin{array}{ccc|c} \mathbf{M}_{11} & \mathbf{M}_{12} & \mathbf{M}_{13} & \mathbf{M}_{14} \\ \mathbf{M}_{21} & \mathbf{M}_{22} & \mathbf{M}_{23} & \mathbf{M}_{24} \\ \mathbf{M}_{31} & \mathbf{M}_{32} & \mathbf{M}_{33} & \mathbf{M}_{34} \\ \hline \mathbf{M}_{41} & \mathbf{M}_{42} & \mathbf{M}_{43} & \mathbf{M}_{44} \end{array}\right] \tag{24}$$

In (24) $\mathbf{M}_{11}$, $\mathbf{M}_{12}$, $\mathbf{M}_{13}$, $\mathbf{M}_{21}$, $\mathbf{M}_{22}$, $\mathbf{M}_{23}$, $\mathbf{M}_{31}$, $\mathbf{M}_{33}$, $\mathbf{M}_{34}$ and $\mathbf{M}_{44}$ are matrices of appropriate dimensions that have all its elements equal to zero. $\mathbf{M}_{14}$, $\mathbf{M}_{24}$, $\mathbf{M}_{32}$, $\mathbf{M}_{41}$, $\mathbf{M}_{42}$ and $\mathbf{M}_{43}$ are defined as:

$$\mathbf{M}_{14} = \mathrm{diag}\left[\mathbf{D} \quad \mathbf{A}\right] \tag{25}$$

$$\mathbf{M}_{24} = \mathrm{diag}\left[\begin{bmatrix}\mathbf{U}^{L}\\ \mathbf{U}^{CP}\end{bmatrix} \quad \mathbf{B}\right] \tag{26}$$

$$\mathbf{M}_{32} = \mathbf{E} \tag{27}$$

$$\mathbf{M}_{41} = \mathrm{diag}\left[\mathbf{I}_{p} \quad \mathbf{C}\right] \tag{28}$$

$$\mathbf{M}_{42} = \begin{bmatrix}\mathbf{H}^{L} & 0 & \mathbf{H}^{CP}\\ 0 & \mathbf{F} & 0\end{bmatrix} \tag{29}$$

$$\mathbf{M}_{43} = \left[\mathbf{V}^{Lac} \quad \mathbf{V}^{NLac} \quad \mathbf{V}^{CPac}\right] \tag{30}$$

The rest of the matrices are defined as follows:

$$\mathbf{A} = \mathrm{diag}\left[\mathbf{A}_{11}, \mathbf{A}_{12}, \mathbf{A}_{13}\right] \tag{31}$$

$$\mathbf{A}_{11} = k_{ssv}d(k_0 + p) \tag{32}$$

$$\mathbf{A}_{12} = k_{ssv}\mathrm{diag}\left[\begin{bmatrix} u(k_0-1) \\ u(k_0) \end{bmatrix} \quad \cdots \quad \begin{bmatrix} u(k_0+m-1) \\ u(k_0+m) \end{bmatrix}\right] \tag{33}$$

$$\mathbf{A}_{13} = k_{ssv}\mathrm{diag}\left[u(k_0),\ldots,u(k_0+m)\right] \tag{34}$$

$$\mathbf{D} = k_{ssv}\mathrm{diag}\begin{bmatrix} d(k_0)+y^{sp}(k_0) \\ \vdots \\ d(k_0+p)+y^{sp}(k_0+p) \end{bmatrix} \tag{35}$$

$$\mathbf{U}^{L} = k_{ssv}\left[\mathbf{U}_1^{L} \quad \ldots \quad \mathbf{U}_l^{L} \quad \ldots \quad \mathbf{U}_p^{L}\right]^{\mathrm{T}} \tag{36}$$

$$\mathbf{U}_l^{L} = \begin{bmatrix} 0_{((p+1-l)\times(l-1))} & u(x)\mathbf{I}_{p+1-l} \\ 0_{((p+1-l)\times(l-1))} & u(x)^2\mathbf{I}_{p+1-l} \end{bmatrix} \tag{37}$$

$$\mathbf{U}^{CP} = k_{ssv}\left[\mathbf{U}_{1,1}^{CP} \quad \mathbf{U}_{1,2}^{CP} \quad \ldots \quad \mathbf{U}_{i,j-1}^{CP} \quad \mathbf{U}_{i,j}^{CP}\right] \tag{38}$$

$$i = 1,\ldots,p-1,\ j = 1,\ldots,p-i$$

$$\mathbf{U}_{i,j}^{CP} = \left[\mathbf{U}_{i,j\,1,1}^{CP} \quad \mathbf{U}_{i,j\,1,2}^{CP}\right] \tag{39}$$

$$\mathbf{U}_{i,j\,1,1}^{CP} = 0_{((p+1-i-j)\times(i+j-1))} \tag{40}$$

$$\mathbf{U}_{i,j\,1,2}^{CP} = u(i+j)u(j)\mathbf{I}_{p+1-i-j} \tag{41}$$

$$\mathbf{B} = \left[k_{ssv}u(k_0+m) \quad k_{ssv}u^2(k_0+m)\right]^{\mathrm{T}} \tag{42}$$

$$\mathbf{C} = \left[\frac{k_{ssv}}{\varepsilon}, \mathrm{diag}\left[\begin{bmatrix} W_i^{\Delta u} & -W_i^{\Delta u} \end{bmatrix}, \frac{k_{ssv}}{u_{\max}(i)}\right]\right] \quad i = 1,\ldots,m \tag{43}$$

$$\mathbf{H}^{L} = \left[\mathbf{H}_1^{L},\ldots,\mathbf{H}_l^{L},\ldots,\mathbf{H}_p^{L}\right] \tag{44}$$

$$\mathbf{H}_l^{L} = \begin{bmatrix} \mathbf{H}_{l\,1,1}^{L} & \mathbf{H}_{l\,1,2}^{L} \\ \mathbf{H}_{l\,2,1}^{L} & \mathbf{H}_{l\,2,2}^{L} \end{bmatrix} \tag{45}$$

$$\mathbf{H}_{l\,1,1}^{L} = \mathbf{H}_{l\,1,2}^{L} = 0_{((l-1)\times(p+1-l))} \tag{46}$$

$$\mathbf{H}_{l\,2,1}^{L} = \mathrm{diag}\left(h_1^{L},\ldots,h_{p+1-l}^{L}\right) \tag{47}$$

$$\mathbf{H}_{l\,2,2}^{L} = \mathrm{diag}\left(h_{1,1}^{NL},\ldots,h_{p+1-l,\,p+1-l}^{NL}\right) \tag{48}$$

$$\mathbf{H}^{CP} = \left[\mathbf{H}_{1,1}^{CP},\mathbf{H}_{1,2}^{CP},\ldots,\mathbf{H}_{i,j-1}^{CP},\mathbf{H}_{i,j}^{CP}\right] \begin{matrix} i = 1,\ldots,p-1 \\ j = 1,\ldots,p-i \end{matrix} \tag{49}$$

$$\mathbf{H}_{i,j}^{CP} = \begin{bmatrix} 0_{((i+j-1)\times(p+1-i-j))} \\ \mathrm{diag}\left(h_{1,i+1}^{NL},\ldots,h_{p+1-i-j,\,p+1-j}^{NL}\right) \end{bmatrix} \tag{50}$$

$$\mathbf{F} = \begin{bmatrix} \frac{k_{ssv}}{\varepsilon}\sum_{i=1}^{p} h_i^{L} & \frac{k_{ssv}}{\varepsilon}\sum_{i=1}^{p}\sum_{j=i}^{p} h_{i,j}^{NL} \end{bmatrix} \tag{51}$$

$$\mathbf{V}^{Lac} = \left[\mathbf{V}_1^{Lac},\ldots,\mathbf{V}_l^{Lac},\ldots,\mathbf{V}_p^{Lac}\right] \tag{52}$$

$$\mathbf{V}_l^{Lac} = \left[0_{((l-1)\times(p+2-l))} \quad \delta h_x^{L}\mathbf{I}_{p+2-l}\right]^{\mathrm{T}} \tag{53}$$

$$\mathbf{V}^{NLac} = \left[\mathbf{V}_1^{NLac},\ldots,\mathbf{V}_l^{NLac},\ldots,\mathbf{V}_p^{NLac}\right] \tag{54}$$

$$\mathbf{V}_l^{NLac} = \left[0_{((l-1)\times(p+2-l))} \quad \delta h_{x,x}^{NL}\mathbf{I}_{p+2-l}\right]^{\mathrm{T}} \tag{55}$$

$$\mathbf{V}^{CPac} = \left[\mathbf{V}_{1,1}^{CPac},\mathbf{V}_{1,2}^{CPac},\ldots,\mathbf{V}_{i,j}^{CPac}\right] \begin{matrix} i = 1,\ldots,p-1 \\ j = 1,\ldots,p-i \end{matrix} \tag{56}$$

$$\mathbf{V}_{i,j}^{CPac} = \left[0_{((i+j-1)\times(p+3-i-j))} \quad \delta h_{i,j}^{NL}\mathbf{I}_{p+3-i-j}\right]^{\mathrm{T}} \tag{57}$$

In order to obtain the matrix **E** it is necessary to build a column vector that contains the Volterra series coefficients according to the following structure:

$$\mathbf{VE} = \left[\mathbf{VE}_1 \quad \ldots \quad \mathbf{VE}_{p+1}\right]^{\mathrm{T}} \tag{58}$$

The matrix **VE** has the following dimensions:

$$\mathbf{VE} = \left(p + p + \sum_{i=1}^{p-1} p - i\right) \times 1 \tag{59}$$

The rule to construct **VE** is as follows:

$$\mathbf{VE}_1 = \left[h_1^{L} \quad \ldots \quad h_p^{L}\right]^{\mathrm{T}} \tag{60}$$

$$\mathbf{VE}_2 = \left[h_{1,1}^{NL} \quad \ldots \quad h_{p,p}^{NL}\right]^{\mathrm{T}} \tag{61}$$

$$\mathbf{VE}_i = \left[h_{1,i-1}^{NL} \quad \ldots \quad h_{p+2-i,p}^{NL}\right]^{\mathrm{T}} \quad i \geq 3 \tag{62}$$

Finally the matrix **E** is constructed according to the following program:

$$\begin{aligned} &\text{for } i = 1,\ldots,p+p+\sum_{q=1}^{p-1} p-q \\ &\quad \text{for } ir = 1,\ldots,p \\ &\quad \text{for } ic = 1,\ldots,p+p+\sum_{iq=1}^{p-1} p-iq \\ &\quad \text{if}\left[\mathbf{H}^{L}\mathbf{H}^{CP}\right]_{ir,ic} = \mathbf{VE}_{i,1} \\ &\quad\quad index_{i,1} = ic \\ &\quad \text{end} \\ &\text{end} \\ &\text{end} \\ &\text{end} \end{aligned} \tag{63}$$

The elements of the matrix **E** are zero except the following:

$$\begin{aligned} &\text{for } ir = 1,\ldots,2\sum_{i=1}^{p} i + \sum_{i=1}^{p-1}\sum_{j=1}^{i} j \\ &\quad \mathbf{E}_{ir,index(ir,1)} = k_{ssv} \\ &\text{end} \end{aligned} \tag{64}$$

OUTPUT-FEEDBACK DISSIPATIVE CONTROL OF EXOTHERMIC CONTINUOUS REACTORS

A. Schaum * **J.A. Moreno** * **J. Alvarez** ** **J. Diaz-Salgado** *

* *Instituto de Ingeniería, Universidad Nacional Autónoma de México (e-mail: {ASchaum,JMorenoP,JDiazS}@ii.unam.mx).*
** *Departamento de Procesos e Hidraulica, Universidad Autónoma Metropolitana de México (e-mail: jac@xanum.uam.mx)*

Abstract: The problem of controlling a (possibly open-loop unstable) continuous exothermic reactor with temperature measurements and manipulation of reactant feed and heat exchange rates is addressed within a passivity-dissipativity framework. The combination of a nonlinear passive state-feedback (SF) controller with a dissipative observer yields the dissipative output-feedback (OF) controller closed-loop stability conditions with: (i) the identification of the underlying gain-behavior interplay, and (ii) simple tuning guidelines. The approach is tested through numerical simulations, with a representative worst-case example: an exothermic reactor with Langmuir-Hinshelwood nonmonotonic kinetics, which must be regulated about an open-loop unstable steady-state which is not observable.

Keywords: Chemical Reactor Models, Output-Feedback Control, Dissipativity, Observability.

1. INTRODUCTION

Continuous exothermic chemical reactors are complex nonlinear dynamical systems with nonlinear behavior, asymmetric MIMO coupling, parametric sensitivity, multiplicity, hysteresis, bifurcation, and limit cycling. Most of the industrial reactors are controlled by combining conventional (ratio, and cascade) feedforward and (P, PI and PID) feedback linear control component with supervisory or advisory material-energy balance and optimizing controllers (Shinskey [1988], Gonzalez and Alvarez [2005]). The process design or redesign to meet tighter safety, productivity, quality and environmental requirements motivates the development of more capable and systematic reactor control designs. Advanced nonlinear control studies have been performed in the chemical process systems engineering field, the related state of the art can be seen elsewhere, and here it suffices to mention that: (i) with a few exceptions (Alvarez et al. [1991], Viel and Jadot [1997], Antonelli and Astolfi [2003]) most of the studies lack rigorous stability and performance assessments, and (ii) only the optimality-based MPC (which stems from industrial control developments) has reached the stage of acceptance for plant scale testing or implementation (Eaton and Rawlings [1990]). Recently, in the context of polymer reactor (Gonzalez and Alvarez [2005], Diaz-Salgado et al. [2007]) and distillation column output-feedback control studies (Castellanos-Sahagun and Alvarez [2006]) with constructive nonlinear control, connections between PI, inventory and MP control designs have been identified, and the closed-loop stability assessment and tuning aspects have been handled either with conceptual arguments or with the small gain theorem. The dissipativity notion offers a unifying framework to handle design-oriented tools in constructive control (Sepulchre et al. [1997]) according to fundamental connections between optimality, passivity, robustness and dissipativity, with emphasis on interlaced observer-control designs and rigorous stability assessments. The dissipativity ideas (i) were originally developed in the context of state-feedback (SF) control problems (Willems [1972]), (ii) have been extended to design of nonlinear observers (Moreno [2005]), and observer-control separation (Moreno [2006]), and (iii) enable the tackling of the difficult problem of estimating and controlling reactors with non-monotonic kinetics, and lack of observability at maximum reaction rate (Schaum et al. [2008]).

The preceding considerations motivate the present reactor output-feedback (OF) control study, where the problem of controlling a continuous exothermic (possibly open-loop unstable) reactor with either monotonic or non-monotonic kinetics, temperature measurements, and manipulation of reactant and heat exchange rates is addresed within a combined passivity-dissipativity approach, including (i) the derivation of rigorous closed-loop stability conditions coupled with easy-to-apply tuning guidelines, and (ii) the identification of the underlying interplay between regulation speed, robustness, and observer-control gains. The proposed approach is tested, through numerical simulations, with an exothermic reactor with nonmonotonic kinetics, open-loop instability, and lack of observability.

In our previous study (Schaum et al. [2008]) the reactor problem was adressed by *ad hoc* combining a passive controller with a dissipative observer, and drawing closed-loop stability conditions with the small gain theorem. However, the passivity (controller) and dissipativity (observer) approaches were methodologically disconnected, and the

stability characterization was not reflected in a practical tuning. In the present work: (i) the controller-observer design and the closed-loop stability assessment are performed with a united framework, and (ii) a simple tuning scheme that is clearly related with closed-loop functioning features is obtained .

2. CONTROL PROBLEM

Consider a continuous chemical reactor where a reactant is converted into product via an exothermic reaction, heat being removed through a diathermal wall with a cooling jacket. Assuming the volume (V) and the jacket temperature (T_c) are controlled with fast (conventional, linear decentralized) feedback loops which manipulate the exit and coolant flowrates (Shinskey [1988]) the *reactor model* is given by the dynamic mass-energy balance:

$$\begin{array}{l} \dot{c} = -r(c,T,\pi) + \theta(c_e - c), \qquad c(0) = c_0 \\ \dot{T} = \beta r(c,T,\pi) + \theta(T_e - T) - \eta(T - T_c), T(0) = T_0 \end{array} \quad (1)$$

where $(\bar{(\cdot)})$ is the steady-state (SS) value of $(\cdot)$)

$$\begin{array}{l} c = C/C^0, \quad \theta = q/V, \quad \beta = (-\Delta H)C^0/(V\rho_m c_p) \\ \eta = (UA_U)/(V\rho c_p), \quad p = (p_a', \pi')', \quad p_a = (c_e, \beta, \eta)' \\ r(\bar{c}, \bar{T}) + \overline{\theta}(\bar{c}_e - \bar{c}) = 0, \\ \beta r(\bar{c}, \bar{T}, \pi) + \overline{\theta}(\bar{T}_e - \bar{T}) - \eta(\bar{T} - \bar{T}_c) = 0 \end{array}$$

The reactant dimensionless concentration c, and the reactor temperature T are the states, the dilution rate q and the jacket temperature T_c are *control inputs*, r is the nonlinear reaction rate function, π is its parameter vector, θ is the inverse residence time, η is the heat transfer coefficient-to-capacity quotient, β is the adiabatic temperature rise, the feed concentration c_e and temperature T_e are the *exogenous inputs*, C (or C^0) is the reactant (or pure reactant) concentration, q is the feed flowrate, $-\Delta H$ is the heat of reaction, ρ_m (or c_p) is the reacting mixture density (or specific heat capacity), U (or A_U) is the heat transfer coefficient (or area), and p is the model parameter. The temperatures (T and T_c) are measured, and the concentrations (c_e and c) are not. In compact vector notation the *reactor model* (1) is given by

$$\begin{array}{l} \dot{x} = f\left[x, d(t), u, p\right], \quad x(0) = x_0, \quad y = Cx, \quad z = x \\ x = [c,T]' \in X = [0,1] \times (T^-, T^+) \subset \mathbb{R}^2, \quad p = (p_a', \pi')' \\ f[\bar{x}, \bar{d}, \bar{u}, p] = 0, \quad d = [c_e, T_e]', \quad T_e = y_e - \tilde{y}_e, \ C = [0,1], \\ u = (\theta, T_c), \ T^- = \min(T_e, T_c), \ T^+ = \max(T_e, T_c) + \beta \end{array} \quad (2)$$

x is the state, u (or d) is the control (or exogenous, possibly time-varying) input, and y (or z) is the measured (or regulated) output. X is an invariant set, meaning that all state motions born in X stay in X (Alvarez et al. [1991]). Since the reactor model (1) contains constant ($\tilde{p}$) and time-varying reactor (or feed) temperature measurement $\tilde{y}$ (or $\tilde{y}_e$), and dilution rate ($\tilde{\theta}$ (or coolant temperature ($\tilde{T}_c$)) actuator bounded errors, the *actual reactor system dynamics* are given by

$$\begin{array}{l} \dot{x} = f[x, d + \tilde{d}(t), u + \tilde{u}(t), p + \tilde{p}], \\ x(0) = x_0, \quad y = Cx + \tilde{y}(t), \quad z = x \\ \tilde{p} = (\tilde{p}_a, \tilde{\pi}), \ \tilde{d}(t) = [\tilde{c}_e(t), \tilde{y}_e(t)]', \ \tilde{u}(t) = [\tilde{\theta}(t), \tilde{T}_c(t)]', \\ \tilde{y}(t) = y - T|\tilde{p}| \leq \delta_p, \quad ||\tilde{d}(t)|| \leq \delta_d, \quad ||\tilde{u}(t)|| \leq \delta_u, \\ ||\tilde{y}(t)|| \leq \delta_y, \quad ||(.)(t)|| = \sup_{t \in [0,\infty)} |(.)(t)|, \end{array} \quad (3)$$

where δ_p, δ_d, δ_u and δ_y are the error sizes, and $|(\cdot)|$ is the Euclidian norm of the vector $(\cdot)$. Our *control problem* consists in designing, on the basis of the reactor model (1) (with parameter approximation p) and flow and temperature measurement, an observer-based dynamical *output-feedback (OF) controller* to regulate the concentration-temperature pair z, about a (possibly opn-loop unstable and unobservable) SS by manipulating the dilution rate-cooling temperature pair u.

3. OUTPUT-FEEDBACK (OF) CONTROLLER

The reactor dynamics represent mass and energy accumulation due to advective, reaction and heat exchange input/output mechanisms. From the abstract energy perspective associated with the dissipativity control (Willems [1972], Sepulchre et al. [1997]) and estimation (Moreno [2005]) framework, our OF control problem amounts to designing the observer-control pair in such a way that the dissipation rate is negative, and robust, and implies nonwasteful control action.

In deviation form referred to the SS regime, the reactor system (1) is written as follows

$$\begin{array}{l} \dot{e} = f_e[e, \tilde{u}_e(t)], \ e(0) = e_0, \ e = x - \bar{x}, \\ \tilde{u}_e = (\tilde{p}', \tilde{d}', \tilde{u}')', \ f_e(0,0) = 0. \end{array} \quad (4)$$

According to the definition of *nonlocal input-to-state stability (ISS)* (Freeman and Kokotovic [1996]), the SS $e = 0$ is said to be *practically uniformly* (P) *stable* if an admissible disturbance size (δ_u) produces an admissible state deviation size (ε_x): given (δ_u, ε_x) there is a KL-class (increasing-decreasing) function β and a K-class (increasing) γ so that the state responses of system (4) are bounded as follows

$$\begin{array}{l} |e_0| \leq \delta_0, |\tilde{u}_e(t)| \leq \delta_u, \\ \Rightarrow |e(t)| \leq \tau(|e_0|, t) + \alpha(||\tilde{u}_e(t)||) \leq \tau(\delta_0, 0) + \alpha(\delta_u) = \varepsilon_x \end{array} \quad (5)$$

where τ (or α) bounds the transient (or asymptotic) response. The (necessary and sufficient) Lyapunov characterization of the ISS property is given by

$$\alpha_1(|e|) \leq V(e) \leq \alpha_2(|e|), \quad \dot{V} = -\alpha_3(|e|) + \alpha_4(|\tilde{u}_e|) \quad (6)$$

where V is a positive definite radially unbounded function and $\alpha_1, \cdots, \alpha_4$ are K-class functions.

3.1 Passive state-feedback (SF) controller

The notion of *passivity* plays a key role in the design of robust nonlinear SF controllers (Khalil [2002]), with: (i) fundamental connections between optimality, robustness and passivity, and (ii) means to analytically construct optimal controllers via inverse optimality. An optimal SF controller is passive and underlien by a minimum phase (MP) system (with relative degree less or equal than one). A nonlinear system is passive if it is *dissipative* (Willems [1972]) with storage function-supply rate pair and MP.

The reactor (1) is feedback-passive (after input coordinate change) with respect to the input-output pair (u, z) and the storage function $V = e^T e$ if and only if the reactor relative degree equal to one condition is met, i.e. (Schaum et al. [2008]):

$$\text{rd}(u, z) = (1, 1), \ z = x \ \Leftrightarrow c_e \neq c \ , \ \eta \neq 0 \quad (7)$$

Thus, the state-input coordinate change $e = x - \bar{x}, v = f(x, d, u)$ takes the reactor into the passive normal form (8)

$$\dot{e} = v, e(0) = e_0, \psi = e; V = e^T e, \dot{V} = 2\psi^T v, \quad (8)$$

with storage function V and input-output pair (v, ψ). The SF controller (9) yields the closed-loop (decoupled, stable, and dissipative) dynamics (10),

$$v{=}f(e,d,u){=}{-}Ke, K{=}\text{diag}(k_c,k_T) \Rightarrow u{=}\mu(x,d,u) \quad (9)$$

$$\dot{e}{=}{-}Ke, e(0){=}e_0, \psi{=}e; V{=}\,e^T e, \dot{V}{=}{-}2eTKe < 0. \quad (10)$$

In original coordinates, *the nonlinear passive SF controller* (9) is given by:

$$\begin{array}{l} \theta = [r(c,T) - k_c(c-\bar{c})]/(c_e - c), \\ T_c = T - [\beta r(c,T) + \theta(T_e - T) + k_T(T - \bar{T})]/\eta \end{array} \quad (11)$$

This controller with state, parameter, and measurement-actuator errors $(\epsilon, \tilde{d}, \tilde{p})$, yields the closed-loop dynamics (13) with dissipation (14)

$$u = \mu(x + \epsilon, d + \tilde{d}, p + \tilde{p}) := [\mu_\theta, \mu_{T_c}]^T \quad (12)$$

$$\dot{e} = -Ke + \tilde{f}\left[e; \epsilon, \tilde{d}(t), \tilde{p}\right], e(0){=}e_0, K{=}\,\text{diag}(k_c, k_T) \quad (13)$$

$$\dot{V} \leq -2\min\{k_c, k_T\}V + e'\tilde{f}\left[e; \epsilon, \tilde{d}(t), \tilde{p}\right] \quad (14)$$

$$\begin{array}{l} \tilde{f}\left(e; \epsilon, \tilde{d}, \tilde{p}\right) = f\left[\bar{x} + e, \bar{d} + \tilde{d}, \mu\left(x + \epsilon, \bar{d} + \tilde{d}, p + \tilde{p}\right), p\right] \\ e = (e_c, e_T)' = x - \bar{x}, \quad \tilde{f}\,(e; 0, 0, 0) = 0. \end{array}$$

Since the reactor has trivially stable nominal zero-dynamics $e = 0$, the errorless closed-loop is asymptotically stable. From the Lipschitz continuity of (f, μ) the system P-stability follows (Khalil [2002]), with a suitable tradeoff between the initial state (δ_0), parameter (δ_p), input (δ_d and $\delta_{\tilde{x}}$) and state excursion (ε_x) sizes, depending on the choice of the control gain pair (k_c, k_T). The P-stable closed-loop reactor dynamics (13) represents: (i) the behavior attainable with any robust controller, and (ii) the recovery target for the OF control design. The related solvability conditions (7) are generically met by the reactor class (1) because: (i) $c < c_e$, and (ii) $\eta > 0$.

3.2 Dissipative observer

The nonlinear global detectability property of any reactor motion (Schaum et al. [2008]) suggests the consideration of a dissipative observer, because (i) its functioning does not require complete observability (Moreno [2005]), and (ii) the structure-oriented approach offers a means to perform the control-estimator design (Section 4). The reactor dissipative observer is given by (Schaum et al. [2008])

$$\begin{array}{l} \dot{\hat{c}} = -r[\hat{c} - \kappa_r(\hat{T} - y), y, \pi] + \theta(c_e - \hat{c}) - \kappa_c(\hat{T} - y), \\ \dot{\hat{T}} = \beta r[\hat{c} - \kappa_r(\hat{T} - y), y, \pi] + \theta(T_e - \hat{T}) - \\ \qquad\qquad - \eta(\hat{T} - T_c) - \kappa_T(\hat{T} - y), \\ \hat{c}(0) = \hat{c}_0, \quad \hat{T}(0) = \hat{T}_0, \end{array} \quad (15)$$

where κ_c (or κ_T) is the usual concentration (or temperature) gain, and κ_r is the gain of an injection in the concentration argument of the reaction rate. The estimation error dynamics are given by the two-subsystem interconnection in Lur'e- Popov form (Khalil [2002], Willems [1972], Schaum et al. [2008])

$$\begin{bmatrix} \dot{\varepsilon}_c(T) \\ \dot{\varepsilon}_T(t) \end{bmatrix} = \begin{bmatrix} -\theta(t) & -\kappa_c \\ 0 & -\lambda_T \end{bmatrix} \begin{bmatrix} \varepsilon_c(T) \\ \varepsilon_T(t) \end{bmatrix} + \begin{bmatrix} 1 \\ -\beta \end{bmatrix} \nu \quad (16)$$

$$\psi = \zeta \triangleq \epsilon_c - \kappa_r \epsilon_T, , \quad \lambda_T \triangleq \theta(t) + \eta + \kappa_T$$

$$\nu = -\rho\,(c, y; \zeta)\,, \quad (17)$$

with (i) a linear-dynamic advective subsystem (16) with input ν and output ζ, and (ii) a nonlinear-static kinetic subsystem (17) with the reaction rate error. Since the rate r is continuously differentiable, there is a continuous secant function φ so that the estimated minus the actual rate is conically bounded (18) with the nonlinearity ρ is encompassed in the conic sector (19)

$$\rho(c, T; \zeta) \triangleq r\,(c + \zeta, T) - r(c, T) = \varphi\,(c, T; \zeta)\,\zeta, \quad (18)$$

$$\begin{array}{l} \zeta \triangleq \epsilon_c - \kappa_r \epsilon_T, \quad -k_1\,(T) \leq \varphi\,(c, T; \zeta) \leq k_2\,(T) \\ -k_1\,(T) = \min\limits_{0 \leq c \leq 1} r_c(c, T, \pi)\,, k_2\,(T) = \max\limits_{0 \leq c \leq 1} r_c(c, T, \pi), \end{array}$$

$$(k_2\zeta - \rho(c, T; \zeta))\,(\rho(c, T; \zeta) + k_1\zeta) \geq 0 \quad (19)$$

(Khalil [2002]). Consequently, the static system (17) is $[-1, 1/2(k_2 - k_1), -k_1 k_2]$-dissipative Moreno [2005], and its dissipation is characterized by the reaction rate slopes: the slope k_1 is positive (or negative) if the reaction rate is monotonic (or non-monotonic). The observer is designed in such a way that: (i) the open-loop estimation error dynamics consist of the feedback interconnection of two adequatly dissipative (passive) subsystems, and (ii) the estimator and control dissipativity properties are structurally compatible. The observer gains $\kappa_c, \kappa_T, \kappa_r$ are chosen so that the system interconnection (16) - (17) is dissipative with respect to the estimation storage function

$$\hat{V} = \frac{1}{2}\epsilon^T \epsilon. \quad (20)$$

The gain pair (κ_c, κ_T) shapes the dissipation of the linear dynamical subsystem, and the gain κ_r determines the interconnection form by setting the output of the linear system. Convergence conditions for the dissipative open-loop observer (15) are given in (Schaum et al. [2008]).

3.3 OF controller

The combination of the SF (9) passive nonlinear controller with the dissipative observer (15) yields the *dynamic OF controller*

$$\begin{array}{l} \dot{\hat{c}} = -r[\hat{c} - \kappa_r(\hat{T} - y), y, \pi_r] + \theta(c_e - \hat{c}) - \kappa_c(\hat{T} - y)\,, \\ \dot{\hat{T}} = \beta r[\hat{c} - \kappa_r(\hat{T} - y), y, \pi_r] + \theta(T_e - \hat{T}) - \\ \qquad\qquad - \eta(\hat{T} - T_c) - \kappa_T(\hat{T} - y), \\ \theta = [r(\hat{c}, T) - k_c(\hat{c} - \bar{c})]/(c_e - \hat{c}), \\ T_c = \hat{T} - [\beta r(\hat{c}, T) + \theta(T_e + \hat{T}) + k_T(\hat{T} - \bar{T})]/\eta \end{array} \quad (21)$$

with five adjustable gains: k_c and k_T for the passive-dissipative controller, and κ_c, κ_T and κ_r for the observer.

4. CLOSED-LOOP STABILITY AND TUNING

In this section, the closed-loop dynamics are characterized, yielding: (i) stability conditions, (ii) tuning guidelines, and (iii) a functioning assessment. The main difficulty resides in an inherent limitation: the unmeasured output concentration (c) must be regulated about a steady-state wich is open-loop unstable and not locally observable.

The application of the OF controller (21) to the actual reactor (3) yields the *closed loop dynamics*

$$\begin{array}{l} \dot{e} = -Ke + \psi(e)\epsilon + \phi\left(e, \epsilon; \tilde{d}(t), \tilde{p}\right), \\ \dot{\epsilon} = M(t)\epsilon + \tilde{g}\left(e, \epsilon; \tilde{d}(t), \tilde{p}\right), \end{array} \quad (22)$$

$$M(t) = \begin{bmatrix} -\theta(t) - \varphi(t) & -\kappa_c \\ \beta\varphi(t) & -\lambda_T \end{bmatrix}, \phi\,(e; 0) = 0$$

where e (or ϵ) is the regulation (or estimation) error, ϕ results from the replacement of ϵ_T by $\tilde{y}$ in the reaction rate term of the error function $\tilde{f}$ (13) associated with the Lyapunov closed-loop stability characterization with SF control. From the continuity of ϕ, $\tilde{f}$, $\tilde{g}$ and the compactness of their domains their Lipschitz continuity and boundedness follow.

Given that the separation principle holds for linear but not for nonlinear systems, the nominal closed-loop stability (i.e. system (22) with $(\tilde{g}, \phi) = (0, 0)$) can be established as follows: since the regulation error dynamics are individually P-stable and the estimation error dynamics are individually convergent, the reactor(1)-OF controller(21) interconnection is uniformly asymptotically stable (Angeli et al. [2004], Moreno [2006]). Motivated by the need of a more constructive stability criterion in the sense of practical applicability for gain tuning and behavior assessment purposes, in the next propositionclosed-loop stability conditions are given in terms of the five-gain set $(k_c, k_T, \kappa_c, \kappa_T, \kappa_r)$ of the proposed OF controller (21).

Proposition 4.1. (Sketch of proof in Appendix A)
The closed-loop reactor (1) with the proposed passive-dissipative OF controller (22) is P-stable if the controller five-gain set $(k_c, k_T, \kappa_c, \kappa_T, \kappa_r)$ and the regulation-estimation error set meet the conditions

$$(i)\ \theta = \mu_\theta(k_c) > -k_1, \qquad (ii)\ k_c > \iota_c(k_c)$$
$$(iii)\ k_T > \iota_T(k_c, \kappa_c, \kappa_r), \quad (iv)\ \kappa_T > \iota_\tau(k_c, k_T, \kappa_T, \kappa_c, \kappa_r),$$

with μ_θ givn in (12) and $\iota_c, \iota_T, \iota_\tau$ in Appendix A.

As it can be seen in Appendix A, the combined passivity-dissipativity approach enables the derivation of the above stability conditions in a rather straighforward way, by using the passive control (V) (13) and dissipative observer $(\hat{V})$ (20) storage functions and applying Lyapunovs direct method. In the absence of modeling error the closed-loop stability becomes asymptotic. Condition (i) is a closed-loop detectability requirement, Condition (ii) ensures the stability of the regulation-estimation concentration dynamics and imposes lower and upper limits ($k_c^- \approx 1, k_c^+ \approx 3$) on the composition control gain k_c (Gonzalez and Alvarez [2005]), and Conditions (iii) and (iv) ensure the stability of the regulation-estimation temperature dynamics and of the entire interconnection. Thus, for $\kappa_r \approx 1/\beta, k_c \approx 3\bar{\theta}$, the preceding inequality conditions can be met by choosing: (i) k_T sufficiently large to dominate $\iota_T(k_c, \kappa_c, \kappa_r)$, and (ii) κ_T sufficiently large to dominate $\iota_\tau(k_c, k_T, \kappa_c, \kappa_r)$.

From the preceding P-stability conditions the conventional-like tuning guidelines follow: (i) set the gains conservatively at $(k_c, k_T) \approx (1, 3), \kappa_r \approx 1\beta, \kappa_c \approx k_c, \kappa_T \approx 10\kappa_c$, (ii) increase the T-estimation gain κ_T until oscillatory response is obtained at κ_T^+, back off and set $\kappa_T = \kappa_T^+/2$-to-3, (iii) in the same way set $k_T = k_T^+/2$-to-3, (iv) carefully increase k_c (sufficiently below $k_c^+ \approx 4\bar{\theta}$) until there is no improvement, and adjust κ_r. If necessary, repeat steps (ii) to (iv).

The solvability of the robust OF reactor control problem is a consequence of: (i) the solvabilities of the OF control (7) and dissipative closed-loop observer (condition (i) in Proposition 4.1) problems, and (ii) the adequate choice of gains according to Proposition 4.1.

5. APPLICATION EXAMPLE

To subject the proposed OF controller to a severe test, let us consider an extreme case of an industrial situation: the operation of the continuous reactor (3) with the Langmuir-Hinshelwood (LH) kinetics model

$$r(c, T, \pi) = \frac{cke^{-(\frac{\gamma}{T})}}{(1 + \sigma c)^2}, \quad r_c = (c^*, T, \pi) = 0, c^* = 1/\sigma$$

adapted from a previous (partial open-loop or asymptotic and full measurement injection) estimation study with EKF and experimental data for the catalyzed carbon monoxide oxidation reaction (Baratti et al. [1993]). With the nominal parameters and inputs
$\bar{d}' = (\bar{c}_e, \bar{T}_e) = (1, 1), \bar{u}' = (\bar{\theta}, \bar{T}_c) = (1, 370), p = (p_a', \pi')'$,
$p_a = (\bar{c}_e, \bar{T}_e, \eta)' = (1, 370, 1), \pi' = (k, \gamma, \sigma) = (e^{25}, 10000, 3)$
the reactor has three steady-states (Diaz-Salgado et al. [2007]: two stable (extinction and ignition), and one unstable at maximum concentration rate $r^* = 0.6614$ with $c^* = 1/3$. The application of the tuning guidelines associated with Proposition 4.1 yielded: $\kappa_c = 0.62$, $\kappa_T = 30$, $\kappa_r = \frac{1}{50}$, $k_c = 2$, $k_T = 3.$, and the initial reactor and estimator conditions were set at $x_0 = [430, 0.28]'$, $\hat{x}_0 = [425, 0.35]'$, about the unstable steady-state with maximum rate. The relative degree (7) and global detectability (Schaum et al. [2008]) conditions are well met, because: $c_e - \bar{c} = 2/3 > 0, \eta = 1 > 0, \bar{\theta} = 1, 1/3 = \theta^- \leq \theta \leq \theta^+ = 3/2$. In the spirit of the nonlocal P-stability framework, the closed-loop reactor with nominal SF, nominal and perturbed OF will be subjected to initial state, and persistent parameter and exogenous input disturbances.

5.1 Nominal behavior with SF control

The closed-loop reactor behavior with exact model-based nonlinear passive SF controller (9) is shown in Figure 1. As expected, the concentration (or temperature) response is about one half (or quarter) settling residence time $(4/\theta = 4)$, with smooth-coordinated dilution rate-coolant temperature control action, safely away from saturation. This agrees with the optimality-based non-wasteful feature of passive SF controllers (Sepulchre et al. [1997]).

5.2 Nominal behavior with OF control

Initially, the reactor was in the above stated deviated initial state, and subjected to known constant feed concentration $c_e = 1$ and temperature $T_e = 370K$. The behavior with exact model-based OF control (21) is shown in Figure 2: (i) the state responses are quite similar to the ones of the nonlinear SF controller (Figure 1), in spite of a sluggish concentration estimate response (about 3/4th of the natural settling time), and (ii) as expected from the FF component of the OF controller, the control inputs practically annihilate the effect of the known oscillatory input, and (iii) the control actions are smooth and efficient, reasonably away from saturation. Thus, the nominal OF controller recovers rather well the behavior of its exact model-based nonlinear SF counterpart. This test verifies

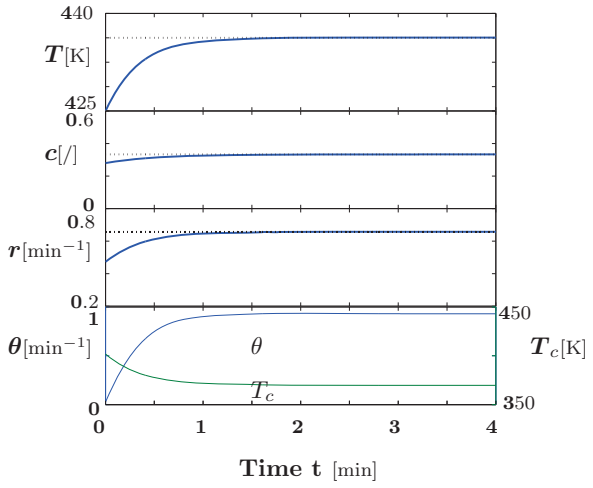

Fig. 1. Closed-loop nominal behavior with nonlinear SF controller: input and response (—) , estimate (− −), and set point (· · ·).

the closed-loop P-stability property with OF dynamic control, with asymptotic convergence to the prescribed SS.

The constant errors in the estimation model correspond to: (i) $\hat{c}_e(t) = 0.991$, (ii) measured feed and reactor temperatures with considerable periodic error $\hat{T}_e(t) - T_e(t) = y(t) - T(t) = 2\cos(40\pi t)$ (four degrees amplitude band and frequency close to natural resonance mechanism), and (iii) -1.5, -10, and $+3$ % errors in the activation energy (γ), heat transfer coefficient (η), and adiabatic temperature rise (β), respectively. These errors represents a worst-case situation to subject the OF controller to a severe robustness test. The resulting closed-loop behavior is presented in Figure 3: (i) the reactor is adequately P-stable with a transient response trend that basically coincides with the one of the errorless model case (see Figure 2), (ii) as expected from the severe modelling errors, the unmeasured concentration exhibits a significant ($\approx -30\%$) asymptotic offset, some reaction rate offset ($\approx -20\%$) and the temperature estimate generated by the linear-dynamical advective (that is mass-energy balance based) estimation component yields an offset-less trend response, and (iii) given the flatness feature of the reaction kinetics in the isotonic branch of the reaction rate function, in spite of the -30% concentration trend offset, the reaction rate trend is only a -20% of its maximum set point value. Should it be necessary, the optimal rate offset can be reduced by online kinetic parameter model calibration on the basis of the occasional or periodic concentration measurements that are usually taken for quality monitoring purposes.

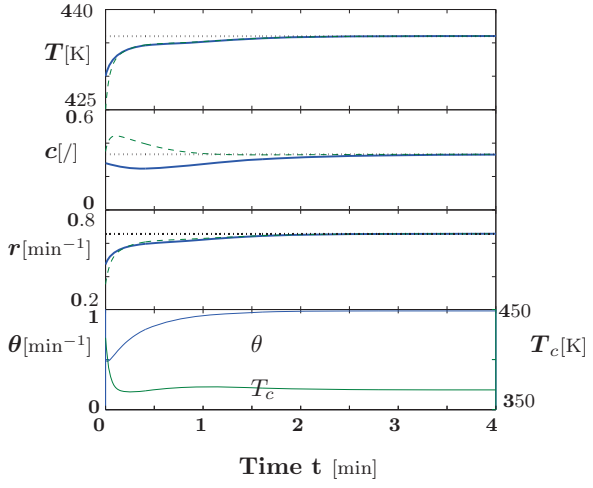

Fig. 2. Closed-loop nominal behavior with nonlinear OF controller: input and response (—) , estimate (− −), and set point (· · ·).

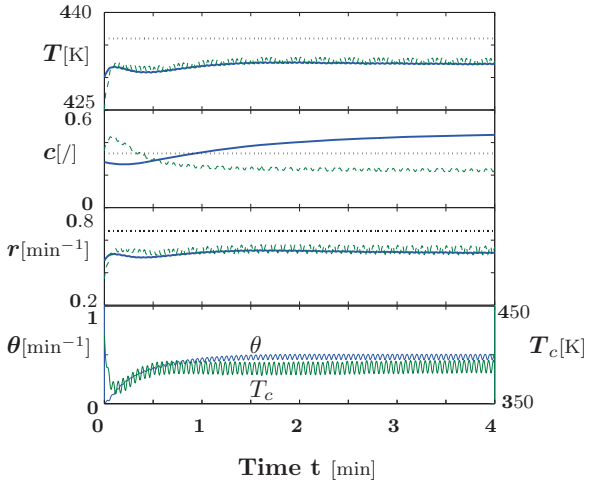

Fig. 3. Closed-loop robust behavior with nonlinear OF controller: input and response (—) , estimate (− −), and set point (· · ·).

5.3 Robust behavior with OF control

To test the robustness of the OF controller, the reactor and the estimator initial states were deviated from the nominal open-loop unstable and maximum reaction rate steady-state, and subjected to the oscillatory feed concentration and temperature inputs

$$c_e = 0.99 + 0.01\cos(4\pi t), \quad T_e = 370 + 2\sin(4\pi t)$$

5.4 Concluding Remarks

In agreement with the theoretically drawn methodology, the proposed passive-dissipative OF controller: (i) recovers rather well the behavior of its exact model-based nonlinear SF counterpart, with optimality-based robustness and control non-wastefulness, and (ii) exhibits P-(robust and non local) stability with respect to model, and measurement

errors. The closed-loop behavior assessment through simulations made quantitative the P-stability features (like transient response speed, overshoot, high frequencies oscillatory components, and asymptotic response offsets), and verified the effectiveness of the gain tuning scheme obtained from the P-stability characterization.

6. CONCLUSIONS

A robust OF control design methodology for continuous reactors with temperature measurements has been presented. Structural (relative degree and global detectability) solvability conditions were identified and exploited to design a nonlinear dynamic dissipative-passive OF controller. The interlaced estimator-control design led to a robust OF control scheme with: (i) a systematic construction procedure, and (ii) a rigorous closed-loop (nonlinear-nonlocal) P-stability criterion, (iii) simple tuning guidelines, and (iv) behavior recovery, up to estimator convergence, of the exact model-based FF-SF nonlinear control. A Langmuir Hinshelwood kinetics (carbon monoxide oxidation) in an open-loop unstable reactor at maximum reaction rate was considered as a representative case example with numerical simulations.

ACKNOWLEDGEMENTS

This work has been supported by DGAPA-UNAM, Project IN112207-3, and CONACyT research grant (Design and Control of Batch Processes) Project 51244. A. Schaum and J. Díaz-Salgado thank CEP-UNAM and CONACyT for financial support.

REFERENCES

Alvarez, J., Alvarez, J., and Suarez, R. (1991). Nonlinear bounded control for a class of continuous agitated tank reactors. *Chem. Eng. Sci.*, 46(12), 3235–3249.

Angeli, D., Ingalls, B., Sontag, E., and Wang, Y. (2004). An output feedback separation principle for input-output and integral-input-to-state stability. *SIAM J. Contr. Optim.*, 43 (1), 256–276.

Antonelli, R. and Astolfi, A. (2003). Continuous stirred tank reactors: easy to stabilise? *Automatica*, 39(10), 1817–1827.

Baratti, R., Alvarez, J., and Morbidelli, M. (1993). Design and experimental identification of nonlinear chemical reactor estimator. *Chem. Eng. Sci.*, 48 (14), 2573–2585.

Castellanos-Sahagun, E. and Alvarez, J. (2006). Synthesis of two-point linear controllers for binary distillation columns. *Chem. Eng. Comm.*, 193, 206–232.

Diaz-Salgado, J., Schaum, A., Moreno, J., and Alvarez, J. (2007). Interlaced estimator-control design for continuous exothermic reactors with non-monotonic kinetics. In *Eighth International IFAC DYCOPS, Cancun, Mexico.*

Eaton, J. and Rawlings, J. (1990). Feedback control of chemical processes using on-line optimization techniques. *Comp. & chemical eng.*, 14(4-5), 469–479.

Freeman, R. and Kokotovic, P. (1996). *Robust Nonlinear Control Design: State-Space and Lyapunov Techniques.* Birkhäuser, Boston.

Gonzalez, P. and Alvarez, J. (2005). Combined pi-inventory control of solution homopolymerization reactors. *Ind. Eng. Chem. Res. J.*, 7147–7163.

Khalil, H. (2002). *Nonlinear Systems (Third Edition).* Prentice Hall, Upper Saddle River, New Jersey.

Moreno, J. (2005). Approximate observer error linearization by dissipativity methods. *Control and Observer Design for Nonlinear Finite and Infinite Dimensional Systems, Springer LNCIS*, 35–51.

Moreno, J. (2006). A separation property of dissipative observers for nonlinear systems. In *45th IEEE Conference on Decision and Control, San Diego, CA, USA*, 1647 – 1652.

Schaum, A., Moreno, J., Alvarez, J., and Diaz-Salgado, J. (2008). Dissipativity-based observer and feedback control design for a class of chemical reactors. *Journal of Process Control*, 18(9), 896 905.

Sepulchre, R., Jankovic, M., and Kokotovic, P. (1997). *Constructive Nonlinear Control.* Springer-Verlag, London.

Shinskey, F. (1988). *Process Control Systems 3rd. Edt.* McGraw-Hill, New York.

Viel, F. and Jadot, G. (1997). Robust feedback stabilization of chemical reactors. *IEEE Trans. Autom. Cont.*, 42(4), 473 – 481.

Willems, J. (1972). Dissipative dynamical systems: Part i - general theory, part ii - linear systems with quadratic supply rates. *Archive for Rational Mechanics and Analysis*, 45, 321–393.

Appendix A. PROOF OF PROPOSITION 4.1

Recall the control (V) (13) and observer ($\hat{V}$) (20) storages, set the composed storage W, and write the corresponding dissipation ($\dot{W}$) along the closed-loop reactor motion:

$$W = V + \hat{V}, \quad \dot{W} = -z^T Q z, z = [e_c, \epsilon_c, e_T, \epsilon_T],$$

$$Q = \begin{bmatrix} k_c & -\iota_c(\theta_r+\varphi) & 0 & \kappa_r\varphi(c_e-c)/[2(c_e-\hat{c})] \\ \star & \theta_r+\varphi & (\beta\varphi)/2 & [\kappa_c-(\kappa_r+\beta)\varphi]/2 \\ \star & \star & k_T & 2\iota_1+\iota_r \\ \star & \star & \star & \kappa_T+\iota_r \end{bmatrix}$$

$$\iota_c(k_c) = \frac{(\theta^* - [k_c-\varphi](c_e-c))^2}{4(c_e-\hat{c})(\theta_r+\varphi)}, \iota_r(\kappa_r) = \mu+\eta+\kappa_r\beta\varphi$$

$$\iota_T(k_c) = \frac{k_c\beta^2\varphi^2}{4(\theta_r+\varphi)(k_c-\iota_c(k_c))}, \iota_1 = \frac{(k_T-\kappa_r\beta\varphi)^2}{4k_T} - \iota_r$$

$$\iota_2 = \frac{\varpi(k_c,\kappa_c,\kappa_r}{(\theta_r+\varphi)} - \iota_r, \quad \iota_\tau = \max\{\iota_1,\iota_2\},$$

and ϖ is a class-$\mathcal{K}$ function of its arguments. The enforcement of the positive defintness property in each of the four leading principal minors $(M_1,\ldots,M_4)$, yields the conditions stated in Proposition 4.1, or equivalently the positive definitness of Q implying the closed-loop P-stability property. QED

Modeling and Simulation

Oral Session

Non-linear model order reduction using input to state Hammerstein structures

O. Naeem, * **A.E.M. Huesman,** ** **O.H. Bosgra.** ***

* *Delft Center for Systems & Control (DCSC), Technische Universiteit Delft, 2628 CD, Delft, the Netherlands (e-mail: O.Naeem@tudelft.nl)*
** *(e-mail: a.e.m.huesman@tudelft.nl)*
*** *(e-mail: o.h.bosgra@tudelft.nl)*

Abstract: In this paper, the focus will be on approximating original model of process systems using block-structured models. The context of model reduction is to improve the computational efficiency (simulation time). The reduced order models are important for online applications. Hammerstein structures have been used to approximate a mathematical non-linear model of a process. Input-Output Hammerstein structure can be defined as classical Hammerstein model but the technique is extended here to Input-State Hammerstein structure. It is shown that Input-State Hammerstein structure can be derived from Taylor series. Approximation accuracy has been improved by approximation for second term. The approximated Input-state Hammerstein block structure model gives good approximation of the original non-linear system. Over an operating domain of a process, the Input-State Hammerstein structure provides opportunities for reducing the computational load by order reduction of states and Jacobians. The methodology has been applied to a high purity distillation benchmark and satisfactory results are obtained as far as approximation is concerned. Reduction in states and Jacobian size by 70% is attained.

Keywords: Nonlinear model order reduction, Hammerstein, Taylor series, high purity distillation column

1. INTRODUCTION

First order principle models (rigorous models) are stiff and large, thus are computationally inefficient. Since the (rigorous) NL models are not always exact match of real processes and there is mismatch at some point between the two, reduced models can be very useful if they match the rigorous NL model over a certain operation window. Advantage of reduced mathematical models for NL processes include low computational effort, better approximation of process within the operating window and beneficial for the real-time applications (e.g; control and optimization purposes).

The rigorous models available for large industrial processes can be characterized as a set of differential and algebraic equations (DAE). DAE class of models is capable to express the majority of processes. Thus the methodology to achieve a reduced model should be capable of handling DAE models. The transformation from DAE to ordinary differential equation (ODE) format is regarded as a major model reduction step; but it is not possible generally. A methodology which involves this step is advantageous for the process models of DAE class.

There is not much literature available on model reductions when it comes to model reduction in context of computational load. Balasubramhanya and Doyle (2000) developed a reduced order model of batch distillation column using travelling waves. The closed loop simulation of this reduced model was six times faster than original model in closed loop. Aling et al. (1997) used POD to get reduced model for rapid thermal processing system. Reduction of computational load by a factor ten was reported. Hahn and Edgar (2000) elaborated on model reduction by balancing empirical Gramians and showed model order reduction but reduction in computational effort and time was limited. Perregaard (1993) simplified and reduced chemical processes models for simulation and optimization purposes. He achieved the reduction by simplifying the calculation of algebraic equations, which resulted in computational effort reduction. Gani et al. (1990) replaced the true (symbolic) Jacobian by approximated Jacobian (from local models). They reported the reduction of computational times by factor of $20 \sim 60$. Empirical modelling has been one of the major approaches for achieving low computational complexity (which allows fast simulations). Ling and Rivera (1998) used a Hammerstein structure for model reduction, but did not report reduction in computational load (on polymerization benchmark). Berg (2005) reported that if computational load has to be reduced, not only model order reduction is to be targeted but the complexity (and stiffness) of reduced model has to be lower; as Gani (Gani et al. (1990)) achieved the computational load reduction by reducing the complexity (discussed above). Block structure models have been used for the identification purposes (see Eskinat et al. (1991); Billings and Fakhouri (1977), Norquay et al. (1999), Harnischmacher and Marquardt (2007) etc.). Though block structure models have been used for the identification purposes, but the block structure models have not been used for the model reduction purposes.

As the literature review shows, there is no reduction technique available directly related to reduction of computational load. Each model reduction technique has its specific purposes which is completely understandable. Not every model reduction methodology works for every process, but it is desired to have a model reduction methodology which is generic and applicable to wide class of processes (represented by DAE class of models). Moreover the literature review indicates that there is not much research material available on model reduction subject; whatever is available, mostly addresses the model order reduction and it does not focuses the reduction in complexity of reduced model (which is major component for computational load). Not many model reduction methodologies have addressed the problem of simplification of reduced model. The field is open for research to achieve reduced models, which are simple and reduced order to achieve computational load reduction.

Block structure models have an advantage over other model approximation methodologies; the structure of approximation model gives insight to the complexity of the process and breaks down the complexity of the NL process. This give handles to feel for the complexity and reduce it. Use of block structure enhances the chances to get a reduced model, which is uncomplicated and is computationally efficient.

In this paper, a block structure (Hammerstein) has been used to achieve reduced model for nonlinear chemical process. In the subsequent section, Hammerstein structure is discussed. In section 3, reduction methodology is discussed. In section 4, implementation on high purity distillation column and its results are considered. The last section 5 concludes the paper with key points and future work.

2. HAMMERSTEIN STRUCTURE

There are different block structures which are known for model reduction (and empirical modeling); Wiener, Hammerstein etc. Chen (1995) has introduced and discussed a wide variety of such block structures. Wiener and Hammerstein block structure models are most widely used structures in literature for the representation of nonlinear physical processes and will be shortly discussed here. Wiener models have limitations (specifically for chemical processes) which give edge to Hammerstein structure for identification purposes (Harnischmacher and Marquardt (2007)). Wiener models not only limit the nonlinearity measure to be approximated, but they also increase the complexity involved in identifying or approximating the process. Harnischmacher (2007) investigated that Wiener models restrict the dynamic NL behavior that can be approximated and identified in comparison to Hammerstein structure.

Hammerstein structure is used for the approximation of NL processes in this study. The methodology is extended further to I/S Hammerstein structure to improve the approximation.

2.1 Classical (Input-Output I/O) Hammerstein structure

Classical Hammerstein model can be seen as nonlinear static gain, followed by linear dynamics.

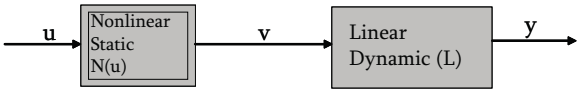

Fig. 1. Classical Hammerstein structure (input-output)

The classical I/O Hammerstein structure shown in figure 1 represents the continuous system/process. A procedure to get Hammerstein structure approximation for a process is to represent the nonlinear static block by interpolation table (lookup table), neural network or spline scheduling (the steady states) and represent linear dynamic block by linear time invariant (LTI) model. The intermediate variable v is a low dimensional vector. Mathematically, classical Hammerstein structure is given as;

$$\begin{aligned} \dot{x} &= A\ x + g(\mathbf{u}) \\ y &= C\ x \end{aligned} \tag{1}$$

where, A is the state matrix, C is the output matrix which can be identified from process data or can be obtained by linearizing the nonlinear system at 'nominal operating point'. Nominal operating point is an operating point within the operating domain, chosen by the input design (discussed in later section 3.1.

The input-output (I/O) Hammerstein model shown can be modified to Input-state (I/S) Hammerstein model under few assumptions (Naeem et al. (2008)). I/S Hammerstein model can be derived from expansion of Taylor series (shown in section 2.3)

2.2 Taylor Series

The Taylor expansion of a function $f(x)$ that is differentiable in the neighborhood of real or complex number 'a' is mathematically given as:

$$f(x) = f(a) + \frac{1}{1!}\left.\frac{\partial f}{\partial x}\right|_a (x-a) + \frac{1}{2!}\left.\frac{\partial f^2}{\partial^2 x}\right|_a (x-a)^2 + \dots \tag{2}$$

Typically process models are of DAE format and transformation from DAE to ODE is a model reduction step (for a large scale process). The ODE can be approximated by I/S Hammerstein structure.

Given an ODE $\dot{x} = f(x, y)$, which is modeled in an environment (gPROMS, MATLAB, SIMULINK), the first order Taylor expansion around point (x^*, u^*) is given mathematically as:

$$\dot{x} = f(x,u) = f(x^*,u^*) + J_x|_{x^*,u^*}\,(x - x^*) + J_u|_{x^*,u^*}\,(u - u^*) + \dots \tag{3}$$

Equation 3 evaluates the function $f(x, u)$ given linearization at $f(x^*, u^*)$. Figure 2 shows the equation 3 in block diagram.

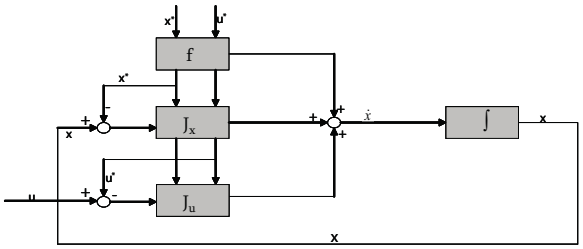

Fig. 2. Block structure for Taylor series of $\dot{x} = f(x, u)$

2.3 Taylor Series expansion

Taylor series illustrated in preceding section can be extended to I/S Hammerstein structure (at steady-state point (x^*, u^*)) under following assumptions:

a. It is assumed, within the operating domain that every u^* leads the system finally to steady-state 'x_{ss}' which means a stable process is considered. Moreover, it is assumed that steady-state is calculated by u. Mathematically, $x_{ss} = g(\mathbf{u})$. Setting $x^* = x_{ss}$ results in output of the (constant) block (f) zero (the system is being evaluated at steady-state x^*).
b. Input u is chosen freely, but is chosen such that it is equal to the input at steady-state, mathematically; $u = u^*$; this implies that gradient input to block $(J(u))$ becomes zero; (since $u - u^* = 0$).

Under above assumptions, adding $g(\mathbf{u})$, removing blocks f and J_u and rearranging the block structure in figure 2, we get the block structure shown in figure 3. Observing this structure it can be considered an *I/S Hammerstein structure*; it has two blocks, a NL steady-state mapping block, followed by linear dynamic block.

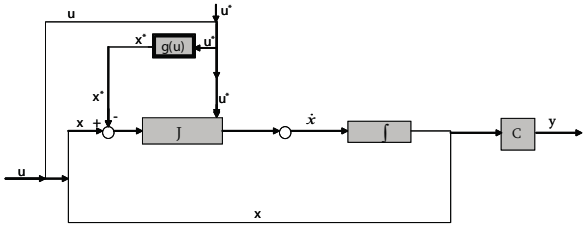

Fig. 3. Taylor series extension to I/S Hammerstein structure

For a linear system, state-space model can be mathematically given as below:

$$\dot{x} = A\ x + B\ u \qquad (4)$$
$$y = C\ x$$

For the state-space linear model (in equation 4), I/S Hammerstein structure can be shown as figure 4.

The block structure shown in figure 4 can be extended for NL processes, shown in figure 5. I/S Hammerstein structure shown in figure 5 is similar to the structure derived by Taylor series expansion (shown in figure 3).

The block structure shown in figure 3 and figure 5 is I/S Hammerstein block structure, with separated NL statics(where NL static mapping takes place), followed by linear dynamic block. The dynamic linear block is driven by difference between the steady state 'x_{ss}' and current state 'x'.

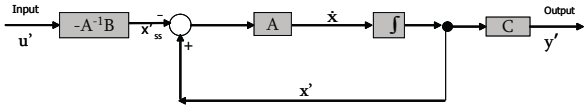

Fig. 4. Input-state Hammerstein structure for linear system

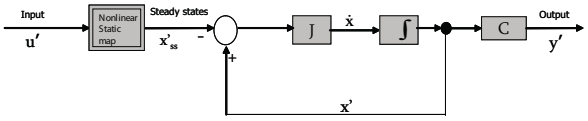

Fig. 5. Input-state Hammerstein structure for non-linear system

Mathematically, for NL case, I/S Hammerstein structure can be given as:

$$\dot{x} = J\ (x - x_{ss}) + g(\mathbf{u}) \qquad (5)$$
$$y = C\ x$$

where, J = *Jacobian*; C = *output state matrix*; y = *output*; x_{ss}= $g(\mathbf{u})$ *is steady-state, scheduling (implemented by lookup table).*

The I/S Hammerstein block structure shown in figures 3 and 5 is used for the approximation of NL processes. The accuracy of approximation of I/S Hammerstein structure is improved by estimating Jacobian online. Jacobian is estimated (and updated) based on information of Jacobian basis J_b, reduced state z and input u. Jacobian basis J_b are calculated by SVD analysis of Jacobian data. Jacobian data is collected by taking snapshots of Jacobians over the operating domain ('*input design*') by exciting the NL system with inputs to acquire most information in operating envelope. Similarly the reduced order states z is calculated by transformation matrix (U_1), obtained by SVD analysis of steady-state and dynamic state (snapshot) data, taken over the operating domain.

First order I/S Hammerstein approximation structure (with updated Jacobian), is shown in figure 6. As figure shows,the Jacobian estimation is based on (reduced) current state information (z).

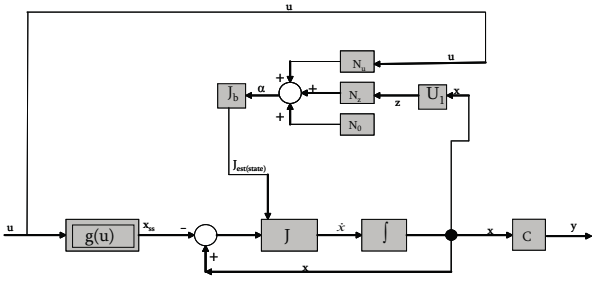

Fig. 6. First order I/S Hammerstein approximation structure

In the figure 6, J = *Jacobian* ; U_1 = *transformation matrix to transform full state x to reduced state z* ; J_b =

Jacobian basis obtained by SVD analysis of snapshots of Jacobians (within operating domain) ; N_0, N_1, N_2 = *the parameters relating Jacobian with reduced-state z, input u and constant.*

It is to be noted, I/S Hammerstein can be derived by extending Taylor expansion as proved above. This is not possible for Wiener structure.

2.4 Accuracy improvement by higher order approximation

First order approximation of NL system by expansion of Taylor series to I/S Hammerstein structure is shown in above section. The approximation accuracy can be improved with higher order terms.

The Taylor series is extended to second order. Taylor series around (steady-state) point (x^*, u^*) is given as:

$$f(x,u) = f(x^*,u^*) + \left.\frac{\partial f}{\partial x}\right|_{x^*,u^*} (x - x^*) + \frac{1}{2!}\left.\frac{\partial f^2}{\partial^2 x}\right|_{x^*,u^*} (x - x^*)^2 \tag{6}$$

Similarly, Taylor series expansion around any point (x, u) is given as below:

$$f(x^*,u^*) = f(x,u) + \left.\frac{\partial f}{\partial x}\right|_{x,u} (x^* - x) + \frac{1}{2!}\left.\frac{\partial f^2}{\partial^2 x}\right|_{x,u} (x^* - x)^2 \tag{7}$$

Equation 6 and equation 7 are the Taylor series expansions at two points (x^* and x), given by Taylor series extension to second order. Rearranging equation 7, we get;

$$f(x,u) = f(x^*,u^*) + \left.\frac{\partial f}{\partial x}\right|_{x,u} (x^* - x) + \frac{1}{2!}\left.\frac{\partial f^2}{\partial^2 x}\right|_{x,u} (x^* - x)^2 \tag{8}$$

Adding equation 6 and equation 8 (while higher order terms are canceled, assuming $\frac{1}{2!}\left.\frac{\partial f^2}{\partial^2 x}\right|_{x,u} = \frac{1}{2!}\left.\frac{\partial f^2}{\partial^2 x}\right|_{x^*,u^*}$), we get;

$$f(x,u) = f(x^*,u^*) + \frac{1}{2}\left[\left.\frac{\partial f}{\partial x}\right|_{x^*,u^*} + \left.\frac{\partial f}{\partial x}\right|_{x,u}\right](x - x^*) \tag{9}$$

Equation 9 is the approximation of $f(x, u)$ using higher order terms. There are two Jacobian evaluations involved in this approach, an approximation using knowledge at steady-state (x^*) and approximation using current state (x) knowledge. The block structure representation of this approximation is shown in figure 7.

3. REDUCED ORDER HAMMERSTEIN STRUCTURE

Approximation block structure shown in figure 7 is full state model. Since it is a prerequisite for the approximation block structure, to be valid within certain operating domain.

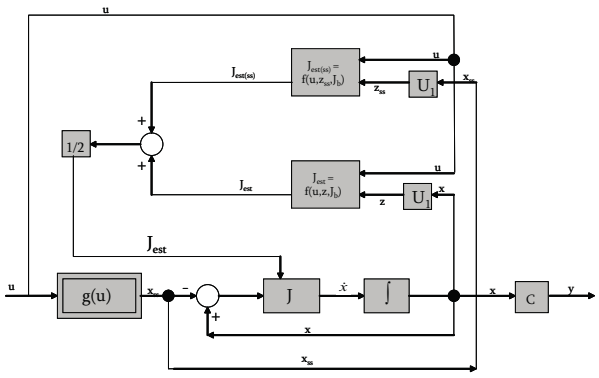

Fig. 7. Approximation model (I/S Hammerstein); Higher order approximation)

3.1 Operating domain/Input Design

Within defined domain, inputs are designed with the purpose to define an input trajectory that travels through complete domain. The process is known as '*input design*'. As the name indicates, it is the process of designing inputs based on constraints on input or output (depending upon a process). In summary, the operating domain is a region, where the approximated model is supposed to be valid, once identified (based on data from the physical process) and input design is the procedure, which defines the boundaries of this operating domain.

The steady-state and dynamic state data is obtained by taking snapshots over the operating domain. Similarly, Jacobian data is collected by taking the snapshots of Jacobians over the operating domain. Jacobian basis J_b are computed by SVD analysis of Jacobian data.

The I/S Hammerstein block structure gives scope to get the reduced order structure by;

i. Reduction in state size.
ii. Reduction in Jacobian size.

i. Reduction in state size.
The singular value analysis on data of states indicates that there is a low dimensional space, such that low order state (z) can represent the whole operating domain. The state reduction is performed by transformation matrix. The transformation matrix U_1 (to obtain reduced state 'z') is obtained by SVD analysis of data over the operating domain. Reduced states are back-transformed to full state by back transformation matrix $\hat{U}_1$. The block structure of the reduced approximation model is shown in figure 8. The Jacobian reduction takes place online (in the block $U_1 * J * U_1^T$).

ii. Reduction in Jacobian size.
The scheme in figure 7 shows that Jacobian estimation takes place using Jacobian basis J_b, state z and input u information. The estimated Jacobian J_{est} is full order Jacobian. There is possibility to obtain reduced size Jacobian, by using reduced order Jacobian basis ($J_{b_{red}}$) and reduced state (z). With reduced basis $J_{b_{red}}$ and reduced states z, estimated Jacobians are also reduced sized and the block structure is a reduced order I/S

Hammersteins approximation model. The block structure is shown in figure 9.

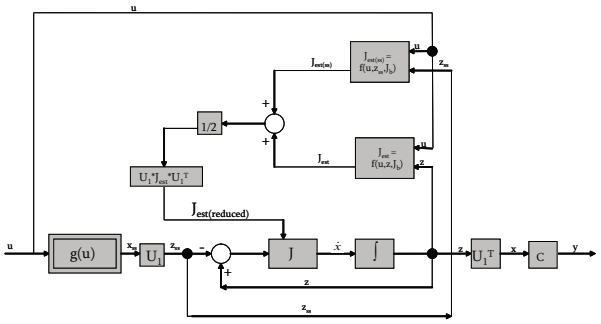

Fig. 8. Reduced order approximation model (I/S Hammerstein); Higher order approximation

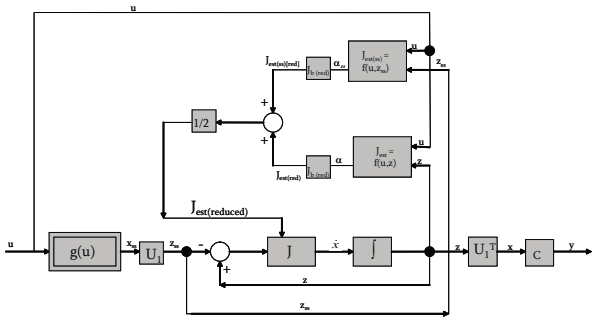

Fig. 9. Approximation block structure with reduced Jacobian and state size

4. APPLICATION TO HIGH PURITY DISTILLATION COLUMN

The approximation block structure and reduced block structure model has been applied to the benchmark. A benchmark is high purity distillation column, and its properties will be discussed in subsequent sections. But before the methodology is implemented on benchmark, a prerequisite for the methodology is to define the operating domain, within which the approximation/reduced model is valid. Input design, discussed in section 3.1 is designed for distillation column; the operating domain has been finalized by constraint in output purity. A set of input variables (reflux (L) and vapour boilup (V)) is chosen, for which output variables are observed. The product purity for output variables sets the boundary for operating domain.

High purity distillation column

A high purity distillation column is used as test case, on which the approximated and reduced model estimation is applied. The distillation column has following properties; The column has 72 trays, a total condenser and partial reboiler. It is a nonlinear system. The thermodynamics of the column are governed by constant relative volatility. The relative volatility for this specific system is 1.33. Pressure is assumed to be constant. Vapour holdups are considered negligible and liquid holdups are considered

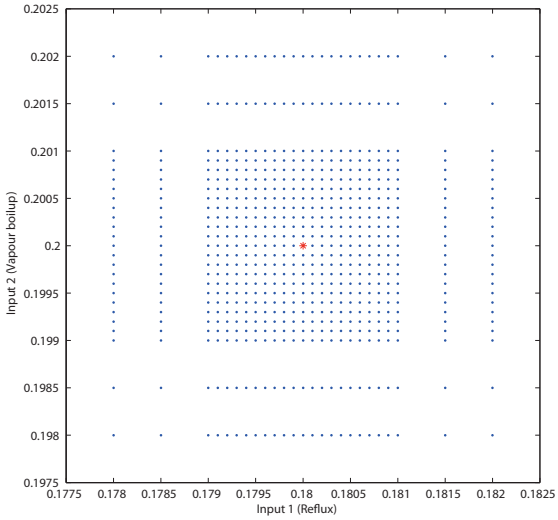

Fig. 10. Figure of operating domain '*input design*'

to be constant. Moreover, the column is assumed to be working with equimolal flow (which results in eliminating energy balances). The distillation benchmark model has been explained in detail by Lévine and Rouchon (1991).

The benchmark is modelled in gPROMS while the approximation model is modelled in MATLAB and SIMULINK. The approximation technique is implemented on the benchmark. The operating domain is finalized (input design) shown in figure 10. The static part consists of lookup table which interpolates the steady-states. The steady-states are fed into the dynamic part. The difference between current state and steady-state is fed to Jacobian block, which is estimated based on state and steady-state data. This represents the linear block as bilinear system.

Two types of changes

There are two types of input signals tested for the validation of approximated (and reduced) model.

a) 'Separation index' (SI) is change in distillation, when both the input variables (reflux rate (L) and vapour boilup (V)) are given *same* steps at the same time, or the rate of flow of distillate D and bottom B does not change.
b) 'Effective Cut Point' (ECP) is change in distillation, when one input variable (reflux rate (L) or vapour boilup (V)) is kept constant and step change is given to the other input variable. This change is known to be highly non-linear for high purity distillation column (in process industry).

Figure 11 show the step in both inputs at the same time (separation index). The approximation model structure (in full state) and reduced order model structure approximate the behavior very well. The mismatch between the approximations and original is cause by offset form lookup table (NL block of approximated model).

Figure 12 show the result comparison of original, full order approximated model and reduced order model, when step in vapour boilup (V) input (effective cut point) is

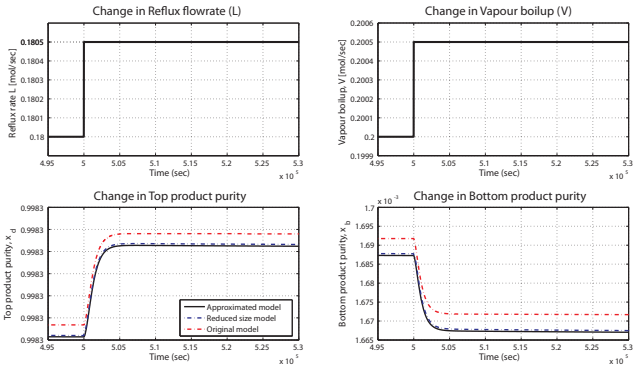

Fig. 11. Results for comparison of SI change between original, approximation '*full*' and '*reduced*' model

applied. The approximation model structure (in full state) and reduced order structure approximates the behavior satisfactorily. There is a very small mismatch in dynamics between the approximation model and original. The offset is acceptable (and sufficiently accurate) for this application.

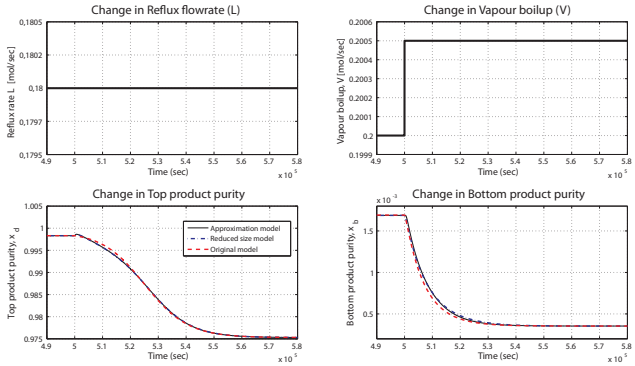

Fig. 12. Results for comparison of ECP change between original approximation '*full*' and '*reduced*' model

5. CONCLUSIONS & FUTURE WORK

In this paper, it is shown that Input-State Hammerstein structure can be derived from a Taylor expansion. The approximation model's accuracy can be improved by including higher order terms. The approximation results were shown for a high purity distillation benchmark are acceptable for the kind of application. Order reduction of 70% is possible using the methodology with satisfactory results (high accuracy).

Work on the following tasks is done presently or is to be considered in future:

i) The computational load reduction for the benchmark example (high purity distillation column) is to be investigated. The computational load and simulation time reduction has to be compared with original NL model.

ii) It is planned to extend the methodology to industrial case. The industrial models make use of dynamic link library (dll) files (as foreign process) to compute different task (such as thermodynamic properties). Such foreign processes buildup overhead costs,resulting in increased computational load. It is anticipated, that transformation of large DAE model to ODE structure will reduce the computational effort (and simulation time), since the algebraic computations are vanished in ODE structure, replaced by NL mapping.

ACKNOWLEDGEMENTS

This work has been supported by the European union within the Marie-Curie Training Network PROMATCH under the grant number MRTN-CT-2004-512441.

REFERENCES

Aling, H., Banerjee, S., Bangia, A., Cole, V., Ebert, J., Emami-Naeini, A., and Jensen, K. (1997). Nonlinear model reduction for simulation and control of rapid thermal processing. *In Proceedings of the American Control Conference*, 2233–2238.

Balasubramhanya, L. and Doyle, F. (2000). Nonlinear model-based control of a batch reactive distillation column. *Journal of Process Control*, 10, 209–218.

Berg, J.V.D. (2005). *Model reduction for dynamic real-time optimization of chemical processes*. OPTIMA, P.O. Box 84115, 3009 CC Rotterdam, The Netherlands.

Billings, S. and Fakhouri, S. (1977). Identification of nonlinear systems- a survey. *IEEE Proc. Pt.D*, 127–272.

Chen, H. (1995). Modelling and identification of parallel nonlinear systems: Structural classification and parameter estimation methods. *P.IEEE*, 83(1), 39–66.

Eskinat, E., Johnson, S., and Luyben, W.L. (1991). Use of hammerstein models in identification of nonlinear systems. *AlChE Journal*, 37, 255–278.

Gani, R., Perregaard, J., and Johansen, H. (1990). Simulation strategies for design and analysis of complex chemical processes. *Trans. IChemE.*, 68 (Part A), 407–417.

Hahn, J. and Edgar, T. (2000). Reduction of nonlinear models using balancing of emperical gramians and galerkin projections. *In Proceedings of the American Control Conference*, 2864–2868.

Harnischmacher, G. and Marquardt, W. (2007). A multivariate hammerstein model for processes with input directionality. *Journal of Process Control*, 17, 539–550.

Harnischmacher, G. (2007). *Block structured modeling for control*. VDI Verlag GmbH, Dusseldorf, Germany.

Lévine, J. and Rouchon, P. (1991). Quality control of binary distillation columns via nonlinear aggregated models. *Chemical Engineering Science*, 27(3), 463–480.

Ling, W. and Rivera, D. (1998). Control relevant model reduction of voltera series models. *Journal of Process Control*, 8(2), 78–88.

Naeem, O., Huesman, A., and Bosgra, O. (2008). Nonlinear model order reduction using input to state hammerstein structures. *In the proceedings of REDUCIT Symposium*.

Norquay, S., Palazoglu, A., and Romangnoli, J. (1999). Application of wiener model predictive control (wmpc) to an industrial c2-splitter. *J. Proc. Control*, 9(6), 461–473.

Perregaard, J. (1993). Model simplification and reduction for simulation and optimization of chemical processes. *Computers and Chemical Engineering*, 17(5/6), 465–483.

A Clean-Coal Control Technology Application Study: Modelling and Control Issues for a Coal Gasifier

S. Bittanti* L. Calloni S. Canevese** A. De Marco* V. Prandoni****

** Dipartimento di Elettronica e Informazione (DEI), Politecnico di Milano, Piazza Leonardo Da Vinci 32, 20133, Milan, Italy (e-mail: sergio.bittanti@polimi.it)*
*** CESI RICERCA, Via Rubattino 54, 20134, Milan, Italy (e-mail: calloni@cesiricerca.it, canevese@cesiricerca.it, prandoni@cesiricerca.it)*

Abstract: The dynamic behaviour of a coal slurry gasifier in an Integrated Gasification Combined Cycle is modelled by means of mass, energy and momentum conservation equations as well as reaction kinetics descriptions. The main phenomena taken into consideration are (i) slurry drying and devolatilisation, (ii) char and volatile gas combustion, char gasification and water-gas shift reaction, and (iii) syngas cooling. The proposed 0-dimensional description is sufficient to capture process dynamics and it is a useful starting point for control design and verification. In particular, basic control strategies are discussed. Both model and control implementation is carried out in the Matlab-Simulink environment. Simulation results are shown to support model reliability and control effectiveness.

Keywords: Process modelling, Process automation, Process control, Process simulators, Power generation, Coal gasification.

1. INTRODUCTION

As it is well known, nowadays the scenario in electric energy production is characterised by a constant increase in demand, a decrease in fossil fuel reserves, more and more demanding restrictions on pollutant levels. Feasible solutions can be increasing efficiency and reducing pollutant emissions in thermoelectric power plants, and contributing to the development of the so called "green energy". Coal can play a major role, especially because of the important amount of its proven reserves worldwide; a main challenge for research is then to develop high-efficiency coal-based energy production systems with near zero emissions. In this paper, reference is made to a 70 MWe coal-fed Integrated Gasification Combined Cycle (IGCC) pilot plant (Fantini et al., 2007), allowing flexible production of electric energy and hydrogen. For the design, work is in progress to build up a simulator of the whole process, in order to obtain reliable predictions of its dynamic behaviour in different operating conditions and to study the operating manoeuvres. Dynamical models of the shift reactor and of the Pressure Swing Adsorption (PSA) unit have already been studied ((Bittanti et al., 2008), (Canevese et al., 2007)). Here, we focus on the gasifier, working out a first-principle model useful for control design.

In Section 2 of this paper, the gasification process is analysed, and its main phases are represented by a dynamical model, based on a thermo-fluid-dynamical and a kinetic-chemical description; such model has been developed in full detail starting from the basic conservation equations and the constitutive equations (including the kinetic equation of char gasification); here, of course, we will present only a partial outline of this model. Section 3 deals with control problems. Section 4 reports some simulation results highlighting control effectiveness. Finally, Section 5 reports some conclusions and hints to future work.

2. PROCESS ANALYSIS

The gasifier under study is an entrained-flow gasifier working at about 65 bar and 1650-1700 K. It is formed essentially by two coaxial cylinders: in the inner one, the gasification process occurs, while the outer one is employed for a first syngas cooling. As illustrated in Fig. 1, the reactor is fed with slurry (pulverized coal mixed with water which can be handled like a liquid fuel) and highly pure oxygen and it produces a gaseous mixture whose main components are CO, CO_2, H_2, N_2, H_2O, and pollutants (COS, H_2S, and dusts). We sketch the overall process of gasification and cooling as composed of the following phases (Smoot and Smith, 1985):

- *drying and devolatilisation*:

slurry can be described as coal powder where each particle is coated with a water film; when it is pumped into the inner cylinder, the high temperature that it meets makes water evaporate, thus yielding dry char, and then makes volatile gases (such as N_2, H_2S, H_2O and several kinds of hydrocarbons, among which CH_4) leave char;

- *oxidation and gasification*:

oxygen burns both the volatile gases and the char, according to the reactions

$$CH_4 + 2O_2 \rightarrow CO_2 + 2H_2O \quad (volatile\ combustion), \tag{1}$$

$$C + \left(1/\phi\right)O_2 \rightarrow 2\left(1 - 1/\phi\right)CO + \left(2/\phi - 1\right)CO_2, \quad 1 \le \phi \le 2 \quad (char\ combustion) \tag{2}$$

(the mechanism factor ϕ indicating whether CO or CO_2 is transported from the particle surface is calculated according to (Wen and Dutta, 1979), (van der Looij, 1988)). The related temperature increase sustains the drying and volatile emission process and the endothermic reactions

$$C + H_2O \rightarrow CO + H_2 \quad (gasification)\,, \tag{3}$$

$$C + CO_2 \rightarrow 2CO \quad (char - CO_2\ reduction)\,, \tag{4}$$

$$CO + H_2O \rightleftarrows CO_2 + H_2 \quad (water - gas\ shift)\,; \tag{5}$$

- *cooling*:

the thus obtained hot syngas (its temperature is around 1760 K) is sent to the bottom of the reactor, where contact with relatively cold liquid water causes a thermal shock which decreases the gas temperature abruptly and stops all reactions still going on; besides, unburned char residuals and char ashes solidify, fall down and are extracted as slag. After bubbling into water, the syngas is pushed by pressure difference (65 bar Vs 62 bar in the considered case) to the outer cylinder, where it is further cooled by a counter-current water spray. Spray temperature and flow rate can be used to control the outlet fluid mixture temperature and humidity. ■

Actually, the first two phases occur in the same region (gasification region). A detailed 3-D description of the phenomena taking place here is suggested, e.g., in (Chen, et al., 2000). Simpler models can be worked out by assuming that both temperature and pressure are uniform in the whole region (0-D assumption). This assumption, motivated by the intense recirculation of gases and adopted also in (Schoen, 1993) for a different type of gasifier, is adopted herein. The proposed model is able to capture the process fundamental dynamics with a low complexity degree, thus ensuring both clear physical insight and short simulation times, in view of the study of control strategies.

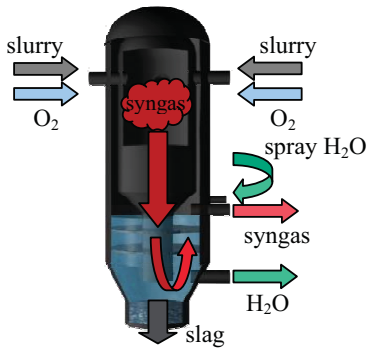

Fig. 1. The GE-Texaco gasifier: schematic view.

The following subsections report the conservation equations employed to model each phase and a reaction kinetic description for the second phase. Table 1 collects the main symbols employed.

Table 1. Nomenclature

Symbol	Description	Unit
c	Specific heat	kJ/(kg·K)
e	Relative energy	kJ/kg
f	Mass fraction	-
h	Relative enthalpy	kJ/kg
$j_k^{(r)}$	Component k stoichiometric coefficient in reaction r=1,..,5	-
p	Pressure	bar
w	Mass flow rate	kg/s
$\tilde{w}$	Molar flow rate	kmol/s
x	Molar fraction	-
A	Area	m^2
L	Length	m
M	Mass	kg
PM_k	Component k molecular weight	kg/kmol
Q	Thermal power	W
S_{ch}	Char active surface	m^2
T	Temperature	K
V	Volume	m^3
β	Mass exchange coefficient	kg/(N·s)
γ	Convective energy exchange coefficient	W/(K·m^2)
ρ	Density	kg/m^3
Ω	Equivalent perimeter	m
Subscripts		
c	Cooling region	
ch	Char	
d/u	Volume under/above the cooling liquid surface	
ev/vol	Resulting from evaporation/devolatilisation	
g/l	Gas/liquid phase	
$g\text{-}l$	Exchange between gas and liquid phases	
in/out	At the inlet/outlet of the region under study	
int/ext	Internal/external chamber	
sat	Saturation	
sh	Shift reaction	
sl	Slurry	
$surf$	Char surface	

2.1 Drying and Devolatilisation

The coal slurry injected into the gasifier forms a jet of length L_{ev} where the water evaporates heated by the hot gases. Then, after water evaporation, the volatile release takes place, due to further heating of the mass of dried coal.

The mass conservation equations for the liquid water and the dry char are respectively

$$\rho_{H_2O}\overline{A}_{H_2O}\dot{L}_{ev} = w_{sl}f_{H_2O,in} - w_{ev}\,, \tag{6}$$

$$\dot{M}_{dry} \equiv \frac{d(\rho_{dry}\overline{A}_{dry}L_{ev})}{dt} = w_{sl}(1 - f_{H_2O,in}) + \\ - M_{dry}u_j/L_{ev} + \rho_{dry}\overline{A}_{dry}\dot{L}_{ev}, \tag{7}$$

where $\overline{A}_{H_2O}$ is the evaporation average equivalent area for water and $\overline{A}_{dry}$ is the equivalent area for char,

$$w_{ev} = \beta_{g-l} L_{ev} \Omega_{ev} (p_{sat}(T_{ev}) - p_{H_2O,g}), \quad (8)$$

$L_{ev}\Omega_{ev}$ is the average evaporation surface and u_j is the particle average velocity in the drying region.

As to energy conservation, a unique average temperature T_{ev} can be adopted for the overall particle (water and char), so

$$\begin{aligned}(\rho_{H_2O}\overline{A}_{H_2O}c_{H_2O} + \rho_{dry}\overline{A}_{dry}c_{dry})[(T_{ev} - T_{sl})\dot{L}_{ev} + \\ +L_{ev}\dot{T}_{ev}] = Q_{ev} - w_{ev}\cdot(h_{g,sat}(T_{ev}) - h_{H_2O}(T_{sl})),\end{aligned} \quad (9)$$

$$Q_{ev} = \gamma_{g-l} L_{ev} \Omega_{ev} \cdot (T_g - T_{ev}). \quad (10)$$

Volatile emission is assumed to occur almost instantaneously after drying, since its dynamics are of the order of few tens of ms ((Thambimuthu and Whaley, 1987), (Kobayashi et al., 1977)); therefore, such dynamics, together with the related heating process, are neglected here. Evaporation is very fast as well, with dynamics of the order of a second at most (Thambimuthu and Whaley, 1987), so it is neglected in the simulations reported in Section 4.

2.2 Oxidation and Gasification

The mass conservation equation for the *k*-th gaseous component in the gasification volume can be written as

$$\begin{aligned}\dot{M}_k = w_{k,in} - w_{g,out} f_{k,out} + \sum_{r=2,3,4} \tilde{w}_{ch}^{(r)} PM_k j_k^{(r)} + \\ +\tilde{w}_{sh} PM_k j_k^{(5)} + \tilde{w}_{CH_4,vol} PM_k j_k^{(1)},\end{aligned} \quad (11)$$

where the component inlet flow rate is

$$w_{k,in} = \begin{cases} w_{ev}, & \text{for } k = H_2O \\ w_{k,vol}, & \text{for } k = CO_2, H_2S \\ 0, & \text{for } k = CO, H_2 \\ w_{N_2,vol} + w_{air} f_{N_2,air}, & \text{for } k = N_2 \end{cases} \quad (12)$$

and $w_{g,out}\, f_{k,out}$ its outlet flow rate. O_2 can be assumed to be completely consumed, and with extremely fast dynamics, by the combustion reactions (1) and (2) (Cotone, 2003); therefore, it is not necessary to write a mass conservation equation for it. For char, which is in the solid phase, we write

$$\dot{M}_{ch} = w_{dry} - \eta_g \frac{w_{g,out} M_{ch}}{\rho_g V_g} + \sum_{r=2,3,4} \tilde{w}_{ch}^{(r)} PM_{ch} j_{ch}^{(r)}, \quad (13)$$

where η_g <<1 is a shape factor (De Marco, et al., 1991) which accounts for the reaction spatial development and which can be identified from experimental results,

$$\tilde{w}_{ch}^{(r)} = \frac{K_r M_{ch} M_r}{V_{\text{int}}}, r = 3,4, M_3 = M_{H_2O}, M_4 = M_{CO_2}, \quad (14)$$

$$\tilde{w}_{ch}^{(2)} = \phi \tilde{w}_{O_2}. \quad (15)$$

$\tilde{w}_{O_2}$ is the difference between the O_2 inlet molar flow rate and the O_2 molar flow rate consumed by reaction (1). We remark that (14) is taken from the unreacted-core-shrinking model described in (Wen and Chaung, 1979); K_r accounts both for reaction kinetics, by means of an Arrhenius-type term, and for component diffusion between the gaseous bulk and the char reacting surface. The reversible shift reaction (5) kinetics is assumed to be at equilibrium on the char surface, so that the gaseous components surface diffusion is the limiting phenomenon, except for H_2, whose diffusion coefficient can be assumed as ideally infinite.

The energy conservation equations, for the gaseous mixture in the gasification volume and for solid char, read as

$$M_g c_g \dot{T}_g = Q_{g,in} - \tilde{w}_{sh}\Delta H_{sh} + w_{vol}\Delta H_{vol} + Q_{ch-g} - Q_{ev}, \quad (16)$$

$$M_{ch} c_{ch} \dot{T}_{ch} = -Q_{ch,in} + Q^{(2)} - Q^{(3)} - Q^{(4)} - Q_{ch-g}, \quad (17)$$

where

$$\begin{aligned}Q_{g,in} = w_{ev}\cdot(h_{H_2O}(T_{ev}) - h_g(T_g)) + w_{O_2}\cdot(h_{O_2}(T_{ev}) + \\ -h_g(T_g)) + w_{ev}\cdot(h_{ev}(T_{ev}) - h_g(T_g)) + w_{dry,out,vol}\cdot \\ \cdot(e_{ch}(T_{ev}) - h_g(T_g)),\end{aligned} \quad (18)$$

$$Q_{ch-g} = \gamma_{ch-g} S_{ch} \cdot (T_{ch} - T_g), \quad (19)$$

$$\begin{aligned}Q_{ch,in} = w_{dry,out,vol}(e_{ch}(T_{ch}) - e_{ch}(T_{ev})) + w_{O_2}\cdot \\ \cdot(e_{ch}(T_{ch}) - h_{O_2}(T_{ev})) + w_{ev}(e_{ch}(T_{ch}) - h_{H_2O}(T_{ev})) + \\ +w_{vol}\cdot(e_{ch}(T_{ch}) - h_{vol}(T_{ev})),\end{aligned} \quad (20)$$

$$Q^{(r)} = \tilde{w}_{ch}^{(r)} PM_{ch} \Delta H^{(r)}, r = 2,3,4 \quad (21)$$

and $\Delta H^{(2)}$ is a function of ϕ, since CO and CO_2 have different heating values.

Finally, as to pressure, the perfect gas law yields

$$p_g = \frac{R T_g}{V_g} \sum_k \frac{M_k}{PM_k}, k = H_2O, H_2, CO, CO_2, N_2, H_2S. \quad (22)$$

2.3 Cooling

The cooling volume is composed of two regions, separated by the liquid water surface: a lower "pool" region, where gas bubbles into water, and an upper spray region, where water droplets further cool humid gas leaving the pool region. Mass and energy conservation equations will be written separately for the gas mixture and for liquid water in each region.

As to the overall gas and to its water part under the surface, first of all, one can write mass conservation as

$$\dot{M}_{gd} = w_b - w_{bout} - w_{g-l}, \quad (23)$$

$$\dot{M}_{H_2O,gd} = w_b f_{H_2O,in} - w_{bout} f_{H_2O,out} - w_{g-l}, \quad (24)$$

where w_b is the gasification outlet flow rate, w_{bout} the flow rate leaving the liquid surface and w_{g-l} the exchanged (usually condensating, anyway) water flow rate inside the gas phase.

Adopting a steady-state model for the gas phase under the free liquid surface, from (23) and (24) we can write

$$w_{bout} = w_{g,out}\,(1 - f_{H_2O,in})\big/(1 - f_{H_2O,out}) \quad (25)$$

$$w_{g-l} = w_b\,(f_{H_2O,out} - f_{H_2O,in})\big/(1 - f_{H_2O,out}), \quad (26)$$

and, adopting an equilibrium model,

$$f_{H_2O,out} = \frac{PM_{H_2O} p_{sat}(T_{ld})}{\overline{PM_{gd}}\,[p_c - p_{sat}(T_{ld})] + PM_{H_2O} p_{sat}(T_{ld})}, \quad (27)$$

where $\overline{PM_{gd}}$ is the average molecular weight of the "dry" gas, i.e. without considering its water contents.

As to energy conservation, we have

$$M_g c_g \dot{T}_{gd} = Q_{g,ex} - Q_{gl} - w_b(h(p_g, T_{in}, f_{gd}) + -h(p_c, T_{gd,out}, f_{gd,out})), \quad (28)$$

$$Q_{g,ex} = w_{g-l}(h_{g,sat}(T_{ld}) - h_g(T_{gd})), \quad (29)$$

$$Q_{gl} = \gamma_{g-l} S_{g-l}(T_{gd} - T_{ld}). \quad (30)$$

In (28), the last product term in the right-hand member describes the heat lost to decrease the inlet gas temperature; p_c is the upper cooling region pressure.

As to the liquid water mass M_{ld} under the surface, one has

$$\dot{M}_{ld} = w_{H_2O\_down} + w_{g-l} - w_{ld,out}, \quad (31)$$

where the three terms on the right-hand member are due to water falling down from the cooling upper region into the pool because of gravity, to the condensating water and to the outlet water respectively. In particular,

$$w_{H_2O\_down} = M_{w\_spr} / \tau_{down}, \quad (32)$$

where the average delay factor τ_{down} (Lydersen, 1983) models the residence time (typically of the order of a few seconds) of spray water (whose mass is M_{w_spr}) in the spray region. $w_{ld,out}$ is a control variable which can be employed for level regulation, by means of a suitable valve.

For the liquid water temperature T_{ld} under the surface, one can write

$$M_l c_l \dot{T}_{ld} = -Q_{H_2O\_down} + Q_{l,ex} + Q_{gl}, \quad (33)$$

$$Q_{H_2O\_down} = w_{H_2O\_down}(h_{H_2O}(T_{lu}) - h_{H_2O}(T_{ld})), \quad (34)$$

$$Q_{l,ex} = w_{g-l}(h_{g,sat}(T_{ld}) - h_l(T_{ld})). \quad (35)$$

For gas mass conservation above the free surface, one has

$$\dot{M}_{gu} = w_{bout} - w_{gas,mix} - w_{cnd}, \quad (36)$$

where $w_{gas,mix}$ is the overall gasifier outlet syngas flow rate, which is assumed, for simplicity, to be regulated by a critical valve, and

$$w_{cnd} = \frac{6 M_{lu} \beta_{g-l,u}}{\rho_{lu} d_{drop}} \cdot \left(\frac{M_{steam} R T_{gu}}{P M_{H_2O} V_{spr}} - p_{sat}\left(\frac{T_{lu} + T_{w\_spr}}{2} \right) \right) \quad (37)$$

is due to humid gas condensation. T_{w_spr} is the spray inlet temperature, d_{drop} the average spray drop diameter (water drops are assumed as spherical), V_{spr} the spray region volume. M_{steam} can be derived from the conservation equation

$$\dot{M}_{steam} = w_{bout} f_{H_2O,out} - w_{cnd} - w_{gas,mix} M_{steam} / M_{gu}. \quad (38)$$

For gas energy conservation above the free surface, one has

$$M_g c_g \dot{T}_{gu} = -Q_{g,sc} - Q_{exch} + w_{bout}(h(T_{gd}, p_c) - h(T_{gu}, p_c)), \quad (39)$$

$$Q_{g,sc} = w_{cnd}(H_{g,sat}(T_{lu}) - h(T_{gu})), \quad (40)$$

$$Q_{exch} = \gamma_{g-l,u} S_{g-l,u}(T_{gu} - T_{lu}). \quad (41)$$

For the liquid water mass M_{lu} and temperature T_{lu} above the surface, respectively, one can write

$$\dot{M}_{lu} = -w_{H_2O,down} + w_{cnd} + w_{spr}, \quad (42)$$

$$M_l c_l \dot{T}_{lu} = Q_{l,sc} + Q_{exch} + w_{spr}(h(T_{w\_spr}) - h(T_{lu})), \quad (43)$$

where w_{spr} is the inlet spray water flow rate and

$$Q_{l,sc} = w_{cnd}(H_{g,sat}(T_{lu}) - h_l(T_{lu})). \quad (44)$$

Again, pressure in the cooling chamber can be derived from the ideal gas law:

$$p_c = R T_{gu} M_{gu} / (V_{spr} \overline{PM_{gu}}). \quad (45)$$

2.4 Model Verification

As for the coal composition and steady-state nominal conditions, we have made reference to the data published in (Cotone, 2003). The main model parameters, especially for the correlations, have been drawn from the literature as well. In particular, the K_r's in (14) have been taken from (Wen and Chaung, 1979). This way, our model has been fully specified. For its verification, the molar fractions supplied by the model have been compared with the molar fractions in the literature. In Table 2 such comparison is carried out by referring to the situation occurring after the thermal shock at T=1077 K.

Table 2. Comparison between literature data (Cotone, 2003) and simulation results at nominal steady state

	Reference data	Simulation results	Relative Error
x_{CO}	34%	38%	12%
x_{H_2O}	14.9%	13%	13%
x_{CO_2}	16%	15.9%	1%
x_{H_2}	33%	30.6%	7%
x_{N_2}	1.8%	2%	11%

3. CONTROL ISSUES FOR THE GASIFICATION PLANT

In this work, attention is focused on problems related to fulfilling the electrical network's needs, such as supplying the requested power variations, in normal operation (load following) or in emergency conditions, taking part in primary frequency control, or even contributing to secondary frequency control. In particular, the problem of coordinate control is dealt with here: the gasifier load and the global plant operating conditions are mastered so as to satisfy power requests from the electrical network, while preserving plant integrity and correct operation, of course. A simplified plant scheme is shown in Fig. 2. It is composed of three main parts: (i) the gasification island; (ii) a lower pressure system for the syngas treatment, together with thermal energy recovery; (iii) a conventional gas turbine, with its own fuel feed system

controlled by valve v_3. A valve, v_2 (or an expansor for power recovery), connects part (i) and part (ii). The symbol θ is adopted for actuator command signals.

We now focus on the problem of supplying fast and relatively large power variations, in order to fulfil the network's requests. For this purpose, the control scheme of Fig. 3 can be considered. Fast power variations are obtained by acting on valve v_3, regulating the turbine inlet flow rate (as in conventional power plants). By means of two feed-forward actions (FFW in Fig. 3), such variation results in corresponding changes in command signals θ_1 and θ_2. Signal θ_1 controls the slurry flow rate as well as the oxygen flow rate. θ_2 determines the flow rate of the outlet syngas. The two feed-forward actions have to be designed so as to keep constant pressure p_1, at the gasifier outlet, pressure p_2, at the turbine inlet, and temperature T_g inside the gasifier. To this purpose, in Fig. 3 a decentralized control scheme is proposed, where control signals θ_1 and θ_2 are adopted for the regulation of p_1 and p_2 (dashed rectangle of Fig. 3). Alternatively, one can resort to a centralized controller, here omitted for reasons of conciseness. As for T_g, the control action is manually operated and indicated in Fig. 3 by a dash-dotted rectangle.

Note that, for the overall control system, variations of θ_3 can be seen as main (measurable) disturbances.

We now conclude with some observations about the regulation problems.

Variable θ_1 acts simultaneously on the slurry and O_2 flow rates. Here the main objective is to keep constant the ratio between the two flow rates. However, these cannot be varied simultaneously, in order to avoid excessive over- or under-elongations in the gasification temperature. More precisely, when there is a load variation, the corresponding variation of the O_2 flow rate must take place with some delay after the variation of the slurry flow rate. The reason is that the oxygen reacts extremely fast, so that the temperature variation occurs abruptly. Such delay is represented in Fig. 3 as well (lag).

Let us finally consider the 2x2 MIMO system where θ_1 and θ_2 are the input signals, and p_1 and p_2 the output signals.

Conventional power plant operating experience would suggest regulating independently p_1 by the gasifier load and p_2 by valve v_2, as shown at the top of Fig. 3. However, the variables under study are rather interacting with each other: for instance, increasing the gasifier inlet load implies an increase in pressure p_1, which makes valve v_2 flow rate increase and therefore pressure p_2 increase as well. The degree of coupling is *quantitatively* captured by the relative gain matrix RGA, whose elements are not far from 0.5. Therefore, a centralized control solution, carried out by a forward decoupling technique, has been also analysed. The open-loop SISO transfer functions employed for controllers tuning have been identified from the system step responses around the chosen steady-state nominal point (see Section 2.4). Summing up, both centralized and decentralized controllers have been designed and simulated. Simulation results are reported in the subsequent section.

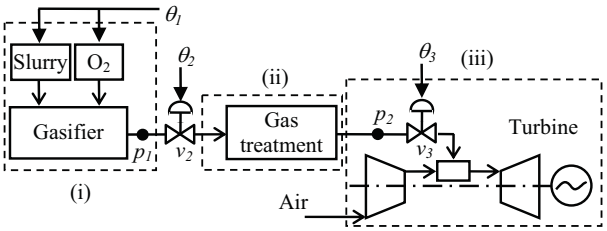

Fig. 2. The controlled simplified plant scheme.

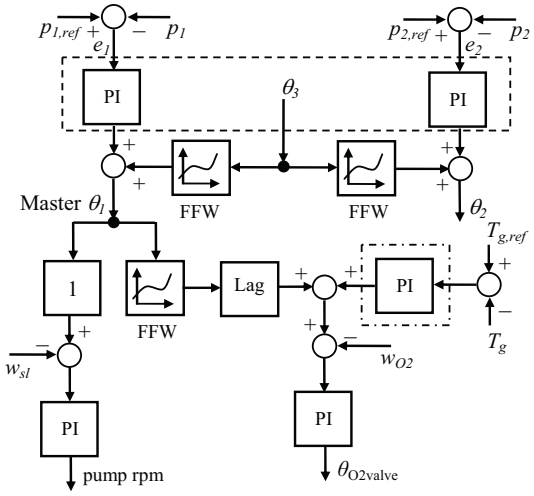

Fig. 3. A controller structure for the plant.

4. SIMULATION RESULTS

The simplified plant depicted in Fig. 2 has been simulated in the Matlab-Simulink environment, with the gasifier model, in particular, implemented by means of an S-function written in the C++ language. Simulations have been carried out both in open loop and in closed loop by considering both the centralized and the decentralized schemes. Integration has been executed in the continuous-time domain, by resorting to the standard Matlab algorithms.

Some of the results of a dynamical simulation with the centralized controller are now reported. Starting from the steady-state nominal conditions, a positive 10% step on the turbine valve position is given, at time t = 1500 s; this simulates a variation of power request from the network, so that the turbogas control system requires more inlet fuel flow rate. The top of Fig. 4 shows the responses of pressure p_1 and temperature T_g: as expected, their steady-state values are unaffected by the disturbance, and elongations around such values are very small. In Fig. 4 - bottom the control variables slurry and oxygen flow rates are depicted: they both increase in a rather slow manner, so as to preserve the integrity of the gasifier itself and of the other devices (with their dynamic operating constraints). Finally, it turns out that also the opening of valve v_2 exhibits a smooth behaviour.

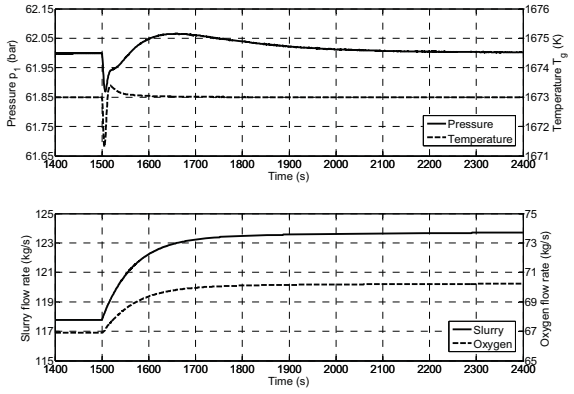

Fig. 4. Simulation results with centralized control.

5. CONCLUSIONS

A control-oriented first-principle dynamical model for a coal slurry gasifier has been proposed. Model parameters have been identified from literature data. Classical control schemes have been proposed for the 2x2 problem of controlling gasifier pressure and turbine inlet pressure by the gasifier inlet slurry and O_2 flow rates and by the gasifier outlet syngas flow rate. Simulations have shown satisfactory performance for disturbance rejection. Also the set-point tracking (not presented in this paper, for brevity) leads to good results. Future activities include model validation in transient conditions and integration of this model and models of other plant devices (see Section 1) into an overall IGCC plant simulator. Then, control strategies will be studied concerning the interaction between the gasifier and the other devices, in normal operating conditions and during startups/shutdowns; such strategies will be implemented both by standard techniques, based on SISO PID controllers, and by more involved MIMO techniques.

ACKNOWLEDGEMENTS

We are grateful to P. D'Adamo and P. De Francesco, formerly students at Politecnico di Milano, for their collaboration in the phase of parameter tuning.

This work has been financed by the Research Fund for the Italian Electrical system under the Contract Agreement between CESI RICERCA and the Ministry of Economic Development - General Directorate for Energy and Mining Resources stipulated on June 21, 2007 in compliance with the Decree n. 73 of June 18, 2007. Research has also been supported by the Italian National Research Project "New Techniques of Identification and Adaptive Control for Industrial Systems" and partially by CNR-IEIIT.

REFERENCES

Bittanti, S., Canevese, S., De Marco, A., Prandoni, V., and Serrau, D. (2008). Towards clean-coal control technologies: modelling conversion of carbon oxide into hydrogen by a shift reactor, *17th IFAC World Congress*, Seoul, South Korea.

Canevese, S., De Marco, A., Murrai, D., and Prandoni, V. (2007). Modelling and control of a PSA reactor for hydrogen purification, *ICPS'07 (1st IFAC Workshop on Convergence of Information Technologies and Control Methods with Power Plants and Power Systems)*, Cluj-Napoca, Romania.

Chen, C., Horio, M., and Kojima, T. (2000). Numerical simulation of entrained flow coal gasifiers. Part I: modeling of coal gasification in an entrained flow gasifier. *Chemical Engineering Science*, 55 (18), 3861-3874.

Cotone, P. (2003). Section D - Basic information for each alternative. In Domenichini, R., *IEA GHG Gasification power generation study, Final Report, Rev. 1*.

De Marco, A., De Michele, G., Miccio, M., Prandoni, W., and Traniello Gradassi, A. (1991). A model for the dynamic simulation of a pilot fluidized bed combustor: Predictions and first validation, *Proceedings of the 11th International Conference on Fluidized Bed Combustion*, vol. 1, 433–438. ASME, New York, NY.

Fantini, V., Mazzocchi, L., Moia, F., Prandoni, V., and Savoldelli, P. (2007). Pre-feasibility study of a flexible hydrogen-electricity co-production IGCC coal-fed plant with CO_2 capture and sequestration, *Third International Conference on Clean Coal Technologies for our Future (CCT 2007)*, Cagliari, Italy.

Kobayashi, H., Howard, J.B., and Sarofim, A.F. (1977). Coal devolatilization at high temperatures, *15th Symposium (International) on Combustion*, 16 (1), 411-425.

Lydersen, A.L. (1983). *Mass transfer in engineering practice*. John Wiley & Sons.

Schoen, P. (1993). *Dynamic modeling and control of integrated coal gasification combined cycle units*. PhD thesis, Delft University of Technology, Delft, The Netherlands.

Smoot, L.D. and Smith, P.J. (1985). *Coal combustion and gasification.* Plenum Press, New York, NY.

Thambimuthu, K.V. and Whaley, H. (1987). The combustion of coal-liquid mixtures. In C.J. Lawn (ed.), *Principles of combustion engineering for boilers*, Chapter 4, 402-408. Academic Press, London.

van der Looij, J.M.P. (1988). *Dynamic modeling and control of coal fired fluidized bed boilers*. PhD thesis, Delft University of Technology, Delft, The Netherlands.

Wen, C.Y. and Chaung, T.Z. (1979). Entrainment coal gasification modeling. *Industrial & Engineering Chemistry Process Design and Development*, 18 (4), 684-695.

Wen, C.Y. and Dutta, S. (1979). Rate of coal pyrolysis and gasification reactions. In C. Wen, Lee (ed's), *Coal conversion technology*, 57-170. Addison-Wesley Publishing Co., Reading, MA.

Identification of Reaction Mechanisms with a Dynamic PFR Model ⋆

Jan C. Schöneberger * **Harvey Arellano-Garcia** *
Holger Thielert ** **Günter Wozny** *

* *Berlin Institute of Technology,Chair of Process Dynamics and Operation, Berlin, Germany (e-mail: jan.schoeneberger@tu-berlin.de)*
** *Uhde GmbH, Dortmund, Germany*

Abstract: In this work, a dynamic model of a catalytic fixed bed reactor (FBR) based on partial differential equations (PDE) is introduced and used for the identification of reaction mechanisms which take place during the oxidation of sulfur dioxide over a vanadium pentoxid catalyst. The measured data is collected from a pilot plant, which uses commercial sized catalyst particles. In order to reduce the experimental effort, a developed framework based on the methods of nonlinear optimal experimental design is applied using a steady state FBR model. The systematic procedure is improved using a dynamic reactor model. This makes the time dependent measurement data valuable for the identification procedure.

Keywords: Catalytic fixed bed reactor (FBR), reaction mechanisms, partial differential equations (PDE), parameter identification, optimal experimental design.

1. INTRODUCTION

Catalytic gas phase reactions have a high relevance in chemical engineering. The majority of chemical processes will not be profitable and in some cases not even viable without the usage of catalysts. An important application represents the utilization of FBR for waste gas treatment processes. In this work, the oxidation of sulfur dioxide to sulfur trioxide is considered, which is converted with water to sulphuric acid. It should be noted that huge effort is made in the development of new catalysts with a higher activity. Commonly, new catalysts are designed and tested at micro scale, i.e. a pulverized catalyst. However, the catalyst used in industrial plants are much larger and the previously identified mechanisms and kinetic parameters can not be transferred without further investigations in a scale up procedure w.r.t. the reactor layout. Thus, measurements with commercial catalyst particles are inevitable implying a high experimental effort. The sized particles require a larger reactor diameter, and thus, high gas flow rates are necessary in order to hold the operation conditions close to the industrial scale reactor. Moreover, corresponding requirements for process automation and safety engineering have to be met. Consequently, in order to reduce the experimental effort while reaching a desired model quality, methods of nonlinear optimal experimental design can be applied. In addition, due to the fact that a good deal of data enhances the mechanism and parameter identification, the proposed framework can still be improved when using a model, which describes the pilot plant dynamic behavior. In this work, a homogeneous and a two-phase FBR model are presented. The latter can be used for dynamic simulations. Both are compared to each other based on a set of measured data taken from an identification campaign. The experiments were performed in a pilot plant (Fig. 1) using a commercially available vanadium pentoxid catalyst.

⋆ This work is supported by the Max-Buchner-Forschungsstiftung.

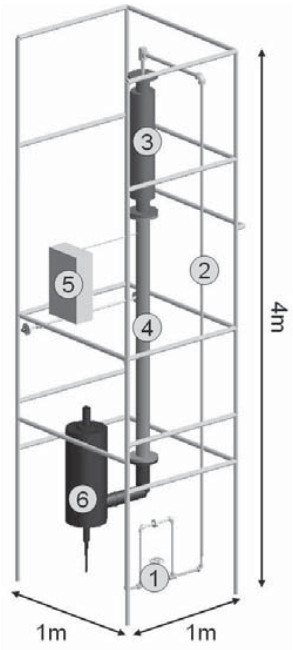

Fig. 1. Pilot plant set-up: (1) Quality measurement, (2) Heating section, (3) Reactor, (4) Tube bundle cooler, (5) Quality measurement, (6) Bubble column.

2. PILOT PLANT DESCRIPTION

The core of the pilot plant is the tubular reactor which has a diameter of $D_R = 0.1$ m and a length of $L_R = 1$ m.

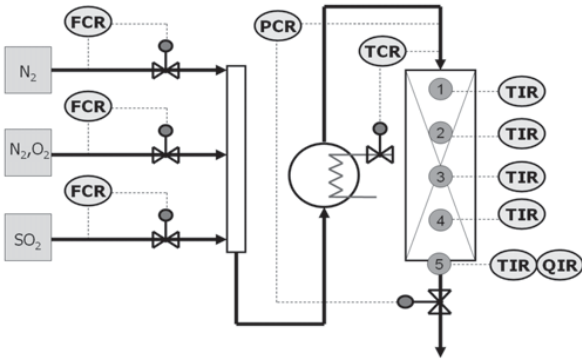

Fig. 2. Control structure: (FCR) Flow control and measurement, (TCR) Temperature control and measurement, (PCR) Pressure control and measurement, (TIR) Temperature measurement, (QIR) Quality measurement.

The diameter results from the size of the catalyst particle, which is about $D_P = 0.005$ m for the examined catalyst. It represents the minimum diameter required in order to get a uniform particle distribution. The reactor consists of five beds of catalyst packing, where each is $H_B = 0.1$ m high. The additional length is used to reduce in and outlet effects. The reactor is operated nearly adiabatic using an electric heated isolation. The majority of the available space is occupied by the secondary units such as the heating, cooling and gas scrubbing. The last two steps are combined in a bubble column. Fig. 1 gives an idea of the pilot plant set-up. The pilot plant is automated using ABB Freelance. Beside the implemented safety engineering procedures, the reactor inlet variables are controlled using the structure given in Fig. 2. The gas flow rate $\dot{V}$ can be varied between 200 and 400 norm liter per minute at inlet temperatures up to $T_{in} = 500$°C.

3. REACTOR MODELS

Two reactor models are presented, which describe the FBR behavior, namely the *homogeneous model* and the *two-phase model*. The chemical reaction is modeled with six different reaction mechanisms for which several steps of parameter identification and model discrimination are performed in order to find the best suitable mechanism. Besides the kinetic parameters in the reaction rate equations, the reactor models contain several parameters. Some of them can be obtained from the particles geometry e.g. the packing porosity ϵ, the relative particle diameter D_P, the specific surface area a, and the catalyst density ρ_C, other parameters are derived from property functions such as the component heat capacities $c_{P,i}$ and $c_{V,i}$, the heat of reaction Δh_R, and the thermodynamic equilibrium constant, K_P. The heat loss can be determined from experimental runs without reactions and is then calculated with the estimated heat transfer coefficient, k_W, and the measured wall temperature, T_W. Four components are considered in the model with the indices as given in Tab. 1.

Table 1. Component indices

Index	1	2	3	4
Component	**SO_2**	**O_2**	**SO_3**	**N_2**

3.1 Homogeneous Model

The model equations composed of mass balances, (1), energy balance, (2), and momentum balance, (3), imply the assumption of a plug flow profile in the reactor and an instant heat and mass transfer between the gas and the solid phase. This means that the temperature of the catalyst particle is the same as the gas phase bulk temperature. Due to this issue the model can not be used for the description of the dynamic behavior, since the heat capacities of gas and solid differ a lot. A detailed description and derivation of the homogeneous model can be found in Arellano-Garcia et al. (2007).

$$\frac{dF_i}{dz} = \nu_i \dot{r} \cdot \rho_C (1-\epsilon) \frac{\pi}{4} D_R^2 \tag{1}$$

$$\frac{dT}{dz} = \frac{-\dot{r} \Delta h_R(T) \rho_C (1-\epsilon) \frac{\pi}{4} D_R^2 - k_W \pi \; D_R \, (T - T_W)}{\sum F_i c_{P,i}} \tag{2}$$

$$\frac{dP}{dz} = -\frac{\sum F_i M_i}{\rho \frac{\pi}{4} D_R^2 D_P} \left(\frac{1-\epsilon}{\epsilon^3}\right) \cdot \left[\frac{150(1-\epsilon)\eta}{D_P} + 1.75 \frac{\sum F_i M_i}{\frac{\pi}{4} D_R^2}\right] \tag{3}$$

In the model equations, F_i denotes the component flow rates, ν_i the stoichiometric coefficient, and M_i, the molar mass. T stands for the gas and the catalyst temperature, P for the gas phase pressure. The viscosity η is calculated assuming an ideal mixing.

Following the simulation results based on this model, the pressure drop can be neglected for the given reactor set-up and is not considered anymore in the two-phase model.

3.2 Two-Phase Model

The key idea of developing a two-phase model is to perform dynamic simulations of the reactor behavior in order to include time variant measurement data in the parameter estimation procedure. Due to the varieties in the resulting time constants in the energy balances, which are mainly influenced by the heat capacity and density in its corresponding phase, a split modeling of the gas and solid phase becomes inevitable. The resulting equation system comprises mass and energy balances for the two phases,(4)- (7), which are coupled via mass and heat transfer correlations,(8)-(10). Instead of the component flow rates (see (1)), the concentrations in the gas phase $c_{G,i}$ and the solid phase $c_{C,i}$ are used here as state variables.

$$\frac{dc_{G,i}}{dt} = D_{ax_i} \frac{\partial^2 c_{G,i}}{\partial z^2} - \frac{\dot{V}}{\epsilon \frac{\pi}{4} D_R^2} \frac{\partial c_{G,i}}{\partial z} - a \frac{1-\epsilon}{\epsilon} \beta (c_{G,i} - c_{C,i}) \tag{4}$$

$$\frac{dc_{C,i}}{dt} = \nu_i \dot{r} \rho_k + a \, \beta (c_{G,i} - c_{C,i}) \tag{5}$$

$$\sum_{i=1}^{4} c_{G,i} c_{V_i} \frac{dT_G}{dt} = a \frac{1-\epsilon}{\epsilon} \alpha (T_C - T_G) - \frac{\dot{V}}{\epsilon \frac{\pi}{4} D_R^2} \cdot \sum_{i=1}^{4} c_{G,i} c_{P_i} \frac{\partial T_G}{\partial z} - k_W \frac{4}{\epsilon \; D_R} (T_G - T_W) \tag{6}$$

$$\frac{dT_C}{dt} = \frac{a\alpha}{\rho_C c_{P,C}} (T_G - T_C) - \frac{\Delta h_R \dot{r}}{c_{P,C}} \tag{7}$$

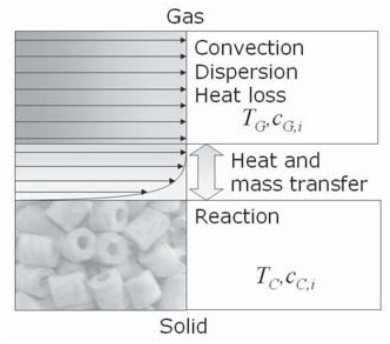

Fig. 3. Control volume of the two-phase model.

The control volume and the considered state variables of the two phases are shown in Fig. 3. The transfer coefficients (α, β, D_{ax}) are calculated with dimensionless numbers (Nusselt number Nu, Sherwood number Sh, axial Peclet number Pe_{ax}) and correlations taken from literature, see e.g. Fogler (2006). Here, $D_{ab,i}$ stands for the diffusion coefficient of the component i in nitrogen and $\bar{\lambda}$ for the mixtures heat conductivity.

$$D_{ax} = \frac{\dot{V} D_P}{Pe_{ax} \epsilon \frac{\pi}{4} D_R^2} \tag{8}$$

$$\beta_i = \frac{Sh_{\epsilon,i}\, D_{ab_i}}{D_P} \tag{9}$$

$$\alpha = \frac{\bar{\lambda} Nu}{D_P} \tag{10}$$

On the one hand, a dynamic simulation becomes possible with the inclusion of the solid phase, but on the other hand, new unknown or not well-known parameters are introduced. Three parameters are used in the transport correlations, one for each equation. In addition, two parameters depend on the catalyst particle properties, namely, the catalyst heat capacity, $c_{P,C}$, and the specific surface area, a. These additional parameters are to be determined from the measurement data, but they are strong correlated with the reaction rate, and thus, with the kinetic parameters of the reaction mechanisms. This problem can be overcome by running experiments without a reaction, i.e. with pure nitrogen or air. By this means the parameter in the heat transfer correlation, and the catalyst properties can be determined independently.

3.3 Reaction Mechanisms

In the open literature, plenty of different reaction mechanisms have been published for the oxidation of sulfur dioxide over vanadium pentoxid, we refer to Mezaki and Kadlec (1972) for an overview. In this work, the five of the most promising rate laws are selected. Additionally, a generic power law mechanism is also considered. All the rate equations describe the reaction stated in equation (11). They are functions of the components partial pressures, P_i, and the temperature, T, which affects the calculation of the velocity constant k, and the equilibrium constants K_P, and K.

$$\mathbf{SO_2} + \frac{\mathbf{1}}{\mathbf{2}}\,\mathbf{O_2} \rightleftharpoons \mathbf{SO_3} \tag{11}$$

Power Law: In the rate equation for the power law mechanism (12), the component exponents a, b, and c are treated as model parameters and have to be determined from the measurements. The temperature dependent velocity constant k is calculated with equation (13), in which the kinetic parameters p_1 and p_2 have to be identified.

Rate 1:

$$\dot{r} = k \left(P_{SO_2}^a P_{O_2}^b P_{SO_3}^c - \frac{P_{SO_2}^{(a-2)} P_{O_2}^{(b-1)} P_{SO_3}^{(c+2)}}{K_P} \right) \tag{12}$$

$$k = exp\left(\frac{p_1}{T} + 0.5\ ln(T) + p_2\right) \tag{13}$$

Mechanistic Rate Equations: The rate equations (14) to (18) can be derived assuming a liquid metal phase on the catalyst particle formed by vanadium, in which the supplied oxygen is dissolved. This is a widely accepted assumption for the oxidation over vanadium pentoxid. The differences in the reaction rates result from different mechanisms of the catalyst activation with oxygen.

Rate 2:

$$\dot{r} = \frac{k K P_{SO_2} P_{O_2}^{1/2}}{\left[P_{SO_3}^{1/2} + (K P_{SO_2})^{1/2}\right]^2} \left(1 - \frac{P_{SO_3}}{K_P P_{SO_2} P_{O_2}^{1/2}}\right) \tag{14}$$

Rate 3:

$$\dot{r} = \frac{k K P_{SO_2} P_{O_2}}{\left[P_{SO_3}^{1/2} + (K P_{SO_2})^{1/2}\right]^2} \left(1 - \frac{P_{SO_3}^2}{K_P^2 P_{SO_2}^2 P_{O_2}}\right) \tag{15}$$

Rate 4:

$$\dot{r} = \frac{k K P_{SO_2} P_{O_2}^{1/2}}{\left[P_{SO_3}^{1/2} + (K P_{SO_2})^{1/2}\right] P_{SO_3}^{1/2}} \left(1 - \frac{P_{SO_3}}{K_P P_{SO_2} P_{O_2}^{1/2}}\right) \tag{16}$$

Rate 5:

$$\dot{r} = \frac{k\,(K P_{SO_2})^{1/2} P_{O_2}}{\left[P_{SO_3}^{1/2} + (K P_{SO_2})^{1/2}\right]} \left(1 - \frac{P_{SO_3}^2}{K_P^2 P_{SO_2}^2 P_{O_2}}\right) \tag{17}$$

Rate 6:

$$\dot{r} = \frac{k K P_{SO_2} P_{O_2}}{\left[P_{SO_3}^{1/2} + (K P_{SO_2})^{1/2}\right] P_{SO_3}^{1/2}} \left(1 - \frac{P_{SO_3}^2}{K_P^2 P_{SO_2}^2 P_{O_2}}\right) \tag{18}$$

All these rate equations utilize the same approach for the velocity constant k, and the equilibrium of the vacant sites K, which are given in the equations (19) and (20).

$$k = exp\left(p_1 - \frac{p_2}{T}\right) \tag{19}$$

$$K = exp\left(p_3 - \frac{p_4}{T}\right) \tag{20}$$

3.4 Numerical Solution

In order to keep the computational effort low, both reactor models were discretized using the orthogonal collocation (OC), see Schöneberger et al. (2009). In the case of the homogeneous model this leads to an algebraic equation system (AE) and in the case of the two-phase model to a system of ordinary differential equations (ODE). The

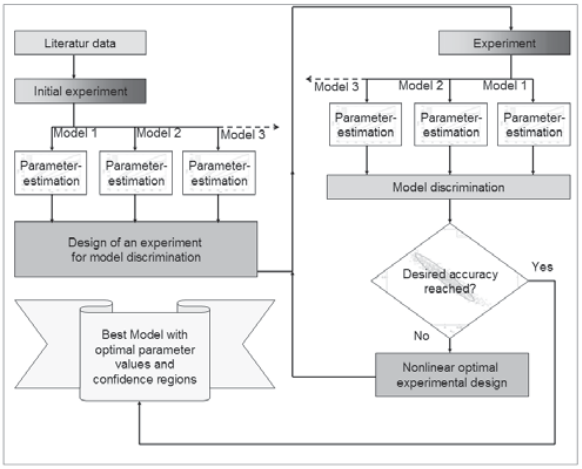

Fig. 4. Model identification framework.

AE is solved with a Newton-Raphson step and the ODE is integrated with an OC based Runge-Kutta algorithm. The use of the numerical solution in an optimization framework requires a very robust solution algorithm, in particular, when the free variables are positioned in exponential terms such as in the case of kinetic parameter estimation. Therefore, specialized initial value generation algorithms and step size control algorithms are required, see Schöneberger et al. (2007). Anyhow, the solution of the homogeneous model is more robust. Consequently, the first parameter estimation is performed with this model in order to get good initial parameter values for the two-phase model.

4. MECHANISM IDENTIFICATION FRAMEWORK

The proposed framework in Fig. 4 is based on the methods of nonlinear experimental design. It is similar to the model building framework proposed by Franceschini and Macchietto (2008), but with some improvements regarding the specific problem. There is only one experiment designed for model discrimination, and this is performed in the beginning of the identification procedure. Further experiments are exclusively designed in order to improve the parameter accuracy until the parameter spreading is in an acceptable region. Please note that all six reaction rates are considered in the steps 'Parameter estimation' and 'Model discrimination' of the loop in Fig. 4, but the 'Nonlinear optimal experimental design' is only performed for the actually best rate model.

4.1 Parameter Estimation Problem

The objective of the parameter estimation procedure is to find the parameter values which set the numerical solution of the model equations (e.g. (1), (2), and (3) for the homogeneous model) as close as possible to the measured data. For this purpose, the problem (21), here stated for the homogeneous model, has to be solved. In this work, a weighted least square functional is used as objective function and it's final value is named LSQ. High values are related to a high lack of fit.

$$\min_{p_1,p_2,a,b,c} \mathsf{LSQ} = \sum_{j=1}^{NM} \frac{\left(T_{ns,j} - T_{md,j}\right)^2}{\sigma^2_{T_j,T_j}} \tag{21}$$

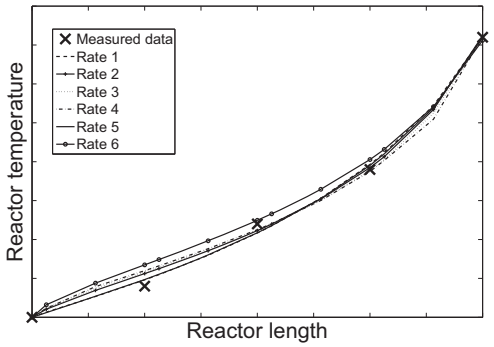

Fig. 5. Initial experiment.

In equation (21) the subscripts ns and md denote numerical solution and measured data, respectively, NM is the number of measured data points, and $\sigma^2_{T_j,T_j}$ is the standard deviation of the measured quantity (here the temperature T) at the measured point j. The calculated temperature profiles for the different rate laws after the parameter estimation are compared to the measured temperature data in Fig. 5. In Tab. 2, the LSQ values for the different rate models are given. All models are able to describe the measured data. This is not surprising, because 4 parameters (5 for rate 1) are fitted to only 5 measured points. Anyhow, the structure of the rate equations does not allow the same good fit for all rates. The best fit is reached with rate 5.
The parameter estimation problem becomes more difficult when more data points are available. The model equations have to be solved separately for each new experiment, making the parameter estimation the most expensive step regarding the computational effort.

Table 2. LSQ values for different rate models.

Rate	1	2	3	4	5	6
LSQ	0.488	0.688	0.821	0.916	0.461	1.901

4.2 Model Discrimination Problem

It is difficult to choose the best suitable rate model from Fig. 5. The discrimination step normally is performed taking the model with the lowest LSQ value. But, after only one experiment the models LSQ values are still close together, see Tab. 2. Thus, in a second step an experiment is designed that drift apart from the calculated temperature profiles for the estimated set of parameters. To do this, the optimization problem given in equation (22) is solved. By this means, the obtained inlet conditions are optimal for the discrimination step. Due to the fact that only one measured variable is considered, here a simpler formulation is chosen as proposed by Akaike (1974) and other authors.

$$\min_{\dot{V},c_{SO_2,in},c_{O_2,in},T_{in}} \Phi_{\text{Disc.}} \text{ , with}$$
$$\Phi_{\text{Disc.}} = \sum_{m=2}^{6} \sum_{i=m}^{6} \sum_{j=1}^{5} \left(T_{ns,Mod=m,j} - T_{ns,Mod=i,j}\right)^2 \tag{22}$$

The temperature profiles calculated with the solution of (22) are plotted in Fig. 6. After the experiment is per-

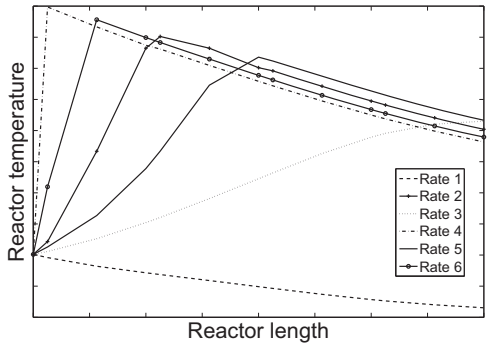

Fig. 6. Model discrimination experiment.

formed and the new parameters for each model are found, the profiles are not separated anymore. However, the experiment forces the rate models parameter values to move, and thus, the models flexibility and arbitrariness is reduced considerably.

Only one experiment is designed for a better model discrimination. After the discrimination experiment the rates 1, 2, and 3 are the most promising candidates. The other rates are still considered in the calculations but not plotted anymore in this paper. Further designs for discrimination are not performed because the focus on the parameter accuracy forces also an increasing difference in the models LSQ values. This means that after the convergence of the loop in Fig. 4 a good distinguishability between the rates is reached in addition.

4.3 Nonlinear Optimal Experimental Design Problem

In this work, the A-Criterion is used in order to increase the parameter accuracy, leading to the objective function given in equation (23). A detailed description of the nonlinear optimal experimental design and the different criteria so as a reason for the selection of the A-Criterion can be found in Schöneberger et al. (2008).

$$\min_{\dot{V},c_{SO_2,in},c_{O_2,in},T_{in}} \Phi_{\mathrm{A}}, \text{ with}$$
$$\Phi_{\mathrm{A}} = \frac{\mathrm{trace}\,(\mathbf{C})}{\dim\,(\mathbf{C})} \tag{23}$$

The covariance matrix of the model parameters $\mathbf{C}$ is approximated with the inverse of the Fisher information matrix $\mathbf{F}$ which can be calculated with equation (24), see Bard (1974). The rate model parameters are summarized in the parameter vector $\mathbf{P}$.

$$\mathbf{C} \geq \mathbf{F}^{-1} = \left[\sum_{j=1}^{NM} \left(\left(\frac{\partial T_{ns,j}}{\partial \mathbf{p}} \right) \frac{1}{\sigma^2_{T_j,T_j}} \left(\frac{\partial T_{ns,j}}{\partial \mathbf{p}} \right)^{\mathbf{T}} \right) \right]^{-1} \tag{24}$$

The parameter's standard deviations $\sigma_{p_n,p_n} = \sqrt{\mathbf{C}(n,n))}$ can be calculated with the diagonal elements of the covariance matrix. The framework is stopped, when a maximal standard deviation of $\sigma_{p_n,p_n,max} \leq 0.02$ is reached. This was accomplished after 8 experiments. The development of the A-Criterion and the maximal parameter standard deviation w.r.t. the experiments is shown in Fig. 7. The development of the LSQ values for the first three rate models

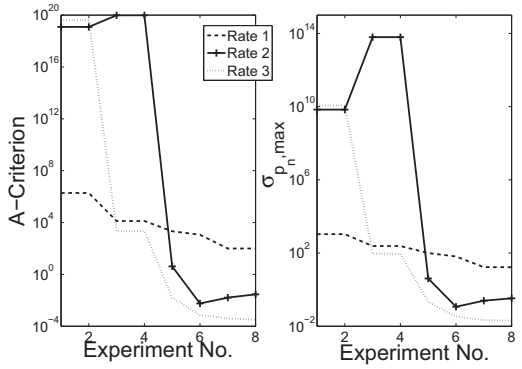

Fig. 7. Development of the parameter accuracy.

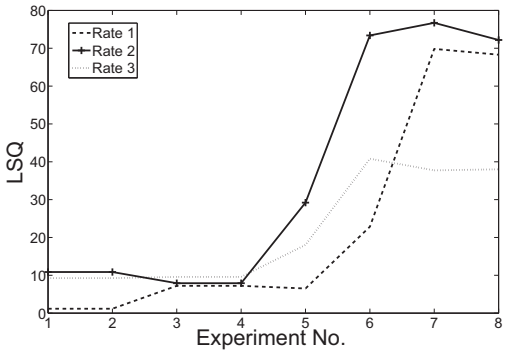

Fig. 8. Development of the lack of fit.

are depicted in Fig. 8. The experiments 1 and 2 and so 3 and 4 are repeated experiments used for the determination of the measured variables standard deviation σ_{T_j,T_j}.

5. RESULTS

In this section, the measured dynamic reactor behavior and the results obtained with the two-phase model are presented.

5.1 Catalyst Properties and Heat Transfer

The specific heat capacity of the catalyst phase $c_{P,k}$ is a model specific property, which has to be determined from experimental data. It should be noted that it is not equal to the heat capacity of the catalysts bulk material since the modeled catalyst phase contains also the particle pores. It can be estimated together with the parameter in the heat transfer correlation from experiments without reaction. This saves reactant gases and reduces the experimental effort because no off-gas treatment is necessary. The transient temperature profiles during the reactor heat up procedure can be used for this issue. They allow the independent estimation of the two parameters because they contain also the initial steady state, when the reactor inlet temperature is reached. These steady state profiles are independent of the catalyst phase heat capacity, but a function of the heat transfer coefficient. In Fig. 9 the numerical solution (surface) is fitted to the measured temperature data (black lines) based on the procedure described in section 4.1.

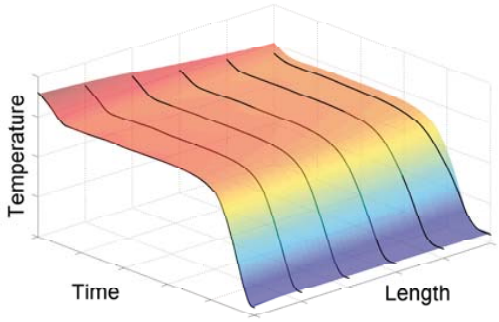

Fig. 9. Time-space surface without reaction.

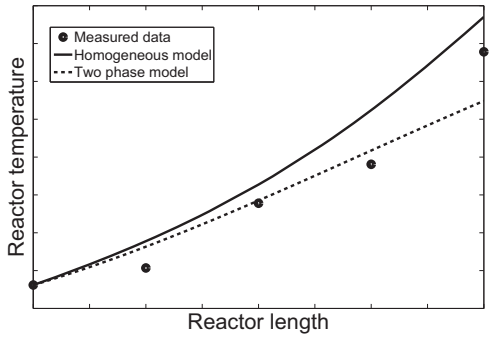

Fig. 10. Steady state comparison of the reactor models.

5.2 Parameter Transfer

Under the assumption of an instantaneous heat and mass transfer and a neglecting of axial dispersion, the model equations of the two-phase model can be rearranged to the form of the homogeneous model in the case of steady state. To show this, the profiles of a solution with the homogeneous model are compared to the steady state solution of the two-phase model in Fig. 10. The differences arise from the stated assumptions, which are not completely fulfilled. However, a steady state examination of a catalyst would not justify the use of the more complex two-phase model.

5.3 Dynamic Reactor Behavior

In Fig. 11, the transient temperature data is plotted. The temperatures after the first and the second bed show a strong overshooting. This behavior can be explained with the two-phase model. The coupled balances for gas and solid phase lead to a PT2 behavior when linearized. This second order element has the potential to produce a swinging solution. The effect is reduced in relation to the distance from the reactor inlet. The last two profiles show inflexion points instead. This can be explained with the increasing reactor wall temperature, which is also disturbing the system as well.

6. CONCLUSIONS

First calculation results show that the two-phase model is able to describe the dynamic reactor behavior. It has been demonstrated that for steady state experiments with a FBR the more complex two-phase model is not required. However, the information content of the transient profiles is much higher than the one from the steady state profiles. The effect on the parameter accuracy still has to be examined, in particular, because of the inclusion of the additional parameters. The knowledge of the dynamic reactor behavior enables the design of optimal transient experiments and their implementation in the proposed identification framework.

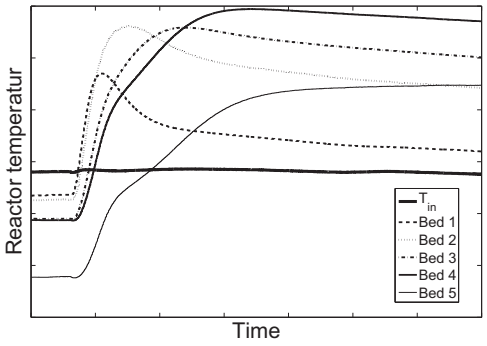

Fig. 11. Transient temperature data with reaction.

ACKNOWLEDGEMENTS

The authors gratefully acknowledge the financial support of the Max-Buchner-Forschungsstiftung, and the provision of the catalyst from the BASF SE.

REFERENCES

Akaike, H. (1974). A new look at the statistical model identification. *IEEE Transactions on Automatic Control*, 19(6), 716–723.

Arellano-Garcia, H., Schöneberger, J.C., and Körkel, S. (2007). Optimale Versuchsplanung in der chemischen Verfahrenstechnik. *Chem. Ing. Tech.*, 79(10), 1625.

Bard, Y. (1974). *Nonlinear Parameter Estimation*. Academic Press, London.

Fogler, H.S. (2006). *Elements of Chemical Reaction Engineering*. Perason International Edition, 4th edition.

Franceschini, G. and Macchietto, S. (2008). Model-based design of experiments for parameter precision: State of the art. *Chem. Eng. Sci.*, 63, 4846.

Mezaki, R. and Kadlec, B. (1972). Remarks on the reduction-oxidation mechanism of sulfur dioxode oxidation on vanadium catalyst. *J. Catal.*, 25, 454.

Schöneberger, J.C., Arellano-Garcia, H., Thielert, H., Körkel, S., and Wozny, G. (2007). An efficient approach to robust simulation of claus processes in coking plants. *Computer Aided Chem. Eng.*, 24, 521.

Schöneberger, J.C., Arellano-Garcia, H., Thielert, H., Körkel, S., and Wozny, G. (2008). Experimental analysis of a fixed bed reactor for catalytic SO2 oxidation. *Ind. Eng. Chem. Res.*, in press.

Schöneberger, J.C., Arellano-Garcia, H., and Wozny, G. (2009). An efficient discretization approach for partial differential equations describing chemical reaction systems. *Computer Aided Chem. Eng.*, in press.

Modeling and Simulation of the Polymeric Nanocapsule Formation Process

Luciane S. Ferreira and Jorge O. Trierweiler

GIMSCOP – Chemical Engineering Department – UFRGS. Rua Luis Englert, s/n. Porto Alegre. RS. Brasil.
(e-mail: {luciane,jorge}@enq.ufrgs.br)

Abstract: In this work the modelling and simulation of nanoparticle formation according to the technique of nanoprecipitation was done. In this method, the particle is formed due to the further diffusion of solvent into the water, resulting in the aggregation of the associated polymer chains. In order to predict the characteristics of the nanoparticle and also to improve the process, it was developed a mathematical model that considers: (a) the type of polymer; (b) interaction between solvent and polymer; and, (c) dynamics of solvent diffusion. The diffusivity between polymer-solvent was modelled by means of the Vrentas & Duda Free Volume Theory, including the Sanchez-Lacombe equation-of-state. The model was written in terms of Partial Differential Equation, and solved with MAPLE for a given initial size distribution. Additionally, it is a moving boundary problem because the diffusion of the solvent out of the droplet leads to its size reduction. Based on a given initial droplet size distribution, the transient behaviour and the final droplet size distribution can be evaluated. The dynamic simulation shows both the evolution of the solvent inside the droplet and the variation of size in time. Additionally, the comparison between experimental and simulated results showed a very good agreement.

Keywords: nanoprecipitation, modeling, simulation, diffusion, moving boundary, droplet size distribution.

1. INTRODUCTION

Polymeric nanoparticles are of especial interest from the pharmaceutical point of view. First, they are more stable in the gastrointestinal tract than other colloidal carriers and can protect encapsulated drugs from gastrointestinal environment. Second, the use of various polymeric materials enable the modulation of physicochemical characteristics (e.g. hydrophobicity, zeta potential), drug release properties, and biological behavior (e.g. targeting, bioadhesion, improved cellular uptake) of nanoparticles. Finally, their submicron size and large specific surface area favor their absorption compared to larger carriers (Des Rieux *et al.*, 2006). For instance, nanoparticles encapsulating proteins and vaccines (Des Rieux *et al.*, 2006) and chemotherapeutic agents (Jabr-Milane *et al.*, 2008) have been investigated in the last years.

One of the methods applied to produce nanoparticles is the so-called Nanoprecipitation. This method, first presented in 1989 (Fessi *et al.*, 1989), was largely applied by other authors in the subsequent years (Guterres *et al.*, 1995, Thioune *et al.*, 1997, Govender *et al.*, 1999, Chorny *et al.*, 2002, Galindo-Rodriguez *et al.*, 2004, Bilati *et al.*, 2005, Galindo-Rodriguez *et al.*, 2005). It consists of a simple procedure for the preparation of nanocapsules (NC) by interfacial deposition of a preformed, well-defined, and biodegradable polymer following displacement of a semi-polar solvent miscible with water from a lipophilic solution. The method of preparation yielded spherical vesicular nanocapsules, which consisted of an oily cavity – where the drug is dissolved - surrounded by a thin wall formed by interfacial deposition of the polymer. When organic and aqueous phases are in contact, it is assumed that solvent diffuses from the organic phase into the water and carries with it some polymer chains, which are still in solution. Then, as the solvent diffuses further into the water, the associated polymer chains aggregate forming NC. Therefore, this method involves the equilibrium among a polymer, its solvent and a non-solvent.

In order to predict the characteristics of the nanoparticle and also to improve the process, it was developed a mathematical model that takes in account: (a) the type of polymer; (b) interaction between solvent and polymer; and, (c) solvent diffusion process. After the description of the nanocapsules preparation, the mathematical model is explained. Then, the numerical simulation and its results are discussed. Finally, in the appendix the Free Volume model, applied to calculate the diffusivity polymer/solvent, is explained.

2. NANOCAPSULES PREPARATION

As mentioned in the previous section, the nanocapsules are prepared according to the method of nanoprecipitation. This method is based on the spontaneous emulsification of the organic internal phase, in which the polymer is dissolved, into the external aqueous phase. In this work nanocapsules of poly(ε-caprolactone) (PCL) containing 3-benzophenon (solar protection factor) were prepared according to the following procedure (Fessi *et al.*, 1989): 100 mg of PCL, 76.6 mg of sorbitan monostearate, 333 mg of Mygliol 810 (caprylic/capric triglyceride) and 30mg of Benzophenon-3 are first dissolved in acetone (27 ml). The resulting organic solution is poured in 53 ml of water containing 76.6 mg of polysorbate 80. The aqueous phase immediately turns milky with bluish opalescence as a result of the formation of nanocapsules, the wall of which is mainly constituted by PCL, and the oily core by the benzophenon-mygliol solution. The size of the nanoparticles is then analyzed by *Dynamic Light Scattering* (Zetasizer Nano, Malvern).

3. MATHEMATICAL MODELLING

It was considered that the nanoprecipitation produces perfect spherical particles and also that each nanoparticle is originated from one droplet formed immediately after the mixing of organic phase and aqueous phases. The major model assumptions are: (a) there is a negligible relative velocity between the droplet and the water; therefore, the external mass transfer is approximated by diffusion. This assumption can be done based on the order of the Stokes number, which is related to the particle velocity and is defined as (Crowe, 2005, Rielly and Marquis, 2001):

$$St \equiv \frac{\tau_v}{\tau_F} = \frac{d_p^{\,2}\rho_p V}{18\mu L} \quad [1] \tag{1}$$

For small Stokes numbers, the particles follow the fluid motion; but for large *St*, the particles follow different trajectories from the fluid elements. The Stokes number (Figure 1) was calculated for fluid velocities between $1x10^{-3}$ and 1 $m.s^{-1}$ (based on CFD simulations for a stirred tank that are not showed here), and particle diameters from 100 to 4000 nm. As the Stoke number is in all cases less than 10^{-5}, the assumption of negligible relative velocity between the droplets and the external phase can be considered valid.

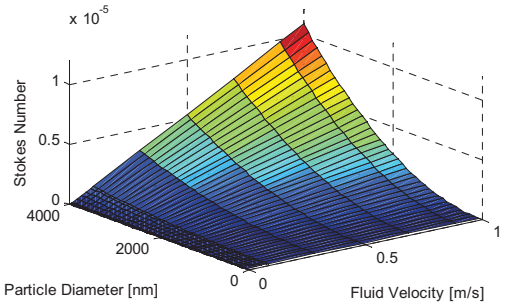

Fig. 1. Stokes Number.

(b) the diffusion is one-dimensional along the radial direction; and, (c) the diffusivity varies with time and concentration only.

Based on these assumptions, the mass balance equation for the solvent, written in spherical coordinates is:

$$\frac{\partial c_1(r,t)}{\partial t} = \frac{D}{r^2}\left(\frac{\partial}{\partial r}\left(r^2\left(\frac{\partial c_1(r,t)}{\partial r}\right)\right)\right)^{2} \tag{2}$$

This is a moving boundary problem, since the size of the droplet reduces because of the diffusion.

As the dimensions of dependent and independent variables are not the same, a variable normalization was be done including new variables τ, rh, and c_{1h} defined as,

$$t_0 = \frac{r_0^2}{D} \tag{3}$$

$$\left\{r = rh \cdot r_0,\ t = \tau \cdot t_0,\ c_1(r,t) = c_{1h}(rh,\tau)\cdot \rho_1\right\}^{3} \tag{4}$$

After the normalization, (2) is then rewritten as:

$$\frac{1}{t_0}\cdot\frac{\partial c_{1h}(rh,\tau)}{\partial \tau} = \frac{D}{r_0^{\,2}\cdot rh^2}\left(\frac{\partial}{\partial rh}\left(rh^2\left(\frac{\partial c_{1h}(rh,\tau)}{\partial rh}\right)\right)\right). \tag{5}$$

3.1 Initial and Boundary Conditions

It is assumed that the solution is well mixed and therefore, the concentration inside the droplet is uniform. Thus the initial condition is,

$$c_{1h}(rh,0) = c_{1h0} \qquad 0 \le rh \le r0\,. \tag{6}$$

Where c_{1h0} is evaluated according to the experimental conditions.

The boundary condition at the center of the droplet (rh=0) arises from the symmetry,

$$\left.\frac{dc_{1h}}{drh}\right|_{rh=0} = 0 \qquad t \ge 0\,. \tag{7}$$

Additionally, the boundary condition at the interface was calculated based on the mass balance and can be written as

$$\left.\frac{dc_{1h}}{dt}\right|_{\text{rh=R}} = \frac{D_{S-W}}{4\pi R^2}\left(c_{1h}(R) - c_{1h}(\infty)\right)^{4} \tag{8}$$

3.2 Boundary Movement

The boundary movement is calculated based on the assumption that both the mass of polymer, oil and drug remain constant during the diffusion process. The volume of the droplet is considered to be

$$V_D = V_2 + V_1 + V_{oil} + V_{drug} \equiv \frac{4}{3}\pi R^{3\,5} \tag{9}$$

Per definition the volume of polymer and solvent inside the droplet are

$$V_2 = m_2/\rho_2 \qquad V_1 = (c_1/\rho_1)V_D^{\,6} \tag{10}$$

Substituting (10) in (9) and isolating for *R*, then the radius can be calculated as

$$R(t) = \sqrt[3]{\left[3\cdot\left(\frac{m_2}{\rho_2} + V_{oil} + V_{drug}\right)\cdot\left(1 - \frac{c_1(t)}{\rho_1}\right)^{-1}\right]\Big/ 4\pi}\,. \tag{11}$$

3.3 Model Parameters

The two main parameters of this model are the diffusivity solvent/polymer and the diffusivity solvent/water.

The experimental data presented by Wild (2003) was adjusted as a polynomial curve to describe the diffusivity of acetone in water.

$$D_{S\text{-}W} = -4.737 w_S + 15.92\, w_S - 14.71\, w_S + 4.738 \tag{12}$$

where w_s is the molar fraction of water in the external phase.

The diffusivity between polymer and solvent was modelled according to the Free Volume Theory (Vrentas and Duda, 1976, Vrentas and Duda, 1977a, Vrentas and Duda, 1977b, Vrentas and Duda, 1979). Those authors applied the Flory–Huggins thermodynamic model in their free volume diffusion theory to describe the polymer solvent enthalpic and entropic

[1] τ_F - characteristic time of the flow field; τ_v - particle relaxation time; d_p - particle diameter; ρ_p - particle density; V - fluid velocity, μ - fluid viscosity; L - characteristic dimension of the obstacle.

[2] c_1 - concentration of solvent; r - particle radius; D - diffusivity; t - time.

[3] r_0 - initial droplet radius; D - diffusivity; ρ_1 - solvent density.

[4] R - actual radius of the droplet; $D_{S\text{-}W}$ - diffusivity of the solvent in the external phase; $c_{1h}(R)$ - concentration of solvent at the interface; $c_{1h}(\infty)$ - bulk concentration.

[5] V_D - volume of the droplet; V_1, V_2, V_{oil}, V_{drug} - volume of solvent, polymer, oil, and drug, respectively.

[6] m_2 - mass of polymer; ρ_2 - polymer density.

interactions. For the estimation of solvent diffusion coefficient in polymer solution systems, free-volume parameters for the both polymer and solvent must be available. The free volume (FV) diffusion model developed by Vrentas & Duda describes the solvent self-diffusion coefficient (D_1) and the polymer/solvent binary mutual diffusion coefficient (D) as given by (13) and (14), respectively.

$$D_1 = D_0 \exp\left(\frac{-E}{RT}\right)\cdot\exp\left(\frac{-\left(w_1\hat{V}_1^* + w_2\xi\hat{V}_2^*\right)}{w_1\left(\frac{K_{11}}{\gamma}\right)\left(K_{21}-T_{g1}+T\right)+w_2\left(\frac{K_{12}}{\gamma}\right)\left(K_{22}-T_{g2}+T\right)}\right) \quad (13)$$

$$D = D_1\left(1-\phi_1\right)^2\left(1-2\chi\phi_1\right) \quad (14)$$

In (13) the first exponential term can be considered as the energy factor, and the second exponential term is the free-volume factor. Eq. (14) contains the following implicit assumptions (Zielinski and Duda, 1992): (a) the mutual-diffusion coefficient is related theoretically to the solvent and polymer self-diffusion coefficients through an expression developed by Bearman (1961); (b) the contribution of the polymer self-diffusion coefficient to the mutual-diffusion is negligible; and, (c) the Flory-Huggins (Flory, 1970) model accurately describes the polymer activity. In addition, the specific free volumes of the polymer and solvent are presumed to be additive (without a volume change on mixing), and thermal expansion coefficients are approximated by average values over the temperature intervals of interest (Frick *et al.*, 1990, Lodge *et al.*, 1990). There are 13 independent parameters to be evaluated in (14). Some of them can be grouped reducing this number to the following variables: K_{11}/γ, $K_{21}-T_{g1}$, K_{12}/γ, $K_{22}-T_{g2}$, $\hat{V}_1^*$, $\hat{V}_2^*$, D_0, E, , ξ, and χ, that must be determined to estimate mutual diffusivities. All of these parameters have physical significance, and therefore one must be able to evaluate every parameter from sources other than diffusion studies. The guidelines to calculate them, clarified by Zielinski and Duda (1992), were used in this work. Additionally the modification proposed by Wang *et al.* (2007), according to the Sanchez-Lacombe equation-of-state (SL EOS), was also taken in account and is explained in Appendix A. The process was considered to be isotermic and isobaric (T=298K, P=1bar and E=0). All the parameters are listed in Table 1 and more details can be found in Appendix A.

Table 1: Model Parameters.

$\hat{V}_1^*$	0.9695 cm^3/mol	(K_{11}/γ)	0.983 x 10^{-3}
$\hat{V}_2^*$	0.8181 cm^3/mol	ρ^*	1.1427 g/cm^3
δ_1	18.29 J$^{1/2}$/cm$^{3/2}$	T^*	668 K
δ_2	20.85 J$^{1/2}$/cm$^{3/2}$	P^*	4035 bar
D_0 x 10^4	14.3 cm^2/s	T_{g2}	213 K
K_{21}-T_{g1}	-12.12		

The numerical values of number- and volume-average (size and standard deviation) – measured with ZetaSizer Nano® from samples all prepared according to the same methodology – are described in Table 2.

4. NUMERICAL SIMULATION

Experimentally the mean diameter is measured by *Dynamic Light Scattering* (ZetaSizer Nano® – Malvern). Typical number and volume density distributions, measured, can be seen in Fig. 2.

According to Table 2 and Fig. 2, it is observed that: (a) The number-average size is always smaller than the volume-average, as the contribution of a spherical particle grows proportionally with D^3; (b) The standard deviation is about 32 – 41% of the averaged value; and, (c) The size distribution does not follow a normal distribution.

Table 2: Number and Volume average sizes.

	Number-average particle diameter	Volume-average particle diameter
Sample 1	222.12 ± 71.25	303.76 ± 103.68
Sample 2	199.23 ± 67.83	285.13 ± 103.97
Sample 3	200.81 ± 73.60	300.90 ± 117.73
Sample 4	200.57 ± 72.48	303.66 ± 126.88

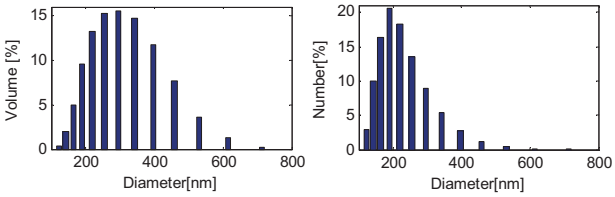

Fig. 2: Measured Number and Volume density distribution.

If it is assumed that the number of droplets/particles remains constant during all the process, the initial distribution can be calculated through the mass balance and based on the experimentally volume density distribution at final time, as explained by Fig. 3.

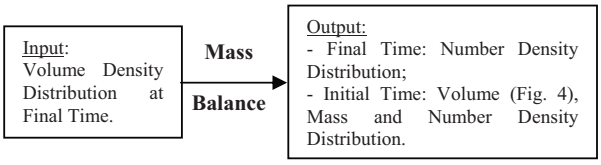

Fig. 3: Measured number and volume size distribution.

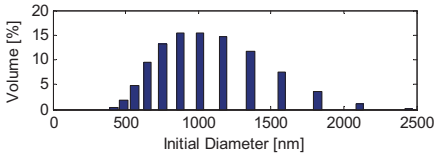

Fig. 4: Calculated Initial Size Distribution.

The calculated number density at final time was compared to the measured one, as can be seen in Fig. 5. The good agreement between both assures that the methodology used in this work is correctly applied.

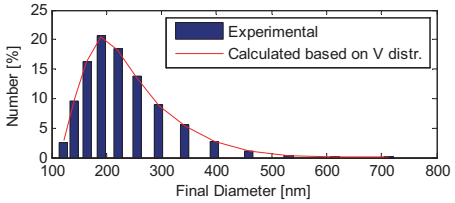

Fig. 5: Comparison between the Experimental and Calculated Number Density Size Distribution.

As the initial size distribution is now available, the diffusion

model can be simulated. It was done in Maple, which is capable of finding solutions for higher order PDE or PDE systems.

Based on the initial size distribution, (5) is solved for each class of particle size. After that, the new radius can be thus calculated. If the relative difference (*ΔDiam*) between the new and old radius is less than $1x10^{-5}$, the process ends; if not, the iteration process goes on as illustrated in Fig. 6.

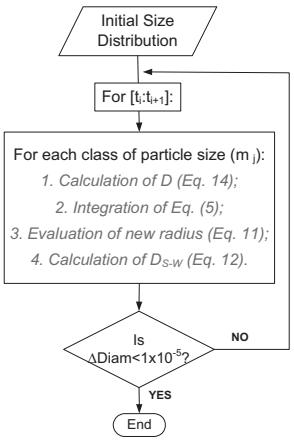

Fig. 6: Scheme of solution implemented in MAPLE.

5. RESULTS AND DISCUSSION

The model predicts that in about 12 ms all the particles reach the final diameter. This result is in qualitative agreement with what is observed experimentally, that is, as the organic phase is mixed in the aqueous phase, the suspension becomes *immediately* (at least for the human eyes) opaque, as a result of the nanoparticle formation.

Throughout the diffusion process, gradients of oil, acetone and polymer arise into the droplet leading to the reduction in size and the formation of the nanoparticle, as can be seen in Fig. 7. Each line represents one class of particle that forms the distribution.

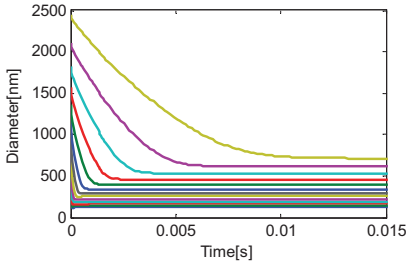

Fig. 7: Evolution of Particle Size in time.

For the smallest particles, it is observed that the diameter reduction is very fast, which is a consequence of the fast diffusion of acetone to the external medium, as can be seen in Fig. 8.

The order of magnitude of the diffusion time is in agreement with that found by Moinard-Chécot *et al.* (2008). They tried to measure the duration of the solvent diffusion step with a stopped-flow apparatus. In this experiment, only the signal corresponding to the final state could be observed, i.e., the diffusion step is less than 20 ms (the acquisition time of the apparatus).

Meanwhile the biggest particles presented a slower diffusion profile. Because of their initial big size, it takes longer for the solvent to reach the interface and consequently, to be transferred to the external medium. As more solvent diffuses out of the droplet, the concentration of polymer inside the droplet increases and consequently, the diffusivity polymer/solvent also grows up. At intermediate steps, the slow reduction in size showed by the largest particles leads almost to a bimodal volume and mass density distribution, as can be seen in Fig. 9.

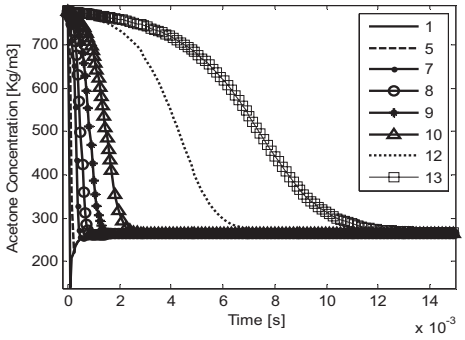

Fig. 8: Acetone concentration at the interface.

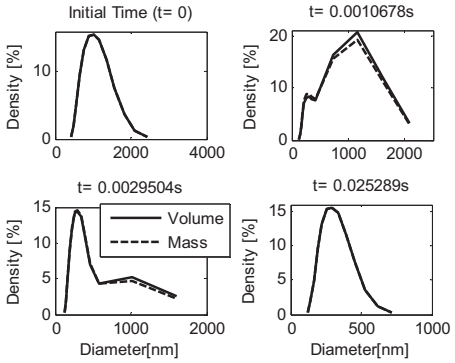

Fig. 9: Volume and Mass Distribution at the initial and final time, and 2 instants of time in-between.

The comparison between the experimental and calculated final volume density distribution (Fig. 10) shows a very good agreement, confirming that the assumptions done in sections 2 and 3 are suitable for modelling the system.

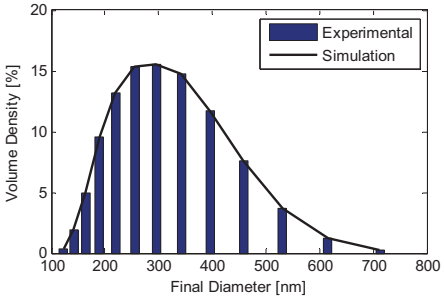

Fig. 10: Comparison between the experimental and simulated volume density distribution.

In order to generalize the model, a probability density

distribution can be employed to describe the initial size of the droplets. Applying the gamma distribution it is possible then to compare the experimental and simulation results, as show in Fig. 11. Analyzing both results and considering the standard deviation of the measurement, it is possible to confirm that the model and the methodology presented in this work are suitable to simulate the nanoprecipitation.

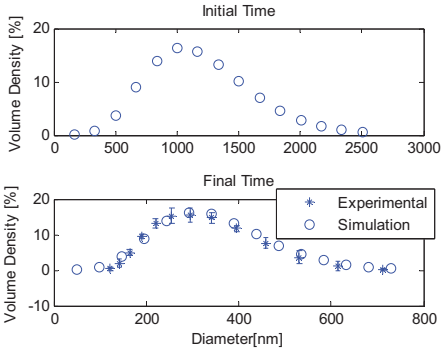

Fig. 11: Results obtained when using a gamma distribution to describe the droplets initial size. (a) Initial size distribution, (b) Final size distribution.

6. CONCLUSIONS

This work shows that it is possible to obtain satisfactory results using a simplified PDE model for the nanoprecipitation. The adopted approach considers several variables that have influence on diffusion, like type of polymer, solvent and non-solvent; affinity among them; and, polymer solubility. As a result, it is then possible to evaluate the particle size distribution during the nanoprecipitation. The comparison between the simulated and measured sizes showed a quite good agreement, suggesting that the employed methodology can describe correctly the nanoprecipitation.

The proposed model can be combined with CFD simulator in order to improve the predictions. From the simulation, one could try to evaluate more accurately the initial droplet distribution. This methodology could thus be applied to study the influence of several kinds and sizes of reactors and mixers in the final properties of the nanoparticles.

Acknowledgments: Prof. Wolfgang Marquardt (PT.AVT – RWTH Aachen) and CNPq/DAAD.

7. REFERENCES

Bearman, R. J. (1961) On the Molecular Basis of some Current Theories of Diffusion. *J. Phys. Chem.,* 65**,** 1961-1968.

Bilati, U., Allemann, E. and Doelker, E. (2005) Development of a nanoprecipitation method intended for the entrapment of hydrophilic drugs into nanoparticles. *European Journal of Pharmaceutical Sciences,* 24**,** 67-75.

Chorny, M., Fishbein, I., Danenberg, H. D. and Golomb, G. (2002) Lipophilic drug loaded nanospheres prepared by nanoprecipitation: effect of formulation variables on size, drug recovery and release kinetics. *Journal of Controlled Release,* 83**,** 389-400.

Crowe, C. T. (2005) *Multiphase Flow Handbook*, CRC Taylor & Francis.

Des Rieux, A., Fievez, V., Garinot, M., Schneider, Y.-J. and Préat, V. (2006) Nanoparticles as potential oral delivery systems of proteins and vaccines: A mechanistic approach. *Journal of Controlled Release,* 116**,** 1-27.

Fessi, H., Puisieux, F., Devissaguet, J. P., Ammoury, N. and Benita, S. (1989) Nanocapsule formation by interfacial polymer deposition following solvent displacement. *International Journal of Pharmaceutics,* 55**,** R1-R4.

Flory, P. J. (1970) Thermodynamics of Polymer Solutions. *Disc. Faraday Soc.,* 49**,** 7 - 29.

Frick, T. S., Huang, W. J., Tirrell, M. and Lodge, T. P. (1990) Probe diffusion in polystyrene/toluene solutions. *Journal of Polymer Science Part B: Polymer Physics,* 28**,** 2629-2649.

Galindo-Rodriguez, S., Allémann, E., Fessi, H. and Doelker, E. (2004) Physicochemical Parameters Associated with Nanoparticle Formation in the Salting-Out, Emulsification-Diffusion, and Nanoprecipitation Methods. *Pharmaceutical Research,* 21**,** 1428-1439.

Galindo-Rodriguez, S. A., Puel, F., Briancon, S., Allemann, E., Doelker, E. and Fessi, H. (2005) Comparative scale-up of three methods for producing ibuprofen-loaded nanoparticles. *European Journal of Pharmaceutical Sciences,* 25**,** 357-367.

Govender, T., Stolnik, S., Garnett, M. C., Illum, L. and Davis, S. S. (1999) PLGA nanoparticles prepared by nanoprecipitation: drug loading and release studies of a water soluble drug. *Journal of Controlled Release,* 57**,** 171-185.

Guterres, S. S., Fessi, H., Barratt, G., Devissaguet, J. P. and Puisieux, F. (1995) Poly (DL-lactide) nanocapsules containing diclofenac: I. Formulation and stability study. *International Journal of Pharmaceutics,* 113**,** 57-63.

Hansen, C. M. (2000) *Hansen solubility parameters: a user's handbook*, CRC Press

Jabr-Milane, L., Van Vlerken, L., Devalapally, H., Shenoy, D., Komareddy, S., Bhavsar, M. and Amiji, M. (2008) Multi-functional nanocarriers for targeted delivery of drugs and genes. *Journal of Controlled Release,* 130**,** 121-128.

Lodge, T. P., Lee, J. A. and Frick, T. S. (1990) Probe diffusion in poly (vinyl acetate) / toluene solutions. *Journal of Polymer Science Part B: Polymer Physics,* 28**,** 2607-2627.

Moinard-Chécot, D., Chevalier, Y., Briançon, S., Beney, L. and Fessi, H. (2008) Mechanism of nanocapsules formation by the emulsion-diffusion process. *Journal of Colloid and Interface Science,* 317**,** 458-468.

Rielly, C. D. and Marquis, A. J. (2001) A particle's eye view of crystallizer fluid mechanics. *Chemical Engineering Science,* 56**,** 2475-2493.

Rodgers, P. A. (1993) Pressure-volume-temperature relationships for polymeric liquids: A review of equations of state and their characteristic parameters for 56 polymers. *Journal of Applied Polymer Science,* 48**,** 1061-1080.

Sugden, S. (1927) Molecular Volumes at Absolute Zero: II. Zero Volumes and Chemical Composition. *Journal of the Chemical Society***,** 1786 - 1798.

Thioune, O., Fessi, H., Devissaguet, J. P. and Puisieux, F. (1997) Preparation of pseudolatex by nanoprecipitation: Influence of the solvent nature on intrinsic viscosity and interaction constant. *International Journal of Pharmaceutics,* 146**,** 233-238.

Van Dijk, M. A. and Wakker, A. (1997) *Polymer Thermodynamics Library - Volume 2: Concepts of Polymer Thermodynamics*.

Van Krevelen, D. W. (1990) *Properties of Polymers*, Elsevier.

Vrentas, J. S. and Duda, J. L. (1976) Diffusion of Small Molecules in Amorphous Polymers. *Macromolecules,* 9**,** 785-790.

Vrentas, J. S. and Duda, J. L. (1977a) Diffusion in Polymer-Solvent Systems. I. Reexamination of the Free-Volume Theory. *J. Polymer Sci., Polymer Phys.,* 15**,** 403 - 416.

Vrentas, J. S. and Duda, J. L. (1977b) Diffusion in Polymer-Solvent Systems. II. A Predictive Theory for the Dependence of Diffusion Coefficients on Temperature, Concentration, and Molecular Weight. *J. Polymer Sci., Polymer Phys.,* 15**,** 417 - 439.

Vrentas, J. S. and Duda, J. L. (1979) Molecular Diffusion in Polymer Solutions. *AIChE J.,* 25**,** 1 - 24.

Wang, B.-G., Lv, H.-L. and Yang, J.-C. (2007) Estimation of solvent diffusion coefficient in amorphous polymers using the Sanchez-Lacombe equation-of-state. *Chemical Engineering Science,* 62**,** 775-782.

Wild, A. (2003) Multicomponent Diffusion in Liquids. TU München.

Zielinski, J. M. and Duda, J. L. (1992) Predicting polymer/solvent diffusion coefficients using free-volume theory. *AIChE Journal,* 38**,** 405-415.

Appendix A. FREE VOLUME THEORY PARAMETERS

$\hat{V}_1^*$ *and* $\hat{V}_2^*$ – The two critical volumes were approximated as the specific volumes of solvent and polymer at absolute zero temperature. The molar volumes at 0K were estimated using a group contribution method (Sugden, 1927).

χ – The interaction parameter in terms of solubility parameters can be calculated through the following equation (Van Dijk and Wakker, 1997):

$$\chi = \frac{V_m}{RT}\left(\delta_1 - \delta_2\right)^2 \tag{15}$$

where V_m is the molar volume, R is the ideal gas constant and δ_1 and δ_2 are the solvent and polymer solubility parameters respectively.

A widely used solubility parameter approach for predicting polymer solubility is proposed by Hansen (2000). The basis of the so-called Hansen Solubility Parameters (HSP) is that the total energy of vaporization of a liquid consists of several individual parts. These arise from (atomic) dispersion forces (E_D), (molecular) permanent dipole-permanent dipole forces (E_P) and (molecular) hydrogen bonding (electron exchange) (E_H). The basic equation which governs the assignment of Hansen parameters is that the total cohesion energy, E, must be the sum of the individual energies which make it up

$$E = E_D + E_P + E_H \tag{16}$$

Dividing each one by the molar volume gives the square of the total solubility parameter.

$$\begin{aligned} E/V &= E_D/V + E_P/V + E_H/V \\ \delta^2 &= \delta_D^2 + \delta_P^2 + \delta_H^2 \end{aligned} \tag{17}$$

The solubility parameter components were predicted from group contribution method, using the following equations (Van Krevelen, 1990).

$$\delta_d = \sum F_{di} \Big/ V \qquad \delta_p = \sqrt{\sum F_{pi}^2} \Big/ V \qquad \delta_h = \sqrt{\sum E_{hi} \Big/ V} \tag{18}$$

D_0, K_{21}-T_{g1}, (K_{11}/γ) – These are solvent parameters (acetone) and the values previously collected by Zielinski and Duda (1992) were used here.

$(K_{12}/\gamma)(K_{22}$-T_{g2}+$T)$*(Wang et al., 2007)* – According to the Vrentas-Duda model (Zielinski and Duda, 1992), the hole free volume of a polymer $\hat{V}_{FH2}$ in its rubbery state can be expressed as

$$\frac{\hat{V}_{FH2}}{\gamma} = \left(K_{12}/\gamma\right)\left(K_{22} - T_{g2} + T\right) \tag{19}$$

Assuming that the hole free volume is equal to the volume defined by the WLF (Williams, Landel and Ferry) theory, at the atmospheric pressure, (19) becomes

$$\frac{\hat{V}_{FH2}}{\gamma} = V\left\{0.025 + \int_{T_{g2}}^{T}\left[\left(1+\frac{\tilde{P}}{\tilde{\rho}^2}\right)\Big/\left(T\left[\frac{\tilde{T}}{1-\tilde{\rho}} - 2\right]\right)\right]_{P0} dT\right\} \tag{20}$$

where $V(=1/\rho)$ is the volume of polymer per gram at temperature T, which can be estimated by the SL EOS according to the equation,

$$\tilde{\rho} = 1 - \exp\left[-\left(\tilde{\rho}^2 + \tilde{P}\right)/\tilde{T} - \tilde{\rho}\right] \tag{21}$$

with the definition

$$\tilde{\rho} = \rho/\rho^*, \qquad \tilde{T} = T/T^*, \qquad \tilde{P} = P/P^* \tag{22}$$

where ρ^*, T^* and P^* are characteristics parameters of mass density, temperature and pressure, respectively. These parameters are listed by Rodgers (1993) and those for PCL used in this work are listed in Table 1. This method eliminates the need to use polymer viscoelastic data for determining the polymer free volume parameters. Additionally, its scope is also extended to include not only temperature and concentration but also pressure influence on solvent diffusivities. The only new parameters introduced by this model (ρ^*, T^* and P^*) are three parameters of the SL EOS (Wang et al., 2007).

Predictive Modeling of Key Process Variables in Granulation Processes based on Dynamic Partial Least Squares

D. Ronen*, C.F.W. Sanders*, H.S. Tan, P. R. Mort***, F.J. Doyle III***

**Department of Chem. Eng., UCSB, Santa Barbara, CA 93106-5080 USA (e-mail: frank.doyle@isb.ucsb.edu)*
*** P & G Technical Centre, Ltd. Whitley road, Longbenton, Newcastle Upon Tyne, NE12 9TS UK (e-mail: tan.h.9@pg.com)*
****Procter & Gamble Co. 5299 Spring Grove Ave, Cincinnati, OH 45217 USA (e-mail:mort.pr@pg.com)*

Abstract: Granulation is a multivariable process characterized by several physical attributes that are essential for product performance, such as granule size and size distribution. An optimally operated granulation process will yield, in a reproducible manner, product with tightly controlled performance attributes. In this paper predictive models of the dynamics of these key variables are developed using a dynamic partial least squares approach. The method, demonstrated here on process simulation as well as on an industrial mixer-granulator process, result in accurate predictions. These models motivate the development of model predictive controllers for these processes.

Keywords: Granulation, Process control, Dynamic modeling, Partial least squares

1. INTRODUCTION

Granulation is a complex process in which many input variables influence many product properties. As Iveson et al. describe in a review paper (2001), the understanding of the fundamental processes that control granulation behavior and product properties have increased in recent years. This knowledge can be used during process design, in choosing the right formulation and operating conditions, and it can also be used to improve process control. Although many variables are set constant during process design, variations during production in input variables occur due to the variable nature of the powder feed. Even if all granule properties, except for size, are ignored for process control, a one dimensional granule size distribution can be constructed by multiple discrete output variables, in order to represent the shape of the distribution (these can be mean sizes (with coefficients of variation), percentile sizes, moments or size bins). Model Predictive Control (MPC) is an effective method to control such multiple input, multiple output processes (García, et al., 1989). The majority of MPC applications in the chemical process industries utilize empirical models that are constructed from plant data. In this work, we explore the use of dynamic partial least squares to construct these empirical models.

2. METHODS

2.1 Partial Least Squares

Partial Least Squares (PLS) methods have been demonstrated as a useful tool for analysis of data and modeling of the systems from which the data are collected (Kaspar and Ray, 1993). Unlike related methods, such as Principal Component Analysis (PCA), which finds factors that capture the greatest amount of variance in the predictor (X) only, the PLS method attempts to find factors which both capture variance and achieve correlation. PLS handles this by projecting the information in high dimensional spaces (X,Y) down to low dimensional spaces defined by a small number of latent vectors (t_1,t_2…t_a). These new latent vectors summarize all the important information contained in the original data sets, by representing the scaled and mean-centered values of X and Y matrices as:

$$X = \sum_{i=1}^{a} t_i p_i^T + E$$
$$Y = \sum_{i=1}^{a} u_i q_i^T + F \qquad (1)$$

where the t_i are latent (score) vectors calculated sequentially for each dimension i=1,2,…a.

In the PLS method, the covariance between the linear combinations of X and the output measurement matrix Y is maximized at each iteration, using the vectors p_i and q_i which are the loading vectors whose elements express the contribution of each variable in X and Y toward defining the new latent vectors t_i and u_i. E and F are residual matrices for X and Y blocks, respectively. The optimal number of latent vectors retained in the model is often determined by cross-validation (Dayal et al. 1994).

In an industrial environment, it is more often the case that many of the predictor variables (X) are highly correlated with one another and their covariance matrix is nearly singular,

which renders classical regression methods intractable. Reduced space methods such as PLS and PCA can overcome this problem (MacGregor and Kourti, 1995). PLS is also robust to measurement noise in the data and can be used in cases where there are random missing data and when the number of input variables is greater than the number of observations (Dayal et al. 1994). Various examples of the implementation of PLS analysis to industrial process modeling and control can be found in the literature (for example, Dayal et al., 1994, MacGregor and Kourti, 1995, and others).

Process dynamics can be incorporated into the PLS model by including columns of lagged outputs and/or inputs into the predictor block (*X*) (Dayal et al., 1994, Kaspar and Ray, 1993, Juricek et al. 2001). The resulting PLS model is actually an ARX type input-output model of the form:

$$A(q^{-1})y_i(k) = \sum_{j=1}^{mu} B_j(q^{-1})u_j(k - nk_j) \tag{2}$$

$$A(q) = 1 + a_1 q^{-1} + a_2 q^{-2} + ... + a_m q^{-m} \tag{3}$$

$$B_j(q) = b_{j,1} q^{-1} + b_{j,2} q^{-2} + ... + b_{j,m} q^{-m} \tag{4}$$

where y denotes the output variable (e.g., median particle size, d_{50}), and u denotes the manipulated variable (e.g., binder flow). The terms A and B contain the autoregressive and exogenous terms of the model, respectively. The autoregressive term captures dynamics through lagged terms of the output, and the exogenous term captures dynamics through lagged terms in the input.

Once the models have been calculated from the plant data, it is useful to evaluate their properties using several key statistical measures. Some of the useful statistics that are associated with reduced space models (Wise et al. 2006) are outlined below:

Q residual – is simply the sum of squares of each row of E (from eq. 1), i.e. for the ith sample in X, x_i:

$$Q_i = e_i e_i^T \tag{5}$$

where e_i is the ith row of E. The Q statistics is a measure of the difference between a sample and its projection into the a principal components retained in the model.

Hotelling T^2 is a measure of the variation in each sample within the model. Its value is the sum of normalized squared scores, defined by:

$$T_i^2 = t_i \lambda^{-1} t_i^T \tag{6}$$

where t_i are the score vectors (eq. 1) and λ is a diagonal matrix containing the eigenvalues corresponding to a eigenvectors (principal components) retained in the model.

Together, the T^2 and Q residual statistics are useful in evaluating the fitness of a PLS model to specific data. It is possible to calculate statistically meaningful confidence limits for both cases.

2.2 Simulation studies

In our previous work, a nonlinear one dimensional population balance model (1D-PBM) was successfully used to model a laboratory continuous drum granulation process with fine particle recycle (Glaser et al., 2008). The same model is used here as a base for a process simulation (Figure 1) for a preliminary evaluation and sensitivity test of the applicability of the dynamic PLS modeling technique for granulation.

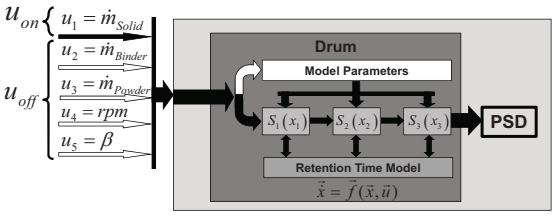

Fig. 1. Simulator structure: five inputs are included in the simulator: binder spray rate, fine powder feed-rate, drum rotation-rate and the drum inclination angle. The model is divided into three well mixed drum compartments, each described by an individual set of ODEs, a retention time model and a set of global parameters that influence the model behavior (taken from Glaser 2008).

Both particle median size (d_{50}) and, separately, particle size distribution width (d_{84}/d_{16}) were used as output variables for this study. The predictor (X) was constructed from 4 manipulated variables (solid feed flow rate, binder feed flow rate, drum rotation speed, recycle rate) and the computed recycle flow as an additional input variable. Process dynamics were incorporated into the X block by including columns of lagged output variables. The lag time was estimated using an autocorrelation function. Delay times of each of the input variables were estimated using cross correlation function, and the predictor matrix was adjusted according to the obtained delay vector. During the simulation, the 4 manipulated variables were randomly perturbed around their nominal values at steady state sequentially, i.e. input variables were perturbed one after the other in fixed time gaps. The resulting PLS-based ARX model's short horizon predictive ability was tested by cross validation with a set of separately calculated simulation sequences with different excitation regimes. For each of these cross validation sequences, the root mean square error of the model based prediction (RMSEP), relative to the simulated plant measurements was calculated for a given short horizon period. In order to make a more representative quantification of the predicting ability of the model, the short horizon start point was moved along the time axis of the data one time step after another thus creating a set of RMSEP measures out of which an average and maximum RMSEP could be calculated. All variables were mean centered and scaled to unit variance prior to processing.

Based on this technique a sensitivity test was performed in order to estimate the required size of the data set needed for reliable process modeling. Figure 2 shows the convergence of RMSEP related to the length of data set used for the PLS model training. This plot is based on averaging 100 multiple simulations and modeling runs for each training length. Sample rate was set to 2 minutes and the simulated process step response time (τ) was set to 4.5 minutes. The prediction horizon was set to 8 samples (i.e., 16 minutes). From this figure one can note that most of the dynamic features are captured by the model in the first 200 minutes of training data, as the mean RMSEP converges to low values. However using training data of up to 600 minutes would improve the model predictions. Notice that these results are not so sensitive to the excitations rate used in the modeling data set (i.e., time between two successive input variable perturbations), as long as this time is in the order of magnitude of the expected variations in process variables. Figure 3 depicts the response of the process model obtained with 520 minutes of training data to the process simulation for a step response in one of the input variables.

All of these models use one lagged output variable (granules median size) in the predictor block and 2 latent variables in the PLS model, which are linear combinations of the time-lagged values of the output variable and the delayed values of the five process variables. Figure 4 shows the prediction abilities of three PLS models obtained using different lengths of data sets for training (120, 220 and 520 minutes long) from a single simulation data, with input variable excitation every 15 minutes. In this example, the predictions of these models are cross-validated using data from a separate simulation run with randomly timed excitations of the inputs. Considering that PLS models captures covariance in X and Y, it is possible to calculated the percentage of variance captured by each of their latent variables by dividing the variance predicted by the latent variables to the total variance in the original data. The percentage of variance captured by the abovementioned 3 PLS models (from the training data) is detailed in Table 1. It is noticeable that the longer the training set used, more fine details of the process dynamics are captured by the models, confirming Figure 2 results. Notice that high values of explained variance do not guarantee good prediction of validation data by these models. The robustness of the PLS based models to measurement noise is demonstrated in Figure 5 and Table 2, where the simulated process was subject to 5% white noise on the output and input variable measurements.

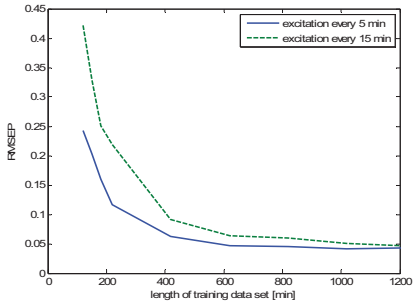

Fig. 2. Root Mean Square Error of Prediction (in validation simulation) versus length of training data set (based on modeling simulation), at different excitation rates.

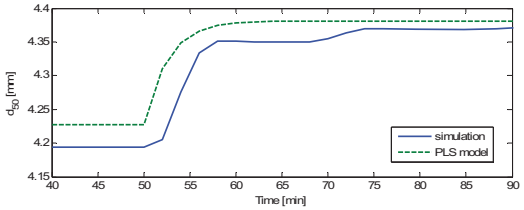

Fig. 3. Step response to a 1.2% step change in Binder feed flow - PLS model based on 520 minutes training data vs. process simulation.

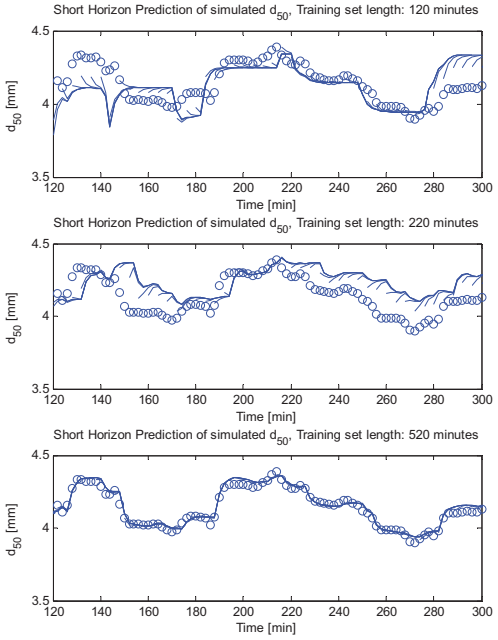

Fig. 4. PLS based dynamic model validation for different training set length. Circles represents simulation results, lines represent 8 point horizon prediction.

Table 1: Percent variance captured by PLS models based on different lengths of training data sets.

Training set length	LVs	X Block		Y Block	
		This	Total	This	Total
120min	1	76.04	76.04	82.44	82.44
	2	7.66	83.7	11.42	93.85
220min	1	59.45	59.45	93.05	93.05
	2	14.21	73.66	2.8	95.85
520min	1	41.35	41.35	97.88	97.88
	2	17.29	58.64	1.04	98.92

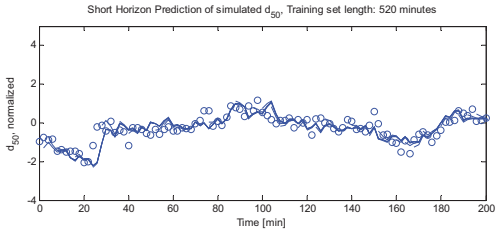

Fig. 5. PLS based dynamic model validation, simulated process with 5% white measurement noise. Circles represents simulation results, lines represent 8 point horizon prediction.

Table 2: Percent variance captured by PLS model, simulated process with 5% white measurements noise.

Training set length	LVs	X Block		Y Block	
		This	Total	This	Total
520 min	1	33.93	33.93	82.75	82.75
	2	33.10	67.03	1.61	84.37

3. DYNAMIC PLS MODELLING OF AN INDUSTRIAL PROCESS PLANT

3.1 Process plant description

In this section, we report on some preliminary studies on granulation model identification for a Procter & Gamble (P&G) industrial granulation process using normalized process data.

A complex industrial granulation process, such as the flowsheet shown in Fig. 6, was subjected to a series of (designed) random perturbations in a number of input parameters. This plant is equipped with an on-line granule size measurement system that measures particle size based on image analysis of 2-D camera images. The analysis constructed size distributions on the basis of the measured cross sectional area of the 2-D images. Granule size data along with all other plant variables were then sent to the UCSB team for modeling.

There are notable distinctions between the P&G study and the one reported in Section 2.2. The P&G process study is not meant to be used as a direct comparison (or validation) for the process simulation studies in Section 2.2. Rather, we present both as separate case studies to demonstrate the feasibility of using PLS methodology as an empirical modeling tool for granulation process control.

The low-shear drum-granulation pilot plant that was used to design the simulator in Section 2.2 produced particles with d_{50}'s of several mm; on the other hand, the medium-high shear mixer-granulation process shown in Fig 6 typically produced particles with d_{50}'s less than 1 mm. While the underlying physical mechanisms of growth and consolidation may be similar, the flow and shear fields are very different for the two processes (the drum granulator is relatively low shear, compared to the medium-high shear mixer-granulation process), the process layouts and control handles are different, as are the material properties. As such, the choices of process variables (manipulated and measured) are unique for each process.

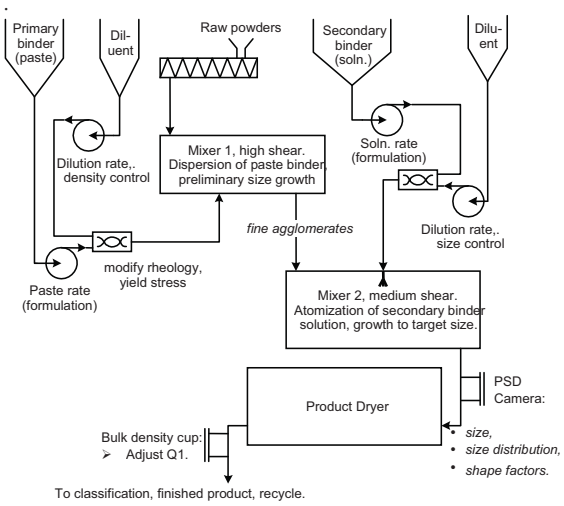

Figure 6. Representative P&G process flow diagram for mixer-granulator (Mort et al. 2001). For simplicity, this diagram omits the usual operations for classification and recycle.

3.2 PLS modeling of real plant data- Case I

Figure 7 describe the dynamic PLS model fitting obtained for the granules median size. The data set obtained from the plant originally contained 147 sampling points, each consist of 81 process variables, together with granules size measurements. Sampling time was 0.4 times the process characteristic time τ. During this time period 4 manipulating variables were subjected to random perturbations around their nominal values at steady states (Fig. 8) in a similar way to the simulation work described earlier (adjusted to the process τ), while other adjustments were continuously made to other plant variables (i.e. normal plant operations). Granules median size (d_{50}) was selected as the output variable. Nine out of the 81 process variables were chosen as predictor variables for the PLS model, based on engineering judgment, GA based variable selection (PLS Toolbox 5.0 by Eigenvector research incorporated), and trial and error. The

output lag time and process variables delay times were evaluated using the auto and cross correlation functions, respectively, as described in section 2.2. The process model uses two latent variables, which are linear combinations of the time-lagged values of the output variable and the delayed values of the nine process measurements. For an independent cross validation of the model, the above data was divided to two sections – the first half was used to train the PLS model, and the second used to test model predictions, yielding RMSEP value of 0.26. These results, as shown in Fig. 9. and Table 3, are very similar to the fitting obtained for the simulation data of the same training length to τ ratio (Fig. 2 and Fig 4. upper plot).

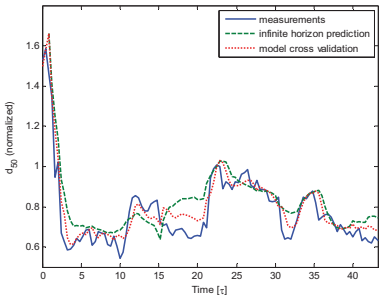

Fig. 7. Dynamic PLS model fitting to plant d_{50} data.

Table 3: Percent variance captured by PLS model, plants' d50 data.

Training set length	LVs	X Block		Y Block	
		LVi	Total	LVi	Total
60τ	1	24.97	24.97	79.34	79.34
	2	25.09	50.06	9.04	88.38
36τ	1	39.46	39.46	72.13	72.13
	2	23.31	62.77	16.8	88.92

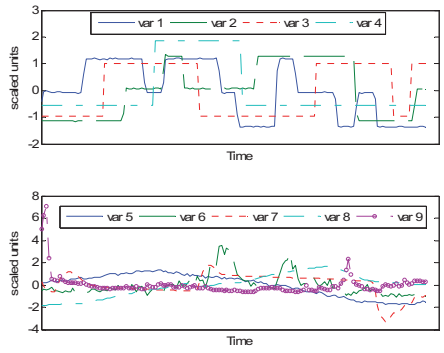

Fig. 8. Values of the 9 predictor variables used in Case I PLS model – 4 manipulated variables (top) and 5 additional process variables (bottom)

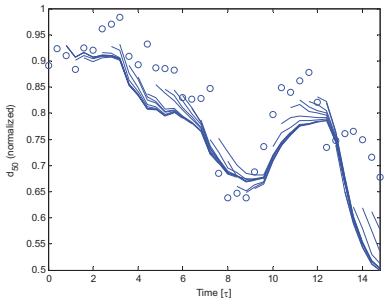

Fig. 9. Cross validation of the dynamic PLS model for plant d_{50} data. Circles represents measurements, lines represent 8 point horizon prediction.

3.3 PLS modeling of real plant data- Case II

In a separate test, the granules distribution width as a function of selected process variables was modeled. This analysis was performed on two limited sets of data, each from a different operating day. A series of step tests were performed on one of the manipulating variables. As in the previous case, other adjustments were continuously made to other plant variables to maintain normal plant operation. The standard deviation of the granules measured area was used as the output variable to be modeled. A dynamic PLS model was built using 3 input variables and one lagged output variable, based on the first data set, and then validated using the second data set, resulting in an excellent fit (Figure 10). In this case, as well, the process model uses two latent variables.

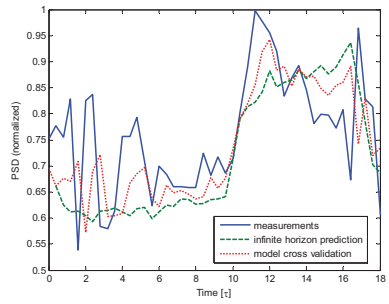

Fig. 10. Actual process data (granules area standard deviation): Cross validation of model based on first data set, tested on second data set

On the scores plot (Figure 11) it is clear, however, that these two sets represent different and distinct operating conditions. If one further examines the contribution of each variable for these two sets (Figures 12) we can see that the main difference is that on the validation set, much lower values of variable 2 were used, compared to the modeling set. It is also interesting to note that the only outlier of the modeling set also exhibits the same low value on variable 2.

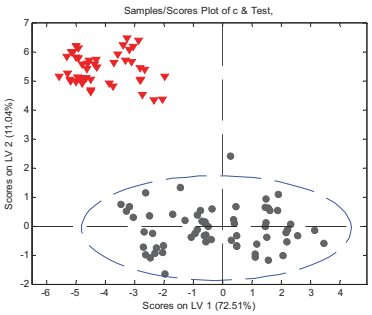

Fig. 11. Score Plots for the PSD width model. Circles are samples from the modeling set; Triangles are samples from the validation set. The ellipse marks the 95% confidence limit for the model.

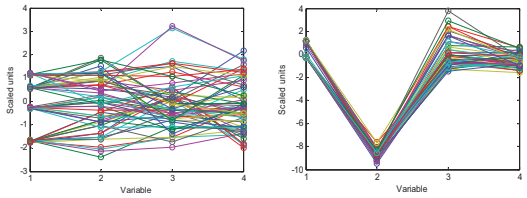

Figure 12: Values of input variables used in the modeling set (left) and in the validation set (right).

Although these results looks promising with respect to the ability to analyze and predict the granulation process variables, a quick look at the high values of Q residuals and Hotelling T^2 (Figure 13) indicates that this model is far from describing the whole complexity of the process, and many more measurements should be done in order to characterize the different operating regimes of this process.

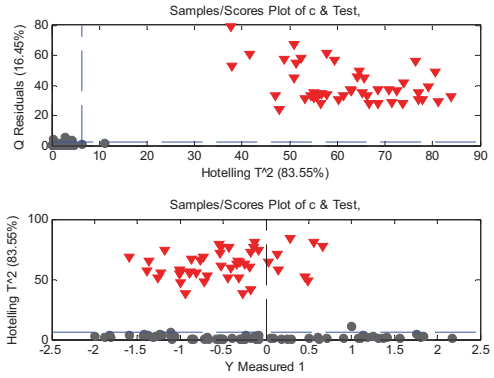

Figure 13: Q Residuals and Hotelling T^2 Values for the PSD width model

4. CONCLUSIONS

Dynamic PLS modeling was proven to be an effective tool in modeling key process variables in an industrial granulation process. Our future work will explore methods to capture the additional dynamics that remain in the plant data. We are also planning longer plant runs with larger input variable excitation to improve the model identification. Longer term goals are to develop a model-based controller for plant testing.

Funding for this work from IFPRI (International Fine Particle Research Institute) is gratefully acknowledged.

REFERENCES

Dayal, B.S., MacGregor, J.F., Taylor, P.A., Kildaw, R. and Marcikic, S. (1994). Application of Feedforward Neural Networks and Partial Least Squares Regression for Modeling Kappa Number in a Continuous Kamyr Digester, *Pulp and Paper Canada*, 95, 26-32.

García, C.E., Prett, D.M. and Morari, M. (1989), Model Predictive Control: Theory and Practice—a Survey, *Automatica*, 25, 335–348.

Glaser, T., Sanders, C.F.W., Wang, F.Y., Cameron, I.T., Litster, J.D., Poon, J.M.H., Ramachandran, R., Immanuel, C.D. and Doyle, F.J. (2008), Model Predictive Control of Continuous Drum Granulation, *Journal of Process Control*, in press.

Iveson, S.M., Litster, J.D., Hapgood, K. and Ennis, B.J. (2001), Nucleation, Growth and Breakage Phenomena in Agitated Wet Granulation Processes: A Review, *Powder Technology*, 117, 3-39.

Juricek, B.C., Seborg, D.E., and Larimore, W. E. (2001), Identification of the Tennessee Eastman Challenge Process with Subspace Methods, *Control Engineering Practice*, 9, 1337-1351.

Kasper, M.H. and Ray, W.H. (1993), Dynamic PLS Modelling for Process Control, *Chemical Engineering Science*, 20, 3447-3461.

MacGregor, J.F. and Kourti, T. (1995), Statistical Process Control of Multivariate Processes, *Control Engineering Practice*, 3, 403-414.

Mort, P.R., Capeci, S.W. and Holder J.W. (2001), Control of Agglomerate Attributes in a Continuous Binder-Agglomeration Process, *Powder Technology*, 117, 173-176.

Wise, B.M., Gallagher, N.B., Bro, R., Shaver, J.M., Windig W. and Koch, R.S. (2006), *PLS_Toolbox 4.0*, Eigenvector Research Incorporated, Wenatchee WA.

Control and Estimation of Distillation Systems

Oral Session

Geometric Estimation of Binary Distillation Columns

Carlos Fernandez and Jesus Alvarez*

Universidad Autónoma Metropolitana-Iztapalapa
Departamento de Ingeniería de Procesos e Hidráulica.
Apdo. 55534, 09340 México, D.F. MEXICO
**(e-mail: jac@xanum.uam.mx)*

Abstract: The problem of designing the estimation structure to perform a specific (entire profile, single/two-effluent, and so son) concentration estimation task in a binary distillation column with two temperature measurements is addressed within a geometric estimation (GE) framework. The structure design involves the choices of: (i) the measurement locations, (i) the complete or truncated estimation model, and (iii) the innovated-noninnovated state partition of the model. First, a structural analysis is performed on the basis of detectability measures in the light of the column characteristics, yielding candidate structures for a specific estimation task. Then, the behavior of the structures is assessed with estimator functioning and dimension considerations, yielding conclusive structural results. The proposed methodology is applied to a representative case example with experimental data.

Keywords: Nonlinear estimator, geometric estimator, nonlinear system realization, distillation column estimation.

1. INTRODUCTION

The study of the concentration estimation problem for distillation columns is motivated by the development of advanced monitoring and control schemes. The estimator design involves decisions on: (i) the structure (sensor number and locations), and (ii) the kind of (EKF, Luenberger, Geometric, etc) algorithm. In the distillation column estimation field: (i) the EKF has been, by far, the most widely employed and accepted algorithm, (ii) the sensor structure has been decided with heuristics (Oisiovici and Cruz, 2000) or observability measures (van der Berg et al. 2000; Singh and Hahn, 2005), (ii) only in a few studies (Alonso et al, 2004; Bian and Henson 2006; Venkateswarlu and Kumar, 2006; Kadu et al, 2008) the measure-based sensor location results have been tested with estimator functioning and is not clear to what extent the results depend on tuning. In principle, the resolution of this drawback requires a unified framework to address the algorithm, sensor location, and tuning aspects.

Recently (Alvarez and Fernandez, 2009), the general-purpose nonlinear geometric estimator (GE) (Alvarez and Lopez, 1999; Alvarez 2000) has been redesigned with: (i) an implementation in terms of model Jacobian matrices (and not of the cumbersome or intractable Lie derivation-based gain of the nonlinear Luenberger observer), (ii) the structure (sensors, complete/truncated model, innovation scheme) as a key design degree of freedom, and (iii) a simple tuning procedure based on a robust convergence criterion, regardless of the structure, and (iv) testing with an experimental binary distillation column. This adjustable-structure GE methodology and the associated nonlinear detectability measures (Lopez and Alvarez, 2004) constitute the methodological points of departure for the present study.

In this work, the problem of designing the best estimation structure (in terms of reconstruction speed, robustness, and algorithm simplicity) to perform a specific (entire profile or two-effluent) concentration estimation task in a binary distillation column with two temperature measurements is addressed, with structure meaning the choices of: (i) the *measurement locations*, (i) the (complete or truncated) *estimation model*, and (iii) the innovated-noninnovated model *state partition*. The proposed methodology is applied to a representative case example with experimental data.

2. ESTIMATION PROBLEM

2.1 Column system and model

Consider an N-stage binary distillation column, with molar feed flow F in tray n_f at (light-component) mole fraction c_F, and bottoms (or distillate) flow B (or D) at composition c_B (or c_D), and a total condenser. Under standard (constant pressure, stage equilibrium, fast holdup dynamics with perfect mixing, evaporator level control, constant molar flow, saturated feed, and adiabatic system) assumptions the *N-composition column model* is given by (Luyben, 1990)

$$\dot{c}_1 = \{(R + F)(c_2 - c_1) - V[\varepsilon(c_1) - c_1]\}/M_1 := f_1, \qquad c_B = c_1$$

$$\dot{c}_i = \{(R + F)(c_{i+1} - c_i) - V[\varepsilon(c_i) - \varepsilon(c_{i-1})]\}/\eta^{-1}(R + F) := f_i,$$
$$1 \le i \le n_f - 1, \qquad \eta(M) = a_\eta(M - M_o)^{b_\eta}$$

$$\dot{c}_{nf} = \{(R + F)(c_{nf+1} - c_{nf}) - V[\varepsilon(c_{nf}) - \varepsilon(c_{nf-1})] + F(c_F - c_{nf})\}/\eta^{-1}(R + F) := f_{nf}$$

$$\dot{c}_i = \{R(c_{i+1} - c_i) - V[\varepsilon(c_i) - \varepsilon(c_{i-1})]\}/\eta^{-1}(R) := f_i, \quad n_f + 1 \le i \le n-1$$

$$\dot{c}_N = \{R[\varepsilon(c_N) - c_N] - V[\varepsilon(c_N) - \varepsilon(c_{N-1})]\}/\eta^{-1}(R) := f_N, \; c_D = \varepsilon(c_N)$$
$$y_1 = T_1 = \beta(c_{l1}), \qquad y_2 = T_2 = \beta(c_{l2})$$

c_i is the i-th stage mol fraction of light component, V (or R) is the vapor (or reflux) flow, M_i is the i-th stage molar holdup, and T_i is the temperature measurement at the l_1-th stage, ε, β, and η are the liquid-vapor, bubble point, and (Francis weir equation) hydraulics functions, respectively. Assuming the feed composition is fixed at $\bar{c}_e$, the *preceding N-composition column model* is written by

$$\dot{c} = f_c(c, u), \quad c(0) = c_o, \quad y = h(c) := [\beta(c_{l_1}), \beta(c_{l_2})] \qquad (1)$$
$$c = (c_1,\ldots, c_N)', \quad u = (F, R, V)', \quad \dim (c, y, u) = (N, m, 3, 1)$$

In virtue of the afore stated modeling assumptions, the *actual column dynamics* are given by

$$\dot{c} = f_c(c, u) + \tilde{f}_c(c, \xi, d), c(t_o) = c_o, \ y = h(c) + \tilde{h}_c(c, \xi) + e_y \quad (2a)$$
$$\dot{\xi} = f_\xi(c, \xi, d, \dot{d}), \qquad \xi(t_o) = \xi_o, \ d = (u, e_u, d_e), \dim \xi = n_\xi \quad (2b)$$

with concentration (or unmodeled) state x (or ξ), actuator error e_u, and unmodeled exogenous input d_e. The unmodeled dynamics (2b) have slow and fast components due to the modeling-measurement errors, including holdup and enthalpy QSS assumptions. Thus, the N-composition model (1) is the actual system (2) with the modeling assumption $(\tilde{f}_c, \tilde{h}_c, e_y) = 0$.

2.2 *Adjustable*-structure estimation model

Following a previous binary distillation column GE (Alvarez and Fernandez, 2009) study with the estimation model regarded as design degree of freedom, rewrite the actual column dynamics (1) in terms of $n \le N$ modeled compositions (x):

$$\dot{x} = f(x,u) + \tilde{f}(x, \chi, d, u), x(t_o) = x_o, \ y = h(x) + \tilde{h}(x, \chi) + e_y \quad (3a)$$
$$\dot{\chi} = f_\chi(x, \chi, d, \dot{d}), \ \chi(t_o) = \chi_o, \ (x, x_\varnothing) = I_c c, \ \chi = (x_\varnothing, \xi) \qquad (3b)$$

where $x_\varnothing$ are the unmodeled concentrations and χ is the augmented unmodeled state. The vector f depends only on the modeled concentrations x, due to a key modeling assumption made for estimator decentralization purposes (Alvarez and Fernandez, 2009): (i) f is the part of f_c that describes x, and is calculated with the unmodeled state at an average constant value ($\bar{x}_\varnothing$), as the related error can be effectively compensated by the GE integral action when the estimation structure is adequately chosen. In terms of κ_1 (or κ_2) *innovated sates* x_1 (or x_2) and (n - κ) *noninnovated states* (x_ι), the *actual dynamics* (2) are given by

$$\dot{x}_1 = f_1(x_1, u) + \tilde{f}_1(x, \chi, d, u), y_1 = h_1(x_1) + \tilde{h}_1(x, \chi) + e_1 \quad (4a)$$
$$\dot{x}_2 = f_2(x_2, u) + \tilde{f}_2(x, \chi, d, u), y_2 = h_2(x_2) + \tilde{h}_2(x, \chi) + e_2 \quad (4b)$$
$$\dot{x}_v = f_v(x_v, x_1, x_2, u) + \tilde{f}_v(x, \chi, d, u), \quad x_v(t_o) = x_{vo} \quad (4c)$$
$$\dot{\chi} = \tilde{f}_\chi(x, \chi, d, \dot{d}), \ \chi(t_o) = \chi_o, \ x_1(t_o) = x_{1o}, \ x_2(t_o) = x_{2o} \quad (4d)$$

where $(x_1, x_2, x_v, x_\varnothing) = I_c c$, $\dim (x_1, x_2, x_v) = (\kappa_1, \kappa_2, \kappa_v)$
$\kappa_1 + \kappa_2 = \kappa_\iota$, $\kappa_1 + \kappa_2 + \kappa_v = n \le N$, $(x_1, x_2) = x_\iota$, $\dim (x_\iota) = \kappa_\iota$

f_1 (or f_2) corresponds to x_1 (or x_2), and is calculated with some (average) constant value [$\bar{x}_1$(or $\bar{x}_2$), $\bar{x}_v$]. From the specialization of the general-purpose definition of model structure [Alvarez and Fernandez, 2009] to the binary column case, the definition of *column model structure* follows

$$\sigma = (\kappa, x_\iota\text{-}x_v), \ \kappa = (\kappa_1, \kappa_2), \ \kappa_1 + \kappa_2 = \kappa_\iota \le n, \ x_\iota = (x_1', x_2')' \quad (5)$$

where κ is the *estimation order* vector, x_ι-x_v is the innovated-noninnovated state partition, and x_1 (x_2) are κ_1 (or κ_2) adjacent concentrations associated with the measurement y_1 (or y_2). Thus, from the enforcement of the modeling assumption

$$(\tilde{f}_1, \tilde{f}_2, \tilde{f}_v) = 0, \qquad (\tilde{h}_1, \tilde{h}_2) = 0, \qquad (e_1, e_2) = 0 \qquad (6)$$

upon the actual subsystem (4a-c), the *estimation model*, with estimation structure σ (5), follows:

$$\dot{x}_1 = f_1(x_1, u), \qquad x_1(t_o) = x_{1o}, \qquad y_1 = h_1(x_1) \qquad (7a)$$
$$\dot{x}_2 = f_2(x_2, u), \qquad x_2(t_o) = x_{2o}, \qquad y_2 = h_2(x_2) \qquad (7b)$$
$$\dot{x}_v = f_v(x_v, x_1, x_2, u), \quad x_v(t_o) = x_{vo} \qquad (7c)$$

2.3 Adjustable-structure geometric estimator (GE)

In virtue of the σ-detectability property of the N-composition staged model (7), the (possibly truncated) model state (x) can be on-line robustly estimated by the *geometric estimator (GE) with structure* σ:

$$\dot{\hat{x}}_1 = f_1(\hat{x}_1, u) + O_1^{-1}(\hat{x}_1, u)\{\pi_1\hat{\iota}_1 + k_1(\zeta_1, \omega_1)[y_1 - h_1(\hat{x}_1)]\},$$
$$\hat{x}_1(t_o) = \hat{x}_{1o}; \qquad \dot{\hat{\iota}}_1 = \omega_1^{\kappa 1+1}[y_1 - h_1(\hat{x}_1)]\}, \quad \hat{\iota}_1(0) = \hat{\iota}_{1o} \qquad (8a)$$
$$\dot{\hat{x}}_2 = f_2(\hat{x}_2, u) + O_2^{-1}(\hat{x}_2, u)\{\pi_2\hat{\iota}_2 + k_2(\zeta_2, \omega_2)[y_2 - h_2(\hat{x}_2)]\},$$
$$\hat{x}_2(t_o) = \hat{x}_{2o}; \qquad \dot{\hat{\iota}}_2 = \omega_2^{\kappa 2+1}[y_2 - h_2(\hat{x}_2)], \quad \hat{\iota}_2(0) = \hat{\iota}_{2o} \qquad (8b)$$
$$\dot{\hat{x}}_v = f_v(\hat{x}_\iota, \hat{x}_1, \hat{x}_2, u) \qquad \hat{x}_v(t_o) = \hat{x}_{vo} \qquad (8c)$$

where: $k_i(\zeta_i, \omega_i) = [a_1^i(\zeta_i)\omega_i, \ldots, a_{\kappa i}^i(\zeta_i)\omega_i^{\kappa i}]'$ (9c)
$O_i'(x_i, u) = [\beta'(c_{l_i})e_i[I, A_i(x_i, u),\ldots,A_i^{\kappa i+1}(x_i, u)], \ i = 1, 2$ (9a)
$A_i(x, u) = \partial_x f(x_i, u), \ \pi_i = (0, \ldots, 0, 1)', \ \dim \pi_i = \kappa_i$ (9b)
$|\beta'(c_{l_1})| \ge \varepsilon_T, \quad |\beta'(c_{l_2})| \ge \varepsilon_T$ (10a-b)

ζ_i (or ω_i) is the damping factor (or characteristic frequency) of the prescribed linear, noninteractive, pole assignable (*LNPA*) output error dynamics

$$\tilde{y}_i^{(\kappa i+1)} + a_1^i(\zeta_i)\omega_i\tilde{y}_i^{(\kappa i)} + \ldots + a_1^i(\zeta_i)\omega_i\tilde{y}_i^{(1)} + \omega_i^{\kappa i+1}\tilde{y}_i = 0, \ i = 1, 2 \quad (11)$$

with coefficient sets $\{a_1,\ldots, a_{\kappa_1}\}_i$ determined by pole placement (Lopez and Alvarez, 1999). The invertibility of O_1 and O_2 is ensured by the tridiagonal state dependency of f_c and the sensor location condition (10) which amounts placing each sensor at a tray with temperature gradient larger than a minimum value (say, two degrees). For any model structure σ (5) (Alvarez and Fernandez, 2009): (i) the afore stated nonlocal robustness convergence feature holds with respect to the N-composition model (1) with decentralization,

truncation, and actuator-measurement errors, and (ii) the rather simple GE tuning scheme applies to any structure. Thus, the adjustable structure-algorithm GE methodological framework offers the means to fairly compare the behavior of different structures, in the sense that the behavior differences are due to the structures itself and not to the tuning.

2.4 Estimation structure design problem

In view of the preceding adjustable-structure column GE approach, *our present problem* consists in, given a specific estimation objective, determining the two-measurement structure, which yields the best estimator behavior in terms of reconstruction speed, robustness and dimensionality. Technically speaking, the problem amounts to choosing the (complete or truncated) estimation model (7) and its σ-detectability structure (5), or equivalently: (i) the location l_1 (or l_2) of the temperature measurement y_1 (or y_2), (ii) the corresponding innovated concentrations x_1 (or x_2), and (iii) the noninnovated state (x_v).

2.5 Structure search methodology

From the perspective of a general-purpose mixed-integer optimization approach, in our 12-stage distillation column example, the N-composition model offers 527, 345 structural possibilities with 4,095 observable (or passive) ones structures, and the number of possibilities grows even more when model truncation is considered. Leaving aside the implementation complexity and difficulties of an optimization-based search method, in the spirit of the constructive control (Sepulchre, 1997) and GE (Alvarez and Fernandez, 2009) approaches, here the structural search will performed by exploiting the column staged feature in the light of the easy to compute version (Alvarez and Fernandez, 2009) of the GE detectability measures (Lopez and Alvarez, 2004), in two steps: (i) first, detectability measures will be used to draw candidate structures for a given estimation objective, and (ii) then, conclusive structural results will be obtained in terms of GE functioning.

2.6 Experimental case example

The proposed methodology will be illustrated and tested with experimental case example employed before to illustrate and test the theoretically drawn features and capabilities of the general-purpose GE approach (Alvarez and Fernandez, 2009): a methanol-water mixture feed F = 40 ml/min, at light component composition c_e = 0.2 and temperature 57°C. Initially, the column was at a steady-state with low reflux ratio (R/D = 0.2) and poor separation ($c_B \approx 0.0$, $c_D \approx 0.57$). Then, at time t = 0, a feed concentration step increase (c_e: 0.2 → 0.4) was introduced, yielding: (i) an overall composition response that settled (≈ 40 min) at an intermediate separation steady-state ($c_B \approx 0.01$, $c_D \approx 0.79$), and (ii) a distillate (or bottoms) composition settling time of ≈ 15 (or 40) min. Finally, at t = 40 min, a reflux step increase (R/D: 0.2 → 1.5) was introduced, yielding: (i) an overall response that settled (≈ 60 min.) at a high-separation steady-state ($c_B \approx 0.15$, $c_D \approx 0.98$), and (ii) a distillate (or bottoms) composition settling time of ≈ 20 (or 50) min. The experimental data can be seen in (Alvarez and Fernandez, 2007 and 2009).

3. STRUCTURAL ANALYSIS

In this section, the dependency of the GE detectability measures (Lopez and Alvarez, 2004; Alvarez and Fernandez, 2007) over sensor location and innovated state dimension are analyzed to draw candidate structures for complete profile and two-effluent estimation purposes.

3.1 Detectability measures

To account for the effect of the decentralization-truncation performed in the passage from the complete N-composition (1) to the truncated-decentralized n-composition estimation model (7) with structure σ (5), the detectability measures (12) for the next N-composition model (13) with innovated-noninnovated state partition will be employed (Alvarez and Fernandez, 2009):

$$s_\iota = 1/\mathrm{msv}(O), \quad c_\iota = \mathrm{cn}(O) \qquad (12a\text{-}b)$$

$$s_v = \mathrm{msv}(F), \quad c_v = \mathrm{cn}(F); \quad \lambda_v = \tfrac{1}{2}\,\mathrm{lev}(F + F') < 0 \qquad (12c\text{-}d)$$

$$\dot{x}_\iota = f_\iota(x_\iota, x_v, u), \quad x(0) = x_{\iota o}, \; y = h(x_\iota), \; \dim(x_\iota) = N \qquad (13a)$$

$$\dot{x}_v = f_v(x_\iota, x_v, u), \quad x_v(t_o) = x_{vo}, \quad \dim(x_v) = N\text{-}n \qquad (13b)$$

where $O(x, u) = \mathrm{bd}(E_1^\dagger, E_2^\dagger)'(x, u)$, $A_i(x_i, u) = \partial_{x_\iota} f_\iota(x, u)$

$F(x, u) = [\partial_{x_v} f_v + \partial_{x_\iota} f_v O^{-1} D](x, u)$, $A_v(x, u) = \partial_{x_v} f_v(x, u)$

$E_i^\dagger(x, u) = \beta'(c_{l_i}) e_i(I, A_i, \ldots, A_i^{\kappa i-1})(x, u)$, $i = 1, 2$

$D'(x, u) = \beta'(c_{l_i}) e_i(I, A_v, \ldots, A_v^{\kappa i-1})(x, u)$, $(x_1^\dagger, x_2^\dagger)' = x_\iota$

s_ι (or s_v) is the singularity measure equal to the inverse of the minimum singular value (msv) of the matrix O (or F), c_ι (or c_v) is the illconditioning measure equal to condition number (cn) of the matrix O (or F), and λ_v is the dominant frequency of the noninnovated dynamics, or equivalently, the negative of the smallest eigenvalue (lev) of the matrix (F + F')/2, O is the estimation matrix of the σ-structure model (13), and F is the Jacobian matrix of the noninnovated dynamics (13b). The illconditioning value c_ι (or c_v) measures the overshoot response of the innovated (or noninnovated) state estimation error to an initial estimate error, and the singularity value s_ι (or s_v) measures the asymptotic offset of the innovated (or noninnovated) state error due to persistent modeling errors, and the number λ_v measures the convergence rate of the noninnovated state error dynamics. In general, these measures can be taken over a column motion x(t) (Lopez and Alvarez, 2004). In our column case, the detectability measures will be computed at the intermidiate steady state (reached after ≈ 40 min).

3.2 Measurement locations

In Figure 1 are presented the singularity (s_ι) and ill conditioning (c_ι) measures (12) of the estimation matrix O (9a) as function of the sensor location pair (l_1, l_2), for a completely observable structure σ (5) with estimation order pair $\kappa = (\kappa_1, \kappa_2) = (6, 6)$ and $\kappa_\iota = \kappa_1 + \kappa_2 = 12 = n = N$ (i.e., complete model with observable structure), showing that: (i) the largest singularity and illconditioning values are obtained with the sensor stage location pair (l_1, l_2) ≈ (1 to 2, 12), (ii) the smallest singularity and illconditioning values are

obtained with the sensor location $(l_1, l_2) \approx (1, 2)$ [or (11, 12)] with two adjacent sensors in the bottom (or top) of the column, followed by the sensor location $(l_1, l_2) \approx (5, 6)$ with two adjacent sensors above or below the feed tray (5). These consideration lead to the *following conclusions*: (i) the two sensors should not be in the same section, and (ii) the best location pair for complete profile estimation is given by

$$(l_1, l_2) = (2, 12) := (l_s, l_e) \tag{14}$$

meaning one sensor in stage $l_s = 2$ (tray one) [or $l_e = 12$ tray 10] of the stripping (or enriching section), precisely in the stage with the largest temperature and concentration stage-to-stage gradient.

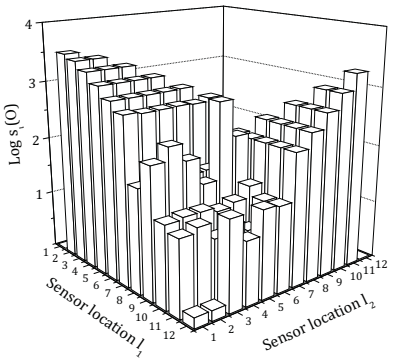

a)

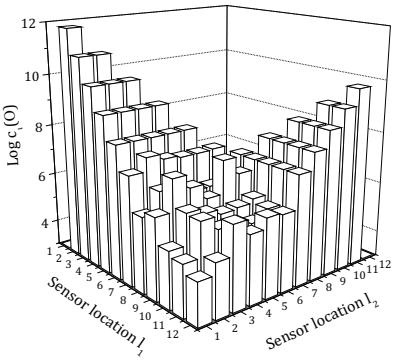

b)

Fig. 1: Dependency of the singularity s_t and ill conditioning c_t of the estimation matrix O on the sensor location pair (l_1, l_2), for comple observable structure σ (5) estimation order pair $\kappa = (\kappa_1, \kappa_2)$ and $\kappa_1 + \kappa_2 = 12$.

These location results are in agreement with location criteria employed in: (i) two-point temperature PI control of distillation columns (Tolliver, 1980; Castellanos-Sahagun et al., 2005), and (ii) previous distillation column studies with EKF (Baratti et al., 1995; Oisiovici and Cruz, 2000).

3.3 Innovated state dimension pair

Next, the sensor pair location (14) determined in the last section for the complete model (1), with observable structure κ (5), is kept fixed, and the dependency of the illconditioning c_t (12a) and the speed parameter λ_v (12c) of the noninnovated dynamics upon the innovated state dimension (or equivalently, estimation order) pair $\kappa = (\kappa_s, \kappa_e)$ is examined, with κ_s (or κ_e) being the number of adjacent innovated states x_s (or x_e) associated with the measurement y_s (or y_e) of the stripping (or enriching) section. The resulting measure c_t (or λ_v) is presented in Figure 2a (or 2b), showing that the illconditioning measure c_t remains within a reasonable bound $(1 \le c_t \le 100)$ for all the estimation order pairs with at most three innovated states per measurement $[(\kappa_s, \kappa_e) \le (3, 3)]$. As expected (Lopez and Alvarez, 2004): (i) the passive structure $(\kappa_s, \kappa_e) = (1, 1)$ yields the smallest possible value $c_t = 1$, and (ii) the speed parameter λ_v of the noninnovated dynamics is minimum ($\lambda_v = 0$) when the structure is observable with $(\kappa_s, \kappa_e) = (6, 6)$. These results are consistent with the general-purpose GE approach (Alvarez y Fernandez, 2009): (i) as the number of innovated states grows, the reconstruction speed grows and the robustness decreases, and (ii) the maximum robustness is obtained with the passive structure $(\kappa_s, \kappa_e) = (1, 1)$, and (iii) the maximum reconstruction speed is obtained with the observable structures $(\kappa_s, \kappa_e) = (6, 6)$.

3.4 Candidate structures

From the preceding structural analysis the next results follow. For *complete profile estimation*, the candidate models are decentralized versions of the N-concentration model (1) with structure σ (5):

$$\dot{c}_s = f_s(c_s, u), \qquad \dot{c}_e = f_e(c_e, u), \quad y = h(c) \tag{15a}$$
$$(\kappa_s, \kappa_e) \le (3, 3), \quad (l_s, l_e) = (2, 12) \tag{15b}$$

For *two-effluent estimation*, the candidate model is the truncated-decentralized model with passive structure σ (5):

$$\dot{c}_1 = \{(R + F)(c_2 - c_1) - V[\varepsilon(c_1) - c_1]\}/M_1, \tag{16a}$$
$$\dot{c}_2 = \{(R + F)(\bar{c}_3 - c_2) - V[\varepsilon(c_2) - \varepsilon(c_1)]\}/\eta^{-1}(R + F), \; y_s = \beta(c_2)$$
$$\dot{c}_{12} = \{R[\varepsilon(c_{12}) - c_{12}] - V[\varepsilon(c_{12}) - \varepsilon(\bar{c}_{11})]\}/\eta^{-1}(R), \quad y_e = \beta(c_{12})$$
$$(\kappa_s, \kappa_e) = (1, 1), \qquad (l_s, l_e) = (2, 12) \tag{16b}$$

4. STRUCTURAL RESULTS

Having as point of departure the suggestive structural results (15, 16) of the last section, in the present section conclusive results are obtained by assessing the candidate structures in terms of reconstruction speed and robustness.

4.1 Estimator tuning and convergence

The column (or holdup) dominant (or fastest) frequency ω_c (or ω_η) was determined from the experimental data and the detailed model (1), the estimator frequency ω is written as n_ω times ω_n, and the adjustable constants (20) are listed next:

$$(\omega_c, \omega_\eta) \approx (1/15, 1)\ \text{min}^{-1};\ \zeta_s, \zeta_e, \omega_s = \omega_e = \omega = n_\omega \omega_c \tag{17-18}$$

Thus: (i) there are three adjustable gains (ζ_s, ζ_e, n_ω), and (ii) the limit upper ω^+ is related to ω_η. From the specialization to

the column case of Lemma and Proposition 1 in (Alvarez and Fernandez, 2009): (i) the GE error dynamics is robustly stable if the stabilizing term λ_s dominates the potentially destabilizing one λ_d (λ_s and λ_d defined in Alvarez and Fernandez, 2009), according to inequality (19), or equivalently, if: (i) the related threshold equation (20) has two strictly positive and sufficiently separated roots (ω^- and ω^+) for ω, and (ii) the gain frequency ω (18) of the prescribed LNPA output error dynamics (11) is chosen so that the low-high gain conditions (21) are met:

$$\lambda_s(\omega, \zeta, \sigma) - \lambda_d(\omega, \zeta, \sigma) := \lambda(\omega, \zeta, \sigma) > 0, \quad \zeta = (\zeta_s, \zeta_e) \qquad (19)$$

$$\lambda(\omega, \zeta, \sigma) = 0 \quad \Rightarrow \quad \exists \quad \omega = \omega^-(\zeta, \sigma), \quad \omega^+(\zeta, \sigma) \qquad (20)$$

$$0 < \omega^-(\zeta, \sigma) < \omega < \omega^+(\zeta, \sigma) \qquad (21)$$

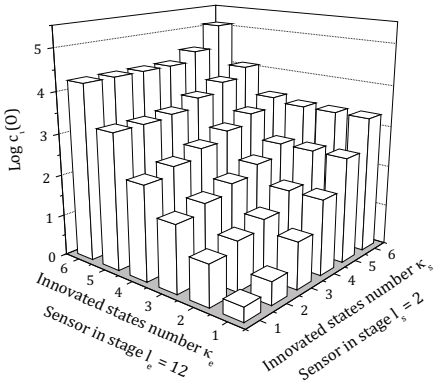

a)

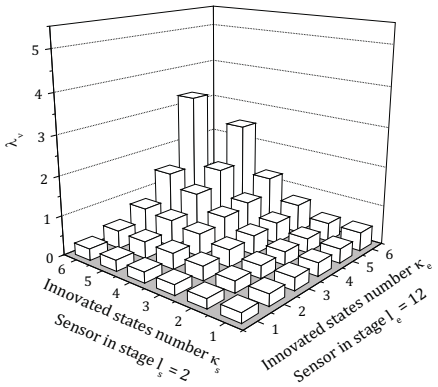

b)

Fig. 2: Dependency of the singularity (or noninnovated-dynamics speed parameter) s_t (or c_t) of the estimation matrix O (or Jacobian matrix F) on the dimension $\kappa = (\kappa_s, \kappa_e)$ of the innovated state pair x_s-x_e, for the sensor location $(l_s, l_e) = (2, 12)$

The meaning of these conditions and their dependency on κ_t ($= \kappa_1, \kappa_2, \kappa_3$ with $\kappa_1 < \kappa_2 < \kappa_3$) are depicted in the Figure 1b of Alvarez and Fernandez (2009): (i) the fulfilment ($\kappa_t = \kappa_1$) or violation ($\kappa_t = \kappa_2, \kappa_3$) of the conditions, and (ii) as the estimation order κ_t grows, the convergence gain (ω^+, ω^-) decreases, and eventually vanishes. In our column problem, we shall be interested in the interplay between structure, behavior, and tuning (ζ_s, ζ_e, ω, ω^-, ω^+, $\Delta\omega$).

4.2 Entire profile estimation

First, the GE estimator (8) was run with the candidate structures $(\kappa_s, \kappa_e) = (1, 1), \ldots (6, 6)$, finding that the best behavior was attained with $(\kappa_s, \kappa_e) = (3, 3)$, followed by (2, 2). In Figure 3 are presented the results for $(\kappa_s, \kappa_e) = (1, 1)$, (3, 3), and (6, 6), and the corresponding gain tuning limit results are listed in Table 1. The structure with three innovated states per measurement yields the best speed versus robustness behavior, with a reasonable gain interval (ω^+, ω^-). In agreement with the convergence-tuning theoretical derivations (Alvarez and Fernandez, 2009): (i) the passive (or observable) structure yields the slowest (or fastest) reconstruction rate with the largest (smallest) robustness, or equivalently, the largest (or smallest) gain interval $\Delta\omega$, and (iii) to avoid oscillatory response, the damping factor $\zeta_{s/e} = 2^{1/2}$ (or 1.5) is used for observable (or passive) innovation (Alvarez and Lopez, 1999).

4.3 Two-effluent estimation

In this case, the three-state model with two decoupled subsystems and passive innovation candidate structure (15) was implemented as well as several other neighbouring structures, finding that, the candidate structure yielded the best behavior with the least number of states, followed closely by some neighboring structures. The corresponding tuning and behavior are listed in Table 2 and Figure 4, respectively. As it can be seen in the Figure 4, for effluent estimation purposes, the truncated model outperforms the complete one, and this verifies the effectiveness of setting the model dimension as design degree of freedom. Comparing with the complete model-based estimation cases, the truncated model with single-stage innovation per measurement yields faster and more robust effluent estimates.

Table 1. Tuning for entire profile estimation.

y	κ	ζ	ω^-	ω	ω^+	$\Delta\omega$	n_ω
T_2, T_{12}	6, 6	$2^{1/2}$	1/15	2/5	8/15	7/15	6
T_2, T_{12}	3, 3	1	1/15	2/3	4/5	11/15	10
T_2, T_{12}	1, 1	3/2	1/15	4/5	14/15	13/15	12

Table 2. Tuning for two-effluent estimation.

n	κ	ζ	ω^-	ω	ω^+	$\Delta\omega$	n_ω
12	1, 1	3/2	1/15	4/5	14/15	13/15	12
3	1, 1	3/2	1/15	14/15	1	14/15	14

5. CONCLUSIONS

The problem of drawing the structure for best estimator behavior with respect to a specific concentration estimation task has been resolved for a binary distillation column with two temperature measurements and experimental data. It was found that: (i) the (12-concentration) profile must be estimated with the complete model, six innovated concentrations (three per measurement), and a 6-concentration open-loop observer module, and (ii) the two-effluent concentration must be estimated with a three-stage truncated model, two innovated concentrations, (one per

measurement), and one noninnovated module. In the complete (or two-effluent) estimation case, the GE consists of 5 (or 14) ODE's, which are considerably less than the 72 ODEs required by an EKF implementation.

The proposed approach: (i) resolves the structure-algorithm estimation design problem in a way that is more effective and simpler than the ones of previous studies, and (ii) is a point of departure to address the multi-component case.

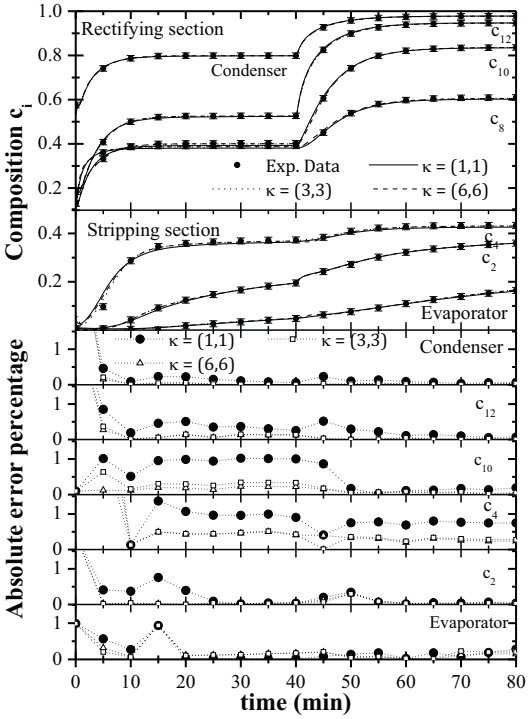

Fig. 3. Profile estimation with two sensors (l_s = 2, l_e = 12) and complete model.

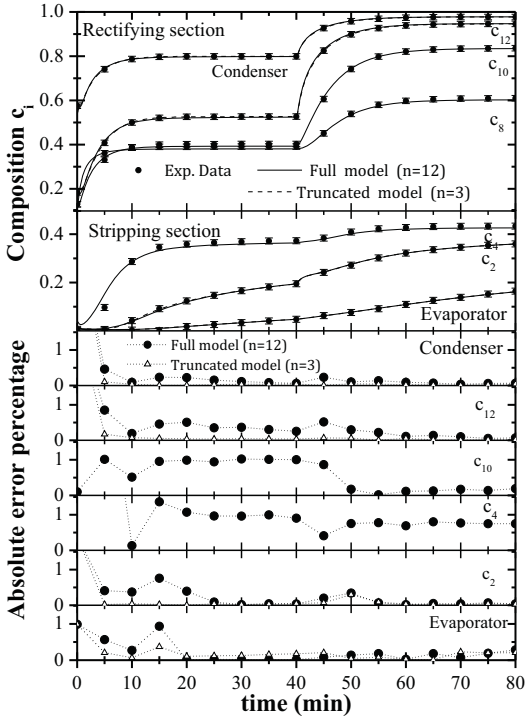

Fig. 4. Two-effluent estimation with two sensors (l_s = 2, l_e = 12) and truncated model.

REFERENCES

Alonso, A. A., Kevrekidis, I. G., Banga, J. R. and Frouzakis, C. E. (2004). Optimal sensor location and reduced order observer design for distributed process systems, *Comput. Chem. Eng.*, 28(1): 27-35

Alvarez, J. and Lopez, T. (1999). Robust Dynamic State Estimation of Nonlinear Plants, *AIChE J.*, 45(1): 107-123

Alvarez, J. (2000). Nonlinear state estimation with robust convergence, *J. Process Control*, 10(1): 59-71

Alvarez, J. and Fernandez, C. (2007). Constructive estimation design for binary distillation columns, *IFAC-DYCOPS 2007*, Preprints (II): 75-80

Alvarez, J. and Fernandez, C. (2009). Geometric estimation of nonlinear process systems, *J. Process Control*, 19(2): 247-260.

Baratti, R., Bertucco, A., Da Rold, A. and Morbidelli, M. (1995). Development of a Composition Estimator for Binary Distillation Columns: Application to a Pilot Plant, *Chem. Eng. Sci.*, 50: 1541-1550

Bian, S. and Henson, M. A. (2006). Measurement selection for on-line estimation of nonlinear wave models for high purity distillation columns, *Chem. Eng. Sci.*, 61(10): 3210-3222

Castellanos-Sahagun, E., Alvarez-Ramírez, J. and Alvarez, J. (2005). Two-point temperature control structure and algorithm design for binary distillation columns, *Ind. Eng. Chem. Res.* 44: 142-152

Kadu, S. C., Bhushan, M. and Gudi, R. (2008). Optimal sensor network design for multirate systems, *J. Process Control*, 18: 594-609

Lopez, T. and Alvarez, J. (2004). On the effect of the estimation structure in the functioning of a nonlinear copolymer reactor estimator, *Journal of Process Control*, 14: 99-109

Luyben, W. L. (1990). *Process modeling, simulation, and control for chemical engineers*. Nueva York, McGraw-Hill.

Oisiovici, R. M. and Cruz, S. L. (2000). State estimation of batch distillation columns using an extended Kalman filter, *Chem. Eng. Sci.*, 55: 4667-4680

Sepulchre, R., M. Janković, P. R.Kokotović. (1997). *Constructive Nonlinear Control*, Communications and Control Engineering Series, Springer - Verlag, London

Singh, A. K. and Hahn, J. (2005). State estimation for high-dimensional chemical processes, *Comput. Chem. Eng.*, 29(11): 2326-2334

Tolliver, T. L. and McCune, L. C. (1980). Finding the Optimum Temperature Control Trays for Distillation Columns, *Instrum. Sci. Technol.* 27(9): 75-80

van den Berg, F. W. J., Hoefsloot, H. C. J., Boelens, H. F. M. and Smilde, A. K. (2000). Selection of optimal sensor position in a tubular reactor using robust degree of observability criteria, *Chem. Eng. Sci.*, 55: 827-837

Venkateswarlu, C. and Jeevan Kumar, B. (2006). Composition estimation of multicomponent reactive batch distillation with optimal sensor configuration, *Chem. Eng. Sci.*, 61: 5260-5274

Distributed Optimization for Predictive Control of a Distillation Column with Output and Control-Input Constraints ⋆

Helton F. Scherer * **Eduardo Camponogara** * **Agustinho Plucenio** *

* *Department of Automation and Systems Engineering, Federal University of Santa Catarina, Florianópolis, SC 88040-900 Brazil (e-mails: scherer@das.ufsc.br, camponog@das.ufsc.br, plucenio@das.ufsc.br)*

Abstract: A distributed predictive control framework based on a state-space model with constraints on the output and control-input is proposed. By a benchmark process, the performance of this framework is analyzed and compared with centralized control strategies in a regulation problem of a distillation column.

Keywords: Model predictive control, distributed optimization, distillation column, convex optimization, interior-point method.

1. INTRODUCTION

Advanced techniques for multivariable control like model predictive control (MPC) have become widespread in the industry, but they are still complex, time-consuming to set-up, and consequently expensive. Further, the centralized approach may not be suitable to the operation of large dynamic networks, either by the communication difficulty between sensors and the central unit, or by the computational limitation to solve optimization problems. Some petrochemical plants are examples of large systems composed by distributed, however coupled subsystems.

An alternative is distributed predictive control (Camponogara et al., 2002), which breaks the static optimization problem into smaller sub-problems to be solved by a network of control/optimization agents. It aims to solve the sub-problems in the most simple form while the final performance is preserved or even improved.

Many studies about distributed formulations are being developed. Mercangöz and Doyle III (2007) propose a distributed formulation that ensures self-sufficient state estimation in each node. Motee and Jadbabaie (2006) present a study of receding horizon control applied to physically decoupled systems with input and state constraints, where the couplings appear through the finite horizon cost function. Li et al. (2005) and Giovanini and Balderud (2006) propose MPC strategies based on Nash optimality to decoupled sub-systems.

Besides this, many algorithms to ensure convergence of distributed problems are being proposed. Dunbar (2007) presents distributed algorithms for dynamically coupled nonlinear systems subject to decoupled input constraints. An iterative procedure based on cooperation that ensures convergence to the global optimum for linear systems with constraints on the local controls is presented by Venkat et al. (2008). Camponogara and Talukdar (2007) present synchronous and asynchronous solutions of optimization problems, proposing a high level optimization framework and safety margins for meeting constraints. Recently, distributed predictive control was specialized to linear dynamic networks and applied to traffic light control, in which the dynamics of the sub-systems are coupled and the constraints are on the local controls (Camponogara and de Oliveira, 2009).

This paper proposes a problem decomposition and distributed algorithm for predictive control of linear networks with dynamic couplings and restrictions on output and control-input signals. Further, it reports on a comparison with existing approaches for the control of a distillation column.

The end result of this research is a distributed predictive control technique for programming control agents which can be deployed to perform regulatory control of linear dynamic networks. Each agent would be responsible for solving a problem of control action, exchanging its local sensor data and control actions with the other agents. The resulting control action is obtained after resolving conflicts with neighboring agents.

Because the algorithms embedded in the agents are much simpler than the centralized one, the distributed approach makes it simpler to modify and reconfigure the plant. Instead of modifying the complex centralized algorithm, it would suffice to add new agents and update only the nearby agents with whom the new agents would have relation. Further, maintenance would be facilitated since the distributed agents are much simpler.

2. DYNAMIC MODEL AND CONTROL PROBLEM

A linear dynamic network is obtained by interconnecting decoupled sub-systems that have local dynamics and controls. The couplings arise from the dynamic interconnections and the constraints on the network's output equations. $\mathscr{M} = \{1, \ldots, M\}$ denotes the set of sub-systems. Each sub-system m is governed by the following discrete-time linear dynamic equation:

$$\mathbf{x}_m(k+1) = A_m \mathbf{x}_m(k) + B_m \mathbf{u}_m(k) \quad (1)$$

⋆ This research has been funded in part by Agência Nacional do Petróleo, Gás Natural e Biocombustíveis (ANP) under grant PRH-34/aciPG/ANP and by Conselho Nacional de Desenvolvimento Científico e Tecnológico (CNPq) under grant 473841/2007-0.

where $\mathbf{x}_m \in \mathbb{R}^{n_m}$ is the state, $\mathbf{u}_m \in \mathbb{R}^{p_m}$ is the control input, and A_m and B_m are matrices of appropriate dimensions. The output from sub-system m depends on the state of the sub-systems in set $I(m) \subseteq \mathscr{M}$ such that $m \in I(m)$:

$$\mathbf{y}_m(k) = \sum_{i \in I(m)} C_{m,i}\mathbf{x}_i(k) \tag{2}$$

and is subject to the output constraints:

$$\mathbf{y}_m^{\min} \leq \mathbf{y}_m(k) \leq \mathbf{y}_m^{\max} \tag{3}$$

with $C_{m,i}$ being matrices of suitable dimensions.

The regulation problem for the overall system subject to output and control-input constraints is:

$$\min \frac{1}{2}\sum_{m=1}^{M}\sum_{k=0}^{\infty}\left[\mathbf{y}_m(k+1)'Q_m\mathbf{y}_m(k+1) + \mathbf{u}_m(k)'R_m\mathbf{u}_m(k)\right] \tag{4a}$$

$$\text{S.to : For } m = 1,\ldots,M,\ k = 0,\ldots,\infty:$$

$$\mathbf{x}_m(k+1) = A_m\mathbf{x}_m(k) + B_m\mathbf{u}_m(k) \tag{4b}$$

$$\mathbf{y}_m(k+1) = \sum_{i \in I(m)} C_{m,i}\mathbf{x}_i(k+1) \tag{4c}$$

$$\mathbf{u}_m^{\min} \leq \mathbf{u}_m(k) \leq \mathbf{u}_m^{\max} \tag{4d}$$

$$\mathbf{y}_m^{\min} \leq \mathbf{y}_m(k+1) \leq \mathbf{y}_m^{\max} \tag{4e}$$

where Q_m are symmetric positive semi-definite and R_m are symmetric positive definite matrices.

Model predictive control solves an optimization problem that approximates the regulation problem for a finite-time horizon. Given the state $\mathbf{x}(k) = (\mathbf{x}_1,\ldots,\mathbf{x}_M)(k)$ of the system at time k, the MPC regulation problem is defined as:

$$P: \min f = \frac{1}{2}\sum_{m=1}^{M}\sum_{j=0}^{T-1}\left[\hat{\mathbf{y}}_m(k+j+1|k)'Q_m\hat{\mathbf{y}}_m(k+j+1|k) + \hat{\mathbf{u}}_m(k+j|k)'R_m\hat{\mathbf{u}}_m(k+j|k)\right] \tag{5a}$$

$$\text{S.to : For } m = 1,\ldots,M,\ j = 0,\ldots,T-1:$$

$$\hat{\mathbf{x}}_m(k+j+1|k) = A_m\hat{\mathbf{x}}_m(k+j|k) + B_m\hat{\mathbf{u}}_m(k+j|k) \tag{5b}$$

$$\hat{\mathbf{y}}_m(k+j+1|k) = \sum_{i \in I(m)} C_{m,i}\hat{\mathbf{x}}_i(k+j+1|k) \tag{5c}$$

$$\mathbf{u}_m^{\min} \leq \hat{\mathbf{u}}_m(k+j|k) \leq \mathbf{u}_m^{\max} \tag{5d}$$

$$\mathbf{y}_m^{\min} \leq \hat{\mathbf{y}}_m(k+j+1|k) \leq \mathbf{y}_m^{\max} \tag{5e}$$

$$\hat{\mathbf{x}}_m(k|k) = \mathbf{x}_m(k) \tag{5f}$$

where $\hat{\mathbf{u}}_m(k+j|k)$ is the prediction for the control input to sub-system m at time $(k+j)$ as predicted at time k, and similarly $\hat{\mathbf{y}}_m$ and $\hat{\mathbf{x}}_m$ are output and state predictions respectively. The variable T is the length of the prediction and control horizons, that have the same length to make the developments simpler.

The term "$|k$" is dropped from all variables for the sake of simplification. Before continuing with the MPC formulation, some terminology will be introduced to simplify the representation. First, it is possible to obtain the state of sub-system m at time $(k+t)$ by using the initial state and the past controls. The future states and outputs are represented as:

$$\hat{\mathbf{x}}_m(k+t) = A_m^t\mathbf{x}_m(k) + \sum_{j=1}^{t} A_m^{j-1}B_m\hat{\mathbf{u}}_m(k+t-j)$$

$$\hat{\mathbf{y}}_m(k+t) = \sum_{i \in I(m)} C_{m,i}\left(A_i^t\mathbf{x}_i(k) + \sum_{j=1}^{t} A_i^{j-1}B_i\hat{\mathbf{u}}_i(k+t-j)\right)$$

By defining the vectors $\hat{\mathbf{x}}_m$, $\hat{\mathbf{u}}_m$, and $\hat{\mathbf{y}}_m$ to represent the predictions over the entire horizon of the states, controls, and outputs, respectively, and the matrices $\overline{CA}_{m,i}$ and $\overline{CB}_{m,i}$ for the dynamics:

$$\hat{\mathbf{x}}_m = \begin{bmatrix}\hat{\mathbf{x}}_m(k+1)\\ \vdots \\ \hat{\mathbf{x}}_m(k+T)\end{bmatrix}, \quad \hat{\mathbf{u}}_m = \begin{bmatrix}\hat{\mathbf{u}}_m(k)\\ \vdots \\ \hat{\mathbf{u}}_m(k+T-1)\end{bmatrix}$$

$$\hat{\mathbf{y}}_m = \begin{bmatrix}\hat{\mathbf{y}}_m(k+1)\\ \vdots \\ \hat{\mathbf{y}}_m(k+T)\end{bmatrix}, \quad \overline{CA}_{m,i} = \begin{bmatrix}C_{m,i}A_i\\ C_{m,i}A_i^2\\ \vdots \\ C_{m,i}A_i^T\end{bmatrix}$$

$$\overline{CB}_{m,i} = \begin{bmatrix} C_{m,i}B_i & 0 & \cdots & 0 \\ C_{m,i}A_iB_i & C_{m,i}B_i & \cdots & 0 \\ \vdots & \vdots & \ddots & 0 \\ C_{m,i}A_i^{T-1}B_i & C_{m,i}A_i^{T-2}B_i & \cdots & C_{m,i}B_i \end{bmatrix}$$

the prediction of the outputs over the entire horizon is written in a compact form as:

$$\hat{\mathbf{y}}_m = \sum_{i \in I(m)}\left(\overline{CA}_{m,i}\mathbf{x}_i(k) + \overline{CB}_{m,i}\hat{\mathbf{u}}_i\right) \tag{6}$$

Defining the matrices $\bar{Q}_m$ and $\bar{R}_m$ with proper dimensions:

$$\bar{Q}_m = \begin{bmatrix} Q_m & 0 & \cdots & 0 \\ 0 & Q_m & \cdots & 0 \\ \vdots & \vdots & \ddots & 0 \\ 0 & 0 & 0 & Q_m \end{bmatrix}, \quad \bar{R}_m = \begin{bmatrix} R_m & 0 & \cdots & 0 \\ 0 & R_m & \cdots & 0 \\ \vdots & \vdots & \ddots & 0 \\ 0 & 0 & 0 & R_m \end{bmatrix}$$

and the vectors $\hat{\mathbf{u}}_m^{\min}$, $\hat{\mathbf{u}}_m^{\max}$, $\hat{\mathbf{y}}_m^{\min}$, and $\hat{\mathbf{y}}_m^{\max}$:

$$\hat{\mathbf{u}}_m^{\min} = \begin{bmatrix}\mathbf{u}_m^{\min}\\ \vdots \\ \mathbf{u}_m^{\min}\end{bmatrix}, \quad \hat{\mathbf{u}}_m^{\max} = \begin{bmatrix}\mathbf{u}_m^{\max}\\ \vdots \\ \mathbf{u}_m^{\max}\end{bmatrix}$$

$$\hat{\mathbf{y}}_m^{\min} = \begin{bmatrix}\mathbf{y}_m^{\min}\\ \vdots \\ \mathbf{y}_m^{\min}\end{bmatrix}, \quad \hat{\mathbf{y}}_m^{\max} = \begin{bmatrix}\mathbf{y}_m^{\max}\\ \vdots \\ \mathbf{y}_m^{\max}\end{bmatrix}$$

problem P is expressed as:

$$P: \min \frac{1}{2}\sum_{m=1}^{M}\left(\hat{\mathbf{y}}_m'\bar{Q}_m\hat{\mathbf{y}}_m + \hat{\mathbf{u}}_m'\bar{R}_m\hat{\mathbf{u}}_m\right) \tag{7a}$$

$$\text{S.to : For } m = 1,\ldots,M:$$

$$\hat{\mathbf{y}}_m = \sum_{i \in I(m)}\left(\overline{CA}_{m,i}\mathbf{x}_i(k) + \overline{CB}_{m,i}\hat{\mathbf{u}}_i\right) \tag{7b}$$

$$\hat{\mathbf{u}}_m^{\min} \leq \hat{\mathbf{u}}_m \leq \hat{\mathbf{u}}_m^{\max} \tag{7c}$$

$$\hat{\mathbf{y}}_m^{\min} \leq \hat{\mathbf{y}}_m \leq \hat{\mathbf{y}}_m^{\max} \tag{7d}$$

The next step is to represent problem P using only the current state and the control predictions. First, let us define f_m as the portion of problem P for a specific m and replace (6) in the objective function:

$$
\begin{aligned}
f_m =& \frac{1}{2}\left(\sum_{i\in I(m)}\left(\overline{CA}_{m,i}\mathbf{x}_i(k)+\overline{CB}_{m,i}\hat{\mathbf{u}}_i\right)\right)'\bar{Q}_m \\
&\cdot\left(\sum_{i\in I(m)}\left(\overline{CA}_{m,i}\mathbf{x}_i(k)+\overline{CB}_{m,i}\hat{\mathbf{u}}_i\right)\right)+\frac{1}{2}\hat{\mathbf{u}}_m'\bar{R}_m\hat{\mathbf{u}}_m \\
=& \frac{1}{2}\left(\sum_{i\in I(m)}\overline{CA}_{m,i}\mathbf{x}_i(k)\right)'\bar{Q}_m\left(\sum_{i\in I(m)}\overline{CA}_{m,i}\mathbf{x}_i(k)\right) \\
&+\left(\sum_{i\in I(m)}\overline{CA}_{m,i}\mathbf{x}_i(k)\right)'\bar{Q}_m\left(\sum_{i\in I(m)}\overline{CB}_{m,i}\hat{\mathbf{u}}_i\right) \\
&+\frac{1}{2}\left(\sum_{i\in I(m)}\overline{CB}_{m,i}\hat{\mathbf{u}}_i\right)'\bar{Q}_m\left(\sum_{i\in I(m)}\overline{CB}_{m,i}\hat{\mathbf{u}}_i\right) \\
&+\frac{1}{2}\hat{\mathbf{u}}_m'\bar{R}_m\hat{\mathbf{u}}_m
\end{aligned}
\tag{8}
$$

Defining vectors $\mathbf{g}_{m,i,j}$, matrices $H_{m,i,j}$, and a constant c_m to represent the terms of f_m:

$$\mathbf{g}_{m,i,j} = \overline{CB}_{m,i}'\bar{Q}_m\overline{CA}_{m,j}\mathbf{x}_j(k) \text{ for } i,j\in I(m) \tag{9a}$$

$$H_{m,m,m} = \overline{CB}_{m,m}'\bar{Q}_m\overline{CB}_{m,m}+\bar{R}_m \tag{9b}$$

$$H_{m,i,j} = \overline{CB}_{m,i}'\bar{Q}_m\overline{CB}_{m,j} \quad \text{for } i,j\in I(m), i\neq m \text{ or } j\neq m \tag{9c}$$

$$c_m = \frac{1}{2}\sum_{i\in I(m)}\sum_{j\in I(m)}\mathbf{x}_i(k)'\overline{CA}_{m,i}'\bar{Q}_m\overline{CA}_{m,j}\mathbf{x}_j(k) \tag{9d}$$

it is possible to redefine problem P as:

$$P: \min\frac{1}{2}\sum_{m=1}^{M}\sum_{i\in I(m)}\sum_{j\in I(m)}\left[\hat{\mathbf{u}}_i'H_{m,i,j}\hat{\mathbf{u}}_j+\mathbf{g}_{m,i,j}'\hat{\mathbf{u}}_i\right]+\sum_{m=1}^{M}c_m \tag{10a}$$

$$\text{S.to}: \text{For } m=1,\ldots,M:$$

$$\hat{\mathbf{u}}_m^{\min}\leq\hat{\mathbf{u}}_m\leq\hat{\mathbf{u}}_m^{\max} \tag{10b}$$

$$\hat{\mathbf{y}}_m^{\min}\leq\sum_{i\in I(m)}\left(\overline{CA}_{m,i}\mathbf{x}_i(k)+\overline{CB}_{m,i}\hat{\mathbf{u}}_i\right)\leq\hat{\mathbf{y}}_m^{\max} \tag{10c}$$

This quadratic programming formulation will be used to solve the problem of control calculation in the centralized approach.

2.1 Logarithmic Barrier Method

The logarithmic barrier method is an *interior-point* method for solving convex optimization problems with inequality constraints (Boyd and Vandenberghe, 2004),

$$\text{minimize } f(\mathbf{x}) \tag{11a}$$

$$\text{subject to } A\mathbf{x}\leq\mathbf{b}, \tag{11b}$$

It is assumed that the problem is solvable, *i.e.*, an optimal solution $\mathbf{x}^\star$ exists, and the constraints delimit a closed set. A *barrier function* is any function $B(\mathbf{x}):\Re^n\to\Re$ that satisfies

- $B(\mathbf{x})\geq 0$ for all $\mathbf{x}$ that satisfy $A\mathbf{x}<\mathbf{b}$, and
- $B(\mathbf{x})\to\infty$ as $\mathbf{x}$ approaches the boundary of $\{\mathbf{x}|A\mathbf{x}\leq\mathbf{b}\}$

Being $\mathbf{a}_i'$ the i-th row of A, the idea of the method is to treat the constraints using a logarithmic barrier function as follows:

$$\phi(\mathbf{x}) = -\sum_{i=1}^{m}\log\left(b_i-\mathbf{a}_i'\mathbf{x}\right) \tag{12}$$

where the domain of ϕ is $\mathbf{dom}\ \phi=\{\mathbf{x}|A\mathbf{x}<\mathbf{b}\}$.

With (12), problem (11) can be approximated by:

$$P(\varepsilon):\ \min\ g(\mathbf{x}) = f(\mathbf{x})+\varepsilon\phi(\mathbf{x}) \tag{13}$$

where $\varepsilon>0$ is a parameter that sets the accuracy of the approximation. As ε decreases, more accurate the approximation $P(\varepsilon)$ becomes, whose optimal solution is $\mathbf{x}(\varepsilon)$. The optimal solution is reached by solving (13) for a decreasing sequence of $\varepsilon\to 0^+$, *i.e.*, $\lim_{\varepsilon\to 0^+}\mathbf{x}(\varepsilon)=\mathbf{x}^\star$. The pseudo-code of the barrier method for solving problem (11) appears in Algorithm 1.

Newton's method can be used to compute the optimal solution to $P(\varepsilon)$ using the gradient and the Hessian of $\phi(\mathbf{x})$ and $f(\mathbf{x})$. Algorithm 2 shows how to use Newton's method with a backtracking line search to choose the step size of each iteration. The gradient and the Hessian of the logarithmic barrier function ϕ are given by:

$$\nabla\phi(\mathbf{x}) = \sum_{i=1}^{M}\frac{1}{(b_i-\mathbf{a}_i'\mathbf{x})}\mathbf{a}_i,\ \nabla^2\phi(\mathbf{x}) = \sum_{i=1}^{M}\frac{1}{(b_i-\mathbf{a}_i'\mathbf{x})^2}\mathbf{a}_i\mathbf{a}_i'$$

Algorithm 1: Barrier method

given: strictly feasible $\mathbf{x}$, $\varepsilon:=\varepsilon^0$, $0<\mu<1$, tolerance $e>0$
repeat
  compute $\mathbf{x}(\varepsilon)$ by minimizing $g(\mathbf{x})$, starting at $\mathbf{x}$;
  update $\mathbf{x}:=\mathbf{x}(\varepsilon)$; $\varepsilon:=\mu\varepsilon$;
until $\varepsilon\leq e$;

Algorithm 2: Newton's method

given: a starting point $\mathbf{x}\in\mathbf{dom}\ g$, tolerance $e>0$
repeat
  compute the Newton step: $\Delta\mathbf{x}_{nt}:=-\nabla^2 g(\mathbf{x})^{-1}\nabla g(\mathbf{x})$;
  choose step size
    given: a descent direction $\Delta\mathbf{x}_{nt}$, $\alpha\in(0,0.5)$, $\beta\in(0,1)$
    $t:=1$;
    while $g(\mathbf{x}+t\Delta\mathbf{x}_{nt})>g(\mathbf{x})+\alpha t\nabla g(\mathbf{x})'\Delta\mathbf{x}_{nt}$ **do**
      $t:=\beta t$;
  end
  update: $\mathbf{x}:=\mathbf{x}+t\Delta\mathbf{x}_{nt}$;
  compute the decrement: $\lambda^2:=\nabla g(\mathbf{x})'\nabla^2 g(\mathbf{x})^{-1}\nabla g(\mathbf{x})$;
until $\lambda^2/2\leq e$;

By approximating problem P given in (10) to the equivalent unconstrained form $P(\varepsilon)$, where the constraints on outputs and controls are put together in $\phi(\hat{\mathbf{u}})$, unconstrained minimization algorithms like those described in this section can be used to solve the problem.

3. DISTRIBUTED OPTIMIZATION AND CONTROL

This paper focuses now on the distributed solution of P, discussing how to perform a decomposition of the problem into a network of coupled sub-problems P_m that will be solved by a network of distributed agents (Camponogara and Talukdar, 2005, 2007), and the use of a distributed iterative algorithm to solve these sub-problems.

Each agent will compute a control vector $\hat{\mathbf{u}}_m$. So, for a perfect decomposition, each agent m must have all the information on problem P that depends on $\hat{\mathbf{u}}_m$. Before giving the decomposition, let us define some special sets:

- $O(m)=\{i: m\in I(i), i\neq m\}$ to represent the set of *output neighbors* of m;

- $C(m) = \{(i,j) \in I(m) \times I(m) : i = m \text{ or } j = m\}$ for the sub-system pairs of quadratic terms in the cost function of sub-system m that depend on $\hat{\mathbf{u}}_m$;
- $O(m,k) = \{(i,j) \in I(k) \times I(k) : i = m \text{ or } j = m\}$ for the pairs of quadratic terms in the cost function of sub-system k, $k \in O(m)$, that depend on $\hat{\mathbf{u}}_m$;
- $N(m) = (I(m) \cup O(m) \cup \{i : (i,j) \in O(m,k), k \in O(m)\}) - \{m\}$, which defines the *neighborhood* of agent m, including input and output *neighbors*;
- $\hat{\omega}_m = (\hat{\mathbf{u}}_i : i \in N(m))$, for the set of control signals of the neighbors of agent m;
- $\hat{\mathbf{z}}_m = (\hat{\mathbf{u}}_i : i \in \mathscr{M} - N(m) \cup \{m\})$, for the set of all control signals that are not in $\hat{\omega}_m$ and $\hat{\mathbf{u}}_m$.

The problem P from the view of agent m is defined as:

$$\begin{aligned} P_m: \ \min \ & \frac{1}{2} \sum_{(i,j) \in C(m)} \hat{\mathbf{u}}_i' H_{mij} \hat{\mathbf{u}}_j + \sum_{i \in I(m)} \mathbf{g}_{mmi} \hat{\mathbf{u}}_m + c_m \\ & + \frac{1}{2} \sum_{k \in O(m)} \sum_{(i,j) \in O(m,k)} \hat{\mathbf{u}}_i' H_{kij} \hat{\mathbf{u}}_j \qquad (14a) \\ & + \sum_{k \in O(m)} \sum_{(m,j) \in O(m,k)} \mathbf{g}_{kmj} \hat{\mathbf{u}}_m \\ \text{S.to}: \ & \hat{\mathbf{u}}_m^{\min} \le \hat{\mathbf{u}}_m \le \hat{\mathbf{u}}_m^{\max} \qquad (14b) \\ & \hat{\mathbf{y}}_i^{\min} \le \sum_{j \in I(i)} \left(\overline{CA}_{i,j} \mathbf{x}_j(k) + \overline{CB}_{i,j} \hat{\mathbf{u}}_j \right) \le \hat{\mathbf{y}}_i^{\max}, \qquad (14c) \\ & \quad \text{for all } i \in O(m) \cup \{m\} \end{aligned}$$

It is possible to simplify the representation of problem P_m by grouping some terms as follows:

$$H_m = H_{mmm} + \sum_{k \in O(m)} H_{kmm} \qquad (15a)$$

$$\begin{aligned} \mathbf{g}_m = \ & \frac{1}{2} \sum_{(i,m) \in C(m): i \ne m} \left(H'_{mim} + H_{mmi} \right) \hat{\mathbf{u}}_i + \sum_{i \in I(m)} \mathbf{g}_{mmi} \\ & + \frac{1}{2} \sum_{k \in O(m)} \sum_{(i,m) \in O(m,k): i \ne m} \left(H'_{kim} + H_{kmi} \right) \hat{\mathbf{u}}_i \qquad (15b) \\ & + \sum_{k \in O(m)} \sum_{(m,j) \in O(m,k)} \mathbf{g}_{kmj} \hat{\mathbf{u}}_m \end{aligned}$$

Using the terms defined above, problem P_m is represented as:

$$\begin{aligned} P_m(\hat{\omega}_m): \ \min f_m(\hat{\mathbf{u}}_m) \ &= \frac{1}{2} \hat{\mathbf{u}}_m' H_m \hat{\mathbf{u}}_m + \mathbf{g}_m' \hat{\mathbf{u}}_m + c_m \qquad (16a) \\ \text{S.to}: \ & \hat{\mathbf{u}}_m^{\min} \le \hat{\mathbf{u}}_m \le \hat{\mathbf{u}}_m^{\max} \qquad (16b) \\ & \hat{\mathbf{y}}_i^{\min} \le \sum_{j \in I(i)} \left(\overline{CA}_{i,j} \mathbf{x}_j(k) + \overline{CB}_{i,j} \hat{\mathbf{u}}_j \right) \le \hat{\mathbf{y}}_i^{\max}, \qquad (16c) \\ & \quad \text{for all } i \in O(m) \cup \{m\} \end{aligned}$$

This quadratic form will be used by each agent m to compute the control signal $\hat{\mathbf{u}}_m$ in the distributed approach.

Some properties about the decomposition are:

- $P_m(\hat{\omega}_m)$ consists of problem P with all the objective terms and constraints that depend on $\hat{\mathbf{u}}_m$;
- each sub-problem $P_m(\hat{\omega}_m)$ is convex.

3.1 Distributed Algorithm

This section describes briefly the distributed algorithm for the agent network to reach a solution. Let $P_m(\varepsilon)$ be the centering problem for $P_m(\hat{\omega}_m)$ with a given ε:

$$P_m(\varepsilon): \ \min \ f_m(\hat{\mathbf{u}}_m) + \varepsilon \phi_m(\hat{\mathbf{u}}_m) \qquad (17)$$

where $\phi_m(\hat{\mathbf{u}}_m)$ is the logarithmic barrier function of the constraints given in (16). It is important to note that the problem to be solved by each agent is much simpler than the one used in the centralized formulation. So, the distributed solution must encompass a sequence of steps before the optimal control sequence is reached (de Oliveira and Camponogara, 2008).

First, define the vector $\hat{\mathbf{u}}^k = \left(\hat{\mathbf{u}}_1^k, \ldots, \hat{\mathbf{u}}_M^k\right)$ with the set of all control variables of P at iteration k. For a given ε, all agents have to *negotiate* to find a solution for each $P_m(\varepsilon)$ in the network. And this process is repeated for a decreasing sequence of $\varepsilon \to 0^+$. The convergence to a stationary solution is ensured by respecting two assumptions:

(1) *Synchronous Work:* if agent m revises its decisions at iteration k, then:
   (a) agent m uses $\hat{\omega}_m^k$ to produce an approximate solution of $P_m(\varepsilon)$;
   (b) all the neighbors of agent m keep their decisions at iteration k: $\hat{\mathbf{u}}_i^{k+1} = \hat{\mathbf{u}}_i^k$ for all $i \in N(m)$.

(2) *Continuous Work:* if $\hat{\mathbf{u}}^k$ is not a stationary point for problems $P_i(\varepsilon)$, $i \in \mathscr{M}$, then at least one agent m for which $\hat{\mathbf{u}}_m^k$ is not a stationary point for $P_m(\varepsilon)$ produces a new iterate $\hat{\mathbf{u}}_m^{k+1}$.

Condition (a) of Assumption 1 and Assumption 2 hold by arranging the agents to iterate repeatedly in a sequence $\langle S_1, \ldots, S_r \rangle$, where $S_i \subseteq \mathscr{M}$, $\cup_{i=1}^r S_i = \mathscr{M}$, and all distinct pairs $m, n \in S_i$ are non-neighbors for all i. The pseudo-code of the distributed barrier method for solving the problem network $\{P_m(\varepsilon)\}$ is given in Algorithm 3.

Algorithm 3: Distributed barrier method

given: strictly feasible $\hat{\mathbf{u}}^0 = (\hat{\mathbf{u}}_1^0, \ldots, \hat{\mathbf{u}}_M^0)$, $\varepsilon = \varepsilon^0 > 0$, $0 < \mu < 1$, tolerance $e > 0$, and a sequence $\langle S_1, \ldots, S_r \rangle$

repeat
- Define the initial group of decoupled agents, $i := 1$;
- Define a flag for the stationary test, $\delta := false$;
- **repeat**
  - each agent $m \in S_i$ receives $\hat{\omega}_m^k$ and computes $\hat{\mathbf{u}}_m^{k+1}$ by solving $P_m(\varepsilon)$ starting at $\hat{\mathbf{u}}_m^k$;
  - each agent j computes $\hat{\mathbf{u}}_j^{k+1} = \hat{\mathbf{u}}_j^k$ for $j \notin S_i$;
  - $\hat{\mathbf{u}}^{k+1} := (\hat{\mathbf{u}}_1^{k+1}, \ldots, \hat{\mathbf{u}}_M^{k+1})$;
  - **if** $\hat{\mathbf{u}}^{k+1}$ *is a stationary point for* $P_i(\varepsilon)$, $\forall i \in \mathscr{M}$ **then**
    - $\delta := true$;
  - **else**
    - $k := k + 1$;
    - $i := (i \mod r) + 1$;
- **until** $\delta = true$;
- $\varepsilon := \mu \varepsilon$;

until $\varepsilon < e$;

4. COMPUTATIONAL ANALYSIS

4.1 Distillation Column

This section presents the application of model predictive control to a benchmark problem, comparing the performance of the centralized and distributed approaches. The model of the heavy oil fractionator utilized is referred in the literature as the Shell Oil's heavy oil fractionator (Prett and Morari, 1987; Camacho and Bordons, 2004). It relates the controlled variables y_1, y_2, and y_3 that correspond to the top endpoint composition, side end composition, and bottom reflux temperature, respectively, with the manipulated variables u_1, u_2, and u_3, corresponding to top draw, side draw, and bottom reflux duties. The discrete model is obtained with a sampling time of 4 minutes, and it is possible to obtain a state space representation in the form:

$$\begin{bmatrix} \mathbf{x}_{11}(k+1) \\ \mathbf{x}_{21}(k+1) \\ \mathbf{x}_{31}(k+1) \\ \mathbf{x}_{12}(k+1) \\ \vdots \\ \mathbf{x}_{33}(k+1) \end{bmatrix} = \begin{bmatrix} A_{11} & & & \\ & A_{21} & \emptyset & \\ & & \ddots & \\ & \emptyset & & A_{33} \end{bmatrix} \begin{bmatrix} \mathbf{x}_{11}(k) \\ \mathbf{x}_{21}(k) \\ \vdots \\ \mathbf{x}_{33}(k) \end{bmatrix} + \begin{bmatrix} B_{11} & 0 & 0 \\ B_{21} & \vdots & \vdots \\ B_{31} & 0 & \\ 0 & B_{12} & 0 \\ \vdots & \vdots & \vdots \\ 0 & 0 & B_{33} \end{bmatrix} \begin{bmatrix} u_1(k) \\ u_2(k) \\ u_3(k) \end{bmatrix}$$

$$\begin{bmatrix} y_1(k+1) \\ y_2(k+1) \\ y_3(k+1) \end{bmatrix} = \begin{bmatrix} C_{11} & 0 & 0 & C_{12} & \cdots & 0 \\ 0 & C_{21} & 0 & 0 & \ddots & \vdots \\ 0 & 0 & C_{31} & 0 & \cdots & C_{33} \end{bmatrix} \begin{bmatrix} \mathbf{x}_{11}(k) \\ \mathbf{x}_{21}(k) \\ \vdots \\ \mathbf{x}_{33}(k) \end{bmatrix}$$

where each group $\mathbf{x}_{ij}$, A_{ij}, B_{ij}, and C_{ij} represents the couplings among the outputs and controls of the transfer function located in line i and column j of the transfer function matrix (Camacho and Bordons, 2004).

This formulation makes the distillation column a special case of the theory developed in the previous sections. For this special case, because the column is fully coupled, the set $I(m)$ is equal to $\{1,2,3\}$ for any m, and the *neighborhood* is equal to the *output* for each agent m. Other sets are given in Table 1.

Table 1. Sets used in the problem decomposition

m	$O(m)$	$C(m)$	$O(m,k)$
1	{2,3}	{(1,1),(1,2),(2,1),(1,3),(3,1)}	$O(1,2) = O(1,3) = C(1)$
2	{1,3}	{(1,2),(2,1),(2,2),(2,3),(3,2)}	$O(2,1) = O(2,3) = C(2)$
3	{1,2}	{(1,3),(3,1),(2,3),(3,2),(3,3)}	$O(3,1) = O(3,2) = C(3)$

Three different algorithms were used to solve the problem for the purpose of comparison:

- *Centralized Quadratic Programming* (cent_{QP}): the solution of P is obtained using a specific solver in Matlab® for problems in the quadratic form with constraints;
- *Centralized Barrier* (cent_{Br}): the solution of P is reached using the logarithmic barrier method and the centralized formulation;

Table 2. Numerical results

	dist_{Br}		cent_{Br}		cent_{QP}	
T	time	objective	time	objective	time	objective
1	0.0332	5.6188	0.0133	5.6188	0.0099	5.6188
2	0.0386	11.5680	0.0200	11.5680	0.0096	11.5680
5	0.0553	40.5596	0.0243	40.5596	0.0096	40.5596
10	0.0857	73.1869	0.0423	73.1868	0.0109	73.1868
15	0.1417	85.9801	0.0670	85.9797	0.0157	85.9797
20	0.2527	91.2292	0.1211	91.2284	0.0197	91.2284
25	0.3880	93.7129	0.2004	93.7115	0.0361	93.7115
30	0.6258	95.0680	0.2657	95.0660	0.0302	95.0660

- *Distributed Barrier* (dist_{Br}): each problem P_m is solved by a different agent and the constraints are treated with the logarithmic barrier method.

The criteria of convergence in Newton's method, which is used in cent_{Br} and dist_{Br} to solve centering problems, is $\lambda^2/2 \leq 10^{-5}$. The convergence criterion for the logarithmic barrier method is $\varepsilon \leq 10^{-4}$, while the stationary test is satisfied with $e \leq 10^{-4}$. The weights on control action and output deviation were set equal because their adjustment is not the focus of this work, but it is clear that the choice of weights affects directly the compromise between performance and robustness.

Ten different feasible start points were chosen at random in the experiments and the initial ε was defined as 10^3. The previous solution was not used as an initial approximation for reoptimization to induce worst-case scenarios. The analyses considered each type of algorithm, different lengths of prediction horizon (T), and rate of decrease $\mu \in \{0.05,\ 0.1,\ 0.3,\ 0.5\}$ for the interior-point methods.

4.2 Numerical Results

The objective function given in (7) is used for comparison as the cost of the computational experiments. Table 2 has the results of the accumulated cost obtained with the ten start points and the four different values for μ. The cost difference between dist_{Br} and the centralized approach is less than 3×10^{-3}, proving that solving the set of distributed problems, $\{P_m\}$, and solving the centralized problem, P, is equivalent. The gap in cost is due to the acceptance range of the convergence criteria.

Table 2 also contains the results about the time spent in the experiments, comparing cent_{QP}, cent_{Br} and dist_{Br}. A computer with an AMD Turion™ 64x2 1.60 GHz processor and 2048 MB of memory was used to perform the experiments. Time is given in seconds and represents the mean time spent to compute the control actions of forty different experiments with each algorithm. As expected, the greater the value of T, more time is necessary to reach the solution, but the time used was always less than one second, which is a very good result, considering real applications.

The iterations between agents to exchange information were also counted. Fig. 1 depicts the average number of iterations for the experiments with varying prediction horizon and decrease rate of the barrier method.

The convergence criterion can be relaxed to minimize the number of iterations between agents. In this case, due to the strong couplings among the variables, the information exchange is considerable. More scattered models will be used in future experiments, which are more suitable for a distributed approach.

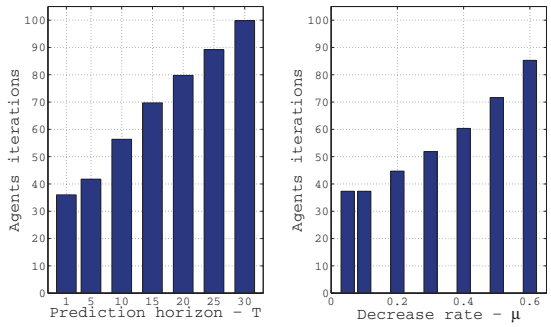

Fig. 1. Algorithm iterations varying T and μ, respectively.

Ending the analyses, it can be said that a network of distributed agents can solve the set of sub-problems $\{P_m\}$, rather than having a single agent solve P in centralized MPC, without incurring great loss of performance. Other adjustments can be made in the algorithm, such as the limit on the number of iterations, to guarantee the fulfillment of the deadlines, but all modifications have a compromise between speed and quality.

5. CONCLUSION

This work presented a distributed MPC framework with constraints on output and control-input signals. The methodology of problem decomposition was outlined and the barrier method was used to deal with the constraints, replacing the constrained minimization problem by a sequence of unconstrained minimization problems. Centralized MPC algorithms and the distributed MPC algorithm were applied to solve a regulation problem in a distillation column model.

The performance of distributed MPC in the distillation column scenario was comparable to the performance obtained with centralized MPC. The computational cost necessary to solve each agent problem was less than the centralized case. This advantage might allow the use of the distributed algorithm in machines with less computational resources.

It is worth emphasizing that distributed predictive control is more appropriate for multivariable problems where the couplings are scattered, which does not happen with the model of the distillation column.

Future works will focus on the implementation of reference tracking and state observers. As well as the whole study of how to introduce these extensions in a distributed algorithm. Another goal is to look into other scenarios that can be more appropriate for the application of distributed algorithms.

REFERENCES

Boyd, S. and Vandenberghe, L. (2004). *Convex Optimization*. Cambridge University Press.

Camacho, E.F. and Bordons, C. (2004). *Model Predictive Control*. Springer-Verlag, London.

Camponogara, E. and de Oliveira, L.B. (2009). Distributed optimization for model predictive control of linear dynamic networks. Accepted by *IEEE Transactions on Systems, Man, and Cybernetics – Part A*.

Camponogara, E., Jia, D., Krogh, B.H., and Talukdar, S.N. (2002). Distributed model predictive control. *IEEE Control Systems Magazine*, 22(1), 44–52.

Camponogara, E. and Talukdar, S.N. (2005). Designing communication networks to decompose network control problems. *INFORMS Journal on Computing*, 17(2), 207–223.

Camponogara, E. and Talukdar, S.N. (2007). Distributed model predictive control: synchronous and asynchronous computation. *IEEE Transactions on Systems, Man, and Cybernetics – Part A*, 37(5), 732–745.

de Oliveira, L.B. and Camponogara, E. (2008). Multi-agent model predictive control for split signaling in urban traffic networks. In *Proceedings of the 5th Workshop on Agents in Traffic and Transportation*, 21–28. Estoril, Portugal.

Dunbar, W.B. (2007). Distributed receding horizon control of dynamically coupled nonlinear systems. *IEEE Transactions on Automatic Control*, 57(7), 1249–1263.

Giovanini, L. and Balderud, J. (2006). Game approach to distributed model predictive control. In *Proceedings of the International Control Conference*. Glasgow, UK.

Li, S., Zhang, Y., and Zhu, Q. (2005). Nash-optimization enhanced distributed model predictive control applied to the Shell benchmark problem. *Inf. Sci.*, 170(2-4), 329–349.

Mercangöz, M. and Doyle III, F.J. (2007). Distributed model predictive control of an experimental four-tank system. *Journal of Process Control*, 17(3), 297–308.

Motee, N. and Jadbabaie, A. (2006). Distributed receding horizon control of spatially invariant systems. In *Proceedings of the American Control Conference*, 731–736.

Prett, D.M. and Morari, M. (1987). *Shell Process Control Workshop*. Butterworths, Boston.

Venkat, A.N., Hiskens, I.A., Rawlings, J.B., and Wright, S.J. (2008). Distributed MPC strategies with application to power system automatic generation control. *IEEE Transactions on Control Systems Technology*, 16(6), 1192–1206.

Comparison of discrete and continuous-discrete observers for composition estimation in distillation columns

A. Aguilera-González *, **A.C. Téllez-Anguiano** *, **C.M. Astorga-Zaragoza** *, **M. Adam-Medina** *

* *Centro Nacional de Investigación y Desarrollo Tecnológico, Interior Internado Palmira s/n, Col. Palmira, A.P. 5-164, C.P. 62490, Cuernavaca, Mor., México*

Abstract: In this paper we present a high-gain observer implemented in its discrete and continuous-discrete versions in order to compare the performance of both algorithms. The comparison is made considering the sampling time used to perform the observer's correction stage in order to establish that the continuous-discrete observer is the best option when a low sampling time is used. Under this condition the continuous discrete observer can process data performing a reliable on-line estimation of the system (a slow dynamics of the process is required). We apply both algorithms to a distillation column that uses the Ethanol-Water binary mixture.

Keywords: High-gain observer, discrete, continuous-discrete, distillation columns.

1. INTRODUCTION

The knowledge of state variables is often required in order to apply the advanced concepts of control and fault diagnosis to practical applications, specially in the chemical process industry. A method to obtain such variables, consists of combining a priori knowledge about physical systems with experimental data to provide an on-line estimator (observer).

The main control problems of distillation columns are caused due to tight interactions between the process variables, nonlinearities of the process, process and measurement delays and the large number of variables involved (see Murray-Gunther (2003)). For these reasons, a significant amount of effort has been devoted to develop algorithms that provide accurate parameter identification and state estimation (state observers) to reconstruct the product composition dynamics by secondary measurements (e.g., temperatures and flows) (see Quintero-Mármol et al. (1991), Deza et al. (1991)), and most recently in Bahar et al. (2006)Jana et al. (2006). The proposed observers are used to estimate unmeasured state variables from on-line and/or off-line measurements, see e.g. Bakir et al. (2005), Hammouri et al. (2006), Yildiz et al. (2005), Astorga et al. (2002) and Nadri et al. (2004).

Estimators are generally dynamic systems obtained from a nominal model by adding a correction term which is proportional to some output deviation. In other words, given a nominal model:

$$\begin{cases} \dot{\mathbf{x}}(t) = \mathbf{f}(\mathbf{x}(t), \mathbf{u}(t)) \\ \mathbf{y}(\mathbf{t}) = \mathbf{h}(x(t)) \end{cases} \tag{1}$$

The state $x(t)$ belongs to an open subset $\mathbf{V}$ of $\mathbb{R}^n$, the input u(t) belongs to a Borelian subset $\mathbf{U}$ of $\mathbb{R}^m$ and the output $y(t) \in \mathbb{R}^p$. An observer for the system represented by Eq. (1) is generally a dynamic system of the form:

$$\begin{cases} \dot{\hat{x}}(t) = \mathbf{f}(\hat{\mathbf{x}}(t), \mathbf{u}(t)) + \mathbf{k}(\mathbf{t})[h(\hat{\mathbf{x}}(\mathbf{t})) - \mathbf{y}(\mathbf{t})] \\ \dot{\mathbf{r}} = \mathbf{F}(\mathbf{r}(\mathbf{t}), \mathbf{u}(\mathbf{t}), \mathbf{y}(\mathbf{t}), \hat{\mathbf{x}}(\mathbf{t})) \\ \mathbf{k}(\mathbf{t}) = \varphi(\mathbf{r}(\mathbf{t})) \end{cases} \tag{2}$$

$r(t)$ and $k(t)$ are called indifferently the gain of the observer (see Hammouri et al. (2002)). An interesting class of nonlinear systems consists of those systems which are observable for every input, called *uniformly observable systems*. For this class of nonlinear systems, we can design an observer whose gain does not depend on the inputs (see Bornard and Hammouri (1991) and Gauthier et al. (1992)). For such systems a canonical (called triangular) form is designed in order to develop an observer. To ensure mathematical convergence, a particular high-gain is required (see Hammouri et al. (2002)).

However, using a high-gain observer may generate the so-called peak phenomena (overshoot problem); moreover, the estimator becomes noise sensitive. Due to nonlinearity of the system, the choice of the gain which gives the best compromise between fast convergence, the noise rejection and the attenuation of the peak phenomena becomes a difficult task, and only simulations allow to determine a possible gain. This paper aims to present a high-gain observer status in its discrete and continuous-discrete versions. We apply this algorithms to a binary distillation column that uses the binary mixture Ethanol-Water.

2. THE BINARY DISTILLATION COLUMN MODEL

The binary distillation column model is derived from the binary distillation column scheme shown in Fig. 1. There are three principal stages considered for a distillation column (condenser, tray and boiler); for every stage, the balances of energy and material should be formulated as well as the equilibrium conditions of the mixture.

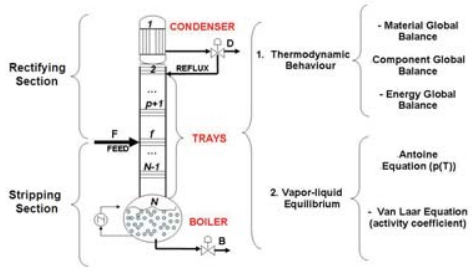

Fig. 1. Distillation column

2.1 General Aspects

The scheme of a typical distillation column is shown in Fig. 1. The binary feeding mixture (molar flow rate F) is introduced toward the middle of the column (the feeding tray). The distilled product (molar flow rate D), which mainly contains the light component, is removed from the top of the column. The bottom product (molar flow rate B), which contains the heavy component in greater concentration, is removed from the bottom of the column. Part of the overhead product is returned into the column to improve purity. Column stages are labeled with an ascendent numeration from the condenser to the boiler: $i = 1, ..., N$. The sections of the column are: the condenser, tray $i = 1$; the rectifying section, trays $i = 2, ..., f - 1$; the feeding tray, tray $i = f$; the stripping section, trays $i = f + 1, ..., N - 1$; the boiler, tray $i = N$.

2.2 Physic Behaviour

Due to its physical structure, a distillation column can be modeled as a set of interconnected stages using the mass balance and vapor-liquid equilibrium relation at every stage. The algebraic and differential equations of the model are formulated to calculate the light component composition of the mixture. The liquid phase and the vapor phase of the light component are designated by x and y, respectively.

Assumptions: The following assumptions, taken from Luyben (1992) and Halvorsen and Skogestad (2000) are considered in the model formulation:(**A1**) Constant pressure; (**A2**) Ideal Liquid-Vapor Equilibrium; (**A3**) Liquid-properties behave as a non-ideal mixture; (**A4**) Negligible molar vapor holdup compared to the molar liquid holdup; (**A5**) Boiler as a theoretical tray; (**A6**) Total condenser; (**A7**) Constant liquid volumetric hold up.

Vapor-liquid equilibrium: If a vapor and a liquid are in intimate contact for a long period of time, equilibrium is attained between the two phases. This concept of vapor-liquid equilibrium is fundamental to model distillation columns. If the vapor-liquid equilibrium exists, then the vapor composition y_i and the liquid composition x_i can be computed by means of correlating equations of the form $(y_i^{eq}, x_i^{eq}) = K_i(T_i, P_T)$, where T_i is the temperature, P_T is the total pressure, y_i^{eq} and x_i^{eq} are the vapor and liquid composition at the equilibrium phase respectively. The equilibrium constant K_i depends on the thermodynamical properties of the mixture.

The non-ideality of a binary mixture is due to different causes, the most frequent is the non-ideality of the liquid phase. In consequence, specially designed models are used to represent these non-idealities. For low pressure systems, the equation that represents the vapor composition is:

$$y_{i,j} P_T = P_{i,j}^{sat} x_{i,j} \gamma_{i,j} \tag{3}$$

where $j = 1$ if the component is ethanol and $j = 2$ if the component is water; $\gamma_{i,j}$ is the activity coefficient for every stage, it is a correction factor highly dependent on the concentration. In this work the vapor composition is calculated as a function of the light component. One method to determine this coefficient in every component of the mixture uses the Van Laar equation (see Perry (1999)).

Mass transfer effects: In order to deal with the mass transfer effects, the Murphree's efficiencies are introduced. The Murphree stage efficiency E_i is the ratio between the current change in vapor composition between two stages and the change that will occur if the vapor is in equilibrium with the liquid leaving the stage (see Murray-Gunther (2003)).

The molar flow rates: In the rectifying section the vapor molar flow V_R and the liquid molar flow L_R are :

$$\begin{cases} V_R = V_S + (1 - q_F)F, & i = 1, ..., f \\ L_R = (1 - R)V_R, & i = 1, ..., f - 1 \end{cases} \tag{4}$$

where

$$q_F = 1 + \frac{C_p(T_b - T_F)}{\lambda} \tag{5}$$

q_F describes the feeding condition. C_{p_j} is the specific heat, T_b is the boiling temperature, T_F is the feeding temperature and λ is the vaporization enthalpy for ethanol and water respectively.

F is the molar flow of the feeding stream:

$$F = F_V[\rho_1 w_1 + \rho_2(1 - w_1)] \left(\frac{x_f}{M_{W_1}} + \frac{1 - x_f}{M_{W_2}} \right) \tag{6}$$

where F_V is the volumetric flow of the feeding stream, ρ_j is the density of the component j, M_{W_j} is the molecular weight, w_1 is the weight fraction of the light component given by:

$$w_1 = \frac{x_f \rho_1}{x_f \rho_1 + (1 - x_f)\rho_2} \tag{7}$$

and x_f is the molar composition of the feeding stream given by:

$$x_f = \left(\frac{V_1 \rho_1 / M_{W_1}}{V_1 \rho_1 / M_{W_1} + V_2 \rho_2 / M_{W_2}} \right) \tag{8}$$

where V_j is the initial volume of the component j on the feeding container.

The distilled product flow rate, $D = 0$ if the three-way ON-OFF reflux valve shown in 1) is totally closed ($r_v = 0$) and $D = V_R$ if this valve is totally open ($r_v = 1$)

In the stripping section (subindex $[\cdot]_S$ is used), the vapor molar flow V_S and the liquid molar flow L_S are, respectively

$$\begin{array}{rcll} V_S & = & \dfrac{Q_b}{\Delta H_1^{vap} x_{1,N} + \Delta H_2^{vap}(1 - x_{1,N})}, & i = f+1, ..., N \\ L_S & = & L_R + q_F F, & i = f, ..., N \end{array} \tag{9}$$

where Q_b is the heating power on the boiler. Finally, the molar flow rate of the bottom product is:

$$B = (L_S - V_S) b_v$$

b_v is a binary variable representing the bottom-valve opening, *i.e.*: $b_v = 0$ if a batch distillation is performed and $b_v = 1$ if the bottom product is totally withdrawn from the boiler.

Molar hold-up: The molar hold-up for every stage must be determined from the distillation plant features and properties of the mixture. This quantity can be approximated as:

$$M_i = v_i \frac{1}{\dfrac{x_1 M_{W_1}}{\rho_1} + \dfrac{(1 - x_2) M_{W_2}}{\rho_2}} \tag{10}$$

2.3 The dynamic model

Tray and distilled product compositions are estimated by using the dynamic model based on material, component and energy balances. Taking into account the assumptions (**A1**) to (**A7**), a set of differential equations can be derived for the light component material balance as follows:

$$\begin{cases} \frac{dM_1}{dt} = V_2 - L_1 - D \\ \frac{dM_i}{dt} = V_{i+1} - L_i - V_i + L_{i-1} + \delta(i) F \\ \frac{dM_N}{dt} = L_{N-1} - V_N - B \end{cases} \tag{11}$$

for $i = 2, 3, ..., N-1$. M_i is the molar holdup of the boiler. The component balances for every stage are given by:

$$\begin{cases} \frac{d(M_1 x_1)}{dt} & = V_2 y_2 - L_1 x_1 - D x_1 \\ \frac{d(M_i x_i)}{dt} & = V_{i+1} y_{i+1} - L_i x_i - V_i y_i + L_{i-1} x_{i-1} + \delta(i) F x_F \\ \frac{d(M_N x_N)}{dt} & = L_{N-1} x_{N-1} - V_N y_N - B x_N \end{cases} \tag{12}$$

where $\delta(i) = 1$ if $i = f$ and $\delta(i) = 0$ if $i \neq f$

The enthalpies of the process are considered constants, therefore the energy balance is not taken into account to develop this model. The state model presented in the following section is based on this dynamic model for the distillation column.

2.4 The state model

The distillation column is a process that belongs to a class of multi-variable nonlinear systems. The process inputs are the heating power applied on the boiler, and the opening period of the reflux valve, this is $\mathbf{u}(t) = [Q_b(t)\ r_v(t)]^T$. F y x_F are considered perturbations in the system, this is $\mathbf{d} = [F, x_F, b_v]$. A state representation can be obtained from Eqs. (11) and (12). Additionally, the nonlinear model has the following triangular form:

$$\begin{cases} \dot{\zeta}_1 = f_1(\zeta_1, \zeta_2, \mathbf{u}) \\ \dot{\zeta}_i = f_i(\zeta_1, ..., \zeta_i, \zeta_{i+1}, \mathbf{u}); \quad (i = 2, ..., f-2) \\ \dot{\zeta}_{f-1} = f_{f-1}(\zeta_1, ..., \zeta_{f-1}, \zeta_f, \mathbf{u}) \\ \dot{\zeta}_f = f_f(\zeta_{f-1}, ..., \zeta_N, \mathbf{u}, \mathbf{d}) \\ \dot{\zeta}_i = f_i(\zeta_{i-1}, ..., \zeta_N, \mathbf{u}, \mathbf{d}); \quad (i = f+1, ..., N-1) \\ \dot{\zeta}_N = f_N(\zeta_{N-1}, \zeta_N, \mathbf{u}, \mathbf{d}) \end{cases} \tag{13}$$

where, ζ represent the states of the process (the liquid compositions of the light component). Subindex f represents the feeding tray number in Eqs. (11) and (12). The model allows to calculate the flows B, D, V_i, L_i and T_i, x_i from inputs Q_b, r_v, b_v, F_V, x_F.

3. OBSERVER DESIGN FOR A CLASS OF NONLINEAR TRIANGULAR SYSTEMS

A special class of nonlinear systems consists of those which are observable for every input, called uniformly observable systems (see Hammouri et al. (2002)). For this class of nonlinear systems, an observer whose gain does not depend on the inputs can be designed. For such systems a canonical (triangular) form is used in order to design an observer. Due to the nonlinearity of the system, it is important to select the gain which gives the best compromise between fast convergence and accuracy. Consider the follow triangular system that can be rewritten in a compact form:

$$\begin{cases} \dot{\zeta}^1 = \mathbf{f^1}(\boldsymbol{\zeta}(t), \mathbf{u}(t)) \\ \dot{\zeta}^2 = \mathbf{f}^2(\boldsymbol{\zeta}(t), \mathbf{u}(t), \mathbf{d}(t), \varepsilon(t)) \\ \boldsymbol{\varrho(t)} = (\varrho_1(t), \varrho_2(t))^T = (\mathbf{C}_{n_1} \boldsymbol{\zeta^1}(t), \mathbf{C}_{n_2} \boldsymbol{\zeta^2}(t))^T \end{cases} \tag{14}$$

where the states $\boldsymbol{\zeta}(t) = \left[\boldsymbol{\zeta}^1(t), \boldsymbol{\zeta}^2(t)\right]^T \in \mathbb{R}^n$ and $n = n_1 + n_2$; $\zeta^j = \left[\zeta_1^j, \zeta_2^j, \ldots, \zeta_{n_j}^j\right]^T \in \mathbb{R}^{n_j}$ for $j = 1, 2$; $y_j = \mathbf{C}_{n_j} \zeta^j = \zeta_1^j$ the first component of ζ^j; $\mathbf{C}_{n_j} = [1, 0, \ldots, 0]$; the input $\mathbf{u} \in \mathbb{R}^m$, and $\varepsilon(t)$ is an unknown and bounded function. The following assumptions are considered in order to design the observer:

- (**A8**) $\mathbf{f}^j$ is globally Lipschitz *w.r.t.* ζ.
- (**A9**) The state variables $\boldsymbol{\zeta}(t)$ are bounded

Considering the following notations:

i) $\mathbf{C}_{n_j} = [1, \ldots, 0] \in \mathbb{R}^{n_j}$ where n_j is the size for every state vector ζ^j.
ii)

$$\mathbf{A}_{n_j}(t) = \begin{bmatrix} 0 & a_1(t) & 0 & 0 \\ \vdots & & a_2(t) & 0 \\ & & & \ddots \\ 0 & & \ddots & a_{n_j-1}(t) \\ 0 & \ldots & 0 & 0 \end{bmatrix},$$

where $a_k(t)$, $k = 1, \ldots, n_{j-1}$ are bounded and unknown functions satisfying the following assumption:

- (**A10**) There are two finite real numbers α, β with $\alpha > 0$, $\beta > 0$ such that $\alpha \leq a_k(t) \leq \beta$.

Lemma 1 *Under assumptions (**A8**) and (**A10**) exist a symmetric positive definite (S.P.D.) matrix $\mathbf{S}_{n_j}$ and a constant $\mu > 0$ s.t.:*

$$\forall t, \mathbf{S}_{n_j}\mathbf{A}_{n_j}(t) + \mathbf{A}_{n_j}^T(t)\mathbf{S}_{n_j} \leq -\mu\mathbf{I}_d \tag{15}$$

where $\mathbf{I}_d$ is the identity matrix.

Then,

$$\mathbf{S}_{n_j} = \begin{bmatrix} s_{11} & s_{12} & 0 & & & 0 \\ & & \ddots & & & \vdots \\ s_{12} & s_{22} & & & & \\ 0 & \ddots & & \ddots & & 0 \\ \vdots & & & \ddots & & s_{(n_j-1)n_j} \\ 0 & \ldots & 0 & s_{(n_j-1)n_j} & & s_{n_j n_j} \end{bmatrix},$$

Assume that the system given in Eq. (14) satisfies hypothesis (**A8**) to (**A10**). Then the observer:

$$\begin{cases} \dot{\hat{\boldsymbol{\zeta}}}^1 = \mathbf{f}^1(\hat{\boldsymbol{\zeta}}, \mathbf{u}) - r_1\boldsymbol{\Delta}_{\theta^{\delta_1}}\mathbf{S}_{n_1}^{-1}\mathbf{C}_{n_1}^T(\mathbf{C}_{n_1}\hat{\boldsymbol{\zeta}}^1 - \varrho_1) \\ \dot{\hat{\boldsymbol{\zeta}}}^2 = \mathbf{f}^2(\hat{\boldsymbol{\zeta}}, \mathbf{u}, \mathbf{d}) - r_2\boldsymbol{\Delta}_{\theta^{\delta_2}}\mathbf{S}_{n_2}^{-1}\mathbf{C}_{n_2}^T(\mathbf{C}_{n_2}\hat{\boldsymbol{\zeta}}^2 - \varrho_2) \end{cases} \tag{16}$$

is an estimator for the system given in Eq. (14), where $r_1 > 0$, $r_2 > 0$; $\theta > 0$; $\boldsymbol{\Delta}_{\theta^{\delta_j}} = diag(\theta^{\delta_j}, \theta^{2\delta_j}, ..., \theta^{n_j\delta_j})$; $\delta_1 > 0$, $\delta_2 > 0$; $\mathbf{S}_{n_1}$ is given by **Lemma 1**.

The following theorem is given:

Theorem 1: *Denote by ε the upper bound of $|\varepsilon(t)|$ i.e. $\varepsilon = \sup_{t>0}|\varepsilon(t)|$, then for $r_1 > 0$, $r_2 > 0$, $\theta > 0$ sufficiently large and $\forall\delta_1 > 0$, $\delta_2 > 0$ s.t.*

$$\frac{2n_1 - 1}{2n_2 + 1}\delta_1 < \delta_2 < \frac{2n_1 + 1}{2n_2 - 1}\delta_1; \tag{17}$$

$$|\hat{\zeta}(t) - \zeta(t)\| \leq \lambda e^{-\mu t} + \lambda'\varepsilon; \tag{18}$$

for some constants $\lambda > 0$, $\mu > 0$ and $\lambda' > 0$. Moreover, $\mu \to +\infty$ as $\theta \to 0$.

Remark 1. *If $\varepsilon = 0$, the system given in Eq. (16) becomes an exponential observer for the system given in Eq. (14). A proof of this result is given in Hammouri et al. (2002).*

3.1 Application of the designed observer to a distillation column

In the previous sections Eqs. (14) to (16) describe the high-gain observer designed for a distillation column, as well as the appropriate model in which this observed is based. In this section, an observer synthesis to the following class of nonlinear systems is developed, which contains the model of binary distillation columns, considering the following notations:

$$\begin{cases} \zeta_i = \zeta_i^1; \ \ 1 \leq i \leq f - 1 \\ \zeta_{N-i+1} = \zeta_i^2; \ \ 1 \leq i \leq N - f + 1 \\ \zeta_F = \zeta_{N-f+2}^2 \end{cases} \tag{19}$$

then, the system given in Eq. (13) can be represented in the following compact form:

$$\begin{cases} \dot{\zeta}^1(t) = \mathbf{f}^1(\boldsymbol{\zeta}(t), \mathbf{u}(t), D(t)) \\ \dot{\zeta}^2(t) = \mathbf{f}^2(\boldsymbol{\zeta}(t), \mathbf{u}(t), \mathbf{d}(t), \varepsilon(t), B(t)) \\ \boldsymbol{\varrho}(t) = (\zeta_1^1, \zeta_1^2)^T = (\zeta_1, \zeta_N)^T \end{cases} \tag{20}$$

where $\varepsilon(t)$ is a bounded and unknown function *s.t.* $\dot{\zeta}_F = \varepsilon(t)$. The liquid flow rates in the stripping section and vapor flow rates in the rectifying section are not known variables. The holdup in the condenser, the boiler and trays (where it is assumed to be constant) is calculated . The weighted error between the estimated and the measured compositions is feed back to the model equation in order to correct the liquid flow rates in the stripping section and the vapor flow rates in the rectifying section (see Halvorsen and Skogestad (2000)).

The hypothesis (**A9**) and (**A10**) must be verified:

- (**A9**) is fulfilled since the flow rates are physically bounded.
- (**A10**) is satisfied because the liquid compositions $x_i \in [0, 1]$

Applying **Theorem 1**, the high-gain observer for the distillation column is:

$$\begin{cases} \dot{\hat{\boldsymbol{\zeta}}}^1 = \mathbf{f}^1(\hat{\boldsymbol{\zeta}}, \mathbf{u}, D(t)) - \mathbf{Q}_{1\theta}(\mathbf{C}_{n_1}\hat{\boldsymbol{\zeta}}^1 - \varrho_1) \\ \dot{\hat{\boldsymbol{\zeta}}}^2 = \mathbf{f}^2(\hat{\boldsymbol{\zeta}}, \mathbf{u}, B(t), \mathbf{d}, \varepsilon(t)) - \mathbf{Q}_{2\theta}(\mathbf{C}_{n_2}\hat{\boldsymbol{\zeta}}^2 - \varrho_2) \end{cases} \tag{21}$$

where $\mathbf{Q}_{j\theta} = r_j\boldsymbol{\Delta}_{\theta^{\delta_j}}\mathbf{S}_{n_j}^{-1}\mathbf{C}_{n_j}^T$, for $j = 1, 2$. The constant parameters are the same described in Eq. (16).

4. EXTENSION OF THE HIGH-GAIN OBSERVER TO THE CONTINUO-DISCRETE CASE

There are processes where the measurement of their variables are performed using long sampling times due to their slow dynamics. In Bahar et al. (2006) it is demonstrated that certain restrictions in the dimension of the sampling period used by a purely discrete observer exist. An alternative of solution for this problem is the use of continuous-discrete observers (see Hammouri et al. (2002)).

Consider a non-linear uniformly observable systems of the form:

$$\begin{cases} \dot{\mathbf{x}}(t) = \mathbf{f}(\mathbf{x}(t), \mathbf{u}(t)) \\ \mathbf{y}(\mathbf{t}) = \mathbf{h}(x(t)) \end{cases} \tag{22}$$

where $x(t) \in \mathbb{R}^n$, $u = (u_1, ..., u_n) \in \mathbb{R}^m$, are measurable inputs and $y \in \mathbb{R}$ is a measurable output. Using the model of the system with $u(t), y(t)$ as known measurements it is possible to estimate the state line in $x(t)$ of the system represented by Ec. 22, this task is performed by a recursive algorithm with the following structure:

i. A prediction period in the time interval $t \in [t_k, t_{k+1}]$:

$$\dot{\hat{x}}_k(t) = \mathbf{f}(\hat{\mathbf{x}}(t), \mathbf{u}(t)) \tag{23}$$

ii. A correction period in the time $t = t_{k+1}$:

$$\dot{\hat{x}}_{k+1}(t) = \hat{\mathbf{x}}_{\mathbf{k+1}}(-) - r\Delta_\theta S_\theta^{-1}C^T(C\hat{x}_{k+1}(-) - y_{k+1}) \tag{24}$$

To make the extension of the high-gain observer to continuous-discrete case, it is assumed that the observations are made at the time $k\triangle t$, where $\triangle t$ is the time between measurements and k is the instant in which the sample is taken. In this case, it is not considered a coordinates change because the triangular structure of the model studied in section 3 is used.

As the observer gain is constant, it is true that:

$$\forall t > 0, \mathbf{A}_k^T(t)\mathbf{S}_k + \mathbf{S}_k\mathbf{A}_k(t) - \rho\mathbf{C}_k^T\mathbf{C}_k \leq\leq -\mu\mathbf{I}_k \quad (25)$$

where S_k is a symmetric positive definite matrix with the following structure:

$$\mathbf{S}_k = \begin{bmatrix} s_{11} & s_{12} & 0 & & 0 \\ & \ddots & & & \vdots \\ s_{12} & s_{22} & \ddots & & \\ & \ddots & & \ddots & 0 \\ \vdots & & & \ddots & s_{(k-1)k} \\ 0 & \dots & 0 & s_{(k-1)k} & s_{kk} \end{bmatrix},$$

C_k is denoted as a vector of k elements:

$$\mathbf{C}_{n_j} = [1, \dots, 0] \quad (26)$$

and A_k is given by:

$$\mathbf{A}_k(t) = \begin{bmatrix} 0 & a_1(t) & 0 & 0 \\ \vdots & & a_2(t) & 0 \\ & & \ddots & \\ 0 & & & a_{k-1}(t) \\ 0 & \dots & 0 & 0 \end{bmatrix},$$

where the terms a_k may be unknown and satisfy the hypothesis **A9**.

5. EXPERIMENTAL VALIDATION OF THE OBSERVER

The distillation pilot plant, located at the Process Control Laboratory of the National Center of Technological Research and Development (CENIDET) in Cuernavaca, Morelos, México, was used to carry out the required experiments. It has twelve trays, where temperature measurements are available through 8 RTD's Pt-100 located at trays 1, 2, 4, 6, 7, 9, 11 and 12. Using these measurements and considering the equilibrium relation (see Section 2.2.2), the respective liquid compositions can be obtained.

The mixture used in these experiments was Ethanol(EtOH)-Water(H_2O) which is considered as a non-ideal mixture. The experimental validation of the observers is done considering: EtOH volume of 2000 ml, H_2O volume of 2000 ml and process total pressure of 105.86 kPa. The specifications of every component of the mixture can be found in Perry (1999). The experiment lasts 82 minutes, once it has reached the stable state. In minute 27 the system goes from total reflux to partial reflux. In minute 54, a change in the input Q_b is applied.

In the discrete observer the sampling time is used to estimate and correct. In the continuous-discrete observer the prediction and correction times can be different in order to use less data, therefore less processing time, performing a reliable online estimation. The observer estimates the liquid composition of the light component (EtOH) for every stage by having the temperature measurements on stage 1 (condenser) and stage 12 (boiler) only.

The high-gain observer is obtained by fixing $r_1 = r_2 = 25$; $\theta = 0.09$ and satisfying (16) with $\delta_1 = 1.2$, $\delta_2 = \frac{1}{2}\left[1 + \left(\frac{2n_1+1}{2n_2-1}\right)^2\right]\delta_1 = 0.0983$(where $n_1 = f - 1 = 6, n_2 = n - f + 2 = 6$). Finally Lemma 1 gives:

$$\mathbf{S}_{n_1} = \mathbf{S}_{n_2} = \begin{bmatrix} 1 & -1 & 0 & 0 & 0 & 0 \\ -1 & 2 & -1.5 & 0 & 0 & 0 \\ 0 & -1.5 & 4 & -2 & 0 & 0 \\ 0 & 0 & -2 & 8 & -3 & 0 \\ 0 & 0 & 0 & -3 & 10.5 & -4 \\ 0 & 0 & 0 & 0 & -4 & 15.5 \end{bmatrix}$$

Fig. 2 shows a comparison between the experimental dat and the estimation performed by the discrete observer in plate 12 (boiler) using a sampling time of $3s$. If the sampling time is slightly increased to $5.4s$ the discrete observer can not perform an adequate estimation, as can be seen in Fig. 3.

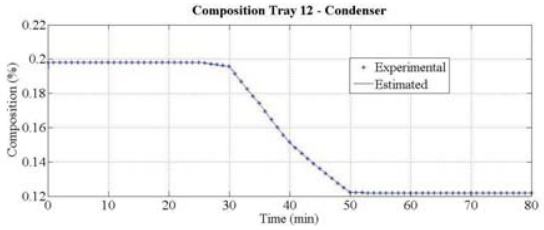

Fig. 2. Composition estimation of tray 12 by the discrete observer using a sampling time of 3 sec

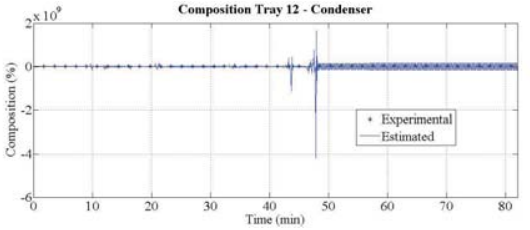

Fig. 3. Composition estimation of tray 12 by the discrete observer using a sampling time of 5.4 sec

In the continuous-discrete observer, a fixed prediction time of $3s$ is used, but different correction times are used in order to validate its performance. Figs. 4 to 6 show the experimental and estimated data when the correction time is 15 seconds, 30 seconds and 1 minute, respectively. In these figures it can be seen the good tracking and quickly convergence of the observer to the experimental data. The observer estimates the compositions of the plant adequately, under different conditions of correction time, having a maximum error of 0.03 and a minimum error 0.0001 between the estimated and the experimental data (the Euclidiean norm was used to estimate the error).

6. CONCLUSIONS

In order to validate the performance of the high-gain observer versions: discrete and continuous-discrete, some experiments were conducted under similar conditions. First,

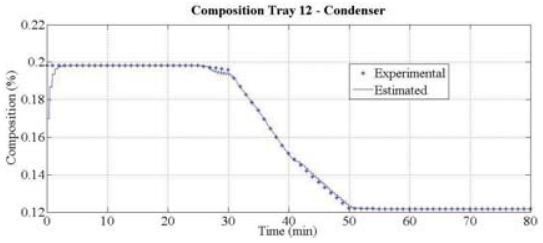

Fig. 4. Composition estimation of tray 12 by the continuous-discrete observer using a correction time of 15 sec

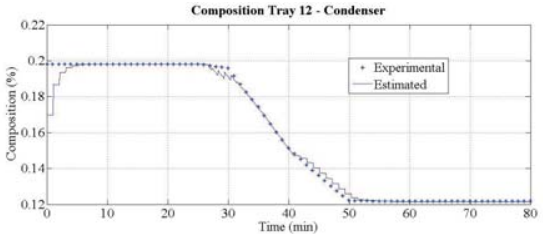

Fig. 5. Composition estimation of tray 12 by the continuous-discrete observer using a correction time of 30 sec

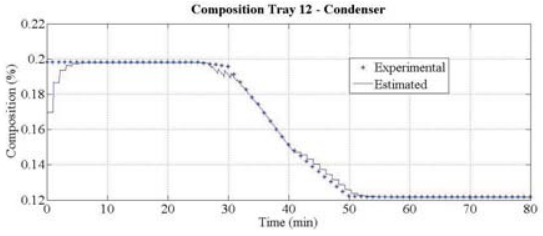

Fig. 6. Composition estimation of tray 12 by the continuous-discrete observer using a correction time of 60 sec

the purely discrete observer was validated, in order to perform, later, an adequate comparison with the continuous-discrete observer and analyze their response. Both validation use the same component specifications and same experimental inputs.

As can be seen in the presented figures the continuous-discrete observer presents a good tracking and quickly convergence to the experimental data, in spite of the sampling time used in the correction stage unlike the purely discrete observer, where the sampling time affects considerably its performance. Therefore, it can be assumed that the continuous-discrete observer is a suitable option to estimate the desired variables when the measurements of the system are performed using a long sampling time due to the slow dynamics of the process, which is the case of a distillation column where the compositions of the light component in a binary mixture of Ethanol-Water are estimated accurately.

REFERENCES

Astorga, C.M., Othman, N., Othman, S., Hammouri, H., and McKenna, T. (2002). Nonlinear continuous-discrete observers: application to emulsion polymerization reactors. *Control Engineering Practice*, 10(1), 3–13.

Bahar, A., Guner, E., Ozgen, C., and Halici, U. (2006). Design of state estimators for the inferential control of an industrial distillation column. In IEEE (ed.), *International Joint Conference on Neural Networks*. Vancouver.

Bakir, T., Othman, S., Puel, F., and Hammouri, H. (2005). Continuous-discrete observer for crystal size distribution of batch crystallization process. In IEEE (ed.), *Proceedings of the 44th IEEE Conference on Decision and Control, and the European Control Conference*, 6240–6244. Seville, Spain.

Bornard, G. and Hammouri, H. (1991). A high gain observer for a class of uniformly observable sytems. In *Proc. of the 30rd IEEE Conf. on Decision and Control*, 130–140. Brighton, UK.

Deza, F., Busvelle, E., and Gauthier, J.P. (1991). Exponentielly converging observers and internal stability using dynamic output feedback for distillation columns. *Chem. Eng. Science*, 47, 3935–3941.

Gauthier, J.P., Hammouri, H., and Othman, S. (1992). A simple observer for nonlinear systems, applications to bioreactors. *IEEE Transactions on Automatic Control*, vol. 37(6), pp. 875–880.

Halvorsen, I.J. and Skogestad, S. (2000). Distillation theory. *Encyclopedy of Separation Science*.

Hammouri, H., Nadri, M., and Mota, R. (2006). Constant gain observer for continuous-discrete time uniformly observable systems. In IEEE (ed.), *Proceedings of the 45th IEEE Conference on Decision and Control*, 5406–5411. San Diego, CA, USA.

Hammouri, H., Targui, B., and Armanet, F. (2002). High gain observer based on a triangular structure. *International Journal of Robust and Nonlinear Control*, 12, 497–518.

Jana, A., Samantab, A.N., and Gangulyb, S. (2006). Observer-based control algorithms for a distillation column. *Chemical Engineering Science*, 61, 4071 4085.

Luenberger, D. (1971). An introduction to observers. *IEEE Transactions on Automatic Control*, vol. 16(6), pp. 596–602.

Luyben, W.L. (1992). *Practical Distillation Control*. Van Nostrand Reinhold, New York, USA.

Murray-Gunther, A. (2003). *Dynamic Mathematical Model of a Distillation Column*. Ph.D. thesis, University of Tenessee at Chattanooga.

Nadri, M., Hammouri, H., and Astorga, C. (2004). Observer design for continuous-discrete time state affine systems up to output injection. *European Journal of Control*, 10(3), .

Perry, R. (1999). *Perrys chemical engineers handbook*. 7 edition.

Quintero-Mármol, E., Luyben, W.L., and Georgakis, C. (1991). Application of an extended luenberger observer to the control of multicomponent batch distillation. *Ind. Eng. Chem. Res.*, 30, 1870–1880.

Yildiz, U., Gurkan, U., Ozgen, C., and Leblebicioglu, K. (2005). State estimator design for multicomponent batch distillation columns. *Chemical Engineering Research and Design*, 83, 433–444.

Composition estimation of a six-component distillation column with temperature measurements

Andrea Frau, * **Roberto Baratti,** * **Jesús Alvarez** **

* *Dipartimento di Ingegneria Chimica e Materiali, Università degli Studi di Cagliari, Piazza d'Armi, 09123 Cagliari*
** *Universidad Autónoma Metropolitana-Iztapalapa, Depto. De Ingegneria de Procesos e Hidraúlica, Apdo. 55534, 09340 México D.F. México*

Abstract: The problem of jointly designing the estimation structure and algorithm to infer all or some composition in a six-component distillation column with temperature measurements is addressed. The structure design involves the choices of: (i) modeled and unmodeled compositions, (ii) the number of measurements and their location, and (iii) the innovated-noninnovated state partition. The algorithm is the dynamic data processor that performs the estimation task. The application of the geometric estimation approach (GE), in the light of the column characteristics, yields a tractable procedure to draw the solution of the estimation structure-algorithm design problem, with an estimation scheme that is considerably simpler than previous ones with extended Kalman Filter (EKF). The proposed methodology is applied to a representative six-component case example through simulations, finding that the estimation task can be performed with a three-component reduced model.

Keywords: Distillation column, nonlinear, estimators, geometric estimators, multicomponent.

1. INTRODUCTION

Distillation is an important energy-intensive industrial operation where many substances are separated and purified. The development of estimation schemes with temperature measurements for multicomponent distillation columns is motivated by: (i) the need of developing monitoring systems and (supervisory, advisory, and feedback) controllers with applicability-oriented requirements on reliability, tractability and maintenance cost, and (ii) the availability of reasonable and reliable multicomponent distillation models, including commercial packages.

The extended Kalman Filter (EKF) (Jazwinsky (1970)) has been by far the most widely used estimation technique in chemical process systems engineering in general, and in multicomponent distillation columns in particular, with successful simulations and experimental implementations for continuous and batch column operations, mostly for binary (Baratti et al. (1995); Yang and Lee (1997)) and ternary systems (Baratti et al. (1998)), and up to four-component systems (Venkateswarlu and Kumar (2006)). Even though adequate multicomponent column models are available, the related EKF construction and implementation for multicomponent systems still rises reliability, complexity, and development-maintenance cost concerns among industrial practitioners, because: (i) the dimensionality of the EKF grows rapidly with the number of stages and components ($\frac{n(n+1)}{2}+n$), (ii) the tuning of the covariance gains of the Riccati equation is a rather complex task, and (iii) due to the lack of formal connections between estimator tuning and functioning, the implementation of the EKF requires extensive testing.

Recently, the geometric estimation (GE) approach (Alvarez (2000)), which does not require the on-line integration of Riccati equations, has been redesigned with the following features (Alvarez and Fernandez (2008)): (i) the obstacle of high order Lie derivations has been removed and replaced by Jacobian model-based gain computations, enabling the consideration of staged systems, (ii) the equivalence between the GE and the EKF has been identified, (iii) the estimation model, its (innovation-noninnovation) detectability structure, and the sensor locations are regarded as structural design degrees of freedom, and (iv) a simple tuning scheme is coupled with a robust convergence criterion. The general-purpose GE approach has been successfully tested with experimental binary columns with complete (Tronci et al. (2005); Fernandez and Alvarez (2007)) or reduced models (Alvarez and Fernandez (2008)), and ternary columns (Pulis et al. (2006)), yielding estimation schemes which are considerably simpler than the EKF-based ones. These considerations motivate the present study on the six-component distillation column problem.

In this work, the problem of simultaneously designing the estimation structure and algorithm to infer all or some composition in a six-component distillation column with temperature measurements is addressed. By structure design we mean the choices of: (i) modeled and unmodeled compositions, (ii) the number of measurements and their locations, and (iii) the innovated-noninnovated composi-

tion state partition which, in conjunction with the model-sensor choice, determines the data assimilation versus error propagation mechanism. By algorithm it is meant the dynamic data processor that performs the estimation task, according to the estimation structure and a suitable gain tuning scheme. The application of afore discussed GE approach, in the light of the six-component column characteristics, yields a tractable procedure to solve the structure-algorithm problem, with an estimation scheme that is considerably simpler than previous EKF-based ones. The proposed methodology is applied to a representative six-component case example through simulations, finding that the estimation task can be performed with a three-component reduced model, a single-stage innovation with passive structure, and without the need of online integrating Riccati equations. The study can be seen as an inductive step towards the consideration of columns with more than six components.

2. ESTIMATION PROBLEM

2.1 Six-component distillation column

Consider a continuous multicomponent column with N stages and C components. Under standard assumptions (energy balance neglected on each tray, constant vapor and liquid flows, holdup dynamics neglected, tight reboiler and condenser level control, and stage liquid-vapor equilibrium), the column dynamics are described by the following set of nonlinear differential equations (Skogestad (1997); Baratti et al. (1998)):

Reboiler ($i = 1$, $j = 1, \ldots, C-1$)

$$\dot{c}_1^j = \frac{(R+F)c_2^j - V\epsilon_j(c_1, P_1) - Bc_1^j}{M_1} = f_1^j(c_1, c_2^j) \quad (1a)$$

Stripping section ($2 \le i \le N_F - 1$, $j = 1, \ldots, C-1$)

$$\dot{c}_i^j = \frac{(R+F)(c_{i+1}^j - c_i^j) - V(\epsilon_j(c_i, P_i) - \epsilon_j(c_{i-1}, P_{i-1}))}{M_i} \quad (1b)$$
$$= f_i^j(c_{i-1}, c_i, c_{i+1}^j)$$

Feed tray ($i = N_F$, $j = 1, \ldots, C-1$)

$$\dot{c}_{N_F}^j = \frac{R(c_{N_F+1}^j - c_{N_F}^j) + F(c_F^j - c_{N_F}^j)}{M_{N_F}} - \frac{V(\epsilon_j(c_{N_F}, P_{N_F}) - \epsilon_j(c_{N_F-1}, P_{N_F-1}))}{M_{N_F}} \quad (1c)$$
$$= f_{N_F}^j(c_{N_F-1}, c_{N_F}, c_{N_F+1}^j, c_F)$$

Enriching section ($N_F + 1 \le i \le N - 1$, $j = 1, \ldots, C-1$)

$$\dot{c}_i^j = \frac{R(c_{i+1}^j - c_i^j) - V(\epsilon_j(c_i, P_i) - \epsilon_j(c_{i-1}, P_{i-1}))}{M_i} \quad (1d)$$
$$= f_i^j(c_{i-1}, c_i, c_{i+1}^j)$$

Condenser ($i = N$, $j = 1, \ldots, C-1$)

$$\dot{c}_N^j = \frac{V\epsilon_j(c_{N-1}, P_{N-1}) - Rc_N^j - Dc_N^j}{M_N} = f_N^j(c_{N-1}, c_N^j) \quad (1e)$$

Temperature measurements ($i = 1, \ldots, m$)

$$T_{s_i} = \beta(c_{s_i}, P_{s_i}) \quad (1f)$$

where m is the number of sensors along the column and s_i is the location of the i-th sensor, c_i^j is the composition of the component j at i-th stage, $c_i = [c_i^1 \ \ldots \ c_i^{C-1}]^T$ is the composition vector at i-th stage, T_{s_i} and P_{s_i} are respectively the temperature and the pressure at s_i-th stage, F is the feed flow rate with composition $c_F = [c_F^1 \ \ldots \ c_F^{C-1}]^T$, D, B, R, and V are respectively the distillate, bottom, reflux and vapor flow rate (V is proportional to reboiler duty Q through the heat of vaporization λ), M_i is the holdup at i-th stage, ϵ_j is the liquid-vapor equilibrium function that determines the vapor composition of the component j, and β is the bubble-point implicit function that sets the temperature. The components c_i^C are determined by the (mass conservation) condition $\sum_{j=1}^{C} c_i^j = 1$, where $i = 1, \ldots, N$. Henceforth, column system (1), will be referred to as the *complete six-component column system*, which in compact vector notation is written as follows:

$$\dot{x}_P = f_P(x_P, u_P, d_P) \qquad y_P = h_P(x_P) \quad (2)$$

where $x_P = [{c_1}^T \ldots {c_N}^T]^T$, $c_i = [c_i^{C2}\, c_i^{C3}\, c_i^{IC4}\, c_i^{NC4}\, c_i^{IC5}]^T$, $u_P = [R\, V]^T$, $d_P = [F\, {c_F}^T]^T$, and $y_P = [T_{s_1} \ \ldots \ T_{s_m}]^T$ are respectively the states, the inputs, the disturbances, and the outputs. The disturbances d_P are assumed to be constant and known.

2.2 Estimation problem

The estimation problem consists in jointly designing the estimation structure (i.e. estimator model, sensor location, innovated states and data assimilation mechanism), and the estimation algorithm (i.e., the dynamic data processor), to infer some of or all the effluent compositions of the six-component distillation column (2) on the basis of a reduced model (to be designed) in conjunction with temperature measurements, according to a specific estimation objective. In virtue of the general-purpose GE approach (Alvarez and Fernandez (2008)) and its applications to binary (Fernandez and Alvarez (2007); Alvarez and Fernandez (2008)) and ternary columns (Pulis et al. (2006)), in the present six-component column estimation study, the emphasis will be placed on: (i) the design of a reduced-component model for estimation, (ii) the employment of a robustness-oriented single-stage innovation scheme with passive structure (Pulis (2007)), (iii) the corresponding decision on the innovated components, meaning the components of the measurement stage with information and error injection, and (iv) the estimation of the effluent (distillate and bottom) impurity compositions as estimation objective.

2.3 Case example

As a representative industrial case example, consider the T110 distillation column located at SARAS refinery (Sarroch, Italy) with $N = 37$ stages and $C = 6$ components: a C3-C4 (propane-butane) splitter fed with propane (C3), iso-butane (IC4), and n-butane (NC4), as well as ethane (C2), iso-pentane (IC5), and n-pentane (NC5) as secondary components (with compositions less than 1%).

The column has a kettle reboiler (1-st stage), a total condenser (37-th stage), 35 nutter float valve trays, the feed is introduced at 19-th stage, the tray spacing is 61 cm, the column diameter is 2 m, and the pressure changes linearly along the column, with the top and bottom pressure being 16.3 Kg·cm^{-2} and 16.6 Kg·cm^{-2}, respectively. This case example represents a sufficiently important class of industrial columns, where two or three main components to be split are present, together with other secondary components in a much smaller amount.

The behavior of the "actual" six-component system (2) was numerically simulated with MATLAB, in the understanding that the same task can be performed with commercial packages (say ASPEN). The thermodynamics was simulated with ideal equilibrium (Reid et al. (1998)). The feed flow and compositions, as well as the reflux flow, and reboiler duty are given in Table 1. In all simulations, the initial conditions for the complete column system correspond to the steady-state determined by the data listed in Table 1.

Table 1. Input values for feed flow and compositions, reflux flow and reboiler duty

F (m^3·h^{-1})	82.9	C2 molar fraction	0.0036
R (m^3·h^{-1})	69.7	C3 molar fraction	0.281
Q (BTU)	19819000	IC4 molar fraction	0.236
		NC4 molar fraction	0.4746
		IC5 molar fraction	0.004
		NC5 molar fraction	0.0008

3. STRUCTURAL ANALYSIS

Motivated by the GE detectability measure-based sensor location criterion employed in previous binary (Tronci et al. (2005); Fernandez and Alvarez (2007); Alvarez and Fernandez (2008)) and ternary columns (Pulis et al. (2006)) as well as by their interpretation in terms of thermodynamic diagrams (Pulis et al. (2006)), in this section the sensor location and innovated composition structure is analyzed on the basis of stage-to-stage temperature gradients and their component-wise contributions.

3.1 Model reduction

The stage-to-stage temperature gradient about a certain operation condition is approximated as follows:

$$\Delta T_i = T_{i+1} - T_i \approx \sum_{j=1}^{C} \frac{\partial T_i}{\partial c_i^j}\bigg|_{c_i} \Delta c_i^j = \sum_{j=1}^{C} \Delta T_{c_i^j} \qquad (3)$$

where $\Delta c_i^j = c_{i+1}^j - c_i^j$, ΔT_i is the temperature gradient at the i-th stage, and $\Delta T_{c_i^j}$ is the contribution of the i-th gradient due to the component j. The idea which underlies the model reduction criterion is to set a data assimilation scheme with a favorable compromise between data assimilation and error propagation: (i) the stages with large temperature gradients are candidates for robustness-oriented single-stage (i.e. passive) innovation, and (ii) the compositions with large contributions to the overall gradient are candidates for being both modeled states and innovated states.

Table 2. Feed compositions for the reduced model

C3 molar fraction	0.2838
IC4 molar fraction	0.2388
NC4 molar fraction	0.4774

On the basis of the steady-state solution of the complete system (2) in conjunction with the total and per-component temperature gradient formula (3), the diagram presented in Figure 1 was obtained, showing that: (i) with respect to stage-to-stage temperature change, the most sensitive zone is the enriching section around the 32-nd stage, (ii) in general, the temperature gradients are due to C3, IC4 and NC4 composition changes, (iii) the IC5, and NC5 components have a rather small contribution to the temperature gradient, and (iv) at the top of the column (around the condenser stage) the C2 has a rather important influence on temperature.

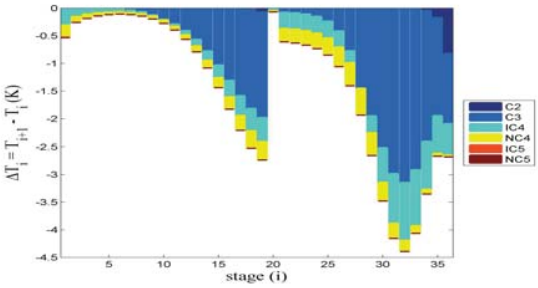

Fig. 1. Complete model-based temperature gradient and its per-component contributions

From the examination of the stage-to-stage temperature gradient and the per-component contributions to such gradient, the following structural conclusions are reached: the reduced model is obtained by retaining the C3, IC4, and NC4 components with appreciable manifestation in the temperature gradient, and discarding the three other ones (C2, IC5, and NC5) with comparatively small manifestation. Thus the reduced model is given by (1) with $C = 3$. In vector notation, the *reduced model* is written as follows:

$$\dot{x} = f(x, u, d) \qquad y = h(x) \qquad (4)$$

where $x = [c_1^{C3} c_1^{IC4} \dots c_N^{C3} c_N^{IC4}]^T$, $u = [R\,V]^T$, $d = [F c_F^{C3} c_F^{IC4}]^T$, and $y = [T_{s_1} \dots T_{s_m}]^T$ are respectively the states, the inputs, the disturbances, and the outputs. The reduced model (4) was set with the feed compositions presented in Table 2.

The behaviors of the reduced three-component model (4) and complete six-component system (2) are presented in Figure 2, showing that the model reduction error has an appreciable (or negligible) manifestation in the distillate (or bottoms) concentrations, and the same is true for the enriching (or stripping) section. This signifies that: (i) the bottom composition can be adequately estimated, without measurement injection, by means of a reduced model-based open-loop observer, and (ii) the distillate compositions can be estimated with a reduced model-based estimator with one temperature measurement, as

the temperature measurement before the top of the column basically reflects C3 and IC4 changes.

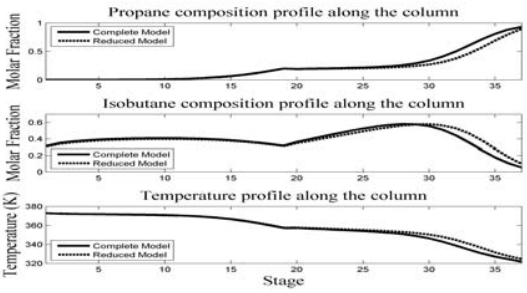

Fig. 2. C3 and IC4 composition and temperature profiles along the column with (six-component) complete and (three-component) reduced models

3.2 Sensor location and innovated states

On the basis of the steady-state solution of the reduced model (4) in conjunction with the total and per-component temperature gradient formula (3), the diagram presented in Figure 3 was obtained, showing that: (i) in the stripping (or enriching) section, the largest temperature gradient, or equivalently, the richest-in-information zone, is located below the feed (or top) tray, and (ii) in the stripping (or enriching) section, the smallest temperature gradient, or equivalently, the poorest-in-information zone, is located above the reboiler (or feed) tray.

From the preceding comments and the findings of Subsection 3.1, the next conclusions on sensor location follow: (i) one temperature measurement should be placed in the stripping section, located at the richest-in-information region (between 29-th and 33-rd stages) with the largest temperature gradient, and (ii) no temperature measurement is needed in the stripping section, as the bottom compositions can be adequately estimated using just the reduced model (without measurements). According to Figure 3, the C3 component has the largest contribution to the temperature gradient in the richest-in-information zone, meaning that the C3 component is an innovated state candidate for a robustness-oriented GE with passive structure (Pulis et al. (2006)).

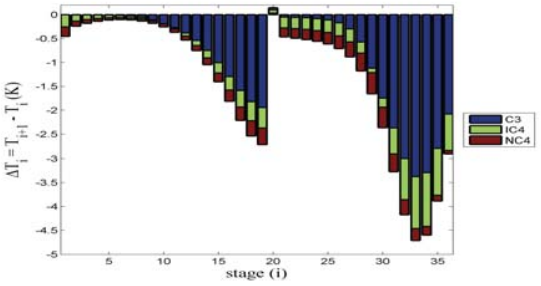

Fig. 3. Reduced model-based temperature gradient and its per-component contributions

3.3 Candidate estimation structures

According to the preceding developments, the two-effluent composition estimation task for the six-component system (2) can be performed using the reduced three-component model with one temperature sensor located between 25-th and 33-rd stages, with the C3 component as innovated state in a robustness-oriented GE with passive structure (Pulis et al. (2006)). To preclude unduly bottom-to-top model and measurement error propagation, no measurement in the stripping section is placed. To have a favorable balance between data assimilation and model-measurement error propagation from the measurement to distillate effluent composition estimate, a measurement should be located in the tray interval between stages 29 and 33, and not in any of the two top trays (stages 35 and 36) as shown in Figure 1. Thus, the preceding considerations lead to the following candidate estimation structure: (i) no sensor in the stripping section, (ii) one sensor in the enriching section between 29-th and 33-rd trays, and (iii) the C3 composition as innovated state. These structural conclusions are suggestive in the sense that: (i) candidate sensor location and innovated C3 compositions around the afore concluded candidates must be examined, and (ii) the conclusive structural assessment will be performed in the next section, on the basis of GE functioning. In order to verify the estimator performance, some different choices for the set of innovated states have been selected by following the considerations above: these innovated state sets will be illustrated and compared in Section 4.

4. STRUCTURE ASSESSMENT WITH ESTIMATOR FUNCTIONING

Having as point of departure the candidate structures identified in the preceding section, in this section the estimation structure for effluent composition estimation aims is assessed on the basis of the structure behavior with a robustness-oriented GE with passive structure (Pulis et al. (2006)). The role of the actual process will be played by the six-component system (2), and the GE will be implemented with the reduced three-component model (4).

4.1 Geometric estimator with passive innovation

Let us recall the adjustable-structure proportional-integral (PI) GE with passive structure (Alvarez and López (1999); Alvarez and Fernandez (2008)):

$$\begin{aligned} \dot{\hat{x}}_I &= f_I(\hat{x},\hat{u}) + \Phi_{x_I}^{-1} P(K_P(y_P - \hat{y}) + z) \\ \dot{\hat{x}}_{II} &= f_{II}(\hat{x},\hat{u}) \qquad \dot{z} = K_I(y_P - \hat{y}) \qquad \hat{y} = h(\hat{x}) \end{aligned} \tag{5}$$

where $\hat{x}$, $\hat{u}$, and $\hat{y}$ are the estimates of x, u, and y, $x_I \in \mathbb{R}^{n_I}$ is the set of the innovated states, $x_{II} \in \mathbb{R}^{n-n_I}$ is the set of the non-innovated states, K_P and K_I are respectively the proportional and integral gain matrices. For this kind of estimator structures, if $x_I = [c_{s_1}^{l_1} \ \dots \ c_{s_1}^{l_1^{n_1}} \ \dots \ c_{s_m}^{l_m^1} \ \dots \ c_{s_m}^{l_m^{n_m}}]^T$, then K_P, K_I, Φ_{x_I}, and P assume the following form:

$$K_P = \begin{bmatrix} K_{P,s_1} & & \\ & \ddots & \\ & & K_{P,s_m} \end{bmatrix} \qquad K_I = \begin{bmatrix} K_{I,s_1} & & \\ & \ddots & \\ & & K_{I,s_m} \end{bmatrix}$$

$$\Phi_{x_I} = \left[\left. \frac{\partial \hat{T}_{s_1}}{\partial \hat{c}_{s_1}^{l_1^1}} \right|_{\hat{c}_{s_1}} \cdots \left. \frac{\partial \hat{T}_{s_1}}{\partial \hat{c}_{s_1}^{l_1^{n_1}}} \right|_{\hat{c}_{s_1}} \cdots \left. \frac{\partial \hat{T}_{s_m}}{\partial \hat{c}_{s_m}^{l_m^1}} \right|_{\hat{c}_{s_m}} \cdots \left. \frac{\partial \hat{T}_{s_m}}{\partial \hat{c}_{s_m}^{l_m^{n_m}}} \right|_{\hat{c}_{s_m}} \right] \cdot \begin{bmatrix} 1 & & \\ & \ddots & \\ & & 1 \end{bmatrix} \qquad P = \begin{bmatrix} 1 \ldots 1 & & \\ & \ddots & \\ & & 1 \ldots 1 \end{bmatrix}^T$$

Note that: (i) the generic composition $c_{s_i}^{l_i^j}$ is innovated only by using temperature at s_i-th stage; (ii) n_i represents the number of innovated components at s_i-th stage and the condition $\sum_{i=1}^{m} n_i = n_I$ holds; (iii) $[x_I \, x_{II} \, z]^T \in \mathbb{R}^{n+m}$; (iv) P is a matrix of 1s and 0s, where for every column $i \in \{1, \ldots, m\}$ there are n_i 1s as shown above. When the integral action state is eliminated, the proportional (P) GE is obtained.

The robust convergence aspects and its connection with the tuning of gains can be seen in Alvarez and Fernandez (2008), and here it suffices to mention that: (i) the convergence criterion is coupled with rather easy-to-apply tuning guidelines, and (ii) the tuning scheme and guidelines apply over all structures. In this way, one has the certainty that the estimator functioning results are due to the structure and not to the tuning scheme.

Next the GE tuning guidelines for the GE PI estimator with passive structure are recalled. Consider an innovated state $c_{s_i}^{l_i^j}$: then, the corresponding temperature used in order to estimate this composition is T_{s_i} and the tuning parameters are:

$$K_{P,s_i} = 2\xi_{s_i}\omega_{s_i} \qquad K_{I,s_i} = {\omega_{s_i}}^2 \tag{6}$$

where ω_{s_i} and ξ_{s_i} are respectively the characteristic frequency and the damping factor of the estimator at s_i-th stage. The characteristic frequency ω_{s_i} must be chosen between 5 and 10 times faster than ω_{o,s_i} (where ω_{o,s_i} is the natural characteristic frequency of composition at s_i-th stage). Following conventional-like filter and control behavior assessments, the estimator functioning will be measured with the IAE index and the steady-state error.

As mentioned before, the estimation task is to infer the effluent impurity compositions (i.e., C3 in the bottom and IC4 in the top). Since the C3 in the reboiler is adequately described by the model without measurement, only the results of the IC4 distillate composition estimates will be presented. Several simulations have been performed, but for sakes of brevity only one of them is reported here. To test the estimator over different structures, a column transient has been induced by some step changes at the reboiler duty ($\Delta Q = +3\%$ at $t = 2$ hrs and $\Delta Q = 0$ at $t = 8$ hrs, with respect to Q value of Table 1)

Two different measures have been employed: (i) the steady-state error (7a), and (ii) the IAE index (7b)

$$e_{i,SS1}^j \quad \text{if} \quad \Delta Q = 0 \quad \text{and} \quad e_{i,SS2}^j \quad \text{if} \quad \Delta Q = +3\% \tag{7a}$$

$$IAE(e_i^j) = \int |e_i^j| dt \tag{7b}$$

where e_i^j is the composition error for the component j at i-th stage. There are two steady-state errors, since two different steady-state conditions are present, as can be seen from Figures 4, 5, and 6. For all the structures considered, the estimator has been tuned with the tuning guidelines sketched in (6), with $\omega_{s_i} = 10\omega_{o,s_i}$ and $\xi_{s_i} = 3$ for $i = 1, \ldots, m$.

4.2 Estimation with one innovated state

On the basis of the structural analysis performed in Section 3, two single-innovated state cases have been considered: $x_I = [c_{29}^{C3}]$ and $x_I = [c_{33}^{C3}]$.

The corresponding GE behavior results are presented in Figure 4 and Table 3, showing that: (i) comparing with the reduced model behavior, in both cases the estimate error undergoes a considerable reduction by measurement injection, and (ii) the case with c_{33}^{C3}-innovation yields a slightly better behavior than with c_{29}^{C3}-innovation. This result is consistent with the conclusion reached in Section 3, as 33-th stage has the largest stage-to-stage gradient and is close to the top stage.

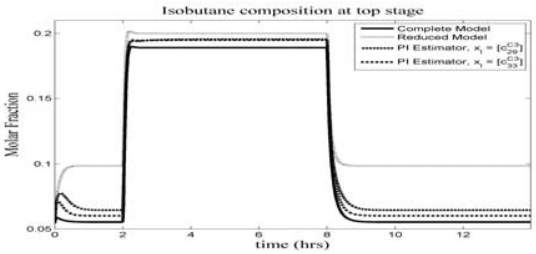

Fig. 4. IC4 distillate composition estimate with one innovated state

4.3 Estimation with two innovated states

Now, let us find out whether the joint consideration of the two previous cases leads to some estimator behavior improvement, this is $x_I = [c_{29}^{C3} \, c_{33}^{C3}]^T$.

The corresponding GE behavior results are presented in Figure 5 and Table 3, showing that there is not an appreciable improvement over the estimation structures with one innovated state discussed in the last subsection (see Figure 4).

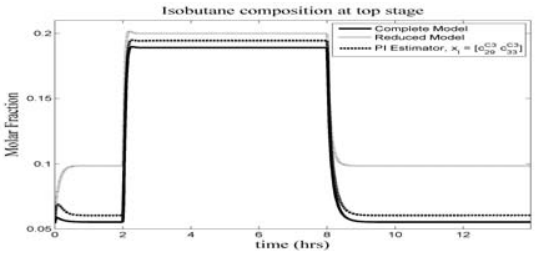

Fig. 5. IC4 distillate composition estimate with two innovated states

4.4 Estimation with three innovated states

Finally, let us investigate if the effluent estimation behavior can be improved by adding one innovated state to the two-innovated state structure presented in Subsection 4.3,

this is $x_I = [c_{29}^{C3}\ c_{31}^{C3}\ c_{33}^{C3}]^T$, with the incorporation of the innovated state c_{31}^{C3} being motivated by the fact that 29-th and 33-rd stages bracket the rich-in-information zone of the enriching section. The corresponding GE behavior results are presented in Figure 6 and Table 3, showing that there is an appreciable improvement over the two-innovated state estimation structure discussed in the last subsection (see Figure 5).

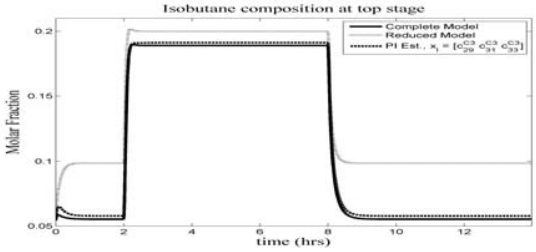

Fig. 6. IC4 distillate composition with three innovated states

Table 3. IAE values and steady-state errors (the subscript T refers to the top stage)

	$e_{T,SS1}^{IC4}$	$e_{T,SS2}^{IC4}$	$IAE(e_T^{IC4})$
Reduced model	−0.0433	−0.0109	20.1124
$x_I = [c_{29}^{C3}]$	−0.0092	−0.0064	5.9306
$x_I = [c_{33}^{C3}]$	−0.0049	−0.0058	3.8622
$x_I = [c_{29}^{C3}\ c_{33}^{C3}]^T$	−0.0052	−0.0054	3.8077
$x_I = [c_{29}^{C3}\ c_{31}^{C3}\ c_{33}^{C3}]^T$	−0.0025	−0.0022	1.7871

4.5 Concluding remarks

The behavior measures of the four estimation structures considered in this section are summarized in Table 3, showing that: the best GE estimator behavior is obtained with the three-innovated state structure, followed by the two-innovated state structure, and by the two single-innovated state structures. It must be pointed out that the steady-state estimation error is smaller than 1% and therefore comparable with typical measurement errors. These results are in agreement with the a priori structural assessments drawn in Section 3. The IC4 distillate composition estimation task can be effectively performed using: (i) a three-component reduced model, (ii) one or more sensors located between stages 29 and 33 in the enriching section, and (iii) passive innovation for component C3.

5. CONCLUSIONS

The problem of jointly designing the estimation structure and algorithm to infer an effluent composition for a six-component distillation column with temperature measurement option has been resolved in a tractable manner within a GE design framework in the light of the staged column system characteristics. The design focused on structural aspects: model reduction, sensor location, and innovation mechanism. The methodology consisted of: (i) one structural analysis step that yielded a few candidate structures and (ii) a step with conclusive structural results on the basis of estimator behavior assessment. The resulting GE (with 75 to 77 nonlinear ordinary differential equations (ODEs), depending on the structure) was considerably simpler than its EKF counterpart (with 2812 ODEs) and of tuning procedure (trial-and-error or optimization for the EKF and well defined for the GE).

Currently, work is underway to apply the proposed approach to estimate the pollutant contents in the outlet streams of an actual industrial column.

ACKNOWLEDGEMENTS

The authors kindly acknowledge the support from Italian and Mexican Foreign Ministries through the Binational Collaboration projectt SAPP01.

REFERENCES

Alvarez, J. (2000). Nonlinear state estimation with robust convergence. *Journal of Process Control*, 10, 59–71.

Alvarez, J. and Fernandez, C. (2008). Geometric estimation of nonlinear process systems. *Journal of Process Control*. doi:10.1016/j.jprocont.2008.04.017.

Alvarez, J. and López, T. (1999). Robust dynamic state estimation of nonlunear plants. *AIChE Journal*, 45(1), 107–123.

Baratti, R., Bertucco, A., Da Rold, A., and Morbidelli, M. (1995). Development of a composition estimator for binary distillation colums. application to a pilot plant. *Chemical Engineering Science*, 50(10), 1541–1550.

Baratti, R., Bertucco, A., Da Rold, A., and Morbidelli, M. (1998). A composition estimator for multicomponent distillation column - development and experimental test on ternary mixtures. *Chemical Engineering Science*, 53(20), 3601–3612.

Fernandez, C. and Alvarez, J. (2007). Constructive estimation design for binary distillation columns. In *International Symposium on Advanced Control of Chemical processes*, 75–80. Cancún, México.

Jazwinsky, A.H. (1970). *Stochastic processes and Filtering Theory*. Academic Press, New York.

Pulis, A. (2007). *Soft sensor design for distillation columns*. Ph.D. thesis, Università degli Studi di Cagliari.

Pulis, A., Fernandez, C., Baratti, R., and Alvarez, J. (2006). Geometric estimation of ternary distillation columns. In *International Symposium on Advanced Control of Chemical processes*, 573–578. Gramado, Brasil.

Reid, R.C., Prausnitz, J.M., and Poling, B.E. (1998). *The properties of gases and liquids*. McGraw-Hill, Singapore, fourth edition.

Skogestad, S. (1997). Dynamics and control of distillation columns: a tutorial introduction. *Trans IChemE, Part A*, 75, 539–559.

Tronci, S., Bezzo, F., Barolo, M., and Baratti, R. (2005). Geometric observer for a distillation column: development and experimental testing. *Ind. Eng. Chem. Res*, 44, 9884–9893.

Venkateswarlu, C. and Kumar, B.J. (2006). Composition estimation of multicomponent reactive batch distillation with optimal sensor configuration. *Chemical Engineering Science*, 61, 5560–5574.

Yang, D.R. and Lee, K.S. (1997). Monitoring of a distillation column using modified extended kalman filter and a reduced order model. *Computers and Chemical Engineering*, 21, 565–570.

Temperature Inferential Dynamic Matrix Control of Reactive Distillation Systems

Deeptanshu Dwivedi and Nitin Kaistha *
Department of Chemical Engineering
Indian Institute of Technology Kanpur India 208016

Abstract: Two-temperature inferential control of the ideal and the methyl acetate double feed reactive distillation (RD) systems operated neat is evaluated using constrained dynamic matrix control (CDMC) and traditional decentralized control. For the ideal RD system, significant improvement in the stripping tray temperature control and the transient deviation in the bottoms purity is observed using CDMC. For the methyl acetate system, CDMC results in significant improvement in the control of the two tray temperatures as well as transient deviations in both the distillate and bottoms purity. Results also show that the magnitude of the maximum through-put change for which the control system fails is noticeably higher using CDMC.

Keywords: Reactive distillation control, dynamic matrix control, temperature inferential control

1. INTRODUCTION

Reactive distillation (RD) is now an established process intensification technology combining reaction and separation in a single column with potentially significant economic savings when the reaction kinetics and component relative volatilities are favorable (Siirola, 1995). When compared to conventional "reactor-separator" processes, the high non-linearity due to direct interaction between reaction and separation combined with fewer control degrees-of-freedom makes the design of an effective control system crucial to the successful implementation of RD technology.

In probably the first paper on RD control, Roat et al (1986) demonstrated that seemingly appropriate control structures succumb to a steady state transition for a moderately large through-put change suggesting the presence of high-non-linearity. Several later articles highlighted the presence of steady state multiplicity in various RD systems (see eg Mohl et al, 1999; Taylor and Krishna, 2000). The presence of steady state multiplicity can result in non-linear dynamic phenomena under open and closed loop operation. Sneesby et al (1997) considered the implications of steady state multiplicity on the operation and control of etherification columns. Kumar and Kaistha (2008a) demonstrated the occurrence of 'wrong' control action and closed loop steady state transition for the hypothetical quaternary ideal RD column studied by Al-Arfaj and Luyben (2000).

Given the high non-linearity in RD systems, the application of non-linear control techniques has been recommended in the literature. Among the prominent non-linear RD control works, Kumar and Daoutiditis (1999) implemented a non-linear inversion based control scheme for an ethylene glycol RD column. Model based gain scheduling has been applied to an ETBE RD column. Gruner et al (2003) report the non-linear control of an industrial RD column operated by Bayer. More recently, Kawathekar and Riggs (2007) have applied a non-linear model predictive control scheme to an ethyl acetate column.

Even as non-linear model based control is widely accepted in the academic community, industrial practice remains strongly biased towards the traditional decentralized PI control and where justifiable, linear model predictive control techniques such as DMC. This is probably due to the difficulty in developing a high fidelity non-linear process model and identifying the model parameters in an industrial setting.

A careful examination of the RD control literature reveals that the control of two-reactant double-feed RD columns operated neat (no excess of a reactant) such as the quaternary ideal RD system and the methyl acetate RD system, is particularly challenging due to the need for stoichiometric balancing of the two fresh feeds. Adjusting one of the fresh feeds to maintain an appropriate tray composition has been shown to be an effective means of maintaining this balance. The use of temperature measurements instead of composition, the former being much more rugged, reliable, cheap and with fast measurement dynamics, however causes the control system to succumb to non-linear dynamic phenomena such as 'wrong' control action in the methyl acetate RD system or a closed loop steady state transition in the quaternary ideal RD system (Kumar and Kaistha, 2008a). Application of linear MPC techniques, which have found industrial acceptance, may significantly improve the performance of a temperature inferential control system for such 'difficult to regulate' processes. This work addresses the same for the quaternary ideal and the methyl acetate RD systems.

2. BASE-CASE COLUMN DESIGN

Figure 1 shows a schematic of the double feed RD columns studied in this work. The reaction $A + B \leftrightarrow C + D$ occurs in the reactive zone. For the methyl acetate system, the components A, B, C and D correspond to methanol, acetic acid, methyl acetate and water respectively. For the ideal RD

system, the component relative volatilities are in the order $\alpha_C > \alpha_A > \alpha_B > \alpha_D$ so that the reactants are intermediate boiling. The reaction kinetics and thermodynamic property models for the methyl acetate and the ideal RD system are taken from Singh et al (2005) and Al-Arfaj and Luyben (2000), respectively. The base-case design and operating conditions for the ideal RD system are taken from Kaymak and Luyben (2006). The internally heat integrated design of the methyl acetate RD system reported in Kumar and Kaistha (2008 b) is studied here. The salient design and operating conditions for the two systems are reported in Table 1.

$$A + B \leftrightarrow C + D$$

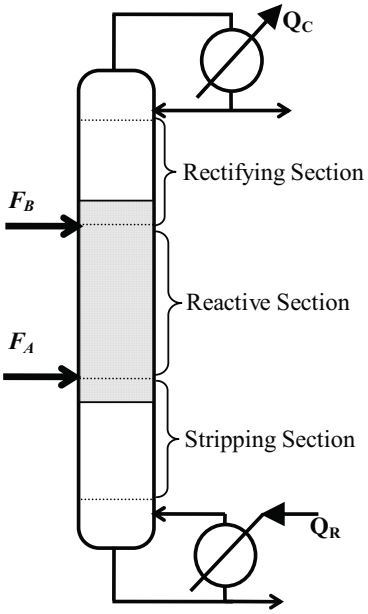

Figure 1. Schematic of a double feed reactive distillation column

Table 1: Design Parameters of Ideal RD system and Methyl Acetate system

	Ideal RD Column	Methyl Acetate RD column
Flow rate of feeds	$F_A = F_B$ = 12.6 mol/s	$F_{HAc}=F_{MeOH}$ =300 kmol/hr
$N_E/N_{RX}/N_S$ design	5/10/5	7/18/10
Feed tray locations	n_{FA} = 9; n_{FB} = 12	n_{FMeOH} =16; n_{FHAc} =28
Catalyst loading per reactive tray	0.7 kmol	300 kg
Pressure	8.5 bar	1.013 bar
Reflux ratio	2.6927	1.4877
Distillate rate	12.6 mol/s	308.63 kmol/h
Reboiler duty	0.8516 MW	3.66387 MW
Product purities	X_C,D = X_D,B = 0.95	X_{MeOAc},D=0.95 X_{H2O},B=0.96

3. TEMPERATURE INFERENTIAL CONTROL

3.1 Control Structures

Figure 2 & 3 plot the tray temperature sensitivities with respect to the two fresh feeds and the reboiler duty at constant reflux ratio for the ideal and methyl acetate columns. The sensitivity plots, suggest two candidate control structures, labeled as CS1 and CS2 for convenience. In CS1, F_A controls a sensitive stripping tray temperature while F_B controls a sensitive reactive tray temperature. The reboiler duty (Q_R) acts as the through- put manipulator. CS2 differs from CS1 in that the Q_R, instead of F_B is used to control a sensitive reactive tray temperature with F_B being the through-put manipulator. The two control structures are schematically depicted in Figure 4. Using bottom-up tray numbering, the temperature of Tray 2 (T_2), a stripping tray, and Tray 12 (T_{12}), a reactive tray, is controlled in the ideal RD column. In the methyl acetate column, the control tray temperature locations are Tray 2 (T_2) and Tray 13 (T_{13}). Note that in the ideal RD system, even as a rectifying tray temperature exhibits higher sensitivity than a reactive tray with respect to F_B (see Figure 2), it is not controlled due an inverse response with respect to F_B (Kaymak and Luyben, 2006) and severe input multiplicity resulting in a steady state transition for moderately large through-put changes (Kumar and Kaistha, 2008a).

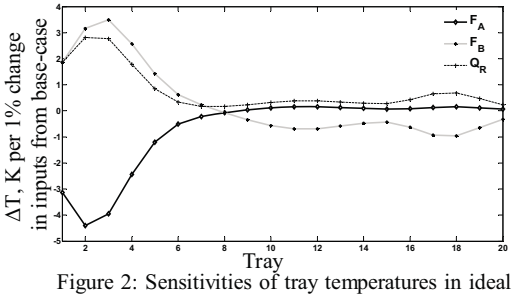

Figure 2: Sensitivities of tray temperatures in ideal RD system with respect to fresh feeds (F_A & F_B) and reboiler (Q_R) duty at fixed reflux ratio

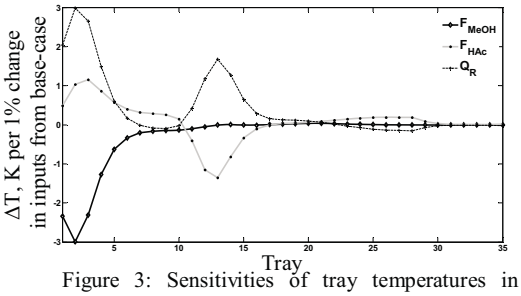

Figure 3: Sensitivities of tray temperatures in methyl acetate system with respect to Methanol feed (F_{MeOH}) and Reboiler Duty (Q_R) at fixed reflux

3.2 Dynamic Simulation and Temperature Controller Details

An in-house dynamic simulator is used to generate the open and closed loop dynamic simulation results for the two RD columns. With the two level controllers and perfect pressure control in place, a 2x2 temperature control system as in structures CS1 and CS2 is implemented. A 1 min lag is applied to the temperature measurements. The performance

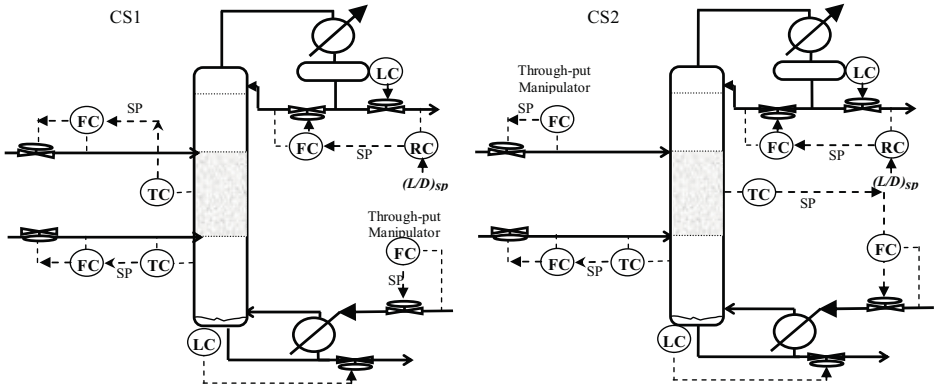

Figure 4. Schematic of used two point temperature inferential control structures

Table 2: CS1 & CS2 controller parameters for the ideal and methyl acetate RD column

Tuning parameters used in CDMC in the two systems						
System	MV	γ	CV	λ	P min	C min
Ideal RD Column with CS1	F_A	1	T_3	5	90	50
	F_B	40	T_{12}	10		
Ideal RD Column with CS2	F_A	1	T_3	5	90	50
	Q_R	4	T_{12}	10		
Methyl Acetate Column with CS1	F_{MeOH}	3	T_2	20	250	125
	F_{HAc}	4	T_{13}	25		
Methyl Acetate Column with CS2	F_{MeOH}	1	T_2	20	250	125
	Q_R	4	T_{13}	25		
Span of temperature measurements = 50K; All valves are 50% open at their design steady state. Slew rate constraints used in CDMC limits the rate of change of manipulated variable from zero to the base-case design value in no less than 2 minutes.						

of a 2x2 decentralized controller is to be compared with that of a 2x2 multivariable constrained dynamic matrix control (DMC) controller. For tuning the two decentralized PI temperature controllers, the relay feedback test is performed to obtain the ultimate gain and ultimate period of the temperature loops. The Tyreus-Luyben controller settings are then applied with appropriate de-tuning, if necessary. In the ideal RD column, both the temperature loops are tuned independently. In the methyl acetate column, sequential tuning is applied where the stripping loop is first tuned. For the DMC controller, appropriate valve saturation and slew rate constraints are applied. The slew rate constraint corresponds to the maximum rate of change of the DMC controller causing the output to saturate in two minutes. The sampling rate of the DMC controller is 0.5 minutes for the ideal RD column and 0.625 minutes for the methyl acetate RD column. The DMC step coefficient matrix is obtained using a +1% step change in the appropriate input. The tuning parameters used for CDMC are shown in Table 2.

4. RESULTS

A through-put change is considered as the primary disturbance to be rejected by the control system. The closed loop performance of the multivariable DMC and decentralized controller is now evaluated for the ideal and the methyl acetate RD columns.

Figure 5 plots the ideal RD column closed loop response to a ±20% through-put change using CS1 as the control structure. The response completion time is about 4 hours for both the controllers. Significantly tighter stripping tray temperature control (T_2) is achieved by the DMC controller while the reactive tray temperature control is comparable. This translates to tighter bottoms purity (x_D,B) control and no appreciable benefit in the distillate purity (x_C,B) control using the DMC controller.

Figure 6 plots the closed loop response to a ±20% through-put change in ideal RD column for CS2 using a decentralized and DMC 2x2 temperature controller. Significantly tighter T_2 and T_{12} temperature control is achieved by the DMC controller.

The closed loop response of the methyl acetate column to a ±20% through-put change is plotted shown in Figure 7. The CDMC temperature controller is far superior to the decentralized controller. The transient deviation in reactive T_{13} control is much smaller for the DMC controller. The tightness of the T_2 control is also better. The tighter temperature control translates to lower transient deviations in both the distillate (x_{MeOAC},D) and bottoms product purity (x_{H2O},B). Notice that with the DMC controller, the two fresh feeds move in tandem for a better stoichiometric feed balance during the transient with consequent improvement in the control performance. Figure 8 plots the closed loop response of CS2 to a ±20% through-put change for the methyl acetate RD column. For this structure also, the DMC achieves much tighter control of the stripping and reactive tray temperatures.

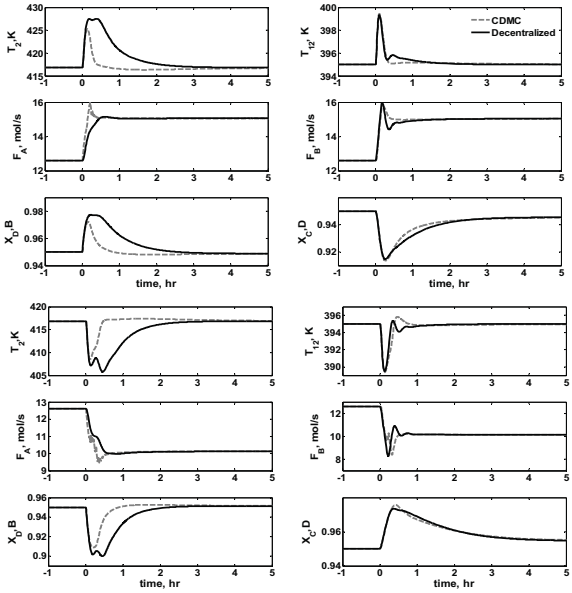

Figure 5. Closed Loop response in Ideal RD system with CS1structure for +20% (Fig A) and -20% (Fig B) change in throughput using CDMC & Traditional decentralized temperature controllers

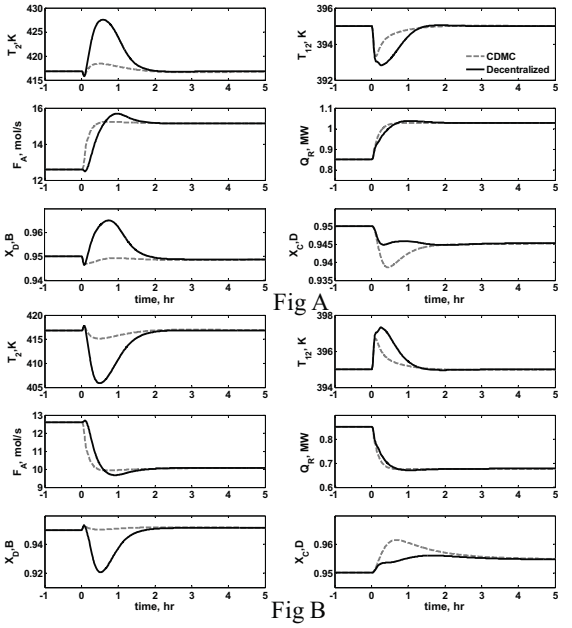

Fig A

Fig B

Figure 6. Closed Loop response in Ideal RD system with CS2 structure for +20% (Fig A) and -20% (Fig B) change in throughput using CDMC & Traditional decentralized temperature controllers

To gain a better perspective on the performance of the controller algorithms and structures, the maximum through-put change that can be handled was studied. In both the ideal and the methyl acetate RD columns, a through-put decrease turns out to be the more severe disturbance with both CS1 and CS2 For the ideal RD column, CS1 using DMC fails for value for the decentralized controller is -45%. CS2 on the a

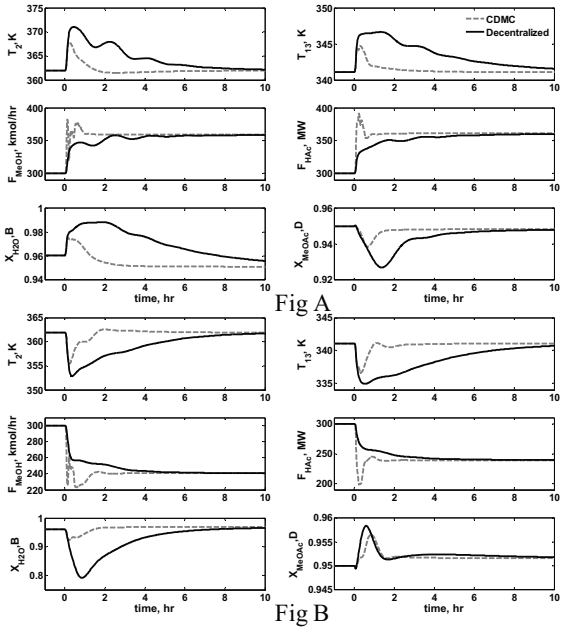

Fig A

Fig B

Figure 7. Closed Loop response in Methyl Acetate RD system with CS1 structure for +20% (Fig A) and -20% (Fig B) change in throughput using CDMC & Traditional decentralized temperature controllers

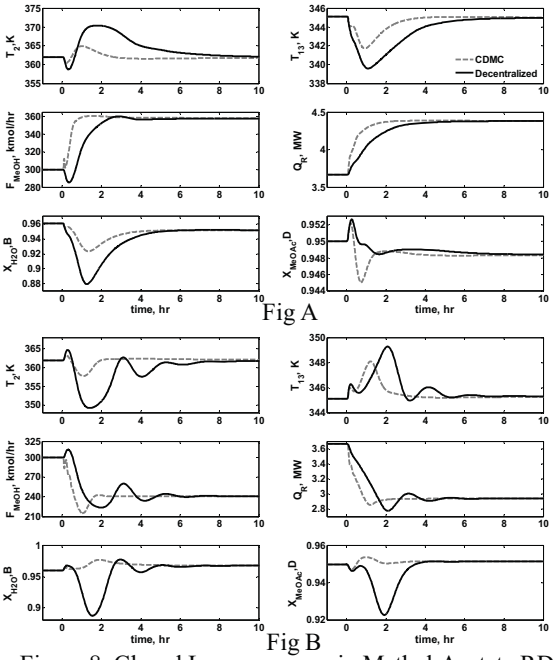

Fig A

Fig B

Figure 8. Closed Loop response in Methyl Acetate RD system with CS2 structure for +20% (Fig A) and -20% (Fig B) change in throughput using CDMC & Traditional decentralized temperature controllers

-70% step change in the through-put. The corresponding other hand fails for -65% and -55% through-put changes using respectively the DMC and decentralized control algorithms. For the methyl acetate system, CS2 with a DMC controller exhibits no improvement in the magnitude of the

maximum through-put decrease handled. Column operation using CS1 with a DMC controller allows for a 60% through-put decrease to be handled where CS1 with decentralized control fails for a 45% through-put decrease.

5 DISCUSSION

The Integral Abslolute Error (IAE) of product purity is plotted in Figure 9 & 10 as the magnitude of the through-put change is increased. Regardless of the control structure and the RD system, the 2x2 DMC control provides tighter product purity controller for large through-put changes.

We have considered a through-put change to be the primary disturbance for the double feed ideal RD systems operated neat. In some situations, variation in the fresh feed composition may also constitute a principal disturbance into the column. To test for the closed loop control performance of the temperature inferential control systems under consideration, we consider a 5 mol% step change in the purity of either feed as a disturbance. For the ideal RD system, component B in F_A and component A in F_B are the feed impurities. For the methyl acetate RD system, water is taken as the impurity in the fresh feeds. Table 3 reports the IAE of the two controlled tray temperatures and the distillate and bottoms purity for the two RD systems using CS1 and CS2. In both the RD systems, the reactive tray temperature control is poorer while the stripping loop temperature is better than decentralized controller. The inferior reactive temperature control is possibly due to the change in the step response coefficients for the altered feed conditions. Inspite of the poorer reactive temperature control, the data in the Table 3 suggests that the deviations in the distillate and bottoms purity for the DMC and decentralized controller are comparable. The DMC controller can thus withstand a feed composition disturbance.

Table 3: Comparison of Controllers for Regulatory Performance with impure fresh feed as disturbance with Integral Absolute Error (IEA's) key control variables

	Disturbance	Control Variable	CS1		CS2	
			CDMC	Decentralized	CDMC	Decentralized
Ideal RD Column	Pure F_A & Impure F_B with Z_B=0.95, Z_A=0.05	T_{12}	72.85	29.285	43.70	46.504
		T_2	334.83	433.47	266.01	695.89
		Top Purity	0.46	0.63	0.703	0.76
		Bottom Purity	0.59	0.88	0.56	1.27
	Pure F_B & Impure F_A with Z_A=0.95, Z_B=0.05	T_{12}	96.28	45.78	35.50	48.65
		T_2	296.61	202.32	143.31	347.67
		Top Purity	1.33	1.09	0.88	0.581
		Bottom Purity	0.612	0.58	0.47	0.35
Methyl Acetate RD Column	Pure F_{H2O} & Impure F_{HAc} with 5 % water	T_{13}	67.26	58.26	68.86	28.94
		T_2	126.38	460.02	120.77	425.32
		Top Purity	0.047	0.046	0.06	0.036
		Bottom Purity	0.429	1.40	0.41	1.20
	Pure F_{HAc} & Impure F_{H2O} with 5 % water	T_{13}	41.19	167.94	52.65	82.71
		T_2	125.61	535.69	137.49	371.41
		Top Purity	0.49	0.51	0.516	0.51
		Bottom Purity	0.45	2.68	0.350	1.62

The asymmetry in the closed loop results (see e.g. Figure 5) suggests the presence of non-linear effects. To investigate this, Figure 11 & 12 plots the variation in the two tray temperatures with respect to the fresh feeds and the reboiler duty at constant reflux ratio. In the ideal RD system, input multiplicity in the stripping tray temperature (T_2) for excess F_B and lower F_A is evident. The reactive tray temperature (T_{12}) exhibits input multiplicity as F_A and F_B are decreased. For the methyl acetate RD system, even as a crossover with respect to base-case steady state does not occur for the range of variation in the column inputs shown, the reactive tray temperature exhibits gain sign reversal with respect to the fresh acetic acid feed. Also, notice the severe directionality in the steady state reactive tray temperature response with respect to the fresh methanol feed with a very small decrease in temperature as the feed rate is increased and very large increase as it is decreased. This extreme directionality, at least partially, explains the asymmetry. The input-output (IO) relations (Figure 11 & 12) can also be used to understand the control system failure mode to large through-put changes. For example, for CS1 with a decentralized controller, for a -50% through-put change, the F_B valve ends up shutting down in slightly under an hour with F_A maintaining T_2 at its set-point. The control system failure mode likely corresponds to 'wrong' control action due to input multiplicity.

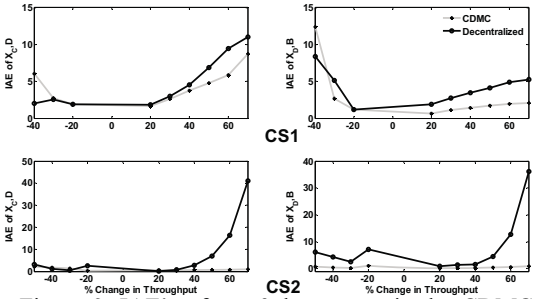

Figure 9: IAE's of top & bottom purity by CDMC and decentralized control using CS1 & CS2 in Ideal RD column for large throughtput changes

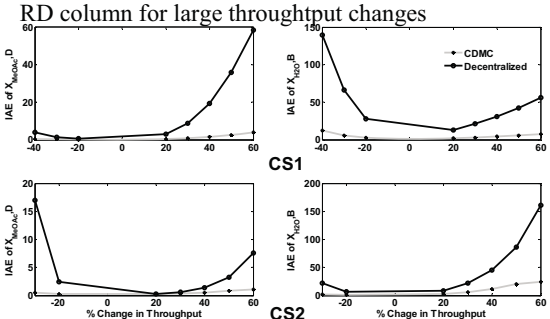

Figure 10: IAE's of top & bottom purity by CDMC and decentralized control by CS1 & CS2 in Methyl Acetate RD column for large throughtput changes

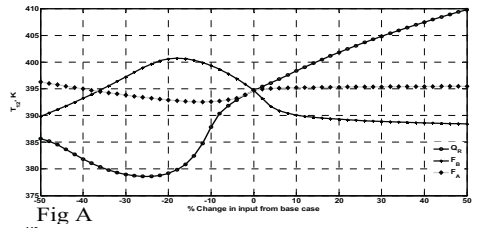

Fig A

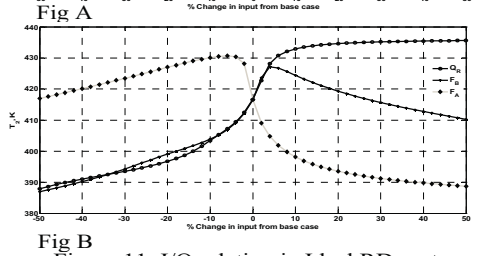

Fig B

Figure 11: I/O relation in Ideal RD system

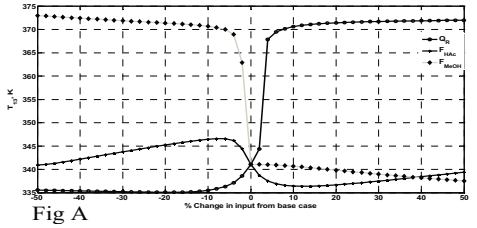

Fig A

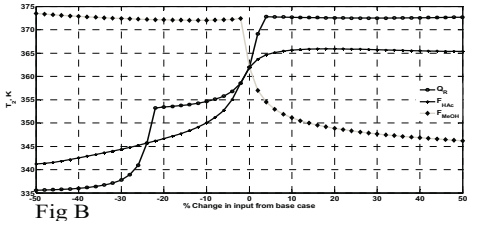

Fig B

Figure 12: I/O relation in Methyl acetate column

It is comforting to note that in spite of the highly non-linear IO relations, a linear control system (decentralized or DMC) effectively rejects such a severe disturbance without succumbing to non-linear dynamic phenomena.

6. CONCLUSIONS

In conclusion, this work demonstrates that the application of constrained dynamic matrix control for two-point temperature inferential control of double feed RD columns operated neat improves the control system performance in terms of the maximum through-put handled and/or the tightness of product purity control achieved. Specifically, in the ideal RD column, significantly tighter bottoms purity control is achieved In the methyl acetate column, tighter control of both the distillate and bottoms purity is achieved using the DMC controller for both the structures. The maximum through-put decrease handled is noticeably higher in CS1 while no such benefit was observed for CS2. These results suggest an overall incentive for the application of linear model predictive control algorithms over conventional decentralized of the highly non-linear RD systems.

REFERENCES

Al-Arfaj, M.A., Luyben, W.L., (2000). Comparison of alternative control structures for an ideal two-product reactive distillation column, *Ind. and Engg. Chem. Res.*, 39, 3298-3307.

Grüner, S., Mohl, K.D., Kienle, A., Gilles, E.D., Fernholz, G., Friedrich, S., (2003). Nonlinear control of a reactive distillation column**,** *Cntl. Engg. Prac., 11,* 915-925.

Kawathekar, R., Riggs, J.B., (2007). Nonlinear model predictive control of a reactive distillation column, *Cntl. Engg. Prac, 15,* 231-239.

Kaymak, D. B., Luyben, W. L., (2006). Evaluation of a Two Temperature Control Structure for a Two-Reactant/Two-Product Type of Reactive Distillation Column, *Chem. Engg. Sc., 61*, 4432-4450.

Kumar, A., Daoutidis, P., (1999). Modeling, analysis and control of ethylene glycol reactive distillation column. *AIChE Journal, 45(1),* 51– 68.

Kumar, M.V.P., Kaistha, N. (2008a). Steady-state multiplicity and its implications on the control of an ideal reactive distillation column. *Ind. and Engg. Chem. Res*, *47*, 2778-2787.

Kumar, M.V.P., Kaistha, N., (2008b), Internal Heat Integration and Controllability of Double Feed Reactive Distillation Columns, 1. Effect of Feed Tray Location, *Ind. and Engg. Chem. Res,* 47, 7294–7303.

Mohl, K., Kienle, A., Gilles, E., Rapmund, P., Sundmacher, K., Hoffmann, U., (1999). Steady-state multiplicities in reactive distillation columns for the production of fuel ethers MTBE and TAME: theoretical analysis and experimental verification, *Chem. Engg. Sc., 54(8)*, 1029-1043.

Roat, S., Downs, J., Vogel, E., Doss, J., (1986). Integration of rigorous dynamic modeling and control system synthesis for distillation columns. In Morari, M., McAvoy, T.J., (Eds), *Chem. Proc. Control; CPC III,* Elsevier: Amesterdam, The Netherlands, 99.

Singh, B.P., Singh, R., Kumar, M.V.P., Kaistha, N., (2005). Steady state analysis of reactive distillation using homotopy continuation method, *Che. Engg. Res. and Des., 83A,* 959-968.

Siirola, J. J., (1995). An industrial perspective on process synthesis, *A.I.Ch.E. Symposium Series, 91 (304),* 222-233.

Sneesby, M.G., Tade, M.O., Smith, T.N. (1997a.). Implications of steady-state multiplicity for operation and control of etherifcation columns. *Distillation and absorption '97, Institute of the Chemical Engineers Symposium Series*, *142*, 205-216.

Taylor, R., Krishna, R (2000). Modelling Reactive Distillation. *Chem. Engg. Sc.*, 55(22), 5183-5229

A General Quadratic Performance Approach to Binary Distillation Control

Ansgar Rehm *

* *University of Applied Sciences Osnabrück,D-49076 Osnabrück, Germany (Tel: ++49-541-9692156; e-mail: a.rehm@fh-osnabrueck.de).*

Abstract: High purity distillation control of a binary mixture in a tray column is considered in the paper at hand. The approach is based on an inferential control idea: dynamics within the column may be described as movements of concentration waves; the position of the wave front on the one hand side can be inferred from few temperature measurements, on the other hand the position implies the product concentrations. Dynamics of wave propagation is derived by simplification of a first principles model of the column. The resulting descriptor model is the basis for a recent LMI based controller design scheme that provides general quadratic performance for descriptor systems.

Keywords: Quadratic performance; descriptor system; binary distillation; inferential Control.

1. INTRODUCTION

Distillation is one of the most common separation processes in the chemical industries and it is also one of the most energy consuming ones. Therefore the control of this kind of processes has been a focus of process control for many years. Most approaches toward control of distillation columns are based on linear models which are based on identification techniques (e.g. Skogestad et al. [1988], Allgöwer and Raisch [1992]). The disadvantage of identified models is the missing physical interpretation. First principle models on the other hand are rather complex and typically not suitable for a direct model based controller computation.

In the paper at hand a reduced model for a distillation column is derived in descriptor form. The control problem is captured as a generalized quadratic performance problem. A solution to this problem is briefly reviewed (see Rehm and Allgöwer [2002] for details) and applied to the problem at hand.

The resulting controller is tested by means of a high order nonlinear model of the distillation process.

2. DESCRIPTOR MODEL

Separation of a binary mixture in a 40 tray distillation column with one feed stream is considered. A schematic representation of the process is given in the left part of Fig. 1. Exemplary the separation of two alcohols (Methanol,n-Propanol) is taken into account. The mixture is fed in the column with the feed flow rate F. Feed flow rate F and feed composition x_F (molar fraction) are determined by upstream processes.

The stationary feed flow rate and feed composition are corrupted by disturbances. The feed stream separates the column into rectifying- (upper part of the column) and stripping section (lower part of the column). Separation is achieved due to intensive heat and mass transfer between liquid flow and countercurrently rising vapor flow.

At the bottom of the column the liquid flow splits up into a liquid product stream which is removed with flow rate B from the column and a stream which is, after being heated in the reboiler, recirculated back to the column as vapor flow with flow rate V.

At the top of the column the vapor flow with the accumulated more volatile product is completely condensed in the condenser. The condensate is partly pumped back in the column with a flow rate L (reflux stream) and is partly removed as the distillate product with a flow rate D (Deshpande [1985]).

We consider the distillation column in "LV" configuration, that is: liquid flow rate L and vapor flow rate V are considered to be control inputs. Measured variables are the concentrations on trays 14 and 28.

2.1 Control Objectives

The main control objective is to stabilize the product concentrations at the top and bottom of the column at their stationary values. Additionally the deviations from the stationary values due to disturbances in the feed flow should be small.

Table 1. Notation for model variables

x_i	... liquid concentration of the more volatile component on the i^{th} tray
y_i	... vapor concentration of the more volatile component on the i^{th} tray
n_i	... liquid holdup of the i^{th} tray
$(\cdot)_{B,M,D}$	... corresponding quantities of reboiler feed tray, and condensor

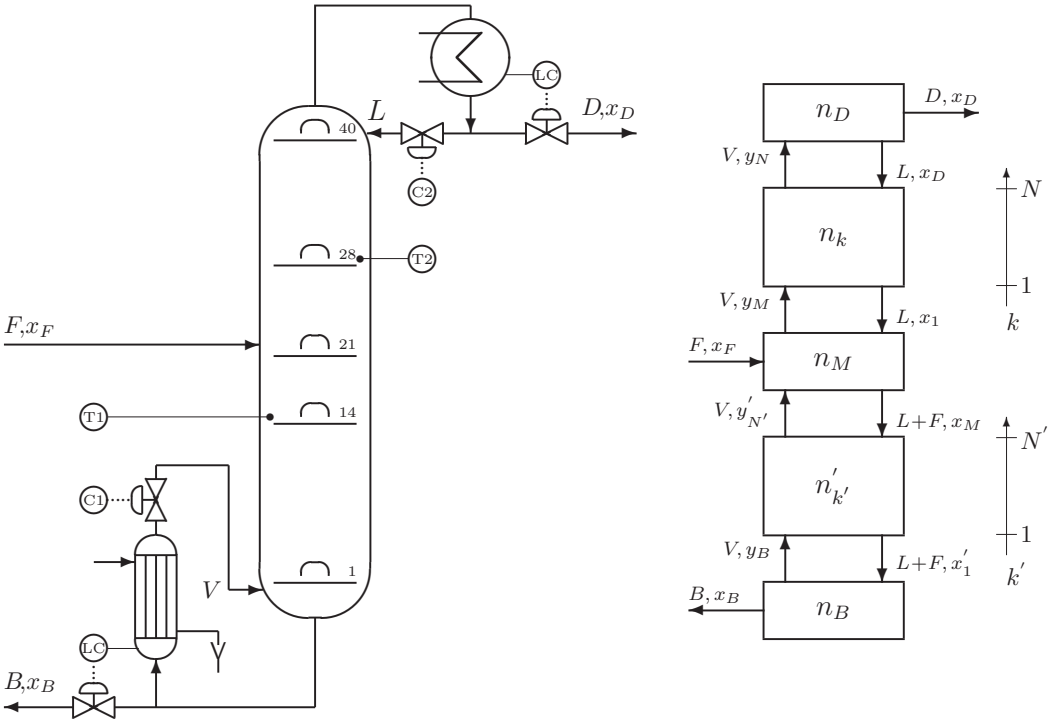

Fig. 1. Scheme of considered 40 tray distillation column (left) and subsystem structure for reduced modelling (right).

2.2 Reference Dynamics

A relatively detailed nonlinear model (CMO model without pressure losses, energy balances, and hydrodynamics (Deshpande [1985])) is used for simulation studies. The modelling equations describe the liquid concentrations of the more volatile component and are derived from the mass balance for every tray and for reboiler and condensor.

$$y_i = \frac{\alpha x_i}{1 + (\alpha - 1)x_i}, \quad \alpha = const. \tag{1}$$

The most important source of nonlinearity in the model are the equations (1) describing the vapor-liquid equilibrium (constant relative volatility α). The resulting model consists of 42 first order differential equations (40 equations from the intermediate trays plus two equations from reboiler and condensor).

2.3 Reduced Dynamics (Descriptor Model)

Starting point for the development of a reduced model in descriptor form of the distillation column is the fact (Retzbach [1986]) that qualitatively the behaviour of the column towards changes in the input values (V, L, F, x_F) can be regarded as motion and distortion of the stationary concentration profile (concentration versus tray number).

Instead of having detailed mass balances for rectifying and stripping section, the idea for a reduced model is thus to capture dynamics just by one position variable for a suitable concentration profile in every column section Due to (1) it is sufficient to consider a moving concentration profile only for the lighter component (measured in molar fractions, denoted by x in the following). Therefore the reduced model will contain two positions (s_r for the rectifying section and s_s in the stripping section) and three

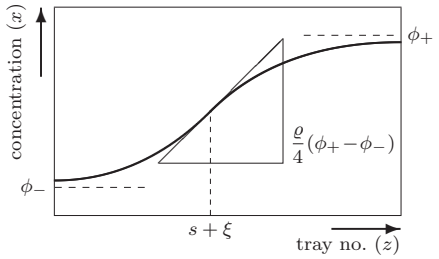

Fig. 2. Illustration of the shape parameters in function (2)

concentrations (concentration x_B in the reboiler, x_M for the feed tray, and x_D in the condenser) as state variables.

Here, only a sketch of the derivation of the reduced model in descriptor form is given, details can be found in Rehm [2004]. Furthermore we restrict ourselves to the presentation of the procedure for one column section, the deviation for the other section is completely analogous. The trays in this section are numbered by $z = 1, \ldots, N$ (see right side of Fig. 1). The concentration profile is modeled with the (continuous) function $x(z)$ (eq. (2), Fig. 2) which is well suited to describe the stationary profile in long packed columns (Kienle [1998]):

$$x(z) = \phi_- + \frac{\phi_+ - \phi_-}{1 + e^{-\varrho(z-s-\xi)}}. \tag{2}$$

With the least squares method the shape parameters ϕ_-, ϕ_+, ϱ, and ξ (see Fig. 2) are calculated such that $x(z)$ matches the stationary concentration profile ($s = 0$, i.e. s denotes the displacement relative to the stationary case) of the tray column for the discrete values $z = 1, \ldots, N$ in a least squares sense.

$$\begin{bmatrix} AY_1+Y_1^{\mathrm{T}}A^{\mathrm{T}}+ & * & * & * \\ B_2\hat{C}_K+(B_2\hat{C}_K)^{\mathrm{T}} & & & \\ (A+B_2\hat{D}_KC_2)^{\mathrm{T}}+\hat{A}_K & X_1^{\mathrm{T}}A+\hat{B}_KC_2+ & * & * \\ & (X_1^{\mathrm{T}}A+\hat{B}_KC_2)^{\mathrm{T}} & & \\ B_1^{\mathrm{T}}+D_{21}^{\mathrm{T}}\hat{D}_K^{\mathrm{T}}B_2^{\mathrm{T}}+ & B_1^{\mathrm{T}}X_1+D_{21}^{\mathrm{T}}\hat{B}_K^{\mathrm{T}}+ & (D_{11}+D_{12}\hat{D}_KD_{21})^{\mathrm{T}}W_P+ & * \\ W_P^{\mathrm{T}}(C_1Y_1+D_{12}\hat{C}_K) & W_P^{\mathrm{T}}(C_1+D_{12}\hat{D}_KC_2) & W_P^{\mathrm{T}}(D_{11}+D_{12}\hat{D}_KD_{21})+V_P & \\ Q_P^{\mathrm{T}}(C_1Y_1+D_{12}\hat{C}_K) & Q_P^{\mathrm{T}}(C_1+D_{12}\hat{D}_KC_2) & Q_P^{\mathrm{T}}(D_{11}+D_{12}\hat{D}_KD_{21}) & -\Sigma_P \end{bmatrix} < 0. \tag{3}$$

$$\begin{aligned} Y_1 &:= RE^{\mathrm{T}}+E^{\mathrm{T}\perp}W_Y,\ R>0, \qquad \begin{bmatrix} R & E^+ \\ E^{\mathrm{T}+} & S \end{bmatrix} > 0 \\ X_1 &:= SE+E^{\perp}W_X, \quad S>0, \end{aligned} \tag{4}$$

$$\begin{pmatrix} * & 0 & 0 & 0 & 0 \\ * & * & * & 0 & 0 \\ 0 & 0 & * & 0 & 0 \\ 0 & 0 & * & * & * \\ 0 & 0 & 0 & 0 & * \end{pmatrix} \begin{pmatrix} \frac{d\Delta x_B}{dt} \\ \frac{d\Delta s_r}{dt} \\ \frac{d\Delta x_M}{dt} \\ \frac{d\Delta s_s}{dt} \\ \frac{d\Delta x_D}{dt} \end{pmatrix} = \begin{pmatrix} * & * & * & 0 & 0 \\ * & * & * & 0 & 0 \\ * & * & * & * & * \\ 0 & 0 & * & * & * \\ 0 & 0 & * & * & * \end{pmatrix} \begin{pmatrix} \Delta x_B \\ \Delta s_r \\ \Delta x_M \\ \Delta s_s \\ \Delta x_D \end{pmatrix} + \begin{pmatrix} 0 & * \\ 0 & * \\ * & * \\ 0 & 0 \\ 0 & 0 \end{pmatrix} \begin{pmatrix} \Delta x_F \\ \Delta F \end{pmatrix} + \begin{pmatrix} * & * \\ * & * \\ * & * \\ * & * \\ 0 & * \end{pmatrix} \begin{pmatrix} \Delta L \\ \Delta V \end{pmatrix}$$

$$\begin{pmatrix} \Delta x_{14} \\ \Delta x_{28} \end{pmatrix} = \begin{pmatrix} * & * & * & 0 & 0 \\ 0 & 0 & * & * & * \end{pmatrix} (\Delta x_B, \Delta s_r, \Delta x_M, \Delta s_s, \Delta x_D)^{\mathrm{T}} \tag{5}$$

However, while ϱ and ξ are kept constant, ϕ_- and ϕ_+ are used as adaptation parameters since concentration profiles not only move but also are distorted. Adaptation of these parameters is based on the requirement that (2) should also match the concentrations for the neighbouring systems when evaluated for $z = 0$ and $z = N + 1$. This adaptation rule implies that the time derivatives of x_B, x_M, and x_D influence the dynamics of wave propagation. The linearisation of the overall reduced descriptor model of the distillation column is given in (5). Here "Δ" implies deviations from the stationary value while "$*$" denotes numerical entries. A detailed derivation of the model and numerical values are given in Rehm [2004].

3. CONTROLLER COMPUTATION

3.1 Synthesis for Generalized Quadratic Performance for Descriptor Systems

The idea of generalized quadratic performance (GQP) control is to impose a general quadratic constraint of the type

$$\int_0^T \begin{bmatrix} \boldsymbol{z}(t) \\ \boldsymbol{w}(t) \end{bmatrix}^{\mathrm{T}} \begin{bmatrix} U_P & W_P \\ W_P^{\mathrm{T}} & V_P \end{bmatrix} \begin{bmatrix} \boldsymbol{z}(t) \\ \boldsymbol{w}(t) \end{bmatrix} dt \ll 0, \tag{6}$$

on the external input/output chanel $\boldsymbol{w} \to \boldsymbol{z}$ of a generalized plant description G_{cl}. Here the notation "$\ll 0$" means that $\int_0^T Q(\boldsymbol{w}(t), \boldsymbol{z}(t))\, dt \le -\epsilon \int_0^T \boldsymbol{w}^{\mathrm{T}}(t)\boldsymbol{w}(t))\, dt$ holds for all $\boldsymbol{w}(\cdot) \in L_2$ and some fixed $\epsilon > 0$.

The rather general GQP problem contains some important control problems as a special case if the objective parameters $U_P \ge 0$, $V_P = V_P^{\mathrm{T}}$, and W_P are chosen accordingly (Scherer et al. [1997]). For example

- the H_∞ constraint $\|G_{cl}\|_\infty < \gamma$, if U_P, V_P, and W_P are specified as $U_P = \frac{1}{\gamma}I$, $V_P = -\gamma I$, $W_P = 0$;
- the strict passivity constraint $G_{cl}(j\omega)+G_{cl}(j\omega)^* > 0$ for all $\omega \in \mathbb{R} \cup \{\infty\}$, when U_P, V_P, W_P are chosen as $U_P = 0$, $V_P = 0$, $W_P = -I$;
- sector constraints of the form

$$\int_0^T (\boldsymbol{z}(t)-\alpha\boldsymbol{w}(t))^{\mathrm{T}} (\boldsymbol{z}(t)-\beta\boldsymbol{w}(t))\ dt \ll 0 \tag{7}$$

for $U_P = I$, $V_P = -\alpha\beta I$, $W_P = -\frac{1}{2}(\alpha+\beta)I$.

We consider a generalized plant description Σ in descriptor form

$$\Sigma: \quad \begin{aligned} E\dot{\boldsymbol{x}}(t) &= A\boldsymbol{x}(t) + B_1\boldsymbol{w}(t) + B_2\boldsymbol{u}(t) \\ \boldsymbol{z}(t) &= C_1\boldsymbol{x}(t) + D_{11}\boldsymbol{w}(t) + D_{12}\boldsymbol{u}(t) \\ \boldsymbol{y}(t) &= C_2\boldsymbol{x}(t) + D_{21}\boldsymbol{w}(t) \end{aligned} \tag{8}$$

with $\boldsymbol{x}(t) \in \mathbb{R}^{n_x}$, $\boldsymbol{w}(t) \in \mathbb{R}^{n_w}$, $\boldsymbol{u}(t) \in \mathbb{R}^{n_u}$, $\boldsymbol{z}(t) \in \mathbb{R}^{n_z}$, and $\boldsymbol{y}(t) \in \mathbb{R}^{n_y}$ denoting the generalized state variables, the external input variables, the control input variables, the external output variables, and the measurement variables, respectively. E and A are square constant matrices where, explicitly, E is allowed to be singular, i.e. $\mathrm{rank}(E) =: r \le n_x$. The remaining matrices are constant matrices of appropriate dimension.

The control problem is, for given matices $U_P \ge 0$, $U_P \in \mathbb{R}^{n_z \times n_z}$, $V_P = V_P^{\mathrm{T}} \in \mathbb{R}^{n_w \times n_w}$, and $W_P \in \mathbb{R}^{n_z \times n_w}$, to find a linear output feedback controller such that the undisturbed closed loop ($\boldsymbol{w} \equiv \boldsymbol{0}$) is an admissible system and such that the transfer matrix from the external input $\boldsymbol{w}$ to the external output $\boldsymbol{z}$ suffices a general quadratic performace bound (6).

The actual design problem therefore consists in the selection of matrices U_P, V_P, W_P such that the transfer matrix from $\boldsymbol{w}$ to $\boldsymbol{z}$ reflects the performance requirements (e.g. robustness, energy dissipation, ...). Since we aim at an admissible close loop, we assume in the following the corresponding necessary stabilizability/detectability properties for descriptor systems, namely stabilizability/detectability at infinity (see also Dai [1989]).

With a controller K_E,

$$K_E: \quad \begin{array}{l} E\dot{\boldsymbol{\zeta}}(t)=A_K\boldsymbol{\zeta}(t)+B_K\boldsymbol{y}(t) \\ \boldsymbol{u}(t)=C_K\boldsymbol{\zeta}(t)+D_K\boldsymbol{y}(t),\ \boldsymbol{\zeta}(t)\in\mathbb{R}^{n_x} \end{array} \tag{9}$$

parametrized by A_K, B_K, C_K, D_K the closed loop system is given by

$$\begin{aligned} E_{cl}\dot{\boldsymbol{\xi}}(t) &= A_{cl}\boldsymbol{\xi}(t)+B_{cl}\boldsymbol{w}(t) \\ \boldsymbol{z}(t) &= C_{cl}\boldsymbol{\xi}(t)+D_{cl}\boldsymbol{w}(t), \qquad \boldsymbol{\xi}(t)\in\mathbb{R}^{2n_x}, \end{aligned} \tag{10}$$

$$\begin{aligned} E_{cl} &= \begin{bmatrix} E & 0 \\ 0 & E \end{bmatrix}, \qquad A_{cl} = \begin{bmatrix} A+B_2D_KC_2 & B_2C_K \\ B_KC_2 & A_K \end{bmatrix}, \\ B_{cl} &= \begin{bmatrix} B_1+B_2D_KD_{21} \\ B_KD_{21} \end{bmatrix}, \quad C_{cl}^{\mathrm{T}} = \begin{bmatrix} C_1^{\mathrm{T}}+C_2^{\mathrm{T}}D_K^{\mathrm{T}}D_{12}^{\mathrm{T}} \\ C_K^{\mathrm{T}}D_{12}^{\mathrm{T}} \end{bmatrix}, \\ D_{cl} &= (D_{11}+D_{12}D_KD_{21}) \end{aligned} \tag{11}$$

Then a sufficient condition for a controller K_E solving the GQP control problem for DAE systems is given by the following theorem:

Theorem 1. Consider a plant (8) and a controller (9). There exists a controller parameterization A_K, B_K, C_K, D_K such that the undisturbed (i.e. $\boldsymbol{w}\equiv 0$) closed loop system (10) is admissible with general quadratic performance if the LMIs (3), (4) [1] admit a solution $\{R, S, W_Y, W_X, \hat{A}_K, \hat{B}_K, \hat{C}_K, \hat{D}_K\}$.

Remark. The preceding theorem constitutes also a necessary condition for the existence of a controller with GQP in the cases, where the corresponding analysis result is necessary for general quadratic performance, i.e. especially in the case of the H_∞ control problem. Therefore the results of Masubuchi et al. [1997] are included in Theorem 1 as a special case.

Theorem 1 is constructive: controller computation consists of three steps:

- Solution of the LMIs (3), (4). This is possible via effective numerical tools tailored for LMI problems arising from control theoretic problem setups (e.g. Gahinet et al. [1994], El Ghaoui et al. [1995]).
- Computation of non-singular matrices X_3, Y_3 such that

$$X_1Y_1+X_2Y_3 = I \tag{12}$$
$$X_3Y_1+X_4Y_3 = 0 \tag{13}$$

  hold together with the coupling condition $E^{\mathrm{T}}X_2 = X_3^{\mathrm{T}}E$. This is a essentially a factorization problem on the range of E which is always solvable provided (3), (4) have a solution.
- Solution of the linear equations

$$\begin{aligned} \hat{D}_K &:= D_K \\ \hat{C}_K &:= C_KY_3+D_KC_2Y_1 \\ \hat{B}_K &:= X_3^{\mathrm{T}}B_K+X_1^{\mathrm{T}}B_2D_K \\ \hat{A}_K &:= X_1^{\mathrm{T}}(A+B_2D_KC_2)Y_1+X_3^{\mathrm{T}}A_KY_3+ \\ &\quad +X_3^{\mathrm{T}}B_KC_2Y_1+X_1^{\mathrm{T}}B_2C_KY_3 \end{aligned} \tag{14}$$

  for the controller matrices D_K, C_K B_K, A_K.

[1] Here E^+ denotes any generalized inverse with the property $EE^+E = E$ and "$*$" is used in order to indicate the symmetric expansion of a block matrix.

3.2 Distillation Control Problem as S/KS Mixed Sensitivity Problem

As a special case of generalized quadratic performance, the H_∞ control problem for the distillation problem is solved. The control objectives are translated into a mixed sensitivity set-up depicted in Fig. 4. with G representing the plant (reduced model in descriptor form), K the controller, and W_1, W_2, V frequency dependent weighting matrices. Controller design by "loop shaping" requires a selection of the weighting matrices such that the solution of the H_∞ control problem

$$\left\| \begin{array}{c} W_1(I+GK)^{-1}V \\ -W_2K(I+GK)^{-1}V \end{array} \right\|_\infty \overset{!}{<} \gamma \tag{15}$$

results in a well behaved closed loop system. In this

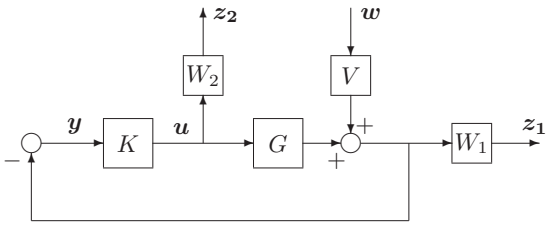

Fig. 4. Mixed sensitivity configuration

setup V can be interpreted as a filter which models the disturbance considered to be relevant for the problem at hand. With $S(s) := (I+GK)^{-1}$ being the sensitivity matrix of the closed loop the expression (15) with $\gamma = 1$ suggests to choose W_1 to be approximately the inverse of the wanted behavior for $S(s)$ and analogously W_2 to be the inverse of $K \cdot S$. General indications on selecting these weighting matrices can be found in Skogestad and Postlewaite [1996].

In case of the distillation control problem at hand an indirect approach is taken: with stabilizing the measured concentrations x_{14}, x_{28} also the stationary profiles are fixed and thus approximately also the product concentrations. In order to realize this idea the descriptor S/KS H_∞ control problem depicted in Figure 4 (with G being the descriptor model (5)) is solved by the outlined descriptor GQP synthesis procedure with specification of W, Q, and Σ as for the H_∞ set-up. The synthesis LMIs are jointly optimized with respect to γ. A final value of $\gamma = 1.01$ shows that the control objectives are approximately met.

The resulting controller has a dynamical order of 9, i.e. equal to the order of the generalized plant description. After removing the fastest two eigen-modes of the controller in order to avoid numerical problems due to stiffness, the controller is tested in simulation studies with the nonlinear CMO model of the distillation column.

4. RESULTS

In Figure 5 the stationary concentration profiles for various severe persistent disturbances for the closed loop are shown. It can be seen that the controller is able to stabilize the profile position although the disturbances result in a distortion of the stationary profile in the vicinity of the feed tray.

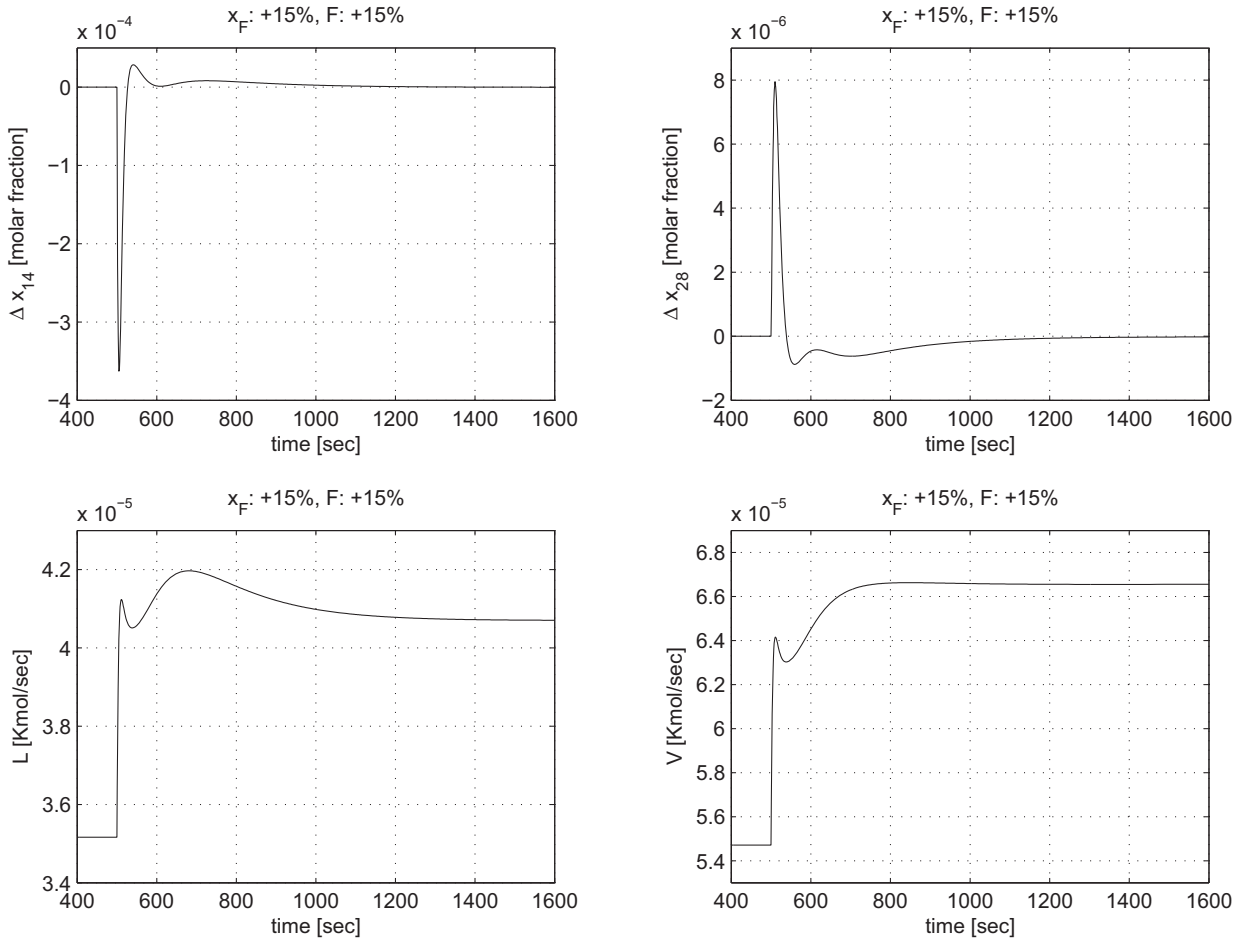

Fig. 3. Step responses for the controlled distillation column (+15% increase in feed flow rate F and +15% increase in feed concentration x_F with respect to stationary values at $t = 500sec$). Top: deviations from the steady state for the controlled variables x_{14} and x_{28}. Bottom: control variables, i.e. liquid flow rate L and vapor flow rate V.

In Figure 3 a detailed view on the control variables and the error in the controlled variables is given for a mutual step in the feed flow rate and feed composition. The plots show a fast transient behavior and small deviations. Furthermore no excessive action in the control variables is needed.

5. CONCLUSION

The generalized quadratic performance control problem for descriptor systems is solved for a reduced model of a distillation control problem. The resulting controller shows rather good results for a nonlinear reference model. The descriptor problem formulation is a direct result of reduced modeling. Furthermore, also standard approaches to build generalized plant descriptions easily fit into the descriptor system set-up. This was demonstrated by means of a S/KS - control problem formulation that directly leads to a descriptor model.

REFERENCES

F. Allgöwer and J. Raisch. Multivariable controller design for an industrial distillation column. In N.K Nichols and D.H. Owens, editors, *The Mathematics of Control Theory*. Clarendon Press, Oxford, 1992.

L. Dai. *Singular Control Systems*, volume 118 of *Lecture Notes in Control and Information Sciences*. Springer, Berlin, 1989.

P. B. Deshpande. *Distillation Dynamics and Control*. Instrument Society of America, Research Triangle Park, NC, 1985.

L. El Ghaoui, F. Delebecque, and R. Nikoukhah. *LMITOOL: A User-Friendly Interface for LMI Optimization*, 1995. Available at ftp.ensta.fr in pub/elghaoui/lmitool.

P. Gahinet, A. Nemirowskii, A.J. Laub, and M. Chilali. The LMI control toolbox. In *Proc. 33rd IEEE Conf. Decision Contr.*, pages 2038–2041, Lake Buena Vista, FL, 1994.

A. Kienle. Reduced models for multicomponent separation processes using nonlinear wave propagation theory. In *CHISA'98, 13th International Congress of Chemical and Process Engineering*, Praha, Czech Republic, 1998. Paper 109.

I. Masubuchi, Y. Kamitane, A. Ohara, and N. Suda. H_∞ control for descriptor systems: A matrix inequalities

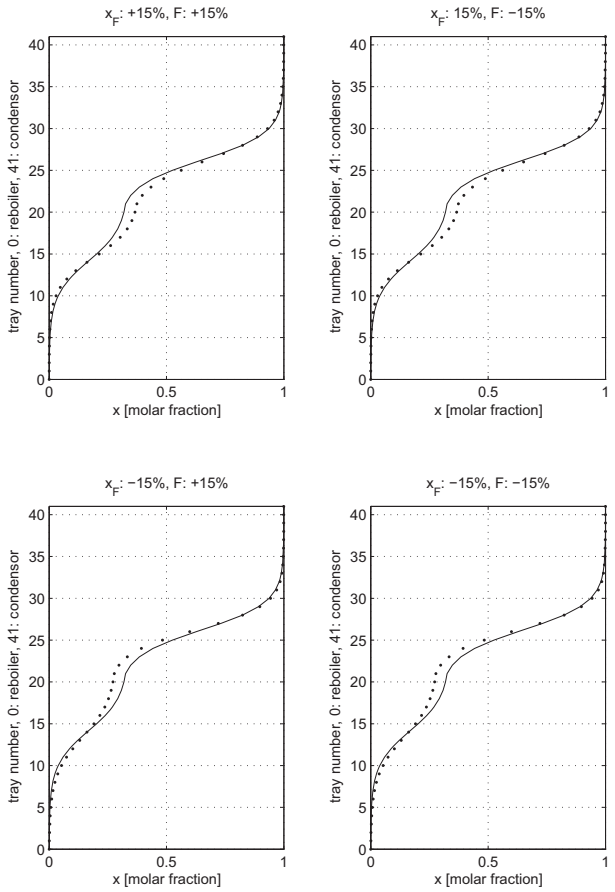

Fig. 5. Liquid concentration profiles in controlled distillation column. Solid lines: undisturbed stationary profile; dotted lines: new stationary profile for non-vanishing disturbances in feed flow rate F and feed concentration x_F (+/- 15% with respect to stationary values).

approach. *Automatica*, 33(4):669–673, 1997.

A. Rehm. *Control of Linear Descriptor Systems: A Matrix Inequality Approach*. Fortschr.-Ber. VDI Reihe 8 Nr. 1019, VDI Verlag, Düsseldorf, 2004.

A. Rehm and F. Allgöwer. General quadratic performance analysis and synthesis of differential algebraic equation (DAE) systems. *J. Proc. Contr.*, 12(4):467–474, 2002.

B. Retzbach. Control of an extractive distillation plant. In *IFAC Symposium Dynamics and Control of Chemical Reactors and Distillation Columns*, pages 225–230, Bournemouth, 1986.

C. W. Scherer, P. Gahinet, and M. Chilali. Multiobjective output - feedback control via LMI optimization. *IEEE Trans. Automat. Contr.*, AC-42(7):896–911, 1997.

S. Skogestad and I. Postlewaite. *Multivariable Feedback Control: Analysis and Design*. John Wiley and Sons, Chicester, GB, 1996.

S. Skogestad, M. Morari, and J.C. Doyle. Robust control of ill-conditioned plants: High-purity distillation. *IEEE Trans. Automat. Contr.*, AC-33(12):1092–1105, 1988.

Advances in Identification

Oral Session

Identification of low-order unstable process model from closed-loop step test

Tao Liu, Furong Gao*

*Department of Chemical and Biomolecular Engineering, Hong Kong University of Science & Technology, Kowloon, Hong Kong (Tel: +852-2358-7139; e-mail address: kefgao@ust.hk)

Abstract: Based on a closed-loop step response test, control-oriented low-order model identification algorithms are proposed for unstable processes. By using a damping factor to the closed-loop step response for realization of the Laplace transform, an algorithm for estimating the process frequency response is developed in terms of the closed-loop control structure used for identification. Correspondingly, two model identification algorithms are derived analytically for obtaining the widely used low-order process models of first-order-plus-dead-time (FOPDT) and second-order-plus-dead-time (SOPDT), respectively. Illustrative examples from the recent literature are used to demonstrate the effectiveness and merits of the proposed identification algorithms.

1. INTRODUCTION

As model-based control strategies have demonstrated apparently improved set-point tracking and load disturbance rejection for open-loop unstable processes, control-oriented identification of low-order process model, e.g., first-order-plus-dead-time (FOPDT) or second-order-plus-dead-time (SOPDT), has been increasingly explored in the process control community (Seborg, Edgar, and Mellichamp, 2003; Liu and Gao, 2008a and 2008b). For safety and economic reasons, unstable processes are usually not allowed to be operated in an open-loop manner. Closed-loop identification methods have been therefore studied in the literature. One of the mostly used identification tests is the close-loop step response test, owing to its implemental simplicity. Based on closed-loop step test in terms of the internal model control (IMC) structure, Häggblom K. E. (1996) demonstrated that closed-loop identification facilitates better representation of the process dynamic response characteristics for closed-loop operation. Using a conventional proportional (P) or proportional-integral-derivative (PID) controller for closed-loop stabilization, recent closed-loop step identification methods can be seen in the references (Paraskevopoulos, Pasgianos and Arvanitis, 2004; Sree and Chidambaram, 2006; Cheres, 2006). Using relay feedback to yield sustained oscillation within an admissible fluctuation of the process output, identification methods based on the resulting limit cycle data have been developed in the papers (Shiu, Hwang and Li, 1998; Marchetti, Scali and Lewin, 2001; Vivek and Chidambaram, 2005; Liu and Gao, 2008a). It was, however, pointed out that the conventional relay feedback structure cannot guarantee periodic oscillation for unstable processes with large time delay (Tan, Wang and Lee, 1998; Thyagarajan and Yu; 2003). Some limiting conditions to form the limit cycle from relay feedback for an unstable process have been disclosed by Liu and Gao (2008b). Besides, using the pseudo-random binary sequence (PRBS) as excitation signal to the set-point, closed-loop identification methods for application of model predictive control (MPC) have been reported in the references (Sung et al, 2001; Saffer and Doyle, 2002; Bindlish, Rawlings and Young, 2003).

In this paper, identification algorithms based on a closed-loop step test are proposed for obtaining low-order models of FOPDT and SOPDT for tuning unstable processes. By using a damping factor to the closed-loop step response for realization of the Laplace transform, an algorithm is first given to estimate the closed-loop frequency response in terms of using a conventional P, PI or PID controller for closed-loop stabilization. Accordingly, the process frequency response can be analytically derived from the closed-loop frequency response with the knowledge of the controller. Then, two identification algorithms are analytically developed for obtaining FOPDT and SOPDT models, respectively. Both the algorithms can give good accuracy if the model structure matches the process. Measurement noise tests are also performed to demonstrate identification robustness of the proposed algorithms.

2. FREQUENCY RESPONSE ESTIMATION

It is commonly known that the Fourier transform of a step response does not exist due to $\Delta y(t) \neq 0$ for $t \to \infty$, where $\Delta y(t) = y(t) - y(t_0)$ and $y(t_0)$ denotes the initial steady output. However, by substituting $s = \alpha + j\omega$ into the Laplace transform to the step response,

$$\Delta Y(s) = \int_0^\infty \Delta y(t) e^{-st} dt \tag{1}$$

we can formulate

$$\Delta Y(\alpha + j\omega) = \int_0^\infty [\Delta y(t) e^{-\alpha t}] e^{-j\omega t} dt \tag{2}$$

Note that if $\alpha > 0$, there exists $\Delta y(t) e^{-\alpha t} = 0$ for $t > t_N$, where t_N may be numerically determined using the condition of $\Delta y(t_N) e^{-\alpha t_N} \approx 0$, since $\Delta y(t)$ reaches a steady value after

the closed-loop transient response to a step change of the set-point. Therefore, by regarding α as a damping factor to the closed-loop step response for Laplace transform, we may compute $\Delta Y(\alpha + j\omega)$ from the N points of step response data as

$$\Delta Y(\alpha + j\omega) = \int_0^{t_N} [y(t)e^{-\alpha t}]e^{-j\omega t}dt \tag{3}$$

For a closed-loop step test with initial steady state, i.e., $y(t) = r(t) = c$ for $t \le t_0$, where $r(t)$ denotes the set-point value, c is a constant and t_0 is the time for step test, we may formulate the step change of the set-point by using a time shift of t_0 (i.e., letting $t_0 = 0$) as

$$\Delta r(t) = \begin{cases} 0, & t \le 0; \\ h, & t > 0. \end{cases} \tag{4}$$

where h is the magnitude of the step change. Its Laplace transform for $s = \alpha + j\omega$ with $\alpha > 0$ can be explicitly derived as

$$\Delta R(\alpha + j\omega) = \int_0^{\infty} he^{-(\alpha + j\omega)t}dt = \frac{h}{\alpha + j\omega} \tag{5}$$

Hence, the closed-loop frequency response can be derived using (3) and (5) as

$$T(\alpha + j\omega) = \frac{\alpha + j\omega}{h}\Delta Y(\alpha + j\omega), \ \alpha > 0 \tag{6}$$

Note that $T(\alpha + j\omega) \to 0$ as $\alpha \to \infty$. On the contrary, $\alpha \to 0$ will cause t_N much larger for computation of (6). A proper choice of α is therefore required for implementation. Considering that all the closed-loop transient response data to a step change of the set-point should be used to procure good estimation of the closed-loop frequency response, the following constraint is suggested to choose α,

$$\Delta y(t_{\text{set}})e^{-\alpha t_{\text{set}}} > \delta \tag{7}$$

where $\Delta y(t_{\text{set}})$ denotes the steady-state output deviation to the step change in terms of the settling time (t_{set}), and δ is a threshold of the computational precision that may be practically taken smaller than 1×10^{-6}. It follows from (7) that

$$\alpha < \frac{1}{t_{\text{set}}}\ln\frac{\Delta y(t_{\text{set}})}{\delta} \tag{8}$$

To ensure computational efficiency with respect to the complex variable, $s = \alpha + j\omega$, for frequency response estimation, the lower bound of α may be simply taken as δ, if there exists no limit on the time length of the step test.

Once α is chosen in terms of the above guideline, the time length, t_N, may be determined from a numerical constraint for computation of (3), i.e.,

$$\Delta y(t_N)e^{-\alpha t_N} < \delta \tag{9}$$

which can be solved as

$$t_N > \frac{1}{\alpha}\ln\frac{\Delta y(t_N)}{\delta} \tag{10}$$

Note that there exists the following Laplace transform with initial steady closed-loop state of $y(0) = r(0) = c$, where c is a constant,

$$L[\int_0^t \Delta y(t)dt] = \frac{\Delta Y(s)}{s} \tag{11}$$

To guarantee identification robustness against measurement noise, we may compute the frequency response by

$$T(\alpha + j\omega) = \frac{\dfrac{\Delta Y(\alpha + j\omega)}{\alpha + j\omega}}{\dfrac{\Delta R(\alpha + j\omega)}{\alpha + j\omega}} = \frac{(\alpha + j\omega)^2}{h}\int_0^{t_N}[\int_0^t \Delta y(\tau)d\tau]e^{-\alpha t}e^{-j\omega t}dt \tag{12}$$

It can be seen from (12) that, rather than use individual output data measured from the step test, a time integral for each measurement point is used to compute the outer-layer integral for obtaining the frequency response estimation. This facilitates reducing measurement errors according to the statistic averaging principle.

Denote the n-th order derivative for a complex function of $F(s)$ with respect to s as

$$F^{(n)}(s) = \frac{d^{(n)}}{ds^n}F(s), \ n \ge 1. \tag{13}$$

It follows from (3) and (6) that

$$T^{(1)}(s) = \frac{1}{h}\int_0^{\infty}(1 - st)\Delta y(t)e^{-st}dt \tag{14}$$

$$T^{(2)}(s) = \frac{1}{h}\int_0^{\infty} t(st - 2)\Delta y(t)e^{-st}dt \tag{15}$$

Hence, by letting $s = \alpha$ and choosing α as well as that for computation of (3), the single integral in (14) and (15) can be computed numerically. The corresponding time lengths of t_N can be respectively determined using the numerical constraints,

$$(1 - \alpha t_N)\Delta y(t_N)e^{-\alpha t_N} < \delta \tag{16}$$

$$t_N(\alpha t_N - 2)\Delta y(t_N)e^{-\alpha t_N} < \delta \tag{17}$$

For a conventional PID controller used in the closed-loop structure to stabilize an unstable process for step test,

$$C(s) = k_C(1 + \frac{1}{\tau_I s} + \frac{\tau_D s}{0.1\tau_D s + 1}) \tag{18}$$

where k_C denotes the controller gain, τ_I the integral constant and τ_D the derivative constant, it can be derived that

$$C^{(1)}(s) = k_C[-\frac{1}{\tau_I s^2} + \frac{\tau_D}{(0.1\tau_D s + 1)^2}] \tag{19}$$

$$C^{(2)}(s) = 2k_C[\frac{1}{\tau_I s^3} - \frac{0.1\tau_D^2}{(0.1\tau_D s + 1)^3}] \tag{20}$$

Note that the closed-loop transfer function can be derived as

$$T(s) = \frac{G(s)C(s)}{1 + G(s)C(s)} \tag{21}$$

It follows from (21) that

$$G(s) = \frac{T(s)}{C(s)[1 - T(s)]} \tag{22}$$

Its first and second derivatives can be derived accordingly as

$$G^{(1)} = \frac{T^{(1)}C + C^{(1)}T(T - 1)}{C^2(1 - T)^2} \tag{23}$$

$$G^{(2)} = \frac{CT^{(2)} + 2C^{(1)}T^{(1)}T + C^{(2)}T(T - 1)}{C^2(1 - T)^2}$$

$$-\frac{2[CT^{(1)}+C^{(1)}T(T-1)][CC^{(1)}(1-T)-C^2T^{(1)}(1-T)]}{C^3(1-T)^3} \quad (24)$$

Therefore, by substituting $s=\alpha+j\omega_k$ ($k=1,2,\ldots,M.$), where M is the number of representative frequency response points in a user specified frequency range, the process frequency response can be numerically estimated for model fitting.

3. MODEL IDENTIFICATION ALGORITHMS

Low-order unstable process models of FOPDT and SOPDT are respectively in the form of

$$G_1(s)=\frac{k_p e^{-\theta s}}{\tau_p s-1} \quad (25)$$

$$G_2(s)=\frac{k_p e^{-\theta s}}{(\tau_1 s-1)(\tau_2 s+1)} \quad (26)$$

where k_p denotes the process gain, θ the process time delay and τ_p (or τ_1 and τ_2) the process time constant(s).

By regarding $s\in\mathbb{R}$ and taking the natural logarithm for both sides of (25) in terms of $0<s<\tau_p$, we obtain

$$\ln[-G_1(s)]=\ln(k_p)-\ln(1-\tau_p s)-\theta s \quad (27)$$

Subsequently, taking the first and second derivatives for both sides of (27) with respect to s yields

$$\frac{1}{G_1(s)}\frac{d}{ds}[G_1(s)]=\frac{\tau_p}{1-\tau_p s}-\theta \quad (28)$$

$$Q_2(s)=\frac{\tau_p^2}{(1-\tau_p s)^2} \quad (29)$$

where $Q_2(s)=d[Q_1(s)]/ds$ and $Q_1(s)$ is the left side of (28).

Substituting $s=\alpha$ into (29), it can be derived that

$$\tau_p=\begin{cases}\dfrac{\sqrt{Q_2}}{\alpha\sqrt{Q_2}-1} \text{ or } \dfrac{\sqrt{Q_2}}{\alpha\sqrt{Q_2}+1}, & \text{if } Q_2>\dfrac{1}{\alpha^2};\\ \dfrac{\sqrt{Q_2}}{\alpha\sqrt{Q_2}+1}, & \text{if } Q_2\le\dfrac{1}{\alpha^2}.\end{cases} \quad (30)$$

Note that for $Q_2\ge 1/\alpha^2$, we may determine a suitable solution based on model fitting accuracy for the closed-loop step response.

It should be noted that the above parameter estimation is without loss of generality since there exists $\alpha<\tau_p$ in general, which may be verified from the guideline for choosing α as given in the earlier section.

Consequently, the other two model parameters can be derived from (28) and (25) using $s=\alpha$ as

$$\theta=-Q_1(\alpha)+\frac{\tau_p}{1-\tau_p\alpha} \quad (31)$$

$$k_p=(\tau_p\alpha-1)G_1(\alpha)e^{\alpha\theta} \quad (32)$$

Hence, the above algorithm named **Algorithm-I** for obtaining a FOPDT model for an unstable process can be summarized as:

(i) Choose $s=\alpha$ and t_N to compute $T(\alpha)$, $T^{(1)}(\alpha)$ and $T^{(2)}(\alpha)$ in terms of (6) (or (12)), (14) and (15);
(ii) Compute $C(\alpha)$, $C^{(1)}(\alpha)$ and $C^{(2)}(\alpha)$ in terms of (18), (19) and (20);
(iii) Compute $G_1(\alpha)$, $G_1^{(1)}(\alpha)$ and $G_1^{(2)}(\alpha)$ in terms of (22), (23) and (24);
(iv) Compute $Q_1(\alpha)$ and $Q_2(\alpha)$ in terms of (28) and (29);
(v) Compute the process time constant, τ_p, from (30);
(vi) Compute the process time delay, θ, from (31);
(vii) Compute the process gain, k_p, from (32).

Following a similar procedure as above, taking the natural logarithm for both sides of (26) in terms of $0<s<\tau_1$, yields

$$\ln[-G_2(s)]=\ln(k_p)-\ln(1-\tau_1 s)-\ln(\tau_2 s+1)-\theta s \quad (33)$$

Accordingly, the first and second order derivatives for both sides of (33) with respect to s can be derived respectively as

$$\frac{1}{G_2(s)}\frac{d}{ds}[G_2(s)]=\frac{\tau_1}{1-\tau_1 s}-\frac{\tau_2}{\tau_2 s+1}-\theta \quad (34)$$

$$Q_2(s)=\frac{\tau_1^2}{(1-\tau_1 s)^2}+\frac{\tau_2^2}{(\tau_2 s+1)^2} \quad (35)$$

where $Q_2(s)=d[Q_1(s)]/ds$ and $Q_1(s)$ is the left side of (34).

Substituting $s=\alpha$ into (35) yields

$$Q_2(\alpha)=[2\alpha^2-\alpha^4Q_2(\alpha)]\tau_1^2\tau_2^2+[2\alpha-2\alpha^3Q_2(\alpha)](\tau_1^2\tau_2-\tau_1\tau_2^2)$$
$$+4\alpha^2Q_2(\alpha)\tau_1\tau_2+[1-\alpha^2Q_2(\alpha)](\tau_1^2+\tau_2^2)+2\alpha Q_2(\alpha)(\tau_1-\tau_2) \quad (36)$$

To solve τ_1 and τ_2 from (36), we reformulate (36) in the LS form of

$$\psi(\alpha)=\phi(\alpha)^T\gamma \quad (37)$$

where

$$\begin{cases}\psi(\alpha)=Q_2(\alpha),\\ \phi(\alpha)=[2\alpha^2-\alpha^4Q_2(\alpha),\ 2\alpha-2\alpha^3Q_2(\alpha),\ -\alpha^2Q_2(\alpha),\ 1,\ 2\alpha Q_2(\alpha)]^T,\\ \gamma=[\tau_1^2\tau_2^2,\ \tau_1^2\tau_2-\tau_1\tau_2^2,\ \tau_1^2+\tau_2^2-4\tau_1\tau_2,\ \tau_1^2+\tau_2^2,\ \tau_1-\tau_2]^T.\end{cases} \quad (38)$$

By choosing 5 different values of α in terms of the guideline given in (8) and denoting $\Psi=[\psi(\alpha_1),\ \psi(\alpha_2),\ldots,\ \psi(\alpha_5)]^T$ and $\Phi=[\phi(\alpha_1),\ \phi(\alpha_2),\ldots,\ \phi(\alpha_5)]^T$, an LS solution can be derived from the linear regression,

$$\gamma=(\Phi^T\Phi)^{-1}\Phi^T\Psi \quad (39)$$

It is obvious that all the columns of Φ are linearly independent with each other, such that Φ is guaranteed non-singular for computation of (39). Accordingly, there exists a unique solution of γ for parameter estimation.

Then, the model parameters can be retrieved from γ as

$$\begin{cases}\tau_1=\dfrac{\gamma(5)}{2}+\dfrac{1}{2}\sqrt{\gamma^2(5)+4\dfrac{\gamma(2)}{\gamma(5)}}\\ \tau_2=\tau_1-\gamma(5)\end{cases} \quad (40)$$

Note that there exist three redundant fitting conditions in the parameter estimation of γ, which can be surely satisfied if the model structure matches the process to be identified. To procure fitting accuracy for a high-order process, we may use $\gamma(1)$, $\gamma(3)$ and $\gamma(4)$ together with $\gamma(2)$ and $\gamma(5)$ to derive

an LS fitting solution for parameter estimation in terms of using the natural logarithm, i.e.,

$$\begin{bmatrix} 2 & 2 \\ 1 & 1 \\ 1 & 0 \\ 0 & 1 \end{bmatrix} \begin{bmatrix} \ln \tau_1 \\ \ln \tau_2 \end{bmatrix} = \begin{bmatrix} \ln \gamma(1) \\ \ln[\dfrac{\gamma(4)-\gamma(3)}{4}] \\ \ln[\dfrac{\gamma(5)}{2}+\dfrac{1}{2}\sqrt{\gamma^2(5)+4\dfrac{\gamma(2)}{\gamma(5)}}] \\ \ln[\dfrac{\gamma(5)}{2}+\dfrac{1}{2}\sqrt{\gamma^2(5)+4\dfrac{\gamma(2)}{\gamma(5)}}-\gamma(5)] \end{bmatrix} \tag{41}$$

Consequently, the other two model parameters can be derived from (34) and (26) as

$$\theta = -Q_1(\alpha) + \frac{\tau_1}{1-\tau_1\alpha} - \frac{\tau_2}{\tau_2\alpha+1} \tag{42}$$

$$k_{\mathrm{p}} = (\tau_1\alpha-1)(\tau_2\alpha+1)G_2(\alpha)e^{\alpha\theta} \tag{43}$$

Hence, the above algorithm named **Algorithm-II** for obtaining an SOPDT model for an unstable process can be summarized as:

(i) Choose $s=\alpha$ and t_N to compute $T(\alpha)$, $T^{(1)}(\alpha)$ and $T^{(2)}(\alpha)$ in terms of (6) (or (12)), (14) and (15);
(ii) Compute $C(\alpha)$, $C^{(1)}(\alpha)$ and $C^{(2)}(\alpha)$ in terms of (18), (19) and (20);
(iii) Compute $G_2(\alpha)$, $G_2^{(1)}(\alpha)$ and $G_2^{(2)}(\alpha)$ in terms of (22), (23) and (24);
(iv) Compute $Q_1(\alpha)$ and $Q_2(\alpha)$ in terms of (34) and (35);
(v) Compute the time constants, τ_1 and τ_2, from (40) (or (41));
(vi) Compute the process time delay, θ, from (42);
(vii) Compute the process gain, k_{p}, from (43).

4. ILLUSTRATION

Example 1. Consider the FOPDT unstable process studied in the recent literature (Padhy and Majhi, 2006),

$$G(s) = \frac{1}{s-1}e^{-0.8s}$$

Based on relay feedback test with two P controllers, Padhy and Majhi (2006) derived a FOPDT model, $G_{\mathrm{m}} = 1.0e^{-0.8033s}/(1.0007s-1)$. For illustration, the unity feedback control structure with a proportional controller of $k_{\mathrm{c}}=1.2$, which is equivalent to that of Padhy and Majhi (2006), is used for closed-loop step test. By adding a step change with a magnitude of $h=0.05$ to the set-point, the closed-loop step response is shown in Fig.1. According to the guidelines given in (8) and (10), $\alpha=0.1$ and $t_N=150$ (s) are chosen to use the proposed Algorithm-I, resulting in a FOPDT model listed in Table 1, which indicates high accuracy. The fitting error is given in terms of the closed-loop transient response in the time interval [0, 50]s.

To demonstrate identification robustness against measurement noise, assume that a random noise of $N(0,\sigma_N^2=0.035\%)$, causing the noise-to-signal ratio (NSR) to 5%, is added to the output measurement which is then used for feedback control. By performing 100 Monte-Carlo tests in terms of varying the 'seed' of the noise generator from 1 to 100, the identified results are listed in Table 1, where the model parameters are respectively the mean of 100 Monte-Carlo tests, and the values in the adjacent parentheses are the sample standard deviation. The results for the noise levels of NSR=10% and 20% are also listed in Table 1 to show the achievable identification accuracy and robustness.

Example 2. Consider the SOPDT unstable process studied by Cheres (2006) and Sree and Chidambaram (2006),

$$G(s) = \frac{1}{(2s-1)(0.5s+1)}e^{-0.5s}$$

Based on a closed-loop step test in terms of a PID controller ($k_{\mathrm{c}}=2.71$, $\tau_{\mathrm{I}}=4.43$ and $\tau_{\mathrm{D}}=0.319$) and a unity step change to the set-point, Cheres (2006) derived only a referential FOPDT model for controller tuning, and so was done in Sree and Chidambaram (2006). By performing the same closed-loop step test, the proposed Algorithm-II based on the choice of $\alpha=0.1, 0.15, 0.2, 0.25, 0.3$ and $t_N=300$ (s) gives a SOPDT model listed in Table 1, again demonstrating good accuracy. The fitting error is given in terms of the closed-loop transient response in the time interval [0, 30]s.

To demonstrate identification robustness against measurement noise, 100 Monte Carlo tests are performed in terms of NSR=5%, 10% and 20%, respectively. The identified results are listed in Table 1 for comparison, which indicate again that good identification accuracy and robustness is therefore obtained.

5. CONCLUSIONS

Low-order model identification methods have been increasingly appealed for improving control system design to operate unstable processes. By applying a damping factor to the closed-loop step response for realization of the Laplace transform, a frequency response estimation algorithm has been proposed for model fitting. Based on the process frequency response estimated from the closed-loop step response with the knowledge of the controller, two model identification algorithms have been analytically developed for obtaining the widely used low-order process models of FOPDT and SOPDT for practical applications. Two illustrative examples from the recent literature have been performed to demonstrate the achievable accuracy of the proposed algorithms. The results under Monte Carlo noise tests have also demonstrated good identification robustness of the proposed algorithms.

ACKNOWLEDGEMENT

This work is supported in part by the Hong Kong Research Grants Council under Project No. 613107.

REFERENCES

Åström, K.J. and T. Hägglund (2005). *Advanced PID Control*. Research Triangle Park, NC, ISA Society of America.

Bindlish, R., J.B. Rawlings and R.E. Young (2003). Parameter estimation for industrial polymerization processes. *AIChE J.*, **49**, 2071-2078.

Cheres, E. (2006). Parameter estimation of an unstable system with a PID controller in a closed loop configuration. *Journal of the Franklin Institute*, **343**, 204-209.

Häggblom, K.E. (1996). Combined internal model and inferential control of a distillation column via closed-loop identification. *Journal of Process Control*, **6**, 223-232.

Liu, T. and F. Gao (2008a). Alternative identification algorithms for obtaining a first-order stable/unstable process model from a single relay feedback test. *Ind. Eng. Chem. Res.*, **47**, 1140-1149.

Liu, T. and F. Gao (2008b). Identification of integrating and unstable processes from relay feedback. *Computers and Chemical Engineering*, **32**, 3038-3056.

Marchetti, G., C. Scali and D.R. Lewin (2001). Identification and control of open-loop unstable processes by relay methods. *Automatica*, **37**, 2049-2055.

Paraskevopoulos, P.N., G.D. Pasgianos and K.G. Arvanitis (2004). New tuning and identification methods for unstable first order plus dead-time. *IEEE Trans. Control Systems Technology*, **12**, 455-464.

Padhy, P.K. and S. Majhi (2006). Relay based PI-PD design for stable and unstable FOPDT processes. *Computers and Chemical Engineering*, **30**, 790-796.

Saffer, D.R. and F.J. Doyle (2002). Closed-loop identification with MPC for an industrial scale CD-control problem. *IET Control Theory & Appl.*, **149**, 448-456.

Seborg, D.E., T.F. Edgar and D.A. Mellichamp (2003). *Process Dynamics and Control, 2nd ed.*, John Wiley & Sons, New Jersey.

Shiu, S.J., S.H. Hwang and M.L. Li (1998). Automatic tuning of systems with one or two unstable poles. *Chemical Engineering Communication*, **167**, 51-72.

Sree, R.P. and M. Chidambaram (2006). Improved closed loop identification of transfer function model for unstable systems. *Journal of the Franklin Institute*, **343**, 152-160.

Sung, S.W., S.Y. Lee, H.J. Kwak and I.-B. Lee (2001). Continuous-time subspace system identification method. *Ind. Eng. Chem. Res.*, **40**, 2886-2896.

Tan, K. K., Q.G. Wang and T.H. Lee (1998). Finite spectrum assignment control of unstable time delay processes with relay tuning. *Ind. Eng. Chem. Res.*, **37**, 1351-1357.

Thyagarajan, T. and C.C. Yu (2003). Improved autotuning using the shape factor from feedback. *Ind. Eng. Chem. Res.*, **42**, 4425-4440.

Vivek, S. and M. Chidambaram (2005). An improved relay auto tuning of PID controllers for unstable FOPTD systems. *Computers and Chemical Engineering*, **29**, 2060-2068.

Yu, C.C. (2006). *Autotuning of PID Controllers: A Relay Feedback Approach, 2nd ed.* Springer-Verlag, London.

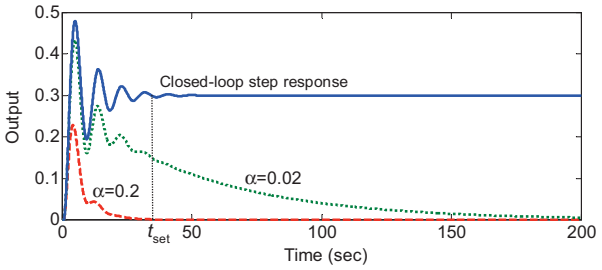

Fig. 1. Illustration of choosing α for example 1

Table 1. Closed-loop step response identification under different measurement noise levels

NSR	Example 1	*err*	Example 2	*err*
0	$\frac{1.0000e^{-0.8008s}}{1.0006s-1}$	8.46×10^{-8}	$\frac{0.9999e^{-0.4996s}}{(2.0000s-1)(0.5000s+1)}$	1.47×10^{-8}
5%	$\frac{1.0001(\pm0.0011)e^{-0.8019(\pm0.045)s}}{1.0015(\pm0.033)s-1}$	4.15×10^{-7}	$\frac{0.9999(\pm0.0025)e^{-0.4998(\pm0.0082)s}}{[2.0002(\pm0.0037)s-1][0.5004(\pm0.0098)s-1]}$	1.72×10^{-7}
10%	$\frac{1.0003(\pm0.0021)e^{-0.8018(\pm0.089)s}}{1.0013(\pm0.066)s-1}$	5.08×10^{-7}	$\frac{0.9999(\pm0.0054)e^{-0.4992(\pm0.023)s}}{[2.0005(\pm0.0087)s-1][0.5009(\pm0.034)s-1]}$	7.61×10^{-7}
20%	$\frac{1.0006(\pm0.0041)e^{-0.7971(\pm0.183)s}}{0.9973(\pm0.136)s-1}$	2.86×10^{-6}	$\frac{0.9995(\pm0.0097)e^{-0.4985(\pm0.026)s}}{[2.0008(\pm0.017)s-1][0.5011(\pm0.026)s-1]}$	2.79×10^{-6}

Multivariable System Identification for Integral Controllability – Computational Issues

Mark L. Darby, Michael Nikolaou

Chemical & Biomolecular Engineering Department, University of Houston, Houston, TX 77204-4004 USA
(darbymark@sbcglobal.net, nikolaou@uh.edu)

Abstract: A process model satisfies the integral controllability (IC) condition if the model can be used in a model-based controller that can be arbitrarily detuned without jeopardizing closed-loop stability. For decoupling multivariable control this requirement is equivalent to the inequality $\mathrm{Re}\left[\lambda\left(\mathbf{G}\hat{\mathbf{G}}^{-1}\right)\right]>0$ for the actual and estimated process steady-state gain matrices $\mathbf{G}$ and $\hat{\mathbf{G}}$. This necessitates experiments for identification of $\hat{\mathbf{G}}$ that satisfies the IC inequality. In this work we explore, via computer simulations, computational issues related to the design of such experiments for an FCC process. The proposed approach is based on a general mathematical optimization framework we presented in prior work.

Keywords: Identification, Integral controllability, multivariable systems

1. INTRODUCTION

A process model satisfies the integral controllability (IC) condition if the model can be used in a model-based controller that can be arbitrarily detuned without jeopardizing closed-loop stability. For decoupling multivariable control this requirement is equivalent to the inequality

$$\mathrm{Re}\left[\lambda\left(\mathbf{G}\hat{\mathbf{G}}^{-1}\right)\right]>0 \tag{1}$$

for the actual and estimated process steady-state gain matrices $\mathbf{G}$ and $\hat{\mathbf{G}}$ (Garcia and Morari 1985). The problem is acute for ill-conditioned processes. This necessitates experiments for identification of a model $\hat{\mathbf{G}}$ that satisfies the IC inequality. "The main weakness of the eigenvalue conditions [eqn. (1)] is that they consist of a coupling between the plant model and the true plant which is highly cumbersome for use in robust control analysis and design." (Featherstone and Braatz 1998b). A number of attempts have been made to address this weakness. Featherstone and Braatz (1998a) showed that for processes with constant rotation matrices in the singular-value decomposition (svd) of their transfer matrix the problem reduces to D-optimal design of experiments. Using insightful geometric reasoning to ensure IC for general linear 2×2 systems, Koung and MacGregor (1993) introduced experiment designs in terms of rotated PRBS input vectors, with power of each component of the rotated input vector reciprocally proportional to the corresponding singular value of $\hat{\mathbf{G}}$. Koung & MacGregor (1994) heuristically extended these design rules to $n\times n$ multivariable systems. The same rules were also used by Bruwer & MacGregor (2006) for the design of identification experiments subject to input and output bounds in the time domain. Darby and Nikolaou (2008) showed that the design rules proposed by Koung and MacGregor (1993; 1994) accept the same deep theoretical justification for both 2×2 and $n\times n$ systems in a number of cases. However, Darby and Nikolaou (2008) also showed that these design rules are not optimal for a number of typical cases, such as when outputs and/or inputs are constrained or when input rather than output variance alone must be maintained at a minimum. Furthermore, the same authors provided rigorous design rules for optimal inputs in a number of such cases. These design rules from solution of corresponding optimization problems. The purpose of this article is to explore the nature of the optimal input designs produced by the mathematical framework introduced by Darby and Nikolaou (2008) when applied to a realistic system, such as a 5×5 fluid catalytic cracking (FCC) unit.

2. BACKGROUND: EXPERIMENT DESIGN FOR IC

Consider a stable, linear, time-invariant, multivariable system with steady-state input-output relationship

$$\mathbf{y}=\mathbf{G}\mathbf{m} \tag{2}$$

where $\mathbf{y},\mathbf{m}\in\mathbb{R}^n$, $\mathbf{G}$ and $\hat{\mathbf{G}}\triangleq[\hat{\mathbf{g}}_1,...,\hat{\mathbf{g}}_n]^T\in\mathbb{R}^{n\times n}$. Because the IC condition, eqn. (1), involves the real process $\mathbf{G}$ and identified model $\hat{\mathbf{G}}$, it cannot directly guide input design for an $n\times n$ system. The following results (Darby and Nikolaou 2008) avoid that difficulty and can be used directly to design experiments pursuing IC.

Theorem 1. Experiment design for IC. Let the model uncertainty matrix $\mathbf{D} = \mathbf{G} - \hat{\mathbf{G}} \in \mathbb{R}^{n\times n}$ *belong to the ellipsoidal uncertainty set*

$$D \triangleq \left\{ [\mathbf{d}_1 ... \mathbf{d}_n]^T \in \mathbb{R}^{n\times n} \middle| \mathbf{d}_k^T \mathbf{M}^T \mathbf{M} \mathbf{d}_k \le c^2, 1 \le k \le n \right\}. \quad (3)$$

Then, an experiment design guarantees IC if the resulting information matrix $\mathbf{M}^T\mathbf{M}$ *and identified model* $\hat{\mathbf{G}}$ *satisfy the inequality*

$$\sum_{k=1}^{n} a_k \sqrt{\hat{\mathbf{v}}_k^T \left(\mathbf{M}^T\mathbf{M}\right)^{-1} \hat{\mathbf{v}}_k} < 1. \quad (4)$$

where

$$a_k \triangleq c \left\| \hat{\mathbf{u}}_k \right\|_1 / \hat{\sigma}_k, \quad k = 1,...,n \quad (5)$$

and $\hat{\sigma}_1 \ge \cdots \ge \hat{\sigma}_n$, $\hat{\mathbf{u}}_k$, $\hat{\mathbf{v}}_k$ *are defined through the svd*

$$\hat{\mathbf{G}} = \hat{\mathbf{U}}\hat{\Sigma}\hat{\mathbf{V}}^T = \sum_{k=1}^{n} \hat{\sigma}_k \hat{\mathbf{u}}_k \hat{\mathbf{v}}_k^T. \quad (6)$$

Eqn. (4) clearly suggests that IC can be satisfied if the information matrix $\mathbf{M}^T\mathbf{M}$ is "large enough". Given bounds on the input vector $\mathbf{m}$, a large enough $\mathbf{M}^T\mathbf{M}$ can be achieved if (a) the identification experiment is run long enough, or (b) $\mathbf{m}$ is shaped appropriately. While the first alternative is straightforward, it is far less desirable than the second one. Therefore, the essence of experiment design for IC is how to *shape process inputs that satisfy eqn. (4) subject to relevant constraints*. Darby and Nikolaou (2008) showed that numerical or analytical solutions can be developed for a number of cases. While for some of these cases the resulting designs are similar to designs that have appeared in literature, for others the resulting designs are entirely different.

2.1. Analytical solutions

Suppose that the quantity $\sum_{k=1}^{n} a_k [\hat{\mathbf{v}}_k^T (\mathbf{M}^T\mathbf{M})^{-1} \hat{\mathbf{v}}_k]^{1/2}$ in eqn. (4) is to be minimized with respect to the zero-mean random input $\mathbf{m}$, subject to the total weighted variance inequality

$$x \operatorname{var}(\mathbf{y}) + (1-x) \operatorname{var}(\mathbf{m}) \le W^2 \quad (7)$$

where $0 \le x \le 1$ and $0 < a_1 < ... < a_n$. Then it can be shown that the optimal input vector $\mathbf{m}$ is

$$\mathbf{m} = \hat{\mathbf{V}}\boldsymbol{\xi}, \quad (8)$$

where $\boldsymbol{\xi}$ is a zero-mean multivariable PRBS with

$$E\left[\xi_k^2\right] = \left(\frac{a_k}{b_k^2}\right)^{2/3} \frac{W^2}{\left[\sum_{j=1}^{n} \left(a_j b_j\right)^{2/3}\right]^2}, \quad k = 1,...,n \quad (9)$$

$$b_k^2 \triangleq x\sigma_k^2 + 1 - x, \quad k = 1,...,n. \quad (10)$$

and $b_1 \ge ... \ge b_n > 0$. Reversing the role of the above objectives and constraints, the minimum of the cost function $x \operatorname{var}(\mathbf{y}) + (1-x) \operatorname{var}(\mathbf{m})$ subject to eqn. (4) can be shown to be attained at an optimal $\mathbf{m}$ satisfying eqn. (8) with

$$E\left[\xi_k^2\right] > \left(\frac{a_k}{b_k^2}\right)^{2/3} \left[\sum_{j=1}^{n} \left(a_j b_j\right)^{2/3}\right]^2, \quad k = 1,...,n. \quad (11)$$

Note that for $x = 1$ (all cost on output variance, as is desirable in early stages of an identification experiment) both eqns. (9) and (11) result in the well known design rule

$$r_{kj} \triangleq \sqrt{\frac{E\left[\xi_k^2\right]}{E\left[\xi_j^2\right]}} = s_{kj} \frac{\hat{\sigma}_j}{\hat{\sigma}_k} \approx \frac{\hat{\sigma}_j}{\hat{\sigma}_k}. \quad (12)$$

where $s_{kj} \triangleq (\| \hat{\mathbf{u}}_k \|_1 / \| \hat{\mathbf{u}}_j \|_1)^{1/3} \approx 1$ for most cases of practical interest, and $1/n^{1/6} \le s_{kj} \le n^{1/6}$ when $\hat{\mathbf{u}}_k$, $\hat{\mathbf{u}}_j$ are any orthonormal vectors in $\mathbb{R}^n$. However, for $x = 0$ (all cost on input variance) we get the new input design

$$r_{kj} \triangleq \sqrt{\frac{E\left[\xi_k^2\right]}{E\left[\xi_j^2\right]}} = s_{kj} \left(\frac{\hat{\sigma}_j}{\hat{\sigma}_k}\right)^{1/3} \approx \left(\frac{\hat{\sigma}_j}{\hat{\sigma}_k}\right)^{1/3}. \quad (13)$$

The above design would keep inputs small to avoid inadvertent loss of IC by failure to excite the process by inputs along directions corresponding to small singular values.

Finally, a D-optimal design subject to eqns. (4) and (7) can be shown to be attained, if feasible, at an optimal $\mathbf{m}$ as in eqn. (8) with

$$E\left[\xi_k^2\right] = W^2 / \left(n b_k^2\right), \quad k = 1,...,n, \quad (14)$$

if eqn. (4) is satisfied by the above ξ_k, or each $E\left[\xi_k^2\right]$ equal to the unique positive solution of the equation

$$\frac{\rho}{t-1}\left(\frac{a_k}{\sqrt{(t-1)E\left[\xi_k^2\right]}} - \frac{1}{n}\right) = b_k^2 E\left[\xi_k^2\right] - \frac{W^2}{n} \quad (15)$$

for a value of $\rho > 0$ such that eqn. (4) is satisfied. It has been shown that eqn. (15) guarantees that $E\left[\xi_{k+1}^2\right] > E\left[\xi_k^2\right]$ and that D-optimality is compatible with IC by Cauchy's inequality (Darby and Nikolaou 2008). Note that as $t \to \infty$ eqns. (14) and (15) coincide asymptotically.

2.2. Numerical solutions

The preceding section 2.1 summarized analytical solutions for simple cases, offering insight into the nature of corresponding solutions. However, in many practical situations individual constraints on m_i and y_i may be present, such as

$$\sum_{\tau=1}^{t} m_{i,\tau}{}^2 = [\mathbf{M}^T\mathbf{M}]_{ii} \le (t-1) M_i^2 \quad (16)$$

$$\sum_{\tau=1}^{t} y_{i,\tau}{}^2 = [\mathbf{Y}^T\mathbf{Y}]_{ii} = [\hat{\mathbf{G}}\mathbf{M}^T\mathbf{M}\hat{\mathbf{G}}^T]_{ii} \le (t-1)Y_i^2 \quad (17)$$

corresponding to bounds on the variance of individual inputs m_k or outputs y_k. In such cases a numerical solution is required. To obtain a numerical solution, assume a zero-mean input vector $\mathbf{m}$, approximate the information matrix as $\mathbf{M}^T\mathbf{M} \approx (t-1)\mathbf{C}_m$, parametrize the input covariance matrix $\mathbf{C}_m$ in terms of the triangular matrix $\mathbf{Q}$ through the Cholesky factorization $\mathbf{C}_m = \mathbf{Q}\mathbf{Q}^T$, and substitute $\mathbf{M}^T\mathbf{M}$ into eqn. (4), to get

$$\frac{c}{\sqrt{t-1}} \underbrace{\sum_{i=1}^{n} \frac{\|\hat{\mathbf{u}}_k\|_1}{\hat{\sigma}_k} \sqrt{\hat{\mathbf{v}}_k^T \left(\mathbf{Q}\mathbf{Q}^T\right)^{-1} \hat{\mathbf{v}}_k}}_{\beta} \triangleq \frac{c}{\sqrt{t-1}} \beta < 1. \quad (18)$$

(Other parametrizations of a symmetric matrix in terms of corresponding basis matrices could be used. This is subject of ongoing investigation.) We can then design experiments for IC using eqn. (18) as a constraint or by minimizing β with respect to $\mathbf{Q}$ subject to input and output constraints such as in eqns. (16) and (17). Then, the corresponding optimal input $\mathbf{m}$ is

$$\mathbf{m} = \mathbf{Q}_{\text{opt}}\mathbf{z} \quad (19)$$

where $\mathbf{z}$ is a zero-mean PRBS with $\text{cov}(\mathbf{z}) = \mathbf{I}$. Even though β is not convex, resulting design problems are not prohibitively large for realistic systems, as demonstrated in section 4. It should be stressed that minimizing β may result to neither uncorrelated rotated inputs $\boldsymbol{\xi}$, nor magnitudes of rotated input components reciprocally proportional to corresponding singular values of the steady-state gain matrix, eqn. (12). In fact, the advantage of the above numerical formulation is that no such underlying assumptions on the nature of optimal inputs are necessary. Rather, the numerical optimization determines the nature of optimal input designs.

3. SUMMARY OF PROPOSED APPROACH

a. Establish constraints commensurate with time t available for identification experiments.

b. Obtain preliminary estimates of $\hat{\mathbf{G}}$ and c^2.

c. Compute the svd of $\hat{\mathbf{G}}$ to get $\hat{\mathbf{U}}$, $\hat{\boldsymbol{\Sigma}}$, $\hat{\mathbf{V}}^T$, eqn. (6).

Case I

d. Compute $\lambda_{k,\text{opt}}$ via eqns. (9) or similar

e. Design $\mathbf{m} = \hat{\mathbf{V}}\boldsymbol{\xi}$ with $\boldsymbol{\xi}$ zero-mean PRBS and $\text{cov}(\boldsymbol{\xi}) = \text{diag}(\lambda_{\ell_1,\text{opt}}^2, ..., \lambda_{\ell_n,\text{opt}}^2)/(t-1)$

Case II

d. Compute $\mathbf{Q}_{\text{opt}} = \arg\min \beta$ subject to constraints.

e. Design $\mathbf{m} = \mathbf{Q}_{\text{opt}}\mathbf{z}$ with $\mathbf{z}$ zero-mean PRBS and $\text{cov}(\mathbf{z}) = \mathbf{I}$ (eqn. (19)).

f. Implement $\mathbf{m}$ and collect data, to update $\hat{\mathbf{G}}$ and c^2.

g. If $\hat{\mathbf{G}}$ is adequate, stop. Otherwise go to step c.

4. CASE STUDY

A steady-state gain matrix is obtained from a linear empirical dynamic model of an industrial reactor-regenerator from a FCC unit, identified from plant testing (Harmse 2007). Note that the specific inputs and outputs are not indicated. Scaling is performed according to the inverse of the typical operating ranges of the inputs and outputs. The resulting gain matrix is

$$\mathbf{G} = \begin{bmatrix} 0.3866 & 0.0 & 0.1192 & 0.0 & 0.0630 \\ 0.0 & -0.6935 & 1.5463 & -0.1311 & -0.2462 \\ 0.0 & 0.0 & 0.5225 & -0.1298 & 0.0 \\ 0.0 & 0.0 & 0.0 & 0.1058 & 0.0 \\ 0.0 & -0.5803 & -0.3669 & -0.2057 & -0.4435 \end{bmatrix} \quad (20)$$

We tested the designs shown in Table 1. The constraints shown in Table 2 were considered.

Table 1. Summary of experimental designs tested

Design	Objective	Constraints
ICmin	$\min_{\mathbf{Q}} \beta$	$\mathbf{Q}$ triangular
KM	(Koung and MacGregor 1994)	
PRBSmax	$\min_{\mathbf{C}_m} -\log(\det \mathbf{C}_m)$	$\mathbf{C}_m \triangleq \text{diag}(v_i) \succ \mathbf{0}$

Table 2. Constraints considered for experiment design

Design case	Bounds	
A	$\text{var}(m_i) \le \infty$	$\text{var}(y_1) \le 0.50$
	$i = 1, ..., 5$	$\text{var}(y_2) \le 0.47$
		$\text{var}(y_3) \le 0.44$
		$\text{var}(y_4) \le 0.41$
		$\text{var}(y_5) \le 0.38$
B	$\text{var}(m_i) \le 0.5$	$\text{var}(y_i) \le 0.5$
	$i = 1, ..., 5$	

In all simulations, parameter estimation is initiated at time step 5 and is performed at each subsequent time step. The IC condition, eqn. (1), is calculated based on the true gain matrix and the inverse of the gain estimate at each time step. For simulations of case A, independent Gaussian noise of zero-mean and unit variance is added to all outputs.

Realizations of the inputs and outputs for each design are shown in Figure 1. We see that due to the high noise levels, the actual output variances are significantly higher than the optimal output variances (which are based on the model without noise). Note that the relatively low signal-to-noise ratio allows us to observe the evolution of gains over a longer period of time.

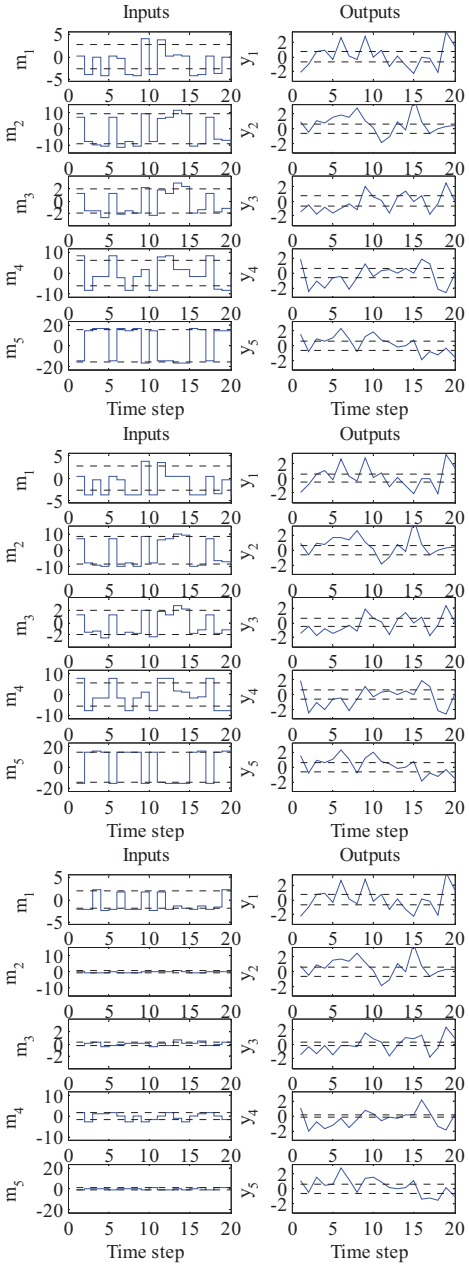

Figure 1 – Example realization of reactor regenerator for the three designs of case A (Table 1). The dotted lines represent $\pm(\mathrm{var}(m_i)^{\mathrm{opt}})^{1/2}$ and $\pm(\mathrm{var}(y_i)^{\mathrm{opt}})^{1/2}$ values.

Trends of the gain errors and an indicator of the IC condition are shown in Figure 2 For this realization, we see that IC is achieved first by ICmin at time step 7, followed by KM at time step 8, and finally PRBSopt at time step 13. The evolution of the gain errors is similar for ICmin and KM, whereas the PRBSopt results show higher gain errors and slower error reduction over time, consistent with the lower value of det(cov(**m**)) for PRBSopt.

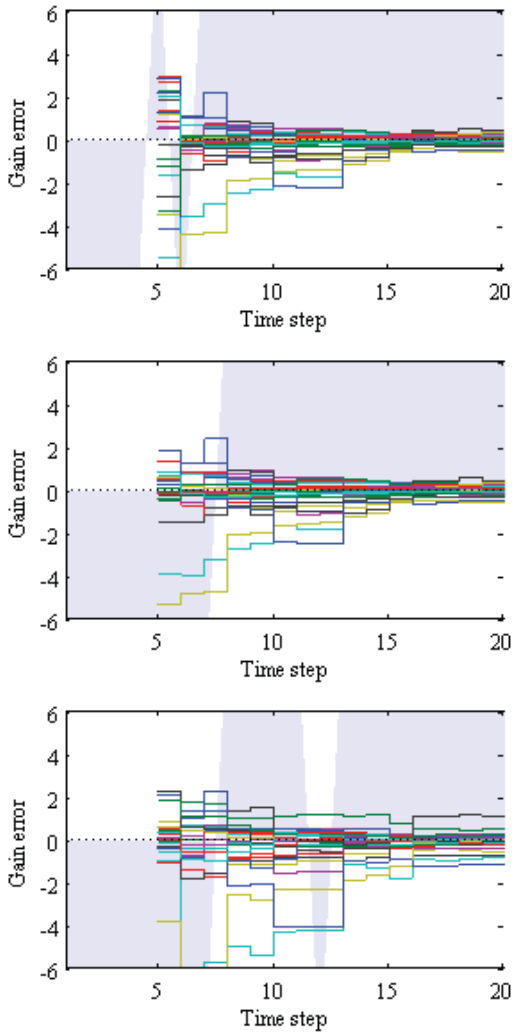

Figure 2 – Gain errors and IC condition for example realization of design case A (Table 1). Satisfaction or violation of the IC condition corresponds to shading above or below 0, respectively.

For the simulations of case B, independent, Gaussian noise of zero mean and variance (0.15^2) is added to all outputs. Realizations of the inputs and outputs for each design are shown in Figure 3. Note that the smaller signals for the KM design, compared to the other two designs, are due to the

fact that inputs must satisfy all inequality constraints, as well as equality constraints on rotated input ratios. The latter are clearly not optimal for case B.

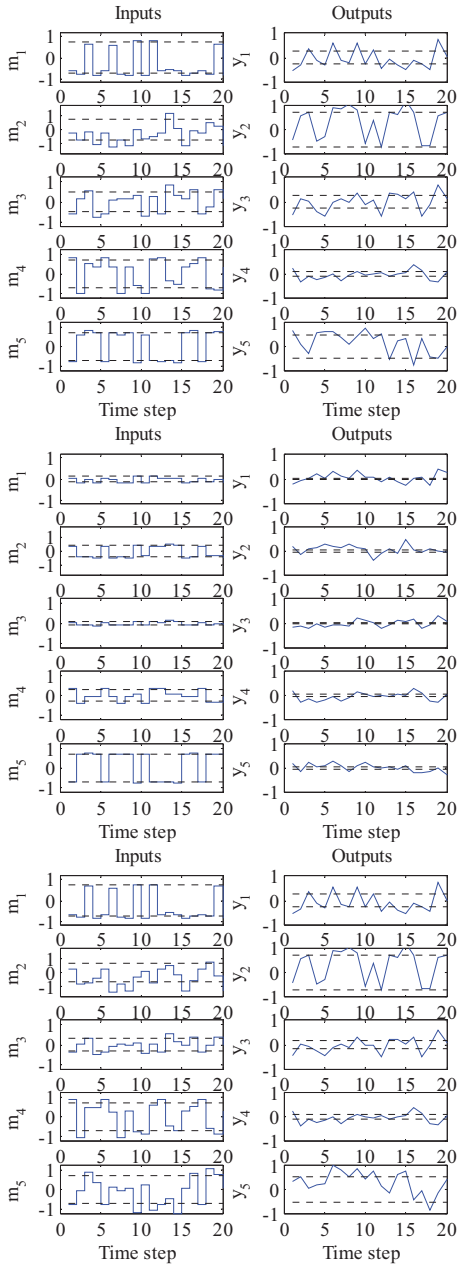

Figure 3 – Example realization of reactor regenerator case B (Table 1). The dotted lines represent $\pm\sqrt{\text{var}(m_i)^{\text{opt}}}$ and $\pm\sqrt{\text{var}(y_i)^{\text{opt}}}$ values.

Trends of the gain errors and an indicator of the IC condition are shown in Figure 4. We see that the parameters estimates for the KM design are significantly inferior to the ICmin and PRBSopt designs, reflecting the much smaller value of det(cov(**m**)) for KM. Further, while IC is achieved by ICmin at time step 6 and by PRBSopt at time step 5, the KM design does not satisfy the IC condition by time step 20 (it is actually achieved at time step 22 – not shown – more then 3 times longer than required for either ICmin or PRBSopt).

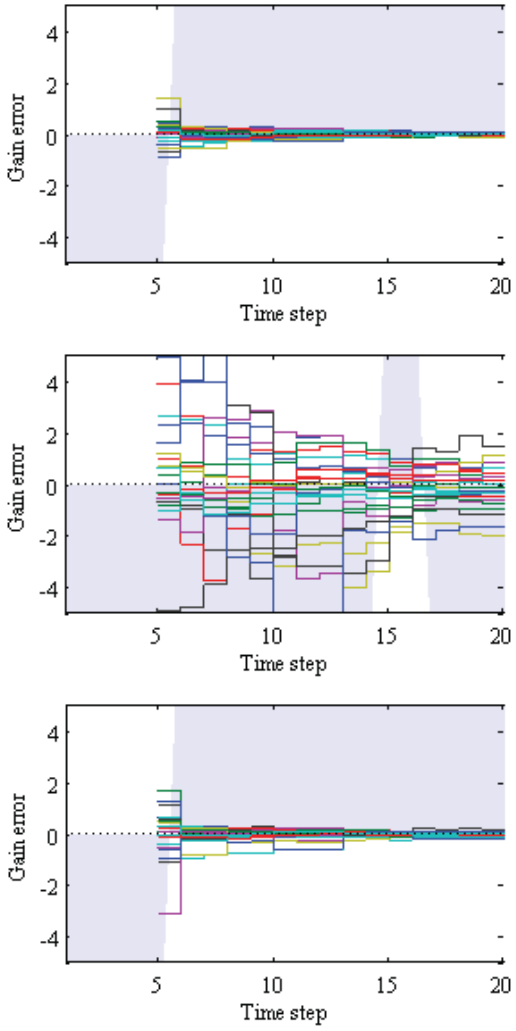

Figure 4 – Gain errors and IC condition for example realization of design case B (Table 1). Satisfaction or violation of the IC condition corresponds to shading above or below 0, respectively.

To develop these designs we used the Matlab routine fmincon with multiple starting points, to reduce the possibility of missing a global optimum for non-convex optimization problems. Run time for all simulations was, on the average, of the order of 0.25 seconds when using the Yalmip interface, and of the order of 0.1 seconds without it.

5. CONCLUSIONS

The purpose of this paper was to explore numerical aspects of a numerical optimization approach proposed in prior work for the design of experiments targeting IC. Given that analytical solutions for this approach are available only for some cases, it is natural to ask how well numerical optimization can work, given that the proposed problems are non-convex. In this work, we develop what appear to be useful designs for a 5×5 multivariable FCC unit. Convergence time appeared not to be an issue. These results suggest that the proposed approach can work reasonably well for problems of that size. Clearly, other optimization methods (either deterministic or probabilistic) can be explored.

Acknowledgments

Partial support from the National Science Foundation (Grant No. CTS-0227232) is gratefully acknowledged.

6. REFERENCES

Bruwer, M. J. and J. F. MacGregor (2006). "Robust multi-variable identification: Optimal experimental design with constraints." Journal Of Process Control **16**(6): 581-600.

Darby, M. L. and M. Nikolaou (2008). "Multivariable system identification for integral controllability." Automatica: submitted.

Featherstone, A. P. and R. D. Braatz (1998a). "Input Design for Large-Scale Sheet and Film Processes." Industrial & Engineering Chemistry Research **37**: 449-454.

Featherstone, A. P. and R. D. Braatz (1998b). "Integrated robust identification and control of large-scale processes." Industrial & Engineering Chemistry Research **37**(1): 97-106.

Garcia, C. E. and M. Morari (1985). "Internal model control: 2. design procedure for multivariate systems." Ind. Eng. Chem. Process Des. Dev. **24**: 472-484.

Harmse, M. (2007). "Personal communication."

Koung, C. W. and J. F. MacGregor (1993). "Design Of Identification Experiments For Robust-Control - A Geometric Approach For Bivariate Processes." Industrial & Engineering Chemistry Research **32**(8): 1658-1666.

Koung, C. W. and J. F. MacGregor (1994). "Identification For Robust Multivariable Control - The Design Of Experiments." Automatica **30**(10): 1541-1554.

Internal Excitation Approaches for Closed-loop Identification of Processes Controlled by MPC

Oscar A. Z. Sotomayor[1], Darci Odloak[2]

[1]*Department of Electrical Engineering*
Center for Exact Sciences and Technology, Federal University of Sergipe (UFS), BRAZIL
E-mail: oscars@ufs.br
[2]*Department of Chemical Engineering*
Polytechnic School of the University of São Paulo (EPUSP), BRAZIL
E-mail: odloak@usp.br

Abstract: This work is concerned with the model re-identification of processes controlled by MPC systems. The MPC system considered here has a two-layer structure, where in the upper layer a steady-state optimization algorithm determines a set of optimal targets for the process inputs and passes this set to the MPC controller that determines the best way to drive the process to such targets. This is the case of several commercial MPC packages applied in industry. In this paper, it is proposed two internal excitation approaches aiming to obtain closed-loop data sufficiently rich for process identifiability. Here, the term internal is used to indicate that the excitation test signal is applied within the MPC control structure. In the first excitation approach, the test signal is introduced as a weighting factor in the objective function of the target calculation layer. In the second approach, the test signal is injected as a dither signal in the objective function of the dynamic controller layer. These two approaches are compared to the usual method where the excitation signal is added to the controller output. The application of the methodologies is illustrated through numerical simulations carried out on a depropanizer column of the oil industry. The results show the effectiveness of the proposed approaches and their good potential to be applied in practice.

1. INTRODUCTION

Model identification has become a bottleneck of MPC technology. It is the most expensive, difficult and time-consuming step of the MPC project. Although industrial processes present nonlinear dynamic characteristics, typically, empirical linear and time-invariant (LTI) models based on process input-output data obtained in open-loop operation are used in MPC implementation (Qin & Badgwell, 2003). While this approach is only acceptable at operating conditions around the operating point where the model was obtained, the control system with this model works satisfactorily in most applications.

However, after some operation time (2-3 years), MPC is seldom performing as when it was commissioned. The main cause of this problem is related to the model deterioration resulting from changes in the dynamics of the plant or persistent unmeasured disturbances that force the plant to a different operating point (Conner & Seborg, 2005). Changes in the dynamics of the plant may result from fatigue conditions, fouling, debottlenecking, etc, or changes in the operating conditions or product specifications. In general, the above listed problems intensify with time and tend to accentuate the plant/model mismatch, leading to poor output prediction and, therefore, degradation of the control system performance. In order to keep the performance of the MPC at an acceptable level, it is essential to carry out the MPC re-commissioning in a periodic basis, which means to re-identify the process model and, if necessary, to retune the MPC considering the new model (Gugaliya et al., 2005). However, due to production goals and safety aspects, model re-identification means, in most cases, to develop a new model based on plant data obtained in closed-loop conditions.

Closed-loop identification is a research subject with growing interest in the last decade (Van den Hof, 1998; Forssell & Ljung, 1999; Hjalmarsson, 2005). Important aspects on model identification have been studied and several identification strategies have been proposed, which can be categorized as variants of the following three approaches (Forssell & Ljung, 1999): direct, indirect and joint input-output methods. Both indirect and joint input-output methods require prior knowledge of the controller or assume that it has a certain LTI structure. Obviously, these methods are not suitable for MPC applications, because MPC presents nonlinear and time-variant features, especially when operating under constraints. For this sort of control strategy, the direct method is the recommended choice for closed-loop identification. See for example Rivera & Flores (1999).

In closed-loop identification, the use of routine operating data would be an ideal goal. But, the inherent reduction in the excitation resulting from the presence of the controller may result in a poor signal-to-noise ratio. In this case, and in order to achieve the necessary and sufficient conditions for process identifiability, an external persistently exciting (PE) test signal is required. External excitation is a dither signal that may be introduced on the controlled variable set-point and/or on the manipulated variable (added to the controller output).

However, adding such a signal is often undesirable or too expensive, and there is no guarantee that the process constraints and product specifications will be attended during the execution of the excitation procedure. On the other hand, an insufficient excitation may compromise the identification requirements.

The main goal of this paper is to compare internal excitation approaches that exploit the two-layer structure of MPC packages. Motivation for this work is due primarily to commercial needs and as an attempt to overcome the significant gap between practical applications and theory in closed-loop identification with MPC. In the proposed methodologies an external PE test signal is applied within the MPC control structure: (a) the test signal is introduced in the objective function of the target calculation layer, and (b) the test signal is injected in the objective function of the dynamic MPC control layer. These approaches does not modify the optimization code and they allows the adequate excitation of the process coupled with the continuous operation of the system as the process constraints and product specification can be satisfied during the test. Results from the proposed excitation methodologies are also compared with the one provided by a conventional external excitation procedure in the closed-loop identification of an industrial depropanizer column.

2. THE TWO-LAYER MPC STRUCTURE

In modern processing plants, MPC control systems are usually implemented in a two-layer scheme (Ying & Joseph, 1999; Qin & Badgwell, 2003; Nikandrov & Swartz, 2009). The two-layer MPC considered here is shown in Figure 1. The upper layer usually corresponds to a simplified steady-state target optimization and the lower layer stands for a constrained dynamic optimization in which the outputs are controlled in specified zones or ranges instead of fixed references. It is at the dynamic layer where the main control objectives (setpoint tracking, disturbance rejection) are pursued. All commercial MPC packages offer the option of zone control. In the target calculation layer, one searches for the optimum steady-state values to the system (input targets), by usually solving a linear or quadratic objective function subject to bound constraints in the inputs and outputs. The outputs at the optimal steady-state are computed through a static model, consistent with the dynamic MPC model, and the available steady-state output prediction computed at the previous time step in the MPC algorithm. The optimal input targets are sent to the dynamic layer, where the control cost is extended with a term that penalizes the distance between the present value of the input and the optimal target. Both layers are executed with the same sampling period.

In this paper, the target calculation layer solves a LP (linear programming) problem where the objective may be to maximize production by forcing one or more inputs to their bounds, while keeping the outputs inside the bounds:

$$\min_{\Delta u_s, \delta_y} W_1^T \Delta u_s + \left| W_2^T \delta_y \right| \tag{1}$$

subject to:

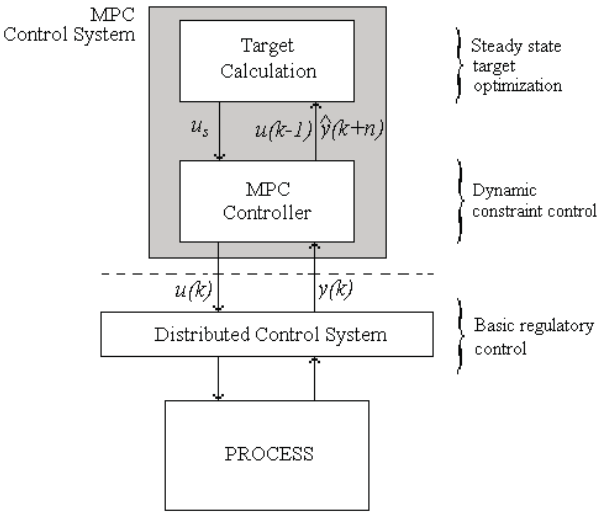

Fig. 1. Two-layer MPC structure

$$\begin{aligned} &\Delta u_s = u_s - u(k-1) \\ &y_s = G_0 \Delta u_s + \hat{y}(k+n) \\ &u_{\min} \le u_s \le u_{\max} \\ &y_{\min} \le y_s + \delta_y \le y_{\max} \end{aligned} \tag{2}$$

where $u(k-1)$ is the last implemented control action, k is the present time, u_s is the vector of steady-state targets for the manipulated inputs, y_s is the vector of predicted output at steady-state, $\hat{y}(k+n)$ is the prediction of the controlled output at time instant $k+n$ (n is the model horizon or settling time of the process in open-loop) computed at time k, δ_y is the vector of slack variables for the controlled outputs, G_0 is the steady state gain matrix model, W_1 and W_2 are weight vector of appropriate dimensions, $u_{\min}$ and $u_{\max}$ are the bounds of the manipulated inputs, $y_{\min}$ and $y_{\max}$ are the bounds of the controlled outputs.

As a result of the solution to the problem formulated in (1) and (2), it is obtained the input target u_s that is passed to the dynamic layer, which typically solves the following QP (quadratic programming) problem:

$$\begin{aligned} \min_{\Delta u} &\sum_{i=1}^{p} \left\| Q\left(\hat{y}(k+i) - y_{sp}\right) \right\|_2^2 + \sum_{j=1}^{m} \left\| R\Delta u(k+j-1) \right\|_2^2 + \\ &\sum_{j=1}^{m} \left\| R_u \left(u(k+j-1) - u_s \right) \right\|_2^2 \end{aligned} \tag{3}$$

subject to:

$$\begin{aligned} &-\Delta u_{\max} \le \Delta u(k+j-1) \le \Delta u_{\max}, \quad j = 1, \cdots, m \\ &u_{\min} \le u(k+j-1) \le u_{\max}, \qquad j = 1, \cdots, m \end{aligned} \tag{4}$$

with $u(k+j-1) = u(k-1) + \sum_{i=1}^{j} \Delta u(k+i-1)$

where $\hat{y}(k+i)$ is the output prediction at time $k+i$, y_{sp} is the setpoint to the system output, $\Delta u = \left[\Delta u(k)^T \quad \Delta u(k+1)^T \quad \cdots \quad \Delta u(k+m-1)^T \right]^T$ is the vector of control moves, $\Delta u_{\max}$ is the upper limit to the control moves, m is the control horizon, p is the prediction horizon, and Q, R and R_u are diagonal weighting matrices of appropriate dimensions. Note that only the first element of the computed input sequence Δu is implemented in the plant, i.e. $u(k) = \Delta u(k) + u(k-1)$.

In this controller, the zone control strategy is implemented as follows: if the prediction of a given output is inside its reference zone or range, the error in this output is considered to be equal to zero and the output is not included in the controller optimization problem. When the output prediction lies outside the corresponding reference range, depending on whether the prediction is above or below the max or min values of this range, one of these bounds is adopted as the output reference. In general, the zone control strategy is used as an attempt to release some degrees of freedom to allow the inputs to approach their optimal targets (constraints pushing) and to smooth out the system response. For more details see Sotomayor et al. (2009).

The two-layer MPC algorithm as described above is similar to the structure of several MPC packages widely applied to control the refining and petrochemical processes. For instance, this MPC algorithm, with slight modifications, is supported by the advanced control package SICON@, which is the standard process control software in the oil refineries of PETROBRAS in Brazil.

3. INTERNAL EXCITATION APPROACHES

To solve the problem of lack of excitation during normal operation of MPC systems, some authors have proposed a new class of excitation methods for MPC that can be considered as internal excitation methods. Genceli & Nikolaou (1996) use the MPCI framework (model predictive control and identification) where the PE characteristic of the inputs is imposed as a constraint in the optimization problem related to the MPC. The drawback of this method is that the additional constraint is non-convex, resulting in a non-convex optimization problem. Since solving non-convex problems is significantly more involved than solving convex problems, the additional non-convex constraints are undesirable and the method cannot be directly applied to existing commercial MPC packages, without extensive modifications of the controller code, which limits its practical application.

On the other hand, a reasonable consideration of the layered MPC is that when the model is biased, the target calculation layer will change the input target to the dynamic layer quite often, and so, the input target could be viewed as a possible test signal. However, to assume that these natural moves on the input targets will be PE is a questionable matter. Here, taking advantage of the layered structure of MPC, and in order to guarantee the necessary excitation of the input targets, an external PE test signal, namely a binary signal of magnitude ± 1, is applied within the MPC control structure according to the following approaches:

Method 1. Introducing the test signal into the LP layer

Given that the weight vector W_1 in the objective function of the target calculation layer is usually available to be set on-line by the user of the MPC package, the external test signal can be introduced in the MPC system as a variable that multiplies W_1. Thus, Equation (1) is re-written as follows:

$$\min_{\Delta u_s, \delta_y} \left(W_{exc} \otimes W_1 \right)^T \Delta u_s + \left| W_2^T \delta_y \right| \tag{5}$$

subject to (2)

where W_{exc} is a vector whose elements are the components of the binary test signal and operator $\otimes$ denotes the Schur (or element-by-element) product. Then, if the product $W_{exc,i} W_{1,i}$ is positive (negative), the solution to the LP problem will tend to reduce (increase) input u_i until it reaches its lower (upper) bound or the output predictions lies outside the control zones. Note that if W_{exc} is set equal to a vector of ones, then the excitation procedure will end and the original objective function (1) is recovered. This method is described with details in Sotomayor et al. (2009).

Method 2. Introducing the test signal into the dynamic layer

In this case, the external test signal, conveniently scaled, is injected as a dither signal in the input target u_s that enters the MPC layer. This is similar to writing the objective function (3) as follows:

$$\min_{\Delta u} \sum_{i=1}^{p} \left\| Q\left(\hat{y}(k+i) - y_{sp} \right) \right\|_2^2 + \sum_{j=1}^{m} \left\| R \Delta u(k+j-1) \right\|_2^2 + \sum_{j=1}^{m} \left\| R_u \left(u(k+j-1) - (u_s + u_{s,dith}) \right) \right\|_2^2 \tag{6}$$

with $u_{s,dith} = \lambda W_{exc}$, subject to (4), where W_{exc} is the excitation vector as defined in Section 3.1 and λ is a scaling factor. Then, the achievement of excitation of the system will largely depend on the value of tuning parameter R_u, which will define if the MPC layer will implement the input target faster than the main process dynamics. Observe that if λ is set equal to zero, the excitation procedure is ended and the original cost function (3) is obtained.

Particularly, Method 1 can be easily implemented in existing MPC packages with a structure similar to the one detailed in Section 2, as the excitation signal is introduced through a tuning parameter of the controller. In both methods the MPC problem is still solved through a QP, and the problem is reduced to design the binary sequence for W_{exc} such that the on-line solution of the problems (5)-(2) and (6)-(4) produces persistent excited inputs, which is the primary requirement for the process identifiability (Ljung, 1999).

As it will be shown in the application section, with the approaches proposed here, the inputs can be adequately excited and if the outputs are controlled within zones, the feedback effect on the test data may be minimized. Also, the approaches attend the process safety requirements and the product specifications can be satisfied adequately.

In the next section it is illustrated the application of the proposed excitation procedures to the closed-loop identification of a depropanizer column. The identification procedure follows same steps as the usual identification methodology applied to industrial processes (Ljung, 1999): design of the test signal and generation of dataset, model structure selection, computation of the model parameters and model validation.

4. APPLICATION: DEPROPANIZER COLUMN

Figure 2 presents the process considered in this work. It is an industrial depropanizer column of the FCC unit at the PETROBRAS Refinery of Cubatão (RPBC), Brazil.

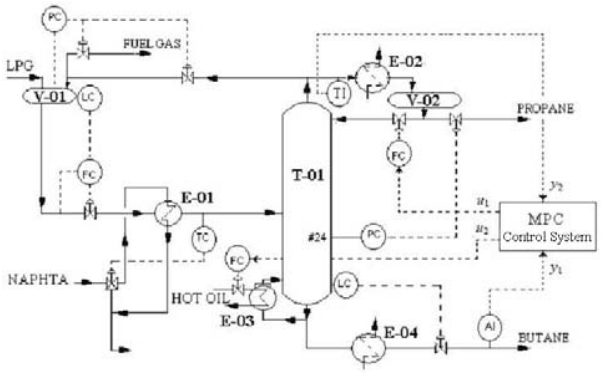

Fig. 2. Schematic diagram of the depropanizer column

In the depropanizer column, the C3 stream (propane and propene) is separated from a C4 stream (butane and butene). The operation of this process is controlled by a commercial MPC system as detailed in Section 2. Basically, it is a 2x2 control system, where the output variables y_1 and y_2 are the molar concentration (%) of C3 in the bottom stream and the temperature (°C) at the first stage of the top section of the column, respectively. The input variables u_1 and u_2 are the reflux flowrate to the top of the column (m^3/d) and the flowrate of hot oil to the reboiler (m^3/d), respectively. Transfer function models of order 2 corresponding to points FD and 1 from Porfirio et al. (2003) are used to simulate the "true" process and to represent the nominal process model (as it is used by the MPC system), respectively. MPC tuning parameters are here omitted but they can be found in Sotomayor et al. (2009).

PE test signal and generation of the dataset

Based on the guidelines provided by Zhu (2001) and a priori knowledge of the process (already existing model in the MPC), two independent GBN (generalized binary noise) (Tulleken, 1990) signals of magnitude ± 1 are designed. These test signals are applied directly to the LP layer of the MPC system if Method 1 is used or they are firstly scaled using $\lambda_1 = 0.065u_{s,1}$ and $\lambda_2 = 0.07u_{s,2}$, respectively, and applied to the MPC dynamic layer if excitation Method 2 is employed. In addition to the these excitation approaches, the system is also perturbed using a conventional external excitation as in MacArthur &. Zhan (2007). For this purpose, the MPC controller first calculates the normal movement for each controller output. New projected outputs are computed by superimposing a dither signal on the moves proposed by the controller. The projected outputs are then compared to the controller's high and low limits (constraints). Projected moves are then modified to ensure that all constraints are honored. In the present case, the dither signals are the GBN test signals scaled to ± 0.0034 and ± 0.0043, respectively. In all the cases, the duration of the excitation test is 4500 min. The data were collected with a sampling time of 1 min, resulting 4500 samples of input-output data.

For better identification results, the dataset is normalized, de-trended and filtered. Next, the dataset is divided into two subsets, where the first one containing 3000 data points is used to identify the model while the second one containing the remaining points is used to cross-validate the model. The PE characteristic of the inputs for the three cases is tested for order $\eta = 4$, which means that 2nd-order transfer functions can be satisfactory identified (Söderström & Stoica, 1989).

Model structure selection

In the present paper, it is considered that the model structure is defined by a continuous-time multi-input and single-output (MISO) output-error (OE) transfer function model, with the stochastic model parameterized as unitary:

$$\hat{y}_j(t,\rho_j) = \sum_{i=1}^{n_u} \hat{G}_{j,i}(s,\rho_{j,i})u_i(t) + \varepsilon_j(t), \quad j = 1,\cdots,n_y \quad (7)$$

where $\hat{G}_{j,i}(s,\rho_{j,i})$ is the (j,i)th transfer function defined as:

$$\hat{G}_{j,i}(s,\rho_{j,i}) = \frac{\hat{B}_{j,i}(s)}{\hat{A}_{j,i}(s)} = \frac{\sum_{k=0}^{m_{j,i}} \hat{b}_{j,i,k}s^k}{\sum_{k=0}^{n_{j,i}} \hat{a}_{j,i,k}s^k} e^{-s\hat{\theta}_{j,i}}$$

with $\hat{a}_{j,i,n_{j,i}} = 1$, $n_{j,i} \geq m_{j,i}$, where $u(t)$ is the input vector, $\hat{y}(t,\rho)$ is the model output, $\hat{\theta}_{j,i}$ is the estimated time-delay between the i_{th} input and the j_{th} output, $\varepsilon(t)$ is the residual or total model error (bias plus variance), n_u and n_y are the number of inputs and outputs, respectively, and $\rho_{j,i} = \left[\hat{b}_{j,i,m_{j,i}} \cdots \hat{b}_{j,i,0}\ \hat{a}_{j,i,(n_{j,i}-1)} \cdots \hat{a}_{j,i,0}\ \hat{\theta}_{j,i}\right]^T \in \mathbb{R}^{q_{j,i}}$, with $q_{j,i} = n_{j,i} + m_{j,i} + 2$, where $n_{j,i}$ and $m_{j,i}$ denotes the denominator and numerator orders of $\hat{G}_{j,i}(s,\rho_{j,i})$, respectively.

Computation of the model parameters

The goal is to build a model as defined in eq. (7) based on closed-loop sampled data, focusing on the parameters of each transfer function $\hat{G}_{j,i}(s,\rho_{j,i})$ rather than on the model error. Thus, the task of the identification procedure is to compute the vector of model parameters:

$$\rho_j = \left[\rho_{j,1}^T \cdots \rho_{j,nu}^T\right]^T \in \mathbb{R}^{q_j \times 1}, \quad q_j = \sum_{i=1}^{n_u} q_{j,i} \tag{8}$$

Here it is used the CONTSID toolbox (Garnier et al., 2008) to find the vector ρ_j for each closed-loop sampled dataset from the depropanizer column, assuming $n_u = n_y = 2$, $n_{j,i} = 2$ and $m_{j,i} = 1$. The identification is carried out off-line considering the values of the parameters of the existing (old) process model as the initial solution to the identification problem.

Three new models are obtained and they are evaluated based on the following performance criteria:

$$FIT = 100 \times \left(1 - \frac{norm(y_j - \hat{y}_j)}{norm(y_j - mean(y_j))}\right)$$

$$R_T^2 = 1 - \frac{\mathrm{var}\left(y_j - \hat{y}_j\right)}{\mathrm{var}\left(y_j\right)}$$

where y is the true system output and $\hat{y}$ the model output. Coefficient FIT indicates the percentage of the output variation that can be associated to the model, while coefficient R_T^2 measures how well the model output explains the behavior of the system output, and this parameter will be close to 1 in low noise conditions.

Model validation

Figure 3 shows the step response comparison between the old model and the new models obtained with the three excitation methods considered here. Observing the responses of the old model used in the controller and the new models obtained with the re-identification procedure, one may conclude that the re-identification of the process model is quite justified not only because of the difference between the gains of the old and new models, but also because of the different dynamics. Also, observing the responses of the re-identified models, one can confirm that the model obtained with excitation method 3 is, in general, inferior to the models obtained with the two other excitation methods, showing a significant bias on the gain of $\hat{G}_{2,1}$. Moreover, from a practical point of view, one may conclude that the internal excitation methods 1 and 2 can be considered equivalent in terms of the model that is obtained, particularly if the step response of the process is to be used as in several MPCs. This result is in concordance with the performance indicators obtained from the cross-validation procedure of the three new models (not presented here).

5. CONCLUSIONS

Three closed-loop excitation methods for systems being controlled by MPCs with a two layer structure were studied here. These excitation methods allow the closed-loop model re-identification that should be used for periodic MPC monitoring and maintenance and for the design of an explicit adaptive MPC. The first two methods are based on the introduction of a persistently exciting signal within the MPC structure. The third method corresponds to the traditional approach of adding the excitation signal to the controller output. The three methods showed equivalence in terms of producing a data set that is adequate for model identification. The main difference between the excitation methods lies in the implementation of the approach in practice. Method 1 introduces the excitation signal in the coefficients of the objective function of the target calculation layer which are usually available as tuning parameters of the controller. So, there is no need of any modification in the controller code and the method does not require any particular attention of the operator while the process excitation is performed. Thus, this method seems to be the most adequate in practical terms. Method 2 adds the excitation signal to the input target of the dynamic layer of the controller. Besides, some new tuning parameters this method requires a slight modification in the controller code and, consequently, can only be implemented if the source code is available. The third or conventional method, that adds the excitation signal to the output of the controller, requires more care in the design stage and more attention of the operator because the control action really injected in the process will not satisfy the process constraints.

REFERENCES

Conner, J.S., D.E. Seborg (2005). Assessing the need for process re-identification. *Industrial & Engineering Chemistry Research*, **44**(8): 2767-2775.

Forssell, U., L. Ljung (1999). Closed-loop identification revisited. *Automatica*, **35**(7): 1215-1241.

Garnier, H., M. Gilson, T. Bastogne, M. Mensler (2008). The CONTSID toolbox: A software support for continuous-time data-based modelling. In. H. Garnier & L. Wang (Eds.), *Identification of continuous-time models from sampled data*. Berlin: Springer.

Genceli, H., M. Nikolaou (1996). New approach to constrained predictive control with simultaneous model identification. *AIChE Journal*, **42**(10): 2857-2868.

Gugaliya, J.K., S.C. Patwardhan, R.D. Gudi, H. Raghavan, R. Yelchuru (2005). Model maintenance for industrial process control. In: *2005 AIChE Annual Meeting*, Cincinnati – OH.

Hjalmarsson, H. (2005). From experiment design to closed loop control. *Automatica*, **41**(3): 393-438.

Ljung, L. (1999). *System identification – Theory for the user* (2nd Ed.), Upper Saddle River, NJ: Prentice-Hall.

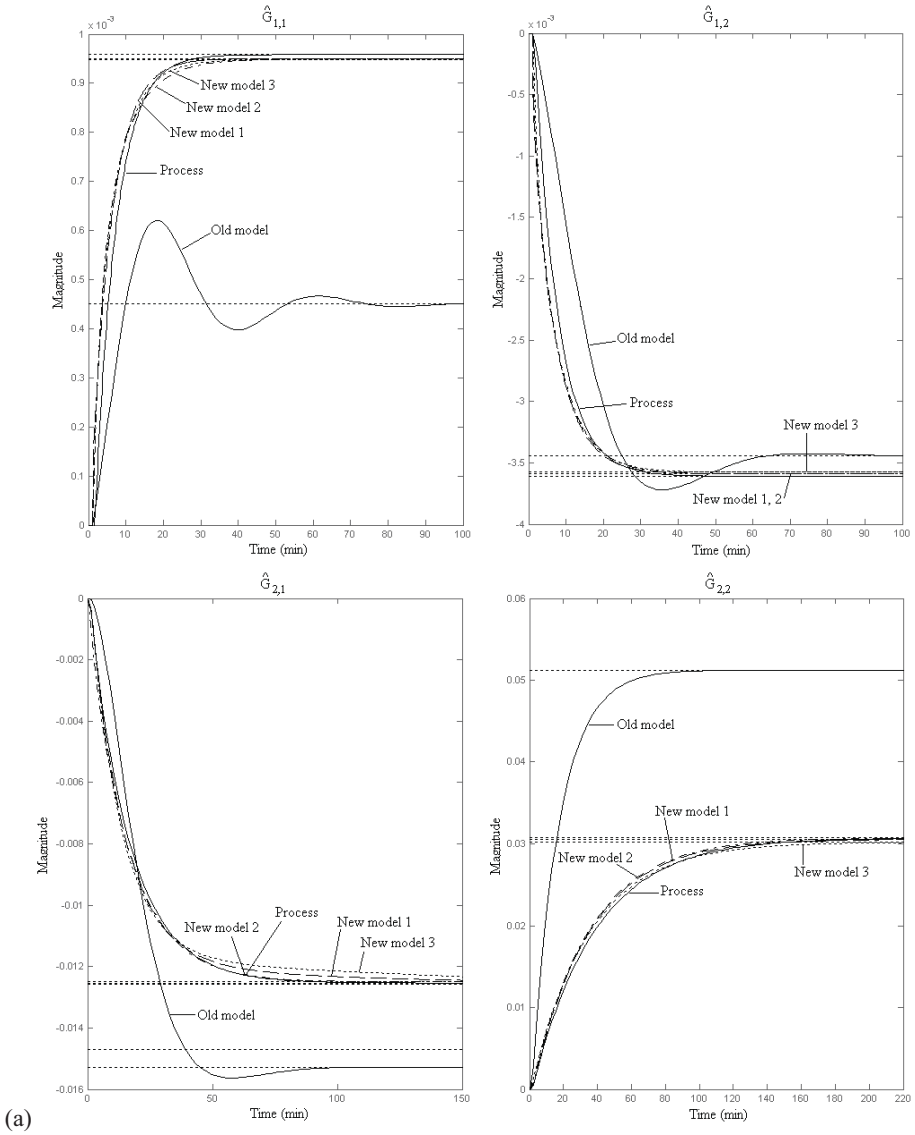

(a)

Fig. 3. Step response for the depropanizer column

MacArthur, J., C. Zhan (2007). A practical global multi-stage method for fully automated closed-loop identification of industrial processes. *Journal of Process Control*, **17**(10): 770-786.

Nikandrov, A., C.L.E. Swartz (2009). Sensitivity analysis of LP-MPC cascade control systems. *Journal of Process Contro,* **19**(1): 16-24.

Porfirio, C.R., E.A. Neto, D. Odloak (2003). Multi-model predictive control of an industrial C3/C4 splitter. *Control Engineering Practice*, **11**(7): 765-779.

Qin, S.J., T.A. Badgwell (2003). A survey of industrial model predictive control technology. *Control Engineering Practice*, **11**(7): 733-764.

Rivera, D.E., M.E. Flores (1999). "Plant-friendly" closed-loop identification using model predictive control. In: *1999 AIChE Annual Meeting*, Dallas – TX.

Söderström, T., P. Stoica (1989). *System identification*. Hemel Hempstead, UK: Prentice-Hall.

Sotomayor, O.A.Z, D. Odloak, L.F.L. Moro (2009). Closed-loop model re-identification of processes under MPC with zone control. *Control Engineering Practice*, **17**(5): 551-563.

Tulleken, H.J.A.F. (1990). Generalized binary noise test-signal concept for improved identification-experiment design. *Automatica*, **26**(1): 37-49.

Van den Hof, P.M.J. (1998). Closed loop issues in system identification. *Annual Reviews in Control*, **22**(1): 173-186.

Ying, C.-M., B. Joseph (1999). Performance and stability analysis of LP-MPC and QP-MPC cascade control systems. *AIChE Journal*, **45**(7): 1521-1534.

Zhu, Y. (2001). *Multivariable system identification for process control*. Oxford, UK: Elsevier Science Ltda.

Identification of Low Order Models for Large Scale Systems ⋆

Satyajit Wattamwar * **Siep Weiland** * **Ton Backx** *

* *All authors are with Dept. Of Electrical Engg. Technical University of Eindhoven, P.O. Box 513, 5600 MB Eindhoven, The Netherlands*

s.wattamwar@tue.nl

Abstract: In this paper we propose a novel procedure for obtaining a low order non-linear model of a large scale multi-phase, non-linear, reactive fluid flow systems. Our approach is based on the combinations of the methods of Proper Orthogonal Decomposition (*POD*), and non-linear System Identification (*SID*) techniques. The problem of non-linear model reduction is formulated as parameter estimation problem. In the first step POD is used to separate the spatial and temporal patterns and in the second step a model structure and it's parameters of linear and of non-linear polynomial type are identified to approximate the temporal patterns obtained by the POD in the first step. The proposed model structure treats POD modal coefficients as states rather than outputs of the identified model. The state space matrices which happens to be the parameters of a black-box to be identified, comes linearly in parameter estimation process. For the same reason, Ordinary Least Square (*OLS*) method is used to estimate the model parameters. The simplicity and reliability of the proposed method gives computationally very efficient linear and non-linear low order models for extremely large scale processes. The method is of generic nature. The efficiency of proposed approach is illustrated on a very large scale benchmark problem depicting Industrial Glass Manufacturing Process (*IGMP*). The results show good performance of the proposed method.

1. INTRODUCTION

Industrial processes involving fluid flows are usually modeled by Navier-Stoke's equations which are solved by some kind of spatial discretization. Due to this modeling approach they are referred to as Distributed Parameter Systems (DPS). Spatial discretization of DPS is done by means of Finite Volume or Finite Element methods and Galerkin or Petro-Galerkin projection techniques and they are simulated in a Computational Fluid Dynamic (CFD) software environment. Although such discretizations approximate the dynamic process behavior reasonably well, it leads to very large order process model. It takes huge computational efforts (time, CPU requirement) to simulate such models and therefore such process models can not be used for online plant optimization and control purposes. Model Order Reduction (MOR) is therefore an important step before proceeding to control design, see e.g. Shvartsman and Kevrekidis [1998]. The method of Proper Orthogonal Decomposition (POD) or Principle Component Analysis (PCA) is widely used for deriving lower dimensional models from the First Principle Model (FPM). The POD method searches for dominant patterns in the given process and defines an optimal, data-dependent basis, that is subsequently used as a projection space to infer reduced order models through Galerkin type of projections, see Astrid [2004] and the references therein. POD methods are empirical (data dependent) in nature and therefore these methods are susceptible to changes in process inputs and process parameters. The reduced model obtained by POD techniques with Galerkin projections are usually very dense and one loses the original sparse model structure. Such a dense model does not always give computational advantage over original full scale CFD model. This motivates one to look for other possible approaches which can give computationally efficient, reliable models which can be used for the online control and optimization purpose. Other motivations for the method proposed in this paper are that in many commercial CFD packages sometimes it becomes impossible to get access to the Partial Differential Equations (PDE) used to implement full scale model and even with access to the PDEs the reduced order modeling efforts can also be very expensive and laborious. In such situations one needs to explore the other possible ways to get a low order model by some identification method. One of such methods is explained in Wattamwar et al. [2008], which uses POD and system identification tools like N4SID algorithms, as explained in e.g. Overschee and Moor [1996], Favoreel et al. [2000]. But the method proposed there results in linear models which are not sufficient for approximating the non-linearities of large scale applications like IGMP. Moreover in the method proposed there, the states of the linear reduced order model have no physical meaning. These problems have motivated us to investigate another model reduction strategy which can approximate process non-linearity. The identification based approach proposed in this paper can be very useful, because it allows to use the available large-scale first principle based detailed non-linear process model in the form of commercial package, not just for the purpose of computationally extremely efficient dynamic

⋆ This work was supported by the European Union within the Marie-Curie Training Network PROMATCH under the grant number MRTN-CT-2004-512441.

process analysis but also for the purpose of design of the process controller and optimization. Therefore the method proposed here helps in minimizing the dependence on the expensive testing of the plant required for the controller design.

This paper is organized as follows. The overall methodology involving necessary tools from system theory like POD, a black-box type of system identification for linear and non-linear polynomial system is explained in section 2. The application/motivation is IGMP and is explained in the section 3. Some results of the proposed method on the motivation problem are presented in the section 4 which is followed by future work and references.

2. THEORY BACKGROUND AND METHODOLOGY

One of the most promising and successful techniques for an efficient reduction of large-scale nonlinear systems in fluid dynamics is the method of Proper Orthogonal Decompositions (POD) also known as the Karhunen-Loève method Holmes et al. [1996]. The method is based on the observation that flow characteristics reveal coherent structures or *patterns* in many processes in fluid dynamics. This has led to the idea that the solutions of model equations may be approximated by considering a small number of dominant coherent structures (called *modes* or *basis*) that are inferred in an *empirical* manner from measurements or simulated data. Given an ensemble of K measurements $\mathbf{T}^k(\cdot), k = 1, \ldots, K$ with each measurement defined on some spatial domain Ω, the POD method amounts to assuming that each observation $\mathbf{T}^k$ belongs to a Hilbert space $\mathcal{H}$ of functions defined on Ω. With the inner product defined on $\mathcal{H}$, it then makes sense to call a collection $\{\varphi_j\}_{j=1}^{\infty}$ an *orthonormal basis* of $\mathcal{H}$ if any element, say $\mathbf{T} \in \mathcal{H}$, admits a representation

$$\mathbf{T}(z) = \sum_{j=1}^{\infty} a_j \varphi_j(z), \quad z \in \Omega \tag{1}$$

Here, the a_j's are referred to as the *modal coefficients*(MC) and the φ_j's are the *modes* or *basis* of the expansion. The truncated expansion

$$\mathbf{T}_n(z) = \sum_{j=1}^{n} a_j \varphi_j(z), \quad z \in \Omega \tag{2}$$

causes an approximation error $\|\mathbf{T} - \mathbf{T}_n\|$ in the norm of the Hilbert space. We will call $\{\varphi_j\}_{j=1}^{\infty}$ a *POD basis* of $\mathcal{H}$ whenever it is an orthonormal basis of $\mathcal{H}$ for which the *total approximation error* in some norm over the complete ensemble is

$$\sum_{k=1}^{K} \|\mathbf{T}^k - \mathbf{T}_n^k\| \tag{3}$$

is minimal for all truncation levels n. This is an *empirical basis* in the sense that every POD basis depends on the data ensemble. Using variational calculus, the solution to this optimization problem amounts to finding the normalized eigenfunctions $\varphi_j \in \mathcal{H}$ of a positive semi-definite operator $R : \mathcal{H} \to \mathcal{H}$ that is defined as

$$\langle \psi_1, R\psi_2 \rangle := \frac{1}{K} \sum_{k=1}^{K} \langle \psi_1, \mathbf{T}^k \rangle \cdot \langle \psi_2, \mathbf{T}^k \rangle \tag{4}$$

with $\psi_1, \psi_2 \in \mathcal{H}$. R is well defined in this manner and corresponds to a positive semi-definite matrix whenever $\mathcal{H}$ is finite dimensional. In that case, a POD basis is obtained from the normalized eigenvectors of R, see e.g. Astrid [2004].

The POD modal coefficients 'a_j' are then obtained by the projection of the ensemble on the span of dominant POD modal coefficients as given by:

$$a_j(k) = \langle \varphi_j(z), \mathbf{T}_n(k, z) \rangle \tag{5}$$

Subsequently, a Galerkin projection is used to obtain the reduced order model as follows. Suppose that the system is governed by a PDE of the form

$$\frac{\partial T_n}{\partial t} = \mathcal{A}(T_n) + \mathcal{B}(u) + \mathcal{F}(T_n, u, d) \tag{6}$$

and let $\mathcal{H}_n$ denote an n dimensional subspace of $\mathcal{H}$ and let $P_n : \mathcal{H} \to \mathcal{H}_n$ and $I_n : \mathcal{H}_n \to \mathcal{H}$ denote the canonical projection and canonical injection maps or operators respectively. The injection map reconstruct the full scale model from reduced space. The reduced model is then given by

$$P_n \frac{\partial T_n}{\partial t} = P_n \mathcal{A}(T_n) + P_n \mathcal{B}(u) + P_n \mathcal{F}(T_n, u, d) \tag{7}$$

where observation $T_n(\cdot, k) = \mathbf{T}_n(k) \in \mathcal{H}_n = P_n \mathcal{H} \quad \forall k$, $\mathcal{A}$ is the spatial operator for convection and diffusion, and is of linear nature $\mathcal{B}$ defines input matrix and $\mathcal{F}$ is nonlinear source term. In the specific case of a POD basis, the finite dimensional subspace $P_n = \text{span}\{\varphi_j\}$, $j = 1, \ldots, n$ where the φ_j's denote POD basis functions. In that case eq. (6) becomes an *ordinary differential equation* in the coefficients $a_j(k)$ in the expansion of T_n as eq. (8) and eq. (9)

$$\frac{\partial \langle P_n, \mathbf{T}_n \rangle}{\partial t} = \mathcal{A}\langle P_n, \mathbf{T}_n \rangle + \mathcal{B}\langle P_n, u \rangle + P_n \mathcal{F}(T_n, u, d) \tag{8}$$

or equivalently,

$$\frac{da_n}{dt} = \mathcal{A}_n a_n + \mathcal{B}_n u + P_n \mathcal{F}(P_n^{-1} a_n, u, d) \tag{9}$$

Eq. (9) is reduced order model (ROM) and the POD modal coefficients 'a_j' are the states of the ROM. Therefore the POD MC can also be viewed as *dominant temporal patterns/dynamics* along which system evolves. The optimization problem to obtain POD basis as mentioned above in eq. (4) equivalently can also be solved for the ensemble $\mathbf{T}_n$ as a 'Singular Value Decomposition' *SVD* which then gives POD basis function (*spatial patterns*) in the form of left singular vectors and POD modal coefficients (*temporal patterns* as singular values multiplied by the right singular vectors. From the property of SVD these patterns are arranged as per their importance, i.e. the first POD basis corresponds to the direction of maximum energy. Usually a tolerance criterion based on amount of energy captured in the reduced model is used to decide the order or the reduced model, i.e. the span of POD basis as defined above in $\mathcal{H}_n$. The criterion is usually called projection energy and is given as below:

$$P_{tol} = \frac{\sum_{k=1}^{r} \lambda_k}{\sum_{k=1}^{n} \lambda_k} \tag{10}$$

where λ_k is the 'k^{th}' eigenvalue of the correlation operator as defined in eq. (4), 'r' is order of ROM and 'n' is order of finite dimensional full scale model. The first two terms of

eq. (9) on RHS are linear and the third non-linear term do not appear for the systems defined by linear PDEs. For the system governed by linear PDEs the differential equation eq. (9) can be transformed in equivalent discrete time form as:

$$a_n(k+1) = A_d a_n(k) + B_d u(k) \tag{11}$$

At this point one can observe that given the ensemble $\mathbf{T}_n$ one can obtain POD basis and corresponding MC, and from this knowledge of MC and system inputs 'u' the system parameters 'A_d' and 'B_d' can be easily estimated by ordinary least square (OLS) estimation techniques. If one now think of the possible approach to identify the system parameters when the governing equations are non-linear like the one in eq. (9), one needs then some approximation for non-linear terms. There are many possible ways to approximate the non-linearities like black-box, neural net, fuzzy logic, grey box, e.g. see Romijn et al. [2008] and many other input-output based fit of Weiner-Hammerstein type. It is also well known that Taylor series expansion of a nonlinear function can be a good approximation of a non-linear function. The use of Taylor Series is not considered in usual input-output identification methods due to the lack of state information. But as explained earlier in the case of model reduction, the states of ROM are accessible and therefore one can make use of Taylor series to approximate the non-linear terms. If one is interested in approximating the original full scale non-linear model then one need to include the Jacobian terms of the Taylor series in ROM. But if the approximation by linear system is not sufficient enough then one must consider the Hessian and other higher terms from the Taylor series. Note that the inclusion of the Hessian terms results into polynomial form of the identified ROM. Replacing the non-linear part by a polynomial system for multi-variable system is cumbersome due to the involvement of the tensor algebra (*Hessian computation*). For this reason we will briefly explain what does a Taylor series expansion for a scalar valued function means and then we will explain it for the vector valued function, and its implementation for the computation purpose. Another interesting feature of he polynomial systems is that they are promising candidates and have structure better suited for analytical analysis and for extension of the notions from linear system theory, e.g. see Ebenbauer et al. [2005]. For a scalar valued function,

$$\dot{x} = f(x)\,, \text{ where } f : \mathcal{R} \to \mathcal{R} \;\; \& f(x^*) = 0 \tag{12}$$

Taylor series expansion in x as a nominal variable and $\tilde{x}$ as a deviation variable, $\tilde{x} = x - x^*$

$$\dot{\tilde{x}} = f(x^*) + f^{'}(x^*)\,\tilde{x} + (1/2!)\,f^{''}(x^*)\,\tilde{x}^2 + ... \tag{13}$$

where, $f^{'}(x) = \mathcal{J}(x) : \mathcal{R} \to \mathcal{R}$, system jacobian operator
$f^{''}(x) = H(x) \; : \mathcal{R} \to \mathcal{R}$, system Hessian operator.
For a vector valued function $f : \mathcal{R}^n \to \mathcal{R}^n$,

the first derivative is defined as a map: $f^{'} : \mathcal{R}^n \to \mathcal{L}(\mathcal{R}^n, \mathcal{R}^n)$, and when the first derivative is evaluated at $x^* \in \mathcal{R}^n$ then $f^{'}(x^*) \in \mathcal{L}(\mathcal{R}^n, \mathcal{R}^n)$, i.e. $f^{'}(x^*)$ is a linear operator, and when it acts on the 'n' dimensional vector 'x' then its image is $\in \mathcal{R}^n$, i.e. $f'(x^*)(x) \in \mathcal{R}^n$. This lets us to understand first derivative as a map, $f' : \mathcal{R}^n * \mathcal{R}^n \to \mathcal{R}^n$. As $f'(x^*)$ is constant term (fixed operator), we better write it as $[f'(x^*)](x) \in \mathcal{R}^n$.

We usually refer the above operator as system Jacobian matrix as, $[f'(x^*)] := \mathcal{J}(x^*)$.

The operator defined in the last expression can be written in terms of partial derivatives as,

$$[f'(x^*)]\,(x) = \begin{bmatrix} \dfrac{\partial f_1}{\partial x_1}(x^*) \ldots \dfrac{\partial f_1}{\partial x_n}(x^*) \\ . \\ \dfrac{\partial f_n}{\partial x_1}(x^*) \ldots \dfrac{\partial f_n}{\partial x_n}(x^*) \end{bmatrix} \begin{bmatrix} x_1 \\ . \\ . \\ . \\ x_n \end{bmatrix} \tag{14}$$

equivalently,

$$[f^{'}(x^*)](x) = \begin{bmatrix} \displaystyle\sum_{k=1}^{n} \frac{\partial f_1(x^*)}{\partial x_k} x_k \\ . \\ \displaystyle\sum_{k=1}^{n} \frac{\partial f_n(x^*)}{\partial x_k} x_k \end{bmatrix} \tag{15}$$

The same procedure is repeated for computing the second derivative of the function,

$f'' : \mathcal{R}^n * \mathcal{R}^n * \mathcal{R}^n \to \mathcal{R}^n$, i.e.
$f'' : \mathcal{R}^n \to \mathcal{L}(\mathcal{R}^n, \mathcal{L}(\mathcal{R}^n, \mathcal{R}^n))$, i.e.
$f''(x^*) \in \mathcal{L}(\mathcal{R}^n, \mathcal{L}(\mathcal{R}^n, \mathcal{R}^n))$, i.e.
$f''(x^*)(x) \in \mathcal{L}(\mathcal{R}^n, \mathcal{R}^n)$, i.e.
$f''(x^*)(x)(x) \in \mathcal{R}^n$, i.e. $[f''(x^*)](x, x) \in \mathcal{R}^n$
$[f''(x^*)] := H(x^*)$, system Hessian operator.

It is clear from the above discussions that the Hessian operator is a tensor with argument from two domains while its codomain remains the same that of the Jacobian operator. The linearity of Hessian operator allows us to compute it like the Jacobian operator as in (15), but now with one more argument as:

$$[f^{''}(x^*)](x, x) = \begin{bmatrix} \displaystyle\sum_{k=1}^{n}\sum_{j=1}^{n} \frac{\partial^2 f_1(x^*)}{\partial x_k \partial x_j} x_k x_j \\ . \\ \displaystyle\sum_{k=1}^{n}\sum_{j=1}^{n} \frac{\partial^2 f_n(x^*)}{\partial x_k \partial x_j} x_k x_j \end{bmatrix} \tag{16}$$

the above expression can be written as:

$$[f^{''}(x^*)](x, x) = A_1(x \otimes x) \tag{17}$$

where, $(x \otimes x)$ is the Kroneckar product.

The complete simplification procedure mentioned above is aimed to express, $f'' : \mathcal{R}^n \to \mathcal{L}(\mathcal{R}^n, \mathcal{L}(\mathcal{R}^n, \mathcal{R}^n))$ as, $f'' : \mathcal{R}^n \to \mathcal{L}(\mathcal{R}^{n^2}, \mathcal{R}^n)$. This is possible due to the notion of the linearity of the tensor operator.

From the discussion above, a nonlinear equation of the form $\dot{x} = f(x, u)$ can be expanded in Taylor series as in (13) which can be approximated by a polynomial of the form,

$$\begin{aligned} \dot{x} =& Ax(t) + Bu(t) + A_1(x(t) \otimes x(t)) \\ &+ B_1(u(t) \otimes u(t)) + Q(x(t) \otimes u(t)) \end{aligned} \tag{18}$$

Where, A_1, B_1, Q are equivalent Hessian operators and $x \in \mathcal{R}^n$, $u \in \mathcal{R}^l$, $A \in \mathcal{R}^{n*n}$, $B \in \mathcal{R}^{n*l}$, $A_1 \in \mathcal{R}^{(n*n)*n}$, $B_1 \in \mathcal{R}^{(l*l)*n}$, $Q \in \mathcal{R}^{(l*n)*n}$ and $\otimes$ is the Kronecker products.

These methodological developments are based on CFD software as plant model, so for the moment we are not considering the output equations here.

Equivalent discrete form of Eq. (18) can be written as:

$$x(k+1) = A_d x(k) + B_d u(k) + A_{1d}(x(k) \otimes x(k)) + B_{1d}(u(k) \otimes u(t)) + Q_d(x(k) \otimes u(k)) \quad (19)$$

As we are considering the discrete identification problem here, for the convenience in remaining part of the paper we have dropped the superscript 'd' from eq. (19).

Please note that the polynomial equation (19) is non-linear in states and inputs but it is linear in all the system parameters (equivalent Jacobian and Hessian terms). This is a big advantage. Because if the states and inputs are known then by fixing the above polynomial model structure we can estimate the system parameters by Least Square parameter Estimation (LSE) techniques.

Coming back to the problem of the reduced model identification, the states in the (18) can be seen as POD modal coefficients (MC) and then linear and non-linear part in (9) can be written as (18).

Another interesting feature of the proposed framework is that for a large scale parameter varying systems, given the knowledge of the variation of the time varying parameter, similar approach as proposed above can be used. But the uncertain parameter should then be treated like process inputs and therefore the corresponding process snapshots due to the parameter excitation need to be included while computing the POD basis functions and MCs. As per the knowledge of the author, this approach of model reduction for very large scale process under process parameter uncertainty is never studied in past.

Once the MC and POD basis are obtained from the full scale CFD model as mentioned earlier, then by using the tensors decomposition as in eq.(16) for eq.(18), the problem of polynomial model parameter estimation is an ordinary least square estimation(*OLS*) problem and if we define,

$$\xi_k := col\,(x(k), u(k), (x(k) \otimes x(k)), (x(k) \otimes u(k)), (u(k) \otimes u(k))) \quad (20)$$

then from (19), $x_{k+1} \simeq \Theta\,\xi_k$ Where, $\Theta = [A\,B\,A_1\,B_1\,Q]$ and define the parameter estimation error at each time instance as

$$e_{k+1} = x_{k+1} - \Theta\,\xi_k \quad (21)$$

similarly the estimation error that is minimized by LSE method over the complete simulation horizon 'N' is

$$E := [x_1 \dots x_N] - \Theta[\xi_0 \dots \xi_{N-1}] \quad (22)$$

equivalently, $E := X - \Theta\Xi$
where, N is the number of samples and , $X \in \mathcal{R}^{n*(N-1)}$, $\Xi \in \mathcal{R}^{(n+l+n*n+l*l+n*l)*(N-1)}$ and $\Theta \in \mathcal{R}^{n*(n+l+n*n+l*l+n*l)}$

The least square solution will be

$$\Theta = X\,\Xi^T\,(\Xi\,\Xi^T)^{-1} \quad (23)$$

Please make a note here that the system parameter vector Θ is rank deficient due to the involved Kronecker product. Nevertheless, there are some simple ways to estimate the parameters for rank deficient problem as well. We simply used *Matlab* routines for our case.

The complete CFD spatio-temporal information can be reconstructed by projecting back the solution of reduced model (19) on the span of dominant POD basis P_n. The reconstructed CFD state space will be:

$$\tilde{\mathcal{I}}_n(k) = I_n\,a_n(k) = P_n^{-1}\,a_n(k), \text{or equivalently} \quad (24)$$

$$\tilde{\mathcal{I}}_n(k) = \sum_{j=1}^{r} \phi_j^{-1}\,a_j(k) \quad (25)$$

As this study is based on software simulations, the outputs can be chosen as per the user choice. In our study we have decided them close to the real life situation. The constructed output equations can be approximated as:

$$\tilde{y}(k) = C\,\tilde{\mathcal{I}}_n(k) \quad (26)$$

Note that the original Navier-Stokes equation (*non-linear PDEs*) modeled in CFD software are continuous in time and in the approach presented above we have proposed to approximate them by using discrete time linear or polynomial type non-linear equations.
The error involved here will be the sum of projection error and the statistical fit in the identification step to the few selected POD modal coefficients corresponding to the maximum energy content as per eq. (10).

One of the serious drawbacks of this approach is that the OLS estimation method for as described earlier can easily lead to an unstable system, although the original system could be a stable one. Notion of stability is discussed here as divergence of simulation results. We think one of the possible explanation could be the small data set, another could be that the POD MC obtained from SVD are right singular vectors and they are orthonormal vectors. These Orthonormal basis functions (MC) are considered as signals while they are being fitted by using a polynomial model. The orthogonality of vectors is equivalent to the property of uncorrelatedness of signals. Or, orthogonality of MC in terms of the inner product is

$$< a_i,\, a_j > \begin{cases} = 1, & i = j \\ = 0, & i \neq j \end{cases} \quad (27)$$

To overcome this drawback of spurious instability one might like to try some other parameter estimation method or to impose the stability in the proposed polynomial model by using some regularization trick. But usually regularization leads to bad performance of the identified model. Moreover regularization if not carried out smartly can lead to completely different dynamics of the identified model. Typically in subspace state space linear model identification techniques, regularization is imposed in the form of forcing the eigenvalues of the identified model to lie in the unit circle, e.g. see Gestel et al. [2000].
In this paper we have not solved the stability issue as the research in polynomial systems is still relatively new and imposing the stability in identification procedure will need considerable amount of further efforts.

3. MOTIVATION: GLASS MANUFACTURING

This section describes the motivating example of Industrial Glass Manufacturing Process, *IGMP*. IGMP is usually carried out in large furnaces which are very well designed in order to have a desired laminar flow pattern of the glass. A 2D view of a typical furnace is shown in figure 1. The flow pattern of glass determines the residence time of the glass in the melting furnace which in turn determines the quality of the glass produced. The process is an example of very large scale integrated systems. Most of the process variables like temperature, velocity, pressure, viscosity are

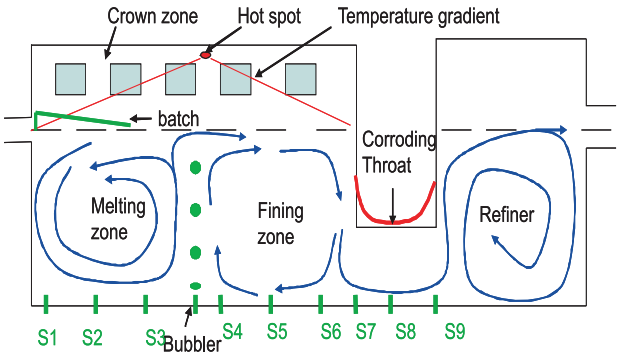

Fig. 1. Glass Manufacturing Furnace

interacting with each other. Due to this interacting nature the control of the furnace has to be done carefully. Usually pull rate (production rate), heat input and pressure valve positions are some of the control variables. Whereas variables of interest are temperature distribution and velocity profiles in the furnace. The product quality is determined by these two factors. The temperature maintained inside the furnace varies between $1400 - 1650\ ^0$C. The glass raw material enters from the left side (inlet) in the form of a batch blanket, it is melted by applying heat from the top. After circulating through the glass furnace for many hours glass passes through the throat and then leaves via the outlet. Based on the process operation there are roughly three regimes - glass melting, fining to remove high concentration of dissolved gases from the molten glass and refining to remove all remaining undissolved gases from the glass. The IGMP shows large variation in the time constants, from minutes to days. The transport of physical quantities in IGMP can be approximated with reasonable accuracy by modeling it by a set of nonlinear Navier-Stokes equations, see Huisman [2005]. There are many different types of glass furnaces and many different ways to manufacture glass depending on the type of glass required. Most of the glass manufacturing process dynamics are series combination of Continuous Stirrer Tank Reactor (CSTR) and Plug Flow Reactor (PFR). Some more details about mathematical modeling of glass can be found in Huisman [2005], Patankar [1980], Post [1988].

Due to very high process temperature and due to the viscous nature of glass, the glass furnace is a hostile environment for sensor systems. Sensors are largely limited to temperature measurements in the bottom refractory of the melting furnace. As 3 dimensional glass furnace model easily consist of $10^4 - 10^6$ finite elements, simulating its steady and/or dynamic behavior takes days for a normal configured PC and therefore it becomes very difficult to generate and process sufficient data that can be used to develop a model reduction method. For this reason we are using an approximate $2D$ glass furnace which mimics the vertical cross section along the length of $3D$ glass furnace and has only 2 grids cells in width direction.

Currently, apart from modeling the process non-linearity in the reduced order model, we are also trying to model the very slow geometric changes that take place in real $3D$ furnace in the form of throat or dam wall corrosion, see figure 1. This corrosion results into back-flow of molten glass from the refining zone to the fining zone. Such back-flow behavior causes undesired changes in the temperature distribution in the furnace which ultimately leads to economic losses. In this paper we are not addressing the corrosion problem but interested readers can refer Wattamwar et al. [2008] and a Linear Parameter Varying (LPV) system approximation in Wattamwar et al. [2009].

4. RESULTS AND DISCUSSION

In this paper a $2D$ benchmark CFD model of the original process is considered. The full scale CFD model has 3000 cells. It has many variables like temperature, velocity, concentration, pressure, etc. in each grid cell. Although most of the variables are interconnected, for the study here we have considered only temperature as variable of the interest. Therefore the order of the full scale model is 3000. From the method explained in the section 2 we have obtained a fourth order linear and non-linear polynomial model. The choice of fourth order approximation is decided based on the stability issue of polynomial model. Approximation order larger than four leads to an unstable ROM. For the linear model as well, there is not much improvement in the parameter fit above fourth order. This means that for the linear reduced model larger than fourth order there is no way to improve its performance merely by increasing its order, and there is need for non-linear reduced order model. The four POD modal coefficients corresponding to the order approximately capture 80% of the total projection energy. Usually it is desired to capture approximately 99% of the energy of the full model. But due to the stability limitation we can not satisfy this requirement.

The input considered for the identification purpose is pull-rate(feed) in terms of tons/day, which varies 5% around the nominal value in the form of +/- steps superimposed by PRBS signal. This is done to excite the slow and fast dynamics. The simulation horizon is 120 hrs and sampling time is 16 mins, therefore we have 450 snapshots. Like most of the POD related methods, this identification process is very sensitive to the type of input excitation signal. For such complex process it is also very important to know what non-linearity the identification input signal excites. If one excites soft non-linearities for such a complex process then one can expect to get a better and stable polynomial model which would fit more POD MC.

Figure 2 shows the identification result for both linear and polynomial models as proposed in this paper. Figure 3 shows zoomed version of the faster dynamics from the figure 2. Plot shows the result for four outputs which are temperature at the bottom of the four main zones of the glass, viz. Melting, Fining, Throat and Refining section. The sensors are assumed to be placed at the bottom of the tank. This is close to the real life situation. The readers can refer to the figure 1 for sensor locations. $S1$ to $S9$ are the sensors in the figure. Plot shows that the both the models approximates the overall trend very well, but the linear model fails to capture the PRBS signal dynamics precisely compared to the polynomial model.

Figure 4 shows the performance of the two models for the validation signal, which is a step input on the raw-material feed rate. Plot shows that both models follows the trend very well, but both models do not match the time constant and the final gain exactly. This is due to the two reasons. First, this is a distributed system and the

excitation signal used for the identification was designed based on the average time constant of the whole glass tank and it was not designed based on only the four location shown in the figure. Reason for the mismatch of the final gain is that these ROM could not capture 99% of the projection energy of the full scale model. One can expect smaller offset if the approximation order of the reduced model is higher. Unfortunately, as explained earlier in 2, approximation order can not be increased more than 4^{th} for the polynomial form of ROM. Nevertheless, for the size and involved complexity in GMP, even the current results seems to be very interesting.

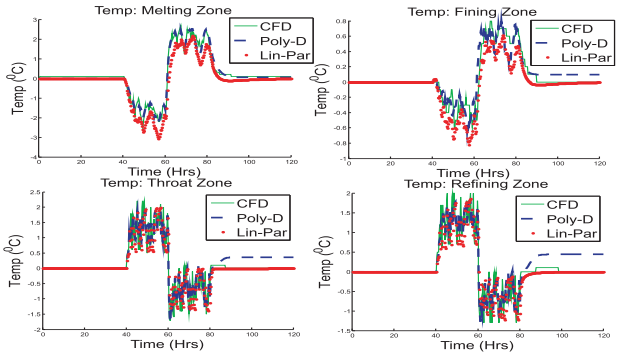

Fig. 2. Model Identification

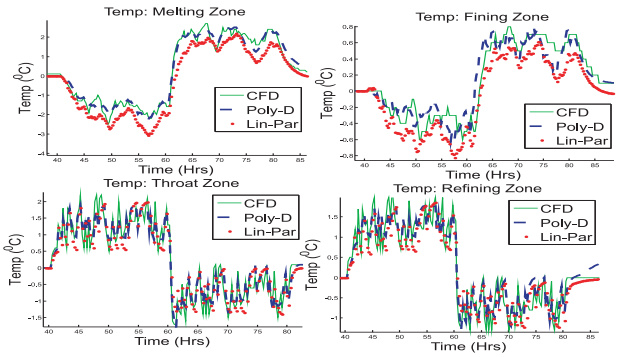

Fig. 3. Model Id: Zoom

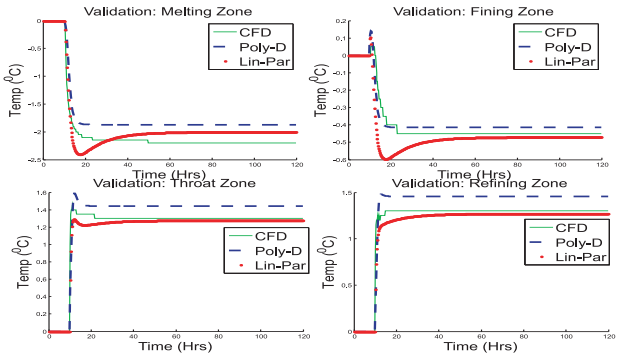

Fig. 4. Model Validation

5. CONCLUSION AND FUTURE RESEARCH

In this paper we have proposed a new model reduction method and its application on large scale industrial application. The proposed method is promising and suited especially for the very large scale processes where complexity reduction by using merely physical insight is not possible. The proposed method is also well formulated in technical aspects and with further improvements in imposing the stability in the identification of polynomial system could make this method of great potential.

We want to explore following topics in near future which has never/rarely been explored in literature like:
1. To investigate the possibility of imposing the stability in the identification process for the polynomial systems.
2. It is also possible to identify multiple linear/polynomial ROM at different working points by the method explained in this paper and construct a non-linear LPV ROM like the one described in Wattamwar et al. [2009].
3. Observer and controller design for polynomial ROM.

REFERENCES

P. Astrid. *Reduction of Process Simulation Models- A proper Orthogonal Decomposition Approach*. PhD report, Technical University of Eindhoven, 2004.

C. Ebenbauer, R. Renz, and F. Allgower. Polynomial feedback and observer design using nonquadratic lyapunov function. *Conference on Decision and Control*, 2005.

W. Favoreel, B. D. Moor, and P. Van Overschee. Subspace state space system identication for industrial processes. *Journal of Process Control*, 10:149–155, 2000.

T. V. Gestel, J. A. K. Suykens, P. V. Dooren, and B. De Moor. Imposing stability in subspace identification by regularization. *Proceedings of IEEE-CDC*, 2000.

P. Holmes, J. L. Lumley, and G. Berkooz. *Turbulence, cohorent structures, dynamical systems and symmetry*. Cambridge University Press: In Cambridge monograph on mechanics, 1996.

L. Huisman. *Control of Glass Melting Processes based on Reduced CFD Models*. PhD report, Technical University of Eindhoven, 2005.

P. Van Overschee and B. De Moor. *Identication for Linear Systems: Theory, Implementation, Applications*. Kluwer Academic, Dordrecht, The Netherlands, 1996.

S.V. Patankar. *Numerical Heat Transfer and Fluid Flow*. Hemisphere, 1980.

L. Post. *Modeling of Flow and Combustion in a Glass Melting Furnace*. PhD report, Technical University of Delft, 1988.

R. Romijn, L. Ozkan, S. Weiland, W. Marquardt, and Ludlage J. A grey-box modeling approach for the reduction of nonlinear systems. *Journal of Process Control*, 18(9):906–914, 2008.

S. Y. Shvartsman and I. G. Kevrekidis. Nonlinear model reduction for control of distributed parameter systems: A computer assisted study. *AIChE Journal*, 44(7):1579–1595, 1998.

S. Wattamwar, S. Weiland, and T. Backx. Identification of low dimensional models for slow geometric parameter variation in an industril glass manufacturing process. *Proceedings of IEEE MSC (CCA)*, 2008.

S. Wattamwar, S. Weiland, and T. Backx. Identification of low dimensional parameter varying models for large scale systems. *sent to the Proceedings of IFAC SYSID*, 2009.

Identification of Nonlinear State-Space Models: The Case of Unknown Model Structure

R.Bhushan Gopaluni *

* *Department of Chemical and Biological Engineering, University of British Columbia, Vancouver, BC, Canada V6T 1Z4, Email: gopaluni@chml.ubc.ca.*

Abstract: This article presents an algorithm for identification of nonlinear state-space models when the "true" model structure of a process is unknown. In order to estimate the parameters in a state-space model, one needs to know the model structure and have an estimate of states. An approximation of the model structure is obtained using radial basis functions centered around a *maximum a posteriori* estimate of the state trajectory. A particle filter approximation of smoothed states is then used in conjunction with expectation maximization algorithm for estimating the parameters. The proposed approach is illustrated through an example.

Keywords: Nonlinear Systems, Maximum Likelihood Parameter Estimation, Expectation Maximization, Particle Filters.

1. INTRODUCTION

Nonlinear models are commonly used to describe the behavior of many chemical processes. Process variables, typically, can be divided into latent variables (that are not measured) and measured variables. A combination of latent and measured variables can be elegantly used to represent the dynamic behavior of a nonlinear process in the following form,

$$\begin{aligned} x_{t+1} &= f(x_t, u_t, \theta) + w_t \\ y_t &= g(x_t, u_t, \theta) + v_t \end{aligned} \tag{1}$$

where $x_t \in \mathbf{R}^n$ is the n-dimensional state vector, $u_t \in \mathbf{R}^s$ is the s-dimensional input vector, $y_t \in \mathbf{R}^m$ is the m-dimensional output or measurement vector, and w_t, v_t are independent and identically distributed Gaussian noise sequences of appropriate dimension and variances Q and R respectively, $\theta \in \mathbf{R}^p$ is a p-dimensional parameter vector and $f(.)$, $g(.)$ are some nonlinear functions that describe the dynamics of the process. The nonlinear functions $f(.)$ and $g(.)$ are typically obtained using physical laws such as energy and mass balance expressions for the process. However, often, due to the complexity of chemical processes, it is difficult to develop accurate and reliable nonlinear functions. This article provides an algorithm for approximation and estimation of $f(.)$ and $g(.)$ using a combination of radial basis functions and Expectation Maximization (EM) algorithm Shumway and Stoffer (2000).

The complexity of the parameter estimation problem considered in this article arises due to unknown nonlinearities, and presence of unmeasured latent variables. If the latent variables are measured, then the model parameters can be estimated using a straightforward nonlinear least squares method Ljung (1999). If the process dynamic functions are linear, then any sub-space approach can be used Van Overschee and Moor (1996). On the other hand, if the process dynamic functions are nonlinear and latent variables are not measured, then approximate maximum likelihood approaches such as the one based on local linearization in Goodwin and Agüero (2005) and the one based on particle filter approximation in Gopaluni (2008) can be used.

The algorithm presented in this article extends the one in author's previous work on parameter estimation for known model structure Gopaluni (2008). The central idea is to find the parameter vector, θ, that maximizes the likelihood function of the observations, y_t. Due to the presence of latent variables, x_t, it is difficult to develop this likelihood function. On the other hand, due to Markov property of latent variables, it is rather straightforward to develop a joint likelihood function of the the latent and measured variables. Hence, expectation maximization, a maximum likelihood approach, that iteratively maximizes the likelihood of the observations by maximizing the joint likelihood function in each iteration, is used. EM algorithm is implemented by iteratively finding the expected value of the joint likelihood function in the first step and maximizing it in the second step Dempster et al. (1977).

This approach using EM algorithm for parameter estimation poses two problems. A structure of the process model (or in other words, the functions $f(.)$ and $g(.)$), and the distribution of noise sequence is needed to develop the joint likelihood function required in EM algorithm. Moreover, since the process is nonlinear, the distribution of latent variables, x_t, and measurements is not Gaussian even if Gaussian noise is assumed. As a result, the expected value of the joint likelihood function required in EM algorithm can not be analytically calculated. In this article, an approach that uses radial basis functions to approximate the process dynamics and particle filters to approximate the expected value of the joint likelihood function is presented.

The rest of this paper is divided into following sections: The problem is mathematically defined in section 2, a summary of expectation maximization algorithm is presented in section 3, the proposed algorithm is presented in section 4, and an example is presented in section 5.

2. PROBLEM DEFINITION AND NOTATION

As explained in the previous section, it is assumed that the process dynamics are unknown and therefore an approximation of the dynamics is needed to apply EM algorithm. It is well-known that any function can be approximated to an arbitrary degree of accuracy using basis functions such as radial basis functions. Hence, the model in (1) is approximated using radial basis functions as follows:

$$x_{t+1} = \sum_{i=1}^{I_x} h_i \rho_i(x_t, u_t, c_i, \Sigma_x) + Ax_t + Bu_t + w_t$$

$$y_t = \sum_{i=1}^{I_y} g_i \gamma_i(x_t, u_t, d_i, \Sigma_y) + Cx_t + Du_t + v_t$$

where $\rho_i(.,.)$ and $\gamma_i(.,.)$ are the radial basis functions centered around c_i and d_i with variance Σ_x and Σ_y respectively, A, B, C, D are appropriate matrices that are used to capture any linear dynamics in the model. w_t, and v_t are identically and independently distributed Gaussian noise sequences with zero mean and covariances Q and R respectively. h_i and g_i are constant vectors of appropriate dimensions. I_x and I_y are the number of basis functions used in the state and observation equations. Theoretically, even linear dynamics in the process can be approximated if sufficiently large number of radial basis functions are used. In order to reduce the total number of parameters, and capture linear dynamics, linear terms involving the matrices A, B, C, and D are added. In this article, radial Guassian basis functions of the following form are used:

$$\rho_i(x_t, u_t, c_i, \Sigma_x) = e^{\left[-(\bar{x}_t - c_i)^T \Sigma_x^{-1} (\bar{x}_t - c_i)\right]}$$

$$\gamma_i(x_t, u_t, d_i, \Sigma_y) = e^{\left[-(\bar{x}_t - d_i)^T \Sigma_y^{-1} (\bar{x}_t - d_i)\right]}$$

where $\bar{x}_t$ is the concatenated vector of states and inputs. The input-output data from the nonlinear model in (1) are denoted by $\{y_{1:T}, u_{1:T}\}$, where $y_{1:T}$ are the observations from time, $t = 1$, to $t = T$, and $u_{1:T}$ are corresponding inputs during that time period. The parameter vector θ includes all the constant parameters in the above model that describe the process behavior, and is defined as $\theta = (\theta_l, \theta_{nl})$, where θ_l consists of all "linear" parameters, h_i, g_i, Q and R, and θ_{nl} consists of all "nonlinear" parameters, c_i, d_i, Σ_x, Σ_y.

The expectation maximization algorithm plays a central role in the method developed in this article, and hence a summary of EM algorithm is presented below. It is an elegant optimization algorithm that constructs a complete likelihood function including the latent states and observations, and maximizes the likelihood function of observed data through iterations. A brief description of the EM algorithm is presented in this section to facilitate the development of the proposed algorithm in later sections.

For the state-space model described in this article, let $p(y_{1:T}|\theta)$ denote the likelihood function of the observed data. The maximum likelihood estimate of the parameter vector is obtained by maximizing this observed data likelihood function. For certain classes of state-space models, such as linear systems, it is possible to derive an explicit expression for this joint density. However, for the model considered in this paper, it is difficult to develop such an expression due to the presence of latent states. Instead, using the Markov property of the states it is straightforward to develop an expression for the complete (including states and observations) likelihood function, $p(x_{1:T}, y_{1:T}|\theta)$. In light of this feature of the Markovian states, the joint probability density function of the states and observations is iteratively maximized to obtain a maximizing θ for $p(y_{1:T}|\theta)$.

This maximization approach is called EM algorithm and can be summarized in four steps:

(1) Choose an initial guess of the parameter vector, say θ_0.
(2) Estimate the states given the parameter vector and the observations and evaluate

$$Q(\theta_i, \theta) = \int \log[p(x_{1:T}, y_{1:T}|y_{1:T}, \theta)] p(x_{1:T}|y_{1:T}, \theta_i) dx_{1:T} \quad (2)$$

where $p(x_{1:T}|y_{1:T})$ is the joint conditional density function of the states given the observations, and θ_i is an estimate of the parameter vector from a previous iteration.
(3) Maximize $Q(\theta_i, \theta)$ with respect to θ. Call the maximizing value θ_{i+1}.
(4) Repeat the above two steps until the change in parameter vector is within a specified tolerance level.

The second step in the above algorithm is called E-step and the third step is called M-step. The likelihood function, $p(y_{1:T}|\theta)$, increases monotonically through these iterations. Due to the nonlinear nature of the dynamics it is not possible to analytically evaluate the Q-function in (2). In the next section, an approximation of the Q-function and an approach to maximize it are presented.

3. MAIN ALGORITHM

3.1 Approximation of Q function

A number of approximations of EM algorithm, involving different approximations of Q function have been proposed in the literature. They either involve approximating the nonlinearities Goodwin and Agüero (2005) or approximating expected value of the joint likelihood function using particle filters and other simulation based approaches Schön et al. (2006); Gopaluni (2008). Methods involving approximation of nonlinearities will fail if the nonlinearities are prominent and on the other hand, methods involving approximation of expected value are usually computationally intensive. In this article, the Q function is approximated using a combination of particle filters and smoothers. The complete details of this approximation and its extension to handle missing data are presented in the author's work in Gopaluni (2008). For continuity a summary of this approach is presented in this section.

The Q function, using Markov property of states, can be expanded to

$$\begin{aligned}
&Q(\theta_i, \theta) \\
&= \int \log[p(x_1|y_{1:T}, \theta)] p(x_1|y_{1:T}, \theta_i) dx_1 \\
&\quad + \sum_{t=2}^{T} \int \log[p(x_t|x_{t-1}, \theta)] p(x_{t-1:t}|y_{1:T}, \theta_i) dx_{t-1:t} \\
&\quad + \sum_{t=1}^{T} \int \log[p(y_t|x_t, \theta)] p(x_t|y_{1:T}, \theta_i) dx_t. \qquad (3)
\end{aligned}$$

From the above expression, it is easy to notice that in order to obtain an approximation of the Q function, the following density functions are needed:

(1) $p(x_1|y_{1:T}, \theta_i)$,
(2) $p(x_{t-1:t}|y_{1:T}, \theta_i)$, and
(3) $p(x_t|y_{1:T}, \theta_i)$.

It is possible to obtain the following particle approximations of the above density functions (please see Gopaluni (2008) for details)

$$\begin{aligned}
p(x_1|y_{1:T}, \theta_i) &= \sum_{i=1}^{N} w_{1|1}^{(i)} \delta(x_1 - x_1^{(i)}) \\
p(x_t|y_{1:T}, \theta_i) &= \sum_{i=1}^{N} w_{t|T}^{(i)} \delta(x_t - x_t^{(i)}) \\
p(x_{t-1}, x_t|y_{1:T}, \theta_i) &= \sum_{i=1}^{N} w_{t-1,t}^{(i)} \delta(x_{t-1} - x_{t-1}^{(i)}) \delta(x_t - x_t^{(i)})
\end{aligned}$$

where $w_{1|1}^{(i)}$, $w_{t|T}^{(i)}$ and $w_{t-1,t}^{(i)}$ are appropriate weights calculated using Bayes rule and importance sampling Klaas et al. (2006), $\delta(.)$ is the Kronecker delta function, and $x_t^{(i)}$ are N samples of states obtained through simulations. Using the above approximations of the density functions in the Q function, one can write the following expression,

$$\begin{aligned}
Q(\theta_i, \theta) \approx &\sum_{i=1}^{N} w_{1|1}^{(i)} \log[p(x_1^{(i)}|y_{1:T}, \theta)] + \sum_{t=2}^{T} \sum_{i=1}^{N} w_{t-1,t}^{(i)} \\
&\log[p(x_t^{(i)}|x_{t-1}^{(i)}, y_{1:T}, \theta)] + \sum_{t=1}^{T} \sum_{i=1}^{N} w_{t|T}^{(i)} \log[p(y_t|x_t^{(i)}, \theta)]
\end{aligned} \qquad (4)$$

In the above approximation, since the noise sequences are assumed to be Gaussian, the density functions, $p(x_t^{(i)}|x_{t-1}^{(i)}, y_{1:T}, \theta)$, and $p(y_t|x_t^{(i)}, \theta)$ can be written in terms of Gaussian density functions and hence,

$$\begin{aligned}
&\log[p(x_t^{(i)}|x_{t-1}^{(i)}, y_{1:T}, \theta)] = \\
&-\frac{1}{2}\log(2\pi) - \frac{1}{2}\log(\det(Q)) - \frac{1}{2}(x_t^{(i)} - \hat{x}_{t-1}^{(i)})^T Q^{-1} \\
&(x_t^{(i)} - \hat{x}_{t-1}^{(i)})
\end{aligned}$$

$$\begin{aligned}
&\log[p(y_t|x_t^{(i)}, \theta)] = \\
&-\frac{1}{2}\log(2\pi) - \frac{1}{2}\log(\det(R)) - \frac{1}{2}(y_t^{(i)} - \hat{\hat{x}}_{t-1}^{(i)})^T R^{-1} \\
&(y_t^{(i)} - \hat{\hat{x}}_{t-1}^{(i)})
\end{aligned}$$

where $\hat{x}_t^{(i)} = \sum_{i=1}^{I_x} h_i \rho_i(x_t^{(i)}, u_t, c_i, \Sigma_x) + Ax_t^{(i)} + Bu_t$, and $\hat{\hat{x}}_t^{(i)} = \sum_{i=1}^{I_y} g_i \gamma_i(x_t^{(i)}, u_t, d_i, \Sigma_y) + Cx_t^{(i)} + Du_t$.

3.2 Maximization of Q function

The maximization of Q function is performed in two steps using separable least squares. It is easy to notice that the parameters in θ_l enter the model linearly, while those in θ_{nl} enter the model nonlinearly. Hence, a two step procedure (called separable least squares) where the linear parameters are estimated in the first step using linear least squares, and the nonlinear parameters are estimated in the second step through nonlinear least squares. The procedure is explained below.

Step 1 Starting with an initial guess for the nonlinear parameter vector, θ_{nl}, the Q function is maximized with respect to θ_l. This maximization can be achieved through linear least squares. Before providing the maximizing value of the linear parameter vector, define the following matrices,

$$\begin{aligned}
\Omega_x &= [h_1 \; h_2 \; \cdots h_{I_x} \; A \; B] \\
s_t &= [I_1 \rho_1(x_t, u_t, c_1, \Sigma_x) \; I_1 \rho_2(x_t, u_t, c_2, \Sigma_x) \cdots \\
&\qquad I_1 \rho_{I_x}(x_t, u_t, c_{I_x}, \Sigma_x) \; x_t \; u_t]
\end{aligned}$$

where I_1 is a vector of ones of appropriate dimensions. Noting that the Q function is quadratic in Ω_x, through straightforward calculations, it can be shown that

$$\Omega_x = \left[\sum_{t=1}^{T} < x_t s_t^T >_{xx}\right] \left[\sum_{t=1}^{T} < s_t s_t^T >_{xx}\right]^{-1} \qquad (5)$$

where $< . >_{xx}$ is used to denote integration with respect to the density function $p(x_{t-1:t}|y_{1:T}, \theta)$. This integration can be approximated using the particle approximation of $p(x_{t-1:t}|y_{1:T}, \theta)$. The state co-variance can be shown to be

$$Q = \frac{1}{T} \sum_{t=1}^{T} \left\langle (x_{t+1} - \Omega_x s_t) x_{t+1}^T \right\rangle_{xx}.$$

Similarly, defining the matrices,

$$\begin{aligned}
\Omega_y &= [g_1 \; g_2 \; \cdots g_{I_y} \; C \; D] \\
r_t &= [I_1 \gamma_1(x_t, u_t, d_1, \Sigma_y) \; I_1 \gamma_2(x_t, u_t, d_2, \Sigma_y) \cdots \\
&\qquad I_1 \gamma_{I_y}(x_t, u_t, d_{I_x}, \Sigma_y) \; x_t \; u_t]
\end{aligned}$$

and noticing that the Q function is quadratic in Ω_y, it can be shown that,

$$\Omega_y = \left[\sum_{t=1}^{T} < y_t r_t^T >_x\right] \left[\sum_{t=1}^{T} < r_t r_t^T >_{yx}\right]^{-1} \qquad (6)$$

where $< . >_x$ denotes integration with respect to the density function $p(x_t|y_{1:T}, \theta)$ and $< . >_{yx}$ denotes integration with respect to the density function $p(y_t|x_t, \theta)$. The measurement noise co-variance can be shown to be,

$$R = \frac{1}{T}\sum_{t=1}^{T} \left\langle (y_t - \Omega_y r_t) y_t^T \right\rangle_x .$$

The parameters in the matrices Ω_x, Ω_y, Q, and R constitute the linear parameter vector, θ_l.

Step 2 : In step one, it is assumed that the centers and widths of the radial basis functions are known. However, in practice, it is difficult estimate them. In this step an approach to estimate centers and radii is presented. The idea is to obtain a *maximum a posteriori* (MAP) estimate of the state trajectory and fix centers and radii that provide the best possible predictions of MAP state estimate and the observations. The MAP estimate of the state is obtained using a modified Viterbi algorithm as described in Godsill et al. (2001). For the sake of completeness, Viterbi algorithm is described below [1] .

Viterbi Algorithm

1. *Initialization*: For $1 \leq i \leq N$, $\delta_1(i) = \log(p(x_1^{(i)}) + \log(p(y_1|x_1^{(i)}))$.
2. *Recursion*: For $2 \leq t \leq T$, and $1 \leq j \leq N$,
$$\delta_t(j) = \log(p(y_t|x_t^{(j)})) + \max_i \left[\delta_{t-1}(i) + \log(p(x_t^{(j)}|x_{t-1}^{(i)}))\right]$$
$$\psi_t(j) = \arg\max_i \left[\delta_{t-1}(i) + \log(p(x_t^{(j)}|x_{t-1}^{(i)}))\right]$$
3. *Termination*: $i_T = \arg\max_i \delta_T(i)$ and $x_{MAP}(T) = x_T^{(i_T)}$.
4. *Backtracking*: For $t = T-1, T-2, \cdots, 1$, $i_t = \psi_{t+1}(i_{t+1})$, and $x_{MAP}(t) = x_t(i_t)$.

An estimate of θ_{nl} is now obtained from the data $\{x_{MAP}(1:T), y_{1:T}, u_{1:T}\}$ by fixing θ_l to its estimated value from step 1 and using nonlinear least-squares. Step 1 and Step 2 are iterated until changes in θ_l and θ_{nl} between iterations are less than a specified tolerance level.

3.3 Proposed Algorithm

The complete proposed identification algorithm is summarized below:

0. **Initialization**: Initialize the parameter vector to θ_0.
1. **Expectation**: Approximate the expected value of the complete log-likelihood function (E-step) using particle filters.
2 **Maximum a Posteriori Estimate**: Obtain a maximum *a posteriori* estimate of the state trajectory using Viterbi algorithm. Using this MAP estimate of the state trajectory, fix the centers and variances of the radial basis functions. In other words, estimate $(\theta_{nl})_{i+1}$, where i denotes the number of EM algorithm iterations performed so far.
3. **Maximization**: Maximize the Q function with respect to θ_l and call the maximizing parameter, $(\theta_l)_{i+1}$. Then set $\theta_{i+1} = [(\theta_l)_{i+1} \;\; (\theta_{nl})_{i+1}]$.
4. **Iterate**: Repeat steps 1, 2, and 3 until the change in parameter vector is within a specified tolerance level.

[1] for notational clarity, the parameter dependence is not shown in the density functions below

4. ILLUSTRATIVE EXAMPLES

The proposed approach is tried on data collected from a real continuous stirred tank reactor. The governing

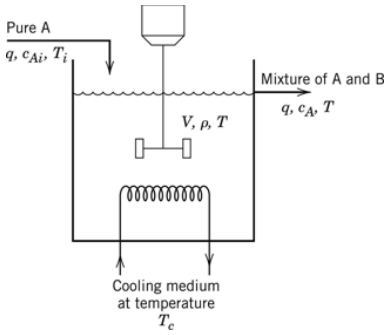

Fig. 1. Continuous Stirred Tank Reactor - Picture taken from Seborg et al. (2004).

equations of this popular CSTR, shown in figure 1, are given below (Morningred et al. (1992); Chen (2004))

$$\frac{dC_A}{dt} = \frac{q}{V}(C_{Ai} - C_A) - k_0 C_A e^{-E_A/T}$$
$$\frac{dT}{dt} = \frac{q}{V}(T_i - T) - \frac{\Delta H}{\rho C_p} k_0 C_A e^{-E_A/T} - \frac{\rho_c C_{pc}}{\rho C_p V} q_c (1 - e^{-\frac{hA}{q_c \rho_c C_{pc}}})(T - T_c)$$

where C_A is the concentration of the reactant in the reactor, T is the temperature in the reactor, q is the flow rate, V is the volume of the reactor, C_{Ai} and T_i are inflow concentration and temperature, $k_0 C_A e^{-E_A/T}$ is the reaction rate, ΔH is the reaction heat, ρ and ρ_c are the densities of the reactant and the cooling fluid respectively, C_p and C_{pc} are the corresponding specific heats, h and A are the effective heat transfer coefficient and area respectively, T_c and q_c are the temperature and flow rate of the cooling fluid. Finite difference discretization of the above continuous time differential equations results in the following model,

$$f(x_t, u_t, \theta) = x_{t-1} + \Delta t \begin{bmatrix} \frac{q}{V}(C_{Ai} - x_{t-1}(1)) - \theta_1 x_{t-1}(1) e^{-E_A/x_{t-1}(2)} \\ \frac{q}{V}(T_i - x_{t-1}(2)) - \theta_2 x_{t-1}(1) e^{-E_A/x_{t-1}(2)} \end{bmatrix} + \begin{bmatrix} 0 \\ \frac{\rho_c C_{pc}}{\rho C_p V} u_{t-1} \left[1 - e^{-\theta_3 A/(u_{t-1}\rho_c C_{pc})}\right](T_c - x_{t-1}(2)) \end{bmatrix}$$

where the state vector is $x_t = [x_t(1) \;\; x_t(2)] = [C_A(t) \;\; T(t)]$, $\theta_1 = k_0$, $\theta_2 = (k_0 \Delta H)/(\rho C_p)$, $\theta_3 = hA$, $u_t = q_c$, $g(x_t, u_t, \theta) = x_t$ and Δt is the discretization sample time. C_{Ai} and q_c are input variables. Real data [2] collected from this reactor is shown in figures 2 and 3. Our goal is to fit a state-space model to this data assuming that the energy and mass balance expressions provided above are unknown.

[2] Please note that this data is available at http://homes.esat.kuleuven.be/ smc/daisy/

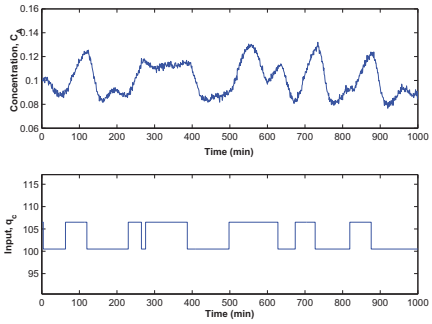

Fig. 2. The concentration, C_A, measurements.

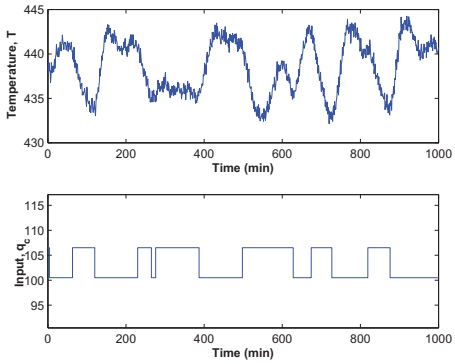

Fig. 3. The temperature, T, measurements.

The proposed algorithm is applied on this data, with a single radial basis function to describe the nonlinearities in the state and observation equations *i.e.,* with $I_x = 1$, $I_y = 1$. The accuracy of the model can definitely be increased by increasing the number of radial basis functions used. The predictions of concentration from this model for different prediction horizons are shown in figure 4. The %-fit, at these prediction horizons, calculated with the estimated model is comparable to that of input-output Hammerstein-Weiner (HW) models built using Matlab system identification toolbox. However, it should be noted that while there is no realistic and fair way to compare the complexities of HW and state space models, an attempt is made to compare the "best" trial and error based HW model with the state-space model estimated using the proposed approach.

The main advantage of the proposed method, over other nonlinear input-output identification methods, is in its ability to handle missing data - both in states and observations. In this article, missing observations are not considered. However, as shown in Gopaluni (2008), it is possible to derive particle approximations of density functions, required to approximate the Q function, even if there are some missing observations. Hence, extension of this approach to handle missing observations is rather straightforward.

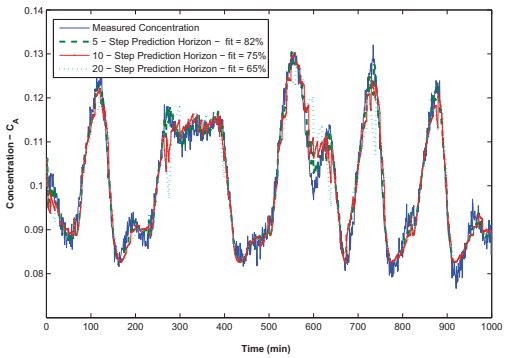

Fig. 4. True and predicted concentration profiles.

5. CONCLUSIONS

An approach to identify stochastic nonlinear systems using a combination of expectation maximization algorithm and particle filters is presented. In the proposed approach it is assumed that the model structure is unknown, and is approximated using radial basis functions. The expectation step in the algorithm is approximated using particle approximations of certain density functions. The maximization step is performed by separable least squares, where linear parameters are estimated using linear least squares, and the nonlinear parameters are estimated by using nonlinear least squares on a sequence of maximum *a posteriori* states and observations. The developed algorithm is applied to a real continuous stirred tank reactor. The proposed approach is easily extendable to handle missing observations.

REFERENCES

Chen, W. (2004). *Bayesian Estimation by Sequential Monte Carlo Sampling For Nonlinear Dynamical Systems.* Ph.d. thesis, Ohio State University.

Dempster, A., Laird, N., and Rubin, D. (1977). Maximum likelihood from incomplete data via the EM algorithm. *J. R. Stat. Soc. B*, 39, 1–38.

Godsill, S., Doucet, A., and West, M. (2001). Maximum a posteriori sequence estimation using Monte Carlo simulations. *Ann. Inst. Stat. Math*, 53(1), 82–96.

Goodwin, G. and Agüero, J. (2005). Approximate EM algorithms for paramter and state estimation in nonlinear stochastic models. *Proceedings of IEEE Conference on Decision and Control*, 368–373.

Gopaluni, R.B. (2008). Identification of nonlinear processes with known structure under missing observations. In *Proceedings of IFAC World Congress*. Seoul, Korea.

Klaas, M., Briers, M., Nando, D., and Doucet, A. (2006). Fast particle smoothing: If I had a million particles. *International Conference on Machine Learning*.

Ljung, L. (1999). *System Identification: Theory for the user*. Prentice Hall.

Morningred, J., Paden, B.E., Seborg, D.E., and Mellichamp, D.A. (1992). An adaptive nonlinear predictive controller. *Chemical Engineering Science*, 47, 755–762.

Schön, T., Wills, A., and Ninness, B. (2006). Maximum likelihood nonlinear system estimation. In *Proceedings*

of IFAC Symposium on System Identification, 1003–1008.
Seborg, D., Edgar, T., and Mellichamp, D. (2004). *Process Dynamics and Control*. John Wiley, New Jersey.
Shumway, R. and Stoffer, D. (2000). *Time Series Analysis and Its Applications*. Springer.
Van Overschee, P. and Moor, B.D. (1996). *Subspace identification for linear systems*. Kluwer.

Subspace closed loop identification using the integration of MOESP and N4SID methods

Santos Miranda, Claudio Garcia

Polytechnic School of the University of São Paulo.
e-mail: santos.borjas@poli.usp.br, clgarcia@lac.usp.br

Abstract: Linear identification of time invariant systems operating in closed loop is of special interest for a large number of engineering applications. There are different techniques and methods to carry out this type of identification. For example, modifying the N4SID method, one can derive a closed loop subspace identification method. The same can be done using the MOESP method. Based on them, the MON4SID method is introduced, which estimates the extended observability matrix and the state sequence directly from a LQ decomposition, using a combination of the techniques contained in both, MOESP and N4SID. This new method uses an algorithm to identify state space model of a plant in a closed loop system, in the same way as in MOESP method. The advantage of the proposed algorithm is that it does not require any knowledge about the controller, whereas such information is essential for other methods (e.g. N4SID). The disadvantage of this algorithm is that it needs a great amount of data to obtain better estimates. A simulated process to show the performance of this algorithm is presented.

Keywords: Subspace identification; closed loop identification; state space models.

1. INTRODUCTION

Great part of the literature referring to system identification deals with how to find polynomial models as Prediction Error Method (PEM). In case of complex systems, there is a parameterization problem in the PEM model, so the state space model appears as an alternative to PEM, such as Multivariable Output-Error State sPace (MOESP) (Verhaegen, 1994), Canonical Variate Analysis (CVA) (Larimore, 1990) and Numerical algorithms for Subspace State Space System Identification (N4SID) (Van Overschee; De Moor, 1996). Statistical properties such as consistency and efficiency of these algorithms were studied by (Bauer, 2003; Bauer; Ljung, 2002; Chiuso; Picci, 2005). One of the main assumptions of theses methods is that the process and the measurement noises are independent of the plant input. This assumption is violated when the system is working in closed loop. The closed loop identification is of special interest for a large number of engineering applications (Ljung, 1999), since closed loop experiments are necessary if the open loop plant is unstable, or the feedback is an inherent mechanism of the system (Forssell; Ljung, 1999; Van den Hof, 1997). Several closed loop identification methods have been suggested in the last years and can be broadly classified into three main groups: direct, indirect and joint input output identification methods (Forssell; Ljung, 1999). The results of any of the N4SID, MOESP and CVA methods cited above are asymptotically biased when closed loop identification is applied. To solve this problem, the MOESP method (Verhaegen, 1993) proposed a closed loop subspace identification method through the identification of an overall open loop state space. Based on it, the plant and the controller models are estimated. To do so, it is necessary to know the order of the controller. In the N4SID case (Van Overschee; De Moor, 1997) it is necessary to know a limited number of impulse response samples of the controller and, via direct identification, the plant model is estimated. There are other possible solutions to the closed loop identification problem; the reader can consult (Huang *et al*., 2005; Katayama, 2005; Katayama *et al.*, 2002; Katayama *et al.*, 2005; Ljung; McKelvey, 1996; Qin *et al.*, 2005).

Combining the MOESP and N4SID methods, we obtain the MON4SID algorithm, which estimates the extended observability matrix in the same way it occurs in the MOESP method, the state sequence is computed through the oblique projection, as it is done in the N4SID method. From this sequence, the past and future states are obtained, and finally a consistent estimate of the system matrices is obtained, applying the least squares method. In this paper, it is proposed an algorithm to identify the state space model of a plant in a closed loop system, in the same way as it was proposed in the MOESP method, that first computes a global model from which is extracted the plant model. **T**his method does not need any knowledge about the controller.

1.1 Open Loop Subspace identification

Consider a time discrete linear time invariant dynamic system described by the state space models in the innovation form:

$$\begin{aligned} x_{k+1} &= Ax_k + Bu_k + Ke_k \\ y_k &= Cx_k + Du_k + e_k \end{aligned} \tag{1}$$

where $u_k \in R^m$ and $y_k \in R^l$ denote the input and output signals, respectively and $x_k \in R^n$ is the vector of states. $e_k \in R^l$ is zero-mean Gaussian white noise and independent of past input and output data. *A*, *B*, *C*, *D* and *K* are matrices with appropriate dimensions.

1.2 Open Loop Subspace identification problem

The subspace identification problem is: given $u = [u_1,..,u_{nd}]$ and $y = [y_1,..,y_{nd}]$ a set of input-output measurements, determine the order *n* of the unknown system, the system matrices (*A*, *B*, *C*, *D*) up to within a similarity transformation and Kalman filter gain *K* (Van Overschee; De Moor, 1996).

1.3 Subspace matrix equation

Making successive iterations in equation (1), one can derive the following matrix equation:

$$Y_f = \Gamma_i X_f + H_i^d U_f + H_i^s E_f \tag{2}$$

where subscript f stands for the "future" and p for the "past". For the definition of the matrices H_i^d and H_i^s given in (2), see (Van Overschee; De Moor, 1996). The past and future input block-Hankel matrices are defined as:

$$\left(\frac{U_p}{U_f}\right) = \left(\begin{array}{cccc} u_0 & u_1 & \cdots & u_{j-1} \\ u_1 & u_2 & \cdots & u_j \\ \cdots & \cdots & \cdots & \cdots \\ u_{i-1} & u_i & \cdots & u_{i+j-2} \\ \hline u_i & u_{i+1} & \cdots & u_{i+j-1} \\ u_{i+1} & u_{i+2} & \cdots & u_{i+j} \\ \cdots & \cdots & \cdots & \cdots \\ u_{2i-1} & u_{2i} & \cdots & u_{2i+j-2} \end{array}\right) \tag{3}$$

where $U_p, U_f \in R^{mixN}$. The output and noise innovation block-Hankel matrices $Y_p, Y_f \in R^{lixN}$ and $E_p, E_f \in R^{mixN}$, respectively, are defined in a similar way to (3).

The states are defined as:

$$X_p = X_0 = \lfloor x_0,..,x_{j-1} \rfloor \tag{4}$$

$$X_f = X_i = \lfloor x_i,..,x_{i+j-1} \rfloor \tag{5}$$

The extended observability matrix Γ_i is given by:

$$\Gamma_i = \begin{pmatrix} C \\ CA \\ \cdots \\ CA^{i-1} \end{pmatrix} \tag{6}$$

The orthogonal projection of the row space of A_x into the row space of B_x is:

$$A_x / B_x = A_x B_x^T (B_x B_x^T)^* B_x \tag{7}$$

where $(\bullet)^*$ denotes the Moore-Penrose pseudo-inverse of the matrix $(\bullet)$.

The projection of the row space of A_x into the orthogonal complement of the row space of B_x is:

$$A_x / B_x^\perp = A_x - A_x / B_x \tag{8}$$

The oblique projection of the row space of *G* along the row space *H* into the row space of *J* is:

$$G /_H J = (G / H^\perp) \cdot (J / H^\perp)^* \cdot J \tag{9}$$

Properties of the orthogonal and oblique projections:

$$A_x / A_x^\perp = 0 \tag{10}$$

$$A_x /_{A_x} C_x = 0 \tag{11}$$

For a proof, see (Van Overschee; De Moor, 1996).

2. PROPOSED IDENTIFICATION METHOD

2.1 MON4SID identification method

In this subsection, the MON4SID method is presented. To solve the problem in section 1.2, it is used the POMOESP method to calculate the extended observability matrix Γ_i and the N4SID method is employed to calculate the matrices *A*, *B*, *C*, *D* through the least squares method. Therefore, it is necessary to eliminate the last two terms in the right side of equation (2). That is done in two steps: first, eliminating the term $H_i^d U_f$ in (2), performing an orthogonal projection of equation (2) into the row space of $U_f^\perp$, which yields:

$$Y_f / U_f^\perp = \Gamma_i X_f / U_f^\perp + H_i^d U_f / U_f^\perp + H_i^s E_f / U_f^\perp \tag{12}$$

And by the property (10), equation (12) can be simplified to:

$$Y_f / U_f^\perp = \Gamma_i X_f / U_f^\perp + H_i^s E_f / U_f^\perp \tag{13}$$

Second, to eliminate the noises in (13), an instrumental variable $Z = (U_p^T Y_p^T)^T$ is defined. Multiplication of (13) by *Z* yields:

$$Y_f / U_f^\perp Z = \Gamma_i X_f / U_f^\perp Z + H_i^s E_f / U_f^\perp Z \tag{14}$$

As it is assumed that the noise is uncorrelated with input and output past data (Verhaegen; Dewilde, 1992), which means that $E_f / U_f^\perp Z = 0$. Therefore, (14) is written as:

$$Y_f / U_f^\perp Z = \Gamma_i \hat{X}_f \tag{15}$$

In equation (15), $X_f / U_f^\perp Z = \hat{X}_f$ is the estimate of the Kalman filter state. Equation (15) indicates that the column space of Γ_i can be calculated by the SVD decomposition of $Y_f / U_f^\perp Z$. For further details, see (Verhaegen; Dewilde, 1992). Γ_i, given in (15), can be derived from a simple LQ factorization of a matrix constructed from the block-Hankel matrices U_f, U_p and Y_f, Y_p, in the form:

$$\begin{pmatrix} U_f \\ Z_p \\ Y_f \end{pmatrix} = \begin{pmatrix} L_{11} & 0 & 0 \\ L_{21} & L_{22} & 0 \\ L_{31} & L_{32} & L_{33} \end{pmatrix} \begin{pmatrix} Q_1 \\ Q_2 \\ Q_3 \end{pmatrix} \tag{16}$$

and the orthogonal projection in the left side of (15) can be computed by matrix L_{32} (Verhaegen; Dewilde, 1992). The SVD of L_{32} can be given as:

$$L_{32} = (U_1\ U_2)\begin{pmatrix} S_n & 0 \\ 0 & S_2 \end{pmatrix}\begin{pmatrix} V_1^T \\ V_2^T \end{pmatrix} = USV^T \tag{17}$$

The order *n* of the system is equal to the number of non-zero singular values in S. The column space of U_1 approximates that of Γ_i in a consistent way (Verhaegen; Dewilde, 1992), that is:

$$\Gamma_i = U_1 \tag{18}$$

The system (1) can be written as:

$$\begin{pmatrix} \widetilde{X}_{i+1} \\ Y_{i|i} \end{pmatrix} = \begin{pmatrix} A & B \\ C & D \end{pmatrix}\begin{pmatrix} \widetilde{X}_i \\ U_{i|i} \end{pmatrix} + \begin{pmatrix} r_i \\ r_2 \end{pmatrix} \tag{19}$$

In equation (19), suppose (ideally) that $\widetilde{X}_{i+1}$ and $\widetilde{X}_i$ are given, then the system matrices (*A*, *B*, *C*, *D*) could be computed through the least squares method. Therefore, the problem now is to find the state sequences.

$\Theta_i = Y_f /_{U_f} Z_p$ is the oblique projection (Van Overschee; De Moor, 1996), which is achieved by performing an oblique projection of equation (2), along the row space U_f onto the row space of Z_p, that is:

$$Y_f /_{U_f} Z_p = \Gamma_i X_f /_{U_f} Z_p + H_i^d U_f /_{U_f} Z_p + \\ + H_i^s E_f /_{U_f} Z_p \tag{20}$$

It is easy to see that the last two terms of equation (20) are zero, by the property of the oblique projection, equation (11); and by the assumption that the noise is uncorrelated with input and output past data (Van Overschee; De Moor, 1996). Thus, equation (20) can be simplified to:

$$Y_f /_{U_f} Z_p = \Gamma_i \widetilde{X}_i \tag{21}$$

where $\widetilde{X}_i = X_f /_{U_f} Z_p$. Then equation (21) is written as:

$$\Theta_i = \Gamma_i \widetilde{X}_i \tag{22}$$

The oblique projection Θ_i given in equation (22) can be computed from (16) by:

$$\Theta_i = Y_f / U_f W_p = L_{32}(L_{22})^{-1}(L_{21}\ L_{22})\begin{pmatrix} Q_1 \\ Q_2 \end{pmatrix}. \tag{23}$$

An estimate of the state sequence X is given by:

$$X = (\Gamma_i)^* L_{32}(L_{22})^{-1} Z_p. \tag{24}$$

The following matrices are defined: $\widetilde{X}_i = X(:,1:N-1)$, $\widetilde{X}_{i+1} = X(:,2:N)$. Thus, the system matrices can be estimated from equation (19). To estimate *K* see (Van Overschee; De Moor, 1996) or (Verhaegen; Dewilde, 1992).

2.2 Closed loop identification method

Figure 1 shows a typical standard closed loop system, where *P* and *C* denote respectively the plant and the controller, r_k is the exogenous input, u_k the input control, y_k the plant output, w_k the plant disturbance and v_k the plant noise.

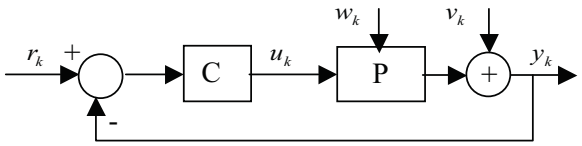

Figure1. Standard closed loop system.

P is given by equation (1) and *C* can be described by the following state equation:

$$\begin{aligned} s_{k+1} &= A_c s_k + B_c(r_k - y_k) \\ u_k &= C_c x_k + D_c(r_k - y_k) \end{aligned} \tag{25}$$

where A_c, B_c, C_c and D_c are matrices with appropriate dimensions.

2.3 Closed loop subspace identification problem

Given (r_k, u_k, y_k), a set of input output measurements finite data, of a well posed problem (Katayama, 2005), one considers the problem of identifying the deterministic part of the plant, that is, one determines the order *n* of the unknown system, the system matrices (*A*, *B*, *C*, *D*) up to within a similarity transformation.

2.3 Identification by joint input output approach

The objective of this paper is to obtain a state space model of the deterministic part of the plant *P*, based on finite measurement data (r_k, u_k, y_k). The present problem is practically the same as it was exposed in Verhaegen (1993), but the approach is quite different, as it is not necessary to know any information about the controller.

Using equations (1) and (25), it is possible to obtain a global state space model (Verhaegen, 1993):

$$\begin{aligned} \Psi_{k+1} &= \widetilde{A}\Psi_k + \widetilde{B}r_k + \Xi_k \\ \Phi_k &= \widetilde{C}\Psi_k + \widetilde{D}r_k + \Lambda_k \end{aligned} \tag{26}$$

where $\Psi_k = [x_k^T\ s_k^T]^T$, $\Phi_k = [u_k^T\ y_k^T]^T$. Ξ_k, Λ_k are noises and $\widetilde{A}, \widetilde{B}, \widetilde{C}, \widetilde{D}$ are matrices with appropriate dimensions.

The method MON4SID is applied to find an estimate of the matrices $\widetilde{A}, \widetilde{B}, \widetilde{C}, \widetilde{D}$, and based on them, to estimate Φ_k. Once Φ_k is known, it is easy to compute the matrices of the plant. To do so, the method POMOESP (Verhaegen, 1994) is used.

3. SIMULATION

In this section, we provide a simulation example to evaluate the performance of the MON4SID algorithm and to compare it with other existing identification algorithms PEM, N4SIDC and ARXS. N4SIDC here denotes the algorithm of Van Overschee and De Moor (1997) and ARXS the algorithm of Ljung and MacKelvey (1996). This example was used by (Huang *et al.*, 2004; Katayama, 2005; Overschee; De Moor, 1997 and Verhaegen, 1993). It is important to stress that the algorithm N4SIDC has three versions (Overschee; De Moor, 1997): two of them are unbiased and one is biased. The version implemented in this paper is the biased one, based on

states. In this version, it is used two different initial conditions, one for past states and the other for future states, what causes the bias. For further details see (Overschee; De Moor, 1997).

The plant is a discrete time model of a laboratory plant setup of two circular plates rotated by an electrical servo motor with flexible shafts. For further details, see (Hakvoort, 1990). The model of the plant is given by equation (1), where:

$$A = \begin{bmatrix} 4.4 & 1 & 0 & 0 & 0 \\ -8.09 & 0 & 1 & 0 & 0 \\ 7.83 & 0 & 0 & 1 & 0 \\ -4 & 0 & 0 & 0 & 1 \\ 0.86 & 0 & 0 & 0 & 0 \end{bmatrix}, \quad B = 10^{-3} \begin{bmatrix} 0.98 \\ 12.99 \\ 18.59 \\ 3.3 \\ -0.02 \end{bmatrix}, \quad C^T = \begin{bmatrix} 1 \\ 0 \\ 0 \\ 0 \\ 0 \end{bmatrix}$$

$$K = \begin{bmatrix} 2.3 \\ -6.64 \\ 7.515 \\ -4.0146 \\ 0.86336 \end{bmatrix} \text{ and } D = 0$$

e_k is the white noise, which generates the disturbance on the plant, with standard deviation equal to 0 (for the case of deterministic system), 0.001 (to denote a system of little noise) and 0.01 (to denote a system of high noise). The controller has a state space description as in the equation (25), where:

$$A_c = \begin{bmatrix} 2.65 & -3.11 & 1.75 & -0.39 \\ 1 & 0 & 0 & 0 \\ 0 & 1 & 0 & 1 \\ 0 & 0 & 1 & 0 \end{bmatrix}, \quad B_c = \begin{bmatrix} 1 \\ 0 \\ 0 \\ 0 \end{bmatrix}$$

$$C_C^T = \begin{bmatrix} -0.4135 \\ 0.8629 \\ -0.7625 \\ 0.2521 \end{bmatrix} \text{ and } D_c = 0.61$$

PRBS was used as an exogenous input signal, that is, persistently exciting of any finite order. There were collected 3000 samples and the number of block rows $i = 20$.

The simulation results for a closed loop deterministic identification without noise is shown in figure 2, where the order of the plant is n = 5. From figure 2, one can observe that all the algorithms had a good performance, apart from the algorithm N4SIDC, which had am improvement using n =7, as it is shown in figure 4. Figure 3 shows the poles of the original open loop plant and the estimated systems, where • denotes the original poles of the plant. One can see that all the algorithms had a good performance in relation to the estimation of the poles, which are on the unit circle.

To see an advantage of the proposed algorithm, a white noise is added to the plant, first with measurement noise variance 0.001 and then with 0.01. The comparison results are shown in figures 5 and 7 respectively.

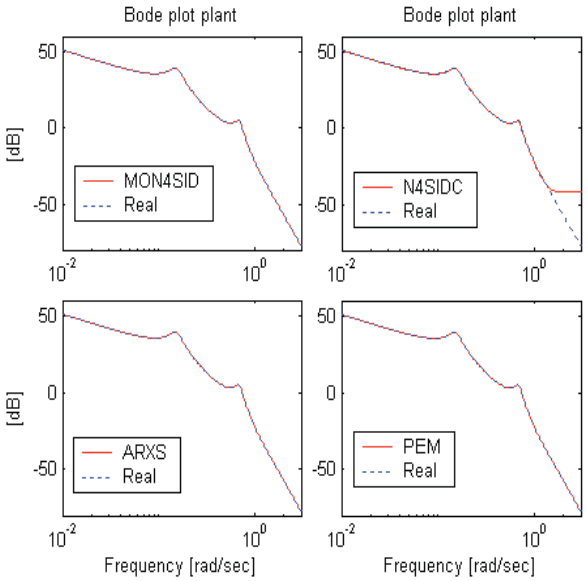

Fig.2. Bode plots of the plant P, to n=5 and no noise.

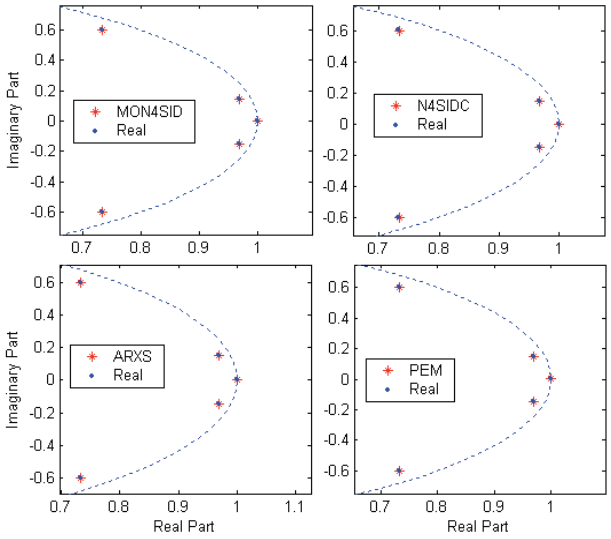

Fig. 3 Poles of the eigenvalues of the estimated A matrix.

From figures 5 and 7 one can see that the algorithm MON4SID performs better in the presence of noise. The order for identification of the plant is $n = 7$. Figures 6 and 8 show the pole estimates and the true poles of the plant. From figure 5 one can see that the algorithm ARXS does not have a good performance.

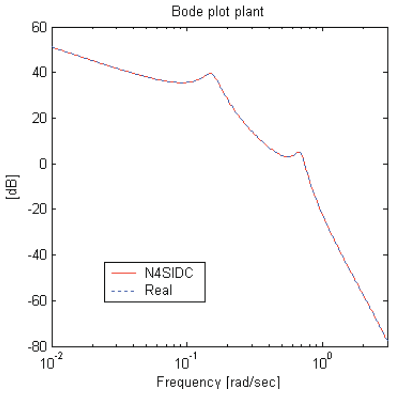

Fig.4. Bode plots of the plant P, to n=7 and no noise.

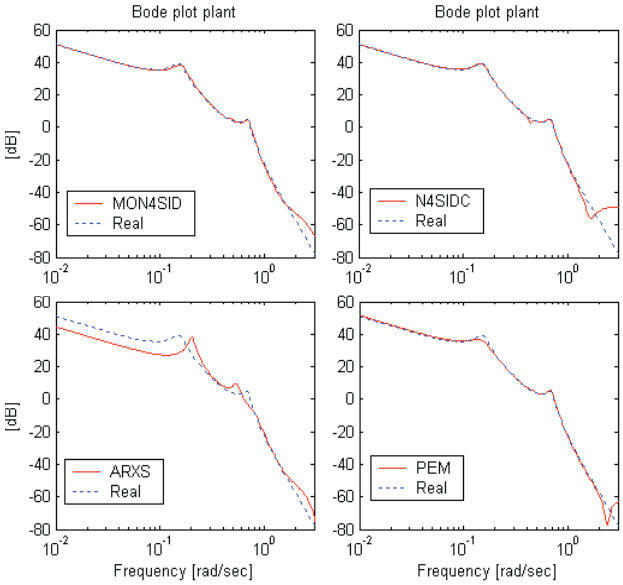

Fig.5. Bode plots of the plant P, to n=7 and little noise.

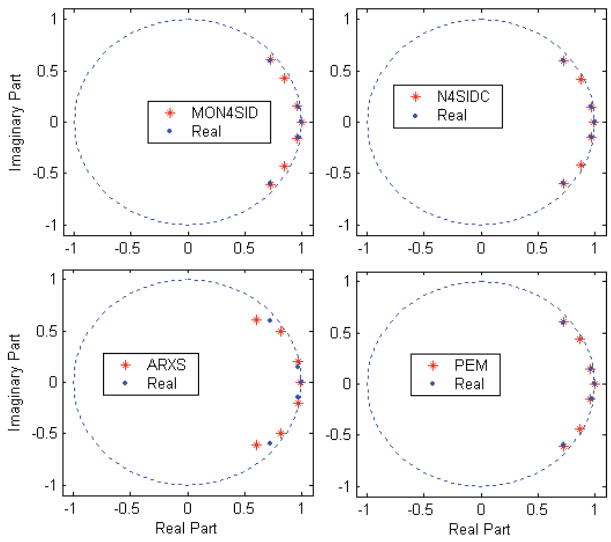

Fig.6 Poles of the eigenvalues of the estimated A matrix.

As can be noticed in figure 6 for the ARXS model, there is a difference between the estimated and real poles, what causes the difference between the real and estimated plots in figure 5.

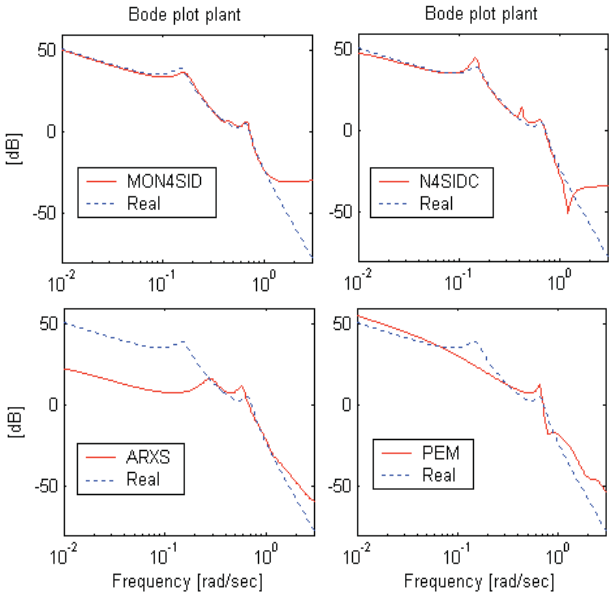

Fig.7. Bode plots of the plant P, to n=7 and high noise.

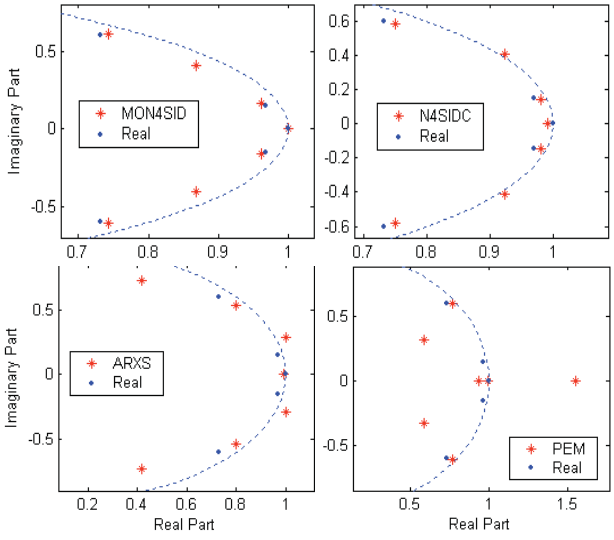

Fig.8 Poles of the eigenvalues of the estimated A matrix.

From figure 8 it can be seen that the MON4SID method provides a better estimation of the most crucial pole and all the poles are inside the unit circle. This does not happen for the other methods. Based on figure 8 one can say that direct identification models do not have a good performance for closed loop identification in the presence of high noises.

6. CONCLUSIONS

In this work, the MON4SID algorithm is presented, which uses LQ factorization in the same way as the MOESP method, which is used to compute the oblique and orthogonal

projections; these projections are used to compute the state sequence and the extended observability matrix, respectively. The past and future state sequences are computed from the state sequences, which have only one initial state. It does not happen in the N4SID method, because for each oblique projection (Θ_i and Θ_{i+1}) different state sequences ($\widetilde{X}_1$ and $\widetilde{X}_{i+1}$) are computed, generating a problem of bias in the estimates.

This algorithm was compared with three identification algorithms (PEM, N4SIDC, ARXS), when applied to a simulated example, which was used in (Van Overschee; De Moor, 1997) to identify a plant model in discrete time state space. Their results were compared by means of Bode plot and the comparison of the estimated poles with the true poles. The algorithm MON4SID presented good performance in all the cases. This algorithm has an advantage over the N4SIDC algorithm in the sense that it does not need any knowledge about the controller.

7. ACKNOWLEDGMENTS

The authors thank the financial support provided by CNPq (Brazil) for the development of this work.

REFERENCES

Bauer, D. (2003) Subspace algorithms. In *Proceedings of the 13th IFAC SYSID Symposium*, pages 1030-1041, Rotterdam, NL.

Bauer, D.; Ljung, L. (2002) Some facts about the choice of the weighting matrices in Larimore type of subspace algorithms. Automatica, volume 38, pages 763–773.

Chiuso, A.; Picci, G. (2005) Consistency analysis of some closed-loop subspace identification methods. Automatica, volume 41, issue 3, pages 377-391.

Forssell, U and Ljung, L. (1999) Closed loop identification revised, Automatica volume 35, issue 7, pages 1215-1241.

Huang, B.; Ding, S.X. and Qin, S. J. (2005) Closed loop subspace identification an orthogonal projection approach, J. Proc. Cont, volume 15, pages 53-66.

Hakvoort, R. (1990) Approximate identification in the controller design problem, Master Thesis, Delft University of Technology, Measurement and control theory section. Mech. Eng., A-538.

Katayama T.; Kawauchi H. and Picci G. (2002) Subspace identification of closed loop systems by stochastic realization, Proc. IFACWorld Congress, Barcelona.

Katayama, T. (2005) Subspace methods for system identification, Springer, London.

Katayama, T; Kawauchi, T. and Picci, G. (2005) Subspace identification of closed loop systems by the orthogonal decomposition method, Automatica, volume 41, issue 5, pages 863-872.

Larimore, W. (1990) Canonical variate analysis in identification, filtering and adaptive control, Proc. 29th Conference on Decision and Control, Hawaii, USA, pages 596-604.

Ljung, L. (1999) System Identification -Theory for the User, Prentice Hall Englewood Cliffs, NJ.

Ljung, L. and McKelvey, T. (1996) Subspace identification from closed loop data, Signal Processing, volume 52, issue 2, pages 209-215.

Qin, S. J.; Lin, W. and Ljung, L. (2005) A novel subspace identification approach with enforced causal models, Automatica, volume 41, issue 12, pages 2043-2053.

Van den Hof, P. (1997) Closed loop issues in system identification, Proc. 11th IFAC Symp. System Identification, Kitakyushu, Japan, pages 1651-1664.

Van Overschee, P. and De Moor, B. (1997) Closed loop subspace systems identification, Proc. 36th IEEE Conference on Decision and Control, San Diego, pages 1848-1853.

Van Overschee, P. and De Moor, B. (1996) Subspace identification for linear systems: Theory, implementation, applications, Dordrecht, Kluwer Academic Publishers.

Verhaegen, M. (1993) Application of a subspace model identification technique to identify LTI systems operating in closed loop, Automatica, volume 29, issue 4, pages 1027-1040.

Verhaegen, M. (1994) Identification of the deterministic part of MIMO state space models given in innovation form from input-output data, Automatica, volume 30, issue 1, pages 61-74.

ADCHEM 2009

IFAC Symposium on

Advanced Control of Chemical Processes

July 12-15, 2009

Koç University, Istanbul, Turkey

Symposium Preprints

Part 2

Editors: Sebastian Engell

Yaman Arkun

International Program Committee

Sebastian Engell (Chair)

Technische Universität Dortmund, Germany

Jorge Mandler (Industrial Co-Chair)

Air Products, USA

IPC Coordination

Christian Sonntag, Thomas Tometzki

Technische Universität Dortmund, Germany

IPC Members

O. Abel (DE), F. Allgöwer (DE), J. Alvarez (MX), H. Arellano-Garcia (DE), T. Backx (NL), T. Badgwell (US), R. Berber (TR), L.Biegler (US), D. Bonvin (CH), R. Braatz (US), M. Çamurdan (TR), T. Chai (CN), M. Chiu (SG), P. Christofides (US), A. Çınar (US), I. Craig (ZA), P. Daoutides (US), C. de Prada (ES), D. Dochain (BE), F. J. Doyle, III (US), G. Dünnebier (DE), F. Forbes (CA), B. Foss (NO), F. Gao (HK), C. Georgakis (US), M. Guay (CA), S. Hasebe (JP), K. Hoo (US), M. Hovd (NO), B. Huang (CA), C. D. Immanuel (UK), S. B. Jorgensen (DK), M. V. Kothare (US), C. Kravaris (GR), J. Lee (US), D. Lewin (IL), P. Li (DE), J. Mandler (US), J. Marchetti (AR), W. Marquardt (DE), M. Nikolaou (US), D. Odloak (BR), C. Özgen (TR), A. Palazoğlu (US), S. Park (KR), M. Perrier (CA), H. Preisig (NO), Raisch (DE), J. Rawlings (US), J. Romagnoli (US), C. Scali (IT), A. R. Secchi (BR), S. L. Shah (CA), S. Skogestad (NO), M. Soroush (US), B. Srinivasan (CA), M. Tade (AU), N. Thornhill (UK), J. O. Trierweiler (BR), M. Türkay (TR), A. Vande Wouwer (BE), E. Ydstie (US), E. S. Yoon (KR), C.-C. Yu (TW), D. Zhou (CN)

National Organizing Committee

Yaman Arkun (Chair)

Koç University, Istanbul, Turkey

NOC Members

Erdoğan Alper, Tahsin Bahar, Ridvan Berber, Mehmet Çamurdan, Devrim Kaymak, Hitay Özbay, Canan Özgen, Metin Türkay, Mustafa Türker

NOC Coordination

Nur Diğdem Burak

Koç University, Istanbul, Turkey

COPYRIGHT CONDITIONS

Contents

Performance Assessment in Closed-loop Systems

Oral Session

Multi-step Prediction Error Approach for MPC Performance Monitoring ⋆

Yu Zhao * **Jian Chu** * **Hongye Su** * **Biao Huang** **

* *State Key Lab. of Industrial Control Technology, Institute of Cyber Systems and Control, Zhejiang University, Hangzhou, China (e-mail: yzhao@iipc.zju.edu.cn).*
** *Department of Chemical and Materials Engineering, University of Alberta, Edmonton, AB, Canada, T6G 2G6 (e-mail: biao.huang@ualberta.ca)*

Abstract: Performance monitoring of model predictive control systems (MPC) has received a great interest from both academia and industry. In recent years some novel approaches for multivariate control performance monitoring have been developed without the requirement of process models or interactor matrices. Among them the prediction error approach has been shown to be a promising one, but it is k-step prediction based and may not be fully comparable with the MPC objective that is multi-step prediction based. This paper develops a multi-step prediction error approach for performance monitoring of model predictive control systems, and demonstrates its application in an industrial MPC performance monitoring and diagnosis problem.

Keywords: Multivariable control systems, Model predictive control, Performance evaluation, Performance monitoring, Prediction error methods.

1. INTRODUCTION

Since early work of Harris (1989), research on control performance assessment (CPA) has achieved a great progress and continues to be an active area. There is a great demand from industry for this research to produce practical solutions, particularly for MPC monitoring. Many algorithms in CPA including commercial software have been developed. There are several interesting reviews addressing related research achievements in different stages (Harris et al., 1999; Huang et al., 1999; Jelali , 2006; Qin , 2007).

Even with great achievements, multivariable CPA still has a number of stumbling blocks in practical applications. Recently some progress has been made towards this direction (Jelali , 2006; Huang et al., 2006). In particular, performance assessment of model predictive control (MPC) has been an interest since MPC is the most effective and widely used advanced multivariate control strategies in modern industries. With the existence of the constraints and economic optimization, the existing CPA is not directly applicable to its performance assessment (Xu et al., 2007).

For multivariable CPA to be practical, it must reduce *a priori* knowledge requirement. Traditional approaches for the multivariable CPA with minimum variance control as the benchmark need to estimate the interactor matrices, which is equivalent to knowing the process model (Huang et al., 1999) or at least the first few Markov parameter matrices. Recently, some new methods have been developed to address the multivariable CPA problems with only the input/output data (Jelali , 2006; Huang et al., 2006).

What simple index may be considered as a measure or one of the most important MPC performance measures? Consider that, if a closed-loop output is highly predictable, one should be able to do better, i.e. to compensate the predictable content by a well designed controller. This is the principle of predictive control. Should a better controller be implemented, the closed-loop output would have been less predictable. Therefore, high predictability of a closed-loop output implies high potential to improve its performance by controller re-tuning and/or re-design, or in other words, the existing controller may not have been satisfactory in terms of exploring its potential.

However, the CPA approach based on the prediction error has an equivalence to minimum variance based performance measure (Huang et al., 2008). Thus it may not be fully comparable with the MPC objective. Motivated by the prediction-error approach of (Huang et al., 2006; Zhao et al., 2008) and multi-step identification of Shook et al. (1992), this paper further develops closed-loop prediction-error measures based on multi-step prediction that is more relevant to model predictive control. Furthermore, applications of the proposed performance measures for an industrial model predictive control system are reported in this paper.

The remainder of this paper is organized as follows: Section 2 revisits the concept of prediction-error and closed-loop potentials for CPA. Section 3 introduces the

⋆ This work is supported in part by the the National Creative Research Groups Science Foundation of China (NCRGSFC: 60421002) and National Basic Research Program of China (973 Program 2007CB714000) and by the 111 Program (B07031) for visiting professorship.

multi-step prediction error. Based on it, new potential measures are defined for the MPC controller performance assessment in Section 4. This is followed by an industrial case study in Section 5 to illustrate the utility of the new performance measures. Finally the conclusion is drawn in Section 6.

2. REVISIT OF CLOSED-LOOP POTENTIAL FOR MULTIVARIATE CPA

In this section, we shall revisit the concepts of prediction error and closed-loop potentials as defined in Huang et al. (2006).

For a multivariable process, the closed-loop output driven by white noise can be described by a time series model:

$$Y_t = G_{cl} a_t \tag{1}$$

where G_{cl} is the time series model and a_t is white noise with mean zero and covariance Σ_a.

Transfer the above time series model to a moving average (MA) form:

$$Y_t = \sum_{k=0}^{\infty} F_k a(t-k) = F_0 a_t + F_1 a_{t-1} + \cdots + F_{i-1} a_{t-(i-1)} + F_i a_{(t-i)} + \cdots \tag{2}$$

Note that this time series model can be estimated without any a priori knowledge about the process.

With the MA model, one can obtain the optimal ith step prediction:

$$Y_{t|t-i} = F_i a_{(t-i)} + F_{i+1} a_{(t-i-1)} + \cdots \tag{3}$$

and the prediction error:

$$e_{t|t-i} = Y_t - Y_{t|t-i} = F_0 a_t + F_1 a_{t-1} + \cdots + F_{i-1} a_{t-(i-1)} \tag{4}$$

where $F_0 = I$. The covariance of the prediction error can be calculated as

$$cov(e_{t|t-i}) = F_0 \Sigma_a F_0^T + F_1 \Sigma_a F_1^T + \cdots + F_{i-1} \Sigma_a F_{i-1}^T \tag{5}$$

Define its scalar measure:

$$s_i = tr(cov(e_{t|t-i})) = tr(F_0 \Sigma_a F_0^T + \cdots + F_{i-1} \Sigma_a F_{i-1}^T) \tag{6}$$

s_i is monotonically increasing with i, as $i \to \infty$, $e_{t|t-i} \to Y_t$, and $s_\infty = tr(cov(Y_t))$. If we plot s_i versus i, the plot reflects how the prediction error increases with the prediction horizon.

A closed-loop potential is defined in Huang et al. (2006) as:

$$p_i = \frac{s_\infty - s_i}{s_\infty} \tag{7}$$

The closed-loop potential can be interpreted as following (Huang et al., 2006): If a deadbeat control action can be applied from time i, then the sum of squared error (SSE) can be reduced by $100 \times p_i$ percent. From stochastic view point, if i is greater than the interactor order d, it is possible that the variance of the multivariate output can be reduced by $100 \times p_i$ percent of the current variance. Since the order of the actual interactor matrix may not be known, one can check the trajectory of the closed-loop potential versus a range of possible time lag d. As s_i is monotonically increasing with i, p_i is monotonically decreasing. When $i \to 0$, $s_0 = tr(cov(Y_t - Y_{t|t})) = 0$, $p_0 = 1$. Therefore, the index p_i starts from 1 at $i = 0$ and monotonically decreases to 0 at $i \to \infty$. Larger the closed-loop potential is, more potential the control performance can be improved.

From the potential plot we can draw the conclusion whether or how much the present closed-loop has potential to improve. Furthermore, with the plot, we can compare performance of a controller between different tuning parameters.

3. CLOSED-LOOP POTENTIAL MEASURES BASED ON MULTI-STEP PREDICTION

3.1 Multi-step optimal prediction and its scalar measure

It is well-known that minimum variance control is an aggressive control and not all controllers are designed towards minimum variance performance. Therefore, in addition to the measure of the optimal i-step prediction error s_i, which is associated with minimum variance performance, we consider a control that achieves optimal prediction performance over multi-steps, i.e. over a window from N_1 to N_2, where N_1 typically equals time delay d. In this way, we consider an optimum that is not based on a single prediction point but based on multiple prediction points.

For the multi-step optimal prediction problem, the minimization of the following multi-step prediction error is of interest (Shook et al., 1992; Huang et al., 2003):

$$s_{N_1,N_2} = \frac{1}{N_p} \sum_{j=N_1}^{N_2} E[Y_{t+j} - Y_{t+j|t}]^T [Y_{t+j} - Y_{t+j|t}] \tag{8}$$

where $Y_{t+j|t}$ is an optimal j-step ahead prediction, N_1 and N_2 are the minimum and maximum prediction step, $N_p = N_2 - N_1 + 1$, and s_{N_1,N_2} is defined as the scalar measure of the optimal multi-step prediction error (from N_1 to N_2). MPC attempts to minimize the error of multi-step predictions, i.e. from the first N_1 step to the N_2 step prediction. Thus the objective function (8) is MPC relevant.

It has been shown in Huang et al. (2003) that the objective function of multi-step prediction error is equivalent to the variance of filtered one-step prediction error:

$$\begin{aligned} s_{N_1,N_2} &= \frac{1}{N_2 - N_1 + 1} \sum_{n=N_1}^{N_2} E||[Y_{t+n} - Y_{t+n|t}]||^2 \\ &= E||[F_{N_1,N_2}(z^{-1})(Y_t - Y_{t|t-1})]||^2 \end{aligned} \tag{9}$$

where the filter $F_{N_1,N_2}(z^{-1})$ is the spectral factor of the following spectrum (Huang et al., 2003):

$$L_{N_1,N_2} = \frac{1}{N_2 - N_1 + 1} \sum_{n=N_1}^{N_2} ||F_n(e^{-nj\omega})||^2 \tag{10}$$

where

$$F_n(z^{-1}) = \sum_{i=0}^{n-1} F_n z^{-i}$$

If $N_1 = 1$ and $N_2 = k$, it is easy to show that $F_{1,k}(z^{-1})$ has the following form:

$$F_{1,k}(z^{-1}) = \tilde{F}_0 + \tilde{F}_1 z^{-1} + \cdots + \tilde{F}_{k-1} z^{-k+1} \tag{11}$$

where $\tilde{F}_i$ is to be determined next.

According to Eqn. 4, the optimal one step prediction error $Y_t - Y_{t|t-1} = a_t$, i.e. white noise. Thus

$$\begin{aligned} s_{1,k} = & \quad E[F_{1,k}(z^{-1})a_t]^T[F_{1,k}(z^{-1})a_t] \\ & = tr\{[(\tilde{F}_0 + \tilde{F}_1 z^{-1} + \cdots + \tilde{F}_{k-1}z^{-k+1})a_t]^T \\ & \quad [(\tilde{F}_0 + \tilde{F}_1 z^{-1} + \cdots + \tilde{F}_{k-1}z^{-k+1})a_t]\} \end{aligned}$$

which can be further written as

$$s_{1,k} = tr(\tilde{F}_0\Sigma_a\tilde{F}_0^T + \tilde{F}_1\Sigma_a\tilde{F}_1^T + \cdots + \tilde{F}_{k-1}\Sigma_a\tilde{F}_{k-1}^T) \quad (12)$$

In the next two sections we will derive univariate and multivariate expressions of the optimal multi-step prediction error, respectively.

3.2 The Univariate Process

For the univariate process, the terms F_i and $\tilde{F}_i$ are both scalars (hence we use f_i and $\tilde{f}_i$ to stand for the scalar values), so the scalar prediction error measures can be simplified to the following forms:

$$s_k = (f_0^2 + f_1^2 + \cdots + f_{k-1}^2)\sigma_a^2 \quad (13)$$

$$s_{1,k} = (\tilde{f}_0^2 + \tilde{f}_1^2 + \cdots + \tilde{f}_{m-1}^2)\sigma_a^2 \quad (14)$$

When $k = 1$, by definition, $s_{1,1}$ is the variance of one step prediction error; thus

$$s_1 = s_{1,1}$$

When $k = 2$, the following result could be obtained:

$$s_{1,2} = (\tilde{f}_0^2 + \tilde{f}_1^2)\sigma_a^2 = \frac{1}{2}(2f_0^2 + f_1^2)\sigma_a^2 = \frac{1}{2}(s_1 + s_2)$$

Similarly, when $N_1 = 1, N_2 = k$, we have

$$\begin{aligned} s_{1,k} &= \frac{\sigma_a^2}{k}\{kf_0^2 + (k-1)f_1^2 + \cdots + f_{k-1}^2\} \\ &= \frac{1}{k}\sum_{i=1}^{k} s_i \end{aligned} \quad (15)$$

Thus

$$\begin{aligned} s_{k,m} = & \frac{1}{m-k+1}[(m-k+1)(f_0^2 + f_1^2 + \cdots + f_{k-1}^2) \\ & + (m-k)f_k^2 + \cdots + f_{m-1}^2]\sigma_a^2 \end{aligned}$$

Proposition 1. For a univariate control loop, the measure of optimal multi-step prediction error from k to m ($s_{k,m}$) is no smaller than that of the optimal k-step prediction error (s_k), and the two measures are asymptotically equal, namely

$$s_{k,m} - s_k \geq 0 \quad (16)$$

$$\lim_{k\to\infty}\{s_{k,m} - s_k\} = 0 \quad (17)$$

Proof.

Recall that the measures of the optimal k-step prediction error and optimal multi-step prediction error are respectively:

$$s_k = (f_0^2 + f_1^2 + \cdots + f_{k-1}^2)\sigma_a^2 \quad (18)$$

and

$$\begin{aligned} s_{k,m} = & \frac{1}{m-k+1}[(m-k+1)(f_0^2 + f_1^2 + \cdots + f_{k-1}^2) \\ & + (m-k)f_k^2 + \cdots + f_{m-1}^2]\sigma_a^2 \end{aligned} \quad (19)$$

Thus

$$\begin{aligned} & s_{k,m} - s_k = \frac{1}{m-k+1}[(m-k+1)(f_0^2 + f_1^2 + \cdots + f_{k-1}^2) \\ & + (m-k)f_k^2 + \cdots + f_{m-1}^2]\sigma_a^2 - (f_0^2 + f_1^2 + \cdots + f_{k-1}^2)\sigma_a^2 \\ & \triangleq \frac{1}{N_p}[(N_p-1)f_k^2 + (N_p-2)f_{k+1}^2 + \cdots + f_{m-1}^2]\sigma_a^2 \quad (20) \\ & \geq 0 \end{aligned}$$

where $N_p = m - k + 1$.

Consider a stable closed-loop response:

$$\begin{aligned} y_t = G_{cl}(z^{-1};\theta)e_t &= \frac{B(z^{-1})}{A(z^{-1})}e_t \\ &= \frac{b_0 + b_1 z^{-1} + \cdots + b_m z^{-m}}{a_0 + a_1 z^{-1} + \cdots + a_n z^{-n}}e_t \end{aligned} \quad (21)$$

Write the above transfer function in the zero-pole form

$$y_t = \frac{b_0(1-\beta_1 z^{-1})(1-\beta_2 z^{-1})\cdots(1-\beta_m z^{-1})}{(1-\alpha_1 z^{-1})(1-\alpha_2 z^{-1})\cdots(1-\alpha_n z^{-1})}e_t \quad (22)$$

where $|\alpha_i| < 1$.

Partial fraction expansion of Eqn. (22) yields

$$\begin{aligned} y_t &= (\frac{c_1}{1-\alpha_1 z^{-1}} + \frac{c_2}{1-\alpha_2 z^{-1}} + \cdots + \frac{c_n}{1-\alpha_n z^{-1}})e_t \\ &= \sum_{p=1}^{n} c_p(1 + \alpha_p z^{-1} + \alpha_p^2 z^{-1} + \cdots)e_t \\ &\triangleq (f_0 + f_1 z^{-1} + \cdots + f_i z^{-i}\cdots)e_t \end{aligned} \quad (23)$$

where

$$f_i = \sum_{p=1}^{n} c_p \alpha_p^i \quad (24)$$

So, the *ith* term of Eqn. (18) can be calculated as

$$\begin{aligned} f_i^2 &= (\sum_{p=1}^{n} c_p\alpha_p^i)^2 \\ &= \sum_{p=1}^{n} c_p^2\alpha_p^{2i} + 2\sum_{p=1}^{n-1}\sum_{q=p+1}^{n} c_p c_q(\alpha_p\alpha_q)^i \end{aligned} \quad (25)$$

According to Eqn. (20)

$$s_{k,m} - s_k = \frac{1}{N_p}\sum_{i=k}^{m-1}(m-i)f_i^2\sigma_a^2 \quad (26)$$

Substituting Eqn. (25) in Eqn. (26), we obtain that

$$\begin{aligned} & s_{k,m} - s_k \\ = & \frac{\sigma_a^2}{N_p}\sum_{i=k}^{m-1}(m-i)(\sum_{p=1}^{n} c_p^2\alpha_p^{2i} + 2\sum_{p=1}^{n-1}\sum_{q=p+1}^{n} c_p c_q(\alpha_p\alpha_q)^i) \\ = & \frac{\sigma_a^2}{N_p}(m\sum_{p=1}^{n} c_p^2\sum_{i=k}^{m-1}\alpha_p^{2i} - \sum_{p=1}^{n} c_p^2\sum_{i=k}^{m-1} i\alpha_p^{2i} \\ & + \sum_{p=1}^{n-1}\sum_{q=p+1}^{n} 2mc_p c_q\sum_{i=k}^{m-1}(\alpha_p\alpha_q)^i \\ & - \sum_{p=1}^{n-1}\sum_{q=p+1}^{n} 2c_p c_q\sum_{i=k}^{m-1} i(\alpha_p\alpha_q)^i) \end{aligned} \quad (27)$$

where the terms $\sum_{i=k}^{m-1}\alpha_p^{2i}$, $\sum_{i=k}^{m-1} i\alpha_p^{2i}$, $\sum_{i=k}^{m-1}(\alpha_p\alpha_q)^i$ and $\sum_{i=k}^{m-1} i(\alpha_p\alpha_q)^i$ can be determined respectively as

$$\sum_{i=k}^{m-1}\alpha_p^{2i}=\frac{\alpha_p^{2k}(1-\alpha_p^{2(m-k)})}{1-\alpha_p^2} \tag{28}$$

$$\sum_{i=k}^{m-1} i\alpha_p^{2i}=\frac{\alpha_p^{2k}(1-\alpha_p^{2(m-k)})}{(1-\alpha_p^2)^2}+\frac{(k-1)\alpha_p^{2k}-(m-1)\alpha_p^{2m}}{(1-\alpha_p^2)} \tag{29}$$

$$\sum_{i=k}^{m-1}(\alpha_p\alpha_q)^i=\frac{(\alpha_p\alpha_q)^k(1-(\alpha_p\alpha_q)^{m-k})}{1-\alpha_p\alpha_q} \tag{30}$$

$$\sum_{i=k}^{m-1} i(\alpha_p\alpha_q)^i=\frac{(\alpha_p\alpha_q)^k(1-(\alpha_p\alpha_q)^{m-k})}{(1-\alpha_p\alpha_q)^2}+\frac{(k-1)(\alpha_p\alpha_q)^k-(m-1)(\alpha_p\alpha_q)^m}{(1-\alpha_p\alpha_q)} \tag{31}$$

Substituting the above four equations in Eqn. (27) yields

$$\begin{aligned}&s_{k,m}-s_k\\ =&\frac{\sigma_a^2}{N_p}\Big(\sum_{p=1}^{n}c_p^2\Big(-\frac{\alpha_p^{2k}(1-\alpha_p^{2(m-k)})}{(1-\alpha_p^2)^2}+\frac{N_k\alpha_p^{2k}-\alpha_m^2}{1-\alpha_p^2}\Big)\\ &+\sum_{p=1}^{n-1}\sum_{q=p+1}^{n}2c_pc_q\Big(-\frac{(\alpha_p\alpha_q)^k(1-(\alpha_p\alpha_q)^{m-k})}{(1-\alpha_p\alpha_q)^2}\\ &+\frac{N_k(\alpha_p\alpha_q)^k-(\alpha_p\alpha_q)^m}{1-\alpha_p\alpha_q}\Big)\Big)\\ \triangleq&\sum_{p=1}^{n}c_p^2\times Sum1+\sum_{p=1}^{n-1}\sum_{q=p+1}^{n}(2c_pc_q)\times Sum2\end{aligned} \tag{32}$$

where

$$Sum1=\frac{\sigma_a^2}{N_p}\Big[-\frac{\alpha_p^{2k}(1-\alpha_p^{2(m-k)})}{(1-\alpha_p^2)^2}+\frac{N_p\alpha_p^{2k}-\alpha_m^2}{1-\alpha_p^2}\Big]$$

$$Sum2=\frac{\sigma_a^2}{N_p}\Big[-\frac{(\alpha_p\alpha_q)^k(1-(\alpha_p\alpha_q)^{m-k})}{(1-\alpha_p\alpha_q)^2}+\frac{N_p(\alpha_p\alpha_q)^k-(\alpha_p\alpha_q)^m}{1-\alpha_p\alpha_q}\Big]$$

When $k\to\infty$, $m\to\infty$ since $m\geq k$. Let $m-k=P\geq 0$. Consequently, $N_p=m-k+1=P+1$. The limits of $Sum1$ and $Sum2$ can be obtained:

$$\begin{aligned}\lim_{k\to\infty}Sum1=&\lim_{k\to\infty}\Big[-\frac{\alpha_p^{2k}(1-\alpha_p^{2(m-k)})}{N_p(1-\alpha_p^2)^2}+\frac{N_p\alpha_p^{2k}-\alpha_p^{2m}}{N_p(1-\alpha_p^2)}\Big]\sigma_a^2\\ =&0\end{aligned} \tag{33}$$

As $|\alpha_i|<1$, obviously $|\alpha_p\alpha_q|<1$. Similarly,

$$\begin{aligned}&\lim_{k\to\infty}Sum2\\ =&\lim_{k\to\infty}\Big(-\frac{(\alpha_p\alpha_q)^k(1-(\alpha_p\alpha_q)^{m-k})}{N_p(1-\alpha_p\alpha_q)^2}+\frac{N_p(\alpha_p\alpha_q)^k-(\alpha_p\alpha_q)^m}{N_p(1-\alpha_p\alpha_q)}\Big)\\ =&0\end{aligned} \tag{34}$$

Consequently,

$$\begin{aligned}&\lim_{k\to\infty}\{s_{k,m}-s_k\}\\ =&\sum_{p=1}^{n}c_p^2\times Sum1+\sum_{p=1}^{n-1}\sum_{q=p+1}^{n}(2c_pc_q)\times Sum2\\ =&0\end{aligned} \tag{35}$$

3.3 The multivariate process

Following a similar procedure as that for the univariate process, the following measure of optimal multi-step prediction error can be derived:

$$\begin{aligned}s_{k,m}=&tr(\tilde{F}_0\Sigma_a\tilde{F}_0^T+\tilde{F}_1\Sigma_a\tilde{F}_1^T+\cdots+\tilde{F}_{m-1}\Sigma_a\tilde{F}_{m-1}^T)\\ =&\sum_{p=0}^{k-1}\sum_{j=1}^{N}\sum_{i=1}^{N}f_{ijp}^2\sigma_j^2+\sum_{p=k}^{m-1}\frac{m-p}{m-k+1}\sum_{j=1}^{N}\sum_{i=1}^{N}f_{ijp}^2\sigma_j^2\end{aligned} \tag{36}$$

A same proposition as in the univariate case can be proved, but is omitted in this shorter version due to space limit.

4. CLOSED-LOOP POTENTIALS BASED ON THE MULTI-STEP PREDICTION

Based on the multi-step prediction error derived in the above section, the following closed-loop potential measure is defined for performance assessment of MPC:

$$p_{k,m}=\frac{s_{\infty,\infty+N_p}-s_{k,m}}{s_{\infty,\infty+N_p}} \tag{37}$$

where $N_p=P+1$ and P represents the prediction horizon. It can be shown that $s_{\infty,\infty+N_p}=s_\infty=trace\{cov(Y_t)\}$.

Here we use the multi-step prediction error scalar measure $s_{k,m}$ instead of the k-step prediction error scalar measure s_k of Huang et al. (2006) to derive closed-loop potential. As has been proven in the last section, with a fixed prediction horizon P, i.e. $m-k=P=N_p-1$, the scalar measure $s_{k,m}$ is monotonically increasing with k. So $p_{k,m}$ is monotonically decreasing. When $k=0$, $s_{k,m}\geq=s_0=0$, so $p_{0,N_p}\leq 1$. Besides, as $s_{\infty,\infty+N_p}\geq s_{k,m}$, consequently, $0\leq p_{k,m}\leq 1$. According to its definition we can see that the $p_{k,m}$ is dimensionless and in addition, the potential measure is more relevant to the MPC control strategy as it is multi-step prediction based. The actual process time delay (that corresponds to k) may not be known in practice. So the trajectory of the potential measure with a range of k will be more useful to assess the performance of the controller.

It is also desirable to know details about the performance of each output. So, the individual scalar potential measure is required. By replacing the operator $tr(\cdot)$ in Eqn. (36) with $diag(\cdot)$, the individual scalar measure is defined as:

$$s_{k,m}^{ind}=diag(\tilde{F}_0\Sigma_a\tilde{F}_0^T+\tilde{F}_1\Sigma_a\tilde{F}_1^T+\cdots+\tilde{F}_{m-1}\Sigma_a\tilde{F}_{m-1}^T)$$

where $s_{k,m}^{ind}\in\mathbb{R}^{N\times 1}$ and N represents the number of controlled variables.

The ith component of $s_{k,m}^{ind}$ can be obtained:

$$s_{k,m}^{ind}(i)=\sum_{p=0}^{k-1}\sum_{j=1}^{N}f_{jip}^2\sigma_i^2+\sum_{p=k}^{m-1}\frac{m-p}{m-k+1}\sum_{j=1}^{N}f_{jip}^2\sigma_i^2 \tag{38}$$

As a result, the individual potential measure can be defined as:

$$p_{k,m}^{ind}(i)=\frac{s_{\infty,\infty+N_p}^{ind}(i)-s_{k,m}^{ind}(i)}{s_{\infty,\infty+N_p}^{ind}(i)} \tag{39}$$

where $s_{\infty,\infty+N_p}^{ind}=diag(s_{\infty,\infty+N_p})=diag(cov(Y_t))$ and $1\leq i\leq N$.

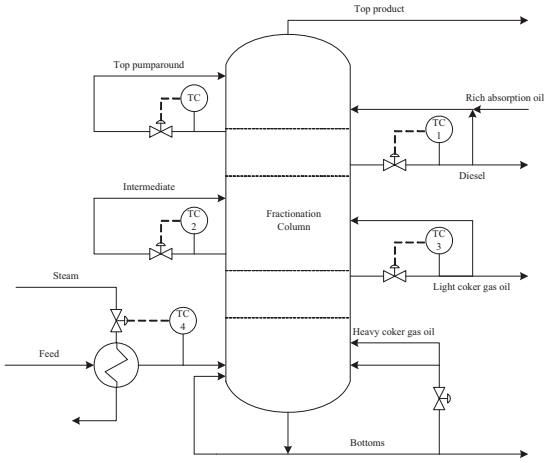

Fig. 1. Schematic diagram of the fractionation column in the delayed coking unit.

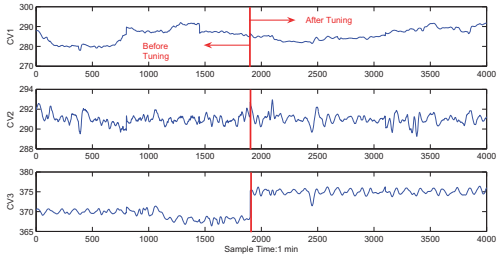

Fig. 2. Output data set under MPC controller.

5. INDUSTRIAL APPLICATION

In this section the proposed multi-step closed-loop potential measures will be applied to evaluate the performance of an industrial control system.

5.1 Process description

This is a control performance assessment and diagnosis problem for a MPC control system in a delayed coking refinery unit. Fig. 1 is a simplified process flow chart.

The control system consists of three manipulated variables (MVs), three controlled variables (CVs) and one disturbance variable (DV), the temperature of the feedstocks. A description of process variables and their corresponding tag names and the parameters for the MPC design is shown in Table 1.

Two different closed-loop operation data sets are collected with 1 min sampling interval under different MPC controller tunings as shown in Fig. 2. All the data is selected without the drum events to avoid unusual upset. The first part of the data from 1 to 1900 is selected before the controller tuning and the rest part is selected after the controller tuning.

5.2 Performance assessment

By using the proposed approach, the scalar potential measure trajectories for each data set are generated and

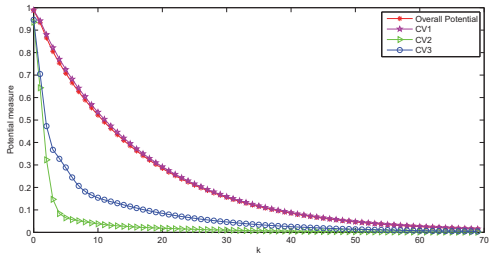

Fig. 3. Scalar potential measures of the system before controller tuning.

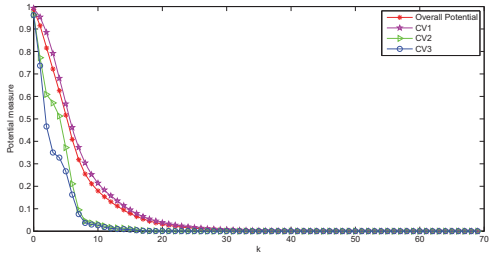

Fig. 4. Scalar potential measures of the system after controller tuning.

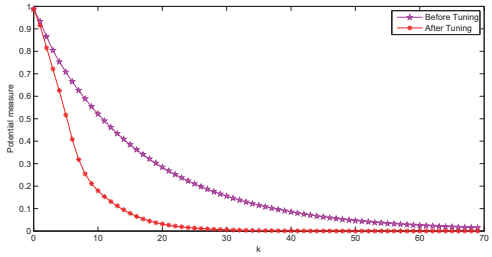

Fig. 5. Overall scalar potential measures of the system under different controller tunings.

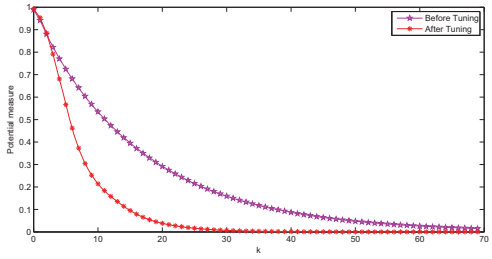

Fig. 6. Individual scalar potential measures of the system under different controller tunings of CV1.

shown in Fig. 3 and 4, respectively. The comparisons of the overall potential and individual potential for each CV are displayed from Fig. 5 to Fig. 8.

With these figures, the following performance analysis conclusions can be obtained:

Table 1. List of process variables and their corresponding tag names and parameters for MPC design.

No.	Tag	Weight	Horizon	Operation Range
CV1	Temperature of diesel	10	20	275-295
CV2	Temperature in the intermediate	1	20	285-295
CV3	Temperature of light coker gas oil	1	20	360-380
MV1	Valve opening of diesel	0.1	3	0-100
MV2	Valve opening of intermediate reflux	0.1	3	0-100
MV3	Valve opening of light coker gas oil reflux	0.1	3	0-100

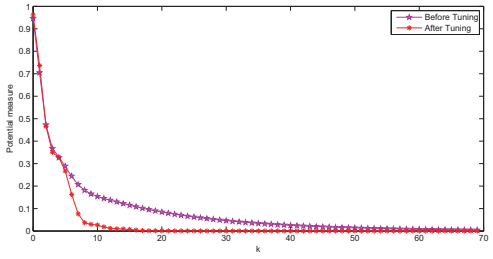

Fig. 7. Individual scalar potential measures of the system under different controller tunings of CV2.

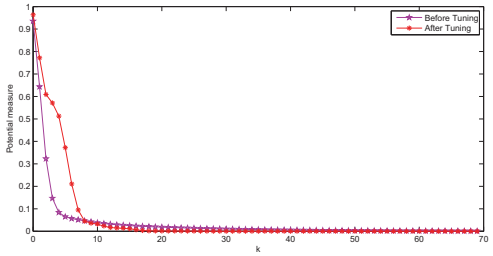

Fig. 8. Individual scalar potential measures of the system under different controller tunings of CV3.

- According to Fig 3, before the controller tuning, the overall scalar potential measure trajectory converges slowly and CV1 contributes the more potential to the overall potential than the other two CVs.
- According to Fig 4, after the controller tuning, the overall scalar potential measure trajectory converges fast and the three individual trajectories come close to each other, although the trajectory of CV1 still lies above the other two.
- According to Fig 5, there is significant improvement of the system's performance after the tuning as there is less potential after the controller tuning than that before tuning.
- According to Fig 6, 7 and 8, performance of both CV1 and CV2 is improved after the controller tuning; however, performance of CV3 is degraded after the tuning.
- The above results indicate that the improvement of the overall performance comes from the improvement of CV1 and CV2 but at some cost of CV3. As CV1 is the most important quality variable (the weight of CV1 is larger than those of the other two in Table 1.), it is worth to improve its performance by slightly deteriorating the performance of CV3.

In summary, after the controller tuning, there is significant improvement of the system's performance.

6. CONCLUSION

The closed-loop potentials are promising measures of model predictive control performance. However, they have certain limitations as they are originally defined. In this paper, new closed-loop potentials are proposed. The proposed performance potentials are multi-step prediction based and thus MPC relevant. Regardless of the dimension of the plant, the closed-loop potentials can be easily calculated, which facilitates the implementation, visualization, and interpretation. Industrial application demonstrates powerfulness of the the proposed performance measures.

REFERENCES

Harris, T.J., C.T. Seppala, and L.D. Desborough. A review of performance monitoring and assessment techniques for univariate and multivariate control systems. *Journal of Process Control*, 9:1-17, 1999.

Harris, T.J. Assessment of closed loop performance. *Can.J.Chem.Eng.*, 67:856-861, 1989.

Huang, B. and R. Kadali. *Dynamic Modeling, Predictive Control and Performance Monitoring: A Data-driven Subspace Approach*. Verlag: Springler, 2008.

Huang, B., S.X. Ding, and N. Thornhill. Alternative solutions to multi-variate control performance assessment problems. *Journal of Process Control*, 16:457-471, 2006.

Huang, B., A. Malhotra, and E.C. Tamayo. Model predictive control relevant identification and validation. *Chemical Engineering Science*, 58:2389-2401, 2003.

Huang, B. and S.L. Shah. *Performance Assessment of Control Loops: Theory and applications*. Springer: New York, 1999.

Jelali, M. An overview of control performance assessment technology and industrial applications. *Control Engineering Practice*, 14:441-466, 2006

Qin, S.J. Recent developments in multivariable controller performance monitoring. *Journal of Process Control*, 17:221-227, 2007.

Shook, D.S., C. Mohtadi and S.L. Shah. A Control-Relevant Identification Strategy for GPC. *IEEE Trans. AC*, 37, 1992.

Xu, F., B Huang, and S. Akande. Performance Assessment of Model Predictive Control for Variability and Constraint Tuning. *Ind. Eng. Chem. Res.*, 46:1208-1219, 2007.

Zhao, Y., Y. Gu, H. Su, B. Huang. Extended prediction error approach for MPC performance monitoring and industrial applications. *17th IFAC World Congress*, Seoul, 2008.

Valve friction and nonlinear process model closed-loop identification

Rodrigo A. Romano * **Claudio Garcia** **

* *Polytechnic School, University of São Paulo, São Paulo, Brazil (Tel: +55 11-30911893, e-mail: rodrigo.romano@poli.usp.br)*
** *Polytechnic School, University of São Paulo, São Paulo, Brazil (Tel: +55 11-30915648, e-mail: clgarcia@lac.usp.br)*

Abstract: Friction in control valves and inadequate controller tuning are two of the major sources of control loop performance degradation. As friction models are needed to diagnose abnormal valve operation or to compensate such undesirable effects, process models play an essential role in controller design. This paper extends existing optimization-based methods that jointly identify the process and friction model parameters, so that a nonlinear process model structure is considered. The procedure is based on data generated from closed-loop experiments with an external test signal. A simulation example indicates that the method accurately quantifies the valve friction, the process dynamics and the nonlinear steady state characteristics, even when the system is subjected to different level of disturbances.

Keywords: Control valves; Nonlinear models; Identification algorithms; Friction.

1. INTRODUCTION

Among several process variability sources (e.g., inadequate controller structure/ tuning, equipment malfunction, poor design, lack of maintenance) valve friction is supposed to be one of the most prevalent (Desborough and Miller, 2001). For this reason, friction quantification methods are highly desirable, since they can be applied in the development of model-based compensators or to diagnose valves that need repair. Moreover, quantification methods based only on controller output (*op*) and process output (*pv*) measurements from closed-loop experiments, are preferable for practical reasons.

Choudhury et al. (2004) dealt with friction quantification by means of the *pv*-*op* plot, but the results produced by this technique depend on the controller tuning. In a method proposed by Srinivasan et al. (2005), an optimization approach is used to jointly estimate the process dynamics and the friction model parameters. This method can be seen as a Hammerstein model identification, since the valve friction is treated as a nonlinear static block ($\mathcal{N}$) followed by a linear dynamic block ($\mathcal{L}$) that represents the process. As the process dynamics is also estimated, the joint procedure previously mentioned can be used for controller retuning. However, in that work, an inappropriate friction model structure that is unable to reproduce important sticky valve characteristics is employed. In a recent work (Choudhury et al., 2008), this drawback was eliminated through the adoption of another friction model structure.

An additional extension to the method originally proposed by Srinivasan et al. (2005) is to model the process with a Wiener structure (Figure 1), built up with a linear dynamic block connected to a nonlinear static function ($\mathcal{L} \rightarrow \mathcal{N}$). In this approach the Hammerstein structure is

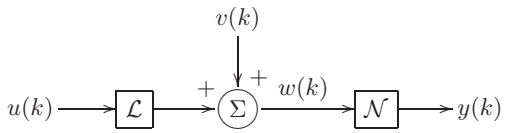

Fig. 1. Wiener model structure with nonlinear disturbance.

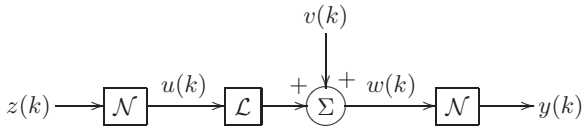

Fig. 2. Hammerstein-Wiener model structure with nonlinear disturbance.

extended to a Hammerstein-Wiener one ($\mathcal{N} \rightarrow \mathcal{L} \rightarrow \mathcal{N}$), i.e., the valve friction is associated with the first nonlinear block, while the remainder blocks represent the process. The Hammerstein-Wiener structure is shown in Figure 2.

This extension intends to provide some features: (*i*) to avoid that process nonlinearities be erroneously incorporated in the friction model, (*ii*) to prevent bias problems in the process model identification and (*iii*) to turn the estimation method suitable to wider operating ranges.

This work proposes a procedure to jointly estimate nonlinear process dynamics and friction model parameters from closed-loop experiments. Actually, it is an extension from previous works (Choudhury et al., 2008; Srinivasan et al., 2005). The paper is organized as follows: the structure that models the valve friction is described in section 2. The parameterization of the nonlinear process, as well as an estimation algorithm suitable for closed-loop data are treated in section 3. The friction and process model joint estimation procedure is presented in section 4. This

procedure is tested through a simulated example in section 5. At last, the conclusions are drawn.

2. VALVE FRICTION MODEL

Several friction models were evaluated using ISA standard tests in Garcia (2008). The best trade-off between accuracy and simplicity was achieved by the data-driven model proposed by Kano et al. (2004). This is a modified version of the model employed in the friction quantification algorithm proposed in Choudhury et al. (2008) and it is characterized by two parameters: S that represents the cummulative input signal $z(k)$ amplitude change necessary to revert the valve movement direction and J that is the size of the stem slip, also referred as slip-jump, observed when the valve starts to move.

Besides the parameters S and J, the friction model uses three auxiliar variables: stp that indicates if the valve is moving ($stp = 0$) or if it is stuck ($stp = 1$), z_s that is updated with $z(k)$ every time the valve sticks and $d = \pm 1$ that denotes the direction of the friction force.

The relationship between the command signal $z(k)$ and the valve stem position $u(k)$ is described in the flowchart shown in Figure 3. After testing whether the valve stopped, so that z_s and stp are eventually updated, a new value is assigned to $u(k)$ if: (i) the valve is moving ($stp = 0$), (ii) the valve changes its direction and overcomes S or (iii) the valve moves in the same direction and overcomes J. On the contrary, the position remains the same.

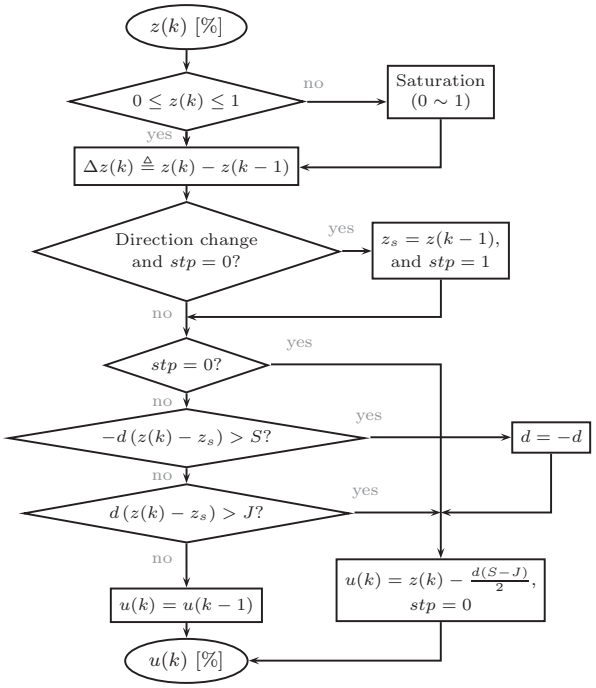

Fig. 3. Flowchart of the data-driven model parameterized by S and J (Kano et al., 2004).

3. NONLINEAR PROCESS MODEL

3.1 Model parameterization

Consider the Wiener model depicted in Figure 1, where the input signal is denoted by $u(k)$, the output signal by $y(k)$ and $v(k)$ represents the process disturbances. Notice that $v(k)$ is applied before the nonlinear block. In this case, the disturbances are also subject to the process nonlinearity. This scheme, proposed by Zhu (1999), is more realistic from a process operation point of view.

The linear dynamic block can be represented by a rational transfer function of order n:

$$G(q) = \frac{b_1 q^{-1} + \ldots + b_n q^{-n}}{1 + a_1 q^{-1} + \ldots + a_n q^{-n}} = \frac{B(q)}{A(q)} \tag{1}$$

where q^{-1} is the backward operator.

When prior knowledge about the process nonlinearity is not available, piecewise polynomials of third degree (cubic spline) provide advantages in respect of polynomials and piecewise linear functions to model the nonlinear block. For a set of m different knots:

$$w_{\min} = w_1 < w_2 < \ldots < w_{m-1} < w_m = w_{\max} \tag{2}$$

A cubic spline can be expressed by (Lancaster and Šalkauskas, 1986):

$$\begin{aligned} y(k) &= f\left(w(k)\right) \\ &= \sum_{i=2}^{m-1} \xi_i \left|w(k) - w_i\right|^3 + \xi_m + \xi_{m+1} w(k) \end{aligned} \tag{3}$$

where $\Xi \triangleq \left(\xi_2, \ldots, \xi_{m+1}\right)^T$ is the cubic spline parameter vector and $w(k)$ denotes the Wiener model intermediate signal.

3.2 Wiener model parameter estimation

In the closed-loop identification of Wiener models, the prediction error approach yields unbiased estimates, provided the process and the disturbance models are built simultaneously and the process model contains at least a delay of one sampling period (Forssell, 1999). To satisfy this condition, the disturbance term is modeled using an Auto Regressive Moving Average (ARMA) structure:

$$\begin{aligned} v(k) &= H(q)e(k) = \frac{C(q)}{D(q)} e(k) \\ &= \frac{1 + c_1 q^{-1} + \ldots + c_{n_c} q^{-nc}}{1 + d_1 q^{-1} + \ldots + d_{n_d} q^{-nd}} e(k) \end{aligned} \tag{4}$$

where $e(k)$ is white noise with zero mean and variance σ^2.

Suppose that the function which describes the process nonlinearity is monotonic and invertible. Hence, analogously to (3), the inverse of the process nonlinearity $f^{-1}(\cdot)$ can be denoted by:

$$w(k) = \sum_{i=2}^{p-1} \gamma_i \left|y(k) - y_i\right|^3 + \gamma_p + \gamma_{p+1} y(k) \tag{5}$$

Furthermore, as the intermediate signal $w(k)$ is unmeasurable, the gain of the Wiener model can be arbitrarily distributed between the dynamic and the static block. For this reason, the constraint $\gamma_{p+1} = 1$ is introduced in (5), so that the parameters can be uniquely determined.

The Wiener model parameters can be obtained from the minimization of the prediction error criterion:

$$V = \sum_k \left(H^{-1}(q)\left(w(k) - G(q)u(k)\right)\right)^2 \tag{6}$$

In order to estimate the Wiener and disturbance model parameters, besides the assumption that the process nonlinearity is invertible, the algorithm considers that the process is open loop stable. Both assumptions are commonly found in many practical situations, e.g., CSTRs, distillation columns and pH neutralization processes. Hence, $G(q)$ can be approximated by a finite impulse response (FIR) model, so that the intermediate signal is expressed by:

$$w(k) = \beta_1 u(k-1) + \ldots + \beta_r u(k-r) + v(k) \tag{7}$$

For more compact notation, consider the regression $\psi(k)$ and the parameter θ vectors:

$$\psi(k) \triangleq \Big(-|y(k) - y_2|^3, \ldots, -|y(k) - y_{p-1}|^3, -1, u(k-1), \ldots, u(k-r)\Big)^T \tag{8}$$

$$\theta \triangleq (\gamma_2, \ldots, \gamma_{p-1}, \gamma_p, \beta_1, \ldots, \beta_r)^T \tag{9}$$

Considering (8) and (9), (6) can be rewritten as:

$$V = \sum_k \left(H^{-1}(q)\left(y(k) - \psi^T(k)\theta\right)\right)^2 \tag{10}$$

Since the criterion (10) is a nonlinear least-squares problem, the following algorithm is employed to calculate $G(q)$, $f(\cdot)$ and $H(q)$:

***Algorithm** 1.* Wiener and ARMA disturbance model parameter estimate.

i. Initialize the disturbance model $H(q)$ with:

$$\hat{C}(q) = \hat{D}(q) = 1 \tag{11}$$

ii. Calculate filtered version of the output and the regression vectors:

$$y_f(k) = \frac{D(q)}{C(q)} y(k)$$

$$\psi_f(k) = \frac{D(q)}{C(q)} \psi(k)$$

iii. Estimate the parameter vector θ from:

$$\hat{\theta} = \left(\sum_k \psi_f(k)\psi_f^T(k)\right)^{-1} \left(\sum_k \psi_f(k) y_f(k)\right) \tag{12}$$

iv. Calculate the residuals $\zeta(k)$ of the Wiener model obtained from the previous step:

$$\zeta(k) = y(k) - \psi^T(k)\hat{\theta} \tag{13}$$

v. Estimate an ARMA model for $\zeta(k)$, i.e., a filter to uncorrelate the residuals:

$$\hat{D}(q)\zeta(k) = \hat{C}(q)e(k) \tag{14}$$

vi. While convergence of $\hat{H}(q)$ does not occur, go to step (ii). Otherwise, go to the next step.

vii. The parameters of $A(q)$ and $B(q)$, defined in (1), are estimated by minimizing the error between the outputs of the FIR model and the transfer function $G(q)$:

$$V_{red} = \sum_k \left(\sum_{i=1}^{r} \hat{\beta}_i u(k-i) - \frac{B(q)}{A(q)} u(k)\right)^2 \tag{15}$$

viii. The nonlinear block parameter vector Ξ estimate is given by:

$$\hat{\Xi} = \arg\min_{\Xi} \sum_k \left(y(k) - \phi^T(k)\Xi\right)^2 \tag{16}$$

where:

$$\phi(k) \triangleq \left(|\hat{w}(k) - w_2|^3, \ldots, |\hat{w}(k) - w_{m-1}|^3, 1, \hat{w}(k)\right)^T$$

$$\hat{w}(k) \triangleq \hat{f}^{-1}(y(k))$$

Correspondingly to the iterative calculation of θ, the linear model reduction (15) and the nonlinear function determination (16) are formulated as linear least squares problems. For this reason, the procedure is considered to be numerically simple and suitable for practical situations.

4. FRICTION AND PROCESS MODEL JOINT IDENTIFICATION ALGORITHM

Consider the process control loop depicted in Figure 4. Since in most of the practical situations only the controller output and the process output are known, the problem to be treated is to identify the friction and process model by means of $z(k)$ and $y(k)$.

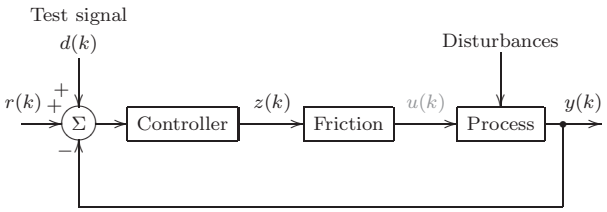

Fig. 4. Process control loop subject to valve friction.

In this work, the friction block is represented by the data-driven model of section 2, while the process dynamics is modeled by a Wiener structure. These parameterizations originate the control loop model shown in Figure 5.

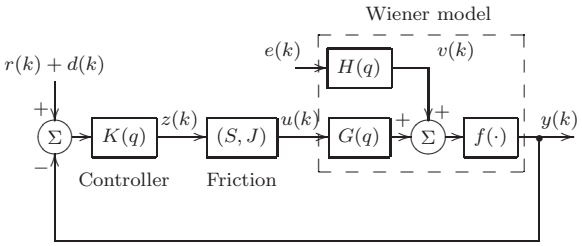

Fig. 5. Control loop where the valve friction and the process are modeled by a Hammerstein-Wiener structure.

In a first moment, suppose that the friction model parameters S and J are known. With this in mind, as the

controller output $z(k)$ is considered to be measurable, it is possible to estimate $u(k)$ with:

$$\hat{u}(k) = \mathcal{F}\left(z(k), \hat{u}(k-1), S, J\right) \tag{17}$$

where $\mathcal{F}(\cdot)$ is the nonlinear transformation described in the flowchart of Figure 3. Hence, the Wiener model parameters can be estimated, using the measured output $y(k)$ and $\hat{u}(k)$ instead of $u(k)$, by means of the algorithm presented in section 3. However, S and J are unknown. To deal with this fact, the following algorithm is proposed:

***Algorithm** 2.* Algorithm that simultaneously estimate the parameters of the friction and nonlinear process model.

i. Generate a set of candidate values for the pair (S, J). Two aspects are considered in order to restrict the set of candidate values: (a) the behavior of most real valves is reproduced by the data-driven model with $\max(J) \leq S$; (b) it is obvious that without stem movement, to estimate the valve friction is an impossible task. If an appropriate excitation $d(k)$ is employed, it is reasonable to consider that the stem velocity reversions are produced by the test signal. Therefore, the controller output imposes an upper bound for S:

$$\max(S) < \max(z(k)) - \min(z(k)) \tag{18}$$

Such constraints yield the geometric locus shown in Figure 6.

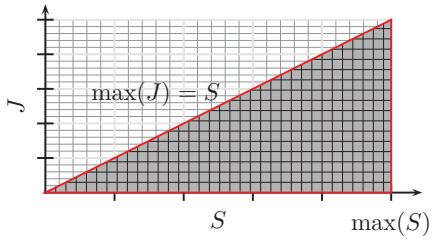

Fig. 6. Geometric locus of the friction model parameter candidate values.

ii. Choose a pair (S_i, J_j) from the set described in the previous step.

iii. Calculate the sequence of values $\hat{u}(k)$ from (17).

iv. Estimate the process model parameters using algorithm *1*, described in section 3.

v. Compute the prediction error of the intermediate signal $w(k)$ through the criterion:

$$\mathcal{C} = \sum_{k} \left(\hat{H}^{-1}(q) \left(\hat{f}^{-1}(y(k)) - \hat{G}(q)\, \hat{u}(k) \right) \right)^2 \tag{19}$$

vi. Until all the candidate values have been tested, back to step (ii). Otherwise, the values of S, J, $G(q)$ and $f(\cdot)$ are supposed to be the ones for which $\mathcal{C}$ is minimum.

Furthermore, note in Figure 4 that a test signal $d(k)$ is introduced into the set-point. Although external interferences are highly undesirable, the test signal guarantees sufficiently informative experiments. A well-known result from the closed-loop identification literature (Ljung, 1999) is that prediction error approach is not consistent if the data have been collected exclusively under feedback. In fact, the variance on the parameter estimate increases with disturbances and decreases the higher $d(k)$ is.

5. SIMULATIONS

To verify the applicability of the friction and process joint identification algorithm, the process loop in Figure 4 is simulated with a PI controller $C(q)$, a process dynamics reproduced by a continuous linear dynamic model $G(s)$ followed by a nonlinear block $f(w(k))$ and a disturbance $v(k)$ given by:

$$C(q) = \frac{0.5\left(1 - 0.5q^{-1}\right)}{\left(1 - q^{-1}\right)}$$

$$G(s) = \frac{5}{(0.5s+1)(s+1)(10s+1)}$$

$$y(k) = f\left(w(k)\right) = \frac{w(k)}{\sqrt{0.1 + 0.9w^2(k)}}$$

$$v(k) = \frac{\rho}{1 - 2.65q^{-1} + 2.335q^{-2} - 0.684q^{-3}} e(k)$$

The simulated friction model parameters are $S = 10\%$ and $J = 2\%$. The algorithm is tested in two distinct situations: low and high disturbances. In the first case, ρ is adjusted so that the disturbance level in $y(k)$ is 1.44% (in variance), while in the high disturbance scenario $v(k)$ provides a ratio of 12.5%.

A randomly switched multi-level signal, GMN (see Zhu, 2001), with average switch time of 25 sampling intervals and amplitude uniformly distributed between $[-0.15, 0.15]$ is applied in $d(k)$. The set-point $r(k)$ is fixed in 0.75. The input-output data of the high disturbance situation, as well as the excitation signal are shown in Figure 7.

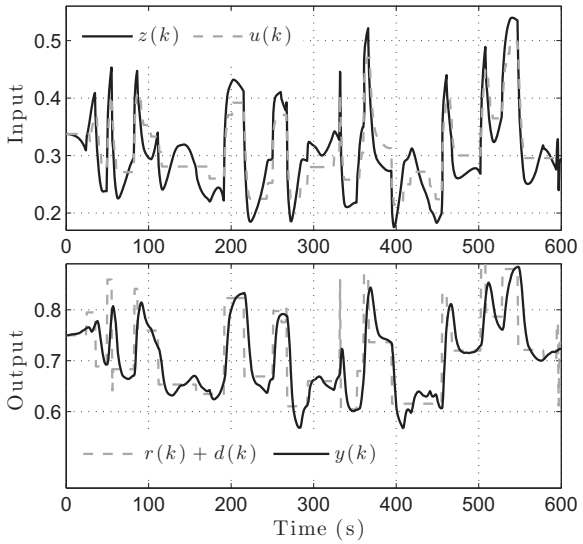

Fig. 7. Input-output data and external test signal of the high disturbance simulation.

The friction and process model parameters are estimated using 600 samples and a 1s sampling period. From (18) one has $\max(S) = 35\%$. A set of candidate values of the pair (S,J) is generated with a resolution of 1% and the process model was estimated using: $m = p = 3$, $r = 35$, $n_c = 0$, $n_d = 6$ and $l = 3$.

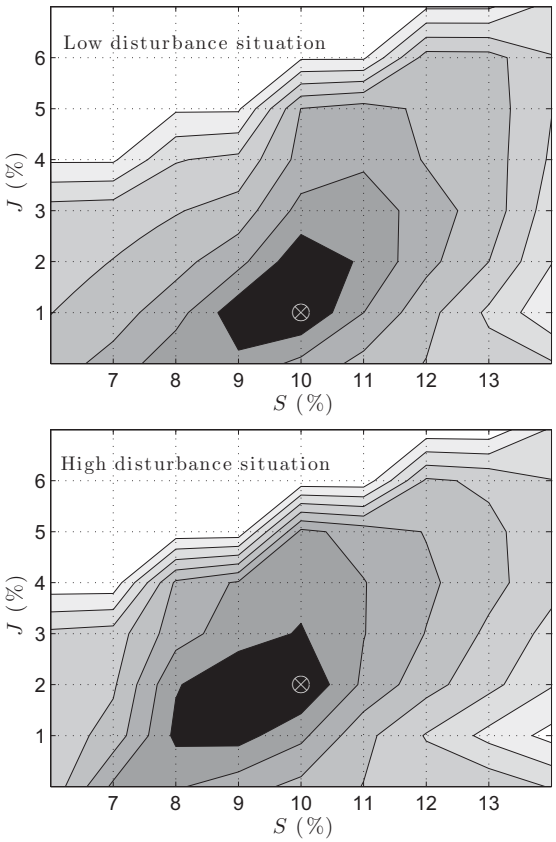

Fig. 8. Level curves of the prediction error $\mathcal{C}$.

The behavior of the prediction error $\mathcal{C}$, in both disturbance situations, is shown in Figure 8. Darker locations indicate lower prediction errors and the symbol "$\otimes$" indicates the minimum. In both disturbance situations, the parameter S is exactly estimated.

On the other hand, $\hat{J} = 1\%$ and 2% for the low and high disturbance scenarios, respectively. The slight misfit obtained in lower disturbance situation has two reasons: (1) the influence of the parameter S is prominent if compared to J and (2) the occurences of slip-jumps in the low disturbance simulation is minor (21 slip-jumps against 26 provided by the major disturbance simulation).

The Nyquist plot of linear block estimate from both disturbances scenarios are compared to the actual one in order to check if the process dynamics were incorporated. From Figure 9 it can be seen that the estimation from the low disturbance dataset provided better results. Therefore, it is clear that the disturbances degrade the accuracy of the identified linear dynamic block.

To get a better insight about frequency domain errors, the Bode plot of the estimates is depicted in Figure 10. Although the Nyquist curves suggest that the dynamic block estimate from the high disturbance simulation data presents a larger misfit, one can see that the errors related to the actual frequency response are acceptable for practical purposes.

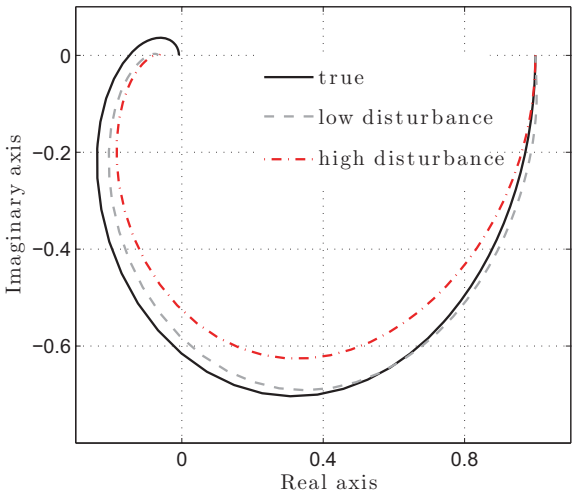

Fig. 9. Nyquist plot of $\hat{G}(q)$ obtained from both disturbance scenarios.

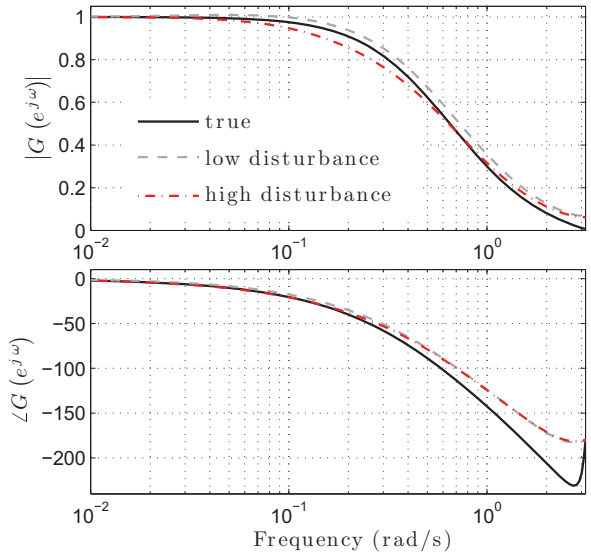

Fig. 10. Bode plot of the estimated dynamic models.

Finally, the nonlinear block fit is investigated. The true process nonlinearity and the estimates from low and high disturbance scenarios, denoted as $\hat{f}_{(low)}(\cdot)$ and $\hat{f}_{(high)}(\cdot)$, are presented in Figure 11. Despite adopting a parameterization different from the cubic splines during the simulations, the process nonlinearity is accurately estimated in both disturbance conditions.

Comparing the results achieved in each of the disturbance situations, one can see that the process steady state curve fit is better when the disturbance level is lower. Nevertheless, the estimation performance deterioration is slight, in spite of the substantial increase (almost 10 times higher) in the disturbance level.

6. CONCLUSIONS

The results provided by the simulated example suggests that the proposed procedure that jontly identifies the

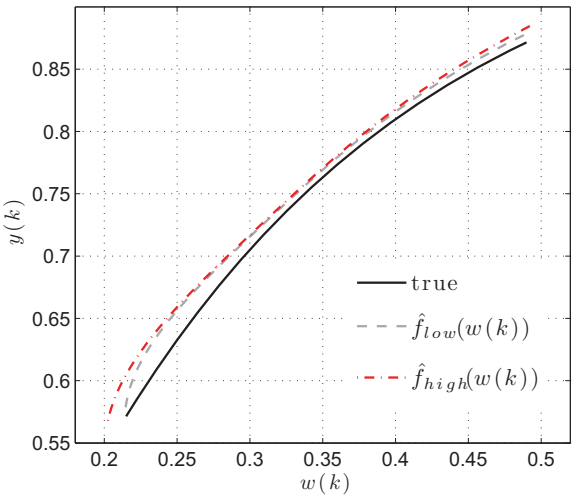

Fig. 11. Actual and estimated process nonlinearity.

friction and the nonlinear process model parameters is promising.

Moreover, the estimation results indicate that the GMN test signal is suitable for the process model identification. On the other hand, this excitation can not be adjusted in order to control the ocurrences of slip jumps. Thus, the GMN is insufficient to guarantee accurate estimates of the parameter J. An alternative to deal with this drawback is to combine a multi-level randon noise with a staircase excitation.

Another aspect that shoud be emphasized is that, when the process nonlinearity is severe, the Wiener model can be used to develop nonlinear controllers, such as gain schedule strategies.

Results of the procedure proposed here applied to industrial data is under development.

ACKNOWLEDGEMENTS

The authors thank CAPES for the Dr. scholarship granted to Rodrigo Alvite Romano.

REFERENCES

M. A. A. S. Choudhury, S. L. Shah, and N. F. Thornhill. Detection and quantification of control valve stiction. In *IFAC Symposium on dynamics and control of process systems (DYCOPS)*, Cambridge, MA, USA, July 5-7 2004.

M. A. A. S. Choudhury, M. Jain, S. L. Shah, and D. S. Shook. Stiction - definition, modelling, detection and quantification. *Journal of Process Control*, 18:232–243, 2008.

L. Desborough and R. Miller. Increasing customer value of industrial control performance monitoring - Honeywell's experience. In *6th International Conference on Chemical Process, CPC - VI*, pages 169–189, Tucson, USA, 2001.

U. Forssell. *Closed-loop Identification: Methods, Theory, and Applications*. Licentiate thesis no. 566, Department of Electrical Engineering, Linköping University, Linköping, Sweden, Mar 1999.

C. Garcia. Comparison of friction models applied to a control valve. *Control Engineering Practice*, 16(10): 1231–1243, 2008.

M. Kano, M. Hiroshi, H. Kugemoto, and K.Shimizu. Practical model and detection algorithm for valve stiction. In *IFAC Symposium on dynamics and control of process systems (DYCOPS)*, Cambridge, MA, USA, July 5-7 2004.

P. Lancaster and K. Šalkauskas. *Curve and Surface Fitting: An introduction*. Academic Press, London, 1986.

L. Ljung. *System Identification: theory for the user*. Prentice Hall, New Jersey, 2nd edition, 1999.

R. Srinivasan, R. Rengaswamy, S. Narasimhan, and R. Miller. Control loop performance assessment. 2. Hammerstein model approach for stiction diagnosis. *Industrial & Engineering Chemistry Research*, 44(17): 6719–6728, 2005.

Y. Zhu. *Multivariable System Identification for Process Control*. Elsevier Science, Oxford, 2001.

Y. Zhu. Distillation column identification for control using Wiener model. In *1999 American Control Conference*, Hyatt Regency San Diego, California, USA, 1999.

Control Loop Performance Monitoring using the Permutation Entropy of Error Residuals

Rachid A. Ghraizi, Ernesto C. Martínez*, César de Prada****

**University of Vallodolid, Department of Systems Engineering and Automatic Control, Valladolid 47011, Spain (e-mails:{rachidag, prada}@autom.uva.es)*
***National Scientific Research Council, INGAR(CONICET), Avellaneda 3657, Santa Fe, S3002 GJC, Argentina (Tel: +54 342 4534451; e-mail: ecmarti@ santafe-conicet.gob.ar)*

Abstract: The predictability of a control-loop behavior beyond its control horizon is an unambiguous indication of loop malfunctioning. Based on the dynamic complexity of the error residual time series the permutation entropy is proposed to define a sensitive index for performance monitoring using data from close-loop operation. A generic framework to understand and quantify the distinctive increase in predictability of the controller error resulting from ill-tuning, sensor errors and actuator faults using a entropy-like index is presented. The dynamic complexity of a well-performing control loop should correspond to the maximum entropy. As loop performance degrades the entropy of its residual time series decreases and any loss of dynamic complexity in the control system gives rise to an increase of the predictability of the control error time series. Results obtained using the proposed performance index along with its confidence interval for industrial data sets are presented to discuss the influence of the sample size, control horizon, and variance estimation in the assessment of close-loop performance.

Keywords: Control-loop performance; Monitoring; Permutation entropy; Fault detection and diagnosis; Error predictability; Ordinal patterns; Time-series analysis.

1. INTRODUCTION

Control loops implementing a hierarchy of functions for process regulation and optimization are the cornerstone of safety and economy in process plants (Thornhill et al., 1999). Many loops are just PID controllers whilst other may be more advanced ones, such as inferential loops, MPCs and real-time optimizers working on top of the regulation layer. It is well known that in most industrial environments the behavior of control loops deteriorate with time due to a number of reasons, e.g. plant-wide perturbations, fouling, utility constraints and raw material variability. Accordingly, process dynamic characteristics change over time and, if not properly maintained, most control loops will perform poorly after some time, which can lead to degraded process operation. In particular, ill-functioning of the regulation layer can easily cancel the benefits of advanced control systems and real-time optimization (Jelali, 2006; AlGhazzawi and Lennox, 2009). With the increasing complexity of control structures and the sheer number of controllers in modern process plants, the automation of performance monitoring tasks is mandatory.

Systematic assessment of SISO control loops can be traced back to the seminal work of Harris (1989) who related the performance of a single-loop control system to the controller errors of a minimum variance controller. The latter, even though it is rather impractical to be implemented, serves as a performance benchmark to provide a lower bound for the variance of the controlled variable. On this basis, the well-known Harris index is defined as the ratio of the variance achievable using minimum variance controller to the variance measured under the current control law (Desborough and Harris, 1992, 1993). As the value of this statistic is reduced then so too does the measured performance of the control system. The key advantage of the Harris approach to control loop monitoring is that only routine close-loop operating data are required to determine the performance of the control system. This fact has made the approach very attractive to industry and it is now applied as a matter of routine by many companies. However, a disadvantage of the Harris index is that it is based on a rather extreme (in terms of cost and energy involved) behaviour and no hints are provided for characterizing the behaviour a well-performing realistic controller based on the control task for which it was designed. Also, it is difficult to pinpoint an informative threshold for the Harris index to differentiate between normal and faulty operation of a control loop.

Based on the insightful concept of control horizon, Thornhill *et al.* (1999) proposed the predictability of the error time series to characterize the performance of a SISO controller. The predictability of a control-loop behaviour beyond its control horizon is an unambiguous indication of loop malfunctioning in biological systems (Li, Ouyang and Richards, 2007). Along this research avenue, Ghraizi *et al*. (2007), proposed a practical index for performance monitoring of a control loop based on the analysis of the predictability of the error time series and emphasizes proper

selection of the control horizon using engineering judgment and the amplitude and frequency of disturbances to which the loop is designed for. To develop ideas further, Martínez and de Prada (2007) resort to ordinal analysis methods of the error time series to define a performance index for performance monitoring based on the permutation entropy.

In this work, the interplay between predictability of controller behaviour and its dynamic complexity for performance monitoring is highlighted by resorting to the residual error time series, which is obtained using a regression model. A generic framework to understand and quantify the distinctive increase in predictability of the controller error resulting from ill-tuning, sensor errors and actuator faults using an entropy-like index is proposed. A well-performing controller should behave so that the sequence of residuals in the error series looks like one generated using *i.i.d.* samples from a random walk and the corresponding dynamic complexity is thus maximum. Accordingly, ordinal patterns in the error residuals will all be equally probable and the corresponding permutation entropy will be then the highest possible.

2. MONITORING METHODOLOGY

2.1 *Predictability analysis*

The performance-monitoring concept revolves around the idea of predictability of controller behaviour beyond a chosen horizon *b*. If a control loop exhibits "good" performance, it should be able to cancel any disturbance entering the loop up to present time *t*, or follow a set point change correctly, after some sensible time interval *b* (expressed in terms of sampling periods). Then, it can be argue that, as from time *t+b* onwards, the error time series cannot be distinguished from a random walk stochastic process so that it cannot be predicted at all using information up to time instant *t* (see Fig. 1 for details). Nevertheless, over the control horizon *b*, the controller behaviour is fully predictable since it corresponds to its own control policy built-in by design. By contrast, error time series of a control loop exhibiting "poor" performance, will show patterns of behaviour (oscillations, steady-state errors, etc.) which can be predicted after time instant *t+b* using present and past measurements.

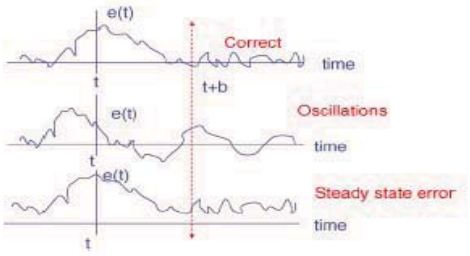

Fig. 1. Error patterns and their predictability

The most sensitive approach to detect patterns of predictability in the time series is analyzing the time series of error residuals $r(t)$ which are obtained using an inductive model to predict future errors.

Let's denote by $e(t)$ the controller error defined as

$$e(t) = \omega(t) - y(t) \tag{1}$$

Where $\omega(t)$ stands for the desired set-point at any time t, and $\hat{e}(t)$ stands for the prediction of such error based on past values of the controller error. The difference between the actual and predicted controller errors is the residue *r(t)* whose time series has a dynamic complexity closely related to the predictability patterns in the controller error time series

$$r(t) = e(t) - \hat{e}(t) \tag{2}$$

The error prediction $\hat{e}(t)$ can be obtained in different ways, but the easiest alternative is using the regression model

$$\begin{aligned}\hat{e}(t+b) = e_o + e_1(t) + e_2(t-2) + e_3(t-3)....\\ + e_m(t-m+1)\end{aligned} \tag{3}$$

Where time indices refer to sampling periods, *m* is the model order and a_i is the unknown parameters, which are fitted using a dataset of size *n* by means of the least-square regression:

$$[a_0, a_1, ..., a_m]^T = (X^T X)^{-1} X^T Y \tag{4}$$

Where

$$X = \begin{bmatrix} 1 & e(1) & e(2) & \cdots & e(m) \\ 1 & e(2) & e(3) & \dots & e(m+1) \\ \vdots & \vdots & \vdots & \vdots & \vdots \\ \vdots & \vdots & \vdots & \vdots & \vdots \\ 1 & e(n-b-m+1) & \cdots & \cdots & e(n-b) \end{bmatrix} \tag{5}$$

And

$$Y = \left[e(m+b)\ e(m+b+1) \cdots e(n)\right]^T \tag{6}$$

It is worth noting that for a well-performing controller in a given time interval the sequence of error residuals is a chaotic, completely random, and non-stationary stochastic process exhibiting maximum dynamic complexity. The reader is referred to the work of Peng et al. (2009) for an interesting discussion on the meaning of regularity and dynamic complexity in physiologic time series from highly controlled biological systems. To quantify the dynamic complexity of residuals there are several options.

In a previous work, the authors, Ghraizi *et al*. (2007), used a performance index based on the ratio between the variance of the residuals and the variance of the errors:

$$PI = \frac{\sigma_r^2}{\sigma_e^2} \tag{7}$$

Assuming that in a perfectly predictable loop the variance of

the residual would be zero, while non-predictable random walk would give a variance similar to the loop error, this expression would provide an index ranging from zero to one that will measure the performance of the controller. In order to obtain a confidence interval of the index the following analysis can be performed:
It is known that the following ratio

$$\frac{(n-1)\hat{\sigma}^2}{\sigma^2} \tag{8}$$

between the estimated and real variance for an stochastic process must follow a χ^2 distribution with n-1 degrees of freedom. Applying this line of reasoning to the residuals and the controller errors and dividing them, we can obtain:

$$\frac{\sigma_r^2\hat{\sigma}_e^2}{\sigma_e^2\hat{\sigma}_r^2} \tag{9}$$

Which will follow a F-distribution with n-1,n-1 degrees of freedom. Hence:

$$\begin{aligned} &P(F_{1-0.5\alpha,n-1} \le \frac{\hat{\sigma}_e^2\sigma_r^2}{\sigma_e^2\hat{\sigma}_r^2} \le F_{0.5\alpha,n-1}) = 1-\alpha \\ &P(\frac{\hat{\sigma}_r^2}{\hat{\sigma}_e^2}F_{0.5\alpha,n-1}^{-1} \le \frac{\sigma_r^2}{\sigma_e^2} \le \frac{\hat{\sigma}_r^2}{\hat{\sigma}_e^2}F_{0.5\alpha,n-1}) = 1-\alpha \end{aligned} \tag{10}$$

Will can be used to compute the 100(1-α) % interval of confidence for the *PI* index defined in (7).

In practice, when this index is computed, large confidence interval appears sometimes, mainly when loop performance degrades, which reduces the interest in the above method. An alternative not based on statistical assumptions, which are always difficult to verify, would be desirable. In this regard, an appealing and sound choice is resorting to an entropy-like index based on ordinal patterns of the residual time series.

2.2 *Residual order patterns*

The complexity of a residual time series can be quantified by means of its symbolic dynamics. A new permutation method was proposed by (Bandt and Pompe, 2002; Bandt, 2005) to map a continuous time series onto a symbolic sequence; the statistics descriptive of the dynamic complexity of the symbolic time series is called permutation entropy. Given a data set for the scalar residual time series $r(t), t = 1,....,n$, the local order of the series can be characterized by patterns in vectors $\Re(t)$ ensembled as follows

$$\Re(t) = [r(t), r(t+\ell),...r(t+(\kappa-1)\ell))] \tag{11}$$

where κ is the embedded dimension parameter and ℓ is the lag parameter (here $\ell = 1$). Then entries in each $\Re(t)$ are arranged in increasing order which allows assigning to it one out of the possible order patterns. For κ different numbers, there will be $\kappa!$ possible order patterns π, which are also called permutations. In Fig. 2 the six order patterns for $\kappa = 3$ are shown. Let $f(\pi)$ denote the frequency of permutation π in the data set whereas $\rho(\pi) = f(\pi)/(n-(\kappa-1)\ell)$ is the relative frequency. For a perfectly working controller the relative frequencies should all be close to $1/\kappa!$

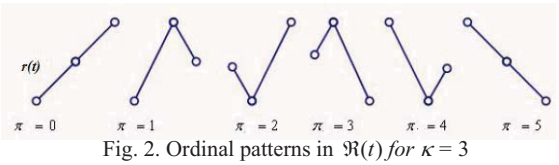

Fig. 2. Ordinal patterns in $\Re(t)$ *for* $\kappa = 3$

2.3 *Permutation entropy and performance monitoring*

The local permutation entropy of order κ for the error residual time series is defined as

$$H_\kappa = -\sum_{\pi=1}^{\kappa!}\rho(\pi)\ln\rho(\pi) \tag{12}$$

The largest possible value for the permutation entropy will correspond to the perfectly working controller where all $\kappa!$ permutations are equally probable which coincides with a residual time series of maximum complexity where the permutation entropy is ln $\kappa!$

Permutation entropy depends on the selection of κ. When κ is too small a value (say less than 3), the scheme will not work, since there are only very few distinct states for characterizing the control system behavior. For too large values of κ (greater than 6), the number $\kappa!$ of permutations which can appear in the time series can result in computer memory problems, due to the large number of data points that need to be examined. In the present work, only values of $\kappa = 3$, 4 or 5 will be used.

For loop monitoring, the permutation entropy of the residual time series is obtained from a sample where the total number of patterns counted is n and the tally number for the *ith* pattern in the sample is denoted by f_i

$$\hat{H}_\kappa^n = -\sum_{i=1}^{\kappa!}\left(\frac{f_i}{n}\ln\frac{f_i}{n}\right) \tag{13}$$

The corresponding variance for this sample estimation of the permutation entropy is (see Moddemeijer, 1989, for details)

$$Var\left(\hat{H}_\kappa^n\right) = \frac{1}{n}\left(\sum_{i=1}^{\kappa!}\frac{f_i}{n}\ln^2\frac{f_i}{n} - \left(\frac{f_i}{n}\ln\frac{f_i}{n}\right)^2\right) \tag{14}$$

Based on equations (13) and (14) and a sample of size n, the following performance index is proposed

$$PI = \frac{\hat{H}_\kappa^n}{\ln\kappa!}, \kappa = 3,4,... \tag{15}$$

Since ln$\kappa!$ is a constant, the variance for the sample estimation of the performance index can be written as

$$Var(PI) = \frac{Var\left(\hat{H}_\kappa^n\right)}{\ln\kappa!}, \kappa = 3,4,... \tag{16}$$

The highest value of *PI* is one, which means the error residual time series is complete random and is its dynamics is very complex; the smallest possible value of *PI* is zero, which

means the error residual time series is highly regular.

Eq. (14) is very important for the following reasons: it is possible to make a very reliable characterization of the variance of a sample-based estimation of the performance index *PI* in Eq. (15). For a well-performing control loop, since the probability for ordinal patterns are all the same, after elementary algebra steps in Eq. (14) an *exact* measure of the variance for the performance index is obtained

$$\frac{\left[\ln\left(\frac{1}{\kappa!}\right)\right]^2(\kappa!-1)}{\ln\kappa!\; n\;\kappa!} \qquad (17)$$

As can be readily calculated, this variance for a properly working loop is very small even for small sample sizes. For example, for n=1000 and κ=3, the variance of *PI* is ≅0.00149 for a perfectly working controller. For a much smaller sample size such n=100 is still rather small (≅0.0149).

To compute a 100(1-α) % confidence interval for the *PI* index estimated through Eq. (15), the Student's *t*-distribution is assumed so that the sample variance in Eq. (16) is used to define upper/lower limits in the usual way as follows

$$\pm t_{1-\alpha/2,n-1}\sqrt{\frac{Var(PI)}{n}} \qquad (18)$$

where α defines the chosen level of confidence.

3. RESULTS

In order to show the applicability of the proposed method, several data sets from an industrial site have been considered. They correspond to routine plant data of a set of typical control loops for pressure, flow, etc. The first one is displayed in Fig.3 and contains 9000 samples of the controlled and manipulated variables as well as the set point of a pressure control loop.

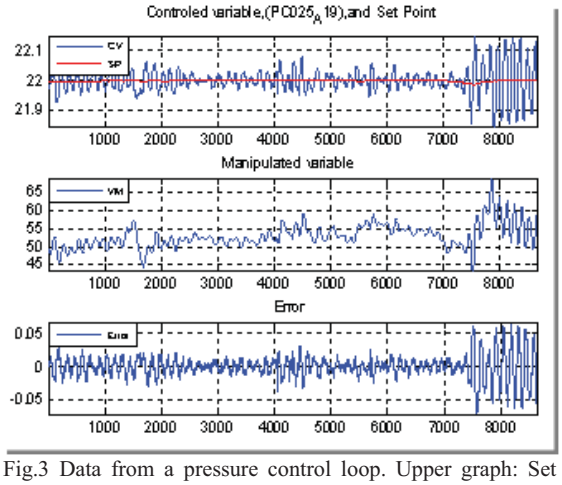

Fig.3 Data from a pressure control loop. Upper graph: Set point (in red) and gauge pressure. Middle graph: control valve signal. Bottom graph: error between set point and pressure readings.

Despite the fact that pressure readings stand close to the set point, the loop experiments an oscillatory behavior, likely as result of a too tight tuning. This can be better observed in a close-up to the data, as the one shown in Fig.4.

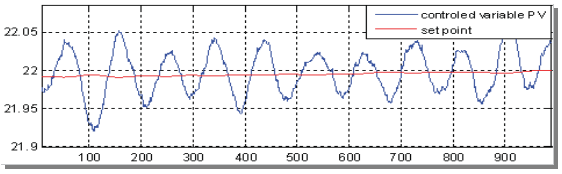

Fig.4. A detailed view of the first 1000 data of the time evolution of pressure and its set point for the example data set shown in Fig.3.

Results obtained from the application of the proposed method to pressure loop are discussed next. Fig.5. displays the actual error and its predictions computed from the expression (3). As can be seen, predictatility is significantly high, as one could expect in a badly tuned control loop whereas residuals are small. The residual time series is displayed in the upper part of Fig. 6, exhibiting a certain regularity, whereas in the bottom part the values of the proposed performance index (15) computed at regular time intervals every 120 data are shown for the case κ = 3 and b = 12.

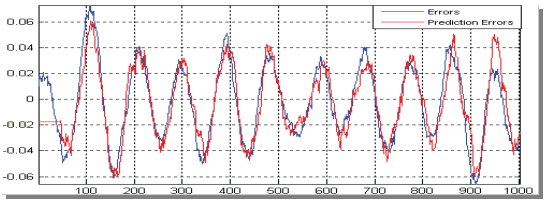

Fig.5. A detailed view of the errors and its predictions (in red) for the first 1000 data using prediction formula (3).

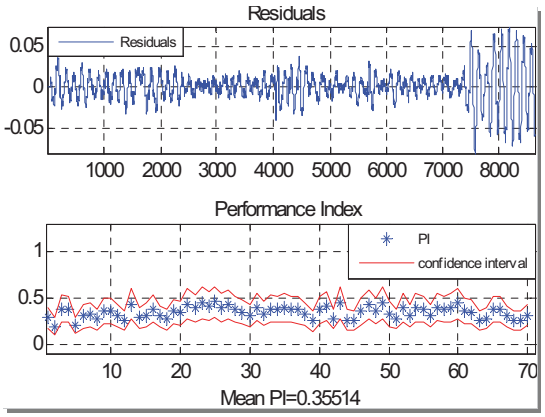

Fig.6. Upper graph: Residuals of the predictions computed with expression (2) for the example of Fig.3. Lower graph: Performance index computed from (16).

As can be seen, in this example, sample estimation the performance index have an average value of 0.35, which is an indication of poor performance of the pressure loop. For the sake of comparison, the *PI* computed from (7) is displayed in Fig.7. Even though consistent results are obtained, but the

confident limits rise up to 1 which creates a great deal of uncertainty in the estimation of this performance index.

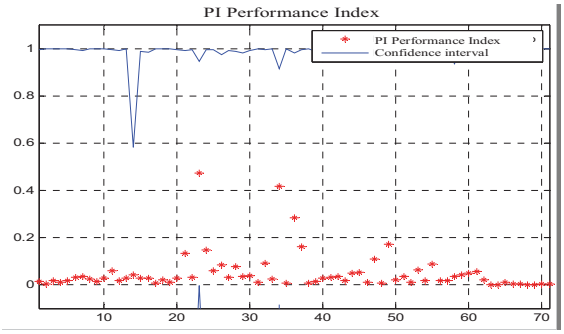

Fig.7. Performance index (in red) computing with expression (7) for the example of Fig.3. Blue line gives the upper confidence limit based on Eqs. (9) and (10).

Data from a second case study are given in Fig. 8. This time data correspond to a flow control loop that is the slave in a cascade configuration. 16,000 data poins are collected and, as can be seen, the loop behaviour is quite good, with fine set point tracking and moderate control signal changes, except in the range for data poins from 12,000 to 13,000, where extreme values of the set point from the master loop lead to saturation of the manipulated variable.

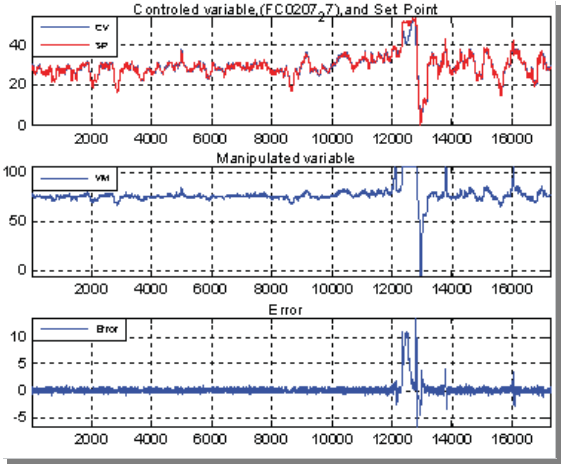

Fig.8. Data from a slave flow control loop. Upper graph: Set point (in red) and flow readins. Middle graph: control valve signal. Bottom graph: error between set point and actual flow.

As can be seen in the close-up displayed in Fig.9, there is a good following of the set point and the predictions of the errors computed with the expression (3) differ from the actual errors, so that the residuals (2), displayed in Fig.10, approach to a random walk, as expected in a loop with good behaviour.

The performance index (15) has been computed using the values $\kappa = 3$ and $b = 12$, at regular time intervals that include 120 data points. The numerical values displayed on the bottom of Fig.10 give regular values around 0.82 that is a reasonable value for this entropy-like index when all patterns are almost equiprobable.

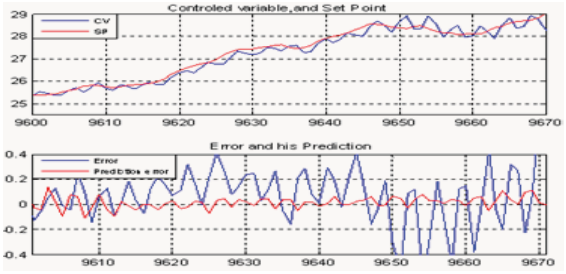

Fig.9. Upper graph: A close-up of data of the time evolution of flow and its set point (in red) for the example of Fig.8. Lower graph: A detailed view of the errors and its predictions (in red) for this range of data using prediction formula (3).

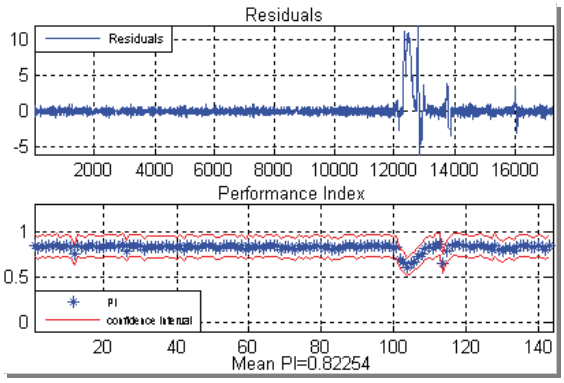

Fig.10. Upper graph: Residuals of the predictions computed with expression (2) for the example of Fig.8. Lower graph: Performance index computed from (16).

Nevertheless, in a set of intervals from data 12,000 on, where the manipulated variable is saturated, the predictions of the errors can be made very well, as can be observed in Fig.11, where the errors and its predictions computed with formula (3) are given.

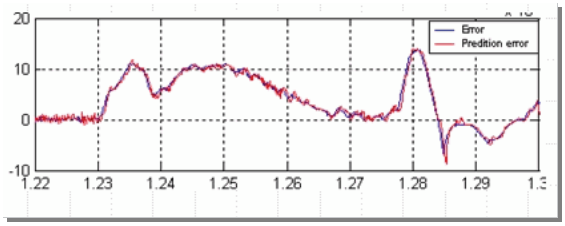

Fig.11. A detailed view of the errors and its predictions (in red) for a range of data above sample 12,000 of the example of Fig.8, using prediction formula (3).

In this case, the residuals are small and do not follow a random walk stochastic process, as can be seen in the corresponding range of variation shown in Fig.10. Accordingly, the *PI* decreases, indicating performance degradation of the loop in this portion of the data set.

For comparison, the *PI* computed with expression (7) and blocks of about 1000 data is given in Fig.12. As we can see, the index is between 0.75 and 0.9 giving consistent indications about the goodness of the loop behaviour, but at

the time intervals where the saturation occurs it drops to 0.1, 0.3 as expected. Nevertheless, the confidence bands increases at this precise times, decreasing the certitude of the diagnosis.

A final test was made to compare previous results with the ones provided by the Harris index for this case study, which are displayed in Fig.13. The values for the Harris index range from 0.3 to 0.5 for most samples, indicating that a margin for improvement exists in relation to the best possible linear controller -the minimum variance one- but it is worth noting that this index does not provide a direct measurement of the loop performance. Notice also that the index drops to 0 and 0.1 in the critical range when the saturation of the manipulated variable occurs.

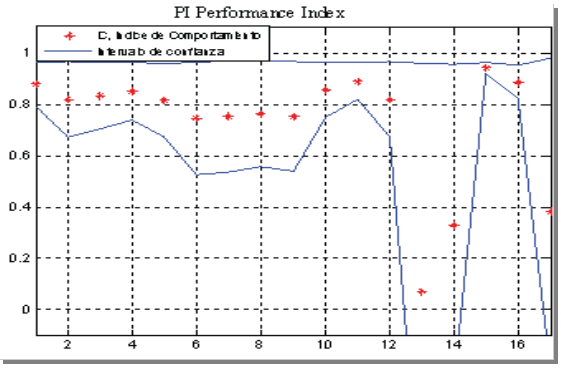

Fig. 12. Performance index (in red) computed with expression (7) for the example of Fig.8. Blue line gives the upper confidence limit.

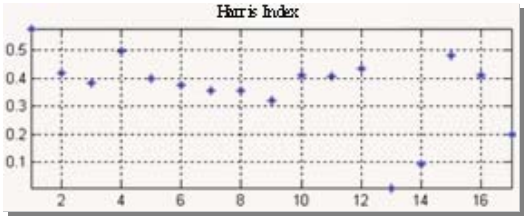

Fig. 13. Sample estimation of the Harris index for the example in Fig. 8 computed from batches of 1,000 data points.

4. CONCLUSIONS

A new index for performance assessment of control loops using normal operating plant data has been proposed. It combines the idea of predictability of the controller error at a point in time beyond the desired settling time of the loop, with an analysis of the corresponding sequence of prediction residuals based on ordinal methods along with the concept of local permutation entropy. The main advantage of the Performance Index defined in this way is the fact that no statistical assumptions are made on the residuals, which allows for a crisp interpretation of sample estimation of the performance index. Moreover, the entropy-like index is easy to compute and can be applied to single isolated loops as well as to cascades or other control configurations including model predictive controllers. For industrial data sets, the proposed *PI* has provides consistent results.

To highlight several advantages some comparisons were made with other indices such the Harris index and a previous *PI* based on the error predictability idea. The proposed method based on the permutation entropy can be applied in real time with minimum computational costs which opens the possibility of automatic supervision of hundreds of control loops of a typical process plant. Also, linking information content with predictability of error residuals is a novel idea for loop monitoring using dynamic complexity.

REFERENCES

AlGhazzawi, A. and Lennox, B. (2008). Model predictive control monitoring using multivariate statistics. *J. of Process Control* (in press).

Bandt, C. (2005). Ordinal time series analysis. *Ecological Modelling* 182, 229–238.

Bandt, C. and B. Pompe (2002). Permutation Entropy: A Natural Complexity Measure for Time Series. *Physical Review Letters* 88, 174102.

Desborough, L., & Harris, T. (1992). Performance assessment measures for univariate feedback control. *Canadian J. of Chemical Engineering* 70, 1186–1197.

Desborough, L., & Harris, T. (1993). Performance assessment measures for univariate feedforward/feedback control. *Canadian J. of Chemical Engineering* 71, 605–616.

Ghraizi, R. A. *et al.* (2007). Performance monitoring of industrial controllers based on the predictability of controller behavior. *Computers and Chemical Engineering* 31, 477-486.

Harris, T. J. (1989). Assessment of control loop performance. *Canadian J. Chemical Engineering*, 67, 856–861.

Jelali, M. (2006). An overview of control performance assessment technology and industrial applications. *Control Engineering Practice,* 14(5).

Li, X., Ouyang, G. and Richards, D. A. (2007). Predictability analysis of absence seizures with permutation entropy. *Epilepsy Research* 77, 70-74.

Martínez, E. C. and de Prada, C. (2007). Control Loop Performance Assessment using Ordinal Time Series Analysis. *Computer-aided Chemical Engineering* 24, 261-266.

Moddemeijer, R. (1989). On the estimation of the entropy and mutual information of continuous distribution. *Signal Processing* 16, 233-248.

Peng, C. K., Costa, M. and Goldberger, A. L. (2009). Adaptive data analysis of complex fluctuations in physiologic time series. *Advances in Adaptive Data Analysis* 1(1), 61-70.

Thornhill, N. F., Oettinger, M., and Fedenczuk, P. (1999). Refinery-wide control loop performance assessment. *J. of Process Control* 9, 109–124.

Performance Assessment of Decentralized Controllers

Antonius Yudi Sendjaja * **Vinay Kariwala** *

* *Division of Chemical and Biomolecular Engineering, Nanyang Technological University, Singapore 637459 (e-mails: ayudi@pmail.ntu.edu.sg, vinay@ntu.edu.sg)*

Abstract: Minimum variance (MV) benchmark is useful for identifying variance reduction opportunities in industrial control systems. During the past two decades, MV benchmarks for single-input single-output (SISO) and multi-input multi-output (MIMO) systems have been proposed. These MV benchmarks do not account for the structure of the decentralized or multi-loop controllers, which are used almost exclusively for regulation purposes in process industries. Due to this drawback, the available MV benchmarks can lead to incorrect conclusions regarding the performance of decentralized controllers. This paper aims to fill this gap. For performance assessment of decentralized controllers on a loop-by-loop basis, we present a simple modification of the available MV benchmark for SISO systems. For simultaneous performance assessment of all loops, we present a method for computing a tight lower bound on the achievable output variance. In the latter approach, the non-convexity of the resulting optimization problem is handled using sums of squares programming. The usefulness of the proposed benchmarks is evaluated using examples drawn from the literature.

Keywords: Decentralized control, Minimum variance control, Performance limits, Performance monitoring, Sums of squares programming.

1. INTRODUCTION

The performance of a well-designed control system can degrade over time due to changes in operating conditions and disturbance dynamics. Controller performance assessment is useful for identifying the opportunities for performance improvement of industrial controllers. Among the various available methods (Qin, 1998; Jelali, 2006), minimum variance (MV) benchmarking is one of the most promising methods for controller performance assessment. In this approach, the controller is deemed to provide satisfactory performance, if MV benchmark (ratio of least achievable and observed output variances) is close to 1. On the other hand, reduction in output variance is considered to be feasible through controller retuning, when the MV benchmark is significantly lower than 1.

The origin of MV benchmark can be traced back to Åström (1970), who demonstrated that the achievable output variance for a single-input single-output (SISO) process under feedback control depends on the first few impulse response coefficients of the disturbance model. Harris (1989) showed that with *a priori* knowledge of time delay, MV benchmark can be estimated using closed loop operating data and established it as a tool for performance assessment of SISO systems. Using the concept of interactor matrices, Harris et al. (1996) and Huang et al. (1997) proposed MV benchmark for multi-input multi-output (MIMO) systems.

This paper focusses on performance assessment of decentralized or multi-loop controllers, which are used almost exclusively for regulation purposes in process industries. Though useful, the available MV benchmarks for SISO and MIMO processes show limitations, when applied to processes under decentralized control. The conventional approaches for performance assessment of decentralized controllers include (see *e.g.* (Harris et al., 1996) and (Huang et al., 1997) for examples):

(1) *Loop by loop analysis*: The performance of individual loops is assessed independent of each other using MV benchmark for SISO processes.
(2) *Simultaneous analysis*: The performance of all loops is assessed simultaneously using MV benchmark for MIMO processes.

The MV benchmark for SISO processes assumes that the loop under consideration is being operated in isolation from the rest of the process and thus inherently views the process as being diagonal; see Figure 1. Due to this assumption, it may be possible to improve the performance of the existing controller further than indicated by the MV benchmark; see Section 3 for details. On the other hand, MV benchmark for MIMO processes ignores the diagonal structure of the decentralized controller and thus has more degrees of freedom for variance minimization than are available in the actual controller. Using a simple 2×2 process, we demonstrate in Section 4 that the least output variance that can be achieved using a diagonal controller can be four times higher than that can be achieved using a full multivariable controller. In summary, ignoring the controller structure can lead to incorrect conclusions regarding performance assessment of decentralized controllers.

The derivation of an approach for MV benchmarking of decentralized controllers requires characterization of the

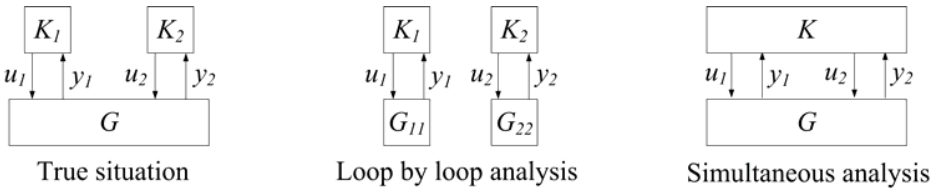

Fig. 1. Insufficiency of available MV benchmarks for performance assessment of decentralized controllers

least achievable output variance and its subsequent estimation from closed-loop data. This paper mainly focusses on the first issue. We first propose an MV benchmark for loop-by-loop analysis, where the presence of other loops is accounted for. The proposed result requires a small modification of the existing MV benchmark for SISO processes. It is further shown that the modified MV benchmark for loop-by-loop analysis can be directly estimated from closed-loop data with *a priori* knowledge of the delays of the different elements of the process model. An interesting insight is that for processes under decentralized control, the pre-whitening of output data using algorithms such as filtering and correlation (FCOR) algorithm (Huang and Shah, 1999) does not necessarily provide the first few impulse response coefficients of the disturbance model, as is traditionally believed.

The derivation of MV benchmark for simultaneous analysis of decentralized controller is more challenging. This happens as the optimization problem involving minimization of output variance becomes non-convex, once the diagonal structure is imposed on the controller (Sourlas and Manousiouthakis, 1995; Rotkowitz and Lall, 2006). With this difficulty, one may alternately look for tight upper and lower bounds on the least achievable output variance using decentralized controllers. Clearly, any suboptimal tuning strategy for the decentralized controller provides an upper bound on the least achievable output variance. Some approaches for finding upper bounds on least achievable output variance have been reported using non-convex optimization (Ko and Edgar, 1998; Jain and Lakshminarayanan, 2007) or by utilizing the structure of the optimization problem (Yuz and Goodwin, 2003; Kariwala et al., 2005). Recently, Kariwala (2007) addressed the more difficult problem involving derivation of a tight lower bound on the least achievable output variance, where an explicit bound is proposed by considering those impulse response coefficients of the closed-loop transfer function between disturbances and outputs, which depend linearly on the controller parameters. In general, however, the lower bound proposed in (Kariwala, 2007) can be conservative due to the neglected impulse response coefficients.

In this paper, we show that though nonlinear, the impulse response coefficients of the closed-loop transfer function between disturbances and outputs can be represented as polynomials in unknown controller parameters. Subsequently, the non-convex optimization problem related to the minimization of output variance is solved using sums of squares (SOS) programming (Parillo, 2000). This result is further extended to find a lower bound on the least achievable output variance, when the individual subcontrollers of the decentralized controller are restricted to be of proportional-integral-derivative (PID) type. The estimation of these lower bounds is difficult from closed-loop data only and the knowledge of process model is required. Nevertheless, the derivation of lower bound on the least achievable output variance can itself be seen as a major step towards systematic performance assessment of decentralized controllers.

2. PROBLEM FORMULATION

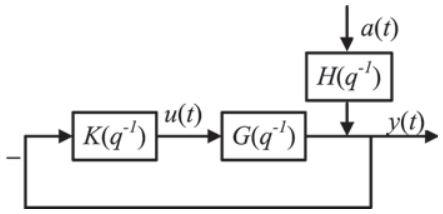

Fig. 2. Block diagram of closed-loop system

We consider the closed-loop system shown in Figure 2. For this system, we denote $G(q^{-1})$ and $H(q^{-1})$ as the process and disturbance models, respectively, such that

$$y(t) = G(q^{-1})\,u(t) + H(q^{-1})\,a(t) \tag{1}$$

Here, $y(t), u(t)$ and $a(t)$ are controlled outputs, manipulated variables and disturbances, respectively. We make the following simplifying assumptions:

(1) $G(q^{-1})$ and $H(q^{-1})$ are stable, causal transfer matrices, contain no zeros on or outside the unit circle except at infinity (due to time delays), and are square having dimensions $n_y \times n_y$.
(2) $a(t)$ is a random noise sequence with unit variance.

When $H(q^{-1})$ contains zeros outside the unit circle, these zeros can be factored through an all pass factor without affecting the noise spectrum (Huang and Shah, 1999). Further, there is no loss of generality in assuming that the system is affected by noise having unit variance, as the disturbance model can always be scaled to satisfy this assumption. For notational simplicity, we drop the arguments q^{-1} and t in the subsequent discussion.

Our objective is to find the least achievable value of $\mathrm{Var}(y)$ with respect to the controller K, *i.e.*

$$J_{\mathrm{decen}} = \min_{K} \mathrm{Var}(y) = \min_{K} E[\mathrm{tr}(y\,y^T)] \tag{2}$$

where K is assumed to have a diagonal structure, *i.e.* $K = \mathrm{diag}(K_1, K_2, \cdots, K_{n_y})$. In (2), $E(\cdot)$ and $\mathrm{tr}(\cdot)$ denote the expectation and trace operators, respectively. The pairings are considered to be selected on the diagonal elements of G.

Based on (2), the MV benchmark for decentralized controller can be defined as

$$\eta_{\text{decen}} = \frac{J_{\text{decen}}}{E[\text{tr}(y\,y^T)]} \tag{3}$$

where $E[\text{tr}(y\,y^T)]$ is the observed output variance.

A related problem involves finding the least achievable variance of the ith output, *i.e.*

$$J_{i,\text{decen}} = \min_{K_i} E[\text{tr}(y_i\,y_i^T)] \tag{4}$$

Similar to (3), the MV benchmark for the ith output can be defined as

$$\eta_{i,\text{decen}} = \frac{J_{i,\text{decen}}}{E[\text{tr}(y_i\,y_i^T)]} \tag{5}$$

where $E[\text{tr}(y_i\,y_i^T)]$ is the observed variance of the ith output.

3. LOOP-BY-LOOP ANALYSIS

We first consider performance assessment of the decentralized controller on a loop-by-loop basis. For clarity of presentation, we limit the discussion to 2×2 systems. The result can be generalized to $n_y \times n_y$ systems using block-partitioning of G and H. We have

$$y_1 = G_{11}\,u_1 + G_{12}\,u_2 + H_1\,a \tag{6}$$

$$y_2 = G_{21}\,u_1 + G_{22}\,u_2 + H_2\,a \tag{7}$$

The time delay associated with G_{ij} is denoted as d_{ij}, *i.e.*

$$G_{ij} = q^{-d_{ij}}\bar{G}_{ij} \tag{8}$$

where $\bar{G}_{ij}$ denotes the invertible part of G_{ij}. Without loss of generality, we consider that the objective is to characterize the least achievable variance of y_1.

3.1 Conventional approach

The traditional approach for loop-by-loop analysis involves using the MV benchmark for SISO systems. Here, H_1 is decomposed using Diophantine identity as

$$H_1 = F_1 + q^{-d_{11}}R_1 \tag{9}$$

Then, the least achievable variance of y_1 is taken as (Åström, 1970; Harris, 1989)

$$J_1 = \min_{K_1} E[\text{tr}(y_1\,y_1^T)] = \|F_1\|_2^2 \tag{10}$$

where $\|\cdot\|_2$ denotes the $\mathcal{H}_2$-norm. The MV benchmark for individual outputs is defined similar to (5). An inherent assumption in the derivation of (10) is that $u_2 = 0$ at all times or in other words, the first loop is being operated in isolation from the rest of the process. We next demonstrate that when the presence of other loops is accounted for, the first d_{11} elements of H_1 are not necessarily feedback invariant and thus the least achievable variance of y_1 can be lower than J_1 in (10).

3.2 Modified MV benchmark

Consider that the second loop is closed with $u_2 = -K_2 y_2$. Under partially closed loop conditions, we have (Skogestad and Postlethwaite, 2005)

$$y_1 = P_{11}\,u_1 + P_{d1}\,a \tag{11}$$

where

$$P_{11} = G_{11} - \frac{G_{12}K_2G_{21}}{1+G_{22}K_2},\; P_{d1} = H_1 - \frac{G_{12}K_2H_2}{1+G_{22}K_2} \tag{12}$$

Since $1/(1+G_{22}K_2)$ and K_2 are rational and invertible, it follows that the delay associated with P_{11} or the effective delay of the first loop is

$$d_1^{'} = \min(d_{11}, d_{12}+d_{21}) \tag{13}$$

Now, let P_{d1} be decomposed using Diophantine identity as

$$P_{d1} = F_1^{'} + q^{-d_1^{'}}R_1^{'} \tag{14}$$

Using (11) and (14), it follows that

$$y_1 = F_1^{'}\,a + q^{-d_1^{'}}(\bar{P}_{11}\,u_1 + R_1^{'}\,a) \tag{15}$$

where $P_{11} = q^{-d_1^{'}}\bar{P}_{11}$ and $\bar{P}_{11}$ denotes the invertible part of P_{11}. Since the first term in (15) cannot be affected by u_1 (invariant of K_1), it follows that

$$J_{1,\text{decen}} = \min_{K_1} E[\text{tr}(y_1\,y_1^T)] = \|F_1^{'}\|_2^2 \tag{16}$$

Note that $\|F_1^{'}\|_2^2$ represents the least achievable variance of y_1, when the presence of second loop is accounted for and can be used readily for performance assessment of decentralized controllers on a loop-by-loop basis.

Remark 1. In general, $J_{1,\text{decen}}$ may depend on K_2. This dependance, however, has no bearing on the loop-by-loop performance assessment, where the objective is to find the least achievable variance of y_i through tuning of K_i. If both controllers are allowed to be tuned simultaneously, using similar analysis as used in this section earlier, it can be shown that the first $d_1^{''} = \min(d_{11}, d_{12})$ impulse response coefficients of H_1 are feedback invariant and thus

$$\min_{K_1,K_2} E[\text{tr}(y_1\,y_1^T)] = \|F_1^{''}\|_2^2 \tag{17}$$

where $H_1 = F_1^{''} + q^{-d_1^{''}}R_1^{''}$. Note that the bound in (17) is independent of controller type (full multivariable or decentralized).

Though the result in (16) may seem entirely mathematical, a physical reasoning with this result can be associated by considering the block diagram of a 2×2 system shown in Figure 3. Here, u_1 can affect y_1 directly through G_{11}, but also through a parallel path involving G_{12} and G_{21} (shown with thick line in Figure 3). Thus, $d_1^{'} = \min(d_{11}, d_{12}+d_{21})$ represents the delay of the fastest path through which u_1 can affect y_1. In this sense, loop interaction can sometimes be beneficial for reducing output variance.

Example 2. To illustrate the findings of this section, we use the case study of a binary distillation column (Wood and Berry, 1973). The continuous-time model is discretized with a sampling time of 1 minute to get

$$G = \begin{bmatrix} \dfrac{0.744q^{-2}}{1-0.942q^{-1}} & \dfrac{-0.879q^{-4}}{1-0.954q^{-1}} \\ \dfrac{0.579q^{-8}}{1-0.912q^{-1}} & \dfrac{-1.302q^{-4}}{1-0.933q^{-1}} \end{bmatrix} \tag{18}$$

$$H = \begin{bmatrix} \dfrac{0.247q^{-9}}{1-0.935q^{-1}} \\ \dfrac{0.358q^{-4}}{1-0.927q^{-1}} \end{bmatrix} \tag{19}$$

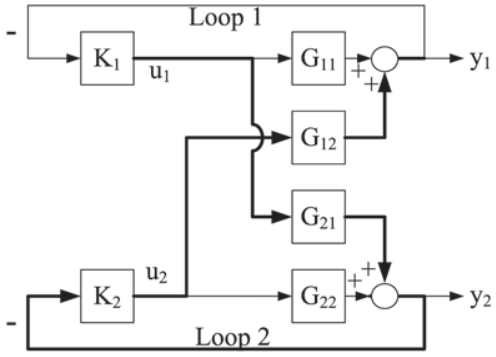

Fig. 3. Presence of parallel path (shown with thick line) from u_1 to y_1 for 2×2 systems

For diagonal pairings, the following decentralized PI controller is tuned using internal model control (IMC) method (Skogestad, 2003)

$$K = \text{diag}\left(\frac{0.652 - 0.571q^{-1}}{1 - q^{-1}}, \frac{-0.124 + 0.115q^{-1}}{1 - q^{-1}}\right) \quad (20)$$

which provides $\text{Var}(y_1) = 0.122$ and $\text{Var}(y_2) = 0.759$. After factoring the time delay of H, the least achievable variances of y_1 and y_2 according to the conventional approach discussed in Section 3.1 are $J_1 = 0.114$ and $J_2 = 0.413$, respectively. Thus, the conventional MV benchmarks for loops 1 and 2 are $\eta_1 = 0.932$ and $\eta_2 = 0.544$, respectively, which indicate that the variance of y_2 can be reduced significantly by re-tuning K_2, but tuning K_1 will not reduce variance of y_1 significantly. Using the modified MV benchmark, we next show that this conclusion is not entirely correct.

We have $d_{11} = 2$, $d_{12} = 4$, $d_{21} = 8$ and $d_{22} = 4$. Thus, $d_1^{'} = \min(d_{11}, d_{12} + d_{21}) = 2$ and $d_2^{'} = \min(d_{22}, d_{12} + d_{21}) = 4$. Since the first $d_2^{'} = d_{22}$ impulse response coefficients of P_{d2} and H_2 are the same, we find that $J_{2,\text{decen}} = J_2 = 0.413$ and $\eta_{2,\text{decen}} = \eta_2 = 0.544$. The first $d_1^{'} = d_{11}$ impulse response coefficients of P_{d1}, however, are different from the corresponding impulse response coefficients of H_1 and we find that $J_{1,\text{decen}} = 0.031$ and $\eta_{1,\text{decen}} = 0.251$. Thus, the modified MV benchmark identifies that the variance of y_1 can be reduced by approximately 4 times through tuning of K_1.

We point out that for this process, the first $d_1^{'}$ impulse response coefficients of P_{d1} and thus $J_{1,\text{decen}}$ depend on K_2. For example, when the gain of K_2 is decreased by a factor of 0.75, $J_{1,\text{decen}}$ increases to 0.037. With this controller tuning the variance of y_1 is 0.126. Thus, we have $\eta_{1,\text{decen}} = 0.293$, which indicates that the variance of y_1 can still be reduced by approximately 3 times.

Remark 3. Although for Example 2, the effective delays for both loops are the same as open-loop delays, *i.e.* $d_1^{'} = d_{11}$ and $d_2^{'} = d_{22}$, this is not true in general. For example, when pairings are chosen on the off-diagonal elements of G in (18), the effective delay for loop 1 is $d_1^{'} = \min(d_{12}, d_{11} + d_{22}) = 6$, which is different from open-loop delay, $d_{12} = 8$.

Remark 4. Based on (11), under closed loop conditions

$$y_1 = \frac{P_{d1}}{1 + P_{11}K_1} a \quad (21)$$

Let $K_1 = M_1/(1 - P_{11}M_1)$, where M_1 is a stable transfer function (Youla parameterization). Then,

$$y_1 = (1 - P_{11}M_1)P_{d1}\, a \quad (22)$$

$$= F_1^{'} a - q^{-d_1^{'}}(\bar{P}_{11}M_1P_{d1} - R_1^{'})a \quad (23)$$

Thus, $F_1^{'}$ and thus $\eta_{i,\text{decen}}$ can be estimated using closed loop data, *e.g.* using the FCOR algorithm (Huang and Shah, 1999), with *a priori* knowledge of the delays of G_{ij}. It is also interesting to note that the use of FCOR algorithm for loop-by-loop analysis of decentralized controllers leads to estimation of the first few impulse response coefficients of P_{d1} and not H_1, as is traditionally believed.

4. SIMULTANEOUS ANALYSIS

The variance of other outputs can increase, when the variance reduction of ith output is attempted through tuning of K_i. This effect is not taken into account by loop-by-loop analysis. To overcome this drawback, we derive an MV benchmark for simultaneous performance assessment of all loops in this section.

4.1 Conventional approach

A multivariable process can be represented as

$$G = D^{-1}\bar{G} \quad (24)$$

such that $\bar{G}$ and D^{-1} contain the invertible and non-invertible parts of G, respectively. We consider that $D(q)$ is a unitary interactor matrix, *i.e.* $D^T(q^{-1})\, D(q) = I$ (Huang and Shah, 1999). Let

$$q^{-d}DH = F + q^{-d}R \quad (25)$$

where d denotes the order of the interactor matrix. Then (Harris et al., 1996; Huang et al., 1997),

$$J_{\text{full}} = \min_K E[\text{tr}(y\, y^T)] = \|F\|_2^2 \quad (26)$$

The MV benchmark for simultaneous analysis is defined similar to (3). The bound on achievable output variance in (26), however, does not take the diagonal structure of the controller into account and thus may classify well-performing decentralized controllers as poorly performing. In the subsequent discussion, we present a lower bound on the achievable output variance for systems under decentralized control.

4.2 MV benchmark for Decentralized controllers

For regulatory control, we have $u = -K\, y$. Thus, the closed loop transfer function between a and y can be written as

$$y = S\, a; \quad S = (I + G\, K)^{-1}\, H \quad (27)$$

Since $E[a(t)a^T(t)] = I$,

$$J_{\text{decen}} = \min_K E[\text{tr}(y\, y^T)] = \min_K \|S\|_2^2 \quad (28)$$

When diagonal structure is imposed on K, the optimization problem in (28) becomes non-convex. A key observation to overcome this difficulty is that

$$\|S\|_2^2 = \sum_{i=0}^{\infty} \mathrm{tr}\,(S_i^T\, S_i) \geq \sum_{i=0}^{n} \mathrm{tr}\,(S_i^T\, S_i) \tag{29}$$

for any finite n. Thus, a lower bound on J_{decen} can be found by minimizing $\sum_{i=0}^{n} \mathrm{tr}\,(S_i^T\, S_i)$. Here, S_i represents the ith impulse response coefficient of S.

When the closed-loop system is stable, (27) can be expanded using Taylor Series expansion to get

$$S = \left[\sum_{i=0}^{\infty} (-1)^i (G\,K)^i\right] H \tag{30}$$

For given n, we define the following $nn_y \times nn_y$-dimensional Hankel matrices

$$G_H = \begin{bmatrix} G_0 & 0 & \cdots & 0 \\ G_1 & G_0 & \cdots & 0 \\ \vdots & \vdots & \ddots & \vdots \\ G_{n-1} & \cdots & G_1 & G_0 \end{bmatrix} \tag{31}$$

$$K_H = \begin{bmatrix} K_0 & 0 & \cdots & 0 \\ K_1 & K_0 & \cdots & 0 \\ \vdots & \vdots & \ddots & \vdots \\ K_{n-1} & \cdots & K_1 & K_0 \end{bmatrix} \tag{32}$$

and the following $nn_y \times nn_d$-dimensional matrices

$$H_v = \begin{bmatrix} H_0^T & H_1^T & \cdots & H_{n-1}^T \end{bmatrix}^T \tag{33}$$

$$S_v = \begin{bmatrix} S_0^T & S_1^T & \cdots & S_{n-1}^T \end{bmatrix}^T \tag{34}$$

Based on (32)-(34), S_v can be compactly written as

$$S_v = \left[\sum_{i=0}^{n} (-1)^i (G_H\, K_H)^i\right] H_v \tag{35}$$

Now, a lower bound on J_{decen} can be found by solving

$$J_{\mathrm{decen}} = \min_K \sum_{i=0}^{\infty} \mathrm{tr}\,(S_i^T\, S_i) \geq \min_K \mathrm{tr}\,(S_v^T\, S_v) \tag{36}$$

for any finite n. Based on (35), we note that S_v and thus $\mathrm{tr}\,(S_v^T S_v)$ depend polynomially on the controller parameters. Thus, the optimization problem in (36) can be seen as finding the global minimal value of a polynomial. For this purpose, we use sums of squares (SOS) programming (Parillo, 2000) in this paper. SOS programming transforms the polynomial minimization problem to a semi-definite program, which is solved using Sedumi (Sturm, 1999) interfaced with Matlab through Yalmip (Löfberg, 2004) in this paper.

SOS programming does not necessarily provide the minimum value of the polynomial, but guarantees a global lower bound (Parillo, 2000). For any controller K, however, since

$$\sum_{i=0}^{n+1} \mathrm{tr}\,(S_i^T\, S_i) \geq \sum_{i=0}^{n} \mathrm{tr}\,(S_i^T\, S_i) \tag{37}$$

tight lower bound on J_{decen} can be found by increasing n sequentially until convergence. In comparison with Kariwala (2007), where only the first $(2d-1)$ impulse response coefficients of S are used to find a lower bound on J_{decen}, the use of SOS programming provides a tighter lower bound, whenever $n > (2d-1)$. A similar approach involving SOS programming has been used earlier by Sendjaja and Kariwala (2009) to characterize the achievable output variance of SISO systems under PID control.

Example 5. We consider the following 2×2 process, where

$$G = \begin{bmatrix} \dfrac{-0.1q^{-2}}{(1-0.1q^{-1})\,(1-0.2q^{-1})} & \dfrac{-0.25q^{-1}\,(1-0.3q^{-1})}{(1-0.1q^{-1})\,(1-0.2q^{-1})} \\ \dfrac{0.5q^{-1}\,(1+0.9q^{-1})}{(1-0.1q^{-1})\,(1-0.2q^{-1})} & \dfrac{-0.1q^{-2}}{(1-0.1q^{-1})\,(1-0.2q^{-1})} \end{bmatrix} \tag{38}$$

and $H = 1/(1-q^{-1})\,I$ (Kariwala, 2007). Then, $D = q\,I$, $F = I$ and $J_{\mathrm{full}} = \|F\|_2^2 = 2$.

By considering the contribution of first $(2d-1)$ impulse response coefficients of S towards $\|S\|_2^2$, Kariwala (2007) found $J_{\mathrm{decen}} \geq 4$. Using the SOS programming approach, however, we find $J_{\mathrm{decen}} \geq 8.023$. Using non-convex optimization with multiple randomized initial guesses, Kariwala (2007) showed that the exact value of J_{decen} is approximately 8.16. This example amply demonstrates the usefulness of the SOS programming approach for finding tight lower bound on least achievable value of output variance for systems under decentralized control. The reader should also note that for this process, the MV benchmark found using conventional approach will be approximately 4 times lower than the MV benchmark found by accounting for the controller structure. Thus, the conventional approach for performance assessment of decentralized controllers may incorrectly classify well-performing controllers as poorly performing.

Remark 6. Unlike loop-by-loop analysis (see Remark 4), it is difficult to estimate η_{decen} directly from closed-loop data. When G is known (or has been identified using open or closed-loop identification experiments), H can be estimated by pre-whitening the pseudo-signal $(y - Gu)$. Then, SOS programming can be used to identify a lower bound on J_{decen} and η_{decen} based on identified model. We point out that the knowledge of G is also required by other available approaches for performance assessment of decentralized controllers (Ko and Edgar, 1998; Jain and Lakshminarayanan, 2007). In practice, the task of identifying G should be undertaken, only when J_{full} differs significantly from the observed output variance.

4.3 MV benchmark for Decentralized PID Controllers

In industrial practice, the individual sub-controllers of the decentralized controller are often fixed to be of PID-type. Clearly, the presence of additional controller structure can further limit the least achievable variance of outputs. Next, we show that the SOS programming approach can be easily extended to derive a tight lower bound on J_{decen} for decentralized PID controllers.

We note that the decentralized PID controller can be expressed as

$$K_{PID} = \frac{1}{\Delta} \sum_{i=0}^{2} C_i\, q^{-1} \tag{39}$$

where C_i has diagonal structure and $\Delta = 1 - q^{-1}$ is the integrator. For

$$\hat{G} = \frac{1}{\Delta} G \tag{40}$$

let us define the Hankel matrices $\hat{G}_H$ and C_H, which have the same structure as G_H and K_H defined in (32). Using similar approach, as used in Section 4.2, it can be shown that for any finite n

$$S_v = \left[\sum_{i=0}^{n} (-1)^i (\hat{G}_H\, C_H)^i\right] H_v \tag{41}$$

Thus, a lower bound on J_{decen} for decentralized PID controller can be found by minimizing $\text{tr}\,(S_v^T\, S_v)$ using SOS programming as before.

Example 7. We revisit Example 5. When individual sub-controllers are restricted to be of PI-type, the lower bound on J_{decen} increases to 9.980 (approximately 25% higher than unrestricted decentralized controller). The following sub-optimal controller is designed using trial and error

$$K_{\text{PI}} = \text{diag}\left(\frac{-0.629 + 0.474\, q^{-1}}{\Delta}, \frac{-2.844 + 1.862\, q^{-1}}{\Delta}\right) \tag{42}$$

which provides $E[\text{tr}(y\, y^T)] = 10.087$. When PID controllers are used, the lower bound on J_{decen} is 9.250 (approximately 15% higher than unrestricted decentralized controller). The following sub-optimal controller

$$K_{\text{PID}} = \text{diag}\left(\frac{-0.884 + 0.924\, q^{-1} - 0.205\, q^{-2}}{\Delta}, \frac{-3.210 + 2.764\, q^{-1} - 0.869\, q^{-2}}{\Delta}\right) \tag{43}$$

provides $E[\text{tr}(y\, y^T)] = 9.421$. For both cases (PI and PID control), the lower bounds are close to the upper bounds, which demonstrates that SOS programming technique can be used to find tight bounds on J_{decen} for decentralized PID controllers efficiently and reliably.

5. CONCLUSIONS AND OPEN ISSUES

The use of decentralized or multi-loop controllers is common in process industries. In this paper, we have shown that the use of existing MV benchmarks for SISO and MIMO systems for performance assessment of decentralized controllers may lead to incorrect conclusions regarding the opportunities for variance reduction through controller retuning. We proposed modified MV benchmarks for loop-by-loop analysis of the decentralized controller, which can be directly estimated from closed-loop data. An MV benchmark for simultaneous analysis of the decentralized controller is also proposed through the novel use of SOS programming, which guarantees a lower bound on the least achievable output variance. In summary, this paper takes a major step towards systematic performance assessment of decentralized controllers.

A limitation of the use of SOS programming approach is that the knowledge of process model is required. Furthermore, SOS programming requires solving large semi-definite programs, whose size and solution time increase rapidly with process dimensions. We are currently exploring the use of alternate approaches to handle the computational complexity of the SOS programming approach.

REFERENCES

Åström, K.J. (1970). *Introduction to Stochastic Control Theory*. Academic Press, London.

Harris, T.J. (1989). Assessment of control loop performance. *Can. J. Chem. Eng.*, 67(5), 856–861.

Harris, T.J., Boudreau, F., and Macgregor, J.F. (1996). Performance assessment of multivariable feedback controllers. *Automatica*, 32(11), 1505–1518.

Huang, B. and Shah, S.L. (1999). *Performance Assessment of Control Loops: Theory and Applications*. Springer-Verlag, London.

Huang, B., Shah, S.L., and Kwok, E.K. (1997). Good, bad or optimal? Performance assessment of multivariate processes. *Automatica*, 33(6), 1175–1183.

Jain, M. and Lakshminarayanan, S. (2007). Estimating performance enhancement with alternate control strategies for multiloop control system. *Chem. Eng. Sci.*, 62, 4644–4658.

Jelali, M. (2006). An overview of control performance assessment technology and industrial applications. *Control Eng. Pract.*, 14(5), 441–466.

Kariwala, V. (2007). Fundamental limitation on achievable decentralized performance. *Automatica*, 43(10), 1849–1854.

Kariwala, V., Forbes, J.F., and Meadows, E.S. (2005). Minimum variance benchmark for decentralized controllers. In *Proc. American Control Conference*, 1437–1442. Portland, OR, USA.

Ko, B. and Edgar, T.F. (1998). Multiloop PID control performance monitoring. In *Proc. The 8th Congress of Aston Pacific Confederation of Chemical Engineering*. Seoul, Korea.

Löfberg, J. (2004). YALMIP : A toolbox for modeling and optimization in MATLAB. In *Proc. the CACSD Conference*. Taipei, Taiwan.

Parillo, P.A. (2000). *Structured Semidefinite Programs and Semialgebraic Geometry Methods in Robustness and Optimization*. Ph.D. thesis, California Institute of Technology, Pasadena, California, USA.

Qin, S.J. (1998). Controller performance monitoring - A review and assessment. *Comput. Chem. Eng.*, 23, 173–186.

Rotkowitz, M. and Lall, S. (2006). A characterization of convex problems in decentralized control. *IEEE T. Automat. Contr.*, 51(2), 274–286.

Sendjaja, A.Y. and Kariwala, V. (2009). Achievable PID performance using sums of squares programming. *J. Proc. Contr.*, In press.

Skogestad, S. (2003). Simple analytic rules for model reduction and PID controller tuning. *J. Proc. Contr.*, 13(4), 291–309.

Skogestad, S. and Postlethwaite, I. (2005). *Multivariable Feedback Control: Analysis and Design*. John Wiley & Sons, Chichester, UK, 2nd edition.

Sourlas, D.D. and Manousiouthakis, V. (1995). Best achievable decentralized performance. *IEEE T. Automat. Contr.*, 40(11), 1858–1871.

Sturm, J. (1999). Using SeDuMi 1.02, A Matlab toolbox for optimization over symmetric cones. *Optim. Method Softw.*, 11(1), 625–653.

Wood, R.K. and Berry, M.W. (1973). Terminal composition control of a binary distillation column. *Chem. Eng. Sci.*, 28(9), 1707–1717.

Yuz, J.I. and Goodwin, G.C. (2003). Loop performance assessment for decentralized control of stable linear systems. *Eur. J. Control*, 9(1), 116–130.

Eliminating Valve Stiction Nonlinearities for Control Performance Assessment ⋆

W. Yu * **D.I. Wilson** ** **B.R. Young** ***

* *Industrial information & Control Centre, The University of Auckland, Auckland, New Zealand (e-mail:* w.yu@auckland.ac.nz*).*
** *Electrical & Electronic Engineering, Auckland University of Technology, Auckland, New Zealand (e-mail:* david.i.wilson@aut.ac.nz*)*
*** *Depart. of Chemical & Materials Engineering, The University of Auckland, Auckland, New Zealand, (e-mail:* b.young@auckland.ac.nz*)*

Abstract: Control performance assessment or CPA is a useful tool to establish the quality of industrial feedback control loops, but this requires establishing the minimum variance lower bound. While reliable algorithms have been developed for linear systems, common nonlinearities such as valve stiction require modifications to the basic strategy.
If the valve gets stuck due to stiction, for stable plants the output will reach steady state until the valve again moves. During this time the nonlinearity due to stiction is essentially removed from the system, and it is possible to compute performance assessment indices in the standard manner.
This paper describes an automated strategy to reliably identify these linear steady-state periods and subsequently compute the minimum variance lower bounds. The results of a simulation example illustrate that the proposed methodology is efficient and accurate enough for the classes of systems and nonlinearities considered to provide statistics for control performance assessment for linear systems with nonlinearities caused by valves.

Keywords: Control performance assessment, Valve stiction, Steady state.

1. INTRODUCTION

It is perhaps not surprising that instrument and control engineers are overwhelmed by the sheer number of loops that need attention on any typical industrial processing plant. Many loops are mis-tuned, if tuned at all, as noted by Bialkowski (1998) and other practitioners, and many control valves are only maintained when something catastrophic occurs. However the economic benefits from improving the performance of control loops, even those operating at a cursory glance acceptably, is often grossly under estimated.

In this paper, we present a strategy to compute the minimum variance lower bound, which is arguably the difficult step in quantifying the performance improvement of a typical control loop that suffers from the specific nonlinear phenomena of valve stiction being a very common cause for poor control performance.

Control performance assessment, or CPA, is a technology to diagnose and maintain operational efficiency of control systems. CPA is routinely applied in the refining, petrochemicals, pulp and paper and the mineral processing industry as noted by Qin (1998), Harris (1999), Huang and Shah (1999), Jelali (2006), although these, and many other publications, are mainly restricted to linear systems.

In the case of nonlinear systems, Harris and Yu (2007) superimposes the nonlinear dynamic model to an additive linear or partially nonlinear disturbance. It is shown that a minimum variance feedback invariant exists and the minimum variance performance can be estimated from routine operating data. Continuing this idea, a semi-parametric method was proposed in Yu et al. (2008) to find the minimum variance lower bound for linear systems with valve stiction. In that work a local smoothing spline approximated the stiction nonlinearity, but given the complexity of the nonlinearity, and the heuristic approach, it must be expected that this strategy will fail for some cases.

In this paper, we will extend CPA to a important practical nonlinear problem, that of control valve stiction. The performance degradation due to stiction prompted Horch (1999), Choudhury et al. (2005, 2006), Thornhill and Horch (2007) to investigate ways to diagnose the issue, while Jelali (2008) and the references therein, attempt the estimation of parametric stiction models, but few have continued the analysis to quantify the performance loss. Consequently, rather than attempt to approximate the nonlinearity, the approach taken here is to develop an automated strategy that extracts the steady state periods resultant once the valve is stuck fast. Based

⋆ Sponsor and financial support from the Industrial Information and Control Centre, AUT University and The University of Auckland, New Zealand.

on readily available input/output data collected during these periods, the minimum variance lower performance bound is computed in the standard manner. This gives an indication of how the control loop, even one suffering from stiction, would perform if it was serviced. Of course this presupposes that one is not allowed the luxury of setting the valve under consideration in manual, or one is charged with assessing many hundreds of operating loops.

The incentive to compute this control performance index is that it delivers a benchmark giving the engineer an idea of the improvement potential if the valve was to be serviced. For example, it could well be that of the hundreds of valves on site that required maintenance, the expected performance improvement, even if the stiction was entirely removed, would not be worth the time and effort.

The layout of the paper is as follows. In Section 2, the problem statement and model including valve stiction is introduced. Section 3 describes the methodology proposed in this paper to first extract, then check the validity of the steady-state linear periods. Section 4 illustrates by way of simulation the performance of the proposed methodology. This is followed by a discussion and conclusions highlighting both the limitations and potential of the method.

2. PROCESS DESCRIPTION

We assume the plant can be adequately modelled by

$$y_t = \frac{B(q^{-1})}{A(q^{-1})} q^{-b} u_t + d_t \tag{1}$$

where $A(q^{-1})$ and $B(q^{-1})$ are polynomials in the backshift operator q^{-1}, and b is the time delay of the system. The disturbance d_t is modelled as the output of a linear Autoregressive-Integrated-Moving-Average (ARIMA) filter driven by white noise a_t of zero mean and variance σ_a^2 of the form

$$d_t = \frac{\theta(q^{-1})}{\phi(q^{-1})\nabla^d} a_t = \psi(q^{-1}) a_t \tag{2}$$

where $\nabla \stackrel{\text{def}}{=} (1 - q^{-1})$ is the difference operator and d is a non-negative integer, typically less than 2. The polynomials $\theta(q^{-1})$ and $\phi(q^{-1})$ are monic and stable.

A common process nonlinearity afflicting control valves is known as 'stiction' which exhibits a range of of nonlinear behaviour including hysteresis, backslash and deadzones, both dynamic and static, and is summarised in de Wit et al. (1995), Lampaert et al. (2004).

Fig. 1 illustrates the typical sawtooth characteristic behaviour of a poorly maintained valve suffering from stick/slip friction using the stiction model developed in Choudhury et al. (2004). It is important to note that under normal industrial operations, the manipulated variable (MV) signal injected into the plant, here denoted as u^v, is unobservable.

We include the nonlinear stiction function $f(\cdot)$ (which represents the relationship between the manipulated variable and the actual valve output), into Eqn. 1 giving

$$y_t = \frac{B(q^{-1})}{A(q^{-1})} q^{-b} f(u_t) + d_t \tag{3}$$

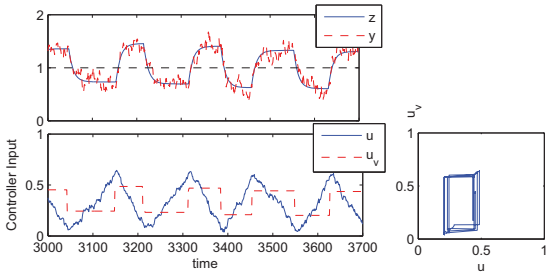

Fig. 1. The output of the controller, u, and the subsequent output of the control valve, u^v, suffering from slip/stick stiction.

Fig. 2 summarises the system considered in this paper. The intended controller output, u, (sometimes referred to as OP), is typically different from the actual valve position, u^v, due to the stiction. In the ideal case however, we can simply assume $u_t^v = f(u_t) = u_t$.

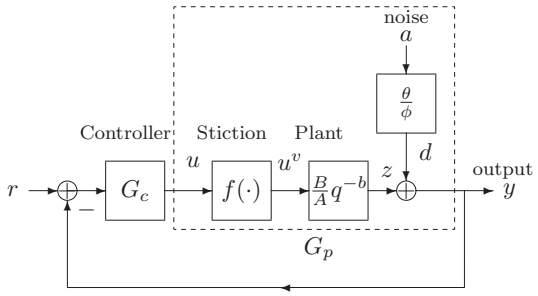

Fig. 2. Closed loop system with valve stiction under consideration

3. MINIMUM VARIANCE PERFORMANCE BOUNDS: VALVE STICTION CASES

The basis for minimum variance performance bounds was developed by Harris (1989) where it was was shown that the minimum variance performance bound for linear systems could be estimated from routine closed-loop data provided the process delay is known in advance. For the system described by Eqn. 1, the minimum variance performance lower bound is simply

$$\sigma_{MV}^2 = (1 + \varphi_1^2 + \cdots + \varphi_{b-1}^2)\sigma_a^2 \tag{4}$$

where the φ weights are the first $b-1$ impulse coefficients of the disturbance transfer function in Eqn. 2.

The minimum variance performance bounds for a class of nonlinear systems described by Eqn. 3 have been reported in Harris and Yu (2007) which used a nonlinear polynomial-AR or polynomial-ARX model to estimate the b-step ahead prediction. The drawback for this application is that it is difficult to find a general function to adequately approximate the valve stiction. Notwithstanding, the non-parametric spline method to approximate the nonlinearity proposed in Yu et al. (2008) partially overcomes the issue of modelling valve stiction/friction, but it too will fail for some cases.

In this paper, we propose a method to find the minimum variance performance bounds for valve stiction cases. Rather than trying to find a parametric or non-parametric function to approximate the nonlinear function as suggested in Yu et al. (2008), we will focus solely on the periods when we know, or at least suspect, that the system is operating in a linear regime. That way, we can simply ignore the now non-existent nonlinearity, and compute the minimum variance lower bound in the standard manner. The success of this strategy depends on how well we can establish that the system is behaving essentially as a linear system.

We can potentially ignore the effects of the nonlinearity by exploiting a unique characteristic of valve stiction. Due to the stick/slip friction, the times that the valve is stuck gives the system a chance to reach steady state and during these periods, we can use linear ARMA techniques to estimate the lower performance bound.

The key problem is how to identify the steady state periods from the closed loop output data. Our approach includes two parts. First we use a heuristic pattern method to select the periods of steady state in the observable time series y, and we validate this by employing a linearity test. Second, given possibly multiple segments of a linear time series, not necessarily contiguous, we can now fit a linear ARMA model and subsequently compute the minimum variance performance bound. The details of the methodology are discussed in the following sections.

3.1 Identifying steady-state periods

The presence of valve stiction induces a limit cycle with a characteristic triangular shape in the controller output as is shown in Fig. 1. This cycling is exacerbated by the integral component of the controller which eventually increases to such an extent that the stuck valve again moves. Unfortunately the valve moves too far, and the cycle begins again as demonstrated in Fig. 3.

Since the information of the actual valve output position, u^v, is not available for most industrial implementations, (if it was, we could simply use this series for the computation), the steady state periods must be identified from the data consisting solely of the process output y and controller output u.

Under the cycling conditions due to stiction, the scaled difference between u and y will describe a sawtooth trend as given in Fig. 4. The discontinuous turning points of the triangle wave indicate when the valve actually moves and it is these instances, (depicted as the vertical dashed and dotted lines) that we need to identify.

Given that most industrial plants have a stable low-pass frequency response that attenuates high frequency noise, and that the plant measurement is disturbed by d, it may be necessary to weight the subtraction to better highlight the trend. Fig. 4 actually trends $cu - y$ where the scale factor c is in this case 10.

After the periods of steady state are identified, an initial segment in each period will be discarded so that the previous input effects will be removed. Then subsequently

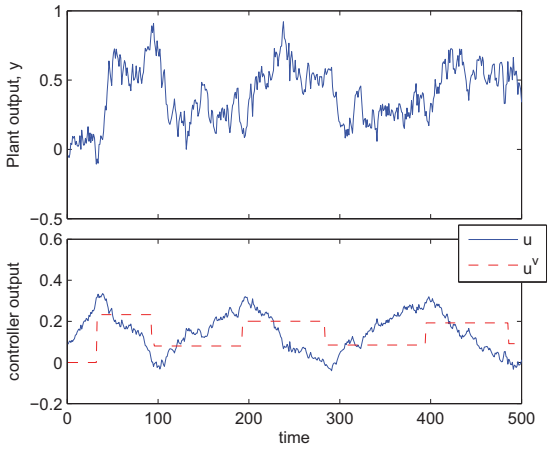

Fig. 3. The plant output, y, the controller output u, and the output of the valve suffering from stiction, u^v.

we can derive a minimum variance controller performance lower bound using these periods of data.

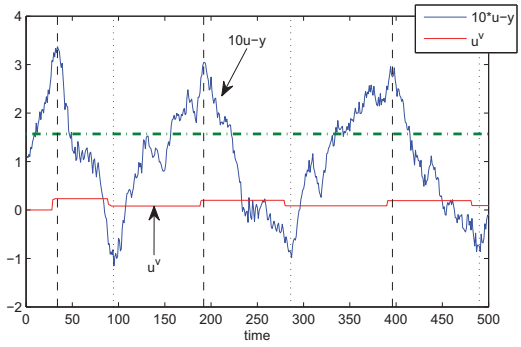

Fig. 4. Establishing the steady-state periods by computing $cu - y$.

An automated procedure to establish the stuck periods relies on reliably identifying the maxima and minima of the sawtooth shaped $cu - y$ trend in Fig. 4. First the times of the zero-crossings and their directions (falling, or raising edges) are established. Then, between each crossing instance, a search is made for the corresponding maximum or minimum.

Of course using such a heuristic approach, this simple algorithm is suspectable to false positives and correspondingly derives estimates of the steady-state periods shorter than the actual period. In cases of excessive suspected false crossings, standard techniques such as data smoothing or a Fourier identification of the dominant period could be applied to the noisy data series. However since these erroneous short periods will not be used for the minimum variance calculation anyway, they do not overly deteriorate the quality of the computed result. They do however, lower the efficiency of the data use.

3.2 Ensuring the removal of any nonlinearities

Notwithstanding the expectation that the valve stiction nonlinearity exhibits little memory, we need to be assured

that the selected period is in fact linear. One way is to do this is to apply a statistical test of linearity proposed by Subba and Gabar (1980), Hinich (1982) and previously used in this context by Choudhury et al. (2004) and Yu et al. (2008). This test, known as the Hinich test, is both nonparametric and reasonably robust.

In the simulations subsequently presented in section 4 it was obvious that the periods were linear so the nonlinear test was not actually employed. However if one is still in doubt, Yu et al. (2008) illustrates how such a validation could be performed.

3.3 Establishing the limit cycle

The proposed strategy works best when the valve is stuck for relatively long periods allowing the system to reach steady state. That is, periods larger than about 10 dominant time constants since we discard the first 3–4 to allow the system to reach steady-state, and then use the remaining data for the ARMAX model identification. Consequently we desire that the period of oscillation due to the valve nonlinearity is long compared to the settling time of the compensated loop and therefore we need to *a priori* establish reasonable conditions when that is likely to occur.

From the literature, and our simulation experience detailed further in section 4, it is found that there are three main factors which will affect the period of oscillation, namely the tuning of the PI controller, the magnitude of the disturbance, and the valve characteristics of the valve stiction.

4. SIMULATION EXPERIMENTS

The purpose of this section is to demonstrate the proposed method for the minimum variance performance assessment for valve stiction cases. A second order single-input, single-output (SISO) system with time constants 10 and 2, and steady-state gain of 3 is sampled at $T_s = 1$ to give

$$G_p = \frac{B}{A} = \frac{0.04338 + 0.03755q^{-1}}{1 - 1.621q^{-1} + 0.6483q^{-2}} \tag{5}$$

with time delay $b = 4$ under feedback control with controller

$$G_c = \frac{0.11 - 0.1q^{-1}}{1 - q^{-1}} \tag{6}$$

was used for generating simulated data. An additive disturbance of

$$d_t = \frac{0.2a_t}{1 - 0.8q^{-1}} \tag{7}$$

where a_t is a sequence of independent and identically distributed Gaussian random variables with zero mean and nominal variance $\sigma_a^2 = 0.1$.

A data-driven model for valve stiction proposed by Choudhury et al. (2004) is used to simulate the valve stiction. The model is characterised by two parameters, s for the valve stickiness and j for the magnitude of the valve jump. The closed loop behaviour with various combinations of s and j are plotted in Fig. 5. Pure deadband occurs when $j = 0$, (b) represents the undershoot case of a sticky valve, $s < j$, (c) illustrates the pure stick-slip situation, $s = j$ and (d) shows the valve output overshooting case, $s < j$. Note that the oscillation period decreases while the j value increases.

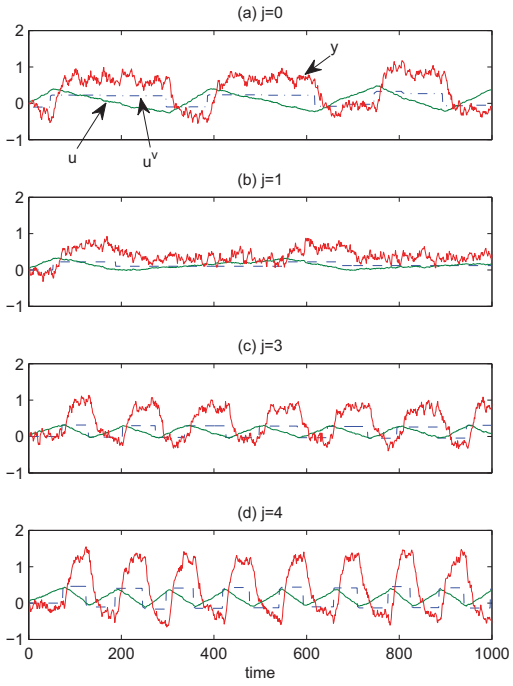

Fig. 5. The closed-loop behavior for $s = 3$ and with various values of j: (a) $j = 0$ (b) $j = 1$ (c) $j = 3$ (d) $j = 4$.

As noted in the pervious section, this strategy is reliant on relatively long periods when the valve is stuck. Given a fixed PI controller, we can vary the magnitude of the disturbance and the stiction jump/slip parameters, j, s and use a Monte-Carlo simulation to establish the largest period on average of the oscillation for each (σ_a^2, s, j) triplet. The resultant contour plots of periods are shown in Fig. 6.

In all cases we are most interested in the 'islands' of high periods apparent in all three examples given in Fig. 6.

Areas with periods less than about 100 are not interesting and are not plotted in Fig. 6. This is because since the plant in Fig. 6 has a dominant time constant of 10 sampled at 1, ten dominant time constants correspond to about 100 samples. We discard 30 to 40 samples to allow time for the system to reach steady-state, leaving a minimum of 60 samples in which to do the ARMA model identification. This data series length is about at the minimum recommended by Ljung (1987).

As expected the 'islands' of large periods occur when both the noise, σ_a^2, and jump parameters are not too big. This makes sense because if both s and j are zero, there is no stiction, and there is no self sustained oscillation due to the nonlinearity. Also for a given stiction, as the noise variance increases beyond the deadband limit, the valve will continually move, lowering, or completely eliminating, the potential steady-state periods.

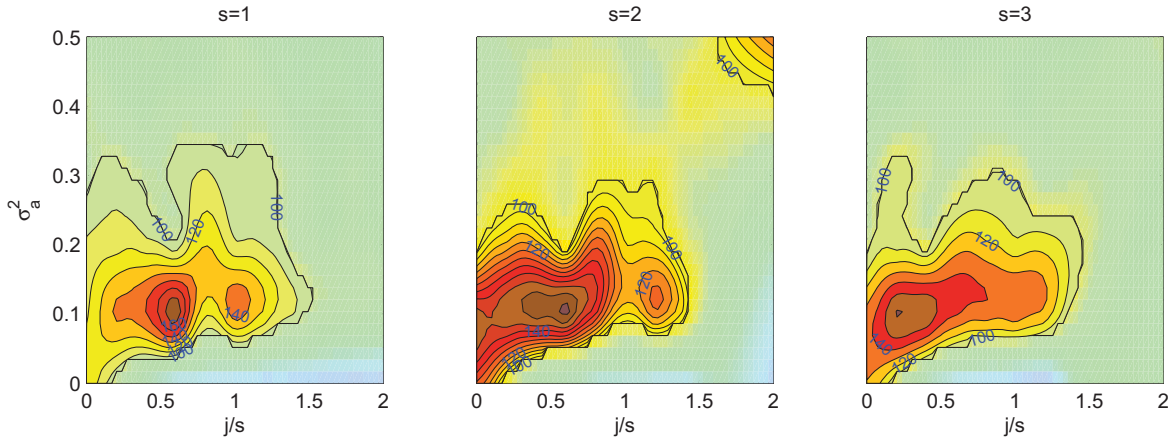

Fig. 6. The period of oscillation as a function stiction jump parameter j, and noise disturbance variance σ_a^2, at differing levels of stiction slip parameter s. Areas where the period is less than about 100 samples are not interesting for t his specific application because they are too short to perform a meaningful identification.

Due to the intractable nature of the nonlinearity, a Monte Carlo method is used to estimate the performance of the proposed strategy to estimate the minimum variance, σ_{MV}^2. 1000 observations generated from the valve stiction simulation are passed to the automated steady-state period identifier described in section 3.1 from which suitable periods are extracted. An ARMA model is fitted to the longest period from which σ_{MV}^2 is directly computed from the parametric model. This procedure is repeated 500 times.

The estimates of σ_{MV}^2 and associated uncertainties for different valve slip/jump conditions are shown in the comparative box plot in Fig. 7 again as in Fig. 5 for the case where $s = 3$ and various values for j. The true value of the minimum performance lower bound for this example is $\sigma_{MV}^2 = 9.2 \times 10^{-3}$.

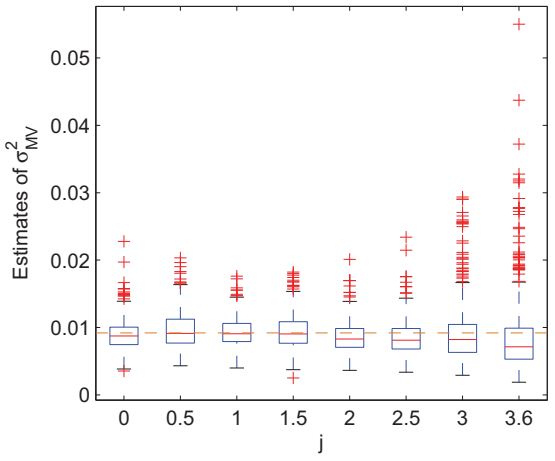

Fig. 7. Comparative box plots of the quality estimates of σ_{MV}^2 for $s = 3$ and for different j models. The horizontal dashed line is the true value of $\sigma_{MV}^2 = 9.2 \cdot 10^{-3}$.

5. DISCUSSION

The results from the numerical experiments to establish the minimum variance performance lower bound from normal operating data given in Fig. 7 show that the proposed strategy does reconstruct the correct σ_{MV}^2. Furthermore it is interesting to note that the quality of the estimate is best for the jump parameter $j \approx 1$, while for values smaller, and particularly larger, it begins to deteriorate. This is consistent with the results presented in Fig. 6 reinforcing the requirement to have reasonably long periods of steady-state to extract statistically significant results.

In the cases where the jump parameter j is larger than the slip s, we experience short periods of the stuck valve coupled with a comparatively large nonlinearity that contributes to the obvious deterioration in the confidence of the estimated minimum variance lower bound.

Similarly, if the zero-crossings are too frequent (and therefore the period available for steady-state consideration is too short compared to the anticipated dominant time constant), then we suggest that the strategy proposed in Yu et al. (2008) which uses smoothing splines to remove the nonlinearity might be more appropriate.

The proposed strategy has some limitations. First of all, as developed, we assume that the plant is stable, and reasonably well-damped. For type 1 plants with integrators, it is of course possible to differentiate the output. Furthermore, we assume that the dominant time constant is approximately known in order to discard the appropriate amount of data while waiting for steady-state. This is unlikely to be an overly onerous requirement for any processing plant. Finally we restrict our attention to those cases with moderate extent of stiction, since of course excessive stiction *must* be addressed, and minimal stiction would probably not be noticed anyway.

6. CONCLUSIONS

Valve stiction is a debilitating feature of many control loops that cannot, nor should not, be corrected by con-

troller tuning. However given the time and energy required to service the valve, it may be prudent for the instrument engineer to first establish what the best controlled performance would be if the valve was serviced.

The strategy proposed in this paper establishes the minimum performance lower bound in the case of excessive valve stiction using only observable signals and estimates of the plant dominant time constants and plant delay. In the case of rapid oscillation in the limit cycle, it is possible to stitch the short periods together to build up enough input/output data to make a reasonable identification.

While the examples considered only nonlinearities introduced by valve stiction, this strategy will work for any system which reaches steady states and stays there for a while.

ACKNOWLEDGMENTS:

Financial support to this project from the Industrial Information and Control Centre, Faculty of Engineering, The University of Auckland, New Zealand is gratefully acknowledged.

REFERENCES

W. L. Bialkowski. Dreams versus reality: A view from both sides of the gap. *Pulp & Paper Canada*, 94(11):19, 1998.

M.A.A.S. Choudhury, N.F. Thornhill, and S.L. Shah. Diagnosis of poor control loop performance using higher order statistics. *Automatica*, 40(10):1719–1728, 2004.

M.A.A.S. Choudhury, N.F. Thornhill, and S.L. Shah. Modelling valve stiction. *Chemical Engineering Progress*, 13(5):641–658, 2005.

M.A.A.S. Choudhury, S.L. Shah, N.F. Thornhill, and D.S. Shook. Automatic detection and quantification of stiction in control valves. *Control Engineering Practice*, 14:1395–1412, 2006.

C. Canudas de Wit, H. Olsson, K. J. Åström, and P. Lischinsky. A New Model for Control of Systems with Friction. *IEEE transactions on automatic control*, 40(3):419–425, March 1995.

T.J. Harris. Assessment of control loop performance. *Canadian Journal of Chemical Engineering*, 67:856–861, 1989.

T.J. Harris. A review of performance monitoring and assessment techniques for univariate and multivariate control systems. *J. Process Control*, 9(1):1–17, 1999.

T.J. Harris and W. Yu. Controller assessment for a class of nonlinear systems. *J. Process Control*, 17:607–619, 2007.

Melvin J. Hinich. Testing for Gaussianity and linearity of a stationary time series. *Journal of Time Series Analysis*, 3(13):169–176, 1982.

A. Horch. A simple method for detection of stiction in control valves. *Control Engineering Practice*, 7:1221–1231, 1999.

B. Huang and S.L. Shah. *Performance Assessment of Control Loops: Theory and Applications*. Springer, 1999.

Mohieddine Jelali. An overview of control performance assessment technology and industrial applications. *Control Engineering Practice*, 14(5):441–466, 2006.

Mohieddine Jelali. Estimation of valve stiction in control loops using separable least-squares and global search algorithms. *Journal of Process Control*, 18(7–8):632–642, 2008. ISSN 0959-1524.

Vincent Lampaert, Jan Swevers, and Farid Al-Bender. Comparison of model and non-model based friction compensation techniques in the neighbourhood of pre-sliding friction. In *Proceedings of the 2004 American Control Conference*, pages 1121–1126, Boston, Massachusetts, June 30 – July 2 2004.

Lennart Ljung. *System Identification: Theory for the User*. Prentice–Hall, 1987.

S. Joe Qin. Control performance monitoring – A review and assessment. *Computers in Chemical Engineering*, 23(2):173–186, 1998.

R.T. Subba and M.M. Gabar. A test for linearity of stationary time series. *Journal of Time Series Analysis*, 1(2):145–158, 1980.

Nina F. Thornhill and Alexander Horch. Advances and new directions in plant-wide disturbance detection and diagnosis. *Control Engineering Practice*, 15:1196–1206, 2007.

Wei Yu, David I. Wilson, and Brent R. Young. Control performance assessment in the presence of valve stiction. In K. Grigoriadis, editor, *The Eleventh IASTED International Conference on Intelligent Systems and Control, ISC 2008*, pages 379–384, Orlando, Florida, USA, 16–18 November 2008. ISBN 978-0-88986-777-2.

Valve Stiction Evaluation Using Global Optimization

M. Farenzena and J. O. Trierweiler

Group of Intensification, Modelling, Simulation, Control and Optimization of Processes (GIMSCOP)
Department of Chemical Engineering, Federal University of Rio Grande do Sul (UFRGS)
Rua Luiz Englert, s/n CEP: 90.040-040 - Porto Alegre - RS - BRAZIL,
Fax: +55 51 3308 3277, Phone: +55 51 3308 4163
E-MAIL: {farenz, jorge}@enq.ufrgs.br

Abstract: Valve stiction is a well known villain in process industry. Quantifying this valve damage is essential to ensure plant stability and profitability. The scope of this work is to propose a new method to compute valve stiction parameters, using a two parameter model, using only routine operating data. The proposed method uses global optimization to evaluate loop and plant parameters. Combining the proposed procedure with an efficient global optimization algorithm, the mean computation time for each valve was about 5 minutes. The method was applied in both simulation and industrial valves, providing reliable results, with relative errors smaller than 3% in all parameters.

Keywords: Performance Monitoring, Valve, Static Friction, Hysteresis, Global Optimization.

1 INTRODUCTION

In the last two decades, control loop performance monitoring has been a fruitful research field, providing automatic tools for process industry, which has great interest in evaluating loop performance in real time. Inside this scope, one topic that has been in focus is valve stiction, whose frequency in control loops is about 30% (Bialkowski, 1993). The effects of stiction are one explanation for these developments: it can cause plant-wide oscillations and increase the variability of the process and products.

Evaluating loop stiction is not a new issue. First studies were dated from 60's (Brown, 1958). However, in the last years, a big effort has been made to diagnose and solve this valve illness. A first group of works aimed at diagnosing stiction automatically, using only process variable (PV) and controller output (OP) (He *et al.*, 2007, Horch, 1999, Rossi and Scali, 2005, Ruel, 2000, Scali and Ghelardoni, 2008, Singhal and Salsbury, 2005, Stenman *et al.*, 2003, Yamashita, 2006). Some works have proposed specific stiction models for diaphragm type valves (Chen *et al.*, 2008, Choudhury *et al.*, 2005). A good survey about stiction models was recently written by Garcia (2008).

Also, some authors have proposed to compute stiction parameters in real time. Choudhury et al. (2006) proposed two methods to quantify stiction parameters, based on ellipse fitting and *c-clustering*, using a 1 parameter empirical model. Subsequently, some authors have proposed to quantify stiction parameters using a more reliable model, with two parameters. Choudhury *et al.* (2008) have proposed a method based on optimization and grid search.

Recently, Jelali (2008) has introduced one methodology to compute both stiction models, based on least-squares and global search algorithms. This method has two drawbacks: it is dependent of initial guess and it is computationally expensive. The scope of this work is to propose an alternative method based on global optimization to compute stiction parameters and linear plant model.

The main difference between our and Jelali's method is the optimization procedure, which is made in a single step, using global optimization. Both plant models and stiction parameters are computed in each optimization step. Combining the proposed procedure with an efficient global optimization algorithm, the computation time for each valve was less than 5 minutes.

The proposed methodology was applied in a set of 1000 simulation valves, with a relative error smaller than 3% in all cases, for all parameters. Then, the proposed method was applied in a group of industrial valves, showing reliable results.

The paper has been organized as follows: in section 2, the stiction definition, model and methodologies to evaluate valve stiction will be briefly discussed. Then, in section 3, the proposed methodology will be detailed. Several simulated and industrial case studies are shown in section 4, to corroborate the applicability of the proposed methodology. The paper ends with the concluding remarks.

2 STICTION: MODEL AND COMPUTATION

Stiction, or high static friction, can be defined as the valve damage that keeps the stem from moving, because the static friction exceeds the dynamic. As a consequence, the force to move the steam is generally larger than the desired new stem value, and the movement is jumpy (Ruel, 2000).

2.1 Stiction: model

A valve "suffering from stiction" has in the phase plot MV versus OP, shown in Fig. 1, four components: deadband (*DB*), stickband (*SB*), slip jump (*J*) and moving phase (*MP*). The method assumes that the process and controller have

linear behaviour, while the sticky valve inserts in the loop nonlinear behaviour.

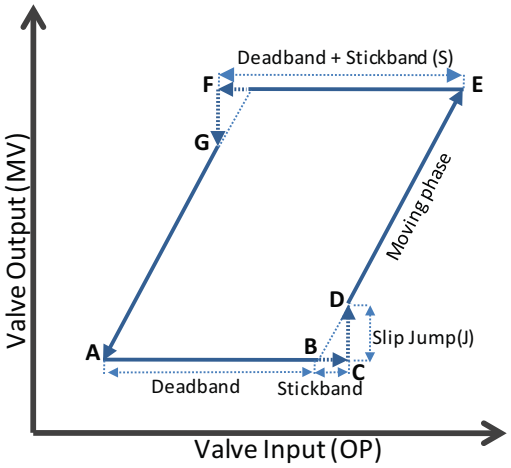

Fig. 1. Relation between controller output (OP) and valve position (MV) for a sticky valve.

When the valve changes the direction (A), the valve becomes sticky. The controller should overcome the deadband (AB) plus stickband (BC), and then the valve jumps to a new position (D). The stiction model consists of these two parameters: *S* (deadband+stickband) and *J* (jump).

Next, the valve starts moving, until its direction changes again or the valve comes to rest, between D and E.

The deadband and stickband represent the behaviour of the valve when it is not moving, although the input of the valve keeps changing. Slip jump represents the abrupt release of potential energy stored in the actuator chambers due to high static friction in the form of kinetic energy as the valve starts to move. The magnitude of the slip jump is crucial to determine the limit cycle amplitude and frequency.

The stiction model used in this work is proposed by Kano (2004), which is an extension of Choudhury's method, where stiction is modeled using two parameters. Their main advantage is that it can deal with both stochastic and deterministic signals. Kano's model flowchart representation is shown in Fig. 2.

The first two branches check the valve bounds. In the Kano's model, two valve states are distinguished: moving (*stp=0*) or resting (*stp=1*). When the valve changes its direction, its actual position state (us) is kept, until the static force is overcome. The friction force direction is denoted by $\pm d$.

2.2 Stiction: computation

In the literature, two methods to compute stiction parameters, using only normal operating data are proposed.

In the method proposed by Jelali (2008), a two step procedure is described. In the first step the stiction parameters are quantified using pattern search methods or genetic algorithms (GA). Next, the low-order linear plant model is identified, using a least-squares estimator. Both simulation and industrial valves are analyzed, and the errors between predicted and actual values for stiction parameters are less than 10%.

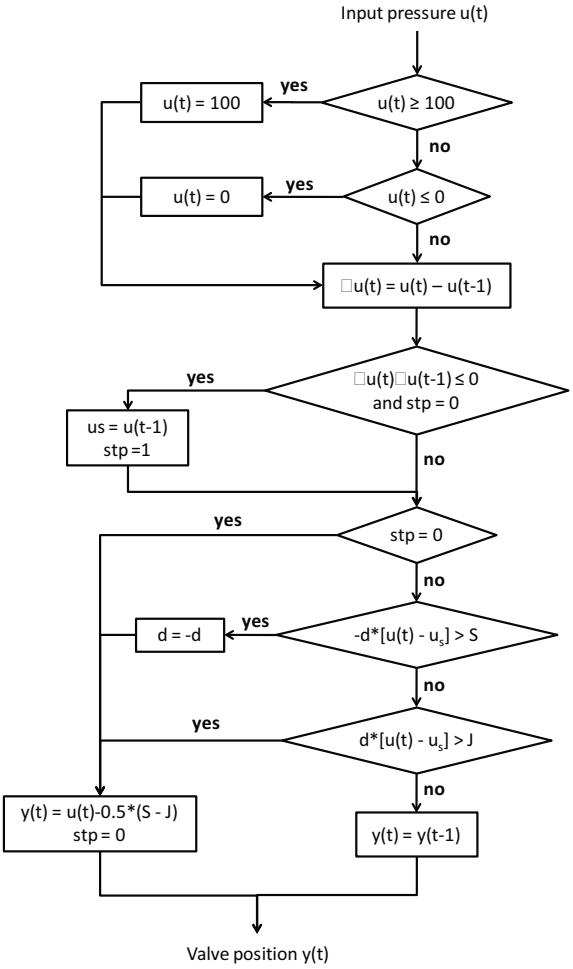

Fig. 2. Flowchart for Kano model.

a second method proposed by Choudhury *et al.* (2008) describes a method based on a grid search. Initially, a grid using several different values of *J* and *S* is built and then based on the process output, the plant model is identified. Based on the mean square error (MSE) between predicted process output and actual output in each grid point, the stiction parameters are estimated.

3 STICTION QUANTIFICATION

This section describes a new method to compute both stiction parameters and plant model, using only normal operating data. Data from process variable (PV) and controller output (OP) are required. Here, only first order with time delay models (FOPTD) will be used. However, the methodology is adequate for second orders, integrating process, among others.

Our approach uses the following assumptions, which are quite similar to the other methods available in the literature:

- The plant model is (locally) linear;
- The loop nonlinearity is caused by the valve;
- The stiction model can be considered a Hammerstein model;

The proposed method computes both plant stiction parameters in a single step, using a global optimization algorithm. This is the first difference between this work and the work proposed by Jelali (2008), where a two step procedure is proposed.

3.1 Optimization problem

The optimization problem to be solved is a non-linear programming type, where the objective function is the mean square error (MSE) of the difference of model output (PV_P) and plant output (PV).

$$MSE = \sum_{i=1}^{n} \frac{\left(PV_i - PV_{P_i}\right)^2}{n}$$

Where *n* is the length of PV.

In this class of problems, the function inside the search space is non-smooth and has some flat areas, where the gradient is zero, or close to this values. Fig 3 illustrates this behavior, using a FOPTD model and a sticky valve. The MSE was computed, varying *J* and *S*. In the process output, white noise is added, with signal-noise ratio equal to 1.

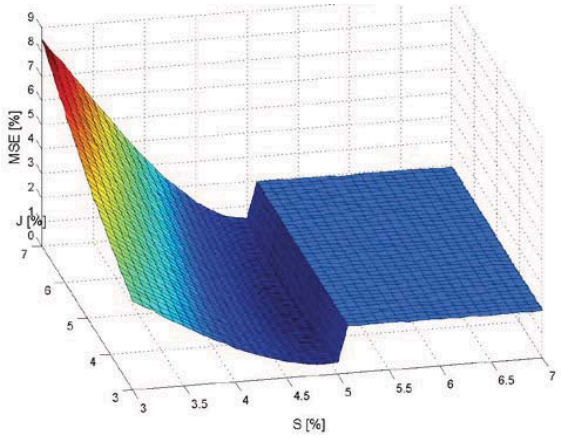

Fig 3: Objective function shape for variable S and J

Fig. 3 clearly shows that this class of function pattern requires global search algorithms; otherwise probably it will stick, depending on the initial guess. One possibility is to use stochastic algorithms, as proposed by Jelali (2008). A second possibility is to use global optimization deterministic algorithms, where the convergence is guaranteed, as proposed in this work.

The optimization problem for a FOPTD model to be solved is:

$$\min_{J,S,K,\tau} (MSE)$$

Where K and τ are the static gain and process time constant, respectively. The time delay is assumed to be known. Several methodologies available in the literature can be used to estimate this loop parameter (Elnaggar *et al.*, 1991, Ahmed *et al.*, 2006, Liang *et al.*, 2003).

The proposed technique can be easily extended to higher order or integrating processes. In this case, the plant model is replaced by an integrating transfer function $\left(\frac{K}{As}\right)$. In this case, the *K* and *A* are estimated by the optimization algorithm.

To allow the industrial application of the proposed method, the computational time should be reasonable. Thus, an efficient global optimization algorithm should be selected. Several optimization methods have been evaluated, and the best obtained by the authors is DIRECT (Finkel and Kelley, 2006). All algorithms are deterministic and deal with bounded decision variables.

4 CASE STUDIES

This section illustrates the applicability of the proposed methodology. Over a thousand simulation systems and a dozen of industrial sticky valves were analyzed and the proposed methodology has shown reliable results, what corroborates its industrial usefulness. Some of these systems will be shown here.

All computations were performed in an Intel Pentium D, 2GHz with 1 GB Ram.

4.1 Simulation case-studies

The objective of this section is to show the applicability of the proposed method in a set of simulation studies. All simulations use a PI controller and a first order plus time delay transfer function. Tab. 1 shows the models used in this work.

Tab. 1: Process and controller models used in the simulation case studies

Parameter	Model
Plant	$G(s) = \frac{1}{\tau s + 1} e^{-3s}$
Controller (PI)	$C(s) = 2\frac{\tau s + 1}{\tau s}$

Here, only twelve cases are shown, where a closed loop system is investigated with variable stiction parameters (*S* and *J*) and different plant time constant. The remaining parameters are maintained constant. Kano's model was used in all cases. The stiction parameters are specified as percentage of input and process variable span (%). Tab. 2 provides the summary of the results obtained by the application of the proposed methodology, where the true plant and valve stiction parameters (τ, *S*, and *J*) were compared with their values obtained by the proposed methodology. (τ_p, S_p, and J_p). The computation time (CPU_t) is also shown. All default settings in the DIRECT algorithm were used, except the maximum number of evaluations of objective functions, which was increased by 1000.

Tab. 2 corroborates the applicability of the proposed method, where the model parameters have deviation less than 3% of

the actual values. These values are comparable with Jelali's simulation cases, where the errors are less than 10%. If the maximum number of evaluations of objective function is increased by 3000, then the deviation reduces by less than 1%, however the CPU time increases to 12 min each.

Tab. 2: Results for process simulations

Case	J (%)	J_p (%)	Error (%)	S (%)	S_p (%)	Error (%)	τ (min)	τ_p (min)	Error (%)	CPU_t (min)
1	2,3	2,3	0,1%	3,0	3,0	0,1%	30,0	30,0	0,0%	4.3
2	2,3	2,3	0,1%	3,0	3,0	0,1%	10,0	10,0	0,0%	4.3
3	3,0	3,0	0,1%	3,0	3,0	0,1%	30,0	30,0	0,0%	4.3
4	3,0	3,0	0,0%	3,0	3,0	0,1%	10,0	10,0	0,0%	4.3
5	3,8	3,8	0,1%	3,0	3,0	0,1%	30,0	30,0	0,0%	4.2
6	3,8	3,7	-1,2%	3,0	3,0	0,0%	10,0	9,9	-1,0%	4.2
7	0,8	0,8	0,6%	1,0	1,0	1,1%	30,0	30,0	0,1%	4.4
8	0,8	0,8	2,9%	1,0	1,0	3,1%	10,0	10,1	1,3%	4.4
9	1,0	1,0	0,0%	1,0	1,0	0,1%	30,0	30,0	0,0%	4.0
10	1,0	1,0	-1,7%	1,0	1,0	-1,2%	10,0	10,0	-0,1%	4.1
11	1,3	1,3	1,3%	1,0	1,0	0,4%	30,0	30,1	0,2%	4.0
12	1,3	1,2	-1,6%	1,0	1,0	-0,9%	10,0	10,0	0,0%	4.3

The second factor also analyzed in this work, was the impact of white noise. Using the same case study of Tab. 1 with $\tau = 20, J = 5$, and $S = 5$, and different level of added white noise to the process variable several optimizations have been performed and the results are summarized in Tab. 3 where SNR is the relationship between Signal-Noise Ratio and the predicted stiction parameters, expressed in percentage of actual value.

Tab 3. White noise impact over the predicted stiction parameters – % change in each parameter

SNR	% S	% J
100	0.09%	-0.23%
50	0.29%	0.87%
5	0.50%	1.23%
0.5	5.9%	25%

As shown in Tab 3, the methodology is not very sensitive to white noise impact. Only when the noise is significant (i.e. SNR = 0.5) the results have been corrupted.

4.2 Industrial case-studies

This section shows some of the industrial application where the proposed methodology was applied. One flow control (case 1) and one pressure control (case 2) with sticky valves, from a Brazilian refinery, are analyzed.

Fig. 4 illustrates the PV and OP for industrial case study 1, where the presence of stiction can be easily seen. The application of the procedure proposed in this work leads to the estimates of $J = 2.6$, $S = 4.0$, and $\tau = 80$ sec. The comparison between the measured and predicted curves is shown in Fig. 5. This comparison shows that the estimated curve is in good agreement with the measured process variable.

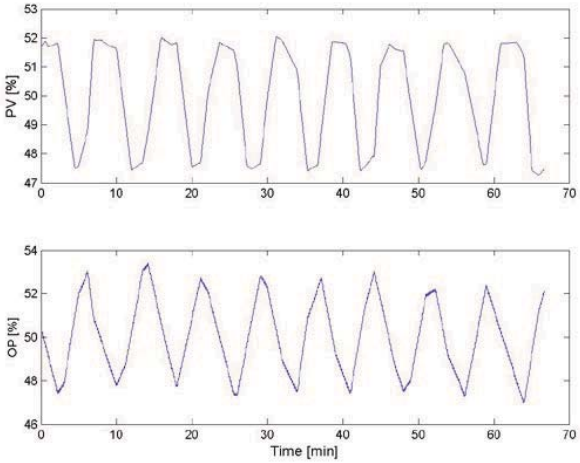

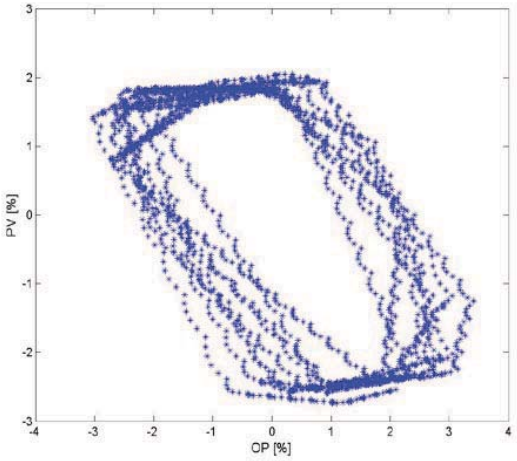

Fig. 4: Data trend for industrial case study 1 – flow control.

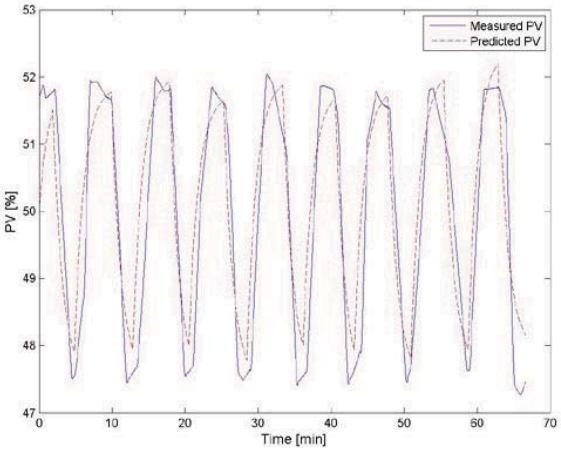

Fig 5: Comparison between measured and predicted PV for industrial case study 1 – flow control.

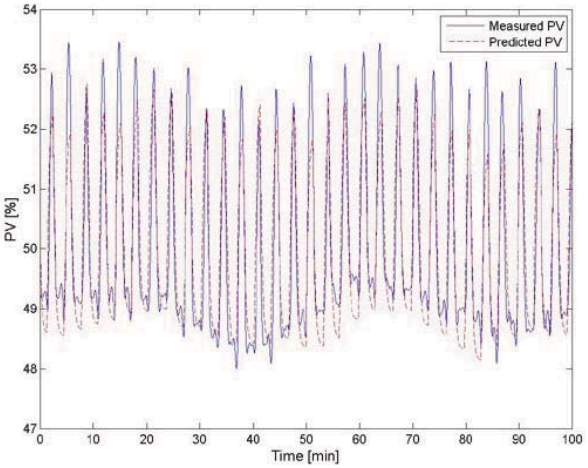

Fig 7 Comparison between measured and predicted PV for industrial case study 2 – pressure control.

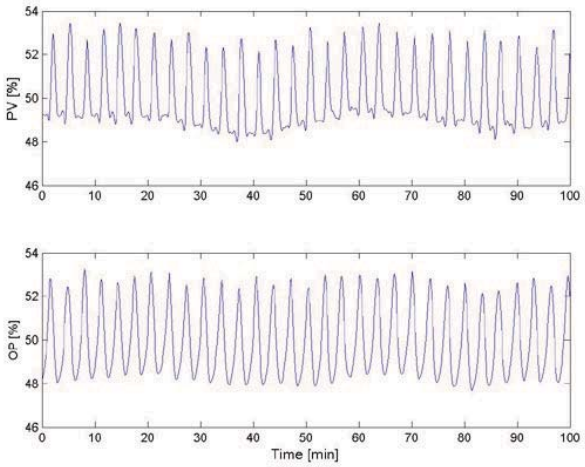

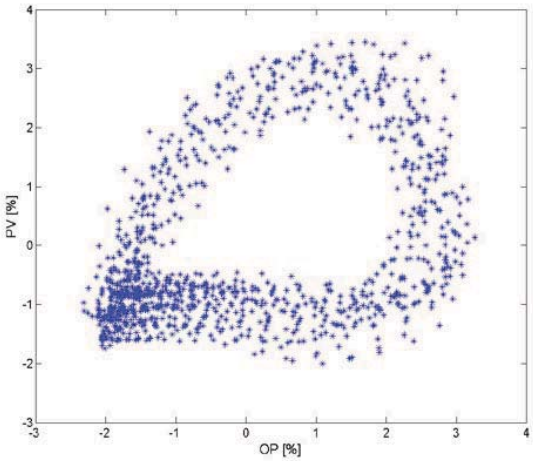

Fig. 6: Data trend for industrial case study 2 – pressure control.

The PV and OP signals for the second industrial sticky valve are shown in Fig. 6. Again, the stiction can be detected by visual inspection of PV versus OP plot, where a parallelogram shape is seen. The proposed estimation algorithm leads to the parameters estimates: $J = 1.6$, $S = 2.9$, and τ=18 sec. The comparison between the measured and predicted curves is shown in Fig. 7.

5 CONCLUSIONS

This work proposes a new method for quantifying valve stiction based on global optimization, using a one-step procedure, where both stiction parameters and plant model are simultaneously quantified, using only process variable (PV) and controller output (OP). The objective function minimized the mean square error between the measured and predicted process output and the optimization algorithm used for this class of problem is called DIRECT (Finkel and Kelley, 2006).

The validity of the method is successfully demonstrated by comparing simulation results, where valves with known stiction parameters were evaluated. Industrial valves were also evaluated, providing very good results. Comparing the actual procedure with the available in the literature, the CPU time is considerably smaller – in this case lower than 5 min against 20 to 30 min – and the quality of the results is comparable – an error lower than 3% against 10%. The industrial applicability of the proposed method has been corroborated by two industrial applications, where reliable results have been obtained.

ACKNOWLEDGMENTS

The authors are very grateful for the grants from CAPES / BRAZIL.

REFERENCES

Ahmed, S., Huang, B. and Shah, S. L. (2006) Parameter and delay estimation of continuous-time models using a linear filter. *Journal of Process Control,* 16**,** 323-331.

Bialkowski, W. L. (1993) Dreams versus reality: A view from both sides of the gap. *Pulp and Paper Canada,* 94**,** 19-27.

Brown, B. P. (1958) Ground Simulator Studies of the Effects of Valve Friction, Stick Friction, Flexibility, and Backlash on Power Control System Quality. IN Aeronautics, N. A. C. F. (Ed.) *Report 1348.* Washington D.C., National Advisory Committee for Aeronautics.

Chen, S. L., Tan, K. K. and Huang, S. (2008) Two-layer binary tree data-driven model for valve stiction. *Industrial and Engineering Chemistry Research,* 47**,** 2842-2848.

Choudhury, M. A. A. S., Jain, M. and Shah, S. L. (2006) Detection and quantification of valve stiction. *Proceedings of the American Control Conference.*

Choudhury, M. A. A. S., Jain, M. and Shah, S. L. (2008) Stiction - definition, modelling, detection and quantification. *Journal of Process Control,* 18**,** 232-243.

Choudhury, M. A. A. S., Thornhill, N. F. and Shah, S. L. (2005) Modelling valve stiction. *Control Engineering Practice,* 13**,** 641-658.

Elnaggar, A., Dumont, G. A. and Elshaefei, A.-L. (1991) Delay estimation using variable regression. *Proceedings of the American Control Conference.*

Finkel, D. E. and Kelley, C. T. (2006) Additive scaling and the DIRECT algorithm. *Journal of Global Optimization,* 36**,** 597-608.

Garcia, C. (2008) Comparison of friction models applied to a control valve. *Control Engineering Practice,* 16**,** 1231-1243.

He, Q. P., Wang, J., Pottmann, M. and Qin, S. J. (2007) A curve fitting method for detecting valve stiction in oscillating control loops. *Industrial and Engineering Chemistry Research,* 46**,** 4549-4560.

Horch, A. (1999) A simple method for detection of stiction in control valves. *Control Engineering Practice,* 7**,** 1221-1231.

Jelali, M. (2008) Estimation of valve stiction in control loops using separable least-squares and global search algorithms. *Journal of Process Control,* 18**,** 632-642.

Kano, M., Maruta, H., Kugemoto, H. and Shimizu, K. (2004) Practical model and detection algorithm for valve stiction. IN Ifac (Ed.) *7th IFAC DYCOPS.* Boston, USA.

Liang, Y., An, D. X., Zhou, D. H. and Pan, Q. (2003) Estimation of time-varying time delay and parameters of a class of jump Markov nonlinear stochastic systems. *Computers & Chemical Engineering,* 27**,** 1761-1778.

Rossi, M. and Scali, C. (2005) A comparison of techniques for automatic detection of stiction: simulation and application to industrial data. *Journal of Process Control,* 15**,** 505-514.

Ruel, M. (2000) Stiction: The hidden menace. *Control Magazine*.

Scali, C. and Ghelardoni, C. (2008) An improved qualitative shape analysis technique for automatic detection of valve stiction in flow control loops. *Control Engineering Practice*.

Singhal, A. and Salsbury, T. I. (2005) A simple method for detecting valve stiction in oscillating control loops. *Journal of Process Control,* 15**,** 371-382.

Stenman, A., Gustafsson, F. and Forsman, K. (2003) A segmentation-based method for detection of stiction in control valves. *International Journal of Adaptive Control and Signal Processing,* 17**,** 625-634.

Yamashita, Y. (2006) An automatic method for detection of valve stiction in process control loops. *Control Engineering Practice,* 14**,** 503-510.

Optimization and Optimal Control

Oral Session

Nonsmooth Optimization of Systems with Varying Structure

Mehmet Yunt, * **Paul I. Barton** **

* *Dept. of Mechanical Engineering, Massachusetts Institute of Technology, Cambridge, MA 02139, USA (e-mail: myunt@mit.edu)*
** *Dept. of Chemical Engineering, Massachusetts Institute of Technology, Cambridge, MA 02139, USA (e-mail: pib@mit.edu)*

Abstract: A novel method based on the generalized gradient and nonsmooth optimization techniques called bundle methods is introduced to optimize the performance of a class of dynamic systems whose governing equations change depending on the values of the parameters, controls and the current state of the system.

Keywords: Nonsmooth Optimization, Generalized Gradient, Bundle Methods, Dynamic Optimization

1. INTRODUCTION

This paper describes a novel method to determine the optimal controls and parameters for a large class of engineering systems with varying structure which have the following characteristics:

(1) The systems evolve according to different ordinary differential equations depending on the values of the states, controls and parameters.
(2) The vector field is unique and continuous.
(3) The values of the continuous states, controls and parameters solely determine the vector field.

Example 1. The liquid level dynamics of a tank with a weir with multiple inlet and outlet flows is

$$\dot{h}(t,\mathbf{p}) = \sum_{i=1}^{n} F_i(t)/A - F_W(h(t,\mathbf{p}),\mathbf{p}) \tag{1}$$

$$F_W(h(t,\mathbf{p}),\mathbf{p}) = \begin{cases} 0 & \text{if } h(t,\mathbf{p}) \le \bar{h} \\ k(h(t,\mathbf{p}) - \bar{h}) & \text{if } h(t,\mathbf{p}) \ge \bar{h} \end{cases}$$

$$\mathbf{p} = (\bar{h}, k, A)^{\mathrm{T}}$$

where h is the liquid level; A is the cross-sectional area of the tank; F_i are volumetric flows; $\bar{h}$ is the weir height; k is an equivalent valve constant for the weir. The governing ordinary differential equations are determined by h and $\bar{h}$. At $h = \bar{h}$, two ordinary differential equations are applicable but the vector field is unique and continuous.

These systems can be expressed in the form,

$$\dot{\mathbf{x}}(t,\mathbf{p}) = \mathbf{f}(\mathbf{x}(t,\mathbf{p}),\mathbf{u}(t),\mathbf{p})$$

where $\mathbf{x}$ represents the continuous-valued states, $\mathbf{p}$ is a finite set of continuous-valued parameters, $\mathbf{u}(t)$ are the bounded controls with possible discontinuities at finitely many points in time. $\mathbf{f}$ is continuous on its domain. The domain of $\mathbf{f}$ is partitioned into finitely many sets, D_k, such that if $(\mathbf{x}(t,\mathbf{p}),\mathbf{u}(t),\mathbf{p}) \in D_k$ then $\mathbf{f}(\mathbf{x}(t,\mathbf{p}),\mathbf{u}(t),\mathbf{p}) = \mathbf{f}_k(\mathbf{x}(t,\mathbf{p}),\mathbf{u}(t),\mathbf{p})$ where $\mathbf{f}_k$ are continuously differentiable with respect to their arguments. As a result of this particular structure $\mathbf{f}$ is piecewise continuously differentiable with respect to its arguments.

In order to formulate a finite dimensional optimization problem, the controls are reformulated as piecewise constant functions of parameters and time with finitely many discontinuities at $t_i,\ i = 1,\ldots,n$ with $t_i < t_{i+1}$, $t_1 = 0$ and $t_n < \infty$. As a result of this reformulation, the dynamics can be represented by a set of equations $\dot{\mathbf{x}}(t,\mathbf{p}) = \mathbf{f}^i(\mathbf{x}(t,\mathbf{p}),\mathbf{p})$ if $t \in (t_i, t_{i+1}]$. Note that each $\mathbf{f}^i$ has a partitioned domain with finitely many partitions, $\{D_k^i,\ k = 1,\ldots,n_i\}$, and corresponding continuously differentiable vector fields $\{\mathbf{f}_k^i\}$.

The mathematical program to be solved is

$$\min_{\mathbf{p}} J(\mathbf{p}) = \sum_{i=1}^{n-1} \int_{t_i}^{t_{i+1}} h(\mathbf{x}(t,\mathbf{p}),\mathbf{p})dt + H(\mathbf{x}(t_n,\mathbf{p}),\mathbf{p}) \tag{2}$$

$$\text{s.t} \sum_{i=1}^{n-1} \int_{t_i}^{t_{i+1}} \mathbf{g}(\mathbf{x}(t,\mathbf{p}),\mathbf{p})dt + \mathbf{G}(\mathbf{x}(t_n,\mathbf{p}),\mathbf{p}) \le \mathbf{0}$$

$$\dot{\mathbf{x}}(t,\mathbf{p}) = \mathbf{f}^i(\mathbf{x}(t,\mathbf{p}),\mathbf{p}),\ \forall t \in (t_i, t_{i+1}], \tag{3}$$

$$\mathbf{x}(0,\mathbf{p}) = \mathbf{f}^0(\mathbf{p}),\ i = 1,\ldots,n-1$$

where H, h, $\mathbf{G}$, $\mathbf{g}$, $\mathbf{f}^0$ are continuously differentiable functions of their arguments that are used to compute values of the objective, values of the constraints and the initial conditions.

Standard numerical methods of dynamic optimization (Betts, 1998) are not applicable to solve (2) because the $\mathbf{f}^i$ are not continuously differentiable. Sensitivity results (Galán et al., 1999) are also not applicable because given $t \in (t_i, t_{i+1}]$, it is not a priori known which $\mathbf{f}_k^i$ govern the dynamics of the system. Furthermore, at $t \in (t_i, t_{i+1}]$ the governing $\mathbf{f}_k^i$ depends on the value of $\mathbf{p}$. The solution of (2) not only determines an optimal $\mathbf{p}$ but prescribes a sequence of $\mathbf{f}_k^i$ in time. This implicit selection complicates the solution process.

The *mixed-integer* (Avraam et al., 1998; Bemporad and Morari, 1999) and the *differential variational inequalities, DVI* (Schumacher, 2004; Pang and Stewart, 2008; Raghunathan et al., 2004) approaches make this selection explicit using transcription. Given $[t_i, t_{i+1}]$, a mesh of time points $\{\tau_j : \ j = 1, 2, \ldots n_i, \ \tau_1 = t_i \ \tau_{n_i} = t_{i+1}\}$ is determined a priori. For each τ_j, a variable, $\mathbf{x}_j$, representing the continuous state is created. In order to make the selection of $\mathbf{f}_k^i$ explicit, (3) needs to be replaced with suitable algebraic relationships and additional constraints. The governing dynamics need to be determined in the intervals $[\tau_j, \tau_{j+1}]$. Both approaches replace (3) with a discretization such as the forward Euler method. Both methods introduce additional variables, μ_j^k, at each τ_j for each $\mathbf{f}_k^i$ and approximate the dynamics between time points using the function; $\sum_k \mu_j^k \mathbf{f}_k^i(\mathbf{x}_j, \mathbf{p})$. For example, if the forward Euler discretization is used, an algebraic relationship replacing (3) is $\mathbf{x}_{j+1} - \mathbf{x}_j = (\tau_{j+1} - \tau_j) \sum_{k=1}^{n_i} \mu_j^k \mathbf{f}_k^i(\mathbf{x}_j, \mathbf{p}), \ j = 1, \ldots, n_i - 1$. Both approaches replace the integral terms in (2) by appropriate quadratures.

The approaches differ in the way the values of μ_j^k are determined. In the mixed-integer approach, μ_j^k are binary variables. Additional constraints enforce that a single μ_j^k is non-zero at a given τ_j and that this is consistent with parameter, $\mathbf{p}$, and state values, $\mathbf{x}_j$ at τ_j. The final formulation is a mixed-integer nonlinear program. In the DVI approach, μ_j^k are part of the solution of an embedded mathematical program of the states and parameters at each τ_j. These programs are replaced with their equivalent KKT conditions.

Both approaches result in large optimization problems as a result of transcription. Only linear and quadratic formulations of the mixed-integer approach can be solved practically. This restricts the underlying ODEs to be linear and the sets D_k to be polyhedral. The DVI approach requires that the embedded programs are convex to guarantee that the KKT conditions are sufficient to determine an optimal solution. Complementarity constraints in the KKT conditions necessitate special solvers because complementarity conditions violate constraint qualifications which are necessary for ordinary nonlinear programming, NLP, algorithms to work. The required special solvers are not as efficient as usual NLP solvers.

This paper describes a method where the selection of dynamics is not handled explicitly. The method is based on *single-shooting*. In single shooting, the dynamics in (3) are solved by an initial value solver, IVP. In the differentiable case, the IVP solver is also used to solve an auxiliary set of equations to obtain parametric sensitivities. These sensitivities are used to calculate gradient information for numerical optimization methods. There are no additional variables or constraints. The resultant optimization problems do not grow with the number of time points in the mesh nor the size of the possible set of ODEs. In addition, the convexity constraints on the dynamics as in the mixed-integer and DVI approaches can be relaxed.

In order to use single-shooting on (2), which is a nonsmooth program, derivative-like information needs to be obtained. Nonsmoothness also prevents the application of standard nonlinear programming solvers. In order to handle these complications, *Clarke's generalized Jacobian* (Clarke, 1990) is employed in conjunction with a class of nonsmooth optimization methods called *bundle methods* (Kiwiel, 1985; Mäkelä, 2001) to solve (2).

In the remainder, the necessary mathematical background is summarized. The method is then described. The paper ends with an illustrative example and directions of further research.

2. MATHEMATICAL BACKGROUND

$\mathbf{F} : \mathbb{R}^n \to \mathbb{R}^m$ is *locally Lipschitz continuous* at $\mathbf{x}$ if there exists a neighborhood, $N_\epsilon(\mathbf{x})$ and a finite positive constant, K, such that $\|\mathbf{F}(\mathbf{y}) - \mathbf{F}(\mathbf{z})\| \leq K\|\mathbf{y} - \mathbf{z}\| \ \forall \mathbf{z}, \mathbf{y} \in N_\epsilon(\mathbf{x})$. Rademacher's theorem states that locally Lipschitz continuous functions are almost everywhere differentiable on their domain (Rockafellar and Wets, 1998). The locally Lipschitz continuous property is preserved under addition and composition of functions.

Let $\mathbf{F} : \mathbb{R}^n \to \mathbb{R}^m$ be locally Lipschitz continuous at $\mathbf{x}$, then the *generalized Jacobian* (Clarke, 1990) at $\mathbf{x}$ is

$$\partial \mathbf{F}(\mathbf{x}) = \text{co}\{ \lim_{\mathbf{x}_i \to \mathbf{x}} J\mathbf{F}(\mathbf{x}_i) : \ \mathbf{x}_i \notin S \cup T\} \quad (4)$$

where co is the convex hull, $J\mathbf{F}$ denotes the Jacobian of $\mathbf{F}$ where it exists; S is the set of measure zero nondifferentiable points and T is an arbitrary set of measure zero. In words, the generalized Jacobian at $\mathbf{x}$ is the convex hull of all the limits of convergent Jacobian sequences with the Jacobians evaluated at points converging to $\mathbf{x}$. In finite dimensional Euclidean spaces, the *generalized gradient* is the generalized Jacobian when $m = 1$ and the elements of the generalized Jacobian are transposed.

Example 2. $\dot{h}(t, \mathbf{p})$ in (1) is locally Lipschitz continuous with respect to $\bar{h}$ and the generalized gradient is:

$$\partial_{\bar{h}} \dot{h}(t, \mathbf{p}) = \begin{cases} 0 & \text{if } h(t, \mathbf{p}) < \bar{h} \\ \text{co}[0, k] & \text{if } h(t, \mathbf{p}) = \bar{h} \\ k & \text{if } h(t, \mathbf{p}) > \bar{h}. \end{cases}$$

Chain rules can be derived for generalized gradients and Jacobians. Implicit function theorems can be formulated. Necessary conditions of optimality for mathematical programs with locally Lipschitz continuous functions can be defined in terms of generalized gradients. For numerical methods, if the generalized gradient at a point is known, a direction of descent can be obtained by using the element of minimum norm.

In general, it is not possible to calculate all the elements of the generalized gradient at a point to determine directions of descent. *Bundle Methods* (Kiwiel, 1985; Mäkelä, 2001) use an approximation to the generalized gradient to solve

$$\min_{\mathbf{z} \in Z} f(\mathbf{z}) \text{ s.t: } g_m(\mathbf{z}) \leq 0, \ m = 1, \ldots, M$$

where f and g_m are locally Lipschitz continuous functions. Bundle methods require that only an element of $\partial f(\mathbf{z})$ and of each $\partial g_m(\mathbf{z})$ are available. The generalized gradient at an iterate is approximated by the convex

hull of a set of generalized gradients of nearby points called the *bundle*. The element of minimum norm of the approximation is used as the descent direction. Using a specialized line search procedure, either the next iterate is determined or another element is added to the bundle to change the direction of descent.

Bundle methods converge to stationary points satisfying KKT type conditions under a *semismoothness* (Mifflin, 1977; Qi, 1993) assumption on f and g_m. Semismoothness guarantees that the iterative line search algorithm in bundle methods terminates after finite number of iterations. Similar to local Lipschitz continuity, semismoothness is conserved under addition, multiplication and composition. Piecewise continuously differentiable functions, finite convex functions and continuously differentiable functions are all examples of functions that are semismooth and locally Lipschitz continuous.

3. METHOD DESCRIPTION

In this section, the theoretical discussion focuses on the dynamic systems,

$$\begin{aligned}&\dot{\mathbf{x}}(t,\mathbf{p}) = \mathbf{f}^i(\mathbf{x}(t,\mathbf{p}),\mathbf{p}),\ \forall t \in (t_i, t_{i+1}] \\ &\mathbf{x}(t_1,\mathbf{p}) = \mathbf{f}^0(\mathbf{p}),\ \mathbf{p} \in P,\ i = 1 \dots n-1\end{aligned} \tag{5}$$

where $\mathbf{f}^i : \mathbb{R}^{n_x} \times \mathbb{R}^{n_p} \to \mathbb{R}^{n_x}$ are piecewise continuously differentiable with respect to their arguments, $\mathbf{f}^0 : \mathbb{R}^{n_p} \to \mathbb{R}^{n_x}$ is continuously differentiable and P is a compact set with non-empty interior. In order to develop a numerical method, the following assumptions are made:

Assumption 1. Equation (5) has a solution on $[t_i, t_{i+1}]$, $i = 1, \dots, n-1$ for each $\mathbf{p} \in P$.

Assumption 2. The domain of each $\mathbf{f}^i$ is partitioned into a finite set of subdomains with nonempty interior, $\{D^i_k,\ k = 1, \dots, n_i\}$ and $D^i_k = \{(\mathbf{v},\mathbf{p}) : d^i_{k,j}(\mathbf{v},\mathbf{p}) \leq 0,\ j = 1, \dots, n_{i,k}\}$ where $d^i_{k,j}$ are continuously differentiable. In other words, the partitions have boundaries that can be expressed using continuously differentiable functions and $d^i_{k,j}(\mathbf{v},\mathbf{p}) = 0$ represent continuously differentiable manifolds of dimension $n_x \times n_p - 1$. There exists a corresponding set of $\{\mathbf{f}^i_k\}$ such that $\mathbf{f}^i(\mathbf{x}(t,\mathbf{p}),\mathbf{p}) = \mathbf{f}^i_k(\mathbf{x}(t,\mathbf{p}),\mathbf{p})$ if $(\mathbf{x}(t,\mathbf{p}),\mathbf{p}) \in D^i_k$ and $\mathbf{f}^i_k$ are continuously differentiable with respect to their arguments.

$\mathbf{x}(t,\mathbf{p})$ is a locally Lipschitz continuous (Coddington and Levinson, 1955) and semismooth function of $\mathbf{p}$ (Pang and Stewart, 2009) as a result of continuity and piecewise continuous differentiability of $\mathbf{f}^i$. The constraints and objective of (2) are composite functions of semismooth and locally Lipschitz functions and $\mathbf{x}(t,\mathbf{p})$. As a result, the constraints and objective of (2) are locally Lipschitz and semismooth functions.

In order to calculate the necessary generalized gradient information for optimization, an element of the generalized gradient of the states with respect to $\mathbf{p}$, $\partial_{\mathbf{p}}\mathbf{x}(t,\mathbf{p})$, is required. The next theorem provides a sufficient condition to detect points where an element can be calculated. It can be deduced from Theorem 7.4.1 in Clarke (1990) using appropriate chain rules and the definition of the Jacobian.

Theorem 1. Let $\mathbf{x}(t,\bar{\mathbf{p}})$ be a solution of (5). If the set-valued mapping, $\partial_{(\mathbf{x},\mathbf{p})}\mathbf{f}^i_{\mathbf{p}}(\mathbf{x}(t,\bar{\mathbf{p}}),\bar{\mathbf{p}})$ is a singleton for almost all $t \in (t_1, t_n]$, then for each $i = 1, \dots, n-1$, there exist unique solutions to the matrix differential inclusions:

$$\begin{aligned}&\dot{Y}_{\mathbf{p}}(t) \in \partial\mathbf{f}^i_{\mathbf{x}}(\mathbf{x}(t,\bar{\mathbf{p}}),\bar{\mathbf{p}})Y_{\mathbf{p}}(t) + \partial\mathbf{f}^i_{\mathbf{p}}(\mathbf{x}(t,\bar{\mathbf{p}}),\bar{\mathbf{p}}), \\ &\qquad\qquad \forall t \in (t_i, t_{i+1}] \\ &\dot{Y}_{\mathbf{x}}(t) \in \partial\mathbf{f}^i_{\mathbf{x}}(\mathbf{x}(t,\bar{\mathbf{p}}),\bar{\mathbf{p}})Y_{\mathbf{x}}(t), \forall t \in (t_i, t_{i+1}] \\ &Y_{\mathbf{p}}(t_1) = 0,\ Y_{\mathbf{x}}(t_1) = I.\end{aligned}$$

The following relations hold for all $t \in (t_i, t_{i+1}]$ except on set of measure zero,

$$\dot{Y}_{\mathbf{p}}(t) = J\mathbf{f}^i_{\mathbf{x}}(\mathbf{x}(t,\bar{\mathbf{p}}),\bar{\mathbf{p}})Y_{\mathbf{p}}(t) + J\mathbf{f}^i_{\mathbf{p}}(\mathbf{x}(t,\bar{\mathbf{p}}),\bar{\mathbf{p}}) \tag{6}$$

$$\dot{Y}_{\mathbf{x}}(t) = J\mathbf{f}^i_{\mathbf{x}}(\mathbf{x}(t,\bar{\mathbf{p}}),\bar{\mathbf{p}})Y_{\mathbf{x}}(t) \tag{7}$$

where $J\mathbf{f}^i_{\mathbf{x}}$ and $J\mathbf{f}^i_{\mathbf{p}}$ are the partial derivatives of $\mathbf{f}^i$ with respect to $\mathbf{x}$ and $\mathbf{p}$ respectively.

Finally, $\partial_{\mathbf{p}}\mathbf{x}(t_n,\bar{\mathbf{p}}) = Y_{\mathbf{x}}(t_n)J\mathbf{f}_0(\bar{\mathbf{p}}) + Y_{\mathbf{p}}(t_n)$.

Definition 1. A trajectory, $\mathbf{x}(t,\mathbf{p})$, is called *singleton* if $\partial\mathbf{f}^i_{(\mathbf{x},\mathbf{p})}(\mathbf{x}(t,\mathbf{p}),\mathbf{p})$ is a singleton for almost all $t \in [t_i, t_{i+1}]$. Otherwise, it is called *non-singleton*.

Note that due to assumption (2) and the piecewise continuous differentiable nature of $\mathbf{f}^i$, the points where $\partial\mathbf{f}^i_{(\mathbf{x},\mathbf{p})}(\mathbf{x}(t,\mathbf{p}),\mathbf{p})$ may not be a singleton are where $d^i_{k,j}(\mathbf{x}(t,\mathbf{p}),\mathbf{p}) = 0$ holds for some k and j. Trajectories that are not singleton have arcs that lie on the surfaces defined by $d^i_{k,j}(\mathbf{x}(t,\mathbf{p}),\mathbf{p}) = 0$.

The next theorem is a result on the occurrence of non-singleton trajectories for autonomous systems with piecewise continuously differentiable vector fields.

Theorem 2. Consider the dynamic system

$$\dot{\mathbf{x}}(t) = \mathbf{f}(\mathbf{x}(t)),\ t \in (0, t_f],\ \mathbf{x}(0) = \mathbf{x}_0,\ \mathbf{x}_0 \in X_0 \subset D \tag{8}$$

where X_0 is an open set in $\mathbb{R}^{n_x}$, D is the bounded domain where all solutions with initial conditions in X_0 remain for $t \in (0, t_f]$. Let $\mathbf{f} : \mathbb{R}^{n_x} \to \mathbb{R}^{n_x}$ be piecewise continuously differentiable on D. Let assumptions (2) hold where all $d^i_{k,j}$ are continuously differentiable functions of $\mathbf{x}$. Then the set of initial conditions producing non-singleton trajectories is a measure zero subset of X_0.

Proof. Since $\mathbf{f}$ is locally Lipschitz continuous on D, the set of points where it is not differentiable is a set of measure zero in D. In addition, due to piecewise continuous differentiability, the generalized Jacobian is a singleton where $\mathbf{f}$ is differentiable. The only points where the generalized Jacobian is not a singleton are on the boundaries of the subdomains which constitute a set of measure zero in D. The solutions of (8) are unique due to the Lipschitz continuous property of $\mathbf{f}$ on D. Due to the autonomous nature of the dynamics, no two solutions intersect for any $t \in (0, t_f]$. Now consider trajectories that pass through boundary points. Since points on the boundaries are a set of measure zero in D, the set of initial conditions producing these trajectories are a set of measure zero in D. Since the set of initial conditions that produce non-singleton trajectories is a subset of the set of initial conditions that produce trajectories passing through boundary points, the set of initial conditions producing non-singleton trajectories is a set of measure

zero in D. Finally the intersection of X_0 which is open in $\mathbb{R}^{n_x}$ with this set of initial conditions is a set of measure zero.

If the initial conditions of (8) are functions of a set of parameters, then the result of the previous theorem may not hold. It is possible that the functions always map the parameters to initial conditions resulting in non-singleton trajectories. Sufficient conditions to determine functions that map parameters to sets of initial conditions for which theorem (2) holds is under investigation.

In the remainder of the paper, the following statement is assumed to hold.

Assumption 3. Let $\tilde{P}$ the set of parameters such that $\mathbf{x}(t, \mathbf{p})$ with $\mathbf{p} \in \tilde{P}$ is not a singleton trajectory. The set $\tilde{P}$ has measure zero in P.

The equations (5), (6) and (7) have to be solved numerically. The solution of (5) poses no problems and can be accomplished with an ordinary IVP solver because $\mathbf{f}^i$ are Lipschitz continuous vector field on their domains. On the other hand, solutions of (6) and (7) require further discussion. Since $\mathbf{f}^i$ are only piecewise continuously differentiable, $J_{\mathbf{p}}\mathbf{f}^i$ and $J_{\mathbf{x}}\mathbf{f}^i$ are not continuous on the domain of $\mathbf{f}^i$. As a result (6) and (7) are differential equations with discontinuities in time. These discontinuities need to be detected for an efficient and correct solution. By virtue of assumption (2), the points where $\mathbf{f}^i$ are not differentiable are on the boundaries of the partitions and satisfy $d^i_{k,j}(\mathbf{x}(t, \mathbf{p}), \mathbf{p}) = 0$ for some values of k and j. Event detection algorithms (Park and Barton, 1996) are used to determine t^* such that $d^i_{k,j}(\mathbf{x}(t^*, \mathbf{p}), \mathbf{p}) = 0$. The event detection algorithm tracks the signs of $d^i_{k,j}(\mathbf{x}(t, \mathbf{p}), \mathbf{p})$ for each i and j. A sign change implies that the state trajectory, $\mathbf{x}(t^*, \mathbf{p})$ crossed a boundary of discontinuity. The event detection algorithm finds the earliest time when the boundary crossing occurred. The integration of (6) and (7) are restarted at t^*.

Event detection algorithms are also used to detect trajectories that are non-singleton. Once t^* is detected where $d^i_{k,j}(\mathbf{x}(t^*, \mathbf{p}), \mathbf{p}) = 0$ for some k and j, $\dot{d}^i_{k,j}(\mathbf{x}(t^*, \mathbf{p}), \mathbf{p})$ is checked. If $\dot{d}^i_{k,j}(\mathbf{x}(t^*, \mathbf{p}), \mathbf{p}) = 0$ for some k and j, this implies that the state trajectory may not leave the surface defined by $d^i_{k,j}(\mathbf{x}(t^*, \mathbf{p}), \mathbf{p}) = 0$ resulting in a trajectory that is possibly non-singleton. Integration is continued until $t + \delta t$ where δt is a small quantity. If there exists any k and j such that $d^i_{k,j}(\mathbf{x}(t^*, \mathbf{p}), \mathbf{p}) = 0$ and $d^i_{k,j}(\mathbf{x}(t^* + \delta t, \mathbf{p}), \mathbf{p}) = 0$, the trajectory is considered to be not a singleton trajectory.

In case $\bar{\mathbf{p}}$ does not correspond to a singleton trajectory, the definition of the generalized Jacobian (4) can be used to approximate an element of the generalized Jacobian. Random parameter values in an ϵ neighborhood, $N_\epsilon(\bar{\mathbf{p}})$, can be used to find a nearby singleton trajectory and calculate an approximate generalized Jacobian.

The necessary generalized gradient information for the objective and constraint functions of (2) is obtained by applying the chain rules for generalized gradients once an element or an approximation of $\partial_{\mathbf{p}}\mathbf{x}(t, \mathbf{p})$ is calculated. The calculated generalized gradient information is used in conjunction with a bundle method to obtain a stationary point of (2).

4. ILLUSTRATIVE EXAMPLE

In this section, a modified version of the cell cycle specific chemotherapy model introduced in Pannetta and Adam (1995) is used to determine an optimal chemotherapy drug schedule. The dynamics,

$$\alpha = a - m - n$$

$$\dot{P} = \alpha P + bQ - F_A(v_A, P) \tag{9}$$

$$F_A(v_A, P) = \begin{cases} 0 & \text{if } v_A - \bar{v}_A \leq 0 \\ k_A(v_A - \bar{v}_A)P & \text{if } v_A - \bar{v}_A \geq 0 \end{cases}$$

$$\dot{Q} = mP - bQ - F_B(v_B, Q) \tag{10}$$

$$F_B(v_B, Q) = \begin{cases} 0 & \text{if } v_B - \bar{v}_B \leq 0 \\ k_B(v_B - \bar{v}_B)Q & \text{if } v_B - \bar{v}_B \geq 0 \end{cases}$$

$$\dot{Y} = \sigma Y(1 - Y/K) - k_A v_A Y - k_B v_B Y \tag{11}$$

$$\dot{v}_A = u_A - \gamma_A v_A \tag{12}$$

$$\dot{v}_B = u_B - \gamma_B v_B \tag{13}$$

represents the behavior of tumor cells and healthy cells in human tissue under chemotherapy. The tissue comprises healthy cells, Y, proliferating tumor cells, P, and quiescent tumor cells, Q. Chemotherapy comprises two drugs; A and B. u_A and u_B are the chemotherapy drug schedules. v_A and v_B are the exponentially decaying drug concentrations in the tissue. Tumor cells develop resistance to drugs. As a result, drugs are effective against the tumor cells only if their concentrations in the tissue are above $\bar{v}_A$ and $\bar{v}_B$. A fraction, n, of proliferating cells die of natural causes and and a fraction, m, of proliferating cells become quiescent cells. The increase in proliferating cell population by cell division is represented as another fraction, a, of the proliferating cell population. In addition, a fraction, b of quiescent cells become proliferating cells. The tumor cell dynamics are in (9) and (10).

A logistic equation (11) governs the healthy cell population to ensure that the number of healthy cells does not exceed the carrying capacity, K. Numerical values for the various parameters are displayed in Table 1. Most of the values are obtained from (Dua et al., 2008) where cell cycle specific chemotherapy with a single drug and without drug resistance is considered. Note that $[D]$ is a unit of drug concentration. The program,

$$\min_{\mathbf{u}_A, \mathbf{u}_B} P(t_f, \mathbf{u}_A, \mathbf{u}_B) + Q(t_f, \mathbf{u}_A, \mathbf{u}_B) \tag{14}$$

$$\text{s.t: } Y(t_f, \mathbf{u}_A, \mathbf{u}_B) \geq Y_{\min} \tag{15}$$

$$u_{\min} \leq u_{A,j} \leq u_{\max},\ j = 1, \ldots, n_f,$$

$$u_{\min} \leq u_{B,j} \leq u_{\max},\ j = 1, \ldots, n_f,$$

$$P(1, \mathbf{u}_A, \mathbf{u}_B) = P_0,\ Q(1, \mathbf{u}_A, \mathbf{u}_B) = Q_0,$$

$$Y(1, \mathbf{u}_A, \mathbf{u}_B) = Y_0,\ v_A(1, \mathbf{u}_A, \mathbf{u}_B) = 0,$$

$$v_B(1, \mathbf{u}_A, \mathbf{u}_B) = 0$$

where $\mathbf{u}_A = \{u_{A,j}\}$ and $\mathbf{u}_B = \{u_{B,j}\}$ are the set of daily drug doses for an n_f-day treatment, is solved to minimize the tumor cell population without totally destroying the healthy cell population. The numerical values used are in Table 2.

DSL48SE is the IVP solver (Tolsma, 2001; Tolsma and Barton, 2002; Feehery et al., 1997) used to integrate the dynamics and the corresponding auxiliary equations to obtain an element of the generalized Jacobian. The event detection algorithm of DSL48SE (Park and Barton, 1996) is used to detect non-singleton trajectories. The necessary Jacobians for the auxiliary system of equations are obtained using automatic differentiation algorithms implemented in DAEPACK (Tolsma and Barton, 2000). The differential equations are integrated with an absolute tolerance of 1×10^{-7} and a relative tolerance of 1×10^{-9}.

A modified proximal bundle method based on the algorithm in (Lukšan and Vlček, 2001) is used to solve (14). A penalty approach to handle (15) is used because the algorithm in (Lukšan and Vlček, 2001) is handles only linear constraints on the decision variables. The objective of (14) is augmented with (15) to obtain

$$J(\mathbf{u}_A, \mathbf{u}_B) = P(t_f, \mathbf{u}_A, \mathbf{u}_B) + Q(t_f, \mathbf{u}_A, \mathbf{u}_B) + \mu_k \max(Y_{\min} - Y(t_f, \mathbf{u}_A, \mathbf{u}_B), 0)$$

where μ_k is the penalty parameter. The modified program is successively solved three times with increasing penalty parameter to an optimality tolerance of 1×10^{-5}. The solution of the preceding programs are used as the initial guesses for the following programs. For the first program, the drug schedules are assigned random values between 0.0 and 5.0. The penalty parameter values are 5000, 25000 and 125000.

The cell population numbers at the beginning and end of the treatment are in Table 3. The tumor cell population is reduced to one percent of its initial size. The drug schedules are shown in Figure 1 and Figure 2. The preference to use drug B is clearly seen. The effects of the drugs are proportional to the corresponding cell populations. Therefore using drug B results in more effective treatment as the population of quiescent cells is greater than that of proliferating cells. In addition, the ratio of tumor cells killed to the ratio of healthy cells killed per unit drug concentration is larger for drug B.

The drug B schedule has four distinctive phases. The initial four-day treatment reverses the increase in the tumor cell population by using drug B as much as possible. In the next week, the drug B concentration is allowed to decay to a tolerable level for the patient. The treatment until the last three days keeps the drug B concentration at that tolerable level. In the last days of the treatment, the drug dose is increased to kill the maximum number of tumor cells. This spike in the drug concentration shows its effect on the healthy cell population after the treatment is over and does not affect (15) significantly.

5. CONCLUSION

In this document, a novel method to optimize the performance of a class of systems with varying structure has been introduced. The theoretical basis and an initial implementation has been described. An illustrative numerical example has been presented.

The implementation of the optimization method will be streamlined in the future. There are different variants of

Table 1. Parameters of equations (9)-(13)

a	$0.500\ \text{day}^{-1}$	$\bar{v}_A$	10.000 [D]
m	$0.218\ \text{day}^{-1}$	$\bar{v}_B$	10.000 [D]
n	$0.477\ \text{day}^{-1}$	k_A	$8.400 \times 10^{-3}\ \text{day}^{-1}[D]^{-1}$
b	$0.100\ \text{day}^{-1}$	k_B	$8.400 \times 10^{-3}\ \text{day}^{-1}[D]^{-1}$
σ	$0.100\ \text{day}^{-1}$	K	$10000M$ cells
γ_A	$0.100\ \text{day}^{-1}$	γ_B	$0.100\ \text{day}^{-1}$

Table 2. Parameters of the mathematical program (14)

t_f	31 days	$Y_{\min}$	$100M$ cells
n_f	30	Y_0	$10000M$ cells
$u_{\max}$	$20.00\ [D]\text{day}^{-1}$	Q_0	$8.00 \times 10^5 M$ cells
$u_{\min}$	$0.00\ [D]\text{day}^{-1}$	P_0	$2.00 \times 10^5 M$ cells

Table 3. Cell Populations at the beginning and end of treatment

	Beginning of Treatment	End of Treatment
Y	$10000M$ cells	$100M$ cells
Q	$8.00 \times 10^5 M$ cells	$4.80 \times 10^4 M$ cells
P	$2.00 \times 10^5 M$ cells	$4.60 \times 10^4 M$ cells

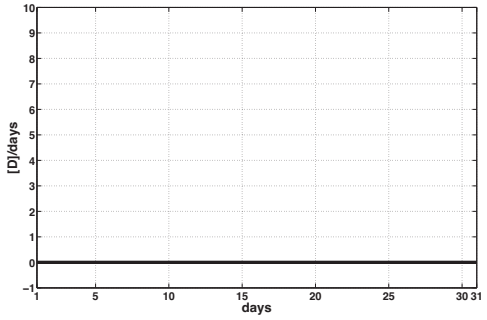

Fig. 1. Drug A Schedule

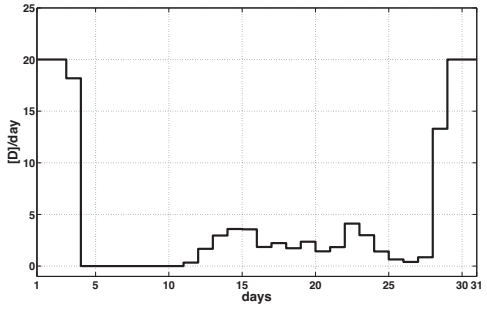

Fig. 2. Drug B schedule

bundle methods available (Mäkelä, 2001). These variants will be investigated in addition to different methods to handle nonlinear constraints. In this paper, a penalty approach is described. Improvements to this approach will be considered and the improvement function approach will be investigated (Mäkelä, 2001).

The performance of the proposed algorithm will be compared to the performance of the available transcription-based algorithms. It is expected that the method introduced in this document can be advantageous in problems with a large number states and candidate dynamics.

REFERENCES

Avraam, M.P., Shah, N., and Pantelides, C. (1998). Modelling and Optimisation of General Hybrid Systems in the Continuous Time Domain. *Computers and Chemical Engineering*, 22(Suppl), S221–S228.

Bemporad, A. and Morari, M. (1999). Control of systems integrating logic, dynamics, and constraints. *Automatica*, 35, 407–427.

Betts, J.T. (1998). Survey of numerical methods for trajectory optimization. *Journal of Guidance Control and Dynamics*, 21(2), 193–207.

Clarke, F.H. (1990). *Optimization and Nonsmooth Analysis*. Number 5 in Classics in Applied Mathematics. SIAM.

Coddington, E.A. and Levinson, N. (1955). *Theory of Ordinary Differential Equations*. McGraw Hill Co., Inc., New York.

Dua, P., Dua, V., and Pistikopoulos, E.N. (2008). Optimal delivery of chemotherapeutic agents in cancer. *Computers & Chemical Engineering*, 32(1-2), 99–107.

Feehery, W.F., Tolsma, J.E., and Barton, P.I. (1997). Efficient sensitivity analysis of large-scale differential-algebraic systems. *Applied Numerical Mathematics*, 25(1), 41–54.

Galán, S., Feehery, W.F., and Barton, P.I. (1999). Parametric sensitivity functions for hybrid / discrete / continuous systems. *Applied Numerical Mathematics*, 31, 17–47.

Kiwiel, K.C. (1985). *Methods of Descent for Nondifferentiable Optimization*, volume 1133 of *Lecture Notes in Mathematics*. Springer-Verlag.

Lukšan, L. and Vlček, J. (2001). Algorithm 811: NDA: Algorithms for nondifferentiable optimization. *ACM Transactions on Mathematical Software*, 27(2), 193–213.

Mäkelä, M.M. (2001). Survey of Bundle Methods for Nonsmooth Optimization. *Optimization Methods and Software*, 17(1), 1 –29.

Mifflin, R. (1977). Semismooth and Semiconvex Functions in Constrained Optimization. *SIAM Journal of Control and Optimization*, 15(6), 959–972.

Pang, J.S. and Stewart, D.E. (2008). Differential variational inequalities. *Mathematical Programming*, 113(2), 345–424.

Pang, J.S. and Stewart, D.E. (2009). Solution dependence on initial conditions in differential variational inequalities. *Mathematical Programming*, 116(1-2), 429–460.

Pannetta, J. and Adam, J. (1995). A mathematical model of cycle-specific chemotherapy. *Mathematical and Computer Modelling*, 22(2), 67–82.

Park, T. and Barton, P.I. (1996). State event location in differential-algebraic models. *ACM Trans. Model. Comput. Simul.*, 6(2), 137–165.

Qi, L. (1993). A nonsmooth version of Newton's method. *Mathematical Programming*, 58, 353–367.

Raghunathan, A., Diaz, M., and Biegler, L. (2004). An MPEC formulation for dynamic optimization of distillation operations. *Computers & Chemical Engineering*, 28(10), 2037–2052.

Rockafellar, R.T. and Wets, R.J.B. (1998). *Variational Analysis*. Number 317 in Grundlehren der mathematischen Wissenschaften. Springer.

Schumacher, J.M. (2004). Complementarity systems in optimization. *Mathematical Programming*, 101(1), 263 – 295.

Tolsma, J. and Barton, P.I. (2000). DAEPACK: an open modeling environment for legacy models. *Industrial & Engineering Chemistry Research*, 39(6), 1826–1839. (http://yoric.mit.edu/daepack/daepack.html).

Tolsma, J.E. (2001). DSL48SE manual (version 1.0). Technical report, Process Systems Engineering Laboratory, Department of Chemical Engineering, Massachusetts Institute of Technology. (http://yoric.mit.edu / daepack / download / Manuals_Pres / dsl48se.ps).

Tolsma, J.E. and Barton, P.I. (2002). Hidden discontinuities and parametric sensitivity analysis. *SIAM Journal on Scientific Computing*, 23(6), 1861–1874.

Real-time Optimization with Estimation of Experimental Gradients

A. Marchetti * **B. Chachuat** ** **D. Bonvin** *

* *Laboratoire d'Automatique, École Polytechnique Fédérale de Lausanne (EPFL), Station 9, CH-1015 Lausanne, Switzerland*
** *Department of Chemical Engineering, McMaster University, 1280 Main Street West, Hamilton, ON L8S 4LT, Canada*

Abstract: For good performance in practice, real-time optimization schemes need to be able to deal with the inevitable plant-model mismatch problem. Unlike the two-step schemes combining parameter estimation and optimization, the modifier-adaptation approach uses experimental gradient information and does not require the model parameters to be estimated on-line. The dual modifier-adaptation approach presented in this paper drives the process towards optimality, while paying attention to the accuracy of the estimated gradients. The gradients are estimated from successive operating points generated by the optimization algorithm. The novelty lies in the development of an upper bound on the norm of the gradient errors, which is used as a constraint when determining the next operating point. The proposed approach is demonstrated in simulation via the real-time optimization of a continuous reactor.

Keywords: Real-time optimization, estimation of experimental gradients, modifier adaptation.

1. INTRODUCTION

Real-time optimization (RTO) of continuous plants aims at improving some steady-state performance index (Marlin and Hrymak [1997]). Since the majority of RTO schemes uses a model of the plant, reaching optimal performance in the presence of plant-model mismatch is a difficult task, which necessitates adaptation based on measured information. Chachuat et al. [2009] proposed a three-way classification of RTO schemes. One class includes the so-called modifier-adaptation approach (Marchetti et al. [2009]), whereby appropriate terms are added to the optimization problem and identified so that the KKT conditions of the model match those of the plant. In this context, the modifier-adaptation approach requires to be able to estimate on-line the experimental gradients, i.e., the derivatives of the plant outputs with respect to the inputs. This paper investigates the estimation of experimental gradients and their use in modifier-adaptation schemes.

A comparison of different approaches for on-line gradient estimation is given in Mansour and Ellis [2003]. Finite-difference techniques can be used to estimate the gradients experimentally. The most straightforward approach consists in perturbating each input individually around the current operating point to get an estimate of the corresponding gradient elements. This is the case, e.g., when forward finite differencing (FFD) is applied at each RTO iteration. An alternative approach, which was introduced in the ISOPE (Integrated System Optimization and Parameter Estimation) literature under the name *dual ISOPE*, is to estimate the gradients based on the current and past operating points (Brdyś and Tatjewski [1994, 2005]). The key issue therein is the ability to estimate the experimental gradients reliably while updating the operating point. Indeed, there are two conflicting objectives: the "primal objective" consists in solving the optimization problem, while the "dual objective" aims at estimating accurate gradients. These conflicting tasks can be accommodated by adding a constraint in the optimization problem so as to ensure sufficiently rich information in the measurements and guarantee gradient accuracy. Brdyś and Tatjewski [1994, 2005] proposed a constraint that prevents ill-conditioning in gradient computation. The present paper goes further and investigates the two main sources of errors, namely the error introduced by numerical approximation of a derivative (truncation error) and measurement noise. A constraint that enforces an upper bound on the gradient error norm is proposed. Since the constraint for ensuring sufficient information might compromise optimality in the vicinity of the optimum, Gao and Engell [2005] suggested using the ill-conditioning measure not to constrain the optimization problem but rather to determine whether an additional input perturbation is needed. Note that such a scheme could also be used in the context of the dual-modifier approach proposed here.

The paper is organized as follows. Section 2 formulates the optimization problem. The modifier-adaptation scheme is reviewed in Section 3. Analysis of the errors in the gradient estimates obtained from past operating points is carried out in Section 4. Based on this analysis, Section 5 proposes a norm-based constraint, which is incorporated into the dual modifier-adaptation algorithm presented in Section 6. The approach is illustrated via the reactor of the Williams-Otto plant in Section 7, and Section 8 concludes the paper and presents directions for future work.

2. PROBLEM FORMULATION

For the sake of simplicity, an unconstrained optimization problem is considered throughout. This way, only the

gradient of the objective function needs to be estimated, while in the constrained case, the constraint gradients would need to be evaluated as well. A possible way of tackling constrained optimization problems will be sketched in the conclusion section.

The unconstrained optimization problem reads:

$$\min_{\mathbf{u}} \quad \Phi_p(\mathbf{u}) := \phi(\mathbf{u}, \mathbf{y}_p(\mathbf{u})) \tag{1}$$

where $\mathbf{u} \in \mathbb{R}^{n_u}$ are the decision (or input) variables, $\mathbf{y}_p \in \mathbb{R}^{n_y}$ are the measured (or output) variables, and $\phi : \mathbb{R}^{n_u} \times \mathbb{R}^{n_y} \to \mathbb{R}$ is the scalar cost function to be minimized. The notation $(\cdot)_p$ will be used for the variables that are associated with the plant. Also, it is assumed that $\phi(\mathbf{u}, \mathbf{y}_p)$ is a known function of $\mathbf{u}$ and $\mathbf{y}_p$. On the other hand, the steady-state input-output mapping of the plant, $\mathbf{y}_p(\mathbf{u})$, is typically unknown, and only the approximate model $f(\mathbf{u}, \mathbf{y}, \boldsymbol{\theta}) = \mathbf{0}$ is available, where $\boldsymbol{\theta} \in \mathbb{R}^{n_\theta}$ is the set of model parameters. Assuming that the model outputs $\mathbf{y}$ can be expressed explicitly as functions of $\mathbf{u}$ and $\boldsymbol{\theta}$, the cost function predicted by the model becomes $\Phi(\mathbf{u}, \boldsymbol{\theta}) := \phi(\mathbf{u}, \mathbf{y}(\mathbf{u}, \boldsymbol{\theta}))$.

It is furthermore assumed that the decision variables $\mathbf{u}$ are of the same order of magnitude, which can be achieved via scaling. For example, if the decision variable u_i remains within the interval $[u_{i,\mathrm{a}}, u_{i,\mathrm{b}}]$, it can be scaled as $u_i^{\mathrm{scaled}} = (u_i - u_{i,\mathrm{a}})/(u_{i,\mathrm{b}} - u_{i,\mathrm{a}})$. For notional simplicity, the superscript indicating a scaled variable will be omitted in the sequel.

3. MODIFIER-ADAPTATION SCHEME

In the modifier-adaptation scheme, a gradient-correction term is added to the cost function of the model-based optimization problem (Marchetti et al. [2009]). At the kth iteration, the next input $\mathbf{u}_{k+1}$ is obtained as:

$$\mathbf{u}_{k+1} = \arg\min_{\mathbf{u}} \Phi_m(\mathbf{u}, \boldsymbol{\theta}) := \Phi(\mathbf{u}, \boldsymbol{\theta}) + \boldsymbol{\lambda}_k^{\mathsf{T}} \mathbf{u} \tag{2}$$

where $\boldsymbol{\lambda}_k$ is the cost-gradient modifier at the kth iteration. This modifier is adapted at each iteration based on the difference between the gradient of the plant and that predicted by the model. For example, upon implementation of a first-order exponential filter, the gradient modifier is calculated as:

$$\boldsymbol{\lambda}_k^{\mathsf{T}} = (1-d)\boldsymbol{\lambda}_{k-1}^{\mathsf{T}} + d\left[\frac{\partial \Phi_p}{\partial \mathbf{u}}(\mathbf{u}_k) - \frac{\partial \Phi}{\partial \mathbf{u}}(\mathbf{u}_k, \boldsymbol{\theta})\right] \tag{3}$$

with the filter gain $d \in (0,\ 1]$. Computation of the modifier $\boldsymbol{\lambda}_k$ requires the knowledge of the plant gradient $\frac{\partial \Phi_p}{\partial \mathbf{u}}(\mathbf{u}_k)$.

An appealing property of the modifier-adaptation scheme is that, upon convergence and in the absence of noise, the optimum $\mathbf{u}_\infty$ for the modified model-based optimization problem (2) satisfies the first-order necessary conditions of optimality of the optimization problem (1) (Marchetti et al. [2009]). Note that this is the case despite plant-model mismatch. Note also that the need to match the plant outputs $\mathbf{y}_p(\mathbf{u})$ by means of a parameter estimation problem, as this is the case for the ISOPE modifier (Roberts [1979]), is removed. However, the downside of modifier adaptation lies in the need to estimate the experimental gradient $\frac{\partial \Phi_p}{\partial \mathbf{u}}$.

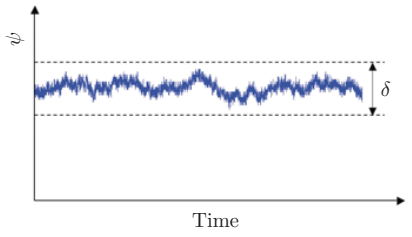

Fig. 1. Noisy cost function at steady state.

4. EXPERIMENTAL GRADIENT COMPUTED FROM PAST OPERATING POINTS

It is assumed that the cost function can be evaluated from the noisy output measurements as follows:

$$\psi(\mathbf{u}) = \phi(\mathbf{u}, \mathbf{y}_p(\mathbf{u}) + \boldsymbol{\nu}) = \Phi_p(\mathbf{u}) + v \tag{4}$$

where $\boldsymbol{\nu}$ is the measurement noise on the outputs and v the induced noise in the cost estimates. Note that, even if $\boldsymbol{\nu}$ is zero mean, v might have a nonzero mean if the function $\phi(\mathbf{u}, \mathbf{y})$ is nonlinear in $\mathbf{y}$.

The forthcoming analysis is conducted assuming that the cost estimates remain within the interval δ at steady-state operation, as illustrated in Figure 1. Based on a statistical description of v, δ could be selected by considering a desired confidence interval. Values that fall outside the selected confidence interval can simply be discarded.

Consider the kth iteration and the n_u past operating points, $\mathbf{u}_{k-j},\ j = 0, \ldots, n_u - 1$, and let us evaluate the cost as a function of the next operating point, which will generically be labeled $\mathbf{u}$. Using a first-order approximation of $\Phi_p(\mathbf{u}_{k-j})$ in the neighborhood of $\mathbf{u}$, the value of ψ at the past operating points is given by:

$$\begin{aligned}\psi(\mathbf{u}_{k-j}) = \Phi_p(\mathbf{u}_{k-j}) + v_{k-j} = (\psi(\mathbf{u}) - v) \\ + \frac{\partial \Phi_p}{\partial \mathbf{u}}(\mathbf{u})[\mathbf{u}_{k-j} - \mathbf{u}] + O\left(\|\mathbf{u}_{k-j} - \mathbf{u}\|^2\right) + v_{k-j}\end{aligned} \tag{5}$$

and, by neglecting the higher-order and noise terms:

$$\psi(\mathbf{u}_{k-j}) = \psi(\mathbf{u}) + \hat{\boldsymbol{\beta}}(\mathbf{u})[\mathbf{u}_{k-j} - \mathbf{u}], \tag{6}$$

where $\hat{\boldsymbol{\beta}}(\mathbf{u})$ is an estimate of the experimental cost gradient $\frac{\partial \Phi_p}{\partial \mathbf{u}}(\mathbf{u})$. $\hat{\boldsymbol{\beta}}(\mathbf{u})$ can be computed from the n_u past operating points $\mathbf{u}_k, \ldots, \mathbf{u}_{k-n_u+1}$ and the corresponding noisy cost values $\psi(\mathbf{u}_k), \ldots, \psi(\mathbf{u}_{k-n_u+1})$ by writing (6) in the following matrix form (Brdyś and Tatjewski [2005]):

$$\hat{\boldsymbol{\beta}}(\mathbf{u}) = \mathcal{Y}(\mathbf{u})\, \mathcal{U}^{-1}(\mathbf{u}) \tag{7}$$

with

$$\mathcal{U}(\mathbf{u}) := [\, \mathbf{u} - \mathbf{u}_k \ \ldots\ \mathbf{u} - \mathbf{u}_{k-n_u+1} \,] \in \mathbb{R}^{n_u \times n_u} \tag{8}$$

$$\mathcal{Y}(\mathbf{u}) := [\, \psi(\mathbf{u}) - \psi(\mathbf{u}_k) \ \ldots\ \psi(\mathbf{u}) - \psi(\mathbf{u}_{k-n_u+1}) \,] \tag{9}$$

The gradient error is defined as $\boldsymbol{\epsilon}(\mathbf{u}) := \hat{\boldsymbol{\beta}}(\mathbf{u}) - \frac{\partial \Phi_p}{\partial \mathbf{u}}(\mathbf{u})$, which, from (7) together with (4), can be split as $\boldsymbol{\epsilon}(\mathbf{u}) = \boldsymbol{\epsilon}^t(\mathbf{u}) + \boldsymbol{\epsilon}^n(\mathbf{u})$, with:

$$\begin{aligned}\boldsymbol{\epsilon}^t(\mathbf{u}) = [\, \Phi_p(\mathbf{u}) - \Phi_p(\mathbf{u}_k) \quad \ldots \\ \ldots \quad \Phi_p(\mathbf{u}) - \Phi_p(\mathbf{u}_{k-n_u+1}) \,]\, \mathcal{U}^{-1}(\mathbf{u}) - \frac{\partial \Phi_p}{\partial \mathbf{u}}(\mathbf{u})\end{aligned} \tag{10}$$

$$\boldsymbol{\epsilon}^n(\mathbf{u}) = [\, v - v_k \quad \ldots \quad v - v_{k-n_u+1} \,]\, \mathcal{U}^{-1}(\mathbf{u}) \tag{11}$$

where $\boldsymbol{\epsilon}^t$ and $\boldsymbol{\epsilon}^n$ represent the errors due to truncation and noise, respectively. Next, we investigate these two components of the gradient error.

Gradient Error due to Truncation. An upper bound on the norm of this error is given in the next proposition.

Proposition 1. Let $\Phi_p(\mathbf{u})$ be twice continuously differentiable with respect to $\mathbf{u}$. Then, given the n_u past operating points $\mathbf{u}_k, \ldots, \mathbf{u}_{k-n_u+1}$, an upper bound on $\|\boldsymbol{\epsilon}^t(\mathbf{u})\|$ is given by

$$\|\boldsymbol{\epsilon}^t(\mathbf{u})\| \leq \mathcal{E}^t(\mathbf{u}), \tag{12}$$

with

$$\mathcal{E}^t(\mathbf{u}) := \frac{\mathsf{d}_2}{2}\Big\| \big[\ (\mathbf{u}-\mathbf{u}_k)^\mathsf{T}(\mathbf{u}-\mathbf{u}_k)\ \ldots \tag{13}$$
$$\ldots\ (\mathbf{u}-\mathbf{u}_{k-n_u+1})^\mathsf{T}(\mathbf{u}-\mathbf{u}_{k-n_u+1})\ \big]\ \mathcal{U}^{-1}(\mathbf{u})\Big\|$$

where d_2 is the largest absolute eigenvalue of the Hessian of $\Phi_p(\cdot)$.

Proof. By Taylor series expansion of $\Phi_p(\mathbf{u}_{k-j})$ at $\mathbf{u}$ and upper bounding of the norm of the Hessian of Φ_p [Marchetti, 2009]. □

Note that d_2 represents an upper bound on the curvature of $\Phi_p(\cdot)$.

Gradient Error due to Measurement Noise. For relating the error norm $\|\boldsymbol{\epsilon}^n(\mathbf{u})\|$ to the location of the new operating point, the concepts of affine subspaces and distance between complement affine subspaces will be used (see Appendix A for a brief review of these concepts).

The largest possible value of $\|\boldsymbol{\epsilon}^n(\mathbf{u})\|$, noted $\|\boldsymbol{\epsilon}^n(\mathbf{u})\|_{\max}$, is computed in the next proposition.

Proposition 2. Given the n_u past operating points $\mathbf{u}_k, \ldots, \mathbf{u}_{k-n_u+1}$ and the interval δ for the noisy function $\psi(\cdot)$, the largest possible value of $\|\boldsymbol{\epsilon}^n(\mathbf{u})\|$ is

$$\|\boldsymbol{\epsilon}^n(\mathbf{u})\|_{\max} = \delta / l_{\min}(\mathbf{u}) \tag{14}$$

where $l_{\min}(\mathbf{u})$ is the shortest distance between all possible pairs of complement affine subspaces that can be generated from $\mathcal{S} = \{\mathbf{u}, \mathbf{u}_k, \ldots, \mathbf{u}_{k-n_u+1}\}$.

Proof. The proof proceeds in two parts: (i) the largest error occurs when the error v is either $\delta/2$ for some of the operating points and $-\delta/2$ for the other points, with each set of points defining an affine subspace; and (ii) the error vector $\boldsymbol{\epsilon}^n(\mathbf{u})$ is normal to both affine subspaces, which results in the largest possible error norm given by (14) [Marchetti, 2009]. □

5. UPPER BOUND ON GRADIENT ERROR

A bound on the condition number of the matrix $\mathcal{U}(\mathbf{u})$ was proposed in Brdyś and Tatjewski [1994, 2005]. This bound ensures that the new operating point does not introduce large errors in the gradient estimates due to ill-conditioning of $\mathcal{U}(\mathbf{u})$. However, the bound is not directly related to the errors resulting from truncation and measurement noise. This section introduces a consistent, although possibly conservative, upper bound on the gradient error norm.

Consider the desired upper bound $\mathcal{E}^U$ on the gradient error norm:

$$\|\boldsymbol{\epsilon}(\mathbf{u})\| \leq \|\boldsymbol{\epsilon}^t(\mathbf{u})\| + \|\boldsymbol{\epsilon}^n(\mathbf{u})\| \leq \mathcal{E}^U \tag{15}$$

Given the n_u past operating points $\mathbf{u}_k, \ldots, \mathbf{u}_{k-n_u+1}$, the following theorem provides a sufficient condition for the location of $\mathbf{u}$ so as to satisfy (15).

Theorem 1. (Sufficient condition for gradient accuracy). The gradient error norm $\|\boldsymbol{\epsilon}(\mathbf{u})\|$ does not exceed the desired upper bound $\mathcal{E}^U$ by choosing $\mathbf{u}$ that satisfies

$$\mathcal{E}(\mathbf{u}) := \mathcal{E}^t(\mathbf{u}) + \|\boldsymbol{\epsilon}^n(\mathbf{u})\|_{\max} \leq \mathcal{E}^U, \tag{16}$$

with $\mathcal{E}^t(\mathbf{u})$ and $\|\boldsymbol{\epsilon}^n(\mathbf{u})\|_{\max}$ given by (13) and (14), respectively.

Proof. The proof follows from (15), inequality (12) and the fact that $\|\boldsymbol{\epsilon}^n(\mathbf{u})\| \leq \delta / l_{\min}(\mathbf{u})$ from (14). □

For given values of δ and d_2, there is a minimal value that $\mathcal{E}(\mathbf{u})$ can take. Hence, $\mathcal{E}^U$ should be selected larger than this minimal value for the constraint (16) to be feasible.

Example 1. Consider the two-dimensional case ($n_u = 2$) with $\delta = 0.2$, $\mathsf{d}_2 = 2$ and the past operating points $\mathbf{u}_k = [0\ \ -0.5]^\mathsf{T}$ and $\mathbf{u}_{k-1} = [0\ \ 0.5]^\mathsf{T}$. The upper bounds $\mathcal{E}^t(\mathbf{u})$ and $\|\boldsymbol{\epsilon}^n(\mathbf{u})\|_{max}$ can be evaluated in terms of the location of the new operating point $\mathbf{u} = [u_1\ \ u_2]^\mathsf{T}$. Figures 2a-c show the contours of the error norms $\mathcal{E}^t(\mathbf{u})$, $\|\boldsymbol{\epsilon}^n(\mathbf{u})\|_{max}$ and $\mathcal{E}(\mathbf{u})$. It is seen that (i) both $\mathcal{E}^t(\mathbf{u})$ and $\|\boldsymbol{\epsilon}^n(\mathbf{u})\|_{max}$ increase as $\mathcal{U}(\mathbf{u})$ becomes more ill-conditioned ($\mathbf{u}$ aligned with $\mathbf{u}_k$ and $\mathbf{u}_{k-1}$), and (ii) the two regions generated by the constraint (16) *are nonconvex.*

Convex Constraint. The objective being to use the constraint (16) in the optimization problem (2), the fact that this constraint is nonconvex creates the possibility of multiple local solutions. Next, we introduce a tight relaxation that makes the constraint convex.

It can be seen that, for a given error level c, the expression $\mathcal{E}^t(\mathbf{u}) = c$ generates two $(n_u - 1)$-dimensional spheres of radius $r = \frac{c}{\mathsf{d}_2}$. The centers of these spheres are located symmetrically on each side of the hyperplane $\mathbf{n}_k^\mathsf{T}\mathbf{u} = b_k$ generated by the n_u past operating points $\mathbf{u}_k, \ldots, \mathbf{u}_{k-n_u+1}$. Considering the new operating point $\mathbf{u}$ located on the sphere, the center point is given by

$$\mathbf{u}_c^\mathsf{T}(\mathbf{u}) = \frac{1}{2}\Big[\ \mathbf{u}^\mathsf{T}\mathbf{u} - \mathbf{u}_k^\mathsf{T}\mathbf{u}_k\ \cdots \tag{17}$$
$$\mathbf{u}^\mathsf{T}\mathbf{u} - \mathbf{u}_{k-n_u+1}^\mathsf{T}\mathbf{u}_{k-n_u+1}\ \Big]\ \mathcal{U}^{-1}(\mathbf{u}).$$

It can be shown that $\|\boldsymbol{\epsilon}^n(\mathbf{u})\|_{\max}$ is convex on each side of the hyperplane $\mathbf{n}_k^\mathsf{T}\mathbf{u} = b_k$ (see also Figure 2b). Hence, non-convexity of the constraint (16) is due to the part of the aforementioned spheres that crosses the hyperplane $\mathbf{n}_k^\mathsf{T}\mathbf{u} = b_k$. The distance (positive or negative) from the center point $\mathbf{u}_c(\mathbf{u})$ to the hyperplane $\mathbf{n}_k^\mathsf{T}\mathbf{u} = b_k$ is given by:

$$l_C(\mathbf{u}) = \frac{b_k - \mathbf{n}_k^\mathsf{T}\mathbf{u}_c(\mathbf{u})}{\|\mathbf{n}_k\|}. \tag{18}$$

Given the n_u operating points $\mathbf{u}_k, \ldots, \mathbf{u}_{k-n_u+1}$, the point $\mathbf{u}_{\mathrm{m},k}$ can be obtained by projecting the center point $\mathbf{u}_c(\mathbf{u})$ on the hyperplane $\mathbf{n}_k^\mathsf{T}\mathbf{u} = b_k$:

$$\mathbf{u}_{\mathrm{m},k} = \mathbf{u}_c(\mathbf{u}) + \frac{l_C(\mathbf{u})}{\|\mathbf{n}_k\|}\mathbf{n}_k \tag{19}$$

It appears that $\mathbf{u}_{\mathrm{m},k}$ is independent of $\mathbf{u}$. For a given upper bound $\mathcal{E}^U$, it is then possible to define convex feasible

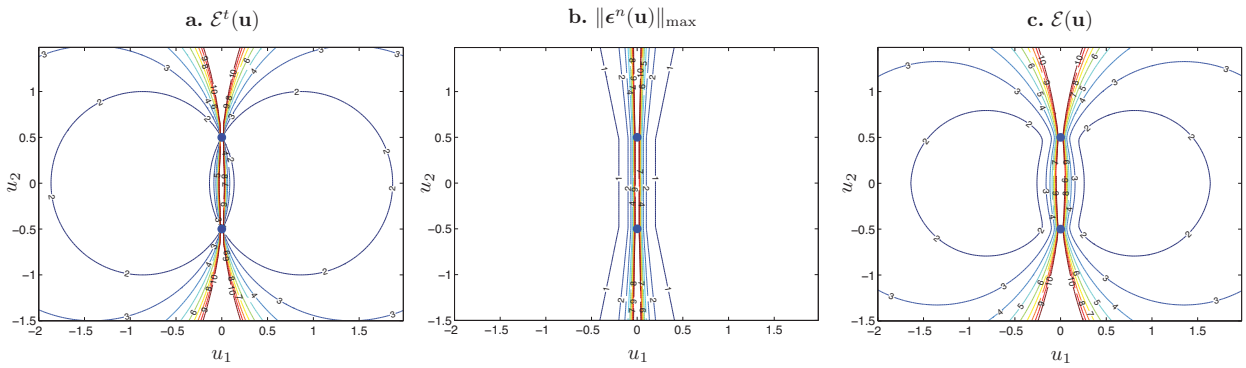

Fig. 2. Contour maps for the norm of the gradient error due to (**a**) truncation error, (**b**) measurement noise, and (**c**) total error.

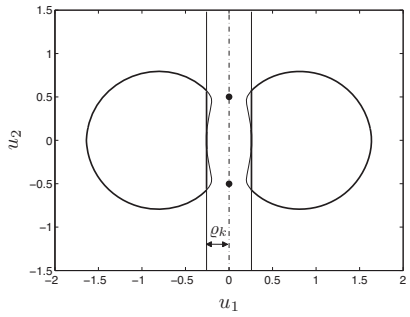

Fig. 3. Convex regions (in bold) corresponding to the constraint $\mathcal{E}(\mathbf{u}) \leq 2$.

regions by adding constraints expressing the minimal distance between the new operating point $\mathbf{u}$ and the hyperplane, which eliminates the non-convex part of the regions generated by (16), as illustrated in Figure 3. The minimal point-to-hyperplane distance ϱ_k can be determined numerically by finding the smallest absolute value solution of the following equation:

$$\mathcal{E}\left(\mathbf{u}_{\mathrm{m},k} + \frac{\varrho_k}{\|\mathbf{n}_k\|}\mathbf{n}_k\right) = \mathcal{E}^U$$

6. DUAL MODIFIER-ADAPTATION SCHEME

The dual modifier-adaptation scheme proposed in this section uses the upper bound on the gradient error defined in Section 5 as a constraint in the optimization problem (2). On each side of the hyperplane $\mathbf{n}_k^\mathsf{T}\mathbf{u} = b_k$ generated by the n_u past operating points, a modified model-based optimization problem is solved. The optimization problem corresponding to the half space $\mathbf{n}_k^\mathsf{T}\mathbf{u} > b_k$ reads:

$$\mathbf{u}_{k+1}^+ = \arg\min_{\mathbf{u}} \Phi_m(\mathbf{u},\boldsymbol{\theta}) = \Phi(\mathbf{u},\boldsymbol{\theta}) + \boldsymbol{\lambda}_k^\mathsf{T}\mathbf{u} \qquad (20)$$
$$\text{s.t.} \quad \mathcal{E}(\mathbf{u}) \leq \mathcal{E}^U, \qquad \mathbf{n}_k^\mathsf{T}\mathbf{u} > b_k + \varrho_k\|\mathbf{n}_k\|$$

while, for the half space $\mathbf{n}_k^\mathsf{T}\mathbf{u} < b_k$, one has:

$$\mathbf{u}_{k+1}^- = \arg\min_{\mathbf{u}} \Phi_m(\mathbf{u},\boldsymbol{\theta}) = \Phi(\mathbf{u},\boldsymbol{\theta}) + \boldsymbol{\lambda}_k^\mathsf{T}\mathbf{u} \qquad (21)$$
$$\text{s.t.} \quad \mathcal{E}(\mathbf{u}) \leq \mathcal{E}^U, \qquad \mathbf{n}_k^\mathsf{T}\mathbf{u} < b_k - \varrho_k\|\mathbf{n}_k\|$$

The modifiers $\boldsymbol{\lambda}_k^\mathsf{T}$ are adapted as in (3). The next operating point is chosen as the value of $\{\mathbf{u}_{k+1}^+, \mathbf{u}_{k+1}^-\}$ that minimizes the augmented cost function $\Phi_m(\mathbf{u},\boldsymbol{\theta})$.

7. OPTIMIZATION OF REACTOR OPERATION

The reactor in the Williams-Otto plant (Williams and Otto [1960]), as modified by Roberts [1979], is used to illustrate the dual modifier-adaptation scheme. This reactor example has also been used to illustrate model adequacy and RTO performance (Forbes et al. [1994], Zhang and Forbes [2000]). It consists of an ideal CSTR in which the following reactions occur:

$$\begin{array}{ll} A + B \longrightarrow C & \bar{k}_1 = 1.660 \times 10^6 e^{-6666.7/(T_R+273.15)} \\ C + B \longrightarrow P + E & \bar{k}_2 = 7.212 \times 10^8 e^{-8333.3/(T_R+273.15)} \\ C + P \longrightarrow G & \bar{k}_3 = 2.675 \times 10^{12} e^{-11111/(T_R+273.15)} \end{array}$$

where the reactants A and B are fed with the mass flowrates F_A and F_B, respectively. The desired products are P and E. C is an intermediate product and G is an undesired product. The product stream has the mass flowrate $F = F_A + F_B$. Operation is isothermal at the temperature T_R. The reactor mass holdup is 2105 kg.

The objective is to maximize profit, which is expressed as the cost difference between the products and the reactants:

$$\phi(\mathbf{u},\mathbf{y}) = 1143.38X_P F + 25.92X_E F - 76.23F_A - 114.34F_B$$

The flowrate of reactant A is fixed at 1.8275 kg/s. The flowrate of reactant B and the reactor temperature are the decision variables, thus $\mathbf{u} = [F_B \; T_R]^\mathsf{T}$.

In this example, the aforementioned reaction scheme corresponds to the simulated reality. However, since it is assumed that the reaction scheme is not well understood, the following two reactions have been proposed to model the system (Forbes et al. [1994]):

$$\begin{array}{ll} A + 2B \longrightarrow P + E & k_1 = 2.189 \times 10^8 e^{-8077.6/(T_R+273.15)} \\ A + B + P \longrightarrow G & k_2 = 4.310 \times 10^{13} e^{-12438/(T_R+273.15)} \end{array}$$

The material balance equations for the plant and the approximate model can be found in Zhang and Forbes [2000].

The inputs are scaled using the intervals $[3, 6]$ for F_B, and $[70, 100]$ for T_R. In this range, the maximal value of d_2 obtained with the scaled inputs is $\mathsf{d}_2 = 1030$ for the model, whereas the (unknown) plant value is $\mathsf{d}_2 = 1221$. The simulations are carried out assuming that the noise v has a Gaussian distribution with standard deviation $\sigma_\phi = 0.5$. The noise interval $\delta = 3$ is chosen. The exponential filter (3) is implemented with $d = 0.5$.

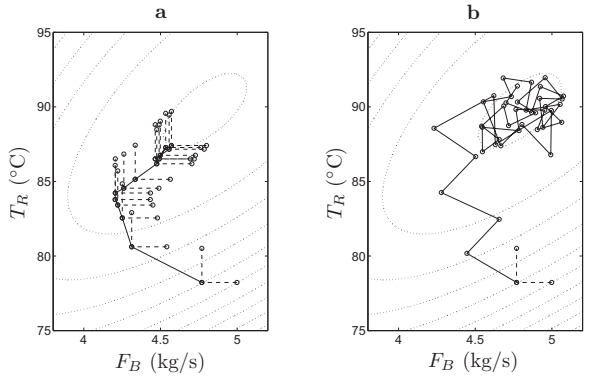

Fig. 4. Input trajectories for 45 operating points. The dotted lines represent the contours of the plant cost function. (**a**) Modifier adaptation using FFD. (**b**) Dual modifier adaptation with bound on gradient error.

Modifier Adaptation using FFD. First, modifier adaptation is applied using the FFD approach, which consists in perturbing the inputs one at the time from the current operating point with the fixed step size h. The gradient error norm, which is a function of h, is found to be minimal for $h^\star = 0.0763$ (scaled value). The corresponding gradient error norm $\mathcal{E}^t(h^\star) + \|\boldsymbol{\epsilon}^n(h^\star)\|_{\max}$ is 111.2 (Marchetti [2009]). Figure 4a shows a resulting input trajectory. The observed offset with respect to the plant optimum results mainly from the gradient error due to truncation.

Dual Modifier Adaptation with Bound on Gradient Error. Dual modifier adaptation is applied with $\mathcal{E}^U = 111.2$ (same value as above). The algorithm is initialized using FFD. Figure 4b shows a resulting input trajectory. Compared with modifier adaptation using FFD, significantly fewer operating points are required to approach the optimum.

Figure 5a shows the evolution of the plant profit and the gradient error norm for 20 noise realizations. At iteration 20, the flowrate F_A is increased from 1.8275 kg/s to 2.2 kg/s. Modifier adaptation tracks the change in the plant optimum. It can be seen in the upper plot of Figure 5a that the neighborhood of the new optimal profit is reached within 6 iterations for all 20 realizations. Also, the lower plot of Figure 5a shows that the gradient error norm is kept below $\mathcal{E}^U$. The observed peak in gradient error occurring at iterations 21 and 22 is due to the fact that, at these points, the gradient is inconsistent in that it is estimated using operating points with different values of F_A.

Dual Modifier Adaptation with Bound on Condition Number. For the sake of comparison, dual modifier adaptation is also applied with a lower bound on the inverse condition number of $\mathcal{U}(\mathbf{u})$, as proposed in Brdyś and Tatjewski [1994, 2005]. The results are shown in Figure 5b. A lower bound of 0.4 gives an adaptation that is similar to that using the gradient error bound in the first iterations. However, as soon as the neighborhood of the plant optimum is reached, the distance between the operating points decreases, and the gradient estimates become much less accurate. Furthermore, the feasible regions given by the condition number constraint decrease proportionally

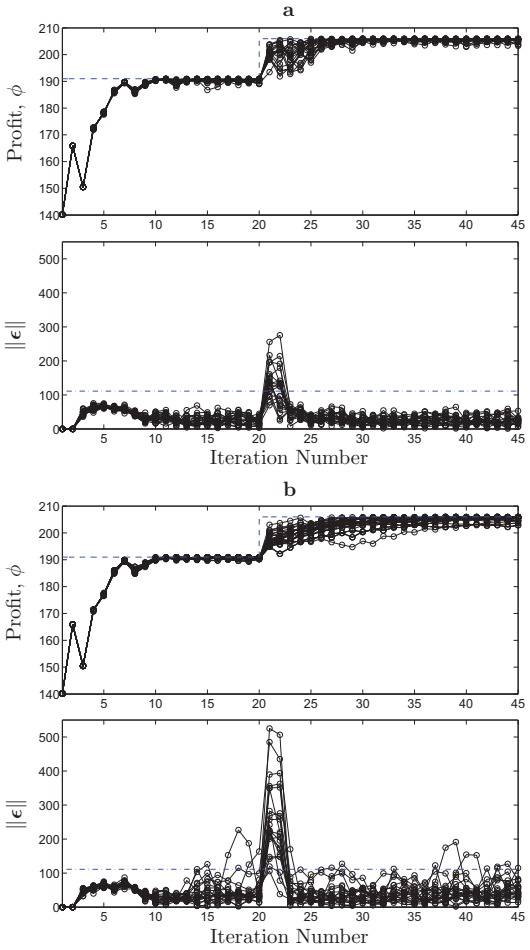

Fig. 5. Optimization for 20 noise realizations; there is a flowrate change at iteration 20. (**a**) Dual modifier adaptation with bound on gradient error norm. (**b**) Dual modifier adaptation with bound on the condition number. Dashed line: Optimal profit for the plant. Dash-dotted line: $\mathcal{E}^U = 111.2$.

to the distance between points. This appropriately prevents taking large steps in the wrong direction, but it also appears less suitable for tracking a changing optimum.

8. CONCLUSIONS

This study has demonstrated the potential of dual modifier adaptation, which pays attention to the accuracy with which the gradients are estimated. The results of the case study indicate that this approach, wherein the gradient error norm is bounded, produces more accurate gradient estimates than with simply bounding the condition number of $\mathcal{U}(\mathbf{u})$, i.e. a measure of the relative position of the successive inputs. In addition, the proposed scheme seems more capable of tracking a changing optimum. The performance depends on the amount of plant-model mismatch, the noise level, the estimated curvature of the cost function d_2, and the filter parameter d.

Future work will consider the extension of this approach to constrained optimization problems. In this case, mod-

ifier adaptation will require an estimate of the cost and constraint gradients of the plant to be available at each iteration. In order to be able to use the upper bound on the gradient error developed in this paper, a possible way is to associate the parameters δ and d_2 to a Lagrangian function, which represents a linear combination of the cost and constraint functions.

REFERENCES

Brdyś, M. and Tatjewski, P. (1994). An algorithm for steady-state optimizing dual control of uncertain plants. In *Proc. 1st IFAC Workshop on New Trends in Design of Control Systems*, 249–254. Smolenice, Slovakia.

Brdyś, M. and Tatjewski, P. (2005). *Iterative Algorithms for Multilayer Optimizing Control*. Imperial College Press, London UK.

Chachuat, B., Srinivasan, B., and Bonvin, D. (2009). Adaptation strategies for real-time optimization. *Comp. Chem. Eng. (in press)*.

Forbes, J.F., Marlin, T.E., and MacGregor, J.F. (1994). Model adequacy requirements for optimizing plant operations. *Comp. Chem. Eng.*, 18(6), 497–510.

Gao, W. and Engell, S. (2005). Iterative set-point optimization of batch chromatography. *Comp. Chem. Eng.*, 29, 1401–1409.

Mansour, M. and Ellis, J.E. (2003). Comparison of methods for estimating real process derivatives in online optimization. *App. Math. Modelling*, 27, 275–291.

Marchetti, A. (2009). *Modifier-Adaptation Methodology for Real-Time Optimization*. Ph.D. thesis, École Polytechnique Fédérale de Lausanne (in preparation).

Marchetti, A., Chachuat, B., and Bonvin, D. (2009). Modifier adaptation methodology for real-time optimization. *Ind. Eng. Chem. Res.*, DOI: 10.1021/ie801352x.

Marlin, T.E. and Hrymak, A.N. (1997). Real-time operations optimization of continuous processes. In *AIChE Symposium Series - CPC-V*, volume 93, 156–164.

Roberts, P.D. (1979). An algorithm for steady-state system optimization and parameter estimation. *Int. J. Systems Sci.*, 10, 719–734.

Williams, T.J. and Otto, R.E. (1960). A generalized chemical processing model for the investigation of computer control. *AIEE Trans.*, 79, 458.

Zhang, Y. and Forbes, J.F. (2000). Extended design cost: A performance criterion for real-time optimization systems. *Comp. Chem. Eng.*, 24, 1829–1841.

Appendix A. AFFINE SUBSPACES

In a n_u-dimensional space, a point is an affine subspace of dimension 0, a line is an affine subspace of dimension 1, and a plane is an affine subspace of dimension 2. An affine subspace of dimension $(n_u - 1)$ is called an hyperplane.

Hyperplane. An hyperplane in n_u-dimensional space is given by

$$n_1 u_1 + n_2 u_2 + \cdots + n_{n_u} u_{n_u} = b, \quad \text{or:} \quad \mathbf{n}^\mathsf{T}\mathbf{u} = b \quad \text{(A.1)}$$

and divides the space into two half-spaces: $\mathbf{n}^\mathsf{T}\mathbf{u} > b$, and $\mathbf{n}^\mathsf{T}\mathbf{u} < b$.

Complement affine subspaces. Given a set of $(n_u + 1)$ points in a n_u-dimensional space, $\mathcal{S} := \{\mathbf{u}_1, \ldots, \mathbf{u}_{n_u+1}\}$, a proper subset $\mathcal{S}^A$, i.e. $\mathcal{S}^A \subsetneq \mathcal{S}$, of $n_u^A \in \{1, \ldots, n_u\}$ points generates an affine subspace of dimension $(n_u^A - 1)$:

$$\mathbf{u} = \mathbf{u}_1 + \lambda_{1,2}\frac{\mathbf{u}_1 - \mathbf{u}_2}{\|\mathbf{u}_1 - \mathbf{u}_2\|} + \cdots + \lambda_{1,n_u^A}\frac{\mathbf{u}_1 - \mathbf{u}_{n_u^A}}{\|\mathbf{u}_1 - \mathbf{u}_{n_u^A}\|} \quad \text{(A.2)}$$

where the parameters $\lambda_{1,2}, \ldots, \lambda_{1,n_u^A}$ represent distances from the point $\mathbf{u}_1$ in the directions $\mathbf{u}_1 - \mathbf{u}_2, \ldots, \mathbf{u}_1 - \mathbf{u}_{n_u^A}$, respectively. The complement subset $\mathcal{S}^C := \mathcal{S} \setminus \mathcal{S}^A$ of $(n_u + 1 - n_u^A)$ points, generates the complement affine subspace of dimension $(n_u - n_u^A)$:

$$\mathbf{u} = \mathbf{u}_{n_u^A+1} + \lambda_{n_u^A+1,n_u^A+2}\frac{\mathbf{u}_{n_u^A+1} - \mathbf{u}_{n_u^A+2}}{\|\mathbf{u}_{n_u^A+1} - \mathbf{u}_{n_u^A+2}\|} + \ldots \quad \text{(A.3)}$$
$$\cdots + \lambda_{n_u^A+1,n+1}\frac{\mathbf{u}_{n_u^A+1} - \mathbf{u}_{n_u+1}}{\|\mathbf{u}_{n_u^A+1} - \mathbf{u}_{n_u+1}\|}$$

Distance between complement affine subspaces.

Definition 1. (Distance between complement affine subspaces). Given a set of (n_u+1) points in a n_u-dimensional space, $\mathcal{S} := \{\mathbf{u}_1, \ldots, \mathbf{u}_{n_u+1}\}$, a proper subset of $\mathcal{S}$, $\mathcal{S}^A \subsetneq \mathcal{S}$ of $n_u^A \in \{1, \ldots, n_u\}$ points, and its complement $\mathcal{S}^C := \mathcal{S} \setminus \mathcal{S}^A$ of $(n_u + 1 - n_u^A)$ points, the distance between complement affine subspaces is defined as the (orthogonal) distance between the affine subspace of dimension $(n_u^A - 1)$ generated by all the points in $\mathcal{S}^A$, and the affine subspace of dimension $(n_u - n_u^A)$ generated by all the points in $\mathcal{S}^C$.

The total number of possible pairs of complement affine subspaces that can be generated from $\mathcal{S}$ is $n_b = 1 + \sum_{s=1}^{n_u-1} 2^s$.

Definition 2. (Nearest complement affine subspaces). The shortest distance between complement affine subspaces is given by $l_{\min} := \min\{l_1, l_2, \ldots, l_{n_b}\}$, where $l_1, l_2, \ldots, l_{n_b}$ are the distances between all possible pairs of complement affine subspaces that can be generated from $\mathcal{S}$.

In the 2-dimensional case ($n_u = 2$), the number of distances to evaluate is $n_b = 3$, which corresponds to the 3 point-to-line distances. In the 3-dimensional case, there are $n_b = 7$ distances to evaluate, which correspond to 4 point-to-plane distances, and 3 line-to-line distances.

In order to compute the distance between the complement affine subspaces (A.2) and (A.3), a vector $\mathbf{n}$ that is normal to both subspaces is required:

$$[\ \mathbf{u}_1 - \mathbf{u}_2\ \ldots\ \mathbf{u}_1 - \mathbf{u}_{n_u^A}\ \ \mathbf{u}_{n_u^A+1} - \mathbf{u}_{n_u^A+2}\ \cdots \quad \text{(A.4)}$$
$$\mathbf{u}_{n_u^A+1} - \mathbf{u}_{n_u+1}\ ]^\mathsf{T}\mathbf{n} = \mathbf{0}, \qquad \text{or,} \qquad \mathsf{U}\mathbf{n} = \mathbf{0}.$$

The matrix $\mathsf{U} \in \mathbb{R}^{(n_u-1)\times n_u}$ is of rank $(n_u - 1)$. The vector $\mathbf{n}$ can be obtained by singular-value decomposition of U.

Given a point $\mathbf{u}^a$ that belongs to the affine subspace (A.2), a point $\mathbf{u}^b$ that belongs to the complement affine subspace (A.3), and a vector $\mathbf{n}$ that is normal to both complement affine subspaces, the distance l_{AC} between the two complement affine subspaces is:

$$l_{AC} = \frac{|\mathbf{n}^\mathsf{T}(\mathbf{u}^b - \mathbf{u}^a)|}{\|\mathbf{n}\|} \quad \text{(A.5)}$$

Optimally Invariant Variable Combinations for Nonlinear Systems

Johannes E. P. Jäschke, Sigurd Skogestad

Norwegian University of Science and Technology (NTNU), Trondheim, Norway (e-mail: skoge@chemeng.ntnu.no).

Abstract: In this article we present an "explicit RTO" approach for achieving optimal steady state operation without requiring expensive online calculations. After identifying regions of constant active constraints, it is shown that there exist some optimally invariant variable combination for each region. If the unknown variables can be eliminated by measurements and system equations, the invariant combinations can be used for control. Moreover, we show that the measurement invariants can be used for detecting changes in the active set and for finding the right region to switch to. This explicit RTO approach is applied to a CSTR described by a set of rational equations. We show how the invariant variable combinations are derived, and use polynomial reduction to eliminate the unknown variables to obtain the measurement invariants which are used for control.

Keywords: Optimizing control, Polynomial systems, Real-time optimization, Explicit RTO, Self-optimizing control, Optimally invariant measurement combinations, Changing active sets

1. INTRODUCTION

Optimal operation of chemical processes becomes increasingly important in order to be able to compete in the international markets and to minimize environmental impact. A well established tool to achieve this goal is real-time optimization (RTO), where the optimal set-points are computed on-line, based on measurements taken at given sample times. This involves setting up and maintaining a real-time computation system, which can be very expensive and time consuming.

An alternative approach is to use off-line calculations and analysis to minimize or avoid complex on-line computations for example by finding optimally invariant measurement combinations ('self-optimizing' variable combinations, (Narasimhan and Skogestad (2007)). Controlling these combinations to their setpoints guarantees to operate the process optimal or close to optimal, with a certain acceptable loss (Skogestad (2000)). The combinations can be controlled by a simple control structure based on PI controllers. The conventional real-time optimization problem can either be replaced completely or partially by controlling invariant variable combinations. In practice, many processes are operated by something similar to this alternative approach, although not always consciously. That is, the optimization problem is not formulated explicitly and the control variables are chosen from experience and engineering intuition.

This publication presents two main results. The first one is extending the idea of self-optimizing control from unconstrained linear problems to constrained nonlinear problems. To the authors knowledge, optimally invariant variable combinations have been considered systematically only for linear plants with quadratic performance index (see e.g. Alstad et al. (2009)). A second contribution is the proof that using controlled variable to identify new sets of active constraints will always identify the correct active set. Although measurement invariants have been used before for active set identification (Manum et al. (2007)), it has not been proved that this holds for nonlinear problems, too.

2. GENERAL PROCEDURE

We consider a plant at steady state and assume the plant performance can be modelled as an optimization problem with a performance index J together with equality and inequality constraints, $g(\mathbf{u}, \mathbf{x}, \mathbf{d})$ and $h(\mathbf{u}, \mathbf{x}, \mathbf{d})$:

$$\min_{\mathbf{u},\mathbf{x}} J \quad \text{s.t} \quad \begin{cases} g(\mathbf{u}, \mathbf{x}, \mathbf{d}) = 0 \\ h(\mathbf{u}, \mathbf{x}, \mathbf{d}) \leq 0 \end{cases} \tag{1}$$

The variables $\mathbf{u}$, $\mathbf{x}$, $\mathbf{d}$ denote the manipulated input variables, the internal states, and the disturbance variables, respectively. In addition, we assume that there are measurements $\mathbf{y}(\mathbf{x}, \mathbf{u}, \mathbf{d})$, which provide information about the internal states and the disturbances of the process.

In order to obtain optimal operation we do not optimize the model on-line at given sample times. Instead, we use the structure of the problem to find optimally invariant variable combinations for the system. Since the available number of degrees of freedom changes when an inequality constraint becomes active, we have to find a new set of invariant measurement combinations for each set of constraints that becomes active during operation of the plant. This makes it necessary to define separate control structures for each region. Therefore, the first step is to partition the operating space into regions defined by the set of active constraints, i.e. the system is optimized for all possible disturbances $\mathbf{d}$ and the active constraints in each region are identified.

In the second step, we determine (nonlinear) variable combinations which yield optimal operation when kept at their constant setpoint. The variables resulting from this step cannot be used for control directly, because they contain unknown disturbance variables and internal states which are not known. To be able to control the system, we attempt to "model" the variable invariants by expressions which only contain known variables. These can then be used for control in feedback loops.

The last step in this procedure is to define rules for detecting and switching regions when the active constraints change. In many cases this can be done by monitoring the controlled variables of the neighbouring region and switching when the controlled variable of the neighbouring region reaches its optimal value.

3. DETERMINING INVARIANT VARIABLE COMBINATIONS

3.1 Invariants for systems with quadratic objective and linear inequality constraints and linear measurements

To illustrate the idea of finding invariant variable combinations we first consider a problem with a quadratic objective and linear constraints. After having identified n_r regions of active constraints, we can define an equality constrained optimization problem for each region.

Given $\mathbf{z} \in \mathbb{R}^{n_z \times 1}$ and $\mathbf{d} \in \mathbb{R}^{n_d \times 1}$, consider the constrained optimization problem:

$$\min_{\mathbf{z}} J = \min_{\mathbf{z}} [\mathbf{z^T}\, \mathbf{d^T}] \begin{bmatrix} \mathbf{J_{zz}} & \mathbf{J_{zd}} \\ \mathbf{J_{zd}}^{\mathbf{T}} & \mathbf{J_{dd}} \end{bmatrix} \begin{bmatrix} \mathbf{z} \\ \mathbf{d} \end{bmatrix} \tag{2}$$

subject to

$$\mathbf{A}_z \mathbf{z} + \mathbf{A}_d \mathbf{d} = \tilde{\mathbf{A}} \begin{bmatrix} \mathbf{z} \\ \mathbf{d} \end{bmatrix} = 0 \tag{3}$$

where we have $\mathbf{A}_z \in \mathbb{R}^{n_c \times n_z}$ has rank n_c, $\mathbf{A}_d \in \mathbb{R}^{n_c \times n_d}$, $\tilde{\mathbf{A}} = [\mathbf{A}_z\, \mathbf{A}_d]$, and $\mathbf{J_{zz}} > 0$.

Eq. (3) may include the model equations as well as active (equality) constraints. Instead of using (3) to eliminate n_c internal states to obtain an unconstrained problem, we keep the constraints explicit in the formulation as this more general formulation will be used later when presenting the nonlinear case (where the internal states are not easily substituted). The Karush-Kuhn-Tucker first order optimality conditions give

$$\nabla_z L = \nabla_z J + \mathbf{A_z^T} \lambda = \tilde{J} \begin{bmatrix} \mathbf{z} \\ \mathbf{d} \end{bmatrix} + \mathbf{A_z^T} \lambda = 0, \tag{4}$$

where $\tilde{J} = [\mathbf{J_{uu}}\, \mathbf{J_{ud}}]$, and λ is the vector of Lagrangian multipliers. Therefore, from (4) we have that

$$\mathbf{A_z^T} \lambda = -\tilde{J} \begin{bmatrix} \mathbf{z} \\ \mathbf{d} \end{bmatrix}. \tag{5}$$

$\mathbf{A}_z$ is not full column rank, so let $\mathbf{N}_z$ be a basis for the null space of $\mathbf{A}_z$ with dimension $n_{DOF} = n_z - n_c$. Then $\mathbf{N_z^T A_z^T} = 0$, and at the optimum we must have

$$\mathbf{c}^v(\mathbf{z}, \mathbf{d}) \triangleq \mathbf{N_z^T} \tilde{J} \begin{bmatrix} \mathbf{z} \\ \mathbf{d} \end{bmatrix} = 0 \tag{6}$$

for the system (5) to be uniquely solvable for λ. Keeping $\mathbf{c}^v(\mathbf{z}, \mathbf{d})$ at zero (in addition to the active constraints), is always optimal. However, it cannot be used for control directly, as it contains unknown (unmeasured) variables. For control, we need a function of measurements $\mathbf{c}(\mathbf{y})$, such that the difference between the invariant and the measurement combination is minimal. Here, we want to "model" $\mathbf{c}^v(\mathbf{z}, \mathbf{d})$ perfectly, such that

$$\mathbf{c}(\mathbf{y}) = \mathbf{c}^v(\mathbf{z}, \mathbf{d}). \tag{7}$$

Then controlling $\mathbf{c}(\mathbf{y}) = 0$ yields optimal operation. If we have $n_z + n_d$ independent linear measurements

$$y = \mathbf{G}^y \begin{bmatrix} \mathbf{z} \\ \mathbf{d} \end{bmatrix}, \tag{8}$$

where $\mathbf{G}^y$ is invertible, we can use them with (6) to give

$$\mathbf{c}(\mathbf{y}) = \mathbf{N^T} \tilde{J} [\mathbf{G}^y]^{-1} \mathbf{y}. \tag{9}$$

However, note that we actually only need $n_z - n_c + n_d = n_{DOF} + n_d$ measurements, since the model equations (3) can be used to eliminate the constrained degrees of freedom (internal states). This is shown in Appendix A.

Remark 1. In the unconstrained case, the optimal invariant variable combination is simply the gradient, such that we have $\mathbf{c}(\mathbf{y}) = \mathbf{H}\mathbf{y} = \nabla_u J$, and $\mathbf{H} = \tilde{J}[\tilde{\mathbf{G}}^y]^{-1}$.

3.2 Invariants for polynomial and rational systems

An analog approach may be taken for obtaining invariant variable combinations for more general systems described by polynomials. Since rational equations can be transformed into polynomials by multiplying with the common denominator, the method is applicable to rational systems, too.

Initially, all regions defined by constant active constraints are determined. For each region we then have:

Theorem 1. (Nonlinear invariants). Given $\mathbf{z}, \mathbf{d}$ as in section 3.1, consider the nonlinear optimization problem

$$\min_{\mathbf{z}} J(\mathbf{z}, \mathbf{d}) \quad \text{s.t} \quad g_i(\mathbf{z}, \mathbf{d}) = 0, \quad i = 1 \dots n_g, \tag{10}$$

and implicit measurement relations

$$m_j(\mathbf{y}, \mathbf{z}, \mathbf{d}) = 0 \quad j = 1 \dots n_y, \tag{11}$$

where $\mathbf{y}$ is the measured variable. If the Jacobian $\mathbf{A}_z(\mathbf{z}, \mathbf{d}) = [\nabla_z g]$ has full rank n_g at the optimum throughout the region, following holds:

(1) There exist $n_{DOF} = n_z - n_g$ independent invariant variable combinations $\mathbf{c}^v$ with

$$\mathbf{c}^v = [\mathbf{N}_z(\mathbf{z}, \mathbf{d})]^{\mathbf{T}} \nabla_z J(\mathbf{z}, \mathbf{d}), \tag{12}$$

where $\mathbf{N}_z(\mathbf{z}, \mathbf{d})$ denotes the null space of the Jacobian of the active constraints $g(\mathbf{z}, \mathbf{d})$.

(2) If there exist polynomials $\alpha_i(\mathbf{z}, \mathbf{d})$ and $\beta_j(\mathbf{z}, \mathbf{d})$, such that element of $\mathbf{c}^v$ can be expressed by

$$c^v = \sum_{i,j} (\alpha_i(\mathbf{z}, \mathbf{d}) g_i(\mathbf{z}, \mathbf{d}) + \beta_j(\mathbf{z}, \mathbf{d}) m_j(\mathbf{y}, \mathbf{z}, \mathbf{d})) + c(\mathbf{y}), \tag{13}$$

then the term $c(\mathbf{y})$ is the desired self-optimizing variable which when controlled to zero yields optimal operation.

Proof. Calculate the Jacobian of the constraints:

$$\mathbf{A}_z(\mathbf{z}, \mathbf{d}) = \left[[\nabla_z g_1(\mathbf{z}, \mathbf{d})]^{\mathbf{T}}, \cdots, [\nabla_z g_{n_g}(\mathbf{z}, \mathbf{d})]^{\mathbf{T}} \right]^{\mathbf{T}} \tag{14}$$

Since $\mathbf{A}_z(\mathbf{z},\mathbf{d})$ has full rank, the null space has a constant dimension and there exist a unique vector λ which satisfies the KKT conditions (Nocedal and Wright (2006)):

$$\begin{aligned} \nabla_z J(\mathbf{z},\mathbf{d}) + [\mathbf{A}_z(\mathbf{z},\mathbf{d})]^{\mathbf{T}} \lambda = 0 \\ g_i(\mathbf{z},\mathbf{d}) = 0, \quad i = 1 \dots n_g \end{aligned} \tag{15}$$

For the existence and uniqueness of λ, we always must have, that

$$[\mathbf{N}_z(\mathbf{z},\mathbf{d})]^{\mathbf{T}} \nabla_z J = -[\mathbf{N}_z(\mathbf{z},\mathbf{d})]^{\mathbf{T}} [\mathbf{A}(\mathbf{z},\mathbf{d})]^{\mathbf{T}} \lambda, \tag{16}$$

where $\mathbf{N}_z(\mathbf{z},\mathbf{d})$ is chosen as a basis for the $n_z - n_g$-dimensional null space of $\mathbf{A}_z(\mathbf{z},\mathbf{d})$. The optimal invariant variable combination to be kept at $\mathbf{c}^v = 0$ is then given by:

$$\mathbf{c}^v = [\mathbf{N}_z(\mathbf{z},\mathbf{d})]^{\mathbf{T}} \nabla_z J(\mathbf{z},\mathbf{d}) \tag{17}$$

The second statement follows from the implicit relations $g_i(\mathbf{z},\mathbf{d}) = 0$ and $m_j(\mathbf{y},\mathbf{z},\mathbf{d}) = 0$. □

Remark 2. This variable combination (17) is not unique in the sense that it can be premultiplied by any nonsingular matrix while still yielding optimal operation. However, since the variable combination is derived from the KKT conditions, it is unique in the sense that for a convex optimization problem $\mathbf{c}^v = 0$ if the system is operated optimally, because the stationary point is unique.

Remark 3. The full rank assumption for $\mathbf{A}_z(\mathbf{z},\mathbf{d})$ at the optimum is valid in most practical cases, as rank deficiency at the optimum implies that the degrees of freedom in the problem change.

Remark 4. The functions α and β can be found using Gröbner theory (Cox et al. (1992)), and the condition for the existence of polynomial functions α_i and β_i is that every variable to be eliminated must appear in the initial ideal generated by all g_i and m_j in lower or equal degree than in $\mathbf{c}^v$.

To illustrate the concept, we present a toy example.

Example 1. (Nonlinear invariants). We consider a cost function $J(z_1, z_2, d) = z_1^2 + z_2^2$ subject to the constraint

$$g = (z_1 - 1)^2 + (z_2 - d)^2 - 5. \tag{18}$$

In addition to the known z_1, z_2, the system has one measurement y with the measurement relation

$$m = z_1 z_2 + z_1 d - y = 0. \tag{19}$$

First we calculate the Jacobian of (18) with respect to z

$$\mathbf{A}(z_1, z_2, d) = [\, 2(z_1 - 1) \;\; 2(z_2 - d) \,], \tag{20}$$

and the basis of its null space:

$$\mathbf{N}(z_1, z_2, d) = [\, -(z_2 - d) \;\; (z_1 - 1) \,]^{\mathbf{T}}. \tag{21}$$

After computing the gradient of the cost function J

$$\nabla J = [\, 2z_1 \;\; 2z_2 \,]^{\mathbf{T}}, \tag{22}$$

we obtain the invariant variable combination as in (17):

$$c^v = \underbrace{[\, -(z_2 - d) \;\; (z_1 - 1) \,]}_{[\mathbf{N}(\mathbf{z},\mathbf{d})]^{\mathbf{T}}} \underbrace{\begin{bmatrix} 2z_1 \\ 2z_2 \end{bmatrix}}_{\nabla J} = 2(z_1 d - z_2) \tag{23}$$

However, c^v contains the unmeasured disturbance d, so it cannot be used for control. Using the measurement relation (19) and equation (13) we see by inspection that $\alpha = 0$ and $\beta = 2$ yield a $c(y)$ which satisfies (7):

$$\begin{aligned} c^v = \underbrace{2(z_1 d - z_2)}_{c^v} = \underbrace{0}_{\alpha} g + \underbrace{2}_{\beta} \underbrace{(z_1 z_2 + z_1 d - y)}_{m} \\ + \underbrace{2y - 2z_2 - 2z_1 z_2}_{\mathbf{c}(\mathbf{y})}. \end{aligned} \tag{24}$$

Since $m = 0$, we have that $c^v = c(y)$. In more complex cases, α and β have to be determined by computing a Gröbner basis for the constraint and measurement relations and by reducing c^v modulo the Gröbner basis.

4. SWITCHING OPERATING REGIONS

After the controlled variables for all regions are identified, the remaining issue is to determine how to switch between operating regions. Under certain assumptions, the switching points can be found using the already defined invariant variable combinations.

Theorem 2. (Switching regions). Assume the system (10) convex and at the optimum $\nabla_z J(\mathbf{z},\mathbf{d}) \neq 0$ wherever a constraint is active. If a disturbance moves the system continuously from one region of active constraints to another, (i.e. the system does not jump over regions) the exact switching points can be detected by monitoring the controlled variables and the constraints of the neighbouring regions.

Proof. We consider to type of changes, denoted type I and II. In changes of type I, a constraint is replaced or added to the current active set. This change is easily detected by monitoring the active constraints of the neighbouring regions. As the system is operated optimally and the disturbance moves the system gradually to the new region, the region boundary is reached, when the constraint is hit.

In changes of type II, a constraint becomes inactive and the released degree of freedom is controlled using a measurement invariant. Detecting a type II change is done by monitoring the invariant variable combinations of the neighbouring regions. If if an invariant variable combination hits the zero value, the region is switched. The invariant variable combinations assume the value zero only at the switching points. This can be seen by contradiction. Consider two regions with c_1^v and c_2^v. Let the system be operated optimally at $(\mathbf{z}_0, \mathbf{d}_0)$ in the constrained region 1 ($c_1^v(\mathbf{z}_0, \mathbf{d}_0) = 0$), and let $c_2^v(\mathbf{z}_0, \mathbf{d}_0) = 0$. The Jacobians of the set of constraints $g^1(\mathbf{z},\mathbf{d})$ and $g^2(\mathbf{z},\mathbf{d})$ are denoted as $\mathbf{A}^1(\mathbf{z},\mathbf{d})$ and $\mathbf{A}^2(\mathbf{z},\mathbf{d})$.

Since $c_1^v(\mathbf{z}_0, \mathbf{d}_0) = c_2^v(\mathbf{z}_0, \mathbf{d}_0) = 0$ we have

$$\underbrace{\left[\mathbf{N}^1(\mathbf{z}_0, \mathbf{d}_0)\right]^{\mathbf{T}} \nabla_z J(\mathbf{z}_0, \mathbf{d}_0)}_{=0} = \underbrace{\left[\mathbf{N}^2(\mathbf{z}_0, \mathbf{d}_0)\right]^{\mathbf{T}} \nabla_z J(\mathbf{z}_0, \mathbf{d}_0)}_{=0}. \tag{25}$$

Since $\nabla_z J(\mathbf{z},\mathbf{d}) \neq 0$, this implies that $\mathbf{A}^1$ and $\mathbf{A}^2$ are row equivalent and the null spaces of $\mathbf{A}^1(\mathbf{z}_0, \mathbf{d}_0)$ and $\mathbf{A}^2(\mathbf{z}_0, \mathbf{d}_0)$ have the same basis. However, this is not possible, because by assumption, $\mathbf{A}^1$ and $\mathbf{A}^2$ have different ranks. Therefore the invariant variable combination of a "less constrained" region cannot become zero in a region which is "more constrained". Thus, the active constraints and the measurement combinations can be used for determining when to switch region. □

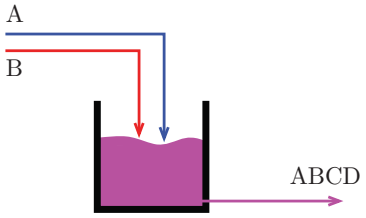

Fig. 1. CSTR with two reactions

Table 1. Variables relevant for control

Measurements $\mathbf{y}$	F, c_B, q
Manipulated variables $\mathbf{u}$	F_A, F_B
Unknown disturbance $\mathbf{d}$	Rate constant k_1
Internal states $\mathbf{z}_{unknown}$	c_A, c_C

5. APPLICATION

We consider an isothermal CSTR with two parallel reactions, Fig. 1, from Srinivasan et al. (2008). Two feed streams F_A and F_B with the concentrations c_A and c_B react in a tank to the desired product C and the undesired side product D. The tank is equipped with one outflow in which all components are present. In order to enable isothermal reaction conditions a temperature loop is closed such that the correct amount of heat is removed from the system. The temperature control is assumed to be perfect. The products C and D are formed by the reactions:

$$\begin{aligned} \mathrm{A} + \mathrm{B} &\xrightarrow{k_1} \mathrm{C} \\ 2\,\mathrm{B} &\xrightarrow{k_2} \mathrm{D} \end{aligned} \tag{26}$$

The optimization objective is to maximize the desired product $(F_A + F_B)c_C$ weighted by a yield factor $(F_A + F_B)c_C/(F_A c_{A,in})$. The amount of heat to remove and the maximum flow rate are limited. This lets us formulate the optimization problem of the system as follows:

$$\max_{F_A, F_B} \frac{(F_A + F_B)c_C}{F_A c_{A_{in}}}(F_A + F_B)c_C \tag{27}$$

subject to

$$\begin{aligned} F_A c_{A_{in}} - (F_A + F_B)c_A - k_1 c_A c_B V &= 0 \\ F_B c_{B_{in}} - (F_A + F_B)c_B - k_1 c_A c_B V - 2k_2 c_B^2 V &= 0 \\ -(F_A + F_B)c_C + k_1 c_A c_B V &= 0 \\ F_A + F_B - F &= 0 \\ k_1 c_A c_B V(-\Delta H_1) + 2k_2 c_B V(-\Delta H_2) - q &= 0 \\ q - q_{max} &\leq 0 \\ F - F_{max} &\leq 0 \end{aligned} \tag{28}$$

The variables k_1 and k_2 are the rate constants for the two reactions, $(-\Delta H_1)$ and $(-\Delta H_2)$ are the corresponding reaction enthalpies, q the heat produced by the reactions, V the reactor volume, and F the total flow rate. The measured variables ($\mathbf{y}$), the manipulated variables ($\mathbf{u}$), the disturbance variables ($\mathbf{d}$), and the internal states are listed in table 1, and the parameter values of the system are given in table 2. The combined vector of states and manipulated variables is

$$\mathbf{z} = [\, c_A,\ c_B,\ c_C,\ F_A,\ F_B \,]^{\mathbf{T}}. \tag{29}$$

5.1 Identifying operational regions

The first step of the procedure, optimizing the system offline for all possible values shows that the system operation

Table 2. Parameters

k_1	l/(mol h)	0.3-1.5
k_2	l/(mol h)	0.0014
$(-\Delta H_1)$	j/mol	7×10^4
$(-\Delta H_2)$	j/mol	5×10^4
$c_{A,in}$	mol/l	2
$c_{B,in}$	mol/l	1.5
V	l	500
$F_{\max}$	l	22
q_{max}	kJ/h	1000

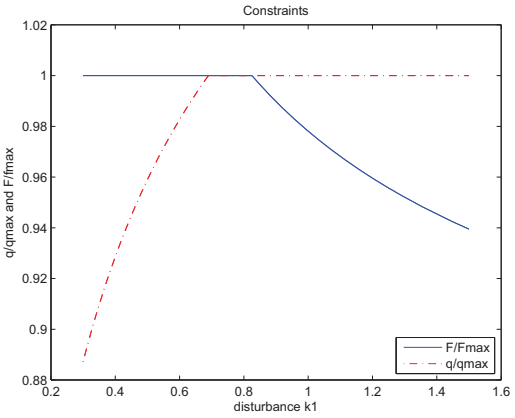

Fig. 2. Optimal values of the constrained variables

space can be partitioned into three regions defined by the set of active constraints. In region 1, for values of k_1 below about $k_1 = 0.65$ only the flow constraint is active (Fig. 2). In region 2 for values between $k_1 = 0.65$ and $k_1 = 0.8$ both constraints are active, and in region 3 above $k_1 = 0.8$ only the heat constraint is active.

After satisfying the active constraints in the regions we are left with $N_{\mathrm{DOF},1} = 1$ for region 1, $N_{\mathrm{DOF},2} = 0$ for region 2, and $N_{\mathrm{DOF},1} = 1$ for region 3.

In region 1, one of the manipulated variables (flow rates) is used to control the active constraint (maximum flow) and the other manipulated variable is used to control the invariant measurement combination of the region. In region 2 we simply control the active constraints, keeping q at $q_{\max}$ and F at $F_{\max}$. In region 3, again one of the manipulated variables is used to control the active constraint (maximum heat removal) and the other one is used to control the invariant measurement combination of region 3.

5.2 Determining the invariant variable combinations

Using the information from the previous section, we determine the invariant variable combinations in each region. First, we calculate the null space of Jacobian of the active set $\mathbf{N}_z^{\mathbf{T}}$ and multiply it with the gradient of the objective function $\nabla_z J(\mathbf{z}, \mathbf{d})$, as in (17) to obtain the invariant variable combination. Generally this is a fractional expression, but since we are controlling it to zero, it is sufficient to consider only the numerator of $\mathbf{N}_z^{\mathbf{T}} \nabla_z J$. For *region 1* we obtain the invariant

$$\begin{aligned}\mathbf{c}_1^v(\mathbf{z},\mathbf{d}) = &-(F_A+F_B)^2c_C\left[-3c_CF_B^2F_A-3c_CF_A^2F_B\right.\\&-4c_Cc_BF_A^2k_2V-4c_Ck_2V^2k_1c_B^2F_A-c_CF_A^3\\&-c_CF_B^3-4c_Ck_2V^2k_1c_B^2F_B-c_Cc_BF_A^2k_1V\\&-4c_Cc_BF_B^2k_2V-c_Cc_BF_B^2k_1V-c_CF_A^2c_Ak_1V\\&-c_CF_B^2c_Ak_1V-8c_CF_Ac_BF_Bk_2V\\&-2c_CF_Ac_BF_Bk_1V-2c_CF_AF_Bc_Ak_1V\\&+8F_Ak_1V^2c_{A,in}k_2c_B^2+2F_A^2k_1Vc_Bc_{A,in}\\&+2F_Ak_1VF_Bc_Bc_{A,in}-2F_A^2k_1Vc_{B,in}c_A\\&\left.-2F_Ak_1VF_Bc_{B,in}c_A\right]\end{aligned} \tag{30}$$

which should be controlled to zero. This invariant can be simplified somewhat further, since we know that $(F_A + F_B)^2c_C \neq 0$. It is therefore sufficient to control the second term in the square brackets in (30) to zero.

As mentioned above, *region 2* does not have any unconstrained degree of freedom, so satisfying all active constraints yields optimal operation. In *region 3* we obtain an expression similar to (30) for $\mathbf{c}_3^v(\mathbf{z},\mathbf{d})$.

5.3 Eliminating unknown variables

The invariant variable combination $\mathbf{c}_1^v(\mathbf{z},\mathbf{d})$ and $\mathbf{c}_3^v(\mathbf{z},\mathbf{d})$ still contain the unknown and internal variables k_1, c_a and c_C, so they cannot be used for feedback control directly. In the next step the unknown variables have to be replaced by expressions in the measured variables, so that this invariant can be used for control. Depending on the type of the system equations, different methods may be applied in this step. The general idea is that we use the measurements together with the equations that are satisfied in the active set to express the invariant. As all equations in this case study are polynomial (rational expressions equal to zero can transformed to polynomials by multiplication with the denominator), we attempt to reduce the invariants modulo the active set with a variable ordering that eliminates the unknowns. To simplify the elimination procedure, k_1 is eliminated by solving the third equality constraint for k_1.

$$k_1 = (F_A + F_B)c_C/(c_Ac_BV) \tag{31}$$

and inserting it into (30). The other unknown variables c_A and c_C are eliminated using polynomial reduction and the resulting measurement invariant in *region 1* becomes:

$$\begin{aligned}c_1(\mathbf{y}) = &-F_{max}(F_{max}c_B+2c_B^2k_2V-F_Bc_{B,in})^2\\&(4c_B^4k_2^2V^2+4F_{max}c_B^3k_2V-6k_2Vc_B^2F_Bc_{A,in}\\&-4k_2VF_{max}c_{B,in}c_B^2+6k_2Vc_B^2F_{max}c_{A,in}\\&+F_{max}^2c_B^2-2F_{max}^2c_{B,in}c_B+2c_BF_{max}^2c_{A,in}\\&-2c_BF_{max}F_Bc_{A,in}-F_B^2c_{B,in}^2+3F_{max}F_Bc_{A,in}c_{B,in}\\&-F_B^2c_{A,in}c_{B,in}+2F_{max}F_Bc_{B,in}^2-2F_{max}^2c_{A,in}c_{B,in})\end{aligned} \tag{32}$$

This expression depends only on known variables and parameters. The measurement invariant for *region 3* is found in the same way:

$$\begin{aligned}c_3(\mathbf{y}) = &-(F_Ac_B+c_BF_B+2c_B^2k_2V-c_{B,in}F_B)^2\\&(-3F_B^2q_{max}c_{B,in}c_B+8c_B^4q_{max}k_2^2V^2\\&+F_B^2q_{max}c_{B,in}^2+2c_B^2F_B^2q_{max}+2F_A^2q_{max}c_B^2\\&+4c_B^4F_Bk_2^2c_{B,in}V^2\Delta H_2+8c_B^3F_Bq_{max}k_2V\\&+2c_B^3F_B^2k_2c_{B,in}V\Delta H_2-6c_B^2F_Bq_{max}k_2c_{B,in}V\\&-2c_B^2F_B^2k_2c_{B,in}^2V\Delta H_2-F_A^2q_{max}c_{B,in}c_B\\&+4F_Ac_B^2F_Bq_{max}+F_AF_Bq_{max}c_{B,in}^2+2F_A^2c_Bq_{max}c_{A,in}\\&+6F_A^2k_2c_{B,in}V\Delta H_2c_B^3+12F_Ak_2^2c_{B,in}V^2\Delta H_2c_B^4\\&+8F_Ac_B^3F_Bk_2c_{B,in}V\Delta H_2+8F_Ac_B^3q_{max}k_2V\\&-2F_Ac_B^2q_{max}k_2c_{B,in}V-6F_Ac_B^2F_Bk_2c_{B,in}^2V\Delta H_2\\&-4F_AF_Bq_{max}c_{B,in}c_B+2F_A^2c_B^2k_2c_{A,in}c_{B,in}V\Delta H_2\\&-F_A^2q_{max}c_{A,in}c_{B,in}+4F_A^2c_B^3k_2c_{A,in}V\Delta H_2\\&+4F_Ac_B^3F_Bk_2c_{A,in}V\Delta H_2-2F_Ac_B^2F_Bk_2c_{A,in}c_{B,in}V\Delta H_2\\&+4F_Ac_B^2q_{max}k_2c_{A,in}V+2F_Ac_BF_Bq_{max}c_{A,in}\\&-F_AF_Bq_{max}c_{A,in}c_{B,in})\end{aligned} \tag{33}$$

Although these expressions seem complicated, they contain only known variables and can therefore be easily evaluated and controlled to their setpoint using a PI controller. In both invariants, the term in the first bracket is never zero (to see this, compare it with the second equality constraint in (28)), so it is sufficient to control the term in the second bracket to zero.

The values of these polynomials vary over order of magnitudes, so they are scaled to avoid numerical problems. The invariant of region 1 was scaled by 10^5 and the invariant of region 3 was scaled by 10^6.

5.4 Using measurement invariants for control and region identification

We use the controlled variables of the neighbouring regions for determining when to switch. Starting in region 1 optimal operation is achieved by using the two inputs F_A and F_B to control $c_1(\mathbf{y}) = 0$ and $F_A + F_B = F_{max}$. If k_1 increases, the amount of heat to be removed (the controlled variable of region 2) increases until it reaches the maximum possible value, q_{max} (Fig 3). When this value is reached, the control structure has to be changed to region 2. Now the inputs are used to control $q = q_{max}$ and $F_A + F_B = F_{max}$. While operating in region 2 the controlled variables of the neighbouring regions, $c_1(\mathbf{y})$ and $c_3(\mathbf{y})$ are monitored. If k_1 increases further, $c_3(\mathbf{y})$ approaches its optimal setpoint for region 3 and we switch region when the optimal value is reached. Switching back from the different regions is done in an analog manner.

6. DISCUSSION

The invariant variable combinations above are obtained by a two-step method, in which first the Lagrangian multipliers are eliminated, and subsequently the unknown variables (disturbances and internal states) are replaced by measurement relations. However, for systems which can be described by rational functions, as the CSTR example, there exists possibilities to eliminate both, the Lagrangian multipliers and the unknown variables simultaneously.

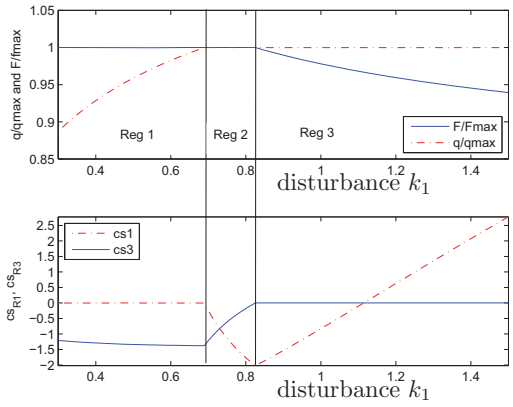

Fig. 3. Optimal values of controlled variables

This is done by defining an ideal which is generated by the polynomials describing the Karush-Kuhn-Tucker conditions and choosing an appropriate term order to eliminate the unknown disturbance and state variables (Cox et al. (1992)) Applying the chosen order to generate the elimination ideal gives a set of equations which are fulfilled at all times when the KKT conditions hold, but which do not contain any of the unknown variables.

Choosing a polynomial from this set which is not a (polynomial) combination of the equality constraints (i.e. which is not in the ideal generated by the equality constraints), gives a candidate for the measurement invariant. However, presently there are two challenges with the simultaneous method. First, the system with the chosen invariant measurement combinations may have (many) more roots than the KKT system. If we use them for control, we might control to "solutions" which do not satisfy the first order optimality conditions. Second, it is generally difficult to determine a term ordering a priori which eliminates the unknown variables and, at the same time ensures that the equations in the elimination ideal are not polynomial combinations of the equality constraints. If this is the case, the chosen variable combination is in the ideal generated by the equality constraints and the invariant will always be zero when the equality constraints are satisfied. This leads to an infinite number of solutions for the system. So far we are not aware of a method to handle these challenges in a systematic way, but we have found invariants in the elimination ideals which yield optimal operation in for the CSTR case study shown above.

The two step method presented in this work fundamentally shows the existence of invariant variable combinations for nonlinear systems and gives an easy way to compute and to use them. Additionally, in contrast to the elimination ideal method, the two-step method is principally not restricted to polynomial or rational models, provided that the unknowns can be eliminated.

7. CONCLUSION

The procedure presented in this paper is applicable to nonlinear steady state optimization problems and consists of four steps. First, regions of constant active constraints are defined. Second, optimally invariant nonlinear variable combinations are determined for each of the regions. Third, the unknown internal variables and disturbances are eliminated from the invariants to obtain variable combinations containing only known variables (measurements). It is proven that these variables can be used to uniquely identify a new active set. This makes the method applicable over a wide disturbance range with changing active sets. Finally, we have applied the method to a case study with a four component isothermal CSTR.

Although designing a self-optimizing control structure may require more work in advance, its implementation and maintenance is easy in practice. After the control structure is designed, optimal operation can achieved by simple PI controllers and there is no need to invest in expensive real-time equipment to operate the process optimally.

REFERENCES

Alstad, V., Skogestad, S., and Hori, E. (2009). Optimal measurement combinations as controlled variables. *Journal of Process Control*.

Cox, D., Little, J., and O'Shea, D. (1992). *Ideals, Varieties, and Algorithms*. Springer-Verlag.

Manum, H., Narasimhan, S., and Skogestad, S. (2007). A new approach to explicit mpc using self-optimizing control, *Internal report*. `www.nt.ntnu.no/users/skoge/publications/2007`.

Narasimhan, S. and Skogestad, S. (2007). Implementation of optimal operations using off-line computations. *8th international IFAC Symposium on Dynamics and Control of Process Systems (DYCOPS), Cancun, Mexico*.

Nocedal, J. and Wright, S.J. (2006). *Numerical Optimization*. Springer.

Skogestad, S. (2000). Plantwide control: The search for the self-optimizing control structure. *Journal of Process Control*, 10, 487–507.

Srinivasan, B., Biegler, L.T., and Bonvin, D. (2008). Tracking the necessary conditions of optimality with changing set of active constraints using a barrier-penalty function. *Computers and Chemical Engineering*, 32, 572–279.

Appendix A. ELIMINATING INTERNAL STATES

We define the combined input and internal state vector as

$$\mathbf{z} = \begin{bmatrix} \mathbf{x^T} & \mathbf{u^T} \end{bmatrix}^{\mathbf{T}}. \tag{A.1}$$

It is assumed that we have $n_u + n_d$ independent measurements for system 3.

$$\mathbf{y} = \tilde{\mathbf{G}}^y \begin{bmatrix} \mathbf{u^T} & \mathbf{d^T} \end{bmatrix} \tag{A.2}$$

with $\tilde{\mathbf{G}}^y$ invertible. Then

$$\begin{bmatrix} \mathbf{z} \\ \mathbf{d} \end{bmatrix} = \begin{bmatrix} \mathbf{x} \\ \mathbf{u} \\ \mathbf{d} \end{bmatrix} = \begin{bmatrix} -\mathbf{A}_x^{-1}\mathbf{A}_u & -\mathbf{A}_x^{-1}\mathbf{A}_s \\ \mathbf{I} & 0 \\ 0 & \mathbf{I} \end{bmatrix} \underbrace{\begin{bmatrix} \mathbf{u} \\ \mathbf{d} \end{bmatrix}}_{=[\tilde{\mathbf{G}}^y]^{-1}\mathbf{y}}, \tag{A.3}$$

and we derive the optimal measurement combination which satisfies (7) as

$$\mathbf{c}(\mathbf{y}) = \mathbf{H}\mathbf{y} \tag{A.4}$$

with

$$\mathbf{H} = \mathbf{N}_z^{\mathbf{T}} \tilde{J} \begin{bmatrix} -\mathbf{A}_x^{-1}\mathbf{A}_u & -\mathbf{A}_x^{-1}\mathbf{A}_s \\ \mathbf{I} & 0 \\ 0 & \mathbf{I} \end{bmatrix} \left[\tilde{\mathbf{G}}^y\right]^{-1}. \tag{A.5}$$

Influence of Differences in System Dynamics in the context of Multi-unit Optimization

François Reney, Michel Perrier, Bala Srinivasan.

Chemical Engineering Department, École Polytechnique, Montreal, Quebec, Canada (e-mail: bala.srinivasan@polymtl.ca).

Abstract: Extremum-seeking methods are unconstrained real-time optimization techniques that control the gradient to zero. The crucial difference between them lies in the gradient estimation method used. Multi-unit optimization technique proposes the use of a multiple units operated with an offset between them and the estimation of the gradient is by finite difference. Though this method gives fast convergence, the major bottleneck is that it assumes the units to be identical. This paper addresses the case where the static curves are indeed identical, while the dynamics are not so. It is shown that if all the units are stable, despite the difference in dynamics, the method would indeed converge to the true optimum. Also, it is shown that the difference in dynamics does not affect stability in the neighborhood of the optimum. In addition, this paper presents a possibility of replacing real units by static models in the calculation of the gradient. Experimental results are presented from a mixing system where an optimal temperature is sought.

Keywords: Real time optimization and control, multi-units optimization.

1. INTRODUCTION

Process optimization is a tool of choice to find the best operating point that balances conflicting objectives such as productivity, selectivity, and operating cost for continuous chemical process. To perform this optimization numerically, it is necessary to have a model of its operation. Though most processes are dynamic in nature, often a steady state model suffices since typically, for continuous process, one is interested in finding the best steady state operation point. However, due to process changes, the optimal operating point varies with time, and to reap the benefits, it is indeed crucial to track these changes.

Without being exhaustive, two main classes of techniques have been employed in the real-time optimization of continuous processes. The first class comprises of the repeated optimization techniques (Marlin & Hrymak, 2000) that alternate between the identification of a steady state model using measurements and numerical computation of the optimal input using the updated model. On the other hand, extremum-seeking methods (Ariyur & Krstic, 2003, Guay et al., 2004) treat the optimization problem as one of controlling the gradient to zero.

In the extremum-seeking framework, various methods have been used for the gradient determination. The perturbation method (Ariyur & Krstic, 2003) deduces the gradient by adding perturbation signal that is very slow compared to the process dynamics. The correlation between the input and output is used to estimate the gradient. In adaptive extremum seeking techniques (Guay et al., 2004), parameters of a dynamic model are adapted and the gradient is computed from the adapted model. All the above mentioned techniques have to respect time-scale separations between gradient estimation and the process dynamics, thereby leading to slow convergence.

The multi-unit optimization technique (Srinivasan, 2007) is an attempt to find another gradient method that would converge faster. The basic method uses two identical units operated with an offset between them and uses finite difference to estimate the gradient. However, the main drawback of this technique is that it needs multiple identical processes working in parallel, which is impossible to get in practice. It has been shown that, if the units are not identical, the stability of the scheme and the convergence toward the true optimum are not guaranteed (Woodward et al., 2009).

Further research (Woodward et al., 2009) has revealed a way to compensate the difference in the curves that represent the steady-state relationship between the input and the objective function. It uses translation in both the input direction and direction of the objective function so as to evaluate correctly the gradient and converge toward the true optimum.

The key advantage of multi-unit optimization technique is that a reliable gradient is available during the transient, and one need not have to wait for the steady state. This advantage arises from the fact that if the process dynamics are the same, the difference of the objective functions is rendered insensitive to the process dynamics. However, if the processes' dynamics are different, even if the static curves are identical, the gradient would be falsified. The stability and convergence to the true optimum are a priori not assured.

In this paper, the case of non-identical dynamics is considered. It is however assumed that the static curves are the same. Such a case occurs when the optimization objective is only a function of the system output whose dynamics is controlled by a controller with integrator. Results from

stability analysis and the equilibrium point are presented. It is shown that the difference in dynamics does not change the equilibrium point but it indeed affects stability and the way it converges. The theoretical results are experimentally verified and the data are also presented in this paper.

This paper also analyses the possibility of replacing a physical unit by a mathematical model. This way, the multi-unit optimization runs with one physical system and one mathematical model. Here, experimental results with a physical dynamic system and a static mathematical model are presented to show that this option is indeed viable.

The rest of this paper is organized as follows. Section 2 of this paper presents briefly the standard multi-unit optimization technique. Section 3 presents the results of the analysis for stability and convergence when the units' dynamic are different. Section 4 presents the methodology and the results for the experimental trials.

2. MULTI-UNIT OPTIMIZATION

2.1 Problem formulation

Mathematically, a standard real time optimization problem is written as follows:

$$\begin{aligned} &\min_{u} \quad J = g(x,u) \\ &\dot{x} = f(x,u) = 0 \end{aligned} \tag{1}$$

J is a twice-differentiable function that is minimized and f represents the dynamics of a stable process. The states of the system are represented by the vector *x* and the inputs by the vector *u*. For the easing of presentation, inequality constraints are ignored.

In order to find the optimal input, it is easier to use the equality constraints to find an expression of x = h(u) and then substitute the same. This transforms the original problem into a unconstrained optimization problem, i.e. min J = p(u). Then, the necessary condition of optimality is then given by:

$$\partial p/\partial u \,|_{u^*} = 0 \tag{2}$$

If it is assumed that the unconstrained optimization problem is convex, then the necessary condition indeed leads to the only minimum. Equation (2) is used in extremum-seeking methods to find the optimal point by gradient control.

2.2 Multi-unit optimization scheme

A schematic representation of a simplified version of the multi-unit optimization framework is shown in Fig. 1 (Srinivasan, 2007). The term "unit" is used to represent a real continuous chemical process, and here they are labeled "0" and "1". A difference of Δ between the inputs "u_0" and "u_1" is necessary to estimate the gradient by a first order finite difference equation $\partial J/\partial u = (J_1 - J_0)/\Delta$. Then, the method uses an integral controller with an appropriate value of gain to push the gradient towards 0. The gain K can be tuned to as a compromise between convergence speed and stability.

$$\dot{u}_0 = \dot{u}_1 = \frac{K}{\Delta}\left(J_1 - J_0\right) \tag{3a}$$

$$u_0 = u - \frac{\Delta}{2} \text{ and } u_1 = u + \frac{\Delta}{2} \tag{3b}$$

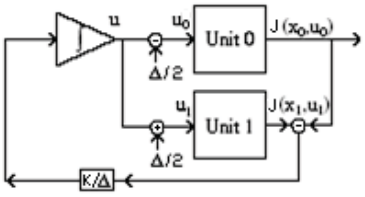

Fig. 1. Standard multi-unit optimization control loop.

In the case of multi-unit optimization, it is necessary to precise the dynamics of each of the units. The two units can be written mathematically as follows:

$$\begin{aligned} \dot{x}_0 &= f_0(x_0,u_0) \\ \dot{x}_1 &= f_1(x_1,u_1) \\ J_0 &= g_0(x_0,u_0) \\ J_1 &= g_1(x_1,u_1) \end{aligned} \tag{4}$$

The steady state for each unit can be described by:

$$\begin{aligned} x_0 &= h_0(u_0) \\ x_1 &= h_1(u_1) \end{aligned} \tag{5}$$

And the objective functions of each of the units at steady-state given by:

$$\begin{aligned} J_0 &= g_0(h_0(u_0),u_0) = p_0(u_0) \\ J_1 &= g_1(h_1(u_1),u_1) = p_1(u_1) \end{aligned} \tag{6}$$

3. MULTI-UNIT OPTIMIZATION WITH DIFFERENT DYNAMICS

In this section, the results of the analyses for stability and convergence are presented for the case when the units' dynamic are different but the static curve for each unit are identical. These analyses are made assuming that the technique is applied without any modification to compensate for the difference in dynamics.

3.1 Analysis for the equilibrium point

Here it is shown that if the scheme is stable, the system will converge toward the true optimum as long as the static curves between the units are identical. The difference between the dynamics does not bias the equilibrium point.

Theorem 1: If (i) the scheme converges, (ii) the static curves of the two units are identical, then despite the difference in the dynamics, the steady state of the multi-units optimization control loop represents the real optimum as Δ tends to zero.

Proof: From (3a), it can be seen that at steady state:

$$\dot{u}_0 = \dot{u}_1 = 0 = \frac{K}{\Delta}\left(J_1 - J_0\right) = \frac{K}{\Delta}\left(p_1(u_1) - p_0(u_0)\right) \tag{7}$$

So, the equilibrium point is determined by:

$$p_0(u_0) = p_1(u_1) \quad (8)$$

As the static curves of two units are considered identical,

$$p_0(u) = p_1(u) = p(u) \quad (9)$$

Let $\bar{u}$ be the value of u at steady state. Then,

$$p\left(\bar{u} + \Delta/2\right) = p\left(\bar{u} - \Delta/2\right) \quad (11)$$

A second order Taylor expansion of the function p is considered:

$$p(\bar{u}) + p'(\bar{u})\frac{\Delta}{2} + p''(\bar{u})\frac{\Delta^2}{4} - p(\bar{u}) + p'(\bar{u})\frac{\Delta}{2} - p''(\bar{u})\frac{\Delta^2}{4} + O(\Delta^3) = 0 \quad (12)$$

$$p'(\bar{u}) = O(\Delta^2) \quad (13)$$

$$\lim_{\Delta \to 0} p'(\bar{u}) = \lim_{\Delta \to 0} O(\Delta^2) = 0 \quad (14)$$

Calculating the limit as Δ tends to zero, it is observed that the derivative becomes zero, indicating that the two units arrive at optimal point. ■

3.2 Analysis for the stability of the scheme.

To analyze the stability of the above scheme, the units are linearized around the current operating point. The transfer function representation is used and normalized transfer function that has a unit steady state gain is derived. Then, the characteristic equation of the loop is obtained and analyzed if the roots of this equation are in the left half of the complex plane.

Theorem 2: If an integral controller with gain K can stabilize the average of the two normalized dynamics, then for a small enough value of Δ, the scheme is locally asymptotically stable around the optimum.

Proof: In order to analyze locally the stability, it is necessary to linearize the dynamics of both units. With the linearization, it is possible to represent directly the relationship between u and J by a transfer function T(s). It is useful to rewrite T(s) as a combination of a dynamic term with a static gain of 1, labeled as N(s), and a static term which represents the steady state gain:

$$T_0(s) = N_0(s)p'(u_0) \text{ and } T_1(s) = N_1(s)p'(u_1) \quad (15)$$

Note that the static gain of the different units is given by the gradient (linearization) of the static curve p(u) at their respective operating points. The above decomposition separates the static behavior of the units from its dynamics. The condition on the characteristic equation for this loop to be stable is given by:

$$Z = 1 + \frac{K}{s\Delta}\left(T_1(s) - T_0(s)\right) = 0 \quad (16)$$

Considering a Taylor expansion approximation of p gives:

$$p'(u_0) = b - \frac{\Delta}{2}M \text{ and } p'(u_1) = b + \frac{\Delta}{2}M \quad (17)$$

where b = p'(u) and M = p''(u). Distributing and rearranging the terms in (16), one gets,

$$s + \frac{KM}{2}\left(N_1 + N_0\right) + \frac{Kb}{\Delta}\left(N_1 - N_0\right) = 0 \quad (18)$$

At the equilibrium point (which has been shown to be the optimum in Theorem 1), as Δ tends to zero, (b/Δ) goes to zero. Then, the third term of the characteristic equation disappears. So, around the optimum, the stability is no more influenced by the value of Δ, nor by the error in the dynamics. The stability of the system around the optimum is then determined by whether or not the integral controller with the given gain stabilizes the average dynamics. ■

Note that the difference in the dynamics would not affect the stability around the optimum. However, the difference in dynamics can affect the characteristic equation considerably when the system is far from the optimum. The characteristic equation (18) is a rich source of information from which two conclusions can be drawn:

Effect of gain K: The value of the gain is crucial to stability in all cases. If the normalized average dynamics is stable and minimum phase, then for small values of gain, the overall scheme would be stable. Moreover, if the value of K is small, it can be seen from (18) that the influence of the difference in dynamics is negligible. In other words, with a small gain, the inputs variations are slow compared to the dynamics, and the two units operate at their respective pseudo-steady states.

Evolution far from the optimum: When the starting point is far from optimum ("b" is not zero), it can be seen from (18) that the dynamic behavior is influenced by the sign of the ratio (b/Δ), rather than the sign of the individual components.

Without loss of generality, suppose unit 0 is faster than unit 1. A negative Δ and a negative b mean that the faster unit is closer to the optimum. The same situation occurs for a positive Δ and a positive b. These two cases would have similar adaptation characteristics, and are shown in Figure 3 with the red dot representing the faster unit 0 and the green representing the slower unit 1.

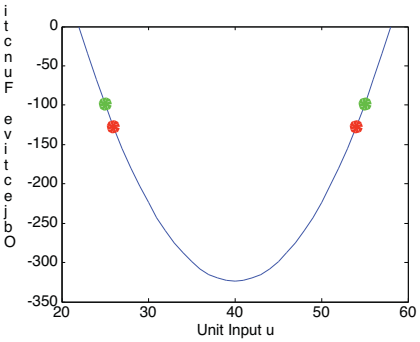

Fig. 3. Analysis of configurations with respect to dynamic behavior. Red faster than green leads to oscillations. Green faster than red leads to slow convergence.

In this configuration, since the system with a rapid dynamics is closer to the optimum, the difference between the outputs will be larger during the transients (for the same change in u). This will overestimate the gradient which, in the best case, will cause the system to converge with oscillations.

A negative Δ and positive b means that the slower unit is closer to the optimum. The same situation occurs for a positive Δ and a negative b. These two cases would have

similar dynamics, and are shown in Figure 3 with the green dot representing the faster unit 0 and the red representing the slower unit 1.

In this configuration, since the system with a slower dynamics is closer to the optimum, the difference between the outputs will be smaller during the transients (for the same change in u). This will underestimate the gradient which will cause the system to converge slowly.

The interesting point is that even if there is an overestimation of the gradient (faster unit closer to the optimum), the system would not in general become unstable. This is due to the fact that once both the units overshoot the optimum, the situation is reversed, i.e., the slower unit is closed to the optimum. So, an under estimation of the gradient occurs, where the return back would be slow and sure.

4. EXPERIMENTAL RESULTS

4.1 Problem Formulation

In order to prove the theoretical results shown in the previous section, an experimental setup has been designed. The setup is composed of two tanks (units) whose temperature is controlled in order to minimize the criterion mentioned below.

$$\min_{F_c} \quad J = (T_{out} - T_c)(T_{out} - T_h)$$
$$\dot{T}_{out} = \frac{F_h}{V}(T_h - T_{out}) + \frac{F_c}{V}(T_c - T_{out}) = 0 \tag{19}$$

Each unit is supplied with water by two pumps: a hot water pump and cold water pump. Hot water at temperature T_h and cold water at temperature T_c are added to these tanks with flow rates F_h and F_c respectively. The hot water pump is fixed with two heads in order to feed the same flow for both units. However, each unit has its own cold water pump (F_{c0} and F_{c1} being the decision variable). The temperatures in the units T_{out0} and T_{out1}, in the hot water tank and in the cold water tank are measured using thermistors. V is the volume of each of the units. The answer to this problem is:

$$T_{out} = \frac{T_h + T_c}{2}; \quad F_c = F_h \tag{20}$$

Also, in order to control the dynamics of each unit independently, cascade control has been implemented. Essentially, the multi-unit scheme sends a temperature set point u to each temperature control loop, which is controlled using a PI controller. This way that the static curves are identical (steady state error is zero). However, by tuning the temperature controllers differently, the two units will have different dynamics.

4.2 Experiments conditions tested

Four experiments are performed for all cases. In Experiment 1, the system is initialized to a value higher than the optimum with a positive value of Δ. Experiment 2 starts with an initial condition that is less than the optimum. Experiment 3 and Experiment 4 start from the initial conditions of Experiment 1 and 2 respectively, but with negative Δ.

It is always arranged that Unit 1 is slower than Unit 0. So, in Experiments 1 and 4, the optimum is closer to the faster unit, while the optimum is closer to the slower unit in the other two experiments. Experiments 1 and 4 show a configuration that overestimates the gradient, while experiments 2 and 3 present a configuration that underestimates the gradient. The gain K is the same for all experiment and is chosen so that the scheme is always stable.

Exp.	Start Temp	Temp Unit 0 (fast)	Temp Unit 1 (slow)
1	47 C	+1 C	-1 C
2	33 C	+1 C	-1 C
3	47 C	-1 C	+1 C
4	33 C	-1 C	+1 C

Table 1: Experimental plan for all experiments

4.3 Experiments with two real units.

In this set of experiments, the controller of "unit 1" has been tuned so that the internal loop (dynamics between the temperature output and temperature set point) is two times slower than its counterpart "unit 0". The results are presented in Figures 5-8.

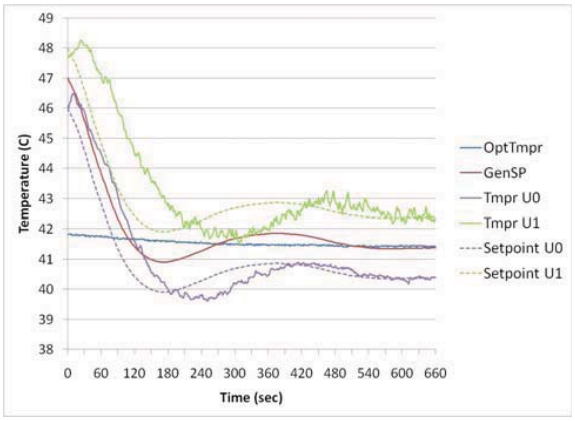

Fig. 5. Evolution for Experiment 1 with real units.

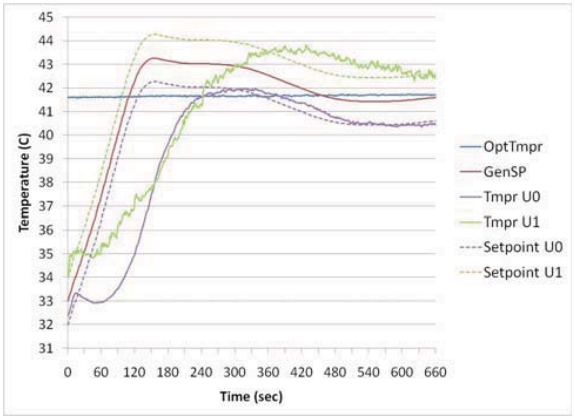

Fig. 6. Evolution for Experiment 2 with real units.

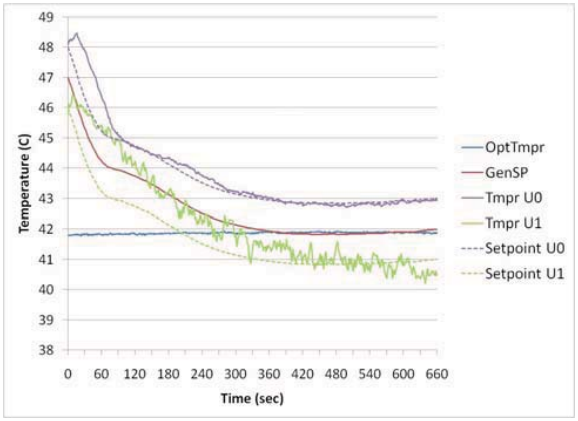

Fig. 7. Evolution of the system for Exp. 3 with real units.

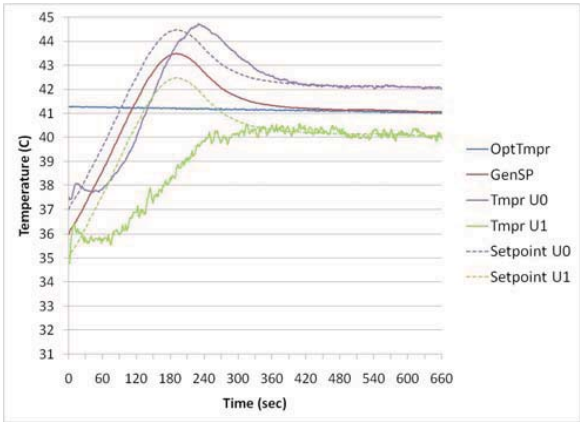

Fig. 8. Evolution of the system for Exp. 4 with real units.

The influence of the sign of Δ can be seen by comparing Fig 5 (Exp1) and Fig 7 (Exp3). The positive value of Δ brings the faster unit closer to the optimum in Exp1 and farther from the optimum in Exp3. Note that in both these experiments, there is a larger difference between the set point and the measured temperature in Unit 1 compared to that of Unit 0. The effect of the transients is more marked when the system is far from the optimum where the set point changes rapidly.

In the case of Exp 1, because of the difference in speed of the respective responses, the gradient is overestimated. This causes the scheme to converge with oscillations. On the contrary, in the case of Exp 3, the gradient is underestimated due the above mentioned speed difference. This underestimation causes the scheme to converge slowly but surely.

The above conclusion can be generalized for the ratio (b/Δ). Comparing Fig 5 (Exp1) and Fig 8 (Exp4), it can be seen that in both these experiments, the faster unit is closer to the optimum ($b/\Delta > 0$). The gradient is overestimated, resulting in an oscillatory response toward the optimum. In contrast, Fig 6 (Exp2) and Fig 7 (Exp3) show slower convergence since the faster unit is farther from the optimum ($b/\Delta < 0$).

Comparing Exp 1 and Exp3, it can be noted that the response for Exp3 is not as smooth as expected. Taking into account that a linear controller was used to control a nonlinear system, such a behavior is expected, The controller parameters are clearly not tuned for all points of operation. The controller settings used favored higher temperatures as can be seen from Figure 3.

4.3 Experiments with a real unit and a virtual unit

The purpose of next series of tests is to check the viability of replacing one of the real units by a mathematical model. This removes one of the major constraints of the scheme, i.e., the availability of two physical identical units in operation. There are two kinds of model that one can use: (i) a first principles/black box dynamic model (ii) a black box static model. Though the dynamic models were tested experimentally, the more interesting and extreme case, i.e., the use of the static model, is presented here.

In this set of experiments, “unit 0” is a static mathematical model whose dynamics is by definition instantaneous and so faster compared to the real unit (unit 1). In practice, it is done by setting the output equal to the set point of the control loop.

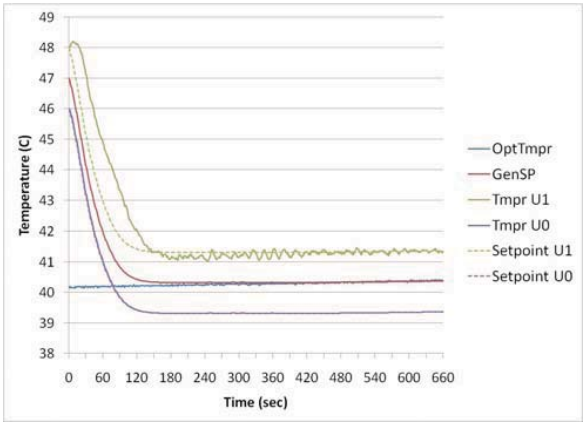

Fig. 9. Evolution for Exp. 1v with real and virtual units.

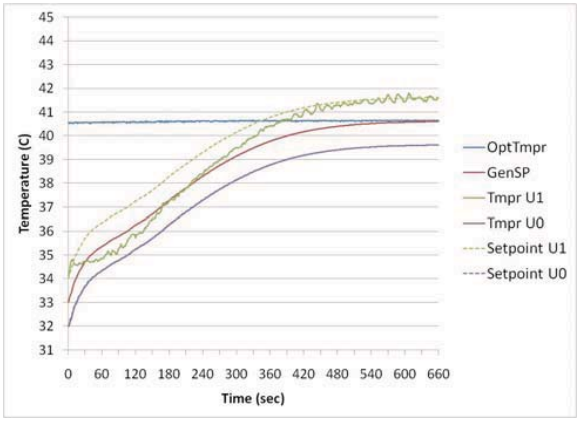

Fig. 10. Evolution for Exp. 2v with real and virtual units.

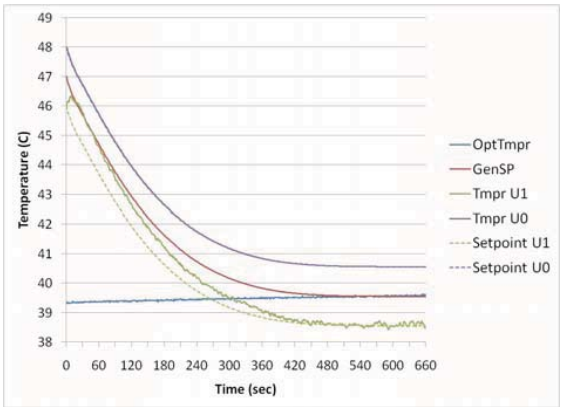

Fig. 11. Evolution for Exp. 3v with real and virtual units.

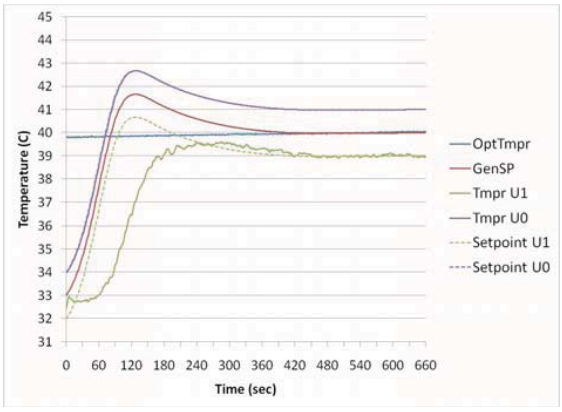

Fig. 12. Evolution for Exp. 4v with real and virtual units.

The results obtained using a system with a real unit and a virtual unit are similar to those obtained with two real units under the same testing conditions. The conditions on stability and convergence remain the same for this series of experiments. Indeed, the comparison of Fig 9 (Exp1v) and Fig 11 (Exp3v) yields the same general conclusion as the comparison of Exp1 and Exp3. It is also true for the comparison of Fig 9 (Exp1v) and Fig 12 (Exp4v) with Exp1 and Exp4 and the comparison of Fig 10 (Exp2v) and Fig 11 (Exp3v) with Exp2 and Exp3. However, for the last comparison, it is easier now to see that the smaller difference between the unit temperatures results in an underestimation of the gradient, thereby leading to slow convergence.

Note that while replacing the real unit by a model, it was assumed that the static characteristics are matched. The only difference between the real and virtual units is at the dynamics level. In this particular example, since the objective function is only dependant on the unit temperature, this assumption of matching the static behavior is easily verified. However, if the objective function is a function of both the output and input (T_{out} and F_c) of the dynamic part, it then becomes mandatory to have a good model of the physical system in order to match the static characteristics.

The conclusion here is that if the static characteristics are matched, then multi-unit optimization can be performed even when the dynamics are not necessarily identical. In extension, a real unit can be replaced by a virtual static model, which has the same static characteristics as the real unit. However, in order to converge to the true optimum, where the static characteristics are different, parameter adaptations are indeed necessary so as to compensate for these differences. In short, the differences in the dynamics can be tolerated, while differences in the static behavior needs to be quantified and compensated.

5. CONCLUSIONS

In this paper, it is shown that it possible to use the multi-unit scheme with differences in dynamics without affect its performance considerably. If the static curves are the same, the equilibrium point and the stability around the optimum are not affected. However, far from the optimum, the choice of the offset plays an important role; it can either make the system converge slowly or make it oscillatory.

Experimentally, it is shown that replacing a real dynamic unit by a simple static mathematical model is indeed viable. This means that the major constraint of having real multiple identical units can be circumvented. A good, not necessarily perfect, approximation of the process is sufficient to this effect.

REFERENCES

Srinivasan B. (2007). Real-time optimization of dynamic systems using multiple units. International Journal of Robust and Nonlinear Control 17, 1183–1193.

Woodward L., Perrier M., Srinivasan B. (2009). Convergence of Multi-Unit optimization with non-identical units: Application to the optimization of a Bioreactor. Journal of Process control, 19(2), 205-215.

Reney F. (2008). Étude de la technique d'optimisation multi-unités avec dynamiques différentes. Master's thesis at École Polytechnique de Montréal.

Guay M, Dochain D, Perrier M. (2004). Adaptive extremum seeking control of continuous stirred tank bioreactors with unknown growth kinetics. Automatica, 40 (5), 881–888

Ariyur K, Kristic M. (2003). Real-time Optimization by Extremum-Seeking Control, John Wiley and Sons.

Marlin T, Hrymak A. (1997). Real-time operations optimization of continuous processes. Vol. 316 of AIChE Symposium Series, p. 156.

A Model-Free Methodology for the Optimization of Batch Processes: Design of Dynamic Experiments

Christos Georgakis*

**Department of Chemical and Biological Engineering and Systems Research Institute*
Tufts University, Medford MA 02155, USA
(Tel: +1-617-627-2573; e-mail: Christos.Georgakis@Tufts.edu).

Abstract: The new methodology presented provides a way to optimize the operation of a variety of batch processes (chemical, pharmaceutical, food processing, etc.) especially when at least one time-varying operating decision function needs to be selected. This methodology calculates the optimal operation without the use of an *a priori* model that describes in some accuracy the internal process characteristics. The approach generalizes the classical and widely used Design of Experiments (DoE), which is limited in its consideration of decision variables that are constant with time. The new approach, called the Design of Dynamic Experiments (DoDE), systematically designs experiments that explore a considerable number of dynamic signatures in the time variation of the unknown decision function(s). Constrained optimization of the interpolated response surface model, calculated from the performance of the experiments, leads to the selection of the optimal operating conditions. Two examples demonstrate the powerful utility of the method. The first examines a simple reversible reaction in a batch reactor, where the time-dependant reactor temperature is the decision function. The second example examines the optimization of a penicillin fermentation process, where the feeding profile of the substrate is the decision variable. In both cases, a finite number of experiments (4 or 16, respectively) lead to the very quick and efficient optimization of the process.

Keywords: Batch Optimization, Design of Experiments, Batch Reactors, Fermentation, Penicillin Production, Batch Modeling.

1. INTRODUCTION

Batch processes are often related to small production rates resulting in processes that are not understood enough to enable the development of an accurate mathematical model describing their inner workings. To accommodate such a lack of detailed understanding, our research group introduced the concept of Tendency Modelling (Fotopoulos, Georgakis, & Stenger, 1996, 1998) which has been applied to several processes with significant success. See for example (Cabassud et al., 2005; Martinez, 2005). On the other hand, François et al. (François, Srinivasan, & Bonvin, 2005) have also introduced a methodology in which the feedback control concept is used to evolve from an initial batch operation to operations that are incrementally better and, after several cycles, arrive at an optimum operation. In the case that a model is available, several model-based optimization techniques can be utilized (Biegler, 2007). We will refer to this model-based approach as the *Classical Approach*.

2. THE CLASSICAL MODEL-BASED APPROACH

The classical approach in optimizing a batch process assumes we have a first-principles model describing our fundamental understanding of the process. Assuming that all important idiosyncrasies of the process are known to make the model quite comprehensive and accurate, one needs only to account for the model's parameters whose values are not well known. Based on the number of unknown parameters, a set of experiments is designed using the classical Design of Experiments (DoE) approach (Box & Draper, 2007; Montgomery, 2005), or any other systematic or not so systematic approach. Once the experimental data are collected, the model parameters can be calculated using a parameter estimation method and related algorithms (van den Bos, 2007). Such a model will often have the form of a set of nonlinear ordinary differential equations (ODEs), as in eq. 1.

$$\frac{d\mathbf{x}}{dt} = \mathbf{f}(\mathbf{x},\mathbf{p},\mathbf{u},t), \quad \mathbf{y}(t) = \mathbf{g}(\mathbf{x}); \quad \text{with } \mathbf{x}(0)=\mathbf{x}_0 \quad \text{and} \quad \mathbf{u}_{\min} \le \mathbf{u}(t) \le \mathbf{u}_{\max} \tag{1}$$

Here, **x** and **y** represent the states and output variables of the system, respectively; **p** the parameters of the model fitted to the experiments; and **u**(t) the decision variable with which we wish to maximize (or minimize) the system's performance index *J*. The performance index is assumed to be only a function of the final values of the state variable at the end of the batch at $t=t_B$:

$$J^* = \max_{\mathbf{u}(t)} J(\mathbf{x}(t_B)) \tag{2}$$

With such a model at hand, one can calculate the optimum value of the decision variable **u**(t) that will yield the optimum value J^* of the performance index *J*. There are

several ways such a calculation can be performed, but here we will follow the method strongly advocated by Professor Biegler's group (Biegler, 2007; Kameswaran & Biegler, 2006, 2008). In such an approach, the interval (0, t_B) is divided into a number of finite elements and inside each element, the method of orthogonal collocations (Biegler, 1984) is used to convert the set of ODEs into a set of algebraic equations. Then, an optimization algorithm, such as sequential quadratic programming, calculates the optimum.

In summary, the Classical Model-based Optimization (CMO) approach involves the following steps: i) Postulation of model, ii) Experiments, iii) Parameter Estimation, and iv) Optimization.

3. THE NEW APPROACH: DESIGN OF DYNAMIC EXPERIMENTS

3.1. The Main Idea

To facilitate the discussion that follows, let us define a dimensionless time τ equal to t/t_B. The decision variable $\mathbf{u}(\tau)$ is considered to be a member of the Hilbert space $\mathcal{L}_2(0,1)$ of square-integrable vector functions. Let us denote with $\{\varphi_i(\tau); i = 1, 2, 3, \ldots\}$ a convenient set of basis-functions in that space. The unknown function $\mathbf{u}(\tau)$ can be written as follows.

$$\mathbf{u}(\tau) = \mathbf{u}_0 + \Delta\mathbf{U}\left(\sum_{i=1}^{\infty}\mathbf{a}_i\phi_i(\tau)\right) \simeq \mathbf{u}_0 + \Delta\mathbf{U}\left(\sum_{i=1}^{N}\mathbf{a}_i\phi_i(\tau)\right)$$
$$\mathbf{u}_0 = (\mathbf{u}^{\max} + \mathbf{u}^{\min})/2, \quad \Delta\mathbf{U} = diag\left((u_i^{\max} - u_i^{\min})/2\right) \tag{3}$$

The summation is truncated to a finite number of *N* terms and the unknowns are the expansion coefficients $\mathbf{a}_i$. If we now expand the performance index $J(\mathbf{x}(\tau=1))$ in terms of the $\mathbf{a}_i$ constants, of the $\mathbf{u}(\tau)$ function can be written as:

$$J(u) = b_0 + \sum_{i=1}^{N} b_i a_i + \sum_{j=i}^{N}\sum_{i=1}^{N} b_{ij} a_i a_j + \sum_{k=j}^{N}\sum_{j=i}^{N}\sum_{i=1}^{N} b_{ijk} a_i a_j a_k + \ldots \tag{4}$$

This will be called the Response Surface Model (RSM). For simplicity's sake, we have assumed in eq. (4) that there is only one decision function u(τ) and that each of the a_i constants is a scalar rather than a vector. The main model parameters are now the constants b_i, b_{ij}, b_{ijk} etc., relating the performance index *J* and the different choices of the decision variable u(τ). In the rare case that the knowledge-based process model is known *a priori*, the constants *b* can be explicitly calculated. Once the *b* constants are known, an optimization can be performed to calculate the optimal values of the parameters a_i (i=1, 2…n) that describe the estimate of the unknown optimal profile $u^*(\tau)$. *Of interest here is the circumstance in which* ***no model*** *for the batch process is available a priori.* In such a case, the novel approach introduced by the present paper consists of the following five steps:

a. Select a functional basis $\varphi_i(\tau)$ to parameterize the input function u(τ).
b. Design a set of time-varied experiments characterized by a properly selected set of constants a_i.
c. Perform the experiments.
d. Estimate the values of the *b* parameters in the RSM (eq. 4), using the values of *J* that correspond to each of the performed experiments.
e. Calculate the values of a_i that optimize *J*. Perform the optimal experiment and compare the results with the response surface model predictions.

The proposed approach is called Model-Free for two reasons. First, the RSM is a rather simple easy-to-develop interpolative model that contains no fundamental information about the process. Second, the process can be still substantially optimized my simply choosing the best of the initial dynamic experiments.

3.2. The Algorithmic Steps

We provide here some additional details of the four steps described before.

1. Define a dimensionless variable $w(\tau)$, referred as coded variable, that varies between -1 and +1 and which characterizes the time dependent process variable, or dynamic factor. For example, if the dynamic factor is the reactor temperature and it is allowed to vary between T_{max} and T_{min}, then the coded variable w(τ) is defined by:

$$w(\tau) = [2T(\tau) - (T_{\max} + T_{\min})]/(T_{\max} - T_{\min}) \tag{5}$$

   In the case that we have more than one decision variable u(τ), we define the coded variable by

$$\mathbf{w}(\tau) = \Delta\mathbf{U}^{-1}\left(\mathbf{u}(\tau) - \mathbf{u}_0\right) \tag{6}$$

2. Select an appropriate functional basis $\{\varphi_i(\tau)|\ i=1, 2,\ldots\}$ defined in the interval [0, 1]. These functions must be a linearly independent set that is complete and thus can serve as a functional basis. This functional basis could be either an orthogonal or a non-orthogonal one. The selection of this basis should be influenced by the expected character of the problem's solution in order to reduce the number of needed expansion terms and thus the number of experiments.

3. The unknown value of the dynamic factors $\mathbf{u}(\tau)$ that maximizes a certain performance index of the process $J(\mathbf{u})$ is denoted by, $\mathbf{u}^*(\tau)$:

$$J(\mathbf{u}^*) = \max_{\mathbf{u}(\tau)} J(\mathbf{u}) \tag{7}$$

   The unknown vector function $\mathbf{u}^*(\tau)$ is expanded in terms of a linear combination of the basis functions $\varphi_i(\tau)$, given in eq. (3).

4. Substitute the optimization with respect to $\mathbf{u}(\tau)$ with an optimization with respect to the constants $\boldsymbol{a}_i$. For each component function $u_q(\tau)$ of $\mathbf{u}(t)$, the corresponding constants $a^q{}_i$ are called the sub-factors that characterize the unknown dynamic factor $u_q(\tau)$. The infinitely dimensional search for the optimal function $\mathbf{u}^*(\tau)$ is then substituted by a finite dimensional search of the *pN* constants *a*, where *p* is the dimensionality of $\mathbf{u}(\tau)$.

5. Design experiments motivated by the classical Design of Experiments (DoE) methodology for the selection of the appropriate values of the sub-factors a^q_i. Each set of values of the sub-factors correspond to a specific time-dependent function $u_j(\tau)$ or $w_j(\tau)$. However, one needs to take into account certain constraints that $u_j(\tau)$ or $w_j(\tau)$ will have to satisfy.
6. Develop an appropriate interpolating response surface model relating J to the values of the a^q_i in the form of eq. (4). The unknown parameters of the model are the coefficients b_j, b_{ij}, b_{ijk} etc. and a linear regression algorithm can be used for their estimation. An analysis of variance (ANOVA) is performed to reveal which of the terms are the most significant based on the accuracy of the experimental measurements.
7. Calculate the optimal values of the a^{q*}_i coefficients that optimize J. This is a constrained optimization task since each of the coefficients a_i is constrained by an upper and lower value (usually $-1 \le a_i \le +1$). The optimal values of the a_j determine the optimal function $u(\tau)$.

The methodology described above substitutes the unknown function $u(\tau)$ by its coefficients a_i. By selecting the appropriate values of the a_i, one designs dynamic experiments with several choices of the input function $u(\tau)$. Each of the experiments results in a value of the performance index J. The set of such values enables the calculation of the response surface model (RSM) of equation (4), which is used to optimize the process with respect to the decision variable(s) $u(\tau)$. The proposed methodology generalizes the classical design of experiments (DoE) (Montgomery, 2005) methodology with respect to dynamically varying processes. For this reason, the term Design of Dynamic Experiments (DoDE) was coined to describe it (Georgakis, 2008).

4. DESIGN OF THE DYNAMIC EXPERIMENTS

Here we present some example designs of the DoDE experiments. We select the (shifted) Legendre polynomial as the basis in the Hilbert space $\mathcal{L}_2(0,1)$. The first three Legendre polynomials are

$$\phi_1(\tau) = P_0(\tau) = 1, \quad \phi_2(\tau) = P_1(\tau) = 1 - 2\tau, \\ \phi_3(\tau) = P_2(\tau) = 1 - 6\tau + 6\tau^2, \ \ldots \tag{8}$$

We will use these orthogonal polynomials to define the dynamic experiments in all the examples discussed here.

4.1. Simple Example of the DoDE Design Approach

The simplest set of DoDE experiments is obtained by selecting the smallest value of N in eq. (3), equal to two. This implies that the dynamic profile of $u(\tau)$, or the coded variable $w(\tau)$, is a linear combination of the first two Legendre polynomials $P_0(\tau)$ and $P_1(\tau)$. This limits our consideration among constant or linear time dependencies. In deciding the values of the a_1 and a_2 sub-factors we can follow the classical DoE approach. If we do level-2 experiments for each sub-factor, we will design the following 2^2=4 experiments:

$$\begin{pmatrix} a_1 \\ a_2 \end{pmatrix} = \left[\begin{pmatrix} +1 \\ +1 \end{pmatrix}, \begin{pmatrix} +1 \\ -1 \end{pmatrix}, \begin{pmatrix} -1 \\ +1 \end{pmatrix}, \begin{pmatrix} -1 \\ -1 \end{pmatrix} \right] \tag{9}$$

Translating, for example, the second experiment to the corresponding dynamic coded variable $w(\tau)$ we have $w(\tau) = P_0(\tau) - P_1(\tau) = 2\tau$. We realize that this profile does not meet its constraints $-1 \le w(\tau) \le +1$. This is easily remedied by imposing the following constraints on the a_1 and a_2 constants: $-1 \le a_1 + a_2 \le +1$ and $-1 \le a_1 - a_2 \le +1$ reducing the values of a_1 and a_2, without changing their relative magnitude so the that the constraints on $w(\tau)$ are met. This leads to the following design of experiments

$$\begin{pmatrix} a_1 \\ a_2 \end{pmatrix} = \left[\begin{pmatrix} +0.5 \\ +0.5 \end{pmatrix}, \begin{pmatrix} +0.5 \\ -0.5 \end{pmatrix}, \begin{pmatrix} -0.5 \\ +0.5 \end{pmatrix}, \begin{pmatrix} -0.5 \\ -0.5 \end{pmatrix} \right] \tag{10}$$

In this case, the four time-variations in $w(\tau)$ are shown in Figure 1.

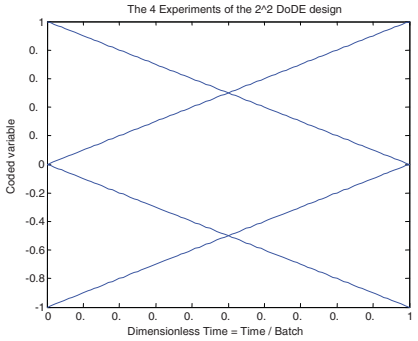

***Figure 1**: The 2^2=4 DoDE experiments*

4.2. Other DoDE Examples

For N=3, we are considering the first three Legendre polynomials, and if we consider only low and high values, we need to perform 2^3= 8 experiments. Here we are considering quadratic dependence on time along with the constant and linear sub-factors considered before. If we add cubic dependence by letting N=4 we need 2^4= 16 experiments and the use of the next Legendre polynomial: $P_3(\tau) = -20\tau^3 + 30\tau^2 - 12\tau + 1$. For N=5 we involve the first five shifted Legendre polynomials. This includes the four polynomials mentioned above along with the fifth one: $P_4(\tau) = 70\tau^4 - 140\tau^3 + 90\tau^2 - 20\tau + 1$. Here we need 2^5= 32 experiments. In the case we design level-3 full factorial experiments we need 3^2= 9 experiments for N=2, and 3^3= 27 experiments for N=3.

We should note that the way the dynamic experiments are designed involves two steps that are similar to the ones presented in section 4.1 for the simplest of the DoDE designs. In the first step, the sub-factors related to the values of the coefficients a_i are treated as independent from each other and are assigned initial values of (-1 , +1) in the level 2 designs and values (-1, 0, +1) in the lever 3 designs. In the second

Table 1: *Details of the Batch Reactor Optimization using the DoDE Methodology*

Dynamic Sub-factors	Levels	Case Number and Number of Experiments	Best Conversion from Initial 2^n or 3^n Experiments	Best Profile from the Initial 2^n or 3^n Experiments: $T(\tau)=308+15u(\tau)$ ^oK with $u(\tau)=a_1P_0+a_2P_1+a_3P_3+\ldots$	RSM-Optimum Conversion of A	Defining Parameters of the Calculated RSM-Optimum Profile $w(\tau)$
Level 2 FULL Factorial Designs						
1	2	DA1:2^1= 2	62.32%	a_1 = -1	62.23%	a_1 = -1
2	2	DA2 : 2^2= 4	73.46%	(a_1, a_2) = (-0.5, 0.5)	76.57%	(a_1, a_2) = (0, 1)
3	2	DA3: 2^3= 8	74.61%	(a_1, a_2, a_3) = (-0.3, 0.3, -0.3)	77.77%	(a_1, a_2, a_3) = (0, 1, 0)
4	2	DA4: 2^4=16	74.82%	(a_1, a_2, a_3, a_4) = (-0.3, 0.3, -0.3, 0.3)	78.10%	(a_1, a_2, a_3, a_4) = (0, 1, 0,- 0.04)
5	2	DA5: 2^5=32	74.43%	(a_1, a_2, a_3, a_4, a_5) = (-0.3, 0.3, -0.3, 0.3, .3)	78.43%	(a_1, a_2, a_3, a_4, a_5) = (0, 0.9, 0,- 0.08, -0.2)
Level 3 FULL Factorial Designs						
1	3	DA6 3^1= 3	73.91%	a_1 = 0	73.92%	a_1 = -0.03
2	3	DA7 3^2= 9	77.35%	(a_1, a_2) = (0, 1)	77.57%	(a_1, a_2) = (0.1, 0.9)
3	3	DA8 3^3=27	77.35%	(a_1, a_2, a_3) = (0, 1, 0)	77.66%	(a_1, a_2, a_3) = (0.05, 0.9, 0.06)

step, all of the a_i values related to a single experiment are scaled up or, in most cases, down by a common factor, so that the coded dynamic variable w(τ) attains values that are inside the [-1, +1] interval. Making the maximum (or minimum) of each profile touch the maximum (or minimum) values of $w(\tau)$ also ensures that the set of DoDE experiments covers all areas on the [-1, +1] x [0, 1] rectangle.

5. BATCH REACTOR WITH REVERSIBLE REACTION

Here we consider the optimization of the operation of a batch reactor in which a reversible reaction between reactant A and product B takes place with the following characteristics:

$$A \underset{k_2}{\overset{k_1}{\rightleftarrows}} B; \quad r = k_1C_A - k_2C_B \quad with$$

$$k_1 = k_{10}\exp(-E_1/RT)\ [1/hr]; \quad k_2 = k_{20}\exp(-E_2/RT)\ [1/hr]$$

$$k_{10}=1.32\text{x}10^7; \quad k_{20}=5.24\text{x}10^{13}; \quad E_1=10,000; \quad E_2=20,000$$

We select the activation energy of the reverse reaction to be larger than that for the forward reaction. This leads to the expectation that the optimum temperature profile is a decreasing one (Rippin, 1983). One needs to note here, that for the development of the fundamental model above, we need to *assume* that the first order kinetic rate is correct. We then perform *at least* 4 experiments to estimate the values of k_{10}, k_{20}, E_1, and E_2.

With such a model at hand, one can optimize the reactor temperature profile to maximize the conversion of reactant A. This is achieved by converting the ODEs into algebraic equations via Radau collocation on finite elements (Biegler, 2007). The reactor temperature is constrained between 20 ^{0}C and 50 ^{0}C and the optimization is achieved by use of the IPOPT algorithm (Wächter & Biegler, 2006).

The optimum profile calculated is constant at the upper temperature constraint for almost 0.4 hrs and then decreases to the minimum constraint at the end of the batch. We select here to fix the batch time to 2.5 hrs and the maximum conversion of the reactant A is calculated to be 77.68%. In Table 1, the results of the different DoDE experiments are presented. They involve up to 5 dynamic sub-factors and include level-2 (low-high) and level-3 (low-medium-high) experiments. In the fourth column the best conversion value of the initial runs is given. In the second to last column, the expected best batch performance, as calculated by the optimization of the response surface model (RSM), is given. In the last column the characteristics of this RSM-optimal profile is given in terms of the coded variable: $w(\tau) = a_1P_0(\tau) + a_2P_1(\tau) + \ldots$ The temperature profile can then be calculated by eq. 5. We observe that in the case denoted as DA2 in Table 1 *only* four experiments described in Figure 1 yield an RSM-optimum with a conversion of 76.57% which is just 1.43% away from the true optimum of 77.68%. We also observe that a larger number of experiments, such as those of cases DA4, DA5, DA7 and DA8, predict a higher conversion, even closer to the true optimum. However, as the number of experiments performed increases, the changes in the predicted optimum conversion becomes smaller and smaller per additional experiment, implying that the true optimum has been reached.

6. PENICILLIN FERMENTATION

Here we simulate the penicillin fermentation model of Bajpai and Reuss (Bajpai & Reuss, 1980) which has been the center of attention in several model-based optimizations (Riascos & Pinto, 2004). The model used to simulate the experiment consists of the equations in the Appendix. To focus on the main idea of calculating the optimum *time-varying* profile, we fix the batch time to t_b=130 hrs and the growth phase of the biomass to t_f=30 hrs. Here we want to demonstrate the application of the DoDE approach to this challenging optimization problem to demonstrate its power in optimizing complex processes. For this reason, we are *not* designing experiments that vary the t_f and t_b values, since they are not time-varying decision variables or factors.

We choose to design 16 experiments with $4=2^2$ variations for the substrate flow in growth phase $0\le t\le t_f$ *(or* $0\le\tau\le\gamma$; $\gamma=t_f/t_b$*)*

and $4=2^2$ additional variations for the production phase $t_f \le t \le t_b$ *(or* $\gamma \le \tau \le 1$*)*, the profiles are depicted in Figure 2. In the growth phase, the average value of the substrate flow is 30 gr/hr, with an allowed change up and down of 20 *gr/hr*. In the production phase, the average flow considered is 7 *gr/hr* and it varies by 3 *gr/hr*, up or down. Each of the four feeding profiles in the first phase is combined with each of the four feeding profiles of the second phase.

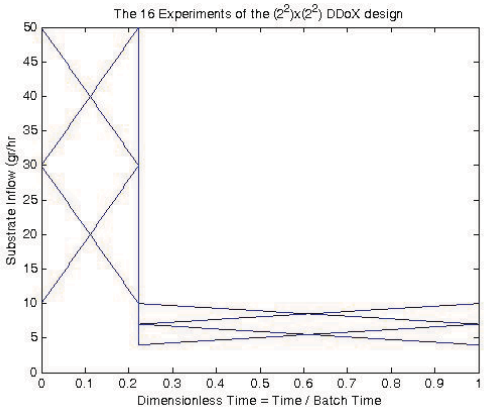

Figure 2: *The $2^2x2^2=14$ DoDE Experiments for Penicillin Fermentation (Total Volume Unconstrained)*

Some of these designs result in an increase in the bioreactor volume by more than 4 lt. from the initial value of 7*lt*. For example, one such profile is the one identified with the following sub-factor coefficients $(a_{11}, a_{12}, a_{21}, a_{22}) = (0.5, 0.5, 0.5, 0.5)$. To meet the final volume constraint of 11*lt*, we impose the following total volume constraint:

$$(u_{1m} + \Delta u_1 * a_{11})t_f + (u_{2m} + \Delta u_2 * a_{21})(t_b - t_f) \le (V_T - V_0)s_f$$

with

$$u_{1m} = 30gr/hr,\ u_{2m} = 7gr/hr,\ \Delta u_1 = 20gr/hr,\ \Delta u_2 = 3gr/hr$$

$$t_b = 130hr,\ t_f = 30hr,\ V_0 = 7lt \text{ and } V_T = 11lt$$

This profile is modified to the (0.44, 0.5, 0.44, 0.5) one (DB16). Three additional profiles need such modification. The resulting time dependencies on the overall feeding profiles are defined in Table 2. The resulting final bioreactor volume and total amount of penicillin produced (i.e. the performance index *J*) are also given in Table 2.

The time evolution of the simulated process during experiments DB9 is given in Figure 3. Using all the data of Table 2, a response surface model is estimated and constrained optimization, $V(t_b)<11$, yields an optimum of the penicillin process with the production of $J=102.30$ grams of product. The calculated optimum feeding profile is characterized by the following values of the 2+2 sub-factor coefficients: $(a_{11}, a_{12}, a_{21}, a_{22}) = (0.19, 0, 0.95, 1.0)$. Simulation of this operation yields 104.17 grams of product, a bit more than predicted.

Here we used a level 2 experimental design which necessitates that the response surface model has only linear and interaction terms. No quadratic terms are allowed. A more accurate response surface model can be constructed if one uses a level 3 DoDE design. In such a case, the response surface model includes quadratic terms.

Table 2: *Definition and Performance Index of the 16 Volume-Constrained Penicillin Experiments*

Run Label	Growth Phase		Production Phase		$V(t_f)$ [lt]	$J=V(t_f)p(t_f)$ [gr]
	a_{11}	a_{12}	a_{21}	a_{22}		
DB1	-0.5	-0.5	-0.5	-0.5	9.3	+58.97
DB2	-0.5	+0.5	-0.5	-0.5	9.3	+59.06
DB3	+0.5	-0.5	-0.5	-0.5	10.5	+57.93
DB4	+0.5	+0.5	-0.5	-0.5	10.5	+57.93
DB5	-0.5	-0.5	-0.5	+0.5	9.3	+54.05
DB6	-0.5	+0.5	-0.5	+0.5	9.3	+54.15
DB7	+0.5	-0.5	-0.5	+0.5	10.5	+51.82
DB8	+0.5	+0.5	-0.5	+0.5	10.5	+51.83
DB9	-0.5	-0.5	+0.5	-0.5	9.9	+84.41
DB10	-0.5	+0.5	+0.5	-0.5	9.9	+84.46
DB11	**+0.44**	**-0.5**	**+0.44**	**-0.5**	**11.0**	**+86.08**
DB12	**+0.44**	**+0.5**	**+0.44**	**-0.5**	**11.0**	**+86.08**
DB13	-0.5	-0.5	+0.5	+0.5	9.9	+81.33
DB14	-0.5	+0.5	+0.5	+0.5	9.9	+81.40
DB15	+0.44	-0.5	+0.44	+0.5	11.0	+80.01
DB16	+0.44	+0.5	+0.44	+0.5	11.0	+80.01

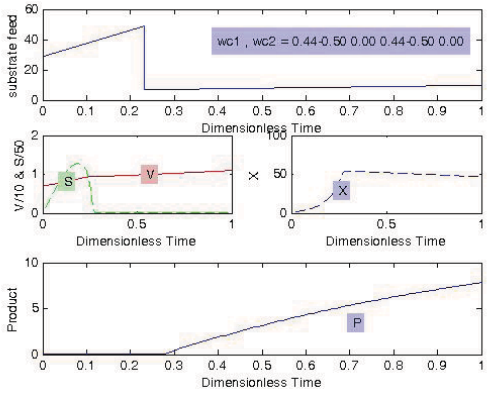

Figure 3: *The time evolution of the state and input variables of the $2^2x2^2=16$ DoDE experiments for penicillin fermentation (total volume constrained)*

We observe that the RSM-optimal run yields a performance index that is 20.82% better than any of the initial 16 experiments. This is very significant but this is not the major result of this investigation. The major result is that the process is significantly optimized with just the 16 initial

systematically designed DoDE experiments. This is a much smaller effort than what is needed to develop a fundamental model describing the process, necessary for the classical approach in process optimization.

7. CONCLUSIONS

We presented a new approach to optimize batch processes with respect to one or more time-varying decision variables. The method, called Design of Dynamic Experiments (DoDE), defines a set of experiments in which time-varying patterns of the decision variable is used. A response surface model, built from the performance index values of each experiment, is used to optimize the process. Two examples, a batch reaction and penicillin fermentation, are used to demonstrate the powerful characteristics of the new methodology. Due to space limitations, we have not presented the related ANOVA analysis. The effect of measurement error (1%-5%) was investigated and it has been convincingly shown that its effect on the process optimization is not at all detrimental to the proposed approach.

8. REFERENCES

Bajpai, R. K., & Reuss, M. (1980). A Mechanistic Model for Penicillin Production. *Journal of Chemical Technology and Biotechnology, 30*(6), 332-344.

Biegler, L. T. (1984). Solution of Dynamic Optimization Problems by Successive Quadratic Programming and Orthogonal Collocation. *Computers & Chemical Engineering, 8*(3-4), 243-247.

Biegler, L. T. (2007). An overview of simultaneous strategies for dynamic optimization. *Chemical Engineering and Processing, 46*(11), 1043-1053.

Box, G. E. P., & Draper, N. R. (2007). *Response Surfaces, Mixtures, and Ridge Analysis*. Hoboken, NJ: Wiley.

Cabassud, M., Cognet, P., Garcia, V., Le Lann, M. V., Casamatta, G., & Rigal, L. (2005). Modeling and optimization of lactic acid synthesis by the alkaline degradation of fructose in a batch reactor. *Chemical Engineering Communications, 192*(6), 758-786.

Fotopoulos, J., Georgakis, C., & Stenger, H. G. (1996, May 05-08). *Effect of process-model mismatch on the optimization of the catalytic epoxidation of oleic acid using tendency models.* Paper presented at the 14th International Symposium on Chemical Reaction Engineering - From Fundamentals to Commercial Plants and Products, Brugge, Belgium.

Fotopoulos, J., Georgakis, C., & Stenger, H. G. (1998). Use of tendency models and their uncertainty in the design of state estimators for batch reactors. *Chemical Engineering and Processing, 37*(6), 545-558.

François, G., Srinivasan, B., & Bonvin, D. (2005). Use of measurements for enforcing the necessary conditions of optimality in the presence of constraints and uncertainty. *Journal of Process Control, 15*(6), 701-712.

Georgakis, C. (2008). Dynamic Design of Experiments for the Modeling and Optimization of Batch Process.

Kameswaran, S., & Biegler, L. T. (2006, Jan 08-13). *Simultaneous dynamic optimization strategies: Recent advances and challenges.* Paper presented at the 7th International Conference on Chemical Process Control (CPC 7), Lake Louise, CANADA.

Kameswaran, S., & Biegler, L. T. (2008). Convergence rates for direct transcription of optimal control problems using collocation at Radau points. *Computational Optimization and Applications, 41*(1), 81-126.

Martinez, E. C. (2005, May 29-Jun 01). *Model discrimination and selection in evolutionary optimization of batch processes with tendency models.* Paper presented at the 15th European Symposium on Computer Aided Process Engineering (ESCAPE-15), Barcelona, SPAIN.

Montgomery, D. C. (2005). *Design and Analysis of Experiments* New York: Wiley.

Riascos, C. A. M., & Pinto, J. M. (2004). Optimal control of bioreactors: a simultaneous approach for complex systems. *Chemical Engineering Journal, 99*(1), 23-34.

Rippin, D. W. T. (1983). Simulation of a Single- and Multiproduct Batch Chemical Plants for Optimal Design and Operation *Computers & Chemical Engineering, 7*(3), 137-156.

van den Bos, A. (2007). *Parameter Estimation for Scientists and Engineers* John Wiley & Sons, Inc. .

Wächter, A., & Biegler, L. T. (2006). On the implementation of an interior-point filter line-search algorithm for large-scale nonlinear programming. *Mathematical Programming 106* (1), 25.

9. ACKNOWLEDGMENTS

The author wishes to acknowledge the assistance of Victor Zavala and Larry Biegler in the selection of the AMPL and IPOPT software environment for calculation of the Model-based Optimum of the first example process. Alex Marvin, a ChBE senior undergraduate student at Tufts University calculated the simulation data used in Table 1.

10. APPENDIX

In this Appendix we present the penicillin model used:

$$x_1 = V: \quad \frac{dV}{dt} = u / s_f$$

$$x_2 = x: \quad \frac{dx}{dt} = \mu x - \frac{x}{s_f V} \qquad \mu = \mu_{\max} \frac{s}{k_x x + s}$$

$$x_3 = s: \quad \frac{ds}{dt} = -\frac{\mu x}{Y_{x/s}} - \rho \frac{x}{Y_{p/s}} - \frac{m_s s}{k_m + s} x + \left(1 - \frac{s}{s_f}\right) \frac{u}{V}$$

$$x_4 = p: \quad \frac{dp}{dt} = \rho x - kd - \frac{p}{s_f V} \mathrm{u} \qquad \rho = \rho \max \left(\frac{s}{k_p + s + s^2 / k_{in}} \right)$$

The model parameters used are the ones reported in (Riascos & Pinto, 2004)

Controller Tuning

Oral Session

An Internal Model Control Approach to Mid-Ranging Control

Sandira Gayadeen*, William Heath*

*Control Systems Centre, School of Electrical and Electronic Engineering, The University of Manchester, PO Box 88, Sackville Street, Manchester M60 1QD UK (e-mail:sandira_vg@hotmail.com, William.Heath@manchester.ac.uk)

Existing tuning rules for mid-ranging control can be improved. In this paper a novel strategy for mid-ranging control based on Internal Model Control (IMC) principles is presented. The design reformulates mid-ranging control specifications in terms of classical bandwidth and sensitivity requirements. The performance of this design is demonstrated through simulation studies. The overall benefits of the IMC design are that it provides transparent and flexible tuning, and that it offers a natural framework for anti-windup. Both classical IMC and modified IMC structures are considered for anti-windup. Their performance during saturation is demonstrated through simulation studies, where minimal degradation is observed.

Keywords: control system analysis, control system design, controller, constraints, saturation

1. INTRODUCTION

The term mid-ranging control typically refers to the class of control problems where two control inputs i.e. actuators are manipulated to control one output. Furthermore there is the condition that one input should return to its midpoint or some setpoint. The inputs usually differ in their dynamic effect on the output and in the relative cost of manipulating each one with the faster input normally being more costly to use than the slower input (Henson et al., 1995). Therefore mid-ranging control schemes seek to manipulate both inputs upon an upset but then gradually reset or mid-range the fast input to its desired setpoint (Allison and Ogawa, 2003).

Mid-ranging control is commonly implemented using the architecture shown in Fig. 1 where u_1 is the fast input and u_2 is the slow input. This structure is referred to as Valve Position Control (VPC) and C_1 is usually chosen as a PI controller and C_2 as an I-only controller. The VPC method for mid-ranging has been found to be sub-optimal (Allison and Isaksson, 1998, Allison and Ogawa, 2003). As such, improvements to the approach of mid-ranging control problems are suggested by many authors. Model predictive control (MPC) has also been suggested by Allison and Isaksson (1998) as an advantageous approach to mid-ranging given that it is inherently a multi-variable control problem. Henson et al. (1995) also propose MPC as well as a Direct Synthesis approach for the design of habituating controllers. The habituating control described by Henson et al. (1995) is essentially a mid-ranging control problem. Allison and Ogawa (2003) put forward a Modified Valve Position Control (MVPC) scheme which combines the simplicity of conventional VPC with the systematic tuning of Direct Synthesis. Allison and Ogawa (2003) compare the performance of MVPC with that of both conventional VPC and Direct Synthesis.

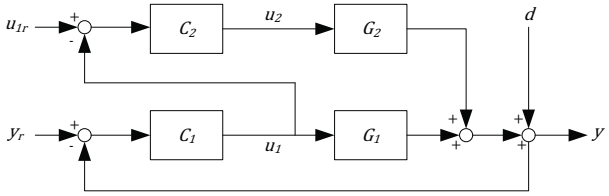

Fig. 1 Block diagram of VPC strategy (Allison and Ogawa, 2003)

For many applications MVPC works fine and has the advantage that it can be implemented using the standard VPC structure in Fig. 1 with PID control blocks. However, MVPC is not optimal; Henson et al. (1995) show that better performance (and implicitly better robustness) can be obtained by using a more general structure which includes both feedforward and feedback elements. This is acknowledged by Allison and Ogawa (2003). The Direct Synthesis design, unlike MVPC, also allows enhanced performance such as decoupling between u_{1_r} and y. MVPC does not achieve this decoupled response though u_1 tracks changes in u_{1_r} correctly.

The mid-ranging design proposed by Henson et al. (1995) uses both feedback and pre-filters. The design criteria are focused on:

- obtaining a desired response from y_r to y
- obtaining a desired response from u_{1_r} to u_1
- obtaining a decoupled response from u_{1_r} to y.

In this paper, a similar general structure is utilised where the decoupling can be achieved through the use of pre-filters.

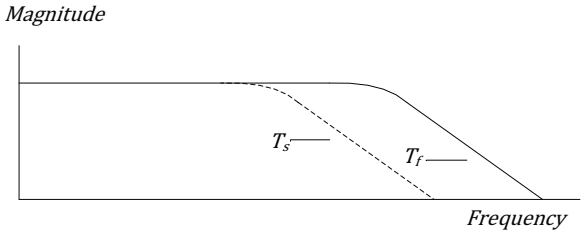

Fig. 2 Desired frequency response of complementary sensitivities

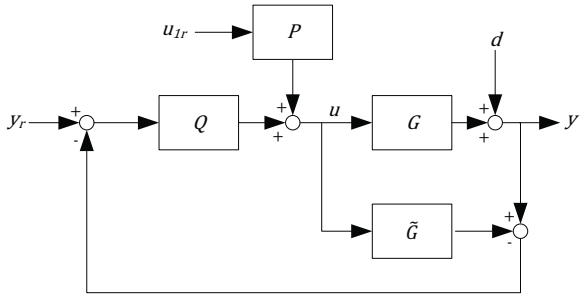

Fig. 3 IMC mid-ranging structure

The mid-ranging design proposed in this paper focuses on the respective disturbance responses of y, u_1 and u_2 and exploits both the structure and tuning methodology of internal model control (IMC). This makes the design trade-offs transparent.

Allison and Ogawa (2003) do not discuss anti-windup for MVPC. However Haugwitz et al. (2005) have shown that for some applications an additional feedback block can significantly improve the anti-windup performance of MVPC. The IMC structure provides a natural framework for both anti-windup (discussed in this paper) and robustness analysis (see Morari and Zafiriou, 1989, for the general case).

In Sections 2 to 5 the IMC tuning method for mid-ranging is presented followed by simulation studies in Section 6 that demonstrate the performance of IMC compared to Direct Synthesis. Anti-windup in IMC mid-ranging is discussed in Section 7 with an example that shows how the classical IMC structure presented in the previous sections and a modified IMC structure perform during saturation of the inputs.

2. MID-RANGING CONTROL OBJECTIVES

The plant model is (see Fig. 1),

$$y = G_1 u_1 + G_2 u_2 + d$$

where u_1 is the fast input and u_2 is the slow input. The objective is to use the both inputs to control y and mid-range u_1 i.e. to return u_1 to its setpoint, u_{1_r}.

The transfer function between y_r and y can be defined as the fast complementary sensitivity, T_f. The response from y_r to y when u_1 is set to zero can be defined as the slow complementary sensitivity, T_s (corresponding to the control action with the slow actuator alone). These are chosen to produce desired responses to setpoint changes such that the frequency response looks like Fig. 2. The proposed IMC mid-ranging design is to specify not only T_f but also T_s. With two degrees of freedom, the rest follows as illustrated in Sections 3 and 4.

3. IMC STRUCTURE FOR MID-RANGING

Firstly the general IMC structure shown in Fig. 3 is considered. Assuming that the model is perfect ($G = \tilde{G}$), y and u can be derived as:

$$y = Gu + d \quad (1)$$

$$u = Q(y_r - y + Gu) + Pu_{1_r} \quad (2)$$

Equations (1) and (2) can expressed as:

$$u = Qy_r - Qd + Pu_{1_r} \quad (3)$$

$$y = GQy_r + (I - GQ)d + GPu_{1_r} \quad (4)$$

For classical feedback control,

$$u = C(y_r - y) + \hat{P}u_{1_r}$$

where C is the equivalent feedback controller and $\hat{P}$ is the equivalent pre-filter.

C can be found by expressing (2) as:

$$u = (I - QG)^{-1}Q(y_r - y) + (I - QG)^{-1}Pu_{1_r} \quad (5)$$

This gives:

$$C = (I - QG)^{-1}Q$$
$$= Q(I - GQ)^{-1} \quad (6)$$

For mid-ranging the following are defined as:

$$u = \begin{bmatrix} u_1 \\ u_2 \end{bmatrix}, G = [G_1 \quad G_2], Q = \begin{bmatrix} Q_1 \\ Q_2 \end{bmatrix} \text{ and } P = \begin{bmatrix} P_1 \\ P_2 \end{bmatrix}$$

4. IMC MID-RANGING DESIGN

From (4), T_f and T_s can be expressed in terms of Q_1 and Q_2. This gives the conditions for the controller design:

Controller Design Conditions:

$$T_f = GQ = G_1Q_1 + G_2Q_2$$

$$T_s = G_2Q_2$$

The sensitivity, S_f is defined as $S_f = 1 - T_f$ such that (4) can be expressed as,

$$y = T_f y_r + S_f d + GPu_{1_r}$$

To achieve the control objectives,

$$T_f|_{ss} = G_1Q_1 + G_2Q_2|_{ss} = 1$$

$$Q_1|_{ss} = 0$$

This means that $T_s|_{ss} = G_2Q_2|_{ss} = 1$.

The decoupling between u_{1_r} and y is achieved through the use of pre-filters. From (4), to obtain a decoupled response between u_{1_r} and y, the following condition must be satisfied:

Pre-filters Design Conditions:

$GP = G_1P_1 + G_2P_2 = 0$

The design algorithm is then as follows:

1. Choose T_s
2. Q_2 is then designed such that $Q_2 = \frac{T_s}{G_2}$
3. Choose T_f
4. Q_1 is then designed such that $Q_1 = \frac{(T_f - T_s)}{G_1}$
5. To design pre-filters, $GP = 0$ must be satisfied. There are different ways to achieve this:
   a. Let $P_1 = 1$ and $P_2 = -G_1/G_2$
   b. Let $P_1 = G_2/G_2|_{ss}$ and $P_2 = -G_1/G_2|_{ss}$
   c. Let $G_2 = {G_2}^-{G_2}^+$ where ${G_2}^+$ is minimum phase and ${G_2}^-$ is non-minimum phase, then let $P_1 = H{G_2}^-$ where $H{G_2}^-|_{ss} = 1$ and $P_2 = -H\,G_1/{G_2}^+$

G_1 and G_2 can be either minimum phase or non-minimum phase. This design above can be extended for non-minimum phase systems as follows:

1. Choose T_s such that $T_s = {T_s}^-\tilde{T}_s$ where ${T_s}^-$ includes the non-minimum phase components (including delays) of both G_1 and G_2 i.e. so that T_s/G_1 and T_s/G_2 are both casual and stable.
2. Q_2 is then designed such that $Q_2 = \frac{T_s}{G_2}$
3. Choose $T_f = {T_f}^-\tilde{T}_f$ where ${T_f}^-$ includes the non-minimum phase component (including delay) of G_1 i.e. so that T_f/G_1 is casual and stable.
4. $Q_1$is then chosen as $Q_1 = \frac{(T_f - T_s)}{G_1}$.
5. P_1 and P_2 are chosen as before.

The IMC approach concentrates on the disturbance responses i.e. the third column of the sensitivities matrices (17) and (28) in Henson et al. (1995) where nine sensitivities are discussed. Equation (7) shows the sensitivities for the IMC design.

$$\begin{bmatrix} y \\ u_1 \\ u_2 \end{bmatrix} = \begin{bmatrix} GQ & GP & (I - GQ) \\ Q_1 & P_1 & -Q_1 \\ Q_2 & P_2 & -Q_2 \end{bmatrix} \begin{bmatrix} y_r \\ u_{1_r} \\ d \end{bmatrix} \quad (7)$$

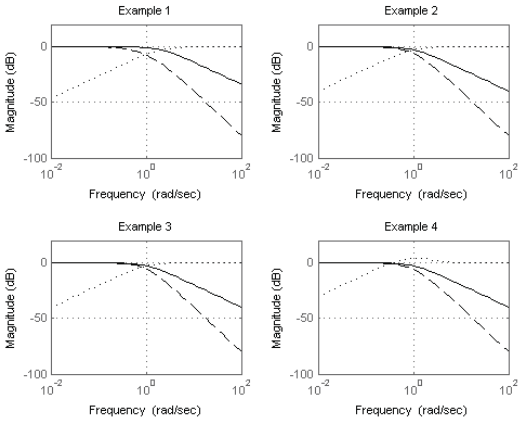

Fig. 4 Complementary sensitivities T_f (solid) and T_s (dashed) and sensitivity, S_f (dotted) for all examples.

From a classical point of view, the disturbance responses correspond to the sensitivity S_f and two control sensitivities, Q_1 and Q_2. For the mid-ranging problem, it is required that the slow actuator should have a control sensitivity that is low bandwidth only; meanwhile the fast actuator should have a control sensitivity that is mid-frequency only and goes to zero at steady state, giving mid-ranging. IMC is advantageous because it gives the control sensitivities of the fast and slow actuators directly as Q_1 and Q_2.

5. IMPLEMENTATION IN VPC STRUCTURE

The IMC mid-ranging design described in Section 4 can be extended for implementation using the VPC structure. This structure is similar to Fig. 1 but includes the pre-filters P_1 and P_2. Without the pre-filters this design does not achieve the decoupled response between u_{1_r} and y; it can only track u_1 to $u_1 = u_{1_r}$.

For the VPC structure in Fig. 1,

$$\begin{bmatrix} u_1 \\ u_2 \end{bmatrix} = \begin{bmatrix} C_1 \\ -C_2C_1 \end{bmatrix} (y_r - y)$$

From (6),

$$\begin{bmatrix} C_1 \\ -C_2C_1 \end{bmatrix} = \begin{bmatrix} Q_1 \\ Q_2 \end{bmatrix} \left[I - \begin{bmatrix} G_1 & G_2 \end{bmatrix} \begin{bmatrix} Q_1 \\ Q_2 \end{bmatrix} \right]^{-1}$$

Therefore,

$$\begin{bmatrix} C_1 \\ -C_2C_1 \end{bmatrix} = \begin{bmatrix} Q_1/(I - G_1Q_1 - G_2Q_2) \\ Q_2/(I - G_1Q_1 - G_2Q_2) \end{bmatrix}$$

This gives,

$$C_1 = \frac{Q_1}{(I - G_1Q_1 - G_2Q_2)}$$

$$C_2 = -\frac{Q_2}{Q_1}$$

6. SIMULATION STUDIES

The performance of the IMC design in the previous sections is demonstrated via simulation of four examples. The examples are all linear, stable systems. Examples 1, 2 and 3 are taken from Henson et al., (1995) to compare the performance of IMC controllers to the Direct Synthesis controllers. Therefore T_f and T_s for examples 1 to 3 are chosen to correspond to g_{y_d} and g_{u_d} given in Henson et al. (1995). In example 1, both G_1 and G_2 are minimum phase systems. For examples 2 and 3, G_1 is minimum phase whereas G_2 has a right half plane zero and a time delay respectively. Example 4 is an original example where both G_1 and G_2 are non-minimum phase. Additional first order setpoint filters are included in both control schemes according to Henson et al. (1995).

The process model transfer functions for the examples are given below.

Example 1: $y = \frac{1}{2s+1}u_1(s) + \frac{1}{5s+1}u_2(s) + \frac{1}{s+1}d(s)$

Example 2: $y = \frac{1}{2s+1}u_1(s) + \frac{-2s+1}{(2s+1)^2}u_2(s) + \frac{1}{s+1}d(s)$

Example 3: $y = \frac{1}{2s+1}u_1(s) + \frac{e^{-2s}}{2s+1}u_2(s) + \frac{1}{s+1}d(s)$

Example 4: $y = \frac{-s+1}{(2s+1)^2}u_1(s) + \frac{-2s+1}{(2s+1)^2}u_2(s) + \frac{1}{s+1}d(s)$

T_f and T_s are as follows:

Example 1: $T_f = \frac{1}{0.5s+1}$ and $T_s = \frac{2}{(2s+1)(s+2)}$

Example 2: $T_f = \frac{1}{s+1}$ and $T_s = \frac{-2s+1}{(2s+1)(s+1)^2}$

Example 3: $T_f = \frac{1}{s+1}$ and $T_s = \frac{e^{-2s}}{(s+1)^2}$

Example 4: $T_f = \frac{-s+1}{(s+1)^2}$ and $T_s = \frac{(-s+1)(-2s+1)}{(2s+1)(s+1)^3}$

The frequency response of sensitivity, S_f and the complementary sensitivities, T_f and T_s for the examples are shown in Fig. 4. T_f is chosen to determine the closed-loop bandwidth and T_s to determine the relative work done by u_1 and u_2.

Figs. 5 to 8 show setpoint and disturbance responses for the IMC controllers (solid line) and Direct Synthesis controllers, both parallel (dashed line) and series (dotted line).

It can be seen from Figs. 5 to 7 that identical output responses are obtained for Direct Synthesis and IMC schemes. This is expected since both pairs of controllers are tuned with the same time constants. The Direct Synthesis parallel architecture and IMC structure are identical when (6) is satisfied where C_1 and C_2 are the habituating controllers, $g_{c_{11}}$ and $g_{c_{21}}$ from Henson et al. (1995).

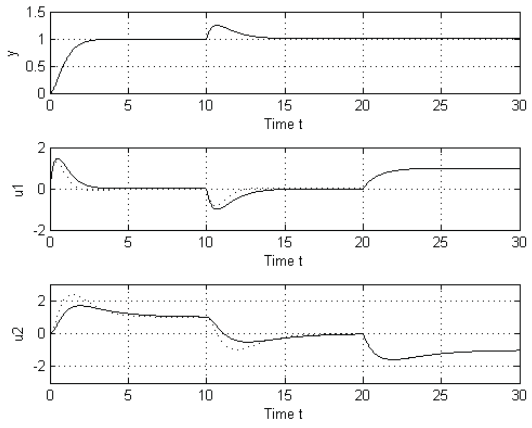

Fig. 5 Example 1: IMC (solid), Direct Synthesis parallel (dashed) and series (dotted) responses to unit changes in y_r at t=0, d at t=10 and u_{1_r} at t=20.

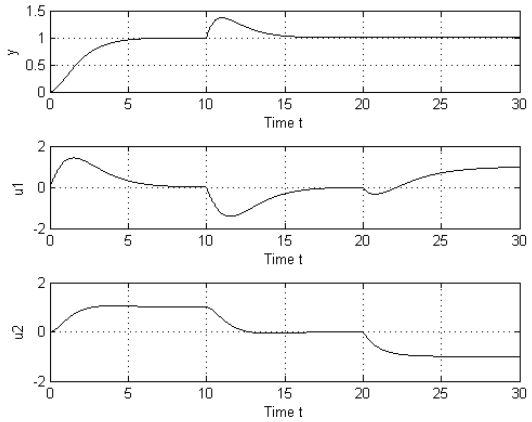

Fig. 6 Example 2: IMC (solid), Direct Synthesis parallel (dashed) and series (dotted) responses to unit changes in y_r at t=0, d at t=10 and u_{1_r} at t=20.

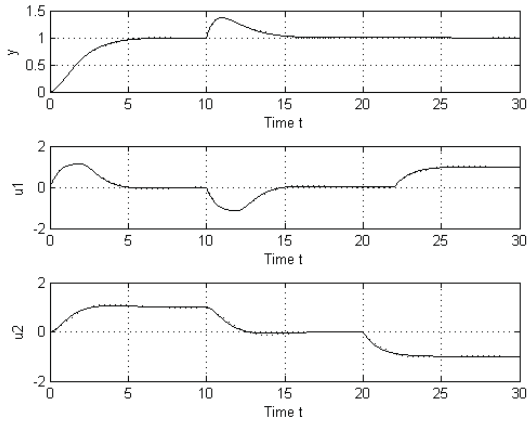

Fig. 7 Example 3: IMC (solid), Direct Synthesis parallel (dashed) and series (dotted) responses to unit changes in y_r at t=0, d at t=10 and u_{1_r} at t=20.

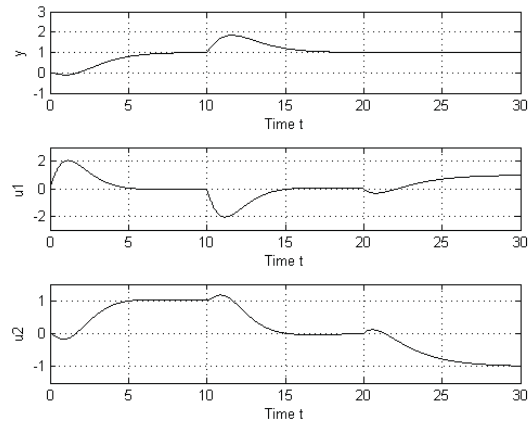

Fig. 8 Example 4: IMC (solid) response to unit changes in y_r at t=0, d at t=10 and u_{1_r} at t=20.

Direct Synthesis implemented in the series architecture responds differently from the IMC and the parallel architecture in example 1 because the relationship given by (11) in Henson et al. (1995) is not satisfied (because of the choice of g_{c21} in the design). For all examples, both methods produce completely decoupled response between u_{1_r} and y. However the IMC design gives more flexibility since H in Section 4 can be adjusted to tune the response to allow faster setpoint tracking of u_{1_r}.

From (7), Q_1 and Q_2 are directly related to the output setpoint and disturbance responses. Therefore it is simple to adjust these controllers because in the absence of model uncertainty, closed loop stability is automatically guaranteed as long as Q_1 and Q_2 are stable (Prett and Garcia, 1988). Henson et al. (1995) state that the controller g_{c21} can also be used to tune the responses of the two inputs to changes in y_r and d. The effect on closed loop performance of adjusting this tuning parameters is however not obvious. Neither is it obvious for what parameter values the closed loop system is stable.

7. ANTI-WINDUP IN MID-RANGING CONTROL

Haugwitz et al. (2005) propose anti-windup schemes for MVPC when u_1 saturates. Guidelines are given on how to tune mid-ranging controllers to maintain the same control action of u_2 in the saturated case as in the unsaturated case. Furthermore a modified anti-windup scheme is presented that achieves increased control action in u_2 to further reduce performance degradation. However, if the MVPC structure is to be modified, then significantly improved performance can be achieved for the saturated case by using the IMC approach in this paper.

In this section, the performance of the classical IMC structure used for mid-ranging (see Fig. 3) is considered when the inputs u_1 and u_2 saturate. This IMC structure works for most cases but as demonstrated by Zheng et al. (1994), sometimes IMC requires a modified structure. The modified IMC structure presented by Zheng et al. (1994) can be utilised for

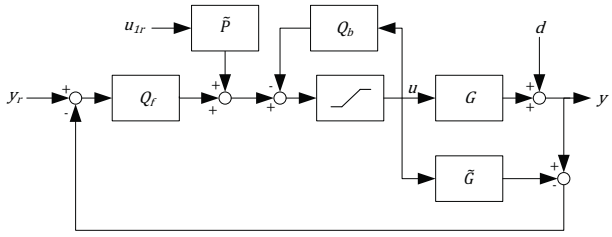

Fig. 9 Modified IMC mid-ranging structure for anti-windup

the proposed IMC mid-ranging design as shown in Fig. 9. The performance during saturation of this modified IMC structure (Fig. 9) is also considered in this section.

7.1 Anti-windup in IMC

As with the controller design, firstly the general case is considered. For the unsaturated case in Fig. 9,

$$u = (1 + Q_b)^{-1} Q_f (y_r - y + Gu) + (1 + Q_b)^{-1} \tilde{P} u_{1_r}$$

From (2),

$$u = Q(y_r - y + Gu) + P u_{1_r}$$

Therefore it is desired that,

$$Q = (1 + Q_b)^{-1} Q_f \tag{7}$$

$$P = (1 + Q_b)^{-1} \tilde{P}$$

For mid-ranging, u, G, Q and P are defined as in Section 3. Additionally, $\tilde{P}$, Q_f and Q_b are as follows:

$$\tilde{P} = \begin{bmatrix} \tilde{P}_1 \\ \tilde{P}_2 \end{bmatrix}, \; Q_f = \begin{bmatrix} Q_{f_1} \\ Q_{f_2} \end{bmatrix} \text{ and } Q_b = \begin{bmatrix} Q_{b_1} & 0 \\ 0 & Q_{b_2} \end{bmatrix}.$$

Extending the general case before for mid-ranging gives:

$$\begin{bmatrix} u_1 \\ u_2 \end{bmatrix} = \left(I + \begin{bmatrix} Q_{b_1} & 0 \\ 0 & Q_{b_2} \end{bmatrix} \right)^{-1} \begin{bmatrix} \bar{u}_1 \\ \bar{u}_2 \end{bmatrix}$$

$$\text{where } \begin{bmatrix} \bar{u}_1 \\ \bar{u}_2 \end{bmatrix} = \begin{bmatrix} \tilde{P}_1 \\ \tilde{P}_2 \end{bmatrix} u_{1_r} + \begin{bmatrix} Q_{f_1} \\ Q_{f_2} \end{bmatrix} \left(y_r - y + [G_1 \quad G_2] \begin{bmatrix} u_1 \\ u_2 \end{bmatrix} \right)$$

Therefore,

$$\begin{bmatrix} u_1 \\ u_2 \end{bmatrix} = \begin{bmatrix} \dfrac{Q_{f_1}}{1 + Q_{b_1}} \\ \dfrac{Q_{f_2}}{1 + Q_{b_2}} \end{bmatrix} (y_r - y + G_1 u_1 + G_2 u_2) + \begin{bmatrix} \dfrac{\tilde{P}_1}{1 + Q_{b_1}} \\ \dfrac{\tilde{P}_2}{1 + Q_{b_2}} \end{bmatrix} u_{1_r}$$

This means that

$$\begin{bmatrix} Q_1 \\ Q_2 \end{bmatrix} = \begin{bmatrix} \dfrac{Q_{f_1}}{1 + Q_{b_1}} \\ \dfrac{Q_{f_2}}{1 + Q_{b_2}} \end{bmatrix} \text{ and } \begin{bmatrix} P_1 \\ P_2 \end{bmatrix} = \begin{bmatrix} \dfrac{\tilde{P}_1}{1 + Q_{b_1}} \\ \dfrac{\tilde{P}_2}{1 + Q_{b_2}} \end{bmatrix}$$

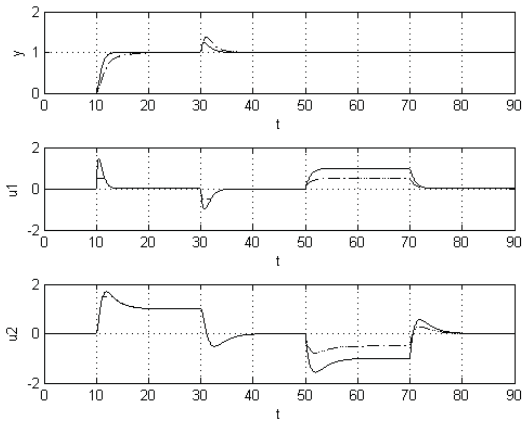

Fig. 10 Example 1: Response of IMC scheme with no saturation (solid), $\lambda = 0$ (dashed) and $\lambda = 1$ (dotted) for a unit changes in y_r at t=10, d at t=30, u_{1_r} at t=50 and t= 70.

From Zheng et al. (1994), Q_f can usually be chosen by the following relationship:

$$Q_f = \lambda Q(\infty) + (1 - \lambda)Q$$

- Condition 1: when $\lambda = 0$, then $Q_f = Q$ and from (7) $Q_b = 0$
- Condition 2: when $\lambda = 1$, then $Q_f = Q(\infty)$ and from (7) $Q_b = (Q(\infty) - Q)/Q$

The classical IMC structure as shown in Fig. 3 corresponds to the condition where $\lambda = 0$ and the modified IMC structure given by the block diagram in Fig. 9 corresponds to $\lambda = 1$. For condition 2 above, Q_{f_1} cannot be chosen to be $Q(\infty)$ because for the mid-ranging control problem it is required that $Q_{f_1}(0) = 0$. To ensure that $Q_{f_1}(0) = 0$, Q_f can be chosen such that,

$$Q_{f_1} = Q_1(\infty)\frac{s}{s + p_1}$$

where p_1 is a pole of Q_1.

Q_{f_2} can simply be chosen as $Q_{f_2} = Q_2(\infty)$. However, if Q_2 is strictly proper then Q_2 can be defined as:

$$Q_2 = Q_{2_b} \times Q_{2_s}$$

where Q_{2_b} is bi-proper and Q_{2_s} is strictly proper so that $Q_{f_2} = Q_{2_b}(\infty) \times Q_{2_s}$.

Fig. 10 shows the response of the system in example 1 defined in Section 6 when u_1 and u_2 saturate. Responses for both the classical IMC structure (Fig. 3) and the modified IMC structure (Fig. 9) are considered. For this example the response when $\lambda = 0$ and $\lambda = 1$ is similar because $Q_{f_1} = Q_1$.

When u_1 saturates, output tracking is still achieved by the slow actuator. The control action of u_2 is the same when u_1 saturates as in the unsaturated case. When u_2 saturates however, the fast actuator compromises between input and output tracking. Therefore the classical IMC structure offers acceptable performance during saturation. In some cases, the modified IMC structure offers even better performance with saturation of u_1 and u_2.

8. CONCLUSION

Many mid-ranging designs have been proposed and of them, MVPC and Direct Synthesis are most appropriate to address the ad hoc nature of conventional mid-ranging tuning procedures. MVPC works sufficiently especially when restricted to conventional mid-ranging structure and PID control. However, when not restricted, the Direct Synthesis (Henson et al., 1995) and IMC approaches give better performance. The IMC mid-ranging design presented in this paper gives the same improved performance over MVPC as Direct Synthesis. Moreover, this approach gives insight to the design trade-offs of MVPC and Direct Synthesis by emphasis on bandwidth considerations. An added benefit of the IMC approach is the ability to integrate anti-windup to mid-ranging control. Other mid-ranging approaches require additional control blocks and further modifications to achieve acceptable performance under saturation of the inputs. IMC mid-ranging is already a natural structure for anti-windup.

REFERENCES

ALLISON, B. J. & ISAKSSON, A. J. (1998) Design and performance of mid-ranging controllers. *Journal of Process Control,* 8**,** 469-474.

ALLISON, B. J. & OGAWA, S. (2003) Design and tuning of valve position controllers with industrial applications. *Transactions of the Institute of Measurement and Control,* 25**,** 3-16.

HAUGWITZ, S., KARLSSON, M., VELUT, S. & HAGANDER, P. (2005) Anti-windup in mid-ranging control. *Fourty-fourth IEEE Conference on Decision and Control, and the European Control Conference 2005.* Seville, Spain.

HENSON, M. A., OGUNNAIKE, B. A. & SCHWABER, J. S. (1995) Habituating Control Strategies for Process-Control. *AIChE Journal,* 41**,** 604-618.

MORARI, M., ZAFIRIOU, E. (1989) *Robust Process Control*, Prentice-Hall, Inc.

PRETT, D. M. & GARCIA, C., E. (1988) *Fundamental Process Control,* Stoneham, Butterworth Publishers.

ZHENG, A., KOTHARE, M. V. & MORARI, M. (1994) Antiwindup Design for Internal Model Control. *International Journal of Control,* 60**,** 1015-1024.

Robust optimization-based multi-loop PID controller tuning: A new tool and an industrial example

Michael Harmse*, Richard Hughes, Rainer Dittmar*****
Harpreet Singh* and Shabroz Gill*

**IPCOSAptitude Ltd., Cambridge, United Kingdom*
(e-mail: info@ipcosaptitude.com)
***SABIC UK Petrochemichals Ltd., Wilton, Middlesbrough, United Kingdom*
**** West Coast University of Applied Sciences, Heide, Germany*
(e-mail: dittmar@fh-westkueste.de)

Abstract: Modern process plants are highly integrated and as a result, decentralized PID control loops are often strongly interactive. The currently used sequential tuning approach is not only time consuming, but does also not achieve optimal performance of the inherently multivariable control system. This paper describes a method and a software tool which allows a control engineer to calculate optimal PID controller settings for multiloop systems. It is based on the identification of a state space model of the multivariable system, and it uses constrained nonlinear optimization techniques to find the controller parameters. The solution is tailored to the specific control system and PID algorithm to be used. The methodology has been successfully applied in several industrial advanced control projects. The tuning results which have been achieved for interacting PID control loops in the stabilizing section of an industrial Gasoline Treatment Unit at SABIC Petrochemicals are presented.

Keywords: PID controller tuning, multi-loop control, decentralized control system design, nonlinear optimization, genetic algorithm, multivariable system identification.

1. INTRODUCTION

One of the most important challenges facing the process industry today is optimizing the operation of complex units, without compromising the safety and integrity of the process equipment. Process complexity has increased significantly over the past two decades due to increased level of heat integration and use of recycle streams. In addition, the need for increased process flexibility to deal with changing raw materials and alternate energy sources, as well as the need to adapt quickly to fluctuating throughput and quality targets, often means that the process dynamics will vary significantly over time and with operating point. The basic control layer of process plants almost always consists of a large number of decentralized SISO PID controllers, although this approach is intrinsically inadequate for multivariable processes. Due to the situation described above, the interactions between these controllers are becoming more important, and tuning these control loops for good performance and adequate robustness is a challenging task.

The industrial practice of PID controller tuning is still dominated by manual trial-and-error tuning. If tuning rules are used at all, it's the "classical" ones like Ziegler-Nichols or Chien-Hrones-Reswick which are based on simplified first order plus dead time (FOPDT) process models and do not consider stability robustness issues, therefore often being not adequate in modern process units with more complex dynamics and nonlinearity. In addition, many tuning rules assume that all PID controller equations work as described in the textbooks, when in fact there is substantial variation between the different vendors. In contrast, different PID controller structures result due to use of either the parallel or the serial form, using the control error or the PV by the Proportional (P) and Derivative (D) terms, and many other quirks like alternative implementations of the derivative filters. Tuning SISO PID controllers in a multivariable environment is usually done in a time-consuming sequential and iterative way, starting with the most important loops, and heuristic detuning in case the interactions are significant.

For a long time, vendors of automation systems such as Distributed Control Systems (DCS) and Programmable Logic Controllers (PLC) have been offering PID self-tuning functionality (tuning on demand). Unfortunately, they have only found limited application. This is also true for model based PID controller tuning software provided by the same or third-party vendors. Moreover, in most cases these tools are restricted to single loop tuning applications, and do not support multi-loop tuning (Li et al., 2006, Espinosa Oviedo et al., 2006 and Zhu, 2004).

The design of interacting PID controllers in a multivariable environment is not a new topic in the process control literature. At least three research directions can be identified: (1) reduction of controller interactions by proper MV-CV pairing, (2) design of decoupling networks and (3) consideration of MIMO interactions in decentralized controller tuning. In this paper, only the third direction is relevant. Several methods have been developed, Luyben's

BLT method being the most popular one (Monica et al., 1988). Here, the individual PI loops are first tuned by the Ziegler-Nichols rules independently. Then, a detuning factor is calculated which assures a certain stability margin for the controlled MIMO system. All individual controller gains are divided by this factor, and the reset times are multiplied by it. The price to be paid for the reduced interaction is a more sluggish behaviour of PI loops. Other methods include the sequential loop closing approach (Hovd and Skogestad, 1994), the independent design method (Hovd and Skogestad, 1993) and the multivariable generalization of the relay-feedback self-tuning method (Halevi et al. 1997). For a discussion of these methods the reader is referred to (Chen and Seborg, 2003).

This paper introduces a new method and a software tool "AptiTune™" for the calculation of optimum PID controller settings in a multivariable system (multivariable loop tuning). The method consists of several steps. First, a set of Finite Impulse Response (FIR) models of the open-loop MIMO plant is being identified and approximated by a reduced-order state space model. In a second step, optimal parameters for the decentralized PID controllers are calculated using constrained optimization. Finally, the setpoint tracking, disturbance rejection and noise attenuation behaviour of the controlled system is simulated.

It was the aim of the development to come up with a software tool which is based on recent identification and control developments, but which does not require in-depth knowledge of identification and control theory by the average user. Furthermore, the optimization solution is tailored to the specific target automation system, e.g. the particular DCS or PLC which is used for control purposes.

The remainder of the paper is organized as follows: In section 2, the identification and optimal tuning methods will be described together with the "AptiTune™" software tool. Section 3 presents some results of multiloop tuning in the stabilizer section of an industrial Gasoline Treatment Unit (GTU). The retuning of the PID controllers was one of the first steps of an advanced control project, which also included the design and commisioning of an MPC controller.

2. METHOD AND TOOL FOR MULTILOOP TUNING

2.1 Identification of the MIMO process model

The first step of model based multiloop tuning is to develop a dynamic model of the multivariable process with n inputs and n outputs, the outputs (u_i) and process variables (y_i) of the PID controllers shown in Fig. 1.

Our preferred approach is to switch all PID controllers to be tuned into manual mode whenever possible and to perform a series of output steps of different duration and amplitude. According to our experience, four to six steps with duration varying between 10% and 100% of the desired closed-loop settling time are usually sufficient. If a test signal generator is available, PRBS (pseudo-random binary sequence) or GBN

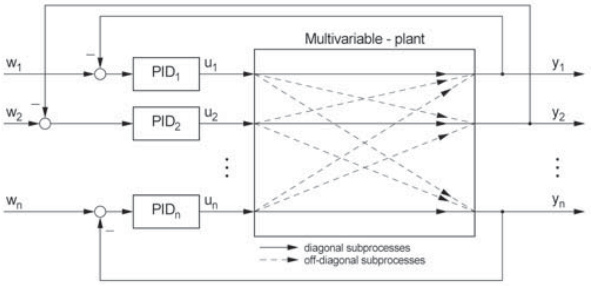

Fig. 1: Decentralized multiloop PID control system

(generalized binary noise), then an automated test may be used as an alternative. Both types of plant tests can be performed in sequential or in time-saving simultanous mode.

If one or more PID controllers cannot be switched to manual mode, then the loop can be kept in automatic mode and multiple setpoint steps can be made. The Projection Method described in (Forsell and Ljung, 2000) can then be used.

After pre-processing the raw test data (detection/rejection of outliers, filtering, decimation, cutting out periods of bad data etc.), the parameters of a MIMO FIR model

$$\vec{g}_{ij} = \left[g_{ij}(0), g_{ij}(1), g_{ij}(2), \ldots, g_{ij}(n_M) \right] \qquad i, j = 1...n \quad (1)$$

are estimated by least squares regression. The user should specify a-priori knowledge such as zero gain, known dead time or integrating behaviour of subprocesses. Although FIR models are estimated, the results are presented as Finite Step Response (FSR) models for easier visualization and understanding. The "AptiTune™" software tool also supports the import of FSR models created by identification tools from MPC packages, but also allows the user to specify a transfer function matrix.

In the next step, the MIMO FIR model is approximated by a linear state-space model of the form

$$\begin{aligned} \dot{x}(t) &= A\,x(t) + B\,u(t) \\ y(t) &= C\,x(t) \end{aligned} \qquad (2)$$

This approximation is not based on the raw or preprocessed plant test data, but on a model-to-model fit. To remove noise and cycles from the FIR model, it can first be smoothed using a central average filter. The state-space model is constructed using the singular value decomposition (SVD) model reduction technique (Maciejowski, 1989). While creating the state-space model, the diagonal model curves are given more preference than the off-diagonal models. As a result, diagonal models normally have higher order than the off-diagonal ones and consequently fit the original FIR model curves more accurately. The step responses calculated based on the stat-space models are graphically displayed.

If it is possible to do a closed-loop step test (or if historical data contain a clear SP step), a practical way of validating the process model is to simulate the closed loop behaviour of the control system with the actual PID controller parameters

currently entered on the DCS , and to compare the simulation results with plant data. If the observed responses are similar to the simulated responses, then we can conclude that the model is sufficiently accurate for loop tuning purposes.

2.2 Calculation of optimal PID controller parameters

The PID controller parameters (controller gains $K_{c,i}$, reset times $T_{r,i}$ and derivative time constants $T_{d,i}$) are calculated solving numerically the nonlinear constrained optimization problem

$$\min_{K_{Pi},T_{Ni},T_{Vi}} \quad J$$
$$g_j(K_{Pi},T_{Ni},T_{Vi}) \le 0 \quad i=1...n,\ j=1...m \tag{3}$$

where J denotes the objective function and g_j are constraints. The objective function J is a weighted sum of three terms $J = J_1 + \alpha J_2 + \beta J_3$ which assess different aspects of the control loop performance. The first part $J_1 = \int_0^{T_f} \left| y(t) - y_r(t) \right| dt$ refers to the Integrated Absolute Error (IAE) criterion for setpoint tracking. Here, the error is defined as the difference between the PV and a user-defined first order reference trajectory $y_r(t)$ connecting the actual PV and the setpoint. By specifying the time constant of the trajectory, the user can affect the speed of the response to setpoint changes. The second part $J_2 = \int_0^{T_f} \left| w(t) - y(t) \right| dt$ denotes the IAE for an input step disturbance. Finally, the third term $J_3 = \int_0^{T_f} \left| \Delta u(t) \right| (t)$ reflects the control effort. By setting the weighting coefficients α and β, the user can balance a compromise between the different performance objectives. Another design parameter allows the user to weight the performance of the n SISO control loops against the necessary degree of decoupling between them.

For each control loop, the user can specify one or more inequality constraints $g_j \le 0$ from the following list: maximum OP deviation after setpoint changes, maximum overshoot, minimum damping ratio, maximal noise amplification, process gain and deadtime margins, maximum/minimum limits of the controller parameters. For level buffering controllers, the maximum setpoint deviation and the minimum return time after a level disturbance can be specified. By careful specification of the constraints, the user can tailor the tuning to process-specific requirements.

For starting the numerical optimization, initial controller parameter values have to be selected. For this purpose, the user can choose to use the actual DCS values or values calculated by the Cohen-Coon tuning rule (for individual controller tuning assuming a SISO model). The degree of difficulty of the nonlinear constrained optimization problem depends on the number of controllers involved, the order of the process model, and the number and nature of the inequality constraints. In general, non-convexity and local minima can occur. Therefore, several search algorithms have been implemented, including a brute force global search in the entire parameter space, a genetic algorithm (both intended for initialization), and a generalized gradient algorithm (Vlachos et al., 2000).

In contrast to some PID controller tuning software available mainly for teaching and training purposes, the "AptiTune™" tool not only calculates "generic" PID controller parameters, but parameters for a specific realization of the PID controller equation for specific commercial control system hardware. The user can select between different control algorithms of widespread DCS systems such as Honeywell, Emerson DeltaV, Foxboro I/A, ABB and several others. For example, six different versions of the PID algorithms are available for the Emerson DCS, for which the optimization results may be quite different. Optimal controller parameters can of course also be calculated for P, I only and PI controllers.

After the optimizer has converged and optimal controller parameters have been found, the design process will be finished by simulation of the dynamic behaviour of the control system. It is useful to study different scenarios: setpoint tracking, input disturbance rejection, and noise attenuation. The "integrity" of the controlled MIMO system should be studied as well, i.e. the behaviour of the controlled system if one or more controllers are in manual mode, or if components like final actuators fail. Finally, the robustness against plant-model mismatch should be evaluated. For this purpose, robustness plots such as in Fig. 2 are helpful. It shows the purple stability limit in a process gain ratio/dead time graph, and the stability region for the minimum required combined gain and deadtime margins as the red polygon (left hand plot, lower left hand corner).

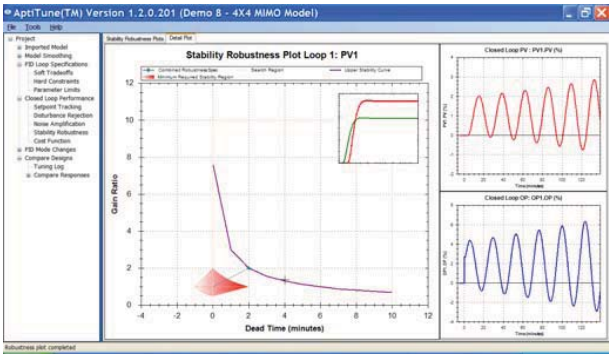

Fig. 2: Robustness plot

3. INDUSTRIAL EXAMPLE

The method and software tool described above have been used successfully in a number of advanced control projects. A good example is the stabilizing section of a GTU process, where improving the PID controller tuning was a prerequisite for successful MPC design and implementation.

The Process and Instrumentation Diagram for the GTU process is shown in Fig. 3. Although the overall system is (8x8), it was possible to decompose it into a (2x2) system on

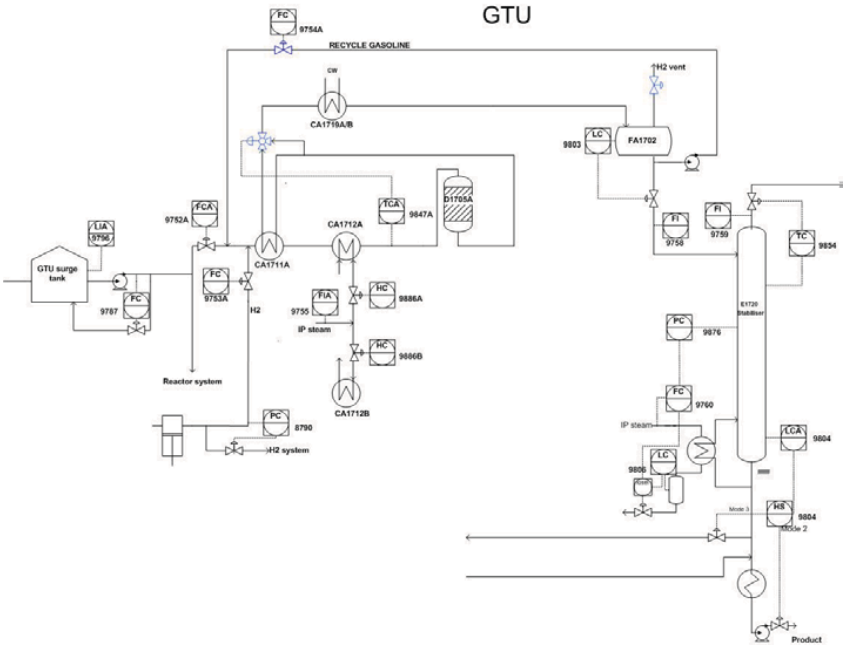

Fig. 3: P&I diagram of the GTU process

the E20 column and (6x6) for the rest of the unit. Due to limited space, the results for the (2x2) system are presented.

The objective of the E20 stabilizer column (on the right hand side of the P&ID) is to remove hydrogen and methane dissolved in the petrol (mostly C5) stream. The column is essentially a degassing drum with trays for improved separation. The current PID control scheme is somewhat unconventional in that the PID loop pairing is the "wrong" way round:

- A tray temperature close to the top of the column is controlled (even though the product specification is on the bottoms stream) by using the overhead vent valve for temperature control. There is no reflux drum, and feed comes in close to the top, providing the internal reflux stream.
- The column pressure controller cascades to the steam flow SP on the reboiler.

One reason for the unconventional PID loop pairing is that controlling pressure with the reboiler duty ensures that the pressure is less likely to go high and lift the safety valve. If the PID was paired the other way around, there is a chance for the pressure to go high if the overhead valve saturates before the column runs out of reboiler duty. Since the degree of interaction between the two loops is quite strong, the pressure loop will go unstable if either the feed drum LIC or the TIC approached unstable (even though there is nothing wrong with the tuning of the PIC). The drum level controller sets the valve position directly without the benefit of a cascaded flow controller. Any change in either upstream or downstream pressure affect the feed flow PV, which then affects the temperature and pressure in the E20 column. Due to the heavy coupling between the three loops, it is not really feasible to tune one loop without due consideration of the remaining two control loops.

Best results were obtained by step testing condensate flow setpoint and vent valve, fitting a 2x2 model and then calculating moderately fast but well damped tuning that takes the strong off-diagonal interaction into account. We tuned it for fast SP tracking but high robustness margins. The standard deviations of the two PVs are now substantially better than before and that both loops are tracking SP well.

The gain for the tray temperature vs. vent valve varies very substantially depending on operating point (from almost zero when the top of the column is perfectly pure, to almost infinite when the column goes rapidly off-spec). This value represents the best model we could identify by keeping the tray temperature in the correct range with the column pressure at the nominal operating point. The dynamic model is shown in Fig. 4.

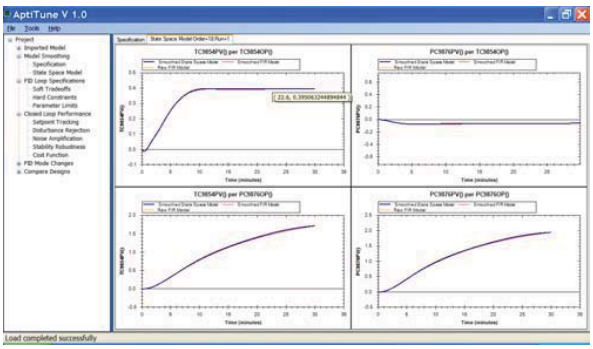

Fig. 4: Step responses of the dynamic model
(Legend: TC.PV=Tray 6 Temperature; PC=Column Pressure; TC.OP=Vent Valve; PC.OP=Steam Flow SP)

Note that the total state-space model order is 18. Fig. 5 shows the optimized PV responses for a step change in both SPs:

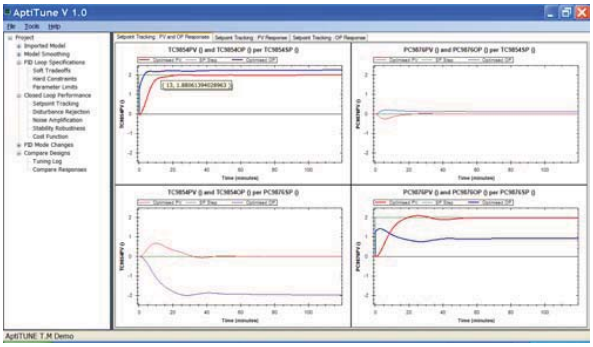

Fig. 5: Response of the 2x2 system to SP step changes
(Legend: PV is shown in red, OP in blue)

Note that PV overshoot is very low and that damping is exceptionally good. The OP value for the vent has a peak value that is almost the same as the steady state value, and the loop has about the same rise time in closed loop as compared to open loop (a speed-up factor of about 1x). The pressure loop is about 2x faster in closed loop compared to open loop. The load disturbance response is shown in Fig. 6:

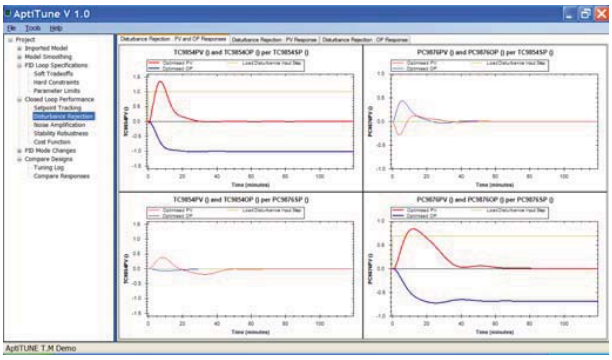

Fig. 6: Response of the 2x2 system to load disturbances

Note that the PV and OP responses have very good damping with peak OP values that are very similar to the steady state values. This will ensure exceptionally good damping on the actual process unit even when the process gain varies significantly. Gain and dead time (stability) margins are very good, see Fig. 7:

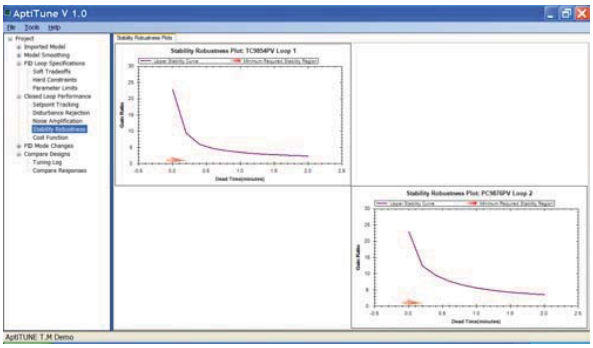

Fig. 7: Robustness plot (gain and deadtime stability margins)

A sensitivity analysis on the tray temperature loop shows that the gain of the process will have to increase by 3x AND the dead time will have to increase by another 12 seconds before the damping of the loops is unacceptable. Instability sets in at a process gain increase of more than 20x. A dead time error of more than 2 minutes is needed to reach instability, and there is no process mechanism for this to occur while the TIC is in the active range. These margins are exceptionally safe.

In order to compare the performance of the loops before and after retuning, we collected a week of normal operating data before we arrived on site, and one week of normal operating data after the re-tuning work was concluded. From these large data sets, we then calculated histograms to show the distribution of the control error (SP-PV). For process reasons, we wanted the loops to be robust and to be able to withstand changes in process dynamics. As a result, some loops were intentionally slowed down, and of course, their probability distributions will be wider than before. However, this compromise is all for a good cause as it will ensure that the loops remain operational for the years to come.

The performance of the pressure control loop PCA9876 is compared in Fig. 8:

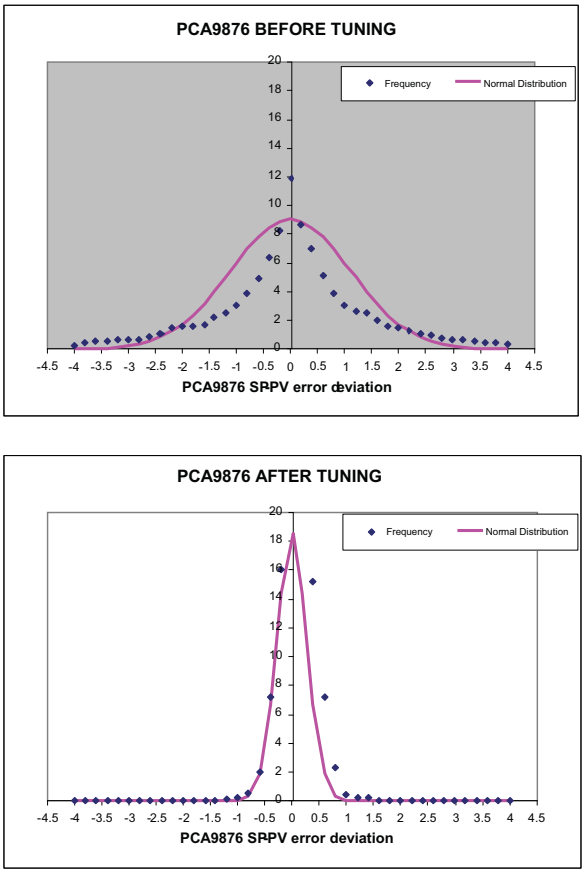

Fig. 8: Control error histograms for PCA9876 before and after retuning

It is clear from the two histograms shown above that the variability in the PV has reduced by about a factor of 4x. This is a big improvement in performance, yet this could be accomplished without compromising the robustness characteristics of the loop. The pink trace shows the best fit for a normal (Gaussian) distribution to the data, assuming a zero mean value. The estimated standard deviation σ reduced from 1.1 to 0.28.

The histograms for temperature loop TC9854 are compared in Fig. 9:

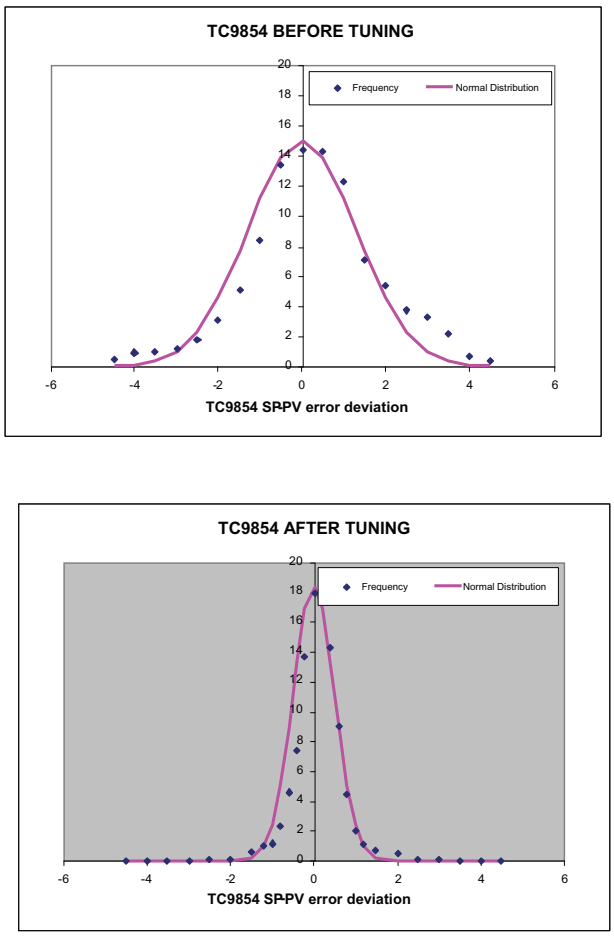

Fig. 9: Control error histograms for TC9854 before and after retuning

The standard deviation reduced from 1.3 down to 0.5, so by a factor of almost 3x. To be honest, these good results are partly due to the very slow initial tuning of some loops we found at the beginning of the project.

4. CONCLUSIONS

The following conclusions can be made. A MIMO model-based approach can be used to successfully tune multiple PID loops that interact strongly. If the open loop model is moderately accurate, then "one-shot" tuning is achievable and the simulated and observed OP and PV responses will be almost identical. The use of sufficiently large gain and dead time robustness margins ensures that the loop will remain stable and well damped even if the process is strongly nonlinear. This also helps to protect us against inaccurate model identification results. The ability to impose hard constraints on damping ratio, maximum PV overshoot, and the maximum OP value means we can ensure that the final design is safe from a process point of view. PID tuning rules cannot achieve this.

REFERENCES

Chen, D., Seborg, D.E. (2003). Design of decentralized PI control systems based on Nyquist stability analysis. *Journal of Process Control* 13(1), 27 – 39.

Espinosa Oviedo, J.J., Boelen, T., van Overschee, P. (2006). Robust advanced PID control. *IEEE Control Systems Magazine* 26(1), 15 – 19.

Forssell, U., Ljung, L. (2000). A projection method for closed-loop identification. *IEEE Trans. On Automatic Control* 45(11) 2101 – 2106.

Halevi, Y., Palmor, Z.J., Efrati, T. (1997). Automated tuning of decentralized PID controllers for MIMO processes. *Journal of Process Control* 7(2), 119 – 128.

Hovd, M., Skogestad, S. (1993). Improved independent design of robust decentralized controllers. *Journal of Process Control* 3(1), 43 – 51.

Hovd, M., Skogestad, S. (1994). Sequential design of decentralized controllers. *Automatica* 30(10), 1601 – 1607.

Li, Y., Ang, K.H., Chong, G. (2006). Patents, software and hardware for PID control. *IEEE Control Systems Magazine* 26(1), 42 – 54.

Maciejowski, J.M. (1989). *Multivariable Feedback Design*. Addison-Wesley

Monica, T.J., Yu, C.-C., Luyben, W.L. (1988). Improved multiloop single-input, single-output (SISO) controllers for multivariable processes. *Ind. Eng. Chem. Res.* 27, 969 – 973.

Vlachos, C., Williams, D., Gomm, J.B. (2000). Genetic approach to decentralized PI controller tuning for multivariable processes. *IEE Proceedings. Control Theory and Applications* 146(1), 58 – 64.

Zhu, Y. (2004). Robust PID tuning using closed-loop identification. Preprints of the International Symposium on Advanced Control of Chemical Processes ADCHEM 2004. vol. 1, 165 – 170

Auto-tuned Predictive Control Based on Minimal Plant Information

G. Valencia-Palomo * **J.A. Rossiter** *

* *Department of Automatic Control and Systems Engineering, University of Sheffield, South Yorkshire, U.K. S1 3JD. (e-mail: g.valencia-palomo@shef.ac.uk, j.a.rossiter@shef.ac.uk).*

Abstract: This paper makes two key contributions. First there is a definition and implementation of a novel auto-tuned predictive controller. The key novelty is that the modelling is based on relatively crude but pragmatic plant information. Secondly, the paper tackles the issue of availability of predictive control for low level control loops. Hence the paper describes how the controller is embedded in an industrial Programmable Logic Controller (PLC) using the IEC 1131.1 programming standard. Laboratory experiment tests were carried out in two bench-scale laboratory systems to prove the effectiveness of the combined algorithm and hardware solution. For completeness, the results are compared with a commercial PID controller (also embedded in the PLC) using the most up to date auto-tuning rules.

Keywords: Predictive control, auto-tuning, programmable logic controller, IEC-1131.1.

1. INTRODUCTION

Control design methods based on the predictive control concept have found wide acceptance in industry and in academia, mainly because of the open formulation that allows the incorporation of different types of models of prediction and the capability of constraint handling in the signals of the system.

Model predictive control (MPC) has had a peculiar evolution. It was initially developed in industry where the need to operate systems at the limit to improve production requires controllers with capabilities beyond PID. Early predictive controllers were based in heuristic algorithms using simple models. Small improvements in performance led to large gains in profit. The research community has striven to give a theoretical support to the practical results achieved and thus the economic argument, predictive control has merited large expenditure on complex algorithms and the associated architecture and set up times. However, with the perhaps notable exception of Predictive Functional Control (PFC) (Richalet, 1993), there has been relatively little penetration into markets where PID strategies dominate, and this despite the fact that predictive control still has a lot to offer in the SISO domain because of its enhanced constraint handling abilities and the controller format being more flexible than PID. The major obstacles cost, complexity and the algorithm not being available in the off the shelf hardware most likely used for local loop control.

Some authors have improved the user-friendliness (complexity) of MPC software packages available for high level control purposes (Froisy, 2006; Zhu *et al.*, 2008). Nevertheless, they have the same implementation drawback in that the development platform is a stand-alone computer running under Windows® OS. Furthermore, these packages involve complex identification procedures which thus requires the control commissioning to be in the hands of a few skilled control engineers; ownership by non control experts is an impediment for more widespread utilization.

Some early industrial work (Richalet, 2007) has demonstrated that with the right promotion and support, technical staff are confident users of PFC where these are an alternative to PID on a standard PLC unit. Technical staff relate easily to the tuning parameters which are primarily the desired time constant and secondly a coincidence point which can be selected by a simple global search over horizons choices. Because PFC is based on a model, the controller structure can take systematic account of dead-times and other characteristics, which are not so straightforward with PID. Also constraint handling can be included to some extent by using predicted violations to trigger a temporary switch to a less aggressive strategy.

The vendors conjecture is that PFC was successfully adopted because of two key factors: first there is effective support in technician training programmes (get it on the syllabus) and second the algorithm is embedded in standard PLC hardware they encounter on the job, thus making it easily accessible (and cheap). However, despite its obvious success academia has shied away from the PFC algorithm because its mathematical foundations are not as systematic or rigorous as other approaches; the performance/stability analysis is primarily an a *posteriori* approach as opposed to the a *priori* one more popular in modern literature. So there is a challenge for the academic community to propose more rigorous but nevertheless intuitive and simple algorithms which could equally be embedded in cheap control units.

On the other hand, in recent specialized conferences authors are often focussing on the level of rigor required in the modelling and tuning procedure for different cases (Morari *et al.*, 2008). However, accessibility and useability

in such a mass market may require different assumptions from those typically adopted in the literature; specifically much less rigor and more automation in the modelling will be essential.

Hence, the first objective of this paper is to develop an auto-tuned MPC controller based on minimal plant information which would be available from staff at technician level only who may be responsible for maintaining and tuning local loops. Secondly, the paper aims to demonstrate how an MPC algorithm, using this model information, can be embedded in a commercial PLC (Valencia-Palomo and Rossiter, 2008); this paper gives some extensions to that developments in (Valencia-Palomo *et al.*, 2008) and of particular interest to readers will be the incorporation of systematic constraint handling within the PLC unit. A final objective is to contrast the auto-tuned MPC with a commercial PID controller in order to show that the MPC is a practical (available and same cost) alternative to PID for local loops.

The paper is organized as follows: Section 2 outlines the controllers and the auto-tuning rules, Section 3 describes the implementation of the controllers in the target hardware, Section 4 presents the simulation results on real hardware and finally in Section 5 are the conclusions and future work.

2. THE CONTROLLERS

This section outlines the auto-tuning rules and modelling assumptions for the MPC and PID strategies adopted. We note that the auto-tuning rules are only applicable to stable systems so discussion of unstable systems is deferred for future work.

2.1 Modelling assumptions

If anything, this paper is more generous with the auto-tuned PID than the MPC because it allows the PID algorithm a large quantity of measurement data and the ability to dither the input substantially during tuning to extract the required information. Moreover, the complexity of this algorithm means that the modelling is done offline. This decision was taken to give a stiff test for the auto-modelled/tuned MPC algorithms.

For MPC we provide crude modelling information only, for instance as could be provided by a technician or plant operator but specifically avoiding the use of a rigorous least squares model estimator which could be expensive if required for large numbers of loops and impractical to put on the PLC unit. The technician should provide estimates of behaviour as compared to standard second order characteristics: rise-time, settling time, overshoot, steady-state gain and dead-time. From this data an approximate second order model with dead-time is determined [1].

2.2 Design point, auto-tuning and constraint handling for PID

A novel auto-tuned PID controller as described in (Clarke, 2006; Gyöngy and Clarke, 2006) is used. A schematic

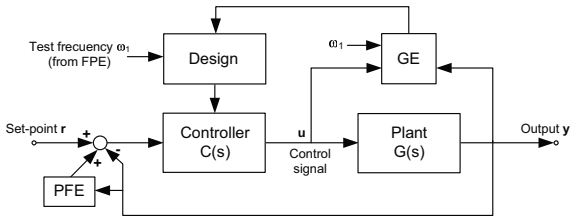

Fig. 1. Schematic diagram of the auto-tuning PID.

diagram of the system is shown in Fig. 1. The objective is to adapt the controller so as to achieve a carefully chosen design point on the Nyquist diagram.

The key components are phase/frequency and plant gain estimators (PFE, GE), described in detail in (Clarke, 2002). In essence a PFE injects a test sinewave into a system and continuously adapts its frequency ω_1 until its phase shift attains a desired value θ_d (in this case the design point). Also forming important part of the tuner, but not shown in Fig. 1, are variable band-pass filters (VBPF) at the inputs of the PFE and GE. These are second-order filters centered on the current value of the test frequency. They are used to isolate the probing signal from the other signals circulating on the loop (such as noise, set-point changes and load disturbances).

The algorithm is initialized using a first-order/dead-time (FODT) approximation $G_a(s)$ for the plant, obtained from a simple step test. The initialization involves the computation of suitable values for the parameters associated with the GE, PFE and the controller.

The controller is based on a design point in the Nyquist diagram. This design point is chosen to obtain the desired closed loop behavior, i.e. rise time, damping value, settling time. In this case, the desired damping value of 0.5 for all the systems is chosen. From this desired damping value, the variables for all the auto-tuning process are obtained as is shown in (Clarke, 2006; Gyöngy and Clarke, 2006).

The PID design does not take explicit account of constraints and thus ad hoc mechanisms are required. Typically input saturation with some form of anti-windup will be used but state constraints are not considered; this is a weakness.

2.3 Basic assumptions for MPC

For the purpose of this paper almost any conventional MPC algorithm can be deployed as the main distinguishing characteristic, **with sensible tuning**, is the model. Hence, assume that the MPC law can be reduced to minimising a GPC [2] cost function of the form:

$$J = \sum_{j=1}^{H_P} \|\hat{\mathbf{y}}(k+j|k) - \mathbf{w}(k+j|k)\|^2 + \sum_{j=1}^{H_C} \|\Delta\mathbf{u}(k+j|k)\|_\lambda^2 \tag{1}$$

where the second term in the eq. (1) is the control effort and λ is the weighting sequence factor. The reference trajectory $\mathbf{w}(k)$, is the desired output in closed loop of the system and is given by:

[1] We accept that for more complex dynamics a slightly more involved procedure may be required.

[2] To simplify some algebra compared to dual-mode approaches, e.g. (Rossiter *et al.*, 1998).

$$\mathbf{w}(k+i|k) = \mathbf{s}(k+i) - \alpha^i [\mathbf{s}(k) - \mathbf{y}(k)]; \ 1 \leq i \leq H_P \quad (2)$$

where $\mathbf{s}(k)$ is the set-point and α determines the smoothness of the approach from the output to $\mathbf{s}(k)$. The objective (1) can be expressed in more compact form in terms of the predicted output:

$$\min_{\Delta \mathbf{u}} \mathbf{J}(\Delta \mathbf{u}) = \frac{1}{2} \Delta \mathbf{u}^T \mathbf{H} \Delta \mathbf{u} + \mathbf{f}^T \Delta \mathbf{u} + \mathbf{b} \quad (3)$$

$$s.t. \qquad \mathbf{R} \Delta \mathbf{u} \leq \mathbf{c} \quad (4)$$

where $\Delta \mathbf{u}$ is the vector of future inputs increments and the other matrix details are omitted for brevity but available in standard references, e.g. (Maciejowski, 2002; Rossiter, 2003; Camacho and Bordons, 2004).

The tuning parameters are usually taken to be the horizons H_P, H_C and weights λ. However, more recent thinking suggests that H_P should be larger than the settling time, H_C is typically 2 or 3 (for practical reasons rather than optimality which requires higher values) and λ becomes the major tuning parameter, albeit some may argue a poor mechanism for tuning. The parameter α will also have a substantial impact but is rarely discussed except in PFC approaches.

2.4 Constraint handling for MPC

The systems considered in this paper are stable, therefore in the absence of output constraints, for a reachable set point the system will only violate the constraints in presence of disturbances or overshoots derived from set point changes. In practice, one may not be able to program a complete QP solver, so a sensible way of handling constraints is to interpolate two control laws (Rossiter and Grieder, 2005), one with good performance (e.g. $\Delta \mathbf{u}_{fast}$) and one with good feasibility (e.g. $\Delta \mathbf{u}_{slow}$) , using:

$$\Delta \mathbf{u} = (1-\beta) \Delta \mathbf{u}_{fast} + \beta \Delta \mathbf{u}_{slow}; \quad 0 \leq \beta \leq 1 \quad (5)$$

The variable β is used to form the mix of fast and slow according to the predicted situation (if feasible $\beta = 0$). Hence, the optimization procedure reduces to simple linear program in one variable that is a set of inequality checks of the form:

$$\min \beta \ \ s.t. \ \ R_i \beta - c_i \leq 0, \quad i = 1, ..., H_C \quad (6)$$

Remark 1. If $\beta = 1$ and the constraints are still being violated, the inputs are saturated. Essentially this means the state is outside the maximal admissible set for the unconstrained control law designed for good feasibility. Such scenarios need more complex strategies not covered in this paper.

2.5 Simple auto-tuning rules for MPC

There are many alternatives for auto-tuning, some with better properties then used here are possible, but the authors felt this paper should initiate discussion with an industrial standard. Thus, the predictive control design and tuning procedure is described next.

For the MPC the prediction horizon H_P is chosen equal to the settling time plus H_C, with $H_C \ll H_P$. Assuming normalisation of input/output signals, $0.1 \leq \lambda \leq 10$, a form of global search can be used to settle on the 'best' parameters against some criteria, however, if we take the criteria to be the cost J of eq. (1) with $\lambda = 1$, then this fixes λ and H_C is chosen to be as large as possible [3] . The design response speed α_{fast} (for $\Delta \mathbf{u}_{fast}$) will be taken as half the open-loop time constant α_0 so that the controller has to deliver some extra speed of response as well as stability and offset free tracking; and α_{slow} (for $\Delta \mathbf{u}_{slow}$) will be taken as 0.95 to have a smooth close loop response and avoid overshooting in set point changes. Thus, the auto-tuning is fixed precisely by the model parameters and the technician role is only to provide best estimates of these parameters (in practice some iteration should take place).

Fig. 2. Allen Bradley PLC – SCL500 processor family.

3. IMPLEMENTATION OF THE ALGORITHMS ON A PROGRAMABLE LOGIC CONTROLLER

This section briefly introduces the PLC and the corresponding implementation of the controllers described in the previous section.

3.1 Allen Bradley — Rockwell Automation Inc. PLC

PLCs are by far the most accepted computers in industry which offer a reliable, safe and robust system; we will not revisit the reasons here. Nevertheless, normally their use is only to implement control sequences in open loop and/or different structures of PID controllers. For the purposes of this paper, the implementation is based on the family of SLC500 processors belonging to the Allen Bradley PLC systems, e.g. see Fig. 2.

The Allen Bradley set of PLC includes the facilities to be programmed in 3 of 5 languages in agreement with the IEC 1131.3 standard using Control Logix 5000^{TM} software programming package. Each of these allows for any combination of programming languages to be used for a single project. These three languages are: (i) *Ladder Diagram*, (ii) *Function Block Diagram* and (iii) *Structured Text*.

3.2 PID

The Control Logix 5000^{TM} software programming package also includes a function block to implement a PID controller. The PID function block is a professional development from Rockwell Inc. used in industry (with a PLC) to control a variety range of processes.

[3] For sensible sample times, a choice of $H_C \geq 5$ implies that this is approximately equivalent in behaviour to a dual-mode approach.

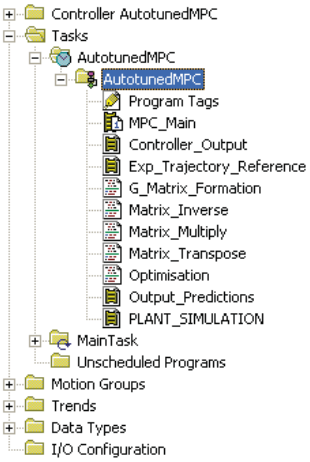

Fig. 3. Structure of the MPC algorithm in the target PLC.

The tuning of the PID is done off-line by the algorithm described in subsection 2.2. The obtained parameters are passed to the PID block before downloading the program to the PLC. As noted earlier, the PID has been unfairly favoured here in that this off-line procedure requires a certain amount and type of experimental data for the model identification of the process.

This controller is going to be used to compare the results obtained with the auto-tuned MPC.

3.3 MPC

For the implementation, is worth mentioning that it is advisable to use a a graphical language such as *ladder logic* or *function block* because technical staff are much more familiar with this than structured text; also it is easier to maintain and debug for the changing nature of bits, timers, counters etc. while being monitored. However, a significant barrier for MPC implementation is that operations between vectors and matrices are not defined in any of the supported IEC 1131.1 languages, thus, all of these operations have to be programmed from scratch.

The complete structure of the proposed MPC program (based on subsections 2.3–2.5) is shown in Fig. 3. The algorithm has been programmed in the High Priority Periodic Execution Group [4] called `AutotunedMPC` which contains the routines summarised in Table 1. The software design, matrix formations, sequence of execution and the computation of the calculated output is described in detail in (Valencia-Palomo and Rossiter, 2008); with the exception of the routine `Optimisation` which is new to this paper and developed to include constraint handling, as described in subsection 2.4.

It can be seen from the properties of the controller with the RSLogix programming tool (Fig. 4) that the programm uses 17% of the available storage of the PLC including memory requirements for I/O, running cache and other necessary subroutines.

Finally, the input parameters for the program are only those who are related with de model, i.e. dead time t_d,

[4] This periodicity is set up with the chosen sample time.

Table 1. Routines and programming languages.

	Routine name	Programming language
1	`MPC_Main`	Ladder logic
2	`Controller_Output`	Ladder logic
3	`Exp_Trajectory_Reference`	Ladder logic
4	`G_Matrix_Formation`	Structured text
5	`Matrix_Inverse`	Structured text
6	`Matrix_Multiply`	Structured text
7	`Matrix_Transpose`	Structured text
8	`Output_Predictions`	Ladder logic
9	`Plant_Simulation`	Ladder logic
10	`Optimisation`	Structured text

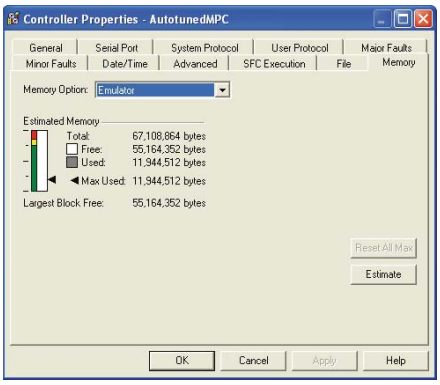

Fig. 4. MPC memory usage in the target PLC.

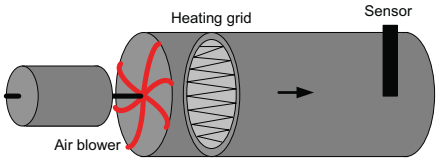

Fig. 5. Heating process.

rise time t_r, settling time t_s, overshoot M_P, gain K and sampling time Ts. The tuning is done online in the first scan of the program and is not repeated after, however, some mechanisms to update the model of the plant and tuning parameters can be embedded.

4. EXPERIMENTAL LABORATORY TESTS

This section shows the experimental results from applying the MPC law via a PLC on a first and a second order plant. For both processes the interest is tracking of step references, which is the most common situation in industry. The PID/MPC experiments ran under the same conditions, in so far as this can be guaranteed.

4.1 First order plant – Temperature control

The first experiment is a heating process consisting of a centrifugal blower, a heating grid, a tube and a temperature sensor, see Fig. 5. The objective is to control the temperature at the end of the tube by manipulating speed of the blower (the input voltage of the D.C. motor).

The model of the plant for the PID off-line tuning is done by a least square estimator assuming a first order plant.

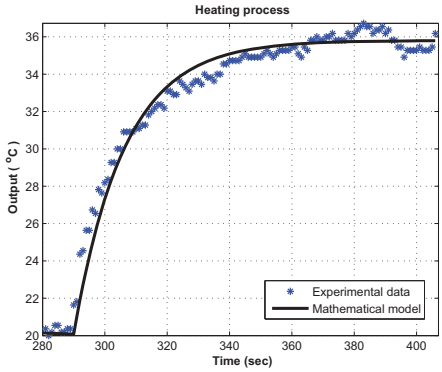

Fig. 6. Model validation of the heating process.

Table 2. Tuning parameters for the PID controller and input parameters for the auto-tuned MPC.

		Heating Proc.	**Speed Proc.**	
Cont.	Par.	Value	Value	Units
PID	P	1.590	0.325	–
	I	0.486	0.799	–
	D	0.0	0.0	–
MPC	Ts	10.0	0.50	Sec
	t_d	2.0	1.00	Samples
	t_r	38.0	4.90	Sec
	t_s	64.0	2.71	Sec
	K	16.0	190.0	–
	M_p	–	–	%

The resulting discrete model, with a sampling time of 10 sec. (which is also roughly the dead-time), is:

$$x(k+1) = 0.94x(k) + u(k)$$
$$y(k) = 0.94x(k)$$

The experimental validation of the mathematical model is shown in Fig. 6.

The tuning parameters for the PID controller and the input parameters for the Auto-tuned MPC are shown in Table 2. The second order approximate model for the predictions is built using standard analysis of the transient response of the plant i.e. nonparametric identification.

The simulation comparisons deploy a step change at $t = 50\,secs$ of the set point from 20 $°C$ to 30 $°C$; after the output reaches a new steady state, the process is disturbed at $t \approx 120\,secs$ by partially blocking the end of the tube. A new change in the set point to 20 $°C$ is required at $t = 180\,secs$ without taking out the disturbance.

It can be seen in Fig. 7 that the plant output is successfully tracking the reference signal for both controllers. Of course this is a simple first order model and thus good control is to be expected. MPC has clearly given better control of overshoot and settling.

4.2 A second order plant – Speed control

This process consists of a motor fitted with a speed sensor, the control objective is to regulate the speed of the motor by manipulation of the input voltage. The same procedure as in the first experiment is applied. The mathematical model of the system with a sampling time of 0.5 sec is:

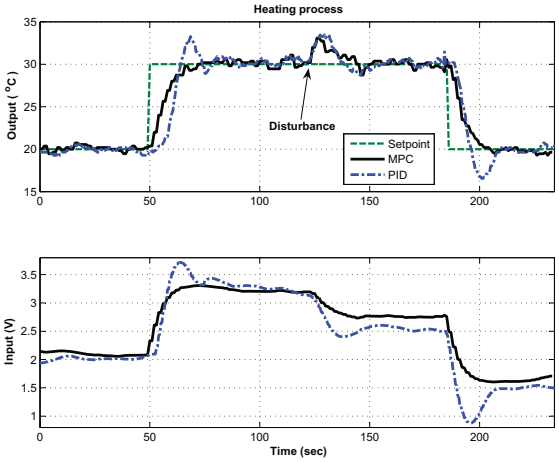

Fig. 7. Experimental test for the heating process.

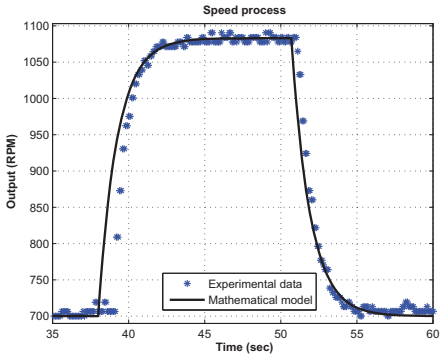

Fig. 8. Model validation of the speed process.

$$x(k+1) = \begin{bmatrix} 0.93 & -0.01 \\ 0.04752 & 0.9964 \end{bmatrix} x(k) + \begin{bmatrix} 1 \\ 0 \end{bmatrix} u(k)$$
$$y(k) = \begin{bmatrix} -0.01 & 3.71 \end{bmatrix} x(k)$$

The experimental validation is shown in Fig. 8 and the tuning parameters are in Table 2. Two set point step changes are demanded; once again, the results in Fig. 9 show that MPC and PID are tracking the set point accurately.

4.3 Performance indexes of the algorithms

The numerical performance indexes of the systems with the two different controller strategies are summarised in Table 3. Specifically the table shows the measures of performance are given by the cost function (J), the settling time (τ_s) and the overshoot (M_p). These numbers show that MPC performs similar to the standard PID controller but,in this case, with a much simpler auto-tuning procedure.

The constraint handling was not tested in a rigorous manner to let the PID controller act in the best possible scenario. Despite that, this simple control task finds its optimal value in saturation (Rojas and Goodwin, 2002).

To complete the analysis of the implemented program, the diagnostics tool from the hardware (shown in Fig. 10)

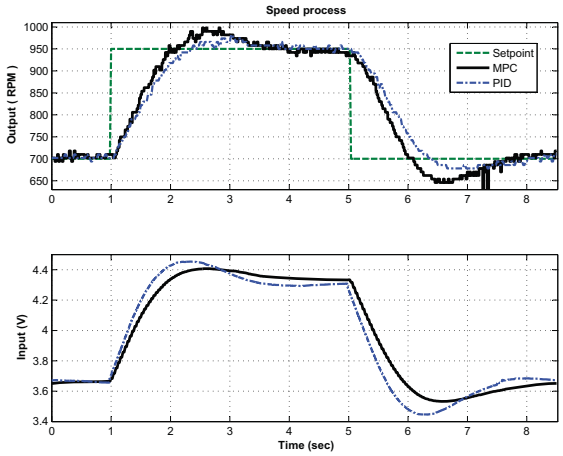

Fig. 9. Experimental test for the speed process.

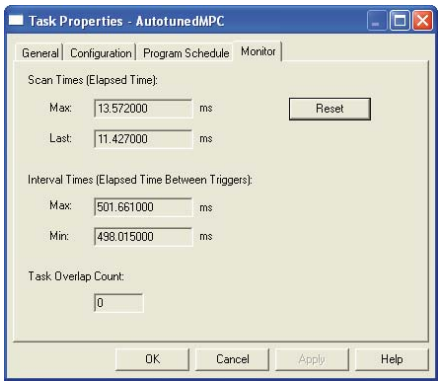

Fig. 10. Execution time and sampling jittering for the speed process.

Table 3. Performance indices for the systems.

	Heating process			Speed process		
	τ_s	M_p	J	τ_s	M_p	J
PI	31 sec	33.45 %	1645	3.3 s	16%	2,615
MPC	20 sec	0.0 %	1629	3.3 s	8%	2,816

displays that the time for scanning the program each sample time oscillates between 11.42 ms and 13.57 ms while the elapsed time between triggers (sampling instants) for the speed process oscillates between 498.01 ms and 501.66 ms. The significance of this is the potential to apply the algorithm on much faster processes.

5. CONCLUSIONS

This paper has made three contributions. First it has demonstrated that an MPC algorithm with systematic, albeit simplistic, constraint handling can be coded in an industrial standard PLC unit and with sample times of milliseconds. Secondly it has demonstrated that such an algorithm can make use of simplistic modelling information in conjunction with basic auto-tuning rules and still outperform an advanced auto-tuned PID whose design relied on far more information. Moreover the MPC includes constraint handling. Thus, thirdly the paper has demonstrated that MPC is a realistic industrial alternative to PID in loops primarily controlled with PLC units. This final contribution opens up the potential for much improved control of loops where PID may be a poor choice.

These results demonstrate the potential for implementing auto-tuned MPC within a PLC. Some issues the authors intend to pursue are: (i) demonstrate the algorithm in more challenging test rigs such as those with non-minimum phase behaviour and/or significant dead-times; (ii) consider extensions for unstable systems; and (iii) implement more advanced dual-mode type MPC algorithms and more advanced constraint handling facilities into the PLC.

REFERENCES

Camacho, E. and C. Bordons (2004). *Model predictive control*. 2nd ed.. Springer Verlag.

Clarke, D.W. (2002). Designing phase-locked loops for instrumentation applications. *Measurement* **32**, 205–227.

Clarke, D.W. (2006). PI auto-tuning during a single transient. IEE *Proceedings Control Theory and Applications* **153**(6), 671–683.

Froisy, J.B. (2006). Model predictive control — building a bridge between theory and practice. *Computer & Chemical Engineering*. **30**, 1426–1435.

Gyöngy, I.J. and D.W. Clarke (2006). On the automatic tuning and adaptation of PID controllers. *Control Engineering Practice* **14**, 149–163.

Maciejowski, J.M. (2002). *Predictive control with constraints*. Prentice Hall.

Morari, M., C. Jones and M. Zeilinger (2008). Low complexity MPC. In: *International Workshop on assessment and future directions in NMPC*. Pavia, Italy.

Richalet, J. (1993). *Practique de la commande predictive*. Hermes, France.

Richalet, J. (2007). Industrial application of predictive functional control. In: *Nonlinear Model Predictive Control, Software and Applications*. Loughborough, U.K.

Rojas, O.J. and G.C. Goodwin (2002). A simple anti-windup strategy for state constrained linear control. In: *IFAC World Congress*. Barcelona, Spain.

Rossiter, J.A. (2003). *Model predictive control: a practical approach*. CRC Press.

Rossiter, J.A. and P. Grieder (2005). Using interpolation to improve efficiency of multiparametric predictive control. *Automatica* **41**, 637–643.

Rossiter, J.A., B. Kouvaritakis and M.J. Price (1998). A numerically robust state-space approach to stable-predictive control strategies. *Automatica* **34**(1), 65–73.

Valencia-Palomo, G. and J.A. Rossiter (2008). The potencial of auto-tuned MPC based on minimal plant information. In: *Assessment and Future Directions of Nonlinear Model Predictive Control*. Pavia, Italy.

Valencia-Palomo, G., K.R. Hilton and J.A. Rossiter (2008). Predictive control implementation in a PLC using the IEC 1131.3 programming standard. *In review for the European Control Conference 2009*.

Zhu, Y., Z. Xu, J. Zhao, K. Han, J. Qian and W. Li (2008). Development and application of an integrated MPC technology. In: *Proceedings of the 17th IFAC Wolrd Congress*. Seoul, Korea.

The Effect of Tuning in Multiple-Model Adaptive Controllers: A Case Study

Ehsan Peymani* Alireza Fatehi**
Ali Khaki Sedigh***

Advanced Process Automation & Control (APAC) Research Group, K. N. Toosi University of Technology
Tehran, Iran.

(e-mail: *ehsan.peymani.f@ieee.org, **fatehi@kntu.ac.ir, ***sedigh@kntu.ac.ir)

Abstract: In this paper, two types of multiple-model adaptive controllers are practically evaluated on a laboratory-scale pH neutralization process. The first one is supervisory switching multiple-model adaptive controller (SMMAC) whose model bank is fixed and selected a priori, and another one is a controller based on multiple models, switching, and tuning strategy (MMST) which uses the possibility of model bank tuning. In addition to investigation of the effect of tuning, the advantage of a disturbance rejection supervisor is studied. Various experiments and exhaustive numerical analyses are provided to assess the abilities of the proposed algorithms.

Key Words: multiple models, adaptive control, pH control, switching control, pole-placement control

1. INTRODUCTION

Multiple-model adaptive control is a promising approach to control complex, nonlinear, and time-variant systems. On the grounds that a very complicated system is decomposed to simpler and smaller ones in this approach, and therefore, a large set of model uncertainty is converted to smaller sets, this approach results in a robust controller. It is, also, called an intelligent approach if intelligence is defined as rapid and appropriate response to large and sudden variations in a system (Narendra and Balakrishnan, 1997).

Multiple-model approaches are well-known not only in control but also in identification and estimation (Johansen and Murray-Smith, 1997). Multiple-modeling means that a set of models describes a dynamical system instead of one lone model. According to the type of contribution of members of this set to construct the global model of the process, switching or interacting multiple-model approaches are obtained. In switching multiple-model control strategies, at each instant, one model of the bank is selected as the global model, and the controller is designed according to the parameters of the model. This kind of control strategy has been evaluated in many subject areas such as robotics (Czlzz and Narendra, 1996), flight control (Boskovic and Mehra, 1999), aerospace applications (Karimi and Landau, 2000), and process control (Pishvaie and Shahrokhi, 2000; Gundala, Hoo, and Piovoso, 2000).

It is obvious that model bank significantly affects control performance. Thus, it is critical to have a model bank that considers all possible operating points. Since all possible operating points are not known a priori, increasing the number of model bank members may be a solution. However, in addition to intensifying computational burden, there is a chance of deteriorating performance owning to excessive competition of unnecessary members (Li and Bar-Shalom, 1996). Another solution is model bank tuning.

Model bank tuning means that beside each fixed models there is an adaptive model which starts to adjust itself from the location of the fixed model after the fixed model was chosen by the supervisor of the control system. Consequently, a quite new control strategy is introduced and called *multiple models, switching, and tuning* (MMST) (Narendra and Balakrishnan, 1997; Narendra and Xiang, 2000).

The main objective of this paper is to study how the possibility of tuning affects the effectiveness of a multiple-model adaptive controller. To accomplish the objective, we experiment two multiple-model controllers on a pH pilot-plant. The pilot-plant was designed and constructed by members of the research group at KNTU. Figure 1 shows this plant. The secondary objective is to investigate practically a disturbance rejection supervisor, introduced firstly in (Peymani et al, 2008). Since there is no buffer stream in the pilot-plant, the process keeps its high nonlinearity such that the static gain of the process can vary more than 70 times for the entire operating range.

The paper is organized as follows. After introduction, the principles of multiple-model adaptive controllers are reviewed. Two control strategies are presented: one has tuning possibility and the other does not. In the next section, section 3, a disturbance rejection supervisor is designed and its specifications are stated. Then, section 4 is allocated for the pH pilot plant description. Application results are, also, provided in this section. Finally, conclusions end the paper.

2. THE BASIS OF MULTIPLE MODELS ADAPTIVE CONTROLLERS

The control strategies utilized in this paper are based on supervisory switching multiple-model adaptive controllers. In these controllers, the whole nonlinear system is divided into several linear systems which can be represented more exactly by a set of simple linear models, called *model bank*.

Fig 1. pH pilot-plant at ACSL, K. N. Toosi University of Technology

That which model and when must be selected is the duty of the *supervisor*. The supervisor determines the appropriate model according to a *switching scheme*.

Let us presume that we have the simplest form of model bank which contains N fixed-parameter models. In fact, each model is a predictor anticipating the future output of the process in accordance with the last measured input and output. The difference between the output of the real plant and of each model is sent to the supervisor to calculate the identification performance index according to eq. (1):

$$J_s(t) = \alpha e_s^2(t) + \beta \sum_{k=1}^{M} \lambda^k e_s^2(t-k), \quad 0 < \lambda \le 1, \alpha, \beta, M > 0 \tag{1}$$

in which $e_s = y - \hat{y}_s$, and α, β, λ and M are the free-design parameters. Pole-placement control design method is utilized in this paper. It is a two-degree of freedom dynamical output feedback controller having the form of:

$$R(q)u(t) = T(q)u_r(t) - S(q)y(t) \tag{2}$$

where R, S, and T are calculated after the process model was selected. The process is viewed as a first order plus time delay model (FOPDT). To find the appropriate values for the controller parameters, it is necessary to define a model reference, a priori, regarding the control objective, and solve a polynomial Diophantine equation on-line. For more details about the controller design method see (Astrom and Wittenmark, 1995; Peymani et al, 2008).

The significance of model bank on the performance of the control system is beyond dispute. The more precise a model bank represents the plant, the better the control system performs. Difficulties arise from the problem of decomposing a plant into efficient smaller linear subsystems. Moreover, a real-world plant inevitably encounters variations which are able to make new operating conditions.

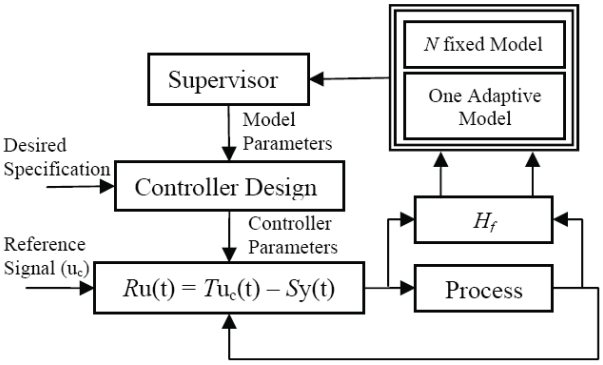

Fig 2. The block diagram of the multiple models, switching, and tuning adaptive controller

If an unpredicted one comes about, the control performance may become weak. To cover more states of the process, the number of members of the model bank should be increased. This solution is not suitable because a bank with too many members may deteriorate the performance in addition to excessive complexity burden (Li and Bar-Shalom, 1996).

Tuning of the current model is another solution to solve this problem. In this idea, after a fixed model is selected, an adaptive model starts to adjust itself to the process condition from the location of the fixed model. Thus, convergence of the adaptation algorithm may be reached soon, and the adaptive model may describe the process more precisely than the selected fixed model does. This model is called *re-initialized adaptive model*, and can be built by a recursive least-squares (RLS) identification method with exponentially forgetting factor (Astrom and Wittenmark, 1995). This control structure containing both fixed and adaptive models in the bank is also called *Multiple Models, Switching, and Tuning* (MMST) control strategy and firstly is introduced by Narendra et al. Thus, this adaptive control strategy possesses a two-stage identification unit: the switching stage to overcome sudden and large changes of the process and the tuning stage to track slow and gradual process variations. Figure 2 shows this control strategy.

Switching Scheme: Decision-making part in MMST is done by supervisor as follows. At each sampling time, performance indexes of N fixed models and one re-initialized adaptive model are updated. Then, in the switching stage, the best fixed model whose index is smaller than the product of other indexes by h_S is selected. The factor h_S is the hysteresis constant for the switching stage. After each change of the best fixed model, the adaptive model is reinitialized by the parameters of the fixed model unless the identification performance of the adaptive model is better than the best fixed model. The decision can be made by comparing their performance indexes.

After the switching stage, the tuning stage triggers. In this stage, the supervisor orchestrates which of the adaptive or the best fixed model is appropriate for control. This stage owns another hysteresis constant, represented by h_T. If the index of

the adaptive model is smaller than the multiplication of the index of the best fixed model by h_T, the adaptive model is used to design the controller. At this time, the process is controlled by an *adaptive pole-placement controller* (APPC). With the same logic, the supervisor determines whether it is appropriate to use the fixed model for control. As mentioned, SMMC is simpler than MMST control strategy and dose not have tuning stage and adaptive model, so switching stage is simpler.

3. DISTURBANCE REJECTION SUPERVISOR

All adaptive controllers need the process information to adapt itself to the current condition. The process has to be excited very well in order to collect appropriate information. In process control, the set-point rarely changes. Nonetheless, disturbances occur occasionally. Hence, disturbances can be considered as the staple source of excitation.

When a disturbance happens, at first the process output deviates from the reference input. Then, the controller reacts against this action. Consequently, it is possible to divide the process output into two parts. The first part is the duration which the disturbance, as an unmeasured input, affects the process output, and the second is the one that the control signal derives the system in spite of disturbance. Excitation resulted from the first part is adverse for identification, but excitation caused by the second part which the control signal dominantly affects the system is proper for process identification.

Then, discarding irrelevant data is vital to enhance on-line system identification. This aim is achieved if the time when a disturbance occurs is detected; that is, the identification stage is interrupted in the first part of excitation caused by a disturbance. An idea to discover disturbance occurrence is proposed in (Hagglund and Astrom, 2000) and is shown in Fig. 3, in which y_f and u_f are high-pass filtered process output and input, respectively. According to this idea which is proposed for positive-gain systems, when filtered process input and output are larger than predefined thresholds and have opposite signs, a disturbance has occurred. The time when the control action is appropriate for identification can be estimated based on the maximum value of the filtered process output.

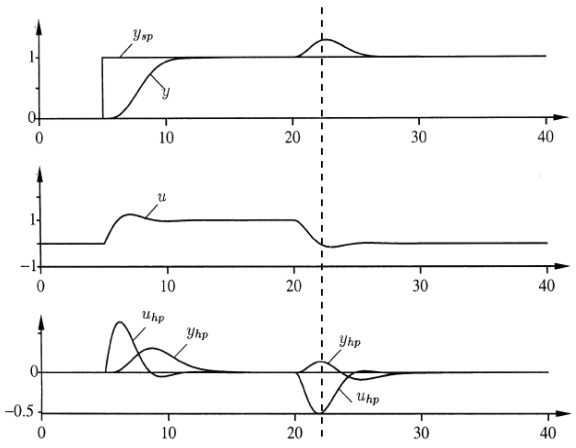

Fig 3. Response of a linear system in close-loop feedback on condition that a disturbance occurs (Hägglund and Astrom, 2000).

According to the extension of this supervisory function for multiple-model controllers, which is proposed by the authors in (Peymani et al, 2008), when a disturbance discovered, both switching and tuning stages are not allowed to work, and the controller is designed based on the best fixed model. After the first part of excitation, the tuning and switching parts are permitted again. In MMST strategy, it is possible to re-initialize the adaptive model to converge rapidly after negative excitation of disturbance.

4. APPLICATION RESULTS

The aim of this paper is to study the effect of tuning in the model bank of multiple-model adaptive control strategies by evaluating two multiple-model based controllers on a pH pilot-plant. After pH pilot plant description, application results are provided.

4.1 pH pilot-plant Description

This plant was designed and constructed in K. N. Toosi University of Technology (Fig. 1). In this process, as shown in Fig. 4, there are four streams: acid, base, water, and effluent. The acid stream is the process stream; its concentration and flow rate are presumably constant. The base stream is the titrating stream whose concentration is constant but flow rate is calculated by the controller to regulate pH of the effluent stream. The effluent stream has a constant flow rate. Moreover, this plant is composed of a continuous stirred tank reactor (CSTR) where chemical components are mixed, a pH sensor, a level sensor, and three dosing pumps which inject water, base, and acid with precise flow rate. To keep the level of the tank constant, a classical PI controller is designed which uses water stream flow rate as the control signal. Figure 5 displays the block diagram of this control system.

It is valuable to mention that aquatic solution of acid acetic (a weak acid) and sodium hydroxide (a strong base) are used as process stream and titrating reagent, respectively. However, there is no buffer stream in this pilot-plant. This feature makes this process highly nonlinear. Figure 6 depicts the titration curve of the process with typical concentrations. As it can be seen, it has a steep and large increase in its derivative. This curve is calculated for a batch process because calculating the titration curve of a continuous process is very difficult owning to inherent nonlinearity and various external disturbances. Figure 7 reveals that the static gain can vary more than 70 times for pH in the range of 5 to 10. It is worth mentioning that the measurement noise of the process varies with pH. It is about 5e-5 outside the range of [7, 8.2], whereas it is about 1e-3 inside the range.

4.2 Experimental Evaluation

In this section, two multiple models adaptive controllers, proposed earlier, are considered and their parameters are presented specifically. To have comparable situations, the parameters of both controllers are chosen the same. Indeed, the only difference between them is that MMST based controller has the possibility of model bank tuning, while supervisory switching multiple models adaptive controllers (SMMC) has a fixed-parameter model bank. Anyway, to construct a fixed model bank, the process is controlled by a classical adaptive pole-placement controller in varying pH values.

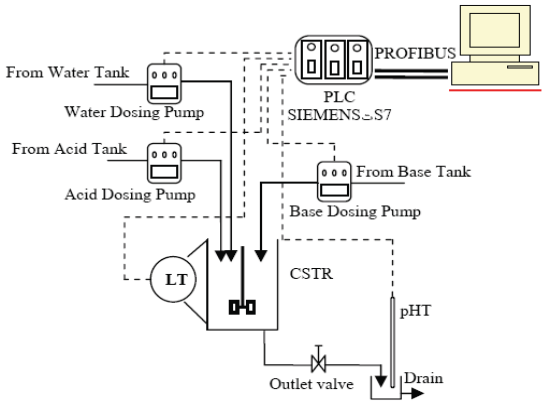

Fig 4. Schematic diagram of pH pilot-plant

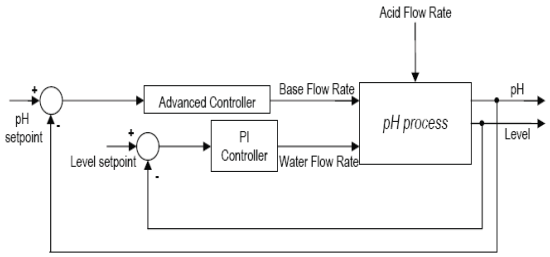

Fig 5. Block diagram of the control system

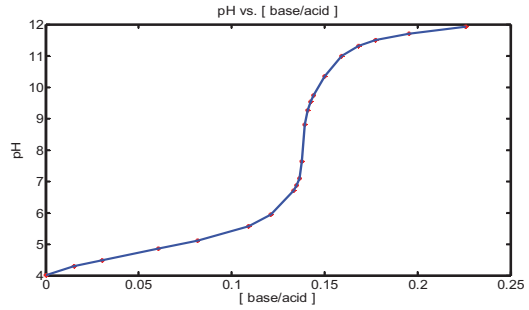

Fig 6. Titration curve of the process stream in the batch form.

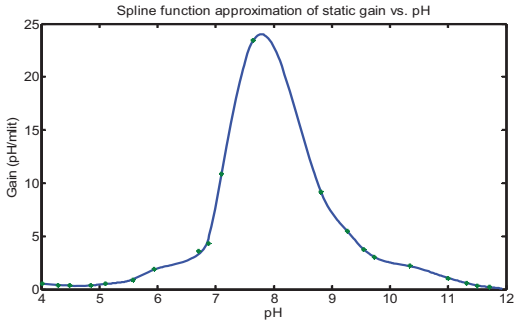

Fig 7. Variations of static gain of pH pilot-plant versus pH

After convergence of the adaptive model, the model is saved as the model of current operating condition. Table I collects models of various operating points. Before identifying, data are passed through a band-pass filter to discard bias and attenuate the adverse effect of noise. Hence, as shown in Fig. 2, filter H_f is located at the beginning of the identification loop, which is:

$$H_f(q) = \frac{(q-1)}{(q-\alpha)^2}(1-\alpha)^2 \tag{3}$$

The parameter α is 0.9652. Then, the model reference for pole-placement control design method is:

$$G_m(q) = \frac{0.0012}{(q-0.9652)^2} q^{-8} \tag{4}$$

The parameters of performance index are selected as $M = 50$, $a = 320$, $b = 100$, $\lambda = 0.985$. Hysteresis factor for SMMAC equals to 0.80, and switching and tuning hysteresis factors in MMST are chosen 0.85 and 0.75, respectively.

We consider a sequence for step-like set-point changes containing three kinds of variations: 1) small changes which means set-point varies from 5 to 10 one by one (Fig. 8.a); 2) medium changes which means set-pint changes from 6 to 8 and to 10, and then returns to 6 in the same manner (Fig. 8.b). These variations are known as the most difficult ones in this process; 3) large changes that contain some variations larger than two units in pH (Fig 8.c). Moreover, the acid feed rate is considered as a measured disturbance. Its nominal value is 30% of maximum power of the corresponding pump. The sequence of 30% → 18% → 42% → 30% is considered as disturbance sequence.

A criterion is defined in order to compare the results numerically, so we choose a two-part measure. Each part is calculated individually for each change in set-point or each disturbance. It is:

$$\begin{aligned} C &= \sum MSWE + 10 \sum O.C. \\ MSWE &= \frac{100}{n-1} \sum \left((y(t) - y_r(t))^2 e^{0.005\,t} \right) \\ O.C. &= 1 - \left| \frac{\sum (y_f)}{\sum |y_f|} \right| \end{aligned} \tag{5}$$

in which *O.C.* is a measure of oscillation. Mean square weighted error (*MSWE*) shows how much the process output is similar to y_r, the model reference output or desired output. It weights the errors exponentially in time.

At first, our aim is to regulate pH of effluent process at different values. Thus, we use the same set-point sequence with various changes to assess how much each controller is able to drive the process similar to the desired output. Fig. 8 shows the results, and table II gathers numerical analysis.

The second test is to evaluate the ability of the controllers to reject external disturbances. Figures 9 to 11 show the results of this test. The effect of disturbance rejection supervisor is demonstrated in Fig. 10 and Fig. 11. Table III compares the disturbance rejection abilities numerically.

4.3 Discussion

This section is allocated for application results. According to Fig. 8, the presence of tuning in the model bank of a multiple-model adaptive control can improve transient response. In this figure, MMST control algorithm has a smoother response, especially for pH around 7.5. Changing from 6 to 8 (and vice versa) is the most difficult change in this plant because the control system has to drive the process from a low-gain operating point to the highest one. The same result can be derived from disturbance rejection part. Hence, it is evident that MMST strategy has a better performance than the other strategy without tuning possibility does.

Figures 9, 10, and 11, and table III demonstrate that the disturbance rejection supervisor can help the supervisor to make a better decision, so this additional supervisory function is satisfactory. Generally, according to Fig. 11, the disturbance rejection supervisor is the reason to a faster rejection.

Table 1 Local models of the process, time delay neglected to be shown equals to 9 sampling times (45 seconds).

Model no.	1	2	3	4
Local Model	$\frac{0.0070}{z-0.985}$	$\frac{0.0166}{z-0.990}$	$\frac{0.0044}{z-0.970}$	$\frac{0.001}{z-0.970}$

5. CONCLUSION

The proposed MMST control strategy is modified slightly from the original version and the switching stage is transparently separated from the tuning phase. Moreover, to constrain the speed of switching, hysteresis constants are used. The presence of tuning in multiple-model adaptive controllers has positive effect in performance. The application results, which are provided for both tracking and disturbance rejection problems by implementation two multiple-model controllers on a pH pilot-plant, prove that the response of MMST is smoother and more similar to desired output. Also, they uncover that the possibility of tuning in identification loop prevents the model bank to be specified to a certain process. In fact, tuning tries to generalize the model bank. Furthermore, the application results reveal that the presence of the disturbance rejection supervisor can augment the effectiveness of multiple-model adaptive controllers to face load disturbances without imposing significant computational burden. The disturbance rejection supervisor is designed for positive-gain systems.

It can be claimed on condition that the model bank has a severe deficiency to describe the process, SMMC may result in instability, while MMST can stabilize the process because of the presence of tuning.

Table 2 Comparison between SMMC and MMST in tracking

	Small	Medium	Large	Overall
SMMC	32.37	52.61	63.29	148.27
MMST	27.81	25.79	63.50	117.10

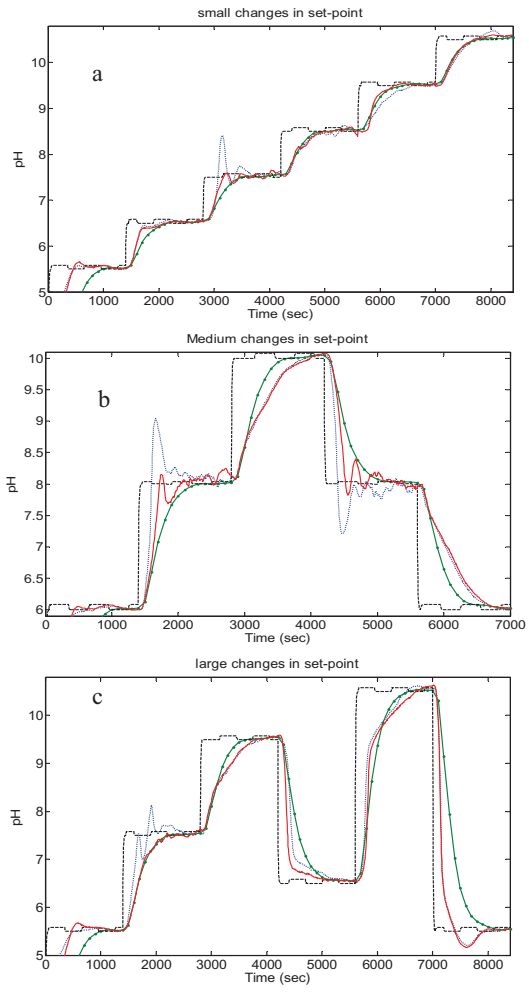

Fig 8. Evaluation of the effect of model bank tuning in tracking problem; a) small, b) medium, c) large changes in set-point; solid line (MMST), dash line (SMMC), and dash-dot line (desired output)

Table 3 Comparison of disturbance rejection ability between SMMC and MMST.

Disturbance Rejection	Disturbance Rejection Supervisor	
	OFF	ON
SMMC	167.38	90.31
MMST	75.07	66.31

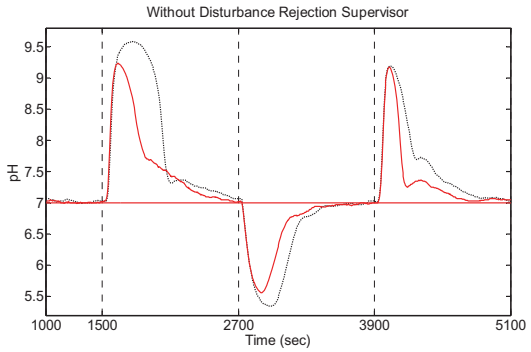

Fig 9. Disturbance rejection of both controllers without disturbance rejection supervisor; solid line (MMST) and dotted line (SMMC)

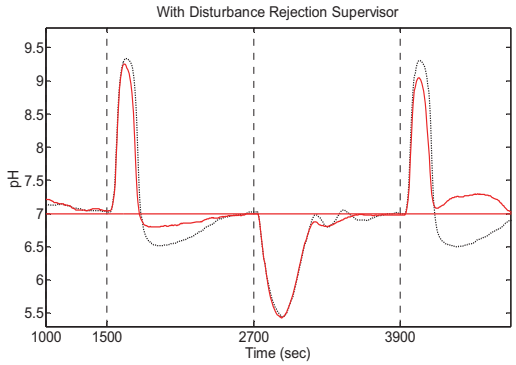

Fig 10. The effect of disturbance rejection supervisor; solid line (MMST) and dash line (SMMC)

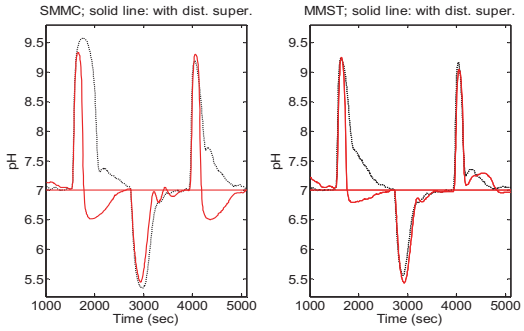

Fig 11. The effect of disturbance rejection supervisor, comparison in each controllers, dash line (without the supervisor) and solid line (with the supervisor); left: SMMC and right: MMST

REFERENCES

Astrom, K. J. and Wittenmark, B. (1995). *Adaptive Control*, 2nd ed.. Addison-Welsey, NY.

Boskovic, J. D., and Mehra, R. K. (1999). Stable multiple model adaptive flight control for accommodation of a large class of control effector failures. In Proceedings of the 1999 American control conference (Vol. 6, pp. 1920-1924), San Diego, CA, June 1999.

Czlzz, M. Kemal and Narendra, K.S., (1996). Intelligent Control of Robotic Manipulators: A Multiple Model Based Approach. The International Journal of Robotics Research, 15(6), 592-610.

Gundala, R., Hoo, K.A., and Piovoso, M.J., (2000). Multiple model adaptive control design for a MIMO chemical reactor. Ind. Eng. Chem. Res., 39(6), 1554-1564.

Hägglund, T. and Astrom, K. J., (2000). Supervision of adaptive algorithms. Automatica, 36(8), 1171-1180.

Johansen, T. A. and R. Murray-Smith (1997). The operating regime approach. In: Multiple Model Approaches to Modelling and Control. (R. Murray-Smith and T. A. Johansen, Eds.). Taylor & Francis Inc.. Bristol, PA. 3-72.

Karimi, A. and Landau, I. D., (2000). Robust Adaptive control of a flexible transmission system using multiple models. IEEE Transactions on Control Systems Technology, 8(2):321-331.

Li, X.R., and Bar-Shalom, Y., (1996). Multiple-model estimation with variable structure. IEEE Transactions on Automatic Control, vol. 41, No. 4, pp. 478-493.

Narendra, K.S. and Balakrishnan, J., (1997). Adaptive Control Using Multiple Models. IEEE Trans. on Automatic Control, 42(2), 171-187.

Narendra, K. S. and Xiang, C., (2000). Adaptive control of discrete-time systems using multiple models. IEEE Trans. on Automatic Control, 45(9), 1669-1686.

Pishvaie, M. R. and Shahrokhi, M., (2000). pH Control Using the Nonlinear Multiple Models, Switching, and Tuning Approach. Ind.& Eng. Chem. Res., 39(5):1311-1319.

Peymani, E., Fatehi, and A., Khaki-Sedigh, A., (2008) A disturbance rejection supervisor in multiple-model based control, proc. of International conference on control, IET, Manchester, UK.

Slug-flow Control in Submarine Oil-risers using SMC Strategies ⋆

Pagano, D. J. * **Plucenio, A.** * **Traple, A.** *

* *Departamento de Automação e Sistemas, Universidade Federal de Santa Catarina, 88040-900 Florianópolis-SC, Brazil*
e-mail: {daniel, plucenio, traple}@das.ufsc.br

Abstract: In this paper we propose different Sliding Mode Control (SMC) strategies to control slug-flow oscillations in submarine oil-risers. The main idea is to design a switching control law that induces a sliding bifurcation on the system, changing its dynamics and, in this way, controlling the amplitude of a limit cycle. Simulation results were obtained using OLGA Scandpower software in order to compare the different SMC strategies.*Copyright©2009 IFAC*

Keywords: Production oil system, Submarine oil-riser, Slug-flow control, Non-smooth dynamical systems, Sliding Mode Control, washout filter

1. INTRODUCTION

Transportation of multiphase fluid (oil, gas and water) is an important task in the oil industry. Nowadays, there is a trend to increase the number of satellite wells and the length of risers between clusters of wells and off-shore production systems. Besides, the increasing depths of oil wells produces several new multiphase transport problems, see Storkaas and Skogestad (2004), Storkaas (2005). In this scenario a common problem is the phenomena so called slug-flow characterized by the intermittent axial distribution of gas and liquid. The pressure and flow rate oscillations induced by the slug-flow can provoke several undesired effects on the surface equipments. These types of disturbances can cause serious problems in the input of the multiphase flow separator, deteriorating the separation quality and causing level overflow (Godhavn et al. (2005)). In short, the slug-flow phenomena in submarine risers cause several problems to the oil off-shore industry. The suppression of this type of oscillations by means of feedback automatic control methods can be applied to stabilize the flow in risers and, consequently, minimize the problems on the separator. At the same time, two other benefits can be obtained: (i) in cases where the oil is pumped from sea bottom, energy consumption is minimized; (ii) in cases of risers connected to wells with natural or artificial lift flows, higher production is obtained by minimizing the pressure in front of the well perforated zones.

A schematic diagram of a riser used in an oil production off-shore system is shown in Fig. 1 with parameters shown in Table 1. This system was simulated in OLGA [1] .

In Fig. 1, bottom and top riser pressures P_1 and P_2, respectively, are measured in [Pa] units and the control action is applied on the production choke. Modelling this system is quit complex since it involves partial differential equations. A simplified third order dynamical model developed in ordinary differential equations can be found in Storkaas and Skogestad (2004), Storkaas (2005). The bifurcation diagram considering the

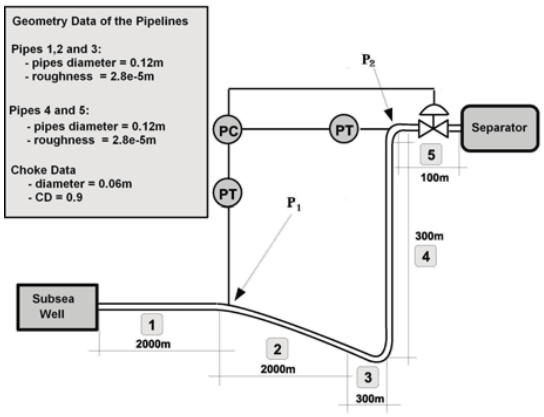

Fig. 1. Oil-riser system set-up simulated in OLGA.

Table 1. Parameter values of the riser setup.

Parameter	value	unit
Mass flow rate entering the riser	5	$Kg.s^{-1}$
Separator pressure	5.10^6	Pa
Gas void fraction	5	%
Temperature in the riser output	22	^oC
Temperatura in the well	62	^oC

choke opening as a bifurcation parameter (see Fig. 2), was obtained based on OLGA data simulations for a mass flow rate entering the riser equal to $5Kg.s^{-1}$ and a pressure separator of $5.10^6 Pa$. The bifurcation diagram of Fig. 2 is qualitatively similar to the diagram shown in Storkaas and Skogestad (2004). The stable and unstable equilibria manifold are depicted in Fig. 3. In this figure we show also the curves corresponding to maximal and minimum values of the limit cycle. A projection

⋆ Partially supported by *Agencia Nacional do Petroleo, Gas Natural e Biocombustiveis* under project PRH34-ANP/MCT. Daniel J. Pagano was partially supported by grant PQ-310281/2006-7 from CNPq - National Council for Scientific and Technological Development/Brazil.

[1] Multiphase flow software simulation commercialized from Scandpower.

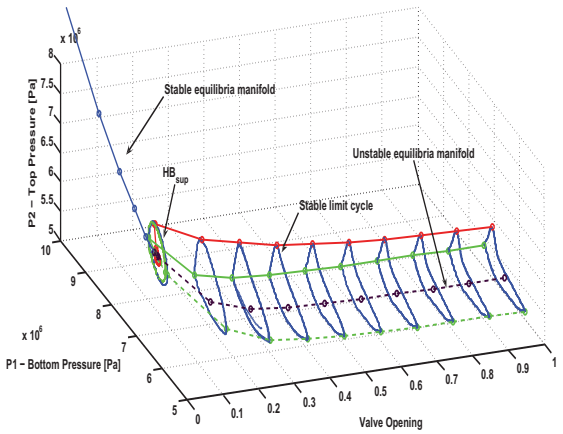

Fig. 2. Bifurcation diagram considering the choke opening as the bifurcation parameter. A stable limit cycle undergoes from a supercritical Hopf Bifurcation (HB_{sup}).

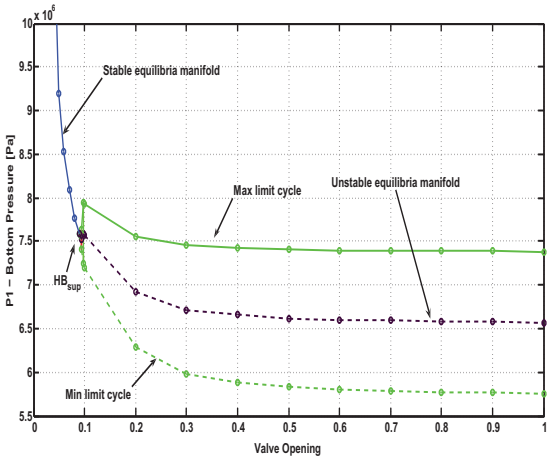

Fig. 3. Bifurcation diagram in $(u(t), P_1)$ plane.

of the limit cycles for different choke openings in the (P_1, P_2)-plane is shown in Fig. 4. As we can observe in this picture, the relation between P_1 and P_2 pressures on the stable (unstable) equilibria manifold can be approximated by a straight line. As can be seen in Figs. 2-4, a supercritical Hopf Bifurcation takes place, at the point HB_{sup} in the diagram, giving rise to a stable limit cycle. Thus, without active feedback control it is necessary to operate the system with choke opening below 10% in order to avoid output system oscillations. The pressure drop around the choke rises for low choke opening and this pressure drop is added to riser's bottom. High pressure for the same mass flow rate means higher energy consumption for sea floor pump applications. On the other hand, risers connected to natural or artificial lift wells may affect the pressure in front of the perforated zones leading to less oil production flow rate. Whatever the case it is desirable to have a steady flow with minimum pressure drop in the surface choke.

Several linear control laws to prevent slug-flow oscillations in submarine oil-risers have been proposed in different works, see

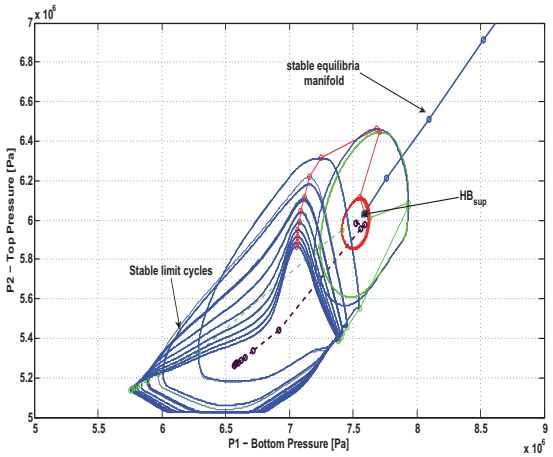

Fig. 4. Bifurcation diagram in (P_1, P_2) plane.

for instance Storkaas (2005), Godhavn et al. (2005). Linear controllers are only local solutions for this complex non-linear control problem. In this paper, as an alternative solution, we propose different non-linear control systems based on the Sliding Mode Control (SMC) theory.

The paper is organized as follows. In Section 2, the Proportional-Integral (PI) control law is revisited showing that it is not robust under disturbances in the input riser flow rate. In Sections 3 and 4, we propose different SMC strategies to control slug-flow oscillations. Our slug SMC washout strategy is presented in Section 5. Finally we discuss some of the limitations of these switching strategies and propose future improvements.

2. REVISITING THE PI CONTROL STRATEGY TO SUPPRESS SLUG-FLOW

In this Section we show by means of simulation results that the PI control law is not robust to disturbances in the input riser flow rate. A simulation test was made to evaluate the efficiency of the PI control. The PI control law is given by

$$u(t) = k_c[e(t) + \frac{1}{T_i}\int_0^t e(\tau)d\tau],$$

where $k_c = -7.92 \cdot 10^{-6} Pa^{-1}$, $T_i = 49.5s$, $e(t)$ is the error and the process variable is the pressure P_1. The PI discrete form implemented is given by

$$u(k) = u(k-1) + s_0 e(k) + s_1 e(k-1)$$

where $s_0 = k_c(1 + \frac{T_s}{T_i})$, $s_1 = -k_c$, $T_s = 1s$ is the sampling time and T_i is the integral time. PI control tuning was made using simple rules of adjusting since no mathematical model of reduced order for control design was available. The simulation setup was defined as:

(1) the choke opening is fixed at 20% and the corresponding operating point calculated from the equilibria manifold curve is $(P_1^*, P_2^*) = (6.93 \cdot 10^6[Pa], 5.56 \cdot 10^6[Pa])$;
(2) at $5000s$ the control is switched ON;
(3) a disturbance in the input riser flow rate is applied at $15000s$;
(4) the control is switched OFF at $25000s$.

Two flow rate disturbances were defined (i) from $5Kg.s^{-1}$ to $3.5Kg.s^{-1}$ and (ii) from $5Kg.s^{-1}$ to $3Kg.s^{-1}$. We use the

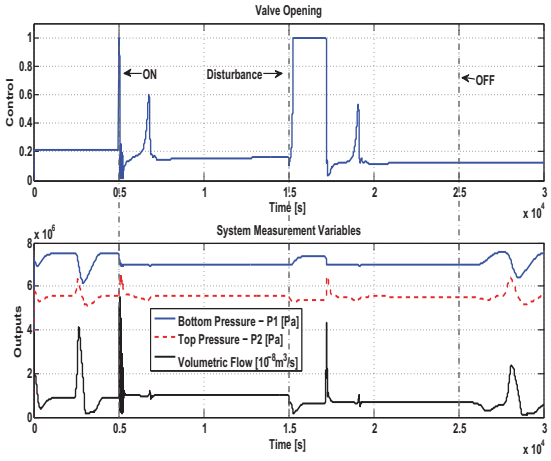

Fig. 5. System time response under *PI* control for a flow rate disturbance from $5Kg.s^{-1}$ to $3.5Kg.s^{-1}$.

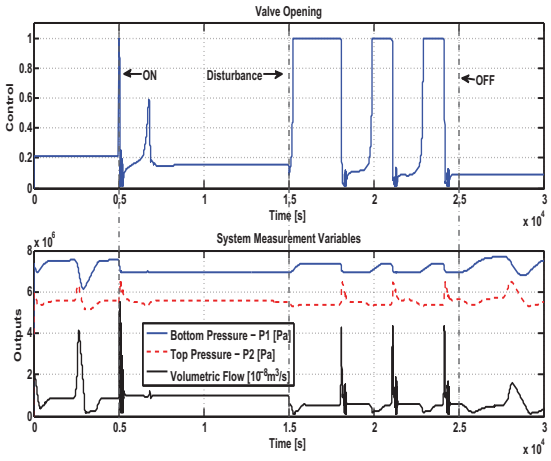

Fig. 6. System time response under *PI* control for a flow rate disturbance from $5Kg.s^{-1}$ to $3Kg.s^{-1}$.

previous simulation setup in order to obtain comparative results between the different slug control strategies.

Simulation results using the PI control are shown in Fig.5 for the first disturbance and in Fig.6 corresponding to the second disturbance. As can be seen, the PI control reject the first perturbation but it is not robust for the second disturbance.

In order to tackle this problem for large flow rate disturbances, three different Sliding Mode Control (SMC) strategies are proposed in the following Sections.

3. SLUG SMC STRATEGY

The main idea is to design a Sliding Mode Control (SMC) law (switching system) that induces a grazing-sliding bifurcation (see Angulo et al. (2005a)) on the system, changing its dynamics and, in this way, the amplitude of the target limit cycle is controlled. This type of non-smooth bifurcation introduces partial sliding motion along a sliding surface, reducing or suppressing the amplitude of the undesired limit cycle. In order to explain these ideas, consider a general system defined by

$$\dot{x} = F(x, u(x)) \tag{1}$$

where $x \in \mathbb{R}^n$ is the state vector of dimension n, and $u(x) \in \mathbb{R}$ is the control signal. The function $F(x) = (F_1, F_2, ..., F_n) : \mathbb{R}^n \rightarrow \mathbb{R}^n$, represents a non-smooth continuous system. We also assume that as a result of a Hopf bifurcation (continuous or not, see di Bernardo et al. (2008)), the system exhibits a steady state oscillatory behavior, where a stable limit cycle is the solution from (1).

The grazing-sliding bifurcation to suppress a limit cycle occurs when the limit cycle is crossed by a sliding surface that generates a grazing-sliding non-smooth transition where part of the trajectory of the limit cycle stands on the sliding surface as shown in Fig. 7.

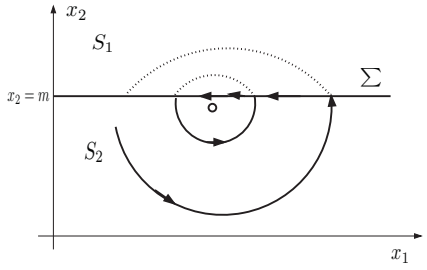

Fig. 7. Grazing-sliding bifurcation induced in the system.

For example, on a system with dimension 2, we consider a region S_1 of the form

$$S_1 := \{x = (x_1, x_2) : x_2 > m\}$$

for arbitrary m, being

$$\Sigma := \sigma(x) = \{x = (x_1, x_2) : x_2 = m\}$$

and

$$S_2 := \{x = (x_1, x_2) : x_2 < m\}.$$

With the variation of m, a grazing-sliding bifurcation occurs and the amplitude of the limit cycle is reduced or even eliminated.

Thus, the sliding mode control suggested is

$$u = u_0 + \Delta u \ \text{sgn}(\sigma(x)) \tag{2}$$

where $\sigma(x) = 0$ is the sliding surface, a function of the system's states that allow the changing of its dynamics; u_0 is the value of the control variable at the operating point and Δu is the maximum value that the control variable can assume from u_0.

The function $sgn(\cdot)$ can be defined as

$$\text{sgn}(\sigma(x)) = \begin{cases} -1, & \text{if } \sigma(x) < 0; \\ 1, & \text{if } \sigma(x) > 0. \end{cases} \tag{3}$$

or

$$\text{sgn}(\sigma(x)) = \begin{cases} 0, & \text{if } \sigma(x) < 0; \\ 1, & \text{if } \sigma(x) > 0. \end{cases} \tag{4}$$

Applying the above equations, we propose the following control law given by

$$u = u_0 + \Delta u \ \text{sgn}(\sigma), \tag{5}$$

$$\sigma(P_1, P_2) = P_2 - P_1 + \beta, \tag{6}$$

where $\beta = P_1^* - P_2^*$; $\Delta u = u_0 - u_{min}$; u_0 is the desired choke opening and u_{min} is the control value at the Hopf Bifurcation point. The switching surface is defined as $P_2 = P_1 - \beta$ and we define the $sgn(\cdot)$ to close the choke whenever $\sigma > 0$. The choke opening bias u_0 is defined at the riser desired operating point. At this point P_1^*, P_2^* are defined on the equilibria manifold curve, for a given mass flow rate of the riser input, as shown in Fig. 3. Choosing the surface choke opening bias u_o has to consider two factors. For one the value should be high enough in order to ensure a minimum pressure drop around the choke. On the other hand the bias should not be too far from values which can cause high pressure drops in order to answer quickly to disturbances. Choke opening close to 100% cause minimum pressure drop but depending on the choke characteristics a significant choke pressure drop can only be obtained for values smaller than 10%.

The control strategy can be interpreted as a mechanism to force an hypothetical steady flow rate which would be obtained without the slug flow behavior. For a constant input gas and liquid mass flow rate the pressure P_1 could be expressed as $P_1 = P_2 + \beta$ where β would take into account the gravity and friction terms of a pseudo stable flow. For instance, the simplest model is the homogeneous model given by

$$P_1 - P_2 = \frac{m_{gr} + m_{lr}}{A} g + \frac{f \bar{\rho} \bar{v}^2}{2 d_r} h, \qquad (7)$$

where A is the section of the pipe; m_{gr} and m_{lr} are the mass of gas and mass of liquid in the riser; $\bar{\rho}$ is the mean density of the flow; $\bar{v}$ is the mean velocity of the flow in the riser; h is the height of the riser; f is the friction function; d_r is the diameter of the pipeline. In (7), first term corresponds to the gravity term and the second is the friction term.

Anytime the relationship is violated action is taken in the choke opening to force the desired P_1, P_2 relationship. Obviously this is done in a way that provides a desired choke opening which minimizes P_1 and consequently the energy used to lift the gas and liquid flow-rates entering the riser.

Time open-loop system responses are shown in Fig. 8. At $t = 5000s$ the proposed control system is turned on. At $t = 15000s$, a disturbance in the flow rate (from $5Kg.s^{-1}$ to $3.5Kg.s^{-1}$) was applied. It can be observed in Fig. 8 and Fig. 9 where the amplitude of the oscillations are decreased around the operating point when the control is switched on. As can be seen in Fig. 8, after the control is switched off, at $t = 250000s$, the oscillations back to the system. State space diagram, in (P_1, P_2)-plane, is depicted in Fig. 9.

The proposed SMC works well for small input riser flow rate disturbances but the control action switches permanently to maintain the equilibrium at the operating point.

4. A MODIFIED SLUG SMC STRATEGY

The SMC strategy development in Section 3 is not efficient to suppress pressure or flow oscillations in the riser since the control action switches permanently to maintain the equilibrium at the operating point. This would be very detrimental to the choke integrity. Another desired control characteristic is to be able to suppress the oscillations while keeping the choke nearly 100% opened. This represents significant less power needed to pump the multiphase fluid to the surface. In this Section, we propose a change in the control algorithm to minimize the switching in the control signal. The idea is to combine two control laws (i)

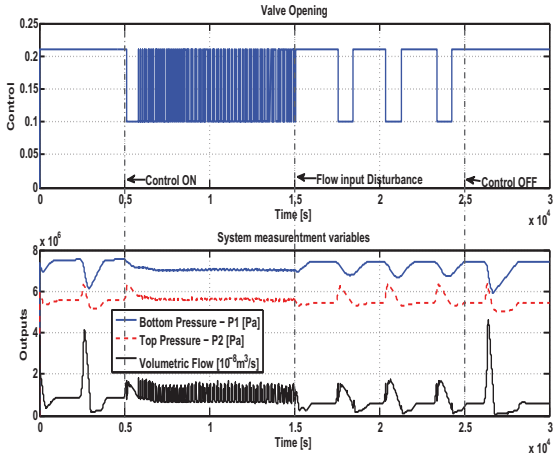

Fig. 8. Time system response (open-loop and with feedback control) with the SMC control strategy. a) choke opening; b) states of the system.

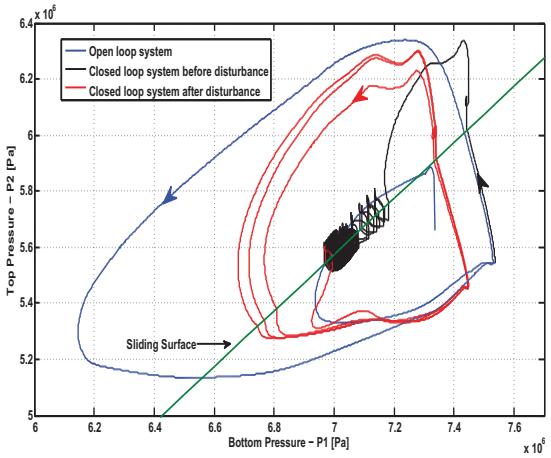

Fig. 9. State space diagram in (P_1, P_2)-plane

the control used in Section 3 and (ii) a discrete form of the PI control law as used in Section 2 by means of a convex function as

$$u(t) = \mu \; u_{SMC} + (1 - \mu) \; u_{PI}, \qquad (8)$$

$$u_{SMC} = u_0 + \Delta u \; sgn(\sigma), \qquad (9)$$

where

$$\sigma = P_2 - P_1 + \beta.$$

$$u_{PI}(k) = u_{PI}(k-1) + s_0 \; e(k) + s_1 \; e(k-1), \qquad (10)$$

where u_{SMC} is the switching control law given by (9) and u_{PI} is the PI control (10), with $e(k) = P_1^*(k) - P_1(k)$.

The parameter $\mu = \mu(P_1, P_2)$ provides a smooth transition between the two control laws in such a way that if the trajectories are far away the equilibrium point then μ is close 1; otherwise μ is close to 0. It is defined as

$$\mu = \frac{1}{1 + e^{\gamma(\lambda - \delta)}}$$

$$\lambda(P_1, P_2) = \left(\frac{P_1}{P_1^*} - 1\right)^2 + \left(\frac{P_2}{P_2^*} - 1\right)^2 \qquad (11)$$

where P_1^* is the operating point for bottom pressure and P_2^* is the desired value for the input choke pressure. Parameter values of (9), (10) and (11) are given in Table 2. Parameter

Table 2. Control law parameters.

Parameter	value	unit
u_0	0.2	
Δu	0.12	
s_0	$-8.08 \cdot 10^{-6}$	Pa^{-1}
s_1	$7.92 \cdot 10^{-6}$	$Pa{-}1$
γ	$8/\delta$	
δ	0.008	

β is defined as $\beta = P_1^* - P_2^*$. The system response with the proposed control law to a disturbance of the well mass flow rate is shown in Fig. 10 and the space state diagram is depicted in Fig. 11. The sample time was chosen as $T_a = 1s$. At

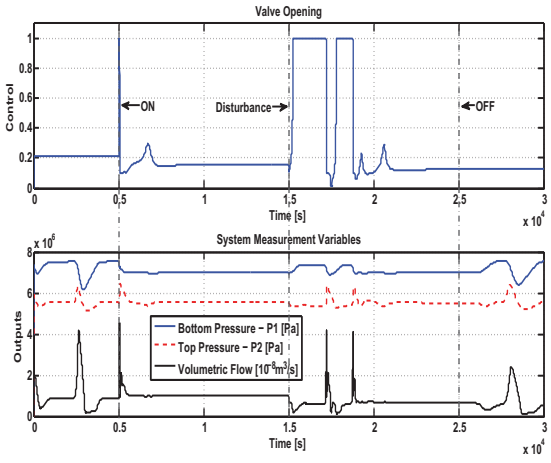

Fig. 10. Control and output system responses with the modified control law (8) for a disturbance input.

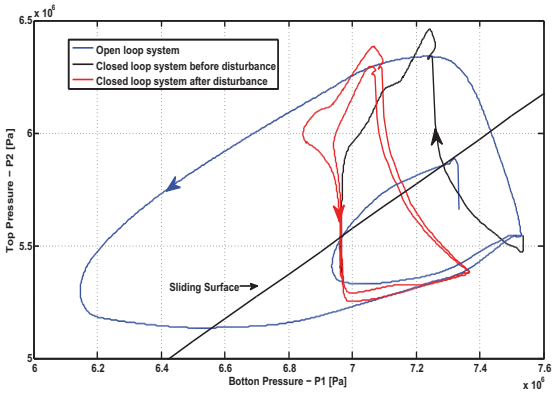

Fig. 11. State-space diagram of the system with the modified control law (8).

$t = 15000s$, the mass flow rate coming from the well is reduced from $5kg/s$ to $3.5kg/s$. This disturbance changes the operating process conditions. The proposed SMC control strategy control the system reduce the amplitude of the oscillations.

At $t = 25000s$, the control is turned off and the system starts to exhibit pressure and flow signal oscillations again. As can be seen the oscillations are back since the choke opening value is now in the instability region.

A disadvantage using the SMC algorithm discussed in this Section is that it is not possible to stabilize the system for large flow rate disturbances.

5. SLUG WASHOUT SMC CONTROL

All approaches presented so far for the slug control have used set-points to derive the control law. These strategies have a problem when there are changes in the fluid mass flow rate entering the riser. Even a stabilized flow rate will exhibit a different value both for P_1 and P_2 since higher mass flow rate will result in higher gravity and friction terms on the riser pressure drop as well as higher pressure drop in the surface choke. For the sliding mode control keeping the set-points for changes in the input mass flow rate means to request the system to operate in a limit cycle not sufficiently collapsed or to ask for an infeasible stabilized flow.

Since the practical objetive is to stabilize the flow keeping the surface choke with a minimum pressure drop, the idea of pressure set-point looses significance. One could say that the control problem is well solved if the pressures and flow rates do not oscillate while the surface choke is kept opened well above the opening which characterizes the beginning of the limit cycle. The idea is to develop a control strategy which supres the oscillation while keeping the choke opening operating around a desired opening value. If the oscillations are suppressed the resultant pressures will be a consequence of the input mass flow rate, fluid characteristics and the system geometry.

In order to attend the former constraints, we propose, in this Section, a new SMC strategy to reject mass flow rate input riser perturbations based on washout filters. Washout filters are intensively used to control chaotic systems by means of techniques based on bifurcation theory Wang and Abed (1995) and in flight control systems Lee and Abed (1991). Recently, washout filters were applied to power electronic converters in conjunction with SMC controllers in order to reject load disturbances Cunha and Pagano (2002). A washout filter is a high-pass linear filter that washes out steady-state inputs while passing transient inputs. The use of washout filters ensures that all the equilibrium points of the original system are preserved in the controlled system, i.e., their location remains unchanged.

The transfer function of a typical washout filter is given by

$$G_F(s) = \frac{s}{s+w} = 1 - \frac{w}{s+w},$$

where w denotes the reciprocal of the filter time constant which is positive for stable filter. We assume that it is possible to filter the inductor current x to achieve a new signal x_F and define an auxiliary variable z so that it is satisfied the output equation

$$x_F = x - z.$$

Then the effect of the washout filter can be represented by means of an additional differential equation, namely

$$\frac{dz}{dt} = w(x - z). \tag{12}$$

In our problem, we use two washout filters in order to filter the signals P_1 and P_2 in such a way that

$$\dot{z}_1 = w_1(P_1 - z) = w_1\tilde{p}_1$$

$$\dot{z}_2 = w_2(P_2 - z) = w_2\tilde{P}_2$$

where $\tilde{p}_1$, $\tilde{p}_2$ are the bottom and top filtered pressures, $w_1 = \frac{2\pi}{5} f_1$ and $w_2 = \frac{2\pi}{5} f_2$ are washout filter constants designed from the oscillatory frequencies f_1, f_2 measurement from the OLGA data simulation.

$$u_{WSMC} = u_0 + \Delta u \ sgn(\sigma), \tag{13}$$

where

$$\sigma(\tilde{P}_1, \tilde{P}_2) = \tilde{P}_2 - \tilde{P}_1. \tag{14}$$

Note that (14) is similar to (6) but now the parameter β is equal to zero. The sliding surface is now defined as $\tilde{P}_2 = -\tilde{P}_1$ and it does not depend on the operating point.

At $t = 10000s$ automatic control is turned on and at $30000s$ a well flow rate is reduced from $5kg/s$ to $3kg/s$.

At $50000s$ the control is again turned off and the system back to the oscillatory behavior. Simulation results are shown in Fig. 12. The state-space diagram in $(P_1 - P_2)$-plane is shown in Fig.

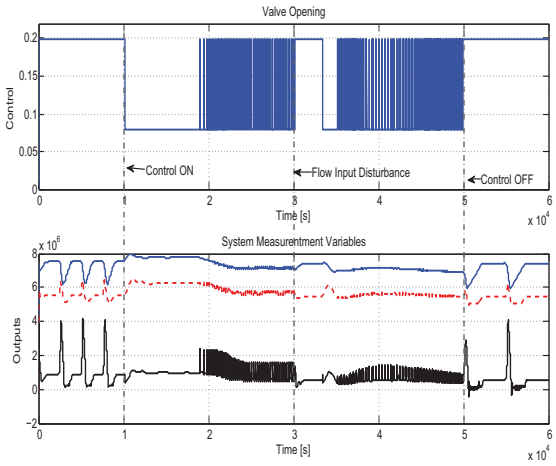

Fig. 12. Control and output system responses with slug washout SMC for a disturbance in the input riser flow rate.

13. As can be seen, the propose control law stabilize the process and at the same time allow to work over the full choke range. A disadvantage to use this propose control law is the resulting

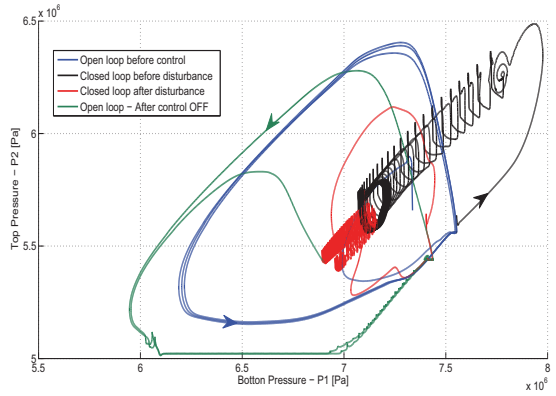

Fig. 13. State-space diagram of the system with slug washout SMC.

chattering produced by the control action signal on the choke. An alternative to overcome the high frequency chattering from the dynamics of the standard sliding mode control presented in the this Section is to design a Higher Order Sliding Mode (HOSM) control.

6. CONCLUSIONS

The lack of robustness to control slug-flow oscillations in submarine oil-risers using classical PI linear control system was tackled in this paper applying SMC techniques. Three different SMC controllers to suppress slug-flow control oscillations were proposed. Simulation results were obtained using OLGA software in order to compare the different SMC strategies subject to mass flow input riser disturbances from $5Kg.s^{-1}$ to $3Kg.s^{-1}$. The SMC technique reveal itself as a robust way of suppressing limit cycles when the mathematical model of the process is not available in practice. The dynamical of the slug system with unknown operating point was treated in this work using washout filters. This situation is manifested in the presence of mass flow rate input riser disturbances.

An existing practical obstacle to apply the standard SMC in the field is the high frequency chattering of the generated control signal. This problem leads to a premature wear down of the choke actuator and could be tackled in future works using High Order Sliding Mode - HOSM controllers.

ACKNOWLEDGEMENTS

The authors would also like to acknowledge *Scandpower* for providing an academical OLGA software license.

REFERENCES

Angulo, F., di Bernardo, M., Fossas, E., and Olivar, G. (2005a). Feedback control of limit cycle: a switching control strategy based on nonsmooth bifurcation theory. *IEEE Transactions on Circuit and Systems-I*, 52(2), 366–378.

Cunha, F.B. and Pagano, D.J. (2002). DC-DC step-up converter controlling by SMC and with an auxiliary washout filter. In *Proc. of Congresso Brasileiro de Automatica, CBA2002*. (in portuguese).

di Bernardo, M., Budd, C., Champneys, A., and Kowalczyk, P. (2008). *Piecewise-smooth Dynamical Systems: Theory and Applications*. Applied Mathematical Sciences 163. Springer.

Godhavn, J., Fard, M.P., and Fuchs, P.H. (2005). New slug control strategies, tuning rules and experiments results. *Journal of Process Control*, 15, 547–557.

Lee, H.C. and Abed, E.H. (1991). Washout filter in the bifurcation control of high alpha flight dynamics. In *Proc. of the American Control Conference*, 206–211. Boston, MA.

Storkaas, E. and Skogestad, S. (2004). Cascade control of unstable systems with application to stabilization of slug flow. *IFAC Symposium ADCHEM 2003*.

Storkaas, E. (2005). *Stabilizing control and controllability. Control solutions to avoid slug flow in pipeline-riser systems*. Ph.D. thesis, Norwegian University of Science and Technology, Norwegian.

Wang, H. and Abed, E.H. (1995). Bifurcation control of a chaotic system. *Automatica*, 31, 1213–1226.

Estimation

Oral Session

A New Process Noise Covariance Matrix Tuning Algorithm for Kalman Based State Estimators

Nina P. G. Salau*, Jorge O. Trierweiler*, Argimiro R. Secchi, Wolfgang Marquardt*****

** Federal University of Rio Grande do Sul, Chemical Engineering Department, Eng. Luiz Englert, s/n°, Campus Central, CEP 90040-040, Porto Alegre - RS, Brazil, (ninas@ enq.ufrgs.br, jorge@ enq.ufrgs.br)*

*** Federal University of Rio de Janeiro, PEQ – COPPE, Av. Horácio Macedo, 2030 - Centro de Tecnologia - Bloco G - Sala G-115, Cidade Universitária, CP: 68502, CEP 21945-970, Rio de Janeiro – RJ, (arge@ peq.coppe.ufrj.br)*

****RWTH Aachen University, Process Systems Engineering,Turmstr. 46, 52064 Aachen, Germany, (wolfgang.marquardt@avt.rwth-aachen.de)*

Abstract: A suitable design of state estimators requires a representative model for capturing the plant behavior and knowledge about the noise statistics, which are generally not known in practical applications. While the measurement noise covariance can be directly derived from the measurement device reproducibility, the choice of the process noise covariance is much less straightforward. Further, processes such as continuous process with grade transitions and batch or semi-batch process are characterized by time-varying structural uncertainties which are, in many cases, partially and indirectly reflected in the uncertainty of the model parameters. It has been shown that the robust performance of state estimators significantly enhances with a time-varying and non-diagonal process noise covariance matrix, which explicitly takes parameter uncertainty into account. For this case, the parameter uncertainty is quantified through the parameter covariance matrix. This paper presents a direct and a sensitivity method for the parameter covariance matrix computation. In the direct method, the parameter covariance matrix is found during the parameter estimation step of the SELEST algorithm, while in the sensitivity method, the parameter covariance matrix is obtained through a time-varying sensitivity matrix. The results have shown the efficacy of these methods in improving the performance of an extended Kalman filter (EKF) for a semi-batch reactor process.

Keywords: state estimator design, noise statistics, parameter estimation, sensitivity analyses.

1. INTRODUCTION

Since usually not all states of a nonlinear dynamic model are measured, they need to be estimated to be used in any control and optimization strategy. State estimators are used to estimate the unmeasured states and to filter the measured ones. Therefore, they are essential for any advanced control and optimization application. Besides an accurate plant model, an appropriate choice of process and measurement noise covariances is crucial in applying state estimators. The measurement error covariance matrix is usually known from the error statistics of the measurement device and is readily available. However, in actual problems, the process-noise statistics are often unknown, do not satisfy the assumptions of normal distribution and are mostly due to the uncertainties in the model that can be either parametric or structural.

Adaptive filtering techniques estimate noise covariances from data and have been used for nonlinear systems (Mehra, 1972; Odelson et al. 2006). The methods in this field can be divided into four general categories (Mehra, 1972): Bayesian, maximum likelihood, covariance matching, and correlation techniques. Bayesian and maximum likelihood methods have fallen out of favor because of their sometimes excessive computation times. Covariance matching is the computation of the covariances from the residuals of the state estimation problem, but has been shown to give biased estimates of the true covariances. The fourth category is correlation techniques, which is the most popular for determining these covariances (Odelson et al. 2006). However, these methods assume constant noise characteristics and the availability of data required to obtain a true representation of noise statistics. For continuous or batch processes with time-varying process dynamics and operating within a wide range of process conditions, these noise statistics are time varying. The use of a fixed value of noise statistics can lead to poor filter performance and even result in filter divergence (Vallapil & Georgakis 1999, 2000, Leu & Baratti, 2000).

Valappil & Georgakis (1999, 2000) introduced two systematic approaches to be used for the calculation of a time-varying and non-diagonal process noise covariance matrix, which explicitly takes parameter uncertainty into account. The first, called linearized approach, is based on a Taylor series expansion of the nonlinear equations around the nominal parameter values, while the second, called Monte Carlo approach, accounts for the nonlinear dependence of the system on the fitted parameters by Monte Carlo simulations that can easily be performed on-line. Both approaches have been compared favorably with the traditional methods of trial-and-error tuning of EKF. For the linearized approach, the process noise covariance matrix for the filter is obtained by a procedure using the known parameter covariance matrix. The main advantage of the linearized approach is that it involves very simple algebraic calculations and can easily be executed on-line. Afterwards this approach was employed successfully in EKF-based NMPC algorithms for batch

processes (Valappil & Georgakis, 2001, 2002; Nagy and Braatz, 2003).

In this work, a new process noise covariance matrix tuning algorithm is proposed. It is an extension of the linearized approach proposed by Valappil and Georgakis (1999, 2000) with two methods for the parameter covariance matrix computation. In the direct method, the parameter covariance matrix is found during the parameter estimation step using SELEST (Secchi et al., 2006), an algorithm for automatic selection of model parameters based on an extension of the identifiability measure of Li et al. (2004). In the sensitivity method, the parameter covariance matrix is obtained through a time-varying sensitivity matrix. Both methods can be successfully applied for state estimator design.

2. PROBLEM FORMULATION AND SOLUTION STRATEGIES

2.1 Hybrid Extended Kalman Filter (H-EKF)

Consider the following nonlinear dynamic system to be used in the state estimator

$$\begin{aligned} \dot{x} &= f(x,u,t,p)+\omega(t) \\ y_k &= h_k(x_k,t_k)+v_k \\ \omega(t) &\sim (0,Q) \\ v_k &\sim (0,R_k) \end{aligned} \tag{1}$$

where u denotes the deterministic inputs, x denotes the states, and y denotes the measurements. The process-noise vector, ω(t), and the measurement-noise vector, v_k, are assumed to be a white Gaussian random process with zero mean and covariance Q and R_k, respectively. The H-EKF formulation uses a continuous and nonlinear model for state estimation, linearized models of the nonlinear system for state covariance estimation, and discrete measurements (Simon, 2006). This is often referred to as continuous-discrete extended Kalman filter (Jazwinski, 1970). Here, the system is linearized at each time step to obtain the local state-space matrices as below:

$$F(t)=\left(\frac{\partial f}{\partial x}\right)_{x,u,t,p_{nom}}, \qquad H(t)=\left(\frac{\partial h}{\partial x}\right)_{x,u,t,p_{nom}} \tag{2}$$

The equations that compose the different steps in the H-EKF are given below.

State transition equation:

$$\hat{x}_{k|k-1}=\hat{x}_{k-1|k-1}+\int_{k-1}^{k} f(\hat{x},u,\tau,p)\,d\tau \tag{3}$$

State covariance transition equation

$$P_{k|k-1}=P_{k-1|k-1}+\int_{k-1}^{k}\left[F(\tau)P(\tau)+P(\tau)F(\tau)^{T}+Q\right]d\tau \tag{4}$$

Kalman gain equation:

$$K_k=P_{k|k-1}H_k^{T}\left[H_kP_{k|k-1}H_k^{T}+R_k\right]^{-1} \tag{5}$$

State update equation:

$$\hat{x}_{k|k}=\hat{x}_{k|k-1}+K_k\left[y_k-h\left(\hat{x}_{k|k-1},t_k\right)\right] \tag{6}$$

State covariance update equation:

$$P_{k|k}=\left[I_n-K_kH_k\right]P_{k|k-1}\left[I_n-K_kH_k\right]^{T}+K_kR_kK_k^{T} \tag{7}$$

2.2 Linearized Approach to Calculate the ω(t) Statistics

As introduced by Valappil & Georgakis (1999, 2000), the linearized approach to calculate the ω(t) statistics of (1) consists in assuming that the process noise vector ω(t) mostly represents the effects of parametric uncertainty. As $\dot{x}(t)$ and $\dot{x}_{nom}(t)$ are desired to be the same, ω(t) can be defined by

$$\omega(t)=f(x,u,t,p)-f(x_{nom},u,t,p_{nom}) \tag{8}$$

Performing a first-order Taylor's series expansion of the right-hand side of (8) around the nominal state trajectory (x_{nom}) and the nominal parameters (p_{nom}), neglecting the higher-order terms, results in following approximation

$$\begin{aligned} \omega(t)=&\left(\frac{\partial f}{\partial x}\right)_{x_{nom},u,t,p_{nom}}\left[x(t)-x_{nom}(t)\right] \\ &+\left(\frac{\partial f}{\partial p}\right)_{x_{nom},u,t,p_{nom}}\left[p-p_{nom}\right] \end{aligned} \tag{9}$$

Assuming that $\left[x(t)-x_{nom}(t)\right]=\left[\hat{x}(t)-x_{nom}(t)\right]\approx 0$, the process noise is calculated from

$$\omega(t)=F_{p_{nom}}(t)\left[p-p_{nom}\right] \tag{10}$$

where $F_{p_{nom}}(t)=\left(\frac{\partial f}{\partial p}\right)_{\bar{x},u,t,p_{nom}}$. Calculating the expected value of both sides of (10) yields

$$\bar{\omega}(t)=F_{p_{nom}}(t)(p_{nom}-p_{nom})=0 \tag{11}$$

indicating that the noise sequence ω(t) has zero mean if the employed linearization in the parameters was accurate. Then the desired computation of the covariance Q(t) of ω(t) is given by

$$Q(t)=F_{p_{nom}}(t)C_pF_{p_{nom}}^{T}(t) \tag{12}$$

where $C_p\in\Re^{n_p\times n_p}$ is the parameter covariance matrix. In this work, we propose two methods to calculate C_p, which are presented in the next subsection.

2.3 Proposed Methods to Calculate the C_p Matrix

Consider the general process model.

$$\dot{x}=f(x,u,t,p_{nom}) \tag{13}$$

Differentiating (13) with respect to the nominal parameter vector, p_{nom}, gives

$$\dot{S}=\left(\frac{\partial f}{\partial x}\right)S+\left(\frac{\partial f}{\partial p_{nom}}\right)=F(t)S+F_{p_{nom}}(t) \tag{14}$$

where S is the sensitivity matrix $(\partial x/\partial p_{nom})$ determined by numerical integration of (14) along with the model of (13).

2.3.1 Direct Method: Parameter Covariance Matrix via Parameter Estimation

In this method, C_p is constant and directly obtained from the parameter estimation procedure. For this purpose, we have selected the SELEST algorithm proposed by Secchi et al. (2006). This algorithm uses a sensitivity matrix, S, based on calculation of the parameters effects on the measured outputs and of a linear-independence metric, as proposed by Li et al. (2004). A predictability degradation index and a parameter correlation degradation index are used as stopping criterion. The definitions of these indexes as well as the SELEST algorithm are presented in Secchi et al. (2006).

2.3.2 Sensitivity Method: Parameter Covariance Matrix via Sensitivity Matrix

As pointed out by Sharma & Arora (1993), the sensitivity matrix, S, can play a role in quantifying how good the estimate of the parameters is. For uncorrelated and normally distributed measurement errors and for nonlinear least-squares problems, a parameter covariance matrix C_p can be estimated from

$$C_p \approx s^2 \left(S^T S\right)^{-1} \tag{15}$$

where s^2 accounts for the accuracy of the data used to fit the parameters ($\hat{Y}$) and is usually represented by the residual mean square

$$s^2 = \frac{\sum \left(\hat{Y}\text{-}Y_p\right)^T \left(\hat{Y}\text{-}Y_p\right)}{n\text{-}np} \tag{16}$$

where Y_p is the estimated data, n is the number of samples and np is the number of estimated parameters. The residual mean square s^2 is also obtained from the parameter estimation using SELEST algorithm. Since the sensitivity matrix, S, is time-varying, C_p is also time-varying, which represents an advantage of this method.

3. MATRIX Q TUNING ALGORITHM

This section presents an algorithm for tuning of the process noise covariance matrix. As mentioned earlier, this algorithm is an extension of the linearized approach proposed by Valappil and Georgakis (1999, 2000) with two methods for the parameter covariance matrix computation.

Since any model is an abstraction of reality, both the structural and parametric uncertainties are present to some degree in most real situations. The structural uncertainties is often captured by uncertainty in the model parameters only. The proposed algorithm requires knowledge about which parameters can be considered time-varying. Afterwards, SELEST algorithm estimates the best possible subset of parameters within a full set of model parameters assumed time-varying.

Parameter estimation is a key ingredient to quantify the parametric model uncertainty. However, most contributions on parameter estimation in process control assume that all model states are measured, which is not true in practical applications. In order to carry out proper parameter estimation, the EKF is used in a previous stage with the nominal parameters to estimate the unmeasured states and to filter the measured ones. Afterwards, the state estimation is carried out a posteriori with the estimated parameters, p_{est}, and a time-varying and non-diagonal matrix Q obtained from the procedure described above. The required covariance matrix C_p is calculated by one of the two methods proposed in this work. The structure of the algorithm for process noise covariance matrix Q tuning is shown in Fig. 1.

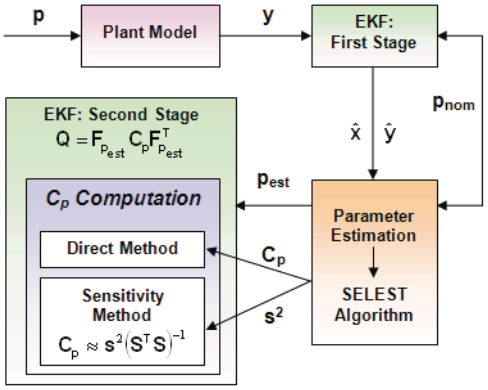

Fig. 1: Process noise covariance matrix Q tuning algorithm.

Note that the matrix Q in our algorithm takes into account the estimated parameters, p_{est}, rather than the nominal parameters, p_{nom}, as introduced by Vallapil and Georgakis (1999, 2000) in (12).

4. CASE STUDY: WILLIAMS-OTTO SEMI-BATCH REACTOR

A description of the Williams-Otto semi-batch reactor, as introduced by Forbes (1994), is provided in this section. The following reactions take place in the reactor:

$$A + B \xrightarrow{k_1} C$$
$$C + B \xrightarrow{k_2} P + E$$
$$P + C \xrightarrow{k_3} G$$

Reactant A is already present in the reactor, whereas reactant B is fed continuously to the reactor. During the exothermic reactions the products P and E as well the side-product G are formed. The heat generated through the exothermic reaction is removed by a cooling jacket, which is controlled by manipulating the cooling water temperature. The manipulated control variables of this process are the inlet flow rate of reactant B (F_B) and the cooling water temperature (T_w), whose values have been kept constant in our study. The model equations are given below and the model parameters are reported in Table 1:

$$\frac{dm_A}{dt} = -\frac{M_A}{M_A} r_1 V \tag{17}$$

$$\frac{dm_B}{dt} = F_B - \frac{M_B}{M_A} r_1 V + \frac{M_B}{M_B} r_2 V \tag{18}$$

$$\frac{dm_C}{dt} = \frac{M_C}{M_A} r_1 V - \frac{M_C}{M_B} r_2 V - \frac{M_C}{M_C} r_3 V \tag{19}$$

$$\frac{dm_P}{dt} = \frac{M_P}{M_B} r_2 V - \frac{M_P}{M_C} r_3 V \quad (20)$$

$$\frac{dm_E}{dt} = \frac{M_E}{M_B} r_2 V \quad (21)$$

$$\frac{dm_G}{dt} = \frac{M_G}{M_C} r_3 V \quad (22)$$

$$\frac{dV}{dt} = \frac{F_B}{\rho} \quad (23)$$

$$\frac{dT_r}{dt} = \frac{H - F_B c_p T_r}{V \rho c_p} \quad (24)$$

where

$$V = \frac{m_A + m_B + m_C + m_P + m_E + m_G}{\rho} \quad (25)$$

$$r_1 = k_1 \frac{m_A m_B}{V^2}; \quad r_2 = k_2 \frac{m_B m_C}{V^2}; \quad r_3 = k_3 \frac{m_C m_P}{V^2} \quad (26)$$

$$k_i = A_i e^{\frac{-E_i}{(T_r + T_{ref})}}; \quad i = 1,2,3 \quad (27)$$

$$H = F_B c_p T_{in} - \Delta H_1 \frac{M_A}{M_A} r_1 V - \Delta H_2 \frac{M_B}{M_B} r_2 V - \Delta H_3 \frac{M_C}{M_C} r_3 V - V \frac{A_0}{V_0} U(T_r - T_w) \quad (28)$$

Table 1. Model Parameters

M_A	100 kg.kmol^{-1}	ΔH_1	-263.8 kJ.kg^{-1}
M_B	200 kg.kmol^{-1}	ΔH_2	-158.3 kJ.kg^{-1}
M_C	200 kg.kmol^{-1}	ΔH_3	-226.3 kJ.kg^{-1}
M_P	100 kg.kmol^{-1}	A_0	9.2903 m^2
M_E	200 kg.kmol^{-1}	V_0	2.1052 m^3
M_G	300 kg.kmol^{-1}	U	0.23082 kJ(m^2.°C.s)$^{-1}$
A_1	1.6599E3 m^{3}kg^{-1}s^{-1}	F_B	5.7840 kg.s^{-1}
A_2	7.2117E5 m^{3}kg^{-1}s^{-1}	T_w	100 °C
A_3	2.6745E9 m^{3}kg^{-1}s^{-1}	$m_A(t_0)$	2000 kg
E_1	6666.7 K	$m_B(t_0)$	0
E_2	8333.3 K	$m_C(t_0)$	0
E_3	11111.1 K	$m_P(t_0)$	0
T_{ref}	273.15 K	$m_E(t_0)$	0
T_{in}	35 °C	$m_G(t_0)$	0
c_p	4.184 kJ.kg^{-1}.°C^{-1}	$V(t_0)$	2 m^3
ρ	1000 kg.m^{-3}	$T_r(t_0)$	65 °C
t_f	1000 s		

In order to illustrate the application of the Q tuning algorithm, the kinetic parameters E_1, E_2, and E_3 were chosen as uncertain parameters. A parametric uncertainty of ±5% is assumed. The correct parameter values ("plant parameters"), p, and the nominal parameters, p_{nom}, are reported in Table 2.

Table 2. Uncertain Parameters

	E_1	E_2	E_3
p	6333.4	7916.3	11666.6
p_{nom}	6666.7	8333.3	11111.1

The application of Q tuning algorithm to the Williams-Otto semi-batch reactor is shown below.

4.1 First Iteration of Q Tuning Algorithm.

4.1.1 Results of State Estimation: First Stage

A first state estimation with nominal parameters is performed to provide information on unmeasured states to be used in the subsequent parameter estimation step. The states and measurements of the Williams-Otto semi-batch reactor are

$$x = [m_A \quad m_B \quad m_C \quad m_P \quad m_E \quad m_G \quad V \quad T_r] \quad (29)$$

$$y = [m_B \quad m_E \quad m_G \quad V] \quad (30)$$

The measurements are obtained from a simulation of the plant model with the plant parameters p. The initial condition and the parameters of the state estimation are

$$x_0 = [2000 \quad 0 \quad 0 \quad 0 \quad 0 \quad 0 \quad 2 \quad 65] \quad (31)$$

$$P_0 = 0.0001^2 I_{8x8} \quad (32)$$

$$\Delta t = t_k - t_{k-1} = 31.25 \quad (33)$$

$$R = \mathrm{diag}(0.1^2 \quad 0.1^2 \quad 0.01^2 \quad 0.01^2) \quad (34)$$

$$Q = \mathrm{diag}(0.1^2 \quad 0.01^2 \quad 0.1^2 \quad 0.01^2 \quad 0.01^2 \quad 0.1^2 \quad 0.1^2 \quad 0.01^2) \quad (35)$$

The state estimation results using the EKF with nominal parameters and a constant-value and diagonal matrix Q are shown in Fig. 2. As expected, in the presence of a constant parametric model mismatch, the estimated states show a bias (cf. Fig. 2b).

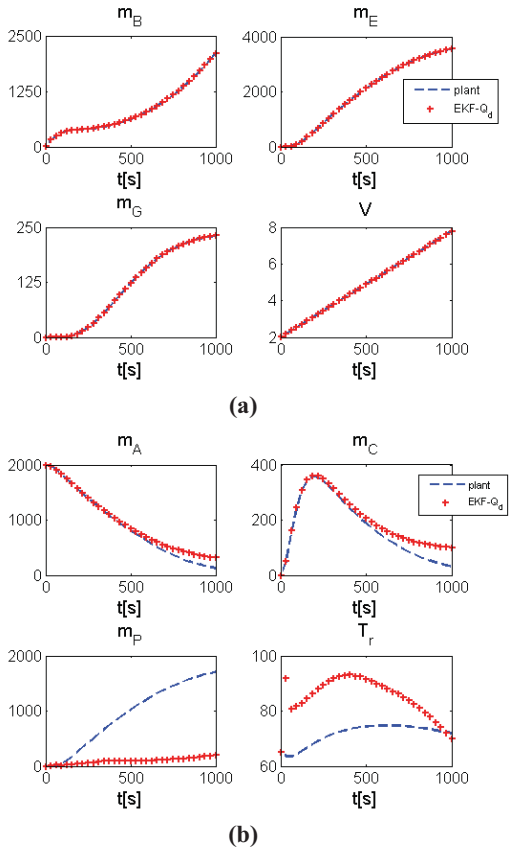

Fig. 2: EKF with nominal parameters (p_{nom}) and a constant-value and diagonal matrix Q (Q_d): (a) filtered measured states and (b) estimated states.

4.1.2 Results of Parameter Estimation Step

Using the SELEST algorithm, the parameter estimation step is based on the nominal parameters, p_{nom}. The data used to fit the parameters are composed of the estimated states and the filtered measured states provided by the first state estimation stage. As a result of the parameter estimation step, the SELEST algorithm provides the estimated parameters, p_{est}, the parameter covariance matrix, C_p, and the residual mean square, s^2

$$p_{est} = \begin{bmatrix} 6333.8 & 7957.9 & 11223.5 \end{bmatrix}$$

$$C_p = \begin{bmatrix} 3.2469E-5 & -8.6175E-6 & -4.2417E-5 \\ -8.6175E-6 & 3.8060E-5 & 8.2221E-6 \\ -4.2417E-5 & 8.2221E-6 & 3.8060E-5 \end{bmatrix}$$

$$s^2 = \frac{\sum\left(\hat{Y}-Y_p\right)^T\left(\hat{Y}-Y_p\right)}{\left(\frac{t_f}{\Delta t}+1\right)-np} = \frac{\sum\left(\hat{Y}-Y_p\right)^T\left(\hat{Y}-Y_p\right)}{\left(\frac{1000}{31.25}+1\right)-3} = 1.66E2$$

where $\hat{Y}$ is composed of the estimated and the filtered measured states resulting from the first state estimation stage and Y_p is calculated by the SELEST algorithm.

4.1.3 Results of State Estimation: Second Stage

At this point, state estimation is carried out with the estimated parameters and the time-varying and non-diagonal Q obtained by C_p. The performance of the EKF with the following choices for calculating Q is compared and the results are shown in Fig. 3.

Direct method: Q is time-varying and non-diagonal, with p_{est} and C_p estimated by means of the SELEST algorithm.

Sensitivity method: Q is time-varying and non-diagonal, with p_{est} and s^2 estimated by means the SELEST algorithm and C_p obtained via sensitivity integration.

Random Variation: Proposed by Valappil and Georgakis (1999, 2000). The parameters in the plant are assumed to vary with time, taking values at each sample interval from a nominal distribution. The mean value of the varying plant parameter is assumed to be different from the nominal value of the model parameter by a fixed amount σ. The parameter covariance matrix used in the filter is given by $C_p = \sigma^2$.

Monte Carlo Approach: Proposed by Valappil and Georgakis (1999, 2000). This approach accounts for the nonlinear dependence of the system on the fitted parameters by Monte Carlo simulations. For the case study, 500 Monte Carlo simulations of different parameter values were used, resulting in 500 evaluations of the process noise.

The initial conditions (31) and the parameters of the state estimation algorithm (32 to 35) remain the same in this stage. According to Fig. 3, the EKF with a time-varying and non-diagonal matrix Q obtained by random variation in the plant parameters presents the worst performance. The sensitivity method performs better compared to the direct method. As mentioned before, an advantage of this method is that the parameter covariance matrix, C_p, is time-varying due to the time-varying sensitivity matrix S. In spite of accounting the nonlinear dependence of the system on the fitted parameters, the Monte Carlo shows a performance slightly inferior to the that of the sensitivity method for estimated states (Fig. 3b) and a performance quite inferior to that of the sensitivity and direct methods for measured states (Fig. 3a), not to mention the high computational effort.

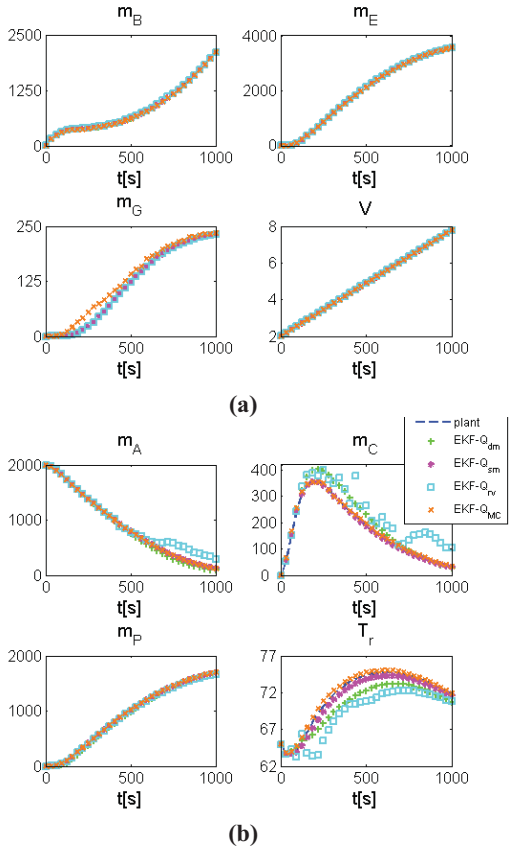

Fig. 3: EKF with estimated parameters (p_{est}) and a time-varying and non-diagonal Q matrix obtained by the proposed methods: direct (Q_{dm}) and the sensitivity (Q_{sm}); and by the literature methods: random variation (Q_{rv}) and Monte Carlo (Q_{MC}): (a) filtered measured states and (b) estimated states.

4.2 Second Iteration of Matrix Q Tuning Algorithm

Since the unmeasured states are unknown in practical applications, the state estimation accuracy shall be quantified. The matrix Q tuning algorithm is hence performed iteratively with the proposed methods for the parameter covariance matrix computation until the state estimation accuracy could not be significantly improved.

The parameter estimation is now taking place with the estimated parameters, p_{est}, and the estimated states and filtered measurements from the first iteration of the proposed algorithm. The parameter estimation results for both methods are given in Table 3.

Table 3. Uncertain Parameters

Method	p_{est}			s^2
	E_1	E_2	E_3	
Direct	6328.1	7952.7	11668.9	7.0880
Sensitivity	6333.9	7921.3	11666.3	0.7785

Disregarding numerical round off, the matrix C_p is the same for both methods, i.e.

$$C_p = \begin{bmatrix} 4.9337E-5 & -4.6902E-6 & 4.3956E-6 \\ -4.6902E-5 & 7.7390E-5 & 4.7829E-6 \\ 4.3956E-5 & 4.7829E-6 & 5.0158E-5 \end{bmatrix}$$

As expected, the residual mean square s^2 is smaller for the sensitivity method which performs better than direct method in an a-posteriori state estimation stage, as shown in Fig. 4.

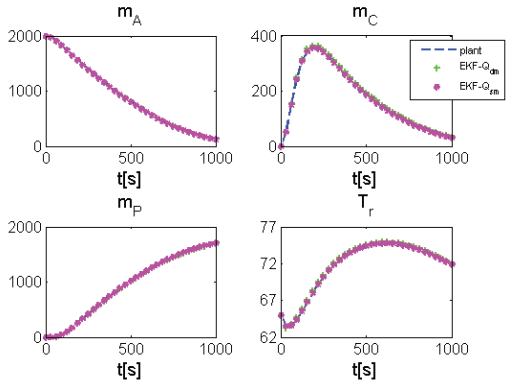

Fig. 4: Estimated states for the EKF with estimated parameters (p_{est}) and a time-varying and non-diagonal Q matrix obtained by the direct (Q_{dm}) and the sensitivity (Q_{sm}) methods.

For this example, a third iteration of the algorithm has not improved significantly the state estimation accuracy.

5. CONCLUSIONS

A new process noise covariance matrix tuning algorithm is presented which incorporates the linearized approach proposed by Valappil and Georgakis (1999, 2000) with two methods for the parameter covariance matrix computation. As pointed out by Valappil and Georgakis (1999, 2000), the investment in a nondiagonal time-varying matrix Q is justified because (a) parametric uncertainties cause significant cross-correlations between the process noises for different states (b) for continuous or batch processes with time-varying process dynamics and operating on wide range of process conditions, the noise statistics are time varying.

The Q tuning algorithm consists of two state estimation steps and a parameter estimation step in between. A first state estimation step with nominal parameters is performed to provide information on unmeasured states to be used in the subsequent parameter estimation step. Afterwards, the state estimation is carried out with the estimated parameters and a time-varying and non-diagonal tuning of matrix Q obtained from the parameter covariance matrix C_p, evaluated by the direct and sensitivity methods. In the direct method, C_p is assumed to be constant and directly obtained from the parameter estimation step using the SELEST algorithm (Secchi et al., 2006). In the sensitivity method, C_p is obtained from the computation of the time-varying sensitivity matrix. Although the EKF with a time-varying and non-diagonal matrix Q obtained from the sensitivity method performs better compared to the direct method, both methods can be successfully applied for state estimator design. Moreover, these methods improve considerably the EKF performance when compared to a) the case of a constant-value and diagonal matrix Q in the presence of constant parametric uncertainty and to b) the methods of prior publications. Successive iterations of the Q tuning algorithm shall improve the state estimation accuracy. For the Williams-Otto semi-batch reactor, only two iterations were necessary to improve the state estimation accuracy, significantly.

The main advantage of the algorithm presented in this work is that it is feasible for practical applications. Besides, of an online EKF tuning, the process model is updated online due to the integration of the state and the parameter estimation steps. Further, the algorithm eliminates an offline, exhaustive, and inexact tuning of EKF by trial and error.

REFERENCES

Forbes, J.F. (1994). Model Structure and Adjustable Parameter Selection for Operations Optimizations. *PhD thesis*, McMaster University, Hamilton, Canada, 1994.

Jazwinski, A. H. (1970). *Stochastic Processes and Filtering Theory*, Academic Press, New York.

Leu, G..; Baratti, R. (2000). An Extended Kalman Filtering Approach with a Criterion to set its Tuning Parameters; Application to a Catalytic Reactor. *Computers & Chemical Engineering*, 23, 1839-1849.

Li, R.; Henson, M.A.; Kurtz, M.J. (2004). Selection of model parameters for off-line parameter estimation. *IEEE Transactions on Control Systems Technology*, 12 (3), 402-412.

Nagy, Z. K.; Braatz, R.D. (2003). Robust nonlinear model predictive control of batch processes. *AIChE J.*, 49(7), 1776- 1786.

Odelson, B.J.; Lutz, Alexander, L; Rawling, J.B. (2006). The autocovariance least-squares method for estimating covariances: Application to model-based control of chemical reactors. *IEEE Transactions on Control Systems Technology*, 14(3), 532-540.

Secchi, A.R.; Cardozo, N.S.M.; Almeida Neto, E.; Finkler, T.F. (2006). An algorithm for automatic selection and estimation of model parameters, *In: Proceedings of International Symposium on Advanced Control of Chemical Processes, ADCHEM 2006*, Gramado, Brazil.

Mehra, R.K. (1972). Approaches to adaptive filtering. *IEEE Trans. Automat. Contr.*, 17(5), 693-698.

Sharma, M.S.; Arora, N.D. (1993). Optima: A nonlinear model parameter extraction program with statistical confidence region algorithms, *IEEE Trans. Comp. Aided Des. Int. Circuits Syst*., 12, 982–987.

Simon, D. (2006). *Optimal State Estimation: Kalman, H Infinity, and Nonlinear Approaches*, Wiley-Interscience, New Jersey.

Valappil, J.; Georgakis, C. (1999). A systematic tuning approach for the use of extended Kalman filters in batch processes. *Proc. of the American Control Conf., IEEE Press,* Piscataway, NJ, 1143.

Valappil, J.; Georgakis, C. (2000). Systematic estimation of state noise statistics for extended Kalman filters. *AIChE J.*, 46(2), 292-398.

Valappil, J.; Georgakis, C. (2001). A systematic tuning approach for the use of extended Kalman filters in batch processes. *Proc. of the American Control Conf., IEEE Press,* Piscataway, NJ, 99.

Valappil, J.; Georgakis, C. (2002). Nonlinear model predictive control of end-use properties in batch reactors. *AIChE J.,* 48(9), 2006-2021.

Observer Design for Systems with Continuous and Discrete Measurements ⋆

C.P. Guillén-Flores * **B. Castillo-Toledo** *
J.P. García-Sandoval ** and **V. González-Álvarez** **

* *CINVESTAV-IPN, Av. Cientifica 1145 , colonia el Bajío, Zapopan , 45015, Jalisco, México (e-mail: [cguillen, toledo]@gdl.cinvestav.mx)*
** *Chemical Engineering Department, University of Guadalajara, Calz. Gral. Marcelino García Barragán 1451, Guadalajara, Jalisco 44430, México (e-mail: paulo.garcia@cucei.udg.mx)*

Abstract: Classical observers are constructed on the basis of the nature of the measurement signals, namely, a continuous observer requires continuous output measurements. In this work, a novel observer which estimates continuous states when continuous and discrete measurements are available is presented. By resetting the initial condition of the observer at each sample instant, the convergence of the continuous states is guaranteed. The application to the the estimation of substrate and biomass concentrations in an anaerobic wastewater treatment process in which continuous and discrete measurements usually appear, shows the feasibility of the proposed scheme.

Keywords: jump observer, anaerobic digestion, discrete measurements

1. INTRODUCTION

Because of the increasing complexity and necessity for safety of industrial processes, efficient monitoring, decision and control systems are becoming more an more important. This is particularly true in the case of bioprocesses where the state of the live organisms of the system must be closely monitored. Extensive surveys have been published on this topic (Dochain, 2008). Furthermore, the last two decades have seen an increasing interest in improving the operation of bioprocesses by applying advanced control schemes. In particular, biological waste treatment process, more efficient that the traditional physicochemical methods but at the same time more complex, call for a consistent good performance,which leads to a needing for more efficient instrumentation, control and automation.

To apply any control strategy it is necessary to measure the process main variables, this can be performed placing sensors (**?**), however, although in many cases continuous measurements are easily available, for example the temperature or pH, due to economical reasons or consuming time techniques, other key variables can be only measured intermittently, or even not measured at all. For this reason the non measurable state variables should be estimated from available measurements (Meleiro and Filho, 2000). To deal with these problems, many solutions have been proposed in the past such as the well known classical Kalman filters and Luenberger observers (Ray, 1980) in both, continuous and discrete approaches. On of the reasons for the popularity of these estimators is that they are easy to implement since the algorithm can be derived directly from the state space model. However, these state observers can not be easily implemented when both continuous and discrete information must be considered. In this direction Scali et al. (1997) have proposed an extended Kalman filter which update some observer parameters each time that the sampled date is available. Using Lyapunov functions , Liu et al. (2008) and Muñoz de la Peña and Christofides (2008) have designed controllers that involve continuous and discrete retarded measurements. Nguang and Shi (2003) also use discrete measurements to design continuous fuzzy control algorithms. Based on this idea in this work it is proposed a continuous observer to be continuously updated from the continuous measurements and also retune the states at each instant when the discrete measurement are available.

This work is organized as follows. A review of jump observers is presented in section 2, then in section 3 the observational problem is formulated, while the proposed solution is developed in section 4. In section 5 we analyze the dynamic behavior through numerical simulations for an anaerobic digestion system. Finally we close the paper with some concluding remarks.

2. BASIC FACTS OF JUMP OBSERVERS

Consider the linear system

$$\dot{x}(t) = Ax(t) + Bu(t) \qquad \forall t \in [0, \infty) \tag{1}$$

$$y(k\delta) = Cx(k\delta) \qquad k = 1, 2, 3, \ldots, \tag{2}$$

where $x \in \mathbb{R}^n$, $u \in \mathbb{R}^m$, and $y \in \mathbb{R}^q$ are the state, input and output vectors, respectively. In this case the outputs are obtained at each sampling time δ.

The usual way to estimate the unknown states of system (1) from output (2) consists in discretizing the system

⋆ Partially Supported by PROMEP under proyect 103.5/08/2919 and CONACYT under grant 43658.

and design a discrete observer. However, the observer thus obtained provides only information at each sampling period. Additionally, to obtain a discrete version of (1) it is necessary to have a well defined input in order to place the appropriate holder (for example a zero holder or a exponential holder), hence unexpected input variations during intersampling periods may produce discrete observer failures (García-Sandoval, 2006). For this reason, an interesting problem would be to construct an observer given by

$$\dot{z}(t) = Az(t) + Bu(t) \qquad \forall t \neq k\delta \tag{3}$$

$$z\left(k\delta^{+}\right) = z(k\delta) - G\left[y(k\delta) - Cz(k\delta)\right] \quad t = k\delta \tag{4}$$

where $z \in \mathbb{R}^n$ are the observer states and $z\left(k\delta^{+}\right)$ denotes the updated observer states at each sampling instant. This is a continuous observer which updates its states at each sampling instant. The next lemma establishes conditions for the existence of such observer.

Lemma 1. Consider system (1)-(2) and suppose the pair $\left(e^{A\delta}, C\right)$ is observable, then an observer of the form (3)-(4) with the matrix gain G such that matrix $(I + GC)\, e^{A\delta}$ is Schur, guaranteeing that $\lim_{t\to\infty}\left[x(t) - z(t)\right] = 0$.

Proof. See Appendix.

Remark 2. The main feature of observer (3)-(4) remains in the fact that the intersampling state information is available at any time and it is not necessary to have a pre-established dynamic behavior for the input. Equation (3) can be seen as a continuous open loop observer in the intersampling period and whose states, according to (4), are reseted each sampling period.

3. PROBLEM FORMULATION

Consider the dynamic system

$$\dot{x}(t) = f\left(x(t), u(t)\right) \quad \forall t \in [0, \infty) \tag{5a}$$

$$y_1(t) = C_1 x(t) \qquad \forall t \in [0, \infty) \tag{5b}$$

$$y_2(k\delta) = C_2 x(k\delta) \qquad k = 1, 2, 3, \ldots \tag{5c}$$

where $x \in \mathbb{R}^n$, $u \in \mathbb{R}^m$ and $y_1 \in \mathbb{R}^{q_1}$, $y_2 \in \mathbb{R}^{q_2}$ are the state, input and output vectors for the dynamic system, respectively. The outputs are divided into continuous (y_1), and discrete (y_2) with sampling time δ. For this system it is desirable to design a continuous observer which uses both discrete and continuous measurements, in order to have continuous information about the full vector state. The following assumption is instrumental for the observer design.

Assumption 3. Defining

$$A = \left.\frac{\partial f}{\partial x}\right|_{x=0,u=0} \quad \text{and} \quad B = \left.\frac{\partial f}{\partial u}\right|_{x=0,u=0}$$

as the linear matrices for system (5), it is assumed that the pair (A, C), with

$$C = \begin{pmatrix} C_1 \\ C_2 \end{pmatrix}$$

is observable but, the pairs (A, C_1) and (A, C_2) related with continuous and discrete measurements, are not necessarily completely observable. That is, the observability matrix of these pairs may not have full rank.

In the following section it is presented a continuous observer for system (5), which is the main result of this work.

4. OBSERVER DESIGN

Assume that there is a transformation $T \in \mathbb{R}^{n\times n}$, such that the linear approximation of system (5a)-(5b) becomes

$$\begin{aligned} \dot{z} &= \bar{A}z(t) + \bar{B}u(t) \\ y_1 &= \bar{C}_1 z(t) \end{aligned} \tag{6}$$

where

$$z = Tx = \begin{pmatrix} z_1 \\ z_2 \end{pmatrix}, \quad \bar{A} = TAT^{-1} = \begin{pmatrix} A_{11} & 0 \\ A_{21} & A_{22} \end{pmatrix}$$

$$\bar{B} = TB = \begin{pmatrix} B_1 \\ B_2 \end{pmatrix}, \quad \bar{C}_1 = C_1 T^{-1} = (C_{11}\ 0)$$

$z_1 \in \mathbb{R}^{n_1}$, $z_2 \in \mathbb{R}^{n_2}$, and the pair (A_{11}, C_{11}) is completely observable. In this case a partial observer for z_1 can be designed in such way that given a matrix G_{11}, $(A_{11} - G_{11}C_{11})$ is Hurwitz. Applying the inverse transformation, the proposed observer is,

$$\dot{\zeta}(t) = f\left(\zeta(t), u(t)\right) - G_1\left(C_1\zeta(t) - y_1(t)\right)$$

where

$$G_1 = T^{-1}\begin{pmatrix} G_{11} \\ 0 \end{pmatrix}.$$

This is a partial observer which only make use of continuous measurements (5b), however, using discrete measurements it is possible to design a jump observer as described in section 2, which include both continuous and discrete measurement. The following theorem states this result.

Theorem 4. Consider the system (5), which has a set of continuous measurements (5b) and a set of discrete measurements (5c) with sampling time δ. Furthermore consider that there is a transformation $T \in \mathbb{R}^{n\times n}$ which transforms the linear approximation of system (5a)-(5b) to its observable canonical form (6), while the matrix $G_1 = T^{-1}\left(G_{11}^T\ 0\right)^T$, is calculated in such a way that $(A_{11} - G_{11}C_{11})$ is Hurwitz and the matrix G_2 is such that $(I + G_2C)\, A_d$ is Schur, with $A_d = e^{(A - G_1C_1)\delta}$. Then, an observer for system (5), which takes continuous measurements and is also updated each sampling period is given by

$$\begin{aligned} \dot{\zeta}(t) &= f\left(\zeta(t), u(t)\right) && \forall t \neq k\delta \\ &\quad -G_1\left(C_1\zeta(t) - y_1(t)\right), \end{aligned} \tag{7a}$$

$$\begin{aligned} \zeta\left(k\delta^{+}\right) &= \zeta(k\delta) && t = k\delta, \\ &\quad +G_2\left(C\zeta(k\delta) - y(k\delta)\right), && k = 1, 2, 3, \ldots \end{aligned} \tag{7b}$$

where $\zeta \in \mathbb{R}^n$ are the observer states and $\zeta\left(k\delta^{+}\right)$ are its updated values at each sampling time and

$$y(k\delta) = \begin{pmatrix} y_1(k\delta) \\ y_2(k\delta) \end{pmatrix}.$$

This observer guarantees that, in a neighborhood of the origin, the error between the system and the observer states tends asymptotically to zero, i.e. $\lim_{t\to\infty}[x(t) - \zeta(t)] = 0$.

Proof. First, consider the linear approximations of both, system (5a) and observer (7a)

$$\dot{x}(t) = Ax(t) + Bu(t) \quad \forall t \in [0, \infty) \tag{8}$$

$$\dot{\zeta}(t) = (A - G_1 C_1)\zeta(t) + Bu(t) + G_1 y_1(t) \tag{9}$$

additionally, consider that there is a matrix T that transforms the system (8) and its output (5b) to its observable canonical form (6), i.e.

$$z = Tx = \mathrm{col}(z_1, z_2),$$
$$\xi = T\zeta = \mathrm{col}(\xi_1, \xi_2),$$

where z_1 and ξ_1 are the observable modes of x and ζ. Then for the observable subsystems of z and ξ defining the error $e_1(t) = z_1(t) - \xi_1(t)$, whose dynamic is

$$e_1(t) = (A_{11} - G_{11}C_{11})e_1(t).$$

Since G_{11} is such that $(A_{11} - G_{11}C_{11})$ is Hurwitz, $e_1(t)$ tends asymptotically to zero. On the other hand, using discrete measurements, $y(k\delta)$, a jump observer (7) which allows the updating of the continuous dynamic observer states in every sampling period it is designed, taking advantage of the discrete information. Defining now the error

$$\eta(t) = x(t) - \zeta(t)$$
$$\eta(k\delta^+) = x(k\delta) - \eta(k\delta^+)$$

its linear dynamic approximation around $\eta = 0$ is

$$\dot{\eta}(t) = (A - G_1 C_1)\eta(t) \qquad \forall t \neq k\delta$$
$$\eta(k\delta^+) = (I + G_2 C)\eta(k\delta) \qquad t = k\delta, \quad k = 1, 2, 3, \ldots$$

As described in Lemma 1, these dynamics are stable if the pair (A_d, C) with $A_d = e^{(A - G_1 C_1)\delta}$ is observable and the gain G_2 is such that the matrix $(I + G_2 C)A_d$ is Schur, thereby ensuring that $\lim_{k\to\infty}[x(k\delta) - \zeta(k\delta)] = 0$ and thus $\lim_{t\to\infty}[x(t) - \zeta(t)] = 0$, which proves the theorem.

Observer (7) can be seen as a hybrid observer since incorporates continuous dynamics (7a) and a discrete event (7b) which modifies the continuous part. It should be also noted that the calculation of the observer part for continuous measurements is independent of the discrete observer part, however, the total discrete observer depends on the gain G_1.

5. STUDY CASE

Last years, the environmental laws have been tightened and it has became mandatory treating wastewater from industries as well households (**?**Huntington, 1998). Because of this, the wastewater treatment control processes have received great importance, especially anaerobic processes are being widely considered as an alternative for the treatment of wastewater because it produces smaller quantities of organic matter and also yields a high-energy gas (Méndez-Acosta et al., 2008). To achieve the control of these processes, state observers are frequently used, however for economical reasons some key variables can just be measured using long sampling times, while others may be measured more often. For this reason, a jump observer is proposed as presented in theorem 4.

There exists many dynamic models to describe anaerobic process (**?**Batstone et al., 2002; Bernard et al., 2006). However, to apply the proposed observer, a macroscopic model of the anaerobic process developed and validated by Bernard et al. (2001) it is considered,

$$\dot{X}_1 = (\mu_1(S_1) - \alpha D)X_1 \tag{10a}$$

$$\dot{S}_1 = -k_1\mu_1(S_1)X_1 + (S_{1in} - S_1)D \tag{10b}$$

$$\dot{X}_2 = (\mu_2(S_2) - \alpha D)X_2 \tag{10c}$$

$$\dot{S}_2 = -k_3\mu_2(S_2)X_2 + k_2\mu_1(S_1)X_1 + (S_{2in} - S_2)D \tag{10d}$$

where X_1, X_2, S_1, S_2, are respectively the concentrations of acidogenic bacteria, methanogenic bacteria, Chemical Oxygen Demand (COD) and Volatile Fatty Acids (VFA), D is the dilution rate, defined by the ratio $D = Q/V$, where Q is the feeding flow and V the digester volume, S_{1in} and S_{2in} are respectively the concentrations of influent organic substrate and of influent VFA. The $k_i s$ are pseudo-stoichiometric coefficients associated to the bioreactions. Parameter $\alpha \in (0, 1]$ represents the fraction of the biomass which is not retained in the digester (Hess and Bernard, 2008). The bacterial growth rates $\mu_1(S_1)$ and $\mu_2(S_2)$, are nonlinear functions given respectively by the Monod and Haldane kinetics (Henze and Harremoes, 1983)

$$\mu_1(S_1) = \mu_{\max 1}\frac{S_1}{S_1 + K_{S1}}$$
$$\mu_2(S_2) = \mu_{\max 2}\frac{S_2}{S_2 + K_{S2} + (S_2/K_{I2})^2}$$

where $\mu_{1\max}$, K_{S1}, $\mu_{2\max}$, K_{S2} and K_{I2} are the maximum bacterial growth rate and the half-saturation constant associated to the substrate S_1, the maximum bacterial growth rate in the absence of inhibition, and the saturation and inhibition constants associated to substrate S_2, respectively. The values of parameters and the input concentrations used for simulations are listed in Tables 1 and 2.

If we consider that VFA concentration (S_2) is a continuous measurement while the COD concentration (S_1) can just be periodically acquired (in fact in real operations, VFA concentration can be obtained up to every hour or less (Méndez-Acosta et al., 2008), hence it can be considered continuous compared with the resident time and the COD concentration that could be measured even just once a

Table 1. Model Parameters (Alcaraz-González et al., 2003)

Parameter	Value
μ_1	$1.2\,\mathrm{d}^{-1}$
$\mu_{\max 2}$	$0.69\,\mathrm{d}^{-1}$
K_{S1}	$4.95\,\mathrm{kg\ COD/\,m^3}$
K_{S2}	$9.28\,\mathrm{mol\ VFA/\,m^3}$
K_{I2}	$20\,\mathrm{mol\ VFA/\,m^3}$
k_1	6.6 kg COD/ kg X_1
k_2	7.8 mol VFA/ kgX_1
k_3	611.2 mol VFA/ kgX_2
α	0.5 (addimentional)

Table 2. Input Concentrations

Substrate	Value
S_{1in}	20 Kg COD/$\mathrm{m^3}$
S_{2in}	100 mol VFA/$\mathrm{m^3}$

day), the jump observer developed in the previous section can be then applied to the dynamic system (10) writing it in the form

$$\dot{x}(t) = \begin{pmatrix} \mu_1(S_1)X_1 \\ -k_1\mu_1(S_1)X_1 \\ \mu_2(S_2)X_2 \\ -k_3\mu_2(S_2)X_2 + k_2\mu_1(S_1)X_1 \end{pmatrix} + \begin{pmatrix} -\alpha X_1 \\ S_{1in} - S_1 \\ -\alpha X_2 \\ S_{2in} - S_2 \end{pmatrix} u(t) \tag{11}$$

$$y_1(t) = (\,0\;0\;0\;1\,)\,x(t)$$
$$y_2(k\delta) = (\,0\;1\;0\;0\,)\,x(k\delta)$$

where

$$x(t) = \begin{pmatrix} X_1 \\ S_1 \\ X_2 \\ S_2 \end{pmatrix}, \quad C = \begin{pmatrix} C_1 \\ C_2 \end{pmatrix} = \begin{pmatrix} 0 & 0 & 0 & 1 \\ 0 & 1 & 0 & 0 \end{pmatrix},$$

and $u\,(t) = D\,(t)$. System (11) can be represented as

$$\dot{x}(t) = f(x) + g(x)u(t). \tag{12}$$

To calculate the jump observer (7) is necessary to linearize the system (12) around a neighborhood of equilibrium points (Hess and Bernard, 2008; Méndez-Acosta et al., 2008) so the system has the form

$$\dot{x}(t) = Ax(t) + Bu(t) + \hat{f}(x,u)$$

where

$$A = \left[\frac{\partial f}{\partial x} + \frac{\partial g}{\partial x}u\right]_{x=0,u=0}, \quad B = g\,(x)|_{x=0}$$

are the linear approximation matrices around the steady state [see (Hess and Bernard, 2008) for a detailed steady state analysis]. In this case, the observability matrices for pairs (A, C_1), (A, C_2) and (A, C) have ranks 4, 2 and 4, respectively, i.e. using S_2 it is possible to estimate the four states, while using S_1 it is just possible to estimate the acidogenic part of the system. This is obvious since system (10) has a cascade dynamic form between acidogenic and methanogenic dynamics.

Considering a sampling time (δ) equal to 1 and parameters listed in Tables 1 and 2, it is easy to verify that A, B and A_d take the values

$$A = \begin{pmatrix} 0 & 0.7900 & 0 & 0 \\ -1.8756 & -5.7825 & 0 & 0 \\ 0 & 0 & 0 & 0.0015 \\ 2.2166 & 6.1622 & -173.6936 & -1.4701 \end{pmatrix},$$

$$B = \begin{pmatrix} -2.7976 \\ 18.4640 \\ -0.1413 \\ 90.0000 \end{pmatrix},$$

$$A_d = \begin{pmatrix} 0.8033 & 0.1145 & 0 & 0 \\ -0.2719 & -0.0349 & 0 & 0 \\ 0.0003 & 0.0008 & 0.9186 & 0.0007 \\ 0.1556 & 0.3069 & -87.2825 & 0.1798 \end{pmatrix},$$

Using LQR techniques to calculate observer gains, observer (7) is designed in order to fulfill theorem 4, obtaining

Table 3. Initial conditions for simulations runs.

State variable	$X_1\,(0)$ kg/ m^3	$S_1\,(0)$ kg/ m^3	$X_2\,(0)$ kg/ m^3	$S_2\,(0)$ mol/ m^3
Plant	1.433	0.1	0.2	0.4
Observer	0.5	0.3	0.1	1

$$G_1 = \begin{pmatrix} -0.0005 \\ 0.0115 \\ -0.9985 \\ 17.2429 \end{pmatrix}, \quad G_2 = \begin{pmatrix} 0.0007 & 0.3923 \\ -0.0002 & -0.1330 \\ 0 & 0.0003 \\ 0 & -0.0002 \end{pmatrix}.$$

5.1 Simulation Results

In order to illustrate the performance of observer (7), some numerical simulations were carried out. Initial conditions and input concentrations for these simulations are listed in Table 3 and 2, while dilution rate was considered as a time varying sinusoidal signal around the nominal value. To verify if the incorporation of the discrete measurement to the continuous observer reduces convergence time, hybrid observer (7) was compared with a continuous observer identical to (7a) without the use of (7b) (or equivalently, for this observer G_2 was settled equal to zero). Figure 1 shows the dynamic behavior of hybrid observer, the discrete actualization is clearly visible in Figure 1a where at time $t = 1$ d there is a jump on the acidogenic biomass estimation. As can be seen, observer states converges after approximately tree days. In contrast, the continuous observer (see Figure 2) converges in approximately twelve days, i.e. four times slower than the hybrid observer. Comparing both observers it easy to see that the hybrid observer obtained a faster convergence rate.

6. CONCLUSIONS

An nonlinear observer which updates the states using continuous and discrete measurements was presented. Despite this is a local observer, since observer gain matrices were calculated using the linear approximation of the original nonlinear system, its application to an anaerobic digestion model presents an excellent performance and stability, obtaining an improvement in convergence rate in comparison with an observer which only uses the continuous information. As future work, the authors are considering to extend this theory to the case where there exists parametric variations in the original plant, as well as the use of these observers to the control of systems with continuous and discrete measurements.

(Chapter head:)*

Bibliography

Alcaraz-González, V., Harmand, J., Dochain, D., Rapaport, A., Steyer, J., Pelayo-Ortiz, C., and González-Alvarez, V. (2003). A robust asymptotic observer for chemical and biochemical reactors. In *Proc. Of the IFAC ROCOND 2003*. IFAC.

Batstone, D., Keller, J., Angelidaki, I., Kalyuzhnyi, S., Pavlostathis, S., Rozzi, A., Sanders, W., Siegrist, H., and Vavilin, V. (2002). *Anaerobic Digestion Model No. 1 (ADM1)*, volume 13 of *Scientific and Technical Report*. IWA Publishing, London.

Bernard, O., Chachuat, B., Hélias, A., and Rodríguez, J. (2006). Can we assess the model complexity for

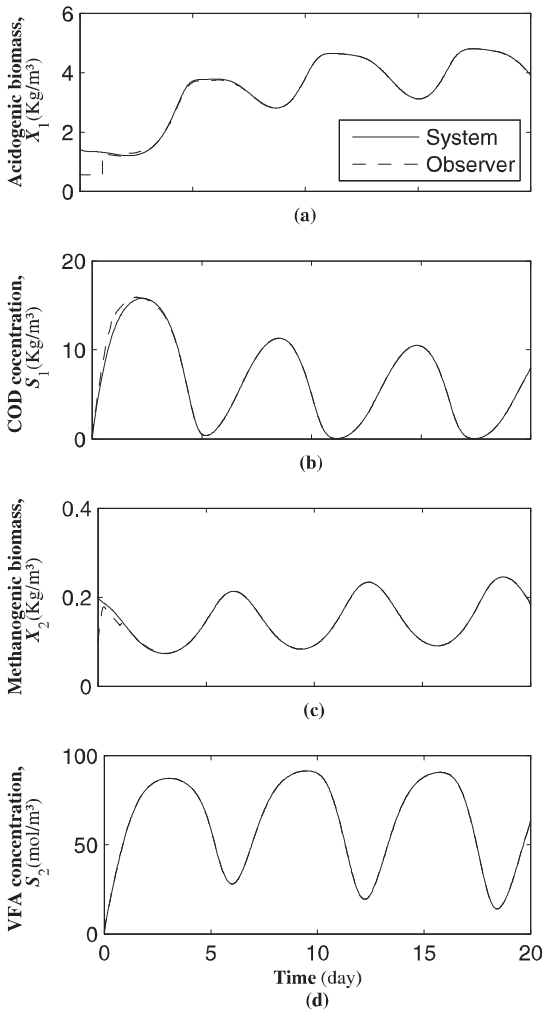

Fig. 1. Hybrid observer simulation.

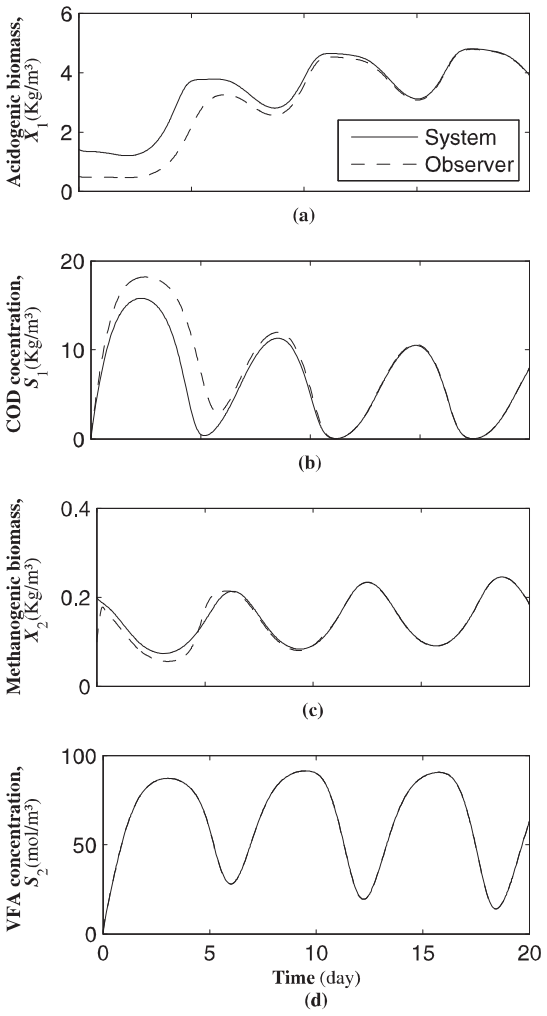

Fig. 2. Continuous observer simulation.

a bioprocess: Theory and example of the anaerobic digestion process. *Water Science Technology*, 53(1), 85–92.

Bernard, O., Hadj-Sadok, Z., Dochain, D., Genovesi, A., and Steyer, J. (2001). Dynamical model development and parameter identification for anaerobic wastewater treatment process. *Biotechnology & Bioengineering*, 75(4), 424–439.

Dochain, D. (2008). *Bioprocess Control*. Control Systems, Robotics and Manufacturing. Wiley.

García-Sandoval, J. (2006). *The Robust Regulation Problem Using Immersions: Reactors Applications*. Ph.D. thesis, CINVESTAV.

Henze, M. and Harremoes, P. (1983). Anaerobic treatment of wastewater in fixed film reactors- a literature review. *Water Science and Technology*, 15(1), 1–101.

Hess, J. and Bernard, O. (2008). Design and study of a risk management criterion for an unstable anaerobic wastewater treatment process. *Journal of Process Control*, 18(1), 71–79.

Huntington, R. (1998). Twenty years development of ICA in a water utility. *Wat. Sci. Technol.*, 37(12), 27–34.

Kailath, T. (1980). *Linear Systems*. Prentice Hall.

Liu, J., Muñoz de la Peña, D., Ohran, B.J., Christofides, P.D., and Davis, J.F. (2008). A two-tier architecture for networked process control. *Chemical Engineering Science*, (63), 5394–5409.

Meleiro, L. and Filho, R. (2000). State and parameter estimation based on a nonlinear filter applied t an industrial process control of ethanol production. *Braz. J. Chem. Eng.*, 17, 4–7.

Méndez-Acosta, H., Palacios-Ruiz, B., Alcaraz-González, V., Steyer, J., González-Álvarez, V., and Latrille, E. (2008). Robust control of volatile fatty acids in a anaerobic digesters. *Industrial and Engineering Chemical Research*, 47(20), 7715–7720.

Muñoz de la Peña, D. and Christofides, P.D. (2008). Output feedback control of nonlinear systems subject to sensor data losses. *Science Direct*, (57), 631–642.
Nguang, S. and Shi, P. (2003). Fuzzy $\mathcal{H}_\infty$ output feedback control of nonlinear systems under sampled measurements. *Automatica*, 39, 2169–2174.
Ray, W. (1980). *Advanced Process Control*. McGraw-Hill.
Scali, C., Morretta, M., and Semino, D. (1997). Control of the quality of polymer products on continuous reactors: Comparison of performance of state estimators with and without updating of parameters. *Journal of Process Control*, 7(5), 357–369.

Appendix A. APPENDIX

Proof. [Lemma 1] Let us define

$$\xi(t) = x(t) - z(t), \quad \text{and } \xi\left(k\delta^+\right) = x(k\delta) - z\left(k\delta^+\right),$$

where $\xi(t)$ represents the continuous error and $\xi\left(k\delta^+\right)$ is the updated error for each sampling period. Note that $x\left(k\delta^+\right) = x(k\delta)$ since system (1) is continuous. Now

$$\dot{\xi}(t) = A\xi(t) \qquad \forall t \neq k\delta \tag{A.1}$$

$$\xi\left(k\delta^+\right) = (I + GC)\,\xi(k\delta) \qquad t = k\delta. \tag{A.2}$$

Solving (A.1) for $t \in \left[k\delta^+, (k+1)\,\delta\right]$, it follows that

$$\xi(k+1) = A_d \xi\left(k\delta^+\right), \tag{A.3}$$

where $A_d = e^{A\delta}$. From (A.2) and (A.3) it is obtained

$$\begin{aligned}\xi\left((k+1)\,\delta^+\right) &= (I + GC)\,\xi(k+1)\\ &= (I + GC)\,A_d \xi\left(k\delta^+\right),\end{aligned}$$

and thus, if the pair (A_d, CA_d) is observable, then a matrix G can be calculated such that $A_d + GCA_d$ is Schur and the error $\xi\left(k\delta^+\right)$ will converge to zero, hence $\lim_{k\to\infty}\left[x(k\delta) - z\left(k\delta^+\right)\right] = 0$; then for $k\delta < t \leq (k+1)\,\delta$ the solution $z(t)$ converges to $x(t)$, that is $\lim\limits_{t\to\infty}\left[x(t) - z(t)\right] = 0$. On the other hand, to prove that the pair (A_d, CA_d) is observable if the pair (A_d, C) is observable, consider its observability matrix

$$\mathcal{O} = \begin{pmatrix} CA_d \\ CA_d^2 \\ \vdots \\ CA_d^n \end{pmatrix},$$

where $A_d \in \mathbb{R}^{n\times n}$, then using the Hamilton-Cailey theorem (Kailath, 1980)

$$A_d^n = a_0 I + a_1 A_d + \cdots + a_{n-1} A_d^{n-1},$$

the observability matrix becomes

$$\mathcal{O} = \begin{pmatrix} CA_d \\ CA_d^2 \\ \vdots \\ a_0 C + a_1 CA_d + \cdots + a_{n-1} CA_d^{n-1} \end{pmatrix}.$$

Since A_d is obtained through a discretization of matrix A then $a_0 \neq 0$ and $\mathcal{O}$ has full rank if the pair (A_d, C) is observable.

Soft sensing for two-phase flow using an ensemble Kalman filter

A. Gryzlov*, M. Leskens, R.F. Mudde***

** Department of Multi-Scale Physics, Delft University of Technology, Delft, 2628 BW, the Netherlands (Tel: 31(0)152783210; e-mail: a.gryzlov@tudelft.nl)*
*** Department of Process Modelling and Control, TNO Science and Industry, Eindhoven, the Netherlands (e-mail: martijn.leskens@tno.nl)*

Abstract: A new approach for real-time monitoring of horizontal wells, which is based on data assimilation concepts, is presented. Such methodology can be used when the direct measurement of multiphase flow rates is unfeasible or even unavailable. The real-time estimator proposed is an ensemble Kalman filter employing a dynamic model of the pipe flow and information from several downhole pressure sensors with a single measurement of the flow velocity and composition. By means of simulation examples it is shown that the proposed algorithm operates quite accurately both for noisy synthetic measurements and artificial data generated by the OLGA simulator.

Keywords: Distributed state estimation, Ensemble Kalman filter, Two-phase flow, Inverse dynamic problem

1. INTRODUCTION

The growing demand for hydrocarbon production has resulted into improved oilfield management with various monitoring and optimization strategies (Glandt, 2003, Jansen *et al.*, 2008). These strategies in turn strongly rely on the efficiency of downhole equipment which is used to obtain real-time oil and gas production rates with sufficient spatial and temporal resolution. In particular, multiphase flowmeters installed downhole can improve the production of long horizontal wells by allocating the zones of oil, gas and water inflow. However, existing multiphase meters are expensive, inaccurate or accurate only within a limited operating range and therefore such monitoring is unrealistic.

To overcome these problems one can use so-called multiphase soft-sensors, i.e. to estimate flow rates from conventional meters, such as downhole pressure gauges, in combination with a dynamic multiphase flow model. Despite the variety of soft-sensing techniques (which are also referred to as data assimilation methods), one can note two principal approaches. Variational data assimilation, which is based on the minimization of a cost function within a certain time interval, and sequential methods or filtering when the state of the system is updated every time instant data becomes available. One way to solve these sequential data assimilation problems is to use Kalman filtering (Kalman, 1960). This method, which was originally developed for linear models, has got numerous extensions (Jazwinski, 1970, Evensen, 1994 and Julier *et al.*, 2000) to deal with non-linearity, which is the case for most industrial processes.

Although there are numerous applications of soft-sensing techniques in oil and gas industry, they mainly deal with the estimation of reservoir properties (Naevdal *et al.*, 2003, Evensen *et al.*, 2007). The range of wellbore flow application includes gas-lift wells (Bloemen *et al.*, 2004) and underbalanced drilling (Lorentzen *et al.*, 2001). Also, the Kalman filter has been used for tuning the parameters of two phase flow models (Lorentzen *et al.*, 2003). Leskens *et al.* (2008) considered the simultaneous estimation of downhole oil, water and gas flow rates from downhole pressure and temperature measurements in a single well. This approach has been extended by de Kruif *et al.* (2008) to the multi-lateral well case both for the two-phase (oil and gas) and three-phase (oil, gas and water) cases.

Despite the variety of applications considered, little attention has been given to the inflow allocation problem. More specific, long horizontal wells with a continuous inflow profile from a reservoir to a wellbore require the use of soft-sensing techniques for the gas breakthrough prediction.

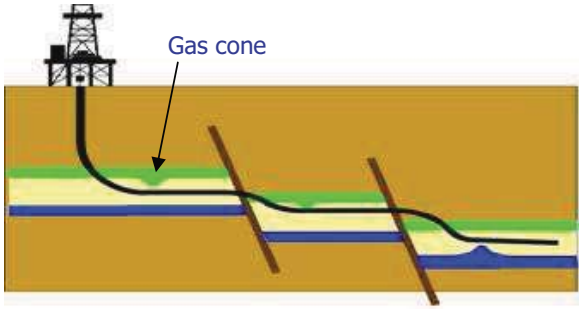

Fig. 1. Schematic view of a horizontal well.

Gas coning is a phenomenon where the gas-oil contact of a reservoir moves towards a producing well (see Figure 1). At a certain moment the gas-oil contact will reach the well and gas breakthrough can happen causing a large gas influx. Consequently, the gas phase may start to dominate production making the well uneconomical. In order to handle or prevent this, several strategies are available. However, the most convenient countermeasure is to isolate gas producing

zones of a wellbore by means of inflow control valves. The purpose of a soft-sensor is to provide the inflow control valves with information of the downhole flow rate distribution.

This study discusses the feasibility of such multiphase soft-sensors. In particular, the required and sufficient set of measurements is defined. Furthermore, the influence of model error and measurement noise on the quality of estimates is studied.

This paper is organized as follows. First, the pipe flow model and the computational setup for soft-sensing are given. Next, the description of the used soft-sensing algorithm is presented. Finally, the simulations results are given.

2. DYNAMIC FLOW MODEL

A model describing one-dimensional two-phase flow in pipes consists of non-linear partial differential equations describing mass and momentum conservation for each phase. This model is obtained from cross-sectional averaging of the Navier-Stokes equations and replacing diffusion terms by empirical correlations. Since the main purpose of this work is the application of estimation techniques, no detailed flow description is required. Therefore, it was assumed that the gas and liquid are travelling with the same velocity u (Vicente, *et al.*, 2001).

The simplified mass conservation equations are

$$\frac{\partial}{\partial t}(\rho_l H) + \frac{\partial}{\partial s}(\rho_l H u) = \Phi_l \tag{1}$$

$$\frac{\partial}{\partial t}(\rho_g (1-H)) + \frac{\partial}{\partial s}(\rho_g (1-H) u) = \Phi_g \tag{2}$$

Where H is the liquid volume fraction, ρ_g is the gas density, ρ_l is the liquid density, t denotes time and s denotes the coordinate along the length of the pipe. Φ_l and Φ_g are the mass sources representing the inflow from a reservoir to the pipe. These sources are normally time dependent.

Although the continuity equations have been written for each phase it is common to write the momentum equation for the mixture.

$$\frac{\partial}{\partial t}(\rho_m u) + \frac{\partial}{\partial s}(\rho_m u^2) = -\frac{\partial p}{\partial s} - S_{fr} \tag{3}$$

Where ρ_m is the mixture density defined by

$$\rho_m = \rho_g (1-H) + \rho_l H \tag{4}$$

A frequently used model for frictional losses in the momentum equation has the form

$$S_{fr} = \frac{\lambda}{2d} \rho_m u^2 \tag{5}$$

Here d is the pipe diameter and λ is the friction factor, which is a function of the Reynolds number and pipe roughness k. In this study the Techo formula is used:

$$\lambda = \left[-0.8685 \ln\left(\frac{1.964 \ln(\mathrm{Re}) - 3.8215}{\mathrm{Re}} + \frac{k}{d \cdot 3.71} \right) \right]^{-2} \tag{6}$$

Here Re is the Reynolds number defined as

$$\mathrm{Re} = u d \rho_m / \mu_m \tag{7}$$

with the mixture viscosity μ_m calculated in terms of liquid volume fraction and gas μ_g and liquid μ_l viscosities

$$\mu_m = \mu_g (1-H) + \mu_l H \tag{8}$$

The gas is treated as a compressible phase with a corresponding equation of state given in the form

$$\rho_g = f(p) \tag{9}$$

The closure of the problem is given by the following boundary conditions.

$$p(s=L,t) = p_{out}, \; p(s,t=0) = p_{out} \tag{10}$$

$$u(s=0,t) = u_{\inf}, \; u(s,t=0) = u_{\inf} \tag{11}$$

$$H(s=0,t) = H_{\inf}, \; H(s,t=0) = H_{\inf} \tag{12}$$

Here the subscripts *inf* and *out* refer to inflow and outflow cross-section of the pipe respectively. L denotes the length of the pipe.

3. DATA ASSIMILATION

3.1 State-space form of the model equations

Due to the nonlinearity of the given equation system (1)-(12) the numerical solution is needed in order to solve it for the dependent variables. For the discretization of the simulation domain a staggered grid approach has been used, meaning that the different grids are used for the continuity and momentum equation. Afterwards, the governing equations are integrated over different control volumes. Any solution procedure can be applied for solving the non-linear system of algebraic equations. Finally, the model can be written in the following state-space notation (Crassidis, 2004):

$$x_k = f(x_{k-1}, u_{k-1}) \tag{13}$$

Here u_{k-1} is the model input representing the inflow from reservoir to wellbore. x_{k-1} is the state vector evaluated on the previous time step. Using the primitive set of variables, the state vector can be written as

$$x = [\, p \; u \; H \,]^T \tag{14}$$

Here p, u and H are the vectors, representing pressure, velocity and liquid volume fraction related to the spatial grid.

3.2 Formulation of the inverse problem

The computational setup for the inverse problem is shown in Figure 2. It should be noted here, that only the horizontal part of the well is being modelled, and the outflow measurements are assumed to be available directly at the outflow cross-section of the horizontal part.

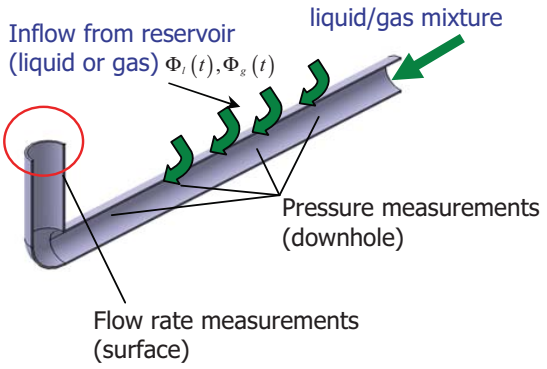

Fig. 2. Scheme of the computational setup for soft-sensing.

For the soft sensing purposes the augmented state vector is introduced:

$$X = \left[p_i \; u_i \; H_i \left| \Phi_{g\,i} \; \Phi_{l\,i} \right. \right]^T \tag{15}$$

Here i indicates the number of the cell defined by the numerical discretization.

It is assumed that several downhole pressure measurements are available. Moreover, outflow information about flow rates is also known, giving the following measurement vector:

$$y = \left[p_i \; u_{out} \; H_{out} \right]^T \tag{16}$$

Finally, the data assimilation problem can be formulated as follows: with the measurements (16) and the flow model (1)-(12) available the components of the augmented state vector should be estimated.

Due to a lack of experimental data, a set of synthetic measurements has been used as a source for soft-sensing. First, a twin experiment concept has been implemented. Here the same mathematical model was used both for generating measurements with predefined inflow distribution and the inverse modelling, when missing dynamic variables are estimated by means of the soft-sensing algorithm. In order to mimic the situation of testing the soft-sensor with "real-life" data, simulation results from the commercially available flow simulator OLGA were used in the second test case.

3.3 Ensemble Kalman filtering

One way to solve estimation problems via the sequential data assimilation algorithm is by using the Kalman filter equations. The Kalman filter is a stochastic recursive estimator, which estimates the values of model states and unknown input by integrating measured data in a mathematical model in real-time. Due to its straightforward numerical implementation and recursive nature, the Kalman filter algorithm is very well adapted to online model calibration.

Kalman filtering was initially developed for linear dynamic systems. Although several extensions of the Kalman filter exist for non-linear system, here the ensemble Kalman filter (EnKF) is used (Evensen, 1994). In this approach, the approximation of the error covariance matrix is calculated using an ensemble of possible model realizations, which are propagated according to the full dynamics of the system.

In order to initialize the filter the initial ensemble is generated. Here a mean value of the initial augmented state vector $\overline{X}_0^a$ and a corresponding covariance matrix Q_o is required. The mean value of the initial ensemble should be a good estimate of the true initial state. The members of the ensemble are generated randomly according to a Gaussian distribution. The j'th member of the ensemble is defined as

$$X_{0,j}^a = \overline{X}_0^a + w_{0,j} \tag{17}$$

With an EnKF the augmented state vector, which also contains the inflow input, is estimated in a recursive manner through the following two steps:

1) The forecast step, which consists in running the flow model one time step forward for each member of the ensemble. This leads to

$$X_{k,j}^f = f\left(X_{k-1,j}^a \right) + w_{k,j} \tag{18}$$

Here $w_{k,j}$ is a Gaussian zero mean white noise with the corresponding covariance matrix Q_k representing the model error. This noise is only added to components of the state vector, which produce the most uncertainty in a simulation. These are in this case the inflow sources Φ_l and Φ_g.

Using the calculated forecast of ensemble states, the error covariance matrix can be calculated using the covariance matrix of the ensemble. The mean value of the ensemble is given by

$$\overline{X}_k^f = \frac{1}{N} \sum_{j=1}^{N} X_{k,j}^f \tag{19}$$

And the error covariance matrix is then calculated as

$$P_k^f = L_k^f (L_k^f)^T \tag{20}$$

With

$$L_k^f = \frac{1}{\sqrt{N-1}} [(X_{k,1}^f - \overline{X}_k^f) \; (X_{k,2}^f - \overline{X}_k^f) ... (X_{k,N}^f - \overline{X}_k^f)] \tag{21}$$

where N is the number of members in the ensemble.

2) The analysis step, which takes into account measurements. The errors in the measurements are assumed to be statistically independent with known variances. This leads to a diagonal covariance matrix for the measurement errors. As it has been pointed out in Burgers *et al.* (1998), it is necessary to define new measurements for the proper error propagation. Therefore, a new observation vector is introduced for each member of the ensemble

$$y_{k,j} = M_k \cdot X_{k,j} + v_{k,j} \tag{22}$$

Here M_k is the measurement matrix and $v_{k,j}$ is the measurement noise generated from a normal distribution with zero mean and covariance matrix R_k.

The Kalman gain is then calculated as follows

$$K_k = P_k^f M_k^T (M_k P_k^f M_k^T + R_k)^{-1} \quad (23)$$

The analyzed state for each member of the ensemble is given by

$$X_{k,j}^a = X_{k,j}^f + K_k (y_{k,j} - M_k X_{k,j}^f) \quad (24)$$

The mean value of the analyzed ensemble is

$$\overline{X}_k^a = \frac{1}{N} \sum_{j=1}^{N} X_{k,j}^a \quad (25)$$

The unknown inflow sources are updated at each time step measurements are available and extracted from the augmented state vector. The analyzed error covariance matrix, from which the estimation error of the inflow parameters can be defined, is then approximated by

$$P_k^a = (I - K_k M_k) P_k^f \quad (26)$$

An important issue with the use of the EnKF is the size of the ensemble. Based on the experience of data assimilation for large-scale atmospheric models (Houtekamer and Mitchell, 1998), 100 ensemble members have been chosen for the ensemble Kalman filtering. The optimal size of the ensemble is, however, not known and it is a subject for future research.

4. RESULTS AND DISCUSSIONS

4.1 Soft sensing under measurement error

A first test case considered uses a twin experiment concept. Here the same mathematical model is used for generating the measurements with predefined inflow distribution. This study deals with two-phase liquid/gas flow and the details of the initial data are given in Table 1. The sketch of the simulation domain is given in Figure 3. The inflow profiles are given only as a reference since they are unknown and have to be estimated via the proposed data assimilation procedure.

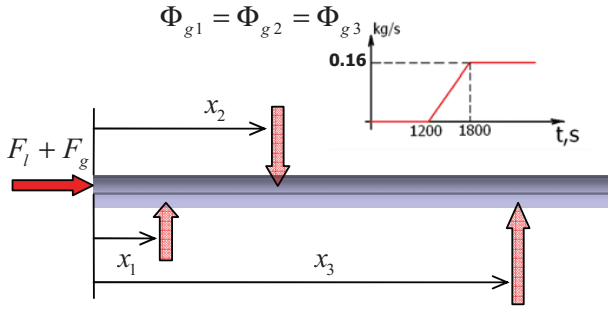

Fig. 3. Computational setup for soft-sensing.

Initially the well produces a mixture of liquid and gas with a total flow rate of 10 kg/s. After 20 minutes of production, gas is injected in three locations of the wellbore. The amount of gas injected increases linearly up to 0.5 kg/s during next 30 minutes and afterwards kept constant for the last 10 minutes of simulation.

The soft-sensor has been tested using the following measurement layout. The number of pressure measurements was taken equal to number of grid nodes obtained from the discretization. The velocity and liquid volume fraction measurements are located at the last grid block of the simulation domain.

Table 1. Initial data for the numerical experiments

Quantity	Value
Pipe diameter, m	0.05
Pipe length, m	100
Liquid density, kg/m^3	1000
Liquid viscosity, Pa·s	0.001
Gas reference density, kg/m^3	118.9
Gas viscosity, Pa·s	$1.82 \cdot 10^{-5}$
Time step, s	60
Inflow liquid rate F_l, kg/s	9.5
Inflow gas rate F_g, kg/s	0.5
x_1, m	15
x_2, m	45
x_3, m	75
Absolute roughness, m	0
Number of grid nodes	12

The Kalman filter initialization is based here on the outflow values of velocity and liquid volume fraction, which are assumed to be known from a flow meter. Since all the pressure measurements are available, pressure is initialized from the current pressure distribution. The synthetic measurements representing downhole pressure and liquid outflow flow rate are generated using equations (1)-(12). A zero mean white Gaussian noise is then added to mimic the uncertainty in measurements.

Table 2. Measurement noise used in simulations

Uncertainty in pressure measurements	0.5%
Uncertainty in outflow velocity measurements	1%
Uncertainty in liquid volume fraction measurements	1%

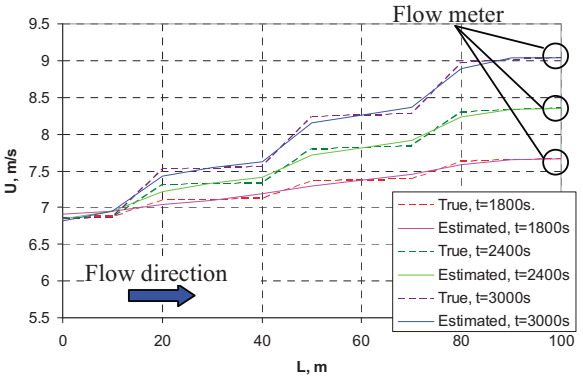

Fig. 4. Comparison of estimated and true flow velocity.

The results of the simulation are given in Figures 4-5. Figure 4 shows the comparison between the estimated and true velocity distributions along the pipe length. Flow velocity is used to allocate the zones where a fluid is entering or leaving the wellbore. In order to identify the type of fluid, the distribution of the estimated liquid volume fraction is required. It is depicted in Figure 5. The results are given for three time instants 30 minutes, 40 minutes and 50 minutes. Since the pressure is available continuously from the measurements it is not depicted as a soft-sensing result.

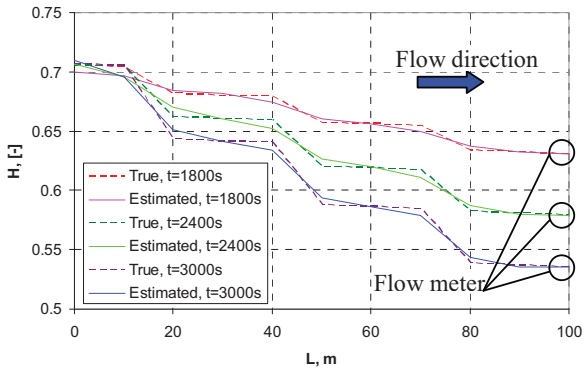

Fig. 5. Comparison of estimated and true liquid fraction.

The results show that the proposed soft-sensor, for the given simplified setup, is very well capable of reproducing the flow rate and liquid volume fraction distributions along the considered well part, even when measured data contains a certain measurement error. Therefore, it is capable to detect multiple fluid sources as it is depicted in the figures.

4.2 Soft sensing under model error

The second study provides an assessment of the influence of the model error on the soft-sensing estimation results. A similar soft-sensing setup was used as depicted in Figure 2 for case study 1. An important difference, however, was that the "true" well was not the same as the model used in the soft-sensor. The true wellbore measurements were obtained from the commercially available simulator OLGA. This was done to assess the inevitable effect of the model error on the soft-sensing estimation results. Here both transient gas and liquid sources are present in a computational setup. Liquid is injected in the first part of the pipe, while a gas source is present close to its outflow cross-section. This situation is a rough approximation of the gas breakthrough scenario. The scheme of the simulation domain is given in Figure 6.

Due to differences between the flow model used in OLGA simulator and the soft-sensor developed, one can point at the following sources of the model error:

- Friction factor correlation

- Fluid properties

- Simulation grid

- Mathematical model

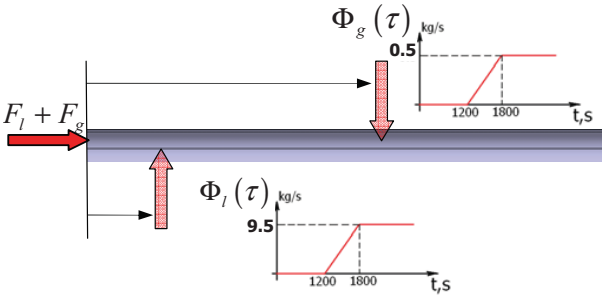

Fig. 6. Computational setup for soft-sensing. Test case 2.

A particularly important modelling assumption for performing OLGA simulations was to keep a dispersed bubble flow regime, since the model used for soft-sensing is valid only for that type of multiphase flow. This was possible using the same set of input parameters, as for the test case 1. The OLGA simulations were performed with 10 grid nodes, where the source term for liquid has been defined in the third grid block, and for gas in the eighth grid block. This consequently led to a soft-sensing setup with 10 available pressure measurements.

Figures 7 and 8 represent the estimated flow velocity and liquid volume fraction.

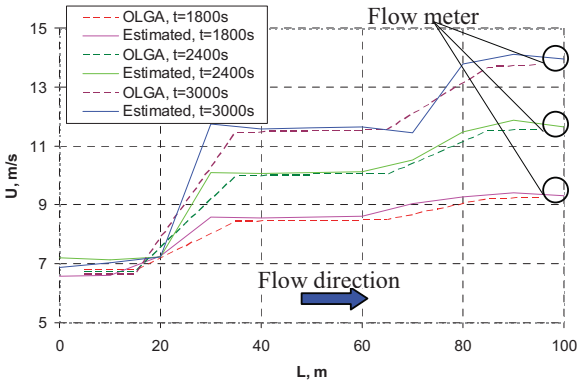

Fig. 7. Estimated velocity profile for the OLGA data.

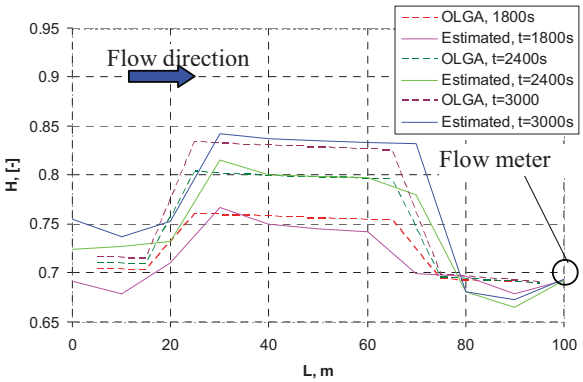

Fig. 8. Estimated liquid fraction profile for the OLGA data.

The results obtained under model error are not as accurate as for the twin-experiment. However, it is still possible to allocate easily zones of liquid or gas inflow. A displacement of the estimated profiles with respect to the true ones is observed. This can be explained by the use of a different grid in the OLGA simulator and different interpolation of the flow variables between grid nodes and edges.

5. SUMMARY AND CONCLUSIONS

By means of two case studies, some limitations and possibilities of soft-sensor multiphase flow meters have been studied. The proposed soft-sensor is based on the ensemble Kalman filter approach and requires as the input the dynamic model of the pipe flow together with pressure measurements available downhole and one composition and velocity measurement at the outflow.

It has been shown, that for a two-phase flow formulation it is possible to reconstruct the distributions of the flow velocity and liquid volume fraction along a pipe and to allocate the inflow of certain fluids in a specific location along it.

The results indicate that the proposed method is quite stable for a certain range of wellbore operational conditions, and capable of taking into account measurement and model error.

6. ACKNOWLEDGEMENTS

This work has been supported by ISAPP knowledge center, which is a joint research project of Shell, TNO and Delft University of Technology. The authors would also like to thank Wouter Schiferli (TNO Science and Industry) for performing the OLGA runs.

REFERENCES

Bloemen, H.H.J., Belfroid, S.P.C., Sturm, W.L., and Verhelst, F.J.P.C.M.G. (2004). Soft Sensing for Gas-Lift Wells. SPE paper 90370, *Proc. SPE Annual Technical Conference and Exhibition*, Houston, Texas, USA.

Burgers, G., van Leeuwen, P.J., and Evensen, G. (1998) On the analysis scheme in the ensemble Kalman Filter. *Monthly Weather review*. Vol. 126, 1719-1734.

Crassidis J.L. and Junkins J.L. (2004). *Optimal estimation of Dynamic systems*. Chapman & Hall/CRC. Florida.

De Kruif, B., Leskens, M., van der Linden, R., Alberts, G., and Smeulers, J. (2008) Soft-sensing for multilateral wells with downhole pressure and temperature measurements. SPE paper 118171, *Proc. Dhabi International Petroleum Exhibition and Conference*, Abu Dhabi, UAE,

Evensen, G. (1994). Sequential data assimilation with a nonlinear quasi-geostrophic model using Monte Carlo methods to forecast error statistics," *J. Geophys. Res*., Vol. 99(C5), 10143–10162.

Evensen, G., Hove J., Meisingset, H.C., Reiso E., Seim, K.S., and Espelid, O. (2007). Using the EnKF for Assisted History Matching of a North Sea Reservoir Model. SPE paper 106184, *Proc. SPE Reservoir simulation symposium*, Woodlands, Texas, USA.

Glandt, C.A. (2003). Reservoir aspects of smart wells. SPE paper 81107, *Proc. SPE Latin American and Caribbean Petroleum Engineering Conference*, Trinidad, West Indies.

Houtekamer, P.L., Mitchell, H.L., (1998). Data assimilation using an ensemble Kalman filter technique. *Monthly Weather review*. Vol. 126, 796-911.

Jansen J.D., Bosgra O.H., and Van den Hof P.M.J. (2008). Model-based control of multiphase flow in subsurface oil reservoirs. *Journal of Process Control*, Vol. 18, 846-855.

Jazwinski, A. H. (1970). *Stochastic Processes and Filtering Theory*. Academic Press, New York.

Julier, S., Uhlmann, J., and Durrant-Whyte, H.F. (2000). A new method for the non-linear transformation of means and covariances in filters and estimators. *IEEE Transcations on Automatic Control*. Vol. 45(3), pp. 477-482.

Kalman, R.E. (1960). A new approach to linear filter and prediction theory. *Trans. ASME, Series D, Journal of Basic Engineering,* Vol. 82, pp. 35 – 45.

Leskens, M., de Kruif, B., Belfroid, S., Gryzlov, A., and Smeulers, J. (2008). Downhole Multiphase Metering in Wells by Means of Soft-Sensing. SPE paper 112046, *proc. SPE Intelligent Energy Conference*, Amsterdam, The Netherlands.

Lorentzen, R.J., Fjelde, K.K.,Frøyen J, Lage A. C. V. M., Nævdal G., and Vefring E.H. (2001). Underbalanced and Low-head Drilling Operations: Real Time Interpretation of Measured Data and Operational Support, *Proc. SPE Annual Technical Conference and Exhibition*, SPE 71384, New Orleans, Louisiana.

Lorentzen, R.J., Nævdal, G., and Lage, A.C.V.M. (2003). Tuning of parameters in a two-phase flow model using an ensemble Kalman filter. *International Journal of Multiphase Flow*. Vol. 29(8), pp. 1283-1309.

Nævdal, G., Johnsen, L.M., Aanonsen, S.I., and Vefring, E.H. (2003). Reservoir Monitoring and Continuous Model Updating Using Ensemble Kalman Filter. SPE paper 84372, *Proc. SPE Annual Technical Conference and Exhibition,* Denver, Colorado, USA.

Vicente, R., Sarica, C., and Ertekin, T. (2001) .A Two-Phase Model Coupling Reservoir and Horizontal Well Flow Dynamics. SPE paper 69570, *Proc. SPE Latin American and Caribbean Petroleum Engineering Conference*, Buenos Aires, Argentina.

Efficient Moving Horizon State and Parameter Estimation for the Varicol SMB Process

Achim Küpper [*], **Moritz Diehl** [***], **Johannes P. Schlöder** [**], **Hans Georg Bock** [**], **Sebastian Engell** [*]

[*] *Process Dynamics and Operations Group, Technische Universität Dortmund, Emil-Figge-Str. 70, 44221 Dortmund, Germany (e-mail: achim.kuepper@bci.tu-dortmund.de).*
[**] *IWR - Interdisciplinary Center for Scientific Computing, Universität Heidelberg, Germany.*
[***] *Electrical Engineering Department (ESAT-SCD), K.U. Leuven, Belgium.*

Abstract: In this paper, a moving horizon state and parameter estimation (MHE) scheme for the Varicol process is presented. The Varicol process is an extension of the Simulated Moving Bed (SMB) process that realizes non-integer column distributions over the separation zones by an asynchronous switching of the inlet and outlet ports (the ports are shifted individually). These additional degrees of freedom can be used to yield an improvement in economical performance compared to SMB operation. The proposed estimation scheme is based on a rigorous SMB model that incorporates rigorous chromatographic columns and port switching. The absence of model simplifications allows the extension of the estimation scheme to the more complex Varicol process. The goal of the estimation scheme is to reconstruct the full state of the system, i.e. the concentration profiles along all columns, and to identify critical model parameters in the presence of noisy measurements. The estimation is based on measurements of the concentrations of the components at the two outlet ports (which are asynchronously switched from one column to the next) and at one fixed location between two columns. The state estimation scheme utilizes a deterministic model within the prediction horizon. State noise is only considered in the state and in the parameters up to the beginning of the horizon. By applying a multiple-shooting method and a real-time iteration scheme for solving the resulting optimization problem, the computation times are reduced and the scheme can be applied online. A numerical simulation for an enantiomer separation system with nonlinear adsorption isotherm is presented.

Keywords: Varicol, Simulated Moving Bed chromatography, moving horizon estimation, state estimation, model identification, real-time application, real-time iteration

1. INTRODUCTION

The Simulated Moving Bed (SMB) process is an efficient chromatographic separation technology that is increasingly applied in the food, fine chemicals, and pharmaceutical industries. Industrial applications have been reported especially for the separation of temperature sensitive components and for the separation of species with similar thermodynamic properties. A SMB process is realized by connecting several chromatographic columns in a closed loop as illustrated by Figure 1. The Varicol process switches the ports indvidually and thereby realizes non-integer column distributions over the zones **?**), see Figure 2.

SMB processes and their variants are characterized by mixed discrete and continuous dynamics, spatially distributed state variables with steep slopes, and slow and strongly nonlinear responses of the concentrations profiles to changes of the operating parameters, therefore, they are difficult to control and to observe. In the literature, relatively few contributions that deal with state estimation of SMB processes can be found. The published work is based upon the approximation of the concentration profiles by a set of truncated exponential functions Alamir and Corriou (2003), or by using the equivalent True Moving Bed (TMB) model Mangold et al. (1994), Kloppenburg and Gilles (1999), or deals with the engineering of tailored estimation schemes Küpper and Engell (2006), Kleinert and Lunze (2005). Recently, a rigorous moving horizon estimation approach for SMB processes was proposed by Küpper et al. (2009). In this formulation of the MHE, a deterministic behaviour of the process on the estimation horizon and Gaussian independent identically distributed measurement noise are assumed. The initial state at the beginning of the horizon and its covariance are computed by an Extended Kalman Filter (EKF). The state noise covariance and the initial error covariance of this EKF are the only tuning parameters of this scheme. A fast online solution of the underlying constrained least-squares optimization problem is obtained by using the direct multiple shooting method Bock (1981, 1987). A full rigorous process

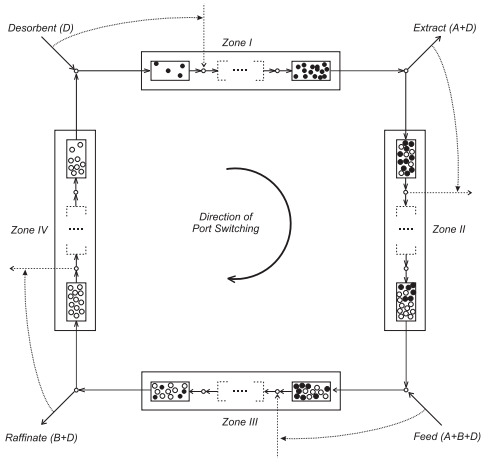

Fig. 1. Principle of the Simulated Moving Bed process

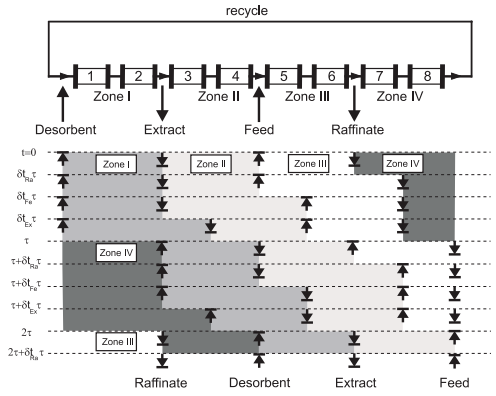

Fig. 2. Asynchronous switching in the Varicol process

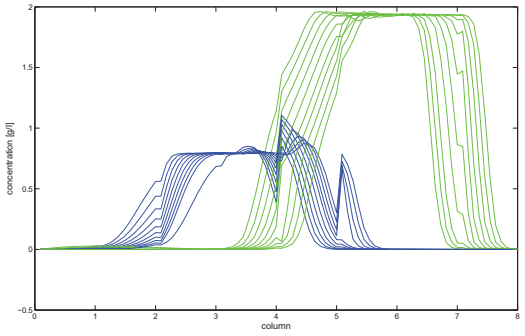

Fig. 3. Concentration profiles of the Varicol process during one period with $\delta\tau_{Ra} = 0.3$, $\delta\tau_{Fe} = 0.6$, $\delta\tau_{Ex} = 0.9$, $\delta\tau_{De} = 1.0$, $\delta\tau_{Re} = 1.0$

model is applied and therefore no assumption that the plant is close to the periodic steady state is needed. Along with the states, key adsorption parameters are estimated online. Simulations demonstrate that the states and critical model parameters can be reconstructed successfully. The scheme also works during transition periods including the start-up phase. The computation times are such that the estimator can be applied online. Since a rigorous full scale SMB model is used, the MHE approach can be extended to more complex variants of the SMB process. In this contribution, the moving horizon state and parameter estimation scheme is applied to the Varicol operation.

2. THE VARICOL SMB PROCESS

Chromatographic separation is based on the different adsorption affinities of the molecules in the liquid to an adsorbent which is packed in a chromatographic solid bed. The SMB process realizes a counter-current movement between the liquid and the adsorbent by switching the ports in the direction of the liquid flow periodically, as illustrated by Figure 1. In the Varicol process, the individual ports i (Eluent, Extract, Feed, Raffinate) are switched individually at the subperiod times δt_i, as illustrated by Figure 2. The individual port switching reduces the impurities by early switching of the Raffinate port and delayed switching of the Extract port. Since the Varicol process offers a larger number of degrees of freedom, it can be operated with better process economics than the SMB process, see Toumi et al. (2002), Toumi et al. (2003).

In the estimation scheme, the counter-current flow of the solid and of the liquid phases is modelled in the same way as it is achieved in the real plant by asynchronously switching the inlet and outlet ports in the direction of the liquid flow after subperiod n with subperiod length $(\delta t_n - \delta t_{n-1})\tau$ has passed. The state variables represent the concentrations in the physical columns and do not exhibit jumps. Only the input flow rates and the inflow concentrations change discontinuously. The dynamic simulation of the Varicol process is achieved by integrating the differential equation over the subperiods n

$$\dot{\mathbf{x}} = f(\mathbf{x}, Q_n, \mathbf{p}) \qquad (1)$$
$$t \in [(m-1)\tau + \delta t_{n-1}\tau,\ (m-1)\tau + \delta t_n \tau]$$
$$\mathbf{x}(t_0) = \mathbf{x}_{m,0} \qquad (2)$$

followed by the switching of the flows $Q_{n,j,\delta t_j}$:

$$Q_{n+1,j,\delta t_j} = M_Q Q_{n,j,\delta t_j} \quad j = \mathrm{De}, \mathrm{Ex}, \mathrm{Fe}, \mathrm{Ra}, \mathrm{Re}, \qquad (3)$$

with differential states $\mathbf{x}(t) \in \mathbb{R}^{n_x}$ and parameters $\mathbf{p} \in \mathbb{R}^{n_p}$. The vector $Q_{n,j,\delta t_j}$ defines the inlet/outlet flow of port j (desorbent, extract, feed, raffinate) and the recycle stream at the individual switching time δt_j in period m (m denotes the full period count). The components of $Q_{n,j}$ represent the flows of the ports j to the columns. M_Q is a permutation matrix that shifts the flow ports after the asynchronous switching time δt_j of port j has passed (with individual period counter n). The recycle flow that defines the total flow rate in the zone in front of the desorbent port is switched with the last port. The zone flow rates result from the port flows and the recycle flow. The concentration profiles during one switching period are illustrated by Figure 3. The asynchronous switching of the feed port and of the extract port can be clearly seen in the profiles. In this paper, three positions where the concentrations of the two substances of the mixture are measured are assumed. The measurements are installed behind the extract port, behind the raffinate port, and behind one column in the process where physically the closing of the loop is realized (six measurements total). The extract and raffinate concentration measurements

move together with the ports. More measurements are not available in production plants.

2.1 Rigorous Dynamic Modelling

From mass balances of the components around the inlet and the outlet ports, the internal flow rates and the inlet concentrations can be calculated according to:

$$\text{Desorbent node: } Q_{\mathrm{IV}} + Q_{\mathrm{De}} = Q_{\mathrm{I}} \tag{4}$$

$$c_{i,\mathrm{out,IV}} Q_{\mathrm{IV}} = c_{i,\mathrm{in,I}} Q_{\mathrm{I}} \quad i = \mathrm{A}, \mathrm{B} \tag{5}$$

$$\text{Extract node: } Q_{\mathrm{I}} - Q_{\mathrm{Ex}} = Q_{\mathrm{II}} \tag{6}$$

$$\text{Feed node: } Q_{\mathrm{II}} + Q_{\mathrm{Fe}} = Q_{\mathrm{III}} \quad i = \mathrm{A}, \mathrm{B} \tag{7}$$

$$c_{i,\mathrm{out,II}} Q_{\mathrm{II}} + C_{i,\mathrm{Fe}} Q_{\mathrm{Fe}} = c_{i,\mathrm{in,III}} Q_{\mathrm{III}} \tag{8}$$

$$\text{Raffinate node: } Q_{\mathrm{Ra}} + Q_{\mathrm{IV}} = Q_{\mathrm{III}}, \tag{9}$$

where $Q_{\mathrm{I-IV}}$ are the flow rates in the corresponding zones, Q_{De}, Q_{Ex}, Q_{Fe}, and Q_{Ra} denote the external flow rates and $c_{i,\mathrm{in}}$ and $c_{i,\mathrm{out}}$ denote the concentrations of the component i in the streams leaving and entering the respective zone. The initial distribution of the columns over the four separation zones is 2/2/2/2 and the individual switching times are $\delta\tau_{Ra} = 0.3$, $\delta\tau_{Fe} = 0.6$, $\delta\tau_{Ex} = 0.9$, $\delta\tau_{De} = 1.0$, $\delta\tau_{Re} = 1.0$ from which the non-integer column distribution 2.1/2.3/2.3/1.3 results.

The chromatographic columns are modelled by the General Rate Model. It is assumed that there are no radial gradients in the column and that the particles of the solid phase are uniform, spherical, porous (with a constant particle porosity ϵ_{p}), and that the mass transfer between the particle and the surrounding layer of the bulk is in local equilibrium. The concentration of component i is denoted by c_i in the liquid phase and by q_i in the solid phase. D_{ax} is the axial dispersion coefficient, u the interstitial velocity, ϵ_{b} the void fraction of the bulk phase, $k_{\mathrm{l},i}$ the film mass transfer resistance, and D_{p} the diffusion coefficient within the particle pores. The concentration within the pores is denoted by $c_{\mathrm{p},i}$. The following partial differential equations of a column can be derived from a mass balance around an infinitely small cross section area of the column assuming a constant radial distribution of the interstitial velocity u and the concentration c_i.

$$\frac{\partial c_i}{\partial t} + \frac{(1-\epsilon_{\mathrm{b}}) 3 k_{\mathrm{l},i}}{\epsilon_{\mathrm{b}} r_{\mathrm{p}}} \left(c_i - c_{\mathrm{p},i}|_{r=r_{\mathrm{p}}}\right) = D_{\mathrm{ax}} \frac{\partial^2 c_i}{\partial x^2} - u \frac{\partial c_i}{\partial x} \tag{10}$$

$$(1-\epsilon_{\mathrm{p}}) \frac{\partial q_i}{\partial t} + \epsilon_{\mathrm{p}} \frac{\partial c_{\mathrm{p},i}}{\partial t} - \epsilon_{\mathrm{p}} D_{\mathrm{p}} \left[\frac{1}{r^2} \frac{\partial}{\partial r} \left(r^2 \frac{\partial c_{\mathrm{p},i}}{\partial r}\right)\right] = 0, \tag{11}$$

with appropriate initial and boundary conditions. It is assumed that the concentration q_i is in thermodynamic equilibrium with the liquid concentrations in the particle and their relationship can be described by an extended Langmuir adsorption isotherm

$$q_i = H_i^1 c_{\mathrm{p},i} + \frac{H_i^2 c_{\mathrm{p},i}}{1 + k_{\mathrm{A}} c_{\mathrm{p,A}} + k_{\mathrm{B}} c_{\mathrm{p,B}}} \quad i = \mathrm{A}, \mathrm{B}, \tag{12}$$

with H_i^j and k_i as isotherm constants. The resulting system of coupled differential equations can be efficiently solved by the numerical approach proposed in Gu (1995) where a Galerkin finite element discretization of the bulk phase is combined with orthogonal collocation for the solid phase. This numerical method was first applied to SMB processes in Dünnebier and Klatt (2000). The bulk phase is divided into n_{fe} finite elements and the solid phase is discretized by n_{c} internal collocation points. As a result, the set of initial values, boundary values, and partial differential equations (PDE) is transformed into a set of initial values and a system of ordinary differential equations (ODE)

$$\dot{\mathbf{x}} = f(\mathbf{x}, \mathbf{u}, \mathbf{p}), \tag{13}$$

where the flows Q are summarized in the input vector $\mathbf{u}(t) \in \mathbb{R}^{n_u}$. The system output is defined as

$$y = h(\mathbf{x}(\mathbf{u}, \mathbf{p})), \tag{14}$$

with $y \in \mathbb{R}^{n_y}$. For $n_{\mathrm{fe}} = 5$, $n_{\mathrm{c}} = 1$, number of components $n_{\mathrm{sp}} = 2$, and number of columns $n_{\mathrm{col}} = 8$ a system order of the SMB process of

$$n_x = n_{\mathrm{col}} * n_{\mathrm{sp}} * (n_{\mathrm{c}} + 1) * (2 * n_{\mathrm{fe}} + 1) = 352 \tag{15}$$

results. The ODE-system is stiff due to large differences in the speeds of the interacting dynamics.

3. ESTIMATION IN THE VARICOL PROCESS

3.1 Moving Horizon Estimation

For the simultaneous estimation of the states and the parameters of SMB processes, we employ the Moving Horizon Estimation scheme introduced by Diehl et al. (2006); Kühl et al. (2008), which is modified in order to handle the shift of the inputs and of the measurements of the SMB process. The Moving Horizon Estimator estimates the states and the parameters based on the past measurements at specific time points that are located in the horizon $T_N = t_K - t_L$. t_K represents the current time and t_L is the time at the beginning of the horizon. A least-squares minimization is performed that minimizes the deviations of the real measurements η_k from the simulated measurements $h(\mathbf{x}(t_k; \mathbf{u}, \mathbf{p}))$ at times t_k. The expression $||.||^2_{V^{-\frac{1}{2}}}$ denotes $||\mathbf{x}||^2_{V^{-\frac{1}{2}}} = \mathbf{x}^T V^{-1} \mathbf{x}$, where the matrix V is the positive semidefinite noise covariance matrix of the variables $\mathbf{x}$. $V^{-\frac{1}{2}}$ can be interpreted as weighting matrix of $\mathbf{x}$. The measurement information prior to the moving horizon is considered in the estimation problem by an arrival cost term that is computed from the expected value of the state and the parameters and the estimation error covariance before the horizon. The optimization problem of the MHE results as:

$$\min_{\mathbf{x}(t_L), p} \left\{ \left\| \begin{matrix} \mathbf{x}(t_L) - \overline{\mathbf{x}}_L \\ \mathbf{p} - \overline{\mathbf{p}}_L \end{matrix} \right\|^2_{P_L^{-\frac{1}{2}}} + \sum_{k=L}^{K} \|\eta_k - h(\mathbf{x}(t_k; \mathbf{u}, \mathbf{p}))\|^2_{V_k^{-\frac{1}{2}}} \right\} \tag{16}$$

$$s.t. \quad \dot{\mathbf{x}}(t) = f(\mathbf{x}(t), \mathbf{u}(t), \mathbf{p}) \tag{17}$$

$$\mathbf{x}_{min} \leq \mathbf{x}(t) \leq \mathbf{x}_{max} \tag{18}$$

$$\mathbf{p}_{min} \leq \mathbf{p} \leq \mathbf{p}_{max} \tag{19}$$

$$t \in [t_L, t_K]\,. \tag{20}$$

The second term represents the prediction errors within the horizon and the first term represents the arrival cost (the penalization of a change of the estimates of the initial values of the states and of the parameters), where $(\overline{\mathbf{x}}_L, \overline{\mathbf{p}}_L)$ are the expected values and $P_L \in \mathbb{R}^{(n_x+n_p)\times(n_x+n_p)}$ is the joint covariance matrix of $\mathbf{x}(t_L)$ and $\mathbf{p}_L$. Note that only the initial values of the states and the parameters are free parameters of the optimization problem because no state

noise is assumed within the horizon. The absence of state noise on the horizon is compensated by the simultaneous estimation of key model parameters which is an appropriate assumption since uncertainties are mostly due to model errors and not to disturbances. Furthermore, the inclusion of state noise at each point within the horizon would lead to a large number of degrees of freedom of the estimation and result in a considerably larger optimisation problem with additional $n_x \times (K - L)$ variables that, taking the system dimension into account, would be hard to solve online reliably. From the solution $\mathbf{x}(t_L)$ and $\mathbf{p}$ of the optimization problem, the deterministic model is simulated forward to obtain the current estimated state $\mathbf{x}_K$. The MHE takes upper and lower bounds on the states and on the parameters into account. The expected value and the covariance of $\mathbf{x}(t_L)$ and $\mathbf{p}_L$ in the arrival cost are determined by an Extended Kalman Filter. The smoothed Extended Kalman Filter Robertson et al. (1996) is employed where the recent state estimation $x_{L+1|K}$ and linearizations of the dynamics $G_{L+1|K}$ and the output matrix $C_{L+1|K}$ are utilized. In order to guarantee positive definite matrices in the presence of numerical errors, the smoothed Extended Kalman update is reformulated by two QR-decompositions yielding the equivalent smoothed Extended Kalman Filtering update in square-root formulation Diehl (2002); Kühl et al. (2008).

$$\begin{pmatrix} \overline{\mathbf{x}}_{L+1} \\ \overline{\mathbf{p}}_{L+1} \end{pmatrix} = \begin{pmatrix} \mathbf{x}(t_{L+1}; t_L, \mathbf{x}_{L|K}, \mathbf{u}_L, \mathbf{p}_{L|K}) \\ \mathbf{p}_{L|K} \end{pmatrix} + G_{L|K} R^{-1} Q^T \begin{pmatrix} P_{L|L-1}^{-\frac{1}{2}} \begin{pmatrix} \mathbf{x}_{L|L} - \mathbf{x}_{L|K} \\ \mathbf{p}_{L|L} - \mathbf{p}_{L|K} \end{pmatrix} \\ V_L^{-\frac{1}{2}} (\eta_L - h(\mathbf{x}_{L|K})) \end{pmatrix} \tag{21}$$

$$P_{L+1|L}^{-\frac{1}{2}} = \overline{Q}^T \begin{pmatrix} 0 \\ W^{-\frac{1}{2}} \end{pmatrix} \tag{22}$$

with the linearizations of the dynamics

$$G_{L|K} = \begin{pmatrix} X_{x,L|K} & X_{p,L|K} \\ 0 & I_{n_p} \end{pmatrix} \tag{23}$$

$$X_{x,L|K} = \left. \frac{d\mathbf{x}(t_{L+1}; \mathbf{x}_{L|K}, \mathbf{p}_{L|K})}{d\mathbf{x}} \right|_{L|K} \tag{24}$$

$$X_{p,L|K} = \left. \frac{d\mathbf{x}(t_{L+1}; \mathbf{x}_{L|K}, \mathbf{p}_{L|K})}{d\mathbf{p}} \right|_{L|K}, \tag{25}$$

the linearization of the output

$$H_{L|K} = \begin{pmatrix} H_{x,L|K} & H_{p,L|K} \end{pmatrix} \tag{26}$$

$$H_{x,L|K} = \left. \frac{dh(\mathbf{x}(t_{L+1}; \mathbf{x}_{L|K}, \mathbf{p}_{L|K}))}{d\mathbf{x}} \right|_{L|K} \tag{27}$$

$$H_{p,L|K} = \left. \frac{dh(\mathbf{x}(t_{L+1}; \mathbf{x}_{L|K}, \mathbf{p}_{L|K}))}{d\mathbf{p}} \right|_{L|K}, \tag{28}$$

the QR-decompositions

$$\begin{pmatrix} P_{L|L-1}^{-\frac{1}{2}} \\ V_L^{-\frac{1}{2}} H_{L|K} \end{pmatrix} = (Q|\breve{Q}) \begin{pmatrix} R \\ 0 \end{pmatrix} \tag{29}$$

$$\begin{pmatrix} R \\ -W^{-\frac{1}{2}} G_{L|K} \end{pmatrix} = (\overline{Q}|\widetilde{Q}) \begin{pmatrix} \overline{R} \\ 0 \end{pmatrix}, \tag{30}$$

and the state noise covariance matrix of the states and of the parameters

$$W = \begin{pmatrix} W_x & 0 \\ 0 & W_p \end{pmatrix}. \tag{31}$$

$\mathbf{x}(t_{L+2}; t_{L+1}, \mathbf{x}_{L+1|K}, \mathbf{u}_{L+1}, \mathbf{p}_{L+1|K})$ denotes the prediction of the system based on the recent estimate at $_{L+1|K}$ while $\mathbf{x}_{L+2|L+1}$ is the smoothed prediction.

The MHE has to cope with jumps in the extract and raffinate measurements that are caused by the port switching. In order to obtain a smooth calculation of the gradients with respect to the simulated measurements which exhibit jumps due to the periodic movement of the ports, virtual measurements at constant positions at the outlet of each chromatographic column are included in the mapping h. In order to account for the actual existence of real measurements at the considered point of time k, the corresponding components on the diagonal of the measurement weight V_k^{-1} are set to $\frac{1}{\sigma_v^2}$ while nonexisting measurements cause zero entries on the diagonal of V_k^{-1}. A zero weight can be interpreted as infinite measurement noise. Thus, the correction terms of nonexisting measurements in the smoothed Extended Kalman Filtering update and in the moving horizon are zero. The switching of the measurement weights at the respective extract and raffinate switching times $\delta t_j \tau$ in period m is realized according to the movement of the extract and raffinate port:

$$\overline{V}_{m,j} = M_V \overline{V}_{m,j} \quad j = Ex, Ra \tag{32}$$

$$\overline{V}_m = \overline{V}_{m,Ex} + \overline{V}_{m,Ra} \tag{33}$$

$$V_m = \mathrm{diag}(\overline{V}_{m+1}(1, \ldots, (n_{\mathrm{col}} - 1) * 2), \sigma_v^2, \sigma_v^2). \tag{34}$$

The permutation matrix M_V for shifting the extract and raffinate measurements around the plant for a new period $m+1$ is similar to the permutation matrix M_Q for shifting the port flows. The last two entries of V_k are the variances of the measurements at the internal measurement position (recycle) which are not shifted.

3.2 Multiple-Shooting Real-Time Iteration Scheme for MHE

The moving horizon optimization problem is solved by the multiple shooting method for parameter estimation Bock (1981, 1987). The basic idea of multiple shooting is to subdivide the time horizon into subintervals and to formulate autonomous initial value problems on each individual subinterval which are coupled by continuity conditions. The computational requirements are largely reduced by applying the *real-time iteration* scheme for the multiple shooting method introduced in Diehl et al. (2002, 2004); Diehl (2002) that updates the sensitivity matrices that are necessary to solve the optimization problem before the most recent measurement η_K is available. Another important feature is that the next optimization problem is initialized well at the current solution such that the number of iterations can be reduced to one.

4. RESULTS

For the demonstration of the performance of the moving horizon estimator, the separation of the enantiomer mixture EMD-53986 is considered which is described by a nonlinear adsorption isotherm of extended Langmuir type (12). Enantiomers are chemical molecules that are mirror images of each other, much as one's left and right hands.

The separation of the enantiomers of EMD-53986 was studied experimentally in a joint project by *Merck* (Germany) and Universität Dortmund in 2001. From this work, an accurate simulation model is available. The parameters of the SMB model were taken from Jupke et al. (2002). More details on the process and the model parameters can be found in Jupke (2004). In order to demonstrate the performance of the MHE estimator, a simulation study is presented in which step changes of the Henry coefficients H_A^2, H_B^2 of the nonlinear adsorption isotherm are assumed. The performance of the moving horizon estimator is illustrated by the evolution of the parameters and of the overall state reconstruction error which is defined as

$$J = \sum_{j=1}^{352} (\mathbf{x}(j) - z(j))^2, \tag{35}$$

where z is the true state. The measurements are corrupted by noise with a standard deviation of 0.025 g/l as observed in Jupke et al. (2002). No cross-correlations between the state noises and between the state noises and the parameters were assumed. Since the concentration profiles move around the simulated plant together with the ports, the same noise variances were assumed for each state. The tuning of the moving horizon estimator was performed by varying the covariances of the state variables and of the free parameters. The weighting matrix W incorporates a standard deviation of 0.00433 g/l for the state noise and a parameter standard deviation of 0.0316 for H_{A}^2 and 0.0265 for H_{B}^2: $W^{\frac{1}{2}} = \mathrm{diag}(0.00433, \ldots, 0.00433, 0.0361, 0.0265)$. The initial weight P_0 is set to $0.005 \times W$. The chosen state and parameter noises represent a compromise between the smooth estimation of the states and a quick adaptation of the parameters. The state and parameter bounds are chosen as -0.25 g/l $\leq x \leq 5$ g/l and $0 \leq H_i^2 \leq 50$ to prevent grossly wrong values. The lower bound on the states is chosen such that it remains inactive in the presence of large measurement noise. The sampling time of the estimator is 1/10 of the period length. The moving horizon length is five sampling intervals (half a period).

In the simulation scenario, H_{A}^2 is increased by 10.6% from 19.90 to 22.00 at $t = 14.58$ min while H_{B}^2 is increased by 10.3% from 5.85 to 6.45 at $t = 68.04$ min. It can be seen from figures 4 to 8, that the state is reconstructed correctly in the presence of the parameter variations and that the parameters are also estimated well. The Henry coefficient H_B^2 is estimated faster than H_A^2 due to the stronger excitation of the raffinate dynamics by the parameter perturbation. The axial concentration profiles are reconstructed correctly by the MHE (not show here due to limited space). The MHE is more robust against measurement noise and wrong initializations of the states and parameters than an EKF, see Küpper et al. (2009). The MHE estimator can be applied online, as can be seen from Figure 8. The CPU times are below the sampling rate at all sampling points. The CPU times of the MHE are around 23 s on a standard PC [1], the maximum and minimum values being 28.0 s and 18.5 s. The CPU times for the estimator varies periodically. It was observed that the estimation problem requires a longer computation time when a shift of one of the inlet/outlet ports occurs within the moving horizon.

[1] Intel Xenon CPU 2.8 GHz, 4.0 GB RAM

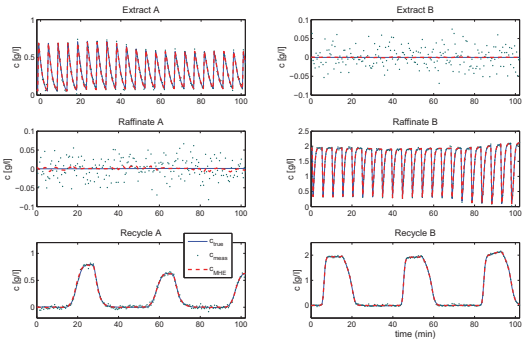

Fig. 4. Measurements (extract, raffinate, recycle)

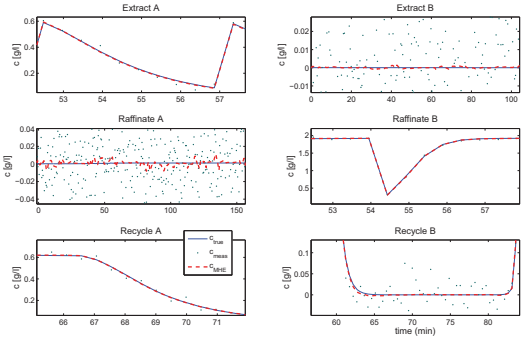

Fig. 5. Enlarged measurements (extract, raffinate, recycle)

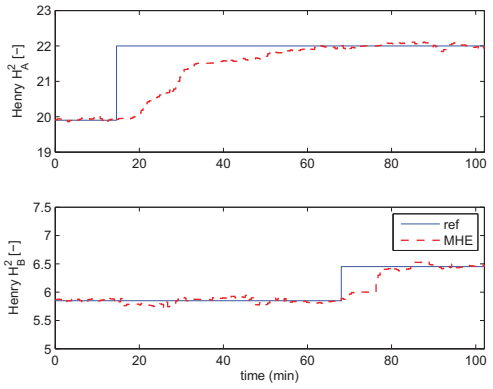

Fig. 6. Parameter estimates

5. ACKNOWLEDGEMENTS

The financial support of the Deutsche Forschungsgemeinschaft (DFG, German Research Concil) in the context of the research cluster "Optimization-based control of chemical processes" (RWTH Aachen, , IWR Heidelberg, Universität Stuttgart, TU Dortmund) is very gratefully acknowledged.

REFERENCES

Alamir, M. and Corriou, J. (2003). Nonlinear receding-horizon state estimation for dispersive adsorption

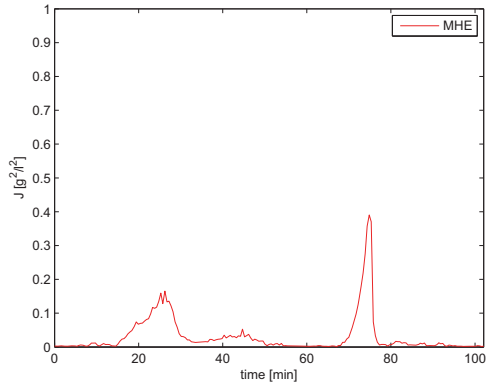

Fig. 7. State reconstruction error

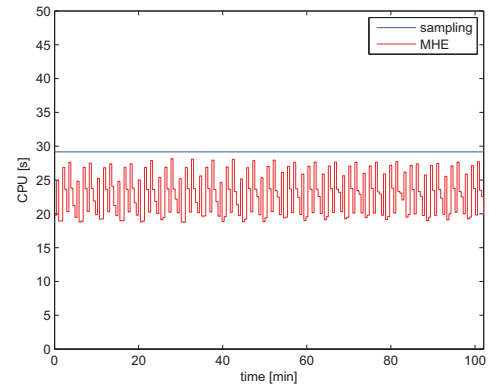

Fig. 8. CPU times of the estimator at each sampling point

columns with nonlinear isotherm. *Journal of Process Control*, 13(6), 517–523.

Bock, H. (1981). Numerical treatment of inverse problems in chemical reaction kinetics. In K. Ebert, P. Deuflhard, and W. Jäger (eds.), *Modelling of Chemical Reaction Systems*, volume 18 of *Springer Series in Chemical Reaction Systems*, 102–125. Springer-Verlag, *Heidelberg*.

Bock, H. (1987). Randwertproblemmethoden zur Parameteridentifizierung in Systemen nichtlinearer Differentialgleichungen. volume 183 of *Bonner Mathematische Schriften*. Universität Bonn, *Bonn*.

Diehl, M. (2002). Real-time optimization of large scale nonlinear processes. volume 920 of *Fortschritt-Berichte VDI Reihe 8, Mess-, Steuerungs- und Regelungstechnik*. VDI Verlag, *Düsseldorf*.

Diehl, M., Bock, H., Schlöder, J., Findeisen, R., Nagy, Z., and Allgöwer, F. (2002). Real-time optimization and nonlinear model predictive control of processes governed by differential-algebraic equations. *Journal of Process Control*, 12(4), 577–585.

Diehl, M., Bock, H., and Schlöder, J. (2004). A real-time iteration scheme for nonlinear optimization in optimal feedback control. *SIAM Journal on Control and Optimization*, 43(5), 1714–1736.

Diehl, M., Kühl, P., Bock, H., and Schlöder, J. (2006). Schnelle Algorithmen für die Zustands- und Parameterschätzung auf bewegten Horizonten. *at-Automatierungstechnik*, 54(12), 602–613.

Dünnebier, G. and Klatt, K.U. (2000). Modelling and simulation of nonlinear chromatographic separation processes: A comparison of different modelling aspects. *Chemical Engineering Science*, 55(2), 373–380.

Gu, T. (1995). Mathematical Modelling and Scale-up of Liquid Chromatography. *Springer Verlag, New York*.

Jupke, A. (2004). Experimentelle Modellvalidierung und modellbasierte Auslegung von Simulated Moving Bed (SMB) Chromatographieverfahren, Dr.-Ing. Dissertation, Fachbereich Bio- und Chemieingenieurwesen, Universität Dortmund. *VDI Reihe 3, Nr. 807*.

Jupke, A., Epping, A., and Schmidt-Traub, H. (2002). Optimal design of batch and simulated moving bed chromatographic separation processes. *Journal of Chromatography A*, 944(1-2), 93–117.

Kühl, P., Diehl, M., Kraus, T., Bock, H., and Schlöder, J. (2008). A real-time algorithm for moving horizon state and parameter estimation. *Journal of Process Control*. (submitted).

Kleinert, T. and Lunze, J. (2005). Modelling and state observation of Simulated Moving Bed processes based on explicit functional wave form description. *Mathematics and Computers in Simulation*, 68(3), 235–270.

Kloppenburg, E. and Gilles, E. (1999). Automatic control of the simulated moving bed process for C8 aromatics separation using asymptotically exact input/output linearization. *Journal of Process Control*, 9, 41–50.

Küpper, A., Diehl, M., Schlöder, J., Bock, H., and Engell, S. (2009). Efficient moving horizon state and parameter estimation for smb processes. *Journal of Process Control*, doi:10.1016/j.jprocont.2008.10.004.

Küpper, A. and Engell, S. (2006). Parameter and state estimation in chromatographic SMB processes with individual columns and nonlinear adsorption isotherms. *Proc. of the IFAC International Symposium of Advanced Control of Chemical Processes, Gramado*, 611–616.

Mangold, M., Lauschke, G., Schaffner, J., Zeitz, M., and Gilles, E.D. (1994). State and parameter estimation for adsorption columns by nonlinear distributed parameter state observers. *Journal of Process Control*, 4(3), 163–172.

Robertson, D., Lee, J., and Rawlings, J. (1996). A moving horizon-based approach for least-squares estimation. *AIChE Journal*, 42(8), 2209–2224.

Toumi, A., Engell, S., Ludemann-Hombourger, O., Nicoud, R.M., and Bailly, M. (2003). Optimization of simulated moving bed and Varicol processes. *Journal of Chromatography A*, 1-2, 15–31.

Toumi, A., Hanisch, F., and Engell, S. (2002). Optimal operation of continuous chromatographic processes: Mathematical optimization of the VARICOL process. *Ind. Eng. Chem. Res.*, 41(17), 4328–4337.

State estimation for large-scale wastewater treatment plants ⋆

Jan Busch [*] [1] **Peter Kühl** [**] [2] **Johannes P. Schlöder** [**]
Hans Georg Bock [**] **Wolfgang Marquardt** [*]

[*] *AVT Process Systems Engineering, RWTH Aachen University, Germany*
[**] *IWR, Heidelberg University, Germany*

AbstractMany relevant process states in wastewater treatment are not measurable, or their measurements are subject to considerable uncertainty. This poses a serious problem for process monitoring and control. Model-based state estimation can provide estimates of the unknown states and increase the reliability of measurements. In this paper, an integrated approach is presented for the estimation problem employing unconventional, but technically feasible sensor networks. Using the ASM1 model in the reference scenario BSM1, the estimators EKF and MHE are evaluated. Very good estimation results for the system comprising of 78 states are found.

Keywords: state estimation, MHE, EKF, wastewater treatment, ASM, BSM1

1. INTRODUCTION

One of the key challenges in the operation of activated sludge wastewater treatment plants (WWTP) is the uncertainty about relevant process state values. E. g. the concentrations of active biomass and of soluble substrate are not measurable online, but they considerably influence process behavior. Some states such as the concentration of total suspended solids are measurable, but their measurements involve significant measurement errors. Reliable estimates of these states are of great value for different operational tasks such as process monitoring, online simulation, and advanced multi-variable control. They are a necessity for model-based control approaches based on dynamic process models (e. g. Busch et al., 2007). Model-based state estimation is one alternative to obtain such estimates. For a given process model, its success depends on the choice of a suitable hardware sensor network and of an appropriate estimation method.

The intention of this paper is to present sophisticated solutions to the state estimation problem for large-scale WWTP and to investigate two distinct state estimation approaches from the practitioner's point of view. First, an optimization-based approach determines the cheapest hardware sensor network that is required for the state estimation task. Second, Extended Kalman Filtering (EKF) and Moving Horizon Estimation (MHE) are employed to estimate the unknown model states of the large-scale WWTP model ASM1 employed in the BSM1 reference scenario (Copp, 2002). Large measurement errors, plant/model-mismatch, and unknown inflow concentrations are considered.

⋆ We thank the German research foundation (DFG) for the financial support in the project "Optimization-based process control of chemical processes" (grant MA 1188/27-1). Also BMBF grant 03BONCHD is gratefully acknowledged.

[1] present address: Bayer Technology Services, Leverkusen, Germany
[2] present address: BASF SE, Ludwigshafen, Germany

State estimation aims at statistically optimal estimates of measurable and unmeasurable process states. Dochain (2003) provides an overview of state and parameter estimation for chemical and biochemical processes focusing on small models. Lubenova et al. (2003) use an adaptive observer for a bioprocess models with 5 states. Goffaux and Vande Wouwer (2005) compare an asymptotic observer, an EKF, and a particle filter (PF) for a bioprocess model with 4 states. A model with approximately 40 states based on the ASM1 successor ASM3 is considered by Chai et al. (2007), who evaluate a KF, an EKF, and an unscented KF (UKF). No rigorous MHE implementation for WWTP has been reported.

Generally speaking, observers prove to be efficient for small-scale models with maybe up to 10 states. For larger models, observer design becomes challenging. An exception are asymptotic observers, which exhibit slow convergence of the estimates to the true values, but which do not require kinetic models. The EKF is the standard choice for large-scale models. It is easy to implement and much experience is available concerning its design and tuning. It is not clear whether the related UKF and PF can significantly outperform the EKF in practical implementations. The MHE is a promising option, but it is not clear whether its increased implementation effort is justified by better estimation results in WWTP applications. Large-scale simulation case studies are rare, and real-life case studies are not available. Also, while the properties of the hardware sensor network are decisive for the success of any state estimation approach, this aspect has not been treated much with respect to WWTP applications.

Ideally, the choice of a sensor network, of a process model, and of the estimator should be considered as an integrated problem. This is beyond our possibilities today. The sensor networks used in this study are obtained by a simple optimization-based sensor network design approach. An observable system for a given large-scale plant model

involving 78 differential states is obtained. An EKF and an MHE are then employed as state estimators.

2. PROCESS AND PROCESS MODEL

The simulation study is based on the BSM1 (Copp, 2002), which has been developed as a benchmark scenario for the evaluation and comparison of different control approaches for WWTP. The plant layout is depicted in Fig. 1. Q_i and $\mathbf{Z}_i$ refer to the flow rate and vector of concentrations for stream i. The inflow is mixed with two recycle streams before entering the plant. Two denitrification basins (each $1000\,\mathrm{m}^3$) are followed by three aerated nitrification basins (each $1333\,\mathrm{m}^3$). The first recycle a is withdrawn from the last nitrification basin. The settler used in the BSM1 is replaced by a membrane filtration unit, which is located in a separate $250\,\mathrm{m}^3$ basin and which is modeled as an ideal splitter. The product stream e as well as a second recycle r and a waste stream w leave the membrane basin. All basins are assumed to be well-mixed.

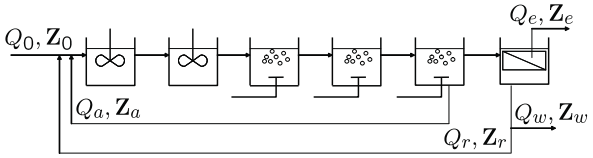

Figure 1. Modified BSM1 plant layout.

The degradation processes in the five biological basins are described by the ASM1 (Henze et al., 1987) with parameters taken from Copp (2002). The ASM1 describes 8 reactions and the component concentrations of inert soluble matter S_I, soluble substrate S_S, inert particulate matter X_I, particulate substrate X_S, heterotrophic biomass $X_{B,H}$, autotrophic biomass $X_{B,A}$, particulate inert metabolism products X_P, dissolved oxygen (DO) S_O, nitrate S_{NO}, ammonia S_{NH}, soluble organic nitrogen S_{ND}, particulate organic nitrogen X_{ND}, and the alkalinity S_{ALK}. The resulting model comprising mass balances and the kinetic model contains 78 differential states. It is formulated as a semi-explicit differential-algebraic model according to

$$\dot{\mathbf{x}} = \mathbf{f}\left(\mathbf{x}, \mathbf{z}, \mathbf{u}, \mathbf{p}\right) \ , \tag{1}$$

$$0 = \mathbf{g}\left(\mathbf{x}, \mathbf{z}, \mathbf{u}, \mathbf{p}\right) \ , \tag{2}$$

$$\mathbf{y} = \mathbf{M} \cdot \mathbf{x} \ . \tag{3}$$

$\mathbf{x}$ are differential and $\mathbf{z}$ are algebraic states, $\mathbf{u}$ are the manipulated variables, and $\mathbf{p}$ are the parameters. $\mathbf{y}$ are the measurable outputs and $\mathbf{M}$ is the measurement matrix. Note that for the BSM1 scenario, $\mathbf{g}(\cdot)$ represents defining equations that can explicitly be solved for $\mathbf{z}$. Generally $\mathbf{g}(\cdot)$ suffices to be of index 1.

The BSM1 benchmark describes a dry weather scenario for a period of 100 days with constant manipulated variables, inflow rates, and inflow concentrations to reach a steady state. This is followed by a period of 14 days with dynamic inflow conditions. One of the three different dynamic scenarios, the *storm scenario*, is used in this paper. It is characterized by dry weather inflow superposed by storm events on days 9 and 11. Exemplarily, the corresponding inflow rate and ammonia inflow concentration are depicted in Fig. 2.

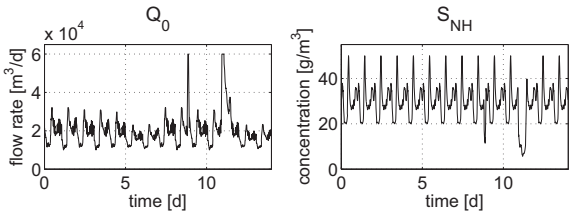

Figure 2. Inflow rate Q_0 and ammonia inflow concentration $Z_{0,S_{NH}}$.

3. SENSOR NETWORK DESIGN

The success of a state estimation approach depends on the process model, on the state estimation algorithm, and on the sensor network which supplies the measurements. Optimal sensor network design aims at the sensor network which leads to optimal state estimates at limited cost, or similarly, reliable state estimates at minimum cost (Singh and Hahn, 2005). So far, systematic approaches to this important aspect of state estimation have been neglected in the literature on WWTP applications. Rather, the sensor network is chosen based on experience and intuition.

The approach to obtain the sensor networks as used in this study is outlined in the following, details are presented in Busch et al. (2009). A sensor network is fully defined by the measurement matrix $\mathbf{M}$ (Eq. (3)), which relates process states $\mathbf{x}$ to measurements $\mathbf{y}$. By assigning prices to the measurement hardware, a cost function $\phi = \phi\left(\mathbf{M}\right)$ is obtained, which describes the cost of the sensor network. The relevant constraint for the sensor network is that it needs to yield an observable system. Hence, the nonlinear process model is linearized at many instances along a typical process trajectory, and observability is checked for each of these instances by a suitable criterium. Finally, a genetic optimization algorithm is employed to find the sensor network with the minimum cost $\phi\left(\mathbf{M}\right)$ which still fulfills the observability constraints (Heyen and Gerkens, 2002). The approach is applied to the simulation scenario described in Section 2. Considering 8 technically feasible measurements in 6 basins gives a total of $2^{6\cdot 8} \approx 2.8 \cdot 10^{14}$ measurement configurations.

The following sensor network is found to give observability at minimum cost: $COD_1, S_{ALK,1}, S_{O,2}, X_{TS,5}$, where the numeric index refers to the basin number. COD is the chemical oxygen demand. This result is quite surprising, as it implies that only four hardware sensors suffice to estimate all 78 model states. Some standard hardware sensors, which are commonly available at WWTP, are added to the sensor network. These are DO sensors in the aerated basins as well as nitrate, ammonia, alkalinity, and COD measurements in the effluent.

4. STATE ESTIMATORS

State estimation refers to retrieving all states of a dynamic system in real-time by utilizing available measurements, possibly in combination with a process model. While the state estimation problem is largely solved for *linear systems*, e. g. , by the Kalman Filter, the problem becomes significantly more difficult for non-linear systems. Most methods are extensions of linear state estimators, such

as the extended Kalman Filter (EKF), described e. g. in Becerra et al. (2001). A *non-linear* version of MHE is presented in Rao et al. (2003). A comparison of EKF and non-linear MHE applied to the BSM1 scenario is presented in Section 5. In the following, main principles and implementation details are reviewed.

4.1 Extended Kalman Filter

The Kalman Filter is a recursive method for state estimation. It consists of a prediction step (time update) and a measurement update. Past data is summarized and carried on by means of suitable statistics. For a non-linear system in discrete-time with measurement noise $\boldsymbol{\upsilon}_k \sim \mathcal{N}(0, \tilde{\mathbf{V}})$ and process noise $\boldsymbol{\mu}_k \sim \mathcal{N}(0, \tilde{\mathbf{W}})$

$$\mathbf{x}_k = \mathbf{f}_k\left(\mathbf{x}_{k-1}, \mathbf{z}_{k-1}, \mathbf{u}_{k-1}, \mathbf{p}_{k-1}\right) + \boldsymbol{\mu}_k \,, \tag{4}$$

$$\mathbf{0} = \mathbf{g}_k\left(\mathbf{x}_{k-1}, \mathbf{z}_{k-1}, \mathbf{u}_{k-1}, \mathbf{p}_{k-1}\right), \tag{5}$$

$$\mathbf{y}_k = \mathbf{M} \cdot \mathbf{x}_k + \boldsymbol{\upsilon}_k \,, \tag{6}$$

where k denotes the sampling instant, the respective filter equations in their most common form are:

Time update:

$$\hat{\mathbf{x}}_k^- = \mathbf{f}_k\left(\hat{\mathbf{x}}_{k-1}, \mathbf{z}_{k-1}, \mathbf{u}_{k-1}, \mathbf{p}_{k-1}\right), \tag{7a}$$

$$\mathbf{P}_k^- = \left.\frac{\partial \mathbf{f}_k}{\partial \mathbf{x}_{k-1}}\right|_{\hat{\mathbf{x}}_{k-1}} \cdot \mathbf{P}_{k-1} \cdot \left.\frac{\partial \mathbf{f}_k}{\partial \mathbf{x}_{k-1}}\right|_{\hat{\mathbf{x}}_{k-1}}^{\mathrm{T}} + \mathbf{W} \,, \tag{7b}$$

Measurement update:

$$\mathbf{K}_k = \mathbf{P}_k^- \cdot \mathbf{M}_d^{\mathrm{T}} \cdot \left(\mathbf{M}_d \cdot \mathbf{P}_k^- \cdot \mathbf{M}_d^{\mathrm{T}} + \mathbf{V}\right)^{-1} , \tag{8a}$$

$$\mathbf{P}_k = \left(\mathbb{I} - \mathbf{K}_k \cdot \mathbf{M}_d\right) \cdot \mathbf{P}_k^- \,, \tag{8b}$$

$$\hat{\mathbf{x}}_k = \hat{\mathbf{x}}_k^- + \mathbf{K}_k \cdot \left(\mathbf{y}_k - \mathbf{M}_d \cdot \hat{\mathbf{x}}_k^-\right), \tag{8c}$$

$$\mathbf{0} = \mathbf{g}_k\left(\hat{\mathbf{x}}_k, \hat{\mathbf{z}}_k, \mathbf{u}_k, \mathbf{p}_k\right). \tag{8d}$$

$\mathbf{f}_k$ typically represents a numerical integration of the continuous system Eq. (1) from time t_{k-1} to t_k with initial values $\mathbf{x}_{k-1}$. The matrix $\mathbf{P}_k$ is the covariance matrix associated with the state estimates $\hat{\mathbf{x}}_k$ at sampling time k. It reflects the confidence one can have in this estimate. The matrices $\mathbf{V}$ and $\mathbf{W}$ describe the assumed covariances of measurement noise and process noise, respectively. The Kalman Filter gain $\mathbf{K}_k$ then reflects the trade-off between the measurements and the process model.

4.2 Moving Horizon Estimation

A drawback of most estimation methods is that they cannot deal with known constraints on the estimated states. In the MHE scheme, such constraints are naturally incorporated in the optimization problem. The formulation also allows to additionally estimate process parameters without reformulating them as dummy states.

Unlike the EKF, the MHE uses more than just the most recent measurements: At a certain time t_j a number of $M+1$ measurements $(\mathbf{y}_{j-M}, \ldots, \mathbf{y}_j)$ associated with past time instants $t_{j-M} < \ldots < t_j$ are explicitly used for estimation. The length L of the time horizon $[t_j, \ldots, t_{j-M}]$ is defined as $L := j - M$. It is assumed that measurement and process noise are normally distributed with zero mean and covariance matrices $\mathbf{V}$ and $\mathbf{W}$. Additionally, a Gaussian distribution is assumed for $\mathbf{x}(t_L)$ and $\mathbf{p}$ at the beginning of the horizon, with expectation value $(\bar{\mathbf{x}}_L, \bar{\mathbf{p}}_L)$ and a block-diagonal covariance matrix $\boldsymbol{\Pi}_L$ with block elements $\boldsymbol{\Pi}_{\bar{x},L}$ and $\boldsymbol{\Pi}_{\bar{p},L}$.

The state estimation problem to be solved at time t_k – given the measurements $\mathbf{y}_j$ for $j = L, L+1, \ldots, k$, the known input $\mathbf{u}(t)$ for $t \in [t_L, t_k]$ and given $(\bar{\mathbf{x}}_L, \bar{\mathbf{p}}_L)$ and $\mathbf{P}_L$ – has the following form:

$$\min_{\mathbf{x}(\cdot),\mathbf{p}} \Big(\|\mathbf{x}(t_L) - \bar{\mathbf{x}}_L\|^2_{\boldsymbol{\Pi}_{\bar{x},L}} + \|\mathbf{p} - \bar{\mathbf{p}}_L\|^2_{\boldsymbol{\Pi}_{\bar{p},L}} + \sum_{j=L}^{k} \|\mathbf{y}_j - \mathbf{M} \cdot \mathbf{x}(t_j)\|^2_{\mathbf{V}} \Big) \tag{9}$$

$$\text{s.t.} \quad \dot{\mathbf{x}}(t) = \mathbf{f}(\mathbf{x}(t), \mathbf{z}(t), \mathbf{u}(t), \mathbf{p}), \quad t \in [t_L, t_k], \tag{10a}$$

$$\mathbf{0} = \mathbf{g}(\mathbf{x}(t), \mathbf{z}(t), \mathbf{u}(t), \mathbf{p}), \tag{10b}$$

$$\mathbf{x}_{\min} \le \mathbf{x}(t) \le \mathbf{x}_{\max}, \tag{10c}$$

$$\mathbf{p}_{\min} \le \mathbf{p} \le \mathbf{p}_{\max}, \tag{10d}$$

where the applied norm is defined as $\|\mathbf{x}\|^2_{\mathbf{V}} := \mathbf{x}^{\mathrm{T}}\mathbf{V}^{-1}\mathbf{x}$.

At each new sampling time t_k, one new measurement vector $\mathbf{y}_k$ enters the set of measurements, while the last one $\mathbf{y}_L$ becomes $\mathbf{y}_{L-1}$ and drops out of the horizon.

The initial weight terms $\|\mathbf{x}(t_L) - \bar{\mathbf{x}}_L\|^2_{\boldsymbol{\Pi}_{\bar{x},L}}$ and $\|\mathbf{p} - \bar{\mathbf{p}}_L\|^2_{\boldsymbol{\Pi}_{\bar{p},L}}$ (often called "arrival costs") summarize information in the MHE problem prior to the horizon beginning at time t_L and also reflect a cumulated effect of process noise on the process. A typical approach is to compute the arrival costs by Kalman Filter updates of $\bar{\mathbf{x}}_L$ and $\bar{\mathbf{p}}_L$. As for the optimal length of the estimation horizon, no general results are available, yet. Horizon length and the weighting matrices $\mathbf{V}^{-1}$, $\boldsymbol{\Pi}^{-1}$ are the tuning parameters. Note that an extended MHE formulation exists that explicitly incorporates process noise (Rao et al., 2003; Diehl et al., 2006).

A necessity for the MHE scheme to work is a fast and reliable numerical scheme for the constrained non-linear dynamic optimization problem (9). The implementation in this work makes use of MUSCOD-II (Leineweber et al., 2003), which is based on a direct multiple shooting approach, see, e. g. , (Bock et al., 2007). For real-time feasibility, the least-squares problem at each time instant t_k is not solved to convergence. Instead, only one Gauss-Newton iteration is performed, combined with a meaningful shift of the problem variables. More information on this so-called *real-time iteration approach* along with other implementational details can be found in Diehl et al. (2006).

5. CASE STUDY

EKF and MHE are applied to the process model and scenario described in Section 2 and the sensor network calculated in Section 3. The estimation task was made increasingly difficult to evaluate the estimation performance under nominal and more realistic conditions.

Only little effort has been devoted to the fine-tuning of the estimators. This is intentional, since the aim of the study is to investigate the practical applicability and general performance of the two estimation methods. The tuning matrices $\mathbf{W}$ and $\mathbf{V}$ for the EKF and the MHE reflect covariances based on an assumed standard deviation of 5% of the initial values $\mathbf{x}_0$ and "initial measurements" $\mathbf{M} \cdot \mathbf{x}_0$. The MHE uses an estimation horizon of 5 measurement samples.

The initial guess for $\hat{\mathbf{x}}_0$ is deliberately set to $1.3 \cdot \mathbf{x}_0$ to introduce a strong initial offset. The measurements are corrupted by white noise $\boldsymbol{\upsilon}$ with a standard deviation of 5% of the initial measurements: $\mathbf{y}_k = \mathbf{M} \cdot \mathbf{x}_k + \boldsymbol{\upsilon}_k$. The sampling interval is set to 15 minutes. In the following, the quality of the estimation results will be illustrated by the estimates of the third basin, which is the one with the least measurements (only DO concentration). The DO concentration is not visualized as the estimates always closely follow the true values.

5.1 Nominal process

In the first scenario, no process noise is added and perfect knowledge of the inflow rate and concentrations is assumed. The estimated state values quickly converge from their initial offset to the true values (not shown). Only the concentration of X_P shows some occasional offset. The root of the cumulated squared relative error (RCSE) averaged over all J samplings is used in the following as a measure to compare the overall estimation performance:

$$\mathrm{RCSE} = \frac{1}{J} \sum_{k=1}^{J} \sqrt{\sum_{i=1}^{N} \left(\frac{\hat{x}_{i,k} - x_{i,k}}{x_{i,k}} \right)^2} , \qquad (11)$$

where J is the number of samples $x_{i,k}$ and $\hat{x}_{i,k}$ and N is the number of states. The RCSE values for the different simulation case studies are stated in Table 1. For the EKF and the MHE with known inputs and no process noise, RCSE of 0.3 and 0.4 are obtained, respectively.

Table 1. RCSE for the estimated states of different simulation scenarios and estimators.

Estimator	Known inputs, no process noise	Known inputs, process noise	Unknown inputs, process noise
EKF	0.3	0.7	1.8
MHE	0.4	0.8	1.6

5.2 Process noise

Process noise is added to introduce plant/model-mismatch to the problem. The process noise $\boldsymbol{\mu}$ has zero mean and a standard deviation of 5% of the initial states and enters the discrete time simulation model according to

$$\mathbf{x}_{k+1} = \mathbf{f}\left(\mathbf{x}_k, \mathbf{z}_k, \mathbf{u}_k, \mathbf{p}_k\right) + \boldsymbol{\mu}_k \, , \qquad (12a)$$

$$\mathbf{0} = \mathbf{g}\left(\mathbf{x}_k, \mathbf{z}_k, \mathbf{u}_k, \mathbf{p}_k\right) . \qquad (12b)$$

Noise-induced negative states representing concentrations are set to zero to ensure that the equations remain physically feasible. The estimation results are similar for the EKF and the MHE. Exemplarily, Fig. 3 shows the results for the third basin using the MHE. Deviations from the true trajectories are observed, but the estimation result averaged over all samples remains satisfactory for both estimators. The RCSE of the EKF and the MHE changes from 0.3 to 0.7 and from 0.4 to 0.8, respectively (Table 1). This result is not surprising, as the process noise now deviates the measured outputs, complicated even further by the process nonlinearities which are not fully captured by the estimators.

5.3 Unknown inflow concentrations

Up to now it has been assumed that the inflow rate and concentrations are perfectly known. This assumption is not realistic. While the inflow rate is indeed well-known, at least part of the inflow concentrations are not. Typically historic data is employed to obtain daily, weekly, and yearly trends and patterns of e. g. the concentrations or the composition of the COD. However, a substantial bias between these predictions and the real inflow concentrations must be expected. A worst case situation is considered in the following: The inflow concentrations of soluble inert matter S_I, soluble substrate S_S, particulate inert matter X_I, particulate substrate X_S, heterotrophic biomass $X_{B,H}$, as well as soluble S_{ND} and particulate organic nitrogen X_{ND} are treated as unknown model inputs. The inflow concentrations of DO S_O, autotrophic biomass $X_{B,A}$, metabolism products X_P, and nitrate X_{NH} are set to zero, and the alkalinity S_{ALK} is set to 7, which corresponds to typical inflow characteristics as well as to the BSM1. The inflow rate Q_0 and the inflow ammonia concentration S_{NH} are measurable. The unknown inputs need to be estimated together with the unknown states.

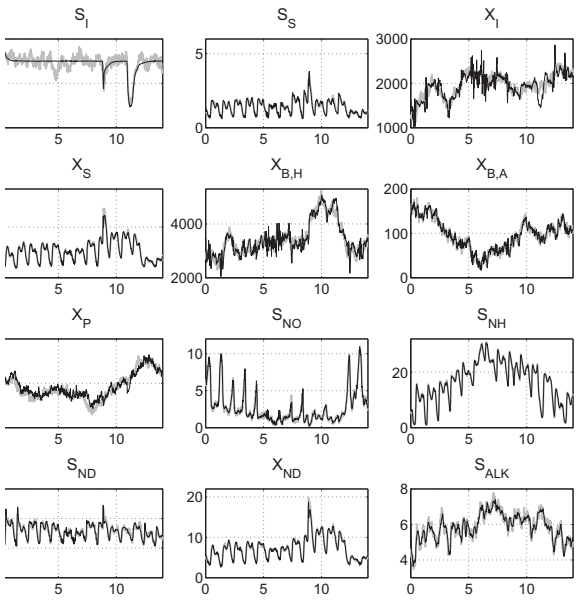

Figure 3. MHE with 5% process noise, third basin. The x-axis shows the time in days, and the y-axis shows the concentrations in [g/m^3]. The alkalinity S_{ALK} is dimensionless. The graphs show the true process state values (light grey) and the estimates (black).

First, a new sensor network is determined by applying the optimization procedure outlined in Section 3 to an extended model, which considers the unknown inflow concentrations as additional model states (Busch et al., 2009). The resulting sensor network is more complex than the network used for the estimation of the nominal process, but still technically and economically feasible:

$$X_{TS,1}, S_{ALK,1}, BOD_2, BOD_3, S_{O,3}, S_{ALK,3} \, , \\ S_{ALK,4}, COD_5, COD_6 \, ,$$

where BOD is the biological oxygen demand. The same standard measurements as discussed in Section 3 are added to the sensor network.

The estimation of the model parameters such as input concentrations is an integrated part of the MHE implementation and thus can be pursued very easily (see Section 4). For the EKF, the effort is slightly higher. Here, to additionally estimate process parameters, these have to be formulated as additional differential states $\mathbf{x}_p$ obeying the trivial differential equation $\dot{\mathbf{x}}_p = \mathbf{0}$ with initial values $\mathbf{x}_p(0) = \mathbf{p}$. The EKF then estimates the augmented state vector $(\mathbf{x}^{\mathrm{T}}\,\mathbf{x}_p^{\mathrm{T}})^{\mathrm{T}}$. Note that the covariance matrix $\mathbf{W}$ has to be adapted to the new state vector. The expected process noise standard deviation of the unknown parameters is specified as 5% of their nominal values. The initial guess for the inflow concentrations is also disturbed by +30%. Fig. 4 depicts the estimated states for the third basin. The estimation performance is again satisfactorily except for two states. The estimation of inert particulate matter X_I shows considerable offset from the true values. This is, however, not severe, as inert matter does not affect the reaction kinetics and is hence irrelevant for process prediction. The second state to exhibit a significant offset is the concentration of heterotrophic biomass $X_{B,H}$. This is more serious as heterotrophic biomass is responsible for the degradation of substrate and nitrate. Whether the offset is critical, e. g. in model-based control approaches, needs to be evaluated in future research. Fine-tuning of the estimator might further minimize the deviation. The overall RCSE is 1.8 for the states (Table 1) and 2.0 for the parameters.

Fig. 5 shows the estimation results for the states in the third basin as obtained by the MHE. The results do not differ much from those of the EKF. Again, the two states inert particulate matter X_I and heterotrophic biomass $X_{B,H}$ show the largest deviations. From visual inspection, the first seems to stay closer to the true value but then exhibits a sudden and sharp drop which is not present in the real trend. The overall RCSE for this case is 1.6 (Table 1) and hence slightly better than for the EKF. The estimated parameters achieve an RCSE of 2.1.

The estimated inflow concentrations are depicted exemplarily for the EKF in Fig. 6. All estimates exhibit high-frequent oscillations, which could probably also be improved by fine-tuning of the estimators. The estimation of the concentration of heterotrophic biomass $X_{B,H}$ again shows a stronger offset during days 11 to 13 following the second storm event but returns to the true value eventually. The graphs of inert particulate matter X_I and particulate organic nitrogen X_{ND} show that the estimates are not able to follow sudden concentration peaks (day 9).

The main trends in the inflow data are captured well, but it is not clear especially with respect to the concentrations of inert particulate matter X_I and heterotrophic biomass $X_{B,H}$ whether these parameter are actually observable. To clarify the issue, additional scenarios have been calculated which show that the parameters are indeed observable, but that their influence on the noisy process and process measurements is small, so that it is not possible to resolve higher frequent variations Busch et al. (2009).

5.4 Computation times

A general belief that can often be found is that optimization-based estimation methods such as MHE are impractical

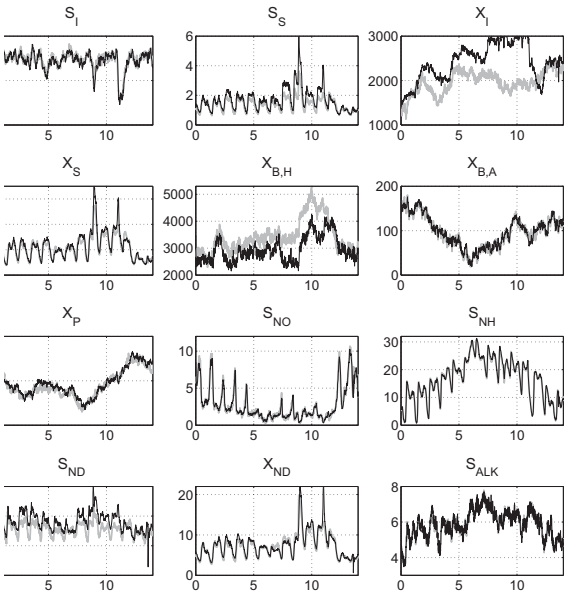

Figure 4. EKF with unknown inflow concentrations and 5% process noise, third basin. The x-axis shows the time in days, and the y-axis shows the concentrations in [g/m^3]. The alkalinity S_{ALK} is dimensionless. The graphs show the true process state values (light grey) and the estimates (black).

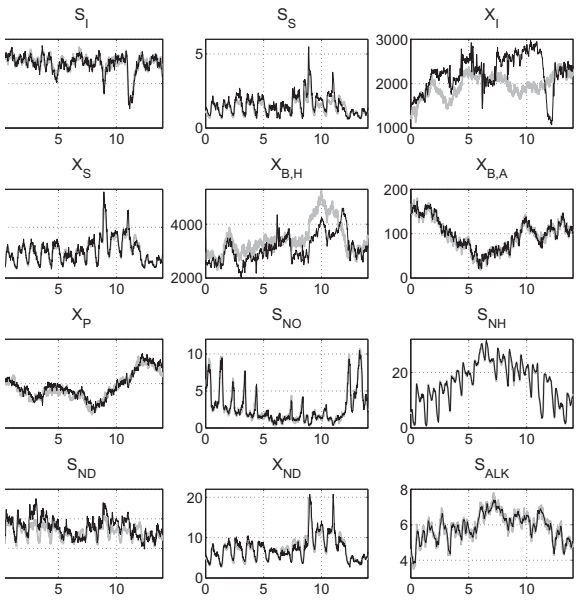

Figure 5. MHE with unknown inflow concentrations and 5% process noise, third basin. The x-axis shows the time in days, and the y-axis shows the concentrations in [g/m^3]. The alkalinity S_{ALK} is dimensionless. The graphs show the true process state values (light grey) and the estimates (black).

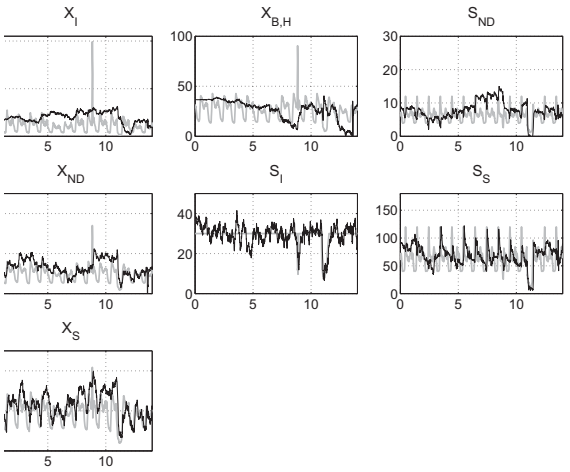

Figure 6. EKF with unknown inflow concentrations and 5% process noise. The x-axis shows the time in days, and the y-axis shows the inflow concentrations in [g/m^3]. The graphs show the true process state values (light grey) and the estimates (black).

because of the excessive computation times to be expected. Indeed the time required to solve a constrained optimization problem to full convergence will necessarily be larger than recursively solving the corresponding unconstrained problem. However, the numerical approach sketched in Section 4 can significantly reduce the computation times. In the case studies described, the average computation time for the MHE was in the range of a few seconds with a maximum lower than 10 seconds on a Pentium 4 machine with 2.8 GHz, 1024 kB L2 cache, 1 GB RAM under Suse Linux 9.3. This is by far fast enough for the estimation tasks for WWTP.

6. CONCLUSIONS

In this paper inflow and state estimation approaches for large-scale wastewater treatment plants are presented. The process is based on the reference scenario BSM1 and employs the dynamic, non-linear process model ASM1. The two prominent state estimators EKF and MHE are evaluated. Large process and measurement disturbances as well as unknown influent conditions have been considered.

The results show that it is possible to yield a fully observable system with an unconventional sensor network of moderate complexity. Both the EKF and the MHE show good estimation performance even in difficult conditions. The EKF shows a marginally better performance for the scenarios with known inflow concentrations. For unknown inflow concentrations, the MHE delivers slightly better state estimates. These do not fully justify the higher implementational effort for the MHE. However, its simple and straightforward handling of unknown inflow conditions and parameters is an advantage over the EKF. The computation times presented here show that the EKF as well as the MHE are real-time feasible for WWTP.

REFERENCES

Becerra, V.M., Roberts, P.D., and Griffiths, G.W. (2001). Applying the extended Kalman Filter to systems described by nonlinear differential-algebraic equations. *Control Eng. Pract.*, 9, 267–281.

Bock, H., Kostina, E., and Schlöder, J.P. (2007). Numerical methods for parameter estimation in nonlinear daes. *GAMM Mitteilungen*, 30/2, 352–375.

Busch, J., Kuehl, P., Gerkens, C., Marquardt, W., Schlöder, J.P., and Bock, H.G. (2009). State estimation for large-scale wastewater treatment plants. *Wat. Res.* (in preparation).

Busch, J., Oldenburg, J., Santos, M., Cruse, A., and Marquardt, W. (2007). Dynamic predictive scheduling of operational strategies for continuous processes using mixed-logic dynamic optimization. *Comput. Chem. Eng.*, 31(5–6), 574–587.

Chai, Q., Furenes, B., and Lie, B. (2007). Comparison of state estimation techniques, applied to a biological wastewater treatment process. In *Proceedings of the 10th IFAC Symposium on Computer Applications in Biotechnology*, 353–358. Cancun, Mexico.

Copp, J.B. (ed.) (2002). *The COST Simulation Benchmark. Description and Simulator Manual*. Office for Official Publications of the European Communities, Luxembourg.

Diehl, M., Kuehl, P., Bock, H.G., and Schlöder, J.P. (2006). Schnelle Algorithmen für die Zustands- und Parameterschätzung auf bewegten Horizonten. *Automatisierungstechnik*, 54(12), 602–613.

Dochain, D. (2003). State and parameter estimation in chemical and biochemical processes: a tutorial. *J. Process Contr.*, 13, 801–818.

Goffaux, G. and Vande Wouwer, A. (2005). Bioprocess state estimation: Some classical and less classical approaches. In T.M. et al. (ed.), *Control and Observer Design*, 111–128. Springer, Berlin, Heidelberg.

Henze, M., Grady Jr., C.P.L., Gujer, W., Marais, G.V.R., and Matsuo, T. (1987). A general model for single-sludge wastewater treatment systems. *Water Res.*, 21(5), 505–515.

Heyen, G. and Gerkens, C. (2002). Application d'algorithmes génétiques à la synthèse de systémes de mesure redondants. In *Proceedings of SIMO 2002 Congress*. Toulouse, France.

Leineweber, D.B., Schäfer, A., Bock, H.G., and Schlöder, J.P. (2003). An efficient multiple shooting based reduced SQP strategy for large-scale dynamic process optimization. Part II: Software aspects and applications. *Comput. Chem. Eng.*, 27, 167–174.

Lubenova, V., Rocha, I., and Ferreira, E.C. (2003). Estimation of multiple biomass growth rates and biomass concentration in a class of bioprocesses. *Bioproc. Biosyst. Eng.*, 25, 395–406.

Rao, C.V., Rawlings, J.B., and Mayne, D.Q. (2003). Constrained state estimation for nonlinear discrete-time systems: Stability and moving horizon approximations. *IEEE T. Automat. Contr.*, 48(2), 246–258.

Singh, A.K. and Hahn, J. (2005). Determining optimal sensor locations for state and parameter estimation for stable nonlinear systems. *Ind. Eng. Chem. Res.*, 44(15), 5645–5659.

Plantwide Control

Oral Session

Feedforward for stabilization

Morten Hovd * **Robert R. Bitmead** **

* *Engineering Cybernetics Department, Norwegian University of Science and Technology, N-7491 Trondheim, Norway (morten.hovd@itk.ntnu.no)*
** *Department of Mechanical and Aerospace Engineering, University of California San Diego, 9500 Gilman Drive, La Jolla, CA 92093-0411, USA*

Abstract: This paper demonstrates how feedforward control can assist in stabilizing unstable systems. Feedback control is necessary for stabilization, but feedforward can be used to avoid input constraints which would otherwise cause the system to go unstable. Thus, if disturbances can be measured, feedforward from disturbances can be a simple and low cost way of avoiding loss of stability due to input constraints.

Keywords: Feedforward, input constraints, stabilization

1. INTRODUCTION

Fundamental limitations in achievable control performance have received a lot of attention in the control literature. A number of important results in this area is covered in Skogestad and Postlethwaite (2005). One such fundamental limitation for unstable systems is that the range of actuation for the inputs must be sufficiently large to avoid saturation. If the inputs saturate, feedback is broken, and hence the stabilizing effect of the controller is lost. Ensuring that the inputs do not saturate is therefore important in order to guarantee closed loop stability, although an unstable system may remain stable despite the inputs being saturated for a limited period, as shown in Favez et al. (2006). If input saturation is avoided, local (linear) stability of the closed loop system is sufficient for stability.

Feedforward is normally used to improve control performance at high frequencies, beyond the achievable bandwidth for stable closed loop control. In this paper, feedforward is instead used to reduce the magnitude of the plant input moves, and therefore to avoid instability due to input constraints.

2. BACKGROUND

Consider a controlled system such as the one illustrated in Fig. 1. For the linear, unconstrained case with only feedback control ($K_f = 0$), we get

$$u = KSr - KSG_d d \tag{1}$$

where $S = (I + GK)^{-1}$. The dependence on the Laplace variable s is suppressed for notational convenience, whenever it is not needed for clarity.

Glover (1986) has shown that for unstable systems, the minimal achievable H_∞ norm of KS is given by

$$\|KS\|_\infty \geq 1/\underline{\sigma}_H(\mathcal{U}(G)^*) \tag{2}$$

where $\underline{\sigma}_H$ denotes the smallest Hankel singular value, and $\mathcal{U}(G)^*)$ denotes the anti-stable part of the plant G, with its unstable pole(s) mirrored into the left half plane.

Observe that for relationships like (2) to have any relevance for evaluating the likelihood of input saturation - with subsequent loss of stabilizing feedback - the plant model G needs to be appropriately scaled. Skogestad and Postlethwaite (2005) recommend scaling plant inputs such that $|u| < 1$ corresponds to inputs within the range of actuation, and scaling outputs such that $|y| < 1$ means that the control offset is acceptable. Similarly, the inputs of the disturbance model G_d should be scaled to get $|d| < 1$ for the expected range of disturbances, and outputs scaled in the same way as for G. In scaled variables, the references are then scaled to give $|r| < R(\omega)$ for the expected range of reference changes. Such scaling is implicitly assumed throughout this paper, and consequently the input saturation limits are assumed to be at ± 1.

Thus, with variables appropriately scaled, sinusoidal reference changes will not cause input saturation provided

$$\|KS\|_\infty < 1/R(\omega) \forall \omega \tag{3}$$

Although reference signals may contain more than a single frequency, and input saturation due to reference changes may therefore occur even if this relationship is fulfilled, this relationship is nevertheless useful in assessing whether

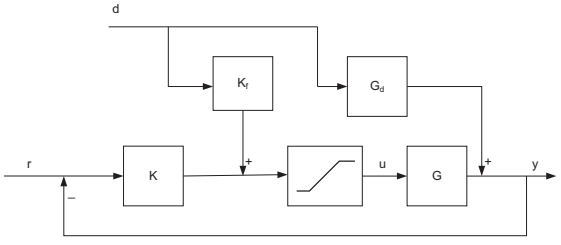

Fig. 1. Feedback and feedforward control, with limited input actuation range.

input saturation is a problem. However, it is also clear from the above that input saturation due to reference changes is not a fundamental problem - one may simply reduce the magnitude of the reference changes to avoid saturation.

On the other hand, it is typically not possible to control the magnitude of external disturbances d. Karivala et al. (2005) extended Glover's result to find that when using feedback only

$$\|KSG_d\|_\infty \geq 1/\underline{\sigma}_H(\mathcal{U}(G_{d,ms}^{-1}G)^*) \tag{4}$$

where $G_{d,ms}$ is the minimum phase and stable version of G_d, i.e., with both RHP poles and RHP zeros mirrored into the left half plane.

Accounting for the feedforward term K_f (but still assuming the saturation element to be inactive), we get

$$u = KSr + S_I(K_f - KG_d)d \tag{5}$$

where $S_I = (I + KG)^{-1}$. Note that $S = S_I$ for SISO systems, but this need not be the case for multivariable systems. From (5) we observe that introducing feedforward gives a new degree of freedom for minimizing input usage in the face of disturbances. Below, we will investigate in what situations this allows for a significant reduction of input usage, thus enabling closed loop stability.

3. STABLE DISTURBANCE MODELS

Consider the case where the plant is unstable from input to output, and hence requires feedback control for stabilization, but the unstable mode is not excited by the disturbances. This is motivated by the following example from Skogestad and Postlethwaite (2005):

Example:

$$G(s) = \frac{5}{(10s+1)(s-1)} \tag{6}$$

$$G_d(s) = \frac{k_d}{(s+1)(0.2s+1)} \tag{7}$$

The transfer functions are assumed to be appropriately scaled, as described above. From (4), we find that for $k_d > 0.54$, $\|KSG_d\|_\infty \geq 1$ for any feedback controller, and hence sinusoidal disturbances can drive the inputs to saturation. This is further illustrated in Skogestad and Postlethwaite (2005), where a stabilizing feedback controller is designed, but where saturation occurs for a step disturbance of magnitude 1 with $k_d = 0.5$. We seem to be in the paradoxical situation where control is not needed to counter the effect of disturbances (since a control offset of 1 is acceptable), but the controller needed to stabilize the system saturates due to the presence of the disturbance. Clearly, it would be better to do nothing to counteract the disturbance, but only manipulate the input to provide stabilization. However, a standard feedback controller does not distinguish the control offset caused by the (stable) disturbance from the offset caused by the unstable mode.

Equation (4) does not distinguish between stable and unstable disturbance models. For stable disturbance models, the feedforward controller K_f can be used to counter the effect of the disturbance on the input. That is, in stead of the conventional (ideal) feedforward

$$K_f = -G^{-1}G_d \tag{8}$$

which cancels the effect of the disturbance on the output [1], the ideal feedforward can from (5) be seen to be

$$K_f = KG_d \tag{9}$$

which cancels the effect of the disturbance on the input.

With this in mind, we revisit the example above, for the case with $k_d = 1$, meaning that feedback alone will not be able to maintain stability in the face of disturbances. The controller

$$K(s) = \frac{(10s+1)^2}{s(0.01s+1)} \tag{10}$$

will stabilize the unconstrained system. However, in Fig 2 we see that a unit step in the disturbance (applied at time $t = 1s$) will drive the input to saturation. Figure 3 shows that the system goes unstable as a result of the saturation. This is exactly as expected. The feedback controller $K(s)$ in (10) contains an integrator, and hence direct application of the ideal feedforward in (9) will mean that K_f will contain an integrator that is not stabilized by feedback. To avoid this problem, the controller is implemented as illustrated in Fig. 4, with the integrator in the block K_2. The corresponding feedforward is $K_f = K_1G_d$, with the overall feedback controller given by $K = K_2K_1$.

With this slight modification, we obtain the results in Figs. 5 and 6. The solid lines represents the 'ideal' feedforward control according to (9), whereas the dash-dot line is conventional feedforward according to (8). Clearly, the conventional feedforward does not avoid the input saturation. On the other hand, the modified feedforward according to (9) simply does nothing to counter the effect of the disturbance. Even though the control offset is acceptable according to the scaling used, most people would probably prefer the responses represented by the dashed line. This is obtained by augmenting the feedforward in (9) with a high pass filter, and results in offset-free control at steady state. Clearly, the pass band of the high pass filter should include frequencies significantly lower than that corresponding to the RHP pole(s).

4. UNSTABLE DISTURBANCE MODELS

It was shown above that it is simple to use feedforward from the disturbance to avoid input saturation and hence loss of stabilizing feedback, when the plant is unstable but the disturbance transfer function is stable. If the disturbance transfer function is unstable, the issue becomes more complicated.

Note, that for stabilization of the unstable disturbance transfer function to make sense, the unstable mode(s) must also be a part of the plant transfer function. That is, it must be possible to reformulate the plant and disturbance transfer functions as indicated in Fig. 7, with $G_3(s)$ a

[1] Neglecting for the moment the effects of possibly unknown initial conditions for the disturbance dynamics.

stable transfer function. In this case, the disturbance will obviously excite the unstable mode, and it therefore does not make sense to avoid the use of the manipulated input when a disturbance occurs.

Furthermore, the direct application of the 'ideal' feedforward in (9) would mean using an unstable feedforward element K_f, which would lead to an internally unstable control system. Instead, we would like to find the *stable* feedforward element K_f which minimizes the term $(K_f - KG_d)$ in (5). The term KG_d can be split into a stable and an anti-stable part. The stable part can be used directly in K_f, whereas we need a *stable approximation to the anti-stable part of* KG_d.

Approximation of an anti-stable transfer function by a stable transfer function (or *vice versa*) is known as a Nehari extension problem. That is, we want to find the optimal stable $Q(s)$ such that $\|Q(s)+R(s)\|_\infty$ is minimized, where $R(s)$ is ant-stable. A solution to this problem can be found in Glover (1984). In Glover (1984), it is also shown that the optimal error is given by $\|R^*\|_H$, where $\|\cdot\|_H$ denotes the Hankel norm, and R^* is the 'stable version of R', with the unstable poles mirrored into the left half plane. Thus, we would like to design a feedback controller K that not only stabilizes the plant, but also makes the Hankel norm of the unstable part of KG_d small. However, with

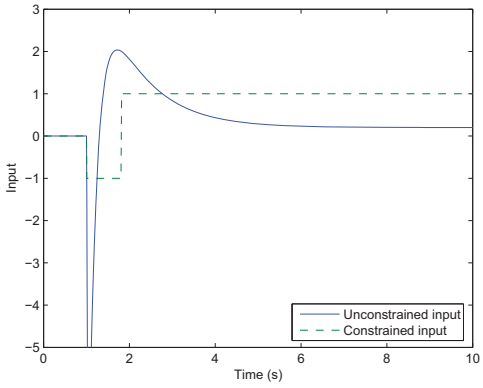

Fig. 2. Response in the input to a unit step in the disturbance as time $t = 1s$, using only feedback control.

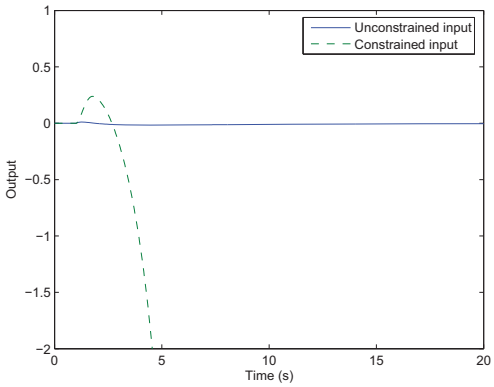

Fig. 3. Response in the output to a unit step in the disturbance as time $t = 1s$, using only feedback control.

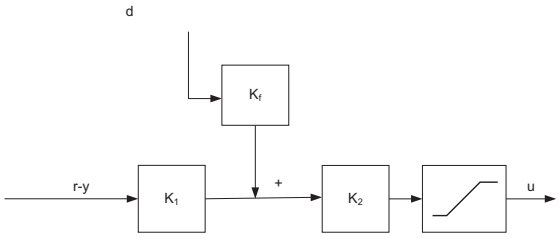

Fig. 4. Implementation of overall feedback/feedforward controller, with the integrator in the block K_2.

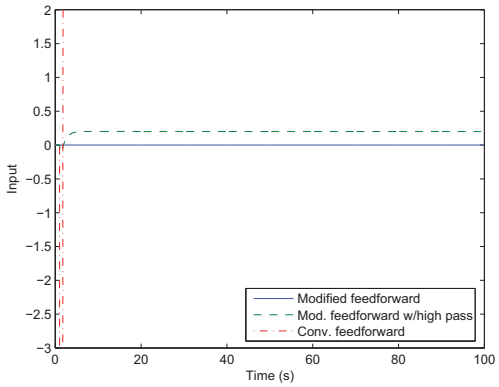

Fig. 5. Response in the input to a unit step in the disturbance as time $t = 1s$, using combined feedback and feedforward control.

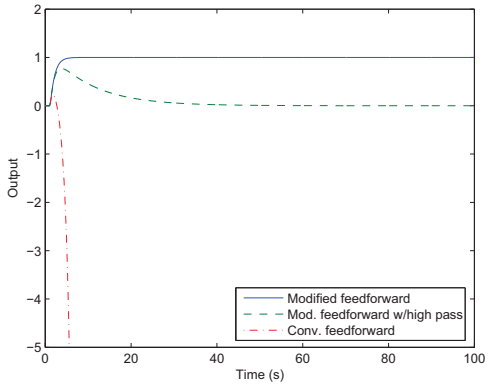

Fig. 6. Response in the output to a unit step in the disturbance as time $t = 1s$, using combined feedback and feedforward control.

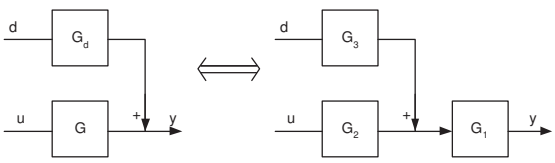

Fig. 7. Reformulation of plant and disturbance transfer functions.

a simple reformulation of the feedforward arrangement, this complication is easily avoided. This rearrangement is illustrated in Fig. 8, and may be regarded more as a 'reference governor' approach than feedforward in the ordinary sense.

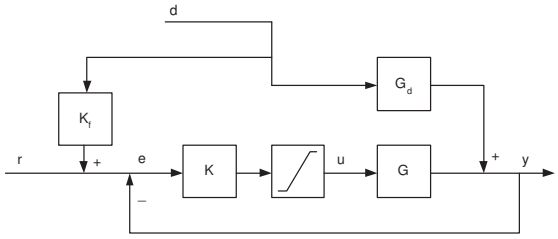

Fig. 8. 'Feedforward' arrangement for an unstable disturbance transfer function.

With the rearranged 'feedforward', the transfer function from the disturbance d to e, the input to the feedback controller K (assuming the saturation element is inactive), is given by

$$e = S(K_f - G_d)d \tag{11}$$

where $S = (I+GK)^{-1}$. Thus, for a given controller K, the controller input (and therefore also the controller output) will be small if the term $(K_f - G_d)$ is small. Next, the validity of the bound (4) and the design of the feedforward controller will be illustrated for two different cases:

- A disturbance transfer function G_d whose only non-minimum phase term is an unstable pole.
- A disturbance transfer function G_d with non-minimum phase terms in addition to the unstable pole.

The benefit of feedforward will be found to be different in these two cases. However, first the H_∞ problem formulation will be briefly explained. For the case with a stable disturbance transfer function, this was not needed, since the design of the feedforward controller was done separately from the design of the feedback controller.

4.1 H_∞ problem formulation

Using feedforward in combination with feedback means that we are using a controller with two degrees of freedom (2-DOF controller)). We wish to investigate the benefit of using a 2-DOF controller for stabilizing the system while minimizing the use of inputs in the face of measured disturbances. However, the resulting H_∞ control synthesis problem violates the standard assumptions. Assumptions A2 and A4 of Zhou et al. (1996), p. 450 are violated.

A small measurement noise n is therefore added, and the magnitude of that measurement noise is reduced until further reduction does not significantly affect the H_∞ norm achieved. The block diagram corresponding to the resulting controller synthesis problem is shown in 9.

4.2 The unstable pole as the only non-minimum phase term in G_d

The same plant transfer function as in (6) is used, whereas the disturbance transfer function is modified to

$$G_d(s) = \frac{k_d}{(s-1)(0.2s+1)} \tag{12}$$

The parameter value $k_d = 1$ is still used. First, a realization of $[G_d \quad G]$ with only one unstable mode is found. Then a 2-DOF controller is designed according to Fig. 9, and compared to a 1-DOF controller (feedback only) designed to minimize KSG_d. For both cases, a H_∞ norm of 1.83 is achieved. This also corresponds to the bound in (4). In this case, there is thus no advantage derived from using a 2-DOF controller with feedforward from disturbances[2].

However, if the feedback controller is designed for some other criterion than minimising $\|KSG_d\|_\infty$, there may be a possible advantage in designing the feedforward using the idea of approximating G_d with a stable transfer function. To illustrate, we first design a feedback controller for minimizing $\|KS\|_\infty$, achieving a H_∞ norm of 4.40 - which agrees with the bound in (2). Using this controller, we would also get $\|KSG_d\|_\infty = 4.40$. Instead, we augment the controller with feedforward as illustrated in Fig. 8. The transfer function G_d can be split into stable and unstable parts, giving

$$G_{d,stable} = \frac{-5k_d}{6(s+5)}$$
$$G_{d,unstable} = \frac{5k_d}{6(s-1)}$$

The task is this to find a stable approximation to $G_{d,unstable}$. The formulae in Glover (1984) for doing so are not directly applicable, since $G_{d,unstable}$ has only one state. However, it is easily verified that a stable approximation which achieves the minimum bound on the approximation error is given by

$$\tilde{G}_{d,unstable} = -\frac{5k_d}{12} \tag{13}$$

With the feedforward $K_f = G_{d,stable} + \tilde{G}_{d,unstable}$ used as illustrated in Fig. 8, and the feedback controller K which minimizes $\|KS\|_\infty$, we achieve an H_∞ norm of 1.83 from disturbance d to input u, while maintaining closed loop stability.

4.3 G_d with non-minimum phase terms in addition to the unstable pole

Consider next the case when the unstable disturbance transfer function is augmented with an all-pass term, giving

[2] And, in order to achieve $|u| < 1$ we would need $k_d < 0.54$, as in the original example in Skogestad and Postlethwaite (2005).

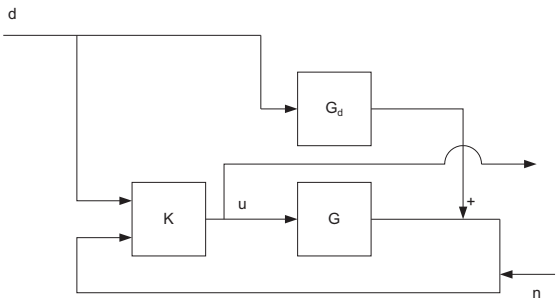

Fig. 9. H_∞ controller synthesis setup for 2-DOF controller.

$$G_d(s) = \frac{k_d(-10s+1)}{(s-1)(0.2s+1)(10s+1)} \quad (14)$$

The all-pass part of G_d cancels in the calculation of the bound in (4), and thus the minimum that can be achieved with feedback control alone is still $\|KSG_d\|_\infty = 1.83$. On the other hand, with a 2-DOF controller we achieve an H_∞ norm from d to u of 1.50. The same is achieved when designing a 1-DOF H_∞ controller minimizing $\|KS\|_\infty$ and subsequently adding feedforward to this controller in a manner similar to the preceding section.

Looking at the unstable part of $G_d(s)$ in (14), the reason for the improvement in input usage when adding the feedforward becomes apparent. One now finds that

$$G_{d,unstable} = \frac{-5k_d}{6(s-1)}\frac{9}{11}$$

The reduction in the unstable part of the disturbance transfer function by the factor 9/11 is a direct result of the all-pass term $(-10s+1)/(10s+1)$, since it modifies the residue at $s = 1$ by that same factor in the partial factor expansion of $G_d(s)$. Note that the improvement in H_∞ norm due to the introduction of feedforward also corresponds to the factor 9/11.

Stable all-pass terms will always reduce all residues in the RHP, and hence always reduce the size of the anti-stable part of $G_d(s)$ if there is a single unstable pole or a single pair of unstable complex conjugate poles. This covers a large fraction of the unstable system dynamics met in engineering practice. However, in general the unstable part of $G_d(s)$ may consist of several terms. The effect of all-pass terms will be different for the different unstable terms in $G_d(s)$, and it may therefore be possible for the unstable part of $G_d(s)$ to increase due to the presence of all-pass terms in the disturbance transfer function.

5. CONCLUSIONS

This paper illustrates how feedforward may be applied to reduce the input usage necessary for stabilizing unstable plants. If the disturbance transfer function is stable, one can thus easily remove the problem that disturbances may cause input saturation - with resulting loss of stabilizing feedback.

For the case of an unstable disturbance transfer function, it is clearly necessary to assume that the unstable mode is shared with the plant transfer function - otherwise it cannot be stabilized by feedback around the plant.

If the unstable pole is the only non-minimum phase term in the disturbance transfer function, feedforward has not been shown to improve on the optimal H_∞ norm achievable by feedback only. The bound on the H_∞ norm from d to u was found to apply for both 1-DOF and 2-DOF controllers in the example studied. However, if the 1-DOF controller is designed according to some other criterion than that of minimizing $\|KSG_d\|_\infty$, feedforward may be used to reduce the usage of inputs.

It is also found in an example that if the disturbance transfer function includes other non-minimum phase terms than the unstable pole, a 2-DOF controller can improve upon the optimal H_∞ norm achievable with feedback only. Feedforward may also in this case be added to a previously designed 1-DOF controller to reduce the usage of inputs.

Further work is necessary to quantify the optimal H_∞ norm from disturbance to plant input that is achievable when using a 2-DOF controller. Also, to simplify the analysis, the factor S has been ignored in (11), focusing instead on keeping $(K_f - G_d)$ small. Accounting for the factor S would lead to a *frequency weighted* Nehari extension problem. The possible benefit in accounting for this frequency weighting is not clear. In the examples studied, the optimal H_∞ norm for the 2-DOF problem has been achieved by appending feedforward (designed without accounting for the frequency weighting) to a 1-DOF controller design.

For the practising engineer, this paper points to the use of feedforward from disturbances to reduce input usage for stabilization. This may be an attractive alternative compared to alternative plant modifications in order to avoid input saturation (leading to loss of stabilizing feedback) in the face of disturbances.

ACKNOWLEDGEMENTS

This work was supported by the Research Council of Norway through grant no. 170636/V30.

REFERENCES

Favez, J.Y., Mullhaupt, P., Srinivasan, B., and Bonvin, D. (2006). Attractor region of planar linear systems with one unstable pole and saturated feedback. *Journal of Dynamical and Control Systems*, 12, 331–355.

Glover, K. (1984). All optimal hankel-norm approximations of linear multivariable systems and their l^∞ error bounds. *Int. J. Control*, 39, 1115–1193.

Glover, K. (1986). Robust stabilization of linear multivariable systems: relations to approximation. *Int. J. Control*, 43, 741–766.

Karivala, V., Skogestad, S., Forbes, J.F., and Meadows, E.S. (2005). Achievable input performance of linear systems under feedback control. *International Journal of Control*, 78, 1327–1341.

Skogestad, S. and Postlethwaite, I. (2005). *Multivariable Feedback Control. Analysis and Design.* John Wiley & Sons Ltd, Chichester, England.

Zhou, K., Doyle, J.C., and Glover, K. (1996). *Robust and Optimal Control.* Prentice-Hall, Upper Saddle River, NJ, USA.

Efficient Cooperative Distributed MPC using Partial Enumeration ⋆

Gabriele Pannocchia * **Stephen J. Wright** ** **Brett T. Stewart** ***
James B. Rawlings ***

* *Dip. Ing. Chim., Chim. Ind. e Sc. Mat. (DICCISM), Univ. of Pisa, Pisa, Italy (e-mail: g.pannocchia@ing.unipi.it)*
** *Computer Science Dept., Univ. of Wisconsin, Madison, WI, USA (e-mail: swright@cs.wisc.edu)*
*** *Chemical and Biological Engineering Dept., Univ. of Wisconsin, Madison, WI, USA (btstewart@wisc.edu, rawlings@engr.wisc.edu)*

Abstract: We discuss in this paper a novel and efficient implementation of distributed Model Predictive Control (MPC) systems for large-scale systems. The method is based on Partial Enumeration (PE), an approach that allows to compute the (sub)optimal solution of the Quadratic Program associated to the MPC problem by using a solution table that stores only a few most recently optimal active sets. This method is applied to the each local MPC system with significant improvements in terms of computational efficiency, and the original PE algorithm is modified to guarantee robust stability of the overall closed-loop system. We also discuss how input constraints that involve different units, e.g. on the summation of common utility consumption, can be appropriately handled. We illustrate the benefits of proposed method by means a simulated example comprising three units.

Keywords: Distributed MPC, Partial Enumeration, Explicit MPC, QP, Plant-wide Control

1. INTRODUCTION AND MOTIVATIONS

Model predictive control (MPC) is the most successful advanced control technique applied in the process industries (Qin and Badgwell, 2003), which nowadays tend to implement MPC systems in more and more plant units. Since units are often interconnected, it is clear that in some extent different MPCs may interfere, and depending on the steady-state and dynamic coupling of the units, these interactions may limit the overall achievable performance. From a pure theoretical point of view, the desire for optimality should push practitioners to implement a smaller number of (larger) MPC systems that encompass several units. From a practical point of view, however, the use of larger number of (smaller) MPC units may be preferred due to increased flexibility of the overall plant-wide control system, e.g. when one unit requires maintenance. Furthermore, depending on the size of the overall plant, a global centralized MPC system may simply be too large and too demanding in terms of computational resources. For these reasons, researchers are investigating so-called distributed MPC strategies, which aim to interconnect different MPC units with a minimal overhead structure and without increasing the complexity of the online problem solved by each MPC unit (Venkat et al., 2007; Dunbar, 2007; Rawlings and Stewart, 2008; Aske et al., 2008).

In the design of distributed MPC systems, several different "flavors" can be considered. The first one is the fully decentralized structure: each MPC unit optimizes its own objective function and no information regarding the computed input is exchanged among the MPC units. The second one is the so-called "non-cooperative" distributed MPC: the different units exchange their optimal input sequence, i.e. each MPC unit considers the other unit's planned input sequences in its optimal control problem. Both these approaches have no proven stability properties in closed-loop. In decentralized MPC the potential for instability comes first of all by the inherent model error induced by neglecting the interactions between different units. Furthermore in both decentralized and "non-cooperative" MPC structures, instability may arise because the different MPC systems optimize over different and competing objectives. When the closed-loop system is stable, "non-cooperative" MPC leads to a so-called Nash equilibrium point, which may be arbitrarily far away from the centralized optimum, also known as Pareto equilibrium point.

These issues are extensively discussed by Venkat et al. (2006a, 2007), who proposed the so-called "cooperative" distributed MPC architecture. In this distributed MPC system, each local controller optimizes, over its inputs, a common (overall) objective function and shares the computed optimal input sequence with all other controllers. As discussed by Venkat et al. (2006a,b), this scheme guarantees nominal stability, constraint satisfaction, and convergence towards the optimal centralized MPC solution, provided that no constraint involves coupling of inputs from different units.

In a recent paper (Pannocchia et al., 2007), we proposed for large-scale centralized MPC systems a novel online solution method called Partial Enumeration (PE) that allows fast evaluation of (a sub-) optimal solution of the MPC problem. Such method shares some ideas with Explicit MPC (Bemporad et al., 2002; Alessio and Bemporad, 2008; Baotic et al., 2008), which however is applicable only to small dimensional systems. In this paper, we investigate the use of PE for the solution of the local MPC problems with the aim of increasing the size and

⋆ This work was supported by National Science Foundation (Grant CTS-0456694)

complexity of problems that can be addressed efficiently by distributed MPC systems. A second objective of the present paper is to address the issue of coupled input constraints, which may limit the achievable performance of distributed MPC systems (Rawlings and Stewart, 2008).

2. COOPERATIVE MODEL PREDICTIVE CONTROL

2.1 Overall system, input constraints and local subsystems

We consider an overall time-invariant system (plant) in the discrete-time form:

$$x^+ = Ax + Bu, \qquad y = Cx\,, \tag{1}$$

in which $x \in \mathbb{R}^n$ and $x^+ \in \mathbb{R}^n$ are the state at a given time and at the successive time, respectively; $u \in \mathbb{R}^m$ is the input and $y \in \mathbb{R}^p$ is the output. Inputs are assumed to be constrained:

$$Du \le d\,, \tag{2}$$

in which the $d \in \mathbb{R}^q$ has non-negative components.

We assume that the plant is divided into $\mathcal{M}$ sub-systems (units), and each unit i has p_i outputs which are affected, in general, by *all* plant inputs. The objective is to design for each unit a Model Predictive Controller (MPC) that optimizes over a subset of inputs denoted with $u_i \in \mathbb{R}^{m_i}$, $i = 1, \ldots, \mathcal{M}$. The complementary input vector is denoted by $\bar{u}_i \in \mathbb{R}^{m-m_i}$. The subvectors u_i are *not* assumed to be disjoint. We define the selection matrices $T_i \in \mathbb{R}^{m_i \times m}$ and $\bar{T}_i \in \mathbb{R}^{(m-m_i)\times m}$ to be row submatrices of the identity, such that

$$u_i = T_i u, \qquad \bar{u}_i = \bar{T}_i u,$$

and thus

$$u = T_i' u_i + \bar{T}_i' \bar{u}_i\,.$$

Then, the dynamic evolution of each unit $i = 1, \ldots, \mathcal{M}$ can then described in the following form:

$$x_i^+ = A_i x_i + B_i u_i + \bar{B}_i \bar{u}_i, \qquad y_i = C_i x_i\,,$$

in which we distinguish the contribution of the inputs that belong to the $i-$th unit from the contribution of the other inputs. The subset of constraints in (2) that involve only u_i can be written as

$$D_i u_i \le d_i\,, \tag{3}$$

with D_i equal to the non-zero rows of (DT_i') and with d_i the corresponding elements of d. Similarly, the subset of constraints in (2) that involve $\bar{u}_i$ can be written as $\bar{D}_i \bar{u}_i \le \bar{d}_i$ with $\bar{D}_i$ equal to the non-zero rows of $(D\bar{T}_i')$ and with $\bar{d}_i$ the corresponding elements of d.

We consider the following assumptions.

Assumption 1. (Properties of subsystems). For each subsystem $i = 1, \ldots, \mathcal{M}$, the pair (A_i, C_i) is detectable, the pair (A_i, B_i) is stabilizable, and the inequality (3) represents *all* and *only* the constraints that involve elements of input vector u_i. The system from the input $\bar{u}_i$ to y_i is stable.

Remark 2. (Shared inputs). Notice that Assumption 1 admits the possibility that some inputs belong to more than one subsystem. It does require that all constraints involving any element of u_i can be written as constraints that do not involve elements of $\bar{u}_i$. Furthermore it assumes that inputs not belonging to unit i, $\bar{u}_i$, do not excite any unstable mode of A_i.

To clarify this point we present the following example.

Example 3. (Coupled constraints). Consider an overall system with four inputs and the following input constraint matrix and right-hand-side vector:

$$D = \left[\begin{array}{cc|cc} 1 & 0 & 0 & 0 \\ 0 & 1 & 0 & 0 \\ 0 & 0 & 1 & 0 \\ 0 & 0 & 0 & 1 \\ -1 & 0 & 0 & 0 \\ 0 & -1 & 0 & 0 \\ 0 & 0 & -1 & 0 \\ 0 & 0 & 0 & -1 \\ \hline 0 & 1 & 1 & 0 \end{array}\right], \qquad d = \begin{bmatrix} 1 \\ 1 \\ 1 \\ 1 \\ 1 \\ 1 \\ 1 \\ 1 \\ \hline 1 \end{bmatrix}.$$

The first eight rows define upper and lower bound on each input whereas the last row defines an upper bound on the sum of second and third input. Suppose that we want to design two MPCs, one of which optimizes over (u_1, u_2) whereas the other one optimizes over (u_3, u_4). Since the last constraint involve both u_2 and u_3 that, in principle, belong to different units, in order to satisfy Assumption 1, we need to include u_3 in the set of inputs for Unit 1 and u_2 in the set of inputs of Unit 2. Thus, for Unit 1 we will consider (u_1, u_2, u_3) as inputs, and for Unit 2, we will consider (u_2, u_3, u_4) as inputs.

2.2 Centralized MPC problem

To simplify the notation and given the time invariance of the system, we consider that the current decision time to be $k = 0$. Let input, state and output targets be given, and satisfy:

$$x^s = Ax^s + Bu^s, \qquad y^s = Cx^s\,.$$

Notice that such targets can be either computed by a plant-wide steady-state optimizer or as the combination of $\mathcal{M}$ local steady-state optimizers. For convenience of notation we define:

$$w = x - x^s, \qquad v = u - u^s\,.$$

We consider a finite-horizon sequence of deviation inputs $\mathbf{v} = (v(0), v(1), \ldots, v(N-1))$ and define the overall cost:

$$V(w(0), \mathbf{v}) = \frac{1}{2}\sum_{k=0}^{N-1} w(k)'Qw(k) + v(k)'Rv(k) + \frac{1}{2}w(N)'Pw(N), \qquad \text{s.t. } w^+ = Aw + Bv\,,$$

Before defining the centralized MPC optimal problem, we make the following assumptions.

Assumption 4. (Properties of overall system). The matrices Q and R are positive definite. The matrix P is the given by $P = S_s'\Pi S_s$ with Π solution to the Lyapunov equation:

$$\Pi = A_s'\Pi A_s + S_s'QS_s\,,$$

where (A_s, S_s) come from the real Schur decomposition of A:

$$A = [S_s \;\; S_u]\begin{bmatrix} A_s & A_{su} \\ 0 & A_u \end{bmatrix}\begin{bmatrix} S_s' \\ S_u' \end{bmatrix}\,,$$

and A_s contains all stable eigenvalues of A.

The centralized MPC controller solves the following problem:

$$\mathbb{P}: \qquad \min_{\mathbf{v}} V(w(0), \mathbf{v}) \qquad \text{s.t.}$$
$$Dv \le d - Du^s, \quad S_u'w(N) = 0\,. \tag{4}$$

Remark 5. The constraint $Dv \le d - Du^s$ is equivalent to $Du \le d$. The terminal constraint $S_u'w(N) = 0$ is present only if the system is open-loop unstable (or integrating) and is needed to zero the unstable modes at the end of the horizon N. Furthermore, the cost function term $\frac{1}{2}w(N)'Pw(N)$ represents the infinite horizon cost-to-go when $v(k) = 0$ for $k \ge N$.

2.3 Distributed cooperative MPC subproblems

Let $\bar{\mathbf{v}}_i$ be a known sequence (in deviation variables) of the inputs that do not belong to Unit i, and define the control problem solved by the $i-$th MPC controller as follows:

$$\mathbb{P}_i: \quad \min_{\mathbf{v}} V(w(0),\mathbf{v}) \qquad \text{s.t.}$$
$$Dv \le d - Du^s, \quad S_u' w(N) = 0, \quad \bar{\mathbf{T}}_i \mathbf{v} = \bar{\mathbf{v}}_i\,, \quad (5)$$

in which $\bar{\mathbf{T}}_i \in \mathbb{R}^{(m-m_i)N \times mN}$ is the block diagonal matrix formed with $\bar{T}_i$, $i = 1,\dots,\mathcal{M}$. Similarly, later we use $\mathbf{T}_i \in \mathbb{R}^{m_i N \times mN}$ to denote the block diagonal matrix formed with blocks equal to T_i. We denote with $\tilde{\mathbf{v}}_i$ the solution to (5).

Remark 6. The last equality constraint enforces the inputs that do not belong to Unit i to be equal to the known value $\bar{\mathbf{v}}_i$.

The problem $\mathbb{P}_i$ (5) contains a large number of decision variables that are fixed, namely, all inputs of the other units. We can eliminate these inputs and reformulate this problem as follows. Let the deviation input sequence $\mathbf{v}$ be expressed as

$$\mathbf{v} = \mathbf{T}_i' \mathbf{v}_i + \bar{\mathbf{T}}_i' \bar{\mathbf{v}}_i\,, \quad (6)$$

in which $\mathbf{v}_i = \mathbf{T}_i \mathbf{v}$ is the sequence of inputs that belong to Unit i, and $\bar{\mathbf{v}}_i = \bar{\mathbf{T}}_i \mathbf{v}$ is the sequence of complementary inputs. We can now write the local control problem as:

$$\mathbb{P}_i: \quad \min_{\mathbf{v}_i} V(w(0),\mathbf{v}) \qquad \text{s.t. (6) and}$$
$$D_i v_i \le d_i - D_i u_i^s, \quad S_u' w(N) = 0\,. \quad (7)$$

Remark 7. We note that in (7) we consider only constraints for the inputs of Unit i, and constraints for the other inputs are assumed to be satisfied, i.e. $\bar{D}_i \bar{v}_i \le \bar{d}_i - \bar{D}_i \bar{u}_i^s$. Moreover, the terminal state constraint may contain equations that are not affected by $\mathbf{v}_i$, and such constraints can be eliminated.

2.4 Algorithm and properties

In distributed MPC, each local MPC unit optimizes and communicates its solution with other MPC units, forming a convex combination of the all $\mathcal{M}$ unit solutions to obtain an overall solution. If decision time permits, this procedure is repeated iteratively until convergence or until a specified maximum number of iterations is reached. The distributed MPC algorithm is initiated with an overall input sequence computed at the previous decision time, as follows:

$$\mathbf{v}^0 = (u^*(1) - u^s, \dots, u^*(N-1) - u^s, 0)\,, \quad (8)$$

in which we emphasize that the terms $u^*(\cdot)$ are the components of the (sub)optimal sequence computed at the previous decision time, whereas u^s is the input target at the current decision time.

Remark 8. Such initial sequence is feasible with respect to the input constraint $Dv \le d - Du^s$, and it is also feasible for the terminal constraint $S_u' w(N) = 0$ if it exists, provided the target has not changed from the previous decision time.

We now describe the distributed cooperative MPC algorithm.

Algorithm 1. (Distributed Cooperative MPC). Data: current target (u^s, x^s), deviation state $w(0) = x - x^s$, an overall initial sequence $\mathbf{v}^0$ as in (8). Relative tolerance parameter ρ, maximum number of iterations $l_{\max}$.

(1) (Local MPC problems) Set $l = 1$ and for each MPC unit i repeat the following steps:
   (a) Define $\bar{\mathbf{v}}_i = \bar{\mathbf{T}}_i \mathbf{v}^{l-1}$, solve problem $\mathbb{P}_i$. Let $\mathbf{v}_i$ be the optimal solution to $\mathbb{P}_i$.
   (b) Construct the "complete" solution obtained by Unit i: $\tilde{\mathbf{v}}_i = \mathbf{T}_i' \mathbf{v}_i + \bar{\mathbf{T}}_i' \bar{\mathbf{v}}_i$.

(2) (Convex Step) Define the "overall" solution as combination of the local solutions $\mathbf{v}^l = \sum_{i=1}^{\mathcal{M}} \lambda_i \tilde{\mathbf{v}}_i$, with $\lambda_i > 0$ and $\sum_{i=1}^{\mathcal{M}} \lambda_i = 1$.

(3) (Convergence Test) If $\frac{\|\mathbf{v}^l - \mathbf{v}^{l-1}\|}{1+\|\mathbf{v}^{l-1}\|} < \rho$ or $l = l_{\max}$, set $\mathbf{v}^* = \mathbf{v}^l$ and stop. Otherwise, increase $l \leftarrow l + 1$ and go to 1.

It is possible to show that such cooperative MPC algorithm converges to the optimal centralized solution in the limit of infinite iterations. Furthermore, we can establish closed-loop stability for any finite number of iterations l.

3. PARTIAL ENUMERATION

3.1 Introduction

Both the centralized problem $\mathbb{P}$ and each problem $\mathbb{P}_i$ can be written as convex Quadratic Programs, and for small to medium scale systems, the solution can be computed efficiently using either Active Set Method (ASM) or Interior Point Method (IPM) solvers (Rao et al., 1998; Bartlett et al., 2002; Milman and Davison, 2003). However, as the system dimension increases, online solvers cannot provide a solution within an acceptable decision time. In order to compute a (suboptimal) solution for large-scale systems that are currently out of the range of QP solvers, we recently proposed an approach called Partial Enumeration (Pannocchia et al., 2007). In Partial Enumeration (PE) we use a solution table that stores a (small) number of optimal active sets and the associated piecewise linear solution (Bemporad et al., 2002). This approach was applied to large-scale centralized MPC problems in (Pannocchia et al., 2007) with average speed-up factors of 80-200 times compared to conventional QP solvers, and with small closed-loop suboptimality. We review PE here and make appropriate modifications for applying it to the distributed MPC problem $\mathbb{P}_i$.

3.2 PE algorithm and properties

We first consider the centralized MPC problem $\mathbb{P}$ and write it as a parametric QP as follows:

$$\min_{\mathbf{v}} \frac{1}{2}\mathbf{v}'\mathbf{H}\mathbf{v} + \mathbf{v}'\mathbf{G}w(0) + \frac{1}{2}w(0)'\mathbf{P}w(0) \qquad \text{s.t.} \quad (9a)$$
$$\mathbf{D}\mathbf{v} + \mathbf{C}u^s \le \mathbf{d}, \quad \mathbf{E}\mathbf{v} + \mathbf{F}w(0) = 0. \quad (9b)$$

Note that $z = [w(0)', \ u^{s\prime}]'$ is the parameter that changes at each decision time point, while all other terms are constant and omitted in the sake of space.

Given a point $\mathbf{v}^*$, we denote by $(\mathbf{D}_a, \mathbf{C}_a, \mathbf{d}_a)$ the stacked rows of $(\mathbf{D}, \mathbf{C}, \mathbf{d})$ such that $\mathbf{D}_a\mathbf{v}^* + \mathbf{C}_a u^s = \mathbf{d}_a$ (i.e. the active constraints). We also denote with $(\bar{\mathbf{D}}_a, \bar{\mathbf{C}}_a, \bar{\mathbf{d}}_a)$ the complementary stacked rows, i.e. such that $\bar{\mathbf{D}}_a\mathbf{v}^* + \bar{\mathbf{C}}_a u^s < \bar{\mathbf{d}}_a$ (i.e. the inactive constraints). Next, we define:

$$\mathcal{G} = [\mathbf{G} \ 0]\,, \quad \mathcal{A} = \begin{bmatrix}\mathbf{D}_a \\ \mathbf{E}\end{bmatrix}, \quad \mathcal{B} = \begin{bmatrix}0 & \mathbf{C}_a \\ \mathbf{F} & 0\end{bmatrix}, \quad \mathbf{b} = \begin{bmatrix}\mathbf{d}_a \\ 0\end{bmatrix}.$$

In order for $\mathbf{v}^*$ to be optimal for (9), the following first-order optimality KKT conditions must hold:

$$\mathbf{H}\mathbf{v}^* + \mathcal{G}z + \mathcal{A}'\lambda^* = 0, \quad (10a)$$
$$\mathcal{A}\mathbf{v}^* + \mathcal{B}z = \mathbf{b}, \quad (10b)$$
$$\lambda_j^* \ge 0, \qquad j \in \{\text{indices of active inequalities}\}, \quad (10c)$$
$$\bar{\mathbf{D}}_a\mathbf{v}^* + [0 \ \bar{\mathbf{C}}_i]z \le \bar{\mathbf{d}}_a. \quad (10d)$$

We now solve the system (10) to derive $\mathbf{v}^*$ as a linear function of the parameter z and we derive the conditions on z for which the considered active set is optimal. To this aim, several

approaches can be followed, and in this paper we use the so-called Null-Space method.

Let $\mathcal{Z}$ be a full rank matrix such $\mathcal{A}\mathcal{Z} = 0$, and consider the point $\mathbf{v}_0 = \mathcal{A}^+(\mathbf{b} - \mathcal{B}z)$, which $\mathcal{A}^+$ is the pseudo-inverse of $\mathcal{A}$. We can express any point that is feasible for (10b) as $\mathbf{v} = \mathbf{v}_0 + \mathcal{Z}p$ and thus rewrite (10a) as follows:

$$\mathbf{H}\mathcal{Z}p + \mathbf{H}\mathbf{v}_0 + \mathcal{G}z + \mathcal{A}'\lambda^* = 0\,.$$

Next, we multiply (on the left) by $\mathcal{Z}'$ (to eliminate the term $\mathcal{Z}'\mathcal{A}'\lambda^*$) and solve for p to obtain

$$\begin{aligned} p &= \left(\mathcal{H}^{-1}(\mathcal{Z}'\mathbf{H}\mathcal{A}^+\mathcal{B} - \mathcal{Z}'\mathcal{G})\right) z - \mathcal{H}^{-1}(\mathcal{Z}'\mathbf{H}\mathcal{A}^+)\mathbf{b} \\ &= \mathbf{\Gamma}_p z + \gamma_p\,, \end{aligned}$$

with $\mathcal{H} = \mathcal{Z}'\mathbf{H}\mathcal{Z}$. Finally, we compute $\mathbf{v}^*$ as follows:

$$\begin{aligned} \mathbf{v}^* &= \mathbf{v}_0 + \mathcal{Z}p = \mathcal{A}^+(\mathbf{b} - \mathcal{B}z) + \mathcal{Z}(\mathbf{\Gamma}_p z + \gamma_p) \\ &= \mathbf{\Gamma} z + \gamma\,. \end{aligned} \tag{11}$$

Now (10a) can be solved for λ^* as follows:

$$\lambda^* = -(\mathcal{A}')^+(\mathbf{H}\mathbf{v}^* + \mathcal{G}z) = -(\mathcal{A}')^+(\mathbf{H}\mathbf{\Gamma} + \mathcal{G})z - (\mathcal{A}')^+\mathbf{H}\gamma.$$

Finally, we write the Primal and Dual inequalities (10c) and (10d) as follows:

$$\begin{bmatrix} \bar{\mathbf{D}}_a\mathbf{\Gamma} + [0\ \bar{\mathbf{C}}_a] \\ [I\ 0]\,(\mathcal{A}')^+(\mathbf{H}\mathbf{\Gamma} + \mathcal{G}) \end{bmatrix} z \le \begin{bmatrix} \bar{\mathbf{d}}_a - \bar{\mathbf{D}}_a\gamma \\ -[I\ 0]\,(\mathcal{A}')^+\mathbf{H}\gamma \end{bmatrix},$$

or more concisely as

$$\begin{bmatrix} \mathbf{\Psi}_P \\ \mathbf{\Psi}_D \end{bmatrix} z \le \begin{bmatrix} \psi_P \\ \psi_D \end{bmatrix}. \tag{12}$$

Furthermore, by inserting the solution (11) into the objective function of (9), we can write the optimal cost for the current active set as: $V^*(z) = \frac{1}{2}z'V_2z + V_1z + V_0$.

In Partial Enumeration we store $(\mathbf{\Psi}_P, \mathbf{\Psi}_D, \mathbf{\Gamma})$, (ψ_P, ψ_D, γ), and also (V_0, V_1, V_2), for a fixed number of active sets that were optimal in the most recent decision time points. Online we scan the table to check if, for the given parameter z, optimality conditions (12) are satisfied, and in such case compute the optimal solution from (11). However, given the fact that not all possible optimal active sets are stored, it is possible that no entry in the table is optimal. In such cases it is necessary to compute a suboptimal solution for closed-loop control. Nonetheless, a QP solver is called afterwards to compute the optimal solution $\mathbf{v}^*$, and thus derive the matrices/vectors $(\mathbf{\Psi}_P, \mathbf{\Psi}_D, \mathbf{\Gamma})$, (ψ_P, ψ_D, γ), (V_0, V_1, V_2) for the corresponding optimal active sets. Whenever this table entry becomes available, it is inserted into the table. When the table exceeds its maximum size (defined by the user), we delete the entry that was optimal least recently. Thus, the table size is fixed and hence the table lookup process is fast, but the table entries are updated to keep track of new operating conditions for the plant.

In order to compute a suboptimal input sequence when the table does include the optimal active set for the current parameter z several options can be considered. It is important to ensure that the given suboptimal solution guarantees, at least, nominal closed-loop stability, and this can be obtained if we ensure a cost decrease from the previous decision time point. Here, we propose a procedure that allows us to prove robust stability of the closed-loop under PE MPC. The procedure requires two points, the first one which needs to be feasible and its computation is discussed later in Algorithm 2. The second point, instead, is a particular minimizer of (9a) subject to the equality constraint (if present) and all the input inequalities that are active at the target point. More specifically, given the input target u^s, let $(\bar{\mathbf{D}}, \bar{\mathbf{d}})$ denote the subset of rows of $(\mathbf{D}, \mathbf{d})$ such that $\bar{\mathbf{C}}u^s = \bar{\mathbf{d}}$. We define $\hat{\mathbf{v}}$ as the solution to:

$$\min_{\mathbf{v}} V(w(0), \mathbf{v}) \text{ s.t. } \bar{\mathbf{D}}\mathbf{v} = 0,\ \mathbf{E}\mathbf{v} + \mathbf{F}w(0) = 0\,. \tag{13}$$

We can show that $\hat{\mathbf{v}} = \hat{\mathbf{\Gamma}}(u^s)w(0)$, where the dependence of the matrix $\hat{\mathbf{\Gamma}}$ on u^s comes from the fact that u^s defines $(\bar{D}, \bar{d})$.

In the following, we denote by $\mathbf{v}^0 = (u^*(1) - u^s, \ldots, u^*(N-1) - u^s, 0)$ the previous shifted optimal sequence, where the inputs $(u(1)^*, \ldots, u^*(N-1))$ were computed at the previous decision time, while u^s is the current input target.

Algorithm 2. (Partial Enumeration). Data: table with M entries, each comprising the terms $(\mathbf{\Psi}_P, \mathbf{\Psi}_D, \mathbf{\Gamma})$, (ψ_P, ψ_D, γ), (V_0, V_1, V_2); current parameter $z = [w(0)',\ u^{s\prime}]'$; candidate sequence $\mathbf{v}^0$ and its cost V^0 if feasible (otherwise $V^0 = \infty$); maximum table size $M_{\max}$. Output: Input sequence $\mathbf{v}^*$ and updated table. Set $j = 0$, $\tilde{V} = V^0$, $\tilde{\mathbf{v}} = \mathbf{v}^0$.

(1) (Table scanning.) Set $j \leftarrow j+1$. If $j > M$ and $\tilde{\mathbf{v}}$ is feasible go to 4. If $j > M$ and $\tilde{\mathbf{v}}$ is infeasible go to 3. Otherwise, perform the following steps for the $j-$th entry:
   (a) If $\mathbf{\Psi}_P z \le \psi_P$ does not hold, go to 1. Otherwise,
   (b) If $\mathbf{\Psi}_D z \le \psi_D$ holds go to 2. Otherwise,
   (c) Compute the cost V. If $V < \tilde{V}$, set $\tilde{\mathbf{v}} = \mathbf{\Gamma}_u(\mathbf{d}_a - \mathbf{C}_a u^s) + \mathbf{\Gamma}_w w(0)$. Go to 1.

(2) (Optimal solution found.) Compute the optimal solution $\mathbf{v}^*$. Inject the optimal input. Put this entry in first position of the table. Stop.

(3) (Feasibility recovery; arrive at this step only if $\tilde{\mathbf{v}}$ is not feasible.) Solve the LP

$$\min_{\mathbf{q},\mathbf{s}} \mathbf{1}'(\mathbf{q} + \mathbf{s}) \qquad \text{s.t. } \mathbf{D}(\mathbf{q} - \mathbf{s}) \le \mathbf{r}_1,$$
$$\mathbf{E}(\mathbf{q} - \mathbf{s}) = \mathbf{r}_2, \quad \mathbf{q} \ge 0, \quad \mathbf{s} \ge 0$$

where $\mathbf{r}_1 = \mathbf{d} - \mathbf{C}u^s - \mathbf{D}\tilde{\mathbf{v}}$, $\mathbf{r}_2 = -\mathbf{F}w(0) - \mathbf{E}\tilde{\mathbf{v}}$, and $\mathbf{1}$ is the vector of ones. Redefine $\tilde{\mathbf{v}} \leftarrow \tilde{\mathbf{v}} + \mathbf{q} - \mathbf{s}$ and compute its cost $\tilde{V}$.

(4) (Solution improvement; $\tilde{\mathbf{v}}$ is feasible at this point.) Evaluate $\hat{\mathbf{v}}$, and compute the largest $t \in [0, 1]$ such that $\mathbf{D}(\hat{\mathbf{v}} - \tilde{\mathbf{v}})t \le \mathbf{d} - \mathbf{C}u^s - \mathbf{D}\tilde{\mathbf{v}}$. Set $\mathbf{v}^* = \tilde{\mathbf{v}}(1-t) + t\hat{\mathbf{v}}$.

(5) (Table update, performed in parallel.) Solve the QP (9), and find the terms $(\mathbf{\Psi}_P, \mathbf{\Psi}_D, \mathbf{\Gamma})$, (ψ_P, ψ_D, γ), (V_0, V_1, V_2) for the optimal active set. Insert this entry in first position of the table, set $M \leftarrow M+1$. If $M = M_{\max}+1$, delete the entry that was optimal least recently, and set $M = M_{\max}$.

Remark 9. The "feasibility recovery" step 3 is required *only if* the system is open-loop unstable *and* either the target changed from the previous decision time or a disturbance occurred. In the nominal case without target change, such step is not performed because $\mathbf{v}^0$ is always feasible. Step 3 is the only "expensive" computation in Algorithm 2 and is justified by closed-loop stability reasons of an open-loop unstable plant. For input bound constraints (i.e., $u_{\min} \le u \le u_{\max}$) further simplifications that allow increased speedup and lower sub optimality can be considered.

It can be shown that PE MPC is nominally stabilizing and robustly stabilizing for sufficiently small measurement noise and additive disturbances (Pannocchia et al., 2009).

3.3 Application of Partial Enumeration to cooperative MPC

Each $\mathbb{P}_i$ in (7) can be written as the following parametric QP:

Table 1. Outputs and inputs of the three units, according to two design schemes: Design A (existing), Design B (optimal).

	Outputs	Inputs	
		Design A	Design B
Unit 1	(y_1, y_2, y_3)	(u_1, u_2, u_3)	$(u_1, u_2, u_3, u_4, u_8)$
Unit 2	(y_4, y_5, y_6)	(u_4, u_5, u_6)	$(u_3, u_4, u_5, u_6, u_8)$
Unit 3	(y_7, y_8)	(u_7, u_8)	(u_3, u_4, u_7, u_8)

$$\min_{\mathbf{v}_i} \frac{1}{2}\mathbf{v}_i'\mathbf{H}_i\mathbf{v}_i + \mathbf{v}_i'\mathcal{G}_i z_i + \frac{1}{2} z_i \mathbf{P}_i z_i \qquad \text{s.t.} \qquad (14a)$$

$$\mathbf{D}_i\mathbf{v}_i + \mathbf{C}_i z_i \leq \mathbf{d}, \quad \mathbf{E}_i\mathbf{v}_i + \mathbf{F}_i z_i = 0\,, \qquad (14b)$$

in which $z_i = [z',\ \bar{\mathbf{v}}_i']'$ is the parameter augmented with the sequence of inputs that do not belong to Unit i, and $\mathbf{H}_i = \mathbf{T}_i\mathbf{H}\mathbf{T}_i'$, $\mathcal{G}_i = \begin{bmatrix}\mathcal{G} & \mathbf{T}_i\mathbf{H}\bar{\mathbf{T}}_i'\end{bmatrix}$, $\mathbf{P}_i = \begin{bmatrix}\mathbf{P} & 0 \\ 0 & 0 & \mathcal{G}'\bar{\mathbf{T}}_i' \\ \bar{\mathbf{T}}_i\mathcal{G} & \bar{\mathbf{T}}_i\mathbf{H}\bar{\mathbf{T}}_i'\end{bmatrix}$, $\mathbf{D}_i = \mathbf{D}\mathbf{T}_i'$, $\mathbf{C}_i = \begin{bmatrix}0 & \mathbf{C} & \mathbf{D}\bar{\mathbf{T}}_i'\end{bmatrix}$, $\mathbf{E}_i = \mathbf{E}\mathbf{T}_i'$, $\mathbf{F}_i = \begin{bmatrix}\mathbf{F} & 0 & \mathbf{E}\bar{\mathbf{T}}_i'\end{bmatrix}$. Notice that several rows of $\mathbf{D}_i$ and $\mathbf{E}_i$ are zero and can be deleted along with the corresponding rows of $\mathbf{C}_i$ and $\mathbf{F}_i$.

We notice that the QP (14) is in the same form of (9), with the main difference that the parameter z is augmented with the known sequence of inputs not belonging to Unit i. Given this increase in dimensionality, a full explicit MPC is impractical even for small systems. On the other hand, PE Algorithm 2 can be readily applied to solve (14). Since PE does not guarantee that each $\mathbb{P}_i$ is solved exactly, no convergence to the optimal centralized solution can be proved. Nonetheless, we can show closed-loop nominal stability and robust stability for sufficiently small disturbances.

4. APPLICATION EXAMPLE

4.1 Overall system and units definition

As an example, we consider a stable system with 8 inputs, 8 outputs and 48 states, whose details are omitted in the sake of space. Each input of the system is constrained in $[-1, 1]$, and the following coupled constraint holds:

$$[0\ 0\ 0\ 1\ 1\ 0\ 0\ 1]\, u \leq 1\,. \qquad (15)$$

In the MPC design we use: $Q = I$, $R = I$, and $N = 30$.

We consider that this overall plant is divided in three units. Outputs and inputs of each unit are reported in Table 1, where we emphasize two different design schemes. In Design A, which can be regarded as the existing scheme for this plant, no inputs belong to more than one unit at a time. However, because of the coupled constraint (15), such input partition scheme does not satisfy Assumption 1. Therefore, for such scheme convergence to the optimal centralized solution cannot be guaranteed. For this reason, we consider an alternative input partition scheme (Design B) in which the inputs (u_3, u_4, u_8) belong to all three units.

4.2 Effect of coupled constraints

First of all we investigate about the different convergence properties for the two distributed MPC architectures. We consider that at decision time 10, the input target changes from 0 to $u^s = (0, 0, 0.5, 0.2, 0, 0, 0, 0.3)'$, thus making the coupled constraint active. We report in Figure 1 the closed-loop response of $u_3 + u_4 + u_8$ obtained by three controllers: CMPC is the centralized controller, DMPC-A is the distributed control structure with $l = 1$ iteration based on Design A, DMPC-B is the distributed control structure with $l = 1$ iteration based on Design B. For this study, we solve the optimal control problems exactly, i.e. we do not use Partial Enumeration. We report in Table 2, the suboptimality of DMPC-A and DMPC-B as the number of iterations l increases, defined by the index:

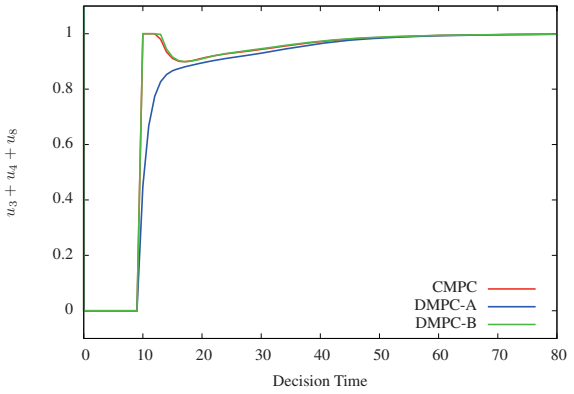

Fig. 1. Effect of coupled input constraints: closed-loop response of $u_3+u_4+u_8$ for centralized MPC (CMPC), distributed cooperative MPC based on Design A (DMPC-A), distributed cooperative MPC based on Design B (DMPC-B). Both DMPC-A and DMPC-B make $l = 1$ iteration.

Table 2. Suboptimality of DMPC-A and DMPC-B for different number of iterations l.

Dec. MPC	S_I			
	$l = 1$	$l = 5$	$l = 10$	$l = 50$
DMPC-A	22.9	0.885	0.682	0.673
DMPC-B	2.29	$4.86 \cdot 10^{-2}$	$5.43 \cdot 10^{-4}$	$1.53 \cdot 10^{-8}$

$$S_I = 100\frac{V_{CL} - V_{CL}^*}{V_{CL}}\,,$$

in which V_{CL} is the closed-loop cost for the considered (distributed) controller and V_{CL}^* is the closed-loop cost for the optimal centralized controller. As expected DMPC-B handles the coupled constraint much better than DMPC-A, and as the number of iterations increases, DMPC-B converges to the optimal centralized MPC solution, whereas the suboptimality index for DMPC-A does not go to zero.

4.3 Comparison of PE-based and QP-based distributed MPC

We now present the results for several decentralized controllers that solve the local MPC problems $\mathbb{P}_i$ either via PE or via an exact (active set) QP solver. We are interested in assessing the suboptimality of each scheme, as well as the computational efficiency quantified by the two indices [1] :

- Average Speed Factor: $A_{SF} = \frac{T_{\text{aver}}^*}{T_{\text{aver}}}$ where T_{aver}^* is the average CPU time required to solve the centralized problem $\mathbb{P}$ via QP solver, and T_{aver} is the average CPU time required to compute the solution using Algorithm 1 (either via PE or via exact QP solver).
- Worst Case Speed Factor: $W_{SF} = \frac{T_{\max}^*}{T_{\max}}$, where $T_{\max}^*$ and $T_{\max}$ are the maximum CPU times for the centralized (QP based) problem $\mathbb{P}$ and for the distributed Algorithm 1 (PE or QP based), respectively.

[1] All computations are performed using GNU Octave on a Pentium-M (1.86 GHz, 1 GB RAM) running Linux.

Table 3. Comparison of suboptimality and computational efficiency for several DMPC-B, based on PE or exact QP solver

	QP based			PE based		
Iter.	S_I	A_{SF}	W_{SF}	S_I	A_{SF}	W_{SF}
$l = 1$	14.7	5.24	12.1	14.8	93.5	285
$l = 5$	0.604	1.25	4.66	0.612	22.0	66.7
$l = 10$	0.0408	0.797	2.37	0.0490	13.9	34.4

We consider a closed-loop simulation of 5000 decision time points, in the presence of random output noise, affecting the state estimate and the target at each decision time, and 14 large target changes. When PE is used, each MPC unit deploys an initially empty table of maximum dimension $M_{\max} = 10$. The results are summarized in Table 3. We can observe, first of all, that as number of iterations l increases, DMPC-B converges to the centralized optimum performance, as indicated by the negligible suboptimality index S_I. Next, we can see that for a given number of iterations l, the suboptimality index obtained by solving the local problems with the QP solver is essentially equal to that obtained with the PE solver. However, the computational requirements using QP and PE solvers are remarkably different. If we compare the distributed controllers using the same number of iterations, DMPC-B based on local PE solvers can compute the solution 17–18 times faster (on average), 14–24 times faster (worst case) than the corresponding DMPC-B based on local QP solvers. In practice, since the time allowed for computation of local solutions and iterations among the distributed controllers may be regarded as fixed, the goal of using local PE solvers is that we can allow more iterations and thus (almost) achieve the centralized optimal performance. If compared with the centralized MPC, most of the computational benefits of using DMPC-B based on PE solvers are achieved with a limited number of iterations, e.g. $l = 5$, which allows one to obtain a suboptimality less than 1% with an average speedup factor of 22 and a worst case speedup factor of 67.

A final remark can be made regarding the possible (apparent) overlap of applicability and scope of Partial Enumeration and distributed MPC, i.e. as alternative means for solving MPC problems in large-scale systems. We want to stress that the main motivation for distributed MPC is organizational rather than computational and, in fact, if the number of iterations l is increased the distributed MPC architecture (based on QP solvers) may be even more time consuming than a centralized MPC architecture (notice the average "speedup" factor less than 1 for DMPC-B based on QP with $l = 10$ iterations). Therefore, distributed MPC should not be considered as a possible competitor of Partial Enumeration centralized MPC which, on the other hand, is motivated by computational issues.

5. CONCLUSIONS

We proposed in this paper an efficient implementation for distributed cooperative Model Predictive Control. The approach is based on Partial Enumeration, that solves the Quadratic Program associated to the MPC problem by means of a small solution table, which includes the most recently optimal active sets. If the optimal solution is not found in the table, a quick suboptimal solution is computed for closed-loop control. In parallel, the optimal active set is evaluated and inserted into the table, possibly deleting the least recently optimal active set. In this way the size of the table is kept small, thus limiting the required time for scanning it. We applied such approach for the solution of "local" MPC problems that are solved in each unit of a distributed MPC system. We also revised the cooperative distributed MPC architecture to optimally handle the case of coupled input constraints. Finally, we presented a simulation example of an 8 input 8 output plant comprising three units in which we achieved relevant speedup factors and negligible suboptimality compared to QP-based MPC.

REFERENCES

Alessio, A. and Bemporad, A. (2008). A survey on explicit model predictive control. In *Proceedings of the International Workshop on Assessment and Future Directions of NMPC*. Pavia, Italy.

Aske, E.M.B., Strand, S., and Skogestad, S. (2008). Coordinator mpc for maximizing plant throughput. *Comp. Chem. Eng.*, 32, 195–204.

Baotic, M., Borrelli, F., Bemporad, A., and Morari, M. (2008). Efficient on-line computation of constrained optimal control. *SIAM J. Control Optim.*, 47, 2470–2489.

Bartlett, R.A., Biegler, L.T., Backstrom, J., and Gopal, V. (2002). Quadratic programming algorithms for large-scale model predictive control. *Journal of Process Control*, 12(7), 775–795.

Bemporad, A., Morari, M., Dua, V., and Pistikopoulos, E.N. (2002). The explicit linear quadratic regulator for constrained systems. *Automatica*, 38, 3–20.

Dunbar, W.B. (2007). Distributed receding horizon control of dynamically coupled nonlinear systems. *IEEE Trans. Auto. Contr.*, 52, 1249–1263.

Milman, R. and Davison, E.J. (2003). Fast computation of the quadratic programming subproblem in model predictive control. In *Proceedings of the American Control Conference*, 4723–4729.

Pannocchia, G., Rawlings, J.B., and Wright, S.J. (2007). Fast, large-scale model predictive control by partial enumeration. *Automatica*, 43(5), 852–860.

Pannocchia, G., Wright, S.J., and Rawlings, J.B. (2009). On the robust stability of partial enumeration model predictive control. *In preparation*.

Qin, S.J. and Badgwell, T.A. (2003). A survey of industrial model predictive control technology. *Contr. Eng. Pract.*, 11, 733–764.

Rao, C., Wright, S.J., and Rawlings, J.B. (1998). Application of interior-point methods to model predictive control. *J. Optim. Theory Applic.*, 99, 723–757.

Rawlings, J.B. and Stewart, B.T. (2008). Coordinating multiple optimization-based controllers: New opportunities and challanges. *J. Proc. Contr.*, 18, 839–845.

Venkat, A.N., Rawlings, J.B., and Wright, S.J. (2006a). Stability and optimality of distributed, linear MPC. Part 1: state feedback. Technical Report 2006–03, TWMCC, Department of Chemical and Biological Engineering, University of Wisconsin–Madison (Available at http://jbrwww.che.wisc.edu/tech-reports.html).

Venkat, A.N., Rawlings, J.B., and Wright, S.J. (2006b). Stability and optimality of distributed, linear MPC. Part 2: output feedback. Technical Report 2006–04, TWMCC, Department of Chemical and Biological Engineering, University of Wisconsin–Madison (Available at http://jbrwww.che.wisc.edu/tech-reports.html).

Venkat, A.N., Rawlings, J.B., and Wright, S.J. (2007). Distributed model predictive control of large-scale systems. In *Assessment and Future Directions of Nonlinear Model Predictive Control*, 591–605. Springer.

Optimality of Process Networks. ⋆

Michael R. Wartmann * **B. Erik Ydstie** *

* *Department of Chemical Engineering, Carnegie Mellon University, Pittsburgh, USA (e-mail: wartmann@cmu.edu, ydstie@cmu.edu).*

Abstract: In this paper we show that conservation laws for extensive quantities and the second law of thermodynamics lead to conditions for stability and optimality of a process network. Interconnections among nodes are represented through connectivity matrices and network graphs. A generalized version of Tellegen's theorem from electrical circuit theory plays a central role in deriving the objective function of the regarded dynamic process networks. The application of irreversible thermodynamics lead to stability and optimality results based on the co-content and content of the regarded process networks. The principle is illustrated in a pipeflow example.

Keywords: dissipation, network theory, irreversible thermodynamics, distributed control, passivity theory.

1. INTRODUCTION

The complexity of process systems arises from the variety of how simple subunits are connected (Hangos et al. (1999)). A crucial component in modeling process systems is therefore to understand how connections between the subunits lead to complex system behavior. Ydstie and Alonso (1997) developed a theoretical framework providing a link between passivity theory and physics using the second law of thermodynamics. They discussed the need to develop passivity based control techniques which focus on input-output properties of the systems. An understanding for complex behavior can then be derived from macroscopic thermodynamic constraints instead of microscopic equations and the complexity that results from using very detailed models can be reduced. Jillson and Ydstie (2007) developed a topological result similar to Tellegen's theorem of electrical circuit theory and passivity theory to derive sufficient conditions under which a network is stabilized using decentralized feedback. The theory shows that it is possible to control very complex networks of process systems without actually modeling the thermodynamics and kinetics explicitly. This is due to inherent passivity properties that follow from the second law of thermodynamics. The conditions for passivity can be checked in a distributed manner. In this work, we will explore if similar ideas can be applied for optimization.

We extend the approaches in Ydstie and Alonso (1997); Jillson and Ydstie (2007) to provide an organizational framework for treating complex process systems concerning optimality using ideas from network theory. The formalism of network theory has been particularly successful for modeling and control of dynamic systems in electrical engineering applications. Classically, electrical circuit theory is not considered an application of non-equilibrium thermodynamics. Nevertheless, electrical circuits are typical irreversible thermodynamic systems. The formalism developed in electrical circuit theory was extended to general thermodynamic systems by Oster et al. (1971); Peusner (1986). In particular the application to complex biological systems has been carried out successfully by Oster and Desoer (1971); Mickulecky (2001). In this paper, we apply the formalism of network theory to describe connected process systems. Network theory brings thermodynamics a degree of mathematical rigor and allows to unify ideas from non-equilibrium thermodynamics, dynamic system theory and control. In the context of dissipativity of process systems, network theory facilitates the extension of irreversible thermodynamics by the system's topological description which is an important part of the dynamic behavior. Looking at mathematical models of many dynamic physical systems, we can identify a certain inherent structure. We can separate the network model into a kinematic structure which addresses the topology of the system and a dynamical structure (Oster and Desoer (1971)). The connectivity properties of the system describe the physical processes where the dynamical structure defines the relationships between the state variables. The paper is organized as follows: In Section 2, we define the type of process systems and describe the connection to network theory, in Section 3, we describe fundamental topological properties of the regarded process networks. In Section 4 and 5, we elaborate the concepts of stability and optimality for the regarded systems and present a pipeflow example to illustrate our findings in Section 6.

⋆ This work was supported by the Center for Integrated Operations in the Petroleum Industry, Trondheim, Norway.

2. PROCESS NETWORKS

Process networks are written as a collection of interconnected sub-systems

$$\dot{x}_i = F(x_i) + \sum_{j=0, j\neq i}^{n} G(u_i, x_i, x_j), \quad i = 0, ..., n \tag{1}$$

$$y_i = H(x_i) \tag{2}$$

x_i is the state of subsystem i and $x_i(0)$ is the initial condition. The function F describes the unforced motion of the system, the function G describes how the system is

connected with other sub-systems, and the output function H relates the state of the system to the measurement functions y_i. The functions u_i represent the manipulated variables. The functions F, G, H are all differentiable at least once. The state of the entire network is given by the vector $x = (x_0^T, x_1^T, ..., x_n^T)^T$.

Subscript zero refers to the reference (exo-) system. Often we are not interested in the dynamics of the exo-system, or more likely, it is too complex to model. The process system is modeled as the reduced system without the reference sub-system. Its state is given by the vector $x = (x_1^T, ..., x_n^T)^T$. The interactions with the exo-system are then established through the boundary conditions.

The network form, as illustrated in Figure 1 is convenient when we model systems with a graph structure. In such systems the interactions between the sub-systems depend on the state of the sub-system itself and the state of its immediate neighbors. Not all dynamical systems can be decomposed in this fashion. However, many large scale systems have sparse interconnections and they can be modeled compactly as networks of sub-systems with interconnections. It is also easy to see that many physical systems, especially those that satisfy the principle of local action, can be decomposed in the manner shown in (1).

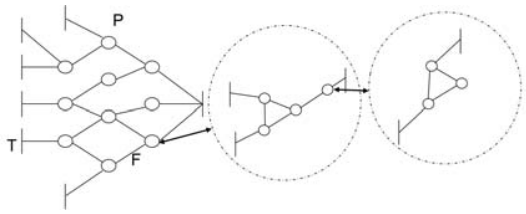

Fig. 1. Graphical network representation: Topological structure of a network consisting of nodes, terminals, and flows. Nodes can contain subgraphs and give rise to a hierarchical, multiscale structure.

We define the inventory Z of a sub-system or a group of systems to be a non-negative, additive function of the state of the corresponding sub-system(s). By additivity we mean that if Z_1 is the inventory of sub-system 1 and Z_2 is the inventory of sub-system 2, then $Z_1 + Z_2$ is the total inventory. Hence for any i, j

$$Z\begin{pmatrix} x_i \\ x_j \end{pmatrix} = Z(x_i) + Z(x_j)$$

By non-negativity we mean that the inventory cannot be less than zero. Examples of physical inventories include mass, energy and charge. More generally, an inventory is any property which is related to an amount.

By referring to (1) and using continuity we derive the conservation law

$$\frac{dZ_i}{dt} = p_i(x_i) + \sum_{j=1, j\neq i}^{n} f_{ij}(u) \tag{3}$$

The *drift* $p_i(x_i) = \frac{\partial Z(x_i)}{\partial x_i} F(x_i)$ measures the rate of production and the function $f_{ij}(u) = \frac{\partial Z(x_i)}{\partial x_i} G(u, x_i, x_j)$ measures the supply of Z between sub-systems j and i. We have the symmetry condition

$$f_{ij}(u) = f_{ji}(u)$$

The term

$$\phi(u, z, d) = \sum_{j=1, j\neq i}^{n} -f_{ij}(u)$$

therefore measures the net rate of supply to sub-system i from all other sub-systems. It is called the *action* on sub-system i.

Definition: Let X_0 be a subset of state-space. An inventory defined by (3) is said to have the

(1) *Clausius-Planck property* if $p(x) > 0$ for x not in X_0
(2) *Conservation property* if $p(x) = 0$ for all x not in X_0
(3) *Dissipation inequality* if $p(x) < 0$ for x not in X_0

The set X_0 associated with the dissipative action ϕ is called the set of *passive states*.

By a graph $\mathbf{G}$ we mean a finite set $\upsilon(\mathbf{G}) = (\upsilon_1, .., \upsilon_{n_P})$, whose elements are called **nodes**, together with the set $\epsilon(\mathbf{G}) \subset \upsilon \times \upsilon$, whose elements are called **branches**. A branch is therefore an ordered pair of distinct nodes.

- If, for all $(\upsilon_i, \upsilon_j) \in \epsilon(\mathbf{G})$, the branch $(\upsilon_j, \upsilon_i) \in \epsilon(\mathbf{G})$ then the graph is said to be **undirected**. Otherwise, it is called a **directed graph**.
- A branch (υ_i, υ_j) is said to be **incoming with respect to** υ_j and **outgoing with respect to** υ_i and can be represented as an arrow with node υ_i as its tail and node υ_j as its head.

Definition 1. A network of nodes $P_i, i = 1, ..., n_p, n_p + 1, ..., n_v$ consisting of nodes and terminals interconnected through branches $E_i, i = 1, ..., n_f$ with topology defined by the graph

$$\mathbf{G} = (\mathbf{E}, \mathbf{P})$$

is called a *process network* if its interconnection structure is described by a directed graph and we have

(1) **First law:** There exists an inventory E (the energy) which satisfies the conservation property
(2) **Second law:** There exists an inventory S (the entropy) which satisfies the Clausius-Planck property

We now develop a compact description of the topology of the network by introducing the incidence matrix.

Definition 2. The $n_t \times n_f$ matrix $\mathbf{A_a}$ is called incidence matrix for the matrix elements a_{ij} being

$$a_{ij} = \begin{cases} 1, & \text{if flow } j \text{ leaves node } i \\ -1, & \text{if flow } j \text{ enters node } i \\ 0, & \text{if flow } j \text{ is not incident with node } i \end{cases}$$

One node of the network is set as reference or datum node P_0 representing the exo-system. The $(n_t - 1) \times n_f$ matrix $\mathbf{A}$, where the row that contains the elements a_{0j} of the reference node P_0 is eliminated, is called reduced incidence matrix.

The connections between nodes through branches can be uniquely defined using the incident matrix $\mathbf{A}$. The conservation laws (3) can now be written

$$\mathbf{AF} = \mathbf{0} \tag{4}$$

for the node-to-branch incident matrix $\mathbf{A}$, where $\mathbf{F^T} = [\frac{dZ_1}{dt}, \frac{dZ_2}{dt}, .., \frac{dZ_t}{dt}, f_{12}, f_{13}..f_{n_{t-1}, n_t}, p_1, .., p_t]$. The flows f_{ij} represent connections between two nodes i.e. f_{ij} connects node i to node j, p_i denotes sources or sinks. The direction of the flows are defined according to the directionality

established in the graph. We now define a vector $\mathbf{W}$ so that

$$\mathbf{W} = \mathbf{A^T w} \tag{5}$$

where $\mathbf{W}$ are the potential differences across flow connections. The variables w are conjugate to Z if they are related via the Legendre transform of a convex potential like the entropy.

A dual structural representation can be derived using mesh analysis (the analysis developed above, which is based on the conservation laws, is called node analysis). Mesh analysis is counter-intuitive in process control applications but frequently used for electrical circuit analysis. When introducing stability and optimality concepts in this work, we will focus on describing the primal problem and its implications but refer to the dual mesh-based problem as proving the equivalent dual case.

2.1 Constitutive Relations

Constitutive equations relate efforts and flows (resistive), flows and displacements (capacitive), and efforts and fluxes (inductive). The constitutive equations describe energy dissipating, irreversible processes (resistive) or energy storing, reversible processes. The constitutive equations define the type of energetic transaction inside the process system or between the process system and the environment. The three main types can be described as

- Capacitive constitutive equation: storage of potential energy, $W = f_C(Z)$
- Inductive constitutive equation: storage of kinetic energy, $p = f_L(W)$
- Resistive constitutive equation: dissipation of energy, $F = f_R(W)$

In the context of process networks, storage of energy usually occurs through capacitive elements. In this work, inductive constitutive equations are neglected due to the fact that we focus on chemical processes or chemical process plants in which inertial effects in mass flow and thus accumulation of kinetic energy are not a significant contributor to the energy balance.

3. TOPOLOGICAL RESULTS, CONTENT AND CO-CONTENT

Consider two networks (a) and (b) with the same topology (identical incidence matrix) but not necessarily the same state. Denote the variables in network (a) with the superscript a and denote variables in the other network with superscript b. Using the conservation laws (4) we can then write $\mathbf{W^{a}}^T\mathbf{F^b} = (\mathbf{A}^T\mathbf{w^a})^T\mathbf{F^b} = \mathbf{w^a}^T\mathbf{A}\mathbf{F^b} = 0$. The equality

$$\mathbf{W^{a}}^T\mathbf{F^b} = 0$$

is often called *Tellegen's theorem.*

Without the reference system Tellegen's theorem is written

$$\mathbf{w^b}^T\frac{d\mathbf{Z^a}}{dt} = -\mathbf{W_R^b}^T\mathbf{F_R^a} - \mathbf{w_T^b}^T\mathbf{F_T^a} - \mathbf{w^b}^T\mathbf{p^a} \tag{6}$$

The term of the left hand side is called the storage. The three terms on the right refer to power dissipation due to transportation, supply from the exo-system through the terminals, and dissipation by production respectively.

If we consider a single network ($a = b$), then we can drop the superscript and we get the common form $\mathbf{W}^T\mathbf{F} = 0$ which represents a powerbalance. If Z represents the energy then we get the classical energy balance for the network. The "balance of entropy dissipation" results if we let one inventory correspond to the thermodynamic entropy defined so that

$$S = k_B \ln \Omega(x)$$

It is important to note that the fundamental equation gives a definition of the classical entropy in terms of extensive and intensive variables through the Pfaffian

$$TdS = dU + PdV - \sum_{i=1}^{n_c} \mu_i dN_i$$

Tellegen's theorem applied to the primal (extensive variable) vector $Z = (U, V, N_1, .., N_n)$ and its Legendre dual (intensive variable) vector $w = (1, P, \mu_1, .., \mu_n)/T$ then gives

$$\dot{S} = \mathbf{W_R}^T\mathbf{F_R} + \mathbf{w_T}^T\mathbf{F_T} + \mathbf{w}^T\mathbf{p}$$

where we used the fundamental equation and (6). The term $p_S = \mathbf{F_R}^T\mathbf{W_R} + \mathbf{w^T p}$ is called the rate of entropy generation.

We define the content of the network as the integral

$$G_R = \int_0^{\mathbf{F_R}} \mathbf{W_R}^T d\mathbf{F_R} + \int_0^{\mathbf{p}} \mathbf{w}^T d\mathbf{p} \tag{7}$$

The co-content is given as

$$G_R^* = \int_0^{\mathbf{W_R}} \mathbf{F_R}^T d\mathbf{W} + \int_0^{\mathbf{w}} \mathbf{p}^T d\mathbf{w} \tag{8}$$

By integration by parts and proper choice of the constant p^* (the constant of integration) we see that

$$G_R + G_R^* = p_S \geq 0$$

The second law dictates that the inequality holds (positive entropy production).

4. STABILITY OF PROCESS NETWORKS

In this section we derive a stability result using a combination of Tellegen's theorem and the co-content as a line integral. First, we note that Tellegen's theorem shows that for each time t the vectors $\mathbf{W}$ and $\mathbf{F}$ lie in fixed and orthogonal spaces. The identity $\dot{\mathbf{W}}^T\mathbf{F} = 0$ is therefore valid for all t and by taking out the sub-system which represent the exo-system we can write as before

$$\dot{\mathbf{Z}}^T\dot{\mathbf{w}} = -\mathbf{F_R^T}\dot{\mathbf{W}}_\mathbf{R} - \mathbf{F_T^T}\dot{\mathbf{w}}_\mathbf{T} - \mathbf{p_T^T}\dot{\mathbf{w}} \tag{9}$$

Due to the concavity of the entropy function we know that there exists a matrix $\mathbf{M} \geq 0$ so that $d\mathbf{w} = \mathbf{M}d\mathbf{Z}$, hence

$$\dot{\mathbf{Z}}^T\dot{\mathbf{w}} = \dot{\mathbf{Z}}^T M\dot{\mathbf{Z}} \geq 0$$

We can also write the co-content as a line integral

$$G_R^* = \int^t (\mathbf{F_R}^T\dot{\mathbf{W}}_\mathbf{R} + \mathbf{p}^T\dot{\mathbf{w}})dt \geq 0$$

Hence, by integrating (9) we get

$$\int_0^t \dot{\mathbf{Z}}^T M\dot{\mathbf{Z}}dt = -G_R^* - \mathbf{F_T^T}\dot{\mathbf{w}}_\mathbf{T}$$

The contribution due the terminal potentials vanish if $\dot{\mathbf{w}}_\mathbf{T} = 0$ and it follows that G^* is integrable and subject the condition of uniform continuity we conclude that G^* converges which implies that $\dot{\mathbf{w}}$ converges to zero.

5. OPTIMALITY OF PROCESS NETWORKS

Maxwell (1892) formulated the minimum heat theorem which states that for linear resistive electrical circuits driven by constant power sources, the flows distribute themselves in a way as to minimize the heat that is dissipated through the resistive elements. Prigogine (1947) observed that the theorem can be generalized to thermodynamic systems with the entropy production σ_S being minimized at steady state. Based on Tellegen's theorem and the content and co-content, we can propose an optimization problem that allows us to find the steady state and dynamic trajectory of a dynamic process network.

For a process network with a graph $\mathbf{G}$, we can define the extended content

$$G = \sum_{i=1}^{b} \int^{F_i} W_i dF_i = \int^{\mathbf{F}} \mathbf{W}^T d\mathbf{F} \tag{10}$$

and the extended co-content:

$$G^* = \sum_{i=1}^{b} \int^{W_i} F_i dW_i = \int^{\mathbf{W}} \mathbf{F}^T d\mathbf{W} \tag{11}$$

The extended content G and co-content G^* represent the sum of contents and co-contents for all branches i.e. reversible, irreversible, production and terminal flow connections of the network.

Lemma 3. For the network content G and the co-content G^*

$$G^*(\mathbf{W}) = \mathbf{W}^T\mathbf{F} - G(\mathbf{F}) \tag{12}$$

Equation (12) is a special form of Tellegen's theorem and can be used to do a variable change corresponding to a Legendre transformation.

Proof. The relation follows directly from integration by parts.

Lemma 4. For the sum of extended content $G = \int^{\mathbf{F}} \mathbf{W}^T d\mathbf{F}$ and extended co-content $G^* = \int^{\mathbf{W}} \mathbf{F}^T d\mathbf{W}$, the following relation holds:

$$G + G^* = 0$$

Proof. Using Tellegen's theorem and Lemma 3, the result follows immediately.

Definition 5. The following set of equations defines the process system:

$$\mathbf{AF} = \mathbf{0} \tag{13}$$
$$\mathbf{W} = \mathbf{A^T w} \tag{14}$$
$$\mathbf{F_R} = \Lambda(\mathbf{W_R}) \tag{15}$$
$$\mathbf{Z} = \mathbf{C w_C} \tag{16}$$
$$\mathbf{F_R} = \mathbf{F} - \mathbf{F_S} \tag{17}$$
$$\mathbf{W_R} = \mathbf{W} - \mathbf{W_S} \tag{18}$$
$$\mathbf{F_S} = \mathbf{F_T} \tag{19}$$
$$\mathbf{W_S} = \mathbf{W_T} \tag{20}$$
$$\mathbf{Z(0)} = \mathbf{Z_0} \tag{21}$$

The first two equations (13) and (14) are the Kirchhoff relations for process networks. Equations (15) are the resistive constitutive equations with Λ being a matrix function and (16) are the capacitive constitutive equations.

We introduced the variables $\mathbf{F_R}$ and $\mathbf{W_R}$ which facilitate writing the resistive constitutive equations in a compact way. The variables $\mathbf{F_R}$ and $\mathbf{W_R}$ allow us to include the terminals as sources or sinks through (19) and (20) for both, terminals where we have the function of the flows $\mathbf{F_T}$ or the potentials $\mathbf{W_T}$ given. For simplicity, we assume the terminal conditions as constant over time. The last equation (21) constitutes the initial conditions for the inventories $\mathbf{Z}$.

The set of equations can be transformed into a system of nonlinear differential algebraic equations (DAE) of the form

$$\frac{d\mathbf{Z}}{dt} = \mathbf{A}(\mathbf{Z}) + \mathbf{B_F^Z}(\mathbf{F_T^{input}}) + \mathbf{B_W^Z}(\mathbf{W_T^{input}}) \tag{22}$$
$$\mathbf{W_T^{output}} = \mathbf{C^W}(\mathbf{Z}) + \mathbf{D_F^W}(\mathbf{F_T^{input}}) + \mathbf{D_W^W}(\mathbf{W_T^{input}}) \tag{23}$$
$$\mathbf{F_T^{output}} = \mathbf{C^F}(\mathbf{Z}) + \mathbf{D_W^F}(\mathbf{W_T^{input}}) + \mathbf{D_F^F}(\mathbf{F_T^{input}}) \tag{24}$$

where nonlinearities are introduced through the constitutive equations. In this dynamic system, each terminal has an input and an output variable. The set of differential equations (22) determines the trajectories of $\mathbf{Z}$ and represent a state space system. The algebraic constraints (23) and (24) compute the output variables at the terminals from the input variables and the state $\mathbf{Z}$.

To find the stationary solutions of the system, we need to solve the set of equations

$$\mathbf{AF} = \mathbf{0} \tag{25}$$
$$\mathbf{W} = \mathbf{A^T w} \tag{26}$$
$$\mathbf{F} - \mathbf{F_T} = \Lambda(\mathbf{W} - \mathbf{W_T}) \tag{27}$$

with the three main sets of constraints: Conservations laws, uniqueness conditions, and the constitutive equations. The inventories and capacitive constitutive equations are only relevant for the dynamic case.

In the following theorem, we introduce the connection between content, co-content and the Kirchhoff laws, and present how duality of the free variables plays a crucial role for the optimization problem that is solved when a process network converges to a steady state solution. The constitutive equations are not directly involved as they are not relevant for the topological properties of the process network.

Theorem 6. For the optimization problem

$$\min_{\mathbf{w}} G^* = \int_0^W \mathbf{F}^T d\mathbf{W} \tag{28}$$
$$s.t. \quad \mathbf{W} = \mathbf{A^T w} \tag{29}$$
$$\mathbf{F} = \Lambda(\mathbf{W}) \tag{30}$$

with the cocontent G^* as objective function, the uniqueness conditions, and resistive constitutive equations as constraints, the solution exhibits a set of equations consisting of the uniqueness condition, the conservation laws, and the constitutive equations. The Langrange multipliers of the optimization problem are the network flow variables $\mathbf{F}$.

Proof. Starting with equations (28) - (30), we first substitute the constitutive equations (30) into the objective function (28) to eliminate the flow variables $\mathbf{F}$. The Lagrange function of the resulting optimization problem is

$$\min L(\mathbf{W}, \mathbf{w}, \lambda) = \int_0^W \Lambda(\mathbf{W})^T d\mathbf{W} + \lambda^T(\mathbf{A^T w} - \mathbf{W}) \quad (31)$$

First order conditions:

$$\frac{\partial L}{\partial \mathbf{W}} = \Lambda(\mathbf{W}) - \lambda = \mathbf{0} \quad (32)$$

$$\frac{\partial L}{\partial \mathbf{w}} = \mathbf{A}\lambda = \mathbf{0} \quad (33)$$

$$\frac{\partial L}{\partial \lambda} = \mathbf{A^T w} - \mathbf{W} = \mathbf{0} \quad (34)$$

comparing (32) and the constitutive equations (30), it follows that $\lambda = \mathbf{F}$. Using $\lambda = \mathbf{F}$ in (32) and (33), the result follows.

In principle, an optimization problem is solved where one set of Kirchhoff equations is omitted. Through the first order conditions, the missing set of equations is derived. The optimization problem with the Kirchhoff voltage law as constraints can be converted to an optimization problem with the Kirchhoff current law and vice versa.

We can now propose the main theorem which allows us to connect the steady state of a process network to the objective function that is simultaneously optimized i.e. we can find the natural optimization problem that a process network solves, when converging to a steady state. We explored the structure of the problem in the previous theorem, however, we need to be able to define boundary conditions and a solution for process networks connected to an exo-system.

Theorem 7. Consider a process network G with given resistive constitutive equations $\mathbf{F_R} = \Lambda(\mathbf{W_R})$ and boundary conditions for each terminal as well as one set of either the conservation laws or the uniqueness conditions. The stationary solution ($\frac{dZ_i}{dt} = 0$) for the network with conservation laws (13) and the uniqueness conditions (14)

$$\mathbf{AF} = \mathbf{0} \quad (35)$$

$$\mathbf{W} = \mathbf{A^T w} \quad (36)$$

$$\mathbf{F} - \mathbf{F_T} = \Lambda(\mathbf{W} - \mathbf{W_T}) \quad (37)$$

can be found by solving the following optimization problem

$$\min_{\mathbf{w}} \quad G^* = \int_0^W \mathbf{F}^T d\mathbf{W} \quad (38)$$

$$s.t. \quad \mathbf{W} = \mathbf{A^T w} \quad (39)$$

$$\mathbf{F_R} = \Lambda(\mathbf{W_R}) \quad (40)$$

$$\mathbf{F_T} = \text{const and/or } \mathbf{W_T} = \text{const} \quad (41)$$

or its equivalent dual optimization problem where (36) is replaced by (35).

Proof. Starting with (38) - (41), we substitute the boundary conditions (41) into the constitutive equations (40) and the constitutive equation into the objective function (38). We then form the Lagrange function using the flows $\mathbf{F}$ as Lagrange multipliers

$$L(\mathbf{W}, \mathbf{w}, \mathbf{F}) = \int_0^W (\Lambda(\mathbf{W} - \mathbf{W_T})^T d\mathbf{W} + \mathbf{W}^T \mathbf{F_T} \quad (42)$$

$$+ \mathbf{F}^T(\mathbf{A^T w} - \mathbf{W}) \quad (43)$$

First order conditions:

$$\frac{\partial L}{\partial \mathbf{W}} = \Lambda(\mathbf{W} - \mathbf{W_T}) + \mathbf{F_T} - \mathbf{F} = \mathbf{0} \quad (44)$$

$$\frac{\partial L}{\partial \mathbf{w}} = \mathbf{AF} = \mathbf{0} \quad (45)$$

$$\frac{\partial L}{\partial \mathbf{F}} = \mathbf{A^T w} - \mathbf{W} = \mathbf{0} \quad (46)$$

Comparing (25) - (27) to (44) - (46) shows the result. Concerning the second order conditions, we observe that convexity of the constraints is trivial for the linear Kirchhoff laws. Non-convexities of the optimization problem are due to non-linearities of the constitutive equations i.e. the constitutive equations are non-positive. For the second order conditions, it is apparent that the first derivative of the constitutive equations has to be analyzed and found positive definite for a global minimum, which corresponds exactly to the findings for passivity in Jillson and Ydstie (2007) for a unique network solution and convergence.

Generally, the objective function is a measure for dissipation of the storage variable over time. We conclude that the steady state of a passive network minimizes the dissipated power subject to the constraints imposed by the constitutive equations, topology, and boundary conditions, i.e. terminal connections.

6. PIPEFLOW NETWORK

A pipeline network example shows how optimization and dynamic simulation are connected. The network consists of two connected pipelines where each pipeline flows through a cylindrical storage tank with volume V_j open to the atmosphere, as shown in Fig. 2. A reference node is introduced representing the environment and connected to the terminals and dynamic nodes.

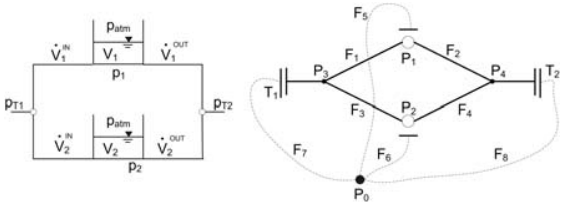

Fig. 2. Graphical network representations: Problem specific representation on the left, a generalized representation on the right including P_0 representing the exo-system.

Each pipeline's cross section is cylindrical with area A_i. The pipeline flow is given as a lumped parameter representation introducing pressure potentials p_j at the nodes and assuming laminar flow ($Re < 2300$). It is assumed that the fluid shows Newtonian behavior as well as being incompressible ($\rho = \text{const.}$). Therefore, the relation between

volumetric flow $\dot{V}_i$ and pressure drop $\Delta p_i = p_j - p_{j+1}$ can be modeled using Hagen-Poiseuille's law $\dot{V}_i = \frac{\pi r_i^4}{8\eta L_i}\Delta p_i$, where r_i is the radius of the pipeline's cross-section and L_i is the length of pipeline i. The potential at the bottom of the tank is given as $p_j = \rho g h_j + p_{atm}$ by hydrostatics. The fluid volume V_j in the tank is connected to the level h_j through $V_j = A_j h_j$ where A_j is the cross-section of the tank. We complete the model with the conservation laws for mass or, for constant density, the conservation of volume:

$$dV_1/dt = \dot{V}_1^{IN} - \dot{V}_1^{OUT} \quad (47)$$

$$dV_2/dt = \dot{V}_2^{IN} - \dot{V}_2^{OUT} \quad (48)$$

$$\dot{V}_{T1} = \dot{V}_2^{IN} + \dot{V}_2^{IN} \quad (49)$$

$$\dot{V}_{T2} = \dot{V}_2^{OUT} + \dot{V}_2^{OUT} \quad (50)$$

Initial conditions for the tank volumes $V_{0,i}$ have to be specified as well as boundary conditions at the terminals. The steady state of (47) - (50) can be found by integrating the differential equations.

The dynamic system given by the previous equations converges to the solution of the following optimization problem ($\frac{dV_1}{dt} = \frac{dV_2}{dt} = 0$):

$$\min \quad \sum_{i=1}^{4} \int_0^{\Delta p_i} \dot{V}_i d(\Delta p_i) \quad (51)$$

$$s.t. \quad (47) - (50) \quad (52)$$

$$\dot{V}_i = \frac{\pi r_i^4}{8\eta L_i}\Delta p_i \ , i = 1, .., 4 \quad (53)$$

$$\dot{V}_{T1} = const., p_{T2} = const. \quad (54)$$

Solving the optimization problem therefore corresponds to minimizing the power dissipated through viscous friction in the pipes subject to the conservation laws and boundary conditions. For each terminal, one boundary condition has to be specified which can be chosen freely ($\dot{V}_{T1} = 0.3$ m^3/s, $p_{T2} = 1.013$ bar). The parameters are given as $d = 0.5$ m and $L_1 = 2500$ m for the upper pipeline segments and $L_2 = 5000$ m for the lower segments. The tanks' cross-sectional diameter is chosen as $d_1 = d_1 = 2$ m. Fig. 3 shows the simulation results. We chose the initial conditions for $V_{0,1} = V_{0,2} = 25$ m ^{3}.

It is apparent that the value of the objective function as well as the flows of the dynamic simulation converge to the optimum determined through the optimization problem for arbitrary initial conditions. The constant inflow $\dot{V}_{T1}$ into the network divides itself into flows through the upper segments and lower segments choosing the path of least resistance.

7. CONCLUSIONS AND DISCUSSION

We introduced a new framework for analysis of optimality and stability of networked process systems in this work. We provide a systematic approach to define stability and optimality conditions for these systems. The objective function minimized by a process systems in its steady state is derived. Although for simplicity, we regard only the steady state in this example, the optimization problem

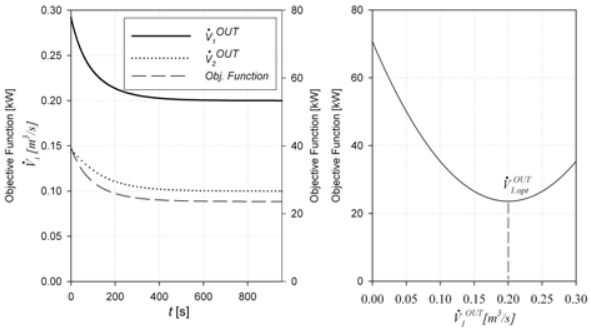

Fig. 3. Flows between tanks and outgoing terminal T_2 and the power dissipation (objective function) as a function of time on the left. Convergence of $\dot{V}_1^{OUT} =$ to 0.2 m^3/s and $\dot{V}_2^{OUT} =$ to 0.1 m^3/s. Objective function values of $\dot{V}_1^{OUT}$ on the right.

is also valid for transient conditions. The findings can explored to design decentralized control structures and hence shape the natural objective function of a process systems towards an economic objective.

REFERENCES

Hangos, K., Alonso, A., Perkins, J., and Ydstie, B. (1999). Thermodynamic approach to the structural stability of process plants. *AICHE*, 45(4), 802–816.

Jillson, K. and Ydstie, B. (2007). Process networks with decentralized inventory and flow control. *Journal of Process Control*, 17, 399413.

Maxwell, J. (1892). *A Treatise on Electricity and Magnetism*. Oxford University Press.

Mickulecky, D. (2001). Network thermodynamics and complexity: a transition to relational systems theory. *Computers and Chemistry*, 25, 369391.

Oster, G. and Desoer, C. (1971). Tellegen's theorem and thermodynamic inequalities. *J. of theor. Biology*, 32, 219–241.

Oster, G., Perelson, A., and Katchalsky, A. (1971). Network thermodynamics. *Nature*, 234, 393–399.

Peusner, L. (1986). *Studies in Network Thermodynamics*. Elsevier, Amsterdam.

Prigogine, I. (1947). *Etude thermodynamique des phenomenes irreversibles*. PhD thesis, Liege.

Ydstie, B. and Alonso, A. (1997). Process systems and passivity via the clausius-planck inequality. *Systems & Control Letters*, 30, 253–264.

Quasi-decentralized Scheduled Output Feedback Control of Process Systems Using Wireless Sensor Networks ⋆

Yulei Sun and Nael H. El-Farra *

* *Department of Chemical Engineering & Materials Science, University of California, Davis, CA 95616 USA (e-mail: nhelfarra@ucdavis.edu)*

Abstract: This paper presents a quasi-decentralized output feedback control structure for multi-unit plants with limited state measurements and distributed control systems that exchange information over a resource-constrained wireless sensor network (WSN). The networked control structure brings together model-based feedback control, state estimation and sensor scheduling to enforce closed-loop stability while simultaneously minimizing the rate of communication over the WSN. Initially, an observer-based output feedback controller is designed for each unit. To conserve the resources of the wireless devices, communication between the local control systems is suspended periodically for extended time periods during which each control system relies on models of the plant units to generate the necessary control action. Communication is then re-established at discrete time instances according to a certain schedule that determines the order and times at which the wireless sensor suites transmit the state estimates needed to update the states of the models embedded in the target units. By analyzing the combined discrete-continuous behavior of the scheduled closed-loop plant, we explicitly characterize the stability of the networked closed-loop system in terms of the communication rate, the sensor transmission schedule, the accuracy of the models, as well as the controller and observer design parameters. The results are illustrated using a chemical plant example where it is shown that by judicious management of the interplays between the control, communication and scheduling design parameters, it is possible to stabilize the plant while simultaneously enhancing the savings in WSN resources beyond what is possible with concurrent transmission configurations.

Keywords: Quasi-decentralized control, wireless sensor networks, model-based control, state estimation, scheduling algorithms, chemical plants.

1. INTRODUCTION

Chemical plants are large-scale dynamical systems that consist of a large number of distributed units which are tightly interconnected through mass and energy flows and recycle. Traditionally, the controller synthesis problem for such plants has been addressed within either the centralized or decentralized control frameworks. Both approaches have been the subject of numerous research studies aimed at understanding their advantages and limitations, as well as the development of strategies to overcome some of those limitations (e.g., see Siljak (1991); Lunze (1992); Sourlas and Manousiouthakis (1995); Katebi and Johnson (1997); Cui and Jacobsen (2002); Camponogara et al. (2002); Huang and Huang (2004); Skogestad (2004); Venkat et al. (2005); Goodwin et al. (2005); Kariwala (2007) and the references therein). Other notable contributions on this problem include the development of plant-wide control strategies based on passivity theory and concepts from thermodynamics (Hangos et al. (1999); Antelo et al. (2007)), the development of agent-based systems to control spatially-distributed reactor networks (Tetiker et al. (2008)), and the analysis and control of integrated process networks using time-scale decomposition and singular perturbations (Baldea et al. (2006)).

An approach that provides a compromise between the complexity of traditional centralized control schemes, on the one hand, and the performance limitations of decentralized control approaches, on the other, is quasi-decentralized control, which refers to a control strategy in which most signals used for control are collected and processed locally, while some signals are transferred between the local units and controllers to adequately account for the interactions and minimize the propagation of process upsets from one unit to another. A key consideration in the design and implementation of quasi-decentralized control systems is the selection of the communication medium over which the local control systems must communicate. While dedicated point-to-point links offer a reliable communication medium, the complexity and costs of installation and maintenance associated with this architecture, as well as the lack of flexibility for real-time reconfiguration, represent major drawbacks especially for large-scale plants with complex interconnections. An alternative solution is the use of wireless communication networks. The viability of this approach stems from the convergence of recent advances in actuator/sensor manufacturing, wireless communications and digital electronics,

⋆ Financial support by NSF CAREER Award, CBET-0747954, is gratefully acknowledged.

which has produced low-cost wireless sensors (e.g., Kumar (2001); Song et al. (2006)) that can be installed for a fraction of the cost of wired devices. Wireless sensor networks (WSNs) offer unprecedented flexibility ranging from high-density sensing capabilities to deployment in areas where wired devices may be difficult or impossible to deploy. Augmenting existing process control and monitoring systems with WSNs has the potential to expand the capabilities of the existing control technology beyond what is feasible with wired architectures alone. These are appealing goals that coincide with the recent calls for expanding the traditional process control and operations paradigm in the direction of smart plant operations (e.g., see Ydstie (2002); Christofides et al. (2007)).

One of the main challenges to be addressed when deploying a low-cost WSN for control is that of handling the inherent constraints on network resources, including the limitations on the computation, processing and communication capabilities. In an effort to address this problem, we developed in Sun and El-Farra (2008a) a quasi-decentralized model-based networked control architecture that enforces closed-loop stability with minimal cross communication between the constituent subsystems. The minimum allowable communication rate was characterized in terms of the plant-models' mismatch for the case when all sensors suites transmit their measurements concurrently and are given simultaneous access to the network. The networked control structure was subsequently generalized in Sun and El-Farra (2008b) to address the problem when only limited state measurements are available (for additional results and references on the design of networked control systems, the reader may refer to Walsh and Ye (2001); Montestruque and Antsaklis (2003); Munoz de la Pena and Christofides (2008) and the references therein).

In addition to transmitting the data at discrete time instances, another important way of conserving the WSN resources is to select and activate only a subset of the deployed sensor suites at any given time to communicate with the rest of the plant. Under this restriction, the stability and performance characteristics of each unit in the plant become dependent not only on the controller design but also on the selection of the scheduling strategy that, at any time, determines the order in which the sensor suites of the neighboring units transmit their data. Forcing the different subsystems to transmit their data at different times creates opportunities for providing a more targeted correction to the models' estimation errors, such that the models with the largest uncertainties can receive more timely updates than is feasible under the simultaneous transmissions configuration.

Motivated by these considerations, we present in this work an integrated approach for model-based control, state estimation and sensor scheduling in plants with limited state measurements and interconnected processing units that communicate over a resource-constrained WSN. The objective is to find a strategy for establishing and terminating communication between the sensors suites of the WSN and the local control systems in a way that minimizes the rate at which each node in the WSN broadcasts data to the rest of the plant without jeopardizing closed-loop stability. The rest of the paper is organized as follows. Following some preliminaries in Section 2, the networked control and scheduling problem is formulated. Section 3 then presents the quasi-decentralized output feedback control structure and describes its implementation over a WSN with the aid of appropriate local state observers, process models and sensor transmission scheduling. The closed-loop system is then formulated and analyzed in Section 4 where precise conditions for closed-loop stability are provided in terms of the communication rate over the WSN, the sensor scheduling strategy, as well as the accuracy of the models and the choice of controller and observer designs. We show how the stability criteria provide systematic tools that can guide the search for optimal transmission schedules that achieve the biggest savings in WSN resource utilization. Finally, the theoretical results are illustrated in Section 5 using a chemical plant example.

2. PRELIMINARIES

2.1 Plant description

We consider a large-scale distributed plant composed of n interconnected processing units, represented by the following state-space description:

$$\begin{aligned}
\dot{x}_1 &= A_1x_1 + B_1u_1 + \sum_{j=2}^{n} A_{1j}x_j, \qquad y_1 = C_1x_1 \\
\dot{x}_2 &= A_2x_2 + B_2u_2 + \sum_{j=1,j\neq 2}^{n} A_{2j}x_j, \; y_2 = C_2x_2 \\
&\vdots \qquad\qquad\qquad\qquad\qquad\qquad \vdots \\
\dot{x}_n &= A_nx_n + B_nu_n + \sum_{j=1}^{n-1} A_{nj}x_j, \qquad y_n = C_nx_n
\end{aligned} \tag{1}$$

where $x_i := [x_i^{(1)} \; x_i^{(2)} \; \cdots \; x_i^{(p_i)}]^T \in \mathbb{R}^{p_i}$ denotes the vector of process state variables associated with the i-th processing unit, p_i is the number of state variables in the i-th unit, $y_i := [y_i^{(1)} \; y_i^{(2)} \; \cdots \; y_i^{(q_i)}]^T \in \mathbb{R}^{q_i}$ and $u_i := [u_i^{(1)} \; u_i^{(2)} \; \cdots \; u_i^{(r_i)}]^T \in \mathbb{R}^{r_i}$ denote the vector of measured outputs and manipulated inputs associated with the i-th processing unit, respectively, x^T denotes the transpose of a column vector x; A_i, B_i, A_{ij} and C_i are constant matrices. The interconnection term $A_{ij}x_j$, where $i \neq j$, describes how the dynamics of the i-th unit are influenced by the j-th unit in the plant. Note from the summation notation in Eq.1 that each processing unit can in general be connected to all the other units in the plant.

2.2 Problem formulation and solution methodology

Referring to plant of Eq.1, we consider a quasi-decentralized control structure in which each unit in the plant has a local control system with its sensors and actuators connected to the local controller through a dedicated wired communication network. An additional suite of wireless sensors is deployed within each unit to transfer data from the local control system to the plant supervisor as well as to the other distributed control systems in the plant. The various sensor suites form a plant-wide WSN through which the plant units and their controllers communicate. The control objective is to stabilize all the plant units at the zero steady-state while simultaneously: (a) keeping the data dissemination and exchange over the WSN to a minimum, and (b) accounting for the lack of full-state measurements within each unit. To address the resource-constraints problem, we develop in the next section an

integrated model-based quasi-decentralized output feedback control and scheduling strategy that reduces the exchange of information between the plant units without loss of stability. This is accomplished by: (a) designing for each local control system an appropriate state observer that generate estimates of the local state variables from the measured outputs, (b) including models within each control system to estimate the interaction terms when measurements are not available through the WSN, and (c) limiting the number of WSN nodes that, at any given time, transmit their data to update the corresponding target models. The problem is to find an optimal scheduling strategy for establishing and terminating communication between the sensor suites and the target controllers. To illustrate the main ideas, we will consider as an example the configuration where only one wireless sensor suite is allowed to transmit its data to the appropriate units at any given time, while the other nodes remain dormant until the next suite is allowed to transmit its data.

3. QUASI-DECENTRALIZED STATE ESTIMATION AND CONTROL WITH SCHEDULED SENSOR TRANSMISSIONS

3.1 Synthesis of distributed output feedback controllers

Referring to the plant of Eq.1, we begin by synthesizing for each unit an output feedback controller of the form:

$$\begin{aligned} u_i &= K_i\bar{x}_i + \sum_{j=1,j\neq i}^{n} K_{ij}\bar{x}_j \\ \dot{\bar{x}}_i &= (A_i - L_iC_i)\bar{x}_i + \sum_{j=1,j\neq i}^{n} A_{ij}\bar{x}_j + B_iu_i + L_iy_i, \end{aligned} \tag{2}$$

where $\bar{x}_i$ is an estimate of the state of the i-th unit generated by an observer embedded within the local control system of the i-th unit, K_i is the local feedback gain responsible for stabilizing the i-th subsystem in the absence of interconnections, K_{ij} is a gain that compensates for the effect of the j-th neighboring subsystem on the dynamics of the i-th unit, and L_i is the observer gain (chosen such that $A_i - L_iC_i$ is Hurwitz). Note that, in addition to $\bar{x}_i$ which is supplied continuously by the local observer, the implementation of the controller of Eq.2 requires the availability of observer-generated state estimates from the other units in the plant, $\bar{x}_j$, which can be transmitted only through the WSN. A copy of the local observer must therefore be included within the wireless sensor suite of each unit in order to generate the state estimates which are then broadcast to the rest of the plant. This setup is possible given the computational capabilities of wireless sensors. An alternative approach, which avoids having the wireless sensors carry the computational load of the observer, is to have the WSN nodes transmit only the output measurements, but include within each control system an observer of the full plant instead (not just an observer of the local subsystem) which then generates the required state estimates of the full plant state. In addition to the complexity of designing a centralized observer for the entire plant, another difficulty with this approach is that the observer must be designed to have hybrid dynamics since the WSN data are transmitted only at discrete time instances while the local measurements are supplied continuously (or at least more frequently).

It should also be noted that the choice to use a Luenberger observer is made only to illustrate the design and implementation of the quasi-decentralized output feedback control architecture. This choice, however, is not unique and any other explicit observer design can be used instead. The only requirement is that the observer possess an explicit evolution equation that relates the dynamics of the state estimate explicitly to the plant matrices, the output and the observer design parameters. As we will see in the next section, this feature permits the derivation of explicit closed-loop stability conditions that depend in a transparent way on the observer design parameters.

3.2 Design of model-based networked control structure

To conserve battery power in the plant-wide WSN, we initially reduce the rate at which the information (i.e., $\bar{x}_j$) is transferred from the wireless sensor suite of each unit to the target control systems in the neighboring units as much as possible without sacrificing closed-loop stability. To this end, and following the idea presented in (Sun and El-Farra (2008b)), we embed in each unit (both in the local controller and in the wireless sensor suite) a set of dynamic models that provide estimates of the evolution of the states of the neighboring units when communication over the WSN is suspended. The model estimates are used to generate both the local state estimates and the local control action. The state of each model is then reset using the state estimate generated by the observer of the corresponding unit when the wireless sensor suite of the latter is allowed to transmit its data at discrete time instances. In mathematical terms, the local control and update laws for unit i are implemented as follows:

$$\begin{aligned} u_i(t) &= K_i\bar{x}_i(t) + \sum_{j=1,j\neq i}^{n} K_{ij}\widehat{x}_j^i(t),\ t\neq t_k^j,\ i=1,2,\cdots,n \\ \dot{\bar{x}}_i(t) &= (A_i - L_iC_i)\bar{x}_i(t) + \sum_{j=1,j\neq i}^{n} A_{ij}\widehat{x}_j^i(t) + B_iu_i(t) + L_iy_i(t) \\ \dot{\widehat{x}}_j^i(t) &= \widehat{A}_j\widehat{x}_j^i(t) + \widehat{B}_j\widehat{u}_j^i(t) + \widehat{A}_{ji}\bar{x}_i(t) + \sum_{l=1,l\neq i,l\neq j}^{n} \widehat{A}_{jl}\widehat{x}_l^i(t), t\neq t_k^j \\ \widehat{u}_j^i(t) &= K_j\widehat{x}_j^i(t) + K_{ji}\bar{x}_i(t) + \sum_{l=1,l\neq i,l\neq j}^{n} K_{jl}\widehat{x}_l^i(t),\ \ t\neq t_k^j \\ \widehat{x}_j^i(t_k^j) &= \bar{x}_j(t_k^j),\ \ j=1,\cdots,n, j\neq i,\ \ k=0,1,2,\cdots \end{aligned} \tag{3}$$

where $\widehat{x}_j^i$ is the estimate of x_j provided by a model of unit j embedded in unit i; $\widehat{A}_j$, $\widehat{B}_j$ and $\widehat{A}_{jl}$ are constant matrices; t_k^j indicates the k-th transmission time for the j-th sensor suite in the WSN. The fact that $\bar{x}_i$ appears directly in the model of the j-th unit follows from: (1) the structure of the plant and the way the i-th and j-th units are interconnected, and (2) the fact that the observer-generated estimates of x_i are assumed to be available continuously to the local control system of the i-th unit. Note that the models used by the i-th controller to recreate the behavior of the neighboring units do not necessarily match the actual dynamics of those processes, i.e., in general $\widehat{A}_j \neq A_j$, $\widehat{B}_j \neq B_j$, $\widehat{A}_{jl} \neq A_{jl}$.

3.3 Scheduling WSN transmissions and model updates

A key measure of the extent of WSN utilization is the update period for each sensor suite, $h^j := t_{k+1}^j - t_k^j$, which determines the frequency at which the j-th node sends observer estimates to the other units through the network to update the corresponding model states. A larger h implies

larger savings in WSN resource utilization. To simplify the analysis, we consider in what follows only the case when the update period is constant and the same for all the units, so that $t_{k+1}^j - t_k^j := h,\ j = 1, 2, \cdots, n$. To further reduce network utilization, we perform sensor scheduling whereby only one wireless sensor suite is allowed to transmit its observer estimates to the appropriate units at any one time, while the other suites remain dormant until the next suite is allowed to transmit its data (the analysis can be generalized to cases where multiple suites transmit at the same time). The transmission schedule is defined by: (1) the sequence (or order) of transmitting nodes: $\{s_j,\ j = 1, 2, \cdots, n\},\quad s_j \in \mathcal{N} := \{1, 2, \cdots, n\}$, where s_j is a discrete variable that denotes the j-th transmitting entity in the sequence, and (2) the time at which each node in the sequence transmits observer estimates. To characterize the transmission times, we introduce the variable: $\Delta t_j := t_k^{s_{j+1}} - t_k^{s_j},\ \ j = 1, 2, \cdots, n-1$, which is the time interval between the transmissions of two consecutive nodes in the sequence. Fig.1 is a schematic representation of how

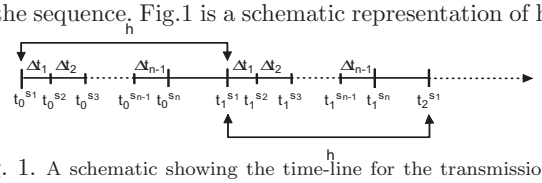

Fig. 1. A schematic showing the time-line for the transmission of each sensor suite in an h-periodic schedule.

sensor scheduling is performed. Note that the schedule is h-periodic in that the same sequence of transmitting nodes is executed repeatedly every h seconds (equivalently, each node transmits its data every h seconds). Note also from the definitions of both h and Δt_j that we always have the constraint $\sum_{j=1}^{n-1} \Delta t_j < h$. Since the update periods for all units are the same, the intervals between the transmission times of two specific units are constant, and within any single execution of the schedule (which lasts less than h seconds), each sensor suite can only transmit its observer estimates through the WSN and update its target models in the local control systems of its neighbors once. This can be represented mathematically by the condition: $s_i \neq s_j$ when $i \neq j$. By manipulating the time intervals Δt_j (i.e., the transmission times) and the order in which the nodes transmit, one can systematically search for the optimal sensor transmission schedule that leads to the largest update period (or smallest communication rate between each sensor suite and its target units).

4. NETWORKED CLOSED-LOOP STABILITY ANALYSIS

4.1 Characterizing the scheduled closed-loop response

In order to derive conditions for closed-loop stability, we need first to express the plant response as a function of the update period and the sensor transmission schedule. To this end, we define the model estimation errors by $e_j^i = \bar{x}_j - \widehat{x}_j^i$, for $j \neq i$, and $e_j^i = 0$, for $j = i$, where e_j^i represents the difference between the state of the observer of unit j (embedded in unit j) and the state of the model of unit j (embedded in unit i). Introducing the augmented vectors: $\mathbf{e}_j := [(e_j^1)^T\ (e_j^2)^T\ \cdots\ (e_j^n)^T]^T$, $\mathbf{e} := [\mathbf{e}_1^T\ \mathbf{e}_2^T\ \cdots\ \mathbf{e}_n^T]^T$, $\mathbf{x} := [x_1^T\ x_2^T\ \cdots\ x_n^T]^T$, $\bar{\mathbf{x}} := [\bar{x}_1^T\ \bar{x}_2^T\ \cdots\ \bar{x}_n^T]^T$, it can be shown that the overall closed-loop plant of Eq.1 and Eq.3 can be formulated as a combined discrete-continuous system of the form:

$$\begin{aligned}
\dot{\mathbf{x}}(t) &= \Lambda_{11}\mathbf{x}(t) + \Lambda_{12}\bar{\mathbf{x}}(t) + \Lambda_{13}\mathbf{e}(t)\\
\dot{\bar{\mathbf{x}}}(t) &= \Lambda_{21}\mathbf{x}(t) + \Lambda_{22}\bar{\mathbf{x}}(t) + \Lambda_{23}\mathbf{e}(t)\\
\dot{\mathbf{e}}(t) &= \Lambda_{31}\mathbf{x}(t) + \Lambda_{32}\bar{\mathbf{x}}(t) + \Lambda_{33}\mathbf{e}(t),\ \ t \neq t_k^j\\
\mathbf{e}_j(t_k^j) &= \mathbf{0},\ \ j = 1, 2, \cdots, n,\ \ k = 0, 1, 2, \cdots,
\end{aligned} \tag{4}$$

where Λ_{ij}'s are constant matrices whose explicit forms are omitted for brevity but can be obtained by substituting Eq.3 into Eq.1. Note that, unlike the case of simultaneous sensor transmissions (where no scheduling takes place) which was investigated in Sun and El-Farra (2008b), not all models within a given unit are updated (and hence not all estimation errors are re-set to zero) at each transmission time. Instead, only the model of the transmitting unit is updated using the observer-generated estimates provided by the wireless sensor suite of that particular unit. Defining the augmented state vector $\xi(t) := [\mathbf{x}^T(t)\ \bar{\mathbf{x}}^T(t)\ \mathbf{e}^T(t)]^T$, the dynamics of the overall closed-loop system can be cast in the following form:

$$\begin{aligned}
\dot{\xi}(t) &= \Lambda_o \xi(t),\ \ t \neq t_k^j\\
\xi(t_k^j) &= \left[\mathbf{x}^T(t_k^j)\ \ \bar{\mathbf{x}}^T(t_k^j)\ \ \mathbf{e}^T(t_k^j)\right]^T,\ k = 0, 1, 2, \cdots\\
\mathbf{e}^T(t_k^j) &= \left[\mathbf{e}_1^T(t_k^j)\ \cdots\ \mathbf{e}_{j-1}^T(t_k^j)\ \ \mathbf{0}\ \ \mathbf{e}_{j+1}^T(t_k^j)\ \cdots\ \mathbf{e}_n^T(t_k^j)\right]^T\\
\Lambda_o &= \begin{bmatrix} \Lambda_{11} & \Lambda_{12} & \Lambda_{13} \\ \Lambda_{21} & \Lambda_{22} & \Lambda_{23} \\ \Lambda_{31} & \Lambda_{32} & \Lambda_{33} \end{bmatrix}
\end{aligned} \tag{5}$$

The following proposition provides an explicit characterization of the scheduled closed-loop response in terms of the update period and the transmission schedule. The proof can be obtained by solving the system of Eq.5 within each sub-interval in Fig.1, and is omitted for brevity.

Proposition 1. Consider the closed-loop system described by Eq.5 with a transmission schedule $\{s_1, s_2, \cdots, s_n\}$ and the initial condition $\xi(t_0^{s_1}) = [\mathbf{x}^T(t_0^{s_1})\ \ \bar{\mathbf{x}}^T(t_0^{s_1})\ \ \mathbf{e}^T(t_0^{s_1})]^T = \xi_0$, with $\mathbf{e}_{s_1}(t_0^{s_1}) = \mathbf{0}$. Then, for $k = 0, 1, 2, \cdots$,

$$\xi(t) = \begin{cases} e^{\Lambda_o(t - t_k^{s_j})}\Gamma_j(\Delta t_j, I_o^{s_j}) M_o^k \xi_0,\ t \in [t_k^{s_j},\ t_k^{s_{j+1}}) \\ e^{\Lambda_o(t - t_k^{s_n})}\Gamma_n M_o^k \xi_0,\ t \in [t_k^{s_n},\ t_{k+1}^{s_1}) \end{cases} \tag{6}$$

where $j = 1, 2, \cdots, n-1$, and

$$\Gamma_j = \prod_{j-1-\mu=0}^{j-2} I_o^{s_{\mu+1}} e^{\Lambda_o \Delta t_\mu}, \text{for } j \geq 2, \text{and } \Gamma_j = I, \text{ for } j = 1 \tag{7}$$

$$M_o = I_o^{s_1} e^{\Lambda_o (h - \sum_{j=1}^{n-1} \Delta t_j)} \Gamma_n \tag{8}$$

$$I_o^{s_j} = \begin{bmatrix} I & O & \cdots & O \\ O & H_1 & \cdots & O \\ \vdots & \vdots & & \vdots \\ O & O & \cdots & H_n \end{bmatrix},\ H_i = \begin{cases} I, & i \neq s_j \\ O, & i = s_j \end{cases} \tag{9}$$

for $j = 1, 2, \cdots, n$, $t_{k+1}^{s_j} - t_k^{s_j} = h$ and $\Delta t_j = t_k^{s_{j+1}} - t_k^{s_j},\ j = 1, 2, \cdots, n-1$.

4.2 Characterizing the maximum allowable update period

Having expressed the overall closed-loop response in terms of the update period, the transmission times (which are determined by Δt_j) and the sequence of transmitting nodes (which determines the structure of $I_o^{s_j}$), we are in a position to state the main result of this section. The following theorem provides a necessary and sufficient condition for stability of the scheduled closed-loop plant under the quasi-decentralized networked output feedback control structure. The proof is omitted for brevity.

Theorem 2. Referring to the scheduled closed-loop system of Eq.5 whose solution is given by Eqs.6-9, the zero solution, $\xi = [\mathbf{x}^T\ \bar{\mathbf{x}}^T\ \mathbf{e}^T]^T = [\mathbf{0}\ \mathbf{0}\ \mathbf{0}]^T$, is globally exponentially stable if and only if the eigenvalues of the matrix in Eq.8 are strictly inside the unit circle.

By examining the structure of the test matrix M_o in Eq.8, it can be seen that its eigenvalues depend on the update period h, the closed-loop matrix Λ_o (which in turn depends on the plant-model mismatch as well as the controller and observer gains for all the units), the time intervals between sensor transmissions $\Delta t_1, \Delta t_2, \cdots, \Delta t_{n-1}$, as well as the sensor transmission sequence $\{s_1, s_2, \cdots, s_n\}$. The stability criteria in Theorem 2 can therefore be used to compare different schedules (by varying the transmission sequence as well as the transmission times) to determine the ones that require the least communication rate between the sensors and the target controllers and therefore produce the biggest savings in WSN battery power utilization. For a fixed schedule, the stability criteria can also be used to compare different models, as well as different controllers and state observers in terms of their robustness with respect to communication suspension (i.e., which ones require measurement updates less frequently than others). Note that choosing $\Delta t_1 = \Delta t_2 = \cdots = \Delta t_{n-1} = 0$ reduces the problem to one where all the nodes in the WSN transmit their observer estimates simultaneously. As expected, in this case stability of the networked closed-loop system depends only on Λ_o and h.

5. SIMULATION STUDY: APPLICATION TO CHEMICAL REACTORS WITH RECYCLE

We consider a plant composed of three non-isothermal continuous stirred-tank reactors (CSTRs) in a cascade. The reactant species A is consumed in each reactor by three parallel irreversible exothermic reactions. The output of the third CSTR is passed through a separator that removes the products and recycles unreacted A to the first CSTR. Under standard modeling assumptions, a plant model of the following form can be derived from conservation laws:

$$\begin{aligned}\frac{dT_j}{dt} &= \frac{F_j^0}{V_j}(T_j^0 - T_j) + \frac{F_{j-1}}{V_j}(T_{j-1} - T_j) \\ &\quad + \sum_{i=1}^{3}\frac{(-\Delta H_i)}{\rho c_p}R_i(C_{Aj}, T_j) + \frac{Q_j}{\rho c_p V_j} \\ \frac{dC_{Aj}}{dt} &= \frac{F_j^0}{V_j}(C_{Aj}^0 - C_{Aj}) + \frac{F_{j-1}}{V_j}(C_{A(j-1)} - C_{Aj}) \\ &\quad - \sum_{i=1}^{3}R_i(C_{Aj}, T_j),\ j = 1, 2, 3\end{aligned}$$

where T_j, C_{Aj}, Q_j, and V_j denote the temperature, the reactant concentration, the rate of heat input, and the volume of the j-th reactor, respectively, $R_i(C_{Aj}, T_j) = k_{i0}\exp\left(\frac{-E_i}{RT_j}\right)C_{Aj}$ is the rate of the i-th reaction, F_j^0 denotes the flow rate of a fresh feed stream associated with the j-th reactor, F_j is the flow rate of the outlet stream of the j-th reactor, with $F_0 = F_r, T_0 = T_3, C_{A0} = C_{A3}$ denoting the flow rate, temperature and reactant concentration of the recycle stream, ΔH_i, k_i, E_i, $i = 1, 2, 3$, denote the enthalpies, pre-exponential constants and activation energies of the three reactions, respectively, c_p and ρ denote the heat capacity and density of fluid in the reactor. Using typical values for the process parameters (see Sun and El-Farra (2008a)), the plant with $Q_j = 0$, $C_{Aj}^0 = C_{Aj}^{0s}$ and a recycle ratio of $r = 0.5$, has three steady-states (two locally asymptotically stable and one unstable). The control objective is to stabilize the plant at the (open-loop) unstable steady-state by manipulating Q_j and C_{Aj}^0, $j = 1, 2, 3$. Only the temperatures of the three reactors are assumed to be available as measurements. A plant-wide WSN composed of 3 wireless sensor suites is deployed. Each sensor suite collects estimates of the local process state variables provided by a state observer embedded within the unit and broadcasts it to the rest of the plant. It is desired to stabilize the plant with minimal data exchange over the WSN to conserve battery power for the wireless devices.

Linearizing the plant around the unstable steady-state yields a system of the form of Eq.1 to which the networked output feedback control and scheduling architecture described in the previous sections is applied. The synthesis details are omitted due to space limitations. In the remainder of this section, we will investigate the interplay between the communication rate and the sensor transmission schedule, and its impact on closed-loop stability. Since closed-loop stability requires all eigenvalues of M_o to lie within the unit circle, it is sufficient to consider only the maximum eigenvalue magnitude, denoted by $\lambda_{\max}(M_o)$.

Table 1. Sensor transmission schedules

Schedule	$s_1, s_2, s_3, s_1, s_2, s_3, \cdots$
1	$1, 2, 3, 1, 2, 3, \cdots$
2	$1, 3, 2, 1, 3, 2, \cdots$
3	$2, 1, 3, 2, 1, 3, \cdots$
4	$2, 3, 1, 2, 3, 1, \cdots$
5	$3, 1, 2, 3, 1, 2, \cdots$
6	$3, 2, 1, 3, 2, 1, \cdots$

We consider first the case when $\Delta t_1 = \Delta t_2 = \Delta t$. Fig.2(a) is a contour plot showing the dependence of $\lambda_{\max}(M_o)$ on both the interval between transmissions, Δt, and the update period, h, under the six possible sensor transmission schedules listed in Table 1 when imperfect models are embedded in the local control systems (each model has 10% parametric uncertainty in the heat of reaction). For each schedule, the area enclosed by the unit contour line is the stability region of the plant. It can be seen that, for sufficiently small Δt (below 0.03 hr), the maximum allowable update periods obtained under sequences 2 and 6 are larger than the one obtained when no scheduling takes place (i.e., with $\Delta t = 0$). As Δt is increased, however, the trend is reversed, indicating that the benefits of scheduling can be limited by a poor choice of the transmission times. For sequences 3 and 5, scheduling yields larger update periods (compared with the concurrent transmission configuration) only when the transmission times are chosen such that $\Delta t > 0.04$ hr. In general, allowing the different sensor suites to transmit their data and update their target models at different times (rather than simultaneously) can help provide a more targeted and timely (though only partial) correction to model estimation errors which in turn helps reduce the rate at which each node in the WSN must transmit its data. These predictions are further confirmed by the closed-loop state profile shown in Fig.2(b), which shows that the linearized plant is stable under sequence 6 but unstable under sequence 2, when $\Delta t = 0.02$ hr and

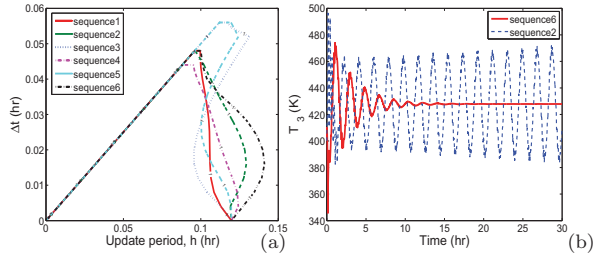

Fig. 2. (a) Dependence of $\lambda_{\max}(M_o)$ on Δt and h for different sensor transmission sequences under a model-based control scheme. (b) Closed-loop temperature profile for CSTR3 under the model-based quasi-decentralized output feedback control strategy using two different sensor transmission schedules with the same update period.

$h = 0.13$ hr (for brevity, only the temperature profile for CSTR 3 is shown; the state and input profiles for the other reactors exhibit similar behavior).

We consider next the more general case where $\Delta t_1 \neq \Delta t_2$. Fig.3(a) is a contour plot showing the dependence of $\lambda_{\max}(M_o)$ on Δt_1 and h for different values of Δt_2, when the WSN nodes transmit according to sequence 2 and an uncertain model is used (nominal value of the heat of reaction is 10% higher than the actual value). It can be seen that a larger update period (and hence larger reduction in WSN utilization) can be obtained by carefully choosing the transmission times for the sensor suites of different units than in the case when $\Delta t_1 = \Delta t_2$. For example, consider the case when $\Delta t_2 = 0.02$ hr and $h = 0.13$ hr. This point lies outside the stability region of schedule 2 when $\Delta t_2 = \Delta t_1 = 0.02$ hr (see Fig.2(a)). If we choose $\Delta t_1 = 0.08$ hr, however, the same update period becomes stabilizing under schedule 2 (the point now lies inside the stability region). These observations are further confirmed by the temperature profiles in Fig.3(b).

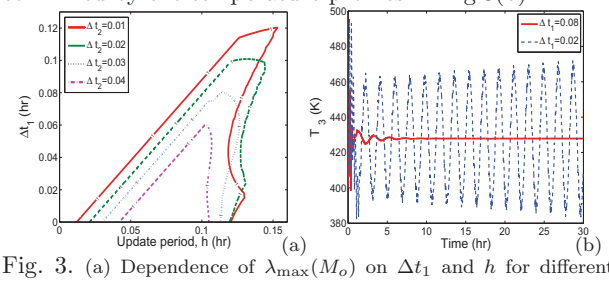

Fig. 3. (a) Dependence of $\lambda_{\max}(M_o)$ on Δt_1 and h for different values of Δt_2 under schedule 2 with a fixed model, and (b) Closed-loop temperature profile for CSTR 3 when $\Delta t_2 = 0.02$ hr and $h = 0.13$ hr for two different values of Δt_1.

REFERENCES

Antelo, L.T., Otero-Muras, I., Banga, J.R., and Alonso, A.A. (2007). A systematic approach to plant-wide control based on thermodynamics. *Comp. & Chem. Eng.*, 31, 677–691.

Baldea, M., Daoutidis, P., and Kumar, A. (2006). Dynamics and control of integrated networks with purge streams. *AIChE J.*, 52, 1460–1472.

Camponogara, E., Jia, D., Krogh, B., and Talukdar, S. (2002). Distributed model predictive control. *IEEE Contr. Syst. Mag.*, 22, 44–52.

Christofides, P.D., Davis, J.F., El-Farra, N.H., Harris, K., Gibson, J., and Clark, D. (2007). Smart plant operations: Vision, progress and challenges. *AIChE J.*, 53, 2734–2741.

Cui, H. and Jacobsen, E. (2002). Performance limitations in decentralized control. *J. Proc. Contr.*, 12, 485–494.

Goodwin, G.C., Salgado, M.E., and Silva, E.I. (2005). Time-domain performance limitations arising from decentralized architectures and their relationship to the RGA. *International Journal of Control*, 78, 1045–1062.

Hangos, K., Alonso, A., Perkins, J., and Ydstie, B. (1999). Thermodynamic approach to the structural stability of process plants. *AIChE J.*, 45, 802–816.

Huang, X. and Huang, B. (2004). Multiloop decentralized PID control based on covariance control criteria: an LMI approach. *ISA Transactions*, 43, 49–59.

Kariwala, V. (2007). Fundamental limitation on achievable decentralized performance. *Automatica*, 43, 1849–1854.

Katebi, M.R. and Johnson, M.A. (1997). Predictive control design for large-scale systems. *Automatica*, 33, 421–425.

Kumar, P.R. (2001). New technological vistas for systems and control: The example of wireless networks. *IEEE Contr. Syst. Mag.*, 21, 24–37.

Lunze, J. (1992). *Feedback Control of Large Scale Systems.* Prentice-Hall, U.K.

Montestruque, L.A. and Antsaklis, P.J. (2003). On the model-based control of networked systems. *Automatica*, 39, 1837–1843.

Munoz de la Pena, D. and Christofides, P.D. (2008). Lyapunov-based model predictive control of nonlinear systems subject to data losses. *IEEE Trans. Automat. Contr.*, 53, 2067–2089.

Siljak, D.D. (1991). *Decentralized Control of Complex Systems.* Academic Press, London.

Skogestad, S. (2004). Control structure design for complete chemical plants. *Comp. & Chem. Eng.*, 28, 219–234.

Song, J., Mok, A.K., Chen, D., and Nixon, M. (2006). Challenges of wireless control in process industry. In *Workshop on Research Directions for Security and Networking in Critical Real-Time and Embedded Systems.* San Jose, CA.

Sourlas, D.D. and Manousiouthakis, V. (1995). Best achievable decentralized performance. *IEEE Trans. Automat. Contr.*, 40, 1858–1871.

Sun, Y. and El-Farra, N.H. (2008a). Quasi-decentralized model-based networked control of process systems. *Comp. & Chem. Eng.*, 32, 2016–2029.

Sun, Y. and El-Farra, N.H. (2008b). Quasi-decentralized state estimation and control of process systems over communication networks. In *Proceedings of the 47th IEEE Conference on Decision and Control*, 5468–5475. Cancun, Mexico.

Tetiker, M.D., Artel, A., Teymour, F., and Cinar, A. (2008). Control of grade transitions in distributed chemical reactor networks: An agent-based approach. *Comp. & Chem. Eng.*, 32, 1984–1994.

Venkat, A.N., Rawlings, J.B., and Wright, S.J. (2005). Stability and optimality of distributed model predictive control. In *Proceedings of the 44th IEEE Conference on Decision and Control*, 6680–6685. Seville, Spain.

Walsh, G. and Ye, H. (2001). Scheduling of networked control systems. *IEEE Contr. Syst. Mag.*, 21, 57–65.

Ydstie, B.E. (2002). New vistas for process control: Integrating physics and communication networks. *AIChE J.*, 48, 422–426.

Bidirectional Branch and Bound Method for Selecting Controlled Variables

Vinay Kariwala * **Yi Cao** **

* *Division of Chemical & Biomolecular Engineering, Nanyang Technological University, Singapore 637459 (e-mail: vinay@ntu.edu.sg)*
** *School of Engineering, Cranfield University, Bedford, UK (e-mail: y.cao@cranfield.ac.uk)*

Abstract: Controlled variable (CV) selection from available measurements through exhaustive search is computationally forbidding for large-scale problems. We have recently proposed novel bidirectional branch and bound (B^3) approaches for CV selection using the minimum singular value (MSV) rule and the local worst-case loss criterion in the framework of self-optimizing control. However, the MSV rule is approximate and worst-case scenario may not occur frequently in practice. In this work, the B^3 approach is extended to CV selection based on the recently developed local average loss metric, which represents the expected loss incurred over the long-term operation of the plant. Lower bounds on local average loss and fast pruning algorithms are derived for the efficient B^3 algorithm. Numerical tests and binary distillation column case study are used to demonstrate the computational efficiency of the proposed method.

Keywords: Branch and bound, Combinatorial optimization, Controlled variable, Self-optimizing control.

1. INTRODUCTION

The selection of controlled variables (CVs) from available measurements is an important task during the design of control systems for complex processes. Traditionally, CVs have been selected based on intuition and process knowledge. To systematically select CVs, Skogestad (2000) introduced the concept of self-optimizing control. In this approach, CVs are selected such that in presence of disturbances, the loss incurred in implementing the operational policy by holding the selected CVs at constant setpoints is minimal, as compared to the use of an online optimizer.

The choice of CVs based on the general non-linear formulation of self-optimizing control requires solving large-dimensional non-convex optimization problems (Skogestad, 2000). To quickly pre-screen alternatives, local methods have been proposed including the minimum singular value (MSV) rule (Skogestad and Postlethwaite, 1996) and exact local methods with worst-case (Halvorsen et al., 2003) and average loss minimization (Kariwala et al., 2008). Though the local methods simplify loss evaluation for a single alternative, every feasible alternative still needs to be evaluated to find the optimal solution. As the number of alternatives grows rapidly with process dimensions, such an exhaustive search is computationally intractable for large-scale processes. Thus, an efficient method is needed to find a subset of available measurements, which can be used as CVs (Problem 1).

Instead of selecting CVs as a subset of available measurements, it is possible to obtain lower losses using combinations of available measurements as CVs (Halvorsen et al., 2003). Recently, explicit solutions to the problem of finding locally optimal measurement combinations have been proposed (Kariwala, 2007; Kariwala et al., 2008; Alstad et al., 2009). It is possible, however, that the use of combinations of a few measurements as CVs may provide similar loss as the case where combinations of all available measurements are used (Kariwala, 2007; Kariwala et al., 2008; Alstad et al., 2009). Though the former approach results in control structures with lower complexity, it gives rise to another combinatorial optimization problem involving the identification of the set of measurements, whose combinations can be used as CVs (Problem 2).

Both Problems 1 and 2 can be seen as subset selection problems, for which only exhaustive search and branch and bound (BAB) method guarantee globally optimal solution. For minimization problems, a BAB approach divides the problem into several sub-problems (nodes) and calculates a lower bound of the selection criterion over all possible solutions of a node. If the lower bound is greater than an upper bound of the optimal solution, then the corresponding node is pruned (eliminated without further evaluation). In this way, the BAB method gains its efficiency in comparison with exhaustive search. The traditional BAB methods for subset selection use downwards approach, where pruning is performed on nodes with gradually decreasing subset size (Narendra and Fukunaga, 1977). Recently, a novel bidirectional BAB (B^3) approach (Cao and Kariwala, 2008) has been proposed for CV selection, where non-optimal nodes are pruned in downwards as well as upwards (gradually increasing subset size) directions simultaneously, which significantly reduces the solution time.

The bidirectional BAB (B^3) approach has been applied to solve Problem 1 with MSV rule (Cao and Kariwala, 2008) and local worst-case loss (Kariwala and Cao, 2009)

as selection criteria. A partially bidirectional BAB (PB^3) method has also been proposed to solve Problem 2 through minimization of local worst-case loss (Kariwala and Cao, 2009). The MSV rule, however, is approximate and can lead to non-optimal set of CVs (Hori and Skogestad, 2008). Selection of CVs based on local worst-case loss minimization can also be conservative, as the worst-case may not occur frequently in practice (Kariwala et al., 2008). Thus, CV selection through minimization of local average loss, which represents the expected loss incurred over the long-term operation of the plant, can be deemed as most reliable.

In this paper, lower bounds on local average loss and fast pruning algorithms are derived to develop an efficient B^3 method for CV selection using the exact local method with average loss minimization. A PB^3 method is also developed to find a subset of available measurements, whose combinations can be used as CVs to minimize local average loss. Numerical tests and binary distillation column case study are used to demonstrate the computational efficiency of the proposed method.

2. BAB METHODS FOR SUBSET SELECTION

Let $X_m = \{x_1, x_2, \cdots, x_m\}$ be an m-element set. The subset selection problem with selection criterion T involves finding an n-element subset $X_n \subset X_m$ such that

$$T(X_n^*) = \min_{X_n \subset X_m} T(X_n) \tag{1}$$

For a subset selection problem, the total number of candidates grows very quickly as m and n increase, which renders exhaustive search unviable. BAB approach can find the globally optimal subset without exhaustive search.

2.1 Unidirectional BAB approaches

Downwards. BAB search is traditionally conducted downwards (gradually decreasing subset size). A downwards solution tree for selecting 2 out of 6 elements is shown in Figure 1(a), where the root node is the same as X_m. Other nodes represent subsets obtained by eliminating one element from their parent sets. Labels at nodes denote the elements discarded there. To describe the pruning principle, let B be an upper bound of the globally optimal criterion, *i.e.* $B \geq T(X_n^*)$ and $\underline{T}_n(X_s)$ be a downwards lower bound over all n-element subsets of X_s, *i.e.* $\underline{T}_n(X_s) \leq T(X_n)\ \forall X_n \subseteq X_s$. Then,

$$T(X_n) > T(X_n^*)\,\forall X_n \subseteq X_s, \text{if } \underline{T}_n(X_s) > B \tag{2}$$

Hence, any n-element subset of X_s cannot be optimal and can be pruned without further evaluation, if $\underline{T}_n(X_s) > B$.

Upwards. Subset selection can also be performed upwards (gradually increasing subset size). An upwards solution tree for selecting 2 out of 6 elements is shown in Figure 1(b), where the root node is an empty set. Other nodes represent supersets obtained by adding one element to their parent sets. Labels at nodes denote the elements added there. To introduce the pruning principle, let the upwards lower bound of the selection criterion be defined as $\underline{T}_n(X_t) \leq T(X_n)\ \forall X_n \supseteq X_t$. Then,

$$T(X_n) > T(X_n^*)\,\forall X_n \supseteq X_t, \text{if } \underline{T}_n(X_t) > B \tag{3}$$

As downwards BAB, if $\underline{T}_n(X_t) > B$, any n-element superset of X_t cannot be optimal and hence can be pruned without further evaluation.

2.2 Bidirectional BAB approach

The upwards and downwards BAB approaches can be combined to form a more efficient bidirectional BAB (B^3) approach. This approach is applicable to any subset selection problem, for which both upwards and downwards lower bounds on the selection criterion are available (Cao and Kariwala, 2008).

Bidirectional pruning. In a B^3 approach, the whole subset selection problem is divided into several subproblems. A sub-problem is represented as the 2-tuple $\mathcal{S} = (F_f, C_c)$, where F_f is an f-element fixed set and C_c is a c-element candidate set. Here, $f \leq n$ and $n \leq f + c \leq m$. The elements of F_f are included in all n-element subsets that can be obtained by solving $\mathcal{S}$, while elements of C_c can be freely chosen to append F_f. In terms of fixed and candidate sets, downwards and upwards pruning can be performed if $\underline{T}_n(F_f \cup C_c) > B$ and $\underline{T}_n(F_f) > B$, respectively. In B^3 approach, these pruning conditions are used together (bidirectional pruning), where the subproblem $\mathcal{S}$ is pruned, if either downwards or upwards pruning condition is met.

The use of bidirectional pruning significantly improves the efficiency as non-optimal subproblems can be pruned at an early stage of the search. Further gain in efficiency is achieved by carrying out pruning on the sub-problems of $\mathcal{S}$, instead of on $\mathcal{S}$ directly. For $x_i \in C_c$, upward pruning is conducted by discarding x_i from C_c, if $\underline{T}_n(F_f \cup x_i) > B$. Similarly, if $\underline{T}(F_f \cup (C_c \backslash x_i)) > B$, then downward pruning is performed by moving x_i from C_c to F_f. Here, an advantage of performing pruning on sub-problems is that the bounds $\underline{T}_n(F_f \cup x_i)$ and $\underline{T}_n(F_f \cup (C_c \backslash x_i))$ can be computed from $\underline{T}_n(F_f)$ and $\underline{T}_n(F_f \cup C_c)$, respectively, for all $x_i \in C_c$ together, resulting in computational efficiency.

Bidirectional branching. In downwards and upwards BAB methods, branching is performed by removing elements from C_c and moving elements from C_c to F_f, respectively. These two branching approaches can be combined into an efficient bidirectional approach by selecting a decision element and deciding upon whether the decision element be eliminated from C_c or moved to F_f. In the B^3 algorithm, the decision element is selected as the one with the largest upwards or downwards upper bound for upward or downward search (best-first search), respectively.

The branching direction (upwards or downwards) is selected by comparing the number of terminal nodes (n-element subsets) of the resulting subproblems with alternate approaches such that the simpler branch is evaluated first, whilst the other branch is kept for possible pruning in future. For downwards branching, removing an element from C_c results in a subproblem with $\mathcal{C}_{c-1}^{n-f}$ terminal nodes, whilst for upwards branching, moving an element from C_c to F_f gives a subproblem with $\mathcal{C}_{c-1}^{n-f-1}$ terminal nodes. Therefore, if $2(n-f) > c$, downwards branching is performed, otherwise upwards branching is selected.

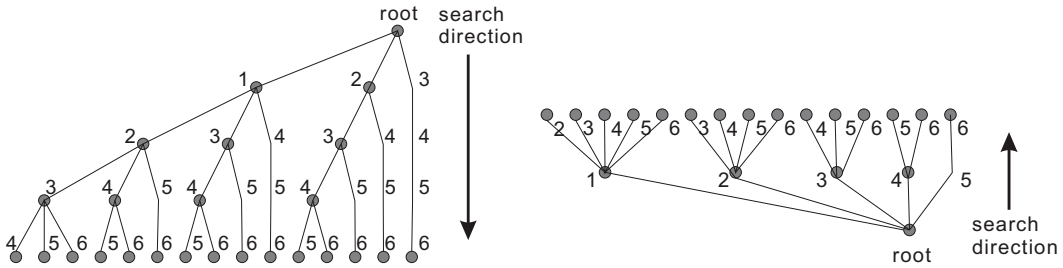

(a) downward search (b) upward search

Fig. 1. Solution trees for selecting 2 out of 6 elements.

3. SELF-OPTIMIZING CONTROL

To present the local method for self-optimizing control, consider that the economics of the plant is characterized by the scalar objective functional $J(\mathbf{u}, \mathbf{d})$, where $\mathbf{u} \in \mathbb{R}^{n_u}$ and $\mathbf{d} \in \mathbb{R}^{n_d}$ denote the degrees of freedom or inputs and disturbances, respectively. The linearized model of the process around the nominally optimal operating point is

$$\mathbf{y} = \mathbf{G}^y \mathbf{u} + \mathbf{G}_d^y \mathbf{W}_d \mathbf{d} + \mathbf{W}_e \mathbf{e} \tag{4}$$

where $\mathbf{y} \in \mathbb{R}^{n_y}$ denotes the process measurements and $\mathbf{e} \in \mathbb{R}^{n_y}$ represents the implementation error including measurement and control errors. Here, the diagonal matrices $\mathbf{W}_d$ and $\mathbf{W}_e$ contain the magnitudes of expected disturbances and implementation errors associated with the individual measurements, respectively. The CVs $\mathbf{c} \in \mathbb{R}^{n_u}$ are given as

$$\mathbf{c} = \mathbf{H}\mathbf{y} = \mathbf{G}\mathbf{u} + \mathbf{G}_d \mathbf{W}_d \mathbf{d} + \mathbf{H}\mathbf{W}_e \mathbf{e} \tag{5}$$

where $\mathbf{G}_d = \mathbf{H}\mathbf{G}_d^y$ and $\mathbf{G} = \mathbf{H}\mathbf{G}^y \in \mathbb{R}^{n_u \times n_u}$ is invertible, a necessary condition for integral control.

When $\mathbf{d}$ and $\mathbf{e}$ are constrained to satisfy

$$\left\| \begin{bmatrix} \mathbf{d}^T & \mathbf{e}^T \end{bmatrix} \right\|_2^T \leq 1 \tag{6}$$

Kariwala et al. (2008) have shown that the average loss over the set (6) is given as

$$L_{\text{average}}(\mathbf{H}) = \frac{1}{6(n_y + n_d)} \left\| (\mathbf{H}\tilde{\mathbf{G}})^{-1}\mathbf{H}\mathbf{Y} \right\|_F^2 \tag{7}$$

where $\tilde{\mathbf{G}} = \mathbf{G}^y \mathbf{J}_{uu}^{-1/2}$ and

$$\mathbf{Y} = \begin{bmatrix} (\mathbf{G}^y \mathbf{J}_{uu}^{-1} \mathbf{J}_{ud} - \mathbf{G}_d^y)\mathbf{W}_d & \mathbf{W}_e \end{bmatrix} \tag{8}$$

When individual measurements are selected as CVs, the elements of $\mathbf{H}$ are restricted to be 0 or 1 and $\mathbf{H}\mathbf{H}^T = \mathbf{I}$. Using index notation, this problem can be stated as

$$\min_{X_{n_u} \subset X_{n_y}} L_1(X_{n_u}) = \left\| \tilde{\mathbf{G}}_{X_{n_u}}^{-1} \mathbf{Y}_{X_{n_u}} \right\|_F^2 \tag{9}$$

Note that the scalar constant $1/(6(n_y+n_d))$ is neglected in (9), as it does not depend on the selected CVs. Instead of 2-norm, as used in (6), if a different norm is used to define the allowable set of $\mathbf{d}$ and $\mathbf{e}$, the resulting expressions for average losses only differ by scalar constants (Kariwala et al., 2008). Thus, the formulation of optimization problem in (9) is independent of the norm used to define the allowable set of $\mathbf{d}$ and $\mathbf{e}$.

Instead of using individual measurements, it is possible to use combinations of measurements as CVs. In this case, the integer constraint on $\mathbf{H} \in \mathbb{R}^{n_u \times n_y}$ is relaxed, but the condition $\text{rank}(\mathbf{H}) = n_u$ is still imposed to ensure invertibility of $\mathbf{H}\mathbf{G}^y$. The minimal average loss over the set (6) using measurements combinations as CVs is given as (Kariwala et al., 2008)

$$\min_{\mathbf{H}} L_{\text{average}} = \frac{1}{6\,(n_y + n_d)} \sum_{i=1}^{n_u} \lambda_i^{-1} \left(\tilde{\mathbf{G}}^T \left(\mathbf{Y}\,\mathbf{Y}^T \right)^{-1} \tilde{\mathbf{G}} \right) \tag{10}$$

Equation (10) can be used to calculate the minimum loss provided by the optimal combination of a given set of measurements. However, the use of all measurements is often unnecessary and similar losses may be obtained by combining only a few of the available measurements. Then, the combinatorial optimization problem involves finding the set of n among n_y measurements ($n_u \leq n \leq n_y$) that can provide the minimal loss for specified n. In index notation, the n measurements are selected by minimizing

$$\min_{X_n \subset X_{n_y}} L_2(X_n) = \sum_{i=1}^{n_u} \lambda_i^{-1} \left(\tilde{\mathbf{G}}_{X_n}^T (\mathbf{Y}_{X_n} \mathbf{Y}_{X_n}^T)^{-1} \tilde{\mathbf{G}}_{X_n} \right) \tag{11}$$

where the scalar constant has been omitted as (9).

4. BAB METHOD FOR CV SELECTION

As shown in Section 3, the selection of CVs using exact local method can be seen as subset selection problems. In this section, the BAB methods for solving these problems are presented. For simplicity of notation, we define the $p \times p$ matrix $\mathbf{M}(X_p)$ and the $n_u \times n_u$ matrix $\mathbf{N}(X_p)$ as

$$\mathbf{M}(X_p) = \mathbf{R}^{-T} \tilde{\mathbf{G}}_{X_p} \tilde{\mathbf{G}}_{X_p}^T \mathbf{R}^{-1} \tag{12}$$

$$\mathbf{N}(X_p) = \tilde{\mathbf{G}}_{X_p}^T (\mathbf{Y}_{X_p} \mathbf{Y}_{X_p}^T)^{-1} \tilde{\mathbf{G}}_{X_p} \tag{13}$$

where $\mathbf{R}$ is the Cholesky factor of $\mathbf{Y}_{X_p} \mathbf{Y}_{X_p}^T$.

4.1 Lower bounds

Individual measurements. L_1 in (9) requires inversion of $\mathbf{G}_{X_{n_u}}$ and thus $L_1(X_p)$ is well-defined only when $\mathbf{G}_{X_p}$ is a square matrix, *i.e.* $p = n_u$. On the other hand, BAB methods require evaluation of loss, when the number of selected measurements differs from n_u. Motivated by this drawback, two alternate representations of L_1 are derived as follows:

$$L_1(X_p) = \sum_{i=1}^{r} \lambda_i^{-1}\left(\mathbf{N}(X_p)\right) = \sum_{i=1}^{r} \lambda_i^{-1}\left(\mathbf{M}(X_p)\right) \quad (14)$$

where $r = \text{rank}(\tilde{\mathbf{G}}_{X_p})$. It is clear that for $r = p = n_u$, (14) is equivalent to (9). However, (14) generally holds for any number of measurements since $\mathbf{Y}_{X_p}\mathbf{Y}_{X_p}^T$ is invertible under the reasonable assumption that every measurement has a non-zero implementation error. Using the generalized expression for L_1 and interlacing properties of eigenvalues (Horn and Johnson, 1985), the downwards and upwards lower bounds required for the application of B^3 algorithm are derived as follows.

Proposition 1. (Lower bounds for L_1). Consider a node $\mathcal{S} = (F_f, C_c)$. For L_1 defined in (14),

$$L_1(F_f) \leq \min_{X_{n_u} \supset F_f} L_1(X_{n_u});\ f < n_u \quad (15)$$

$$L_1(F_f \cup C_c) \leq \min_{X_{n_u} \subset (F_f \cup C_c)} L_1(X_{n_u});\ f + c > n_u \quad (16)$$

To illustrate the implications of Proposition 1, let B represent the best available upper bound on $L_1(X^*_{n_u})$. Then (15) implies that, if $L_1(F_f) > B$, the optimal solution cannot be a superset of F_f and hence all supersets of F_f need not be evaluated. Similarly, if $L_1(F_f \cup C_c) > B$, (16) implies that the optimal solution cannot be a subset of $F_f \cup C_c$ and hence all subsets of $F_f \cup C_c$ need not be evaluated. Thus, upwards and downwards pruning can be conduced using (15) and (16) and the optimal solution can be found without complete enumeration.

Measurements combinations. The expression for L_2 in (11) is the same as the expression for L_1 in (14). Thus, similar to Proposition 1, it can be shown that

$$L_2(F_f \cup C_c) \leq \min_{X_n \subset (F_f \cup C_c)} L_2(X_n); \quad f + c > n \quad (17)$$

For selecting measurements, whose combinations can be used as CVs, the result in (17) is useful for downwards pruning. Equation (16), however, also implies that when $n_u \leq f < n$, $L_2(F_f)$ decreases as the subset size increases. Thus, unlike L_1, the expression for L_2 cannot be directly used for upwards pruning. In the following proposition, a lower bound on L_2 is derived, which can instead be used for upwards pruning, whenever $n - n_u < f < n$.

Proposition 2. (Upwards lower bound for L_2). For the node $\mathcal{S} = (F_f, C_c)$, let

$$\underline{L}_2(F_f) = \sum_{i=1}^{f+n_u-n} \lambda_i^{-1}\left(\mathbf{N}(F_f)\right) \quad (18)$$

where $f > n - n_u$. Then, $\underline{L}_2(F_f)$ represents a lower bound on the loss corresponding to combinations of any n measurements obtained by appending indices to F_f, *i.e.*

$$\underline{L}_2(F_f) \leq \min_{\substack{X_n \supset F_f \\ X_n \subset (F_f \cup C_c)}} L_2(X_n) \quad (19)$$

Proposition 2 implies that the lower bound of L_2 defined in (18) can be used for upwards pruning. In this case, upwards pruning can only be applied when the size of fixed set of the node under consideration is greater than $n - n_u$. Thus, the BAB algorithm based on $\underline{L}_2$ in (18) is referred to as partially bidirectional BAB (PB^3) algorithm. Development of fully bidirectional BAB algorithm for selection of measurement combination as CVs is an open problem.

4.2 Fast pruning and branching

Propositions 1 and 2 can be used to prune the non-optimal nodes quickly. Thus, the optimal solution can be found with evaluation of fewer nodes, but the solution time can still be large, as direct evaluation of L_1 in (14) and L_2 in (11) requires eigenvalue decomposition, which is computationally expensive.

Individual measurements. When $f < n_u$, $\mathbf{M}(F_f)$ in (12) is invertible. Similarly when $s = f + c > n_u$, $\mathbf{N}(S_s)$ in (13) for $S_s = F_f \cup C_c$ is invertible. Thus,

$$L_1(F_f) = \sum_{i=1}^{r} \lambda_i^{-1}(\mathbf{M}(F_f)) = \text{trace}(\mathbf{M}^{-1}(F_f)) \quad (20)$$

$$L_1(S_s) = \sum_{i=1}^{r} \lambda_i^{-1}(\mathbf{N}(S_s)) = \text{trace}(\mathbf{N}^{-1}(S_s)) \quad (21)$$

The use of (20) and (21) for evaluation of lower bounds on L_1 avoids computation of eigenvalues. The next two propositions relate the bounds of a node with the bounds of sub-nodes allowing pruning on sub-nodes directly and thus improving efficiency of the B^3 algorithm further.

Proposition 3. (Upwards pruning for L_1). Consider a node $\mathcal{S} = (F_f, C_c)$ and index $i \in C_c$. Then

$$L_1(F_f \cup i) = L_1(F_f) + \frac{\|\mathbf{z}_i^T\mathbf{Y}_{F_f} - \mathbf{Y}_i\|_2^2}{\eta_i} \quad (22)$$

where $\mathbf{z}_i = (\tilde{\mathbf{G}}_{F_f}\tilde{\mathbf{G}}_{F_f}^T)^{-1}\tilde{\mathbf{G}}_{F_f}\tilde{\mathbf{G}}_i^T$ and $\eta_i = \tilde{\mathbf{G}}_i(\mathbf{I} - \mathbf{G}_{F_f}^T(\tilde{\mathbf{G}}_{F_f}\tilde{\mathbf{G}}_{F_f}^T)^{-1}\tilde{\mathbf{G}}_{F_f})\tilde{\mathbf{G}}_i^T$.

Proposition 4. (Downward pruning for L_1). For a node $\mathcal{S} = (F_f, C_c)$, let $S_s = F_f \cup C_c$, where $s = f + c$. For $i \in C_c$,

$$L_1(S_s \setminus i) = L_1(S_s) + \frac{\|\mathbf{x}_i\mathbf{N}^{-1}(S_s)\|_2^2}{\zeta_i - \mathbf{x}_i\mathbf{N}^{-1}(S_s)\mathbf{x}_i^T} \quad (23)$$

where $\mathbf{x}_i = \mathbf{Y}_i\mathbf{Y}_{S_s\setminus i}^T(\mathbf{Y}_{S_s\setminus i}\mathbf{Y}_{S_s\setminus i}^T)^{-1}\mathbf{G}_{S_s\setminus i} - \mathbf{G}_i^T$ and $\zeta_i = \mathbf{Y}_i(\mathbf{I} - \mathbf{Y}_{S_s\setminus i}^T(\mathbf{Y}_{S_s\setminus i}\mathbf{Y}_{S_s\setminus i}^T)^{-1}\mathbf{Y}_{S_s\setminus i})\mathbf{Y}_i^T$.

In comparison with the direct calculation of L_1, the use of (22) and (23) is computationally less demanding. This happens as in (22), the inverse $(\tilde{\mathbf{G}}_{F_f}\tilde{\mathbf{G}}_{F_f}^T)^{-1}$ needs to be evaluated only once for all c sub-nodes, whilst in (23), two inverses $(\tilde{\mathbf{Y}}_{S_s\setminus i}\tilde{\mathbf{Y}}_{S_s\setminus i}^T)^{-1}$ and $N^{-1}(S_s)$ are evaluated only once for all c sub-nodes.

Measurements combinations. As the downwards pruning criteria for minimization of L_1 and L_2 are the same, Proposition 4 can be used for fast downwards pruning for selection of a subset of measurements, whose combinations can be used as CVs. The fast upwards pruning criteria for minimization of L_2 is presented in the next proposition.

Proposition 5. (Upwards pruning for L_2). Consider a node $\mathcal{S} = (F_f, C_c)$ and index $i \in C_c$. Then

$$\underline{L}_2(F_f \cup i) \geq \sum_{j=1}^{f+n_u-n+1} \frac{1}{\lambda_j(\mathbf{N}(F_f)) + t_j} \quad (24)$$

where $t = [t_1 \ \cdots \ t_{f+n_u-n+1}]^T$ is determined by solving the following linear equations:

$$t_j - t_{j+1} = \lambda_{j+1} - \lambda_j, \ j = 1, 2, \cdots, f + n_u - n \quad (25)$$

$$\sum_{j=1}^{f+n_u-n+1} t_j = \|\mathbf{s}_i\|_2^2/\beta_i \quad (26)$$

with $\mathbf{s}_i = \mathbf{Y}_i\mathbf{Y}_{F_f}^T(\mathbf{Y}_{F_f}\mathbf{Y}_{F_f}^T)^{-1}\mathbf{G}_{F_f} - \mathbf{G}_i^T$ and $\beta_i = \mathbf{Y}_i(\mathbf{I} - \mathbf{Y}_{F_f}^T(\mathbf{Y}_{F_f}\mathbf{Y}_{F_f}^T)^{-1}\mathbf{Y}_{F_f})\mathbf{Y}_i^T$.

Note that the relationship in (24) is an inequality, which can be conservative. As a BAB method spends most of its time in evaluating nodes that cannot lead to the optimal solution, we use the computationally cheaper albeit weaker pruning criteria in this paper.

5. NUMERICAL EXAMPLES

To examine the efficiency of the proposed BAB algorithms developed in this work and listed in Table 1, numerical tests are conducted using randomly generated matrices and binary distillation column case study. All tests are conducted on a Windows XP SP2 notebook with an Intel® Core™ Duo Processor T2500 (2.0 GHz, 2MB L2 Cache, 667 MHz FSB) using MATLAB® R2008a.

Table 1. BAB programs for comparison

program	description
UP	upwards pruning (22)
DOWN	downwards pruning (23)
B^3	bidirectional BAB by combining (22) and (23)
PB^3	partially B^3 by combining (23) and (24)

5.1 Random tests

To evaluate the efficiency of the different BAB algorithms developed in this work, we consider selection of n_u out of $n_y = 36$ variables, where n_u varies between 1 and 35 with $n_d = 5$. Six random matrices are generated: three full matrices, $\mathbf{G}^y \in \mathbb{R}^{n_y \times n_u}$, $\mathbf{G}_d^y \in \mathbb{R}^{n_y \times n_d}$ and $\mathbf{J}_{ud} \in \mathbb{R}^{n_u \times n_d}$, and three diagonal matrices, $\mathbf{W}_e \in \mathbb{R}^{n_y \times n_y}$, $\mathbf{W}_d \in \mathbb{R}^{n_d \times n_d}$ and $\mathbf{J}_{uu} \in \mathbb{R}^{n_u \times n_u}$. The average computation time and number of nodes evaluated over the 100 random cases are summarized in Figure 2.

From Figure 2, it can be seen that all the developed algorithms (UP, DOWN and B^3) show much superior performance than the currently used brute force method. As one may expect, upwards pruning based algorithm (UP) shows better efficiency for problems involving selection of a few variables from a large candidate set, whilst downwards pruning based algorithm (DOWN) is more efficient for problems, where a few among many candidate variables need to be discarded to find the optimal solution. The solution times for the B^3 algorithm is similar to the better of UP and DOWN algorithms, however, its efficiency is insensitive to the kind of selection problem. Within 1000 seconds, both UP and DOWN algorithms can only handle problems with $n_u < 9$ or $n_y - n_u < 9$. For all cases,

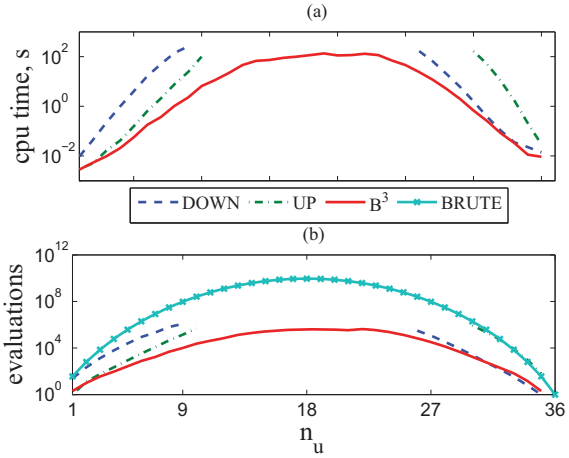

Fig. 2. Random test: (a) computation time and (b) number of nodes evaluated against n_u.

however, the B^3 algorithm exhibits superior efficiency and is able to solve the problem with $n_u = 18$ within 200 seconds.

5.2 Distillation column case study

To demonstrate the efficiency of the developed PB^3 algorithm, we consider self-optimizing control of a binary distillation column (Skogestad, 1997). The objective is to minimize the deviation of the distillate and bottoms composition from their nominal steady-state values in presence of disturbances in feed flow rate, feed composition and vapor fraction of feed. Two degrees of freedom (reflux and vapor boilup rates) are available and thus two CVs are required for implementation of self-optimizing control strategy. It is considered that the temperatures on 41 trays are measured with an accuracy of $\pm 0.5^o$ C. The combinatorial optimization problem involves selection of n out of 41 candidate measurements, whose combinations can be used as CVs. The reader is referred to Hori and Skogestad (2008) for further details of this case study.

The PB^3 algorithm is used to select the 10 best measurement combinations for $2 \leq n \leq 41$. The trade-off between the losses of the 10 best selections and n is shown in Figure 3(a). It can be seen that when $n \geq 14$, the loss is less than 0.075, which is close to the minimum loss (0.052) by using a combination of all 41 measurements. Furthermore, the reduction in loss is negligible, when combinations of more than 20 measurements are used.

Figures 3(b) and (c) show the computation time and number of node evaluations for PB^3 and DOWN algorithms. Overall, both algorithms are very efficient and are able to reduce the number of node evaluations by 5 to 6 orders of magnitude, as compared to the brute force search method. For example, to select 20 measurements from 41 candidates, evaluation of a single alternative requires about 0.15 ms on the specified notebook computer. Thus, a brute force search methods would take more than one year to evaluate all possible alternatives. However, both PB^3 and DOWN algorithms are able to solve this problem within 100 seconds. Hence, without algorithms developed here, it

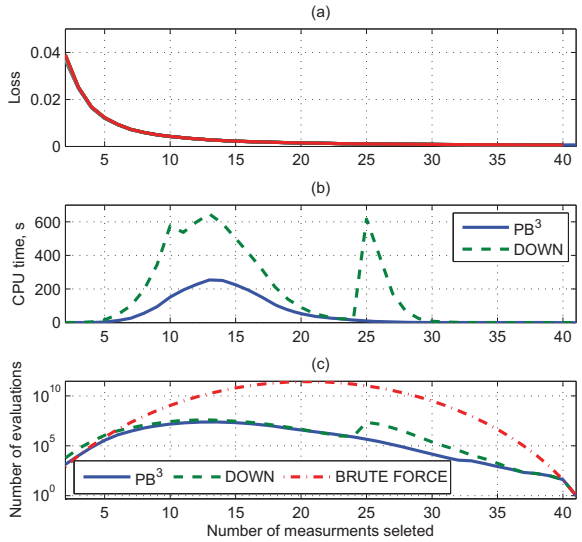

Fig. 3. (a) Average losses of 10-best measurement combinations against the number of measurements, (b) Comparison of computation time, and (c) Comparison of number of node evaluations

would be practically impossible to generate of the trade-off curve shown in Figure 3(a).

Due to the conservativeness of the pruning condition (24), the PB^3 algorithm is only able to reduce the number of node evaluations and hence computation time up to a factor of 2 for selection problems involving selection of a few measurements from a large candidate set. It is expected that a less conservative or fully upwards pruning rule would improve the efficiency, but the derivation of such a rule is currently an open problem.

6. CONCLUSIONS

In this paper, the concept of bidirectional branch and bound (BAB) proposed in Cao and Kariwala (2008) has been further developed for selection of controlled variables (CVs) using the local average loss minimization criterion for self-optimizing control (Kariwala et al., 2008). The numerical tests using randomly generated matrices and binary distillation column case study show that the number of evaluations for proposed algorithms is 4 to 5 orders of magnitude lower than the current practice of CV selection using brute force search.

The computational efficiency of the algorithms developed in this paper based on bidirectional pruning and branching principles and fast pruning algorithms is compatible to the BAB approach for CV selection based on minimum singular value (MSV) rule (Cao and Kariwala, 2008) and the local worst-case criterion (Kariwala and Cao, 2009). Despite the availability of the exact local criteria (the worst case and average loss), one of the apparent reasons for continued use of the approximate MSV rule is its computational efficiency. This work makes CV selection using the local average loss criterion computationally tractable so that it can be adopted as a standard tool for CV selection in the self-optimizing control framework.

While the algorithm for selection of individual measurements as CVs is fully bidirectional, the algorithm for selection of subset of measurements, whose combinations can be used as CVs, is only partially bidirectional. It is expected that the development of a fully bidirectional BAB algorithm for the latter problem would improve the computational efficiency further. Furthermore, the combination matrix H that minimizes average loss also minimizes worst-case loss (Kariwala et al., 2008). This super-optimality, however, only holds for a given subset of measurements and in general, different measurement subsets can be optimal for these two criteria. An extension of the bidirectional BAB algorithm to select CVs based on the bi-objective minimization of local worst-case and average losses for self-optimizing control is currently under consideration.

ACKNOWLEDGEMENTS

The first author gratefully acknowledges the financial support from Office of Finance, Nanyang Technological University, Singapore through grant no. RG42/06.

REFERENCES

Alstad, V., Skogestad, S., and Hori, E.S. (2009). Optimal measurement combinations as controlled variables. *J. Proc. Control*, 19(1), 138–148.

Cao, Y. and Kariwala, V. (2008). Bidirectional branch and bound for controlled variable selection: Part I. Principles and minimum singular value criterion. *Comput. Chem. Engng.*, 32(10), 2306–2319.

Halvorsen, I.J., Skogestad, S., Morud, J.C., and Alstad, V. (2003). Optimal selection of controlled variables. *Ind. Eng. Chem. Res.*, 42(14), 3273–3284.

Hori, E.S. and Skogestad, S. (2008). Selection of controlled variables: Maximum gain rule and combination of measurements. *Ind. Eng. Chem. Res.*, 47(23), 9465–9471.

Horn, R.A. and Johnson, C.R. (1985). *Matrix Analysis*. Cambridge University Press, Cambridge, UK.

Kariwala, V. (2007). Optimal measurement combination for local self-optimizing control. *Ind. Eng. Chem. Res.*, 46(11), 3629–3634.

Kariwala, V. and Cao, Y. (2009). Bidirectional branch and bound for controlled variable selection: Part II. Exact local method for self-optimizing control. *Comput. Chem. Eng.*, Accepted for publication.

Kariwala, V., Cao, Y., and Janardhanan, S. (2008). Local self-optimizing control with average loss minimization. *Ind. Eng. Chem. Res.*, 47(4), 1150–1158.

Narendra, P. and Fukunaga, K. (1977). A branch and bound algorithm for feature subset selection. *IEEE Trans. Comput.*, C-26, 917–922.

Skogestad, S. (1997). Dynamics and control of distillation columns - A tutorial introduction. *Trans. IChemE Part A*, 75, 539–562.

Skogestad, S. (2000). Plantwide control: The search for the self-optimizing control structure. *J. Proc. Control*, 10(5), 487–507.

Skogestad, S. and Postlethwaite, I. (1996). *Multivariable Feedback Control: Analysis and Design*. John Wiley & sons, Chichester, UK, 1st edition.

Plantwide control of fruit concentrate production

Mark van Dijk, Sander Dubbelman, Peter Bongers *

**Unilever Research Vlaardingen Netherlands, Process Systems Engineering.*
(E-mail: mark-van.dijk@unilever.com).

Abstract: Fruit concentrates are key ingredients in many fruit based Unilever products. We have designed a novel continuous fruit concentration process involving a decanter, an evaporator and a recombination process. In order to ensure best product quality and highest capacity a methodology for control structure design for complete processing plants (plantwide control) was applied. This included defining the control objectives, degrees of freedom analysis, definition of inventory and production rate control and the development of a non-linear dynamic model. Using the methodology, control alternatives were systematically analyzed and eliminated. The chosen control structure was successfully applied and implemented in a Unilever factory.

Keywords: Control structure design; Plantwide control; Dynamic control model; Decanter; Evaporator.

1. INTRODUCTION

Plantwide control is viewed as a strong methodology to design effective control structures in complex food plants.[1]

This paper presents the conceptual process control design of a novel fruit concentration method using a separation and recombination step. It involves the development of a dynamic control model of the system, the design of a suitable control strategy with the help of this model, the implementation of the control strategy in an actual factory process control system and evaluation of its performance.

1.1 Background

Traditionally fruit purees are produced by concentrating the fruit pulp in a forced recirculation evaporator, which are known to be detrimental to product quality because of their large residence time and high temperatures.

We have developed a novel fruit concentration process involving the use of a separation step to separate the fruit pulp into a cake fraction and a serum fraction. Because of the absence of fibres in the serum fraction, the serum fraction can be concentrated at lower temperatures, thus maintaining its freshness. Simultaneously, the fibres are not exposed to high shear and will therefore better maintain their water-binding properties.

A draw-back of the novel fruit concentration process is that the cake fraction and the concentrated serum fraction need to be recombined into a homogeneous fruit paste in a controlled way. At the same time, the Brix and viscosity of the resulting fruit concentrate need to be maintained within normal food standards. For this reason, a systematic approach is required in order to design an effective control strategy.

1.2 Approach

Plantwide control is a concept or methodology to systematically build control structures of large, continuous processes with complex interactions [1, 2, 3]. Process modelling and simulation form an important aspect of the method. It follows a series of logical steps which are easy to apply in practice:

1. Definition of Operational Control Objectives
2. Manipulated Variables and Degrees Of Freedom
3. Primary Controlled Variables
4. Production Rate
5. Regulatory Control Layer
6. Supervisory Control Layer
7. Optimization Layer
8. Validation

We applied most steps of this methodology in conjunction with a conceptual process design methodology [4] to ensure that the integration of process, equipment and control design is optimal. This paper will focus on the first five steps. In chapter 2 we will go systematically through steps 1 to 5 given above based on the process given in figure 2.1. Next, we will present the assumptions behind the underlying mathematical model that we used to determine the best control strategy. Finally we will present the results from the industrial process that we implemented in one of our factories.

2. PLANTWIDE CONTROL PROCEDURE

2.1 STEP 1: Overall control objective. Identify operational constraints.

The process control aims at producing high grade, constant quality fruit paste. Good quality paste has a nice red

[1] This is in contrast with plantwide automation which addresses the design and implementation of Industrial Process Control and Automation Systems (IPCAS).

colour, constant Brix (sugars) and Bostwick (viscosity) values and also good taste and flavour. In order to achieve this, it is necessary to control the product flow throughout the plant smoothly and to minimise the hold-up time of product in the system. The following process and control system requirements were considered:

Process Requirements

Maximization of assets. Maximization of plant output is a key objective since fruit concentration processes are mostly seasonal continuous operations. It is therefore important that the bottleneck is 100% utilised. In our case, the evaporator is the bottleneck of the process.

Process reliability. There are many factors in the process not directly related to the control system or strategy, which influence the control performance. A major factor is the overall factory reliability (equipment and utilities). The novel process is more complex and especially vulnerable for unplanned stoppages. Both factory reliability and the control system robustness towards unplanned stoppages are essential aspects to consider in the design process.

Equipment restrictions. It is industry practice to operate decanters with a constant in-flow in order to get a stable liquid/solid separation. It is recommended that feed flow variations are less than ±20%. It is also industry practise to operate forced recirculation evaporators with a constant steam supply (constant evaporation rate).

Fruit quality fluctuations. The fibre- and sugar content of raw fruit juice is known to vary up to ±20% on an hourly basis. The fibre- and sugar content vary independently.

Control system requirements

End-product variability Brix. The Brix boundaries should be less than 1.0 Brix from controller setpoint for commercial purposes.

End-product variability Bostwick. The Bostwick should be the same or lower as normal variations in standard paste (typically +/- 0.5 cm). This implies that there should not be *more* variation in the ratio of sugars to fibers in the puree as in the original fruit.

Simple control. The control strategy must be able to be implemented in the SIEMENS Control System and must be relatively easy to understand for the operators. For this reason, the control strategy is based on standard PID-controllers.

2.2 STEP 2: Manipulated variables and degrees of freedom.

According to the principles by Skogestad, we will identify dynamic and steady-state Degrees Of Freedom (DOF) based on the process given in figure 2.1 according to the equation below:

$$N_{ss} = N_m - (N_{0m} + N_{0y})$$

In which:

N_{ss}	Number of steady state DOFs
N_m	Number of dynamic (control) DOFs (valves, pumps)
N_{0m}	Number of manipulated input variables with no steady state effect
N_{0y}	Number of output variables with no steady state effect (product levels)

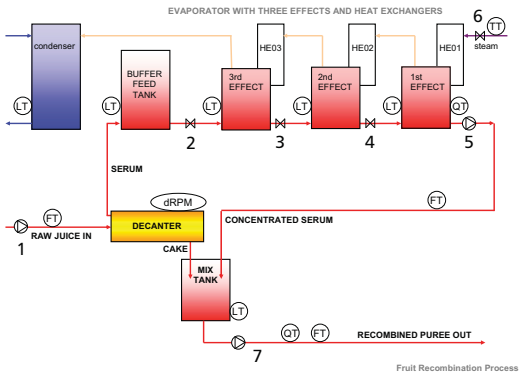

Figure 2.1: Process Flow Diagram of novel fruit concentration process with Degrees Of Freedom (DOFs).

As can be seen from figure 2.1, 7 dynamic DOFs (N_m) can be identified. Since the process consists of 5 tanks, there are 5 tank levels that need to be controlled (N_{0y}), but that do not contribute to the steady state mass- and composition balance. This means that there are two remaining DOFs (N_{ss}) to control the whole process. This is identical to an existing fruit concentrate process in which the two DOFs are used to control the Brix of the puree and the production rate. However we know that the dynamics of the novel process have changed, because we have combined a slow evaporation process with a fast separation process in one additional process step (the mix tank). Therefore a dynamic model is essential to evaluate the new process dynamics and possible process control structures.

2.3. STEP 3: Primary controlled variables.

Skogestad states that the primary variable to control is the active constraint. According to our control objectives, this is overall production rate as set by the evaporator. Another key primary controlled variable is the Brix of the resulting fruit puree. The Brix is given by the following equation:

$$\phi_{puree} \cdot Brix_{puree} = \phi_{cake} \cdot Brix_{cake} + \phi_{concentrated\ serum} \cdot Brix_{concentrated\ serum}$$

in which:

ϕ_{puree}	Flow of puree [kg/s]
$Brix_{puree}$	Brix of puree [Brix]
ϕ_{cake}	Flow of cake [kg/s]
$Brix_{cake}$	Brix of cake [Brix]
$\phi_{concentrated\ serum}$	Flow of concentrate serum [kg/s]
$Brix_{concentrated\ serum}$	Brix of concentrate serum [Brix]

The flow rate of cake is mainly driven by the amount of fibres in the fruit juice as well as the way the decanter is operated (level of drying of the cake), whereas the Brix of the cake is driven by the fruit variety, ripeness and other agronomical factors. Both Brix and flow rate of concentrated serum are highly dependent on the way that

the evaporator is operated and controlled. The chance of product that is out of specification is high since it is dependent on four variables.

2.4 STEP 4: Set of production rate.

The choice where to set the production rate determines the structure of the remaining inventory (level) control system. The production rate should be set at the (dynamic) bottleneck of the process as explained in section 2.3. For the traditional fruit concentrate process, the production rate is determined by the slow evaporator (dynamic bottle-neck). The evaporator is operated at a fixed steam pressure (constant evaporation rate). The up-stream and down-stream processes follow the evaporation rate. Since the end product Brix is controlled through manipulating the evaporator out-feed pump, this means the product flow through all unit operations is changing constantly dependent on the incoming Brix of the raw juice.

On the other hand, it is industry experience that decanters require a constant feed (within 20% of the main flow) to have the best performance. This requires controlling the flow towards the decanter and setting the production rate here, through a flow controller.

In order to control the level in the evaporator feed tank, therefore two options do exist:

A. **Control the level via manipulation of the steam supply** (thus via manipulation of the evaporation rate). No constant steam supply means that the evaporator cannot be operated at constant evaporation rate and temperatures. The potential negative impact should be evaluated and preferably minimized.

B. **Control the level via manipulation of the inflow to the decanter.** It is clear that in this scenario no constant inflow to the decanter can be guaranteed and that the potential negative impact on separation performance should be evaluated and minimized. It is noted that controlling the level through decanter serum outflow will disturb the separation process and therefore is not feasible.

Either scenario clearly forced us to deviate from the industry practice w.r.t equipment operation.

Already at this stage of the methodology we decided to develop a dynamic model based on the following arguments:

- The choice of setting the production rate highly influences the dynamics of the overall process
- There is a direct correlation between productivity and end-product composition in concentration processes
- The recombination process is highly vulnerable to variations
- We deviate from the industry standard w.r.t. equipment operation for either the decanter or the evaporator.
- The design of the control system will influence the process design, like the design of the recombination tank.

The model must involve the complete regulatory control layer in order to decide on the best control strategy. In section 2.5, we will provide the results from the model simulations and we will demonstrate how we used this to evaluate the various control strategies.

2.5. STEP 5, 6 and 8: Regulatory and Supervisory Control layers and Validation.

Section 2.4 showed that the production rate could not be defined because of the strong interactions between production rate, inventory control and product composition. It was also shown that there are two DOFs. With these two DOFs, a steady state analysis demonstrates that we can control the production rate and the Brix of the fruit puree in the following way:

1. Puree Brix control through manipulation of the concentrated serum Brix. Steady state mass- and composition balances show that an increase in concentrated serum Brix will increase the Brix of the resulting puree. Based on this, a cascade control loop can be designed. In this way, no extra DOF needs to be created and no additional equipment is required.

However, if the dynamics of this control structure prove to be unsuitable to control the Brix of the fruit puree, one additional DOF will be required in order to make the process controllable. This DOF should have sufficiently fast response time and a sufficient process gain. We have designed two alternative ways to create one extra DOF:

2. Puree Brix control through manipulation of decanter settings. By changing the differential speed of the screw inside the decanter [5] the amount of juice incorporated inside the cake can be controlled. Reducing the differential speed will send less water via the cake to the recombination tank and the Brix of the resulting puree will increase.

3. Puree Brix control through addition of juice to recombination tank. A third stream of juice can be added to the recombination tank to dilute a slightly over-concentrated puree to the specified composition.

All scenarios are summarized in table 2.1.

Table 2.1: Overview of control scenarios.

Production rate Brix control	Extra DOF created?	A. Control the level via steam supply	B. Control the level via inflow to the decanter.
1. Puree Brix control through manipulation of the concentrated serum Brix	No	A1	B1
2. Puree Brix control through manipulation of decanter settings.	Yes	A2	B2
3. Puree Brix control through addition of juice to recombination tank	Yes	A3	B3

Despite the fact that scenarios A1 and B1 are feasible based on steady state, an inverse response occurs initially: Upon increasing of the concentrated serum Brix (see figure 2.2 at t=10 hours), the outflow pump first slows down in order to increase the residence time in the first effect. The result is an inverse response of the puree Brix. This clearly demonstrates that in concentration processes, flow and concentration level are inversely proportional.

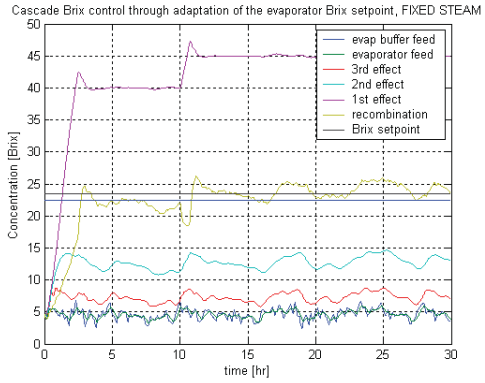

Figure 2.2: Dynamic model simulation of scenario A1. The inverse response in puree Brix (denoted in yellow-green as 'recombination') at t=10 hours is clearly visible.

The conclusion is that the additional DOF is required (Scenarios A2, B2, A3 and B3). In order to decide on the optimal control strategy, we will first evaluate the A2 and B2-strategies against the A3 and B3-strategies.

For strategies A2 and B2 the dynamic behaviour and operating window of the decanter needs to be known. Based on step response measurements on the serum exiting the decanter (see figure 2.3), we estimated that the response time of the cake fraction upon changes in differential speed is in the order of 300 seconds (three times the response time of the serum fraction).

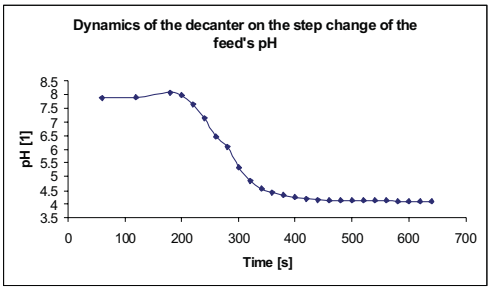

Figure 2.3: Response time of decanter serum exit on a step change in pH via citric acid addition (at 170 s).

Figure 2.4 shows the response behaviour of the solids concentration in the cake exiting the decanter as a function of changes in the differential speed (courtesy of GEA Westfalia). It can be seen that there is a strong response, but only in a small operating window. Also can be seen that the machine operation is highly non-linear.

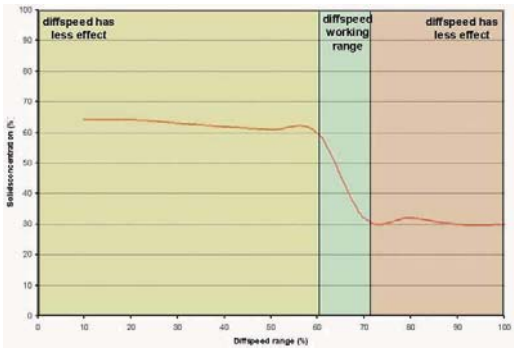

Figure 2.4: Response of solids concentration in the cake from a decanter. Courtesy of GEA Westfalia GmbH.

The results of the simulations with the above time delay and response behaviour are shown for scenario A2 in figure 2.5. As can be seen the fruit puree Brix cannot be kept within the desired range. Scenario B2 (not shown) behaved in a similar way. This means that the decanter is too slow to be used in a control loop, thus rendering strategies A2 and B2 ineffective.

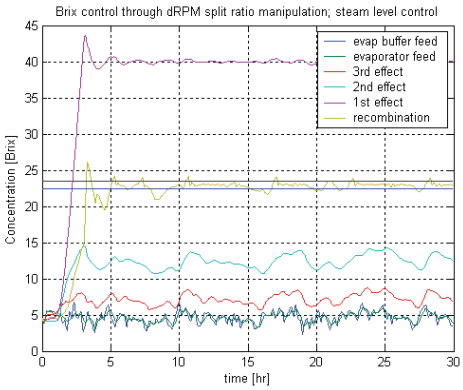

Figure 2.5: Dynamic model simulation of scenario A2. Fruit puree Brix control through manipulation of decanter settings. It can be seen that the Brix of the fruit puree (denoted in yellow-green as 'recombination') cannot be maintained within the desired range of ±1 Brix around setpoint.

We now need to decide between the scenarios A3 and B3. For a stable process, it is important that both concentrated serum and cake are recombined according to its natural ratio. This means that there cannot be an excess flow of either cake or concentrated serum in the mix tank. In this way no changes in hold-up volume of either the cake fraction or the serum fraction should occur. The only location where significant changes in hold-up volume can occur is the evaporator feed tank.

Figure 2.6 shows the level in the evaporator feed tank for scenarios A3 and B3. It can be seen that both control

strategies can control the level in this tank, but control strategy A3 requires a much longer time upon start-up to reach a stable level (> 5 hours). This means that this strategy is very slow due to the slow response of the evaporator upon changes in steam supply. For this reason, this control strategy is very vulnerable to disturbances and not recommended.

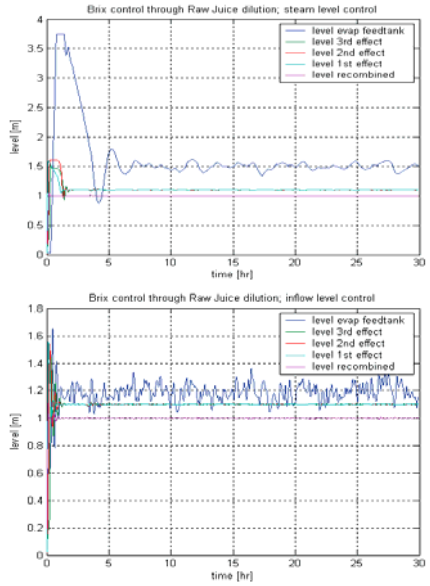

Figure 2.6: Dynamic model simulation of scenarios A3 (top) and B3 (bottom). It can be seen that the time delay to reach a setpoint of the evaporator feed tank is in the case of scenario A3 is in the order of 5 hours and in scenario B3 in the order of 1 hour.

Scenario B3 gave the right dynamic behaviour to control the evaporator feed tank, allowing for a proper recombination of concentrated serum and cake. Figure 2.7 demonstrates that this strategy is also able to control the Brix of the fruit puree. Also, it can be seen that the variation of the ratio of sugars to fibers is within variations found in the raw material. Thus control strategy B3 is most suitable for this process.

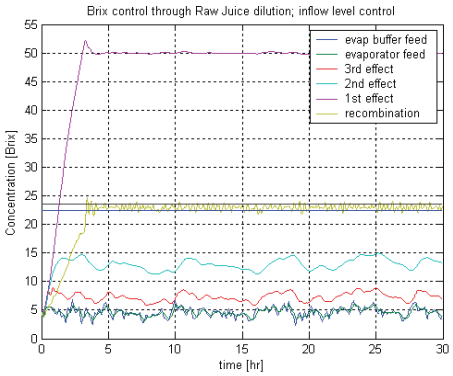

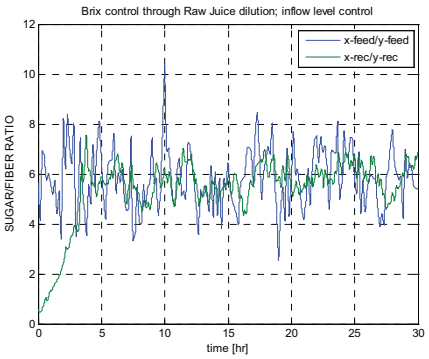

Figure 2.7: Dynamic model simulation of scenario of control strategy B3. It can be seen that the Brix of the fruit puree (denoted in yellow-green as 'recombination') can be maintained within the desired range of ±1 Brix around setpoint (left bottom). The ratio of sugars to fibers in the feed (x-feed/y-feed) and in the fruit puree (x-rec/y-rec) are shown above.

Proper tuning of the level control loop of the evaporator feed tank further contributes to the overall process stability. In order to minimize fast fluctuations in decanter inflow, it was decided to use a P-algorithm and to set the gain value relatively low. In this way, the evaporator feed tank can be used as a real buffer without impacting on the ratio of sugars to fibers. Also feed fluctuations to the decanter are minimised.

The resulting process flow diagram for strategy B3 with all sensors, actuators and control loops is given in figure 2.8.

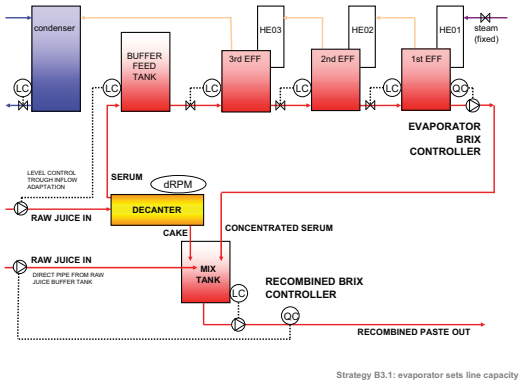

Figure 2.8: Process flow diagram with for strategy B3 with sensors, actuators and the final control structure.

3. DYNAMIC MODEL

We built a non-linear dynamic model in Matlab/Simulink [6] based on:

- Dynamic mass- and composition balance for all tanks
- Dynamic heat balance for all heat exchangers with the heat transfer coefficient estimated based on real-time factory data
- Steady state equations for the decanter with a first order transfer function with lag time
- Band-limited white noise in feed sugar and fibre levels of ±20% around the average
- PID-feedback control

4. IMPLEMENTATION INTO THE FACTORY

4.1 IPCAS implementation

The process and control strategy as defined before was implemented in a Unilever factory. To this purpose a "User Requirements Specification of the Industrial Process Control and Automation System (IPCAS)" was written. It specifies the Industrial Process Control System (PLC/SCADA process computer hardware and software), instrumentation and installation infrastructure.

4.2 Evaluation of control strategy B3 under factory conditions

The performance of the selected control strategy that was implemented in the SIEMENS PLC/SCADA system was evaluated during actual production.

Figure 4.1 shows that for the given day, the whole production was within specifications. During one whole season, the average Brix was 22.92 (with a setpoint of 23) with a standard deviation of only 0.3.

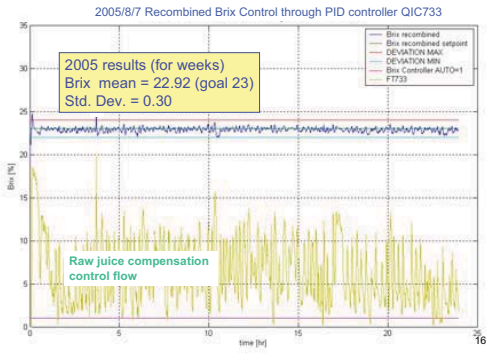

Figure 4.1: Factory data of fruit puree Brix (named QIC 733 in factory control system). Also the flow rate (named FT733 in the factory control system; raw juice compensation control flow) of the added juice is depicted. This flow rate should be multiplied by 100 and is expressed in kg/hour.

5. CONCLUSIONS

In this paper we presented a novel fruit concentrate production process involving a decanter, an evaporator and a recombination process. The choice for this process results in complex, non-linear, process dynamics. Such processes can be difficult to control and a systematic methodology was required.

We demonstrated that a strategy in which the Brix is controlled via addition of a third juice stream was the best choice for the given process. Evaluation of the control strategy under real factory conditions showed that the control strategy is very robust and that end-product specifications are met.

This case demonstrated to us that it is important to integrate control strategy design in an early stage with process and equipment design. Furthermore we required a non-linear dynamic model to understand the complex dynamics of the process and to design an appropriate control strategy.

REFERENCES

[1] Skogestad S., ″Control Structure Design for Complete Chemical Plants″, Computers and Chemical Engineering, 28 (2004), pp. 219-234.

[2] Luyben M.L., Tyreus B.D., Luyben W.L., ″Plantwide Control Design Procedure″, AIChE Journal, 43 (1997), pp. 3161-3174.

[3] E. M. Vasbinder, K. A. Hoo and U. Mann, Computer Aided Chemical Engineering, Volume 17, 2004, Pages 375-400 ; ″Synthesis of plantwide control structures using a decision-based methodology″.

[4] Douglas J.M., ″Conceptual Design of Chemical Processes, McGraw-Hill″, New York (1988).

[5] Records A., Sutherland K. ″Decanter Centrifuge Handbook″, Elsevier, Oxford (2001).

[6] Matlab/Simulink, Dynamic modelling and simulation software. The MathWorks, Inc.

Emerging Methods and Technologies

Oral Session

Monitoring, Analysis and Diagnosis of Distributed Processes with Agent-Based Systems ⋆

Ali Çinar * **Sinem Perk** * **Fouad Teymour** * **Michael North** **
Eric Tatara ** **Mark Altaweel** **

* *Department of Chemical and Biological Engineering, Illinois Institute of Technology, Chicago, IL 60616 USA (e-mail: perksin@iit.edu)*
** *Argonne National Laboratory, Argonne, IL 60439 USA (e-mail: north@anl.gov)*

Abstract: Multiagent systems provide a powerful framework for developing real-time process supervision and control systems for distributed and networked processes by automating adaptability and situation-dependent rearrangement of confidence to specific monitoring and diagnosis techniques. An agent-based framework for monitoring, analysis, diagnosis, and control with agent-based systems (MADCABS) is developed and tested by using detailed models of chemical reactor networks. MADCABS is composed of three main hierarchical layers, the physical communication layer, the supervision layer and the agent management layer. The supervision layer consists of agents and methods for data preprocessing, process monitoring, fault diagnosis, and control. The agent management layer conducts the assessment of agent performances to assign the priorities for selecting the most useful methods of process supervision for specific types of situations. The paper illustrates the operation of MADCABS for monitoring and fault detection.

Keywords: Multi-agent systems, process monitoring, fault detection, fault diagnosis, process supervision, process control, distributed systems, distributed artificial intelligence, autocatalytic reactions.

1. INTRODUCTION

Multi-layered and adaptive multiagent systems (MAS) provide a powerful framework for developing a new generation of real-time supervision and control systems for distributed and networked processes. The strategy, techniques and tools are being developed at IIT for monitoring, analysis, diagnosis, and control with agent-based systems (MADCABS) that automates knowledge extraction from data, analysis, and decision making. This distributed artificial intelligence framework is expected to enable the consideration of novel configurations for manufacturing such as distributed reactor networks to produce high-value-added specialty chemicals.

There are strong reasons for distributing the activities and intelligence in software for supervision of distributed process operations:

- The complex layout of a manufacturing process yields a problem that is physically distributed,
- The supervision problem is distributed and heterogeneous in functional terms,
- The complexity of the supervision problem dictates a local point of view that contributes to the development of system-wide decisions that may force reexamination of local decisions,
- The supervision system must be able to adapt to changes in the structure or environment of the supervised process or network.

Agents are capable of acting, communicating with other agents, perceiving their environment, and determining behavior to satisfy their objectives. They are endowed with autonomy and they possess resources. However, the MAS framework offers challenges as well: Agents have only partial information about their environments, they may act "selfishly" or initiate actions that may conflict with actions of other agents. This may lead to undesirable or harmful behavior in MADCABS or the supervised process, compromising its profitability and safety.

The nature of the supervision problem dictates the use of multiple layers of agents where lower-level agents perform local well-defined tasks such as information validation from sensors and higher-level agents perform more global tasks over wider regions of the supervised system. Several agents can be used to perform a specific task, each using different methods to enable not only decision by consensus-building but also to reduce the influence of the weaker methods over time. Intelligence and adaptation is provided both at agent and at system level.

MADCABS is composed of three main hierarchical layers, the *physical communication* layer, the *process supervision* layer and the *agent management* layer. The physical layer is where two-way information communication between the

⋆ This work is supported by the National Science Foundation CTS-0325378 of the ITR program.

process and MADCABS takes place. Process information, such as the flowchart of the process is mapped to MADCABS through the physical communication layer. The supervision layer consists of agents and methods for data preprocessing, process monitoring, fault diagnosis, and control. Data preprocessing agents filter the process data, check for outliers and missing data, and provide estimates for them. Monitoring agents detect deviations from normal operation and trigger the fault detection and diagnosis (FDD) agents. When abnormal process operation is validated, FDD is carried out using contribution plots, statistical methods, and process knowledge. Control agents range from simple local PI controllers to decentralized plant-wide grade transition agents. Some agents collaborate to help each other, while others work in a competing manner to satisfy a global objective. The performances of different agents and methods are evaluated in the topmost agent management layer. The agent management layer is responsible for selecting the best performing agents for process monitoring, fault detection and diagnosis, and process control for the current operating conditions. The assessment of agent performances guide the priorities assigned to select the most useful methods of process supervision for specific types of situations.

In this paper, MADCABS modules for monitoring and fault detection, and the information flow among them is discussed. The paper focuses on the architecture and functionality of MADCABS, the automated tools for assessing the success of its various functions, the redundancies in MADCABS, and the adaptation of MADCABS based on the current state of process operations. The communication and cooperation between different MADCABS modules is demonstrated with case studies using autocatalytic CSTR networks. The capabilities of MADCABS in detecting and diagnosing various types of faults are shown.

2. PROCESS MONITORING, FAULT DETECTION AND DIAGNOSIS

2.1 Statistical Process Monitoring Techniques

Multivariate statistical process monitoring (SPM) techniques are used in this study. Multivariate techniques that extract the correlation among variables based on principal component analysis (PCA) provide the basic tool for monitoring continuous processes (Kourti and MacGregor (1996); Cinar et al. (2007); Jackson (1980)). PCA is a multivariate projection method that extracts strong correlations among the variables in a data set, and based on that information defines a new orthogonal coordinate space where the coordinate axes are the highest variance directions. For chemical processes, where large highly-correlated process datasets need to be monitored, singularity problems may arise. PCA is well-suited for reducing the dimensionality of the data and capturing the essential information in the data.

For large processes that involve many processing units and many process variables with different correlation structures, a single PCA model for the whole process may not give sufficient explanation about the process behavior, may provide unreliable information based on many false and missed alarms, and may have difficulty localizing the source cause among so many variables when a fault is detected. Multiblock methods have been proposed in literature for large processes, where the process can be separated into meaningful process blocks, to increase the efficiency and interpretability of the statistical monitoring model. Algorithms to handle multiple data blocks include hierarchical PCA (HPCA) and consensus PCA(CPCA) (Qin et al. (2001); Wangen and Kowalski (1988); Westerhuis et al. (1998); Wold et al. (1996)). Multiblock algorithms enable monitoring of the process both locally and globally. The CPCA method is designed for comparing several blocks of descriptor variables measured on the same objects (Wold et al. (1996); Westerhuis et al. (1998)).

Dynamic PCA (DPCA) is an extension of conventional PCA to deal with multivariate process data that is correlated in time, using a time-lag shift method (Ku et al. (1995)). The flow of action, namely, monitoring, fault detection and diagnosis, is the same for all SPM methodologies independent of which monitoring algorithm is employed.

2.2 Fault Detection, Monitoring and Diagnosis Framework in MADCABS

MADCABS is written in Java, using Repast Simphony as the agent building platform (ROAD (2005)). Among the important features of Repast that MADCABS uses are its object oriented structure, scheduling tools and its built-in automated Monte Carlo simulation framework. Repast also allows users to change, add, delete agents in run time.

In Repast Simphony, a *context* is defined as a container where the agents reside. There are three contexts for monitoring, fault detection and diagnosis agents in MADCABS. The communications between different agents in these contexts are shown in Figure 1. Statistical models are built by the monitoring agents. The fault detection agents, which are the monitoring statistics, assign themselves to the fault detection organizer agents responsible for each subsystem that is monitored. A fault is flagged when a consensus is formed among different fault detection agents on the existence of a fault in the system. The fault flag triggers the diagnosis agent. Diagnosis agent uses information from the neighboring fault detection organizers, finds the most contributing process variables to the fault on the faulty subsystem, and investigates the potential reasons behind the fault.

Monitoring Agents. The monitoring agents are PCAStarter, DPCAStarter and MultiblockStarter agents and a monitoring organizer (Figure 2). After the system reaches steady state and a sufficient amount of normal operation data is available, monitoring starters are scheduled to form models. For all process units, a local statistical model is built using both PCA and DPCA. In the distributed framework, this is achieved by creating as many PCAStarters and DPCAStarters as the number of operating units. Each PCAStarter agent builds a separate PCA model since the data and the PC number that is used to build the models are different for each unit. DPCAStarters work identical to PCAStarters. There is only one MultiblockStarter for the whole process. In this case, the data blocks consist of data from each operating unit. The MultiblockStarter forms a single multiblock model, which

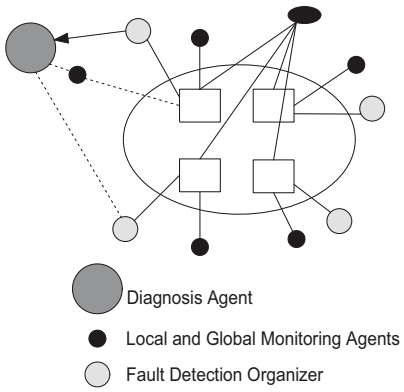

Fig. 1. Monitoring, fault detection and diagnosis agents in a four reactor network

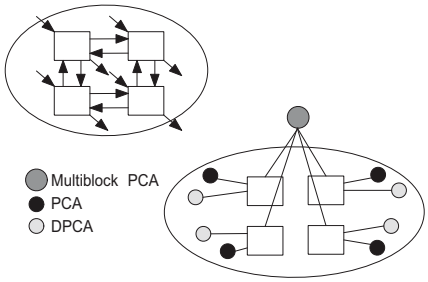

Fig. 2. Monitoring agents. The upper figure represents a four reactor network, which is simplified in the lower figure.

enables the monitoring of the process both locally and globally through block statistics and super statistics. Since there is only one model, the size retained in the model is the same for each block.

The starter agents are subclasses of MonitoringStarterParent class. Consequently, each of the starters extend some of the characteristics from the parent class and they also have class specific properties. The methods in each starter such as the buildModel and startProjection are common methods inherited from the parent, as well as the user-specified parameters. The number of principal components to be retained in the model is a superclass variable and it is overridden in each child class. Each model generates two monitoring statistics for each subsystem, a T^2 statistic and an SPE statistic. Three monitoring methods generate a total of six fault detection agents for each subsystem. The fault detection agents are contained in the fault detection context.

Fault Detection Agents. The fault detection agents, which are the T^2 and SPE statistics for each subsystem, assign themselves to the fault detection organizer of their subsystem (Figure 3). The fault detection organizer is responsible for keeping count of its fault detection agents, declaring consensus fault, keeping history of the performances of different fault detection agents under different fault scenarios, and in case of a consensus fault decision, triggering the diagnosis agent.

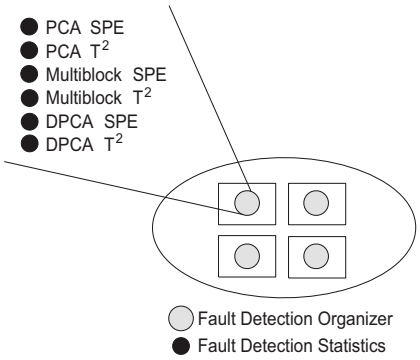

Fig. 3. Fault detection agents.

Statistics values and confidence limits are among the class variables for each fault detection agent. If the value of the statistic goes outside of the limits, the agent flags a fault. Fault detection organizer keeps track of all the fault flags given by its statistics. There are several criteria to form a consensus among different fault detection agents. The simplest would be to flag a fault, if the majority of the fault detection agents are flagging fault. This would require four of the six agents to flag a fault in order to declare that there is a fault in the unit. In the following, this strategy will be referred to as the "*number weighted*" consensus criteria.

Another criterion is based on the performances of fault detection agents over time, and based on their reliability, their decision is given more weight compared to less reliable fault detection agents. This is referred to as the "*reliability weighted*" consensus criteria. At each time point, when a new observation is available and new monitoring statistics are calculated, fault detection agents either detect a fault or not. Based on their decisions, they are given an instantaneous performance reward. The rewarding strategy is designed so that a missed alarm is penalized the most and the correct detection of fault is rewarded the most. A set of instantaneous performance rewards or penalties is given in Table 1, where the rows show the consensus and columns show the individual agent decisions. If the fault detection agent flags a fault but the consensus decision indicates otherwise, the agent is penalized for a false alarm. If the agent does not flag a fault, but the consensus flags a fault, then the agent is penalized for a missed alarm. A missed alarm is considered to be worse than a false alarm, and this is reflected in the instantaneous performance calculations. The instantaneous performances are summed in time for each detection agent, and makes up the accumulated performances. The reliability of an agent is determined by the accumulated performance values divided by the total accumulated performance value of all agents in that unit. The reliability weights are then considered in the consensus decision making.

Table 1. Instantaneous performance rewards

	Not faulty	Faulty
Not faulty	0.5	-0.5
Faulty	-1	1

The challenging problem of SPM methods is the missed and false alarm rates. For some cases, where the fault is

diffusing in the process and affecting the neighboring units and also with minor faults, the consensus flag may be oscillatory. This oscillation affects the performance mechanism in an undesired way such that an agent that has been flagging fault in the oscillatory period may not be reliable enough at that point to affect the consensus decision, and it will be penalized for flagging fault although the flag was right. Or an insensitive method could be rewarded if it did not flag the fault and again this would affect the consensus in an undesired way. In order to prevent these, the performances of agents are updated after fault episodes. A fault episode starts when a consensus fault is flagged. And the episode continues until no consensus fault is flagged for eight consecutive time points. At that point, looking back in history, the performances of agents are updated.

In order to design an automated fault detection framework, where the decisions of fault detection and diagnosis highly influence the succeeding tasks, reliability of the decisions is very important. Some of the monitoring methods may perform better than the others for various states of the process. Use of agent-based cooperation between different methods that are competing for the same task results in better overall performance than if these methods were used independently. Several monitoring agents have been implemented in MADCABS to provide diversity. The aim is to design an automated fault detection framework that can detect the faults on time, and that gives fewer false and missed alarms than if the monitoring methods were used independently. Comparison of different combinations of monitoring methods and the false and missed alarm rates of the corresponding monitoring statistics indicates that cooperation among agents improved the false and missed alarm rates.

Table 2. False and missed alarm summary of different fault detection agent combinations, using reliability weight condition

Agent	Missed Alarm	False Alarm
PCA	1.09	0.17
Multiblock PCA	20.98	0.01
DPCA	0.18	0.02
PCA-Multiblock PCA	1.21	0.06
DPCA-Multiblock PCA	0.75	0.07
PCA-DPCA	0	0.03
ALL	0	0.03

Diagnosis Agent. Diagnosis agent works in an event-driven way. It is activated when a consensus fault is flagged by a fault detection organizer. The responsibility of the diagnosis agent is to investigate the type and severity of the fault under consideration. Contribution plots are used as a diagnostic tool. The contributions of process variables to each fault detection statistic are calculated for different monitoring methods. The contribution plots do not indicate the source cause of the fault, but identify the variables that have contributed to the inflation in the SPM statistic. The diagnosis agent performs contribution plot analysis and determines the variables that inflated the SPM statistic that went out-of-control. At this point a sequence of events is activated. First, the most contributing variable to each statistic is chosen by checking if the variable contribution value is beyond the 3-*sigma* confidence limits and if it makes up a significant amount of the contributions. Each fault detection agent identifies their most contributing variables, and the common top most contributor to all is identified. That variable is then eliminated from the monitoring model data matrix and a new statistical model is built using the remaining variables. The aim is to detect if the fault is a sensor fault or a process fault. The assumption that is made here is, that a process fault usually has a fault signature and is realized in more than one variable. On the other hand, a sensor fault, especially a single sensor fault does not affect the other variables if it is not being used for control.

If the new observation, after the variable is eliminated, is in-control with the new model, it is declared as a potential sensor fault, however, the projection onto the new model continues in parallel to check if it will turn out to be a process fault later since some of the minor process faults can be misinterpreted as sensor faults in the beginning. If the new observation is not in-control with the new model, this means other variables have also been affected from the fault, and it is declared as a potential process fault. In addition to discriminating the types of faults, diagnosis agent estimates the severity of the fault by looking at how much the variable contributions have gone outside the confidence limits, how many of the neighboring fault detection organizer are signaling fault and how many of the fault detection statistics in the unit have identified the same fault signature.

3. MONITORING AND FAULT DETECTION OF A REACTOR NETWORK

3.1 Autocatalytic CSTR Network

Reactor networks hosting multiple species have a very complex behavior (Figure 2). As the number of steady states of the network increases, autocatalytic species are allowed to exist in the network that would otherwise not exist in a single CSTR. The cubic autocatalytic reaction for a single autocatalytic species is

$$R + 2P \rightarrow 3P \quad \text{and} \quad P \rightarrow D \tag{1}$$

R is the resource concentration, P is the species concentration, D is a dead species. The reaction rate for the first reaction, species growth rate constant, is k and k_d is the species death rate constant. The feed flow rates and interconnection flow rates are treated as manipulated variables. Each reactor has an inlet and outlet flow. The resource concentration in each reactor along with species concentrations is also available.

MADCABS is designed to work with process data from a real process plant or a process simulator. The data are stored in a database in MADCABS for use by MADCABS agents. For the case studies, the data are obtained from a simulator of the CSTR network, where multiple competing species coexist in the network and consume the same single resource. The ordinary differential equations modeling the operation of the reactors are written in C and connected to Repast Simphony through a Java Native Interface (JNI).

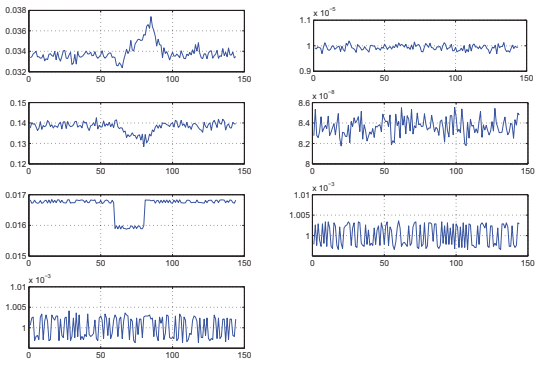

Fig. 4. A 5% process fault in the top right corner reactor 3.(a) Resource concentration in the reactor, (b) Species 1 concentration in the reactor, (c) Species 2 concentration in the reactor, (d) Species 3 concentration in the reactor (e) Feed flow rate into the reactor (Variable 5), (f) Outflowing interconnection to reactor 2 (g) Outflowing interconnection to reactor 7.

3.2 Monitoring and Fault Detection with MADCABS

The case studies use a four-by-five rectangular CSTR network, where three species coexist feeding from the same resource. Faults with different magnitudes and types are simulated to show the effectiveness of the agent-based monitoring, fault detection and diagnosis framework in MADCABS.

Fault Detection and Diagnosis. In Figure 4, a step decrease in the feed flow rate is introduced to reactor 3. The process fault affected the host species in the reactor since they start to die. The resource concentration in the reactor has increased after a delay after the dominant species start dying. From the figure, the variables that have been contributing to the fault are seen in the first three rows of the first column, the resource concentration in the reactor, dominant species concentration in the reactor and the feed flow rate to the reactor, which was reset to its original value after some time.

The contribution plots are given in Figure 5. For the five fault detection statistics that detected the existence of a fault in the system, PCA T^2, DPCA statistics and multiblock SPE showed that the main contributor to the fault is variable 5. PCA-SPE statistic had a smearing effect, where the signature of the fault could not be seen. Therefore, having multiple statistics improved diagnosis results as well. The fault has been detected on time by five fault detection agents.

Multiblock T^2 agent is insensitive to faults with magnitude less than 10%. A contribution chart that shows how many fault detection agents detected a contributing variable (Figure 6) indicates that variable 5, the feed flow rate to Reactor 3, is the common most contributor.

Table 2 provides a summary of 100 runs for each scenario. Multiblock PCA suffered from its insensitive T^2 agent, which had the highest missed alarm rate. The effect of the

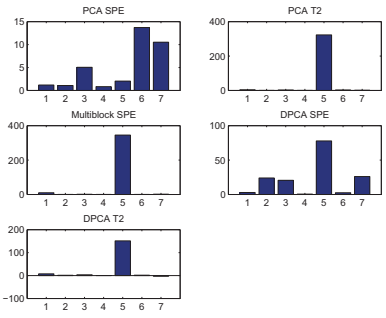

Fig. 5. Contribution plots for reactor 3 at the time of detection.

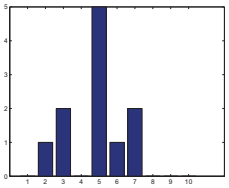

Fig. 6. Number of fault detection agents and common contributors for reactor 3.

insensitive statistic to the performance is realized in the performance of every combination with multiblock PCA. Combinations with DPCA improved the false and missed alarm rate. Especially PCA-DPCA performance is superior to any of the other less diverse combinations and seems to have a large impact on the combined performance when all three are used together. In summary, the results show that having multiple methods working together improves the effectiveness of the combined monitoring and fault detection.

Another type of fault in processes is sensor faults, where sensors might be defective and may provide false readings. A sensor fault should be identified in a timely manner since the measured variable can be used in computing the control actions and an erroneous reading may move the process to an undesired state, and may even destabilize the system. In general, correct and timely diagnosis and communication between control and diagnosis is required. A sensor fault in the form of a ramp decrease is given to the resource concentration sensor, variable 1 in reactor 6 (the figure is not provided because of space limitations). This sensor fault does not affect the other variables since it is not used for control.

The contribution plots show that the most contributing variable to the fault is variable 1. When this variable is taken out of the statistical model data, and a new model is built with one less variable, the new model reveals that the process is in-control. This indicates a potential sensor fault. The diagnosis results for reactor 6 are shared with control agents and also preprocessing agents in MADCABS so that preprocessing agents can provide reliable estimates instead of the faulty sensor, and control agents will continue to provide the necessary control actions to continue the desired operation level.

As another fault scenario, four consecutive faults are introduced to reactor 3. The fault is again introduced to the feed flow, and is of magnitude 1%. The fault introduction times and the detection times of the best performing combinations are given in Table 3. The reliability weight based consensus formation is shown to provide much earlier detection times than the majority based consensus criteria. Since the adapting reliability weight of the fault detection agents are taken into consideration, the first criteria provided earlier detection times, for consecutive faults. The results showed some kind of a learning pattern. However, this is going to be tested with different validation cases, where the training is followed by validation with different fault magnitudes. In Table 2, performance of DPCA-PCA combination was the same as the ALL combination, however, in Table 3, the detection times showed that when ALL of the monitoring agents are used in fault detection the fault is detected earlier than DPCA-PCA combination.

Table 3. Fault detection times (four consecutive process faults)

Agents	Fault#1	Fault#2	Fault#3	Fault#4
Actual Fault Times	220	250	290	330
PCA-DPCA (reliability)	221.9	250.9	290.4	330.8
ALL(reliability)	221.8	250.6	290.1	330.1
ALL(number)	223.1	254.4	294.0	333.6

The average number of agents that are flagging a fault when the consensus gives a fault flag is listed in Table 4 where two different consensus forming criteria are compared. When the agents' reliabilities increase with fault detection, less agents are required to declare a fault. When the presence of the majority of the fault detection agents is required to give a fault flag, the missed alarm rates increase and detection is delayed.

Table 4. Number of agents that flag fault at the time of detection (four consecutive process faults)

Agents	Fault#1	Fault#2	Fault#3	Fault#4
ALL(reliability)	4.06	3.46	3.48	3.25
ALL(number)	4.26	4.19	4.13	4.20

When the performances of different monitoring methods are compared the worst performing method is the multiblock PCA method because of the insensitive T^2 statistic. The overall performance of the PCA method is close to DPCA, but inferior because of the sensitive SPE statistic that gives many false alarms. The methods and the statistics are ranked and the results are provided in Table 5.

Table 5. Performances of the monitoring agents

Rank	Agent
1	DPCA SPE
2	Multiblock PCA SPE
3	PCA T^2
4	PCA SPE
5	DPCA T^2
6	Multiblock PCA T^2

4. SUMMARY AND CONCLUSIONS

PCA, DPCA and multiblock PCA methods are widely used multivariate SPM methods in process industries. However, all these methods are prone to false and missed alarms. The common practice in SPM is to test different monitoring tools form the literature, improve and tune the algorithms and find the best method that provides reliable monitoring. Considering the shortcomings of relying on a single SPM tool, consensus from several SPM tools is desirable. This is especially important for distributed and networked processes. Since there are multiple units, a monitoring system that is giving frequent false alarms on different operating units will be misleading and will not be relied on.

In order to improve the effectiveness of monitoring, several monitoring methods have been used together in the proposed framework. Some of the methods performed well on minor faults and disturbances, but had problems in contribution charts. Others gave good diagnostic results. Combining all these methods improved the effectiveness of the proposed overall monitoring, fault detection and diagnosis framework.

MADCABS provides an excellent environment to assess the performance of various SPM and fault detection methods for specific regions of process operation and adapt the reliance to different techniques based on prior experience and recursive assessment of performances. The agent management layer offers the tools and metrics to assess the performance of the monitoring, detection and diagnosis tools and dynamically update the confidence to specific techniques in a context-dependent way.

REFERENCES

Cinar, A., Palazoglu, A., and Kayihan, F. (2007). *Chemical Process Performance Evaluation*. CRC Press, Boca Raton, FL.

Jackson, J.E. (1980). Principal components and factor analysis: Part I-principal components. *J Qual Technol*, 12, 201–213.

Kourti, T. and MacGregor, J. (1996). Multivariate SPC methods for process and product monitoring. *J Qual Technol*, 28, 409–428.

Ku, W., Storer, R.H., and Georgakis, C. (1995). Disturbance detection and isolation by dynamic principal component analysis. *Chemometr Intell Lab*, 30, 179–196.

Qin, S., Valle, S., and Piovoso, M. (2001). On unifying mutliblock analysis with application to decentralized process monitoring. *J Chemometr*, 15, 715–742.

ROAD (2005). Repast organization for architecture and design. *Repast Simphony*. Available at http://repast.sourceforge.net.

Wangen, L. and Kowalski, B. (1988). A multiblock partial least squares algorithm for investigating complex chemical systems. *J Chemometr*, 3, 3–20.

Westerhuis, J., Kourti, T., and MacGregor, J. (1998). Analysis of multiblock and hierarchical PCA and PLS models. *J Chemometr*, 12, 301–321.

Wold, S., Kettaneh, N., and Tjessem, K. (1996). Hierarchical multiblock PLS and PC models for easier model interpretation and as an alternative to variable selection. *J Chemometr*, 10, 463–482.

Guaranteed Steady-State Bounds for Uncertain Chemical Processes

Jan Hasenauer [*], **Philipp Rumschinski** [**], **Steffen Waldherr**[*], **Steffen Borchers**[**], **Frank Allgöwer**[*], and **Rolf Findeisen**[**]

[*] *Institute for Systems Theory and Automatic Control, Universität Stuttgart, Germany (e-mail: {hasenauer,waldherr,allgower}@ist.uni-stuttgart.de)*

[**] *Institute for Automation Engineering, Otto-von-Guericke-Universität Magdeburg, Germany (e-mail: {philipp.rumschinski, steffen.borchers,rolf.findeisen}@ovgu.de)*

Abstract: Analysis and safety considerations of chemical and biological processes frequently require an outer approximation of the set of all feasible steady-states. Nonlinearities, uncertain parameters, and discrete variables complicate the calculation of guaranteed outer bounds. In this paper, the problem of outer-approximating the region of feasible steady-states, for processes described by uncertain nonlinear differential algebraic equations including discrete variables and discrete changes in the dynamics, is adressed.
The calculation of the outer bounding sets is based on a relaxed version of the corresponding feasibility problem. It uses the Lagrange dual problem to obtain certificates for regions in state space not containing steady-states. These infeasibility certificates can be computed efficiently by solving a semidefinite program, rendering the calculation of the outer bounding set computationally feasible. The derived method guarantees globally valid outer bounds for the steady-states of nonlinear processes described by differential equations. It allows to consider discrete variables, as well as switching system dynamics.
The method is exemplified by the analysis of a simple chemical reactor showing parametric uncertainties and large variability due to the appearance of bifurcations characterising the ignition and extinction of a reaction.

Keywords: Steady-states, nonlinear dynamical systems, discrete variables, hybrid dynamics, semidefinite programming, CSTR

1. INTRODUCTION

In the chemical and biochemical processing industry one frequently has to face large modelling uncertainties and process disturbances. Precise reaction mechanisms and kinetic parameters might be unknown and operating conditions, e.g. feed flowrate, or feed temperature, can be time dependent. Additionally, many of the substances handled in a chemical plant are potentially dangerous, e.g. inflammable or explosive. Reactions can lead to the disposal of large amounts of thermal energy, what makes safety considerations necessary. Stationary temperature and pressure have to stay below critical values and for instance in pharmaceutical processes the variability within the drug production has to be restricted. Hence, a detailed analysis of the process uncertainty is essential.

In this paper we address the problem of determining the set of all feasible steady-states of a process, for a class of uncertain hybrid nonlinear differential algebraic systems. Using the set of feasible steady-states the stationary process uncertainty can be upper bounded. Furthermore, it can be used to check whether for all possible disturbances, parameter variations, and operating conditions the process operates within previously defined constraints. One exemplary question to be asked is whether thermal runaway of a chemical reactor can be avoided under specific failure situations.

The physical processes taking place in chemical plants mostly behave in a continuous fashion. There are, however important discrete phenomena like changes in the physical system, e.g. phase transitions, imposed qualitative changes caused by limitation of the equipment, e.g. limited tank capacity, discontinuous input signals and process faults (Engell et al., 2000). To capture continuous as well as discrete phenomena, regime based approaches are used to model the process behavior (Seborg et al., 1989; Murray-Smith and Johansen, 1997; Lennartson et al., 1996). Frequently, one refers to this kind of models as hybrid models, because they contain both discrete and continuous dynamical components and an interface describing the interaction of them.

For most nonlinear systems an analytical calculation of the set of steady-states is impossible. Therefore, during the last decade several methods have been developed for approximating the set of feasible states, in the context of reachability analysis. Those methods are rather efficient if the considered system is linear time-invariant (Girard

and Guernic, 1996) and also for uncertain linear systems some results exist (Girard, 2005). However, if the systems under consideration are nonlinear, the approximation of the feasible set is more difficult. Asarin and coworkers developed an approach for two-dimensional systems based on piecewise linear approximation (Asarin et al., 2003) and Ramdani et al. (2008) proposed a method for high dimensional uncertain nonlinear systems using guaranteed set integration, which yields good results for cooperative systems. Nevertheless, the performance of these methods strongly depends on the particular structure of the nonlinear system and in many cases the results are very conservative.

Due to this drawback of set-based approaches, for the analysis of nonlinear systems, often simple Monte-Carlo type methods are employed (Robert and Casella, 2004). However, such approaches only provide the complete set of possible steady states in the limit of infinite many samples, i.e. important solutions might be left out, especially for highly nonlinear systems.

The method derived in this paper follows the idea presented in the work of Waldherr et al. (2008). There, recent advances in the field of semidefinite programming (SDP) (Parrilo, 2000; Chesi et al., 2003) are employed to compute certificates that a given set in state space cannot contain a steady-state for any feasible model parameterization. A very similar approach was earlier proposed by Kuepfer et al. (2007) for parameter estimation and later extended to dynamical systems by Borchers et al. (2009). However, all these methods are restricted to systems described by polynomial vector fields, which is rarely the case for chemical processes. Furthermore, discrete variables or parameters, as might occur in the analysis of chemical and biological processes, have not been considered.

In the following, an approach will be presented, which overcomes this shortcoming and allows the outer approximation of the set of all feasible steady-states of a process described by uncertain hybrid nonlinear differential algebraic equations with non-polynomial vector fields. Thus, systems combining continuous dynamics with logic or discrete components can be studied. Furthermore, a more elaborate algorithm is proposed to obtain a more precise approximation of the set of feasible steady-states, in cases the considered system has multiple steady-states.

The remainder of this paper is structured as follows: In Section 2 the problem of bounding the set of steady-states for processes described by non-polynomial hybrid differential algebraic equations is presented. Section 3 formalizes the problem statement. In Section 4 the resulting feasibility problem is relaxed to a semidefinite program which is used by the algorithm outlined in Section 5 to estimate the set of feasible steady-states. In Section 6 we provide as an example the analysis of a CSTR, before final conclusions are provided

Mathematical notation: The space of real symmetric $n \times n$ matrices is denoted as $\mathcal{S}^n$. N_a^b denotes the discrete set $\{1, \ldots, n_a^b\}$, where n_a^b is the number of considered variables. The positive semidefiniteness of a quadratic matrix $X \in \mathcal{S}^n$ is denoted $X \succeq 0$ and the trace of X by tr X. The transposed vector $(x^d)^T$ is written as x^{dT}.

2. PROBLEM STATEMENT

The processes under consideration are supposed to be described by hybrid differential algebraic systems which exhibit both continuous and discrete dynamical behavior. Such a process description is quite general. It covers for instance reaction networks which allow phase transitions, as well as discrete variables/inputs such as the opening of a valve or the on/off status of a heater. Mathematically, we assume that the process is described by

$$0 = F^d(\dot{x}^d, x^d, p^d, u^d), \qquad x^d(0) = x_0^d \tag{1}$$

Here $x^d \in \mathbb{R}^{n_x^d}$ is the state vector, $p^d \in \mathbb{R}^{n_p^d}$ the vector of parameters, $u \in \mathbb{R}^{n_u^d}$ the vector of inputs (externally manipulated variables), and $F^d : \mathbb{R}^{n_x^d} \times \mathbb{R}^{n_x^d} \times \mathbb{R}^{n_p^d} \times \mathbb{R}^{n_u^d} \to \mathbb{R}^{n_x^d}$ the mapping for a given discrete decision variable $d \in \mathbb{N}$. The decision variable d is assumed to be time dependent with $d(t) \in \mathcal{D}$.

To derive such hybrid differential algebraic descriptions in which each node captures the dynamics under certain operating conditions and to define switching surfaces is often easier than deriving ordinary differential equation models, holding for all process configurations.

In the following we are interested in the steady-state behavior of (1). The problem under consideration is to find all possible, or at least an outer bound of all, steady states of (1):

Problem 1. (Set of feasible steady states): Given the sets $\mathcal{D} \subset \mathbb{N}$, $\mathcal{P}^d \subset \mathbb{R}^{n_p^d}$ and $\mathcal{U}^d \subset \mathbb{R}^{n_u^d}$, compute the set $\mathcal{X}_s^*$ which contains all feasible steady-states of (1).

Note that the set of feasible steady-states for a given decision variable $d \in \mathcal{D}$ is defined by

$$0 = F^d(0, x^d, p^d, u^d). \tag{2}$$

Hence problem 1 can be split into n_d subproblems, where n_d is the cardinality of $\mathcal{D}$. For each subproblem one obtains a set of feasible steady states

$$\mathcal{X}_s^{d,*} = \{x^d \in \mathbb{R}^{n_x^d} \mid \exists\, p^d \in \mathcal{P}^d, u^d \in \mathcal{U}^d : f^d(x^d, p^d, u^d) = 0\}, \tag{3}$$

in which $f^d(x^d, p^d, u^d) = F^d(0, x^d, p^d, u^d)$. The whole set of feasible steady-states is given by the union of all steady-states

$$\mathcal{X}_s^* = \bigcup_{d \in \mathcal{D}} \mathcal{X}_s^{d,*}. \tag{4}$$

In the following the problem of computing an outer-approximation of $\mathcal{X}_s^*$ is considered. This was previously done by Waldherr et al. (2008) for differential equations with polynomial right hand sides. The main contribution of this paper is a generalization of these results to hybrid non-polynomial DAE systems.

3. BOUNDING BY PIECEWISE-POLYNOMIAL FUNCTIONS

The computational method we propose allows to handle uncertain systems that are described by polynomial equations. Therefore, (2) is transformed to a set of uncertain polynomial equations. In the case that f^d is rational, this can be trivially achieved by multiplying with the denominator. In cases in which the systems are non-rational, it is more difficult.

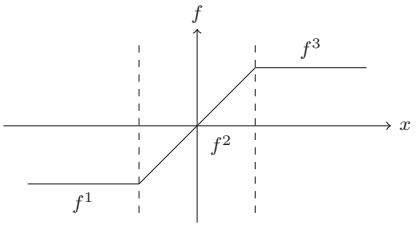

Fig. 1. Saturation function as example for the partitioning of piece-wise polynomial functions.

Savageau and Voit (1987) showed that any system with smooth non-polynomial nonlinearities can be converted to a polynomial system of larger state dimension, which is restricted via equality constraints to a manifold of the dimension of the original system. Unfortunately, in many cases the equality constraints are non-polynomial and so their method is not applicable for our approach. Instead, we apply a different method, which achieves a comparable result without enlarging the state space.

Piece-wise polynomial functions: In case that f^d is piece-wise polynomial, e.g. piece-wise linear, the state space can be partitioned into different intervals. This leads to an increase in the number of decision variables of the hybrid system and is illustrated in Figure 1 for the saturation function, which appears for instance if a process contains flow limiting valves. It has to be emphasized that in cases like this, the partitioning depends on the state. Thus, for a given region in state space $\mathcal{X}$ only a subset of decision variables $d \in \mathcal{D}$ is accessible.

General nonlinear functions: For functions which are not piece-wise polynomial, e.g. the exponential terms in the Arrhenius like rate constant, polynomial lower and upper bounds can be introduced as

$$\begin{aligned} g_1^d(x^d,p^d,u^d) \leq & f^d(x^d,p^d,u^d) \leq g_2^d(x^d,p^d,u^d) \\ & \forall x^d \in \mathcal{X}^d,\ p^d \in \mathcal{P}^d,\ u^d \in \mathcal{U}^d, \end{aligned} \tag{5}$$

in which $\mathcal{X}^d$ is the set in state space of interest. Using these bounds it can be shown that

$$\begin{aligned} \mathcal{X}_s^{d,*} \subseteq \{\, & x^d \in \mathbb{R}^{n_x^d} | \exists\, p^d \in \mathcal{P}^d, u^d \in \mathcal{U}^d, c \in [0,1] : \\ & c g_1^d(x^d,p^d,u^d) + (1-c) g_2^d(x^d,p^d,u^d) = 0 \} . \end{aligned} \tag{6}$$

Hence, the steady-state constraint $f^d(x^d,p^d,u^d) = 0$ can be substituted by the polynomial constraint

$$c g_1^d(x^d,p^d,u^d) + (1-c) g_2^d(x^d,p^d,u^d) = 0, \quad c \in [0,1], \tag{7}$$

where c has to be appended to p^d. This step corresponds to a constraint relaxation and $||f^d(x^d,p^d,u^d) - g_i^d(x^d,p^d,u^d)|| \ll 1$ should be enforced to keep the difference between $\mathcal{X}_s^{d,*}$ and the set of solutions of the relaxed problem small.

Combinations of the methods, e.g. rational, polynomial and nonlinear functions are possible, see Section 6.

4. BOUNDING STEADY STATES

In this section a method to compute an outer approximation of the state space region containing all steady-states is derived. For this purpose we define the feasibility problem,

$$(P): \begin{cases} \text{find} & d \in \mathcal{D},\ x^d \in \mathbb{R}^{n_x^d}, p^d \in \mathbb{R}^{n_p^d}, u^d \in \mathbb{R}^{n_u^d} \\ \text{subject to} & f^d(x^d,p^d,u^d) = 0 \\ & x^d \in \mathcal{X}^d,\ p^d \in \mathcal{P}^d,\ u^d \in \mathcal{U}^d, \end{cases}$$

which is in the following used for the classification of $\mathcal{X}^d$. If (P) is infeasible, $\mathcal{X}^d$ cannot contain any equilibrium points. (P) is called a mixed integer nonlinear program. Unfortunately, the feasibility problem (P) is in general non-convex and NP-hard.

Kuepfer et al. (2007) proposed a framework for relaxing a polynomial non-convex feasibility problem to a semidefinite program (SDP). Due to inherent convexity of SDPs, these problems can be solved computationally efficient, e.g. via primal-dual interior point methods. In the following, we present an approach which is based on the work of Kuepfer et al. (2007) and has been used for analysis of the set of feasible steady states in the case of biochemical reaction networks in Waldherr et al. (2008).

For the relaxation of (P) to a SDP, the original feasibility problem is at first rewritten as a quadratic feasibility problem (QP), for each d. Therefore, the vectors $\xi^d \in \mathbb{R}^{n_\xi^d}$ are introduced, which consists of the monomials of the model equation (1), i.e.

$$\xi^d = (1,\ x_i^d,\ p_j^d,\ u_k^d,\ x_i^d p_j^d,\ x_i^d u_k^d,\ p_i^d u_k^d, \ldots)^T \tag{8}$$

for all $i \in N_x^d$, $j \in N_p^d$, and $k \in N_u^d$. Using this monome vectors ξ^d, the equality constraints $f^d(x^d,p^d,u^d) = 0$ can be transformed to

$$0 = f_i^d(x^d,p^d,u^d) = \xi^{dT} Q_i^d \xi^d, \quad i \in N_x^d, \tag{9}$$

in which $Q_i \in \mathcal{S}^{n_\xi}$. Note that for higher order terms, additional constraints have to be introduced. For instance if ξ^d contains the second order term $x_1^d p_1^d$, the constraint $x_1^d p_1^d = x_1^d \cdot p_1^d$ must be introduced to express the dependency of the higer order monomial on the first order monomials. This leads to additional constraints of the form,

$$\xi^{dT} Q_i^d \xi^d = 0, \quad i \in N_c^d, \tag{10}$$

in which $Q_i \in \mathcal{S}^{n_\xi}$, $N_c^d = \{n_x^d + 1, \ldots, n_x^d + n_c^d\}$, and n_c^d is the number of dependencies. To simplify the notation we set $N_{xc}^d = N_x^d \cup N_c^d$.

To further simplify the notation we restrict $\mathcal{X}^d$, $\mathcal{P}^d$, and $\mathcal{U}^d$ to be generated by the intersection of half-spaces, e.g. $\mathcal{X}^d$, $\mathcal{P}^d$, and $\mathcal{U}^d$ can be convex polytopes. In this case, $x^d \in \mathcal{X}^d$, $p^d \in \mathcal{P}^d$, and $u^d \in \mathcal{U}^d$ can be written as

$$B^d \xi^d \geq 0, \tag{11}$$

in which $B^d \in \mathbb{R}^{n_b^d \times n_\xi^d}$, and n_b^d is the sum of constraints on x^d, p^d, and u^d.

The original feasibility problem (P) can then be restated as

$$(QP): \begin{cases} \text{find} & \xi^d \in \mathbb{R}^{n_\xi^d},\ d \in \mathcal{D} \\ \text{subject to} & \xi^{dT} Q_i^d \xi^d = 0,\ i \in N_{xc}^d \\ & B^d \xi^d \geq 0 \\ & \xi_1^d = 1. \end{cases}$$

Using the ideas suggested by Parrilo (2003), the (QP) is subsequently relaxed to a SDP, for each d, by introducing the matrices $X^d = \xi^d \xi^{dT}$ and dropping the appearing non-convex constraint $\text{rank}(X^d) = 1$. This leads to the relaxed feasibility problem

$$(RP): \begin{cases} \text{find} & X^d \in \mathcal{S}^{n_\xi^d},\ d \in \mathcal{D} \\ \text{subject to} & \operatorname{tr}(Q_i^d X^d) = 0,\ i \in N_{xc}^d \\ & B^d X^d e_1^d \geq 0 \\ & B^d X^d B^{dT} \geq 0 \\ & \operatorname{tr}(e_1^d e_1^{dT} X^d) = 1 \\ & X^d \succeq 0, \end{cases}$$

in which $e_1^d = (1, 0, \ldots, 0)^T \in \mathbb{R}^{n_\xi^d}$. Note that the relaxation may induce additional solutions. To reduce conservatism, the redundant constraint $B^d X B^{dT} \geq 0$ is added, which is fulfilled by every solution of the problem (QP) (Kuepfer et al., 2007).

From (RP) one can derive the Lagrange dual problem (DP_d) for each d,

$$(DP_d): \begin{cases} \text{maximize} & \nu_1^d \\ \text{subject to} & e_1^d \lambda_1^{dT} B^d + B^{dT} \lambda_1^d e_1^{dT} + B^{dT} \lambda_2^d B^d \\ & \quad + \lambda_3^d + \nu_1^d e_1^d e_1^{dT} + \sum_{i \in N_{xc}^d} \nu_{2,i}^d Q_i^d = 0 \\ & \lambda_1^d \geq 0,\ \lambda_2^d \geq 0,\ \lambda_3^d \succeq 0, \end{cases}$$

in which the Lagrange multipliers are $\lambda_1^d \in \mathbb{R}^{n_b^d}$, $\lambda_2^d \in \mathcal{S}^{n_b^d}$, $\lambda_3^d \in \mathcal{S}^{n_\xi^d}$, $\nu_1^d \in \mathbb{R}$ and $\nu_2^d \in \mathbb{R}^{n_x^d + n_c^d}$ (Waldherr et al., 2008). Using the dual problem, one can obtain an infeasibility certificate for the original problem.

Lemma 2. Let $\nu_1^{d,*}$ be the optimal cost of (DP_d). If

$$\inf \left\{ \nu_1^{d,*} \mid d \in \mathcal{D} \right\} = \infty, \tag{12}$$

then the original feasibility problem (P) is infeasible.

This follows directly from weak duality. Only if the Lagrange dual problem is unbounded from above for all $d \in \mathcal{D}$ the infeasibility of (P) can be guaranteed. The advantage of the formulation using the Lagrange duals is that all subproblems are convex and can be solved efficiently.

In case that $\operatorname{card}(\mathcal{D}) \gg 1$, checking all the distinct combinations of decision variables can become very costly. One possibility to reduce the problem size is to divide $\mathcal{D}$ into subsets $\mathcal{D}_i$. The subsets $\mathcal{D}_i$ can be merged to a common node and the analysis can be performed for all subsets instead of for all nodes. This approach can also be combined with a hierachical refinement of the subsets $\mathcal{D}_i$, which reduces the computational demand significantly.

5. ALGORITHM

Using the Lagrange dual problem (DP_d), certificates for the infeasibility of (4) can be computed. This allows to exploit (DP_d) to determine an outer approximation $\mathcal{X}_s$ of $\mathcal{X}_s^*$. In this work, this is done via simple a multi-dimensional bisection algorithm (Jaulin et al., 2001). Compared to the work by Waldherr et al. (2008) this allows a better approximation of $\mathcal{X}_s^*$ but is computationally more demanding. The basic implementation can be summarized as follows:

Algorithm: $\mathcal{X}_s = \text{Approximation-}\mathcal{X}_s^*(\mathcal{X}, \mathcal{P}, \mathcal{D})$

1. If volume$(\mathcal{X}) < \epsilon$, return $\mathcal{X}_s = \mathcal{X}$
2. Check feasibility of $DP_d(\mathcal{X}, \mathcal{P}, \mathcal{D})$, $\forall d \in \mathcal{D}$
3. If $\inf \left\{ \nu_1^{d,*} \mid d \in \mathcal{D} \right\} = \infty$, return $\mathcal{X}_s = \emptyset$
4. If $\inf \left\{ \nu_1^{d,*} \mid d \in \mathcal{D} \right\} \neq \infty$:

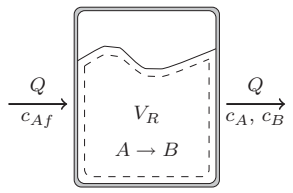

Fig. 2. Schematic of the considered simple CSTR.

4.1. Bisection of $\mathcal{X}$ in $\mathcal{X}_1$ and $\mathcal{X}_2$
4.2. $\mathcal{X}_{1,s} = \text{Approximation-}\mathcal{X}_s^*(\mathcal{X}_1, \mathcal{P}, \mathcal{D})$
4.3. $\mathcal{X}_{2,s} = \text{Approximation-}\mathcal{X}_s^*(\mathcal{X}_2, \mathcal{P}, \mathcal{D})$
4.4. Return $\mathcal{X}_s = \mathcal{X}_{1,s} \cup \mathcal{X}_{2,s}$

Remark 3. Note that for the application of this algorithm an initial set $\mathcal{X}_0$ must be chosen. If we want to guarantee that an outer approximation of $\mathcal{X}_s^*$ is found containing all feasible equilibrium points, $\mathcal{X}_s^* \subseteq \mathcal{X}_0$ must hold. This is not a restriction because a suitable $\mathcal{X}_0$ can often easily be determined from physical insight into the problem.

6. BOUNDING THE STEADY STATES OF A CSTR

In order to illustrate the proposed scheme the steady-state behavior of a CSTR is analyzed. The reactor considered is a simple tank filled with fluid stirred by an impeller, an inflow and an outflow, as depicted in Figure 2.

6.1 System description

Specifically we consider an adiabatic, constant volume CSTR in which the first-order, exothermal liquid-phase reaction

$$A \xrightarrow{k} B$$

takes place. The conversion rate is given by $R = k(T)c_A$, in which the reaction rate constant is modelled using Arrhenius' equation,

$$k(T) = k_\infty e^{-\frac{E}{RT}}. \tag{13}$$

Simple mass and energy balances lead to the following set of ordinary differential equations:

$$\begin{aligned} \frac{dc_A}{dt} &= \frac{1}{\theta}(c_{Af} - c_A) + k(T)c_A \\ \frac{dT}{dt} &= \frac{1}{\theta}(T_f - T) - \frac{\Delta H_R}{C_p \rho} k(T) c_A, \end{aligned} \tag{14}$$

which captures the dynamics of the CSTR (Rawlings and Ekerdt, 2002). The state variables are the concentration c_A of reactant A, and the reactor temperature T. The parameters are the mean residence time $\theta = V_R/Q$, the reactor volume V_R, the flowrate Q, the concentration of A in the feed stream c_{Af}, the feed stream temperature T_f, the reaction enthalpy ΔH_R, the heat capacity of the fluid C_p, and the fluid density ρ. The numerical values of the nominal parameters are provided in Table 1.

6.2 Analysis of the nominal CSTR

In case that all parameters are known, one can exactly predict how the reactor behaves in different operating conditions. Hereby, since the mean residence time θ is the easiest parameter to manipulate, the operating condition will be defined in terms of θ. The other parameters are assumed to be fixed.

Table 1. Parameter values.

Parameter	Value	Units	Uncertainty
T_f	298	K	3K
C_p	4.0	KJ/kg K	5%
c_{Af}	2.0	kmol/m^3	5%
k_∞	5.0×10^8	min^{-1}	5%
E/R	8.0×10^3	K	–
ρ	10^3	kg/m^3	–
ΔH_R	-3.0×10^5	kJ/kmol	5%

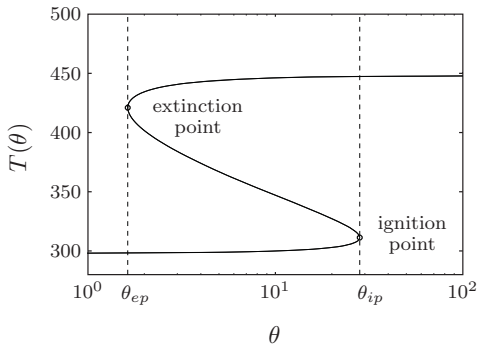

Fig. 3. Bifurcation diagram of CSTR without parameter uncertainties.

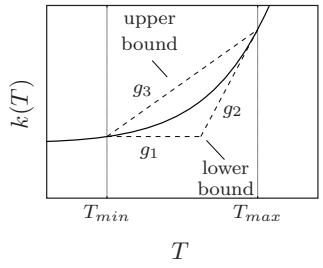

Fig. 4. Bounding of $(-)$ Arrenhius term with $(--)$ linear functions.

Using continuation methods it is possible to numerically compute the steady-state curve (bifuraction diagramm) for varying residence times (Dhooge et al., 2003), as shown in Figure 3. θ_{ep} and θ_{ip} denote the mean residence time at the extinction and the ignition point respectively.

6.3 Analysis of CSTR with parameter uncertainties

If one or more parameters are uncertain, which is in practice always the case, calculating the set of steady-state is significantly more challenging. Typically, sampling based techniques such as Monte-Carlo like methods are used. These allow the approximation of the union of all feasible equilibrium points $\mathcal{X}_s^*$. However, as for all Monte-Carlo like methods no bounds for the obtained sets can be provided. Our approach overcomes this problem and enables us to compute an outer approximation of the set of feasible equilibrium points of the uncertain system.

Approximation of the rate constant: Applying the proposed method requires in a first step to bound the Arrhenius-like rate constant from below and from above using polynomial functions. In this paper $k(T)$ is bounded via three linear functions,

$$\max(g_1, g_2) \leq k \leq g_3, \quad \forall T \in [T_{min}, T_{max}], \tag{15}$$

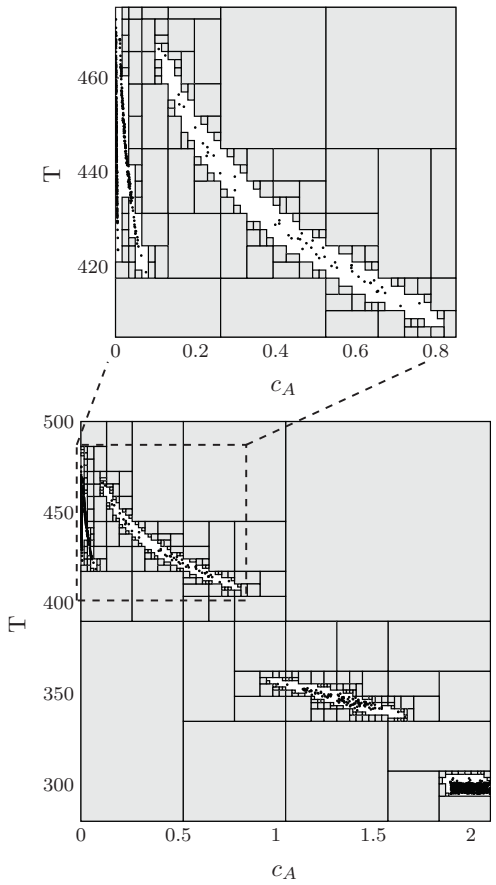

Fig. 5. Region in state space which cannot contain steady-states for given parameter uncertainties and $\theta \in \{1, 10, 100\}$ versus $(\cdot)$ steady-states computed using Monte-Carlo sampling.

as depicted in Figure 4. This approach is very simple and has the disadvantage that the approximation of $k(T)$ is less precise if the difference of T_{min} and T_{max} becomes large. Therefore, we don't use a static approximation but rather select g_1, g_2 and g_3 in each interation of the bisection algorithm dependent on the box $\mathcal{X}$ in state space currently under consideration. This allows to keep the overestimation of the set of feasible steady-states small as will be seen later.

One could of course choose other methods to bound $k(T)$, for instance based on high order polynomials and the Taylor series expansion, but in many cases the computational effort to solve the semidefinite program once will increase significantly and the presented simplistic approach will be more efficient.

Set of feasible steady-states: The above derived theory and the bounding of $k(T)$ allow to compute the set of feasible steady-states of the CSTR. As decision variable we consider besides the temperature interval also the mean residence time θ. Additionally, most parameters are uncertain. The amounts of uncertainty with respect to the nominal values are provided in Table 1.

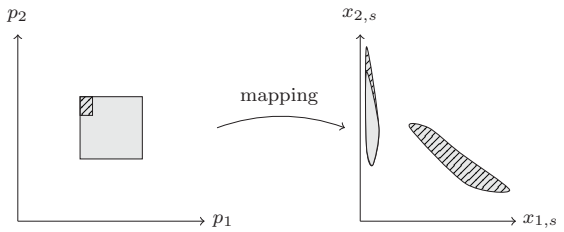

Fig. 6. Illustration of the nonlinear mapping from parameter to steady-states.

The algorithm outlined in Section 5 is in the following used to estimate the set of all feasible equilibrium points of (14) for the given parameter uncertainties and $\theta \in \{1, 10, 100\}$. The results are shown in Figure 5, where the part of the state space which is certified infeasible is marked light gray. To compare our results with classical approaches, five thousand equally distributed Monte-Carlo samples for the accessible parameter set were taken and the steady-states were determined.

Computation of the set of feasible steady-states: As one can see, the results match with each other. However, a closer look at the results reveals several disadvantages of the sampling based approach. First of all, the number of samples in some regions of the state space is small compared to other regions, where the sampling density is extremely high. This indicates that many parameters lead to steady-states in the region with high sampling density, but there are still some regions that cannot be explored unless even higher numbers of samples are used. This might represent a problem, whenever the set of all feasible steady-states has to be computed, since normally a homogeneous sampling rate is more desireable. However, the Monte-Carlo method is not able to guarantee under such a condition that the whole state space is explored, due to the highly nonlinear mapping between parameters and steady-states, illustrated in Figure 6. Therefore, the set of feasible equilibrium points is always underestimated, even for exhaustive Monte-Carlo sampling, while the proposed method guarantees that all equilibrium points are contained in the determined set.

7. CONCLUSION

In this work we studied the problem of outer bounding the region in state space containing all equilibrium points of uncertain hybrid differential algebraic systems. The proposed method is based on the formulation as a feasibility problem and a relaxation to a SDP. It is shown that guaranteed outer bounds of the feasible set of equilibrium points can be determined.

The advantage of the proposed methodology in comparison to Monte-Carlo based approaches is explained and shown considering a simple CSTR process. In particular, the developed method does not rely on sampling and can deal with strongly nonlinear and non-unique mappings from parameters to steady-states.

The computed set is guaranteed to contain all feasible steady-states, thus worst case scenarios can be analyzed. This is of certain interest to evaluate controller performance in fault situations.

8. ACKNOWLEDGEMENTS

This work was supported by the Forschungseinheiten der Systembiologie (FORSYS) [grant 0315280D]; the International Max Planck Research School Magdeburg; and by the Stuttgart Research Centre for Simulation Technology.

REFERENCES

Asarin, E., Dang, T., and Girard, A. (2003). Reachability analysis of non-linear systems using conservative approximations. *Hybrid Systems: Computation and Control*, 2623, 20–35.

Borchers, S., Rumschinski, P., Bosio, S., Weismantel, R., and Findeisen, R. (2009). Model invalidation and system identification of biochemical reaction networks. *Proceedings of the 16th IFAC Symposium on Identification and System Parameter Estimation (SYSID 2009)*. To appear.

Chesi, G., Garulli, A., Tesi, A., and Vicino, A. (2003). Characterizing the solution set of polynomial systems in terms of homogeneous forms: an lmi approach. *International Journal of Robust and Nonlinear Control*, 13(13), 1239–1257.

Dhooge, A., Govaerts, W., and Kuznetsov, Y. (2003). Matcont: A Matlab package for numerical bifurcation analysis of odes. *ACM Transactions on Mathematical Software*, 29(2), 141–164.

Engell, S., Kowalewski, S., Schulz, C., and Stursberg, O. (2000). Conitinuous-discrete interactions in chemical processing plants. *Proceedings of the IEEE*, 88(7), 1050–1068.

Girard, A. (2005). Reachability of uncertain linear systems using zonotopes. *Hybrid Systems: Computation and Control*, 3414, 291–305.

Girard, A. and Guernic, C.L. (1996). Zonotope/hyperplane intersection for hybrid systems reachability analysis. *IEEE control systems*, 16(5), 45–56.

Jaulin, L., Kieffer, M., Didrit, O., and Walter, E. (2001). *Applied interval analysis*. Springer, Heidelberg.

Kuepfer, L., Sauer, U., and Parrilo, P. (2007). Efficient classification of complete parameter regions based on semidefinite programming. *BMC Bioinformatics*, 8, 12.

Lennartson, B., Tittus, M., Ehardt, B., and Pettersson, S. (1996). Hybrid systems in process control. *IEEE control systems*, 16(5), 45–56.

Murray-Smith, R. and Johansen, T.A. (1997). *Multiple Model Approaches to Modelling and Control*. Taylor and Francis, London.

Parrilo, P. (2000). *Structured Semidefinite Programs and Semialgebraic Geometry Methods in Robustness and Optimization*. Ph.D. thesis, Caltech, Pasadena, CA.

Parrilo, P. (2003). Semidefinite programming relaxations for semialgebraic problems. *Math. Program., Ser. B*, 96, 293–320.

Ramdani, N., Meslem, N., and Candau, Y. (2008). Reachability analysis of uncertain nonlinear systems using guaranteed set integration. *Proceedings of the 17th IFAC World Congress*, 8972–8977.

Rawlings, J. and Ekerdt, J. (2002). *Chemical reactor analysis and design fundamentals*. Nob Hill Publishing, Madison, WI 53705.

Robert, C.P. and Casella, G. (2004). *Monte Carlo Statistical Methods*. Springer-Verlag.

Savageau, M.A. and Voit, E.O. (1987). Recasting nonlinear differential equations as S-systems: a canonical nonlinear form. *Mathematical Biosciences*, 87, 83–115.

Seborg, D., Edgar, T., and Mellichamp, D. (1989). *Process Dynamics and Control*. Wiley.

Waldherr, S., Findeisen, R., and Allgöwer, F. (2008). Global sensitivity analysis of biochemical reaction networks via semidefinite programming. *Proceedings of the 17th IFAC World Congress*, 9701–9706.

Extremely Fast Catalyst Temperature Pulsing: Design of a Prototype Reactor

Jasper Stolte * **Ton Backx** * **Okko Bosgra** *

* *Eindhoven University of Technology, PO Box 513, 5600 MB Eindhoven, the Netherlands (e-mail: j.stolte@tue.nl).*

Abstract: This paper discusses a novel principle of advanced process control strategy: the extremely fast and local pulsing of temperature. This strategy leads to some interesting potential applications, but there are no devices implementing it available yet. One such device currently under construction by the authors is introduced in this paper. It operates by converting electrical energy into heat by forcing a very high current through a very thin resistive element, which also acts as the catalyst for heterogeneous reactions. A design procedure for the key parameters is developed and a simulation of heat distribution in the design under construction is presented. The simulation shows that it should be possible to get local temperature peaks of 500 K which exist for only about 20 μs.

Keywords: Process Control, Pulses, Heterogeneous Catalysis, Temperature Forcing, Periodic Control, Non-Steady State.

1. INTRODUCTION

For various reasons, chemical reaction engineers prefer to operate reactions in steady state. In modeling and design of chemical processes, reactors are almost always assumed to be ideally mixed. Control of such processes boils down to maintaining constant reaction conditions as best as possible. However, chemical reaction systems can be seen as systems of highly nonlinear partial differential equations, which are typically full of transient dynamics. If we know that these dynamics can be present, is it not possible to find cases where the dynamics can be exploited?

Attempting to exploit the dynamics demonstrated by chemical processes is not new. Horn and Lin (1967) already introduces periodic reactor operation, and it is shown there that there are reaction complexes for which periodic operation is fundamentally better than any steady state operation. This idea was picked up by researchers all over the world, and in the following decades there have been numerous studies showing there exist reaction complexes for which non steady state operation gives fundamental advantages, see Bailey (1973); Matsubara et al. (1973); Silveston et al. (1995); Silveston and Hudgins (2004) for excellent reviews of this research field.

Although there are plenty examples of academic (often theoretic) research, there are few known examples of practical applications in industry. One promising direction of research which has already shown significant improvements in a number of studies is microwave assisted chemistry, sometimes called microwave enhanced chemistry Wan et al. (1990); Wan (1993); Will et al. (2004). When some parts of a reactor subjected to microwave irradiation are more susceptible than others, they will heat up more and create gradients in temperature. Wan (1993) specifically considers heating the catalyst particles directly. Microwave assisted catalysis is not very accessible to most scientists, as powerful microwave equipment is expensive, it is difficult to model due to inhomogeneities, and measurements are difficult also. Still, microwave heating has shown to allow modes of operation that are impossible using steady state operation.

Silveston and Hudgins (2004) state that the field of temperature forcing is relatively underdeveloped compared to the periodic feed forcing, even though the reaction complexes show more strong non-linear behavior as a function of temperature. The reason given is that due to the large time constants and energy flows involved it is difficult to apply temperature forcing to large amounts of matter. That paper also indicates that the advance of micro-reactors may change allow for better heat transfer paving the way for new studies in the forced temperature direction.

The authors of this paper have started a project on dynamic operation of heterogeneous catalysis. A first theoretical result showed that very fast and local pulsing of temperature may in some cases fundamentally improve attainable results, see Stolte et al. (2008). Also, Wan et al. (1990) state that the fastest and most intense pulses of microwave energy shows the most interesting results for the important methane coupling reaction complex. Work has started on a setup that will create very fast and intense temperature pulses, of several hundred degrees Kelvin in tens of microseconds. To our knowledge this is orders of magnitudes faster than any setups reported in literature have realized.

This paper considers the considerations in designing a setup for heterogeneous catalysis capable of such temperature pulses, delivered directly at the catalyst. Section 2 describes the general reactor setup, as well as a design procedure to decide upon the critical design parameters. Section 3 considers a simulation of the heat distribution

within the reactor, which suggests that heating and cooling within such short timescales is possible. Section 4 discusses a few potential pitfalls that may be encountered when designing such a reactor.

2. REACTOR CONCEPT

The goal of this setup is to create a reactor which is capable of operating heterogeneous catalysis reactions where the catalyst is turned into an actuator which creates very fast and large pulses in temperature. Pulse shaped temperature profiles indicate that very fast heating as well as very fast cooling are required. A very schematic 2D-view of the reactor under construction is given in figure 1.

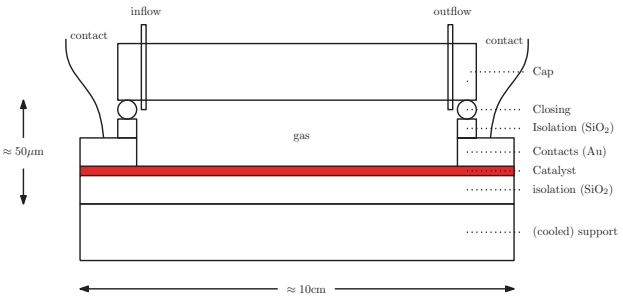

Fig. 1. Schematic view of the prototype reactor concept (not to scale). A channel is created where gas can flow through, with a floor consisting of a thin catalyst layer which is heated.

The concept is based upon a micro-flow-channel reactor, but it has a 'floor' consisting of a thin layer of catalyst through which an electrical current can be driven. Contacts are mounted at the sides to connect a source of electrical energy. For this general heterogeneous catalysis setup the catalyst is chosen to be platinum, which has excellent conductive properties. The reactor heating is supplied by the electrical source, but the cooling cannot be done actively. The heat simply has to flow to cooler areas to cool down the catalyst layer. The bulk of the energy in the catalytic layer will be conducted through the SiO_2 layer to the the cooled support which consists of pure silicon. To get a nice pulse like temperature profile it is desired to have the time constant for cooling approximately equal to the time constant for heating. If it is too small, the energy will flow away already while the pulse is still being applied, and if it is too large it will simply take a long time to cool down. The thickness of especially the catalyst layer and the SiO_2 layer supporting it are critical degrees of freedom to shape the time constant for cooling.

Reasons to choose for this design are:

- Energy is by definition directly added to the catalyst
- Fast creation of electrical currents is a well developed field
- Platinum resistance dependends on temperature almost linearly. By measuring voltage over and current through the catalyst layer an indication for its temperature can be found.
- By electrochemical deposition very thin layers of other catalyst can be deposited on the platinum, giving flexibility in using different catalysts.
- There are no fundamental reasons preventing this design from being scaled up for application in industry.

2.1 Basics of Electrical Heating

This subsection will summarize the basics of electrical heating as needed for this application. When voltage and current are used to heat a layer of resistive material and no heat is lost to the environment, all electrical energy is directly converted into temperature and the following relation holds:

$$\frac{dT}{dt} = \frac{P}{\rho c_p V} \tag{1}$$

where T is temperature [K], P is electrical power [W], ρ is material density [kg/m^3], c_p is specific heat [J/kg K] and V is volume [m^3]. Since the layer is rectangular in shape it can be described by a certain length l [m], height h [m] and width w [m], which together make up the layer volume as given in (2). Also there are the basic electrical relations for power and resistance given in (3) and (4):

$$V = lhw \tag{2}$$

$$P = \frac{U^2}{R} \tag{3}$$

$$R = \frac{l}{\sigma wh} \tag{4}$$

where R is the electrical resistance [Ω] and σ is the electrical conductivity [S/m]. Combining all the equations above, the following relation is found for the temperature gradient due to electrical heating:

$$\frac{dT}{dt} = \frac{\sigma}{\rho c_p}\frac{U^2}{l^2} \tag{5}$$

The relation as stated in (5) is used in the simulation of section 3. It can be seen from (5) that the heating is dependent on some material parameters, and on the applied voltage squared per unit length squared. This means that if a higher temperature gradient is desired for a given setup the voltage should be increased, or the length should be decreased.

The limiting factor is the electrical current. The voltage in the formulas above can only exist if the corresponding current runs through the material. The electrical current I [A] for a voltage applied to a layer of material is given by Ohms law:

$$I = \frac{U}{R} \tag{6}$$

From this relation it is evident that by increasing the voltage, the current increases also. Furthermore making the length smaller decreases the resistance according to (4) and therefore will also increase the current. Although there is no fundamental limit to the current, there is a practical limit in how quickly a large current can be created and switched.

2.2 Resonant Circuit for Energy Transfer

To create short bursts of energy, a resonant circuit is used. The basic resonant circuit is shown in figure 2, where R represents the resistance of the catalyst layer. This layer is connected to two external components, a capacitor C and an inductance L. The capacitor is charged to a certain

voltage separately, and then connected to the other two components resulting in the circuit of figure 2. Due to the charge in the capacitor, current will flow and through the inductance and the resistance dissipating energy which is released as heat.

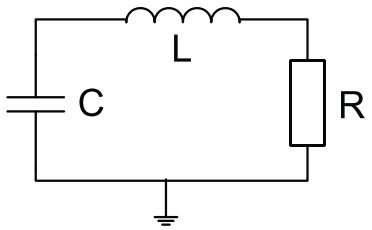

Fig. 2. Basic resonant circuit consisting of a capacitance, an inductance and a resistance. The resistance represents the catalytic layer.

From linear circuit theory, the circuit of figure 2 is governed by (7):

$$U_R = \frac{sRC}{s^2LC + sRC + 1} U_{C0} \tag{7}$$

where U_R is the voltage over the catalytic layer [V], U_{C0} is the initial voltage over the capacitor [V] and s is the Laplace operator. This equation shows second order dynamics in the numerator, which can be associated with a natural frequency ω_0 [rad/s] and a quality factor Q [-] as given in (8).

$$s^2/\omega_0^2 + s/\omega_0 Q + 1 = s^2LC + sRC + 1 \tag{8}$$

The natural frequency gives the frequency of the oscillation in the circuit, and the quality factor roughly indicates how many periods can be seen before the oscillation is gone and all the energy from the capacitor is dissipated in the resistance. From (8) the natural frequency and quality factor for a given circuit can be calculated:

$$\omega_0 = \frac{1}{\sqrt{LC}} \tag{9}$$

$$Q = \frac{1}{R}\sqrt{\frac{L}{C}} \tag{10}$$

In this application it is desired to release the energy stored in the capacitor as quickly as possible in the catalyst layer. A quality factor of 0.5 together with a high natural frequency is considered optimal.

2.3 Design Strategy

The question of how to choose values for R,L,C etcetera is an important one. This subsection proposes a strategy for consistent selection of most of the free parameters. The simulation introduced in section 3 is needed to verify the time constant for cooling and verifying validity of the thickness of the catalyst layer. The following design strategy is proposed:

(1) Fix resistance R and its dimensions: The value for the resistance should be the dominant resistance in the circuit. Wires and connections can easily account for up to 1 Ω, and the catalyst layer should have significantly more resistance. A value of 100 Ω is chosen. For this laboratory setup it is desired that the amount of energy needed to create a significant heat pulse is not too large, so volume should be kept small. At the same time it is desired that the width and length of the layer are much larger than the height, such that the energy loss to the sides can be neglected. Also the sizes should be chosen such that the device can be created using integrated circuit techniques. The layer should be very thin, a value of 100 nm is chosen for the height h. To make the resistance approximately 100 Ω, we choose w to be 0.5 mm and l to be 5 cm.

(2) The next step is to determine the pulse amplitude. Since we want to significantly influence kinetics for a very short time, the temperature pulse should be large. A value of 1000 K is chosen. Since the dimensions are already specified, the amount of energy needed to make the platinum layer temperature rise by this amount can easily be calculated. For the selected dimensions, this energy is 7.1 mJ. This value holds under the assumption that no energy is lost during the application of the pulse, which in practice will be the case. In the next section it is shown that for this design the simulation predicts an actual rise of 500 K which the authors find satisfactory.

(3) Determine the maximum available voltage. The voltage is limited mostly by the switching devices needed to open and close the current loop. In this design a MOSFET type device will be used for switching. Even high voltage MOSFETs can typically not deal with voltages greater than 1000 V. This will be the voltage used. For higher voltages spark gap switches can be applied if necessary. The voltage determines the size of the capacitance C needed by the basic relation of (11).

$$E = \frac{1}{2} C U_{C0}^2 \tag{11}$$

In this case the capacitance needed is 14 nF. Using this capacitance value, the corresponding inductance can be computed from (10) to get the proper quality factor for the resonance circuit. The natural frequency that corresponds to this network can be computed using (9), in this case it is 1.32 Mrad/s. That means the period length is approximately 4.75 μs, which is excellent for this application. If the natural frequency would have been too low, the applied voltage would have to be increased further.

Table 1. Design Parameters Chosen

Description	Parameter	Value	Unit
Resistance	R	106	[Ω]
Catalyst length	l	50	[mm]
Catalyst width	w	0.5	[mm]
Catalyst height	h	100	[nm]
Temperature rise	ΔT	1000 (500)	[K]
Pulse energy	E	7.1	[mJ]
Quality factor	Q	0.5	[−]
Capacitance	C	14	[nF]
Inductance	L	40	[μH]
Natural Frequency	ω_0	1.32	[Mrad/s]

Table 1 summarizes the choices made using this design procedure.

3. HEAT SIMULATION MODEL

The previous section introduced the design of a pulsed reactor, and in this section the heat distribution within that design is simulated. Since the design is developed in such a way that heat loss to the sides should be negligible in comparison to the heat loss to the support of the catalytic layer, only the vertical dimension is simulated. Figure 3 schematically shows the layers (not drawn to scale), with their respective sizes in one dimension which is named the x dimension.

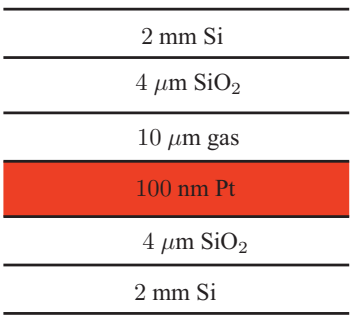

Fig. 3. Schematic view of the layers in the vertical dimension. In this dimension the heat distribution will be simulated. BC stands for boundary condition.

Heat distribution by conduction and diffusion in the model is simulated, as a lower limit to the cooling. The partial differential equation that is being solved is the standard heat diffusion equation given as (12), where κ is the local thermal conductivity [m^2/s].

$$\frac{dT}{dt} = \kappa(x)\frac{\partial^2 T}{\partial x^2} \tag{12}$$

Since this is a very straightforward geometry, the pseudo spectral method is used for collocation (Trefethen (2000); Weideman and Reddy (2000)) to get the benefit of spectral accuracy. Each of the layers is collocated separately, with energy preserving von Neumann boundary conditions at the layer boundaries. Only at the very top and bottom there are fixed temperatures (Dirichlet boundary conditions). Initially, all the layers have a temperature of 300 K. When heat enters the system in the catalytic layer, conduction will transport the heat through the other layers to the outer boundary where it is eventually lost to the surroundings.

After collocation, a system of ordinary differential equations which pose an initial value problem that is solved in Matlab using the built-in stiff ODE solvers.

3.1 Simulation Results

An RLC circuit is also simulated in parallel with the heating simulation. The RLC parameters are chosen identical to those find using the design procedure described in the previous section. The capacitor discharges via the inductance into the catalytic layer. The power that is released as heat into the catalytic layer is shown in figure 4. The peak power is about 5 kW which creates an enormous temperature gradient in the thin catalyst layer.

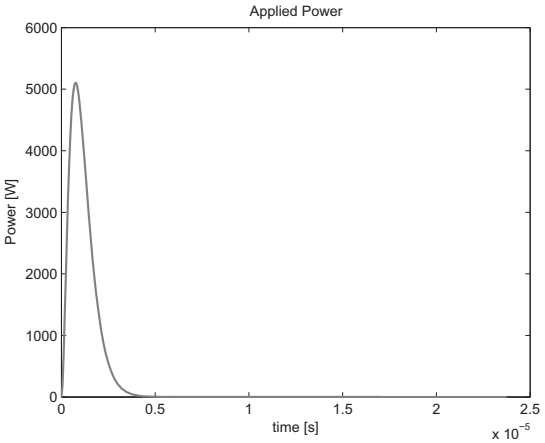

Fig. 4. Power supplied to the catalytic layer by the resonant circuit. The shape is very much like a pulse, with the peak power at about 5 kW.

This heat will result in a temperature rise of the catalytic layer, which will therefore have a temperature gradient with respect to the other layers. Transport of heat to the other layers will result. The temperature at the boundary between the catalytic layer and the gas layer is the surface temperature, which is critical for the catalytic reactions taking place. The simulated surface temperature resulting from the energy pulse is shown in figure 5. The surface temperature rises by about 500 K and not with the 1000 K for which this amount of energy (7.1 mJ) was computed in the previous section. This is due to the loss of energy to the other layers while the pulse is still in progress. About half the energy is lost to the other layers before the pulse is finished, so the heating and cooling time constants are approximately equal. If this is undesired, raising the voltage used in the design procedure will give a smaller capacitance and a faster resonance frequency. The applied energy pulse will then be shorter and higher. For the current laboratory application losing half of the 7.1 mJ is not a problem so the design is left as it is.

The heat will quickly spread into the gas layer and the SiO_2 (silica) layer supporting the catalyst. Figure 6 shows how the heat spreads through the silica supporting layer in time. The conduction within the metal layer that lies beneath the silica layer is so fast that, even though the Si layer is 2 mm thick, it does not allow for high internal temperature gradients. The whole Si layer remains at approximately 300 K and has a maximum at the boundary with the silica layer of only 301.5 K. The whole temperature gradient between the Si layer and the catalyst layer exists in the supporting silica layer, which very quickly builds up a linear temperature profile, due to the fact that the silica has a much lower thermal conductivity than the catalyst or Si layer.

The other side of the catalyst layer loses heat to the gas layer. Figure 7 shows the heat profile within the gas layer. The heat conductivity for gas is even lower than the one for the top silica layer and thus much lower than that of the metallic catalyst layer. Just like with the supporting silica layer at the bottom, the majority of the temperature gradient at the top side of the catalyst will be in the layer

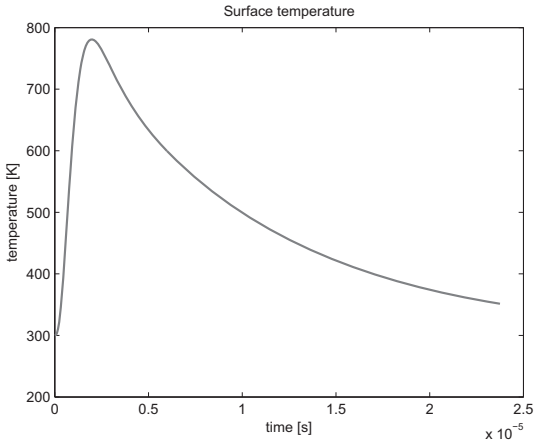

Fig. 5. Surface temperature when pulse is applied. The pulse causes the temperature to rise by about 500 K. The cooling time constant and the heating time constant are approximately equal for the parameters of table 1.

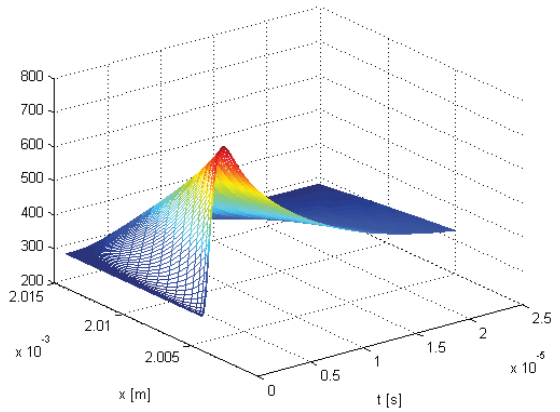

Fig. 7. The gas layer temperature profile over time. Like with the supporting SiO_2 layer a gradient leads to a linear profile, but the time taken for the linear profile to build up is longer.

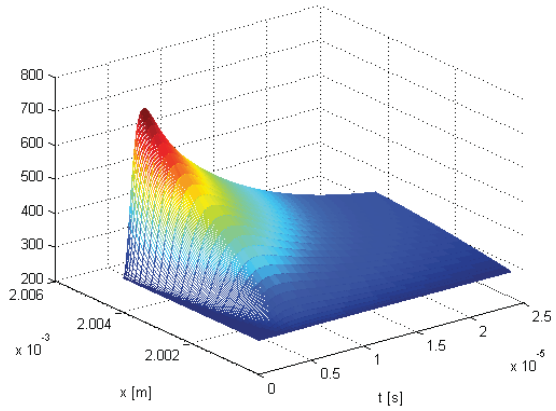

Fig. 6. Heat profile of the SiO_2 layer supporting the catalyst. A large temperature gradient over this layer quickly leads to a linear temperature profile.

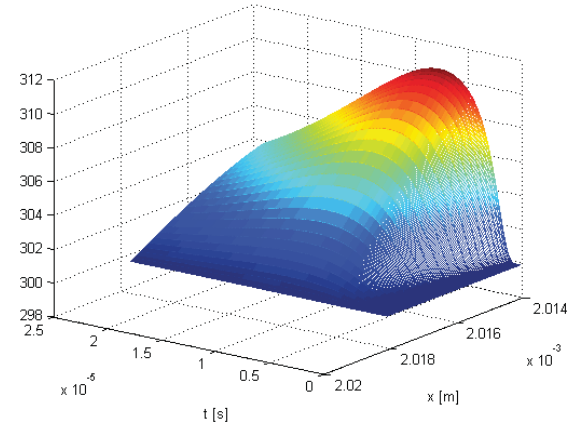

Fig. 8. Temperature profile within the top SiO_2 layer over time. The peak temperature is only about 10 K above the ambient temperature. Heat entering this layer from the gas layer is quickly transported to the top Si layer.

with the poorest heat conductivity which is the gas layer. Since the gas layer is thicker than the silica layer and even poorer in conducting heat, it takes a bit longer for the linear profile to build up. Due to the low conductivity of the gas, much less heat is lost to the gas than is lost through the supporting silica layer.

Figure 8 shows the top silica layer, which is heated through the gas layer. The maximum rise of temperature in the top silica layer is only 10 K even though the catalyst surface was heated by almost 500 K. The heat that ends up in the top silica layer is quickly lost to the top Si layer.

Just to confirm the results, the heat distribution within the platinum catalyst layer is shown in figure 9. From this figure it is clear that there exists almost no gradient within the catalyst layer, due to the superior heat conductivity of platinum.

The heating of the platinum layer is achieved through ohmic heating a resonant circuit with a high natural frequency and a low quality factor. By using higher voltages and adjusting the capacitance and inductance accordingly the heating can be made as fast as parasitic effects allow for. The cooling of the catalyst layer however cannot be forced, and the cooling time constant is created as an interplay between the different layers thicknesses and their values for thermal conductivity. By manipulating the thickness of the catalyst layer and the supporting silica layer the time constant for cooling can be shaped. A thickness of 100 nm for the catalyst layer and 4 µm for the supporting silica layer give a feasible time constant in this design.

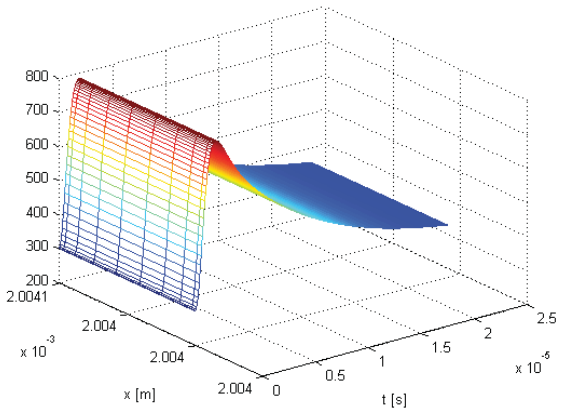

Fig. 9. The temperature profile within the catalytic layer. There exists almost no gradient within the catalyst layer, resulting in a flat profile.

4. POTENTIAL PITFALLS

Apart from the design variables already considered there are some miscellaneous design considerations that need to be included. This section mentions the most important ones.

4.1 Mechanical Strength

The heated metal layer will go up and down in temperature by hundreds of Kelvin. Metals normally expand when they become hot, and shrink when they cool down again. Unfortunately it is difficult to say whether this will physically break the layer or not. Since nobody ever tried this before there is no data on such high gradients in such thin supported metal layers. If mechanical strength is found to be a problem the pulses will need to be less intense.

4.2 Discharge Through SiO_2 Support

In the current design there is a 4 µm SiO_2 layer between the catalytic layer and the silicon support. The silicon support is electrically grounded for safety reasons. The catalytic layer is subjected to a high voltage. This voltage should not become so high that discharge occurs straight through the quartz layer because this will not only lead to pulse energy loss, but also break the device.

4.3 Electro Migration

When extremely high current densities are applied to any material, a phenomenon called electro migration will occur. The atoms of the metal start to physically move to one of the contacts, which in time will break the catalyst layer. To prevent this effect the current direction should be reversed between pulses.

4.4 Electromagnetic Interference

The high frequency currents are associated with a high frequency electromagnetic field. For any industrial application this field should be contained to such values that other electronic devices are not disturbed, and the radio spectrum is not polluted.

5. CONCLUSION

A new prototype reactor is presented to create extremely fast temperature pulses in heterogeneous catalysis. The authors intend to use this prototype to improve understanding of the effects of temperature pulsing on complex reaction schemes. The availability of such a reactor can help understanding the results of microwave enhanced catalysis as well. There appear to be no fundamental problems preventing a temperature pulse of 1000 K in less than 10^{-5} s, which is orders of magnitudes faster than what is known from literature.

REFERENCES

Bailey, J. (1973). Periodic operation of chemical reactors: A review. *Chemical Engineering Communications*, 1, 111–124.

Horn, F. and Lin, R. (1967). Periodic processes: A variational approach. *Industrial & Engineering Chemistry*, 6, 21–30.

Matsubara, M., Nishimura, Y., and Takahashi, N. (1973). Periodic operation of CSTR - I idealized control. *Chemical Engineering Science*, 28, 1369–1377.

Silveston, P. and Hudgins, R. (2004). Periodic temperature forcing of catalytic reactions. *Chemical Engineering Science*, 59, 4043–4053.

Silveston, P., Hudgins, R., and Renken, A. (1995). Periodic operation of catalytic reactors–introduction and overview. *Catalysis Today*, 25, 91–112.

Stolte, J., Vissers, J., Backx, T., and Bosgra, O. (2008). Modeling local/periodic temperature variation in catalytic reactions. In *IEEE International Conference on Control Applications*.

Trefethen, L. (2000). *Spectral Methods in Matlab*. SIAM.

Wan, J. (1993). Microwaves and chemistry: the catalysis of an exciting marriage. *Research on Chemical Intermediates*, 19, 147–158.

Wan, J., Tse, M., Husby, H., and Depew, M. (1990). High-power pulsed microwave catalytic processes: decomposition of methane. *Journal of Microwave Power and Electromagnetic Energy*, 25, 32–38.

Weideman, J. and Reddy, S. (2000). A matlab differentiation matrix suite. *ACM Transactions on Mathematical Software*, 26(4), 465–519.

Will, H., Scholz, P., and Ondruschka, B. (2004). Microwave-assisted heterogeneous gas-phase catalysis. *Chemical Engineering & Technology*, 27, 113.

Decision Oriented Bayesian Design of Experiments

Farminder S. Anand*, Jay H. Lee,**
Matthew J. Realff***

**School of Chemical & Biomolecular Engineering*
Georgia Institute of Technology, Atlanta, GA 30332 USA
(Tel:404-642-9151 ; e-mail: farminder.anand@ chbe.gatech.edu).
***(e-mail: jay.lee@chbe.gatech.edu)*
**** (e-mail: matthew.realff@chbe.gatech.edu)}*

Abstract: Experimental design is a fundamental problem in science and engineering. Traditional 'Design of Experiment' (DOE) approaches focus on minimization of variance. In this work, we propose a new "decision-oriented" DOE approach, which takes into account how the generated data, and subsequently the developed model, will be used in decision making. By doing so, the variance will be distributed in a manner such that its impact on the targeted decision making will be minimal. Our results show that the new decision-oriented experiment design approach significantly outperforms the standard D-optimal design approach. The new design method should be a valuable tool when experiments are conducted for the purpose of making R&D decisions.

Keywords: Decision making, optimal experiment design.

1. INTRODUCTION

Design of experiments (DOE) as a field has evolved over the period of last few decades. Its importance has grown significantly because of the increasing need to reduce the resource requirement for achieving the target. The targets historically perceived by the scientists in performing experiments have been driven towards understanding the underlying phenomenon or estimating the parameters. Consequently, the traditional DOE tools have been geared towards maximization of some measure of information or towards the minimization of the variance in the parameter estimates.

It is our opinion that this way of thinking over a long period of time has led the field to lose sight on the ultimate purpose of experiments in many applications. If one looks back into the history of the evolution of design of experiments one finds the answers in Bernardo (1979): "*Scientists typically does not have, nor can be normally expected to have, a clear idea of the utility of his results. An alternative is to design an experiment to maximize the expected information to be gained from it*". Bernardo (1979), further goes on proving that any *f* (function of the parameters, θ), in informational theoretical terms is '*garbling of θ*'. Hence follows the conclusion that maximization of information of θ is better than maximizing information on *f*.

This practice, while seeming logical, does not directly address the intended purpose of the experiments in many engineering applications. Today much of industrial research is driven by investment decisions, i.e., experiments are conducted with a specific objective in mind. For example, experiments can be conducted to aid decisions for the maximization of revenue function when investigating a new process or for the selection of a few processes among the large alternatives. In such scenarios, following the traditional route for design of experiments may be significantly suboptimal.

2. BACKGROUND

Traditionally there have been two major classes for the design of experiments (DOE) approaches: Classical approach and Bayesian approach. Historically, Classical DOE approaches like the factorial design have been more popular due to the computational complexities of the Bayesian approach. But recent developments in sampling techniques such as Markov Chain Monte Carlo (MCMC) (Kass (1998), Cowles (1996)) have rejuvenated the interest in the Bayesian approaches. In addition, the Bayesian approaches provide an added advantage of enabling the designer to incorporate the prior expert opinions. Hence, we will focus on the Bayesian approaches for design of experiments from here on.

To elaborate on the traditional Bayesian design strategies, we would follow Chaloner's (1995) approach, as it does justice to the inherent decision aspect hidden in the Bayesian approach. The idea of Bayesian DOE has evolved from information acquisition concepts in decision theory. Raiffa (1961) presented a decision theoretic approach for optimal information acquisition strategy using Expected Value of Information (EVOI) approach for investment decision problems. EVOI is defined as the expected difference between the expected posterior and prior utility, if one is to acquire information. Lindley (1956) introduced his seminal work on the use of Shannon information as a measure of information provided by an experiment. Following this, several authors (Stone (1959), DeGroot (1962) and Bernardo (1979)) presented a decision theoretic approach to experimental design, which was basically the maximization of EVOI with the utility function being replaced by Shannon information.

Consider a utility function (U), optimal decision (u) under posterior distribution, design matrix (η), parameters (θ) and observations (Y). Application of Lindley's EVOI maximization approach results in the maximization of expected pre-posterior utility as the expected value of the prior utility function is constant. The optimal expected pre-posterior utility is given in (1). Fig.1 demonstates how (1) can be solved numerically. Based on a given design (η) and the prior distribution of the parameters (θ_{prior}), potential observations (Y) are found via Monte Carlo simulation. For each of these potential realizations, posterior estimates (and covariances) for the parameters are obtained ($\theta_{Posterior}$) and corresponding to these posterior parameter estimates optimal decision variable (u) is estimated. Next step is to calculate the posterior expected utility(U) value corresponding to each of these potential realizations (Y). The average of the posterior utility values for each potential realization (Y) gives a utility of the design (η). The design that maximises this average utlity value is the optimal design.

$$U(\eta^*) = \max_{\eta} \int_{y} \max_{u} \int_{\Theta} U(\theta, \eta, Y, u) p(\theta \mid Y, \eta) p(Y \mid \eta) d\theta dY \quad (1)$$

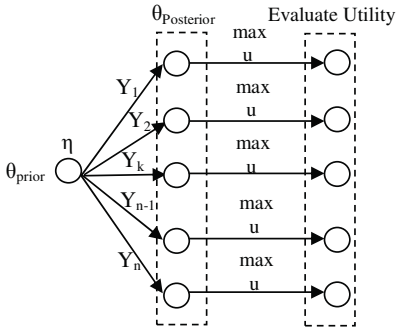

Fig. 1. Demonstrating the calculation of optimal design based on Lindley's EVOI concept.

Now, if one considers the Shannon information as the utility function, as suggested by Lindley, the above simplifies to (2). As both Fig. 2 and (2) show the calculations become much more tangible as the 'max' step drops out.

$$U(\eta^*) = \max_{\eta} \int_{y} \int_{\Theta} \log\{ p(\theta \mid Y, \eta) \} p(Y, \theta \mid \eta) d\theta dY \quad (2)$$

The rest of the Bayesian DOE methodologies, follow a similar line as (2) with some small changes to the utility function. In a broad sense, there exist three categories of Bayesian DOE approaches. First is the information maximization approach, which consists of maximizing the Kullback - Leibler distance between the prior and the posterior distribution. This approach consists of D-optimal and Ds-optimal designs. The second category is the set of designs, where the objective is to obtain a point estimate of the parameter values. This category consists of A-optimal and C-optimal designs. The third category is the minimax type of designs, where the objective is to minimize the maximum

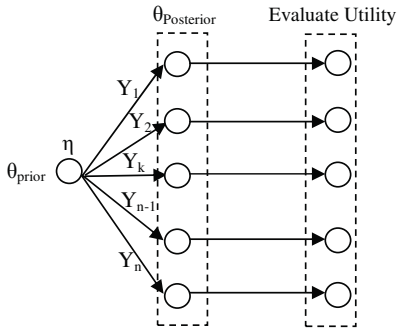

Fig. 2. Demonstrating the calculation of optimal design based on Shannon information criterion.

possible variance for all the linear combinations of the parameters under consideration. These various designs are further explained in details as follows:

D - Optimal: Maximize information gain for the parameters (Uses Kullback-Leibler distance between the prior and posterior distribution as a measure of gain in information).

Ds-optimality: Maximize gain in Shannon information of Ψ (= $S^T\theta$), where 'S' is a known constant vector.

A- Optimal: The objective of the experiment is to obtain a point estimate of the parameters. A design is chosen to maximize the following utility function:

$$U(\eta) = -\int \left(\theta - \hat{\theta}\right)^T A \left(\theta - \hat{\theta}\right) p(y, \theta \mid \eta) d\theta dy \quad (3)$$

Here 'A' is a symmetric nonnegative definite matrix. This design minimizes expected squared error of loss for estimating $C^T\theta$ or Minimizing square error of predicting at C, where C is not necessarily a fixed and a distribution is specified on it.

C- Optimal: Special case of A-optimality, where C is a constant.

E- Optimal: It is a minimax approach for variance. The maximum posterior variance of all possible normalized linear combinations of parameter estimates is minimized. An, E-optimal design minimizes:

$$\sup_{\|c\|=\omega} c^T \left(\eta^T \eta + R\right)^{-1} c = \omega^2 \lambda_{\max} \left[\left(\eta^T \eta + R\right)^{-1} \right] \quad (4)$$

G- Optimal: Closely related to E-optimal deign is G-optimal design, which minimizes $\sup_{x \in D} x^T \left(\eta^T \eta + R\right)^{-1} x$. An equivalence theorem [see Atkinson (1992)] states that continuous G-optimal designs are numerically identical to a corresponding continuous D-optimal design.

It is important to note that, among the above mentioned designs, D-, Ds- A- and C-optimal design have a utility function, which justifies its decision theoretic sense. On the other hand, E- and G-optimal designs though are considered

Bayesian design don't have any decision-theoretic sense, Chaloner (1995).

The rest of the document is structured as follows: Section 3 discusses in more detail the setup for the decision oriented design, section 4 presents the numerical results, and section 5 concludes the paper.

3. SELECTION/REJECTION DESIGN

As elaborated in the previous section the traditional design criterions either try to maximize the information gain or minimize the variance. Consider the case when the objective of the experimentation is to select/reject processes from a large set of potential processes. In this scenario traditional overall variance reduction design techniques may not be the optimal solution. For example, assume that the selection criterion is based on a cut-off value of operating profit margins, say \$10M/yr and processes that have operating profit margins equal or above the cut-off are worth pursuing. The question at this juncture may be: Should one be more focused towards reducing the overall parameter uncertainty or towards designing experiment strategies that directly target this objective?

In order to design experiments focused on this target, we propose to design experiments that maximize the expected operating profit margin. The premise here is that the designs that try to obtain the maximum operating profit margins would inherently be able to obtain values closer to the true optimal operating profit margin values. In order to obtain such a DOE we substitute the operating profit margin function in place of the utility function 'U' in (1).

3.1 Problem Formulation

Assume an initial model structure and prior estimates for the process models are available from the prior experimental results. The decision-maker wants to perform more experiments to select the few processes with the most potential.

Assume the yield (Y_1) of the process has a linear model, $Y_1 = \tilde{X}^T\tilde{\theta}_1 + \varepsilon$, where $\tilde{X}$ is the vector of the operating conditions to be optimized and ε is the Gaussian noise, $N(0,\sigma)$ with known variance(σ^2). We assume that the quality of the product also varies linearly, $Y_2 = \tilde{X}^T\tilde{\theta}_2 + \varepsilon$, with the operating conditions and the target quality is μ. We consider the operating profit margin function (*f*) in Eq. (5), which depends linearly on the yield value, has a quadratic penalty for the quality deviation, and a quadratic penalty (Q) for higher operating conditions.

$$f = \alpha * Y_1 - \beta * (Y_2 - \mu)^2 - \frac{1}{2}\tilde{X}^T * Q * \tilde{X} \qquad (5)$$

To obtain a DOE which maximizes the operating profit margins, we substitute *f*, operating profit margin function in place of the utility 'U' in (1) and follow the algorithm as explained in Fig.1 and section 2.

To evaluate the new design criterion, we consider $\tilde{X} = [x_1, x_2]^T$ to be a two dimensional vector and hence both the prior parameter estimates $\tilde{\theta}_1 = [\theta_{1,1}, \theta_{1,2}]^T$ & $\tilde{\theta}_2 = [\theta_{2,1}, \theta_{2,2}]^T$ are also two dimensional vectors. We consider the range of the operating conditions to be in the range of [1e-5, 10]. We consider the prior estimates of the parameters (θ_1 and θ_2) to be normal distributions with mean $\bar{\theta}_1 = [\bar{\theta}_{1,1}, \bar{\theta}_{1,2}]^T$, $\bar{\theta}_2 = [\bar{\theta}_{2,1}, \bar{\theta}_{2,2}]^T$ and covariance matrices $\Sigma_{\theta 1}$ and $\Sigma_{\theta 2}$ respectively.

In order to statistically evaluate the performance of our DOE approach against the traditional D-optimal DOE approach, we consider the following distributions for the parameter values:

$$\bar{\theta}_{1,1} \sim U[-100, 100] \qquad (6)$$

$$\bar{\theta}_{1,2} \sim U[\max(-100, -\bar{\theta}_{1,1}), 100] \qquad (7)$$

$$\bar{\theta}_{2,1} \sim U[-100, 100] \qquad (8)$$

$$\bar{\theta}_{2,2} \sim U[\max(-100, -\bar{\theta}_{2,1}), 100] \qquad (9)$$

$$\Sigma_{\theta 1} = [(0.1*\bar{\theta}_{1,1})^2 \;\; 0 \;;\; 0 \;\; (0.1*\bar{\theta}_{1,2})^2] \qquad (10)$$

$$\Sigma_{\theta 2} = [(0.1*\bar{\theta}_{2,1})^2 \;\; 0 \;;\; 0 \;\; (0.1*\bar{\theta}_{2,2})^2] \qquad (11)$$

$$\sigma = \sqrt{\min((0.1*\bar{\theta}_{1,1})^2, (0.1*\bar{\theta}_{1,2})^2)} \qquad (12)$$

$$\mu = U[0.5*1e\text{-}5*\min(\bar{\theta}_{2,1}, \bar{\theta}_{2,2}),\ 1.5*10*\max(\bar{\theta}_{2,1}, \bar{\theta}_{2,2})] \qquad (13)$$

The idea behind choosing the above parameter space is not only to have a sufficiently broad range of the parameter space but also to have some realistically sensible parameter values. The quadratic penalty matrix (14), Q, for higher operating conditions is chosen appropriately so that it is both positive definite and a practically reasonable value.

$$Q = [q_{11}\ q_{12};\ q_{21}\ q_{22}], \text{ where} \qquad (14)$$

$$q_{11} = U[1e^{-5}, \alpha * |(\bar{\theta}_{1,1} + \bar{\theta}_{1,2})/2|] \qquad (15)$$

$$q_{22} = U[1e^{-5}, \alpha * |(\bar{\theta}_{2,1} + \bar{\theta}_{2,2})/2|] \qquad (16)$$

$$q_{12} = U[1e^{-5}, \sqrt{(q_{11}*q_{22})}] \qquad (17)$$

$$q_{21} = U[1e^{-5}, \; q_{11}*q_{22}/q_{12}] \qquad (18)$$

Lastly the true parameter values, unknown to the decision-maker, are considered to be drawn randomly from the prior parameter distributions.

3.2 Solution Approach

To obtain the optimal design solution for the above mentioned problem, we need to solve (19). In (19) Y is the two dimensional vector $[Y_1, Y_2]^T$, each term corresponding to the yield and the quality value. And Θ is the vector of the corresponding parameters for the yield ($\tilde{\theta}_1 = \left[\theta_{1,1}, \theta_{1,2}\right]^T$) and quality ($\tilde{\theta}_2 = \left[\theta_{2,1}, \theta_{2,2}\right]^T$) respectively. Algorithm to calculate the optimal design via (19) is shown in Fig. (3).

$$U(\eta^*) = \max_{\eta} \int_y \max_u \int_\Theta f(\theta, \eta, Y, u)\, p(\theta \mid Y, \eta)\, p(Y \mid \eta)\, d\theta dY \quad (19)$$

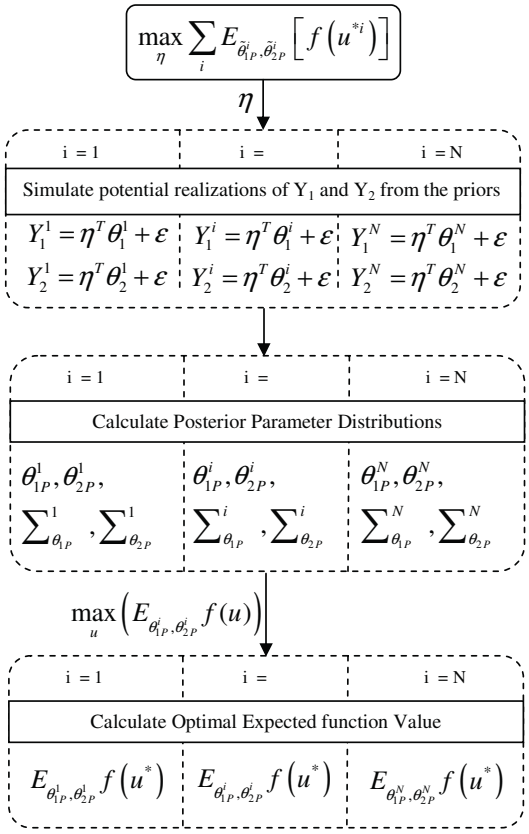

Fig. 3. Algorithm to calculate the optimal decision oriented design of experiment.

The calculation algorithm consists of two stages of optimization. The outer optimization is for selecting the optimal design and the inner optimization is for obtaining the optimal posterior operating conditions. The details for evaluating a given design 'η' are explained as follows:

Step 0: Assume an initial design 'η'

Step 1: Based on the given design and the prior distributions for the parameters $\tilde{\theta}_1 = \left[\theta_{1,1}, \theta_{1,2}\right]^T$ and $\tilde{\theta}_2 = \left[\theta_{2,1}, \theta_{2,2}\right]^T$ generate potential realizations of Y_1^i and Y_2^i for i = 1, 2,..., N (we consider N = 500).

Step 2: For each given realization estimate the posterior mean and covariance matrix for the parameters $\tilde{\theta}_1$ and $\tilde{\theta}_2$.

Step 3: For each posterior distribution estimate, obtain the optimal operating condition and hence the optimal function '*f*' value. Since the function '*f*' has nice structure in our case, the optimization has an analytical solution. But due to the constraints on the operating conditions, the optimal operating conditions are either at the boundary of the constraints or are given by the analytical solution.

Step 4: Calculate the expected value of the optimal function '*f*' value for each of the distributions.

Step 5: Calculate the average of all the optimal expected function values calculated in Step 4.

The value obtained in Step 5 is the value signifies potential of the given design ''. In order to obtain the optimal design, maximization is performed over the design space. This maximization is performed using the inbuilt function '*fmincon*' in MATLAB.

4. RESULTS

To compare the results given by our new design approach and the D-optimal design approach, we took 100,000 runs for different randomly sampled parameter values. To measure the performance of different designs, we measure the closeness of the predicted operating profit margin value to the true optimal operating profit margin value. The percentage of times the true value is closer to the predicted value by a design is reported as the 'Performance Index' of that design.

Table 1 Comparison of performance of new- and D-optimal designs for the 10% noise case.

Type of Prior Distribution	'Performance Index'	
	New Design	D Design
Strongly Informative	45.2290	25.9920
Informative	53.5120	22.8120
Mildly Informative	58.2250	21.1130
Un-Informative	63.5690	17.3060

In order to check if the kind of prior distribution has an effect on the performance of the new-design approach, we measure four levels of prior distributions. An '*Informative*' prior distribution is the one with square root of the diagonal elements of the prior covariance matrix being 10% of the prior mean of the respective parameter. This kind of prior distribution is the one we have shown in (10) and (11). A '*Strongly Informative*' prior distribution is the one with a small covariance and we depict it by replacing the 0.1 values

by 0.05 in (10) and (11). A '*Mildly Informative*' prior distribution is the one with a relatively high variance and is depicted by replacing 0.1 values by 0.15 in (10) and (11). A '*Un-Informative*' prior distribution is the one with a relatively high variance and is depicted by replacing 0.1 values by 0.30 in (10) and (11). The comparison of the performance measure for our decision-oriented and the D-optimal design is shown in Table 1. The above results clearly show ~20-35% improvement in the prediction power of the Decision-oriented design compared to the D-optimal design of experiments.

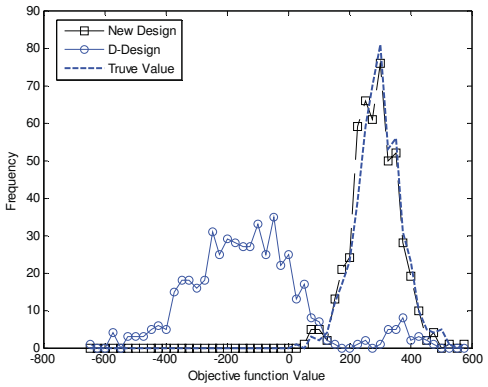

Fig. 4. Histogram comparing the prediction of the Decision oriented and D-optimal design to the true objective value for a '*Mildly Informative*' prior distribution.

Table 2 Comparison of performance of the Decision-oriented design and the D-optimal designs for the 5% noise case

Type of Prior Distribution	'Performance Index'	
	New Design	D Design
Strongly Informative	52.8330	23.3690
Informative	60.5130	18.2910
Mildly Informative	63.9620	16.4300
Un-Informative	67.3060	14.0870

To give more insight to the results we plot the histogram of the optimal operating margin values for the decision oriented and D-optimal design along with the optimal operating margin values (determined assuming that the 'true' parameter values are known), for a particular set of parameter values with 500 different 'true' parameter values being sampled from the prior distribution. To be precise, these are the operating margins for the 'true' plant (with 'true' parameter values) with the optimal operating conditions determined based on the parameter estimates resulting from the respective DOEs. Fig 4 shows the histogram for a '*Mildly Informative*' prior distribution, with 500 'true' parameter values sampled from the prior distribution.

Similarly Fig. 5, Fig. 6 and Fig. 7 show the histogram plots for the '*Informative'*, '*Strongly Informative*' and '*Un-Informative*' prior distributions respectively. Fig 4, 5, 6 & 7 clearly demonstrate the better performance of the decision-oriented DOE strategy compared to traditional D-optimal design strategy.

Table 3 Comparison of performance of the Decision-oriented design and the D-optimal designs for the 15% noise case

Type of Prior Distribution	'Performance Index'	
	New Design	D Design
Strongly Informative	39.5190	25.4060
Informative	49.3160	24.8090
Mildly Informative	53.5440	22.6560
Un-Informative	60.2590	19.1200

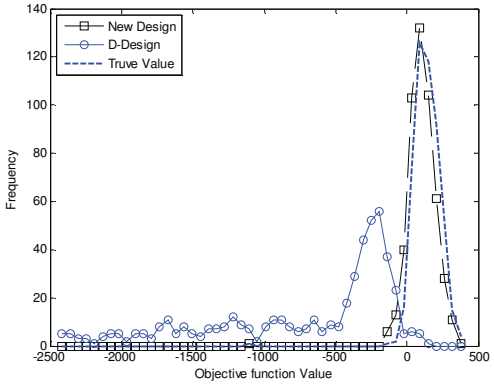

Fig. 5. Histogram comparing the prediction of the Decision oriented and D-optimal design to the true objective value for an '*Informative*' prior distribution.

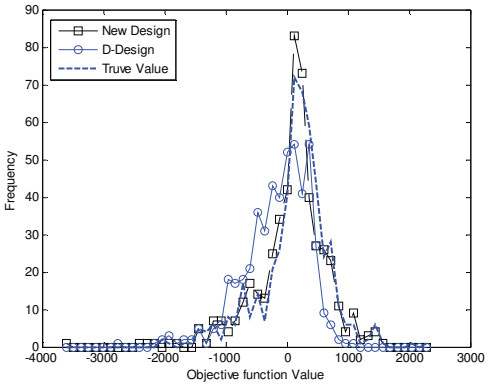

Fig. 6. Histogram comparing the prediction of the Decision oriented and D-optimal design to the true objective value for a '*Strongly Informative*' prior distribution.

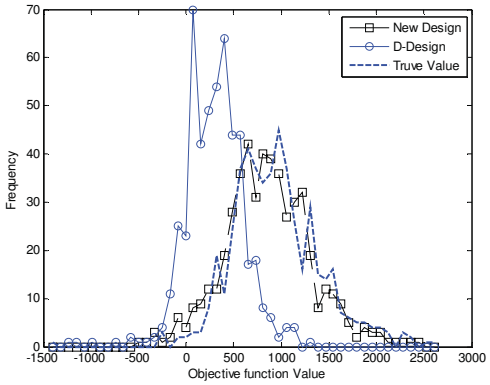

Fig. 7. Histogram comparing the prediction of the Decision oriented and D-optimal design to the true objective value for a '*Un-Informative*' prior distribution.

In order to check if noise has any significant impact on the performance of the decision-oriented designs, we vary the noise measured by the variance of the Gaussian noise in (12). In comparison to the initial noise of 10% as depicted by the value '0.1' in (12) we test two other levels of noise 5% and 15% , which correspond to changing '0.1 value in (12) to '0.05' and '0.15' respectively. The results for the 5% and the 15% noise cases are shown in the Table 2 and Table 3 respectively. The results clearly demonstrate that the decision-optimal design outperforms the D-optimal design regardless of the noise level.

5. CONCLUSIONS

We have introduced a new decision oriented design of experiment strategy, which significantly improves the prediction of a process's optimal objective function value compared to that of a D-optimal design of experiment strategy. These types of DOE strategies are expected to be of significant importance in improving the R&D decisions, especially in bio-fuel related research where one faces multiple process alternatives. Moreover, in addition to the design criterion considered in this work, one can consider alternative Acceptance/Rejection design criterion. For example, in the problem discussed in this work, we were mainly concerned with the mean value of '*f*', but an alternat-

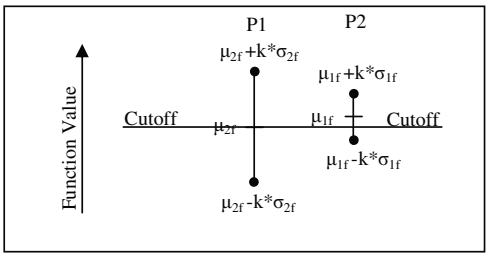

Fig. 8. An alternative Acceptance/Rejection criterion

-ive design criterion can be based on both the mean and the variance of '*f*' along with a cut-off value. Consider two processes P1 and P2, shown in Fig. 8. The selection criterion of the decision maker for these processes is that $\mu - k*\sigma$ be greater than the 'Cutoff' and the rejection criterion being that $\mu + k*\sigma$ be less than the 'Cutoff', where μ is the posterior mean and σ is the posterior standard deviation of the objective function '*f*'. To design experiments for selection/rejection of processes based on this type of criterion can be done by maximising $|\Sigma\delta_i|$, where δ_i is defined as follows:

$$\delta_i = \begin{Bmatrix} +1, if\ \mu_{fi} - k*\sigma_i > Cutoff \\ -1, if\ \mu_{fi} + k*\sigma_i < Cutoff \\ 0, Otherwise \end{Bmatrix}$$

The subscript 'i' represents the potential random samples with value ranging form i = 1, 2.., N, as explained earlier in section 3.2. Similarly various other design criterions can be created based on the decision maker's objective function. We will evaluate these and similar acceptance/rejection decision criterions in our future work.

REFERENCES

Atkinson, A.C. and Donev, A.N. (1992). *Optimum Experimental Designs*, Pg. 114, Ch.10. Oxford Science Publications, United States

Bernardo, J.M.(1979). Expected information as expected utility. *Annals of Statistics*, 7 686-690

Chaloner, K. and Verdinelli, I. (1995). Bayesian Experimental Design: A Review, *Statistical Science*, 10 273-304

Cowles, Mary K. and Carlin, Bradley P. (1996), Markov Chain Monte Carlo Convergence Diagnostics: A comparative Review, *Journal of the American Statistical Association*, 91 883-904.

DeGroot, M.H. (1962). Uncertainty, information and sequential experiments, *The Annals of Mathematical Statistics*, 33 404-419

Kass, Robert E., Carlin, Bradley P., Gelman, Andrew, and Neal, Radford M., Markov Chain Monte Carlo in Practice: A Roundtable Discussion, *The American Statistician*, 52 93-100.

Lindley, D.V. (1956). On the measure of information and provided by an experiment. *Annals of Statistics*,27 986-1005

Raiffa, H. and Schlaifer, R. (1961). Applied statistical decision theory, Division of Research, Graduate School of Business Administration, Harvard University, Boston, United States

Stone, M. (1959). Application of a measure of information to the design and comparison of regression experiment. *The Annals of Mathematical Statistics, 30 55-70*

Correlation-Based Pattern Recognition and Its Application to Adaptive Soft-Sensor Design

Koichi Fujiwara * **Manabu Kano** * **Shinji Hasebe** *

* *Dept. of Chemical Engineering, Kyoto University, Katsura Campus, Nishikyo-ku, Kyoto 615-8510, Japan*
(e-mail: manabu@cheme.kyoto-u.ac.jp)

Abstract: Although soft-sensors have been widely used for estimating product quality or other key variables, they do not always function well in practice due to changes in process characteristics. The Correlation-based Just-In-Time (CoJIT) modeling has been proposed to cope with changes in process characteristics. In the CoJIT modeling, the samples used for local modeling are selected on the basis of correlation together with distance, since changes in process characteristics are expressed as the difference of the correlation. In addition, the individuality of production devices should be considered when they are operated in parallel. However, the CoJIT modeling cannot cope with the individuality of production devices because it is only applicable to time-series data. In the present work, a new pattern recognition method, referred to as the Nearest Correlation (NC) method is proposed, and it selects samples whose correlations are similar to the query. In addition, the proposed NC method is integrated with the CoJIT modeling. The advantages of the proposed CoJIT modeling with the NC method are demonstrated through a case study of a parallelized CSTR process.

Keywords: Soft-sensor, Estimation, Prediction, Just-In-Time modeling, Pattern recognition, Principal component analysis

1. INTRODUCTION

A soft-sensor, or a virtual sensor, is a key technology for estimating product quality or other important variables when on-line analyzers are not available. Partial least squares (PLS) regression and artificial neural network (ANN) have been widely accepted as useful techniques for soft-sensor design (Kano and Nakagawa (2008), Mejdell and Skogestad (1991), Kresta et al. (1994), Kano et al. (2000), Kamohara et al. (2004) and Radhakrishnan and Mohamed (2000)). In addition, the application of subspace identification (SSID) to soft-sensor design has been reported in Amirthalingam and Lee (1999) and Kano et al. (2008) for achieving higher estimation performance.

Generally, building a high performance soft-sensor is very laborious, since input variables and samples for model construction have to be selected carefully and parameters have to be tuned appropriately. In addition, even if a good soft-sensor is developed successfully, its estimation performance deteriorates as process characteristics change. In chemical processes, for example, process characteristics are changed by catalyst deactivation or fouling. Such a situation may deteriorate product quality. Therefore, maintenance of soft-sensors is very important in practice to keep their estimation performance. Ogawa and Kano (2008) indicate that soft-sensors should be updated as the process characteristics change, and also manual, repeated construction of them should be avoided due to its heavy workload.

To update statistical models automatically when process characteristics change, recursive methods such as recursive PLS (Qin (1998)) were developed. These methods can adapt models to new operating conditions recursively. However, when a process is operated within a narrow range for a certain period of time, the model will adapt excessively and will not function in a sufficiently wide range of operating conditions. In addition, recursive methods cannot cope with abrupt changes in process characteristics.

On the other hand, the individuality of production devices should be taken into account. In semiconductor processes, for example, parallelized production devices are used, and they have different characteristics even if their catalog specifications are the same. Therefore, a soft-sensor developed for one device is not always applicable to another device, and it is very laborious to customize soft-sensors according to their individuality.

The Just-In-Time (JIT) modeling has been proposed to cope with process nonlinearity (Bontempi et al. (1999) and Atkeson et al. (1997)) and changes in process characteristics (Cheng and Chiu (2004)). In the JIT modeling, a local model is built from past data around the query only when an estimate is required. The JIT modeling is useful when global modeling does not function well. However, its estimation performance is not always high because the samples used for local modeling are selected on the basis of the distance from the query and the correlation among variables is not taken into account. How should we determine the samples used for local modeling to build

a highly accurate statistical model? Distance is not the most important. A good model cannot be developed when correlation among input-output variables is weak, even if the distance between samples is very small. Conversely, a very accurate model can be developed when the correlation is strong even if the distance is large.

Recently, a new JIT modeling method based on the correlation among variables, referred to as the correlation-based JIT (CoJIT) modeling, has been proposed by Fujiwara et al. (2008). In the CoJIT modeling, the samples used for local modeling are selected on the basis of correlation together with distance. The CoJIT modeling can cope with abrupt changes of process characteristics and also achieve high estimation performance. However, it is applicable to only time-series data because it uses moving windows to generate data sets for local modeling. In other words, the original CoJIT modeling cannot generate a data set consisting of such data that represent characteristics of a query sample and are obtained from various devices operated in parallel.

To make the CoJIT modeling applicable to soft-sensor design for parallelized production devices, samples obtained from various devices have to be discriminated on the basis of the correlation among variables. This discrimination problem is one of the unsupervised pattern recognition problems because the teacher signal is not used for sample classification.

The Nearest Neighbor (NN) method and k-means method are well-known conventional unsupervised pattern recognition algorithms. The NN method can detect samples that are similar to the query, and k-means method can cluster samples without the teacher signal. However, they are distance-based methods and do not take into account the correlation among variables. Self organizing map (SOM) also has been used as an unsupervised pattern recognition method (Kohonen (2001)). SOM is a machine learning process that imitates the brain ' s learning process, and it not only can classify samples but also can visualize high dimensional data. However, it requires high computational load, and the preprocessing data are complicated.

In the present work, to cope with the individuality of production devices as well as changes in process characteristics, a new unsupervised pattern recognition method based on the correlation among variables, referred to as the Nearest Correlation (NC) method, is proposed. The proposed NC method can detect samples that have correlation similar to the query on the basis of sample geometry. In addition, the proposed NC method is integrated with the CoJIT modeling. The usefulness of the integration is demonstrated through a case study of a parallelized CSTR process.

2. INDICES OF CORRELATION

In this section, several measures for quantifying correlation among variables are briefly explained.

2.1 Correlation coefficient

The correlation coefficient $C_{i,j}$ can be used as an index of the similarity between two vectors $\boldsymbol{x}_i$ and $\boldsymbol{x}_j \in \Re^M$.

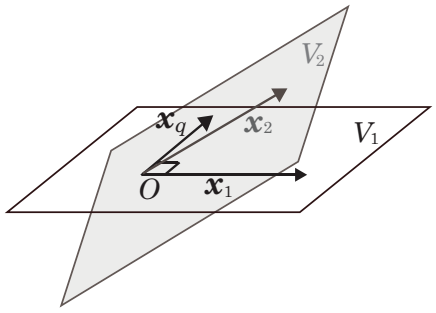

Fig. 1. An example of vector geometry in 3-dimensional space

$$C_{i,j} = \frac{\boldsymbol{x}_i^{\mathrm{T}} \boldsymbol{x}_j}{||\boldsymbol{x}_i|| ||\boldsymbol{x}_j||} = \cos\theta \tag{1}$$

where, θ is the angle between two vectors.

Suppose that the samples in the three-dimensional data consist of two classes K_1 and K_2, and samples belonging to classes K_1 and K_2 span the two-dimensional linear subspaces V_1 and V_2, respectively, as shown in Fig. 1.

Now, the query $\boldsymbol{x}_q$ is newly measured, and its class should be identified as K_1 or K_2. The correlation coefficients can be used as the index of sample discrimination. For example, $\boldsymbol{x}_1 \in K_1$ and $\boldsymbol{x}_2 \in K_2$ are selected from each class in a random manner, and the correlation coefficients between $\boldsymbol{x}_q$ and them are calculated respectively, and the class including the sample with the largest correlation coefficient can be identified as the class of $\boldsymbol{x}_q$.

In many cases, however, this method is inappropriate. In Fig. 1, the selected sample $\boldsymbol{x}_1$ and the query $\boldsymbol{x}_q$ are orthogonal to each other even though both vectors belong to K_1. In such a case, $\boldsymbol{x}_q$ is identified as an element of K_2 because the correlation coefficient between $\boldsymbol{x}_q$ and $\boldsymbol{x}_2$ is larger than the correlation coefficient between $\boldsymbol{x}_q$ and $\boldsymbol{x}_1$.

2.2 The Q statistic

In this work, the Q statistic is used as an index of sample discrimination.

The Q statistic is derived by principal component analysis (PCA), and it expresses the distance between the sample and the subspace spanned by principal components (Jackson and Mudholkar, 1979). The Q statistic is defined as

$$Q = \sum_{m=1}^{M} (x_m - \hat{x}_m)^2 \tag{2}$$

where x_m and $\hat{x}_m$ are the mth measurement and its estimate by the PCA model, respectively. The Q statistic is a measure of dissimilarity between the sample and the modeling data from the viewpoint of the correlation among variables.

In addition, to take into account the distance between the sample and the origin, Hotelling's T^2 statistic can be used. The T^2 statistic is defined as

$$T^2 = \sum_{r=1}^{R} \frac{t_r^2}{\sigma_{t_r}^2} \tag{3}$$

where σ_{t_r} denotes the standard deviation of the rth score t_r. The T^2 statistic expresses the normalized distance from the origin in the subspace spanned by principal components. The Q and T^2 statistics can be integrated into a single index for sample selection as proposed by Raich and Cinar (1994):

$$J = \lambda T^2 + (1 - \lambda)Q \tag{4}$$

where $0 \leq \lambda \leq 1$.

3. NEAREST CORRELATION METHOD

The NN method and the k-means method can discriminate or cluster samples on the basis of the distance without a teacher signal. However, they do not take into account the correlation among variables. In this section, a new unsupervised pattern recognition method based on the correlation among variables, referred to as the nearest correlation (NC) method, is proposed. In the proposed NC method, sample geometry is used for sample discrimination.

3.1 Concept of the NC method

Suppose that the hyper-plane P in Fig. 2 (left) expresses the correlation among variables and the samples on P have the same correlation. Although samples $\boldsymbol{x}_1$ to $\boldsymbol{x}_5$ have the same correlation and they are on P, samples $\boldsymbol{x}_6$ and $\boldsymbol{x}_7$ have different correlation from the others. The NC method aims to detect samples whose correlation is similar to the newly measured query $\boldsymbol{x}_q$. In this example, $\boldsymbol{x}_1$ to $\boldsymbol{x}_5$ on P should be detected.

At first, the whole space is translated so that the query becomes the origin. That is, $\boldsymbol{x}_q$ is subtracted from all samples $\boldsymbol{x}_i (i = 1, 2, \cdots, 7)$. Since the hyper-plane P is translated to the plane containing the origin, it becomes the linear subspace V.

Next, a line connecting each sample and the origin is drawn. Suppose another sample can be found on this line. In this case, $\boldsymbol{x}_1$-$\boldsymbol{x}_4$ and $\boldsymbol{x}_2$-$\boldsymbol{x}_3$ satisfy such a relationship as shown in Fig. 2 (right). The correlation coefficients of these pairs of samples must be 1 or -1. On the other hand, $\boldsymbol{x}_6$ and $\boldsymbol{x}_7$ that are not the elements of V cannot make such pairs. Therefore, the samples of the pairs whose correlation coefficients are ± 1 are thought to have the same correlation as $\boldsymbol{x}_q$.

However, $\boldsymbol{x}_5$ that does not make a pair cannot be detected by this method even though it is on V. To detect $\boldsymbol{x}_5$, a linear subspace is derived from the selected pairs by using PCA, and the derived linear subspace corresponds to V.

Finally, the Q statistics for all samples $\boldsymbol{x}_i$ $(i = 1, 2, \cdots, 7)$ are calculated by using the PCA model expressing V. The samples with small Q statistics are located close to the linear subspace V, and such samples have correlation similar to the query. Although $\boldsymbol{x}_5$ cannot be detected in the previous step, it can be detected in this step because its Q statistic is 0. On the other hand, $\boldsymbol{x}_6$ and $\boldsymbol{x}_7$ are not detected in this step since they have large Q statistics.

In addition, the T^2 statistic can be used to take into account the distance from the origin. In the present work,

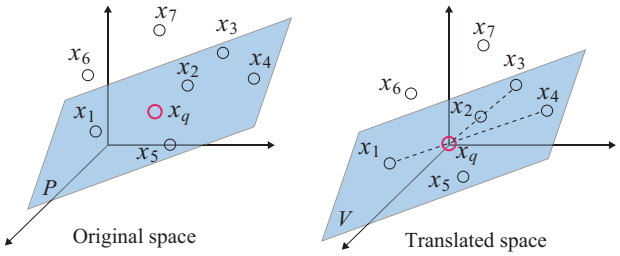

Fig. 2. An example of the procedure of the NC method

J in Eq. (4) is used as the index for sample selection. The samples with small J are selected as the samples similar to the query.

In the implementation of the above procedure, the threshold of the correlation coefficient γ $(1 \geq \gamma > 0)$ has to be used since there are no pairs whose correlation coefficient is strictly ± 1. That is, the pairs should be selected when the absolute values of their correlation coefficients are larger than γ.

3.2 Algorithm of the NC method

Assume that the samples stored in the database are $\boldsymbol{x}_n \in \Re^M$ $(n = 1, 2, \cdots, N)$ and the query is $\boldsymbol{x}_q \in P$ $(\dim(P) = R)$. The samples belonging to P should be detected in a manner similar to $\boldsymbol{x}_q$. The algorithm of the proposed NC method is as follows:

(1) Set R, $\gamma(1 \geq \gamma > 0)$, $\delta(\delta > 0)$ and K or $\bar{J}$.
(2) $\boldsymbol{x}'_n = \boldsymbol{x}_n - \boldsymbol{x}_q$ for $n = 1, 2, \cdots, N$.
(3) Calculate the correlation coefficients $C_{k,l}$ between all possible pairs of $\boldsymbol{x}'_k$ and $\boldsymbol{x}'_l$ $(k \neq l)$.
(4) Select the pairs satisfying $|C_{k,l}| \geq \gamma$, and set the number of the selected pairs S.
(5) If $S < R$, then $\gamma = \gamma - \delta$ $(\delta > 0)$ and return to step 4. If $S \geq R$, then go to the next step.
(6) Arrange the samples of the pairs selected in step 4 as the rows of the matrix $\boldsymbol{X}'$.
(7) Derive the linear subspace V from $\boldsymbol{X}'$ by using PCA. The number of principal components is R.
(8) Calculate the index J of $\boldsymbol{x}'_n$, and $J_n = J$ for $n = 1, 2, \cdots, N$.
(9) Detect the first K samples in ascending order of J_n or the samples whose J_n is smaller than $\bar{J}$ as samples similar to the query $\boldsymbol{x}_q$, where $\bar{J}$ is the threshold.

In step 5, when S is smaller than R, the threshold γ has to be relaxed to increase the number of selected pairs since the linear subspace V is not spanned by the samples of the selected pairs. R can be used as the tuning parameter.

3.3 Numerical example

The discrimination performance of the proposed NC method is compared with that of the NN method through a numerical example. In this example, data consist of three classes that have different correlations, and the samples belonging to the same class as the query should be detected. The discrimination rate is defined as

$$\text{Discrimination Rate [\%]} = \frac{L}{K} \times 100 \tag{5}$$

where K is the number of detected samples and L ($L \leq K$) is the number of samples that belong to the same class as the query among the detected samples. Samples in each of three classes are generated by using the following equation.

$$\boldsymbol{x}_i = \boldsymbol{A}_i \boldsymbol{s} + \boldsymbol{n} \ (i = 1, 2, 3) \tag{6}$$

$$\boldsymbol{s} = [s_1 \ s_2 \ s_3]^T \tag{7}$$

$$\boldsymbol{n} = [n_1 \ n_2 \ n_3]^T \tag{8}$$

where $\boldsymbol{A}_i$ is a coefficient matrix, $s_i \sim N(0, 10)$ and $n_i \sim N(0, 0.1)$. $N(m, \sigma)$ is the random number following the normal distribution whose mean is m and standard deviation is σ. The coefficient matrices are as follows:

$$\boldsymbol{A}_1 = \begin{bmatrix} 1 & 2 \\ 1 & 4 \\ 1 & 1 \\ 2 & 3 \\ 1 & 3 \end{bmatrix}, \ \boldsymbol{A}_2 = \begin{bmatrix} 3 & 3 \\ 2 & 1 \\ 3 & 1 \\ 3 & 2 \\ 2 & 0 \end{bmatrix}, \ \boldsymbol{A}_3 = \begin{bmatrix} 2 & 1 \\ 3 & 4 \\ 1 & 3 \\ 0 & 4 \\ 3 & 1 \end{bmatrix}. \tag{9}$$

100 samples are generated in each of three classes. In addition, a query belonging to each class is prepared. The number of detected samples K is fixed at 20.

In this example, the number of principal components is $R = 2$, the threshold is $\gamma = 1 - 10^{-4}$, the parameters are $\lambda = 0$ and $\delta = 0.9999$. Sample generation and sample detection by the NN method and the NC method are repeated 100 times and the average discrimination rates [%] and the average CPU time [ms] are calculated. The computer configuration used in this numerical example is as follows: OS: Windows Vista Business (64bit), CPU: Intel Core2 Duo 6300 (1.86GHz×2), RAM: 2G byte, and MATLAB® 7.5.0 (2008a).

Table 1 shows the discrimination results of the NN method and the NC method. The proposed NC method can achieve higher discrimination performance than the NN method. On the other hand, the computational load of the NC method is relatively heavy since singular value decomposition (SVD) is used for calculating the correlation among variables. In fact, the computation of SVD occupies most of the computation time of the NC method.

4. CORRELATION-BASED JUST-IN-TIME MODELING

The conventional JIT modeling uses the distance for sample selection when a temporary local model is constructed. However, its estimation performance is not always high since it does not take into account the correlation among variables. Recently, The Correlation-based JIT (CoJIT) modeling that selects samples for local modeling on the basis of the correlation among variables has been proposed by Fujiwara et al. (2008).

Figure 3 shows the difference of sample selection for local modeling between the JIT modeling and the CoJIT modeling. The samples are classified into two groups that have

Table 1. Discrimination performance of the NC method and the NN method

	Discrimination rate [%]			CPU time [ms]
	Class 1	Class 2	Class 3	
NC method	97.5	95.9	96.9	13.9
NN method	78.7	68.0	51.1	1.1

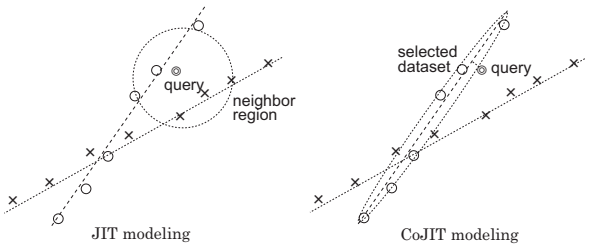

Fig. 3. Sample selection in the JIT modeling (left) and the CoJIT modeling (right)

different correlations. In conventional JIT modeling, samples are selected regardless of the difference of correlation as shown in Fig. 3 (left), since a neighbor region around the query point is defined only by distance. On the other hand, the CoJIT modeling can select samples whose correlation is best fit for the query as shown in Fig. 3 (right).

The procedure of the CoJIT modeling is as follows: 1) several data sets are generated from data stored in the database. 2) The index J is calculated from the query and each data set. 3) The data set whose J is the smallest is selected. 4) A temporary local model is constructed from the selected data set. In the above procedure, each data set is generated so that it consists of successive samples included in a certain period of time, because the correlation in such a data set is expected to be very similar (Fujiwara et al. (2008)).

However, the NC method can detect samples that have correlation similar to the query regardless of whether the objective data is time-series data or not. This is the motivation for integrating the proposed NC method with the CoJIT modeling.

Assume that the sampling interval of the output is longer than that of the input, and the output at time t, $\boldsymbol{y}_t$, should be estimated. Now, the input and the output measured at the same time are stored in the database, and the sth input-output sample $\boldsymbol{x}^{\{s\}} \in \Re^M$ $(s = 1, 2, \cdots, S)$ and $\boldsymbol{y}^{\{s\}} \in \Re^L$ are stored as matrices $\boldsymbol{X}_S \in \Re^{S \times M}$ and $\boldsymbol{Y}_S \in \Re^{S \times L}$, respectively. To cope with process dynamics, measurements at different sampling times can be included in $\boldsymbol{x}^{\{s\}}$. The algorithm of the proposed CoJIT modeling with the NC method is as follows:

(1) When the input at time t, $\boldsymbol{x}_t$, is measured, the index J is calculated from $\boldsymbol{x}_t$ and $\boldsymbol{X}_{t-1}$ that was used for building the previous local model f_{t-1}, and $J_I = J$.
(2) If $J_I \leq \bar{J}_I$, $f_t = f_{t-1}$, $\boldsymbol{X}_t = \boldsymbol{X}_{t-1}$, and f_t is used for estimating the output $\boldsymbol{y}_t$. Then, return to step 1. If $J_I > \bar{J}_I$, go to the next step. Here, $\bar{J}_I$ is the threshold.
(3) K input samples whose correlation is similar to the query are detected from $\boldsymbol{X}_S$ by the NC method, and they are arranged as the rows of $\boldsymbol{X}_t \in \Re^{K \times M}$. In addition, K output samples corresponding to the detected input samples are selected from $\boldsymbol{Y}_S$, and they are arranged as the rows of $\boldsymbol{Y}_t \in \Re^{K \times L}$, where K is the number of the detected samples.
(4) A new local model f_t whose input is $\boldsymbol{X}_t$ and output is $\boldsymbol{Y}_t$ is built.
(5) The output $\boldsymbol{y}_t$ is estimated by using f_t.

(6) The above steps 1 through 5 are repeated until the next output sample $\boldsymbol{y}_{S+1}$ is measured. When $\boldsymbol{y}_{S+1}$ is measured, $\boldsymbol{y}_{S+1}$ and its corresponding input $\boldsymbol{x}_{S+1}$ are stored in the database, and return to step 1.

In the above algorithm, any modeling method can be used for building a local model f. In the present work, partial least squares regression (PLS) is used to cope with the colinearity problem. In addition, steps 1 and 2 control the model update frequency. When the threshold $\bar{J}_I$ is large, the update frequency becomes low. The local model is updated every time when new input measurements are available in the case where $\bar{J}_I = 0$.

5. CASE STUDY

In this section, the estimation performance of the proposed CoJIT modeling with the NC method is compared with that of the conventional JIT modeling through their applications to product composition estimation for a parallelized CSTR process. The detailed CSTR model used in this case study is described in Johannesmeyer and Seborg (1999).

5.1 Problem setting

In this process, CSTR1 and CSTR2 are operated in parallel. Although these CSTRs have the same structure

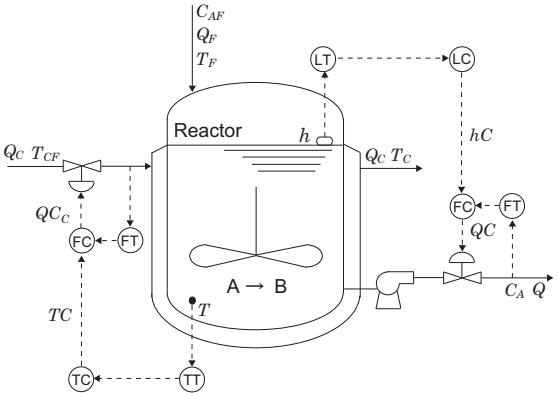

Fig. 4. Schematic diagram of CSTR with cascade control systems

Table 2. Process variables of the CSTR processes

Variable	Caption
C_A	Reactant concentration [mol/m^3]
T	Reactor temperature [K]
T_C	Coolant temperature [K]
h	Reactor level [m]
Q	Reactor exit flow rate [m^3/min]
Q_C	Coolant flow rate [m^3/min]
Q_F	Reactor feed flow rate [m^3/min]
C_{AF}	Feed concentration [mol/m^3]
T_F	Feed temperature [K]
T_{CF}	Coolant feed temperature [K]
hC	Level controller instruction
QC	Outlet flow rate controller instruction
TC	Temperature controller instruction
QC_C	Colorant flow rate controller instruction
T_{set}	Reactor temperature set point [K]

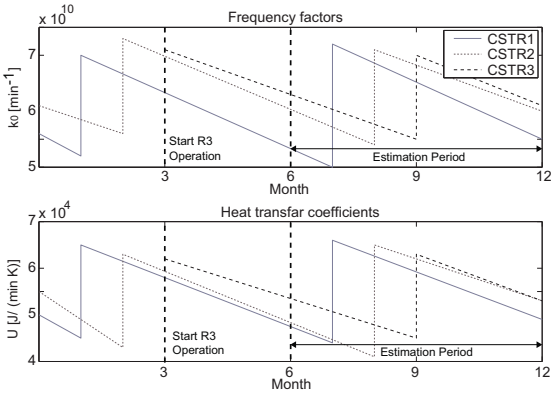

Fig. 5. Changes of overall heat transfer coefficients and frequency factors of the CSTRs

as shown in Fig. 4, they have different characteristics. In each CSTR, an irreversible reaction A $\longrightarrow$ B takes place. The set point of the reactor temperature $T^{[d]}(d = 1, 2)$ is independently changed between $\pm$2K every ten days. Although 15 process variables listed in Table 2 are calculated in the simulations, measurements of only five variables $T^{[d]}$, $h^{[d]}$, $Q^{[d]}$, $Q_C^{[d]}$, $Q_F^{[d]}$ are used for analysis, and their sampling interval is one minute. In addition, reactant concentration $C_A^{[d]}$ is measured in a laboratory once a day.

In this case study, to take into account catalyst deactivation and fouling as changes in process characteristics and individuality of each CSTR, the frequency factor $k_0^{[d]}$ and the heat transfer coefficient $UAc^{[d]}$ are assumed to decrease with time. In addition, each CSTR is maintained every half year (180 days). Figure 5 shows changes of the frequency factors $k_0^{[d]}$ and heat transfer coefficients $UAc^{[d]}$. The operation data of each CSTR for the half years (180 days) were stored in the database.

The soft-sensor for estimating reactant concentration of the newly developed CSTR3 is designed. The estimation of CSTR3 starts the 90th day after the start of its operation, and the soft-sensor is updated in the next half year. Although CSTR3 has only a small amount of data due to its short operation term, the soft-sensor is updated searching samples similar to the current operation of CSTR3 from the other CSTR operation data in the past.

5.2 Estimation result

The reactant concentration $C_A^{[3]}$ is estimated by the JIT modeling and the proposed CoJIT modeling with the NC method. To take into account process dynamics, the input data consist of the present sample and the sample measured one minute before.

In the JIT modeling, linear local models are built and Euclidean distance is used as the measure for selecting samples to build local models. The MATLAB Lazy Learning Toolbox developed by Bontempi et al. (1999) is used.

In the CoJIT modeling, samples for local modeling are selected by the NC method, and PLS is used for model building. The parameters of the NC method are deter-

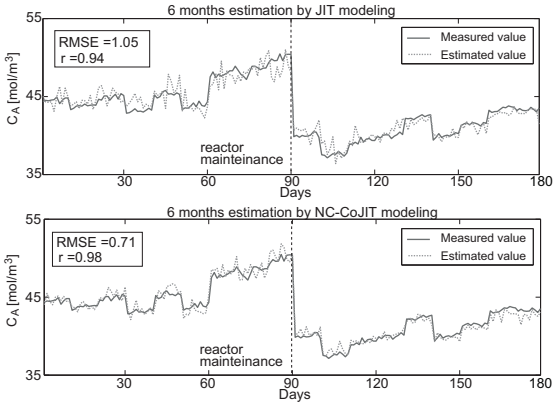

Fig. 6. Prediction result of $C_A^{\{3\}}$ by the JIT modeling (top) and the CoJIT modeling (bottom)

mined by trial and error, the threshold is $\gamma = 1 - 10^4$, the parameter is $\lambda = 0.01$, and the parameter for update frequency $\bar{J}_I = 0$.

The soft-sensor design results are shown in Fig. 6. Although $C_A^{[3]}$ is estimated every minute, only estimates corresponding to the measurements are plotted. In this figure, r denotes the correlation coefficient between measurements and estimates, and RMSE is the root-mean-squares error.

This result shows that the JIT modeling does not function well. On the other hand, the estimation performance of the proposed CoJIT modeling with the NC method is very high. With the proposed CoJIT modeling, RMSE is improved by about 35% in comparison with the JIT modeling. These results of this case study clearly show that the proposed CoJIT modeling can cope with not only abrupt changes in process characteristics but also the individuality of production devices. In addition, it can construct a high performance soft-sensor for a newly develop device, even if only a small amount of operation data is available.

6. CONCLUSION

A new unsupervised pattern recognition method that can detect samples whose correlation is similar to the query is proposed. In addition, the JIT modeling is integrated with the proposed the NC method. The proposed CoJIT modeling with the NC method can cope with not only changes in process characteristics but also the individuality of production devices and improve the estimation performance of a soft-sensor since it can select samples for local modeling by appropriately accounting for the correlation among variables. The proposed CoJIT modeling has the potential for realizing efficient maintenance of soft-sensors.

REFERENCES

Atkeson, CG., Moore, AW., and Schaal, S. (1997). Locally Weighted Learning, Artificial Intelligence Review, 11, 11-73.

Amirthalingam, R., and Lee J. (1999). Subspace Identification Based Inferential Control Applied to a Continuous Pulp Digester. J Proc Cont, 9,397-406.

Bontempi, G., Birattari, M., and Bersini, H. (1999). Lazy Learning for Local Modeling and Control Design. Int J Cont, 72, 643-658.

Bontempi, G., Birattari, M., and Bersini, H. (1999). Lazy Learners at Work: The Lazy Learning Toolbox. EUFIT'99: The 7th European Congress on Intelligent Techniques and Soft Computing, Aachen, Germany. Sep.13-16.

Cheng C., and Chiu, MS. (2004). A New Data-Based Methodology for Nonlinear Process Modeling. Chem Engng Sci, 59, 2801-2810.

Fujiwara, K., Kano, M., and Hasebe, S. (Accepted). Soft-Sensor Development Using Correlation-Based Just-In-Time Modeling. AIChE J.

Jackson, JE., and Mudholkar, GS. (1979). Control Procedures for Residuals Associated with Principal Component Analysis. Technometrics, 21, 341-349.

Johannesmeyer, M., and Seborg, DE. (1999). Abnormal Situation Analysis Using Pattern Recognition Techniques and Histrical Data. AIChE Annual meeting, Dallas, TX, Oct.31-Nov.5.

Kamohara, H., Takinami. A., Takeda. M., Kano, M., Hasebe, S., and Hashimoto, I. (2004). Product Quality Estimation and Operating Condition Monitoring for Industrial Ethylene Fractionator. J Chem Eng Japan, 37, 422-428.

Kano, M., Lee, S., and Hasebe, S. (2008). Two-Stage Subspace Identification for Softsensor Design and Disturbance Estimation. J Proc Cont, 1016/j.jprocont.2008.04.004.

Kano, M., Miyazaki, K., Hasebe, S., and Hashimoto, I. (2000). Inferential Control System of Distillation Compositions Using Dynamic Partial Least Squares Regression. J Proc Cont, 10, 157-166.

Kano, M., and Nakagawa, Y. (2008). Data-Based Process Monitoring, Process Control, and Quality Improvement. Recent Developments and Applications in Steel Industry, Comput Chem Engng, 32, 12-24.

Kohonen, T. (2001). Self-organizing maps. New York, Springer, 3rd edition.

Kresta, VJ., Marlin, TE., and MacGregor, JF. (1994). Development of Inferential Process Models Using PLS. Comput Chem Engng, 18, 597-611.

Mejdell, T., Skogestad, S. (1991). Estimation of Distillation Compositions from Multiple Temperature Measurements Using Partial-Least-Squares Regression. Ind Eng Chem Res, 30, 2543-2555.

Ogawa, M., and Kano, M. (2008). Practice and Challenges in Chemical Process Control Applications in Japan. The 17th IFAC World Congress, Paper WeC25.3.

Qin, SJ. (1998) . Recursive PLS Algorithms for Adaptive Data Modeling. Comput Chem Engng, 22, 503-514.

Raich, A. and Cinar, A. (1994). Statistical Process Monitoring and Disturbance Diagnosis in Multivariable Continuous Processes. AIChE J, 42, 995-1009.

Radhakrishnan, V., and Mohamed, A. (2000). Neural networks for the identification and control of blast furnace hot metal quality. J Proc Cont, 10,509-524.

Vesanto, J., Himberg, J., Alhoniemi, E., and Parhankangas, J. (1999). Self-Organizing Map in Matlab: the SOM Toolbox. The Matlab DSP Conference 1999, Espoo, Finland, Nov.16-17.

Process Monitoring

Oral Session

On-line statistical monitoring of batch processes using Gaussian mixture model

Tao Chen [*], **Jie Zhang** [**]

[*] *School of Chemical and Biomedical Engineering, Nanyang Technological University, Singapore 637459 (e-mail: chentao@ntu.edu.sg).*
[**] *School of Chemical Engineering and Advanced Materials, Newcastle University, Newcastle upon Tyne, NE1 7RU, U.K. (e-mail: jie.zhang@ncl.ac.uk)*

Abstract: The statistical monitoring of batch manufacturing processes is considered. It is known that conventional monitoring approaches, e.g. principal component analysis (PCA), are not applicable when the normal operating conditions of the process cannot be sufficiently represented by a Gaussian distribution. To address this issue, Gaussian mixture model (GMM) has been proposed to estimate the probability density function of the process nominal data, with improved monitoring results having been reported for continuous processes. This paper extends the application of GMM to on-line monitoring of batch processes, and the proposed method is demonstrated through its application to a batch semiconductor etch process.

Keywords: Batch processes, mixture model, principal component analysis, probability density estimation, multivariate statistical process monitoring.

1. INTRODUCTION

Batch processing is of great importance in many industrial applications due to its flexibility for the production of low-volume, high-value added products. With increasing commercial competition it is crucial to ensure consistent and high product quality, as well as process safety. These requirements have resulted in wide acceptance of the technique of multivariate statistical process monitoring (Martin et al., 1999; Qin, 2003). The basis of the monitoring schemes is historical data that has been collected when the process is running under normal operating conditions (NOC). This data is then used to establish confidence bounds for the monitoring statistics, e.g. Hotelling's T^2 and squared prediction error (SPE), to detect the onset of process deviations. The primary objective of process monitoring is to identify abnormal behavior as early as possible, in addition to keeping an acceptably low false alarm rate.

As a result of the multi-way characteristic of batch process data, special tools are required for the modelling and monitoring purposes, including multi-way principal component analysis (MPCA) (Nomikos and MacGregor, 1995b), hierarchical PCA (Rannar et al., 1998) and multi-way partial least squares (MPLS) (Nomikos and MacGregor, 1995a). The methods for on-line monitoring of batch process can be classified into two categories. The first does not require measurements on the entire batch duration to be available. Techniques that are within this class include hierarchical and two-dimensional dynamic PCA (Rannar et al., 1998; Lu et al., 2005). In the other category, the entire batch data is required for the calculation of the monitoring statistics, whilst the data from a new batch is available only up to the current time. Therefore the future data must be predicted in some way (Nomikos and MacGregor, 1995b). In this paper the latter of the two approaches is considered, and the details will be discussed subsequently in Section 2.

However, the afore reviewed conventional process monitoring methods are based on a restrictive assumption that the NOC can be represented by a multivariate Gaussian distribution. Specifically the confidence bounds for T^2 and SPE are calculated by assuming the PCA/PLS scores and prediction errors are Gaussian distributed. This assumption may be invalid when the process data is collected from a complex manufacturing process. To address this issue, Gaussian mixture model (GMM) (Chen et al., 2006; Choi et al., 2004; Thissen et al., 2005), which is capable of approximating any probability density function (*pdf*), has been proposed for the monitoring of continuous processes, as well as batch-wise monitoring of batch processes.

The major contribution of this paper is to extend the application of GMM to on-line monitoring of batch processes. As the first step MPCA is applied to the nominal batch data to extract the low-dimensional representation of the process. The challenge with on-line monitoring is that the scores and SPE must be predicted based on available process measurements up to the current time step. Clearly the predicted scores and SPE are not identical to the values that are calculated from the entire batch duration, and thus the predictions may not conform to the nominal distribution even if the process is running normally. We follow the approach of Nomikos and MacGregor (1995b) to pass the nominal batches through the monitoring procedure and collect the predicted scores and SPE at each time step. Then GMM is employed to estimate the joint *pdf* of these predicted scores and SPE from MPCA at each

time step, as opposed to the traditional T^2 and SPE where the process data is assumed to be Gaussian distributed.

The rest of this paper is organized as follows. Section 2 gives a summary of the PCA and GMM tools for process monitoring, followed by the discussion of the on-line monitoring strategy in Section 3. Section 4 demonstrates the application of the on-line monitoring techniques to a batch semiconductor manufacturing process. Finally Section 5 concludes this paper.

2. PCA AND GAUSSIAN MIXTURE MODEL FOR PROCESS MONITORING

This section presents a brief overview of the PCA and GMM techniques. A number of issues related to the application to process monitoring are discussed, including model selection and the construction of confidence bound.

2.1 PCA

Principal component analysis (PCA) (Jolliffe, 2002) is a general multivariate statistical projection technique for dimension reduction, where the original data is linearly projected onto low-dimensional space such that the variance is maximized. Formally the D-dimensional data $\mathbf{x}$ is represented by a linear combination of the Q-dimensional scores $\mathbf{t}$ plus a noise vector $\mathbf{e}$: $\mathbf{x} = \mathbf{W}\mathbf{t} + \mathbf{e}$, where $\mathbf{W}$ are the eigenvectors of the sample covariance matrix having the Q largest eigenvalues ($Q \leq D$). Consequently normal process behavior can be characterized by the first Q principal components, which capture the main source of data variability.

The proper number of principal components can be selected using a number of criteria, including variance ratio, cross-validation and the "broken-stick" rule (Jolliffe, 2002). This is essentially a model selection problem. The "broken-stick" rule is adopted in this paper due to its low computation and good results reported in the literature (Nomikos and MacGregor, 1995b). According to this rule, the q-th principal component should be retained if the percentage of variance explained by it exceeds the corresponding G value given by

$$G(q) = \frac{100}{C} \sum_{i=q}^{C} \frac{1}{i} \tag{1}$$

where $C = \min(D, N)$.

In statistical process monitoring, the next step is to define the monitoring statistics and the corresponding confidence bounds. Traditionally two metrics are used: $T^2 = \mathbf{t}^{\mathrm{T}}\mathbf{\Lambda}^{-1}\mathbf{t}$ and SPE as $r = \mathbf{e}^{\mathrm{T}}\mathbf{e}$, where $\mathbf{\Lambda}$ is a diagonal matrix comprising the Q largest eigenvalues.

As discussed previously, the first issue with T^2 and SPE is that the corresponding confidence bounds are calculated based on restrictive Gaussian distribution. Secondly two separate metrics are required for process monitoring. Practically the process is identified as deviating from normal operation if either T^2 or SPE moves outside the confidence bounds. This empirical solution could potentially increase the false alarm level [1]. The technique of GMM is suitable for addressing the two issues simultaneously. In our previous work (Chen et al., 2006) we have demonstrated that a unified monitoring statistic can be obtained by estimating the joint *pdf* of the PCA scores and log-SPE using GMM, i.e. the *pdf* of a $(Q+1)$-dimensional vector $\mathbf{z} = (\mathbf{t}^{\mathrm{T}}, \log r)^{\mathrm{T}}$. The logarithm operator is used to transform the non-negative SPE onto the whole real axis on which the GMM is defined.

In this paper the methodology in (Chen et al., 2006) is followed to establish the confidence bounds for process monitoring based on PCA and GMM techniques. GMM is described in detail in the next subsection.

2.2 Gaussian mixture model

As a general tool for *pdf* estimation, Gaussian mixture model (GMM) has been used in a wide variety of problems in applied statistics and pattern recognition. A GMM is a weighted sum of M component densities, each being a multivariate Gaussian with mean $\boldsymbol{\mu}_i$ and covariance matrix $\mathbf{\Sigma}_i$:

$$p(\mathbf{z}|\boldsymbol{\theta}) = \sum_{i=1}^{M} \alpha_i G(\mathbf{z};\, \boldsymbol{\mu}_i, \mathbf{\Sigma}_i) \tag{2}$$

where the weights satisfy the constraint: $\sum_{i=1}^{M} \alpha_i = 1$. A GMM is parameterized by the mean vectors, covariance matrices and mixture weights: $\boldsymbol{\theta} = \{\alpha_i, \boldsymbol{\mu}_i, \mathbf{\Sigma}_i; i = 1, \ldots, M\}$.

Given a set of training data $\{\mathbf{z}_n, n = 1, \ldots, N\}$, the parameters can be estimated by maximizing the likelihood function: $L(\boldsymbol{\theta}) = \prod_{n=1}^{N} p(\mathbf{z}_n|\boldsymbol{\theta})$. In the context of process monitoring, $\mathbf{z}_n$ is the $(Q+1)$-dimensional vector of PCA scores and log-SPE: $\mathbf{z}_n = (\mathbf{t}_n^{\mathrm{T}}, \log r_n)^{\mathrm{T}}$. The maximization is typically implemented iteratively using the expectation-maximization (EM) algorithm (Dempster et al., 1977).

The number of mixture components, M, must be selected prior to the training of a GMM. This is a model selection problem that can be addressed using a number of methods, including cross-validation and Bayesian information criterion (BIC) (Schwarz, 1978). BIC is widely applied in model selection problems for its effectiveness and low computational cost. According to BIC the model is selected such that $L - (H/2)\log N$ is the largest, where L is the log-likelihood of the data and H is the total number of parameters within the model. The motivation of BIC is that a good model should be able to sufficiently explain the data (the log-likelihood) with low model complexity (the number of parameters). In this study BIC is adopted for the selection of number of mixtures.

One of the advantages of the GMM for process monitoring is that it provides the likelihood value as the single statistic for the construction of confidence bounds, as opposed to the confidence bounds for two statistics (i.e. the T^2 and SPE) in conventional process monitoring techniques. In

[1] Suppose 95% confidence bound is used, and thus by definition the false alarm rate is 5% for both T^2 and SPE. The probability of either T^2's bound or SPE's bound being exceeded, when the process is runing normally, will be equal to or greater than 5%.

practice a single monitoring statistic simplifies the plant operators' decision effort, and it may be more sensitive to some subtle process faults (Chen et al., 2006).

On the basis of the *pdf* $p(\mathbf{z}|\boldsymbol{\theta})$ for the normal operating data, the $100\beta\%$ confidence bound is defined as a likelihood threshold h that satisfies the following integral (Chen et al., 2006):

$$\int_{\mathbf{z}:p(\mathbf{z}|\boldsymbol{\theta})>h} p(\mathbf{z}|\boldsymbol{\theta})d\mathbf{z} = \beta \tag{3}$$

To determine the confidence bound, we can calculate the likelihood of all the nominal data, and then find h that is less than the likelihood of $100\beta\%$ (e.g. 99%) of the nominal data (Thissen et al., 2005). This approach is applicable to most continuous processes where the number of nominal data points can be up to several thousand; however it may be unreliable when the nominal data is very limited as in batch process monitoring. The estimation of the confidence bound based on limited batches would be very sensitive to the data, and thus a small perturbation in the data would result in very different estimation of the h.

To address this issue, we resort to numerical Monte Carlo simulation to approximate the integral in Eq. (3) (Chen et al., 2006). Specifically we generate N_s random samples, $\{\mathbf{z}^j, j = 1, \ldots, N_s\}$, from $p(\mathbf{z}|\boldsymbol{\theta})$. These samples serve as the "pseudo data" (since the real data is not sufficient) to represent the normal process behavior. Thus the Monte Carlo samples, in conjunction with nominal process data, are used to calculate the confidence bound h. Then a new batch $\mathbf{z}$ is considered to be faulty if $p(\mathbf{z}|\boldsymbol{\theta}) < h$ (or equivalently $-p(\mathbf{z}|\boldsymbol{\theta}) > -h$). The number of Monte Carlo samples required (N_s) to approximate the confidence bounds is dependent on the dimension of $\mathbf{z}$, and it can be determined heuristically.

3. MONITORING OF BATCH PROCESSES

To analyze the three-way batch data ($N \times J \times K$) (N, J and K denote the number of batches, process variables at each time instance, and time steps, respectively), multiway analysis methods have been proposed to unfold the data array into a two-way matrix on which conventional PCA is then performed (Nomikos and MacGregor, 1995b). This study unfolds the data array into a large matrix ($N \times JK$) such that each batch is treated as a "data point". This two-way matrix is then pre-processed to zero mean and unit standard deviation on each column, prior to the application of PCA to extract the scores $\mathbf{t}_n$ and SPE r_n, $n = 1, \ldots, N$. Then a Gaussian mixture model is developed for the joint vector $\mathbf{z}_n = (\mathbf{t}_n^{\mathrm{T}}, \log r_n)^{\mathrm{T}}$, followed by the calculation of confidence bound using Monte Carlo simulation.

3.1 On-line monitoring

In the on-line monitoring stage, it is necessary to project the new batch onto the PCA space to obtain the scores and SPE, and then to calculate the likelihood value under the GMM to identify possible process anomaly. The issue is that, at time step t, the batch measurements are only available up to the current time. It is possible to develop multiple PCA and GMM models at each time step; however this strategy requires excessive computation and computer memory. A more reasonable and widely accepted method is to predict the scores and SPE using the available measurements.

More specifically, let $\bar{\mathbf{x}}_{1:t}$ be the vector of a new batch with available measurements from time step 1 to t. Note $\bar{\mathbf{x}}_{1:t}$ is a vector of order Jt. According to Nomikos and MacGregor (1995b), the least square prediction of the scores is:

$$\bar{\mathbf{t}}_{1:t} = \left(\mathbf{W}_{1:t}^{\mathrm{T}}\mathbf{W}_{1:t}\right)^{-1}\mathbf{W}_{1:t}^{\mathrm{T}}\bar{\mathbf{x}}_{1:t} \tag{4}$$

where $\mathbf{W}_{1:t}$ is the sub-matrix of $\mathbf{W}$ having the rows corresponding to time step 1 to t. In Eq. (4) the matrix to be inverted is well conditioned due to the orthogonality of the loading $\mathbf{W}$. Since the future measurements are not available, the prediction error can only be calculated up to time step t:

$$\bar{\mathbf{e}}_{1:t} = \bar{\mathbf{x}}_{1:t} - \mathbf{W}_{1:t}\bar{\mathbf{t}}_{1:t} \tag{5}$$

The SPE is then obtained as $\bar{\mathbf{e}}_{1:t}^{\mathrm{T}}\bar{\mathbf{e}}_{1:t}$. It was suggested to use the "instantaneous" SPE associated with the latest on-line measurements for process monitoring (Nomikos and MacGregor, 1995b), i.e. $\bar{\mathbf{e}}_t^{\mathrm{T}}\bar{\mathbf{e}}_t$, which is expected to increase the sensitivity of fault detection method. However the instantaneous SPE leads to an excessive number of false alarms in the case study of this paper (see details in Section 4). This phenomenon could be due to the non-Gaussian distribution of the process data. The SPE calculated from Eq. (5), which in a sense is a smoothed version of the instantaneous SPE, may be a more appropriate monitoring metric. We will discuss this issue through the application study in Section 4.

Clearly the predicted scores and SPE from Eqs. (4)(5), based on current available measurements, are not identical to the values that are calculated should the entire batch be available. As a result the predicted scores and SPE may not conform to the *pdf* developed based on the entire duration of nominal batches, even if the process being monitored is running normally. This is a serious issue particularly in the initial stage of a batch processing, when only a small number of measurements are available to calculate the scores and SPE. We follow the standard approach in on-line batch process monitoring (Nomikos and MacGregor, 1995b) to pass each of the nominal batches through the monitoring procedure to collect the predicted scores and SPE at each time step from Eqs. (4)(5), and then apply GMM to estimate the joint *pdf* of these predicted scores and log-SPE at each time step, and to establish the confidence bounds as presented in Section 2. Essentially we propose to replace the confidence bounds for T^2 and SPE in (Nomikos and MacGregor, 1995b), where the process data is assumed to be Gaussian distributed, with more powerful Gaussian mixture model. For on-line monitoring of a new batch, the scores and SPE are calculated from Eqs. (4)(5), and the likelihood value is calculated under the GMM for the current time step. If this likelihood value is lower than the confidence bound, the process under monitoring is considered to be in a faulty condition.

Table 1. Variables used for the monitoring of the semiconductor process.

1	Endpoint A detector	7	RF impedance
2	Chamber pressure	8	TCP tuner
3	RF tuner	9	TCP phase error
4	RF load	10	TCP reflected power
5	RF Phase error	11	TCP Load
6	RF power	12	Vat valve

4. CASE STUDY

The manufacture of semiconductors is introduced as an example of the on-line monitoring of batch processes. This study focuses specifically on an Al-stack etch process performed on the commercially available Lam 9600 plasma etch tool (Wise et al., 1999). Data from 12 process sensors, listed in Table 1, was collected during the wafer processing stage which run for 80 s. A sampling interval of 1 s was used in the analysis. Thus for each batch, the data is of the order (12×80). A series of three experiments, resulting in three distinct data groups, were performed where faults were intentionally introduced by changing specific manipulated variables (TCP power, RF power, pressure, plasma flow rate and Helium chunk pressure). There are 107 normal operating batches and 20 faulty batches. Twenty batches were randomly selected from the normal batches to investigate the effect of false alarms. The remaining 87 nominal batches were used to build the MPCA and GMM models.

4.1 Off-line analysis

According to MPCA, the three-way nominal data array $(N \times J \times K = 87 \times 12 \times 80)$ is unfolded into a large two-way matrix of the order (87×960), which is then mean-centered and scaled to unit standard deviation on each column. Then PCA is applied to the pre-processed data, where two principal components are retained according to the broken-stick rule (Jolliffe, 2002). Considering there are 960 columns in the unfolded matrix, it is not surprising to find that two principal components explain only 45.50% of the total variance (similar results can be found in the literature, e.g. (Nomikos and MacGregor, 1995b)).

Figure 1 gives the scatter plot of the PCA scores corresponding to the first two principal components. It is clear that the nominal data exhibits the characteristic of multiple groups, and it cannot be adequately approximated by a single multivariate Gaussian distribution. As a result, the 99% confidence bound does not capture the region of NOC accurately. In addition to the normal testing batches, 17 out of 20 faulty batches are within the confidence bound, resulting in 17 missing errors. Clearly more complex models are required to represent the nominal behavior of the process.

To develop a GMM for the PCA scores and log-SPE, the appropriate number of mixtures must be selected. According to the BIC, the GMM with three mixture components is utilized for the analysis of the semiconductor process. Once the GMM is developed, the 95% and 99% confidence bounds is calculated using Monte Carlo simulation presented in Section 2.2, where the number of random samples is heuristically determined to be 10,000. Despite the large sample size, the CPU time for the Monte Carlo simulation

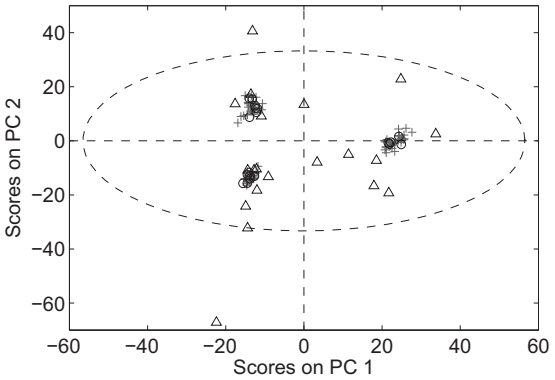

Fig. 1. Bivariate scores plot for principal components 1 and 2 with 99% confidence bound (− − −−): nominal (+), normal (○) and faulty (△).

Table 2. Off-line monitoring results.

	T^2	SPE	T^2 + SPE	GMM
False alarms	0	0	0	0
Missing errors	17	7	7	4

was only 0.03 s (Matlab implementation under Windows XP with Pentium 2.8 GHz CPU). In the literature the 95% is treated as "warning bound" and 99% "action bound". Throughout this section the process is classified as faulty if the 99% confidence bound is violated.

Table 2 summarizes the off-line batch-wise monitoring results for both conventional PCA and the GMM approach. Both methods incur no false alarms in this example. The large number of missing errors from T^2, as depicted in Figure 1, is the result of over-estimation of the confidence bound. It appears that SPE is more sensitive to the fault and it attains seven missing errors. By combining T^2 and SPE in the way that the process is identified as faulty if either metric is exceeded, the number of missing errors is still seven. Table 2 clearly indicates that GMM outperforms the conventional PCA in terms of smaller number of missing errors through the direct estimation of the joint *pdf* of the PCA scores and log-SPE.

4.2 On-line monitoring

The on-line monitoring results are given in Table 3. A normal testing batch is considered to be a false alarm if it is identified as faulty within the batch duration. A missing error means a faulty batch is not detected during the entire duration. Similar to the off-line monitoring, T^2 fails to detect most of the faulty batches because the scores do not conform to a multivariate Gaussian distribution. A comparison between Table 3 (a) and (b) suggests that the instantaneous SPE can detect more faulty batches than the smoothed SPE; however the increased sensitivity is at the cost of dramatically decreased robustness. The number of false alarms for instantaneous SPE is excessively large (13 out of total 20 batches), and thus the smoothed SPE is adopted for the rest of this paper. Table 3 indicates that the GMM approach gives better results than the conventional MPCA in terms of smaller number of false alarms and missing errors.

Table 3. On-line monitoring results. (a) SPE is calculated based on process measurements at current time step (instantaneous SPE); (b) SPE is calculated based on process measurements from batch beginning to current time step (smoothed SPE).

(a)

	T^2	SPE	T^2 + SPE	GMM
False alarms	0	13	13	8
Missing errors	17	2	2	0

(b)

	T^2	SPE	T^2 + SPE	GMM
False alarms	0	3	3	1
Missing errors	17	4	4	2

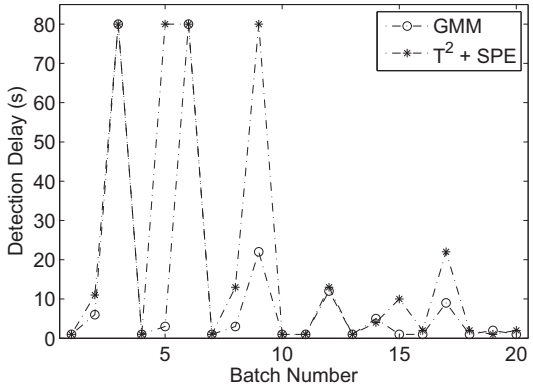

Fig. 2. Delay in the detection of the faulty batches.

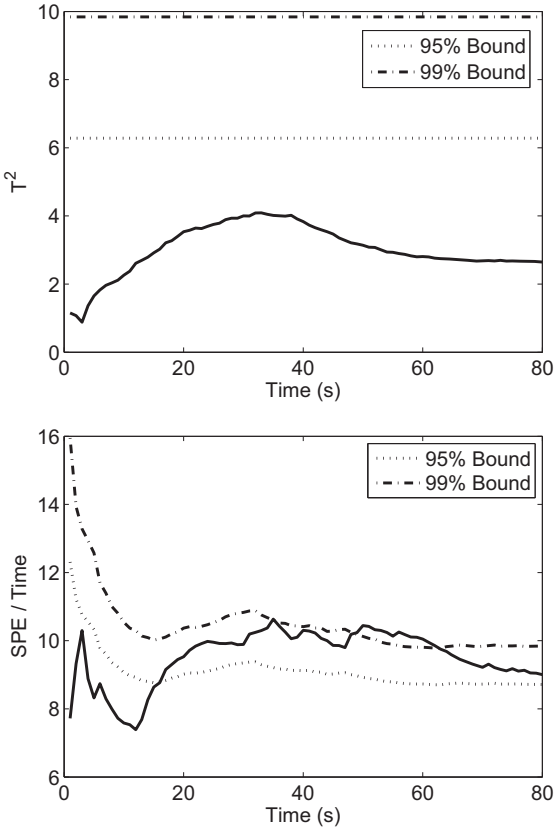

Fig. 3. On-line monitoring of a normal batch using T^2 and SPE.

It should be noted that the number of missing errors in on-line monitoring is not the only index to evaluate the monitoring performance. Of greater practical importance is the time delay between the occurrence and the detection of the fault. Figure 2 illustrates the detection delay of the 20 faulty batches using MPCA and GMM. To facilitate the calculation of average delay for comparison, the detection delay is artificially set to the batch duration (i.e. 80 s) if a faulty batch is not detected by the monitoring system. Essentially this is to assume that the abnormal behavior will be identified in some way (e.g. the presence of off-specified product) when the batch finishes. In practice plant operators are often not able to identify the fault until much later than the end of batch duration. On average, the detection delay for GMM is 11.6 s that is significantly shorter than 20.3 s obtained by the PCA method. Since the process is operating relatively fast, the reduction of delay in 9 s (equivalently 9 time steps) may not be sufficient for the operators to take appropriate actions in practice. Nevertheless if the proposed approach is applied to monitor a slow process, for example batch fermentation that takes several days to complete where data is sampled every half day, a shorter detection delay of 9 time steps would provide significant advantage in terms of reduced operational cost and improved process safety and product quality.

Figure 3 illustrates the on-line monitoring charts of a normal batch, which is false-alarmed by conventional PCA. Since the value of on-line SPE increases with time, we plot SPE divided by time for better illustration in the figure. The T^2 indicates that this batch is under normal operation; however T^2 is not a reliable index for the monitoring of this process as discussed previously. The SPE metric appears to be susceptible to process disturbance; it exceeds the 95% confidence bound from 17 s and is over the 99% bound between 50 s to 60 s, despite the fact that the process is running normally. Figure 4 shows the GMM based monitoring chart, where the negative likelihood value is plotted. The GMM approach correctly recognizes that this batch is within the region of NOC during the whole batch duration.

Figure 5 and 6 give the on-line monitoring charts of a faulty batch (batch 5 as in Figure 2), using conventional PCA and the GMM approach, respectively. Both T^2 and SPE fails to detect this fault. In contrast, the likelihood value from the GMM is becoming outside the 99% confidence bound since time 3 s.

5. CONCLUSIONS

This paper extends the GMM technique for the modelling and on-line performance monitoring of batch manufacturing processes. The handling of the unobserved future batch measurements is discussed for the purpose of on-line monitoring. The GMM provides a probabilistic approach to estimating the *pdf* of the nominal process data and therefore enables more accurate calculation of the

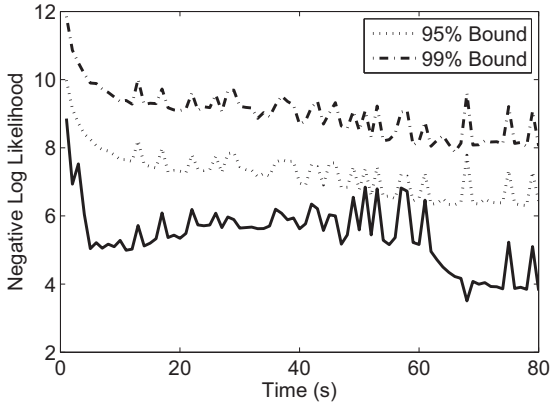

Fig. 4. On-line monitoring of a normal batch using GMM.

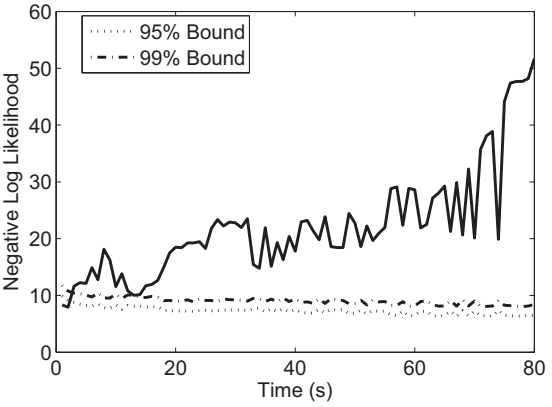

Fig. 6. On-line monitoring of a faulty batch using GMM.

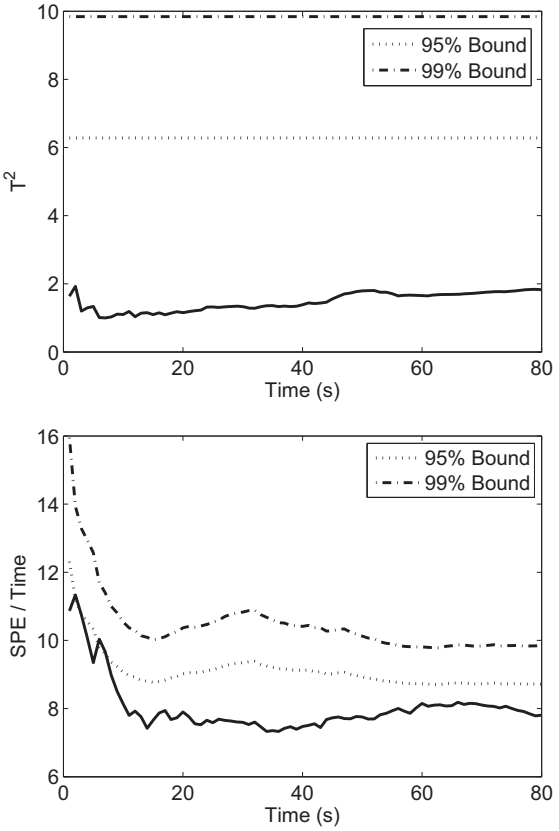

Fig. 5. On-line monitoring of a faulty batch using T^2 and SPE.

confidence bounds. The case study confirms that through accurate modelling of the process historical data collected from NOC, GMM is a promising approach to maintaining a low rate of both false alarms and missing errors in process performance monitoring.

REFERENCES

Chen, T., Morris, J., and Martin, E. (2006). Probability density estimation via an infinite Gaussian mixture model: application to statistical process monitoring. *Journal of the Royal Statistical Society C (Applied Statistics)*, 55, 699–715.

Choi, S.W., Park, J.H., and Lee, I.B. (2004). Process monitoring using a Gaussian mixture model via principal component analysis and discriminant analysis. *Computers and Chemical Engineering*, 28, 1377–1387.

Dempster, A.P., Laird, N.M., and Rubin, D.B. (1977). Maximum likelihood from incomplete data via the EM algorithm. *Journal of Royal Statistical Society B*, 39, 1–38.

Jolliffe, I.T. (2002). *Principal Component Analysis*. Springer, 2nd edition.

Lu, N., Yao, Y., and Gao, F. (2005). Two-dimensional dynamic pca for batch process monitoring. *AIChE Journal*, 51, 3300–3304.

Martin, E.B., Morris, A.J., and Kiparrisides, C. (1999). Manufacturing performance enhancement through multivariate statistical process control. *Annual Reviews in Control*, 23, 35–44.

Nomikos, P. and MacGregor, J.F. (1995a). Multi-way partial least squares in monitoring batch processes. *Chemometrics and Intelligent Laboratory Systems*, 30, 97–108.

Nomikos, P. and MacGregor, J.F. (1995b). Multivariate SPC charts for monitoring batch processes. *Technometrics*, 37, 41–59.

Qin, S.J. (2003). Statistical process monitoring: basics and beyond. *Journal of Chemometrics*, 17, 480–502.

Rannar, H., MacGregor, J.F., and Wold, S. (1998). Adaptive batch monitoring using hierarchical PCA. *Chemometrics and Intelligent Laboratory Systems*, 41, 73–81.

Schwarz, G. (1978). Estimating the dimension of a model. *Annals of Statistics*, 6, 461–464.

Thissen, U., Swierenga, H., de Weijer, A.P., Wehrens, R., Melssen, W.J., and Buydens, L.M.C. (2005). Multivariate statistical process control using mixture modelling. *Journal of Chemometrics*, 19, 23–31.

Wise, B.M., Gallagher, N.B., Butler, S.W., White, D.D., and Barna, G.G. (1999). A comparison of principal component analysis, multiway principal component analysis, trilinear decomposition and parallel factor analysis for fault detection in a semiconductor etch process. *Journal of Chemometrics*, 13, 379–396.

Variability Matrix: A Novel Tool to Prioritize Loop Maintenance

Marcelo Farenzena*, Jorge O. Trierweiler*, Sirish L. Shah**

** Department of Chemical Engineering, Federal University of Rio Grande do Sul (UFRGS)*
Porto Alegre, RS, CEP: 90.040-040, BRAZIL (Tel:+555133084072; e-mail:{farenz,jorge}@enq.ufrgs.br)
*** Department of Chemical and Materials Engineering, University of Alberta, Edmonton, AB, T6G 2G6, Canada*
(e-mail: sirish.shah@ualberta.ca)

Abstract: It is now common knowledge that as many as 40% of the control loops in most industrial processes have considerable potential for improving control performance by reducing variability. Because of the large number of control loops in an industrial plant, controller performance monitoring is indispensable, but equally important is how to prioritize their maintenance. It is well known that variance reduction in a loop occurs by transferring variability to other variables or loops. The focus of this study is to propose a methodology to prioritize loop maintenance based on the potential improvement of each loop and the variability transfer among them. The central point of this work is the Variability Matrix (VM), an array that shows the impact of performance improvement of a given loop on the whole plant. Based on the VM, a methodology to translate this array into a potential loop economic benefit metric is also introduced. The VM can be quantified in the ideal scenario where plant model and controller are available and also when they are not, thus allowing the application of these ideas in industry. The efficacy of proposed methodology is illustrated by successful application to two case studies.

1. INTRODUCTION

The main requirement for a control system is to ensure process stability and robustness. This is the key reason for the widespread industrial interest in performance assessment methodologies and tools. A typical plant has hundreds or thousands of controllers and most of them have potential for improvement (Bialkowski, 1993). Many good reviews on assessment of control loops are available in the literature (Huang and Shah, 1999, Jelali, 2006). A common problem in controller performance monitoring is how to prioritize loop maintenance. The answer should not only be based on the performance potential, but also on the economic benefits that can be realized in improving the performance of each loop.

The main motivation for improving the performance of the plant is simple: reduction in process variability allows achieving a more profitable operating point, closer to the constraints, as shown in Fig. 1. In scenario I, the process has large variability and therefore the setpoint or the target has to be significantly far away from the economically optimal operating point. If the variability is reduced, due to controller or process improvement (scenario II) the process operating point can be moved to a more profitable setpoint (scenario III).

The literature is relatively sparse in terms of quantification of economic benefits due to improvement of controller performance. Muske (2003) proposed the idea of potential reduction in control loop variability. The economic benefit is quantified based on the shift in the mean operation toward a product specification or process constraint. The variance reduction can be based on a fixed or user-specified benchmark, e.g. minimum variance benchmark or a desired

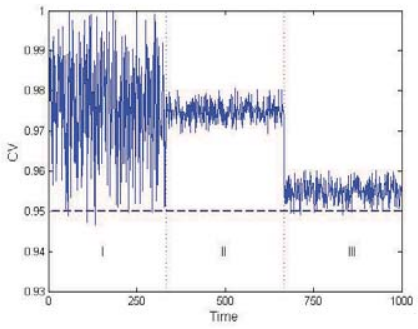

Fig. 1: Variability reduction impact: (I) normal operating variability (II) variability reduction and (III) operating point shift.

rise time or settling time benchmark. Craig and Henning (2000) proposed another methodology to quantify the economic benefit of Advanced Process Control (APC) projects. The authors mention that the whole part of the benefits come from the steady-state optimization. They assume that the variance of the products can be reduced by 35% to 50%. Mascio and Barton (2001) proposed a methodology to quantify the control quality in economic terms based on the Taguchi Framework.

All available methodologies agree that reduction in variability means shifting the operating point to a more profitable point. The main drawback is that they consider each loop as an isolated case, i.e. if performance of one loop is improved then the whole plant will not suffer its effect.

All modern industrial plants have significant interaction among loops due to tighter heat integration. Because of this,

one cannot assume that the variance reduction in one loop will occur without impacting other loops adversely. Typically, variability is transferred from loops where it should be reduced to loops that have the room or the buffer to accommodate large fluctuations (e.g. level loops). In many cases, if one variable has its variability reduced and its operating point shifted, then it is likely that other interacting or complementary loops will have their variability increased, shifting the operating point away from the constraints. This implies that "part of the profit" realized by variability reduction in a given loop "will be offset" by the loops where the variability increases. This is why a control loop should not be considered in isolation and the potential economic benefit should be computed by analyzing the whole plant and not only a specific loop. The common idea that the improvement of a given controller performance will increase the performance of the whole plant is not always true. Sometimes in an interacting system, the coupling between the channels can help or hinder overall performance. For example, decrease in the variability of a given controller can also reduce the variability in other loops in which case, one can say that the interaction helps. In other cases, the interaction may affect performance of associated loops adversely.

The main contribution of this work is the introduction of the notion of the Variability Matrix (VM). This array shows how the variability will transfer between the loops and the impact of one specific loop on the variances of all other interacting or complementary loops. The potential economic benefit of each loop can be quantified based on VM.

This paper is structured as follows: section 2 introduces the concept of Variability Matrix. In section 3, practical issues in computing the VM are discussed. The methodology to quantify the economic benefit of each control loop and prioritize loop maintenance is shown in section 4. The complete methodology is illustrated by successful application on two case studies (section 5). The paper ends with concluding remarks.

2. VARIABILITY MATRIX: CONCEPTS AND DEFINITION

2.1 Preliminary Definitions

To quantify the economic impact, it is interesting to consider the classification of control loops into the following two categories:

Main Loops: Loops that directly control the products specification. Their performance improvement affects the product variability, which can be directly translated into profitability.

Auxiliary Loops: Loops that do not directly control product quality, but can indirectly affect the product variability.

2.2 Variability Matrix Structure

The structure of the variability matrix consists of the following:

Rows: The rows show the influence of each loop on the same final product. The number of rows is the same as the products or the number of main loops.

Columns: Shows the influence of a specific loop on all other loops that may impact or influence the specification of the final product. The number of columns is the same as the number of control loops implemented in the plant. The first columns correspond to the main loops and the adjacent set of columns corresponds to the auxiliary loops as shown in Figure 2.

		Main Loops				Auxiliary Loops		
		Mn_1	Mn_2	…	Mn_m	Aux_1	⋯	Aux_{l-m}
Main	Mn_1	$VM_{1,1}$	$VM_{1,2}$	…	$VM_{1,m}$	$VM_{1,m+1}$	…	$VM_{1,l}$
	Mn_2	$VM_{2,1}$	$VM_{2,2}$	…	$VM_{2,m}$	$VM_{2,m+1}$	…	$VM_{2,l}$
	⋮	⋮	⋮	…	⋮	⋮	…	⋮
	Mn_m	$VM_{m,1}$	$VM_{m,2}$	…	$VM_{m,m}$	$VM_{m,m+1}$	…	$VM_{m,l}$

Fig. 2: Schematic representation of Variability Matrix

In Fig. 2 Mn_i is the main loop i and Aux_j is the auxiliary loop j. The total number of loops in the plant is l and it has m main loops. For example, column 1 (Mn_1) shows the impact of variability reduction in main controller 1 on all other main loops. Row 1 shows the impact on the variability of Mn_1 when the performance of all other loops is changed.

2.3 VM Computation

This section discusses the methodology for computing each element *VM(i,j)* of the Variability Matrix. In the first scenario, the following assumptions are taken: (I) the plant model (G) is available; (II) the controller model (C) is also available; and (III) the controlled variables (y) and control outputs (u) are available. For the sake of simplicity, we consider that the setpoint is fixed and set to zero.

Based on the previous assumptions, the procedure to quantify the VM is described below:

1. Read process data y_j ($j = 1…l$) and u_j ($j = 1…l$) with all loops closed (with actual performance);
2. Select main and auxiliary loops;
3. Compute the actual variance for each main loop ($\text{var}_{\text{act,i}}$, $i = 1…m$);
4. For each loop j ($j = 1…l$)
    1. Calculate the best performance achievable (see section 3.2) for loop j;
    2. Apply the controller;
    3. Calculate the new variance for each main loop i ($var_{best,i,j}$, $i = 1…m$)
    4. Compute the elements of VM j^{th} column using eq. 1.

$$VM(i,j) = \frac{\text{var}_{act,i} - \text{var}_{best,i,j}}{\text{var}_{act,i}} \quad (1)$$

This structure for VM elements was chosen because for two main reasons: 1) it provides a direct measure of the

variability improvement potential for each loop; and 2) it is dimensionless, a fact that allows the comparison of the impact of two or more loops in the plant. For example, consider the VM of:

$$\begin{bmatrix} 0.3 & 0 & -1.2 \\ -0.7 & 0.9 & -1.5 \end{bmatrix} \quad (2)$$

Initially, we can verify that this plant has 2 main loops and one auxiliary loop. From this VM, by examining column 1, we can conclude that: if the performance of main controller 1 is improved, its variance will decrease 30%; however, it has a negative and strong impact on another loop: its variance will increase by 70%. Is this healthy for the process? Clearly the answer to this question depends on the economic impact of each main loop. In column 2, the main loop 2 has potential reduction in variability of 90%. This controller has no influence on the main loop 1 variance; furthermore improving the performance of the auxiliary loop (3rd column) will lead to variability increase in both main loops.

In complement with the VM, the concept of the complementary VM arises (CVM). It is not necessary for all controllers to have fast performance, many loops have to play the role of accommodating or buffering disturbances. Based on this assumption, we define the Complementary Variability Matrix (*CVM*). The values are computed with actual loop variance ($var_{act,i}$) and the variance of the loop with the worst performance acceptable ($var_{wor,i,j}$). The structure is the same as shown before, and the elements are computed as follows:

$$CVM(i,j) = \frac{\text{var}_{act,i} - \text{var}_{wor,i,j}}{\text{var}_{act,i}} \quad (3)$$

The same procedure as considered earlier can be used to evaluate the Complementary Variability Matrix (*CVM*). Only step 4.1 is replaced by the slowest accepted performance (see Smith, 2002) and the worst accepted performance (var_{wor}) should be quantified.

The proposed computational steps may not be easily applicable in an industrial setting, because the required information (controller and process model) is generally unavailable. The algorithm to compute VM where the controller and plant model are not available is shown in section 3.

2.4 VM Dependence of the System Parameters

From a preliminary inspection, VM seems to be analogous to static the RGA (Skogestad and Postlethwaite, 2005), where only the process static gains have impact in the analysis. However, VM is not only a function of process gains, but also depends on process behavior (dynamics and time delays), disturbance patterns and correlation among the disturbances, controller structure (e.g. PI, PID, MPC, among others), closed loop performance, and best performance achievable. The VM values are specific for each process: even two systems where the models and controllers are the same can have a completely different VM, because of the disturbance pattern.

2.5 Some Peculiar Behaviour

Intuitively, the diagonal elements of the VM should have a positive sign and the off-diagonal elements negative sign, i.e.: improving the performance of a given controller will reduce its variability; and transfer variability to the other loops, increasing their variability. However, this may not always be the case:

Proposition 1*: Diagonal elements of VM can have negative sign, i.e. the performance improvement of a given controller can increase its variability.*

Proof: Consider a SISO system with linear PI type controller that is affected by an output disturbance (*d*). Suppose that the disturbance is a pure white-noise random signal. Considering that *d* is random, it is not possible to predict its future values based on the past values. In this case increasing loop gains will likely increase *y* variability. In this case, the diagonal VM element will have a negative sign.

Proposition 2*: Off-diagonal elements can have positive sign, i.e. the performance increase of a given controller can also decrease the variability in other interacting loops. Typically this happens when interactions help in accommodating disturbances.*

Proof: Consider the triangular system shown in Fig. 3.

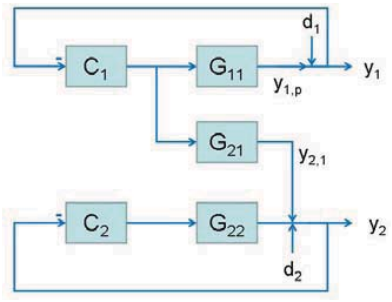

Fig. 3: Schematic representation of the triangular system

Consider the case when C_1 reduces the output variability when it is compared with the open loop case (i.e. $\sigma^2(d_1 + y_{1,p}) < \sigma^2(d_1)$), and upon improving C_1 performance, y_1 will also decrease its variability.

$$\sigma^2(d_1) > \sigma^2(d_1 + y_{1,p1}) > \sigma^2(d_1 + y_{1,p2}) \quad (4)$$

Where p_1 and p_2 are the controllers performance and $p_2 > p_1$ (i.e. closed loop performance in the second scenario (p_2) is faster than p_1). Considering the case when:

$$\begin{aligned} G_{11} &= G_{21} \\ d_1 &= d_2 \end{aligned} \quad (5)$$

Then $y_{1,p} = y_{2,1}$. From the loop 2 and $y_{2,1}$, it is clear that improving the performance of loop 1, will also have the effect of reducing the variability of y_2. This will occur as $y_{2,1}$ will help offset the effect of d_2 (in the same way as $y_{1,p}$ offsets d_1). Thus leads to:

$$\sigma^2(d_2) > \sigma^2(d_2 + y_{2,1,p1}) > \sigma^2(d_2 + y_{2,1,p2}). \quad (6)$$

3. PRACTICAL ISSUES IN COMPUTING VM

3.1 Computing the VM

This section presents the methodology to evaluate VM in industrial settings where process and/or controller models may not be available.

The first analyzed scenario is where a Model Predictive Controller is implemented. In this case, the controller model is not available, because most industrial MPCs are "closed box solutions". However, the plant model is available. In this case, setpoint variations in MPC controllers are quite common, because of the optimization layer. In this scenario, the controller model can be extracted (identified) using the *Asymptotic Method* (Zhu, 1998) or *Subspace Identification* (Overschee and Moor, 1996).

A second scenario contemplates the case where only low order controllers (PI and PID) are present and setpoint activity is available in all loops. For this case, the following steps are contemplated: (I) identify the controller order and parameters (*C*) using *structured target factor analysis* (STFA) (Fotopoulos et al., 1994); (II) estimate the time delay (Tuch et al., 1994); (III) identify the process model (*G*) using *Subspace Identification* (Overschee and Moor, 1996); (IV) identify the disturbance model (*d*) using *Subspace Identification*; (V) with *G*, *C*, and *d* available, the VM can be estimated applying the methodology shown in section 2.3.

Based on our limited experience, we can affirm that the VM is not extremely dependent on the accuracy of the plant and controller. Even for a visible mismatch in the plant model, the obtained results are fairly good, comparing with the case where accurate controller and plant models are available.

3.2 Best and Worst Controller Performances

A natural question that arises is: how can the best and worst performance be computed for a given system? The answer clearly depends on the controller that is implemented on the process.

For MPC controllers, the best achievable performance can be computed using the methodology proposed by Trierweiler and Farina (2003). If the desired performance is attainable, this methodology provides the tuning parameters for the chosen performance. Otherwise, if it's not achievable, the best achievable performance is quantified. In this work, we assume that the "best performance" is based on the open and closed loop rise time ratio, and a convenient value for this ratio is 3.

For low order (PI and PID) decentralized controllers, the best performance can be estimated using the methodology proposed by Faccin and Trierweiler (2004). The worst performance can be evaluated based on the methodology to tune buffer tank controllers (Smith, 2002).

4. QUANTIFYING THE ECONOMIC BENEFITS BASED ON VM

The economic benefits of improving control performance of each loop can be computed in two ways. The first method considers that the best performance can be achieved. In this case the VM can be used as follows. We represent the column *j* of the VM as VM_j. The economic benefit can be easily quantified using the relationship:

$$CLEB = D \cdot VM \quad (7)$$

where *CLEB* is the *Control Loop Economic Benefit* array. It has the same number of elements as the number of loops in the plant (*l*).

$$CLEB = \begin{bmatrix} D \cdot VM_1 & D \cdot VM_2 & \cdots & D \cdot VM_l \end{bmatrix} \quad (8)$$

Where *D* is the array that translates variability reduction into $ per unit time.

$$D = \begin{bmatrix} D_1 & D_2 & \cdots & D_m \end{bmatrix} \quad (9)$$

where *m* is the number of main loops in the plant. This array can be quantified as a function of plant throughput increase, utilities reduction, etc. This value can be provided by the commercial department of the plant or the optimization layer weights used in MPC design.

However, as previously mentioned, not all controllers need to have high or tight tuning and the economic benefit, considering the worst performance of each one, can also be quantified. This vector is defined as *Complementary Control Loop Economic Benefit:*

$$CCLEB = \begin{bmatrix} D \cdot CVM_1 & D \cdot CVM_2 & \cdots & D \cdot CVM_l \end{bmatrix} \quad (10)$$

For example, suppose a plant where the VM and D are:

$$VM = \begin{bmatrix} 0.7 & -0.6 \\ -0.3 & 0.8 \end{bmatrix} \quad (11)$$

$$D = [100 \quad 50] \quad (12)$$

the *CLEB* is then be computed as:

$$CLEB = \begin{bmatrix} 55 & -20 \end{bmatrix} \quad (13)$$

The CLEB indicates that improvement in loop 1 performance means increase the plant profitability. However, the opposite behavior is expected when loop 2 performance is improved.

5. CASE STUDIES

5.1 Wood and Berry Distillation Column Model

The pilot-scale distillation column proposed by Wood and Berry (1973) is the first case study. The plant model is given by:

$$\begin{bmatrix} x_D(s) \\ x_B(s) \end{bmatrix} = \begin{bmatrix} \frac{12.8}{16.7s+1}e^{-1s} & \frac{-18.9}{21s+1}e^{-3s} \\ \frac{6.6}{10.9s+1}e^{-7s} & \frac{-19.4}{14.4s+1}e^{-3s} \end{bmatrix} \begin{bmatrix} R(s) \\ S(s) \end{bmatrix} \quad (14)$$

where x_D and x_B are the overhead and bottom products composition, and R and S are the reflux and steam flow rates, respectively. The time constants and time delays are expressed in minutes.

Two decentralized PI type controllers were applied in this case study. The disturbance was generated by passing a random signal through a first order transfer function with unitary gain and 50 minute time constant. The VM analysis of this case study is presented next under 3 scenarios: 1) controller and plant models are assumed to be available; 2) only plant model is available; 3) neither the plant model nor controller models are available. However setpoint activity is assumed. This serves as good excitation for closed loop identification. For case 3), details of closed-loop based subspace identification method are not included here due to lack of space. The PI controllers were tuned to have a performance where the desired closed loop rise time is twice faster the open loop case. We consider here the best achievable performance when the rise time is 6 times faster than open loop.

The *D* vector for this case is hypothetically set as:

$$D = \begin{bmatrix} 100 & 30 \end{bmatrix} \tag{15}$$

In the first scenario, the controller and plant model were available. The VM was computed using the methodology shown in section 2.3.

$$VM = \begin{bmatrix} 0.57 & -0.17 \\ -0.18 & 0.41 \end{bmatrix} \tag{16}$$

The *CLEB* for this case is:

$$CLEB = \begin{bmatrix} 52 & -5 \end{bmatrix} \tag{17}$$

Based on *CLEB*, loop 1 should have its performance improved (top composition), increasing the plant profitability. Loop 2 shows the opposite behavior, improvement in its performance is likely to result in decreased plant profitability.

In the second scenario, the controller model is assumed to be unavailable. Initially, using a scenario where two setpoint variations in each variable are available, the controller model was identified (see section 3.1). In this scenario, the VM was estimated to be:

$$VM = \begin{bmatrix} 0.60 & -0.19 \\ -0.19 & 0.46 \end{bmatrix} \tag{18}$$

Notice that the estimated VM closely matches the true VM shown in (16). In the third scenario, both controller and plant model were identified using closed loop data. The estimated VM for this scenario is:

$$VM = \begin{bmatrix} 0.60 & -0.19 \\ -0.18 & 0.46 \end{bmatrix} \tag{19}$$

Even for this case, where controller and plant model were first identified using subspace identification, a good estimate of VM was obtained.

5.2 Shell Benchmark Process

The Shell Control Problem benchmark was proposed by Prett and Morari (1987). The system is characterized by the high interaction among channels and large time delays.

It involves one heavy oil fractionator. It has three product draws, three side circulating loops and a gaseous feed stream. The system consists of seven measured outputs, three manipulated inputs and two unmeasured disturbances. In this case study, we will reduce the problem to a 3 input and 3 output case. The three controlled variables are: top end point (*y1*); side endpoint (*y2*); bottom reflux temperature (*y3*). The manipulated variables are: top draw (*u1*); side draw (*u2*); bottom reflux duty (*u3*). The system has also two disturbances: upper reflux (*d1*); intermediate reflux (*d2*). The process output can be written as:

$$y = Gu + G_d d \tag{20}$$

Where G is the plant model

$$G = \begin{bmatrix} \frac{4.05}{50s+1}e^{-27s} & \frac{1.77}{60s+1}e^{-28s} & \frac{5.88}{50s+1}e^{-27s} \\ \frac{5.39}{50s+1}e^{-18s} & \frac{5.72}{60s+1}e^{-14s} & \frac{6.9}{50s+1}e^{-15s} \\ \frac{4.38}{33s+1}e^{-20s} & \frac{4.42}{44s+1}e^{-22s} & \frac{7.2}{19s+1} \end{bmatrix} \tag{21}$$

and G_d is the disturbance model:

$$Gd = \begin{bmatrix} \frac{1.2}{45s+1}e^{-27s} & \frac{1.44}{40s+1}e^{-27s} \\ \frac{1.52}{25s+1}e^{-15s} & \frac{1.83}{20s+1}e^{-15s} \\ \frac{1.14}{27s+1} & \frac{1.26}{32s+1} \end{bmatrix} \tag{22}$$

Where the time constant and time delays are reported in minutes. The MPC from Matlab® (MPC toolbox V. 2.2.2) was applied in this study. The analysis for this case is reported under two scenarios: (I) where controller and plant models are available and (II) when both are unavailable.

The *D* vector for this case is (hypothetically set):

$$D = \begin{bmatrix} 100 & 50 & 20 \end{bmatrix} \tag{23}$$

The actual performance in this case was computed based on closed loop rise time when it is set equal to the open loop case. The desired performance for each channel is three times faster than open loop. The VM for this scenario is:

$$VM = \begin{bmatrix} -0.39 & 0.10 & 0.26 \\ -0.12 & -0.16 & 0.28 \\ -0.24 & -0.60 & 0.32 \end{bmatrix} \tag{24}$$

The VM shows that improving the performance of controller 1 and 2 will result in an increase in the variance of all main loops. Retuning loop 1 means increase its variance by 39% and increase in the variances of loops 2 and 3 by 12% and 24% respectively. On the other hand, improvement of loop 3 performance means decrease in its variance by 32% and

corresponding reductions in variances in loop 1 and loop 2 by 26% and 28%, respectively. The *CLEB* for this case is:

$$CLEB = \begin{bmatrix} -50 & -10 & 46 \end{bmatrix} \quad (25)$$

The answer to improving plant profitability lies not only in VM but also the CVM, i.e. some controllers should not have their performance improved, but rather detuned. The CVM for this case is:

$$CVM = \begin{bmatrix} 0.15 & 0.13 & -0.12 \\ 0 & 0.28 & -0.13 \\ -0.30 & -0.29 & -0.44 \end{bmatrix} \quad (26)$$

The *CCLEB* for this case is:

$$CCLEB = \begin{bmatrix} 9 & 21 & -27 \end{bmatrix} \quad (27)$$

The maintenance list for this hypothetical case indicates that the most important controller to maintain or improve performance is loop 3. The second loop in the maintenance list should be loop 2 followed by loop 1.

In the second scenario, both controller and plant are assumed to be unavailable, only setpoint activity is assumed. In this case, the VM is estimated using the procedure shown in section 3.1. The estimated VM is:

$$VM = \begin{bmatrix} -0.42 & 0.06 & 0.26 \\ -0.15 & -0.27 & 0.28 \\ -0.32 & -0.74 & 0.32 \end{bmatrix} \quad (28)$$

Both plant model and controller are identified using subspace identification from Matlab® (system identification toolbox version 6.1.1, function n4sid). Both models have 9 states.

Eq. 28 shows that the estimated VM compared with the original (eq. 24) is fairly good. We attribute the success of this fairly accurate VM estimation to the direct closed loop subspace identification method under reasonable level of setpoint activity.

6. CONCLUDING REMARKS

The main conclusions of the proposed work can be summarized as:

- industrial plants have many loops with considerable potential for performance improvement and therefore a methodology to prioritize loop maintenance is required;
- the concept of Variability Matrix was introduced in this work and has been shown to highlight the potential improvement in each loop and its impact on the whole plant;
- the methodologies to compute VM where neither the controller nor plant model are available has also been presented; in this scenario Subspace Identification can be used; even for this case the methodology has been shown to yield very good results based on closed loop identification;
- the proposed methodology was applied to two case studies providing good results;
- the proposed scenarios where the VM can be computed allows the application of these ideas in an industrial setting.

ACKNOWLEDGMENT

The first two authors wish to thank CAPES, PETROBRAS and FINEP for supporting this work.

REFERENCES

BIALKOWSKI, W. L. (1993) Dreams versus reality: A view from both sides of the gap. *Pulp and Paper Canada,* 94**,** 19-27.

CRAIG, I. K. & HENNING, R. G. D. (2000) Evaluation of advanced industrial control projects: a framework for determining economic benefits. *Control Engineering Practice* 8**,** 12.

FACCIN, F. & TRIERWEILER, J. O. (2004) A Novel Tool for multi-model PID Controller Design. *7th IFAC Symposium on Dynamics and Control of Process Systems.* Boston- USA, IFAC.

FOTOPOULOS, J., GEORGAKIS, C. & STENGER, H. G., JR (1994) Structured target factor analysis for the stoichiometric modeling of batch reactors. *American Control Conference, 1994.*

HUANG, B. & SHAH, S. L. (1999) *Performance assessment of control loops : theory and applications,* London, Springer.

JELALI, M. (2006) An overview of control performance assessment technology and industrial applications. *Control Engineering Practice,* 14**,** 441-466.

MASCIO, R. D. & BARTON, G. W. (2001) The economic assessment of process control quality using a Taguchi-based method. *Journal of Process Control,* 11**,** 8.

MUSKE, K. R. (2003) Estimating the economic benefit from Improved Process Control. Ind. Eng. Chem. Res.,42, 4535-4544.

OVERSCHEE, P. V. & MOOR, B. L. R. D. (1996) *Subspace identification for linear systems : theory, implementation, applications,* Boston, Kluwer Academic Publishers.

PRETT, D. M. & MORARI, M. (1987) *The Shell Process Control Workshop,* Boston, Butterworths.

SKOGESTAD, S. & POSTLETHWAITE, I. (2005) *Multivariable feedback control : analysis and design,* Chichester, England ; Hoboken, NJ, John Wiley.

SMITH, C. A. (2002) *Automated continuous process control,* New York, J. Wiley.

TRIERWEILER, J. O. & FARINA, L. A. (2003) RPN tuning strategy for model predictive control. *Journal of Process Control,* 13**,** 591-598.

TUCH, J., FEUER, A. & PALMOR, Z. J. (1994) Time delay estimation in continuous linear time-invariant systems. *IEEE Transactions on Automatic Control,* 39**,** 823-827.

WOOD, R. K. & BERRY, M. W. (1973) Terminal composition control of a binary distillation column. *Chemical Engineering Science,* 28**,** 11.

ZHU, Y. (1998) Multivariable process identification for MPC: the asymptotic method and its applications. *Journal of Process Control,* 8**,** 15.

Soft sensor models: Bias updating revisited

André D. Quelhas* and José Carlos Pinto**

**Petrobras – Corporate University, Rio de Janeiro - Brazil*
(Tel: +55-21-3487-3467; e-mail:quelhas@ petrobras.com.br).
***Chemical Engineering Program, COPPE-UFRJ, Rio de Janeiro - Brazil*
(e-mail:pinto@peq.coppe.ufrj.br)

Abstract: Bias updating is a widespread adaptive procedure to allow inference models to pursue time variant features of a real world process. The aim of this work is to clarify the statistical consequences of bias updating to soft sensor estimates as well to point up the need of careful analysis of the effect of unmeasured disturbances on the true values of the variable of interest. It is shown that bias updated inferences are unbiased estimates of the true value but yields estimates whose variance are 100% larger than the ones obtained with no use of bias updating. It is suggested the use of a weighting factor to bias updating in order to balance statistical benefits and penalties. A case study of a soft sensor for weathering of LPG in oil refinery exemplifies the concepts discussed.

Keywords: Soft sensor, Bias Updating, Error Analysis, Statistics.

1. INTRODUCTION

The main goal of an industry is to operate as close as possible to the point where profit is maximum. It means that there should be no off-spec product and the lowest degree of product quality give-away should be achieved. Maximum profit is also related to the fact that the set of manipulated variables leads to lower costs by minimizing use of heat, steam, electricity, water etc..

It may be hard if not impossible to accomplish this goal. Real processes are likely to be nonlinear and highly integrated causing modeling and identification prone to errors. In addition, long term operation makes processes more susceptible to hardware upsets (corrosion, fouling, mechanical failures) and to experience environmental disturbances as well qualitative/quantitative changes in physical-chemical properties of feed streams.

Accurate knowledge of process actual model structure and parameters is essential if one intends to predict future states (for control and optimizing) or to diagnose safety risks. Unfortunately many relevant process variables are not available as frequently as desirable or even not available at all. For example, it is very common that physical-chemical properties related to quality control are measured by laboratory tests performed with a very low frequency when compared to process variables acquired by online sensors. Such process with differing sample rates for measured variables are known as multirate process (Ragahavan *et al.*, 2006).

Most of times the long period of time to be awaited before new information about low frequency variables become available is unacceptable. It is necessary to make use of some inferential knowledge based on high frequency information about the process. If a sufficiently accurate model is available, the variable of interest can be estimated from high frequency process measurements $\mathbf{x}$ as long as model structure and parameters $\boldsymbol{\alpha}$ are known:

$$\hat{y} = f(\mathbf{x}, \boldsymbol{\alpha}) + bias \tag{1}$$

Every time a new measurement of the *true* value of y is available, an adaptive procedure can be used to adapt the inferential model. The only parameter updated through this one parameter correction is the independent coefficient in (1): $bias = y - f(\mathbf{x}, \boldsymbol{\alpha})$. This simple strategy is very common in industry as well in literature for optimizing purposes (Mercangöz and Doyle 2008; Jesus 2004; Singh 1997) or for soft sensors inferences (Sharmin *et al.* 2006; Mu *et al.* 2006; Tran *et al*. 2005).

Some questions should be posed regarding the use of inferences as (1) for anyone who has to cope with a multirate process:

- What is the best model structure $f(\mathbf{x},\boldsymbol{\alpha})$?
- How often should bias be updated?
- How are inference errors affected by bias updating?
- What are the effects of unmeasured disturbances on inference errors?

Those questions usually receive unequal importance. A lot of effort has been spent along time to answer the first question. Models have progressively become more complex by using the mathematical weaponry of process modeling

(multivariable regression, PCA, neural networks, fuzzy logic). The second question is often answered based on practical matters as availability of laboratory technicians. The last two questions are normally disregarded in spite of their huge consequences on the estimates.

The aim of this work is to pay attention to those usually forgotten questions by remembering the mathematical considerations implicit in models as (1) and answering, from a statistical point of view, what the benefits and penalties of bias updating are.

2. MATHEMATICAL FOUNDATIONS OF BIAS UPDATING

For a steady state system, the generic mathematical relationship linking the output variable, y, and all pertinent process variables, **w**, required by fundamental physical laws, may be expressed as:

$$F(y, \mathbf{w}, \mathbf{c}) = 0 \tag{2}$$

where **w** represents the NW necessary variables to perfectly predict the unknown behavior of y given the NC constants in the vector of parameters, **c**.

Two practical reasons explain why it is unlike that any real model would incorporate the whole set of NW necessary variables. The first one is the fact that NW may be large and would conflict with science´s parsimony principle. In this sense, a less complete description would be acceptable in a trade-off for simplicity under a certain allowable tolerance. The other reason is that several of the NW variables either are not measured or are not considered relevant by the scientist due to a methodological error.

Taking these reasons under consideration one can split **w** into the subsets **x** and **z**. The first subset contains the NX measured variables that were chosen as relevant for the model. The second subset contains the remaining NZ = NW-NX variables. It contains measured and unmeasured variables that should be part of a perfect model but were set apart. The complete description of the system behavior is then expressed as:

$$F(y, \mathbf{x}, \mathbf{z}, \mathbf{c}) = 0 \tag{3}$$

In the process of justifying the possibility of a correction as proposed in (1) it is required that (3) be partially separable with respect to addition at least with respect to y. It requires that $(1/F)\partial \exp(F)/\partial y$ depends only on y (Viazminsky 2008). If this condition is satisfied one can express (3) as:

$$g(y) = F_1(\mathbf{x}, \mathbf{z}, \mathbf{c}_1) \tag{4}$$

Additionally, if the inverse function g^{-1} exists, then:

$$y = g^{-1}(F_1(\mathbf{x}, \mathbf{z}, \mathbf{c}_1)) = F_2(\mathbf{x}, \mathbf{z}, \mathbf{c}_2) \tag{5}$$

Physical knowledge or empirical insight may lead to an attempt to predict *y* based on measurements **x** and parameters $\boldsymbol{\alpha}$ by means of a model $f(\mathbf{x}, \boldsymbol{\alpha})$. If **z** is an empty set and the whole influence of **x** on *y* is taken into account by $f(\mathbf{x}, \boldsymbol{\alpha})$ we have a perfect model. Otherwise one should expect a relationship as (6), where $F_3(\mathbf{x}, \mathbf{z}, \mathbf{c}_3)$ plays the role of bias as in (1). It should be noticed that (6) is derived from (5) if $F_3(\mathbf{x}, \mathbf{z}, \mathbf{c}_3)$ is a separable function with respect to the set **z**.

$$y = f(\mathbf{x}, \boldsymbol{\alpha}) + F_3(\mathbf{x}, \mathbf{z}, \mathbf{c}_3) \tag{6}$$

The model built by the experimenter is $f(\mathbf{x}, \boldsymbol{\alpha})$. The invisible part of the true model is $F_3(\mathbf{x}, \mathbf{z}, \mathbf{c}_3)$. This term is captured by the bias term in a very common pragmatic approach assuming the form (1).

Inference structure (6) is very attractive but it is valid only if the assumptions that allowed disregarding more generalized expressions (3)-(5) are true. If not, there will be no guarantee that successive inferred values will express the true values y even if no further disturbances alter the values of the set **z**. This can be seen by comparing two simple models. One represents a model as expressed in (5) (type A model) and the other one represents the less generic model expressed in (6) (type B model), for instance:

type A true model: $y = (x+z)/x$

type B true model: $y = x + z$

It should be noticed that the type B true model in this example shows no dependence of F_3 on x. This class of true models yields the best possible performance for an adaptive experimental model as (1).

Assuming that: 1) experiments to identify the inference $f(x, \alpha)$ were carried out under controlled conditions in order to keep z at a constant value z_0 in both cases and 2) perfect model identification led to inferences with the same mathematical structure than true models:

type A inferred model: $\tilde{y} = (x+ z_0)/x$

type B inferred model: $\tilde{y} = x + z_0$

If the inferred models were parameterized by means of proper statistical criticism both inferred models will adequately represent the behavior of the variable of interest. However, as time passes, it is possible that z assumes values different of the one kept controlled along identification phase. So, if z assumes the value z_1 and $x=x_1$ at the moment of correction in both cases, according to the bias updating routine:

type A true value: $y_1 = (x_1+z_1)/ x_1$,

type A inferred value: $\tilde{y}_1 = (x_1 + z_0)/ x_1$

$\Rightarrow$ bias = $y_1 - \tilde{y}_1 = (z_1 - z_0)/x_1$

corrected inference: $\hat{y}_1 = (x + z_0)/x + ((z_1 - z_0)/x_1)$

type B true value: $y_1 = x_1 + z_1$,

type B inferred value: $\tilde{y}_1 = x_1 + z_0$

$\Rightarrow$ bias = $y_1 - \tilde{y}_1 = z_1 - z_0$, corrected inference: $\hat{y}_1 = x + (z_1 - z_0)$

It is clear that, after bias correction, inferences derived from type B models will produce results as close to the truth as they were before the change of z value as long as this variable is kept constant from this change on. On the other hand, inferences derived from type A models will not behave this way because accuracy of the corrected inference will be affected not only by further changes of z value but also by additional changes in the x value because the nonlinear behavior is not captured by a single point correction.

3. BIAS UPDATING PROCEDURE

In order to describe the behavior of predictions of the value *y* along time it is interesting to write inference model to allow time course to be taken into account:

$$\tilde{\mathbf{y}} = f(\mathbf{X}, \boldsymbol{\alpha}), \quad \mathbf{X} = \begin{bmatrix} \mathbf{x_1} \\ \mathbf{x_2} \\ \dots \\ \mathbf{x_{NS}} \end{bmatrix}, \quad \mathbf{x_i} = \begin{bmatrix} x_{i1} & x_{i2} & x_{i3} & \dots & x_{i,NX} \end{bmatrix},$$

$$\tilde{\mathbf{y}} = \begin{bmatrix} \tilde{y}_1 \\ \tilde{y}_2 \\ \dots \\ \tilde{y}_{NS} \end{bmatrix} \tag{7}$$

where NS is the number of time samples of the process variable signals.

Corrected values of *y* along time are obtained from bias updating according to:

$$\hat{\mathbf{y}} = \tilde{\mathbf{y}} + \mathbf{bias} \tag{8}$$

where the array of time values of bias is built according to:

$bias_1 = 0$

$bias_k = \left(y_k^m - \tilde{y}_k\right) s_k + (1 - s_k) bias_{k-1}$

leading to:

$$\mathbf{bias} = \begin{bmatrix} 0 \\ \left(y_2^m - y_2\right) s_2 + (1 - s_2) bias_1 \\ \left(y_3^m - y_3\right) s_3 + (1 - s_3) bias_2 \\ \dots \\ \left(y_{NS}^m - y_{NS}\right) s_{NS} + (1 - s_{NS}) bias_{NS-1} \end{bmatrix} \tag{9}$$

Vector $\mathbf{y^m}$ contains measurements of the true values **y** sampled with period at a lower rate, T_{meas}, than primary variables of the model. Vector **s** is a binary set that indicates when true values $\hat{y}$ are available:

$$\mathbf{y^m} = \left[[0]_{1x(Tmeas-1)} \; y_{Tmeas} \; [0]_{1x(Tmeas-1)} \; y_{2Tmeas} \dots \right]^T$$

$$\mathbf{s} = \left[[0]_{1x(Tmeas-1)} \; 1 \; [0]_{1x(Tmeas-1)} \; 1 \dots \right]^T$$

4. STATISTICAL IMPACT OF BIAS UPDATING

Although equations (7-9) indicate the *modus operandi* of inference correction, it is not clear how our expectation about error values is affected. Since corrections are made at a low frequency the duration of their benefits will be affected by the probability of occurrence of new disturbances before a new gold standard measurement is ready, thus making possible another correction. A reasonable question would be: what benefits are obtained with periodic bias updating comparing with no bias correction at all?

In fact, bias updating and no updating schemes are extreme points of a continuous range of possible single point corrections. Considering the weight parameter $\varphi \in \Re$, $\varphi \subset [0\ 1]$, the time values $\bar{\mathbf{y}}$ are a weighted mean of bias corrected values (8) and values from the original inference model (7):

$$\bar{\mathbf{y}} = \varphi \hat{\mathbf{y}} + (1 - \varphi) \tilde{\mathbf{y}} \tag{10}$$

If samples of true values are taken with period T_{meas} the n^{th} element suffers the effects of the last bias updating made at sample $i = \text{int}(n/T_{meas})T_{meas}$, where int(x) retains the integer part of the floating point real number x:

$$\overline{y_n} = \varphi\left(\tilde{y}_n + bias_n\right) + (1 - \varphi)\tilde{y}_n \tag{11}$$

$$\overline{y_n} = \varphi\left(\tilde{y}_n + y_i - \tilde{y}_i\right) + (1 - \varphi)\tilde{y}_n = \tilde{y}_n + \varphi\left(y_i - \tilde{y}_i\right) \tag{12}$$

Inference error at the n^{th} element will be:

$$\varepsilon_n = y_n - \overline{y_n} = y_n - \tilde{y}_n - \varphi y_i + \varphi \tilde{y}_i \quad (13)$$

Since n^{th} and i^{th} elements of the true values come from the same sample space as well n^{th} and i^{th} elements of the inferred values, their statistical moments are the same, i.e., $E[y_n] = E[y_i]$ and $E[\tilde{y}_n] = E[\tilde{y}_i]$. Dropping indexes to simplify notation, it is possible to say that the expected error value is:

$$E[\varepsilon] = (1-\varphi)E[y] + (\varphi - 1)E[\tilde{y}] \quad (14)$$

$$if \begin{cases} \varphi = 1, & E[\varepsilon] = \varepsilon_{\min} = 0 \\ \varphi = 0, & E[\varepsilon] = \varepsilon_{\max} = E[y] - E[\tilde{y}] \end{cases}$$

It can be seen that the bias update scheme expressed in (8) ($\varphi = 1$) guarantees mean error value of zero if length of **y** tends to infinity. If no correction is made ($\varphi = 0$), long term error mean depends on the ability of model $f(\mathbf{X}, \boldsymbol{\alpha})$ to be an unbiased estimate of the true value. It is also possible to investigate the dependence of error variance on the choice of φ. From (13) it is possible to write:

$$\mathrm{var}(\varepsilon_n) = \mathrm{var}(y_n - \tilde{y}_n - \varphi y_i + \varphi \tilde{y}_i) \quad (15)$$

$$\begin{aligned} \mathrm{var}(\varepsilon_n) = {} & \mathrm{var}(y_n) + \mathrm{var}(\tilde{y}_n) + \varphi^2 \mathrm{var}(y_i) + \varphi^2 \mathrm{var}(\tilde{y}_i) \\ & - 2\,\mathrm{cov}(y_n, \tilde{y}_n) + 2\varphi\,\mathrm{cov}(y_n, \tilde{y}_i) - 2\varphi\,\mathrm{cov}(y_i, \tilde{y}_n) \\ & - 2\varphi^2\,\mathrm{cov}(y_i, \tilde{y}_i) \end{aligned} \quad (16)$$

For the same reason explained above $\mathrm{var}(y_n) = \mathrm{var}(y_i)$ and $\mathrm{var}(\tilde{y}_n) = \mathrm{var}(\tilde{y}_i)$, making it more convenient to drop subscripts and simplify (16):

$$\begin{aligned} \mathrm{var}(\varepsilon) = {} & \mathrm{var}(y) + \mathrm{var}(\tilde{y}) + \varphi^2(\mathrm{var}(y) + \mathrm{var}(\tilde{y})) - 2\mathrm{cov}(y, \tilde{y}) \\ & - 2\varphi^2\,\mathrm{cov}(y, \tilde{y}) \end{aligned} \quad (17)$$

At the extreme points of φ:

$$if \begin{cases} \varphi = 1, & \mathrm{var}(\varepsilon) = v\varepsilon_{\max} = 2\,\mathrm{var}(y) + 2\,\mathrm{var}(\tilde{y}) - 4\,\mathrm{cov}(y, \tilde{y}) \\ \varphi = 0, & \mathrm{var}(\varepsilon) = v\varepsilon_{\min} = \mathrm{var}(y) + \mathrm{var}(\tilde{y}) - 2\,\mathrm{cov}(y, \tilde{y}) \end{cases}$$

With respect to the error variance the progressive updating ($\varphi = 1$) doubles the value obtained when no correction is made ($\varphi = 0$). Confronting this result with the expected value of the error one can see that bias updating is associated with an expectation of unbiased mean value of estimates but it also causes a 100% increase in error variance. There would be a choice of φ to cope with these consequences? In order to answer this question it is necessary to create a single objective function that combines both effects.

As an example, a possible choice for such function could be $\psi = E[\varepsilon] + \mathrm{var}(\varepsilon)$, choosing φ that minimizes its value. However this function is too dependent of the problem specificities and units of measurement. In fact even the choice the objective function depends on the problem to be solved and on the needs of the plant personnel in order to fulfill several goals related to the industrial process.

Taking this into consideration, it is suggested a very simple objective function, derived from the previous one. It represents an attempt to equalize the importance of the effects of φ regarding each statistical moment. Such function could assume the normalized form:

$$\psi = E[\varepsilon]_{norm} + \mathrm{var}(\varepsilon)_{norm} \quad (18)$$

where

$$E[\varepsilon]_{norm} = \frac{E[\varepsilon] - \varepsilon_{\min}}{\varepsilon_{\max} - \varepsilon_{\min}} \quad (19)$$

and

$$\mathrm{var}(\varepsilon)_{norm} = \frac{\mathrm{var}(\varepsilon) - v\varepsilon_{\min}}{v\varepsilon_{\max} - v\varepsilon_{\min}} \quad (20)$$

Substituting (19-20) in (18):

$$\begin{aligned} \psi = {} & \frac{(1-\varphi)E[y] + (\varphi - 1)E[\tilde{y}]}{E[\hat{y}] - E[y]} \\ & + \frac{\varphi^2(\mathrm{var}(y) + \mathrm{var}(\tilde{y})) - 2\varphi^2\,\mathrm{cov}(y, \tilde{y})}{\mathrm{var}(y) + \mathrm{var}(\tilde{y}) - 2\,\mathrm{cov}(y, \tilde{y})} \end{aligned} \quad (21)$$

The choice of φ is made in order to minimize ψ and is represented by the solution of:

$$\frac{\partial \psi}{\partial \varphi} = 1 - \varphi - \varphi^2 = 0 \;\Rightarrow\; \varphi = 1/2 \quad (22)$$

It is interesting to see how formalism of (21) and (22) conducts to a common sense value of ½ for the weighting factor in this case.

5. CASE STUDY

In this section it will be shown the statistical features of bias updating in a soft sensor to be implemented in an oil refinery. The process unity at study is a FCC debutanizer showed in figure 1. In order to improve quality control of liquefied petroleum gas (LPG) it is desirable to have online information about the relative amount of molecules with more than four carbon atoms present on LPG stream. A laboratory or field test usually carried out a few times a day measures weathering of LPG, expressed in temperature units, which is correlated to the ratio of heavier molecules.

An empirical mathematical model of LPG weathering based on NX = 3 process variables feeds the model predictive control of the process unity with inferred values along time as in (7).

For the purposes of this work, actual behavior of the unity is represented by data from customized process simulation software. The discrete mathematical space of operating scenarios has its basis formed by the N_{inp} = 4 process simulation input parameters as shown in figure 1.

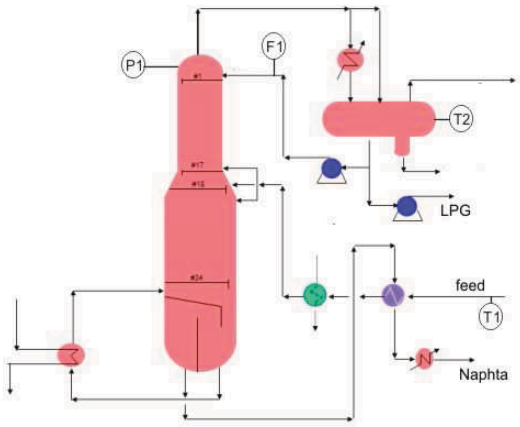

Figure 1 – FCC debutanizer. Process variables used as inputs for the process simulator: P1, F1, T1, T2.

The subregion of operation considered for analysis was the regular mesh **S** (N_{sc} x N_{inp}) of equally spaced points around nominal condition of operation. This region of operation induces the subregion $\boldsymbol{\chi}$ (N_{sc} x NX) of the input variables of the empirical model of weathering. For simulation of long term operation a string of scenarios, $\mathbf{S}^{str}$ (L_{sc} x N_{inp}), representing the time course of conditions of operation, was assembled:

$ind_i \sim \text{Unif}(1, N_{sc})$; $ind_i \in \mathbb{N}$; i = [1 2 ... L_{sc}]

Each choice ind_i is a uniformly distributed random variable that indicates where, in the subregion **S**, is the i^{th} line of $\mathbf{S}^{str}$ and, as consequence, maps **X** (L_{sc} x NX) as in (7):

$$\begin{aligned} &\mathbf{S}(ind_i, \mathbf{j}) \rightarrow \boldsymbol{\chi}(ind_i, \mathbf{k}) \\ &\mathbf{S}^{str} = \mathbf{S}(\mathbf{ind}, \mathbf{j}) \rightarrow \mathbf{X} = \boldsymbol{\chi}(\mathbf{ind}, \mathbf{k}) \\ &\mathbf{j} = [1 \quad 2 \quad \ldots \quad N_{inp}] \; \mathbf{k} = [1 \quad 2 \quad \ldots \quad NX] \end{aligned} \tag{22}$$

Since quality of the feed is a major unmeasured disturbance the set of variables **z** is represented by the ratio of the slope of the true boiling point curve of the actual feed related to the one at nominal operating condition. If feed stream may have three different compositions symmetrically disturbed:

$\mathbf{r}$=[0.95 1 1.05]

$ind_i \sim \text{Unif}(1, 3)$; $ind_i \in \mathbb{N}$; i = [1 2 ... L_{sc}]

$$\mathbf{z} = \mathbf{r}(\mathbf{ind}) \tag{23}$$

In order to allow a better understanding of the different effects observed in the results there will be considered two cases of study. In the more generic case A it is supposed that the set of variables **z** is represented by (23) and that the inference model is the actual one used in industrial practice. Case B will also take disturbances as in (23) into account but it is supposed that the inference model was perfectly modeled in the absence of disturbances. It is perfect in the sense that all the effects of the model input variables perfectly propagate to the output variable. In other words, at $z=z_{nominal}$, $F_3 = F_3(z,c3)$ as in (6) and the inference is correct for any value of **x**.

As it can be seen in figure 2, in both cases bias updating procedure yields an expected mean value of zero although values show less dispersion when no bias correction is used.

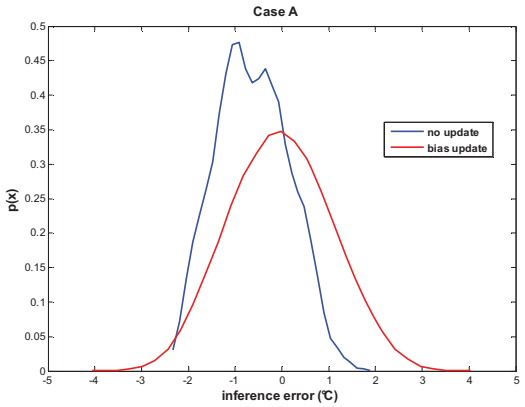

Figure 2 – Estimated probability density function of inferred weathering values for case A.

Estimated probability density function for case B (fig. 3) shows additional features. In this case it is clear that, with no update, the inference will be correct every time $z=z_{nominal}$ whatever the **x** values. The two triangular areas under the blue line around the central peak in figure 3 are originated when $z= z_{nominal} \pm \Delta z$. It should be noticed that the fact that those areas are not as thin as the central peak is due to the dependence of F3 (6) on **x**. When bias update is implemented, two more regions appear as well all regions become flatter. It is because bias expected values will be the result of the difference of all possible two random samples respectively chosen from the sample space of the non corrected inferred values and from the sample space of true values. These bias values will be summed to the inferred ones creating the oscillations of the red line at extreme inference errors observed in figure 3.

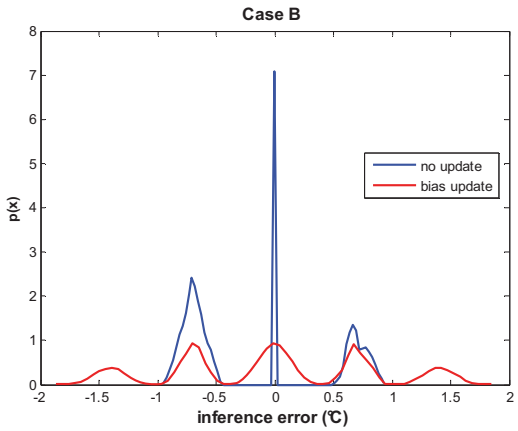

Figure 3 – Estimated probability density function of inferred weathering values for case B.

6. CONCLUSIONS

This work addressed the problem of continuous time monitoring in processes with differing sample rates for measured variables. Bias updating is a common adaptive procedure to periodically correct soft sensor models estimates. It was shown that this strategy is associated with long term zero mean error but at very high cost of 100% increase in variance of estimates. Our intention was to shown that a procedure to implement periodical parameter update should be problem-specific. It means to take into account statistical impact on estimates based on prior knowledge of probability density of disturbances as well error magnitude of soft sensor estimates.

ACKNOWLEDGMENT

The authors are grateful to Eng. Cristina Neves Passos, from Petrobras, for providing simulation files from FCC plant that were used as templates for our work.

REFERENCES

Jesús, R.A.J. (2004), *Modelación y Optimización del Mezclado de Petróleo Crudo con Redes Neuronales*, Master thesis, Centro de Investigación y de Estudos Avanzados del Instituto Politécnico Nacional de Mexico.

Mercangöz, M., Doyle, F.J. (2008), Real-time optimization of the pulp mill benchmark problem, *Computers and Chemical Engineering*, 32, 789-804.

Mu, S., Zeng, Y., Liu, R., Wu, P., Su, H., Chu, J. (2006), Online dual updating with recursive PLS model and its application in predicting crystal size of purified terephthalic acid (PTA) process, *Journal of Process Control*, 16, 557-566

Ragahavan, H.; Tanrigala, A.K.; Gopaluni, B.; Shah, S. (2006), Identification of chemical processes with irregular output sampling, *Control Engineering Practice*, 14, 467-480.

Sharmin, R., Sundararaj, U., Shah, S., Griend, L.V., Sun, Y. (2006), Inferential sensors for estimation of polymer quality parameters - Industrial application of a PLS-based soft sensor for a LDPE plant, *Chemical Engineering Science*, 61, 6372-6384.

Singh, A. (1997). *Modeling and Model Updating in the Real-Time Optimization of Gasoline Blending*, Master thesis, University of Toronto.

Tran, M., Varvarezos, D.K., Nasir, M. (2005), The importance of first-principles, model-based steady-state gain calculations in model predictive control - a refinery case study, *Control Engineering Practice*, 13, 1369-1382.

Viazminsky, C.P. (2008). Necessary and sufficient conditions for a function to be separable. *Applied Mathematics and Computation*, 204, 658-670.

Data derived analysis and inference for an industrial deethanizer

Francesco Corona [*] **Michela Mulas** [**] **Roberto Baratti** [***]
Jose A. Romagnoli [***,1]

[*] *Dept. of Computer and Information Science, Helsinki University of Technology, Finland, (e-mail: francesco.corona@hut.fi).*
[**] *Dept. of Bio and Chemical Technology, Helsinki University of Technology, Finland, (e-mail: michela.mulas@hut.fi)*
[***] *Dept. of Chemical Engineering and Materials, University of Cagliari, Italy, (e-mails: baratti@dicm.unica.it, jose@lsu.edu)*

Abstract: In this paper, we present an application of data derived approaches for analyzing and monitoring an industrial deethanizer column. The discussed methods are used in visualizing process measurements, extracting operational information and designing an estimation model. Emphasis is given to the modeling of the data obtained with standard paradigms like the Self-Organizing Map (SOM) and the Multi-Layer Perceptron (MLP). The SOM and the MLP are classic methods for nonlinear dimensionality reduction and nonlinear function estimation widely adopted in process systems engineering; here, the effectiveness of these data derived techniques is validated on a full-scale application where the goal is to identify significant operational modes and most sensitive process variables before developing an alternative control scheme.

Keywords: Process monitoring, Process supervision, the Self-Organizing Map

1. INTRODUCTION

A modern process plant is under tremendous pressure to maintain and improve product quality and profit under stringent environmental and safety constraints. For efficient operation, any decision-making action related to the plant operation requires the knowledge of the actual state of the process. The availability of easily accessible displays and intuitive knowledge of the states is thus indispensable, with immediate implications for profitability, management planning, environmental responsability and safety.

Due to the advances in measuring and information technology, historical data are available in abundance. Remarkable characteristics of the data acquired in industrial facilities are redundancy and possibly insignificance, not to mention the presence of disturbances that corrupt the measurements. Very often, the amount and quality of the data together with their high-dimensionality can be a limiting factor for the analysis; therefore, it is necessary the availability of effective methods that: i) model the data to extract the structures existing in the measurements, ii) identify and reconstruct the most relevant structures for the scope at hand and, iii) allow for easily interpretable displays where the states' information is presented to the plant operators. Intuitive knowledge of all visited states is invaluable for safe plant operation and trustworthy methods become necessary when considering statistical process monitoring as part of a supervision and control strategy.

In this paper, we discuss the implementation and direct application of a strategy to model, visualize and analyze the information encoded in industrial process data. The approach is based on a classical machine learning method for dimensionality reduction and quantization, the Self-Organizing Map, SOM (Kohonen, 2001). The SOM combines many of the main properties of other general techniques and shares many commonalities with two standard methods for data projection (Principal Components Analysis, PCA (Jolliffe, 2002)) and clustering (K-means, (Hartigan et al., 1979)). In addition, the SOM is also provided with a set of tools that allow for efficient data visualization in high-dimensional settings.

The use of the Self-Organizing Map in the exploratory stage of data analysis is discussed in (Kaski, 1997; Vesanto, 2002) and it is widely employed in many fields. In general terms, the main contributions in applying the SOM on industrial process data are collected by Alhoniemi (2002) and Laine (2003), whereas more domain specific developments can be found in the SOM's bibliography (Oja et al., 2003). Here, the SOM is used as a framework for the identification of the process modes with their time of occurence and present the information on simple displays.

To support the presentation, the analysis is discussed on a full-scale deethanizer where the goal is to identify significant operational modes and most sensitive process variables before developing an alternative control scheme. The study relies on an regression model for estimating an important quality variable (the ethane concentration in the bottom) otherwise difficult to measure in real-time from a set of easily measurable process variables. Inference is based on the Multi-Layer Perceptron Haykin (1998).

[1] On leave from the Department of Chemical Engineering, Louisiana State University, Baton Rouge LA 70803, USA.

2. THE SELF-ORGANIZING MAP

The Self-Organizing Map (Kohonen, 2001) is an adaptive formulation of vector quantization performing in unison:

- a reduction of the data dimensionality by projection; that is, the reduction of the dimensionality of the data by mapping all the observations onto a meaningful subspace with lower dimensionality;
- a reduction of the amount of data by clustering; that is, the retention of the original dimensionality of the data space while reducing the amount of observations by prototyping them by similarity.

The SOM nonlinearly projects vast quantities of high-dimensional data onto a low-dimensional array of few prototypes in a fashion that aims at preserving the topology of the observations. By choosing a conventional bi-dimensional array of prototypes, the main advantage of the map is in a wealth of visualization techniques that allows the analysis of the structures existing in the data.

The following overviews the SOM algorithm and its analogies with other projection and clustering methods. A brief presentation of the most common SOM-based visualization methods for exploratory data analysis is also reported.

Algorithm and properties The basic Self-Organizing Map consists of a low-dimensional and regular array of K nodes, where a prototype vector $\mathbf{m}_k \in \mathbb{R}^p$ is associated with each node k. Each prototype acts as an adaptive model vector for the N observations $\mathbf{v}_i \in \mathbb{R}^p$. During the computation of the SOM, the observations are mapped onto the array of nodes and the model vectors adapted according to:

$$\mathbf{m}_k(t+i) = \mathbf{m}_k(t) + \alpha(t) h_{k,c(\mathbf{v_i})} \Big(\mathbf{v}_i(t) - \mathbf{m}_k(t) \Big). \quad (1)$$

In the learning rule in Equation 1, t denotes the discrete-time coordinate of the mapping steps and $\alpha(t) \in (0,1)$ is the monotonically decreasing learning rate. The scalar multiplier $h_{k,c(\mathbf{v_i})}$ denotes a neighborhood kernel centered at the Best Matching Unit (BMU); that is, at the model vector $\mathbf{m}_c(t)$ that, at time t, best matches with the observation vector $\mathbf{v}_i$. The matching is based on a competitive criterion on the Euclidean metric $d(\mathbf{m}_k(t), \mathbf{v}_i(t))$, for all $k = 1, \ldots, K$. At each step t, the BMU is thus the prototype $\mathbf{m}_k(t)$ that is the closest to observation $\mathbf{v}_i(t)$:

$$c(t) = \underset{k}{\operatorname{argmin}} \Big(d(\mathbf{m}_k(t), \mathbf{v}_i(t))^2 \Big), \ \forall k \text{ and } \forall i. \quad (2)$$

The kernel $h_{k,c(\mathbf{v_i})}$ centered at $\mathbf{m}_c(t)$ is often a Gaussian:

$$h_{k,c(\mathbf{v_i})} = \exp\Big(- \frac{||\mathbf{r}_k - \mathbf{r}_c||^2}{2\sigma^2(t)} \Big), \quad (3)$$

where the vectors $\mathbf{r}_k$ and $\mathbf{r}_c$ represent the geometric location of the nodes on the array and $\sigma(t)$ denotes the monotonically decreasing width of the kernel. The effect of the kernel decreases with the distance from the BMU.

The SOM is computed recursively for each observation. As $\alpha(t) h_{k,c(\mathbf{v_i})}$ tends to zero with t, the set of prototype vectors $\{\mathbf{m}_k\}_{k=1}^K$ are adaptively updated to represent similar observations in $\{\mathbf{v}_i\}_{i=1}^N$, and converge toward their asymptotic limits. The resulting model vectors learn a nonlinear manifold in the original embedding space such that the relevant topological and metric properties of the observations are preserved on the map. Thus, the SOM is to be understood as an ordered image of the original high-dimensional data modeled onto a low-dimensional manifold, where the complex data structures are represented by simple geometric relationships.

A rigorous analysis of the SOM has demonstrated difficult. However, in the case of the basic algorithm with a fixed kernel function, also the SOM algorithm can be understood from the optimization of a cost function:

$$\mathtt{E(SOM)} = \sum_{i=1}^{N} \sum_{k=1}^{K} h_{k,c(\mathbf{v_i})} d(\mathbf{m}_k, \mathbf{v}_i)^2. \quad (4)$$

The cost function in Equation 4 is closely related to the objective optimized with the K-mean algorithm (Lloyd, 1982). The only difference is in the neighborhood function that smoothly weights all the distances between the observations and the prototypes, instead of just the closest one. In that sense, the SOM operates as the conventional clustering method where the width of the kernel is zero. Moreover, there is no need to explicitly specify the number of taxonomies; in fact, the number of prototypes in the SOM can be chosen without any specific concern on the actual number of clusters. The SOM has also neat projection properties. In fact, the cost in Equation 4 closely resembles the objective optimized by Curvilinear Components Analysis CCA (Demartines et al., 1997); CCA is a modification of metric Multi-Dimensional Scaling MDS (Cox et al., 2000) and Principal Components Analysis PCA (Jolliffe, 2002). Similarity is in the decreasing and smoothing nature of the neighborhood function that emphasizes smaller distances in the projection. Conversely, the notion of locality in the SOM does not correspond to the global concern on small distances characterizing CCA.

Data exploration methods In the typical case of projections onto 2D arrays, the SOM offers excellent techniques for data exploration. In that sense, the approach to data analysis with the SOM is mainly visual and focuses on the low-dimensional displays specifically designed for the map.

The data visualization techniques based on the SOM assume that the prototype vectors are representative models for groups of similar observations, and projecting the data onto the low-dimensional array allows for an efficient display of the dominant relationships existing between them. For instance, the displays permit to identify the shape of the data distribution, cluster borders, projection directions and dependencies between variables. The visualizations techniques considered here are i) the component planes and ii) the distance matrix. Such techniques were thoroughly studied by Kaski (1997) and Vesanto (2002).

A component plane shows on the SOM's array the coordinates of the prototype vectors along a specific direction in the data embedding space; that is, each component plane is associated to one original variable and there are as many planes as directions in the embedding. The coordinate values are encoded into gray levels or colors, and the area of each unit on the array is dyed with the color associated to the component value. A component plane thus displays the distribution of the corresponding variable among the prototype vectors. The component planes are useful in order to visually identify possible dependencies between variables. The dependencies between variables can be seen as similar patterns (the colors corresponding to the values

of the variables) in identical locations on the component planes. Such representations can be also used to quantify dependencies. In that sense, the SOM reduces the effect of noise and outliers in the observations and, therefore, may actually make any existing dependence simpler to detect.

A distance matrix visualizes on the SOM's array the average distance between each prototype vector and its adjacent neighbors. In a distance matrix, distances are encoded into gray levels or colors and each unit on the array is dyed with the color associated to the distance with the neighbors. The most widely used distance matrix for the SOM is the Unified Distance Matrix, or U-matrix (Ultsch, 1993). Here, the dominant clustering structure of the observation can be seen as clearly separated areas (large distances) characterized by a homogeneous coloring. In the U-matrix, visualization of the clusters is improved by augmenting the distance matrix with additional entries (nodes) between each prototype vector and each of its neighbors. Unconventional alternatives to the U-matrix are reported by Oja et al. (2003) but not considered here.

3. CASE STUDY

To illustrate the potentialities of topological data analysis using the Self-Organizing Map, the overviewed methods are applied on a set of measurements from a full-scale process. The monitoring problem consists of modeling and analyzing the operational behaviour of an industrial deethanizer, starting from a set of online process measurements. The objective of the deethanizer (in Figure 1) is to separate ethane from the feed stream (a light naphta) while minimizing the ethane extracted from the bottom of the column (an economical constraint for the subsequent unit in the plant). Such a constraint is quantified by the maximum amount of ethane lost from the column bottom; the operational threshold is set be smaller than 2%. The

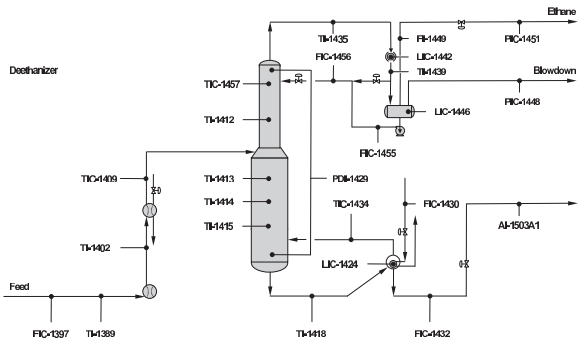

Fig. 1. Deethanizer: Simplified flowsheet.

motivation for choosing this unit is merely illustrative; in fact, the considered deethanizer offers an ample variety of behavior that reflects the operational usage; hence, an interesting groundwork for presentation and discussion.

TAG/Variable	TAG/Variable
FIC-1397/Inlet Flowrate	FIC-1430/Vapor Flowrate
TI-1389/Inlet Temp.	LIC-1424/Reboiler Level
TI-1402/Inlet Temp.	FIC-1432/Bottom Flowrate
TI-1409/Inlet Temp.	FI-1449/Distillate Flowrate
TI-1435/Top Temp.	PIC-1451/Distillate Pressure
TIC-1457/Enriching Temp.	TI-1452/Reflux Temp.
TI-1412/Enriching Temp.	FIC-1455/Bypass Flowrate
TI-1413/Exhausting Temp.	TI-1439/Condensed Temp.
TI-1414/Exhausting Temp.	LIC-1442/Top Drum Level
TI-1415/Exhausting Temp.	PIC-1448/Blowdown Pressure
TI-1418/Bottom Temp.	LIC-1446/Bottom Drum Level
FIC-1456/Reflux Flow.	AI-1503A1/Ethane Conc.
TIC-1434/Vapor Temp.	AI-1503A2/Butane Conc.
PDI-1429/Delta Pressure	

Table 1. Deethanizer: Process variables

In order to analyze the behaviour of the unit, a set of process variables was collected from the plant's distributed control system (DCS). The measurements correspond to three weeks of continuous operation in winter asset and three weeks in summer asset. The data are available as 3-minute averages and 27 process variables (in Table 1) are available for a macroscopic characterization of the unit.

In addition, there are a number of control loops in the process. Briefly, the temperature $TIC-1457$ and the vapor temperature $TIC-1434$ out of the reboiler are controlled by manipulating the reflux flow $FIC-1456$ and the steam rate $FIC-1430$ to the reboiler, respectively; with both loops cascaded with the corresponding flowrates. The distillate pressure $PIC-1451$ is controlled by the distillate flowrate $FI-1449$ and the level in the reboiler $LIC-1424$ by the bottom flowrate $FIC-1432$.

3.1 Analysis and inference

The operational objective of the column is to produce as much ethane as possible (minimizing concentration of propane from the top of the column) while satisfying the constraint on the amount of impurity from the bottom (maximum concentration of ethane in the bottom $\leq 2\%$). With respect to the loss of ethane from the bottom, such considerations led to the definition of 3 operational modes:

- a *normal* status, corresponding to the operation of the column, where the concentration of ethane is within allowable bounds (within the $1.8-2.0\%$ range)
- a *high* status, corresponding to the operation of the column, where the concentration of ethane is exceeding the allowable upper bound (above 2%)
- a *low* status, corresponding to the operation of the column, where the concentration of ethane is below the allowable lower bound (below 1.8%).

The two abnormal conditions have a direct and important economic implication. In fact, when at low status, the process is delivering a product out of specifications whereas, when at high status the product is within the specifications, but an unnecessary operational cost is observed.

To understand under which conditions such modes are experienced, in a recent study (Corona et al., unpublished) we analyzed the clustering structure of the data and visualized the operating conditions of the unit. Starting from a selection of important process variables, we expanded this

subset by incorporating an additional *dummy* indicator, specifically calculated to indicate the status. As such, the new variable was defined as to take values $+1$, -1 or 0, according to the operational status of the process. Value 0 is assigned to the normal operation, whereas values $+1$ and -1 correspond to high and low operations, respectively. Notice that the calculation of the *dummy* variable requires the availability of a real-time measurement for the ethane concentration; such a variable ($AI - 1503A1$) is presently acquired from a continuos-flow chromatograph. The subset of selected process variables augmented by the *dummy* indicator was used to calibrate a SOM over which the resulting component planes and U-matrix were analyzed; the exploration was perfomed as a direct application of the techniques discussed by Alhoniemi (2002). The study allowed us to extract the clustering structure of the data and illustrate on simple displays how it corresponds to the operational modes of the unit.

However, the delay associated with the analytical measurements of the ethane concentration from the bottom of the column can pose severe limitations to the online analysis. Moreover, the existing instrumentation setup available for the unit may benefit from a backup measurement for such an important variable. In this study, we are thus extending the analysis of the operational modes of the deethanizer, by validating the functionality of the approach when replacing the analytical measurements of ethane with online estimates. In that sense, the availability of an inference model would allow the development of a fully automated system to be implemented online in the plant's DCS.

For the purpose, a soft sensor based on the standard Multi-Layer Perceptron MLP (Haykin, 1998) with one hidden layer and sigmoidal activation functions was developed to infere the ethane concentration from the bottom. The estimates are obtained starting from the same input subset of easily measurable process variables used for the SOM and selected according to the guidelines provided by Baratti et al. (1995). The parameters of the MLP (that is, number of hidden nodes, one, and the connection weights) were optimized using the Levemberg-Marquard method and cross-validation. In Figure 2, the response of the soft sensor on a set of independent testing observations is reported for about a week of continuous operation.

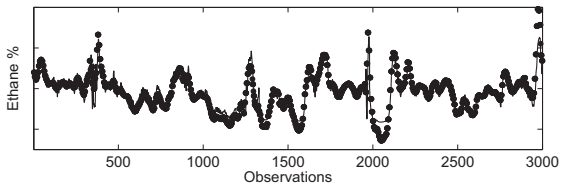

Fig. 2. Ethane concentration from the bottom: Analytical measurements ($\cdot$) and MLP estimates ($-$).

Based on the MLP estimates, a bidimensional Self-Orgaznizing Map was calibrated using only the winter data. The map consists of a hexagonal array of prototype vectors initialized in the space spanned by the eigenvectors corresponding to the two largest eigenvalues of the covariance matrix of the data. As usual, the ratio between the two largest eigenvalues was used to calculate the ratio between the two dimensions of the SOM; the resulting map consists of a 70×24 array of 15-dimensional prototype vectors, where the dimensionality of the vectors equals the number of variables used for calibration. On the SOM, we analyzed the clustering structure of the data and visualized the operating conditions of the unit using the U-matrix.

The U-matrix is based on distances between each prototype vector and its immediate neighbors. A common way to visualize it consists of an initial projection of all the distances onto a color axis and the subsequent display with colored markers between each prototype vector. On the display, areas with homogeneous coloring correspond to small within-cluster distances (recognized as clusters), whereas cluster borders are areas with homogeneous coloring but corresponding to large between-cluster distances. The use of the U-matrix in clustering the operational regimes of the deethanizer column is shown in Figure 3.

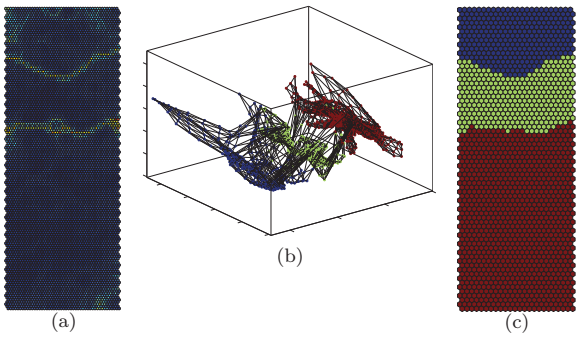

Fig. 3. The U-Matrix (a), the clustered SOM projected onto the 3D principal components space (b) and the SOM colored according to the K-means clustering (c).

In Figure 3(a), distances are depicted with dark blue colors shading toward dark red as the proximity between the prototypes decreases. The visualization permits to clearly recognize the presence of three distinct clusters of prototypes, as well as several other data substructures. An analogous visualization of the grouping is achieved by projecting the map onto a low-dimensional subsapce; in Figure 3(b), a tridimensional principal components space learned by the metric MDS. Indeed, also this visualization permits to illustrate the actual clustering structure of the process measurements and displays a good separateness also in this space of reduced dimensionality. However, to obtain a quantitative characterization of the clustering structure, the prototypes of the SOM should be regarded as a reduced data set and modeled with a standard clustering algorithm. For simplicity, we are here adopting a standard K-means algorithm coupled by the Davier-Bouldin index, a measure of cluster validity to identify an optimal number K of taxonomies from data Milligan et al. (1985). As expected, optimality was found for $K = 3$ clusters, corresponding to the modes of the unit.

On the SOM, such clusters are located in the lower, middle and upper part of the map. After coloring the SOM according to the cluster membership obtained by using the K-means algorithms, in Figure 3(c), and comparing it with the component plane of the *dummy* variable (and equivalently, the MLP estimated ethane concentation), it is straightforward to associate the three taxonomies to the

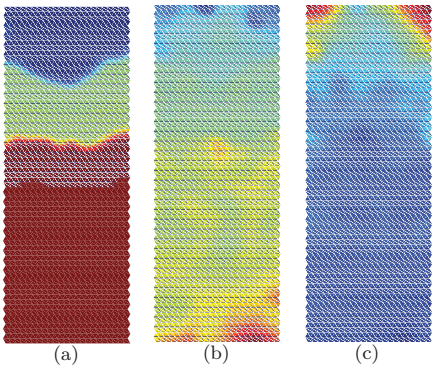

(a) (b) (c)

Fig. 4. The component planes for the *dummy* variable (a), the estimated ethane concentration (b) and the temperature $TI-1414$ (c), with a coloring scheme that assigns blue to high values of the variables fading toward red as the values decrease. This scheme differs from the what defined for the clustering with blue and red corresponding to -1 and $+1$, respectively.

three main operational modes of the deethanizer, Figure 4. Specifically, Figure 3(c) shows the clusters on the SOM as distinct regions dyed in blue, green and red with a cloring scheme that assignes those colors to the operational modes ($+1$, 0 and -1, respectively). As expected, a similar structure is also retrieved from the component plane for the *dummy* variable, Figure 4(a). Though apparently less evident, the same structuring is retrieved from the component planes of the estimated ethane concentration (Figure 4(b)) and one of the temperatures in the exhausting section of the dethanizer; namely, $TI-1414$ in 4(c). Looking for similar patterns in similar positions in such components planes allows the visualization of a neat dependence between the ethane composition and such temperature indicator. Such pair of variables shows near identical but reversed component planes, thus highlighting the inherent inverse correlation that exists between them.

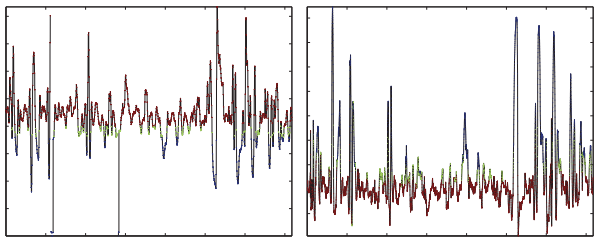

(a) AI-1503A1 (b) TI-1414

Fig. 5. The colored time series (3 winter weeks) for the ethane concentration $AI-1503A1$ (a) and the temperature in the enriching section $TI-1414$ (b). The actual values of the variables could not be reported because of the confidentiality agreement.

Information about this dependence can be further enhanced by applying the coloring scheme resulting from clustering directly to the original observations in the time domain. In fact, all points can be dyed using the cluster color of the corresponding Best Matching Unit, as in Figure 5. The figure shows how $TI-1414$ is mostly responsible for the transition between the aformentioned operational

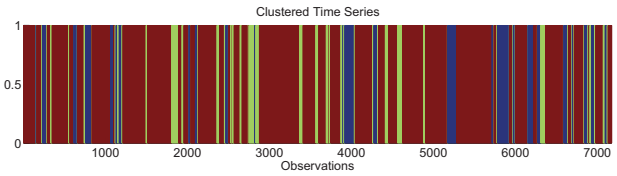

Fig. 6. The temporal evolution of the winter operational modes colored according to the SOM clustering.

conditions. The correspondence with the ethane concentration is observed as clear banded regions and indicates that, in order to maintain the column at optimality (withing the $1.8-2.0\%$ range of ethane from the bottom), such a temperature should be controlled (possibily, within the $52-55°C$ range). A possible variable to manipulate is the steam flowrate $FIC-1430$. However, such a variable is not used in the present control scheme and induces an overall 85% of off-spec operation of the unit, during the given winter period. Such information is obtained by calculating the number of point measurements that falls outside the normality conditions over the total count and pictorially depicted also as clustered time series (in Figure 6).

So far, we have restricted the analysis only to the measurements observed under winter asset. However, it is also possible to directly use the calibrated SOM as a reference model for new and unseen observations; in our setting, the three weeks of data corresponding to the summer operation of the deethanizer column. To validate this idea, the winter SOM was used to explore the behaviour of the deethanizer under summer asset. Again, the summer measurements from $AI-1503A1$ were replaced by the estimates from the soft sensor. The analysis was accomplished by initially projecting the new data onto the calibrated SOM, being the mapping based on a nearest neighbor criterion between the new sample vectors and the prototype vectors of the SOM. In this respect, novelty detection using the SOM is based on finding the BMU. Once the mapping is completed, the inspection is performed for the new data.

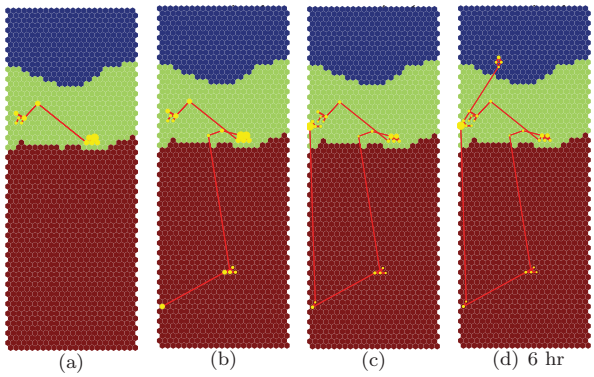

(a) (b) (c) (d) 6 hr

Fig. 7. Trajectory of a selection the summer observations (approximatively, 6hr) displayed on the winter SOM.

The results in extrapolation are presented by illustrating another technique for visualization on the SOM. The approach allows to follow operational changes in the process and tries to provide a simple display for identifying reasons of specific behaviors. For the purpose, the map calibrated on the winter data can be enhanced by the inclusion of

the summer point trajectories followed by the process. The trajectory permits to intuitively indicate the current mode of the process and observe how it has been reached. In Figure 7, the process trajectory is sequentially reported for a small time window corresponding to six hours of continuous summer operation of the deethanizer. The process trajectory on the SOM's domain passes through all the BMUs of each new data vector and it is shown as red line connecting the visited prototypes (the nodes are marked as yellow dots and thicken with the count of visits).

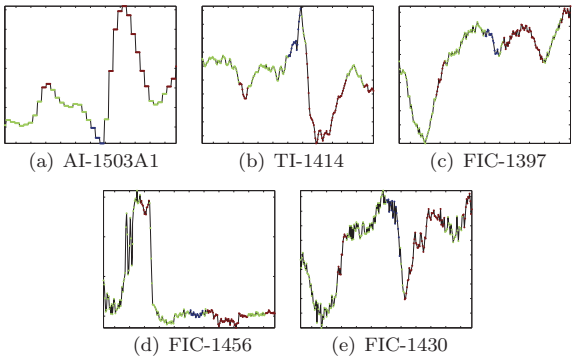

(a) AI-1503A1 (b) TI-1414 (c) FIC-1397

(d) FIC-1456 (e) FIC-1430

Fig. 8. Status transitions on the time domain (approximatively, 6hr), for a set of relevant process variables.

Following the temporal evolution from Figure 7 and 8, the diagrams show a process that is initially operated in the green area, or *normal* condition (as for the ethane in the bottom and reference temperature). As the process has moved further in time, new prototype vectors are visited and added to the trajectory until the column eventually leaves the normality region and crosses the boundary towards the region of high ethane composition (in red). In a similar fashion, all the process variables changed coloring to match the visited modes allowing to appreciate that the change in the operation was mainly due to an abrupt change in the feed flowrate ($FI-1397$), in Figure 8(c), and possibly its composition. In turns, the variation triggered the action on steam to reboiler flowrate ($FIC-1430$), in Figure 8(e), as well as the reflux to control the top temperature ($FIC-1456$), in Figure 8(d). The events initiated a sequence of oscillations around normality that could be reestablished only after several hours.

4. CONCLUSIONS

In this work, we implemented and discussed a strategy to model, visualize and analyze the information encoded in industrial process data. In particular, the proposed strategy was applied to a full-scale distillation column.

From a methodological point of view, the process monitoring problem was casted in a topological framework by using the Self-Organizing-Map. On the SOM, the identification of the process modes was approached as a clustering task rather than classification; that is, in an unsupervised rather than supervised fashion. Moreover, in order to overcome the limitations associated with the time delay and costs of the analytical instrumentation, a software sensor based on a Multi-Layer Perceptron was developed to infer a primary process variable, thus favoring the possibility to directly use such a strategy also for online monitoring.

The application allowed the definition of simple displays capable to present meaningful information on the actual state of the process and also suggested an alternative control strategy for maintaining the unit in normal conditions.

ACKNOWLEDGEMENTS

J. Romagnoli kindly acknowledges Regione Sardegna for the support through the program *Visiting Professor 2008*.

REFERENCES

E. Alhoniemi. Unsupervised pattern recognition methods for exploratory analysis of industrial process data. *Doctoral Dissertation*, Lab. of Computer and Information Science. Helsinki University of Technology, Finland, 2002.

R. Baratti, G. Vacca, and A. Servida. Neural network modeling of distillation columns. *Hydrocarbon Processing*, 74:35–38, 1995.

F. Corona, M. Mulas, R. Baratti, and J.A. Romagnoli. On the topological analysis of industrial process data. PSE 2009 International Symposium on Process Systems Engineering, to appear.

T.F. Cox, and M.A.A. Cox. *Multidimensional scaling, Second edition*. Chapman & Hall, 2000.

P. Demartines, and J. Herault. Curvilinear component analysis: a self-organizing neural network for nonlinear mapping of data sets. *IEEE Transaction on Neural Networks*, 8:148–154, 1997.

S. Haykin. *Neural Networks: A Comprehensive Foundation, Second Edition*. Prentice Hall, 1998.

I.T. Jolliffe. *Principal Components Analysis, Second edition*. Springer, 2002.

S. Kaski. Data exploration using Self-Organizing Maps. *Doctoral Dissertation*, Lab. of Computer and Information Science. Helsinki University of Technology, Finland, 1997.

T. Kohonen. *Self Organizing Maps, Second edition*. Springer, 2001.

A. Hartigan, and M.A.A. Wong. K-means clustering algorithm. *Applied Statistics*,28:100–108, 1979.

S. Laine. Using Visualization, Variable selection and feature extraction to learn from industrial data. *Doctoral Dissertation*, Lab. of Computer and Information Science. Helsinki University of Technology, Finland, 2003.

P. Lloyd. Least squares quantization in PCM. *IEEE Transaction on Information Theory*, 28:129–137, 1982.

G.W. Milligan, and M.C. Cooper. An examination of procedures for determining the number of clusters in a dataset. *Psychometrika*, 50:159–179, 1985.

M. Oja, S. Kaski, and T. Kohonen. Bibliography of Self-Organizing Map (SOM) papers: 1998-2001 addendum. *Neural Computing Surveys*, 3:1–156, 2003.

A. Ultsch. Self-organizing neural networks for visualization and classification. *Information and Classification*, 307–313. Springer, 1993

J. Vesanto. Data exploration process based on the Self-Organizing Map. *Doctoral Dissertation*, Lab. of Computer and Information Science. Helsinki University of Technology, Finland, 2002.

Stiction Identification in Nonlinear Process Control Loops

U. Nallasivam [*] **B. Srinivasan,** [**] **R. Rengaswamy** [***]

[*] *Dept. of Chemical Engineering, Clarkson University, Potsdam, NY, US 13699. (e-mail: nallasu@clarkson.edu).*
[**] *Dept. of Chemical Engineering, Texas Tech University, Lubbock, Texas, US 79409. (e-mail: babji.srinivasan@ttu.edu)*
[***] *Dept. of Chemical Engineering, Texas Tech University, Lubbock, Texas, US 79409. (e-mail: raghu.rengasamy@ttu.edu)*

Abstract: Nearly 20-30% of all process control loops oscillate due to stiction and lead to loss of productivity. Thus, the detection and quantification of stiction in control valves using just the raw operating data is an important component of any automated controller performance monitoring application. Many techniques have been proposed for the detection and quantification of stiction. Pattern based identification approaches use unique shapes of the PV and OP data to identify stiction. Other approaches that include some measure of nonlinearity index have also been used to identify stiction. A solution technique for stiction detection in nonlinear processes with known process models is also available. In this paper, one possible approach to detect stiction in nonlinear process control loops with unknown process models is discussed.

1. INTRODUCTION

Research on developing automated controller performance monitoring systems has been increasing in the past decade. Control strategies such as Model Predictive Control (MPC) or other supervisory control are crucial for optimization of process operations. Performance gains from such advanced control techniques depend on how effectively the lowest control elements in the control strategy track the desired set points. A spate of surveys on the performance of control loops [Bialkowski, 1993, Ender, 1993, Entech, 2005, Desborough and Miller, 2001] indicate that a majority of control loops in processing industries perform poorly. Performance demographics of 26,000 PID controllers collected across a wide variety of processing industries in a two year time span indicate that the performance of 16% of the loops can be classified as excellent, 16% as acceptable, 22% as fair, 10% as poor, and the remaining 36% are in open loop [Desborough and Miller, 2001]. The impact of this has to be seen from the fact that PID is the dominant control algorithm in the industry accounting for 97% of the regulatory loops [Desborough, 2003]. This has led to increasing interest in automated Controller Performance Assessment (CPA) tools in recent years. The three major reasons for deterioration of control performance are: badly tuned controllers, oscillating load disturbances, or nonlinearities in control valves. 20% to 30% of all control loops oscillate due to valve problems caused by static friction or hysteresis [Bialkowski, 1993, Miller, 2000] resulting in performance deterioration. It was found that over 80% of all valves adjusted by Entech Control Engineering failed dynamic performance standards due to stiction, backlash or oversized design. Thus the task of detecting stiction or other nonlinearities in valves from routine operating data is a challenging task and is an important component in any CPA suite.

⋆ Corresponding Author: R. Rengaswamy, Dept. of Chemical Engineering, Texas Tech University, Lubbock, Texas, US 79409. Adjunct Faculty, Dept. of Chemical Engineering, Clarkson University.

2. PROBLEM DEFINITION

A typical process control loop with stiction in the control valve can best be depicted as shown in the Figure 1. As seen, the stiction precedes the control valve dynamics and the process transfer function also includes the valve dynamics. The fundamental problem that is being solved in this paper is one of identifying the root cause of oscillation in the process variable (PV) as being due to either stiction or external oscillations. In this work, the focus is on a model-based solution approach to this problem. There are solutions for stiction detection based on the analysis of the input-output data such as the shape based analysis proposed by Rengaswamy et al. [2001], Srinivasan et al. [2005a] and higher order statistics based approach proposed by Choudhury et al. [2004]. Most of these approaches rely on the process being linear. For non-linear process Nallasivam and Rengaswamy [2008] proposed a solution strategy that works when the process model is known. However, there is no work on detecting stiction in nonlinear control loops when the process model is not known.

Previous attempts at quantifying stiction were mostly based on measures developed from the data characteristics such as the span of controller output (OP) data, apparent stiction, maximum width of the ellipse fitted by PV-OP plot etc. The first attempt at quantifying stiction through a joint identification procedure was by Srinivasan et al. [2005b]. Srinivasan et al. [2005b] proposed a model-based approach and solved this problem for a linear process. Their approach is based on the identification of a Hammerstein model of the system comprising of the sticky valve and the process (see Figure 1(b)). The identification of the linear dynamics is decoupled from the nonlinear element. The decoupling between the nonlinear and the linear component is achieved by an iterative procedure. The solution proposed in Srinivasan et al. [2005b] is shown in Figure 2. Several stiction quantification attempts based on this approach have started to appear. A similar approach but

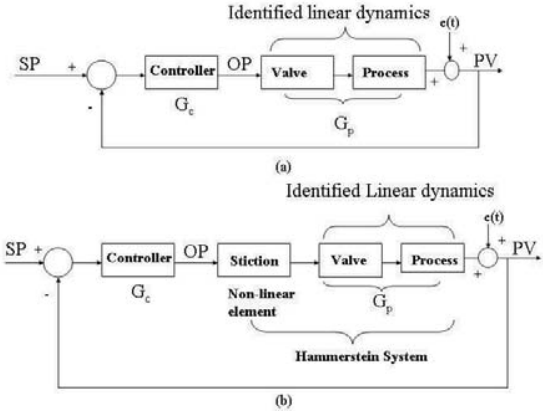

Fig. 1. (a) General process control loop, (b) Process control loop with stiction element

with a two parameter model to quantify stiction is discussed in Choudhury et al. [2008]. Another work using a Hammerstein ID approach with a two parameter model can be found in Jelali [2008]. The difference between Choudhury et al. [2008] and Jelali [2008] seem to be that while a gird search, similar to Srinivasan et al. [2005b], is used in Choudhury et al. [2008], genetic algorithms (GAs) are used to identify the stiction parameters in Jelali [2008]. However, all these methods assume that the process is linear. Nallasivam and Rengaswamy [2008] have shown that these approaches fail if the underlying process is nonlinear and solved this problem for the nonlinear case when the process model is known. The present work is on detecting stiction in nonlinear control loops when the process model is unknown.

Figure 3 depicts the control loop that is being addressed in this work. From this figure,

$$\begin{aligned} y &= y_p + y_d \\ y &= N(u) + y_d \\ y &= N(V(v)) + y_d \end{aligned} \tag{1}$$

where y is the measured process variable pv, which includes the process component y_p and the disturbance component y_d, which are additive. N is the non linear process transfer function and u is the valve output, which might not be a measured variable. The valve output u is a function (V) of the op (v) dictated by the stiction phenomenon. In this paper, the detection, quantification and isolation of stiction from external disturbances for the system given in equation 1 is addressed.

$$x(t) = \begin{cases} x(t-1) & if\ |u(t) - x(t-1)| \le d, \\ u(t) & otherwise \end{cases} \tag{2}$$

3. SOLUTION APPROACH

A single parameter stiction model is given by equation 2. In this model, the value of the parameter d goes to zero when stiction is absent in the valve. Thus a non-zero value for this parameter d indicates the presence of stiction and also quantifies the stiction level. The estimation of this parameter is achieved by decoupling the stiction parameter estimation from the estimation of the process dynamics. This is achieved by

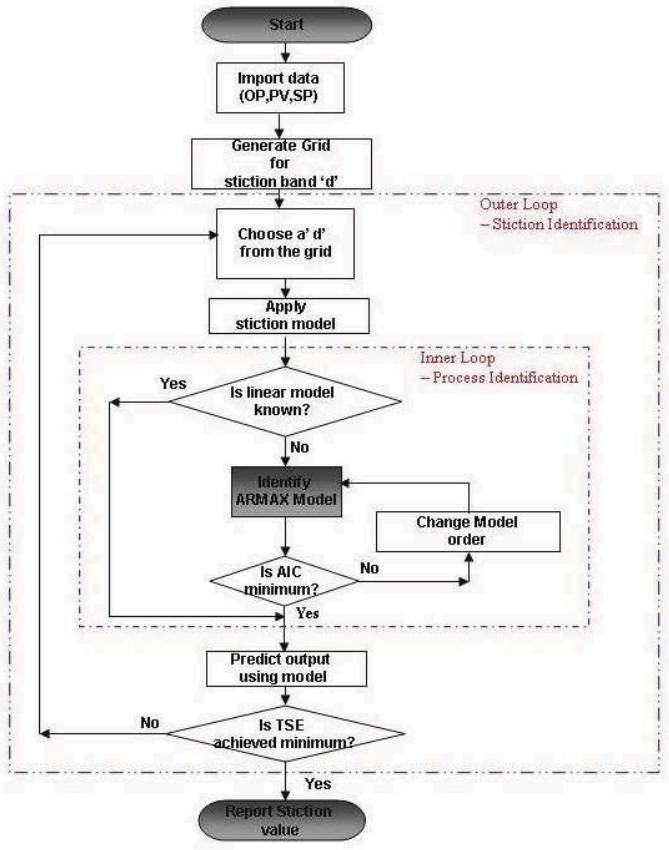

Fig. 2. Solution algorithm proposed by Srinivasan et al. [2005b]

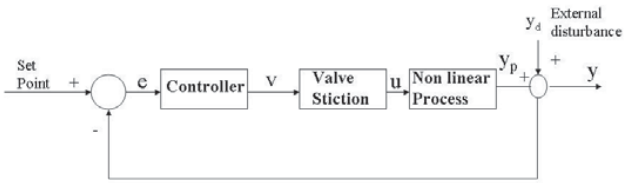

Fig. 3. Nonlinear control loop in presence of stiction

an iterative process in which a value for d is assumed in an outer loop and the best fit model for the remaining dynamics in the inner loop is identified. From Figure 3, since the controller parameters θ_c are known, v (op) can be calculated from y. Using the equation 2 for a given selected value of d, u can be calculated. Thus the identification problem becomes,

$$\begin{aligned} y &= y_p + y_d \\ y &= N(u) + y_d \end{aligned}$$

Since the process model is not known, by considering y_d as a moving average process, we can write

$$A(q)y(t) = B(u,q) + C(q)e(t) \tag{3}$$

where

$$A(q) = [1 + a_1 q^{-1} + ... + a_{n_a} q^{-n_a}]$$
$$C(q) = [1 + c_1 q^{-1} + ... + c_{n_c} q^{-n_c}]$$

$B(u,q)$ represents a general nonlinear process. As before u is known based on the actual output, the controller parameters and the assumed d value. A predictor form can be obtained for the system given by equation 3. In the linear model case, this will lead to a pseudolinear regression problem. One approach to retain the pseudolinear regression framework in the nonlinear case would be to parameterize the nonlinear function using a N^{th} order discrete Volterra series approximation as below

$$B(u,q) = \sum_{n=1}^{N} \sum_{i_1=1}^{M_1} ... \sum_{i_n=1}^{M_n} h_n(i_1,...,i_n) q^{-i_1} u(k) ... q^{-i_n} u(k)$$

With this expression, equation 3 now represents a Volterra MA model. By considering only the first and second order terms in the above Volterra series,

$$B(u,q) = \sum_{i=1}^{n_b} h_1(i) q^{-i} u(k) + \sum_{i=1}^{n_b} \sum_{j=1}^{n_b} h_2(i,j) q^{-i} u(k) q^{-j} u(k)$$

Now the predictor for equation 3 can be derived as

$$y(k/k-1) = B(u,q) + [1 - A(q)]y(k) + [C(q) - 1]e(k)$$

which is

$$y(k/k-1) = \sum_{i=1}^{n_b} h_1(i) q^{-i} u(k) + \sum_{i=1}^{n_b} \sum_{j=1}^{n_b} h_2(i,j) q^{-i} u(k) q^{-j} u(k) - a_1 y(k-1) - a_2 y(k-2) - ... - a_{n_a} y(k-n_a) + c_1 e(k-1) + c_2 e(k-2) + ... + c_{n_c} y(k-n_c)$$

When this predictor is applied to n samples, one would get n equations which results in the following equation in the matrix form

$$Y = XH$$

This equation can be solved iteratively till the solution converges for a given given selected model order of n_a, n_b and n_c using the following relationship.

$$H = [X^T X]^{-1} X^T Y$$

Based on this second order approximation of the Volterra series, an approach similar to the one that was used by Nallasivam and Rengaswamy [2008] for the known model case can be followed. However, now the model parameters and the MA process parameters have to be jointly estimated and evaluated through the AIC criteria. The overall best fit could then be chosen based on the d parameter that results in the minimum TSE. This approach is shown in Figure 4.

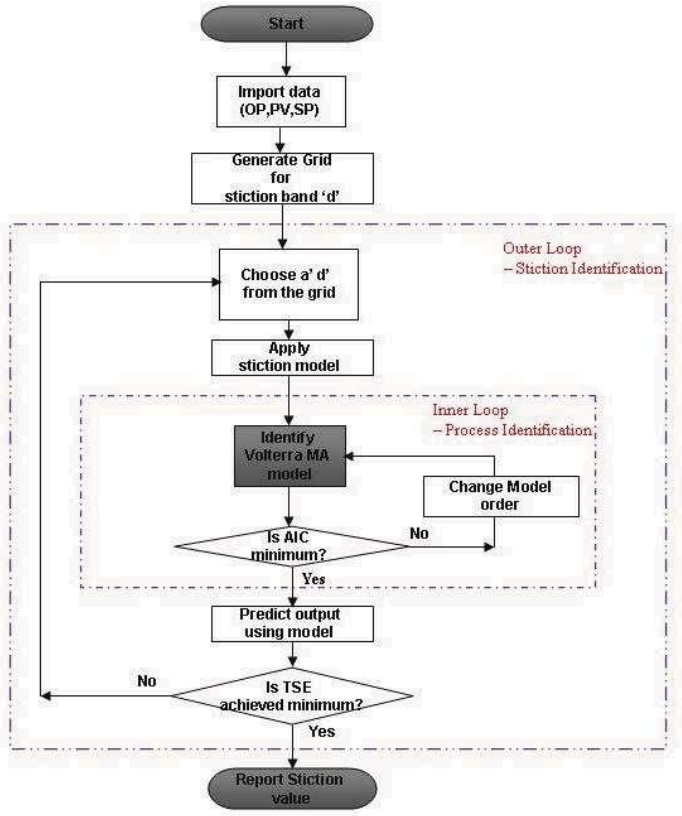

Fig. 4. Proposed approach

4. CASE STUDY

In this case study, a nonlinear polymerization reactor process from Doyle et al. [1995] is used. In this nonlinear process a polymerization reaction takes place in a jacketed CSTR where the controlled variable is the number-average molecular weight and the manipulated variable is the volumetric flowrate of the initiator. A second-order Volterra model in the frequency domain as given below describes this non-linear process.

$$P_1 = c_1^T (sI - A_{11})^{-1} b_1$$
$$P_2 = c^T [(s_1 + s_2)I - A]^{-1} N (s_1 - A)^{-1} b \tag{4}$$

Details on the matrices c, A, N, b can be found in Doyle et al. [1995].

4.1 Data for testing of the solution approach

This case study is used to demonstrate the effectiveness of the proposed solution approach in three different scenarios for stiction detection. These are:

(a) No stiction case
(b) Stiction alone case
(c) Stiction and external oscillation case

Three datasets were generated by using equation 4 as the nonlinear process in Figure 3 to address all the above three scenarios. A PI controller with $K_p = 0.3$, $T_i = 1.0$ was used. Data were

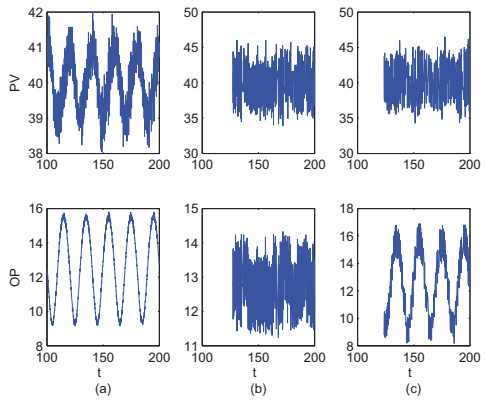

Fig. 5. Data for (a) No stiction (b) Stiction alone (c) Stiction and external oscillation

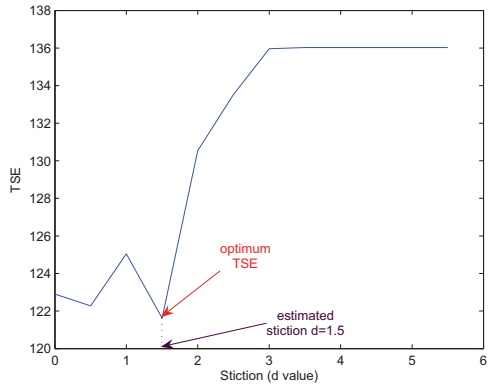

Fig. 6. Result for the approach of Srinivasan et al. [2005b]

simulated for scenario (a) using an external sine oscillation disturbance of amplitude 20 at a frequency of $0.3142 rad/sec$ as y_d. For scenario (b), a stiction value of $d = 1.5$ was used. For scenario (c), both the sine oscillation of scenario (i) and a stiction value of $d = 1.5$ were used. The data that are generated are shown in Figure 5.

4.2 Discussion on the existing approaches

The existing techniques based nonlinearity detection as in Choudhury et al. [2004] and qualitative pattern matching approaches as the one proposed in Rengaswamy et al. [2001] will not work for this dataset. As shown in Nallasivam and Rengaswamy [2008], the model-based approach proposed by Srinivasan et al. [2005b] is also not likely to work for this dataset. To verify this, the data shown in Figure 5(a) for the no stiction case is tested using the approach suggested in Srinivasan et al. [2005b] (approach shown in Figure 2). The resulting d vs TSE plot is shown in Figure 6. As expected, the value of d is incorrectly identified. In other words, stiction is detected where it is not actually present.

5. RESULTS

The dataset (Figure 5(a)), where the approach of Srinivasan et al. [2005b] failed is used to test the performance of the

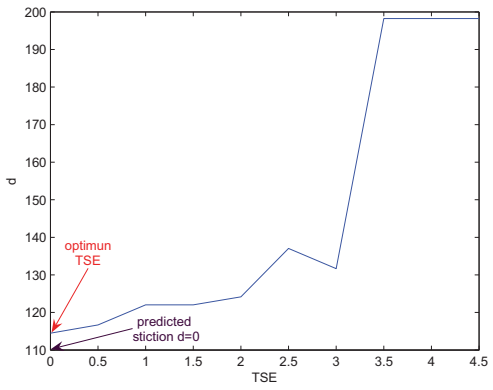

Fig. 7. Result for the no stiction case

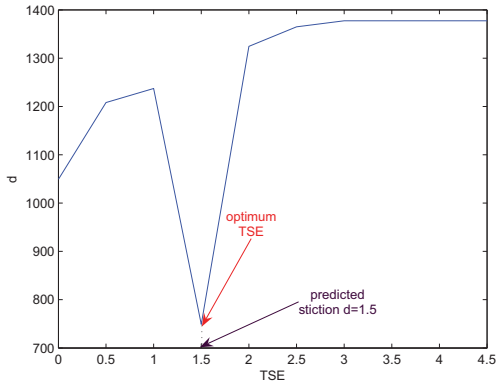

Fig. 8. Result for the stiction alone case

proposed approach shown in Figure 4. Figure 7 shows the result and as seen, it is clear that the scenario is correctly diagnosed as being a no stiction case. The minimum TSE is achieved at $d = 0$.

The dataset for the other two scenarios (Figures 5(b) and 5(c)) are also tested using this proposed approach. The results are shown in Figures 8-9. It can be seen from Figure 8, the case of stiction is also correctly identified with an accurate estimation of the stiction level. The more difficult third scenario is where both stiction and an external oscillating disturbance are present, with the process being nonlinear. The result for this case is shown in Figure 9. In this case also, not only is stiction detected but the magnitude of stiction is also accurately estimated. From these observations, it clear that the proposed solution approach works well in detecting and isolating the root cause of oscillation in nonlinear SISO loops.

6. VALIDATION USING DATA FROM PHYSICAL STICTION MODEL

The aim of this section is to verify how the proposed approach works when process data is generated by considering physical stiction model instead of single parameter stiction model. The physical stiction model that was used for this simulation is the same as the one used by Srinivasan et al. [2008]. The various parameters that were used for the physical stiction model are given in Table 1.

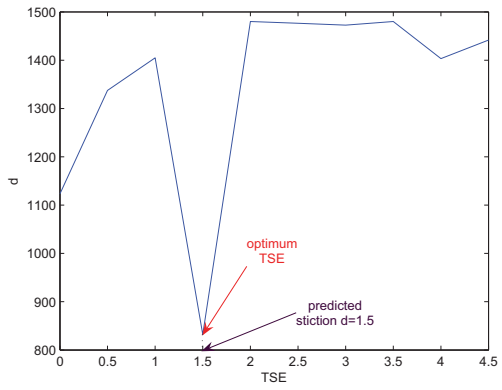

Fig. 9. Result for the case of both stiction and an external oscillating disturbance case

Table 1. Valve Parameters

Parameter	Description	Value
P	Applied Actuator Pressure	psi
A	Effective Diaphragm Surface area	100 in^2
m	Mass of Stem and Plug	3 lb
K	Spring rate	300 lbf/in
b	Viscous coefficient	0.15 lb/s
F_c	Coulomb friction	24 lbf
F_s	Static friction	34 lbf
v_s	Stribeck constant	0.01 in/s

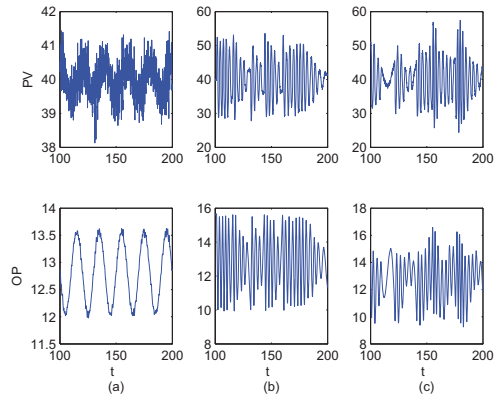

Fig. 10. Data set 2 for (a) No stiction (b) Stiction alone (c) Stiction and external oscillation

Data were simulated for scenarios (a) and (c) using an external sine oscillation disturbance of amplitude 5 at a frequency of $0.3142 rad/sec$ as y_d. A PI controller with $K_p = 0.01$, $T_i = 0.5$ was used for this data generation. The data that are generated are shown in Figure 10.

This data are tested using the proposed approach and the results are given in the Table 2. As seen, the absence or presence of stiction is predicted correctly in all the scenarios as indicated by a zero or non zero d value respectively. However the d parameter estimated for scenarios b and c are not the same as one would expect because of the use of the physical stiction model in generating the data. The reason for this is that the single parameter stiction model used in the detection algorithm is only an approximation of the physical stiction model. Nonetheless, stiction detection is not compromised.

Table 2. Validation Results

Scenario	Predicted stiction
No stiction case	d=0
Stiction alone case	d=3
Stiction and disturbance case	d=0.5

7. DISCUSSION

The proposed approach takes advantage of the fact that the stiction nonlinearity is discontinuous, whereas the process transfer function is continuous for stiction detection. It was shown that it might be possible to detect and isolate stiction in some cases in nonlinear SISO control loops when the process model is not known. However, extensive studies are needed before any definite conclusions can be drawn. There are several possible extensions to the proposed approach. The obvious ones include the use of two parameter stiction model for stiction quantification, the use of optimization algorithms such as GA for estimating the stiction parameters and validation with industrial data. Also, further theoretical work is needed to formalize the approach proposed in this paper.

8. CONCLUSIONS AND FUTURE WORK

In this paper, the problem of detection of stiction and isolation of stiction from external oscillations in nonlinear process control loops was addressed for the unknown model case. While Nallasivam and Rengaswamy [2008] have demonstrated the solution strategy for known nonlinear model case, almost no work exists in the case of unknown nonlinear processes. A solution approach for the unknown model case was proposed. The advantages and the limitations of the proposed approach were discussed.

It is essential to analyze the theoretical basis of the proposed method for using Volterra models. In addition, it would be interesting to study the use of Volterra second-order models to higher order nonlinear systems or linear systems. The former results in under-modeling of the original process while the latter results in over-modeling of the underlying linear process. We are in the process of developing a theoretical basis to analyze these interesting phenomena [Nallasivam et al. [2009]]. In future, the efficacy of the proposed approach along with the underlying theory needs to be further validated with other examples for different types of disturbances and different stiction models.

ACKNOWLEDGEMENTS

The authors thank the National Science Foundation (USA) for financial support for this work through the Grant CBET-0553992.

REFERENCES

W. L. Bialkowski. Dreams versus reality: A view from both sides of the gap. *Pulp and Paper Canada.*, 94(11):19–27, 1993.

M. A. A. S. Choudhury, M. Jain, and S. L. Shah. Stiction - definition, modelling, detection and quantification. *Journal of Process Control*, 18:232–243, 2008.

M. A. A. S. Choudhury, S. L. Shah, and N. F. Thornhill. Diagnosis of poor control loop performance using higher order statistics. *Automatica*, 40(10):1719–1728, 2004.

L. D. Desborough. Control loop economics. *Honeywell Proprietary report*, 2003.

L. D. Desborough and R. M. Miller. Increasing customer value of industrial control performance monitoring – honeywell's experience. Arizona, USA, 2001. CPC-VI.

F. J. Doyle, B. A. Ogunnaike, and R. K. Pearson. Nonlinear model-based control using second-order volterra models. *Automatica*, 31(5):697–714, 1995.

D. B. Ender. Process control performance: Not as good as you think. *Control Engineering*, 9:180–190, 1993.

Entech. Control valve dynamic specification. version 3.0. Entech Control, Division of Emerson Electric Canada Limited, Canada, Toronto, 2005.

M. Jelali. Estimation of valve stiction in control loops using separable least-squares and global search algorithms. *article in press, Journal of Process Control*, 2008.

R. M. Miller. Loop scout regulatory control performance study. *Honeywell*, unpublished report, 2000.

U. Nallasivam and R. Rengaswamy. Blind identification of stiction in nonlinear process. Seattle, USA, 2008. American Control Conference.

U. Nallasivam, B. Srinivasan, and R. Rengaswamy. On the detection of stiction in closed-loop systems. *Automatica*, to be submitted, 2009.

R. Rengaswamy, T. Hägglund, and V. Venkatasubramanian. A qualitative shape analysis formalism for monitoring control loop performance. *Engineering Applications of Arti.cial Intelligence*, 14:23–33, 2001.

R. Srinivasan, R. Rengaswamy, and R. M. Miller. Control loop performance assessment 1: A qualitative pattern matching approach for stiction diagnosis. *Industrial and Engg. Chemistry Research*, 44:6708–18, 2005a.

R. Srinivasan, R. Rengaswamy, U. Nallasivam, and V. Rajavelu. Issues in modelling stiction in process control valves. Seattle, USA, 2008. American Control Conference.

R. Srinivasan, R. Rengaswamy, S. Narasimhan, and R. M. Miller. Control loop performance assessment 2: Hammerstein model approach for stiction diagnosis. *Industrial and Engg. Chemistry Research*, 44:6719–28, 2005b.

Stochastic dynamical nonlinear behavior analysis of a class of single-state CSTRs

S. Tronci*, M. Grosso*, J. Alvarez*[+] and R. Baratti*

*Dipartimento di Ingegneria Chimica e Materiali, Università degli Studi di Cagliari, I-9123 Cagliari, Italy
(Tel: +39-0706755056; e-mail: tronci;baratti;grosso@ dicm.unica.it)
[+] On leave from Departamento de Ingenieria de Procesos e Hidraulica, Universidad Autonoma Metropolitana - Iztapalapa, 09340 Mexico D.F., Mexico (e-mail:jac@xanum.uam.mx)

Abstract: Motivated by the need of developing stochastic nonlinear model-based methods to characterize uncertainty for chemical process estimation, control, identification, and experiment design purposes, in this paper the problem of characterizing the global dynamics of single-state nonlinear stochastic system is addressed. An isothermal CSTR with Langmuir-Hinshelwood kinetics is considered as representative example with steady state multiplicity. The dynamics of the state probability distribution function (PDF) is modeled within a Fokker-Planck's (FP) global nonlinear framework, on the basis of FP's partial differential equation (PDE) driven by initial state and exogenous uncertainty. A correspondence between global nonlinear deterministic (stability, multiplicity and bifurcation) and stochastic (PDF stationary solution and mono/multimodality) characteristics is identified, enabling the interpretation of tunneling-like stationary-to-stationary PDF transitions, and the introduction of a bifurcation diagram with the consideration of stochastic features in the context of the CSTR case example.

Keywords: isothermal CSTR, multistability, nonlinear system, stochastic model, Fokker-Planck

1. INTRODUCTION

The study of stochastic nonlinear systems is motivated by the need of characterizing the effect of model uncertainty for model-based applications such as chemical process modeling, system identification, experiment design, estimation and control purposes, process safety assessment. While the deterministic approaches for nonlinear chemical processes are a rather mature field, the development of nonlinear stochastic approaches lags far behind. Deterministic descriptions suffice for chemical processes described by nonlinear models over the neighborhood of a steady-state (or nominal motion) for a continuous (or batch) process, but the same cannot be said for processes which evolve over ample (nonlocal) state-space domains, where nonlinearities become significant, and consequently, the inexorable presence of uncertainty due to measurement and modeling errors and its effect on the stability, observability and controllability features must be regarded within a stochastic global nonlinear framework. In chemical processes, the combination of measurement errors with high-frequency unmodeled dynamics manifests itself as random-like uncertainty, which imposes limits of estimation and control behavior.

In most of previous studies in chemical process engineering, the issue of uncertainty characterization has been performed with the so-called model sensitivity analysis with respect to initial values and/or parameters (Morbidelli and Varma, 1989, Dutta *et al*., 2001), on the basis of a linear model truncation. The drawback of this approach is that it does not allow the assessment of the combined effect of the uncertainties caused by the neglected nonlinear dynamics, which manifest itself when testing or implementing the model with the data generated by the actual nonlinear process (Horenko *et al.*, 2005).

In the nonlinear systems theory field, there are rather well established approaches to address the model uncertainty problem for multi-state nonlinear processes, with rigorous probability distribution function (PDF) evolution descriptions in terms of a set of Fokker-Planck (FP) partial differential equations (Risken, 1996). In fact, the nonlinear EKF estimator design can be seen as a second-order statistics approximation of the FP equation approach. However, in spite of being the EKF the most widely used estimation technique in chemical process systems engineering, its employment for uncertainty assessment purposes has been rather limited, and the consideration of the full nonlinear statistics FP equation approach has been circumscribed to a rather limited set of studies.

While the rigorous FP equation approach has been successfully applied in a diversity of problems in applied science, including physics, medical sciences (Mei *et al*., 2004; Lo, 2007), biology (Soboleva and Pleasants, 2003; Huang *et al*., 2008) and electronic circuits (Hanggi and Jung, 1988), in the chemical process systems engineering field only a few chemical reactor studies have been performed according to the FP equation approach. In a pioneering work, Pell and Aris (1969) studied the local-stochastic behavior of a

chemical reactor on the basis of a linear model truncation. In spite of the limited nature of the local results, recognized by the authors themselves, this work evidenced the benefit and possibilities of modeling the presence of random fluctuations within a stochastic framework. Later, Rao *et al.* (1974) addressed the same problem with a numerical algorithm to solve the associated nonlinear equation drawing nonlocal results and establishing that the linearization approach breaks down when the system is close to a saddle-node bifurcation. In a subsequent study, Ratto (1998) applied the FP equation approach to the linearization of a stable closed-loop reactor with PI temperature control subjected to measurement noise, sufficiently away from the possibility of Hopf bifurcations (whose consideration is a central point of the present study). This study evidenced the advantages of the FP equation-based theoretical approach (with quasi-analytical solutions), with respect to Monte Carlo methods (Ratto and Paladino 2000, Paladino and Ratto 2000, Sherer and Ramkrishna, 2008; Hauptmanns, 2008).

In the context of a combustion engineering science problem, Oberlack *et al.* (2000) studied the stationary solution of the FP equation associated to a multistable homogeneous adiabatic flow reactor described by a one-dimensional deterministic system. In spite of having addressed only the steady-state aspect of the problem, this study further evidenced the capabilities and possibilities of the FP equation-based approach to tackle the chemical reactor stochastic modeling problem. These considerations on the employment of the FP equation-based approach for the treatment of dynamical nonlinear systems, in general, and of chemical reactor, in particular, motivate the present study on the global-stochastic dynamical behavior of chemical reactors with emphasis on: the presence of multistability, transient behavior and the connection between deterministic and stochastic modeling approaches.

As an inductive step towards the development of nonlocal, global, nonlinear stochastic uncertainty characterization methodology, in this work the problem of characterizing the concentration stochastic dynamical behavior of single-state nonlinear isothermal CSTR with Langmuir-Hinshelwood kinetics as representative case example with multistability phenomena has been addressed. The problem is treated within a global-nonlinear framework by combining deterministic multiplicity and bifurcation analysis tools with a FP equation-based stochastic behavior characterization, in the light of the particular system characteristics. The stochastic dynamical behavior is studied by looking at the response solution of the dynamic FP partial differential equation (PDE) to: (i) initial state uncertainty and (ii) modeling error described as a white noise exogenous input injection. As a result, a correspondence between stochastic features (mono or multimodality, potential, quasi-stability, and escape time) and deterministic features (stability, multiplicity and bifurcation) is established, enabling a better understanding of the nonlinear stochastic behavior and opening the possibility of extending the approach to multi-state chemical processes.

2. THE STOCHASTIC MODEL

Consider the single-state (x) nonlinear stochastic dynamical system:

$$\dot{x} = f[x, u(t)] + w(t), \quad x(0) = x_o, \qquad w(t) \sim N[0, q(x)] \qquad (1)$$
$$x \in X = [0, \infty)$$

with exogenous deterministic input u, and driven by input uncertainty modeled as white noise with intensity $q(x)$. In the absence of noise, with $w(t) = 0$, the (single or multiple) steady-states satisfy, for the nominal input $\bar{u}$, the static-algebraic equation $f(\bar{x}, \bar{u}) = 0$. Due to the nonlinearity of $f(x)$, the deterministic system (i.e. when $w(t)=0$) can show structural instability, meaning the existence of steady-state bifurcation points as system parameters or inputs are varied. In the one-dimensional case, the more generic bifurcation is the saddle-node, which may imply the presence of multistability regions. This means that the deterministic system reaches one of the stable equilibrium points, depending on initial conditions and system input (Wiggins, 1990). Assuming the noise intensity $q(x)$ is constant for a fixed value of the input, $u(t) = \bar{u}$, the dynamics of the concentration (normalized) probability density function (PDF) $p(x,t)$ is governed by the Fokker-Planck partial differential equation (Risken, 1996):

$$p_t(x, t) = [d\, p_x(x, t)]_x - \{f(x, \bar{u})\, p(x, t)\}_x, \; 0 \le x < \infty, \; t > 0 \qquad (2a)$$

$$x = 0: \; d\, p_x(0, t) - f(0, \bar{u})\, p(0, t) = 0, \quad x = \infty: \; p_x(\infty, t) = 0 \qquad (2b\text{-}c)$$

$$t = 0: \; p(x, 0) = p_0(x), \qquad d = q^2/2 \qquad (2d)$$

where d is the "diffusion constant" set by the noise intensity, (2b)-(2c) is the boundary condition pair and (2d) is the initial condition with initial PDF p_o. Condition (2b) establishes that x can have only positive values (Gardiner, 1997), in the understanding that this condition is easily met by writing the chemical process states in suitable scales.

2.1 Stationary probability density function

The stationary solution of (2) is given by:

$$p_s(x) = N_0 e^{-\frac{\phi(x)}{d}}, \quad \phi(x) = -\int_x f(s)ds \qquad (3a\text{-}b)$$

where N_0 is the integration constant associated to the normalization of $p_s(x)$ and $\phi(x)$ is the potential function.

From the examination of the stationary solution (3) in the light of multiplicity features of the deterministic system, the next conclusions follow. When the deterministic system has a unique global attractor $\bar{x} \in X$, the potential function $\phi(x)$ has a single well shape with minimum at $\bar{x}$, and the stationary PDF $p_s(x)$ is monomodal with maximum at $\bar{x}$, meaning that the solution $\bar{x}$ is the more probable state over X. As noise intensity decreases (d tends to zero) the monomodal PDF tends to the Dirac Delta function $\delta(x - \bar{x})$ about $\bar{x}$. When the deterministic system has multiple steady state $\bar{x}_1, \ldots, \bar{x}_m \in X$,

with domains of attraction $X_1,\ldots, X_m$ such as $\bigcup_{i=1}^{m} X_i = X$: (i) the potential function $\phi(x)$ has a multi well shape potential with minima at $\bar{x}_1,\ldots, \bar{x}_m$, (ii) the multivalued stationary PDF $p_s(x)$ has maxima at $\bar{x}_1,\ldots, \bar{x}_m$, (iii) the most probable steady state solution is the one with the deepest potential well $\phi(\bar{x}_m)$ and therefore with the largest maximum, and (iv) the difference among PDF maxima grows exponentially with the decrease of d. As a consequence of (iv), at low d values the distribution appears monomodal and tends to a Dirac Delta when the noise intensity tends to zero. Multimodality is maintained, even at low d values, when the potential minima are equal and in this case the limit as d tends to zero is a multi Dirac Delta.

2.3 *Probability distribution function evolution*

The right hand side of (2a) can be written as follows:

$$p_t = d\, p_{xx} - f(x, \bar{u})\ p_x - f_x(x, \bar{u})\, p \tag{4}$$

evidencing that: (i) the shape of the PDF over time is due to a source/sink mechanism $-f_x\ p$ combined with two transport mechanisms, one diffusive $d\ p_{xx}$ and one convective $-f\ p_x$, and (ii) the PDF temporal evolution is obtained by giving an initial value $p(x,0) = p_0(x)$ and integrating numerically the FP equation. If the deterministic system has a unique global attractor, the potential function has a single minimum, and the PDF reaches asymptotically a monomodal distribution, regardless the initial PDF shape. Otherwise, when there is deterministic steady-state multiplicity with multiple potential minima, the PDF evolution may exhibit some behaviors, which seem atypical from a deterministic nonlinear system perspective. In fact, the PDF settles at some multimodal PDF with largest maximum at (probability around) the attractor $\bar{x}_1$, then after some time, the PDF eventually starts moving and reaches another multimodal shape with a different largest maximum at (probability around) the attractor $\bar{x}_2$. In fact, for the case of steady-state multiplicity with an asymptotic (stationary) bimodal PDF, the time necessary for a state x at the steady state $x = \bar{x}_1$, with domain of attraction X_1, to escape to the steady-state $x=\bar{x}_2$, with domain of attraction X_2, is approximated by the formula (Gardiner, 1997):

$$T \propto \exp[(\phi(\bar{x}_2)-\phi(\bar{x}_1))/d] \tag{5}$$

which resembles Arrhenius' equation in chemical kinetics.

Thus stationary-to-stationary ($\bar{x}_1$-to-$\bar{x}_2$) state transition probability is favored by: i) a small well potential difference $[\phi(\bar{x}_1)-\phi\bar{x}_2)]$ and (ii) a well potential with large minima. When the minima have the same ordinate, there is not a dominant attractor and the probability of leaving one of the wells is the same.

3. STOCHASTIC MODEL OF AN ISOTHERMAL CSTR

3.1 CSTR with Langmuir-Hinshelwood kinetics

As a representative example in catalytic reactors, let us consider an isothermal CSTR with Langmuir – Hinshelwood kinetics, with the corresponding mass balance being described by the nonlinear differential deterministic system:

$$\dot{x} = f(x, Da, \sigma),\ x(0) = x_o, \tag{6}$$
$$f(x, Da, \sigma) = (1 - x) - Da(1 + \sigma)^2\, x/(1 + \sigma x)^2$$
$$x = c/c_i,\quad \tau = t/(V_R/Q),\quad Da = (V_R/Q)k/(1 + \sigma)^2,\ \sigma = K\, c_i.$$

x is the dimensionless concentration (referred to the feed concentration c_i), t and τ are, respectively, the actual and dimensionless time, Q the volumetric feedrate, V_R the reactor volume, k the reaction-rate constant, K the equilibrium adsorption constant and Da the Damkohler number. In spite of its simplicity, the above single-state system exhibits a rather rich behavior over the parameter space pair (Da, σ), showing multiple steady-states for a specified range of parameter values. In the case of multiplicity, there are two (low and high concentration) stable steady-states and one (intermediate concentration) unstable steady-state. Moreover system (6) captures the important nonlinearities which underline the lack of global and local observability at the value $x = 1/\sigma$ (where the reaction rate is maximum), in the understanding that this feature makes difficult the design of nonlinear observers and controllers of an important class of chemical reactors with nonmonotonic kinetics (Schaum *et al*., 2008).

The stochastic system associated to the deterministic reactor (6) is given by (1) replaced by $f(x,Da,\sigma)$, and the corresponding stationary PDF is given by:

$$p_s(x) = N_0 \exp\left[-\frac{1}{d}\left(-x + \frac{x^2}{2} + \frac{Da(1+\sigma)^2}{\sigma^2(1+\sigma x)} + \frac{Da(1+\sigma)^2 \ln(1+\sigma x)}{\sigma^2}\right)\right]. \tag{7}$$

3.1 *Deterministic nonlinear dynamics*

The bifurcation analysis of system (6) evidences the occurrence of saddle-node bifurcation when $Da > 0$ (see Figure 1) and, on the parameter space (Da, σ), the deterministic reactor steady-state (SS) exhibits either: (i) a unique global attractor $\bar{x}$ with domain of attraction X[0, 1], or (ii) three-SS multiplicity, with two (low and high concentration) stable and one (intermediate concentration) unstable steady-state.

In the multiplicity case, there are two basins of attraction (X_1 and X_2), one per attractor. Thus, in the single SS case any state motion $x(t)$ beginning in $x_0 \in X$ remains in X, and asymptotically converges to the steady state $\bar{x}$ in X (see Figure 2a):

$$x_o \in X = [0, 1] \Rightarrow\ x(t) \in X,\ x(t) \to \bar{x}$$

In the three-SS case (with two stable attractors $\bar{x}_i$, i = 1, 2 with domain of attraction X_i) any state motion $x(t)$ beginning in $x_o \in X_i$ remains in X_i, and asymptotically converges to the steady-state $\bar{x}_i$ in X_i, this is (see Figure 2b):

$$x_o \in X_i = [0, 1] \Rightarrow x(t) \in X_i,\ x(t) \to \bar{x}_i,\ i = 1, 2$$

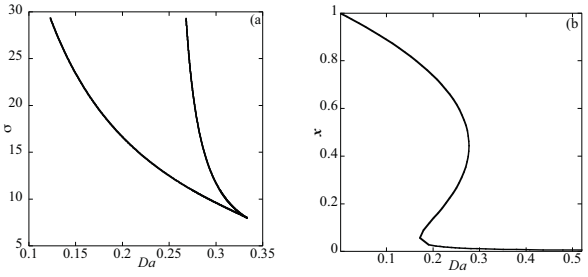

Figure 1: a) bifurcation diagram of system (6) and b) corresponding solution diagram at σ=20.

In particular, for σ = 20, the deterministic reactor system (6) exhibits: (i) a low (or high) concentration unique global attractor for $0 < Da < Da^- \approx 0.172$ (or $Da > Da^+ \approx 0.277$), (ii) three steady-states for $Da^- < Da < Da^+$, and (iii) two saddle-node bifurcations at Da equal to Da^- and Da^+ (see Figure 1).

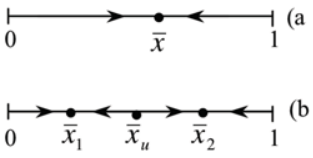

Figure 2: Phase diagram (a) in the single-SS case and (b) in the three-SS case.

3.2 *Stationary stochastic behavior*

The stationary (asymptotic) behavior of the PDF which satisfies the FP equation was investigated by setting σ equal to 20 (cf. Section 3.1), varying the value of Damkohler number $0 < Da < 1.0$ and the noise-related diffusion coefficient $10^{-5} < d < 10^{-3}$ (Ratto, 1998). The normalization constant in (3a) was calculated through the orthogonal collocation method on finite elements.

In Figure 3a (or 3b) the stationary PDF for $Da = 0.226$ (or $Da = 0.231$) with three SSs and two attractors, for two noise levels $d = 5.0\ 10^{-4}$ (continuous line) and $5.0\ 10^{-3}$ (dashed line) is shown. At the lowest d value only one peak is clearly detectable at $x \approx 0.683$ (or $x \approx 0.0178$), while the second peak corresponding to $x \approx 0.018$ (or $x \approx 0.671$) becomes evident only at the highest d value.

In Figure 4a (or 4b) is presented the potential function $\phi(x)$ (or stationary PDF for $d = 10^{-4}$) at three values of Da: 0.226 (dotted line), 0.229 (continuous line), and 0.231 (dashed line). In accordance with the deterministic bistability properties there are two attracting minima for the potential $\phi(x)$, meaning the possibility of well-to-well steady-state transition with longer residence in the deepest well. As expected, at low diffusion value only one peak is clearly visible for $Da = 0.226$ (extinction) and for $Da = 0.231$ (ignition). When the two minima have the same value, $Da \approx 0.229$, the stationary PDF exhibits bimodality made of nearly non overlapping monomodal PDFs or equivalently, a well-to-well potential without a dominant attractor.

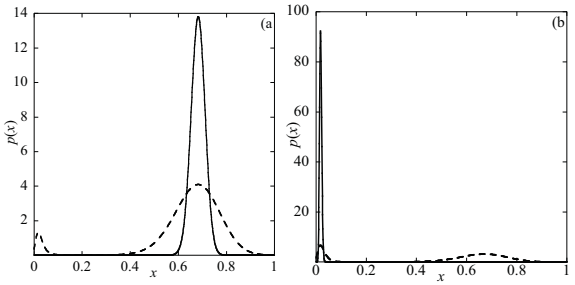

Figure 3: Stationary PDF when a) $Da = 0.226$ and b) $Da = 0.231$ for $d = 5.0\ 10^{-4}$ (solid line) and $d = 5.0\ 10^{-3}$ (dashed line).

The latter case could be considered as an important bifurcation characteristic related to the stochastic behavior, and not to the deterministic one. This Damkohler critical number Da_C is determined by the enforcement of the next equipotential conditions:

$$\left.\frac{d\phi}{dx}\right|_{(\bar{x}_1;Da_C)} = \left.\frac{d\phi}{dx}\right|_{(\bar{x}_2;Da_C)} = 0 \qquad (\bar{x}_1 \neq \bar{x}_2)$$
$$\phi(\bar{x}_1;Da_C) = \phi(\bar{x}_2;Da_C) \qquad (8)$$

In conclusion, the Da_C value corresponds to a transition between two qualitatively different behaviors of the stochastic reactor system. This transition appears smooth for high d values, meaning that a bimodal distribution is apparent in a wider neighborhood of Da_C, and becomes sharper as the diffusion coefficient tends to zero.

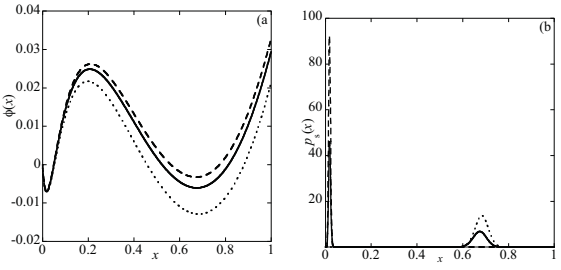

Figure 4: a) Potential function and b) stationary PDF (d=10^{-4}) for different Da values: Da=0.226 (dotted line), Da=0.229 (solid line), Da=0.231 (dashed line).

The one-dimensional manifold satisfying (8) can be derived by resorting to standard continuation algorithms (Doedel *et*

al., 1997), and the stochastic bifurcation diagram, over the (*Da*-σ) plane, was constructed and reported in Figure (5) together with the bifurcation diagram of (6).

Observe that the passage from the deterministic (Figure 1a) to the stochastic (Figure 5) bifurcation diagram evidences: (i) the correspondence between the deterministic steady-state and stochastic stationary nonlinear features, and (ii) the kind of information contained in the stochastic diagram and not in the deterministic one.

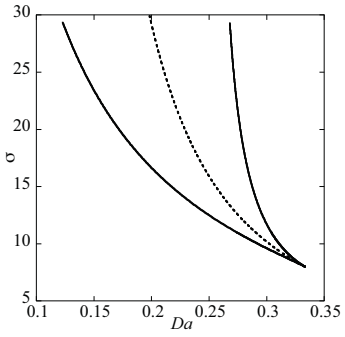

Figure 5: Diagram of the saddle-node bifurcation of the deterministic system (solid line) and the (Da_C, σ) curve (dashed line).

3.3 *Dynamic behavior*

According to the preceding developments, in a deterministic framework, the domain of attraction determines the steady-state which will be reached asymptotically by the system. However, from a stochastic point of view it may happen that one of the deterministic steady states has a low or negligible asymptotic probability of being reached, regardless the initial condition.

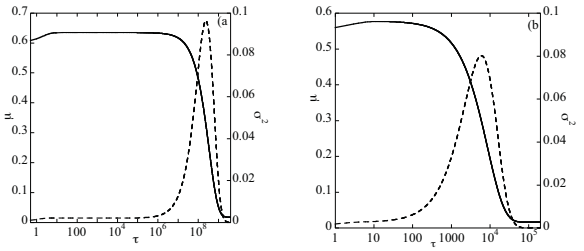

Figure 6: Dynamic behavior of mean (solid line) and variance (dashed line) of the PDF when $d = 10^{-3}$ at a) Da = 0.244 and b) Da = 0.260. The time scale is logarithmic.

Figure 6 represents the transient of mean and variance of the probability distribution function when $d = 10^{-3}$, and the initial condition is a Gaussian distribution with mean equal to 0.6 and variance equal to 0.02, at Da = 0.244 (Figure 6a) and Da = 0.260 (Figure 6b). In both cases, the absolute minimum of the potential function is positioned on the lower branch of the solution diagram, but the initial distribution is inside of the basin of attraction of the other solution, meaning that the probability that the initial condition is outside the weaker attractor is almost negligible.

The responses of the PDF show that during the transient, the mean of the distribution does not directly move towards its steady state value in the ignited zone, but first approaches the higher solution. It should be noted that, at Da = 0.244 (Figure 6a), mean and variance are almost constant for a wide interval of time (the time scale in Figure 6 is logarithmic), looking as if a stable stationary solution was definitely reached. Thus, the high concentration solution appears as a *quasi-stationary* solution. In other words, only after a long transient the system departs from the extinction steady-state and eventually reaches the ignited region. The variance reaches a maximum during the transition from the quasi-stationary to the stationary solution, implying that the PDF becomes bimodal with its two peaks corresponding to the two deterministic attractors. As time elapses, one of the peaks becomes negligible and the other one finally prevails. When Da = 0.260 (Figure 6b), the system again moves first towards the solution contained in the attraction basin where the initial distribution is centered (low conversion solution), but after a while the mean starts decreasing towards its stationary value. Some snapshots of the evolving probability distribution are shown in Figure 7 for Da = 0.244. It must be pointed out that the *quasi-stationary* condition duration can range from several to orders of magnitude the reactor natural deterministic dynamics (set by the residence time), depending on the noise intensity, and this is a fact that must be carefully accounted for in long-term prediction assessments, with applicability in safe process design.

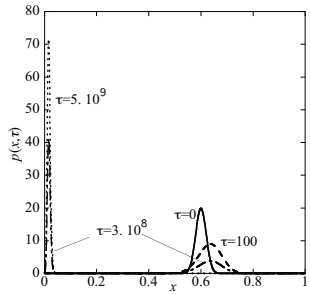

Figure 7: Snapshots of the PDF at τ=0 (solid line), τ =100 (dashed line), τ =3.0 10^8 (dashed-dotted line) and τ =5.0 10^9 (dotted line).

The duration of the *quasi-stationary* state can be related to the escape time, evaluated by means of (5). Calculating the escape time for Da = 0.244 and Da = 0.260 we found, respectively, T_1=4.3 10^8 and T_2=8.4 10^3. These results establish that stationary conditions are reached for a time greater than the calculated escape time, as confirmed by the simulation. The decreasing of the escape time as Da approaches the bifurcation value reflects the fact that the relative minimum is less and less deep until it disappears at the bifurcation point.

6. CONCLUSIONS

The global-nonlinear stochastic behavior of the concentration in an isothermal CSTR reactor with multistability has been characterized on the basis of standard deterministic tools in conjunction with FP equation theory. In addition to issues considered in previous studies in chemical reactor (Pell and Aris, 1969; Ratto 1998) and combustion engineering (Oberlack, 2000), in this study the presence of multistability, transient behavior, and the connection between deterministic and stochastic modeling approaches were considered. In particular, the interplay between the stochastic (mono or multimodality, potential, quasi-stability, and escape time) and deterministic (stability, multiplicity and bifurcation) features was identified. The stationary analysis revealed that, even when multistability was expected for the deterministic model, the probability distribution function usually appeared as monomodal, indicating that there is one dominant attractor, with higher probability of being reached asymptotically. However, the occurrence of multi-stabilities in the deterministic model did affect the behavior of the transient dynamics and the system could stay in a neighborhood of the weaker attractor for a long time interval, thus appearing as a *quasi-stationary* state.

The results of this paper constitute a point of departure: (i) to study the multi-state nonlinear stochastic system case, and (ii) to explore the implications and applications for global nonlinear estimation, control, and safe process designs.

*A*cknowledgement.

J. Alvarez kindly acknowledges Regione Sardegna for the support, through the program "Visiting Professor 2008", for the realization of this work at the Dipartimento di Ingegneria Chimica e Materiali of the University of Cagliari.

REFERENCES

Doedel, E. J., Champneys, A. R., Fairgrieve, T. F., Kuznetsov, Y. A., Sanstede, B., and Wang, X., (1997). "AUTO97: continuation and bifurcation software for ordinary differential equations".

Dutta, S., Chowdhury, R., and Bhattacharya, P., (2001). Parametric sensitivity in bioreactor: an analysis with reference to phenol degradation system. *Chem. Eng. Sci*., 56, 5103-5110.

Gardiner, C. W., (1997). *Handbook of stochastic methods*. Springer-Verlag, Germany.

Hanggi, P. and Jung, P., (1988). Bistability in active circuits: Application of a novel Fokker-Planck approach. *IBM J. Res. Develop*., 32(1), 119-126.

Hauptmanns, U., (2008). Comparative assessment of the dynamic behaviour of exothermal chemical reaction including data uncertainties. *Chem. Eng. J*., 140, 278-286.

Horenko, I., Lorenz, S., Schutte, C., and Huisinga, W., (2005). Adaptive approach for nonlinear sensitivity analysis of reaction kinetics. *J. Comp. Chem.*, 26(9), 941-948.

Huang, D. W., Wang, H. L., Feng, J.F. , and Zhu, Z.W., (2008). Modelling algal densities in harmful algal blooms (HAB) with a stochastic dynamics. *Applied Mathematical Modelling,* 32(7), 1318-1326.

Lo, C. F., (2007). Stochastic Gompertz model of tumor cell growth. *Journal of Theoretical Biology* 248, 317-321.

Mei, D. C., Xie , C.W. and Zhang, L., (2004). The stationary properties and the state transition of the tumor cell growth model. *European Physical Journal B* 41(1) 107-112.

Morbidelli, M., and Varma, A., (1989). A generalized criterion for parametric sensitivity: Application to a pseudohomogeneous tubular reactor with concecutive or parallel reactions. Chem. Eng. Sci., 44, 1675-1696.

Oberlack, M., Arlitt, R., and Peters, N., (2000). On stochastic Damkohler number variations in a homogeneous flow reactor. *Combust. Theory Modelling*, 4, 495-509.

Paladino, O., and Ratto, M., (2000). Robust stability and sensitivity of real controlled CSTRs. *Chem. Eng. Sci*., 55, 321-330.

Pell, T. M., and Aris, R., (1969). Some problems in chemical reactor analysis with stochastic features. *I&EC Fundamentals*, 8(2), 339-345.

Rao, N. J., Ramkrishna, D., and Borwanker, J. D., (1974). Nonlinear stochastic simulations of stirred tank reactors. *Chem. Eng. Sci*., 29, 1193-1204.

Ratto, M., (1998). A theoretical approach to the analysis of PI-controlled CSTRs with noise. *Comp. Chem. Eng.*, 22(11), 1581-1593.

Ratto, M., and Paladino, O., (2000). Analysis of controlled CSTR models with fluctuating parameters and uncertain parameters. *Chem. Eng. Sci*., 79, 13-21.

Risken, H., (1996). *The Fokker-Planck equation: Methods of solutions and Applications*. Springer-Verlag, Berlin.

Schaum A, Moreno J. A., Díaz-Salgado, J., and Alvarez J. (2008). Dissipativity-based observer and feedback control design for a class of chemical reactors. *Journal of Process Control*, 18(9): 896–905

Sherer E., Ramkrishna, D., (2008). Stochastic analysis of multistate systems. *Ind. Chem. Eng. Res*., 47(10), 3430-3437.

Soboleva, T. K., and Pleasants, A.B., (2003). Population growth as a nonlinear stochastic process. *Mathematical and Computer Modelling,* 38(11-13), 1437-1442.

Wiggins, S., (1990). *Introduction to applied nonlinear dynamical systems and chaos*, Springer-Verlag, New York.

Process Control and Optimization

Poster Session

Nonlinear Model Predictive Control Using Multiple Shooting Combined with Collocation on Finite Elements

Jasem Tamimi and Pu Li

Simulation and Optimal Processes Group, Institute of Automation and Systems Engineering, Ilmenau University of Technology, P. O. Box 10 05 65, 98684 Ilmenau, Germany. (Tel.:+49-3677-691427, e-mail:{jasem.tamimi/pu.li}@tu-ilmenau.de)

Abstract: A new approach to nonlinear model predictive control (NMPC) is proposed in this paper. The multiple shooting method is used for discretizing the dynamic system, through which the optimal control problem is transformed to a nonlinear program (NLP). To solve this NLP problem state variables and their gradients at the end of each shooting need to be computed. Here we employ the method of collocation on finite elements to carry out this task. Due to its high numerical accuracy, the computation efficiency for the integration of model equations can be enhanced, in comparison to the existing multiple shooting method where an ODE solver is applied for the integration and the chain-rule for the gradient computation. The numerical solution framework is implemented in C++. Two examples are taken to demonstrate the effectiveness of the proposed NMPC algorithm.

Keywords: Optimal control, NMPC, multiple shooting, collocation on finite elements.

1. INTRODUCTION

Solving optimal control problem is highly motivated nowadays, since these solutions are very important in almost all industrial fields such as chemical, electrical, mechanical, and economical systems. One of the optimal control algorithms is MPC which refers to a class of computer control strategies that utilize an explicit process model to predict the future response of the plant (Qin and Badgwell, 2003). MPC, also known as receding horizon control, has the ability to handle input as well as output constraints and transparent tuning capabilities (Gatlu and Zafiriou, 1992).

The main goal of MPC is to find an optimal vector of control functions that minimize or maximize a performance index subject to a given process model (usually a nonlinear differential equation system) as equality constraints, and boundary conditions as inequality constraints on the states and controls. Simple problems can be solved by the so-called *indirect method* which is based on the first order optimality condition of variation (Diehl *et al.,* 2006, Schäfer *et al.*, 2007). This leads to a two-point-boundary value problem in ordinary differential equations (ODE). For more details see e.g. Bryson and Ho (1975), Kirk (1970), and Lewis and Syrmos (1995).

On the other hand, the *direct method* which follows the philosophy of "first discretize then optimize", transforms the optimal control problem into a NLP problem which can then be solved by the method of sequential quadratic programming (SQP). In this way inequality constraints and equality path constraints can be easily treated, and we can also successfully deal with highly nonlinear complex optimal control problems (Diehl *et al.*, 2006, Schäfer *et al.*, 2007).

In all direct methods, the control trajectory will be parameterized and the state trajectories computed using either sequential or simultaneous approaches. In the *sequential approach*, the state variables are considered as an implicit function of control trajectories, where the ODEs are addressed as an initial value problem using one of the dedicated integration methods like Runge-Kutta or Euler algorithms (Sargent and Sullivan, 1977; Kraft, 1985; Biegler *et al.,* 2002). In the *simultaneous approach*, state trajectories are parameterized, too, and we deal with all of parameterized variables (states and controls) as optimization variables in the NLP. The ODEs will be represented as equality constraints, either with collocation on finite elements (Biegler *et al.,* 2002; Hong *et al.,* 2006; Li, 2007) or with multiple shooting (Bock and Plitt, 1984; Leineweber, 1995; Diehl, 2001; Diehl *et al.,* 2002a; Diehl *et al*., 2002b).

In this work, we propose a new approach to the solution of nonlinear model predictive control (NMPC) problems. This control strategy is a combination of the multiple shooting and the collocation method. We use multiple shooting for discretizing the dynamic system, so that the optimal control problem is transformed to a NLP problem in which continuity conditions in each shooting are considered as equalities and state constraints at the end of each shooting as inequalities. To solve this NLP problem the values of state variables and their gradients at the end of each shooting have to be computed. Here we employ collocation on finite elements to carry out this task. Due to its high numerical accuracy, the computation efficiency for the integration of the ODEs can be enhanced, in comparison to the existing multiple shooting method where an ODE solver is applied for the integration and chain-rules for the gradient computation. We implement the proposed approach with a numerical solution framework in C++. Two examples are taken to demonstrate the effectiveness of the proposed NMPC algorithm. The results from our approach are compared with

those achieved from the multiple shooting method (using the software MUSCOT II (Diehl *et al.*, 2001)).

2. NONLINEAR MODEL PREDICTIVE CONTROL

2.1 Optimal control problem

We will consider the following optimal control problem

$$\min \int_{t_0}^{t_f} L(x(t),u(t),t)dt + E\left(x(t_f)\right)$$

s.t.

$$\begin{aligned} &\text{(i)} && x(t_0) = x(0), \\ &\text{(ii)} && \dot{x}(t) = f(x(t),u(t),t),\ t \in [t_0,t_f] \\ &\text{(iii)} && g(x(t),u(t),t) \geq 0\ ,\ t \in [t_0,t_f] \\ &\text{(iv)} && r\left(x(t_f)\right) = 0, \end{aligned} \tag{1}$$

where $x(t), u(t)$ are the state and control variables, respectively, t_0 and t_f are initial and final time of the receding horizon, and constraint (i) is the initial value condition, (ii) the nonlinear ODE model, (iii) the path constraint, and (iv) the terminal constraint.

2.2 Direct multiple shooting scheme

The direct multiple shooting algorithm proposed by Bock and Plitt (1984) for solving problem (1) can be summarized in the following steps:

1) Discretize the time horizon $[t_0, t_f]$ into equal subintervals $[t_i, t_{i+1}]$, such that

$$t_0 < t_1 < \cdots < t_n = t_f \tag{2}$$

where *n* is the total number of subintervals.

2) Parameterize the control function $u(t)$ for each subinterval:

$$u(t) = v_i \quad for \quad t \in [t_i, t_{i+1}] \tag{3}$$
$$i = 0,1,\dots,n-1$$

3) Parameterize the initial condition of the state vector for each subinterval:

$$x(t_i) = h_i \tag{4}$$
$$i = 0,1,\dots,n-1$$

4) Evaluate the state trajectories in each subintervals and the value of h_i from the final state subinterval considering the parameterized state initial value in the previous step:

$$\dot{x}_i(t) = f(x_i(t),v_i,t),\ t \in [t_i, t_{i+1}] \tag{5a}$$
$$x_i(t_i) = h_i \tag{5b}$$

5) Define the continuity constraints:

$$h_{i+1} - x_i(t_{i+1}; h_i, v_i) = 0 \tag{6}$$

6) Compute the objective function for each subinterval, so we need to solve the following NLP

$$\min_{h_i,v_i} \sum_{i=0}^{n-1} \int_{t_i}^{t_{i+1}} L(x_i(t),v_i)dt + E\left(x_n(t_n)\right)$$

s.t. (7)

$$h_0 - x(0) = 0$$
$$h_{i+1} - x_i(t_{i+1}; h_i, v_i) = 0,\ i = 0,1,\dots,n-1,$$
$$g(h_i, v_i) \geq 0$$

Eq. (7) can be described as

$$\min_w\ A(w) \qquad s.t. \qquad \begin{cases} B(w) = 0 \\ C(w) \geq 0 \end{cases} \tag{8}$$

where $w = [h_0, v_0, h_1, v_1, \dots, h_n, v_{n-1}]$,

$$B(w) = \begin{bmatrix} h_0 - x(0) \\ h_1 - x_0(t_1; h_0, v_0) \\ \vdots \\ h_{n-1} - x_{n-2}(t_{n-1}; h_{n-2}, v_{n-2}) \end{bmatrix},$$

$$C(w) = \begin{bmatrix} g(h_0, v_0) \\ g(h_1, v_1) \\ \vdots \\ g(h_{n-1}, v_{n-1}) \end{bmatrix}.$$

We can use the spars nonlinear optimizer (SNOPT) to solve the above NLP problem. In SNOPT equality constrains will be transformed into inequality constraints by introducing a set of slack variables, i.e.

$$\min_w A(w)$$

s.t. (9)

$$\left(\begin{pmatrix} B(w) \\ C(w) \end{pmatrix} - s = 0\right), \text{ and } \ l \leq \begin{pmatrix} w \\ s \end{pmatrix} \leq u$$

where $s = (s_0, \cdots, s_{n-1}, s_n, \cdots s_{2n-2})^T$. For more information on SNOPT see Gill *et al.* (2005) and Gill *et al.* (2008). Consequently, problem (8) can now be rewritten as:

$$\min_w A(w)$$

s.t. (10)

$$l \leq D(w) \leq u$$

$$\text{where, } D(w) = \begin{bmatrix} h_0 - x(0) \\ h_1 - x_0(t_1; h_0, v_0) \\ \vdots \\ h_{n-1} - x_{n-2}(t_{n-1}; h_{n-2}, v_{n-2}) \\ g(h_0, v_0) \\ g(h_1, v_1) \\ \vdots \\ g(h_{n-1}, v_{n-1}) \end{bmatrix},$$

$$l = \begin{bmatrix} l_0 \\ \vdots \\ l_{n-1} \\ l_n \\ \vdots \\ l_{2n-2} \end{bmatrix} = \begin{bmatrix} 0 \\ \vdots \\ 0 \\ 0 \\ \vdots \\ 0 \end{bmatrix} and\ u = \begin{bmatrix} u_0 \\ \vdots \\ u_{n-1} \\ u_n \\ \vdots \\ u_{2n-2} \end{bmatrix} = \begin{bmatrix} 0 \\ \vdots \\ 0 \\ \infty \\ \vdots \\ \infty \end{bmatrix}.$$

2.3 SQP iteration

Fig. 1 shows all of the information needed for each SQP iteration.

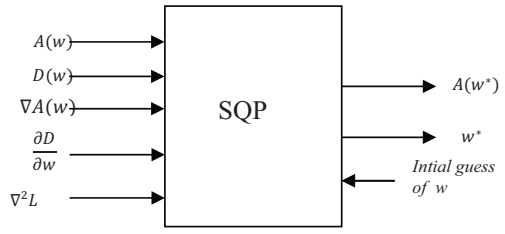

Fig. 1: Inputs and outputs of each SQP iteration.

In Fig. 1, $\nabla A(w)$ and $\frac{\partial D}{\partial w}$ are the gradient of the objective function and Jacobian of the equality constraints in (7), respectively. $A(w^*)$ and w^* are the objective function value and the optimization variables at the solution. ∇^2L denotes the Hessian of the Lagrangian. The sensitivity information, i.e. $\nabla A(w)$ and $\frac{\partial D}{\partial w}$, plays the most important role in the SQP iteration and its computation requires much CPU-time. In the existing multiple shooting algorithm it is done by integrating the ODEs with an ODE solver and then using the chain-rule for the sensitivity computation. In this work we employ the method of collocation on finite elements to carry out the ODE integration and compute these sensitivities for each shooting. This proposed method is described in the next section.

3. SOLVING ODE AND SENSITIVITIES

To solve NLP (9) we have to solve the set of ODEs (5a). If we use piece-wise constant parameters for v_i, we can rewrite the ODE in each subinterval as

$$\begin{pmatrix}\dot{x}_i(t)\\ \dot{v}_i\end{pmatrix} = \begin{pmatrix}f(x_i(t), v_i, t)\\ 0\end{pmatrix} \Rightarrow \begin{matrix}\dot{z}_i = f(z_i(t), t)\\ z_i(t_i) = [x_i\ v_i]^T\end{matrix} \quad (11)$$

Using collocation method the state variables $z_i(t)$ will be approximated by the following Lagrangian polynomials (Finlayson, 1980)

$$z(t) = \sum_{j=0}^{M}\left[\prod_{\substack{k=0\\ j\neq k}}^{M}\frac{(t-t_k)}{(t_j-t_k)}\right] z_j \quad (12)$$

where M is the number of the collocation points. Using the three-point-collocation to compute the vector z, we yield

$$z(t) = T_0 z_0 + T_1 z_1 + T_2 z_2 + T_3 z_3 \quad (13)$$

where $T_j = \prod_{\substack{k=0\\ k\neq j}}^{3}\frac{t-t_k}{t_j-t_k}$.

To define the end time point of a subinterval to be the beginning point of the next one, we yield inside each shooting

$$t_0 = t_i, \quad t_1 = \alpha_1(t_{i+1} - t_i),$$
$$t_2 = \alpha_2(t_{i+1} - t_i), \text{ and } t_3 = t_{i+1} \quad (14)$$

where $\alpha_1 = 0.127$ and $\alpha_2 = 0.5635$. Then

$$\dot{T}_{i,k} Z_{i,k} + \dot{T}_{i,0} Z_{i,0} - f_{i,k}(z_i(t), t) = 0 \quad (15)$$

where $T_{i,k} = \begin{bmatrix} T_{i,1}(t_1) & T_{i,2}(t_1) & T_{i,3}(t_1)\\ T_{i,1}(t_2) & T_{i,2}(t_2) & T_{i,3}(t_2)\\ T_{i,1}(t_3) & T_{i,2}(t_3) & T_{i,3}(t_3)\end{bmatrix}, Z_{i,k} = \begin{bmatrix} z_{i,1}\\ z_{i,2}\\ z_{i,3}\end{bmatrix}$

$$T_{i,0} = \begin{bmatrix} T_{i,1}(t_0) & 0 & 0\\ 0 & T_{i,2}(t_0) & 0\\ 0 & 0 & T_{i,3}(t_0)\end{bmatrix}, Z_{i,0} = \begin{bmatrix} z_{i,0}\\ z_{i,0}\\ z_{i,0}\end{bmatrix}$$

We solve the nonlinear equations (15) on the collocation points by using the Newton-Raphson method to find $Z_{i,k}$ and z_i. The first Taylor-expansion of (15) leads to

$$\dot{T}_{i,k}\frac{\partial Z_{i,k}}{\partial z_{i,0}} + \dot{T}_{i,0} - \frac{\partial f_{i,k}(z_i(t),t)}{\partial z_{i,0}} = 0 \quad (16)$$

We define $\frac{\partial Z_{i,k}}{\partial z_{i,0}} = \Psi_{i,k}$, then

$$\dot{T}_{i,k}\Psi_{i,k} + \dot{T}_{i,0} - \frac{\partial f_{i,k}(z_i(t),t)}{\partial z_{i,k}}\Psi_{i,k} = 0 \quad (17)$$

or

$$\Psi_{i,k} = -\left[\dot{T}_{i,k} - \frac{\partial f_{i,k}(z_i(t),t)}{\partial z_{i,k}}\right]^{-1}\dot{T}_{i,0} \quad (18)$$

In fact, equation (18) is a linear equation system and thus can be solved by a LU factorization using forward and backward substitution, for more details see Golub and van Loan (1996). From the computed value of $\Psi_{i,3}$ we receive the Jacobian $\frac{\partial D}{\partial w}$, since

$$\frac{\partial D}{\partial w} = \begin{bmatrix} I & 0 & 0 & 0 & 0 & 0 & 0 & 0 & \cdots & 0\\ \Psi_{0,3} & I & 0 & 0 & 0 & 0 & 0 & 0 & \cdots & 0\\ 0 & 0 & \Psi_{1,3} & I & 0 & 0 & 0 & 0 & \cdots & 0\\ 0 & 0 & 0 & 0 & \Psi_{2,3} & I & 0 & 0 & \cdots & 0\\ \vdots & \vdots & \vdots & \vdots & \vdots & \vdots & \vdots & \vdots & \ddots & 0\\ 0 & 0 & 0 & 0 & 0 & 0 & 0 & 0 & \Psi_{n-1,3} & I\end{bmatrix} \quad (19)$$

where I is a unit matrix. In the same way, we can calculate the gradient vector of $\nabla A(w)$.

4. THE PROPOSED ALGORITHM

As we have seen above, the multiple shooting method depends mainly on the SQP iteration. Inside each SQP iteration the gradient values of the objective function and Jacobian of the constraints as well as the approximated Hessian need to be computed. Based on the theoretical development in Sections 2 and 3, we propose the following algorithm to solve the nonlinear optimal control problem.

Algorithm 1:

1. *Initialize SQP*
   - 1.1. *Time horizon.*
   - 1.2. *Subintervals.*
   - 1.3. *Upper and lower bounds for states, controls and constraints.*
   - 1.4. *Fixed initial value constraint.*
   - 1.5. *Initial guess.*

2. *Define the continuity constraints $B(w)$ (8).*
3. *Define the continuity constraints $C(w)$ (8).*
4. *Initialize the three collocation points for each subinterval (14).*
5. *Compute the constraint equations and their sensitivities*
   5.1. *Define collocation equations (15).*
   5.2. *Solve (15) using Newton-Raphson.*
   5.3. *Define sensitivity equations (1).*
   5.4. *Solve (17) using LU factorization.*
6. *Compute objective function and its sensitivity.*
7. *Solve SQP iteration*
   7.1. *If KKT is not satisfied go to 4.*
8. *End*

This algorithm is realized in the framework of the numerical algorithm group (NAG) library Mark 8 (Numerical Algorithms Group Ltd, 2005) and IPOPT (Wächter, 2008) for SQP and in C/C++ for the rest of computations.

5. A CASE STUDEIS

We consider the following optimal control problems to demonstrate the performance of the proposed algorithm.

Example 1: Batch reactor - temperature profile. Maximize yield of x_2 after one hour's operation by manipulating a transformed temperature $u(t)$. This example is taken from Diehl *et al.* (2001).

$$\max_{u,x1,x2} \quad x_2(t_f)$$

s.t. (20)

$$\dot{x}_1(t) = -(u(t) + \frac{u^2(t)}{2})x_1(t)$$
$$\dot{x}_2(t) = u(t)x_1(t), \qquad t \in [0,1]$$
$$x_1(0) = 1, x_2(0) = 0.$$
$$0 \le x_1(t), x_2(t) \le 1$$
$$0 \le u(t) \le 5$$

We discretize the dynamic system with 20 subintervals. The computation was done using a PC with an intel processor "Pentium 4", 3 GHz and 1G Byte RAM. The solution took 350 ms and provides the final value of objective function with $x_2(t_f) = 0.57329$. Fig. 2 shows the optimal control trajectory and Fig. 3 the corresponding state trajectory x_1 while x_2 is shown in Fig. 4. These profiles of states (x_1 and x_2) and optimal control trajectory are identical, by using both MSCOD II and the proposed algorithm.

If we solve this problem with different number of subintervals, e.g. 5, 10, 20, 40, 80 and 160 subintervals, we can note from the results, as shown in Table 1, that the number of optimization variables (z) and the number of constrains will be increased when the number of subintervals increases. The CPU-time will increase exponentially. However, if we compare the CPU-time taken by MUSCOD II with that of the proposed algorithm, it can be seen at a large number of subintervals (i.e. a high dimension of the NMPC), the proposed algorithm will be more effective.

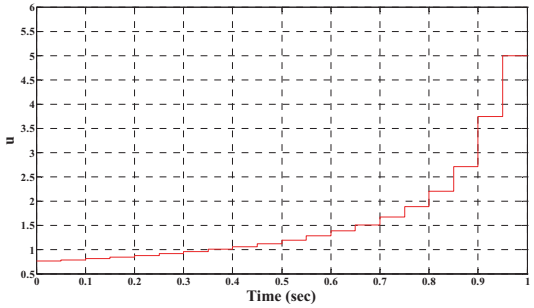

Fig. 2: The optimal control trajectory $u(t)$

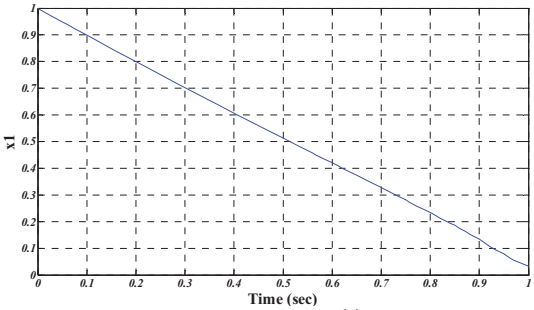

Fig. 3: The optimal state trajectory $x_1(t)$

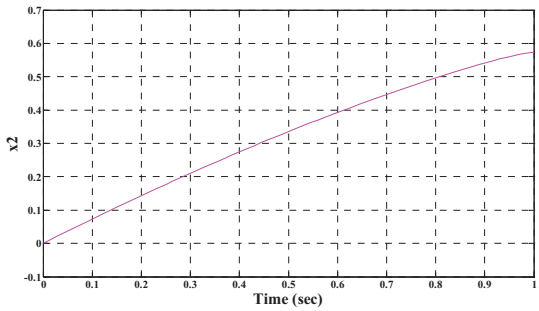

Fig. 4: The optimal state trajectory $x_2(t)$

Table 1: Results of using different number of subintervals

n	*z's*	*Co. eq.*	MUSCOD II		Algorithm 1	
			CPU-Time (ms)	*J*	CPU-Time (ms)	*J*
5	18	12	43	0.573117	188	0.568171
10	33	22	53	0.573080	290	0.572162
20	63	42	146	0.573527	350	0.573290
40	123	82	940	0.573544	480	0.573478
80	243	162	3620	0.573545	547	0.573528
160	483	322	21612	0.573545	735	0.573541

n: number of subintervals; *z's*: total number of variables; *Co. eq.*: total number of constraints; *J*: value of objective function.

Example 2: Optimal control of a continuous stirred tank reactor (CSTR): We consider a CSTR as shown in Fig. 5.

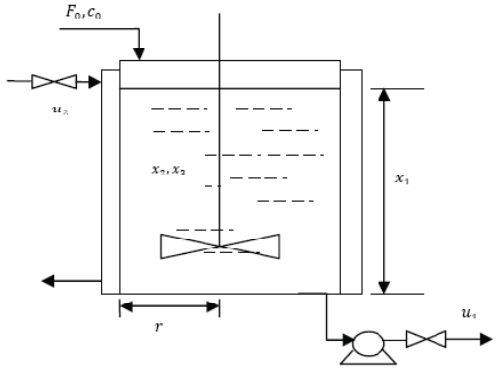

Fig. 5: CSTR example

An exothermic, irreversible, first order reaction A B occurs in the liquid phase and the temperature is regulated with external cooling. This highly nonlinear example is taken form Henson and Seborg (1997) or Pannocchia and Rawlings (2003) with the assumption that the level liquid is not constant. The constrained optimal control problem is formulated as follows:

$$\min_{x,u} \int_0^{t_f} [(x_1 - x_1^s)^2 + 100(x_2 - x_2^s)^2 + 0.1(u_1 - u_1^s)^2 + 0.1(u_2 - u_2^s)^2]dt$$

s.t. (21)

$$\dot{x}_1 = \frac{F_0 - u_1}{\pi r^2}$$

$$\dot{x}_2 = \frac{F_0(c_0 - x_2)}{\pi r^2 x_1} - k_0 x_2 e^{-E/RT}$$

$$\dot{x}_3 = \frac{F_0(T_0 - x_3)}{\pi r^2 x_1} + \frac{-\Delta H}{\rho C_p} k_0 x_2 e^{-E/RT} + \frac{2U}{r\rho C_p}(u_2 - x_3)$$

$$x_1(0) = 0.659, \quad x_2(0) = 0.877 \text{ and } x_1(0) = 324.5$$

$$0.5 \le x_1 \le 2.5, \quad 0.8 \le x_2 \le 1.0$$

$$85 \le u_1 \le 115, \quad 299 \le u_2 \le 301$$

where x_1 is the level of the tank in meter, x_2 the product concentration in mol and x_3 the reaction temperature in (K), and the controls are u_1 and u_2 the outlet flow rate in (L/min) and coolant liquid temperature, respectively. In addition the inlet flow rate F_0 or the inlet concentration c_0 is acting as a disturbance to CSTR. The desired steady-state operating points: x_1^s, x_2^s, u_1^s and u_2^s are 0.659 meter, 0.877 mol/L, 100L/min and 300K, respectively. The model parameters in nominal conditions are shown in Table 2. We consider the operation case that at the tenth minute a disturbance enters the plant at a level of 0.05 mol/L on the inlet molar concentration c_0. A time horizon of $t_f = 50$ min is considered.

Table 2: Parameters of the CSTR

F_0	100 L/min	E/R	8750 K
T_0	305 K	U	915.6 $Wm^{-2}K^{-1}$
c_0	1.0 mol/L	ρ	1 kg/L
R	0.219	C_p	0.239 $Jg^{-1}K^{-1}$
k_0	0.219	ΔH	-5×10^4 J/mol

To solve problem (21) using the proposed algorithm we divide the time horizon into 50 subintervals and so that the number of resulted NLP will be 306 variables with 204 constraints, and the same PC is used to make the optimization. We used the IPOPT 3.4.0 to solve the NLP and NAG mark 8 to solve the Newton-Raphson equations and linear equation systems.

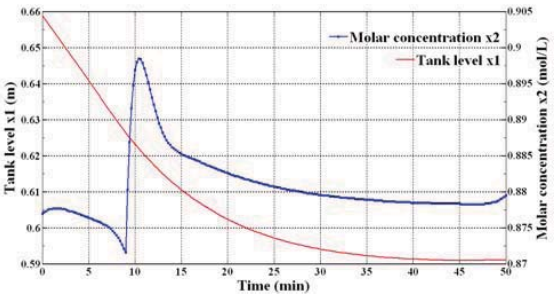

Fig. 6: The optimal output flow $x_1(t)$ and coolant temperature $x_2(t)$.

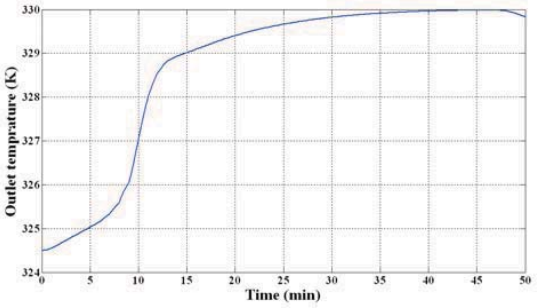

Fig. 7: The optimal outlet temperature $x_3(t)$.

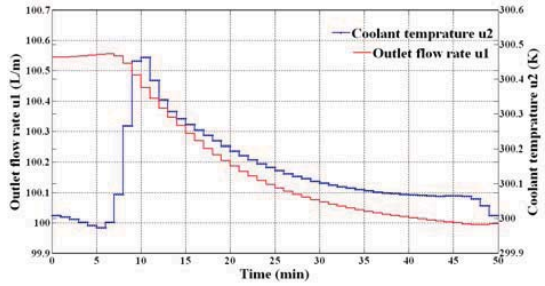

Fig. 8: The optimal control profiles $u_1(t)$ and $u_2(t)$.

Figures 6 and 7 show the optimal control profiles of the states $x_1(t)$, $x_1(t)$ and $x_3(t)$, respectively and Fig. 8 shows the optimal control profiles $u_1(t)$ and $u_2(t)$. The objective function value at the optimum is 0.9015886. Moreover, the algorithm was converged in 35 iterations and with the CPU-time in 0.954s. In comparison, this problem was also solved by Hong *et al.* (2006) using a quasi-sequential approach and it was converged in 16 iterations and 5.56 s of CPU time of SUN Ultra 10 Station with identical solutions.

6. CONCLUSIONS

In this paper we proposed a novel algorithm for NMPC. It is a combination of the multiple shooting, where the NLP problem will be handled, with the collocation method, where function values and gradients required in the NLP will be computed. We use piecewise constant for controls and the three-point collocation for states to parameterize the vector of optimization variables. The proposed algorithm has been realized in the framework of the numerical algorithm group (NAG) and IPOPT in the C/C++ environment. In addition, two demonstrative examples have been taken as case studies to show and compare the results from our algorithm and the well known MUSCOD II code. From these results it can be seen that the proposed algorithm is more efficient when a large-scale NMPC problem is to be solved. Stability and error control issues as well as practical applications of this algorithm will be considered in our future work.

7. ACKNOWLEDGEMENT

The financial support from the German Academic Exchange Service (DAAD) for this work is gratefully acknowledged.

8. REFERENCES

Biegler, L. T., Cervantes, A. M. and Wächter, A. (2002). Advances in simultaneous strategies for dynamic process optimization. *Chemical Engineering Science*. 4(57), 575–593.

Bock, H.G. and Plitt, K.J. (1984). A multiple shooting algorithm for direct solution of optimal control problems. *In: Proceedings 9th IFAC World Congress Budapest*. Pergamon Press, 243-247.

Bryson, A. E. and Ho, Y.C. (1975). *Applied Optimal control*, Hemisphere publication corporation, Levittown.

Diehl, M. (2001). Real-time optimization for large scale nonlinear processes. PhD Thesis, *University of Heidelberg*.

Diehl, M., Findeisen, R., Schwarzkopf, S., Uslu, I., Allgöwer, F., Bock, H.G., Gilles, E.D., and Schlöder, J.P. (2002a). An efficient algorithm for nonlinear model predictive control of large-scale systems. Part I: Description of the method. *At-Automatisierungstechnik.* 50(12), 557-567.

Diehl, M., Bock, H.G. Schlöder, J.P., Findeisen, R., Nagy, Z., and Allgöwer, F. (2002b) Real-time optimization and nonlinear model predictive control of processes governed by differential-algebraic equations. *Journal of Process Control.* 12(4)**,** 577-585.

Diehl, M., Schäfer, A. and Leineweber, D. B. (2001). *MOSCOD II user manual*, Interdisciplinary Center for Scientific Computing (IWR), University of Heidelberg.

Diehl, M., Bock, H.G., Diedam, H. and Wieber P.B. (2006). Fast direct multiple shooting algorithms for optimal robot control. LNCIS, *Fast Motions in Biomechanics and Robotics*, 340, 65-93.

Finlayson, B. A. (1980). *Nonlinear analysis in chemical engineering*, McGraw-Hill, New York.

Gill, P. E., Murray, W. and Saunders, M. A. (2002). SNOPT: an SQP algorithm for large-scale constrained optimization. *SIAM J. Optim*. 12(1). 979–1006.

Gill, P. E., Murray, W. and Saunders, M. A. (2008). *User's Guide for SNOPT version 7: Software for large-scale nonlinear programming.* Department of Mathematics, University of California, San Diego.

Gatlu, G. and Zafiriou, E. (1992). Nonlinear quadratic dynamic matrix control with state estimation. *Ind. Eng. Chem. Res*. 31(4), 1096-1104.

Golub, G. H. and van Loan, C. F. (1996). *Matrix computations.* (3rd ed.). Johns Hopkins University Press. Baltimore.

Henson, MA., Seborg, DE. (1997). *Nonlinear Process Control. Upper Saddle River.* NJ, Prentice Hall.

Hong, W. R., Wang, S. Q., Li, P., Wozny, G., Biegler, L.T. (2006), A quasi-sequential approach to large-scale dynamic optimization problems, *AIChE Journal*, 52(1), 255-268.

Kirk, D. E. (1970). *Optimal Control*, Prentice Hall Inc, Englewood Cliffs.

Kraft, D. (1985). On converting optimal control problems into nonlinear programming problems. *In K. Schittkowski. Computational Mathematical Programming,* vol. F15 of NATO ASI, 261–280. Springer.

Leineweber, D. B. (1995). Analyse und Restrukturierung eines Verfahrens zur direkten Lösung von Optimal-Steuerungsproblem, The Theory of MUSCOD II in a Nutshell. Master Thesis, University of Heidelberg.

Lewis, F. L., and Syrmos, V. L. (1995). *Optimal Control Theory*, Wiley Interscience.

Li, P. (2007). Prozessoptimierung: Methoden, Anwendungen und Herausforderungen, *Chemie Ingenieur Technik*. 79(10), 1567-1580.

Numerical Algorithms Group Ltd. (2005), *NAG C Library Manual, Mark 8.* Oxford, UK.

Pannocchia, G., Rawlings, J., Disturbance models for offset-free model predictive control. *AIChE J*. 49, 426-437

Qin, S.J., Badgwell, T.A. (2003). A survey of industrial model predictive control technology, *Control Engineering Practice.* 11(7), 1096-1104.

Sargent, R.W.H. and Sullivan, G.R. (1977). The development of an efficient optimal control package. In J. Stoer, *Proceedings of the 8th IFIP Conference on Optimization Techniques,* Part 2. **7**(1978), 158-168. Springer. Heidelberg.

Schäfer, A., Kühl, P. Diehl, M., Schlöder, J. and Bock, H.G. (2007). Fast reduced multiple shooting methods for nonlinear model predictive control. *Chemical Engineering & Processing*, 46(11), 1200–1214.

Wächter, A. (2008), Introduction to IPOP: A tutorial for downloading, installing and using IPOPT. Department of Mathematical Sciences, IBM T.J. Watson Research Center, Yorktown Heights, NY.

Schäfer, A., Kühl, P. Diehl, M., Schlöder, J. and Bock, H.G. (2007). Fast reduced multiple shooting methods for nonlinear model predictive control. *Chemical Engineering & Processing*, 46(11), 1200–1214.

Robust Control of Yeast Fed-Batch Cultures for Productivity Enhancement

D. Coutinho [*,**] **L. Dewasme** [*] **A. Vande Wouwer** [*]

[*] *Service d'Automatique, Faculté Polytechnique de Mons, Boulevard Dolez 31, B-7000 Mons, Belgium (e-mails: Daniel.Coutinho(Alain.VandeWouwer,Laurent.Dewasme)@fpms.ac.be)*
[**] *On leave from the Group of Automation and Control Systems, Faculty of Engineering, Pontifícia Universidade Católica do Rio Grande do Sul, Av. Ipiranga 6681, Porto Alegre-RS, 90619-900 Brazil*

Abstract: This work proposes a robust control strategy for the optimizing control of fed-batch cultures of S. cerevisae. The process dynamics is characterized by a nonlinear kinetic model based on the bottleneck assumption and ethanol inhibition for a possible excess of substrate feeding. The control strategy is based on the feedback linearization technique, where the resulting free linear dynamics is designed so as to ensure a certain robustness to plant parameter variations. A feedforward loop achieves the correct critical substrate value, which is a function of the ethanol and oxygen in the culture medium. In addition, a robust Luenberger-like observer is designed taking plant parameter variations into account. Numerical experiments demonstrate the potential of the proposed approach as a tool for control design of fed-batch cultures.

Keywords: robust control, feedback linearisation, Luenberger observer, fermentation process.

1. INTRODUCTION

The culture of host recombinant micro-organisms is probably the only economical way of producing pharmaceutical biochemicals. The cell cultures or the culture of micro-organisms are basically operated in three different modes – batch, fed-batch and continuous. The fed-batch operation is popular in industrial practice, because it is advantageous from an operational and control point of view (Roeva and Tzonkov, 2005). In this mode of operation, the bioreactor is manipulated by controlling its feeding rate. The off line design of the optimal feeding profile in general does not give high productivity, since in open-loop an excess of substrate leads to the accumulation of by-products (ethanol for yeast and acetate for bacteria), which in turn yields an inhibition of the cell respiratory capacity.

To avoid high concentrations of inhibitory by-product, a closed-loop solution is in general applied leading to a wide diversity of approaches (Chen et al., 1995; Boskovic and Narendra, 1995; Hisbullah et al., 2002; Rocha et al., 2004; Renard and Vande Wouwer, 2008; Ignatova et al., 2008). Nevertheless, the closed-loop control optimization of yeast fed-batch process is still a challenging task for two main reasons. Firstly, the process kinetics is governed by highly nonlinear functions with uncertain model parameters. Secondly, there is a lack of reliable and low cost online sensors for the measurement of key state variables.

In the control context, many researchers are applying online algorithms to cope with time-varying model uncertainties by either adaptive control (Renard and Vande Wouwer, 2008; Dewasme and Vande Wouwer, 2008; Ignatova et al., 2008) or computational intelligence based algorithms (Rocha et al., 2004; Karakuzu et al., 2006). However, the use of online adaption schemes may lead to closed-loop instability in the presence of unmodeled dynamics. In this paper, we follow a different direction by applying the robust control theory to design a nonlinear controller (with a fixed parametrization) taking model uncertainties into account. The control strategy is based on the classical feedback linearizing technique which is widely applied in fermentation process (Bastin and Dochain, 1990). However, feedback linearizing control schemes are very sensitive to model uncertainties. To handle the lack of robustness, the resulting linear dynamics is designed in order not only to improve the overall performance but also to achieve robustness against model uncertainties.

On the other hand, complex control methods need in general full state information which in most of the situations is not practical. In this case, many approaches have been proposed in the process control literature to estimate some unavailable key states based on Luenberger observer (LO) and Kalman filter (KF) (Bastin and Dochain, 1990; Klockow et al., 2008). However, these state estimators are implemented iteratively (e.g., extended LO and KF) to deal with the nonlinearities exhibited in the fermentation dynamics making difficult the task of tuning the observer gain in order to achieve a nice convergence behaviour. In this paper, we propose a robust nonlinear observer for which a nonlinear static gain is designed to improve the estimation convergence as well as to cope with model uncertainties. The rest of this paper is as follows. Section 2 introduces the problem to be addressed in this paper. The control strategy is proposed in Section 3 and the robust observer design is derived in Section 4. Numerical experiments are carried out in Section 5 to validate the approach and Section 6 ends the paper.

2. PRELIMINARIES

The yeast strain *S. cerevisiae* presents a metabolism that is macroscopically described as follows (Bastin and Dochain, 1990):

$$\text{Substrate oxidation:} \quad S + k_5 O \xrightarrow{r_1} k_1 X + k_7 P \tag{1}$$

$$\text{Substrate fermentation:} \quad S \xrightarrow{r_2} k_2 X + k_4 E + k_8 P \tag{2}$$

$$\text{Ethanol oxidation:} \quad E + k_6 O \xrightarrow{r_3} k_3 X + k_9 P \tag{3}$$

where X, S, E, O and P are, respectively, the concentration in the culture medium of biomass, substrate (typically glucose), ethanol, dissolved oxygen and carbon dioxide. The k_i, $i = 1, \ldots, 9$, are the constant yield coefficients and the r_i, $i = 1, 2, 3$, are the specific growth rates. We model these rates by the following discontinuous functions:

$$r_1 = \min\{r_S, k_5^{-1} r_O\} \tag{4}$$

$$r_2 = \max\{0, r_S - k_5^{-1} r_O\} \tag{5}$$

$$r_3 = \max\left\{0, \frac{r_O - k_5 r_S}{k_6} \cdot \frac{E}{E + K_E}\right\} \tag{6}$$

where the kinetic terms related to the substrate consumption r_S, the oxidative or respiratory capacity r_O and the ethanol oxidative rate r_E are represented as follows

$$r_S = \mu_S \ \frac{S}{S + K_S} \tag{7}$$

$$r_O = \mu_O \ \frac{O}{O + K_O} \cdot \frac{K_{i_E}}{K_{i_E} + E} \tag{8}$$

$$r_E = \mu_E \ \frac{E}{E + K_E} \tag{9}$$

with the constants μ_S, μ_O and μ_E being the maximal values of the specific growth rates and K_S, K_O and K_E expressing the saturation of the respective elements. Note that we are taking the effect of ethanol on the cells growth into account by considering the inhibition ethanol constant K_{i_E} in (8).

The component-wise mass balances of the above reaction scheme lead to the following state-space representation (Dewasme and Vande Wouwer, 2008)

$$\dot{x} = K r(x) x_1 + A x - u x + B(u) \tag{10}$$

where $x = [\, x_1 \ x_2 \ x_3 \ x_4 \ x_5 \ x_6 \,]' = [\, X \ S \ E \ O \ P \ V \,]'$ is the state vector with $x_6 = V$ being the culture medium volume, $r(x) = [\, r_1 \ r_2 \ r_3 \,]'$ is the vector of reaction rates, and $u = F_{in}/x_6$ is the control input (the dilution rate) with F_{in} denoting the inlet feed rate. The matrices K and A, and the vector function $B(\cdot)$ are given by:

$$K = \begin{bmatrix} k_1 & k_2 & k_3 \\ -1 & -1 & 0 \\ 0 & k_4 & -1 \\ -k_5 & 0 & -k_6 \\ k_7 & k_8 & k_9 \\ 0 & 0 & 0 \end{bmatrix}, \ B(u) = \begin{bmatrix} 0 \\ S_{in} \ u \\ 0 \\ k_L a \ O_{sat} \\ k_L a \ P_{sat} \\ 0 \end{bmatrix}, \tag{11}$$

$$A = \begin{bmatrix} 0_3 & 0_{3\times 2} & 0_{3\times 1} \\ 0 & -k_L a \ I_2 & 0 \\ 0_{1\times 3} & 0_{1\times 2} & 0 \end{bmatrix},$$

where $k_L a$ is the volumetric transfer coefficient, S_{in} is the feeding substrate concentration, and O_{sat} and P_{sat} are respectively the saturations of dissolved oxygen and carbon dioxide concentrations.

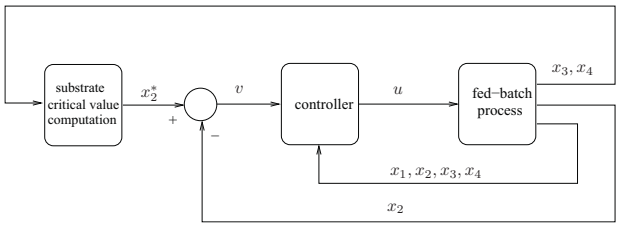

Fig. 1. Control Scheme for Optimal Operation Regime.

To analyze the biomass productivity, we recall the Sonnleitner's bottleneck assumption (Sonnleitner and Käppeli, 1986) which states that during a culture the yeast cells are likely to change their metabolism because of limited respiratory capacity. When the substrate concentration is large, the yeast cells produce ethanol (respiro-fermentative regime). If the substrate concentration becomes small, the available substrate (and possibly the ethanol) are oxidized (respirative regime). Thus, the optimal operating point to maximize the biomass productivity is at the boundary of the two regimes (Valentinotti et al., 2004), i.e., when the fermentation and oxidation reaction rates are equal to zero. Hence, the optimal operating point can be easily computed through the equality $r_O = k_5 r_S$ leading to the following equation

$$x_2^* = \frac{K_S \ r_O}{k_5 \mu_S - r_O} \tag{12}$$

where x_2^* refers to the substrate critical value.

In view of (8), we note that the operating point x_2^* is in fact a nonlinear function of x_3 and x_4. To simplify the control problem, many references either consider a constant set-point (Klockow et al., 2008) or alternatively choose a sub-optimal solution by imposing a low-level of ethanol concentration (Renard and Vande Wouwer, 2008).

3. CONTROL STRATEGY

In this paper, we aim at maintaining the system as close as possible to its optimal operating condition. To this end, we have to determine on-line the value of x_2^* and design a controller such that x_2 tracks approximately x_2^*. In addition, to simplify the analysis, we suppose in this section that all states are available on-line for feedback. For practical purposes, a nonlinear observer is proposed in the next section to estimate some state variables which are difficult to measure.

The proposed control scheme is illustrated in Figure 1. The internal feedback loops correspond to a standard feedback linearizing controller, where the free linear dynamics is designed to give a good tracking response as well as to assure a certain level of robustness against plant parameter variations. The external feedforward loop is to compute on-line the substrate critical level. We stress that instead of computing an adaptive controller to handle plant parameter variations (as, e.g., Dewasme and Vande Wouwer (2008)), we design a fixed controller that will have a guaranteed performance in the admissible parameter space.

To control the substrate level, consider the following dynamics for x_2 taken from (10)

$$\dot{x}_2 = -(r_1 + r_2)x_1 + (S_{in} - x_2)u \tag{13}$$

where r_1 and r_2 are nonlinear functions of x_2, x_3 and x_4 as given by (4) and (5). With respect to the above system dynamics, we assume that the values of $x_1, \ldots, x_6$ are bounded to a given polytopic region $\mathcal{X}$ with know vertices, that is, $x \in \mathcal{X} \subset \mathbb{R}^6$.

A feedback linearizing control law can be easily derived:

$$u = \frac{F_{in}}{x_6} = \frac{1}{S_{in} - x_2}((\tilde{r}_1 + \tilde{r}_2)x_1 + v) \tag{14}$$

where $\tilde{r}_1$ and $\tilde{r}_2$ are respectively the nominal values of r_1 and r_2, which may vary due to parameter variations, and v is the new input of the resulting linearized system.

In view of (13) and (14), we obtain the following dynamics for x_2

$$\dot{x}_2 = v - (e_{r_1} + e_{r_2})x_1 \tag{15}$$

where $e_{r_1} := r_1 - \tilde{r}_1$ and $e_{r_2} := r_2 - \tilde{r}_2$ are nonlinear functions of (x_2, x_3, x_4) representing possible inexact cancelations of nonlinear terms due to uncertain model parameters.

Borrowing the ideas of the *Quasi-LPV* approach (Leith and Leithead, 2000), we bound the term $e_{r_1} + e_{r_2}$ by a time-varying parameter $\delta = \delta(t)$ which is supposed to belong to a known set $\Delta := \{\delta : \underline{\delta} \leq \delta \leq \overline{\delta}\}$ with $\underline{\delta}$ and $\overline{\delta}$ respectively representing the minimal and maximal admissible uncertainty.

To approximately track the time-varying reference signal x_2^*, we consider the following additional control loop

$$v = \lambda(x_2^* - x_2) \tag{16}$$

where $\lambda \in \mathbb{R}$ is a free parameter to be designed.

In this paper, we design the parameter λ to ensure some robustness and a certain tracking performance to the overall closed loop system. To this end, we model the closed loop system as follows

$$\mathcal{M} : \begin{cases} \dot{x}_2 = -\lambda x_2 + a(\lambda, \delta)w \\ z = -x_2 + c\,w\ ,\ \delta \in \Delta \end{cases} \tag{17}$$

where $w = [\, x_2^* \quad x_1 \,]' \subset \mathcal{L}_{2,[0,T]}$ is a disturbance input to the system $\mathcal{M}$, $z = x_2^* - x_2$ the performance output and

$$a(\lambda, \delta) = [\, \lambda \quad -\delta \,]\ ,\ c = [\, 1 \quad 0 \,]\ .$$

Now, consider the following definition for the finite horizon $\mathcal{L}_2$-gain of system $\mathcal{M}$:

$$\|\mathcal{M}_{wz}\|_{\infty,[0,T]} = \sup_{\delta \in \Delta, 0 \neq w \subset \mathcal{L}_{2,[0,T]}} \frac{\|z\|_{2,[0,T]}}{\|w\|_{2,[0,T]}} \tag{18}$$

Thus, we design the parameter λ based on the $\mathcal{H}_\infty$ control theory (Skogestad and Postlethwaite, 2001). In other words, we solve the following optimization problem

$$\min_{\lambda, \delta \in \Delta}\ \gamma : \|\mathcal{M}_{wz}\|_{\infty,[0,T]} \leq \gamma \tag{19}$$

while ensuring the robust stability of system (17).

Note 1. The parameter λ can be easily obtained through the LMI framework either via a quadratic Lyapunov function (Boyd et al., 1994) or a parameter dependent one (de Souza et al., 2000) if we assume $\dot{\delta}$ is also bounded, since we can easily perform a line search on λ. □

4. ROBUST OBSERVER

To implement the control law proposed in the latter section, we have to measure several state variables such as X, S, E and O. In spite of existing specific probes to measure all these signals on-line, some sensors can be quite expensive and are not always available in a practical set-up. Particularly, in the proposed control strategy, we are dealing with very low levels of substrate (glucose) and ethanol concentrations making their measurements expensive and inaccurate.

Alternatively, we propose a robust Luenberger-like nonlinear observer to estimate the substrate and ethanol concentration levels from the measurement of $x_1 = X$, $x_4 = O$, $x_5 = P$ and the dilution rate $u = F_{in}/x_6$. As we are dealing with a nonlinear system, the exponential observability property of the system is state dependent (Bastin and Dochain, 1990). In other words, for large estimation errors, the observer may diverge from the system operating point since the exponential observability is lost. To overcome this problem, we assume the initial conditions $x_2(0)$ and $x_3(0)$, which are respectively the initial substrate and ethanol concentration levels, are partially known (likely through inaccurate off-line measurements).

Firstly, we model the reaction rates by the following uncertain functions:

$$r_i(x) \cong r_i(\theta_i) = \alpha_i(1 + \beta_i\theta_i)\ ,\ \theta_i \in [-1, 1] \tag{20}$$

where, for $i = 1, 2, 3$, α_i is the steady-state value of r_i, θ_i is an uncertain time-varying parameter which models the displacement of r_i from its steady-state regime and also a possible inaccuracy on the system parameters, and β_i is a given constant added in light of the unitary normalization of the uncertain parameter space. Then, we propose the following state space representation for the observer

$$\begin{cases} \dot{\hat{x}} = K\hat{r}\hat{x}_1 + \hat{A}(u)\hat{x} + \hat{B}(u, y) + L(y, u)(y - \hat{y}) \\ \hat{y} = C_y\hat{x} \\ \hat{z} = C_z\hat{x} \end{cases} \tag{21}$$

where $\hat{x} \in \mathbb{R}^6$ is the state estimation, $y = C_y x$ is the on-line measurement, $\hat{y}$ is the measurement estimation, $\hat{z}$ is the signal to be estimate, K is as in (11), $L(y, u) \in \mathbb{R}^{6\times 4}$ is a nonlinear matrix function of y and u to be determined, $\hat{r}$ is as defined in (24), and

$$\begin{aligned} \hat{A}(u) &= -\mathrm{diag}\{0, u, u, k_L a, k_L a, 0\} \\ \hat{B}(u, y) &= [\, -x_1 u \quad S_{in}u \quad 0 \quad (k_L a O_{sat} - x_4 u) \\ &\qquad (k_L a P_{sat} - x_5 u) \quad -x_6 u \,]' \end{aligned} \tag{22}$$

$$C_y = \begin{bmatrix} 1&0&0&0&0&0 \\ 0&0&0&1&0&0 \\ 0&0&0&0&1&0 \\ 0&0&0&0&0&1 \end{bmatrix}\ ,\ C_z = \begin{bmatrix} 0&1&0&0&0&0 \\ 0&0&1&0&0&0 \end{bmatrix}\ .$$

Accordingly to (20), we define the estimates of $r_i(\theta_i)$ as follows

$$\hat{r}_i := \alpha_i \tag{23}$$

where, for $i = 1, 2, 3$, $\hat{r}_i$ is the estimate of the approximate reaction rates.

Now, considering the following notation

$$r(\theta) = \begin{bmatrix} \alpha_1(1+\beta_1\theta_1) \\ \alpha_2(1+\beta_2\theta_2) \\ \alpha_3(1+\beta_3\theta_3) \end{bmatrix}\ ,\ \theta = \begin{bmatrix} \theta_1 \\ \theta_2 \\ \theta_3 \end{bmatrix}\ ,\ \hat{r} = \begin{bmatrix} \alpha_1 \\ \alpha_2 \\ \alpha_3 \end{bmatrix}\ , \tag{24}$$

we can approximate the error dynamics as follows

$$\begin{aligned}\dot{e} &\cong (K\hat{r}N_r + \hat{A}(u) - L(y,u)C_y)e + K(r(\theta) - \hat{r})x_1 \\ &\cong (K\hat{r}N_r + \hat{A}(u) - L(y,u)C_y)e + K\Omega(x_1)\theta\end{aligned}$$

where $N_r = [\,1\ 0\ \cdots\ 0\,]$, $\theta \in \Theta := \{\theta \in \mathbb{R}^3 : |\theta_i| \leq 1\ ,\ i = 1,2,3\}$ and $\Omega(x_1) = x_1 \cdot \mathrm{diag}\{\alpha_1\beta_1, \alpha_2\beta_2, \alpha_3\beta_3\}$.

In light of the above developments, we can pose the problem of determining $L(y,u)$ in an ℓ_1 optimal control setting (Dahleh and Diaz-Bobillo, 1995). To this end, consider the following error dynamics representation:

$$\mathcal{E} : \begin{cases} \dot{e} &= A_e e + B_e \theta \\ z_e &= C_z e\ ,\ \|\theta\|_\infty \leq 1 \end{cases} \tag{25}$$

where θ is an energy-peak bounded disturbance signal, z_e the estimation error to be minimized and

$$A_e = K\hat{r}N_r + \hat{A}(u) - L(y,u)C_y\ ,\ B_e = K\Omega(x_1)\ .$$

In this paper, we consider the following definition for the ℓ_1-norm of system (25):

$$\|\mathcal{E}_{\theta z_e}\|_1 = \sup_{\substack{e \in \mathbb{E}, e(0) = 0 \\ \|\theta\|_\infty \leq 1}} \|z_e\|_\infty \tag{26}$$

where $\mathbb{E} := \{e : V(e) \leq 1\}$ is an estimate of the reachable set and $V(e)$ is a Lyapunov function for system $\mathcal{E}$, which guarantees the system internal stability.

An upper-bound σ on $\|\mathcal{E}_{\theta\ e_z}\|_1^2$ can be determined via the following optimization problem (Nagpal et al., 1994)

$$\min_{\substack{V(e),\eta \\ e \in \mathbb{E}}} \sigma : \begin{cases} V(e) > 0\ ,\ \eta > 0 \\ \dot{V}(e) + \eta(V(e) - \theta'\theta) < 0 \\ V(e) - \dfrac{z_e' z_e}{\sigma} \geq 0 \end{cases} \tag{27}$$

Notice the set invariance property of $\mathbb{E}$ is guaranteed for zero initial conditions and the constraints on (27) may not hold when $e(0) \neq 0$. As a result, the error state trajectory may leave $\mathbb{E}$ and do not return since the state observer is nonlinear and the stability properties are not necessarily global. In this paper, we assume the initial error is sufficiently close to zero such that $\mathbb{E}$ is attractive.

5. NUMERICAL EXPERIMENTS

In this section, we perform several numerical experiments considering small-scale culture conditions. In particular, we borrow the 20 $[l]$ bioreactor studied in (Dewasme and Vande Wouwer, 2008), where the initial and operating conditions are:

$$\begin{gathered} x_1(0) = 0.4\ [g/l]\ ,\ x_2(0) = 0.5\ [g/l]\ ,\ x_3(0) = 3\ [g/l]\ , \\ x_4(0) = O_{sat} = 0.035\ [g/l]\ ,\ x_5(0) = P_{sat} = 1.286\ [g/l]\ , \\ x_6(0) = 6.8\ [l] \quad \text{and} \quad S_{in} = 350\ [g/l]\ . \end{gathered}$$

We study two different scenarios. Firstly, supposing the state variables are available online for feedback, we design the robust linearizing feedback controller proposed in Section 3 aiming for tracking as close as possible the estimation of the substrate critical value. In this setup, we consider a noisy ethanol measurement, since the level of ethanol is likely to be very close to zero making difficult its measurement. Secondly, we design a robust observer to estimate the substrate and ethanol concentration levels, which in the proposed strategy are very low and difficult to measure in current practice, applying the result proposed in Section 4. In this case, we analyze the observer robustness and verify the set of initial conditions in which the convergence properties hold.

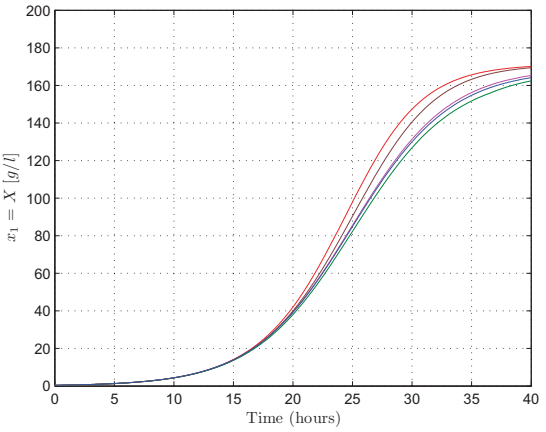

Fig. 2. Biomass concentration – state feedback case.

5.1 State Feedback

We refer to state feedback the control law proposed in (14) and (16), where x_1, x_2, x_3, x_4 and u are available online. To design the parameter λ in (16) via the optimization problem (19), we suppose the parameters K_S, K_E, K_O and K_{i_E} may vary $\pm 20\%$ from their nominal values. Simulating the operating conditions of the control strategy in (14), we may infer that $\overline{\delta} = -\underline{\delta} = 1.0$, which in light of (17) and (19) yields $\lambda = 44.8511$.

Figures 2 to 4 show the closed-loop response of biomass x_1, substrate x_2 and ethanol x_3 concentrations, for five different values of K_S, K_E, K_O and K_{i_E} (which were randomly chosen). In all simulations, we have added a white noise on the ethanol concentration measurement with a maximal amplitude of ± 0.25 $[g/l]$. Notice in all cases the biomass productivity does not significantly vary against parameter uncertainty and noise measurement.

5.2 Output Feedback

In order to design the state observer as proposed in Section 4, we have considered

$$\begin{gathered} \alpha_1 = 3.2 \times 10^{-5}\ ,\ \alpha_2 = 1.3 \times 10^{-6}\ ,\ \alpha_3 = 4 \times 10^{-7}\ , \\ \beta_1 = \beta_2 = \beta_3 = 1\ ,\ x_1 \in [0.4, 180]\ ,\ F_{in} \in [10^{-7}, 10^{-4}]\ , \end{gathered}$$

which are obtained from the noiseless simulations of the state-feedback case.

We can compute the observer gain through the LMI framework, see for instance (Coutinho et al., 2005). Assuming that u is available online, we have chosen an observer gain as follows:

$$L(y,u) = L(u) = L_0 + uL_1\ ,$$

where L_0 and L_1 are constant matrices to be determined. In addition, to simplify the computations, we constraint the Lyapunov function to be quadratic, i.e., $V(e) = e'Pe$ with $P = P' > 0$.

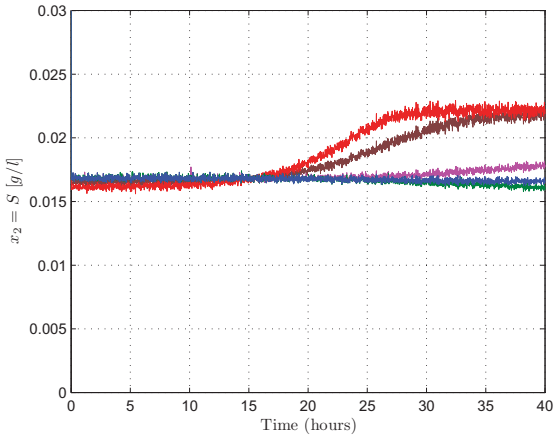

Fig. 3. Substrate concentration – state feedback case.

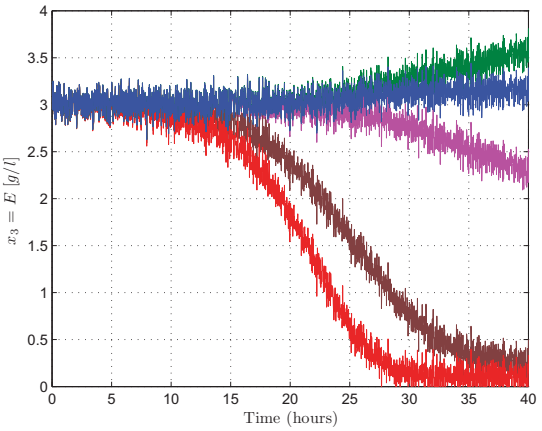

Fig. 4. Ethanol concentration – state feedback case.

Thus, solving (27) for all $(x_1, u) \in \mathcal{V}([0.4, 180] \times [10^{-7}, 10^{-4}])$ with the parametrization $Q(u) = PL(u)$ and a line search on η, we obtain the following matrices

$$L_0 = 10^6 \times \begin{bmatrix} 0.267 & -0.380 & 1.006 & 0.000 \\ -0.208 & 1.421 & -3.759 & 0.000 \\ 0.058 & -0.341 & 0.903 & 0.000 \\ -0.041 & 0.283 & -0.747 & 0.000 \\ 0.109 & -0.747 & 1.978 & 0.000 \\ 0.000 & 0.000 & 0.000 & -2\times10^{-7} \end{bmatrix}$$

$$L_1 = 10^2 \times \begin{bmatrix} 0.143 & -0.256 & 0.679 & 0.000 \\ -0.172 & 1.217 & -3.220 & 0.000 \\ 0.045 & -0.290 & 0.768 & 0.000 \\ -0.034 & 0.241 & -0.639 & 0.000 \\ 0.090 & -0.639 & 1.690 & 0.000 \\ 0.000 & 0.000 & 0.000 & 0.000 \end{bmatrix}$$

where $\mathcal{V}(\cdot)$ stands for the set of vertices of $(\cdot)$.

From several simulations, the observer initial conditions that guarantee the stability of the error system are as follows

$$\hat{x}_2(0) = x_2(0) \pm 50\% \ , \ \hat{x}_3(0) = x_3(0) \pm 50\% \ . \qquad (28)$$

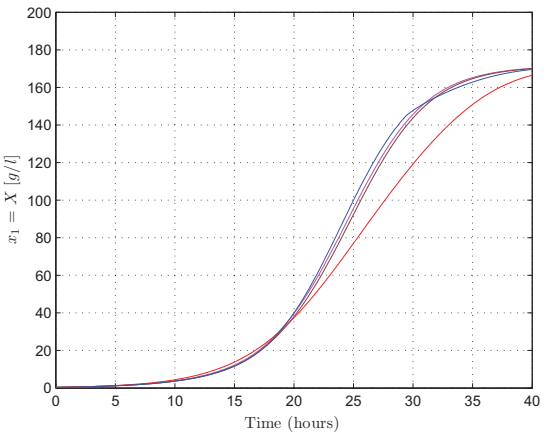

Fig. 5. Biomass concentration – output feedback case.

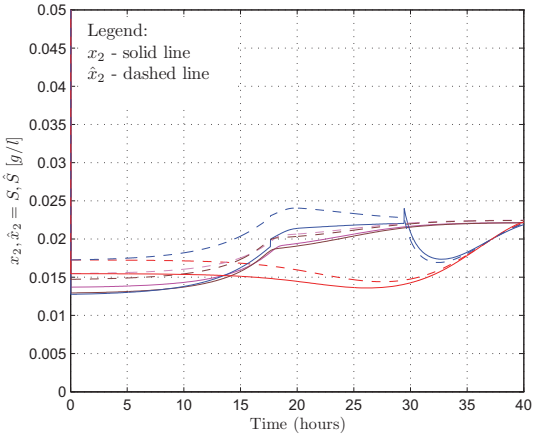

Fig. 6. Substrate concentration – output feedback case.

To test the output feedback closed-loop performance, we carried out several simulations for randomly chosen values of K_S, K_E, K_O, K_{i_E} and $\hat{x}_2(0), \hat{x}_3(0)$ from the admissible parameter space leading to the results detailed in Figures 5, 6 and 7.

5.3 Remarks and Future Research

The simulations indicate that the overall performance of the biomass concentration productivity is robust against uncertainties on model parameters and some initial condition estimates. The biomass productivity is similar to the one obtained in (Dewasme and Vande Wouwer, 2008), where an adaptive control is applied for a similar setup, but the proposed approach achieved a better transient performance. However, the ethanol concentration level does not always converge to zero indicating an error on the estimation of x_2^*. Notice we determine x_2^* from (12) which is a function of some partially known parameters. Further developments are needed to improve the estimation of the substrate concentration critical level.

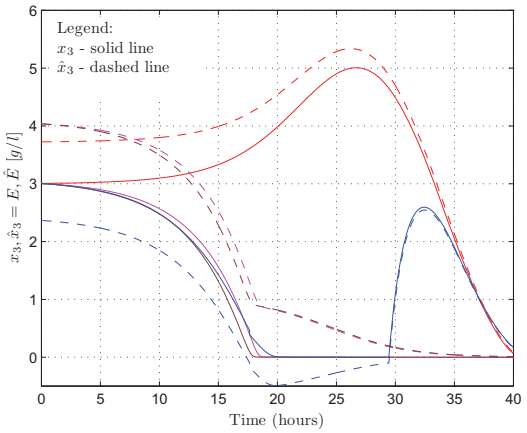

Fig. 7. Ethanol concentration – output feedback case.

6. CONCLUSION

This paper has proposed a robust control strategy to optimize the production of yeast cultures in fed-batch operation. Firstly, assuming full state information, a robust controller is designed for ensuring a guaranteed performance in spite of parameter uncertainty. Then, a nonlinear robust observer is derived in order to estimate the states that are not available online for feedback. Numerical examples have demonstrated the applicability of the proposed approach to control yeast fed-batch fermentation processes.

ACKNOWLEDGEMENTS

This paper presents research results of the Belgian Network DYSCO (Dynamical Systems, Control, and Optimization), funded by the Interuniversity Attraction Poles Programme, initiated by the Belgian Federal Science Policy Office (BELSPO). The scientific responsibility rests with its authors. D. Coutinho is beneficiary of a fellowship granted by BELSPO.

REFERENCES

Bastin, G. and Dochain, D. (1990). *On-line Estimation and Adaptive Control of Bioreactors*. Elsevier, Amsterdam, The Netherlands.

Boskovic, J. and Narendra, K. (1995). Comparion of linear, nonlinear and neural network-based adaptive controllers for a class of fed-batch fermentation processes. *Automatica*, 31, 817–840.

Boyd, S., El-Ghaoui, L., Feron, E., and Balakrishnan, V. (1994). *Linear Matrix Inequalities in System and Control Theory*. SIAM, Philadelphia, PA.

Chen, L., Bastin, G., and van Breusegem, V. (1995). A case study of adaptive nonlinear regulation of fed-batch biological reactors. *Automatica*, 31, 55–65.

Coutinho, D., Curcio, M., Mladic, J., and Bazanella, A. (2005). Robust Observer Design for a Class of Nonlinear Systems. In *Proc. 44th IEEE Conf. Decision Contr. and European Contr. Conf.*, 2640–2645. Seville, Spain.

Dahleh, M. and Diaz-Bobillo, I. (1995). *Control of Uncertain Systems: A Linear Programming Approach*. Prentice-Hall, Englewwod-Cliffs, NJ.

de Souza, C., Trofino, A., and de Oliveira, J. (2000). Robust H_∞ Control of Uncertain Linear Systems via Parameter-Dependent Lyapunov Functions. In *Proc. 39th IEEE Conf. Decision and Contr.*, 3194–3199. Sydney, Australia.

Dewasme, L. and Vande Wouwer, A. (2008). Adaptive extremum-seeking control applied to productivity optimization in yeast fed-batch cultures. In *Proc. 17th IFAC World Congress*, 9713–9718. Seoul, Korea.

Hisbullah, M., Hussain, K., and Ramachandran, K. (2002). Comparative evaluation of various control schemes for fed-batch fermentation. *Bioprocess and Biosystems Engineering*, 24, 309–318.

Ignatova, M., Lyubenova, V., Garcia, M., Vilas, C., and Alonso, A. (2008). Indirect adpative linearizing control of a class of bioprocess – Estimator tuning procedure. *Journal of Process Control*, 18, 27–35.

Karakuzu, C., Türker, M., and Öztürk, S. (2006). Modelling, on-line state estimation and fuzzy control of production scale of fed-batch baker's yeast fermentation. *Control Engineering Practice*, 14, 959–974.

Klockow, C., Hüll, D., and Hitzmann, B. (2008). Model based substrate set point control of yeast cultivation processes based on FIA measurements. *Analytica Chimica Acta*, 623, 30–37.

Leith, D. and Leithead, W. (2000). Survey of gain-scheduling analysis and design. *International Journal of Control*, 73, 1001–1025.

Nagpal, K., Abedor, J., and Poola, K. (1994). An LMI Approach to Peak-to-Peak Gain Minimization: Filtering and Control. In *Proc. Am. Contr. Conf.*, 742–746. Baltimore, MA.

Renard, F. and Vande Wouwer, A. (2008). Robust adaptive control of yeast fed-batch cultures. *Computers and Chemical Engineering*, 32, 1238–1248.

Rocha, M., Neves, J., Rocha, I., and Ferreira, E. (2004). Evolutionary algorithms for optimal control in fed-batch fermentation processes. In G.R. et al (ed.), *Applications of Evolutionary Computing - LNCS*, volume 3005, 84–93. Springer-Verlag, Berlin, Germany.

Roeva, O. and Tzonkov, S. (2005). Optimal Feed Rate Control of Escherichia coli Fed-batch Fermentation. *Bioautomation*, 2, 30–36.

Skogestad, S. and Postlethwaite, I. (2001). *Multivariable Feedback Control – Analysis and Design*. John Willey & Sons, New York, NJ.

Sonnleitner, B. and Käppeli, O. (1986). Growth of Saccharomyces cerevisiae is controlled by its limited respiratory capacity: Formulation and verification of a hypothesis. *Biotechnology and Bioengineering*, 28(6), 927–937.

Valentinotti, S., Srinivasan, B., Holmberg, U., and Bonvin, D. (2004). An Optimal Operating Strategy for Fed-Batch Fermentations by Feeding the Overflow Metabolite. In *Proc. IFAC Int'l Symp. Advanced Contr. Chemical Processes – ADCHEM'03*. Kowloon, Hong Kong.

Human Operator Based Fuzzy Intuitive Controllers Tuned with Genetic Algorithms

Filipe Leandro de F. Barbosa*, Ming Tham, Jie Zhang**, André Domingues Quelhas***

**Petrobras SA – Petróleo Brasileiro SA – Rio de Janeiro – RJ, Brazil*
Rua Visconde de Duprat s/n – 8o andar, CEP: 20211-230 – Rio de Janeiro – RJ, Brazil
(Tel: +55 21 3487-3474; e-mail: filipeleandro@petrobras.com.br, quelhas@petrobras.com.br)
*** School of Chemical Engineering and Advanced Materials, Newcastle University,*
Newcastle upon Tyne NE1 7RU, UK (e-mail: ming.tham@ncl.ac.uk, jie.zhang@newcastle.ac.uk)

Abstract: A recent study (Desborough and Miller, 2001) revealed that a great majority of the control loops that operate in industry use the PID (Proportional-Integral-Derivative) controllers. Furthermore, the study has shown that more than one third of these loops were switched to manual for a considerable period of time, indicating poor behaviour of the controllers' performance. As was also reported, the gap between the industrial practice and the process control theory remains unchanged over the years, indicating that industry is looking for simple and easy to use technologies. The present research offers an alternative control scheme that intends to be a step towards introducing a new technology for practical implementation in industry. The controller is developed aiming to emulate human operators' actions when manually controlling SISO systems, subject to disturbances. The developed control scheme is based on an intuitive hypothetical model that describes the way human operators (HO) act in a manual control loop, generating the Human Operator Based Intuitive Controller (HOBIC). Since human operators typically use vague terms when describing control actions, it is natural to use fuzzy logic to express manual control actions. The HOBIC is then extended using the Fuzzy Logic theory. Membership functions within Fuzzy-HOBIC are tuned using a genetic algorithm (GA). The tuning does not require a process model. It is based on historical process operation data containing manual operation actions from experienced operators. The traditional GA is modified to cope with real valued optimisation variables and their constraints. Results show that the hypothetic model created for the HO's actions is appropriate, since the generated control actions by the HOBIC and Fuzzy-HOBIC can approximate those of human operators. The control signal generated has the same discontinuous nature of the HO's one.

Keywords: advanced control strategy, human operator model, auto-tuning, fuzzy logic, genetic algorithm

1. INTRODUCTION

Process Control theory has been well explored over decades to, at first, automate the manual control loops and thereafter, to maintain and improve them. However, it is observed that there is a gap between the Industry and the state of the art theory (Desborough and Miller, 2001). Industry presents, very often, a high resistance to put into practice what was recently developed. As a result, the vast majority of the control loops observed operates using traditional PID (Proportional-Integral-Derivative) controllers. Such kinds of controllers are very simple to apply and understand, when compared to other more advanced approaches.

However, recent studies have revealed that a great part of those PID control loops are having a poor behaviour or are operating in manual. As an example, Desborough and Miller (2001) published a survey showing that 97% of the regulatory controllers from over 11,000 control loops of refining, chemicals, pulp and paper industries use the PID strategy. Furthermore, this work mentions that only one third of these controllers provide an acceptable performance. It is also commented that this fact is in accordance with the work of Bialkoski (1993).

This leads to the challenge of investigating those control loops to verify if they can be improved by simply reviewing the applied PID strategies or, in some cases, by studying the applicability of new techniques. Nevertheless, being aware of Industry's inertia to new developments, the challenge is even greater: to develop a control strategy with a great practical appeal, so it can be easy to understand and apply.

In the authors' experience, very often, newly developed control strategies are difficult to understand by the operators, the end users of the controllers. Hence, at the first indication of bad behaviour of the loop, the operators simply switch the controller to manual and if the process engineer does not verify what caused the problem, the operator normally will not turn it into automatic again. This will reinforce the statistics of loops in manual in Industry and quickly put the new technology into disrepute.

The review by Desborough and Miller (2001) also explicitly shows that 36% of the analysed PID loops are operating in manual for at least 30% of the observed data (5,000 samples

at the dominant system time constant). Hence, almost 4,000 controllers have been switched to manual for a considerable amount of time.

This work has the objective of developing a technique which is easily understandable by the operators. By doing so, the end users of the control loop will tend to support the idea and maintain the controller in automatic.

One way of getting support of the operators is to make the control loop behave as if the loop is in manual. In other words, the controller has to give actions to the final control element in the same way as the operator would do, if he was controlling the loop. If the new controller manages to mimic this behaviour, it is less likely that the operator will switch the controller to manual.

Nevertheless, trying to emulate the operator's actions in a control scheme is not something new. Until 1966, over 200 works related to this subject were published, according to Costello and Higgins (1966).

The great majority of the research on Human Operator (HO) modelling in the past was for application in mechanical systems, such as aircrafts and vehicles dynamics (Kleinman, Baron and Levison, 1970). Investigating more recent papers in this field, it can be noticed that this area of modelling the human behaviour for applications in control systems still attracts the researchers' attention as can be seen by the works of Enab (1995); Zapata, Galvão and Yoneyama (1999); Ertugrul and Hizal (2005). However, there is still a lack of real applications of such control technique in the Process Control field.

The present research aims to construct a control system with direct application in the continuous Process Control Industry, also by modelling Human Operator actions. However, it is different from the vast majority of the previous works in this modelling field. Due to the fact that the system dominant time-constants in the Process Control area are, in general, greater than in the mechanical systems, the concern about the HO's reaction time becomes negligible. Hence, the HO modelling techniques applied by Kleinman, Baron and Levison (1970a, b) are not suitable for sluggish Process Control applications. In the same manner, Zapata, Galvão and Yoneyama (1999) presented a mechanical application where the system time-constant had the same order of magnitude of the HO responses. As a result, an ARMA (autoregressive with moving average) model for the HO had to be identified to smooth the operator actions, considered to be noisy and less consistent than the ARMA model ones.

Another important issue to be discussed is the implementation strategy that the recent works used to model the HO control actions. They applied a model-free type technique. In other words, the model was extracted based upon input-output data, either by using Neural Networks approach (Enab, 1995), Neuro-Fuzzy techniques (Ertugrul and Hizal, 2005) or simply by extracting Fuzzy rules directly (Zapata, Galvão and T. Yoneyama, 1999).

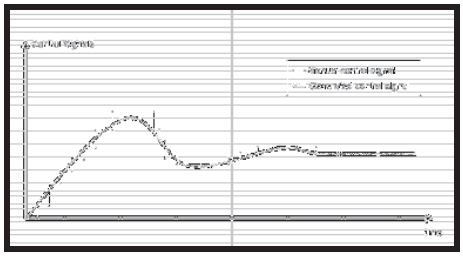

Fig. 1: Fictitious representation of a Manual control signal and a generated control signal using a model-free approach.

Although the model-free approach is able to approximate the HO behaviour, as the results of these works show, it fails to present a clear and easily understandable description of how the HO behaves and which rule system it uses to generate the actions. Even when applying Fuzzy Logic (FL) technique directly, as done by the work of Zapata, Galvão and T. Yoneyama (1999), the model-free approach generated a set of 15625 rules, which is quite difficult to understand and maintain in a practical application.

In the present work, a model-based approach is applied using the FL theory. Hence, the number of generated Fuzzy rules is expected to be much less than when using the model-free approach, and therefore easier to understand and apply in the Process Industry.

The work developed by Enab (1995) is of particular interest because it was related specifically to Process Control. The application presented was the control of the level in a tank, which has a nonlinear behaviour. This paper shows that the manual operation can be approximated using a Neural Networks approach. However, the generated control signal is continuous, compared with a "stair-like" manual signal, as can be seen by Fig.1. The difference in the signal's nature is clear. On the other hand, a FL model-based approach would be able to produce a "stair-like" signal, if the proposed rules that comprise the Human Operator model are designed to perform this task. Nevertheless, one disadvantage of the FL model-based system is that the resultant Fuzzy Logic Controller (FLC) will need to have its parameters adjusted so it will be able to reflect the behaviour of a given operator. Thus, these Membership Functions (MFs) have to be appropriately adjusted so that the generated control signal approximates the HO behaviour.

One way to cope with this disadvantage of the model-based FL approach is to come up with an automatic procedure for finding the appropriate adjustments of the MFs. In this work, this procedure is called "tuning". As there are many possible combinations for the MFs parameters, the search space for the tuning procedure is inevitably large. To solve such kind of high dimensional search space problems, Genetic Algorithms can be applied (Orvosh and Davis, 1994). In this work, a Genetic Algorithm (GA) is developed to tune and validate the proposed FL model.

The remainder of this work is organised as follows. Section 2 gives a general idea of the desired behaviour of the developed controller based on a hypothetic model for the way the HO acts in a manual control loop. In Section 3, the controller is

formally presented and its natural extension, via FL approach is achieved. In Section 4, a Genetic Algorithm (GA) is used to select the appropriate FLC parameters. A nonlinear Process Control application is tested with the developed FLC to compare the generated control actions with the manual operation in Section 5, where the results of the system simulation and discussion are presented. Section 6 summarises the conclusions of this paper and recommendations for future work.

2. HUMAN OPERATOR BASED INTUITIVE CONTROLLER DEVELOPMENT

2.1 Human Operator tasks and responsibilities

In a process plant, commonly, the HO has the responsibility of maintaining the plant under control, mainly by manipulating the final control elements, in manual loops, or by changing the controllers' set-point (SP) values.

The first concern of the operators is about safety. Right after the security concern is the production task. The production throughput should not decrease in time. Supervisors are always checking for production problems and possible causes of such incidents.

2.2 Human Operator's behaviour model

Two modes of operation may be defined for the HO:

A. When changing the operating conditions (SP-Tracking);

B. When rejecting disturbances (Disturbance Rejection).

In the first mode of operation (Mode A), the operator, to not disturb the system, will change the operating conditions only when necessary by slow changes in the final control element. This tends to minimise some problems such as interactions between loops, for example. This manual procedure is equivalent to changing the controller SP, when it is in automatic. Hence, Mode A is called SP-Tracking mode of operation. In Mode B, to reject a given disturbance, the behaviour of the operator is normally more aggressive. This is natural, since his task is to maintain the process plant under control.

An intuitive algorithm to describe the way the operator adjusts the final control element (Control Valve, for example), considering a single input single output system, subject to disturbances, can be described as follows:

1) Is the PV following the desired path (SP)?

If 'Yes' then "Do nothing. The process is under control"

Else

If Mode A: - apply Mode A procedure;

If Mode B: - apply Mode B procedure;

End

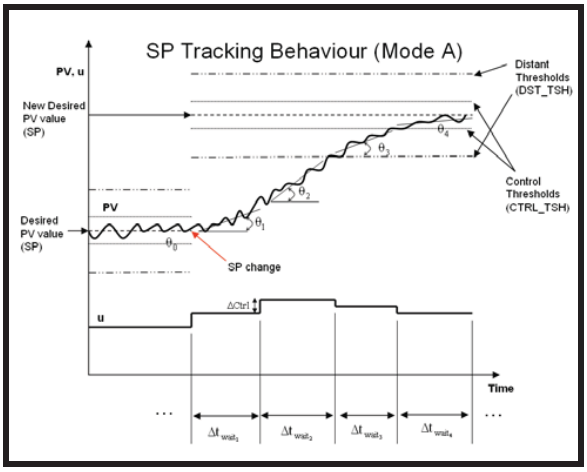

Fig.2: Intuitive HO behaviour when in Mode A of operation.

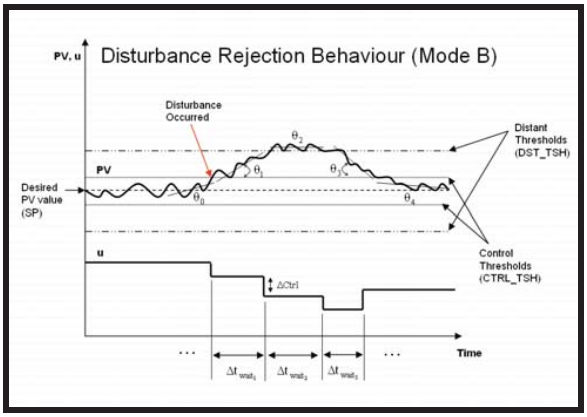

Fig. 3: Intuitive HO behaviour when in Mode B of operation.

2) When in Mode A:

Manipulate the Control Valve appropriately and wait for the system to react. If the trend of the PV is already going to the desired SP with an appropriate "velocity" do not change the Control Valve value. However, if the PV trend is going too "fast" or too "slow" to the desired SP, change the Control Valve appropriatelly and wait for the system's response

3) When in Mode B:

Perform the same actions done in Mode A, but with more aggressiveness, that depends upon the value of the PV.

From Fig. 2 and Fig. 3, some subjective terms mentioned in items 1, 2 and 3 such as "velocity", "slow" and "fast", are clarified. It can be observed that as the operator inspects the PV, he determines if the PV is under control by observing three variables, mainly:

- Variable 1 – Angle that the PV trend makes with respect to the desired SP;
- Variable 2 – Distance between the PV and SP;
- Variable 3 – Is the error increasing or decreasing?

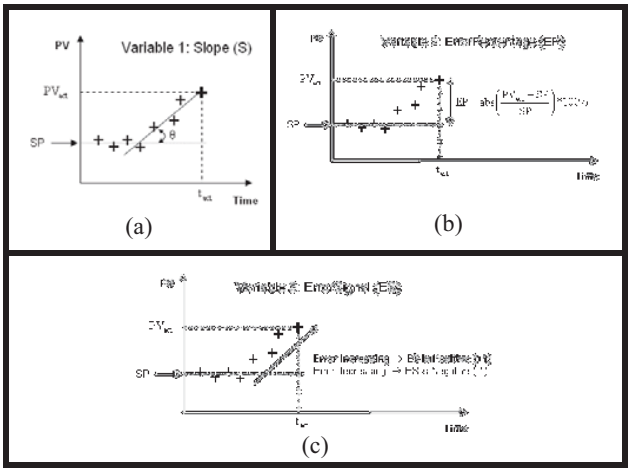

Fig.4: Variables used to encapsulate the HO's behaviour in the HOBIC.

Hence, the action taken in the Control Valve will be generated after analysing these three variables. After the action, the operator has to wait some time until the system reacts to it. The minimum time to wait (Δt_{wait}) should be greater than the Process time-delay. Thus, after observing the result of his action, the HO judges again the variables 1, 2 and 3 and takes another action or waits, if the PV is already under control again or if the PV trend is behaving as intended.

The PV is considered to be "behaving as intended" if it is approaching the SP within a given range of angles ("velocity") at a given distance from the SP that the operator establishes in his mind for that specific system. Therefore, if the angle is not within the desired range of values for a specific distance away from SP, then the control action is increased or reduced appropriately. From Fig.2 and Fig.3 it is clear that for SP-tracking (Mode A) the actions are less aggressive than when rejecting disturbances (Mode B). These figures also show that the HO has in his mind imaginary thresholds to determine how far from the SP the PV is (CTRL_TSH and DST_TSH).

2.3 The HOBIC and its natural extension –Fuzzy-HOBIC

Fig. 4 suggests the way variables 1, 2 and 3 are obtained. Variable 3, denoted as ErrorSignal (ES), reflects whether the error between SP and PV is increasing ("+1") or decreasing ("-1"). Variable 2, shown in Fig. 4(b), defines the absolute value of the error percentage between PV_{act} and SP, i.e. ErrorPercentage (EP). The reason for defining the distance between PV and SP as an error percentage measure is because the operator tends to analyse the PV value relatively to its desired value to judge if the PV is close or far from the SP. For example, for SP values of 100 units, deviations of 3 units can be considered to be "small" (3%) by the operator, and no action would be taken. However, if the SP is zero, the EP will be, by definition, the absolute value of the PV times 100%. Variable 1 defines the angle, in degrees, that the PV trend makes with the SP, denoted by Slope (S) in Fig.4(a).

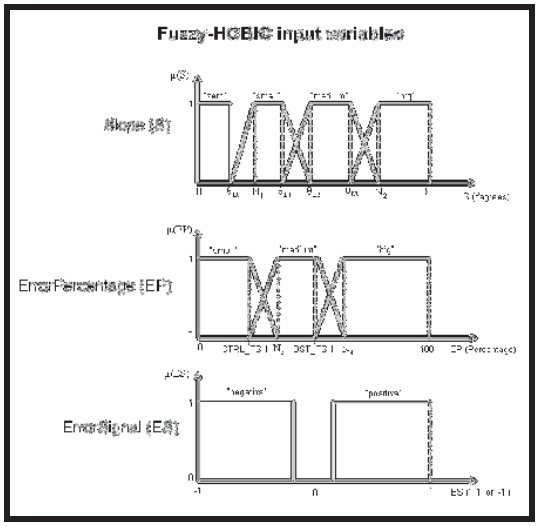

Fig. 5: Fuzzy-HOBIC Linguistic variables.

The Slope can be obtained numerically using Multi-variable Least Squares (LS). From Fig. 4(a), one can notice that the angle is obtained by using five samples (PV_{act} and the past four samples). This is a good compromise between being less sensitive to the presence of noise and getting the actual PV trend. It is being assumed here that the sampling period used is sufficiently low to capture the system dynamics (eg.: 10% of the dominant time-constant) and sufficiently high to not to capture only the noise dynamics.

After defining how the variables 1, 2 and 3 are determined in the HOBIC, the next step is to specify the thresholds CTRL_TSH and DST_TSH. The Control Threshold is, by definition, the limits within which the operator judges that the system is under control and no action is taken, when the PV has "small" Slope values. The Distant Threshold is obtained by determining the distance between PV and SP, when the operator's actions start to increase significantly. These limits are also automatically detected (Section 3).

2.4 Determining the HOBIC's rules

To be able to embed in the HOBIC the rules that the operator is using, four angle limits are defined: $\theta_{L0}, \theta_{L1}, \theta_{L2}, \theta_{L3}$. The first angle limit (θ_{L0}) is a dead band limit. In other words, the HOBIC will consider that the Slope is zero if S is less than θ_{L0}. The other three limits are distributed from θ_{L0} to 90 degrees, dividing this region into intervals. For each region of Slope values and considering the EP and ES variables, a specific action is taken in the Control Valve. Judgment about what action is to be taken given the system state (S, EP, ES) is performed by a set of 20 rules. However, these rules can be simplified by applying the FL approach.

The actual HOBIC variables S, EP and ES are considered to be linguistic input variables. The Linguistic values for these variables are as follows:

Table 1: Fuzzy-HOBIC rules definition.

Rule N°	Rule Definition	*Abs (deltaAction)*
1	IF (S is zero) and (EP is small)	*zero*
2	IF (S is zero) and (EP is medium)	*small*
3	IF (S is zero) and (EP is big)	*medium*
4	IF (S is small) and (EP is small)	*small*
5	IF (S is small) and (EP is medium)	*small*
6	IF (S is small) and (EP is big)	*medium*
7	IF (S is medium) and (EP is small)	*small*
8	IF (S is medium) and (EP is medium) and (ES is negative)	*Zero*
9	IF (S is medium) and (EP is medium) and (ES is positive)	*medium*
10	IF (S is medium) and (EP is big) and (ES is negative)	*zero*
11	IF (S is medium) and (EP is big) and (ES is positive)	*big*
12	IF (S is big) and (EP is small)	*medium*
13	IF (S is big) and (EP is medium)	*medium*
14	IF (S is big) and (EP is big) and (ES is negative)	*small*
15	IF (S is big) and (EP is big) and (ES is positive)	*max*

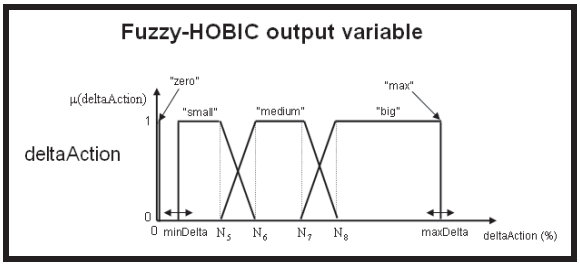

Fig. 6: Fuzzy-HOBIC output variable description.

• Slope (S): “zero”, “small”, “medium”, “big”

• ErrorPercentage (EP): “small”, “medium”, “big”

• ErrorSignal (ES): “positive”, “negative”

The Fuzzy-HOBIC input variables are described in Fig. 5. Each linguistic value is mathematically defined as a MF. Applying FL approach, the rules number is reduced to 15. They are shown in Table 1. This happens without loss of generality because of the advantage that the fuzzy rules give of activating more than one rule at a time.

It is important to notice that the control action is shown in Table 1 as an absolute value. The sign of deltaAction, is determined by observing the ES value. The Fuzzy-HOBIC output variable (deltaAction) is shown in Fig.6. About Fig. 6, the linguistic values “zero” and “max” are applied to force the Defuzzification process to give the numeric outputs zero and maxDelta, according to its respective fuzzy rules.

The process time-delay, minDelta and maxDelta values are assumed to be known inputs that depend upon the application and the HO’s behaviour, as well as the times involved to wait for the system to react, after the control actions are given.To cope with the disadvantage of having many parameters to tune for this controller, an automatic method of tuning the developed Fuzzy-HOBIC using a Genetic Algorithm (GA) is developed.

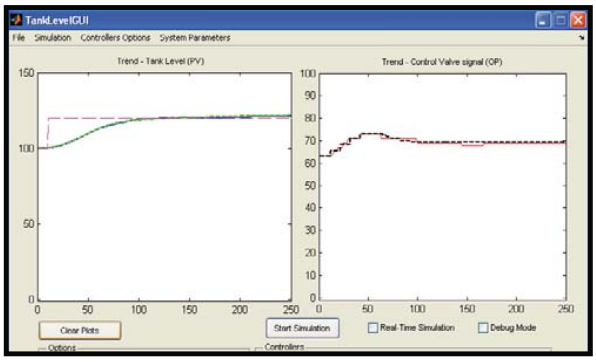

Fig. 7: Fuzzy-HOBIC (dashed lines) vs. Manual Operation (solid lines). Step up test (+20%).

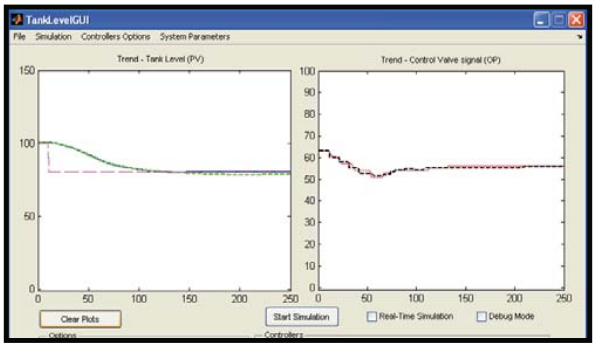

Fig. 8: Fuzzy-HOBIC (dashed lines) vs. Manual Operation (solid lines). Step down test (-20%).

3. APPLYING A GENETIC ALGORITHM TO TUNE THE FUZZY-HOBIC

The objective of the GA is to find values of the 14 parameters (P1-P14) that will make the Fuzzy-HOBIC approximate a given HO’s behaviour. The closer the Fuzzy-HOBIC’s actions are to the HO’s ones the better is the tuning. A suitable objective function, is given by (1), where $U_{man}(i)$ and $U_{FHOBIC}(i)$ represent the sample ‘i’ of the manual and the Fuzzy-HOBIC actions from a total of N

available samples, respectively.

$$J = \sum_{i=1}^{N} \frac{(U_{man}(i) - U_{FHOBIC}(i))^2}{N} \qquad (1)$$

For the developed GA, an elitist strategy is used (Chipperfield, Fleming, Pohlheim and Fonseca, 1994). The initial population is split into two sets which are used to compose three sub-populations. The first set is composed of the best individuals of the population (smallest J values). This set composes the first and the second sub-populations. The first one has a low mutation rate, while in the second a high mutation rate is applied. The low mutation rate in the first sub-population is used to search for local minimums, while the high mutation rates for the second population is applied to find new regions of minimums, trying to avoid getting trapped in local minimums.

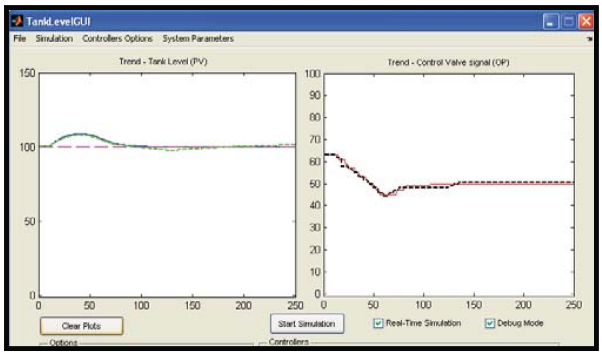

Fig. 9: Fuzzy-HOBIC (dashed lines) vs. Manual Operation (solid lines). Disturbance Rejection up test (+20%).

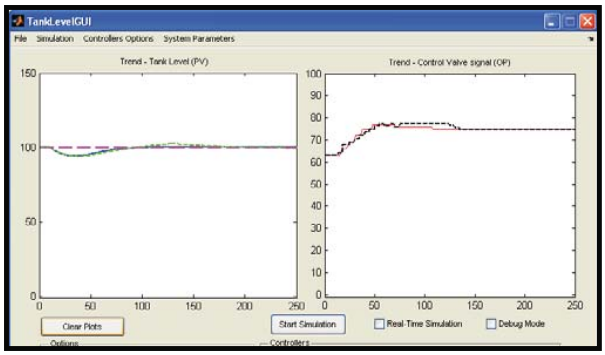

Fig. 10: Fuzzy-HOBIC (dashed lines) vs. Manual Operation (solid lines). Disturbance Rejection down test (-20%).

A third sub-population is composed of the second set of the population. In this case, a high mutation is applied, because of the same reasoning used for the second population.

The convergence criteria applied in this work is either when the best individual from the population does not change for more than 10 generations or when the maximum number of generations is exceeded.

4. RESULTS AND DISCUSSION

The application chosen for testing the Fuzzy-HOBIC is controlling the level of liquid in a Tank, in the same manner as performed by Enab (2005). This is a very common nonlinear application in the process industry. For this specific application, it is also supposed that the level needs a tight control. The input flow control valve is used to regulate the tank level, while the output flow control valve generates the non-measured disturbance. After defining the application to test the Fuzzy-HOBIC it is necessary to develop a simulation environment that reflects the proposed system to be controlled. A Graphical User Interface (GUI) was implemented to simulate the tank level system.

Figures 7-10 show the results obtained when tuning the Fuzzy-HOBIC using the GA approach. It is important to notice, however, that two different tunings where used here: one for sp-tracking and the other for disturbance rejection. The manual operations where generated using the developed GUI, by an operator that got experienced by using the system. When controlling the level in manual, two objectives where followed: 1) Do not produce any overshoot, when tracking set-point; 2) Try to eliminate the disturbance as fast as possible without making large changes in the control valve. These objectives are in accordance with the HO's behaviour, described in sub-section 2.2. As can be seen by the results, the operator's behaviour could be well approximated the tuned Fuzzy-HOBICs, showing its "stair-like" signals nature.

5. CONCLUSIONS

The results of applying the Fuzzy-HOBIC in a process control simulation have indicated that:

• The rules used to describe the HO's behaviour were adequate for approximating his manual operations in the application tested;

• A process model is not needed to tune the Fuzzy-HOBIC.

As recommendations for future work, it is suggested to test the developed controller in a real Process Control Application. Another possible application of Fuzzy-HOBIC would be to train apprentice operators, as already suggested by Zapata, Galvão, and Yoneyama (1999).

REFERENCES

Bialkowski, W. L. (1993). Dream versus Reality: a view from both sides of the gap, Pulp and Paper Canada, 94 (11), pp. 19-27.

Costello, R. G. and Higgins, T. J. (1966). An Inclusive Classified bibliography pertaining to modelling the human operator as an element in an automatic control system. *VII IEEE Symp. On Human Factors in Electronics*, Minneapolis, Minn.

Chipperfield, A., Fleming, P., Pohlheim, H. and Fonseca, C. (1994). Genetic Algorithm Toolbox: For use with MATLAB - Software and User's Guide. Department of Automatic Control and Systems Engineering. University of Sheffield. UK.

Desborough, L. and Miller, R. (2001). Increasing Customer Value of Industrial Performance Monitoring – Honeywell's Experience. Honeywell Hi-Spec Solutions.

Enab, Y. M. (1995). Controller Design for an unknown process, Using simulation of a Human Operator, *Engineering Appl. of Artificial Intelligence* 8(3), pp. 299-308.

Ertugrul, S. E. and Hizal, N. A. (2005). Neuro-Fuzzy controller design via modelling human operator actions. *Journal of Intelligent & Fuzzy Systems* 16, 133-140, IOS Press.

Kleinman, D. L., Baron, S. and Levison, W. H. (1970). An Optimal Control Model of Human Response – Part I: Theory and Validation. *Automatica*, vol. 6, pp. 357-369.

Orvosh, D. and Davis, L. (1994). Using a Genetic Algorithm to Optimize Problems with Feasibility Constraints. *IEEE Conference on Evolutionary Computation - Proceedings* (2/-), pp. 548-553.

Zapata, G. O. A., Galvão, R. K. H. and Yoneyama, T. (1999). Extracting Fuzzy Control Rules from Experimental Human Operator data. *IEEE Trans. On Systems, Man and Cybernetics-PartB: Cybernetics* 29(3), pp. 398-406.

Considerations on Set-Point Weight choice for 2-DoF PID Controllers

Víctor M. Alfaro [*] **Ramon Vilanova** [**] **Orlando Arrieta** [*,**]

[*] *Departamento de Automática, Escuela de Ingeniería Eléctrica Universidad de Costa Rica, San José, 11501-2060 Costa Rica. e-mail: {Victor.Alfaro, Orlando.Arrieta}@ucr.ac.cr*

[**] *Departament de Telecomunicació i d'Enginyeria de Sistemes, ETSE Universitat Autònoma de Barcelona, 08193 Bellaterra, Barcelona, Spain. e-mail: {Ramon.Vilanova, Orlando.Arrieta}@uab.cat*

Abstract: This paper's aim is to present an analysis of the influence of the 2-DoF controllers proportional set-point weight over the servo-control performance and to show that the removal of the existing constraint for its selection ($0 \leq \beta \leq 1.0$) will allow to improve its performance when a high robust regulatory control system is required. A concrete analysis is conducted by using 2-DoF PID tuning approaches that explicitly take the desired robustness level as a design parameter. It is seen that as the desired robustness increases the tuning methods suggest values $\beta > 1.0$. Performance looses are evaluated if we are to be constrained to the case $\beta \leq 1.0$.

Keywords: PID Control, Two-Degree-of-Freedom, Set-Point Weights

1. INTRODUCTION

Since their introduction in 1940 (Babb, 1990; Bennett, 2000) commercial *Proportional - Integrative - Derivative* (PID) controllers have been with no doubt the most extensive option found on industrial control applications. Their success is mainly due to its simple structure and meaning of the corresponding three parameters. This fact makes PID control easier to understand by the control engineers than other most advanced control techniques.

With regard to the design and tuning of PID controllers, there are many methods that can be found in the literature over the last sixty years. Special attention is made of the IFAC workshop PID'00 Past, Present and Future of PID Control held in Terrassa, Spain, on April 2000, where a glimpse of the state-of-the-art on PID control was provided. It can be seen that most of them are concerned with feedback controllers which are tuned either with a view to the rejection of disturbances (Cohen and Coon, 1953; López et al., 1967; Ziegler and Nichols, 1942) or for a well-damped fast response to a step change in the controller set-point (Martin et al., 1975; Rivera et al., 1986; Rovira et al., 1969). The Two-Degree-of-Freedom (2-DoF) formulation is aimed at trying to met both objectives. This second degree of freedom is aimed at providing additional flexibility to the control system design. See for example (Araki, 1984a,b, 1985) and its characteristics revised and summarized in (Taguchi and Araki, 2000, 2002) and (Taguchi et al., 2002), as well as different tuning methods that have been formulated over the last years (Alfaro et al., 2008; Åström et al., 1992; Åström and Hägglund, 2004; Åström et al., 1998; Gorez, 2003; Hang and Cao, 1996; Hägglund and Åström, 2002; Taguchi and Araki, 2000).

This second degree of freedom is found on the presented literature as well as in commercial PID controllers under the form of the well known set-point weighting factor (usually called β) that ranges within $0 \leq \beta \leq 1.0$, being the main purpose of this parameter to avoid excessive proportional control action when a set-point change takes place. Therefore the use of *just a fraction* of the set-point.

There is however a shift of perspective with the introduction of Robustness considerations (Åström and Hägglund (1995, 2004, 2006)). As a result, less aggressive control actions are generated and smooth responses are achieved. However, if the desired level of robustness is high, step response performance can be seriously degraded. This is the analysis conducted in this paper that leads us to conclude that the use of values of β that are beyond the constraint, are definitively needed in order to get better step response performance. The analysis is conducted by using two existing tuning rules for 2-DoF PID controllers that include, as an explicit design parameter, the desired robustness level in terms of the Maximum Sensitivity value. This allows to analyze the effect of going on increasing the desired robustness level. The suggested value for β goes to values $\beta > 1.0$ in many of the cases therefore constraining the achievable performance if we are to be limited to a maximum of $\beta = 1.0$.

It is worth to notice that even the suggestion of allowing $\beta > 1.0$ seems quite common sense and natural, to the knowledge of the authors it has not still been considered. In this paper this proposal is raised within the motivation of the increased use of robustness considerations on what we could call *modern* control design approaches.

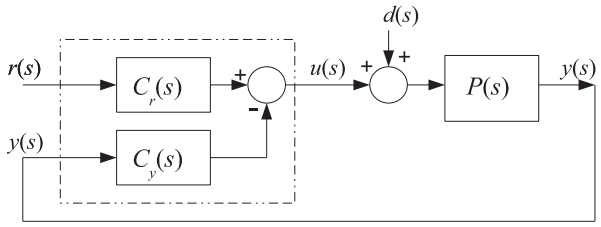

Figure 1. Closed-loop Control System

The paper is organized as follows. Section 2 introduces the control setup and the 2-DoF PID formulation. Discussion about the selection of the β parameter is also introduced. Section 3 analyzes the effects of constraining the set-point weight on robustness based tuning rules and suggests to relax that constraint in order to met a high demanding robustness-performance *tradeoff*. On Section 4 an example illustrates how performance increases if larger values of β are allowed. The paper ends in Section 5 with some conclusions.

2. 2-DOF PID FORMULATION

Consider the closed-loop control system of Fig. 1, where $P(s)$ is the *controlled process* transfer function, $C_r(s)$ the *set-point controller* transfer function, $C_y(s)$ the *feedback controller* transfer function, and $r(s)$ the *set-point*, $d(s)$ the *load-disturbance*, and $y(s)$ the *controlled variable* (process output).

The output of the controller is given by

$$u(s) = C_r(s)r(s) - C_y(s)y(s) \tag{1}$$

Without loss of generality we will use an error feedback *Ideal* PID controller which equation is

$$\begin{aligned} u(s) = & K_c \left(1 + \frac{1}{T_i s}\right) r(s) \\ & - K_c \left(1 + \frac{1}{T_i s} + \frac{T_d s}{T_d/N s + 1}\right) y(s) \end{aligned} \tag{2}$$

where K_c is the *controller gain*, T_i the *integral time constant*, T_d the *derivative time constant* and N the *derivative filter constant* (usually $N = 10$ (Visioli, 2006)). Then, the controllers' transfer functions are

$$C_r(s) = K_c \left(1 + \frac{1}{T_i s}\right) \tag{3}$$

and

$$C_y(s) = K_c \left(1 + \frac{1}{T_i s} + \frac{T_d s}{0.1 T_d s + 1}\right) \tag{4}$$

The closed-loop control system response to a change in any of its inputs, will be given by

$$y(s) = \frac{C_r(s)P(s)}{1 + C_y(s)P(s)} r(s) + \frac{P(s)}{1 + C_y(s)P(s)} d(s) \tag{5}$$

or in a compact form by

$$y(s) = M_{yr}(s)r(s) + M_{yd}(s)d(s) \tag{6}$$

where $M_{yr}(s)$ is the transfer function from set-point to controlled process variable: the *servo-control* closed-loop transfer function or complementary sensitivity function; $T(s)$; and $M_{yd}(s)$ is the one from load-disturbance to controlled process variable: the *regulatory control* closed-loop transfer function or disturbance sensitivity function $S(s)$.

Since all parameters of $C_r(s)$ are identical to the ones of $C_y(s)$ it is not possible to specify the dynamic performance of the control system to set-point changes, independently of the performance to load-disturbances changes.

If the degrees of freedom in control system are defined as the number of closed-loop transfer functions that may be selected independently (Horowitz, 1963), we have in this case a *One-Degree-of-Freedom* (1-DoF) control system.

The above constraint forces the designer to use a tuning rule developed for the specific required application (servo-control o regulatory control) finding in the literature tuning rules for regulatory control (Cohen and Coon, 1953; López et al., 1967; Ziegler and Nichols, 1942), for servo-control applications (Martin et al., 1975; Rivera et al., 1986; Rovira et al., 1969) or separate tuning rules for both applications (Chien et al., 1952; Kaya, 2004; Sung and Lee, 1999) only to mention a few. Alternatively the 1-DoF can be forced to operate in order to provide a balanced performance with respect to both operation modes. This is the so called *implicit* 2-DoF PID and has been presented in (Arrieta and Vilanova (2007b,c); Arrieta et al. (2008)). A collection of tuning methods may be found in O'Dwyer (2003).

It has been widely reported elsewhere that a control system with a controller optimized for load-disturbance rejection, normally presents high overshoots to set-point step inputs requiring a detuning with the consequential reduction in its regulatory performance. In such case, considerations about performance degradation of optimal tunings have to be taken into account (Arrieta and Vilanova (2007a)).

In order to provide additional flexibility for the control system design, a second degree of freedom was introduced into the PID algorithms in Araki (1984a,b, 1985) and its characteristics revised and summarized in Taguchi and Araki (2000, 2002) and Taguchi et al. (2002).

Consider now the PID controller equation (Åström and Hägglund, 2006)

$$\begin{aligned} u(s) = & K_c \left(\beta + \frac{1}{T_i s} + \frac{\gamma T_d s}{0.1 T_d s + 1}\right) r(s) \\ & - K_c \left(1 + \frac{1}{T_i s} + \frac{T_d s}{0.1 T_s s + 1}\right) y(s) \end{aligned} \tag{7}$$

where β and γ are the *set-point weights*.

The γ parameter is more frequently applied as a derivative mode *switch* (0 or 1) for the signal reference r. To avoid extreme instantaneous change in the controller output signal when a set-point step change occurs normally γ is set to zero. In this case the new set-point controller transfer function is

$$C_r(s) = K_c \left(\beta + \frac{1}{T_i s}\right) \tag{8}$$

and the one for the feedback controller

$$C_y(s) = K_c \left(1 + \frac{1}{T_i s} + \frac{T_d s}{0.1 T_d s + 1}\right) \tag{9}$$

which is the same as (4) above.

In commercial controllers the proportional set-point weight β may be selected only in the $0 \leq \beta \leq 1.0$ range.

Given a controlled process $P(s)$, the feedback controller $C_y(s)$ parameters (K_c, T_i, T_d) may be selected to achieve a target performance for the regulatory control $M_{yd}(s)$,

and then using the proportional set-point weight (β), in the set-point controller $C_r(s)$, to modify the servo-control performance $M_{yr}(s)$.
Under the above degree of freedom definition, we have now a *Two-Degree-of-Freedom* (2-DoF) control system. This option allowed the development of sets of tuning methods for the 2-DoF controllers as the ones found in (Alfaro et al., 2008; Åström et al., 1992; Åström and Hägglund, 2004; Åström et al., 1998; Gorez, 2003; Hang and Cao, 1996; Hägglund and Åström, 2002; Taguchi and Araki, 2000).
With regard to the commercial implementation of the PID algorithms, it is usually to find that most of them are of 1-DoF type like the ones described in (ABB ((n.d.); Foxboro (1998); Fuji (2001); Honeywell (2007); Rockwell (2003, 2005)) a few include a set-point filter ((Omron, 2007; Yokogawa, (n.d.)) and very few have 2-DoF capabilities ((Emerson, 2008; Mitsubishi, 2002)). In particular, the 2-DoF PID controller in (Emerson (2008)) allows both weights in (7) (β and γ) to be selected in the full 0 to 1 range.

3. PROPORTIONAL SET-POINT WEIGHTING ANALYSIS

From (5) and (6) the servo-control closed-loop transfer function is

$$M_{yr}(s) = \frac{C_r(s)P(s)}{1 + C_y(s)P(s)} \tag{10}$$

and the one for the regulatory control

$$M_{yd}(s) = \frac{P(s)}{1 + C_y(s)P(s)} \tag{11}$$

which are related by

$$M_{yd}(s) = C_r(s)M_{yr}(s) \tag{12}$$

Using (8) in (12) we have

$$M_{yd}(s) = K_c\left(\frac{\beta T_i s + 1}{T_i s}\right) M_{yr}(s) \tag{13}$$

On the other hand, the characteristic polynomial of the closed-loop control system is

$$p(s) = 1 + C_y(s)P(s) \tag{14}$$

from where it can be obtained the closed-loop poles location; therefore the closed-loop stability; depends only on the $C_y(s)$ parameters, hence not affected by β.
This fact makes possible to design first the feedback controller considering the *regulatory control performance* and the *closed-loop control system robustness* and, on a second step to modify the set-point controller considering only the *servo-control performance* (by the introduction of β).
Although, the instant change in the controller output signal to a step set-point change is given by

$$\Delta y_r = K_c\beta\Delta e_r = K_c\beta\Delta r \tag{15}$$

Since the performance optimization of a regulatory control system requires controllers' gains higher than the optimization of the same loop for servo-control operation, the use of a proportional set-point weight $\beta < 1$ allows to shift to the left the controller integral mode zero to a desired position to reduce the controlled signal overshoot and also to decrease the instant change in the controller output.
From the above presented analysis, it is clear that the use of a 2-DoF controller improves the servo-control performance and no questions arise about the manufactures imposed constraint on the proportional set-point weight selection range. It is along this framework that the above indicated tuning rules for 2-DoF PI and PID controllers; including the ones that take into consideration the control system robustness; constraint the set-point weight to $0 \leq \beta \leq 1$ respecting the allowed range in commercial controllers (see for example (Alfaro et al., 2008; Åström and Hägglund, 2004; Åström et al., 1998; Gorez, 2003; Hägglund and Åström, 2002; Taguchi and Araki, 2000)).
However, within a more *modern* framework robustness considerations are an integral part of practically every design approach. In such cases, as it will be explicitly shown in next section, extending the allowed range for the set-point weight will be definitively needed in order to be able to improve the servo-control performance. When a highly robust control system is required due to the expected variations in the controlled process characteristics, a significant reduction in the controller gain is needed and the performance of the control-loop will decrease. The system responses to load-disturbance and set-point changes will be slower.
This situation motivates the analysis of the proportional set-point weighting effect over the control system performance when the set-point changes, using two of the available tuning rules for 2-DoF controllers. The choice of the presented tuning rules is based on the fact that they include, as an explicit design parameter, the desired robustness level for the closed-loop control system. This setup allows for a more concrete and objective analysis. However the analysis can be easily extended to other tuning rules as the effect of getting a more robust feedback system is by sure to generate more conservative responses.

3.1 ART_2 PI Controller Tuning

The *Analytical Robust Tuning* for 2-DoF PI controllers (ART_2) follows (Alfaro et al., 2008) and is outlined here:

- *Controlled Process Model:*
$$P(s) = \frac{K_p e^{-Ls}}{Ts + 1} \tag{16}$$
where K_p is the *process gain*, T is the *time constant*, and L is the *dead-time*. It will be referred to $\tau_o = L/T \leq 1.0$ as the controlled process *normalized dead-time*.
- *Controller's Parameters:* The ART_2 tuning equations are
$$\kappa_c = K_c K_p = \frac{2\tau_c - \tau_c^2 + \tau_o}{(\tau_c + \tau_o)^2} \tag{17}$$
$$\tau_i = \frac{T_i}{T} = \frac{2\tau_c - \tau_c^2 + \tau_o}{1 + \tau_o} \tag{18}$$
where κ_c and τ_i are the controller *normalized parameters* and $\tau_c = T_c/T$ the *design parameter* (T_c is the target regulatory control closed-loop time constant).
- *Set-point Weighting:* The proportional set-point weight selection criteria is
$$\beta = \min\left\{\frac{1}{K_c}, \frac{\tau_c T}{T_i}, 1\right\} \tag{19}$$
- *Design Parameter:* The design parameter τ_c may be selected within the range
$$\max(0.50, \tau_{cmin}) \leq \tau_c \leq 1.50 + 0.3\tau_o \tag{20}$$
where τ_{cmin} is given by

$$\tau_{cmin} = k_{11}(M_s) + \left[\frac{k_{21}(M_s)}{k_{22}(M_s)}\right]\tau_o \qquad (21)$$

$$k_{11}(M_s) = 1.384 - 1.063M_s + 0.262M_s^2$$

$$k_{21}(M_s) = -1.915 + 1.415M_s - 0.077M_s^2$$

$$k_{22}(M_s) = 4.382 - 7.396M_s + 3.0M_s^2$$

allowing to design the control system with a robustness higher than the minimum required (give it by the maximum sensitivity M_s).

Using (20) and (21), the lower limits for the design parameter τ_c may be estimated. These are shown in Table 1 for robustness $1.2 \leq M_s \leq 2.0$ and controlled process model normalized dead-time $0.1 \leq \tau_o \leq 1.0$.
As it can be seen in Table 1 the lower and higher recommended limits in (20) were reached for the extreme cases (low normalized dead-time and robustness and high normalized dead-time and robustness). For the first case this means that, slow responses with high robustness system requirements will be obtained, and for the second one, that it is not possible to obtain a system with the high robustness specified.
The controller's proportional set-point weight may be obtained with (19) and they are shown in Table 2. As can be seen in this Table the existing upper limit constraint of 1.0 for β was intentionally relaxed (bold).

According to the ART_2 tuning rules, when the normalized dead-time is in the upper side of the range ($\tau_o \approx 1$) and the required system robustness is high, the recommended proportional weight would be higher than 1.0. As it can be seen in the last column of Table 2, this is the situation for practically all values of τ_o when a robustness $M_s = 1.2$ is specified. Therefore, the imposed constraint for the β value selection, in the available commercial Two-Degree-of-Freedom PID controllers, does not allow the designer to use the full capabilities of these controllers.

Table 1. Higher Close-loop Speed Allowed τ_{cmin}

	M_s				
τ_o	2.0	1.8	1.6	1.4	1.2
0.1	0.500	0.500	0.500	0.501	0.675
0.2	0.500	0.500	0.500	0.593	0.864
0.3	0.500	0.500	0.553	0.685	1.054
0.4	0.500	0.513	0.620	0.777	1.243
0.5	0.500	0.562	0.686	0.869	1.432
0.6	0.535	0.610	0.753	0.961	1.622
0.7	0.573	0.659	0.819	1.053	1.710
0.8	0.611	0.707	0.886	1.145	1.740
0.9	0.650	0.756	0.952	1.236	1.770
1.0	0.688	0.804	1.019	1.328	1.800

Table 2. Proportional Set-Point Weight Factor β

	M_s				
τ_o	2.0	1.8	1.6	1.4	1.2
0.1	0.424	0.424	0.424	0.425	0.604
0.2	0.516	0.516	0.516	0.608	0.878
0.3	0.609	0.609	0.654	0.742	**1.056**
0.4	0.609	0.618	0.691	0.806	**1.298**
0.5	0.600	0.644	0.735	0.879	**1.636**
0.6	0.619	0.674	0.783	0.962	**2.138**
0.7	0.642	0.707	0.835	**1.054**	**2.431**
0.8	0.667	0.743	0.892	**1.158**	**2.501**
0.9	0.694	0.780	0.954	**1.274**	**2.573**
1.0	0.723	0.820	**1.019**	**1.404**	**2.647**

3.2 Integrated Absolute Error (IAE) Optimized PID Tuning

A tuning method for 2-DoF PI and PID controllers that optimizes their performance under a IAE cost functional ensuring at the same time a minimum closed-loop robustness (M_s) is described in Méndez (2008). Bellow are presented the controller parameters for one particular robustness level, say $M_s = 1.4$.

- *Controlled Process Model:*
$$P(s) = \frac{K_p e^{-Ls}}{(Ts+1)(aTs+1)} \qquad (22)$$
where K_p is the process gain, T is the dominant time constant, a is the *time constants ratio* and L is the dead-time ($\tau_o = L/T$).
- *Controller's Set-Point Weight:* Table 3 shows the PID_2 controller's set-point weighting factor for the $M_s = 1.4$ case corresponding to different values of τ_o and a. As shown in this table for this robustness most of the recommended proportional set-point weights exceed the 1.0 upper limit (bold).

Table 3. $IAE - M_s$ PID_2 Controller Set-Point Weight β

	τ_o						
a	0.1	0.25	0.50	0.75	1.0	1.50	2.0
0.25	0.636	0.819	**1.073**	**1.256**	**1.413**	**1.665**	**1.839**
0.50	0.585	0.731	0.992	**1.189**	**1.338**	**1.630**	**1.778**
0.75	0.588	0.695	0.921	**1.104**	**1.261**	**1.550**	**1.755**
1.0	0.567	0.662	0.871	**1.052**	**1.210**	**1.412**	**1.663**

4. EXAMPLE

This section provides an example to show the effect of the proportional set-point weighting over the servo-control system performance.
In order to have simulation results more close to industrial practice, in the example it is assumed that all variables can vary in the 0 to 100% normalized range and that in the normal operation point, the controlled variable, the set-point and the control signal, have all values close to 70%. For the tests a 20% change in set-point followed by a 10% change in load-disturbance will be used in all cases.
Performance: Performance will be evaluated for a set-point change and under the presence of a load-disturbance. The Integrated-Absolute-Error (IAE) that is defined as

$$J_{IAE} \doteq \int_0^\infty |r(t) - y(t)|\, dt \qquad (23)$$

and provides a measure for control system *output performance.*
Control input usage: On the other hand to evaluate the manipulated input usage, the total variation of the control effort $u(t)$ (TV_u) is computed. This value is defined, for a discrete signal as the sum of the size of its increments

$$TV_u \doteq \sum_{k=1}^{\infty} |u_{k+1} - u_k| \qquad (24)$$

This quantity should be as small as possible and provides a measure of the *smoothness of the control signal.*
Robustness: The maximum sensitivity value

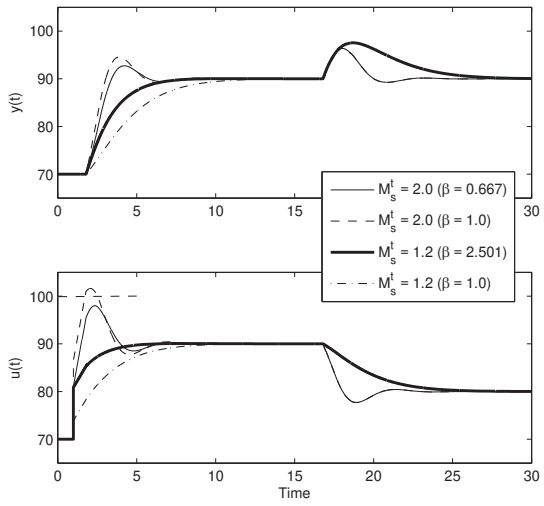

Figure 2. PI Control System Responses

Table 4. ART_2 PI Controller Parameters

M_s^t	τ_c	K_c	T_i	β
2.0	0.611	0.828	0.916	0.667
1.2	1.740	0.194	0.988	2.501

$$M_s = \max_{\omega} |S(\mathrm{j}\omega)| = \max_{\omega} \frac{1}{|1 + C_y(\mathrm{j}\omega)P(\mathrm{j}\omega)|} \qquad (25)$$

is used as a measure of the control system *robustness*. Recommended values for M_s are typically within the range 1.2 - 2.0.

Consider the particular case of controlled process (16) with $K_p = 1.0$, $T = 1.0$ and $L = 0.80$ ($\tau_o = 0.80$). The PI_2 controller's parameters obtained with the ART_2 tuning method in Section 3.1, in order to have a low robustness ($M_s^t = 2.0$) and a high robustness ($M_s^t = 1.2$) control system, are shown in Table 4 (the upper limit constraint for β was not taken into account).
System responses are shown in Fig. 2. The figure includes also the responses obtained with $\beta = 1.0$ in both cases.
The servo-control performance (J_{IAEr}) and control effort smoothness (TV_{ur}) as well as the obtained control system robustness (M_s^r) are shown in Table 5.
For the low robustness case ($M_s^t = 2.0$) the use of a proportional set-point weight lower than 1.0 ($\beta = 0.667$) allows to reduce: the servo-control controlled variable overshoot, the control effort upper value and helps to made it smoother compared with the $\beta = 1.0$ case. This last case is equivalent to the use of a 1-DoF PI controller.
In the high robustness case ($M_s^t = 1.2$) the use of a proportional set-point weight higher than 1.0 ($\beta = 2.501$) allows to improve the servo-control performance reducing J_{IAEr} without deterioration of the control effort behavior TV_{ur} compared with the case of $\beta = 1.0$. This is when the use of the set-point weight, in the 2-DoF PI controller, is setted to the upper limit allowed by the manufacturer.

Table 5. PI Control Performance and Robustness

M_s^t (β)	J_{IAEr}	J_{IAEr}(%)	TV_{ur}	TV_{ur}(%)	M_s^r
2.0 (0.667)	0.363	100%	0.398	81%	2.009
2.0 (1.0)	0.363	100%	0.489	100%	2.009
1.2 (2.501)	0.471	66%	0.201	101%	1.239
1.2 (1.0)	0.717	100%	0.200	100%	1.239

5. CONCLUSIONS

The use of a Two-Degree-of-Freedom (2-DoF) PID controller must allow the control-loop designer to take into consideration the *regulatory control performance* and *control effort* requirements in conjunction with the *control system robustness* and then improve the *servo-control performance*.
However the analysis of the recommended tuning for its proportional set-point weight has shown that the established constraint by controller's manufactures for its values to the $0 \leq \beta \leq 1.0$ range, avoids the designer to exploit the full potential of these controllers.
The allowed range for the proportional set-point weight could make sense when the controller design main objectives were only to optimize its performance but nowadays, the *performance-robustness trade-off* is taken into account within the *modern* control design formulations. Even included explicitly into the tuning equations as it has been shown in the concrete tuning rules analyzed in this paper. It has been shown that this constraint reduces the performance of the control-loop responses, to a set-point step change, when a high robustness control system is required.
The control system designer will be able to use the full inherent capabilities of the Two-Degree-of-Freedom PID controllers, only when the existing constraint in the set-point weight selection will be removed by the manufacturers.

ACKNOWLEDGEMENTS

This work has received financial support from the Spanish CICYT program under grant DPI2007-63356.
The financial support from the University of Costa Rica and from the MICIT and CONICIT of the Government of the Republic of Costa Rica is greatly appreciated.

REFERENCES

ABB ((n.d.)). *Protonic 100/500/550 Digitric 500 Configuration and Parametrization Manual*. ABB Automation Products. 42/62-500 12EN.

Alfaro, V.M., Vilanova, R., and Arrieta, O. (2008). Analytical Robust Tuning of PI controllers for First-Order-Plus-Dead-Time Processes. In *13th IEEE International Conference on Emerging Technologies and Factory Automation*. Hamburg-Germany.

Araki, M. (1984a). On Two-Degree-of-Freedom PID Control System. Technical report, SICE Research Commitee on Modeling and Control Design of Real Systems.

Araki, M. (1984b). PID Control Systems with Reference Feedforward (PID-FF Control System). In *Proc. of 23rd SICE Anual Conference*, 31–32.

Araki, M. (1985). Two-Degree-of-Freedom Control System - I. *Systems and Control*, 29, 649–656.

Arrieta, O. and Vilanova, R. (2007a). Performance degradation analysis of Optimal PID settings and Servo/Regulation *tradeoff* tuning. *CSC07, Conference on Systems and Control, Marrakech-Morocco*.

Arrieta, O. and Vilanova, R. (2007b). PID Autotuning settings for balanced servo/regulation operation. *MED07, 15th IEEE Mediterranean Conference on Control and Automation, Athens-Greece*.

Arrieta, O. and Vilanova, R. (2007c). Servo/Regulation tradeoff tuning of PID controllers with a robustness consideration. *CDC07, 46th IEEE Conference on Decision and Control, New Orleans, Louisiana-USA*.

Arrieta, O., Vilanova, R., Alfaro, V., and Moreno, R. (2008). Considerations on PID Controller Operation: Application to a Continuous Stirred Tank Reactor. In *13th IEEE International Conference on Emerging Technologies and Factory Automation*. Hamburg-Germany.

Åström, K. and Hägglund, T. (1995). *PID Controllers: Theory, Design and Tuning*. Instrument Society of America, Research Triangle Park, NC, USA.

Åström, K. and Hägglund, T. (2004). Revisiting the Ziegler-Nichols step respose method for PID control. *Journal of Process Control*, 14, 635–650.

Åström, K. and Hägglund, T. (2006). *Advanced PID Control*. ISA - The Instrumentation, Systems, and Automation Society.

Åström, K., Hang, C.C., Persson, P., and Ho, W.K. (1992). Towards Intelligent PID Control. *Automatica*, 28(1), 1–9.

Åström, K., Panagopoulos, H., and Hägglund, T. (1998). Design of PI controllers based on non-convex optimization. *Automatica*, 34, 585–601.

Babb, M. (1990). Pneumatic Instruments Gave Birth to Automatic Control. *Control Engineering*, 37(12), 20–22.

Bennett, S. (2000). The Past of PID Controllers. In *IFAC Digital Control: Past, Present and Future of PID Control*. Terrassa, Spain.

Chien, I., Hrones, J., and Reswick, J. (1952). On the automatic Control of generalized passive systems. *Trans. ASME*, 175–185.

Cohen, G.H. and Coon, G.A. (1953). Theoretical Considerations of Retarded Control. *ASME Transactions*, 75, Jul.

Emerson (2008). *DeltaV BooksOnLine9.3*. Emerson Process Managment. Web-based version http://www.easydeltav.com/BOL/.

Foxboro (1998). *Instruction 762 CNA Single Station Micro Controller*. The Foxboro Company. MI 018-885.

Fuji (2001). *Instruction Manual - Compact Controller M*. Fuji Electric. INP-TN1PDA 3cE.

Gorez, R. (2003). New desing relations for 2-DOF PID-like control systems. *Automatica*, 39, 901–908.

Hägglund, T. and Åström, K. (2002). Revisiting the Ziegler-Nichols tuning rules for PI control. *Asian Journal of Control*, 4, 354–380.

Hang, C. and Cao, L. (1996). Improvement of Transient Response by means of variable set point weighting. *IEEE Transaction on Industrial Electronics*, 4, 477–484.

Honeywell (2007). *UDC 3500 Universal Digital Controller Product Manual*. Honeywell International. 51-52-25-120.

Horowitz, I.M. (1963). *Shynthesis of Feedback Systems*. Academic Press.

Kaya, I. (2004). Tuning PI controllers for stable process with specifications on gain and phase margings. *ISA Transactions*, 43, 297–304.

López, A.M., Miller, J.A., Smith, C.L., and Murrill, P.W. (1967). Tuning Controllers with Error-Integral Criteria. *Instrumentation Technology*, 14, 57–62.

Martin, J., Smith, C.L., and Corripio, A.B. (1975). Controller Tuning from Simple Process Models. *Instrumentation Technology*, 22(12), 39–44.

Méndez, V. (2008). *Performance and Robustness of PID Control Loops*. Licenciatura Thesis, Escuela de Ingeniería Eléctrica, Universidad de Costa Rica. (in Spanish).

Mitsubishi (2002). *System Q Programmable Controller Logic Control Programming Manual*. Mitsibishi Electric. 149256.

O'Dwyer, A. (2003). *Handbook of PI and PID Controller Tuning Rules*. Imperial College Press, London, UK.

Omron (2007). *Instructions Reference Manual Programmable Controllers SYSMAC CS Series*. Omron Electronics LLC.

Rivera, D.E., Morari, M., and Skogestad, S. (1986). Internal Model Control. 4. PID Controller Desing. *Ind. Eng. Chem. Des. Dev.*, 25, 252–265.

Rockwell (2003). *MicroLogix 1200 and 1500 Programmable Controllers Bulletin 1762 and 1764 Instruction Set Reference Manual*. Rockwell Automation.

Rockwell (2005). *Logix 5000 Controllers Process Control and Drivers Instructions User Manual*. Rockwell Automation. PN 957955.

Rovira, A., Murrill, P.W., and Smith, C.L. (1969). Tuning Controllers for Setpoint Changes. *Instrumentation & Control Systems*, 42, 67–69.

Sung, S.W. and Lee, I.B. (1999). *PID Controllers and Automatic Tuning*. A-JIN Publishing Co., Seul, Korea.

Taguchi, H. and Araki, M. (2000). Two-Degree-of-Freedom PID controllers - Their functions and optimal tuning. In *IFAC Digital Control: Past, Present and Future of PID Control*. Terrassa, Spain.

Taguchi, H. and Araki, M. (2002). Survey of researches on Two-Degree-of-Freedom PID controllers. In *The 4th Asian Control Conference*. Singapore.

Taguchi, H., Kokawa, M., and Araki, M. (2002). Optimal tuning of two-degree-of-freedom PD controllers. In *The 4th Asian Control Conference*. Singapore.

Visioli, A. (2006). *Practical PID Control*. Springer Verlag Advances in Industrial Control Series.

Yokogawa ((n.d.)). *YS 1500 Indicating Controller User Manual*. Yokogawa Electric Company. IM 01B08B01-02E.

Ziegler, J.G. and Nichols, N.B. (1942). Optimum Settings for Automatic Controllers. *ASME Transactions*, 64, 759–768.

A nonlinear control strategy for a Bidirectional Flow Process

Pablo Zúñiga Salas Héctor Ramírez Estay Daniel Sbarbaro Hofer

Department of Electrical Engineering, Universidad de Concepción,
Concepción, Chile (Tel: +56 41 2204353; e-mail: pablozuniga, hectrami, dsbarbar @udec.cl).

Abstract: A nonlinear control strategy based on Interconnection Damping Assignment Passivity Based Control (IDA-PBC) is proposed for a process with bidirectional flow. The bidirectional flow condition introduces singularities in the control action under certain operation conditions. A solution to this problem is proposed such that operation through the singular points is possible and the stability conditions around the desired operation point are exactly preserved. In addition, a passivity based integral action is included in order to take into account the effects of model uncertainties and unknown step like disturbances. A description of the process and the controller design methodology is presented along with some numerical simulations illustrating the closed-loop behavior of the proposed controller.

1. INTRODUCTION

There are many applications where the characteristic of the process changes and there is the possibility of having singular points associated to the control variable. This condition means that the states of the process are not controllable at the singular point and the control variable became unbounded. This condition can be found for instance in chemical reactors (E.J. McColm and M. T. Tham, 1995) and in electromechanical systems (F. Zhang and B. Fernandez, 2006). In most cases this problem is overcome by modifying the control law such that the singular point is eliminated. There are two approaches for dealing with this problem: the first one is based on differentiation (E. J. McColm and Ming T. Tham, 1995), and the second one on a modification of the control law (H. Xu and P.A. Ioannou, 2004). In this work, the second option is used to design an IDA-PB controller that can deal with singular points without affecting the closed loop stability when the system is outside the set of singular points.

Port-Hamiltonian (PH) systems and Interconnection Damping Assignment Passivity Based Control (IDA-PBC) are two powerful approaches for modeling and control of nonlinear systems. PH representations are physical motivated, since they are based on models representing mass and energy balances; where the structure of the model takes into account the interaction between the system and it environment.

IDA-PBC control approach relies on the notions of interconnections, dissipation and energy balance, (Ortega et al., 2001, 2002). The capability to define precisely the interconnections and energy dissipations of non-linear processes makes the use of PH representation an attractive modeling tool and hence, IDA-PBC an effective alternative to design high performance non-linear controllers for complex processes.

The IDA-PBC approach has been shown to be very effective when the system characteristics changes from one operation mode to another. For instance, in (Ramírez et al., 2008) the same IDA-PB controller is used to stabilize a minimum and a non-minimum phase system, and in (Batlle et al., 2005) this approach is used to stabilize a bidirectional power systems, where the direction of power is reversed depending on the operation mode of a power converter. In this work, a nonlinear bidirectional flow process with singular points operation is used as an application example. The process consists of three serials tanks at same height; hence flow inversion between tanks is possible. The process also considers an unknown disturbance.

This paper is organized as follows: Section 2 describes a process comprising three tanks in series with the possibility of having reversing flow, and the model of this system. Section 3 presents the design of a IDA-PBC plus integral action. In section 4, a solution to the singular point operation is proposed and the system stability is analyzed. Some simulations results are presented in section 5 and finally, in section 6, some closing remarks are given.

2. THE THREE TANKS CONTROL PROBLEM

The multi tank serial circuit is a multivariable system, fully actuated and minimum phase. This process has three tanks of the same height in a serial arrangement, as depicted in Fig. 1.

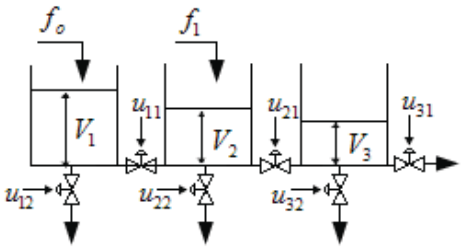

Fig. 1. Proposed system of serial tanks

In Fig. 1 the control valves are u_{11}, u_{21} and u_{31}. The remaining valves, u_{12}, u_{22} and u_{32} are manual valves, whose openings remain constant during the entire operation. On other hand, the feed flow rate into the first tank is measurable and the feed flow rate into the second tank is unknown. The last tank does not have any independent feed flow rate.

The control objective is to operate the tanks at different heights by allowing flow reversing operations.

The tanks are at the same height so the flow direction between tanks depends on the bottom pressure on each of them; i.e. the flow will go from the tank with higher water level to the tank with lower one. This reversing flow phenomenon occurs only in the first and second tanks because they are the only ones with an independent feed flow rate, f_o and f_1 respectively. The maximum water level in the third tank is the level of the second tank, because it does not have an independent water flow rate. Another phenomenon, that arises during the flow reversing process, is the lack of controllability, this occurs when the water level in the first and second tank are the same.

Physically, given a set of feed flow rates the processes always operate in one of these modes. In order to model the process using mass balance equations, the following variables are defined: $x_i \in \mathbb{R}_+$ is the volume inside of a tank i, A_i the cross section (they are constant and the same for all tanks) and $k_{ij}(u_{ij}) = u_{ij}$ linear valve opening functions. Thus, the equations representing the system are:

$$\dot{x}_1 = f_o - u_{11} \cdot sign(x_1 - x_2) \cdot a_1 - b_1 , \quad (1)$$

$$\dot{x}_2 = f_1 + u_{11} \cdot sign(x_1 - x_2) \cdot a_1 - u_{21} \cdot sign(x_2 - x_3) \cdot a_2 - b_2 , \quad (2)$$

$$\dot{x}_3 = u_{21} \cdot sign(x_2 - x_3) \cdot a_2 - u_{31} \cdot a_3 - b_3 , \quad (3)$$

where, for notational convenience, we have defined:

$$a_1 = \sqrt{2g\left(\frac{x_1}{A_1} - \frac{x_2}{A_2}\right)} \; ; \; a_2 = \sqrt{2g\left(\frac{x_2}{A_2} - \frac{x_3}{A_3}\right)} \; ; \; a_3 = \sqrt{2g\frac{x_3}{A_3}}$$

$$b_1 = \sqrt{2g\frac{x_1}{A_1}} \cdot u_{12} \; ; \; b_2 = \sqrt{2g\frac{x_2}{A_2}} \cdot u_{22} \; ; \; b_3 = \sqrt{2g\frac{x_3}{A_3}} \cdot u_{32} .$$

In order to invert the flow rate direction, between the first and second tank, the feed flow rate in the first tank must satisfy $f_o \le b_1$. This can be obtained by calculating the operation point for u_{11}

$$u_{o11} = \frac{f_o - b_1}{a_1 \cdot sign(x_{o1} - x_{o2})} . \quad (4)$$

Thus, in order to have $u_{o11} \ge 0$, for a operation point $x_{o1} < x_{o2}$ with $x_{o1}, x_{o2} \in \mathbb{R}_+$, the following inequality has to be satisfied that $f_o - b_1 \le 0$. To get a flow from the first to the second tank we need $f_o - b_1 \ge 0$.

We will also define the set of singular points as all the $x_1, x_2 \in \mathbb{R}_+$, such that $x_1 = x_2$.

From the knowledge of the process and given a set of possible combinations of feed flow rates, the following operating modes can be identified:

Operation Mode 1: The feed flows are: $f_o > b_1, f_1 \ge 0$, the initial state $x_1^0 > x_2^0 > x_3^0$, with $x_1^0, x_2^0, x_3^0 \in \prod \subset \mathbb{R}_+$ and references $x_1^* > x_2^* > x_3^*$, with $x_1^*, x_2^*, x_3^* \in \mathbb{R}_+$. The set $\prod$ represents the physical admissible levels. The flow goes from the first to the second tank.

Operation Mode 2: The feed flows are: $f_o \le b_1, f_1 > 0$, the initial state $x_1^0 > x_2^0 > x_3^0$, with $x_1^0, x_2^0, x_3^0 \in \prod \subset \mathbb{R}_+$ and references $x_1^* < x_2^*$ and $x_3^* < x_2^*$, with $x_1^*, x_2^*, x_3^* \in \mathbb{R}_+$. The flow is inverted and goes from the second to the first tank.

Operation Mode 3: The feed flows are: $f_o \le b_1, f_1 > 0$, the initial state $x_1^0 < x_2^0$ and $x_3^0 < x_2^0$, with $x_1^0, x_2^0, x_3^0 \in \prod \subset \mathbb{R}_+$ and references $x_1^* < x_2^*$ and $x_3^* < x_2^*$, with $x_1^*, x_2^*, x_3^* \in \mathbb{R}_+$. The flow goes from the second to the first tank.

Operation Mode 4: The feed flows are: $f_o > b_1, f_1 \ge 0$, the initial state $x_1^0 < x_2^0$ and $x_3^0 < x_2^0$, with $x_1^0, x_2^0, x_3^0 \in \prod \subset \mathbb{R}_+$ and references $x_1^* > x_2^* > x_3^*$, with $x_1^*, x_2^*, x_3^* \in \mathbb{R}_+$. The flow is inverted and goes from the first to the second tank.

3. CONTROLLER DESIGN USING IDA-PBC

It is convenient to represent the system in a PH form, to simplify the application of the IDA-PBC.

Consider a process described by a PH system of the form

$$\dot{x} = \left[J(x) - \Re(x)\right]\frac{\partial H}{\partial x}(x) + g(x)u + q(x)f \quad (5)$$

Where $x \in \mathbb{R}^n$ and $u \in \mathbb{R}^m$ are the mass (volume) variables and the control, respectively. The smooth function $H(x)$ typically represents the total stored mass, $f = \begin{bmatrix} f_o & f_1 \end{bmatrix}^T \in \mathbb{R}^m$ represents constant disturbances and $q(x)$ defines the interaction between the system and *f*. the skew-symmetric matrix $J(x) = -J^T(x)$ represents the interconnection between the different system's components, and $\Re(x) = \Re^T(x) \ge 0$ is the dissipation matrix, while $g(x)$ defines the interconnection of the system with its

environment. A detailed overview of PH systems can be found in (van der Shaft, 2004).

To represent the tank processes as PH model, the following storage function is selected, which represents the total mass (volume) in the system

$$H(x) = x_1 + x_2 + x_3 \geq 0 \,. \tag{6}$$

The IDA-PBC methodology allows to find a static control feedback $u = \beta(x)$ such that the desired performance is specified by a closed loop dynamic as

$$\dot{x} = \left[J_d(x) - \Re_d(x)\right]\frac{\partial H_d(x)}{\partial x}, \tag{7}$$

where $H_d(x)$ is the desired total mass function fixed by the designer and which has a strict minimum in x^*. The matrices $J_d(x) = -J_d{}^T(x)$ and $\Re_d(x) = \Re_d{}^T(x) \geq 0$ are the desired interconnection and damping matrices respectively. In order to get decoupled outputs, the closed loop port Hamiltonian system has to have a null interconnection matrix and a diagonal damping matrix. For accomplishing this objective, it is possible to define the open-loop PH system such that it satisfies these characteristics. The PH matrixes are

$$J(x) = -J^T(x) = 0 \,, \tag{8}$$

$$\Re(x) = \Re^T(x) = diag\{b_1, b_2, b_3\} \,, \tag{9}$$

$$g(x) = \begin{bmatrix} -sign(x_1 - x_2)\cdot a_1 & 0 & 0 \\ sign(x_1 - x_2)\cdot a_1 & -sign(x_2 - x_3)\cdot a_2 & 0 \\ 0 & sign(x_2 - x_3)\cdot a_2 & -a_3 \end{bmatrix}, \tag{10}$$

$$q(x) = \begin{bmatrix} 1 & 0 & 0 \\ 0 & 1 & 0 \end{bmatrix}^T \,. \tag{11}$$

The closed loop interconnection and damping matrices have to be equal to the open loop matrices; i.e. $J_d(x) = J(x)$ and $\Re_d(x) = \Re(x)$. If this is satisfied, the closed-loop process has decoupled outputs. The references levels are constant, so the following desired storage function (Ramírez *et al,* 2008) can be used,

$$H_d(x) = \sum_{i=0}^{n} x_i + \sum_{i=0}^{n} -(1-k_i)x_i - k_i x_i^* \ln(x_i)$$

$$= \sum_{i=0}^{n}\left[x_i - k_i x_i^* \ln(x_i)\right]. \tag{12}$$

For the given desired storage function and for previously defined open and closed loop PH matrices, by matching (5) and (7) the following control law, where $\hat{f}_1$ is an estimation of f_1, is obtained

$$u_{11} = \frac{f_o - b_1 + b_1 \cdot k_1\left(1 - \dfrac{x_1^*}{x_1}\right)}{sign(x_1 - x_2)\cdot a_1}, \tag{13}$$

$$u_{21} = \frac{\hat{f}_1 - b_2 + b_2 k_2\left(1 - \dfrac{x_2^*}{x_2}\right) + u_{11}\cdot a_1 \cdot sign(x_1 - x_2)}{sign(x_2 - x_3)\cdot a_2}, \tag{14}$$

$$u_{31} = \frac{-b_3 + b_3 k_3\left(1 - \dfrac{x_3^*}{x_3}\right) + u_{21}\cdot a_2 \cdot sign(x_2 - x_3)}{a_3} \,, \tag{15}$$

If the control inputs (13), (14) and (15) are replaced in (5), then the time derivate of the desired storage function, will be negative, thereby the closed-loop system is asymptotically stable.

Equations (13) and (14) require to know the system parameters and flow rates f_o and f_1. In order to compensate the lack of knowledge about the values of these flow rates, an integral action is considered in the final control law. The solution used in this paper was presented in (Ortega and García-Canseco, 2004) and consists in adding an integral term of the passive output to the control.

Let's consider the system presented in (5) in closed loop with $u = \beta(x) + \upsilon$, where υ is an integral action added to the system trough a state variable and defined as

$$\dot{\upsilon} = -K_I g^T(x)\nabla H_d(x) \tag{16}$$

With $K_I = K_I{}^T > 0$. Then, all stability properties of x^* are preserved. In fact the closed loop clearly takes the PCH form

$$\begin{bmatrix} \dot{x} \\ \dot{\upsilon} \end{bmatrix} = \begin{bmatrix} J_d(x) - \Re_d(x) & g(x)K_I \\ -K_I g^T(x) & 0 \end{bmatrix}\begin{bmatrix} \nabla_x W \\ \nabla_\upsilon W \end{bmatrix} \,, \tag{33}$$

where

$$W(x,\upsilon) = H_d(x) + \frac{1}{2}\upsilon^T K_I{}^{-1}\upsilon \tag{17}$$

is the new total storage function which now qualifies as Lyapunov function. For this application it is convenient to use a diagonal gain matrix, i.e. $K_I = diag\ \{k_{I1}, k_{I2}, k_{I3}\}$, $g(x)$ like in (10) and $H_d(x)$ like in (12).

4. SINGULAR POINT REGULARIZATION

The control action (13), (14) and (15), have singulars points arising when two tanks have the same level. In this case, the flow between these tanks becomes null and the control action becomes inexistent. Operating the system on this singulars point is not required in this application. However, if the controller attempts to invert the flow between two contiguous tanks, it is necessary to pass from a state $x_1 > x_2$ to a state

$x_1 < x_2$. Along the trajectory is necessary to pass trough $x_1 = x_2$, which make the control law unfeasible. This only happens between the first and second tank, hence, the solution is only used in the first control input.

Based on the work of Haojian and Ioannou (2004), a singular point solution is proposed. Assume a function $\eta(x) \in \mathbb{R}$ such that $\eta(0) = 0$. The inverse of $\eta(x)$ is undetermined at zero. To avoid this, the following solution is proposed:

$$\frac{1}{\eta(x)} \Rightarrow \frac{\eta(x)}{\eta^2(x) + \delta(x)}, \tag{18}$$

where $\delta(x)$ is defined as follows:

$$\delta(x) = c_1 \cdot \left(1 - \frac{1}{1 + e^{-c_2 \cdot |x_1 - x_2|}}\right) \cdot \left| e_{ctrl}(x, x^*) \right| \cdot k_{sp}, \tag{19}$$

where k_{sp}, c_1 and c_2 are real positive constants and they are considered as tuning parameters. Equations (19) means that $\delta(x)$ will be zero if x is at the reference x^*. Of course, the references x_1^* and x_2^* must be different, otherwise (18) will be unbounded.

The control input (13) including the singular point solution becomes:

$$u_{11} = \frac{sign(x_1 - x_2) \cdot a_1 \cdot \left(f_o - b_1 + b_1 \cdot k_1 \left(1 - \frac{x_1^*}{x_1}\right)\right)}{a^2{}_1 + \delta(x)} \quad . \tag{20}$$

The control variables u_{21} and u_{31} do not require changes since they do not have singular points.

4.1 Stability Analysis

In this section a brief and simple stability analysis is carried out. Replacing (20), (14) and (15) in (1), (2) and (3), respectively, the closed loop system takes the form:

$$\dot{x}_1 = -\frac{a_1^2}{a_1^2 + \delta(x)} b_1 k_1 \left(1 - \frac{x_1^*}{x_1}\right) + \left(f_o - b_1\right) \frac{\delta_1(x)}{a_1^2 + \delta(x)} \tag{21}$$

$$\dot{x}_2 = -b_2 k_2 \left(1 - \frac{x_2^*}{x_2}\right) + \Delta f_1 \tag{22}$$

$$\dot{x}_3 = -b_3 k_3 \left(1 - \frac{x_3^*}{x_3}\right) \tag{23}$$

where $\Delta f_1 = f_1 - \hat{f}_1$ is the estimation error of the unknown disturbance in the second tank.

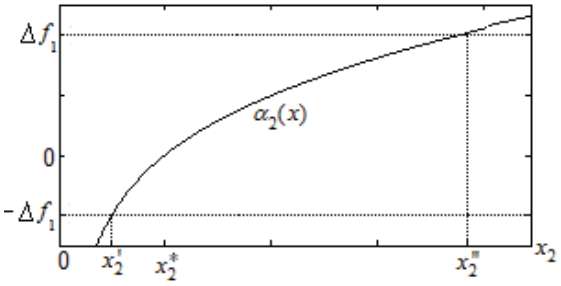

Fig. 2. Right hand terms of equation (22)

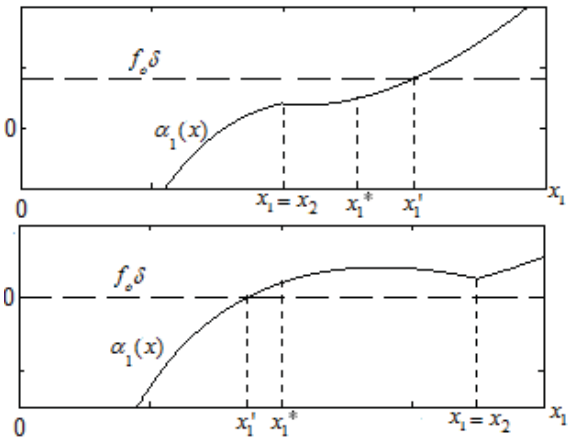

Fig. 3. Right hand terms of equation (21) for a constant δ

Then stability of the closed-loop system can be analyzed as follows: Since equation (23) only depends on x_3 and the term $b_3 k_3$ is positive, x_3^* will be an asymptotically stable equilibrium point. From equation (22) we have that the dynamic only depends on x_2. The stability analysis can be carried out by analyzing the right hand terms, as they are depicted in Fig. 2., where Δf_1 and the term $\alpha_2(x) = b_2 k_2 (1 - x_2^*/x_2)$ have been drawn in terms of x_2. From this plot can be seen that the system will converge to a unique equilibrium point x_2'', so that $\|x_2'' - x_2^*\| < \gamma$, where $\gamma(\Delta f_1) > 0$ is a real positive constant that depends on Δf_1. If $\Delta f_1 = 0$, then x_2^* will be asymptotically stable equilibrium point, as x_3^*. The analysis for x_1 consider the perturbation term $(f_o - b_1)\delta/(a_1^2 + \delta(x))$, which vanishes at the equilibrium, hence x_1 could converge asymptotically to x_1^*. In fact, the expression for the equilibrium point is:

$$\left(f_o - b_1\right) \delta(x) - a_1^2 b_1 k_1 \left(1 - \frac{x_1^*}{x_1}\right) = 0 . \tag{24}$$

Equation (24) can be verified at the desired operation point x_1^* or if $(f_o - b_1) = 0$ and $a_1 = 0$. The last case can only be possible if the system is at the singular point; i.e. if $x_1^* = x_2^*$ and $f_o = b_1 = (2g x_1)^{1/2}$. Fig. 3 depicts the right hand terms of (21); $\alpha_1(x)$ defined as:

$$\alpha_1(x) = b_1 \delta(x) + a_1^2 b_1 k_1 \left(1 - \frac{x_1^*}{x_1}\right), \tag{25}$$

and for both condition $(f_o - b_1) > 0$ and $(f_o - b_1) < 0$. From this figure can be seen that there exist only one asymptotically stable equilibrium point x_1^*, which is not the desired reference value, the steady state error will depend on δ and f_o. Fig. 5, shows the effect of making δ dependant on the variable x, as in (20). In this case, the desired reference value is an asymptotically stable equilibrium point.

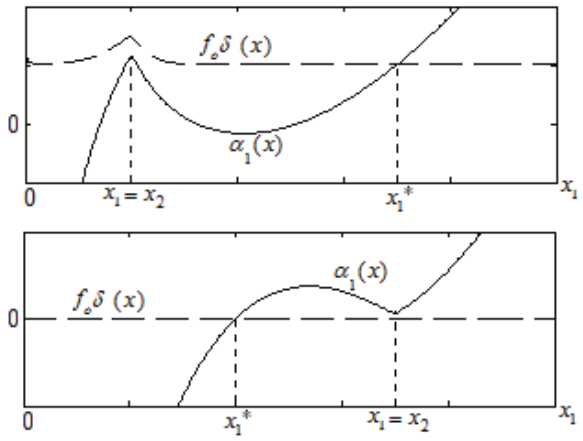

Fig. 4. Right hand terms of equation (21) for a variable δ (x)

5. NUMERICAL SIMULATIONS

In this section, some simulation results illustrating the controller characteristics are presented. The tuning parameters were selected to obtain a closed loop response with overshoots smaller than 15% and small settling times according with the open loop dynamics.

This simulation considers the following: linear control valves, i.e. $k_{ij}(x) = u_{ij}$ and the cross section of all tanks are the same and constant, i.e. $A_1 = A_2 = A_3 = 1731.3$. The tuning parameters for the singular points solution where selected as $C_1 = 500$ y $C_2 = 0.0004$. The feed flows rates have their maximum value at 4000 cm^3/s and are represented in percentage values.

If the flow direction, between the first and second tank, is inverted, then the system go through a singular point. The following simulations show the performance of the system with a flow rate inversion. The parameters were k_1=4, k_2=2, k_3=1 and the integrator parameter were set at k_{I1}=0.0001, k_{I2}=0.01, k_{I3}=0.01.

In the first part, the system is working with a level of 10cm in the first tank and 5 cm in the second one, and the flow between the tanks goes from the first to the second. Fig.5 depicts the closed loop behavior. At 4250 the both set points were increased at the same time. to 35cm and 25cm respectively. At 5000 sec. the level reference of the first tank is set to 15cm and for the second one is kept at 25cm, leading to an inversion of the flow direction. From Fig. 5 can be seen that while the level in the first tank changes, the control tries to maintain the level in the second tank constant, and it invert the flow direction without discontinuities in the control inputs. The coupling between the outputs is due to the integrator compensation, since the static feedback was designed considering a null interconnection matrix. These good results are achieved due to the joint action of the integral action and the methodology used to deal with the singular point.

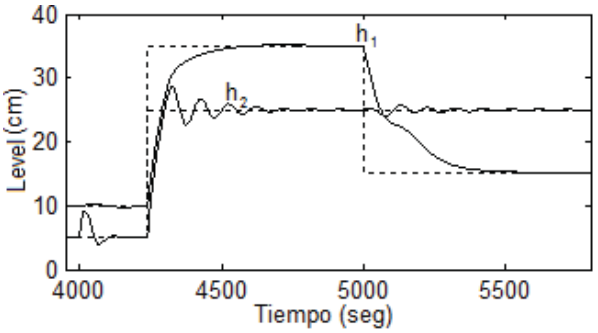

Fig. 5. Levels in first and second tank. Integral action and flow rate inversion

From Fig. 6, can be seen that the control input, in both tanks (1 and 2), are smooth, continuous and bounded. Beside, Fig. 7 shows the flow rate inversion (5070 seconds approx.), and the sudden changes of the flow rate when the control inputs changes their values due to references changes.

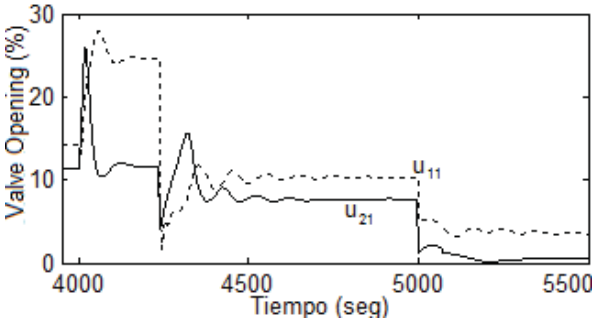

Fig. 6. Control input of the first and second tank. Integral action and flow rate inversion

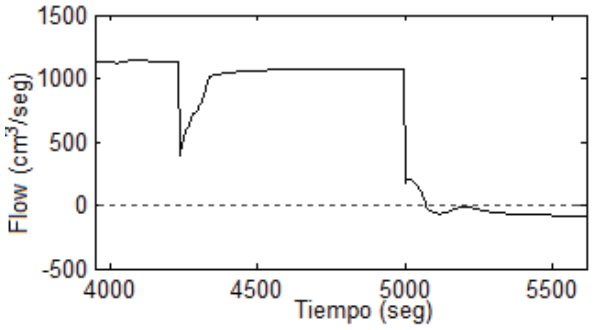

Fig. 7. Flow rate between the first and second tank. Integral action and flow rate inversion

A simple PI controller can not deal with reversing flows, since the process open-loop gain changes sign when the flow changes direction.

6. CONCLUDING REMARKS

This paper presents a novel nonlinear control strategy based on IDA-PBC for a non-linear process with bidirectional flow. The process was modeled as PH model, and by a proper selection of the process closed-loop matrices. A passivity based strategy was designed, and in order to deal with model uncertainties and unknown disturbances, integral action was also considered in the control law. Since the process exhibits uncontrollable operation conditions; i.e. singular points in the control law, a singular point solution was proposed without compromising the stability conditions of the closed-loop process. A nice feature of the proposed singular point solution is that outside the set of singular points the desired closed-loop interconnection and damping specifications are preserved, hence no special considerations must be taken into account when selecting the desired closed-loop PH system in the IDA-PBC design. The closed-loop behavior of the proposed controller has been illustrated by numerical simulations.

Future works will consider a more detailed stability analysis for the general case, including integral actions. Implementation of the controller in a laboratory application is also part of the future work to be carried out.

ACKNOWLEDGEMENTS

This work was supported by Fondecyt Project 1070491

REFERENCES

E. J. McColm and M. T. Tham (1995). "On Globally Linearising Control about Singular Points", *Proceedings of the American control conference*, pp. 2229-2233.

R. Ortega, A. van der Schaftb, I. Mareels and B. Maschke. (2001). "Putting Energy Back in Control", *Control Systems Magazine, IEEE*, vol. 21, pp. 18-33.

R. Ortega, A. van der Schaft, B. Maschke, G. Escobar (2002). "Interconnection and damping assignment passivity-based control of port controlled Hamiltonian systems". Automatica 38, pp. 585-596.

R. Ortega and E. García-Canseco (2004). "Interconnection and damping assignment passivity based control: A survey", *European Journal of Control*, vol. 10, pp. 432-450.

H. Xu and P. Ioannou (2004). "Robust Adaptive Control of Linearizable Non-linear Single Input Systems with Guaranteed Error Bounds", *Automatica,* vol. 40, pp. 1905-1911.

A.J. van der Schaft (2004). "Port-Hamiltonian systems: network modeling and control of nonlinear physical systems", *In: H. Irschik, K. Schlacher (Eds.), Advanced Dynamics and Control of structures and Machines, pp. 127–168.*

C. Batlle, A. Doria - Cerezo and E. Fossas (2005). "IDA-PBC Controller for a Bidirectional Power Flow Full-Bridge Rectifier", *Decision and Control, 2005 and 2005 European Control Conference. CDC-ECC '05. 44th IEEE Conference on*, pp. 422-426.

J. Johnsen and F. Allgöwer (2006). "Interconnection and Damping Assignment Passivity-Based Control of a Four-Tank System", *F. Bullo y K. Fujimoto (Eds.), Preprints of the IFAC 3rd Workshop on Lagrangian and Hamiltonian Methods for Nonlinear Control*, vol. 60, pp. 69–74.

F. Zhang and B. Fernandez, 2006. "Feedback Linearization control of System with Singularities: A Ball Beam Revisit", *International conference on Complex Systems (ICCS2006).*

H. Ramírez, D. Sbarbaro and R. Ortega (2008). "On the control of non-linear processes: An IDA–PBC approach", *Journal of Process Control*, vol 19, pp. 405-414.

J.K. Johnsen, F. Döorer, and F. Allgöwer (2008). "L2-gain of Port-Hamiltonian systems and application to a biochemical fermenter". *Proceedings of the American Control Conference 2008*, pages 153-158.

Characteristics-based MPC of a fixed bed reactor with catalyst deactivation

Leily Mohammadi * **Ilyasse Aksikas** * **J. Fraser Forbes** *

* *Chemical and Materials Engineering department, University of Alberta, Edmonton, AB Canada*
(e-mail: {leily, aksikas, fraser.forbes }@ualberta.ca).

Abstract: In this work characteristics-based model predictive control (CBMPC) of a fixed bed reactor with catalyst deactivation is studied. Performance of CBMPC has been analyzed for two cases: one that incorporates the catalyst deactivation within the reactor model and another that ignores the deactivation. Simulation results show that the performance of first controller that incorporates the catalyst deactivation is better than the controller that ignores the deactivation.

Keywords: Fixed bed reactor, Catalyst deactivation, Characteristics-based model predictive control

1. INTRODUCTION

A catalyst loses its activity during operation. Catalyst deactivation can have variety of consequences. It may cause thermal instability of the reactor. It also affects the conversion and selectivity of the desired reaction. Consequently, it will affect the productivity and energy efficiency of the plant. In order to compensate for the effect of catalyst deactivation, the operating conditions are changed gradually to ensure maintaining the quality of product and the rate of production. Then designing a controller that can ensure changing optimal process operating conditions are tracked as they vary, is an important issue in operation of catalytic reactors.

Integration of the catalyst deactivation dynamics into the reaction system model results in a model that can describe the dynamical behavior of the system more precisely. By using this model in model-based algorithms, one can design a more efficient controller.

The objective of this work is to study the control of a fixed bed reactor with catalyst deactivation. In order to capture all of the main "macroscopic" phenomena (i.e., reactions, diffusion, convection, and so forth), the model of a fixed bed reactor takes the form of a mixed set of partial differential, ordinary differential, and algebraic equations. Such systems and many others (e.g., systems modeled by partial difference equations, integral equations and delay differential equations) are called distributed parameter systems (DPS) or infinite dimensional systems. Since we will consider the catalyst deactivation in the reactor's model, the resulting infinite dimensional system will be time varying.

Aksikas et al. (2009) and Aksikas et al. (2008) studied the control of the time varying infinite dimensional systems. In these works linear-quadratic controllers are developed by solution of the classical Riccati equation. This work is extended by Mohammadi et al. (2009) to cover the two-time scale property of the fixed bed reactors.

Model Predictive Control (MPC) is an optimal control technique that uses a model of the system to predict the future plant behavior and determines a sequence of control moves so that the predicted response moves to the desired set point in an optimal manner. Unfortunately, MPC algorithms for distributed parameter systems are relatively scarce. For diffusion-reaction systems, which are described by parabolic PDEs, Dubljevic et al. (2005) used modal decomposition to derive finite-dimensional systems that capture the dominant dynamics of the original PDE and are subsequently used for controller design. For the convection dominated parabolic PDEs, the modal decomposition methods result in high-order finite dimensional systems. MPC for high-order systems is computational demanding and cannot be applied on-line. For hyperbolic systems, the eigenvalues of the spatial differential operator cluster along vertical or nearly vertical asymptotes in the complex plane[Christofides (2001)], and the modal decomposition methods may not be used. Dubljevic et al. (2005) used the finite difference method to convert the hyperbolic equations to a set of ODEs and the MPC is designed for the resulting model. Using discretization methods may result in improperly capturing the dynamics of the system. More-

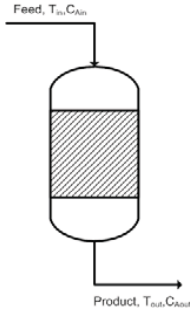

Fig. 1. Schematic diagram of Fixed-Bed reactor

over, the resulting ODEs are high-order and may result in an MPC that has high computational computational requirements.

Characteristics-based MPC is an approach for model predictive control of DPS proposed by Shang et al. (2004) and Shang et al. (2007). The method of characteristic allows controller design for linear, quasilinear, nonlinear low dimensional PDEs. In this method, partial differential equations are transformed to a set of ordinary differential equations along the characteristic curves, which exactly describe the original DPS. Then the controller design can be performed on ODEs instead of PDEs without approximation.

The process considered in this work is a catalytic hydrotreating reactor. Hydrotreating is the conventional means for removing sulfur from petroleum fractions. A schematic diagram of this reactor is shown in Fig.1. An important feature of a fixed bed reactor is the two time scale property of the system. In the other words, the dynamic behavior of the material balance is faster than the energy dynamics. Due to this property, the system has two characteristic curves. Furthermore, by incorporating the catalyst deactivation equation within reactor's model another very slow dynamic will be added to the system.

In this work the problem of controlling a fixed-bed catalytic reactor with catalyst deactivation is considered. We applied nonlinear characteristic-based MPC on-line algorithm to control the temperature of the reactor at the desired setpoint during the reactor's operation. Two cases have been considered. In the first one, the designed MPC uses a model of the system that considers the catalyst deactivation. In the second one, the catalyst deactivation is ignored for model predictive control development. Then performance of the two cases has been compared.

2. MODEL DESCRIPTION

The dynamics of a fixed-bed reactor can be described by partial differential equations derived from mass and energy balances. To model the reactor, a plug-flow pseudo-homogeneous model is considered. Moreover, we consider a one-spatial dimension model where there are no gradients in the radial direction. In the simplified system considered here, a lumped reaction kinetics equation was assumed and has the following form (see Chen et al. (2001)):

$$r_A = k(t)e^{\left(-\frac{E}{RT}\right)}C_A^{n_1}C_H^{n_2} \tag{1}$$

Under the above mentioned assumptions, the dynamics of the process are described by the following energy and mass balance partial differential equations (PDE's).

$$\epsilon\frac{\partial C_A}{\partial t} = -u\frac{\partial C_A}{\partial z} - \rho_B k(t)e^{-\frac{E}{RT}}C_A^{n_1}C_H^{n_2} \tag{2}$$

$$\frac{\partial T}{\partial t} = -u\frac{\partial T}{\partial z} + \frac{\rho_B \Delta H_r}{\rho C_p}k(t)e^{-\frac{E}{RT}}C_A^{n_1}C_H^{n_2} \tag{3}$$

Initial and boundary conditions are:

$$\begin{array}{lll} C_A(0,t) & = C_{A,in}, & C_A(z,0) = C_{A0}(z), \\ T(0,t) & = T_{in}, & T(z,0) = T_0(z) \end{array} \tag{4}$$

In the equations above, $C_A, T, \epsilon, \rho_B, \rho, C_p, E, C_H, \Delta H_r, u$ denote the reactant concentration, the temperature, the porosity of the reactor packing, the catalyst density, the fluid density, the heat capacity, the activation energy,the hydrogen concentration, the enthalpy of reaction, and the superficial velocity respectively. k is the pre-exponential factor. Catalysts lose their activity with time and as a result this coefficient varies with time. The parameter k is proportional to the catalyst activity, which is a function of time and the operating conditions and can be described by an ODE (see Furimsky and Massoth (1999)). Here, we assume that the operating conditions are maintained in narrow ranges and in this case k is only a function of time, which can be described by:

$$k = k_0 + k_1 e^{-\alpha t} \tag{5}$$

The above expression for the kinetics of naphtha hydrotreating reaction is in agreement with the observations that after a rapid initial deactivation of the hydrotreating catalyst there is a slow deactivation phase and finally a stabilization of the catalyst activity phase.

3. CHARACTERISTICS-BASED MPC

The method of characteristics is a technique for solving hyperbolic partial differential equations. The idea is that every hyperbolic PDE has characteristic curves along which the dynamics evolve and as a result, the PDE can be represented as an equivalent ODE.

Consider a quasilinear system of first-order equations with two dependent variables ν_1,ν_2 and two independent variables t and x.

$$\begin{aligned} \frac{\partial \nu_1}{\partial t} + a_1\frac{\partial \nu_1}{\partial z} &= f_1(\nu_1, \nu_2, u) \\ \frac{\partial \nu_2}{\partial t} + a_2\frac{\partial \nu_2}{\partial z} &= f_2(\nu_1, \nu_2, u) \end{aligned} \tag{6}$$

if $a_1 \neq a_2$, the system has two different characteristics determined by:

$$\begin{aligned} \text{Characteristic C}_1: \quad & \frac{dz}{dt} = a_1 \\ \text{Characteristic C}_2: \quad & \frac{dz}{dt} = a_2 \end{aligned} \tag{7}$$

along these characteristics dynamic of the system is described by:

$$\begin{aligned} \frac{d\nu_1}{dt} &= f_1(\nu_1, \nu_2, u) \quad \text{along characteristic C}_1 \\ \frac{d\nu_2}{dt} &= f_2(\nu_1, \nu_2, u) \quad \text{along characteristic C}_2 \end{aligned} \tag{8}$$

Then, by using the method of characteristics, the set of partial differential equations (6) is transformed to a set of ODEs along the characteristic curves. This set of ODEs can be used to predict the future behavior of the system.

For a fixed-bed reactor which is modeled by equations (2) and (3) the characteristic curves are:

$$\text{C}_1 = \frac{dz}{dt} = \frac{u}{\epsilon} \tag{9}$$

$$\text{C}_2 = \frac{dz}{dt} = u \tag{10}$$

and the state variables C_A and T are described by the following ODEs along the characteristic curves:

$$\frac{\partial C_A}{\partial t} = -\frac{\rho_B}{\epsilon} k(t) e^{-\frac{E}{RT}} C_A^{n_1} C_H^{n_2} \tag{11}$$

$$\frac{\partial T}{\partial t} = \frac{\rho_B \Delta H_r}{\rho C_p} k(t) e^{-\frac{E}{RT}} C_A^{n_1} C_H^{n_2} \tag{12}$$

The characteristic ODEs are coupled with respect to the two characteristic curves, and the future state variables at one spatial point should be determined by simultaneous integration of both characteristic ODEs along two nonparallel characteristic curves. Fig. 2 illustrates the calculation of the future output variables using method of characteristics. This method for prediction of the future behavior is proposed by Shang et al. (2004). The idea is that at $t = t_k$ the measurements of the state variables are available at discretization points and these measurements are used to determine the value of the state variables at intersections of the characteristic curves. This algorithm provides us with the future values of the output variable. For example for point P we have:

$$C_A(P) = \int_{t(Q)}^{t(P)} f_1(Q) \tag{13}$$

$$T(P) = \int_{t(R)}^{t(P)} f_2(R) \tag{14}$$

where:

$$t(P) = \frac{a_1 t(Q) - 2a_2 t(Q) + a_2 t(R) + Z(R) - Z(Q)}{a_1 - a_2} \tag{15}$$

and a_1 and a_2 are $\frac{u}{\epsilon}$ and u respectively. The position of the point P is calculated by:

$$Z(P) = \frac{a_1 Z(R) - a_2 Z(Q) + a_1 a_2 [t(R) - t(Q)]}{a_1 - a_2} \tag{16}$$

This procedure is repeated for all nodes and then values of the future output variables are available and one can use common NMPC algorithm to compute the control action. The control action is calculated by solving the following optimization problem in receding horizon manner.

$$\min \int_t^{t+H_p} (T - T_{sp})^2 dt + \int_t^{t+H_c} \lambda (\Delta u)^2 \tag{17}$$

Where H_p is the prediction horizon, H_c is the control horizon, and λ is the weight of the input in the objective function. These parameters are tuning parameters for MPC.

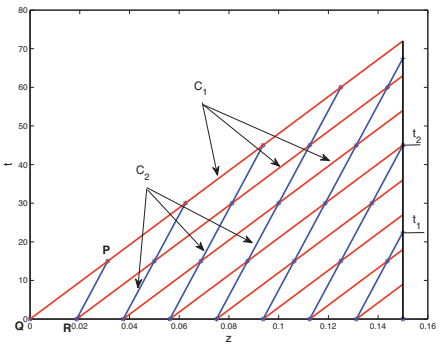

Fig. 2. Calculation of future outputs using characteristic curves

The values of T in the objective function are calculated using the method that described in this section. Since f_1 and f_2 in equations (13) and (14) are nonlinear functions, this optimization problem is a nonlinear optimization and can be solved numerically.

4. NUMERICAL SIMULATIONS

Our case study is a naphtha hydrotreating reactor. The simulation of the reactor was performed using COMSOL® Multi-physics. Using the MPC controller formulated in section 3, the control of the outlet temperature can be achieved. The manipulated variable is the superficial velocity of the feed.

To simulate the closed loop behavior of the system, we performed two cases. In the first one, we considered the deactivation equation of the catalyst and applied the MPC controller to time-varying equations.

In the second case, the model of the system that is used for MPC ignores the catalyst deactivation and assumes constant activity over operation time of the reactor.

Model parameters are given in Table 1. The objective is to control the reactor's outlet temperature at specified setpoint. The objective function is given in Equation (17).

The characteristic curves (9) and (10) are functions of the input variable. Then for the cases that the control horizon, H_c, is greater than one, the characteristic curves will not have constant slope and the calculation of the future values of the output variable will be challenging. In order to simplify the calculations, for the purpose of this example, we assumed that the control horizon is equal to 1, so the MPC problem becomes the following optimization problem:

$$\min \int_t^{t+H_p} (T - T_{sp})^2 dt + \lambda(\Delta u)^2 \tag{18}$$

$$\frac{\partial C_A}{\partial t} = -\frac{\rho_B}{\epsilon} k(t) e^{-\frac{E}{RT}} C_A^{n_1} C_H^{n_2} \quad \text{along characteristic } C_1$$

$$\frac{\partial T}{\partial t} = \frac{\rho_B \Delta H_r}{\rho C_p} k(t) e^{-\frac{E}{RT}} C_A^{n_1} C_H^{n_2} \quad \text{along characteristic } C_2$$

The number of discretization points was taken to be $m = 9$. The prediction horizon is set to the residence time of the reactor, and λ is 1×10^3. The difference between the two cases is in the characteristic equations (11) and (12), which for the first case are functions of time.

This optimization problem can be solved by any optimization method for differential algebraic equations (DAE). Here we used sequential approach, which assumes piecewise constant inputs at each time interval and integrates the differential equations in each interval. This method is an easy method for solving optimization problems for MPC, but it is slower than other algorithms such as that proposed by Bock et al. (2000). The sequential algorithm is good enough for purpose of this illustration example, but for actual implementation the optimization algorithm should be improved.

Fig. 3 illustrates the performance of the CBMPC for the first and second case. This figure shows that the performance of the standard MPC algorithm for the first case is better than the second one. The second case, which considers a constant activity for the catalyst results in an steady state offset. Fig. 5 is the plot of the outlet concentration for two cases and Fig. 4 illustrates the computed control actions for two cases. As Fig. 4 shows, for the second case the input trajectory is almost constant except for first few time intervals; For the first case, due to inclusion of the time varying catalyst activity, the MPC provides more accurate control. Since we assumed

Table 1. Model Parameters

Parameter	Values	unit
ϵ	0.4	
ρ_B	700	$\mathrm{kg_{cat}/m^3}$
C_H	587.4437	$\mathrm{mol/m^3}$
n_1	1.12	
n_2	0.85	
E	81000	J/mol
R	8.314	J/mol K
C_{A0}	0.419344	$\mathrm{mol/m^3}$
C_{Ain}	0.419344	$\mathrm{mol/m^3}$
T_0	523	K
T_{in}	523	K
ρ	2.7	$\mathrm{Kg/m^3}$
C_p	147.49	J/Kg K
ΔH	101.3×10^3	J/mol
α	0.005	
k_1	1.2384	
k_2	2.8896	

piecewise constant profiles for input variable, resulting output trajectory for the first case is non-smooth. But the fluctuations are not greater than $\pm 0.01 \times Y_{sp}$.

In order to deal with the steady state offset problem in the second case, one should implement offset elimination algorithms on standard MPC. These algorithms increase the computational demand of the MPC. Moreover the best offset elimination algorithm may achieve a performance similar to that of the first case.

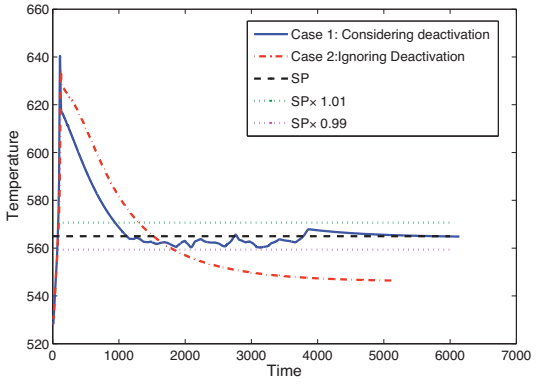

Fig. 3. Outlet temperature(Controlled variable)

Fig. 6 compares the conversion of the reactor for two cases. Although the conversion of the second case is higher at beginning, after a while the reactor's conversion decreases. Lower conversion results in decrease in the profitability of the plant.

5. CONCLUSION

In this work we studied the model predictive control of a naphtha hydrotreating reactor with catalyst deactivation. A characteristic-based MPC is developed to control the reactor. Two different case studies are studied: One that

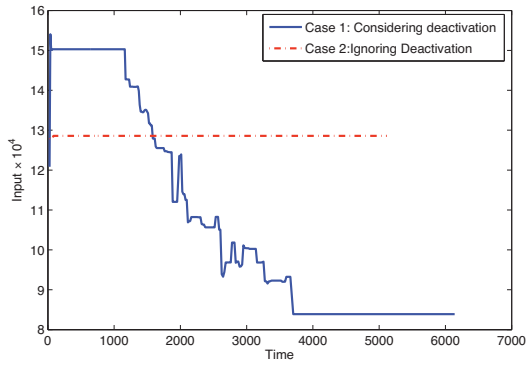

Fig. 4. Computed Input variable

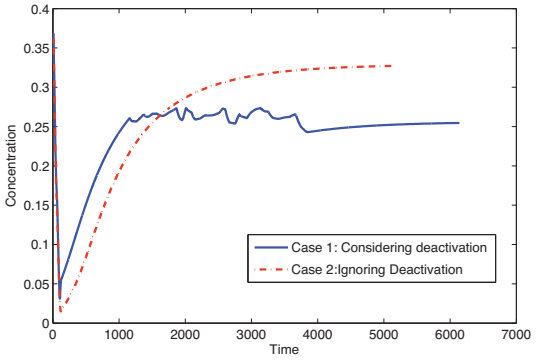

Fig. 5. Computed Input variable

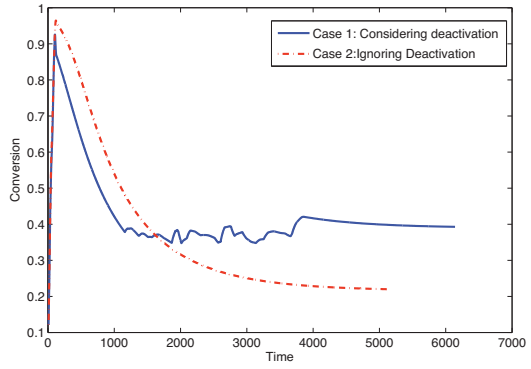

Fig. 6. Conversion at reactor outlet

incorporates the catalyst deactivation kinetics in the controller model and the second one that ignores the catalyst deactivation. The performance of two controllers are compared. The key result of this study is that integration of the catalyst deactivation kinetics with the reactor model, provides improved performance of the characteristic based MPC. This improvement in temperature control results in an improvement in conversion of the reaction, which may increase the plant profitability.

REFERENCES

Aksikas, I., Fuxman, A., Forbes, J.F., and Winkin, J.J. (2009). LQ-Control Design of a Class of Hyperbolic PDE Systems: Application to Fixed-Bed Reactor. *Automatica, in Press.*

Aksikas, I., Fuxman, A.M., and Forbes, J.F. (2008). Control of Time Varying Distributed Parameter Plug Flow Reactor by LQR. In *Proceedings of the IFAC World Congress, Seoul Korea.*

Bock, H., Diehl, M., Leineweber, D., and Scholder, J. (2000). *A direct multiple shooting method for real time optimization of nonlinear DAE processes.* Nonlinear Predictive control. Birkhäuser.

Chen, J., Ring, Z., and Dabros, T. (2001). Modeling and simulation of a fixed-bed pilot-plant hydrotreater. *Ind. Eng. Chem. Res.*, 40, 3294–3300.

Christofides, P.D. (2001). *Nonlinear and Robust Control of PDE Systems:Methods and Applications to Transport-Reaction Processes.* Birkhäuser.

Dubljevic, S., Mhaskar, P., El-Farra, N.H., and Christofides, P. (2005). Predictive control of transport-reaction processes. *Computers & Chemical Engineering*, 29, 2335–2345.

Furimsky, E. and Massoth, F.E. (1999). Deactivation of hydroprocessing catalysts. *Catalysis Today*, 52, 381–495.

Mohammadi, L., Aksikas, I., and Forbes, J.F. (2009). Optimal Control of a Time-Varying Catalytic Fixed Bed Reactor With Catalyst Deactivation. *American Control Conference 2009.*

Shang, H., Forbes, J.F., and Guay, M. (2004). Model predictive control for quasilinear hyperbolic distributed parameter systems. *Ind. Eng. Chem. Res.*, 43, 2140–2149.

Shang, H., Forbes, J.F., and Guay, M. (2007). Computationally efficient model predictive control for convection dominated parabolic systems. *Journal of Process Control*, 17, 379–386.

Hierarchical Economic Optimization of Oil Production from Petroleum Reservoirs

Gijs M. van Essen [*] **Paul M.J. Van den Hof** [*]
Jan Dirk Jansen [**]

[*] *Delft Center for Systems & Control, Delft University of Technology, Mekelweg 2, 2628 CD Delft, the Netherlands, (e-mail: g.m.vanessen@tudelft.nl, p.m.j.vandenhof@tudelft.nl).*
[**] *Department of Geotechnology, Delft University of Technology, Stevinweg 1, 2628 CN Delft, the Netherlands / Shell International E&P, Kesslerpark 1 ,2288 GS Rijswijk, the Netherlands (e-mail: jan-dirk.jansen@shell.com).*

Abstract: In oil production *waterflooding* is a popular recovery technology, which involves the injection of water into an oil reservoir. Studies on model-based dynamic optimization of waterflooding strategies have demonstrated that there is a significant potential to increase life-cycle performance, measured in Net Present Value. However, in these studies the complementary desire of oil companies to maximize daily production is generally neglected. To resolve this, a hierarchical optimization structure is proposed that regards economic life-cycle performance as primary objective and daily production as secondary objective. The existence of redundant degrees of freedom allows for the optimization of the secondary objective without compromising optimality of the primary objective.

Keywords: Optimal control, hierarchical structures, redundant DOF, numerical simulation, oil recovery, waterflooding.

1. INTRODUCTION

Oil is produced from subsurface reservoirs. In these reservoirs the oil is contained in the interconnected pores of the reservoir rock under high pressure and temperature. The depletion process of a reservoir generally consists of two production stages. In the primary production stage the reservoir pressure is the driving mechanism for the production. During this phase, the reservoir pressure drops and production gradually decreases. In the secondary production stage liquid (or gas) is injected into the reservoir using injection wells. The most common secondary recovery mechanism involves the injection of water and is referred to as *waterflooding*. It serves two purposes: sustaining reservoir pressure and sweeping the oil out of pores of the reservoir rock and replacing it by water.

Due to heterogeneity of the reservoir rock, the flowing fluids do not experience the same resistance at different points and in different directions in the reservoir. As a result, the oil-water front may not move uniformly towards the production wells, but has a rather irregular shape as depicted schematically in Figure 1. Due to this phenomenon - referred to as *fingering* - the oil-water front may reach the production wells while certain parts of the reservoir are not be properly drained. The produced water must be disposed of in an environmentally friendly way, bringing along additional production costs. At some point the production is no longer economically viable and the wells are closed (shut-in). At the end of the life of the reservoir all production wells are shut-in, while large amounts of oil may still be present in the reservoir.

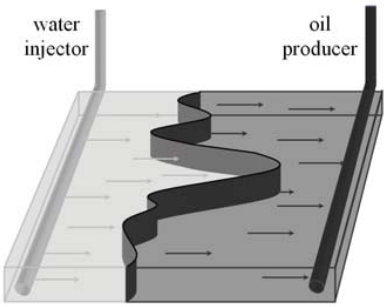

Fig. 1. *Process of waterflooding using a (horizontal) injection and production well. The irregular-shaped oil-water front is a result of the heterogeneous nature of the reservoir, after Brouwer and Jansen (2004).*

Although the injection and production rates of the wells can be manipulated dynamically, they are generally held constant at the maximum capacity of the wells until they are shut-in. Replacing this reactive waterflooding strategy by a dynamic, more proactive one can vastly improve sweep efficiency. Different optimization studies have demonstrated using a numerical reservoir model that there is a potential increase possible of up to 15%, see Brouwer and Jansen (2004) and Jansen et al. (2008). In these optimization studies the objective function is usually of an economic type, most often Net Present Value (NPV), evaluated over the life of the reservoir.

Although many oil companies acknowledge the need for improving economic efficiency over the entire life of the

waterflooding project, many of them adopt maximizing daily production as objective, due to the uncertainty in future economic circumstances. These two objectives, the long-term (life-cycle) objective and the short-term (daily) objective, lead to different, generally conflicting waterflooding strategies.

The goal of this paper is to address the problem of multiple objectives in the optimization of oil recovery from a petroleum reservoir. To that end, a hierarchical optimization structure is proposed that requires a prioritization of the objectives.

This paper proceeds as follows. In Section 2 the properties and characteristics of the reservoir model are described. In Section 3 the life-cycle optimization problem is presented and a hierarchical optimization procedure is proposed. Section 4 deals with identifying redundant degrees of freedom in the optimization problem. The hierarchical optimization procedure is applied to a 3D reservoir model in Section 5. Finally, in Section 6 the results are discussed and alternative approaches are proposed.

2. RESERVOIR MODELING

Reservoir simulators use conservation of mass and momentum equations to describe the flow of oil, water or gas through the reservoir rock. For simplicity reasons, in the oil reservoirs models used within this work only the oil and water phase are assumed to be present.

The mass balance is expressed as follows:

$$\nabla \left(\rho_i u_i\right) + \frac{\partial}{\partial t}\left(\phi \rho_i S_i\right) = 0, \quad i = o, w, \tag{1}$$

where t is time, ∇ the divergence operator, ϕ is the porosity (volume fraction of void space), ρ_i is the density of the phase i, u_i the superficial velocity and S_i the saturation, defined as the proportion of the pore space occupied by phase i.

Conservation of momentum is governed by the Navier-Stokes equations, but is normally simplified for low velocity flow through porous materials, to be described by the semi-empirical Darcy's equation as follows:

$$u_i = -k\frac{k_{ri}}{\mu_i}\nabla p_i, \quad i = o, w, \tag{2}$$

where p_i is the pressure of phase i, k is the absolute permeability, k_{ri} is the relative permeability and μ_i is the viscosity of phase i. The permeability k is an inverse measure of the resistance a fluid experiences flowing through the porous medium. The relative permeability k_{ri} relates to the additional resistance phase i experiences when other phases are present, due to differences in viscosity. As a result, it is a strongly non-linear function of the saturation S_i. In (2) gravity is discarded for simplicity reasons. However, within the 3D example presented in this paper, gravity does play a role. For a more complete description of Darcy's equation we refer to literature, see Aziz and Settari (1979).

Substituting (2) into (1) results into 2 flow equations with 4 unknowns, p_o, p_w, S_o and S_w. Two additional equations are required to complete the system description. The first is the closure equation requiring that the sum of phase saturations must equal 1:

$$S_o + S_w = 1 \tag{3}$$

Second, the relation between the individual phase pressures is given by the capillary pressure equation:

$$p_{cow}(S_w) = p_o - p_w \tag{4}$$

Common practice in reservoir simulation is to substitute (3) and (4) into the flow equations, by taking the oil pressure p_o and water saturation S_w as primary state variables:

$$\nabla(\tilde{\lambda}_o \nabla p_o) = \frac{\partial}{\partial t}\left(\phi \rho_o \cdot [1 - S_w]\right), \tag{5}$$

$$\nabla\left(\tilde{\lambda}_w \nabla p_o - \tilde{\lambda}_w \frac{\partial p_{cow}}{\partial S_w}\nabla S_w\right) = \frac{\partial}{\partial t}\left(\phi \rho_w S_w\right), \tag{6}$$

where $\tilde{\lambda}_o = k\frac{k_{ro}}{\mu_o}$ and $\tilde{\lambda}_w = k\frac{k_{rw}}{\mu_w}$ are the oil and water mobilities. Flow equations (5) and (6) are defined over the entire volume of the reservoir. It is assumed that there is no flow across the boundaries of the reservoir geometry over which (5)-(6) is defined (Neumann boundary conditions).

Due to the complex nature of oil reservoirs, (5)-(6) generally cannot be solved analytically, hence they are evaluated numerically. To this purpose the equations are discretized in space and time. The discretization in space leads to a system built up of a finite number of blocks, referred to as *grid blocks*. This results in the following state space form:

$$\mathbf{V}(\mathbf{x}_k) \cdot \mathbf{x}_{k+1} = \mathbf{T}(\mathbf{x}_k) \cdot \mathbf{x}_k + \mathbf{q}_k, \quad \mathbf{x}_0 = \bar{\mathbf{x}}_0, \tag{7}$$

where k is the time index and $\mathbf{x}$ is the state vector containing the oil pressures (p_o) and water saturations (S_w) in all grid blocks. Vector $\bar{\mathbf{x}}_0$ contains the initial conditions, which are assumed to be known. In the discretization of (5)-(6), the units are converted from $[\frac{kg}{m^3 s}]$ to $[\frac{m^3}{s}]$. In (7) a source vector $\mathbf{q}_k$ is added to model the influence of the wells on the dynamic behavior of the reservoir. The source terms are usually represented by a so-called well model, which relates the source term to the pressure difference between the well and grid block pressure:

$$q_k^j = w^j \cdot (p_{bh,\,k}^j - p_k^j), \tag{8}$$

where $p_{bh,\,k}$ is the well's bottom hole pressure, j the index of the grid block containing the well and p_k^j the grid block pressure in which the well is located. The term w is a well constant which contains the well's geometric factors and the rock and fluid properties of the reservoir directly around the well.

The geological properties inside each grid block are assumed to be constant. The strongly heterogeneous nature of the reservoir can be characterized by assigning different property values to each of the grid blocks. Usually a very large number of grid-blocks is required ($10^3 - 10^6$) to adequately describe the fluid dynamics of a real petroleum reservoir.

The reservoir simulations used within this study are performed using the reservoir simulation software package MoReS, which has been developed by Shell.

3. WATERFLOODING OPTIMIZATION PROBLEM

Flooding a reservoir with water to increase oil production is essentially a batch process, with the additional characteristic that there is no repetition involved. Due to the fact that performance is evaluated at the end of the process and the time constants associated with the nonlinear dynamics are very long, a receding horizon approach will most likely not result in optimal depletion of a reservoir. Dynamic optimization over the entire life of the reservoir is required which can be expressed by the following mathematical formulation:

$$\max_{\mathbf{u}} J(\mathbf{u}), \tag{9}$$

$$s.t.\ \mathbf{x}_{k+1} = \mathbf{f}\left(\mathbf{x}_k, \mathbf{u}_k\right),\ k = 1, .., K, \quad \mathbf{x}_0 = \bar{\mathbf{x}}_0, \tag{10}$$

$$\mathbf{g}(\mathbf{u}) \leq 0 \tag{11}$$

where $\mathbf{u}$ is the input trajectory, $\mathbf{f}$ represents the system equations as described in (7) and $\bar{\mathbf{x}}_0$ is a vector containing the initial conditions of the reservoir. The inequality constraints $\mathbf{g}(\mathbf{u})$ relate to the capacity limitations of the wells.

The objective function J is of an economic type, generally Net Present Value:

$$J = \sum_{k=1}^{K} \left[\frac{r_o \cdot q_{o,k} - r_w \cdot q_{w,k} - r_{inj} \cdot q_{inj,k}}{(1+b)^{\frac{t_k}{\tau_t}}} \cdot \Delta t_k \right], \tag{12}$$

where r_o is the oil revenue $[\frac{\$}{m^3}]$, r_w the water production costs $[\frac{\$}{m^3}]$ and r_{inj} the water injection costs $[\frac{\$}{m^3}]$, which are all assumed constant. K represents the total number of time steps k of a fixed time span and Δt_k the time interval of time step k in $[day]$. The term b represents the discount rate for a certain reference time τ_t. The terms $q_{o,k}$, $q_{w,k}$ and $q_{inj,k}$ represent the total flow rate of respectively produced oil, produced water and injected water at time step k in $[\frac{m^3}{day}]$. An economic objective functions like (12) does not necessarily provide a unique solution to the optimization problem. Although it relates to realistic business conditions, it may well cause ill-posedness of the problem.

Several methods are available for dynamic optimization of large scale problems, see Bryson (1999), Schlegel et al. (2005) and Biegler (2007). *Simultaneous* methods have attractive convergence and constraint handling properties, but even though their capacity to cope with large-scale problems has increased considerably over the recent years, models of order 10^6 still remain very difficult to handle. Although *sequential* methods require repeated numerical integration of the model equations, only the control vector is parameterized and as a result can deal with larger problems. Secondly, due to the fact that the flooding process is very slow much time is available to perform the usually large number of required simulations. However, if the number of control parameters grows the required simulation time may still become unfeasible at some point, unless a method is available to efficiently calculate the gradients of the objective function with respect to the control parameters. This can be done by integration of the adjoint equations or directly through sensitivity equations of model equations.

In the reservoir simulation package used within this work, the adjoint equations are implemented to calculate the gradients. For simplicity reasons, a Steepest Ascent (SA) algorithm is adopted to determine improving control parameters.

3.1 Hierarchical optimization

In the life-cycle waterflooding problem as expressed by (9)-(11), the desire of many oil companies to maximize short-term (daily) production is discarded. A balanced objective provides a possibility to address both objectives in a single function. However, finding an suitable weighting between the objectives may prove to be difficult. Alternatively, we propose a hierarchical (or lexicographic) optimization structure that requires a prioritization of the multiple objectives, as described in Haimes and Li (1988) and Miettinen (1999). In this structure, optimization of a secondary objective function J_2 is constrained by the requirement of the primary objective function J_1 to remain close to its optimal value J_1^*. This structure can be expressed mathematically as follows:

$$\max_{\mathbf{u}} J_2(\mathbf{u}), \tag{13}$$

$$s.t.\ \mathbf{x}_{k+1} = \mathbf{f}\left(\mathbf{x}_k, \mathbf{u}_k\right),\ k = 1, .., K, \quad \mathbf{x}_0 = \bar{\mathbf{x}}_0 \tag{14}$$

$$\mathbf{g}(\mathbf{u}) \leq 0 \tag{15}$$

$$J_1^* - J_1(\mathbf{u}, \mathbf{x}) \leq \varepsilon \tag{16}$$

where ε is an arbitrary small value compared to J_1^*. Solving (13) - (16) requires the knowledge of J_1^*, which is obtained through solving optimization problem (9) - (11).

4. REDUNDANT DEGREES OF FREEDOM

In Jansen et al. (2009) it was observed that significantly different optimized waterflooding strategies result in nearly equal values in NPV. They concluded that the flooding optimization problem is ill-posed and contains many more control variables than necessary. This suggests that optimality of an economic life-cycle objective in waterflooding optimization does not fix all degrees of freedom (DOF) of the decision variable space $\mathcal{D}$, i.e. there exist redundant DOF in the optimization problem. Huesman et al. (2008) found similar results for economic dynamic optimization of plant-wide operation.

A consequence of these redundant DOF is that even if ε in (16) is chosen equal to 0, DOF are left to improve the secondary objective function J_2. A straightforward way of investigating this is to imbed (16) as an equality constraint in the adjoint formulation by means of an additional Lagrange multiplier. Unfortunately, the adjoint functionality in MoReS is not yet capable of dealing with (additional) state constraints. Alternatively, unconstrained gradient information can be used to investigate the redundant DOF, as described in the next section.

4.1 Quadratic approximation of the objective function

A solution $\mathbf{u}$ for which no constraints are active is an optimal solution $\mathbf{u}^*$ if and only if the gradients of J with respect to $\mathbf{u}$ are zero, i.e. $\frac{\partial J}{\partial \mathbf{u}} = 0$. As a result, at $\mathbf{u}^*$ the

gradients do not provide any information on possible redundant degrees of freedom under the optimality condition on J.

Second-order derivatives of J with respect to $\mathbf{u}$ are collected in the Hessian matrix $\mathbf{H}$. If $\mathbf{H}$ is negative-definite, the considered solution $\mathbf{u}$ is an optimal solution, but no DOF are left when the optimality condition on J holds. If $\mathbf{H}$ is negative-semidefinite it means that the Hessian does not have full rank. An orthonormal basis $\mathbf{B}$ for the indetermined directions of $\mathbf{H}$ can than be obtained through a singular value decomposition:

$$\mathbf{H} = \mathbf{U} \cdot \mathbf{\Sigma} \cdot \mathbf{V} \tag{17}$$

The orthonormal basis $\mathbf{B}$ consists of those columns of $\mathbf{V}$ that relate to singular values of zero, i.e. $\mathbf{B} = \{\mathbf{v}_i \mid \sigma_i = 0, \quad i = 1, \ldots, N_{\mathbf{u}}\}$, where $N_{\mathbf{u}}$ is the number of parameters that represent the DOF in the input.

Not all orthogonal directions spanned by the columns of $\mathbf{B}$ will be redundant DOF. These directions are redundant DOF, if they are linear and all higher order derivatives are zero as well, which at this point in time is impossible to proof for reservoir models. $\mathbf{B}$ is however a basis for redundant DOF for a quadratic approximation $\hat{J}$ of objective function J. As $\hat{J}$ can be considered to be an acceptable approximation for small deviations from $\mathbf{u}^*$, $\mathbf{B}$ can be regarded as an acceptable basis for the redundant DOF for small deviations from $\mathbf{u}^*$.

Approximate Hessian matrix Unfortunately, no reservoir simulation package is currently capable of calculating second-order derivatives. However, using the gradient information second-order derivatives can be approximated. Within this work a forward-difference scheme is adopted:

$$\frac{\partial^2 J}{\partial u_i \partial u_j} \approx \frac{\nabla J_i(\mathbf{u} + h_j \mathbf{e}_j) - \nabla J_i(\mathbf{u})}{2h_j} + \frac{\nabla J_j(\mathbf{u} + h_i \mathbf{e}_i) - \nabla J_j(\mathbf{u})}{2h_i} \tag{18}$$

Where $\mathbf{e}_i$ is a canonical unit vector, i.e. a vector with a 1 at element i and 0 elsewhere and h_i is the perturbation step size that relates to parameter u_i of $\mathbf{u}$. In total $N_{\mathbf{u}} + 1$ simulations (function evaluations) are required to obtain the approximate Hessian matrix $\hat{\mathbf{H}}$ at a particular optimal solution $\mathbf{u}^*$.

4.2 Hierarchical optimization method

Adopting the approximation of $\mathbf{H}$ as described in Subsection 4.1, the following iterative procedure is proposed to attack the hierarchical optimization problem (13) - (16) with $\varepsilon = 0$:

(1) Find a (single) optimal strategy $\mathbf{u}^*$ to primary objective function J_1 and use $\mathbf{u} = \mathbf{u}^*$ as starting point in the secondary optimization problem.
(2) Approximate the Hessian matrix $\mathbf{H}$ of J_1 with respect to the input variables at (initial input) $\mathbf{u}$ and determine an orthonormal basis $\mathbf{B}$ for the null-space of $\hat{\mathbf{H}}$.
(3) Find the improving gradient direction $\frac{\partial J_2}{\partial \mathbf{u}}$ for the secondary objective function J_2.

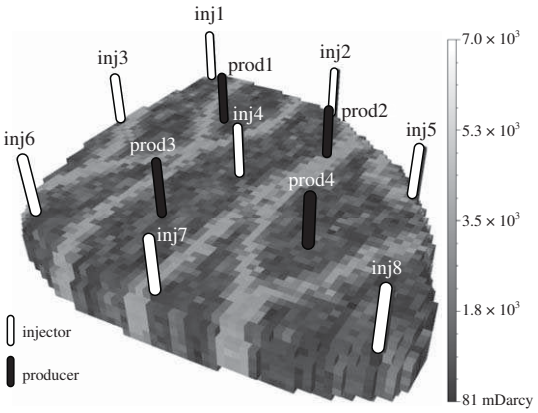

Fig. 2. *3D reservoir model with 4 production and 8 injection wells. The geological structure involves a network of meandering channels in which the fluids flows experience less resistance, due to higher permeability.*

(4) Project $\frac{\partial J_2}{\partial \mathbf{u}}$ onto the orthonormal basis $\mathbf{B}$ to obtain projected direction $\mathbf{d}$, such that $\mathbf{d}$ is an improving direction for J_2, but does not affect J_1. The projection is performed using projection matrix $\mathbf{P}$, see Luenberger (1984):

$$\mathbf{d} = \mathbf{P} \cdot \left(\frac{\partial J_2}{\partial \mathbf{u}} \right)^T \tag{19}$$

$$\mathbf{P} = \mathbf{B} \cdot \left(\mathbf{B}^{\cdot T} \mathbf{B} \right)^{-1} \cdot \mathbf{B}^T \tag{20}$$

(5) Update $\mathbf{u}$ using projected direction $\mathbf{d}$ in a SA method.

$$\mathbf{u}_{new} = \mathbf{u}_{old} + \tau \cdot \mathbf{d}, \tag{21}$$

where τ is an appropriately small step size such that the quadratic approximation of J_1 is justified.
(6) Perform steps 2 through 6 until convergence of J_2.

In the next section a numerical example is presented where the iterative hierarchical optimization structure is tested on a 3D heterogeneous reservoir model.

5. NUMERICAL EXAMPLE

The hierarchical optimization procedure is applied to a 3-dimensional oil reservoir model, introduced in Van Essen et al. (2006). The life-cycle of the reservoir covers a period of 3,600 days and is chosen such that all oil can be produced within that time frame. The length of the life-cycle is in this example not incorporated as additional optimization parameter. The reservoir model consists of 18,553 grid blocks, as depicted in Figure 2, and has dimensions of $480 \times 480 \times 28$ meter. Its geological structure involves a network of fossilized meandering channels in which the flowing fluids experience less resistance, due to higher permeability. The average reservoir pressure is 400 $[bar]$.

The reservoir model contains 8 injection wells and 4 production wells. The production wells are modeled using a well model (8) and operate at a constant bottom hole pressure p_{bh} of 395 $[bar]$. The flow rates of the injection wells can be manipulated directly, i.e. the control input $\mathbf{u}$ involves injection flow rate trajectories for each of the 8

injection wells. The minimum rate for each injection well is 0.0 $[\frac{m^3}{day}]$, the maximum rate is set at a rate of 79.5 $[\frac{m^3}{day}]$.

The control input $\mathbf{u}$ is re-parameterized in time using a zero-order-hold scheme with input parameter vector θ. For each of the 8 injection wells, the control input $\mathbf{u}$ is re-parameterized into 4 time periods t_{θ_i} of 900 days over which the injection rate is held constant at value θ_i. Thus, the input parameter vector θ consists of $8 \times 4 = 32$ elements.

5.1 Life-cycle optimization

The objective function for the life-cycle optimization is defined in terms of NPV, as defined in Equation (12), with $r_o = 126\,[\frac{\$}{m^3}]$, $r_w = 19\,[\frac{\$}{m^3}]$ and $r_i = 6\,[\frac{\$}{m^3}]$. The discount rate b is set to 0. Thus, the life-cycle objective relates to undiscounted cash flow.

The optimal input - denoted by ${\mathbf{u}_\theta}^*$ - obtained after approximately 50 iterations, is shown in Figure 3. None of the input constraints (11) are active for ${\mathbf{u}_\theta}^*$. The value of the objective function corresponding to input ${\mathbf{u}_\theta}^*$ is 47.6×10^6 \$.

5.2 Hierarchical optimization

A secondary objective function J_2 was defined to emphasize the importance of short-term production. To that end, J_2 is chosen identical to the primary objective function but with the addition of a very high annual discount rate b of 0.25. As a result, short-term production is weighed far more heavily than future production. Note that due to the very high discount rate, the actual value of J_2 no longer has a realistic meaning in an economic sense.

The hierarchical approach as presented in Subsection 4.2 is applied. The total number of simulation runs needed to approximate the Hessian ($\hat{\mathbf{H}}$) is 33. However, the required simulation time was vastly reduced by parallel processing the simulations.

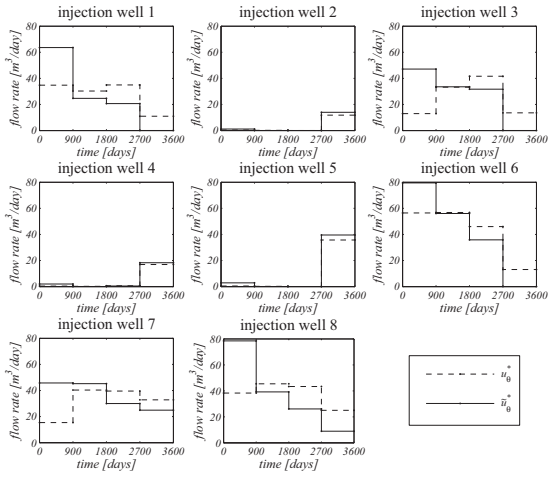

Fig. 3. *Input trajectories for each of the 8 injection wells for the initial optimal solution ${\mathbf{u}_\theta}^*$ to J_1 (dashed line) and the optimal solution $\tilde{\mathbf{u}}_\theta^*$ after the constrained optimization of J_2 (solid line)*

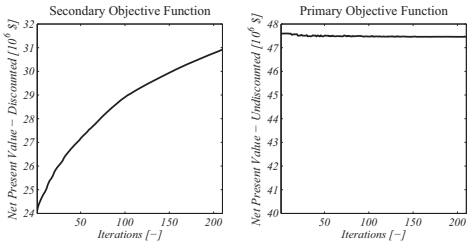

Fig. 4. *Values of the secondary J_2 and primary J_1 objective function plotted against the iteration number for the constrained secondary optimization problem.*

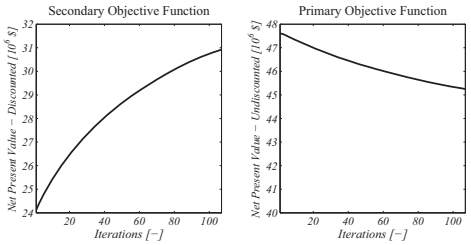

Fig. 5. *Values of the secondary J_2 and primary J_1 objective function plotted against the iteration number for the secondary optimization problem, no longer constrained by the orthonormal basis $\mathbf{B}$.*

Due to the fact that this example involves a numerical model and an approximation of the second-order derivatives, the selection criterion for $\mathbf{B}$ is relaxed. Those columns $\mathbf{v}_i$ of $\mathbf{V}$ were selected that correspond to singular values for which $\frac{\sigma_i}{\sigma_1} < 0.02$ instead of $\sigma_i = 0$. The projected gradients $\mathbf{d}$ were again used in a steepest-ascent scheme. For the quadratic approximation of J_1 to be justified, $\mathbf{u}_{\theta,new}$ must remain close to $\mathbf{u}_{\theta,old}$. To achieve that, $\mathbf{d}$ was normalized and a constant step size τ of 1 was used. Due to time restrictions, the hierarchical optimization of J_2 was terminated after 210 iterations with final control input $\tilde{\mathbf{u}}_\theta^*$. To evaluate the results of the hierarchical optimization, a second optimization case was carried out, where optimization of J_2 was performed *without* projection on $\mathbf{B}$. As a result, the obtained control input - denoted by $\tilde{\mathbf{u}}_\theta$ - does in this case not ensure optimality of J_1.

Figure 4 displays the values of J_1 and J_2 plotted against the iteration number for the hierarchical optimization problem. It shows a considerable increase of J_2 of 28.2% and a slight drop of J_1 of -0.3%. In Figure 3 the input strategy after the final iteration step is presented. It can be observed that the injection strategy shows a substantial increase in injection rates at the beginning of the production life and a decrease at the end. The values of J_1 and J_2 plotted against the iteration number for the *unconstrained* optimization of J_2 are shown in Figure 5. Again an increase of J_2 of 28.2% is realized, but now at a cost of a decrease of J_1 of -5.0%. Finally, Figure 6 shows the value of the primary objective function J_1 over time until the end of the producing reservoir life for ${\mathbf{u}_\theta}^*$, $\tilde{\mathbf{u}}_\theta^*$ and $\tilde{\mathbf{u}}_\theta$. Input $\tilde{\mathbf{u}}_\theta^*$ shows a steeper ascent of J_1 than ${\mathbf{u}_\theta}^*$, while their final values are nearly equal. Input $\tilde{\mathbf{u}}_\theta$ shows initially the same steep ascent as $\tilde{\mathbf{u}}_\theta^*$, but J_1 drops at the end of the life of the reservoir.

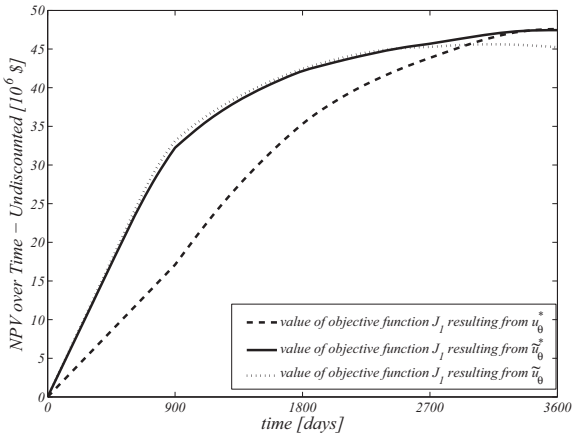

Fig. 6. *Value of the primary objective function J_1 over time for initial optimal input $\mathbf{u}_\theta{}^*$ to J_1 (dashed line), the optimal input $\tilde{\mathbf{u}}_\theta^*$ after the constrained optimization of J_2 (solid line) and input $\tilde{\mathbf{u}}_\theta$ after the unconstrained optimization of J_2 (dotted line)*

6. CONCLUSION

Model-based optimization is a relatively new approach to oil recovery from petroleum reservoirs. Optimization studies have shown a considerable potential increase in life-cycle performance. However, increased understanding of the optimal control problem and characteristics of the optimal solutions is necessary to take the next step towards a real-life application.

Within this work the issue of multiple objectives in oil production is addressed. A hierarchical approach is investigated by means of a simulation experiment. For the presented experiment we conclude that:

- There exist redundant DOF in the input strategy $\mathbf{u}$ with respect to the optimality of the life-cycle objective. This implies the existence of an optimal subset $\mathcal{S}$ of connected optimal solutions within the solution space $\mathcal{D}$.
- The redundant DOF create enough freedom to significantly improve the secondary objective function. Moreover, the difference between the initial and final input strategy to the secondary optimization problem is substantial. This suggest that $\mathcal{S}$ occupies a considerable space within decision variable space $\mathcal{D}$.
- The presented hierarchical optimization procedure provides a method to incorporate short-term performance objectives into problem setting of maximizing life-cycle performance of oil recovery. Using the hierarchical structure, optimization of the secondary objective may be executed without significantly compromising the primary objective.

Under which conditions these conclusions also apply to different life-cycle waterflooding problems and/or different reservoir models will be subject for further investigation.

6.1 Discussion

The presented hierarchical optimization approach is computationally very demanding and becomes infeasible for more realistic reservoir models with an increased number of input parameters. A different method to approximate the Hessian requiring less simulation runs may be considered to resolve this, e.g. the secant method. However, calculating second-order derivatives may be avoided altogether when the hierarchical optimization problem is imbedded in the adjoint formulation, as mentioned in Section 4. This approach will be the focus of future research.

Within this work, uncertainty - of the model and/or the objective function parameters - was neglected. In literature, a number of methods are presented to attack the problem of life-cycle optimization under uncertainty, using a closed-loop approach. For a good overview see Jansen et al. (2008). Without considerable effort, the presented hierarchical optimization structure can be integrated into this closed-loop framework.

REFERENCES

Aziz, K. and Settari, A. (1979). *Petroleum Reservoir Simulation*. Applied Science Publishers.

Biegler, L.T. (2007). An overview of simultaneous strategies for dynamic optimization. *Chemical Engineering and Processing: Process Intensification*, 46(11), 1043–1053. doi:10.1016/j.cep.2006.06.021.

Brouwer, D.R. and Jansen, J.D. (2004). Dynamic optimization of waterflooding with smart wells using optimal control theory. *SPE Journal*, 9(4), 391–402. doi: 10.2118/78278-PA. SPE 78278-PA.

Bryson, A.E. (1999). *Dynamic Optimization*. Addison Wesley Longman.

Haimes, Y.Y. and Li, D. (1988). Hierarchical multiobjective analysis for large-scale systems: Review and current status. *Automatica*, 24(1), 53–69. doi:10.1016/0005-1098(88)90007-6.

Huesman, A.E.M., Bosgra, O.H., and Van den Hof, P.M.J. (2008). Integrating mpc and rto in the process industry by economic dynamic lexicographic optimization; an open-loop exploration. In *AIChE Annual Meeting*. Philadelphia, U.S.A.

Jansen, J.D., Bosgra, O.H., and Van den Hof, P.M.J. (2008). Model-based control of multiphase flow in subsurface oil reservoirs. *Journal of Process Control*, 18(9), 846–855. doi:10.1016/j.jprocont.2008.06.011.

Jansen, J.D., Douma, S.D., Brouwer, D.R., Van den Hof, P.M.J., Bosgra, O.H., and Heemink, A.W. (2009). Closed loop reservoir management. In *SPE Reservoir Simulation Symposium*. The Woodlands, Texas, U.S.A. doi:10.2118/119098-MS. SPE 119098-MS.

Luenberger, D.G. (1984). *Linear and nonlinear programming*. Addison-Wesley.

Miettinen, K.M. (1999). *Nonlinear Multiobjective Optimization*. Kluwer Academic Publishers, Boston.

Schlegel, M., Stockmann, K., Binder, T., and Marquardt, W. (2005). Dynamic optimization using adaptive control vector parameterization. *Computers & Chemical Engineering*, 29(8), 1731–1751. doi: 10.1016/j.compchemeng.2005.02.036.

Van Essen, G.M., Zandvliet, M.J., Van den Hof, P.M.J., Bosgra, O.H., and Jansen, J.D. (2006). Robust waterflooding optimization of multiple geological scenarios. In *SPE Annual Technical Conference and Exhibition*. San Antonio, Texas, U.S.A. doi:10.2118/102913-MS. SPE 102913-MS.

Expected Cost Optimization using Asymmetric Probability Density functions

Bertrand Pigeon*. Michel Perrier*. Bala Srinivasan*

**NSERC Environmental Design Engineering Chair in Process Integration,*
Department of Chemical Engineering, École Polytechnique de Montréal,
C.P. 6079, Succ. Centre Ville, Montréal, Québec, Canada, H3C 3A7,
(e-mail: bertand.pigeon@ polymtl.ca)

Abstract: In the stochastic context, expected value of the cost function is optimized either by changing the mean values of the manipulated variables or by reducing their variance. An extension is to look for an optimal shape for the entire probability density function (PDF). Though the use of asymmetric PDFs is proposed in the literature, no formal proof that justifies their use has been provided. In this paper, it is shown that an asymmetric PDF is required if and only if the cost function is asymmetric and the manipulated variable is penalised. The proof uses an analytical solution of the Fokker-Planck-Kolmogorov equation derived to calculate the shape the output PDF for scalar systems. In particular, this analytical solution is adapted to a switching proportional controller. The theoretical concepts are illustrated on a simulation example, where the advantage of choosing an asymmetric PDF is shown.

Keywords: Stochastic control, Optimization, Probability Density Functions, Switching Algorithms

1. INTRODUCTION

Optimization in a stochastic context involves studying the influence of decisions variables on the expected value of the objective function. In the stochastic context, not only the mean values of the decision variables but the entire distribution plays a role in optimization. Typically, in the presence of constraints, variability is reduced first using appropriate controllers, and secondly by shifting the set point closer to the constraint. Use of minimum variance controllers for optimization purposes has been well studied in the literature (Muske, 2003).

However, shaping the entire probability density function (PDF) could be a viable option to reduce costs. The first mention of this possibility was made in Kàrnỳ (1996). Then, Wang (1998) developed a PDF shaping algorithm based on the weights of a neural B-Spline that parameterized the output PDF. This method has been improved ever since by the same authors (Wang ,2002; Wang & Zhang 2002; Wang & Wang, 2002; Guo & Wang 2005). Crespo and Sun (2002) used an analytical solution of Fokker-Plank-Kolmogorov equation in steady-state to develop a PDF shaping algorithm. On the other hand, Forbes et al. (2004) developed an algorithm based on the parametrization of the target PDF using Gram-Charlier basis functions. In all the above cited works, though the motivation is to improve an optimization objective, only the sub-problem of getting close to a target PDF is addressed. No indication is given on how to compute a target PDF that is suited for the optimization problem at hand.

It has been argued in all the above works that the advantage of PDF shaping lies in shaping it in an asymmetric manner. The necessity of an asymmetric PDF arises from the asymmetry of the objective function. This is normally due to the presence of process and operational constraints. With constraints, typically, an approach based on penalty (barrier) function is used for resolution. An additional cost is added when the constraint is violated (or in the barrier function case an additional cost is added when operated close to the constraint), which inturn causes asymmetry.

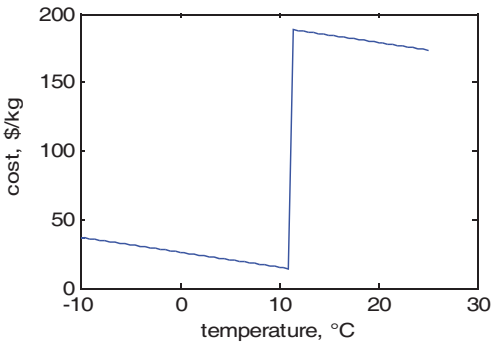

Figure 1: Example of an asymmetric objective function

Figure 1 shows an example with a penalty function where a constant penalty is added if the manipulated variable is above the constraint set at 11°C. As seen, such penalty/barrier functions cause a huge asymmetry around the optimal solution. The optimal solution without any stochastic behaviour would be on the constraint 11°C. However with process noise, a controller needs to be used to reduce the variance of the manipulated variable, and the set point must be lower than 11°C, so that only a small

part of the distribution violates the constraint. The minimum variance controller tries to squeeze and shift the distribution towards the constraint. On the other hand, the PDF shaping solution tries to match the asymmetry in the objective function using an asymmetric PDF with its tail on the opposite side of the constraint.

Though intuitive arguments were given for using asymmetric PDFs, no formal results are available to distinguish the cases where an asymmetric PDF would be more beneficial than the symmetric one. So, the main question asked in this paper is, "which class of problems requires an asymmetric PDF?" It is shown that not only the asymmetry of the objective function but also an input weighting is needed to necessitate an asymmetric PDF. The importance of input weighting is one of the core contributions of this paper. In the minimum variance controller, by reducing the variability of the output variable, the variability of the manipulated variables would increase, straining the process equipment. Contrarily, with an asymmetric PDF, the set point can be shifted toward the constraint and with less impact on the manipulated variables.

This paper first presents an analytical solution of the Fokker-Planck-Kolmogorov (FPK) equation for general scalar systems. This analytical solution is then applied to the switching controller case, using which, the optimality or non-optimality of symmetric solution is ascertained. The last section is devoted to a simulation example where the improvement in cost using an asymmetric controller is shown.

2. PROBLEM FORMULATION

2.1Optimization problem formulation

Consider the dynamic system given by equation (1), where u is the scalar manipulated variable, x the scalar state variable, and w the zero-mean Gaussian process noise input with standard deviation η .

$$\dot{x} = f(x) + g(x)u + w \tag{1}$$

The functions *f(x)* and *g(x)* represent the unforced and the forced parts of the system dynamics. Consider the optimization of the above system at steady state:

$$\begin{matrix} \min_{u} \Phi(x,u) \\ C(x,u) \leqslant 0 \\ f(x) + g(x)u = 0 \end{matrix} \quad , \tag{2}$$

where Φ is the function to be optimized, C the constraints. Note that the optimization considers the system equations without noise at steady state as equality constraints.

In the context of this paper, a penalty function is introduced to handle the constraints as show below:

$$\begin{matrix} \min_{u} [\bar{\Phi}(x,u) + D(C(x,u))] = \phi(x,u) \\ f(x) + g(x)u = 0 \end{matrix} \quad , \tag{3}$$

where *D(.)* is any appropriate penalty function and $\phi(.)$ the augmented cost. As discussed earlier, *D(.)* is asymmetric which would lead to an asymmetry in the cost function.

In the context of this paper, x is considered stochastic due to the presence of the noise term w. So, the expectation of the cost function needs to be calculated for optimization purposes. The cost function that is minimized is given by:

$$J = \int_{-\infty}^{+\infty} \int_{-\infty}^{+\infty} \phi(x,u)\, p(x,u)\, dx du \quad , \tag{4}$$

where *p(x,u)* is the joint probability density function.

2.3 Controllers for PDF shaping

In this section, the nonlinear controller used for PDF shaping is presented. Nonlinearity is crucial since, if the process and the controller were linear, and the input is Gaussian, the output PDF would just be Gaussian.

In order to have a full control on the nonlinearity, all the system nonlinearities are eliminated by feedback linearization. In addition, the controller *h(x)* is used to bring the state to its desired set point. Then, the controller would introduce the nonlinearities required to shape the PDFs. For the system under consideration, the linearizing feedback is given by:

$$u = \frac{-f(x) + h(x)}{g(x)} \quad . \tag{5}$$

Here, a switching controller of the following form will be studied. The nonlinearity arises from the gain schedule and results in an asymmetrical PDF.

$$h(x) = \begin{Bmatrix} k_1(x_{sp} - x) & if & x < x_{sp} \\ k_2(x_{sp} - x) & if & x > x_{sp} \end{Bmatrix} \quad . \tag{6}$$

To simplify the development, no measurement noise is considered, while a zero-mean Gaussian measurement noise, z, with standard deviation λ will be added to the set point. Thus, the the system reads

$$\begin{matrix} \dot{x} = h(x) + w + k_{cont}(x) z \\ k_{cont}(x) = \begin{Bmatrix} k_1 & if & x < x_{sp} \\ k_2 & if & x > x_{sp} \end{Bmatrix} \end{matrix} \tag{7}$$

3.ANALYTICAL SOLUTION OF THE SCALAR FPK EQUATION FOR SWITCHING CONTROLLER

In this section, the analytical solution of the FPK equation will be developed for the general *h(x)* and later exploited to suit the switching controller.

3.1 General case

Consider the system (8) where the two random variables are Brownian processes :

$$dx = h(x)dt + \eta\ d\beta_w + k_{cont}(x)\lambda\ d\beta_z, \quad t \geq t_0 \quad , \qquad (8)$$

where η and λ are the standard deviations of the process and measurement noise respectively, $d\beta_w$ and $d\beta_z$ are unit variance Brownian processes. These two noises can be clubbed together into a general equation as follows:

$$dx = h(x)dt + \rho(x)\ d\beta, \quad t \geq t_0 \qquad (9)$$

where $\rho(x)$ represents the agglomerated standard deviation.

The evolution of its probability density function of *x* is given by the Fokker-Planck-Kolmogorov equation (Jazwinsky (1968)):

$$\frac{\partial p(x,t)}{\partial t} = \frac{-\partial[p(x,t)h(x)]}{\partial x} + \frac{1}{2}\frac{\partial^2[p(x,t)\rho(x)^2]}{\partial x^2} \quad . (10)$$

with boundary conditions $lim_{x\to\infty} p = lim_{x\to-\infty} p = 0$

$lim_{x\to\infty} \frac{\partial p}{\partial x} = lim_{x\to-\infty} \frac{\partial p}{\partial x} = 0$, $\int_{-\infty}^{\infty} p(x)\,dx = 1$.

At steady state, this equation reads

$$\frac{d\,ph}{dx} = \frac{1}{2}\frac{d^2\rho^2 p}{dx^2} \quad . \qquad (11)$$

By integrating both sides of the equation:

$$2\,ph = \frac{d\rho^2 p}{dx} + c \quad . \qquad (12)$$

Using the boundary conditions it can be seen that, $c = 0$. Rearranging the terms gives,

$$\frac{dp}{p} = \left(\frac{2h}{\rho^2} - \frac{2}{\rho}\frac{d\rho}{dx}\right)dx \quad . \qquad (13)$$

The solution of the above equation is given by:

$$p(x) = p_0\, e^{\int_{-\infty}^{\infty}\left(\frac{2h}{\rho^2} - \frac{2}{\rho}\frac{d\rho}{dx}\right)dx} \quad , \qquad (14)$$

where p_0 is the normalizing constant to render the integral of the probability to 1.

3.2 Switching controller case

The analytical solution developed in Section 3.1 is applied to a case of the switching controller. Let p_{sp} be the value of the probability density function at $x = x_{sp}$. From (6) and (7) it can be seen that to the left of the set point

$$h(x) = k_1(x - x_{sp}),\ \rho^2(x) = \eta^2 + k_1^2\lambda^2 \quad , \qquad (15)$$

and to the right

$$h(x) = k_2(x - x_{sp}),\ \rho^2(x) = \eta^2 + k_2^2\lambda^{2.} \quad . \qquad (16)$$

Thus, it can be seen that

$$p(x) = \begin{cases} p_{sp}\, e^{\frac{-2k_1(x-x_{sp})^2}{\eta^2 + k_1^2\lambda^2}} & \text{for } x < x_{sp} \\ p_{sp}\, e^{\frac{-2k_2(x-x_{sp})^2}{\eta^2 + k_2^2\lambda^2}} & \text{for } x \geq x_{sp} \end{cases} \quad . \qquad (17)$$

This can be interpreted as Gaussian function where the two branches are not symmetric. The variance on one side is different from that of the other. The variances on either side can be computed as follows:

$$\sigma_1 = \frac{\sqrt{\eta^2 + k_1^2\lambda^2}}{2\sqrt{k_1}} \quad \text{and} \quad \sigma_2 = \frac{\sqrt{\eta^2 + k_1^2\lambda^2}}{2\sqrt{k_2}} \quad . \qquad (18)$$

Also, the normalisation constant can be computed analytically as follows:

$$p_{sp} = \frac{2}{\sqrt{2\pi}(\sigma_1 + \sigma_2)} \quad . \qquad (19)$$

From the expression of *h(x)* it can also be shown that

$$p(h) = \begin{cases} p_{h0}\, e^{\frac{-2h^2}{k_1(\eta + k_1\lambda)^2}} & \text{for } h < 0 \\ p_{h0}\, e^{\frac{-2h^2}{k_2(\eta + k_2\lambda)^2}} & \text{for } h \geq 0 \end{cases} \qquad (20)$$

with

$$\sigma_{1h} = \frac{\sqrt{\eta^2 + k_1^2\lambda^2}\sqrt{k_1}}{2} \quad , \quad \sigma_{2h} = \frac{\sqrt{\eta^2 + k_2^2\lambda^2}\sqrt{k_2}}{2} \qquad (21)$$

$$p_{h0} = \frac{2}{\sqrt{2\pi}(\sigma_{1h} + \sigma_{2h})} \quad . \qquad (22)$$

4.NON-OPTIMALITY OF THE SYMMETRIC SOLUTION

In this section, it is be shown that a symmetric PDF is sufficient even for an asymmetric objective function, when there is no input weighting. Also, when the objective function is symmetric, with or without input weighting a symmetric PDF is indeed optimal. However, when there is asymmetry and input weighting, then it is shown that a symmetric solution is not optimal.

Consider equation (4). Since, *u* is a function of *x*, the objective function $\phi(x,u)$ is just a function of *x*. In particular, consider a special case where the squared deviation of the control action *h(x)* is included in the cost function. The remaining part of the objective function is termed *l(x)*. So,

$$\phi(x,u) = l(x) + \gamma h^2(x) \qquad (23)$$

Due to the imposed control structure, the degree of freedom for the optimization problem is no longer u, but the parameters x_{sp}, k_1 and k_2. So, the optimization problem reads,

$$\min_{x_{sp},k_1,k_2} J=\int_{-\infty}^{+\infty} l(x)\,p(x)\,dx+\int_{-\infty}^{+\infty}\gamma h^2\,p(h)\,dh \quad . \tag{24}$$

The proof of non-optimality proceeds by deriving the necessary conditions of optimality of the above optimization problem by considering that k_1 and k_2 are varied independently. Then an additional condition of symmetry, i.e. $k_1 = k_2$ is imposed. This gives four conditions (3 necessary conditions and one condition of symmetry) for three variables. If these four conditions are consistent then the symmetric solution is indeed optimal. On the other hand, if it leads to an inconsistency or contradiction then it shows that the symmetric solution is not optimal in the case considered.

Theorem 1: The symmetric switching controller is locally optimal if and only if (i) l(x) is symmetric around the optimum, i.e., the third derivative evaluated at the optimum is zero, or (ii) the input weighting γ is zero.

Proof: Without loss of generality let $x = 0$, $l(x) = 0$, $J = 0$ be the optimum in the absence of noise. Consider the third order Taylor series expansion of $l(x)$ around $x = 0$. The first two terms are zero since $l(0) = 0$ and the first derivative is zero due to optimality. Thus the expansion is given by

$$l(x)=\alpha x^2+\delta x^3 \quad , \tag{25}$$

where α and δ are the second and third derivatives, respectively, at the origin. The expected cost (5) is then given by,

$$J=\alpha\int_{-\infty}^{+\infty} x^2\,p(x)dx+\delta\int_{-\infty}^{+\infty} x^3\,p(x)\,dx+\gamma\int_{-\infty}^{+\infty} h^2\,p(h)\,dh \quad .(26)$$

Analytical expressions for all the three terms can be obtained.

$$\int_{-\infty}^{+\infty} x^2\,p\,dx=x_{sp}^2-\frac{4\,x_{sp}(\sigma_1-\sigma_2)}{\sqrt{2\pi}}+(\sigma_1^2-\sigma_1\sigma_2+\sigma_2^2) \tag{27}$$

$$\int_{-\infty}^{+\infty} x^3\,p\,dx=x_{sp}^3-\frac{6\,x_{sp}^2}{\sqrt{2\,\pi}}(\sigma_2-\sigma_1)+3\,x_{sp}(\sigma_2^2-\sigma_1\sigma_2+\sigma_1^2)\frac{+4}{\sqrt{2\,\pi}}(\sigma_2-\sigma_1)(\sigma_1^2+\sigma_2^2) \tag{28}$$

$$\int_{-\infty}^{+\infty} h^2\,p(h)\,dh=(\sigma_{h1}^2-\sigma_{h1}\sigma_{h2}+\sigma_{h2}^2)-\frac{2}{\pi}(\sigma_{h1}-\sigma_{h2})^2 \tag{29}$$

The optimality condition requires that the derivatives of J with respect to x_{sp}, k_1 and k_2 be zero, the expressions for which can be readily obtained. To analyse the symmetric solution, consider $k_1 = k_2 = k$. Substituting this in the derivatives leads to

$$\frac{\partial J}{\partial x_{sp}}=2\alpha x_{sp}+3\delta x_{sp}^2+\frac{3\delta}{4k}(\eta^2+k^2\lambda^2)=0 \quad , \tag{30}$$

$$\frac{\partial J}{\partial k_1}-\frac{\partial J}{\partial k_2}=\frac{(\eta^2-k^2\lambda^2)}{\sqrt{2\pi k^3}}\left(2\alpha x_{sp}+3\delta x_{sp}^2+\frac{\delta}{k}(\eta^2+k^2\lambda^2)\right)=0 \quad , \tag{31}$$

and

$$\frac{\partial J}{\partial k_1}+\frac{\partial J}{\partial k_2}=\frac{\eta^2-k^2\lambda^2}{4k^2}(\alpha+3\delta x_{sp})+\frac{\gamma}{4}(\eta^2+3k^2\lambda^2)=0 \quad . \tag{32}$$

It can be seen that there are 3 equations for 2 unknowns, k and x_{sp}. Replacing the terms with x_{sp} in (31) using (30), it can be seen that

$$\frac{\partial J}{\partial k_1}-\frac{\partial J}{\partial k_2}=\frac{(\eta^2-k^2\lambda^2)}{\sqrt{2\pi k^3}}\frac{\delta}{4k}(\eta^2+k^2\lambda^2)=0 \quad . \tag{33}$$

Only if part: $\delta\neq 0,\gamma\neq 0\Rightarrow non-optimality$

When $\delta\neq 0$, the only solutions of (33) are $k=\pm\eta/\lambda$ But, plugging these values of k in the sum of derivatives lead to $\gamma=0$. So, if $\gamma\neq 0$ the symmetric controller is not optimal .

If part: $\gamma=0\Rightarrow optimality$

When $\gamma=0$ note that $k=\pm\eta/\lambda$ satisfies all the three necessary conditions of optimality .

If part: $\delta=0\Rightarrow optimality$

Since $\delta=0$, (31) gives $x_{sp} = 0$. (33) is not useful in determining k. However from (32), it can be seen that the following 4th order equation can be used to compute k.

$$3\gamma\lambda k^4+(\gamma\eta+\lambda\alpha)k^2-\alpha\eta=0 \tag{34}$$

■

5. EXAMPLE

In this section, an asymmetric example with input weighting is presented. The optimal switching controller is computed using the output PDF obtained through the analytical solution. It will be shown that such a controller indeed leads to an asymmetric PDF.

A cost function analogous to the one in Figure 1 is considered here.

$$\begin{gathered}\phi(x)=26-10x+D(c(x))+10h^2(x)\\ D(c(x))=0\ if\ x\leq 11\\ D(c(x))=10^5\ if\ x>11\end{gathered} \tag{35}$$

The system dynamics is given by

$$\dot{x}=-0.4\mathrm{x}+0.2\mathrm{u}+w \quad , \tag{38}$$

where the process noise w has a mean of 0 and a standard deviation $\eta=1$. A measurement noise of standard deviation $\lambda=0.01$ was considered. Though it is unrealistic to consider a ratio of 100 between the standard deviations of

process and measurement noises, it is required in this case to prove the principle. The asymmetric PDF gives better results only in a narrow range of parameter values and so is such a choice made.

5.1 Controller design

The controller (6) is used here. It has 3 parameters; gains k_1, k_2 and the set point x_{sp}. These parameters are found via non linear programming where the equation (24) is minimized. Equation (24) for the given example can be written as follows:

$$J = 26 - 10\int_{-\infty}^{+\infty} x\,p(x)dx + 10^5\int_{11}^{+\infty} p(x)dx + 10\int_{-\infty}^{+\infty} v^2\,p(v)dv \tag{39}$$

Also, in this case an analytical expression for all the three terms can be derived using *p(x)* given in (20). The analytical expression of the last term is already provided in (31). The expressions for the other terms are given as follows:

$$\int_{c}^{+\infty} p(x)dx = \frac{\sigma_2}{\sigma_1+\sigma_2}\left(1+\mathrm{erf}\left(\frac{x_{sp}-c}{\sqrt{2}\sigma_2}\right)\right) \tag{48}$$

$$\int_{-\infty}^{+\infty} x\,p(x)dx = x_{sp} + \sqrt{\frac{2}{\pi}}\left(\sigma_2-\sigma_1\right) \quad . \tag{49}$$

5.2 Results

The optimal parameters for a switching controller and a constant gain control have been found numerically. For calculating the optimal single-gain controller, the same calculations are used with $k_1 = k_2$. The optimal gains and the value of the cost function are presented in Table 1. It can be seen that with the switching controller, the cost is reduced by around 6.7%. It is because by having 2 gains, the controller can be aggressive on one side, the side of the constraint, while having a low gain and thereby low input variance on the other side.

Table 1: Results of the example

Controller type	Switching controller	Single gain controller
Set point	10.6	10.53
k_1	0.41	2.94
k_2	4.99	2.94
Cost	5.39	5.78

Figure 2 shows the output PDF for the both controllers. It can be seen that the single proportional controller leads to a symmetric Gaussian PDF, while with the switching controller results in an asymmetric PDF. It is equally interesting to see in Figure 3 that the asymmetry in the input PDF is reversed. It can be explained by the fact that closer to the constraint, the input works hard and has a larger variance, while far from the constraint, the input does not work in order to reduce the cost by decreasing its variance.

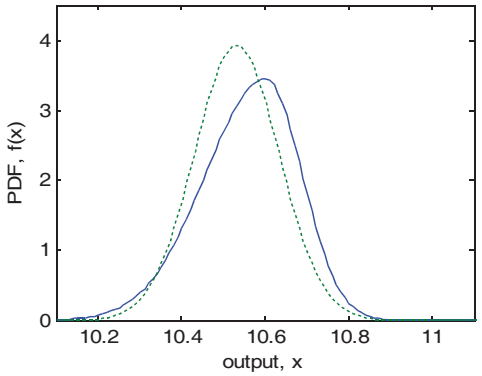

Figure 2: Output PDF with a switching controller (solid line) and with a non-switching controller (dotted line)

Several tests were performed with varying penalties, with varying input weights, and varying measurement noise levels. Figure 4 shows the effect changing the penalty. It can be seen that increasing the weighting for the penalty increases the difference between the cost functions of the symmetric and asymmetric PDF. This tendency can be attributed to the fact that increasing the penalty increases the asymmetry of the cost function. Note that the x axis is logarithmic, i.e, a small increase in the difference calls for a order of magnitude change in the weighting.

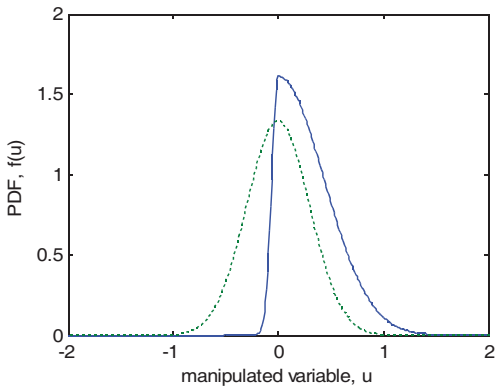

Figure 3: Manipulated variable PDF with a switching controller (solid line) and with a non-switching controller (dotted line)

Figure 5 shows the effect of changing the input weight. An interesting effect can be observed here. The difference first increases, while it decreases after reaching a maximum. Intuitively, when the input weight is zero, the symmetric solution is indeed optimal and there can be no gain by using an asymmetric controller. On the other hand, since the input weighting is symmetric, for large input weightings the asymmetry of the cost function becomes negligible and so a symmetric controller is again optimal.

Figure 6 shows the influence of measurement noise on the difference. The larger the measurement noise, lesser is the gain that can be obtained by using an asymmetric PDF. This is due to the fact that with increasing measurement noise the minimum variance controller as such has a fairly low gain and not much manoeuvrability is left.

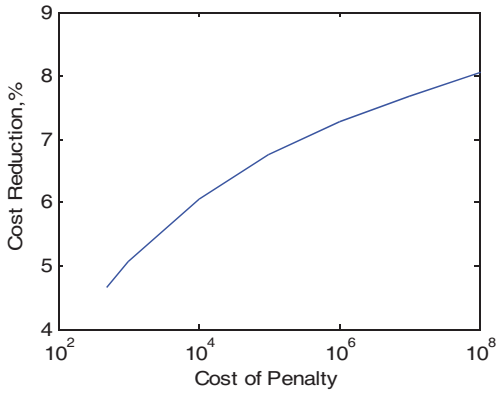

Figure 4: Effect of the weighting of the penalty on the cost reduction due to switching controller

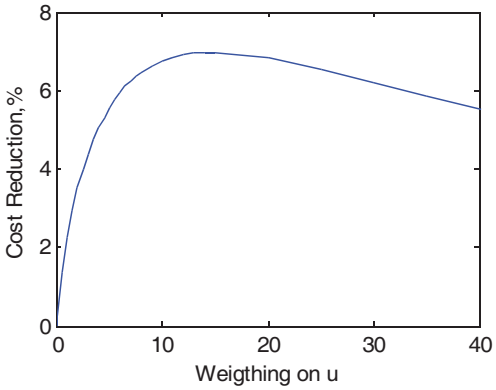

Figure 5 Effect of the input weighting on the cost reduction due to switching controller

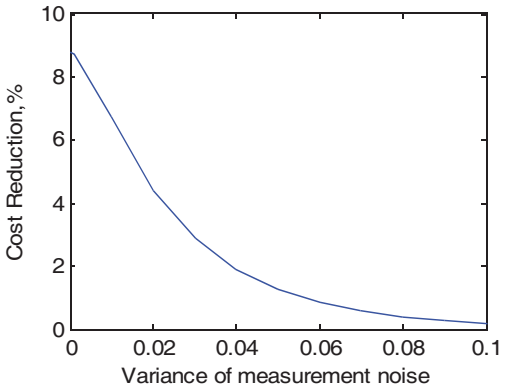

Figure 6: Effect of the measurement noise on the cost reduction due to switching controller

6. CONCLUSION

This paper showed the non-optimality of a symmetric PDF when the cost function was asymmetric and the manipulated variable was constrained. The result is derived using the analytical solution of the FPK equation for a scalar system and a switching controller. Finally, a numerical example was shown where the asymmetric PDF gave a better result than the symmetric one.

The importance of this result lies in the fact that it clearly demarks the cases where an asymmetric PDF is required. Also, a simple switching controller structure for PDF shaping is proposed that can be easily implemented in an industrial context. Finally, the analytical solution of the FPK equation is not only limited to PDF shaping, but could have more impact in the general context of stochastic optimization.

ACKNOWLEDGEMENTS

This work was supported by the Natural Sciences and Engineering Research Council of Canada (NSERC), Environmental Design Engineering Chair at École Polytechnique and Le Fonds Québécois de Recherche sur la Nature et les Technologies (FQRNT).

REFERENCES

Crespo, L.G., Sun, J.Q. (2002). Nonlinear Stochastic Control via Stationary Probability Density Functions. Proceedings of the American Control Conference. Volume 3. 2029-2034

Forbes, M.G. , Guay M., Forbes, J.F. (2004). Control Design for First-order Processes: Shaping the Probability Density of the Process State. *Journal of Process Control.* 14(4). 399-410

Guo, L., Wang, H. (2005*)*. Generalized discrete-time PI control of output PDF using square root B-spline expansion. *Automatica.* 41(1). 159-162

Jazwinski, A. H. 1970. *Stochastic Processes and Filtering Theory.* New-York: Dover Publications.376 p.

Kàrnỳ, M. (1996). Towards Fully Probabilistic Control Design. *Automatica.* 32(12). 1719-1722

Muske, K.(2003). Estimating the Economic Benefit from Improved Process Control. *Industrial Engineering Chemical Research.* 42(20). 4535-4544

Wang, H. (1998). Robust Control of the Output Probability Density Functions for Multivariable Stochastic Systems. *Proceedings of the 37st Conference on decision on control.* volume 2. 1305-1310

Wang, H. (2002). Minimum Entropy Control of Non-Gaussian Dynamic Stochastic Systems. *IEEE Transactions on Automatic Control.* 47(2). 398-403

Wang, H., Zhang, J. H. (2002). Control of the Output Stochastic Distributions via Lyapunov Function Analysis. *Proceedings of the 2002 IEEE International Conference on Control Applications.* 927-931.

Application of Near-infrared Spectroscopy in Batch Process Control

H. Lin*. O. Marjanovic. B. Lennox ***. A. Shamekh******

** Control Systems Centre, School of Electrical and Electronic Engineering, The University of Manchester, UK (e-mail: haishenglin318@yahoo.com.cn).*
*** Control Systems Centre, School of Electrical and Electronic Engineering, The University of Manchester, UK (e-mail: mchssom2@manchester.ac.uk).*
**** Control Systems Centre, School of Electrical and Electronic Engineering, The University of Manchester, UK (e-mail: barry.lennox@manchester.ac.uk).*
***** Electrical Engineering Department, University of Garyounis, Benghazi-Libya (e-mail: awshamekh@yahoo.com)*

Abstract: While batch processes are gaining ever increasing importance in the manufacturing industries, control of the product quality remains to be a serious challenge. To improve overall process understanding and control, new analytical techniques, such as Near-Infrared (NIR) Spectroscopy, are starting to be employed in industry. Currently, these techniques are primarily used for process monitoring purposes and have not yet been explicitly included in feedback control systems. This paper investigates the ability of three different control systems to adequately control a simulated batch reactor using the NIR spectra as feedback information such that the product meets quality specifications. The particular problem considered in this paper is adequate representation of the NIR spectrum using a single variable that is then controlled by employing Model Predictive Controller (MPC). It is shown that the resulting controller performances are highly variable if the controlled variable is chosen by selecting a single peak in the NIR spectrum to represent that variable. On the other hand, by using Principal Component Analysis (PCA) to extract information from all of the wavenumbers and represent it using a single composite variable, which is then controlled, it is shown that the process can be adequately regulated.

Keywords: Batch Process, Near Infrared Spectroscopy, Model Predictive Control, Chemical Reactor

1. INTRODUCTION

Batch processes are gaining ever increasing importance in the manufacturing industries. They are particularly prevalent in the polymer, pharmaceutical and specialty chemicals industries where the focus is on the production of low-volume, high-value added products. However, a major problem that is faced by those involved in batch processing is the application of reliable control systems. The characteristics associated with batch processes that make them particularly challenging to control include the presence of time-varying and nonlinear dynamics, multitude of unmeasured disturbances such as concentrations of various raw materials, and the presence of irreversible behaviour (Bonvin 1998).

This paper deals with the application of control systems to a chemical batch reactor for which the requirement to manufacture high quality product often translates into the control problem of tracking the reference temperature profile (Cott and Macchietto 1989). This is because the reaction rates involving raw materials, intermediates and products are highly dependent on the temperature. As a result, the composition of the product is also highly dependent on the reactor temperature. The reference profile design consists of characterising, in terms of the reactor temperature, the following three main stages of batch reactor operation: heating up the reactor; controlling the reactor temperature to meet the process requirement and then cooling down the reactor. However, temperature control of batch reactors can be a difficult task due to the process nonlinearities and the absence of the steady-state operation (Shinskey 1996). Aziz et al. (2000) analyzed the performance of different types of controllers in terms of their ability to track a reference profile of reactor temperature.

Even if the adequate temperature control system is in place and the reactor temperature does follow closely its reference profile, there is no guarantee that the final product will meet its specifications. For example, changes in the reaction rates and/or inclusion of a new raw material (as an impurity) can introduce new reaction pathways, which may cause the final composition of the product to change significantly. As a result, product quality can deteriorate even in the presence of a satisfactory temperature control system. Hence, it would be highly useful to construct a control system that would focus on regulating not the reactor temperature but some other variables that are much more directly related to product quality. As a result, such control system should be able to maintain high quality product in the presence of disturbances.

Near-infrared (NIR) spectroscopy represents a set of non-destructive analytical techniques that have been extensively used to extract chemical and physical information from a product sample based on scattered light (Reich 2005). NIR spectroscopy has been widely used in the pharmaceutical industry to test raw materials, control product quality and

monitor processes (M. Blanco 1998; Donald A. Burns 2001; Luypaert, Massart 2007). In the food industry there have been several applications of NIR spectroscopy being used for continuous process monitoring and control (Huang 2008).

Since the NIR spectra reflect the composition of the product, they represent excellent feedback information that could be used by control system to ensure the high quality of a product. So far NIR spectroscopy has been widely used for monitoring of manufacturing processes (Reich 2005; Jorgensen 2004; Scarff 2006). However, there is currently no publication proposing a method of explicitly using NIR spectra as feedback information to control the temperature of a reactor in order to ensure that the manufactured product conforms to high quality standards.

One clear problem in using NIR spectra as feedback information is the large number of variables that are needed to replicate information contained within the NIR spectrum. Arguably the number of variables should be equal to the number of spectral channels (wavenumbers) in order to completely characterise a given NIR spectrum. However, if this guideline is followed then the resulting control problem will potentially have several hundred controlled variables which could not be simultaneously controlled using typically only a handful or even just one or two manipulated variables.

In this paper, the problem of incorporating NIR spectrum as feedback information is addressed by using two different approaches. Both approaches utilise Model Predictive Control (MPC) framework but with a different definition of a controlled variable. The first approach is based on an idea of selecting wavenumber corresponding to one of the spectral peaks as a controlled variable. However, there are currently no clear guidelines regarding the selection of the peak to be considered as a controlled variable. The second approach is to use multivariate statistical analysis tools, namely Principal Component Analysis (PCA), in order to extract the information from NIR spectrum and represent it in a format of a single composite variable. This composite variable can then be regulated by means of a control system. Assessment of the controllers' performances is conducted using a simulated chemical batch reactor. The NIR spectrum is simulated by assuming that it is a linear combination of pure spectra related to individual compounds.

2. PRELIMINARIES

In this section the general concepts of Model Predictive Control (MPC) and Principal Component Analysis (PCA) are briefly introduced in order to facilitate the understanding of the control methodologies employed in the paper.

2.1 Model Predictive Control (MPC)

MPC (Maciejowski 2002) refers to a class of control algorithms that utilise an explicit process model to predict the future response of a plant. At each sampling instant, the MPC algorithm attempts to optimise future process behaviour by computing a sequence of adjustments that should be made to the manipulated variables. The first input in the optimal sequence is then implemented, and the entire calculation is repeated at the next sampling instant.

The key ingredient of the MPC controller is a prediction model used to forecast future process behaviour. In this paper the ARX structure (auto regressive with exogenous inputs) is chosen as the prediction model, and it is given as follows:

$$y(k) = -\sum_{i=1}^{n_y} a_i y(k-i) + \sum_{j=1}^{n_u} b_j u(k-j) + e(k) \qquad (1)$$

where $y(k)$ and $u(k)$ are the controlled and manipulated variable, respectively, at a sampling instant k. The model error is represented by $e(k)$. The order of the ARX model is determined by the values of n_y and n_u.

This cost function for the selection of the appropriate control action is given in (2).

$$J = \sum_{i=1}^{p} \alpha \left(y_r(k+i/k) - \hat{y}(k+i/k) \right)^2 + \sum_{j=1}^{m} \beta \Delta u(k+j-1/k)^2 \qquad (2)$$

Where J is the cost function to be minimized, p and m are the prediction and control horizons, respectively. y_r and $\hat{y}$ are the reference (set-point) values and estimated future output values, respectively, α and β are the weighting parameters for the controlled and manipulated variables, respectively. Finally, Δu is the change in manipulated variable (incremental control move) that is to be computed by the MPC algorithm.

The target of the cost function in (2) is to force the future output to track the reference trajectory over the specified prediction window p, while taking into account the balance between error energy and incremental control energy.

2.2 Principal Component Analysis (PCA)

The primary objective of Principal Component Analysis (PCA) is to capture the majority of variation present in data using a minimal number of composite variables, named principal components (PCs) (Johansson 2001; Berrar 2003). This dimensionality reduction is performed by exploiting the inter-dependence between measured process variables, such as individual wavenumbers in the NIR spectra.

For the analysis of spectroscopic data, such as that obtained from the NIR instruments, the power of PCA lies in its ability to condense the correlated information from hundreds of wavenumbers into a small number of mutually orthogonal principal components (PCs). Formally, PCA performs the following matrix decomposition:

$$\mathbf{X} = \mathbf{T}\mathbf{P}^{\mathbf{T}} + \mathbf{E} \qquad (3)$$

where $\mathbf{X}$ represents measured process data organised in n rows and m columns. PCA decomposes this data matrix into

the product of two matrices **T** and **P**, as shown in (3). **T** and **P** matrices contain as columns the so-called PCA scores and PCA loadings, respectively. **E** matrix represents the information contained within the matrix **X** that is not represented in the first nc principal components. Normally, each column of the data matrix **X** corresponds to a particular process variable, while the particular row is related to a specific sampling instant in time. In the context of NIR spectra, the columns of **X** represent specific spectral channels or wavenumbers while the rows contain data related to the whole NIR spectrum measured at a particular instance in time.

Due to the fact that the columns of the loadings matrix P are orthogonal, the expression for the calculation of scores is given as:

$$\mathbf{T} = \mathbf{XP} \tag{4}$$

It is the expression in equation (4) that will be utilised in this paper in order to condense information from hundreds of wavenumbers present in **X** into a single composite variable, namely the score associated with the first principal component.

3. CONTROL METHODOLOGY

3.1 Temperature Cascade Control (TCC)

A standard control problem in chemical reactor operation is that of controlling reactor temperature such that it follows a certain pre-computed reference trajectory, which should in turn ensure that the product quality will be satisfactory. Ultimately, reactor temperature is controlled by manipulating the flow of coolant or steam into the reactor's jacket. However, due to the presence of numerous disturbances, such as the feed temperature and the temperature of the incoming coolant, this control problem is addressed by employing two controllers in master-slave configuration, as shown in Fig.1.

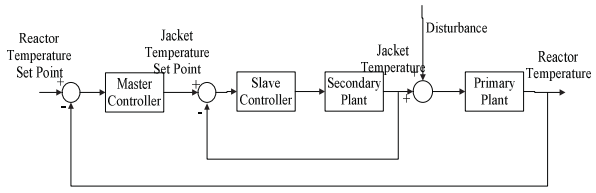

Fig. 1. Control of Reactor Temperature Using TCC System

The primary control loop, also known as the Master control loop, controls reactor temperature by adjusting the inlet jacket temperature set-point. The secondary control loop, known as the slave control loop, regulates jacket temperature by manipulating the flow of either coolant or steam into the jacket. Hence, the manipulating variable of the master control loop is the set-point for the slave control loop. This method of cascading controllers is very popular in the process industries and is particularly useful when there are disturbances associated with the slave controller's manipulated variable (Seborg 2004).

In this paper, a PI controller is used in the primary (slave) control loop while the PID controller is employed in the master (primary) control loop.

Note that the TCC system controls product quality implicitly, through the regulation of reactor temperature. The main problem with such implicit control arises with the occurrence of specific disturbances and process dynamics' changes, which adversely affect the underlying relationship between the reactor temperature and the product quality. As a result, optimal temperature profile will change. However, unless the optimal profile is calculated in real-time, TCC system will typically not have access to it. Instead, TCC will use existing reference trajectory, which is sub-optimal and may result in unsatisfactory product quality as demonstrated in the results section of this paper.

3.2 Wavenumber-Based MPC Control (Wn-MPC)

Spectroscopic instrumentation is being increasingly used to provide measurements, such as NIR spectra, that are in some way closely related to the product quality. By incorporating these measurements as feedback information into the control system the product quality control is addressed more explicitly when compared to the TCC scheme. One possible control system structure that incorporates NIR spectra as feedback information is shown in Fig. 2.

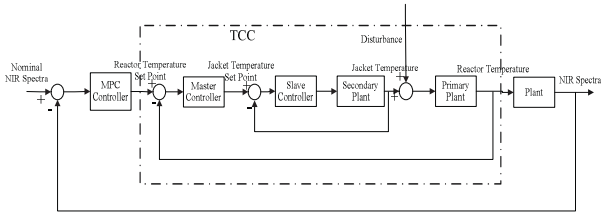

Fig. 2. Basic Structure of Wn-MPC Control

This new control structure incorporates the TCC system from Fig. 1 and augments it with the additional outer control loop, namely MPC control loop. The manipulated variable of the MPC controller is the reactor temperature set-point while controlled variables are the intensities of NIR spectra at a particular set of wavenumbers. Hence, within this control system structure, the TCC system can be viewed as a slave controller while MPC can be viewed as a master controller. This control system structure will be referred to as Wn-MPC.

The reference profile for the wavenumber is obtained by collecting NIR spectra from a 'nominal' batch, during whose progression no major disturbances were present and the standard TCC control scheme was used.

Since each wavenumber in the NIR spectra represents a candidate variable to be used as feedback information, there may be hundreds of potential controlled variables. Therefore, serious practical problem that arises when attempting to implement Wn-MPC is to decide on the set of wavenumbers that will be used as controlled variables. Currently, there are no clear guidelines as to which wavenumber should be selected for control purposes. In this paper a range of

wavenumbers was selected and their suitability was evaluated by incorporating them into Wn-MPC as controlled variables.

3.3 PCA Score-Based MPC Control (Sc-MPC)

In order to incorporate information from all of the wavenumbers into a feedback signal, a modified control system structure is used, as shown in Fig. 3.

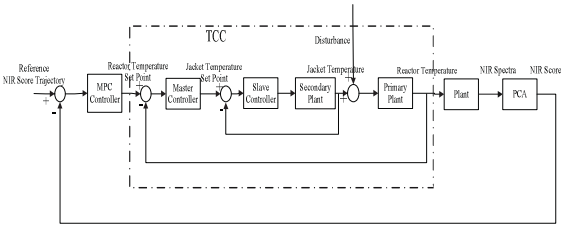

Fig. 3. Basic Structure of the Sc-MPC Control

This control scheme differs from Wn-MPC in that it includes a block containing the PCA model that pre-processes feedback information, namely NIR spectra. The result of PCA processing is a small set of variables, called scores, that contain information related to all of the measured wavenumbers. This is in contrast to Wn-MPC where the feedback information relates to only a few wavenumbers.

In this paper it is assumed that a PCA model is constructed using NIR spectra collected from a nominal batch. This nominal batch is run in the absence of any major disturbances using TCC control scheme. Hence, the resulting NIR spectra are assumed to represent reference profile that is to be replicated by Sc-MPC. In order to extract the main features from the highly multivariate NIR spectral data into a single variable, PCA model is applied. The resulting score trajectory is used as a reference profile that Sc-MPC is required to follow.

4. CASE STUDY

4.1 Chemical Reactor Simulation

This paper documents the application of three different control systems to a simulated chemical batch reactor taken from Cott (Cott and Macchietto 1989). The reactions taking place are given as follows:

$$A + B \xrightarrow{k_1} C;\ A + C \xrightarrow{k_2} D \qquad (5)$$

where *A*, *B* are the raw material, *C* is the desired product and *D* is the waste product, while k_1 and k_2 are the rates of the two reactions.

The control objective is to track the reactor temperature T_r reference trajectory by adjusting the jacket temperature T_{jsp}.

4.2 Disturbance Description

Three different control systems, described in section 3, were evaluated by injecting large disturbance and observing the control system response. Disturbance was chosen to be a reduction in a value of a reaction rate constant k_1 by 8%.

4.3 Prediction Model Identification

Training data for the Recursive Least Squares (RLS) algorithm was obtained using the TCC system structure, shown in Fig. 1. To excite the process dynamics, reference temperature trajectory was perturbed for three batches by adding a PRBS signal of amplitude 0.1 degrees C and switching time of 60 seconds.

In this particular case study ARX based prediction models were developed with $n_y = 2$ and $n_u = 80$. The data-driven identification method of RLS was used to develop dynamic models for both Wn-MPC and Sc-MPC controllers.

The output signal considered during the prediction model identification is the deviation of a controlled variable from its nominal trajectory. This controlled variable may be spectral intensity at the particular wavenumber (in the case of Wn-MPC control) or the value of the PCA score (in the case of Sc-MPC control).

4.4 Wavenumber Selection

In the case of Wn-MPC, candidate controlled variables were taken to be those wavenumbers that corresponded to a local peak of the measured NIR spectrum. In this particular case study the wavenumbers corresponding to the local peaks in the NIR spectra and, therefore, representing the candidate controlled variables were 2, 77, 98, 127, 161 and 232, as illustrated in Fig. 4.

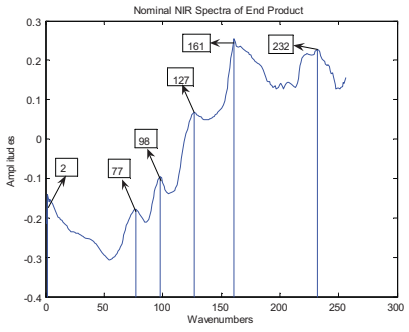

Fig. 4. Selection of spectral peaks as controlled variables

For each of these wavenumbers prediction model was identified and the corresponding MPC controller was constructed and evaluated. The corresponding controllers are designated with a chosen wavenumber written within brackets following a label Wn-MPC. For example, Wn-

MPC(127) designates Wn-MPC controller that utilises wavenumber 127 as the controlled variable.

4.5 PCA Model Development

A PCA model was developed using NIR spectra collected from a single nominal batch. The first PCA score captured 93.8% of the variation present in the NIR spectra and was used as a reference trajectory in the subsequent implementation of Sc-MPC controller. The loadings vector associated with the first PCA score was then used in real-time to compute score value from the measured NIR spectra according to equation (4).

4.6 Results and Discussion

For each controller (TCC, Wn-MPC and Sc-MPC) the process was perturbed using the identical large disturbance described in section 4.2. The resulting NIR spectra that corresponded to particular controllers along with the reference spectrum are plotted in Figures 5 and 6.

Fig. 5 shows the NIR spectra obtained when the controllers used to regulate the batch reactor were TCC, Sc-MPC and Wn-MPC(77). Sc-MPC can be seen to outperform both TCC and Wn-MPC(77). In fact, the NIR spectrum obtained when using Sc-MPC controller was found to be very similar to the reference spectrum, as shown in Fig. 5. On the other hand, both TCC and Wn-MPC(77) clearly failed to reject the disturbance as evidenced by considerable deviation of their respective NIR spectra from the reference spectrum.

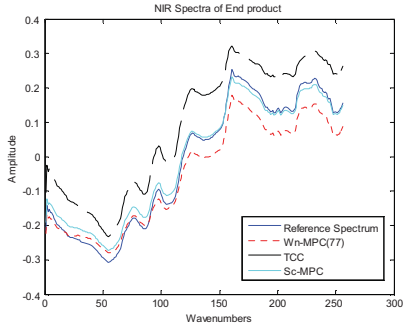

Fig. 5. NIR spectra of end product obtained when using TCC, Wn-MPC(77) and Sc-MPC

The reason for the discrepancy in performance between the TCC and Sc-MPC lies in the fact that the TCC control system does not consider NIR spectra as its feedback information and, furthermore, its reference temperature profile is not adjusted to account for the presence of the large disturbance, which has modified the underlying relationship between temperature and product quality. On the other hand, Sc-MPC explicitly considers regulation of the NIR spectra by using the composite of spectral measurements as its feedback information. Wn-MPC(77) also delivered sub-optimal performance because the spectral data contained in wavenumber 77 appeared not to be sufficient to characterise the majority of information contained in the entire NIR spectrum. Wn-MPC(77) is an example of Wn-MPC controller with its controlled variable obtained by randomly selecting one of the prominent peaks in the NIR spectrum, which is not an unlikely scenario in real applications.

The performances obtained by controlling NIR trajectories at different wavenumbers (77 127 161) using Wn-MPC controllers change largely, as demonstrated in Fig. 6.

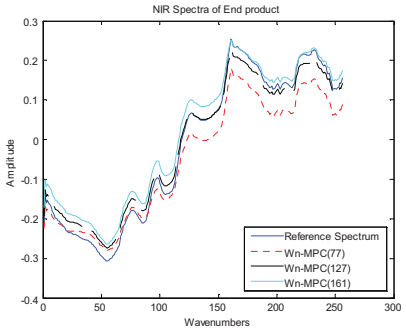

Fig. 6. NIR spectra of end product obtained when using Wn-MPC(127), Wn-MPC(161) and Wn-MPC(77)

The sum of square errors of the NIR spectra and its nominal values by Wn-MPC at every wavenumber are calculated and showed in Fig. 7. This figure shows a large variation in performance achieved by Wn-MPC controllers that utilise different wavenumbers (2, 77, 98, 127, 161, 232) as their controlled variables.

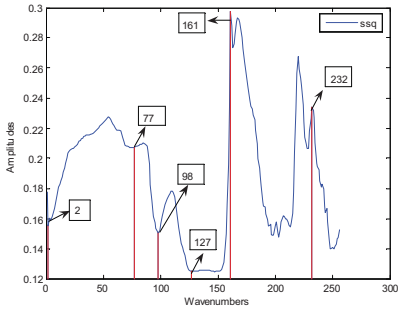

Fig. 7. The sum of square errors (ssq) by Wn-MPC at different wavenumbers

Even if the Wn-MPC is used with an optimally selected wavenumber, which is wavenumber 127 in this particular case study, the resulting control performance was found to be very similar to the performance of the Sc-MPC controller. This is demonstrated in Fig. 8 where the NIR spectra shown were obtained when the process was being controlled using Sc-MPC and Wn-MPC(127).

Hence, the improvement in performance delivered by Wn-MPC(127) is not considerable while the trial-and-error procedure involved in selection of the wavenumber to be controlled may be prohibitively time-consuming and expensive. On the other hand, Sc-MPC delivered satisfactory

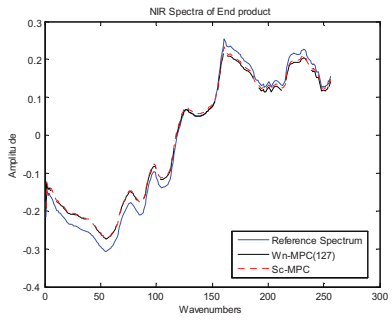

Fig. 8. NIR spectra of end product obtained when using Wn-MPC(127) and Sc-MPC

performance that was similar to that of the Wn-MPC(127) controller. In addition, the controlled variable is automatically selected requiring no trial and error in the case of Sc-MPC. Hence, Sc-MPC controller was found to require minimal user interaction when selecting appropriate controlled variable while also delivering a highly satisfactory performance.

Observed variability in performance can be explained by the fact that all of the considered Wn-MPC controllers focus on the feedback information contained within a single wavenumber. Hence, there may be cases where a chosen wavenumber conveys little information related to other segments of the overall NIR spectrum, such as the wavenumber 77. In these cases the resulting Wn-MPC will not deliver satisfactory performance, as is the case with Wn-MPC(77). Similarly, there may be cases where a single wavenumber does reflect many of the features of the entire NIR spectrum, such as the wavenumber 127. Resulting controller, namely Wn-MPC(127), will then deliver a satisfactory performance.

5. CONCLUSIONS

This paper investigated the ability of three different control systems to adequately control a simulated batch reactor using the NIR spectra as feedback information such that the product meets quality specifications. The first of the three controllers ignored the presence of NIR spectra and was solely concerned with the regulation of reactor temperature such that it follows pre-specified reference trajectory. This controller was found to be inadequate when the large disturbances altered the underlying relationship between reactor temperature and product quality. The other two controllers utilised aspects of the measured NIR spectrum in their formulations. One of these two controllers used spectral intensities at specific wavenumbers (spectral channels) that corresponded to local peaks in NIR spectra as feedback information and was referred to as Wn-MPC. The other controller used multivariate statistical tool, namely Principal Component Analysis (PCA) in order to extract the main features present in all of the wavenumbers and condense this information into a single composite variable that was controlled. This controller was referred to as Sc-MPC. Results of implementing these three controllers on a simulated batch reactor reveal that the Sc-MPC achieved satisfactory control while also requiring no user interaction when deciding on the variable to be controlled. On the other hand, performance achieved by Wn-MPC was found to be highly dependent on the choice of the wavenumber that is to be controlled. However, due to the lack of rigorous guidelines when selecting appropriate wavenumber and the resulting trial and error necessary to determine optimal wavenumber, it is questionable whether Wn-MPC can be used as a practical solution in industrial process control area.

REFERENCES

Aziz, N., Hussain, M.A., and Mujtaba, I.M. (2000). Performance of different types of controllers in tracking optimal temperature profiles in batch reactors. Computers & Chemical Engineering, 24(2-7), 1069-1075.

Berrar, D.P., Dubitzky, W., and Granzow, M. (2003). Singular value decomposition and principal component analysis. A Practical Approach to Microarray Data Analysis, Kluwer: Norwell, MA.

Blanco, M., Coello, J., Iturriaga, H., Maspoch, S., and Pezuela, C.d.l. (1998). Near-infrared spectroscopy in the pharmaceutical industry. Analyst, 123, 135-150.

Burns, D.A., and Ciurczak, E.W. (2001). Handbook of Near-Infrared Analysis, CRC.

Cott, B.J., and Macchietto, S. (1989). Temperature Control of Exothermic Batch Reactors Using Generic Model Control. Industrial & Engineering Chemistry Research, 28(8), 1177-1184.

Huang, H.B., Yu, H.Y., Xu, H.R., and Ying, Y.B. (2008). Near infrared spectroscopy for on/in-line monitoring of quality in foods and beverages: A review. Journal of Food Engineering, 87(3), 303-313.

Johansson, E., Ettaneh-Wold, N., and Wold, S. (2001). Multi- and Megavariate Data Analysis. Umetrics Academy.

Jorgensen, P., Pedersen, J.G., Jensen, E.P., and Esbensen, K.H. (2004). On-line batch fermentation process monitoring (NIR): introducing 'biological process time'. Journal of Chemometrics, 18(2), 81-91.

Luypaert, J., Massart, D.L. (2007). Near-infrared spectroscopy applications in pharmaceutical analysis. Talanta, 72(3), 865-883.

Maciejowski, J. (2002). Predictive Control With Constraints, Addison Wesley Longman.

Reich, G. (2005). Near-infrared spectroscopy and imaging: Basic principles and pharmaceutical applications. Advanced Drug Delivery Reviews, 57(8), 1109-1143.

Scarff, M., Arnold, S.A., Harvey, L.M., and McNeil, B. (2006). Near Infrared Spectroscopy for bioprocess monitoring and control: Current status and future trends. Critical Reviews in Biotechnology, 26(1), 17-39.

Seborg, D.E., Edgar, T.F., and Mellichamp, D.A. (2004). Process dynamics and control. Wiley.

Shinskey, F.G. (1996). Process control systems. McGraw-Hill, New York, USA.

Profitability and Re-usability: An Example of a Modular Model for Online Optimization

Margret Bauer*. Moncef Chioua.*
Jörg Schilling*.
Guido Sand*. Iiro Harjunkoski*.

**ABB Corporate Research, Ladenburg 68526, Germany*
(Tel: +49-6203-716284; e-mail: margret.bauer@de.abb.com)

Abstract: In this article, we describe the development of a modular online optimization solution. This solution can be configured to deal with different plant layouts and therefore allows for a re-usable and hence profitable advanced optimization solution. The industrial process for which the model was developed is divided into separate stages. Each stage represents a production step, which may or may not be present in a particular plant. Inputs and outputs of each stage are defined in a flexible way to ensure that the sequence of the production stages can vary and can be easily connected. Optimization results are shown for two alternative plant configurations and are discussed together with the benefits and cost that come with the pursuit of a modular solution.

Keywords: Online optimization, modularity, advanced solutions, nonlinear optimization, multi-stage processes, configuration.

1. INTRODUCTION

Most advanced industrial control and optimization solutions are developed on a case-by-case basis and are tailored to a production process at a particular plant. A large part of the implementation is spent on expert manpower; to model the plant behaviour with a deterministic or stochastic model and to adjust the control algorithm of the model (Bauer and Craig, 2008).

From a vendor's point of view, the business case of developing advanced solutions will often only achieve a breakeven if the model and the control algorithm can be re-used and installed multiple times without long and tedious adaptation of the model and algorithm. The development cost can then be split between the several implementation projects and the solutions is offered at a price that will result in an acceptable net present value (NPV) – both for the vendor and the customer.

Achieving re-usable and thus profitable advanced control and optimization solutions, however, are as rare as hen's teeth. Darby and White (1988) point out that this can be a question of modelling the process with one single model or in a decentralized approach. A modular approach is often easier to implement and maintain, especially when model updates are required.

In some industrial plants, production stages resemble each other and show enough common features to be generalized by a basic building block. A modular approach is achieved by configuring and connecting the basic building blocks. Other processes might be constructed by the same basic building block with different parameterization that is configured to adjust to the plant layout, including the use of a different number of blocks.

In this article, we describe a modular nonlinear real-time optimization approach that maximizes the throughput in a production process. Nonlinear online optimization is still not applied as widely as linear optimization problems in industry but some applications have been reported (De Gouvea and Odloak, 1998, Jockenhövel et al., 2003). The approach has been developed for an industrial environment to be implemented for online application.

Here, we describe an example of a production process for which a modular model will be developed. This model is derived using the following steps.

- Identify a basic building block;
- Define the block equations;
- Define the block connections;
- Define the process' objective function;
- Package the basic building block.

If a model is available in such a way, it significantly reduces the effort required to adapt the model to a new plant configuration. The solution can be re-used once implemented on an appropriate platform. One of the keys to a profitable advanced solution is furthermore the easy configuration and implementation of any modelling approach. An example is ABB's Expert Optimizer that provides the framework for implementing hybrid model predictive controllers. An example of such an implementation is given by Stadler and co-workers (2007).

The paper is structured as follows. In the next section, the process is described and two examples of possible configur-

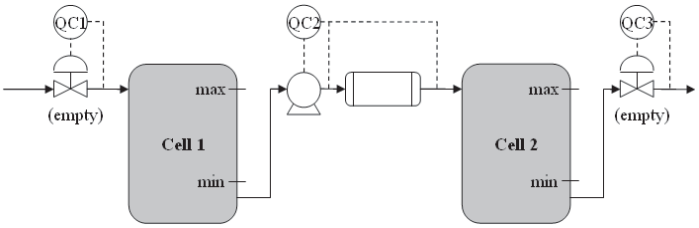

Fig. 1. Process schematic of Configuration I consisting of two cells.

ations are given together with the objective of the optimization problem. The different types to which the basic building block can be configured are identified and listed. Section 3 describes the model derivation along the steps stated above. Results are given in Section 4 together with a discussion on the advantages and disadvantages of the modular solution.

2. PROCESS DESCRIPTION

The continuous process under consideration consists of a set of sequential cells. An example of a configuration of this process is shown in Fig. 1. The medium flows from one cell with a certain flow rate. Valves or pumps control the flow rate into each cell. The flow rate is limited and so is the volume contained in the cell. What makes the process particular and difficult to control is the fact that the medium to be processed changes almost completely and abruptly. The medium consists, in fact, of different separate products with different attribute affecting the flow rate. The products do not mix but instead are processed successively. Thus, the flow rate changes whenever the next product enters a cell. A sensor therefore measures the consistency at the entry of the cell and the flow rate is adjusted accordingly.

The particular are characteristics concerning the operation of the two cells. The first cell has to be emptied before a new product enters it. Thus, the valve or alternatively pump is closed off for a period of time until the tank has been emptied to a certain level. The second cell is preceded by a heat exchanger that warms up the medium before it enters the cell. While the first part of the medium is in the heat exchanger, the heat has to be adjusted to a certain temperature and the flow rate has to be lower than its normal maximum. In any configuration, an outflow valve controls the last flow in the process. The outflow is interrupted as one product is filled into a container, the container is sealed off, removed and a new container is placed in this position.

Altogether, there are four basic cell types, each with or without a heat exchanger and/or emptying during transition, as listed in Table 1. A plant can consist of a number of sequential cells, ranging from two up to about eight cells.

The process is very difficult to control as all cells interact and disturbances directly travel through the process. Minimum and maximum constraints of the level in the cells and of the flow rate are hard and cannot be violated without causing a complete shut-down of the plant. An important process characteristic is that the flow rates have to be constant while one product is filled into a cell. The level is therefore constantly increasing or decreasing, depending on the difference between the in- and outflow of the cell. If in- and outflow are identical for a certain period of time the level stays constant for that period of time. Determining the optimal set-points is therefore crucial for an uninterrupted operation of the process that also maximizes the throughput.

2.1 Configuration 1

The process can have different setups of the basic cell types described in Table 1. The one such configuration is shown in Fig. 1 and, as described earlier, consists of two cells where Cell 1 has to be emptied before the next product can enter it (Case B). During this period, the valve is closed off. Cell 2 is preceded by a heat exchanger (Case C). The consistency is measured before and after the heat exchanger so that a product change is noticed thereafter so that the flow rate can be adjusted when the medium enters and exits the heat exchanger. The opening and closing of the cells in- and outflow depends on the different material and the control is indeed already very complex when considering only these two cells.

2.2 Configuration II

Fig. 2 shows the process schematic of the second configuration to be investigated in this paper. Here, three cells are connected where the first cell has to be emptied after a product changeover (Case B). The second cell adjusts the speed according to a product change but neither has it a heat exchanger nor is it emptied (Case A). The third case has a heat exchanger but does not have to be emptied between product changeovers (Case C). The plant parameters such as maximum flow rate and cell volume differ from Configuration I. This naturally affects the different operational routines.

Table 1. Alternative cell types

		Emptying during transition	
		No	Yes
Heat exchanger	No	Case A	Case B
	Yes	Case C	Case D

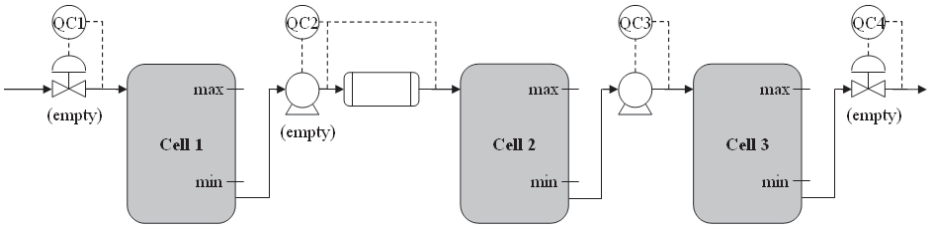

Fig. 2. Process schematic of Configuration II consisting of three cells.

2.3 Online process optimization

The described process is somewhat different to a standard continuous chemical process. Here, we deal with different products in operation with changing attributes. The controller has to deal with different states that alter with a product changeover: emptying, heating and normal operation. The aim of this study is to determine the flow rate set-points for a sequence of products under the given constraints, that is, limits of the constant flow rates and minimum and maximum cell levels. The objective is to maximize the outflow of the last cell. New setpoints are determined repeatedly, either:

a) Time based, that is, on a fixed time grid for example every ten seconds;
b) Event based, that is, if a defined event occurs, for example if a new product enters the process.

If an event occurs, the time grid is reset and restarted after the event. The high update frequency requires a fast result from the online optimization routine.

3. MODULAR MODELLING

The processes described in the previous section can be modelled as one single problem since the number of variables is limited. However, in order to re-use the optimization solution for both Configuration I and II and possibly other configurations, it is advantageous to model a basic building block and then configure and connect the blocks using the same description and connections. In the following, the basic building block is identified, the equations are identified, connections established and the objective function for the complete process is derived.

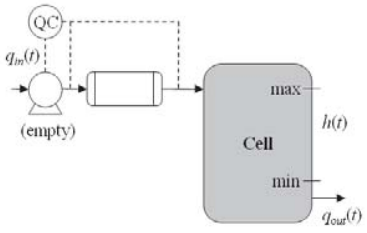

Fig. 3. Basic building block from which Configuration I and II can be constructed.

3.1 Identification of basic building block

By looking at Fig. 1 and Fig. 2 one can easily identify the repeating elements in the process such as the cell and inflow control. A basic building block that describes all cells and their inflow control is shown in Fig. 3. It consists of one cell and the adjustable flow rate of the inflow. The heat exchanger preceding the cell is included in the generic block and its parameters and equations will be set to zero if no heat exchanger is present. Variables are also introduced for emptying the cell. In case that the cell does not have to be emptied, these variables are also set to zero.

3.2 Building block equations

First, the decision variables to be optimized are introduced for each cell. These variables are noted with lower case letters and include the following. There are p products with $p=\{1...P\}$.

$h(t)$	Cell level
$q_p^{in}(t)$	Inflow to cell
$q_p^{out}(t)$	Outflow of cell
τ_p	Time duration during which the product flows into the cell
τ_p^{empty}	Time duration during which the cell and the heat exchanger are emptied
τ_p^{warmup}	Time duration during which the product is warmed up in the heat exchanger

The flow rates are fixed for the duration while processing product p. If the flow rate is constant then the level is a linear function. The durations are auxiliary variables.

Parameters to be configured for each cell are as follows.

V_p	Volume of product p
V^C	Volume of cell C
V^{HE}	Volume of the heat exchanger
$Q_p^{\min}$, $Q_p^{\max}$	Minimum and maximum flow rate

$H^{\min}$, $H^{\max}$ Minimum and maximum cell level

If no heat exchanger is located ahead of the cell (Case A and B) then volume V^{HE} is set to zero.

The duration during which the product flows into the cell is defined as the volume of product *p* minus the volume of the heat exchanger divided by the flow rate of product *p*. When the next product enters the cell the flow rate changes to q_{p+1}^{in}.

$$\tau_p = \frac{V_p - V^{HE}}{q_p^{in}} \tag{1}$$

This equation is nonlinear and thus can cause difficulties for most solvers. It is therefore necessary to reformulate this equation as well as the following into a bilinear form by multiplication ($\tau \cdot q_p^{in} = V_p - V^{HE}$).

When emptying the cell, the valve or pump is closed off and the inflow rate is hence set to zero. The duration during which the tank is emptied is determined by the outflow rate. The volume to be emptied is the volume in the cell plus the volume in the heat exchanger.

$$\tau_p^{empty} = \frac{V^C + V^{HE}}{q^{out}} \tag{2}$$

The duration during which the product is warmed up is defined by the volume of the heat exchanger divided by the inflow rate. It is independent from the outflow rate as one might initially expect.

$$\tau_p^{warmup} = \frac{V^{HE}}{q_p^{in}} \tag{3}$$

The level is proportional to the difference between the in- and outflow rate. The proportional coefficient depends on the area of the cell.

$$h(t) \sim q^{in}(t) - q^{out}(t) \tag{4}$$

Eq. (1)–(4) describe the dynamics of the cell. Inflow, outflow and level have to be defined for each time point for which a switch occurs, that is, when a new product reaches a measuring point. There are two measuring points in case of the presence of a heat exchanger, one before and one after. At these switching points, the level reaches its minimum or maximum value as the function increases and decreases only linearly. If the cell level does not violate the constraints at two consecutive switching points, it will not violate the constraints at any time between those switching points. The reformulation of the inflow, outflow and level for these switching points is rather cumbersome in notation but straight forward otherwise. It will therefore not be detailed in this article.

In addition to the equations describing the process dynamics there are also constraints that determine the operation of the cells. These constraints are considered for the inflow rate q^{in} and for the cell level *h*.

$$Q_p^{\min} \le q_p^{in}(t) \le Q_p^{\max} \tag{5}$$

Table 2. Parameter adaptation for cell types

		Emptying during transition	
		No	Yes
Heat exchanger	No	$V^{HE} = 0 ; \tau_p^{empty} = 0$	$V^{HE} = 0$
	Yes	$\tau_p^{empty} = 0$	none

$$H^{\min} \le h(t) \le H^{\max} \tag{6}$$

The constraints on the outflow rate do not have to be considered as they are defined in the successive cell.

3.3 Connection of building blocks

The cells are connected by the flow through the process. The connection is formulated by equating the outflow rate of cell *C* with the inflow rate of the subsequent cell *C*+1.

$$q^{out,C}(t) = q^{in,C+1}(t) \tag{7}$$

3.4 Objective function

The objective of the optimization problem is to maximize the throughput of the process. As the throughput is determined by the outflow rate of the last cell, this is the quantity to be maximized.

$$\max \int q^{out,C=C_{last}}(t)dt \tag{8}$$

Alternatively, it is possible to minimize the sum of all durations defined in Eq. (1)–(3). In some cases, a better solution is obtained by maximizing the flow rate in all cells and not only the one of the last. This is particularly valid for very short product sequences as the first cells may not process with the highest rate as the finishing of the product sequence in the last cell does not depend on it. As a result, the objective function is set to Eq. (8) plus an additional term including the flow rates in the other cells multiplied by a weighting factor smaller than one.

3.5 Configuration

The basic building block can be packaged into a stand alone function with input and output variables as shown in Fig. 4.

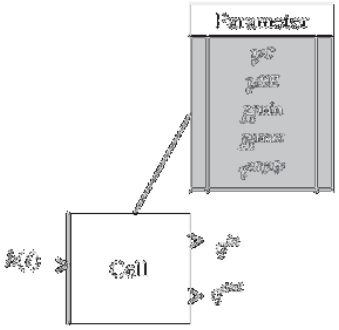

Fig. 4. Configuration block for implementation.

The parameters have to be set for each block. The differentiation between the cell types as given in Table 1. leads to a parameter configuration that is summarized in Table 2. The final step is the connection between the in- and outflows of the consecutive cells as given in Eq. (7) to derive the complete plant setups of Fig. 1 and Fig. 2.

4. OPTIMIZATION RESULTS

The same model is applied for both Configuration I and II with only changes to the parameters and the number of cells. The optimization problem was implemented in GAMS and as a nonlinear program solved with CONOPT. CONOPT is based on the generalized reduced gradient method which transforms inequality constraints into equality constraints by introducing slack variables. The solver then searches along the steepest slope of the super-basic variables.

In some instances, nonlinear models can easily lead to infeasibility. However, as the initialization of the optimization routine is already close to the optimum results can be found reliably. Upper constraints of flow rate and level are used as initial values. The solution is also not necessarily the global optimum. This decision is left to the writer of the GAMS code and the model developer.

Fig. 5 shows the results of Configuration I of Fig. 1. Here, two cells were connected with a heat exchanger between the cells. The first cell had to be emptied/flushed in preparation for a product change. The outflow of the process was also interrupted to allow the product to be filled into tanks. The tanks have to be removed and the process outflow closed off during that period. The process operation can be best seen in the flow rates. The left hand side of Fig. 5 shows the three flow rates, q_1-q_3 for three products. The first flow rate is the process inflow and is interrupted each time a new product enters the cell. The maximum flow rate into the first cell is large for both products, however, the set point is set to a lower level to not exceed the level in the cell as the outflow of the first cell is limited by significantly lower constraints. Flow rate $q_2(t)$ is at its maximum constraint as it poses, together with $q_3(t)$ the bottle neck in the process. While the first part of a product is processed in the second cell, a reduced flow rate is applied. The flow rate $q_3(t)$ is at a higher value than $q_2(t)$ but a stop time interrupts the flow during the product changeover.

The cell levels shown in the right hand side of Fig. 2 indicate that the cell level of the first cell is in the region of its upper limit, i.e., the cell is filled during most time of the operation. The second cell, on the other hand, hits on some occasions the lower constraints.

The results of the optimization routine of Configuration II are shown in Fig. 6. Here, four flows and three cell levels are shown for three products. The first cell is emptied with every product changeover, as can be seen in $q_1(t)$. A heat exchanger is placed ahead of the second cell which affects the flow rate $q_2(t)$. The flow rate $q_3(t)$ changes only with the different products while the last flow rate includes stops during which a new tank is replaced. The stop times for the tanks are constant.

The last cell level is somehow cyclic as the cell is emptied for the new product and then filled up again. The cycle would be repeated if the optimization would have been carried out for more products. The level $h_1(t)$ shows similar features while $h_2(t)$ decreases and then stays at its minimum level for the last product as the in- and outflow rates are identical.

Because of the modular approach, the same model could be re-used for both configurations. The model changes are only changes to the input parameters but not the model equations. In both cases, the outflow rate was optimized which ensures that the flow rates are at their maximum for the bottleneck cells.

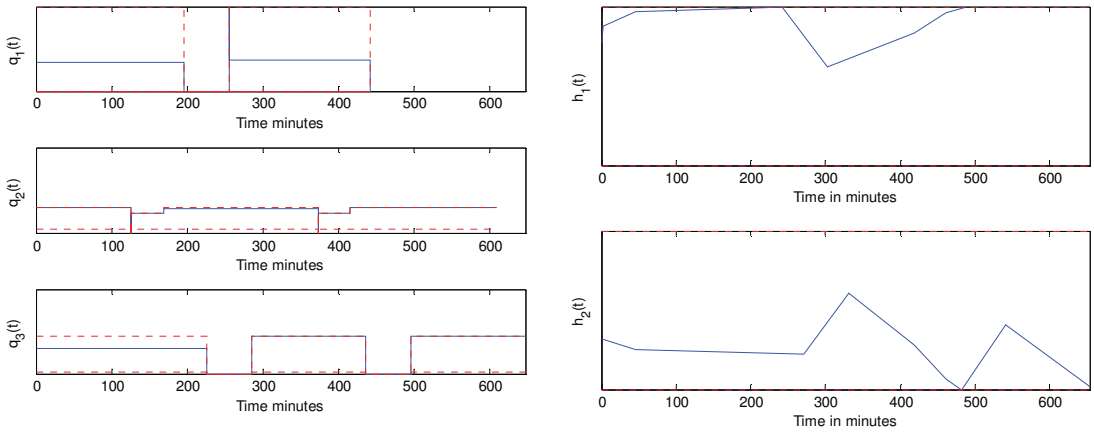

Fig. 5. Results for process Configuration I: cell inflow rates $q(t)$ and levels $h(t)$. Dashed lines indicate the upper and lower constraints.

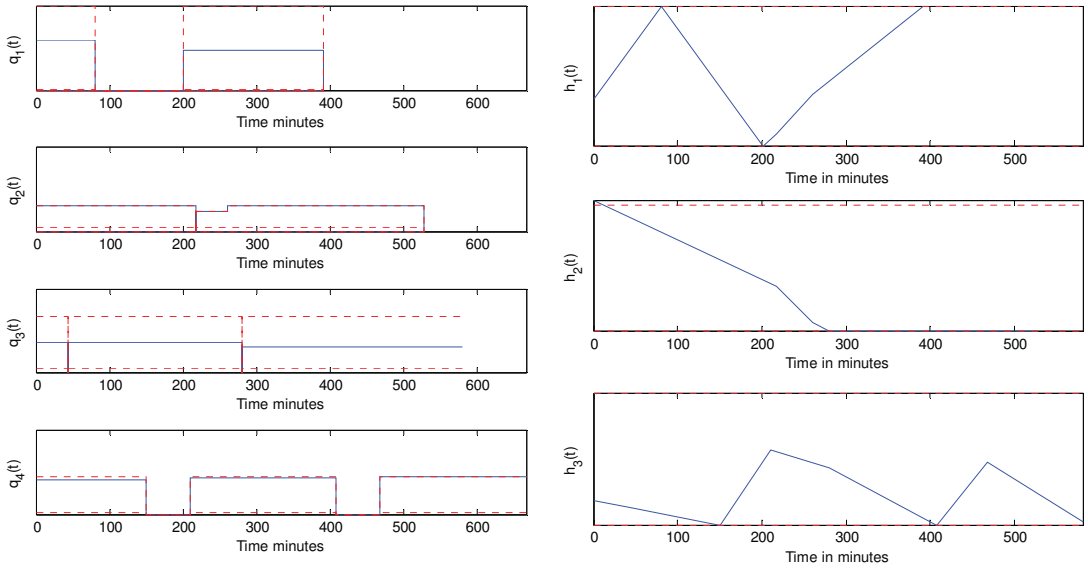

Fig. 6. Results for process Configuration II: cell inflow rates $q(t)$ and levels $h(t)$. Dashed lines indicate the upper and lower constraints.

5. CONCLUSIONS

To achieve a viable business model of advanced control and optimization solutions the modelling, implementation and maintenance effort has to be as small as possible. Re-usable solutions do not only decrease the modelling effort but also make it easier to maintain the solution as the development and commissioning engineers have to be familiar with one solution type. It is therefore attractive to build a modular solution that can be applied to different process setups. In this article a modular solution for a process with different configurations has been derived. The model has been applied to industrial processes and is currently in the process of deployment.

The key steps followed were as follows. A basic building block was identified and the equations introduced, including the connection between the blocks. Optimization results were discussed. Deriving this kind of modular approach is key when developing solutions that can be easily adapted and therefore have the potential to become a business success.

REFERENCES

Bauer, M. and Craig, C., 2008. Economic assessment of advanced process control – A survey and framework. *Journal of Process Control*, 18, 2-18.

Darby, M.L. and White, D.C., 1988. On-line optimization of complex process units. *Chemical Engineering Progress*, 84, 51-59.

Jockenhövel, T., Biegler, L.T. and Wächter, A., 2003. Dynamic optimization of the Tennessee Eastman process using OptControlCentre. *Computers & Chemical Engineering*, 27, 1513-1531.

De Gouvea, M.T. and Odloak, D., 1998. One-layer real time optimization of LPG production in the FCC unit: Procedures, advantages and disadvantages. *Computers & Chemical Engineering*, 22, S191-S198.

Stadler, K.S., Wolf, B. and Gallestey, E., 2003. Model predictive control of the calciner at Holcim's Lägerdorf plant with the ABB Expert Optimizer. *ZKG International*, 60, 66-67.

A PID automatic tuning method for distributed-lag processes ⋆

Massimiliano Veronesi * **Antonio Visioli** *

* *Dipartimento di Elettronica per l'Automazione, University of Brescia, Italy*
e-mail: antonio.visioli@ing.unibs.it

Abstract: In this paper we present an automatic tuning methodology for PID controllers for distributed-lag processes. The technique is based on the evaluation of a closed-loop set-point or load disturbance step response and it can be therefore employed with process routine operating data. Further, a performance assessment index is also proposed in order to establish when the performance of a PID controller can be improved by retuning it according to the proposed method. Simulation results show the effectiveness of the approach.

1. INTRODUCTION

Distributed-lag processes are frequently encountered in the process industry. For example, transmission lines, heat exchangers, stirred tanks and distillation columns might have a dynamic characteristic so that they can be modelled as an infinite series of infinitesimally small interacting lags and therefore as a distributed lag (Shinskey, 1994). Despite this fact, this kind of processes are rarely considered in the academic literature (Shinskey, 2002), with the notable exception of the works of Shinskey (see, for example, (Shinskey, 2001)). Therein a tuning tule for Proportional-Integral-Derivative (PID) controllers has been proposed based on process parameters that are obtained by evaluating an open-loop step response.
Indeed, many tuning rules have been developed for PID controllers (O'Dwyer, 2006) and the great majority of them are based on a first-order-plus-dead-time (FOPDT) or second-order-plus-dead-time (SOPDT) model of the process that can be obtained typically by evaluating an open-loop step response. However, this experiment can be time-consuming and, above all, it can imply that the normal process operations are stopped, which is obviously not desirable. For this reason, automatic tuning methodologies have been developed also based on closed-loop experiments, usually by considering a relay-feedback experiment (Yu, 1999).

In this paper we present a methodology for the automatic tuning of PID controllers for distributed-lag processes which is based on the evaluation of a *closed-loop* set-point or load disturbance step response. In particular, we assume that a (possibly badly tuned) PID controller is operating and the evaluation of the step response is employed to retune the PID controller if the achieved performance is not satisfactory, as in (Veronesi and Visioli, 2009). In order to assess the performance of the controller, a performance index is proposed, so that the methodology can be applied both for tuning-on-demand (namely, the controller is tuned after an explicit request of the operator) and for self-tuning (namely, the controller itself determines that the control performance is not satisfactory and a new tuning is provided). It is worth stressing that the tuning rule applied is devoted to the load disturbance rejection task which is usually of main concern in the above mentioned processes.

The paper is organised as follows. A model for distributed-lag processes is given in Section 2. The autotuning method is presented in Section 3, where we explain how the relevant process parameters can be obtained and how the PID parameters can be selected. Finally, the practical implementation of the method is addressed. Simulation results are given in Section 4, and conclusions are drawn in Section 5.

2. MODELLING

A distributed-lag process can be described by the following transfer function (Shinskey, 1994)

$$P(s) = \frac{2\mu}{e^{\tau s} + e^{-\tau s}} = \frac{\mu}{\cosh\sqrt{\tau s}} \tag{1}$$

where μ is the process gain. The hyperbolic cosine can be expanded into an infinite-product series, so that we obtain

$$P(s) = \frac{\mu}{[1 + (2/\pi)^2\tau s][1 + (2/3\pi)^2\tau s][1 + (2/5\pi)^2\tau s]\cdots} \tag{2}$$

It is worth noting that the sum of all time constants, denoted as T_0, is equal to 0.5τ. If a unit step is applied to the process input, the sum of all time constants can be estimated easily as the time the process variable takes to attain the 63.2% of its steady-state value (see Figure 1). Then, the process gain can be estimated easily by considering the steady-state value of the process output and the amplitude of the step input (Visioli, 2006a). However, the open-loop experiment can be time-consuming and, in order to perform it, it can be necessary to stop the routine process operations. Thus, we propose a method to estimate the value of T_0 and of the process gain μ with a closed-loop experiment, namely by employing a PID controller with any values of the parameters (provided that the closed-

⋆ This work was partially supported by MIUR scientific research funds.

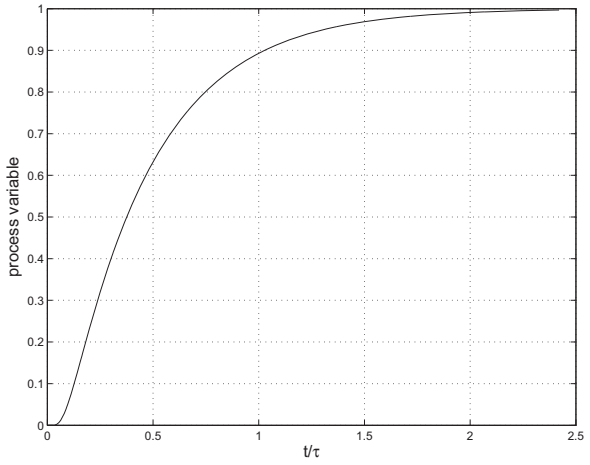

Fig. 1. Open-loop step response of a distributed-lag process. The process variable attains the 63.2% of its steady-state value at time $t = T_0 := 0.5\tau$.

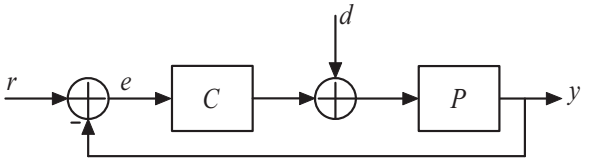

Fig. 2. The considered control scheme.

loop system is asimptotically stable).
Note that, for the purpose of simulation, transfer function (2) can be written as

$$P(s) = \frac{\mu}{\prod_{i=0}^{n-1}\left[1 + \left(\frac{2}{(2i+1)\pi}\right)^2 \tau s\right]} \tag{3}$$

with n at least equal to 20, because the dynamics of the process does not change significantly for $n > 20$ (Shinskey, 2001).

3. AUTOMATIC TUNING

3.1 Estimation of the process parameters from set-point step response

We consider the unity-feedback control system of Figure 2 where the process P is controlled by a PID controller whose transfer function is in series ("interacting") form:

$$C(s) = K_p\left(\frac{T_i s + 1}{T_i s}\right)(T_d s + 1). \tag{4}$$

The series form has been chosen for the sake of simplicity, however, the use of other forms is straightforward by suitably applying translation formulae to determine the values of the parameters (Visioli, 2006a). Note also that the use of a first-order filter that makes the controller transfer function proper has been neglected for the sake of clarity but it can be easily selected so that it does not influence the PID controller dynamics significantly.
We assume that the PID controller has been (roughly) tuned and a step signal of amplitude A_s is applied to the set-point. The process gain μ can be determined by considering the following trivial relations which involve the final steady-state value of the control variable u and of the control error e:

$$\lim_{t\to+\infty} u(t) = \frac{K_p}{T_i}\int_0^\infty e(t)dt = \frac{A_s}{\mu} \tag{5}$$

and therefore we have

$$\mu = A_s\frac{T_i}{K_p\int_0^\infty e(t)dt}. \tag{6}$$

The determination of the sum of the time constants T_0 of the process can be performed by considering the following variable:

$$e_u(t) = \mu u(t) - y(t). \tag{7}$$

By applying the Laplace transform to (7) and by expressing u and y in terms of the reference signal r we have

$$E_u(s) = \mu U(s) - Y(s) = \frac{C(s)(\mu - P(s))}{1 + C(s)P(s)}R(s). \tag{8}$$

At this point, for the sake of clarity, it is convenient to write the controller and process transfer functions respectively as

$$C(s) = \frac{K_p}{T_i s}\tilde{C}(s) \tag{9}$$

where

$$\tilde{C}(s) := (T_i s + 1)(T_d s + 1) \tag{10}$$

and (see (3))

$$P(s) = \frac{\mu}{q(s)} \tag{11}$$

where

$$q(s) = \prod_i(\tau_i s + 1) = \prod_i \tau_i s^n + \cdots + \sum_i \tau_i s + 1 \tag{12}$$

with

$$\tau_i := \left[\frac{2}{(2i+1)\pi}\right]^2 \tau, \qquad i = 0, 1, \ldots. \tag{13}$$

Then, expression (8) can be rewritten as

$$E_u(s) = \frac{\mu K_p\tilde{C}(s)}{T_i s q(s) + \mu K_p\tilde{C}(s)}(q(s) - 1)R(s). \tag{14}$$

By applying the final value theorem to the integral of e_u when a step is applied to the set-point signal we finally obtain (see (12))

$$\begin{aligned}\lim_{t\to+\infty}\int_0^t e_u(v)dv &= \lim_{s\to 0} s\frac{A_s}{s}\frac{\mu K_p\tilde{C}(s)}{T_i s q(s) + \mu K_p\tilde{C}(s)}\frac{q(s) - 1}{s} \\ &= A_s\lim_{s\to 0}\frac{q(s) - 1}{s} \\ &= A_s\sum_i \tau_i \\ &= A_s T_0.\end{aligned} \tag{15}$$

Thus, the sum of the time constants of the process can be obtained by evaluating the integral of $e_u(t)$ at the steady-state when a step signal is applied to the set-point and by dividing it by the amplitude A_s of the step.
Remark 1. It is worth noting that both the value of the gain μ and of sum of the time constants T_0 of the process are determined by considering the integral of signals and therefore the method is inherently robust to the measurement noise.
Remark 2. Note also that the set-point step signal can be applied just for the purpose of (re)tuning the PID

controller (in this case its amplitude should be as small as possible in order perturb the process as less as possible) but also a step response during routine process operations can be employed. This issue will be further discussed in subsection 3.5.

Remark 3. It is worth stressing that the value of T_0 is obtained independently on the values of the PID parameters. This is an advantage with respect to the use of other methods for the identification of the process transfer function, whose result depends on the control variable and process variable signals.

3.2 Estimation of the process parameters from load disturbance step response

The process parameters can be estimated by evaluating also a load disturbance step d of amplitude A_d. However, in this case the amplitude A_d is not known and therefore must be estimated as well. This can be determined by considering the final value of the integral of the control error. In fact, the expression of the Laplace transform of the control error is:

$$E(s) = -\frac{P(s)}{1+C(s)P(s)}D(s) = -\frac{T_i s\mu}{T_i s q(s) + K_p\tilde{C}(s)\mu}\frac{A_d}{s}, \tag{16}$$

and therefore we obtain

$$\begin{aligned}\lim_{t\to+\infty}\int_0^t e(v)dv &= \lim_{s\to 0} s\frac{1}{s}\frac{A_d}{s}\left(-\frac{T_i s\mu}{T_i s q(s) + K_p\tilde{C}(s)\mu}\right)\\ &= -\frac{A_d T_i}{K_p}.\end{aligned} \tag{17}$$

Thus, the amplitude of the step disturbance can be determined as

$$A_d = -\frac{K_p}{T_i}\int_0^\infty e(t)dt. \tag{18}$$

Once the amplitude of the step disturbance has been determined, the process gain μ can be determined by first considering the Laplace transform of the process input $i = u + d$, that is:

$$\begin{aligned}I(s) &= U(s) + D(s)\\ &= -\frac{C(s)P(s)}{1+C(s)P(s)}D(s) + D(s)\\ &= \frac{1}{1+C(s)P(s)}\frac{A_d}{s}\\ &= \frac{T_i s q(s)}{T_i s q(s) + K_p\tilde{C}(s)\mu}\frac{A_d}{s}.\end{aligned} \tag{19}$$

Thus, if we integrate $i(t)$ and we determine the limit for $t \to +\infty$ we obtain

$$\lim_{t\to+\infty}\int_0^t i(v)dv = \lim_{s\to 0} s\frac{1}{s}\frac{T_i s q(s)}{T_i s q(s) + K_p\tilde{C}(s)\mu}\frac{A_d}{s} = \frac{T_i A_d}{\mu K_p} \tag{20}$$

The process gain μ can be therefore found easily, once the value of A_d has been determined by using (18), as

$$\mu = A_d\frac{T_i}{K_p\int_0^\infty (u(t)+A_d)dt}. \tag{21}$$

Finally, the determination of the sum of the time constants of the process can be performed by initially considering the variable

Table 1. Tuning rules for distributed-lag processes.

	K_p	T_i	T_d
PI	$5/\mu$	$0.54T_0$	0
PID	$100/15/\mu$	$0.25T_0$	$0.10T_0$

$$e_i(t) := \mu(u(t)+d(t)) - y(t). \tag{22}$$

By applying the Laplace transform to (22) and by expressing u and y in terms of d we have

$$\begin{aligned}E_i(s) &= \frac{\mu - P(s)}{1+C(s)P(s)}D(s)\\ &= \frac{\mu - P(s)}{1+C(s)P(s)}\frac{A_d}{s}\\ &= \frac{\mu T_i A_d s}{T_i s q(s) + K_p\mu\tilde{c}(s)}\frac{q(s)-1}{s}.\end{aligned} \tag{23}$$

By twice integrating e_i and by applying the final value theorem we obtain (see (15))

$$\begin{aligned}&\lim_{t\to+\infty}\int_0^t\int_0^{v_2} e_i(v_1)dv_1dv_2\\ &= \lim_{s\to 0} s\frac{1}{s^2}\frac{\mu T_i A_d s}{T_i s q(s) + \mu K_p\tilde{C}(s)}\frac{q(s)-1}{s}\\ &= \frac{T_i A_d}{K_p}T_0.\end{aligned} \tag{24}$$

Thus, T_0 can be obtained as

$$T_0 = \frac{K_p}{T_i A_d}\int_0^\infty\int_0^t e_i(v)dvdt. \tag{25}$$

Remark 4. Note that also in this case the estimation of the process parameters is based on the integral of signals and therefore the method is inherently robust to the measurement noise. Further, the process parameters are obtained independently on the values of the PID parameters, because the estimation is based on steady-state values of the variables. Finally, as for the set-point step response, the step disturbance signal can be applied just for the purpose of (re)tuning the PID controller (in this case its amplitude should be as small as possible in order to perturb the process as less as possible) but also a step response during routine process operations can be employed.

Remark 5. In the proposed method, the occurrence of an abrupt (namely, step-like) load disturbance has been assumed. Indeed, this is the most relevant case for the control system, as the disturbance excites significantly the dynamics of the control system itself. Thus, the performance assessment technique has to be implemented together with a procedure for the detection of abrupt load disturbances. Methods for this purpose have been proposed in (Hägglund and Åström, 2000; Veronesi and Visioli, 2008).

3.3 Tuning of the controller

Once the sum of the time constants has been estimated by evaluating the set-point or the load disturbance step response, the PID controller can be tuned properly by considering the load disturbance rejection task, which is usually of main concern in practical applications. We propose to use the tuning rules devised by Shinskey and explained in (Shinskey, 1994, 2001). They are reported in Table 1, for the sake of clarity, for both PI and PID controller.

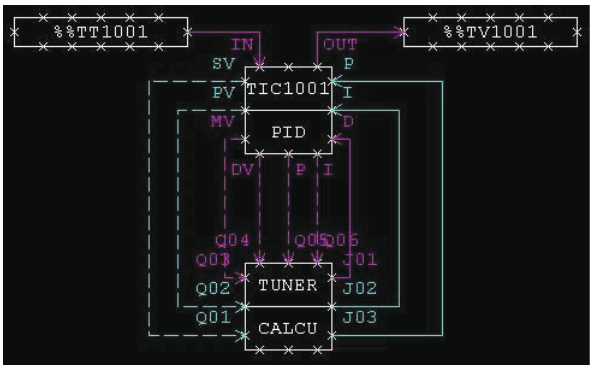

Fig. 3. The implementation of the proposed technique by means of the Yokogawa Centum VP Distributed Control System (courtesy of Yokogawa Italia).

3.4 Practical implementation

If a set-point step response is employed for estimating the process parameters, the proposed methodology can be easily implemented in a DCS with a suitable software development environment, as shown in Figure 3. The PID block (TIC1001) executes the standard PID control: its input and output are indicated respectively as TT1001 and TV1001. The calculation block TUNER determines the value of T_0 by computing the integral of the process variable (PV) and of the control output (MV) it receives from the PID block. Further, it computes the process gain. For this reason it needs also the setpoint (SV) and the PI parameters, namely, the proportional gain (or, equivalently, the proportional band) and the integral time constant. Finally the block TUNER computes the new values of the PID parameters by implementing the tuning rules shown in Table 1 and send them back to the PID block. Note that Q01..08 and J01..03 are the conventional name of the ports that the calculation block uses for exchanging data with the other function blocks.
If a load disturbance response is employed, the estimation procedure has to be estimate first the step amplitude A_d and then its value has to be employed to determine the μ and T_0 as indicated in (21) and (25).

3.5 Performance assessment

In a practical context it is also useful to evaluate the performance of a (PID) controller in order to determine if it has to be retuned or not. This is especially necessary if a self-tuning procedure has to be implemented, namely, the control system itself evaluates the control performance during process routine operations and a new tuning is provided in case it is not satisfactory. In this context, a measure of the performance of a control system can be effectively based on the integrated absolute error

$$IAE = \int_0^\infty |e(t)|dt \tag{26}$$

which implicitly considers both the peak error value and the settling time. For the technique proposed in this paper it is of interest to assess the control performance when a load disturbance occurs. For this purpose, the integrated absolute error obtained by applying the tuning rules of Table 1 to distributed-lag processes (2) with different

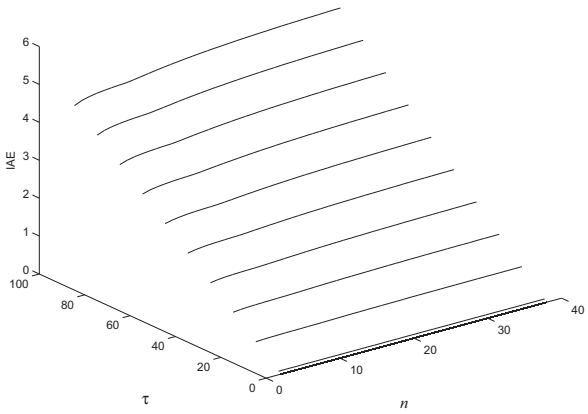

Fig. 4. Values of IAE for different values of τ and n (process order) with a PI controller tuned according to Table 1.

values of μ and τ, and different process order n has been computed. Results for $\mu = 1$ are shown in Figure 4 and 5 for PI and PID controller respectively. By interpolating these results, we obtain that the value of IAE achieved by applying the tuning rules of Table 1 are (for PI and PID controllers respectively):

$$IAE_{PI} = 0.058\tau\mu = 0.116T_0\mu \tag{27}$$

$$IAE_{PID} = 0.02\tau\mu = 0.04T_0\mu \tag{28}$$

Thus, the integrated absolute error achieved by a PI(D) controller should be ideally that expressed in (27) and (28). A performance index can be therefore defined as

$$J_{PI} = \frac{IAE_{PI}}{\int_0^\infty |e(t)|dt} \tag{29}$$

$$J_{PID} = \frac{IAE_{PID}}{\int_0^\infty |e(t)|dt} \tag{30}$$

and it can be determined, once the process parameters have been estimated by applying the technique described previously, by considering the obtained integrated absolute error.
In principle, the performance obtained by the control system is considered to be satisfactory if $J_{PI} = 1$ or $J_{PID} = 1$. From a practical point of view, however, the controller can be considered to be well-tuned if J_{PI} or J_{PID} is greater than a threshold (less than one) which can be selected by the user depending on how tight are its control specifications. In any case a sensible default value of 0.8 can be fixed.
Remark 6. It turns out from the presented results that using the derivative action allows to improve the performance significantly with respect to a PI controller.
Remark 7. It is worth noting that a performance index J greater than one can result because of the (small) interpolation error in determining (29) and (30) and because in any case the tuning formulae of Table 1 does not guarantee that the integrated absolute error is globally minimized.

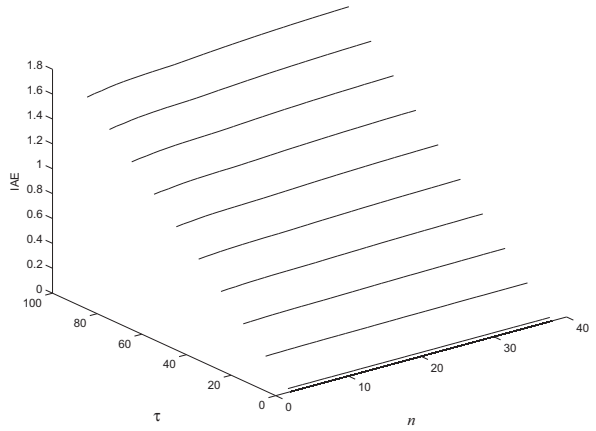

Fig. 5. Values of *IAE* for different values of τ and n (process order) with a PID controller tuned according to Table 1.

4. SIMULATION RESULTS

4.1 Example 1 - PID control

As a first example we consider a process with $\mu = 1$, $\tau = 10$ and $n = 30$ lags. Initially, the PID controller parameters are selected as $K_p = 3.3$, $T_i = 1.9$, $T_d = 0.25$. Then, a unit step load disturbance is applied to the process and the amplitude of the disturbance, the gain of the process and the sum of the time constants are estimated as $A_d = 1$, $\mu = 1.0$, and $T_0 = 4.97$. Based on these values, the PID parameters are retuned, according to Table 1, as $K_p = 6.66$, $T_i = 1.24$, $T_d = 0.5$. The load disturbance step response provided by the new values of the PID controller parameters is shown as a solid line in Figure 6, where the load disturbance step response provided by the initial values is also plotted as a dashed line. The control signal is not shown for the sake of brevity, in any case there are no significant differences between the two cases. By retuning the controller, the performance index is improved from $J_{PID} = 0.32$ to $J_{PID} = 1.03$ while the integrated absolute error decreases from IAE = 0.62 to IAE = 0.19. It is worth noting that the same result is achieved if a set-point step response is employed for estimating the process parameters.

4.2 Example 2 - PI control

As a second example we consider the same process of Example 1, but the use of a PI controller is assumed. Initially, the controller parameters are selected as $K_p = 7$ and $T_i = 2$ (note that the controller is aggressive). Then, a unit step load disturbance is applied to the process and the amplitude of the disturbance, the gain of the process and the sum of the time constants are estimated as $A_d = 1$, $\mu = 0.99$, and $T_0 = 4.97$ (the same parameters are estimated by considering a set-point step response). Based on these values, the PI parameters are retuned, according to Table 1, as $K_p = 5.06$ and $T_i = 2.68$. The load disturbance step responses provided by the initial and new values of the PI controller parameters are shown in Figure 7 as a dashed and solid line respectively. As

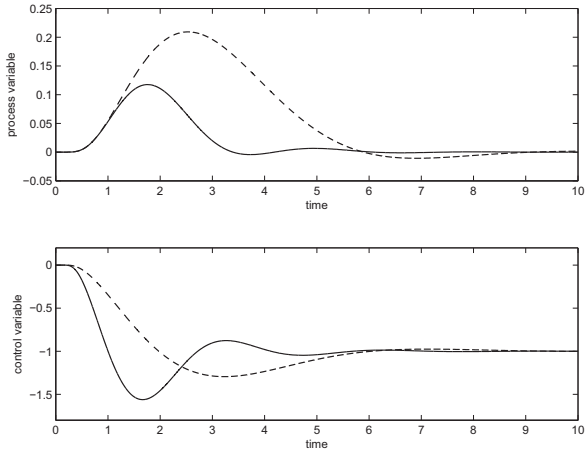

Fig. 6. Load disturbance step response for example 1. Dashed line: initial tuning. Solid line: automatic tuning.

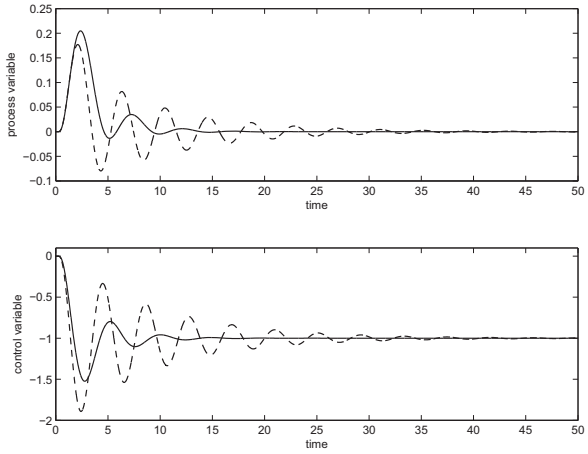

Fig. 7. Load disturbance step response for example 2. Dashed line: initial tuning. Solid line: automatic tuning.

in Example 1, retuning the controller allows to increase the performance. In particular, the performance index is improved from $J_{PI} = 0.64$ to $J_{PID} = 1.01$ while the integrated absolute error decreases from IAE = 0.88 to IAE = 0.56.
It turns out that the proposed autotuning method is effective and, by comparing these results with those of Example 1, it appears that the use of the derivative action allows to increase the controller performance significantly.

4.3 Example 3 - Measurement noise

As a third example we consider again the same process of Example 1, but the process output is corrupted with zero-mean white noise with a variance of $0.1 \cdot 10^{-3}$. The load disturbance step response obtained by selecting the controller parameters as $K_p = 3$, $T_i = 2$, and $T_d = 0.5$ is shown in Figure 8. In order to determine the performance index J_{PID} correctly, it is necessary to discard from the computation of the integrated absolute error those areas

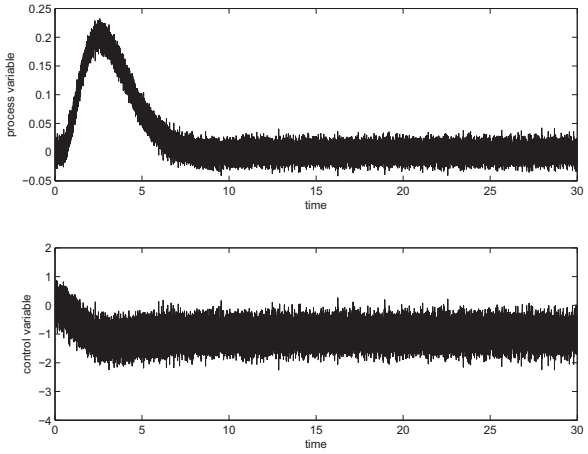

Fig. 8. Load disturbance step response for example 3 with $K_p = 3$, $T_i = 2$, and $T_d = 0.5$.

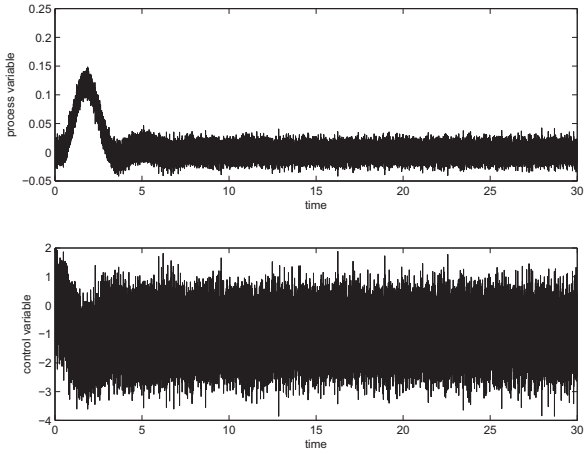

Fig. 9. Load disturbance step response for example 3 with $K_p = 6.87$, $T_i = 1.26$, and $T_d = 0.51$.

whose value is less than a predefined threshold (because they are actually due to the noise) (Visioli, 2006b). It results $J_{PID} = 0.29$, which suggests that the controller needs to be retuned. The gain of the process and the sum of the time constants are then estimated as $A_d = 1$, $\mu = 0.97$, and $T_0 = 5.06$ (once again, note that virtually the same values are obtained by considering a set-point step response). Based on these values, the PID parameters are retuned, according to Table 1, as $K_p = 6.87$, $T_i = 1.26$, and $T_d = 0.51$. The load disturbance step response obtained with the new PID controller is shown in Figure 9. In this case the performance index is $J_{PID} = 1.06$. By retuning the controller the integrated absolute error is decreased from IAE = 0.68 to IAE = 0.19. It turns out that the presence of noise does not impair the effectivess of the method, as expected because the considered variables are integrated.

5. CONCLUSIONS

In this paper we have proposed an automatic tuning methodology for distributed-lag processes based on a closed-loop experiment. Being based on the evaluation of a set-point or load disturbance step response, the technique can employ process routine operating data and can therefore be extended straightforwardly as a self-tuning method. Indeed, a performance index has been devised in order to assess the performance of the controller based on the achieved integrated absolute error. Illustrative examples have shown the effectiveness of the method and that it is robust to the measurement noise. Thus, the methodology appears to be suitable to implement in an industrial setting.

REFERENCES

T. Hägglund and K. J. Åström. Supervision of adaptive control algorithms. *Automatica*, 36(2):1171–1180, 2000.

A. O'Dwyer. *Handbook of PI and PID Tuning Rules*. Imperial College Press, 2006.

F. G. Shinskey. *Feedback Controllers for the Process Industries*. McGraw-Hill, New York, USA, 1994.

F. G. Shinskey. PID-deadtime control of distributed processes. *Control Engineering Practice*, 9(11):1177–1183, 2001.

F. G. Shinskey. Process control: as taught vs as practiced. *Industrial and Engineering Chemistry Research*, 41(16): 3745–3750, 2002.

M. Veronesi and A. Visioli. Performance assessment and retuning of pid controllers. *Industrial and Engineering Chemistry Research*, 48(5):2616–2623, 2009.

M. Veronesi and A. Visioli. A technique for abrupt load disturbance detection in process control systems. In *Proceedings 17th IFAC World Congress*, Seoul, ROK, 2008.

A. Visioli. *Practical PID Control*. Springer, London, UK, 2006a.

A. Visioli. Method for proportional-integral controller tuning assessment. *Industrial and Engineering Chemistry Research*, 45:2741–2747, 2006b.

C. C. Yu. *Autotuning of PID Controllers*. Springer-Verlag, London, Great Britain, 1999.

New tuning rules for PI and fractional PI controllers

Juan J. Gude and Evaristo Kahoraho

Faculty of Engineering – ESIDE
University of Deusto
Avda. de las Universidades 24, 48007 Bilbao (Spain)
(Tel: +34 944139000; Fax: +34 944139101; e-mail: jgude@eside.deusto.es)

Abstract: This paper presents new tuning rules for PI and fractional PI control of processes that are typically found in process control. The rules are based on characterization of process dynamics by three parameters that can be obtained from a simple step response experiment. The rules are obtained by minimizing a frequency objective function subject to a constraint on the maximum sensitivity. Comparisons with classical tuning rules show that they are very simple but give substantially better performance.

Keywords: Fractional control, PID control, design, tuning methods, optimization, process control.

1. INTRODUCTION

In spite of all the advances in process control over the past several decades, the proportional integral (PI) and the proportional integral derivative (PID) controller remains to be certainly the most extensive option that can be found on industrial control applications, see Åström and Hägglund (2001). The transparency of the PID control mechanism, the availability of a large number of reliable and cost-effective commercial PID modules, and their widespread acceptance by operators are among the reasons of its success, see Gude and Kahoraho (2007).

Over the last half-century, a great deal of academic and industrial effort has focused on improving PID control, primarily in the area of tuning rules. In fact, since Ziegler and Nichols proposed their popular tuning rules, Ziegler and Nichols (1942), an intensive research has been done. Works include from modifications of the original tuning rules, see Chien *et al.* (1952), Hang *et al*. (1991), and Åström and Hägglund (2004), to a variety of new techniques, see Åström and Hägglund (1995).

Fractional calculus, which is the expansion to fractional orders, has been known since the development of the regular calculus. However, fractional-order control was not incorporated into control engineering mainly due to the lack of sufficient mathematical knowledge and the limited computational power available at that time.

More recently, Podlubny (1999) has proposed a generalization of the PI and PID controllers, namely the PI^{λ} and $PI^{\lambda}D^{\mu}$ controllers, involving an integrator of order λ and a differentiator of order μ (the orders λ and μ may assume real non-integer values). Podlubny has also demonstrated the better response of these types of controllers, in comparison with the classical PI and PID controllers, when used for the control of fractional-order systems. A frequency domain approach by using fractional PID controllers has also been studied in Vinagre et al. (2000). However, the design methods for fractional controllers are a recent research area, see Capponetto *et al.* (2002) and Monje *et al.* (2005).

Given that the most common control structure used in the process industry is the PI controller, Åström and Hägglund (2001), an immediate approach that should be taken into account is to use the fractional PI^{λ} controller. Because of the widespread use of PI controllers and the potentials of fractional PI^{λ} controllers, see Gude and Kahoraho (2009), it is interesting to have simple but efficient methods for tuning these kind of controllers.

In this paper, we have developed new simple tuning methods for PI and PI^{λ} controllers that give significantly better performance for a wide range of processes.

The layout of this paper is the following. The different controllers and the test batch considered in this paper are presented in Section 2. The design method is treated in Section 3. This is followed by the main results obtained in this paper: new tuning rules for PI and PI^{λ} controllers in Section 4. In Section 5 the developed tuning rules are applied to a process and a comparison between different tuning rules is made. Finally conclusions and final remarks are drawn in Section 6.

2. CONTROLLERS AND TEST BATCH

2.1 Plant knowledge

To be accepted in industrial applications controller tuning rules must be based on a limited amount of plant knowledge that is easy to obtain. The plant can the be characterized by its τ value:

$$\tau = \frac{L}{L+T} \quad (1)$$

This parameter is usually called the *normalized dead time*. It is essentially the classical *controllability ratio* L/T, but the parameter τ has the advantage that it is in the range from 0 to 1. The *controllability ratio* was often mentioned in the early process control literature, see Cohen and Coon (1953). This parameter can be used to characterize the difficulty of controlling a process. Roughly speaking, processes with small τ can be considered easy to control and the difficulty in controlling the system increases as τ increases.

2.2 The test batch

The design method presented in the next section requires the transfer function of the process to be known. The results of this investigation depend critically on the chosen test batch. To apply the method we therefore have to choose process models that are representative for the dynamics of typical industrial processes. Processes with the following transfer functions have been used:

$$G_1(s) = \frac{e^{-s}}{(1+sT)^2}$$

T = 0.01, 0.05, 0.1, 0.2, 0.3, 0.5, 0.7, 1, 2, 4, 6, 8, 10

$$G_2(s) = \frac{1}{(s+1)^n}$$

n = 3, 4, 5, 6, 7, 8

$$G_3(s) = \frac{1}{(1+s)(1+\alpha s)(1+\alpha^2 s)(1+\alpha^3 s)} \quad (2)$$

α = 0.1, 0.2, 0.5, 0.7

$$G_4(s) = \frac{1-\alpha s}{(s+1)^3}$$

α = 0.1, 0.2, 0.5, 1, 2

$$G_5(s) = \frac{1}{(1+s)(1+sT)}$$

T = 0.02, 0.05, 0.1, 0.2, 0.5

The process (3) is the standard model that has been used in many investigations of PID tuning.

$$G(s) = K_P \frac{e^{-Ls}}{(1+sT)} \quad (3)$$

The test batch (2) does, however, not include this transfer function because this model is not representative for typical industrial processes, see Åström and Hägglund (1995). Tuning based on the model (3) typically gives controller gains that have a different behaviour from the other processes in the test batch, see Hang *et al.* (1991). This is remarkable because tuning rules have traditionally been based on this model.

The processes selected in the test batch (2) are representative for many of the processes typically found in process control, see for example Åström and Hägglund (2000) and Gorez (2003), suggested as standard benchmark models for testing PID controllers. The test batch includes processes that range from delay-dominated to lag-dominated processes. They include all kinds of plants with poles strictly on the negative real axis, such as plants with time delay or non-minimum phase zeros, plants of high and low orders, plants with multiple and spread poles, etc. All processes are normalized to have unit steady state gain and have a parameter that can be changed to influence the response of the process. The parameter ranges have been chosen to give a wide variety of responses. The normalized time delay ranges from 0.17 to 1 for G_1. The rest of the processes have values of τ in the range $0 < \tau < 0.5$

2.3 PI and PI$^{\lambda}$ controllers

In this paper, two different controllers are considered: the PI and the fractional PI$^{\lambda}$ controller, which is a generalisation of the PI controller. It is a non-integer order controller of the form:

$$C(s) = K + \frac{k_i}{s^{\lambda}} \quad (4)$$

where K is the proportional gain, k_i the integral gain, and λ the fractional order of the integral part.

The interest of this kind of controller is justified by a better flexibility, since it exhibits a fractional integral part of order λ. Thus, three parameters can be tuned in this structure (K, k_i, and λ), that is, one more parameter than in the case of conventional PI controller (λ = 1). We can take advantage of the fractional order λ to improve the performance.

3. THE DESIGN METHOD

Within the process industry, regulation performance is often of primary importance since most controllers operate as regulators, see Shinskey (1996). Regulation performance is often expressed in terms of the control error obtained for certain disturbances. A load disturbance is typically applied at the process input. Typical criteria are to minimize a loss function of the form:

$$I = \int_0^{\infty} t^n |e(t)|^m dt \quad (5)$$

where the error is defined as e(t) = r(t) – y(t). Common cases are IAE (n = 0, m = 1), ISE (n = 0, m = 2), or ITSE (n = 1, m = 2).

However, Kristiansson and Lennartson (2002) defined another performance criterion in the frequency domain as an alternative to the above criteria based on a function of the error signal. It is formulated as:

$$J_v = \left\| \frac{1}{s} G(s) S(s) \right\|_{\infty} = \max_{\omega} \left| \frac{1}{j\omega} \cdot \frac{G(j\omega)}{1 + L(j\omega)} \right| \quad (6)$$

The proposed performance criterion is mainly a measure of the system ability to handle low-frequency load disturbances.

Robustness is an important consideration in control design. There are many different criteria for robustness. Many of them can be expressed as restrictions on the Nyquist curve of

the loop transfer function L(s) = G(s)C(s). Åström and Hägglund (1995) introduced the maximum sensitivity function of the closed-loop system, M_S, as a tuning parameter for PID controllers. The constraint (7) that sensitivity function S(jω) is less than a given value M_S implies that the loop transfer function should be outside a circle with radius $1/M_S$ and center at –1.

$$\|S(s)\|_\infty = \max_\omega |S(j\omega)| = \max_\omega \left|\frac{1}{1+L(j\omega)}\right| \le M_S \qquad (7)$$

The design problem discussed in this paper can be formulated as an optimisation problem: *Find parameters of the different controllers that minimize performance criterion (6) subject to the robustness constraint (7).*

A reasonable ambition in all control design is to keep the control signal as small as possible. Control system design very often deals with the trade-off between performance and control effort, provided that a reasonable mid-frequency robustness is guaranteed, see for example Gude and Kahoraho (2009). Therefore, introduce the control effort criterion:

$$J_u = \|C(s)S(s)\|_\infty = \max_\omega \left|\frac{C(j\omega)}{1+L(j\omega)}\right| \qquad (8)$$

4. RESULTS

An empirical method is used to develop the new tuning rules. The design method proposed in Section 3 with $M_S = 1.4$ was applied to all processes in the test batch (2). This value of M_S provides a good compromise between performance and robustness. This gave the corresponding parameters K, T_i, for the PI, and K, T_i, and λ, for the fractional PI controller. The process parameters K_P, L and T were also computed from the step response experiment. The controller gain is normalized by multiplying it either with the static process gain K_P or with the parameter $a = K_P L/T$. Integration time is normalized by dividing by T or by L. We will represent normalized controller parameters as functions of τ. Data obtained can be well approximated by functions having the form:

$$f(\tau) = a\tau^b + c \qquad (9)$$

4.1 PI controller

Simplified tuning rules for PI controllers will be first obtained. Figures 1 and 2 show the normalized proportional gains and integration times, respectively, as a function of normalized time delay τ when the design procedure is applied to all processes in the test batch (2). The curves drawn correspond to the results obtained by curve fitting. Both figures show that there appears to be a good correlation between the normalized controller parameters and the normalized time delay τ. This indicates that it is possible to develop good tuning rules based on the *KLT*-model. However, Figures 1 and 2 also show that parameters KK_P, aK, T_i/L, and T_i/T range from 0.16 to 23.8, from 0.21 to 3.15, from 0.34 to 8.2, and from 0.1 to 6.8, respectively.

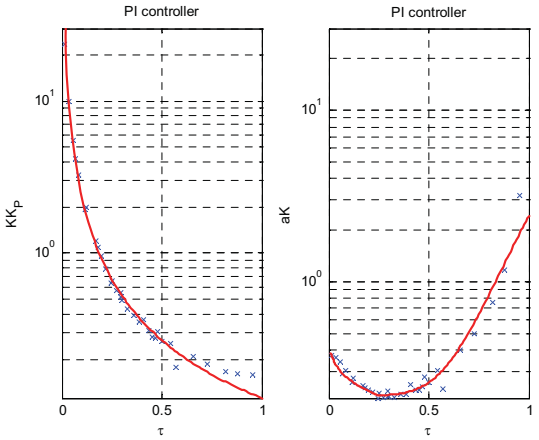

Fig. 1. Normalized PI controller proportional gains plotted versus normalized time delay τ for the test batch. The solid lines correspond to the tuning rules obtained in Table 1.

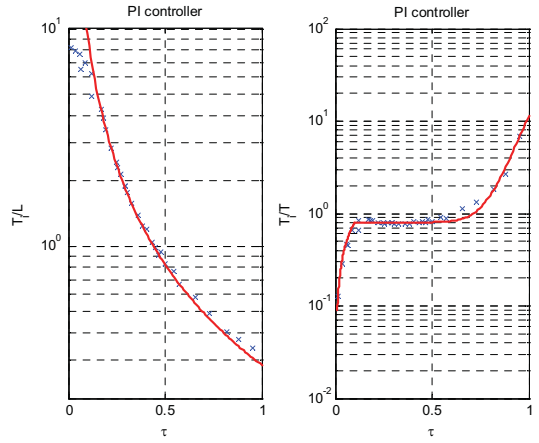

Fig. 2. Normalized PI controller integration times plotted versus normalized time delay τ for the test batch. The solid lines correspond to the tuning rules obtained in Table 1.

This indicates clearly that it is not possible to obtain good tuning rules that do not depend on τ. The deviations from the solid lines in the figure is about ± 15%

Table 1. Tuning formulae for the PI controller. The table gives the parameters of the functions of the form (9) for the normalized controller parameters and $M_S = 1.4$.

f(τ)	a	b	c	τ
KK_P	0.09793	–1.3676	0.01378	$0 < \tau < 1$
aK	–0.6473	0.1128	0.77	$0 < \tau < 0.25$
	2.212	5.7	0.2163	$0.25 < \tau < 1$
T_i/L	0.2967	–1.497	–0.01252	$0 < \tau < 1$
T_i/T	5.479	0.8154	–0.03853	$0 < \tau < 0.1$
	10.7	11.79	0.8028	$0.1 < \tau < 1$

Table 1 gives the coefficients for functions of the form (9) fitted to the data available in Figures 1 and 2. The corresponding graphs are shown in solid lines in figures.

4.2 *PI$^{\lambda}$ controller*

Simplified tuning rules for fractional PI controllers will be now obtained. Figures 3, 4, and 5 show the normalized proportional gains, the normalized integration times, and the controller fractional order, respectively, as a function of normalized time delay τ when the design procedure is applied to all processes in the test batch (2). The curves drawn correspond to the results obtained by curve fitting. Both figures show that there appears to be a good correlation between the normalized controller parameters and the normalized time delay τ. This indicates that it is possible to develop good tuning rules for fractional PI controllers based on the *KLT*-model.

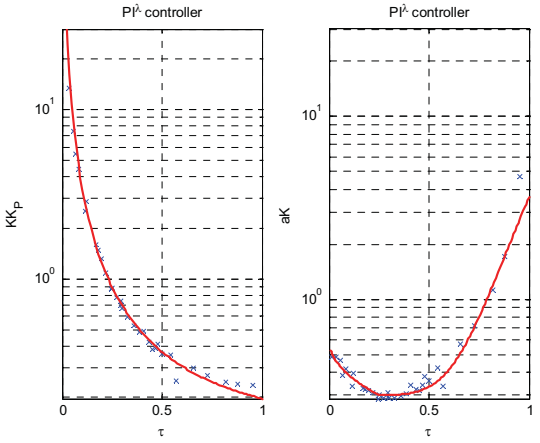

Fig. 3. Normalized PI$^{\lambda}$ controller proportional gains plotted versus normalized time delay τ for the test batch. The solid lines correspond to the tuning rules obtained in Table 2.

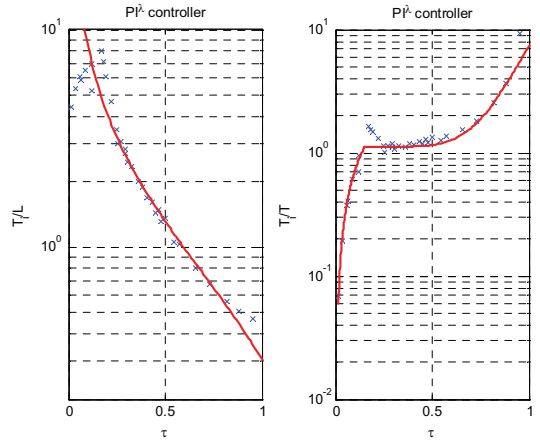

Fig. 4. Normalized PI$^{\lambda}$ controller integration times plotted versus normalized time delay τ for the test batch. The solid lines correspond to the tuning rules obtained in Table 2.

As in the case of the PI controller, it is not possible to obtain good tuning rules that do not depend on τ. The deviations from the solid lines in the figure is about ± 15%. Table 2 gives the coefficients of functions of the form (9) fitted to the data available in Figures 3, 4, and 5. The corresponding graphs are shown in solid lines in these figures.

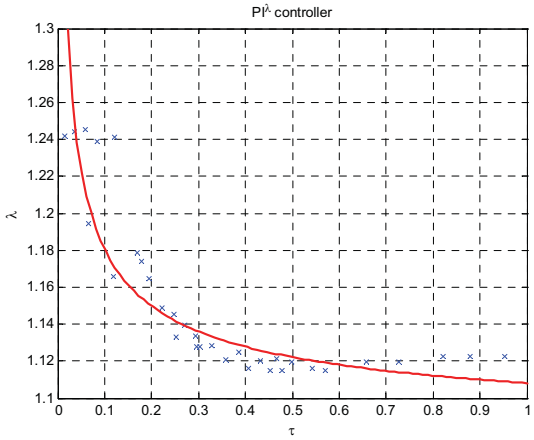

Fig. 5. Fractional order λ plotted versus normalized time delay τ for the test batch. The solid lines correspond to the tuning rules obtained in Table 2.

Table 2. Tuning formulae for the fractional PI$^{\lambda}$. The table gives the parameters of the functions of the form (9) for the normalized controller parameters and M_S = 1.4.

f(τ)	a	b	c	τ
KK_P	0.08621	–1.594	0.1096	0 < τ < 1
aK	–0.5643	0.2715	0.6866	0 < τ < 0.25
	3.327	6.593	0.2983	0.25 < τ < 1
T_i/L	1.17	–0.8997	–0.8666	0 < τ < 1
T_i/T	8.549	1.052	–0.04380	0 < τ < 0.15
	6.271	7.304	1.12	0.15 < τ < 1
λ	0.03512	–0.4862	1.073	0 < τ < 1

Figure 6 shows the ratio between the optimal J_v–values obtained with a PI$^{\lambda}$ and PI controller applied to the processes in the test batch. It shows that the benefit in using a PI$^{\lambda}$ instead a PI controller is more than 12% for delay–dominated processes, about 11% for balanced lag and delay processes, and tends to 18% for lag–dominated processes.

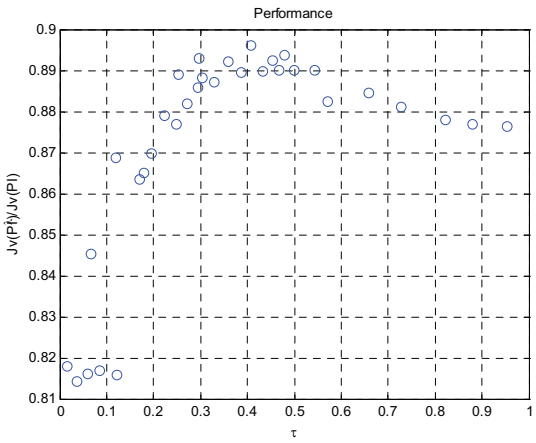

Fig. 6. Ratio of the J_v–values obtained for a PI$^{\lambda}$ and a PI controller for different values of τ applied to the processes of the test batch.

4.3 A simpler tuning rule for PI$^\lambda$ controllers

As can be seen in Figure 5, optimal λ–value is approximately equal to 1.12 for $0.3 < \tau < 1$. Provided that the maximum difference between the optimal value of λ and 1.12 is, in the worst case, equal to 0.12, i.e. 10%, we will try to develop simple tuning rules for PI$^\lambda$ controllers, fixing the value of λ to 1.12. Figures 7 and 8 show the optimal normalized proportional gains and integration, for a constant value of $\lambda = 1.12$, as a function of the normalized time delay τ. The curves drawn correspond to the results obtained by curve fitting in Table 3.

Figure 9 shows the ratio between the optimal J_v–values obtained with a PI$^\lambda$ with all its parameters free and a PI$^\lambda$ with $\lambda = 1.12$ applied to the test batch. It shows that the J_v–values obtained in both cases are nearly the same for $0.3 < \tau < 1$, and the loss for lag–dominated processes increases but it is, in all cases, less than 5%.

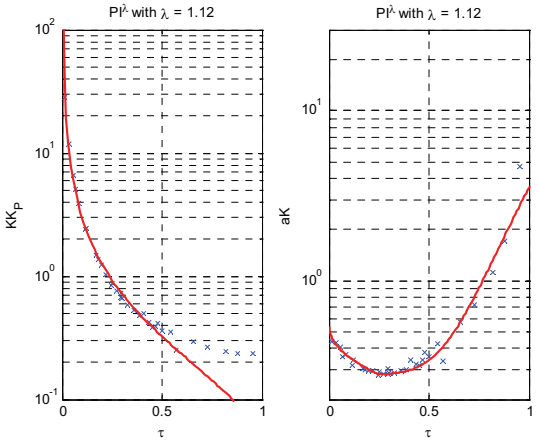

Fig. 7. Normalized PI$^\lambda$ controller proportional gains plotted versus normalized time delay τ for the test batch. The solid lines correspond to the tuning rules obtained in Table 3.

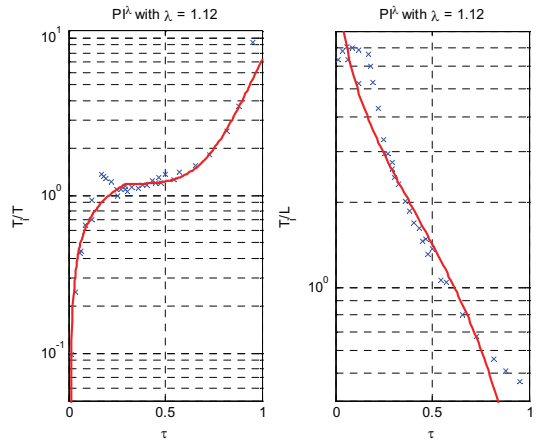

Fig. 8. Normalized PI$^\lambda$ controller integration times plotted versus normalized time delay τ for the test batch. The solid lines correspond to the tuning rules obtained in Table 3.

Table 3. Tuning formulae for fractional PI$^\lambda$ controllers. The table gives the parameters of the functions of the form (9) for the normalized controller parameters, $\lambda = 1.12$ and $M_S = 1.4$.

f(τ)	a	b	c	τ
KK_P	0.2154	–1.169	–0.1592	$0 < \tau < 1$
aK	–0.4645	0.3182	0.5795	$0 < \tau < 0.25$
	3.271	5.75	0.28	$0.25 < \tau < 1$
T_i/L	9.242	–0.1966	–9.171	$0 < \tau < 1$
T_i/T	5.479	0.8154	–0.03853	$0 < \tau < 0.3$
	6.06	7.066	1.18	$0.3 < \tau < 1$
λ	$\lambda = 1.12$			$0 < \tau < 1$

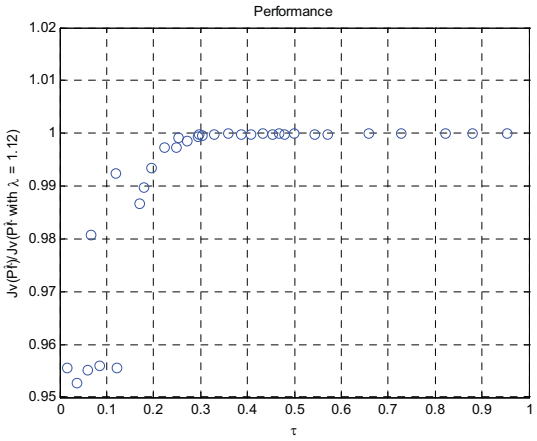

Fig. 9. Ratio of the J_v–values obtained for a PI$^\lambda$ and a PI$^\lambda$ with $\lambda = 1.12$ for different values of τ applied to the processes of the test batch.

5. COMPARISON WITH OTHER DESIGN METHODS

Extensive simulations have been done. Comparisons with classical tuning rules show that proposed tuning rules are very simple but give substantially better performance. However, due to page limitations, only one simulation has been included in this paper. There are many methods for tuning PI controllers. In this Section, the proposed methods for PI and PI$^\lambda$ controllers are compared with the Ziegler-Nichols step response method, Ziegler and Nichols (1942), the Cohen-Coon method, Cohen and Coon (1953), and optimal controllers in terms of J_v, IAE, J_u, and M_S.

For simplicity we will denote the Ziegler Nichols step response method by ZN, the Cohen-Coon method by CC, the optimal PI and PI$^\lambda$ controller obtained using the design method by opt-PI and opt-PI$^\lambda$, respectively, the proposed method for PI controllers by GK, the one for PI$^\lambda$ controllers by f-GK, and the approximation for PI$^\lambda$ controllers with $\lambda = 1.12$ by af-GK.

Consider the process with the following transfer function: $G(s) = 1/(1+s)(1+0.5s)$. We find that the apparent time delay and time constants are $L = 0.193$ and $T = 1.407$. Hence, the controllability index is $L/T = 0.1372$ and $\tau = 0.12$ for this process.

Table 4 contains the values of the different controller parameters obtained with the considered design methods. This table shows that results obtained by GK, f-GK and af-GK are very close to their respective optimal values. The performance obtained for PI^{λ} is substantially better than for PI. ZN and CC give controllers that reduce load disturbances very effectively, however they exhibit a very poor robustness and excessively large control effort.

Table 4. Controller parameters obtained for the different design methods for the considered transfer function.

Method	K	T_i	λ	k_i	M_S	J_u	J_v	IAE
ZN	6.56	0.58	1	11.34	3.11	22.59	0.12	0.16
CC	6.65	0.50	1	13.32	3.62	28.90	0.14	0.18
GK	1.78	1.13	1	1.58	1.38	2.65	0.63	0.63
opt-PI	2.04	1.21	1	1.68	1.40	3.02	0.59	0.59
f-GK	2.62	1.24	1.17	2.12	1.41	3.58	0.45	0.58
opt-PI^{λ}	2.86	1.34	1.24	2.13	1.40	3.79	0.46	0.61
af-GK	2.40	1.32	1.12	1.82	1.39	3.28	0.50	0.60

Parameters obtained by f-GK and optimal PI^{λ} are very close which indicates that little is lost by not using the full transfer function. The improvement in J_v of using a PI^{λ} instead of a PI is about 22%. The value of J_v for GK is about 28% higher compared with f-GK. These improvements are also evaluated in Gude and Kahoraho (2009).

6. CONCLUSIONS

This paper presents new tuning rules for PI and fractional PI control of typical processes found in process control. The rules are based on characterization of the process dynamics by three parameters, i.e. gain K_P, apparent time constant T and apparent time delay L, that can be obtained by a simple step response experiment. The design method consists on minimizing a frequency objective function subject to a constraint on the maximum sensitivity function. Based on these parameters it is possible to develop very simple tuning rules for PI and PI^{λ} controllers that only depend on the normalized time delay τ.

In this paper it is also demonstrated that substantially better performance can be obtained using PI^{λ} instead of PI controllers. These tuning rules are shown to give good results compared to a couple of well established classical tuning methods, especially when simplicity, performance and robustness are emphasized.

Future investigation should rely on extending these tuning rules to fractional PID controllers.

ACKNOWLEDGEMENTS

This paper has mainly been written during a stay of the first author at the Laboratory IMS Bordeaux (France) from June to October 2008, which has been supported by DEIKER – *Agencia para la Promoción y Gestión de la Investigación*, University of Deusto.

REFERENCES

Åström, K.J. and Hägglund, T. (1995). *PID Controllers: Theory, Design, and Tuning.* Instrument Society of America. Research Triangle Park, NC.

Åström, K.J. and Hägglund, T. (2000). Benchmark systems for PID control. *Proceedings of IFAC workshop on Digital Control*, pp. 165-166. Terrassa, Spain.

Åström, K.J. and Hägglund, T. (2001). The future of PID control. *Control Engineering Practice*, Vol. 9 (11), pp. 1163-1175.

Åström, K.J. and Hägglund, T. (2004). Revisiting the Ziegler-Nichols step response method for PID control. *Journal of Process Control*, Vol. 14(6), pp. 635-650.

Capponetto, R., Fortuna, L., and Porto, D. (2002). Parameter tuning of a non integer order PID controller. *Proceedings of 15th Int. Symp. on Mathematical Theory of Networks and Systems*. Notre Dame, IN.

Chien, K.L., Hrones, J.A. and Reswick, J.B. (1952) On the automatic control of generalized passive systems, *Transactions ASME*, Vol. 74, pp. 175-185.

Cohen, G.H. and Coon, G.A. (1953). Theoretical consideration of retarded control, *Transactions ASME*, Vol. 75, pp. 827-834.

Gorez, R. (2003). New design relations for 2-DOF PID-like control systems. *Automatica*, Vol. 39 (5), pp. 901-908.

Gude, J.J. and Kahoraho, E. (2007). PID control: Current status and alternatives. *In 2nd Seminar for Advanced Industrial Control Applications – SAICA 2007*, pp. 247-253. UNED Ediciones.

Gude, J.J. and Kahoraho, E. (2009). Performance comparison between PI(D) and fractional PI controllers. *In IFAC Workshop on Control Applications and Optimization – CAO'09*. University of Jyvaskyla, Finland.

Hang, C.C., Åström, K.J., and Hägglund, T. (1991). Refinements of the Ziegler-Nichols tuning formula. *IEE Proc., Part D,* Vol. 138 (2), pp. 111-118.

Kristiansson, B. and Lennartson, B. (2002). Robust and optimal tuning of PI and PID controllers. *IEE Proc., Part D*, Vol. 149 (1), pp. 17-25.

Monje, C.A., Vinagre, B.M., Chen, Y.Q., Feliu, V., Lanusse, P., and Sabatier, J. (2005). Optimal tunings for fractional $PI^{\lambda}D^{\mu}$–controllers. *Fractional Differentiation and its Applications*. Le Mehauté, A., Tenreiro Machado, J.A., Trigeassou, J.C., and Sabatier, J. (eds.) Ubooks Verlag, Augsburg, pp. 675-686.

Podlubny, I. (1999). Fractional-order systems and $PI^{\lambda}D^{\mu}$-controllers. *IEEE Trans. Autom. Control*. Vol. 44 (1), pp. 208-214.

Shinskey, F.G. (1996). *Process Control Systems. Application, design, and tuning*. 4th edition. McGraw-Hill

Vinagre, B.M., Podlubny, I., Dorcak, L. and Feliu, V. (2000). On fractional PID controllers: A frequency domain approach. *Proceedings of IFAC workshop on Digital Control,* pp. 51-56. Terrassa, Spain.

Ziegler, J.G. and Nichols N.B. (1942). Optimum settings for automatic controllers. *Transactions ASME,* Vol. 64, pp. 759-768.

On A New Approach for Self-optimizing Control Structure Design

S. Heldt *

* *Linde AG, Linde Engineering Division, Dr.-Carl-von-Linde-Str. 6-14 82049 Pullach (Tel: +498974453536; e-mail: steffen.heldt@linde-le.com).*

Abstract
In this paper, a new method for the identification of self-optimizing control structure designs (CSDs) based on generalized singular value decomposition (GSVD) is proposed. The method is primarily dedicated to find optimal CSDs where all controlled variables (CVs) are represented by a common set of linear combinations of process variables (PVs). It is shown that the implementation of the GSVD into iterative solution approaches is beneficial in order to find CSDs where an individual PV subset is mapped to each CV. The developments will be tested on a simple process.

Keywords: Control system design; Linear control systems; Controlled variables; Optimal control; Self-optimizing control

1. INTRODUCTION

With more than 4000 completed plant projects, the Engineering Division of the Linde AG ranks among the leading international plant contractors, with focus on the key market segments olefin plants, natural gas plants, air separation plants, as well as hydrogen and synthesis gas plants. This paper relates to new process developments for liquefied natural gas plants whose steady state and dynamic behavior are currently under investigation in order to provide design guidelines and to ensure reliable and economic operation. In the context of this work, new methods for the identification of regulatory control structure designs (CSDs) have been developed. They will be presented in this paper.

Steady state process optimization by regulation was first motivated by Morari et al. [1980]. They articulated the idea that a constant set point policy will lead to optimal operation if the underlying control structure is properly designed. Skogestad and Postlethwaite [1996, p. 428-433] extended this idea and gave an approximate criterion for finding CSDs with self-optimizing abilities, the so-called minimum singular value (MSV) rule. Assuming a linear process model and a quadratic cost function, an exact local criterion for the worst-case loss of CSDs was developed by Halvorsen et al. [2003]. Based on the resulting worst-case loss criterion, a multivariate non-convex problem subject to structural constraints needs to be solved in order to obtain a self-optimizing CSD. These structural constraints refer to limitations on the size of the process variable (PV) subset and the particular selection of PVs. For instance, it must be decided whether only PV selection or PV combination is taken into account. Several methods have been developed which solve the constrained optimization problem. An optimal CSD subject to PV selection can be found by either screening all possible PV combinations or applying branch and bound (BAB) algorithms in order to avoid time consuming calculations as proposed by Cao and Saha [2005], Kariwala and Skogestad [2006/07/09-13], Cao and Kariwala [2008], Kariwala and Cao [2009]. PV combination methods have been published by Alstad and Skogestad [2007], Alstad et al. [2008], Kariwala [2007] and Kariwala et al. [2008]. They all have in common that the same PV subset is considered for all CVs.

In Section 2, the mathematical framework of self-optimizing control theory will be briefly introduced. In the following sections, two variants of a new PV combination method will be proposed. In Section 3 the focus is on CSDs where a common PV subset is considered for all CVs. Section 4 is dedicated to CSDs where individual PV subsets are mapped to each CV. For illustration, the new developments will be applied to a process example in Section 5. Concluding remarks are given in Section 6.

2. MATHEMATICAL FRAMEWORK

The scheme in Figure 1 represents a general regulatory CSD applied to an arbitrary process plant. Based thereon the exact local method by Halvorsen et al. [2003] will be introduced. The vectors $\boldsymbol{u} \in \mathbb{R}^{n_{\boldsymbol{u}}}$, $\boldsymbol{d} \in \mathbb{R}^{n_{\boldsymbol{d}}}$, $\boldsymbol{y} \in \mathbb{R}^{n_{\boldsymbol{y}}}$ and $\boldsymbol{c} \in \mathbb{R}^{n_{\boldsymbol{u}}}$, respectively, correspond to the manipulated variables (MVs), disturbance variables (DVs), measured process variables (PVs) and controlled variables (CVs). A constant set point policy is applied. That is, the MVs are adjusted by the controller(s) until, feasibility provided, the CVs equal the set point vector $\boldsymbol{c}_s$. To account for measurement errors, the PVs and CVs are affected by the implementation errors $\boldsymbol{n}^{\boldsymbol{y}} \in \mathbb{R}^{n_{\boldsymbol{y}}}$ and $\boldsymbol{n}^{\boldsymbol{c}} \in \mathbb{R}^{n_{\boldsymbol{u}}}$.

Morari et al. [1980], the inventors of self-optimizing control, state that it is desirable "(...) to find a function of PVs which when held constant, leads automatically to the optimal adjustments of the MVs, and with it, the optimal operating conditions." In other words, self-optimizing con-

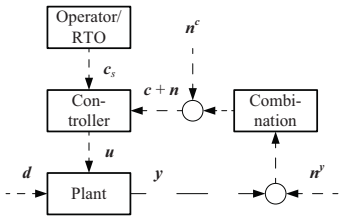

Figure 1. General representation of regulatory CSDs in chemical plants (after Alstad et al. [2008]).

trol may be achieved by an appropriate mapping of PVs towards CVs, denoted by $\boldsymbol{c} = \mathcal{H}(\boldsymbol{y})$, where $\mathcal{H} \in \mathbb{R}^{n_u}$ represents the "combination" block in Figure 1. For deriving the exact local method, Halvorsen et al. [2003] considered a linear map $\boldsymbol{H} = \frac{\partial \boldsymbol{c}}{\partial \boldsymbol{y}^T}$. The cost function of a plant denoted by J are usually affected by both, MVs and DVs. In order to operate the plant optimally (at minimum cost), MVs need to be adjusted subject to variations in DVs. The solution to the problem

$$\boldsymbol{u}_{\text{opt}}(\boldsymbol{d}) = \arg\left(\min_{\boldsymbol{u}} J(\boldsymbol{u}, \boldsymbol{d})\right) \text{ s.t. } g(\boldsymbol{y}, \boldsymbol{u}, \boldsymbol{d}) = 0 \qquad (1)$$

gives the best input leading to the lowest achievable cost. Problem (1) will be referred to as feed-forward re-optimization. Here $g \in \mathbb{R}^{n_y}$ denotes the steady-state model equations of the plant. The following simplifying assumptions are made.

(1) Nonlinearities of the plant are treated as locally negligible. Then, the steady-state I/O model of the plant can be represented as

$$\boldsymbol{y} = \boldsymbol{G^y}\,\boldsymbol{u} + \boldsymbol{G_d^y}\,\boldsymbol{d}, \qquad (2)$$

where $\left[\,\boldsymbol{G^y}\;\boldsymbol{G_d^y}\,\right] = -\left(\frac{\partial g}{\partial \boldsymbol{y}^T}\right)^{-1} \frac{\partial g}{\partial\left[\,\boldsymbol{u}^T\;\boldsymbol{d}^T\,\right]}$.

(2) The cost function J is locally approximated by a second order Taylor series.

(3) The number of MVs might be reduced as some of them need to be spend in "a priori" controller loops in order to either stabilize the plant or fulfill optimally active constraints. It is assumed that $\boldsymbol{u}$ represents only the remaining MVs available for self-optimizing CSD. The "a priori" controller loops are considered part of the model equations g.

Figure 2 shows exemplarily the operational cost of a process plant versus one DV. The cost of feed-forward re-optimization is indicated by the solid line and gives the lower bound for the cost of feedback control with constant set points. It is thus convenient to define a loss function as

$$L(\boldsymbol{d}) = J(\boldsymbol{u_H}(\boldsymbol{d}), \boldsymbol{d}) - J(\boldsymbol{u}_{\text{opt}}(\boldsymbol{d}), \boldsymbol{d}).$$

Here $\boldsymbol{u_H}(\boldsymbol{d})$ represents the influence from DVs to MVs for feedback control, easily derived for the linear case. From $\boldsymbol{c} = \boldsymbol{H}\,\boldsymbol{y} \overset{!}{=} \boldsymbol{c}_s = \boldsymbol{0}$ and (2) it follows that

$$\boldsymbol{u_H} = -(\boldsymbol{H}\,\boldsymbol{G^y})^{-1}\;\boldsymbol{H}\,\boldsymbol{G_d^y}\,\boldsymbol{d}.$$

According to Halvorsen et al. [2003] the worst-case loss is given by

$$L_{\text{worst}} = \frac{1}{2}\,\boldsymbol{z}^T\,\boldsymbol{z}, \qquad (3)$$

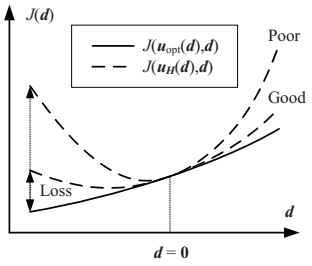

Figure 2. Objective functions for a poor and a good self-optimizing CSD compared with the case of re-optimized MVs (after Skogestad [2000]).

where the loss variables $\boldsymbol{z}$ are given by

$$\boldsymbol{z} = \boldsymbol{M}\,\boldsymbol{f}, \qquad (4)$$

for feedback control with

$$\boldsymbol{M} = J_{\boldsymbol{uu}}^{1/2}\;(\boldsymbol{H}\,\boldsymbol{G^y})^{-1}\;\boldsymbol{H}\,\tilde{\boldsymbol{F}}$$
$$\tilde{\boldsymbol{F}} = \left[\,-\left(\boldsymbol{G^y}\,J_{\boldsymbol{uu}}^{-1}\,J_{\boldsymbol{ud}} - \boldsymbol{G_d^y}\right)\,\boldsymbol{W_d}\;\boldsymbol{W_{n^y}}\,\right].$$

Here, the matrices $J_{\boldsymbol{uu}}$ and $J_{\boldsymbol{ud}}$ indicate the second derivatives (Hessians) of the cost function J with respect to $\boldsymbol{u}$ and $\boldsymbol{d}$. The disturbance variation $\Delta\boldsymbol{d}$ and the implementation error $\boldsymbol{n_y}$ are commonly represented by the scaled variable $\boldsymbol{f}$, *i.e.*,

$$\begin{bmatrix}\Delta\boldsymbol{d}\\ \boldsymbol{n_y}\end{bmatrix} = \begin{bmatrix}\boldsymbol{W_d} & \boldsymbol{0}\\ \boldsymbol{0} & \boldsymbol{W_{n^y}}\end{bmatrix}\boldsymbol{f} \text{ with } \|\boldsymbol{f}\|_2 \le 1,$$

where the matrices $\boldsymbol{W_d}$ and $\boldsymbol{W_{n^y}}$ are diagonal scaling matrices. From observation of (3) and (4) it is evident that a self-optimizing CSD with least worst-case loss may be obtained by solving the problem

$$\boldsymbol{H} = \arg\min_{\boldsymbol{H}} \overline{\sigma}(\boldsymbol{M}), \qquad (5)$$

where $\overline{\sigma}$ indicates the largest singular value. In a more recent work, Kariwala et al. [2008] proved that the average loss given by

$$L_{\text{average}} = \frac{1}{6\,(n_{\boldsymbol{y}} + n_{\boldsymbol{d}})}\;\|\boldsymbol{M}\|_{\text{F}}^2 \qquad (6)$$

is a better estimate of the loss as the worst-case loss (3) tends to overestimation. Here, $\|.\|_F$ indicates the Frobenius norm also known as the Euclidean norm. Besides, Kariwala et al. [2008] proved that the average loss is super-optimal in the sense that it also minimizes the worst-case loss. According to (6), they suggested solving

$$\boldsymbol{H} = \arg\min_{\boldsymbol{H}} \|\boldsymbol{M}\|_{\text{F}} \qquad (7)$$

instead of (5).

The solution of problems (5) and (7) is nontrivial since the matrix $\boldsymbol{M}$ depends in a nonlinear fashion on $\boldsymbol{H}$. Moreover, the problem may be structurally constrained, as indicated in Section 1. *E.g.*, the dimension of the PV subset could be limited or special PVs may be excluded from PV subset etc. Many authors such as Alstad and Skogestad [2007], Alstad et al. [2008], Kariwala [2007] and Kariwala et al. [2008] addressed the problem of finding a global solution to either (5) or (7) with focus on PV combination. All of these

methods are limited to the structural constraint that the same PV subset is used for each CV. Based on the method developed in the next section, iterative solution strategies will be developed which focus on finding CSDs without structural limitations except for rank $(\boldsymbol{H}) = n_{\boldsymbol{u}}$.

3. THE GSVD METHOD

In this section a new solution method is presented for the worst-case and average loss problem, (5) and (7), subject to a common PV subset for all CVs. It will be referred to as the GSVD method. In a first step, (4) is restated as

$$\boldsymbol{z}^T \left(\boldsymbol{G}_{\boldsymbol{z}}^{\boldsymbol{y}}\right)^T \boldsymbol{H}^T = \boldsymbol{f}^T \tilde{\boldsymbol{F}}^T \boldsymbol{H}^T, \tag{8}$$

where

$$\boldsymbol{G}_{\boldsymbol{z}}^{\boldsymbol{y}} = \boldsymbol{G}^{\boldsymbol{y}} J_{\boldsymbol{uu}}^{-1/2}.$$

Suppose, that the rank condition

$$\operatorname{rank}\left(\begin{bmatrix} \left(\boldsymbol{G}_{\boldsymbol{z}}^{\boldsymbol{y}}\right)^T \\ \tilde{\boldsymbol{F}}^T \end{bmatrix}\right) = n_{\boldsymbol{y}} \tag{9}$$

is satisfied which will be generally the case if the condition $n_{\boldsymbol{u}} + n_{\boldsymbol{f}} \geq n_{\boldsymbol{y}}$ holds (the case $n_{\boldsymbol{u}} + n_{\boldsymbol{f}} < n_{\boldsymbol{y}}$ is discussed below in Remark 4). Then, according to Hogben [2007, p. 15.12f], the generalized singular value decomposition (GSVD) of the matrix pair $\left\{\left(\boldsymbol{G}_{\boldsymbol{z}}^{\boldsymbol{y}}\right)^T, \tilde{\boldsymbol{F}}^T\right\}$ exists and (8) can be written as

$$\boldsymbol{z}^T \boldsymbol{U} \boldsymbol{\Sigma} \boldsymbol{V}^T \boldsymbol{H}^T = \boldsymbol{f}^T \tilde{\boldsymbol{U}} \tilde{\boldsymbol{\Sigma}} \boldsymbol{V}^T \boldsymbol{H}^T, \tag{10}$$

where the decomposed matrices have the following properties.

The matrices $\boldsymbol{U} \in \mathbb{R}^{n_{\boldsymbol{u}} \times n_{\boldsymbol{u}}}$ and $\tilde{\boldsymbol{U}} \in \mathbb{R}^{n_{\boldsymbol{f}} \times n_{\boldsymbol{f}}}$ are unitary, *i.e.*, $\boldsymbol{U}^T \boldsymbol{U} = \boldsymbol{I}_{n_{\boldsymbol{u}}}$ and $\tilde{\boldsymbol{U}}^T \tilde{\boldsymbol{U}} = \boldsymbol{I}_{n_{\boldsymbol{f}}}$. The matrix $\boldsymbol{V} \in \mathbb{R}^{n_{\boldsymbol{y}} \times n_{\boldsymbol{y}}}$ is regular. The matrix $\boldsymbol{\Sigma} \in \mathbb{R}^{n_{\boldsymbol{u}} \times n_{\boldsymbol{y}}}$ is tailing diagonal, with $\boldsymbol{\Sigma}^T \boldsymbol{\Sigma} = \operatorname{diag}\left(\alpha_1^2, \alpha_2^2, ..., \alpha_{n_{\boldsymbol{y}}}^2\right)$ and $0 \leq \alpha_i \leq \alpha_{i+1} \leq 1$. The matrix $\tilde{\boldsymbol{\Sigma}} \in \mathbb{R}^{n_{\boldsymbol{f}} \times n_{\boldsymbol{y}}}$ is leading diagonal, with $\tilde{\boldsymbol{\Sigma}}^T \tilde{\boldsymbol{\Sigma}} = \operatorname{diag}\left(\beta_1, \beta_2, ..., \beta_{n_{\boldsymbol{y}}}\right)$ and $1 \geq \beta_i \geq \beta_{i+1} \geq 0$. Note that the number of $r = \max\left(0, n_{\boldsymbol{y}} - n_{\boldsymbol{u}}\right)$ leading α_i and β_i are 0 and 1, respectively, and that the number of $s = \max\left(0, n_{\boldsymbol{y}} - n_{\boldsymbol{f}}\right)$ tailing α_i and β_i are 1 and 0, respectively. For more information on GSVD and on how the resulting matrices can be computed, the reader is referred to standard linear algebra textbooks, *e.g.*, Golub and VanLoan [1996, pp. 465-467].

Theorem 1. If $n_{\boldsymbol{y}} \geq n_{\boldsymbol{u}}$, the minimum worst-case and average loss are given by

$$L_{\text{worst}} = \frac{1}{2}\left(\frac{\beta_{r+1}}{\alpha_{r+1}}\right)^2 \tag{11}$$

and

$$L_{\text{average}} = \frac{1}{6\ (n_{\boldsymbol{y}} + n_{\boldsymbol{d}})} \sum_{i=r+1}^{n_{\boldsymbol{y}}} \left(\frac{\beta_i}{\alpha_i}\right)^2, \tag{12}$$

respectively. They may be obtained by selecting

$$\boldsymbol{H} = \boldsymbol{M}_{\boldsymbol{n}} \begin{bmatrix} \boldsymbol{p}_{r+1} & \cdots & \boldsymbol{p}_{n_{\boldsymbol{y}}} \end{bmatrix}^T,$$

where $\boldsymbol{p}_i$ is the i^{th} column of $\boldsymbol{P} = \boldsymbol{V}^{-T}$ and $\boldsymbol{M}_{\boldsymbol{n}} \in \mathbb{R}^{n_{\boldsymbol{u}} \times n_{\boldsymbol{u}}}$ is an arbitrary regular matrix.

Proof. By selecting $\boldsymbol{H} = \boldsymbol{M}_{\boldsymbol{n}} \begin{bmatrix} \boldsymbol{p}_{r+1} & \cdots & \boldsymbol{p}_{n_{\boldsymbol{y}}} \end{bmatrix}^T$ it follows that

$$\boldsymbol{V}^T \boldsymbol{H}^T = \boldsymbol{V}^T \begin{bmatrix} \boldsymbol{p}_{r+1} & \cdots & \boldsymbol{p}_{n_{\boldsymbol{y}}} \end{bmatrix} \boldsymbol{M}_{\boldsymbol{n}}^T = \begin{bmatrix} \boldsymbol{0}_{r \times n_{\boldsymbol{u}}} \\ \boldsymbol{I}_{n_{\boldsymbol{u}}} \end{bmatrix} \boldsymbol{M}_{\boldsymbol{n}}^T. \tag{13}$$

and

$$\boldsymbol{\Sigma}\, \boldsymbol{V}^T \boldsymbol{H}^T = \operatorname{diag}\left(\alpha_{r+1}, ..., \alpha_{n_{\boldsymbol{y}}}\right) \boldsymbol{M}_{\boldsymbol{n}}^T$$

$$\tilde{\boldsymbol{\Sigma}}\, \boldsymbol{V}^T \boldsymbol{H}^T = \begin{bmatrix} \boldsymbol{0}_{r \times n_{\boldsymbol{u}}} \\ \operatorname{diag}\left(\beta_{r+1}, ..., \beta_{n_{\boldsymbol{y}}}\right) \\ \boldsymbol{0}_{\bar{s} \times n_{\boldsymbol{u}}} \end{bmatrix} \boldsymbol{M}_{\boldsymbol{n}}^T,$$

where $\bar{s} = \max\left(0, n_{\boldsymbol{f}} - n_{\boldsymbol{y}}\right)$. Inserting these results into (10) yields

$$\boldsymbol{z}^T = \boldsymbol{f}^T \underbrace{\tilde{\boldsymbol{U}} \begin{bmatrix} \boldsymbol{0}_{r \times n_{\boldsymbol{u}}} \\ \operatorname{diag}\left(\sigma_{r+1}, ..., \sigma_{n_{\boldsymbol{y}}}\right) \\ \boldsymbol{0}_{\bar{s} \times n_{\boldsymbol{u}}} \end{bmatrix}}_{=\boldsymbol{M}^T} \boldsymbol{U}^T,$$

where $\sigma_i = \beta_i / \alpha_i$ indicate the i^{th} largest generalized singular value of the matrix pair $\left\{\left(\boldsymbol{G}_{\boldsymbol{z}}^{\boldsymbol{y}}\right)^T, \tilde{\boldsymbol{F}}^T\right\}$. Note that the maximum singular value and the Frobenius norm of a matrix are invariant to unitary transformations thereof. Thus, the worst-case loss (3) and the average loss (6) depend only on the selected generalized singular values and the derivation of (11) and (12) is trivial. As the minimum generalized singular values were selected, both, the worst-case loss and the average loss are minimal.

Remark 2. The GSVD method is written in terms of the complete PV set $\mathcal{Y}$. Note that it work as well for a selected PV subset $\mathcal{Y}_{\text{c}} \subseteq \mathcal{Y}$. Then, in all formulas stated above the respective rows in $\boldsymbol{G}_{\boldsymbol{z}}^{\boldsymbol{y}}$ and $\tilde{\boldsymbol{F}}$ must be extracted and $n_{\boldsymbol{y}}$ must be substituted by $n_{\mathcal{Y}_{\text{c}}}$.

Remark 3. For perfect disturbance rejection, *i.e.*, $\boldsymbol{M} = \boldsymbol{0}$, it is required that at least $n_{\boldsymbol{u}}$ tailing β_i are 0. As indicated above, the number of $s = \max\left(0, n_{\boldsymbol{y}} - n_{\boldsymbol{f}}\right)$ tailing β_i are in fact 0. Thus, perfect disturbance rejection occurs if the inequality

$$s \geq n_{\boldsymbol{u}}$$

is satisfied. The necessary condition therefore is $s > 0$, *i.e.*, $n_{\boldsymbol{f}} < n_{\boldsymbol{y}}$, which can only be satisfied if the implementation error is disregarded, *i.e.*, $\boldsymbol{W}_{\boldsymbol{n}^{\boldsymbol{y}}} = \emptyset$ and $n_{\boldsymbol{f}} = n_{\boldsymbol{d}}$. The sufficient condition for perfect disturbance rejection is then $n_{\boldsymbol{y}} \geq n_{\boldsymbol{u}} + n_{\boldsymbol{d}}$. This is in agreement with the combination methods from Alstad and Skogestad [2007], Alstad et al. [2008] and Kariwala [2007], Kariwala et al. [2008].

Remark 4. If $n_{\boldsymbol{u}} + n_{\boldsymbol{f}} < n_{\boldsymbol{y}}$, the rank condition (9) is violated and the GSVD as stated above cannot be performed. Note that this is only a formal issue and will not be treated here for the sake of brevity.

Remark 5. The GSVD method is related to the method by Kariwala et al. [2008] and the "constrained average loss minimization" method by Alstad et al. [2008]. It can be shown that all three methods minimize the average loss subject to the same structural constraint and thus provide the same results. However, it will be omitted here for the sake of brevity.

4. BEYOND COMMON PV SUBSETS

For better legibility of this section, definitions for CSDs will be introduced.

Definition 6. A CSD is said to be *column-structured*, if all CVs are linear combinations of the same PV subset $\mathcal{Y}_\mathrm{c}$ of size $n_{\mathcal{Y}_\mathrm{c}} = \dim(\mathcal{Y}_\mathrm{c})$. A *common-sized* CSD refers to a CSD in which the i^{th} CV is a linear combination of an individual PV subset $\mathcal{Y}_i$ with the constraint that all PV subsets have the same set size $n_\mathrm{s} = \dim(\mathcal{Y}_i)\,\forall i \in \{1,\ldots,n_{\boldsymbol{u}}\}$. In a more general *loosely-structured* CSD, the i^{th} CV is a linear combination of an individual PV subset $\mathcal{Y}_i$ with individual set size $n_{\mathcal{Y}_i} = \dim(\mathcal{Y}_i)$.

Theorem 7. Let $\boldsymbol{H}_\mathrm{c}$ represent a column-structured CSD of size $n_{\mathcal{Y}_\mathrm{c}}$ with finite worst-case/average loss, *i.e.*, $\operatorname{rank}(\boldsymbol{H}_\mathrm{c}) = n_{\boldsymbol{u}}$. Then, for every $\boldsymbol{H}_\mathrm{c}$ there exists a common-sized CSD $\boldsymbol{H}_\mathrm{s}$ with a PV subset size of $n_\mathrm{s} = n_{\mathcal{Y}_\mathrm{c}} - (n_{\boldsymbol{u}} - 1)$ and the same worst-case/average loss as $\boldsymbol{H}_\mathrm{c}$. The proof will be omitted due to the lack of space.

Corollary 8. Let $\boldsymbol{H}_\mathrm{c}$ be a column-structured CSD with PV subset size $n_\mathrm{c} = n_{\boldsymbol{u}}$ and finite loss. Then, the worst-case/average loss of $\boldsymbol{H}_\mathrm{c}$ is independent of the coefficients in $\boldsymbol{H}_\mathrm{c}$. Rather, the worst-case/average loss of $\boldsymbol{H}_\mathrm{c}$ depends only on the selection of the PV subset $\mathcal{Y}_\mathrm{c}$. The proof will be omitted due to the lack of space.

Some advantages of common-sized and loosely-structured CSDs over column-structured CSDs are pointed out below.

(1) A smaller PV subset size is, on the one hand, favorable due to better practical acceptance but, on the other hand, usually accompanied by a larger worst-case/average loss. From Theorem 7 it can be concluded that for $n_{\boldsymbol{u}} > 1$ a reduction in PV subset size without affecting the worst-case/average loss can be achieved if, instead of a column-structured CSD, a common-sized CSD is taken into account. In particular, the PV subset size reduction with invariant worst-case/average loss can be as large as $n_{\boldsymbol{u}} - 1$ PVs.
(2) By implication of the first argument, it is evident that a smaller worst-case/average loss can be achieved if, instead of a column-structured CSD, a common-sized CSD with equal PV subset size is taken into account.
(3) For $n_{\mathcal{Y}_\mathrm{c}} = n_{\boldsymbol{u}}$ the optimality of column-structured CSDs is only a matter of PV subset selection as pointed out in Corollary 8 presented above.
(4) Column-structured CSDs $\boldsymbol{H}_\mathrm{c}$ fail if $n_{\mathcal{Y}_\mathrm{c}} < n_{\boldsymbol{u}}$ holds. This is due to the fact that $\operatorname{rank}(\boldsymbol{H}_\mathrm{c}) < n_{\boldsymbol{u}}$ which leads to a singular $\boldsymbol{H}_\mathrm{c}\,\boldsymbol{G}^{\boldsymbol{y}}$ and, by observation of (4) and (5), to infinite loss.
(5) Input/output (I/O) selection based on heuristic rules is a common practice. Physical closeness between CVs and MVs is probably the most common rule, in order to achieve good cause and effect between MVs and CVs. If decentralized controllers are used and the MVs are far apart from each other (*e.g.*, in large scale processes), it is desirable to have an individual PV subset for every CV as in common-sized and loosely-structured CSDs.
(6) PV combinations including different measurement units have poor practical acceptance. If the structural constraint was imposed on the prospective CSD that only PVs of the same type can be selected for each CV, then, in the case of a column-structured CSD with $n_{\boldsymbol{u}} > 1$, one would be forced to omit information of all PVs not part of the selected unit group. In common-sized and loosely-structured CSDs, for each CV another PV subset can be selected which allows to use information of more than only one unit group.

For loosely-structured CSDs, no explicit expression for $\boldsymbol{H}$ can be derived by the solution to problems (5) and (7). Thus, iterative solution methods need to be applied. In the following, a framework for advanced iterative methods will be presented.

In order to take loosely-structured CSDs into account, (4) is restated as

$$\boldsymbol{z}^T \sum_{i=1}^{n_{\boldsymbol{u}}} (\boldsymbol{G}_{\boldsymbol{z}}^{\boldsymbol{y}})^T\, \boldsymbol{h}_i\, \boldsymbol{e}_i^T = \boldsymbol{f}^T \sum_{i=1}^{n_{\boldsymbol{u}}} \tilde{\boldsymbol{F}}^T\, \boldsymbol{h}_i\, \boldsymbol{e}_i^T, \tag{14}$$

where $\boldsymbol{h}_i^T \in \mathbb{R}^{n_{\boldsymbol{y}}}$ is the i^{th} row vector of $\boldsymbol{H}$, *i.e.*, $\boldsymbol{H}^T = [\,\boldsymbol{h}_1\ \ldots\ \boldsymbol{h}_{n_{\boldsymbol{u}}}\,]$, and $\boldsymbol{e}_i \in \mathbb{R}^{n_{\boldsymbol{u}}}$ is the i^{th} standard basis vector. The vector $\boldsymbol{h}_i$ represents the map from the PVs of the subset $\mathcal{Y}_i$ towards the i^{th} CV, hence $h_{ij} = 0 \forall j \notin \mathcal{Y}_i$. It is thus convenient to write (14) as

$$\boldsymbol{z}^T \sum_{i=1}^{n_{\boldsymbol{u}}} (\boldsymbol{G}_{\boldsymbol{z}}^{\boldsymbol{y}})_{\mathcal{Y}_i}^T\, \boldsymbol{h}_{i\mathcal{Y}_i}\, \boldsymbol{e}_i^T = \boldsymbol{f}^T \sum_{i=1}^{n_{\boldsymbol{u}}} \tilde{\boldsymbol{F}}_{\mathcal{Y}_i}^T\, \boldsymbol{h}_{i\mathcal{Y}_i}\, \boldsymbol{e}_i^T, \tag{15}$$

where the subscript $\mathcal{Y}_i$ denotes that those columns/elements of $(\boldsymbol{G}_{\boldsymbol{z}}^{\boldsymbol{y}})^T$, $\tilde{\boldsymbol{F}}^T$ and $\boldsymbol{h}_i$ are selected whose index is part of $\mathcal{Y}_i$.

By performing the GSVD of the corresponding matrix pairs $\left\{(\boldsymbol{G}_{\boldsymbol{z}}^{\boldsymbol{y}})_{\mathcal{Y}_i}^T, \tilde{\boldsymbol{F}}_{\mathcal{Y}_i}^T\right\}$, (15) can be written as

$$\boldsymbol{z}^T \underbrace{\sum_{i=1}^{n_{\boldsymbol{u}}} \boldsymbol{U}_i\, \boldsymbol{I}_{n_{\boldsymbol{u}} \times n_{\mathcal{Y}_i}}\, \tilde{\boldsymbol{h}}_i\, \boldsymbol{e}_i^T}_{=\boldsymbol{X}} = \boldsymbol{f}^T \sum_{i=1}^{n_{\boldsymbol{u}}} \tilde{\boldsymbol{U}}_i\, \boldsymbol{\mathcal{S}}_i\, \tilde{\boldsymbol{h}}_i\, \boldsymbol{e}_i^T, \tag{16}$$

where $\boldsymbol{\mathcal{S}}_i = \left[\, \boldsymbol{0}_{n_{\mathcal{Y}_i} \times r_i}\ \operatorname{diag}\left(\sigma_{i1}, \ldots, \sigma_{in_{\mathcal{Y}_i}}\right)\ \boldsymbol{0}_{n_{\mathcal{Y}_i} \times \bar{s}_i}\, \right]^T$, $r_i = \max(0, n_{\mathcal{Y}_i} - n_{\boldsymbol{u}})$, $\bar{s}_i = \max(0, n_{\boldsymbol{f}} - n_{\mathcal{Y}_i})$ and $\sigma_{ij} = \begin{cases} \alpha_{ij}/\beta_{ij} & \text{if } \beta_{ij} \neq 0 \\ 1 & \text{otherwise} \end{cases}$; $\boldsymbol{U}_i \in \mathbb{R}^{n_{\boldsymbol{u}} \times n_{\boldsymbol{u}}}$ and $\tilde{\boldsymbol{U}}_i \in \mathbb{R}^{n_{\boldsymbol{f}} \times n_{\boldsymbol{f}}}$ are unitary; $\boldsymbol{I}_{n_{\boldsymbol{u}} \times n_{\mathcal{Y}_i}}$ is the $n_{\boldsymbol{u}} \times n_{\mathcal{Y}_i}$ tailing diagonal identity matrix; and $\tilde{\boldsymbol{h}}_i = \operatorname{diag}\left(\beta_{i(r_i+1)}, \ldots, \beta_{in_{\mathcal{Y}_i}}\right) \boldsymbol{V}_i^T\, \boldsymbol{h}_{i\mathcal{Y}_i}$, with $\boldsymbol{V}_i \in \mathbb{R}^{n_{\mathcal{Y}_i} \times n_{\mathcal{Y}_i}}$ if $n_{\boldsymbol{u}} + n_{\boldsymbol{f}} \geq n_{\mathcal{Y}_i}$. The decomposed formulation (16) has several advantages over (10) as pointed out below.

(1) From observation of (16) it can be seen that the first $r_i = \max(0, n_{\mathcal{Y}_i} - n_{\boldsymbol{u}})$ elements in $\tilde{\boldsymbol{h}}_i$ do not contribute to $\boldsymbol{X}$. It is generally close to optimal to set them to zero as the corresponding columns in $\tilde{\boldsymbol{U}}_i\, \boldsymbol{\mathcal{S}}_i$ vanish. Thus, if any $r_i > 0$ then one can reduced the variable space from $\sum_{i=1}^{n_{\boldsymbol{u}}} n_{\mathcal{Y}_i}$ to $\sum_{i=1}^{n_{\boldsymbol{u}}} n_{\mathcal{Y}_i} - r_i$. The maximum dimension of the reduced space is $n_{\boldsymbol{u}} \times n_{\boldsymbol{u}}$. (16). This approach will be referred to as the reduced space (RC) method. The starting values for the RC method will be $\tilde{\boldsymbol{h}}_i = \boldsymbol{e}_{n_{\mathcal{Y}_i}}$ which corresponds to the selection of the smallest generalized singular values.
(2) From (16), it can be shown that a suboptimal solution to (7) can be obtained by setting the first r_i elements in $\tilde{\boldsymbol{h}}_i$ are zero and solving the substitute problem

$$\boldsymbol{X} = \arg\min_{\boldsymbol{X}} \sum_{i=1}^{n_{\boldsymbol{u}}} \boldsymbol{X}_i^T\, \tilde{\boldsymbol{\mathcal{S}}}_i^T\, \tilde{\boldsymbol{\mathcal{S}}}_i\, \boldsymbol{X}_i \text{ s.t. } \boldsymbol{X}^T\, \boldsymbol{X} = \boldsymbol{I}, \tag{17}$$

where $\tilde{\boldsymbol{\mathcal{S}}}_i = \boldsymbol{\mathcal{S}}_i\, \boldsymbol{I}_{n_{\boldsymbol{u}} \times n_{\mathcal{Y}_i}}^T\, \boldsymbol{U}_i^T$ and $\boldsymbol{X}_i$ is the i^{th} column of $\boldsymbol{X}$. Problem (17) is still nonconvex but has the

advantage that an efficient steepest descend method can be developed. Due to the lack of space, the method cannot be outlined here but will be an issue of a subsequent publication. It will be referred to as the unitary matrix constraint (UMC) method. The starting value for the iterative solution of $\boldsymbol{X}$ will be the identity matrix.

(3) From (16) a lower bound for the minimum worst-case/average loss can be derived. This is particularly helpful in reducing computational expense as described below.

The large number of alternative control structures can be reduced by excluding candidate CVs which cannot lead to an optimal solution. This strategy is known as the BAB principle. BAB algorithms have been formerly applied to CSD problems by several authors such as Cao and Saha [2005], Kariwala and Skogestad [2006/07/09-13], Cao and Kariwala [2008] and Kariwala and Cao [2009]. Lower bounds on the minimal worst-case/average loss are helpful for discriminating candidate CVs. From the conclusion that the lower bounds corresponds to the ideal case that $\tilde{\boldsymbol{h}}_i = \boldsymbol{e}_{n_{\mathcal{Y}_i}}$, $\boldsymbol{U}_{i\mathcal{Y}_i} \perp \boldsymbol{U}_{j\mathcal{Y}_j}$ and $\tilde{\boldsymbol{U}}_{i\mathcal{Y}_i} \perp \tilde{\boldsymbol{U}}_{j\mathcal{Y}_j} \forall i \neq j$ it follows from observation of (16) that

$$\boldsymbol{M} = \sum_{i=1}^{n_{\boldsymbol{u}}} \sigma_{in_{\mathcal{Y}_i}} \boldsymbol{e}_i \boldsymbol{e}_i^T.$$

This yields the inequalities

$$L_{\text{worst}} \geq \frac{1}{2} \max_i \left(\sigma^2_{in_{\mathcal{Y}_i}} \right) \tag{18}$$

$$L_{\text{average}} \geq \frac{1}{6\ (n_{\mathcal{Y}_\cap} + n_{\boldsymbol{d}})} \sum_{i=1}^{n_{\boldsymbol{u}}} \sigma^2_{in_{\mathcal{Y}_i}}. \tag{19}$$

Note that $n_{\mathcal{Y}_\cap}$ indicates the size of the merged PV subset $\mathcal{Y}_1 \cap \cdots \cap \mathcal{Y}_{n_{\boldsymbol{u}}}$. It is important to state that (18) and (19) also hold for incomplete set of candidate CVs, *i.e.*, the lower bound of one candidate CV is also the lower bound of all possible control structures which include this CV. If an upper bound for the worts-case/average loss of all alternatives L_{ub} is known, the evaluation of structures (and substructures) can be omitted which show a lower bound $L_{\text{lb}} > L_{\text{ub}}$. Unfortunately, the bounds given above are not very tight, so that computational savings are relatively small.

5. EVAPORATOR CASE STUDY

In this section, the proposed CSD methods will be applied to the evaporation process presented in Figure 3. This forced-circulation evaporation was originally treated by Newell and Lee [1989] and has been investigated subsequently by Heath et al. [2000] and Kariwala et al. [2008], among others. The purpose of the process is the concentration of dilute liquor from the feed to the product stream by evaporation and separation of the solvent. The analytic model equations including the cost function and operational constraints can be found in Kariwala et al. [2008]. The process model has three state variables, the level L_2, the composition X_2 and the pressure P_2 with eight degrees of freedom. Table 1 lists the important stream properties, their value at the nominal operating point and

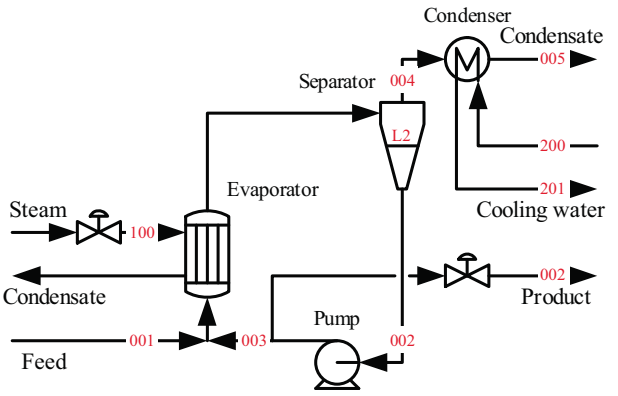

Figure 3. Evaporation process scheme

Var.	Description	Nominal value	Classification
F_1	Feed flow rate	9.469 kg/min	MV, PV (±2 %)
F_2	Product flow rate	1.334 kg/min	MV†, PV (±2 %)
F_3	Circulating flow rate	24.721 kg/min	MV†, PV (±2 %)
F_4	Vapor flow rate	8.135 kg/min	
F_5	Condensate flow rate	8.135 kg/min	PV (±2 %)
X_1	Feed composition	5.00 %	DV (±5 %)
X_2	Product composition	35.50 %	
T_1	Feed temperature	40.0 °C	DV (±20 %)
T_2	Product temperature	88.4 °C	PV (±1 °C)
T_3	Vapor temperature	81.066 °C	PV (±1 °C)
p_2	Operating pressure	51.412 kPa	PV (±2.5 %)
F_{100}	Steam flow rate	9.434 kg/min	PV (±2 %)
T_{100}	Steam temperature	151.52 °C	
p_{100}	Steam pressure	400.0 kPa	MV†
Q_{100}	Heat duty	345.292 kW	
F_{200}	Water flow rate	217.738 kg/min	MV, PV (±2 %)
T_{200}	Water inlet temp.	25.0 °C	DV (±20 %)
T_{201}	Water outlet temp.	45.55 °C	PV (±1 °C)
Q_{200}	Condenser duty	313.21 kW	
J	Operational cost	-582.233 $/h	

Table 1. Key process variables in the evaporation process

their classification into MVs, DVs and PVs. Three out of five MVs indicated by † are used to keep the three PVs L_2, X_2 and P_{100} at their set points. Note that the level in the separator L_2 has no steady-state effect but needs to be controlled for stabilization. The other two controlled PVs need to be kept at their constraints in order to achieve optimality over the given disturbance region. Generality is not lost by this particular selection of the unconstrained MVs. In Table 1, the (embraced) expected variations of the DVs and measurement errors of the PVs are given in % from their nominal value except for temperature measurement errors which are indicated on an absolute scale.

The model equations were implemented in a modeling environment (ME) of the in-house tool OPTISIM® [1], an equation-oriented process simulator. The model has been optimized with respect to the DVs' nominal values given in Table 1 and operational constraints. This led to the operating conditions of the MVs and DVs presented in Table 1. As the ME provides first derivatives by automatic differentiation, the linear I/O gains $G_{\boldsymbol{u}}^{\boldsymbol{y}}$ and $G_{\boldsymbol{u}}^{\boldsymbol{y}}$ at the operating point are directly available. Second derivatives $J_{\boldsymbol{uu}}$ and $J_{\boldsymbol{ud}}$ were estimated by finite difference approx-

[1] OPTISIM® is a registered trademark of the Linde AG. (Burr [1991/4/7-11])

$n_{\mathcal{Y}_c}$	Best PV set	L_{average} (in \$/h)	L_{worst} (in \$/h)
2	F_3, F_{200}	3.8079	56.7126
3	F_2, F_{100}, F_{200}	0.6533	11.6643
4	F_2, T_{201}, F_3, F_{200}	0.4545	9.4516
...			
10	All PVs	0.1941	7.5015

Table 2. Worst-case/average loss of best column-structured CSDs

imation and the use of the NAG routine E04XAF. The numerical results of the I/O gains and the Hessians are in agreement with those of Kariwala et al. [2008]. CSDs for the evaporation process have been identified using the methods presented in Sections 3 and 4. The calculations were conducted in Matlab®R2008b using a Windows XP SP2 desktop with an Intel®Core™Duo CPU E8400 (3.0 Ghz, 3.5 GB RAM).

At first, column-structured CSDs were identified by average loss minimization using the GSVD method. The best control structure was determined by screening over all possibilities satisfying the PV subset size condition imposed. Some results are given in Table 2. They reproduce the results by Kariwala et al. [2008] with an deviation of less than 0.6 %. Both, the minimum worst-case and average loss of the best structure decrease with the PV subset size and approach a lower bound (at $n_{\mathcal{Y}_c} = 10$) asymptotically. According to Corollary 8, the case $n_{\mathcal{Y}_c} = n_{\boldsymbol{u}} = 2$ indicates as well the best PV selection structure.

Next, common-sized CSDs PVs were sought. According to Theorem 7, for each $n_{\mathcal{Y}_c}$-sized column-structured CSD there exists a common-sized CSD of size $n_s = (n_{\mathcal{Y}_c} - n_{\boldsymbol{u}} + 1)$ which can be obtained by a simple linear transformation of the former. Thus, the results in Table 2 indicate also possible common-sized CSDs of PV subset size n_s from one to nine. For instance, Table 3 shows the transformation of the best column-structured CSD with set size three, indicated by $\boldsymbol{H}_{c3}$, into $\boldsymbol{H}_{s2}$ where only combinations of two PVs per CV occur. Despite its small PV subset size, $\boldsymbol{H}_{s2}$ achieves a considerably small average loss. Note that CSDs obtained by this approach are generally not the best among all CSDs satisfying the particular structural constraint of a common-sized set with set size two. In order to find a CSD with lower average loss, the RC method was applied. The best solution found among the $\left(C_{10}^2\right)\left(C_{10}^2 - 1\right)/2 = 990$ alternatives is indicated as $\hat{\boldsymbol{H}}_{s2}$ in Table 3. Due to the BAB algorithm only 103 problems with an average of 0.07 s expense per problem had to be solved. The total computation time was 8.3 s. Using the UMC method, the computational efficiency could be reduced to 6 ms expense per problem leading to a total computation time of 3.3 s at 144 iterative problem solutions. The solution $\tilde{\boldsymbol{H}}_{s2}$ showed a larger average loss than $\hat{\boldsymbol{H}}_{s2}$ structurally identical though.

Suppose that due to cost issues, only one flow meter can be afforded. Since temperature and pressure indicators are rather cheap, their numbers are not limited by cost considerations. In this situation, the task is to find the two best CVs out of $C_6^1 + 2$ candidates, *i.e.*, one out of six flows, one pressure and one temperature set. The best CSD indicated as $\boldsymbol{H}_{s1F}$ in Table 3 was found by applying

CSD	L_{average} (in \$/h)
$\boldsymbol{H}_{c3} = \begin{bmatrix} -0.99 & 0.15 & 0.00 \\ -0.99 & -0.12 & 0.01 \end{bmatrix} \begin{bmatrix} F_2 & F_{100} & F_{200} \end{bmatrix}^T$	0.6533
$\boldsymbol{H}_{s2} = \begin{bmatrix} -6.27 & 1.0 & \\ -143.08 & & 1.0 \end{bmatrix} \begin{bmatrix} F_2 & F_{100} & F_{200} \end{bmatrix}^T$	0.6533
$\hat{\boldsymbol{H}}_{s2} = \begin{bmatrix} -6.27 & 1.0 & & \\ & & 1.0 & -23.30 \end{bmatrix} \begin{bmatrix} F_2 & F_{100} & F_{200} & F_1 \end{bmatrix}^T$	0.5673
$\tilde{\boldsymbol{H}}_{s2} = \begin{bmatrix} -6.22 & 1.0 & & \\ & & 1.0 & -13.34 \end{bmatrix} \begin{bmatrix} F_2 & F_{100} & F_{200} & F_1 \end{bmatrix}^T$	0.6682
$\boldsymbol{H}_{s1F} = \begin{bmatrix} 1.0 & & & \\ & 0.36 & 0.33 & 0.87 \end{bmatrix} \begin{bmatrix} F_3 & T_2 & T_3 & T_{201} \end{bmatrix}^T$	2.9704
$\boldsymbol{H}_{c3T} = \begin{bmatrix} 0.59 & 0.53 & -0.61 \\ 0.02 & 0.01 & 1.0 \end{bmatrix} \begin{bmatrix} T_2 & T_3 & T_{201} \end{bmatrix}^T$	3.6573

Table 3. CSD results

the RC method. It shows slightly better average loss than $\boldsymbol{H}_{c3T}$ which is the best column-structured CSD where all temperatures are used.

6. CONCLUSION

In this paper new insights into the identification problem of self-optimizing CSDs were given. The GSVD method was proposed which allows finding CVs, altogether linear combinations of a common PV subset. It minimizes the average loss super-optimal to the worst-case loss by taking expected disturbances and measurement errors into account. The GSVD method can be beneficially implemented into iterative solution approaches in order to find loosely-structured CSDs where for each CV an individual PV subsets is taken into account. The new methods were successfully applied to an evaporation process. It could be shown that loosely structured CSDs are favorable in terms of flexibility, practical acceptance and economic considerations.

REFERENCES

E04XAF. In *NAG Fortran library manual: Mark 21*. 2006. ISBN 1852062045.

V. Alstad and S. Skogestad. *Ind. eng. chem. res.*, 46(3):846–853, 2007.

V. Alstad, S. Skogestad, and S. E. Hori. *J. proc. cont.*, 2008.

S. P. Burr. AIChE spr. nat. meet., Houston, Texas, 1991/4/7-11.

Y. Cao and V. Kariwala. *Comp. chem. eng.*, 32(10):2306–2319, 2008.

Y. Cao and P. Saha. *Chem. eng. sci.*, 60(6):1555–1564, 2005.

H. G. Golub and F. C. VanLoan. Johns Hopkins Univ. Press, Baltimore, Maryland, 3rd ed. edition, 1996. ISBN 0801854148.

J. I. Halvorsen, S. Skogestad, C. J. Marud, and V. Alstad. *Ind. eng. chem. res.*, 42:3273–3284, 2003.

A. J. Heath, K. I. Kookos, and D. J. Perkins. *AIChE*, 46(10):1998–2016, 2000.

L. Hogben. Chapman & Hall/CRC, Boca Raton, Florida, 2007. ISBN 1584885106.

V Kariwala. *Ind. eng. chem. res.*, 46(46):3629–3634, 2007.

V. Kariwala and Y. Cao. *Comp. chem. eng.*, in print, 2009.

V. Kariwala and S. Skogestad. PSE/ESCAPE, Garmisch-Partenkirchen, Germany, 2006/07/09-13.

V. Kariwala, Y. Cao, and S. Janardhanan. *Ind. eng. chem. res.*, 47 (4):1150–1158, 2008.

M. Morari, Y. Arkun, and G. Stephanopoulos. *AIChE*, 26(2):220–232, 1980.

B. R. Newell and L. P. Lee. Prentice-Hall, New York, NY, 1989. ISBN 0130409405.

S. Skogestad. *J. proc. cont.*, 10(5):487–507, 2000.

S. Skogestad and I. Postlethwaite. Wiley, Chichester, UK, 1996. ISBN 0471942774.

An Online Algorithm for Robust Distributed Model Predictive Control

Walid Al-Gherwi. Hector Budman. Ali Elkamel

Chemical Engineering Department, University of Waterloo, Waterloo, Canada

Abstract: Distributed Model Predictive Control (DMPC) has received significant attention in the literature. However, the robustness of DMPC with respect to model errors has not been explicitly addressed. In this paper, an online algorithm that deals explicitly with model errors for DMPC is proposed. The algorithm requires decomposing the entire system into *N* subsystems and solving *N* convex optimization problems to minimize an upper bound on a robust performance objective by using a time-varying state-feedback controller for each subsystem. Simulations on two typical examples were considered to illustrate the application of the proposed method.

Keywords: Distributed Model Predictive Control; Robust Control.

1. INTRODUCTION

Distributed model predictive control (DMPC) has received significant attention in the literature in recent years. The key potential advantages of DMPC are: i) it can provide better performance than fully decentralized control especially when the interactions ignored in the latter are strong, and ii) it can maintain the flexibility with respect to equipment failure and partial plant shutdowns that may jeopardize the successful operation of centralized MPC. The basic idea of DMPC is to partition the total system of states and controlled and manipulated variables into smaller subsystems and to assign an MPC controller to each subsystem. The design of all the reported DMPC strategies is composed of three parts: (1) Modeling; each controller has access to a local dynamic model of the corresponding subsystem along with an interaction dynamic model that represents the influence of the other subsystems. These models can be obtained by directly decomposing a centralized model of the process (Rawlings and Stewart 2008). (2) Optimization; each MPC solves a local optimization problem. Some reported strategies use modified objective functions that take into account the goals of other controllers to achieve full coordination (Venkat 2006; Zhang and Li 2007) whereas some others use strict local objectives (Li *et al.* 2005), e.g. a Nash-equilibrium objective. (3) Communication; at every control time interval all the controllers exchange the measurements of their local states that are used for subsequent local optimization. These 3 steps are executed at each time interval in an iterative manner until convergence among the controllers is reached. Venkat (2006) showed that increasing the iterations allows the DMPC strategy to reach the optimal centralized solution and the termination at any intermediate iteration maintains system-wide feasibility. Zhang and Li (2007) analyzed the optimality of the iterative DMPC scheme and derived closed-form solution for an unconstrained DMPC and showed that it is identical to centralized MPC solution. The common feature of the reported strategies is that they employ a nominal model of the plant and rely on feedback to account for plant-model mismatch. However, plant–model mismatch may have a significant impact on stability and performance. Thus, the robustness of DMPC to model errors has been identified as a key factor for a successful application of DMPC (Rawlings and Stewart 2008). Kothare *et al.* (1996) proposed a methodology for robust centralized constrained MPC design that maintains robust stability and minimizes a bound on performance in the presence of model errors. The problem is formulated as a convex optimization problem with linear matrix inequalities LMI that is solved efficiently using available algorithms (Boyd *et al.* 1994) and can be used for on-line implementations. This method has been recognized as a good potential candidate for use in process industry to handle the issue of plant-model mismatch (Qin and Badgwell 2003).

The aim of this paper is to present a methodology for Robust DMPC (RDMPC) that explicitly deals with model errors. An LMI-based predictive control formulation (Kothare *et al.* 1996) has been modified to design an on-line iterative algorithm for RDMPC. Issues of robust stability and convergence are analyzed and discussed. Two case studies are used to illustrate the algorithm: a distillation column example (Venkat 2006) when "bad" input-output pairings are chosen and a high-purity column example (Skogestad and Morari, 1988) with high condition number.

2. Definitions and Methodology

2.1 Models

In this work, it is assumed that the process model is given by a linear time-varying (LTV) model of the form:

$$\boldsymbol{x}(k+1) = \boldsymbol{A}(k)\boldsymbol{x}(k) + \boldsymbol{B}(k)\boldsymbol{u}(k) \tag{1}$$

where the real plant lies within a polytope that is represented by the convex hull:

$$[\boldsymbol{A}(k)\ \boldsymbol{B}(k)] = \sum_{l=1}^{L} \beta_l [\boldsymbol{A}^{(l)}\ \boldsymbol{B}^{(l)}] \quad ; \sum_{l=1}^{L} \beta_l = 1;\ \beta_l \geq 0 \tag{2}$$

Each vertex l corresponds to a linear model obtained from linearizing a nonlinear model or identification of a linear model in the neighbourhood of a particular operating point. It is assumed that the states are fully measured. The states and the controlled and manipulated variables in model (1) can be decomposed into N subsystems as follows:

$$\begin{bmatrix} \boldsymbol{x}_{11}(k+1) \\ \vdots \\ \boldsymbol{x}_{ii}(k+1) \\ \vdots \\ \boldsymbol{x}_{NN}(k+1) \end{bmatrix} = \begin{bmatrix} \boldsymbol{A}_{11}(k) & \cdots & \cdots & \cdots & \boldsymbol{A}_{1N}(k) \\ \vdots & \ddots & & & \vdots \\ \boldsymbol{A}_{i1}(k) & \cdots & \ddots & \cdots & \boldsymbol{A}_{iN}(k) \\ \vdots & & & \ddots & \vdots \\ \boldsymbol{A}_{N1}(k) & \cdots & \cdots & \cdots & \boldsymbol{A}_{NN}(k) \end{bmatrix} \begin{bmatrix} \boldsymbol{x}_{11}(k) \\ \vdots \\ \boldsymbol{x}_{ii}(k) \\ \vdots \\ \boldsymbol{x}_{NN}(k) \end{bmatrix} + \begin{bmatrix} \boldsymbol{B}_{11}(k) & \cdots & \cdots & \cdots & \boldsymbol{B}_{1N}(k) \\ \vdots & \ddots & & & \vdots \\ \boldsymbol{B}_{i1}(k) & \cdots & \ddots & \cdots & \boldsymbol{B}_{iN}(k) \\ \vdots & & & \ddots & \vdots \\ \boldsymbol{B}_{N1}(k) & \cdots & \cdots & \cdots & \boldsymbol{B}_{NN}(k) \end{bmatrix} \begin{bmatrix} \boldsymbol{u}_1(k) \\ \vdots \\ \boldsymbol{u}_i(k) \\ \vdots \\ \boldsymbol{u}_N(k) \end{bmatrix} \tag{3}$$

where $i \in \{1,\cdots,N\}$; $\boldsymbol{x}_{ii} \in \Re^{n_{ii}}$; $\boldsymbol{u}_i \in \Re^{m_i}$. For example, in model (3) the i[th] controller for the i[th] subsystem is based on the following model:

$$\boldsymbol{x}_i(k+1) = \boldsymbol{A}_i(k)\boldsymbol{x}_i(k) + \boldsymbol{B}_i(k)\boldsymbol{u}_i(k) + \sum_{\substack{j=1 \\ j\neq i}}^{N} \boldsymbol{B}_j(k)\boldsymbol{u}_j(k) \tag{4}$$

and similar to the representation given in (2) it is assumed that for the i[th] subsystem (4):

$$[\boldsymbol{A}_i(k)\ \boldsymbol{B}_i(k)..\ \boldsymbol{B}_j(k)..] = \sum_{l=1}^{L} \beta_l [\boldsymbol{A}_i^{(l)}\ \boldsymbol{B}_i^{(l)}..\ \boldsymbol{B}_j^{(l)}..] \quad \forall j \in \{1,...,N\},\ j \neq i \tag{5}$$

where $\boldsymbol{x}_i' = \left[\boldsymbol{x}_{11}', \cdots\cdots, \boldsymbol{x}_{ii}', \cdots\cdots, \boldsymbol{x}_{NN}'\right]'$ is the vector of states of subsystem i containing states $\boldsymbol{x}_{ii}$ that can be measured locally augmented with states $\boldsymbol{x}_{jj}$ that affect subsystem i measured in the other subsystems and communicated among the subsystems. Therefore the matrix $\boldsymbol{A}_i(k)$ contains all the elements of the matrix $\boldsymbol{A}(k)$. Model (4) also includes the effect of local controller $\boldsymbol{u}_i$ and the other controllers $\boldsymbol{u}_j$ with their corresponding matrices defined as:

$$\begin{aligned} \boldsymbol{B}_i'(k) &= \left[\boldsymbol{B}_{1i}'(k), \cdots\cdots, \boldsymbol{B}_{Ni}'(k)\right]' \\ \boldsymbol{B}_j'(k) &= \left[\boldsymbol{B}_{1j}'(k), \cdots\cdots, \boldsymbol{B}_{Nj}'(k)\right]' \end{aligned} \tag{6}$$

The model in (4) is general and can be used to represent special limiting cases such as the decentralized case where all the interactions are ignored, e.g. $\boldsymbol{B}_j' = [\boldsymbol{0}]\ \forall j \in \{1,...,N\},\ j \neq i$.

2.2 Robust Performance Objective

Kothare *et al.* (1996) proposed a formulation for a centralized problem whereby an upper bound on a robust performance objective is minimized. In the current work a similar formulation is used but the minimization is simultaneously done for every subsystem i defined by (4) for which the following min-max problem is solved:

$$\begin{aligned} &\min_{\boldsymbol{u}_i(k+n|k)} \ \max_{[\boldsymbol{A}_i(k+n)\ \boldsymbol{B}_i(k+n)\ \boldsymbol{B}_j(k+n)],n\geq 0} J_i(k) \\ &s.t. \\ &\left|\boldsymbol{u}_i(k+n|k)\right| \leq \boldsymbol{u}_i^{max},\ n \geq 0 \end{aligned} \tag{7}$$

In general, the local objective $J_i(k)$ is defined as follows:

$$\begin{aligned} J_i(k) = \sum_{n=0}^{\infty} [&\boldsymbol{x}_i'(k+n|k)\mathbb{Q}_i\boldsymbol{x}_i(k+n|k) \\ &+ \boldsymbol{u}_i'(k+n|k)\boldsymbol{R}_i\boldsymbol{u}_i(k+n|k) \\ &+ \sum_{\substack{i=1 \\ i\neq j}}^{N} \boldsymbol{u}_j^{\bullet\prime}(k+n|k)\boldsymbol{R}_j\boldsymbol{u}_j^{\bullet}(k+n|k)] \end{aligned} \tag{8}$$

where $\mathbb{Q}_i > 0$, $\boldsymbol{R}_i > 0$, $\boldsymbol{R}_j > 0$. The local objective given in (8) takes into account the goals of the other controllers, third summation in the RHS, in order to achieve the global objective of the entire system. The superscript "$\bullet$" indicates that the solution was obtained in a previous iteration and remains fixed in the current iteration as will be explained later. It should be pointed out that one can easily modify the problem in (8) to solve particular objectives such as Nash equilibrium or decentralized control. Both strategies are based on minimizing strictly local objectives of the subsystems. The difference is that for Nash the interaction information is shared among the subsystems while for decentralized control the interaction information is neglected. Accordingly, for both Nash and decentralized control $\mathbb{Q}_i$ and $\boldsymbol{R}_i$ in (8) are modified to contain all zeros except for the weights corresponding to the local subsystem and the third summation in the RHS of (8) is excluded. On the other hand the interaction term in (4) is included for Nash but it is ignored for decentralized control.

Since the objective in (8) has an infinite horizon, the problem of finding infinite $\boldsymbol{u}_i$ is computationally intractable. Instead, a state-feedback law is sought for each subsystem i as follows:

$$\begin{aligned} \boldsymbol{u}_i(k+n|k) &= \boldsymbol{F}_{ii}\boldsymbol{x}_{ii}(k+n|k) + \sum_{\substack{j=1 \\ j\neq i}}^{N} \boldsymbol{F}_{ij}\boldsymbol{x}_{ij}(k+n|k) \\ &= \boldsymbol{F}_i\boldsymbol{x}_i(k+n|k) \end{aligned} \tag{9}$$

similarly,

$$\begin{aligned} \boldsymbol{u}_j^{\bullet}(k+n|k) &= \boldsymbol{F}_{jj}^{\bullet}\boldsymbol{x}_{jj}(k+n|k) + \sum_{\substack{i=1 \\ i\neq j}}^{N} \boldsymbol{F}_{ji}^{\bullet}\boldsymbol{x}_{ji}(k+n|k) \\ &= \boldsymbol{F}_j^{\bullet}\boldsymbol{x}_i(k+n|k) \end{aligned} \tag{10}$$

Using these state-feedback laws in (4) leads to the following closed loop model:

$$\boldsymbol{x}_i(k+1) = \left(\tilde{\boldsymbol{A}}_i(k) + \boldsymbol{B}_i(k)\boldsymbol{F}_i\boldsymbol{u}_i(k)\right)\boldsymbol{x}_i(k) \tag{11}$$

where $\tilde{A}_i(k) = A_i(k) + \sum_{\substack{j=1 \\ j\neq i}}^{N} B_j(k)F_j^{\bullet}$

It is assumed that there exists a quadratic function $V_i(k) = \boldsymbol{x}_i'(k)\boldsymbol{P}_i\boldsymbol{x}_i(k)$, $\boldsymbol{P}_i > 0$, so that, for any plant in (6), this function satisfies the following stability constraint:

$$\begin{aligned} V_i(k+n+1|k) - V_i(k+n|k) \leq -[&\boldsymbol{x}_i'(k+n|k)\mathbb{Q}_i\boldsymbol{x}_i(k+n|k) \\ &+ \boldsymbol{u}_i'(k+n|k)\boldsymbol{R}_i\boldsymbol{u}_i(k+n|k) \\ &+ \sum_{\substack{i=1 \\ i\neq j}}^{N} \boldsymbol{u}_j^{\bullet\prime}(k+n|k)\boldsymbol{R}_j\boldsymbol{u}_j^{\bullet}(k+n|k)] \\ n \geq 0 \end{aligned} \tag{12}$$

Using (11), the robust stability constraint in (12) becomes:

$$\begin{aligned} V_i(k+n+1|k) - V_i(k+n|k) \leq -[&\boldsymbol{x}_i'(k+n|k)\tilde{\mathbb{Q}}_i\boldsymbol{x}_i(k+n|k) \\ &+ \boldsymbol{u}_i'(k+n|k)\boldsymbol{R}_i\boldsymbol{u}_i(k+n|k)] \end{aligned}$$

where $\tilde{\mathbb{Q}}_i = \mathbb{Q}_i + \sum_{\substack{i=1 \\ i\neq j}}^{N} \boldsymbol{F}_j^{\bullet\prime}(k+n|k)\boldsymbol{R}_j\boldsymbol{F}_j^{\bullet}(k+n|k)$ (13)

which, for all $n \geq 0$, turns out to be:

$$\begin{aligned} \left[\tilde{\boldsymbol{A}}_i(k+n) + \boldsymbol{B}_i(k+n)\boldsymbol{F}_i\right]'\boldsymbol{P}_i\left[\tilde{\boldsymbol{A}}_i(k+n) + \boldsymbol{B}_i(k+n)\boldsymbol{F}_i\right] \\ - \boldsymbol{P}_i + \boldsymbol{F}_i'\boldsymbol{R}_i\boldsymbol{F}_i + \tilde{\mathbb{Q}}_i \leq 0 \end{aligned} \tag{14}$$

By defining an upper bound, i.e.

$$J_i(k) \leq \boldsymbol{x}_i'(k)\boldsymbol{P}_i\boldsymbol{x}_i(k) = V_i(k) \leq \gamma_i \tag{15}$$

and substituting the parameterization $\boldsymbol{F}_i = \boldsymbol{Y}_i'\boldsymbol{Q}_i^{-1}$, $\boldsymbol{Q}_i = \gamma_i\boldsymbol{P}_i^{-1}$, followed by performing Schur complements (Boyd et al. 1994) on (14) and (15) it can be easily shown that the minimization of $J_i(k)$ is equivalent to the minimization of its upper bound γ_i as in the following linear minimization problem with LMI constraints (Kothare *et al.* 1996):

$$\begin{aligned} &\min_{\gamma_i, \boldsymbol{Q}_i, \boldsymbol{Y}_i} \ \gamma_i \\ &s.t. \\ &\begin{bmatrix} 1 & \boldsymbol{x}_i'(k) \\ \boldsymbol{x}_i(k) & \boldsymbol{Q}_i \end{bmatrix} \geq 0 \\ &\begin{bmatrix} \boldsymbol{Q}_i & \boldsymbol{Q}_i\tilde{\boldsymbol{A}}_i^{\prime(l)} + \boldsymbol{Y}_i'\boldsymbol{B}_i^{\prime(l)} & \boldsymbol{Q}_i\tilde{\mathbb{Q}}_i^{1/2} & \boldsymbol{Y}_i'\boldsymbol{R}_i^{1/2} \\ * & \boldsymbol{Q}_i & \boldsymbol{0} & \boldsymbol{0} \\ * & * & \gamma_i\boldsymbol{I} & \boldsymbol{0} \\ * & * & * & \gamma_i\boldsymbol{I} \end{bmatrix} \geq 0 \\ &\qquad \forall l \in \{1,\ldots,L\} \\ &\begin{bmatrix} \left(\boldsymbol{u}_i^{max}\right)^2\boldsymbol{I} & \boldsymbol{Y}_i \\ \boldsymbol{Y}_i' & \boldsymbol{Q}_i \end{bmatrix} \geq 0 \end{aligned} \tag{16}$$

The key difference between the centralized control algorithm proposed by Kothare *et al.* (1996) and the distributed strategy proposed in this work is that every controller in the set $i \in \{1,\cdots,N\}$ solves a local problem as in (16) and then the solutions are exchanged in an iterative scheme that is further explained in the next subsection. It should be remembered that one of the key reasons to use distributed MPC strategies is to address real time computation issues when dealing with large-scale processes (Li *et al.* 2005). Although the proposed iterative scheme tends to increase the computational time, the problem defined in (16) is numerically advantageous as compared to solving the same problem for the whole system (centralized control). The reason is that the state feedback controller for each subsystem i is obviously of smaller dimensions than a state feedback controller of the centralized MPC strategy. For instance, $\boldsymbol{Y}_i$ for subsystem i is of dimension $(n \times m_i)$ instead of $(n \times m)$ for centralized system where m is the total number of manipulated variables of the entire process.

2.3 Robust DMPC Algorithm

This section presents the main result of the paper where an on-line algorithm for RDMPC is proposed. It is assumed that there is an ideal communication network available so that the controllers can exchange their information with no delays. The goal of performing communication and exchanging solutions among controllers is to achieve the optimal solution of the entire system in an iterative fashion. The algorithm proceeds according to the Jacobi iteration method used for the solution of systems of algebraic equations. The procedure is summarized in *Algorithm 1* below.

Algorithm 1 (RDMPC)

Step0 (initialization)*: at control interval k=0 set* $\boldsymbol{F}_i$*=0.*

Step1 (updating) *at control interval (k) all the controllers exchange their local states measurements and initial estimates* $\boldsymbol{F}_i$*'s via communication, set iteration t = 0 and* $\boldsymbol{F}_i = \boldsymbol{F}_i^{(0)}$.

Step2 (iterations)

while $t \leq t_{max}$

Solve all N LMI problems (16) in parallel to obtain the minimizers $\boldsymbol{Y}_i^{(t+1)}, \boldsymbol{Q}_i^{(t+1)}$ *to estimate the feedback solutions* $\boldsymbol{F}_i^{(t+1)} = \boldsymbol{Y}_i'^{(t+1)}\boldsymbol{Q}_i^{-1(t+1)}$. *If problem is infeasible set* $\boldsymbol{F}_i^{(t)} = \boldsymbol{F}_i^{(t-1)}$. *Check the convergence for a specified error tolerance* ε_i *for all the controllers*

if $\left\|\boldsymbol{F}_i^{(t+1)} - \boldsymbol{F}_i^{(t)}\right\| \leq \varepsilon_i \quad \forall i \in \{1,\ldots,N\}$

break

end if

Exchange the solutions ($\boldsymbol{F}_i$*'s) and set t = t + 1*

end while

Step3 (implementation) *apply the control actions* $\boldsymbol{u}_i = \boldsymbol{F}_i\boldsymbol{x}_i$ *to the corresponding subsystems, increase the control interval* $k = k + 1$*, return to step1 and repeat the procedure.*

Algorithm1 is implemented in MATLAB® and problem (16) is solved via MATLAB® LMI solver. Convergence of the iterations in Step 2 and stability properties are discussed in the following subsection.

2.4 Convergence and Robust Stability Analysis of RDMPC Algorithm

Regarding convergence, it can be shown that at each time interval, each one of the *N* convex problems defined in *Algorithm1* will converge to the same solution which is the solution of the centralized problem, i.e. $\gamma_1 = \gamma_2 = \cdots = \gamma_i = \cdots = \gamma_N = \gamma$ where γ is the performance upper bound of centralized MPC. For brevity, a two subsystem situation, i.e. *N*=2 is considered without loss of generality. It is also assumed that the solutions are feasible.

Define:

$$\textit{for subsystem 1} \quad \gamma_1^{(t)} = \min_{\boldsymbol{F}_1^{(t)}} \gamma_1(\boldsymbol{F}_1^{(t)}, \boldsymbol{F}_2^{(t-1)})$$

$$\textit{for subsystem 2} \quad \gamma_2^{(t)} = \min_{\boldsymbol{F}_2^{(t)}} \gamma_2(\boldsymbol{F}_1^{(t-1)}, \boldsymbol{F}_2^{(t)})$$

$$\textit{Then,} \quad \gamma_1^{(t)} \le \gamma_2^{(t-1)} \tag{a}$$

and the reason being that both sides of this inequality are using the same value of $\boldsymbol{F}_2 = \boldsymbol{F}_2^{(t-1)}$ but the LHS minimizes γ with respect to $\boldsymbol{F}_1$ whereas the RHS of the inequality uses a not necessarily optimal value of $\boldsymbol{F}_1 = \boldsymbol{F}_1^{(t-1)}$. Following the same argument:

$$\gamma_2^{(t)} \le \gamma_1^{(t-1)} \tag{b}$$

Thus, the γ_i's decrease until (a) or (b) become equalities. Since the minimizations are convex and lead to global optimal solutions, this occurs only when $\boldsymbol{F}_1^{(t)} = \boldsymbol{F}_1^{(t-1)}$ and $\boldsymbol{F}_2^{(t)} = \boldsymbol{F}_2^{(t-1)}$ and consequently $\gamma_{sub1}^{(t)} = \gamma_{sub2}^{(t)} = \gamma$, i.e. the minimization with respect to both $\boldsymbol{F}_1$ and $\boldsymbol{F}_2$ give the same solution which must be, following convexity of problem (16), equal to the global optimum of the centralized control problem that has an identical formulation to (16). The robust stability of *Algorithm1* follows from the fact that for each subsystem, a robust stability related constraint is enforced by one of the linear matrix inequalities in problem (16). Thus each one of the *N* controllers satisfies robust stability. Although theoretical convergence of the Jacobi iteration can be proven, it was found that numerical noise exists due to inaccuracies of the LMI solvers in obtaining the solution of problem (16). Consequently, to speed up convergence in the presence of this numerical noise when *Algorithm1* is implemented, the *successive Relaxation* (SR) method is employed (Hageman and Young 1981). The SR method is applied to the solution obtained from (16) for each subsystem to estimate a weighted average between the current and previous iterate solutions. The method is given by the following recurrence formula:

$$\boldsymbol{F}_i^{(t+1)} = \alpha\bar{\boldsymbol{F}}_i^{(t+1)} + (1-\alpha)\boldsymbol{F}_i^{(t)} \tag{17}$$

where α is a parameter to be specified by the user in order to accelerate convergence. $\bar{\boldsymbol{F}}_i^{(t+1)}$ denotes the solution obtained at the current iteration from (16) whereas $\boldsymbol{F}_i^{(t+1)}$ is the estimate to be used in the next iteration. Typically, α can be chosen from values between 0 and 2 and when it is set to 1 the normal iterative scheme is retrieved. Since there is no systematic way to select a value for α in advance, simulations with different values of α have to be performed as shown in the first example.

3. Case Studies

3.1 Example 1

A distillation column control problem studied by Venkat (2006) is considered with the difference that uncertainties in the steady-state gains of the model are added to illustrate the robustness of the proposed algorithm. Accordingly, the real model lies within a polytope defined within the two vertices:

$$G_1 = \begin{bmatrix} \dfrac{32.63}{(99.6s+1)(0.35s+1)} & \dfrac{-33.89}{(98.02s+1)(0.42s+1)} \\ \dfrac{34.84}{(110.5s+1)(0.03s+1)} & \dfrac{-18.85}{(75.43s+1)(0.3s+1)} \end{bmatrix}$$

$$G_2 = \begin{bmatrix} \dfrac{326.3}{(99.6s+1)(0.35s+1)} & \dfrac{-338.9}{(98.02s+1)(0.42s+1)} \\ \dfrac{348.4}{(110.5s+1)(0.03s+1)} & \dfrac{-188.5}{(75.43s+1)(0.3s+1)} \end{bmatrix} \tag{21}$$

A state-space model, not shown for brevity, is obtained from a canonical realization of equation (21). To demonstrate the effectiveness of the proposed method the bad pairings, according to the *Relative Gain Array* RGA, are selected, i.e. the RGA element λ_{11} is -1.0874 and accordingly the "bad" pairings are u_1-y_1 (*subsystem1*) and u_2-y_2 (*subsystem2*). The physical constraints on manipulated variables are given by:

$$|u_1(k+n)| \le 1.5; \quad |u_2(k+n)| \le 2; \quad n \ge 0 \tag{22}$$

For the purpose of comparison between different cases, a cost function is defined as follows:

$$J_{cost} = (1/2Ns)\sum_{j=0}^{Ns}\sum_{i=1}^{N}\left(\boldsymbol{x}_i'(j)\mathbb{Q}_i\boldsymbol{x}_i(j) + \boldsymbol{u}_i'(j)\boldsymbol{R}_i\boldsymbol{u}_i(j)\right) \tag{23}$$

where *Ns* is the simulation time. The following parameters are used for the two controllers: $\mathbb{Q}_{y1} = \mathbb{Q}_{y2} = 50$ so that $\mathbb{Q}_i = \boldsymbol{C}_i'\mathbb{Q}_{yi}\boldsymbol{C}_i + 10^{-6}\boldsymbol{I}$ where $\boldsymbol{C}_i$ is the measurement matrix such that $\boldsymbol{y}_i = \boldsymbol{C}_i\boldsymbol{x}_i$; $\boldsymbol{R}_1 = \boldsymbol{R}_2 = 1$; $\alpha = 0.95$. The value of α is selected, as mentioned above, based on simulations by trial and error to speed convergence of the Jacobi iteration. The number of iterations that was required to satisfy the convergence criteria of *Algorithm1* for different values of α

is given in Table1. α=*0.95* resulted in the fastest convergence.

Table 1. Effect of α on convergence with $\varepsilon_1=\varepsilon_2=10^{-3}$

α	# iterations
1.05	55
1.00	38
0.95	28
0.90	32
0.8	38

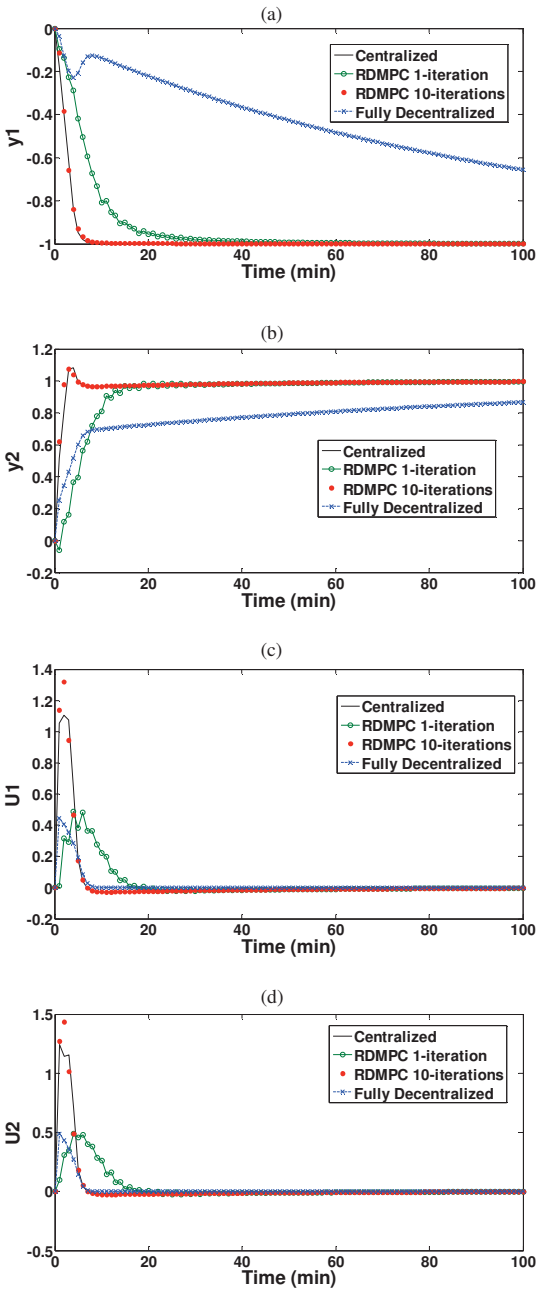

Fig. 1. Dynamic response in controlled and manipulated variables for set-point changes in y1 and y2.

Three cases are considered for the application of *Algorithm1*; fully decentralized, RDMPC with one iteration, and RDMPC with 10 iterations. It should be remembered that as indicated in section 2, the cost γ decreases monotonically with the number of iterations. Thus, even after one iteration, a performance improvement is expected. The motivation for using a small number of iterations, as mentioned earlier, is to use distributed MPC strategies to address real time computation issues when dealing with large scale processes. The decentralized strategy used in this study is obtained, as explained in Section 2.2, with *Algorithm1* by ignoring interactions in equation (4). Then, the performance of *Algorithm1* with these 3 different schemes was compared to the centralized strategy in Figure1. The simulations correspond to simultaneous changes in set-points of both controlled variables y1 and y2 by -1 and 1; respectively.

In comparison with the centralized scheme, the performance of RDMPC approaches that of the centralized scheme as the number of iterations is increased. The fully decentralized case resulted as expected in the worst performance. A comparison of the cost in (23) for different schemes is given in Table2. This table illustrates that *Algorithm1* can be used, depending on the chosen number of iterations, to obtain a performance that varies between two extremes corresponding to the fully decentralized and the centralized strategies; respectively. It is also clear, from figures 1(c) and 1(d), that the constraints given in (22) are satisfied.

Table 2. Cost for different strategies (example1)

Strategy	Cost (23)
Centralized	0.92
RDMPC (10 iteration)	0.93
RDMPC (1 iteration)	2.43
Fully decentralized	35.9

3.2 Example 2

This example considers the high-purity column originally studied by Skogestad and Morari (1988). The nominal transfer function of this system is given by:

$$\begin{bmatrix} y_1 \\ y_2 \end{bmatrix} = \frac{1}{75s+1}\begin{bmatrix} 0.878 & 0.864 \\ 1.082 & 1.096 \end{bmatrix}\begin{bmatrix} u_1 \\ u_2 \end{bmatrix} \qquad (24)$$

A state-space model is obtained based on a canonical realization of equation (24) and not shown for brevity. Due to the high condition number, this process has been used in the past to illustrate closed-loop sensitivity to model errors. The model uncertainty is given by errors in steady-state gains. The gains in the first column of the transfer matrix in (24) are expected to change by up to +80% whereas the gains in the second column are expected to change by up to -80%. The constraints on manipulated variables are represented by $|\boldsymbol{u}(k+n)| \le 1$, $n \ge 0$. The system given above was decomposed into two subsystems; *viz.*, y_1-u_1 (*subsystem1*) and y_2-u_2 (*subsystem2*). The controllers parameters used in simulation are; $\mathbb{Q}_1 = \mathbb{Q}_2 = 1$, $R_1 = R_2 = 1$, $\alpha = 1$, $\varepsilon_1 = \varepsilon_2 = 10^{-2}$.

Figure 2 depicts the performance of *Algorithm1* compared with centralized MPC for a unit set-point change in y_1 and it illustrates that RDMPC algorithm results in an identical response as the centralized MPC. For this example, the RDMPC algorithm converges very quickly in about three iterations after which the error tolerances specified above ($\varepsilon_1=\varepsilon_2=10^{-2}$) are met. Figure 3 shows the convergent behaviour of the RDMPC algorithm obtained in the first sampling interval. The upper bounds γ_1 and γ_2 for subsystems 1 and 2 respectively, obtained by solving (16) in parallel and by applying *Algorithm1*, converge to the same value after about 3 iterations and this value is identical to that obtained for centralized MPC. The cost, defined by equation (23), for both strategies, is equal to *7.48*. To show the ability of the method to deal with different objective functions an RDMPC with a Nash equilibrium objective and a robust decentralized MPC were designed by proper choice of the weights $\mathbb{Q}_i$ and $\boldsymbol{R}_i$ as explained in section 2.2. The results with the Nash-equilibrium based controller, shown also in Figure 2, are similar to the centralized case and the cost was *7.55*, slightly larger than the centralized MPC cost. The decentralized MPC, not shown in the Figure, resulted as expected in a slightly higher cost than Nash of *7.73*.

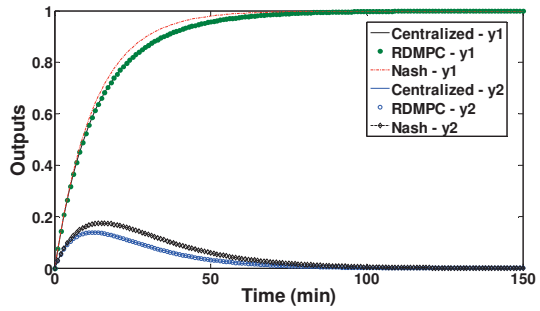

Fig. 2. Dynamic response to unit set-point change in y1.

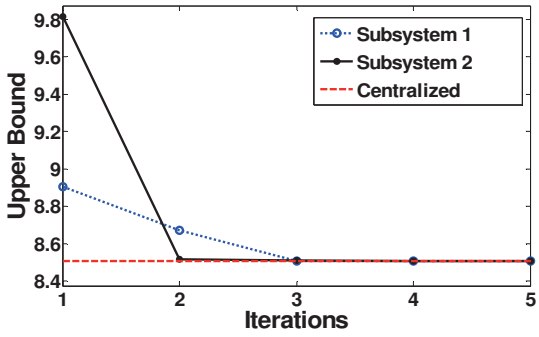

Fig. 3. Convergence characteristics of *Algorithm1* at the first sampling time.

4. CONCLUSIONS

The main goal of this work was to propose an on-line algorithm for DMPC strategy that explicitly considers model errors. The main idea of the proposed method is to decompose the model of the whole system into *N* subsystems and then obtain a local state feedback controller by minimizing an upper bound on a robust performance objective for each subsystem. The subsystem performance takes into account the objectives of the other subsystems in order to achieve the goal of the entire system. The method was also suitable for pursuing other objectives such as Nash equilibrium or decentralized control in the presence of model errors. The problem was converted into *N* convex problems with linear matrix inequalities and solved iteratively by using the Jacobi iteration method with successive relaxation (SR). Although convergence of the iterative solution was proven, the SR feature was helpful for filtering numerical noise in the LMI solutions resulting in faster convergence. When convergence was reached, the algorithm led to the same solution of the centralized MPC problem. The examples showed that RDMPC can achieve, after a sufficient number of iterations, equivalent performance to centralized control. Moreover, the examples illustrated that improvements in RDMPC performance as compared to decentralized control can be achieved with a relatively small number of iterations.

ACKNOWLEDGMENT

The first author would like to thank the General Secretariat of Higher Education of Libya for financial support. Also, the authors acknowledge additional support of Natural Sciences and Engineering Research Council of Canada (NSERC).

REFERENCES

Boyd, S., El.Ghaoui, L., Feron, E., and Balakrishnan, V. (1994). *Linear matrix inequalities in system and control theory*, SIAM, USA.

Hageman, L. and Young, D. (1981) *Applied iterative methods.* Academic Press, NY.

Kothare, M. V., Balakrishnan, V., and Morari, M. (1996) Robust constrained model predictive control using linear matrix inequalities. *Automatica*, **32** (10), 1361-1379.

Li, S., Zhang, Y., and Zhu, Q. (2005). Nash-optimization enhanced distributed model predictive control applied to the shell benchmark problem. *Information science,* **170,** 329-349.

Qin, S. J. and Badgwell, T. A. (2003). A survey of industrial model predictive control technology. *Control engineering practice,* **11,** 733-764.

Rawlings, James B. and Stewart, Brett T. (2008). Coordinating multiple optimization-based controllers: new opportunities and challenges. *Journal of Process Control,* **18,** 839-845.

Skogestad, S. and Morari, M. (1988). Robust control of ill-conditioned plants: high-purity distillation. *IEEE transactions on automatic control,* **12,** 1092-1104.

Venkat, A. N. (2006). *Distributed model predictive control: theory and applications*, PhD thesis, USA.

Zhang, Y., and Li, S. (2007). Networked model predictive control based on neighbourhood optimization for serially connected large-scale processes. *Journal of Process Control,* **17,** 37-50.

.

Advances in Modeling, Estimation, and Identification

Poster Session

Multirefinery and Petrochemical Networks Design and Integration

K. Al-Qahtani*, A. Elkamel**
E. Alper***

** Saudi Aramco, Dhahran, Saudi Arabia 31311*
(Tel.: (966)-875-4828. e-mail: Khalid.qahtani.7@aramco.com)
*** Department of Chemical Engineering, University of Waterloo, Ontario, Canada N2L 3G1*
(Tel.: (519)-888-4567 ext. 37157. e-mail: aelkamel@uwaterloo.ca)
**** Department of Chemical Engineering, Hacettepe University, Beytepe, Turkey 06800*
((Tel.: (312)-297-7400. e-mail: ealper@hacettepe.edu.tr)

Abstract: In this paper we propose a model for the design of an optimal network integration of multisite refinery and petrochemical systems under uncertainty. The proposed model was formulated as a two-stage stochastic mixed-integer problem with the objective of minimizing the refining cost over a given time horizon and maximizing the added value by the petrochemical network. Uncertainties considered in this study were in terms of imported crude oil price, refinery product price, petrochemical product price, refinery market demand, and petrochemical lower level product demand. The proposed method adopts the sample average approximation (SAA) method for scenario generation and optimal gap statistical bounding. The model performance was tested on an industrial case study of multiple refineries and a polyvinyl chloride (PVC) complex.

Keywords: Integration, petrochemical planning, multirefinery optimization, planning under uncertainty

1. INTRODUCTION

Process integration in the refining and petrochemical industry includes many intuitively recognized benefits of processing higher quality feedstocks, improving value of byproducts, and achieving better efficiencies through sharing of resources. This is evidently seen from the current projects around the world for building integrated refineries and the development of complex petrochemical industries that are aligned through advanced integration platforms.

Despite the fact that petroleum refining and petrochemical companies have recently engaged in more integration projects, relatively little research in the open literature have been reported mostly due to confidentiality reasons. Such concerns render the development of a systematic framework of network integration and coordination difficult. Pervious research in the field assumed either no limitations on refinery feedstock availability for the petrochemical planning problem or fixed the refinery production levels assuming an optimal operation. In this paper, we present a mathematical model for the determination of the optimal integration and coordination strategy for a refinery network and synthesize the optimal petrochemical network required to satisfy a given demand from any set of available technologies. Therefore, achieving a global optimal production strategy by allowing appropriate trade offs between the refinery and the downstream petrochemical markets. The refinery and petrochemical systems were modeled as MILP problems that will also lead to an overall refinery and petrochemical process production levels and detailed blending levels at each refinery site. Furthermore, we apply the sample average approximation (SAA) method within an iterative scheme to generate the required scenarios. The solution quality is then statistically evaluated by measuring the optimality gap of the final solution.

2. MODEL FORMULATION

The proposed formulation addresses the problem of the simultaneous design of an integrated network of refineries and petrochemical processes. The proposed model is based on the formulations proposed by Al-Qahtani and Elkamel (2008) and Al-Qahtani et al. (2008). All material balances are carried out on a mass basis with the exception of refinery quality constraints of properties that only blend by volume where volumetric flowrates are used instead. Uncertainty was accounted for using two-stage stochastic programming with recourse approach. Parameters uncertainties considered in this study included uncertainties in the imported crude oil price $CrCost_{cr}$, refinery product price Pr_{cfr}^{Ref}, petrochemical product price Pr_{cp}^{Pet}, refinery market demand $D_{Ref_{cfr}}$, and petrochemical lower level product demand $D_{Pet_{cp}}^{L}$. Uncertainty is modeled through the use of mutually exclusive scenarios of the model parameters with a finite number N of outcomes. For each $\xi_k = (CrCost_{cr,k}, Pr_{cfr,k}^{Ref}, Pr_{cp,k}^{Pet}, D_{Ref_{cfr,k}}, D_{Pel_{cp,k}}^{L})$ where $k = 1,2,...,N$, there corresponds a probability p_k. The generation of the scenarios will be briefly explained in a later section. The proposed stochastic model is as follows:

$$
\begin{aligned}
Min\ & \sum_{cr\in CR}\sum_{i\in I}\sum_{k\in N} p_k\ CrCost_{cr,k}\ S^{Ref}_{cr,i} + \sum_{p\in P}\sum_{cr\in CR}\sum_{i\in I} z_{cr,p,i}\ OpCost_p \\
& + \sum_{cir\in CIR}\sum_{i\in I}\sum_{i'\in I} InCost_{i,i'}\ ypipe^{Ref}_{cir,i,i'} + \sum_{i\in I}\sum_{m\in M_{Ref}}\sum_{s\in S} InCost_{m,s}\ yexp^{Ref}_{m,i,s} \\
& - \sum_{cfr\in PEX}\sum_{i\in I}\sum_{k\in N} p_k\ Pr^{Ref}_{cfr,k}\ e^{Ref}_{cfr,i} - \sum_{cp\in CP}\sum_{m\in M_{Pet}}\sum_{k\in N} p_k\ Pr^{Pet}_{cp,k}\ \delta_{cp,m}\ x^{Pet}_{m} \\
& + \sum_{cfr\in CFR}\sum_{k\in N} p_k\ C^{Ref+}_{cfr}\ V^{Ref+}_{cfr,k} + \sum_{cfr\in CFR}\sum_{k\in N} p_k\ C^{Ref-}_{cfr}\ V^{Ref-}_{cfr,k} \\
& + \sum_{cp\in CFP}\sum_{k\in N} p_k\ C^{Pet+}_{cp}\ V^{Pet+}_{cp,k} + \sum_{cp\in CFP}\sum_{k\in N} p_k\ C^{Pet-}_{cp}\ V^{Pet-}_{cp,k}
\end{aligned} \tag{1}
$$

Subject to

$$
z_{cr,p,i} = S^{Ref}_{cr,i} \qquad \forall\ cr\in CR,\ i\in I \text{ and } p\in P' = \{\text{Set of CDU processes} \forall \text{ plant i}\} \tag{2}
$$

$$
\begin{aligned}
& \sum_{p\in P}\alpha_{cr,cir,i,p}\ z_{cr,p,i} + \sum_{i'\in I}\sum_{p\in P}\xi_{cr,cir,i',p,i}\ xi^{Ref}_{cr,cir,i',p,i} \\
& - Fi^{Pet}_{cr,cir\in RPI,i} - \sum_{i'\in I}\sum_{p\in P}\xi_{cr,cir,i,p,i'}\ xi^{Ref}_{cr,cir,i,p,i'} \\
& - \sum_{cfr\in CFR} w_{cr,cir,cfr,i} - \sum_{rf\in FUEL} w_{cr,cir,rf,i} = 0
\end{aligned} \qquad \forall\ cr\in CR,\ cir\in CIR,\ i'\ \&\ i\in I \text{ where } i\neq i' \tag{3}
$$

$$
\begin{aligned}
& \sum_{cre\in CR}\sum_{cir\in CB} w_{cr,cir,cfr,i} - \sum_{cre\in CR}\sum_{rf\in FUEL} w_{cr,cfr,rf,i} \\
& - \sum_{cre\in CR} Ff^{Pet}_{cr,cfr\in RPF,i} = x^{Ref}_{cfr,i}
\end{aligned} \qquad \forall\ cfr\in CFR,\ i\in I \tag{4}
$$

$$
\sum_{cre\in CR}\sum_{cir\in CB}\frac{w_{cr,cir,cfr,i}}{sg_{cr,cir}} = xv^{Ref}_{cfr,i} \qquad \forall\ cfr\in CFR,\ i\in I \tag{5}
$$

$$
\begin{aligned}
& \sum_{cir\in FUEL} cv_{rf,cir,i}\ w_{cr,cir,rf,i} + \sum_{cfr\in FUEL} w_{cr,cfr,rf,i} \\
& - \sum_{p\in P}\beta_{cr,rf,i,p}\ z_{cr,p,i} = 0
\end{aligned} \qquad \forall\ cr\in CR,\ rf\in FUEL,\ i\in I \tag{6}
$$

$$
\begin{aligned}
& \sum_{cre\in CR}\sum_{cir\in CB}\left(\begin{array}{l} att_{cr,cir,q\in Qv}\dfrac{w_{cr,cir,cfr,i}}{sg_{cr,cir}} + att_{cr,cir,q\in Qw} \\ \left[\begin{array}{l} w_{cr,cir,cfr,i} - \sum_{rf\in FUEL} w_{cr,cfr,rf,i} \\ - \sum_{cre\in CR} Ff^{Pet}_{cr,cfr\in RPF,i} \end{array}\right] \end{array}\right) \\
& \geq q^{L}_{cfr,q\in Qv}\ xv^{Ref}_{cfr,i} + q^{L}_{cfr,q\in Qw}\ x^{Ref}_{cfr,i}
\end{aligned} \qquad \forall\ cfr\in CFR,\ q=\{Qw,Qv\},\ i\in I \tag{7}
$$

$$
\begin{aligned}
& \sum_{cre\in CR}\sum_{cir\in CB}\left(\begin{array}{l} att_{cr,cir,q\in Qv}\dfrac{w_{cr,cir,cfr,i}}{sg_{cr,cir}} + att_{cr,cir,q\in Qw} \\ \left[\begin{array}{l} w_{cr,cir,cfr,i} - \sum_{rf\in FUEL} w_{cr,cfr,rf,i} \\ - \sum_{cre\in CR} Ff^{Pet}_{cr,cfr\in RPF,i} \end{array}\right] \end{array}\right) \\
& \leq q^{U}_{cfr,q\in Qv}\ xv^{Ref}_{cfr,i} + q^{U}_{cfr,q\in Qw}\ x^{Ref}_{cfr,i}
\end{aligned} \qquad \forall\ cfr\in CFR,\ q=\{Qw,Qv\},\ i\in I \tag{8}
$$

$$
\begin{aligned}
MinC_{m,i} & \leq \sum_{p\in P}\gamma_{m,p}\sum_{cr\in CR} z_{cr,p,i} \\
& \leq MaxC_{m,i} + \sum_{s\in S} AddC_{m,i,s}\ yexp^{Ref}_{m,i,s}
\end{aligned} \qquad \forall\ m\in M_{Ref},\ i\in I \tag{9}
$$

$$
\begin{aligned}
& \sum_{cre\in CR}\sum_{p\in P}\xi_{cr,cir,i,p,i'}\ xi^{Ref}_{cr,cir,i,p,i'} \\
& \leq F^{U}_{cir,i,i'}\ ypipe^{Ref}_{cir,i,i'}
\end{aligned} \qquad \forall\ cir\in CIR,\ i'\ \&\ i\in I \text{ where } i\neq i' \tag{10}
$$

$$
\begin{aligned}
& \sum_{i\in I}\left(x^{Ref}_{cfr,i} - e^{Ref}_{cfr',i}\right) + V^{Ref+}_{cfr,k} \\
& - V^{Ref-}_{cfr,k} = D_{Ref_{cfr},k}
\end{aligned} \qquad \forall\ cfr\in CFR,\ cfr'\in PEX,\ k\in N \tag{11}
$$

$$
IM^{L}_{cr} \leq \sum_{i\in I} S^{Ref}_{cr,i} \leq IM^{U}_{cr} \qquad \forall\ cr\in CR \tag{12}
$$

$$
\begin{aligned}
& Fn^{Pet}_{cp\in NRF} + \sum_{i\in I}\sum_{cre\in CR} Fi^{Pet}_{cr,cp\in RPI,i} \\
& + \sum_{i\in I}\sum_{cre\in CR} Ff^{Pet}_{cr,cp\in RPF,i} + \sum_{m\in M_{Pet}}\delta_{cp,m,k}\ x^{Pet}_{m} \\
& + V^{Pet+}_{cp\in CFP,k} - V^{Pet-}_{cp\in CFP,k} = D_{Pet^{L}_{cp\in CFP,k}} + xi^{Pet}_{cp\in CIP}
\end{aligned} \qquad \forall\ cp\in CP,\ k\in N \tag{13}
$$

$$
\begin{aligned}
& Fn^{Pet}_{cp\in NRF} + \sum_{i\in I}\sum_{cre\in CR} Fi^{Pet}_{cr,cp\in RPI,i} \\
& + \sum_{i\in I}\sum_{cre\in CR} Ff^{Pet}_{cr,cp\in RPF,i} \\
& + \sum_{m\in M_{Pet}}\delta_{cp,m}\ x^{Pet}_{m} \leq D_{Pet^{U}_{cp\in CFP}}
\end{aligned} \qquad \forall\ cp\in CP \tag{14}
$$

$$
B^{L}_{m}\ yproc^{Pet}_{m} \leq x^{Pet}_{m} \leq K^{U}\ yproc^{Pet}_{m} \qquad \forall\, m\in M_{Pet} \tag{15}
$$

$$
\sum_{cp\in CIP} yproc^{Pet}_{m} \leq 1 \qquad \forall\, m\in M_{Pet} \text{ that produces } cp\in CIP \tag{16}
$$

$$
\sum_{cp\in CFP} yproc^{Pet}_{m} \leq 1 \qquad \forall\, m\in M_{Pet} \text{ that produces } cp\in CFP \tag{17}
$$

$$
Fn^{Pet}_{cp} \leq S^{Pet}_{cp} \qquad \forall\ cp\in NRF \tag{18}
$$

The above formulation is a two-stage stochastic mixed-integer linear programming (MILP) model. Objective function (1) represents a minimization of the annualized cost which consists of crude oil cost, refineries operating cost, refineries intermediate exchange piping cost, refinery production system expansion cost, less the refinery export revenue, added value by the petrochemical processes, plus the recourse variables of refinery and petrochemical networks; respectively. Inequality (2) corresponds to each refinery raw materials balance where throughput to each distillation unit $p\in P'$ at plant $i\in I$ from each crude type $cr\in CR$ is equal to the available supply $S_{cr,i}$. Constraint (3) represents the intermediate material balances within and

across the refineries where the coefficient $\alpha_{cr,cir,i,p}$ can assume either a positive sign if it is an input to a unit or a negative sign if it is an output from a unit. The multirefinery integration matrix $\xi_{cr,cir,i,p,i'}$ accounts for all possible alternatives of connecting intermediate streams $cir \in CIR$ of crude $cr \in CR$ from refinery $i \in I$ to process $p \in P$ in plant $i' \in I'$. The variable $xi^{Ref}_{cr,cir,i,p,i'}$ represents the transshipment flowrate of crude $cr \in CR$, of intermediate $cir \in CIR$ from plant $i \in I$ to process $p \in P$ at plant $i' \in I$. Constraint (3) also considers the petrochemical network feedstock from the refinery intermediate streams $Fi^{Pet}_{cr,cir,i}$ of each intermediate product $cir \in RPI$. The material balance of final products in each refinery is expressed as the difference between flowrates from intermediate steams $w_{cr,cir,cfr,i}$ for each $cir \in CIR$ that contribute to the final product pool and intermediate streams that contribute to the fuel system $w_{cr,cfr,rf,i}$ for each $rf \in FUEL$ less the refinery final products $Ff^{Pet}_{cr,cfr,i}$ for each $cfr \in RPF$ that are fed to the petrochemical network as shown in constraint (4). In constraint (5) we convert the mass flowrate to volumetric flowrate by dividing it by the specific gravity $sg_{cr,cir}$ of each crude type $cr \in CR$ and intermediate stream $cir \in CB$. This is needed in order to express the quality attributes that blend by volume in blending pools. Constraint (6) is the fuel system material balance where the term $cv_{rf,cir,i}$ represents the caloric value equivalent for each intermediate $cir \in CB$ used in the fuel system at plant $i \in I$. The fuel production system can either consist of a single or combination of intermediates $w_{cr,cir,rf,i}$ and products $w_{cr,cfr,rf,i}$. The matrix $\beta_{cr,rf,i,p}$ corresponds to the consumption of each processing unit $p \in P$ at plant $i \in I$ as a percentage of unit throughput. Constraints (7) and (8), respectively, represent a lower and an upper bounds on refinery quality constraints for all refinery products that either blend by mass $q \in Q_w$ or by volume $q \in Q_v$. Constraint (9) represents the maximum and minimum allowable flowrate to each processing unit. The coefficient $\gamma_{m,p}$ is a zero-one matrix for the assignment of production unit $m \in M_{Ref}$ to process operating mode $p \in P$. The term $AddC_{m,i,s}$ accounts for the additional refinery expansion capacity of each production unit $m \in M_{Ref}$ at refinery $i \in I$ for a specific expansion size $s \in S$. The integer variable $y_{exp}{}^{Ref}_{m,i,s}$ represents the decision of expanding a production unit and it can take a value of one if the unit expansion is required or zero otherwise. Constraint (10) sets an upper bound on intermediate streams flowrates between the different refineries. The integer variable $y_{pipe}{}^{Ref}_{cir,i,i'}$ represents the decision of exchanging intermediate products between the refineries and takes on the value of one if the commodity is transferred from plant $i \in I$ to plant $i' \in I$ or zero otherwise, where $i \neq i'$. When an intermediate stream is selected to be exchanged between two refineries, its flowrate must be below the transferring pipeline capacity $F^{U}_{cir,i,i'}$. Constraint (11) stipulates that the final products from each refinery $x^{Ref}_{cfr,i}$ less the amount exported $e^{Ref}_{cfr',i}$ for each exportable product $cfr' \in PEX$ from each plant $i \in I$ must satisfy the domestic demand $D_{Ref_{cfr}}$. The recourse variables $V^{Ref+}_{cfr,k}$, $V^{Ref-}_{cfr,k}$, $V^{Pet+}_{cp,k}$ and $V^{Pet-}_{cp,k}$ in equations (11) and (13) represent the refinery production shortfall and surplus as well as the petrochemical production shortfall and surplus, respectively, for each random realization $k \in N$. These variables will compensate for the violations in equations (11) and (13) and will be penalized in the objective function using appropriate shortfall and surplus costs C^{Ref+}_{cfr} and C^{Ref-}_{cfr} for the refinery products, and C^{Pet+}_{cp} and C^{Pet-}_{cp} for the petrochemical products, respectively. Resources are limited by constraint (12)

Constraints (13) and (14) represent the material balance that governs the operation of the petrochemical system. The petrochemical network receives its feed from potentially three main sources. These are, 1) refinery intermediate streams $Fi^{Pet}_{cr,cir,i}$ of an intermediate product $cir \in RPI$, 2) refinery final products $Ff^{Pet}_{cr,cfr,i}$ of a final product $cfr \in RPF$, and 3) non-refinery streams Fn^{Pet}_{cp} of a chemical $cp \in NRF$. For a given subset of chemicals $cp \in CP$, the proposed model selects the feed types, quantity and network configuration based on the final chemical and petrochemical lower and upper product demand $D_{Pet}{}^{L}_{cp}$ and $D_{Pet}{}^{U}_{cp}$ for each $cp \in CFP$, respectively. Furthermore, in equation (13) an additional term xi^{Pet}_{cp} was added to the left hand side representing the flow of intermediate petrochemical stream of $cp \in CIP$. In constraint (15), defining a binary variables $y_{proc}{}^{Pet}_{m}$ for each process $m \in M_{pet}$ is required for the process selection requirement as $y_{proc}{}^{Pet}_{m}$ will equal 1 only if process m is selected or zero otherwise. Furthermore, if only process m is selected, its production level must be at least equal to the process minimum economic capacity B^{L}_{m} for each $m \in M_{pet}$, where K^{U} is a valid upper bound. Finally, we can specify limitations on the supply of feedstock Fn^{Pet}_{cp} for each chemical type $cp \in NRF$ through constraint (18).

3. SCENARIO GENERATION

The solution of stochastic problems is generally very challenging as it involves numerical integration over the random continuous probability space of the second stage variables (Goyal & Ierapetritou, 2007). An alternative approach is the discretization of the random space using a finite number of scenarios. In our study, the Sample Average

Approximation (SAA) method, also known as stochastic counterpart, is employed. The SAA problem can be written as (Verweij et al., 2003):

$$v_N = \min_{x \in X} c^T x + \frac{1}{N} \sum_{k \in N} Q(x, \xi^k) \quad (19)$$

It approximates the expectation of the stochastic formulation (usually called the "true" problem) and can be solved using deterministic algorithms. Problem (19) can be solved iteratively in order to provide statistical bounds on the optimality gap of the objective function value. The validation procedure was originally suggested by Norkin et al. (1998) and further developed by Mark et al. (1999).

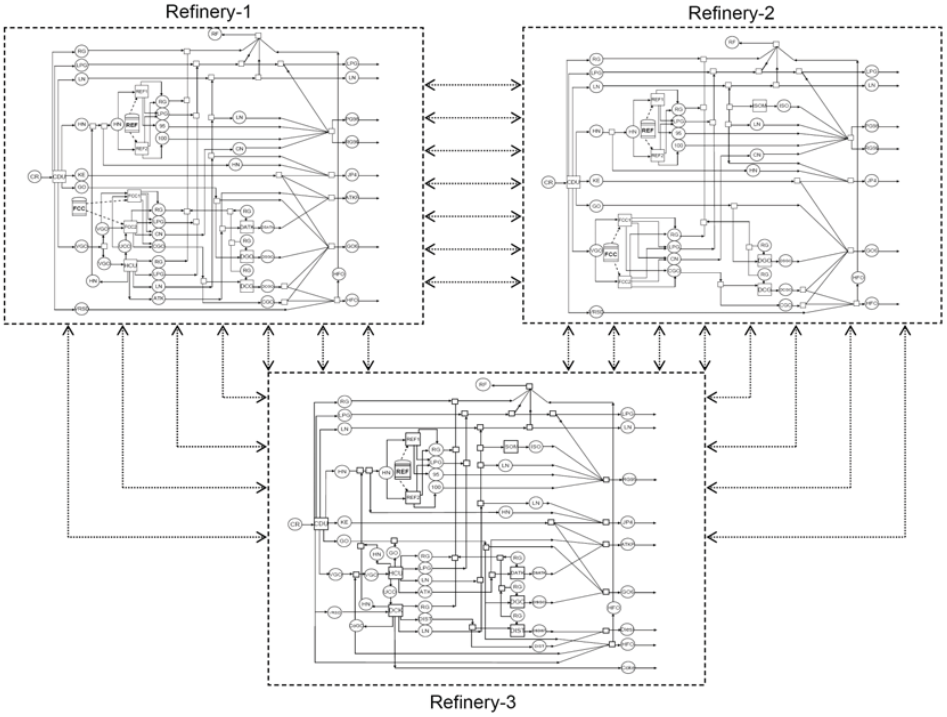

Fig. 1. Refinery Integration Network

originally suggested by Norkin et al. (1998) and further developed by Mark et al. (1999).

Table 1. Major refinery network capacity constraints

Production Capacity	Higher limit (10^3 ton/yr)		
	R1	R2	R3
Distillation	45000.	12000.0	9900.0
Reforming	700.0	2000.0	1800.0
Isomerization	200.0	-	450.0
Fluid catalytic cracker	800.0	1400.0	-
Hydrocracker	-	1800.0	2400.0
Delayed coker	-	-	1800
Des gas oil	1300.0	3000.0	2400.0
Des cycle gas oil	200.0	750.0	-
Des ATK	-	1200.0	1680.0
Des Distillates	-	-	450.0
Crude availability			
Arabian Light		31200.0	
Local Demand			
LPG		$\mathcal{N}(432,20)$	
LN		-	
PG98		$\mathcal{N}(400,20)$	
PG95		$\mathcal{N}(4390,50)$	
JP4		$\mathcal{N}(2240,50)$	
GO6		$\mathcal{N}(4920,50)$	
ATK		$\mathcal{N}(1700,50)$	
HFO		$\mathcal{N}(200,20)$	
Diesel		$\mathcal{N}(400,20)$	
Coke		$\mathcal{N}(300,20)$	

4. ILLUSTRATIVE CASE STUDY

This section presents the computational results of the proposed model and sampling scheme. The case study considers a subsystem of the petrochemical industry for the integration problem with the refinery network as apposed to considering the full scale petrochemical industry, which might have limited applications. The case study will examine the integration between a multirefinery network with a polyvinyl chloride (PVC) petrochemical complex. PVC is a major ethylene derivative with many important applications and uses (e.g. pipe fittings, automobile bumpers, toys, bottles, etc.).

In this paper, we consider the planning for three refineries in one industrial location, which is a common situation in many

areas around the world. The state equipment network (SEN) representation of the three refineries is shown in Fig. 1. The final products of the three refineries network consists of liquefied petroleum gas (LPG), light naphtha (LT), two grades of gasoline (PG98 and PG95), No. 4 jet fuel (JP4), military jet fuel (ATKP), No.6 gas oil (GO6), diesel fuel (Diesel), heating fuel oil (HFO), and petroleum coke (coke). The major capacity constraints for the refinery network are given in Table 1. The petrochemical complex, on the other hand, starts with the production of ethylene from the refineries feedstocks by steam cracking. The main feedstocks

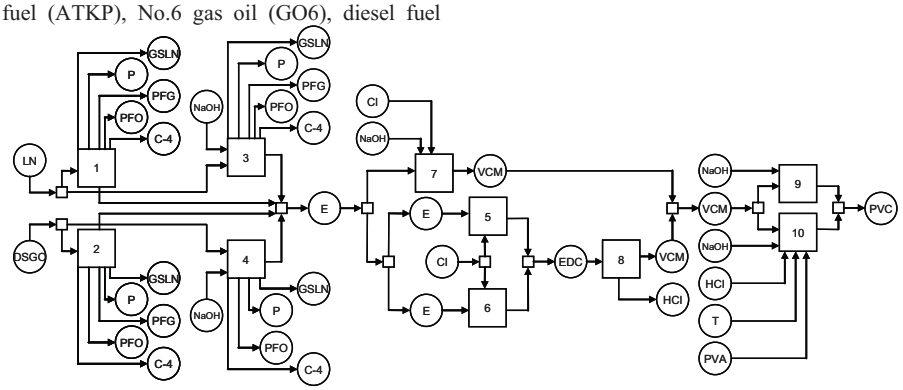

Fig. 2. PVC complex possible production alternatives

to the ethylene plant in our study are light naphtha (LN) and gas oil (GO). The selection of the feedstocks and hence the process technologies is decided upon based on the optimal balance and trade-off between the refinery and petrochemical markets. The process technologies considered in this study for the production of PVC are list in Table 2. The overall topology of all petrochemical technologies for the PVC production is shown in Fig. 2. The modeling system GAMS (Brooke et al., 1996) is used for setting up the optimization models and the MILP problems were solved with CPLEX (CPLEX Optimization Inc., 1993).

Table 2 Major products and processes in PVC complex

Product	Price ($/ton)	Process Technology	Index	Min. Prod. (10^3 ton/yr)
Ethylene (E)	$\mathcal{N}$(1570,10)	Pyrolysis of naphtha (LS)	1	250
		Pyrolysis of gas oil (LS)	2	250
		Steam cracking of naphtha (HS)	3	250
		Steam cracking of gas oil (HS)	4	250
Ethylene Dichloride (EDC)	$\mathcal{N}$(378,10)	Chlorination of ethylene	5	180
		Oxychlorination of ethylene	6	180
Vinyl chloride monomer (VCM)	$\mathcal{N}$(1230,10)	Chlorination and Oxychlorination of ethylene	7	250
		Dehydrochlorination of ethylene dichloride	8	125
Polyvinyl chloride (PVC)	$\mathcal{N}$(1600,10)	Bulk polymerization	9	50
		Suspension polymerization	10	90

In our study, we considered uncertainty in the imported crude oil price, refinery product price, petrochemical product price, refinery market demand, and petrochemical lower level product demand. In the presentation of the results, we focus on demonstrating the sample average approximation computational results as we vary the sample sizes and compare their solution accuracy and the CPU time required for solving the models.

Table 3 Computational results of stochastic model

		Lower bound sample size=N		
UB Samples	Number of Samples (R=30)	1000	2000	3000
N'=5000	LB estimate: $\overline{v}_N$	8802837	8804092	8804456
	LB error: $\widetilde{\varepsilon}_l$ (α=0.975)	3420	2423	1813
	UB estimate: $\hat{v}_{N'}$	8805915	8805279	8805578
	UB error: $\widetilde{\varepsilon}_u$ (α=0.975)	7776	7715	7778
	95% Conf. Interval	[0,14274]	[0,11324]	[0,10713]
	CPU (sec)	65	112	146
N'=10000	LB estimate: $\overline{v}_N$	8800071	8802080	8804305
	LB error: $\widetilde{\varepsilon}_l$ (α=0.975)	3356	2527	2010
	UB estimate: $\hat{v}_{N'}$	8803310	8803204	8803414
	UB error: $\widetilde{\varepsilon}_u$ (α=0.975)	5473	5833	5410
	95% Conf. Interval	[0,12068]	[0,9484]	[0,7420]
	CPU (sec)	196	224	263
N'=20000	LB estimate: $\overline{v}_N$	8796058	8801812	8802511
	LB error: $\widetilde{\varepsilon}_l$ (α=0.975)	3092	2345	1755
	UB estimate: $\hat{v}_{N'}$	8802099	8804121	8802032

UB error: $\widetilde{\varepsilon}_u$ (α=0.975)	3837	3886	3880
95% Conf. Interval	[0,12970]	[0,8540]	[0,5635]
CPU (sec)	1058	1070	1114

The problem was solved for different sample sizes N and N' to illustrate the variation of optimality gap confidence intervals, while fixing the number of replications R to 30. The replication number R need not be very large to get an insight of $\bar{v}_N$ variability. Table 4 shows different confidence interval values of the optimality gap when the sample size of N assumes values of 1000, 2000, and 3000 while varying N' between 5000, 10000, and 20000 samples. As the sample sizes N and N' were limited to these values due to computational considerations. In our case study, we ran into memory limitations when N and N' values exceeded 3000 and 20000, respectively. The solution of the three refineries network and the PVC complex using the SAA scheme with N = 3000 and N'=20000 required 1114 CPU sec to converge to the optimal solution.

Table 4. Model results integrated network

Process variables				Results (10^3 ton/yr) R1	R2	R3
Refinery	**Crude Oil Supply**			4500	12000	9900
	Production levels	Crude unit		4500	12000	9900
		Reformer		612.5	1824.6	1784.6
		Isomerization		160	-	450
		FCC		378	1174.2	-
		Hydrocracker		-	1740.4	2400
		Delayed coker		-	-	1440
		Des Gas oil		1300	3000	2400
		Des cycle gas oil		168.6	600	-
		Des ATK		-	1200	1654.8
		Des Distillates		-	-	366.2
	Intermediate streams exchange	From **R1**	VGO	-	-	576.1 to HCU
		From **R2**	LN	-	-	112.4 to Isom
		From **R3**	VGO	-	274.8 to FCC	-
	Exports	PG95			439.8	
		JP4			1101.9	
		GO6			2044.2	
		HFO			1907.8	
		ATK			1887.6	
		Coke			110.7	
		Diesel			5.1	
Petrochemical	**Refinery feed to PVC complex**	Gas oil		788.6	1037.0	71.3
	Production levels	S. Crack GO (4)			486.8	
		Cl & OxyCl E (7)			475.4	
		Bulk polym. (9)			220.0	
	Final	PVC			220.0	
Total cost ($/yr)					$8,802,000	

Table 4 depicts the results of the optimal integration network between the three refineries and the PVC petrochemical complex. As shown in Table 5, the proposed model designed the refinery network and operating policies and also devised the optimal production plan for the PVC complex from all available process technologies. The model selected gas oil as the refinery feedstock to the petrochemical complex. PVC production was proposed by first high severity steam cracking of gas oil to produce ethylene. Vinyl chloride monomer (VCM) is then produced through the chlorination and oxychlorination of ethylene and finally, VCM is converted to PVC by bulk polymerization. The annual production cost across the refineries and the PVC complex was $8,802,000.

REFERENCES

Al-Qahtani, K., and Elkamel, A. (2008). Multisite Facility Network Integration Design and Coordination: An Application to the Refining Industry. *Computers & Chemical Engineering*, 32, 2198.

Al-Qahtani, K., Elkamel, A. and Ponnambalam, K. (2008). Robust Optimization for Petrochemical Network Design under Uncertainty, *Industrial & Engineering Chemistry Research*, 47, 3912.

Brooke, A., Kendrick, D., and Meeraus, A., Raman, R. (1996). *GAMS—A User's Guide*, GAMS Development Corporation: Washington DC.

CPLEX Optimization, Inc. (1993). *Using the CPLEX Callable Library and CPLEX Mixed Integer Library*, CPLEX Optimization Inc: Incline Village, NV.

Goyal, V., and Ierapetritou, M. G. (2007). Stochastic MINLP optimization using simplicial approximation. *Computers and Chemical Engineering*, 31, 1081.

Mark, W. K., Morton, D. P., and Wood, R. K. (1999). Monte Carlo bounding techniques for determining solution quality in stochastic programs. *Operational Research Letters*, 24, 47.

Norkin, W. I., Pflug, G. Ch., and Ruszczysk, A. (1998). A branch and bound method for stochastic global optimization. *Mathematical Programming*, 83, 425.

Verweij, B., Ahmed, S., Kleywegt, A. J., Nemhauser, G., and Shapiro, A. (2003). The sample average approximation method applied to stochastic routing problems: A computational study. *Computational Optimization & Applications*, 24, 289.

Nonlinear State Estimation of Differential Algebraic Systems

Ravi K. Mandela * **Raghunathan Rengaswamy** **
Shankar Narasimhan ***

* *Department of Chemical and Biomolecular Engineering, Clarkson University, Potsdam, NY 13699 USA (Tel: 315-268-3808; e-mail: mandelrk@clarkson.edu)*
** *Department of Chemical Engineering, Texas Tech University, Lubbock, TX 79409 USA (Tel: 806-742-3553; e-mail: raghu.rengasamy@ttu.edu)*
*** *Chemical Engineering Department, IIT Madras, India (e-mail:naras@iitm.ac.in)*

Abstract: Kalman filter and its variants have been used for state estimation of systems described by ordinary differential equation (ODE) models. Moving Horizon Estimation (MHE) has been a popular approach in chemical engineering community for the estimation of both ODE and differential algebraic equation (DAE) systems but is computationally demanding. There has been some work on applying Extended Kalman filter for state estimation of DAE systems with measurements as functions of only the differential states. This work describes the estimation of nonlinear DAE systems with measurements being a function of both the differential and algebraic states. An Unscented Kalman filter (UKF) formulation is also derived for semi-explicit index 1 DAE systems. The utility of these formulations are demonstrated through a case study.

1. INTRODUCTION

Differential algebraic equation (DAE) models naturally arise in several chemical/physical systems, where some rate processes are much faster than the others and admit quasi steady-state approximations. Common examples of these can be found in separation and reaction systems. Many chemical engineering systems can be modeled as DAE systems. Examples of algebraic equations include mole fraction summations, vapor-liquid equilibrium relationships and so on. The algebraic equations can be either linear or nonlinear. Other areas where DAE models arise are mechanical systems, electrical systems and biological systems. A DAE system is characterized by the index of the system. The index of a DAE system is defined as the number of differentiations that are required to convert the DAE system into an explicit ODE system. It is not always possible and easy to convert DAE into ODE systems [Petzold, 1988]. In this paper. the focus is on estimation of nonlinear index one DAE systems that are common in chemical engineering.

The Kalman filter (KF) is an optimal estimator for linear dynamical systems in the presence of state and measurement uncertainties [Gelb, 1988, Sorenson, 1985]. Extended Kalman filter (EKF) is an extension of the Kalman filter for nonlinear systems described by a class of ordinary differential equations. Simultaneous parameter and state estimation is achieved in KF and EKF by augmenting the states [Jazwinski, 1970].

The KF has been used by several researchers for state estimation of systems describing linear DAE models [Nikoukhah et al., 1992, Chisci and Zappa, 1992]. The state estimation of nonlinear DAEs has already been studied by Albuquerque and Biegler [1997] using Moving -horizon estimation technique. Moving-horizon estimation (MHE) is considered as an efficient optimization based method for state estimation. Moving-horizon estimation can also be extended to parameter estimation of nonlinear DAEs [Tjoa and Biegler, 1991].

Moving-horizon estimator can handle constraints and bounds at every sampling instant [Rao et al., 2003]. However, questions remain about the computational complexity for on-line implementation of MHE estimators. The main advantage of the EKF lies in their predictor-corrector recursive form that has the potential for online deployment [Muske and Edgar, 1997].

There has been some work on the application of EKF for nonlinear DAE systems. One of the first attempts at this can be found in Becerra et al. [1999]. Becerra et al. [2001] extend this work further and demonstrate their approach on an experimental case study. They also explore the use of square root formulation of the EKF which has better numerical stability than the standard EKF [Park and Kailath, 1995]. However, the measurements available to the estimator are all assumed to be functions of differential states. In this paper, we extend Becerra et al. [2001] approach to cases where the measurements are functions of both the differential and algebraic states. Further, we develop an approach for the use of Unscented Kalman filter (UKF) for estimation in index 1 nonlinear DAE systems.

The paper is organized as follows. Section 2 provides an introduction to DAE systems. EKF and UKF algorithms

for DAE systems are discussed in section 3 and section 4 respectively. Simulation results with discussions are presented in section 5 followed by conclusions in section 6.

2. DIFFERENTIAL ALGEBRAIC SYSTEMS

As discussed in the previous section, DAE systems consist of both differential and algebraic equations. DAE systems are characterized by the index of the system. The index of the DAE system is defined as the number of differentiations required to convert the DAE into an ODE. As a simple example, consider

$$\dot{y_2}(t) = y_1(t) + \lambda_1(t) \tag{1}$$

$$0 = y_2(t) + \lambda_2(t) \tag{2}$$

Differentiating the algebraic equation 2 once, we get

$$0 = \dot{y_2}(t) + \dot{\lambda_2}(t) \tag{3}$$

Differentiating the algebraic equation 3 once more yields

$$0 = \ddot{y_2}(t) + \ddot{\lambda_2}(t) \tag{4}$$

Putting these equations together we now get an ODE as shown in equation .

$$\begin{aligned} \dot{y_2}(t) &= y_1(t) + \lambda_1(t) \\ \dot{y_1}(t) &= -\dot{\lambda_1}(t) - \ddot{\lambda_2}(t) \end{aligned} \tag{5}$$

Since the equations had to be differentiated twice this is an index 2 DAE system. While there are DAE systems of orders higher than 1 in chemical engineering, index 1 DAE systems are common as seen in electrochemistry, reactive distillation and biochemical engineering applications. As mentioned before, this work considers index 1 DAE systems.

3. EKF FOR DAE SYSTEMS

While EKF has been studied extensively for ODE systems, the application of EKF approaches to DAE systems are not many. Becerra et al. [2001] developed an EKF estimation approach for for nonlinear index 1 DAEs. The EKF approach follows the same predictor-corrector form with some modifications. In the prediction step, a DAE solver is used for propagating the prior state through the system model. This is in contrast to the use of an ODE solver in standard EKF. The covariance matrix of the differential states are propagated by linearizing the system model. The correction step is performed only for the differential states through a linearization of the measurement model. This is possible because it is assumed that the measurements are functions of differential states alone. Once the corrected differential states are available, the corrected algebraic states are calculated using the algebraic portion of the system model. The corrected covariance matrix for the differential states is calculated using the standard EKF procedure. The mathematical details of the algorithm are explained below. The nonlinear DAE system is considered with discrete measurements sampled at regular intervals with sampling period Δt

$$x_{k+1} = x_k + \int_{(k)\Delta t}^{(k+1)\Delta t} f(x(\tau)), z(\tau))\, d\tau + w_{k+1} \tag{6}$$

$$g(x_{k+1}, z_{k+1}) = 0 \tag{7}$$

$$y_{k+1} = h(x_{k+1}) + v_{k+1} \tag{8}$$

where w_{k+1} and v_{k+1} are assumed to be independent Gaussian white noise processes with known covariance matrix Q_{k+1} and R_{k+1}

For a fixed input, the linearized equation is given by

$$\dot{x} = Ax \tag{9}$$

where

$$A = (J_1 - J_2 J_4^{-1} J_3) \tag{10}$$

$$\begin{bmatrix} J1 & J2 \\ J3 & J4 \end{bmatrix} = \begin{bmatrix} \frac{\partial f}{\partial x} & \frac{\partial f}{\partial z} \\ \frac{\partial g}{\partial x} & \frac{\partial g}{\partial z} \end{bmatrix} \tag{11}$$

Following are the steps involved in the algorithm

- The differential states are propagated by integrating the DAE model from time t_k to t_{k+1}. The predicted state estimate $\hat{x}_{k+1/k}$ is obtained with u_k, which is the constant input between sampling intervals.
- The predicted covariance matrix in differential states is propagated using
$$P_{k+1/k} = \bar{A}_k P_{k/k} \bar{A}_k^T + Q_k \tag{12}$$
where $\bar{A} = exp(A\Delta t)$
- The kalman gain is computed using
$$K_{k+1} = P_{k+1/k} G_{k+1}^T (G_{k+1} P_{k+1/k} G_{k+1}^T + R_{k+1})^{-1} \tag{13}$$
where G_{k+1} is the linearized measurement model and the actual measurement model is a function of only differential states.
- The updated differential estimates are obtained from kalman update equation
$$\hat{x}_{k+1/k+1} = \hat{x}_{k+1/k} + K_{k+1}(y_{meas} - h(\hat{x}_{k+1/k})) \tag{14}$$
- The updated estimate $\hat{z}_{k+1/k+1}$ is obtained from the set of algebraic equations defining the DAE system once differential state estimate $\hat{x}_{k+1/k+1}$ is obtained
- The updated covariance matrix is computed as
$$P_{k+1/k+1} = (I - K_{k+1} G_{k+1}) P_{k+1/k} \tag{15}$$
In this method, $\hat{z}$ is computed only from the $\hat{x}$ using algebraic equation and there is no dependence or use of prior estimates of z (algebraic states). This method cannot be applied to cases where there is an availability of algebraic states measurements.

4. PROPOSED APPROACH: EXTENDED KALMAN FILTER FOR DAE SYSTEMS

In DAE systems, the measurements can, in general, be a function of both the differential and algebraic states. In the proposed work, we extend the EKF approach to this case. The algorithm deviates from the work of Becerra et al. [2001] in that the EKF works with an augmented system (with both the differential and algebraic states). A linearized ODE model involving both differential and

algebraic states (augmented) is derived. This linearized ODE model is used for the covariance propagation of augmented state as opposed to just the differential states as in Becerra et al. [2001]. The gain matrix is calculated form the augmented predicted covariance matrix and the linearized measurement model which is a function of both the differential and algebraic measurements. The corrected augmented state is computed. From these corrected augmented states, only the differential states are retained. As the algebraic constraints are to be met, the algebraic states are calculated from the corrected differential states using algebraic equations. The details of the algorithm are explained below. The nonlinear DAE system is considered with discrete measurements sampled at regular intervals with sampling period Δt

$$x_{k+1} = x_k + \int_{(k)\Delta t}^{(k+1)\Delta t} f(x(\tau)), z(\tau))\, d\tau + w_{k+1} \tag{16}$$

$$g(x_{k+1}, z_{k+1}) = 0 \tag{17}$$

$$y_{k+1} = h(x_{k+1}) + v_{k+1} \tag{18}$$

where w_{k+1} and v_{k+1} are assumed to be independent Gaussian white noise processes with known covariance matrix Q_{k+1} and R_{k+1}

Linearizing the differential equations and algebraic equations of index 1 DAE system, we get

$$\begin{aligned} \dot{x} &= Ax + Bz \\ 0 &= Cx + Dz \end{aligned} \tag{19}$$

where

$$\begin{bmatrix} A & B \\ C & D \end{bmatrix} = \begin{bmatrix} \frac{\partial f}{\partial x} & \frac{\partial f}{\partial z} \\ \frac{\partial g}{\partial x} & \frac{\partial g}{\partial z} \end{bmatrix} \tag{20}$$

Differentiating the linearized algebraic equation once , we get

$$0 = C\dot{x} + D\dot{z} \tag{21}$$

Then

$$\dot{z} = -D^{-1}C\dot{x} \tag{22}$$

$$\dot{z} = -D^{-1}CAx - D^{-1}CBx \tag{23}$$

Writing in matrix form

$$\begin{bmatrix} \dot{x} \\ \dot{z} \end{bmatrix} = \begin{bmatrix} A & B \\ -D^{-1}CA & -D^{-1}CB \end{bmatrix} \begin{bmatrix} x \\ z \end{bmatrix} \tag{24}$$

The augmented form is

$$\dot{X}^{aug} = A^{aug} X^{aug} \tag{25}$$

The transition matrix is evaluated as

$$\phi = exp(A^{aug}\Delta t) \tag{26}$$

The algorithm consists of following steps

- Both differential and algebraic states are propagated using a DAE solver from t_k to t_{k+1} starting from the latest updated estimate $\hat{X}_k^{aug}$ and the latest input u_k.
- The predicted covariance matrix of the augmented states is computed as
$$P_{k+1/k}^{aug} = \phi P_{k/k}^{aug} \phi^T + \Gamma Q_{k+1} \Gamma^T \tag{27}$$
where
$$\Gamma = \begin{bmatrix} I \\ -D^{-1}C \end{bmatrix} \tag{28}$$
- The augmented Kalman gain is computed as
$$K_{k+1}^{aug} = P_{k+1/k}^{aug} G_{k+1}^T (G_{k+1} P_{k+1/k}^{aug} G_{k+1}^T + R_{k+1})^{-1} \tag{29}$$
where G_{k+1} is the linearised measurement model.
- The updated state estimate is given by
$$X_{k+1/k+1}^{aug} = X_{k+1/k}^{aug} + K_{k+1}^{aug} (y_{meas} - h(X_{k+1/k}^{aug}) \tag{30}$$
- As the algebraic constraints are to be met, differential terms (x) of the updated estimate are retained and the updated estimates of the algebraic states (z) are calculated from the algebraic equation of DAE system.
- The updated covariance matrix is calculated as
$$P_{k+1/k+1}^{aug} = (I - K_{k+1}^{aug} G_{k+1}) P_{k+1/k}^{aug} \tag{31}$$

5. UNSCENTED KALMAN FILTER FOR DAE SYSTEMS

Unscented Kalman filter (UKF) is an approach that was developed to improve on EKF. The UKF approach uses the idea of unscented transforms for predicting the mean and covariance when a random variable passes through a nonlinear transformation. In EKF, linearization of the nonlinear transformation is used to predict the mean and covariance of the transformed variable. Unscented transformation is a sampling technique where a small number of deterministic samples are chosen such that their weighted mean and covariance exactly equal the mean and covariance of the random variable undergoing the nonlinear transformation. The transformed sample points are used to calculate the *a posteriori* mean and covariance. This results in much better accuracy than the linearization approach [Julier et al., 2000].

UKF estimation for ODE systems is well developed and several application studies have appeared [Romanenko and Castro, 2004, Romanenko et al., 2004, van der Merwe et al., 2000, Julier, 2002, Wan et al., 2000, Wan and van der Merwe, 2000]. In this paper, we extend the UKF approach for semi-explicit index 1 DAE systems. The proposed approach also follows the predictor-corrector form. First, unscented samples are chosen for the differential states. The unscented samples for the algebraic states are generated from the algebraic equations. This makes all the sigma points consistent. These sigma points are propagated through the system through a DAE solver. Unscented samples for the differential and algebraic states are again generated using the propagated covariance matrix. The sample points for the measurements are calculated by passing the unscented differential and algebraic state samples through the measurement function. The sample covariances are used to calculate the Kalman gain. Using the Kalman gain, the corrected differential states are obtained. The corrected algebraic states are calculated using the algebraic equations in the system model. This algorithm of unscented Kalman filter for DAE systems is

explained below. The nonlinear DAE system is considered with discrete measurements sampled at regular intervals with sampling period Δt

$$x_{k+1} = x_k + \int_{(k)\Delta t}^{(k+1)\Delta t} f(x(\tau)), z(\tau)) \, d\tau + w_{k+1} \quad (32)$$

$$g(x_{k+1}, z_{k+1}) = 0 \quad (33)$$

$$y_{k+1} = h(x_{k+1}, z_{k+1}) + v_{k+1} \quad (34)$$

where w_{k+1} and v_{k+1} are assumed to be independent Gaussian white noise processes with known covariance matrix Q_{k+1} and R_{k+1}

- The first step is the generation of sigma points. At the k^{th} instant, $\hat{x}_{k/k}$ is the filtered estimate of differential states and $P_{k/k}$ is the covariance matrix associated with it. A set of 2n+1 sigma points $\hat{X}_{k/k,i}$ with associated weights are chosen symmetrically about $\hat{x}_{k/k}$ where n is the dimension of the state.

$$\hat{X}_{k/k,0} = \hat{x}_{k/k}; W_0 = \frac{\kappa}{(n+\kappa)} \quad (35)$$

$$\hat{X}_{k/k,i} = \hat{x}_{k/k} + (\sqrt{(n+\kappa)P_{k/k}})_i; W_i = \frac{1}{2(n+\kappa)} \quad (36)$$

$$\hat{X}_{k/k,i+n} = \hat{x}_{k/k} - (\sqrt{(n+\kappa)P_{k/k}})_i; W_{i+n} = \frac{1}{2(n+\kappa)} \quad (37)$$

where $(\sqrt{P_{k/k}})_i$ is the i^{th} column of matrix square root of $P_{k/k}$ and W_i is the weight associated with the corresponding point. The parameter κ is a tuning parameter. The weights W_i add to one and the weighted mean of the set X is same as $\hat{x}_{k/k}$. The weighted covariance matrix of the sample is equal to $P_{k/k}$.

$$P_{k/k} = \sum_{i=0}^{2n} W_i (\hat{X}_{k/k,i} - \hat{x}_{k/k})(\hat{X}_{k/k,i} - \hat{x}_{k/k})^T \quad (38)$$

- Calculate $\hat{Z}_{k/k,i}$ from $g(\hat{X}_{k/k,i}, \hat{Z}_{k/k,i}) = 0$
- Propagate $\hat{X}_{k/k,i}$ and $\hat{Z}_{k/k,i}$ through DAE system to get $\hat{X}_{k+1/k,i}$ and $\hat{Z}_{k+1/k,i}$

  The predicted differential state estimate $\hat{x}_{k+1/k}$ is given by

$$\hat{x}_{k+1/k} = \sum_{i=0}^{2n} W_i \hat{X}_{k+1/k,i} \quad (39)$$

- Calculate $P^{xx}_{k+1/k}$

$$P^{xx}_{k+1/k} = \sum_{i=0}^{2n} W_i (\hat{X}_{k+1/k,i} - \hat{x}_{k+1/k}) (\hat{X}_{k+1/k,i} - \hat{x}_{k+1/k})^T + Q_{k+1} \quad (40)$$

- Do unscented sampling with $\hat{x}_{k+1/k}$ as mean and $P^{xx}_{k+1/k}$ as covariance matrix
- Recalculate $\hat{Z}_{k+1/k,i}$ from $g(\hat{X}_{k+1/k,i}, \hat{Z}_{k+1/k,i}) = 0$
- Form $\hat{X}^{aug}_{k+1/k,i}$ by augmenting $\hat{X}_{k+1/k,i}$ with $\hat{Z}_{k+1/k,i}$
- Calculate $\hat{x}^{aug}_{k+1/k}$

$$\hat{x}^{aug}_{k+1/k} = \sum_{i=0}^{2n} W_i \hat{X}^{aug}_{k+1/k,i} \quad (41)$$

- The predicted sigma points are propagated through the nonlinear measurement equation to obtain the predicted measurement as

$$Y_{k+1,i} = h(\hat{X}^{aug}_{k+1/k,i}) \quad (42)$$

Using the set of predicted measurements, the covariance matrix of innovations and the cross covariance between predicted state estimate errors and innovations are computed as

$$P_{\nu\nu,k+1} = \sum_{i=0}^{2n} W_i (Y_{k+1,i} - \hat{y}_{k+1}) (Y_{k+1,i} - \hat{y}_{k+1})^T + R_{k+1} \quad (43)$$

$$P_{x\nu,k+1} = \sum_{i=0}^{2n} W_i (\hat{X}^{aug}_{k+1,i} - \hat{x}^{aug}_{k+1/k})(Y_{k+1,i} - \hat{y}_{k+1})^T \quad (44)$$

where

$$\hat{y}_{k+1} = \sum_{i=0}^{2n} W_i Y_{k+1,i} \quad (45)$$

- The Kalman gain matrix is computed as

$$K_{k+1} = P_{x\nu,k+1} (P_{\nu\nu,k+1})^{-1} \quad (46)$$

- The Kalman gain corresponding to differential states is K^{diff}_{k+1}
- The updated differential estimates are obtained using the linear update equation as in Kalman filter

$$\hat{x}_{k+1/k+1} = \hat{x}_{k+1/k} + K^{diff}_{k+1} (y_{k+1} - \hat{y}_{k+1}) \quad (47)$$

- The updated estimate $\hat{z}_{k+1/k+1}$is obtained from the set of algebraic equations defining the DAE system once differential state $\hat{x}_{k+1/k+1}$ is obtained
- The covariance matrix of error in the updated differential estimates is computed using

$$P_{k+1/k+1} = P_{k+1/k} - K^{diff}_{k+1} P_{\nu\nu,k+1} K^{diff\,T}_{k+1} \quad (48)$$

6. CASE STUDY

The utility of the proposed approaches is tested on an electrochemical case study. The case study considers the galvanostatic charge /open-circuit/ discharge processes of a thin film nickel hydroxide electrode [Celik et al., 2002]. The modeling equations are

$$\frac{\rho V}{W} \frac{dy_1}{dt} = \frac{j_1}{F} \quad (49)$$

$$j_1 + j_2 - i_{app} = 0 \quad (50)$$

where

$$j_1 = i_{01}[2(1-y_1) exp(\frac{0.5F}{RT}(y_2 - \phi_{eq,1})) - 2y_1 \times exp(\frac{-0.5F}{RT}(y_2 - \phi_{eq,1}))] \quad (51)$$

$$j_2 = i_{02}[exp(\frac{F}{RT}(y_2 - \phi_{eq,2})) - exp(\frac{-F}{RT}(y_2 - \phi_{eq,2}))] \quad (52)$$

The first equation is the species balance equation, the second equation is the charge balance equation and j_1 and j_2 are derived using the Butler-Volmer kinetics. For the purpose of demonstrating the utility of the proposed approaches we assume that the differential state is corrupted with process noise w_{k+1} and the algebraic equation is exact. The values of parameters used are $F = 96487$, $R = 8.314$, $T = 298.15$, $\phi_{eq,1} = 0.420$, $\phi_{eq,2} = 0.303$, $\rho = 3.4$, $W = 92.7$, $V = 1 \times 10^{-5}$, $i_{app} = 1 \times 10^{-5}$, $i_{01} = 1 \times 10^{-04}$, $i_{02} = 1 \times 10^{-08}$. The units of parameters and variables are omitted for the simplicity. y_1 is the mole fraction of Nickel hydroxide and y_2 is potential difference between at the solid-liquid interface.The initial guess to the estimator is $[x0, z0] = [0.5322, 0.4254]$ and the actual value is [0.35024, 0.4071]. The tuning parameters used in EKF are

The following parameters are used

$$\Delta t = 15$$
$$P_0 = \begin{bmatrix} 0.005 & 0 \\ 0 & 0.005 \end{bmatrix}$$
$$Q_{k+1} = 0.00001$$
$$R_{k+1} = 0.0001$$

where Δt is the sampling time , P_0 is the error covariance matrix of differential and algebraic states, Q_{k+1} is the process noise associated with differential states and R_{k+1} is the measurement covariance matrix. The measurement in this case study is y_2, which is the potential difference at the solid-liquid interface. The important point to note is that the augmented covariance matrix should be taken into consideration if the measurement model is a function of differential and algebraic states. Figure 1 and Figure 2 show the estimates for the mole fraction and potential difference.

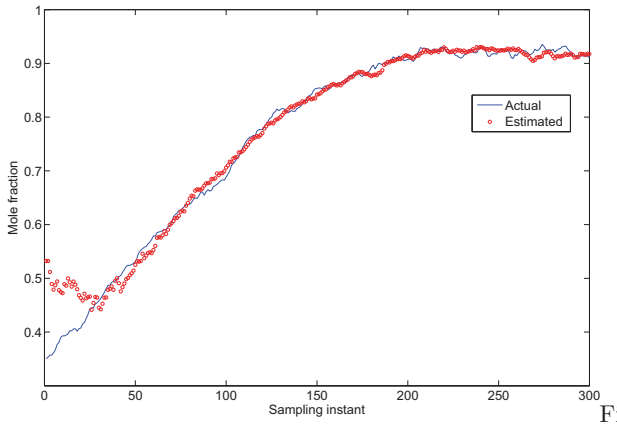

Fig. 1. EKF estimates of mole fraction for case study

The same differential algebraic system is considered and the UKF approach proposed in this paper is tested. The main advantage of UKF lies in the fact that it does not require linearization to compute covariance matrices. The UKF estimator gives very good estimates of mole fraction and potential difference as shown in Figure 3 and Figure

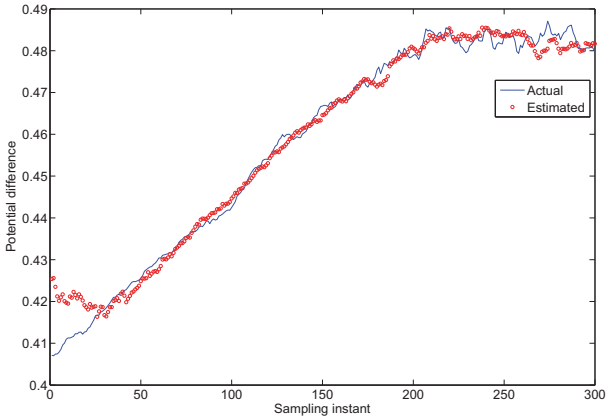

Fig. 2. EKF estimates of potential difference for case study

4. The tuning parameters for the UKF are same as used in EKF implementation. Figure 5 shows the comparison of UKF and EKF estimates and the their performances are compared by computing the root mean square error (RMSE) of the two states. Table 6 shows the RMSE values of estimates of UKF and EKF. It can clearly be seen that the UKF performs better than the EKF for this case study. Further, the UKF also avoids linearization in the computation of the covariance matrices.

RMSE values of EKF and UKF		
Method	RMSE y_1	RMSE y_2
EKF	0.0305	0.0035
UKF	0.0035	0.0035

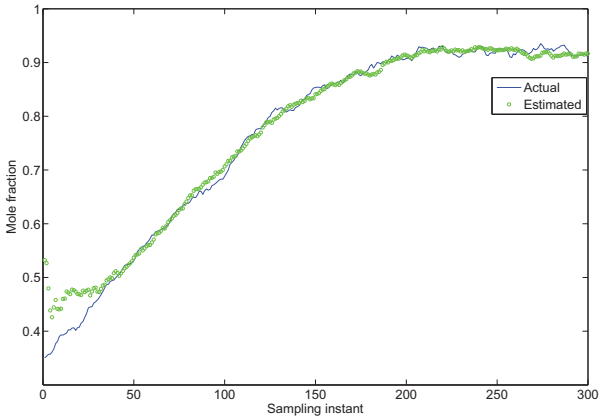

Fig. 3. UKF estimates of mole fraction for case study

7. CONCLUSIONS

In this paper, EKF and UKF formulations for nonlinear DAEs were proposed. The proposed EKF approach handles the case where the measurement functions are a function of both the differential and algebraic states. While UKF for ODE systems are well studied, there is very little work on the application of the UKF approach to DAE

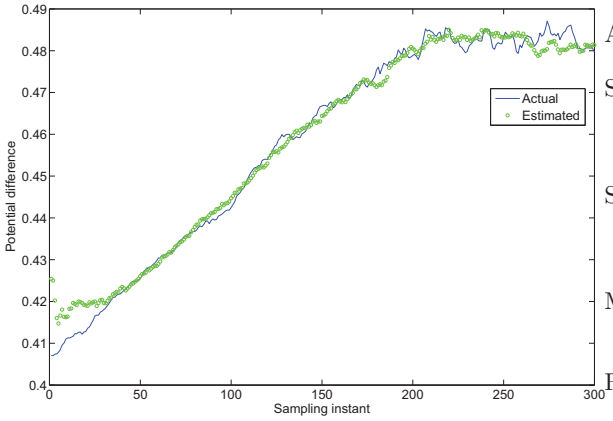

Fig. 4. UKF estimates of potential difference for case study

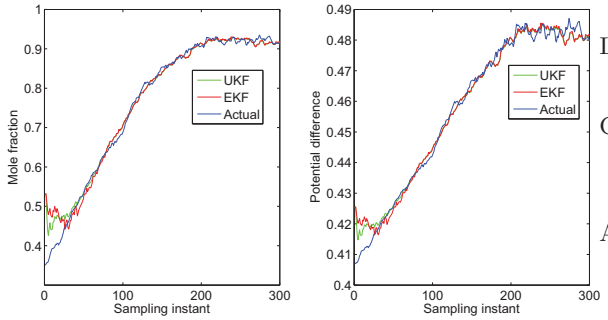

Fig. 5. Comparison of UKF and EKF estimates

systems. One possible approach to use unscented transformation in the estimation of DAE systems is proposed in this work. A case study is presented to demonstrate both the approaches. In this case study, the algebraic state is directly measured. It is shown that while both the proposed approaches provide satisfactory estimation, the UKF approach outperforms the EKF approach.

REFERENCES

J. S. Albuquerque and L. T. Biegler. Decomposition algorithms for on-line estimation with nonlinear models. *Computers in Chemical Engineering*, 21:283–299, 1997.

V. M. Becerra, P. D. Roberts, and G. W. Griffiths. Dynamic data reconciliation for a class of nonlinear differential algebraic equation models using the extended kalman filter. *Proceedings of the 14th IFAC world congress*, pages 303–308, 1999.

V. M. Becerra, P. D. Roberts, and G. W. Griffiths. Applying the extended kalman filter to sytems described by nonlinear differential-algebraic equations. *Control Engineering Practice*, 9:267–281, 2001.

E. Celik, E. Karaduman, and B. Mustafa. Numerical method to solve chemical differential algebraic equations. *International journal of quantum chemistry*, 89: 447–451, 2002.

L. Chisci and G. Zappa. Square root kalman filtering of descriptor systems. *Systems and Control Letters*, 19(4): 325–334, 1992.

A. Gelb. *Applied optimal estimation*. MIT Press, Cambridge, 1988.

A. Jazwinski. *Stochastic processes and filtering theory*. Academic Press, New York, 1970.

S. Julier, J. Uhlmann, and H. Whyte. A new method for the nonlinear transformation of means and covaraiances in filters and estimators. *IEEE Trans. Automat. Control*, 45:477–482, 2000.

S. J. Julier. The scaled unscented transformation. In *Proceedings of American Control Conference 2002*, volume 6, pages 4555–4559. American Control Conference, 2002.

M. Muske and T. Edgar. *Nonlinear state estimation. In: Henson, M.A, Seborg D.E, eds. Nonlinear Process Control*. Prentice Hall, Upper Saddle River, NJ, 1997.

R. Nikoukhah, A. Willsky, and B. C. Levy. Kalman filltering and riccati equations for descriptor systems. *IEEE Transactions on Automatic Control*, 37(9):1325–1342, 1992.

P. Park and T. Kailath. New square root algorithms for kalman filtering. *IEEE Transactions on Automatic Control*, 40(5):895–899, 1995.

L. R. Petzold. Differerential algebraic equations are not ode's. *SIAM Journal of Science and Statistical Computing*, 3:367–384, 1988.

C. Rao, J. Rawlings, and D. Mayne. Constrained state estimation for nonlinear discrete-time systems: stability and moving horizon approximations. *IEEE Trans. Automat. Control*, 48:246–258, 2003.

A. Romanenko and J. A. A. M. Castro. The unscented filter as an alternative to the ekf for nonlinear state estimation: A simulation case study. *Comput. Chem. Eng.*, 28(3):347–355, 2004.

A. Romanenko, L. O. Santos, and P. A. F. N. A. Afonso. Unscented kalman filtering of a simulated ph system. *Ind. Eng. Chem. Res.*, 43(23):7531–7538, 2004.

H. Sorenson. *Kalman filtering theory and applications*. IEEE Press, New York, 1985.

I. B. Tjoa and L. T. Biegler. Simultaneous solution and optimization strategies for parameter estimation of differential-algebraic equation systems. *Industrial and Engineering Chemistry Research*, 30(2), 1991.

R. van der Merwe, A. Doucet, J. F. G. de Freitas, and E. A. Wan. The unscented particle filter. Technical report, Cambridge University Engineering Department, 2000.

E. A. Wan and R. van der Merwe. The unscented kalman filter for nonlinear estimation. In *Proceedings of IEEE Symposium 2000(AS-SPCC)*, Alberta, Canada, October 2000.

E. A. Wan, R. van der Merwe, and A. T. Nelson. Dual estimation and the unscented transformation. *Neural Information Processing Systems*, 12:666–672, 2000.

RIVER WATER QUALITY MODEL VERIFICATION THROUGH A GIS BASED SOFTWARE

M. K. Yetik*, M. Yüceer, R. Berber***, E. Karadurmuş******

** Turkish Statistical Institute Regional Office, Zonguldak, Turkey, (e-mail: kazim.yetik@tuik.gov.tr).*
*** Department of Chemical Engineering, Faculty of Engineering Inonu University, 44280 Malatya, Turkey, (e-mail:myuceer@inonu.edu.tr)*
**** Department of Chemical Engineering, Faculty of Engineering Ankara University, Tandoğan 06100 Ankara, Turkey (e-mail: berber@eng.ankara.edu.tr)*
***** Department of Chemical Engineering, Faculty of Engineering Hitit University, Çorum, Turkey (e-mail: erdalk@gazi.edu.tr)*

Abstract: Research and development attempts on water quality models created valuable resources in the sense of model calibration and verification techniques. Recognizing the current degree of pollution in rivers and the importance of the sustainable water resources management, the interactive river monitoring appears to be at the center of recent focus. However the available information in this area is still far from expectations. On one side, the Geographical Information Systems (GIS) are gaining widespread acceptance and on the other side fast and reliable water quality models and parameter estimation techniques are becoming available. However, previous work on integrating water quality models and GIS is very limited. This work brings an integrated platform on which ArcMap as a GIS and a water quality model in Matlab™ are brought together in an interactive and user-friendly manner. The software developed allows the user to enter the data collected from the river, runs the dynamic model in the Matlab™ environment, predicts the values of pollution constituents along the river, extracts the results and displays the water quality on the map in different forms. The software thus provides a considerable ease in future real time application for on site river monitoring and environmental pollution assessment.

Keywords: water quality modeling, GIS, GUI, water management, systems analysis.

1. INTRODUCTION

Water pollution is gradually becoming one of major threats for aquatic as well as human life. In order to assess the impact of wastewater discharges into the surface waters, mathematical models are of great importance. Over the past there have been considerable developments in the area of water quality modeling for rivers. A summary can be found in the review by Rauch *et al.* (1998) who gave the then state of the art in river water quality modeling. The most widely used model in the world is pronounced to be QUAL2E, which was developed by US Environmental Protection Agency (EPA), and known as almost the standard for river water quality modeling (Shanahan *et al.* 1998). In addition; WASP, SALMANQ and SIMCAT are probably the ones that have been frequently referred to in the literature. The water quality models can be classified from many perspectives, ranging from model complexity to the simulation method employed, and the number and type of water quality indicators incorporated. Just to give an idea, Cox (2003), for example, selected 6 models in conceptualization and solution for detailed comparison. Three of them were steady state and the rest was of dynamic character. Cox (2003) noted that water quality modeling was an active area of research around the world, and underlined that only few papers referred to specific models with majority of the papers reporting applications with QUAL2E.

In the authors' research group, a dynamic modeling strategy based on QUAL2E and coupled with a parameter estimation technique was introduced by Karadurmus and Berber (2004). The suggested strategy assumed that river reach could be modeled as a single CSTR. The model predicted and compared to the field data for 10 quality constituents observed; except those for the total coliform, total chloride and BOD_5, good agreement was obtained. Later a user-interactive software code in Matlab™ (The MathWorks Inc., USA) named as RSDS (River Stream Dynamics and Simulation) for the implementation of the suggested technique was presented, and the model predictions were compared against experimental data collected in field observations along the Yesilirmak river basin in Turkey and predictions from QUAL2E (Yuceer *et al.* 2007). In a following work, a water reach was represented by a series of CSTRs rather than a single one. Taking the trade-off between the computing load and the prediction accuracy into account, the number of CSTRs to be used to represent a river section was determined. Then, for simulating a 500 m long reach of the river between the two sampling stations, 20 CSTRs were used (Berber *et al.* 2009). Furthermore, this work included a parameter identification study.

Despite the progress that has been observed in the field of modeling, only few reports are available in the current literature on integrated software development for river water quality monitoring. It is seen that the recent efforts are now concentrating on the incorporation of a geographical information system to water quality models. Within this framework, Marsili–Libelli *et al.* (2001) described the interfacing of a Matlab™ based quality model to a popular geographical information system ArcView™ (ESRI Inc., USA) by a communication protocol through which data could be exchanged between the two platforms. The same research group later provided a new software package developed entirely in the Matlab™ platform based on the Mapping Toolbox™ and reported enhanced interactivity and portability. The features of the program are illustrated through a case study (Marsili–Libelli *et al.* 2002).

From the perspective of using web-based technologies for remote monitoring, Cianchi *et al.* (2000) used internet technologies to follow water quality with river quality sensors. Data from sensor signals were transmitted to information warehouse by internet. In a more recent work, web based Geological Information System was used to visualize and assess water quality over the web for end user with minimum knowledge and computing experience (Ganapathy and Ernest, 2004). The spatial 'Decision Support System' developed for their study focused on the lower Rio Grand river basin.

The use of Geographical Information System (GIS) computing platforms, as they represent a process for looking at geographic patterns in data and provide nice display options, has been increasing. GIS incorporates computer hardware, software, and geographic data for capturing, managing, analyzing, and displaying all forms of geographically referenced information. This rapidly growing technological field brings graphical features with tabular data in order to assess real-world problems. The opportunities that GIS systems provide may range from simple applications where one layer data display and analysis is done on a digital map, to more complex cases that mimic the real world by combining many data layers (Mitchell, 1999). Distributions of nitrate, nitrite and ammonium at various monitoring sites across the Humber basin were examined by Davies and Neal (2004) within a GIS framework. Empirical relationships between land characteristics and water quality for the whole catchment draining to each water quality monitoring site were established. The main water quality data source was the Land Ocean Interaction Study dataset. The land characteristics were classfied as lowland arable, urban, upland and coniferous woodland. The relationship between water quality and the catchment characteristics were assessed using linear regression. The study has proved success in showing the broad patterns across the region based on regression analysis of environmental measurements on the nitrogen species and simple land characteristics. (Davies and Neal, 2004). In a particular work by Ruelland *et al.* (2007) the Riverstrahler model that describes the biological functioning of an entire river system was coupled to a GIS interface to make the model entirely generic to be run on any river system for which a suitable database was available. They examined the effect of increasing the spatial resolution of the drainage network representation on the performance of the Riverstrahler model.

In this study we have developed an interactive GIS based software for water quality monitoring in rivers. The water quality model that has been previously developed in our research group was used for simulation and prediction. The software created has been tested with off-line water quality data gathered from a 36.5 km long section of Yesilirmak river in the central northern region of Turkey.

2. GIS PLATFORM INTEGRATING A WATER QUALITY MODEL IN MATLAB

A software has been created in this work to analyze the river water quality data in GIS platform. The program, called RSDS-C, and particularly designed to simulate Yesilirmak river in the central northern part of Turkey, allows user interaction and visual effects so that the predictions for pollution constituents can be represented on a digital map of the river. The River Stream Dynamic Simulation (RSDS) software previously developed in Matlab™ in our research group (Yuceer *et al.* 2007) was used as the water quality model, and was incorporated into the GIS platform ArcMap™ 9.1.

One critical point in combining a Matlab model with a GIS system is integrating the geographical data (which come from digital maps of GIS) with river pollution variables that are handled in Matlab. Data exchange between these two platforms requires that the graphical indications used to represent the geographical object in GIS be adapted to the data structure in the model embodied in Matlab. We used the data transfer strategy depicted in Fig. 1, which shows that the ASCII formatted text files were the medium of transfer between GIS (ArcMap™) and Matlab™. As ArcMap™ employs database files for displaying the digital maps, Microsoft Access™ was employed as the database-handling platform.

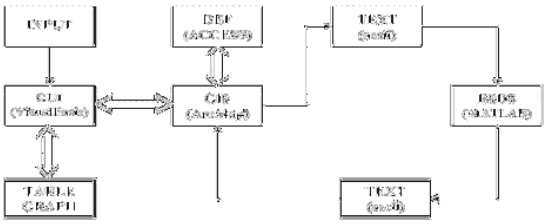

Fig. 1. ASCII file transfer strategy between different computing platforms.

A special graphical user interface (GUI) was designed for data input related to the river. The input comprise initial conditions for simulation, parameters related to integration of differential equations, flow characteristics of the river, or real measured data that has been observed at a particular location along the river (particularly when a parameter estimation study is intended). The GUI allows the user to interactively enter the observed quality of the river, which may be used as

the initial conditions at the beginning of simulations, or as the experimental value for the embedded simulation algorithm in case if parameter identification is to be performed. As for the water quality constituents, we use 11 variables comprising dissolved oxygen, carbonaceous BOD, four nitrogen forms (organic, ammonia, nitrite, and nitrate), two phosphorus forms (organic and dissolved), coliforms, nonconservative constituent chloride and phytoplanktonic algae. Those are the state variables of the embedded rigorous water quality model (Yuceer *et al.* 2007). The entered data also include variables related to the physical conditions in the river such as flow rate, temperature, cross-sectional area; and numerical parameters pertaining to the simulation (integration time, step size, method, etc.). The data was combined with the GIS system and transferred to Matlab™ platform for simulation. The simulations run on the Matlab platform determine the predictions of water quality along the river. Simulation results are relayed back to the GIS platform, and combined with the geographical data for display and analysis. The GUI was coded in Visual Basic™. The software allows the ArcMap and Access package programs to run interactively. This was accomplished through interlinking the ArcMap with Access (mdb) files, thus the data can be handled interactively. All graphics and tables were created from 'mdb' files.

In the previous work reported by Marsili–Libelli *et al.* (2002) data was transferred between the platforms by special 'avenue' script. This was appropriate in their case because the GIS platform that they used, ArcView (ESRI, 1996a), has a procedural language called Avenue (ESRI, 1996b) to define "scripts" that can implement the dynamic data exchange (DDE) procedure. However, the ArcMap™ 9.1 used here reads 'txt' files, so the data conveyed in ASCII format from Matlab are known. This data is then converted into dimensional variables in Visual Basic to be represented in tabulated form. For this procedure, the following SQL statements were used. These database connection statements make the data such that it can be viewed in graphs and tables, and also be used for color coding of the river information in GIS system.

```
Set m_pAdoCon = New ADODB.Connection
        m_pAdoCon.Open
"Provider=Microsoft.Jet.OLEDB.4.0; Data
            Source=C:\...\....mdb;Persist Security Info=False"
        Set pRecset = New ADODB.RecordSet
```

First of these statements opens database connections, second shows 'mdb' file path, name and table; and the third one starts the actual connection procedure. With these SQL statements, data become interconnected to ArcMap tables.

All windows and menus of the GUI, which are illustrated in the following figures, were designed in Visual Basic editor of ArcMap. The opening menu of the program is depicted in Fig. 2 together with the input sheet for entering initial water quality conditions. The table on the left hand side of the window lists the water quality variables that can be monitored on the screen. Prior to any run for simulation and prediction, the user is expected to enter the initial water quality conditions at starting point of working area where the simulation will begin. If there is a point source to the river, it can also be taken into account and respective values can be entered via additional input sheets that will open.

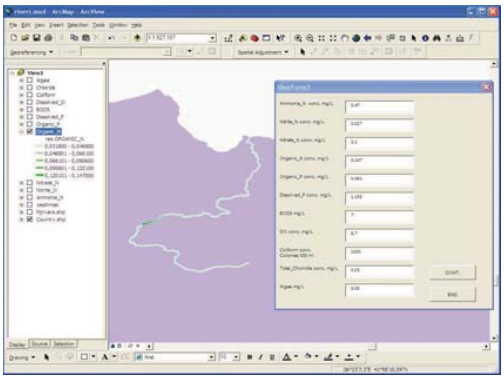

Fig. 2. View of the opening menu of the software (with the map of Yesilirmak river indicating the study area, and user input sheet).

Once the simulation is run, the user can select any variable from the list, shown in left hand side of the menu, to be displayed in table or graphical form.

The working area was divided into 100 parts of equal length to illustrate water quality variables, and thus the user can follow the concentration of the selected quality variable in different color at desired locations on map. The geographical point where the variables are sought is selected by the movement of the mouse along the river displayed on map. It then becomes possible to follow the water quality in terms of the selected pollutants along the river. For example, Fig. 3 depicts the change in the ammonia nitrogen concentration following a point source. With this feature, the simulation results are linked to the GIS database, and thus the user can easily follow the spatial distribution of the major constituents of river water quality. It is also possible to display more than one quality variable in graphical or table form at any location indicated.

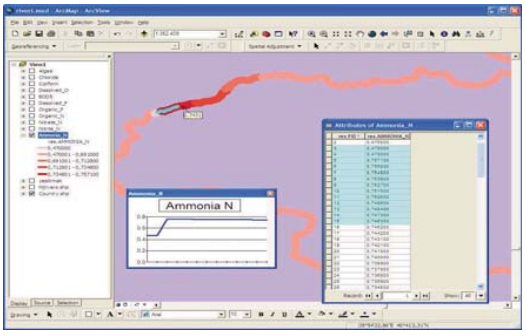

Fig. 3. Water quality display in table and graph form on the map.

In Fig. 3 the list on the left hand side shows the water quality variables considered. The user can select a location on the river map by moving the mouse, and if it is a point on the river the data table associated with this particular location opens on the screen. On the other hand, if the user scans a

region along the river, the software allows the user to see the changes in the concentration of the selected quality variables along this site by different colors. The color intensity on the map changes from light to dark with increased concentration, and this feature makes keeping track of water quality very easy. The user can select the concentration range (maximum and minimum values) and the number of intervals between. The color codes corresponding to those selected concentrations may be also determined by the user. If no choice has been made, the software picks up the maximum and minimum concentration values encountered in the simulations, and allocates five intermediate color codes (as default) to 5 intermediate values between the maximum and minimum. This feature of the GUI is illustrated in Fig. 4. It is also possible to see the changes in concentration in graphical form.

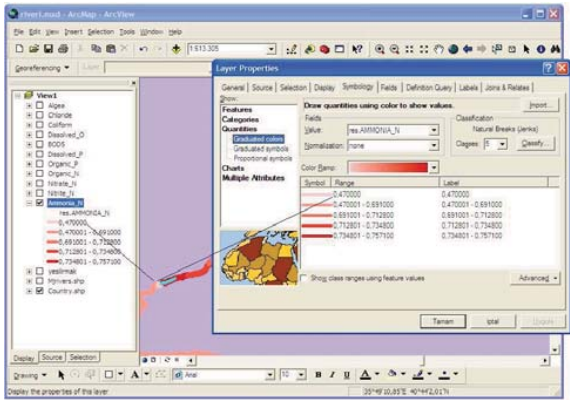

Fig. 4. Selection of color codes between maximum and minimum concentration intervals.

3. TESTING ON YESILIRMAK RIVER IN TURKEY

The software developed was tested with off line data collected from field studies around the city of Amasya along Yesilirmak river in Turkey. Yesilirmak is one of the major rivers in Turkey with 519 km length, and a basin of 36114 km^2 comprising 4.63 % of the territorial area of Turkey. Fig. 5 shows the study area on the river map. Pollution level in Yesilirmak affects the agricultural and rural development directly by distorting the ecological balance. The basin is a predominantly rural area and suffers from quite high level of pollution, in particular from agriculture, urban and industrial sources. Water quality in the river is classified in III and IV level according to the Water Pollution Control Act of Turkey, when physical, chemical, organic and bacteriological parameters are considered. An interactive river management decision support system for the region in order to protect the river from pollution becomes important for sustainable development in the future. Therefore, Yesilirmak was chosen as the study area, where our previous studies had also been concentrated.

The concentrations of ten water-quality constituents indicative of the level of pollution in the river were determined either on-site by portable analysis systems or in laboratory after careful conservation of the samples. For determination of dissolved oxygen, YSI Model 51/B portable oxygen meter in compliance with the Turkish Standard-TS 5677 were used. Nitrite, nitrate and ammonia forms of nitrogen were analyzed with HACH (Model DR2000) portable spectrophotometer. Total nitrogen was determined by Kjeldahl method. The organic nitrogen was calculated as the difference between the total nitrogen and the sum of ammonia, nitrite and nitrate forms. Phosphorous was analyzed by the methods of colorimetric ascorbic acid amino reduction and molibdo vanado phosphate (Greenberg, 1992) in the same spectrophotometer. BOD analysis and coliform analysis were done in the laboratory, after careful transportation of the samples, with manometric method in HACH spectrophotometer, and with multiple tubes and filtering method respectively. The chloride analysis was done in HACH spectrophotometer for free chloride and total chloride. Out of the 11 state variables, 10 were determined from field measurements. Only a representative data for the concentration of algae was taken from literature (Brown, 1987).

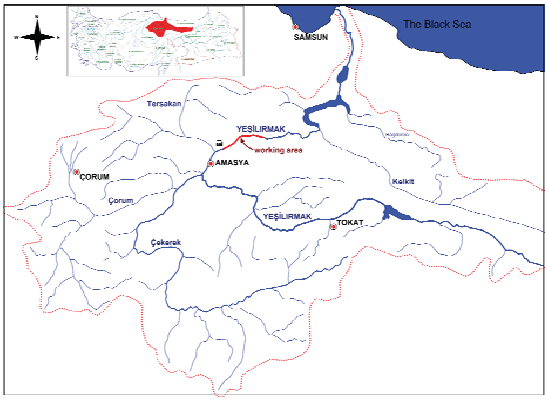

Fig. 5. Yesilirmak river basin and the study area.

During the dynamic sample collection period, the effluent from the wastewater treatment plant of a baker's yeast production plant was being discharged right beyond the starting point. Therefore, the results of the study indicated the extent of the pollution caused by the discharge from this industrial plant. In the simulations, addition of this discharge was considered as a continuous disturbance to the system, and its effect on the water quality, thus, was determined. Table 1 gives the characteristics of discharge from this local industrial plant.

Water quality data was collected for a 36.5 kms long section of the river adjacent to the city of Amasya. The study area started from the location 8.9 kms east of the city center where a baker's yeast plant was situated. The treated wastewater of this plant was considered as a point source to the river. The river water was sampled at 7 different locations in the downstream direction towards Durucasu gauging station of State Hydraulic Works (DSI) and the town of Tasova.

The initial conditions of the river and the characteristics of the point source as measured from points 1 and 2 indicated on Fig. 6 were introduced into the software, and dynamic simulation was run.

Table 1. Characteristics of discharge from the local baker's yeast plant

Variables	Waste water of baker's yeast plant
Temperature (^oC)	25.3
Flow (m^3/s)	0.25
Ammonia-N (mg/L)	27.4
Nitrite-N (mg/L)	1.3
Nitrate-N (mg/L)	52
Organic-N (mg/L)	0
Organic-P (mg/L)	0.52
Dissolved-P (mg/L)	12.4
BOD (mg/L)	210
DO (mg/L)	7.2
Coliform, (colonies/100 ml)	2900
Chloride (mg/L)	0

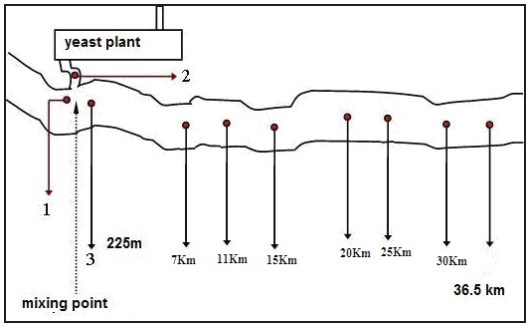

Fig. 6. Experimental study area for model verification, and sample collection points (distances indicated are measured from point 1).

Predictions from the software were compared to field data for a section of 36.5 kms of the river after the point source. Measured and predicted profiles of the pollution variables are shown in the following figures. Fig. 7, 8 and 9 reveal the pollution load due to the point source, and indicate that after some distance from the point where the effluent enters, remarkable recovery was observable. Fig. 10 shows the change in dissolved oxygen concentration along the study area. The points in the Figs. 7-8 indicate measurements whereas the continuous lines are predictions from the model.

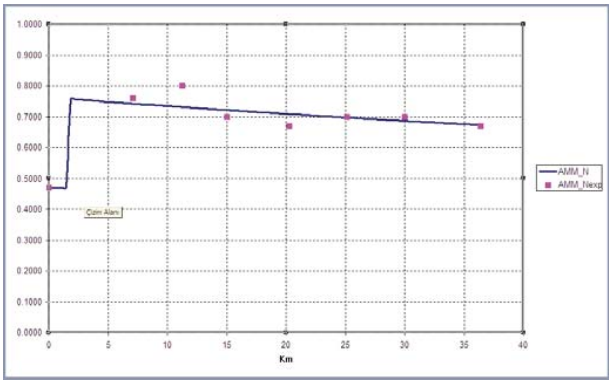

Fig. 7. Ammonia nitrogen profile.

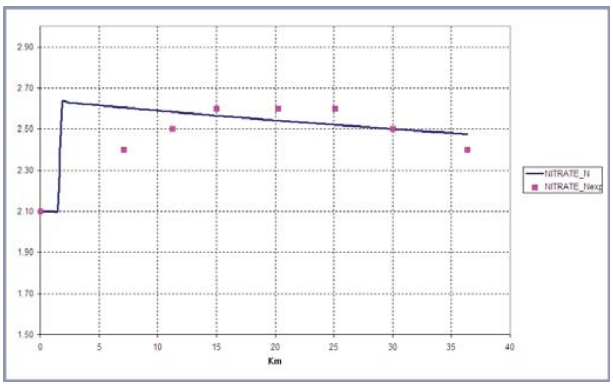

Fig. 8. Nitrate nitrogen profile.

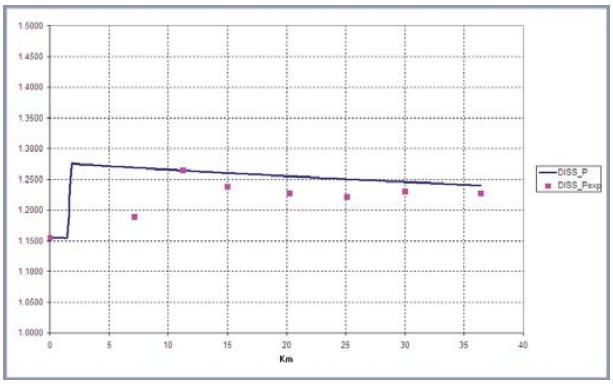

Fig. 9. Dissolved phosphorus profile.

For quantitative evaluation and comparison, Absolute Average Deviation (AAD) values were calculated. Table 2 indicates that, except nitrite nitrogen and chloride, the predicted values of all quality variables are in compliance with measured values.

Fig. 11 presents the predicted water quality results in tabulated form as a function of geographical space indicated on the first row. The columns represent the water quality variables predicted. The water quality data displayed can be viewed in graphical form or as color coded displays on the river map.

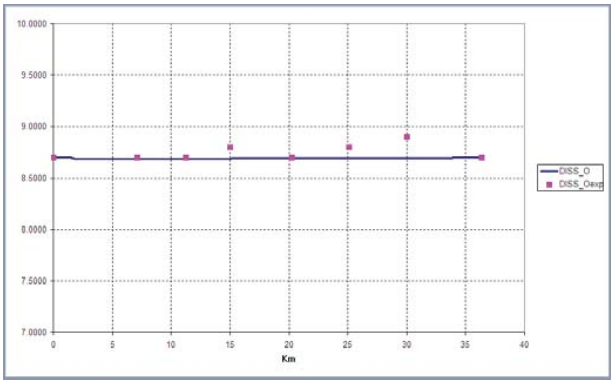

Fig. 10. Dissolved oxygen profile.

Table 2. Absolute Average Deviation (AAD) values for comparison of pollution variables

Water Quality Variables	(AAD %)
Ammonia Nitrogen	2.86
Nitrite Nitrogen	29.59
Nitrate Nitrogen	2.71
Organic Nitrogen	9.01
Organic Phosphorus	2.09
Dissolved Phosphorus	1.89
BOD	5.49
Dissolved Oxygen	0.64
Coliform	6.87
Chloride	20.19

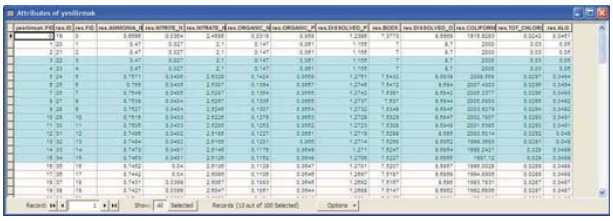

Fig. 11. Simulation results in tabulated form.

4. CONCLUSION

Although many models have been developed, they appear to be available to limited number of professionals who are capable of using and interpreting water quality simulation models. However, increased awareness in surface water pollution dictates that these models be used by non-experts who may be interested in knowing the consequences of various scenarios on river pollution. Availability and affordability of GIS systems offer alternative solutions to this problem.

Starting from this point, a software integrating a Geographical Information System and a water quality model in a single convenient package has been developed in this study. The effects of a discharge on the river can be predicted by simulation and the results are displayed on the map. The software was tested off-line with data collected from field measurements on Yesilirmak river in Turkey.

The integration strategy developed and the GUI created provide an interactive environment for the user and will help decision making process in river basin management systems, and can be fairly easily adapted to other rivers.

The results indicated that the model was able to satisfactorily estimate the water quality along the downstream section of a point load.

In our ongoing work, the software has been implemented for real time applications, and these results will be reported later.

REFERENCES

Berber, R., Yuceer, M. and Karadurmus, E. (2009). A parameter identifiability and estimation study in Yesilirmak River. *Water Science and Technology*, 59(3), 515–521.

Brown, L. C. (1987). Uncertainty analysis in water quality modelling using QUAL2E, EPA/Technical Report Data, Athens, GA.

Cianchi, P., Marsili–Libelli, S., Burchi, A. and Burchielli, S. (2000). Integrated river quality management using internet technologies. *Watermatex.* Gent(B), 18-20.

Cox, B.A. (2003). A review of available in-stream water quality models and their applicability for simulating dissolved oxygen in lowland rivers. *The Science of the Total Environment.* 314-316, 335-377.

Davies, H. and Neal, C. (2004). GIS-based methodologies for assessing nitrate, nitrite and ammonium distribution across a major UK basin, the Humber. *Hydrology and Earth System Sciences.* 8(4), 823-833.

ESRI (1996a) ArcView GIS. *The geographic information system for everyone*. Environmental Systems Research Institute, USA.

ESRI (1996b) ArcView Spatial Analyst. *Advanced spatial analysis using raster and vector data*. Environmental Systems Research Institute.

Ganapathy, C. and Ernest, A.N.S. (2004). Water quality assessment using web based GIS and distributed database management systems. *Environmental Informatics Archives*. 2, 938-945.

Greenberg, A.E., Clesceri, L.S., Lenore, S. and Eaton, A.D. (1992). Standard methods for the examination of water and wastewater. *American Public Health Assoc.* Washington D.C.

Karadurmus, E. and Berber, R. (2004). Dynamic simulation and parameter estimation in river streams. *Environmental Technology*. 25, 471-479.

Marsili–Libelli, S., Caporali, E., Arrighi, S. and Becattelli, C. (2001). A georeferenced water quality model. *Water Sci. Tech.* 43(7), 223-230.

Marsili–Libelli, S., Pacini, G., Barresi, C., Petti, E. and Sinacori, F. (2002). An interactive georeferenced water quality model. *Hydroinformatics: Proc. of the 5th Int. Conf. on Hydroinformatics*, Cardiff, UK.

Mitchell, A. (1999). *The ESRI Guide to GIS Analysis*. Vol. 1, Esri Press, USA.

Rauch, W., Henze, M., Koncsos, L. Reichert, P., Shanahan, P., Somlyody, L. and Vanrolleghem, P. (1998). River water quality modelling: I. State of the art. *IAWQ Biennial Int. Conf.* Vancouver-Canada, 21-26.

Ruelland, D.,Billen, G., Brunstein, D., Garnier, J. (2007). SENEQUE: A multi-scaling GIS interface to the Riverstrahler model of the biogeochemical functioning of river systems. *Science of the Total Environment.* 375, 257-273.

Shanahan, P., Henze, M., Koncsos, L. Rauch, W., Reichert, P. Somlyody, L. and Vanrolleghem, P. (1998). River water quality modelling: II. Problems of the art. *IAWQ Biennial Int. Conf.* Vancouver-Canada, 21-26.

The MathWorks Inc. Natick- MA. (2003).

Yuceer, M., Karadurmus, E. and Berber, R. (2007). Simulation of River Streams: Comparison of a New Technique to QUAL2E. *Mathematical and Computer Modelling.* 46, 292–305.

Unscented Kalman Filter state and parameter estimation in a photobioreactor for microalgae production ⋆

Giancarlo Marafioti * **Sihem Tebbani** ** **Dominique Beauvois** **
Giuliana Becerra** ,*** **Arsene Isambert** *** **Morten Hovd** *

* *Department of Engineering Cybernetics, Norwegian University of Science and Technology, N-7491 Trondheim, Norway* {giancarlo.marafioti, morten.hovd}@itk.ntnu.no
** *Control Department, SUPELEC, Plateau de Moulon, 91192 Gif sur Yvette, France* {sihem.tebbani, dominique.beauvois, giuliana.becerra}@supelec.fr
*** *LGPM, Ecole Centrale Paris, 92295 Chatenay-Malabry, France* arsene.isambert@ecp.fr

Abstract: Microalgae have many applications such as the production of high value compounds (source of long-chain polyunsaturated fatty acids, vitamins, and pigments), in energy production (e.g. photobiological hydrogen, biofuel, methane) or in environmental remediation (especially carbon dioxide fixation and greenhouse gas emissions reduction). However, the photobioreactor microalgae process needs complex and costly hardware sensors, especially for biomass measurement. Thus, state and parameter estimation seems to be a critical issue and is studied in this paper in the case of a culture of the microalga Porphyridium purpureum. This paper is an extension of the previous work of Becerra-Celis et al. (2008) where the principal objective is to design a biomass estimator of this microalga production in a photobioreactor based on the total inorganic carbon measurement.
Unscented Kalman filtering is applied to estimation of states and model parameters, producing better performances in comparison with Extented Kalman filtering. Numerical simulations in batch mode, and real-life experiments in continuous mode have been carried out. Corresponding results are given in order to highlight the performance of the proposed estimator.

Keywords: Unscented Kalman Filter, state and parameter estimation, microalgae photobioreactor

1. INTRODUCTION

In chemical and biochemical processes, often chemical reactions have to be monitored and controlled using different sensor measurements. Typically, measurements of reactant and product concentrations, operating temperatures, pressures, and other parameters are needed. In general, a measurement has to be reliable, i.e. it has to be available and accurate. However, there are several reasons why required measurements may not be reliable. Some of such reasons are the impracticability of building an appropriate sensor due to lack of technology, the difficulty to position the sensor, the associated cost. In such cases, an attempt to use estimation techniques may be done.

Dochain (2003) presents an interesting overview of available results on state and parameter estimation in chemical and biochemical processes. A comparison of several traditional state and parameter estimation approaches is given, discussing pros and cons in different cases, and describing how the most common implementation problems are solved (see Dochain (2003) and references therein). In this work particular attention is given to Kalman filtering. Its application to nonlinear systems is tipically implemented by the well known and widely used Extended Kalman Filter (EKF). Even though there are issues due to the inherent linearization procedure in the algorithm, the scientific and industrial communities have obtained successful EKF applications. However, it is the authors' opinion that in systems with strong nonlinearities it could be interesting to exploit the benefits of the Unscented Kalman Filter (UKF). Thus, the UKF is introduced as a valid EKF alternative, and it is shown how to obtain improvement due to its implementation flexibility, extending then its applicability. The first works introducing the Unscented transformation idea and the UKF algorithm are Julier and Uhlmann (1996), and Julier and Uhlmann (1997). In Wan and Van Der Merwe (2000) several UKF algorithms are described, which could be used for state estimation, parameter estimation, and joint state and parameter estimation. This work aims to present UKF advantages in terms of performance and implementation ease, compared to the EKF. The work of Becerra-Celis et al. (2008) is considered as starting point, where it is shown how to implement an

⋆ The authors wish to acknowledge support from the French-Norwegian research cooperation project AURORA

EKF for state estimation in a photobioreactor. Moreover, experimental data is used to validate the results.

Next section explains how to use the UKF for joint state and parameter estimation. Section 3 describes the photobioreactor used for microalgae production, and its model. Section 4 analyzes the application of the UKF to the photobioreactor. In addition, it is shown that when parameter estimation is considered, the UKF produces improved results, particularly when experimental data, collected from continuous cultures, is used. Finally, conclusions and future work are presented.

2. STATE AND PARAMETER ESTIMATION

Consider the following nonlinear system

$$\begin{aligned}\dot{\xi}(t) &= g(\xi(t), u(t), v_\xi(t)) \\ y(t) &= l(\xi(t)) + n(t)\end{aligned} \tag{1}$$

where ξ is the state vector, u is the input vector, y is the measurement vector, v_ξ is the process noise vector, n is the measurement noise vector, of appropriate dimensions, respectively. Simply stated, the state estimation problem consists to reconstruct the state vector knowing the measurement and input vectors, some information on noise distributions, and the nonlinear functions $g(\cdot)$ and $l(\cdot)$. When the parameters used in the model (1) are uncertain the estimation problem may be more difficult to solve. One method to obtain sufficiently good estimates is to make the estimator algorithm robust with respect to the parameter variations. Another method is to try to estimate the uncertain parameters improving the model accuracy. However, joint parameter and state estimation may lead to observability problems. A general framework to introduce the parameter estimation is to extend the state with the uncertain parameters vector and then estimate the augmented state. In cases where the actual parameters are slowly varying, it is common to model the parameters vector η as a random walk driven by a white noise process $v_\eta(t)$. Thus the following differential equation

$$\dot{\eta}(t) = v_\eta(t) \tag{2}$$

is used to augment the system (1). Associating then a relatively small covariance to $v_\eta(t)$, it is possible to consider the slowly varying nature of the parameters. The section below describes the particular UKF used in this work. The algorithm describes the case of joint parameter and state estimate. The equations are still valid if only state estimate is considered. However, the procedure to augment the state vector and covariance matrix, with the parameter vector and its covariance matrix, respectively, must be omitted.

2.1 Unscented Kalman Filter algorithm

Consider the following discretization of the system (1-2)

$$\begin{aligned}\xi_{k+1} &= f(\xi_k, u_k, v_k^\xi, \eta_k) \\ \eta_{k+1} &= \eta_k + v_k^\eta \\ y_k &= h(\xi_k, \eta_k) + n_k\end{aligned} \tag{3}$$

obtained using an appropriate numerical integration routine. To estimate jointly the state and parameters of the system (3), the following augmented vector is defined:

$$\hat{x}_k^a = [\hat{x}_k',\ v_k']' \tag{4}$$

where $\hat{x}_k = [\hat{\xi}_k',\ \hat{\eta}_k']'$ has as elements the state and parameter estimates, respectively. The vector $v_k = [v_k^{\xi'}, v_k^{\eta'}]'$ contains the process noises in the evolution of ξ and η. Analogously, the augmented covariance matrix is defined as

$$P_k^a = \begin{bmatrix} P_k^x & P_k^{x,v} \\ P_k^{v,x} & P_k^v \end{bmatrix} \tag{5}$$

where P_k^x consists of the state and parameter error covariances, while P_k^v includes the process noise covariance associated to state and parameters. In addition, the off diagonal entries are cross covariance terms represented by the notation $P_k^{\cdot,\cdot}$. Obviously, all elements of $\hat{x}_k^a$ and P_k^a are of appropriate dimensions.

Given the initial conditions

$$\hat{x}_0^a = \begin{bmatrix} \hat{x}_0 \\ 0_v \end{bmatrix}, \qquad P_0^a = \begin{bmatrix} P_0^x & 0 \\ 0 & P_0^v \end{bmatrix}, \tag{6}$$

the dimension L of the augmented system state $\hat{x}^a$, and the following scalar weigths W_i

$$W_0^{(m)} = \lambda/(L+\lambda) \tag{7}$$

$$W_0^{(c)} = \lambda/(L+\lambda) + (1-\alpha^2+\beta) \tag{8}$$

$$\begin{aligned}W_i^{(m)} &= W_i^{(c)} \\ &= 1/[2(L+\lambda)]\end{aligned} \tag{9}$$

for $i = 1, \ldots, 2L$, $\lambda = \alpha^2(L+\kappa) - L$, and where α, β, κ are parameters to be chosen.

For $k = 1, \ldots, \infty$

- Calculate the sigma points defined as

$$\begin{aligned}\left(\mathcal{X}_{k-1}^a\right)_0 &= \hat{x}_{k-1}^a \\ \left(\mathcal{X}_{k-1}^a\right)_j &= \hat{x}_{k-1}^a + \gamma\left(\sqrt{\mathrm{P}_{k-1}^a}\right)_j \\ \left(\mathcal{X}_{k-1}^a\right)_{j+L} &= \hat{x}_{k-1}^a - \gamma\left(\sqrt{\mathrm{P}_{k-1}^a}\right)_j\end{aligned} \tag{10}$$

  where $\left(\sqrt{\mathrm{P}_{k-1}^a}\right)_j$ is the j-th column ($j = 1, \ldots, L$) of the square root of the augmented covariance matrix (5) at the previous time step. The parameter $\gamma = \sqrt{L+\lambda}$ can be interpreted as a scaling factor used to move the position of sigma points around the mean value $\hat{x}_{k-1}^a$. Finally, the sigma points are regrouped in the following matrix of L rows and $2L+1$ columns:

$$\mathcal{X}_{k-1}^a = \begin{bmatrix} \mathcal{X}_{k-1}^x \\ \mathcal{X}_{k-1}^v \end{bmatrix} \tag{11}$$

  where $\mathcal{X}_{k-1}^x$ contains the sigma point rows associated to state and parameters, and $\mathcal{X}_{k-1}^v$ the sigma point rows associated to the state and parameters process noises.

- Propagate the sigma points through the nonlinear dynamics F[·], and compute the predicted state estimate, where the index i is used to select the appropriate sigma point column:

$$\mathcal{X}_{k|k-1} = \mathrm{F}\left[\mathcal{X}^a_{k-1}, u_{k-1}\right] \tag{12}$$

$$\hat{x}^-_k = \sum_{i=0}^{2L} W_i^{(m)} \mathcal{X}_{i,k|k-1} \tag{13}$$

- Compute the predicted covariance:

$$P^-_k = \sum_{i=0}^{2L} W_i^{(c)} \left[\mathcal{X}_{i,k|k-1} - \hat{x}^-_k\right] \left[\mathcal{X}_{i,k|k-1} - \hat{x}^-_k\right]' \tag{14}$$

- Using the predicted mean (13) and covariance (14), recompute a new set of sigma points as defined in (10-11):

$$\mathcal{X}^-_k = \left[\mathcal{X}^{x\prime}_k, \mathcal{X}^{v\prime}_k\right]' \tag{15}$$

- Instantiate the new sigma points through the observation model H[·], and calculate the predicted measurement:

$$\mathcal{Y}_{k|k-1} = \mathrm{H}\left[\mathcal{X}^-_k\right] \tag{16}$$

$$\hat{y}^-_k = \sum_{i=0}^{2L} W_i^{(m)} \mathcal{Y}_{i,k|k-1} \tag{17}$$

- Obtain the innovation covariance and the cross covariance matrices:

$$P_{\tilde{y}_k\tilde{y}_k} = \sum_{i=0}^{2L} W_i^{(c)} \left[\mathcal{Y}_{i,k|k-1} - \hat{y}^-_k\right] \left[\mathcal{Y}_{i,k|k-1} - \hat{y}^-_k\right]' + P^n \tag{18}$$

$$P_{y_k x_k} = \sum_{i=0}^{2L} W_i^{(c)} \left[\mathcal{X}_{i,k|k-1} - \hat{x}^-_k\right] \left[\mathcal{Y}_{i,k|k-1} - \hat{y}^-_k\right]' \tag{19}$$

where P^n is the measurement noise covariance;

- Perform the measurement update using the regular Kalman filter equations:

$$\mathcal{K}_k = P_{y_k x_k} P^{-1}_{\tilde{y}_k\tilde{y}_k} \tag{20}$$

$$\hat{x}_k = \hat{x}^-_k + \mathcal{K}_k\left(y_k - \hat{y}^-_k\right) \tag{21}$$

$$P^x_k = P^-_k - \mathcal{K}_k P_{\tilde{y}_k\tilde{y}_k} \mathcal{K}'_k \tag{22}$$

In (12), F[·] is the modified nonlinear dynamics of (3). The changes are made to consider the discretization and the augmented state, and also to guarantee the proper propagation of each sigma point. Analogously, in (16) H[·] is the modified observation function. Due to the fact that measurement noise is assumed additive with zero mean, it is possible to write (18). Thus, the algorithm computational complexity is reduced because there is no need to associate more sigma points. Regarding filter design parameters, in most cases typical values are $\beta = 2$, and $\kappa = 0$ or $\kappa = 3 - L$, leaving only the parameter α as free parameter. Moreover, considering that $1 \leq \alpha \leq 10^{-4}$ the tuning of the UKF becomes simpler. For a finer tuning and a more accurate description about the meaning of the UKF parameters one can refer to Wan and Van Der Merwe (2000). Finally, in (11) and (15) a square root of a matrix has to be calculated, thus an appropriate algorithm must be used, for instance the Cholesky factorization.

3. PHOTOBIOREACTOR FOR MICROALGAE PRODUCTION

3.1 Strain and growth conditions

The photobioreactor is used to produce the red microalgae *Porphyridium purpureum* SAG 1830-1A obtained from the Sammlung von Algenkulture Pflanzenphysiologister Institut Universität Göttingen, Germany. The strain is growth and maintained on Hemerick medium (Hemerick (1973)). The pH of the Hemerick medium is adjusted to 7.0 before autoclaving it for 20 minutes at 121 °C. Cultures are maintained at 25 °C in 500 ml flask containing 400 ml culture under continuous light intensity of 70 $\mu E m^{-2} s^{-1}$ and aerated with air containing 1% (v/v) CO_2 at 100 rpm on an orbital shaker. During the exponential growth phase, within an interval of two weeks, 200 ml of culture are transferred to a new flask containing fresh medium.

3.2 Culture conditions and measurements

Figure 1 illustrates the photobioreactor diagram where the growth of cultures is performed. The bubble column photobioreactor has a working height of 0.4 m and a diameter of 0.1 m. The total culture volume is 2.5 l, and the cylindrical reactor, made of glass, has an illuminated area of 0.1096 m^2. To agitate the culture an air mixture with 2% (v/v) CO_2 is continuously supplied at a flow rate of 2.5 $V.V.H$ (gas volume per liquid culture volume per hour). 0.22 μm Millipore filters, appropriate valves and flowmeters are used to filter and to control the air flow rate entering the photobioreactor. Four OSRAM white fluorescent tubes (L30W/72) and three OSRAM pink fluorescent tubes (L30W/77) are arranged around the bubble column as an external light source. The incident light intensity on the reactor surface is measured at ten different locations with flat surface quantum sensors (LI-COR LI-190SA). The average light intensity is computed by the weighted average of all measurements. The optimal value of irradiance on surface for the reactor is 120 $\mu E m^{-2} s^{-1}$. A transparent jacket connected to a thermostat unit allows the temperature control, which is regulated at 25 °C. Other sensors are a pH sensor (Radiometer Analytical) and a dissolved oxygen sensor (Ingold type 170). A sampling port is applied to the top of the column, from where samples for off line analysis are collected after 6, 8, and 12 hours. The number of cells is counted using an optical microscope ZEISS Axioplan-2 on Malassez cells. The total inorganic carbon (T.I.C.) in the culture medium is calculated by gas phase chromatography. This method, proposed by Marty et al. (1995), is used to measure low inorganic carbon concentrations down to ($10^{-6} mol\ l^{-1}$) within an accuracy of 10%.

3.3 Mathematical model

In this work the bioprocess model presented in Baquerisse et al. (1999) is used. It consists of two sub models, one describing the growth kinetics, and one representing the gas-liquid mass transfer in the photobioreactor. This

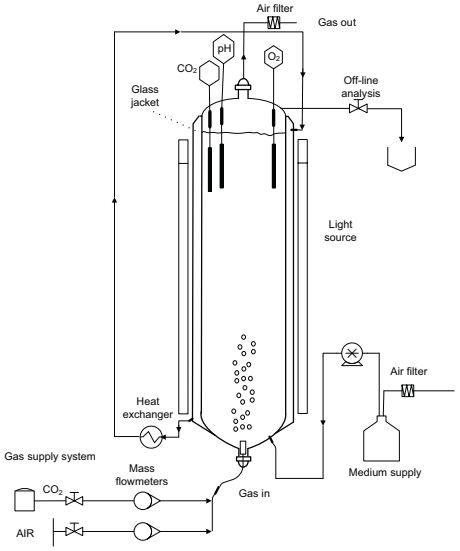

Fig. 1. Photobioreactor diagram.

results in two differential equations describing the state of the reactor:

$$\begin{aligned}\frac{dX}{dt} &= \frac{F_{in}}{V}X_{in} + \mu X - \frac{F_{out}}{V}X \\ \frac{d[TIC]}{dt} &= \frac{F_{in}}{V}[TIC]_{in} - \frac{F_{out}}{V}[TIC]_{out} - \mu\frac{X}{Y_{X/S}} \\ &\quad - mX + k_L a\left([CO_2^*] - [CO_2]\right) \end{aligned} \tag{23}$$

where X is the biomass, and $[TIC]$ is the inorganic carbon concentration associated with cell density increase. The subscripts $[\cdot]_{in}$ and $[\cdot]_{out}$ indicate quantities flowing into, and out from the reactor, respectively. V is the culture volume, and F is the medium flow rate. The mass conversion yield is defined by $Y_{X/S}$, m is the maintenance coefficient, and $k_L a$ is the gas-liquid transfer coefficient. The carbon dioxide concentration in the medium fresh is defined as:

$$[CO_2^*] = \frac{PCO_2}{\mathcal{H}} \tag{24}$$

where PCO_2 is the partial pressure of carbon dioxide, and $\mathcal{H}$ is the Henry's constant for Hemerick medium. Moreover, the carbon dioxide concentration in the medium is given by:

$$[CO_2] = \frac{[TIC]}{\left[1 + \frac{K_1}{[H^+]} + \frac{K_1 K_2}{[H^+]^2}\right]} \tag{25}$$

where K_1, K_2 are kinetics constants, and $[H^+]$ is defined as:

$$[H^+] = 10^{-pH} \tag{26}$$

representing the hydrogen ions concentration in the culture media.

In addition, a light transfer model is considered, which describes the evolution of incident and outgoing light intensity:

$$E = \frac{(I_{in} - I_{out})A_r}{VX} \tag{27}$$

$$I_{out} = C_1 I_{in} X^{C_2} \tag{28}$$

where E is the light "energy" accessible per cell, I_{out} is the outgoing light intensity, I_{in} is the ingoing light intensity. C_1, C_2 are constants depending on the reactor geometry, and A_r is its area.

The light intensity and the total carbon concentration influence the specific growth rate, defined as

$$\mu = \mu_{max}\frac{E}{E_{opt}}e^{\left(1-\frac{E}{E_{opt}}\right)}\frac{[TIC]}{[TIC]_{opt}}e^{\left(1-\frac{[TIC]}{[TIC]_{opt}}\right)} \tag{29}$$

where μ_{max}, E_{opt}, and $[TIC]_{opt}$ are model parameters identified from the batch data experiments. Finally, in (29) substrates limitation effect is taken into account.

3.4 Batch and continuous operating conditions

The photobioreactor can work in two different operating conditions, batch mode and continuous mode. In batch mode:

$$F_{in} = F_{out} = 0; \qquad [TIC]_{in} = 0; \qquad X_{in} = 0. \tag{30}$$

In continuous mode, instead:

$$F_{in} = F_{out} \neq 0. \tag{31}$$

3.5 Model parameters

The model parameters used in this work are the ones identified in Becerra-Celis et al. (2008). For more details on the system identification procedure the reader is referred to their work. Tables 1 and 2 contain the parameters for the microalgae and the total inorganic carbon dynamics, respectively.

Table 1. Model parameters for *Porphyridium purpureum* at 25 °C.

Parameter	Unit	Value
μ_{max}	h^{-1}	0.0337
E_{opt}	$\mu Es^{-1}(10^9 cell)^{-1}$	1.20
$[TIC]_{opt}$	$mmolel^{-1}$	12.93
$k_L a$	h^{-1}	41.40
C_1		0.28
C_2		−0.55

Table 2. Model parameters for [TIC] dynamics.

Parameter	Unit	Value
K_1		$1.02 \cdot 10^{-6}$
K_2		$8.32 \cdot 10^{-10}$
m	$h^{-1}mmole(10^9 cell)^{-1}$	0.004
$Y_{X/S}$	10^9 *cell per mole TIC*	198.1
$\mathcal{H}$	*atm l mole*$^{-1}$	34.03

4. BIOMASS ESTIMATION

Controlling a photobioreactor has some difficulties associated to the implicit nonlinear and time varying nature of the system. There are also problems with the practicability

to find reliable online sensors able to measure the state variables (Shimizu (1996)). To overcome the lack of online sensors, Becerra-Celis et al. (2008) show how to implement an Extended Kalman Filter (EKF) to estimate the biomass for the photobioreactor, described in Section 3, using the measurement of T.I.C.. In this work, it is shown how the use of an UKF gives better performance, particularly for continuous cultures. There are several reasons for which the UKF may be considered as an EKF alternative. There is no linearization procedure in the UKF, as can be seen in section 2.1. This is relevant when strong nonlinearities are present in the process because no linearization error is introduced. It is straightforward to extend the state estimation to joint estimation, just augmenting the estimated vector and covariance matrix, while calculation of system derivatives with respect to the parameters, are required in an EKF algorithm.

4.1 UKF applied to the photobioreactor

Using the UKF, described in Section 2.1, the main objective is to estimate the biomass X in the photobioreactor of Section 3. Focusing on the two different working conditions defined in Section 3.4, it is observed how in batch mode the UKF has an excellent performance, which also is the case for the EKF designed in Becerra-Celis et al. (2008). This is due to the fact that the model parameters are identified in batch mode, and the measurements have a constant sampling time. A more complex scenario appears for continuous cultures. The model parameters are still the ones from the batch experiments, and the experimental data are collected at variable instant intervals. Due to the variable time steps, Becerra-Celis et al. (2008) implements a continuous discrete version of the EKF. In this work, this problem is tackled in two steps. Firstly, a zero order hold is applied to the measurements, secondly the standard UKF algorithm is properly modified. More in detail, the discrete UKF algorithm with an augmented state to consider parameter estimation and process noise is implemented. The sigma points are recomputed in (15) and then used to obtain the predicted measurement in (16-17). Those modifications give the possibility to use the discrete algorithm with the irregular measurement sampling time of the continuous culture case. Furthermore, the parameter μ_{max} in (29) is chosen to be estimated. Finally, despite the fact that a zero order hold is used to permit a discrete UKF implementation, the UKF accuracy and speed of convergence are improved with respect to the EKF ones.

4.2 Simulation results with experimental data

The following results show the efficiency of the proposed method when the photobioreactor works either in batch mode or in continuous mode. Figure 2 illustrates the convergence of the UKF in simulated batch mode, for which conditions (30) hold. In this case the nonlinear model (23) is discretized at sampling time $T_s = 0.5\ h$ and used to simulate the state of the process, starting from initial conditions $X_0 = 2.44 \cdot 10^9 cell/l$, $[TIC]_0 = 2.55\ 10^{-3} mole/l$. After that, $[TIC]$ is corrupted by additive Gaussian white noise with standard deviation $\sigma = 0.2\ 10^{-3} mole/l$, and used as measurement for the UKF. Thus, the state is

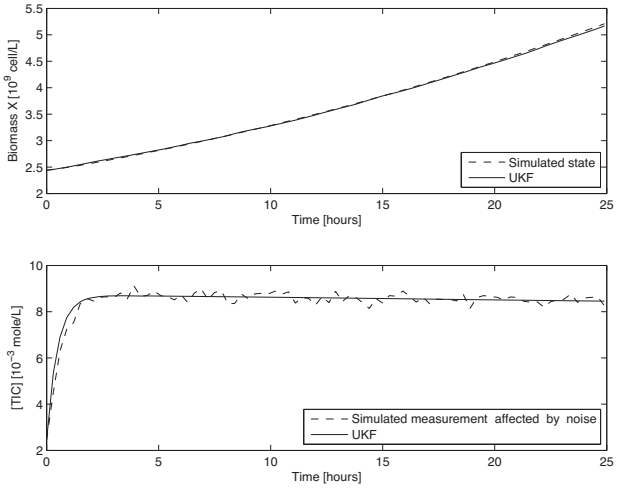

Fig. 2. UKF estimation for simulated batch mode.

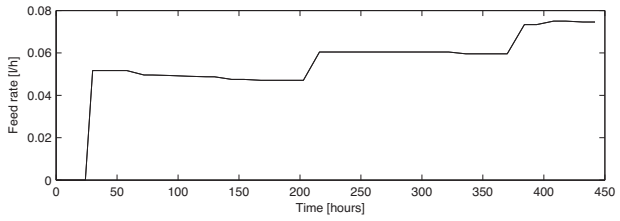

(a) Culture medium feeding profile

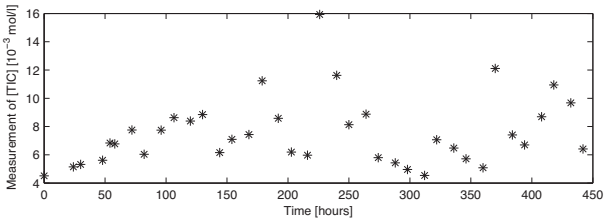

(b) Measurement of [TIC]

Fig. 3. Experimental data: input and output of the photobioreactor collected in continuous mode.

estimated successfully with excellent noise rejection in T.I.C.. The results obtained for continuous cultures are even more interesting. Initial conditions are $X_0 = 1.8 \cdot 10^9 cell/l$, $[TIC]_0 = 4.51 \cdot 10^{-3} mole/l$, and in addition real experiment data, presented in Figure 3, are used as input to the filters. The EKF designed in Becerra-Celis et al. (2008), the UKF with only state estimation, and the UKF with joint state and parameter estimation are simulated. The results obtained are shown in Figure 4 and here discussed. In Figure 4(a) it is noticeable how both UKF implementations have faster speeds of convergence than the EKF. In Figure 4(b) the state estimation error of the three different approaches are compared, and it is evident how the UKFs give smaller estimation errors. Moreover the mean squared error (MSE) between the biomass and its estimate is computed. Table 3 shows the MSE index, which is obtained averaging the MSE along the entire simulation period. From both figures it is noticeable how the UKF performs better than the EKF, and how the introduction

Table 3. Mean Squared Error Index

EKF	UKF	UKF with par. est.
13.60	6.12	6.12

of parameter estimation in the UKF improves the accuracy of the estimation in the final part (after 300 hours), although slightly reduces the speed of convergence. Since the parameters are identified from batch experiments, as shown in Becerra-Celis et al. (2008), adding parameter estimation may be useful when the photobioreactor is run in continuous mode. Figure 5 shows the evolution of the μ_{max} estimation, the estimated value is compared with the identified value and moreover the UKF error covariance is shown.

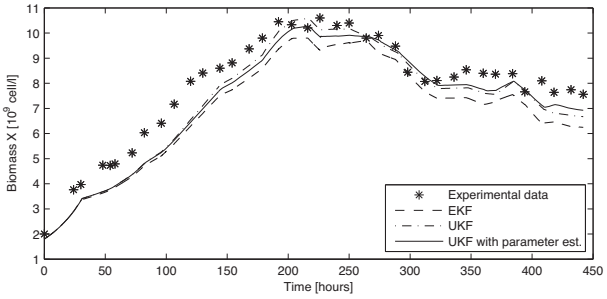

(a) Biomass estimate

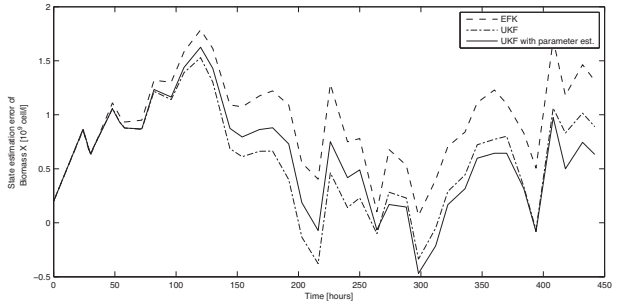

(b) State Estimation Error

Fig. 4. Biomass estimation comparison for continuous cultures.

5. CONCLUSION

This work can be considered as an extension of Becerra-Celis et al. (2008), where the main objective is to design an efficient, reliable and applicable biomass estimator for a microalgae photobioreactor. A more recent nonlinear estimator (UKF) is used, obtaining improved results. In both batch and continuous mode, the approach presented produces a faster estimate convergence and a better estimate accuracy. The capacity and ease to introduce parameter estimation jointly with state estimation, the absence of linearization, the comparable computational complexity make the UKF an attractive estimator for nonlinear systems. The particular UKF framework described in section 2.1 showed to be well suited for the case when measurements, arriving at variable time instants, are subject to a zero holder filter. The extra set of sigma points calculated in (15) are needed to obtain a smoother estimate. Future work is needed to design a feedback based controller using

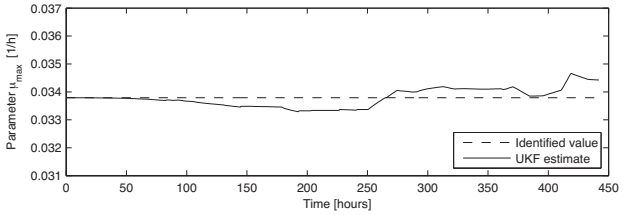

(a) UKF estimate and identified value of μ_{max}

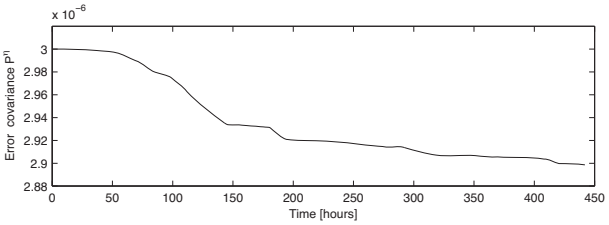

(b) UKF error covariance of μ_{max}

Fig. 5. UKF parameter estimate and its covariance for continuous culture.

the UKF estimate, and to better understand which parameter would improve the filter performance without introducing observability issues. It is also interesting to explore how the UKF performs with other processes compared to the traditional methods in use in practice.

REFERENCES

Baquerisse, D., Nouals, S., Isambert, A., dos Santos, P.F., and Durand, G. (1999). Modelling of a continuous pilot photobioreactor for microalgae production. *Journal of Biotechnology*, 70(1-3), 335 – 342.

Becerra-Celis, G., Tebbani, S., Joannis-Cassan, C., Isambert, A., and Boucher, P. (2008). Estimation of microalgal photobioreactor production based on total inorganic carbon in the medium. *17th IFAC W.C., Seoul*.

Dochain, D. (2003). State and parameter estimation in chemical and biochemical processes: a tutorial. *Journal of process control*, 13, 801 – 818.

Hemerick, J. (1973). Culture methods and growth measurements. In J. Stein (ed.), *Handbook of Physiological Methods*, 250–260. Cambridge University Press, UK.

Julier, S. and Uhlmann, J.K. (1996). A general method for approximating nonlinear transformations of probability distributions. Technical report, .

Julier, S.J. and Uhlmann, J.K. (1997). A new extension of the kalman filter to nonlinear systems. In *Int. Symp. Aerospace/Defense Sensing, Simimulation and Controls*, 182–193.

Marty, A., Cornet, J., Djelveh, G., Larroche, C., and Gros, G. (1995). A gas phase chromatography method for determination of low dissolved CO_2 concentration and/or CO_2 solubility in microbial culture media. *Biotechnology Technique*, 9(11), 787–792.

Shimizu, K. (1996). A tutorial review on bioprocess systems engineering. *Computers and Chemical Engineering*, 20, 915–941.

Wan, E.A. and Van Der Merwe, R. (2000). The unscented kalman filter for nonlinear estimation. *Adaptive Systems for Signal Processing, Communications, and Control Symposium*, 153–158.

Dynamic model of NOx emission for a fluidized bed sludge combustor

S. Li[1], C. Cadet[1], P.X. Thivel[2], F. Delpech[2]

[1]GIPSA-lab, Dep Automatique, UMR 5216 CNRS-INPG-UJF
BP46, 38402 Saint Martin d'Heres Cedex, France (tel. +33(0)476826412,
e-mail: shi.li@lagep.univ-lyon1.fr, catherine.cadet@gipsa-lab.inpg.fr
[2]LEPMI, UMR 5631 CNRS-INPG-UJF
BP 76, 38402 38402 Saint Martin d'Heres Cedex (tel. +33(0)476826733,
e-mail: pierre-xavier.thivel@ujf-grenoble.fr, francoise.delpech@ujf-grenoble.fr

Abstract: Sludge incineration in fluidized bed is a very complex process, producing gaseous pollutants (carbon monoxide (CO) and nitrogen oxides (NOx)). The legislative norms need to be respected in spite of variations of sludge in composition and in quantity. The NOx formation, due to lots of chemical reactions from sludge nitrogen, is partly unknown. This paper deals with the design of a dynamic model of NOx emissions for a fluidized bed sludge combustor to be used in control strategy. The model is validated with industrial data, and the simulation results validate the simplification hypotheses, but need the reconstruction of sludge composition.

Keywords: sludge incineration, fluidized bed, NOx, chemical reaction, modelling, validation.

1. INTRODUCTION

The treatment and disposal of sewage sludge is an expensive and environmentally sensitive problem. It is also a growing worldwide problem since sludge production will continue to increase and since environmental quality standards become more stringent. Compared with landfill and agricultural compost, incineration presents some advantages: large volume reduction, stabilized ash production (heavy metals included) and toxic organic matters destruction. However to be economically viable, sludge has to be burned without fuel supply locally in wastewater treatment plant (Reimann, 1999).

Fluidized bed combustors are industrially largely used for coal, wastes and sewage sludge combustion (Werther and Ogada, 1999). The incineration process produces gaseous pollutants, mainly carbon monoxide (CO) and nitrogen oxides (NOx), which have to respect the legislative norms. Carbon monoxide formation can be limited by oxygen supply regulation, which is widely used in industrial plants. However, nitrogen oxides emissions should be controlled during combustion because its post-treatments are rather expensive. Linear dynamic models of coal combustion to be used in control strategy (Muir et al., 1997), (Bittanti et al., 2000) (Ikonen and Kortela, 1994), have showed that the combustion process presents a highly non linear behaviour, which needs a control strategy based on nonlinear models. Therefore, a suitable model has to be developed.

Models of coal combustion for simulation purpose (Gogebakan and Selçuk, 2004), (Huilin et al., 2000), (Adanez et al., 2001), and models of other fuels, as waste combustion (Marias et al., 2001), are based on accurate considerations on combustor hydrodynamics, which are highly complex and lead to models that do not fit to be used in control strategy. In addition, most of them target combustion efficiency without considering pollutant formation.

The sludge thermal decomposition in fluidized bed is based on the reference (Werther et Ogada, 1999). The NOx formation and reduction, due to lots of chemical reactions from sludge nitrogen, are partly unknown. Only one model, dedicated to biomass combustion (Liu and Gibbs, 2002), includes many chemical reactions of NOx formation and reduction, and will be our reference for reaction scheme. The proposed model is based on the molar and energy conservation balances, and is validated with industrial data.

2. MODEL DEVELOPMENT

2.1 Sludge thermal decomposition

A typical sludge analysis is shown in Table 1.

Table 1. Sludge analysis (Werther and Ogada, 1999).

Proximate analysis	
moisture (f_{H2O} wt% raw)	76.0
char (f_{char} wt% dry)	3.6
volatiles (f_{vol} wf% dry)	45.4
ash (f_{ash} wf% dry)	51.0

After entering the furnace, sludge is decomposed into four phases under heat effect: water vapour, char, volatiles and ash, which play different roles:

- To guarantee self-combustion, the sludge produced by the wastewater treatment process sludge is dewatered mechanically to about 76% of moisture (f_{H2O}).

- Sludge char, in a solid phase that can burn, presents a very low fraction (f_{char}), unlikely carbon and biomass chars. Based on numerous laboratory analyses, J. Werther and T. Ogada (Werther and Ogada, 1999) concluded that sludge combustion behaviour is mostly governed by the gaseous phase of volatiles. So char particles can be neglected.
- Volatiles fraction (f_{vol}) is large, the volatiles combustion lead to exothermic combustion and dominate the sludge combustion process, the furnace temperature and the air input.
- Ash fraction (f_{ash}) is large.

A composition of volatiles gas, issued from off-line studies, is presented in Table 2.

Table 2. Volatiles gas composition after sludge devolatilization at temperature 760°C (Werther and Ogada, 1999).

f_{CO} wt%	43.43
f_{CO2} wt%	15.39
f_{CnHm} wt%	31.12
f_{H2} wt%	3.20
Others	6.86

The chemical species, ammonia (NH_3) and cyanide (HCN), are responsible of NOx formation, and are generally not represented in volatiles. At a relatively low combustion temperature, and with a few char but many volatiles in fuel composition, NH_3 is the dominant specie (Aho *et al.*, 1993).

2.2 Fluidized bed combustor

The fluidized sludge combustor can be divided into two beds: bubbling fluidized bed and post-combustion bed, shown in fig. 1.

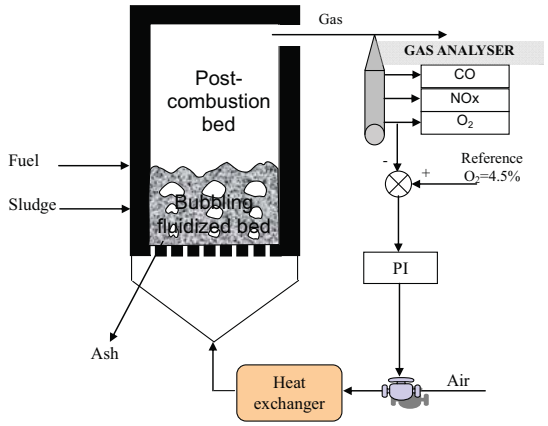

Fig. 1. Fluidized sludge combustor.

Sludge is introduced at the bottom of the furnace, i.e. the bubbling fluidized bed. Some fuel may be used as supply for starting combustion or for compensating sludge disturbances in composition or in flow. Air is preheated by a heat exchanger, and then injected with a sufficient velocity to insure the fluidization of inert sand in bubbling fluidized bed. High weight sand guarantees thermal inertia of the furnace and provides a great surface for sludge combustion and maintains a uniform temperature (~760°C). In the higher section, the post-combustion bed, volatiles gases continue post-combustion which increase the bed temperature (850°C-900°C). Temperature at the top of the furnace is limited up to 920°C, to avoid both furnace overheating and NOx formation.

The oxygen concentration is regulated up to 4.5% by air flow rate. This regulation loop provides an excess of oxygen which guaranties complete gas combustion, so as to avoid carbon monoxide (CO) formation.

On-line industrial measurements are sludge flow input in dry basis ($Q_{b,MS}^{in}$); air temperature input (T_a^{in}), air flow input (F_{am}^{in}), two bed temperatures (T^B, T^P), gas concentrations output (y_{O2} %, y_{CO} ppmv, y_{NO} mg.Nm^{-3}). As CO concentration is very low and its measurement presents lots of noise, unfortunately, this measurement can't be used for parameter estimation.

2.3 Modeling strategy and main hypothesis

The temperature and CO behaviors are described by combustion reactions. NOx formation and reduction can be considered as a separated model, using temperatures as input variables. Considering that two models has some advantages: they can be used simultaneously for simulation purpose, or separately for control purpose.

A difficulty is that sludge input flow is as constant as possible, and that sludge composition is not available on-line. So the dynamical behavior is only measured on the furnace outputs. We propose to reconstruct this composition with output measurements in the model.

As char particles can be neglected, the bubbling fluidized bed can be supposed perfectly mixed. The post-combustion bed is also approximated to a perfectly mixed reactor for model simplicity, but it is rather a plug flow reactor.

2.4 Chemical reactions

The reference (Liu and Gibbs, 2002) proposes 25 chemical reactions describing biomass combustion, including 20 reactions for NOx and N_2O formation and reduction. These reactions are selected and simplified with consideration on sludge specificities, as listed bellow:

- Due to low char content, the reactions using char as reactant and catalyst are all neglected.
- C_nH_m is supposed to be only CH_4. Its reaction is supposed to be complete in bubbling fluidized bed.
- Reaction of H_2 is supposed to be instantaneous and complete in bubbling fluidized bed.

- Catalyst as limestone (CaO), which is not used in sludge combustion, is not included.
- The lack of knowledge both on ash composition and its catalytic role (Tran et al., 2007) leads to suppose it chemically inert.
- N_2O can be decomposed rapidly in the post-combustion area where the temperature reaches 900°C. So N_2O is not considered in the model.

Five reactions are finally retained, as shown in table 3. The first reaction is NOx reduction, the second is NOx formation, and the last three are combustion reactions, which are independent from the NOx reactions. The first three reactions are supposed to be dynamically available, and the last two ones are supposed to be complete, so they do not need kinetic expression. The reactions R22, R23 and R24 are endothermic, their reaction enthalpies are noted as ΔH_{22}, ΔH_{23} and ΔH_{24}. The energy consumed or produced by the reactions R1 and R2 are negligible.

Table 3. Chemical reactions of sludge combustion model

No.	Reaction	Reaction rate r_i (mol.m^{-3}.s^{-1})	Enthalpies
R1	$NO + NH_3 + {}^1/_4O_2 \rightarrow N_2 + {}^3/_2 H_2O$	$r_1 = k_1[NH_3]^{0.5}[NO]^{0.5}[O_2]^{0.5}$	Negligible
R2	$NH_3 + {}^5/_4O_2 \rightarrow NO + {}^3/_2 H_2O$	$r_2 = k_2[NH_3][O_2]$	Negligible
R22	$CO + ½\ O_2 \rightarrow CO_2$	$r_{22} = k_{22}[CO][O_2]^{0.5}[H_2O]^{0.5}$	ΔH_{22}
R23	$CH_4 + {}^3/_2\ O_2 \rightarrow CO_2 + {}^3/_2 H_2O$	complete	ΔH_{23}
R24	$H_2 + ½\ O_2 \rightarrow H_2O$	Instantaneous	ΔH_{24}

The reaction rate r_i depends on the kinetic constant k_i and on the reactant concentrations. The kinetic constant k_i is given by the Arrhenius equation:

$$k = k_0 \exp(-\frac{Ea}{RT}) \quad (1)$$

Where k_0 is the pre-exponential factor or simply the *prefactor*, E_a is the activation energy, R is the perfect gas constant, R=8.31 J.mol^{-1}.K^{-1}, and T is the temperature (in Kelvin).

To simplify validation procedure, kinetic constant k_i is supposed to be constant in one bed, so the rate constant of reaction j in bubbling fluidized bed and post-combustion bed are named as k_j^B and k_j^P.

2.5 Combustion modelling

Combustion reactions are mostly responsible of temperature and oxygen concentration in the furnace. As the combustion reactions are independent of the NOx reactions, a model of combustion can be proposed individually.

After entering the furnace, sludge particles are decomposed physically and chemically at high temperature. Firstly, drying and devolatilization take place simultaneously, splitting sludge into species described previously in table 1 and table 2. Flux of gas species can be reconstructed:

$$\begin{bmatrix} F_{H_2O}^{in} \\ F_{CO}^{in} \\ F_{CH_4}^{in} \\ F_{H_2}^{in} \end{bmatrix} = \begin{bmatrix} Q_{b,MS}^{in} \dfrac{f_{H_2O}}{1-f_{H_2O}} / M_{H_2O} \\ Q_{b,MS}^{in} f_{vol} f_{CO} / M_{CO} \\ Q_{b,MS}^{in} f_{vol} f_{CH_4} / M_{CH_4} \\ Q_{b,MS}^{in} f_{vol} f_{H_2} / M_{H_2} \end{bmatrix} \quad (2)$$

Where F_i^{in} is the molar flow rate of component i after sludge drying and devolatilization, mol.h^{-1}; M_i is the molecular weight of component i, kg.mol^{-1}.

The volatile gas repartition is taken from table 2 without adaptation, though some relations between species fractions and temperature and fuel composition should be more realistic. With this assumption, only two sludge characteristics are needed: water fraction (f_{H2O}) and volatile fraction (f_{vol}). They are calculated by two static global balances: one is the balance of oxygen; the other is the balance of thermal energy, as shown in fig. 2.

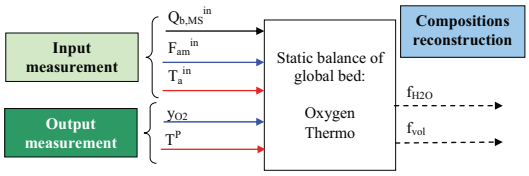

Fig. 2. Reconstruction f_{H2O} and f_{vol} from measurements (dashed line: unmeasured data, solid line: measured data).

Figure 3 presents the model structure. Three macroscopic inputs that can be easily measured (solid line): sludge flow rate in dry basis ($Q_{b,MS}^{in}$), air flow rate (F_{am}^{in}), input air temperature (T_a^{in}). State variables are gaseous species concentrations (C_{H2O}^B, C_{CO}^B, C_{O2}^B and C_{H2O}^P, C_{CO}^P, C_{O2}^P) and bed temperatures (T^B and T^P). Only four variables are measured (solid lines: C_{CO}^P, C_{O2}^P, T^B and T^P).

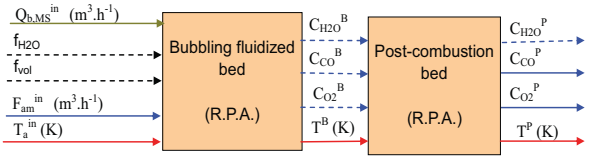

Fig. 3. Structure of combustion model (dashed line: unmeasured data, solid line: measured data).

The combustion model is written by molar and energy conservation balances (^{B} bubbling bed, ^{P} post-combustion):

$$\begin{pmatrix} \dfrac{dC_{H_2O}^B}{dt} \\ \dfrac{dC_{CO}^B}{dt} \\ \dfrac{dC_{O_2}^B}{dt} \end{pmatrix} = \begin{bmatrix} F_{H_2O}^{in} \\ F_{CO}^{in} \\ F_{O_2}^{in} \end{bmatrix} / V_B - \begin{pmatrix} C_{H_2O}^B \\ C_{CO}^B \\ C_{O_2}^B \end{pmatrix} \times \frac{F_g^B}{V^B} + \begin{pmatrix} \varphi_{H_2O}^B \\ \varphi_{CO}^B \\ \varphi_{O_2}^B \end{pmatrix} \quad (3)$$

$$\begin{pmatrix}\varphi^B_{H_2O}\\ \varphi^B_{CO}\\ \varphi^B_{O_2}\end{pmatrix}=\begin{bmatrix}0\\ -1\\ -0.5\end{bmatrix}\times r^B_{22}+\begin{pmatrix}F^{in}_{H_2}+2F^{in}_{CH_4}\\ F^{in}_{CH_4}\\ -0.5F^{in}_{H_2}-1.5F^{in}_{CH_4}\end{pmatrix}/V_B \quad (4)$$

Where F_{O2}^{in} is the oxygen molar flow rate brought by input air flow, mol.h^{-1}; F_g^{in} is the global gas flow rate (calculated by a global static balance on input and output flows), m^3.h^{-1}; V_B is the bubbling bed volume, m^3; φ_i^B is the production or consumption flux of component i by chemical reactions; r_{22}^B is the reaction rate of R22 (see table 3).

$$\begin{aligned}c_{ps}m_s^B\frac{dT^B}{dt}&=\left(c_{pa}F^{in}_{am}\rho_{a(T^{in}_{am})}T^{in}_a+c_{pb}\frac{Q^{in}_{b,MS}}{1-f_{H_2O}}T^{in}_b\right)\\&-\left(c_{pg}\rho_{g(T^B)}F^B_gT^B+c_{p,ash}Q^{in}_{b,MS}(1-f_{vol})T^B\right)\\&-\left(F^{in}_{H_2O}L_{H_2O}\right)-\left(r^B_{22}\Delta H_{R22}V^B+F^{in}_{CH_4}\Delta H_{R23}+F^{in}_{H_2}\Delta H_{R24}\right)\end{aligned} \quad (5)$$

Where c_{ps}, c_{pa}, c_{pg} and $c_{p,ash}$ are specific heat capacities of sand, air, gas and ash, J.kg^{-3}.K^{-1}; m_s^B is the sand mass in bubbling fluidized bed, kg; ρ is the density, kg.m^{-3}; L_{H2O} is the water latent heat of vaporisation, J.mol^{-1}.

Post-combustion balances can be similarly written:

$$\begin{pmatrix}\frac{dC^P_{H_2O}}{dt}\\ \frac{dC^P_{CO}}{dt}\\ \frac{dC^P_{O_2}}{dt}\end{pmatrix}=\begin{pmatrix}C^B_{H_2O}F^B_g-C^P_{H_2O}F^P_g\\ C^B_{CO}F^B_g-C^P_{CO}F^P_g\\ C^B_{O_2}F^B_g-C^P_{O_2}F^P_g\end{pmatrix}/V^P+\begin{pmatrix}\varphi^P_{H_2O}\\ \varphi^P_{CO}\\ \varphi^P_{O_2}\end{pmatrix} \quad (6)$$

$$\begin{pmatrix}\varphi^P_{H_2O}\\ \varphi^P_{CO}\end{pmatrix}=\begin{bmatrix}0\\ -1\end{bmatrix}\times r^P_{22} \quad (7)$$

$$\begin{aligned}c_{pg}m_g^P\frac{dT^P}{dt}&=\left(c_{pg}\rho_{g(T^B)}F^B_gT^B-c_{pg}\rho_{g(T^P)}F^P_gT^P\right)\\&-\left(r^P_{22}\Delta H_{R22}V^P\right)\end{aligned} \quad (8)$$

Only kinetic parameters (k_{22}^B and k_{22}^P) need to be estimated, other parameters are known from literature.

2.6 NOx modelling

As the combustion model has modelled the bed temperatures and the oxygen concentrations, which can be used as inputs of the NOx model. They are provided either from the combustion model or directly by measurements.

The NOx model can be then established and simulated independently of the combustion model, as shown in fig.4.

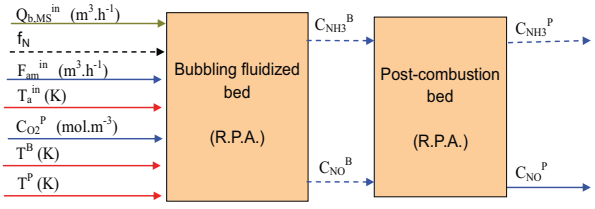

Fig. 4. Structure of NOx model.

One input cannot be measured on-line: the sludge nitrogen content (f_N), it is supposed to change slightly, and may be an additional parameter to be estimated. State variables are gaseous nitrogen species (C_{NH3}^B, C_{NO}^B, C_{NH3}^P and C_{NO}^P) among which only one is measured (C_{NO}^P).

After devolatilization, flux of NH_3 is reconstructed:

$$F^{in}_{NH_3}=Q^{in}_{b,MS}f_{vol}f_N/M_N \quad (9)$$

The balance equations are:

$$\begin{pmatrix}\frac{dC^B_{NH_3}}{dt}\\ \frac{dC^B_{NO}}{dt}\end{pmatrix}=\begin{pmatrix}F^{in}_{NH_3}\\ 0\end{pmatrix}/V_B-\begin{pmatrix}C^B_{NH_3}\\ C^B_{NO}\end{pmatrix}\times\frac{F^B_g}{V^B}+\begin{pmatrix}\varphi^B_{NH_3}\\ \varphi^B_{NO}\end{pmatrix} \quad (10)$$

$$\begin{pmatrix}\varphi^B_{NH_3}\\ \varphi^B_{NO}\end{pmatrix}=\begin{bmatrix}-1 & -1\\ -1 & 1\end{bmatrix}\times\begin{pmatrix}r^B_1\\ r^B_2\end{pmatrix} \quad (11)$$

$$\begin{pmatrix}\frac{dC^P_{NH_3}}{dt}\\ \frac{dC^P_{NO}}{dt}\end{pmatrix}=\begin{pmatrix}C^B_{NH_3}F^B_g-C^P_{NH_3}F^P_g\\ C^B_{NO}F^B_g-C^P_{NO}F^P_g\end{pmatrix}/V^P+\begin{pmatrix}\varphi^P_{NH_3}\\ \varphi^P_{NO}\end{pmatrix} \quad (12)$$

$$\begin{pmatrix}\varphi^P_{NH_3}\\ \varphi^P_{NO}\end{pmatrix}=\begin{bmatrix}-1 & -1\\ -1 & 1\end{bmatrix}\times\begin{pmatrix}r^P_1\\ r^P_2\end{pmatrix} \quad (13)$$

Only kinetic parameters (k_1^B, k_1^P, k_2^B and k_2^P) need to be estimated, other parameters are known from literature.

3. VALIDATION

3.1 Validation strategy

Because of bad numerical results, it is not possible to simulate the model with the parameters at their literature values. The proposed validation strategy is based on some physical considerations and sensitivity analysis. As the number of parameters is numerous, only some kinetic parameters are estimated. This choice is made on the consideration that they influence directly the dynamic behaviour of the model, and that the literature values were proposed from chemical engineering laboratory analysis of coal combustion, which means that the identified values may very different.

Another important choice was to identify the parameters with two separated models or with a global one. In the first step, we choose the first solution considering that NOx content can't influence the furnace temperature. In addition, temperature is difficult to be estimated accurately with a model, though its measurement is quite reliable. Some attempts for identification with the global model have not improved the results. The main drawback of validation is that part of sludge composition (f_N, f_H) has to be fixed for each data set. Now it is adjusted by trial and error, but it would have to be further included in global parameters.

3.2 Industrial data file for parameter estimation

Two industrial data files of an industrial fluidized sludge combustor with different events are used for parameters estimation and model validation. The data used for identification corresponds to the introduction of fat matters in furnace. Model input measurements are shown in fig. 5.

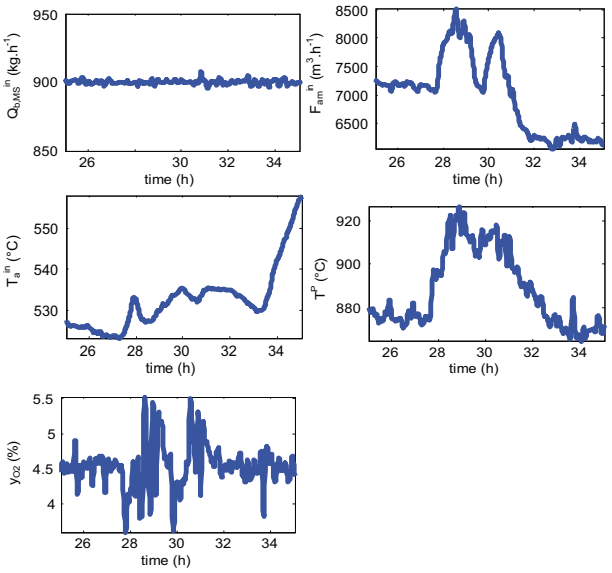

Fig. 5. Measurements of model input of data file 1.

Sludge flow ($Q_{b,MS}^{in}$) in Fig. 5 is constant, which is a necessity as sludge has to be treated continuously. The dynamic event is revealed by output measurements, which affect the input by the heat exchanger (T_a^{in} is defined by T^P) and the oxygen control loop (F_{am}^{in} is the action which regulates y_{O2}). The post-combustion temperature presents an increasement due to the dynamic event. The oxygen concentration (y_{O2}) is regulated at reference point 4.5%.

3.3 Parameter estimation methodology

For parameter estimation, minimisation of a least square criterion on the difference between the measured value and the model value has been carried out.

For combustion model, only temperature to be used is T^B, as T^P is used to reconstruct the sludge compositions f_{H2O} and f_{vol}. Consequently, the parameter k_{22}^P, can't be estimated. Some additional measurements, such as y_{CO}, may be useful for estimating this parameter. In the model, k_{22}^P is taken as a great value to guarantee a complete CO combustion, because CO in the measurement is almost null in the sake of oxygen regulation.

For NOx model, four kinetic parameters k_1^B, k_2^B, k_1^P and k_2^P need to be identified. Their literature values, calculated from steady temperature values (T^B=752°C, T^P=870°C) are presented in table 4.

Table 4. Literature values of parameters to be estimated

$k_1^B = 0.4$	$k_1^P = 7.2$
$k_2^B = 0.02$	$k_2^P = 0.87$

Because of the great number of parameters to be estimated with only one measured data y_{NO}, a sensitivity analysis is made to select the more influent parameter. Figure 6 shows that k_1^P is the most sensitive parameter with respect to y_{NO}. Finally, only the parameter k_1^P is estimated as a constant, the others are used with their reference values.

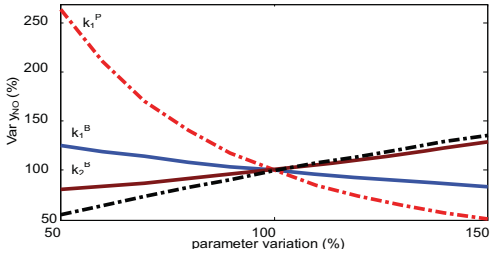

Fig. 6. Sensitivity analysis of k_1^B, k_2^B, k_1^P and k_2^P with respect to y_{NO}.

3.4 Estimated Parameters

The initial value of k_{22}^B=$3.25\times10^7\exp(-15098/T^B)$ (14)

Which lead the equation (15) after estimation:

k_{22}^B=$(2211\pm5)\exp(-(7743\pm2)/T^B)$ (15)

The estimated value of k_1^P:

k_1^P=0.9981 ± 0.0035 (16)

The estimated values are all very small compared to the literature values. These differences can be attributed to the great simplifications of chemical reactions: neglected char, instantaneous and complete reactions of H_2 and CH_4 in the bubbling bed, which need to slow the global combustion reactions. For post-combustion, perfectly mixed reactor may also be revised. Some tests with other initial values have leading the same results. However, the precision interval points out that no better values can be estimated.

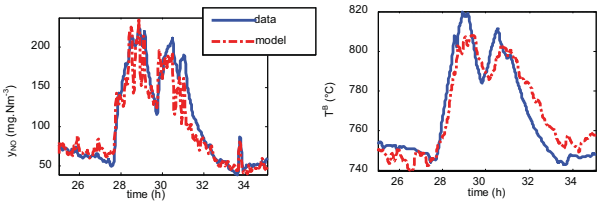

Fig. 7. Comparison of data file and model with kinetic parameter estimated k_{22}^B and k_1^P.

With the estimated values in equation (15) and (16), simulation results are shown in fig. 7. Bubbling fluidized bed temperature (T^B) in combustion model is tracking well the measurement, and NOx model fits also very well the measured data. In conclusion, we can consider that the model

is realistic and these results are good enough to continue a validation step.

3.5 Validation with data file 2

The main characteristic of data file 2 (fig. 8) is an increase of the operating point: NOx concentration exceeds the norm of 400 mg.Nm^{-3}, post-combustion bed temperature (T^P) is upper the limitation value of 920°C. The sludge flow rate ($Q_{b,MS}^{in}$) remains constant at 900 kg.h^{-1} and is not represented. The air flow rate (F_{am}^{in}) and the oxygen concentration present small fluctuations around a reference point.

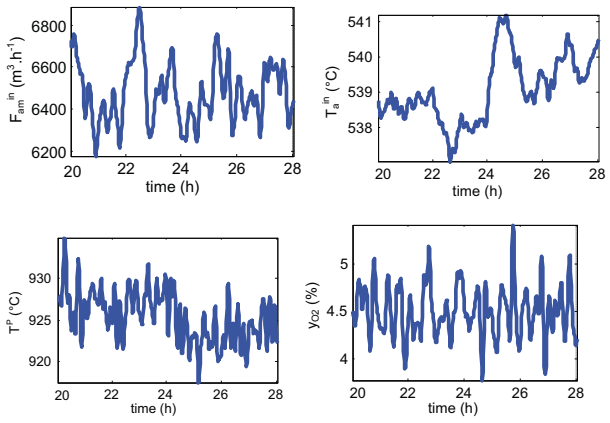

Fig. 8. Measurements of model input of data file 2

When analysing the measurements, we can notice that the bed temperatures increase greatly but fewer oxygen is consumed due to perturbation reconstruction of water fraction and volatile fraction. Trying to translate this behaviour in the model, the following adjustments are made: the hydrogen fraction (f_{H2}) after devolatilization is decreased from 3.2% to 2% (see table 2), the nitrogen fraction (f_N) is increased from 1% to 2.5%. Both corrections are used to fill up the unknown perturbations.

Figure 9 compares the simulation results with the measurements. We can see that the global tendency is good, and that means that our model is able to fit the data. The fluctuations observed for the model are due to algebraic equations for the reconstruction of f_{H2O} and f_{vol}. The main drawback is that the lack of knowledge on the input composition is a major obstacle to such modelling.

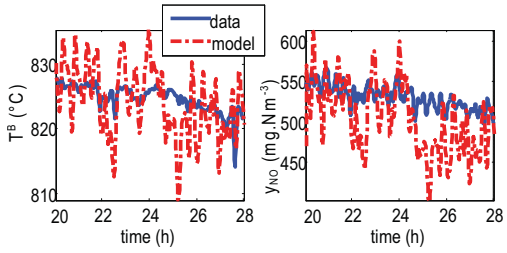

Fig. 9. Model validation.

4. CONCLUSIONS

A dynamic model of fluidized bed sludge combustor has been designed to predict NOx emissions. The main hypothesis is the lack of reactant particles in the furnace, leading to only five chemical reactions and simplifying hydrodynamics into two perfectly mixed reactors. As the sludge composition is not available, it has been reconstructed with output measurements. This point represents the main drawbacks of the model: more knowledge on devolatilization and/or more output measurements would be very helpful to have a deterministic model. However this model has been partly validated with industrial data files, and it is sufficiently representing the NOx formation behaviour, to be used in a control strategy and therefore to contribute to improve combustion quality and control NOx emissions.

REFERENCES

Adanez J., Gayán P., Grasa G., Diego L.F., Armesto L., Cabanillas A., (2001), Circulating fluidized bed combustion in the turbulent regime: modelling of carbon combustion efficiency and sulphur retention, *Fuel*, 80, 1405-1414.

Aho M.J., Hämäläinen J.P., Tummavuor J.L., (1993), Importance of solid-fuel properties to nitrogen-oxide formation through HCN and NH3 in small-particle combustion. *Combustion Flame*, 95, 22-30.

Bittanti S., Bolzern P., Campi M.C., Marco A., Poncia G., Prandoni W., (2000), A model of a bubbling fluidized bed combustor oriented to char mass estimation, *IEEE transactions on control systems technology*, 8 (2).

Gogebakan Y., Selçuk N., (2004), Assessment of a model with char attrition for a bubbling atmospheric fluidized-bed combustor, *Combust. Sci. and Tech.*, 176, 799-818.

Huilin L., Guangbo Z., Rushan B., Yongjin C., Gidaspow D., (2000), A coal combustion model for circulating fluidized bed boilers, *Fuel*, 79, 165-172.

Ikonen E. and Kortela U., (1994), Dynamic model for a bubbling fluidized bed coal combustor, *Control Eng. Practice*, 2 (6), 1001-1006.

Liu H., Gibbs B.M., (2002), Modeling of NO and N2O emissions from biomass-fired circulating fluidized bed combustors, *Fuel*, 81, 271-280.

Marias, F., Puiggali, J.R., Flamant, G., (2001), Modelling for Simulation of Fluidized-Bed Incineration Process, *AIChE Journal*, 47, 1438-1460.

Muir J.R., Brereton C., Grace J.R. and Lim C.J., (1997), Dynamic modeling for simulation and control of a circulating fluidized bed combustor, *AIChE Journal*, 43 (5).

Reimann D.O., (1999), Problems about sludge incineration, *Proceedings of the Workshop on "Problems around sludge", session 3: Technology and innovative options related to sludge management*, Stresa, Italy, 3, 173-183.

Tran K.Q., Kilpinen P., Kumar N., (2007), In-situ catalytic abatement of NOx during fluidized bed combustion – a literature study, *Applied Catalysis B: Environmental*, 2007.

Werther J., Ogada T., Sewage sludge combustion, *Progress in energy and combustion science*, 25, pp. 55-116, 1999.

Comparison of Different Modeling Concepts for Drying Process of Baker's Yeast

U. Yüzgeç* M. Türker **

**Kocaeli University Department of Electronics & Telecom. Engineering, 41040 Kocaeli, Turkey*
(uyuzgec@kocaeli.edu.tr)
***Pakmaya, P.O. Box 149, 41001, Kocaeli, Turkey*
(mustafat@pakmaya.com.tr)

Abstract: This study investigates different modeling approaches and compares for drying of baker's yeast in a fluidized bed dryer. Four modeling concepts were investigated: modeling based on the mass and energy balance, modeling based on diffusion mechanism in the granule, modeling based on recurrent Artificial Neural Network (ANN) and modeling based on Adaptive Neural Network Fuzzy Inference System (ANFIS). Dry matter of product, product temperature and product quality were predicted using these model structures. To evaluate performances of the modeling structures, industrial scale drying process data were used.

Keywords: Drying process, spatial distribution, product quality, modeling, ANN, ANFIS

1. INTRODUCTION

Biological products, such as agricultural products, foods, pharmaceuticals, enzyme preparations, bacterial and yeast cultures, are particularly sensitive to drying conditions, including moisture content and temperature (Yüzgeç et al., 2008). There are different modeling concepts for the drying processes reported in the literature. In general, three possible approaches can be taken to the modeling: a physical approach based on energy and mass balance (Temple et al., 2000; Türker et al., 2006), black-box modeling (Castellanos et al., 2002; Köni et al., 2009) and hybrid modeling (Ciesielski et al., 2001). In contrast with the physical approach, the black-box modeling approach does not require prior theoretical knowledge.

The objective of this study is to examine alternative and novel modeling techniques based on the physical approaches and based on mathematical approaches, such as ANN and ANFIS structures, for an industrial-scale drying process of baker's yeast. Four model structures which are different from each other were investigated. First model was developed by using mass and energy balances in the fluid-bed. The second mathematical model is based on the spatial distribution of moisture, temperature and quality. In the third model, the recurrent ANN structure was selected according to the results of the regression analysis in their study presented by Köni et al.(2009). The last model is constructed using ANFIS architecture. The vast numbers of industrial data (570 data sets) used for training and testing of the models were collected from a production-scale baker's yeast drying process. As a result of this work, advantages and disadvantages of the model structures investigated for drying process were presented.

2. MATHEMATICAL MODELS

2.1 Model based on mass and energy balances

Model equations are constructed by combining mass and energy balances (Temple and Boxtel, 1999; Kanarya, 2002).

The model equations consist of four basic balance equations: Dry solid balance, water conservation, air conservation and energy balance. All of these equations are presented below:

$$\frac{dM_{b,y}}{dt} = m_y^i - m_y^o \tag{1}$$

$$\frac{dW_{b,y}}{dt} = w_y^i - r_w - w_y^o \tag{2}$$

$$\frac{dM_{b,a}}{dt} = m_a^i - m_a^o \cong 0 \tag{3}$$

$M_{b,y}$ is dry solid mass of product in the bed and m_y^i is the flow rate of the product into the bed and m_y^o is the flow rate of the product out of the bed. $W_{b,y}$ represents the water mass inside the bed, w_y^i is the flow rate of water in product fed to the system, r_w is the flow rate of water removed from product by means of evaporation, and w_y^o represents the flow rate of water in product entrained through cyclones. $M_{b,a}$ is the mass of air in the bed, m_a^i, m_a^o represent the flow rates of the inlet and outlet air.

The energy accumulation of the process H is assumed as adiabatic. The energy accumulation in the bed can be written as dynamic balance between energy flows to and from the system as given in Eq.(4):

$$H = h_y^i + h_a^i - h_y^o - h_a^o. \tag{4}$$

In this equation, h_a^i represents the energy introduced by air, h_y^i is the energy introduced by yeast, h_a^o is the energy removed by air and h_y^o represents the energy removed by yeast. The detail informations related to this model can be found in the paper presented by Türker et al. (2006).

2.2 Model based on spatial distributions of moisture and quality

This modeling of the drying comprises four main parts: moisture diffusion equation, heat balance equation, shrinking model, product activity in the granule. The model also includes dependence of the moisture and temperature of granules on several parameters like moisture diffusion coefficient, heat and mass transfer coefficients and water activity. The batch fluidized bed is assumed to be an ideally mixed bed, with uniform temperature and humidity of the air which equal the outgoing air conditions. The particles are all at the same stage of drying at any instant of the batch operation. Furthermore, there is no interaction between the particles, as far as drying is concerned (Yüzgeç et al., 2008).

A generalized formulation of the moisture diffusion equation is presented by a nonlinear partial differential equation (Schoeber, 1976) as given below:

$$\frac{\partial(\rho_s X)}{\partial t} = \frac{1}{r^v}\frac{\partial}{\partial r}\left(r^v \rho_s D(X,T)\frac{\partial X}{\partial r}\right). \tag{5}$$

X (*kg water/kg dry solid*) is the moisture content inside the granule, *D* (m^2/s) is the moisture diffusion coefficient which is the function of material's moisture content (*X*) and temperature (*T*) and *v* represents geometry factor with *v* = 0 slab, *v* = 1 cylinder, *v* = 2 sphere. The initial and boundary conditions:

$$t = 0; 0 \le r \le R_d \Rightarrow X(0,r) = X_0 \tag{6}$$

$$t > 0 \Rightarrow \left.\frac{\partial X}{\partial r}\right|_{r=0} = 0 \tag{7}$$

$$t > 0 \quad r = R_d \Rightarrow j_{m,i} = -D\rho_s \left.\frac{\partial X}{\partial r}\right|_{r=R_d} = k\left(\rho_{wv,i} - \rho_{wv,g}\right). \tag{8}$$

$j_{m,i}$ is the moisture flux at the interface, *k* is the liquid film mass transfer coefficient around the granule, $\rho_{wv,i}$ represents the water vapor concentration at the interface and $\rho_{wv,g}$ represents the water vapor concentration in the bulk air.

The heat balance can be described as heat transfer both to and from the surface and within the material. The equation of the heat balance inside a granule is described by the following non-linear partial differential equation (Quirijns et al., 1998; Quirijns et al., 2000),

$$\frac{\partial(T(\rho_s c_{p,s} + \rho_m c_{p,m}))}{\partial t} = \frac{1}{r^v}\frac{\partial}{\partial r}\left(r^v \lambda \frac{\partial T}{\partial r}\right) \tag{9}$$

where *T* is the temperature, ρ_m is the moisture concentration, ρ_s is the dry solid concentration inside the granule, $c_{p,s}$ and $c_{p,m}$ are the heat capacities of the solid and moisture, λ is the thermal conductivity of the granule. The initial and boundary condition are given by

$$t = 0; 0 \le r \le R_d \Rightarrow T(0,r) = T_0 \tag{10}$$

$$t > 0 \Rightarrow \left.\frac{\partial T}{\partial r}\right|_{r=0} = 0 \tag{11}$$

$$t > 0 \quad r = R_d \Rightarrow j_{T,i} = -\lambda \left.\frac{\partial T}{\partial r}\right|_{r=R_d} \tag{12}$$

$$j_{T,i} = \alpha(T(t,R_d) - T_a) + \Delta H_v\big|_{T(t,R_d)}\, j_{m,i} \tag{13}$$

where $j_{T,i}$ is the heat flux at the interface, α is the heat transfer coefficient, T_a is the inlet air temperature and ΔH_v is the evaporation enthalpy of water.

The product quality can be described as first-order kinetics (Lievense, 1991):

$$\frac{dQ}{dt} = -k_e Q \tag{14}$$

where *Q* is the concentration of the active product and k_e is the specific rate of product activity. According to the Arrhenius equation, the rate of the product activity can be expressed as a function of the temperature (Liou et al., 1984). Lievense (1991) has described that following equation for dependency of $\ln(k_e)$ on temperature and moisture:

$$\begin{aligned}\ln(k_e) = &\left[\left(a_1 - \frac{a_2}{RT}\right)X + \left(b_1 - \frac{b_2}{RT}\right)\right] \\ &+ \left[1 - \exp\left(pX^q\right)\right]\left[\left(a_3 - \frac{a_4}{RT}\right)X + \left(b_3 - \frac{b_4}{RT}\right)\right]\end{aligned} \tag{15}$$

where *p, q, a_i, b_i* are the parameter values in the equation. If *p<0* and $q \ge 1$, at high moisture content, $\exp\left(pX^q\right) \approx 0$ and $\ln(k_e)$ consists of the linear sum of the two parts; at low moisture content, $\exp\left(pX^q\right) \approx 1$ and $\ln(k_e)$ is described with the first linear part of the equation.

The volume of the granule consists of volumes of both moisture and solid:

$$V = V_m + V_s \tag{16}$$

According to Coumans (1987), the volume of the granule is a linear function of the average moisture content $\overline{X}$ during shrinkage that is expressed by

$$V = V_s\left(1 + \tau \frac{d_s}{d_m}\overline{X}\right) \tag{17}$$

where τ is the shrinkage coefficient within $0 \le \tau \le 1$. The detail informations related to this model can be found in the paper presented by (Yüzgeç et al., 2008).

2.3 Model based on Artificial Neural Network (ANN)

The fifteen different ANN structures were investigated in the study introduced by Köni et al. (2009) in order to determine the suitable model which represents drying process. The essential differences for all of the proposed ANN structures are in the input layer and in the relations of the hidden layers. The ANN-9 model had the best performance according to the results of regression analysis of all model approaches. Fig.1 presents the architecture of this ANN model. This recurrent neural network model has nine layers each of whose hidden neurons are twelve and it consists of five inputs and three outputs (*DM* is dry matter of product (%), T_m is product temperature (^oC) and ΔDM is change in dry matter of product).

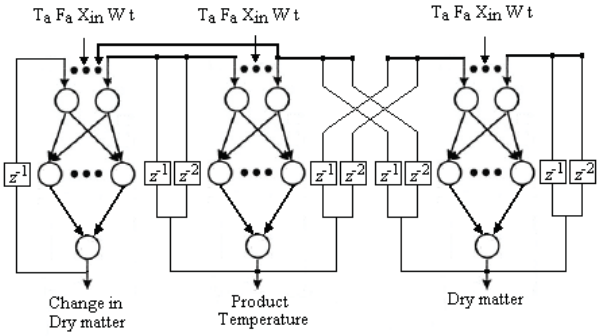

Fig.1. Drying model architecture designed using recurrent ANN. *t*: the drying time (s), *W*: loading (kg), X_{in}: moisture content of inlet air (kg water/kg air), F_a: flow rate of inlet air (m^3/h) and T_a: temperature of inlet air (^oC).

The drying process should be performed under optimal conditions in order to minimize quality loss. The change in the quality loss (ΔQ) is given as:

$$\Delta Q = \frac{Q_n - Q_f}{Q_n} \tag{18}$$

where Q_n is the quality at the beginning of the drying and Q_f is final quality at the end of the drying. In the industrial scale production, product quality is measured at the beginning and at the end of the drying process. In this study, a neural network model with three layers was used as quality model based on the results of regression analyses done by Köni et al. (2009). In this model shown in Fig.2, the inputs were considered as the process output variables, such as dry matter of product (*DM*) and product temperature (T_m). The values of dry matter and product temperature were stored in each drying time and a database forms for the product quality obtained at the end of the process. The inputs of quality model are all sampled values of dry matter of product *DM(i)* and product temperature $T_m(i)$, i denotes the sample in a drying period (Köni et al., 2009).

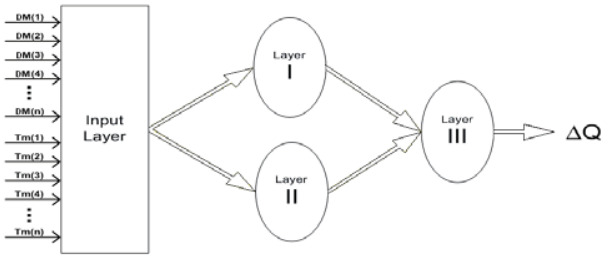

Fig. 2. Architecture of ANN model for quality.

The first layer represents the quality effect of drying on baker's yeast and the second layer denotes the effect arising from fermentation process. The tansig functions in layer 1 and layer 3 and logsig function in layer 2 are used as activation functions.

2.4 Model based on Adaptive Neural Network-Based Fuzzy Inference System (ANFIS)

The basic difference between ANFIS and ANN architecture is that ANFIS has a single output. This means that different ANFIS structures are constructed for each output parameter to be predicted, without changing the input parameters. Five input parameters were applied to the proposed ANFIS model approach: drying time, loading weight, moisture content of inlet air, flow rate of inlet air and temperature of inlet air. ANFIS structures were constructed separately for fuzzy modeling to predict the dry matter of the product (*DM*), the product temperature (T_m) and the change in dry matter of the product (ΔDM). In Fig. 3, the ANFIS architecture proposed for the dry matter of the product is given in detail. A_i, B_i, C_i, D_i and E_i (i = 1,2,3) represent the drying time (t), loading weight (W), moisture content of inlet air (X_{in}), flow rate of inlet air (F_a) and temperature of inlet air (T_a) membership functions, respectively.

All of the outputs are predicted by linear output functions. The ANFIS structures are the same for the other two output parameters, namely, *Tm* and *ΔDM*. Only output parameters change, while the inputs are kept the same. In this model, all of the ANFIS structures have five inputs and a single output, using the Sugeno-type fuzzy model. Three membership functions are defined for each input parameter. Although the model causes overloads during operation, all output membership functions were defined as first-order (linear). In the neuro-fuzzy model, the parameters associated with each membership function were adjusted by a hybrid learning algorithm consisting of a combination of least-squares and back propagation gradient descent methods. This algorithm used back propagation for the parameters related to the input membership functions and least squares estimation for the parameters related to the output membership functions (Jang, 1993; Azeem et al., 2000). As a result of using the hybrid learning algorithm, the training error decreased during the learning process.

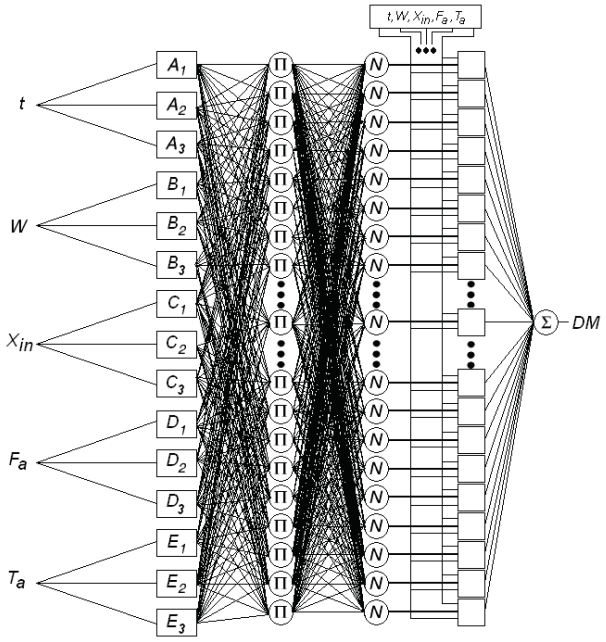

Fig. 3. Inputs and output of fuzzy model structure for dry matter of product (*DM*).

3. MATERIALS & METHODS

Data obtained from an industrial scale drying plant, which is produced baker's yeast (*Saccharomyces cerevisiae*), were used to test the models in this study. Yeast cake was extruded into the dryer through a perforated plate of a different diameter to obtain the desired granule size (Türker et al., 2006). In general, baker's yeast with a value of 33-34% dry matter prior to loading in the dryer eventually dried to a value of 94-96% dry matter. The fluid bed contained a centrifugal fan to supply air drawn from the ambient air. There are two essential output parameters for the drying processes: moisture content and product temperature. The product temperature was measured by Pt-100 sensors in the fluid bed. The temperature on the dryer outlet was also measured regularly. Moisture content is more difficult to measure than temperature. Infrared sensors are used to measure the moisture content in the drying material at third drying stage. The data set consisted of measurements obtained from the dryer under different loading conditions and different air profiles over one year of training and testing for the ANN and ANFIS model approaches. The sampling period of the data collection was 30 seconds.

The quality of the product was defined as the volume of carbon dioxide produced per unit time upon introduction of the yeast into the dough. This method is commonly used in the yeast industry to assess the performance of baker's yeast (Yüzgeç et al., 2008). To measure product quality, yeast samples are taken from the dryer at specific times during the drying, and then the volume of carbon dioxide in the laboratory is measured. Relative activity is expressed as the ratio of the activity of the product at time t to the activity of the yeast cake at the beginning time of the drying. A database which consists of 570 data was divided into the two parts: 60% training and 40% testing (Köni et al., 2009).

The first mathematical model is based on the first order ordinary differential equation with initial and boundary conditions. Therefore Runge-Kutta finite difference method has been used for the solution of the equation describing product temperature (Türker et al., 2006). There are two nonlinear partial differential equations in the second mathematical model. Due to the complex nature of the analytical solutions, numerical methods especially Crank-Nicholson method were used for the solution of non-linear partial temperature and moisture diffusion (Yüzgeç et al., 2008). The equations were subject to a Robin boundary condition. The mass flux at the interface is variable in the Robin type boundary condition. The sample time was chosen as one second and the particle was divided into ten grids.

4. RESULTS & DISCUSSION

To evaluate the performances of developed model structures, outputs of the models (dry matter of product and product temperature) were compared with the industrial scale data obtained from drying process of baker's yeast. Fig.4 show the simulation results for the energy and mass balance based model and the spatial distributions of moisture and quality based model.

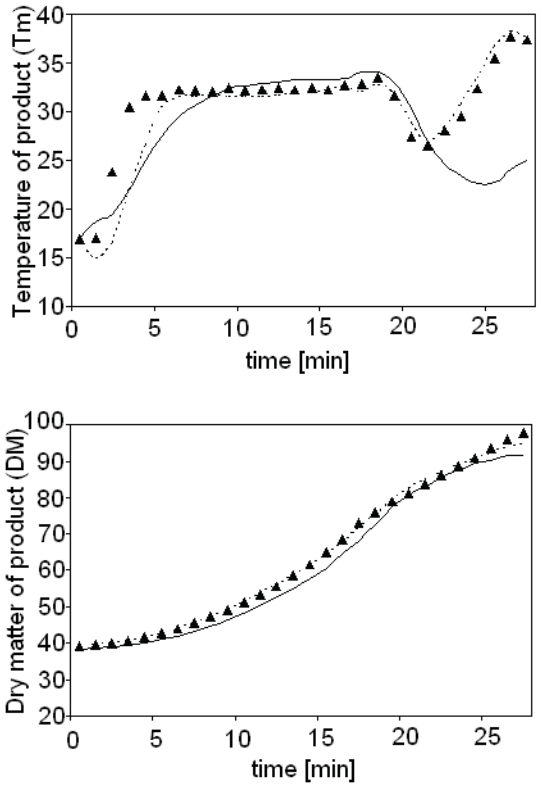

Fig. 4. Simulation results of the energy and mass balance based model (—) and granule based model (---). Industrial data (▲).

Note from this figure that there is good correspondence between the results obtained by developed model approaches and experimental data. Compared to the energy and mass balance based model, the granule based model significantly improves the predictions during the drying of granular product with spatial distribution of moisture. The simulation result of ANN based model is shown in Fig.5, together with experimental data chosen randomly from the database. The features of this experimental data is: loading weight 550-650 kg, moisture content of inlet air 0.0037-0.0056 kg water/kg air, flow rate of inlet air 34000-47500 m^3/h and temperature of inlet air 54-132 ^{0}C. In these figures, the predicted values for the drying process match very well with the experimental data; the differences can only be seen on a much finer scale. Comparison between the simulation results obtained by ANFIS based model and experimental data set is presented in Fig. 6. It can be seen from these figures that the ANFIS based model approach has a little more performance than that of the ANN based model. There is no vital difference between the results of the last two model structures. Both of them can be used as alternatives to one another with respect to response time and system definition. ANFIS based models have more advantages due to their adaptive structure.

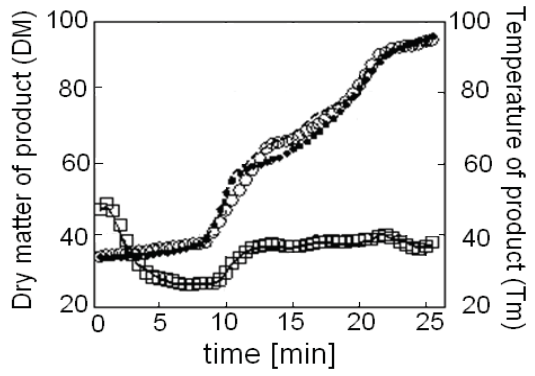

Fig. 5. The simulation results of the ANN based model. *DM* experimental, (o) *DM* simulation (---), *ΔDM* simulation (•••), T_m experimental (□),T_m simulation (—).

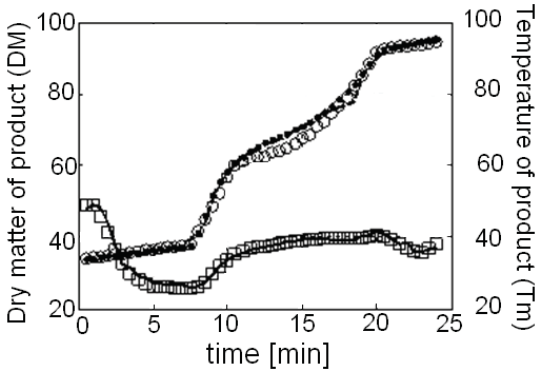

Fig. 6. The simulation results of the ANFIS based model. *DM* experimental, (o) *DM* simulation (---), *ΔDM* simulation (•••), T_m experimental (□),T_m simulation (—).

For modeling of the product quality loss or product activity using ANN and ANFIS approaches, which is the most difficult variable in the design of a proper physical model for biomass drying, only the ANN based model was used because ANFIS based model has a serious operational load in the training process. In energy and mass balance based model and ANFIS based model, the product quality is not used among the model outputs. Fig.7 shows the profiles of the product activity, which was obtained by drying model based on spatial distribution of quality and moisture inside the granule, according to the drying time and radial distance. The average product activity during drying is also presented in this figure with experimental data. As can be noted this figure, the product activity is retained at the surface of the granule due to the diffusion limitation of the drying process. Accordingly, the product activity is preserved in a thin layer at the surface of the granule. The product activity is decreased from the surface of the granule to the center. Fig. 8 shows that the comparison of real industrial data related to the change of the quality loss and simulation results of the ANN based quality model. For entire experimental data, it can be shown from this figure, the performance of the ANN based model is quite satisfactory.

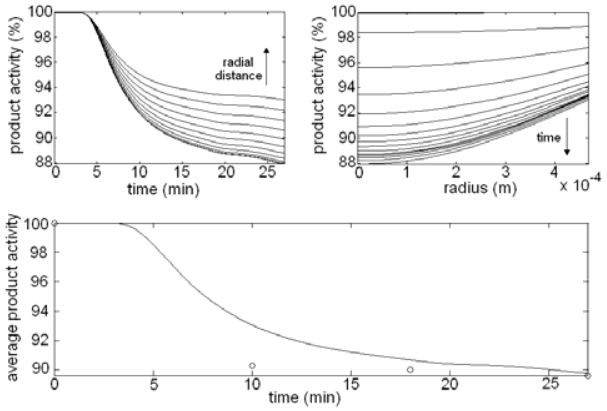

Fig. 7. The profiles of the product activity in the granule and average product activity for the model based on the spatial distribution of product activity. Experimental data (o), drying time 27 min, $R_0 = 5.10^{-4}$m, $X_0 = 1.563$ kg/kg, $T_0 = 16.9^oC$.

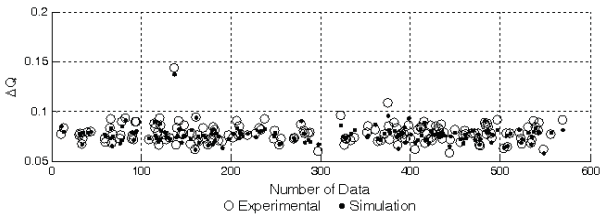

Fig.8. The change in the quality loss (ΔQ) obtained by ANN based quality model with experimental data.

The average root mean square error (RMSE) of ANN based quality model for five experimental data was calculated as 0.004742. For the second model based on spatial distributions of moisture and quality, the RMSE value is 0.005976. ANN based quality model has better performance than the

performance of the other model according to RMSE values. The coefficient of determination R^2 is the proportion of variability in a data set, as given below:

$$R^2 = \left(1 - \frac{SSE}{SST}\right) \tag{19}$$

SSE represents the sum of squared errors and *SST* denotes the total sum of squares. y_i and f_i denote a data set and the modeled values, respectively, and $\overline{y}$ represents the mean of the modeled values. Table 1 represents the R^2 values associated with all of the model approaches for only one experimental data selected randomly from database. An R^2 of 1.0 indicates that the regression line perfectly fits the data.

Table 1. The performance results of the all model approaches

Model	Dry matter of product R^2	Product temperature R^2
Model_1	0.97925	0.62711
Model_2	0.98743	0.72643
Model_3	0.98387	0.85256
Model_4	0.98525	0.81776

Model_1: Model based on the mass and energy balance,
Model_2: Model based on the spatial distribution in granule,
Model_3: Model based on ANN
Model_4: Model based on ANFIS

As can be noted from Table 1, R^2 values are fairly good for the dry matter of product, but R^2 values related to the product temperature are different from the each other. ANN and ANFIS based model approaches have better performances than the others.

5. CONCLUSIONS

In this study, four different modeling structures were considered for an industrial scale drying process. In all of the models, dry matter of product and the product temperature were used as model outputs. As comparing to the mass and energy balance based model, the second drying model provides significantly improved predictions by providing spatial distributions of moisture and quality inside the granule. Besides, the model accurately predicts the change of granule size during drying by the effect of the shrinkage of the granule. In the production plant, the product quality is measured with offline laboratory conditions as the amount of carbon dioxide produced upon introduction of the yeast into dough per unit time. The product quality is only predicted in ANN based model and the model based on spatial distributions of moisture and quality. It has been provided that the product activity can be observed online by these proposed model structures such as a soft sensor. In contrast with the physical approach based modeling, ANN or ANFIS based modeling approaches does not need prior theoretical knowledge. In order to overcome modeling difficulties, easily self-updating modeling structures can be designed to capture all of the system's operating conditions, as well as details that may have escaped observation. The investigated modeling structures may be an alternative to predict many parameters, such as the moisture content, dry matter of product, product temperature and the product quality or quality loss, in the biomass drying process industry.

REFERENCES

Azeem, M. F., Hanmandlu, M. and Ahmad, N. (2000). Generalization of adaptive neuro-fuzzy inference systems. *IEEE Trans. on Neural Networks*, *11*(6), 1332-1346.

Castellanos, J. A., Palancar, M. C. and Aragon, J. M. (2002). Designing and optimizing a neural network for the modeling of a fluidized-bed drying process. *Industrial and Engineering Chemistry Research*, *41*, 2262-2269.

Ciesielski, K. and Zbicinski I. (2001). Hybrid neural modeling of fluidized bed drying process. *Drying Technology, 19*(8), 1725-1738.

Coumans, W.J. (1987). Power law diffusion in drying processes. Ph.D. Thesis, Technical University Eindhoven, The Netherlands.

Jang, J. S. R. (1993). ANFIS: Adaptive-network-based fuzzy inference system. *IEEE Transactions on Systems Man and Cybernetics*, *23* (3), 665-685.

Kanarya, A. (2002). Mathematical modelling of fluidized bed drying process, *MSc Thesis*, Gebze Institute of Technology, Gebze, Turkey (in Turkish).

Köni, M., Türker, M., Yüzgeç, U., Dinçer, H. and Kapucu, H. (2009). Adaptive modeling of the drying of baker's yeast in a batch fluidized bed. *Control Engineering Practice*, *17* (4), 503-517.

Lievense, L.C. (1991). The inactivation of Lactobacillus Plantarum during drying. Ph.D. Thesis, Wageningen University, The Netherlands.

Liou, J.K., Luyben, K. Ch. A. M. and Bruin, S. (1984). A simplified calculation method applied to enzyme inactivation during drying. *Biotechn. Bioeng., 27*,109-116.

Quirijns, E.J., van Boxtel, A.J.B. and van Straten, G. (1998). The Use of moisture and temperature profiles in predicting product quality for optimal control of drying process. *Proceedings on Automatic Control of Food and Biological Processes IV*. Göteborg, Skjöldebrand, C. and G. Trystam (Eds.), Sweden, 485-490.

Quirijns, E.J., van Willigenburg, L.G., van Boxtel, A.J.B. and van Straten, G. (2000). The significance of modeling spatial distributions of quality in optimal control of drying processes. *Journal A. Benelux Quarterly Journal on Automatic Control*, *41*(3), 56-64.

Schoeber, W.J.A.H. (1976). Regular regimes in sorption processes.*Ph.D. Thesis*, Technical University Eindhoven, The Netherlands.

Temple, S. J., Tambala, S. T. and van Boxtel, A. J. B. (2000). Monitoring and control of fluid-bed drying of tea. *Control Engineering Practice*, *8*,165-173.

Temple, S.J. and van Boxtel, A.J.B. (1999). Modeling of Fluidized Bed Drying of Black Tea, *Journal of Agricultural Engineering Research*, *74,* 203-212.

Türker, M., Kanarya, A., Yüzgeç, U., Kapucu, H. and Şenalp Z. (2006). Drying of baker's yeast in batch fluidized bed. *Chemical Engineering and Proc.*, *45* (12), 1019-1028.

Yüzgeç, U., Türker, M. and Becerikli, Y. (2008). Modelling spatial distributions of moisture and quality during drying of granular baker's yeast. *The Canadian Journal of Chemical Engineering*, *86* (4), 725-738.

Dynamic Modeling and Control Issues on a Methanol Reforming Unit for Hydrogen Production and Use in a PEM Fuel Cell

Dimitris Ipsakis[1,2], Spyros Voutetakis[1], Panos Seferlis[3], Simira Papadopoulou[1,4]

[1]Chemical Process Engineering Research Institute (C.P.E.R.I.), CEntre for Research and Technology Hellas (CE.R.T.H.), P.O. Box 60361, 57001 Thermi-Thessaloniki, Greece (Tel: +30-2310-498 317; e-mail:paris@cperi.certh.gr).

[2]Department of Chemical Engineering, Aristotle University of Thessaloniki, P.O. Box 1517, 54124 Thessaloniki, Greece (Tel: +30-2310-498 353; e-mail:ipsakis@cperi.certh.gr).

[3]Department of Mechanical Engineering, Aristotle University of Thessaloniki, P.O. Box 484, 54124 Thessaloniki, Greece (Tel: +30-2310-994 229; e-mail:seferlis@cperi.certh.gr).

[4]Department of Automation, Alexander Technological Educational Institute of Thessaloniki, P.O. Box 14561, 54101 Thessaloniki, Greece (Tel: +30-2310-498 319; e-mail:shmira@teithe.gr).

Abstract: The presented research work focuses on the mathematical description and control analysis of an integrated power unit that uses hydrogen produced by methanol autothermal reforming. The unit consists of a reformer reactor where methanol, air and water are co-fed to produce a hydrogen rich stream through a series of reactions. The hydrogen main stream is fed to a preferential oxidation reactor (PROX) for the reduction of CO at levels below 50ppm with the use of air. In the end, the PROX outlet stream enters the anode of a PEM fuel cell where power production takes places to serve a load demand. The operation of the two reactors is described by a combination of partial differential equations (mass and energy balances) and non-linear equations (kinetic expressions of the reactions), while the power production in the fuel cell is based on the inlet hydrogen flow and on operational characteristics. A simple case sceanrio is employed when a step change on methanol flowrate is imposed. Main target is to identify and analyze the changes occuring in the main variables of concern (H_2, CO and temperature levels) that affect the overall system operation. Based on the results, an insight on the challenging control scheme will be applied in order to identify possible ways of setting up a reliable and robust control structure according to the developed mathematical model.

Keywords: methanol reforming, preferential oxidation, hydrogen, PEM fuel cell, dynamic modeling

1. INTRODUCTION

Hydrogen can be considered an energy carrier for the future and when derived from renewable energy sources can be totally non-polluting when used in fuel cells (Ipsakis D. et al., 2008). Fuel cells advantages include (Larminie J. and Dicks A., 2003) the low operation temperatures (~ 80^{o}C), the CO_2 tolerance by the electrolyte, the fast cold start and their few moving parts, which enhances their role as back-up units in vehicles. Nevertheless, the main disadvantage of fuel cells refers to the hydrogen supply. Natural gas, gasoline and higher hydrocarbons have been proposed for hydrogen production via steam reforming, but methanol carries the most advantages from all (Lindström B. and Petterson L.J., 2001). Methanol is a liquid that does not require special conditions of storage, while it is also free from high reforming temperatures and sulphur oxides that are met in methane and gasoline reforming. Moreover, methanol has a high H:C ratio and no C:C ratio and thus, prevents the soot formation (Lindström B. and Petterson L.J., 2001), while biomass resources can be used to produce methanol (bio-methanol). Production of hydrogen from methanol can be achieved in three ways: (i) steam reforming of methanol, (ii) partial oxidation of methanol and (iii) autothermal reforming of methanol (Lindström B. and Petterson L.J., 2001). Autothermal reforming has the asset of eliminating the disadvantages of steam reforming (endothermic process which requires a heating source) and partial oxidation (highly exothermic process which leads to the formation of hot spots in the catalyst) by properly selecting the reactants ratios in such a way, so that adiabatic conditions can be achieved. One of the drawbacks of hydrocarbons reforming however, is the production of CO at high levels that degrade the electrochemical performance of low temperature PEM fuel cells. Several processes used for the minimization of CO content at acceptable levels (less than 50ppm) have been discussed in the past, where among them preferential oxidation is considered to be the simplest and the least expensive method (Cipitì F. et al., 2007).

Most of the simulation and modeling studies on methanol reforming, focus on each subsystem as an individual part. Steam reformers have been modelled using axial distribution models (Suh J. S. et al., 2007), while PROX reactors have also been modelled using 2D models (Cipitì F. et al., 2007). In one of the very few papers that deal with an integrated system, Stamps A. T. and Gatzke E.P. (2006), developed and implemented a system level model of a vehicular reformer PEM fuel cell stack power system without the use however, of a hydrogen purification system, while the dynamic operation results were not provided explicitly. As can be seen, literature references lack in studies that deal with the detailed mathematical description of all the involved subsystems and on their overall dynamic interactions. The objective of this study is to analyze the dynamic behaviour of the two reactors based on a step change imposed in methanol flowrate. The reactors temperature and CO content will be continuously monitored, since they mostly affect the power production of the fuel cell. In the end, an analysis on the demanding task of the control of such an integrated power system will be applied, in order to identify all the necessary actions need to be taken for the development of a robust control scheme.

2. DESCRIPTION OF THE INTEGRATED POWER SYSTEM

Figure 1, shows the overall process flow diagram of the methanol autothermal reforming unit.

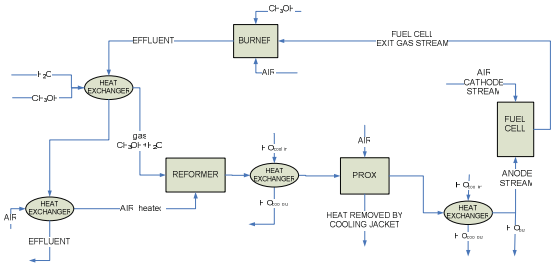

Fig. 1: Overall operation scheme of the methanol autothermal reforming unit.

Methanol, air and water are co-fed to the reformer (0.15m length and 0.1m diameter) after they are preheated by the effluent gases of a burner. The main reaction that takes place at the reformer is the steam reforming of methanol (R1), but because it is an endothermic reaction, oxygen also reacts with methanol (R2) to provide the necessary heat to the system.

Table 1. Reactions taking place at the reformer

$CH_3OH + H_2O \rightarrow CO_2 + 3H_2$ $\Delta H_{R,298} = 49kJ/mol$, (R1)	$CH_3OH + 0.5O_2 \rightarrow CO_2 + 2H_2$ $\Delta H_{R,298} = -193kJ/mol$, (R2)
$CO + H_2O \leftrightarrow CO_2 + H_2$ $\Delta H_{R,298} = -41.2kJ/mol$, (R3)	$CH_3OH \rightarrow CO + 2H_2$ $\Delta H_{R,298} = 90.1kJ/mol$, (R4)

The autothermal reforming of methanol is based on the effective selection of the reactants ratios at the inlet of the reformer. For the current study, it was found from steady-state simulations using Aspen Plus® (Ouzounidou M. et al., 2008a) that the optimum values for H_2O/CH_3OH and O_2/CH_3OH are between 1.5-1.7 and 0.1-0.15 respectively. Steam reforming is considered as the sum of the water gas shift (R3) and methanol decomposistion (R4) reactions.

The reduction of CO after steam reforming, takes place at the PROX reactor (0.1m length and 0.1m diameter). There, besides CO oxidation, H_2 oxidation also takes place, but it is kept at low rate through the effective selection of the catalyst. The reactions of the PROX can be seen in table 2:

Table 2. Reactions taking place at the PROX

$CO + 0.5O_2 \rightarrow CO_2$ $\Delta H_{R,298} = -283kJ/mol$, (R5)	$H_2 + 0.5O_2 \rightarrow H_2O$ $\Delta H_{R,298} = -242kJ/mol$ (R6)

The main objective of the PROX reactor is to keep the CO concentration at a maximum limit of 50 ppm by using efficiently the O_2/CO ratio. From ASPEN Plus® simulations (Ouzounidou M. et al., 2008a), its optimum value is 1, but could vary severely with CO concentration. The PROX reactor due to the presence of the two highly exothermic reactions is surrounded by a jacket to cool the system from undesirable extreme heat generation. The kinetic expressions for all the involved reactions can be found in (Ouzounidou M. et al., 2008b) where an analysis on their selection is provided.

Finally, the hydrogen rich stream is fed to the anode of the fuel cell where it ionises releasing protons (H^+) and electrons (e^-). Protons pass through the proton exchange membrane to the cathode, while electrons flow through an external electric circuit and produce current. In the cathode, oxygen is fed via air supply and reacts with the protons and electrons to form water (Table 3).

Table 3. Reactions taking place at the PEM fuel cell

$H_2 \rightarrow 2H^+ + 2e^-$ Anode, (R6)	$0.5O_2 + 2H^+ + 2e^- \rightarrow H_2O$ Cathode, (R7)

3. MATHEMATICAL DESCRIPTION OF THE SUBSYSTEMS

In this section, the mathematical models of the involved subsystems will be presented and discussed. All parameters, variables and symbols are explained in the nomenclature section. gPROMS® was used to simulate the operation of the integrated power system (PSE®, 2002).

3.1 Reformer and PROX Reactors

The model equations for the catalytic reactors consist of the standard material and energy balances for a pseudo-homogeneous system (packed-bed type). These equations are in partial differential form with spatial and radial distributions. In order to simplify the model and reduce the computational effort needed to simulate all the subsystems, a number of assumptions have been made. It is highlighted, that the description of the system does not lose its accuracy

and the crucial phenomena can be easily described by the developed mathematical model.

- The ideal gas law is applied for all gas components.
- No diffusion phenomena are assumed to take place from the gas phase to the surface of the catalyst.
- Constant reactor pressure and fluid velocity.
- Constant physical properties (component density and heat capacity) over the range of conditions.
- The temperature in the cooling jacket of the PROX reactor is approximately uniform and the resistance to heat transfer occurs primarily between the reactor contents and the wall of the tube (being at the cooling medium temperature).

Material Balance Equation

$$\frac{\partial \mathrm{C_i}}{\partial \mathrm{t}} + \mathrm{u}\cdot\frac{\partial \mathrm{C_i}}{\partial \mathrm{z}} - \varepsilon_{\mathrm{cat}}\cdot D_z\frac{\partial^2 C_i}{\partial z^2} - \varepsilon_{\mathrm{cat}}\cdot D_r\cdot\left(\frac{\partial^2 C_i}{\partial r^2}+\frac{1}{r}\cdot\frac{\partial C_i}{\partial r}\right) = \sum_{i=1}^{N}\sum_{j=1}^{R}\nu_{i,j}\cdot R_j \quad (1)$$

Energy Balance Equation

$$\sum_{\mathrm{i}=1}^{\mathrm{N}}\rho_{\mathrm{i}}\cdot \mathrm{C_{p,i}}\cdot\frac{\partial \mathrm{T}}{\partial \mathrm{t}} + \sum_{\mathrm{i}=1}^{\mathrm{N}}\rho_{\mathrm{i}}\cdot \mathrm{C_{p,i}}\mathrm{u}\cdot\frac{\partial \mathrm{T}}{\partial \mathrm{z}} - k_z\frac{\partial^2 T}{\partial z^2} - k_r\left(\frac{\partial^2 T}{\partial r^2}+\frac{1}{r}\cdot\frac{\partial T}{\partial r}\right) = -\sum_{\mathrm{j}=1}^{\mathrm{R}}\mathrm{R_j}\cdot(\Delta \mathrm{H}_{R,T,j}) \quad (2)$$

Coolant Energy Balance Equation

$$\rho_c\cdot V_c\cdot Cp_c\cdot\frac{\partial \mathrm{T_c}}{\partial \mathrm{t}} = F_c\cdot Cp_c\cdot(T_{c,in}-T_c)+Q \quad (3)$$

$$Q = U\cdot A\int_0^{\mathrm{Reactor\,Length}}(T-T_c)\cdot dz \quad (4)$$

Ideal Gas Law

$$P_i\cdot V = n_i\cdot R\cdot T \Rightarrow P_i = C_i\cdot R\cdot T \quad (5)$$

Species Flowrate

$$F_i = C_i\cdot Q_o \quad (6)$$

$$Q_o = u\cdot S = \frac{\sum F_{i,in}\cdot R\cdot T_{in}}{P_{reactor}} \quad (7)$$

Boundary Conditions (Eqs. 1-4)

z=0

$C_i=C_{i,in}$ *and* $T=T_{in}$, r ε [0,R] (8)

z=L

$$\frac{\partial \mathrm{C_i}}{\partial \mathrm{z}} = 0 \text{ and } \frac{\partial \mathrm{T}}{\partial \mathrm{z}} = 0 \text{ , r ε [0,R]} \quad (9)$$

r=0

$$\frac{\partial \mathrm{C_i}}{\partial \mathrm{r}} = 0 \text{ and } \frac{\partial \mathrm{T}}{\partial \mathrm{r}} = 0 \text{ , z ε (0,L)} \quad (10)$$

r=R

$$\frac{\partial \mathrm{C_i}}{\partial \mathrm{r}} = 0 \quad and \quad -k_r\cdot\frac{\partial \mathrm{T}}{\partial \mathrm{r}} = h_w\cdot(T-T_c), z\varepsilon(0,L) \quad (11)$$

In the solution of the reformer, h_w is 0 and for the PROX ≠0. For the discretization of the distributions the method of centered finite difference (2nd order) was used. The discretization of the axial and radial distribution was performed for 50 and 5 intervals, respectively. More intervals showed that the results are not affected, but the increase in the required computational effort leads to inefficient solution procedure.

3.2 PEM Fuel Cell

Larminie J. and Dicks A., (2003), presented an equation that relates the power production with the hydrogen flow and the operational characteristics of the fuel cell:

$$\mathrm{P_{fc}} = \mathrm{F_{H2}}\cdot n_e\cdot F\cdot\eta_F\cdot V_{cell} \quad (12)$$

The hydrogen flow predicted by the reactors mathematical model is used in the above equation to predict the power production as a function of time. V_{cell} is usually around 0.7V/cell (Larminie J. and Dicks A., 2003).

The same authors also concluded that if all the enthalpy of reaction of a hydrogen fuel cell was converted into electrical energy then the output voltage would be 1.48V (water in liquid form) or 1.25V (water in vapour form). Therefore, the difference between the actual cell voltage and this voltage represents the energy that is converted into heat instead. For the vapour case in our fuel cell, heat is calculated as:

$$\mathrm{Q_{fc}} = \mathrm{P_{fc}}\cdot\left(\frac{1.25}{V_{cell}}-1\right) \quad (13)$$

3.3 Model validation

Based on the experimental results presented in (Ouzounidou M. et al., 2008b), validation with the above mathematical model (kinetic parameters and the axial and radial distributed paramaters were estimated) has been performed, where it has been found that the model accurately simulates the performance of both reactors. Figures 2 and 3 show the comparison between the experimental data and mathematical model for the two reactors, respectively and the deviation between simulated and experimental values is within the expected error (less than 5%). Only in low PROX temperatures a higher deviation is detected but considered negligible, since PROX operates in temperatures >150°C.

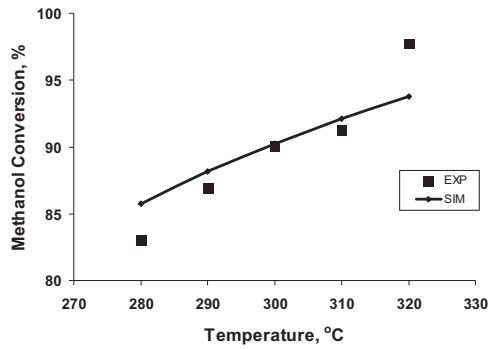

Fig. 2. Comparison between simulated and experimental results for the reformer

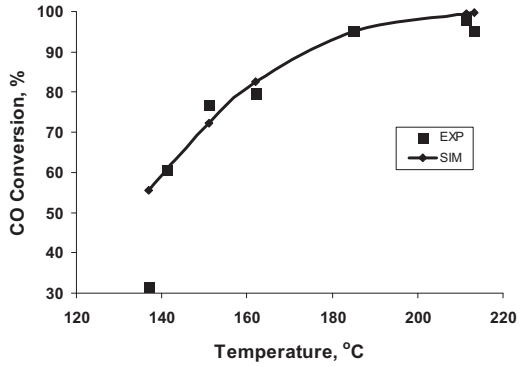

Fig. 3. Comparison between simulated and experimental results for the PROX

4. SIMULATION RESULTS FROM THE DYNAMIC OPERATION OF THE INTEGRATED POWER SYSTEM

The dynamic operation of the integrated power unit will be presented based on an imposed step change. The conditions of the simulated case study are: inlet methanol at 0.02mol/s, reformer temperature at 300°C, PROX temperature at 200°C, H_2O/CH_3OH at 1.5, O_2/CH_3OH at 0.14 and O_2/CO at 2. It is noted that the flowrates of the reactants and reactor temperature at the inlet of the reformer do not have a sharp constant value at the start of the simulation time, but a value that increases smoothly with time and reaches its steady state value after a few seconds. Fig.4 shows the 50% step change on the inlet methanol flowrate at t=30s (inlet water and oxygen flowrates are also increased based on the selected ratios). As can be seen, at the same time an increase at the exit hydrogen flowrate starts to appear and after 80s the increase in hydrogen flowrate is calculated at 49.6%, which shows that methanol conversion is practically unaffected by the increase in the methanol flowrate for the selected conditions.

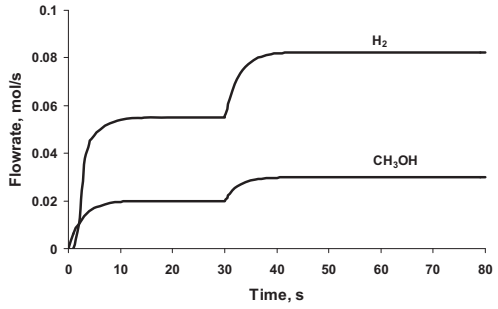

Fig. 4. Methanol inlet and hydrogen outlet flowrates

Similarly Fig.5 shows the CO content (ppm) where a 13% decrease is observed at the time that the step change occurs. This decrease is excpected due to the fact that water flowrate is increased (according to the methanol step change) and the water gas shift reaction is favored. This can also be concluded by the fact that CO flowrate increase is calculated at 22.5% which differs significantly from the 50% increase detected in other products, such as hydrogen.

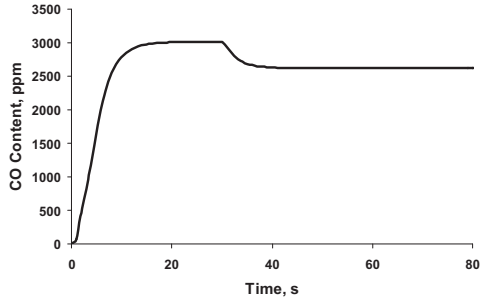

Fig. 5. Carbon monoxide content at the reformer exit

Fig.6 shows the reformer inlet and outlet temperature levels. The inlet gas temperature follows a smooth increase in order to prevent hot spots due to the rigorous exothermic partial oxidation of methanol.

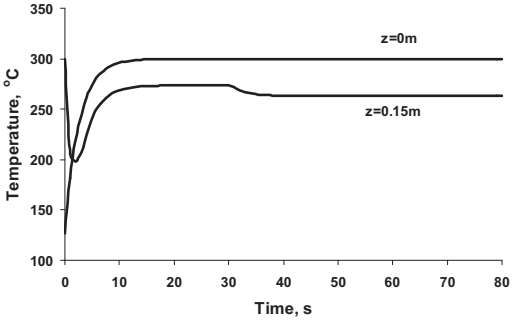

Fig. 6. Temperature levels at the reformer inlet and outlet

This smooth increase is based on the operation of the assumed preheater that heats the reactants mixture. On the

other hand, the outlet temperature of the reformer (at t=0s the reformer is assumed to be at 300°C) is initially decreased due to the fact that low temperature gas mixture exits the reactor at t<10s, but as the reformer operation proceeds, the exit temperature is gradually increased to 260-270 °C. As can be seen for the present conditions, the endothermic reactions prevail and the exit temperature is 30-40 °C lower than the inlet (at steady-state conditions) and also the step change seems to affect the temperature levels by lowering them by 10 °C.

Unlike the reformer, where negligible changes are observed in the radial domain, in the PROX the species concentration and temperature varies severely along the reactor radius. Fig.7 shows the CO content at the wall of the reactor, at its center and the average value that indicates the exit flow. As can be seen, the CO content is higher away from the center due to the lower temperature at that region (see Fig.8). As we move to the reactor center, the CO levels are quite low (practically zero at the reactor center) due to the increased temperature while the average value is always lower than 50ppm for the current conditions. It is highlighted that the CO at the exit of the reformer is measured and according to the selected O_2/CO ratio, the air feed rate is manipulated and introduced to the PROX reactor, so as to always provide a constant O_2/CO ratio. If the O_2 flow was constant based on the initial conditions, then the CO levels would have been higher indicating a possible fuel cell deterioration.

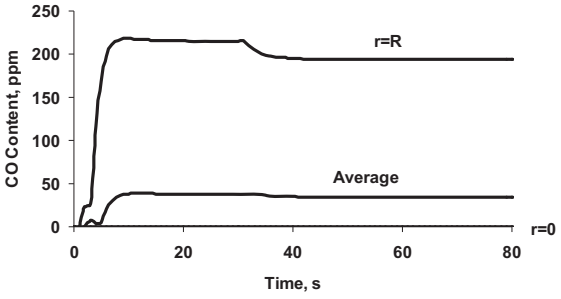

Fig. 7. Carbon monoxide content at the PROX wall, center and average value in the radial domain

Fig.8 shows the temperature levels at the wall of the reactor, at the center and the average (exit) value. Initially (t=0s), the reactor is assumed to be at 200°C and as the oxidations take place, the reactor center is found to have increased temperature in contrast with the reactor wall temperature that is maintained at low levels due to the presence of the cooling medium. Eventually, the exit (average) temperature is initially decreased, but as the gas mixture approaches the reactor exit, the temperature levels are increased. It can also been said, that at t=30s, a small increase is detected due to the increased flowrate at the inlet of the PROX which is not considered severe (less than 15°C). The presence of a controller to maintain the reaction temperature at specific levels is of primary importance and the manipulated value will be the coolant flowrate. It is noted that the hydrogen main stream is assumed to be cooled down before entering the PROX and the fuel cell, but the dynamic simulation of the heat exchangers is omitted for this study, since we focus on the main subsystems.

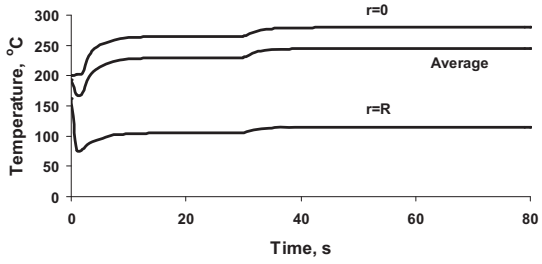

Fig. 8. Temperature levels at the PROX wall, center and average value in the radial domain

Finally, Fig. 9 shows the power and heat production levels based on the inlet hydrogen flow. As can be seen, at t=30s a 49.8% increase in power and heat production is detected, which should be taken into consideration at the developed control scheme that will always try to meet the load demand (see next section).

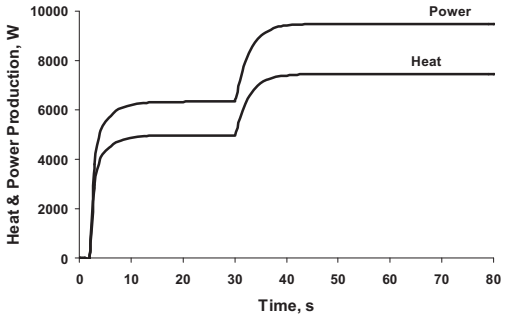

Fig. 9. Power and heat production in the fuel cell

5. CONTROL ISSUES ON THE INTEGRATED POWER SYSTEM

As it is obvious from the above analysis, the operation of the integrated power system, requires the development of a robust control scheme. The variables that constantly need to be monitored are: the reactor temperatures, the CO levels and finally, the power to be supplied to the load. In the reformer, the temperature will be controlled by the O_2/CH_3OH ratio and in the PROX through the coolant flowrate. The CO composition will be controlled by the effective selection of the H_2O/CH_3OH and O_2/CO ratios. Nevertheless, the main variable of concern is the power that needs to be provided to the load. Changes in the demanded load power level will be handled by manipulating the methanol flowrate in order to produce the hydrogen needed in the fuel cell to operate. As was presented, step changes in methanol flowrate affect the overall operation and model predictive control (MPC) is the more suitable control scheme of such an integrated power system. The control algorithm must also satisfy the bounds for CO and temperature levels in order to protect the various subsystems from deterioration (mainly PROX and fuel cell).

All these consequent changes will be decided based on the minimization of an objective function (MPC) that will take into account all the system necessary constraints. Special care, however, should be given to the fact that that slow and fast dynamics occur in the system (e.g. the fast PROX oxidation versus the slow coolant effect) that might need to be specially treated. Perturbation Theory is proposed to alleviate such problems, because it can be applied to mathematical systems that combine non-linear algebraic equations and differential ones (Kumar A. and Daoutidis P., 1999).

6. CONCLUSIONS

An integrated power system for the production of hydrogen via autothermal reforming of methanol has been studied in this paper. The developed mathematical model for the two reactors was validated and used for the simulation of the operation of the power unit where a step change was imposed. The next step will be the integration of the heat management system (burner and heat exchangers), while the developed control scheme will try to maintain the operational variables of concern at their desired values (set points).

Nomenclature

A:	heat transfer area, m^2
C_i:	concentration of the component i, mol/m^3
Cp_c:	coolant specific heat capacity, J/ K Kg
C_{pi}:	component i specific heat capacity, J/K kg
D_r:	radial effective diffusivity, m^2/s
D_z:	axial effective diffusivity, m^2/s
F:	Faraday's constant, Cb/mol
F_c:	coolant flowrate, kg/s
F_i:	flowrate of the component i, mol/m^3
h_w:	wall heat transfer coefficient, W/m^2 K
i:	component that takes part at the system
in:	inlet conditions
j:	number of reaction at the reactors
k_r:	radial thermal conductivity, W/m^2 K
k_z:	axial thermal conductivity, W/m^2 K
n_c:	number of cells of the PEM fuel cell
n_e:	number of electrons
n_F:	Faraday's efficiency, %
P_i:	parital pressure of the component i, bar
P_{fc}:	fuel cell power, Watt
$P_{reactor}$:	reactor pressure, bar
Q:	heat removed by the cooling jacket, Watt
Q_o:	volumetric flow, m^3/s
Q_{fc}:	heat, W
r:	radius of the reactor, m
R:	universal gas constant bar m^3/ mol K
R_j:	kinetic expression of the reaction j, mol/kg_{cat} s
S:	cross section of the reactor, m^2
t:	time, s
T:	temperature, K
T_c:	coolant temperature, K
u:	superficial gas velocity, m/s
U:	overall heat transfer coefficient, W/m^2 K
V_c:	coolant jacket volume, m^3
V_{cell}:	cell voltage, V/cell
z:	length of the reactor, m
$\Delta H_{R,T,j}$:	enthalpy of reaction j at temperature T, J/mol
ε_{cat}:	void fraction of the catalyst
$\nu_{i,j}$:	coefficient of the component i in the reaction j
ρ_i:	density of the component i, kg/m^3
ρ_c:	coolant density, kg/m^3

REFERENCES

Cipitì, F., Pino, L., Vita, A., Laganà, M., and Recupero V. (2007). Model-based investigation of a CO preferential oxidation reactor for polymer electrolyte fuel cell systems. *International Journal of Hydrogen Energy*, Volume 32, Pages 4040-4051

Ipsakis, D., Voutetakis, S., Seferlis, P., Stergiopoulos, F., Papadopoulou, S., and Elmasides C. (2008). The Effect of the Hysteresis Band on Power Management Strategies in a Stand-Alone Power System. *Energy*, Volume 33, Pages 1537-1550

Kumar A., and Daoutidis P. (1999). Control of nonlinear differential algebraic equation systems. Chapman & Hall/CRC, New York, Washington D.C.

Larminie J., and Dicks A. (2003). Fuel Cell Systems Explained. 2nd Edition, John Wiley & Sons Ltd

Lindström B., and Petterson L.J. (2001). Hydrogen generation by steam reforming of methanol over copper-based catalysts for fuel cell applications. *International Journal of Hydrogen Energy*, Volume 26, Pages 923-933.

Ouzounidou, M., Ipsakis, D., Voutetakis, S., Papadopoulou, S., and Seferlis P. (2008a). Experimental Studies and Optimal Design for a Small-Scale Autonomous Power System Based on Methanol Reforming and a PEM Fuel Cell. T*he AIChE 2008 Annual Meeting*, Philadelphia, PA, U.S.A., November 16-21, 2008

Ouzounidou, M., Ipsakis, D., Voutetakis, S., Papadopoulou, S., and Seferlis P. (2008b). A combined methanol autothermal steam reforming and PEM fuel cell pilot plant unit: Experimental and simulation studies, (submitted in Energy, Special Issue for PRES08)

Process Systems Enterprise Ltd, gPROMS Introductory User Guide, London, United Kingdom, Release 2.1.1.-15 March 2002.

Stamps, T., and Gatzke, E.P., (2006). Dynamic modeling of a methanol reformer—PEMFC stack system for analysis and design. *Journal of Power Sources*, Volume 161, Pages 356-370

Suh, J. S., Lee, M. T., Greif, R., and Grigoropoulos, C. P. (2007). A study of steam methanol reforming in a microreactor. *Journal of Power Sources*, Volume 173, Pages 458-466

Dynamic modelling of a three-phase catalytic slurry intensified chemical reactor

S. Bahroun*, C. Jallut*, C. Valentin*, F. De Panthou**

** Université de Lyon, F-69622, Lyon, France;*
Université Lyon 1, Villeurbanne;
LAGEP, UMR 5007, CNRS, CPE, 43, Bd du 11 Novembre 1918, 69100 Villeurbanne cedex, France;
(e-mail: bahroun@lagep.univ-lyon1.fr, Tel: (+33)4 72 43 18 81, Fax: (+33)4 72 43 18 99).
*** AETGROUP SAS, 6 montée du Coteau, 06800 Cagnes-sur-mer, France,*
(e-mail: fabrice.depanthou@aetgroup.com, Tel: (+33)6 24 05 25 83, Fax: (+33)4 92 08 53 40).

Abstract: Three-phases chemical reactions are widely applied industrially. They are highly non-linear, multivariable, exothermal processes. The aim of the present work is to propose a dynamic model of an intensified continuous three-phases mini-reactor. This model is developed to enable the transient phase monitoring of the mini-reactor. The reactor is treated as an association of J stirred tank reactors in series with back mixing effect. The model is used to describe the dynamic behaviour of the reactor during the hydrogenation of o-cresol on Ni/SiO_2 catalyst. The model consists in mass and energy balance equations for the catalyst particles, the gas and liquid bulk phases. The transient heat transfers between the metal body of the reactor, the coolant fluid and the bulk fluid are also taken into account.

Keywords: Intensification; Three-phase reactor; Hydrogenation; Dynamic modelling; Control; Dynamic behaviour.

1. INTRODUCTION

The pharmaceutical and the fine chemical industries produce molecules of high added values mainly in batch or fed-batch agitated reactors. Indeed, batch reactors, even if they provide the characteristics of flexibility and versatility required in the field of fine chemicals production, have a number of limitations: in particular, poor conditions of heat released by the chemical reactions leads to a serious safety problem for highly exothermal chemical reactions.

For some years, there is an alternative in the use of batch reactors, thanks to process intensification progresses and to mini-reactors development. The idea is to perform the reactions in continuous intensified reactors. On the one hand, the intensification leads to a better control of heat transfer that allows concentrating the reagent and thus limiting the quantities of solvent to be treated. On the other hand, intensification leads to reduce mass transfer limitations in the case of multiphase chemical reactors.

Nowadays, the control and safety of these reactors are important features in the design as well as in the operation of industrial processes. Such processes carry out complex reactions with constraints on thermal stability and/or selectivity as, for example, exothermal hydrogenation reactions (Vasco de Toldeo *et al.*, 2001).

Hydrogenation reactions are widely applied industrially. Development of efficient and reliable models for three phase reactors is still a difficult task because it involves many aspects including hydrodynamics, gas-liquid and liquid-solid mass transfer, heat transfer, reaction kinetics (Bergault *et al*, 1997).

In the literature, we can find many studies proposing dynamic modelling of catalytic three phase reactors (P.A Ramachandran and J.M. Smith, 1976; R.J. Wärnä and T. Salmi, 1995; Vasco de Toldeo *et al.*, 2001) but as far as we know, the problem of mini-reactors modelling is not addressed.

The aim of this paper is to propose a dynamic model of a continuous three-phases intensified mini-reactor. This model is developed to enable the transient period monitoring of the three phases mini-reactor. It will allow better predictions of the behaviour of the system and therefore secure and effective studies of the reactor control.

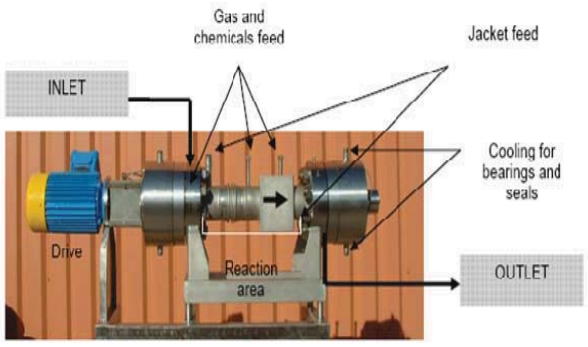

Fig.1. The "RAPTOR® (***R**éacteur **A**gité **P**olyvalent à **T**ransfert **O**ptimisé **R**ectiligne)*".

The mini-reactor under consideration, the "RAPTOR®" (presented by the figure 1) is developed by AETGOUP SAS Company a French society whose main activity is to offer a broad range of services mainly focused on chemical process industrialisation, in the field of pharmaceuticals, fragrances and aromas, cosmetics and specialty chemicals. For confidentiality reasons, we cannot give here a detailed description of the RAPTOR®.

2. MATHEMATICAL MODELLING

The model is used to describe the dynamic behaviour of the reactor during the hydrogenation of o-cresol on Ni/SiO_2 catalyst, taken as an example. A three-phase catalytic reactor is a system in which gas and liquid phases are in contact with a porous solid phase. The reaction occurs between a dissolved gas and a liquid-phase reactant in presence of a catalyst on the surface of the porous solid support (P.A. Ramachandran and R.V. Chaudhari, 1983), according to the following global stoichiometric equation:

$$A_{(g)} + \nu_B B_{(l)} \rightarrow \nu_C C_{(l)} \quad (1)$$

The chemical process involves several steps in series (see figure 2):

- diffusion of A from gas-liquid interface to the bulk liquid;
- diffusion of A and B from bulk liquid through liquid-solid interface;

- intraparticle diffusion of A and B into the pores of the solid;
- adsorption of the reactants;
- adsorbed phase reaction.

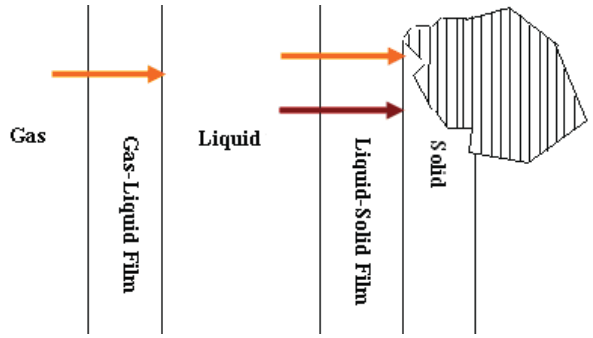

Fig.2. Steps of catalytic reaction.

The reactor is treated as an association of J stirred tank reactors in series with back mixing effect. Similarly, the jacket is treated as an association of J perfectly stirred tank reactors series. This way to consider the flows in the reactor is highly flexible and leads to a finite dimension model. Since an intensified reactor has to be compact, the influence of the reactor body itself may be significant with respect to the thermal transient behaviour of the system. Consequently, a piece of reactor body is associated to each perfectly mixed reactors used to model the flows (see figure 3).

The model consists in mass and energy balance equations for the catalyst particles, the gas phase and liquid-bulk phase, and also energy balance equations for the body of the reactor and for the coolant fluid into the jacket.

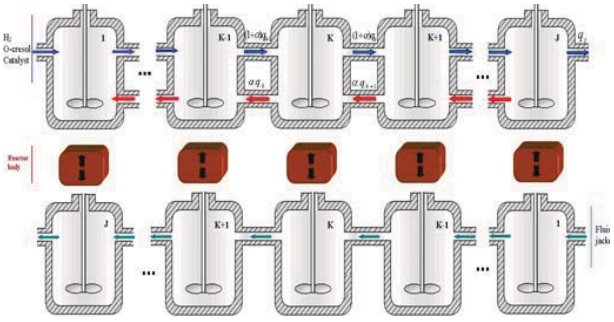

Fig.3. Flow model of the mini-reactor.

2.1 Kinetic model

Hydrogenation of o-cresol on Ni/SiO_2 catalyst (Hichri *et al.*, 1991) is taken as an example of chemical process that can be intensified. In this case, hydrogen reacts with o-cresol without any solvent due to the high heat and mass transfer capacities of the mini-reactor. The reaction can be represented by equation (1). In this case, A stands for hydrogen, B for o-cresol, C for 2-methylcyclohexanol.

Langmuir-Hinshelwood model represents in a realistic way the adsorption phenomena involved in heterogeneous catalysis processes. The reaction rate is calculated as follows (Hichri *et al*, 1991):

$$R = k\frac{K_A K_B C_{As} C_{Bs}}{(1+K_A C_{As})(1+K_B C_{Bs})} \quad (2)$$

C_{As} and C_{Bs} are respectively the hydrogen and o-cresol concentrations within the catalyst pores. The Arrhenius law gives the variation of the rate constants k with temperature while adsorption constants K_A and K_B variations derive from mass action law. The following expressions are taken from (Hichri *et al.*, 1991):

$$k(mol/kg.cat.s) = 5{,}46.10^{8}\exp(-82220/RT_s) \quad (3)$$

$$K_A(m^3/mol) = 10{,}55.10^{-3}\exp(+5003/RT_s) \quad (4)$$

$$K_B(m^3/mol) = 7{,}54.10^{-6}\exp(+16325/RT_s) \quad (5)$$

where $T_s\,(K)$ is the catalyst pellet temperature.

2.2 Mini-reactor model

The following assumptions are considered to derive the model (Vasco De Toledo *et al.*, 2001; Santana, 1999):

- the liquid and gas phases homogeneous suspension is considered as a pseudo-fluid with respect to the temperature;

- a global mass transfer coefficient is used to represent hydrogen transfer from the liquid surface to the bulk. Equilibrium conditions at the liquid surface are assumed;

- the pressure variations are negligible;

- the resistances to mass and heat transfer at the catalyst pellet surface and within the pores are lumped into global heat and mass transfer coefficients;

- the material balance in the gas phase, that is assumed to be pure hydrogen, is written at steady state.

Mass balance of reactant A in the gas phase

$$F_{Ag}^{0k} + V_k k_l a^k \left(C_{Al}^{k*} - C_{Al}^k\right) = F_{Ag}^{Ik} \tag{6}$$

Mass balance of reactant A in the liquid phase

$$\varepsilon_l^k V_k \frac{dC_{Al}^k}{dt} = (1+\alpha) q_l^{k-1} C_{Al}^{k-1} + \alpha q_l^{k+1} C_{Al}^{k+1} - (1+2\alpha) q_l^k C_{Al}^k$$
$$- V_k k_s a \left(C_{Al}^k - C_{As}^k\right) + V_k k_l a^k \left(C_{Al}^{*k} - C_{As}^k\right) \tag{7}$$

Mass balance of reactant A in the solid phase

$$\varepsilon_s V_k \frac{dC_{As}^k}{dt} = (1+\alpha) q_s^{k-1} C_{As}^{k-1} + \alpha q_s^{k+1} C_{As}^{k+1} - (1+2\alpha) q_s^k C_{As}^k$$
$$+ V_k k_s a \left(C_{Al}^k - C_{As}^k\right) - \nu_A \varepsilon_s \rho_s V_k R(C_{As}^k, C_{Bs}^k, T_s^k) \tag{8}$$

Mass balance of reactant B in the liquid phase

$$\varepsilon_l^k V_k \frac{dC_{Bl}^k}{dt} = (1+\alpha) q_l^{k-1} C_{Bl}^{k-1} + \alpha q_l^{k+1} C_{Bl}^{k+1}$$
$$- (1+2\alpha) q_l^k C_{Bl}^k - V_k k_s a (C_{Bl}^k - C_{Bs}^k). \tag{9}$$

Mass balance of reactant B in the solid phase

$$\varepsilon_s V_k \frac{dC_{Bs}^k}{dt} = (1+\alpha) q_s^{k-1} C_{Bs}^{k-1} + \alpha q_s^{k+1} C_{Bs}^{k+1} - (1+2\alpha) q_s^k C_{Bs}^k$$
$$+ V_k k_s a (C_{Bl}^k - C_{Bs}^k) - \nu_B \varepsilon_s \rho_s V_k R(C_{As}^k, C_{Bs}^k, T_s^k) \tag{10}$$

Energy balance in the fluid (gas + liquid) phase

$$V_k (\varepsilon_g^k \rho_g C_{pg} + \varepsilon_l^k \rho_l C_{pl}) \frac{dT_f^k}{dt} = hS (T_m^k - T_f^k)$$
$$+ V_k h_s a_{ls} (T_s^k - T_f^k) - (\varepsilon_g^k \rho_g C_{pg} + \varepsilon_l^k \rho_l C_{pl})$$
$$\left((1+\alpha) q_{k-1} (T_f^k - T_f^{k-1}) + \alpha q_{k+1} (T_f^k - T_f^{k+1})\right) \tag{11}$$

Energy balance in the solid phase

$$\varepsilon_s V_k \rho_s C_{ps} \frac{dT_s^k}{dt} = V_k h_s a_{l:s} (T_f^k - T_s^k)$$
$$- (\rho_s C_{ps}) \left((1+\alpha) q_{sk-1} (T_s^k - T_s^{k-1}) + \alpha q_{sk+1} (T_s^k - T_s^{k+1})\right)$$
$$- \varepsilon_s V_k \rho_s \Delta_r HR(C_{A,s}^k, C_{B,s}^k, T_s^k). \tag{12}$$

Energy balance of the body of the mini-reactor

$$(V_k \rho C_p)_m \frac{dT_m^k}{dt} = hS(T_f^k - T_m^k)$$
$$+ h_j S(T_j^k - T_m^k) \tag{13}$$

Energy balance of the refrigerant fluid into the jacket

$$(V_k \rho C_p)_j \frac{dT_j^k}{dt} = h_j S(T_m^k - T_j^k)$$
$$- (\rho C_p)_j q_j^{k-1} (T_j^k - T_j^{k-1}). \tag{14}$$

3. SIMULATION RESULTS

Kinetic and thermodynamic parameters are taken from (Hichri *et al.*, 1991). The other physical parameters are taken from (Vasco de Toledo *et al.*, 2001; Adriano Pinto Mariano *et al.*, 2005).

We have performed a sensitivity study to define the optimum conditions that enable to achieve a high conversion rate under the constraint of the thermal runaway. One can see on the figure 5 the dynamic behaviour of the reactor and on the figure 4 the steady-state conversion profile that we have obtained. The operating conditions resulting from the sensitivity analysis lead to a conversion up to 90% at the reactor outlet, which is a very common industrial target.

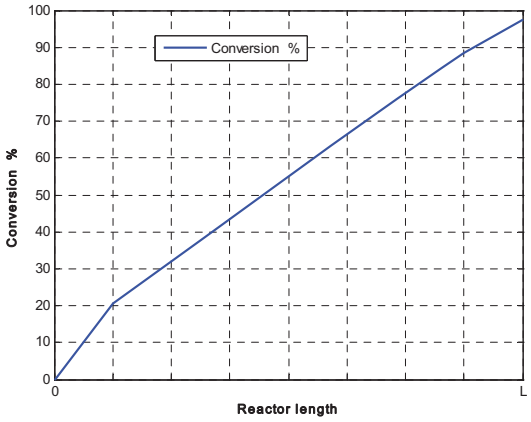

Fig.4. The steady-state conversion profile along the mini-reactor.

In figure 5, the dynamic behaviour of the reactor outlet temperature is represented. We observe that the fluid temperature is limited and increases by 24 %.

The catalyst temperature is slightly higher than that of reactant fluid since the reaction takes place in the pores catalyst. We also observe that the jacket temperature remains nearly constant while the temperature of the reactor body heats up by 15%. In fact the reactor body tends to store up the energy released by the reaction; it therefore appears that the reactor can work in hard reactive conditions, but safely.

When the optimum operating conditions have been established, we performed a steady-state characterization of the model; this feature allows not only steady analysis of model sensitivity with respect to the variation of input variables, but also consistency verification of the model.

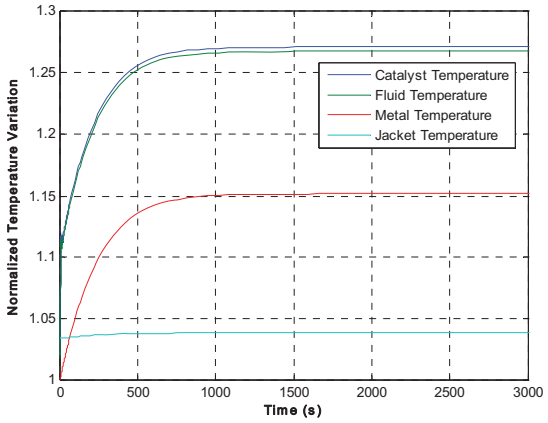

Fig.5. The dynamic behaviour of outlet reactor temperatures.

As far as intensified reactors are concerned, where the reaction takes place at very high temperature, the jacket plays a dual role in the evolution of the reaction. On the one hand, it is related to safety problems since the jacket fluid allows cooling the temperature of the bulk in order to avoid thermal runaway. On the other hand, it allows the indirect control of the outlet conversion by controlling the temperature of the bulk.

Figure 6 illustrates the steady-state characterization of outlet temperatures and conversion with respect to the inlet jacket fluid temperature (variations ranging from -5% to 5% around T_{j0}).

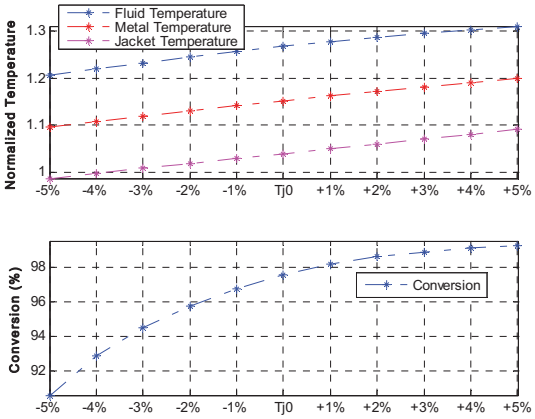

Fig.6. The steady-state characterization of outlet temperatures and conversion with respect to the inlet jacket fluid temperature.

From this figure, it is observed that both of outlet temperatures and conversion are very sensitive to changes in the inlet temperature of the jacket fluid. This sensibility of the dynamic behaviour of the reactor in relation to changes in the coolant fluid is observed mainly in industrial situations.

Figure 7 shows the steady characterization of outlet temperatures and conversion with respect to the inlet gas flow (ranging from -30% to 30% around q_{A0}). We can observe that the variations of q_{A0} have more impact on the conversion than the outlet temperatures.

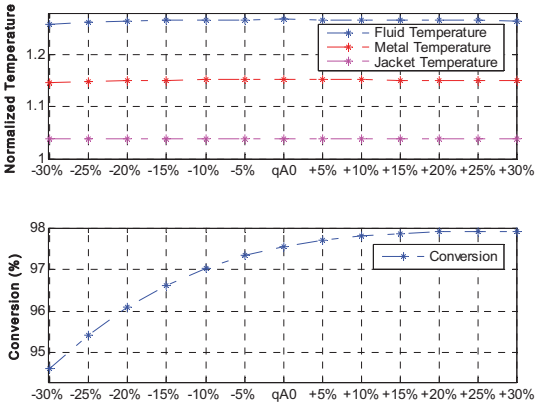

Fig.7. The steady-state characterization of outlet temperatures and conversion with respect to the inlet gas flow.

Figure 8 shows the effect of the inlet fluid temperature on the behaviour of outlet temperatures and conversion (variations ranging from -5% to 5% around T_{f0}). This figure points out that only conversion is sensitive to the variations of T_{f0}, as a result, disturbance on the inlet fluid temperature greatly affects the quality of the output product.

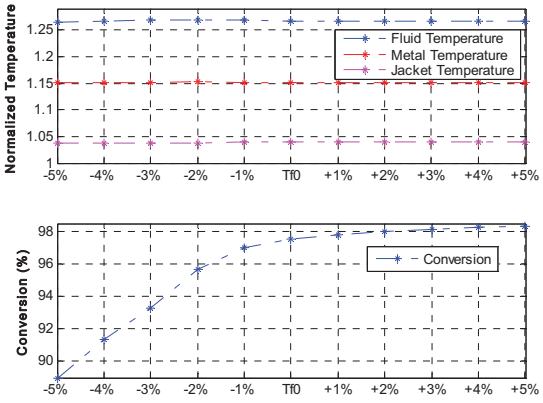

Fig.8. The steady-state characterization of outlet temperatures and conversion with respect to the inlet fluid temperature.

In figure 9, the steady-state characterization of outlet temperatures and conversion with respect to the inlet fluid flow (ranging from -30% to 30% around q_{f0}) is highlighted. We remark that the temperatures and conversion are very sensitive to q_{f0}. In fact, a decrease in the inlet fluid flow (-30%) allows obtaining a good conversion (=99.9%) with better thermal conditions. However this result leads to lower productivity.

According to the observations of these figures, the steady-state characterization of the model confirms the consistency of the model sets.

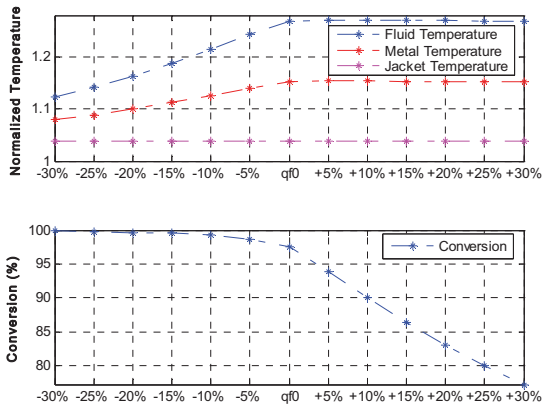

Fig.9. The steady-state characterization of outlet temperatures and conversion with respect to the inlet Fluid flow.

We observed that system's output variables are very sensitive to the variations of inlet jacket temperature. We could also highlight the fact that the conversion is very sensitive to the variations of inlet gas flow. Thus it may be concluded that these two variables may be chosen as an efficient control variables.

4. CONCLUSION

Reactions performed in multiphase catalytic intensified reactors have a complex behaviour due to heat and mass transfers and chemical kinetic interactions. The objective of the dynamic mathematical model developed in this work is to perform a detailed study of the process dynamic behaviour in order to define a suitable control structure. This structure has to control the outlet conversion and preserve safety conditions of the reactor. Others objectives such as high product quality and economy gain can also be considered.

ACKNOWLEDGMENTS

This project devoted to intensification of fine chemicals workshop is supported by the French research agency ANR (Agence Nationale de la Recherche). The authors thank warmly Shi Li for his discussions.

NOTATION

a	interfacial area, m^{-1}
C_A	concentration of the component A, mol m^{-3}
C_A^*	solubility of the component A, mol m^{-3}
C_B	concentration of the component B , mol m^{-3}
C_p	heat capacity, J K^{-1} kg^{-1}
F	molar flow, mol s^{-1}
h	heat transfer coefficient, W m^{-2} K^{-1}
k	kinetic constant, mol kg^{-1} s^{-1}
K	adsorption constant, m^3 mol^{-1}
k_l	mass transfer coefficient gas–liquid, m s^{-1}
k_s	mass transfer coefficient liquid–solid, m s^{-1}
q	volume flow, m^3 s^{-1}
R	reaction rate, mol kg^{-1} s^{-1}
S	surface, m^2
T	temperature, K
v	volume, m^3

GREEK LETTERS

$\Delta_r H$	heat of reaction, j mol^{-1}
ν	stoichiometric coefficient
α	back mixing
ρ	density, kg m^{-3}
ε_g	gas hold up
ε_l	bulk hold up
ε_s	solid hold up

SUBSCRIPT

A	component A
B	component B
j	jacket fluid
f	fluid
g	gas
k	reactor number
l	liquid
m	metal
s	solid

SUPERSCRIPT

k	reactor number
I	Inlet
O	Outlet

REFERENCES

Bergault, I., Rajashekharam, M. V., Chaudhari, R. V., Schweich, D. and Delmas, H. (1997). Modeling and comparison of acetophenone hydrogenation in trickle-bed and slurry airlift reactors. *Chemical Engineering Science*, 52, 4033–4043.

De Toledo, E. C. V., De Santana , P. L., Wolf Maciel, M. R., Filho , R. M. (2001). Dynamic modelling of a three-phase catalytic slurry reactor. *Chemical Engineering Science*, 56, 6055–6061.

Hichri, H., Armand, A., and Andrieu, J. (1991). Kinetics and slurry-type reactor modelling during catalytic hydrogenation of o-cresol on Ni/SiO2. *Chemical Engineering Process*, 30, 133–140.

Julcour, C., Stüber, F., Le Lann, J. M., Wilhelm, A. M., and Delmas, H. (1999). Dynamics of a three-phase up-flow fixed-bed catalytic reactor. *Chemical Engineering Science*, 54, 2391–2400.

Pinto Mariano A., De Toledo, E. C. V., Da Silva, J. M. F., Wolf Maciel, M. R. and Filho ,R. M.(2005). *Computers and Chemical Engineering*, 29, 1369–1378

Ramachandran, P. A., and Chaudhari, R. V. (1983). *Three-phase catalytic reactors*. Gordon and Breach, New York.

Ramachandran, P. A., and Smith, J. M. (1977). Dynamics of three phase slurry reactor. *Chemical Engineering Science*, 32, 873–880.

Santana, P. L., De Toledo, E. C. V., Meleiro, L. A. C., Scheffer, R., Freitas Jr., N. B., Wolf Maciel, M. R., and

Filho, R. M. (2001). A Hybrid mathematical model for a three-phase industrial hydrogenation reactor, *European symposium on computer aided process engineering*, Vol. (11), 279–284.

Wärnä, J., and Salmi, T. (1996). Dynamic modelling of catalytic three phase reactors. *Computers in Chemical Engineering*, 20(1), 39–47.

Identification of an Ill-Conditioned Distillation Column Process using Rotated Signals as Input

M.S. Sadabadi and J. Poshtan

Electrical Engineering Department, Iran University of Science and Technology, Tehran, Iran
(e-mails: sadabadi@iust.ac.ir, jposhtan@iust.ac.ir)

Abstract: The standard uncorrelated test signals estimate the low-gain direction of ill-conditioned multivariable systems poorly. Therefore, the low-gain information needs to be excited more. In this paper, identification of an ill-conditioned distillation column process using rotated signals is proposed. Rotated input signals allow more excitation to be applied in the weak gain direction of the process and less excitation in the strong gain direction. In this approach, the singular value decomposition (SVD) of the steady state gain matrix is used to rotate the input signals along the directions of the right singular vectors. Simulation results show good accuracy of the proposed method in identifying low and high gain directions.

Keywords: Rotated Input Design, Ill-conditioned Process, System Identification, Subspace Method, Distillation Column.

1. INTRODUCTION

Unlike SISO processes, MIMO processes may show ''directions'' (in the input vector space) in which the (steady-state or dynamic) effect of the inputs on the process outputs is much larger than in other directions (Zhu *et al.*, 2001, 2006). In such situations the process is said to be ill-conditioned. An ill-conditioned problem is a specific problem for multivariable processes.

Control-relevant identification of an ill-conditioned system requires special techniques. The directionality of such systems should be taken into account in the identification test signal design. Traditional uncorrelated open-loop step tests tend to excite the system mostly in high-gain directions. Therefore, the input test signals should be selected correctly (Zhu *et al.*, 2001, 2006).

In MIMO processes, the existing input test signal design methods can be divided in two categories, sequential input testing and simultaneous input testing (Conner *et al.*, 2004).

In sequential input testing, one signal, often PRBS (pseudo random binary sequence) or GBN (generalized binary noise) signal, is applied to each input separately while the other inputs are kept at their nominal values (Conner *et al.*, 2004). This input excitation usually takes a long time because the inputs are perturbed one at a time (Li *et al.*, 2008).

Simultaneously input testing excites more than one input at a time (Conner *et al.*, 2004). This method leads to more efficient use of the plant testing time (Conner *et al.*, 2004). Gevers *et al*. (Gevers *et al*., 2006) using variance analysis shows that it is better to excite all inputs simultaneously. However, simultaneous uncorrelated open-loop tests cannot usually excite the ill-conditioned processes in low-gain direction (Zhu *et al.*, 2001, 2006). In these systems, the information of low gain direction is dominated by the noise (low SNR) and no good identification results can be achieved. This problem is caused by poor data not related to identification methods or model structure (Zhu *et al.*, 2001, 2006).

In order to increase the SNR in the low gain direction, one can replace the standard uncorrelated PRBS or GBN inputs with highly correlated signals as inputs. Koung and MacGregor (Koung *et al.*, 1993) proposed rotated inputs. These signals allow more excitation to be applied in the weak gain direction of the process and less excitation in the strong gain direction (Conner *et al.*, 2004). In their approach, the singular value decomposition (SVD) of the steady state gain matrix is used to rotate the input signals along the directions of the right singular vectors (Li *et al.*, 2008). Therefore, for constructing a rotated input signal, preliminary knowledge of the steady-state gain matrix is needed (Conner *et al.*, 2004).

In this paper, MIMO rotated input design for an ill-conditioned distillation column process identification is proposed.

The paper is organized as follows: In Section 2 and 3, ill-conditioned processes and rotated input design are respectively described. In Section 4, the application of the proposed method is carried out on high-purity distillation column as an ill-conditioned process. Finally, section 5 concludes the paper.

2. ILL-CONDITIONED PROCESS

Consider the multivariable (MIMO) system with n inputs and n outputs as follows

$$y(j\omega) = G(j\omega)u(j\omega) \tag{1}$$

The singular value decomposition (SVD) of G can be written (Skogestad *et al.*, 2001) as:

$$G(j\omega) = U(j\omega)\Sigma(j\omega)V^H(j\omega) \tag{2}$$

where U and V are the left and the right singular unitary matrices, respectively. Matrix Σ is the singular value matrix which is diagonal containing the singular values σ_i in decreasing order. The complex frequency $j\omega$ denotes that the SVD in general is a frequency dependent measure. For 2×2 processes, we can write (Jacobsen, 1994)

$$U = [\bar{u}\ \ \underline{u}],\ \ \Sigma = diag(\bar{\sigma},\underline{\sigma}),\ \ V = [\bar{v}\ \ \underline{v}] \tag{3}$$

and

$$G\bar{v} = \bar{\sigma}\bar{u},\ G\underline{v} = \underline{\sigma}\underline{u} \tag{4}$$

where $\bar{\sigma}$ denotes the maximum gain of G (in terms of 2-norm), $\bar{v}$ and $\bar{u}$ are the corresponding input and output directions, respectively. Similarly, $\underline{\sigma}$ is the minimum gain of G with corresponding input direction $\underline{v}$ and output direction $\underline{u}$. Note that the singular values and the corresponding input and output directions are frequency dependent; however, for simplicity $j\omega$ is omitted.

The condition number of gain matrix G is given by the ratio of the upper and lower singular values as follows (Jacobsen, 1994)

$$\gamma(G) = \bar{\sigma}/\underline{\sigma} \tag{5}$$

A process is said to be ill-conditioned if $\gamma(G) >> 1$ in some frequency range (Jacobsen, 1994).

In these processes, the process gain is strongly dependent on the direction of the input vector (Jacobsen, 1994). Therefore, the response of the plant is much stronger if input vector is in the high gain direction than if it lies along the low gain direction (Jacobsen, 1994). This can cause difficulties in the identification of ill-conditioned processes. In other words, ill-conditioned processes represent one of the most difficult kinds of linear processes to be identified (Micchi *et al*. 2008).

The ill-conditioned processes also have strongly interactions. The relative gain array (RGA), proposed by Bristol (Bristol, 1966), is a valuable criterion for evaluating the degree of interactions or directionality. The elements of the RGA is defined as follows (Zhu *et al.*, 2006)

$$\lambda_{ij}(j\omega) = g_{ij}(j\omega)[G^{-1}(j\omega)]_{ji} \tag{6}$$

where g_{ij} is the i,j element of G. As the elements in each row and column in the RGA adds up to unity, it is sufficient to consider the 1,1 element for the 2×2 case (Jacobsen, 1994). When one refer to the RGA, it means the 1,1 element of the RGA, i.e., λ_{11}. Large value of λ_{11} denotes that the process is strongly interactive (Jacobsen, 1994).

Note that there are differences between strongly interactive and ill-conditioned processes. A strongly interactive process is always ill-conditioned while the opposite is not always true (Jacobsen, 1994).

3. ROTATED INPUT DESIGN

Consider the singular value decomposition (SVD) of the steady state gain matrix $\bar{G}$.

$$\bar{G} = \bar{U}\bar{\Sigma}\bar{V}^H \tag{7}$$

Using the above equation, the steady state output of process, with N input-output data, can be written as (Conner *et al.*, 2004)

$$\bar{Y}^T = \bar{G}\hat{U}^T = \bar{U}\bar{\Sigma}\bar{V}^H\hat{U}^T \tag{8}$$

where

$$\bar{Y} = [\bar{Y}_1\ \bar{Y}_2 \dots \bar{Y}_n] \tag{9a}$$

$$\hat{U} = [U_1\ U_2 \dots U_n] \tag{9b}$$

and

$$\bar{Y}_i = [\bar{y}_i(1)\ \bar{y}_i(2) \dots \bar{y}_i(N)]^T \tag{10a}$$

$$U_j = [u_j(1)\ u_j(2) \dots u_j(N)]^T \tag{10b}$$

In theses equations, an overbar indicates steady state of a variable if inputs are held constant from the current time forward.

Now, the original inputs, $\{U_i\}$, are scaled by the singular values $\{\sigma_i\}$ to give new inputs $\tilde{U}$ (Conner *et al.*, 2004).

$$\tilde{U} = [U_1\ \ U_2(\frac{\sigma_1}{\sigma_2})\ \ U_3(\frac{\sigma_1}{\sigma_3})\ \ \dots\ \ U_n(\frac{\sigma_1}{\sigma_n})] \tag{11}$$

Then the rotated inputs are produced as follows (Conner *et al.*, 2004)

$$\Xi = \alpha\tilde{U}V^H \tag{12}$$

where α is a factor that should be adjusted so that the outputs do not exceed prespecified limits.

By using the rotated inputs, Ξ, instead of the original inputs, $\hat{U}$, equation (8) can be rewritten as (Conner *et al.*, 2004)

$$\bar{Y}^T = \alpha\bar{U}\bar{\Sigma}\tilde{U}^T \tag{13}$$

Therefore, the modes of the steady-state gain matrix are individually excited by scaled, uncorrelated PRBS or GBN signals (Conner *et al.*, 2004).

A generalization of the rotated inputs design procedure to non-square multivariable systems of arbitrary dimensions is presented at Micchi *et al*., 2008.

4. CASE STUDY: HIGH-PURITY DISTILLATION COLUMN

A binary distillation column as in Fig. 1 is considered as an ill-conditioned process. The column is running in LV-configuration.

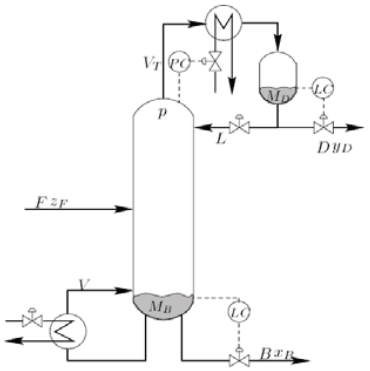

Fig. 1. High-purity distillation column

In this study, reflex (L) and boilup (V) flow rates are considered as the inputs and distillate (y_d) and bottom (x_b) compositions are considered as the outputs of the distillation column. For more detailed description, one can refer to Skogestad, 1997.

High-purity distillation is a challenging process application for system identification because of its nonlinear and strongly interactive dynamics (Rivera *et al*., 2007). Despite their nonlinear behavior, the ability to control high-purity distillation columns using linear controllers is desirable in practice for reasons of simplicity (Rivera *et al*., 2007). Thus, in many studies like this study, a linearized model is used.

The linear model of a distillation column can be described as (Jacobsen, 1994)

$$\begin{bmatrix} y_1(j\omega) \\ y_2(j\omega) \end{bmatrix} = G(j\omega) \begin{bmatrix} u_1(j\omega) \\ u_2(j\omega) \end{bmatrix} \tag{14}$$

where the state space model of *G* is as follows

$$\dot{x} = \begin{bmatrix} -0.0051 & 0 & 0 & 0 & 0 \\ 0 & -0.0737 & 0 & 0 & 0 \\ 0 & 0 & -0.1829 & 0 & 0 \\ 0 & 0 & 0 & -0.4620 & 0.9895 \\ 0 & 0 & 0 & -0.9895 & -0.4620 \end{bmatrix} x + \begin{bmatrix} -0.629 & 0.624 \\ 0.055 & -0.172 \\ 0.030 & -0.108 \\ -0.186 & -0.139 \\ -1.230 & -0.056 \end{bmatrix} u \tag{15a}$$

$$y = \begin{bmatrix} -0.7223 & -0.5170 & 0.3386 & -0.0163 & 0.1121 \\ -0.8913 & 0.4728 & 0.9876 & 0.8425 & 0.2186 \end{bmatrix} x \tag{15b}$$

Fig.2 and Fig.3 respectively show the singular values and RGA plotted as functions of frequency for the high-purity distillation column.

It can be seen that the process has large condition number and high RGA in the low frequency range.

At steady state, the high-gain singular value and the low-gain singular value are equal to $\bar{\sigma} = 198.2$ and $\underline{\sigma} = 1.36$, respectively. Steady state condition number is $\gamma \approx 146$.

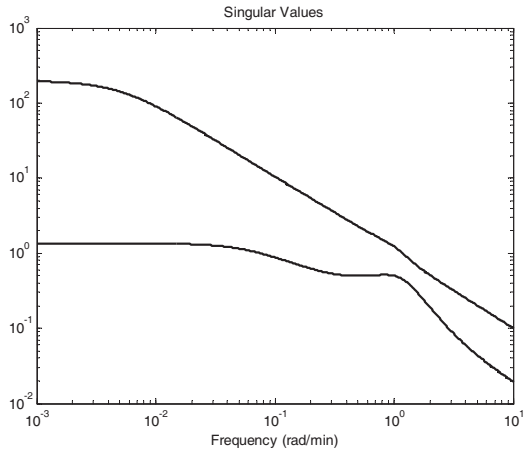

Fig. 2. Singular values of the distillation column

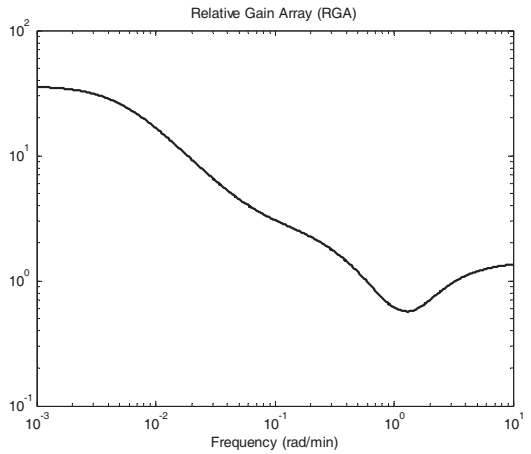

Fig. 3. RGA of the distillation column

Therefore, the largest effect on the outputs is obtained by moving the inputs in opposite directions which causes the two outputs to move in the same direction. The smallest effect is obtained by moving the inputs in the same direction which moves the two outputs in opposite directions.

4.1 Input Test Signals

For identification of the high purity distillation column, two open-loop test signals are considered: uncorrelated signals and rotated signals as outlined in Section 3.

Identification data are constructed by using generalized binary noise (GBN) signals as inputs, both uncorrelated and correlated in the case of rotated inputs. GBN signals, proposed by Tulleken (Tulleken, 1990), have many favorable features, in particular in terms of frequency content, which is typically superior to that of pseudo-random binary noise (PRBS) and of step signals (Zhu, 2001).

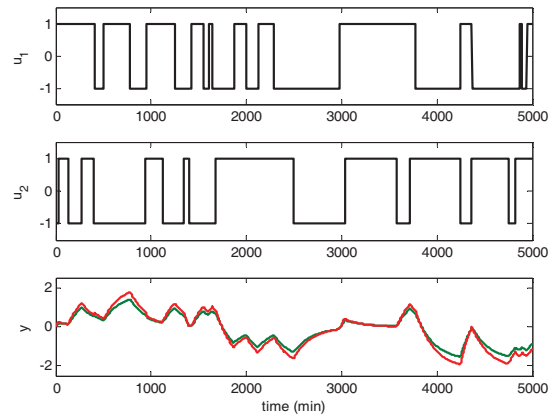

Fig. 4. Data collected using uncorrelated GBN signals as inputs

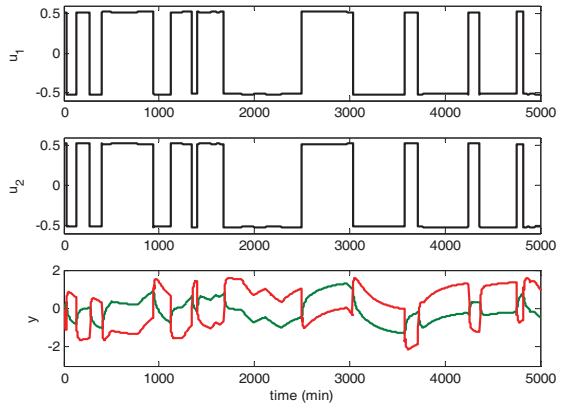

Fig. 5. Data collected using rotated GBN signals as inputs

Hence, two independent GBN signals with amplitude ± 1, switching time $T_{sw} = 300\,\text{min}$, and final time $T_f = 5000\,\text{min}$ are applied on the inputs of the plant simultaneously. The sampling time is selected to be 1 min.

Normally, distributed output noise with a signal-to-noise ratio (SNR) of 10 is added to both outputs. The input-output data from the two experiments are shown in Fig. 4 and Fig. 5.

Fig. 6 and Fig. 7 show the excitations of output directions in the uncorrelated and the correlated tests.

It can be seen that the uncorrelated test inputs only excite the high gain direction. In other words, in this case, the outputs of the process have no information about the low-gain direction of the model. It is clear that the low-gain direction information needs to be excited more in order to obtain good estimates of model. Therefore, strongly correlated test inputs with larger amplitudes are needed (see Fig. 7).

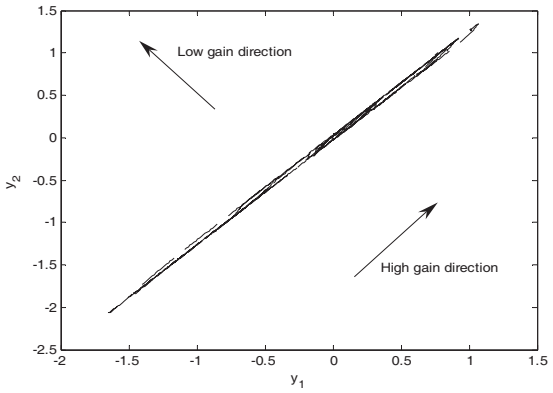

Fig. 6. Excitation of output directions in the uncorrelated test

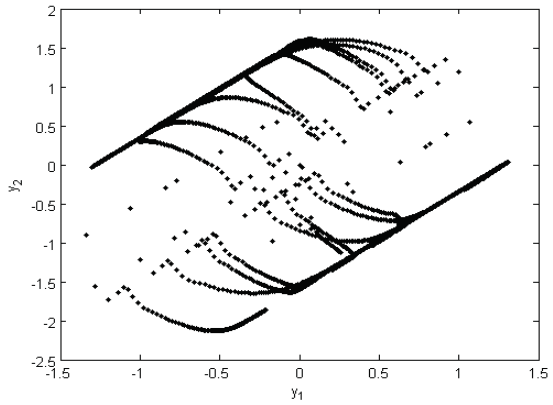

Fig. 7. Excitation of output directions in the rotated test

4.2 Subspace Identification

In this paper, a MIMO structure for the model is considered. In other words, there is a common model for all outputs. System identification is performed using subspace identification (SID) method. This method involves particular matrices obtained from output and input data and performs projection operations to cancel out the noise contributions. Thus, the system model is obtained in state-space form using these projected data matrices. A detailed treatment of this method can be found in Van Overschee *et al.*, 1996.

For identifying the system using subspace method, model order should be selected. In this paper, the model order is determined using number of nonzero singular values of matrix M given by (Misra *et al.*, 2003)

$$M = Y_f \underset{U_f}{/} W_p \prod\nolimits_{U_f^T}^{\perp} \tag{16}$$

$$= Y_f \prod\nolimits_{U_f^T}^{\perp} \left[[W_p \prod\nolimits_{U_f^T}^{\perp}]^{+} [W_p \prod\nolimits_{U_f^T}^{\perp}] \right]$$

where

$$Y_f \underset{U_f}{/} W_p = [Y_f \prod_{U_f^T}^{\perp}][W_p \prod_{U_f^T}^{\perp}]^{+} W_p;\ W_p = \begin{bmatrix} U_p \\ Y_p \end{bmatrix} \quad (17a)$$

$$\prod_{U_f^T}^{\perp} = I - \prod_{U_f^T}^{\perp} \quad (17b)$$

$$= I - U_f (U_f^T U_f)^{+} U_f^T$$

(Y_f, U_f) and (Y_p, U_p) are future and past output-input data, respectively, that is:

$$Y_f = \begin{bmatrix} y_r & y_{r+1} & \cdots & y_{r+M-1} \end{bmatrix} \quad (18a)$$
$$U_f = \begin{bmatrix} u_r & u_{r+1} & \cdots & u_{r+M-1} \end{bmatrix}$$

$$Y_p = \begin{bmatrix} y_0 & y_1 & \cdots & y_{M-1} \end{bmatrix} \quad (18b)$$
$$U_f = \begin{bmatrix} u_0 & u_1 & \cdots & u_{M-1} \end{bmatrix}$$

where r is greater than the system order n ($r > n$) and $M = N - 2r + 1$. The order of system is determined using singular value decomposition of matrix M in equation (16) as follows:

$$M = \begin{bmatrix} \hat{Q}_s & \hat{Q}_n \end{bmatrix} \begin{bmatrix} \hat{S}_s & 0 \\ 0 & \hat{S}_n \end{bmatrix} \begin{bmatrix} \hat{V}_s^T \\ \hat{V}_n^T \end{bmatrix} \quad (19)$$

In the absence of noise, the rank of this matrix is exactly *n*. Thus there are exactly *n* nonzero singular values in the SVD in equation (19). In the presence of noise, however, the data matrix on the left hand side of (19) becomes a full rank matrix. The selection of the sizes of $\hat{S}_s$ and $\hat{S}_n$ then requires determining which singular values can be considered small, hence essentially zero, and which ones large. If the noise level is not too high, there is usually a significant difference between noise and signal singular values, and their separation is easily achieved (Misra *et al*., 2003). However, for ill-conditioned systems, even a small magnitude of noise can make it very difficult to determine the system order correctly (Misra *et al*., 2003).

For solving this problem, additional requirements must be posed on the input signals. In other words, input signals must excite ill-conditioned system in order to produce output signals as uncorrelated as possible. Therefore, rotated input signal is one of the most appropriate input signals to be used in subspace identification of ill-conditioned multivariable systems.

Fig.8 shows the singular values of the matrix M (for $r = 6$) in the rotated inputs case. As can be observed in this figure, the system order is 5.

After model order determination, subspace method MOESP is used to identify the system. Identification for both types of input test is performed over 20 simulation runs. For estimated model validation, the singular values and RGA are checked. Fig. 9-12 show the singular values and RGA of 20 simulation runs.

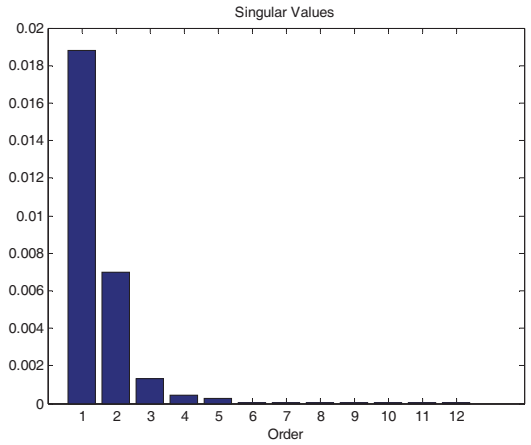

Fig. 8. Singular-value plot for distillation column using rotated input test

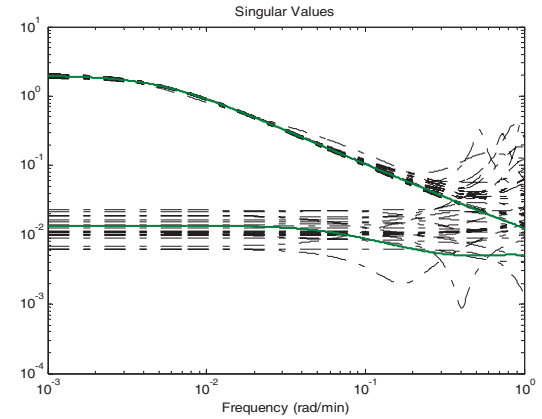

Fig. 9. Singular values of MIMO MOESP models from 20 simulations using uncorrelated test

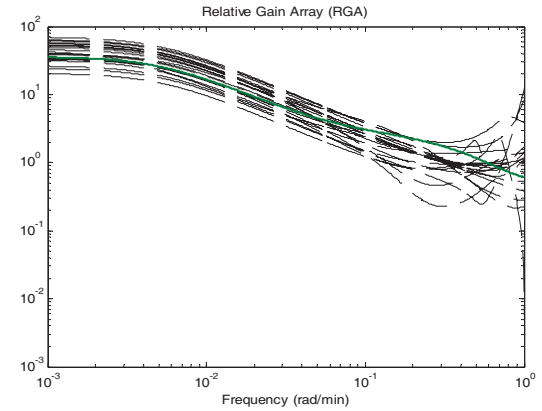

Fig. 10. RGA of MIMO MOESP models from 20 simulations using uncorrelated test

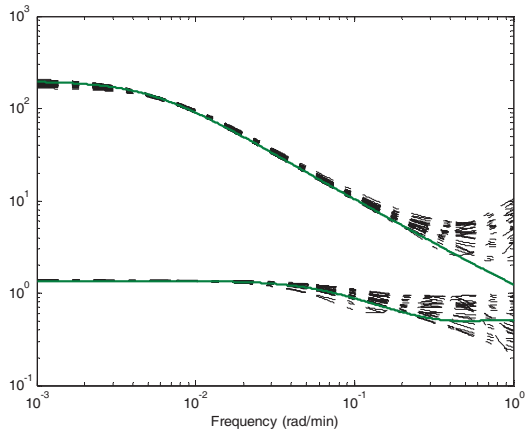

Fig. 11. Singular values of MIMO MOESP models from 20 simulations using rotated input test

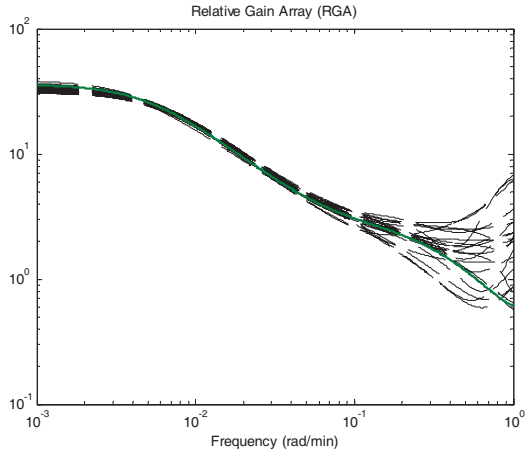

Fig. 12. RGA of MIMO MOESP models from 20 simulations using rotated input test

Note that in these figures, solid lines are the true values and dashed lines are the estimates. It can be seen that the high gain of process is easily estimated whereas the low-gain is very poorly estimated using the uncorrelated test signals. However, by using rotated input signal, good estimates of both low and high gain directions are achieved.

5. CONCLUSIONS

The standard uncorrelated test signals estimate the low-gain direction of ill-conditioned systems poorly. Therefore, the low gain information needs to be excited more in order to obtain good estimates. In this paper, MIMO rotated input design for ill-conditioned process identification was described. Rotated input signals allow more excitation to be applied in the weak gain direction of the process and less excitation in the strong gain direction. In this approach, the singular value decomposition (SVD) of the steady state gain matrix is used to rotate the input signals along the directions of the right singular vectors. The application of the proposed method was carried out on a high-purity distillation column as an ill-conditioned process. Simulation results show good accuracy of the proposed method in identifying both low and high gain directions.

REFERENCES

Bristol, E.H. (1966). On a new measure of interactions for multivariable process control. *IEEE Trans. Automatic Control*, AC-11, 133-134.

Conner, J.S. and Seborg, D.E. (2004). An evaluation of MIMO input design for process identification. *Ind. Eng. Chem. Res.*, 43, 3847-3854.

Gevers, M., Miskovic, L., Bonvin, D., and Karimi, A. (2006). Identification of multi-input systems: variance analysis and input design issues. *Automatica*, 42, 559-572.

Jacobsen, E.W. (1994). Identification for control of strongly interactive plants. *AIChE Annual Meeting*, San Francisco.

Koung, C.W. and MacGregor, J.F. (1993). Design of identification experiments for robust control. A geometric approach for bivariate processes. *Ind. Eng. Chem. Res.*, 32, 1658-1666.

Li, T. and Georgakis, C. (2008). Dynamic input signal design for the identification on constrained systems. *Journal of Process Control*, 18, 332-346.

Micchi, A. and Pannocchia, G. (2008). Comparison of input signals in subspace identification of multivariable ill-conditioned systems. *Journal of Process Control*, 18, 582-593.

Misra, P. and Nikolaou, M. (2003). Input design for model order determination in subspace identification. *AIChE Journal*, 49, 2124-2132.

Rivera, D.E., Lee, H., Mittelmann, H.D., and Braun, M.W. (2007). High-purity distillation: using plant-friendly multisine signals to identify a strongly interactive process. *IEEE Control Systems Magazine*, 28, 72-89.

Skogestad, S. and Postlethwaite, I. (2001). *Multivariable feedback control, Analysis and design*, Second Edition, John Wiley & Sons.

Skogestad, S. (1997). Dynamic and control of distillation columns- A tutorial introduction. *Trans. IChemE*, 75, 539-562.

Tulleken, H.J.A.F. (1990). Generalized binary noise test-signal concept for improved identification-experiment design. *Automatica*, 26, 1, 37-49.

Van Overschee, P. and Demoor, B. (1996). *Subspace identification for linear systems: theory-implementation-applications*, Kluwer, Dordrecht, Netherlands.

Zhu, Y. and Stec, P. (2006). Simple control-relevant identification test methods for a class of ill-conditioned processes. *Journal of Process Control*, 16, 1113-1120.

Zhu, Y. (2001). *Multivariable system identification for process control*, Elsevier Science.

A Sampling based method for linear parameter estimation from correlated noisy measurements

Ugur Guner*. Jay H. Lee**
Matthew J. Realff***

**Georgia Institute of Technology, Atlanta, GA 30332 USA (Tel: 404-388-2149; e-mail: Ugur.Guner@chbe.gatech.edu).*
***Georgia Institute of Technology, Atlanta, GA 30332 USA (e-mail: Jay.Lee@chbe.gatech.edu)*
**** Georgia Institute of Technology, Atlanta, GA USA (e-mail: matthew.realff@chbe.gatech.edu)*

Abstract: We address the problem of linear parameter estimation in discrete time state space models in the presence of serially correlated error in variables. The common way to solve parameter estimation problem is least squares (LS) methods. LS method is not considered to be effective when both dependent and independent variables are contaminated by noise. Total Least Squares (TLS) has been introduced as the method for parameter estimation in the case of noisy response and predictor variables. However, TLS solution is not optimal when number of data is limited and noise is correlated. Constrained TLS is a variant of TLS that considers correlation of noise in the data as additional constraints. We introduced a novel method based on a stochastic sampling method to solve estimation problem from correlated noisy measurements, and we compared it with the existing methods through in silico examples. Our method demonstrates significant improvement over other common estimation algorithms, LS, TLS and Constrained TLS under the different amount of correlated noise and data points. It has the potential to be the valuable tool for the difficult real life problems, such as, biological systems where data is limited and noisy.

Keywords: Linear parameter estimation; Least Squares; Total Least Squares; Constrained Total Least Squares; Multiplicative noise; additive noise; correlation; state space models; stochastic.

1. INTRODUCTION

The problem of linear parameter estimation arises in a broad class of scientific disciplines such as signal processing, automatic control, system theory, general engineering, statistics, physics, economics, biology, medicine, etc (Huffel ,1991). Linear estimation problem becomes challenging in the presence of correlated noise. Errors are unavoidable and can be related to many sources, such as modelling, human or instruments. They may appear in different forms depending on the source of error and nature of the system. Noise can be proportional to the signal itself (multiplicative),simply additive or it can include both components. In this paper, we will particularly focus on parameter estimation in linear discrete time state space models in the presence of measurements that include both multiplicative and additive error terms. One can write the linear discrete time system as follows;

$$\hat{x}_i^{k+1} = a_{i1}\hat{x}_i^k + a_{i2}\hat{x}_2^k + ,...,+a_{iN}\hat{x}_N^k \qquad i = 1,...,N \tag{1}$$

In this equation this equation, value of observed state at time $k+1$ is linear function of all N observed states at time point, k . This model can be extended for all states and time points in a compact form as follows:

$$\hat{X}' = A^{(N\times N)}\hat{X} \tag{2}$$

$$\hat{X}'^{(N\times(M-1))} = \{\vec{x}^{\,2},..., \vec{x}^{\,M}\} \qquad \hat{X}^{(N\times(M-1))} = \{\vec{x}^{\,1},..., \vec{x}^{\,(M-1)}\}$$

where M is the number of time points and N is the number of states. Each column of X and X' is represented with the vector,

$$\vec{x}^{\,j} = [\hat{x}_1^{\,j},..., \hat{x}_N^{\,j}]^T . \tag{3}$$

The parameters are collected in matrix,

$$A^{(N\times N)} = \{ a_{ij} \}. \tag{4}$$

This paper is organized as follows. In next section we will briefly summarize common methods to solve linear estimation problem. Furthermore, we will introduce our novel approach based on a sampling algorithm. Section 3 will summarize assessment of the performance of our method compared to some common existing methods. Finally, section 4 will present the concluding remarks.

2. METHODS

2.1 Common methods

Many methods have been introduced to solve the linear estimation problem (Ljung ,1987 and Huffel ,1991). The classic way to solve the linear estimation problem is least squares. In the classical least squares regression theory, the errors are assumed to be confined only to $\hat{X}'$ (response variables) , and $\hat{x}$ (predictor variables) are assumed to be error free. One can write least squares estimate for parameters as follows,

$$A^T = \left(\hat{X}\hat{X}^T\right)^{-1}\hat{X}\hat{X}'^T \tag{5}$$

However, in our problem, it is not realistic to assume $\hat{X}$ to be error free as it shares the same columns with $\hat{x}'$except for the first column. (See (2)). This results in serial correlation between $\hat{X}$, and $\hat{X}'$.

Total least squares (TLS) is another method of linear parameter estimation when there are errors in both sides of the equation ($\hat{X}$ and $\hat{X}'$) (Huffel ,1991).

$$\hat{X}' = X' - \Delta X' \qquad \hat{X} = X - \Delta X$$

$$\Delta X' = \left[\Delta x^2,...,\Delta x^M\right] \qquad \Delta X = \left[\Delta x^1,...,\Delta x^{M-1}\right] \tag{6}$$

where, $\Delta X'$ and ΔX are the noise terms. Since X and $X'$are not known, for each state ($i = 1,...,N$), equation (2) can be written in the following format;

$$x_i + \Delta x_i = a^{(1\times N)}\left(\hat{X} + \Delta\hat{X}\right)$$

(7)

where $x_i = \left[x_i^2,...,x_i^M\right]$ and $\Delta x_i = \left[\Delta x_i^2,...,\Delta x_i^M\right]$ are the i^{th}rows of $\hat{X}'$ and $\Delta X'$respectively (See (2, 6)). $a = \left[a_{i1},..,a_{iN}\right]$ is the i^{th} row of A .

Let,

$$C = \left[\hat{X}^T\ x_i\right] \text{ ,and } \quad \Delta C = \left[\Delta\hat{X}^T\ \Delta x_i^T\right] \tag{8}$$

Then, equation (6) can be written as;

$$\left(C + \Delta C\right)\cdot\begin{bmatrix} a^T \\ -1 \end{bmatrix} = 0$$

where a is the i^{th} row of A . The TLS problem then can be posed as follows;

$$\min\left\|\Delta C\right\|_2^F \quad \text{subject to} \quad (C+\Delta C)\cdot\begin{bmatrix} a^T \\ -1 \end{bmatrix} = 0 \tag{9}$$

The solution to this problem given as;

$$a^T = \left(\hat{X}\cdot\hat{X}^T - \lambda^2 I\right)^{-1}\hat{X}\cdot\hat{X}'^T \tag{10}$$

where λ is the smallest singular value of C . Compared to least squares solution (5), the TLS solution has a correction term, λ at the inverse of the matrix. This reduces the bias in the solution which is caused by noise in X (Kim et al, 2007). However, TLS solution inherently assumes that the noise terms, $\Delta X'$and Δx_i are independent , which is not the case here.

The correlation between two noise term requires the total least squares solution to have additional constraints instead merely satisfying the existence of a solution (Cadzow and Wilkes, 1985). Recently, Kim et al. (2007) applied constrained least squares algorithm in the context of gene network identification problem on a linear discrete time model. In their model, they rewrite error term, ΔC in an open form and as follows;

$$\Delta C^{(M-1)\times(N+1)} = \left[\Delta\hat{X}^T\ \Delta x_i^T\right] = \begin{bmatrix} \Delta x_1^1 & ... & \Delta x_i^1 & .... & \Delta x_N^1 & \Delta x_i^2 \\ . & . & . & . & . & . \\ . & . & . & . & . & . \\ . & . & . & . & . & . \\ \Delta x_1^{M-1} & ... & \Delta x_i^{M-1} & ... & \Delta x_N^{M-1} & \Delta x_i^M \end{bmatrix} \tag{11}$$

They introduced the vector, $e_i^{(N\times 1)} = [0,...,1,..,0]^T$ whose elements are zero except for the i^{th} element, which is equal to 1. All error terms are rewritten in a vector form as follows;

$$\Delta Y^{1\times(N(M))} = \left[\left(\Delta x^1\right)^T,...,\left(\Delta x^M\right)^T\right] \tag{12}$$

The first N columns of ΔC can be written as follows;

$$\Delta C^i = G_i\cdot\Delta Y^T \tag{13}$$

Where $G_i = \left[\left(I_{M-1}\otimes e_i\right)^T\ 0_{(M-1)\times N}\right]$ and I_{M-1} denotes the identity matrix of size $(M-1)\times(M-1)$ and the symbol, $\otimes$, denote Kronecker product of two matrices. $0_{(M-1)\times N}$ represents the matrix of zeros with size, $(M-1)\times(N)$

After several steps and simplifications, they posed this as optimization problem as follows;

$$\min\left\|\Delta C\right\|^2 = \min_a\left[a\ \ -1\right]C^T\left(H_a^{-1}\right)^T\left(H_a^{-1}\right)C\begin{bmatrix} a^T \\ -1 \end{bmatrix} \tag{14}$$

where $H_a = \sum_i a_i\cdot G_i$. This is a nonlinear, non-convex optimization problem without constraints. They initialized the optimization problem with least squares solution.

2.2 Our method

In this paper, we introduced a new method to solve linear parameter estimation problem when both sides of the equation are contaminated by error. This method based on a stochastic sampling approach. In this method, observations $(\hat{X}, \hat{X}')$ are perturbed by adding a negative noise term in each sample.

$$ {}^{(j)}y_i^k = \hat{x}_i^k - {}^{(j)}\varepsilon_i^k \qquad {}^{(j)}\varepsilon_i^k \propto N\left(0, \sigma_i^k\right) \tag{15} $$

$$ i = 1,...,N \qquad j = 1,...,S \qquad k = 1,...,M $$

Where ${}^{(j)}y_i^k$ is the j^{th} perturbed observation for i^{th} state at time point k and ${}^{(j)}\varepsilon_i^k$ is the amount of perturbation sampled from Gaussian distribution of zero mean and σ_i^k variance in the j^{th} sample. N is the number of states, S is the number of samples and M stands for the number of time points. Variance for perturbation σ_i^k is chosen roughly close to variance of the observation error in i^{th} state and k^{th} time point. (μ_{ik} , see equation (20)). The amount of perturbation , ${}^{(j)}\varepsilon_i^k$, is selected through Monte Carlo Sampling procedure.

Finally, all data points for each state i at each sample j are collected in a vector form. This is performed for both sides of equation (2). Let,

$$ {}^{(j)}y_i = \left[{}^{(j)}y_i^1,...,{}^{(j)}y_i^k,...,{}^{(j)}y_i^{M-1}\right]^T $$

$$ {}^{(j)}y_i' = \left[{}^{(j)}y_i^2,...,{}^{(j)}y_i^k,...,{}^{(j)}y_i^M\right]^T \tag{16} $$

Equation (16) can be written in a matrix form for all states, $i = 1,...,N$

$$ Y^{(j)} = \left[{}^{(j)}y_1 \ldots {}^{(j)}y_i \ldots {}^{(j)}y_N\right]^T $$

$$ Y'^{(j)} = \left[{}^{(j)}y_1' \ldots {}^{(j)}y_i' \ldots {}^{(j)}y_N'\right]^T \tag{17} $$

Next, equation (17) can be written for all samples, $j = 1,...,S$;

$$ Y^{Total} = \left[Y^{(1)} \ldots Y^{(j)} \ldots Y^{(S)}\right] $$

$$ Y'^{Total} = \left[Y'^{(1)} \ldots Y'^{(j)} \ldots Y'^{(S)}\right] \tag{18} $$

The parameters are estimated using least squares solution;

$$ A^T = \left(\left(Y^{Total}\right)^T \cdot Y^{Total}\right)^{-1}\left(Y^{Total}\right)^T Y'^{Total} \tag{19} $$

3. ASSESSING THE PERFORMANCE

To test the performance of our method against least squares (LS), Total Least Squares , and Constrained TLS solutions, we created ensemble of 50 linear time discrete systems with different parameters, each consisting of 10 states. This is achieved by creating random $A^{10\times10}$ matrices. We assumed sparse structure for each $A^{10\times10}$ matrix, therefore the number of non-zero elements are fixed to 30 out of 100 total connections. Each system is simulated for certain number of time points (M) starting from a random initial condition. However, we assumed limited number of data for the systems, as most of the real systems have small number of data (Most biological systems, gene networks, etc.). Multiplicative and additive noise terms are added to the simulation results as follows;

$$ \hat{x}_{ik} = x_{ik} + x_{ik}\mu_{ik} + \eta_{ik} $$

$$ \mu_{ik} \approx N(0, \sigma_1) \qquad \eta_{ik} \approx N(0, \sigma_2) \tag{20} $$

In this equation, $\hat{x}_{ik}$ is the observed value of i^{th} state at k^{th} time point. ε_{ik} and η_{ik} are random variables assumed to have Gaussian distribution with zero mean and variances σ_1 and σ_2 respectively. The term, $x_{ik}\mu_{ik}$ corresponds to the multiplicative noise term, whereas η_{ik} stands for the additive noise term. Our algorithm is tested against the other algorithms for different level of noise and number of time points. Performances of methods for parameter estimation are quantified as the Frobenius norm of the deviation of estimated parameters from their true values relative to the Frobenius norm of true parameters according the following formula;

$$ E_A = \frac{\left\|A - A^R\right\|_F}{\left\|A^R\right\|_F} \tag{21} $$

where A^R and A stand for the true and estimated parameters respectively. In addition, fitness of the system is evaluated and compared to true values of states similar to (15);

$$ E_X = \frac{\left\|X - X^R\right\|_F}{\left\|X^R\right\|_F} \tag{22} $$

where X and X^R indicates estimated and true values of states, respectively. E_A and E_X are calculated for ensemble of 50 different systems at each number of sample point and averaged. In figure 1, one can see the comparison of the methods with respect to number of samples when multiplicative and additive noise terms are set to $\sigma_1 = 0.10$, and $\sigma_2 = 0.0001$ and number of time points is 10.

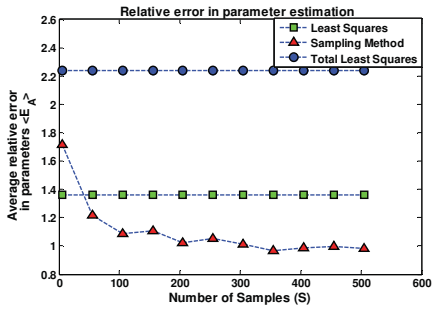

Fig.1. Relative error in parameter estimation vs number of samples for 10 time points at $\sigma_1 = 0.10$

Our method shows significant decrease in relative error in parameters compared to total least squares and least squares with increasing number of samples.

Methods	M=12	M=18	M=24
Least Squares	2730.1	1.1925	0.59776
Sampling Method **(at S=500)**	**0.11563**	**0.48125**	**0.44043**
Total Least squares	200.95	29.465	35.352
Constrained TLS	0.72001	289.98	3.7678

Table1. Average relative error in fitness for different methods for different time points at $\sigma_1 = 0.10$

Table 1 depicts the average relative error in fitness across the different methods and for different number of data. Our method outperforms all methods for 500 samples.

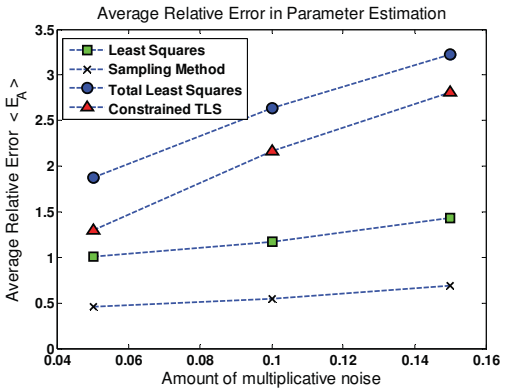

Fig.2. Average relative error in parameters versus amount of multiplicative noise for 18 time points

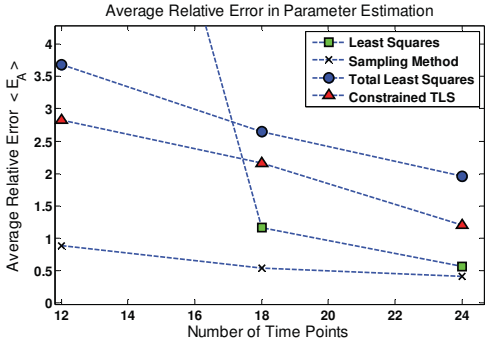

Fig.3. Average relative error in parameters versus number of time points at $\sigma_1 = 0.10$

Figure 2 indicates that our method performs significantly better than LS, TLS and constrained TLS across different levels of noise. TLS is expected to perform better in the case of noisy dependent and independent variables if enough data points are available. However, in this particular problem, due to the serially correlated multiplicative error and limited number of data, its performance is even below least squares solution. We assumed relatively small number of data, because for most of the interesting real systems, data is usually limited and noisy. Constrained TLS solution resolves the serial correlation problem and performs better than TLS, however, its performance still falls behind least squares solution because of limited data. When the number of data increases, the performances of all methods converge (See Figure (3)).

In Fig.3, one can observe that sampling method gives least amount of error in parameters at different number of time steps.

Methods	$\sigma_1 = 0.05$ $\sigma_2 = 0.0001$	$\sigma_1 = 0.10$ $\sigma_2 = 0.0001$	$\sigma_1 = 0.15$ $\sigma_2 = 0.0001$
Least Squares	7.3e+007	2730.1	9.9e+10
Sampling Method **(at S=500)**	**0.059484**	**0.11563**	**0.16913**
Total Least squares	11.331	200.95	21.864
Constrained TLS	1.2951	0.72001	8.4658

Table 2. Average relative error in fitness for different methods for 10 time points at different levels of noises.

In table 2, it is seen that the fitness of our method is much better than other methods for different noise levels.

4. CONCLUSIONS

The contribution of this work can be summarized in two ways. First, our method outperforms the common estimation methods in parameter estimation in the presence of correlated noise. Second, fitness of the estimated parameters through our method is significantly better than LS, TLS and Constrained TLS method. This method is particularly promising in the application of gene network identification problem. The biological measurements are notorious for having a high level of multiplicative noise which makes the network identification problem difficult. Our method has the potential to be the valuable tool for this difficult problem.

REFERENCES

Cadzow, J. A., Wilkes, D. M. (1985). *IEE international conference on Acoustics, Speech and Signal Processing,* 10, 1341-1344.

Huffel, S. V. (1991). *The total least squares problem: computational aspects and analysis,* Society for Industrial and Applied Mathematics, Philadelphia.

Kim, J., Bates, D. G., Postlethwaite, I., Harrison, P., and Cho, K. (2007). *BMC Bionformatics,* 8, 8.

Ljung, L. (1987). *System identification: theory for the user: computational aspects and analysis,* Prentice Hall information and system science series, Englewood Cliff, NJ.

Experimental and Modeling Studies for a Reactive Batch Distillation Column

Almıla Bahar*. Canan Özgen**

Department of Chemical Engineering, Middle East Technical University,
Ankara, 06531, Turkey
e-mail: *abahar@metu.edu.tr, **cozgen@metu.edu.tr

Abstract: Modeling of esterification reaction of ethanol with acetic acid in a reactive batch distillation column is investigated. The dynamic model developed is verified using the data of a theoretical study available in the literature. However, the existing models are found to be inappropriate for this system when compared with the experimental data. Then the model is improved using the data obtained from the experiments performed on a lab-scale column. In the model, different rate expressions and different thermodynamic models ($\phi-\phi$, EOS-G_{ex}, and $\gamma-\phi$ methods) considering different equations of state (EOS), mixing rules and activity coefficient models are used. It is found that the $\gamma-\phi$ approach considering van der Waals mixing rule and NRTL activity coefficient model gives the best fit between the dynamic model and the results of the experiments for the system under study.

Keywords: Reactive Distillation, Batch Column, Mathematical Modeling, Dynamic Simulation, Ethyl Acetate Production.

1. INTRODUCTION

Reactive distillation, which is combination of reaction and separation operations in a single unit, has many advantages over conventional processes. Modeling of this process is a challenging task due to its complex dynamics, highly nonlinear behaviour, complex interactions between vapor-liquid equilibrium (VLE) and chemical kinetics.

The system studied in this work is an esterification reaction where ethanol (EtOH) reacts with acetic acid (AcAc) to produce ethyl acetate (EtAc) and water (H_2O). In this quaternary system, azeotropes are formed between EtOH-H_2O, EtAc-H_2O, EtAc-EtOH, and EtAc-H_2O-EtOH. In the literature, most of the studies on this reaction utilized the numerical methods of solution (Chang and Seader, 1988; Bogacki et al., 1989; Simandl and Svrcek, 1991) and some others worked on its thermodynamics for phase equilibrium (Okur and Bayramoglu, 2001; Park et al., 2006) with very simple models in simulation. Assumptions considered are; ideal plates with constant molar holdup, negligible tray hydrodynamics and steady state condition. Alejski and Duprat (1996) dealt with the dynamic simulation of a reactive distillation column for EtAc system in presence of a catalyst. Tang et al. (2003) showed that, NRTL activity coefficient model parameters predict the VLE data of this system well. Both of these dynamic studies are done on continuous column. On the other hand, unlike continuous columns very few studies are done for modeling of reactive batch columns. Mujtaba and Macchietto (1997) developed an optimization algorithm and Monroy-Loperena and Alvarez-Ramirez (2000) developed an output-feedback control algorithm for a reactive batch column. However, in their studies they used very simplified VLE models and the model is not checked with experimental data.

The objective of this study is to develop a dynamic mathematical model for the esterification reaction of EtOH and AcAc in a reactive batch distillation column (RBDC) by verifying it with experimental data. Thus, different thermodynamic models are used for VLE calculations in order to obtain a good fit with the experimental data.

2. EXPERIMENTAL

The batch distillation column (Fig. 1) used in this study (Bahar, 2007) has an inner diameter of 5 cm, a height of 40 cm, and 8 sieve plates. The overall column parameters and experimental operating conditions are given in Table 1. The column is first operated at total reflux. After steady state is reached, reflux ratio is set to a predefined value. Analyses of the collected samples are done through Gas Chromatography.

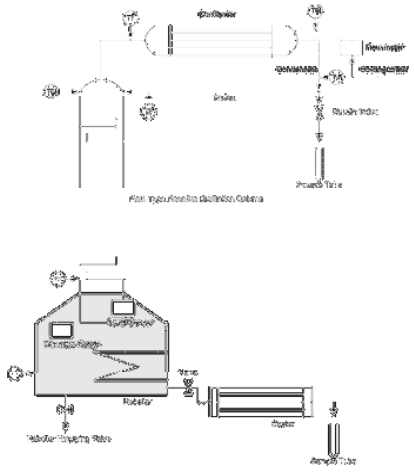

Fig. 1. Reactive Batch Distillation Column.

Table 1. Experimental Column Parameters and Operating Conditions

Total fresh feed, mol	311.67
Feed composition (EtAc, EtOH, H_2O, AcAc), mole fraction	0.0, 0.5, 0.0, 0.5
Column holdup, mol	
condenser+drum	30
internal plates	0.779
Reboiler heat duty, J/h	2.016×10^6
Column pressure, bar	1.013
Cooling water flow rate, lt/min	1.0

3. RBDC MODELING

The unsteady state model of RBDC is based on model of Yıldız et al. (2005). The assumptions employed are negligible vapour holdup, constant volume of tray liquid holdup, constant liquid molar holdup in the reflux drum, total condenser, negligible fluid dynamic lags, linear pressure drop profile, Murphree tray efficiency, approximated enthalpy derivatives and adiabatic operation. The balance equations for column reboiler, trays and reflux-drum-condenser system are given as follows:

Reboiler: j = 1,…,NC

$$dM_1/dt = L_2 - V_1 \qquad (1)$$

$$d(M_1 x_{1j})/dt = L_2 x_{2j} - V_1 y_{1j} + \varepsilon_j R_1 M_1 \qquad (2)$$

$$d(M_1 h_1)/dt = L_2 h_2 - V_1 H_1 + Q_1 \qquad (3)$$

where the reboiler holdup, M_1, is as given in (4) where M_f^0 is the molar amount of feed initially charged to the column.

$$M_1 = M_f^0 - \sum_{n=2}^{NT+2} M_n - \int_0^t D(\tau)d\tau \qquad (4)$$

Trays: i = 2,…,N_{T+1}; j = 1,…,NC

$$dM_i/dt = L_{i+1} + V_{i-1} - L_i - V_i \qquad (5)$$

$$d(M_i x_{ij})/dt = L_{i+1}x_{i+1,j} + V_{i-1}y_{i-1,j} - L_i x_{ij} - V_i y_{ij} + \varepsilon_j R_i M_i \qquad (6)$$

$$d(M_i h_i)/dt = L_{i+1}h_{i+1} + V_{i-1}H_{i-1} - L_i h_i - V_i H_i \qquad (7)$$

where $M_i = (\rho_i^{avg} / Mw_i^{avg})v_i$ is the molar holdups on trays where ρ_i^{avg} is the average density of the mixture on the i[th] tray, Mw_i^{avg} is the average molecular weight of the mixture on the i[th] tray, v_i is the volume of the liquid tray holdup.

Reflux-drum-condenser system: j = 1,…,NC

$$dM_{NT+2}/dt = V_{NT+1} - L_{NT+2} - D \qquad (8)$$

$$\frac{d(M_{NT+2}x_{NT+2,j})}{dt} = V_{NT+1}y_{NT+1,j} - L_{NT+2}x_{NT+2,j} - Dx_{NT+2,j} + \varepsilon_j R_{NT+2} M_{NT+2} \qquad (9)$$

$$\frac{d(M_{NT+2}h_{NT+2})}{dt} = V_{NT+1}H_{NT+2} - L_{NT+2}h_{NT+2} - Dh_{NT+2} - Q_{NT+2} \qquad (10)$$

where R_i is the reaction rate at i[th] stage in mol/h and can be expressed as given in (11) and the rate expression, r_i, without catalyst is expressed as $r = k_1 x_2 x_4 - k_2 x_3 x_1$. The forward and backward reaction rate constants in lt/gmol.min are k_1=29100exp(-7190/T(K)) and k_2=7380exp(-7190/T(K)), respectively (Alejski and Duprat, 1996).

$$R_i = r_i \rho_i / MW_i \quad \text{for i = 1,…,}N_{T+2} \qquad (11)$$

The reflux ratio is defined as $R = L_{NT+2}/D$. The subscripts i and j are for stage and component numbers, respectively. i=1 for reboiler, i=2,.,N_{T+1} for trays and i=N_{T+2} for reflux-drum-condenser unit. The components are numbered in the subscripts as follows: EtAc-1, EtOH-2, H_2O-3, and AcAc-4.

In energy balance equations, no additional term for the heat of reaction is included because, the enthalpies are referred to their elemental state for which the heat of reaction is accounted automatically and thus, no separate term is needed (Mujtaba and Macchietto, 1997). The linear pressure drop profile is given as $P_i = P_1 - i(P_1 - P_{NT+2})/NT$ where P_i is the pressure in i[th] tray, P_1, the pressure in the reboiler and P_{NT+2}, the pressure in the reflux drum.

4. MODELS FOR VAPOR-LIQUID EQUILIBRIUM

In modeling of batch distillation column, the selection of proper thermodynamic model affects the estimation of compositions highly and therefore is very crucial. In simulation studies, four different models are used for phase equilibrium and these models are explained below in detail.

4.1 Model-I:Phase Equilibrium Using VLE data in Literature

VLE data for EtAc-EtOH-H_2O-AcAc system given in Table 2 is taken from literature (Suzuki et al., 1971). This data is utilized in the simulation as a preliminary check.

Table 2. Vapor Liquid Equilibrium Data.

EtAc	log K = -2.3 x 10^3/T + 6.742
EtOH	log K = -2.3 x 10^3/T + 6.588
H_2O	log K = -2.3 x 10^3/T + 6.484
AcAc	K = (2.25 x 10^{-2})/T - 7.812 for T > 347.6 K
	K = 0.001 for T ≤ 347.6 K

4.2 Model-II: Phase Equilibrium Using $\phi - \phi$ Approach

In this approach, Peng Robinson EOS (PR) with van der Waals one-fluid mixing rule is used to calculate the fugacity of species for both liquid and vapor phases. The binary interaction parameters are given in Table 3 (Burgos-Solorzano, 2004).

Table 3. Binary interaction parameters, k_{ij}.

k_{ij}	EtAc	EtOH	H_2O	AcAc
EtAc	0.0	0.022	-0.280	-0.226
EtOH	0.022	0.0	-0.935	-0.0436
H_2O	-0.280	-0.935	0.0	-0.144
AcAc	-0.226	-0.0436	-0.144	0.0

4.3 Model-III: Phase Equilibrium Using Combination of EOS with Excess Free Energy Models (EOS-G_{ex} Approach)

In this method, activity coefficient models are incorporated into EOS. NRTL, Wilson, and UNIQUAC models are used

and performances for the system under consideration are compared. The parameters for these models are obtained from Tang et al. (2003), Okur and Bayramoğlu (2001), and Kang et al., (1992).

In this study, as EOS; PR and Peng-Robinson-Stryjek-Vera (PRSV) (Stryjek and Vera, 1986) are used. κ_1 parameters for components are given in Table 4 (Stryjek and Vera, 1986). As the mixing rule, van der Waals one-fluid mixing rule, Huron-Vidal (Original) Mixing Rule (HVO), and Orbey-Sandler modification of the Huron-Vidal mixing rule (HVOS) are used.

Table 4. PRSV EOS parameters, κ_1 .

Components	κ_1
EtAc	0.0693
EtOH	-0.03374
H_2O	-0.06635
AcAc	-0.19724

4.4 Model-IV: Phase Equilibrium Using $\gamma-\phi$ Approach

In VLE descriptions with the $\gamma-\phi$ approach, an activity coefficient model can be used for the liquid phase and an EOS is used for the vapor phase.

5. RESULTS AND DISCUSSION

This study is done in three phases. In first phase, modeling studies are done and then checked with a simulation study found from the literature which has the same reactive system. In second phase, experimental studies are done and data is collected for total and different reflux ratios. In third phase, the experimental findings and the simulation results are compared and the dynamic model is finalized by selecting the appropriate thermodynamic model for VLE calculations.

The properties of the column which is used in simulation are given in Table 5. Monroy-Loperena and Alvarez-Ramirez (2000) used the VLE data of Model-I and temperature independent rate constants with k_1 of $4.76\text{x}10^{-4}$ lt/(gmol.min) and k_2 of $1.63\text{x}10^{-4}$ lt/(gmol.min). The comparison of dynamic model using same rate expression at total reflux is given in Fig. 2. As can be seen, the results are almost the same. This indicates that the developed dynamic model is quite satisfactory to represent this non-linear and complex problem of RBDC behaviour.

Table 5. RBDC Specifications

No. of stages (including reboiler and total condenser)	10
Total fresh feed, kmol	5.0
Feed composition (EtAc, EtOH, H_2O, AcAc), mole fraction	0.0, 0.45, 0.1, 0.45
Column holdup, kmol	
condenser	0.1
internal plates	0.0125
Condenser vapor load, kmol/h	2.5
Column pressure, bar	1.013

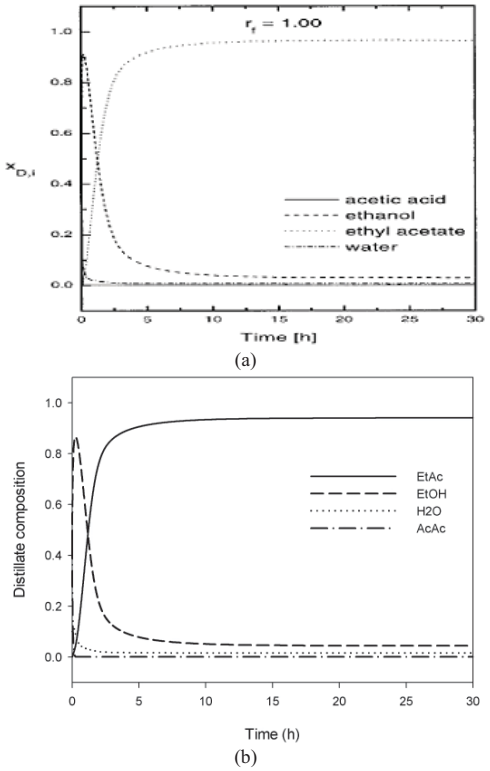

Fig. 2. Distillate compositions at total reflux. (a) Results from literature (b) Results from the simulation in this study.

After obtaining similar results with literature, experiments are performed in order to improve the model. Column is first operated at total reflux until the steady state is reached. Then it is operated with arbitrary reflux ratios and data for distillate and reboiler compositions are collected with respect to time.

5.1 Dynamic Analysis of the Results of Experimental and Simulation Studies

There is a difference in initialization of the experiments and simulation program. Therefore, although the trends of the profiles of compositions are similar, they cannot be compared up to steady state point. Consequently, if the two results match at total reflux steady state, then comparisons of dynamic response can be done. Thus, for each model explained in Section 4, the experimental data collected is checked with the simulation results.

Model-I: In Table 6, simulation result of Model-I and experiments at total reflux steady state are given. It can be seen that, when steady state values are compared, they are too different from each other and there is no need to check the dynamic behaviour. More accurate VLE model is needed.

Table 6. Total Reflux Steady State Composition Values

Comp.	Distillate		Reboiler	
	Exp.	Sim.	Exp.	Sim.
EtAc	0.5222	0.9384	0.1434	0.2582
EtOH	0.2408	0.0476	0.3189	0.1829
H_2O	0.2371	0.0135	0.1918	0.3684
AcAc	0.0000	$5.61\text{x}10^{-4}$	0.3459	0.1906

Model-II: The results of simulation that uses Model-II and experiments are given in Fig. 3. It is found that total reflux steady state values are better compared to Model-I. The comparison is further continued dynamically for a constant reflux ratio of 5.72. The time at total reflux steady state is shown as zero. It can be seen that there are great differences in the distillate and reboiler liquid composition trends with respect to time.

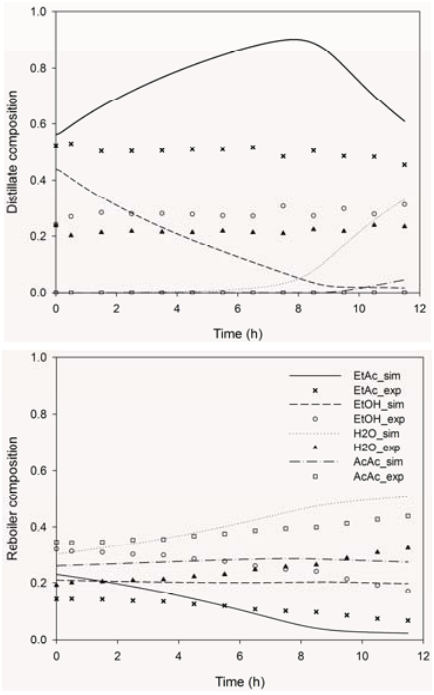

Fig. 3. Results with Model-II

Model-III: In Model-III, first of all PR with HVO mixing rule and NRTL activity coefficient model (Model-III-A) is tested. It can be seen from Fig. 4 that the results are somewhat improved compared to Model-II, especially for the reboiler compositions. However, the results for distillate compositions are not satisfactory. Therefore, EOS is changed to PRSV with same mixing rule and activity coefficient model; the performance of the system with this model (Model-III-B) is given in Fig. 5. Distillate compositions are much better than that of Model-III-A. However, reboiler compositions become worse and therefore this result is also found to be not satisfactory. As a further step, mixing rule is changed to HVOS and it is used together with PRSV and NRTL activity coefficient model (Model-III-C). The results are given in Fig. 6. The results for both distillate and reboiler compositions are improved significantly with this thermodynamic model.

In order to see the effects of different activity coefficient models, Wilson and UNIQUAC models are used in EOS-G_{ex} approach. The distillate and reboiler liquid compositions with Wilson model (Model-III-D) and UNIQUAC model (Model-III-E) are given in Fig. 7 and Fig. 8, respectively. It can be seen from the figures that, while NRTL and Wilson models give similar results, UNIQUAC performs poorly. NRTL model is selected to be the most proper activity coefficient model for this system, since it gives slightly better results than Wilson model, and will be used also in Model-IV.

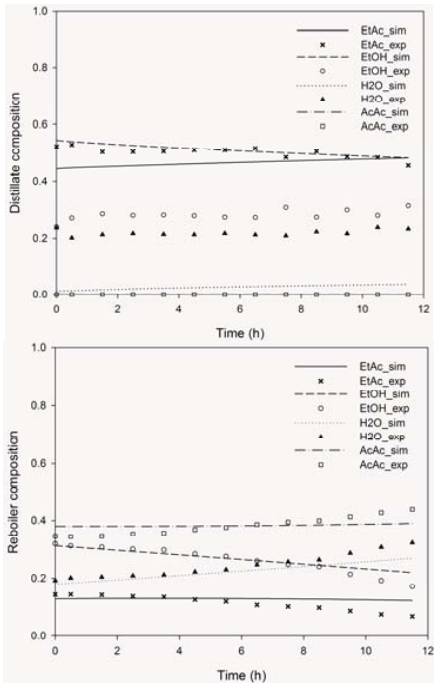

Fig. 4. Results with Model-III-A

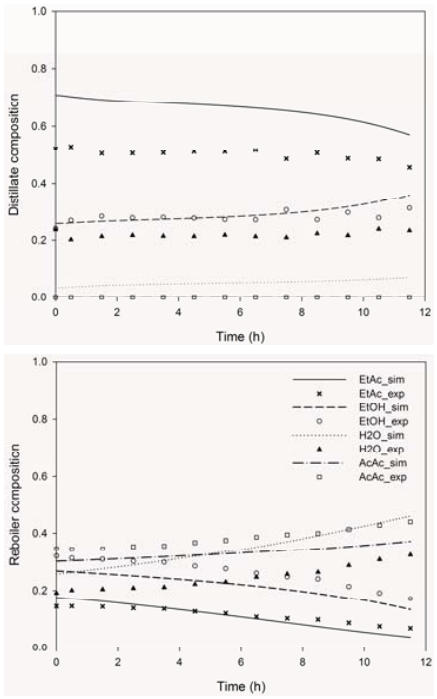

Fig. 5. Results with Model-III-B

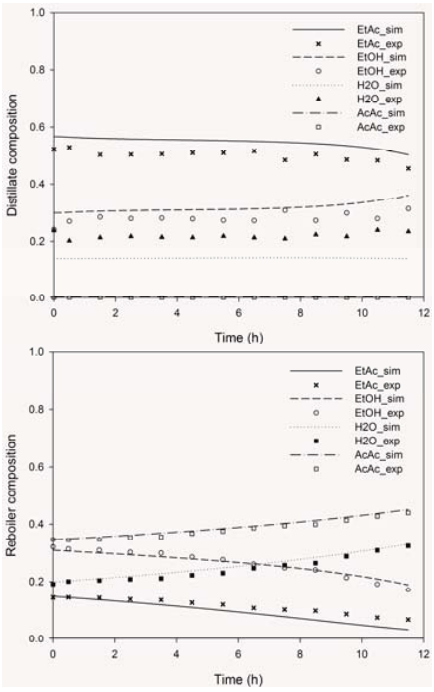

Fig. 6. Results with Model-III-C

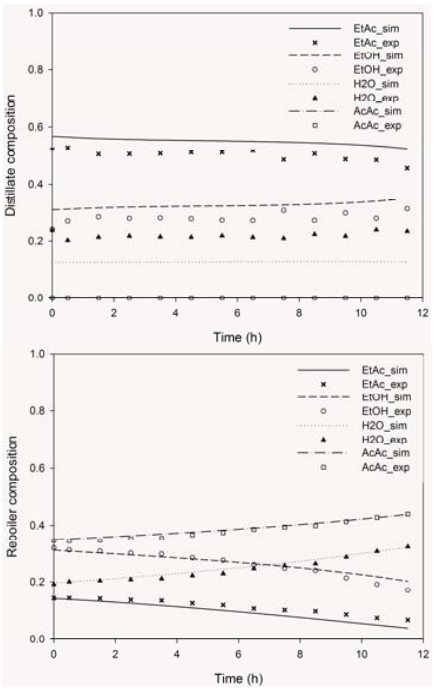

Fig. 7. Results with Model-III-D

Model-IV: In Model-IV, NRTL activity coefficient model is used for liquid phase, PRSV (Model-IV-A) and PR (Model-IV-B) with van der Waals mixing rule is used for vapor phase. It can be seen from Fig. 9 that the distillate compositions are improved compared to Model-III. Although the reboiler compositions become a little worse, they are in an acceptable range. Unlike Model-III, PR also gives similar results with PRSV in Model-IV as can be seen in Fig. 10.

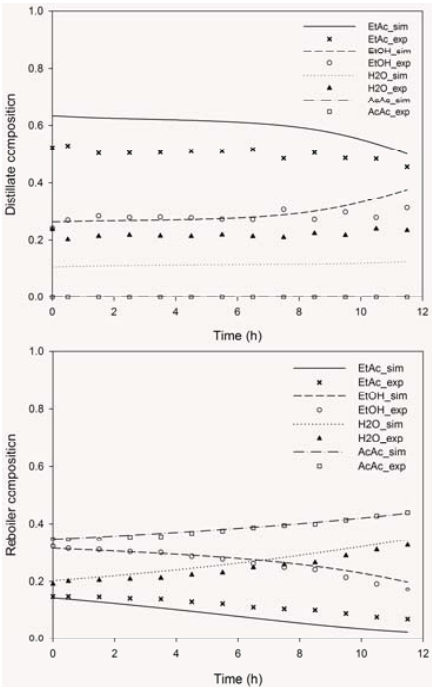

Fig. 8. Results with Model-III-E

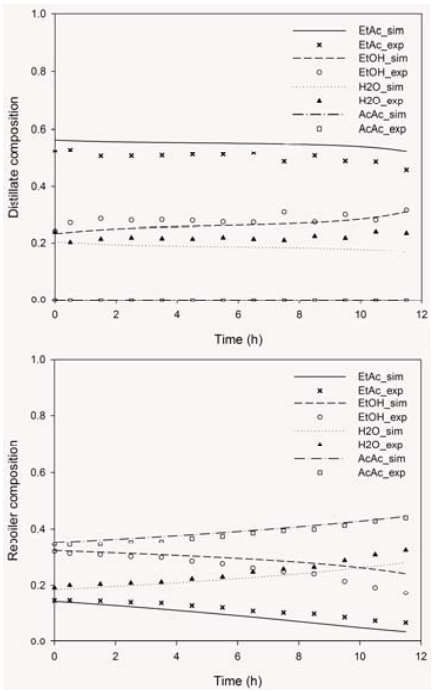

Fig. 9. Results with Model-IV-A

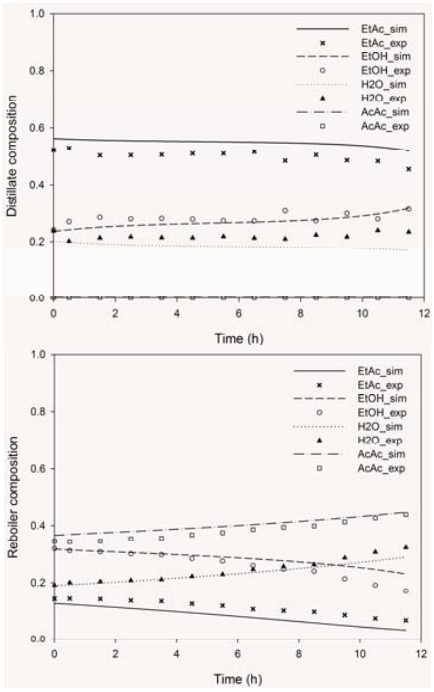

Fig. 10. Results with Model-IV-B

Table 7. Summary of Thermodynamic Models.

Model	*Description*	*IAE Scores*		
		Distillate	*Reboiler*	*Overall*
Model-I	VLE data from literature	-	-	-
Model-II	$\phi-\phi$ method (PR+van der Waals)	-	-	-
Model-III-A	EOS-G^{ex} method (PR + HVO + NRTL)	6.080	1.049	7.129
Model-III-B	EOS-G^{ex} method (PRSV + HVO + NRTL)	4.514	2.805	7.320
Model-III-C	EOS-G^{ex} method (PRSV+HVOS+NRTL)	2.131	0.621	2.751
Model-III-D	EOS-G^{ex} method (PRSV+HVOS+Wilson)	2.437	0.552	2.989
Model-III-E	EOS-G^{ex} method (PRSV+HVOS+UNIQUAC)	2.915	0.877	3.791
Model-IV-A	$\gamma-\phi$ method (PRSV+van der Waals+NRTL)	1.321	1.026	2.347
Model-IV-B	$\gamma-\phi$ method (PR+van der Waals+NRTL)	1.279	1.072	2.351

6. CONCLUSIONS

A summary of results for different thermodynamic models are given in Table 7 with Integral Absolute Error (IAE) scores of response curves. Model-IV-A, which uses traditional $\gamma-\phi$ approach with NRTL activity coefficient model for liquid phase and PRSV for vapor phase gives the smallest IAE score for the quaternary EtOH-AcAc-EtAc-H_2O system. Nevertheless, Model-IV-B which uses the traditional approach with NRTL activity coefficient model for the liquid phase and the PR-EOS for the vapor phase, which is simple to use also gives similar result with a slightly higher IAE score. Thus, both methods are suggested to be used in the simulation of EtOH esterification reaction with AcAc in a RBDC system.

REFERENCES

Alejski, K., Duprat, F. (1996). Dynamic Simulation of the Multicomponent Reactive Distillation. Chem Eng Sci, 51 (18), 4237-4252.

Bahar, A. (2007). Modeling and Control Studies for a Reactive Batch Distillation Column, in Ph.D. Thesis, Chemical Engineering Department, Middle East Technical University, Ankara.

Bogacki, M.B., Alejski, K., Szymanowski, J. (1989). The Fast Method of the Solution of a Reacting Distillation Problem. Comput Chem Eng, 13 (9), 1081-1085.

Burgos-Solorzano, G.I., Brennecke, J.F., Stadtherr, M.A. (2004). Validated Computing Approach for High-Pressure Chemical and Multiphase Equilibrium. Fluid Phase Equilibr, 219 (2), 245-255.

Chang, Y.A., Seader, J.D. (1988). Simulation of Continuous Reactive Distillation by a Homotopy-Continuation Method. Comput Chem Eng, 12 (12), 1243-1255.

Kang, Y. W., Lee, Y. Y., Lee, W. K. (1992). Vapor-Liquid Equilibria with Chemical Reaction Equilibrium - Systems Containing Acetic Acid, Ethly Alcohol, Water, and Ethyl Acetate. J Chem Eng Jpn, 25 (6), 649-655.

Monroy-Loperena R., Alvarez-Ramirez, J. (2000), Output-Feedback Control of Reactive Batch Distillation Columns. Ind Eng Chem Res, 39, 378-386.

Mujtaba, I.M., Macchietto, S. (1997). Efficient Optimization of Batch Distillation with Chemical Reaction Using Polynomial Curve Fitting Techniques. Ind Eng Chem Res, 36, 2287-2295.

Okur, H. and Bayramoglu, M. (2001), The Effect of the Liquid-Phase Activity Model on the Simulation of Ethyl Acetate Production by Reactive Distillation. Ind Eng Chem Res, 40, 3639-3646.

Park J., Lee, N., Park, S., Cho, J. (2006). Experimental and Simulation Study on the Reactive Distillation Process for the Production of Ethyl Acetate. J Ind Eng Chem, 12(4), 516-521.

Simandl, J. Svrcek, W.Y. (1991). Extension of the Simultaneous-Solution and Inside-Outside Algorithms to Distillation with Chemical Reactions. Comput Chem Eng, 15 (5), 337-348.

Stryjek R., Vera J.H. (1986). An Improved Peng-Robinson Equation of State for Pure Compounds and Mixtures, 64 (2), 323-333.

Suzuki, I., Yagi, H., Komatsu, H., Hirata. M. (1971). Calculation of Multi-component Distillation Accompanied by a Chemical Reaction. J Chem Eng Jpn, 4 (1), 26-32.

Tang, Y. T., Huang, H., Chien, I. (2003). Design of a Complete Ethyl Acetate Reactive Distillation System. J Chem Eng Jpn, 36 (11), 1352-1363.

Yıldız, U., Gürkan, U.A., Özgen, C., Leblebicioğlu, K. (2005), State Estimator Design for Multicomponent Batch Distillation Columns. Chem Eng Res Des, 83(A5), 1-12.

Process Control Applications

Poster Session

Application of the IHMPC to an industrial process system

O. L. Carrapiço[1], M. M. Santos[2], A. C. Zanin[1] and D. Odloak[3]
1. Petrobras, Refinery of Cubatão, Pça Stênio Caio de Albuquerque Lima,1, 11555-900, Cubatão, SP - Brazil
2. Chemtech, a Siemens Company, Av. Ermano Marchetti, 1435, 05038-001, São Paulo, SP - Brazil
3. Department of Chemical Engineering - University of São Paulo, PO.B. 61548, 05424-970, São Paulo, SP – Brazil

Abstract: This paper addresses the application of a new MPC to a distillation system where isobutane and light butenes are separated from butane and heavier compounds. This system is located in the alkylation unit of an oil refinery. The MPC considered here is based on the infinite horizon MPC extended to the case where the system has stable and integrating modes. The controller is developed based on a particular state space model in the incremental form, which considers the existence of time delays. The proposed controller provides nominal stability to the closed loop system. Practical tests in a distillation system show that the performance of the new controller, which can be extended to consider robustness to model uncertainty is similar to the performance of the conventional MPC with finite prediction horizon.

Keywords: Predictive control; Stability; Infinite horizon; Integrating system.

1. INTRODUCTION

One of the key issues in the application of MPC to industrial processes is the requirement that the closed loop system should remain stable for a large set of tuning parameters and any possible control structure in terms of active controlled outputs and available manipulated inputs. Rawlings & Muske (1993) have demonstrated that, in the regulator operation of stable systems, the infinite horizon MPC preserves stability even in the presence of constraints in the inputs and states. These ideas have been extended to the case of output tracking of stable systems (Odloak, 2004) and to systems with stable and integrating modes (Carrapiço & Odloak, 2005; González et al., 2007). However, a recent review by Qin & Badgwell (2003) points out that these developments have not been incorporated into the available MPC technology. Thus, the main scope of this work is to report the application of an infinite horizon MPC with nominal stability to an industrial system of small dimension but that presents the typical ingredients of a practical application: time delay, measured and unmeasured disturbances and integrating modes.

The state space model considered here is an extension of the model developed by Gouvêa & Odloak (1997) and Rodrigues and Odloak (2003) and implemented by Porfírio et al. (2003) to include time delays and integrating modes and is represented as follows:

$$\begin{aligned} x(k+1) &= Ax(k) + B\Delta u(k) \\ y(k) &= Cx(k) \end{aligned} \tag{1}$$

where

$$x(k) = \left[y(k|k)^T \quad y(k+1|k)^T \quad \cdots \quad y(n+np|k)^T \quad x^s(k)^T \quad x^d(k)^T \quad x^i(k)^T \right]^T \tag{2}$$

$$A = \begin{bmatrix} 0 & I_{ny} & 0 & \cdots & 0 & 0 & 0 & 0 \\ 0 & 0 & I_{ny} & \cdots & 0 & 0 & 0 & 0 \\ \vdots & \vdots & \vdots & \ddots & \vdots & \vdots & \vdots & \vdots \\ 0 & 0 & 0 & \cdots & I_{ny} & 0 & 0 & 0 \\ 0 & 0 & 0 & \cdots & 0 & I_{ny} & \Psi((np+1)\Delta t) & I^*((np+1)\Delta t) \\ 0 & 0 & 0 & \cdots & 0 & I_{ny} & 0 & I_{ny}\,\Delta t \\ 0 & 0 & 0 & \cdots & 0 & 0 & F & 0 \\ 0 & 0 & 0 & \cdots & 0 & 0 & 0 & I_{ny} \end{bmatrix} \tag{3}$$

$$B = \left[S(\Delta t)^T \quad S(2\Delta t)^T \quad \cdots \quad S((np+1)\Delta t)^T \quad [D^0 + \Delta t\, D^i]^T \quad [D^d F\ N]^T \quad [D^i]^T \right]^T$$

$$C = \left[I_{ny} \quad 0 \quad \ldots \quad 0 \right]$$

In the model defined in (1), $u \in \Re^{nu}$ is the manipulated input. The first np components of the state vector defined in (2) correspond to the output predictions computed at time k based solely on past control actions and disturbances, x^s are the state components associated with the integrating modes created by the incremental form of the model, x^d are the state components associated with the stable modes of the system and x^i are the state components associated with the integrating modes of the system. To represent systems with time delays, it is assumed that $np \geq m + \text{int}\left\{\max(\theta_{i,j}/\Delta t)\right\}$, where m is the control horizon of the MPC, Δt is the sampling time and $\theta_{i,j}$ is the time delay associated with output y_i and input u_j. In the state matrix defined in (3), one has

$$\Psi\left((np+1)\Delta t\right)=$$
$$\begin{bmatrix} \Phi_1\left((np+1)\Delta t\right) & & & \\ & \Phi_2\left((np+1)\Delta t\right) & & 0 \\ 0 & & \ddots & \\ & & & \Phi_{ny}\left((np+1)\Delta t\right) \end{bmatrix}$$

$$\Phi_i\left((np+1)\Delta t\right)=\begin{bmatrix} f_{i,1,1} & \cdots & f_{i,1,na} & f_{i,2,1} & \cdots & f_{i,2,na} \\ \cdots & f_{i,nu,1} & \cdots & f_{i,nu,na} \end{bmatrix}$$

where $f_{i,j,g}=r_{i,j,g}^{(np+1)\Delta t-\theta_{i,j}}$, r is a stable pole of the system. States $y(k/k),\ y(k+1/k),\ ....,\ y(k+np/k)$ correspond to the output predictions calculated at time k based solely on past control actions and disturbances.

$$I^*[(np+1)\Delta t]=\begin{bmatrix} (np+1)\Delta t-\theta_1 & 0 & \cdots & 0 \\ 0 & (np+1)\Delta t-\theta_2 & \cdots & 0 \\ \vdots & \vdots & \ddots & \vdots \\ 0 & 0 & \cdots & (np+1)\Delta t-\theta_{ny} \end{bmatrix} \in \Re^{ny\times ny}$$

θ_i is the time delay associated with the integrating mode related to output y_i.

$D^0\in\Re^{ny\times nu}$ and $D^i\in\Re^{ny\times nu}$

$$F=\text{diag}\left(r_{1,1,1}\cdots r_{1,1,na}\cdots r_{1,nu,1}\cdots r_{1,nu,na}\cdots r_{ny,1,1}\cdots r_{ny,1,na}\cdots r_{ny,nu,1}\cdots r_{ny,nu,na}\right),$$

$F\in C^{nd\times nd}$

$$D^d=\text{diag}\left(d^d_{1,1,1}\cdots d^d_{1,1,na}\cdots d^d_{1,nu,1}\cdots d^d_{1,nu,na}\cdots d^d_{ny,1,1}\cdots d^d_{ny,1,na}\cdots d^d_{ny,nu,1}\cdots d^d_{ny,nu,na}\right),$$

$D^d\in C^{nd\times nd}$

$$N=\begin{bmatrix} J_1 \\ J_2 \\ \vdots \\ J_{ny} \end{bmatrix},\ N\in\Re^{nd\times nu};\ J_i=\begin{bmatrix} 1 & 0 & \cdots & 0 \\ \vdots & \vdots & \ddots & \vdots \\ 1 & 0 & \cdots & 0 \\ & & \ddots & \\ 0 & 0 & \cdots & 1 \\ \vdots & \vdots & \ddots & \vdots \\ 0 & 0 & \cdots & 1 \end{bmatrix},$$

$J_i\in\Re^{nu\,na\times nu}$, $i=1,2,\ldots,ny$

In the above matrix, it is assumed that either output y_i integrates only input u_i, or if this output integrates other inputs, the time delays between the integrated inputs and the output are the same for all the inputs. If this condition is not satisfied, the model proposed above is not observable. The step response of the system can be calculated by the following equation

$S(t)=D^0+\Psi(t)D^dN+I^*(t)D^i$

where t is supposed to be larger than any time delay included in the process model.

2. THE INFINITE HORIZON MPC

The infinite horizon MPC considered here is based on the following control cost

$$V_k=\sum_{j=0}^{\infty}\left[e(k+j|k)-\delta_k^s-j\Delta t\delta_k^i\right]^T Q\left[e(k+j|k)-\delta_k^s-j\Delta t\delta_k^i\right]+\sum_{j=0}^{m-1}\Delta u(k+j|k)^T R\,\Delta u(k+|k)+\delta_k^{sT}S_1\delta_k^s+\delta_k^{iT}S_2\delta_k^i \quad (4)$$

where

$e(k+j|k)=\tilde{y}(k+j|k)-y^{sp}$ and $\tilde{y}(k+j|k)$ is the output prediction at time $k+j$ computed at time k and considering the future control actions. Weight matrices Q, R, S_1 and S_2 are assumed positive definite.

The control objective defined in (4) can be expanded as follows

$$V_k=V_k^{(1)}+V_k^{(2)}+\sum_{j=0}^{m-1}\Delta u(k+j|k)^T R\,\Delta u(k+j|k)+\delta_k^{sT}S_1\delta_k^s+\delta_k^{iT}S_2\delta_k^i \quad (5)$$

where

$$V_k^{(1)}=\sum_{j=0}^{np}\left[e(k+j|k)-\delta_k^s-j\Delta t\delta_k^i\right]^T Q\times\left[e(k+j|k)-\delta_k^s-j\Delta t\delta_k^i\right]$$

$$V_k^{(2)}=\sum_{j=1}^{\infty}\left[e(k+np+j|k)-\delta_k^s-(np+j)\Delta t\delta_k^i\right]^T Q\times\left[e(k+np+j|k)-\delta_k^s-(np+j)\Delta t\delta_k^i\right] \quad (6)$$

It can be shown that

$$V_k^{(1)}=\left[\bar{C}\,x(k|k)+\tilde{C}\Delta u_k-y_1^{sp}-\bar{I}\,\delta_k^s-\tilde{I}\,\delta_k^i\right]^T\bar{Q}\times\left[\bar{C}\,x(k|k)+\tilde{C}\Delta u_k-y_1^{sp}-\bar{I}\,\delta_k^s-\tilde{I}\,\delta_k^i\right] \quad (7)$$

where

$$\bar{C}=\begin{bmatrix} C \\ CA \\ \vdots \\ CA^{np} \end{bmatrix},\ \tilde{C}=\begin{bmatrix} 0 & 0 & 0 & \cdots & 0 \\ CB & 0 & 0 & \cdots & 0 \\ CAB & CB & 0 & \cdots & 0 \\ \vdots & \vdots & \vdots & \cdots & \vdots \\ CA^{np-1}B & CA^{np-2}B & & \cdots & CA^{np-m}B \end{bmatrix},$$

$\Delta u_k=\left[\Delta u(k|k)^T\quad \Delta u(k+1|k)^T\quad\cdots\quad \Delta u(k+m-1|k)^T\right]^T$

$\bar{Q}=diag(\left[Q\quad Q\quad ...\quad Q\right])\in\Re^{np.ny\times np.ny}$,

$y_1^{sp}=[y^{spT}\quad y^{spT}\quad ...\quad y^{spT}]^T\in\Re^{np.ny}$

$\bar{I}=[I_{ny}\quad I_{ny}\quad ...\quad I_{ny}]^T\in\Re^{np.ny\ x\ ny}$,

$\tilde{I}=[0\quad \Delta t\,I_{ny}\quad ...\quad np\Delta t\,I_{ny}]^T\in\Re^{np.ny\ x\ ny}$

In order to develop the infinite sum defined in (6), one needs to consider an expression for the calculation of the output prediction at time steps beyond time *np*. Using the model expressions defined in (1) to (3), the output prediction at time step *np*+1 can be written as follows:

$$\tilde{y}(k+np+1|k) = \tilde{x}^s(k+m|k) + \Psi((np+1)\Delta t)\tilde{x}^d(k+m|k) + (np+1)\Delta t\, I_{ny}\tilde{x}^i(k+m|k)$$

where $\tilde{x}^s$, $\tilde{x}^d$ and $\tilde{x}^i$ are computed considering the future control actions. Analogously, the prediction at any time step *np+j* can be written as follows:

$$\tilde{y}(k+np+j|k) = \tilde{x}^s(k+m|k) + \Psi((np+1)\Delta t)F^{j-1}\tilde{x}^d(k+m|k) + (np+j)\Delta t\ \tilde{x}^i(k+m|k)$$

In order to guarantee that $V_k^{(2)}$ will be bounded, it is necessary to force the state components related to the integrating modes to be zero at the end of the control horizon:

$$\tilde{x}^s(k+m|k) - y^{sp} - \delta_k^s = 0 \quad (8)$$

$$\tilde{x}^i(k+m/k) - \delta_k^i = 0 \quad (9)$$

If constraints (8) and (9) are satisfied, $V_k^{(2)}$ can be written as follows:

$$V_k^{(2)} = \sum_{j=1}^{\infty} \tilde{x}^d(k+m/k)^T (F^{j-1})^T \left(\Psi((np+1)\Delta t)\right)^T Q \times \Psi((np+1)\Delta t)F^{j-1}\tilde{x}^d(k+m/k)$$

$$V_k^{(2)} = \tilde{x}^d(k+m/k)^T \tilde{Q}\tilde{x}^d(k+m/k) \quad (10)$$

where $\tilde{Q}$ satisfies

$$F^T\tilde{Q}F - \tilde{Q} = \left(\Psi((np+1)\Delta t)\right)^T Q\Psi((np+1)\Delta t)$$

and

$$x^d(k+m/k) = F^m x^d(k/k) + F_u \Delta u_k$$

$$F_u = \left[F^{m-1}B^d \quad F^{m-2}B^d \quad \cdots \quad B^d\right], \quad B^d = D^d F\, N$$

Substituting (7) and (10) in (4), the control objective becomes

$$V_k = \left[\Delta u_k^T \quad \delta_k^{sT} \quad \delta_k^{iT}\right] H \begin{bmatrix}\Delta u_k \\ \delta_k^s \\ \delta_k^i\end{bmatrix} + 2C_f^T \begin{bmatrix}\Delta u_k \\ \delta_k^s \\ \delta_k^i\end{bmatrix}_k + c \quad (11)$$

where

$$H = \begin{bmatrix} H_{11} & H_{12} & H_{13} \\ H_{12}^T & H_{22} & H_{23} \\ H_{13}^T & H_{23}^T & H_{33}\end{bmatrix}$$

$$C_f = \begin{bmatrix} \left[x(k/k)^T\bar{C}^T\bar{Q}\tilde{C} - y_1^{spT}\bar{Q}\tilde{C} + x^d(k/k)^T F^{mT}\tilde{Q}F_u\right]^T \\ \left[-x(k/k)^T\bar{C}^T\bar{Q}\bar{I} + y_1^{spT}\bar{Q}\bar{I}\right]^T \\ \left[-x(k/k)^T\bar{C}^T\bar{Q}\tilde{I} + y_1^{spT}\bar{Q}\tilde{I}\right]^T \end{bmatrix}$$

$$H_{11} = \tilde{C}^T\bar{Q}\tilde{C} + F_u^T\tilde{Q}F_u + \bar{R}$$

$$c = x(k/k)^T\bar{C}^T\bar{Q}\bar{C}x(k/k) - 2y_1^{spT}\bar{Q}\bar{C}x(k/k) + y_1^{spT}\bar{Q}y_1^{sp} + x^d(k/k)^T F^{mT}\tilde{Q}F^m x^d(k/k)$$

$$\bar{R} = diag(\left[R \quad R \quad \ldots \quad R\right]) \in \Re^{m.nu \times m.nu}$$

$$H_{12} = -\tilde{C}^T\bar{Q}\bar{I}, \quad H_{13} = -\tilde{C}^T\bar{Q}\tilde{I}, \quad H_{22} = \bar{I}^T\bar{Q}\bar{I} + S_1,$$
$$H_{23} = \bar{I}^T\bar{Q}\tilde{I}, \quad H_{33} = \tilde{I}^T\bar{Q}\tilde{I} + S_2$$

It is easy to show that for the model defined in (1), the constraint defined in (8) can be written as follows

$$x^s(k/k) - y^{sp} + m\Delta t\, x^i(k/k) + \tilde{D}\Delta u_k - \delta_k^s = 0 \quad (12)$$

where

$$\tilde{D} = [D^0 + m\Delta t\, D^i \quad D^0 + (m-1)\Delta t\, D^i \quad \ldots \quad D^0 + \Delta t\, D^i]$$

Analogously, the constraint defined in (9) becomes

$$x^i(k/k) + \tilde{D}^i\ \Delta u_k - \delta_k^i = 0 \quad (13)$$

where

$$\tilde{D}^i = \left[\underbrace{D^i \quad \cdots \quad D^i}_{m}\right]$$

Therefore, the infinite horizon MPC that is implemented here is based on the following optimization problem:

$$\min_{\Delta u_k, \delta_k^s, \delta_k^i} V_k \quad (14)$$

subject to

(12), (13) and

$\Delta u(k+j) \in \mathbb{U},\ j \geq 0$,

where

$$\mathbb{U} = \left\{ \Delta u(k+j) \left| \begin{array}{l} -\Delta u^{\max} \leq \Delta u(k+j) \leq \Delta u^{\max} \\ \Delta u(k+j) = 0; \quad j \geq m \\ u^{\min} \leq u(k-1) + \sum_{i=0}^{j} \Delta u(k+i) \leq u^{\max}; \\ j = 0,1,\cdots,m-1 \end{array} \right. \right\}$$

Carrapiço & Odloak (2005) showed that the problem defined in (14) produces a nominally stable MPC if it is solved in a two step approach. In the first step, the objective is to minimize slack δ_k^i, which is related to the integrating modes. Then, in the second step, the objective is to minimize V_k while δ_k^i is kept at the same value computed in the first step. In practical terms, the two step approach would be equivalent to adopting the value of the slack weight S_2 large enough to force the controller to minimize δ_k^i before considering the other control objectives. Thus, the IHMPC, which is implemented here, is obtained through the solution to the problem defined in (14) with suitable tuning parameters that produce the nominal stability of the controller.

3. PROCESS OVERVIEW AND CONTROL STRATEGY

A schematic representation of the de-isobutanizer distillation column where the infinite horizon MPC was implemented is illustrated in Figure 1. The system is part of an alkylation unit in the PETROBRAS/Cubatão oil refinery. The feed stream distillation column comes from the FCC unit and consists of a mixture of isobutane, 1-butene, cis-2-butene, trans-2-butene, n-butane and n-pentane. The top product, which is sent to the alkylation reactor, is composed mainly of isobutane and light butenes. The bottom stream that is

composed of n-butane and heavy butenes is sent to storage and sold as a special product.
The feed flowrate is defined by the refinery production plan and usually remains constant over long periods of time. The feed temperature is the main disturbances to the control system. A recycle stream of isobutane and steam are used as sources of heat to the reboiler. The pressure in the top drum is controlled by manipulating the bypass of the top condenser. In the original regulatory strategy, a PID controller of the temperature of tray 68 cascades the steam flowrate to the reboiler and there was no control on the level of liquid in the top drum. The main control objective is to keep the composition of the top product composition at desired values.

As shown in Figure 1, in the control strategy implemented in the IHMPC there are two manipulated inputs: u_1 (ton/h) is the steam flowrate to the reboiler and u_2 (m^3/d) is the reflux flowrate. The feed temperature d_1 (ºC) is a measured disturbance. The outputs of the distillation column are: y_1 (%) the level of liquid in the top drum, y_2 (ºC) the temperature of tray 68 and y_3 (%) the percentage of flooding in the column. The flooding is calculated based on the measured values of some variables of the process. The two degrees of freedom (inputs) are used to control the liquid level in the drum at a fixed set-point and the other two outputs are controlled by zone: the column flooding has to be kept below an upper limit and the temperature in tray #68 has to be kept above a minimum value. Two other outputs that will be included in this control strategy in the near future are the volumetric ratio iC4/(∑ olefin components) in the top product and the volumetric fraction of iC4 in the bottom stream.
Step tests were performed in the distillation column and the resulting transfer function model is the following:

$$\begin{bmatrix} y_1(s) \\ y_2(s) \\ y_3(s) \end{bmatrix} = \begin{bmatrix} \frac{2.3}{s} & \frac{-0.7\times10^{-3}}{s} \\ \frac{4.7e^{-7s}}{9.3s+1} & \frac{1.4\times10^{-3}e^{-2s}}{6.8s+1} \\ \frac{1.9e^{-s}}{10.1s+1} & \frac{61\times10^{-3}e^{-3s}}{6.6s+1} \end{bmatrix} \begin{bmatrix} u_1(s) \\ u_2(s) \end{bmatrix} + \begin{bmatrix} \frac{0.2}{s} \\ \frac{0.4e^{-3s}}{11.6s+1} \\ \frac{0.2e^{-3s}}{12.3s+1} \end{bmatrix} d_1(s)$$

During the identification tests, it was observed that the control valve of the reflux flow rate has shown an erratic behavior probably due to stickiness. Although, this problem could be easily repaired, we found it interesting to perform the evaluation test of the proposed IHMPC in these conditions, as this scenario may be frequently found in industry. So, the sticking reflux control valve becomes an unmeasured disturbance to the MPC controller. The transfer functions represented above relates the outputs to the set points to the regulatory flow control loops.

4. PRACTICAL RESULTS

Figures 2 and 3 show the typical responses of the industrial system with IHMPC when a step disturbance is introduced in the set point of the liquid level. The tuning parameters of the controller are the following: $m = 2$, $\Delta t = 1$, $Q = diag(6,4,1)$, $R = diag(0.1,5)$, $S_1 = S_2 = diag(1,1,1)\times10^3$.

In this case, the column flooding (y_3) was controlled at a fixed set point of 91%, while the temperature in tray #68 (y_2) was kept above the minimum constraint (52ºC). Fig. 3 clearly shows that there is a sticking problem in the valve of the reflux flow rate (u_2), where the process variable (*PV*) has a significant delay in comparison to the corresponding set point (*SV*). The consequence is a continuous cycling of this variable with a period of about 30min. This disturbance is transferred to the controlled variables of the system, but the IHMPC can cope with this situation quite nicely as the amplitude of the resulting oscillation is largely attenuated. Concerning the tuning parameters of the proposed IHMPC, they can be borrowed from the conventional MPC, except the prediction horizon, which is infinite, and the slack weights S_1 and S_2. Typically, these parameters should be two or three orders of magnitude larger than the output weights. The main point related to the slack weights is that they should be large enough to make the hessian matrix H defined in (11) positive definite. If this condition is not satisfied, the integrating outputs may become unbounded or the stable outputs may show offset.

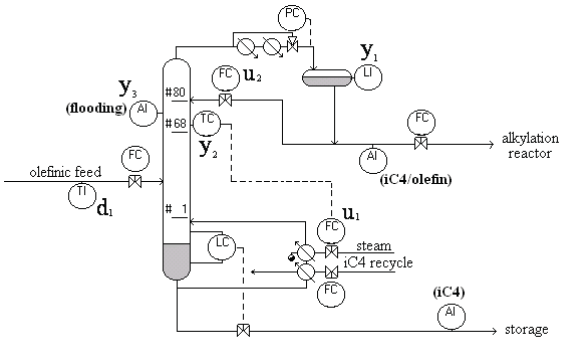

Fig. 1. Schematic diagram of the de-isobutanizer column.

There was a question if the proposed IHMPC would amplify this sort of periodic disturbance, as the controller includes equality constraints (12) and (13) related to cancellation of the integrating modes. Apparently, the inclusion of slacks δ_k^s and δ_k^i greatly reduced this problem. To verify if the gain in stability associated with the use of an infinite prediction horizon would result in a loss of performance, the proposed controller was compared with the conventional MPC. For this purpose, a finite horizon MPC was also implemented in this distillation column. Although, in practice, one cannot repeat exactly the experiment reported above but considering the conventional MPC, Figures 4 and 5 show the responses of the conventional MPC for a similar step disturbance in the set point of the liquid level. The tuning parameters for the two controllers are the same except, for the prediction horizon, which is infinite in the IHMPC and the slacks weights, which do not exist in the conventional MPC. Observing figs. 4 and 5, one may conclude that there is no significant difference between the performances of the two controllers and consequently, there is no practical disadvantage in implementing the infinite horizon MPC that introduces nominal stability.

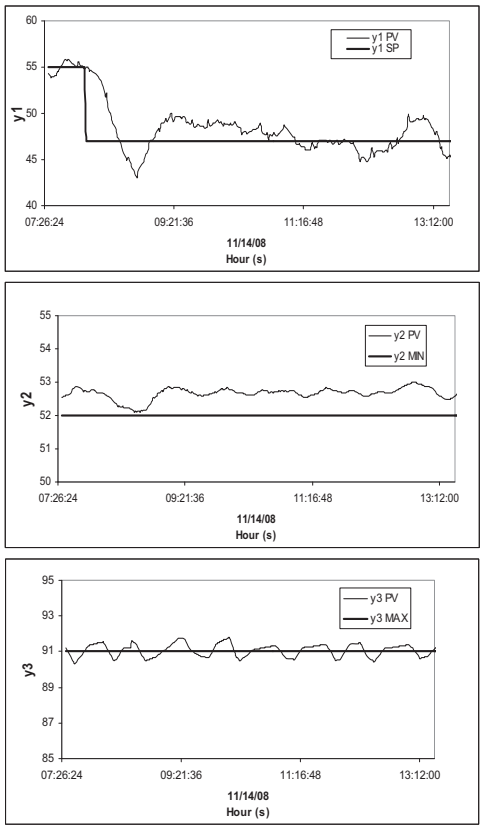

Fig. 2 – Outputs for the IHMPC. Step change in the liquid level set-point.

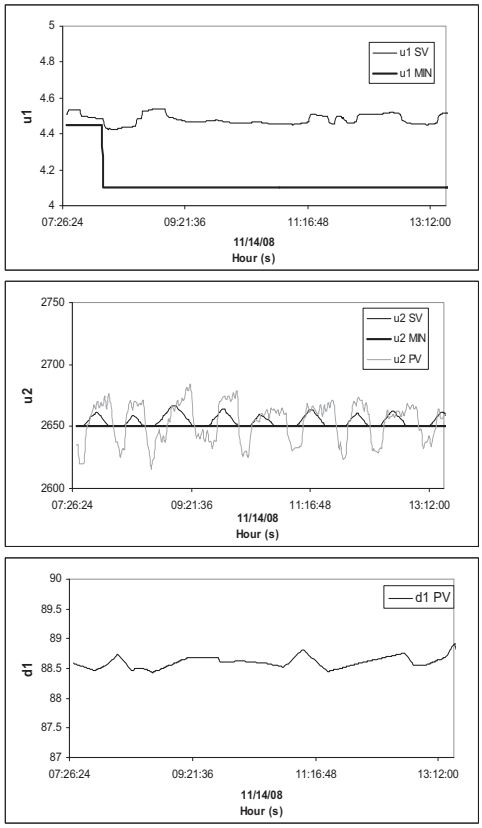

Fig. 3 – Inputs for the IHMPC. Step change in the liquid level set-point.

Another practical experiment performed with the IHMPC is shown in figures 6 and 7. In this case, the set point to the flooding percentage (y_3) in the column is successively decreased along a series of step changes, while the set point to liquid level in the reflux drum (y_1) is fixed and the column temperature (y_2) is controlled by zone. Although the performance of the controller can be considered satisfactory, the sticking problem in the reflux control valve seems more serious and heavily affects the behavior of the system, mainly the reflux flow rate (u_2) and the column flooding. It is not represented here, but the same kind of behavior is observed when the system is controlled with the conventional MPC.

5. CONCLUSIONS

A MPC with infinite prediction horizon was successfully implemented in an industrial distillation column and has been in continuous operation for several months. The proposed controller can be applied to systems with stable and integrating outputs. The IHMPC was compared to the conventional finite horizon MPC and the performances of the two controllers seem quite similar. The new controller has some additional parameters related to the weighting of slack variables that are introduced in the control problem in order to guarantee that this control problem will remain always

REFERENCES

Carrapiço, O. L. & Odloak, D. (2005), A stable model predictive control for integrating processes, *Comp. & Chem. Engng*, 29, 1089–1099.

González, A. H., Marchetti, J. L. & Odloak, D. (2007), Extended robust model predictive control of integrating systems, *AIChE Journal* 53 (7), pp. 1758-1769.

Gouvêa, M. T. & Odloak, D. (1997), Rossmpc: A new way of representing and analysing predictive controllers, *Chem. Engng Research and Design*, 75(7), 693-708.

Odloak, D. (2004), Extended robust model predictive control, *AIChE Journal*, 50(8), 1224-1236.

Porfírio, C. R., Neto, E. A. & Odloak, D. (2003), Multi-model predictive control of an industrial C3/C4 splitter, *Control Engng Practice*, 11 (7), 765-779.

Qin, S. J. & Badgwell, T.A. (2003), A survey of model predictive control technology, *Control Engng Practice* 11(7), 733–764.

Rawlings, J. B., & Muske, K. R. (1993), The stability of constrained receding horizon control, *IEEE Transaction on Automatic Control*, 38, 1512–1516.

Rodrigues, M.A. & Odloak, D. (2003). An infinite horizon model predictive control for stable and integrating processes. *Comp. & Chem. Engng*, 27, 1113-1128.

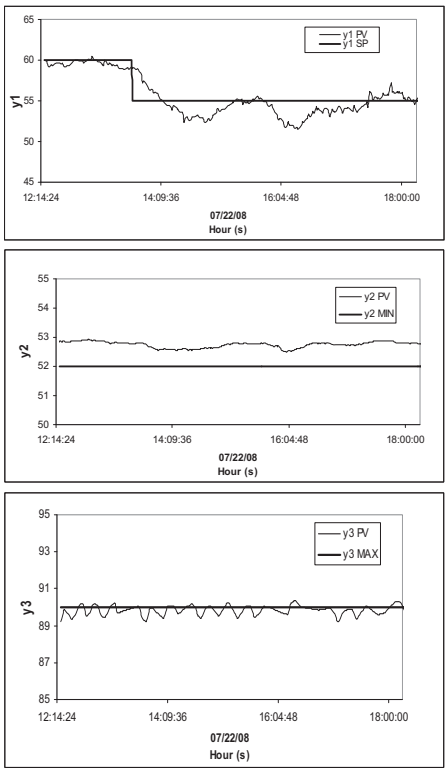

Fig. 4–Outputs for the conventional MPC. Step change in the liquid level set-point.

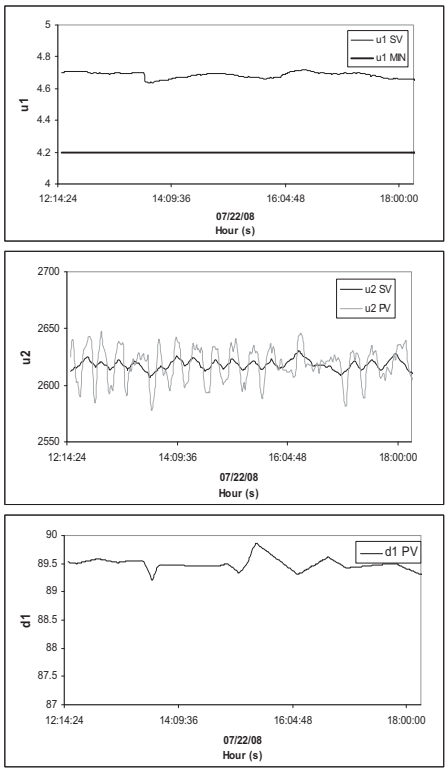

Fig. 5 – Inputs for the conventional MPC. Step change in the liquid level set-point.

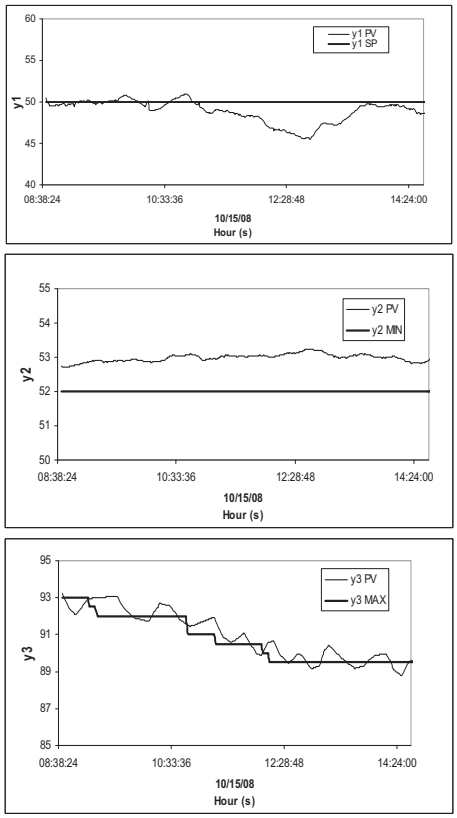

Fig. 6 – Outputs for the IHMPC. Step changes in the set point to column flooding.

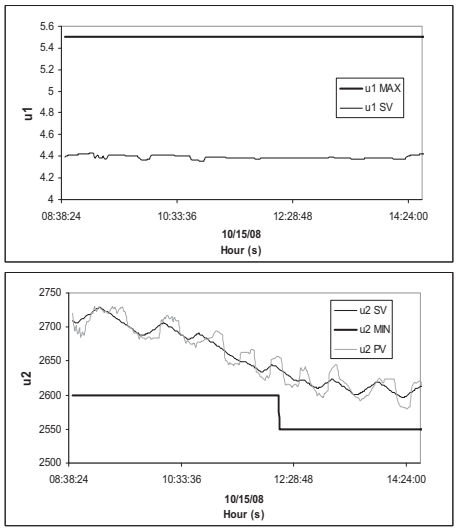

Fig. 7 – Inputs for the IHMPC. Step changes in the set point to column flooding.

Multivariable control with adjustment by decoupling using a distributed action approach in a distillation column

Cintia Marangoni[1]. Joel G. Teleken[2]. Leandro O. Werle[3]. Ricardo A. F. Machado[4]. Ariovaldo Bolzan[5]

Federal University of Santa Catarina State – UFSC . Chemical Engineering Department.
P.O. Box 476 – Trindade, Florianópolis, SC – Zip Code 88010-970 – Brazil. Fone/ Fax: +55 (48) 3721-9554
[1](e-mail:sissi@enq.ufsc.br). [2](e-mail: joel_teleken@yahoo.com.br). [3](e-mail:leandro@enq.ufsc.br).
[4](e-mail:ricardo@enq.ufsc.br) [5](e-mail:abolzan@enq.ufsc.br).

Abstract: This paper presents an approach which uses a multivariable control strategy with distributed action in order to minimize operation transients in distillation columns when a disturbance in the temperature feed is introduced. Experiments were carried out adjusting multivariable PID controllers by static decoupling of the temperature loops of the bottom and distillate trays, characterizing a 2 x 2 system. The dynamics was compared to the distributed approach (same controllers on the bottom and top and an additional control loop on a tray). The controllers adjustment of this new system (3 x 3) was carried out considering the temperature control loop stage in two different ways: decentralized and coupled with the bottom and top temperature control loops. The minimization of transients was verified in both distributed approaches.

Keywords: control schemes, distillation columns, dynamics, multivariable systems, transient analysis.

1. INTRODUCTION

A well designed and adjusted control system is not sufficient to eliminate operation transients of a distillation process. One aspect that contributes to this situation, besides the column operation stage, is the centralization of the control system in the bottom and top column variables. In this way there is the propagation of the corrective control action through the whole unit, generating a production period out of the desired specification. The formation of transients in a distillation column occurs when the process is disturbed and its characteristics reduce the control system efficiency or when an external factor induces the modification of the unit operation point. In the first case there are factors such as variable coupling, nonlinearities, deadtime, high time constants and process constrains. In the second case there are aspects such as the mixture to be distillated, feed composition changes and operation transitions that are necessary due to changes in the market. In both cases, the process dynamics influences the way the transient operation will be generated and what the final result will be.

The current proposals to minimize the transient time of distillation columns use control techniques which consider process dynamics only to study the efficiency of these algorithms, without changing the process conception or evaluating the minimization of transients (Zhu and Liu, 2005). Stricter product specifications and greater demands in terms of environmental control, together with the design of more and more integrated units, require a better performance of these systems. Thus, economic incentives for the development and application of high performance control systems in industrial plants have grown considerably.

The proposal here developed, which is the object of this study, consists of the distribution of the control action throughout the column stages aiming at the minimization of the transient operation. This approach is based on the study of diabatic distillation columns (Koeijer, Rosjorde and Kjestrup, 2005), where intermediate heating points are used instead of only one heat input (reboiler) and one heat remover (condenser). These additional points keep a certain desired temperature profile throughout the column. Previous research (Marangoni and Machado, 2007) has demonstrated the feasibility of this proposal with the use of classic controllers (PID). The unit dynamics was evaluated and the results showed a reduction in the operation transition time when feed disturbances are introduced into the distillation column. Although 90% of industrial processes use classic controllers (Astrom and Hagglun, 2001), it was also necessary to evaluate the use of advanced controllers (model-based) which consider the process dynamics. Multivariable and predictive control seem to be the most used techniques due to their great flexibility. Here, it is worth mentioning the studies carried out with model-based controllers: Model Predictive Control (MPC) (Bezzo et al., 2005); Dynamic Matrix Control (DMC) (Jana et al., 2005); and Generalized Predictive Control (GPC) (Karanca, 2003). On the other hand, some studies have been carried out with proportional-integral-derivative (PID) controllers, aiming at a more flexible adjustment considering the distillation characteristics (Zhu and Liu, 2005). However, even in these recent studies, the controllers used to obtain the quality profile are implemented with the control action only in the bottom and top column stages.

Thus, aiming at the application of easy implementation strategies, the objective of this study was to evaluate the use of a 2 x 2 control system (controllers of the temperature loops

of the bottom and distillate trays) and compare it to a new distributed approach (same controllers on the bottom and top and an additional temperature control loop on a tray) implemented in two different ways: the first considering the additional control stage without interaction with the other two control loops (decentralized), and the second considering the system as 3x3 multivariable.

2. MATERIALS AND METHODS

Experiments were carried out in a pilot unit processing an ethanol-water mixture. The conditions used are summarized in Table 1. Composition measurements were carried out during the experiments using a densimeter for alcohol.

Table 1. Operation conditions used in the experiments.

Variable	Value
Ethanol feed volumetric fraction	0.15
Feed Temperature	92°C
Volumetric feed flow	300 $L.h^{-1}$
Column top pressure	1.25 bar
Drop pressure	0.25 bar
Reflux ratio (Reflux stream/Distillate)	5
Bottom Holdup	4 L
Accumulator Holdup	5 L

2.1 The pilot unit

The unit, illustrated in Figure 1, represents a tray distillation process. It operates in a continuous way and thus there is a main tank responsible for the feed.

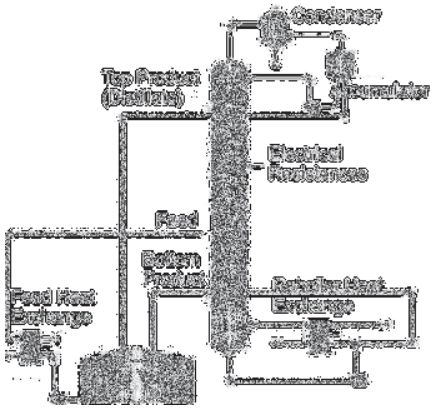

Fig. 1. Schematic illustration of the experimental unit's.

The column has 13 equilibrium stages and each module has one point for temperature measurement, one for sample collection and a third for the distributed heating adaptation. The latter was carried out by means of electrical resistances designed with up to 3.5kW power each. Temperature sensors (Pt-100) were used to monitor this variable in all equilibrium stages, as well as the main tank and the reflux accumulator. The feed was carried out on the fourth tray, with the reboiler as the zero stage.

The control configuration of the distillation column was formulated based on Nooraii et al. (1999), and is illustrated in Figure 2. The following control loops were defined: (1) bottom level control through the bottom product flow rate adjustment; (2) reflux accumulator level control by manipulating the top product flow rate; (3) feed flow rate control as a function of the adjustment of the same stream flow rate; (4) feed temperature control through the fluid flow rate adjustment in the heat exchanger of this stage; (5) last tray (distillate) temperature control by means of the manipulation of the reflux flow rate; (6) reboiler temperature control through the vapor flow rate in the heat exchanger of this stage; and (7) temperature control of pre-defined stages of the column through the adjustment of the dissipated power in the tray electrical resistance.

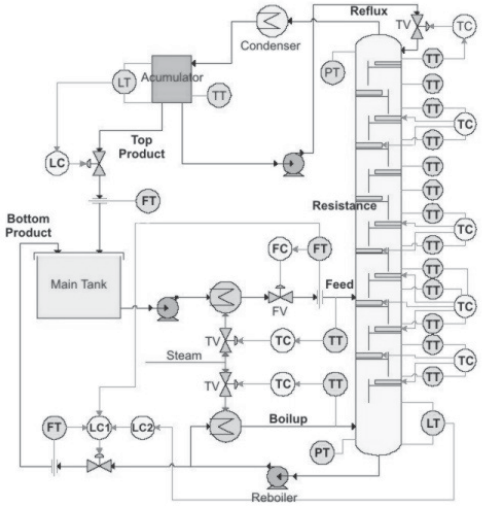

Fig. 2. Control configuration of the distillation unit.

The first, second and third loops represent the column mass balance (inventory) control. The fifth and sixth loops comprise the quality control – in this case represented by the temperature. The use of these two loops in combination is referred to herein as conventional control. When these two loops are combined with the seventh loop mentioned above, it is considered herein as the distributed strategy.

All control loops are instrumented with fieldbus protocols, along with the acquisition and indication of the bottom and distillate stream flows and the pressures at the same stages. The temperatures of all the trays, reboiler, accumulator and feed are monitored by a programmable logic controller and used in the dynamic study of the distributed control. The pressures were monitored in order to assure the proper functioning of the equipment and the process.

2.2 The control strategies tested

For this study, the experiments were carried out with three different control strategies: (1) conventional 2 x 2 – with multivariable control applied to the reboiler and distillate temperatures; (2) distributed 2 x 2 – with multivariable control applied to the reboiler and distillate temperatures and decentralized control in only one stage (PID without interaction with the other loops); and (3) distributed 3 x 3 – with multivariable control applied to the reboiler, second stage and distillate temperatures.

2.3 Controller's tuning

PID controllers are used in the three strategies tested. This kind of controller was employed since it is the most widely used (Astrom and Hagglund, 2001). Multivariable tuning was applied as the experiments consider both loops (reboiler and distillate temperatures) coupled to control the process.

Thus, for strategies 1 and 3 a static decoupler was used (Lee et al, 2005) to cancel the undesired effects of the interaction and adjustment of the multivariable controllers. This procedure can be designed from steady-state process gains, which are easier to obtain and can be tuned in the field. As an initial estimate the PID controller parameters were calculated using the criterion of the integral absolute error (ITAE). A fine adjustment was then made in the plant.

For strategy 2, the same controllers obtained in strategy 1 were used for the reboiler and distillate temperature loops. For the tray temperature controller the ITAE criterion was used to estimate the parameters followed by a fine adjustment (considering this loop decentralized from others, i.e., with weak interaction).

2.4 Stage selection

To identify the most sensitive stage for the consequent application of the distributed control, three different methods were applied (Luyben, 2006). In the first method, the difference between the temperatures of two successive trays was calculated throughout the column and the most sensitive tray was that which presented the greatest difference in relation to its adjacent tray. In the second method, a temperature profile for a given value of the manipulated variable (in this case, the reflux flow and the reboiler heat) is obtained. The most sensitive tray gives a symmetrical response to positive and negative equally variations. Finally, the third method analyzes the tray with the highest derivative of the temperature in relation to the stage when the process is disturbed. To analyze the first method, the temperature profile for three different conditions of ethanol feed composition (15, 25 and 35%) was observed. In the second and third methods it was necessary to disturb the process and evaluate its behavior. The feed flow used was 400L.h^{-1} as the standard condition, which was increased to 600L.h^{-1} and also decreased to 200L.h^{-1}.

It is important to emphasize that the different methods can produce different answers. The definition was based on this analysis together with the characteristics of the plant.

2.5 Disturbances

To analyze the control strategies, changes in the temperature feed were introduced, decreasing this variable by around 15^{o}C (from 92^{o}C to 77^{o}C). This was achieved by controlled cooling of this stream.

This study aimed to interfere in the column temperature profile in order to minimize the response time when some disturbance occurs. Thus, it was not tested for set point tracking.

3. RESULTS

The first step of this study was to determine the stage were distributed heating could be applied. As cited before, this was achieved through a sensitivity analysis employing three different methods. The results obtained with the first method (successive trays) using three feed ethanol composition conditions demonstrated the possibility of using trays 1, 2, 3, 5 and 7. As the fifth and seventh trays are located in the rectifying section, they were discarded. It was assumed, following diabatic studies upon which this proposal was based, that in this section it is better to remove heat than supply it.

In addition, as this is an initial study, it was defined that only one tray will be used to test the proposal. To define this stage, since method 1 was not conclusive, the analysis of symmetrical response and maximum derivative (methods 2 and 3) was used. The derivative method again pointed to stages 5 and 7, which were previously discarded, but the symmetrical response method indicated tray 2 as the most appropriate for this study. Figure 3 shows this analysis, where it can be observed that tray 2 is almost the same distance from steady state when the process is disturbed with positive and negative perturbations in the feed flow.

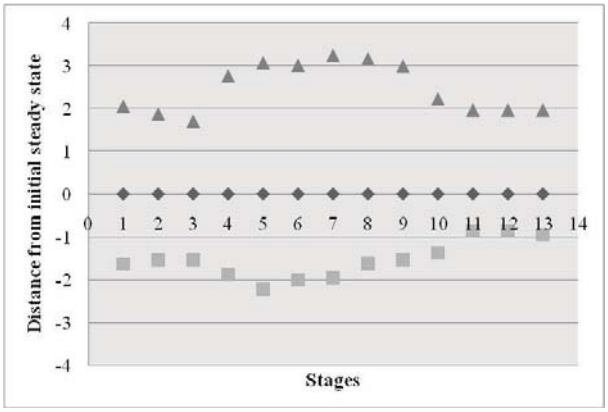

Fig. 3. Results of sensitivity analysis using symmetrical response method (■ negative disturbance, ◆ steady state, ▲ positive disturbance).

Based on this sensitivity analysis, the distributed action of the proposal was used only in tray 2. The simultaneous action of the trays was not tested because the main objective was to analyze the distributed proposal with a multivariable system, and its behavior, through the coupling of control loops.

In sequence, the process transfer functions were determined and the relative gain array matrix was evaluated.

Multivariable control algorithms were studied since the process has multiple inputs and outputs and it is characterized by the high coupling degree among the variables. These kinds of controllers require process models for which an approximated model was used, obtained by the transfer

functions of the reboiler, second stage and distillate temperature control loops. In fact, a multivariable system can be easily modeled through transfer functions. These functions associate the system outputs (Y) with the disturbances (L) and the inputs (U), and integrate the transfer function matrix with the disturbance (G_L) and inputs (G).

The transfer functions were obtained by means of experimental tests, through input and output data collection and later numeric treatment of this information, disturbing the variables that are used for the manipulation of the control loops. The equations obtained are presented below (time values expressed in seconds and deadtime obtained by Taylor series approximation).

Equation (1) presents the matrix which represents the 3 x 3 system, where Tb is the reboiler temperature, Td the distillate temperature and T_2 the second stage temperature, corresponding to the system outputs. Q_b (steam valve opening at the reboiler entrance), R (reflux flow valve opening) and Q_2 (dissipated power at the electrical resistance stage), represent the inputs.

$$\begin{bmatrix} Y_1 = Tb(s) \\ Y_2 = Td(s) \\ Y_3 = T_2(s) \end{bmatrix} = \begin{bmatrix} G_{11}(s) & G_{12}(s) & G_{13}(s) \\ G_{21}(s) & G_{22}(s) & G_{23}(s) \\ G_{31}(s) & G_{32}(s) & G_{33}(s) \end{bmatrix} \begin{bmatrix} U_1 = Qb(s) \\ U_2 = R(s) \\ U_3 = Q_2(s) \end{bmatrix} \quad (1)$$

Equations (2) to (10) present the transfer functions obtained, which consist of the input/output relations presented in (1). For the calculations, the deadtime of these functions were expressed using a simple first-order Taylor series approximation.

$$G_{11} = \frac{0.69}{112s+1} \quad (2)$$

$$G_{12} = \frac{3.12e^{-13s}}{203s+1} \quad (3)$$

$$G_{13} = \frac{0.56e^{-1s}}{145s+1} \quad (4)$$

$$G_{21} = \frac{-0.08e^{-26s}}{172s+1} \quad (5)$$

$$G_{22} = \frac{-0.04e^{-4s}}{364s+1} \quad (6)$$

$$G_{23} = \frac{-0.06e^{-17s}}{135s+1} \quad (7)$$

$$G_{31} = \frac{0.02e^{-1s}}{74s+1} \quad (8)$$

$$G_{32} = \frac{0.14e^{-2s}}{407s+1} \quad (9)$$

$$G_{33} = \frac{0.02}{85s+1} \quad (10)$$

Experimental tests were carried out, data were evaluated and with the process equations the existing interactions were verified by controlling the process with and without the proposed approach. Experiments were carried out in order to construct the relative gain array matrix (RGA) (Shinskey, 1996) for the 2 x 2 system (reboiler and distillate temperature control loops) and for the 3 x 3 systems (reboiler, second stage and distillate temperature control loops). In this case, the cited method was used to identify the degree of coupling among the proposed systems and not to define the control structure, which is the usual purpose. This evaluation is important since the intermediate column stages also influence the temperature profile and the process composition.

Equation (11) presents the matrix obtained for the 2 x 2 system and (12) the matrix for the 3 x 3 system.

$$\Lambda = \begin{bmatrix} 0.89 & 0.11 \\ 0.11 & 0.89 \end{bmatrix} \quad (11)$$

$$\Lambda = \begin{bmatrix} 0.77 & 6.80 & -6.57 \\ -4.92 & -0.07 & 6.03 \\ 5.50 & -5.69 & 1.54 \end{bmatrix} \quad (12)$$

Although the selection of the best control structure is not the main objective of this study, the 2 x 2 system is adequate as shown in (11), where the sum of the matrix columns and lines are 1 (one).

In (12) we can observe some values above one for seven of the nine possible combinations of control loops, which indicates strong interactions in these combinations. It is well known that the closer the element is to +1, the weaker the interaction between the loops, and the elements with high modulus values indicate strong interactions between the loops, or it could be that the system is sensitive to parameter changes (less robustness).

With this phase completed, the studies were followed by experimental tests using multivariable control algorithms. As mentioned above, the common technique of controller adjustment by decoupling was used. This tuning was defined since it provides good results (Waller, et al. 2003, Liu et al., 2006). It is important to note that the objective is to improve the control of a new column and the operation approach, and therefore the application of techniques used industrially is the aim.

In decoupled control, it is implicit that the design objective is to obtain a system that reduces the interaction between the loops through specific additional controllers, called decouplers. These are used to improve the performance of multivariable control systems through interaction compensation, though they are sensitive to changes in the process and require detailed process models, which are often difficult to obtain. These disadvantages often limit the use of multivariable controllers industrially. However, the static decouplers approach can be designed from the gains in the process in steady state, which are easy to obtain and can be adjusted in the field (Lee et al. 2005). Because of these

advantages, the static decouplers approach was used, based on the gain of each control loop.

Besides the objective of the implementation and study of advanced techniques using the distributed approach, these studies were carried out to evaluate whether or not it is possible to work with the hypothesis that the interactions caused by the tray can be eliminated when the reboiler interactions are reduced or eliminated.

Figures 4 and 5 show the reboiler and distillate temperature profiles for the strategies applied. In these experiments, the disturbance was applied by decreasing the feed temperature.

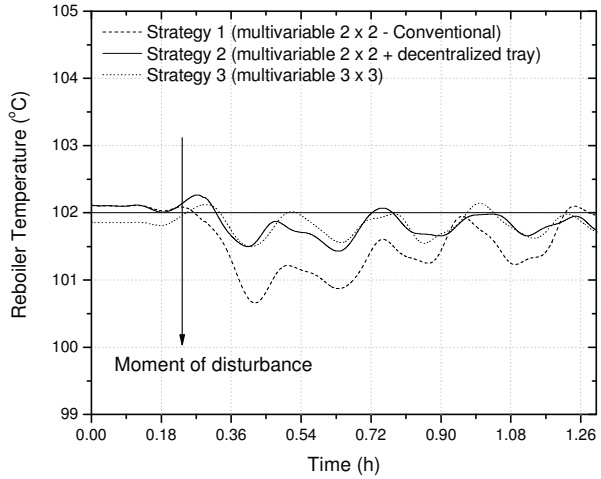

Fig. 4. Effect of the disturbance on reboiler temperature control loop response in relation to setpoint.

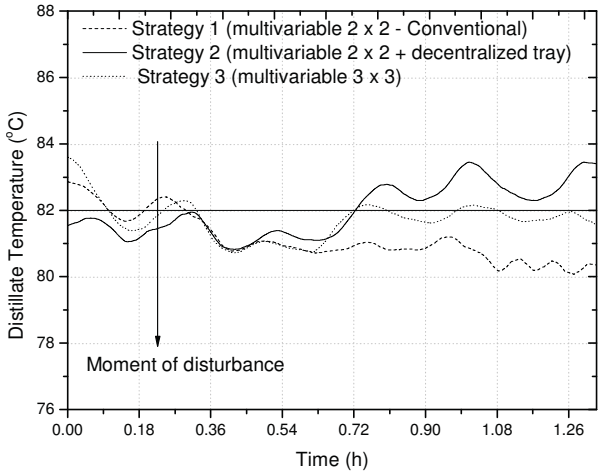

Fig. 5. Effect of the disturbance on distillate temperature control loop response in relation to setpoint.

It can be observed, in both figures, that the disturbance is quickly rejected when the distributed approach is used. Both strategies 2 (2 x 2 multivariable adjustment and decentralized adjustment at stage 2) and 3 (3 x 3 multivariable adjustment) showed that the steady state was reached faster than with strategy 1 (conventional multivariable control – 2 x 2 system). This result indicates that the distributed control action maintains the temperature profile in the column and thus it allows the reduction of the transients generated.

However, strategy 2, which assumes that the interactions between the tray temperature control loops and the other quality controllers is weak, leads to a value slightly higher than that desired. This case is better observed in relation to the distillate temperature. For this same variable, the disturbance applied was not completely rejected using the conventional control, and the distillate temperature stabilized at a lower value.

When reboiler and distillate temperature loops are evaluated together, the 3 x 3 distributed approach allows a better performance. It is possible that this adjustment, considering the interactions between the three control loops, made the system a bit slower, although it is still faster and less oscillatory than the conventional approach.

Figure 6 gives the second stage temperature profile, where the distributed control was implemented. As expected, the performance of the 2 x 2 multivariable adjustment strategy with decentralized adjustment at stage 2 leads to a value closer to the set point. In fact, using a decentralized PID controller at this stage, leads to faster dynamics than applying a multivariable 3 x 3 system which consider all interactions of this tray with the reboiler and distillate temperature control loops. However, strategy 3 showed a slight overshoot and rejected the disturbance quickly, in contrast to the conventional strategy.

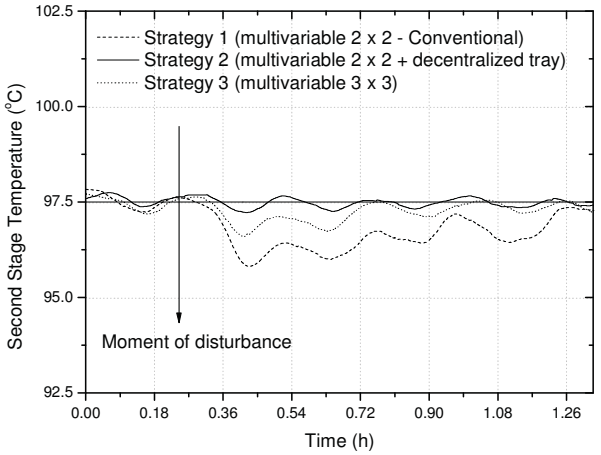

Fig. 6. Effect of the disturbance on the tray 2 temperature control loop response in relation to the setpoint.

In order to carry out a final evaluation regarding which strategy leads to the best performance, the effect of the disturbance on the temperature of the accumulator tank was studied. Since this is the last unit stage, it is the one with the highest transition time. Therefore, its behavior was observed by analyzing the temperature derivative in relation to the time required for the disturbance rejection, as illustrated in Figure 7.

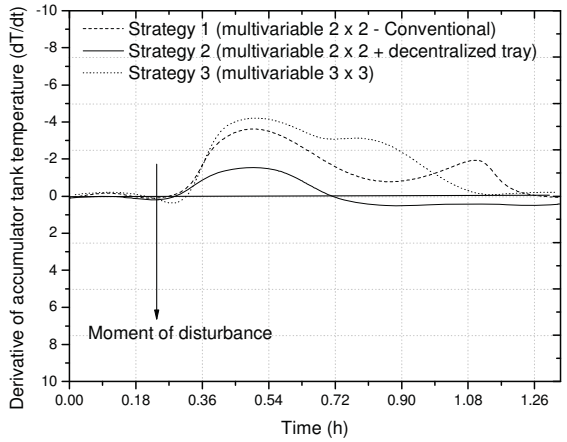

Fig. 7. Derivative of the temperature of the reflux accumulator tank in relation to the setpoint.

The figure demonstrates that the time required to reduce the effects on feed temperature disturbance is shorter when the distributed control approach is applied, considering the second stage temperature control loop not interacting with the others. This hypothesis will be true if the interaction at this stage can be eliminated by the reboiler temperature control loop decoupling. However, it is important to note that the value of the accumulator tank temperature did not return to the same steady state present before the disturbance. It is possible that the use of a PID decentralized controller at stage 2 allowed the production of a greater vapor phase inside the column as the temperature of the last stage was higher in this case. If this occurred, the condenser would produce more distillate and the accumulator temperature tank would stabilize at a different value, as was in fact observed.

4. CONCLUSIONS

The evaluation of the conventional and distributed approach, for a feed temperature disturbance, allowed a reduction in the column transition time and in the oscillations of the controlled variable when the strategy with control at stage 2 was used (independent of the tuning of this loop – decentralized or not).

It is also necessary to consider that the decentralized utilization of the temperature control loop which comprises the distributed approach gives better results than the conventional control system. This is an important result since most industrially implemented controllers are considered decentralized (Garelli et al. 2006).

The comparison between the use of a distributed control loop, decentralized or not with the reboiler and distillate temperature loops, shows that the hypothesis of weak interaction of an intermediate stage can be assumed. When a decoupler was used to tune the quality controllers of the base and top it is possible that the interactions with the trays were reduced. Thus, with the application of an advanced control algorithm, it is observed that the introduction of heat to one of the column stages allows a reduction in the operation time out of the desired conditions. As with classic controllers tested in previous research studies, the introduction of distributed heat throughout the column was shown to be a valid option for the reduction of transients, enabling faster dynamics and lower volumes of products processed out of the pre-defined quality parameters.

ACKNOWLEDGMENTS

The authors are grateful for the financial support of the National Agency of the Petroleum - ANP - and of the funding agency - FINEP - through the Program of Human Resources of ANP for the Petroleum and Gas Sector - PRH-34-ANP/MCT and to the National Council of Research - CNPq.

REFERENCES

Astrom, K.J.; Hägglund, T. (2001) The future of PID control. *Control Engineering Practice*, v. 9, p. 1163-1175.

Bezzo, F; Micheletti, F.; Muradore, R. Barolo, M. (2005) Using MPC to control middle-vessel continuous distillation columns. *Journal of Process Control.* v.15, p. 925-930.

Garelli, F., Mantz, R. J., Battista, H. De. (2006) Limiting interactions in decentralized control of MIMO processes. *Journal of Process Control.* v. 5, p. 473-483.

Jana, A. K.; Samantha, A. N.; Ganguly, S. (2005) Globally linearized control system design of a constrained multivariable distillation column. *Journal of Process Control.* v. 15, p., 169-181.

Karaca, S. (2003) Application of a non-linear long range predictive control to a packed distillation column. *Chemical Engineering and Processing*, v. 42, p. 943-953.

Koeijer, G.; Røsjorde, A.; Kjelstrup, S. (2005) Distribution of heat exchange in optimum diabatic distillation columns. *Energy*. v. 29, p. 2425-2440.

Lee, J., Dong, H. K.; Edgar, T. F. (2005) Static decouplers for control of multivariable processes. *AICHE Journal.* v. 51, p. 2712-2720.

Liu, T., Zang, W., Gao, F. (2006) Analytical decoupling control strategy using unit feedback control structure for MIMO processes with time delays. *Journal of Process Control***.** v. 17, p. 173-186.

Luyben, W.L. (2006) Evaluation of criteria for selecting temperature control trays in distillation columns. *Journal of Process Control* v. 16, p. 115-134.

Marangoni, C. Machado, R. A. F. (2007) Distillation tower with distributed control strategy: Feed temperature loads. *Chemical Engineering an. Technoly.* v 30, p 1292-1297.

Nooraii, A.; Romagnoli, J. A.; Figueroa, J. (1999) Process, identification, uncertainty characterization and robustness analysis of a pilot scale distillation column. *Journal of Process Control*, v. 9, n. 3, p. 247-264.

Shinskey, F. G. (1996) Process Control Systems. McGraw-Hill, 4a edition, New York, 439p.

Waller, M., Waller, J. B., Waller, K. V., (2003) Decoupling revisited. *Industrial & Engineering Chemical Research.* v. 42, p. 4575-4577.

Zhu, Y. & Liu, X. G. (2005) Dynamics and control of high purity heat integrated distillation columns. *Industrial & Engineering Chemical Research.* v. 44, p.8806-8814.

Simultaneous Synthesis, Design and Control of Processes Using Model Predictive Control

M. Francisco*, S. Revollar, **, P. Vega*, R. Lamanna**

**Departamento de Informática y Automática. Universidad de Salamanca. Spain (e-mail: mfs@usal.es).*
***Departamento de Procesos y Sistemas. Universidad Simón Bolívar. Venezuela (e-mail: srevolla@usb.ve)*

Abstract: This work presents the simultaneous synthesis, design and control of an activated sludge process using a Multivariable Model-based Predictive Controller (MPC). The process synthesis and design are carried out simultaneously with the MPC tuning to obtain the most economical plant which satisfies the controllability indices that measure the control performance (H∞ and l1 norms of different sensitivity functions of the system). The mathematical formulation results into a mixed-integer optimization problem with non-linear constraints that is solved using a real coded genetic algorithm. The solutions reflects the effect of applying different bounds over the controllability norms. The results are encouraging for the development of integrated design approaches with advanced control schemes which usually results in complex optimization problems difficult to solve with conventional techniques.

Keywords: Process Design, Controllability indices, Model Based Predictive Control, Genetic Algorithms.

1. INTRODUCTION

The fact that the incorporation of controllability issues at the early stage of process design improves the dynamical behaviour of the plants have motivated the development of different methodologies to deal with the simultaneous process and control system design as Kookos and Perkins (2001), Revollar et al. (2004), Sakizlis et al (2004), Francisco et al. (2005) and more recently Tlacuahuac-Flores and Biegler (2007) and Tlacuahuac-Flores and Biegler (2008).

The simultaneous process and control system design leads to a non linear optimization problem where economic objectives, operability specifications and control performance are considered. The most comprehensive applications contemplate, also, the process synthesis or the control structure selection resulting into a mixed-integer-non-linear optimization problem (MINLP). The controllability analysis might require the evaluation of dynamic performance indices, which translates the problem into a mixed-integer-dynamical optimization (MIDO).

Even thought, the contribution in the field of integrated design is considerable, most of the approaches use conventional PID controllers. Only few works (Sakizlis et al., 2003; Sakizlis et al., 2004; Francisco and Vega, 2006) have been addressed to the application, in the integrated design, of advanced control techniques as Model-Based Predictive Controllers (MPC). The reason is that the advanced control schemes involve solving an optimization problem on-line, leading to a drastic increase in the complexity of the design framework (Sakizlis, et al, 2003; Sakizlis, et al, 2004).

Model based predictive control (MPC or MBPC) makes use of a process model to calculate the optimal control law. The MPC have been mainly accepted due to its natural way of incorporating operating constraints in multivariable process and the successful results in industrial applications (Maciejowsky, 2002; Qin and Badgwell, 2003). The shortcomings of conventional control schemes can be overcome by pursuing an advanced model-based predictive control (MPC) scheme (Sakizlis et al, 2003).

There are several strategies to deal with automatic tuning of MPC based on optimization of dynamical performance index (Ali et al., 1993; Francisco et al, 2005; Li and Du, 2002) but its evaluation requires time-consuming dynamical simulations which is an important drawback of these methodologies. Vega et al (2007) proposed the use of frequency domain methods as controllability indexes to speed up the MPC automatic tuning procedure by solving a mixed sensitivity problem with constraints. It avoids dynamical simulations but the use of linearized models, caused some problems of stability and robustness in the presence of nonlinearities and load disturbances on the process.

The aim of this work is to perform the integrated synthesis and design of a process using model-based predictive controllers (MPC) that will be tuned automatically using the strategy proposed by Vega et al (2007). The activated sludge process of the Manresa's plant was selected to apply the integrated design methodology as has been done in previous work using a conventional PI control technique (Revollar, et al., 2004, Revollar, et al., 2005). Francisco and Vega (2006) applied advanced control techniques for the integrated design of the

mentioned plant, but the structure selection was not taken into account in the problem formulation.

The main difficulty for solving the problem is the existence of continuous process and MPC variables, integers for the prediction and control horizon and binary variables for the structural decisions, which leads to a complex mixed integer non linear optimization problem. Therefore, it is necessary the use of advanced algorithms that handle both, continuous and discrete decisions, to lead the optimization to economically optimal processes operating in an efficient dynamic mode around the nominal working point.

Several deterministic mathematical programming optimization techniques have been used for solving the simultaneous design and control problem (Sweiger and Floudas, 1997; Kookos and Perkins, 2001, Sakizlis et al, 2003; Sakizlis et al, 2004) but complex formulations and a considerable computational effort are required for its implementation. On the other hand, stochastic optimization methods as genetic algorithms have been a good alternative for solving such difficult problems with a minimum effort for its implementation. A genetic algorithm has been proposed for the solution of this non linear mixed integer optimization problem.

The paper is organized containing, first, the description of the MPC and the controllability metrics used for the automatic tuning in the integrated design procedure, the formulation of the optimization problem and the description of the process and in section 3. The analysis of the results is presented in section 4. Finally, conclusions and different projections of this work are included.

2. MPC FORMULATION AND CONTROLLABILITY METRICS

The basic MPC formulation consists of the on-line calculation of the future control actions by solving the following optimization problem subject to constraints on inputs, predicted outputs and changes in manipulated variables.

$$\min_{\Delta\hat{u}} V(k) = \sum_{i=Hw}^{Hp} \left\| \hat{y}(k+i\,|\,k) - r(k+i\,|\,k) \right\|_{Wy}^2 + \sum_{i=0}^{Hc-1} \left\| \Delta\hat{u}(k+i\,|\,k) \right\|_{Wu}^2 \qquad (1)$$

where k denotes the current sampling point, $\hat{y}(k+i\,|\,k)$ is the predicted output vector at time $k+i$, depending of measurements up to time k, $r(k+i\,|\,k)$ is the reference trajectory, $\Delta\hat{u}$ are the changes in the manipulated variables, *Hp* is the upper prediction horizon, *Hw* is the lower prediction horizon, *Hc* is the control horizon, *Wu* and *Wy* are positive definite matrices representing the weights of the change of control variables and the weights of the set-point tracking errors respectively. In this work the matrices *Wy* and *Wu* are diagonal but not time dependent, so the error vector $\hat{y}(k+i\,|\,k) - r(k+i\,|\,k)$ is penalized at every point in the prediction horizon and the changes in the control signal $\Delta\hat{u}(k+i\,|\,k)$ are penalized at every point in the control horizon.

The problem (1) is a Quadratic Programming (QP) problem that gives a sequence of control moves $\Delta\hat{u}(k+i\,|\,k)$. The first component of this sequence is applied to the system in time $k+1$, and the optimization problem (1) is repeated at the next sampling time (receding horizon strategy).

The MPC prediction model used in this paper is a linear discrete state space model of the plant obtained by linearizing the first-principles nonlinear model of the process Maciejowsky (2002):

$$\begin{cases} x(k+1) = Ax(k) + Bu(k) + B_d d(k) \\ y(k) = Cx(k) \end{cases} \qquad (2)$$

where *x(k)* is the state vector, *u(k)* is the input vector and *d(k)* the disturbance vector. Matrices ***A***, ***B***, ***Bd*** and ***C*** are of adequate dimensions. For this model the prediction is:

$$\hat{y}(k+i|k) = C\hat{x}(k+i|k) = C\left[A^i x(k) + \sum_{j=1}^{i} A^{j-1} Bu(k+i-j|k) \right] \qquad (3)$$

One reason for choosing state space models is that a significant part of the recent research literature on MPC shows contributions based on this type of models. Connections between the standard linear quadratic regulator (LQR) theory and unconstrained MPC when the horizons approach infinity could be another reason for that.

When the MPC controller is linear and unconstrained, it can be represented with a transfer function KMPC. The corresponding transfer function is:

$$u = \begin{pmatrix} K_1 & K_2 & K_3 \end{pmatrix} \cdot \begin{pmatrix} r \\ y \\ d \end{pmatrix} = K_1 r + K_2 y + K_3 d \qquad (4)$$

where Ki are the transfer functions between the control signal and the different inputs (r,y,d) which depend on the control system tuning parameters (Wu, Hp, Hw and Hc). Particularly, in our MPC formulation $K_2 = -K_1$ (Maciejowsky, 2002), then, control law can be stated as:

$$u = K_1(r - y) + K_3 d \qquad (5)$$

Consequently, taking into account control law and the transfer function of the open loop system, the closed loop response can be obtained from

$$y = \frac{GK_1}{1+GK_1} r + \frac{1}{1+GK_1} \tilde{d} \qquad (6)$$

where $\tilde{d}$ are the filtered disturbances

$$\tilde{d} = \left(GK_3 + G_d \right) d \qquad (7)$$

In order to state the automatic tuning problem, is necessary to define: The Sensitivity function *S(s)* between the load disturbances (*d*) and the outputs (*y*) and the Control Sensitivity transfer function *M(s)* between the load disturbances (*d*) and the control signals (*u*) when the reference is zero .

$$S(s)=\frac{y(s)}{d(s)}=\frac{k_3G+G_d}{1+GK_1} \tag{8}$$

$$M(s)=\frac{u(s)}{d(s)}=\frac{K_3-K_1G_d}{1+GK_1} \tag{9}$$

For solving the MPC optimization problem, MPC Toolbox of MATLAB has been used, with some specific modifications (Maciejowsky, 2002) implementing an extended state space representation.

Regarding to the controllability indices, some norm based metrics were considered. The first controllability index considered in this work is:

$$\|N\|_\infty=\max_w|N(jw)| \tag{10}$$

where N is a mixed sensitivity index that takes into account both disturbance rejection and control effort objectives. The function N is defined as:

$$N=\begin{pmatrix} Wp\cdot S \\ Wesf\cdot s\cdot M \end{pmatrix} \tag{11}$$

Wesf(s) is chosen to penalize control efforts adequately, and *Wp(s)* is chosen based on the spectra of disturbances to ensure proper disturbance rejection. *Wp(s)* and *Wesf (s)* are suitable weights for optimization. The selection of *Wp(s)* is explained below, and the weight *Wesf(s)* is selected to complete the H∞ mixed sensitivity problem and allows for the significance of control efforts. Note that control efforts rather than magnitudes of control are included in the objective function by considering the derivative of the transfer function *M(s)*.

In order to ensure disturbance rejection we need (considering normalized disturbances):

$$|S(jw)|\cdot|d(w)|<1 \tag{12}$$

in the disturbances frequency range where *S(jw)* is the frequency response of the sensitivity function, and *d(w)* is the disturbance spectra. By choosing a weight *Wp(s)* satisfying

$$20\cdot\log|Wp(jw)|^{-1}<20\cdot\log|d(w)|^{-1} \tag{13}$$

disturbance rejection can be assured imposing the following constraint in the optimization tuning procedure:

$$\|Wp\cdot S\|_\infty<1 \tag{14}$$

A typical choice for the weight *Wp(s)* is a rational function with one zero and one pole. *B* is the weight gain for high frequencies, *a* is the gain for low frequencies and w_b represents the required bandwidth for the closed loop system. The parameter *a* is very small to impose integral action to the system but avoiding numerical problems.

$$Wp(s)=\frac{\frac{s}{B}+w_b}{s+w_ba} \tag{15}$$

The maximum value of the manipulated variables (for the worst case of disturbances) can be constrained to be less than u_{max}, by means of the *l1* norm and the following condition:

$$\|M\|_1<u_{\max} \tag{16}$$

3. PROCESS DESCRIPTION AND PROBLEM FORMULATION

The activated sludge process was selected to study the simultaneous synthesis and control system design methodology. A simple model (Moreno et al., 1992) was selected, to avoid the excessive complexity of models like the ASM1 developed by the IAWPRC.

Moreno et al. (1992) model is based on the wastewater treatment process of the Manresa plant (Spain). It is founded in the classical Monod and Maynard-Smith model. It is assumed that the reactions take place in only one perfectly-mixed tank. However, in this work two possible structural alternatives consisting in one or two aeration tanks are considered.

The activated sludge process corresponds to the secondary wastewater treatment stage. In the aeration tanks or bioreactors, the activity of a mixture of microorganisms is used to reduce the substrate concentration in the water. The dissolved oxygen required is provided by a set of aeration turbines. Water coming out of each reactor goes to the settler, where the clean water is separated from the activated sludge that is recycled to both bioreactors. The control of this process aims to keep the substrate at the output (s_1 or s_2) below a legal value despite the large variations on the incoming substrate concentration (*si*) using the recycling flows qr_1 and qr_2 as manipulated variables (Moreno et al, 2002). The frequency and magnitude of the disturbances at the *si* input make the control of the plant a difficult task. The set of disturbances used for evaluate the control performance while tuning the MPC has been determined by COST 624 program Copp (2002).

3.1. Mathematical Optimization Problem

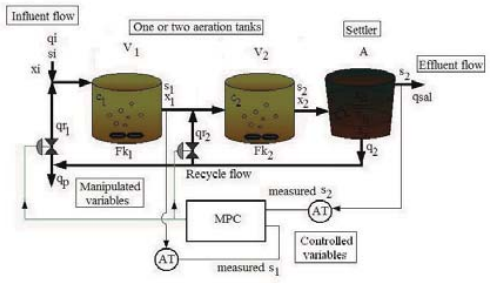

Fig. 1. Activated sludge process superstructure

The simultaneous synthesis, design and control of the activated sludge process pretend to obtain the most economical plant that satisfies the desired control performance. A cost function is defined to measure the economical issues while a predictive controller is tuned to achieve the desired closed loop behaviour according to the controllability norms described in section 2.

The two possible structural alternatives proposed for the plant are represented in a superstructure shown in figure 1. The model equations take the appropriated values for each structural alternative according to the binary y_1.

The mathematical formulation results into a mixed-integer-non-linear optimization problem where the objective is to minimize a cost function considering as decision variables: the structure (y_1), dimensions and controller parameters. Some constraints based in process model are set to find dimensions and initial working point, together with constraints over the norms used to measure the controllability of the plant with the actual controller parameters.

The cost function is:

$$f = p_1 \cdot (v_1 + v_2)^2 + p_2 \cdot A^2 + p_3 \cdot Fk_1^2 + p_3 \cdot Fk_2^2 + p_4 \cdot q_2^2 \qquad (11)$$

where v_1, v_2 are the reactor volumes and A is the cross-sectional area of the settler, Fk_1 and Fk_2 are the aeration factors for each reactor and q_2 is the overall recycle flow. The first three terms are associated to the construction cost that is proportional to the volume of the reactors and the area of the settler. The terms proportional to Fk_1, Fk_2 represent the aeration turbines costs, and the term proportional to q_2 represents pumping costs (purge and recycling).

Logical conditions must be imposed to guarantee the mathematical coherence of the model for any possible structure: if the second reactor does not exist: $y_1=0 \Rightarrow v_2=0$, $x_1=x_2$, $s_1=s_2$, $c_1=c_2$, $Fk_2=0$, $qr_2=0$, if the second reactor exist, then, $y_1=1$ and all the variables take values within their ranges.

The constraints imposed over mass balances in aeration tanks and the settler, are used to define the plant dimensions and the initial stationary working point.

$$\left| v_1 \frac{dx_1}{dt} \right| = \left| \mu_{\max} Y \frac{s_1 x_1}{(K_s + s_1)} v_1 - K_d \frac{x_1^2}{s_1} v_1 - K_c x_1 v_1 + q_{12} (xir_1 - x_1) \right| \le \varepsilon \qquad (17)$$

$$\left| v_1 \frac{ds_1}{dt} \right| = \left| -\mu_{\max} \frac{s_1 x_1}{(K_s + s_1)} v_1 + f_{kd} K_d \frac{x_1^2}{s_1} v_1 + f_{kd} K_c x_1 v_1 + q_{12} (sir_1 - s_1) \right| \le \varepsilon \qquad (18)$$

$$\left| v_1 \frac{dc_1}{dt} \right| = \left| K_{la} Fk_1 (c_s - c_1)\, v_1 - K_{01} \mu_{\max} \frac{s_1 x_1}{(K_s + s_1)} v_1 - q_{12} c_1 \right| \le \varepsilon \qquad (19)$$

$$\left| v_2 \frac{dx_2}{dt} \right| = \left| \mu_{\max} Y \frac{s_2 x_2}{(K_s + s_2)} v_2 - K_d \frac{x_2^2}{s_2} v_2 - K_c x_2 v_2 + q_{22} (xir_2 - x_2) \right| \le \varepsilon \qquad (20)$$

$$\left| v_2 \frac{ds_2}{dt} \right| = \left| -\mu_{\max} \frac{s_2 x_2}{(K_s + s_2)} v_2 + f_{kd} K_d \frac{x_2^2}{s_2} v_2 + f_{kd} K_c x_2 v_2 + q_{22} (sir_2 - s_2) \right| \le \varepsilon \qquad (21)$$

$$\left| v_2 \frac{dc_2}{dt} \right| = \left| K_{la} Fk_2 (c_s - c_2) v_2 - K_{01} \mu_{\max} \frac{s_2 x_2}{(K_s + s_2)} v_2 - q_{22} c_2 + W_1 \right| \le \varepsilon \qquad (22)$$

$$\left| AL_d \frac{dx_d}{dt} \right| = \left| q_{sal} x_b - q_{sal} x_d - A \cdot nnr \cdot x_d \exp(aar \cdot x_d) \right| \le \varepsilon \qquad (23)$$

$$\left| AL_b \frac{dx_b}{dt} \right| = \left| \begin{matrix} q_{22} x_2 - q_{22} x_b + A \cdot nnr \cdot x_d \exp(aar \cdot x_d) \\ -A \cdot nnr \cdot x_b \exp(aar \cdot x_b) \end{matrix} \right| \le \varepsilon \qquad (24)$$

$$\left| AL_r \frac{dx_r}{dt} \right| = \left| q_2 x_b - q_2 x_r + A \cdot nnr \cdot x_b \exp(aar \cdot x_b) \right| \le \varepsilon \qquad (25)$$

If the second reactor does not exist ($y_1=0$), the values of the variables given by the logical conditions mentioned above, annul the equations (20) and (21), a $W_1 = q_{22} \cdot c_2$ term is used to cancel equation (22).

The operation constraints for the activated sludge process are:

Residence times:

$$2.5 \le \frac{v_1}{q_{12}} \le 8 \qquad (26)$$

$$2.5 \le \frac{v_2 + (1 - y_1) \cdot W_2}{q_{22}} \le 6 \qquad (27)$$

where W_2 annul de constraint for $y_1=0$.

Mass loads in the aeration tanks:

$$0.001 \le \frac{q_i s_i + qr_1 s_2}{v_1 x_1} \le 0.12 \qquad (28)$$

$$0.001 \le \frac{q_{12} s_1 + qr_2 s_2 - (1 - y_1) W_3}{v_2 x_2} \le 0.12 \qquad (29)$$

where W_3 annul de constraint for $y_1=0$.

Sludge age in the settler:

$$2 \le \frac{v_1 x_1 + v_2 x_2 + AL_r x_r}{q_p x_r 24} \le 10 \qquad (30)$$

Limits in hydraulic capacity:

$$\frac{q_{22}}{A} \le 1.5 \qquad (31)$$

Limits in the relationship between the input, recycled and purge flow rates:

$$0.03 \le \frac{q_p}{q_2} \le 0.3 \qquad (32)$$

$$0.05 \le \frac{q_2}{q_i} \le 0.9 \qquad (33)$$

The controllability constraints are the limits over the norms described in section 2 where the transfer functions are referred to s_2 as the output, si y qi as the disturbances, and recycling flows qr_1, qr_2 as control variables. The parameter u_{max} is an upper bound for the magnitude of control variables. These constraints: $\|N\|_\infty < 1$, $\|Wp \cdot S\|_\infty < 1$, $\|M\|_1 < u_{\max}$ ensure a satisfactory control performance with the tuned MPC.

The main difficulties when solving this problem is the existence of continuous, integer and binary variables and the evaluation of controllability norms that implies the linearization of the process model for each possible solution. GA are particularly suitable, due to its robustness and the straightforward method to compute the objective function and constraints avoiding gradient evaluation.

4. RESULTS

For solving the problem using genetic algorithms (Gen and Cheng, 2000), a fixed length real coded chromosome is defined, containing the continuous normalized process variables, the controller parameters (Wu, Hp, Hc) and a binary variable to set the structure of the plant: [x_1, x_2, S_{sab}, xd xb xr qr_1 qr_2 qp Fk_1 Fk_2 v_1 v_2 A Wu Hp Hc y_1].

The location of the variables in the chromosome is important for the objective function and constraints evaluation procedure.

The genetic algorithm starts by generating randomly a population of possible solutions, that contains the same quantity of individuals for the two structural alternatives ($y_1=0$ and $y_1=1$). Each solution is manipulated to fulfil the logical conditions mentioned in section 3.1, according to the actual value of y_1. The new candidate solutions are manipulated also, according to the logical conditions. The population in the succeeding generation consists of 50% of the best individuals from the previous generation and 50% of the individuals generated by crossover.

The problem is solved using a population size of 200 individuals and 300 maximum iterations. Roulette selection and arithmetic crossover were used. The mutation rate decreases with generations from 0.1 to 0.02 and the crossover probability used is 85%. A penalization strategy is applied to deal with constraints. The genetic algorithm was run 10 times for each case study, giving optimal feasible solutions for each run with an average computing time of 9657 seconds.

Two scenarios with different demands on control performance were proposed. For the case 1 the norm $\|M\|_1 < 1000$ and for the case 2 the norm $\|M\|_1 < 1500$. The weights Wp for both cases are: $Wp(s) = \frac{8s+19.2}{s+0.0001}$

Table 1. Numerical results for integrated synthesis and design with MPC for the case 1

Cost (MU)	0.13	Wu	0.0122
V_1 (m^3)	8640	Hp	9
A (m^2)	2728.9	Hc	3
S_1 (mg/l)	115.66	$\|N\|_\infty$	0.97
Qr_1 (l/hr)	371.47	$\|M\|_1$	987.47
Fk1	0.035	$\|Wp \cdot S\|_\infty$	0.92
Residence times	2.5		
Mass loads	0.08		
Hydraulic capacity	0.55		
Sludge age	2.08		

The results for the two scenarios are presented in tables 1 and 2. In both cases, the transfer functions and weights are referred to disturbances in si and qi. It is observed that the solution gives small economical plants that satisfy all the process and control constraints. It is important to notice the flexibility of the method for different limits imposed over the constraints leading to plants of different dimensions. In the case 1, where an stringent bound is imposed over l1 norm is obtained a plant with 8640m^3 reactor while, for the case 2, with a relaxed bound in l1 norm is possible to obtain an smaller plant with a reactor of 5858.1 m^3 which is reflected in cost.

The optimization case 1 produces a plant with better disturbance rejection because the weight Wp_1 is more restrictive for sensitivity function S. On the other hand, with a smaller bound for $\|M\|_1$, the magnitude of control is less relaxed than in case 2 giving a smaller range of action to the manipulated variable to reject disturbances. The values of Wesf for qr_1 and qr_2 control sensitivity functions are fixed to:

$$Wesf_{qr1}(s) = \frac{0.0117s+0.14}{s+0.0004} \qquad Wesf_{qr2}(s) = \frac{0.0183s+0.22}{s+0.0004}$$

Table 2. Numerical results for integrated synthesis and design with MPC for the case 2

Cost (MU)	0.064	Wu	0.0069
V_1 (m^3)	5858.1	Hp	8
A (m^2)	2178.4	Hc	3
S_1 (mg/l)	118.06	$\|N\|_\infty$	0.979
Qr_1 (l/hr)	273.9	$\|M\|_1$	1454.9
Fk1	0.021	$\|Wp \cdot S\|_\infty$	0.786
Residence times	4.11		
Mass loads	0.0856		
Hydraulic capacity	0.65		
Sludge age	5.03		

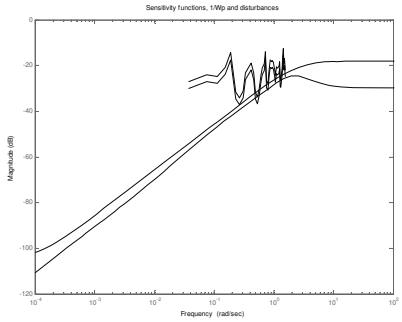

Fig.2. Sensitivity function S, Wp^{-1} and disturbances inverse spectrum for case 1

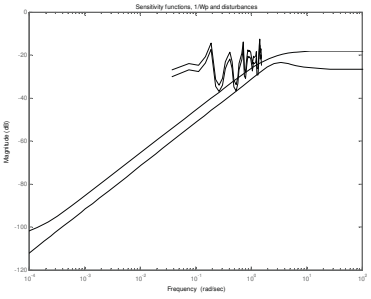

Fig.3. Sensitivity function S, Wp^{-1} and disturbances inverse spectrum for case 1

In figures 2 and 3 sensitivity functions S are presented for both cases. In the case 1 the inverse spectrum of disturbances is over Wp^{-1}, and in case 2 this weight is a bit more relaxed representing worse disturbance rejection. In figures 4 and 5 the dynamical responses of the optimal plants for both cases are

presented, to illustrate the better disturbance rejection for case 1 as have been previously mentioned.

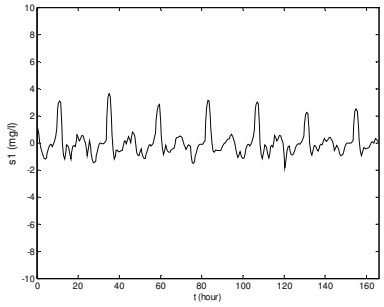

Fig. 4. Substrate response for case 1

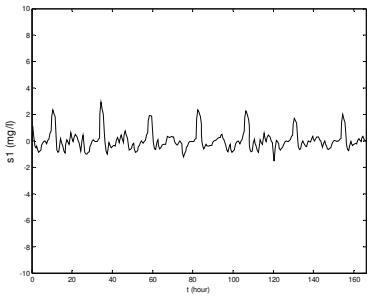

Fig. 5. Substrate response for case 2

5. CONCLUSIONS

In this work, the synthesis and integrated design of an activated sludge process with an advanced controller (MPC) was addressed. The problem was translated into a mixed-integer-non-linear optimization problem, with the evaluation of controllability norms to ensure the most economical design with a suitable control performance.

The MINLP was solved using a real-coded genetic algorithm which leads to good quality feasible solutions with desired disturbance rejection, which is the main control objective. The solutions obtained are sensible to the bounds imposed over controllability indices.

The controllability norms were set as constraints in the formulation of the optimization problem, but it could be formulated as a multiobjective optimization problem considering costs and controllability.

These results are encouraging for the development of simultaneous design and control approaches with advanced control schemes which usually results in complex optimization problems difficult to be solved. In this framework, the use of advanced control techniques represent a significant advance due to the advantages of these control strategies respect to conventional PID.

REFERENCES

Ali, E. and E. Zafiriou, 1993. On the tuning of Nonlinear Model Predictive Control Algorithms. Proceedings of the American Control Conference, pp. 786-790.

Copp, J.B., 2002, The COST Simulation Benchmark: Description and Simulator Manual. Office for Official Publications of the European Community.

Francisco, M., Vega, P. and O. Pérez, 2005. Process Integrated Design within a Model Predictive Control framework. IFAC'05 World Congress, Prague.

Francisco, M. and Vega, P., 2006, Diseño Integrado de procesos de depuración de aguas utilizando Control Predictivo Basado en Modelos. RIAI. Vol. 3, nº 4. 88-98.

Gen, M. and R. Chen, 2000, Genetic algorithms and engineering optimisation. J. W. and Sons.

Kookos I. and J. Perkins, 2001, An algorithm for simultaneous process design and control, Ind. Eng. Chem. Res. 40, 4079.

Li, S. and G. Du, 2002. On-line tuning scheme for generalized predictive control via simulation-optimization. IEEE International Conference on Fuzzy Systems, 1381-1386.

Maciejowsky, J. M. Predictive Control with Constraints. Prentice Hall, 2002.

Moreno, R. De Prada, C., Lafuente, J. Poch, M. and Montague, G. , 1992, Non-linear predictive control of dissolved oxygen in the activated sludge process. IFAC BIO 2pp. 289-298. Ed. Pergamon Press.

Qin, S. J. and Badgwell, 2003, T. A. A survey of industrial model predictive control technology. Control Engineering Practice11, 733-764

Revollar, S, Vega, P. and R. Lamanna, 2004, Algorithmic synthesis and integrated design of chemical reactor systems using genetic algorithms. Proceedings of World Automation Conference Vol 17, 493. Sevilla.

Revollar, S, Lamanna, R. and P Vega, 2005, Algorithmic synthesis and integrated design for activated sludge processes using genetic algorithms. ESCAPE. Barcelona

Sakizlis, S., Perkins, J., and E. Pistikopoulos, 2003. Parametric controllers in simultaneous process and control design optimization. Ind. Eng. Chem. Res., 42, 4545-4563.

Sakizlis, S., Perkins, J., and E. Pistikopoulos, 2004, Recent advances in optimization-based simultaneous process and control design. Computers and Chemical Engineering, 28, 2069-2086.

Schweiger, C and Floudas, C., 1997. Interaction of design and control: Optimization with dynamic models. In W. Hager and P. Pardalos (Eds.) Optimal control: Theory, algorithms and Applications. 388-435. Kluwer Academic Publishers.

Vega, P., Francisco, M., and E. Sanz, 2007. Norm based approach for automatic tuning of Model Predicitive Controllers. Proceedings of ECCE-6, Copenhagen.

Tlacuahuac-Flores, A and Biegler, L., 2008, Integrated Control and Process Design During Optimal Polymer Grade Transitions Operations. Computers and Chemical Engineering, In press.

An efficient multi-objective model predictive control framework of a PEM fuel cell

Ziogou Chrisovalantou[1], Simira Papadopoulou[1,3], Panos Seferlis[1,2] , Spyros Voutetakis[1]

[1]*Chemical Process Engineering Research Institute (C.P.E.R.I.), CEntre for Research and Technology Hellas (CE.R.T.H.), P.O. Box 60361, 57001 Thermi-Thessaloniki, Greece (Tel: +30-2310-498 317; e-mail:ziochr@cperi.certh.gr, paris@cperi.certh.gr)*

[2]*Department of Mechanical Engineering, Aristotle University of Thessaloniki, P.O. Box 484, 54124 Thessaloniki, Greece (Tel: +30-2310-498 169; e-mail:seferlis@cperi.certh.gr)*

[3]*Department of Automation, Alexander Technological Educational Institute of Thessaloniki, P.O. Box 14561, 54101 Thessaloniki, Greece (Tel: +30-2310-498 319; e-mail:shmira@teithe.gr)*

Abstract: Fuel cell systems can produce clean energy and have attracted the interest of both industrial and basic research in the recent years. They are part of a promising benign and environmentally friendly technology and they can be used both in mobile and stationary applications. A dynamic model was constructed and validated using experimental data based on a specific application, consisting of a high temperature PEM Fuel Cell (FC) working at a constant pressure and a Power Conversion Device that controls the current drawn from the FC. An integrated framework that consists of an online maximum power point prediction algorithm and a non-linear model based control scheme is presented. The proposed framework aims to maintain the fuel cell close to the optimum power point and the corresponding oxygen excess ratio level. Simulation studies show that the proposed control framework results in improved performance regarding the efficient and safe fuel cell operation under varying operating conditions.

Keywords: fuel cell control, model predictive control, power management

1. INTRODUCTION

Fuel cells are electrochemical devices that convert the chemical energy of a fuel directly into electricity and are under intensive development by several manufacturers. They are categorized according to the type of electrolyte used, operating conditions or fuel. The Polymer Electrolyte Membrane or Proton Exchange Membrane fuel cells (PEMFC) are currently considered by many to be in a relative more developed stage for ground vehicle applications and portable devices. PEMFC's have high power density, solid electrolyte, long cell and stack life, as well as low corrosion. Lately PEM fuel cells working at higher temperatures of up to 200°C have appeared such as those that use phosphoric acid doped polybenzimidazole (PBI) membrane, which is considered one of the most successful membrane systems so far [Jensen, 2007]. The benefits of operation at elevated temperature are mainly the tolerance to carbon monoxide concentration at the hydrogen feed, commonly present when operating with reformate streams, that can be increased by many orders of magnitude compared to that of a common PEM and also the water management which is a lesser issue, since the water is in vapor state. Additionally, the PBI membranes are conductive at very low relative humidity and consequently no moisture management is needed. Moreover, the high working temperature eliminates the possibility of water condensation in pores or channels of the fuel cell. Due to the higher temperature difference to the surroundings thermal management can be satisfactorily performed by a smaller cooling system [Jensen, 2007]. However, due to material limitations, the power of the fuel cell cannot be arbitrary used without prior consideration on the internal effects such as the provision for fuel and oxidant supply, temperature gradients, condition of the membrane (humidity) and so forth. The choice of the operating region leads to different characteristics for the unit regarding its profitability, effectiveness and safety. The dynamic response of a fuel cell is affected when the power demand fluctuates or when the fuel cell does not operate at its optimal steady-state design point [Golbert, 2007]. An optimization algorithm is used to search off-line for the optimum excess oxygen ratio level and the corresponding near maximum power. The primary objective of this paper is to demonstrate that model-based predictive control (MPC) is a suitable approach for efficient and safe fuel cell operation. The paper is organized as follows: Section 2 gives an overview of the dynamic fuel cell mathematical model. In section 3, the model validation procedure is presented. Section 4 presents the model-based predictive control structure along with the conventional control that is present for the pressures of the anode and the cathode compartments of the FC. Section 5 discusses the maximum power targeting algorithm The simulated results of the proposed MPC framework are presented and discussed in section 6.

2. MODELING AND ANALYSIS

The application is consisting of a high temperature PEM Fuel Cell working at a constant pressure and a Power Conversion Device capable of controlling the current drawn from the FC. In order to define a model based control strategy it is important to have an accurate model that reflects the transient dynamics and fuel cell system behavior and in the same time fast in execution in order to be useful for a real-time application. The mathematical model equations that describe the operation of the fuel cell consists of the voltage-current characteristics and a relationship for the consumption of the reactants as a function of the current drawn from the fuel cell. The main purpose of the detailed model is to describe the dynamic behavior in a way that the fundamental operating parameters current and pressure are established as manipulated variables and temperature as disturbance and power and excess oxygen ratio as controlled variable.

2.1 General

The main components of a PEM fuel cell are three - an anode, typically featuring platinum-containing catalyst, a thin, solid polymeric layer which acts as electrolyte, and a cathode, also coated with platinum [Mann, 2000]. In the PEM fuel cell the only reaction that takes place is the production of water from hydrogen and oxygen. In order to accurately describe the fuel cell behavior the mass balance and the equations that affect the voltage calculation are analyzed in the following section. The development of the fuel cell model is based on some assumptions. The gases are ideal and uniformly distributed inside anode and cathode. The stack is fed with hydrogen and air. The temperature is constant and uniform for each experiment. The gas channels along the electrodes have a fixed volume with small lengths, so that it is only necessary to define one single pressure value in their interior.

2.2 Electrochemistry and Voltage Calculation

Typical characteristics of FC are normally given in the form of polarization curve, which is a plot of cell voltage versus cell current density. To determine the voltage-current relationship of the cell, the cell voltage has to be defined as the difference between an ideal, Nernst voltage and a number of voltage losses and it is described in the current section. The main losses are categorized as activation, ohmic and concentration losses. The activation losses are caused by the slowness of the reactions taking place on the surface of the electrodes. A portion of the voltage generated is lost in driving the chemical reaction that transfers the electrons to or from the electrodes. The activation losses are described by the Tafel equation, which can be calculated as [Mann, 2000]:

$$\Delta V_{act} = \xi_1 + \xi_2 T + \xi_3 T \ln(C_{O_2}) + \xi_4 T \ln(i) \quad (1)$$

where ξ(i = 1–4) are parametric coefficients for each cell model. The term C_{O_2} is the concentration of oxygen on the electrolyte membrane at the gas/liquid interface (mol/cm^3), which can be expressed as [Zhong, 2008]:

$$C_{O2} = \frac{p_{O2}}{5.08 \cdot 10^6 e^{\left(\frac{-498}{T}\right)}} \quad (2)$$

The ohmic losses are caused by the resistance to the flow of electrons through the material of the electrodes and the various interconnections, as well as by the resistance to the flow of protons through the electrolyte. The ohmic losses are given by:

$$\Delta V_{ohm} = R_{mem} \cdot i \quad (3)$$

The ohmic resistance is described by:

$$R_{mem} = \frac{r_m \cdot mem_{thick}}{A} \quad (4)$$

where r_m is membrane resistivity (Ωcm) to proton conductivity, mem_{thick} is the membrane thickness (cm) and A is the active cell area (cm^2). Membrane resistivity depends strongly on membrane humidity and temperature, and can be described by an empirical expression given by Mann et. al. [Mann, 2000]. Finally the mass transport or concentration losses result from the change in concentration of the reactants at the surface of the electrodes as the fuel is used [Larminie J., 2003]:

$$\Delta V_{conc} = me^{ni} \quad (5)$$

where m and n are constants that can be estimated to give better fit to measured results. Thus, the actual voltage will be less due to the aforementioned losses that occur because of the various electrochemical phenomena. The Nernst voltage or open circuit voltage falls as the current supplied by the stack increases. The reversible thermodynamic potential is calculated using the Nerst equation and can be expressed as:

$$E = E^0 + \frac{RT}{2F} \ln\left[\frac{P_{H2} P_{O2}^{\frac{1}{2}}}{P_{H2O}}\right] \quad (6)$$

where F is the Faraday's constant (C/kmol) and p_i are the partial pressures (atm) (with i=H_2, O_2, H_2O). The equation that combines the above irreversibilities expresses the actual cell voltage:

$$V_{cell} = E - V_{act} - V_{ohm} - V_{conc} \quad (7)$$

The above equation is able to predict the voltage output of PEM fuel cells of various configurations. Depending on the amount of current drawn the fuel cell produces the output voltage according to (7). The electric power delivered by the system equals the product of the stack voltage V_{cell} and the current drawn I:

$$P = I \cdot V_{cell} \quad (8)$$

2.3 Mass Balance Equations

The model equations consist of the standard material balance of each component. Every individual gas follows the ideal gas equation. Therefore mass is described through partial pressures of each gas in the material balances:

$$\frac{d}{dt}p_g = \frac{R \cdot T}{V}\left[q_g^{in} - q_g^{out} - q_g^r\right] \quad (9)$$

where R is the universal gas constant (J (kmol K)$^{-1}$)), T is the temperature (K), V is the anode or cathode volume (1). For each gas q_g^{in} is the input flow, q_g^{out} is the output flow and q_g^r is the consumption or production due to the reaction. The same expression is used for oxygen, hydrogen and the produced water by replacing the term g with the corresponding gas. The amount of hydrogen consumed due to reaction is calculated as:

$$q_{H2}^r = \frac{I}{2F} \quad (10)$$

and for the oxygen :

$$q_{O2}^r = \frac{1}{2}\frac{I}{2F} \quad (11)$$

while the water production can be described by :

$$q_{H2O}^r = -\frac{I}{2F} \quad (12)$$

The water production rate is the same as the hydrogen's reaction rate, since water is produces as hydrogen is consumed. The oxygen reaction rate is the half of that of the hydrogen due to the stoichiometry of the reaction. As the load draws current, the reactants become depleted in the fuel cell and partial pressure of oxygen and hydrogen drop accordingly. A common practice to protect the fuel cell from reactants starvation is to supply it with excessive amounts of hydrogen and oxygen.

2.4 Oxygen Excess Ratio

There are two phenomena that can deteriorate or even destroy the fuel cell, flooding and oxygen starvation. Flooding is related to temperature and humidity, which are assumed constant and stable in the developed model since it is a high temperature FC where flooding is rather avoidable. The second one, the oxygen starvation, when it occurs the operation of the FC must be stopped in order to prevent fuel cell malfunction. The lack of oxygen is a complicated phenomenon that occurs when oxygen falls below a critical level at any location within the cathode. This phenomenon entails a rapid decrease in cell voltage, which in severe cases can cause a hot spot, or even burn-through on the surface of a membrane. To prevent this catastrophic event, the system must either remove the current from the stack or trigger a shut-down procedure. For all these reasons in a PEM fuel cell it is considered important to control the amount of available oxygen in the cathode. The air flow needs to be controlled rapidly and efficiently to avoid oxygen starvation and extend the life of the stack [Pukrushpan, 2004]. Although the oxygen concentration is not homogenous throughout the cathode, the control can be achieved by defining a parameter that indicates the oxygen level status in the cathode, named excess oxygen ratio level λ_{O2}. The excess ratio level is an unmeasured but observable variable that can be expressed as the inlet flow q_{O2}^{in} to the rate of oxygen consumption q_{O2}^r :

$$\lambda_{O2} = \frac{q_{O2}^{in}}{q_{O2}^r} \quad (13)$$

As can be observed by (11) and (13) the oxygen excess ratio level depends on the current drawn from the cell. This relationship can cause an abrupt and momentarily drop of the λ_{O2}, while it is related to the fuel consumption High values of λ_{O2}, and thus higher partial oxygen pressure improves the overall power. Low values of λ_{O2} indicate low oxygen concentration that could lead to oxygen starvation. Moreover, the temperature within the fuel cell may rapidly increase when oxygen concentration is too low. Therefore, the oxygen should be replenished quickly as it is depleted in the cathode [Vahidi, 2006].

3. PARAMETER IDENTIFICATION

The dynamic process model described in the previous section is validated using experimental data from a high temperature PEMFC. Nonlinear regression techniques are used to estimate the model parameters. The selected estimated parameters are the following: the parametric coefficient in activation losses (ξ_1) and the parameters in concentration losses (m, n). The characteristic cell voltage and the applied current density were measured through an on-line supervisory control and data acquisition system. Experiments were performed at the single cell system at constant temperatures between 170°C to 200°C. The activation area of the cell is 25cm2. The estimated values of the parameters are presented in Table 1.

Table 1 Estimated parameters

Parameter	Estimated value
ξ_1	-1.771
m	7.04E-05 V
n	9.44 E-03 cm^2 mA

Fig 1 compare the model predictions with the experimental data for various operating temperature levels for the polarization curves Fig 1 reveal that model predictions are in good agreement with the experimental data. As can be observed in the experimental results, a temperature increase raises cell voltage and consequently the fuel cell power output.

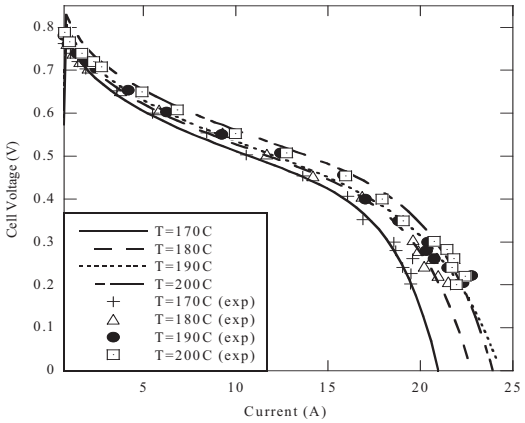

Fig. 1 Model predicted and experimental polarization curves

4. MAXIMUM POWER TARGETING

The power of the fuel cell depends nonlinearly on the applied current. As it is observed from the power curve there exists a unique operating point for each set of operating conditions, where the delivered power reaches a maximum power point (MPP). The operation of the system beyond MPP is not safe and should be avoided. The purpose of the control strategy is to deliver a near optimum power and at the same time to choose the proper operating region to ensure high fuel cell efficiency and avoid oxygen starvation. Thus a MPP tracking algorithm is developed that calculates the highest possible power as operating conditions vary. Fuel cell operation at the MPP is not very beneficial because the corresponding fuel efficiency is at best 50%. [Zhong, 2008]. As illustrated in Fig. 2 there exists an area where the power is near its MPP and the corresponding oxygen excess ratio level guarantees a safe and efficient fuel cell operation. The calculation of the MPP from process measurements is not possible as it depends on numerous factors that change during operation (e.g., relative humidity, gas mole fractions) and furthermore the entire power curve needs to be inferred to identify its maximum. Therefore, the fuel cell mathematical model is used in order to determine a desired trajectory towards the near MPP.

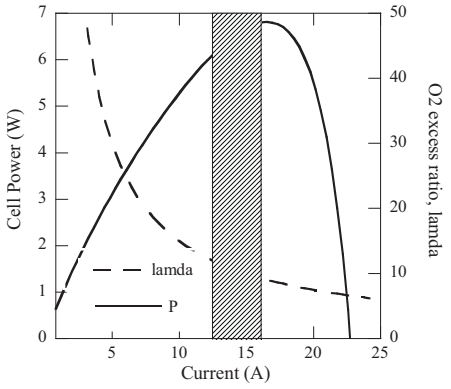

Fig. 2 Power curve and λ_{O2} (lamda) trajectory. Desired area of operation is shadowed.

Numerous methods have been proposed for maximum power tracking such as the perturbation and observe, adaptive extremum seeking algorithm, artificial intelligence methods and model-based methods to name a few [Zhong 2008, Krstic, 2000]. The current approach utilizes the developed non-linear dynamic model to determine off-line the near optimum region of operation and calculate the corresponding oxygen concentration level at the specific operating point usually defined as a function of temperature and pressure. The higher oxygen excess ratio level leads to a safer operation. The resulting strategy aims to an operation where a compromise between the maximum achievable power output and the optimal oxygen excess ratio is sought.

5. MODEL PREDICTIVE CONTROL FRAMEWORK

A Model Predictive Control (MPC) framework is formulated for the satisfaction of the control objectives described in the previous section. The fuel cell system presents a number of control challenges, the most significant of which is the nonlinearity in the area of the maximum power. Also an important control objective is the effective regulation of the oxygen concentration in the cathode. Furthermore, it is of interest to ensure safe operation during transients and sudden load changes. MPC is able to satisfy multiple control objectives under the presence of changes in process characteristics. Another important feature is its ability to deal with constraints. When a fuel cell operates near the MPP and consequently close to its operation limits constraints violations are critical in the achieved control performance.

5.1 Anode and Cathode Pressure Control

To regulate the anode and the cathode pressure a fast proportional-integral (PI) controller is implemented as used in the real system. The conventional PI controllers are used independently of the MPC scheme, which assumes that the anode and cathode pressure is held at a constant level as the dynamics of the PI control system are relatively fast. In the performed experiments it is assumed that the cathode and anode pressure is at 2 barg. These secondary loops are tightly controlled and assumed not to interact with the main control objectives of the system.

5.2 Model Predictive Control

Model predictive control (MPC) is part of a family of optimization-based control methods, which are based on on-line optimization of future control moves. Also MPC is based on the fact that past and present control actions affect the future response of the system. Using a process model, the optimizer predicts the effect of past inputs on future outputs. The deviation of the model prediction from the actual response is recorded and considered as the error of the process model, as shown in the block diagram of the MPC framework. The calculated error defines a bias term that is used to correct future predictions and it is constant for the entire prediction horizon. The block diagram describing the MPC scheme and the near optimum power targeting scheme is illustrated in Fig. 3.

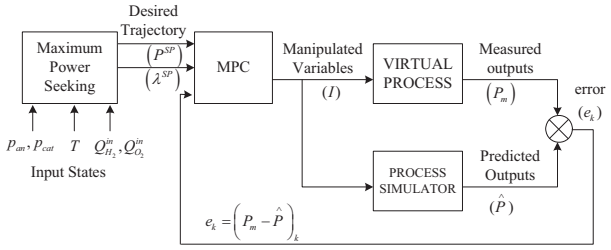

Fig. 3 Block diagram of the MPC control framework

The control structure utilizes two instances of the aforementioned dynamic model; the one corresponds to the Virtual Process (VP) and the second one to the Process Simulator (PS) or Model, and they are concurrently executed. Successive iterations between the optimizer, that evaluates the optimum value for the manipulated variable, and the model, that calculate the response of the process to the imposed control action are performed. The mathematical representation of the MPC algorithm is as follows:

$$\min_{k+j-1} J = \sum_{j=1}^{Np} \left\| \hat{P}_{k+j} - P_{k+j}^{SP} \right\|_{w_P}^2 + \left\| \hat{\lambda}_{k+j} - \lambda_{k+j}^{SP} \right\|_{w_\lambda}^2 \quad (14)$$

Subject to :

$$e_{k+j-1} = \left(y^{meas} - y^{pred} \right)_{k+j-1}, \; y_k = P_k \quad (15)$$

$$\hat{y}_{k+j} = y_{k+1}^{pred} + e_{k+j-1} \quad (16)$$

$$N_c = (T_c - T_k) / \Delta t_c \quad (17)$$

$$N_p = (T_p - T_k) / \Delta t_p \quad (18)$$

Where vectors $\hat{P}_k^{SP}$ and $\hat{\lambda}_k^{SP}$ denotes the desired response trajectories. The difference e_k between the measured variables y^{meas} and their predicted values y^{pred} at time instance *k* is assumed to persist constant for the entire number of time intervals N_p of the prediction time horizon T_p. While T_c denotes the control horizon reached through N_c time intervals. Also this minimization is subject to constraints on the manipulated and controlled variables:

$$I_{\min} \le I_{k+j-1} \le I_{\max} \quad (19)$$

$$\lambda_{O_2,\min} \le \lambda_{O_2} \le \lambda_{O_2,\max} \quad (20)$$

Eq (19) imposes a constraint to the input variables that corresponds to their physical limits. Eq (20) imposes a constraint on lamda to avoid starvation. Tuning parameters of the algorithm are the weight factors in the objective function (w_p, w_λ) and the length of the prediction and control horizon. The selection of the appropriate prediction horizon is mainly dictated by the time scale characteristics of the system. The computational time to reach a solution of the nonlinear dynamic program may affect the duration of the control interval.

6. SIMULATION RESULTS

The performance of the proposed MPC framework is evaluated through a number of simulated examples for a high temperature PEMFC. In all cases, unless otherwise stated, the system operates at constant temperature ($T_{sim} = T_{process} = 180^\circ C$) and constant cathode pressure ($p_{an} = p_{cat} = 2\text{barg}$). The influence of the controller tuning parameters on the closed-loop performance of the MPC is investigated. The main parameters are the control and the prediction horizons and the weighting factors of the power and oxygen concentration terms. Both prediction and control horizons were chosen equal to 15 seconds while the intervals of the control actions were chosen equal to 5 seconds. The length between two consecutive control actions (Δt_c) was selected according to the required computational time of the optimization problem.

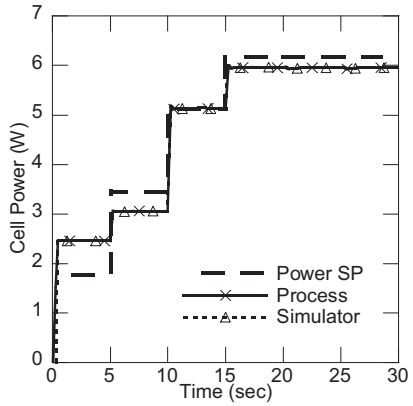

Fig. 4 Power response with unequal weights $w_p = 0.8,\ w_\lambda = 0.2$

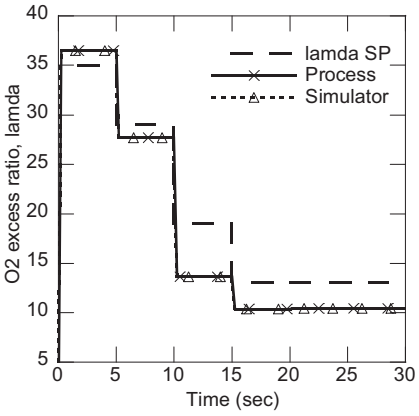

Fig. 5 Oxygen excess ratio level with unequal weights $w_p = 0.8,\ w_\lambda = 0.2$

Fig 4-7 show the sensitivity of the MPC performance on the weighting factors in the objective function. In the first case (Fig 4-5) more importance is given on the tracking of the power output while in the second case (Fig 6-7) an equal importance to both control objectives is imposed. In both

cases the desired setpoints were followed satisfactorily. However, in the first case excess O_2 is quite low which may cause difficulties in the fuel cell operation (i.e. oxygen starvation). The power output offset is small in the first case where a larger weight is used for the power output difference term. A better compromise is achieved in the second case with the excess oxygen closer to the desired level.

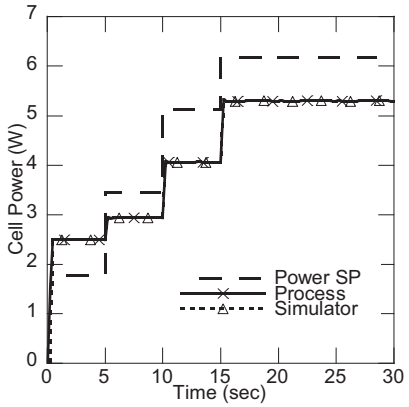

Fig. 6 Power response with equal weights $w_p = 0.5,\ w_\lambda = 0.5$

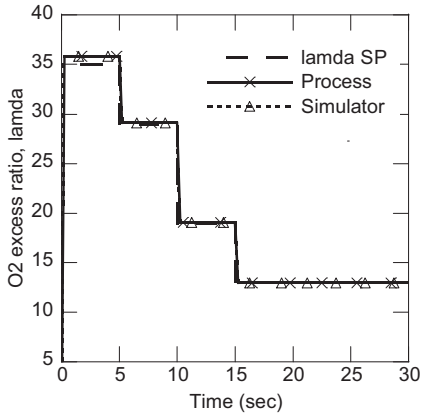

Fig. 7 Oxygen excess ratio level with equal weights $w_p = 0.5,\ w_\lambda = 0.5$

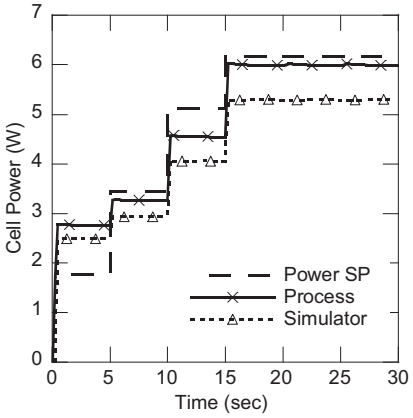

Fig. 8 Power response with altered process temperature

In another case study (Fig 8), significant mismatch in the fuel cell temperature between the Virtual Process and Process Model ($T_{sim} = 180^{\circ}C, T_{process} = 140^{\circ}C$) is deliberately introduced in order to asses the robustness of the proposed strategy to a significant disturbance. Fig. 8 illustrates the ability of the nonlinear MPC scheme to compensate for the temperature variation and successfully satisfy the control objective by close tracking of the desired power output level. The application of the constrained MPC framework allowed for an accurate targeting of the desired oxygen concentration and was able to give a near maximum power.

7. CONCLUSIONS

In this work a dynamic model for a high temperature PEM fuel cell stack based on single cell was developed and an advanced constrained predictive control framework was implemented. Having tested and verified some selected operational parameters a reliable MPC scheme was resulted. The MPC framework that combines two contradictive operational objectives, can safely lead to an operation that maximizes the power of a given size FC. The proposed MPC will be implemented and verified in the experimental fuel cell system. In order to improve the overall efficiency and safe operation, the controller would further include mathematical models for the auxiliary subsystems.

REFERENCES

Bordons Carlos, et. al (2006), Constrained Predictive Control Strategies for PEM fuel cells, *Proceedings of the 2006 ACC*, Minnesota, USA, June 14-16, 2486-2491

Jensen Jens Oluf, et al. (2007), High temperature PEMFC and the possible utilization of the excess heat for fuel processing, *International Journal of Hydrogen Energy*, 32 2007, 1567 – 1571

Golbert J., Lewin, D.R. (2007) Model-based control of fuel cells: optimal efficiency, *Journal of Power Sources,* 173 (1), 298-309

Krstic M., H.-H. Wang (2000), Stability of extremum seeking feedback for general nonlinear dynamic systems, *Automatica*, 36 (4) 2000, 595–601

Larminie J, Dicks A. (2003), *Fuel Cell Systems Explained*, 2nd Edition, John Wiley & Sons Ltd

Mann Ronald F., et. Al (2000), Development and application of a generalized steady-state electrochemical model for a PEM fuel cell, *Journal of Power Sources*, 86,173–180

Pukrushpan J., et. al (2004), Control of Fuel Cell Breathing, *IEEE Control Systems Magazine*, 0272-1708/04, 30-46

Vahidi A., et. al (2006), Current Management in a Hybrid Fuel Cell Power System: A Model-Predictive Control Approach, *IEEE Transactions on Control Systems,* vol. 14, no 6 2006, 1047-1057

Zhong Zhi-dan, et. al (2008), Adaptive maximum power point tracking control of fuel cell power plants, *Journal of Power Sources*, 176 2008, 259–269

Design of an Adaptive Self-Tuning Smith Predictor for a Time Varying Water Treatment Process

Khaled Gajam*, Zoubir Zouaoui,**
Philip Shaw*, Zheng Chen******

**Engineering Department, Glyndwr University, Mold Road, Wrexham, LL11 2AW, UK (e-mail: khaledgajam@hotmail.com)*
***Engineering Research Centre, Glyndwr University, Mold Road, Wrexham, LL11 2AW, UK (Tel. +44-1978-293151; e-mail: z.zouaoui@glyndwr.ac.uk)*
****United Utilities PLC, Huntington WTW, Chester Road, Huntington, Chester, CH3 6EA, UK (e-mail: philip.shaw@uuplc.co.uk)*
*****Engineering Research Centre, Glyndwr University, Mold Road, Wrexham, LL11 2AW, UK (e-mail: z.chen@glyndwr.ac.uk)*

Abstract: This paper presents the simulation and real time implementation of an adaptive predictive PI controller for the control of Chlorine dosing in secondary water disinfection rigs. This trial is part of a project that looks at the optimisation of process control specifically in the water industry. As one of the main treatment processes, Chlorine dosing is one of the processes that naturally imposes very long dead times for the controller to deal with. Although PI controllers are still commonly used for controlling this process, previous literature as well as trials carried as part of this project proved that the performance of PI controllers, no matter how tuned they are, is very sluggish and unreliable. A pilot rig was used instead of a live secondary disinfection rig, and a number of open loop step tests were performed for system identification. Once the process dynamics became known, complementary functions that estimate the process transfer function based on the water flow were introduced. A standard tuned PI controller configuration was simulated for the process, and then a Smith predictor was used in order to be able to compare the performance of the predictive PI with a standard PI controller. Tuning functions were derived for the PI to make it a self-tuning predictive controller, and parameter estimation functions were also used so that the final outcome is an adaptive self-tuning system. This system was then implemented on the same pilot rig, and real time implementation proved the findings obtained from the simulation. Both simulation and pilot rig tests show a very good dynamic response with excellent accuracy.

Keywords: Water process control; Chlorine dosing; PI tuning; Smith predictor; adaptive self-tuning.

1. INTRODUCTION

Process dead time is one of the most challenging issues in process control system design, as it makes the process difficult to control using standard feedback techniques mainly because the control action takes some time affect the controlled variable, and therefore the control action that is applied based on the actual error tries to correct a situation that originated some time before [1]. There can be several causes of this time delay, but in most process industries, the delay is caused by mass or energy transportation (also known as transport delay).

Processes with long dead times can not often be controlled effectively using a simple PI/PID controller. This is because the additional phase lag caused by the time delay tends to destabilise the closed loop system. The stability of such system can be improved by decreasing the controller gain, but that will certainly slow the controller down and make the response very sluggish [2]. Most water treatment processes incur relatively long transport delays, simply because the process variable is controlled by the addition of certain chemicals where a reaction time (Time taken for the chemical to dissolve/react in water) is to be allowed before the process variable can be sampled. It therefore, becomes part of the design requirements to allow enough distance between the chemical dosing and sampling points, and the time delay is then a function of the water flow within this distance as well as the flow in the sample line. A valid estimation of the delay may be expressed as:

$$Td = V/Q \quad (1)$$

Where Td is time delay, V is the volume of the pipe work between the dosing and sampling points, and Q is the water flow rate through the pipe. Another element that may have to be considered is the delay that might be caused by the sample line unless this delay is much smaller than the time delay caused by the pipe work. Previous research showed that PI controllers have been used to control dead-time processes, and the performance was acceptable when the dead time was small, but the performance deteriorates as the dead time increases, and in such cases a significant amount of detuning is required to maintain closed loop stability [5, 6].

2. THE CHLORINATION PROCESS

This research project focused on the implementation of predictive control for time varying water treatment processes that can generally be represented by a first order plus dead time (FOPDT) transfer function. Chlorine dosing is one of the essential treatment processes in most treatment plants as Chlorine is the most commonly used disinfectant and has been for the last hundred years [4]. The disinfection process takes place mainly in the main treatment plant, but there are usually secondary disinfection points spread around the distribution network in order to ensure that water provided to customers is microbiologically safe. Chlorine has many advantages that make it a more desirable disinfectant to use than other disinfectants (e.g. Ozone), but there are also disadvantages on using Chlorine. One of the main concerns in using Chlorine as a disinfectant is the formation of disinfection by products (DBP). Chlorine reacts with natural organic matter in water to form DBP's, and researchers are becoming increasingly concerned about the health problems those products can cause. A trade-off between the protection from infectious diseases and limiting exposure to DBP's has to be considered when using chlorine as a disinfectant [4]. This highlights the sensitivity of the Chlorination process, and the importance of having a reliable accurate control system to ensure that the amounts of Chlorine dosed in drinking water is what is needed.

3. PARAMETER ESTIMATION

The process described here is implemented on a pilot rig to study the effects of time varying processes on the performance of the controller. The advantage of using this pilot rig is the flexibility it gives in terms of controlling the parameters defining the dynamics of the process (i.e. water flow, pressure, and incoming Chlorine residual). These parameters have a direct impact on the process transfer function, and are normally hard to control in live disinfection rigs as they depend on water consumption by consumers.

Open loop step tests were performed at various flow rates and repeated several times. As expected, the variation of flow affected the dead time and the process time constant. Theoretically the dead time can be calculated using equation (1) provided that the precise volume of the pipe work as well as the precise flow rate are both known. Because of the relatively small size of the rig where even small inaccuracies in either the flow or the volume would affect the estimated process parameters, it was necessary to estimate the dead time using the open loop step test results. Figure 1 shows the relationship between the water flow rate and the process parameters.

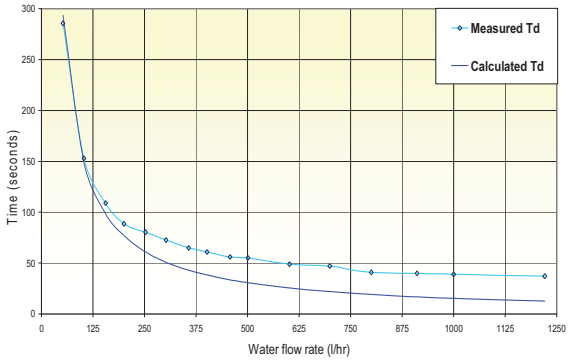

Fig. 1. Calculation and measurement of process dead time in relation to water flow rate.

It can be clearly noticed that at low flow rates, the measured dead time is almost identical to the calculated values, but as the flow increases beyond the lower 10% of this trial's flow range, the decrease in process dead time is not as expected. This highlights the importance of using real time data analysis when optimising the control system in this application.

4. PROCESS SIMULATION

Based on the open loop step test results, a model was built to represent both the process and the PI controller as implemented in most water treatment processes. Most chemical dosing process in water treatment use feedback plus feed forward control in a layout known in industry as Flow paced plus trim (Compound) control. The idea here is to combine the outputs of the feedback controller (usually a standard PI controller) and the feed forward controller (a gain element that is proportional to the water flow rate) in what will become the manipulated variable. In an ideal case, the feed forward controller output should keep the process variable equal to or very close to the set point. However, due to offsets in the dosing and measurement equipment, mismatch between the nominal and actual Chlorine strength, as well as the usual possibility of Chlorine presence in the incoming water, the feed forward controller will have to be supported by a feedback controller to act as a final trim and make up for all existing offsets.

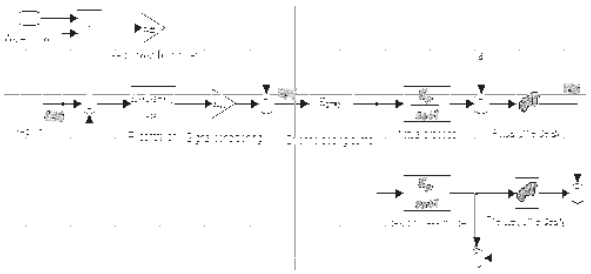

Fig. 2. Layout of Chlorine Dosing control loop.

A Smith predictor layout is shown in figure 2 combined with the PI controller and a proportional flow pacing function for feed forward control. The two main disturbances that can affect the process are the variation of water flow over time, and the incoming residual to the process. Many secondary disinfection rigs are installed on varying flow lines, where the flow rate changes over time by a ratio of up to 1:8. Therefore, it's important to consider the effect such big changes will have on the transfer function of the process, especially on the dead time of the process. Figure 3 shows a plot of real time data collected over a week from a time varying secondary dosing rig that is controlled by a PI controller.

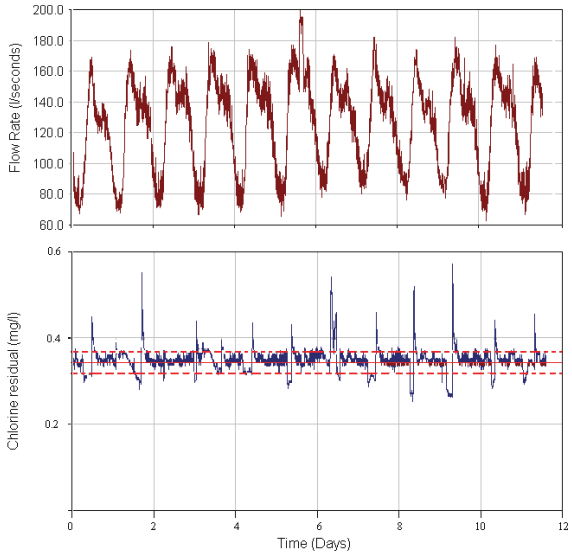

Fig. 3. Effect of time varying flow on the process variable (Chlorine residual).

The plot in figure 3 shows a clear link between changes in the water flow rate and variation in the Chlorine residual. Ideally, the Chlorine residual is supposed to remain within the band defined by the dashed lines for 99 % of the time for the system performance to be considered acceptable. Open loop step tests proved that the process time constant is also affected considerably by significant changes in the water flow rate. It is, therefore, obvious that in real applications, the practical approach would be to design a controller that will compensate for the inherent long dead times, and that will also be robust enough to the two major disturbances (i.e. Water flow rate changes, and incoming residual). For processes that are not time varying or where the variation is not that significant, PI controllers could produce what can be considered an acceptable performance. The more realistic scenario is the process where either one or sometimes all disturbances are significant, and that was the focus of this trial. The model in figure 2 was simulated. The process gain, time constant and dead time were all replaced with functions of the water flow rate that would make this an adaptive predictive controller. All the other gains are representative of the actual dosing and flow pacing constants. Figure 4 shows the closed loop step response of the simulated Smith predictor.

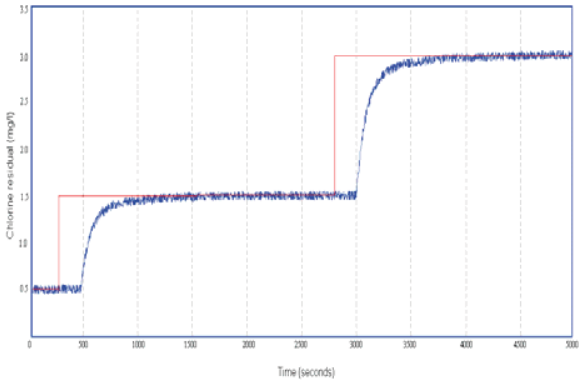

Fig. 4. Closed loop response of a simulated Smith predictor.

As mentioned earlier, the process parameters are flow dependent. A relatively low flow rate of 100 l/hr was chosen here to be able to simulate a challenging operational condition compared to a fast process. The above response shows that the controller performs well at set point tracking, and that accuracy and stability are maintained. The speed of response of the controller to the step changes is also very good considering the fact the dead time in this particular case was around 3 minutes. The same process model was simulated in closed loop using a standard PI controller that was also tuned using the same method that was used to tune the Smith predictor. It was noticed that at low flow rates, the dynamic response exhibits large un-damped oscillations as shown in figure 5.

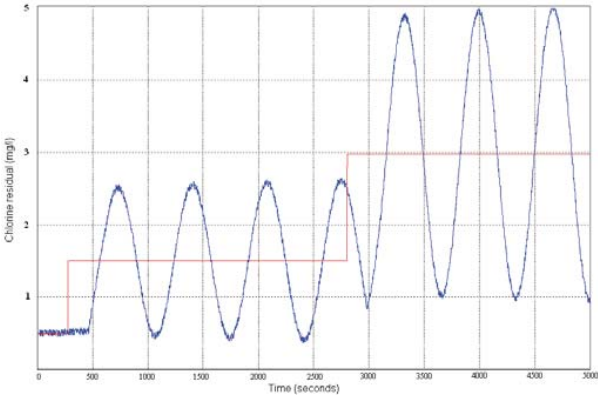

Fig. 5. Performance of a standard PI controller for a relatively long dead time process.

PI controllers are still being widely used in such processes. The only explanation as to why they are still being used is that in most cases the controller gain will be kept at a minimum value that is enough to allow the controller to track large process variable offsets, but at a very low speed of response. In a particular real time test on a live dosing rig, the response to a closed loop step test using a standard PI controller with a low gain took more than four hours to be completed due to the sluggish response of the controller.

5. IMPLEMENTATION AND TESTING

The water industry like most other process industries uses a combination of conventional analogue (4 – 20 mA) instruments and actuators with digital control PLC's, which nowadays have the resolution that allows them to control continuous processes. That said, PLC's still have their limitations when it comes to the implementation of advanced control methods as they seem to lack some important functionalities needed for continuous process control. It was also noticed with this particular application that offsets in the analogue modules interfacing between the PLC and the equipment (water flow meter, Chlorine analyser, and Chlorine dosing pump) can either exaggerate or dampen signals to and from the controller respectively. It is therefore important to obtain a process model that is a valid representation of the actual process so that the effect of the above mentioned offsets will be minimal; otherwise, those offsets will add to the uncertainties caused by the mismatch between the actual process and the process model and make the control system design process much more complicated.

The control algorithm was written in PLC ladder logic. Therefore, all continuous functions and the process model had to be written in that form. The dead time was then implemented using a data array that stores data in sequence at a frequency that is equal to the process sampling frequency, and the length of this array is equivalent to the predicted process dead time. To be able to test the Smith predictor for different flow rates, the control algorithm included functions to calculate the process parameters from online water flow rate measurements, and update the process model as well as the length of the delay array accordingly. There is also a tuning routine that uses the minimisation of the Integral of Absolute Error (IAE) tuning method to calculate the PI parameters (Kc and Ti). Many tuning methods have been suggested for Smith predictor applications, and many of them seem to have produced a robust performance [3, 5-8]. The following equations provide a good starting point for the minimum IAE method which is used to obtain the optimum PI parameters:

$$Kc = 0.984/Kp*(\tau/Td)^{0.986} \quad (2)$$

$$Ti = \tau/0.608*(Td/\tau)^{0.707} \quad (3)$$

Where Kc is the controller gain, Kp is the process gain, τ is the process time constant, Td is the process dead time, and Ti is the controller integration time. To make the controller self-tuning, these formulae were written in the control algorithm, and as part of the cyclic scan sequence, the PLC would calculate the process parameters based on the online flow rate measurement, then calculate the PI parameters as shown above and update them in the PI controller function block instantly. The following plot of real time data of closed loop step tests of the Smith predictor as explained above also shows the effect of sudden variation in the water flow rate on the process:

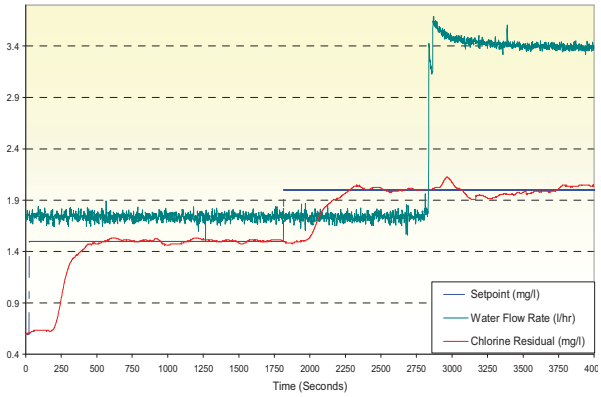

Fig. 6. Setpoint tracking performance of the Smith Predictor and its response to a major (Flow rate) disturbance.

The response achieved here conforms to the simulation results in terms of setpoint tracking, stability of the system, and the speed of its response. Also, the disturbance caused by the change in water flow rate did not have a significant effect on the process dynamics. The same test rig was used to test the same process under the same operating conditions using just a tuned PI controller in order to compare it to the performance of the Smith predictor, and the response is shown below.

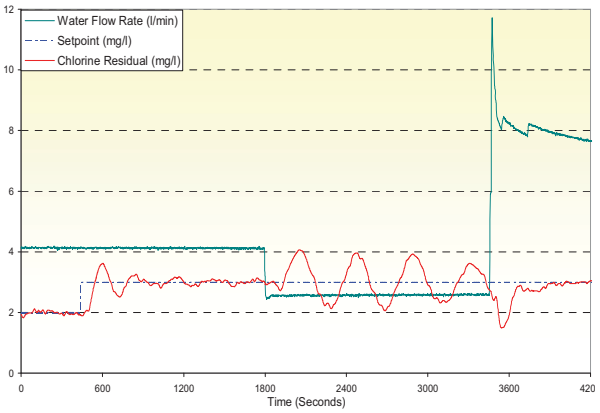

Fig. 7. Performance of a PI controller at various water flow rates.

The controller here was tuned well enough to produce an acceptable performance at a medium flow rate of 4.2 l/min, but when the flow was reduced to about 1.7 l/m, the controller became incapable of keeping the process variable at steady state until the flow was increased to a much high rate, where the controller slowly tracked the setpoint. Retuning the controller at this flow rate, would produce a faster response than the response shown, but at the low flow rate, the only option was to detune the controller (by keeping the controller gain as low as possible) so that it will respond to the step input, but at a relatively low speed of response, and hence not causing the oscillations seen in figure 7.

It is important to emphasise that without an accurate process model, the Smith predictor performance deteriorates. During this trial, initially the dead time was under estimated by around 20% and as a result the controller reacted earlier than required causing an overshoot in the Process variable of nearly 15%.

6. CONCLUSION

Simulation of PI controllers on FOPDT processes shows that the performance of the PI controller is dependent on the process dead time. In this trial the PI controller was found incapable of handling very long time delays regardless of the method used to tune it. The Smith predictor provides a reliable solution as long as the process model used is an accurate estimation of the actual process. In challenging process control applications where the process is time varying, adaptive Smith predictor configurations can be used effectively to overcome the uncertainty caused by the changes in process dynamics. Simulations and practical tests have shown that this method can be implemented successfully in water treatment processes.

REFERENCES

[1] Normey-Rico, J., & Camacho, E. (2008). Dead-time compensators: A survey. *Control Engineering Practice*, 16, 407-428.

[2] Kaya, I. (2002). A new Smith predictor and controller for control of processes with long dead time. *ISA Transactions*, 42, 101-110.

[3] Nortcliffe, A., & Love, J. (2003). Varying time delay Smith predictor process controller. *ISA Transactions*, 43, 61-71.

[4] Galal-Gorchev, H. (1996). Chlorine in water disinfection. *Pure & Appl. Chem.*, 68(9), 1731-1735.

[5] Guzman, J. L., Garcia, P., Hägglund, T., Dormido, S., Albertos, P., Berenguel, M (2007). Interactive tool for analysis of time-delay systems with dead-time compensators. *Control Engineering Practice*, 16, 824-835.

[6] Ingimundarson, A., & Hägglund, T. (2002). Performance comparison between PID and dead time compensating controllers. *Journal of Process Control*, 12, 887-895.

[7] Normey-Rico, J., & Camacho, E. (2008). Unified approach for robust dead-time compensator design. *Journal of Process Control*, 19(1), 38-47.

[8] Kaya, I. (2003). Obtaining controller parameters for a new PI-PD Smith predictor using autotuning. *Journal of Process Control*, 13, 465-472.

MODEL PREDICTIVE CONTROL OF A CRUDE DISTILLATION UNIT AN INDUSTRIAL APPLICATION

Serdar Kemaloğlu Emre Özgen Kuzu
Dila Gökçe Özgur Çetin

Turkish Petroleum Refineries Corporation, Izmit 41780
Turkey

Abstract: This paper reviews the application of a model predictive controller algorithm to a crude oil unit in Izmit Refinery of Turkish Petroleum Refineries Corporation as a summary of nearly eight months of practical study. The controller is designed to control the crude heating via process flows followed by furnace heating and distillation column with product strippers. After a process overview, the fundamental control loop considerations are discussed. Steps of determining inferred qualities and step test response tests are outlined. The controller design considerations, constraint handling and economic variables are presented. Finally, a comparison of before and after commissioning in the kerosene quality and rate is tabulated as well as simulation results of the system response for different set point changes in the product qualities.

Keywords: Advanced process control, multivariable predictive control, crude distillation processes, model identification.

1. INTRODUCTION

Model predictive control (MPC) strategies have found a wide range of applications from refineries to food processing and become a standard control algorithm for process industries. In 1999 nearly five thousand applications were reported with an increase of about 80 % in the following years (Qin and Bagdwell, 2003). MPC algorithm utilizes an explicit process model to optimize an open loop performance objective to constraints over a future time horizon, based on current measured variables and the current and the future inputs (Rossitier, 2003).

Turkish Petroleum Refineries Corporation (TUPRAS) is the largest industrial enterprise in Turkey. TUPRAS controls all of Turkey's refining capacity with operating four refineries with a total annual process capacity of 28.1 million tons crude oil. TUPRAS Izmit Refinery is the biggest refinery of four with annual refining capacity of 11.0 million tons of crude oil.

After privatization in 2006, implementation of advanced process control (APC) applications were initiated to increase operational excellence with many other projects. In this paper, an APC application to one of the crude units in Izmit Refinery is presented. After the process overview, base layer control strategies developed to sustain healthy layer for APC studies are explained. The main elements of the controller, controlled, manipulated and disturbance variables are discussed. Following the methods for obtaining inferred qualities, response tests and dynamic modelling strategies are outlined. The dynamic models obtained during tests are used in the commercial MPC algorithm SMOCPro. The control strategies, economic concerns and commissioning issues are discussed in the Section 4. The results of the commissioned plant data is tabulated as well as simulation of the controller for different set point changes in product qualities.

It is desired to give an outline of an industrial MPC application, but also some practical issues on implementation details. Finally, Section 5 outlines the study.

2. PROCESS OVERVIEW AND BASE LAYER CONTROL STRATEGIES

Plant-5 is one of the three crude oil units in TUPRAS Izmit Refinery and its simplified flow diagram is depicted in Figure1.

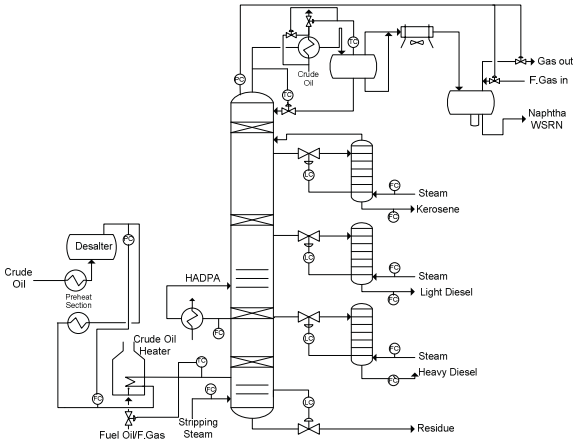

Fig. 1. CDU layout

The crude unit consists of mainly five operations. Advanced control strategies of steps 1,2 and 3 are in the scope of this paper:

1. Before and after desalter operation, the crude is heated via the hot streams available in the plant.
2. The crude is heated at a temperature around 320-350 ºC in two parallel furnaces.
3. The heated crude oil is distilled into products. Kerosene, light diesel and heavy diesel are drawn off after strippers. The bottom product, residue, is the feed to the vacuum unit.
4. The upstream of distillation column, a mixture of LPG, light straight run naphtha and heavy straight run naphtha, is fed to the naphtha splitter column where LPG and light naphtha are separated from heavy naphtha.
5. The liquid product of naphtha splitter upstream is separated into light naphtha and LPG in the debutanizer column.

Before implementation of advanced process control algorithm, a preliminary study comprising a base layer PID-based control is running successfully in normal operation. This study includes check of all instrumentation, checking for sticky valves, process feedback effects, process interactions, noisy measurements, retuning of PID controllers and possible configuration changes in the control strategies. In this scope, 56 regulatory PID controllers were retuned before starting testing.

Two base layer enhancements were carried out in distillation column control. There has been no bottom flow controller in the distillation column. Operators would manipulate the residue flow manually to keep level at operating ranges. This resulted continuous monitoring by operators and also discrete sudden changes in residue flow, which is the feed of vacuum unit as well. In the reviews, a new base layer of a level controller cascaded to the bottoms flow controller is implemented. With an appropriate tuning, the level is controlled while the bottoms flow does not vary significantly to create big disturbances to the vacuum unit.

The overhead drum temperature was manually controlled via bypassing from crude oil preheat heat exchangers at above 102 ºC to avoid corrosion problems. A new temperature controller has been implemented that closes the bypass valve in the line directing overheads product through the overheads cooler / crude preheat exchange.

3. CONTROLLER DESIGN

3.1 Variables

At the beginning of an APC project, the controller design requires selection of manipulated (MV), disturbance (DV) and controlled (CV) variables. These variables in this project:

- 28 manipulated variables are considered, 17 of which are for preheat and 11 for crude distillation column. These manipulated variables are feed flow controllers, furnace coil flow controllers and distillation column pressure, temperature and flow controllers.
- 3 disturbance variables are selected; amount of total feed and inlet flow rates to two furnaces.
- 19 controlled variables, where 4 variables are in preheat section and remaining in the crude distillation column.

Controlled variables for preheat section are desalter temperature and pressure and furnace outlet temperatures for the preheat section.

Some key variables are tabulated in Table 1 at the end of the paper. Distillation column controlled variables can be classified in three categories; inferred qualities, variables of economic importance and operational constraints.

The inferred qualities are the four main product qualities, heavy naphtha, light diesel and heavy diesel 95% distillation points and kerosene flash point. In order to control these qualities, inferential measurements have been developed. All the qualities have been inferred based on statistical regression of empirical data. The data was collected during a test period of two weeks, where manipulated variables and important column dynamics were changed one by one and held constant for two to three hours, while subsequent lab results were gathered. This data was used as a training period and inferential measurements were modelled using RQE Pro, software in the Process Control Technology Package (PCTP) of Shell Global Solutions International BV. Various combinations of process variables were regressed and good fits were achieved. Regular laboratory data of nearly eight months was also used to validate the model. The inferred qualities are mainly functions of pressure compensated temperatures. In some cases, vapour / liquid ratio below the draw-off tray of the product of which the quality was to be inferred. In the online application, the inferred qualities' equations' biases are updated with regular laboratory results. Before defining these qualities as a CV to the controller, several lab results were introduced to obtain a healthy estimation. These results correct any prediction error in the calculation that might arise in a local problem occurred during tests. Reducing the laboratory analysis amount after a certain period is another advantage of this method. Also in the online application, sudden change in bias may result in a change in the predicted quality, hence an aggressive MV output. To overcome this local disturbance, a filter time of thirty minutes to one hour has been applied to smoothen the update mechanism.

Operational constraints are usually the design specifications. Controlling column pressure valve opening prevents any loss of gas during operation. Reflux and heavy diesel pump around amount and top drum level as a CV sustains a safe operation. The level in the strippers is a major constraint where light diesel stripper level can be operated successfully to only a certain amount and is the main drawback of the light diesel amount.

Although they are not a part of the controller, reducing stripping steam amount and transferring the maximum heat from heavy diesel pump around are two economically beneficial CV's. The controller controls the stripping steam / feed ratio and heavy diesel inlet/outlet temperature difference multiplied by heavy diesel pump around amount at certain ranges.

3.2 Response Testing

During the commissioning of a predictive controller, testing and modelling efforts can take up to 90 % of the cost and time (Andersen and Kummel, 1992). Successful modelling engenders controller stability and performance on the predictive capability of the process model used. The most important element of a good modelling is the high quality clean data obtained form response testing. Also it should be noted that data analysis and model identification enhances process understanding and behaviour.

In the APC application in TUPRAS Izmit Refinery crude distillation unit, the response tests were carried out for three weeks in two shifts. For each of the 28 manipulated variables, tests were carried out separately in sequence, groups of six to eight steps were made in each. The sequence was repeated afterwards, obtaining a test data of sixteen to twenty moves for each variable. Repeating sequence allows preventing unmeasured disturbances that might happen in one of the sequences. The step sizes were defined in a way to see clear effects in the other variables, and steps were held for periods of one to one and a half of the settling time. The step sizes were changed sometimes to identify the presence of nonlinearities.

During step testing, it is very important to carefully observe the steps. The correlation of the independent variables, possible operator interventions and insufficient move sizes may result in poor data, hence poor modelling. Good signal-to-noise ratio enables that the effects of test changes in inputs could be clearly visible in process outputs. To overcome possible operator interventions, trainings were carried out before start of tests. Also changes in the regulatory configuration, PID tunings and possible controller saturations must be prevented during the test period.

3.3 Dynamic Modelling

Majority of industrial MPC applications use linear empirical models (Qin and Bagdwell, 2003). While analyzing the plant data, such an empirical dynamic process-modelling tool, AIDAPro –another PCTP software- was used. The results of step tests were analyzed and mathematically fit to obtain predictive process models.

In dynamic modelling, the interactions of all variables are taken into account, hence the effect of intermediate variables and disturbances can be tolerated in identification. Basically, multivariable higher order parametric models were created for each variable. These models are then approximated and reduced to a parametric model on individual relationship basis of two variables. Based on the data analyzed, the process knowledge and step test experience dynamic response of the variables are determined. Numerical representation of these dynamic response curves can be of any degree from first order zero gain to second order beta.

During modelling 31(28 manipulated and 3 disturbance variables) X 19 response curves were fitted. Of these 589 possible independent / dependent variable response curves, 53 responses are identified for the controller design. The other responses are either zero gain or insignificant.

4. CONTROLLER COMISSIONING

4.1 Controller Design

The dynamic models from observed plant data were used to design the controller. Shell Multivariable Optimizing Controller, SMOCPro is used to implement predictive controller in TUPRAS Izmit Refinery Crude Unit. SMOCPro, a part of the Process Control Technology Package (PCTP) of Shell Global Solutions International BV, and its algorithm was summarized by Qin and Bagdwell (2003) :

- An explicit disturbance model described the effect of unmeasured disturbances; the constant output disturbance was simply a special case,
- A Kalman filter was used to estimate the plant states and unmeasured disturbances from output measurements,
- A distinction was introduced between controlled variables appearing in the control objective and feedback variables that were used for state estimation
- Input and output constraints were enforced via a quadratic program formulation

As well as most advanced process control algorithms, SMOC algorithm also follows a reference trajectory by the future outputs on the prediction horizon and penalizes the control effort on the control horizon. General objective function of the controller can be written as

$$\min_{\Delta u(n)\ldots\Delta u(n+C-1)} \sum_{i=1}^{P} \left\| \hat{y}(n+i) - r(n+i) \right\|^2 w_1 + \sum_{j=1}^{C} \left\| \Delta u(n+i-1) \right\|^2 w_2 \quad (1)$$

in which 'u' represents inputs, 'y' is used to define outputs and the superscript ^ denotes the predicted values. Δu is the input variation and r is the reference trajectory of the outputs. In this optimization problem, the first term is used to minimize the error resulting from the difference between predicted outputs and reference trajectory during prediction horizon, P. The second term is the difference of control actions taken at each time step during control horizon, C. Weighting matrices w_1 and w_2 are positive definite matrices, with different magnitudes for all MV's and CV's. These matrices were used in controller tuning. The optimal input sequence's only first input is implemented to the system and the calculations are re-executed in the next sampling time.

The controller was tuned in offline program with simulations. While simulating both control considerations and economic variables, discussed in the next part, were considered.

Increasing w1, CV weights, increases the priority in decreasing the deviation in set point and reference trajectory, in other words makes the control tighter. Low w1 values allow bigger trade-offs. Increasing w2, MV weights, prioritizes minimum input variation and results in smoother moves.

As a base decision, the weights for column pressure, column top temperature and furnace outlet temperature controllers were given higher values than other MV's. The controller was expected to move these MV's smoother. CV weights for kerosene flash point, heavy diesel 95 % distillation and level of light diesel stripper were set higher than other weights to sustain tighter control. The weight tunings were completed by evaluating simulations.

4.2 Economic Variables

A key factor of SMOCPro is the economic function. Economic function is a bilinear function that the controller minimises. As long as the control objectives are met, the controller drives the defined economic function to minimum. Economic function in crude distillation unit consists of:

- Minimizing column top temperature, column pressure and stripping steam ratio to the feed
- Maximizing heavy diesel pump around duty, product draws to stripper level constraints and furnace heater duties. Maximizing the amount of heavy diesel by letting heavier cuts into heavy diesel and leaning to high limit. Maximizing the amount of kerosene by letting heavy naphtha into kerosene and approaching to low limit.

The constants of elements of economic function can be changed based on the plant needs or operational conditions.

4.3 Commissioning and Online Tuning

The controller was commissioned over a three- week period. The controller tunings determined in the offline studies were rechecked to prevent any model-process mismatch. After sustaining successful control, economic variables were commissioned by extending / restricting the limits. Operator trainings were also a major part of the commissioning period. All operators were trained to understand the basics of controller's function and philosophy.

4.4 Results

Over a two months period of controller running, the overall throughput of desired products increased significantly. Figure 2 shows the decrease in the naphtha yield, whole straight run naphtha (WSRN), and increase in the kerosene yield for a five weeks period of pre-commissioning and four weeks period of post-commissioning of the controller. The crude oil density was assumed to be constant, 32.46 and 32.43 API for pre and post-commissioning respectively. As seen from the figure, 11 % increase in the kerosene yield was achieved as a result of decrease in naphtha yield.

The change in the naphtha yield was also observed in the kerosene flash point. The naphtha in the kerosene product decrease the flash point of kerosene and by the high weight in the kerosene quality, the quality approaches to low limit. This approach shown in Figure 3 resulted in very significant economic benefits.

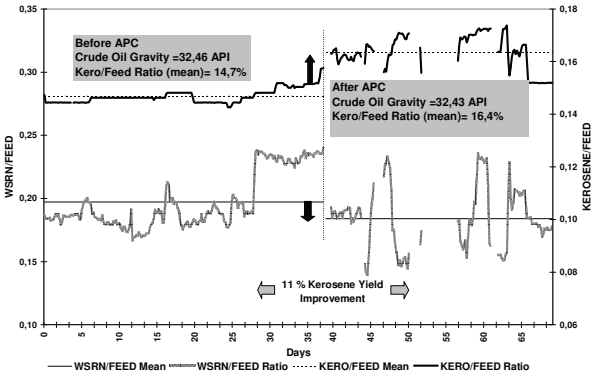

Fig. 2. Change in the naphtha yield before and after commissioning.

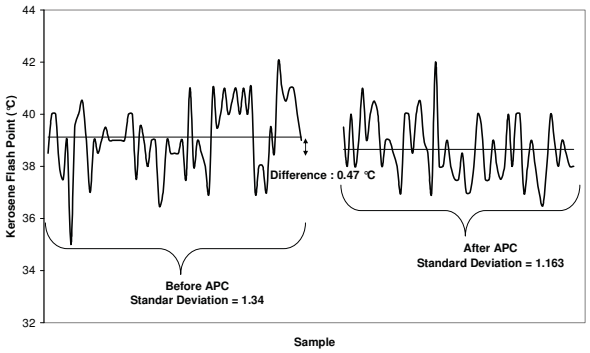

Fig. 3. Change in kerosene flash point before and after commissioning.

To illustrate the controller's performance on different situations, a simulation was studied using real plant data and specifications. When analyzing the results, a few points in controller tuning should be noted. Highest priority was assigned to kerosene and heavy diesel. Controller objective was to keep these qualities to low limit for kerosene and high limit for heavy diesel. On the other hand light diesel was assigned a low priority that its product rate was manipulated mainly in control of heavy diesel quality.

Figure 4 shows the changes in the product quality set points for kerosene flash point, heavy diesel, heavy naphtha and light diesel 95 % distillation points and their responses to these changes. The changes in critical column dynamics were reported in Figure 5. Figure 6 illustrates the product rate changes occurred during these set point changes.

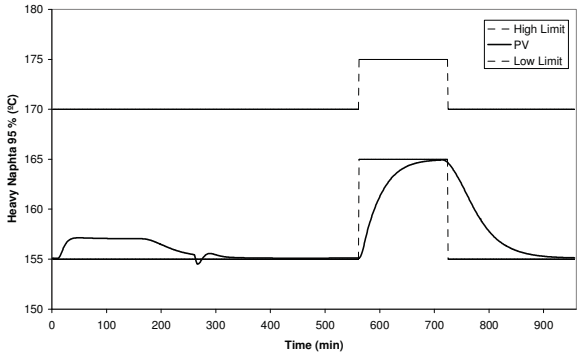

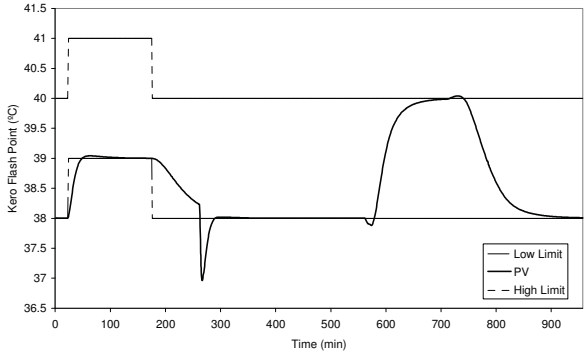

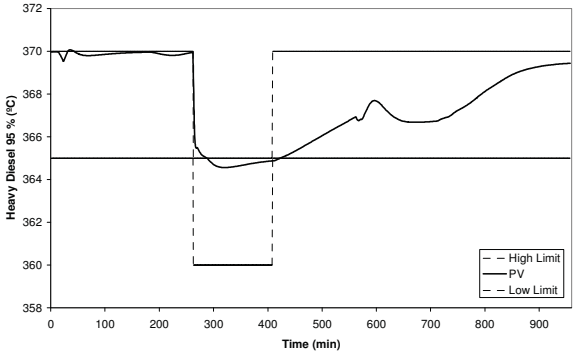

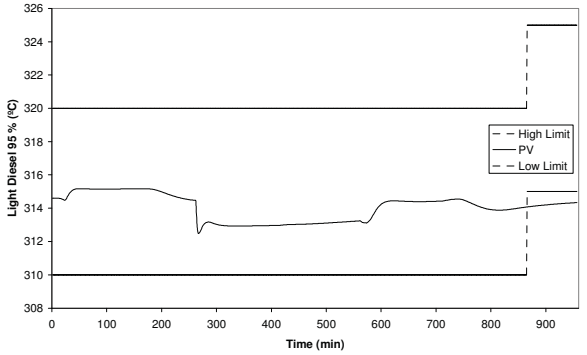

Fig. 4. Controller results in the qualities for the changes in the product quality limits.

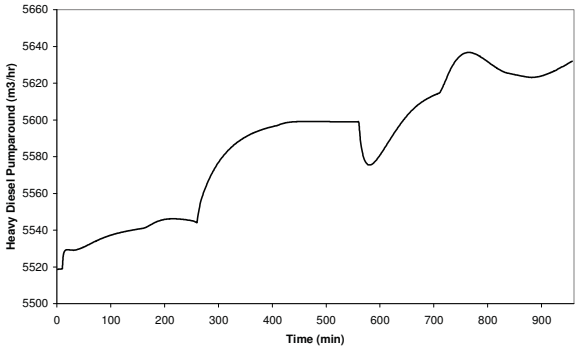

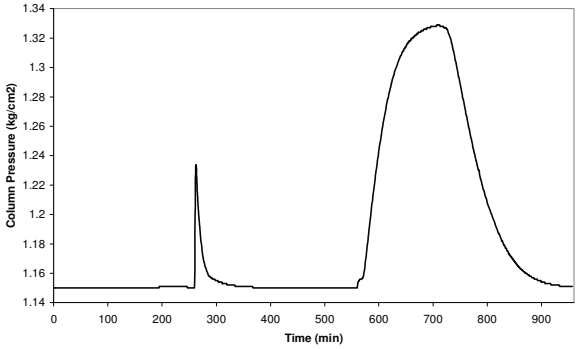

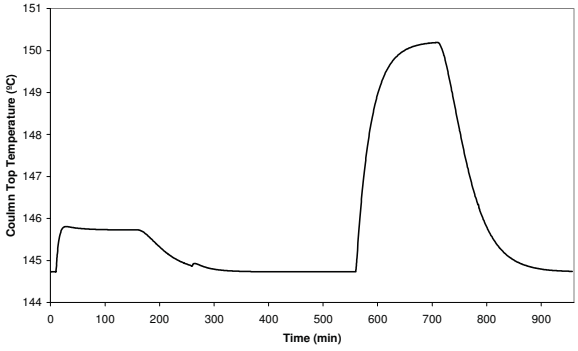

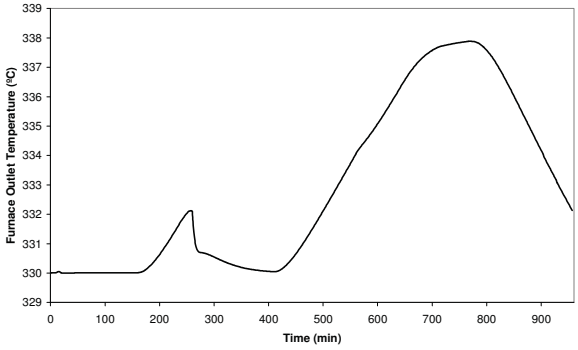

Fig. 5. Controller results in the distillation column critical controllers for the changes in the product quality limits.

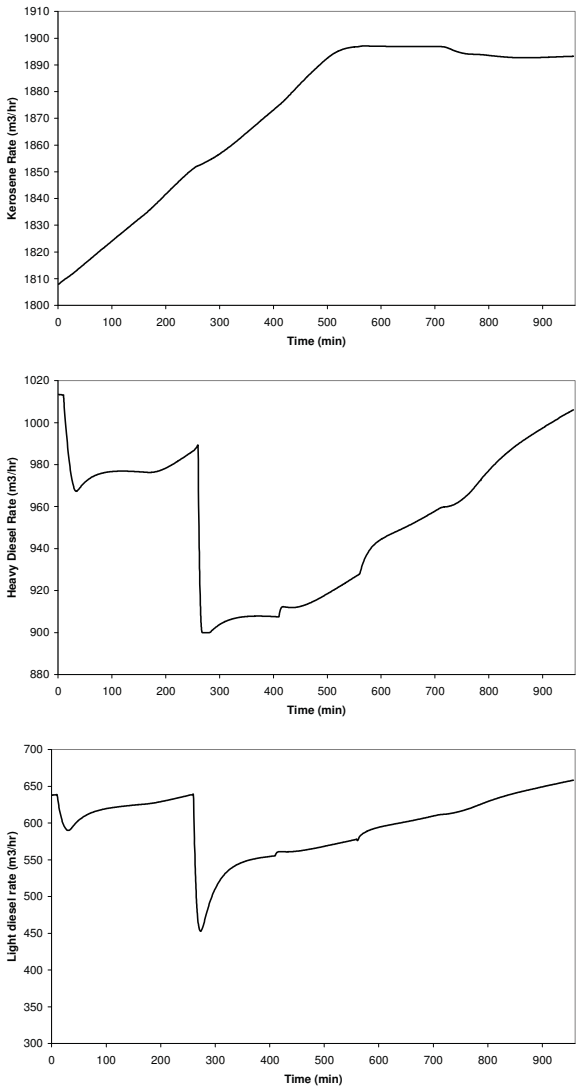

Fig. 6. Controller results in the product flow rates for the changes in the product quality limits.

5. CONCLUSIONS

In this paper, an industrial application of a model predictive controller algorithm has been presented. The controller has been designed for predictive control of crude oil preheat and distillation column of a crude oil unit in Izmit Refinery of Turkish Petroleum Refineries Corporation. A base layer control study has been performed to observe any nonconformity in the present control scheme. Tests have been carried out to obtain a mathematical model of the inferred product qualities. Dynamic step tests have been done for determined 28 manipulated variables. Dynamic modelling showed 53 responses to validate the controller.

Priorities for controlled variables and desired variation limits of manipulated variables were determined and the controller performance was tested using simulations in SMOCPro. Obtained model was commissioned for a three week period. It has been observed that the product throughputs and its economic benefit have been increased significantly.

Table 1. Control Variables of CDU Atmospheric Column

	Loop Description	MV	CV	DV
1	Heater Outlet Temperature	√		
2	Heavy Diesel Pump Around (HADPA) Duty		√	
3	Atm. Column Top Temperature	√		
4	Atm. Column Top Pressure	√		
5	Kerosene Draw-off Flow	√		
6	Light Diesel Draw-off Flow	√		
7	Heavy Diesel Draw-off Flow	√		
8	Stripping Steam Flow	√		
9	Heavy Naphtha 95% Distillation		√	
10	Kerosene Flash Point		√	
11	Kerosene 95% Distillation		√	
12	Light Diesel 95% Distillation		√	
13	Heavy Diesel 95% Distillation		√	
14	Kerosene Stripper Level Control Valve Opening		√	
15	Light Diesel Stripper Level Control Valve Opening		√	
16	Heavy Diesel Stripper Level Control Valve Opening		√	
17	Atm. Column O/H Drum Level Control Valve Opening		√	
18	Atm. Column O/H Drum Pressure Control Valve Opening		√	
19	HADPA Flow			√
20	Stripping Steam Duty		√	
21	Feed to Atm. Column			√

REFERENCES

Andersen, H.W. and Kummel, M. (1992). Evaluating estimation of gain directionality – Part 2: a case study of binary distillation, *Journal of Process Control*, 2, 67-86.

Rossitier, J.A. (2003). *Model based predictive control – A practical approach*, CRC Press, London.

Qin, S.J. and Badgwell, T.A., (2003). A survey of industrial model predictive control technology, *Control Engineering Practice,* 11, 733-764.

Inferential Control of Depropanizer Column Using Wave Propagation Model

S. Gupta*, A. N. Samanta, S. Ray*****

*M. W. Kellogg Ltd, Greenford, UK UB6 0JA
UK (e-mail: Sourabh.Gupta@mwkl.co.uk)
**Indian Institute of Technology, Kharagpur, India 721 302
(Tel: 91-3222-283948 ;e-mail: amar@che.iitkgp.ernet.in)
*** Indian Institute of Technology, Kharagpur, India 721 302
(e-mail: sray@che.iitkgp.ernet.in)

Abstract: In the present work a novel inferential control strategy cascaded with a nonlinear profile position controller is employed to control the top and bottom product compositions of a simulated depropanizer column. The inferential model for estimating product compositions is developed using the wave propagation model, and the composition profile position of both rectifying and stripping section is calculated using one temperature measurement from the respective section of the column. It is found that the estimation of the end product compositions using proposed technique may lead to an offset. The accuracy of the proposed inferential model can be further improved by providing an intermittent feedback of composition measurement in the form of an integral action. The wave propagation model of the depropanizer column is used in the Generic Model Control (GMC) architecture to design the profile position controllers.

Keywords: distillation column, nonlinear control, inferential control, profile position observer.

1. INTRODUCTION

A depropanizer column is used to separate propane from a mixture of components ranging from ethane to hexane. It is important to maintain the column product qualities on specification, to limit the negative effects of disturbances and upsets, and to reduce the switching time from one operating condition to another. An effective control strategy is therefore needed to control the depropanizer column. In this work, an inferential model based generic model control strategy is used which can handle disturbances and input uncertainties.

An inferential model is often used in process control when a measurement of the true variable being controlled is not available in real time. Reasons for the lack of real-time measurement include cost, reliability, and long analysis times or long dead times for sensors located far downstream. In these cases, an inferential model provides an estimate of the process variable, which can be used in the design of a controller to provide approximate regulation of the true variable. Tray temperatures are commonly used inferential measurements for product compositions. The temperature control is based on the assumption that the product composition can satisfy its specification when an appropriate tray temperature is kept constant at setpoint. In ideal situation, for a binary distillation column at constant pressure, the temperature at an end of the column is an indicator of the corresponding product composition. However, in case of a multi-component distillation column, tray temperatures do not uniquely determine the product composition. As a result, for these cases it is essential that an on-line analyzer or, at least, periodic laboratory analysis be used to adjust the tray temperature set point to the proper level.

In a Brosilow estimator [Weber and Browsilow (1972), Joseph and Brosilow (1978)] temperatures and flow rates were used for estimating unmeasured disturbances and then the derived disturbance values were used to estimate the product compositions. This estimator is based on a linearized process model. Mejdell and Skogestad (1991a, b) found that the steady state Brosilow estimator was very sensitive to modeling error for the ill-conditioned plant. In the last few decades, the development of composition estimators using partial least squares (PLS) regression have been proposed [Kresta et al. (1994)]. Furthermore, Mejdell and Skogestad dealt mainly with binary distillation columns. For a multicomponent column, tray temperatures do not correspond exactly to the product compositions. Mejdell and Skogestad have shown that the performance of the steady state PLS model for a multicomponent column is worse than that for a binary column. From the results, Mejdell and Skogestad seem to indicate the necessity of a dynamic regression estimator, which was implemented by Kano et al. (2000) in the form of dynamic partial least squares regression.

Gilles et al. (1980) reported the presence of a temperature front within a small area of the column in their extensive experimental study and showed that the locus of the temperature front is related to the product compositions. Gilles and Retzbach (1983) and Marquardt (1988, 1989) characterized the nonlinear behavior of distillation columns by the propagation of concentration profile (C-profile) and temperature profile (T-profile) in the column sections. Lang and Gilles (1990) presented an estimation technique that can be applied to complex processes in chemical industries. Adapting well advanced theories of fixed bed adsorption,

Hwang (1991) proposed a nonlinear wave theory for distillation columns which views the movement of composition and temperature profiles as nonlinear waves. They reported that these waves tend to sharpen for most situations and become constant pattern waves. Han and Park (1993) proposed a model based composition controller design incorporating Hwang's nonlinear wave model into the generic model control (GMC) framework of Lee and Sullivan (1988). To overcome the difficulty of composition measurements, Shin et al. (2000) proposed a C-profile position observer based on the temperature measurements. However, their proposed profile position estimation algorithm is applicable only for a binary system. Recently Gupta et al. (2009) has extended the application of profile position control to a debutanizer column.

In this work distillate and bottom propane compositions of a simulated depropanizer column are controlled by using composition to C-profile position cascaded controllers (Figure 1). The compositions are inferred from the C-profile position observer using one temperature measurement from each section (rectifying/ stripping). The objective of this article is to present a new approach to infer and control product compositions using the C-profile position of a depropanizer column, which uses one temperature measurement from the respective (rectifying/stripping) section.

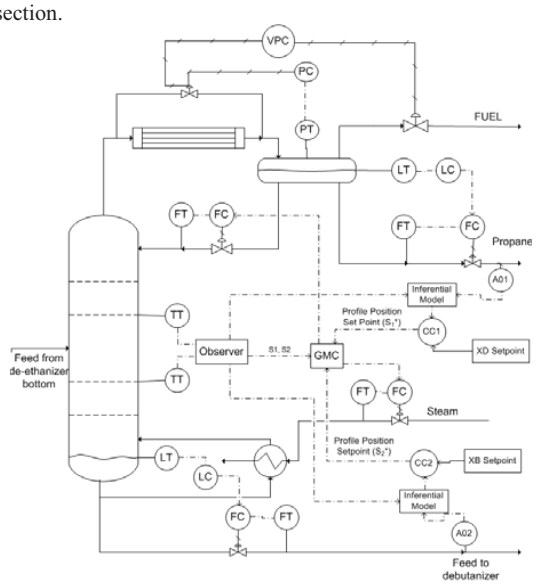

Figure 1: Depropanizer column with control strategy

2. PROCESS DESCRIPTION AND CONTROL STRATEGY

The depropanizer column of a gas recovery unit is simulated in this work [Huang and Riggs (2002)]. The depropanizer column consists of 40 trays, and feed, a mixture of C_2-C_6 components, is fed to the column at 22nd tray (counted from the bottom). The column has a partial condenser and the pressure is controlled via a hot vapor bypass around the overhead condenser. The distillate accumulator level is controlled by adjusting propane product flow rate. In a depropanizer column, the control objective should be to remove impurities (C_4+ components) in the distillate and maintain minimum possible propane loss in the bottom product to maximize the yield of propane in the distillate. This is a separate optimal control problem and is not in the scope of this work. Here the control is achieved by controlling the propane compositions in the distillate and bottom product to their already known optimum targets. The control scheme is shown in Figure 1 and the nominal values required for the distillation column simulation is presented in Table 1. The composition controllers (CC1 & CC2) are PI controllers which generate the profile position setpoints by using the inferred values of propane composition from the inferential model.

reflux rate (k mol/sec)	0.30		
reboiler duty (k joule/sec)	5248.8		
condenser duty (k joule/sec)	-4881.7		
Stream Details			
	feed	*distillate*	*bottoms*
flowrate (k mol/sec)	0.21	0.06	0.15
Temperature (°C)	86	43	112
pressure (k pascal)	3052	1515	1612
Composition (mol %)			
C_2	0.6	2	-
C_3	30	95.1	1.2
C_4	54.2	2.9	76.8
C_5	8.1	-	11.7
C_6	7.1	-	10.3

Table 1: Operating variables for depropanizer column

3. NONLINEAR WAVE MODEL

The dynamic behavior of distillation columns is characterized by the propagation of concentration or temperature profile in the column sections. Numerical simulation results of this typical dynamic behavior for the depropanizer column presented in figure 2 for 10% heavier and 10% lighter feed (Table 2). Propane composition and temperature profile moves up or down to the column ends as a result of increase or decrease of heavier components in the feed. It is also evident from the figure that both the waves ultimately tend to become steep and constant pattern as they move up or down the column.

The travel of such a constant-pattern self-sharpening wave can be characterized by the 'shock wave' velocity [Hwang (1991)] tracking the propagation of specific value of concentration. This wave velocity is derived from the material balance across the wave:

$$u_{\Delta} \equiv \left(\frac{\partial \sigma}{\partial \tau}\right)_{\Delta} = \frac{V}{F} \cdot \frac{\Delta y / \Delta x - L/V}{1 + r\left(\Delta y / \Delta x\right)} \qquad (1)$$

where r is vapor to liquid holdup ratio, τ is normalized time ($\tau = tF / NM$), and σ is normalized distance from bottom of the column ($\sigma = k / N$). Assuming the liquid flow is so slow that local equilibrium is attained, y in equation (1) can be

substituted with the vapor liquid equilibrium relation. The concentration and temperature waves will travel to either one of the column ends unless the balance of convective transports is carefully maintained to have a zero shock wave velocity with the compositions and flow rates of all streams entering the column sections including feed, reflux, and reboiler vapor flow. Therefore, the behavior of the column is severely nonlinear and sensitive since even a small upset of the balanced condition will lead to a large shift of the composition/temperature profile, giving dramatic changes in the product purity. By analyzing the profile positions for each section and the compositions at the column ends (distillate/bottoms) a model equation can be obtained to correlate the profile position with the compositions from the steady state data for the profile position and the top/bottom compositions collected from the steady state plant model simulation.

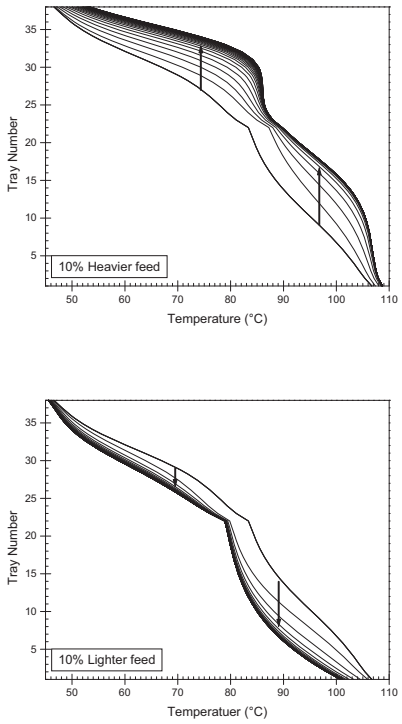

Figure 2: Dynamic profiles of the depropanizer column to a step disturbance (10% heavier feed and 10% lighter feed) of feed composition in open loop (each curve is separated by 5 minutes).

Feed composition

Composition (mol %)	normal	10% lighter	10% heavier	20% heavier	30% heavier
C2	0.6	0.64	0.56	0.52	0.48
C3	30	32.12	27.96	25.99	24.10
C4	54.2	52.51	55.83	57.39	58.90
C5	8.1	7.85	8.34	8.58	8.80
C6	7.1	6.88	7.31	7.52	7.72

Table 2: Feed composition in different scenarios

4. DEPROPANIZER CONTROLLER DESIGN

4.1. Profile position controller

The profile position controller is a nonlinear model-based controller, and is designed by embedding a nonlinear wave model directly into the generic model control (GMC) control framework.

The GMC equation can be written as the following in the case that state vector is a composition profile position S.

$$\frac{dS}{dt} = K_1\left(S^* - S\right) + K_2 \int_0^t \left(S^* - S\right) dt' \tag{2}$$

where, S and S^* are the profile position and its setpoint respectively; dS/dt is the propagation rate of profile. S is expressed in terms of the normalized distance from the bottom of the column ($S = 0$ at the bottom; $S = 1$ at the top). The propagation rate can be expressed from the nonlinear wave model as follows:

$$\frac{dS}{dt} = u = \frac{V}{F}\frac{\Delta y/\Delta x - L/V}{1 + r\left(\Delta y/\Delta x\right)} \tag{3}$$

Distillation columns, in general, have two sections: one is the rectifying section and other is the stripping section. Combining equations (2) and (3) gives one equation for each section as follows:

$$\frac{V}{F}\frac{\Delta y/\Delta x - L/V}{1 + r\left(\Delta y/\Delta x\right)} - K_{11}\left(S_1^* - S_1\right) - K_{12}\int_0^t \left(S_1^* - S_1\right) dt' = 0 \tag{4}$$

$$\frac{\bar{V}}{F}\frac{\Delta \bar{y}/\Delta \bar{x} - \bar{L}/\bar{V}}{1 + r\left(\Delta \bar{y}/\Delta \bar{x}\right)} - K_{21}\left(S_2^* - S_2\right) - K_{22}\int_0^t \left(S_2^* - S_2\right) dt' = 0 \tag{5}$$

where, subscripts 1 and 2 represent rectifying section and stripping section respectively, and L and V are the liquid and vapor flow rates respectively in the rectifying section and $\bar{L}$ and $\bar{V}$ in the stripping section. The profile position and the slope of the equilibrium curve at the representative concentration can be estimated by the profile position observer. Mass balance around the feed tray gives

$$\bar{L} = L + qF \tag{6}$$

$$V = \bar{V} + (1 - q)F \tag{7}$$

where, q is the liquid mole fraction of the feed. Knowing the feed conditions L, V, $\bar{L}$ and $\bar{V}$ is calculated from equations (4)-(7).

4.2. Online estimation of the profile position

The success of the inferential controller is mainly dependent on the ability to estimate the profile positions for both rectifying and stripping sections. The profile position in each section can be regarded as the location of the constant pattern wave representing a single point corresponding to a representative temperature. The profile position of the constant pattern wave can be determined by tracking the representative temperature instead of the entire wave.

In this case, the profile position observer is designed using the nonlinear wave model for the depropanaizer with an

additional feedback of weighted output error of temperature(s) feedback.

$$\dot{S} = \frac{dS}{dt} = \frac{V}{F}\frac{\Delta y/\Delta x - L/V}{1 + r\left(\Delta y/\Delta x\right)} + \sum_{i=l}^{m} k_1\left(T_i\right)\left(T_i - \hat{T}_i\right) \quad (8)$$

$$\frac{\Delta y}{\Delta x} = \frac{\dot{S} + L/F}{V/F - r\dot{S}} \quad (9)$$

$$\hat{T}_i = k_2\left(S_i - S\right) + T_s \quad (10)$$

$$k_1\left(T_i\right) = k_0 \exp\left[-b\left(T_i - T_s\right)^2\right] \quad (11)$$

where, i is the measurement tray number and l and m are the number of first measurement tray and the number of last measurement tray in a column section respectively. For $\Delta y/\Delta x$ and T relationship the steady state plant data can be used which will be associated with the tray efficiencies also. The tray temperature measurement location (26th and 18th tray) in each section is selected based on the inflection points in the temperature waves. The above equations are solved with initial estimates of the profile position S and representative slope $\Delta y/\Delta x$ to obtain the profile position. The sample time for the composition controller has been taken as 2 seconds while that of the profile position controller was 0.2 seconds.

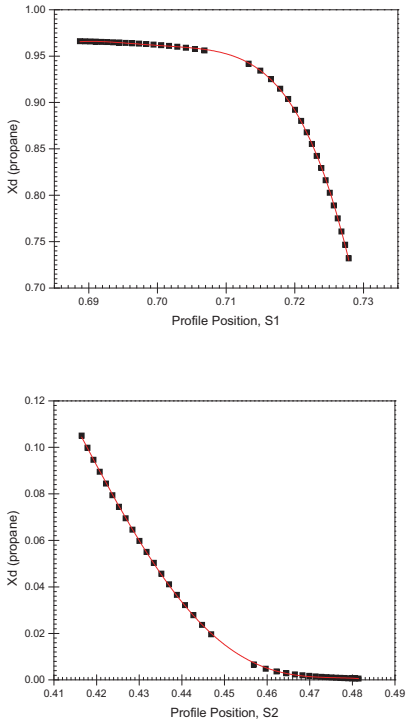

Figure 3: Graphical representation of steady state data set, of rectifying section profile position vs X_D (propane), and stripping section profile position vs X_B (propane).

5. INFERENTIAL CONTROL

In earlier work, the column end compositions were estimated using more than one measurement in the form of temperature, flow rate, and heat duty etc. In the proposed estimator one temperature measurement from each section (rectifying/ stripping) is used to find out the distillate and bottom composition of propane in the depropanizer.

5.1. Model identification using profile position

In this section we are proposing a model based inferential control using the profile position estimation. By analyzing the profile positions for each section and the compositions at the column ends (distillate/bottoms) a model equation can be obtained to correlate the profile position with the compositions. The steady state data for the profile position and the top/bottom compositions collected from the steady state plant model. Figure 3 shows that the data obtained from the plant model can be expressed by a 3rd order polynomial.

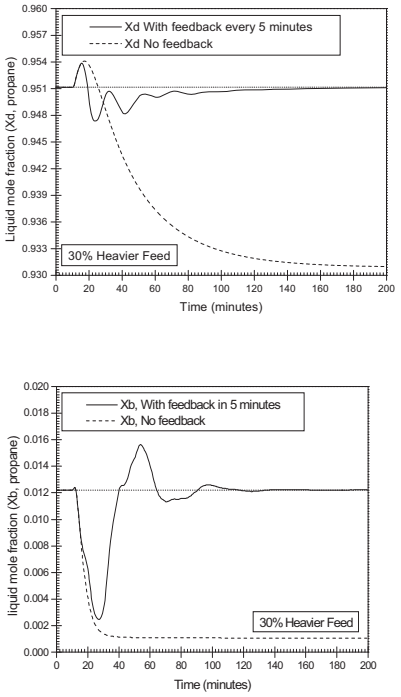

Figure 4: Closed loop transient response of the distillate composition (propane) and bottoms composition (propane) for 30% heavier feed using inferential control, with feedback /no feedback to the inferential composition estimator for the depropanizer column

Figure 4 shows that the proposed model is fair enough to control the end compositions of the depropanizer column. However, the current structure of the model leads to an offset with the final setpoint compositions.

5.2. Model identification using profile position with feedback

Our study leads that the composition measurements are required for the tight control of the end compositions of the depropanizer column. To remove the offset, an integral action

as a feedback to the estimator is proposed. The final form of the composition estimator can be expressed as follows:

$$x^{est.} = x^{\text{model}} + k' \int \left(x^{\text{last measurement}} - x^{\text{model}} \right) dt \quad (8)$$

where, k' is a tuning parameter. Figure 4 shows that the proposed model with feedback is able to control the end compositions of the column without any offset. For the depropanizer column value of tuning parameter k' is tuned at 1 and 0.1 for rectifying section and stripping section respectively, and a lag of 5 minutes allowed for the composition measurement.

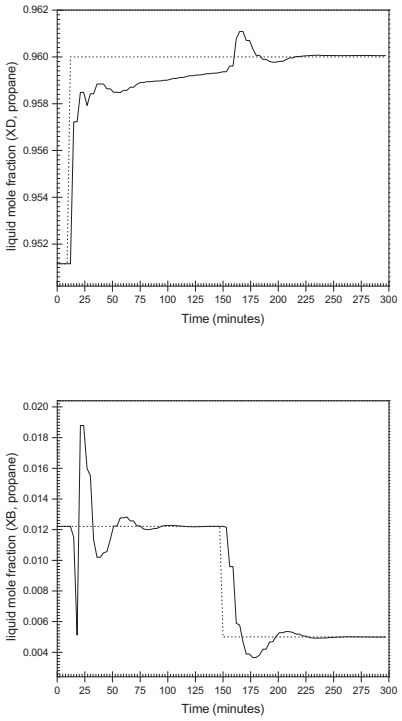

Figure 5: Closed loop transient response for the distillate and bottoms composition (propane) for setpoint change in X_D (propane) of 0.009 (0.951 to 0.96) at 10 minutes followed by a setpoint change in X_B (propane) of 0.007 (0.012 to 0.005) at 150 minutes, with feedback to the inferential composition estimator

6. RESULTS AND DISCUSSION

The depropanizer column with all control loops is simulated to verify the proposed control strategy.

6.1. Effect of composition setpoints change

Two concurrent setpoint changes are implemented to the top and bottom composition controllers. Closed loop transient response for the distillate and bottoms composition (propane) for a setpoint change in X_D (propane) of 0.009 mole fraction (0.95 to 0.96) at 10 minutes followed by a setpoint change in X_B (propane) of 0.007 mole fraction (0.012 to 0.005) at 150 minutes is shown in Figure 5. Increasing the propane purity in the distillate caused an immediate loss in propane content in the bottom causing a shift in the profile position. To maintain the propane composition in the bottom product the GMC controller has to put back the profile position in place which causes a sluggish response in the top composition response after the initial jump. When the bottom composition setpoint is also changed, both the controllers acted speedily because the changes are in favored direction from the viewpoint of the process dynamics.

6.2. Effect of noise and input uncertainty

To examine the robustness aspects of the controller about input uncertainty and temperature measurement noise, a simulation experiment is conducted on the depropanizer controlled by the proposed control strategy. During the simulation experiment following setpoint changes and disturbances are given to the system:

Setpoint change in X_D (propane) at 10 minutes (from 0.95 to 0.96).

Setpoint change in X_B (propane) at 150 minutes (from 0.012 to 0.01).

Step disturbance in the feed composition at 300 minutes (20% heavier feed, Table 2).

The following uncertainties have been taken into account during the simulation experiment:

Random disturbance in the feed flowrate (±5%)

Random disturbance in the reboiler heat duty (±10%) and reflux rate (±10%)

Temperature measurement noise (±0.5 °C)

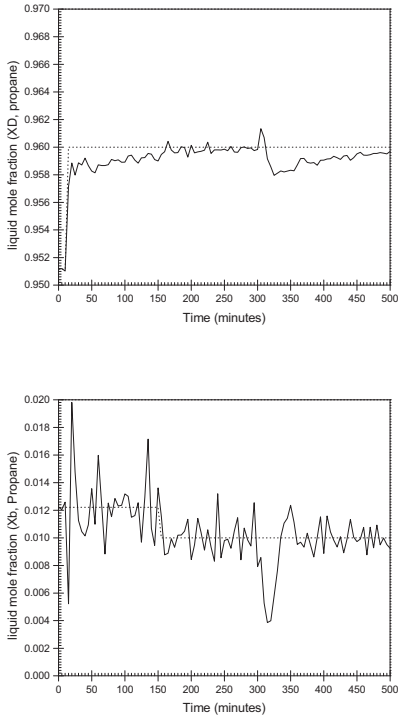

Figure 6: Effect of noise and input uncertainty: closed loop transient response in X_D (propane) and X_B (propane)

The distillate and bottom propane composition responses are shown in Figure 6. In spite of the severe input disturbances and measurement noise, the proposed controller is able to control the product propane compositions with reasonable speed of response and accuracy.

7. CONCLUSIONS

This study has shown a method of developing an inferential model for process control of depropanizer column using the observed profile position. A nonlinear profile position observer has also been developed to estimate the profile position of the column section with sufficient accuracy using temperature measurement. The profile position has been shown to be a powerful approach to building such models and uses the existing available measurements in the depropanizer. However, steady state plant data is needed for design of such models which may be collected while the process is operating under a feedback structure. Under a process/model mismatch, cascaded inferred composition to nonlinear profile position controller performed adequately well in controlling the depropanizer column. It will be interesting to compare the performance of the proposed controller with other nonlinear controller using input-output linearization controller or nonlinear model predictive controller which are much more computationally intensive than the proposed controller.

8. REFERENCES

Weber, R. and Brosilow, C. B. (1972), The use of secondary measurements to improve control. AIChE Journal, 18(3), 614-623.

Joseph, B. and Brosilow, C. B. (1978), Inferential control of processes. AIChE Journal, 24 (3), 485-509.

Mejdell, T. and Skogestad, S. (1991a), Estimation of distillation compositions from multiple temperature measurements using partial least squares regression. Industrial & Engineering Chemistry Research, 30, 2543-2555.

Mejdell, T. and Skogestad, S. (1991b), Composition estimator in a pilot plant distillation column using multiple temperatures. Industrial & Engineering Chemistry Research, 30, 2555-2564.

Kresta, J. V., Marlin, T. E. and MacGregor (1994), J. F., Development of inferential process models using PLS. Computers & Chemical Engineering, 18(7), 597-611.

Kano, M., Miyazaki, K., Hasebe, S. and Hashimoto, I. (2000), Inferential control system of distillation compositions using dynamic partial least squares regression. Journal of Process Control, 10, 157-166.

Gilles, E. D., Retzbach, E. and Silberberger, F. (1980), Modeling, simulation, and control of an extractive distillation column. Computer Applications to Chemical Engineering, 481-491.

Gilles, E. D., and Retzbach, B. (1983), Reduced models and control of distillation columns with sharp temperature profiles. IEEE Transactions on Automatic Control, 28 (5), 628-630.

Marquardt, W. (1988), Nonlinear model reduction for binary distillation. IFAC Symposium DYCORD ’86-Dynamics and Control of Chemical Reactors and Distillation Columns, Bournemouth, UK. Pergamon Press, Oxford, 123-128.

Marquardt, W. (1989), Concentration profile estimation and control in binary distillation. IFAC Workshop Model-Based Process Control, Atlanta, USA. Pergamon Press, Oxford, 137-144.

Lang, L. and Gilles, E. D. (1990), Nonlinear observers for distillation columns. Computers & Chemical Engineering, 14(11), 1297-1301.

Hwang, Y. L. (1991), Nonlinear wave theory for dynamics of binary distillation columns. AIChE Journal, 37 (5), 705-723.

Han, M. and Park, S. (1993), Control of high-purity distillation column using a nonlinear wave theory. AIChE Journal, 39(5), 787-796.

Lee, P. L. and Sullivan, G. R. (1988), Generic Model Control (GMC). Computers & Chemical Engineering, 12(6), 573-580.

Shin, J., Seo, H., Han, M. and Park, S. (2000), A nonlinear profile observer using tray temperatures for high-purity binary distillation column control. Chemical Engineering Science, 55, 807-816.

Gupta, S., Ray, S. and Samanta, A. N. (2009), Nonlinear Control of debutanizer column using profile position observer. Computers and Chemical Engineering.

Huang, H. and Riggs, J. B. (2002), Comparison of PI and MPC for control of a gas recovery unit. Journal of Process Control, 12, 163-173.

Advanced Process Control Wide Implementation in Alunorte Digestion Unit

Rafael Lopes*, Leonardo Vieira*, Ayana Oliveira, Jedson Santos**, Márcia Ribero**, Jorge Aldi**, Jorge Charr***,**

** Honeywell do Brasil. Av. Tamboré, 576 - Barueri – São Paulo – Brazil (e-mail: rafael.lopes@honeywell.com)*
*** Alunorte - Alumina do Norte do Brasil. Rodovia PA 481 km 12 – Distrito do Murucupi Barcarena – Pará – Brazil (e-mail: jorge.aldi@alunorte.net)*
**** Honeywell Venezuela. Av. Ppal Los Cortijos con 4ta Transversal. Edif. Honeywell. Los Cortijos de Lourdes. Caracas – Venezuela (e-mail: jorge.charr@honeywell.com)*

Abstract: The most competitive environment generated the need of process performance optimization. Performance optimization means produce the same amount of product, more effectively and spending less money. On the alumina market, that's fundamental in this economy scenario. Robust Multivariable Predictive Control Technology becomes one of the main tools to optimize this class of plants. This paper will discuss the application and benefits of this technology to alumina digestion units, implemented in 5 interconnected digesters. This digestion interconnection is a whole digestion train, and the plant has 5 of those. The APC philosophy is based on process variability reduction, and consequently operations optimization, against plant constraints. Since alumina – caustic ratio (A/C) is the key plant variable, it has a fundamental role in this variability reduction. The main challenge in this project was to coordinate the use of 5 bauxite grinders and 2 more grinder bauxite flows to the 5 digesters. The implementation was made in 3 phases and the project length was approximately 18 months, generating more than 1.00% increase in overall production, rather than A/C variability reduction.

Keywords: Advanced Process Control, Alumina, Alunorte, Honeywell, Multivariable, RMPCT

1. INTRODUCTION

Significant economic savings can be generated to alumina plants, through the utilization of new control technologies that uses the existing infrastructure and require a reduced support team. The global market and supplier consolidation created a more competitive environment, which drives the need of production and performance optimization. The multivariable predictive control becomes one of the main tools in this scenario. This paper will discuss the application and benefits of this technology to the alumina digestion units.

The challenge to any alumina refinery is to minimize the cost of production per tonne of alumina, consistently with safety and environmental considerations. It is translated into alumina production maximization (plant flow and yield) and energy costs per tonne of alumina minimization.

In this scenario, the digestion process is the one that has the biggest potential to the robust multivariable predictive control technology (RMPCT) implementation. Rather than this, the digestion is considered by most of refineries as a key-unit to the production and also is the one that offers the best data for an APC modelling.

1.1 Process Description

The process for obtaining alumina from bauxite ore was developed and patented by Karl Josef Bayer in 1888. Typically, depending on the quality of the ore, between 1.9 and 3.6 tonnes of bauxite are required to produce 1 tonne of alumina.. Bayer process is cyclical and involves many unit operations, like digestion, solid – liquid separation and crystallization.

Overall, bauxite ore is digested in caustic solution concentrate in temperatures ranging from 145 to 270°C, depending on the nature of the ore. Under these conditions, most mineral species that contains aluminum is dissolved, forming sodium aluminate, soluble, as shown in equations (1) and (2).

$$Al(OH)_3 + NaOH \rightarrow NaAlO_2 + 2H_2O \quad (1)$$

$$AlO(OH) + NaOH \rightarrow NaAlO_2 + H_2O \quad (2)$$

The portion of the ore that is insoluble in caustic solution after digestion (red mud) is removed by sedimentation and filtration process. The pregnant liquor in alumina is send to the precipitation, which is almost pure crystals of $Al(OH)_3$. The hydrate precipitate is removed, washed and sorted. Alumina is then obtained by their calcination.

1.2 RMPCT (Robust Multivariable Predictive Control Technology)

RMPCT technology represents an advance of the traditional MPC technologies. Like the others, this technology models the process, calculate the necessary predictions and use multivariable control movements in order to: optimize the process, maintain the variables inside operational limits and respect the process and plant constraints. The performance gain and robustness is due to a feature called "range control algorithm" (RCA), which makes that the disturbances and prediction errors inherent to the process are considered in the future movement plan. Figure 1 sketches how the RCA technology works.

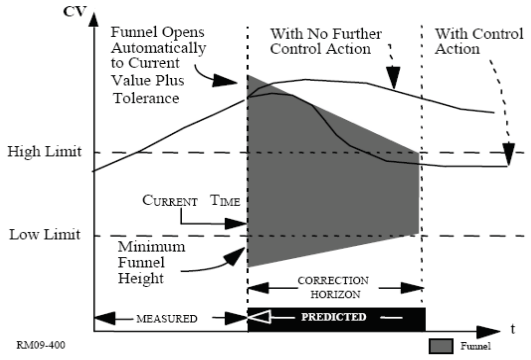

Figure 1 - RCA Technique Controlling a CV Inside Limits

The correction horizon concept is that CV errors are reduced to zero at the correction horizon in the future. Prior to the correction horizon, the controller is free to determine any trajectory for the CV as long as the CV is brought within limits or to setpoint at the correction horizon. Because no trajectory is imposed on the controller, the controller has the freedom to determine a trajectory that requires minimum MV movement and is least sensitive to model error.

However, the correction horizon by itself does not say anything about what happens to the CV prior to the horizon. It is important that the controller does not transiently move a CV farther outside a limit while correcting other CV errors, even though all CVs are brought to zero error by their correction horizons. Limit funnels are used to prevent the controller from introducing transient errors prior to the correction horizons, by defining constraints on the CVs that are imposed at intervals from the current interval out to the horizon.

These features drives the application to deal smoother and more efficiently with model mismatches (gain inversion, colinearities, bigger or smaller gains than the real, dynamic errors). Rather than this, the tuning in this technology is based on the controlled variables and not in the manipulated variables.

2. APPLICATION OF RMPCT IN ALUNORTE DIGESTION UNIT

2.1 Digestion Process Description

The digestion unit is designed to extraction alumina from bauxite using caustic solution in high temperature and remove dissolved silica from the liquor leaving the digesters to ensure product hydrate of the desired quality.

The alumina extraction is carried out in a train consisting of five vertical digesters arranged in series. The first step is to dissolve a most part of alumina in ore mixing slurry bauxite and heater spent liquor, in small digesters, equipped with agitators. The large digesters, without agitators, in series are to keep the residence time to reduce the silica dissolved by desilication reaction to a tolerable level.

The five vertical digesters are sized to provide a total of 60 minutes nominal retention time. Varying the liquor outlet temperature from the second live steam heater controls the digestion temperature. In occasion when one digester is taken out of operation the temperature is increased approx 1°C to compensate.

2.2 General Control Strategies

The Advanced control strategies of the Bayer plant are used to control blow off ratio, caustic concentration and to keep productivity and quality.

Alumina refineries generally operates with advanced A/C ratio control systems, involving feed forward with feedback trim and utilizing on-line measurement of liquor properties, such as electrical conductivity and density.

In 2006, ALUNORTE concluded the project of expansion 2 with five lines, in operate, with total liquor flow of 5610 m3/hr and installed capacity of 4.3 Mt/year.
The project to implement RMPCT control is divided in three phases:

- Phase I : Implementation of control on digestion 3.
- Phase II : Implementation of control on digestions 1 and 2.
- Phase III: Implementation of control on digestions 4 and 5.

2.3 Controller Objectives

The advanced control objectives for the digestion section are described below:

- Control A/C ratio to operator specified target
- Maximize productivity (bauxite and liquor flows), subject to process constraints
- Provide safe and stable operation
- Protect the unit when possible from defined, measurable constraints such as hydraulic, mechanical and environmental constraints.

2.4 Application Methodology

The RMPCT implementation consisted on the following steps:
Data and information gathering → Pre-Step Test → Step Test → Mathematical Modeling → Installation and sustaining

The implementation methodology is detailed bellow:

- Collection of: historical data, operation screens, process flow diagrams, engineers and operators information by interviews;
- Instrumentation review, control strategy setup and related loops tuning;
- After the analysis of all data, a preliminary controller design matrix is defined and discussed. This matrix will drive the initial plant tests (Pre-Step test);
- Prior to starting a test, the process and control system must be brought to a suitable starting condition, and allowed to settle if any changes were made. This will involve ensuring that the process is away from limits or "wind-up" conditions, and making sure that all control loops are in the correct modes.
- Pre-Step Testing is necessary to determine the steady state gain and settling times to be able to conduct precise Step Testing. After analyze of the collected data, final decisions of controller structure and step size will be issued in a report that acts as the basis for the formal step testing
- After the Pre-Step test, the Step Test is performed, applying steps to the considered manipulated variables. The steps are applied with variable time and amount, in order to indentify the actual interactions that will build the definitive multivariable control matrix.
- Using the data gathered on the Step Test, the models are constructed and the RMPCT is built. The matrix is validated, analyzing the predictions and controller offline simulation.
- After the matrix and control construction, the software connections with DCS are configured and an initial software tuning is performed.

2.5 Basic Controller Structure

The main manipulated variables are:
- Bauxite slurry flow
- Liquor flow
- Steam flows of relevant plant heat exchangers

The main controlled variables are:
- Alumina/Caustic Amount Ratio
- Digestion Conditions (temperatures, pressures and volume controls)
- Feed to digestion conditions.

The following table represents the controller gain matrix. MVs 1 to 4 refer to the unit mass balance variables. MVs from 5 to 7 refer to the unit energy balance variables. CVs from 3 to 6 refer to the unit energy balance variables. Other CVs are related to the unit mass balance parameters.

Table 1 – RMPCT Gain Matrix to the Digestion

	MV1	MV2	MV3	MV4	MV5	MV6	MV7
CV1	+	+	-	-			
CV2	-	-	-	-			
CV3	-	-	-	-	+	+	
CV4	-	-	-	-	+	+	
CV5	-	-	-	-	+	+	
CV6	+						
CV7		+					
CV8			+				
CV9				+			
CV10					+		
CV11							
CV12							
CV13						+	
CV14							-
CV15	+	+					

For example, MV1 is the bauxite flow and CV1 is the Alumina – Total Caustic ratio. If the bauxite flow is increased, the A/TC ratio is increased, after a dead time. CV2 is the residence time and the CV's 3, 4 and 5 are digestion temperatures. It can be noticed that, if the bauxite flow is increased, the residence time on the digestion system decreases and the digestion temperature decreases, too. In this controller, the A/TC ratio is controlled on a target, not inside operational limits.

MV3 is the liquor flow to the digestion system. This variable has a significant influence on the A/TC ratio as is one of the main handles for it. For the digestion temperature and residence time, it can be expected the same behaviour as on the interaction between the bauxite MV and the same controlled variables.

CV's from 6 to 13 are valves and they are controlled as constraints on the controller.

3. MODELLING RESULTS

3.1 Modelling Achievement

The historical data gathered was enough to get good models to build the control matrix. To the mass balance variables, around 10 steps were used and to the energy balance variables, around 6 steps were used. This difference is due to the bigger relevancy of the mass balance, since the main variable (A/C) is influenced by this group of variables.

The following figure represents one of the models between the manipulated and controlled variables. In this case, the model represents the behaviour of the Alumina – Caustic Concentration ratio, against on of the mass balance manipulated variables.

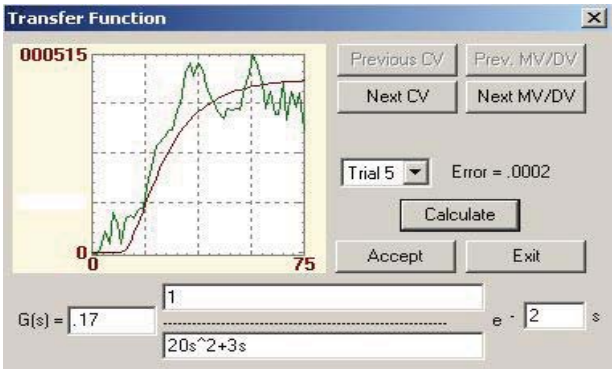

Figure 2 – Model Between Bauxite and the Alumina-Caustic Concentration Ratio (CV)

The unit studied has some valve opening problems on the liquor and pulp heating section. These problems are due plugging, caused by the material that goes inside the heat exchanger tubes. In order to minimize this problem, the valves were modelled, against their steam flows. A model example is showed on the Figure 3.

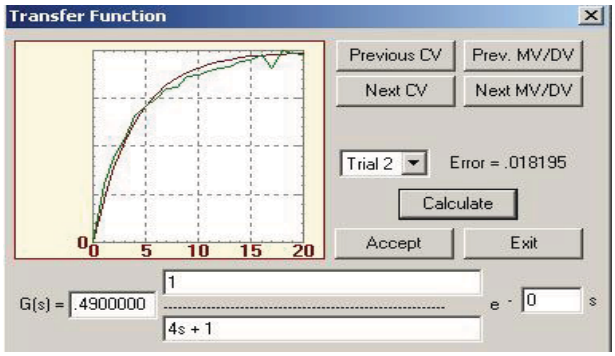

Figure 3 – Valve modelling against the steam flow

3.2 Model Validation

After the modelling, the predictions were analyzed, in order to check if the model is coherent with the real process data, found on the plant test. This validation is one of the last steps, before the controller implementation. The following pictures show the prediction results.

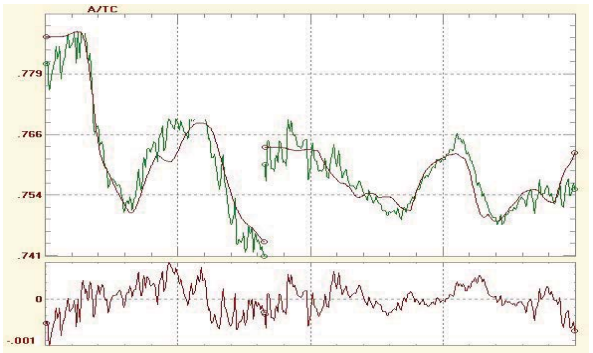

Figure 4 –A/TC Prediction

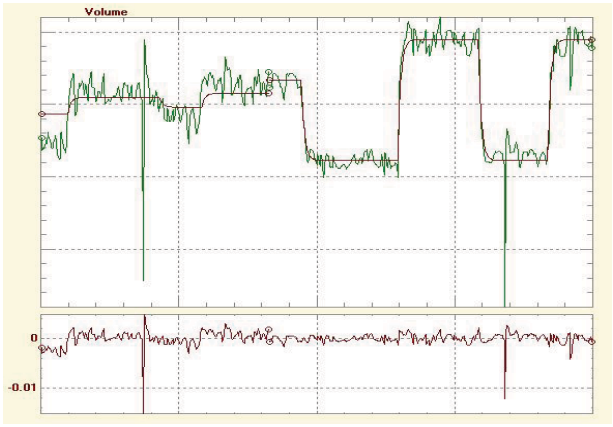

Figure 5 – Digestion Volume Prediction

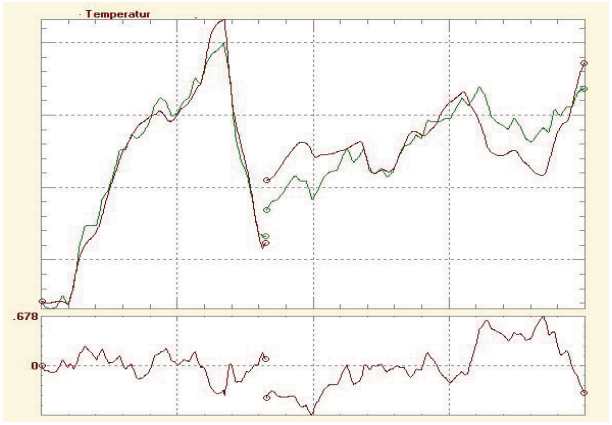

Figure 6 – Temperature Prediction

The Figures show good prediction results. Thus, the proposed and modelled matrix could be tested on the offline controller simulations. In the simulation mode, the control strategies and controller tuning are tested. Rather than this, the controller behaviour against critical situations can be validated. After this last validation, the controller was ready to be implemented on this alumina digestion unit

4. IMPLEMENTATION RESULTS

4.1 Overview

The main reason to implement RMPCT in digestion unit is to keep A/C control at the set point, decrease variability of the system, to increase digestion yield and to keep safety and stable operational conditions.

The main controllers are: DG4B_CLT (Digestion 3 controller). The others controllers are called: DG4A1_CLT, for digestion 1 and DG4A2_CLT, for digestion 2, DG4C1_CTL, for digestion 4 and DG4C2_CTL for digestion 5.

In order to evaluate digestion operation results with RMPCT, it's necessary to consider two parameters:

- Digestion Blow Off (DBO) ratio;
- Digestion Yield

4.2 Digestion Blow off (DBO) ratio

DBO ratio is the main parameter to determinate digestion yield. A good control of this parameter means smaller variability, which allows a higher yield at the digestion outlet. For digestion lines 1,2 and 3, the set point DBO ratio is 0,750. For the digestion lines 4 and 5, the set point DBO ratio is 0,759.

4.3 Digestion Yield

To calculate the digestion yield, the equation 3 is used:

$Y = (((C_{SL}\text{-}S_l)\ .\ A/C_{DBO})\text{-}(C_{SL}.A/C_{SL}))\text{-}C_{STT}$ (3), where:

CSL = Spent liquor caustic concentration (g/l)
SL = Silica lost
A/CDBO = Digestion blow off ratio
A/CSL = Spent liquor ratio
CSTT = Spent liquor solids concentration

5. RMPCT PERFORMANCE

5.1 DG4B_CTL

Controller performance was evaluated through the comparison between two different periods of digestion 3 operation. Those periods represent the time when RMPCT was turned on and off.

In the digestion operation without RMPC, the average DBO standard deviation was 0,005 higher, when compared with the digester operation with RMPC (0,002). It represents that the controller performed satisfactorily. Table 2 shows draft of DBO ratio performance with and without RMPCT operation.

Table 2- Draft DBO ratio performance

RMPCT Operation	Average DBO Ratio	Average δDBO
Controller off	0,748	0,005
Controller on	0,751	0,002

This improvement on the DBO represented a gain of 1,02% on the digestion yield. The total time spent for this project phase was 8 months.

Figure 9 and 10 show DG04B_CLT performance when RMPCT was on and off. When RMPCT was on, A/C values were more stable than when the controller was off. A DBO standard deviation of 0,003 was achieved when the Profit Controller was turned on, instead of 0,006, when controller was off.

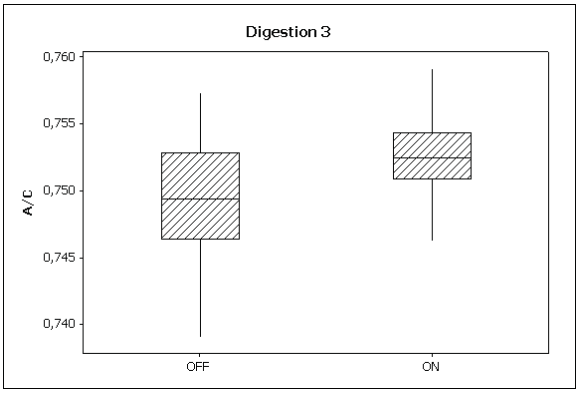

Figure 7 – Digestion 3 A/C when RMPCT on and off

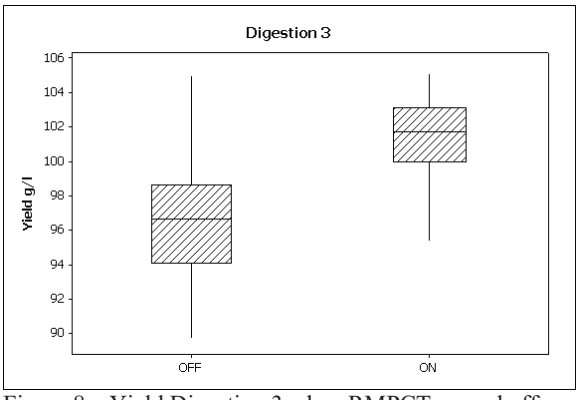

Figure 8 – Yield Digestion 3 when RMPCT on and off

5.2 DG4A1_CTL and DG4A2_CTL

RMPCT for digestion 1 and 2 was evaluated, in order to define a gain with controller in these units. The evaluation followed the same methodology as in the digestion 3.
Figure 11 shows behaviour of A/C in periods when RMPCT is off and on, with average of 0.749 and 0.753, respectively. Standard deviation of the DBO in periods where RMPCT was turned on was better than when the controller was turned off, with averages of 0,02 and 0,01, respectively.

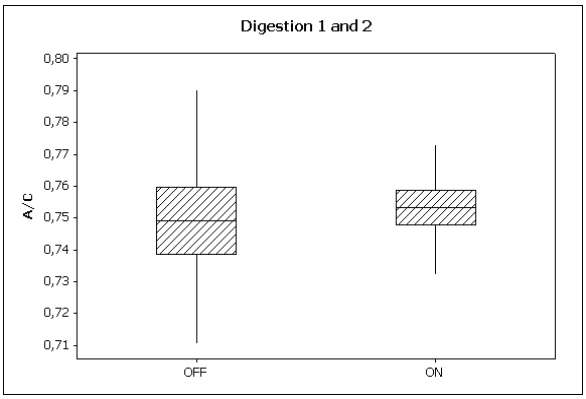

Figure 9 – Digestion 1 and 2 A/C when RMPCT on and off

Figure 12 shows an yield digestion gain of 1,85%. The yield when the controller was turned off was 98,93 g/l and when the controller was turned on was (100,77 g/l).

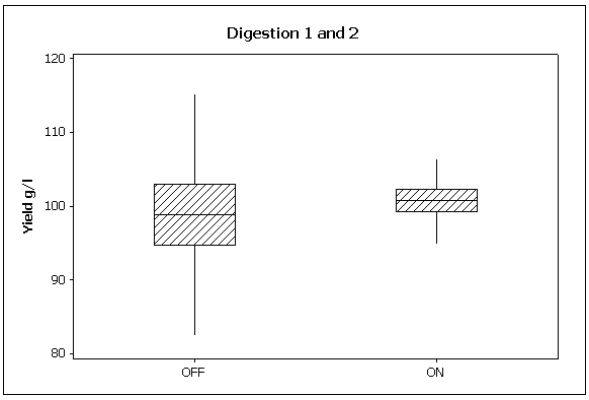

Figure 10 – Yield Digestion 1 and 2 when RMPCT on and off

5.3 DG4C1_CTL and DG4C2_CTL

RMPCT for digestion 4 and 5 was evaluated, in order to measure the gain obtained with its implementation. The evaluation follows the same methodology as in the other digestion trains.

Figure 13 shows behaviour of A/C in periods when RMPCT is off and on, with average of 0.756 and 0.759, respectively. Standard deviation δDBO in periods where RMPCT is on is better than it's off, with average of 0,02 and 0,01.

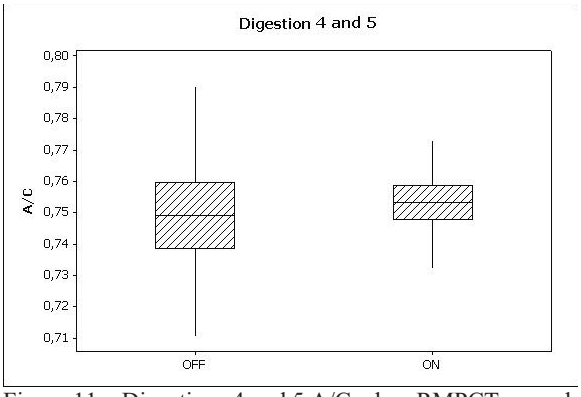

Figure 11 – Digestions 4 and 5 A/C when RMPCT on and off

Figure 14 shows yield digestion gain of 1,69%. The yield when the controller was turned off was 99,72 g/l and when the controller was turned on was 101,44 g/l.

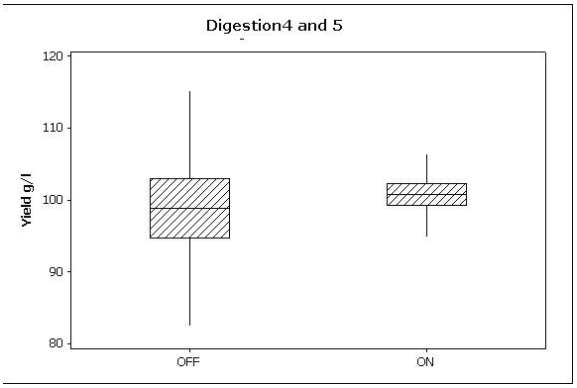

Figure 12 – Yield Digestion 4 and 5 when RMPCT on and off

6. CONCLUSION

A good RMPCT implementation on Alumina Digestion was described. The A/TC variability reduction and a bigger operation stability were proven. Also, the opportunity to operate the plant close to the operational constraints represents a productivity increase and a plant debottlenecking. The steam and liquor consumption didn't change significantly, since the objective was to use the debottlenecking to increase alumina production.

Nevertheless, in this application the liquor flow was maintained constant, due to operational restrictions. If the liquor could move, probably the results would be better than the achieved. Other source of improvement (which wasn't explored in this work) is the increase of operator training on this tool. Since the operators are the heaviest users of the system, training them to help on the optimization, pushing constraints and widening the operation limits can generate a bigger production improvement, than it was achieved.

REFERENCES

Garcia, C.E., D.M. Prett and M. Morari (1989). "Model predictive control: Theory and practice - a survey". Automatica 25(3), 335–348.

Qin, J., Badgwell, T., "An Overview of Industrial Model Predictive Control Technology". Department of Chemical Engineering, Rice University, USA (1997)

Lopes, R., Charr, J. ,"Alunorte Digestion Phase I Detail Design V2.1", Belém, Brasil (2007).

Ribeiro, M., "Benefícios Encontrados com Implementação RMPCT Honeywell", Belém, Brasil (2007).

Den Hond R., Hiralal I., Rijkeboer A., "Alumina Yield in the Bayer Process; Past, Present and Prospects". TMS (The Minerals, Metals & Materials Society), 2007.

www.solucoesavancadas.com.br – More advanced solutions business cases

Dynamic Models and Open-Loop Control of Blood-Glucose for Type 1 Diabetes Mellitus

Hsiao-Ping Huang*¶, Shih-Wei Liu*, I-Lung Chien, Yi-Hao Lin**, Miao-Ju Huang*****

** Department of Chemical Engineering, National Taiwan University, Taipei 106, Taiwan*
¶ (Tel: 886-2-23638999; e-mail: huanghpc@ntu.edu.tw)
*** Department of Chemical Engineering, National Taiwan University of Science and Technology, Taipei 106, Taiwan*
**** College of Medicine, Chang Gung University, Tao-Yuan, Taiwan*

Abstract: Type 1 diabetes mellitus must rely on daily insulin injection/infusion for the control of blood glucose. The treatments on those patients to maintain their blood glucose within an acceptable level is thus of essential importance. A good mathematical model of blood glucose may facilitate such a control. In this research, modeling and open-loop control of blood glucose for a type-1 patient using a model extended from the works of Hovorka and his coworkers (Hovorka *et al*., 2002; Hovorka *et al.*, 2004; Wilinska *et al*., 2005) are studied. Clinical data from a continuous glucose monitoring system is used to develop the model for such use. Open-loop control strategies for patients that use basal and bolus subcutaneous infusions via an insulin pump are presented.

1. INTRODUCTION

Some relevant studies indicate that good metabolic control of diabetes may decrease the risk of chronic complications. The averaged blood glucose (BG) levels as reflected by the HAb1c levels are generally considered an indication of goodness of such a control. Nevertheless, a good control in terms of HAb1c levels is only necessary but not sufficient, because, high glycemic excursion can not be detected by measuring the HAb1c values only. Recently, a system known as CGMS (Continuous Glucose Monitoring System) has been available for continuously measuring glucose concentrations in subcutaneous tissue. Clinic physicians can make uses of the recorded continuous profiles to learn the excursion of BG and modify their treatments on the patients. Meanwhile, the appearing of real time CGMS on the market also provides a basis for implementation of on-line blood glucose control in the future.

The motivation of this paper is to show, by making uses of a modification to the Harvoka's model (Hovorka *et al*., 2002; Hovorka *et al.*, 2004; Wilinska *et al*., 2005) and real CGMS data, an open-loop control that aims to desired HAb1c and blood glucose levels for type 1 patients can be developed.

2. MODEL DESCRIPTIONS

As mentioned, many physiological models have been proposed that describe glucose and/or insulin dynamics. In this paper, the model for study is based on the works of Hovorka and his coworkers (Hovorka, *et al*. ,2002; Hovorka, *et al*. ,2004; and Wilinska *et al*. ,2005). The reasons that this model is adopted for study is due to the inclusion of more detail insulin action that describes the physiological effect of insulin on glucose transport, removal and endogenous glucose production. Also it provides the insulin absorption through two compartmental channels that can be used to model the short acting and long acting effects from the bolus and basal insulin. Two subsystems are used to describe the glucose concentrations in the accessible compartment such as vein and organs, where measurements are made, and the inaccessible compartment such as tissue in human body, where measurements are not made. The insulin action describes the physiological effect of insulin on glucose transport, removal and endogenous glucose production. The original Harvokal model for IVGTT test is given as the following:

$$\frac{dQ_1}{dt} = -F_{01}^c - x_1(t)Q_1 + k_{12}Q_2(t) - F_R + U_G + \mathrm{W}\cdot EGP_0\left[1 - x_3(t)\right]; \quad (1)$$

$$\frac{dQ_2}{dt} = x_1(t)Q_1(t) - \left[k_{12} + x_2(t)\right]Q_2(t) \quad (2)$$

$$U_G = \sum_{i=1}^{N} \frac{D_G A_G (t - T_i) e^{\frac{-(t-T_i)}{t_{\max,G}}}}{t_{\max,G}^2} S(t - T_i); \quad T_i, i = 1, \cdots, M \quad (3)$$

$$F_R = \begin{cases} 0.003(G-9)V_G \cdot W & \text{, for G} \geq 9 mmole/L \\ 0 \text{ , else} \end{cases};$$

$$F_{01}^c = \begin{cases} F_{01} \cdot W & \text{; if } G \geq 4.5 mmole/L \\ F_{01} G \cdot W / 4.5 & \text{; otherwise} \end{cases};$$

and $G(t) = \dfrac{Q_1}{V_G W}$ $(mmole/L)$

$$\frac{dq_{1a}}{dt} = k_{ba}u_{ba} + k_{bo}\sum_i \frac{u_{bo,i}}{\tau}\exp\left\{-\frac{(t-T_i)}{\tau}\right\} - k_{a1^*}\cdot q_{1a} - \frac{V_{\max,LD}q_{1a}}{\left(k_{M,LD}+q_{1a}\right)} \quad (4)$$

$$\frac{dq_{1b}}{dt} = \left(1-k_{ba}\right)u_{ba} + (1-k_{bo})\sum_i \frac{u_{bo,i}}{\tau}\exp\left\{-\frac{(t-T_i)}{\tau}\right\} - k_{a2^*}\cdot q_{1b} - \frac{V_{\max,LD}q_{1b}}{\left(k_{M,LD}+q_{1b}\right)} \quad (5)$$

$$\frac{dq_2}{dt} = k_{a1^*}q_{1a} - k_{a1^*}q_2 \quad (6)$$

$$\frac{dq_3}{dt} = k_{a1^*}q_2 + k_{a2^*}q_{1b} - k_e q_3 \quad (7)$$

$$\frac{dx_1}{dt} = -k_{a1}x_1(t) + \frac{k_{a1}S_{IT}^f q_3}{V_I \cdot W} \quad (8)$$

$$\frac{dx_2}{dt} = -k_{a2}x_2(t) + \frac{k_{a2}S_{ID}^f q_3}{V_I \cdot W} \quad (9)$$

$$\frac{dx_3}{dt} = -k_{a3}x_3(t) + \frac{k_{a3}S_{IE}^f q_3}{V_I \cdot W} \quad (10)$$

where, Q_1 and Q_2 (*mmole/l*) represent the glucose in accessible and non-accessible compartments, G (*mmole/l*) is the measurable glucose concentration, k_{12} represents the transfer rate constant from non-accessible to accessible compartment, V_G represents the distribution volume of the accessible compartment, and EGP_0 represents endogenous glucose production at the zero insulin concentration. F_{01}^c is the non-insulin-dependent glucose flux and F_R is the renal glucose clearance thresholds of 9 mmol/L. W is the patient's weight. U_G is the gut absorption rate, $t_{\max,G}$ is the time-of-maximum appearance rate of glucose in the accessible glucose compartment, D_G is the amount of carbohydrates (CHO) digested and A_G is the carbohydrate bioavailability. Variable q_2 represents the insulin mass (mU) in the nonaccessible subcutaneous compartment, q_3 represents the insulin mass (mU) in the plasma compartment. The quantities q_{1a} and q_{1b} represent the masses of insulin administered as continuous infusion (mU) through the slow and fast compartment channels (Wilinska *et al*. 2005). The variable u represents the basal insulin input (mU/min). The parameters k_{a1^*}, k_{a2^*}, and k_e are transfer rates ($\min^{-1}$), $V_{\max,LD}$ is the saturation level (mU/min) for Michaelis-Menten dynamics of insulin degradation, $k_{M,LD}$ is the value of insulin mass (mU) at which insulin degradation is equal to half of its maximal value for continuous infusion. The dimensionless constant k and $1-k$ represent the proportions of the total input flux of insulin passing through the slower and faster compartment channels, respectively. The variables, x_1, x_2, and x_3 represent the (remote) effects of insulin on glucose distribution/transport, glucose disposal and endogenous glucose production (Harvoka, *et al*. 2002). Finally, k_{ai}, i=1,⋯,3, represent the deactivation rate constants.

The modeling form given above is based on the work of Seborg and his coworkers (2008). On this basis, the addition of carbohydrates in-take from different meals (i.e. Eq.(3)) and the basal insulin and bolus insulin infusion/injection at different times (i.e. Eq.(4) and Eq.(5)) are considered as an extensions to the original model. Notations u_{ba} and u_{bo} are used to designate the quantities of basal insulin and bolus insulin, respectively.

The complete model for modelling the BG consists of equations from Eq.(1) through Eq.(10). V_G and A_G are assumed to be constant as: V_G=0.16 (L^{-1}·kg) and A_G=0.8. Totally seventeen parameters in the model will be determined:

F_{01}, k_{12} ,EGP_0, k_{a1^*}, k_{a2^*}, $t_{MAX,G}$, S_{IT}^f/V_I, S_{ID}^f/V_I, S_{IE}^f/V_I, $V_{\max,LD}$, $k_{M,LD}$, k_{ba}, $k_{bo,}$ k_e, k_{a1}, k_{a2}, k_{a3}

For patient undertaking same insulin in basal and bolus injections, k_{ba} and k_{bo} in the model are assumed to have the same value.

3. PARAMETER ESTIMATION FOR MODELING

The model described above was applied to one real patient who has type-1 diabetes. The subject undergoing the experiment weighted 55kg and wore an insulin pump for insulin infusion. She also wore the MiniMed CGMS for five days during the experiment period. During that period, the meal contents and the insulin doses were recorded on a diary. These meal contents then were quantified by a dietician. No special arrangement was made for this experiment. The patient was asked to live on her normal way with meals and works as usual. The data from the patient accompanied with a complete diary on meals and insulin dosages are recorded. These data are then fitted into the model abovementioned. The modelling is aimed to find the parameters that minimize the sum of squares of the output errors. To compute these output errors, BG is computed by integrating the modified Hovorka model described in Section 2, starting with a set of parameters and initial conditions. The initial parameters are taken from the parameters of Marchetti *et al*. (2008). The steady-states values of the modified Hovorka model which correspond to a fasting level of BG are prepared in advance from the same model and are taken to initiate the integration for optimization. These initial states for integration are then updated from iteration to iteration using the resulted states in the last fasting stage of the previous run.

The modelling starts to fit themodel to the CGMS data of the first two days by making uses of the reported quantified CHOs and insulin doses. The parameters thus obtained are given as follows:

Parameter	Value	Unit	Parameter	Value	Unit
S_{IT}^f / V_I	0.019	$Min^{-1} \cdot mU^{-1} \cdot kg$	k_{12}	0.237	min^{-1}
S_{ID}^f / V_I	0.003	$Min^{-1} \cdot mU^{-1} \cdot kg$	k_{a1}	0.017	min^{-1}
S_{IE}^f / V_I	0.052	$mU^{-1} \cdot kg$	k_{a2}	0.273	min^{-1}
EGP_0	0.051	$mmole \cdot kg^{-1} \cdot min^{-1}$	k_{a3}	0.128	min^{-1}
F_{01}^c	1.899	$mmole \cdot min^{-1}$	k_e	0.036	min^{-1}
k	0.34	–	$t_{MAX,G}$	22.91	min
$V_{MAX,LD}$	2.156	$mU \cdot min^{-1}$	k_{a1^*}	0.005	min^{-1}
$k_{M,LD}$	64.182	mU	k_{a2^*}	0.054	min^{-1}

With the resulting parameters, the fitting of the real CGMS data to the model is shown in Figure 1. In this figure, the fitting of the model to the reported CGMS data in the first 48 hours looks good. The model is then used to predict the blood glucose in the remaining days. Figure 2 shows that the fitting is not good enough, but the trend is alright. The lack of fit in the extending time horizon is due to imprecise quantification of CHO intakes. If the remaining CHOs are allowed for some modifications, the fitting turns out to be more satisfactory (see Figure 3).

4. OPEN-LOOP CONTROL VIA SUBCUTANEOUS INSULIN INFUSION/INJECTION

Using an artificial pancreas, subcutaneous infusion of insulin according to a pre-programmed basal and bolus dosages is one approach to control the blood glucose of a type-1 diabetic patient in an open-loop manner. However, artificial pancreas is somewhat an expensive device that most of the patients may not afford. Fortunately, due to the availability of effective long acting insulin, the pre-programmed subcutaneous insulin injection can also be applied to patients who do not use artificial pancreas. The multiple subcutaneous injections with long acting and short acting insulin can be used to mimic the insulin secretions in a normal body. The basal insulin rate is aimed to maintain a given fasting level of blood glucose (e.g. 100 mg/dl). The bolus insulin dose is taken to enhance the control of blood glucose at each CHO intake.

4.1 Development of bolus dosage plan for Prandial CHO-uptake

While planning the bolus dosage under a prandial condition, some constraints should be considered. These constraints come from clinical demands for normal control of blood glucose. For example,

(1). Fasting blood glucose ≤ 100 mg/dl (≤ 5.6 mmol/l)

(2). Two-hour Post-prandial blood glucose $\leq$ 120 mg/dl

(3). In all time, blood glucose $\geq$ 70 mg/dl and never less than 50 mg/dl

The above standards may not be achievable by a type-1 diabetic patient in real practice. Apart from keeping patients from a hyperglycemia status, type-1 diabetic patient should be cautious to keep from having hypoglycaemia, especially during midnight (i.e. approx. 6 hours after dinner). Thus, in order to accommodate properly the blood glucose concerns in many aspects, the determination of bolus dosage for a CHO-intake is thus formulated as the problem of the following:

$$\underset{u_{bo}}{Min}\left\{\left|G_{av}(t^*,u_{bo}(x_i))-\gamma_1^*\right| \text{ given } |\, CHO=x_i \text{ and } G_{fasting}=\gamma_o\right\} \quad (13)$$

$$s.t. \quad \begin{cases} (1)\ G(t)\geq \gamma_*, \\ (2)\ G(t)<\gamma^* \ \forall t\geq 0\ , \end{cases}$$

Where, x_i, i=1, 2, 3 is the grams of CHO-intake in each meal, $\gamma^*, and\ \gamma_*$ are parameters to be assigned, which may vary according to the physician on a patient-to-patient basis for constraining blood glucose. Notice that, here, γ_* is taken as 70mg/dl. In other words, $\underline{G}\geq 70\ mg/dl$ is a hard constraint for patient to avoid from having hypoglycemia. The value of t^* is taken as 6hrs, since each meal is usually 6 hours apart from one to the other. $G_{av}(6hrs,u_{bo}(x_i))$ is the average value of G in a 6-hours period with x_i CHO-intake and $u_{bo}(x_i)$ bolus dosage.

To solve the problem in Eq. (13), first, we need the function $u_{bo}(x_i)$ and a basal insulin amount, $u_{ba}(G_{fasting})$, to maintain the blood glucose at a specified fasting level. The latter is used to mimic the secretion of the basal insulin in a normal human body. Mathematically, basal insulin can be considered as a step dose lasting for 24 hours a day that leads G to a fasting level. In fact, this value can be obtained by solving the set of algebraic equations obtained from setting the derivatives in the extended Hovorka model to zeros. The fasting glucose to mimic the effect of the secretion of basal insulin in a normal human body is taken as 100 mg/dl in this study (γ_0=100 mg/dl). A lower value may also be taken, however, a too low value may lead Eq.(13) without having feasible solution. Based upon this basal insulin amount (or, in other words, the targeting blood glucose) the bolus dosage plan will then be computed.

Next, we need to develop the function, $u_{bo}(x_i)$, which describes the required bolus dosage to a CHO intake from meals. The parameters $\gamma^*, and\ \gamma_1^*$ are considered for type-1 diabetic patients to have an acceptable glycated hemoglobin (i.e., hemoglobin HbA_{1c} or, simply, A1c) value. The use of hemoglobin A1c for monitoring the degree of control of glucose metabolism in diabetic patients was proposed in 1976 by Koenig and coworkers. A buildup of A1c within the red cell reflects the average level of glucose to which the cell has been exposed during its life cycle (approx. 120 days). Thus,

the A1c level is proportional to the averaged blood glucose concentration over the previous four weeks to three months. According to ADA (American Diabetes Association), the mean plasma glucose concentration (MPG) is related to HbA_{1c} with an empirical equation of the following:

MPG (mg/dl) = (35.6* HbA_{1c}) - 77.3, or, MPG (mmol/l) = (1.98* HbA_{1c}) - 4.29 (14)

A simpler and approximately equivalent formula can also be written as:

$$MPG(mg/dl) = 35*(A1c-5)+100 \quad (15)$$

Where, MPG is the mean plasma glucose concentration in the last three months. Thus,

$$A1c = \left(MPG-100\right) \div 35+5 \quad (16)$$

If the daily average blood glucoses (i.e. $G_{av}(24hrs)$) are equal from day to day in a period of at least three months, the MPG will equal to its daily time-average. Notice that the glucose concentration in the plasma is higher than the glucose concentration in the whole blood by about 11%. In the mathematical model, the glucose concentration G is referred to the whole blood. As a result, in terms of blood glucose as described by the model, Eq.(16) needs to be updated as:

$$A1c \cong \left[G_{av}(24hrs)\times 1.1-100\right] \div 35+5 \quad (17)$$

For easier application, one may consider to replace the $G_{av}(24hrs)$ with the following:

$$G_{av}(24hrs) \cong \left[\sum_{i=1}^{3} G_{av}(6hrs, u_{bo}(x_i)) + G_{fasting}\right] * 0.25 \quad (18)$$

And,

$$A1c \cong \left[\left\{\sum_{i=1}^{3} G_{av}(6hrs, u_{bo}(x_i)) + G_{fasting}\right\} * 0.25\times 1.1-100\right] \div 35+5 \quad (19)$$

Where, x_1, x_2, x_3 are CHO amounts in terms of grams taken from the daily three meals. Eq.(18) compute the mean BG by assuming that daily BG has a level at $G_{av}(6hrs)$ in a period of three meals (i.e.18 hours) and at 100mg/dl in the fasting period (i.e. another 6 hrs). Thus, specifying γ_1^* in Eq.(13) is to specify the target A1c as shown in Figure 4. An effective control of blood glucose should make this A1c value to remain below 7. In practical treatment, the values of γ^*, and γ_1^* may differ from subject to subject. If a bolus-to-CHO relation is available, then, given a daily CHO-plan, the average blood glucose can be computed from integrating the model. A graphical approach to the solution of a bolus-to-CHO relation will be demonstrated in the example that follows.

4.2 Case study

As mentioned, the basal insulin amount versus the fasting blood glucose levels can be calculated from the steady-state solution to the modified Hovorka model given in Section 2. For this case, the basal insulin amounts corresponding to each possible fasting glucose level are prepared and plotted in Figures 4. On the other hand, under a basal dose that leads to a fasting glucose of 100mg/dl, the responses of the blood glucose to different CHO intakes are computed. Based on these responses, the average blood glucoses at 4hrs and 6 hrs, together with maximum and minimum values under the same dosage are computed and plotted in Figure 5 and Figure 6, , with an insulin increment of 0.5 unit. The values of γ^*, and γ_1^* are then specified in order to obtain the bolus dose. As an example in this case, they are selected as 320, and 120, respectively.

The feasible regions to satisfy condition (1) and condition (2) of Eq. (13) are plotted for specific CHO intakes, starting from 15grams to 60grams, with an increment of 15grams. As shown in Figure 5, the feasible region that satisfies condition (1) and condition (2) is the region spanned by the pink and red lines. In each case (e.g. Figure 5 and Figure 6), there is u_{bo} that corresponding to the given CHO value, x. However, in case there is no feasible solution exists that will give $G_{av}(6hrs)$ exactly at 120 mg/dl, the bolus dosage at the boundary of the feasible region will be taken. By increasing the CHO amount, x, at an increment of 15 grams, a curve of bolus insulin required for different prandial CHOs can be obtained as shown in Figure 7. Thus, under a give basal insulin amount, the bolus dosage required for each CHO-intake can be read from these curves. If, a CHO meal-plan is taken (e.g., breakfast: 30gm, lunch: 60gm, dinner:60gm) with the bolus dosage plan as shown in Fig. 7 (e.g. breakfast: 1.05U, lunch: 2.1U, dinner: 2.1U), the averaged blood glucose could be expected to be 113.5 which gives 5.76 for the A1c value. Compared to the current record from the CGMS, the A1c value as well as the blood glucose could be significantly improved.

5. CONCLUSIONS

Modeling glucose-insulin interactions with real CGMS data and a model extended from Hovorka and his coworkers (Hovorka *et al*., 2002; Hovorka *et al.*, 2004) are studied. Using the mathematical model as a frame work, dynamic models are built for a case study. Data from a continuous glucose monitoring system (CGMS, MiniMed) are used to estimate the parameters in the model. As the CHO contents in various foods are fuzzy due to natural language, the CHO values thus quantified are subject to certain extent of uncertainties. As a result, during the parameter estimation, these quantified CHO values need to be modified. The resulting models are then used to determine the daily basal and bolus dosages to mimic the secretion of insulin of a human body and control the blood glucose to an acceptable level. The basal amount is to be determined to maintain the fasting glucose value at a given level. The bolus dosage is then determined based upon this basal insulin and the CHO intake in each meal. The bolus is aimed to keep the blood glucose within upper and lower bounds. The lower bound is

70 mg/dl which is normally considered in medical treatment to prevent the occurrence of hypoglycermia. The upper bound can be considered on a person-to-person basis. Besides setting the glucose value in the upper/lower bounds, the bolus dosage plan is also aimed to have a targeted A1c value, which is normally less than 7.0 in general medical treatments for the diabetes patients. The basal insulin amount and the bolus dosage plan are demonstrated with the utilization of the developed models.

REFERENCES

1. Hovorka, R. F. Shojaee-Moradie, P. V. Carroll, L. J. Chassin, I. J. Gowrie, N. C. Jackson, R. S. Tudor, A. M. Umpleby, and R. H. Jones, "Partitioning glucose distribution/transport, disposal, and endogenous production during IVGTT," *Am J Physiol Endocrinol Metab*, vol. 282, no. 5, pp. E992–1007, May 2002.

2. Hovorka R., V. Canonico, L. J. Chassin, U. Haueter, M. Massi-Benedetti, M. O. Federici, T. R Pieber, H. C Schaller, L. Schaupp, T. Vering and M. EWilinska", Nonlinear model predictive control of glucose concentration in subjects with type 1 diabetes" Physiol. Meas. vol.25(2004), pp.905–920.

3. Koenig RJ, Peterson CM, Jones RL, Saudek C, Lehrman M, Cerami A (1976). "Correlation of glucose regulation and hemoglobin AIc in diabetes mellitus". *N. Engl. J. Med.* **295** (8): 417–20.

4. Gianni Marchetti , M. Barolo , L. Jovanovic , H. Zisser , D. E. Seborg, "A feedforward-feedback glucose control strategy for type 1 diabetes mellitus", JPC, 18 (2008) 149-162.

5. Wilinska M. E., L. J. Chassin, H. C. Schaller, L. Schaupp, T. R. Pieber, and R. Hovorka, "Insulin kinetics in type–1 diabetes: Continuous and bolus delivery of rapid acting insulin," IEEE Trans. Biomed. Eng., vol. 52, no. 1, pp. 3–12, 2005.

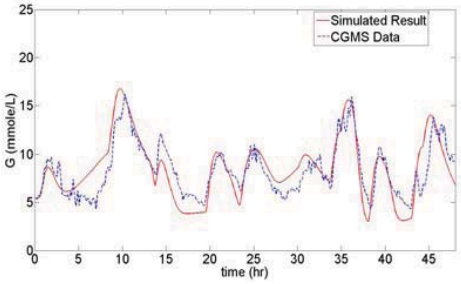

Figure 1. Fitting of the CGMS data to the model

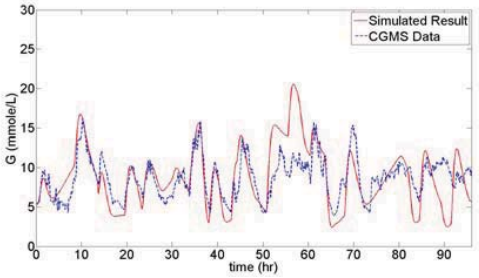

Figure 2. Validation of model using the original CHO and insulin data (case 1)

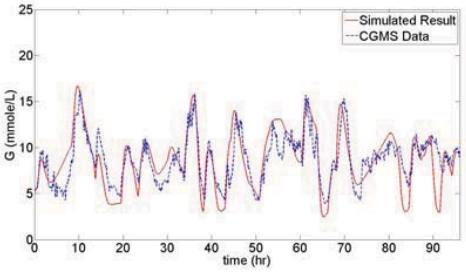

Figure 3. The blood glucose excursions after meal CHO being modified (Case 1).

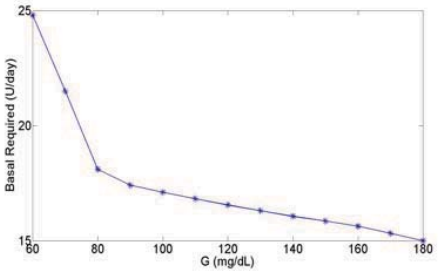

Figure 4. The basal dose for fasting blood glucose

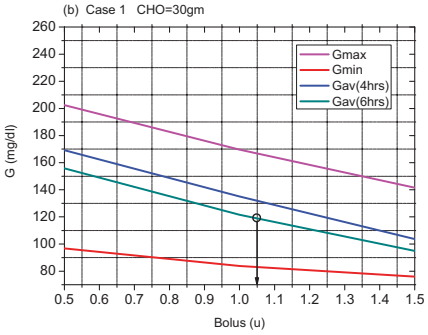

Figure 5. Graphical solution to Eq.(13), CHO intakes at 30gms.

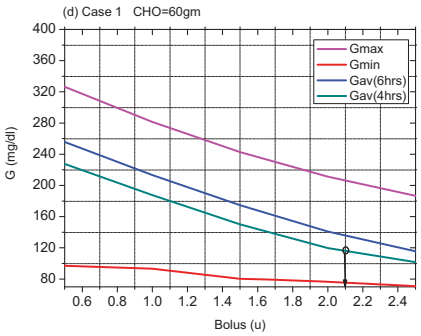

Figure 6. Graphical solution to Eq.(13), CHO intakes at 60gms.

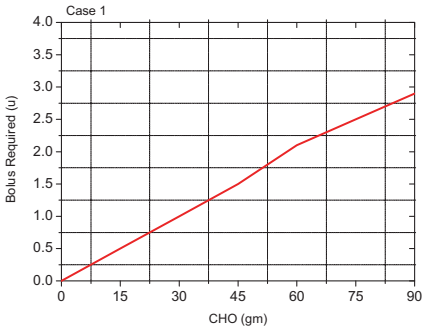

Figure 7. Bolus dose v.s. CHO for Case 1 ($G_{fasting}$=100mg/dl)

Table 4. CHO-plans vs A1c for Case 1

A1c*: computed from G_{av}(6hrs)

CHO-plan (g)			MG (24hr)	MPG (24hr)	A1c	A1c*
B	L	D	mg/dL			
15	45	45	114.52	125.97	5.7	5.7
15	45	60	113.94	125.33	5.7	5.7
15	60	45	111.58	122.74	5.6	5.7
15	60	60	111.22	122.35	5.6	5.7
30	45	45	112.39	123.62	5.7	5.7
30	45	60	111.94	123.14	5.7	5.7
30	60	45	110.63	121.70	5.6	5.7
30	60	60	110.35	121.39	5.6	5.7

Nonlinear Model-Based Control of an Experimental Reverse Osmosis Water Desalination System ⋆

Alex R. Bartman, [*] **Panagiotis D. Christofides,** [*,**,1] **Yoram Cohen** [*]

[*] *Department of Chemical and Biomolecular Engineering, University of California, Los Angeles, CA 90095-1592 USA.*
[**] *Department of Electrical Engineering, University of California, Los Angeles, CA 90095-1592, USA.*

Abstract: This work focuses on the design and implementation of a nonlinear model-based control system on an experimental reverse osmosis (RO) membrane water desalination system in order to deal with large set-point changes and variations in feed water salinity. A dynamic nonlinear lumped-parameter model is derived using first-principles and its parameters are computed from experimental data to minimize the error between model predictions and experimental RO system response. Then, this model is used as the basis for the design of a nonlinear control system using geometric control techniques. The nonlinear control system is implemented on the experimental RO system and its set-point tracking capabilities are successfully evaluated.

Keywords: Process control, process monitoring, model based control, nonlinear process systems

1. INTRODUCTION

Reverse osmosis (RO) membrane desalination has emerged as one of the leading methods for water desalination due to the low cost and energy efficiency of the process (Rahardianto et al. (2007)). Lack of fresh water sources has necessitated further development of these desalination plants, especially in areas with dry climates. Even with advances in reverse osmosis membrane technology, maintaining the desired process conditions is essential to successfully operating a reverse osmosis desalination system. Seasonal, monthly, or even daily changes in feed water quality can drastically alter the conditions in the reverse osmosis membrane modules, leading to decreased water production, sub-optimal system performance, or even permanent membrane damage. In order to account for the variability of feed water quality, a robust process control strategy is necessary. In a modern reverse osmosis (RO) plant, automation and reliability are elements crucial to personnel safety, product water quality, meeting environmental constraints, and satisfying economic demands. Industrial reverse osmosis desalination processes primarily use traditional proportional and proportional-integral control to monitor production flow and adjust feed pumps accordingly (Alatiqi et al. (1999)). While such control strategies are able to maintain a consistent product water (permeate) flow rate, they may fail to provide an optimal closed-loop response with respect to set-point transitions owing to the presence of nonlinear process behavior (Chen et al. (2005)). In some cases, permeate production can decrease due to scaling or fouling on the membrane surface. When this occurs, traditional control algorithms force the feed pumps to increase feed flow rate leading to an increased rate of scaling, irreversible membrane damage, and eventual plant shutdown. Traditional process control schemes are also unable to monitor plant energy usage and make adjustments toward energy-optimal operation. Model based control is a promising alternative to traditional RO plant control strategies. Several model based methods such as model-predictive control (MPC) and Lyapunov-based control have been evaluated via computer simulations for use in reverse osmosis desalination (Abbas (2006); McFall et al. (2008); Bartman et al. (2009b); Gambier and Badreddin (2002)). Experimental system identification and MPC applications can also be found in the literature (Assef et al. (1997); Burden et al. (2001)). Model based control methods have also been used in conjunction with fault detection and isolation schemes to improve robustness of control methods in the presence of sensor and actuator failures (McFall et al. (2008)). Other automatic control methods utilize model based control based on a linear model (Alatiqi et al. (1989)); using step tests to create a model that is a linear approximation around the desired operating point. Several other traditional control methods have also been studied in the context of RO system integration with renewable energy sources (Herold and Neskakis (2001); Liu et al. (2002)). Motivated by these considerations, the goal of this work is to evaluate the effectiveness of a feedback linearizing nonlinear model-based controller through application to an experimental reverse osmosis desalination system. The nonlinear model-based controller is shown to possess excellent set-point tracking capabilities. The nonlinear controller is also shown to outperform a proportional-integral control system.

⋆ Financial support from NSF and the California Department of Water Resources is gratefully acknowledged.
[1] Corresponding author: P.D. Christofides, pdc@seas.ucla.edu

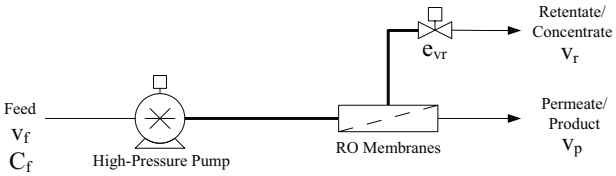

Fig. 1. Reverse osmosis system used for model development

2. RO SYSTEM MODEL

In this section, a fundamental model of a representative RO desalination system is developed including all of the basic elements present in UCLA's experimental RO desalination system. In this system, shown in Fig. 1, water enters the feed pump, which is equipped with a variable frequency drive (VFD), and is pressurized to the feed pressure P_{sys}. The pressurized stream enters the membrane module where it is separated into a low-salinity product (or permeate) stream with velocity v_p, and a high-salinity brine (or retentate) stream with velocity v_r. In the model, the individual spiral-wound membranes in series are assumed to be one large spiral-wound membrane in one large vessel, where any effects of individual membrane vessel interconnections are neglected. The pressure downstream of the actuated valve and at the permeate outlet is assumed to be equal to atmospheric pressure.

The model is based on a mass balance taken around the entire system and an energy balance taken around the actuated retentate valve. In the model derivation, it is assumed that the water is an incompressible fluid, all components are operated on the same plane (so potential energy terms due to gravity can be neglected), and the density of the water is assumed to be constant. It is also assumed that the effective concentration in the membrane module is a weighted average of the feed concentration and the brine stream concentration (see Eq. 6 below). The model derivation results in a nonlinear ordinary differential equation for the retentate stream velocity and an algebraic relation for the system pressure. This model is an adaptation of a model developed in our previous work used to describe a similar reverse osmosis desalination system (McFall et al. (2008)). In the previous work, the system utilized a feed pump with a constant feed flow rate, but used a separate bypass stream with an actuated valve to control the velocity of the water feeding to the membrane units. An equation for the osmotic pressure based on effective concentration and temperature in the membrane unit was also developed in (Lu et al. (2007)), and is used as an estimate in the model. Specifically, an energy balance is first taken around the retentate valve which leads to the following differential equation:

$$\frac{dv_r}{dt} = \frac{P_{sys}A_p}{\rho V} - \frac{1}{2}\frac{A_p e_{vr} v_r^2}{V} \tag{1}$$

where v_r is the retentate stream velocity, P_{sys} is the system pressure, A_p is the pipe cross-sectional area, ρ is the fluid density, V is the system volume and e_{vr} is the retentate valve resistance. To compute an expression for the system pressure in terms of the other process variables, an overall steady-state mass balance is taken to yield:

$$0 = v_f - v_r - v_p \tag{2}$$

where v_f is the feed stream velocity and v_p is the permeate stream velocity. In order to get an expression for the system pressure, the following classical expression is used for the computation of the permeate stream velocity:

$$v_p = \frac{A_m K_m}{\rho A_p}(P_{sys} - \Delta\pi) \tag{3}$$

where A_m is the membrane area, K_m is the membrane overall mass transfer coefficient, and $\Delta\pi$ is the difference in osmotic pressure between the feed side of the membrane and the permeate side. Substituting Eq. 3 into Eq. 2, the following expression for the system pressure (P_{sys}) is obtained:

$$P_{sys} = \frac{\rho A_p}{A_m K_m}(v_f - v_r) + \Delta\pi \tag{4}$$

where the osmotic pressure ($\Delta\pi$) and effective average concentration at the membrane surface (C_{eff}) on the feed side can be computed from the following relations:

$$\Delta\pi = \delta C_{eff}(T + 273) \tag{5}$$

$$C_{eff} = C_f(a + (1-a)((1-R) + R(\frac{v_f}{v_r}))) \tag{6}$$

where C_f is the amount of total dissolved solids (TDS) in the feed, a is an effective concentration weighting coefficient, δ is a constant relating effective concentration to osmotic pressure, T is the water temperature in degrees Celsius, and R is the fractional salt rejection of the membrane. Substituting Eq. 4 into the energy balance equation of Eq. 1 yields the following nonlinear ordinary differential equation for the dynamics of the retentate stream velocity:

$$\frac{dv_r}{dt} = \frac{A_p^2}{A_m K_m V}(v_f - v_r) + \frac{A_p}{\rho V}\Delta\pi - \frac{1}{2}\frac{A_p e_{vr} v_r^2}{V} \tag{7}$$

Using the above dynamic equation, various control techniques can be applied using the valve resistance value (e_{vr}) as the manipulated input. As the valve resistance goes to zero, the valve behaves as an open pipe; as the valve resistance approaches infinity, the valve behaves as a total obstruction and the flow velocity goes to zero (Bird et al. (2002)). To accurately model the valve dynamics and to relate the experimental results to the concept of valve resistance value (e_{vr}), the concept of valve C_v is used. The definition of C_v for a valve in a water system is:

$$C_v = \frac{Q_r}{\sqrt{P_{sys}}} \tag{8}$$

where Q_r is the volumetric flow rate ($Q_r = A_p v_r$) through the retentate valve. In order to obtain an expression for C_v as a function of the retentate valve resistance (e_{vr}), we consider the steady state form of the energy balance of Eq. 1, solve the resulting equation for P_{sys} and substitute the resulting expression for P_{sys} into Eq. 8 to yield:

$$C_v = \frac{A_p}{\sqrt{\frac{1}{2}\rho e_{vr}}} \tag{9}$$

Depending on the type of valve and its flow characteristics, it is assumed that the C_v values (and in turn, the e_{vr}

values) can be related to the valve position (percentage open) through the following empirical logarithmic relation based on commercially available valve data (Bartman et al. (2009b)):

$$O_p = \mu \ln e_{vr} + \phi \tag{10}$$

where μ and ϕ are constants depending on the valve properties. The values of μ and ϕ for this model are taken from a paper based on the same experimental system at UCLA (Bartman et al. (2009b)). For the model presented in this paper, the curve relating valve position (O_p) to resistance value (e_{vr}) is shown in Fig. 2. It can be seen in Fig. 2 that as the valve position goes to zero (fully closed), the valve resistance values begin to grow at an increasing rate; and as the valve approaches the fully-open position, the resistance values change slowly. The data from the experimental system is also plotted on the figure, and it can be seen that the data does not fit the same logarithmic relation as the ideal valve curve. Due to the shape of the experimental data curve, the data is fit in three segments with curve fits following a similar form as the theoretical curve. The first curve fit is applied to valve resistance (e_{vr}) values of approximately 205 to 212 and takes the form:

$$O_p = -84.428 \ln(e_{vr}) + 459.21 \tag{11}$$

For e_{vr} values between 212 and 6200, O_p is computed by:

$$O_p = -2.0473 \ln(e_{vr}) + 18.141 \tag{12}$$

while for e_{vr} values above 6200, O_p is computed by:

$$O_p = -0.0778 \ln(e_{vr}) + 0.9476 \tag{13}$$

This treatment of the valve characteristics allows for conversion of the experimental values of O_p to values of e_{vr} in the model-based nonlinear control algorithm, and allows for values of e_{vr} generated by the control algorithm to be translated to values of O_p to be sent to the actuated valve on the experimental system. Capturing the nonlinearity present in the valve is extremely crucial when applying the control algorithms to the experimental system.

2.1 Computation of Nonlinear Model Parameters Based on Experimental Data

Most of the parameters of the model of Eqs. 7-13 such as the membrane area (A_m), water density (ρ), pipe cross-sectional area (A_p), and system volume (V) have constant values which can be obtained from the experimental system. Another key model parameter, the overall mass transfer coefficient (K_m) was computed to match the model response to experimental step-test data. Specifically, K_m was computed using steady state data from the experimental system by minimizing the difference between the model steady state and the experimental system steady state for various step tests. The computed values of K_m were then averaged to determine the best value for use in the model used for controller design. The values of the model parameters can be found in Table 1.

3. CONTROL ALGORITHMS

Two separate control loops are present in the control problem formulation. The first loop regulates the system pressure by adjusting the variable frequency drive (VFD) speed directly (effectively changing the feed flow rate). This control loop will be termed "loop I". In each set of experiments presented below, a proportional-integral (PI) feedback controller is used to keep the system pressure (P_{sys}) at the set-point value (P_{sys}^{sp}) of 150 psi. This control algorithm takes the form:

$$S_{VFD} = K_f(P_{sys}^{sp} - P_{sys}) + \frac{K_f}{\tau_f}\int_0^{t_c}(P_{sys}^{sp} - P_{sys})dt \tag{14}$$

where S_{VFD} is the control action applied to the variable frequency drives (VFD speed), K_f is the proportional gain and τ_f is the integral time constant. The second control loop (termed "loop II") uses a nonlinear model-based controller (for the purposes of comparison, and a PI controller is also used in loop II). The nonlinear controller utilizes the error between the retentate velocity and its corresponding set-point, but it also takes into account many additional system variables (El-Farra and Christofides (2001, 2003); Christofides and El-Farra (2005)). Specifically, the nonlinear model-based controller manipulates the actuated retentate valve position by using measurements of the feed flow velocity (v_f), feed salinity (C_f), and retentate flow velocity (v_r). The nonlinear controller is designed following a feedback linearization approach. To derive the controller formula, the following linear, first-order response in the closed-loop system between v_r and v_r^{sp} is requested:

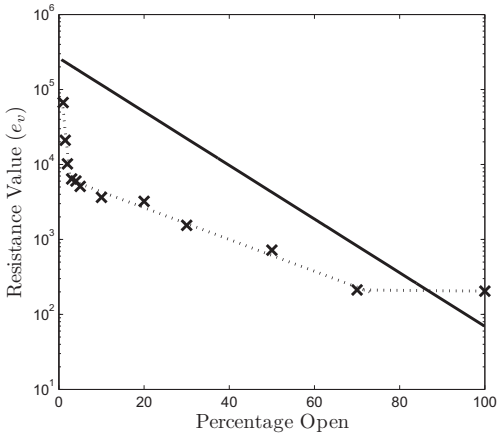

Fig. 2. Correlation between valve resistance value (e_{vr}) and valve percentage open (O_p) : commercial theoretical data (solid line), experimentally measured data (x), and curve fittings to experimental data (dashed lines) using Eqs. 11-13.

Table 1. Process model parameters based on experimental system data.

ρ	=	1007	kg/m^3
V	=	0.6	m^3
A_p	=	0.000127	m^2
A_m	=	15.6	m^2
K_m	=	6.4×10^{-9}	s/m
C_f	=	4842	mg/L
a	=	0.5	
T	=	22	$^\circ C$
R	=	0.97	

$$\frac{dv_r}{dt} = \frac{1}{\gamma}(v_r^{sp} - v_r) \tag{15}$$

It is noted that a first-order response is requested because the relative degree between v_r and e_{vr} is one (Christofides and El-Farra (2005)). Using this approach, the following formula is obtained for the nonlinear controller:

$$e_{vr} = \frac{\frac{1}{\gamma}(v_r^{sp} - v_r) - \frac{A_p^2}{A_m K_m V}(v_f - v_r) - \frac{A_p \delta (T+273)}{\rho V} C_{eff}}{\frac{-A_p}{2V}(v_r^2)} \tag{16}$$

To achieve offset-less response, integral action is added to the controller in Eq. 16 and the resulting controller takes the form:

$$e_{vr} = \frac{\frac{1}{\gamma}(v_r^{sp} - v_r) + \frac{1}{\tau_{NL}}\int_0^{t_c}(v_r^{sp} - v_r)dt}{\frac{-A_p}{2V}(v_r^2)} + \frac{-\frac{A_p^2}{A_m K_m V}(v_f - v_r) - \frac{A_p \delta (T+273)}{\rho V} C_{eff}}{\frac{-A_p}{2V}(v_r^2)} \tag{17}$$

As a baseline, the performance of the nonlinear controller is compared to a traditional form of control. Loop II, using PI control, uses the retentate (or concentrate) stream flow velocity to manipulate the actuated valve in order to regulate the retentate stream velocity/flow rate. Under PI control, the control system for loop II takes the form:

$$O_p = K_r(Q_r^{sp} - Q_r) + \frac{K_r}{\tau_r}\int_0^{t_c}(Q_r^{sp} - Q_r)dt \tag{18}$$

where Q_r is the retentate stream volumetric flow rate and Q_r^{sp} is the retentate stream flow rate set-point. In the experiments, the performance of the nonlinear controller implemented on the experimental system is compared to the performance of the nonlinear controller implemented on the process model and to the performance of the proportional-integral controller implemented on the experimental system. The control algorithms were programmed into the data acquisition and control software to operate in real-time with a sampling time of 0.1 seconds. Additionally, the actuated retentate valve is powered by an electric motor with a maximum operating speed which must be taken into account when attempting to simulate the nonlinear controller action. From testing on the experimental system, it was found that the actuated valve could travel its entire range in approximately 45 seconds; this provides an important constraint on the speed of valve opening/closing in the simulations of the form:

$$\left|\frac{dO_p}{dt}\right| \leq 2.22\frac{\%}{s} \tag{19}$$

To derive the constraint of Eq. 19, it is assumed that the valve speed is independent of valve position (valve always turns at maximum speed). This is a physical constraint which is intrinsically accounted for in the experimental results and is programmed into the nonlinear model-based controller simulation as well (to facilitate comparison). Additionally, when using the experimental system, the valve position is not allowed to fall under 1%, and any values sent to the valve above 100% are translated to the max value of 100% open. The lower constraint ($< 1\%$) is enforced so that the system pressure will not rise too rapidly. A constraint on the variable frequency drive is also placed to avoid pressure spikes (a maximum VFD speed of 4.5/10 is used). In the experiments presented in this work, the actuators do not reach these constraints.

4. EXPERIMENTAL SYSTEM DESCRIPTION

The experimental reverse osmosis water desalination system constructed at UCLA's Water Technology Research (WaTeR) Center was used for conducting the control experiments. This experimental system is comprised of a feed tank, two low-pressure feed pumps in parallel which provide enough pressure to pass the feed water through a series of cartridge filters while also providing sufficient pressure for operation of the high-pressure pumps, two high-pressure pumps in parallel (each capable of delivering approximately 4.3 gallons per minute at 1000 psi), and a bank of 18 pressure vessels containing Filmtec spiral-wound RO membranes. The high-pressure pumps are outfitted with variable frequency (or variable speed) drives which enable the control system to adjust the feed flow rate by using a 0-10V output signal. The bank of 18 membranes are arranged into 3 sets of 6 membranes in series; and for the control experiments presented below, only one bank of 6 membrane units was used. The experimental system uses solenoid valves controlled by the data acquisition and control hardware to enable switching between multiple arrangements of the membrane modules (2 banks of 6 in parallel to one bank of 6 in series, or any number of the modules in series) while also allowing for control of the flow direction through the membrane banks. After the membrane banks, an actuated valve is present to control the cross-flow velocity (v_r) in the membrane units, while also influencing system pressure. This valve is used as an actuator for the control system utilizing the control algorithms presented in section 3. The resulting permeate and retentate streams are currently fed back to the tank in an overall recycle mode, but for field operation the system can be operated in a one-pass fashion. The experimental system also has an extensive sensor and data acquisition network; flow rates and stream conductivities are available in real-time for the feed stream, retentate stream and permeate stream. The pressures before each high pressure pump, as well as the pressures before and after the membrane units (feed pressure and retentate pressure) are also measured. The system also includes sensors for measuring feed pH, permeate pH, in-tank turbidity, and feed turbidity after filtration (in real-time). A centralized data acquisition system takes all of the sensor outputs (0-5V, 0-10V, 4-20mA) and converts them to process variable values on the local (and web-accessible) user interface where the control system is implemented. The data is logged on a local computer as well as on a network database where the data can be accessed via the internet, while the control portion of the web-based user interface is only available to persons with proper authorization. The data acquisition and control system uses National Instruments software and hardware to collect the data at a sampling rate of 10 Hz and perform the necessary control calculations needed for the computation of the control action to be implemented by the control actuators. A photograph of the system can be seen in Fig. 3.

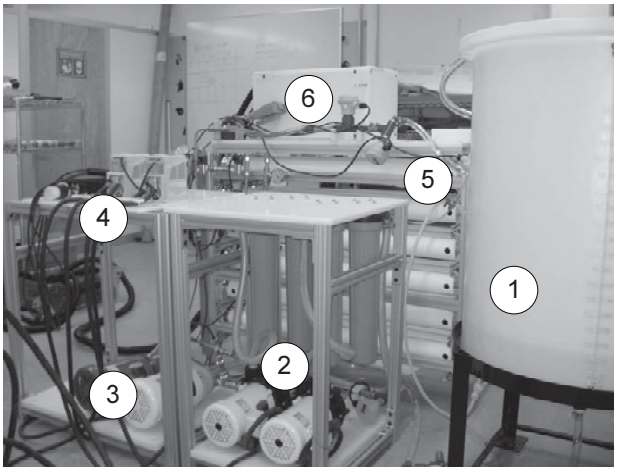

Fig. 3. UCLA experimental RO membrane water desalination system: (1) Feed tank, (2) Low-pressure pumps and prefiltration, (3) High-pressure positive displacement pumps, (4) Variable frequency drives (VFDs), (5) Pressure vessels containing spiral-wound membrane units (3 sets of 6 membranes in series), (6) National Instruments data acquisition hardware and various sensors.

5. EXPERIMENTAL CLOSED-LOOP RESULTS

In the control experiments presented in this paper, the experimental system was turned on and the PI loop controlling the variable frequency drives (loop I) was activated to bring the system pressure to a set-point of $P_{sys} = 150$ psi. The retentate flow rate was set to 1.5 gallons per minute (gpm). After the system had been operating at this steady state for a sufficient period of time, loop II was activated to manipulate the retentate valve. All data taken from the experimental system was averaged (after the experiments) using a 19 point moving average to remove most of the measurement noise. The following sets of experiments compare the performance of the nonlinear controller with the performance of the proportional and proportional-integral controllers. The closed-loop response observed for the nonlinear controller applied to the dynamic process model is used as a baseline for comparison of controller performance, as well as to determine an approximate range of controller tunings for the experimental system. In this set of experiments, the retentate flow rate set-point was changed from an initial value of 1.5 gpm to a new value of 0.8 gpm, while the VFD control loop is again maintained at a pressure set-point of 150 psi. In this set of experiments, the performance of the nonlinear controller with integral term is evaluated against the performance of a proportional-integral (PI) controller (both of these controllers are implemented experimentally), and the performance of the nonlinear controller with integral action applied to the dynamic process model via simulations. The feed salt concentration for these experiments was approximately 8200 ppm of NaCl. The tuning parameters for the controllers in this set of experiments can be found in Tables 2 and 3.

The results for these experiments are plotted in Figs. 4 - 5. In Fig. 4, it can be seen that all of the closed-loop results (simulated and experimental) decrease at the same rate initially (due to the valve opening/closing rate constraint). As expected, the simulated nonlinear model-based controller with integral term immediately converges to the set-point with no offset since it is not subject to any plant-model mismatch or measurement noise. As it is evident in Table 2, the integral time constant for the simulated controller is slightly different ($\tau_f = 0.01$, $\tau_f^{sim} = 0.0091$). The simulations where the nonlinear controller was applied to the process model were used to find an approximate range of controller parameters, but these values were implemented on the experimental system and changed slightly to achieve better closed-loop performance in the presence of plant-model mismatch. The speed of the closed-loop response under the nonlinear controller applied to the experimental system is slower in terms of convergence to the set-point than the one in the simulated case and the retentate flow rate reaches the set-point in about 145 seconds. The proportional-integral

Table 2. Loop I PI controller tuning parameters.

K_f	=	0.01
τ_f	=	0.1
K_f^{sim}	=	0.0091
τ_f^{sim}	=	0.1

Table 3. Loop II controller tuning parameters (both PI and nonlinear controllers).

K_r	=	1
τ_r	=	5
γ	=	0.6
τ_{NL}	=	10
γ^{sim}	=	0.6
τ_{NL}^{sim}	=	10

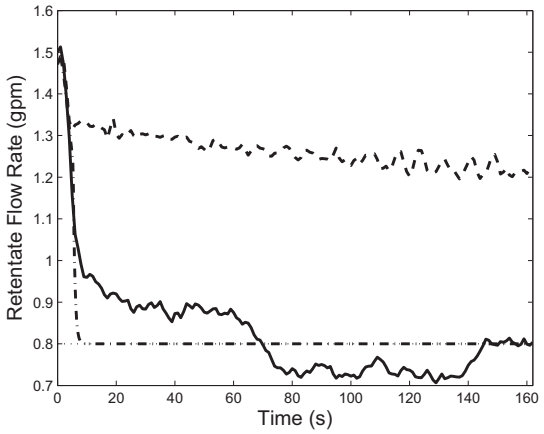

Fig. 4. Profiles of retentate flow rate (Q_r) with respect to time for retentate flow rate set-point transition from 1.5 to 0.8 gpm under proportional-integral control (dashed line), nonlinear model-based control with integral action (solid line) and nonlinear model-based control with integral action implemented via simulation on the process model (dash-dotted line). The horizontal dotted line denotes the retentate flow rate set-point ($Q_r^{sp} = 0.8$ gpm).

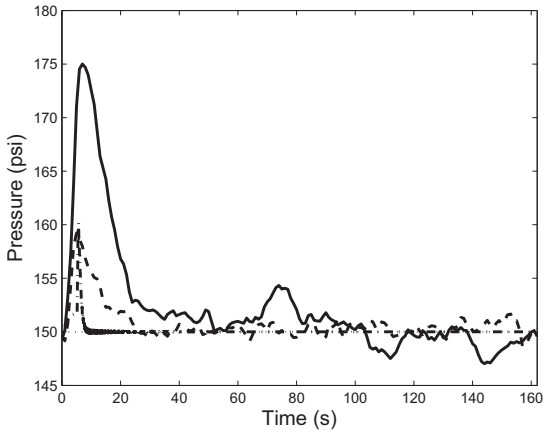

Fig. 5. Profiles of system pressure (P_{sys}) with respect to time for retentate flow rate set-point transition from 1.5 to 0.8 gpm under proportional-integral control (dashed line), nonlinear model-based control with integral action (solid line) and nonlinear model-based control with integral action implemented via simulation on the process model (dash-dotted line). The horizontal dotted line denotes the system pressure set-point ($P_{sys}^{sp} = 150$ psi).

(PI) controller with $\tau_r = 5$ leads to an extremely slow convergence to the set-point (on the order of 10 minutes). It is also seen that when a smaller integral time constant is used, it results in significant oscillations around the set-point due to the coupling between the two control loops. These oscillations cause large fluctuations in the feed flow rate (due to the VFD control loop) and could damage the feed pumps and cause fatigue on system components. Similar results are evident in Fig. 5. The application of the nonlinear controller to the experimental system causes the most deviation from the pressure set-point due to the speed at which it converges to the set-point. It can be seen that the PI controller causes almost no deviation from the set-point (approximately the same as the simulated nonlinear controller) because the convergence (change in valve position) is much slower. As the valve closes, it causes the system pressure to rise, forcing loop I to take action in order to keep the system pressure at the set-point. Slower valve actions allow more time for loop I to act and keep the system pressure at the set-point, such as in the case of the PI control with $\tau_r = 5$. Additional results from the experiments can be seen in the submitted journal paper (Bartman et al. (2009a)).

REFERENCES

Abbas, A. (2006). Model predictive control of a reverse osmosis desalination unit. *Desalination*, 194, 268–280.

Alatiqi, I., Ettourney, H., and El-Dessouky, H. (1999). Process control in water desalination industry: an overview. *Desalination*, 126, 15–32.

Alatiqi, I.M., Ghabris, A.H., and Ebrahim, S. (1989). System identification and control of reverse osmosis desalination. *Desalination*, 75, 119–140.

Assef, J.Z., Watters, J.C., Deshpande, P.B., and Alatiqi, I.M. (1997). Advanced control of a reverse osmosis desalination unit. *J. Proc. Cont.*, 4, 283–289.

Bartman, A.R., Christofides, P.D., and Cohen, Y. (2009a). Nonlinear model-based control of an experimental reverse osmosis water desalination system. *Industrial & Engineering Chemistry Research,* submitted.

Bartman, A.R., McFall, C.W., Christofides, P.D., and Cohen, Y. (2009b). Model predictive control of feed flow reversal in a reverse osmosis desalination process. *J. Process Contr.*, 19, 433–442.

Bird, R.B., Stewart, W.E., and Lightfoot, E.N. (2002). *Transport Phenomena, Second Edition.* John Wiley and Sons.

Burden, A.C., Deshpande, P.B., and Watters, J.C. (2001). Advanced control of a B-9 Permasep permeator desalination pilot plant. *Desalination*, 133, 271–283.

Chen, J., Wang, F., Meybeck, M., He, D., Xia, X., and Zhang, L. (2005). Spatial and temporal analysis of water chemistry records (19582000) in the Huanghe (Yellow River) basin. *Global Biogeochem. Cycles*, 19, GB3016.

Christofides, P.D. and El-Farra, N.H. (2005). *Control of Nonlinear and Hybrid Process Systems: Designs for Uncertainty, Constraints and Time-Delays,* 446 pages. Springer, New York.

El-Farra, N.H. and Christofides, P.D. (2001). Integrating robustness, optimality, and constraints in control of nonlinear processes. *Chemical Engineering Science*, 56, 1841–1868.

El-Farra, N.H. and Christofides, P.D. (2003). Bounded robust control of constrained multivariable nonlinear processes. *Chemical Engineering Science*, 58, 3025–3047.

Gambier, A. and Badreddin, E. (2002). Application of hybrid modeling and control techniques to desalination plants. *Desalination*, 152, 175–184.

Herold, D. and Neskakis, A. (2001). A small PV-driven reverse osmosis desalination plant on the island of gran canaria. *Desalination*, 137, 285–292.

Liu, C.C.K., Park, J., Migita, R., and Qin, G. (2002). Experiments of a prototype wind-driven reverse osmosis desalination system with feedback control. *Desalination*, 150, 277–287.

Lu, Y., Hu, Y., Zhang, X., Wu, L., and Liu, Q. (2007). Optimum design of reverse osmosis system under different feed concentration and product specification. *Journal of Membrane Science*, 287, 219–229.

McFall, C.W., Bartman, A.R., Christofides, P.D., and Cohen, Y. (2008). Control and monitoring of a high-recovery reverse-osmosis desalination process. *Industrial & Engineering Chemistry Research*, 47, 6698–6710.

Rahardianto, A., Gao, J., Gabelich, C.J., Williams, M.D., and Cohen, Y. (2007). High recovery membrane desalting of low-salinity brackish water: Integration of accelerated precipitation softening with membrane RO. *Journal of Membrane Science*, 289, 123–137.

Periodic Control of Gas-phase Polyethylene Reactors

Al-haj Ali, M., Ali, E.

Chemical Engineering Department, King Saud University
P.O.Box: 800, 11421 Riyadh, Saudi Arabia, (alhajali@ksu.edu.sa)

Abstract: Nonlinear model predictive control algorithm is used for the on-line control of polymer molecular weight distribution. The control of chain-length distribution is achieved by selecting a collection of points in the distribution and using it as set points for the control algorithm. An on-line Kalman filter is used to incorporate infrequent and delayed off-line molecular weight measurements. Through simulation; the control algorithm is evaluated, under tracking conditions as well as plant-model mismatch. The results demonstrate that the control algorithm can regulate the entire molecular weight distribution with high computational efficiency and minimum steady state error.

Keywords: Molecular weight distribution, nonlinear model predictive control, Kalman filter, polymerization reactor control, fluidized bed reactor, polyethylene

1. INTRODUCTION

Polymers today are crucial products that are used in all parts of our daily life. The range of applications includes standard applications as packaging materials and textile fibers, and special ones in the automobile and electrical industries. Molecular weight distribution (MWD) is considered as one of the fundamental properties that determines polymer properties and thus its applications. Therefore, it is important to monitor and control MWD during the industrial production of polymers. A significant amount of research has been done in the area of control, monitoring and modelling of polymerization reactors; Excellent reviews have been given by several researchers (Elicabe and Meira, 1988, Embirucu et al., 1996, Congalidis and Richards, 1998, Richards and Congalidis, 2006). A careful study of previous works, with focus on the description of polymer MWD, results in the following conclusions:

1. Most of the work that was done described polymer MWD by the weight average molecular weight (M_w), in addition to polydispersity index (PDI). Few researchers used the entire molecular weight distribution in their control studies. The use of Mw and PDI to describe polymer quality is helpful. However, sometimes, the molecular weight averages can be misleading when the molecular weight distribution shows bimodalities and/or it has high molecular weight tails. Besides, it is very useful to describe polymer quality by using the entire molecular weight distribution because in many polymer applications such as paints and paper coatings, it is required to specify such distribution properly (Sayer et al., 2001).

2. In polyolefins polymerization, the work done to control the entire MWD of the produced polymer used mixtures of different metallocenes (Chatzidoukas et al., 2007, Heiland and kaminsky, 1992) or a hybrid catalyst of Ziegler-Natta and metallocene catalysts in a one stage process (Shamshoum et al., 2003). The use of single reactor to produce the desired polymer is cost-efficient alternative. However, the mixture of different catalysts may lead to complex undesirable catalyst interactions and non-reproducible catalyst behaviour due to the high variability of the polymerization rate of each catalyst (Nele and Pinto, 2000). Additionally, the implementation of such catalyst systems requires a deep understanding of polymerization mechanisms using these catalysts; which is not a simple task. Finally, this method is still in the research phase and, it may take a long time before it can be (if it is developed successfully) widely implemented in industry. An alternative approach is to vary the polymerization conditions periodically in a single polymerization reactor. The periodic operation of continuous chemical reactors can improve the performance of the reacting system and allow better design and control of the molecular weight distribution in a single reactor (Nele and Pinto, 2000, Schiffino, 1995).

The scope of this work is to investigate the production of polyethylene, in a fluidized bed reactor, with a well-defined molecular weight distribution using nonlinear model predictive controller (NLMPC).

2. PROCESS MODEL

In fluidized-bed polyethylene reactors, the co-polymerization of ethylene and -olefin monomers is carried out using a multi-site Ziegler-Natta catalyst, which consists of three different types of active sites. Each active site produces polymer with molecular weight distribution that can be described by Schulz-Flory distribution. The polyethylene reactor process is depicted in Fig 1. The process model was

developed by (McAuley et al., 1995), modifications made in this model were described in (Ali et al., 2003).

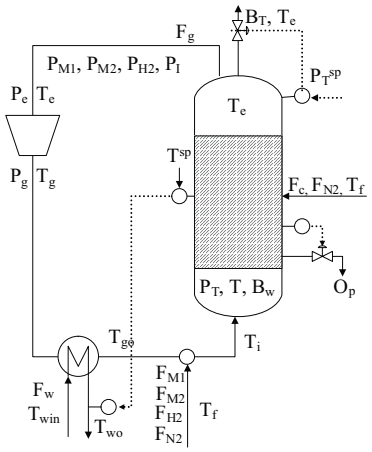

Fig. 1. Polyethylene reactor.

2.1 Molecular Weight Distribution Model

The instantaneous molecular weight distribution for each type of active sites can be described by Flory-Schulz exponential function (Kissin et al., 2005)

$$y_j^d = j \cdot q^2 \cdot \exp(-j \cdot q) \tag{1}$$

with q is the termination probability, j is the number of repeating units and y_j^d instantaneous weight distribution. As assumed above, the catalyst consists of three different active sites and the distribution of the polymers produced by each site type can be represented by Flory's most probable distribution. Thus, the overall distribution of the produced polymer can be calculated by the weighted sum of the three distributions as given below

$$y_{j,ins} = \sum_{i=1}^{3} w_i \cdot (y_j^d)_i \tag{2}$$

where $y_{j,ins}$ is the overall instantaneous molecular weight distribution, and w_i is the mass fraction of each site. The molecular weight distribution of the polymer accumulated in the reactor after a certain polymerization time can be calculated using the following equation:

$$\frac{dy_j}{dt} = \frac{O_p \cdot (y_{j,ins} - y_j)}{B_w} \tag{3}$$

here y_j is the cumulative molecular weight distribution, O_p is polymer production rate and B_w is mass of polymer in the reactor bed. Finally the GPC reading of the MWD is calculated by the following equation:

$$GPC = j \cdot y_j \cdot ln(10) \tag{4}$$

3. ON-LINE NLMPC ALGORITHM

In this work, the structure of the MPC version developed by Ali and Zafiriou (1993) that utilizes directly the nonlinear model for output prediction is used. A usual MPC formulation solves the following on-line optimization:

$$\min_{\Delta u(t_k),\ldots,\Delta u(t_{k+M-1})} \sum_{i=1}^{P} \left\| \Gamma(y(t_{k+i}) - R(t_{k+i})) \right\|^2 + \sum_{i=1}^{M} \left\| \Lambda \Delta u(t_{k+i-1}) \right\|^2 \tag{5}$$

subject to

$$A^T \Delta U(t_k) \le b \tag{6}$$

For nonlinear MPC, the predicted output, y over the prediction horizon P is obtained by the numerical integration of:

$$\frac{dx}{dt} = f(x,u,t) \tag{6}$$

$$y = g(x) \tag{7}$$

from t_k up to t_{k+P} where x and y represent the states and the output of the model, respectively. The symbols || . || denotes the Euclidean norm, k is the sampling instant, Γ and Λ are diagonal weight matrices and $R = [r(k+1) \ldots r(k+P)]^T$ is a vector of the desired output trajectory. $\Delta U(t_k)=[\Delta u(t_k) \ldots \Delta u(t_{k+M-1})]^T$ is a vector of M future changes of the manipulated variable vector u that are to be determined by the on-line optimization. The control horizon (M) and the prediction horizon (P) are used to adjust the speed of the response and hence to stabilize the feedback behavior. Γ is usually used for trade-off between different controlled outputs. The input move suppression, Λ, on the other hand, is used to penalize different inputs and thus to stabilize the feedback response. The objective function (Eq. 5) is solved on-line to determine the optimum value of $\Delta U(t_k)$. Only the current value of Δu, which is the first element of $\Delta U(t_k)$, is implemented on the plant. At the next sampling instant, the whole procedure is repeated.

To compensate for modeling error and eliminate steady state offset, a regular feedback is incorporated on the output predictions, $y(t_{k+1})$ through an additive disturbance term. Therefore, the output prediction is corrected by adding to it the disturbance estimates. The latter is set equal to the difference between plant and model outputs at present time k as follows:

$$d(k) = y_p(k) - y(k) \tag{7}$$

The disturbance estimate, d, is assumed constant over the prediction horizon due to the lack of an explicit means of predicting the disturbance. However, for severe modeling errors, or open-loop unstable processes the regular feedback is not enough to improve the NLMCP response. Hence, state or parameter estimation is necessary to enhance the NLMPC performance in the face of model-plant mismatch. In this work, Kalman filtering (KF) will be incorporated to correct the model state and thus, to address the robustness issue. Utilization of the NLMPC with KF requires adjusting an additional parameter, σ. More details on the integration of KF

with the NLMCP algorithm are given elsewhere (Ali and Zafiriou, 1993). In addition to state estimation by KF, the predicted output will be also corrected by the additive disturbance estimates of Eqn.7.

The main objective of the NLMPC is to control the entire MWD. It is also necessary to maintain acceptable polymer production rate. Process stability is another important issue which is handled through regulating the total gas pressure and the bed temperature. These two controlled variables are adapted via separate PI control loops. The design and tuning parameters of these loops are given elsewhere (Ali et al., 2003).

4. RESULTS AND DISCUSSION

It is worth mentioning that determining input trajectories that provide the desired distribution is difficult as the final polymer quality is sensitive to hydrogen concentration (X) value and the mass of the produced polymer. In this sense, maintaining the desired MWD during process operation is even more challenging. In the presence of model-plant mismatch and/or when unmeasured disturbances enter the plant, the situation becomes more complex. The control objective here is to produce broad polyethylene with well-defined MWD starting from narrow distribution and maintain it there. The results of this case are shown in Figs. 2 and 3. Four manipulated variables, which are the monomer, hydrogen, nitrogen and catalyst flow rates, are used. The weighting factors for these inputs are Λ=[0 0 20 50]. Four controlled variables, which represent specific points in the target MWD, are considered as shown by the dots in Fig 3. The weighting factor for all outputs is given the same value of Γ=[1 1 1 1]×100. The lower limit for the manipulated variables is set to zero and the upper limit is set to twice their nominal values. The MWD target function contains 103 points, however only four points were selected as controlled outputs to reduce the computation effort consumed by the NLMPC calculations. The input horizon (M) and output horizon (P) are taken equal to 1 and 4, respectively. A sampling time of 1 hr is used. Usually the GPC measurements are available at low frequency. Advanced measurement sensors that can provide measurements in the order of minutes are available but at high cost.

Fig. 3 demonstrates the ability of NLMPC to maintain the new set point for the polymer distribution with minor distortion in the distribution function. More interesting is the response of the manipulated variables as shown in Fig. 2. The resulted response of the manipulated variables is in the form of periodic functions. Long prediction and moving horizon capability of NLMPC helped the controller to understand the dynamic nature of the process to an extent that it produced cyclic input sequences. Moreover, Fig. 2 shows how the bleed flow rate (B_T) and the cooling water inlet temperature (T_w) varies by separate PI controllers to maintain the total pressure at 20 atm and the reactor temperature at 82 ^oC. Note that the manipulated variables used by NLMPC are plotted in discrete form because the NLMPC works in discrete time fashion.

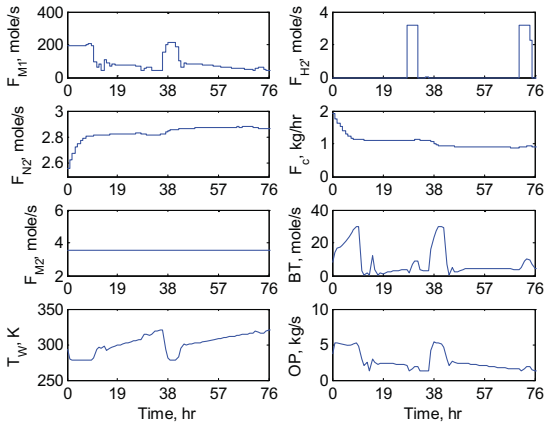

Fig. 2. Manipulated variable response using NLMPC.

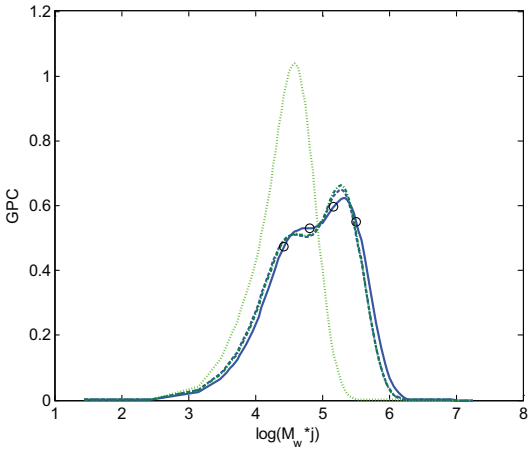

Fig. 3. MWD using NLMPC. Dotted line: initial distribution, solid: target, dashed: controlled distribution.

Next the algorithm was tested for targeting another MWD. In this case, seven points on the GPC curve is taken as the controlled variables with their weights are fixed at G=[1 100 100 200 100 50] ×102. The lower limit of F_{M1} is set to 40 mole/s to keep high monomer concentration in the reactor. The value of the rest of the parameters remains the same as before. The simulation results are shown in Figs. 4 - 5. Evidently, NLMPC generated suitable periodic input sequences that produce MWD close to the desired one as shown in Fig. 5. The MWD suffered from minor distortion; however exact match of the target function is not necessary especially when we know that the relative error in GPC measurements is around 10%. This outcome can be obtained at shorter simulation time. The small production rate is obvious from Fig. 4; in fact, the average production rate is found to be 2.42 kg/s. To improve the production rate, the latter is incorporated as a controlled variable in the NLMPC algorithm. Using γ=0.1 for the production rate, NLMPC managed to increase the polymer production to 2.86 kg/s but with notable loss of the MWD. Results are not shown here for simplicity. Increasing the weight of the designated

controlled output further will of course propagates the production rate but the MWD will depart away from the desired set point. Our investigation revealed the existence of trade-off between the production rate and broadening the MWD. Widening the distribution requires pronounced changes in hydrogen concentration inside the reactor. Increasing hydrogen concentration is achieved by feeding more hydrogen to the reactor this reduces ethylene polymerization rate and as a consequence reduces the overall production rate. Whereas, reducing hydrogen concentration is achieved by opening the vent (Lo and Ray, 2006) that allows hydrogen concentration in the reactor to escape, causing hydrogen concentration to fall quickly. Such reduction in the concentration affects positively on the production rate.

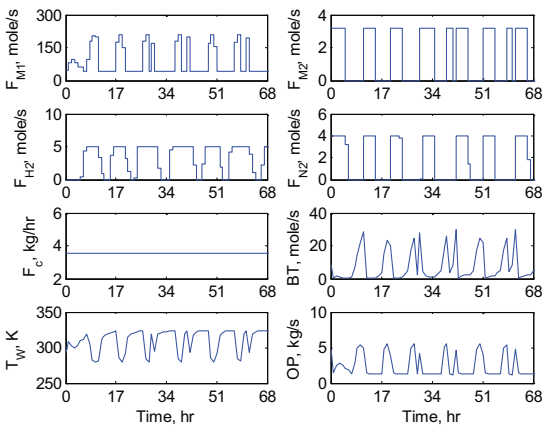

Fig. 4. Manipulated variable response using NLMPC. Decreasing polymer average molecular weight.

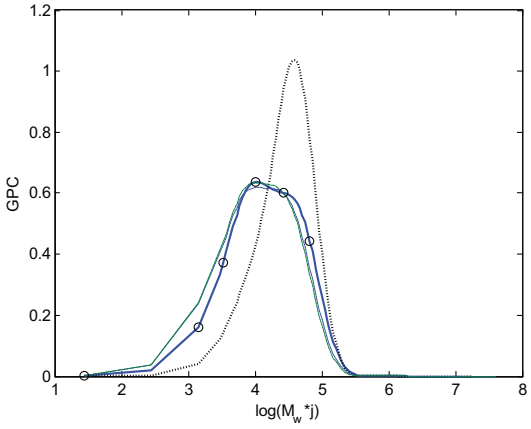

Fig. 5. MWD using NLMPC. Dotted line: initial distribution, solid: target, dashed: controlled distribution.

The previous simulations are carried out assuming perfect model. However, this is not always true in real practice. To test the robustness of NLMPC to reject the effect of modeling errors, the simulation of targeting higher molecular weight is repeated with−20% error in the reaction rate constant and catalyst activity. The results are shown in Figs. 6 - 7. It is evident that NLMPC is able to keep good control performance despite minor loss of controller performance.

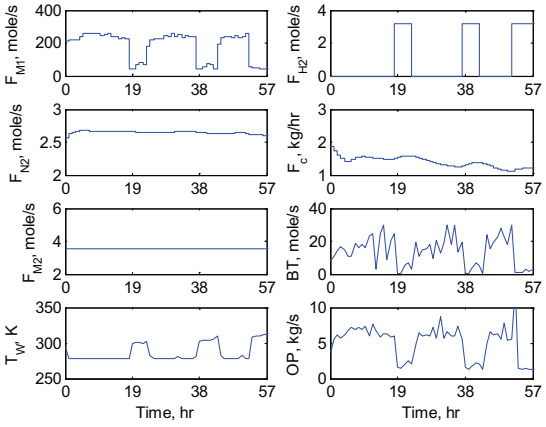

Fig. 6. Manipulated variable response using NLMPC in the presence of -20% in catalyst activation and reaction rate constant.

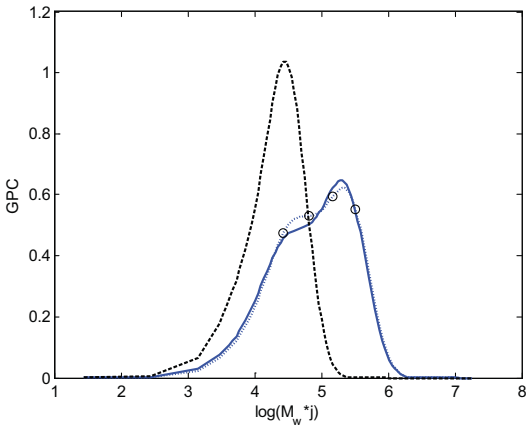

Fig. 7. MWD using NLMPC in the presence of -20% error in catalyst activation and reaction rate constant. Dotted line: initial distribution, solid: target, dashed: controlled distribution.

It is worth mentioning that controller performance could be improved more if the dynamics of hydrogen is faster. Since, hydrogen is not consumed in the reactor and large fluctuations in hydrogen concentration are required to broaden polymer distribution, improving controller performance would not be an easy task. This challenge can be solved using either a catalyst that is highly-sensitive to hydrogen as metallocenes or hydrogen consuming agent. The first approach depends on implementing a relatively new catalyst that is not widely used industrially (Galli and Vecellio, 2001). The second approach still needs more investigation to prove its applicability for the studied process. Finally, note that venting is usually used to reduce hydrogen concentration, as described above, however; venting reactor contents is not an economical choice because monomer also

escapes from the reactor. Nonetheless, no other choices are available.

5. CONCLUSIONS

In industrial applications, the molecular weight distribution of the produced polymer is usually measured using molecular weight averages and polydispersity index. In this article, we have presented an on-line MWD control technique to produce polymers with a target distribution in a fluidized-bed polymerization process. This strategy uses detailed polymerization process model, and Kalman filter to correct model states. A NLMPC controller is designed to control polymer MWD and polymerization process productivity. For the calculation of the MWD, selected points in polymer distribution curve are used as set-points for the controller that manipulates monomer, hydrogen, nitrogen and catalyst feed rates. To test the feasibility of the proposed MWD control technique, simulations have been carried out for ethylene gas-phase polymerization using conventional Zielger-Natta catalyst. The simulations suggest that the proposed control strategy can be useful new technique to control the MWD of polymer in continuous polymerization processes. The performance of the developed control algorithm can be improved more if the dynamic response of hydrogen concentration inside the polymerization reactor is less sluggish.

ACKNOWLEDGMENT

The financial support from Saudi Basic Industries Company (SABIC), (grant number 7/429), is greatly appreciated.

REFERENCES

Ali, E. M., Al-Humaizi, K. and Ajbar, A. (2003).Multivariable Control of a Simulated Industrial Gas-Phase Polyethylene Reactor. *Industrial and Engineering Chemistry Research,* **42,** 2349-2364.

Ali, E. M. and Zafiriou, E. (1993).Optimization-based Tuning of Non-linear Model Predictive Control with State Estimation. *J. of Process Control,* **3,** 97-107.

Chatzidoukas, C., Kanellopoulos, V. and Kiparssides, C. (2007).On The Production of Polyolefins with Bimodal Molecular Weight and Copolymer Composition Distributions in Catalytic Gas-phase Fluidized-bed Reactors. *Macromolecular Theory and Simulation,* **16,** 755-769.

Congalidis, J. P. and Richards, J. R. (1998).Process control of polymerization reactors: An industrial perspective. *Polymer Reaction Engineering,* **6,** 71-111.

Elicabe, G. E. and Meira, G. R. (1988).Estimation and Control in Polymerization Reactors. A Review. *Polymer Engineering and Science,* **28,** 121-135.

Embirucu, M., Lima, E. L. and Pinto, J. C. (1996).A Survey of Advanced Control of Polymerization Reactors. *Polymer Engineering and Science,* **36,** 433-447.

Galli, P. and Vecellio, G. (2001).Technology: Deriving Force Behind Innovation and Growth of Polyolefins. *Progress in polymer Science,* **26,** 1287-1336.

Heiland, K. and kaminsky, W. (1992).Comparison of Zirconocene and Hafnocene Catalysts for the Polymerization of Ethylene and 1-Butene. *Makromoleculare Chemie-Macromolecular Chemistry and Physics,* **193,** 601-610.

Kissin, Y. V., Mirabella, F. M. and Meverden, C. C. (2005).Multi-Center Nature of Heterogeneous Ziegler–Natta Catalysts: TREF Confirmation. *Journal of Applied Polymer Science,* **43,** 4351-4362.

Lo, D. P. and Ray, W. H. (2006).Dynamic Modeling of Polyethylene Grade Transitions in Fluidized bed Reactors Employing Nickel-Diimine Catalysts. *Industrial and Engineering Chemistry Research,* **45,** 993-1008.

McAuley, K. B., McDonald, D. A. and McLellan, P. J. (1995).Effects of Operating Conditions on Stability of Gas-phase Polyethylene Reactors. *AIChE,* **41,** 868-879.

Nele, M. and Pinto, J. C. (2000).Retrofitting of Industrial Olefin Polymerization Plants: Producing Broad MWDs Through Multiobjective Periodic Operation. *Journal of Applied Polymer Science,* **77,** 437-452.

Richards, J. R. and Congalidis, J. P. (2006).Measurement and Control of Polymerization Reactors. *Computers and Chemical Engineering,* **30,** 1447-1463.

Sayer, C., Arzamendi, G., Asua, J. M., Lima, E. L. and Pinto, J. C. (2001).Dynamic Optimization of Semicontinuous Emulsion Copolymerization Reactions: Composition and Molecular Weight Distribution. *Computers and Chemical Engineering,* **25,** 839-849.

Schiffino, R. S. (1995) USA.

Shamshoum, E. S., Chen, H. and Margarito, L. (2003) USA.

Control of Nonlinear System – Adaptive and Predictive Control

Jiri Vojtesek*, Petr Dostal*, Vladimir Bobal*

**Department of Process Control, Faculty of Applied Informatics,*
Tomas Bata University in Zlin, Czech Republic
(Tel: 00420576035199; e-mail: {vojtesek,dostalp,bobal}@fai.utb.cz)

Abstract: The goal of this paper is to propose suitable control methods for controlling of the highly nonlinear system represented by the mathematical model of the continuous stirred tank reactor (CSTR) with so called van der Vusse reaction inside. Temperature of the reactant is controlled by the heat removal of the cooling liquid in the reactor's jacket. Two control strategies were suggested – adaptive control and predictive control. The adaptive approach uses recursive identification for the optimal setting of the controller. The predictive control computes input sequence by the minimizing of the cost function constructed by the difference between output variable and reference signal. Both control strategies shows good control results and pertinence for the controlling of such type of systems.

Keywords: Adaptive control, Predictive Control, Polynomial methods, Recursive estimation, Nonlinear systems, CSTR, Simulation.

1. INTRODUCTION

Unfortunately, most of the processes in the technical praxis have nonlinear properties. Typical example of the nonlinear system can be found in the chemical or the biochemical industry where so called chemical reactor is used for production of the several chemicals or drugs (Corriou, 2004).

Controlling of these devices with the conventional methods where parameters of the controller are set at the beginning fixed during the control could result in non-optimal control responses because of changing parameters of the system. This inconvenience could be overcome with use of other control strategies which takes into account these changes, for example adaptive or predictive control. These two control strategies are compared in this paper in order to compare obtained simulation results.

The basic idea of adaptive control is that parameters or the structure of the controller are adapted to parameters of the controlled plant according to the selected criterion (Bobál *et al.*, 2005). Adaptation can be done for example by the modification of the controller's parameters by the change of the controller's structure or by generating an appropriate input signal, which is called "adaptation by the input signal".

The polynomial synthesis (Kučera, 1993) is one of the methods used in adaptive control for control synthesis of the system. This method is based on the input-output model of the controlled system or its transfer function. It can be classified as an algebraic method and is based on algebraic operations in the ring of polynomials. Polynomials are usually described in *s*-plane for continuous systems, in *z*-plane for discrete systems and in δ-plane for systems which come from δ-models of both the controlled system and the controller too (Middleton and Goodwin, 2004) and (Mukhopadhyay *et al.*, 1992).

One of the biggest advantages of the polynomial method compared to the conventional method is that it provides not only relations for computing of the controller's parameters but the structure of the controller too. This structure fulfils general requirements for control systems and input signals (reference signal and disturbance) and it can be used for controlling of the systems with negative properties from the control point of view, such as non-minimum phase systems or unstable systems. Another advantage is that the resulted relations are easily programmable.

Polynomials in the numerator and denominator of the transfer function of the controller result from the solution of Diophantine equations, which have so called characteristic polynomial of the closed loop system on the right side of the equation. The roots of this polynomial are then poles of the closed-loop system, which affects the quality of control. The method of choosing the poles is called Pole-placement or Pole-assignment (Kučera, 1991).

The idea of the predictive control is based on the calculation of the control sequence from the actual time point minimizing the deviation of the reference signal and the output signal of the plant in the future horizon (Clarke *et al.*, 1987). The future values of the reference signal are given in advance or are assumed to be equal to the present one. The future values of the plant can be predicted from a process model. If disturbances are measurable, then their future values are predicted using some assumptions.

All approaches are verified by the simulation in the simulation program Matlab®, version 6.5.

2. ADAPTIVE CONTROL

The adaptive approach in this work is based on choosing an external linear model (ELM) of the original nonlinear system

whose parameters are recursively identified during the control. Parameters of the resulted continuous controller are recomputed in every step from the estimated parameters of the ELM (Bobál *et al.*, 2005).

2.1 External Linear Model

The main types of ELM are continuous-time (CT) models and discrete-time (DT) models.

The general description of the CT ELM can be formulated via transfer function $G(s)$:

$$G(s)=\frac{b(s)}{a(s)}=\frac{Y(s)}{U(s)}=\frac{b_m s^m+b_{m-1}s^{m-1}+\ldots+b_1 s+b_0}{a_n s^n+a_{n-1}s^{n-1}+\ldots+a_1 s+a_0} \tag{1}$$

The continuous-time ELM is supposed to be more accurate and corresponding to the real model because data are estimated continuously during the control. On the contrary, CT identification is difficult.

On the other hand, identification of the DT models are easy to realize. We can say that discrete models are used in the cases where the usage of continuous ones is complicated or the realization is impossible. An important variable in the discrete-time models is sampling period T_v.

The transfer function G in this case is defined as Z-transform of the output variable y to the input variable u

$$G(z)=\frac{Y(z)}{U(z)}=\frac{b(z)}{a(z)}=\frac{b_m z^m+b_{m-1}z^{m-1}+\ldots+b_1 z+b_0}{a_n z^n+a_{n-1}z^{n-1}+\ldots+a_1 z+a_0} \tag{2}$$

where $a(z)$ and $b(z)$ are discrete polynomials and $U(z)$ and $Y(z)$ are Z-transform images of the input and output variables.

2.2 Identification

The use of the discrete model for nonlinear system can cause problems with the sampling period T_v. This sampling period cannot be small because of the stability and the big sampling period is unacceptable because we do not know what will happen with the system during this sample.

The inconvenience with the sampling period could be overcome with the use of so called delta (δ-) models. Although the delta operator belongs to the class of discrete models with the operator described as

$$q\cdot x(k)\triangleq x(k+1) \tag{3}$$

it can been seen from

$$\delta=\frac{q-1}{T_v} \tag{4}$$

that this operator is related to sampling period T_v and it means that δ-models are close to the continuous ones in d/dt.

A new complex variable in "δ" plane called "γ", which is defined for example in (Mukhopadhyay *et al.*, 1992) as

$$\gamma=\frac{z-1}{\beta\cdot T_v\cdot z+(1-\beta)\cdot T_v} \tag{5}$$

need to be introduced. We can obtain an infinite number of δ–models for different values of optional parameter β in Equation (5) from the range $0\le\beta\le 1$.

The forward δ-model described for $\beta = 0$ by

$$\gamma=\frac{z-1}{T_v} \tag{6}$$

is dealt with in this work.

The Recursive Least-Squares (RLS) method is used for the parameter estimation in this work. The RLS method is well-known and widely used for the parameter estimation (Fikar and Mikleš, 1999). It is usually modified with some kind of forgetting, exponential or directional (Kulhavý and Karny, 1984), because parameters of the identified system can vary during the control which is typical for nonlinear systems and the use of some forgetting factor could result in better output response.

The RLS method with exponential forgetting is describe by the set of equations:

$$\begin{aligned}
&\varepsilon(k)=y(k)-\varphi^T(k)\cdot\hat{\theta}(k-1)\\
&\gamma(k)=\left[1+\varphi^T(k)\cdot\mathbf{P}(k-1)\cdot\varphi(k)\right]^{-1}\\
&\mathrm{L}(k)=\gamma(k)\cdot\mathbf{P}(k-1)\cdot\varphi(k)\\
&\mathbf{P}(k)=\frac{1}{\lambda_1(k-1)}\left[\mathbf{P}(k-1)-\frac{\mathbf{P}(k-1)\cdot\varphi(k)\cdot\varphi^T(k)\cdot\mathbf{P}(k-1)}{\lambda_1(k-1)+\varphi^T(k)\cdot\mathbf{P}(k-1)\cdot\varphi(k)}\right]\\
&\hat{\theta}(k)=\hat{\theta}(k-1)+\mathrm{L}(k)\varepsilon(k)
\end{aligned} \tag{7}$$

Several types of exponential forgetting can be used, e.g. like RLS with constant exponential forgetting, RLS with increasing exp. forgetting etc. RLS with the changing exp. forgetting is used for parameter estimation, where the changing forgetting factor λ_1 is computed from the equation

$$\lambda_1(k)=1-K\cdot\gamma(k)\cdot\varepsilon^2(k) \tag{8}$$

Where K is small number, in our case $K = 0.001$.

2.3 Polynomial Synthesis

The structure of the controller is designed via polynomial synthesis. The simple one degree-of-freedom (1DOF) control configuration was used. The block scheme of this configuration in Fig. 1.

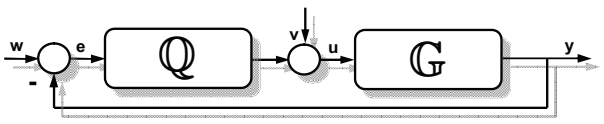

Fig. 1 1DOF control configuration

Block Q in Fig. 1 represents the transfer function of the controller, G denotes the transfer function of the plant, w is

the reference signal, e is used for the control error, v is the disturbance at the input to the system, u determines the input variable, and finally y is the output variable.

Transfer functions of the controller and controlled plant could be described in the continuous time by equations:

$$Q(s)=\frac{q(s)}{s\cdot p(s)};\ G(s)=\frac{b(s)}{a(s)} \tag{9}$$

where polynomials $p(s)$ and $q(s)$ are designed by the polynomial approach and parameters of these polynomials are computed by the Method of uncertain coefficients which compares coefficients of individual s-powers from Diophantine equation (Kučera, 1993):

$$a(s)\cdot s\cdot p(s)+b(s)\cdot q(s)=d(s) \tag{10}$$

Although parameters of the polynomials $a(s)$ and $b(s)$ are reflected to be in continuous-time, the identification runs recursively in discrete time periods related to the sampling period T_v. This simplification is supported by the use of δ-models where each input and output variable is recomputed to this sampling period, T_v, which shifts these discrete polynomials closer to the continuous ones. It was proofed for example in (Stericker and Sinha, 1993) that the parameters of the delta model for the small sampling period approach to the continuous ones in (9).

The feedback controller $Q(s)$ in Fig. 1 ensures all basic control requirements – i.e. stability, load disturbance attenuation and asymptotic tracking of the reference signal. It is required that each controller could be tuned somehow. This option can be found in this controller in the stable optional polynomial $d(s)$ on the right side of the Diophantine equation (10). As it is mentioned above, there are several methods for choosing of this polynomial. The method used here is Pole-placement or Pole-assignment method. Polynomial $d(s)$ can be divided into two parts – $m(s)$ and $n(s)$, so

$$d(s)=m(s)\cdot n(s) \tag{11}$$

where polynomial $n(s)$ is computed from the spectral factorization of polynomial $a(s)$ in the denominator of the transfer function $G(s)$ (9)

$$n^*(s)\cdot n(s)=a^*(s)\cdot a(s) \tag{12}$$

and polynomial $m(s)$ is a stable one $m(s)=(s+\alpha_i)^{\deg d-\deg n}$ and $\alpha_i>0$ are (deg d – deg n) optional stable roots, usually called poles of the control system. A disadvantage of this method can be found in the uncertainty of the polynomial $m(s)$ – there is no general rule how to choose roots α_i.

3. PREDICTIVE CONTROL

3.1 Generalized Predictive Control

Generalized Predictive Control (GPC) is one of the most popular predictive methods based on Model Predictive Control (MPC) (Clarke *et al.*, 1987), and has been successfully used in praxis for different types of control problems from this time.

The GPC has many common ideas with the ordinary predictive methods but it has some differences to such as the solution of the GPC controller is analytical, it can be used for unstable and non-minimum phase systems etc.

The general single-input single-output (SISO) after linearization can be described through the discrete backshift operators z^{-1} as

$$A(z^{-1})\cdot y(t)=z^{-d}\cdot B(z^{-1})\cdot u(t-1)+C(z^{-1})\cdot e(t) \tag{13}$$

where $u(t)$ is control variable, $y(t)$ output variable, $e(t)$ denotes a zero mean white noise, and d is dead time of the system. Polynomials $A(z^{-1})$, $B(z^{-1})$ and $C(z^{-1})$ are

$$\begin{aligned}A(z^{-1})&=1+a_1z^{-1}+a_2z^{-2}+\ldots+a_{n_a}z^{-n_a}\\ B(z^{-1})&=b_0+b_1z^{-1}+b_2z^{-2}+\ldots+b_{n_b}z^{-n_b}\\ C(z^{-1})&=1+c_1z^{-1}+c_2z^{-2}+\ldots+c_{n_c}z^{-n_c}\end{aligned} \tag{14}$$

Equation (23) is called the *Controller Auto-Regressive Moving-Average* (CARMA) *model*. This model is not suitable in most industrial processes where disturbances are non-stationary. In these cases, the integrated CARMA (CARIMA) model is more suitable

$$A(z^{-1})\cdot y(t)=z^{-d}\cdot B(z^{-1})\cdot u(t-1)+C(z^{-1})\cdot\frac{e(t)}{\Delta} \tag{15}$$

where $\Delta=1-z^{-1}$.

The GPC algorithm can be then formulated as minimization of the cost function

$$\begin{aligned}J_{GPC}=&\sum_{j=N_1}^{N_2}\delta_u(j)\left[\hat{y}(t+j|t)-w(t+j)\right]^2+\ldots\\ &\ldots+\sum_{j=1}^{N_u}\lambda_u(j)\left[\Delta u(t+j-1)\right]^2\end{aligned} \tag{16}$$

where $\hat{y}(t+j|t)$ is an optimum j-ahead prediction of the output on data up to time t, further, N_1 and N_2 denote minimum and maximum costing horizons, respectively, N_u is control horizon, $w(t+j)$ means reference signal, Δu stands for manipulated variable and finally $\delta_u(j)$ and $\lambda_u(j)$ denote weighting sequences.

The values of these factors are for simplification assigned as $\delta_u=1$, and λ_u is constant through the whole time interval of the control.

4. MODEL OF THE PLANT

The nonlinear system under the consideration is the Continuous Stirred Tank Reactor (CSTR). The reaction inside the reactor is called *van der Vusse* reaction can be described by the following reaction scheme (Chen, *et al.*, 1995):

$$A \xrightarrow{k_1} B \xrightarrow{k_2} C$$
$$2A \xrightarrow{k_3} D \qquad (17)$$

The graphical scheme of this reactor can be seen in Fig. 2

The mathematical model of this reactor is described by the following set of ordinary differential equations (ODE):

$$\frac{dc_A}{dt} = \frac{q_r}{V_r}\left(c_{A0} - c_A\right) - k_1 c_A - k_3 c_A^{\,2} \qquad (18)$$

$$\frac{dc_B}{dt} = -\frac{q_r}{V_r} c_B + k_1 c_A - k_2 c_B \qquad (19)$$

$$\frac{dT_r}{dt} = \frac{q_r}{V_r}\left(T_{r0} - T_r\right) - \frac{h_r}{\rho_r c_{pr}} + \frac{A_r U}{V_r \rho_r c_{pr}}\left(T_c - T_r\right) \qquad (20)$$

$$\frac{dT_c}{dt} = \frac{1}{m_c c_{pc}}\left(Q_c + A_r U\left(T_r - T_c\right)\right) \qquad (21)$$

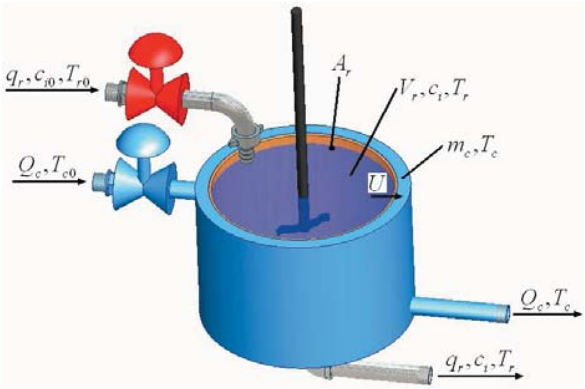

Fig. 2: Continuous Stirred Tank Reactor (CSTR)

This set of ODE together with simplifications then mathematically represents examined CSTR reactor. The model of the reactor belongs to the class of *lumped-parameter nonlinear systems*. Fixed parameters of the system are shown in Table 1 (Chen, *et al*., 1995).

Table 1 Fixed parameters of CSTR

$k_{01} = 2.145 \cdot 10^{10}\ min^{-1}$	$k_{02} = 2.145 \cdot 10^{10}\ min^{-1}$
$k_{03} = 1.5072 \cdot 10^{8} min^{-1}.mol^{-1}$	$E_1/R = 9758.3\ K$
$E_2/R = 9758.3\ K$	$E_3/R = 8560\ K$
$h_1 = -4200\ kJ.kmol^{-1}$	$h_2 = 11000\ kJ.kmol^{-1}$
$h_3 = 41850\ kJ.kmol^{-1}$	
$V_r = 0.01\ m^3$	$\rho_r = 934.2\ kg.m^{-3}$
$c_{pr} = 3.01\ kJ.kg^{-1}.K^{-1}$	$q_r = 2.365 \cdot 10^{-3}\ m^3 min^{-1}$
$c_{pc} = 2.0\ kJ.kg^{-1}.K^{-1}$	$Q_c = -18.5583\ kJ.min^{-1}$
$U = 67.2\ kJ.min^{-1}m^{-2}K^{-1}$	$A_r = 0.215\ m^2$
$c_{A0} = 5.1\ kmol.m^{-3}$	$c_{B0} = 0\ kmol.m^{-3}$
$T_{r0} = 387.05\ K$	$m_c = 5\ kg$

The reaction heat (h_r) in eq. (20) is expressed as:

$$h_r = h_1 \cdot k_1 \cdot c_A + h_2 \cdot k_2 \cdot c_B + h_3 \cdot k_3 \cdot c_A^2 \qquad (22)$$

where h_i means reaction enthalpies.

Nonlinearity can be found in reaction rates (k_j) which are described via Arrhenius law:

$$k_j\left(T_r\right) = k_{0j} \cdot \exp\left(\frac{-E_j}{RT_r}\right), \text{ for } j = 1,2,3 \qquad (23)$$

where k_0 represent pre-exponential factors and E are activation energies.

Static analysis has shown (Vojtesek, *et al.*, 2004), that system has an optimal working point for volumetric flow rate of the reactant $q_r = 2.365 \times 10^{-3}\ m^3.min^{-1}$ a heat removal $Q_c = -18.56\ kJ.min^{-1}$. The difference between actual and initial temperature of the reactant T_r was taken as controlled output and changes of the heat removal Q_c was set as control input, i.e.

$$y(t) = T_r(t) - T_r^s(t)\,[K]$$
$$u(t) = 100 \cdot \frac{Q_c(t) - Q_c^s(t)}{Q_c^s(t)}\,[\%] \qquad (24)$$

On the other hand, dynamic analysis results in ELM represented by a second order transfer function with relative order one, which is generally:

$$G(s) = \frac{b(s)}{a(s)} = \frac{b_1 s + b_0}{s^2 + a_1 s + a_0} \qquad (25)$$

Equation (25) can be rewritten for the identification to the form of the differential equation

$$y_\delta(k) = -a_1 y_\delta(k-1) - a_0 y_\delta(k-2) + \\ + b_1 u_\delta(k-1) + b_0 u_\delta(k-2) \qquad (26)$$

where y_δ is recomputed output to the δ-model:

$$y_\delta(k) = \frac{y(k) - 2y(k-1) + y(k-2)}{T_v^2}$$
$$y_\delta(k-1) = \frac{y(k-1) - y(k-2)}{T_v} \quad y_\delta(k-2) = y(k-2) \qquad (27)$$
$$u_\delta(k-1) = \frac{u(k-1) - u(k-2)}{T_v} \quad u_\delta(k-2) = u(k-2)$$

where T_v is the sampling period, the data vector is

$$\phi^T(k-1) = \left[-y_\delta(k-1), -y_\delta(k-2), u_\delta(k-1), u_\delta(k-2)\right] \qquad (28)$$

and the vector of estimated parameters

$$\hat{\Theta}^T(k) = \left[\hat{a}_1, \hat{a}_0, \hat{b}_1, \hat{b}_0\right] \qquad (29)$$

could be computed from the ARX (Auto-Regressive eXogenous) model

$$y_\delta(k) = \hat{\Theta}^T(k)\phi(k-1) \qquad (30)$$

by the recursive least squares methods described in part 2.2.

The ELM is of the second order, which means that degrees of polynomials $p(s)$, $q(s)$, and $d(s)$ are then:

$$\deg q = 2; \deg p = 1; \deg d = 4 \qquad (31)$$

and polynomials $m(s)$ and $n(s)$ in the equation (11) are

$$n(s) = s^2 + n_1 s + n_0; \quad m(s) = \left(s + \alpha_i\right)^{\deg d - \deg n} = \left(s + \alpha_i\right)^2 \qquad (32)$$

and coefficients of the polynomial $n(s)$ are computed via spectral factorization (12) as

$$n_0 = \sqrt{a_0^2}, n_1 = \sqrt{2n_0 + a_1^2 - 2a_0} \tag{33}$$

Transfer functions of the feedback and feedforward parts of the controller for 1DOF and 2DOF configurations are

$$Q(s) = \frac{q_2 s^2 + q_1 s + q_0}{s(s + p_0)} \tag{34}$$

Where parameters of the polynomials $q(s)$ and $p(s)$ by the comparison of the coefficients of the s-powers a in diophantine equations (10).

The identified parameters of the delta ELM from the predictive control were recomputed to the discrete-time ELM:

$$G(z^{-1}) = \frac{-0.0021z^{-1} + 0.0010z^{-2}}{1 - 1.5851z^{-1} + 0.6197z^{-2}} \tag{35}$$

which was used for computation of the predictive controller in Equation (25). Zero mean white noise $e(t)$ is not take into account.

5. SIMULATION RESULTS

Both control strategies were verified by simulation experiments. The sampling period was set to $T_v = 0.3$ *min*, all simulations took 500 min and 5 different step changes $w = [2, -1, 1\ -1, 1.5]$ were done during this interval.

The first simulation study was done for adaptive controller with the various values of the root α_i = 0.05, 0.1 and 0.2 in Equation (32). The predictive controller was verified again for different values of the weighting factor λ_u = 0.05, 0.5 and 2 in (16).

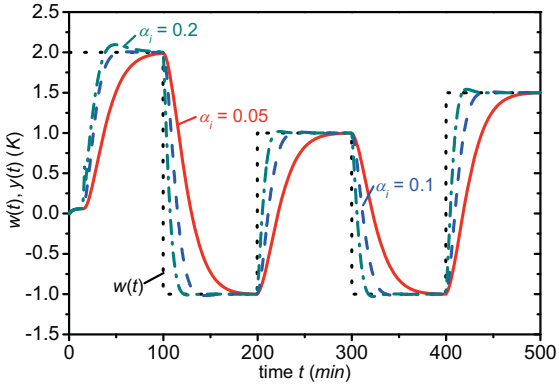

Fig. 3: Course of the reference signal $w(t)$ and the output variable $y(t)$ for various of the root α_i in adaptive control

Figures 3 and 4 represents simulation results for adaptive control. It can be clearly seen, that the increasing value of the parameter α_i results in the quicker output response, $y(t)$, but small overshoots. On the other hand, lower value of this root position is parsimonious to the input variable, $u(t)$, in Fig. 4 which could be in this case considered as a twist of the valve on the feeding of the cooling pipe.

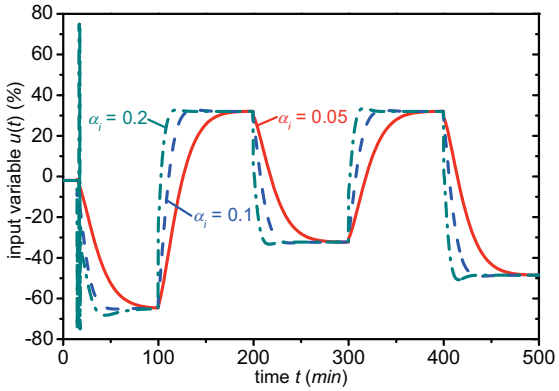

Fig. 4: Course of the input variable $u(t)$ for various of the root α_i in adaptive control

The quality of control was evaluated by the quality criteria S_u and S_y computed for a time interval as:

$$S_u = \sum_{i=2}^{N} \left(u(i) - u(i-1)\right)^2 [-]; \quad S_y = \sum_{i=1}^{N} \left(w(i) - y(i)\right)^2 [K^2] \quad \text{,for } N = \frac{T_f}{T_v}. \tag{36}$$

The results for both control strategies are shown in Table 2.

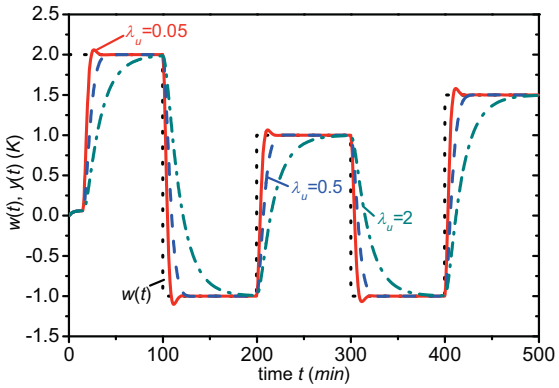

Fig. 5: Course of the reference signal $w(t)$ and the output variable $y(t)$ for various of the root λ_u in predictive control

The simulation results of the second control strategy, predictive control, are shown in Fig. 5 and Fig. 6. This controller is tuned via weighting parameter λ_u which is constant during the control and the second weighting parameter is δ_u = 1 as it is written above in the theoretical part. In this case, increasing value of the λ_u results in slower response of the output variable $y(t)$.

The last two graphs in Fig. 7 and Fig. 8 compares the best results for both control strategies – adaptive control with α_i = 0.1 and predictive control with λ_u = 0.5.We can say, that in this case both control strategies are comparable but the output response $y(t)$ in the predictive control reaches the reference signal (wanted value) $w(t)$ a little bit quicker than the adaptive controller.

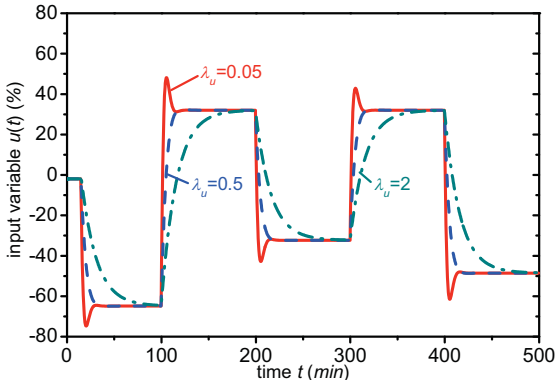

Fig. 6: Course of the input variable $u(t)$ for various of the root λ_u in predictive control

Table 2 The results of control quality criteria S_u and S_y

	Adaptive control, α_i =			**Predictive control, λ_u =**		
	0.05	0.1	0.4	0.05	0.5	2
S_u[-]	192.4	492.3	8571.5	3265.1	868.3	265.3
S_y[K^2]	1664.4	934.7	532.7	430.3	653.3	1194.8

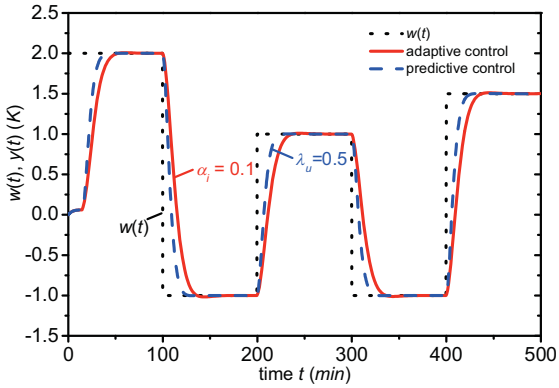

Fig. 7: The best courses of the output variable $y(t)$ for adaptive and predictive control

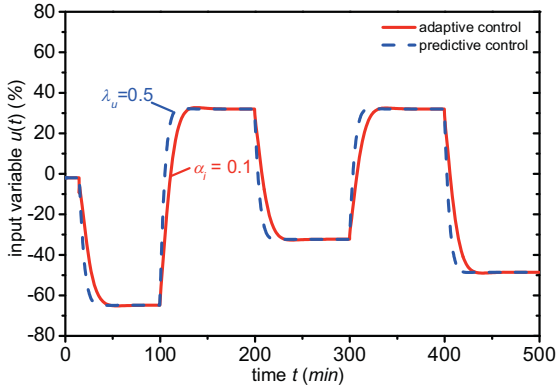

Fig. 8: The best courses of the input variable $u(t)$ for adaptive and predictive control

6. CONCLUSIONS

This paper presents two approaches which could be used for controlling of the temperature of the reactant inside the CSTR which is typical member of the nonlinear process with lumped parameters. Both, adaptive and predictive, controllers have good control results although the system has negative properties from the control point of view. The adaptive controller could be tuned by the parameter α_i while predictive controller has its weighting factor λ_u as a tuning parameter too. Final comparison of both control techniques results better for the predictive controller but the difference is minimal. The future work will be focused on the verification of the obtained results on the real plant which could increase reliability of these methods.

ACKNOWLEDGMENT

This work was supported by the Ministry of Education of the Czech Republic under grants No. MSM 7088352101 and No. 1M0567

REFERENCES

Bobál, V., Böhm, J., Fessl, J., Macháček, J. (2005) *Digital Self-tuning Controllers. Algorithms, Implementation and Applications*. Springer

Corriou, J.-P. (2004). *Process control. Theory and applications.* Springer-Verlag London.

Clarke, D.W., Mohtadi, C., Tuffs, P.S. (1987) Generalized predictive control – Part I. The basic algorithm. *Automatica*. 23(2), 137-148

Chen, H., Kremling, A., Allgöwer, F. (1995) Nonlinear Predictive Control of a Benchmark CSTR. *In: Proceedings of 3rd European Control Conference. Rome, Italy*

Fikar, M., Mikleš J. (1999) *System identification* (in Slovak). STU Bratislava.

Kučera, V. (1991) *Analysis and Design of Discrete Linear Control Systems*. Prentice-Hall, London

Kučera, V. (1993) Diophantine equations in control – A survey. *Automatica*, 29, 1361-1375

Kulhavý, R., Kárný, M. (1984) Tracking of slowly varying parameters by directional forgetting, *In: Proc. 9th IFAC World Congress*, vol. X, Budapest, p. 78-83

Middleton, R.H., Goodwin, G.C. (2004) *Digital Control and Estimation - A Unified Approach*. Prentice Hall, Englewood Cliffs.

Mukhopadhyay, S., Patra, A.G., Rao, G.P. (1992) New class of discrete-time models for continuos-time systeme. *International Journal of Control*, vol.55, 1161-1187

Stericker, D.L., Sinha, N.K. (1993) Identification of continuous-time systems from samples of input-output data using the δ-operator. *Control-Theory and Advanced Technology*, vol. 9, 113-125

Vojtesek, J., Dostal, P., Haber, R. (2004). Simulation and Control of a Continuous Stirred Tank Reactor. *In: Proc. of Sixth Portuguese Conference on Automatic Control CONTROLO 2004*. Faro. Portugal, p. 315-32

Gas-lift Optimization and Control with Nonlinear MPC

A. Plucenio * **D. J. Pagano** * **E. Camponogara** * **A. Traple** * **A. Teixeira** **

* *Departamento de Automação e Sistemas, Universidade Federal de Santa Catarina, 88040-900 Florianópolis-SC, Brazil*
e-mail: {plucenio, daniel, camponog, traple}@das.ufsc.br
** *CENPES-Petrobras, Rio de Janeiro, RJ, Brazil*
e-mail: alex.teixeira@petrobras.com.br

Abstract: More than 70% of the oil production in Brazil employs gas-lift as the artificial lift method. An effort is being done by some operators to complete new gas-lift wells with down hole pressure gages. This paper proposes a Non-Linear MPC algorithm to control a group of wells receiving gas from a common Gas-Lift Manifold. The objective is to maximize an economic function while minimizing the oscillations of the pressures at the manifold and at the bottom of the wells.

Keywords: Gas-Lift, Nonlinear MPC,

1. INTRODUCTION

Advanced Control Techniques like Nonlinear MPC have not arrived yet at the upstream processes of the oil industry. Many gas-lift wells with significant daily production are operating with manual driven gas injection and production chokes. In the last few years some Petroleum Exploration and Production companies have initiated efforts to introduce automation and control techniques in the operation of production wells. These initiatives resulted in technical approaches with names as smart wells, intelligent wells, smart fields or Digital Oilfield Management-GEDIG in Petrobras, Campos et al. (2006). The introduction of Information Technology in the oil production system is slow mainly due to the prohibitive cost of well intervention to install new sensors and actuators. Apart from that, sensors and actuators to be used in oil wells will have to cope with very harsh conditions caused by high pressure, temperatures and vibrations. There are several important works related to modeling, control and optimization of gas-lift wells operations like Boisard et al. (2002), Eikrem et al. (2004), L. Singre and Lemetayer (2006), Imsland et al. (2003), Camponogara and Nakashima (2006), Plucenio et al. (2006) to cite only a few. Not all control and optimization techniques discussed in the literature will be ready to be applied with the present instrumentation level of most gas-lift wells. This work discuss the automation of gas-lift wells equipped with downhole pressure measurement sensor, gas injection control valve and manually operated production choke. This is a realistic scenario in Brazil for new gas-lift wells. To our knowledge this is the first work that attempts to control the Gas Lift Manifold and the wells connected to it using Nonlinear MPC (NMPC). Section 2 discusses the NMPC formulation, section 3 presents and discusses the main results and section 4 concludes the paper.

⋆ A. Plucenio and A. Traple are supported by *Agência Nacional do Petróleo, Gás Natural e Biocombustiveis* under project PRH34-ANP/MCT. Daniel J. Pagano and E. Camponogara are supported by CENPES-Petrobras under the project *Development of control algorithms for artificial lifting*. A. Teixeira is a researcher at CENPES-Petrobras

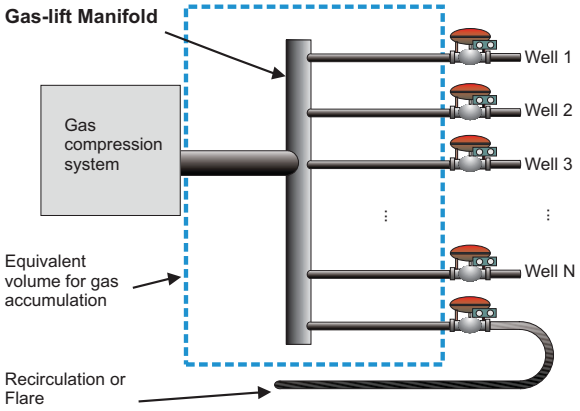

Fig. 1. Gas-lift Manifold

2. THE NMPC FORMULATION

We deal with a system where N gas-lifted wells with downhole pressure measurement and gas injection valves receive gas from a common Gas-lift Manifold (GLM). Gas from the compressor system enters the GLM and is distributed to the gas-lift wells and to an output which can be directed to the flare or to the recirculation of the compressor system. This output is a mechanism which allows gas to be discharged in cases where the gas flow-rate entering the GLM is higher than what is needed to operate the wells at their unconstrained optimum. This will be referred in the paper as the excess gas flow rate. The pressure at the GLM has to be kept at level high enough to allow injection in the annular of all gas-lift wells. For such a system shown in Figure 1 we wish

- to keep the GLM pressure close to a set-point designed according to the needs of the gas-lift wells,
- to distribute the gas flow-rate delivered by the compressor system among the gas lift wells in a way that maximizes an economic objective and

- to minimize the production oscillations caused by changes in the gas injection flow-rates. These oscillations cause problems to the separation process.

Some constraints should be introduced.

- To keep the gas injection flow rate of each well above a minimum value.
- To keep the pressure at the GLM between an upper and lower bound.

Table 1 presents the nomenclature used.

Table 1. Nomenclature

Symb.	Variable description	Unit
qo_i	Well i oil flow rate	std $m^3.d^{-1}$
$qliq_i$	Well i liquid flow rate	std $m^3.d^{-1}$
qw_i	Well i water flow rate	std $m^3.d^{-1}$
qg_i	Well i gas flow rate	std $m^3.d^{-1}$
p_{wf}	Bottom hole pressure with well flowing	$kgf.cm^{-2}$
$\bar{p}$	Average reservoir pressure	$kgf.cm^{-2}$
p_{sat}	Oil saturation pressure	$kgf.cm^{-2}$
q_{sat}	Liquid flow rate at $p_{wf} = P_{sat}$	std $m^3.d^{-1}$
q_{max}	Maximum well liquid flow rate ($p_{wf} = 0$)	std $m^3.d^{-1}$
qo_{max}	Maximum well oil flow rate	std $m^3.d^{-1}$
$qinj_i$	Well i gas injection flow rate	std $m^3.d^{-1}$
q_{exc}	GLM excess gas flow rate (flare or recirc.)	std $m^3.d^{-1}$
P_m	Gas Lift Manifold Pressure	$kgf.cm^{-2}$
P_{msp}	Gas Lift Manifold Pressure set point	$kgf.cm^{-2}$
p^*_{wf}	Value of p_{wf} used for normalization	$kgf.cm^{-2}$
$qinj^*$	Value of $qinj$ where $p_{wf} = p^*_{wf}$	std $m^3.d^{-1}$
q_{out}	Mass flow rate exiting the GLM	kgs^{-1}
q_{in}	Mass flow rate entering the GLM	kgs^{-1}
$\widetilde{x}$	Predicted or modeled value of x	

Symb.	Constants	Unit
V	Equivalent GLM volume	m^3
R	Universal Gas Constant, 8.314472	$Pa.m^3/Kmol$
M	Gas molecular weight	$kg.mol^{-1}$
BSW	Water saturation	-
GOR	Gas Oil Ratio	-

2.1 The NMPC Cost Function

The NMPC Cost Function should be tailored in such a way that its minimization provides the objectives discussed previously. There are several economic objectives that can be introduced in the Cost Function. A more general economic objective should express the net economic result of the gas lift operation taking into account the revenue from the oil production, gas production and the costs associated with the gas compression, water treatment, etc. Every well i has a maximum attainable oil production rate, qo_{maxi} , which can be obtained with an unique gas injection flow rate. Since there is a cost to implement the gas injection flow rate it becomes interesting to consider an economic objective which takes into account the gas compression cost and the revenue due to the oil produced. This is done at every sample time kTs computing the total amount of oil that will not be produced and the total amount of gas that will be injected between the actual time kTs and the future time T defined by the prediction horizon p and the sampling time Ts, $T = (k+p) * Ts$. An expression for the revenue loss due to oil production below unconstrained optimum is

$$L = P_o \sum_{i=1}^{N} \sum_{j=1}^{p} [qo_{maxi} - qo_i(k+j)]\, Ts, \text{ where} \quad (1)$$

P_o is the oil price per 1 $stdm^3$. The gas injection compression cost can be expressed as

$$C_{comp.} = C_c \sum_{i=1}^{N} \sum_{j=0}^{p-1} [qinj_i(k+j)]\, Ts, \text{ where} \quad (2)$$

C_c is the cost to compress $1stdm^3$ of gas to the GLM nominal pressure P_{msp}. The economic objective can be obtained by determining for every well i the vector

$$\Delta \mathbf{Q}inj_i = [\, \Delta qinj_i(k)\ \Delta qinj_i(k+1)\ \ldots\ \Delta qinj_i(k+m-1)\,]^T, \quad (3)$$

that minimize the objective function J_1, or,

$$\min_{\Delta \mathbf{Q}inj} J_1 \quad (4)$$

$$J_1 = \sum_{i=1}^{N} \sum_{j=1}^{p} [qo_{maxi} - qo_i(k+j)] + \frac{p}{m} \frac{C_c}{P_o} \sum_{i=1}^{N} \sum_{j=0}^{m-1} [qinj_i(k+j)]$$

The factor $\frac{p}{m}$ compensates the fact that the accumulated production loss is computed along an interval of time pTs while the total gas injected is computed along the time mTs where p and m are respectively the prediction and control horizon length. This formulation, in the absence of constraints is equivalent to the equal slope method, Kanu et al. (1981). One way to implement the cost function in matrix representation is to define for each well i the oil production loss qo_{Li},

$$qo_{Li} = qo_{maxi} - \tilde{qo}_i(p_{wfi}), \quad (5)$$

where $\tilde{qo}(p_{wf}))$ is computed with the predicted p_{wf}. We assemble the vector $\tilde{\mathbf{Qo}}_L$ with the difference between the maximum attainable oil flow rate and the predicted flow rate for every well i along the prediction horizon p.

$$\tilde{\mathbf{Qo}}L = [\, qo_{L1}(1)\ \cdots\ qo_{L1}(p)\ \cdots\ qo_{LN}(1)\ \ldots\ qo_{LN}(p)\,]^T \quad (6)$$

In order to damp the production oscillations we propose to minimize the sum of the time differential square of the production losses of all wells along the prediction horizon.

$$J_2 = \sum_{i=1}^{N} \sum_{j=1}^{p} \left(\frac{dqo_{Li}(k+j)}{dt} \right)^2 \quad (7)$$

The time differential is obtained using the matrix T equivalent to the $\Delta = 1 - z^{-1}$ operator.

$$T = \begin{bmatrix} -1 & 1 & 0 & 0 & \cdots & 0 \\ 0 & -1 & 1 & 0 & \cdots & 0 \\ \vdots & \vdots & \vdots & \vdots & \cdots & 0 \\ 0 & 0 & 0 & \cdots & -1 & 1 \end{bmatrix} \quad (8)$$

The final Cost Function used is

$$J = \mathbf{W_1}\tilde{\mathbf{Qo}}_L + \mathbf{W_2}\mathbf{Qm_{out}} + (\mathbf{P}_{msp} - \tilde{\mathbf{P}}_m)^T \mathbf{W}_3 (\mathbf{P}_{msp} - \tilde{\mathbf{P}}_m) + \left(\mathbf{T}\tilde{\mathbf{Qo}}_L\right)^T \mathbf{W}_4 \left(\mathbf{T}\tilde{\mathbf{Qo}}_L\right) + \Delta \mathbf{Qm}_{out}^T \mathbf{W}_5 \Delta \mathbf{Qm}_{out}, \text{where}$$
$$\mathbf{Qm}_{out} = [\, \mathbf{Q}inj_1;\ \mathbf{Q}inj_2;\ \cdots\ \mathbf{Q}inj_N;\ \mathbf{Q}_{exc.}\,], \text{ and}$$
$$\mathbf{Q}_{exc.} = [\, q_{exc}(k)\ q_{exc}(k+1)\ \ldots\ q_{exc}(k+m-1)\,]^T \quad (9)$$

The first two terms implement the economic objective, the third term forces the pressure at the GLM to its nominal value or set-point, the fourth term minimizes the production losses oscillation and consequently the oil production rate oscillations and the fifth term minimizes the changes in the gas injection flow-rates. The vectors $\mathbf{W}_1$ and $\mathbf{W}_2$ can be adjusted to implement the economic objective in steady state. The matrix $\mathbf{W}_3$, $\mathbf{W}_4$ and $\mathbf{W}_5$ must be adjusted to weight the dynamic response objectives against the economic objective. There is no doubt that the optimum gas distribution is reached in steady state since in this case terms 3, 4 and 5 vanish but a proper tuning should provide optimization also during production transients. An excessive requirement for the oil production oscillation attenuation may induce a production loss compared to softening this objective.

2.2 Prediction models

The main purpose of applying automatic control to a group of gas-lift wells is to maximize an economic objective. That means to distribute the available gas flow rate entering the GLM among the wells in order to maximize the oil production for instance. Using the available downhole pressure measurements, the parameters of the Inflow Performance Relationship (IPR) of each well as well as parameters like BSW and GOR, it is possible to estimate the oil production flow rate entering the well. For under-saturated reservoir (formation pressure above the bubble point pressure),

$$qo = J(\bar{p} - p_{wf}), \tag{10}$$

where J is the productivity index, p_{wf} is the well flowing pressure in front of the perforated zone, $\bar{p}$ is the static pressure, and qo is the oil flow rate produced by the well. For saturated reservoirs, Vogel's formula Vogel (1968) gives

$$qo = qv_{max}\left[1 - 0.2\frac{p_{wf}}{\bar{p}} - 0.8\left(\frac{p_{wf}}{\bar{p}}\right)^2\right], \tag{11}$$

where qv_{max} is the maximum oil flow rate (for $p_{wf} = 0$). Defining the bubble pressure as p_{sat}, Patton and Goland (1980) proposed an expression considering the case where $\bar{p} > p_{sat}$ and the well operating with $p_{wf} \geq p_{sat}$ or $p_{wf} < p_{sat}$:

$$\text{if } p_{wf} \geq p_{sat}$$

$$q_{liq} = \frac{q_{sat}}{\bar{p} - p_{sat}}(\bar{p} - p_{wf}), \tag{12}$$

$$\text{if } p_{wf} < p_{sat}$$

$$q_{liq} = q_{sat} + (q_{max} - q_{sat})\left[1 - 0.2\frac{p_{wf}}{p_{sat}} - 0.8\left(\frac{p_{wf}}{p_{sat}}\right)^2\right]$$

$$qw = BSW\, q_{liq}. \tag{13}$$

$$qo = (1 - BSW)q_{liq}, \tag{14}$$

$$qg = RGO q_o \tag{15}$$

where q_{liq} is an IPR relationship that accounts for liquid flow rate in saturated and under-saturated wells, qw is the water flow rate, qo is the oil flow rate and qg is the gas flow rate. Other IPR models are found in Fetkovich (1973), Richardson and Shaw (1982), Raghavan (1993), Wiggins et al. (1996), and Maravi (2003). Due to the difficulty to have on line measurements for oil, water and gas flow rate of each well, and taking advantage of the availability of downhole pressure measurements an effort was done to derive an empirical model relating steady state gas injection flow rate to downhole pressure. For a real application the cost to obtain steady state values of downhole pressure and gas injection rate is significant since the well will have to operate at downhole pressures which translate into lower oil flow rate. Therefore it is highly desirable that the steady state model relating $p_{wf} = f(q_{inj})$ could be adjusted with measurements close to the point (p^*_{wf}, q^*_{inj}) where the production loss is minimum. A mathematical model with good extrapolation capability is most welcome. Most gas-lift wells do not produce naturally and for those the knowledge of the average reservoir static pressure, even with some uncertainty, gives an important information that can be used in the model since $p_{wf}(q_{inj} = 0) = \bar{p}$. In order to avoid numerical problems the relationship proposed uses normalized variables. Downhole pressure and injection flow rate are normalized to the pair (p^*_{wf}, q^*_{inj}). This would be an operational point corresponding to an observed lowest downhole pressure. The exact point chosen to normalization is not too important as long as the curve adjustment can use points to the right and left of (p^*_{wf}, q^*_{inj}).

$$u = \frac{q_{inj.}}{q^*_{inj.}}$$

$$y = \frac{p_{wf}}{p^*_{wf}}$$

$$y = \Theta_1 e^{-\Theta_2 u^m} + \Theta_3 + \Theta_4 u^2$$

$$\tilde{p}_{wf} = p^*_{wf} y. \tag{16}$$

A simplified SQP algorithm was developed for the curve fitting

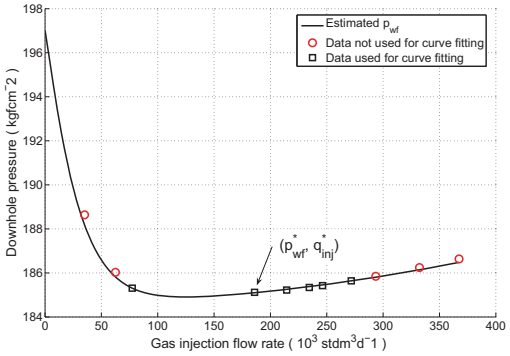

Fig. 2. Estimated p_{wf}

which uses the information about the average reservoir static pressure and its uncertainty. Figure 2 shows an example of curve fitting for data obtained from a rigorous steady state gas lift simulator. In order to verify the model extrapolation capability some points with lower values of downhole pressure were not used for the curve parameters adjustment. All points are plotted to show that the model adjusts well to the data even with a narrow data range used for the curve fitting. The points used for the curve fitting present downhole pressure close to the minimum which means that the production loss for obtaining these measurements would be minimum. Because one of the control objectives is to damp the oil production flow rate oscillations caused by changes in gas injection flow rates, it is also important to have a dynamic model for prediction. Since the main objective is economic, the dynamic prediction

model needs to exhibit a very accurate steady state relationship. Modern wells are being completed with Venturi gas-lift operating valves. These valves can provide critical flow for the injection gas at very low pressure drops (about 10% of the upstream pressure). This is normally enough to make sure that the gas-lift flow will be critical for most of its operating range. Critical flow in the gas-lift operating valve eliminates the heading phenomena but does not help to avoid the density wave oscillations, Hu (2004). In order to take advantage of the steady state model developed for $p_{wf} = f(q_{inj.})$ a Hammerstein model is proposed to be used for prediction. Figure

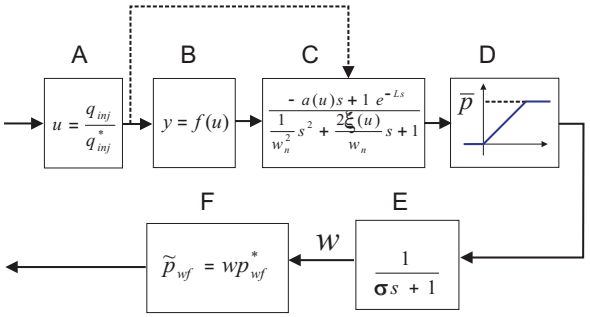

Fig. 3. Hammerstein dynamic model $p_{wf}(t) = f(q_{inj}(t))$

3 shows the dynamic model structure. Block A performs the normalization to the gas injection flow rate, block B applies the steady state function shown in equation (16), block C is a second order transfer function with transport delay and an adaptive zero and damping factor. Block D applies a saturation limiting the pressure values between zero and static pressure $\bar{p}$. Block E filters the saturation effect and block F multiplies the incoming signal by p^*_{wf} to recover the final estimated $\tilde{p}_{wf}$. It is assumed that the operating valve is working in critical mode so the gas flow rate crossing it is approximately the same gas flow rate that entered the casing head L seconds earlier. An approximate expression for L, ξ and the zero a are

$$L = \frac{H}{\sqrt{\frac{\gamma RT}{M}}},$$
$$\xi = k_1(.99 - e^{-3u(t-L)^2}) \text{ and}$$
$$a = \frac{k_2}{k_3 + u(t-L)}, \text{ where} \quad (17)$$

H is the distance from the casing head to the operating valve, γ is the gas ratio $\frac{c_p}{c_v}$, R is the universal gas constant, T is the gas temperature, $u(t-L)$ is the normalized gas injection flow rate at the casing head L seconds before the actual time and the constants k_1, k_2 and k_3 need to be tuned for each well together with the natural frequency w_n. In order to develop this empirical model several well cases were simulated with the OLGA^{TM} [1]. The pressure at the manifold, (P_m) is modeled as the pressure of a volume (V) filled with gas that results from the balance of gas that arrives from the compressor system and gas leaving to the wells and to the flare or to recirculation depending on the setup. The volume V is the sum of the internal volumes of all pipes between the compressor system and wells casing head. The pressure at the GLM is modeled as

[1] http://www.sptgroup.com/Products/olga/

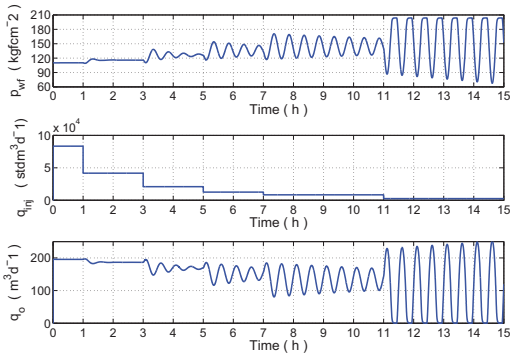

Fig. 4. Dynamic model response

$$\dot{P}_m = k_{GLM}(q_{in} - q_{out}),$$
$$k_{GLM} = \frac{RT}{MV}, \text{where} \quad (18)$$

T is the gas temperature, R is the gas universal constant and M is the gas molecular weight. The compressibility factor is assumed to be one. It is assumed that the gas mass flow rate entering the GLM is measured.

3. RESULTS AND DISCUSSION

In order to test the strategy proposed a total of 4 wells were modeled. These wells were simulated with a rigorous steady state simulator and the parameters of the empirical model given by equation (16) were tuned. The wells details are shown in table 2. A hypothetical dynamic model was added according to the model structure shown in figure 3. The Nonlinear MPC

Table 2. Well data

Parameter	*Well 1*	*Well 2*	*Well 3*	*Well 4*
$qmax[\frac{m^3}{d}]$	871.38	7.739e+003	5.177e+003	1.558e+003
BSW	0.341	0.676	0.03	0.488
$p^*_{wf}[kgf/cm^2]$	110.0	185.1	182.9	146.5
$q^*_{inj}\ [m^3/d]$	8.33e+4	1.859e+5	2.661e+5	9.98e+4
$\bar{p}\ [kgf/cm^2]$	203.7	199	217.2	205
a_1	.9038	0.067	0.4003	0.3885
a_2	3.5039	8.0042	0.6133	5.8235
a_3	0.9666	0.9972	0.7751	0.9972
a_4	0.0075	0.0026	0.0082	0.0052
m	0.56	1.11	0.09	1.04

algorithm used is discussed in Plucenio et al. (2008b) and with more details in Plucenio et al. (2008a). The NMPC algorithm, named PNMPC, employs a continuous linearization technique where the vector of the predicted variable $\tilde{\mathbf{Y}}$ is represented by

$$\tilde{\mathbf{Y}} = \mathbf{F} + \mathbf{G}\Delta\mathbf{u} + \Gamma. \quad (19)$$

The matrix $\mathbf{G}$ is the Jacobian of $\tilde{\mathbf{Y}} = f(\Delta\mathbf{u})$ and is obtained by a numerical procedure realized in two steps at every iteration. The first step uses the matrix $\mathbf{G}$ of the previous iteration to produce an intermediate $\Delta\mathbf{u}$. Next, another matrix $\mathbf{G}$ is obtained using the $\Delta\mathbf{u}$ just computed. The matrix $\mathbf{G}$ used to compute the final $\Delta\mathbf{u}$ is an average of the two matrix. The vector Γ represents the correction factors which are an explicit version of the CARIMA error treatment.

3.1 NMPC Tuning

One way to tune the NMPC objective function weights is to start by the economic function as described by equation (4). Next the other weights are tuned to balance production oscillation attenuation with the economic objective. For numerical efficiency it may be interesting to multiply all weights by a common factor. The tuning parameters are shown in table 3. Controlling the system composed by the GLM and the wells

Table 3. NMPC Tuning Parameters

Symb.	Variable description	Value
Ts	Sampling time	5s
p	Prediction horizon for qo_L	150
p_1	Prediction horizon for P_m	18
w_1	Element of vector $\mathbf{W}_1$ $1 \times 4p$	.020
w_2	Element of vector $\mathbf{W}_2$ $1 \times 5m$	5e-4
w_3	Diagonal element of Matrix $\mathbf{W}_3$ $p_1 \times p_1$	(1)
w_4	Diagonal element of Matrix $\mathbf{W}_4$ $4p \times 4p$	(2)
w_5	Diagonal element of Matrix $\mathbf{W}_5$ $5m \times 5m$	(3)

(1) $w_3(i)$ varies linearly from 1 to 10 for $i = 1 : 18$
(2) w_4 is a linear function of the filtered and normalized gas mass flow rate q_{in} entering the GLM. 1 for $q^*_{in} = 1$ and 12 for $q^*_{in} = 0.25$
(3) $\mathbf{W}_5(i,i) = 1x10^{-5}$ for i=1:12. For Δu_{flare}, $\mathbf{W}_5(i,i)$ for i=13:15, a linear function of the filtered and normalized gas mass flow rate q_{in} entering the GLM was used. $\mathbf{W}_5(i,i)$ goes from $1x10^{-5}$ for $q^*_{in} = 0.25$ to $15x10^{-5}$ for $q^*_{in} = 0.25$.

has a great advantage of eliminating the gas lift availability constraint. Many gas-lift optimization studies consider gas lift availability as a constraint while this information is not always available. Another advantage is the possibility to apply optimization during the transients which can be more or less frequent depending on the setup used. On the other hand the GLM pressure dynamic behavior is highly dependent on the associated pipe internal volume and it will be normally faster than the downhole pressure. This requires the sampling time to be adjusted based on the GLM pressure dynamics. To overcome a bit the problem the qo_L predictions were done every 3 sampling time resulting in a prediction horizon p equal to 150. A constraint was used to make sure that the excess gas flow rate would be always positive. Besides, a minimum flow rate was imposed to all wells to avoid entering in the density wave limit cycle. A constraint was used to imposed a limit on the GLM Pressure deviation from the set point at +- 5%.

3.2 Results obtained

In order to test the control strategy proposed an operation of 24 hours was simulated covering different gas-lift availabilities. It was assumed an equivalent volume for the GLM (sum of all associated pipes internal volume) equal to 1 m^3. The initial gas injection flow rate was the sum of all gas flow rates values which corresponded to the values used for normalization. This value was considered as the nominal input GLM flow rate. Next the gas entering the GLM was changed to 50%, 25% and 110% of nominal value as shown on figure 5. Figure 6 top shows all the wells downhole pressure (normalized values) and the GLM pressure (normalized to the set-point value). It can be noticed that they change smoothly. The GLM pressure presents a small deviation from its set-point at moments of significant ramp type changes on the gas flow rate entering

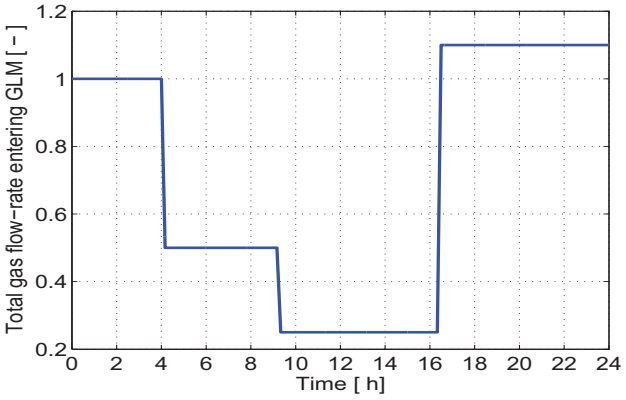

Fig. 5. Normalized gas flow-rate entering the GLM

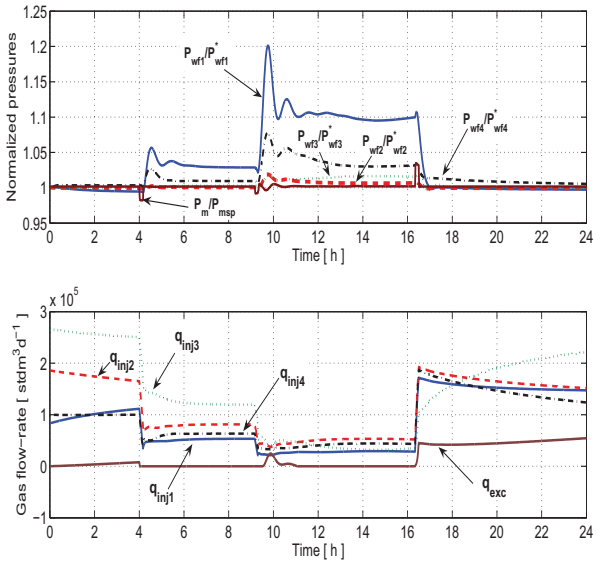

Fig. 6. GLM and gas lift wells behavior

the GLM although not enough to exceed the constraints. The bottom plot of figure 6 shows all the gas injection flow rates for the four wells and the excess gas flow rate. It is interesting to observe that when the gas flow rate entering the GLM goes to 110% of the nominal value the excess gas flow rate rises to keep the GLM pressure at its reference and to avoid production losses. When the gas entering the GLM decreases from 50% to 25% of the nominal value, the excess gas flow rate helped on avoiding too much change in the wells gas injection flow rate what would cause excessive oil production oscillation. This behavior can be controlled by tuning the Cost Function parameters. Figure 7 shows the evolution of the total oil production flow rate as the gas entering the GLM was changed. Both, 100% and 110% of nominal GLM input flow-rate give the same total oil production flow-rate. The gas flow rate not used for injection in the wells returns on the recirculation line as excess gas as shown in figure 6. The oil production flow rate of all the four wells is shown in figure 8. The solid lines were obtained with the simulation including the

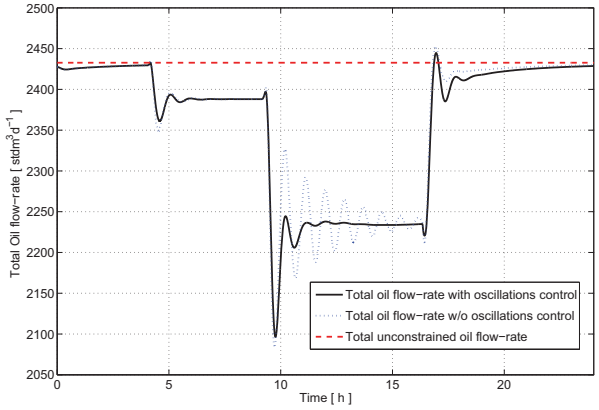

Fig. 7. Total oil production flow rate

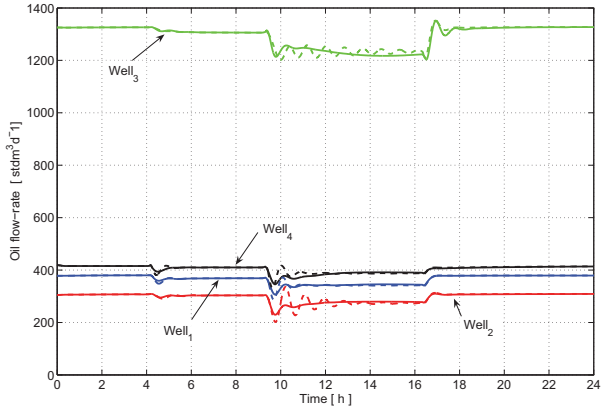

Fig. 8. Oil Production flow rate for all wells

oscillation attenuation control while the dashed lines not. The well 3 is the main producer. It is interesting to notice that the production decay is not much affected by the decrease in the total gas injection flow rate due to the appropriate gas allocation made by the NMPC algorithm. Despite the limited degree of freedom (only gas injection flow-rate manipulation) all the objectives are met; optimum gas distribution, GLM pressure control and attenuation of oil production oscillations.

4. CONCLUSION

Downhole permanent pressure measurement is becoming a reality for new wells. This work proposes the utilization of the PNMPC control technique discussed in Plucenio et al. (2008b) and demonstrates its applications on the control of 4 gas-lift wells using simulation. More work has to be done to investigate the quality of the empirical gas lift well dynamical model proposed.

ACKNOWLEDGEMENTS

The authors also acknowledge Scandpower for providing an academical OLGA2000 software license.

REFERENCES

Boisard, O., Makaya, B., Nzossi, A., Hamon, J., and Lemetayer, P. (2002). Automated well control increases performance of mature gas-lifted fields, Sendji case. In *Proc. 10^{th} Abu Dhabi International Petroleum Exhibition and Conference*. Abu Dhabi,. Paper SPE 78590.

Camponogara, E. and Nakashima, P.H.R. (2006). Optimizing gas-lift production of oil wells: Piecewise linear formulation and computational analysis. *IIE Transactions*, 38(2), 173–182.

Campos, S.R., Junior, M.F.S., Correa, J.F., Bolonhini, E.H., and Filho, D.F. (2006). Right time decision of artificial lift management for fast loop control. In *SPE Intelligent Energy Conference and Exhibition*. Amsterdam, Netherlands.

Eikrem, G.O., Imsland, L., and Foss, B. (2004). Stabilization of gas-lifted wells based on state estimation. *Proc. of International Symposium on Advanced Control of Chemical Processes-ADCHEM, Hong Kong*.

Fetkovich, M. (1973). The isochronal testing of oil wells. In *Proceedings of the SPE Annual Fall Meeting*. Las Vegas, Nevada.

Hu, B. (2004). *Characterizing gas-lift instabilities*. Master's thesis, Department of Petroleum Engineering and Applied Geophysics, Norwegian University of Science and Technology University, Trondheim, Norway.

Imsland, L., Eikrem, G.O., and Foss, B. (2003). State feedback control of a class of positive systems: Application to gas lift control. *Proc. of European Control Conference, Cambridge*.

Kanu, E.P., Mach, J., and Brown, K.E. (1981). Economic approach to oil production and gas allocation in continuous gas lift. *Journal of Petroleum Technology*, 33, 1887–1892. Paper SPE 9084.

L. Singre, N. Petit, T.S.P. and Lemetayer, P. (2006). Active control strategy for density-wave in gas-lifted wells. *International Symposium on Advanced Control of Chemical Processes-ADCHEM*, 2(ADCHEM 2006), 1075–1080.

Maravi, Y.D.C. (2003). *New Inflow Performance Relationships for Gas Condensate Reservoirs*. Master's thesis, Department of Petroleum Engineering, Texas A&M University.

Patton, D. and Goland, M. (1980). Generalized IPR curves for predicting well behavior. *Petroleum Engineering International*, 52(7), 74–82.

Plucenio, A., Mafra, G.A., and Pagano, D.J. (2006). A control strategy for an oil well operating via gas-lift. *International Symposium on Advanced Control of Chemical Processes-ADCHEM*, 2(ADCHEM 2006), 1081–1086.

Plucenio, A., Normey-Rico, J.E., Pagano, D.J., and Bruciapaglia, A.H. (2008a). Controle preditivo não linear na indústria do petróleo e gás. *IV Congresso Brasileiro de P & D em Petróleo e Gás - PDPetro*.

Plucenio, A., Pagano, D.J., Bruciapaglia, A.H., and Normey-Rico, J.E. (2008b). A pratical approach to predictive control for nonlinear processes. *NOLCOS 2008*.

Raghavan, R. (1993). *Well Test Analysis*. Prentice Hall, Englewood Cliffs, NJ.

Richardson, J.M. and Shaw, A.H. (1982). Two-rate IPR testing – a practical production tool. *Journal of Canadian Petroleum Technology*, 57–61.

Vogel, J.V. (1968). Inflow Performance Relationships for Solution-Gas Drive Wells. In *JPT*.

Wiggins, M.L., Russel, J.E., and Jennings, J. (1996). Analytical development of vogel-type inflow performance relationships. *SPE Journal*, 355–362.

Application of a New Scheme for Adaptive Unfalsified Control to a CSTR with Noisy Measurements ⋆

Tanet Wonghong and Sebastian Engell *

* *Process Dynamics and Operations Group, Department of Biochemical and Chemical Engineering, Technische Universität Dortmund, 44221 Dortmund, Germany*
(e-mail: {t.wonghong, s.engell}@bci.tu-dortmund.de)

Abstract:
In this paper, a new scheme for adaptive unfalsified control with non-ideal measurements is presented and demonstrated for a well-known example of a nonlinear plant, the continuous stirred tank reactor (CSTR) with the van-der-Vusse reaction scheme. In our adaptive control algorithm, there are two adaptation mechanisms: 1. Switching of the active controller in a fixed set of candidate controllers by the ϵ-hysteresis switching algorithm. 2. Adaptation of the set of controllers performed by a population-based evolutionary algorithm. In this paper, the effect of measurement errors on the adaptive control scheme is investigated. The total least squares method is used to perform the deconvolution of noisy signals.

Keywords: Adaptive Control; Unfalsified Control; Nonlinear Control, Reactor Control, Measurement Error

1. INTRODUCTION

The adaptive unfalsified control scheme was initially introduced by Safonov et al. (1997). The basic idea is to switch among candidate controllers in a predefined set of controllers. This approach does not require a plant model but uses the observed plant input-output data while one controller is active to decide on the switching to the next active controller. Further developments by Wang et al. (2005) led to the concept of cost-detectability, the proposal of a cost-detectable cost function, and the ϵ-hysteresis switching algorithm. Stability of the adaptive system was proven in Wang et al. (2005) in the sense that if the set of controllers contains stabilizing controllers with satisfactory performance, the scheme will ultimately switch to one of them. In Engell et al. (2007), Manuelli et al. (2007) and Dehghani et al. (2007), it was pointed out that the scheme in Wang et al. (2005) cannot detect instability of controllers that are not in the loop and may temporarily switch to destabilizing controllers. For this reason, the cost function proposed in Wang et al. (2005) is not suitable for evaluating controllers that are not in the loop, and cannot be used to adapt the controllers in the set.

To resolve this problem, a new scheme of adaptive unfalsified control was proposed in Engell et al. (2007). The key point was the introduction of a new fictitious error signal that can be computed using the estimated sensitivity function obtained by deconvolution between the fictitious reference signal and the fictitious error signal. This new signal is used in a new cost function that can measure the true performance of non-active controllers correctly. Based upon this new cost function, an adaptation of the set of controllers using evolutionary algorithm was performed. The scheme was demonstrated to work for the well-known non-minimum phase CSTR example with undisturbed measurements in Wonghong and Engell (2008).

In this paper, we extend the approach in Engell et al. (2007) to the case of noisy measurements. In the next section, we first review the new concept of unfalsified control with the ϵ-hysteresis switching algorithm as a switching mechanism for the active controller and the adaptation of the set of candidate controllers using evolution strategies. Then we investigate the effect of noise added to the plant output signal on the observed plant input-output data, the fictitious reference signal, and the fictitious error signal. We introduce the total least squares technique to solve the noisy deconvolution problem. This leads to an estimation of the sensitivity function in the non-ideal situation. In section 5, we present simulation studies for the CSTR example. We show that the adaptation of the controller parameters can be performed successfully under non-ideal measurements.

2. A NEW SCHEME FOR ADAPTIVE UNFALSIFIED CONTROL

We consider a SISO adaptive unfalsified control system $\Sigma(P, \hat{K})$ mapping r into (u, y). The system is defined on $\Sigma(P, \hat{K}) : \mathcal{L}_{2e} \rightarrow \mathcal{L}_{2e}$. The scheme of an adaptive unfalsified control system $\Sigma(P, \hat{K})$ is shown in Fig. 1.

The disturbed unknown plant $P : \mathcal{U} \rightarrow \mathcal{Y}$ is defined by

$$\mathbf{P} = \{(u, y, w) \subset \mathcal{U} \times \mathcal{Y} \times \mathcal{W} \mid y = Pu + w\}. \quad (1)$$

⋆ This work was supported by the NRW Graduate School of Production Engineering and Logistics at Technische Universität Dortmund.

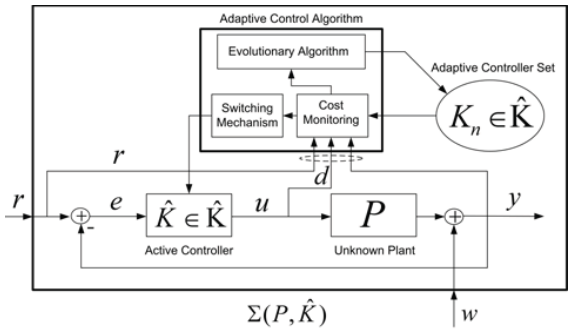

Fig. 1. Adaptive Unfalsified Control Scheme

The set of controllers $K : \mathcal{R} \times \mathcal{Y} \to \mathcal{U}$ is defined by

$$\hat{\mathbf{K}} = \{(r, u, y) \subset \mathcal{R} \times \mathcal{U} \times \mathcal{Y} \mid u = K_n \begin{bmatrix} r \\ y \end{bmatrix}\}, n = 1, 2, ..., N. \tag{2}$$

The signals $r(t), u(t), y(t)$ are assumed to be square-integrable over every bounded interval $[0, \tau], \tau \in \mathbb{R}_+$. The adaptive control algorithm maps vector signals $d = [r(t), u(t), y(t)]^T$ into a choice of a controller $K_n \in \hat{\mathbf{K}}$, where K_n satisfies the *stable causal left invertible* (SCLI) property [Wang et al. (2005)]. The true error signal is

$$e(t) = r(t) - y(t). \tag{3}$$

The adaptive control law has the form:

$$u(t) = \hat{K}(t) * e(t) \tag{4}$$

where $\hat{K} = K_{n(t)}$ denotes the active controller. $n(t)$ is a piecewise constant function with a finite number of switchings in any finite interval and $*$ denotes the convolution integral.

Let $d = (r(t), u(t), y(t)), 0 \le t \le T$ denote experimental plant data collected over the time interval T, and let $\mathbf{D}$ denote the set of all possible vector signals d. d_τ denotes the truncation of d, e.g., all past plant data up to current time τ. The data set $\mathbf{D}_\tau$ is defined by

$$\mathbf{D}_\tau = \{(r, u, y) \subset \mathcal{R} \times \mathcal{U} \times \mathcal{Y} \mid d_\tau = (r_\tau, u_\tau, y_\tau)\}.$$

We consider linear time-invariant control laws of the form:

$$K_n = \{(r, u, y) \subset \mathcal{R} \times \mathcal{U} \times \mathcal{Y} \mid u = c_n * e\} \tag{5}$$

where c_n is the impulse response of the n^{th} controller. $C_n(s)$ denotes the Laplace transform of c_n.

We assume that we have observed the excitation r_τ, the plant input data u_τ and the plant output data y_τ.

In unfalsified control, these data are used to evaluate whether the controller K_n meets a specified closed-loop performance criterion

$$J_n^*(r_\tau, u_\tau, y_\tau) \le \alpha \tag{6}$$

where α is called the unfalsification threshold. If this condition is not met, the control law switches to a different controller and the previous controller is discarded. After at most N switchings, a suitable controller is found, if there is such a controller in the set.

The key idea of unfalsified control is to compute the cost $J_n^*(d_\tau, \tau)$ based upon the available measurements. For this purpose,

$$\tilde{r}_n = c_n^{-1} * u + y \tag{7}$$

and

$$\tilde{e}_n = \tilde{r}_n - y \tag{8}$$

are defined where c_n^{-1} is the impulse response of the inverse controller transfer function $C_n^{-1}(s)$. These signals are called the *fictitious reference signal* and the *fictitious error signal*, respectively. $\tilde{r}_n$ is the reference signal that produces the measured plant input u and output y if the controller K_n is in the loop instead of the currently active controller.

In Engell et al. (2007), the *new fictitious error signal*

$$e_n^* = \tilde{s}_n * r \tag{9}$$

where $\tilde{s}_n$ is the impulse response of the sensitivity function with the n^{th} controller in the loop,

$$\tilde{S}_n(s) = \frac{1}{1 + C_n P} \tag{10}$$

was introduced. e_n^* is the error that results for the true reference signal r with the controller K_n in the loop. As $\tilde{S}_n(s) = \frac{\tilde{E}_n(s)}{\tilde{R}_n(s)}$, $\tilde{s}_n$ can be computed via the deconvolution of $\tilde{r}_n$ and $\tilde{e}_n$ [Engell et al. (2007)].

When $J_n^*(e_{n_\tau}^*, d_\tau, \tau) > \alpha$, this implies that if the controller K_n were in the loop, it would not satisfy the performance criterion (6). In this case, it is said that the controller K_n is a *falsified* controller. Otherwise the controller K_n is an *unfalsified* controller.

The new adaptive control algorithm consists of two adaptation mechanisms:

1. Switching of the active controller
The closed-loop performances of all candidate controllers are computed using sampled signals

$$J_n^*(d_{\tau_k}, \tau_k) = \max_{\tau_j \le \tau_k} \frac{\sum_{i=0}^{j} |e_n^*(i)|^2 + \gamma \cdot \sum_{i=0}^{j} |u(i)|^2}{\sum_{i=0}^{j} |r(i)|^2} \tag{11}$$

where γ is a positive constant.

The ϵ-hysteresis switching algorithm of Morse et al. (1992) is applied for the switching of the active controller:

(1) Initialize: Let $k = 0, \tau_0 = 0$; choose $\epsilon > 0$. Let $\hat{K}(0) = K_1, K_1 \in \hat{\mathbf{K}}(0)$, be the first active controller in the loop.
(2) $k = k + 1, \tau_k = \tau_{k+1}$
If $J^*(\hat{K}(k-1), d_{\tau_k}, \tau_k) \ge \min_{K_n \in \hat{\mathbf{K}}(k)} J_n^*(d_{\tau_k}, \tau_k) + \epsilon$,
then $\hat{K}(k) \leftarrow \arg\min_{K_n \in \hat{\mathbf{K}}(k)} J_n^*(d_{\tau_k}, \tau_k)$,
else $\hat{K}(k) \leftarrow \hat{K}(k-1)$.
(3) Go to 2.

2. Adaptation of the set of controllers $\hat{\mathbf{K}}(t^*)$
An evolutionary algorithm (EA) is used for the adaptation of the set of controllers because EA manipulate a population of candidate controllers and can handle nonconvex cost functions and are able to escape from local minima. The EA is executed only at units of time t^* after a sufficiently large change of $r(t)$ was detected. For accurate results, t^* should approximately match the settling time of the controlled system. Insufficient excitation leads to numerical problems due to an ill-conditioned matrix in the deconvolution. Thus, we restrict the activation of the EA to a suitable interval after a sufficient excitation by a change of $r(t)$. In this work, the evolutionary algorithm is a so-called *evolution strategy* where each individual is

represented by a vector of controller parameters and by a vector of strategy parameters that control the mutation strength.

The *evolution strategy* as introduced by Rechenberg (1965) and later developed by Schwefel (1975) is based on a population P of μ individuals $\mathbf{a} = (\mathbf{x}, \mathbf{s})$, which represent search points $\mathbf{x} = (x_1, \ldots, x_m) \in \mathbb{R}^m$ and vectors of strategy parameters $\mathbf{s} = (s_1, \ldots, s_m) \in \mathbb{R}_+^m$ that handle the evolution of the population. The size of the population is equal to the number of candidate controllers $\mu = N$. The μ parent individuals in the parent set are randomly selected from the population. The new offspring λ are generated by recombination of two parent individuals and by subsequent perturbation of single variable $x_j, j \in \{1, ..., m\}$ with a random number drawn from a Gaussian distribution $\mathcal{N}(0, s_j)$ by

$$x_j' = x_j + s_j \cdot \mathcal{N}(0, 1). \tag{12}$$

According to the self adaptation mechanism of evolution strategies, each strategy s_j is modified log-normally

$$s_j' = s_j \cdot \exp(\delta \cdot \mathcal{N}(0, 1)) \tag{13}$$

where δ is an external parameter. Normally it is inversely proportional to the square root of the problem size ($\delta \propto \frac{1}{\sqrt{N}}$). To preserve a constant number of individuals, the survivor selection chooses the μ best ($1 \leq \mu < \lambda = 7 \cdot \mu$) individuals out of the set of λ offspring ((μ, λ)-selection) or out of the union set of parents and offspring ($(\mu + \lambda)$-selection). The quality of each individual is evaluated by the fitness function $f(\mathbf{a}) = J^*(\mathbf{x}, d_{t^*}, t^*)$. As long as a fitness improvement ($\Delta f > min_{\Delta f}$) of the best individual within a certain number of generations can be observed, the termination criterion of the evolution strategy is not fulfilled and the μ selected individuals from the previous generation are used for the next iteration.

3. CONSIDERATION OF NOISE AT THE PLANT OUTPUT

For the scheme in Fig. 1 with a linear plant and a linear controller, in the Laplace domain,

$$\begin{aligned} Y(s) &= P(s)U(s) + W(s) \\ &= P(s)\hat{C}(s)(R(s) - Y(s)) + W(s) \\ &= \hat{T}(s)R(s) + \hat{S}(s)W(s) \\ &= Y_{true}(s) + Y_w(s) \end{aligned} \tag{14}$$

with the active complementary sensitivity function,

$$\hat{T}(s) = \frac{\hat{C}(s)P(s)}{1 + \hat{C}(s)P(s)} \tag{15}$$

and the active sensitivity function,

$$\hat{S}(s) = \frac{1}{1 + \hat{C}(s)P(s)}. \tag{16}$$

The observed disturbed plant input signal is,

$$\begin{aligned} U(s) &= \hat{C}(s)(R(s) - Y(s)) \\ &= \hat{C}(s)(R(s) - Y_{true}(s)) - \hat{C}(s)Y_w(s) \\ &= U_{true}(s) - \hat{C}(s)Y_w(s). \end{aligned} \tag{17}$$

Hence $y(t)$ and $u(t)$ consist of deterministic and stochastic components,

$$y(t) = y_{true}(t) + y_w(t) \tag{18}$$

$$u(t) = u_{true}(t) - \hat{c}(t) * y_w(t) \tag{19}$$

where

$$y_{true}(t) = \hat{t}(t) * r(t) \tag{20}$$

$$u_{true}(t) = \hat{c}(t) * (r(t) - y_{true}(t)) \tag{21}$$

$$y_w(t) = \hat{s}(t) * w(t). \tag{22}$$

Therefore, the error propagation in the measured plant input-output data depends on the closed-loop performance of the active controller.

4. STOCHASTIC DECONVOLUTION

4.1 Stochastic Fictitious Signals

Using (7), the stochastic fictitious reference signal $\tilde{R}_{i,w}$ of C_i using the noisy observed plant input-output data (U, Y) while controller $\hat{C}$ is active results as

$$\begin{aligned} \tilde{R}_{i,w} &= C_i^{-1}U + Y \\ &= C_i^{-1}\hat{C}(R - Y) + Y \\ &= C_i^{-1}\hat{C}(R - Y_{true} - Y_w) + Y_{true} + Y_w \\ &= \tilde{R}_{i,true} + \Delta\tilde{R}_i \end{aligned}$$

where $\Delta\tilde{R}_i = (1 - C_i^{-1}\hat{C})\hat{S}W$. Note that $\Delta\tilde{R}_{\hat{C}} = 0$.

Using (8), the stochastic fictitious error signal $\tilde{E}_{i,w}$ of C_i can be computed from (U, Y),

$$\begin{aligned} \tilde{E}_{i,w} &= C_i^{-1}U \\ &= C_i^{-1}\hat{C}(R - Y) \\ &= C_i^{-1}\hat{C}(R - Y_{true} - Y_w) \\ &= \tilde{E}_{i,true} + \Delta\tilde{E}_i \end{aligned}$$

where $\Delta\tilde{E}_i = -C_i^{-1}\hat{C}\hat{S}W$. Note that $\Delta\tilde{E}_{\hat{C}} = -Y_w \neq 0$.

Using (9), the new fictitious error signal $e_{i,w}^*(t)$ of C_i is

$$E_{i,w}^* = \tilde{S}_{i,w}R. \tag{23}$$

$\tilde{S}_{i,w}$ can be obtained using (10),

$$\begin{aligned} \tilde{E}_{i,w} &= \tilde{S}_{i,w}\tilde{R}_{i,w} \\ \tilde{e}_{i,w}(t) &= \tilde{s}_{i,w}(t) * \tilde{r}_{i,w}(t). \end{aligned} \tag{24}$$

From (24), $\tilde{s}_{i,w}(t)$ can be computed from $u(t)$ and $y(t)$ via $\tilde{e}_{i,w}(t)$ and $\tilde{r}_{i,w}(t)$. The noisy deconvolution is performed using sampled signals:

$$\begin{aligned} \tilde{\mathbf{R}}_{i,w} \cdot \tilde{\mathbf{s}}_{i,w} &= \tilde{\mathbf{e}}_{i,w} \\ (\tilde{\mathbf{R}}_{i,true} + \Delta\tilde{\mathbf{R}}_i) \cdot \tilde{\mathbf{s}}_{i,w} &= \tilde{\mathbf{e}}_{i,true} + \Delta\tilde{\mathbf{e}}_i \end{aligned} \tag{25}$$

where

$$\tilde{\mathbf{R}}_{i,true} = \begin{bmatrix} \tilde{r}_{i,true}(0) & 0 & \cdots & 0 \\ \vdots & \tilde{r}_{i,true}(0) & 0 & 0 \\ \tilde{r}_{i,true}(l-1) & \ddots & \tilde{r}_{i,true}(0) & 0 \\ \tilde{r}_{i,true}(l) & \tilde{r}_{i,true}(l-1) & \cdots & \tilde{r}_{i,true}(0) \end{bmatrix}$$

and $\tilde{\mathbf{e}}_{i,true} = [\tilde{e}_{i,true}(0) \ \cdots \ \tilde{e}_{i,true}(l-1) \ \tilde{e}_{i,true}(l)]^T$. The unknown matrix $\Delta\tilde{\mathbf{R}}_i$ is defined similar to $\tilde{\mathbf{R}}_{i,true}$ and the unknown vector $\Delta\tilde{\mathbf{e}}_i$ is defined similar to $\tilde{\mathbf{e}}_{i,true}$. Examples

of the computation of $\tilde{\mathbf{R}}_{i,true}, \tilde{\mathbf{e}}_{i,true}, \tilde{\mathbf{s}}_{i,true}$ can be seen in Engell et al. (2007) and Wonghong and Engell (2008).

The deconvolution problem (25) contains error terms both in the matrix and in the right hand side, and therefore it is not adequate to approach it as an ordinary least squares problem. Instead we employ the *total least squares* (TLS) method.

The total least squares method was originally proposed by Golub et al. (1980). The motivation comes from the asymmetry of the *least squares* (LS) method where no error term in the matrix $\tilde{\mathbf{R}}$ is taken into account. The idea of TLS is to find the minimal (in the Frobenius norm sense) error terms $\Delta\tilde{\mathbf{R}}$ and $\Delta\tilde{\mathbf{e}}$ in the matrix $\tilde{\mathbf{R}}$ and in the vector $\tilde{\mathbf{e}}$ that make the linear equations system (25) solvable, i.e.,

$$\{\tilde{\mathbf{s}}_{TLS}, \Delta\tilde{\mathbf{R}}_{TLS}, \Delta\tilde{\mathbf{e}}_{TLS}\} = \arg \min_{\tilde{\mathbf{s}}, \Delta\tilde{\mathbf{R}}, \Delta\tilde{\mathbf{e}}} \|\Delta\tilde{\mathbf{R}} \;\; \Delta\tilde{\mathbf{e}}\|_F$$

$$\text{subject to } (\tilde{\mathbf{R}} + \Delta\tilde{\mathbf{R}}) \cdot \tilde{\mathbf{s}} = \tilde{\mathbf{e}} + \Delta\tilde{\mathbf{e}}.$$

4.2 Solution of the Total Least Squares Problem

The conditions for the existence and the uniqueness of a TLS solution can be found in Markovsky et al. (2007):

$$\mathbf{Z} = [\tilde{\mathbf{R}} \;\; \tilde{\mathbf{e}}] = \mathbf{U}\Sigma\mathbf{V}^T$$

where $\Sigma = diag(\sigma_1, ..., \sigma_{l+1})$ is a singular value decomposition of $\mathbf{Z}$, $\sigma_1 \geq \cdots \geq \sigma_{l+1}$ are the singular values of $\mathbf{Z}$. Partitioned matrices are defined as

$$\mathbf{V} = \begin{bmatrix} \mathbf{V}_{11} & \vdots & \mathbf{v}_{12} \\ \cdots & & \cdots \\ \mathbf{v}_{21} & \vdots & v_{22} \end{bmatrix}, \Sigma = \begin{bmatrix} \Sigma_{11} & \vdots & \mathbf{0}_{12} \\ \cdots & & \cdots \\ \mathbf{0}_{21} & \vdots & \sigma_{l+1} \end{bmatrix},$$

where $\mathbf{V}_{11}, \Sigma_{11} = diag(\sigma_1, ..., \sigma_l) \in \mathbb{R}^{l\times l}, \mathbf{v}_{12}, \mathbf{0}_{12} \in \mathbb{R}^{l\times 1}, \mathbf{v}_{21}, \mathbf{0}_{21} \in \mathbb{R}^{1\times l}, v_{22}, \sigma_{l+1} \in \mathbb{R}$. A TLS solution exists if and only if v_{22} is not zero. In addition, it is unique if and only if $\sigma_l \neq \sigma_{l+1}$. In the case when a TLS solution exists and is unique, the solution is given by

$$\tilde{\mathbf{s}}_{TLS} = -\frac{\mathbf{v}_{12}}{v_{22}}. \tag{26}$$

Therefore, the new fictitious error signal $e^*_{i,w}(t)$ for controller C_i can be computed by

$$\mathbf{e}^*_{i,w} = \mathbf{R} \cdot \tilde{\mathbf{s}}_{i,w} = \mathbf{R} \cdot \tilde{\mathbf{s}}_{i_{TLS}}. \tag{27}$$

4.3 Ill-conditioned Matrix $\tilde{R}_{i,w}$

In the error-free case, the computation fails if $\tilde{\mathbf{R}}_{i,true}$ is ill-conditioned, in particular if $\tilde{r}_{i,true}(0) \to 0$. Using the relationship of $\tilde{r}_{i,true}(t)$ and $r(t)$

$$\tilde{R}_{i,true} = \frac{\hat{C}}{C_i} \frac{1 + C_i P}{1 + \hat{C} P} R \tag{28}$$

and applying the initial value theorem,

$$\tilde{r}_{i,true}(0) = \lim_{s\to\infty} s \frac{\hat{C}}{C_i} \frac{1 + C_i P}{1 + \hat{C} P} R. \tag{29}$$

If a unit step function is applied to $r(t)$ and P is strictly proper and $C_i(s) = k_{p_i}(1 + \frac{1}{T_{n_i} s})$,

$$\tilde{r}_{i,true}(0) = \frac{\hat{k}_p}{k_{p_i}}, \tag{30}$$

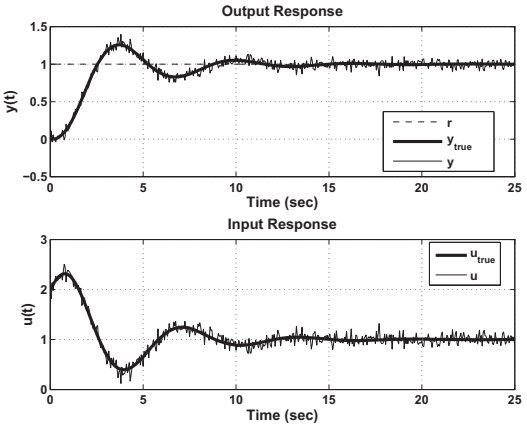

Fig. 2. The measured plant input-output data

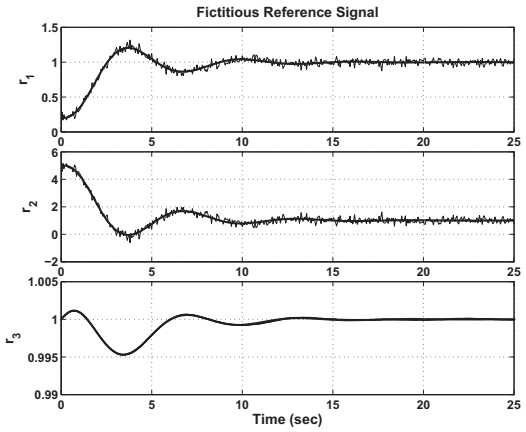

Fig. 3. Fictitious reference signals

so $|k_{p_i}| \gg |\hat{k}_p|$ leads to ill-conditioned matrices $\tilde{\mathbf{R}}_{i,true}$. For $\tilde{\mathbf{R}}_{i,w}$

$$\tilde{r}_{i,w}(0) = \tilde{r}_{i,true}(0) + \Delta\tilde{r}_i(0) = \frac{\hat{k}_p}{k_{p_i}} + \Delta\tilde{r}_i(0). \tag{31}$$

Hence the presence of measurement noise alleviates the ill-conditioning problem for the deconvolution technique.

4.4 Example of Estimated Fictitious Error Signals

We assume that $P = \frac{1}{(s+1)^3}$ and $\hat{C} = 2(1 + \frac{1}{3s})$ and a unit step was applied to $r(t)$. $d_\tau = (r_\tau, u_\tau, y_\tau)$ was observed up to $\tau = 25s$. We assume measurement errors in the plant output data as shown in Fig. 2. Three candidate controllers are tested: 1. $C_1 = 10(1+\frac{1}{3s})$ 2. $C_2 = 0.4(1+\frac{1}{3s})$ 3. $C_3 = 2(1 + \frac{1}{3s})$. $\tilde{r}_{i,true}(t)$ and $\tilde{r}_{i,w}(t)$ result as shown in Fig. 3. Note that the computation of $\tilde{r}_{3,w}(t)$ is error-free. $e^*_{i,true}(t)$ and $e^*_{i,w}(t)$ are shown in Fig. 4. The closed-loop instability of the loop with C_1 is detected and the performances of C_2 and C_3 are estimated well.

5. ADAPTIVE CONTROL OF A CSTR WITH NONMINIMUM PHASE BEHAVIOR

As an example of the application of the new adaptive control scheme to a nonlinear process we investigate the

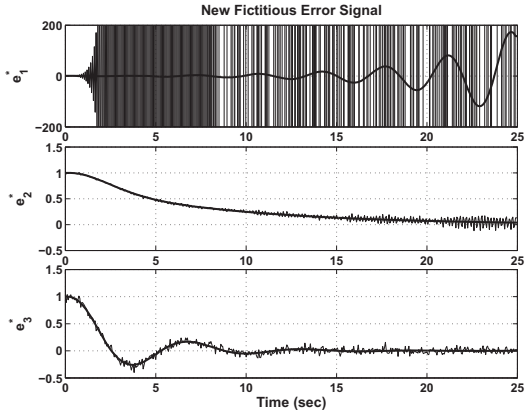

Fig. 4. New fictitious error signals

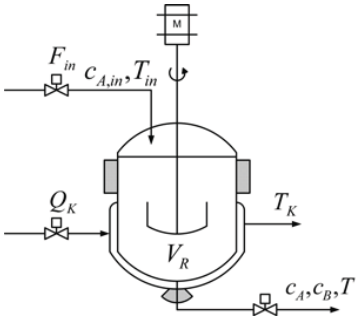

Fig. 5. Continuous Stirred Tank Reactor

well-known case study of the control of a CSTR with the van-der-Vusse reaction scheme. The parameters of the model are the same as in Engell et al. (1993), Klatt et al. (1998).

A sketch of the reactor is shown in Fig. 5. The reaction scheme is

$$A \overset{k_1}{\rightarrow} B \overset{k_2}{\rightarrow} C,$$
$$2A \overset{k_3}{\rightarrow} D.$$

The reactor is operated at a constant holdup, i.e., the volume of the contents is constant. The manipulated input $u(t)$ is the flow through the reactor, represented by the inverse of the residence time (F_{in}/V_R). u is in the range $0 \leq u(t) \leq 30h^{-1}$. We assume that the temperature control is tight so that the dependency of the kinetic parameters on the reactor temperature can be neglected. Under these assumptions, a SISO nonlinear model results from mass balances for the components A and B:

$$\begin{aligned} \dot{x}_1 &= -k_1 x_1 - k_3 x_1^2 + (x_{1,in} - x_1)u \\ \dot{x}_2 &= k_1 x_1 - k_2 x_2 - x_2 u \\ y &= x_2 \end{aligned} \tag{32}$$

where x_1 is the concentration of component A, x_2 is the concentration of component B and $x_{1,in}$ is the feed concentration of A, assumed to be constant. The parameter values are $k_1 = 15.0345h^{-1}, k_2 = 15.0345h^{-1}, k_3 = 2.324l \cdot mol^{-1} \cdot h^{-1}, x_{1,in} = 5.1mol \cdot l^{-1}$.

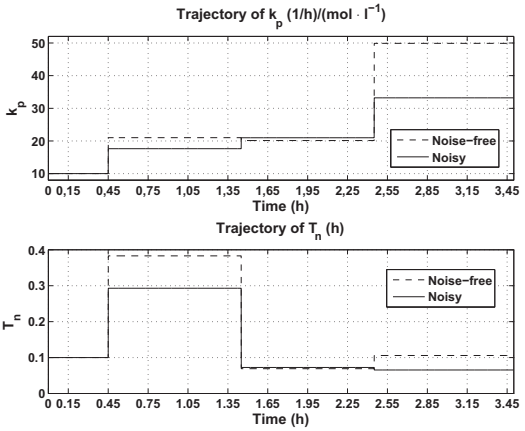

Fig. 6. Evolution of the active controller

We assume that the unknown plant P consists of the continuous stirred tank reactor as described by the above model plus a delay of $0.02h$ for the analytic instrument. The controller structure is a PI-controller defined by

$$C(s) = k_p(1 + \frac{1}{T_n s}).$$

The initial set of the controller parameters is given by the proportional gains $\mathbf{k}_{p_a} = \{10, 50, 100\}$ and the integral times $\mathbf{T}_{n_b} = \{0.1, 0.5, 1\}$. The initial set of candidate controllers consists of 9 candidate controllers with PI-controller parameter vectors $\Theta = \{\theta_i = [k_{p_a}, T_{n_b}]^T, 1 \leq a, b \leq 3\}$. The first active controller assigned to the feedback loop is $\theta_1 = [10, 0.1]^T \in \Theta$. All initial conditions at $\tau = 0$ are zero and the simulation horizon is $t_f = 3.5h$. The constant ϵ in the ϵ-hysteresis switching algorithm is 0.1 and $\gamma = 10^{-9}$ in the cost function J_i^*.

The reference signal is

$$r(t) = \begin{cases} 0mol \cdot l^{-1} & : \quad 0 \leq t < 0.15h; \\ 0.7mol \cdot l^{-1} & : \quad 0.15h \leq t < 1.15h; \\ 0.9mol \cdot l^{-1} & : \quad 1.15h \leq t < 2.15h; \\ 1.09mol \cdot l^{-1} & : \quad 2.15h \leq t < 3.5h. \end{cases}$$

EA activation times are at $t^* = 0.3h$ after each change of $r(t)$ at $t = 0.15h, 1.15h, 2.15h$.

CSTR with adaptation of the set of controllers with noisy measurements

The EA is executed three times at $0.45h$,$1.45h$, and $2.45h$. The EA used is a standard evolution strategy (ES) with adaptation of the search parameters according to Schwefel (1995) and Quagliarella et al. (1998). In this application, the size of the population is equal to the number of candidate controllers $\mu = N$. The $(\mu + \lambda)$ selection is chosen with $\mu = 9$ and $\lambda = 63$. This means that the best controllers are kept from the set of the old controllers and 63 offspring. The search space of solutions $\mathbf{k}_p \times \mathbf{T}_n$ is restricted to $[-100, 100] \times [0.01, 1]$ and the initial strategy parameters are set to 10% of the ranges of the variables. We assume Gaussian i.i.d. measurement errors and the TLS solution is used to compute the estimated sensitivity functions.

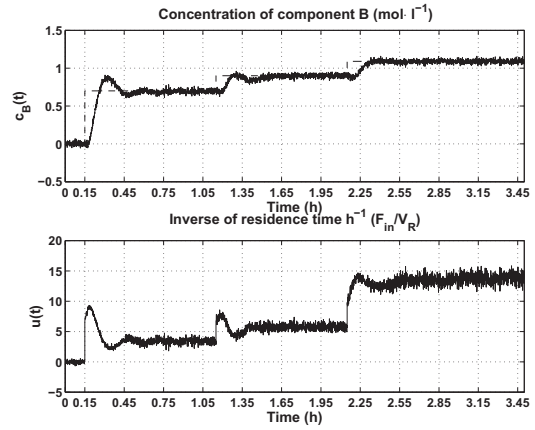

Fig. 7. Noisy control performance

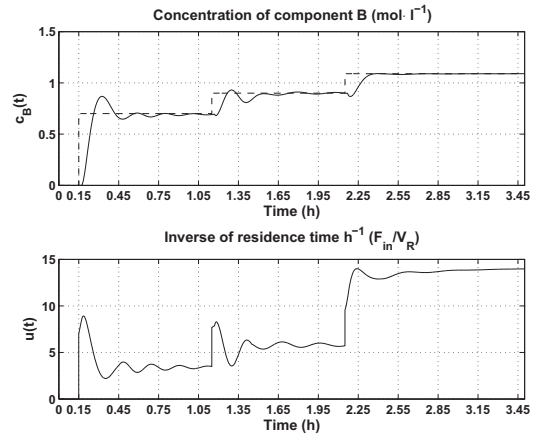

Fig. 8. Noise-free control performance

The first execution of the evolutionary algorithm was performed using measured data $d_{(0.15h,0.45h)}$ obtained with the first active controller θ_1 that was in the loop during $t \in (0.00h, 0.45h)$. At the first execution of the ES at $t = 0.45h$, the evolution strategy returns a new set of controllers for the first operating point after 38 generations. As shown in Fig. 6, the new active controller is $\theta^*_{p_{1_w}} = [17.6214, 0.2929]^T$.

The evolutionary algorithm was executed for the second time using the data $d_{(1.15h,1.45h)}$ with the active controller $\theta^*_{p_1}$. After 19 generations, the new active controller is $\theta^*_{p_{2_w}} = [20.9662, 0.0725]^T$ (see Fig. 6).

The evolutionary algorithm was executed for the third time using the data $d_{(2.15h,2.45h)}$ with the active controller $\theta^*_{p_2}$. After 12 generations the ES returned a new set of controllers and the new active controller is $\theta^*_{p_{3_w}} = [33.1989, 0.0652]^T$ (see Fig. 6). The control performance and the manipulated variable for the case with measurement noise are shown in Fig. 7 and can be compared with the noise-free case in Fig. 8. We can see that the active controller is well adapted to the change of the dynamics of the unknown plant under measurement error.

6. CONCLUSIONS

In this paper, the new scheme for adaptive unfalsified control was investigated for the case with noisy measurement. The deconvolution with noisy plant data can be solved by the total least squares method. The example of a CSTR with nonminimum phase nonlinear dynamics showed that a good performance can still be achieved for noisy measurements.

REFERENCES

A. Dehghani, B.D.O. Anderson and A. Lanzon. Unfalsified adaptive control: A new controller implementation and some remarks. *Proc. European Control Conf.*, Kos, 709-716, 2007.

S. Engell and K. U. Klatt. Nonlinear control of a non-minimum-phase CSTR. *Proc. American Control Conf.*, San Francisco, 2941 - 2945, 1993.

S. Engell, T. Tometzki and T. Wonghong. A new approach to adaptive unfalsified control. *Proc. European Control Conf.*, Kos, 1328-1333, 2007.

G. Golub and C. Van Loan An analysis of the total least squares problem. *SIAM J. Numer. Anal.*, 1980.

K.-U. Klatt and S. Engell. Gain-scheduling trajectory control of a continuous stirred tank reactor. *Computers & Chemical Engineering 22*, 491-502, 1998.

C. Manuelli, S.G. Cheong, E. Mosca and M.G. Safonov. Stability of unfalsified adaptive control with non $SCLI$ controllers and related performance under different prior knowledge. *Proc. European Control Conf.*, Kos, 702-708, 2007.

I. Markovsky and S. Van Huffel. Overview of total least squares methods. *Signal Processing*, 87, 2283-2302, 2007.

A.S. Morse and D.Q. Mayne and G.C. Goodwin. Application of Hysteresis Switching in Parameter Adaptive Control. *IEEE Transactions on Automatic Control*, 37:1343-1354, 1992.

D. Quagliarella, J. Periaux, C. Poloni and G. Winter. Genetic Algorithms and Evolution Strategy in Engineering and Computer Science: Recent Advances and Industrial Applications. *John Wiley & Sons*, 1998.

I. Rechenberg. Cybernetics Solution Path of an Experimental Problem. *Royal Aircraft Extablishment Library Translation*, 1965.

M.G. Safonov and T.C. Tsao. The Unfalsified Control Concept and Learning. *IEEE Transactions on Automatic Control*, 42(6):843-847, 1997.

H.-P. Schwefel. Evoluionstrategie und Numerische Optimierung. *Dissertation*, 1975.

H.-P. Schwefel. Evolution and Optimum Seeking. *John Wiley & Sons, New York*, 1995.

R. Wang, A. Paul, M. Stefanovic and M.G. Safonov. Cost-detectability and Stability of Adaptive Control Systems. *Proc. IEEE CDC-ECC*, Seville, 3584-3589, 2005.

T. Wonghong and S. Engell. Application of a New Scheme for Adaptive Unfalsified Control to a CSTR. *Proc. IFAC World Congress*, Korea, 13247-13252, 2008.

Model Based Control of Large Scale Fed-Batch Baker's Yeast Fermentation

Akif Hocalar and Mustafa Türker

Pakmaya, P.K. 149, 41001 İzmit, Kocaeli, Türkiye
akifh@pakmaya.com.tr
mustafat@pakmaya.com.tr

Abstract : Two different control methods are applied to the technical scale (25 m^3) fed-batch baker's yeast fermentation. Feedback linearizing control design is used to manipulate the substrate feeding rate in order to maximize the biomass yield and minimizing the production of ethanol. Firstly, the specific growth rate controller is developed and applied to maintain the specific growth rate at specified trajectory. Secondly, the minimal ethanol controller is developed to maximize biomass productivity, by controlling specific growth rate just above the maximum oxidative growth rate by controlling ethanol concentration. The both controllers worked successfully and can be combined to follow required specific growth rate trajectory and respond successfully to disturbances in overflow fermentations such as *Saccharomyces cerevisiae.*

Keywords: Nonlinear control, feedback linearizing control, fed-batch, baker's yeast, specific growth rate, ethanol concentration, biocalorimetry.

1. INTRODUCTION

Fed-batch bioprocesses have extensive applications in industry for production of baker's yeast, enzymes, antibiotics, growth hormones, microbial cells, vitamins, amino acids and other organic acids (Perulekar and Lim, 1985; Yamane and Shimizu, 1984). *Saccharomyces cerevisiae* is used in many applications such as beverage products (beer, wine), baker's yeast for bread production, heterologous protein production, bio-transformations, flavour components, single cell protein, bio-ethanol, glycerol and food additives (Walker, 1998; Renard and Wouwer, 2008). The specific growth rate is a key variable for the growth-associated biotechnological processes and determines the physiological state of the cells and the capacity of cell's protein-synthesizing machinery that is important for recombinant protein production or biomass production in several fermentations (Cannizzaro et. al., 2004; Gnoth et. al., 2008). Similarly, *Escherichia coli* show similar metabolic behaviour in the presence of excess substrate and shortage of oxygen. In the production of recombinant proteins with *E. coli*, acetate is produced as an overflow metabolite both when *E.coli* grown under anaerobic or oxygen limiting conditions. It is important to maintain the specific growth rate below a certain threshold in order to avoid the accumulation of acetate throughout the fermentation (Rocha and Ferreira, 2002; Jana and Deb, 2005).

In the literature, many works have been reported by several authors for the control of fed-batch fermentation, most of these studies report experimental results either at laboratory scale or simulation results (Chen and Bastin, 1995; Pomerleau and Viel, 1992; Soons et al., 2006; Rocha and Ferreira, 2002; Cannizzaro et al., 2004; Valentinotti et al., 2003).

The main objective of this study is to develop a robust control scheme to cope with changing process dynamics during fermentation, set point tracking, required minimum process measurements and batch-to-batch consistency for the technical scale fed-batch baker's yeast fermentation. The control methods are based on previously developed and verified state estimation model and reliable measurement system (Hocalar et. al., 2006).

In this work, different key process variables are controlled with the state feed-back linearizing control scheme at technical scale fermentations: 1. nonlinear control of specific growth rate, 2. nonlinear control of ethanol concentration. In the first part, the derivation of nonlinear specific growth rate controller ant its results are discussed. The restrictive conditions of the controlling of specific growth rate are given at the end of first section. In the second part, the control of nonlinear ethanol concentration is presented. By means of controlling of overflow metabolite concentration at minimal concentration, specific growth rate can be maintained near the maximum values.

2. STOICHIOMETRY OF THE PROCESS

General stoichiometry of the baker's yeast fermentation process can be written with respect to reaction rates as (Türker, 2003; Türker, 2004):

$$r_s CH_2ON_{0.0125} + r_n NH_3 + r_o O_2 \rightarrow r_x CH_{1.8}O_{0.5}N_{0.2} + r_p CH_3O_{0.5} + r_c CO_2 + r_w H_2O + r_q \quad (1)$$

and the rate vector is

$$r = (-r_s\ ,\ -r_n\ ,-r_o\ ,\ r_x\ ,\ r_p\ ,\ r_c\ ,\ r_w\ ,\ r_q)^T \quad (2)$$

Metabolic heat production rate is added to reaction rates. The unknown process states are determined by the metabolic black-box modeling and the integration of estimated reaction rates. The redundant reaction rates are used in the derivation of reconciliated reaction rates *(Hocalar et. al., 2006)*.

3. RESULTS AND DISCUSSIONS

3.1. Nonlinear Control of Specific Growth Rate

The feedback linearizing control of the specific growth rate is based on the assumption of the presence of sufficient oxygen concentration and the absence of ethanol in the fermentation broth (Claes, 1999). In order to implement the control approach, the oxygen concentration has to be maintained high enough not to run into oxygen limitation throughout fermentation and the specific growth rate has to be below the critical value in order not to form ethanol.

The starting point for the derivation of the controller expression is the general dynamical mass balance equation for the substrate feeding as shown in Eq. 3.

$$\frac{dS}{dt} = D\,(S_{in} - S) - \left(\frac{\mu_x^{ox}}{Y_{X/S}^{ox}} + \frac{q_{e,pr}}{Y_{E/S}^{red}} + m \right) X \quad (3)$$

By rearranging the Eq. 3, Eq. 4 can be written as;

$$\frac{dC_s}{dt} = -\sigma X + \frac{F_s}{V}(C_{s,in} - C_s) \quad (4)$$

where $\sigma = \left(\frac{\mu_x^{ox}}{Y_{X/S}^{ox}} + \frac{q_{s,red}}{Y_{E/S}^{red}} + m \right)$, C_s is substrate concentration, X biomass, F substrate feed rate. The second step is to set up a stable linear reference model for tracking error. The reference model determines to the decreasing trajectory of the tracking error.

$$\frac{d}{dt}(C_s' - C_s) + \lambda\,(C_s' - C_s) = 0 \quad (5)$$

The λ is arbitrary adjustment coefficient and have to be chosen such that the differential equation (Eq. 5) is stable. At steady state conditions, the substrate concentration can be accepted zero, $(\frac{dC'}{dt} \approx 0)$ and Eq. 5 can be written as $\lambda\,(C_s' - C_s) = \frac{dC_s}{dt}$ and by substituting the Eq. 4 in the Eq. 5,

$$F_s = \frac{\sigma X - \lambda (C_{s,in} - C_s')}{C_{s,in} - C_s'} V \quad (6)$$

obtained as a final controller equation. Under oxidative conditions and in the absence of ethanol in the fermentation broth, specific growth rate is a function of substrate concentration. Therefore, specific growth rate (μ) can be written instead of substrate concentration term in Eq. 6. By rearranging the Eq. 6, the expression for substrate feed rate controller can be written as follows;

$$F_s = \frac{\frac{\mu_x}{Y_{X/S}^{ox}} X - \lambda\,(\mu_s - \mu')}{C_{s,in}} V \quad (7)$$

where λ is the arbitrary adjustment coefficient for the decrease of tracking error. When the Eq. 7 is applied to the fermentation, steady state errors are observed between the estimated specific growth rate and set profiles. In order to eliminate this difference, an integral term is added to the Eq. 7. and the obtained results are presented in Fig. 1 for the controlling of time varying specific growth rate profile.

$$F_s = \frac{\frac{\mu_x}{Y_{X/S}^{ox}} X - \lambda_P \left\{ (\mu_s - \mu') - \frac{1}{\lambda_i} \Sigma (\mu_s - \mu') \right\}}{C_{s,in}} V \quad (8)$$

The results of the implementation of Eq. 8 in a fed-batch fermentation are given Fig. 1. The adjustment parameters are $\lambda_p = 0.14$, $\lambda_i = 1800$ for the ascending and $\lambda_p = 0.27$, $\lambda_i = 1800$ for the descending specific growth rate region.

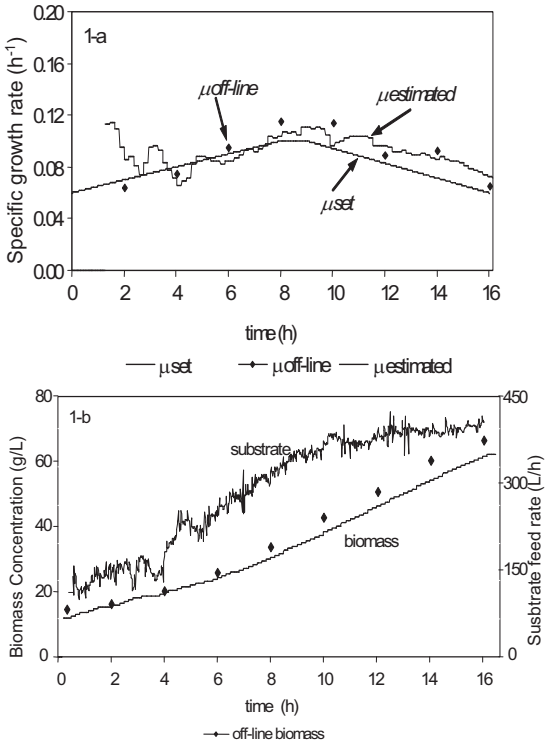

Figure 1.a- Specific growth rate b- biomass concentration and substrate.

The estimation of biomass concentration can be accepted successfully (Fig. 1-b) and is used in the calculation of specific growth rate (fig. 1-a). The specific growth rate estimations and off-line measurements are close to each other

with acceptable accuracy. The time varying specific growth rate profile is controlled successfully by the controller and obtained substrate feed rate resemble the predetermined substrate feeding profiles widely used in practice.

In Fig. 2, the results of different specific growth rate controlled fermentation are given. In this fermentation, ethanol formation is observed at the different times during the process and cause's decrease in the specific growth rate. The controller increased the substrate feed rate in order to compensate the decrease in the specific growth rate that caused more ethanol formation (Fig. 2-a). The unexpected decreases in the specific growth rate estimation are given in Fig. 2-b. The excess in the substrate feed rate puts the process more instability and results in failure of the control of specific growth rate. As a result, the substrate feed rate is manually intervened to consume the ethanol in the broth.

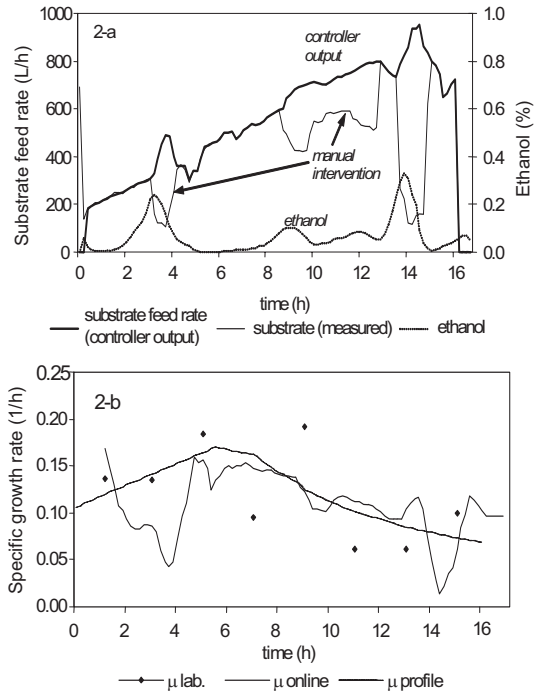

Figure 2.a- substrate feed rate and ethanol concentration, b-specific growth rate.

This controller has successfully controlled the specific growth rate at trajectory under defined conditions as shown in Fig. 1. Once the fermentation went to beyond the restrictive conditions the controller failed as shown in Fig. 2.

3.2. Nonlinear Control of Minimum Ethanol Concentration

An alternative way to control the specific growth rate at maximum oxidative rate is to use the overflow metabolite as an indicator of how close the actual value to critical growth rate to maximize biomass production. If ethanol concentration can be controlled at constant minimal concentration, it is possible to keep the specific growth rate slightly above the critical value (Cannizzaro et. al., 2004). In order to control the ethanol concentration, the regulator design is based on a feedback linearization of a reduced-order model of the process obtained by singular perturbation of the state space model under the following assumptions: the stoichiometric (yield) coefficients are known, the gaseous outflow rates (ethanol, CO_2, O_2) are measured on-line, the influent substrate concentration S_{in} is fixed and known, the specific growth rate is unknown. The singular perturbation techniques can be used for systems in which some reactions proceed at much faster rates than the others (Bastin and Dochain, 1990; Pomerleau and Viel, 1992; Chen et. al., 1995).

The dynamical process equations for five process states with known yield coefficients can be given as follows;

$$\frac{d}{dt}\begin{bmatrix} X \\ S \\ E \\ O \\ C \end{bmatrix} = \begin{bmatrix} 1 & 1 & 1 \\ -Y^{ox}_{X/S} & -Y^{red}_{X/S} & 0 \\ 0 & Y^{red}_{X/E} & -Y^{eth}_{X/E} \\ -Y^{ox}_{X/O} & 0 & -Y^{eth}_{X/O} \\ Y^{ox}_{X/C} & Y^{red}_{X/C} & Y^{eth}_{X/C} \end{bmatrix} \begin{bmatrix} \mu^{ox}_x \\ \mu^{red}_x \\ \mu^{ox}_e \end{bmatrix} X - D \begin{bmatrix} X \\ S \\ E \\ O \\ C \end{bmatrix} + \begin{bmatrix} 0 \\ DS_{in} \\ 0 \\ r_o \\ -r_c \end{bmatrix} \tag{9}$$

The general state space dynamical model can be written as follows (Bastin and Dochain, 1990);

$$\frac{d\xi}{dt} = K\varphi(\xi) - D\xi + F - Q \tag{10}$$

$$\xi^T = [X, S, E, O, C]$$

where ξ, Q, F involves n components, φ involves m reaction rates ve K is (NxM) size yield coefficient matrix. In Eq. 9, the first term $K\varphi(\xi)$ describes the kinetics of microbiological reactions, the remaining term $-D\xi + F - Q$ describes the transport dynamics of the components through the bioreactor. The yield coefficients used in the design is shown in Table 1.

Table 1. Parameters used in nonlinear controller design (Cmol/mol) (Beşli et. al. 1995).

k_1, $Y^{ox}_{X/S}$	3.65	k_2, $Y^{red}_{X/S}$	0.36
k_3, $Y^{red}_{X/E}$	0.19	k_4, $Y^{eth}_{X/E}$	1.35
k_5, $Y^{ox}_{X/O}$	1.56	k_6, $Y^{eth}_{X/O}$	0.83
k_7, $Y^{ox}_{X/C}$	1.45	k_8, $Y^{red}_{X/C}$	0.2
k_9, $Y^{eth}_{X/C}$	1.99		

By the systematic application of singular perturbation technique, fully reduced model can be established and in the case of $\dim(\xi_F) = M$ and K_F full rank, the process states can be partitioned as slow $\xi^T_S = [X, E]$ and fast varying state variables $\xi^T_F = [S, O, C]$. The substrate, oxygen and carbon-dioxide are fast varying state variables and biomass and ethanol are slow varying state variables for the fed-batch yeast fermentation process. The general dynamical model can be written as given in Eq. 11 by the assumption of the fast

varying state variables dynamics allow the singular perturbation (Bastin and Dochain, 1990);

$$\frac{d\xi_S}{dt} = K_S\,\varphi - D\,\xi_S + F_S - Q_S$$
$$K_F\,\varphi + F_F - Q_F = 0 \tag{11}$$

The reaction rate vector , $\varphi(\xi)$, can be written as;

$$\varphi(\xi) = -K_F^{-1}\,(F_F - Q_F) \tag{12}$$

By substituting Eq. 12 in Eq. 11, the dynamics of slow varying state variables can be obtained as in Eq. 13.

$$\frac{d}{dt}\begin{bmatrix} X \\ E \end{bmatrix} = -D\begin{bmatrix} X \\ E \end{bmatrix} + \begin{bmatrix} 1 & 1 & 1 \\ 0 & k_4 & -k_3 \end{bmatrix} * inv(K_F) \begin{bmatrix} DS_{in} \\ r_o \\ -r_c \end{bmatrix} \tag{13}$$

In steady state, singular perturbation allows the fast varying state's dynamics to consider to equal to zero and unknown reaction rates can be determined by simple matrixes operations as shown below if the inverse of the yield coefficient matrices can be calculated (Hocalar, 2007).

$$\begin{bmatrix} \mu_s^{ox} \\ \mu_s^{red} \\ \mu_e^{ox} \end{bmatrix} = -K_F^{-1} \begin{bmatrix} DS_{in} \\ r_o \\ -r_c \end{bmatrix} \tag{14}$$

By inserting the Eq. 14 in Eq. 13, slow varying process states can be calculated by means of basic matrice operations:

$$\psi = det(K_F) = \left(k_7 k_6 k_2 - k_5 k_9 k_2 - k_1 k_8 k_6\right)$$
$$\upsilon_1 = \left(-k_4 k_1 k_6 + k_3 k_2 k_5\right)\psi^{-1}$$
$$\upsilon_2 = \left(-k_4 k_1 k_9 + k_3 k_2 k_7 - k_3 k_1 k_8\right)\psi^{-1}$$
$$\upsilon_3 = \left(k_4 k_5 k_9 - k_4 k_6 k_7 + k_3 k_5 k_8\right)\psi^{-1}$$
$$\frac{dE}{dt} = -D\,E + \upsilon_3\,DS_{in} + \upsilon_2\,r_o - \upsilon_1\,r_c \tag{15}$$

By inserting the Eq. 15 into the first order reference model equation in Eq. 16, the controller law for substrate feed rate can be obtained as in Eq. 17.

$$\frac{d}{dt}(y^* - y) + (\lambda_1 + \lambda_2 x)(y^* - y) = 0 \quad (\lambda_1, \lambda_2 > 0) \tag{16}$$

$$F_s = \frac{1}{\upsilon_3}\left\{\frac{dE^*}{dt} + (\lambda_1 + \lambda_2 \hat{X})(E_s - E) + DE + \upsilon_1 r_c - \upsilon_2 r_o\right\} \tag{17}$$

The tracking ethanol error is tried to minimize using λ adjustment parameters. Several fed-batch experiments were conducted in a 25 m^3 fermentor to validate the control strategy. The results are given in Fig. 3.

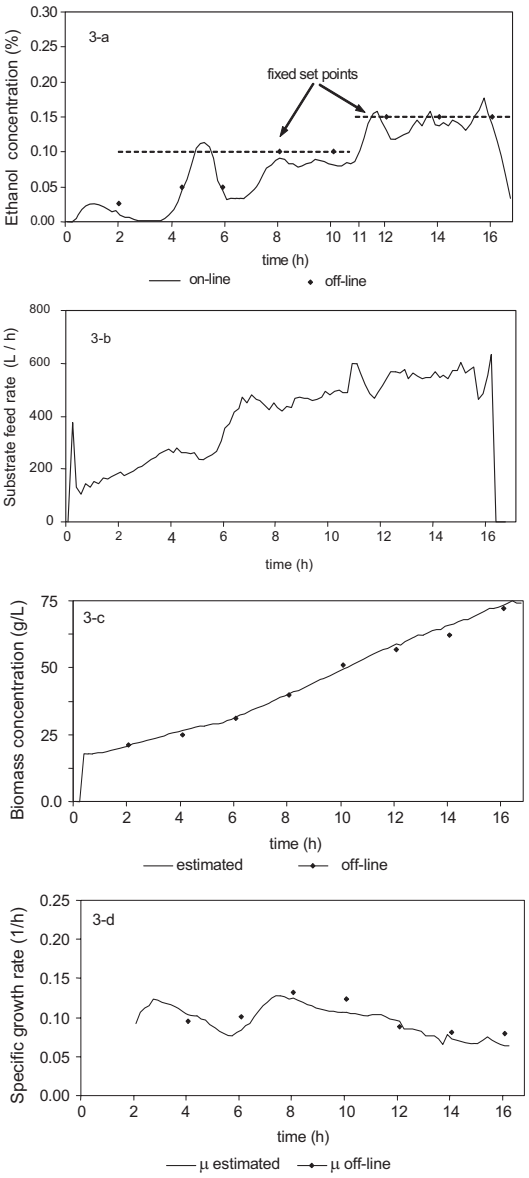

Figure 3: a- Ethanol concentration, b- substrate feed rate, c- biomass concentration and d- specific growth rate curves obtained from the industrial fermentation.

The controller was started at second hour and two fixed set points were tried to control for certain periods with ethanol set values E_s= % 0.10 and then with E_s= % 0.15. The ethanol concentration was successfully controlled at different set values from the 7th hour to the end of fermentation. The manipulated variable substrate feed rate and biomass concentration are given in Fig. 3-b and 3-c respectively. The biomass concentration increased exponentialy (Fig. 3.c) and the specific growth rate estimation is given in Fig. 3-d and quite close to experimental results. The controller developed stable response to the step change in the ethanol set point. The controller automatically adapted the feed rate of substrate to compensate for step changes. The difficulty of controlling the ethanol concentration can be seen in first

hours of fermentation (exponential growth phase). During the first hours, the controller increased the substrate feed rate and because of the time delay of the ethanol formation, slightly excess substrate feeding suggested by the controller.

4. CONCLUSION

The state feedback linearizing control strategy is applied to the industrial fed-batch baker's yeast fermentations. The control of specific growth rate and minimal ethanol concentration are attempted at technical scale fermentations. The control of specific growth rate at specificed trajectory is required in many fermentation processes. In this work, this approach has been successfully applied to baker's yeast fermentation. In order to maximize biomass concentration and productivity, the process has to be controlled at its maximum oxidative growth rate, minimizing by-product ethanol formation. This strategy is applied in second controller and specific growth rate was maintained slightly above maximum oxidative growth rate by maintaining and controlling by product ethanol at minimal concentration. This approach can also be applied to similar overflow processes such as the growth of *E. coli*. The ethanol concentration was controlled successfully at minimal concentrations. Both controllers can be combined to control specific growth rate at any trajectory and to minimize ethanol production.

NOMENCLATURE

C_i	concentration of i (kg/m^3)
D	dilution rate (1/h)
F_i	flow rate of i (m^3 / h)
K	yield coefficient matrices
M_i	molar weight of i (kg)
q_i	specific conversion rates of i (kg/kgh, C-mol/ C-mol h)
S	substrate concentration (kg/m^3)
X	biomass (kg/m^3)
V	volume (m^3)
$Y_{i/j}$	yield of i over j

Subscripts

ox	oxidative
red	reductive
eth	ethanol
m	maintenance
ae	aerobic
in	inlet
out	outlet
T	transpose
n	nitrogen
o	oxygen
e	ethanol
c	carbon
q	metabolic heat production
s	substrate
p	product
x	biomass
w	water

Greek Letters

μ	specific growth rate, (h^{-1})
ξ	state variable
λ	adjustment coefficient

REFERENCES

Bastin, G. and Dochain, D. (1990) On-line estimation and adaptive control of bioreactors. *Elsevier*.

Beşli, N., Türker, M., Gül, E. (1995). Design and simulation of a fuzzy controller for fedbatch yeast fermentation. *Bioprocess Engineering*. 13:141-148.

Cannizzaro, C., Valentinotti, S., von Stockar, U. (2004). Control of yeast fed-batch process through regulation of extracelluler ethanol metabolite. *Bioprocess Biosystem Engineering*. 26: 377-383.

Chen, L. (1992). Modelling, identifiability and control of complex biotechnological systems. *PhD Thesis*. Faculte des Sciences Appliquees. Universite Catholique de Louvan.

Chen, L., Bastin, G., Van Breusegem, V. (1995). A case study of adaptive nonlinear regulation of fed-batch biological reactors. *Automatica*. 31:1: 55-65.

Claes, J.E. (1999). Optimal adaptive control of the fed-batch bakers yeast fermentation process. *PhD Thesis*. Katholieke Universiteit Leuven.

Gnoth, S., Jenzsch, M., Simutis, R., Lubbert, A. (2008). Control of cultivation processes for recombinant protein production: a review. *Bioprocess and Biosystems Engineering*. 31: 21–39.

Hocalar, A. (2007). Model based control of industrial fed-batch baker's yeast fermentation process. *PhD Thesis*. University of Kocaeli, Turkey.

Hocalar, A., Türker, M., Öztürk, S. (2006). State estimation and error diagnosis in industrial fed-batch yeast fermentation. *AIChE Journal*. 52:11: 3967-3980.

Jana, S., and Deb, J. (2005). Strategies for efficient production of heterologous proteins in

Escherichia coli. *Applied Microbiology and Biotechnology*. 67: 289-298.

Perulekar, S.J. and Lim, H.C. (1985). Modeling, optimization and control of semi-batch bioreactors. *Advances in Biochemical Engineering*. 32: 207–258.

Pomerleau, Y., Viel, G. (1992). Industrial application of adaptive nonlinear control for baker's yeast production. *IFAC Modelling and Control of Biotechnological Processes*. Colorado, USA.

Renard, F. and Wouwer, A.V. (2008). Robust adaptive control of yeast fed-bacth cultures. *Computers and Chemical Engineering*. 32: 1246–1256.

Rocha, I. and Ferreira, E.C. (2002). Model-based adaptive control of acetate concentration during the production of recombinant protein with *E. Coli*. *IFAC 15th Triennial World Congress*. Barcelona, Spain.

Soons, Z.I.T.A., Voogt, J.A., Van Straten, G., Van Boxtel, A.J.B. (2006). Constant specific growth rate in fed-batch cultivation of *Bordetella Pertussis* using adaptive control. *Journal of Biotechnology*. 125: 252-268.

Türker, M. (2003). Measurement of metabolic heat in a production scale bioreactor by continuous and dynamic calorimetry. *Chemical Engineering Communication*. 190: 573-598.

Türker, M. (2004). Development of biocalorimetry as a technique for process monitoring and control in technical scale fermentations. *Thermochimica Acta*. 419: 73-81.

Valentinotti, S., Srinivasan, B., Holmberg, U., Bonvin, D., Cannizzaro, C., Rhiel, M., Von Stockar, U. (2003). Optimal operation of fed-batch fermentations via adaptive control of overflow metabolite. *Control Engineering Practice*. 11: 665-674.

Walker, G.M. (1998). *Yeast Physiology and Biotechnology*. Wiley. ISBN: 978-047196446-9.

Yamane, T. and Shimizu. S. (1984). Fed-batch techniques in microbial processes. *Advances in Biochemical Engineering*. 30: 148–194.

Modeling and Control of Free Radical Co-Polymerization

Harshad Ghodke, Siddarth Raman, B. Erik Ydstie

Department of Chemical Engineering, Carnegie Mellon University, Pittsburgh, USA (e-mail: ydstie@cmu.edu).

Abstract: In this work, we develop a model and a control system for a 4 monomer acrylate - methacrylate - styrene free-radical co-polymerization reaction. The model was implemented in PREDICI, and parameter estimation was carried out using nonlinear optimization from semi-batch experiments. Molecular weight distribution (MWD) determine utility. Stringent control over reactor conditions is critical. An inventory control scheme was demonstrated to work well for this complex polymerization process. A correlation mapping among the steady state initiator and monomer concentrations, molecular weight distributions and poly-dispersity was used to assign set-points for the inventory controller.

Keywords: polymerization, process control, passivity, automotive paint.

1. INTRODUCTION

We have developed a kinetic model for the free-radical polymerization of the Hydroxypropyl acrylate/ Styrene/ Butyl acylate/ Butyl methacrylate (HPA/ Sty/ BA/ BMA) copolymerization system. Unknown model parameters were estimated using data from semi-batch experiments and an inventory control strategy has been proposed for operation in continuous mode. The kinetic model has been implemented in PREDICI while the control system was implemented in MATLAB. The motivation of this current work stems from the need for effective operation of industrial continuous polymerization reactors to make resins from acrylates, methacrylates and styrene. These resins are an important constituent of automotive coatings.

Homopolymerization and butyl acrylate systems have previously been studied, and rate-constants are available in literature (Beuermann and Buback (2002), Maeder and Gilbert (1998), Curteanu (2003), Curteanu and Bulacovschi (2005)). For example, Congling Quan and Grady (2003) have developed a kinetic model of the high-temperature free-radical polymerization of butyl acrylate capable of predicting polymer molecular weight for a semi-batch process. D. Li and Hutchinson (2005) developed kinetic models for butyl acrylate - butyl methacrylate free radical polymerization system. In this study, the modeling tool PREDICI was used to show good predictions for the outputs, without a need for further refinement of the kinetic parameters. However, it is uncommon to find models with parameters that have been refined using a combination of experimentation and parameter optimization for this system.

The processability and utility of polymer products depend upon reactor operating conditions, and, good control is needed to achieve desired properties (Amrehn (1977), Elicabe and Meira (1988), MacGregor (1986)). Several promising control strategies applied to polymerization processes such as adaptive control (W. R. Cluett (1985)), optimal control (Choi (1997)), output feedback control (Soroush and Zambare (2000)) and nonlinear model predictive control (H. Seki (2001)) have been proposed. None of these approaches however, have been applied to very complex polymerization systems with several monomer inputs and few advanced schemes have found industrial application.

The purpose of our paper is to investigate the feasibility of using inventory control to control polymer properties. Inventory control is based on the idea of manipulating process flows so that the inventories follow their set points. The operator mapping flows to inventories in a macroscopic system is passive and any input strictly passive (ISP) feedback controller can be used in order to achieve input-output stability. The inventory control approach, which can be viewed as a way to chose candidate measured and manipulated variables for output linearization, was proposed by C. A. Farschman (1998). The method has been applied to transport reaction systems by M. Ruszkowski (2005). M. D. Díez (2007) applied the method to control particulate systems and Ydstie and Jiao (2006) applied the method to control a float glass plant for automotive windshield production. The HPA/ Sty/ BA/ BMA copolymerization system central to our work, has not been previously studied in literature from a modeling and control point of view. The model we propose combines literature data with experimental studies using nonlinear optimization.

2. KINETIC MODEL FOR FREE-RADICAL POLYMERIZATION

The model for free-radical polymerization consists of the following sets of reactions: Initiation, Propagation, Chain-transfer and Termination.

⋆ This work was supported by PPG Inc.

Initiation: The initiator used in this study is Di-*t*-amyl peroxide (DTAP) with a half life of 2 minutes at 160 °C (AkzoNobel (2006)). It decomposes with an efficiency f, to form two free radicals that can initiate propagation by reaction with any of the four monomers present in the system, abstract hydrogen atoms from other species in the system or recombine to form the initiator. Equation (1) represents the initiator decomposition reaction

$$I \xrightarrow{k_d} 2\,f\,I^{\cdot} \tag{1}$$

The dissociation rate constant k_d for DTAP is known to be given by eq (2) (AkzoNobel (2006))

$$k_d = 4.08 \times 10^{15} e^{-\frac{17831.36}{T}} \quad (s^{-1}) \tag{2}$$

The free radicals generated by initiator decomposition can initiate polymerization by reacting with the monomer species present in the solution. This process is described by the initiation reactions as shown in eq (3).

$$I^{\cdot} + M_i \xrightarrow{k_{p_{ii}}} P_1^{i\cdot} \tag{3}$$

Propagation: The polymer chain is then propagated by the products of the initiation reactions by reaction with monomers via the propagation reactions given in eq (4).

$$P_n^{i\cdot} + M_j \xrightarrow{k_{p_{ij}}} P_{n+1}^{j\cdot} \tag{4}$$

The rate constants for the homo-polymerization reactions, $k_{p_{ii}}$ (Asua (2007); D. Li and Hutchinson (2005)) were evaluated at 433 K and 10 psi. $k_{p_{11}}$ was assumed to be identical to $k_{p_{33}}$ because of lack of literature values. $k_{p_{33}}$ (and hence $k_{p_{11}}$) was assumed to be insensitive to pressure. Where possible, $k_{p_{ii}}$ were calculated using (6) and (5).

$$k_{p_{ii}} = A_i\, e^{-\frac{E_i + 1\times10^{-6}\Delta V_p\, P}{R\,T}} \qquad \forall i \in \{2,4\} \tag{5}$$

$$k_{p_{ii}} = A\, e^{-\frac{E_a}{R\,T}} \qquad \forall i \in \{1,3\} \tag{6}$$

The rate constants for the hetero-propagation reactions, $k_{p_{ij}}$, are obtained by defining reactivity ratios, r_{ij}, as shown in (7)

$$r_{ij} = \frac{k_{p_{ii}}}{k_{p_{ij}}} \tag{7}$$

Reactivity ratios were obtained from literature (Ham (1964); Chow (1975)). For the particular set of monomers present in the HPA/Sty/BA/BMA system, it was difficult to obtain reactivity ratios at the desired temperature. The values obtained from literature or calculated from *Q-e* data are available at temperatures different from the reactor temperature and hence, were treated as estimates.

Chain Transfer: Chain transfer in the context of free-radical polymerization involves the transfer of the radical from a live polymer chain to any other species present in the system which may be initiator, monomer, solvent molecules, dead polymer or live polymer or another species specifically added to the system which behaves as a chain transfer agent (CTA) (Asua (2007)). In this work, three types of chain transfer reactions are considered - chain transfer to monomer, chain transfer to solvent and chain transfer to live polymer.

Chain Transfer to Monomer: Chain transfer to monomers that contain aliphatic hydrogens such as acrylates and methacrylates involves H-atom abstraction to form an unsaturated radical (Asua (2007)). This unsaturated radical may then undergo further reaction as shown in eq (8). Transfer to monomer rates were not available in literature and were calculated using eq (9).

$$P_n^{i\cdot} + M_j \xrightarrow{k^{mon}_{tr_{ij}}} P_1^{j\cdot} + D_n \tag{8}$$

$$k^{mon}_{tr_{ij}} = \frac{k_{p_{ij}}}{C^{mon}_{tr}} \tag{9}$$

C^{mon}_{tr} is the coefficient for chain-transfer to monomer and typically lies in the range $1 - 50 \times 10^{-5}$ (Asua (2007)). For this work, the value C^{mon}_{tr} was taken to be 1×10^{-5}.

Chain-transfer to solvent: Chain transfer to solvent occurs according to reactions eq (10) and eq (11). In this system, for lack of literature values, we assume that both the solvents behave identically, and hence, have identical rate constants. The rate constants for chain transfer to solvent are obtained from eq (12) using a value for $C^{S_k}_{tr}$ is taken to be 3.16×10^{-5}, which is the logarithmic mean of the range in which it lies in 1×10^{-6} - 1×10^{-3}.

$$P_n^{i\cdot} + S_k \xrightarrow{k^{S_k}_{tr_{ii}}} S_k^{\cdot} + D_n \tag{10}$$

$$S_k^{\cdot} + M_i \xrightarrow{k^{S_k}_{ii}} P_1^{i\cdot} \tag{11}$$

$$k^{S_k}_{tr_{ii}} = \frac{k_{p_{ii}}}{C^{S_k}_{tr}} \tag{12}$$

Further, for lack of literature values, the rate constants $k^{S_k}_{ii}$, are assumed to be identical to the rate constant for propagation.

Chain transfer to Polymer: Chain transfer to polymer occurs according to reaction eq (13). In this system, for lack of literature values, we assume that the chain transfer to polymer is similar to chain transfer to monomer, and hence, has similar rate constants. The rate constants for chain transfer to polymer are obtained from eq (14), using a value of C^{pol}_{tr} equal to 1×10^{-5} which is the logarithmic mean of the range in which it lies 1×10^{-6} - 1×10^{-4}.

$$P_n^{i\cdot} + D_m \xrightarrow{k^{pol}_{tr_{ij}}} P_m^{j\cdot} + D_n \tag{13}$$

$$k^{pol}_{tr_{ij}} = \frac{k_{p_{ij}}}{C^{pol}_{tr}} \tag{14}$$

Termination: Termination occurs via two competing routes - combination (eqn (15)) and disproportionation (eqn (16)). Termination by combination results in the formation of a single dead polymer chain from two live polymer chains, whereas, termination by disproportionation results in the formation of one dead polymer chain and a live polymer chain with an unsaturated terminal residue which may react further.

$$P_n^{i\cdot} + P_r^{j\cdot} \xrightarrow{k_{tc_{ij}}} D_{n+r} \tag{15}$$

$$P_n^{i\cdot} + P_r^{j\cdot} \xrightarrow{k_{td_{ij}}} D_n + D_r \tag{16}$$

The termination rate constant is defined as the sum of the individual rate constants for termination by combination and disproportionation (eq (17)).

$$k_t = k_{tc} + k_{td} \tag{17}$$

Termination rates for free radical polymerization are diffusion controlled (Asua (2007)) and any available estimates are system specific. Thus, for the HPA/Sty/BA/BMA system, termination rates that were obtained from literature (Asua (2007)) were treated as estimates. The rate constant

for homo-termination for M_1 was not available in literature and was assumed to be identical to that of M_3.

The relative importance of the mechanism of termination by disproportionation versus termination by combination is measured using a parameter δ, which is defined in eq (18).

$$\delta = \frac{k_{td}}{k_{tc} + k_{td}} \tag{18}$$

δ_{ij} values for styrene and acrylates lie in the range of 0.05 - 0.2 while those for methacrylates lie in the range 0.5 - 0.8 (Asua (2007)). In this work, δ_{ii} for acrylates and styrene is taken to be 0.05, while that for methacrylates is taken as 0.65 (D. Li and Hutchinson (2005)). δ_{ij} value was evaluated as the arithmetic mean of δ_{ii} and δ_{jj}. The values for δ_{ii} were taken to be 0.05 for acrylates, 0.65 for methacrylates.

For the copolymerization reactions, $k_{tc_{ij}}$ and $k_{td_{ij}}$ are calculated using equations (19), (20) and (21). Equation (19) was obtained by generalizing eq (16) from D. Li and Hutchinson (2005) for the case of more than 2 monomers. Here, f_i represents the instantaneous mole fraction of M_i.

$$k_{t,copo_{ij}} = k_{t_{ii}}^{f_i}\, k_{t_{jj}}^{f_j} \tag{19}$$

$$k_{tc_{ij}} = (1 - \delta_{ij})\, k_{t,copo_{ij}} \tag{20}$$

$$k_{td_{ij}} = \delta_{ij}\, k_{t,copo_{ij}} \tag{21}$$

3. EXPERIMENTAL DATA AND PARAMETER ESTIMATION

Polymerization of the HPA/Sty/BA/BMA system was carried out in a well mixed, semi-batch reactor. The feed to the reactor consists of four monomers and an inhibitor dissolved in two solvents. The polymerization is carried out in semi-batch mode, in a 4000 mL vessel isothermally at a temperature of 160 °C and pressure of 10 Psi. The temperature of the vessel is maintained constant using electrical heating.

The reactor is initially charged with solvent mix (76 g S_1, 549.4 g S_2) and heated to 210 °C and then allowed to cool to 160 °C at atmospheric pressure. Feed A (293.6 g S_1 and 65 g I) and Feed B (827.2 g M_1, 393.9 g M_2, 374.2 g M_3 and 374.3 g M_4) are then fed to the reactor simultaneously for a period of 125 min and 120 min respectively. For the semi-batch process the outputs of interest are the residual monomer concentrations, weight average molecular weight (MW_w), number average molecular weight (MW_n), z-average molecular weight (MW_z) and the polydispersity index (PDI). Experimental data was obtained from two different sets of experiments. In one set, only data for the first 1000 seconds was collected and in the second set, data for times from 1000 - 7000 seconds was collected.

This model was implemented in PREDICI (Polyreaction Distributions by Countable System Integration), a comprehensive simulation package for the numerical integration of differential equations arising out of the kinetic equations describing polymerization systems. The results for the integration of the differential equations generated for the semi-batch process model in PREDICI are compared with the experimental data. The integration was performed in the *moment mode* with the values for the rate constants as listed in the tables and the relevant outputs were tracked. The model matches the experimental results poorly using literature data for the kinetic parameters.

Sensitivity and Estimability Analyses: The kinetic model for the HPA/Sty/BA/BMA system has a total of 79 parameters which can be estimated. To improve the fit of the model predictions and the experimental data, parameter estimation was carried out. The set of estimable parameters was obtained following the methodology of K. Zhen Yao (2003). Hence, as a first step toward identifying estimable parameters, a sensitivity study was carried out to identify the sensitivity of the model outputs with respect to the set of parameters as functions of time. The estimable parameters represent the set of parameters that affect the relevant set of outputs the most, among all the parameters, based on the initial values of the parameters at which the sensitivity derivatives are evaluated. The algorithm use to identify this set is called the Estimability analysis (K. Zhen Yao (2003)).

In order to be able to compare the measure of the sensitivity of a parameter, the sensitivity derivatives are non-dimensionlized using a scaling factor φ_{ijk} defined so that

$$\tilde{S}_{ijk} = \varphi_{ijk} \frac{\Delta y_{i,k}}{\Delta \theta_j}, \quad \varphi_{ijk} = \frac{\hat{\theta}_j}{\hat{y}_{i,k}} \tag{22}$$

$\hat{\theta}_j$ and $\hat{y}_{i,k}$ are used for scaling because they reflect the approximate magnitudes of changes in parameter estimates and model predictions respectively. Here, θ_j represents the j^{th} paramater and $y_{i,k}$ represents the value of the i^{th} output at the k^{th} time point.

It is important to note that the number of estimable parameters depends on the number of output variables, the number of observations per output variable and the linear dependence of the parameters on each other. Further, the global identifiability of the parameters depends on the size of the space of input-output variable values in which experimental data is available. For the purpose of estimability calculations, the scaled sensitivity derivatives defined in eq (**??**) were used to construct the *Scaled Sensitivity Matrix,* $\tilde{S}$ given in eq (23).

$$\tilde{S} = \begin{bmatrix} \varphi_{111}\dfrac{\partial y_{1,1}}{\partial \theta_1} & \cdots & \varphi_{1p1}\dfrac{\partial y_{1,1}}{\partial \theta_p} \\ \vdots & \ddots & \vdots \\ \varphi_{r11}\dfrac{\partial y_{r,1}}{\partial \theta_1} & \cdots & \varphi_{rp1}\dfrac{\partial y_{r,1}}{\partial \theta_p} \\ \varphi_{112}\dfrac{\partial y_{1,2}}{\partial \theta_1} & \cdots & \varphi_{1p2}\dfrac{\partial y_{1,2}}{\partial \theta_p} \\ \vdots & \ddots & \vdots \\ \varphi_{r1n}\dfrac{\partial y_{r,n}}{\partial \theta_1} & \cdots & \varphi_{rpn}\dfrac{\partial y_{r,n}}{\partial \theta_p} \end{bmatrix} \tag{23}$$

The cut-off (ϵ) value for which the algorithm is terminated is fairly arbitrary. From the estimability analysis for an $\epsilon = 1 \times 10^{-2}$, only 8 parameters may be estimated with $\mathcal{L} \equiv \{f, k_{t_{22}}, k_{p_{23}}, k_{p_{21}}, k_{p_{11}}, \delta_{22}, k_{p_{31}}, k_{p_{24}}\}$ in order of estimability.

Parameter Estimation: The parameter estimation algorithm was implemented by combining PREDICI and MATLAB using an MS Excel interface. The PREDICI-Excel link was set up to integrate the differential equations

based on initial conditions for parameters obtained from literature values. Updated estimates for the parameters were obtained from a weighted non-linear least squares Gauss - Newton algorithm with line search implemented in MATLAB. Table 1 shows the optimized values of the parameters.

Table 1. Optimized values of the estimable parameters

Parameter	Optimal value
f	0.95
$k_{t_{22}}$	1×10^9
$k_{p_{23}}$	8483. 5
$k_{p_{21}}$	426. 6
$k_{p_{11}}$	3.5114×10^5
δ_{22}	0.2
$k_{p_{31}}$	100
$k_{p_{24}}$	2136

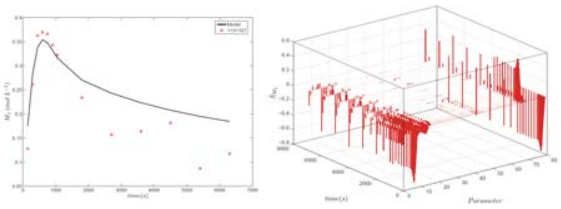

Fig. 1. Model results (solid) vs experiments (circles) for Monomer 1 (Left). Scaled sensitivity for Mononmer 1 shown with respect to time and the 79 parameters (Right).

Comparison plots shows that the model over-predicts some of the outputs and under-predicts some others. A typical result is shown in Figure 3.The sensitivity plot Figure 3 in shows that the sensitivity derivatives for the set of estimable parameters are of the same sign. This necessarily implies, that there is a trade-off between the outputs for which the model over-predicts and those for which the model under-predicts. This means that we can only obtain 'good' fits for either the set of outputs which are over-predicted or the set of outputs which are under-predicted. We conclude that the model we have developed misses some reaction mechanisms and that good fit with the semi-batch data is not possible.

4. CONTROL SYSTEM FOR THE COPOLYMERIZATION SYSTEM

Let the vector x represents the state of a process system, m a vector of control variables, d a vector of disturbance variables and y a vector of measurements. An inventory for the system described above is defined to be an additive continuous function v: $\mathbf{X} \rightarrow \Re$. For the system described above and using the nomenclature introduced in C. A. Farschman (1998) we have:

$$\frac{\mathrm{d}v}{\mathrm{d}t} = \phi(m, x, d) + p(x), \qquad v = g(z) \tag{24}$$

where $v \in \mathbb{R}_{+}^{dimv}$ are the inventories (mass, component mass,...). C. A. Farschman (1998) showed that the synthetic input and output pair

$$u = \phi + p + \frac{\mathrm{d}v^*}{\mathrm{d}t} \qquad e = (v - v^*) \tag{25}$$

is passive with the storage function $\psi = \frac{1}{2}(v-v^*)^T(v-v^*)$. C. A. Farschman (1998) implement a feedback-feedforward control in the form

$$u = -\mathbf{C}(e) = \phi(m, z, d) + p(z, d) + \frac{\mathrm{d}v^*}{\mathrm{d}t} \tag{26}$$

This control law is input strictly passive (ISP). Khalil (2002) showed that when a passive system is connected in feedback with an ISP controller, the closed loop is also passive. Hence the operator $\mathbf{C}$(e), which maps errors into synthetic controls, should be strictly passive. Most controllers in use are strictly passive. The control law is easy to implement if the inventories can be estimated from process data and the mapping $\phi(m, z, d)$ can be inverted with respect to the control variables m. In the simulations below we use a proportional controller ($\mathbf{C}(e) = Ke$ where K is a positive constant). It can be observed that an inventory controller linearizes the system dynamics.

In our application, the manipulated variables are the input flows of monomers (F_{M_1} to F_{M_4}) and initiator (F_I). The concentrations of the monomers and initiator are selected as the inventories and are forced to track their respective set-points. This gives a 5×5 multivariable control system for our system. Using the differential equation model (Equations 24 and 25), we generate the control equations for the required manipulated variables which force the concentration of the initiator and the respective monomers to its set-point. The control scheme generated is shown below: Control equation for initiator I,

$$F_{I_{in}} = F_{I_{out}} + k_d I V - K(I - I^*) \tag{27}$$

Control equations for the monomers,

$$F_{M_{1,in}} = F_{M_{1,out}} + \Big(2fk_dI + \sum_{j=1}^{4} P_n^{j\cdot} M_1 (k_{p_{j1}} + k_{tr_{j1}} + \sum_{l=1}^{2} k_{11}^{S_l} S_l M_1)\Big)V - K(M_1 - M_1^*) \tag{28}$$

$$F_{M_{2,in}} = F_{M_{2,out}} + \Big(2fk_dI + \sum_{j=1}^{4} P_n^{j\cdot} M_2 (k_{p_{j2}} + k_{tr_{j2}} + \sum_{l=1}^{2} k_{22}^{S_l} S_l M_2)\Big)V - K(M_2 - M_2^*) \tag{29}$$

$$F_{M_{3,in}} = F_{M_{3,out}} + \Big(2fk_dI + \sum_{j=1}^{4} P_n^{j\cdot} M_3 (k_{p_{j3}} + k_{tr_{j3}} + \sum_{l=1}^{2} k_{33}^{S_l} S_l M_3)\Big)V - K(M_3 - M_3^*) \tag{30}$$

$$F_{M_{4,in}} = F_{M_{4,out}} + \Big(2fk_dI + \sum_{j=1}^{4} P_n^{j\cdot} M_4 (k_{p_{j4}} + k_{tr_{j4}} + \sum_{l=1}^{2} k_{44}^{S_l} S_l M_4)\Big)V - K(M_4 - M_4^*) \tag{31}$$

In the above equations, K is a positive constant and I^* and $M_i^*(i \in \{1, 2, 3, 4\})$ are the predetermined set-points for the initiator and monomer concentrations. The theory provides guidance for how to chose K since $1/K$ corresponds to the closed loop time-constant. The control

system assumes that the initiator and four monomer concentrations are measured. If these variables are not measured then it is necessary to develop an estimator to estimate these variables from the model.

To illustrate the performance of the control system we have introduced set point changes, first in M_1 at time 330 seconds and then in I at time 510 seconds to study how the system responds to these set point changes after the effect of initial conditions have died out. The results for the setpoint tracking performance for initiator and 3 monomers are shown in Figure 2 [1] . The proportional gain for all four controllers is $K = 0.01$ so that the closed loop time constant for all the four outputs is equal to 100 secs. The results show that the inventory controller decouples the response so that a setpoint change in one variable does not lead to a change in the other variables [2] . In practice there will be a mismatch between the real system and the controller equations and it may not be possible to achieve perfect decoupling.

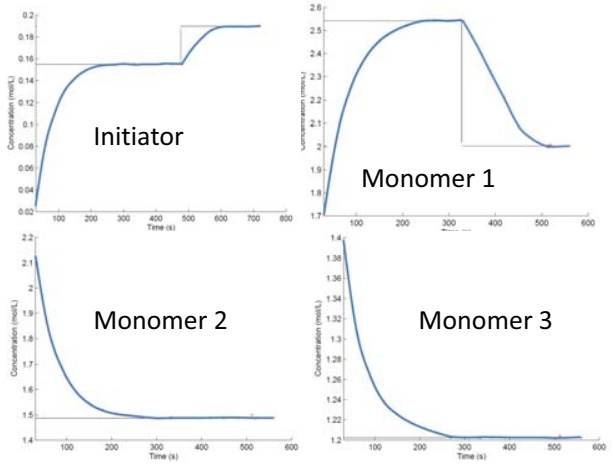

Fig. 2. Initiator, 3 Monomer Concentrations and Setpoints

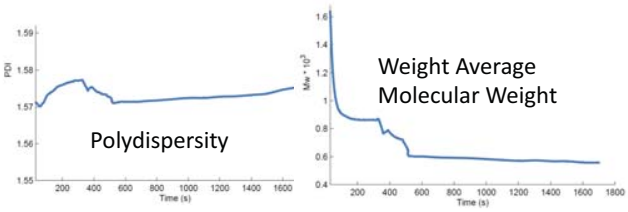

Fig. 3. Polydispersity and Weight Average Molecular Weight

5. THE CORRELATION MAPPING

The inventory control scheme allows the user to define setpoints in terms of inventories. In our case these are the initiator concentration and concentrations of monomers inside the reactor. These variables are related to the flow variables in a passive manner and they are easy to control. In practice it is often necessary to control secondary variables like molecular weight and polydispersity. These variables are more difficult to control since the relative degree of the control system now may be much higher. In this work we have solved the problem by developing a correlation mapping to identify how the steady state monomer set points correspond to target molecular weights and polydispersity for use in the inventory control scheme. The idea now is to use the mapping to generate inventory setpoint and control to the calculated setpoints. Model uncertainty can be compensated for using a separate estimation algorithm to fit the mapping to the data in real time.

One example of such a correlation is shown in Figure 4. The x-axis consists of the different molecular weight distributions. the numbers 1 to 3 are indices corresponding to M_w, M_n and M_z respectively. The z-axis shows the number value of each of the molecular weight distributions, while the y-axis shows the values of the input flow rates. These maps provide a means to chose set points for monomer inventories to achieve desired polymer properties. Similar plots were developed for the initiator and the other monomers.

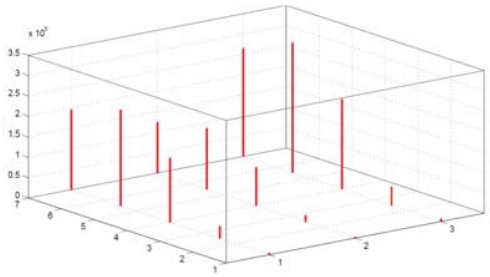

Fig. 4. M1-MWD correlation plot

Table 2. Simulation Results for varying M1

Flow rate of $M1$(kg/s)	M_w	M_n	M_z
1	4574	2439	6844
2.5	30003	15813	44928
4	158560	93652	219070
5.5	235980	149230	319110
7	195670	123340	264750

6. CONCLUSIONS

A kinetic model for free radical polymerization of the monomers in HPA/Sty/BA/BMA was developed and implemented in PREDICI. Kinetic parameters obtained from literature were found to predict the experimental data poorly. Further refinement was carried by implementing a parameter estimation algorithm based on nonlinear optimization. A sensitivity study and an estimability analysis were carried out to identify the set of estimable parameters. The estimable parameters were then optimized using a weighted, constrained non-linear least squares Gauss-Newton algorithm with backtracking line search. The optimized values of the parameters were found to yield better fits for the experimental data. However, there seems to be

[1] Due to space limitation we do not show the 4th monomer which is similar to the third and fourth.

[2] The simulated controller used a sampling time of 30 sec during the period when the setpoints were constant. It was decreased to one sample every 2 seconds for a brief period during the setpoint change

a trade-off between the two types of outputs (molecular weights and residual monomer concentrations) that may be optimized. It is possible to fit only either set of outputs very well, using this model. Certain features of the experimental data were not captured, indicating that the need for further refinement of the model by adding other reactions that are relevant to the process. An inventory control approach was proposed to force monomer concentrations to track some pre-determined set points. These set points can be appropriately selected based on the requirements using a correlation mapping such as the one performed in this study.

NOMENCLATURE

I ≡ Initiator
M_i, M_j ≡ Monomer
S_k ≡ Solvent
$P_n^{i\cdot}$, $P_r^{i\cdot}$, $P_{n+r}^{i\cdot}$, $P_m^{i\cdot}$ ≡ Live Polymer Chain
D_n, D_r, D_m, D_{n+r} ≡ Dead Polymer Chain
φ_{ijk} ≡ Scaling factor

Sets

$\mathcal{M} \equiv \{M_1, M_2, M_3, M_4\}$ ≡ set of all monomers
$\mathcal{A} \equiv \{M_1, M_2, M_3\}$ ≡ set of Acrylate monomers
$\mathcal{MA} \equiv \{M_4\}$ ≡ the set of Methacrylate monomers
$\mathcal{P} \equiv \{P_n^{i\cdot}, P_r^{i\cdot}, P_m^{i\cdot}, P_{n+r}^{i\cdot}\}$ represents the set of Live Polymer Chains
$\mathcal{S} \equiv \{S_1, S_2\}$ represents the set of solvents
$\mathcal{D} \equiv \{D_n, D_r, D_m, D_{n+r}\}$ represents the set of dead polymer chains

Indices

$i, j \in \{1,2,3,4\}$, $k \in \{1,2\}$, $n, r, m \in [1, \ldots, \infty)$

REFERENCES

AkzoNobel (2006). *Initiators for High Polymers.* Akzo Nobel Polymer Chemicals, june edition.

Amrehn, H. (1977). Computer Control in Polymerization Industry. *Automatica*, 13, 533.

Asua, J.M. (2007). *Polymer Reaction Engineering.* Blackwell Publishing.

Beuermann, S. and Buback, M. (2002). Rate coefficients of free-radical polymerization deduced from pulsed laser experiments. *Prog. Polym. Sci*, 27, 191 – 254.

C. A. Farschman, K. P. Viswanath, B.E.Y. (1998). Process systems and inventory control. *AIChE Journal*, 44(8), 1841–1857.

Choi, T.J.C..K.Y. (1997). Discrete Optimal Control of Molecular Weight Distribution in a Batch Free Radical Polymerization Process. *Ind. Eng. Chem. Res.*, 36, 3676–3684.

Chow, C.D. (1975). Monomer Reactivity Ratio and Q-e Values for Copolymerization of Hydroxyalkyl Acrylates and 2-(1-Aziridinyl)ethyl Methacrylate with Styrene. *Journal of Polymer Science*, 13, 309 – 313.

Congling Quan, M.S. and Grady, M.C. (2003). Product Quality Improvement in a High-Temperature Free-Radical Polymerization Reactor. *Proceedings of the American Control Conference*, 3980 – 3985.

Curteanu, S. (2003). Modeling and Simulation of Free Radical Polymerization of Styrene under Semibatch Reactor conditions. *Central European Journal of Chemistry*, 1, 69 – 90.

Curteanu, S. and Bulacovschi, V. (2005). Free Radical Polymerization of Methyl Methacrylate: Modeling and Simulation under Semibatch and Nonisothermal Reactor Conditions. *Journal of Applied Polymer Science*, 74(11), 2561 – 2570.

D. Li, M.C.G. and Hutchinson, R.A. (2005). High-Temperature Semibatch Free Radical Copolymerization of Butyl Methacrylate and Butyl Acrylate. *Ind. Eng. Chem. Res.*, 44, 2506 – 2517.

Elicabe, G.E. and Meira, G.R. (1988). Estimation and Control in Polymerization Reactors - A Review. *Poly. Eng. & Sci.*, 28, 121.

H. Seki, M. Ogawab, S.O.K.A.M.O..W.Y. (2001). Industrial application of a nonlinear model predictive control to polymerization reactors. *Control Engineering Practice*, 9, 819 – 828.

Ham, G.E. (1964). *Copolymerization*, volume XVIII. Interscience Publishers.

K. Zhen Yao, B. M. Shaw, B.K.K.B.M..D.W.B. (2003). Modeling Ethylene/Butylene Copolymerization with Multi-Site Catalysis: Parameter Estimability and Experimental Design. *Polymer Reaction Engineering*, 11 (3), 563 – 588.

Khalil, H.K. (2002). *Nonlinear Systems, Third Ed.* Prentice Hall.

M. D. Díez, B. E. Ydstie, M.F.B.L. (2007). Inventory control of particulate processes. *Computers and Chemical Engineering*, 32, 46–67.

M. Ruszkowski, V. Garcia-Osorio, B.E.Y. (2005). Passivity based control of transport reaction systems. *AIChE Journal*, 51, 3147–3166.

MacGregor, J.F. (1986). Control of polymerization reactors. *Poly. Eng. & Sci.*, 31.

Maeder, S. and Gilbert, R.G. (1998). Measurement of transfer constant for butyl acrylate free-radical polymerization. *Macromolecules*, 31(14), 4410 – 4418.

Soroush, M. and Zambare, N. (2000). Nonlinear output feedback control of a class of polymerization reactors. *IEEE Trans. Control Systems Technology*, 8(2), 310–320.

W. R. Cluett, S.L.S..D.G.F. (1985). Adaptive Control of a Batch Reactor. *Chemical Engineering Communications*, 38, 67–78.

Ydstie, B.E. and Jiao, Y. (2006). Passivity based control of the float glass process: Multi-scale decomposition and real-time optimization of complex flows. *IEEE Control Systems Magazine*, 26(6), 64–72.

Simultaneous Regulation of Surface Roughness and Porosity in Thin Film Growth

Gangshi Hu * **Gerassimos Orkoulas** * **Panagiotis D. Christofides** *,**,[1]

* *Department of Chemical and Biomolecular Engineering, University of California, Los Angeles, CA 90095 USA.*
** *Department of Electrical Engineering, University of California, Los Angeles, CA 90095 USA.*

Abstract: This work focuses on simultaneous control of surface roughness and film porosity in a porous thin film deposition process modeled via kinetic Monte Carlo simulation on a triangular lattice. The microscopic model of the thin film growth process includes adsorption and migration processes. Vacancies and overhangs are allowed inside the film for the purpose of modeling thin film porosity. Appropriate closed-form dynamic models are first derived to describe the evolution of film surface roughness and porosity and used as the basis for the design of a model predictive control algorithm that includes penalty on the deviation of surface roughness and film porosity from their respective set-point values. Closed-loop simulations demonstrate that when simultaneous control of surface roughness and porosity is carried out, a balanced trade-off is obtained in the closed-loop system between the two control objectives of surface roughness and porosity regulation.

Keywords: thin film processing, roughness, porosity, model predictive control

1. INTRODUCTION

Thin film deposition processes play an important role in the semiconductor industry. Thin film microstructure, including surface roughness and film porosity, strongly affects the electrical and mechanical properties of thin films and of the resulting devices. Motivated by this, recent research efforts on modeling and control of thin film microstructure have focused mostly on thin film surface roughness on the basis of microscopic thin film growth models which utilize a square lattice. Specifically, kinetic Monte Carlo (kMC) models based on a square lattice and utilizing the solid-on-solid (SOS) approximation for deposition were initially employed to develop an effective methodology to describe the evolution of film microstructure and design feedback control laws for thin film surface roughness (Lou and Christofides (2003); Christofides et al. (2008)). This control methodology was successfully applied to surface roughness control of: a) a gallium arsenide (GaAs) deposition process (Lou and Christofides (2004)), and b) a multi-species deposition process with long range interactions (Ni and Christofides (2005a)). Furthermore, a method that couples partial differential equation (PDE) models and kMC models was developed for computationally efficient multiscale optimization of thin film growth (Varshney and Armaou (2005)). However, kMC models are not available in closed-form and this limitation restricts the use of kMC models for system-level analysis and design of model-based feedback control systems. To overcome this problem, model identification of linear deterministic models from outputs of kMC simulators was used for controller design using linear control theory (Siettos et al. (2003); Armaou et al. (2004)). However, deterministic models are only effective in controlling the expected values of macroscopic variables, i.e., the first-order statistical moments of the microscopic distribution. For higher statistical moments of the microscopic distributions such as the surface roughness (the second moment of height distribution on a lattice), deterministic models are not sufficient, and stochastic differential equation (SDE) models may be needed.

SDEs arise naturally in the modeling of surface morphology of ultra thin films in a variety of thin film preparation processes (Edwards and Wilkinson (1982); Villain (1991); Vvedensky et al. (1993)). Advanced control methods based on SDEs have been developed to address the need of model-based feedback control of thin film microstructure. Specifically, methods for state feedback control of surface roughness based on linear (Lou and Christofides (2005); Ni and Christofides (2005b)) and nonlinear (Lou and Christofides (2008)) SDE models have been developed. However, state feedback control assumes full knowledge of the surface morphology at all times, which may be a restrictive requirement in certain practical applications. To this end, output feedback control of surface roughness was recently developed (Hu et al. (2008)) by incorporating a Kalman-Bucy type filter, which utilizes information from a finite number of noisy measurements.

In the context of modeling of thin film porosity, kMC models have been widely used to model the evolution of porous thin films in many deposition processes and to investigate the influence of the macroscopic parameters on the porous thin film microstructure (Wang and Clancy (1998); Zhang et al. (2004)). Deterministic and stochastic ordinary differential equation (ODE) models of film porosity were recently developed (Hu et al. (2009a)) to model the evolution of film porosity and its fluctuation and design model predictive control (MPC) algorithms to control film porosity to a desired level and reduce run-to-run porosity variability. Despite recent significant efforts on modeling and control of surface roughness and film porosity, simultaneous regulation of surface roughness and film porosity within a unified control framework has not been investigated.

[1] Corresponding author: Tel: +1(310)794-1015; Fax: +1(310)206-4107; (e-mail: pdc@seas.ucla.edu). Financial support from NSF, CBET-0652131, is gratefully acknowledged.

Motivated by these considerations, the present work focuses on simultaneous regulation of surface roughness and film porosity in a porous thin film deposition process modeled via kMC simulation on a triangular lattice. The definition of surface height profile is first introduced and the dynamics of surface height of the thin film are described by an Edwards-Wilkinson (EW)-type equation. Subsequently, an appropriate definition of film site occupancy ratio (SOR) is introduced to represent the porosity and a deterministic ODE model is derived to describe the time evolution of film SOR. The model parameters are estimated on the basis of data obtained from the kMC simulator of the deposition process using least-square methods. The developed dynamic models are used as the basis for the design of a model predictive control algorithm that includes penalty on the deviation of surface roughness square and film SOR from their respective set-point values. Simulation results demonstrate the applicability and effectiveness of the proposed modeling and control approach in the context of the deposition process under consideration.

2. PROCESS DESCRIPTION AND MODELING

2.1 On-lattice kinetic Monte Carlo model of film growth

The thin film growth process considered in this work includes two microscopic processes: an adsorption process, in which particles are incorporated into the film from the gas phase, and a migration process, in which surface particles move to adjacent sites (Wang and Clancy (1998); Levine and Clancy (2000); Yang et al. (1997)). Specifically, the film growth model used in this work is an on-lattice kMC model in which all particles occupy discrete lattice sites. The on-lattice kMC model is valid for temperatures $T < 0.5T_m$, where T_m is the melting point of the crystal. At high temperatures ($T \lesssim T_m$), the particles cannot be assumed to be constrained on the lattice sites and the on-lattice model is not valid. In this work, a triangular lattice is selected to represent the crystalline structure of the film, as shown in Fig.1. All particles are modeled as identical hard disks and the centers of the particles deposited on the film are located on the lattice sites. The diameter of the particles equals the distance between two neighboring sites. The width of the lattice is fixed so that the lattice contains a fixed number of sites in the lateral direction. The new particles are always deposited vertically from the top side of the lattice where the gas phase is located; see Fig.1. Particle deposition results in film growth in the direction normal to the lateral direction. The direction normal to the lateral direction is thus designated as the growth direction. The number of sites in the lateral direction is defined as the lattice size and is denoted by L. The lattice parameter, a, which is defined as the distance between two neighboring sites and equals the diameter of a particle (all particles have the same diameter), determines the lateral extent of the lattice, La.

The number of nearest neighbors of a site ranges from zero to six, the coordination number of the triangular lattice. A site with no nearest neighbors indicates an unadsorbed particle in the gas phase (i.e., a particle which has not been deposited on the film yet). A particle with six nearest neighbors is associated with an interior particle that is fully surrounded by other particles and cannot migrate. A particle with two to five nearest neighbors is possible to diffuse to an unoccupied neighboring site with a probability that depends on its local environment. In the triangular lattice, a particle with only one nearest neighbor is considered unstable and is subject to instantaneous surface relaxation.

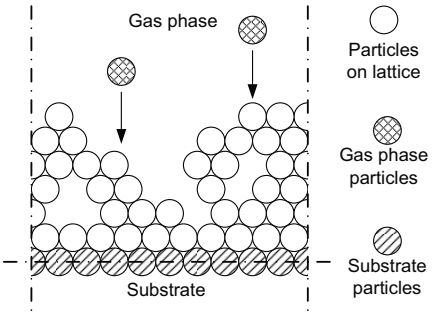

Fig. 1. Thin film growth process on a triangular lattice.

In the simulation, a bottom layer in the lattice is initially set to be fully packed and fixed, as shown in Fig.1. There are no vacancies in this layer and the particles in this layer cannot migrate. This layer acts as the substrate for the deposition and is not counted in the computation of the number of the deposited particles, i.e., this fixed layer does not influence the film surface roughness and porosity (see Section 2.2 below). All microscopic processes (Monte Carlo events) are assumed to be Poisson processes. These Monte Carlo events occur randomly with probabilities proportional to their respective rates. The events are executed instantaneously upon selection and the state of the lattice remains unchanged between two consecutive events. The specific rules used to carry out the adsorption and migration processes and their simulation are discussed in detail in Hu et al. (2009b) and are not presented here due to space limitations.

2.2 Definitions of surface roughness and site occupancy ratio

Utilizing the continuous-time Monte Carlo algorithm, simulations of the kMC model of a porous silicon thin film growth process can be carried out. Snapshots of film microstructure, i.e., the configurations of particles within the triangular lattice, are obtained from the kMC model at various time instants during process evolution. To quantitatively evaluate the thin film microstructure, two variables, surface roughness and film porosity, are introduced in this subsection.

Surface roughness, which measures the texture of thin film surface, is represented by the root mean square (RMS) of the surface height profile of the thin film. Determination of surface height profile is slightly different in the triangular lattice model compared to a SOS model. In the SOS model, the surface of thin film is naturally described by the positions of the top particles of each column. In the triangular lattice model, however, due to the existence of vacancies and overhangs, the definition of film surface needs further clarification. Specifically, taking into account practical considerations of surface roughness measurements, the surface height profile of a triangular lattice model is defined based on the particles that can be reached from abobe in the vertical direction, as shown in Fig.2. In this definition, a particle is considered as a surface particle only if it is not blocked by the particles in both neighboring columns. Therefore, the surface height profile of a porous thin film is the line that connects the sites that are occupied by the surface particles. With this definition, the surface height profile can be treated as a function of the spatial coordinate. Surface roughness, as a measurement of the surface texture, is defined as the standard deviation of the surface height profile from its average height. The definition expression of surface roughness is given later in Section 3.1.

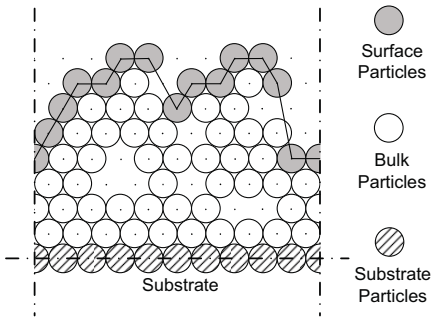

Fig. 2. Definition of surface height profile. A surface particle is a particle that is not blocked by particles from both of its neighboring columns in the vertical direction.

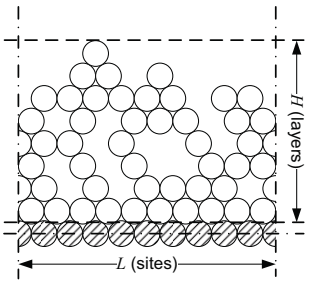

Fig. 3. Illustration of the definition of film SOR of Eq.1.

In addition to film surface roughness, the film site occupancy ratio (SOR) is introduced to represent the extent of the porosity inside the thin film. The mathematical expression of film SOR is defined as follows:

$$\rho = \frac{N}{LH} \tag{1}$$

where ρ denotes the film SOR, N is the total number of deposited particles on the lattice, L is the lattice size, and H denotes the number of deposited layers. Note that the deposited layers are the layers that contain only deposited particles and do not include the initial substrate layers. The variables in the definition expression of Eq.1 can be found in Fig.3. Since each layer contains L sites, the total number of sites in the film that can be contained within the H layers is LH. Thus, film SOR is the ratio of the occupied lattice sites, N, over the total number of available sites, LH. Film SOR ranges from 0 to 1. Specifically, $\rho = 1$ denotes a fully occupied film with a flat surface. The value of zero is assigned to ρ at the beginning of the deposition process since there are no particles deposited on the lattice.

3. DYNAMIC MODEL CONSTRUCTION AND PARAMETER ESTIMATION

3.1 Edwards-Wilkinson-type equation of surface height

An Edwards-Wilkinson (EW)-type equation can be used to describe the surface height evolution in many microscopic processes that involve thermal balance between adsorption (deposition) and migration (diffusion). In this work, an EW-type equation is chosen to describe the dynamics of the fluctuation of surface :

$$\frac{\partial h}{\partial t} = r_h + \nu \frac{\partial^2 h}{\partial x^2} + \xi(x,t) \tag{2}$$

subject to PBCs:

$$h(-\pi,t) = h(\pi,t), \quad \frac{\partial h}{\partial x}(-\pi,t) = \frac{\partial h}{\partial x}(\pi,t) \tag{3}$$

and the initial condition:

$$h(x,0) = h_0(x) \tag{4}$$

where $x \in [-\pi,\pi]$ is the spatial coordinate, t is the time, r_h and ν are the model parameters, and $\xi(x,t)$ is a Gaussian white noise with the following expressions for its mean and covariance:

$$\begin{aligned} \langle \xi(x,t) \rangle &= 0 \\ \langle \xi(x,t)\xi(x',t') \rangle &= \sigma^2 \delta(x-x')\delta(t-t') \end{aligned} \tag{5}$$

where σ^2 is a parameter which measures the intensity of the Gaussian white noise and $\delta(\cdot)$ denotes the standard Dirac delta function.

To proceed with model parameter estimation and control design, a stochastic ODE approximation of Eq.2 is first derived using Galerkin's method. Consider the eigenvalue problem of the linear operator of Eq.2, which takes the form:

$$\begin{aligned} A\bar{\phi}_n(x) &= \nu \frac{d^2\bar{\phi}_n(x)}{dx^2} = \lambda_n \bar{\phi}_n(x) \\ \bar{\phi}_n(-\pi) &= \bar{\phi}_n(\pi), \quad \frac{d\bar{\phi}_n}{dx}(-\pi) = \frac{d\bar{\phi}_n}{dx}(\pi) \end{aligned} \tag{6}$$

where λ_n denotes an eigenvalue and $\bar{\phi}_n$ denotes an eigenfunction. A direct computation of the solution of the above eigenvalue problem yields $\lambda_0 = 0$ with $\psi_0 = 1/\sqrt{2\pi}$, and $\lambda_n = -\nu n^2$ (λ_n is an eigenvalue of multiplicity two) with eigenfunctions $\phi_n = (1/\sqrt{\pi})\sin(nx)$ and $\psi_n = (1/\sqrt{\pi})\cos(nx)$ for $n = 1,\cdots,\infty$. Note that the $\bar{\phi}_n$ in Eq.6 denotes either ϕ_n or ψ_n. For fixed positive value of ν, all eigenvalues (except the zero-th eigenvalue) are negative and the distance between two consecutive eigenvalues (i.e. λ_n and λ_{n+1}) increases as n increases.

To this end, the solution of Eq.2 is expanded in an infinite series in terms of the eigenfunctions as follows:

$$h(x,t) = \sum_{n=1}^{\infty} \alpha_n(t)\phi_n(x) + \sum_{n=0}^{\infty} \beta_n(t)\psi_n(x) \tag{7}$$

where $\alpha_n(t)$, $\beta_n(t)$ are time-varying coefficients. Substituting the above expansion for the solution, $h(x,t)$, into Eq.2 and taking the inner product with the adjoint eigenfunctions, $\phi_n^*(x) = (1/\sqrt{\pi})\sin(nx)$ and $\psi_n^*(x) = (1/\sqrt{\pi})\cos(nx)$, the following system of infinite stochastic ODEs is obtained:

$$\begin{aligned} \frac{d\beta_0}{dt} &= \sqrt{2\pi} r_h + \xi_\beta^0(t) \\ \frac{d\alpha_n}{dt} &= \lambda_n \alpha_n + \xi_\alpha^n(t), \frac{d\beta_n}{dt} = \lambda_n \beta_n + \xi_\beta^n(t), n = 1,\ldots,\infty \end{aligned} \tag{8}$$

where

$$\xi_\alpha^n(t) = \int_{-\pi}^{\pi} \xi(x,t)\phi_n^*(x)dx, \quad \xi_\beta^n(t) = \int_{-\pi}^{\pi} \xi(x,t)\psi_n^*(x)dx. \tag{9}$$

The covariances of $\xi_\alpha^n(t)$ and $\xi_\beta^n(t)$ can be computed as follows: $\langle \xi_\alpha^n(t)\xi_\alpha^n(t') \rangle = \sigma^2\delta(t-t')$ and $\left\langle \xi_\beta^n(t)\xi_\beta^n(t') \right\rangle = \sigma^2\delta(t-t')$.

Since the stochastic ODE system is linear, the analytical solution of state variance can be obtained from a direct computation as follows:

$$\begin{aligned} \left\langle \alpha_n^2(t) \right\rangle &= \frac{\sigma^2}{2\nu n^2} + \left(\left\langle \alpha_n^2(t_0) \right\rangle - \frac{\sigma^2}{2\nu n^2} \right) e^{-2\nu n^2 (t-t_0)} \\ \left\langle \beta_n^2(t) \right\rangle &= \frac{\sigma^2}{2\nu n^2} + \left(\left\langle \beta_n^2(t_0) \right\rangle - \frac{\sigma^2}{2\nu n^2} \right) e^{-2\nu n^2 (t-t_0)} \\ & n = 1,2,\ldots,\infty \end{aligned} \tag{10}$$

where $\langle \alpha_n^2(t_0) \rangle$ and $\langle \beta_n^2(t_0) \rangle$ are the state variances at time t_0. The analytical solution of state variance of Eq.10 will be used in the parameter estimation and the MPC design.

When the dynamic model of surface height profile is determined, surface roughness of the thin film is defined as the standard deviation of the surface height profile from its average height and is computed as follows:

$$r(t) = \sqrt{\frac{1}{2\pi}\int_{-\pi}^{\pi} [h(x,t) - \bar{h}(t)]^2 dx} \tag{11}$$

where $\bar{h}(t) = \frac{1}{2\pi}\int_{-\pi}^{\pi} h(x,t)dx$ is the averaged surface height. According to Eq.7, we have $\bar{h}(t) = \beta_0(t)\psi_0$. Therefore, $\langle r^2(t) \rangle$ can be rewritten in terms of $\langle \alpha_n^2(t) \rangle$ and $\langle \beta_n^2(t) \rangle$ as follows:

$$\langle r^2(t) \rangle = \frac{1}{2\pi}\left\langle \int_{-\pi}^{\pi} (h(x,t) - \bar{h}(t))^2 dx \right\rangle$$

$$= \frac{1}{2\pi}\left\langle \sum_{i=1}^{\infty} (\alpha_i^2(t) + \beta_i^2(t)) \right\rangle = \frac{1}{2\pi}\sum_{i=1}^{\infty} \left[\langle \alpha_i^2(t) \rangle + \langle \beta_i^2(t) \rangle \right] \tag{12}$$

where $\bar{h} = \frac{1}{2\pi}\int_{-\pi}^{\pi} h(x,t)dx = \beta_0(t)\psi_0$ is the average of surface height. Thus, Eq.12 provides a direct link between the state variance of the infinite stochastic ODEs of Eq.8 and the expected surface roughness of the thin film. Note that the model parameter r_h does not appear in the expression of surface roughness, since only the zeroth state, β_0, is affected by r_h but this state is not included in the computation of the expected surface roughness square of Eq.12.

3.2 Deterministic dynamic model of film site occupancy ratio

Since film porosity is another control objective, a dynamic model is necessary in the MPC formulation to describe the evolution of film porosity, which is represented by the film SOR of Eq.1. The dynamics of the expected value of the film SOR evolution are approximately described by a linear first-order deterministic ODE as follows:

$$\tau \frac{d\langle \rho(t) \rangle}{dt} = \rho^{ss} - \langle \rho(t) \rangle \tag{13}$$

where t is the time, τ is the time constant and ρ^{ss} is the steady-state value of the film SOR. The deterministic ODE system of Eq.13 is subject to the following initial condition:

$$\langle \rho(t_0) \rangle = \rho_0 \tag{14}$$

where t_0 is the initial time and ρ_0 is the initial value of the film SOR. Note that ρ_0 is a deterministic variable, since ρ_0 refers to the film SOR at $t = t_0$. From Eqs.13 and 14, it follows that

$$\langle \rho(t) \rangle = \rho^{ss} + (\rho_0 - \rho^{ss})\, e^{-(t-t_0)/\tau}. \tag{15}$$

3.3 Parameter estimation

Referring to the EW equation of Eq.2 and the deterministic ODE model of Eq.13, there are several model parameters, ν, σ^2, ρ^{ss} and τ, that need to be determined as functions of the substrate temperature. These parameters describe the dynamics of surface height and of film SOR and can be estimated by comparing the predicted evolution profiles from the dynamic models of Eqs.2 and 13 and the ones from the kMC simulation of the deposition process in a least-square sense (Hu et al. (2009a,b)).

Since surface roughness is a control objective, we choose the expected surface roughness square of Eq.12 as the output for the parameter estimation of the EW equation of Eq.2. Thus, the model coefficients, ν and σ^2, can be obtained by solving the minimization problem as follows:

$$\min_{\nu,\sigma^2} \sum_{i=1}^{n_1} \left[\langle r^2(t) \rangle - \frac{1}{2\pi}\sum_{i=1}^{\infty} \left(\langle \alpha_i^2(t) \rangle + \langle \beta_i^2(t) \rangle \right) \right]^2 \tag{16}$$

where n_1 is the number of the data samplings of surface height profile and surface roughness from the kMC simulations. The predictions of model state variance, $\langle \alpha_i^2(t) \rangle$ and $\langle \beta_i^2(t) \rangle$, can be solved from the analytical solution of Eq.10.

With respect to the parameters of the equation for film porosity, ρ^{ss} and τ can be estimated similarly from the solutions of Eq.15 as follows:

$$\min_{\rho^{ss},\tau} \sum_{i=1}^{n_2} \left[\langle \rho(t_i) \rangle - \left(\rho^{ss} + (\rho_0 - \rho^{ss})\, e^{-(t-t_0)/\tau} \right) \right]^2 \tag{17}$$

where n_2 is the number of the data samplings of film SOR from the kMC simulations. We note that since the dynamic models of film surface height and film SOR may have different dynamics, different numbers of data samplings at different time instants may be used to estimate the parameters of the dynamic models.

The data used for the parameter estimation are obtained from the open-loop kMC simulation of the thin film growth process. The process parameters, i.e., the substrate temperature and the adsorption rate, are fixed during each open-loop simulation. The predictions from the dynamic models with the estimated parameters are close to the open-loop simulation profiles. Detailed data and plots can be found in Hu et al. (2009b).

The parameters that are estimated from fixed operating conditions are suitable for the feedback control design in this work. This is because the control input in the MPC formulation is piecewise, i.e., the manipulated substrate temperature remains constant between two consecutive sampling times, and thus, the dynamics of the microscopic process can be predicted from the dynamic models with estimated parameters. The dependence of the model parameters on substrate temperature is used in the formulation of the model predictive controller in the next section. Thus, parameter estimation from open-loop kMC simulation results of the thin film growth process for a variety of operation conditions is performed to obtain the dependence of the model coefficients on substrate temperature. In this work, the deposition rate for all simulations is fixed at 1 layer/s. The range of T is between 300 K and 800 K, which is from room temperature to the upper limit of the allowable temperature for a valid on-lattice kMC model of silicon film. The dependence of the model parameters on the substrate temperature can be found in Hu et al. (2009b).

4. MODEL PREDICTIVE CONTROL DESIGN

We consider the problem of regulation of surface roughness and of film SOR to desired levels within a model predictive control framework. State feedback control is considered in this work, i.e., the surface height profile and the value of film SOR are assumed to be available to the controller. Real-time film roughness and SOR can be estimated from in-situ thin film thickness measurements (Buzea and Robbie, 2005) in combination with off-line film porosity measurements. Since surface roughness and film SOR are stochastic variables, the expected values, $\langle r(t)^2 \rangle$ and $\langle \rho \rangle$, are chosen as the control objectives. The substrate temperature is used as the manipulated input and the deposition rate is fixed at a certain value, W_0, during the entire closed-loop simulation. To account for a number of prac-

tical considerations, several constraints are added to the control problem. First, there is a constraint on the range of variation of the substrate temperature. This constraint ensures validity of the on-lattice kMC model. Another constraint is imposed on the rate of change of the substrate temperature to account for actuator limitations. The control action at a time t is obtained by solving a finite-horizon optimal control problem. The cost function in the optimal control problem includes penalty on the deviation of $\langle r^2 \rangle$ and $\langle \rho \rangle$ from their respective set-point values. Different weighting factors are assigned to the penalties of the surface roughness and of the film SOR. Surface roughness and film SOR have very different magnitudes, ($\langle r^2 \rangle$ ranges from 1 to 10^2 and $\langle \rho \rangle$ ranges from 0 to 1). Therefore, relative deviations are used in the formulation of the cost function to make the magnitude of the two terms comparable. The optimization problem is subject to the dynamics of the surface height of Eq.2 and of the film SOR of Eq.13. The optimal temperature profile is calculated by solving a finite-dimensional optimization problem in a receding horizon fashion. Specifically, the MPC problem is formulated as follows:

$$\begin{aligned} \min_{T_1,\ldots,T_i,\ldots,T_p} J = \sum_{i=1}^{p} \Big\{ & q_{r^2,i} \left[(r^2_{set} - \langle r^2(t_i) \rangle)/r^2_{set} \right]^2 \\ & + q_{\rho,i} \left[(\rho_{set} - \langle \rho(t_i) \rangle)/\rho_{set} \right]^2 \Big\} \\ \text{subject} \quad & \text{to} \\ \frac{\partial h}{\partial t} = r_h + \nu \frac{\partial^2 h}{\partial x^2} + \xi(x,t), & \tau \frac{d\langle \rho(t) \rangle}{dt} = \rho^{ss} - \langle \rho(t) \rangle \\ T_{min} < T_i < T_{max}, & |(T_{i+1} - T_i)/\Delta| \le L_T \\ i = 1, 2, \ldots, p & \end{aligned} \tag{18}$$

where t is the current time, Δ is the sampling time, p is the number of prediction steps, $p\Delta$ is the specified prediction horizon, t_i, $i = 1, 2, \ldots, p$, is the time of the ith prediction step ($t_i = t + i\Delta$), respectively, T_i, $i = 1, 2, \ldots, p$, is the substrate temperature at the ith step ($T_i = T(t + i\Delta)$), respectively, W_0 is the fixed deposition rate, $q_{r^2,i}$ and $q_{\rho,i}$, $i = 1, 2, \ldots, p$, are the weighting penalty factors for the deviations of $\langle r^2 \rangle$ and $\langle \rho \rangle$ from their respective set-points at the ith prediction step, T_{min} and T_{max} are the lower and upper bounds on the substrate temperature, respectively, and L_T is the limit on the rate of change of the substrate temperature.

The optimal set of control actions, (T_1, T_2, …, T_p), is obtained from the solution of the multi-variable optimization problem of Eq.18, and only the first value of the manipulated input trajectory, T_1, is applied to the deposition process during the time interval $(t, t+\Delta)$. At time $t+\Delta$, a new measurement of ρ and h is received and the MPC problem of Eq.18 is solved for the next control input trajectory.

The MPC formulation proposed in Eq.18 is developed on the basis of the EW equation of surface height and the deterministic ODE model of the film SOR. The EW equation, which is a distributed parameter dynamic model, contains infinite dimensional stochastic states. Therefore, it leads to a model predictive controller of infinite order that cannot be realized in practice (i.e., the practical implementation of such a control algorithm will require the computation of infinite sums which cannot be done by a computer). To this end, a finite dimensional approximation of the EW equation of order $2m$, derived using modal decomposition, is used in the simulations below.

5. SIMULATION RESULTS

In this section, the model predictive controller is applied to the kMC model of the thin film growth process described in Section 2. The value of the substrate temperature is obtained from the solution of the MPC problem at each sampling time and is applied to the closed-loop system until the next sampling time. The optimization problem is solved using a local constrained minimization algorithm using a broad set of initial guesses.

The constraint on the rate of change of the substrate temperature is imposed onto the optimization problem, which is realized in the optimization process in the following way:

$$\left| \frac{T_{i+1} - T_i}{\Delta} \right| \le L_T \Rightarrow T_i - L_T\Delta \le T_{i+1} \le T_i + L_T\Delta \qquad i = 1, 2, \ldots, p. \tag{19}$$

The desired values (set-point values) in the closed-loop simulations are $r^2_{set} = 10.0$ and $\rho_{set} = 0.95$. The order of finite-dimensional approximation of the EW equation in the MPC formulation is $m = 20$. The deposition rate is fixed at 1 layer/s and initial temperature of 600 K. The variation of temperature is from 400 K to 700 K. The maximum of change of the temperature is $L_T = 10$ K/s. The sampling time is fixed at $\Delta = 1$ s. The number of prediction steps is set to be $p = 5$. The simulation duration is determined on the basis of a desired film thickness and the fixed adsorption rate and is chosen as 1000 s for the closed-loop simulations in this work. All expected values are obtained from 1000 independent simulation runs.

Closed-loop simulations of separately regulating film surface roughness and porosity are first carried out. In these control problems, the control objective is to only regulate one of the control variables, i.e., either surface roughness or film SOR, to a desired level. The cost functions of these problems contain only penalty on the error either of the expected surface roughness square, or of the expected film SOR, from their set-point values. The corresponding MPC formulations can be realized by assigning different values to the penalty weighting factors, $q_{r^2,i}$ and $q_{\rho,i}$.

In the roughness-only control problem, the weighting factors take the following values: $q_{r^2,i} = 1$ and $q_{\rho,i} = 0$, $i = 1, 2, \ldots, p$. Fig.4 shows the closed-loop simulation results of the roughness-only control problem. From Fig.4, we can see that the expected surface roughness square is successfully regulated at the desire level, 10. Since no penalty is included on the error of the expected film SOR, the final value of expected film SOR at the end of the simulation, $t = 1000$ s, is 0.988, which is far from the desired film SOR, 0.95.

In the SOR-only control problem, the weighting factors are assigned as: $q_{r^2,i} = 0$ and $q_{\rho,i} = 1$, $i = 1, 2, \ldots, p$. Fig.5 shows the closed-loop simulation results of the SOR-only control problem. Similar to the results of the roughness-only control problem, the desired value of expected film SOR, 0.95, is approached at large times. However, since the error from the expected surface roughness square is not considered in the cost function, $\langle r^2 \rangle$ reaches a very high level around 125 at the end of the simulation.

Finally, closed-loop simulations of simultaneous regulation of surface roughness and film SOR are carried out by assigning non-zero values to both penalty weighting factors. Specifically, $q_{r^2,1} = q_{r^2,2} = \cdots = q_{r^2,p} = 1$ and $q_{\rho,1} = q_{\rho,2} = \cdots = q_{\rho,p} = q_{SOR}$ and q_{SOR} varies from 1 to 10^4. Since substrate temperature is the only manipulated input, the desired-values of r^2_{set} and ρ_{set} cannot be achieved simultaneously. With different assignments of penalty weighting factors, the MPC evaluates and strikes a balance between the two set-points. Fig.6 shows the expected

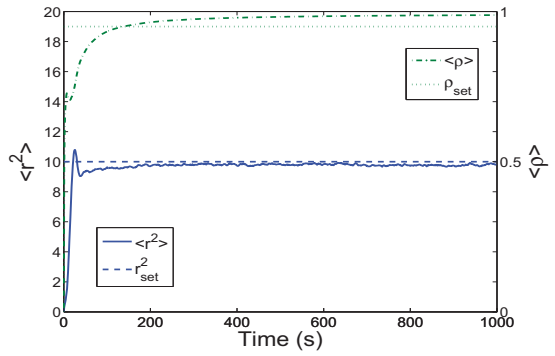

Fig. 4. Profiles of the expected values of surface roughness square (solid line) and of the film SOR (dash-dotted line) under closed-loop operations with cost function including only penalty on surface roughness.

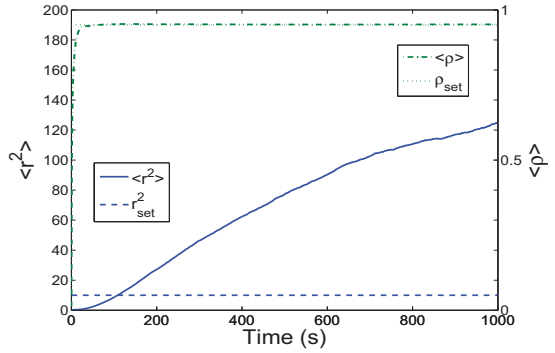

Fig. 5. Profiles of the expected values of surface roughness square (solid line) and of the film SOR (dash-dotted line) under closed-loop operation with cost function including only penalty on the film SOR.

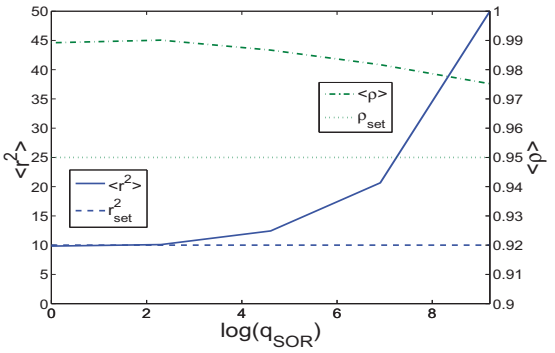

Fig. 6. Profiles of the expected values of surface roughness square (solid line) and of the film SOR (dash-dotted line) at the end of the closed-loop simulations ($t = 1000$ s) with the following penalty weighting factors: $q_{r^2,i}$ fixed at 1 for all i and for different values of q_{SOR}.

values of r^2_{set} and ρ_{set} at the end of closed-loop simulations of the simultaneous control problem with respect to different weighting factors. It is clear from Fig.6 that as the weighting on expected film SOR increases, the expected film SOR approaches its set-point value of 0.95, while the expected surface roughness square deviates from its set-point value of 10.

REFERENCES

Armaou, A., Siettos, C.I., and Kevrekidis, I.G. (2004). Time-steppers and 'coarse' control of distributed microscopic processes. *International Journal of Robust and Nonlinear Control*, 14, 89–111.

Buzea, C. and Robbie, K. (2005). State of the art in thin film thickness and deposition rate monitoring sensors. *Reports on Progress in Physics*, 68, 385–409.

Christofides, P.D., Armaou, A., Lou, Y., and Varshney, A. (2008). *Control and Optimization of Multiscale Process Systems*. Birkhäuser, Boston.

Edwards, S.F. and Wilkinson, D.R. (1982). The surface statistics of a granular aggregate. *Proceedings of the Royal Society of London Series A - Mathematical Physical and Engineering Sciences*, 381, 17–31.

Hu, G., Lou, Y., and Christofides, P.D. (2008). Dynamic output feedback covariance control of stochastic dissipative partial differential equations. *Chemical Engineering Science*, 63, 4531–4542.

Hu, G., Orkoulas, G., and Christofides, P.D. (2009a). Modeling and control of film porosity in thin film deposition. *Chemical Engineering Science,* accepted.

Hu, G., Orkoulas, G., and Christofides, P.D. (2009b). Simultaneous regulation of surface roughness and porosity in thin film deposition. *Industrial & Engineering Chemistry Research,* accepted.

Levine, S.W. and Clancy, P. (2000). A simple model for the growth of polycrystalline Si using the kinetic Monte Carlo simulation. *Modelling and Simulation in Materials Science and Engineering*, 8, 751–762.

Lou, Y. and Christofides, P.D. (2003). Estimation and control of surface roughness in thin film growth using kinetic Monte-Carlo models. *Chemical Engineering Science*, 58, 3115–3129.

Lou, Y. and Christofides, P.D. (2004). Feedback control of surface roughness of GaAs (001) thin films using kinetic Monte Carlo models. *Computers & Chemical Engineering*, 29, 225–241.

Lou, Y. and Christofides, P.D. (2005). Feedback control of surface roughness using stochastic PDEs. *AIChE Journal*, 51, 345–352.

Lou, Y. and Christofides, P.D. (2008). Nonlinear feedback control of surface roughness using a stochastic PDE: Design and application to a sputtering process. *Industrial & Engineering Chemistry Research*, 45, 7177–7189.

Ni, D. and Christofides, P.D. (2005a). Dynamics and control of thin film surface microstructure in a complex deposition process. *Chemical Engineering Science*, 60, 1603–1617.

Ni, D. and Christofides, P.D. (2005b). Multivariable predictive control of thin film deposition using a stochastic PDE model. *Industrial & Engineering Chemistry Research*, 44, 2416–2427.

Siettos, C.I., Armaou, A., Makeev, A.G., and Kevrekidis, I.G. (2003). Microscopic/stochastic timesteppers and "coarse" control: a kMC example. *AIChE Journal*, 49, 1922–1926.

Varshney, A. and Armaou, A. (2005). Multiscale optimization using hybrid PDE/kMC process systems with application to thin film growth. *Chemical Engineering Science*, 60, 6780–6794.

Villain, J. (1991). Continuum models of crystal growth from atomic beams with and without desorption. *Journal de Physique I*, 1, 19–42.

Vvedensky, D.D., Zangwill, A., Luse, C.N., and Wilby, M.R. (1993). Stochastic equations of motion for epitaxial growth. *Physical Review E*, 48, 852–862.

Wang, L. and Clancy, P. (1998). A kinetic Monte Carlo study of the growth of Si on Si(100) at varying angles of incident deposition. *Surface Science*, 401, 112–123.

Yang, Y.G., Johnson, R.A., and Wadley, H.N. (1997). A Monte Carlo simulation of the physical vapor deposition of nickel. *Acta Materialia*, 45, 1455–1468.

Zhang, P., Zheng, X., Wu, S., Liu, J., and He, D. (2004). Kinetic Monte Carlo simulation of Cu thin film growth. *Vacuum*, 72, 405–410.

A Strategy for Controlling Acetaldehyde Content in an Industrial Plant of Bioethanol

Fabio R. M. Batista*. Antonio J. A. Meirelles**

** Laboratory EXTRAE, Department of Food Engineering, Faculty of Food Engineering, University of Campinas - UNICAMP, Brazil (e-mail: f.fabio.batista@gmail.com).*
*** Laboratory EXTRAE, Department of Food Engineering, Faculty of Food Engineering, University of Campinas - UNICAMP, Brazil (Phone: 55-19- 3521-4037, e-mail: tomze@fea.unicamp.br).*

Abstract: This work presents a strategy for controlling acetaldehyde content in Brazilian bioethanol, based in simulation results of a typical industrial distillation plant. The major problem of acetaldehyde in bioethanol is that, during the storage period, it can oxidize to acetic acid, increasing fuel acidity above the legislation limit. This work tested, by dynamic simulation, simple loops to control acetaldehyde in bioethanol. The dynamic simulation generated a disturbance in the wine to be distilled by increasing acetaldehyde content, and verified how those loops were able to control the acetaldehyde level in bioethanol. Two different column system configurations were investigated. The first one includes a degassing system and a second one that produces pasteurized alcohol without or with a degassing system. Suggestions for the best control system of acetaldehyde contamination in bioethanol were formulated according to the acetaldehyde level in the wine.

Keywords: Fuel ethanol, bioethanol, dynamic simulation, degassing system, aspen plus.

1. INTRODUCTION

There is an increasing interest in bioethanol as a renewable energy source as well as a commodity to be used in other industrial branches, such as the chemical, pharmaceutical, and beverage industries. Brazil is one of the largest bioethanol producers and the largest exporter. For more than 30 years bioethanol is used directly as a biofuel, in this case with a concentration close to the azeotropic one, or added to petrol and, in this last case, it should be anhydrous. The rapid increase in its use as biofuel, the increase of its exports and of its use in other industrial branches is requiring a better control of product quality. Several minor components are generated during bioethanol production by fermentation and most of them are contaminants present in the end product. Although ethanol distillation is a largely investigated subject, most of the research works focus on energy consumption, alternative dehydration techniques and control strategies for separating the binary mixture ethanol-water, not taking into account the series of minor components that influence the distillation process. Those research works also rarely consider the peculiarities of the column systems used for ethanol distillation in the industrial practice.

Some recent works are applying simulations tools in order to investigate spirits and bioethanol distillation, taking into account at least part of the complexity of the multicomponent alcoholic mixture and of the industrial equipments used for its distillation. GAISER et al. (2002) used the commercial software Aspen Plus for simulating a continuous industrial unit for whiskey distillation, validating the results against industrial data. MEIRELLES et al. (2008) simulated a continuous distillation column for spirits production from sugar cane fermented must. DECLOUX and COUSTEL (2005) simulated a typical distillation plant for neutral alcohol production, using the software ProSim Plus. Neutral alcohol is a very pure ethanol product that requires a series of distillation columns to be produced.

Taking into account the increasing importance of bioethanol and the largely untreated subject of controlling its contaminants, this work is focused on investigating strategies for controlling the acetaldehyde content in bioethanol. Acetaldehyde is the contaminant responsible for the increase in biofuel acidity during storage time.

2. DESCRIPTION OF PROCESS

A typical industrial installation for bioethanol production in Brazil, according to MARQUINI et al. (2008), is shown in Fig. 1. This industrial installation is composed by 3 columns, two stripping ones (A and B1) and the rectifying column B. Column A, a equipment for wine stripping, is composed by 22 plates, 1 reboiler and no condenser. These plates have Murphree efficiency of 0.65, the total pressure drop of this column is 18437 Pa, the pressure of stage 1 is 138932 Pa and the reboiler pressure 157369 Pa. The wine or beer, industrial denominations of the fermented sugar cane must, is represented by the standard solution given in Table 1. This mixture is fed into the top of column A. The stream named PHLEGM, a vapor stream with ethanol concentration within the range 35-45 mass%, is fed into the bottom of column B. STILLAGE and WHITE STILLAGE, streams withdrawn from the bottoms of columns A and B1, respectively, must have an ethanol content not larger than 0.02 mass%.

Column B, the phlegm rectification column, is composed by 45 plates plus a condenser, has Murphree efficiency of 0.50, a total pressure drop of 38932 Pa, condenser pressure of

100000 Pa and bottom stage pressure of 138932 Pa. Bioethanol is extracted as top product of column B with 93 mass% of ethanol. Column B1, the phlegm stripping column, is fed with the bottom product of column B. This column is composed by 18 plates plus a reboiler, has Murphree efficiency of 0.60, total pressure drop of 8042 Pa, and the reboiler pressure equal to 146974 Pa.

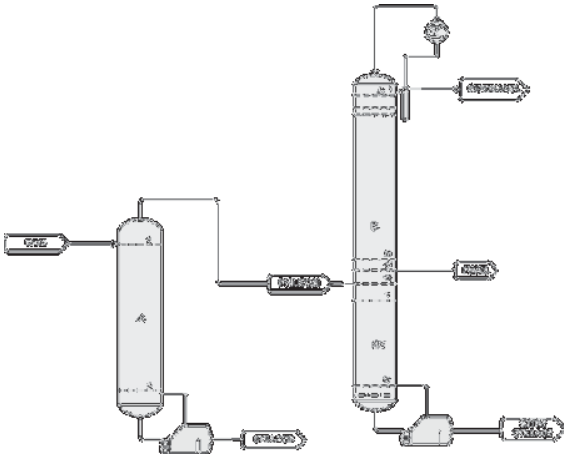

Fig. 1 - Brazilian Bioethanol Industrial Plant

Table 1. Typical composition of industrial wine used in the simulations.

Component	Concentration (mass fraction)	Reference
Water	0.93495357	By difference.
Ethanol	6.450×10^{-2}	Oliveira (2001)
Methanol	3.200×10^{-7}	Boscolo et al. (2000)
Isopropanol	1.020×10^{-6}	Cardoso et al. (2003)
Propanol	3.000×10^{-5}	Oliveira (2001)
Isobutanol	2.780×10^{-5}	Oliveira (2001)
Isoamyl alcohol	4.250×10^{-5}	Oliveira (2001)
Ethyl Acetate	7.690×10^{-6}	Oliveira (2001)
Acetaldehyde	2.000×10^{-6}	Oliveira (2001)
Acetic Acid	4.351×10^{-4}	Oliveira (2001)

3. MATERIALS AND METHOD

The first part of the present work focused on the steady-state simulation of a typical industrial unit, such as that shown in Fig. 1. The simulations were conducted using the commercial software Aspen Plus, by Aspen Tech, and aimed to investigate the operation of the industrial system by analyzing the effects of operational conditions upon the concentration profiles in columns A, B and B1. The second part was conducted using the module Aspen Dynamic, by Aspen Tech, so that some control strategies could be tested in order to keep the acetaldehyde level in bioethanol within the required limits. In this way the acidity increase of the biofuel during storage period could be prevented. The package RADFRAC for simulating distillation columns within Aspen Plus was selected in order to represent the whole industrial system. This package uses a rigorous method of calculation for solving the set of balance and equilibrium equations based on the MESH system described in detail by KISTER (1992). According to a detailed and rigorous analysis (Meirelles et al., 2008), previously performed for the vapor-liquid equilibrium of the binary mixtures formed by the wine components (Table 1), the NRTL model and a corresponding set of parameters were selected for representing the liquid phase non-ideality and the Virial equation, together with the approach based on HAYDEN-O'CONNELL (1975), for estimating the vapor phase fugacities.

Wine was fed into column A (see Fig. 1) with a mass flow of 202542 kg/h, at 94 ºC and the composition given in Table 1. The ethanol concentration in the bottom product of column A was fixed in 200 mg/kg (0.02 mass %) and the mass flow of bioethanol was varied around 14000 kg/h with at least 93 mass% of ethanol, corresponding to an approximately daily production of 465 m^3. In the bottom of column B1 the ethanol concentration was not fixed but it level was ever less than 200 mg/kg. In accordance with industrial information, the fusel stream mass flow was fixed in 41 kg/h, almost 0.3% of the bioethanol mass flow. Reflux and bioethanol stream mass flows were varied and the corresponding concentration profiles investigated.

For the dynamic simulation, in a first step a PID controller was used with the aim of controlling the acetaldehyde content (controller variable) in bioethanol, by manipulating the reflux stream and bioethanol mass flows (manipulated variables), after a perturbation in acetaldehyde concentration was imposed to the feed stream (wine). In a second step, the degassing system was tested to control the acetaldehyde content in bioethanol.

The degassing system is based on the association of two or more partial condensers in the top of column B. The vapor stream of each partial condenser is fed into the next one and the liquid streams return to the top of the column. In the last condenser, a small amount of vapor phase is withdrawn as a DEGASSING stream. According to the maximum level of allowed acetaldehyde contamination, the temperature of the last condenser can be varied and more or less mass of degassing can be generated.

4. RESULTS AND DISCUSSION

Almost all bioethanol fed into column A was stripped from the liquid phase and transferred via the PHLEGMA stream to column B. Except for acetic acid, all congeners (minor components in wine) are concentrated in the PHLEGMA stream and also transferred to column B. Fig. 2 shows the concentration profiles of water and ethanol along columns B (stages 1, condenser, to 46) and B1 (stages 47 to 65, reboiler). An alcoholic graduation of 93.0 mass% was obtained. Note that this value is within the concentration range required by the Brazilian legislation for hydrous bioethanol (Table 2).

Fig. 3 shows the concentration profiles for high alcohols. High alcohols, containing mainly isoamyl alcohol, are extracted from column B as a side stream named FUSEL stream.

Fig. 4 shows the concentration profile for acetaldehyde and acetic acid in columns B and B1. Acetaldehyde profile

indicates that this contaminant is concentrated in the biofuel stream.

ANP, the Brazilian National Petroleum Agency, is the public institution responsible for setting quality standards for fuels and biofuels. Copersucar, one of the largest Brazilian trading companies for sugar and bioethanol export, also sets specific quality standards according to the requirements of its clients. Table 2 shows the main specifications for bioethanol according to ANP (AEHC) and Copersucar (H1 and H2), and also some of the results obtained by steady-state simulation of the industrial plant (SIM). According to the simulation results the bioethanol produced fulfil the requirements of the Brazilian legislation and even most of the requirements set by Copersucar.

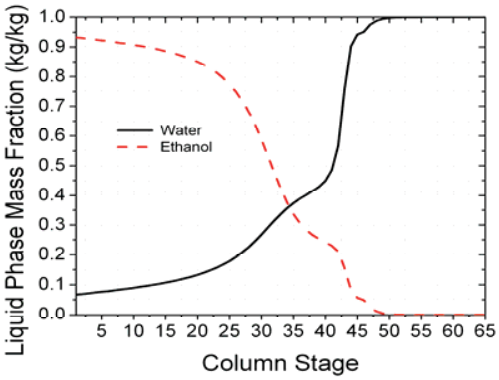

Fig. 2. Concentrations profile of ethanol and water in columns B (stages 1-46) and B1 (stages 47-65).

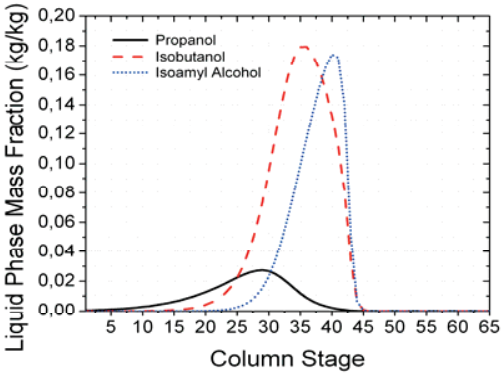

Fig. 3. High alcohols profiles in columns B (stages 1-46) and B1 (stages 47-65).

Acetaldehyde concentration is not a quality parameter fixed by ANP for the biofuel (Table 2). In case of the simulation results, the obtained acidity values, were far below the limit set by the Brazilian legislation. However, during the storage period acetaldehyde can oxidize to acetic acid and deteriorate the biofuel quality, increasing its acidity. If all acetaldehyde content present in the simulated fuel ethanol (Table 2) oxidizes to acetic acid, the product acidity would be increased to 33.5 mg/L. With this value, the biofuel would be outside the standards qualities established by the Brazilian legislation (Table 2). For this reason, the concentration of acetaldehyde in biofusel must be strictly controlled to prevent that the acidity level exceeds the legislation limits along the storage time. On the other hand, Brazil is nowadays the largest bioethanol exporter and the use of this bioproduct is increasing worldwide not only as an alternative energy source as well as an input material for chemical, pharmaceutical, perfume and beverage industries. Although these other uses may require further purification steps, sometimes conducted at the importing country, the Brazilian exporters are opting for defining stricter quality standards, such as the values specified by Copersucar (see Table 2). This highlights the importance of monitoring and controlling the contamination levels of minor components, such as acetaldehyde and high alcohols, in bioethanol.

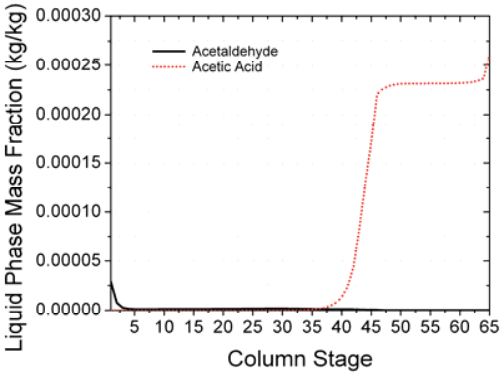

Fig. 4. Acetaldehyde and acetic acid profiles in columns B (stage 1-46) and B1 (stages 47-65)

Table 2. Bioethanol quality standards, ANP (AEHC), Copersucar (H1 and H2) and the simulation results (SIM).

Spec.	Unities	Bioethanol			
		AEHC	H1	H2	SIM
Alcoholic Graduation	mass%	92.6-93.8	≥ 92.8	≥ 93.8	93.2
Acidity (Acetic Ac.)	mg/L	≤ 30	≤ 20	≤ 10	Trace
Density (20ºC)	kg/m^3	807.6-811.0	-	-	807.1
Acetaldehyde	mg/L	-	≤ 50	≤ 10	24.6
High Alcohols	mg/L	-	≤ 400	≤ 50	332.5

Data on the mechanism and kinetics of acetaldehyde oxidation to acetic acid can be found in WANG et al. (1992) and XU et al. (2000). In order to avoid the risk of this oxidation during biofuel storage one of the possible strategies is to reduce acetaldehyde content in biofuel to a minimal value. In the second part of this work, some strategies to control the acetaldehyde content were investigated. All the strategies were based in a PID loop control, with the aim of keeping acetaldehyde concentration in bioethanol constant even if a perturbation increases its content in the wine. Figure 5 shows the simplest configuration of column simulated in the present work. As acetaldehyde is a very light component, the total amount of this substance present in the wine will

contaminate bioethanol if this configuration is used. For this reason no control strategy would be able to avoid an increase of acetaldehyde contamination in bioethanol in case of a slight increase in its concentration in the wine. In fact, attempts to avoid this contamination, by using reflux and/or bioethanol flow, according to the loop control represented in Fig. 5, failed. Thus two alternative solutions are suggested and they include changes in the industrial installation.

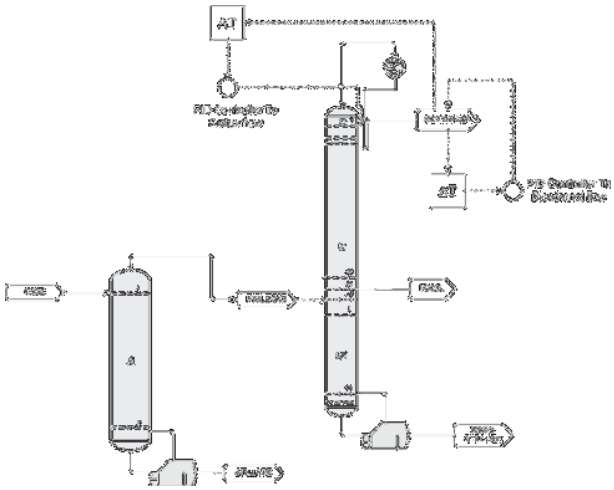

Fig. 5. Loop control for acetaldehyde concentration in bioethanol

The first alternative installation includes a degassing system, as that shown in Fig. 6 and explained above. Such a system makes easier the control of acetaldehyde content in bioethanol. As a very light component, acetaldehyde concentrates in the vapor streams and is eliminated by the DEGASSING stream. Controlling the DEGASSING flow makes possible to eliminate part of the acetaldehyde contamination, although this also causes small losses of the bioproduct.

Fig. 7 shows steady-state results for DEGASSING flow, ethanol mass flow in degassing and acetaldehyde content in bioethanol as a function of the last condenser temperature. The increase of this temperature increases the degassing flow, and by consequence increases the mass flow of ethanol in degassing stream, and decreases the acetaldehyde concentration in the bioethanol. These results show that the control of the temperature of the last condenser in the degassing system can control the concentration of acetaldehyde in the bioethanol. Taking this into account, a simple PID controller was developed to control the temperature of the last condenser of the degassing system (see Fig. 6). In this loop control, the controller variable was the acetaldehyde content in bioethanol and the manipulated variable was the temperature of the last condenser. The stack point (maximum level of the acetaldehyde in bioethanol) was fixed in 25.3 ppm (2.530×10^{-5} kg/kg). With this concentration, even if all the acetaldehyde oxidize to acetic acid, the mass of acid formed will not be sufficient to exceed the acidity maximum level fixed by ANP (Table 2). In order to better represent the industrial process, carbon dioxide (CO_2) produced during fermentation was included in the wine composition in a concentration of 0.0011 kg/kg. This value was determined assuming that the alcoholic fermentation industrial process is performed in closed vat with light over pressure (600 to 800 mm of water) and temperatures close to 35 °C. Considering that gas phase inside the vat is composed of saturated CO_2 with vapors of ethanol and water, the NRTL model and the Henry constant for CO_2 (Dalmolin et al., 2006) was used in order to estimate the solubility of CO_2 in the wine. The estimated values varied within the range 1050 to 1150 mg/kg. The acetaldehyde concentration in the wine was increased to 2.100×10^{-6} kg/kg and after 3 hours decreased to 1.900×10^{-6} kg/kg, in order to demonstrate the efficiency of the degassing system. The concentration of the other wine components were kept constant in the values indicated in Table 1, except for water whose value was appropriately adjusted. The results are present in the Fig. 8.

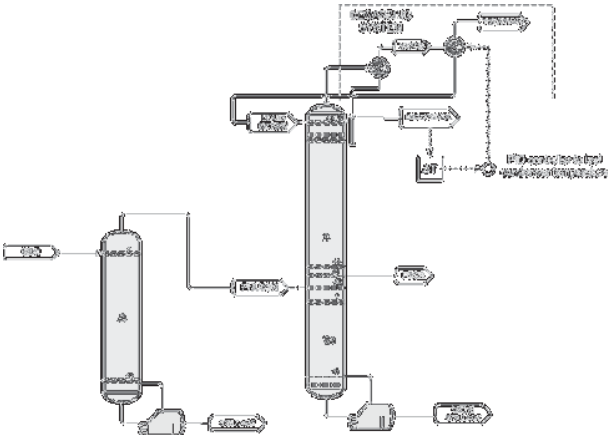

Fig. 6. Industrial plant with degassing system

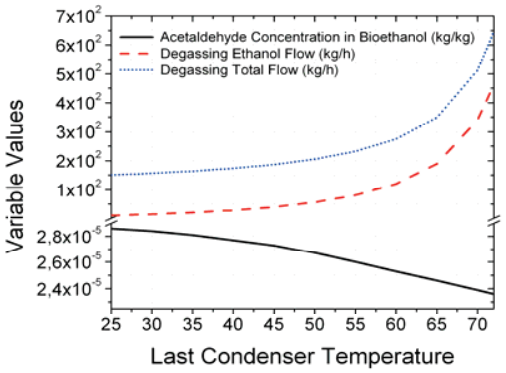

Fig. 7. Acetaldehyde content and degassing flow as a function of last condenser temperature

As is possible to observe in Fig. 8, the control system based in a PID controller has a good performance in avoiding a contamination of acetaldehyde in bioethanol. A direct dependence between the controller variable (biofuel acetaldehyde concentration) and the manipulated variable (last condenser temperature) was observed. In case of an

increase of acetaldehyde concentration in the wine the PID controller increases the last condenser temperature and, in consequence, a large degassing flow is withdrawn of the equipment. The acetaldehyde level in bioethanol reaches safe values after 40 minutes and stabilizes after one hour. The reverse process occurs when the concentration of acetaldehyde in wine is decreased (see Fig. 8).

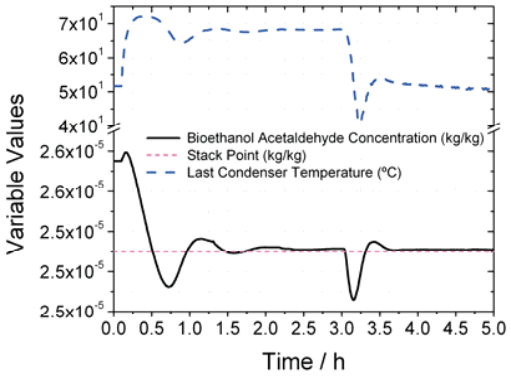

Fig. 8. Results of PID controller in degassing system (industrial installation)

Despite this good performance, the configuration with a degassing system may exhibit some difficulties in case of a large wine contamination with acetaldehyde. Large concentrations of acetaldehyde in wine require larger flow of degassing stream in order to reduce the biofuel contamination. A larger degassing mass flow increases ethanol losses (see Fig. 7). Therefore, the total loss of the ethanol in the production system can reach levels higher than those accepted by industry. An alternative configuration better for a wine with larger acetaldehyde contamination is the pasteurized bioethanol installation shown in Fig. 9. In this kind of installation two news columns (D and A1) are added to the original system. These columns concentrate the major part of wine volatile compounds, including acetaldehyde, and eliminate part of them via the SECOND ALCOHOL stream withdrawn from the top of column D.

In column B bioethanol is withdrawn from a tray close to the column top. In the top of Column B a further SECOND ALCOHOL stream is also withdrawn. According to Fig. 4 acetaldehyde is concentrated in the trays located close to the top of column B. For this reason streams such as the two SECOND ALCOHOL ones are concentrated in acetaldehyde and other light minor components, for instance ethyl acetate. These contaminants are taken away by the top streams and bioethanol, withdrawn from column B as a side stream, has its acetaldehyde content decreased. On the other hand, small amounts of ethanol are not recovered as the main product (bioethanol), being extracted in those byproduct streams. Such scheme is more appropriate for producing bioethanol from a wine with larger contamination of light components or in case the bioproduct must have a higher purity.

Fig. 10 shows the results of steady state simulations performed for the pasteurized bioethanol installation. For this simulation acetaldehyde concentration in the wine was increased to approximately 10 times the value of the previous simulations (new concentration equal to 1.900×10^{-5} kg/kg), representing a larger contamination, closer to the industrial wine, according to Oliveira (2001).

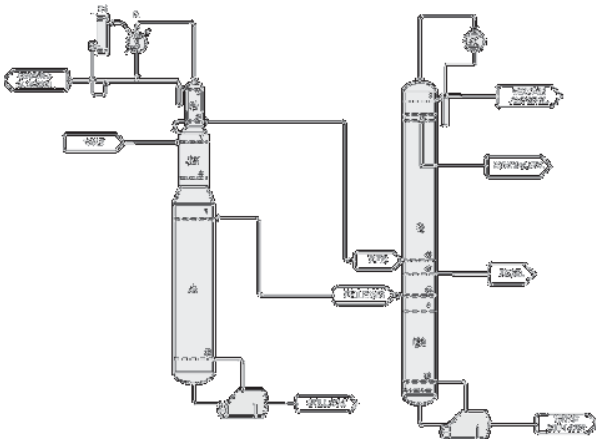

Fig. 9. Industrial plant for bioethanol with second alcohol streams.

The main objective of those simulations was to show that, varying the mass flow of the second alcohol stream in column B, it is possible to reduce considerably the concentration of acetaldehyde in bioethanol. According to Fig. 10, the increase of the mass flow of the second alcohol stream reduces acetaldehyde contamination without influencing, in a significant way, the bioproduct alcoholic graduation. In these simulations only the second alcohol stream in top of column B was varied, keeping the second alcohol stream in top of column D fixed at the value 400 kg/h.

This means that a relative larger acetaldehyde contamination is contained in the second alcohol stream, a result that makes easier the control of this contamination in the main product (pasteurized bioethanol) by means of the degassing system. For this reason a loop control similar to that of Fig. 6, connecting the acetaldehyde concentration in pasteurized bioethanol (controller variable) to the last condenser temperature (manipulated variable), was tested. The wine acetaldehyde concentration was increased to 2.000×10^{-5} kg/kg and the last partial condenser temperature was varied to stabilize the bioethanol acetaldehyde concentration at 2.450×10^{-5} kg/kg. With this value, the problem of acetaldehyde oxidation during storage time was eliminated. The result of this simulation was presented in Fig. 11.

The results show that in almost 2 hours the acetaldehyde concentration reaches the required value although the stabilisation time is approximately 7 hours. This result suggests that the degassing system is an excellent alternative for acetaldehyde control in bioethanol, provided that the wine contamination with acetaldehyde is not too large.

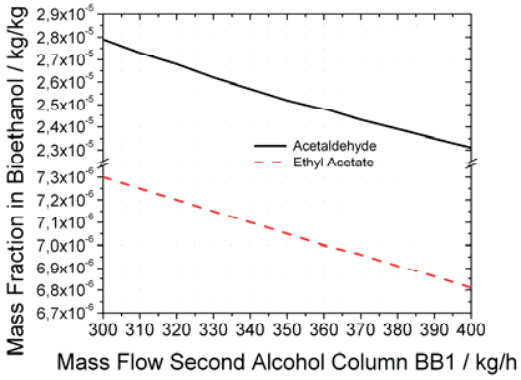

Fig. 10. Volatiles content in bioethanol in function of second alcohol flow of column BB1

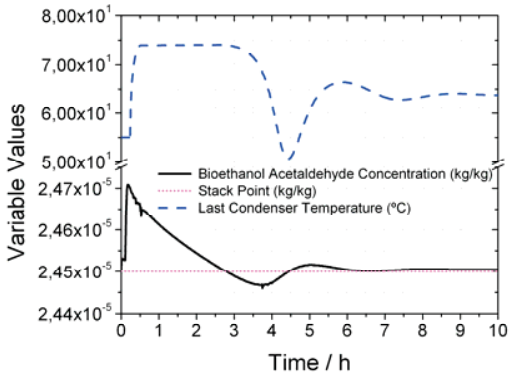

Fig. 11. Results of PID controller in degassing system (pasteurized bioethanol installation)

5. CONCLUSION

Production of bioethanol as a renewable fuel or as an input commodity to be used in other industrial branches requires the reduction and control of several contaminants contained in the fermented must. In the present work special attention was focused on controlling acetaldehyde contamination. Analyzing the results presented it is possible to conclude that the wine (must) acetaldehyde concentration will determine the type of industrial installation and the type of control to be used to regulate the acetaldehyde in bioethanol and prevent problems with its oxidation during storage. Thus, for wine with less than 2.0×10^{-6} kg/kg of acetaldehyde, the industrial installation without degassing system is appropriate. For wine concentrations within the range 2.0×10^{-6} to 2.2×10^{-6} kg/kg, the degassing system is required. In case of wine concentrations within the range 2.2×10^{-6} to 2.0×10^{-5} kg/kg, the pasteurized bioethanol installation is the most appropriate one. For concentrations within the range 2.0×10^{-5} to 2.2×10^{-5} kg/kg the degassing system should be included in the pasteurized bioethanol installation. Finally, for musts with higher acetaldehyde concentration ($\geq 2.2\times10^{-5}$ kg/kg) the pasteurized bioethanol installation with a PID controller to regulate the mass flow of second alcohol is probably the best way to prevent problems with acetaldehyde oxidation during storage.

ACKNOWLEDGMENTS

The authors acknowledge the financial support of FAPESP (05/53095-2 + 08/56258-8), CNPq (306250/2007-1) and CAPES.

REFERENCES

Boscolo, M., Bezerra, C.W.B., Cardoso, D.R., Neto, B.S.L., and Franco, D.W. (2000). Identification and Dosage by HRGC of Minor Alcohols dnd Esters in Brazilian Sugar-Cane Spirit. *Journal of The Brazilian Chemical Society*. 11(1), 86.

Cardoso, D.R., Lima-Neto, B.S., Franco, D.W., Nascimento, R.F. (2003). Influência do Material do Destilador na Composição Química das Aguardentes de Cana – Parte II. *Química Nova*, 26(2), 165.

Dalmolin, I., Skovroinski, E., Biasi, A., Corazza, M.L., Dariva, C., Oliveira, J. V. (2006). Solubility of carbon dioxide in binary and ternary mixtures with ethanol and water. *Fluid Phase Equilibria*. 245, 193-200.

Decloux, M. and Coustel, J. (2005). Simulation of a neutral spirit production plant using beer distillation. *International Sugar Journal*, 107 (1283), 628-643.

Gaiser, M., Bell, G. M., Lima, W., Roberts, N. A., Faraday, D. B. F., Schulz, R. A., Grob, R. (2002). Computer simulation of a continuous whisky still. *Journal of Food Engineering*, 51(1), p. 27-31.

Hayden, J. G. and O'Connell, J. P. (1975) A Generalized Method for Predicting Second Virial Coefficients. *Ind. Eng. Chem.. Process Des. Dev*., V 14(3), 209-216.

Kister. Henry Z. (1992). *Distillation Design*. United States: McGraw-Hill. Inc. 709 p.

Marquini, M.F., Maciel Filho, R., dos Santos, O.A.A., Meirelles, A.J.A., Jorge, L.M.M. (2008). Reduction of Energy Comsumption and Effluent Generation in Ethanol Distilleries., 09/2008, *XVII Brazilian Congress on Chemical Engineering - COBEQ - 2008*,Vol. 1, pp.1-3, Recife, PE, Brazil.

Meirelles, Antonio J.A., Batista, E.A.C., Scanavini, H.F.A., Batista, Fabio R.M., Ceriani, R. Distillation Applied to the Processing of Spirits and Aromas. In: M. Angela A. Meireles (Ed.). *Extracting Bioactive Compounds: Theory and Applications*. New York: CRC Press, 2009. Chapter 3, 75-136.

Oliveira, E. S. (2001). PhD thesis (in potuguese), Faculty of Food Engineering, University of Campinas, Campinas, Brazil.

Wang, S.Q., Zhang, R.F., Wang, J.C. (1992). Mathematical model of the process for the oxidation of acetaldehyde to acetic acid. *Computers in Industry*, 18 (2), 213-219.

Xu, L., Boring, E., Hill, C.L. (2000). Polyoxometalate-Modified Fabrics: New Catalytic Materials for Low-Temperature Aerobic Oxidation. *Journal of Catalysis*, 195(2), 394-405.

Process Monitoring and Diagnosis

Poster Session

Sensor fault detection and isolation for single, multiples and simultaneous faults: Application to a waste water treatment process

Fragkoulis D. * **, Roux G. * ** and Dahhou B. * **

* LAAS-CNRS ; Université de Toulouse ;
7, Avenue du Colonel Roche, F-31077 Toulouse, France (e-mail: roux@laas.fr).
** Université de Toulouse;

Abstract: In this paper, sensor fault detection, isolation and identification model-based approach is designed. We introduce a new state variable so that an augmented system can be constructed to treat sensor faults as actuator faults. The approach uses the model of the system and a bank of adaptive observers to generate residuals. Structured residuals are defined in such way to isolate the faulty sensor after detecting the fault occurrence. The advantage of this method is that we can treat single, multiple and simultaneous sensor faults. In this study, we consider that only abrupt faults in the system sensor can occur. The proposed strategy is validated by simulation results of a nonlinear model of a waste water treatment process.

1. INTRODUCTION

In all industrial processes the reliability and the security of the system is a very important task. A fault may occur in all possible location, such as actuators, sensors and system's parameters. Fault detection techniques could prevent from all the undesirable consequences. In order to improve efficiency, the reliability can be achieved by fault-tolerant control, which relies on early fault detection, using fault detection and isolation (FDI) procedures. So FDI is becoming an attractive topic. Model based fault detection and diagnosis systems have found extensive use because of the fast response to abrupt failure and the implementation of the model based FDI in real-time algorithms. A comprehensive review of the different methods for FDI and their applicability to a given physical system has been presented in ([Iserman, 1994] and [Venkatasubramanian *et al.* 2003]). A variety of effective methods can be used to realize FDI, such as differential geometric approach [De Persis and Isidori 2001], sliding mode observer ([Edwards and Spurgeon 1994] and [Xing-Gang and Edwards 2005]), and adaptive control technique ([Frank, 1994] and [Hammouri *et al.* 1999]).

The progressive deterioration of the water resources and the great quantity of polluted water produced in the industrialized companies, give to the waste water treatments (WWT) a great importance in the safeguarding of water quality. The new directives and regulations (the directing 91/271/CEE referring itself to the European countries) impose the adoption of specific indices for the quality of treated waste water. Taking into account the current ecological problems, it is realistic to believe that this tendency will continue. At the same time, the existing factories increase thanks to the growth of the urban sectors and this situation requires more effective treatments of the used water. Consequently, we want that such an industry, almost always, operates with the maximum effectiveness.

Generally, the recent evolution of the legislation of some countries, about the use of surface or subsoil waters, is such that the total reuse of the water used in the processes became a very important issue. So the waste water treatment became a part of the production process, where the quality control of effluent is very important. Since the weak operation of the treatment can carry out to an important loss of production and to ecological problems.

The paper is organized as follows. In Section 2, we present the class of the nonlinear systems that we study, the filter that we apply to form the new extended system and the formulation of the fault problem. Then we give the principle of the fault detection and isolation scheme and the synthesis of the observer. Section 3 describes the waste water treatment process which is used to show the effectiveness of the proposed method. In Section 4, we give simulation results that illustrate the method for single, multiple and simultaneous faults. Conclusion and perspectives end the paper.

2. EXTENTED MODEL AND PROPOSED METHOD

2.1 Filter for the system's output

We consider the following class of nonlinear systems:

$$\begin{cases} \dot{x} = f(x) + g(x)u \\ y = Cx \end{cases} \qquad (1)$$

where $f(x)$ is a nonlinear vector function from $\Re^n$ to $\Re^n$, $g(x) \in \Re^{n\times m}$ is a matrix function whose elements are nonlinear functions, $C \in \Re^{p\times n}$ is a matrix, $u \in \Re^m$ is the input vector and $y \in \Re^p$ is the output vector. Throughout

this paper, we assume that only constant sensor faults can occur $y_j^f(t) = y_j(t) + f_{sj}$, that is $y_j^f \equiv \theta_j$ for $t \geq t_f$, $j \in 1, 2, \cdots p$, and $\lim_{t\to\infty} | y_j(t) - \theta_j | \neq 0$, where θ_j is a constant and $y_j^f(t)$ is the actual output of the j^{th} sensor when it is faulty, while $y_j(t)$ is the expected output when it is healthy.

In [Chee and Edwards 2003] the authors presents a method for the linear system where the output vector passes through two orthogonal matrices $T_{r,1}$ and $T_{r,2}$. At the same time these matrices make the separation of the outputs at $y_1 \in \Re^{p-h}$ and $y_2 \in \Re^h$ where y_1 are the outputs without fault and y_2 are the outputs with a fault. The same manipulation of the outputs for the nonlinear system (1) is impossible but there is a similar method proposed in [Chen and Saif 2006] for the class of the nonlinear systems (1) that we presented above. We will apply to the output vector y a filter of the form:

$$\dot{\xi} = A_f \xi + B_f y \quad (2)$$

Where the state vector is $\xi \in \Re^p$, we select $A_f \in \Re^{p\times p}$ as a Hurwitz matrix and $B_f \in \Re^{p\times p}$ is chosen as an invertible matrix. We form the new input $w = \begin{bmatrix} u \\ y \end{bmatrix}$ and we define the extended system of the form:

$$\dot{z} = \underline{f}(x, \xi) + \underline{g}(x) w \qquad (3)$$

Where the vector $z \in \Re^{n+p}$ is the new state $z = \begin{bmatrix} x \\ \xi \end{bmatrix}$, $\underline{f}(x, \xi) \in \Re^{n+p}$ is a vector with nonlinear and linear elements ($\underline{f}(x, \xi) = \begin{bmatrix} f(x) \\ A_f \xi \end{bmatrix}$). The matrix $\underline{g}(x) \in \Re^{(n+p)\times(m+p)}$ is a matrix with nonlinear and linear elements ($\underline{g}(x) = \begin{bmatrix} g(x) & 0_{n\times p} \\ 0_{p\times m} & B_f \end{bmatrix}$) and finally the vector $w \in \Re^{m+p}$ is the new input vector. So, as we have seen with this transformation we have extended the system and the initial sensor fault problem has become, after the transformation, an actuator fault problem. The output vector y of the system has become a part of the input vector w of the new system. Based on the approach developed in [Blanke *et al.* 2003], it is easy to build the corresponding extended faulty model:

$$\begin{cases} \dot{z} = \underline{f}(x, \xi) + \sum_{j\neq l} \underline{g}_j(x) w_j + \underline{g}_l(x) \theta_l \\ y = \begin{bmatrix} C & 0_{p\times p} \end{bmatrix} z \end{cases} \qquad (4)$$

where we have a fault in the l^{th} actuator and $\underline{g}(x) = [\underline{g}_1(x) \cdots \underline{g}_{m+p}(x)]$.

The new system input as we already mentioned is the vector *w*. This vector includes the inputs and the outputs of the system (1), $w^T = [u_1 \ \cdots \ u_m \ | \ y_1 \ \cdots \ y_p]$. In this paper, we are focusing only in sensors faults. As the method that it will be used is an actuator fault detection and isolation method, the inputs of the new vector *w* that we are interested are from w_{m+1} to w_{m+p}.

2.2 The fault detection and isolation scheme

After this transformation, the problem has become an actuator fault detection and isolation problem where the faults have the same properties with the ones presented in the begin of the subsection *2.1*; only that in the place of the output y we have the input w. For the fault detection and isolation, we will develop a bank of p adaptive observers, where $\hat{\theta}$ is the fault estimation [Chen and Saif 2005]. The form of the adaptive observer that we will use in this bank for the l^{th} actuator is:

$$\begin{cases} \dot{\hat{z}}_l = \underline{f}(x, \xi) + \sum_{j\neq l} \underline{g}_j(x) w_j + \underline{g}_l(x) \hat{\theta}_l + H_l(\hat{z} - z) \\ \dot{\hat{\theta}}_l = -2\gamma(\hat{z}_l - z)^T P_l \underline{g}_l(x) \quad m+1 \leq l \leq m+p \end{cases} \qquad (5)$$

Where H is a Hurwitz matrix that it can be chosen freely, γ is a design constant and P is a positive definite matrix. We can calculate the matrix P and H with the help of the following Lyapunov equation:

$$H^T P + PH = -Q \qquad (6)$$

where Q is a positive definite matrix that it can be chosen freely. The analysis of the method can be found in [Chen and Saif 2005] along with all the proofs and details. An application of this method for an actuator fault detection and isolation to the same system that we studied can be found in [Fragkoulis *et al.* 2007]. The residual r_i that it is proposed in this paper is the difference between the estimation of the fault $\hat{\theta}_i$ determined in (5) and the output of the system so:

$$r_i = \hat{\theta}_{m+i} - y_i, i \in [1 \ldots p] \quad (7)$$

The residuals are designed to be sensitive to a fault that comes from a specific sensor and as insensitive as possible to all the others sensor faults. This residual will permit us to treat not only with single faults but also with multiple and simultaneous faults. To facilitate the isolation of the fault the structured residual will be used, and in particular the Boolean method introduced in [Gertler 1998] with simple thresholds δ_{si}.

$$\varepsilon_i(t) = \begin{cases} 1 & if \quad |r_i(t)| \geq \delta_{si} \\ 0 & if \quad |r_i(t)| < \delta_{si} \end{cases} \qquad (8)$$

$$\Phi = [\varepsilon_1(t)\ \varepsilon_2(t) \ldots \varepsilon_p(t)] \quad (9)$$

$$r_s \leftarrow \Phi f_s \qquad (10)$$

So the five steps for this new FDI scheme are:

1. we determine the filter as in (2) for the augmented space.
2. we form the new faulty model (4) and the new input vector *w*.
3. we build a bank of p observers as in (5) for the detection and isolation of the fault.
4. we generate the residuals r_i (7).
5. from the thresholds δ_{si} we elaborate the structural matrix Φ and then
6. from (10) we generate the structured residuals r_s for the fault isolation and identification.

3. WASTE WATER TREATMENT PROCES MODEL

The process of water treatment by activated sludge, invented in Manchester in 1914, industrially reproduced the purifying effect of the rivers, and became the principal current process of purification. It consists of an aerobic biological system in which the biological floc (biofloc) are continuously recycled and given in contact with organic waste water in the presence of oxygen. Oxygen is usually provided by bubbles of air, insufflated in the mixture of liquid and sludge under conditions of turbulence or by units of surface mechanics or by other aeration types.

A plant of water purification with activated sludge generally consists of a system of treatment in two phases (figure 1). The first phase of the treatment consists in eliminating pollutant in suspension, which mainly includes the degreasing, the de-sanding and the de-oiling. Now, we present the second phase which can be described by three reactors placed in cascade. The first reactor called primary decanter receives polluted water coming from the urban or industrial environments. Water penetrates then in a second reactor, called aerated basin, which constitutes the heart of the plant. The treatment is based on setting in contact of a bacterial population (micro-organisms) with organic matter contained in the effluent to treat. In the aerated basin occur initially a fast adsorption and flocculation of the colloidal matters in suspension and of the organic matter soluble by the activated sludge. Then there is a progressive oxidation of a synthesis of the adsorbed organic matter and of the extracted organic matter. Finally, water undergoes a last treatment in the third reactor, called settling tank. This one delivers purified water after the decantation of sludge. A part of this latter is recycled in the aerated basin (recycled sludge) and sludge in excess is evacuated for a suitable external treatment.

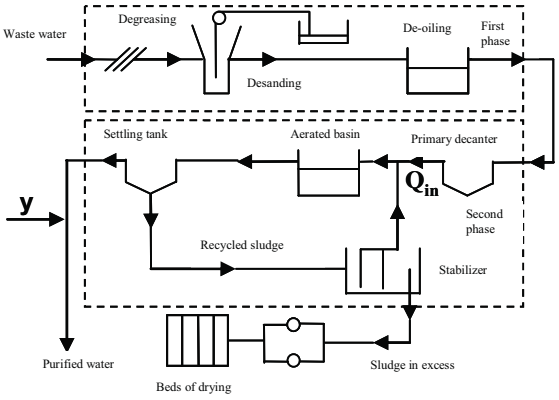

Figure.1 Waste water treatment process

The mathematical model for the activated sludge process (aerated basin and settling tank) is based on the equations, resulting from mass balance considerations, carried out on each of the reactant of the process.

$$Variation = \pm Conversion + Feeding - Drawing\ off$$

All the details about the system and the values of the model parameters can be found in ([Nejjari 2001] and [Fragkoulis *et al.* 2007]). The FDI scheme will monitor the sensors S_I, S_S, X_I, X_S, X_H and S_O, measuring the output vector y of the settling tank (cf. figure 1), by using a bank of adaptive observers. The algorithm for this model is constituted by a bank of six adaptive observers for the fault detection, isolation and identification. More details about the observer synthesis can be found in [Fragkoulis *et al.* 2008].

4. SIMULATION RESULTS

In this section, we will give the results obtained from the developed method for one or more sensor faults. We have to mention that in the case of multiple and simultaneous faults, while the second fault occurs the first fault still acts in the system. The banks of adaptive observers run simultaneously with the system. The considered installation is a closed loop system. So the presence of the controller makes the sensor fault problem more complex. In this case, the fault affects not only the faulty sensors but also the system's dynamic (the other outputs of the system). The sampling period is one sample per hour, the value of all the constant thresholds are $\delta_{si} = 0.5$. Finally we have to mention that all the outputs and so all the faults are in *mg/l*.

4.1 Single fault

We have applied a fault with magnitude $f_{s5} = -2.2\, mg/l$ at time $t = 50$ days in the fifth sensor X_H. In Figure 2, we present the six residuals r_i associated to the six observers. The six residuals in the begin needs a short time period to

converge. This time depends on the initialisation time of the observer's bank, so as to be ready for a fault detection and isolation. After, they reach a constant value and stays there until the fault occurrence.

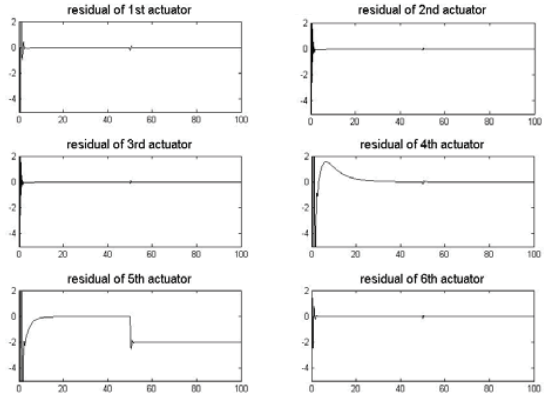

Figure.2 Residuals r_i for a single fault

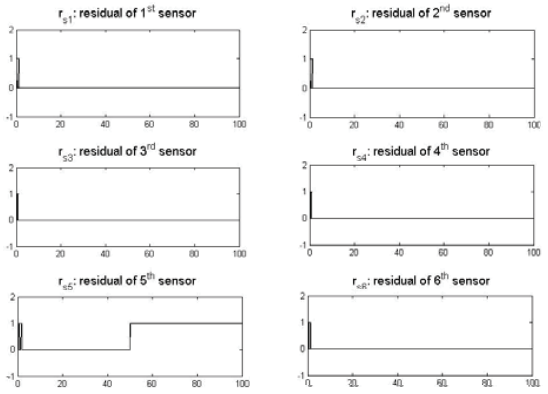

Figure.3 Structured residuals r_{si} for a single fault

At time $t = 50$ days, we can see that the residual of all the six observers leave zero but after a very short period (one day maximum), all of them return to their initial values, except from the residual associated to the fifth observer that corresponds to the output X_H that it takes a new constant value and remains there. In figure 3 we present the structured residuals for this fault. As expected all the residuals stay at zero except from the residual r_{s5} associated to the fifth sensor that at time $t = 51$ days takes and stays at the value "1". Thus, this fact indicates that this is the faulty sensor. Therefore, we isolate the faulty sensor correctly and rapidly enough. As we already mention, this method not only isolates the fault but also identify its value, which can be used for the system reconfiguration. In this case, the actual value of the fault is $f_{s5} = -2.2\, mg / l$ and the estimated value is $\hat{f}_{s5} = -2.1\, mg / l$, so we had identified the fault very accurately.

4.2 Multiple faults

We have applied a constant fault with magnitude $f_{s3} = -5\, mg / l$ at time $t = 50$ days in the third sensor X_I and one with magnitude $f_{s1} = -3\, mg / l$ in the first sensor S_I at time $t = 60$ days. The fault at the third sensor is still occurred when the fault at first sensor has been introduced. Figure 4 shows, the six residuals associated to the observers, where after the initialisation, they have a constant value until $t = 50$ days. There, all the residuals leave their initial values and only the residual associated to the third observer that corresponds at the third sensor stays to the new value. The other five residuals return to their initial values.

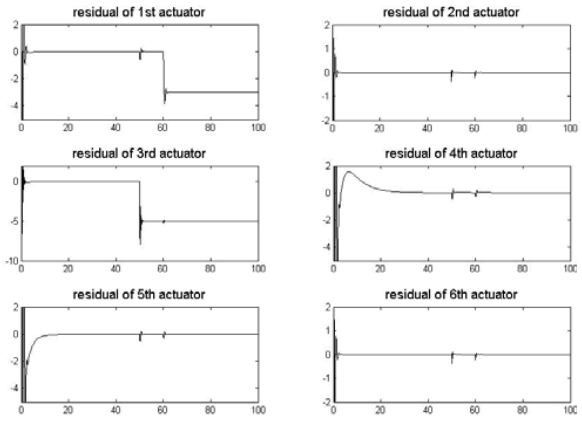

Figure.4 Residuals r_i for multiple faults

At time $t = 60$ days, where the second fault has been entered, the residual that corresponds to the first sensor S_I change from his initial value. It stays at the new value but the other five residuals leave their value and returns to them after a short time period. The third residual, which corresponds to the third sensor where the first fault still occurs, has not been affected by the new fault.

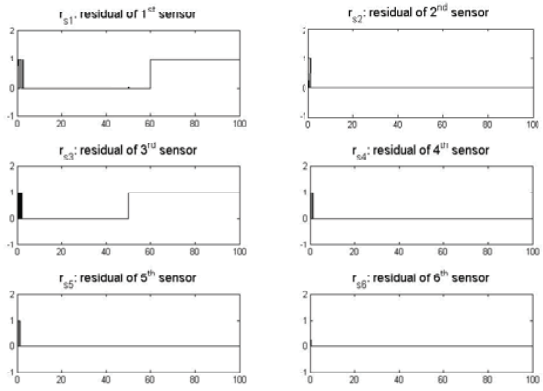

Figure.5 Structured residuals r_{si} for multiple faults

In figure 5, we can see the structured residuals where only the residuals r_{s3} and r_{s1} at time $t = 51$ days and $t = 61$ days respectively leave zero and stay at their new value "1". More generally each fault affects only the corresponding residual and the isolation of the multiple faults has been done. For the fault identification we have: the estimation of the first fault is $\hat{f}_{s3} = -4.5\, mg/l$ and the actual value is $f_{s3} = -5\, mg/l$; the estimation of the second fault is $\hat{f}_{s1} = -2.85\, mg/l$ and the actual value is $f_{s1} = -3\, mg/l$. So we have a good estimation of the fault, not only for the first one where we have a single fault but also for the second one, the multiple fault case.

4.3 Simultaneous faults

We illustrate the case where more than one faults occur at the same time on the system or briefly the simultaneous faults. We have applied two faults: one on the fourth sensor X_S with magnitude $f_{s4} = -13\, mg/l$ and one on the sixth sensor S_O with magnitude $f_{s6} = -2\, mg/l$ at the same time $t = 50$ days.

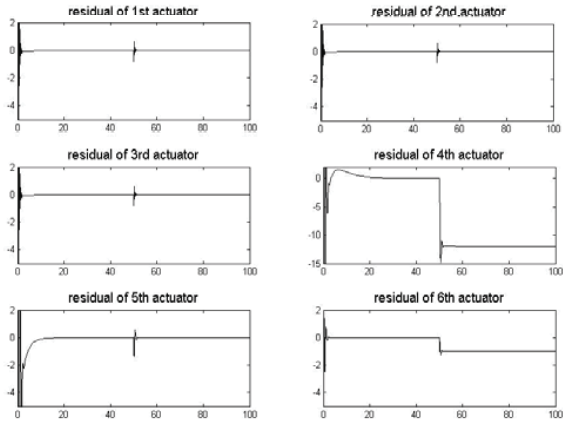

Figure.6 Residuals r_i for simultaneous faults

In Figure 6, we give the residuals associated to the observers and we can see that their values are equal to a constant value until $t = 50$ days where the two faults occur on the system. At that time, all the residuals leaves their initial values and only the residual associated to the fourth observer that correspond to the fourth sensor and the residual associated to the sixth observer that correspond to the sixth sensor stays to their new value; the other four residuals returns to their initials values. Figure 7 presents the structured residuals where only the residuals r_{s4} and r_{s6} leaves zero at time $t = 51$ days, therefore we isolate the two faulty sensors. The identification of the two faults is quite accurate, so for the fourth sensor the estimation is $\hat{f}_{s4} = -12.5\, mg/l$ and for the other one the estimation is $\hat{f}_{s6} = -1.8\, mg/l$.

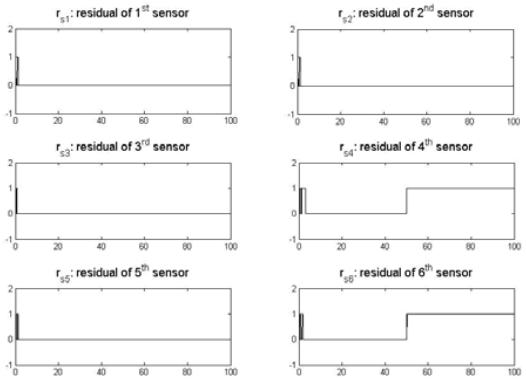

Figure.7 Structured residuals r_{si} for simultaneous faults

4.4 Single fault with real data

We will present the case where the input Q_{in} which is the flow rate input of the aerated basin (cf. figure 1) take his values from a file with real data. These data are collected from a benchmark installed in Terrassa Spain [Nejjari 2001], while the other three inputs have a constant value as in reality. Thus a single fault occurs in one of the six sensors and the method's validity will be presented. In figure 6 we present the input Q_{in}.

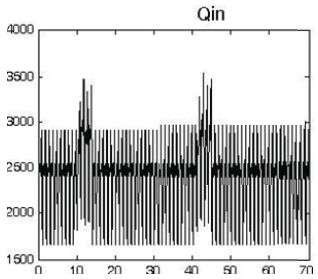

Figure.8 Input Q_{in} with real data

The duration of these data is 70 days and during this time we have two intermittent perturbations, one at the 9th day until the 13th day and another one at the 40th day until the 45th day, caused by the rain. A single fault with magnitude $f_{s4} = -15$ has been occurred at time $t = 50$ days in the fourth sensor X_S.

In figure 9, we show the six residuals associated to the six sensors. As we can see the two perturbations that occurred on the system have a little influence on them. Mainly the first, fourth and fifth residuals have been a little bit affected by them, but the effect can not be misjudged as a fault as long as the residuals remain in the zone defined by the two thresholds δ_{si}. The structured residuals, figure 10, stay at zero during the perturbations.

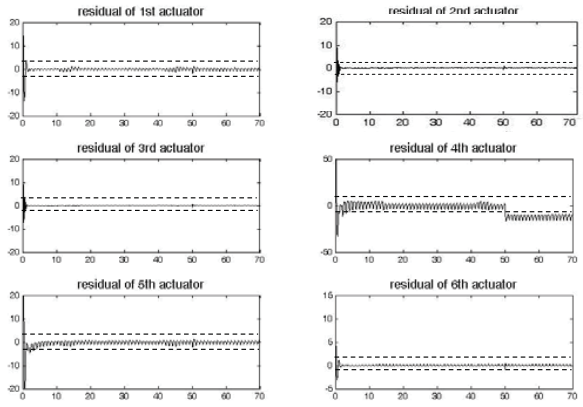

Figure.9 Residuals r_i for single fault with real data

Then at time $t = 50$ days the fourth residual, in both figures, indicates us that there is a fault in the fourth sensor. The simple residual leaves his initial value and gives us the estimation of the fault and the structured residual takes the value "1", so we can easily conclude the source of the fault. For the estimation of the fault we have to use the mean value on a sliding window due to the fact that we have a small oscillation of the value; this mean value is $\hat{f}_{s4} = -16\, mg/l$. In this case the thresholds value is $\delta_{si} = 2$ and they are chosen empirically, also we have to mention that the use of structured residuals facilitates the automatic isolation.

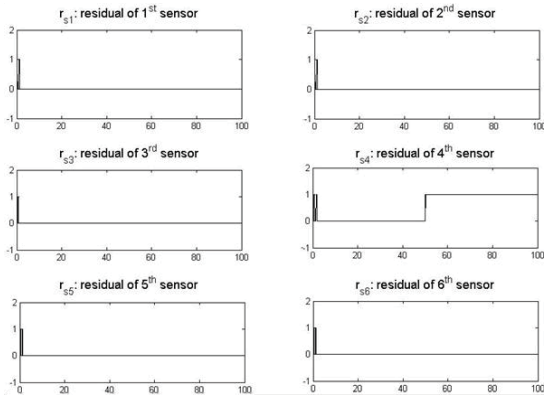

Figure.10 Structured residuals r_{si} for single fault with real data

5. CONCLUSIONS

In this paper, a new method, for sensor fault detection isolation and identification, based on nonlinear observers has been developed. We have reformulated the initial sensor fault problem, by using a transformation filter, to an actuator fault problem. We have designed a known bank of adaptive observers to treat the FDI procedure. Simulation results illustrate the effectiveness of the method for the isolation of single faults, multiple and simultaneous faults. Finally we have validated the proposed method with real data collected from a waste water treatment process benchmark. Our future considerations are to improve the fault estimation in the case of measurement noise by using a better filtering method of the residual. Finally the comparison with the simple method of adaptive observers and mainly the comparison between the isolation time and the fault identification is one of our highly concerns.

ACKNOWLEDGMENTS

The first author would like to thank his sponsor, the Greek State Scholarships Foundation (I.K.Y.), for the financial support.

REFERENCES

Blanke, M., Kinnaert, M., Lunze, J. and Staroswiecki, M. (2003). *Diagnosis and Fault-Tolerant Control*, Springer-Verlag, Berlin.

Chee, P. T. and Edwards, C. (2003). Sliding mode observers for reconstruction of simultaneous actuator and sensor faults, *Proceeding of the 42nd CDC*, December 9-12, Maui, USA.

Chen, W. and Saif, M. (2005). An Actuator Fault Isolation Strategy for Linear and Nonlinear Systems, *American Control Conference*, June 8-10, Portland, USA.

Chen, W. and Saif, M. (2006). Fault detection and isolation based on novel unknown input observer design, *American Control Conference*, June 14-16, Minneapolis, Minnesota, USA.

De Persis, C. and Isidori, A. (2001). A geometric approach to nonlinear fault detection and isolation, *IEEE Transactions on Automatic Control*, 46(6), pp. 853-865.

Edwards, C. and Spurgeon, S. (1994). On the development of a discontinuous observer, *International Journal of Control*, 59, pp. 1211-1229.

Fragkoulis, D., Roux, G. and Dahhou, B. (2007). Actuator fault isolation strategy to a waste water treatment process, *Conference on Systems and Control*, Mai 16-18, Marrakech, Morocco.

Fragkoulis, D., Roux, G. and Dahhou, B. (2008). Sensor fault detection and isolation scheme for single and multiple faults, *Internal Report LAAS N°08317*.

Gertler, J. J. (1998). *Fault Detection and Diagnosis in Engineering Systems*, Marcel Dekker Inc..

Frank, P. M. (1994). Online fault detection in uncertain nonlinear systems using diagnostic observers: a survey, *International Journal of System Science*, 12, pp. 2129-2154.

Hammouri, H., Kinnaert, M. and EI Yaagoubi, E. H. (1999). Observer based approach to fault detection and isolation for nonlinear systems, *IEEE Transactions on Automatic Control*, 44(10), pp. 1879-1884.

Isermann, R. (1994). On the applicability of Model-based fault detection for technical processes, *Control Engineering Practice*, 2, pp. 439-450.

Nejjari, F. (2001). Benchmark of an Activated Sludge Plant, *Internal report*, Terrassa, Spain.

Venkatasubramanian, V., Rengaswamy, R., Yin, K. and Kavuri, S. N. (2003). A review of process fault detection and diagnosis Part I: Quantitative model-based methods, *Computers and Chemical Engineering*, 27, pp. 293-311.

Xing-Gang, Y. and Edwards, C. (2005). Robust sliding mode observer-based actuator fault detection and isolation for a class of nonlinear systems, *Conference on Decision and Control*, and the *European Control Conference*, Seville, Spain, 12-15 December .

Batch Process Monitoring and Fault Diagnosis Based on Multi-Time-Scale Dynamic PCA Models

Yuan Yao* and Furong Gao**

** Dept. of Chemical and Biomolecular Engineering, Hong Kong University of Science and Technology, Clear water bay, Kowloon, Hong Kong SAR, P. R. China,*
*** Dept. of Chemical and Biomolecular Engineering, Hong Kong University of Science and Technology, Clear water bay, Kowloon, Hong Kong SAR, P. R. China*
(Tel: +852-2358-7139, Fax:+852-2358-0054, e-mail: kefgao@ust.hk).

Abstract: Dynamics are inherent characteristics of batch processes, which can be divided into short time-scale dynamics within a batch duration and long time-scale dynamics across several batches. The interactions between process variables make different types of dynamics confounded. Under such situations, it is difficult to perform efficient fault diagnosis. In this paper, a batch process monitoring scheme is proposed to separate different types of process variations for modeling and perform monitoring and fault diagnosis with multi-time-scale dynamic principal component analysis (PCA) models. Simulation results show that the fault diagnosis efficiency is enhanced.

Keywords: batch process, monitoring, fault diagnosis, principal component analysis, dynamics.

1. INTRODUCTION

In today's industrial manufacturing, batch processes are widely applied to manufacture high-value-added products. To ensure operation safety and product quality, the multivariate statistical monitoring methods, such as multiway principal component analysis (MPCA) (Nomikos and MacGregor, 1994; Nomikos and MacGregor, 1995) which is an extension of principal component analysis (PCA), have been utilized in batch process monitoring and fault diagnosis.

Dynamics are inherent characteristics of batch processes, including short time-scale dynamics within a batch duration and long time-scale dynamics across several batches. Different types of batch dynamics are usually caused by different values of variable response time which measures the time process variables take to react to given inputs. Fast-response variables have small response time constant, while slow-response variables have large values which may be longer than a batch duration. To model batch process dynamics better, several multivariate statistical monitoring methods have been proposed. Batch dynamic principal component analysis (BDPCA) (Chen and Liu, 2002) captures within-batch dynamic information, while two-dimensional dynamic principal component analysis (2-D-DPCA) (Lu, et al., 2005) can model both long and short time-scale dynamics in a two-dimensional (2-D) model structure.

In batch processes, variable correlations always exist. Especially, changes in slow-response variables can also affect fast-response variable trajectories. This makes different types of variable dynamics confounded, and causes difficulties in process fault diagnosis, as shown later. Therefore, it is desirable to have a method which can decouple process variation information according to dynamic time scales and monitor different types of variations separately. Thus, the fault diagnosis efficiency and accuracy can be enhanced.

Several existing multivariate statistical methods can divide process variations into blocks, scales or levels, but none of them can be utilized directly to handle the situation mentioned above. Multiblock PCA or partial least squares (PLS) methods (Westerhuis et al., 1998) group process variables into meaningful blocks and concern both the inner relationship within each block and the inter relationship among blocks. Although the variables with different response time can be divided into different blocks, two kinds of dynamics information are not separated due to variable correlations. Multiscale PCA (Bakshi, 1998) makes use of wavelet analysis techniques to transform each variable signal from time domain to frequency domain, and performs PCA on wavelet coefficients at each scale. However, the different dynamics characteristics of each variable are not taken into consideration. Multilevel component analysis (MLCA) and multilevel simultaneous component analysis (MLSCA) (Timmerman, 2006) separate within-batch variations and between-batch variations. But only the static variations are extracted, while process dynamics are not modeled. Besides, none of the methods reviewed in this paragraph can deal with long time-scale dynamics across several batches.

In this paper, a batch process monitoring scheme is developed. This scheme makes use of variable response time information which can be easily achieved, and separate process variations into different levels corresponding to dynamics time scales. 2-D-DPCA method is adopted to build multi-time-scale models. Thus, faults occurring to a certain level can be accordingly detected with the level model. Then, diagnosis can also be performed in the corresponding level, indicating the causing of the fault more clearly.

The article is organized as following. In section 2, the 2-D-DPCA method is reviewed. Then, a multi-time-scale batch process monitoring scheme is proposed and described detail in section 3. Simulation results are given in section 4. A batch process with both long time-scale and short time-scale dynamics is simulated to compare the monitoring and diagnosis efficiencies between the conventional 2-D-DPCA method and the proposed scheme. Finally, a conclusion is given in section 5 to summarize the paper.

2. TWO-DIMENSIONAL DYNAMIC PCA (2-D-DPCA)

2-D-DPCA method proposed by the authors can model both long and short time-scale batch process dynamics with a parsimonious two-dimensional (2-D) time series model structure together with PCA technique (Lu, et al., 2005).

Process dynamics can be indicated by the correlations between current measurements and lagged measurements. Long time-scale dynamics often behave as a kind of two-dimensional (2-D) dynamics, which means the current measurements are dependent not only on lagged measurements in the past time direction in the same batch, but also on lagged measurements in some past batches. These lagged variables form a region called the support region or the region of support (ROS). In 2-D-DPCA, an expanded data matrix $\tilde{\mathbf{X}}$ is formed by including all the lagged measurements in ROS, together with current measurements. For more details about ROS determination, please refer to Yao et al.'s work (2008).

Suppose $\tilde{\mathbf{X}}$ has been normalized to have unit variances and zero means. PCA algorithm is performed on it:

$$\tilde{\mathbf{X}} = TP^T + E \,. \tag{1}$$

where T and P are score matrix and loading matrix respectively, and E is the residual matrix. The number of scores retained in the score space can be determined using cross-validation (Wold, 1978). Thus, the original process data are divided into two subspaces. Score space extracts systematic variation information, including both 2-D dynamics and cross-correlation information among variables, while normal distributed noises are retained in residual space. Therefore, *SPE* statistic and corresponding control limits can be calculated for process monitoring in residual space. After a fault is detected by the *SPE* control plot, contribution plots with control limits (Westerhuis et al., 2000) are used in fault diagnosis to find the causes of the faults.

When a batch process only has short time-scale dynamics, its ROS is selected as a region containing several steps of lagged measurements in current batch. In such a case, 2-D-DPCA model is similar to BDPCA model (Chen and Liu, 2002).

3. MULTI-TIME-SCALE MONITORING SCHEME

3.1 Motivations

As mentioned in introduction section, in batch processes, fast-response variable trajectories are often affected by disturbances in slow-response variables. Take injection molding process as an example. In that process, temperature variables' response time constants are often longer than a batch duration, while pressure variables response fast. Suppose a disturbance occurs to barrel temperature. It takes a long time for barrel temperature to recover. During this period, the material properties, such as viscosity and density, change gradually due to the temperature change. This further causes slow drifts in pressure variable trajectories, although pressures are fast-response variables. From this example, it can be seen that both short and long time-scale dynamics are confounded in fast-response variable trajectories.

As shown in the simulation example in section 4, such confounding leads to difficulties in fault diagnosis results. Therefore, it is desirable to decouple process variation information into several levels according to dynamic time scales. Then, level models can be built and different types of variations can be monitored and diagnosed separately, so that the fault diagnosis efficiency and accuracy can be enhanced.

3.2 Variable classification

As a kind of external information, variable response time is easy to be estimated from process open-loop tests which are regular steps in controller designs. Such information is used to classify variables into groups. It is the first step of multi-time-scale modeling and monitoring.

In many cases, the variables can be simply divided into two groups. One contains fast-response variables, while the other contains slow-response variables which can cause long time-scale dynamics beyond a batch. In some other situations, it may be desired to further divide the above two groups into sub-groups. Suppose there are M number of variable divided into the fast-response variable group. Take each variable's response time constant as a pattern. The k-means clustering algorithm (Jain et al., 1999) is adopted for partitioning the M number of patterns. The final cluster number is determined automatically with a specified threshold of the minimal distance between two cluster centers or the maximal radius of a cluster. A larger threshold results in fewer variable groups; vice versa. The slow-response variable group can also be further divided in the same way. By doing so, the process variables with similar response time constants are clustered into the same group.

3.3 Multi-time-scale level separation

Without losing generality, first, suppose the process variables are divided into two groups. As discussed in section 3.1, two types of dynamics may confound in the trajectories of the variable in the fast-response variable group. To solve this problem, the operation data in this group should be decomposed into two parts: one part can be explained by the variable measurements in the slow-response variable group, and the other part can not be explained by them and only contains short time-scale dynamics. The level separation is based on the idea of external analysis, which was originally proposed by Takane and Shibayama (1991) and further

discussed by Yoon and MacGregor (2001). Kano et al. (2004) made use of this idea to distinguish faults from normal changes in operating conditions.

Consider a batch process data matrix $\hat{X}(I \times J \times K)$, where I, J, K are the number of batches, variables and time intervals respectively. Unfold this three-way data matrix into a two-way matrix $X(IK \times J)$ by keeping the variable dimension and merging the other two dimensions. Suppose X have been normalized. After variable classification, X can be described as $X = [F \ S]$, where F consists of J_F number of fast-response variables and S consists of $J_S = J - J_F$ number of slow-response variables. To decompose F, regression analysis is performed by regarding S and F as inputs and outputs respectively. If variables in S are independent of each other, the ordinary least square (OLS) regression can be used:

$$\Phi = (S^T S)^{-1} S^T F, \tag{2}$$

where Φ is the regression coefficient matrix. The significance of regression can be tested (Montgomery, 2005) to show whether there are correlations between S and F. If there is no correlation, the levels are naturally seperated. The short time-scale level consists of $D^S = F$, while the long time-scale level consists of $D^L = S$. Otherwise, calculate (3).

$$E = F - S\Phi, \tag{3}$$

where $S\Phi$ contains a part of information in F which is explained by slow-response variable, while the filtered data matrix E dose not contains long time-scale dynamics. When the slow-response variables are not independent, PLS or principal component regression (PCR) can be utilized to avoid the collinearity problem. Thus, the process variation information is separated into two levels according to different time scales of dynamics: $D^S = E$ and $D^L = [S\Phi \ \ S]$.

When there are more than two groups, the time-scale level separation is performed in an iterative way. Unfolded data matrix X is described as $X = \left[X_1^0 \quad X_2^0 \quad \cdots \quad X_C^0 \right]$, where X_i^j is the filtered data matrix of the ith variable group after the jth iteration run in time-scale level separation, consisting of J_i number of variables. When $j = 0$, X_i^j represents the data before performing iteration steps. C is the total number of variable groups, and the variables in X_i^j response faster than the variables in X_{i+1}^j. In the jth run, let $S^j = X_{C-j+1}^{j-1}$ and $F^j = \left[X_1^{j-1} \quad X_2^{j-1} \quad \cdots \quad X_{C-j}^{j-1} \right]$. Φ^j is then calculated in the similar way as (2), and the data are filtered as

$$\begin{aligned} E^j &= F^j - S^j \Phi^j = \left[X_1^{j-1} \quad X_2^{j-1} \quad \cdots \quad X_{C-j}^{j-1} \right] - X_{C-j+1}^{j-1} \Phi^j \\ &= \left[X_1^j \quad X_2^j \quad \cdots \quad X_{C-j}^j \right] \end{aligned}. \tag{4}$$

After C-1 cycles of iteration, all levels are separated. The shortest time-scale level consists of $D^1 = E^{C-1}$. The second shortest time-scale level consists of $D^2 = [S^{C-1}\Phi^{C-1} \ \ S^{C-1}]$. … The longest time-scale level consists of $D^C = [S^1\Phi^1 \ \ S^1]$.

3.4 Multi-time-scale dynamic PCA modeling, monitoring and fault diagnosis

After level separation, 2-D-DPCA is adopted to construct level models for online monitoring and fault diagnosis.

Take a C level separation as an example. In level j (j>1), $D^j = [S^{C-j+1}\Phi^{C-j+1} \ \ S^{C-j+1}]$. Since $S^{C-j+1}\Phi^{C-j+1}$ is completely dependent on S^{C-j+1}, it only represents redundant information in a process monitoring context. Therefore, the variation information in each level is reorganized as $G^1 = E^{C-1}$, $G^2 = S^{C-1}$, …, $G^C = S^1$ with matrix dimensions of ($IK \times J_1$), ($IK \times J_2$), …, ($IK \times J_C$) respectively. These matrices are rearranged into three-dimensional arrays with dimensions of ($I \times J_1 \times K$), ($I \times J_2 \times K$), …, ($I \times J_C \times K$). Then, following ordinary procedures, 2-D-DPCA models can be established for each level. The *SPE* control limits are calculated for online monitoring. For a level belonging to short time-scale dynamics, the 2-D-DPCA model reduces to a BDPCA model. For these levels, the T^2 control limits can also be calculated, since there is no batch-wise dynamics.

In online monitoring, the new data are firstly filtered based on (4) using coefficient matrices Φ^1, Φ^2, …, Φ^{C-1} in turns. Thus, the variations contained in the new data are separated into different time-scale levels. The corresponding 2-D-DPCA model is utilized to monitor each level. After faults are detected in some levels, the contribution plots can be used for fault diagnosis in these levels accordingly.

4. SIMULATION EXAMPLE

4.1 Batch process modeling

In this section, a simulated batch process with both long and short time-scale dynamics is utilized to compare the monitoring and fault diagnosis efficiency of the proposed multi-time-scale dynamic PCA models with the conventional 2-D-DPCA model. The process model is given as below,

$$\begin{aligned} x_1(i,k) &= 0.5 * x_1(i,k-1) + 0.8 * x_1(i-1,k) - 0.3 * x_1(i-1,k-1) \\ x_2(i,k) &= 0.44 * x_2(i-1,k) + 0.67 * x_2(i,k-1) - 0.11 * x_2(i-1,k-1) \\ x_3(i,k) &= 0.4 * x_3(i,k-1) + 0.25 * x_1(i,k) + 0.35 * x_2(i,k) \\ x_4(i,k) &= 0.8 * x_4(i,k-1) + 0.53 * x_1(i,k) - 0.33 * x_2(i,k) \end{aligned}, \tag{5}$$

where i is the batch index; k is the time index; x_1 and x_2 are two independent slow-response variables with long time-scale dynamics described in a 2-D structure; x_3 and x_4 are fast-response variables correlated to their own values at one step before in the current batch, which are also affected by x_1, x_2. Gaussian noises with variance 0.01 are added into the data.

For conventional 2-D-DPCA modeling, the ROS is determined as $\mathbf{x}(i,k-1), \mathbf{x}(i-1,k), \mathbf{x}(i-1,k-1)$, where $\mathbf{x}(i,k-1) = \left[x_1(i,k) \quad x_2(i,k) \quad x_3(i,k) \quad x_4(i,k) \right]$. So that, there are totally 16 variables in the augmented data matrix $\tilde{\mathbf{X}}$, including 4 current variables and 12 lagged variables in the ROS.

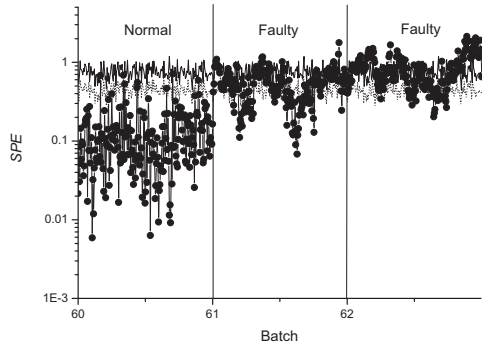

(a)

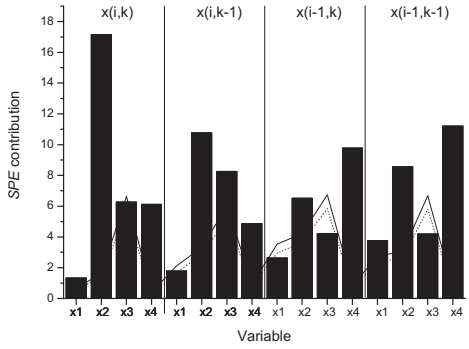

(b)

Fig. 1. Monitoring and diagnosis results of fault 1 based on 2-D-DPCA: (a) monitoring result; (b) fault diagnosis result.

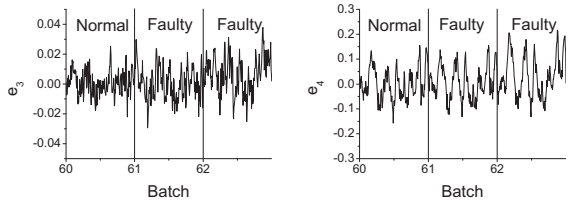

(a) (b)

Fig. 2. Filtered variable trajectories in fault 1: (a) e_3; (b) e_4.

For multi-time-scale dynamic PCA modeling, x_1 and x_2 belong to the slow-response variable group *S*, while x_3 and x_4 are divided into the fast-response variable group *F*. The regression model between *F* and *S* is built to remove the effects of x_1 and x_2 from x_3 and x_4, as described in (2) and (3). Supposing e_3 and e_4 are the filtered values of x_3 and x_4, the variation information is separated into $G^S = \begin{bmatrix} e_3 & e_4 \end{bmatrix}$ as the short time-scale level and $G^L = \begin{bmatrix} x_1 & x_2 \end{bmatrix}$ as the long time-scale level. Then, 2-D-DPCA is performed on each level to model the two different types of dynamics. Let $\hat{\mathbf{x}}(i,k-1) = \begin{bmatrix} x_1(i,k) & x_2(i,k) \end{bmatrix}$. In the long time-scale level, the ROS is selected as $\hat{\mathbf{x}}(i,k-1), \hat{\mathbf{x}}(i-1,k), \hat{\mathbf{x}}(i-1,k-1)$.

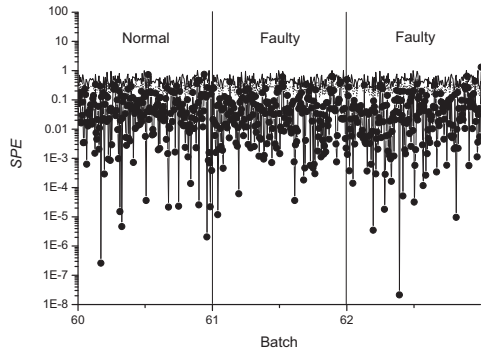

(a)

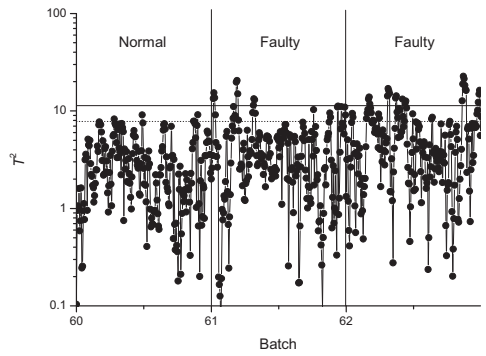

(b)

Fig. 3. Monitoring results of fault 1 based on short time-scale level model: (a) *SPE* plot; (b) T^2 plot.

The 2-D-DPCA model is calculated based on 2 current variables in $\hat{\mathbf{x}}(i,k)$ and 6 lagged variables in the ROS. In the short time-scale level, the algorithm is performed on 4 variables including $e_3(i,k), e_4(i,k), e_3(i,k-1), e_4(i,k-1)$.

4.2 Online modeling and fault diagnosis

Two faults are introduced into the process. Fault 1 occurs to the slow-response variable x_2. From batch 61, x_2 is formulated as (6) to simulate a fault:

$$x_2(i,k) = 0.6 * x_2(i-1,k) + 0.3 * x_2(i,k-1) + 0.2 * x_2(i-1,k-1) . \quad (6)$$

Fig. 1 shows the monitoring and the fault diagnosis results based on conventional 2-D-DPCA, respectively. The *SPE* control chart shows that the fault can be detected from the beginning of batch 61. However, from the contribution plot of batch 61, Fig. 1(b), it is hard to say which variable is faulty. Due to the variable correlations, many variables (including the lagged variables) are outside the control limits.

In multi-time-scale monitoring, variable x_1 and x_2 are filtered to get short time-scale dynamic signals e_3 and e_4. Since the fault occurs to the slow-response variable x_2, and the effects

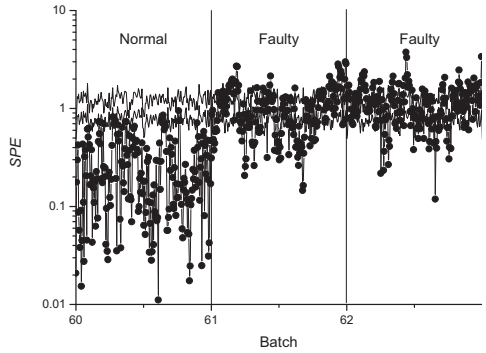

(a)

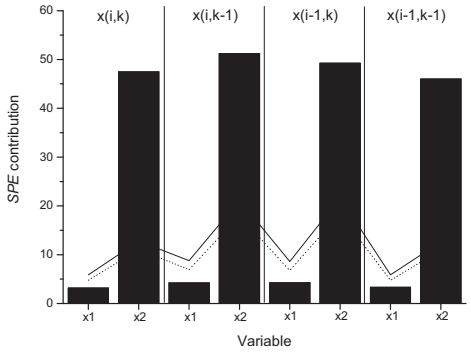

(b)

Fig. 4. Monitoring results of fault 1 based on long time-scale level model: (a) monitoring; (b) diagnosis.

of x_1 and x_2 have been removed from the short time-scale level, there is no significant difference between the trajectories of e_3 and e_4 in a normal cycle and those in the faulty cycles, as shown in Fig. 2. The monitoring results in Fig. 3 confirm this. Neither *SPE* nor T^2 plot in this level is affected by the fault significantly. At the same time, the *SPE* control plot in the other level detects the fault efficiently, as Fig. 4(a) shows. This points out that the fault happens in the long time-scale level. Then, contribution plot in this level is plotted to find out the reason of the fault. From Fig. 4(b), it is very easy to conclude that x_2 is the faulty variable.

Fault 2 is about the fast-response variable x_3. From batch 61, the formulation of x_3 becomes:

$$x_3(i,k) = 0.5 * x_3(i-1,k) + 0.25 * x_1(i,k) + 0.35 * x_2(i,k). \quad (7)$$

As shown in Fig. 5, again, the conventional 2-D-DPCA detects the fault very quickly, but the contribution plot can not give a clear indication about the reason of the fault.

Fig. 6 shows the trajectories of e_3 and e_4. Obviously, significant magnitude differences exist between the trajectory of e_3 in a normal batch and that in faulty batches. So that, this fault is hopefully to be detected by the T^2 control chart in the short time-scale level, which is confirmed by Fig. 7(a). The

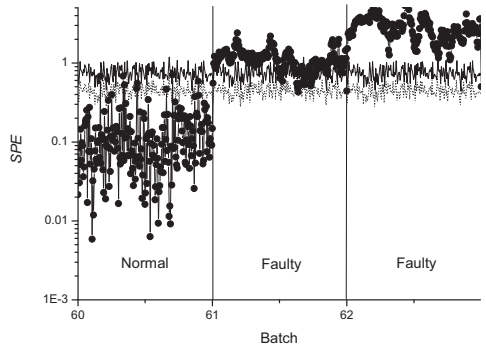

(a)

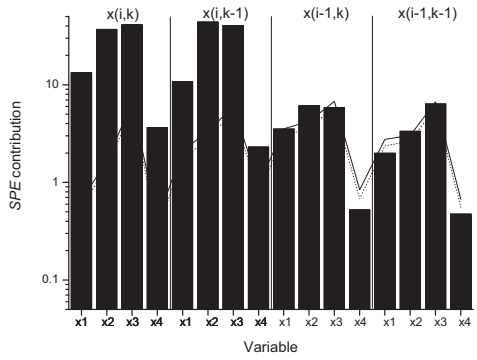

(b)

Fig. 5. Monitoring and diagnosis results of fault 2 based on 2-D-DPCA: (a) monitoring; (b) diagnosis.

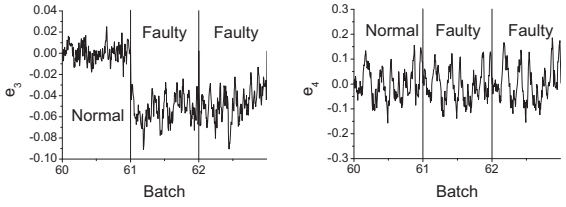

(a) (b)

Fig. 6. Filtered variable trajectories in fault 2: (a) e_3; (b) e_4.

monitoring in the other level, as shown in Fig. 8, dose not show the fault, as it only occurs to a fast-response variable and dose not affect the long time-scale dynamics. The fault diagnosis is only needed to be performed in the short time-scale level. The contribution plot diagnoses the reason of the fault clearly and correctly, as Fig. 7(b) shows.

5. CONCLUSIONS

Batch process variables have various response time constants, causing dynamics with different time scales. The trajectories of the fast-response variables are often affected by the slow-

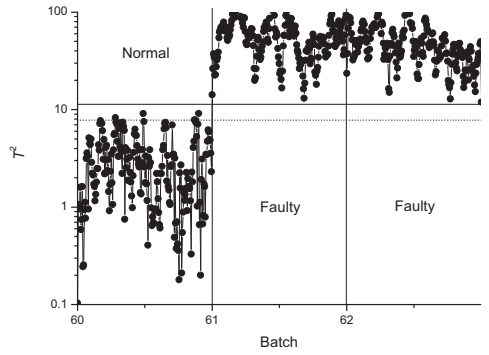

(a)

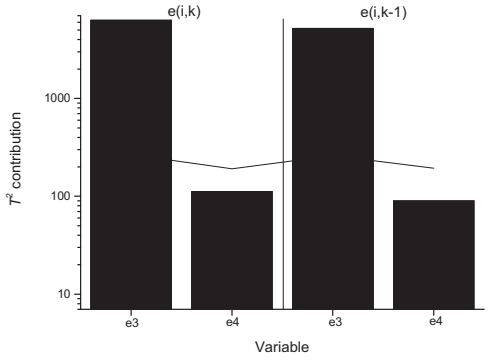

(b)

Fig. 7. Monitoring and diagnosis results of fault 2 based on short time-scale level model: (a) monitoring; (b) diagnosis.

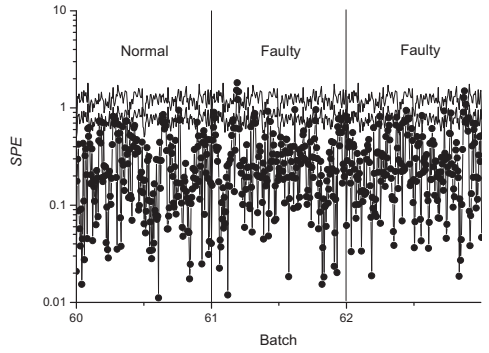

Fig. 8. Monitoring results of fault 2 based on long time-scale level model

response variables, confounding different types of dynamics and causing trouble in fault diagnosis.

A multi-time-scale dynamic PCA monitoring scheme is proposed in this paper. The process variations are separated into different levels according to the dynamics time scales. Then 2-D-DPCA method is adopted to model each level for online monitoring. The simulation results show that the fault diagnosis accuracy is largely improved.

In this paper, variable response time constants are assumed to be known as a kind of external information. It is better if such information can be achieved from the analysis of the operation data. This issue will be studied in the future researches to make the method completely data-based.

REFERENCES

Bakshi, B.R. (1998). Multiscale PCA with application to multivariate statistical process monitoring. *AIChE Journal*, 44, 1596-1610.

Chen, J. and Liu K.C. (2002). On-line batch process monitoring using dynamic PCA and dynamic PLS models. *Chemical Engineering Science*, 57, 63-75.

Jain, A.K., Murty, M.N., and Flynn, R.J. (1999). Data clustering: a review. *ACM Computing Surveys*, 31, 264-323.

Kano, M., Hasebe, S., Hashimoto, I. and Ohno, H. (2004). Evolution of multivariate statistical process control: application of independent component analysis and external analysis. *Computers and Chemical Engineering*, 28, 1157-1166.

Lu, N., Yao Y., and Gao F. (2005). Two-dimensional dynamic PCA for batch process monitoring. *AIChE Journal*, 51, 3300-3304.

Montgomery, D.C. (2005). *Design and analysis of experiments*, *6th ed*, New York: Wiley.

Nomikos, P. and MacCregor J.F. (1994). Monitoring batch processes using multiway principal component analysis. *AIChE Journal,* 40, 1361-1375.

Nomikos, P. and MacCregor J.F. (1995). Multivariate SPC charts for monitoring batch processes. *Technometrics,* 37**,** 41-59.

Takane, Y. and Shibayama, T. (1991). Principal component analysis with external information on both subjects and variables. *Psychometrika*, 56, 97–120.

Timmerman, M.E. (2006). Multilevel component analysis. *British Journal of Mathematical and Statistical Psychology*, 59, 301-320.

Westerhuis, J.A., T. Kourti, and J.F. MacGregor (1998). Analysis of multiblock and hierarchical PCA and PLS models. *Journal of Chemomet*rics, 12, 301-321.

Westerhuis, J.A., S.P. Gurden and A.K. Smilde (2000). Generalized contribution plots in multivariate statistical process monitoring. *Chemometrics and Intelligent Laboratory Systems*, 51, 95-114.

Wold, S. (1978). Cross-validatory estimation of the number of components in factor and principal components models. *Technometrics*, 20, 397-405.

Yao, Y., Diao, Y., Lu, N., Lu, J., and Gao, F. (2008). Two-dimensional dynamic principal component analysis wieht auto-determined suppert region. *Industrial & Engineering Chemistry Research*, in print.

Yoon, S. and MacGregor, J.F. (2001). Incorporation of external information into multivariate PCA/PLS models. *Proc. of 4th IFAC Workshop on On-line Fault Detection and Supervision in the Chemical Industries*, 121-126.

FAULT DECTION AND VARIATION SOURCE IDENTIFICATION BASED ON STATISTICAL MULTIVARIATE ANALYSIS

Ming-Da Ma*. Chun-Cheng Chang. Shi-Shang Jang**. David Shan-Hill Wong****
Sheng-Tsaing Tseng***

**Center for Control and Guidance Technology, Harbin Institute of Technology*
Harbin, China, (e-mail: mamingda@hit.edu.cn).
*** Department of Chemical Engineering, National Tsing-Hua University, Hsin-Chu, Taiwan*
(e-mail: ssjang@mx.nthu.edu.tw; dshwong@che.nthu.edu.tw)
**** Institute of Statistics, National Tsing-Hua University, Hsin-Chu, Taiwan,*
(e-mail: sttseng@stat.nthu.edu.tw)

Abstract: This paper aims to solve the problems of fault diagnosis and variation reduction by using multivariate statistical techniques when the quality measurements are scarce. Both single stage process and multi-stage process are considered. For the single stage process, the nonparametric statistical method, Wilcoxon rank-sum test is used to identify the key variable/step that causes the fault of the un-qualified wafers. For the multi-stage process, the most important variables are first picked out by systematic statistical analysis, and the specifications of these key variables are designated using nonparametric method to improve the product yield. Gene map which gives visual images is used to assist the analysis. Industrial examples are given to show the effectiveness of the proposed method.

Keywords: semiconductor manufacturing, fault detection, Wilcoxon rank-sum test, cluster analysis, stepwise regression.

1. INTRODUCTION

State-of-the-art semiconductor processes are often pushed to the limits of current technologies, resulting in processes that have little or no margin for error. Advanced process control (APC) and fault detection and classification (FDC) are widely applied in semiconductor industries to reduce cycle-time and improve yield. The focus of this paper is on the fault detection algorithms to find out the variation source and root-cause of scrap wafers by using statistical multivariate analysis techniques.

Detection of process and tool faults in the shortest possible time is critical for minimizing scrap wafers and improving product yields for semiconductor manufacturing. However, most of wafer-states lack in situ sensor to provide real time information and usually are measured offline and less frequently than every wafer, which can lead to a number of scrapped wafers before a fault is detected. In the meanwhile, fortunately, more and more real time measurements of manufacturing equipments like temperature, pressure, power and flow rate, etc., are available due to the advances in metrology technology. These real time measurements provide valuable information about the tool status and can be used to predict final wafer characteristics. Further, it also provides a way to improve product quality by detecting and identifying equipment malfunctions in real time without interrupting the normal operations. The difficulty is, with such an abundant amount of data available, it is usually not clear which tool-state variable is critical or closed related with the final product quality.

Principal component analysis (PCA) and partial least squares (PLS) have drawn increasing interest and have been studied extensively in semiconductor manufacturing industry. PCA and PLS are useful tools for data compression and information extraction and have the advantages of dealing with high dimension and collinearities. PCA/PLS methods find linear combinations of variables that describe major trends in a data set. Considering the batch nature of semiconductor manufacturing, multi-way PCA is usually used to unfold three dimensions data into 2-D data array (Macgregor, 1994). Yue et al. applied multi-way PCA method to optical emission spectra for plasma etchers.

Most of the methods mentioned above require a large amount of training data to build a reliable statistical model to capture the key characteristics of the process. However, in real practice, many fabs are operating with diversified products of small account (Ma, et al., 2008) which means that one has to find out the causes of un-qualified wafers with limited quality data. Compared with principal components which are combined by all process variables, engineers are more eager to know which variable exactly, or linear combinations of several variables, plays an important role on the product quality. It is also of interest to know which step is critical to the whole streamline.

In this paper, a systematic approach is proposed for fault diagnosis and variation reduction by using statistical multivariate techniques. Both single stage process and multi-

stage process are considered. For the single stage process, the nonparametric statistical method, Wilcoxon rank-sum test is used to identify the key variable/step that causes the fault of the un-qualified wafers. For the multi-stage process, homogeneous process variables are first grouped by using cluster analysis, and representative variables or linear combinations of variables of each group are picked out. Then the key clusters are selected by stepwise regression method. Further, the upper and lower limits of these selected representative variables are designated to reduce product variation. It is shown that the proposed method improves the product yield substantially.

Recently, combinatory and high throughput experiments have received widespread attention in biology. Synopsis of large amount of experiment data and subsequent information mining from such data has become a special branch of study known as bioinformatics (Baldi and Brunak, 2001). The key experimental technique that is responsible for the advancement of bioinformatics is the microarray which enables expressions of tens of thousands of genes be measured and represented on a small array of colored image dots. In this paper, we demonstrate that quick diagnosis of the key variable/step that causes the fault in final quality can be achieved by simple statistical analysis of measured values of different sensors and graphical synopsis of results of such analysis. Furthermore, specifications for the key variables, which are usually far from optimal in original settings, can be designated to improve the product yield.

2. FAULT DETECTION FOR SINGLE STAGE PROCESS

2.1 Problem statement

Consider quality data of n wafers are collected from a tool, n_1 wafers are qualified, and n_2 wafers are un-qualified, hence $n_1+n_2=n$. Let's denote that m steps with v variables are implemented during the whole process. It is assumed that in each step t_s seconds are carried out for some certain objective (for instance temperature ramped up, current ramped down,…,etc.), where s=1,…,m. Suppose that the total time for all steps is t, then $t_1 + t_2 + \cdots + t_m = t$; let $T_r = t_1 + \cdots + t_r$, where r=1,…,m. Now, let's define $X_{i,j,k,l}$ to be the kth independent variable at batch time l of jth wafer, where j=1,…,n_i, k=1,…,v, l=1,…,t, and i=1 means the wafer is qualified, i=2 indicates the wafer is not qualified. Now, the problem is what is the p-value of $X_{i,j,k,l}$ to distinguish the wafer is qualified or unqualified in case n_1 and n_2 are small.

2.2 Statistical analysis

It is general to apply t-test to distinguish two set of data whether or not their mean is equal to each other. However, in this case n_1 and n_2 are small, a two sample t-test is not appropriate since the above two set of data may not be in normal distribution. Therefore, a nonparametric analysis, Wilcoxon rank-sum test, is used here.

The Wilcoxon rank-sum test is a nonparametric alternative to the two-sample t-test which is based solely on the order in which the observations from the two samples fall (Higgins, 2004). It is valid for data from any distribution, whether normal or not, and is much less sensitive to outliers than the two-sample t-test. The Wilcoxon test is based upon ranking the n_1+n_2 observations of the combined sample. Each observation has a rank: the smallest has rank 1, the 2nd smallest rank 2, and so on. The Wilcoxon rank-sum test statistic is the sum of the ranks for observations from one of the samples.

In this work, we implement Wilcoxon rank-sum test to find the p-value of the hypothesis of

$$H_0 : \mu_{1,k,l} = \mu_{2,k,l} \quad vs. \quad H_a : \mu_{1,k,l} \neq \mu_{2,k,l} \qquad (1)$$

where $\mu_{1,k,l}$ and $\mu_{2,k,l}$ are the mean of qualified and un-qualified wafers of the kth variable at time l respectively. It is assumed that there is not much prior knowledge of the product and no evidence shows that $\mu_{1,k,l}$ is greater or smaller than $\mu_{2,k,l}$. Therefore, a two-side test is implemented here.

Let $p_{k,l}$ be the above p-value of the kth variable at time l, three different approaches to evaluate the above approach can be implemented

(i) Evaluate the p-value of a process variable by finding the average p-value of the process variable in the whole time horizon:

$$P_k = \sum_{l=1}^{t} p_{k,l} \Big/ t \qquad (k=1,2,\ldots,v) \qquad (2)$$

(ii) Evaluate the average of p-value of each variable at each step

$$P_{k,b} = \sum_{l=T_{b-1}+1}^{T_b} P_{k,l} \Big/ t_b \qquad (k=1,2,\ldots,v\ ; b=1,2,\ldots.m,) \qquad (3)$$

(iii) Direct observe the p-value $p_{k,l}$ of each variable at each different time.

From the statistical analysis of the above approaches, we can determine which process variable, which step, plays an important role on the quality of the wafers, and more specifically, which second is critical for the final product quality. All these information is valuable to the engineers for their further improvement of the product quality.

2.3 Illustrative example

The proposed algorithm is applied to a high-density plasma chemical vapor deposition (HDP-CVD) process. HDP-CVD, which is used as the gap-filling process for the dielectric in semiconductor circuits, features a high gap-fill capability compared with conventional plasma CVD by the excitation

of a high-density plasma. The schematic diagram of the HDP-CVD reactor is shown in Fig. 1.

There are 33 process variables for this manufacturing process. 9 steps are implemented for this process and the processing time is shown in Table 1. The quality data obtained from WAT test of 25 wafers are collected, among which 21 wafers are qualified and 4 wafers are un-qualified.

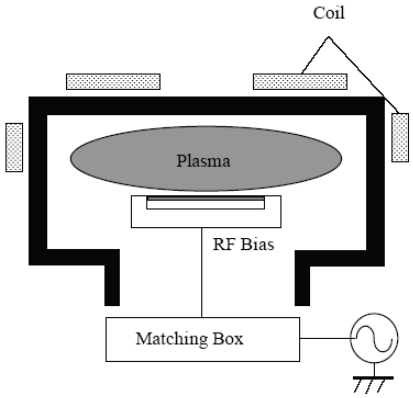

Fig. 1. Schematic diagram of the HDP-CVD reactor.

Table 1 Processing time of each step

Step	1	2	3	4	5	6	7	8	9	Total
Seconds	5	30	53	3	67	5	10	15	5	193

The proposed statistical method is applied to this process. The p-value of hypothesis (1) is calculated for process variables. To find out the key process variable that plays an important role on the process, equation (2) is implemented and the image plot of 1-P_k is shown in Fig. 2. From Fig. 2, we can determine which process variable is more influential for the product quality. This industrial gene map can help engineers to determine which process variable is important and which one is less important at a first glance. Engineers can grasp as much as information in the shortest time with the help of industrial gene map.

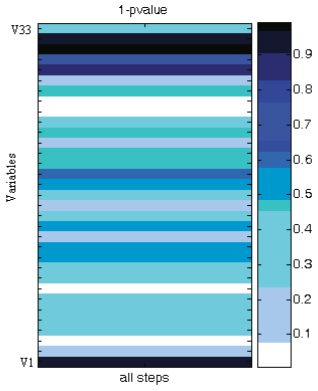

Fig. 2. Image of 1-P_k of total average approach

To further know which step is critical for the process, equation (3) is evaluated for the profile variables of the process and the result is shown in Fig. 3. Similarly, Fig. 3 corresponds to a matrix of dimension 33 by 9. Obviously, the industrial gene map is more visual and straightforward. From Fig. 3, it is observed that most of critical steps are also related with the settings of temperature. The p-value of the profile variables in second are shown in Fig. 4. It can help engineers know when a fault is most likely to happen.

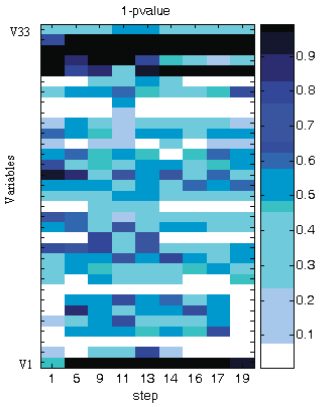

Fig. 3. Image plot of 1-$P_{k,b}$ of step average approach

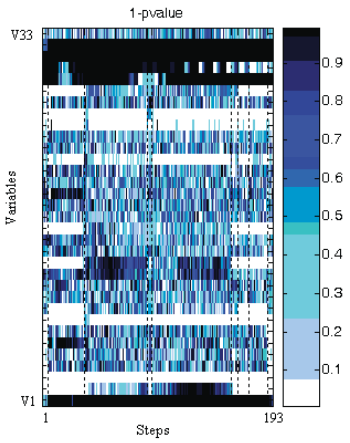

Fig. 4. Image plot of 1-$p_{k,l}$

3. VARIATION REDUCTION FOR MULTI-STAGE PROCESS

3.1 Problem statement

In this section, a statistical method is proposed to find out the key variables that have essential effects on the product quality for the multi-stage manufacturing process. Similarly, the basic assumption is that there is relatively few quality data available compared with process variables. Then, specifications for the key variables which are usually far from optimal in original settings are designated to improve the

product yield. This framework provides a systematic method of drawing inferences from the available evidence without interrupting the normal process operation. The proposed method is directly illustrated by an industrial example. The statistical methods used in the following analysis include cluster analysis, canonical correlation analysis and stepwise regression.

3.2 Statistical analysis and illustrative example

Consider a CVD process. Every wafer must be processed by three chambers A, B, and C successively. Denote the process variables of chamber A, B and C as X_A, X_B and X_C, respectively. The final quality variable is denoted as Y which may contain wafer thickness measurements and wafer electrical measurements. In the following analysis, the method is illustrated for the wafer thickness y, which is one of the most important characteristics of wafers.

The numbers of steps and process variables for chamber A, B and C are list in Table 2. The data set includes measurements of 526 wafers from 22 batches. In this analysis, we want to know which variable, of which chamber, on which step, has an essential effect on the wafer thickness. Every process variable from different chambers on different is treated as an independent variable. Therefore, it is still the case that there are much more process variables than the quality data. Furthermore, process variables are usually highly correlated because of physical and chemical principles governing the process operation. To pick out the most influential variables for the quality variable y, the first step is to reduce the redundancy of the original data set.

Table 2 Number of steps and variables of the three chambers

Chambers	Number of steps	Number of variables
A	13	79
B	5	19
C	12	79

Cluster analysis is a useful technique used for combining observations into groups or clusters such that each group or cluster is homogeneous with respect to certain characteristics. Simultaneously, each group should be different from other groups with respect to the same characteristics (Sharma, 1996). The definition of similarity or homogeneity varies from analysis to analysis, and depends on the objectives of the study. In this study, it is desired to combine variables that are highly correlated into one group. Therefore, the similarity measure is defined as

$$d_{ij} = 1 - \left| r_{ij} \right| \qquad (4)$$

where r_{ij} is the correlation coefficient of variables x_i and x_j. For variables that are highly correlated, d_{ij} would be small which represents similarity and vice versa. The clustering method adopted here is average-linkage method, one of the hierarchical clustering methods.

To determine the number of clusters, the rule that the correlation coefficient of the variables from the same groups should be greater than 0.9 is used. The result of cluster analysis is shown in Fig. 5-7. In these figures, variables that are filled with the same color or indicated with the same number are of the same group.

Then, the next step is to select representative variables from each group. The variables picked out should give good variance explanation which is usually evaluated by the R^2 statistics of the wafer thickness y. For example, the R^2 statistics of one variable selected from group 8 is 0.352 and the total R^2 of the whole group is 0.361. In such case, one process variable is capable of representing the group.

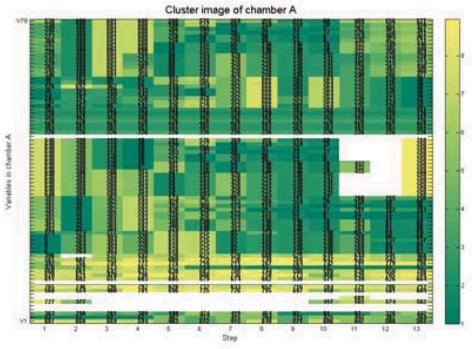

Fig. 5. Cluster image of chamber A.

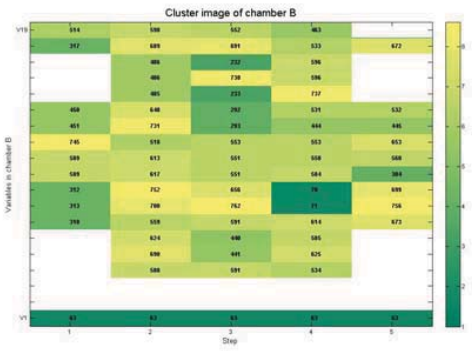

Fig. 6. Cluster image of chamber B.

However, in some circumstances, the R^2 of each individual variable is quite low yet the linear combination of these variables contributes a high R^2. In this case, it is more appropriate to use linear composites of the original variables to represent the group. This problem actually belongs to the field of canonical correlation analysis. The new variables, the linear composites, are called canonical variates. The coefficients of the canonical variates are determined to make the correlation between the linear composites maximum. For this special case, there is only one quality variable, the wafer thickness y. Therefore, canonical correlation analysis is essentially equal to the linear multiple regression.

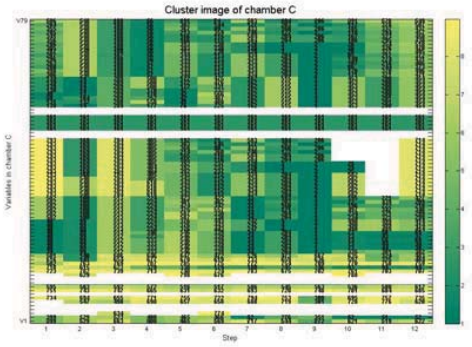

Fig. 7. Cluster image of chamber C.

Then, the question is, when a single variable should be used and when a linear composite should be used to represent a group. In this application, the following rules are adopted: if the R^2 of individual variable is more than eighty percent of the total R^2, then the single variable which has the largest R^2 is used to represent the whole group; otherwise, a linear composite is used. The number of variables in the canonical variate is increased till the R^2 of the linear composite is more than eighty percent of the total R^2. The coefficients of the linear composite are obtained from canonical correlation analysis.

After picking out the representative variable from each group, the next step is to select important representative variables from all the groups. The method used is stepwise regression. Stepwise regression is a statistical method used for variable selection in linear regression. The procedure iteratively constructs a sequence of regression models by adding or removing variables at each step. The criterion for adding or removing a variable at any step is usually expressed in terms of a partial F-test Montgomery, et al., 2001). The changes of R^2 and adjusted R^2 of stepwise regression are shown in Fig. 8. There are 68 representative variables selected by the stepwise regression.

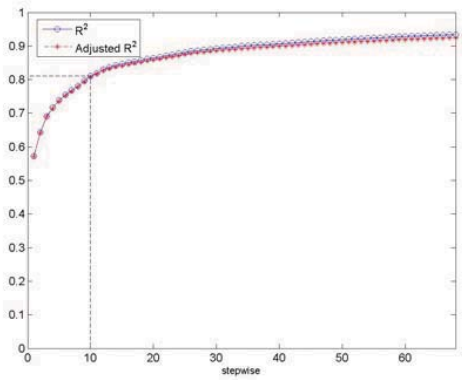

Fig. 8. Representative variables selected by stepwise regression method.

It is not an easy task to monitor 68 variables online simultaneously. Therefore, the first ten representative variables selected by stepwise regression are picked out and analyzed. The first ten representative variables listed in Table 8 give a good variance explanation because the R^2 and adjusted R^2 are higher than 0.8 which can be seen from Fig. 8.

In fact, all the 526 wafers are qualified wafers. To reduce the variance of wafer thickness further, we define $\left[\overline{y}-1.5s_y, \overline{y}+1.5s_y\right]$ as the acceptable region for the wafer thickness. Here, $\overline{y}$ is the average value of y and s_y is the standard deviation of y, respectively. The wafers fall out of this region is treated as "un-qualified" now. Among all the 526 wafers, there are 455 wafers fall into the acceptable region. Therefore, the yield is 0.865. In the following analysis, we will develop a nonparametric method to find out the new specifications for the above ten important representatives to improve the product yield.

First, the center point for all the qualified wafers in a space defined by the 10 important representative variables is determined. The Mahalanobis distance of each qualified wafer from the center point is calculated as

$$MD_i = \left(X_i - \mu\right)^T S \left(X_i - \mu\right) = c_i \quad (5)$$

where X is a 10×1 vector of coordinates and S is a 10×10 covariance matrix, μ is the center point. Then, the yield can be viewed as an implicit function of the Mahalanobis distance. Each value of Mahalanobis distance corresponds to a value of yield which is defined as the ratio between the number of qualified wafers and the number of all the wafers within the Mahalanobis distance. A graphical interpretation of this relationship is shown in Fig. 9. In this figure, the solid line is the relationship between the yield and the Mahalanobis distance and the dashed line is its 95% confidence interval.

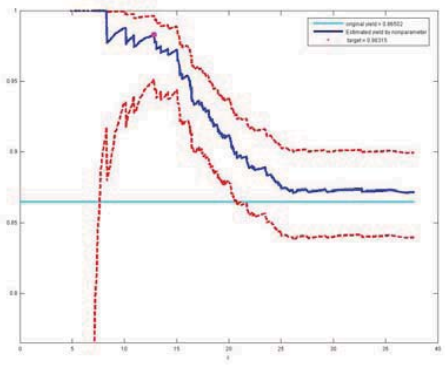

Fig. 9. Plot of Mahalanobis distance versus product yield.

It can be observed that the yield is not reliable when c_i is small because the samples within the corresponding Mahalanobis distance are few. To get a balance between reliability and high yield, the point corresponds to one third of the maximum of c_i which is marked as a dot in Fig. 9 is

used to derive the specifications of the ten representative variables. Once c_i is determined, the joint boundary of the ten representative variables is also determined.

However, the joint boundary which is a function of ten independent variables can not be easily monitored. Therefore, the projections of the joint boundary onto the axes of coordinates are used as the new specifications of the ten representative variables. The yield increased greatly when the upper and lower bounds of the first representative variable are designated. A graphical interpretation of the increase of the yield is shown in Fig. 10. The increases of the yield are not obvious after the designation of the specification of the third representative variable.

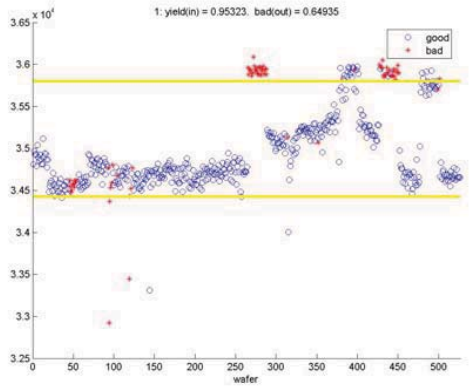

Fig. 10. Specifications of the first representative variable.

It is of interest to study the improvement of process capability ratio after the specifications of the ten representative variables are designated. The process capability ratio (PCR, or C_p) is defined as

$$C_p = \frac{USL - LSL}{6\sigma} \qquad (6)$$

where USL and LSL are the upper and lower specification limits, respectively. Since σ is unknown, it is replaced by the standard deviation s. If the process capability ratio and standard deviation are treated as a function of Mahalanobis distance, then we can get

$$\frac{C_p(c_i)}{C_p} = \frac{s}{s(c_i)} \qquad (7)$$

The relationship between $C_p(c_i)/C_p$ and the Mahalanobis distance is shown in Fig. 11. It can be observed that there is about 40% improvement of process capability ratio for the point we used to designate the specifications of the representative variables. The changing trend of $C_p(c_i)/C_p$ is consistent in the area where the point we used also indicates that the value of c_i we chose is appropriate.

4. CONCLUSIONS

Nowadays, many semiconductor manufacturing foundries are operating with diversified products of small account which makes the fault detection and variation reduction difficult. In this paper, systematic statistical methods are proposed to solve this difficulty. Both single stage process and multi-stage process are considered. The effectiveness of the proposed methods are illustrated by industrial examples.

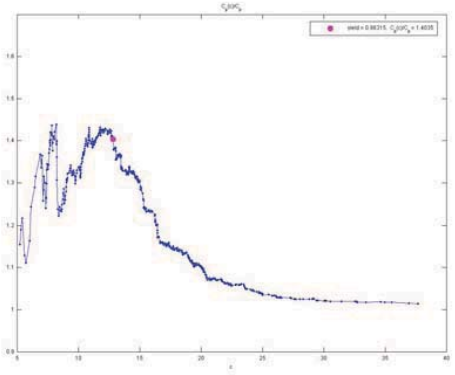

Fig. 11. Plot of Mahalanobis distance versus $C_p(c_i)/C_p$.

REFERENCES

Cherry, G.A. and Qin, S.J. (2006). Multiblock principal component analysis based on a combined index for semiconductor fault detection and diagnosis. *IEEE Trans. Semiconduct. Mnauf.*, 19 (2), pp 159-172.

Ma, M.D., Chang, C.C., Wong, D.S.H., and Jang, S.S. (2008). Identification of tool and product effects in a mixed product and parallel tool environment. *J. Process Contr.*, doi:10.1016/j.jprocont.2008.07.009.

Montgomery, D.C. (1993). *Introduction to Statistical Quality Control (3ed.)*. Wiley, New York.

Montgomery, D.C., Peck, E.A., and Vining, G.G. (2001). *Introduction to Linear Regression Analysis (3ed.)*. Wiley, New York.

Nomikos, P. and MacGregor, J.F. (1994). Monitoring batch processes using multiway principl analysis. *AIChE Journal*, 40 (8), pp 1361-1375.

Sharma, S. (1996). *Applied Multivariate Techniques*. Wiley, New York.

Wong, J. (2006). Batch PLS analysis and FDC process control of within lot SiON gate oxide thickness variation in sub-nanometer range. *Proc. AEC/APC Symp. XVIII*, Westminster, CO, Sep.

Yue, H.H., Qin, S.J., Markle, R.J., Nauert, C., and Gatto, M. (2000). Fault detection of plasma etchers using optical emission spectra. *IEEE Trans. Semiconduct. Mnauf.*, 13 (3), pp 374-385.

Baldi, P. and S. Brunak. (2001). *Bioinformatics: The Machine Learning Approach*. MIT Press.

Higgins, J.J. (2004). *Introduction to Modern Nonparametric Statistics*, Brooks.

Fault Detection and Diagnosis using Multivariate Statistical Techniques in a Wastewater Treatment Plant. ⋆

D. Garcia-Alvarez * **M.J. Fuente** * **P. Vega** ** **G. Sainz** *

* *Department of Systems Engineering and Automatic Control, University of Valladolid, 47011 Valladolid, Spain*
[dieggar@cta,maria@autom,gresai@eis].uva.es
** *Department of Computer Science and Control, University of Salamanca, ETSII, 37700 Bejar (Salamanca), Spain* pvega@usal.es

Abstract: In this paper Principal Components Analysis (PCA) is used for detecting faults in a simulated wastewater treatment plant (WWTP). Diagnosis tasks are treated using Fisher discriminant analysis (FDA). Both techniques are multivariate statistical techniques used in multivariate statistical process control (MSPC) and fault detection and isolation (FDI) perspectives. PCA reduces the dimensionality of the original historical data by projecting it onto a lower dimensionality space. It obtains the principal causes of variability in a process. If some of these causes change, it can be due to a fault in the process. FDA provides an optimal lower dimensional representation in terms of a discriminant between classes of data, where, in this context of fault diagnosis, each class corresponds to data collected during a specific and known fault. A discriminant function is applied to diagnose faults using data collected from the plant.

Keywords: Fault detection, Fault diagnosis, Statistical process control, Wastewater treatment plant, Discriminant analysis

1. INTRODUCTION

Multivariate statistical methods for the analysis of process data have recently been used successfully for monitoring and fault detection. The safe operation and the production of high quality products are two of the main objectives in industry. Modern control techniques have resolved many problems, but when a special cause occurs in a process, it cannot operate under control. The development of an industrially reliable online scheme for such processes would be a step toward effectiveness and robustness.

Conventional univariate Statistical Process Control (SPC) uses typical control charts, such as Shewhart charts, for monitoring a single variable. When univariate control charts are applied to multivariate systems, with hundreds of variables, the results are improper because, when there is a fault or an abnormality in the operation, several of these charts set off an alarm in a short period of time or simultaneously. This situation is because the process variables are correlated, and a special cause can affect more than one variable at the same time. Multivariate Statistical Process Control (MSPC) uses latent variables instead of every measured variable. All these methods use historical databases to calculate empirical models that describe the system's trend. They are able to extract useful information from the historical data, calculating the relationship between the variables. When a problem appears, it changes the covariance structure of the model and can be detected.

Multivariate statistical approaches, and principal component analysis (PCA) in particular, have been investigated to deal with this problem. Jackson and Mudholkar investigated PCA as a tool of MSPC (Jackson and Mudholkar, 1979) two decades ago. The objective of this approach is to reduce the dimensionality of the original historical data by projecting it onto a lower dimensionality space. PCA finds linear combinations of variables that describe major trends in a data set. Mathematically, PCA is based on an orthogonal decomposition of the covariance matrix of the process variables along the directions that explain the maximum variation of the data. PCA can be studied from two perspectives, one is the cited MSPC, and other is the fault detection and isolation (FDI) perspective, which is discussed by Venkatasubramanian (Venkatasubramanian et al., 2003a,b,c). The author divides the fault detection and diagnosis techniques into three parts: quantitative model-based methods, qualitative models and search strategies and process history-based methods. PCA falls into the third category because it uses historical databases to derive the statistical model (PCA model) (Hwang and Han, 1999; Kourti, 2002; Tien et al., 2004).

The charts most commonly used with PCA techniques are Hotelling statistics, T^2, and the sum of squared residuals, SPE, or Q statistic. The T^2 statistic is a measure of the variation in the PCA model and the Q statistic is a

⋆ This work was supported in part by the national research agency of Spain (CICYT) through the project DPI2006-15716-C02-02 and the regional government of Castilla y Leon through the project VA052A07

measure of the amount of variation not captured by the PCA model.

Once the fault is detected using monitoring techniques, it can be diagnosed by determining the fault region in which the observations are located. The approach used in this paper for fault diagnosis is pattern classification. When the data collected during the *out-of-control* operations have been previously diagnosed, the data can be categorized into separate classes when each class pertains to a particular fault (Chiang et al., 2000).

Fisher discriminant analysis (FDA) is a linear pattern classification method used to find the linear combination of features which best separate two or more classes. It is an empirical method based on observed attributes over the collected examples. FDA provides an optimal lower dimensionality representation in terms of a discriminant between classes of data, where, for fault diagnosis, each class corresponds to data collected during a specific, known fault. FDA has been studied in detail in the pattern classification literature (Duda et al., 2001), but its use for analyzing chemical process data had not been explored until recently (Chiang et al., 2000; He et al., 2005; Fuente et al., 2008).

The purpose of this article is to implement a method for fault detection and diagnosis using multivariate statistical methods and to apply it to a wastewater treatment plant (WWTP). Theoretical aspects of PCA and FDA will be presented and finally the wasterwater treatment plant, the considered faults and the results obtained will be explained and discussed.

2. PRINCIPAL COMPONENT ANALYSIS

Principal component analysis (PCA) is a vector space transformation often used to transform multivariable space into a subspace which preserves maximum variance of the original space in a minimum number of dimensions. The measured process variables are usually correlated to each other. PCA can be defined as a linear transformation of the original correlated data into a new set of uncorrelated data, so, PCA is a good technique to transform the set of original process variables into a new set of uncorrelated variables that explain the trend of the process.

Consider a data matrix $X \in \Re^{n\times m}$ containing n samples of m process variables collected under normal operation. This matrix must be normalized to zero mean and unit variance with the scale parameter vectors $\bar{x}$ and s as the mean and variance vectors respectively. Then next step to calculate the PCA is to construct the covariance matrix R:

$$R = \frac{1}{n-1} X^T X \tag{1}$$

and to perform the SVD decomposition on R:

$$R = V \Lambda V^T \tag{2}$$

where Λ is a diagonal matrix that contains the eigenvalues of R in its diagonal sorted in decreasing order ($\lambda_1 \geq \lambda_2 \geq \ldots \geq \lambda_m \geq 0$). Columns of matrix V are the eigenvectors of R. The transformation matrix $P \in \Re^{m\times a}$ is generated by choosing a eigenvectors or columns of V corresponding to a principal eigenvalues. Matrix P transforms the space of the measured variables into the reduced dimension space.

$$T = XP \tag{3}$$

The columns of matrix P are called *loadings* and the elements of T are called *scores*. Scores are the values of the original measured variables that have been transformed into the reduced dimension space.

Operating in equation (3), the scores can be transformed into the original space.

$$\hat{X} = TP^T \tag{4}$$

The residual matrix E is calculated as:

$$E = X - \widehat{X} \tag{5}$$

Finally the original data space can be calculated as:

$$X = TP^T + E \tag{6}$$

It is very important to choose the number of principal components a, because TP^T represents the principal sources of variability in the process and E represents the variability corresponding to process noise. There are several proposed procedures for determining the number of components to be retained in a PCA model, such as Zumoffen and Basualdo (2007) and Jackson (1991):

a) The SCREE procedure (Jackson, 1991): It is a graphical method in which one constructs a plot of the eigenvalues in descending order and looks for the *knee* in the curve. The number of selected components are the components between the high component and the *knee*. An example of this graph is shown in Fig. 2.
b) Cumulative Percent Variance (CPV) approach Zumoffen and Basualdo (2007). A measure of the percent variance ($CPV(a) \geq 90\%$) captured by the first a principal components is adopted:

$$CPV(a) = \frac{\sum_{i=1}^{a} \lambda_i}{trace(R)} 100 \tag{7}$$

c) Cross validation.

Having established a PCA model based on historical data collected when only common cause variations are present, multivariate control charts based on Hotelling's T^2 and square prediction error (SPE) or Q can be plotted. The monitoring can be reduced to these two variables (T^2 and Q) characterizing two orthogonal subsets of the original space. T^2 represents the major variation in the data and Q represents the random noise in the data. T^2 can be calculated as the sum of the squares of a new process data vector x:

$$T^2 = x^T P \Lambda_a^{-1} P^T x \tag{8}$$

where Λ_a is a squared matrix formed by the first a rows and columns of Λ.

The process is considered *normal* for a given significance level α if:

$$T^2 \leq T_\alpha^2 = \frac{(n^2-1)a}{n(n-a)} F_\alpha(a, n-a) \tag{9}$$

where $F_\alpha(a, n-a)$ is the critical value of the Fisher-Snedecor distribution with n and $n-a$ degrees of freedom

and α the level of significance. α takes values between 90% and 95%.

T^2 is based on the first a principal components so that it provides a test for deviations in the latent variables that are of the greatest importance to the variance of the process. This statistic will only detect an event if the variation in the latent variables is greater than the variation explained by common causes.

New events can be detected by calculating the squared prediction error SPE or Q of the residuals of a new observation. The Q statistic (Jackson and Mudholkar (1979), Jackson (1991)) is calculated as the sum of the squares of the residuals. The scalar value Q is a measurement of *goodness of fit* of the sample to the model and is directly associated with the noise:

$$Q = r^T r \tag{10}$$

with:

$$r = (I - PP^T)x$$

The upper limit of this statistic can be computed as follows:

$$Q_\alpha = \theta_1 \left[\frac{h_0 c_\alpha \sqrt{2\theta_2}}{\theta_1} + 1 + \frac{\theta_2 h_0 (h_0 - 1)}{\theta_1^2} \right]^{\frac{1}{h_0}} \tag{11}$$

with:

$$\theta_i = \sum_{j=a+1}^{m} \lambda_j^i \qquad h_0 = 1 - \frac{2\theta_1 \theta_3}{3\theta_2^2}$$

where c_α is the value of the normal distribution, with α being the level of significance.

When an unusual event occurs and it produces a change in the covariance structure of the model, it will be detected by a high value of Q.

3. FISHER DISCRIMINANT ANALYSIS

For fault diagnosis, data collected from the plant during specific faults are categorized into classes, where each class contains data representing a particular fault. Define n as the number of observations, m as the number of measurement variables, p as the number of classes and n_j as the number of observations in the j^{th} class. The training data for all classes have been stacked into the matrix $X \in \Re^{n \times m}$. The total-scatter matrix is:

$$S_t = \sum_{i=1}^{n} (x_i - \bar{x})(x_i - \bar{x})^T \tag{12}$$

where $\bar{x}$ is the total mean vector whose elements correspond to the means of the columns of X. Let the matrix X_j be defined as the set of vectors x_j which belong to class j, then the within-scatter matrix for class j is given by:

$$S_j = \sum_{x_i \in X_j} (x_i - \bar{x}_j)(x_i - \bar{x}_j)^T \tag{13}$$

where $\bar{x}_j$ is the mean vector for class j:

$$\bar{x}_j = \frac{1}{n_j} \sum_{x_i \in X_j} x_i \tag{14}$$

The within-class-scatter matrix is:

$$S_w = \sum_{j=1}^{p} S_j \tag{15}$$

and the between-class-scatter matrix is:

$$S_b = \sum_{j=1}^{p} n_j (\bar{x}_j - \bar{x})(\bar{x}_j - \bar{x})^T \tag{16}$$

The total-scatter matrix is equal to the sum of the between-scatter matrix and the within-scatter matrix: $S_t = S_b + S_w$. The objective of the first FDA vector, w_1, is to maximize the scatter between classes while minimizing the scatter within classes:

$$\max_{w_1 \neq 0} \frac{w_1^T S_b w_1}{w_1^T S_w w_1} \tag{17}$$

with $w_1 \in \Re^m$. The second FDA vector, w_2, is computed so as to maximize the scatter between classes while minimizing the scatter within classes on all axes perpendicular to the first FDA vector, and so on for the remaining FDA vectors. These vectors are equal to the eigenvectors w_k of the generalized eigenvalue problem:

$$S_b w_k = \lambda_k S_w w_k \tag{18}$$

where the eigenvalues λ_k indicate the degree of separability between the classes. As it is the direction and not the magnitude of w_k which is important, the norm is usually chosen to be $\|w_k\| = 1$. The first FDA vector is the eigenvector associated with the largest eigenvalue and so on.

Then, the linear transformation of the data x from the m-dimensional space to the reduced space a-dimensional generated by the FDA vectors is:

$$z_i = W_a^T x_i \tag{19}$$

where $W_a \in \Re^a$ has the a FDA vectors as columns, and $z_i \in \Re^a$. FDA computes the matrix W_a that as the data $x_1, \ldots, x_n$ for the p classes are optimally separated when projected into the a-dimensional space.

There are several methods to choose the number of FDA vectors. These methods are very similar to PCA selection methods, cited in section 2. For example, cross validation or the SCREE procedure.

In order to diagnose the faults, FDA takes into account data collected during different faulty conditions, and uses a discriminant function that takes into account the similarity between the actual data and the data belonging to each class. An observation is assigned to the class i when the maximum discriminant function value, g_i, satisfies:

$$g_i(x) > g_j(x) \ \forall j \neq i \tag{20}$$

where $g_i(x)$ is the discriminant function for class i given a measured vector $x \in \Re^m$. The discriminant function that minimizes the error rate, when the event v_i occurs (for example, the fault i), is (Duda et al., 2001):

$$g_i(x) = P(v_i|x) \tag{21}$$

where $P(v_i|x)$ is the *a posteriori* probability of x belonging to class i. It can be shown that identical classification occurs when the equation (21) is replaced by:

$$g_i(x) = \ln p(x|v_i) + \ln P(v_i) \tag{22}$$

Using the Bayes' rule, considering that the data for each class are normally distributed and characterizing the data to this case, i.e., considering $W_a \in \Re^{m \times a}$ containing the eigenvectors $w_1, w_2, \ldots, w_a$ computed from equation (18), the discriminant function for each class can be derived as:

$$g_j(x) = -\frac{1}{2}(x - \bar{x}_j)^T W_a (\frac{1}{n_j - 1} W_a^T S_j W_a)^{-1} W_a^T (x - \bar{x}_j) + \ln(p_j) - \frac{1}{2} \ln[\det(\frac{1}{n_j - 1} W_a^T S_j W_a)] \quad (23)$$

where S_j, $\bar{x}_j$ and n_j are defined in equations (13) and (14) respectively.

4. APPLICATION

The approach presented in this paper has been tested in a simulated wastewater treatment plant (WWTP). This plant is based on the COST benchmark (Copp, -; Alex et al., 2008). This benchmark was developed for the evaluation and comparison of different activated sludge wastewater treatment control strategies. The model is implemented using MATALAB© and SIMULINK©.

Fig. 1 shows an overview of this plant. It is composed of a two-compartment activated sludge reactor consisting of two anoxic tanks followed by three aerated tanks. This type of plant combines nitrification with predenitrification in a configuration that is usually built for achieving biological nitrogen removal in full-scale plants. The reactor is followed by a secondary settler. The settler is modeled as a 10 layer non-reactive unit. The 6^{th} layer is the feed layer. Table 1 shows the physical parameters of the plant.

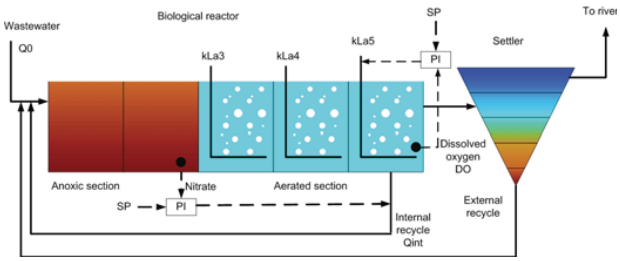

Fig. 1. General overview of the wastewater treatment plant (WWTP)

Table 1. Physical parameters

Elements	Values	Units
Volume - Anoxic section	2000 (2×1000)	m^3
Volume - Aerated tank	4000 (3×1333)	m^3
Volume - Settler (10 layers)	6000	m^3
Area - Settler	1500	m^2
Height - Settler	4	m

The influent used was the dry influent data file Copp (-). In this file, the variation of influent flow is between $15000 - 35000$ m^3/d. The plant, as Fig. 1 shows, has two reflux: external refluxes, from settler to input, which is approximately equal to the influent flow, and internal reflux, from the last aerated tank to input, which is approximately equal to three times the influent flow, but which is a controlable variable.

The objective of the control strategy is to control the dissolved oxygen level in the aerated reactor by manipulation of the oxygen transfer coefficient ($K_L a_5$) and to control the nitrate level in the anoxic tank by manipulation of the internal recycle flow rate. The controllers are of PI type. Tab. 2 shows the principal controller settings.

Table 2. Controllers settings

Variables	Oxygen loop	Nitrate loop
Controller type	PI	PI
Controlled variable	DO $[g/m^3]$	S_{NO} $[gN/m^3]$
Manipulated variable	$K_L a5$ $[1/hr]$	Q_{int} $[m^3/d]$
Setpoint	2 $[g/m^3]$	1 gN/m^3

The model of the plant is formed by 13 state variables. The variables involved are concentrations of:

1. Alkalinity (S_{ALK}).
2. Soluble biodegradable organic nitrogen (S_{ND}).
3. Ammonia nitrogen (S_{NH}).
4. Nitrate (S_{NO}).
5. Dissolved oxygen (S_O).
6. Readily biodegradable substrate (S_S).
7. Active autotrophic biomass ($X_{B,A}$).
8. Active heterotrophic biomass ($X_{B,H}$).
9. Particulate biodegradable organic nitrogen (X_{ND}).
10. Particulate products from biomass decay (X_P).
11. Slowly biodegradable substrate (X_S).
12. Particulate inert organic matter (X_I).
13. Soluble inert organic matter (S_I).

In this case, three faults have been considered. They are not sensors or actuators faults, they are faults in the process. The faults considered are:

- **Toxicity shock.** This fault is due to a reduction in the normal growth of heterotrophic organisms. This type of fault can be produced by toxic substances in the water coming from textile industries or pesticides. This fault is simulated by reducing the maximum heterotrophic growth rate (μ_H).
- **Inhabitation.** This fault can be produced by hospital waste that can contain bactericides, or metallurgical waste that can contain cyanide. This type of fault is due to a reduction in the normal growth of the heterotrophic organisms and an increase in the decay factor of this type of organisms. This fault is similar to toxicity shock but is more drastic. In this case, the fault is caused by reducing the maximum heterotrophic growth rate (μ_H) and increasing the heterotrophic decay rate (b_H).
- **Bulking.** This type of fault is produced by the growth of filamentous microorganisms in the active sludge. This phenomenon causes the impossibility of decantation in the settler. To simulate this fault the settling velocity in layer (v_{sj}) is reduced.

More information about these parameters and mathematical models can be consulted in Copp (-). But in this example the benchmark has been modified in order to introduce the fault parameters.

There are several groups working on fault detection in wastewater treatment plants using PCA (Rosen and Lennox, 2001) or using other fault detection approaches (Genovesi et al., 2000).

Using this dynamic model, the results were obtained in steady state. For this, the plant model has to simulate $100 - 150$ days in open-loop configuration and determines this steady state. Then, the simulation in closed-loop is simulated for 14 days and faults are caused on the 7^{th} day. The samples for monitoring experiments were taken 100 times per day.

The selected variables to calculate principal components analysis (PCA) and Fisher discriminant analysis (FDA) are the first eleven state variables and the effluent flow rate (Q_0). The concentration of particulate inert organic matter (X_I) and soluble inert organic matter (S_I) are not relevant to this study (Tomita et al., 2002).

The number of principal components, calculated using the CPV approach with 95% maximum variance level, are five, but Fig. 2 shows that seven principal components can be a better option because they capture more variability of the process.

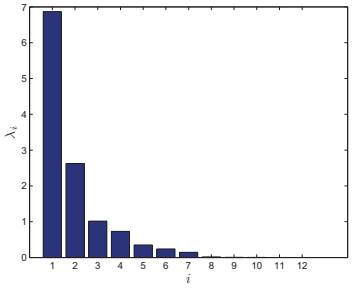

Fig. 2. SCREE graph for principal component selection

The process monitoring under toxicity shock fault can be seen in Fig. 3. The thresholds of both statistics T^2 and Q rise when the fault occurs. In this case, the Q statistic detects this fault better than the T^2 statistic, as this figure shows.

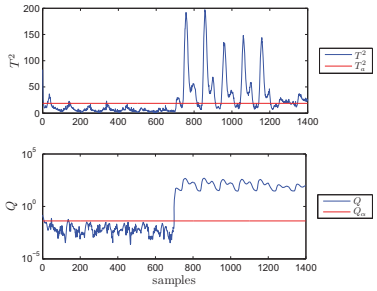

Fig. 3. Toxicity shock fault detection. Logarithmic scale for Q statistic.

The inhabitation fault detection is more effective than the detection of the toxicity shock fault because this type of fault is more drastic, as can be seen in Fig. 4. Finally, the bulking fault detection using PCA is shown in Fig. 5.

The number of selected FDA vectors for fault diagnosis tasks was two using the the SCREE graph method. Fig. 6 shows the discriminant functions (g_i, eq. 23) when a toxicity shock fault has been caused. The solid line corresponds

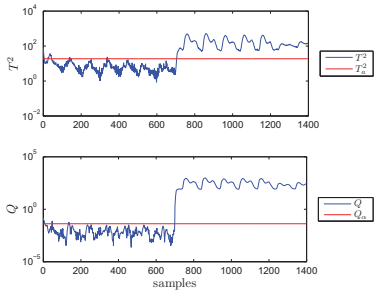

Fig. 4. Inhabitation detection. Logarithmic scale for T^2 and Q statistics.

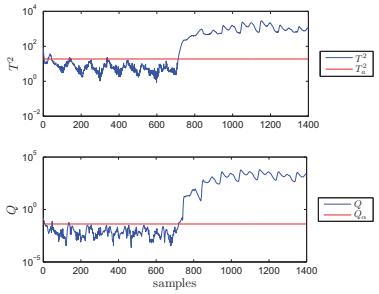

Fig. 5. Bulking fault detection. Logarithmic scale for T^2 and Q statistics.

to the discriminant function for toxicity shock fault, the dotted line corresponds to the discriminant function for inhabitation fault and the dashed line corresponds to the discriminant function for the bulking fault. In this case, once the fault has been detected (7^{th} day) the discriminant function for the toxicity shock fault is greater than the rest of the discriminant functions, so the fault is correctly diagnosed. The experimented faults used to find results are different from the considered faults used in the training data.

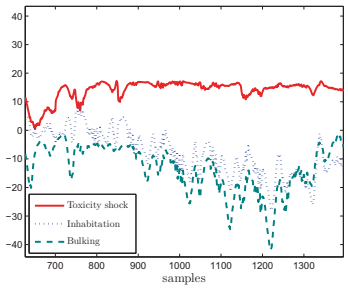

Fig. 6. Toxicity shock fault diagnosis

Fig. 7 shows the discriminant function graphs in the case where the inhabitation fault has occurred. In this situation, the discriminant function for the inhabitation fault is the greatest, so the fault is correctly diagnosed.

Finally, Fig. 8 shows the evolution of the discriminant function for the bulking fault. In this case, the evolution for the bulking fault is always greater than for the rest of the discriminant faults.

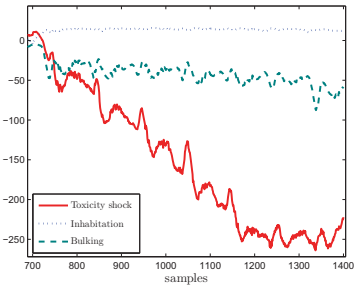

Fig. 7. Inhabitation fault diagnosis

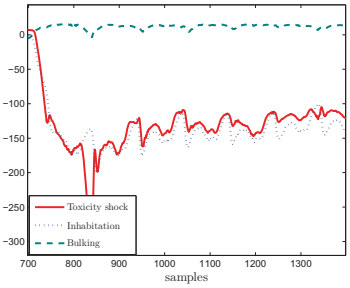

Fig. 8. Bulking fault diagnosis

5. CONCLUSIONS

This paper proposes an approach to deal with the fault detection and diagnosis using statistical techniques, concretely, the principal component analysis (PCA) is used in detection tasks and the Fisher discriminant analysis (FDA) is implemented in diagnosis tasks.

The approach has been proved in a simulated wastewater treatment plant (WWTP) based on the COST benchmark. The considered faults are critical process faults that affect some plant parameters. Data are collected from the plant for normal conditions in order to calculate the PCA model and the thresholds of the T^2 and Q statistics, used to detect the faults. Data for different classes (parameter faults) are also collected to calculate the FDA models for diagnosis. The used approach shows good results because the faults was detected and correctly diagnosed.

A useful update to this work can be to obtain data when two or more faults occur simultaneously. New discriminant functions can be calculated using this data and these new situations could be diagnosed.

ACKNOWLEDGEMENTS

The authors would like to express their gratitude to the department of industrial electrical engineering and automation of Lund University for the implementation of BSM1 model.

REFERENCES

Alex, J., Benedetti, L., Copp, J., Gernaey, K., Jeppsson, U., Nopens, I., Pons, M., Rieger, L., Rosen, C., Steyer, J., Vanrolleghem, P., and Winkler, S. (2008). *Benchmark Simulation Model no. 1 (BSM1)*. Dept. of Industrial Electrical Engineering and Automation. Lund University.

Chiang, L., Russell, E., and Braatz, R. (2000). *Fault Detection and Diagnosis in Industrial Systems*. Springer, Nueva York.

Copp, J. (-). *The COST Simulation Benchmark: Description and Simulator Manual (a product of COST Action 624 & COST Action 682)*. European Cooperation in the field of Scientific and Technical Research.

Duda, R., Hart, P., and Stork, D. (2001). *Pattern Clasification*. Wiley, New York, 2nd edition.

Fuente, M., Garcia, G., and Sainz, G. (2008). Fault diagnosis in a plant using fisher discriminant analysis. *16th Mediterranean Conference on Control and Automation Congress Centre, Ajaccio, France*, 53–58.

Genovesi, A., Harmand, J., and Steyer, J. (2000). Integrated fault detection and isolation: Application to a winery's wastewater treatment plant. *Applied Intelligence*, 13, 59–76.

He, Q., Qin, S., and Wang, J. (2005). A new fault diagnosis method using fault directions in fisher discriminant analysis. *AIChE Journal*, 51(2), 555–571.

Hwang, D. and Han, C. (1999). Real-time monitoring for a process with multiple operating modes. *Control Engineering Practice*, 7, 891–902.

Jackson, J. (1991). *A user's guide to principal components*. Wiley.

Jackson, J. and Mudholkar, G. (1979). Control procedures for residuals associated with principal component analysis. *Technometrics*, 21, 341–349.

Kourti, T. (2002). Multivariable dynamic data modeling for analysis and statistical process control of batch processes, start-ups and grade transitions. *Journal of Chemometrics*, 17, 93–109.

Rosen, C. and Lennox, J. (2001). Multivariate and multiscale monitoring of wastewater treatment operation. *Water research*, 35, 3402–3410.

Tien, D., Lim, K., and Jun, L. (2004). Compartive study of pca approaches in process monitoring and fault detection. *The 30th annual conference of the IEEE industrial electronics society*, 2594–2599.

Tomita, R., Park, S., and Sotomayor, O. (2002). Analysis of activated sludge process using multivariate statistical tools - a pca approach. *Chemical Engineering Journal*, 90, 283–290.

Venkatasubramanian, V., Rengaswamy, R., Kavuri, S., and Yin, K. (2003a). A review of process fault detection and diagnosis. part i: Quantitative model-based methods. *Computers & Chemical Eng.*, 27, 291–311.

Venkatasubramanian, V., Rengaswamy, R., Kavuri, S., and Yin, K. (2003b). A review of process fault detection and diagnosis. part ii: Qualitative models and search strategies. *Computers & Chemical Eng.*, 27, 313–326.

Venkatasubramanian, V., Rengaswamy, R., Kavuri, S., and Yin, K. (2003c). A review of process fault detection and diagnosis. part iii: Process history based methods. *Computers & Chemical Eng.*, 27, 327–346.

Zumoffen, D. and Basualdo, M. (2007). From large chemical plant data to fault diagnosis integrated to decentralized fault tolerant control. *Industrial & Eng. Chemistry Research*, 47, 1201–1220.

On the structure determination of a dynamic PCA model using sensitivity of fault detection

Mohamed Guerfel * **Kamel Ben Othman** *
Mohamed Benrejeb *

* *LARA Automatique, ENIT, BP 37, 1002 Tunis Belvédère, Tunisia*
(e-mail: guerfel_mohamed@yahoo.fr, kamel.benothman@enim.rnu.tn, mohamed.benrejeb@enit.rnu.tn)

Abstract: This work proposes a dynamic PCA modeling method for dynamical non-linear processes. This method uses fault free data to construct data matrix used to compute the correlation matrix and faulty system data in order to fix the dynamic PCA model parameters (the time-lag and the number of principal components). It is shown that the sensitivity of dynamic PCA-based fault detection depends on the parameters used in the model. This method is tested on a three serial interconnected tanks and subject to fluid circulation faults in its pipes.

Keywords: Process and control monitoring; Modeling; Static PCA; Dynamic PCA; Time-lag; Number of components; System fault detection.

1. INTRODUCTION

The use of multi statistical process control tools also known as MSPC became frequent for the modeling, control and diagnosis of complex and over-instrumented processes (chemicals, microelectronics, pharmaceutical..., see Venk (2003)). Static principal component analysis (PCA) is one among the most popular statistical methods, it was used successfully as a modeling tool for statical and slow dynamics processes in linear or non-linear cases, (see Qin (2003)). The extension of PCA for the dynamical modeling, called DPCA, was proposed in Ku (1995). Other work tackled this subject, like in Lee (2004), Li (2003), Mina (2007), Treasure (2004), Xie (2006). In all methods presented in scientific litterature, the model used as reference in the diagnosis procedure is obtained via the minimization of a criterion depending on the nominal data of the process. However, the obtained model can be inadequate for changes detection purposes since the minimized criterion does not necessarily maximize the changement impact of the process on the computed model (see Tamura (2007), Kano (2002)). Many changement types can affect the process, among them one distinguishes : sensors/actuators failures (see Huang (2000)), performance degradation (see Kano (2002)), operating point changes (see Zhao (2004)) and process structure modification or "system fault" (see Huang (2007)). These changes can be highlighted by various statistical tests chosen according to the changement type to be detected. For further details on these tests (also called residuals), the reader can consult Harkat (2006), Kano (2001), Singhal (2005), Guerfel (2008). This work proposes a modeling method of dynamic, linear or non-linear processes via DPCA. This method jointly uses nominal process data to build the correlation matrix to diagonalize and system fault type data to fix the time-lag and the principal component number to retain for the DPCA model. The paper is divided into the following sections. Section 2 recalls shortly the static PCA modeling and its structural parameter. Section 3 defines the dynamic PCA modeling and its structural parameters. The different changes which can affect a process and the statistical test used in this work to detect the system fault type are defined in section 4. The proposed modeling method permitting the choice of the time-lag and the number of principal component to retain for the DPCA model in the case of dynamical non-linear process is presented in section 5. Section 6 illustrates the application of the method on a three serial tanks subject to fluid circulation faults in their pipes. Finally, the last section provides a concluding summary of this work.

2. STATIC PRINCIPAL COMPONENT ANALYSIS

For the vector $z(k) = [z_1(k)\ z_2(k)\ \dots\ z_m(k)]^t$, scaled to zero mean and unity variance and containing the m observed inputs/outputs of the process in the instant k, the data matrix Z_N resulting from the juxtaposition of $z(k)$ in different instants is written :

$$Z_N = [\, z(k)\ \cdots\ z(k+N-1)\,]^t \tag{1}$$

The subscripts N designates the number of observations used in the construction of the matrix Z_N.
Modeling a process via static PCA consists in seeking an optimal linear transformation (with respect to a variance criterion) of the original data matrix Z_N into a new one called T and defined as follows :

$$T = Z_N P \quad ; \quad T = [\, t_1\ \cdots\ t_m\,] \in \mathbb{R}^{N\times m} \tag{2}$$

The vectors $t_q \in \mathbb{R}^N$, $q \in \{1, \dots, m\}$, called principal components are uncorrelated and arranged in the decreasing variance order. The column vectors p_q of the matrix P

represent the eigenvectors corresponding to the eigenvalues λ_q obtained from the diagonalization of the correlation matrix Σ of Z_N :

$$\Sigma = P\Lambda P^t \quad ; \quad PP^t = P^tP = I_m \tag{3}$$

the notation $\Lambda = diag(\lambda_1 \dots \lambda_m)$ designates the diagonal matrix of eigenvalues arranged in the decreasing magnitude order $\lambda_1 \geq \lambda_2 \geq \dots \geq \lambda_m$. With the triple partitioning :

$$\Lambda = \begin{bmatrix} \hat{\Lambda} & 0 \\ 0 & \tilde{\Lambda} \end{bmatrix}, \quad P = \left[\, \hat{P} \middle| \tilde{P} \,\right], \quad T = \left[\, \hat{T} \middle| \tilde{T} \,\right] \tag{4}$$

The data matrix can be decomposed in the following form :

$$Z_N = \hat{Z}_N + E_N \text{ with } \hat{Z}_N = Z_N\hat{C} \ ; \ E_N = Z_N\tilde{C} \tag{5}$$

The matrices $\hat{C} = \hat{P}\,\hat{P}^t$ and $\tilde{C} = I_m - \hat{C}$ form the static PCA model of the process (for further details see Jollife (2003)). The matrices $\hat{Z}_N$ and E_N represent, respectively, the modeled and the non modeled variations of Z_N from ℓ components ($\ell < m$). The first ℓ eigenvectors forming the matrix $\hat{P} \in \mathbb{R}^{m\times\ell}$ constitute the representation space whereas the last $(m-\ell)$ eigenvectors forming the matrix $\hat{P} \in \mathbb{R}^{m\times\ell}$ constitute the residual space.
The identification of the static PCA model thus consists in estimating its parameters by an eigenvalue/eigenvector decomposition of the matrix Σ and determining its structural parameter which is the number of principal components ℓ to retain. An incorrect choice (too large or too small) of ℓ could mask the changes occurring in the modeled process or gives false alarms which affect the change detection procedure (see Qin (2003)). Many methods were proposed to fix ℓ in the static PCA model. The reader can find more details in Valle (1999). Most of these methods are heuristic and give a subjective number ℓ (see Harkat (2005)). In order to mitigate the disvantages of the heuristic methods, Qin and Dunia have proposed to fix ℓ via the minimization of a criterion called VNR which represents the variance of the reconstruction error of the process variables (see Qin (2000)). However, it is noted that the VNR criterion underestimates the number ℓ exact to retain in real applications cases (see Valle (1999)). All the methods aiming at the determination of ℓ seek to find its theoretical or exact value called (ℓ_{th}) which represents the theoretical number of linear or quasi-linear relations existing between the different components of $z(k)$. These methods are sensitive to the signal noise ratio and depend on the nature of the process non linearity. It is also noted that ℓ can be different from ℓ_{th} in the case of models built for diagnosis purposes provided that the static PCA model (constructed with ℓ components) can detect changes (see Frank (2000)). From this idea was born a new process modeling method via static PCA. Proposed in Tamura (2007), this method uses nominal process data to build the correlation matrix which will be diagonalized and faulty data in order to fix ℓ.

3. DYNAMIC PRINCIPAL COMPONENT ANALYSIS

Dynamic principal component analysis proposed in Ku (1995) and known as DPCA aims at finding dynamical linear relations between the process variables. The principle of this method is identical to the static PCA. Starting from a scaled to zero mean and unity variance data vector $z^d(k) = [z^t(k)\ z^t(k-1)\ \dots\ z^t(k-s)]$, where s designates the used time-lag, the data matrix $Z_N^d(k,s) \in \mathbb{R}^{N\times m(s+1)}$ is built as follows :

$$Z_N^d(k,s) = \begin{bmatrix} z^t(k) & \dots & z^t(k-s) \\ z^t(k+1) & \dots & z^t(k-s+1) \\ \vdots & \ddots & \vdots \\ z^t(k+N-1) & \dots & z^t(k+N-1-s) \end{bmatrix} \tag{6}$$

with $N > m(s+1)$ and $k > s$.
The correlation matrix obtained from $Z_N^d(k,s)$, noted Σ_d, is computed and diagonalized in order to obtain the eigenvectors and the eigenvalues matrices noted respectively P_d and Λ_d. Each one of these two matrices is divided into two parts the first corresponding to the representation space $(\hat{\Lambda}_d,\ \hat{P}_d)$ and the second corresponding to the residual space $(\tilde{\Lambda}_d,\ \tilde{P}_d)$. The principal components vector noted $t^d \in \mathbb{R}^{1\times m(s+1)}$, can be computed in an instant k as follows :

$$t^d(k) = \left[\, \hat{t}^d(k) \mid \tilde{t}^d(k) \,\right] = z^d(k)P_d = z^d(k)\left[\, \hat{P}_d \mid \tilde{P}_d \,\right] \tag{7}$$

The structural parameters in DPCA modeling are the number of principal components ℓ and the time-lag s. The number ℓ can be fixed via the methods used in static PCA after the choice of s which is a very delicate problem. The modeling of data obtained from dynamic process via static PCA constructs an approximate static model of the real process and does not reveal its exact structure (see Ku (1995)). It is possible to detect modifications in dynamical processes via static PCA as in Harkat (2006) and Sharmin (2008), but the theoretical bases of the method are lost since the principal components are no longer uncorrelated and do not follow a normal multivariate statistical distribution. In this case, it will be very difficult to detect small changes in the process parameters as long as the variation domain of the process variales remain the same before and after the change. For a well chosen time-lag $s = s_{min}$, all the static and dynamic relations ruling the process will be represented by the last eigenvectors corresponding to the smallest eigenvalues of Σ_d computed from $Z_N^d(k, s_{min})$. Taking a time-lag s higher than s_{min} in the construction of $Z_N^d(k,s)$ used for the computation of the DPCA model will not bring any supplementary information but will add redundant relations which were obtained from the construction of the DPCA model using the matrix $Z_N^d(k, s_{min})$ (see Ku (1995)). Many methods were proposed for the choice of s. They seek to find the theoritical $s = s_{min}$, most of them are heuristic as in Ku (1995) or resulting from the identification techniques as AIC, see Akaike (1974), Larimore (1990), Li (2003) and MDL, see Simoglou (2002), Rissanen (1978) which privilege the approximation of the data matrix. None of those methods was built in the purpose of minimization of s compared to fault detection.

4. STATISTIC USED FOR SYSTEM FAULT DETECTION

The physical processes are subject to changes in their operating conditions. In the case of non stationary processes, these changes can be sensors/actuators failures (see Huang (2000)), operating point changes, performance degradation or process structure modification. The operating point

changes are characterized by an augmentation in the mean of one or many inputs (see Zhao (2004)). The process performance degradation can be expressed as an augmentation in the variance of one or many process variables under the hypothesis of independent and identically distributed noise (see Kano (2002)). The process structure modifications known as "system fault" appear as changes in the structure or a modification in its model parameters (see Huang (2007)). All these changes can be highlighted by various statistical tests chosen according to the changement type to be detected. Only the system fault type is included in this work. The best indices for the detection of such modification are the ones based on the residual space (see Guerfel (2008)). For this reason, one proposes the use of the D_i statistic, $i = 1, 2, \ldots, (m(s+1) - \ell)$, which is defined in Harkat (2006) as the sum of squared last principal components. This statistic is computed every instant k :

$$D_i(k) = \sum_{j=m(s+1)-i+1}^{m(s+1)} \left(\tilde{t}_j^d(k)\right)^2 \tag{8}$$

The variable $\tilde{t}_j^d(k)$ designates the j^{th} principal component obtained at the instant k. The index D_i represents an SPE (see box (1954)) computed from a DPCA model with $(m(s+1)-i)$ components, its detection threshold $\tau_{i,\alpha}^2$, can be computed in the following way :

$$\tau_{i,\alpha}^2 = g^{(i)} \chi_{h^{(i)},\alpha}^2 \tag{9}$$

The notation χ^2 designates the Chi-square distribution, α designates the used confidence limit, $g^{(i)}$ and $h^{(i)}$ are defined as follows :

$$g^{(i)} = \frac{\sum_{j=m(s+1)-i+1}^{m(s+1)} \lambda_j^2}{\sum_{j=m(s+1)-i+1}^{m(s+1)} \lambda_j} \quad h^{(i)} = \frac{\left(\sum_{j=m(s+1)-i+1}^{m(s+1)} \lambda_j\right)^2}{\sum_{j=m(s+1)-i+1}^{m(s+1)} \lambda_j^2} \tag{10}$$

The quantities $\lambda_j,\ j \in \{m(s+1) - i + 1, \ldots, m(s+1)\}$, designate the j^{th} eigenvalues of Σ_d. A system fault is detected if the D_i index is higher than its threshold $\tau_{i,\alpha}^2$.

5. PROPOSITION FOR DYNAMICAL PROCESSES MODELING

The proposed method is similar to the one defined in Tamura (2007) and called MDM abreviation of *Multi Dimensionnal Monitoring*. Contrary to the MDM, the proposed method allows not only the choice of ℓ but also the choice of the minimum time-lag s to retain for the data matrix $Z_N^d(k, s)$ used in the construction of the DPCA process model. The principle of the method is the following :

(1) Begin method
(2) Initialization $S_{init} = 0$ and $\ell = 0$
(3) Build $Z_N^d(k, S_{init})$, Compute Σ_d, P_d and Λ_d
(4) Compute D_i from system fault data for i varying from 1 to the number of column in $Z_N^d(k, s)$ minus 1
(5) If the fault is detected with any of D_i then go to step 7 else go to step 6
(6) $S_{init} = S_{init} + 1$ go to step 3
(7) $s = S_{init}$ and ℓ is equal to the difference between the number of column in $Z_N^d(k, s)$ and the largest value of i which permits the fault detection.
(8) End method

The disadvantage of the proposed method lies in the fact that a knowledge of information on the system fault is necessary to ensure the choice of structural parameters (s and ℓ) to be retained for the DPCA model. From another point of view, if information on the system fault is available, this method becomes very attractive because it determines the simplest model allowing the system fault detection. Figure (1) summarizes the algorithm of the method in the case of a single system fault "j" affecting the modeled process.

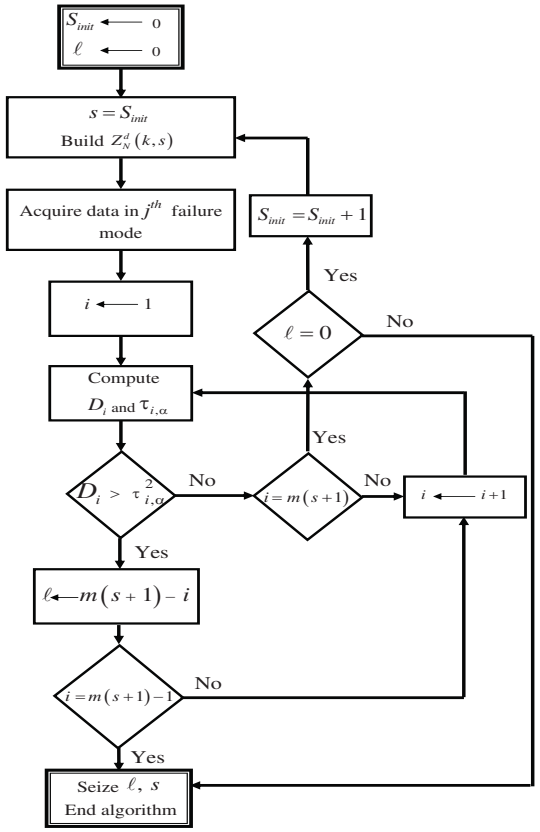

Fig. 1. Algorithm of the proposed method for the determination of s and ℓ in the DPCA model

In order to supress false alarms, the process is considered in failure mode ($D_i > \tau_{i,\alpha}^2$), if D_i has shown eight succeeding values larger than $\tau_{i,\alpha}^2$. The value "eight" is determined in an empirical way and must be adjusted according to the treated application.

6. APPLICATION IN THE MODELING OF THREE TANK SYSTEM

The modeled process illustrated in figure (2), is formed by three identical serial tanks. It contains two inputs : flows q_1, q_2 and three outputs H_1, H_2 and H_3 representing respectively the heights in the first, second and third tanks.

These tanks are interconnected at the bottom by pipes. Two valves V_3 and V_2, separating respectively tank 2 from tank 3 and tank 2 from the outside are introduced in order to model the flows perturbations in the pipes. For a sampling period equal to one second, the discrete process equations are :

$$\left\{\begin{array}{c} H_1(k) = A^{-1}\left(q_1(k) + q_{31}(k) - q_{10}(k)\right) + H_1(k-1) \\ H_2(k) = A^{-1}\left(q_2(k) - q_{23}(k) - q_{20}(k)\right) + H_2(k-1) \\ H_3(k) = A^{-1}\left(q_{23}(k) - q_{31}(k)\right) + H_3(k-1) \\ q_{10}(k) = K_1\sqrt{H_1(k)} \\ q_{20}(k) = K_2\sqrt{H_2(k)} \\ q_{31}(k) = K_{31} f\left(H_3(k) - H_1(k)\right) \\ q_{23}(k) = K_{23} f\left(H_2(k) - H_3(k)\right) \end{array}\right. \tag{11}$$

where A equal to $0.01539\, m^2$, designates the tank section. The constants K_1, K_2, K_{31} and K_{23} respectively equal to $1.816\, e^{-4}$, $9.804\, e^{-5}$, $1.005\, e^{-4}$ and $7.804\, e^{-5}$ are the process characteristics. The term $f(.)$ designates a non linear function defined as follows :

$$f(x) \triangleq sign(x)\sqrt{|x|} \tag{12}$$

The measured process variables are the inputs z_1^b, z_2^b and

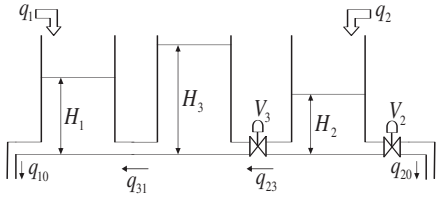

Fig. 2. Three tanks system

the outputs z_3^b, z_4^b and z_5^b. Theses measures are related in the instant k to the physical values via the following equations :

$$\left\{\begin{array}{l} z_1^b(k) = H_1(k) + \varepsilon_1(k) \\ z_2^b(k) = H_2(k) + \varepsilon_2(k) \\ z_3^b(k) = H_3(k) + \varepsilon_3(k) \\ z_4^b(k) = q_1(k) + \varepsilon_4(k) \\ z_5^b(k) = q_2(k) + \varepsilon_5(k) \end{array}\right. \tag{13}$$

The quantities $\varepsilon_r(k)$, $r \in \{1, \ldots, 5\}$ designate gaussian centered measurement noise. Its standard deviation is equal to 3% of that of the entries. The flows q_1 and q_2 are expressed in m^3/s. They are chosen to be random durations crenels with variable amplitudes respectively in $[3.20,\ 6.71] \times 10^{-5}$ for q_1 and in $[5.73,\ 9.57] \times 10^{-5}$ for q_2. The tanks initial heights are expressed in meter. Their values are 0.147, 0.276 and 0.195 respectively for the first, second and third tank. The system is firstly simulated under nominal operation during 4000 samples. After centering and reducing the inputs/outputs measures, the vector z is built at each instant k as follows :

$$z(k) = \left[\, z_1(k)\ z_2(k)\ z_3(k)\ z_4(k)\ z_5(k) \,\right]^t \tag{14}$$

where $z_r(k)$ designates the centered and reduced value of $z_r^b(k)$. The data matrix is constructed via (1). It will be used in the computation of the matrices Λ and P.

In the dynamical case, the vector z^d is constructed in an instant k for a time-lag s using time-lagged vectors z obtained in the static case as following :

$$z^d(k) = \left[\, z^t(k)\ z^t(k-1)\ \ldots\ z^t(k-s) \,\right] \tag{15}$$

The data matrix $Z_N^d(k,s)$ is built via (6). It will be used for the computation of the matrices Λ_d and P_d.

Figure 3 shows the process scree plot for a time-lag s respectively equal to zero, one and two. The eigenvalues of Σ (built for $s = 0$) are not null and do not indicate the presence of any linear or quasi linear relation between the measured process variables at the same instant. The last three eigenvalues of Σ_d built for $s = 1$ are quasi null and show the existance of three quasi linear relations verified by the measured process variables between two sampling instants. The correlation matrix Σ_d built for $s = 2$ shows six quasi null eigenvalues. They indicates the presence of six quasi linear relations verified by the measured process variables between three sampling instants. The approximation of the non linear relations verified by the measured process variables may be better if one uses time-lags higher than two but the computation complexity will increase as well.

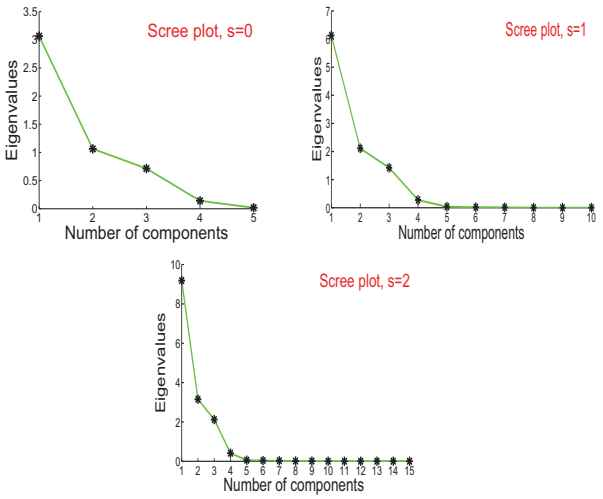

Fig. 3. Scree plots for $s = 0$, $s = 1$ and $s = 2$

Twenty measures representing a system fault are generated in order to fix the time-lag s used for the construction of $Z_N^d(k,s)$. This system fault represents a variation of 1.1 of K_2 from its nominal value. The application of the algorithm in section 5 gives that $s = 1$ and $\ell = 7$ are sufficient to detect such a fault.

A second simulation shown in figure 4 is realized during 4000 instants and perturbations in flows circulation are introduced by varying K_2 in the following way. For the first 1000 instants, K_2 is equal to its nominal value. In the second 1000 instants, K_2 is equal to 1.1× its nominal value. In the third 1000 instants, K_2 is equal to 1.2× its nominal value. For the latest 1000 instants, K_2 is equal to 1.3× its nominal value.

The evolution of the statistics D_i, $i \in \{i, \ldots, 4\}$, respectively for $s = 0$ and $s = 1$ in the case of the second simulation are shown in figure 5 and 6. On one hand, the flows perturbations are not detectable with the statical PCA model. The statistics D_i obtained from its application on

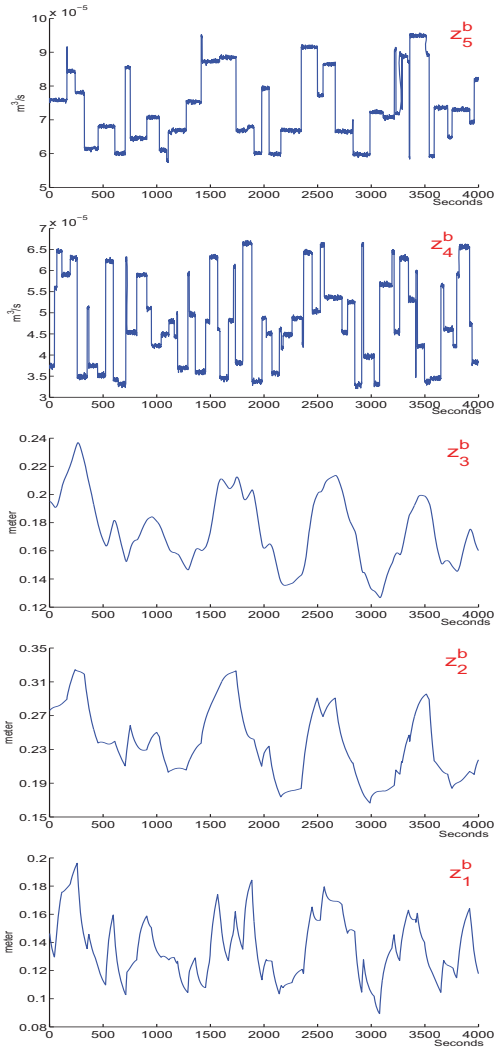

Fig. 4. Evolution of flows z_5^b, z_4^b and heights z_3^b, z_2^b and z_1^b in the second simulation

the current process data are always under their thresholds (figure 5) excepting some aberrant values. On the other hand, the flows perturbations are well detected with a DPCA built with $s = 1$. The statistics D_i, $i \in \{1, \ldots 3\}$, obtained from its application on the current process data allow the detection of all the system faults that were simulated. The maximal dimension of the residual space that can detect the perturbations is equal to three. The time-lag s used to construct the data matrix from which the DPCA model is built depending on the magnitude of the system fault to be detected. Increasing the value of s may lead to a better linear approximation of the real non linear relations existing between the time-lagged process measurements which can reduce the magnitude of the system fault to be detected.

7. CONCLUSION

The proposed method permits the estimation of the time-lag s and the choice of the principal component number ℓ used in the process modeling via DPCA. Contrary to the

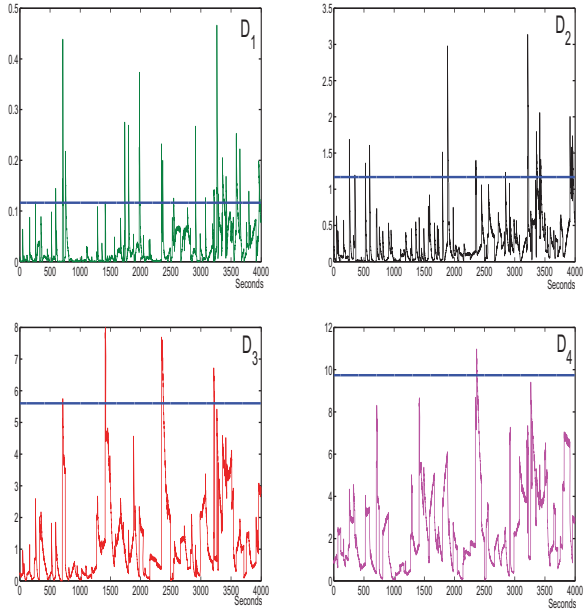

Fig. 5. Evolution of $D_i, i \in \{1, \ldots, 4\}$ in the case of $s = 0$

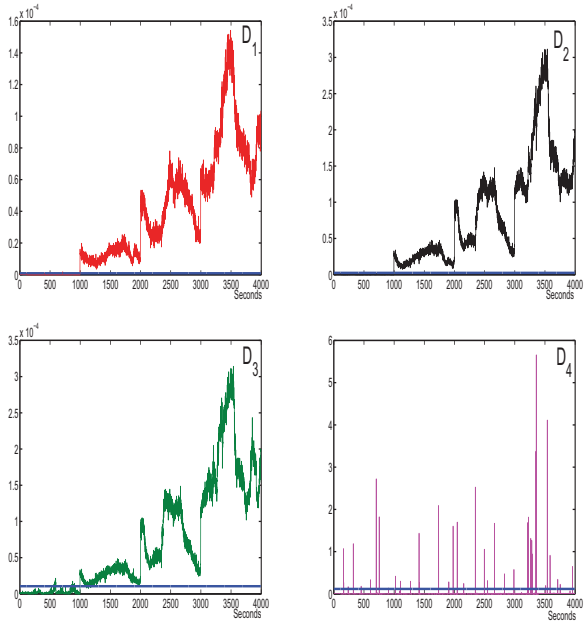

Fig. 6. Evolution of $D_i, i \in \{1, \ldots, 4\}$ in the case of $s = 1$

majority of the existing methods which use data gathered during nominal operation conditions to estimate s and ℓ, the proposed method uses data representing nominal process operating condition to build the data matrix which is used in the computation of DPCA model and other process data belonging to the system fault type to compute the structural parameters s and ℓ. The suggested method proves to be interesting if information relating to the system fault mode is a priori available. In this case, the method determines the least complex model allowing the detection of the considered system fault. Built around a

particular operating point, this method can be sensitive to operating point changes. In the abscence of a system fault, the obtained model presents a risk of generating false alarms due to a shift of the current process variables operating point. The extension of the method to multiple system fault cases and the minimization of the false alarms due to the operating point shift will be considered in forthcoming works.

REFERENCES

H. Akaike. A new look at the statistical model identification. *IEEE Transactions on Automatic Control*, volume 19, pages 716–723, 1974.

G. E. P. Box. Some theorems on quadratique forms applied in the study of analysis of variance problems : Effect of inequality of variance in one-way classification. *The Annals of Mathematical Statistics*, volume 25, pages 290–302, 1954.

P.M. Frank, E. A. Garcia, B. Köppen-Seliger. Modelling for fault detection and isolation versus modelling for control. *Mathematics and Computers in Simulation*, volume 53, pages 259–271. 2000.

M. Guerfel, G. Mourot, J. Ragot, M. Benrejeb, K. Benothman. Comparaison des indices de détection de changements des modes de fonctionnement par ACP. Cas des indices basés sur l'estimation d'état. *1st International Workshop on Systems Engineering Design & Applications, SENDA'08*, Monastir, Tunisia 24-26 October, 2008.

M. F. Harkat, G. Mourot, J. Ragot. Diagnostic de fonctionnement de capteurs d'un réseau de surveillance de la qualité de l'air par analyse en composantes principales. *Journal européen des systèmes automatisés*, volume 39. pages 417–436, 2005.

M. F. Harkat, G. Mourot, J. Ragot. An improved PCA scheme for sensor FDI: Application to an air quality monitoring network. *Journal of Process Control*, volume 16, pages 625–634, 2006.

Y. Huang, J. Gertler, T. McAvoy. Sensor and actuator fault isolation by structured partial PCA with nonlinear extensions. *Journal of Process Control*, volume 10, pages 444-459, 2000.

H.P. Huang, C.C. Li, J.C. Jeng. Multiple multiplicative fault diagnosis for dynamic processes via parameter similarity measures *Industrial and Engineering Chemistry Research*, volume 46, pages 4517-4530, 2007.

I. T. Jolliffe. *Principal component analysis.* Springer-Verlag, New York, 2003.

M. Kano, H. Ohno, S. Hasebe, I. Hashimoto. New multivariate statistical process monitoring method using principal component analysis. *Computers and Chemical Engineering*, volume 25, pages 1103–1113, 2001.

M. Kano, K. Nagao, S. Hasebe, I. Hashimoto, H. Ohno, Strauss R. Comparison of multivariate statistical process control monitoring methods with applications to the Eastman challenge problem. *Computers and Chemical Engineering*, volume 26, pages 161–174, 2002.

W. Ku, R. H. Storer, C. Georgakis. Disturbance detection and isolation by dynamic principal component analysis. *Chemometrics and Intelligent Laboratory Systems*, volume 30, pages 179–196, 1995.

W. E. Larimore. Canonical variate analysis in identification, filtering and adaptative control. *29th Conference on Decision and Control*, Honolulu, Hawai Islands December, pp. 635–639, 1990.

C. Lee, S. W. Choi, I. B. Lee. Sensor fault identification based on time-lagged PCA in dynamic processes. *Chemometrics and Intelligent Laboratory Systems*, volume 70, pages 165–178, 2004.

W. Li, S. J. Qin. Consistent dynamic PCA based on errors-in-variables subspace identification. *Journal of Process Control*, volume 11, pages 661–678, 2003.

J. Mina, C. Verde. Fault detection for large scale systems using dynamic principal components analysis with adaptation. *International Journal of Computers, Communications & Control*, volume 2, pages 185–194, 2007.

S. J. Qin, R. Dunia. Determining the number of principal components for best reconstruction. *Journal of Process Control*, volume 10, pages 245–250, 2000.

S. J. Qin. Statistical process monitoring: basics and beyond. *Journal of Chemometrics*, volume 17, pages 480–501, 2003.

R. Sharmin, S. L. Shah, U. Sundararaj. A PCA Based Fault Detection Scheme for an Industrial High Pressure Polyethylene Reactor. *Macromolecular Reaction. Engineering*, volume 2, pages 12–30, 2008.

A. Singhal, D. E. Seborg. Clustering multivariate time-series data. *Journal of chemometrics*, volume 19, pages 427–438, 2005.

A. Simoglou, E. B. Martin, A.J. Morris. Statistical performance monitoring of dynamic multivariate process using state space modelling. *Computers and Chemical Engineering*, volume 26, pages 909–920, 2002.

J. Rissanen. Modelling by shortest data description. *Automatica*, volume 14, pages 465–471, 1978.

M. Tamura, S. Tsujita. A study on the number of principal components and sensitivity of fault detection using PCA. *Computers and Chemical Engineering*, volume 31, pages 1035–1046, 2007.

R. J. Treasure, U. Kruger, J. E. Cooper. Dynamic multivariate statistical process control using subspace identification. *Journal of Process Control*, volume 11, 661–678, 2004.

S. Valle, L. Weihua, S. J. Qin. Selection of the number of principal components : The variance of the reconstruction error criterion with a comparison to other methods. *Industrial and Engineering Chemistry Research*, volume 38, pages 4389–4401, 1999.

V. Venkatsubramanian, R. Rengaswamy, K. Yin, S. N. Kavuri. A review of fault detection and diagnosis; part I: quantitative model-based methods. *Computers and Chemical Engineering*, volume 27, pages 293–311, 2003.

M. Wax, I. Ziskind. Detection of the number of coherent signals by the MDL principle. *IEEE Transactions on Acoustic, Speech and signal processing*, volume 37, pages 1190–1195, 1989.

L. Xie, J. Zhang, S. Wang. Investigation of Dynamic Multivariate Chemical Process Monitoring. *Chinese Journal of Chemical Engineering*, volume 14, pages 559–568, 2006.

S. J. Zhao, J. Zhang, Y. M. Xu. Monitoring of processes with multiple operating modes through multiple principle component analysis models. *Industrial Engineering Chemical Research*, volume 43, pages 7025–7035, 2004.

LoopRank: A Novel Tool to Evaluate Loop Connectivity

M. Farenzena and J. O. Trierweiler

Group of Integration, Modelling, Simulation, Control and Optimization of Processes (GIMSCOP)
Department of Chemical Engineering, Federal University of Rio Grande do Sul (UFRGS)
Rua Luiz Englert, s/n CEP: 90.040-040 - Porto Alegre - RS - BRAZIL,
Fax: +55 51 3308 3277, Phone: +55 51 3308 4163
E-MAIL: {farenz, jorge}@enq.ufrgs.br

Abstract: Since the number of loops in refineries or petrochemical plants is very large and the number of loops with poor performance is equally large, to prioritize their maintenance is essential to ensure plant profitability. This work proposes a methodology called *LoopRank* to compute the importance factor of each loop, aiming to prioritize their maintenance. The algorithm is based on the connection among them, which is computed using partial correlation. The algorithm is based on *PageRank*, which analyses connections among nodes recursively and computes a rank for each node using partial correlation. The *LoopRank* assigns an individual score for each loop ranging from 0% to 100%. Based on this score, the loop maintenance can be ranked. The *LoopRank* algorithm is computationally efficient, thus allowing its industrial large-scale application. The proposed algorithm was applied both on simulation and industrial case studies, providing fruitful results.

Keywords: Performance Monitoring, Data correlation, Loop Rank, Partial Correlation, Data-mining.

1. INTRODUCTION

Nowadays, it is a common knowledge the positive impact of control loop performance assessment tools over industrial plants. In the last twenty years, many methodologies and tools have been developed to diagnose the main loops problems:

- Poor performance (Harris, 1989, Huang *et al.*, 1997, Jelali, 2006);
- Plant-wide disturbances (Jiang *et al.*, 2007, Thornhill and Horch, 2007, Xia *et al.*, 2005);
- Valve hysteresis (Choudhury *et al.*, 2004, Hagglund, 2002, Hagglund, 2007, Rossi and Scali, 2005, Ruel, 2000);

It is also well known that most of industrial loops do not perform well (Paulonis and Cox, 2003). However, improve and maintain all loops in their optimal performance are impossible and economically infeasible because of the small number of engineers responsible to maintain a large number of loops. Therefore, a methodology to prioritize loop maintenance is required.

Methodologies to prioritize loop maintenance or to evaluate loop interaction are scarce in the literature. Tangirala et al. (2005) proposed a method based on spectral correlation between loops. Thornhill et al. (2002) proposed tools based on spectral principal component analysis.

The scope of this work is to provide an importance score for each control loop to prioritize its maintenance. Fig. 1 shows one simple case with four loops.

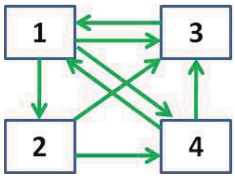

Fig. 1: Case study with four control loops interconnected.

In Fig. 1 scheme, it is easy to see that loop 3 has the most connections from others (3). So, is it the most important loop? On the other hand, loop 1 receives 2 connections, where one of them is very important, coming from loop 3, and it is the only loop 3 connection. Which is more important, loop 1 or 3? It is clear that an algorithm to systematize this procedure that provides an importance score for each loop is strongly required.

In this work is proposed an algorithm, called *LoopRank* that provides a grade based on loops connections. The loops that receive more connections from others, i.e. the loops that have stronger correlation with the remaining should have more importance than a loop that does not have any correlation with the others. To quantify these bounds, partial correlation is used. Subsequently, the priority of each loop is ranked using *PageRank* algorithm (Bryan and Leise, 2006).

The paper is segmented as follows: in section 2 the necessary background will be summarized. In section 3, the methodology to prioritize loop maintenance, proposed in this work is described. In section 4, the methodology is applied in simulation and industrial case studies. The paper ends with the concluding remarks.

2. BACKGROUND

This section provides the necessary background to understand the proposed methodology described in section 3.

2.1 Correlation and Partial Correlation

Correlation can be described as the linear dependence between two random variables (Bilodeau and Brenner, 1999). The correlation (ρ_{XY}) between two variables can be computed as follows:

$$\rho_{XY} = \frac{cov(X,Y)}{\sqrt{var(X)var(Y)}} \quad (1)$$

Where $cov(X,Y)$ is the covariance between X and Y and $var\,var$ is the variance. The correlation is a measurement of variable interaction, independently of the scale which it is measured.

In the case where the inputs and outputs are correlated, a better measure of the interaction is the partial correlation. It provides the degree of association of X and Y, with the effect of a set controlling variables (Z) removed. The partial correlation between X and Y with Z fixed ($\rho_{XY|Z}$) is computed by:

$$\rho_{XY|Z} = \frac{\rho_{XY} - \rho_{XZ}\rho_{YZ}}{\sqrt{(1-\rho_{XZ}^2)(1-\rho_{YZ}^2)}} \quad (2)$$

2.2 Importance score

To rank the relative importance of elements is essential when resources are limited. Rank algorithms have a broad class of applications including financial decisions, searching tools, among others. One rank algorithm that has been highlighted recently is *PageRank* (Bryan and Leise, 2006), which is used by the Google®'s search engine to rank pages relevance. It gives an importance score for each webpage according to an eigenvector of a weighted link matrix. It is based on the links made to a given page from other pages, and the relative impact of each source page.

The algorithm can be summarized as follows. Suppose n elements where the relative connectivity of them (x_k) should be computed, where k is the indexing element ($1 \leq k \leq n$), where this value corresponds to the arrows in each element. In the example (Fig. 1) x_1=2, x_2=1, x_3=3, x_4=2. Thus, loops can be ranked as follows 3, 1 and 4, and 2, based only on the connections. Following, the relative importance of k (x_k) is computed using the number of back links for this page. If page j contains n_j links to other pages, and one of them links to element k, then it will be boosted by a score x_j/n_j. Let $L_k \subset \{1,2,\dots,n\}$ denote the set of pages with link to page k. The relative weight for each k is computed by:

$$x_k = \sum_{j \in L_k} \frac{x_j}{n_j} \quad (3)$$

It is also assumed that the link from a page to itself has zero weight. For loop 1, its impact can be written as $x_1 = \frac{x_3}{1} + \frac{x_4}{2}$, since pages 3 and 4 have back-links to 1 and loops 3 and 4 have 1 and 2 links, respectively.

This linear relation can be written as $Ax = x$, where A is called "link matrix" and $x = [x_1 \;\; x_2 \;\; x_3 \;\; x_4]$. $A(i,j)$ provides the relative weight from loop j to loop i, where the rows show the relative weight of each connection that goes to a given loop and columns show the relative importance of the connections that come from the same loop.

In the scheme of Fig. 1, the A matrix can be written as:

$$A = \begin{bmatrix} 0 & 0 & 1 & \frac{1}{2} \\ \frac{1}{3} & 0 & 0 & 0 \\ \frac{1}{3} & \frac{1}{2} & 0 & \frac{1}{2} \\ \frac{1}{3} & \frac{1}{2} & 0 & 0 \end{bmatrix} \quad (4)$$

In the case of loop 1 (Fig 1): three arrows come out this loop. Then the relative importance added in each loop is $\frac{1}{3}$, as shown in the first column of A.

This procedure transforms the problem into a simple eigenvector problem ($Ax = \lambda x$). It can be proved that λ has always a unitary eigenvalue for this kind of matrices. Thus, the eigenvector x with eigenvalue 1 for matrix A is seek. The importance score (*IS*) for each page is given by the mentioned eigenvector just normalizing each elements by the sum of all components so that at the end the final sum is equal to 1. For the case study, the already normalized importance score are x_1=0.387, x_2=0.129, x_3=0.290, x_4=0.194.

More information about *PageRank* algorithm can be found in Bryan and Leise (2006).

3. METHODOLOGY DESCRIPTION

This section describes the *LoopRank* algorithm to evaluate loop importance.

Initially the loop output data is collected. Only routine data is required and no further information about the loop is required.

The first step is to compute the links between loops and its relative weight, where the impact of a single variable over each other should be computed. The measure of loops connectivity used in this work is the linear dependence among them.

Industrial loops generally have high correlation between them. To overcome this constraint and isolate the individual loop impact over each other, partial correlation is used. Simple correlation between loops has also been tested and results were poorer. This comparison will be shown in the case studies section. Thus, the relative weight between loops i

and j is provided by the partial correlation between these loops, removing the effect of the remaining loops ($\rho_{ij|LI}$), where $L = \{1,2,\dots,n\}$, $LA = \{i,j\}$, and $LI = L \cap LA$. Each element of the relative weight matrix (A_{ij}) is given by the partial correlation between loop i and loop $_j$ ($\rho_{ij|LI}$) :

$$A_{ij} = \rho_{ij|LI} \tag{5}$$

The next step is to evaluate *the LoopRank (LR)*, based on *relative weight matrix* (A), using *PageRank* algorithm that can quantify the relative importance of each loop, allowing to rank the loops for maintenance purposes. This class of algorithm was chosen because of its capacity to prioritize elements based on the connections among them and its computational/numerical efficiency. The *LoopRank* output is then normalized to limit each grade between 0 and 100%, where always the worst important loop has $LR = 0\%$ and the most important $LR = 100\%$.

Some loops can have more impact in plant profitability or help to smooth the operation. The loops that have connections with these "important ones" should have stronger weights. Thus, it is necessary to assign a *loop weight* (w_k), which is dependent on the source loop. The w_k is assigned heuristically, depending on loop type and its profitability. One heuristics is here suggested: flow and level loops are least important ($w=1$), pressure loops have middle importance ($w=1.5$) and temperature and composition are the highest importance ($w=2$). The *connection weight* k is then multiplied by all links where the source is loop k, in A.

The application of *LoopRank* algorithm can be summarized as follows:

1. Collect routine operating data of the loops;
2. Compute the partial correlation between each loop and build the *relative weight matrix (A)*;
3. Based on A, compute the *LoopRank*, using *PageRank* algorithm;
4. To the result in 3, multiply each loop by the corresponding loop weight (w);
5. Normalize the final results to express the result in relative percentage, where each importance is bounded between 0% and 100%.

4. CASE STUDIES

This section shows the application of *LoopRank* algorithm both on simulation and industrial case studies.

4.1 Simulation example I

In the first case study, a set of 10 loops will be analyzed. The first one has oscillatory behaviour. The other loops have been generated from the first loop by a simple addition of different noise levels followed by normalization in the amplitude. Fig. 2 shows the time trends for all loops.

Applying the proposed algorithm with $w = 1$ for all loops produces the results shown in Tab. 1. As it was already expected, the results of Tab. 1 clearly indicates that the source of oscillatory behaviour is related to the most important loop, which is in this case is the first one.

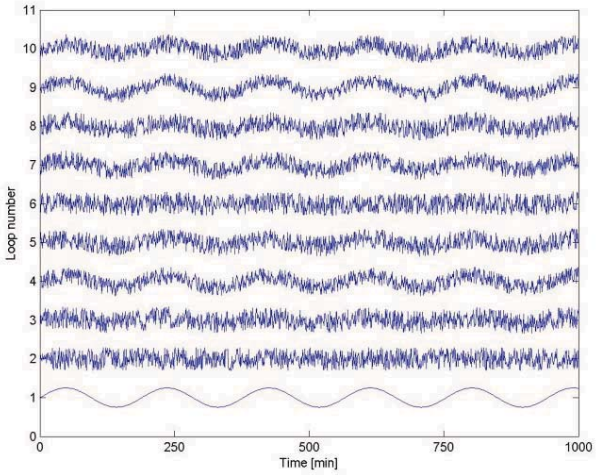

Fig. 2: Time trends of 10 data series.

Tab. 1: *LoopRanks* for case study 1.

k	LR_k	k	LR_k
1	100	**6**	16
2	3	**7**	10
3	1	**8**	20
4	21	**9**	11
5	13	**10**	0

Following, the impact of w_k will be analyzed. In this case study, w_5 will be increased and its impact over loop 4 (LR_4) and loop 8 (LR_8) are shown in Tab. 2. Since interaction between loop 5 and 1 is stronger than all remaining loop 5 connections, it is expected that increase the weight of loop 5, the LR of loop 1 will increase while the LR of all others will decrease, because the connections between loop 5 and all others will become weaker.

Tab. 2: Impact of w_5 in LR_4 and LR_8 *LoopRanks.*

w_5	LR_4	LR_8
1	21.0	20.0
1.5	20.0	18.6
2	19.3	17.3
5	16.1	12.3
10	13.7	8.3

The previous claim is corroborated by Tab. 2, where increasing w_5, the importance factors LR_4 and LR_8 decreased. LR_1 remains for all cases equal to 100%.

4.2 Simulation example II

In the second case study a set of 100 loops are be analyzed. The time trend for each loop is generated using the following procedure:

- Loop 1, loop 2, and loop 4 have oscillatory behaviour with different frequencies;
- Loop 3 and loop 5 data trends are obtained passing white-noise through a first order transfer function with different time constants;
- Loops 6, 7, and 8 are random signals;
- Other 92 data trends are generated by the linear combination of the first 8 data trends. Following, white noise is added in each one of the 92 data trends. Time trends 1, 2, and 3 impact all 92 loops using a random weight between 0.5 and 1.
- Time trends 4 to 8 impact some of 92 loops using a random weight between 0.5 and 1. The probability of each time trend to impact each loop is 50%.

Fig. 3 shows the 8 time trends for the source loops and Fig. 4 shows loops 9 to loop 18 time trends, generated using the previous loops.

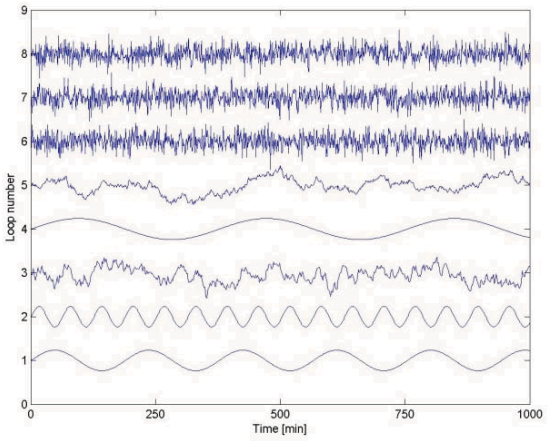

Fig. 3: Time trends for loops 1 to 8 in case study 2.

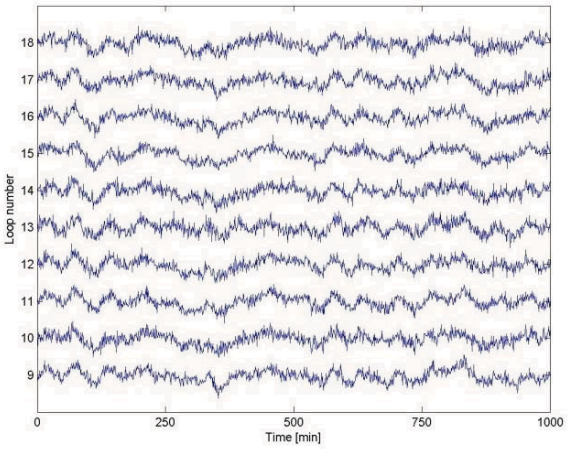

Fig. 4: Time trends for loops 9 to 18 in case study 2.

Applying the *LoopRank* algorithm, the following importance, shown in Fig. 5, is computed:

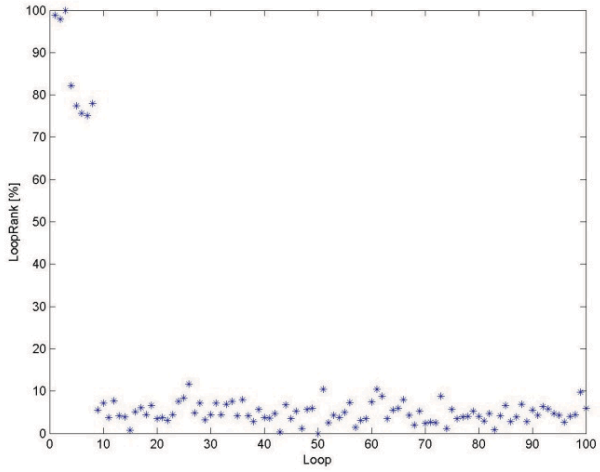

Fig. 5: *LoopRank* for case study 2, using 100 loops.

Fig. 5 reflects the expected result – loops 1, 2, and 3 have the highest importance, because of their impact in all loops. Loops 4 to 8 are less important than loops 1 to 3, but they are more important than the remaining. The remaining loops are less important, because the impact of a single one is not transferred to others.

One question can arise: If instead of partial correlation the correlation would be used, the results would be different? The comparison between *LoopRanks* using partial correlation and correlation is shown in Fig. 6.

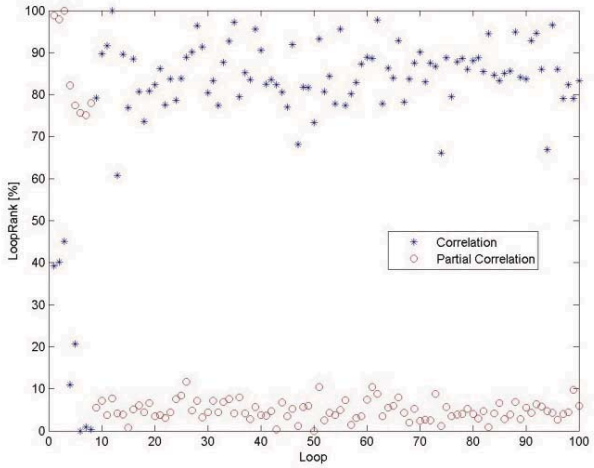

Fig. 6: *LoopRank* for case study 2, using both correlation and partial correlation.

Fig. 6 shows contrasting results, while correlation shows small importance of loops 1-8, partial correlation showed that these loops are the most important. Similar results have been seen in all tests, where correlation cannot point out the loops with major interaction among them, reason why partial correlation is used.

4.3 Industrial data

An industrial data set was provided by the courtesy of a Brazilian refinery. The system is an atmospheric distillation column of a petroleum refinery. The provided data set consists of 25 process variables: 6 level, 12 flow, 5 pressure, and 2 temperature controllers. The whole dataset has 1000 samples with a sampling time of 1 min. Fig. 7 shows the time trends of the variables.

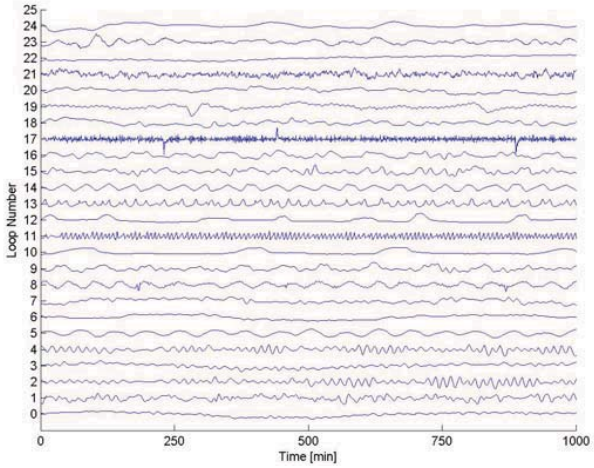

Fig. 7: *Time trends of industrial case study with 19 process variables.*

The *LoopRank* algorithm is then applied, providing the ranking shown in Fig. 8.

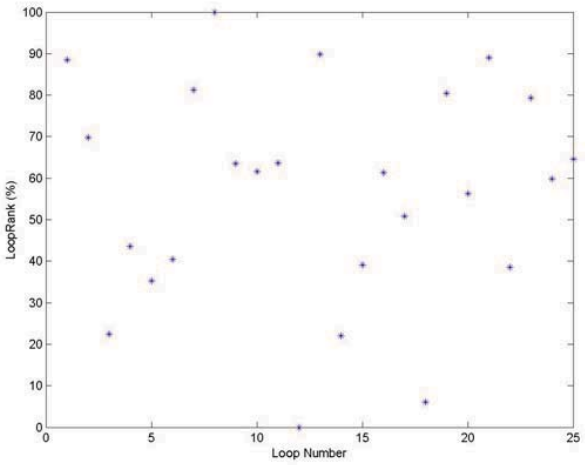

Fig. 8: *LoopRank* for industrial case study.

Fig. 8 clearly ranks the loop importance. It shows that loops 1, 8, 13, and 21 are the most important, because of its impact over the others. Loops 3, 12, 14, and 18 are the least important.

There previous results can be explained by the positions in the process flow diagram. The most important loop, in this case, is the flow of the intermediate recycle in the atmospheric tower (loop 8). The remaining most important loops are:

- Loop 1: crude oil inlet flow;
- Loop 13: Total reflux flow;
- Loop 21:Kerosene flow side-withdraw.

5. CONCLUSIONS

The main conclusions of the proposed work can be summarized as:

Loop ranking is an important tool for loop maintenance – Loop ranking for maintenance is required because of the large number of loops with poor performance in process plants. Unfortunately, the number of methodologies to evaluate loop impact is scarce. In this work a methodology for loop ranking aiming their maintenances, called *LoopRank*, is proposed.

It is better use partial correlation than correlation – *LoopRank* is based on loop interaction, measured by partial correlation. Correlation was also tested, however the results were poorer, therefore should not be used.

The proposed algorithm is similar to the Pagerank algorithm used by Google search engine – the relative importance score for each loop is computed using the *PageRank* algorithm. When the impact of a given loop should be emphasized, a loop weight can be assigned.

Successful applications of the LoopRank algorithm – the proposed algorithm was applied in 3 case studies, where reliable results were provided. One industrial case study was

presented to demonstrate the efficacy of the algorithm. The computational time for all case studies was negligible.

ACKNOWLEDGMENTS

The authors would like to thank CAPES / Brazil for supporting this work.

REFERENCES

Bilodeau, M. and Brenner, D. (1999) *Theory of multivariate statistics,* New York, Springer.

Bryan, K. and Leise, T. (2006) The $25,000,000,000 eigenvector: The linear algebra behind Google. *SIAM Review,* 48**,** 569-581.

Choudhury, M. A. A. S., Shah, S. L. and Thornhill, N. F. (2004) Diagnosis of poor control-loop performance using higher-order statistics. *Automatica,* 40**,** 1719-1728.

Hagglund, T. (2002) A friction compensator for pneumatic control valves. *Journal of Process Control,* 12**,** 897-904.

Hagglund, T. (2007) Automatic on-line estimation of backlash in control loops. *Journal of Process Control,* 17**,** 489-499.

Harris, T. J. (1989) Assessment of control loop performance. *Canadian Journal of Chemical Engineering,* 67**,** 856-861.

Huang, B., Shah, S. L. and Kwok, E. K. (1997) Good, bad or optimal? Performance assessment of multivariable processes. *Automatica,* 33**,** 1175-1182.

Jelali, M. (2006) An overview of control performance assessment technology and industrial applications. *Control Engineering Practice,* 14**,** 441-466.

Jiang, H., Shoukat Choudhury, M. A. A. and Shah, S. L. (2007) Detection and diagnosis of plant-wide oscillations from industrial data using the spectral envelope method. *Journal of Process Control,* 17**,** 143-155.

Paulonis, M. A. and Cox, J. W. (2003) A practical approach for large-scale controller performance assessment, diagnosis, and improvement. *Journal of Process Control,* 13**,** 155-168.

Rossi, M. and Scali, C. (2005) A comparison of techniques for automatic detection of stiction: simulation and application to industrial data. *Journal of Process Control,* 15**,** 505-514.

Ruel, M. (2000) Stiction: The hidden menace. *Control Magazine*.

Tangirala, A. K., Shah, S. L. and Thornhill, N. F. (2005) PSCMAP: A new tool for plant-wide oscillation detection. *Journal of Process Control,* 15**,** 931-941.

Thornhill, N. F. and Horch, A. (2007) Advances and new directions in plant-wide disturbance detection and diagnosis. *Control Engineering Practice,* 15**,** 1196-1206.

Thornhill, N. F., Shah, S. L., Huang, B. and Vishnubhotla, A. (2002) Spectral principal component analysis of dynamic process data. *Control Engineering Practice,* 10**,** 833-846.

Xia, C., Howell, J. and Thornhill, N. F. (2005) Detecting and isolating multiple plant-wide oscillations via spectral independent component analysis. *Automatica,* 41**,** 2067-2075.

Operational Flexibility of Heat Exchanger Networks

M. Escobar and J.O. Trierweiler

Group of Intensification, Modelling, Simulation, Control and Optimization of Processes (GIMSCOP), Department of Chemical Engineering, Federal University of Rio Grande do Sul (UFRGS) Porto Alegre, Brazil (*e-mail: escobar@enq.ufrgs.br/ jorge@enq.ufrgs.br*)

Abstract Process integration is motivated from economic benefits, but it also impacts on the plant behavior introducing interactions and in many cases making the process more difficult to control and operate. A prerequisite for optimal operation is that the HEN is sufficiently flexible, i.e. it must have the ability to operate over a range of conditions while satisfying performance specifications. In this work it is defined the Operational Flexibility related not only to the size of the feasible region but also to the costs involved to put the HEN into operation. In order to provide an appropriated metric, the operational flexibility index is defined. Five different networks structures designed for the nominal conditions of a case study are used to illustrate the proposed ideas. It was noticed that a great feasible region does not point out the more economic operation, and the costs must be considered together with the flexibility analysis. These characteristics are taken into account by the novel proposed operational flexibility index, which can also consider during the analysis the increasing in the utility duties, extra utility exchangers and bypass installation. These results clearly point out for the need of a simultaneous framework for flexible design and profitability.

Keywords: Heat Exchanger Networks, Optimal Operation, Operational Flexibility.

1. INTRODUCTION

Operability issues are very important for heat integrated process, since the economic performance of a process is greatly affected by process variations and the ability of the system to satisfy its operational specifications under external disturbances or inherent modelling uncertainty.

Methods based on pinch analysis and mathematical programming for fixed operating conditions hve been largely developed. An extensive review of these methods can be found in Furman and Sahinidis (2002). Compared to design of HENs for nominal operating conditions, less effort has been dedicated to the operability and controllability aspects of such networks.

Since the concept of resilient HENs firstly developed by Marselle et al. (1982) and the introduction of the flexibility index by Swaney and Grossmann (1985) several design methods based on the multiperiod approach were proposed. Floudas and Grossmann (1986) introduced a multiperiod case based on the synthesis with decomposition. Papalexandri and Pistikopoulos (1994) and Konukman et al. (2002) extended the simultaneous synthesis to the multiperiod case in an MINLP problem.

All these works relates the flexibility with the size of the feasible region and they do not take into account explicitly all the trade-offs involved in a HEN design. In this work a new metric for comparing different HEN structures is proposed based on the concept of operational flexibility. A case study with 5 different synthesized HENs is used to illustrate the proposed metric.

2. OPERATION OF HENs

A HEN is considered optimal operated if the targets temperatures are satisfied at steady state (main objective); the utility cost is minimized (secondary goal); and the dynamic behaviour is satisfactory (Glemmestad, 1997).

During HEN operation, degrees of freedom or manipulated inputs are needed for control and optimization. The different possibilities are shown in Figure 1: 1-Utility Flowrates; 2-Bypass fraction; 3-Split fraction; 4-Process Streams flowrates; 5-Exchanger area (e.g. flooded condenser); 6-Recycle (e.g. if exchanger fouling is reduced by increased flowrates).

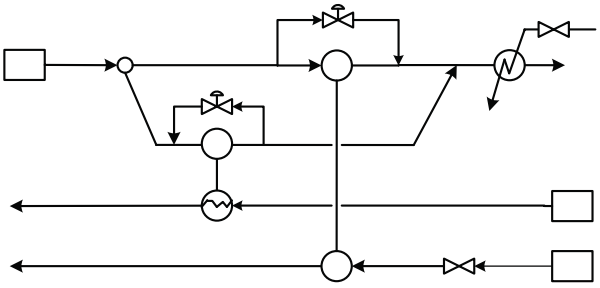

Fig. 1. Possible manipulated inputs in HENs.

In this work, we will consider the outlet target temperatures as controlled variables and utility loads, bypasses or splits, when they are present, as manipulated variables. The idea is to maintain the targets temperatures using the minimal

increase of the external utilities. The best HEN is the one where the effect of a given set of disturbances can be accommodated internally without requiring too much external "help" from the utilities heat exchangers. These ideas are illustrated through the case study of the next section.

3. CASE STUDY

To analyze the flexibility problem we have synthesized 5 different HENs for the plant illustrated in Figure 2.

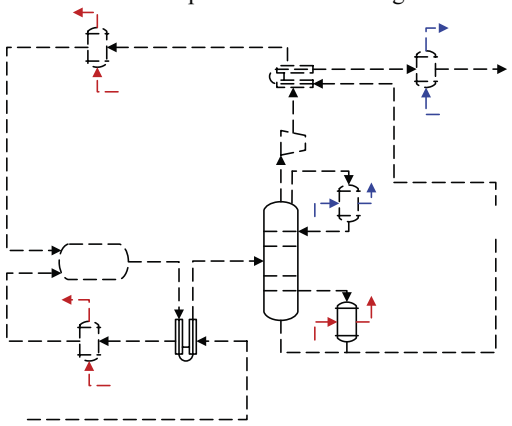

Fig. 2. Simple process with reaction, separation and heat exchangers.

Table 1. Nominal operating condition for the Case Study.

Stream	T_{in} (°C)	T_{out} (°C)	F (kW°C^{-1})	h (kW m^2 °C^{-1})
H1	270	160	18	1
H2	220	60	22	1
C1	50	210	20	1
C2	160	210	50	1
CU	15	20		1
HU	250	250		1

Cost of Heat Exchangers (y^{-1}) = 4000+500[Area (m^2)]$^{0.83}$
Cost of Cooling Utility = 20 (kW^{-1}y$^{-1})
Cost of Heating Utility = 200 (kW^{-1}y$^{-1})

Table 1 summarizes the corresponding data of the nominal operating conditions. This data and a ΔT_{min} of 10 °C were used to design the 5 different HENs depicted in Fig. 3. The five HENs have been designed by the following approaches:

S01-Pinch Technology (Linnhoff & Hindmarsh, 1983);

S02-NLP Superstructure proposed by Floudas, Ciric, and Grossmann (1986) using Pinch Technology as initial guesses;

S03-NLP Superstructure in the Sequential procedure (Floudas, Ciric, and Grossmann, 1986);

S04-Hyperstrucutre proposed by Ciric and Floudas (1991); and

S05- the stage-wise Synheat model proposed by Yee and Grossmann (1990) with the assumption isothermal mixing.

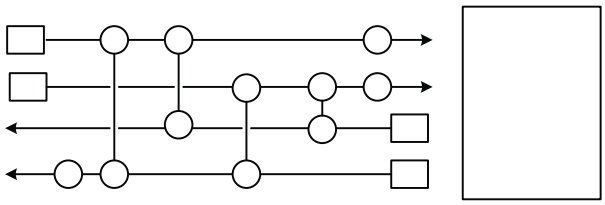

S01: Pinch Technology

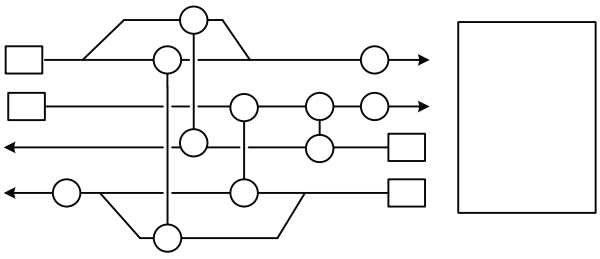

S02: NLP Superstructure (initial point by Pinch Technology)

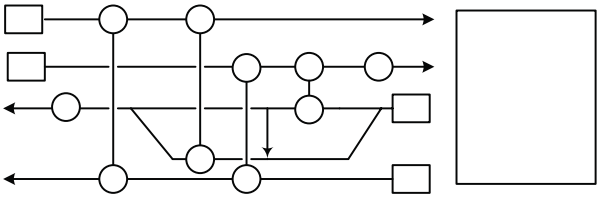

S03: NLP Superstructure (Sequential Procedure)

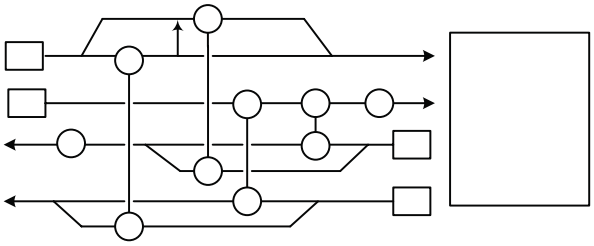

S04: MINLP Hyperstrucuture (Simultaneous Procedure

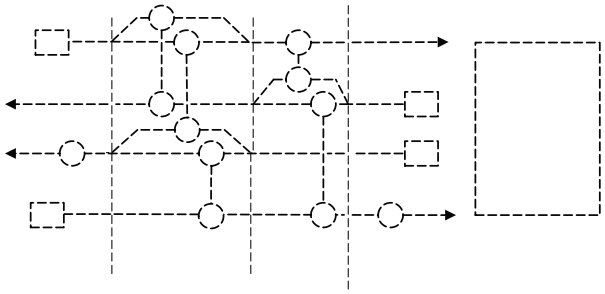

S05: MINLP Synheat Model (Isothermal Mixing)

Fig. 3. Synthesized HENs for the Case Study using different approaches.

4. OPERATIONAL FLEXIBILITY

The flexibility is defined by Swaney and Grossmann (1985) as the size of the region of feasible operation in the space of possible deviations of the parameters from their nominal values. In order to analyze the flexibility, a disturbance scenario is explored on the basis of the vertices of the polyhedral region of uncertainty (Konukman et al., 2002) trough a scalar δ (flexibility target). For a fixed HEN topology and design the 'flexibility index' is defined by Swaney and Grossmann (1985) as the maximum scalar δ* (Figure 4).

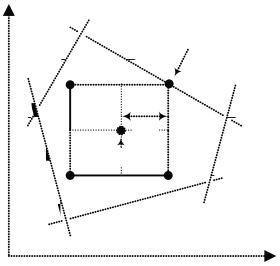

Fig. 4. Geometric representation of vertex-based flexibility target.

As the feasible region is convex when it is considered the inlet temperatures as uncertain parameters, the critical point that limits the operation lies at a vertex of the polyhedral region of uncertainty. For non-convex region the vertex-based formulation should be replaced by a more general active-constraint-strategy-based on MINLP formulation (Floudas, 1995).

Considering the four inlet temperatures as disturbances, a total of 16 vertices are enumerated. Each vertex represents an operating condition and it is formed by a deviation of ±δ from the nominal values In order to calculate the expected variations in the operating conditions that potentially could happen for a given flexibility target, each HEN configuration was implemented in Excel® using the heat exchanger model described by the set of equations (1), (2), and (3) and notation shown in Fig. 5.

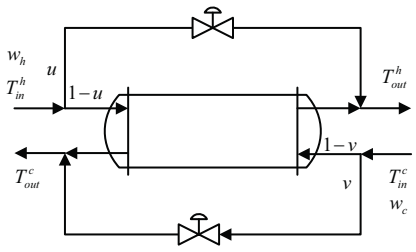

Fig. 5. General structure of a heat exchanger with bypasses.

$$T^h_{out} = (1-u)\left[\frac{(R_h-1)}{R_h-a}T^h_{in} + \frac{(1-a)}{R_h-a}T^c_{in}\right] + uT^h_{in} \quad (1)$$

$$T^c_{out} = (1-v)\left[\frac{R_h(1-a)}{R_h-a}T^h_{in} + \frac{a(R_h-1)}{R_h-a}T^c_{in}\right] + vT^c_{in} \quad (2)$$

Where

$$R_h = \frac{w_h(1-u)}{w_c(1-v)}; NTU_h = \frac{UA}{w_h(1-u)}; a = e^{NTU_h(1-R_h)} \quad (3)$$

The individual heat exchanger model was connected according to the topology for each HEN structure and the outlet temperatures deviations from their target values are calculated together with the additional utility requirement. A free simulation for fixed bypass and split fractions was carried out for each operating condition. Positive values encountered of heat duties at the stream where no utility exchanger exist mean that an extra utility exchanger must be included. Moreover, the negative values indicate an infeasible operation without any structural modifications, even for adding a new utility exchanger.

4.1 Optimal Operation of HENs

To overcome an infeasible operation it is possible to use the degrees of freedom, such as split fractions and bypasses placement in order to increase the feasible region and ensure that the optimal operation can be achieved by minimizing the utility consumption. The optimal steady-state operation or network optimization problem (Marselle et al., 1982):

Optimal Steady State Operation: *(For each operating point n)*

Minimum Utility Consumption ***(secondary objective)***

$$\min_{u,v} \sum_{i=1}^{NH} Q^{CU}_{i,n} + \sum_{j=1}^{NC} Q^{HU}_{j,n}$$

subject to.

Hot and Cold target temperatures ***(primary goal)***

$$T^{out}_{i,n} - T^{sp}_{i} = 0; T^{out}_{j,n} - T^{sp}_{j} = 0$$

Positives or zero heat loads coolers and heaters

$$T^{sp}_{i} - T^{out}_{i-1,n} \le 0; T^{out}_{j,n} - T^{sp}_{j} = 0$$

Hot and Cold Utility loads

$$Q^{HU}_{i,n} = w^{H}_{i}\left(T^{out}_{i-1,n} - T^{out}_{i,n}\right)$$

$$Q^{CU}_{j,n} = w^{C}_{j}\left(T^{out}_{j,n} - T^{out}_{j-1,n}\right)$$

Heat Exchanger Static Model (3), (4), and (5)

*Topology Constraints**

Bypass bounds

$$0 \le u, v \le 1$$

** The topology constraints define the configuration, and are expressed as appropriated model variables connections.*

The optimal optimization problem for each configuration was implemented using the software GAMS and solved using the solver CONOPT considering δ_T is equal to 10°C (flexibility target). The new requirements for the each HEN structure are exhibited in Table 2.

According to the initial analysis, the maximum or critical utility exchanger operation is not a good metric since it was not able to distinguish the configurations S01 and S02. Furthermore, comparing the configurations S03 and S04, even though the critical loads are greater for the first one the total heat load (summation for each operation point) and the averages are not.

Table 2. Utility loads (kW) for a feasible operation for each case study using extra utility units.

Struc.	Utility	Maximum	Average	Total
S01	cold	1000	446	7584
	hot	1300	646	10984
S02	cold	1000	445	7563
	hot	1300	645	10963
S03	cold	1300	570	9886
	hot	1480	769	13073
S04	cold	1287	586	9966
	hot	1466	782	13306
S05	cold	1000	497	8455
	hot	1480	696	11840

According to the results the configurations S03 and S04 are the worst from a flexibility point of view, since they require more utility to a feasible operation. On the other hand, S04 is the HEN with lowest TAC (3.619 x10^5 \$/year) as shown in Fig. 3, but considering the flexibility this is not the best option and clearly points out that flexibility issues must be considered in an early stage of the process design, since the nominal optimum .

4.2 Optimal Operation with no extra utility units

The solution provided in the previous analysis is trivial and may guarantee the operation for a large range. Furthermore, it is an expensive solution. Providing a more reasonable analysis, a second optimal operation problem was considered. The new problem definition differs from the previous one by the addition of constraints that ensure no extra utility exchangers. The general results are presented in Table 3.

Table 3. Utility loads (kW) for a feasible operation for each case study using no extra utility units.

Struc.	Utility	Maximum	Average	Total
S01	cold	1000	494	8425
	hot	1714	694	11825
S02	cold	1003	502	8534
	hot	1540	702	11934
S03*(8)	cold	1058	521	8851
	hot	1480	721	12251
S04*(14)	cold	902	499	8410
	hot	1480	699	11810
S05*(7)	cold	1000	530	9011
	hot	1587	730	12411

* (*ni*) indicate *ni* infeasible operating points.

Due to extra constraints, greater utility consumption in general was need. Moreover, how it was expected not always a feasible solution could be found. The main difficult faced by the configurations S03, S04 and S05 was the presence of only two utility exchangers, i.e. these configurations are more penalized with the additional constraints. The bad performance of the configuration S05 may be also explained possibly by the "inflexible" isothermal mixing constrain applied to the design.

A new analysis was made considering the possibility of variation for the extra degrees of freedom, when they take place. Whereas the configuration S01 has no one split fraction, the best possible results has already presented in Table 3. Conversely, all other configurations have split fractions. For the configurations S03 and S04 was also considered as an extra degree of freedom the recycle stream, from the outlet of a heat exchanger to another. The results are presented in Table 4.

Table 4. Utility loads (kW) for a feasible operation for each case study using no extra utility units but using extra degrees of freedom (split and recycle fractions).

Struc.	Utility	Maximum	Average	Total
S01	cold	1000	494	8425
	hot	1714	694	11825
S02	cold	900	435	7396
	hot	1430	635	10796
S03*(7)	cold	990	458	7780
	hot	1383	658	11180
S04*(8)	cold	780	417	7088
	hot	1368	641	10904
S05	cold	900	456	7745
	hot	1431	656	11145

* (*ni*) indicate *ni* infeasible operating points.

Like it was expected the extra degrees may be used to achieve the targets and decreases the utility consumption increasing the feasible region, which is proven by the increase of the number of feasible operating points. For the configuration S05, allowing the manipulation of the split fractions automatically removes the isothermal mixing assumption and hence increases considerably the flexibility.

Comparing the results, the configurations S03 and S04 must be discarded because they do not provide a suitable operation. The results are a sign of designs with splits are good from the flexibility viewpoint because these extra degrees of freedom can be used to decrease the investment cost during the design phase and be used to decrease the utility consumption during operation. In addition, the installed areas are utilized completely for all operating points, which not occurs using bypasses. In the overall design the dynamic behaviour must be analysed carefully once split fractions can give competitive effects.

4.3 Flexibility Range

All the previous analysis considered the flexibility target (δ_T) of 10°C, in order to analyze the flexibility range, the total utility consumption (δQ) levels corresponding to the critical operating conditions versus the flexibility targets (δ_T) for structures S01, S02 and S05 and the virtual structure (Maximum Energy Recovery) MER were calculated and they are shown in Figure 6.

The illustration reveals plateaus of total utility requirements levels for a given value of δ, under the correspondent δQ level the configuration is operable, i.e. it will not violate the temperatures specifications as long as the deviations in the

source streams temperatures along the vertex directions have magnitudes within $0 < \delta_T < \delta$.

The analysis reveals the trade-off between the flexibility target and the total utility load need to maintain a feasible operation pointing out that a more flexible is more expensive. For practical purposes, increasing the flexibility target trough penalization of total utility consumption is possible until a limit (δ*), which is reached when at least one bypass saturation occurs.

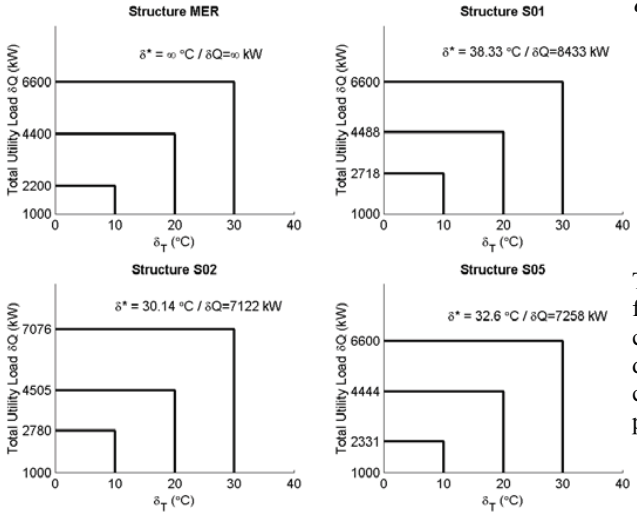

Fig. 6. Total utility consumptions at the critical operating conditions versus the flexibility ranges for structures MER, S01, S02 and S05.

In Table 4, the structure S02 (δ*=38.33^{0}C) depicted the lowest total utility load in general (considering all operating points) and the lowest average utility load. Therein, the critical loads define the feasibility operational range and it must be checked, but a selection of a structure using purely the analysis provided by the Figure 6 will not be appropriated because it would assume that most of the time the process would operate in the critical conditions what is not correct.

5. OPERATIONAL FLEXIBILITY INDEX

An appropriated metric to compare different HENs is based on the operational flexibility that is reached if the operation is possible and the maximum energy recovery is obtained for the entire feasible region with a minimum investment cost.

The structure of the HEN has a direct influence on the flexibility. Disintegrated structures are highly flexible, but that trivial solution is not interesting under an economic point of view. The other highly flexible possibility is a totally integrated structure, with the maximum number of units and maximum areas with bypasses across all units, but very expensive from an investment point of view.

Here we introduce the operational flexibility index to take into account in addition to the feasible range related with a flexibility target the most important costs involved during a "flexible operation". The Operational Flexibility Index for a specific flexibility target (OF_δ) is defined in equation (4), where the two terms correspond to operating cost (φ_{oc}) and the investment cost (φ_{ic}) penalties for an operational flexibility, and these terms are defined in equations (5) and (6). The operational flexibility index varies form 0 to 100%. Its upper bound indicates feasible operation without much economic penalty. On the other hand, when bypasses, new units, increased areas, and increased utility consumption are considered the indice will be penalized.

$$OF_\delta(\%) = 100(1 - \varphi_{oc} - \varphi_{ic}) \tag{4}$$

$$\varphi_{OC} = w_1 \frac{1}{2(V+1)} \sum_{n=1}^{V} \frac{\sum_{k=1}^{NH+NC} \delta q_{k,n}^{U} - \sum_{k=1}^{NH+NC} \delta q_{k,n}^{U,\min}}{\sum_{k=1}^{NH+NC} \delta q_{k,n}^{U,\max} - \sum_{k=1}^{NH+NC} \delta q_{k,n}^{U,\min}} \tag{5}$$

$$\varphi_{IC} = w_2 \frac{N_{bp}}{N_{hx,retrofit}} + w_3 \left(1 - \frac{N_{hx}}{N_{hx,retrofit}}\right) + w_4 \left(N_{hx} - \sum_{m=1}^{N_{hx}} \frac{A_{m,installed}}{A_{m,retrofit}}\right) \tag{6}$$

The parameters w_i (7) correspond to the normalized weight for each contribution to the penalty. A suggested set may be calculated by the constants k_i (8) that depends on economic data from the process, i.e. the utility costs and the exchanger costs, considering the bypass cost. For the case study these parameters are provided in Table 1.

$$w_i = \frac{k_i}{\sum_{i=1}^{4} k_i} \tag{7}$$

$$k_1 = \frac{cu.}{2(V+1)} \left(\sum_{k=1}^{NH+NC} \delta q_{k,n}^{U,\max} - \sum_{k=1}^{NH+NC} \delta q_{k,n}^{U,\min} \right)$$
$$k_2 = 0.2aN_{hx,ret}; k_3 = aN_{hx,ret}; k_4 = b\sum_{m=1}^{N_{hx}} A_{m,ret}^{\beta} \tag{8}$$

The parameters N_{bp}, N_{hx} and A_m correspond to the number of bypasses placed, the number of heat exchangers and the area of the heat exchanger m, respectively. Moreover, the subscript 'retrofit' indicates the variable in the flexible operation, i.e. the retrofitted design.

To evaluate the potential of each structure, the operational flexibility index was calculated. The calculation requires the bounds for the utility loads. It was used the LP transshipment model (Papoulias and Grossmann, 1983) for each operating point to estimate the minimum utility consumption for the design case (ΔT_{min}=10^{0}C) and the minimum case (ΔT_{min}=0^{0}C). Furthermore, it was calculated the utility loads for the no heat integration case; all the targets are exhibited in Table 5.

Table 5. Utility loads (kW) for a feasible operation for each case study using no extra utility units.

Case	*Utility*	*Max.*	*Average*	*Total*
MER	*cold*	900	412	7000
ΔT_{min}=10^{0}C	*hot*	1300	612	10400
MER	*cold*	900	219	3720
ΔT_{min}=0^{0}C	*hot*	1080	360	6120
No Heat	*cold*	5900	5500	93500
Integration	*hot*	6400	5700	96900

The main results are expressed in Table 6. The term corresponding to the energy cost is dominant due to its greater economic impact in the total cost; the investment cost is worthless for most cases. The structure S02 showed the best performance for the required flexibility target. The interpretation inside the context of a feasible operation is that a greater index indicates that operation occurs inside a more economic way, using a lower average utility consumption with the lower investment cost. Otherwise different conditions will penalize the operational flexibility.

Table 6. Operational Flexibility Index for the structures S01, S02 and S05.

	S01	*S02*	*S05*
φ_{oc}	0.0605691	0.0498255	0.0536638
φ_{ic}	0.00203939	0.00271918	0.00000000
$OF_{\delta=10}$	93.73916%	94.74553%	94.63362%

5.1 Flexibility x Installed Area

All the previous analysis was carried out using the areas as fixed parameters, and these areas were designed at nominal conditions. If it was considered the whole feasible region, trough a multi-period design these areas would have better usage in order to reduce the utility consumption in the entire region. A new optimization problem was performed for the structure S01, considering varying areas. In order to avoid extreme solutions, a practical consideration for the areas bounded between 1 and 1000 m^2 were imposed and new optimizations were performed. The areas for each operating point are presented in Table 7. In order to satisfy all operating points, the maximum areas obtained in Table 7 where fixed and the optimal operation problem was solved with the increased areas.

Table 7. Nominal and maximum areas (m^2) for the HEN structure S01.

	$A_{H1,C1}$	$A_{H1,C2}$	$A_{H2,C1}$	$A_{H2,C2}$
Nominal	318.12	56.55	609.97	209.79
Maximum	1000.00	97.46	1000.00	1000.00

Comparing the values obtained with the results presented in Table 4 for the structure S01, the total utility loads decreased from 8425.3kW to 4370.9 kW (cold utility) and 11825.3 kW to 7770.9 kW (hot utility); and the average consumption decreased from 494kW to 257kW(cold utility) and 694kW to 457kW (hot utility). The flexibility index (δ*) provided in the Figure 6 increased from 38.33^{0}C to 49.8^{0}C, i.e. the feasible region increased. Furthermore, the operational flexibility index (OF_δ) exhibited in Table 6 increased from 93.73916% to 98.197858% considering only the energy cost and considering the capital cost for the oversize of the areas the index is 97.02954%.

6. CONCLUSIONS

The flexibility analysis of different structures previously designed was accomplished through optimal operation problem taking into account the trade-offs between energy cost, capital cost and the flexibility in order to ensure an economic operation. The formulation presumed that the feasible region in the space of uncertain input parameters was convex, and thus the optimal solution was explored based on the vertices of the polyhedral uncertainty region in the space of source-stream temperatures. It was defined the operational flexibility index as a measure of operational flexibility that was assumed to be different of structural flexibility. The first one considers the impacts on the total annual cost, since infinity areas, high levels of utility loads and disintegrated structures are according with this work highly structural flexible but present a poor (expensive) operation and hence a low operational flexibility.

The HEN structure provides an upper bound for the flexibility that should be expected during operation. The increasing of flexibility target reveals the flexibility dependent on structural modifications and total utility consumption until the unfeasible operation may be achieved. It was showed that more important that the size of the feasible region it is the cost involved in a feasible operation around the desired flexibility target. It has shown the real need of taking into account the flexibility in a simultaneous framework, once the utility loads, heat exchangers (units and areas), and the arrange (configuration of flows, temperatures) are determined in only one step, and all these variables strongly affect the flexibility.

REFERENCES

Ciric, A. R. & Floudas, C. A. (1991). Heat exchanger network synthesis without decomposition. Computer and Chemical Engineering15, 385.

Floudas, C. A., Ciric, A. R. & Grossmann, I. E. (1986). Automatic synthesis of optimum heat exchangers network configurations. American Institute of Chemical Engineering Journal 32, 276.

Floudas, C.A., Grossmann, I.E., (1986). Synthesis of flexible heat exchanger networks for multiperiod operation. Computers & Chemical Engineering 10 (2), 153–168.

Furman K.C. and N.V. Sahinidis,(2002). A critical review and annotated bibliography for heat exchanger network synthesis in the 20th century, Industrial and Engineering Chemistry Research 41 (10), pp. 2335–2370.

Glemmestad, B. (1997). Optimal Operation of Integrated Processes, Studies on Heat Recovery Systems. Ph.D. thesis, Norwegian University of Science and.

Konukman A.E.S., M.C. Camurdan, U. Akman, (2002). Simultaneous flexibility targeting and synthesis of minimum-utility heat exchanger networks with superstructure-based MILP formulation, Chem. Eng. Processing 41 501–518.

Linnhoff B., E. Hindmarsh, (1983) The pinch design method for heat exchanger networks, Chem. Eng. Sci. 38 (5) 745–763.

Marselle, D.F., Morari, M., Rudd, D.F., (1982). Design of resilient processing plants—II, design and control of energy management systems. Chemical Engineering Science 37 (2), 259–270.

Papalexandri, K.P., Pistikopoulos, E.N., (1994). Synthesis and retrofit design of operable heat exchanger networks—I, flexibility and structural controllability aspects. Industrial & Engineering Chemistry Research 33 (7), 1718–1737.

Papoulias, S. A., & Grossmann, I. E. (1983). A structural optimization approach in process synthesis-I. utility systems. Computers and Chemical Engineering, 7, 695–706.

Swaney R.E., and I.E. Grossmann (1985). An index for operational flexibility in chemical process design. AIChE J. 31 (4) (1985) 621–630.

Yee, T. F., & Grossmann, I. E. (1990). Optimization models for heat integration-II. Heat exchanger network synthesis. Computers and Chemical Engineering, 14, 1165–1184.

GPC Controller Performance Monitoring and Diagnosis Applied to a Diesel Hydrotreating Reactor

A. C. Carelli* M. B. da Souza Jr.**

*Chemical Engineering Department, Federal University of Rio de Janeiro, Rio de Janeiro Brazil (e-mails: *alain.carelli@gpi.ufrj.br, **mbsj@eq.ufrj.br)*

Abstract: Control systems tend to lose performance over time if their responses are not monitored and thus there is no support information on to how to make adjustments on them. Reliable controllers have complementary systems to identify and diagnose reductions in performance and also to implement predetermined solutions vis-à-vis the desirable type of output. The goal of this work was to analyze controller performance monitoring and causes diagnosis methods based in two indexes: historical benchmark and model based performance measurement. These methods were applied to situations of degraded performance simulated in the predictive control of a hydrotreating reactor, aiming the identification of the reduction in the controller performance and the discrimination of its causes. The obtained results can also be extended to several other chemical processes, once that the investigated process presents first order with dead-time dynamics, typical of these processes.

Keywords: 1. Process control. 2. Performance reduction detection and diagnosis. 3. Control audit. 4. Refinery.

1. INTRODUCTION

In recent years, the performance requirements for process plants have become increasingly difficult to satisfy. Stronger competition, tougher environmental and safety regulations, and changing economic conditions have been key factors in tightening product quality specifications. A further complication is that modern plants have become more difficult to operate because of their complex and highly integrated processes. The largest emphasis recently given to safety has naturally improved the importance of the process control area. Without process control systems integrated with computers, it would be impossible to operate modern plants safely and lucratively while achieving product quality and environmental requirements. Therefore, it becomes important for chemical engineers to have an understanding both of the theory and of the process control practice. (Seborg, Edgar and Mellichamp, 2004).

Controller performance assessment and monitoring are necessary in order to assure the process control effectiveness and profit of the plant. The initial design of control systems includes many uncertainties caused by approximations in process model, estimations of disturbance dynamics and magnitudes, and assumptions about operating conditions. Many factors can cause their abrupt or gradual performance deterioration overtime. Around 60% of all industrial controllers have some kind of performance problem (Schäfer and Cinar, 2004).

All controllers need to be retuned as the dynamic of the process suffer natural or continuous alterations. The controllers performance should be monitored, because, even though they may have been adequately adjusted, it is expected that their performance decays along years due to variations in the materials, deterioration of the instrumentation, changes in the plant, etc. This reduction in the performance should also be diagnosed, enabling the identification of the needs to readjust the controller tuning parameters.

The main benefit of applying advanced control strategy to catalytic processes in refineries can be related to quality giveaway. For hydrotreating units, quality giveaway is mainly obtained by reducing over-desulphurization. Experimental results showed clearly that the sulfur content of the product is strongly related to the severity of the reaction, which is determined by reactor bed temperatures and the residence time. Operating at higher temperatures yields better product quality, but at the same time shortens the catalyst cycle. Therefore, the better the reaction control is (so as to guarantee only the necessary conversion), the better the utilization of the catalyst cycle and the lower the operational cost of the process (Lababidi, Alatiqi and Ali, 2004). Additionally, in case of accident, the replacement of a reactor and the reconstruction of other damaged equipments can take up to 12 months and the cost of lost production can exceed US$ 50 millions (Ancheyta and Speight, 2007).

2. CONCEPTUAL ASPECTS

This work is structured under three main themes: dynamic process control, process control performance assessment and diesel hydrotreating.

2.1 Model Predictive Control – Generalized Predictive Control

The general set of the available Generalized Predictive Control (GPC) algorithms cover a large variety of control goals in contrast to other methods, so that some of them can even be considered GPC specific cases.

In the SISO case (single-input *u*, single output *y*), a linearized time-invariant discrete process is assumed, where the relations between input and output are described by the following equation:

$$A(q^{-1})y(t) = q^{-d}B(q^{-1})u(t-1) \quad (1)$$

A and *B* are polynomials in the backward shift operator q^{-1} with, respectively, degrees *m* and *n*, and *d* is the dead-time.

With the premise that all process natural disturbances can be characterized by a stochastic disturbance, the principle of the superposition can be used to represent all disturbances as a unique influence in the output. Then, the process can be described by the following CARIMA (controlled auto-regressive and integrated moving average) model:

$$A(q^{-1})y(t) = q^{-d}B(q^{-1})u(t-1) + C(q^{-1})e(t)/\Delta \quad (2)$$

where *C* is also a polynomial in the backward shift operator q^{-1}, *e(t)* is an uncorrelated random sequence and $\Delta(q^{-1})$ is the differencing operator $1 - q^{-1}$.

The CARIMA model may be considered the most appropriated model for many industrial applications with non-stationary disturbances. In practice, it has two main types of disturbance: occurrence of random steps in random intervals (e.g. changing of the product quality) and Brownian motion which is met in plants that depend on the energy balance (Clarke, 1988).

The following Diophantine Equation is employed for the development of the solution:

$$C(q^{-1}) = E(q^{-1})A(q^{-1})\Delta + q^{-d} * F(q^{-1}) \quad (3)$$

where, *E* and *F* are polynomials in the backward shift operator q^{-1} with degrees *d-1* and *m*, respectively.

Multiplying the term $E(q^{-1})\Delta q^{j}$ in the components of (2); considering $C(q^{-1}) = 1$ (alternatively *C* is truncated and absorbed inside the polynomials *A* and *B*); and, assuming the future error values equal to zero, because they do not depend on the past values of *y(t)* and *u(t)*, the following equation is obtained:

$$y(t+j) = G(q^{-1})\Delta u(t+j-d-1) + F(q^{-1})y(t) \quad (4)$$

where, $G(q^{-1}) = E(q^{-1})B(q^{-1})$.

In the GPC, the predictions *y(t+j)* are estimated in order to compare them with a reference trajectory, and to calculate the optimum control actions. The system outputs will be influenced by signals in *u(t)* after of the sampling periods *d+1*, due to the system dead-time of *d* sampling periods.

The following cost function is assumed:

$$J = (Gu + f - w)^T (Gu + f - w) + \lambda u^T u \quad (5)$$

where, *w* is the reference trajectory or *set-point* and λ is a weighting sequence.

Assuming that there are no constraints in the control signals, the minimum of *J* can be met by equating the *J* gradient to zero. Therefore, the following result is used in order to obtain the future control actions:

$$\Delta u = \left(G^T G + \lambda I\right)^{-1} G^T (w - f) \quad (6)$$

2.2 Predictive Control Performance Monitoring and Diagnosing

In order to perform performance reduction diagnosis of the controller, its performance shall initially be monitored preferable on-line. There is a set of techniques conceived for this purpose, named controller performance monitoring (CPM) techniques.

The objective of the CPM is to develop and implement technologies that provide information of the plant to determine if the appropriated performance and the characteristics of behavior are being reached through the controlled variables. For the case SISO, the normalized performance index is an elegant method, which compares the theoretic absolute lower limit in the output variability with the achieved values. This index could configure itself as a benchmark appropriated to measure the performance of a feedback control system (Cinar, Palazoglu and Kayihan, 2007).

Nevertheless, mostly for multivariable MPC controllers, other CPMs methods have been studied based in the calculation of the cost function, which in most cases is the objective function minimized to determine the MPC's strategy. Cinar, Palazoglu and Kayihan (2007) introduced two methods based on monitoring of the cost function values for the controller performance reduction diagnosis, called of historical benchmark and model-based performance measurement.

The cost function J_{ach} is obtained with plant real values that can be described in the following form:

$$J_{ach} = \frac{1}{Pc}\left\{\sum_{j=1}^{Pc}\left[e^T(k+j-Pc)Qe(k+j-Pc) + \Delta u^T(k+j-Pc)R\Delta u(k+j-Pc)\right]\right\} \quad (7)$$

Where, *Pc* is the moving horizon of past data; *e(k)* is the vector of control errors at time *k* (difference between the controlled variable and the reference trajectory); Δu is the change in manipulated variables at time *k*; and, *Q* and *R* are weighting matrices representing the relative importance of each controlled and manipulated variable.

The historical benchmark requires a priori knowledge of good performance during a certain time period according to some expert assessment. The cost function applied in historical benchmark has the same form of (7), where the input and output data are taken from that period. So, the value

achieved through this function is constant until a better performance is reached (Schäfer and Cinar, 2004).

The historical benchmark index is described by the following expression, which supports the control performance reduction or increase detection:

$$\gamma_{his}(t) = J_{his} / J_{ach}(t) \quad (8)$$

The model-based performance measure index compares the achieved performance with the performance in the design case that is characterized by inputs and outputs given by the model (Schäfer and Cinar, 2004).

The model-based performance measure index is described by the following expression:

$$\gamma_{des}(t) = J_{des}(t) / J_{ach}(t) \quad (9)$$

Both cost functions used in the calculation of the model-based performance measure index have the same form of (7).

Monitoring the model-based performance measure is useful in diagnosing causes that affect the design case controller. Two groups of causes may be devised. For instance, increases in unmeasured disturbances, actuator faults, or increase in the model mismatch do not influence the design case performance (group II causes). Accordingly, J_{des} remains constant while J_{ach} increases, reducing the model-based performance measure. Root cause problems such as input saturation or increase in measured disturbance, on the other hand, affect the design case performance as well (group I causes). This lead to an approximately constant value of the model-based performance measure, if the effect is quantitatively equal (Cinar, Palazoglu and Kayihan, 2007).

This diagnostic sequence assumes that only one source cause occurs. If γ_{des} doesn't change significantly, while the model performance and achieved performance decrease quantitatively equal, the diagnosis of the root cause is in the group I. If γ_{des} presents a considerable decrease, the diagnosis of the root cause is in the group II. In the case that multiple causes can occur simultaneously, the diagnosis logic becomes more complex.

Subgroups are defined to further distinguish between the root cause problems in group I. All changes in the controller (e.g. tuning parameters, estimator, constraints) are assumed to be performed manually. These changes are known and their effects can be monitored. However, the action taken is known and the root cause of the effect does not need to be identified by diagnosis tools (subgroup Ia causes). The remaining two root cause problems (change in measured disturbances and input saturation) belong to subgroup Ib. Additional information is needed to distinguish between the two root cause problems in subgroup Ib. Looking at the manipulated variables, input saturation can be determined by visual inspection. A saturation effect in a manipulated variable indicates input saturation as underlying root cause and rules out the increase in measured disturbances (Cinar, Palazoglu and Kayihan, 2007).

2.3 Diesel Hydrotreating

The hydrotrating unit considered in this work is the Trickle Bed Reactor (TBR) with two reactors in series, each reactor formed by two fixed bed, as showed in Figure 1.

The oil feed is combined with makeup hydrogen and recycle hydrogen and heated to the reactor inlet temperature. Heat is provided from heat exchange with the reactor effluent and by a furnace. The reaction of hydrogen and oil occurs in the reactors in the presence of the catalyst. To prevent reactor temperatures from getting too high, quench gas (cold recycled hydrogen gas) is added between reactors and between catalyst beds of multiple-bed reactors to maintain reactor temperatures in the desired range.

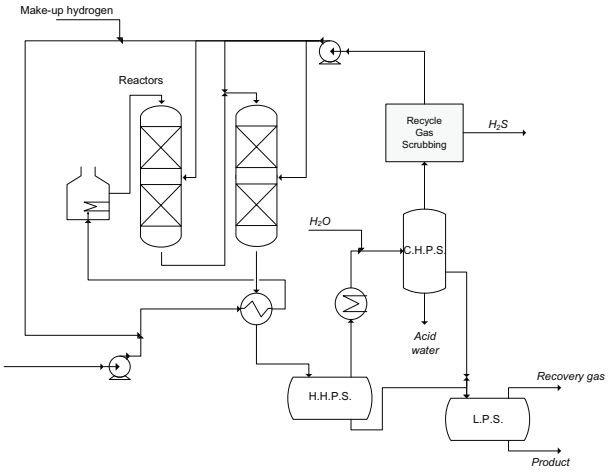

Figure 1 – Diesel hydrotreating process

The second reactor effluent is cooled (by exchange with the reactor feed) to recover the heat released from the hydrotreating reactions. After cooling, the reactor effluent is flashed in the hot, high-pressure separator (HHPS) to recover hydrogen and to make a rough split between light and heavy reaction products. The liquid from HHPS has its pressure lowered, than it is sent to the low-pressure separators, and on to the product fractionator. The HHPS vapor is cooled and water is injected to absorb hydrogen sulfide and ammonia produced in the reactors by the hydrotreating reactors. The mixture is further cooled to condense the product naphtha and gas oil and is flashed in the cold, high-pressure separator (CHPS). The CHPS separates the vapor, liquid water, and the liquid light hydrocarbons. The pressure of the hydrocarbon liquid is lowered and it is sent to the low-pressure separators. The water is sent to a sour water recovery unit for removal of the hydrogen sulfide and ammonia. The hydrogen-rich gas from the CHPS flows to the H_2S absorber. The purified gas flows to the recycle compressor where it is increased in pressure so that it can be used as quench gas and recombined with the feed oil. Liquid from the low-pressure separators is fed to the atmospheric fractionator, which splits the hydroprocessed oil from the reactors into the desired final products.

The model adopted in this work to represent the HDT's process was the model presented by Carneiro (1992) which applies the concept proposed by Hlavácek (1982) in representing fixed beds through the CSTR-CELL model. The CSTR-CELL in series describes the adiabatic fixed bed reactors dynamic. In Figure 2, a scheme of this model is shown.

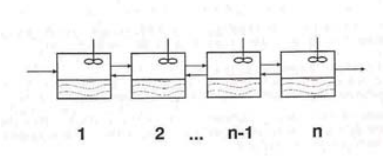

Figure 2 – CSTR-CELL reactor model

The CSTR-CELL reactor model considers mass and heat axial dispersion in the bed, mass diffusion and heat transportation between fluid and solid phases, as illustrated in Figure 3. The following assumptions are adopted in the CSTR-CELL: only one first order reaction – with respect to the mean concentration of a pseudo-reagent "A" in the solid phase porous – occurs and the reaction rate can be described by the Arrhenius equation; there is no volume variation in the reactor; the reactors are adiabatic; there is only one liquid and one solid phase with constant physical-chemical properties; there is only longitudinal transport phenomena; and, there are non-linear interactions between kinetic and thermal processes.

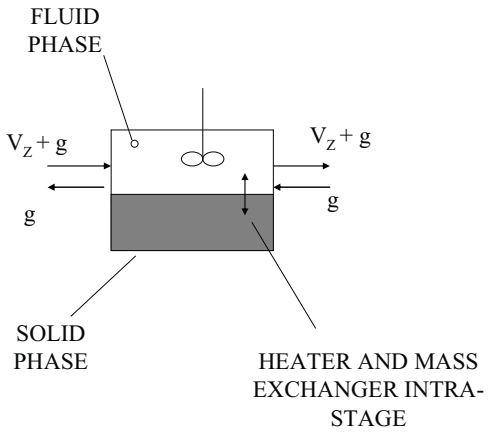

Figure 3 – CSTR-CELL stages

The Carneiro (1992) model was employed in this work for being at the same time able to represent the main process dynamics and simple, as it is composed by ordinary differential equations.

4. METHODOLOGY

This paper focus on the primary controller of the cascade control system applied to the first bed of the first reactor of the HDT unit, which can be seen in the top left hand corner of the diagram shown in Figure 4. This controller controls the bed outlet temperature through the manipulation of the set-point that is sent to the secondary controller. The secondary controller controls the inlet temperature of the bed through the manipulation of the fuel flow that enters the furnace.

The primary controller was performed by the GPC algorithm, using no explicit constraints and weighting in the cost function. The tuning parameters were the prediction horizon (N), the control horizon (NU) and the reference trajectory parameter (α).

The GPC was projected with a first order internal model with dead-time. The function considered for reference trajectory was a first order equation, which has only one tuning parameter: α. The larger α, the more cautious the control actions. If α is zero, the trajectory is constant and equal to the set-point, as can be noticed in the equation to follow:

$$w(t+1) = \alpha\, y(t) + (1-\alpha)SP \qquad (10)$$

As a default option, α was chosen in this study as equal to 0.7.

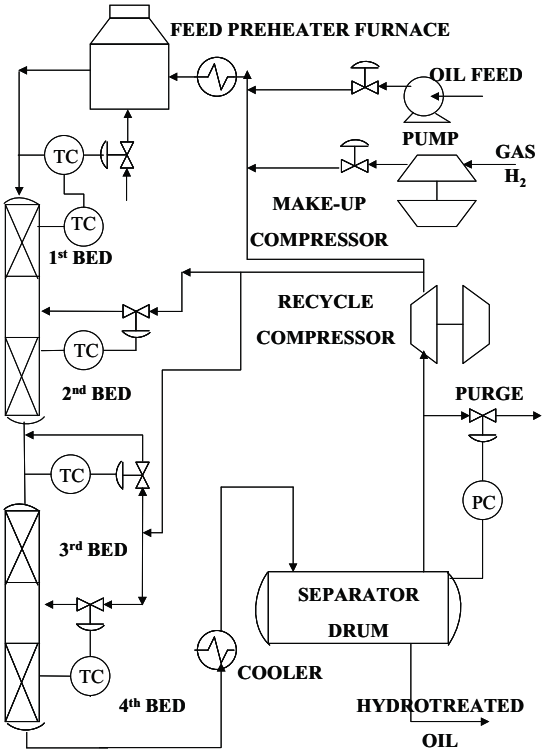

Figure 4 – Diesel Hydrotreating Unit Diagram (De Souza Jr., Campos and Tunala, 2009)

In respect to the assumed performance reduction scenarios, four cause diagnosis cases were tested based in the method presented previously: increased controlled variable variability (group II causes), mismatch between the model and the phenomenological model based simulator (group II causes), saturation of manipulated variable (group Ib causes) and change of the control tuning parameters (group Ia causes).

5. RESULTS

The events responsible for the reductions in performance were introduced in the 80th sampling time, as can be observed in the following figures. Figures 5, 6, 7 and 8 present, respectively, the following situations: increase in the controlled variable variability, mismatch between the internal model of the controller and the phenomenological model based simulator, saturation of the manipulated variable and change of the control tuning parameter. In all figures, the first graph presents the cost functions calculated to obtain the historical benchmark and model-based performance measure indexes. The second graph presents the historical benchmark index (monitoring index), and the third graph presents the model-based performance measure index (diagnosis index).

With the controlled variable variability increased in 5 times (in the phenomenological simulator), the achieved cost function was increased, while the others remained at the same level, as shown in Figure 5. In consequence, both the monitoring and diagnosis indexes had their values reduced. So, these behaviors agree with the expected for causes belonging to the group II which is the case for increases in unmeasured disturbances.

Figure 6 represents the change of CARIMA model parameters – *a* and *b* of (2) – which were multiplied by 20, causing an increase of the achieved cost function. The cost function applied to the model remained at the same level, because the internal model of the controller was affected in the same way.

As the mismatch between the internal model of the controller and the phenomenological simulator belongs to the causes of group II, the monitoring and diagnosis indexes decrease as can be seen in Figure 6.

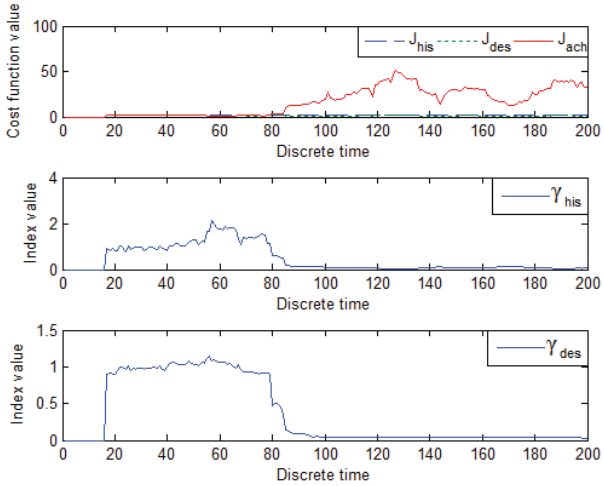

Figure 5 – Control performance reduction diagnosis caused by the controlled variable variability increase

When a constraint in the manipulated variable was applied to limit its lower value to 236.1ºC, the achieved cost function and the based-model cost function showed an increase which resulted in the decrease of the monitoring index and in the maintenance of the diagnosis index (see Figure 7). The observed behavior agrees with the causes belonging to group I, as was expected. Among the causes of group I, this particular cause can be diagnosed by monitoring the control actions, such as presented in the Figure 8, where from the 80th sampling time ahead the manipulated variable did not decrease beyond the value -0.2.

Figure 9 represents the control tuning change situation, where the prediction horizon varied from 4 to 50. In this situation, it can be observed that the indexes presented a similar behavior to the previous situation, due to the fact that this kind of cause also belongs to group I, where the same change affects the internal model and the model of the phenomenological simulator. This cause would not need to be diagnosed, because the modification in the tuning parameters of the controller – and, therefore, the reason of the performance reduction – would be previously known.

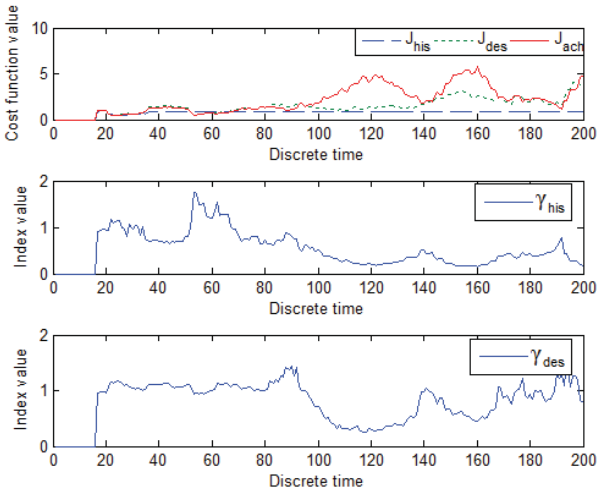

Figure 6 – Control performance reduction diagnosis caused by the mismatch between the model and the phenomenological model based simulator

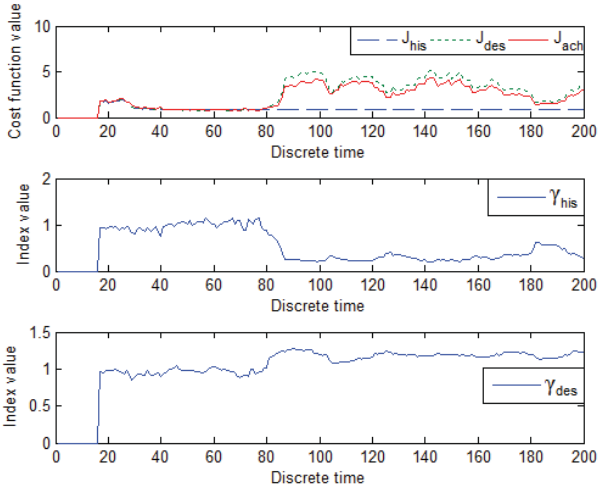

Figure 7 – Control performance reduction diagnosis caused by the saturation of the manipulated variable

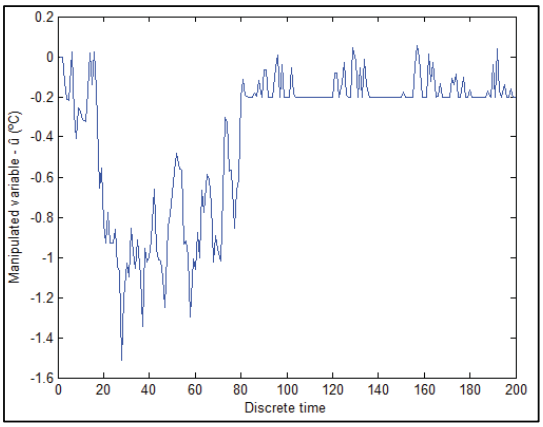

Figure 8 – Saturation of manipulated variable

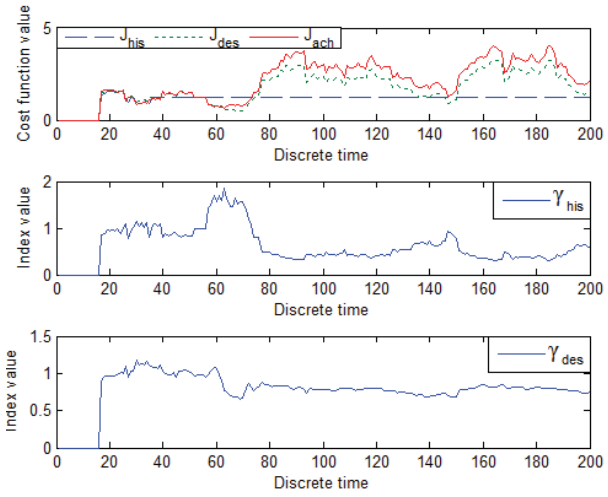

Figure 9 – Control performance reduction diagnosis caused by the change of the control tuning parameter

Even though some situations were potentially easier (e.g. the saturation of the manipulated variable) to detected and diagnose than others (e.g. the mismatch between the model and the phenomenological model based simulator), all the simulated scenarios were safely diagnosed. However, the situations studied in this paper were magnified in order to allow the verification of the differences that were expected for each case in the figures.

6. CONCLUSIONS

Monitoring and diagnosis methods were successfully applied to study control performance reduction scenarios using a GPC algorithm. Four types of performance reduction causes were diagnosed: increase in the controlled variable variability, mismatch between the model and the phenomenological simulator, saturation of manipulated variable and change in the control tuning parameter.

As future developments, it is suggested the implementation of operation support tools that enable the automatic performance monitoring and diagnosis.

Finally, it is expected that – with environmental concern, development of the industrial safety area and evolution of human intellectual capacity – more and more technologies will be developed in order to enable the correction, the prevention and, mostly, the failures prediction, allowing the man to dedicate his work to nobler activities, like process optimization.

REFERENCES

Ancheyta, J., Speight, J. G. (2007). *Hydroprocessing of heavy oils and residua*. CRC Press. USA.

Carneiro, H. P. (1992). Robust control of a fixed bed chemical reactor. 1992. 142 p. Dissertation (Chemical Engineering Master) – Engineering Pos-Graduation Program Coordination (COPPE), Federal University of Rio de Janeiro, Rio de Janeiro.

Cinar, A., Palazoglu, A., and Kayihan, F. (2007). *Chemical process performance evaluation*. CRC Press. USA.

Clarke, D. W. (1998). Application of generalized predictive control to industrial processes. *IEEE Control Systems Magazine*. April. p. 49 – 55.

De Souza Jr., M. B., Campos, M. C. M. M., and Tunala, L. F. (2009). Dynamic Principal Component Analysis Applied to the Monitoring of a Diesel Hydrotreating Unit. In Ferrarini, L. and Veber, C. (ed.). *Modeling, control and diagnosis of complex industrial and energy systems*. ISA, USA.

Hlavácek, V. (1982). *Fixed bed reactors, flow and chemical reaction*. Verlag Chemic. Germany.

Lababidi, H. M. S., Alatiqi, I. M., and Ali, Y. I. (2004). Constrained model predictive control for a pilot hydrotreating plant. *Chemical Engineering Research and Design*, v. 82 (A10), p. 1293 – 1304.

Schäfer, J. and Cinar, A. (2004). Multivariable MPC system performance assessment, monitoring and diagnosis. *Journal of Process Control*, v. 14, p. 113 – 129.

Seborg, D. E., Edgar, T. F., and Mellichamp, D. A. (2004). *Process dynamic and control*. Wiley, 2nd Edition. USA.

ACKNOWLEDGMENTS

This work was sponsored by 'Brazilian Research and Projects Financing Agency' (FINEP) and PETROBRAS (Grant 01.04.0902.00). Professor M. B. de Souza Jr acknowledges CNPq for a research fellowship.

Early determination of toxicant concentration in water supply using MHE

F. Ibrahim [*] **B. Huang** [*] **J. Xing** [**] **B. Jayasankar** [*]

[*] *Department of Chemical and Material Engineering, University of Albert, Canada T6G 2G6. fadi.ibrahim@ualberta.ca, biao.huang@ualberta.ca, jayasank@ualberta.ca*
[**] *Department of Laboratory Medicine and Pathology, University of Alberta, Canada T6G 2S2. jzxing@ualberta.ca*

Abstract: In this paper, a novel application of state estimation in environmental engineering is presented. Filtering techniques including moving horizon estimator (MHE) and extended Kalman filter (EKF) are used for early concentration estimation of toxic agents existing in water supply. The purpose is to integrate the filtering techniques with an early warning system enabling an early detection of the presence of toxicants in the water supply system and quantifying their concentrations. The estimation is based on dynamic measurements generated by a real-time cell electronic sensor (**RT-CES**) and cytotoxicity dynamic models.

Keywords: state estimation, extended Kalman filter, moving horizon state estimation, cytotoxicity, real-time cell electronic sensor, early warning, water protection.

1. INTRODUCTION

Drinking water may be contaminated by a range of chemical, microbial and physical hazards that could pose risks to health if they are present at high levels. Examples of chemical hazards include mercury, chromium, arsenic, etc. The sources of these toxicants differ with respect to the toxicant. Mercury for instance, occurs as a result of both natural (volcanic, forest fires and oceanic releases) and anthropogenic sources (mining, smelting and other industrial activities) in our environment as mentioned by Wang et al. (2004).

The effects of toxicants on the human cells are referred to as cytotoxicity. In other words, cytotoxicity is the characteristic of being toxic to living cells, including cell killing, cell lysis and certain cellular pathological changes, such as cellular morphological change and adhesion change as reported in Xing et al. (2005). Therefore, citizens must be alerted as early as possible when water is contaminated. For this purpose, an early warning system is necessary for detection of any sudden deterioration in the quality of water supply. An efficient detection must include the ability of an early determination of the presence of a toxicant at low concentration. Thus, our main objective in this paper is to use filtering techniques, such as moving horizon estimation (MHE) and extended Kalman filter (EKF) to determine on-line the concentration of such a toxicant in water supply. To achieve this purpose, mathematical modeling and real-time measurements are necessary. Two mathematical models have been developed and validated by Huang and Xing (2006) to predict cell toxicity response to mercury (II) chloride and sodium dichromate [chromium (VI)] toxicity. The measurements of toxicity response were recorded using Real-Time Cell Electronic Sensor (**RT-CES**). These two models are able to predict cell responses to different values of toxicant concentration and allow assessment of the biological consequences of toxic chemicals in environmental contamination. In this paper, we reverse the modeling procedure. We are interested in the estimation of toxicant concentration for a given dynamic model through on-line monitoring data sampled from **RT-CES**. The organization of this paper is as follows. The monitoring procedure and the mathematical models are revisited in Section 2 and Section 3 respectively. The procedure of concentration estimation and the validation results are presented in Section 4 including concentration estimation using both MHE and EKF. Concluding remarks are given in Section 5.

⋆ The authors gratefully acknowledge the support of the Natural Sciences and Engineering Research Council of Canada (NSERC).

2. EQUIPMENT AND MONITORING PROCEDURE REVISIT

1) ***Equipment***: The RT-CES system (ACEA Biosciences, CA, U.S.A.) is used for this study and has been described in (Xing et al., 2005; Huang and Xing, 2006). Briefly, as shown in Fig. 1, it consists of a 16x microelectronic sensor devices having 16 plastic wells in microtiter plate format, a device station and an electronic sensor analyzer. Cells are grown onto the surfaces of microelectronic sensors. In operation, the sensor devices with cultured cells are mounted to a device station placed inside a CO2 incubator. Electrical cables connect the device station to the sensor analyzer. Under the control of RT-CES software, the sensor analyzer automatically selects wells to be measured and continuously conducts measurements. The electronic impedance can then be transferred to a computer and recorded. A parameter termed cell index (CI) is derived to represent cell status based on the measured electrical impedance. The frequency dependent

electrode impedance (resistance) without or with cells present in the wells is represented as $R_b(f)$ and $R_{cell}(f)$, respectively. The CI is calculated by:

$$CI = \max_{i=1,\ldots,n} \left[\frac{R_{cell}(f_i)}{R_b(f_i)} - 1 \right] \quad (1)$$

where n is the number of the frequency points at which the impedance is measured. Several features of the CI can be derived: (1) Under the same physiological conditions, if more cells attach onto the electrodes, the larger impedance value leading to a larger CI value will be detected. If no cells are present on the electrodes or if the cells are not well-attached onto the electrodes, $R_{cell}(f)$ is the same as $R_b(f)$, leading to $CI = 0$; (2) A large $R_{cell}(f)$ value leads to a larger CI. Thus, CI is a quantitative measure of the number of cells attached to the sensors; (3) For the same number of cells attached to the sensors, changes in cell status, such as morphological change, lead to change of CI.

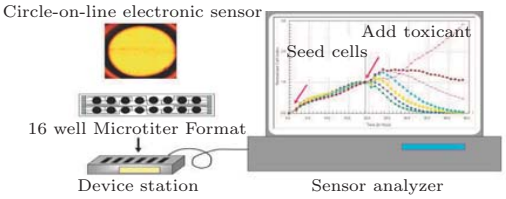

Fig. 1. *The Real-Time Cell Electronic Sensor*

In addition to cell numbers, the impedance also depends on the extent to which cells attach to the electrodes. For example, if cells spread, there will be a greater cell/electrode contact area, resulting in larger impedance. Thus, the cell biological status including cell viability, cell number, cell morphology and cell adhesion will all affect the measurements of electrode impedance that is reflected by CI on the RT-CES system. Therefore, a dynamic pattern of a given CI curve can indicate sophisticated physiological and pathological responses of the living cells to a given toxic compound (Xing et al., 2005).

2) ***Dynamic growth with toxicity***: Two environmental toxicants, mercury (II) chloride and sodium dichromate [chromium (VI)], were used for cytotoxicity assessment on the 16 sensor device. The cell line NIH 3T3 was tested. The starting cell number was 10 000 cells per sensor wells. The cell growth on the sensor device was monitored every hour up to 24 h in real-time by the RT-CES system. When the CI values reached a range between 1.0 and 1.2, the cells were then exposed to either mercury (II) chloride, or chromium (VI) at different concentrations. Fig. 2 shows dynamic cytotoxic response to different doses of chromium (VI). Fig. 3 shows dynamic cytotoxic response to mercury (II) chloride. In both cases the cytotoxicity response is dose dependent and increasing dose leads to decreasing (CI).

3. MATHEMATICAL MODELING

As mentioned in the introduction, the cytotoxicity mechanism is complex and cell response to toxicity depends on cell type, toxicant type, toxicant concentrations and the time of exposure to the toxicant. In Huang and Xing (2006), two types of models were developed and validated

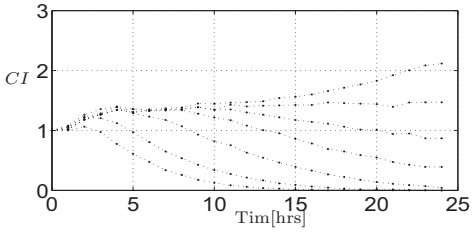

Fig. 2. *Dynamic cytotoxic response of NIH 3T3 cells to different doses of* ***chromium (VI)****: 0; 0.62; 0.91; 1.97; 2.89; 4.25; 5.78 in the unit of μM. Increasing dose leads to decreasing (CI).*

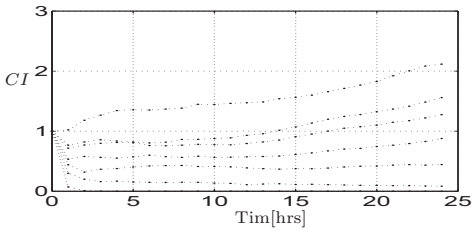

Fig. 3. *Dynamic cytotoxic response of NIH 3T3 cells to different doses of* ***mercury (II)****: 0; 10.43; 15.2; 22.35; 32.8; 48.3; 71 in the unit of μM. Increasing dose leads to decreasing (CI).*

to predict cell toxicity response to mercury (II) chloride, and sodium dichromate [chromium (VI)] stimulations. In both models, it was suggested that the process of cytotoxicity follows two-step mechanism: (1) uptake of toxicant by cells and (2) killing of the cells. The uptake mechanism describes the transport process of the toxicant into a cell as illustrated in Fig. 4 (Huang and Xing, 2006). This mechanism relates the extracellular concentration c_e (representing the concentration of a toxicant in the environment) and the intracellular concentration c_i (concentration inside the cell) and it is described by El-Kareh and Secomb (2005) as follows :

$$\dot{c_i} = k_1(k_2 c_e + \frac{k_3 c_e}{k_4 + c_e} - c_i) \quad (2)$$

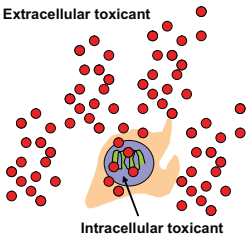

Fig. 4. *Schematic of transport process of toxicant onto cell.*

The first step in cytotoxicity (the uptake mechanism) is supposed to be rather consistent; however the second step (cell killing) differs with respect to the toxicant and can be described through cell population dynamics as $\dot{N} = f(C, N)$ where N is the cell population and C can be the intracellular or the extracellular concentration of the toxicant or a combination of them. It depends on the type of the toxicant. In the following, we present the mathematical models of cell killing under the effect of two toxicants, mercury (II) chloride, and sodium dichromate [chromium (VI)] as described in Huang and Xing (2006).

3.1 Mathematical modeling of [chromium (VI)] toxicity

The cell exposed to dichromate [chromium (VI)] is killed by *apoptosis* mechanism which is a highly regulated process and is described as programmed cell death. The apoptosis mechanism mainly depends on the intracellular concentration of the toxicant. This is described by the dynamics of cell pullulation given by Eliaz et al. (2004) as $\dot{N} = N(k_s - kc_i)$. As proposed by Huang and Xing (2006), this mechanism yields the following system of differential equations for describing dichromate [chromium (VI)] effects on cells population dynamics:

$$\begin{aligned} \dot{c_i} &= k_1(k_2 c_e + \frac{k_3 c_e}{k_4 + c_e} - c_i) \\ \dot{N} &= N(k_s - kc_i) \end{aligned} \tag{3}$$

The parameters of this model (3) are estimated from the experiment data and presented in Table 1.

Table 1. Estimated parameters for model (3)

k_1	k_2	k_3	k_4	k_s	k
0.0146	2.9399	0.0080	29.2418	0.0425	0.1041

3.2 Mathematical modeling of mercury (II) chloride toxicity

In Huang and Xing (2006), mercury cytotoxicity has both necrosis mechanism and apoptosis mechanism. The necrosis describes an accidental cell death caused, for example, by chemical or physical assault to the cell which may make cells die by direct disruption of cell membrane. Thus necrosis mechanism mainly depends on extracellular concentration of the toxicant. The cell population dynamics, together with the uptake mechanism expressed by eqn. (2), under mercury (II) chloride toxicity effect is described as follows:

$$\begin{aligned} \dot{c_i} &= k_1(k_2 c_e + \frac{k_3 c_e}{k_4 + c_e} - c_i) \\ \dot{N} &= N(k_5 + k_6 c_i + k_7 c_e) \end{aligned} \tag{4}$$

The parameters of model (4) are presented in Table 2.

Table 2. Estimated parameters for model (4)

k_1	k_2	k_3	k_4	k_5	k_6	k_7
7.735	1.108	3.21	12.8	0.0312	0.2084	-0.2364

4. RAPID TOXICANT CONCENTRATION ESTIMATION

The on-line estimation of the key parameter (the concentration of toxicant c_e) is critical due to two reasons. First, as being well known the concentration itself is usually not easily measurable due to technical or economical limitations especially for biomedical processes. The key toxicants are usually measured by high performance liquid chromatography (**HPLC**) and liquid chromatography-mass spectrometry (**LC-MS**) which are expensive equipments. Second, an early determination (detection) of the concentration of such a toxicant is important for an early warning system (which we aim to develop) in order to detect any sudden deterioration in the quality of water supply. Deterioration in water quality mainly means increase of the concentrations (or even the presence) of toxicants . For the early warning system, it is necessary to do on-line estimation of c_e.

For on-line estimation, several methods for state estimation are available such as EKF and MHE. EKF is a popular state estimation technique and considered as the standard choice for estimating state for nonlinear systems due to lower computation load and more stable property. However, additional physical insights about the process may help in state estimation to prevent negative concentration for instance. This kind of insights can not be considered in EKF. On the other hand, this physical insights can be added as inequality constraints and integrated with an optimal state estimation scheme formulated as a quadratic problem such as MHE (Rao et al., October 2001).

We use mainly MHE for on-line estimation of the key parameter c_e and we also use EKF as an alternative (usually a quicker method) of the estimation. This may be considered as a comparison to demonstrate by biological application examples the benefits of using MHE on one hand. On the other hand, the EKF is also imbedded in the MHE and is naturally used for a comparison. The superiority of MHE has also been pointed out by several authors through a number of applications such as in Rao and Rawlings (2002) and Haseltine and Rawlings (2005) for instance.

Before starting the procedure of on-line state estimation of the key parameter (the extracellular concentration c_e) for our biological application, an identifiability test is necessary. We present in the next section an identifiability test for mercury (II) chloride toxicity model (4) for an illustration. An identifiability test for chromium (VI) toxicity model (3) can be performed similarly.

4.1 Identifiability

A mathematical model is identifiable if there exist no two parameter sets which have the same input-output behavior. In other words, a model is not identifiable if there exists no unique parameter set to explain the input-output behavior. Identifiability is a pre-analysis for parameter estimation problem to determine the uniqueness of the parameter solution obtained from the estimation process. A number of methods are available for testing identifiability of parametric models. For testing the identifiability of the mercury (II) toxicity model (4), the Taylor series approach is utilized (see Walter and Pronzato (1996)). A brief description of the approach is given below. Consider the following model :

$$\begin{aligned} \dot{x}(t) &= f(x(t), u(t), t, p), \quad x(0) = x_0(p) \\ y(t, p) &= h(x(t), p) \end{aligned} \tag{5}$$

where p is the model parameters set.

If $a_k(p) = \lim_{t \longrightarrow 0+} \frac{d^k}{dt^k} y(t, p)$ then a sufficient condition for model (5) to be uniquely identifiable is :

$$a_k(\hat{p}) = a_k(p^*), \quad k = 0, 1, ..., k_{max}, \Longrightarrow \quad \hat{p} = p^*$$

where k_{max} is a positive integer, small enough for the computations to remain tractable.

Since mercury (II) toxicity model (4) has only one parameter (the concentration c_e), checking for identifiability reduces to checking for conditions under which the parameter can be observed from the Taylor series coefficients. The first two coefficients of the series for the mercury (II) toxicity model can be determined as:

$$a_0(p) = N(0)$$
$$a_1(p) = \dot{N}(0) = N(0)(k_5 + k_6 c_i(0) + k_7 c_e) \quad (6)$$

Solving the equation (6) for c_e yields,

$$c_e = \frac{k_6 c_i(0) N(0) + k_5 N(0) - \dot{N}(0)}{-k_7 N(0)}$$

Therefore c_e is identifiable if:

$$-k_7 N(0) \neq 0 \quad \text{and} \quad (7)$$
$$k_6 c_i(0) N(0) + k_5 N(0) - \dot{N}(0) \neq 0 \quad (8)$$

Measurements evolution shown in Fig. 2 and values of the estimated parameters in table 2 satisfy both conditions, equations 7 and 8.

4.2 Extended Kalman Filter (EKF) formulation

Before presenting EKF formulation, considering the problem of estimating the state of system modeled by the nonlinear state space equation :

$$x_{k+1} = f(x_k, u_k, k) + G w_k \qquad k = 0, 1, 2... \quad (9)$$
$$y_k = g(x_k, k) + v_k$$

where, $x_k \in \mathbb{R}^n$ is the state vector, $y_k \in \mathbb{R}^p$ the measured output, $w_k \in \mathbb{R}^n$ state disturbance and $v_k \in \mathbb{R}^p$ the measurement noise. The EKF linearizes the nonlinear system and then applies the Kalman filter to obtain the state estimation. The method can be summarized in a recursion structure similar to linear Kalman filter for a nonlinear system described above by equations (9) (see Haseltine and Rawlings (2005)):

Prediction step

$$\hat{x}_{k|k-1} = f(\hat{x}_{k-1|k-1}, u_{k-1}, w_{k-1})$$
$$P_{k|k-1} = A_{k-1} P_{k-1|k-1} A_{k-1}^T + G_{k-1} Q_{k-1} G_{k-1}^T$$

Update step

$$\hat{x}_{k|k} = \hat{x}_{k|k-1} + K_k(y_k - g(\hat{x}_{k|k-1}))$$
$$K_k = P_{k|k-1} C_k^T [C_k P_{k|k-1} C_k^T + R_k]^{-1}$$
$$P_{k|k} = P_{k|k-1} - K_k C_k P_{k|k-1}$$

in which, the following linearizations are made

$$A_k = \frac{\partial f(x_k, u_k, k)}{\partial x_k^T}, \quad G_k = \frac{\partial f(x_k, u_k, k)}{\partial w_k^T}, \quad C_k = \frac{\partial g(x_k)}{\partial x_k^T}$$

4.3 Moving Horizon State Estimation (MHE) formulation

The MHE strategy belongs to a class of optimization methods for on-line determination of state. The optimization problem is formulated as a least-squares problem where the decision variables are chosen to minimize the sum of the squared errors between the available measurements and model prediction. When a new measurement becomes available, this optimization is repeated by adding the new measurement to the past measurements each sampling time. This leads to growing computational burden of solving the least-squares optimization, known as full information estimation problem. MHE reduces this computational cost by considering a finite horizon of only the last N_h measurements in the optimization problem and information provided by past data beyond the horizon is captured by arrival cost. This optimization is repeated each sampling time by including a new measurement and discarding the first measurement while keeping a fixed horizon length (N_h). In other words, the MHE algorithm is a least square optimization problem solved over a window of fixed horizon length (N_h). This window moves one step ahead each time after solving an optimization problem with a quadratic cost function (Ψ_k) of the following form (for more details see Rao et al. (2003)):

$$\min_{\{\hat{w}_{k-N_h-1|k}, \ldots, \hat{w}_{k-1|k}\}} \Psi_k : \Psi_k = \hat{w}_{k-N_h-1|k}^T Q_{-N_h|k}^{-1} \hat{w}_{k-N_h-1|k} + \sum_{j=k-N_h}^{k-1} \hat{w}_{j|k}^T Q^{-1} \hat{w}_{j|k} + \sum_{j=k-N_h}^{k} \hat{v}_{j|k}^T R^{-1} \hat{v}_{j|k}$$

subject to the state equality constrains:

$$\hat{x}_{k-N_h|k} = \bar{x}_{k-N_h|k} + \hat{w}_{k-N_h-1|k}$$
$$\text{with} \quad \bar{x}_{k-N_h|k} = f(\hat{x}^*_{k-N_h-1|k-1}, u_{k-N_h-1}, k)$$
$$\hat{x}_{j+1|k} = f(\hat{x}_{j|k}, u_j) + \hat{w}_{j|k}, j = k - N_h, ..., k-1$$
$$y_j = g(\hat{x}_{j|k}, k) + \hat{v}_{j|k}, j = k - N_h, ..., k$$

with the possibility to incorporate inequality constraints on the state, state disturbance and process noise:

$$w_{min} < A w_j < w_{max}, \quad x_{min} < A x_j < x_{max},$$
$$v_{min} < A v_j < v_{max}, \quad j = k - N_h - 1, ..., k-1$$

where Q is the covariance of the state disturbance and R is the covariance of process noise.

The term $\hat{w}_{k-N_h-1|k}^T Q_{-N_h|k}^{-1} \hat{w}_{k-N_h-1|k}$ approximates the arrival cost which summarizes the effects of the past information before $t = k - N_h$. The weighting term $Q_{-N_h|k}$ initially represents the covariance of the prior state estimate $\bar{x}_{k-N_h}$ and is computed according to EKF covariance update formula (Rao et al., 2003):

$$Q_{-N_h|k+1} = A_k Q_{-N_h|k} A_k^T + G_k Q_k G_k^T - A_k Q_{-N_h|k} C_k^T [C_k Q_{-N_h|k} C_k^T + R_k]^{-1} C_k Q_{-N_h|k} A^T \quad (10)$$

where A_k, C_k and G_k result from linearizing the model (9) around the estimated trajectory.

In the full information problem there is no arrival cost because the whole information (all available measurements) is used each sampling time in the optimization while in MHE, only a subset of the information is used and the rest is approximated by the arrival cost. Thus, MHE is an approximation of the full information problem and therefore stability issue arises. The key to preserving

stability is how to approximately summarize the old data, equivalently, how to find the best approximation of the arrival cost, an explicit expression which rarely exists in nonlinear or constrained system. One strategy is to use the EKF covariance update formula as presented in equation (10) (Rao et al., 2003).

Next we present a state estimation based approach for rapid determination of concentrations of mercury (II) and chromium (VI) from the measurement of cell population responses provided by the **RT-CES**.

4.4 Concentrations estimation of chromium (VI)

The key parameter we aim to estimate is the extracellular concentration (c_e) of chromium (VI). This parameter is added to the toxicity equation (3) of chromium (VI) as an augmented state as follow :

$$\begin{aligned} \dot{c_i} &= k_1(k_2 c_e + \frac{k_3 c_e}{k_4 + c_e} - c_i) \qquad (11) \\ \dot{N} &= N(k_s - k c_i) \\ \dot{c_e} &= 0 \quad ; \quad y = N \end{aligned}$$

where, c_i is the intracellular concentration, N is the cell population and y is the observation. We estimate toxicant concentrations from three toxicity responses corresponding to toxicant doses c_e =(0.62; 1.97; 4.25)μM. Note these data have not been used for modeling purpose and thus serve as cross validation data for state estimation. The results presented in Fig. (5-7) show that MHE in general has a better estimation than EKF. In addition, MHE is able to prevent an estimation of negative concentration at all time but EKF can not. It is also observed from these figures that the extracellular concentration can be correctly estimated between 10 to 15 hrs, instead of 24 hrs as traditional the method needs. Thus a rapid estimation is achieved.

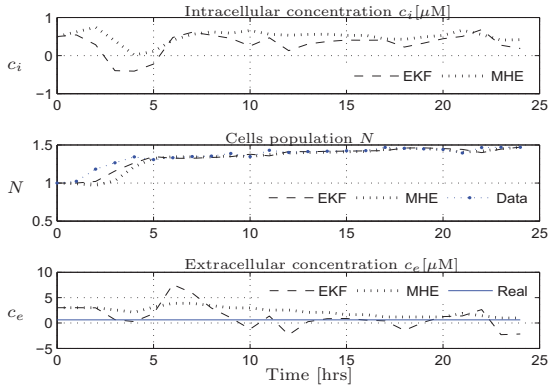

Fig. 5. *Concentration estimation of chromium (VI) corresponding to real $c_e = 0.62\mu M$. Bottom plot : Estimation of c_e converges to the real value (0.62μM) using both estimators. Top plot shows the estimation of c_i which is not measured. The middle plot shows the estimation of cell population that is measured.*

4.5 Concentrations estimation of mercury (II) chloride

Similar to the procedure adopted for estimating the concentration of chromium VI presented in the previous section, we aim here to estimate the concentration of mercury (II) chloride from the available data. The concentration c_e is added to the toxicity equation (4) of mercury (II) chloride as an augmented state similar to the augmented model (eqn. 11) for chromium (VI). We estimate the toxicant concentrations from three toxicity responses corresponding to the toxicant concentration c_e =(10.43; 22.35; 48.3)μM. The results presented in Fig. (8-10) show that both estimators (EKF and MHE) provide a good estimation of c_e while preventing negative concentration estimation when using MHE. This shows clearly the benefits of using constraints by MHE.

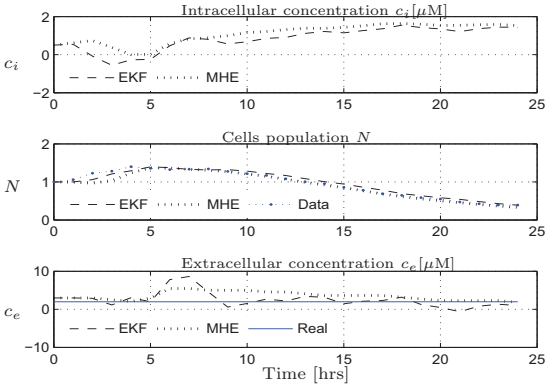

Fig. 6. *Concentration estimation of chromium (VI) corresponding to real $c_e = 1.97\mu M$. Bottom plot : Estimation of c_e converges to the real value (1.97μM) using both estimators. Top plot shows the estimation of c_i which is not measured. The middle plot shows the estimation of cell population that is measured.*

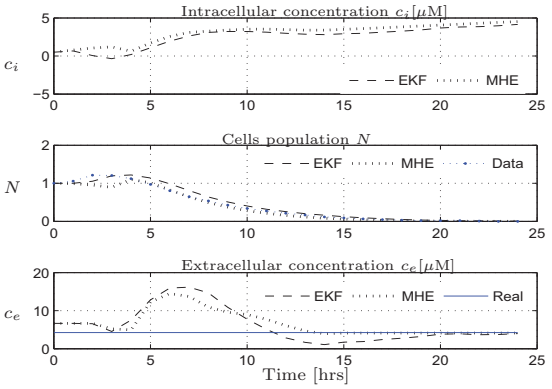

Fig. 7. *Concentration estimation of chromium (VI) corresponding to real $c_e = 4.25\mu M$. Bottom plot : Estimation of c_e converges to the real value (4.25μM) using both estimators. Top plot shows the estimation of c_i which is not measured. The middle plot shows the estimation of cell population that is measured.*

Our experience shows that tuning EKF is simpler. Using MHE requires a more careful tuning of a several parameters, namely, Q, R, Q_{-N_h}, horizon length (N_h), the constraints w_{min}, w_{max} and also the initial conditions. In addition, the tuning may vary from different experiments. The evolution of the estimation converges by using horizon length $N_h = 1$ for mercury (II) chloride case while at least $N_h = 2$ is needed for chromium IV case.

In the selection of the covariance, the Q matrix reflects the uncertainty of the state equations while the R matrix reflects the uncertainty in the measurement of CI due to other phenomena that also affect CI in addition to cell numbers.

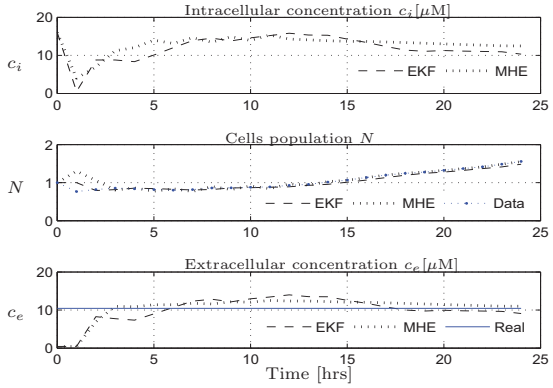

Fig. 8. *Concentration estimation of mercury (II) chloride corresponding to real $c_e = 10.43\mu M$. Bottom plot : Estimation of c_e converges to the real value (10.43μM) using both estimators. Top plot shows the estimation of c_i which is not measured. The middle plot shows the estimation of N that is measured.*

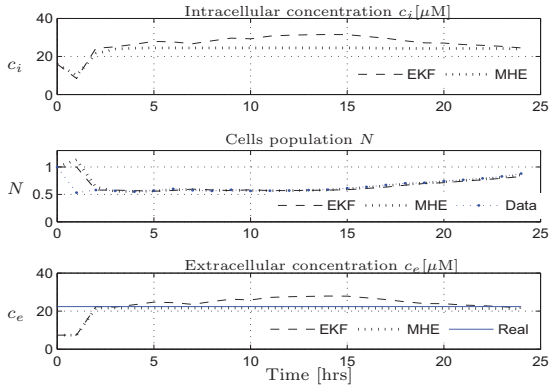

Fig. 9. *Concentration estimation of mercury (II) chloride corresponding to real $c_e = 22.35\mu M$. Bottom plot : Estimation of c_e converges to the real value (22.35μM) using both estimators. Top plot shows the estimation of c_i which is not measured. The middle plot shows the estimation of N that is measured.*

5. CONCLUSION

An early warning system for water supply is our main goal of the work presented. This includes an early determination of the presence of specific toxicants in water by on-line estimation of their concentrations. We use mainly MHE as an on-line estimation tool in this paper. Determination of the concentration is only one of the features of the aimed early warning system. This system will also include prediction of future evolution of toxicity response using only initial measurements and prediction of cells response when the concentration of a toxicant varies. Integrating all these prediction features is the ultimate goal. Intuitively, this includes also the development of toxicity mathematical models for other kinds of common water toxicants such as sodium arsenite [As (III)] for instance.

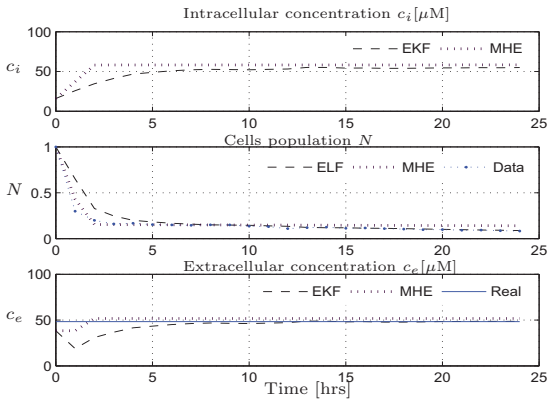

Fig. 10. *Concentration estimation of mercury (II) chloride corresponding to real $c_e = 48.3\mu M$. Bottom plot: Estimation of c_e converges to the real value (48.3μM) using both estimators. Top plot shows the estimation of c_i which is not measured. The middle plot shows the estimation of N that is measured.*

In addition, as has been discussed, the cell index also reflects other sophisticated physiological and pathological responses in addition to cell numbers. A model that considers other properties of the cell index will further improve on-line state estimation.

ACKNOWLEDGEMENTS

The authors gratefully acknowledge the support of the Natural Sciences and Engineering Research Council of Canada (NSERC).

REFERENCES

El-Kareh, A. and Secomb, T. (2005). Two-mechanism peak concentration model for cellular pharmacodynamics of doxorubicin. *Neoplasia*, 77, 705–713.

Eliaz, R., Nir, S., Marty, C., and Szoka, J. (2004). Determination and modeling of kinetics of cancer cell killing by doxorubicin and doxorubicin encapsulated in targeted liposomes. *Birches. J.*, 64, 711–718.

Haseltine, E. and Rawlings, J. (2005). A critical evaluation of extended kalman filtering and moving horizon estimation. *Ind. Eng. Chem. Res.*, 44, 2451–2460.

Huang, B. and Xing, J. (2006). Dynamic modeling and prediction of cytotoxicity on microelectronic cell sensor array. *Canadian Journal of Chemical Engineering*, 86, 393–405.

Rao, C. and Rawlings, J. (2002). Constrained process monitoring: Moving - horizon approach. *IChE Journal*, 48, 97–109.

Rao, C., Rawlings, J., and Lee, J. (October 2001). Constrained linear state estimation - a moving horizon approach. *Automatica*, 37, 1619–1628.

Rao, C., Rawlings, J., and Mayne, D. (2003). Constrained state estimation for nonlinear discrete-time systems: stability and moving horizon approximations. *Automatic Control, IEEE Transactions on*, 48, 246–258.

Walter, E. and Pronzato, L. (1996). On the identifiability and distinguishability of nonlinear parametric models. *Mathematics and Computers in Simulation*, 42, 125–134.

Wang, Q., Kim, D., Dionysiou, D., Sorial, G., and Timberlakeb, D. (2004). Sources and remediation for mercury contamination in aquatic systems - a literature review. *Environmental Pollution*, 131, 323–336.

Xing, J., Zhu, L., Jackson, J.A., Gabos, S., Sun, X.J., b. Wang, X., and Xu, X. (2005). Dynamic monitoring of cytotoxicity on microelectronic sensors. *Chem. Res. Toxicol*, 18 (2), 154–161.